SMITHSONIAN INSTITUTION LIBRARIES

SMITHSONIAN INSTITUTION LIBRARIES

TWENTY-THIRD ANNUAL REPORT

OF THE

NATIONAL ADVISORY COMMITTEE FOR AERONAUTICS

1937

INCLUDING TECHNICAL REPORTS

Nos. 577 to 611

UNITED STATES
GOVERNMENT PRINTING OFFICE
WASHINGTON: 1938

For sale by the Superintendent of Documents, Washington, D. C. - - - - - - - - - - - - Price, $2.50 (Buckram)

TECHNICAL REPORTS

	Page
No. 577. Prechamber Compression-Ignition Engine Performance. By Charles S. Moore and John H. Collins, Jr	49
No. 578. Flight Measurements of the Dynamic Longitudinal Stability of Several Airplanes and a Correlation of the Measurements With Pilots' Observations of Handling Characteristics. By Hartley A. Soulé	69
No. 579. A Study of the Two-Control Operation of an Airplane. By Robert T. Jones	75
No. 580. Heat Transfer to Fuel Sprays Injected Into Heated Gases. By Robert F. Selden and Robert C. Spencer	91
No. 581. Measurements of Intensity and Scale of Wind-Tunnel Turbulence and Their Relation to the Critical Reynolds Number of Spheres. By Hugh L. Dryden, G. B. Schubauer, W. C. Mock, Jr., and H. K. Skramstad	109
No. 582. A Theory for Primary Failure of Straight Centrally Loaded Columns. By Eugene E. Lundquist and Claude M. Fligg	141
No. 583. The Rolling Friction of Several Airplane Wheels and Tires and the Effect of Rolling Friction on Take-Off. By J. W. Wetmore	169
No. 584. Strength of Welded Aircraft Joints. By W. C. Brueggeman	177
No. 585. Span Load Distribution for Tapered Wings With Partial-Span Flaps. By H. A. Pearson	209
No. 586. Airfoil Section Characteristics as Affected by Variations of the Reynolds Number. By Eastman N. Jacobs and Albert Sherman	227
No. 587. Blower Cooling of Finned Cylinders. By Oscar W. Schey and Herman H. Ellerbrock, Jr	269
No. 588. Fuel Spray and Flame Formation in A Compression-Ignition Engine Employing Air Flow. By A. M. Rothrock and C. D. Waldron	281
No. 589. An Analysis of Lateral Stability In Power-Off Flight With Charts For Use In Design. By Charles H. Zimmerman	297
No. 590. Pressure-Distribution Measurements of An O–2H Airplane In Flight. By H. A. Pearson	319
No. 591. An Analytical and Experimental Study of the Effect of Periodic Blade Twist on the Thrust, Torque, and Flapping Motion of an Autogiro Rotor. By John B. Wheatley	353
No. 592. Full-scale Tests of N. A. C. A. Cowlings. By Theodore Theodorsen, M. J. Brevoort, and George W. Stickle	361
No. 593. Cooling of Airplane Engines At Low Air Speeds. By Theodore Theodorsen, M. J. Brevoort, and George W. Stickle	391
No. 594. Characteristics of Six Propellers Including the High-Speed Range. By Theodore Theodorsen, George W. Stickle, and M. J. Brevoort	401
No. 595. Full-Scale Tests of A New Type N. A. C. A. Nose-Slot Cowling. By Theodore Theodorsen, M. J. Brevoort, George W. Stickle, and M. N. Gough	439
No. 596. Cooling Test of A Single-Row Radial Engine With Several N. A. C. A. Cowlings. By M. J. Brevoort, George W. Stickle, and Herman H. Ellerbrock, Jr	449
No. 597. Air Propellers In Yaw. By E. P. Lesley, George F. Worley, and Stanley Moy	459
No. 598. Alternating-Current Equipment For the Measurement of Fluctuations of Air Speed In Turbulent Flow. By W. C. Mock, Jr	475
No. 599. Flight Tests of the Drag and Torque of the Propeller in Terminal-Velocity Dives. By Richard V. Rhode and Henry A. Pearson	493
No. 600. An Analysis of the Factors That Determine the Periodic Twist of an Autogiro Rotor Blade, With A Comparison of Predicted and Measured Results. By John B. Wheatley	503
No. 601. Torsion Tests of Tubes. By Ambrose H. Stang, Walter Ramberg, and Goldie Back	515
No. 602. Wind-Tunnel and Flight Tests of Slot-Lip Ailerons. By Joseph A. Shortal	537
No. 603. Wind-Tunnel Investigation of Wings With Ordinary Ailerons and Full-Span External-Airfoil Flaps. By Robert C. Platt and Joseph A. Shortal	563
No. 604. Pressure-Distribution Measurements At Large Angles of Pitch On Fins of Different Span-Chord Ratio on A 1/40-Scale Model of the U. S. Airship "Akron". By James G. McHugh	585
No. 605. Résumé and Analysis of N. A. C. A. Lateral Control Research. By Fred E. Weick and Robert T. Jones	605
No. 606. Electrical Thermometers For Aircraft. By John B. Peterson and S. H. J. Womack	633
No. 607. Spinning Characteristics of the XN2Y–1 Airplane Obtained From the Spinning Balance and Compared With Results From the Spinning Tunnel and From Flight Tests. By M. J. Bamber and R. O. House	649
No. 608. Stress Analysis of Beams With Shear Deformation of the Flanges. By Paul Kuhn	669
No. 609. Experimental Investigation of Wind-Tunnel Interference On the Downwash Behind an Airfoil. By Abe Silverstein and S. Katzoff	689
No. 610. Tests of Related Forward-Camber Airfoils in the Variable-Density Wind Tunnel. By Eastman N. Jacobs, Robert M. Pinkerton, and Harry Greenberg	697
No. 611. Wind-Tunnel Investigation of Tapered Wings With Ordinary Ailerons and Partial-Span Split Flaps. By Carl J. Wenzinger	733

LETTER OF TRANSMITTAL

To the Congress of the United States:

In compliance with the provisions of the act of March 3, 1915, establishing the National Advisory Committee for Aeronautics, I transmit herewith the Twenty-third Annual Report of the Committee covering the fiscal year ended June 30, 1937.

Franklin D. Roosevelt.

The White House,
January 7, 1938.

LETTER OF SUBMITTAL

National Advisory Committee for Aeronautics,
Washington, D. C., November 29, 1937.

Mr. President:

In compliance with the provisions of the act of Congress approved March 3, 1915 (U. S. C., title 50, sec. 153), I have the honor to submit herewith the Twenty-third Annual Report of the National Advisory Committee for Aeronautics covering the fiscal year 1937.

During the past year the United States has maintained its position in the forefront of progressive nations in the technical development of aircraft for both military and commercial purposes. This has been due chiefly to sound organization and liberal support of scientific laboratory research in aeronautics in this country.

The War, Navy, and Commerce Departments, having equal representation on the Committee, cooperate in every way in its work, and each receives the results of the scientific investigations conducted. Thus the research needs of all branches of aviation are met without overlapping or duplication of effort. The Committee's activities, however, are limited to research. They do not include experimental engineering in the application of research results to the development of military, naval, or commercial aircraft.

The greatly increased interest of the major powers in fostering aeronautical research and their determined efforts to excel in this rapidly advancing engineering science constitute a scientific challenge to America's present leadership. It is the responsibility of the National Advisory Committee for Aeronautics to see to it that the United States will not become dependent upon any foreign nation for fundamental scientific data on which to base the design of American aircraft. To do this effectively it will be necessary that this Committee continue to have the liberal and far-sighted support of the President and of the Congress.

Respectfully submitted.

Joseph S. Ames, *Chairman.*

The President,
The White House, Washington, D. C

NATIONAL ADVISORY COMMITTEE FOR AERONAUTICS

HEADQUARTERS, NAVY BUILDING, WASHINGTON, D. C.

LABORATORIES, LANGLEY FIELD, VA.

Created by act of Congress approved March 3, 1915, for the supervision and direction of the scientific study of the problems of flight (U. S. Code, Title 50, Sec. 151). Its membership was increased to 15 by act approved March 2, 1929. The members are appointed by the President, and serve as such without compensation.

JOSEPH S. AMES, Ph. D., *Chairman*,
Baltimore, Md.

DAVID W. TAYLOR, D. Eng., *Vice Chairman*,
Washington, D. C.

WILLIS RAY GREGG, Sc. D., *Chairman, Executive Committee*,
Chief, United States Weather Bureau.

WILLIAM P. MACCRACKEN, J. D., *Vice Chairman, Executive Committee*,
Washington, D. C.

CHARLES G. ABBOT, Sc. D.,
Secretary, Smithsonian Institution.

LYMAN J. BRIGGS, Ph. D.,
Director, National Bureau of Standards.

ARTHUR B. COOK, Rear Admiral, United States Navy,
Chief, Bureau of Aeronautics, Navy Department.

FRED D. FAGG, JR., J. D.,
Director of Air Commerce, Department of Commerce.

HARRY F. GUGGENHEIM, M. A.,
Port Washington, Long Island, N. Y.

SYDNEY M. KRAUS, Captain, United States Navy,
Bureau of Aeronautics, Navy Department.

CHARLES A. LINDBERGH, LL. D.,
New York City.

AUGUSTINE W. ROBINS, Brigadier General, United States Army,
Chief Matériel Division, Air Corps, Wright Field, Dayton, Ohio.

EDWARD P. WARNER, M. S.,
Greenwich, Conn.

OSCAR WESTOVER, Major General, United States Army,
Chief of Air Corps, War Department.

ORVILLE WRIGHT, Sc. D.,
Dayton, Ohio.

GEORGE W. LEWIS, *Director of Aeronautical Research*

JOHN F. VICTORY, *Secretary*

HENRY J. E. REID, *Engineer-in-Charge, Langley Memorial Aeronautical Laboratory, Langley Field, Va.*

JOHN J. IDE, *Technical Assistant in Europe, Paris, France*

TECHNICAL COMMITTEES

AERODYNAMICS
POWER PLANTS FOR AIRCRAFT
AIRCRAFT MATERIALS
AIRCRAFT STRUCTURES
AIRCRAFT ACCIDENTS
INVENTIONS AND DESIGNS

Coordination of Research Needs of Military and Civil Aviation

Preparation of Research Programs

Allocation of Problems

Prevention of Duplication

Consideration of Inventions

LANGLEY MEMORIAL AERONAUTICAL LABORATORY

LANGLEY FIELD, VA.

Unified conduct, for all agencies, of scientific research on the fundamental problems of flight.

OFFICE OF AERONAUTICAL INTELLIGENCE

WASHINGTON, D. C.

Collection, classification, compilation, and dissemination of scientific and technical information on aeronautics.

38548—38——2

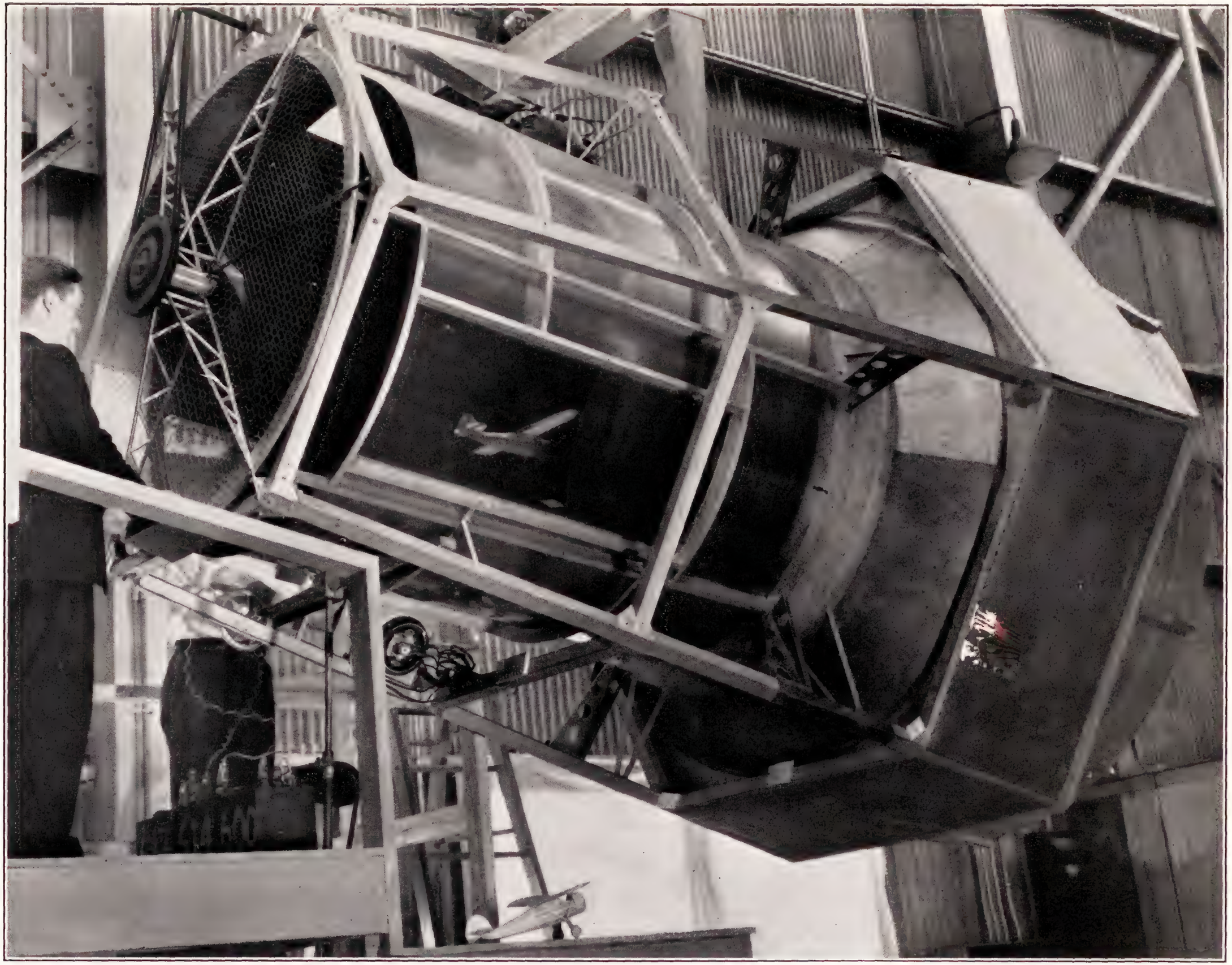

THE NEW N. A. C. A. FREE FLIGHT WIND TUNNEL IN WHICH INVESTIGATIONS OF AIRPLANE STABILITY AND CONTROL CHARACTERISTICS CAN BE MADE ON AN AIRPLANE MODEL IN FREE FLIGHT.

TWENTY-THIRD ANNUAL REPORT

OF THE

NATIONAL ADVISORY COMMITTEE FOR AERONAUTICS

WASHINGTON, D. C., *November 10, 1937.*

To the Congress of the United States:

In accordance with the act of Congress approved March 3, 1915 (U. S. C., title 50, section 151), which established the National Advisory Committee for Aeronautics, this Committee submits herewith its twenty-third annual report, covering the fiscal year 1937.

Responsibilities of this organization.—The prescribed functions of this organization are to "supervise and direct the scientific study of the problems of flight, with a view to their practical solution," and to "direct and conduct research and experiment in aeronautics." In the discharge of its functions under the law the primary responsibilities of the National Advisory Committee for Aeronautics are: (1) To recognize in advance the trend of aeronautical development, civil and military; (2) to anticipate the research problems that will arise; and (3) to design and provide research equipment to meet the needs of this rapidly advancing engineering science, and then to conduct the necessary scientific investigations.

Created by law in 1915 as an independent Government establishment, the Committee, with the consistent and liberal support of the President and of the Congress, has gradually developed a large and well-equipped aeronautical research laboratory at Langley Field, Virginia. In this laboratory it has conducted fundamental scientific research in aeronautics with the sincere and indispensable cooperation and assistance of the War, Navy, and Commerce Departments. As a result, the scientific basis for aircraft design in the United States for both military and civil uses is not excelled in any other country. Long adherence to sound policy has won for the United States general recognition as a leader among the progressive nations in improving the performance, efficiency, and safety of aircraft.

The continued improvement in the performance of both military and commercial aircraft has confronted this Committee with a variety of problems that are pressing for immediate solution. Among examples of such problems may be mentioned the need for devising a method for studying the stalling characteristics of highly tapered wings; the determination of the necessary load factors and their variation with size and speed; the problem of reducing or eliminating if possible the formation of ice on wings, propellers, and control surfaces, and of providing effectively for the automatic removal of ice when it does form; problems involved in the design of wings, control surfaces, and flaps, as well as other devices to secure better control at low speeds incident to taking off and landing; problems of suppressing vibration and flutter, improving engine and propeller efficiency, capacity, and dependability, extending the range, enlarging the capacity, and at the same time constantly increasing the speed and safety of aircraft.

In addition to meeting urgent needs of the present, the Committee tries to look into the future and to anticipate some of the problems that may arise. For example, what are the maximum requirements for military and commercial aircraft going to be? Will speeds in excess of 400 miles per hour be required? How much will the size of commercial aircraft exceed 50 tons within the next few years? What are the problems that will require scientific analysis before such craft can be successfully designed and constructed? Will airships be further developed for naval use or for transoceanic transportation and, if so, what are fundamental problems this Committee should investigate?

The organization of research.—To analyze the present and probable research needs of aviation, civil and military, the N. A. C. A. has set up standing technical subcommittees on aerodynamics, power plants for aircraft, aircraft materials, and aircraft structures. The subcommittees are organized along lines similar to the main Committee and include specially qualified representatives of all the governmental agencies concerned with aeronautical development, as well as experts from private life. The members of the subcommittees, like the members of the main Committee, serve as such

without compensation. The subcommittees prepare and recommend research programs. The more fundamental problems are usually assigned for investigation at the Committee's laboratory at Langley Field, Virginia, primarily because of its special equipment for aeronautical research. Problems are also assigned to the National Bureau of Standards, so as to make the best use of available Government facilities and at the same time to avoid duplication in the field of aeronautical research. In the same manner problems are assigned and funds transferred to universities and technical schools. In this way aeronautical research is stimulated and coordinated.

Advances in the science of aeronautics have given rise to various trends, as the possibilities of aircraft increase. At the present time the trend of design of aircraft in all nations is definitely toward higher speeds and larger structures, with greater range and carrying capacity. This is true in both the military and commercial fields. Scientific and technical problems do not diminish but on the contrary increase in number and in difficulty with each advance in speed or size. It is the duty of this Committee to supply the fundamental data on which the design of new aircraft is based. If the Committee does not meet this responsibility adequately, the United States will quickly fall behind, because of the great emphasis now being placed on aeronautical research and development by other progressive nations.

Research facilities.—Up to 1932 the Committee had constructed at its laboratories at Langley Field, Virginia, known as the Langley Memorial Aeronautical Laboratory, special equipment such as the variable-density tunnel, the propeller-research tunnel, the full-scale tunnel, and the hydrodynamic laboratory—a seaplane towing basin. They were at the time of construction the only such pieces of equipment in the world. The possession of such equipment was one of the chief factors in enabling the United States to become the recognized leader in the technical development of aircraft. Since 1932 this research equipment has been reproduced by foreign countries and in some cases special research equipment for the study of problems in aeronautics has been developed and constructed abroad which is more modern than and superior to the equipment existing at Langley Field.

Since 1932 the importance of scientific research in aeronautics has been more generally appreciated by European nations and several of the larger powers have greatly augmented their research facilities and activities. The competition in the development of research equipment and facilities between the progressive nations is just as intense as the competition in the production of aircraft of superior performance. This condition has impressed the Committee with the advisability of providing additional facilities promptly as needed for the study of problems that are necessary to be solved, in order that American aircraft development, both military and commercial, will not fall behind.

In answering this scientific challenge the Committee has under construction at its laboratories at Langley Field a new wind tunnel having a diameter of 19 feet that can be operated under a pressure of three or more atmospheres at an air speed of more than 200 miles per hour. This tunnel will permit the investigation of the characteristics of large models of aircraft at much higher values of Reynolds Number than can be obtained in any of the Committee's existing wind tunnels. The Committee also has under construction a refrigerated wind tunnel for the investigation of the problems of ice formation on aircraft. This tunnel has throat dimensions of 7½ by 3 feet and will embody features and principles which, it is believed, will make it an effective instrument for the purpose intended.

The Committee during the past year developed an entirely new type of wind tunnel. The experience of the Committee in the operation of the free-spinning wind tunnel indicated the advantage of being able to reproduce and observe aircraft motion under controlled conditions in a wind tunnel. Methods of studying stability, control, and motion of an aircraft in previous types of wind tunnels, where the model is fixed on a balance, are long and laborious, and leave much to be desired in accuracy. Realizing the need for studying stability, control, and motion of a model of an aircraft when flying unrestrained, the Committee developed in the past year a new form of wind tunnel known as a "free-flight wind tunnel."

The first tunnel of this type constructed was 5 feet in diameter, and was so arranged that by tilting the tunnel its longitudinal axis could be set parallel to the glide path of the model under test. To do this the tunnel was suspended from above at a single point so that the axis of the wind tunnel could be varied through a wide range of angles, making this tunnel what might be called a "tilting wind tunnel."

The results obtained with this small tunnel were so encouraging that the Committee proceeded with the construction of a free-flight wind tunnel having a diameter of 20 feet.

With the establishment of commercial service across the Pacific Ocean by seaplane transports and the early prospect of such service across the Atlantic, operators and designers are focusing their attention on aircraft of larger sizes having improved efficiency and carrying more passengers and a heavier mail and express load. The design of the seaplane hull is a most important factor affecting the efficiency of transoceanic transports. Anticipating the need for extensive investigation of seaplane hull models in connection with the develop-

ment of larger seaplanes, the Committee during the past year modernized its hydrodynamic laboratory. The towing basin was lengthened from 2,000 feet to 2,900 feet. The towing carriage was enlarged and the operating speed increased so that investigations can now be made at speeds corresponding to the higher take-off and landing speeds of seaplanes.

The Committee's laboratories are on a portion of Langley Field assigned to this organization by the Secretary of War and are under the direct control of the Committee. The Committee believes that its laboratories, despite the recent great expenditures on research organizations abroad, are as yet unexcelled by those of any other single nation. In addition to the new research equipment under construction as noted above, the Committee's laboratories include: An 8-foot 500-mile-per-hour wind tunnel; a 60- by 30-foot full-scale wind tunnel; a 20-foot propeller-research tunnel; a 5-foot variable-density wind tunnel; a 7- by 10-foot wind tunnel; a 5-foot vertical wind tunnel; a 15-foot free-spinning wind tunnel; two high-velocity jet-type wind tunnels of 11- and 24-inch throat diameters, respectively; a hydrodynamic laboratory; an engine research laboratory; a flight research laboratory; and an instrument research laboratory.

Relation of Committee's work to national defense.—The relationship of the work of this organization to national defense has long been recognized and appreciated by the War and Navy Departments. The Army and Navy air organizations rely upon the N. A. C. A. to anticipate and to meet their research needs and thus to enable them to achieve and maintain leadership in the highly competitive field of military aircraft development. The safety and security of our country in time of war may depend upon a decision in the air. The course of a war will certainly be influenced in favor of that side which can gain supremacy in the air. Sound tactical organization, large numbers of aircraft, sufficient trained personnel, and ample productive capacity in the industry are not in themselves sufficient. The aircraft that engage the enemy in action must, if possible, be superior in performance. The hope of retaining our present superiority in technical development, in the face of the increasing emphasis being placed upon aeronautical research and development abroad, will depend largely upon the ability of this organization to solve promptly and effectively the fundamental problems attendant upon rapid progress in this branch of engineering science.

In this connection, the economic value of the work of this organization is worthy of reference. The procurement programs of the Army and Navy call for the expenditure of large sums to carry into effect the national defense policy approved by the Congress. Unless the aircraft procured are at least equal in performance to those possessed by other nations, their net value to the Army and Navy in time of war would be almost at the vanishing point. A national investment in inferior military aircraft would not only invite the risk of loss of the aircraft in time of war, but also the trained flying personnel. It would be as disappointing and disastrous as it usually is to try to win on the second-best hand in a poker game. Without up-to-date, reliable results of scientific laboratory research, our Army and Navy would not be able, even with the most sincere cooperation of the industry, to design and procure aircraft with any assurance that they would not be "second best" in time of war.

Commercial aviation.—The continued search for trends of development, and the effort to meet these trends by the provision of adequate research facilities and investigation of the right problems, also have a very important bearing upon the development of commercial aviation. Researches initiated primarily to meet military needs are in many cases broadened in scope to meet the needs of commercial aviation. Research problems peculiar to commercial aviation alone are also investigated. The Committee is materially assisted in this respect by suggestions from the Bureau of Air Commerce and from the air transport lines. Aircraft manufacturers also offer research suggestions and are alert to incorporate changes which the Committee's researches indicate will improve the safety or efficiency of aircraft. That the United States leads the world in the development and operation of commercial aircraft is due not alone to this healthy condition, but also in large measure to the national policy of air mail payment and to the indispensable assistance of the Bureau of Air Commerce in providing unexcelled air navigation facilities and otherwise helping in every practicable way to promote the safety and efficiency of air navigation. We cannot in this connection underestimate the importance of the meteorological service of the Weather Bureau in aid of safety, nor the numerous and valuable contributions to commercial aviation that have resulted from the experiments and developments on aircraft, engines, instruments, and accessories by the Army and Navy.

Our growing air transport business finds a healthy reflection in an aircraft production industry better equipped to respond to the needs of national defense in time of emergency. A healthy nucleus of an aircraft industry capable of rapid expansion in time of need is essential to our national defense. If it were not for the stimulation and support given the manufacturers by the growth of commercial air transportation in the United States, the aircraft industry would be so much weaker that, in view of disturbed world conditions at this time, there would be need for some form of artificial stimulation and development of productive ca-

pacity. That we are not confronted with such a problem at this time is due partly to the fact that the results of the Committee's researches have made possible the development of commercial air transports in the United States superior to those of any other country. This has not only facilitated a rapid growth of commercial air transportation in this country, but has given to the American aircraft industry an advantage in world markets, evidenced by orders received from foreign countries for commercial airplanes of American manufacture.

The improved efficiency and safety of American air transports have permitted economies in operation, which in turn have resulted in material lessening of the cost of carrying air mail and of passenger fares.

Economic value of research.—No money estimate can be placed upon the economic value of greater national security through development of the means of producing superior military aircraft. Nor can a money estimate be placed upon the economic value of lives and property saved through improvements in the safety of aircraft. Nor can the educational advantages offered by air travel, the time saved, and the pleasure afforded to passengers be evaluated, nor the value to the nation of extending its national influence through world trade routes of the air. The researches of this Committee, however, do have a tremendous economic value that can be measured in dollars and cents. Improvements in aircraft that have resulted from the Committee's investigations and that have a definite economic value are numerous. Careful computations have been made of the economic value of a few of the more important contributions of this organization. These indicate that the annual savings in money made possible by the Committee's researches exceed the total appropriations for this organization since its establishment in 1915.

Summary.—With the rapid expansion of aviation in national defense, it is more than ever necessary that facilities be available for the prompt and adequate study of those fundamental problems in aeronautics that influence the speed, range, capacity, and control of aircraft.

The Committee believes that the future development of American aeronautics is largely dependent upon the support and effort given to the orderly and sustained prosecution of fundamental scientific research. It is the confident hope of the Committee that the United States will never be in a position where fundamental information necessary for the design of aircraft of maximum performance, efficiency, and safety will have to be imported from any foreign nation.

In commercial aviation the major problem is one of improving safety without penalizing those factors that are necessary to increase the speed, efficiency, operating range, and comfort of aircraft. When this Committee was established over twenty-two years ago there was but little appreciation of the value of aeronautics to national defense and practically no appreciation of the possibilities of aircraft in commerce.

Aviation has now become such an important factor in national defense, in the promotion of transportation in the United States, and in the extension of international commerce and good will that the organization and conduct of aeronautical research have attained the greatest significance and importance.

Foreign nations are making determined efforts to design and produce superior research facilities and to develop superior aircraft, both civil and military. The Committee in order fully to meet its responsibilities is endeavoring to modernize, improve, and augment its research facilities so as to maintain the present advantage of the United States.

To assure effective functioning on the urgent problems of the Army and Navy in time of war means for stabilizing the personnel of this organization must be found. From a study of the problem thus far it appears that enactment of legislation for this purpose may be necessary.

The Committee believes that the results achieved in the past and the problems to be faced justify a continuation of the liberal support of its work, and it further believes that in order to secure the best results there should be no change in its functions or in its status as an independent Government establishment.

PART I

REPORTS OF TECHNICAL COMMITTEES

In order to carry out effectively its principal function of the supervision, conduct, and coordination of the scientific study of the problems of aeronautics, the National Advisory Committee for Aeronautics has established a group of technical committees and subcommittees. These technical committees prepare and recommend to the main Committee programs of research to be conducted in their respective fields, and as a result of the nature of their organization, which includes representation of the various agencies concerned with aeronautics, they act as coordinating agencies, providing effectively for the interchange of information and ideas and the prevention of duplication.

In addition to its standing committees and subcommittees, it is the policy of the National Advisory Committees for Aeronautics to establish from time to time special technical subcommittees for the study of particular problems as they arise.

During the past year there has been a major change in the organization of the Committee's standing technical committees. The Committee on Aircraft Structures and Materials, which was one of the three principal technical committees, its Subcommittee on Structural Loads and Methods of Structural Analysis and the latter's Subcommittee on Research Program on Monocoque Design have been replaced by two coordinate committees, both reporting direct to the main Committee, namely, the Committee on Aircraft Materials and the Committee on Aircraft Structures. This change was made in recognition of the greatly increased importance of the problems of structural design in the field of aeronautics, and of the need for greater concentration of effort on these problems.

With this change in organization, the Committee has four principal technical committees—the Committee on Aerodynamics, the Committee on Power Plants for Aircraft, the Committee on Aircraft Materials, and the Committee on Aircraft Structures. Under these committees there are six standing subcommittees. The membership of these technical committees and subcommittees is listed in Part II.

The Committees on Aerodynamics and Power Plants for Aircraft have direct control of the aerodynamic and aircraft-engine research, respectively, conducted at the Committee's laboratory at Langley Field, and of special investigations conducted at the National Bureau of Standards. Most of the research under the supervision of the Committee on Aircraft Materials is conducted by the National Bureau of Standards. The greater part of the research under the cognizance of the Committee on Aircraft Structures is carried on by the National Bureau of Standards, but a number of structural investigations, especially those of a theoretical nature, are conducted at educational institutions and at the Committee's laboratory at Langley Field. The four technical committees recommend to the main Committee the investigations in their respective fields to be undertaken by educational institutions under contract with the National Advisory Committee for Aeronautics, and keep in touch with the progress of the work and the results obtained. The experimental investigations in aerodynamics, aircraft power plants, aircraft materials, and aircraft structures undertaken by the Army Air Corps, the Bureau of Aeronautics of the Navy, the National Bureau of Standards, and other Government agencies are reported to these four committees.

REPORT OF COMMITTEE ON AERODYNAMICS

LANGLEY MEMORIAL AERONAUTICAL LABORATORY

LANDING SPEED AND SPEED RANGE

Flaps.—The use of wing flaps on high-performance airplanes is now almost universal. The research that has been conducted by the Committee during the past several years on the most promising forms of flaps has resulted in establishing their relative merits and has made possible the selection of the most satisfactory type for a given design. During the past year, attention has been directed mainly toward obtaining more specific design data for flap application.

In the variable-density wind tunnel, tests of ordinary and split flaps of 20-percent wing chord on the N. A. C. A. 23012 airfoil have been made with a large range of flap settings at a value of the effective Reynolds Number of about 8,000,000, for the purpose of providing designers with more reliable data as to the airfoil section characteristics for these combinations at large values of the Reynolds Number. While the results have not been completely analyzed, they corroborate, in general, the conclusions drawn from previous tests at lower values of the Reynolds Number.

The split flap is somewhat more favorable to speed range and landing speed than is the ordinary flap.

In the 7- by 10-foot wind tunnel a study of slotted flaps is under way in which tests of flaps of various shapes with slots of various forms are being conducted on an N. A. C. A. 23012 wing of 3-foot chord. With this installation, airfoil characteristics corresponding to a Reynolds Number of about 2,500,000 are being determined. The results to date indicate that with a properly designed slotted flap, unusually high maximum lift coefficients may be obtained. In addition, very low profile drag coefficients at high lift coefficients may be obtained with the flap deflected, which should result in improved take-off and climb characteristics. For controlling the glide-path angle, the slotted flap may be deflected beyond the angle for maximum lift without appreciably changing the lift coefficients. With this type of operation, the flap is similar to the glide-control flap previously described in Technical Note No. 552.

The results of the investigation in flight and in the full-scale wind tunnel, of a Zap flap mounted on a Fairchild 22 airplane, previously mentioned, have been published in Technical Note No. 596. Results of a similar investigation on the external-airfoil flap are presented in Technical Note No. 604.

Tests have also been made in the 7- by 10-foot wind tunnel for private companies and for the Bureau of Aeronautics of the Navy Department of the aerodynamic characteristics of several models equipped with flaps.

Maxwell slot.—The results of tests of another device for the improvement of speed range, the Maxwell leading-edge slot, mentioned in last year's report, have been published in Technical Note No. 598.

Measurement of minimum speed.—Opportunity was afforded during the year, in connection with the investigation of the maximum lift coefficient of a $2R_1 12$ wing on a Fairchild 22 airplane, to obtain a comparison between the flow conditions in flight and in the full-scale wind tunnel and thus study the effect of various test procedures and conditions on the measured minimum speed of an airplane. The main flight program covered the effect of wing loading and altitude on minimum speed. By extension of the program the effects of propeller position, throttle setting, wing-surface roughness, and the rate at which the angle of attack was increased were investigated. It was found that for a constant weight the minimum speed might vary by 5 percent, depending on the factors. The maximum lift coefficient obtained with one loading cannot be directly applied to the computation of the minimum speed with another loading, because of the variation of the lift coefficient with speed.

CONTROL AND CONTROLLABILITY

For a number of years the Committee has been engaged in a systematic wind-tunnel investigation of lateral control with special reference to the improvement of control at low air speeds and at high angles of attack. Many different ailerons and other lateral-control devices have been subjected to the same systematic investigation in the 7- by 10-foot wind tunnel and the devices that seemed most promising have been tested in flight. As has been stated in previous reports, the wind-tunnel and flight results were not always in agreement and indicated that, in determining actual control effectiveness from wind-tunnel results, it was necessary to include what had been previously considered secondary factors. A mathematical method of analysis was consequently developed to include those secondary factors and this method of analysis has been in use for about two years.

The experience gained has resulted in a revised basis of comparison of lateral-control devices and on this revised basis a critical résumé and analysis of the Committee's research to date on lateral control has been made and has been published in Technical Report No. 605. The analysis indicates that for normal-flight conditions, ordinary ailerons with the gap between the aileron and the wing sealed are the most generally satisfactory. An added advantage of these ailerons is that they appear to be practically free from icing hazards.

Slot-lip ailerons.—The complete results of the wind-tunnel and flight investigation of slot-slip ailerons have been published in Technical Report No. 602. It was stated in the last annual report that slot-lip ailerons installed on a Fairchild 22 airplane produced unsatisfactorily sluggish control, although such sluggishness was not detected by the pilots when these ailerons were installed on the W1–A airplane. An analysis made during the year has shown that the difference between the response of the two airplanes is explainable by the difference in their lateral-stability characteristics. Although some reduction in the drag of the slot-lip ailerons over that previously reported was obtained with a modified slot shape, the drag of this type of aileron is still considered excessive for modern high-performance airplanes.

The wind-tunnel investigation mentioned last year of the special form of slot-lip aileron, consisting of a plain aileron forming the trailing edge of an airfoil equipped with an external-airfoil flap, has been completed. The characteristics of these ailerons on an N. A. C. A. 23012 wing equipped with 20 and 30 percent chord full-span external-airfoil flaps of the same section were measured and are reported in Technical Report No. 603. These ailerons were found to be capable of developing large rolling moments but the hinge moments had cer-

tain undesirable characteristics and should receive further study.

Ailerons on tapered wings.—At the request of the Army Air Corps an investigation of the effectiveness of conventional ailerons on a tapered wing was made for direct comparison with a straight wing having ailerons of the same size. A 2:1 tapered wing with conventional flap-type aileron was mounted on a Fairchild 22 airplane and investigated in flight and in the full-scale wind tunnel. Conventional ailerons on this wing were found to be slightly more effective than ailerons of the same dimensions on a straight wing. The improvement was of the order of only 5 percent at low speed, and was so slight that it was not apparent to the pilots in the handling of the airplane. The results are being prepared for publication.

An investigation of ordinary sealed ailerons on two wings having medium and high taper ratios and partial-span split flaps has been described in Technical Report No. 611. The report presents aerodynamic information necessary for aileron design, including rolling, yawing, and hinge moments, as well as the aerodynamic characteristics of the wings.

Floating wing-tip ailerons.—Comparative tests were made in the full-scale wind tunnel and in flight to determine the relative effectiveness of floating-tip ailerons and conventional trailing-edge ailerons. The tests were made on a Fairchild 22 airplane equipped with a 2:1 tapered wing the wing tips of which could be removed and replaced by floating-tip ailerons. The floating-tip ailerons were made as large as seemed reasonable from considerations of structural weight. These ailerons were found to be approximately one-half as effective in producing rolling moment as conventional ailerons on the same wing. The floating-tip ailerons produced small favorable yawing moments while the trailing-edge ailerons produced appreciable unfavorable yawing moments.

Combinations of spoilers.—At the request of the Bureau of Aeronautics of the Navy Department, the lateral-control possibilities of combinations of spoilers arranged in tandem were investigated in the 7- by 10-foot wind tunnel. Since the time of response with such an arrangement was questionable, the investigation consisted primarily of measuring the response characteristics by means of a motion-picture study of the motion of a wing model restrained by springs but free to move when the control device was operated. The rolling moments produced by the control devices were measured with the same installation. It was found that while a combination of front and rear spoilers without lag was possible, no improvement in control was obtained over that with the rear spoiler or retractable aileron alone when the wing was equipped with a full-span flap.

Reduction of aileron control forces.—With the increase in size and speed of airplanes, increased interest has been shown in means of reducing the forces required to operate ailerons. On a large percentage of airplanes aerodynamic balances of the Frise or slotted types are used, with an accompanying loss in control effectiveness. In addition, such balances, with their projecting surfaces, are subject to icing difficulties.

The use of trailing-edge tabs in the conventional manner to balance the control forces of ailerons is accompanied by a sacrifice of some control effectiveness. A less conventional but apparently more successful method of applying tabs to ailerons is to use a very narrow-chord full-span tab to increase the up-floating angle of the ailerons by deflecting the tabs downward on both ailerons in conjunction with a proper differential movement of the ailerons. A study of aileron hinge moments as affected by differential linkages has been made and the results published in Technical Note No. 586. The value of a tab and differential linkage system has been investigated with a large wing in the 7- by 10-foot wind tunnel and on a Fairchild 22 airplane in flight. The ability of the arrangement to reduce the control forces to any desirable value was verified in both installations.

The flight investigation, in addition to verifying, in general, the principles involved in the theoretcal analysis, has indicated certain practical details requiring further study. The effect of the tabs on the aileron floating angle appears to be critically dependent on the tab shape. Tabs consisting of flat plates extending back of the aileron trailing edge were found to have very little effect on the aileron floating angle and consequently little effect on the control forces, whereas tabs inset within the aileron contour are satisfactory.

Wind-tunnel tests have shown that the effectiveness of a given aileron may be increased considerably by sealing the gap between the aileron leading edge and the wing to prevent leakage of air at this point. The effectiveness of the seal is greatest for narrow-chord ailerons, the increase being of the order of 50 percent when the aileron chord is about 10 percent of the chord. The increase in effectiveness may be utilized to improve the controllability or, if the controllability is satisfactory, to reduce the control forces by the substitution of a smaller sealed aileron for one having a gap at the hinge.

The actual application of this system of improving lateral control or reducing aileron stick forces depends on how much leakage occurs at the hinge in a normal aileron installation. In order to study this problem, measurements were made of the lateral control of the Fairchild 22 airplane, which has ailerons having a chord of 18 percent of the wing chord, with the original aileron installation and with a fabric seal

over the gap at the hinge. A 30-percent improvement in the control effectiveness was obtained. On the basis of these findings, sealed ailerons of half the chord of the original ailerons, or 9 percent of the wing chord, were installed on the airplane. These ailerons are about as effective as the original unsealed ailerons but require less than half the operating effort.

Two-control operation of an airplane.—Control of an airplane by means of two controls instead of the three normally used has appeared to offer promise of simplifying the operation of an airplane. Flights have been made with airplanes in which both aileron-elevator and elevator-rudder combinations were utilized for two-control operation, but considerable uncertainty remains as to which of these modes of operation is likely to prove the better and also whether either of them is capable of affording the controllability required for safety in flight.

In order to obtain additional information on the subject, an analytical study was made of two-control operation of a conventional airplane by the method of the theory of disturbed motion and is presented in Technical Report No. 579. Control maneuvers were computed for various combinations of rolling and yawing moments with an airplane for which the lateral-stability derivatives were varied. It was concluded that, while the most desirable control characteristics would depend somewhat on the lateral-stability characteristics and on the rate of application of the control device, the two-control operation of an airplane would be most generally satisfactory with controls which gave primarily a rolling moment with a slight amount of favorable yawing moment.

Flying qualities of large airplanes.—As was mentioned in the last annual report, a research is in progress to determine how much is known quantitatively regarding the actual stability, controllability, and maneuverability of large airplanes, and also what the procedure should be in any investigation to determine these characteristics in quantitatve form. During the past year a program of investigation in flight covering the measurement of all the quantities believed to be of importance with respect to flying qualities, has been formulated, the instrumentation developed, and the program successfully tried with a single-engine five-place high-wing cabin monoplane. Some modifications in the original program regarding the measurement of the general stability and the effectiveness of the rudder control were indicated to be desirable. The modified program and certain items referring to asymmetric power conditions that could not be investigated with a single-engine airplane are being studied with a twin-engine bombardment monoplane, and the measurements have been initiated on modern transport airplanes.

Flight with unsymmetrical power.—The problem of flight with only the propellers on one side operating was investigated as part of the investigation of the power-on characteristics of large multi-engine models in the full-scale tunnel.

Flight with zero yaw, accomplished by banking the airplane slightly to balance the side forces due to the propellers and rudder, was found preferable to balancing the side forces by yawing without banking, both as regards the maximum ceiling and the rudder deflection required. For unsymmetrical power conditions, the losses in performance, aside from the reduction of the thrust, are due to the drag of the inoperative propellers and the deflected rudder. The propeller drag is the major item unless the propeller is feathered or allowed to free-wheel.

MANEUVERABILITY

At the request of the Bureau of Aeronautics, Navy Department, the Committee is undertaking an investigation of the maneuverability of several Navy airplanes primarily for the purpose of determining the maximum angular accelerations in pitch and roll to which the machines may be subjected. The tests have been completed on two airplanes. The investigation includes measurements of the angular accelerations in rolling produced by abrupt use of the ailerons alone and also by combined use of the ailerons and other controls. Pitching accelerations are investigated in abrupt pull-ups from level flight and in recoveries from vertical dives. In all cases the angular accelerations are correlated with the linear accelerations of the center of gravity. In addition to the measurements of angular acceleration, information is being obtained on the pressure inside the wings during vertical dives and data are obtained to compare the loss of altitude in recoveries from dives with that predicted by means of charts developed as a result of previous investigations.

In connection with the study of the vertical-dive maneuver, the velocity-altitude relations for airplanes have been studied. Charts have been prepared (Technical Note No. 599) that present in a readily usable form the solution of the relation between time, velocity, and altitude for airplanes having various terminal velocities. The variation of density with altitude is taken into account on these charts.

STABILITY

A review of all available previous and contemporary work on stability, which was mentioned in the last annual report, has been completed and an extensive program outlined for systematic research in the various facilities available to the Committee. Work is now in progress upon several of the projects deemed to be the most urgent.

The investigation of new equipment for the study of stability is being continued. An experimental 5-foot free-flight wind tunnel has been developed to a point

of satisfactory operation. This tunnel can be used to study the free-flight behavior of models up to 22 inches in span. With a tunnel of this type it is possible to investigate inherent and controlled stability, motion in gusty air, stalling characteristics, the power of controls, and many other factors directly related to the actual free-flight behavior of the airplane. Even at the very low scale of tests possible in the present 5-foot tunnel, observation of model behavior has led to very interesting conclusions regarding the effects of such factors as the adverse yawing moments of ailerons, the effect of the position of the wing wake on the damping of longitudinal oscillations, the behavior of an aircraft when the tail is in the violent wake behind deflected split flaps, etc. The free-flight tunnel, of which the present 5-foot experimental version is the first and only one of the type, gives promise of greatly facilitating the entire study of aircraft motion.

Lateral stability.—Most existing work on stability deals with the inherent stability of the craft itself with the controls either fixed or free. Actually, the most usual condition of flight is that in which the aircraft is held to a definite course by either a human pilot or a compass-controlled automatic pilot. The pilot endeavors to bring the craft back to the course after a disturbance and in so doing alters the stability characteristics. A study of the stability of controlled motion along a definite course is now in progress and should show the effects of various ways of using the controls. It may also lead to a modification of present ideas regarding the importance and proper values of certain factors which affect the motion, since the present ideas are based on requirements for inherent stability.

In any study of stability with reference to a certain course, it is of great practical importance to know how the factors that govern the stability influence the magnitude and violence of the motion when an atmospheric disturbance is encountered. A mathematical study of motion in gusty air is being carried out and is approaching completion for the case of lateral motion.

A report on lateral stability in power-off flight has been published as Technical Report No. 589. This report parallels Technical Report No. 521, which deals with longitudinal stability. It includes discussions of the problem and of the individual factors involved. A number of charts are presented from which the lateral stability of a new design can be quickly and easily estimated.

One of the factors that most critically affects the lateral-stability characteristics is the rate of change of yawing moment with change in sideslip. There has been considerable uncertainty as to what allowance to make for the effect of the fuselage when this factor is estimated. During the past year, the Committee has undertaken a study of all readily available data on this factor with a view to developing suitable empirical relationships for its estimation. A technical note is being prepared giving the results of this investigation.

The investigation of the effect of tip shape and dihedral of rectangular monoplane wings on the lateral-stability characteristics, reported last year, has yielded basic information on the subject. For practical application to complete airplanes, however, the wing-fuselage interference would seem to be an important factor in determining the stability characteristics. Quantitative information on this effect will be obtained from an investigation that has been started in the 7- by 10-foot wind tunnel with fuselages of various cross sections and with tapered, swept-back, swept-forward, and rectangular wings.

Longitudinal stability.—Work is now in progress on a general study of longitudinal stability with power on. An attempt is being made to prepare charts similar to those in Technical Reports 521 and 589 to enable the designer to estimate quickly the effect of power on the stability.

The investigation of wing-fuselage interference in progress in the variable-density wind tunnel has been extended to include the study of the effects of adding tail surfaces to typical combinations. Conventional tail surfaces and horizontal tail surfaces with end plates are both being investigated with a view toward exploring the parameters of combination as affecting the aerodynamic interference, particularly as regards longitudinal stability. The effect on the moment of the tail surfaces entering the wing wake is noticeable but small, particularly when compared with the effect of the wing stall.

The analysis, reported last year, of the horizontal tail surface required for airplanes equipped with wing flaps, has been completed. A rational system for computing the horizontal tail area was evolved and has been presented in Technical Note No. 597.

A comprehensive investigation has been undertaken in the Committee's full-scale wind tunnel to determine the effect of propeller operation on the important characteristics of airplanes, such as the lift, stability, control, balance, etc. Full-scale data have been obtained for five airplanes having different geometrical arrangements, and a report presenting an analysis of these results is in preparation. These tests include measurements of the air-stream velocities and downwash angles in the region of the tail plane, and a study is being made to determine the variation of these quantities with the propeller thrust.

Stalling.—The problem of avoiding excessive danger from the stall has been a recurrent one. Most airplane manufacturers dealt with the problem rather satisfactorily several years ago, either empirically or through a

reasonably sound understanding of the phenomenon, gained as the result of research work both here and abroad.

In general, the solutions embodied the use of increased static longitudinal stability, thus providing a definite warning of the approaching stall through the backward movement, position, and forces on the control column, together with a gradually developing stall secured either by allowing the upper or lower wing of a biplane to stall first or by the use of monoplanes with little or no taper and with "poor" wing-fuselage junctures, which further tended to bring about a gradually developing stall, beginning at mid-span. These measures assured that the stalled condition would develop progressively after a reasonably definite warning; furthermore, lateral control was often maintained up to or beyond the stall (wing maximum lift), owing to the fact that the essentially effective parts of the wing system remained unstalled even after the angle of attack had exceeded that of maximum lift. Inasmuch as the pilot has little incentive to go beyond this point, such a solution was and still is considered satisfactory.

With such satisfactory solutions in common use, attention has for the past few years been diverted from the problem of minimizing stalling dangers. Recently however, modern design trends are bringing the problem back again in an acute form. These trends are toward higher wing loadings and landing speeds; the substitution of efficient high-speed sections having more sudden and hence less desirable stalling characteristics; the almost exclusive use of tapered-wing monoplanes; the use of increased taper; the low-wing position which contributes to reduced longitudinal stability with increasing lift; the use of "good" wing-fuselage junctures; and, finally, high-lift devices. The high-lift devices may further add to the dangers of tip stalling, add to balance and stability difficulties, and usually cause a vicious section stall corresponding to a sudden, large, and usually unsymmetrical loss of lift.

These trends have already gone so far that it now appears that many airplanes in common use cannot be considered reasonably safe, even for experienced pilots. The worst offenders may give no indication of an approaching stall which, when it occurs, is manifested by a vicious uncontrolled rolling dive, that results from a sudden loss of lift on the right or left wing and a simultaneous loss of lateral control.

During the year practical methods of avoiding these conditions in modern types of airplanes have been sought. The investigations have proceeded mainly on the theory that the vicious stall may best be avoided in monoplanes by causing the wing to stall progressively from the center toward the tips. Not only are the sudden loss of lift and violent roll thus avoided, but lateral control is maintained through the first stages of the stall and the tendency toward an upwash on the tail surfaces associated with the loss of lift near the center of the wing may be used to bring about a marked increase in longitudinal stability as the stall is approached.

In the first investigation conducted in flight, sharp leading-edge strips extending out along the wing from either side of the fuselage were employed to bring about the desired symmetrical center-stalling characteristic. Wind-tunnel experiments with airfoils having sharp leading-edge sections over a small portion near their midspan had indicated how the flight investigation should proceed. The flight investigations for the power-off condition showed that an airplane having vicious stalling characteristics could be improved as expected by thus bringing about a gradually and symmetrically developing center stall. The extreme maximum lift coefficient was, of course, slightly reduced, but the practical gliding or approach speed was not increased; in fact, it was actually reduced. This phase of the flight investigation is, however, only preliminary in that the airplane tested had no flaps or other high-lift devices, whereas the problem is of most practical interest and is probably more difficult when high-lift devices are employed. The investigations are being extended.

The method employed to start center stalling may be objectionable on the grounds that the sharp leading edges will always tend to reduce the maximum lift. An investigation in the variable-density tunnel of methods of accomplishing the same result without loss of maximum lift led to the development of a new device known as the "stall-control flap." The flap tends to produce a well-rounded lift curve similar to that produced by the sharp leading edge but, together with a split flap or other conventional high-lift device, high maximum lift coefficients may be obtained. A special wing incorporating a stall-control flap has been constructed and installed on an F–22 airplane converted to a low-wing type. Flight tests are now being started on this airplane and from preliminary results it appears that, besides bringing about the desired center stall, several attendant advantages, such as favorable induced yawing moments from the ailerons, may be realized through its use.

SPINNING

The 15-foot free-spinning wind tunnel has been kept busy with routine testing of scale models of specific airplanes. The Matériel Division of the Army Air Corps, and the Bureau of Aeronautics of the Navy Department, are requiring spinning tests of models of new designs that are expected to be spun extensively in service. Four such models have been tested during the past year and three more are being prepared for testing in the immediate future. The work carried on

in this connection includes not only tests of the particular design, but also investigation of changes necessary to improve the spinning characteristics where such changes appear to be necessary.

The free-spinning tunnel is available for the testing of models for commercial concerns, and two such models have been tested during the year.

A certain amount of general information is being gleaned from the test results with specific designs. Conclusions stated in the last annual report regarding the importance of the tail unit in spinning have been confirmed and amplified during the past year. As a result of tests of a number of models of modern low-wing monoplanes, it now appears possible to draw certain conclusions about the effect of changes in mass distribution on such designs. In most cases the spinning characteristics of low-wing types have been improved, and in no case have they been impaired, by moving weight from the fuselage to the wings. This fact is of special significance in view of the present trend toward multi-engine airplanes with the engines in the wings.

During the past year a method has been developed for measuring, on free-spinning models, the hinge moment required to reverse completely the rudder during the spin. Such measurements have been made on three models. Indications are that the requirements of rapid recovery from the spin and reasonably low rudder moments are in certain cases very difficult to meet with a rudder that is also satisfactory in normal flight.

In addition to the spinning of models of specific airplanes, a systematic investigation is being carried out in the free-spinning tunnel to determine the effects of changes in wing arrangement, in tail arrangement and mass distribution. This investigation is about 20 percent completed. It is designed to reveal the relative importance of the various factors which affect spinning and to show which of these factors is most deserving of more detailed study. The results to date tend to confirm the conclusion that the tail arrangement is the most important single item. The effects of wing plan form and tip shape are, however, of considerably greater importance than has hitherto been thought to be the case. The effect of wing section appears to be relatively slight.

Tests of a model of the Fleet airplane on the spinning balance, reported last year, have been published as Technical Report No. 607. An investigation on the spinning balance of effect of wing plan form on the spinning characteristics has also been completed and the results published in Technical Note No. 612. The tests included a rectangular wing with square tips and with rounded tips and a tapered wing with rounded tips. An investigation in progress will show the effect of airfoil section on the spinning characteristics of monoplanes with rounded tips.

An investigation on the spinning balance of the effect of stagger of rectangular biplane cellules has been completed and will be the subject of a report. The range of stagger investigated was from negative 25 percent stagger to positive 25 percent stagger. While no general conclusions can be drawn regarding the effect of stagger, the results can be used in studying the steady spinning characteristics of particular airplanes.

Tests for the purpose of making a direct comparison between the actual spinning behavior of a low-wing monoplane and the behavior of a model of the same airplane in the spinning tunnel have been started. Some difficulty and delay have been encountered in obtaining a suitable airplane for the tests. Two have been tried in flight. With one, the oscillating nature of the spin made measurements impossible. With the second airplane, the rudder forces built up to such a magnitude on the entry into the spin as to make it extremely uncertain that the pilot could supply the force necessary to assure that the airplane would recover from the prolonged spins required for the measurements. The mechanical advantage available to the pilot in operating the rudder of this airplane was increased and the forces that the pilot had to apply were reduced to the extent that it was possible to continue the tests.

TAKE-OFF

The results of the investigation of the rolling friction of airplane wheels, mentioned in last year's report, have been published in Technical Report No. 583.

In the calculated prediction of the take-off performance of airplanes, common practice has been either to neglect the transition period between the end of the ground run and the beginning of the steady climb or to take it into account by assuming a simple motion, since the actual motion is too complex for simple mathematical treatment. This lack of knowledge regarding the motion of the airplane in the transition introduces, of course, a degree of uncertainty into the results. As mentioned last year, an investigation of this phase of the take-off was undertaken in an effort to eliminate this uncertainty. The study is now completed and the results are being prepared for publication. It was found that the calculated value of the air-borne distance required in taking off over a 50-foot obstacle might be subject to an error of about 10 percent if the transition is neglected.

The investigation served also to emphasize the difficulties which are encountered in attempting to obtain representative comparisons directly from take-off tests and which arise from the fact that it is practically impossible for a pilot to conform exactly to a prescribed procedure throughout a series of complete take-offs, particularly if the air conditions are not absolutely steady. At present an attempt is being made to

develop a method whereby the true take-off capabilities of an airplane may be evaluated without consideration of the personal element or the air conditions. One solution that appears promising is to determine from individual tests the relation between ground run, distance, and speed, and the relation between angle of climb and speed, the latter to be measured at some altitude where smooth-air conditions prevail. These quantities should not be appreciably affected by piloting and when properly combined, together with a suitable allowance for the transition, should provide an accurate measure of the take-off performance of an airplane. An investigation has been made to determine the feasibility of this system and the results are being analyzed.

The characteristics of the propeller producing the thrust are an important influence on the take-off. Available propeller data have to a great extent been rendered inadequate because of the changes in design necessitated by higher engine power and airplane speeds, requiring larger propellers of higher pitch and with three or more blades. For the purpose of establishing the design factor for propellers in this category, an extensive investigation on full-scale propellers has recently been made in the propeller-research wind tunnel. The investigation is more completely covered in a later section of this report.

The above-mentioned investigation that was made in the variable-density wind tunnel of ordinary and split flaps of 20 percent of the wing chord on N. A. C. A. 23012 airfoils indicates that neither of these flaps can be considered a satisfactory high-lift device for use in take-off because of the high profile drag caused by these flaps at high values of the lift coefficient. In this respect the ordinary flap is inferior to the split flap. At any value of the lift coefficient where the flaps are useful, a lower value of the profile drag coefficient can be obtained with the split flap than with the ordinary flap.

The stall-control flap previously mentioned, especially when combined with a low-drag trailing-edge high-lift device, appears to offer improvements in the take-off characteristics of flying boats and airplanes equipped with three-wheel landing gears, because this flap permits high lift coefficients to be obtained with the airplane in a level attitude.

LANDING

Landing loads.—At the request of the Bureau of Air Commerce and the Army Air Corps, the Committee is undertaking the accumulation of statistical information on the loads sustained by the landing gear in landings. Investigations have been made with four airplanes and one autogiro. Measurements of the attitude and vertical velocities immediately prior to contact and simultaneous measurements of the linear accelerations of the center of gravity and the angular accelerations in pitch are made in order to correlate the magnitude and direction of the resultant ground reaction and the approximate distribution of force between the main and tail wheels with the motion and attitude of the airplane at contact. The investigation will be continued as more aircraft become available. A preliminary analysis is being made of the data obtained thus far.

Stable landing gears.—The tricycle landing gear has recently been receiving considerable attention because of its possibilities for greatly improving the stability and handling characteristics of the airplane on the ground and for increasing the ease with which landings may be made. A study of the various factors affecting the geometrical arrangement of the landing gear has been made.

With the use of tricycle landing gears, the shimmy of the castering nose wheel has presented a problem. The Committee has made an analytical investigation of the stability of castering wheels as a result of which information was obtained as to the cause of wheel shimmy and several means of overcoming it were suggested. The allowance of a certain amount of lateral freedom of the wheel on its axle was indicated as a remedy. Model tests, and full-scale tests with the W1–A airplane, verified the indications of the analytical investigation and have shown that the shimmy of the castering wheel may be overcome by allowing a relatively small amount of lateral freedom of the wheel. To center the wheel, damping of the sidewise motion should be provided, which in the investigation described was done by curving the axle slightly.

The accelerations in landing of an airplane with a tricycle landing gear have been studied to ascertain whether the passengers might experience relatively severe accelerations in an emergency landing. The study revealed that the predominant acceleration was due to braking forces applied to the main wheels and that the vertical acceleration due to nosing over on the nose wheel should not be serious from the standpoint of passenger comfort.

AIRFOILS

The work on airfoils carried on by the Committee during the past year has been confined mainly to the consolidation of the large amount of data obtained in recent years and to the extension of its usefulness by providing more diversified and accurate methods of its application to practical problems.

Section characteristics.—Airfoil data obtained in the variable-density wind tunnel since 1930 have been corrected by the empirical method mentioned last year, to give more accurate section characteristics than it has been possible to obtain previously from tests of

rectangular airfoils in the variable-density wind tunnel. These corrected data are to be presented in two reports. The first of these (Technical Report 610) presents the complete results obtained from the investigation of related forward-camber airfoils, of which the N. A. C. A. 23012 airfoil is representative. The second report, now in preparation, will contain the complete results for a large number of miscellaneous airfoils investigated since 1930 and will also include a table giving the improved section characteristics for the airfoils on which data are presented in Technical Report No. 460. These results are reasonably complete at one value of the Reynolds Number. Since airfoil data must be employed in practice at widely different values of the Reynolds Number, scale effect must also be taken into account.

The results of an investigation of airfoil scale effect which have been available only in condensed form as a confidential report have been published in full in Technical Report No. 586. These data give the most reliable basis available for the prediction of airfoil-section data at values of the Reynolds Number other than that at which the section data published in the reports mentioned in the preceding paragraph were obtained. However, uncertainties in the present knowledge must be admitted, and it appears that entirely satisfactory results must await future research at full scale in a nonturbulent air stream. The difficulty is the lack of knowledge about the transition from laminar to turbulent flow in the boundary layer of the airfoil.

Many of the effects of scale, turbulence, and surface condition are intimately connected with the transition from laminar to turbulent flow in the boundary layer. The importance of these effects may be realized from an analysis of the effects of transition on the drag of airfoil sections. If it is assumed that the boundary layer over the surface of an airfoil is entirely laminar, remarkably low drag coefficients are found for the higher values of Reynolds Number. The drag coefficient for a flat plate with laminar boundary layer is 0.0008 at a Reynolds Number of 10,000,000. If the boundary layer is assumed to be turbulent from the leading edge onward, the drag coefficient is more than seven times as large as the laminar value at the same value of Reynolds Number, actually amounting to 0.0057.

It is known, however, that it is not possible to have a laminar boundary layer over the entire airfoil surface. Calculations made by the method given in Technical Report No. 504 show that at zero lift on the N. A. C. A. 0012 airfoil section separation would be expected if the boundary layer were laminar at about 55 percent of the chord back of the leading edge, because of the adverse pressure gradient existing over the rearward portion of the airfoil. If transition occurs at this point, the drag will be intermediate between the values given for the completely laminar and the completely turbulent flows, but will still be markedly less than that for the completely turbulent layer.

Some experimental results, including data from recent tests in the 8-foot high-speed wind tunnel and some theoretical considerations as well, indicate that with very smooth wings in an air stream having zero turbulence the transition may tend to remain near the laminar separation point. If such is the case, savings of approximately 40 percent of the wing profile drag at a Reynolds Number of 10,000,000 are indicated, as compared with that predicted from a normal extrapolation of data from the variable-density wind tunnel.

In this connection some direct evidence on the nature of transition has been obtained from an investigation carried out in the nonturbulent N. A. C. A. smoke tunnel. Boundary-layer surveys were made throughout the transition region on a smooth flat plate having an adverse pressure gradient. The investigation showed that while the extent of the transition region decreased considerably with an increase in Reynolds Number, the point at which marked changes in the laminar boundary-layer flow first occurred was independent of the Reynolds Number throughout the range included in the investigation. The transition region was close to the position at which separation of the laminar boundary layer was to be expected unless premature transition was brought about by slight roughness near the leading edge of the plate. The tests were carried to a Reynolds Number of 150,000 based on the distance from the leading edge to the calculated point of separation. Visual observation of the flow over the plate indicates that similar conditions may exist over the range of Reynolds Number up to 500,000. A technical note is being prepared presenting the results of this investigation.

Wing characteristics.—The calculation of the characteristics of tapered wings from airfoil section data has been continued with several wings of varying aspect ratio and taper ratio. The basic section data and the data on scale effect, if applied by the method described in Technical Report No. 572, will enable the user to reduce the wind-tunnel data and to estimate the best wing for a given airplane. The calculated characteristics of 20 tapered wings will be compared with the experimental results for the same wings.

Measurement of profile drag in flight.—It has been feasible to investigate the profile drag of an airfoil section in flight by means of the pitot traverse method. This method has been used in an investigation of the comparison of air-flow conditions in flight and in the full-scale wind tunnel, the data obtained being evaluated to determine the profile drag from the momentum loss in the wake of an airfoil. The airfoil was an N–22

section and was first investigated with a smooth surface that was later modified by the addition of a thread having a diameter of 0.01 inch and located on the upper surface about 5 percent of the chord back of the leading edge. The results indicated that the addition of the small thread increased the profile drag of the smooth airfoil by about 18 percent. The addition of another small thread to the under surface of the airfoil at the same chordwise location further increased the profile drag, the total increase due to the two threads being about 32 percent.

EFFECT OF RIVETS AND OTHER SURFACE IRREGULARITIES ON WING DRAG

Past investigations in the full-scale and variable-density wind tunnels have shown that rivet heads and other surface irregularities increase the drag of wings appreciably. As aircraft have been made otherwise more efficient, the importance of the increases in drag due to small surface irregularities has become more apparent and a need has arisen for more complete information on the magnitude of such drag increases.

An investigation has been made in the 8-foot high-speed wind tunnel to provide data on the effect on wing drag, over a comprehensive range, of rivet size, type, and arrangement, lap type and arrangement, and surface roughness. This investigation was made with a model of an N. A. C. A. 23012 airfoil of 5-foot chord at air speeds from 80 to 500 miles per hour at values of the Reynolds Number up to 18,500,000.

Rivets.—During the investigation tests were made of $\frac{3}{32}$- and $\frac{1}{16}$-inch brazier-head rivets, $\frac{3}{32}$-inch thin brazier-head rivets, and $\frac{3}{32}$-inch countersunk rivets in various chordwise and spanwise arrangements. The $\frac{3}{32}$-inch brazier-head rivets in a typical arrangement increased the drag of the smooth airfoil 27 percent at 225 miles per hour. The drag increases due to the other protruding rivet heads were approximately proportional to the height of the heads, indicating that rivets with the thinnest practical heads should be used. The countersunk rivets increased the drag 6 percent under the same conditions. Increasing the spanwise pitch of the rivets had little effect unless it was made more than 2.5 percent of the wing chord. The investigation showed that more than 70 percent of the rivet drag was due to the rivets on the forward 30 percent of the wing. About 66 percent of the rivet drag was due to the rivets on the upper surface of the airfoil.

Lapped joints.—A typical arrangement of conventional plain laps facing aft increased the drag over that for the smooth airfoil by 8 percent. Joggled laps increased the drag only half as much. Plain laps facing forward were found to be slightly inferior to plain laps facing aft, but if they were faired by rounding the edges of the sheets, the increase in drag was less than that with conventional laps facing aft. Rivets and laps employed together increased the drag only slightly more than rivets alone.

Surface roughness.—The effect of five different degrees of surface roughness on airfoil drag was investigated. At 225 miles per hour the drag of the smooth airfoil was increased 44 percent by covering the surface with 0.0013-inch carborundum grains. Even the roughness due to spray painting increased the drag 14 percent at this speed. Sandpapering the painted surface with No. 400 sandpaper made the drag as low as that of the highly polished airfoil. The investigation showed that there is considerable scale effect on the drag due to roughness.

Effect on drag of wing due to manufacturing discrepancies.—In order to determine the effect on the drag of a wing due to manufacturing discrepancies, such as waves in the metal covering sheets and inaccuracies in the profile, tests were made on a model wing constructed to represent average present-day tolerances and workmanship. The drag of this "service wing" was 11 percent greater than that of the truer wind-tunnel model when both had the same arrangement of rivets and laps, and was 42 percent greater than the drag of the smooth-surface wind-tunnel model without rivets or laps. This excess in drag of 42 percent is equivalent to 273 extra horsepower on airplanes of the size and speed of those used on present air lines.

AERODYNAMIC INTERFERENCE

Wing-fuselage interference.—A report is now being prepared on the interference investigation recently completed in the full-scale wind tunnel with an Air Corps YO–31A observation monoplane. The airplane was first tested with the original gull wing and then with parasol wing arrangements in which the wing was placed at various heights above the fuselage. When the parasol tests were made the gull-wing roots were replaced by a straight center section. For the purpose of determining the interference effects the principal component parts of the airplane were tested separately in addition to the tests of the complete machine for each wing arrangement.

An investigation of the effects of triangular and elliptical cross-sectional fuselage shapes on the aerodynamic interference between wing and fuselage has been completed in the variable-density wind tunnel, together with tests of a special shape of juncture. During the course of the tests it was shown that ordinary critical combinations could be sometimes benefited, as regards the occurrence of the interference burble, by very smoothly finished surfaces at the wing junctures. In this respect one special shape of juncture showed a very powerful effect, its use resulting in the suppression of the premature interference burble entirely, with no increase in the minimum drag.

An investigation has also been made to obtain a comparison between a combination including the airfoil-type fuselage, and an efficient conventional wing-fuselage combination. Tail surfaces have been added to typical combinations in an investigation comprising an extension of the program of wing-fuselage interference. An interesting development of this phase thus far is the surprisingly low drag found possible for such a complete model combination.

FORCED VIBRATIONS AND AIR DAMPING OF A WING SYSTEM

A theoretical study has been made of the vibration response and air damping of a wing-aileron system in a uniform air stream to impressed alternating forces and moments. The mathematical treatment is a direct continuation of that presented in Technical Report No. 496 to analyze the flutter problem. The response characteristics of the vibrating wing-aileron system in a complete range of velocities and frequencies up to the critical flutter conditions can be determined in any specific case without extensive calculations. Thus not only are the critical flutter velocity and frequency readily determined, but also the vibration response and the air damping at intermediate conditions. The study thus presents a more complete picture of the phenomenon of flutter than has previously been available in aerodynamic literature. In particular, it is shown that in the case of forced vibrations large responses may often be expected when flutter conditions are approached, even when actual flutter cannot occur. The results of this work are being prepared for publication.

PROPELLERS

Investigation of full-scale propellers.—The results of the investigation of six full-scale propellers in conjunction with a standard nacelle unit equipped with six different N. A. C. A. cowlings have been published in Technical Report No. 594. The investigation covered the complete range of flight conditions, including ground operation, take-off, climbing, and high-speed flight. The range of the advance-diameter ratio was extended far beyond that of earlier full-scale experiments, blade angles of 45° at 75 percent radius being included, which are equivalent to air speeds of more than 300 miles per hour for propellers of normal size and diameter.

An extensive investigation of full-scale propellers, which was planned last year and which will provide considerable data in addition to those just mentioned, has been proceeding for several months in the 20-foot propeller-research tunnel. A large number of tests of propellers of 10-foot diameter driven by a 600-horsepower engine have been made in conjunction with a cowled nacelle such as would house a radial air-cooled engine. A number of tests have been made also in conjunction with a nacelle for liquid-cooled engines.

The propellers on which this investigation is being made are of modern type, with the blade gradually fairing into the hub section, in contrast to the older type with airfoil sections carried in very close to the hub. Comparative tests indicate a small aerodynamic advantage for the latter type, but their use is precluded by the characteristics of existing engines.

In this investigation blade-angle settings up to 45° at 75-percent radius were also used and in several cases blade-angle settings up to 60°. A maximum efficiency was obtained under the conditions of this investigation at a setting of about 30° and there was little falling off even at 60°. This investigation gives further evidence that the old practice of designing propellers with a low basic pitch and then setting the blades at much higher angles should be modified for high-pitch propellers. It appears that high-pitch propellers should be designed to have a constant pitch when the blades are set at 20° to 30° at the 75-percent radius. This method will result in a smaller washout of pitch toward the hub at the higher blade-angle settings, which is of some advantage in obtaining the best thrust distribution for minimum energy loss.

During this investigation particular attention has been paid to the effect of tip speed on the efficiency in the take-off and climbing range of propeller operation. A small progressive loss in efficiency begins to appear when the tip speed reaches approximately 700 feet per second. There seems to be some variation with the airfoil section of the propeller, the Clark Y section holding its efficiency under these conditions to higher tip speeds than does the R. A. F. 6 section. Calculations from the data obtained show, however, that when applied to the controllable propeller the change in power coefficient is such that the propeller must be set at a lower blade angle than would be required if no tip-speed effect were present, with the result that the tip-speed effect is practically eliminated.

Analysis of the data obtained with propellers differing in airfoil sections, but otherwise similar, shows that the differences in characteristics are very small, as was expected. The analysis is not yet complete and other deductions may be possible after further examination.

A definite improvement is noted with a spinner on the propeller of a liquid-cooled engine, in contrast to radial-engine installations, where it was found that the use of a spinner over the hub had a negligible effect. An improvement of about 4 percent in the net efficiency of the liquid-cooled installation was caused by the spinner. In this connection a spinner just covering the hub and having the nacelle lines faired into it was found to be as good as a larger spinner.

A number of tests have been made in the negative torque (windmilling) region covering the conditions from zero thrust to propeller locked at blade-angle settings from 0° to 90°. The data from these tests will

provide information on the drag of idling and stopped propellers and on the braking effect of the propeller in the diving of military types of aircraft. It appears that the stopped propeller feathered to a blade-angle setting of 90° causes the least drag, but an idling propeller set at 50° and operating against normal engine friction has nearly as low a drag.

A series of five reports, each covering a section of this propeller investigation, is now being prepared. The many factors involved in a study of this scope require a division of the subject for the sake of clarity of presentation, as well as facility in use. Other reports may be required to present analyses of minor phases and data yet to be obtained.

Investigation of oppositely rotating tandem propellers.—The continual increase in the power ratings of airplane engines and the large propellers required, as well as the effect of torque reaction when large geared engines are used in small high-performance airplanes, have turned attention to the possibilities of oppositely rotating tandem propellers. The Army Air Corps requested an investigation of the problem, and Stanford University, which is a pioneer in propeller testing in the United States, agreed to make the investigation under contract with the Committee as a part of the Committee's program of cooperation with universities.

The investigation was made with model propellers of 3-foot diameter, and the results indicate that a 4-blade propeller is slightly inferior in performance to two 2-blade propellers of the same diameter and blade dimensions rotating in opposite directions. Both are, of course, inferior to normal 2-blade propellers. The spacing of the tandem propellers was varied from 8 to 30 percent of the propeller diameter, and practically no effect of spacing was noted except that the closer spacings produced more noise. At the lower blade-angle settings the rear propeller had to be set at a smaller angle than the front one in order to absorb the same power, but, as the blade-angle settings of the propeller were increased to give higher pitches, the rear propeller gradually required a setting higher than the front propeller. Increasing the propeller spacing of the tandem propellers when the blade-angle settings were in the low range also required an increase in the setting of the rear propeller. It is proposed to extend this investigation to compare a 6-blade propeller with two oppositely rotating 3-blade propellers.

Investigation of model propellers in yaw.—The characteristics of propellers whose axes are at an angle to the air stream are of considerable importance in the study of airplane stability with power on, and to some extent in the calculation of airplane performance. A series of tests of model propellers of 3-foot diameter in yaw has been made at Stanford University under contract with the Committee to provide data of this nature, and the results have been published in Technical Report No. 597.

Prediction of propeller performance from airfoil section data.—The analysis of airfoil section data as applied to the selection of sections for propeller blades has been continued during the past year. In addition methods for predicting the performance of propellers from the section data are being devised and further analysis made of the distribution of energy losses for conventional propellers. The characteristics of three propellers having different blade sections have been analytically determined from the section data obtained in the variable-density wind tunnel and the smaller high-speed wind tunnels, and three full-scale propellers of the same design will be tested in the 20-foot wind tunnel. The experimental data obtained should provide an excellent check on the method of predicting the performance analytically.

Propeller vibration.—The model method of determination of the dangerous vibration frequencies of propellers mentioned in the twenty-first anual report of the Committee has been verified and superseded by a method applicable directly to any propeller in question. The method consists in the use of a carbon-resistance strain gage attached to the propeller and a means for producing artificially forced vibrations of any mode, the propeller being electrically driven at full speed in a partial vacuum.

Propeller noise.—Experimental work on the sound emission from propellers has been continued, particularly with a view to obtaining greater absolute accuracy in the measurements. The intensity of the sound emitted from the propeller in various directions has been measured for the five lowest harmonics for the purpose of obtaining data for use as a basis for theoretical work. The measurements have been completed for the range of propeller tip speeds below the speed of sound in air and will be continued into the supersonic speed range.

A paper has been published (Technical Note No. 605) indicating the effect of blade thickness on propeller noise. The theoretical relations given in the paper permit calculation of sound intensity of long wave lengths from a propeller with symmetrical sections at zero blade angle. With the aid of experimental data, an empirical factor was introduced into the theoretical relations to make possible the calculations of higher harmonics of the rotation noise.

THEORETICAL AERODYNAMICS

Compressible flow.—The study of compressible flow about symmetrical Joukowsky profiles has been continued, and expressions have been developed for determination of the velocity and therefore the pressure distribution over the airfoils. In particular, lift and

pitching-moment formulas have been obtained for thin profiles at large angles of attack. It has been found that the expression for lift is analogous to that for incompressible flow, but that the expression for pitching moment, in addition to being analogous to that for incompressible flow, contains a term which amounts to a shift in the center of pressure toward the leading edge. In addition to developing the expressions for lift and pitching moment, the limiting value of the ratio of the air-stream velocity to the velocity of sound in an undisturbed stream has been calculated for several Joukowsky profiles, and the effect of angle of attack and thickness upon this ratio has been determined.

Pressure distribution on flapped airfoils.—A method has been devised for calculating the chordwise pressure distribution over airfoils with ordinary flaps. The distribution has been determined by altering the theoretical distribution and may be applied to airfoil sections having more than one flap. Technical Reports Nos. 360 and 563 show a disagreement between experimental and theoretical forces and pressure distribution. In the more recent analysis the empirical correction to the theory was determined through knowledge of the lift, pitching moment, and flap deflection. Work is continuing on this method of analysis to develop an expression for airfoils with split flaps.

WIND-TUNNEL CORRECTIONS

The interference of the wind-tunnel boundaries on the downwash behind an airfoil has been experimentally investigated, and the results have been compared with the available theoretical results for open-throat wind tunnels. This investigation has yielded results that are particularly valuable in correcting the downwash angle in the region of the tail plane. The experimental results show that the theoretical assumption of an infinite free jet at the test section of the wind tunnel may lead to erroneous conclusions if applied to the downwash in the region behind an airfoil where the tail surfaces would normally be located. The results of a theory based on the more accurate concept of an open-jet wind tunnel as a finite length of free jet provided with a closed exit passage gave good qualitative agreement with the experimental results. The results of this investigation have been presented in Technical Report No. 609.

The investigation to determine the scale effect on the maximum lift of an airfoil has been extended by additional tests in flight and in the full-scale wind tunnel. The investigation was made with a $2R_1 12$ airfoil mounted on a Fairchild 22 airplane, and the variations of Reynolds Number in flight were obtained chiefly by varying the wing loading of the airplane and by varying the altitude at which the tests were made. The maximum lift as obtained in flight and in the full-scale wind tunnel agreed within 2 percent, the results thus further substantiating the agreement obtained with sphere tests, which indicated a low percentage of turbulence in the full-scale wind tunnel.

The investigation of the factors leading to discrepancies between the power-on performance of an airplane as predicted from wind-tunnel data and as measured in flight is being continued. In order to avoid the difficulties usually experienced in obtaining precise measurements of climbing performance, the excess horsepower available for climb is being determined in level flight.

This determination is accomplished by the towing of parachutes of various sizes to absorb the excess horsepower at various speeds. The horsepower is computed from the tension in the towing line and the velocity of the airplane. This method avoids, in particular, the errors usually experienced in climb owing to variations in the wind velocity with altitude. A second airplane is being equipped to study quantitatively the effect on climbing performance of variations in the wind velocity with height by correlating the excess horsepower measured in level flight with the rates of climb actually experienced in several climb tests. The results will be checked by tests of the same airplanes in the full-scale wind tunnel under power-on conditions.

COMPRESSIBILITY EFFECTS DUE TO HIGH SPEED

Aerodynamic phenomena encountered at high speeds have heretofore been considered of importance mainly in relation to the adverse effects on propellers operating at high tip speeds. It has now been established that marked adverse effects due to compressibility may occur on other parts of airplanes when the forward speed of the airplane is approximately one-half the speed of sound. Investigations conducted in both the 24-inch and the 8-foot high-speed tunnels have shown that the compressibility burble results in a large energy loss. A large increase in drag may therefore occur when the flow about any part of the airplane produces a local velocity equal to the speed of sound. A bluff body and one having a high curvature produce high induced velocities, and therefore the critical speed of such bodies is low.

The results from an investigation in the 11-inch high-speed tunnel on the drag of circular and elliptical cylinders and prisms of triangular and square cross sections show that the critical velocities or, in other words, the forward speed at which compressibility effects become noticeable, may be as low as 0.4 the velocity of sound.

Similar results have been obtained in the 8-foot high-speed tunnel on a wing-nacelle combination. One-fifth-scale models of a family of radial-engine cowlings were tested on a nacelle with a wing of 2-foot chord.

Five of the cowling shapes had previously been tested in the propeller-research tunnel, and at the lower speed possible in the propeller-research tunnel these cowlings were considered satisfactory. One cowling shape was found to have a critical speed between 280 and 350 miles per hour, depending upon the attitude of the cowling and nacelle. When the compressibility burble, or shock wave, occurred at the critical speed the drag of the combination was increased from 50 to 200 percent, with only a slight increase in the tunnel speed.

During the investigation it had been found that if the pressure distribution over the cowling was known, the critical speed could be accurately predicted. Therefore, two cowlings were designed with the nose curvatures proportioned to reduce the peak negative pressure and obtain a uniform negative pressure distribution over the nose. By so changing the nose shape the critical speed of the cowling was increased to more than 500 miles per hour and approached the critical speed of the N. A. C. A. 23012 wing, which was used for the investigation. It was found that when the critical speed of the cowlings was increased other advantages were obtained. The cowling with the highest critical speed also had the lowest drag throughout the entire speed range, and the drag remained substantially constant over a larger range of angle of attack.

In order to determine at a large scale the possible variation in pitching moment with speed, four wings of 2-foot chord were tested in the 8-foot high-speed wind tunnel through a range of speeds up to that at which the compressibility burble was experienced. The four wings tested had the following N. A. C. A. sections: 0012, 23012, 23012–64, and 4412. The N. A. C. A. 23012 and 23012–64 airfoils were chosen as sections of low pitching moment and the N. A. C. A. 4412 as a section of high pitching moment. All the sections tested showed an increase in pitching-moment coefficient with increased speed, the increase amounting to as much as 45 percent at 500 miles per hour. This change in pitching moment has little practical significance in the case of an airplane on which a wing section having low pitching moments is used, because the resulting absolute change in pitching moment at high speeds would be of little importance in the design of the wing or tail surfaces. In the case of an airplane with a wing section of high pitching moment the change may be very important in high-speed dives.

BOUNDARY-LAYER CONTROL

The investigation of boundary-layer control has been continued in the propeller-research tunnel, and tests have been completed on a tapered wing of N. A. C. A. 8318 section with upper-surface suction slots to control the boundary layer. Tapering the slot was found to be very effective in producing an even distribution of control over the span, and the suction power required was intermediate between the low power required for a thick wing and the high power required for a thin wing. Measurements of boundary-layer thickness were made both with and without the control in operation.

ICE PREVENTION

In view of the fact that several accidents during the last year may be directly attributed to ice formation on the airplanes, a survey has been made of the ice-prevention investigations that have been conducted by the various Government and commercial organizations. A compilation of these data is being made so as to make available to all concerned information that may be valuable in preventing accidents due to ice formation.

In order to determine the effect of rubber de-icers on the aerodynamic characteristics of a wing, a model of a 5-tube de-icer was tested on an N. A. C. A. 23012 wing of 5-foot chord in the 8-foot high-speed tunnel. The results show that for both the inflated and deflated conditions the de-icers did not appreciably affect the lift or pitching moment for high-speed or cruising conditions, but with either two or three tubes of the de-icer inflated the drag of the wing was increased in the order of 80 percent. The conventional de-icer equipment deflated increased the drag of the wing 16 percent at 200 miles per hour. At air speeds greater than 200 miles per hour the de-icer lifted from the wing and in some cases breaks in the rubber were produced. In order to reduce the drag of the de-icer in the deflated condition a flush installation was made by the use of a metal attachment strip, which on the full-scale airplane would be 1/32-inch thick. With this installation the drag increment was reduced from 16 to 9 percent, but the same difficulty was experienced in the lifting of the de-icer from the wing at speeds greater than 200 miles per hour.

ROTATING-WING AIRCRAFT

The development of the direct-control type of autogiro has been delayed to some extent by the introduction of certain secondary difficulties connected with the provision of a satisfactory variation of control forces with air speed and with the elimination of vibration. A study of the effect on certain rotor characteristics of a periodic variation in blade-pitch angle has been made, and the results have been published in Technical Report No. 591. The predicted value of the flapping motion of the rotor blade was radically altered when the periodic pitch variation was inserted in the rotor analysis, and an appreciable influence of the periodic pitch on the rotor thrust coefficient was indicated. An analysis has been made of the factors involved and a method developed of predicting the periodic variation of the pitch angle. The results have been published in Technical Report No. 600.

An investigation has recently been conducted both in flight and in the full-scale wind tunnel on a direct-control autogiro to determine the lift, drag, control forces, flapping motion of the rotor blade, and periodic variation in pitch angle. The tests in the full-scale wind tunnel were made on the complete autogiro, on the rotor alone, and on the machine without the rotor to determine the interference effects between various parts. The data obtained from these tests are being analyzed for use in the study of any desired variation of the location of the center of pressure on the rotor.

An investigation has been started in the propeller-research tunnel on a series of model autogiro rotors having airfoil sections of different thickness and different mean camber lines, and will include two rotors that differ only in plan form of the rotor blades. This work is an extension of an investigation previously made in which the effect of airfoil section and plan form on the lift-drag ratio of an autogiro rotor was studied.

The analysis of the results obtained during the autogiro jump take-off tests has been completed and published in Technical Note No. 582. The report covers a theoretical study of the jump take-off without forward speed and includes an experimental verification.

An analytical study of the rotor-blade oscillations in the plane of the rotor disk has been made, and the results have been published in Technical Note No. 581.

A study of the autogiro rotor-torque equation has been made, and a report is in preparation which will include a solution of the problem in chart form.

MISCELLANEOUS TESTS OF COMPLETE MODELS OF AIRPLANES

The improved aerodynamic efficiency of the modern airplane has made it increasingly important to make tests on a complete model of a projected airplane before it is constructed. Consequently a large number of complete models have been tested in the 7- by 10-foot, the 20-foot, and the full-scale wind tunnels. Most of these tests have been conducted at the request of the Army and Navy, but several models have been tested for manufacturers at their expense.

The models tested in the full-scale tunnel have been ½ and ¼ scale, and the tests have included considerable development work that could be conveniently carried out on these large-scale models at considerably less cost than would be involved in doing the same work on the actual airplane after it has been constructed. Although this development work has restricted to some extent the research programs in the tunnels, it is felt that the tests have resulted in a large saving of money to the Government. It might also be pointed out that the development work in the wind tunnel will save much of the time required to take an airplane through the experimental stages and place it in production.

NATIONAL BUREAU OF STANDARDS

WIND-TUNNEL INVESTIGATIONS

The aerodynamic activities of the National Bureau of Standards have been conducted in cooperation with the National Advisory Committee for Aeronautics.

Wind-tunnel turbulence.—Within the last few years the equipment used in the study of wind-tunnel turbulence has been redesigned for use with an alternating-current power supply instead of storage batteries. A description of the new equipment and of its performance has been published in Technical Report No. 598.

As mentioned in last year's report, the investigation of turbulence has been extended to include the measurement of the scale or eddy size of the turbulence as well as the intensity. The most satisfactory method of introducing turbulence into the wind-tunnel stream was found to be by means of screens placed across the stream, the scale being controlled by the size of the screen and the intensity by the distance downstream from the screen. The measurements of scale and intensity have been made and the aerodynamic effect of these two factors has been determined. The results of this work have been published as Technical Report No. 581. The screens described in this report are now regarded as standard equipment in the Bureau's 4½-foot wind tunnel and are used to introduce turbulence of the desired scale and intensity within the limits obtainable.

Preparations are being made to continue the study of turbulence by measuring the distribution of energy in turbulent motion with the wave length of the turbulence. According to recent theories the spectral distribution of energy is a characteristic property of turbulence related to the intensity and scale.

Boundary layer near an elliptic cylinder.—During the past year boundary-layer investigations have been in progress with an elliptic cylinder of 12-inch major axis and 4-inch minor axis, placed with the major axis parallel to the wind. The laminar boundary layer formed about the cylinder was previously studied and the results were published as Technical Report No. 527.

The recent work has consisted of the measurement of velocity distributions in the boundary layer with the air speed in the tunnel high enough to produce transition from laminar to turbulent flow in the layer before separation occurred. Two cases were investigated: the first with the low turbulence normally prevailing in the wind tunnel and the second with the stream turbulence raised to about 4 percent by means of the 1-inch screen placed 18 inches ahead of the cylinder.

Marked differences were found between the types of transition occurring in the two cases. Transition with the low stream turbulence was the result of a laminar separation, and occurred within a very short length of the surface, about an inch ahead of the point of separa-

tion of the turbulent layer. Work with the higher stream turbulence gave no evidence of a laminar separation, but showed a gradual transition extending over about a third of the distance from the leading to the trailing edge of the cylinder (i. e., over about 4 inches). This latter type of transition was very difficult to detect by any single means and was found only by careful study of the velocity distributions in the layer. In order to throw more light on the transition phenomena at the higher stream turbulence measurements were made of the fluctuations in velocity throughout the layer at various points about the surface. These measurements also showed the gradual nature of the transition.

Studies of transition.—The two different types of transition found on the elliptic cylinder suggested an extension of the work to cover the general effects of turbulence and Reynolds Number on transition, the purpose of the extension being to learn under what conditions each type of transition exists and how the region of transition shifts with changes in Reynolds Number and changes in scale and intensity of the stream turbulence.

As was pointed out previously, the location of the transition region could be determined with the available equipment only by extensive measurements of the distribution of mean velocity or fluctuation of velocity across the boundary layer. In order to facilitate the investigation, a new device for quickly and easily detecting transition was sought. Previous work has shown that transition occurs in the neighborhood of the point where the intensity of skin friction is a minimum. This immediately suggested the use of some device, such as the Stanton surface tube developed in England, by which the surface friction may be measured. However, the adaptation of the surface tube was not considered feasible on the elliptic cylinder. Instead a sliding steel band 6 inches wide and 0.002 inch in thickness was fitted about the cylinder so that the heated element of a hot-wire anemometer, fixed at the center of the band, could be moved around the contour of the ellipse at a small fixed distance from the surface.

While an actual measurement of the velocity by this means is not readily possible, the wire can be used to detect where the speed is a minimum as the band is slipped around the surface. In the tests already made a platinum wire 0.016 millimeter in diameter and 13 millimeters long was mounted 0.21 millimeter from the surface of the band. The device has proved quite satisfactory and shows sufficient promise to justify further development. It may be possible to use a device of this sort for locating transition on an airplane wing in flight.

Investigation of boundary layer by diffusion of heat.—The method of thermal diffusion described in Technical Report No. 524 has been applied to the study of velocity fluctuations in a thick turbulent boundary layer formed on the surface of a flat plate 10 feet wide and 24 feet long. The procedure consists of measuring with a thermocouple the spread of the heated wake downstream from a fine but long heated wire placed transverse to the flow in the boundary layer. The spread of the wake is caused by the components of turbulent motion normal to the mean direction of flow, and the purpose of the work is to compute the magnitude of the components from the measured spread. By this means the magnitude of the velocity fluctuations normal to the surface has been determined. In a similar manner it is planned to determine the magnitude of the component parallel to the surface. By the usual hot-wire equipment the component in the direction of the mean flow will be measured so that finally a comparison between all three components of the fluctuations will be possible.

AERONAUTIC-INSTRUMENT INVESTIGATIONS

The work on aeronautic instruments has been conducted in cooperation with the National Advisory Committee for Aeronautics and the Bureau of Aeronautics of the Navy Department.

Reports on aircraft instruments.—A report on the pressure drop in tubing used to connect aircraft instruments to vacuum pumps and pitot-static tubes has been published as Technical Note No. 593, and a report on electrical thermometers is being published as Technical Report No. 606.

An experimental investigation of the performance characteristics of venturi tubes used in aircraft for operating air-driven gyroscopic instruments has been completed and a report prepared.

Progress has been made on reports on the effect of vibration on service aircraft instruments and on gyroscopic instruments for aircraft.

Tests and test methods.—It was originally planned to measure humidity in the aerograph test apparatus by the dew-point method. A simpler method has been developed in which advantage is taken of the fact that completely saturated salt solutions have a characteristic vapor pressure so that a particular salt solution produces a practically constant relative humidity when placed in a closed chamber. Corrections can be applied for the relatively small variation of the relative humidity with temperature.

Altitude mercurial barometers for field use should withstand shipment without breakage and should be designed so that the accumulation of gas above the mercury column is easily removable. Principally for these reasons it is advisable to fill the barometer tube in the

field. Experiments with the Barnes type, which meets these requirements, indicate that the procedure to be followed is too complicated. In cooperation with an instrument manufacturer, the common-type altitude barometer has been modified to make it possible for the tube to be filled in the field by following a relatively simple procedure. The barometer must be designed so that the end of the tube is always well covered with mercury while the barometer is tipped from the normal to the upside-down position. The usual capillary restriction in the end of the tube must be of such size that the passage of gas is not impeded by mercury sticking in the capillary.

Laboratory test methods have been developed, and data on the performance obtained, on fuel-air-ratio indicators of the thermal conductivity type. In these tests known mixtures of nitrogen and hydrogen and of nitrogen and carbon dioxide were passed through the instrument subject to various conditions, such as temperature, pressure, and voltage.

New instruments.—Instruments designed and constructed for the Bureau of Aeronautics include: a helium purity meter utilizing a porous plug of a type recently developed commercially; a superheat meter of the electrical-resistance type for a K airship; an experimental pitot-static tube for installation on the wing tip of monoplanes. Development of a fuel flowmeter of the orifice type is in progress.

SUBCOMMITTEE ON AIRSHIPS

The Subcommittee on Airships formulates and recommends programs of airship investigations to be undertaken at the Langley Memorial Aeronautical Laboratory and maintains close contact with the work in progress.

The Committee recently published as Technical Report No. 604 the results of the investigation conducted by the laboratory at the request of the Bureau of Aeronautics of the Navy to determine the pressure distribution at large angles of pitch on fins of different span-chord ratios on a large model of the airship *Akron*. This investigation was requested by the Bureau to provide information particularly desired by the Special Committee on Airships of the Science Advisory Board, of which Dr. W. F. Durand, of Stanford University, is chairman. Mention is made here of the publication of the technical reports of this committee, which cover certain phases of airship technical problems.

Models and apparatus are being prepared for the investigation in the Committee's 20-foot wind tunnel of boundary-layer control on airship forms. This investigation will include a form with blower in the nose, and also a form with propeller in the rear with control of the boundary layer by both suction and discharge jets.

At a meeting of the Subcommittee on Airships held in January 1937, plans were discussed for the extension of the investigation of the forces acting on an airship during ground handling, as published in Technical Report No. 566, to include a study of the effect of wind gradient and also of the effect of fin angle. Consideration was also given to the desirability of conducting an investigation at the Committee's laboratory on the loads on the tail surfaces of an airship in flight, and also an investigation of the forces on a large airship model with tail surfaces of the form used on the *Hindenburg*.

SUBCOMMITTEE ON METEOROLOGICAL PROBLEMS

The Subcommittee on Meteorological Problems keeps in contact with the progress of investigations being conducted by the various agencies on problems relating to the atmospheric conditions which are of particular importance in connection with aircraft design and operation.

Atmospheric disturbances in relation to airplane accelerations.—Extensive measurements of gusts have been made by the Langley Memorial Aeronautical Laboratory by means of flights to altitudes of 19,000 feet with a large military-type airplane and flights with a small light airplane. From partial analysis of the data obtained, it appears that it may be possible to correlate the gust strength and gradient with the energy available for turbulence in the atmosphere. The new results do not invalidate the conclusions previously reached tentatively that, in stable atmospheric conditions, with large wind gradients, vertical gust velocities of the order of 30 feet per second are reached in a horizontal distance of about 100 feet, and that the gust gradient increases with decreasing gust intensity.

Surveys of clouds of cumulus type indicate, in general, stronger downward-acting than upward-acting gusts. On one occasion a downward gust of 53 feet per second, which reached maximum intensity in a distance of 53 feet, was experienced.

The development of a special acceleration-altitude recorder for installation at various Weather Bureau stations throughout the country is nearing completion. When available, these instruments will be used in conjunction with air-speed recorders to obtain data on the relation between gust intensity and altitude.

The accumulation and analysis of records of accelerations on transport airplanes in regular operation is being continued with the cooperation of a number of the air transport operators. The records obtained represent conditions encountered in operation over practically every part of the United States, in transpacific operation, and in operation over the Andes Mountains in South America. Records from flying boats in the transpacific service indicate effective gust velocities as great as 33 feet per second, which is substantially equal to the maximum recorded on flying boats in service

between Florida and the West Indies and South America and on land transports.

Investigation of wind gustiness.—The study of wind gustiness, including both atmospheric turbulence under ordinary conditions and the fluctuations of wind velocity during the passage of cold fronts, conducted by the Daniel Guggenheim Airship Institute at Akron, Ohio, in cooperation with the Weather Bureau and the Bureau of Aeronautics of the Navy, has been continued. Additional measurements are being made by means of instruments installed on the radio tower at Akron and on movable towers placed at various positions in relation to the radio tower and to each other, with supplementary records obtained by the use of balloons and theodolites.

Ice formation.—The problem of ice formation is receiving considerable attention at the Langley Memorial Aeronautical Laboratory, and a report has recently been issued to American manufacturers giving the results of a study of the prevention of ice formation on propellers. In this report information is given as to the conditions under which ice forms on propellers, and an investigation conducted by the Committee on the propeller de-icer developed under the sponsorship of the Bureau of Air Commerce in cooperation with the B. F. Goodrich Company and Transcontinental and Western Air, Incorporated, is described.

The problem of ice formation on wings and ailerons is also being studied, and a report is being prepared presenting all the information at present available. In addition, a program is being formulated for the study of the effect on the aerodynamic characteristics of a wing, of ice particles that adhere after the de-icer has acted. Data on the shape and location of such particles for use in the preparation of this program have been supplied through the cooperation of the Air Transport Association of America.

Electrical phenomena.—The question of the possible effect of electrical phenomena on airplanes has been brought to the Committee's attention and will be discussed at a meeting of the Subcommittee on Meteorological Problems to be held in the near future. Observations of pilots on the subject have been obtained from a number of sources, and the question will be thoroughly studied by the subcommittee.

SUBCOMMITTEE ON SEAPLANES

World-wide interest in seaplanes has grown at an accelerated rate and almost every month has brought word of the launching of new craft of greater size and speed. Designers are discussing with confidence the construction of flying boats of magnitudes that would have been considered impracticable a few years ago and are looking forward to the construction of even larger and faster flying boats within a relatively short time.

With the increases in size and range have come increased get-away speeds and heavier loads on the hulls. The power required for the take-off of such large flying boats is sometimes 100 percent greater than that ordinarily used in flight, and in such cases the designer is confronted with the necessity of choosing between the use of larger engines involving a serious increase in weight and the possibility of shortened engine life as a result of running at excessive power during take-off.

The cost of these large flying boats makes it essential that the form of hull selected shall be the best possible compromise between the requirements of low drag in flight and good performance on the water. Research in the N. A. C. A. tank has therefore been directed toward the improvement of the over-all performance of flying boats and seaplanes by the reduction of the resistance on the water and the general improvement of the form of the hull. In contrast to previous work, the aerodynamic improvement is being given consideration at the same time.

Improvements to N. A. C. A. tank.—In anticipation of the demand for tests of models of larger hulls at higher take-off speeds, the Committee is enlarging the N. A. C. A. tank and increasing the speed of the towing carriage. When the work now under way is completed the tank will have 2,880 feet of water at a depth of 12 feet, which is an increase of 900 feet. The extension has been specially constructed to permit the generation and propagation of waves for use in testing models in waves and the simulation of operation in rough water.

The increase in length has been matched by an increase in the speed of the towing carriage. It is expected that when the alterations are completed the carriage will have a maximum speed of about 80 miles per hour. The carriage will also be able to tow much larger models.

At lower speeds, with models of the same size, it will be possible to increase the amount of testing per day because the ratio of the distance that can be used in testing and obtaining readings to the distance required for stopping and starting the carriage will be considerably increased.

A two-story office building has been built at the southern end of the tank and the shop spaces have been extended 100 feet.

Effect of variation in dimensions and form of hull on take-off.—The result of incorporating longitudinal steps on the forebody of a V-bottom hull was determined by an investigation of a series of models in which the form and number of steps were systematically varied. In general, the longitudinal steps were found to decrease resistance at high speeds by reducing the area in contact with the water, but to increase resistance at low speeds where the bottom is wetted out to the chines. One longitudinal step on each side of the keel was

superior to two longitudinal steps, except at high speeds and very light loads. Spray strips fitted along the steps reduced both the resistance and spray if they were set at the proper angle. This investigation is described in Technical Note No. 574.

Various methods of artificial ventilation of the step were investigated on two typical hull forms, one having straight V sections and one having chine flare on both forebody and afterbody. In both cases the chines aft of the step were clear of the water at the hump speed and above. When the chines were clear the step was ventilated by air flowing in from the sides and the introduction of additional air through ducts or slots produced no further change in resistance or trim. In the case of the form with chine flare, natural ventilation was delayed at speeds below the hump speed and artificial ventilation through ducts aft of the step resulted in an appreciable reduction in resistance and trim. The results of this investigation have been published in Technical Note No. 594.

Tests of models of representative flying-boat hulls.—The hull of the U. S. Navy PB–1 flying boat, which was built by the Boeing Aircraft Company in 1925, had two transverse steps very close together and a long extension carrying the tail surfaces. The forebody was much like that of the NC hull, from which it was apparently derived. Comparisons of its water performance as obtained in the N. A. C. A. tank with that of the NC hull and the Sikorsky S–40 hull are presented in Technical Note No. 576.

A model of the hull of the British Singapore II–C flying boat was investigated in the N. A. C. A. tank in response to suggestion of the Director of Research, British Air Ministry. This investigation made it possible to determine the hydrodynamic characteristics of a typical British hull form over an extensive range of loadings and speeds. It was found that the Singapore hull had higher resistance at the hump speed and lower resistance at higher planing speeds than the American hull with which it was compared. The results of this investigation, together with a comparison with similar results obtained in the British R. A. E. tank with the same model, are presented in Technical Note No. 580.

A large model of the hull of the British Short Calcutta flying boat was made from lines supplied by the British manufacturers and investigated in the N. A. C. A. tank. The form is the immediate predecessor of the Singapore hull, and is representative of British flying-boat design in 1928. The results of these tests, together with calculated comparisons of its take-off performance with that of typical American forms, are published in Technical Note No. 590.

Trim-angle indicator.—The importance of holding a seaplane at the trim angles that would give least resistance during the process of take-off was described in Technical Note No. 486, issued in 1934. In that publication there is described and illustrated a trim indicator for showing the pilot of a seaplane the trim angle at which the craft is traveling. Several versions of this type of trim-angle indicator have since been constructed and tested in service. It has been found that if a pilot has a trim-angle indicator and the information obtained from tank tests of the hull as to the trim angles that give least resistance during the take-off, it is possible for him regularly to take off in much shorter time than he requires when no such instrument and data are available. The pilot of a heavily loaded amphibian operating in the tropics reported that he attributed the uniformly successful operation of his craft, especially the ease with which it took off in smooth water, to the use of a trim-angle indicator that had been supplied by the Committee. In another case the use of a trim-angle indicator by a test pilot is credited with so greatly improving the take-off characteristics that a seaplane which at first appeared very unsatisfactory gave very good performance.

REPORT OF COMMITTEE ON POWER PLANTS FOR AIRCRAFT

LANGLEY MEMORIAL AERONAUTICAL LABORATORY

ENGINE POWER

The recent demand of aircraft designers for engines of increased power output has been fulfilled by the supplying of radial air-cooled engines developing 1,500 horsepower during take-off. This large increase in power has been obtained by increasing the number of engine cylinders and by designing the engines to take the greatest possible advantage of the antidetonating quality of the improved fuels now available for aircraft engines. These large engines will be used in aircraft designed to transport greater loads at increased speeds over present airways. The several investigations of the Committee on the cooling of air-cooled engines have indicated that it will be possible to cool satisfactorily engines of even greater power.

Engine performance with high octane fuels.—The greater percentage of the recent increase in power of aircraft engines is due to the use of fuels having increased antidetonating quality. An investigation to determine the maximum engine performance with fuels having a range of octane numbers from 87 to somewhat greater than 100 has been in progress at the Committee's laboratory during the past year, under the cognizance of the Subcommittee on Aircraft Fuels and Lubricants, and will be described in the report of that subcommittee.

Valve overlap.—The power of aircraft engines may be increased by removing the exhaust gases from the cylinder clearance volume. An efficient method of removing the exhaust gas is to operate with a large valve overlap

38548—38——3

and low boost pressure. At the request of the Bureau of Aeronautics of the Navy Department, the Committee is determining on a single-cylinder test engine the performance and optimum valve overlap to give efficient scavenging of a radial air-cooled fuel-injection engine operating at a maximum speed of 2,200 r. p. m.

The results indicate that satisfactory scavenging can be obtained with a valve overlap of 130°. From the tests on the single-cylinder engine it was found that as the boost pressure was increased the gain in power with the two-valve cylinder was slightly less than that obtained in previous tests with a cylinder having four valves. The results showed that an engine operating with valve overlap would develop 25 percent more power at the same cylinder temperature than an engine operating with normal valve timing. The tendency to detonate was reduced so that the engine with valve overlap, for the one fuel tested, showed an increase in brake mean effective pressure of 25 percent without detonation as compared with the normal valve timing.

The 2-stroke-cycle engine.—Increased power output can be obtained from a given engine displacement by operation on the 2-stroke cycle instead of on the 4-stroke cycle. The availability of improved fuels having increased antiknock values has renewed the interest in the 2-stroke-cycle spark-ignition fuel-injection engine. An investigation has been conducted to determine the optimum location of the fuel-injection valve and the best arrangement of fuel-valve orifices for injecting the fuel into the engine cylinder. Favorable results have been obtained in a limited series of tests, and the research program is being continued to obtain information on the operating characteristics of this type of engine as affected by speed, scavenging pressures, and induction and exhaust conditions. With fuel of 100 octane number, scavenging pressure of 3 pounds per square inch, and a speed of 1,650 r. p. m., the single-cylinder engine developed an indicated mean effective pressure of 166 pounds per square inch, the corresponding fuel consumption being 0.37 pound per horsepower-hour. A maximum indicated mean effective pressure of 193 pounds per square inch has been developed with a fuel consumption of 0.44 pound per horsepower-hour. A positive valve-operating mechanism for this engine is being developed that will permit the maximum engine speed to be increased from 1,800 to 2,500 r. p. m.

Air intercoolers.—An analysis has been made of data from laboratory tests for the purpose of selecting the most desirable intercooler for various operating conditions—the cooling, drag, pressure drop through cooler, and weight of core being considered. On the basis of this analysis, a program of tests for intercoolers has been prepared that includes both full-scale tests in a wind tunnel and tests of promising cores in the engine laboratory.

COMBUSTION RESEARCH

A study of combustion both in spark-ignition and in compression-ignition engines has been undertaken with the object of obtaining new knowledge concerning the combustion phenomena. The problem of detonation in internal-combustion engines is being attacked with the aid of high-speed schlieren photographs to indicate the temperature variations in the front and rear of the combustion zone following ignition.

Ignition lag in compression-ignition engines.—The investigation of the effect of air temperature and density on the auto-ignition and combustion of Diesel fuel with a constant-volume bomb has been extended. Very little reduction in ignition lag is possible for the particular fuel under test by the use of temperatures and pressures in excess of those attained in compression-ignition engines. The combustion process, however, is more satisfactory at densities corresponding to considerable boost. A concentration of combustion products several times greater than that corresponding to the residuals in a compression-ignition engine is capable of definitely increasing the ignition lag. Technical Report No. 580 has been published giving the results of this investigation.

Compression-ignition engine with air flow.—The investigation of the fuel-spray and flame formation occurring in a compression-ignition engine having air flow that was set up by a displacer on the piston crown has been described in Technical Report No. 588.

Detonation in engines.—With a schlieren set-up and a high-intensity electric spark as the light source, by means of which 10 photographs are taken at rates up to 2,000 pictures a second with an exposure interval for each picture of approximately one-millionth second, photographs have been obtained that show clearly the depth of the combustion zone and also the burning of the end gases in normal combustion. No evidence has been obtained of any sonic wave preceding the combustion front. Such waves were artificially produced in the chamber and, although their effect on the combustion front was visible, they did not cause the charge to detonate. Even with very severe detonation, the combustion reaches all, or nearly all, the way across the combustion chamber before the detonation occurs. The results of this investigation are being prepared for publication.

An apparatus has been constructed and is being used for preliminary tests of the detonation of gasoline-air mixtures. The combustible mixture is prepared in a reservoir heated to a temperature below the auto-ignition point but sufficiently high to vaporize all the fuel. A portion of this mixture is then admitted by means of a poppet-valve mechanism to an evacuated tubular bomb heated to a temperature such that auto-ignition of the charge will occur after a relatively long

time. If this mixture is spark-ignited at one end in such a way that the normal flame can traverse the tube within this lag period, no detonation occurs. On the other hand, when the spark is so applied to the mixture that the flame travels only a large portion of the tube length, then severe vibrations, presumably due to detonation, are set up in the optical pressure indicator attached to the tube at the end opposite the sparking end.

Analysis of engine cycle.—The calculated ideal engine cycle does not include consideration of the actual combustion process, so that the results depart considerably from those obtained from engine tests. In order to obtain better correlation between theoretical and experimental results, a study of the spark-ignition engine cycle was made and a thermodynamic cycle set up closely approximating the actual operating cycle. From a consideration of this cycle, equations for the cycle characteristics, such as indicated horsepower and fuel consumption, maximum cylinder pressure, and point at which the maximum cylinder pressure occurs in the cycle, were written as functions of three combustion parameters that specify the rate, the completeness, and the position in the cycle at which combustion occurs. The variation of the combustion parameters with engine operating conditions was obtained from indicator cards. The cycle characteristics calculated from the combustion parameters agree closely with those obtained in the engine tests.

Air flow in cylinders.—An investigation has been started to determine the effect of air flow on combustion in spark-ignition engines. The air flow is set up by shrouds placed on the inlet valves. Preliminary tests have shown that with an orderly swirl in the combustion chamber the entire combustion front is rotated, but that there is little apparent effect on the combustion velocity.

FUEL CONSUMPTION

Any reduction in the fuel consumption of engines used in long-range or transport aircraft can be utilized to increase the useful load or the range of the aircraft. Large savings in fuel have resulted from the use of mixture indicators by commercial operators. The improvement in cylinder cooling has progressed to such a point that aircraft engines are capable of operating at mixtures leaner than are accurately indicated by commercial mixture indicators. The use of fuels of high octane number has also resulted in an appreciable reduction in fuel consumption.

Mixture distribution.—The results obtained from an investigation of the distribution of fuel to each cylinder of a single-row radial air-cooled engine by chemically analyzing the exhaust gases have been published as Technical Note No. 583.

Fuel distribution.—The use of a fuel-injection system instead of the conventional carburetor requires that additional air flow be set up within the cylinder to assist in mixing the fuel and air. A study has been started to determine the effect of air movement on the distribution of the fuel spray during the suction and compression strokes. The apparatus consists of a glass cylinder clamped between the jacket and the cylinder head of an N. A. C. A. single-cylinder test engine. The piston side thrust is taken on the steel liner, and a dummy piston screwed in the main piston moves in the glass cylinder with very small clearance. The air flow is made visible by goose down introduced with the inlet air and is recorded by high-speed motion pictures taken at a rate of 2,400 frames per second. Tests have been completed with a pent-roof cylinder head in which the inlet valves were shrouded to give different degrees of air movement. With the shrouds arranged to give a tangential swirl, the photographs show that the tangential swirl persists throughout the compression stroke. With the shrouds arranged to direct the air parallel to the cylinder diameter, a decided vertical swirl is produced. With the shrouds radially arranged, a general indiscriminate air movement similar to that obtained without shrouds is obtained. The data are being prepared for publication.

Decreased fuel consumption.—A study of the fuel-consumption characteristics of modern air-cooled engine cylinders at various values of engine speed and torque has been completed. The determination of these characteristics was made on two single-cylinder air-cooled test engines having compression ratios of 5.6 and 6.9, respectively. The results showed that to secure best fuel economy an engine should be operated at high torque and at 65 percent of rated speed. Increasing the compression ratio from 5.6 to 6.9 decreased the fuel consumption but did not change the air-fuel ratio that produced maximum power or minimum fuel consumption. A report is being prepared giving the results of this investigation.

Mixture-ratio indicators.—With transport aircraft maximum range is obtained by operating the engines at the air-fuel ratio giving minimum specific fuel consumption. The Committee is investigating the more promising types of mixture-ratio indicators suitable for aircraft. The use of these instruments is limited, however, to air-fuel ratios from 15 to 9. Since aircraft engines under cruising conditions are already operating at air-fuel ratios of approximately 18, there is need for an improved instrument that will include the full-range of mixture ratios. An investigation has been started to determine possible methods of operating such an instrument.

Exhaust-gas analysis.—As most commercial instruments for indicating air-fuel ratio depend upon one or

more constituents of the exhaust gases, it is important in connection with the development of such an instrument to know the correlation of these constituents with air-fuel ratio. The most reliable method of determining this correlation is by chemical analysis of the exhaust gases. An investigation to determine the correlation for a number of engines and a range of engine-operating conditions has been completed, and the results are in process of publication as Technical Report No. 616.

ENGINE COWLINGS

The N. A. C. A. cowling.—The results of the comprehensive investigation carried out with full-scale models of the N. A. C. A. cowlings in the N. A. C. A. 20-foot wind tunnel have been published in Technical Reports Nos. 592, 593, and 594. The effect of cowlings on the cooling characteristics of a Pratt & Whitney Wasp S1H1–G engine is reported in Technical Report No. 596.

Nose-slot cowling.—The preliminary results obtained with the nose-slot cowling in the wind tunnel have been described in Technical Report No. 595. This cowling is characterized by the fact that the exit opening discharging the cooling air is not, as usual, located behind the engine but at the foremost extremity or nose of the cowling. This nose-slot cowling is inherently capable of producing two to three times the pressure head obtainable with the normal type of cowling, because the exit opening is located in a low-pressure field. Thus identical conditions of cooling can be obtained at correspondingly lower air speeds. In general, the efficiency is found to be high, owing to the fact that higher velocities may be used in the exit opening.

Investigation of the nose-slot cowling has been extended to include flight tests on the XBFC–1 airplane. A two-slot design with an adjustable nose section controllable from the cockpit has given very good results. This cowling compares very favorably with the original installation of the conventional N. A. C. A. cowling. Greater pressure is available for cooling on the ground, while the top speed of the airplane is increased 8 miles per hour. This investigation is being continued to improve the ground cooling further and to eliminate some conditions of local heating caused by the change in direction of the air flow. In the second design of the nose-slot cowling tightly fitting baffles were used. These baffles were much superior to the service-type baffles, lowering the temperature of the cylinder heads 40° and requiring the expenditure of only one-fifth the power.

The in-line air-cooled engine.—With increase in the power output of the air-cooled in-line engine the difficulties of obtaining satisfactory cooling and low drag have increased. The Committee is investigating the problems connected with the cowling and cooling of a 6-cylinder in-line air-cooled engine. In the in-line engine the opening available for the entrance of the cooling air is quite small, so that the air must enter at relatively high speed. The air must be turned through 90° in order to flow over the engine cylinders. Owing to the relatively high velocity, it was found that 30 percent of the available pressure was lost in turning the air before it entered the cylinder baffles. The energy required for cooling was therefore high compared to the energy required in the radial engine.

A new cowling has been constructed that will insure a smooth flow of air over the cowling. Enlarged openings and passages on the air-entrance side of the cylinders will be used to reduce the turning loss of the air. From the results obtained in the tests on this cowling a supplementary investigation will be planned.

ENGINE COOLING

Aircraft engines must be operated at approximately one-half the rated power and with lean mixtures to obtain maximum range. Any improvement made in the cooling of air-cooled engines can be utilized in operating the engine at higher power output during take-off and in cruising with leaner mixtures.

Fin dimensions.—An analysis has been made to determine the best proportions for metal fins for given rates of heat flow, consideration being given to the minimum pressure drop across the fins, the minimum power required for cooling, and the minimum weight of the fins.

This investigation has shown that: A considerable improvement in the heat transfer of conventional aluminum fins is possible by the use of correctly proportioned fins; correctly proportioned aluminum fins will transfer more than 2.25 times as much heat as steel fins for the same weight and pressure drop; the best fin proportions for maximum heat transfer for a given fin weight and pressure drop are also best for obtaining a high heat transfer for a given power expenditure in cooling.

As a result of the investigation of fin dimensions it was found that, for a given width of fin and velocity, there was an optimum spacing below which the heat transfer rapidly decreased. In order to determine the cause of this decrease, an investigation has been started in which the type of flow of air around large-scale model cylinders is determined by means of smoke-flow pictures. A hot-wire anemometer is also used to determine the change from laminar to turbulent flow. The effect of cylinder diameter, fin space, and fin width on the type of flow is being determined.

Heat-transfer coefficients.—The calculation of the heat flow from air-cooled finned surfaces depends upon the experimentally determined heat-transfer coefficients. An investigation to determine the surface heat-transfer

coefficients of closely spaced fins from wind-tunnel tests with and without baffles and with blower cooling has been described in Technical Note 602.

An investigation has been made to determine the heat-transfer coefficients of closely spaced aluminum-alloy fins having a width of 1.22 inches and copper fins having a width of 3 inches. The primary object of these tests was to determine whether the heat transfer as calculated from a theoretical equation checked the experimental values for finned surfaces constructed of metals having different thermal conductivities. The optimum fin spacing with wide fins was also investigated.

Cylinder baffles.—A study has been completed of the aerodynamics of cooling air-cooled engine cylinders with baffles. The air passage was recognized to be a venturi and was studied from this point of view. The use of a baffle approximating the best venturi possible under the conditions imposed by a radial air-cooled engine resulted in an improvement of 20 percent in cooling on a model cylinder. When the results of this study were applied in the baffling of a modern 2-row radial engine the cooling on the head was improved 28 percent.

Further work is in progress on the problem of improving the cooling by changing the cylinder contour. An attempt is being made to overcome some of the difficulties in constructing a good venturi in the conventional circular engine cylinder. Although the study is being made for convenience on a model simulating the barrel of the cylinder, the results are applicable to the head of the cylinder. Since 80 percent of the heat is dissipated through the head, and since contour changes are more easily made on the head than on the barrel, the results will be applied to the head of the cylinder.

Blower cooling.—The results of an investigation on a cylinder with fins 1.22 inches in width and with spacings varying from 0.022 to 0.21 inch have been published in Technical Report 587. The cylinders were enclosed in jackets and cooled with air supplied by a blower. The results showed that maximum cooling was obtained with a fin spacing of 13 fins per inch and that the heat-transfer coefficient was not sensitive to the fin spacing for values near the maximum, whether more or less. With 11 or 16 fins per inch the heat transfer was 95 percent of that obtained with a fin spacing of 13 fins per inch.

The results of the investigation to determine the effect of fin width, fin spacing, entrance and exit areas of the jacket around the cylinder, separator plates, and fillets on the pressure drop and power required to force air around finned cylinders at air speeds from 15 to 230 miles per hour have been prepared for publication and will be released as Technical Note 621. An analysis has been made of the losses occurring around the cylinder. As a supplement to this work, some miscellaneous tests are being made to determine the effect of certain special jacket and baffle designs on the heat transfer and pressure drop of finned cylinders.

Cylinder-temperature correction factors.—The results of an investigation to determine the effect of engine power, weight velocity of the cooling air, and atmospheric temperature on the cylinder temperatures of a Pratt & Whitney 1535 engine under flight conditions have been published in Technical Note 584.

The study of the factors for correcting cylinder temperatures of air-cooled engines to a standard atmospheric temperature has been extended to include the correction factors for various flight and test conditions, such as level flight, climb, take-off, airplane stationary on ground, and conditions of constant mass flow of cooling air and of constant velocity of cooling air. The correction factors range from approximately a change in cylinder temperature of 0.6° to 1.1° per degree change in atmospheric temperature, the value of the factor depending on the flight or test condition. A report covering this work is being prepared.

Heat transfer.—The study of the cooling of air-cooled engines has been continued. A report has been prepared and will be published as Technical Report 612, presenting an analysis in which equations for the rate of heat transfer from the engine gases to the cylinder and from the cylinder to the cooling air, as well as equations for the average head and barrel temperatures, as functions of the important engine and cooling variables, are obtained. Data obtained in tests of single-cylinder engines of cylinders from Pratt & Whitney 1535 and 1340–H engines for checking the analysis and for providing the empirical constants in the equations for these cylinders are presented in the report. An illustration of the application of the equations to the correlation of cooling data obtained in flight tests of a Grumman Scout (XSF–2) airplane is also given in the report.

An investigation of the effect of turbulence in the cooling air stream on the cooling of the Pratt & Whitney 1535 cylinder showed that in some cases the turbulence caused an increase of as much as 30 percent in the heat-transfer coefficient of the fins for the same pressure drop across the cylinder. These data are included in the report.

Further cooling tests have been made on a cylinder from a Wright 1820–G engine for obtaining the constants of the heat-transfer equations for this engine.

Radiators.—A study of radiator design has been undertaken. The entrance and exit conditions are being studied with a view to improving their aerodynamic performance. The study has revealed that 50 percent of

the power required to cool a radiator is lost in the exit of the air from the radiator tubes in the conventional honeycomb tube radiator. The results show that an important part of this loss can be avoided. Further, the diameter and length of tubes for the minimum power to cool is being determined. The results will give the optimum dimensions for several operating conditions and installations.

COMPRESSION-IGNITION ENGINES

The compression-ignition engine is of particular interest as a power plant for transport aircraft because of its inherently low fuel consumption. The criticism previously made of the compression-ignition engine was that it could not produce the necessary high power outputs for take-off and that the weight of the engine would be excessive because of the high maximum cylinder pressures. The results obtained by the Committee in tests of single-cylinder engines with the N. A. C. A. displacer-type combustion chamber showed that the boosted performance of this compression-ignition engine was equal to that obtained from the latest type of air-cooled engines operating with fuel of 100 octane number. Under take-off conditions the maximum cylinder pressures developed in conventional air-cooled engines have been found to equal those in the compression-ignition engine. The two types of engines should therefore weigh approximately the same.

Prechamber type of combustion chamber.—The results of the investigation of the prechamber type of combustion chamber for compression-ignition engines have been published in Technical Report 577.

Integral type of combustion chamber.—The investigation of engine performance at 2,500 r. p. m. with a displacer piston and a vertical-disk form of combustion chamber has been continued. In order to accommodate the increase in the engine rotative speed from 2,000 to 2,500 r. p. m. the air induction and exhaust systems were altered and development work conducted to determine the proper air-flow passages and the arrangement of fuel sprays in the combustion chamber. Test results showed that with existing fuel-injection equipment the injection period was too long, as evidenced by late burning and a smoky exhaust. Even without the correct rate of fuel injection an indicated mean effective pressure of 260 pounds per square inch was developed at 2,500 r. p. m. for a boost pressure of 10 pounds per square inch. The corresponding specific fuel consumption was 0.42 pound per indicated horsepower-hour.

Altitude performance.—An investigation of the performance of a compression-ignition engine under altitude conditions has been completed, and the results showed the Diesel engine to be under no handicap when compared with the carburetor engine. Tests were conducted at pressure altitudes up to 30,000 feet and at temperature and pressure conditions up to 14,000 feet. Boosted performance was also determined at constant inlet-air temperature from boost pressures of 0 to 10 pounds per square inch over a range of exhaust pressures corresponding to altitudes from 0 to 19,000 feet. The scope of the research was expanded to include the investigation of the effect of single variables of temperature and pressure of the inlet air and exhaust back pressure. A report presenting the results of the work is in process of publication.

Single-cylinder and multicylinder engines.—An air-cooled compression-ignition cylinder having a push-rod-valve mechanism suitable for use on a radial engine has been designed by the Committee and is being supplied by the Bureau of Aeronautics, Navy Department, for investigation. The cylinder has the displacer form of combustion chamber developed by the Committee and will be used to investigate its adaptation to air-cooled cylinders. Information will also be obtained on the factors of multicylinder compression-ignition engine performance and the problem of air-cooling a compression-ignition engine cylinder.

The 2-stroke-cycle engine.—The investigation of the 2-stroke-cycle compression-ignition engine has been continued, and tests have been made to determine the effect of the shape of the inlet ports on engine performance. A cylinder liner providing 62 inlet ports, each of $^{11}/_{32}$-inch diameter arranged in three staggered rows and drilled at an angle of 56° from the radial, has been tested for several length-diameter ratios of the ports. Best performance was obtained when the length-diameter ratio was 0.7 and was approximately equal to that with the eight large rectangular ports previously used. Work is in progress to determine the effect of varying the timing and duration of exhaust on engine performance.

Fuel-injection rates.—The results obtained from the investigation of the rates of discharge from a single-cylinder fuel-injection pump connected to two injection valves have been published in Technical Note 600.

The increase in rotative speeds of the compression-ignition engines has resulted in inferior performance of the fuel-injection equipment. Special apparatus has been constructed whereby accurate and convenient determination of injection rates has been made for a group of available fuel pumps, plungers, and cams in various combinations. The tests included variations of engine speed and quantity of fuel injected for the several injection-system combinations. Results indicated the unsuitability of any available injection equipment to give satisfactory introduction of the fuel charge into the cylinder at engine speeds in excess of 2,000 r. p. m. and the urgent need for further injection-system tests and development.

Fuel-injection pumps.—An improvement in the performance of several compression-ignition engines has resulted from changes in the rate of fuel injection. A knowledge of the rate of injection of the various fuel-injection systems has been obtained only after investigation of their characteristics. A unit type of injection system was investigated to obtain a direct control over the injection rate by variation in the cam outline. A cam-operated injection pump was closely coupled to the injection valve, and the effect of changes in orifice diameter, injection-tube length, throttle setting, pump speed, type of injection valve, and cam outline was studied.

The cam outline directly controlled the injection rate during the first five pump degrees of injection for a large orifice diameter and a differential-area valve. After this time interval, leakage at the pump affected the control. An open nozzle in combination with a ball-check valve reduced the initial rate of discharge to about half that of the differential-area valve. This rate increased with fuel quantity to a maximum at cut-off. With the differential-area valve, the rate of injection reached a maximum a few degrees after the beginning of injection and an increase in fuel quantity did not increase this rate. An increase in pump speed decreased the maximum rate and increased the period in degrees. Increase in injection-tube length had less effect on the open-nozzle valve. Secondary discharges were not obtained under any operating conditions with short injection tubes, but were obtained with increase in tube length under operating conditions in which a high initial pressure wave was obtained. The orifice diameter materially affected the injection rate, owing primarily to the high leakage rate at the injection pump. The maximum rate decreased with decrease in orifice diameter. With a suitable pressure seal at the pump and a relatively large orifice diameter in a differential area valve, the rate of discharge should be controllable by the cam outline for the unit-type injector.

Fuel and combustion accelerators.—The efficiency of the compression-ignition engine at increasing loads is reduced by late burning during the power stroke. Some evidence has been presented that the problem of eliminating the late burning may not be entirely the mechanical process of fuel and air mixing but one also of overcoming chemical retardants. The use of chemical combustion accelerators in the fuel has been suggested as a possible means of overcoming this handicap. A tetranitromethane Diesel oil dope has been obtained and tested in various percentages in the standard laboratory fuel. The small improvement in performance (2 to 3 percent) was considered economically undesirable. A sample of a second combustion accelerator has been ordered for test. A program is also under way to determine the relative merits of combinations of fuel oil and alcohol in various percentages, particularly with respect to more complete utilization of the air charge.

Fuel investigation.—The correlation of engine-performance data requires a knowledge of the heat of combustion of the fuel used. The determination of this factor and the distillation characteristics of the fuel make possible the recognition of changes in fuels due to aging or replacement. The heating values of five samples of Diesel fuel used by the Committee for engine testing have been determined. The values found vary from 19,790 B. t. u. to 19,930 B. t. u. per pound.

The smoky exhaust obtained with compression-ignition engines operating at air-fuel ratios richer than the theoretical (15 pounds of air to one pound of fuel) indicates that considerable fuel is wasted in unburned carbon. An investigation is being made to determine the amount of this carbon and its variation with air-fuel ratio. The method used is to determine the actual hydrogen-carbon ratio of the fuel from complete combustion tests and the apparent hydrogen-carbon ratio from exhaust-gas analysis, the difference in the two values being the carbon in the exhaust. The actual hydrogen-carbon ratio of five samples of Diesel fuel oil representative of the fuels used during the past two years by the Committee has been determined. The values found varied from 0.160 to 0.161.

INSTRUMENTS

Fuel flowmeter.—Flight testing of the electrical type of indicating fuel flowmeter which has been developed by the Committee has been conducted by the Materiel Division of the Army Air Corps. The fuel flowmeter is being altered to incorporate desirable changes indicated as a result of the flight tests.

High-speed camera.—The design of a high-speed motion-picture camera to photograph combustion at rates up to 40,000 frames per second has been completed, and construction of the camera has been started. The operating principle of the camera has been checked by means of a mock-up of the camera.

Fuel-injection pressure indicator.—A piezo-electric pick-up unit has been adapted to a fuel-injection valve to obtain instantaneous values of the fuel pressure at the discharge orifice. The pressures are shown on a cathode-ray tube. Photographic records are made of these instantaneous pressure traces. The rates of fuel discharge calculated from the pressure records show a very close agreement with the rates measured on the rate-of-discharge apparatus. This unit allows a rapid determination of rates of fuel discharge and of any cyclic variations in the discharge.

NATIONAL BUREAU OF STANDARDS

Phenomena of combustion.—A spherical explosion vessel with central ignition and auxiliary apparatus for obtaining simultaneous records of flame travel and pressure development has been constructed. The bomb consists of two flanged hemispheres, about 10 inches in diameter, clamped together on a short ring of glass which affords a view of the flame in a narrow, vertical center-section of the bomb.

The progress of the flame as it spreads from the central spark gap is photographed on a film which is carried on a drum rotating at a known speed on a vertical axis. The movement of the film under the lengthening image of the narrow flame section produces a time-displacement record of the flame front.

Six diaphragm pressure indicators, designed with a view to securing high accuracy throughout the pressure range of the explosion, are mounted on the bomb. Each indicator is set to close an electric contact the instant some predetermined pressure is reached in the bomb. When the contact is closed a neon lamp of high intensity is lighted, which photographs on the rotating film as a line beside the flame trace. In addition to the six lamps corresponding to the six indicators, there is a lamp which flashes 1,000 times a second under the control of a tuning fork and a lamp which burns continuously to provide a reference line for the measurement of flame displacements. The film thus contains all the information necessary for plotting time-displacement and time-pressure curves for the explosion.

Formulas have been developed for calculating from these curves (1) the "transformation velocity" or fundamental speed at which the flame front advances into and transforms the unburned charge; and (2) the "expansion ratio" or ratio of the volume of burned gas to the volume of the same mass of gas before explosion at constant pressure. Experiments will be conducted with this apparatus to investigate the separate effects of charge composition, temperature, and pressure on transformation velocity and expansion ratio.

Some experiments were made in which a cylindrical glass bomb was used with no pressure indicator to determine the effect of water vapor on the period of subnormal flame velocity just after the occurrence of the spark. In equivalent mixtures of carbon monoxide and oxygen saturated with moisture at atmospheric pressure this delay period is very short and high-film speeds must be used to detect it. Constant flame velocity is attained much more slowly when the moisture content is reduced below about one percent by volume. The cause of the delay is not known and it is hoped that new information concerning it will be obtained with the spherical bomb.

A brief mimeographed circular outlining the combustion experiments which have been conducted at the Bureau in engines, soap bubbles, and bombs, and containing a list of published reports on these experiments has been prepared for distribution to visitors and to others interested. A mimeographed bibliography containing 162 references on high-speed pressure indicators, classified according to type, is also available.

Investigation of piston cooling.—As the output of aircraft engines is raised the problem of heat dissipation from the piston head becomes increasingly serious. A program has been outlined for determining the heat flow in suitable test specimens under conditions similar to those encountered in service by aircraft-engine pistons. Preliminary static experiments showed greatly improved heat transfer for a hollow steel specimen with internal cooling over a solid aluminum specimen of approximately equal strength, size, and weight.

SUBCOMMITTEE ON AIRCRAFT FUELS AND LUBRICANTS

Engine performance with iso-octane fuels.—As mentioned in the report of the Langley Memorial Aeronautical Laboratory above, an investigation is being conducted at that laboratory to determine the maximum engine performance with fuels having octane numbers ranging from 87 to somewhat greater than 100. In this investigation the engine performance has been determined with the N. A. C. A. high-speed single-cylinder test engine having a cylinder bore of 5 inches and a stroke of 5.75 inches. The tests have been made at an engine speed of 2,500 r. p. m. and a coolant temperature of 250° F. The desired octane number of the fuel has been obtained by using commercial iso-octane blended with a gasoline having an octane number of 18. For octane numbers greater than 100, tetraethyl lead has been added to the iso-octane.

Tests have been completed with fuels of 87, 91, 95, and 100 octane number as determined by the C. F. R. method. In addition, tests are almost completed on the iso-octane with 1 cubic centimeter of tetraethyl lead. The limiting performance of these fuels has been determined at maximum power and at best fuel economy for both incipient and audible knock. The results show that as the inlet-air temperature is increased for any one compression ratio the effectiveness of the fuels of higher octane number appreciably decreases. Only at the lower inlet-air temperatures are the greatest increases in performance realized for the fuels of higher octane number. The tests have shown that the power of the engine does not vary as the inverse square root of the inlet-air temperature, but as an approximately lineal function.

Stability of aviation oils.—The investigation of the stability of aircraft-engine lubricating oil, conducted by the National Bureau of Standards in cooperation with the Bureau of Aeronautics of the Navy, has been extended to include laboratory tests of the stability of oils

in an apparatus in which the oil flows in a thin film down the walls of a heated cylinder and thus simulates engine conditions. The investigation of this method is not yet completed, but the data obtained thus far indicate a correlation between the results of these tests and the results of tests which have been made in a Pratt and Whitney Hornet engine.

An investigation of the stability of compounded oils has been initiated in cooperation with the Subcommittee on Aircraft Fuels and Lubricants, and the effect of a number of compounding materials on the stability of the base oil has been studied. The results of this investigation will serve as a basis for the choice of compounded oils to be used in connection with the study of wear and oiliness characteristics of aviation engine lubricating oils.

Oil acidity and bearing corrosion.—The investigation, conducted by the National Bureau of Standards in cooperation with the Bureau of Aeronautics of the Navy, of the effect of increase in oil acidity during service on the corrosion of master-rod bearings has been continued. Study of oils in the apparatus for forming acids in oils has indicated that this apparatus can be used to produce changes in the acidity of oils similar to changes which occur during service in aviation engines. It has been found desirable to construct additional apparatus for use in this investigation and this apparatus is being designed.

Aviation engine wear.—The investigation of the relative wear with different oils in actual aircraft engines, carried out at the National Bureau of Standards in cooperation with the Bureau of Aeronautics and certain petroleum organizations, has been continued throughout the fiscal year. The assembly of the operating equipment for engine control and absorption of power is essentially completed. Considerable precautions have been taken to insure reproducibility of operating conditions. Special fixtures for use with the precision instruments required for measuring the engine parts are under construction.

Wear and oiliness characteristics of aviation engine lubricating oils.—The investigation of the oiliness and wear characteristics of mineral and compounded lubricating oils, conducted by the National Bureau of Standards in cooperation with the Army Air Corps and the Bureau of Aeronautics, was continued throughout the fiscal year. An apparatus for determining the differences in piston-ring and cylinder-wall wear with various oils and compounding agents under conditions approximating those of actual engine operation has been completed, and preliminary tests are in progress. Construction of a second wear apparatus of different type has been begun. The design and construction of a machine for the study of oiliness as related to friction in master-rod bearings is under way.

REPORT OF COMMITTEE ON AIRCRAFT MATERIALS

SUBCOMMITTEE ON METALS USED IN AIRCRAFT

Weathering of aircraft structural sheet metals—light alloys.—The series of atmospheric exposure tests of aluminum-alloy sheet materials was completed during the spring of 1937 after four years' duration at three test sites, typical of conditions prevailing at a tropical marine, a temperate marine, and an inland location. The results amply confirm the tentative conclusions announced in last year's report concerning the most corrosion-resistant types of alloys and satisfactory coating treatments for all alloys of this general kind. A report intended for publication summarizing the essentials of the test and the important facts established is in progress.

Preparations are approaching completion for a new series of tests. This series, which is on a somewhat smaller scale than the two previous ones, will be conducted at only one location, a marine one. Hampton Roads Naval Air Station is the site selected. Both aluminum and magnesium alloys are included in the program of tests scheduled, which are intended primarily for investigating the effects of riveting, welding, and contact between unlike metals, as well as the merits of newly developed protective surface treatments. The manufacturers of these materials are cooperating actively in the preparations, and this will insure that the industrial aspects of the problem will receive the careful consideration they deserve.

Corrosion-resistant steel.—The trend toward the use in aircraft of corrosion-resistant steel in thin sheet form has led to the inauguration of a similar program on this type of material. Deterioration of this material, if it occurs, takes place in a different manner from that of the light alloys, and the inspection and testing procedure must be correspondingly different. In both programs the effect of continuous exposure to the marine atmosphere as well as intermittent exposure to sea-water (the so-called "tide-water" tests) is to be determined.

Surface treatment for improving the durability of magnesium.—The ultimate aim in this investigation is to produce a tightly adherent surface film, highly impervious to corrosive agents, particularly chlorides, to which paint and other applied coatings will adhere over long periods of time without peeling or flaking. Anodic treatment in a dichromate-phosphate bath by the method developed in cooperation with the Bureau of Aeronautics, according to repeated laboratory tests at the National Bureau of Standards, continues to be the preferred method for the surface treatment of magnesium and its alloys. Studies on the improvement of the anodic treatment have been continued, and the

results have indicated certain modifications by which further improvement appears possible. "Sealing" of the pores in the anodic film after it has been formed is important to produce a highly impervious film. This may be accomplished either by chemical means or by immersion in a hot oil or resin bath. Tests along this line are continuing. Initial cleaning before anodic treatment is also important in obtaining a film on the treated specimen of superior resistance. Tests on paint adherence as affected by the sealing treatment and other surface characteristics are in progress in the laboratory and on the outdoor exposure rack.

Sub-zero temperature and aircraft metals.—The original program, undertaken in cooperation with the Bureau of Aeronautics, has been completed and a report rendered, copies of which are available to all interested Government agencies. The only important adverse effect of low temperature, down to −80° C., is the decreased impact resistance of ferritic steels, which is in marked contrast to the aluminum alloys and the austenitic steels. Study of the factors responsible for this lowered impact resistance of ferritic steels is being continued with the aim of reducing and possibly eliminating the effect by suitable initial heat treatment of the steel. The investigation has been extended to include a study of the impact resistance at low temperatures of welded joints in steel members.

Elastic properties of high-strength aircraft metals.—The elastic properties of metals which owe their high-strength properties to strengthening by cold working are only nominal and vary greatly with the precision of the method used for their determination. An outstanding example is austenitic steel, such as 18–8 stainless steel, which because of its high corrosion resistance is favored for many important uses in aircraft. The method used in this work is essentially an "over-load" or "proof-stress" method, consisting in the determination of yield strength after various degrees of cold working by stretching immediately prior to testing. A rise in proof stress with increase in prior cold work is indicative of an improvement in the material, and vice versa for a decrease in proof stress. A report summarizing this phase of the work will be forthcoming shortly. Hysteresis measurements, such as those which may be obtained in the ordinary tensile-testing machine, are now in progress.

Structural changes in aircraft metals occurring as a result of service stressing.—The principal aim in this investigation is expressed in the question, Does continued fatigue-stressing below the endurance limit adversely affect aircraft metals? The widely used aluminum propeller alloy, 25S, is the material used in this study. A variety of approaches to the problem have been made, some of which were abandoned at early stages for more promising ones. The project is still in the stage of attempts to detect *significant* changes (other than crack formation and propagation) in physical properties, microstructure, and X-ray diffraction pattern as results of continued repeated stressing in the range of maximum fibre stress from 5,000 to 26,000 pounds per square inch. Up to the present no nondestructive method of inspection has been found which shows a significant difference between the metal not stressed and the same metal after it has been subjected to fatigue stressing. Special mention may be made of the failure to detect a lowering of impact resistance which could be attributed to prior fatigue stressing.

Propeller materials.—The possible deleterious effect of fabrication defects on the endurance properties of steel used in hollow steel propellers merits serious study. Also, the influence on the endurance of propellers of surface coatings, such as chromium plating as a finish, should not be overlooked.

The fatigue limit of such steel is approximately one-half of the tensile strength, which is considered to be normal for this material. Determinations of the fatigue limit of sound weld metal showed this to be about 60 percent of that of the parent metal. Scaling and surface decarburizing, such as may be present accidentally on the inside of the welded structure and cannot be removed, reduced the fatigue limit to one-half that of the polished steel, i. e., not much below that of the weld metal. The effect of accidental defects in the weld is variable; such defects may cause a very sharp reduction in the fatigue limit of the weld metal.

The effect of chromium plating varies with the condition of the steel and thickness of the plating. Specimens of normalized steel (previously polished) bearing relatively thick coatings showed no significant reduction in fatigue limit and a thinner coating had only a slightly greater effect. On specimens of the same steel in quenched-and-tempered condition, however, a reduction in fatigue limit was noted, which appeared to be of more significance and was greater for a very thin coating than for a coating ten times as thick, the plating in each case being applied directly to the previously polished steel. The use of a nickel "under coat," in accordance with commercial usage, prior to plating the quenched-and-tempered steel, gave similar results. The subject is receiving further study.

Further study of the unusual structural features previously reported for aluminum-alloy propeller blades has failed to show that any practical significance can be attached to them.

Miscellaneous.—The fact is well established that the corrosion resistance of many of the aluminum alloys which are strengthened by heat treatment is dependent in large measure upon the control of the conditions of heat treatment. A simple rapid test to determine in advance of service whether structural materials of this

kind have been suitably heat-treated so as to develop maximum corrosion resistance should serve a very useful purpose. A study is being made of a proposed method, the essential feature of which is a determination of the solution potential of the material under consideration.

A relatively inexpensive method of preparing small fittings of unusual shape is to use transverse sections of an extruded shape of the proper size and contour. A study of extruded aluminum fittings made in this manner is under way, with a two-fold purpose, namely, (a) the improvement of such fittings with respect to certain features which have not proved entirely satisfactory under all service conditions, and (b) the determination of the practical significance of certain suspected structural features.

The need for a certain degree of ductility in a structural member, as in an aircraft assembly, is well recognized. The amount and the manner in which it is specified are, however, matters on which difference of opinion exists. Determinations of the ductility of various structural steels under various conditions of stress application have been continued, in cooperation with the Bureau of Aeronautics of the Navy. Interpretations as to the practical significance of differences in this property observed under various conditions are yet to be made.

SUBCOMMITTEE ON MISCELLANEOUS MATERIALS AND ACCESSORIES

The problems under the cognizance of this subcommittee during the past year which are being investigated at the National Bureau of Standards include the development of a flexible substitute for glass and the development of substitutes for linen webbing and silk shroud lines for parachutes. Consideration has also been given to the possibilities of plastics as a material for aircraft structures and to the adequacy of thermal and acoustical insulation.

Development of flexible substitute for glass.—Commercial and experimental transparent plastics which have been investigated to determine their suitability for aircraft windshields and windows include cellulose acetate, acrylate resins, cellulose nitrate, ethylcellulose, vinyl chloride-acetate, vinyl acetal, glyceryl-phthalate, styrene, phenol-formaldehyde, and cellulose acetobutyrate.

The tests included light transmission, haziness, distortion, resistance to weathering, scratch and indentation hardnesses, impact strength, dimensional stability, resistance to water and various cleaning fluids, bursting strength at normal and low temperatures, and flammability.

The two types of transparent plastics which are now in use on aircraft, namely, cellulose acetate and acrylate resin, were found to have certain defects which, it is believed, can be overcome in part by suitable modification of the composition and processing of the material.

Cellulose-acetate plastic was found to have excellent impact strength, bursting strength, and flexibility, but the commercial products tested varied considerably in resistance to weathering and were all subject to marked shrinkage in one year's time. The shrinkage produces warping and sets up strains in the plastic sheets, which cause them to craze and crack. These strains are believed to be the cause of the spontaneous cracking of cellulose-acetate windshields after they have been in service for six months or longer. This is particularly true of windshields which are exposed to low temperatures, as by ascent to high altitudes, as additional strains are thereby introduced in the windshield because of thermal contraction. Considerable variation was observed in the weathering resistance between cellulose-acetate sheets received from different manufacturers and also between different lots of the material from the same manufacturer.

The acrylate-resin plastic was found to be remarkably transparent, more stable to light and weathering, and more resistant to scratching than cellulose acetate, but its impact strength and flexibility are much poorer. Surface crazing of the acrylate resins was noted after one year's exposure on the roof and also after storage for a similar period. It is claimed, however, that a method of processing has been developed which eliminates this tendency to craze. Further tests on modified samples of both cellulose acetate and acrylate resins are in progress to determine whether more uniformly durable products than have been on the market to date can be made available to the aircraft industry.

Certain of the other materials, which are not now commercially available, appear very promising.

Tests for impact resistance were developed on a scale commensurate with service conditions. Soft rubber balls, five inches in diameter, loaded to weigh three pounds, were fired from guns at the Naval Proving Grounds. The muzzle velocity was approximately 300 feet per second. No material, whether plastic or laminated glass, was found able to withstand a direct hit with such a projectile. The experimental pieces were, of course, limited as to weight and thickness by practical considerations of airplane design. It was therefore concluded that the windshield alone cannot be regarded as a protection against ducks.

Substitute for linen webbing.—An all-cotton webbing which meets the requirements for breaking strength, weight, width, and thickness contained in U. S. Army Specification No. 15–11–D for linen webbing has been produced commercially. While the construction is not identical with that of the Type-G webbing, the cotton webbing appears to be a satisfactory substitute.

Substitute for silk shroud lines.—Attempts to make shroud lines from some material other than silk have not been successful to date. Whether cotton or rayon was used, the strength-weight ratio of the line has not equalled that obtainable with silk. Experiments are being continued to obtain information on the effect of variations in the construction of the line.

Development of plastic material for aircraft structures.—A survey of the literature on this subject was completed and a report presented to the Committee. The report contains data on density, tensile and compressive strengths, modulus of elasticity, fatigue, energy absorption, corrosion, and methods of fabrication. The Committee is now studying this report with a view to deciding whether or not to go further into the matter.

Materials for acoustical and thermal insulation.—A report bringing together some of the information available on this subject has been presented to the Committee. Plans have been made to ascertain the practical importance of this subject, and upon the answer to this question will depend future developments.

REPORT OF COMMITTEE ON AIRCRAFT STRUCTURES

LANGLEY MEMORIAL AERONAUTICAL LABORATORY

Applied loads on airplane structures—gust loads.—Coordinated measurements of acceleration and air speed on transport airplanes have been continued during the past year, and the total flying time represented on the records has been extended to over 30,000 hours. The maximum accelerations previously recorded have not, however, been exceeded and the maximum effective gust velocities for normal transport operations remain at ±35 feet per second.

Gust research.—The measurements of gust intensities and gradients on light airplanes, begun last year, have been continued and the data greatly extended. The new results do not invalidate the previous tentative conclusions, that in stable atmospheric conditions with large wind gradients, vertical gust velocities of the order of 30 feet per second are reached in a horizontal distance of about 100 feet and that the gust gradient increases with decreasing gust intensity.

Surveys of cumulus types of clouds indicate, in general, stronger downward-acting than upward-acting gusts. On one occasion a downward gust of 53 feet per second, which reached maximum intensity in a distance of 53 feet, was experienced.

Gust tunnel.—During the past year an apparatus for catapulting dynamically scaled models through artificial gusts has been developed to the point of satisfactory operation. In this apparatus the model is launched into a condition of steady glide, following which it flies through an air jet whose angle relative to the flight path can be controlled. The model carries a small optically recording accelerometer, and as it flies through the gust the acceleration is recorded and synchronized with external photographic measurements of the speed, path angle, and attitude angle.

Although this equipment is not ideally suited to the investigation of some of the important fundamental problems of unsteady flow, it can be used and was designed for the direct determination of the effects of changes in the several airplane and gust variables on the airplane motion and wing loads. This function is justification for the equipment in view of the rapid trend toward larger transport airplanes, to which the statistical data obtained on past and present types of airplanes do not apply.

Gust-relief devices.—A preliminary analytical study of the merit of two devices for reducing accelerations due to gusts has been made. The more effective arrangement appears to be a trailing-edge flap operated by a small vane located somewhat ahead of the wing. This arrangement responds more quickly and reduces the acceleration further than the other device studied, which was simply a mass-overbalanced flap.

Load distribution.—The results of a previously reported investigation of the span-load distribution on wings with partial-span flaps have been published as Technical Report No. 585. This report includes a simple set of computing forms for determining the distribution by the Lotz method with sufficient harmonics retained for good precision. The work on wings with partial-span flaps has been extended to include the calculation of the angle of zero lift, the pitching moment, and the induced drag. Wing models are now being constructed for investigation to provide data for comparison with the calculations.

Several pressure-distribution tests have been made in the 7- by 10-foot wind tunnel of wings with various flap arrangements, including Fowler flaps with chords 30 and 40 per cent of the wing chord.

Several reports describing investigations conducted prior to this year have been issued and include a report on pressure-distribution measurements on an O–2H observation airplane in flight (Technical Report No. 590), a report presenting an empirical method for determining tip corrections to the theoretical span-load distribution (Technical Note No. 606), and a report on the theoretical span loading and moments of tapered wings produced by aileron deflection (Technical Note No. 589).

Fuel tank vents.—During a dive from high altitudes the pressure changes rapidly on the outside of an airplane. Unless the venting tubes to the fuel tanks and plugs are of the correct size, a pressure difference may be built up that will be sufficient to collapse the fuel tanks or plugs.

The Committee has been requested by the Bureau of Aeronautics, Navy Department, to investigate these pressure differences for a range of diameters and lengths of vent tubes. Apparatus has been assembled in the laboratory that makes possible the rapid determination of the pressure difference between a tank of given volume and the atmosphere during a dive. The laboratory tests have been made at constant temperature, as calculations show that this does not introduce an appreciable error.

Tests have been made for terminal velocities of 300, 400, and 500 miles per hour for dives starting at 10,000 to 40,000 feet altitude with float and tank volumes from 10 to 60 cubic feet. Several lengths of vent tubes 1.5 inches in diameter and 0.75 inch in diameter have been investigated. Pressure differences of 10.5 pounds per square inch have been recorded with a tube 0.5 inch in diameter and 12 feet long.

Stressed-Skin Design—stress analysis of beams with shear deformation of the flanges.—The rapidly increasing size of aircraft structures is forcing designers to rely increasingly, for economic reasons, on mathematical stress analysis rather than on static tests. It is well known that the classic methods of analysis are not always sufficiently accurate and efforts are being made to correct these methods.

As a step in this direction, the bending action of box beams such as airplane wings has been examined. It has been realized for some time that the flanges of such beams deform sufficiently under shear stress to alter the stress distribution materially. The mathematical theory of this action has been developed to the point of practical applicability and has been partially verified by tests. Further tests are under way to determine under what conditions the theory can be used without modification and, for cases in which modifications are necessary, to lead over into the range of the classic engineering theory of bending.

Strength of stiffeners.—A theory for primary failure of straight centrally loaded columns has been published as Technical Report No. 582. In the report the theory for twisting failure of open-section stiffeners, as presented by Herbert Wagner (Technical Memorandums Nos. 807 and 784), has been elaborated to include the twisting failure of open-section stiffeners attached to a skin, with stresses carried above the elastic range. An illustrative computation of the column curve for the twisting failure of an I-section skin-stiffener combination is also included.

Work is being continued on the twisting failure of other types of stiffener sections, notably the Z section and the U section, with and without flanged edges. Consideration is being given to the manner of shift of the axis of rotation in twisting failure, both in and above the elastic range, in order to establish the extent of refinement necessary for practical application.

Besides the study of twisting failure, which is a primary failure, the local failure of various types of stiffener sections is being investigated, and the theoretical strength curves are being compared with such experimental data as become available from time to time.

Stability of structural systems.—A report has been prepared and published as Technical Note No. 617 dealing with the stability criterion for structural systems. The Hardy Cross method of moment distribution is employed. In order to simplify the application of the stability criterion, detailed tables are given for the ready evaluation of the stiffness and carry-over factors. Sample problems are also included to illustrate the use of the method.

NATIONAL BUREAU OF STANDARDS

Tubes under loads other than torsion.—Considerable time has been spent during the year in revising and bringing into conformity with latest Navy Department specifications a report which has been written on the fixation of struts; that is, the column strength of tubing elastically restrained at the ends. This report is now completed and will be published by the National Advisory Committee for Aeronautics as a technical report. It gives the column strength of chromium-molybdenum steel, 17ST aluminum alloy, stainless steel, and heat-treated chromium-molybdenum-steel tubing, and suggests a method by which planar trusses that are continuous at the joints may be analyzed and designed for stability. Two numerical examples are given.

In order to determine the minimum ratio of slenderness below which thin tubes fail by crinkling rather than as columns, and to determine the crinkling strength, tests of short tubes must be made under axial load. The crinkling strength under axial load of relatively short specimens of round 17ST aluminum-alloy tubing has been determined for values of the diameter-thickness ratio approximately from 15 to 100. Work is in progress and has been almost completed to determine the crinkling strength of chromium-molybdenum-steel tubing.

The modulus of rupture of round 17ST aluminum-alloy tubing has been determined for values of the diameter-thickness ratio approximately from 15 to 100. This has been done under third-point loading with the load applied (1) in such a way that failure occurred in the free length between loads, and (2) in such a way that failure occurred under a load. The latter method of loading simulates practical conditions occasionally encountered under which the load is applied

through a compression member tending to dent the tube. Two empirical formulas involving the tensile yield strength of the tube material and the dimensions of the tube were derived to describe the modulus of rupture for the two series of tests.

The modulus of rupture obtained with the first method of loading does not depend to any marked extent on the position of the loading points, and the empirical formula for this method of loading may be used with safety whenever the maximum bending moment occurs in the free length of tube between loading points (including supports). The results are conservative for all other cases except in those relatively few instances in which the load is applied through a compression member tending to dent the tube. Under these conditions the empirical formula obtained from the tests with the second method of load should be used. The results of the second series of tests can be extended rationally to apply to other than third-point loading.

Work is in progress and has almost been completed to determine the modulus of rupture of round chromium-molybdenum-steel tubing under the same conditions of test as obtained for the 17ST aluminum-alloy tubing.

Determination of elastic constants on stainless-steel sheet material.—A study was made of the elastic properties of stainless-steel sheet of three thicknesses (0.007, 0.016, and 0.022 inch) in order to determine effective values of Young's modulus and of Poisson's ratio which could later be used in calculating stresses from the deformation under load of a model structure of this material.

The variation of Poisson's ratio and of Young's modulus with stress, sheet thickness, direction of rolling, and prestressing was measured by cutting tensile specimens in the direction of rolling and at right angles to that direction and measuring the ratio of transverse strain to axial strain with a set of four pairs of Tuckerman optical strain gages suitably placed to eliminate the effects of nonuniformity of stress distribution.

The values of Poisson's ratio were found to range from about 0.2 to 0.3. On the 0.007-inch specimen the Poisson's ratio in the direction of rolling was about 0.27, while at right angles to that direction it was only about 0.21. In some cases a considerable difference in values was found for the second run as compared to the first, showing the effect of prestressing on the elastic properties of the material.

Large variations in the value of Young's modulus with direction of rolling, sheet thickness, and stress were also found. In the case of the 0.007-inch specimens tested in the direction of rolling the Young's modulus dropped from around 28.5 10^6 pounds per square inch at a stress of around 5,000 pounds per square inch to a value less than 26.0 10^6 pounds per square inch at a stress of around 30,000 pounds per square inch.

The test results indicated the anisotropy of the stainless-steel sheet material. Stresses determined from strain measurements on a model constructed from such material would be subject to a probable error of several percent due to the variations in elastic properties alone.

Flat plates under normal pressure.—Experimental work was confined to tests of circular plates under normal pressure. The stress-strain curve of the material in the center of the plate was derived from the measured strains and the measured contours under load for two of the plates. In both cases the stress-strain curve obtained was found to differ from the tensile stress-strain curve of a coupon cut from the plate in that the stress continued to rise after passing the knee of the stress-strain curve; the mechanism of yielding in bilateral tension seemed to be different from that in straight tension.

The experimental work was paralleled by an extension of Stewart Way's analysis of clamped circular plates of medium thickness under normal pressure to greater deflections than the deflections of 1.2 times the thickness of the plate to which Way carried his tables. The deflections in the present plates amounted to about four times the plate thickness before yielding became appreciable. With the derivation of the curves of maximum stress and of deflection at the center of this order it will be possible to make an instructive comparison between the observed and the calculated deformation of circular flat plates, which it is hoped will lead to an understanding of the yielding in the rectangular plates also.

Inelastic behavior of duralumin and alloy steels in tension and compression.—The investigation of stress-strain curves of sheet material in tension and compression has been continued. A large number of tensile and "pack" compressive tests have been made on specimens cut with and across the direction of rolling from sheet ranging in thickness from 0.032 to 0.081 inch. Stress-strain curves have been obtained for aluminum alloys 17ST, 24ST, 24SRT, Alclad 17ST, and Alclad 24 ST. The difference in yield strength in compression as compared to tension was found to be of the order of 10 to 15 percent. The data suggest that the compressive yield strength of sheet material in the direction of rolling can, in general, be approximated roughly by the tensile yield strength at right angles to that direction, and vice versa.

The accuracy of the pack compression test was investigated by comparing the stress-strain curves obtained on solid specimens of cold-rolled steel, aluminum alloy, and brass 0.7 by 0.7 inch in section, with stress-

strain curves from pack compression tests on packs built up from leaves cut from the same bar stock. The two sets of stress-strain curves were found to agree within ±2 percent.

The pack compression tests on 24SRT aluminum alloy had shown a value of Young's modulus which was consistently higher by about 3 percent than the Young's modulus in tension. This difference could not be ascribed to errors in the compression tests. Preliminary tests indicated it to be due to a continuous increase in the slope of the stress-strain curve in passing from small tensile stresses through zero to small compressive stresses.

Tubes with torsional loads.—The report on torsion tests of 61 chromium-molybdenum-steel tubes and of 102 17ST aluminum-alloy tubes was completed and will be published as Technical Report No. 601 of the National Advisory Committee for Aeronautics.

A comparison of the empirical formulas proposed in this report with the torsional strength of tubes of 17ST and 51SW aluminum alloy as tested at the Aluminum Research Laboratories showed close agreement, although the tubes tested by the Aluminum Research Laboratories were considerably shorter and in the case of the 51SW material had considerably different mechanical properties than the tubes tested at this Bureau. The agreement may be ascribed to the use in the empirical formulas of ratios involving the tensile properties of the tube material.

Beams and stressed-skin research.—The program on wing beams has been continued with the completion of tests under axial load, transverse load, combined axial and transverse loads, of eight wing-beam specimens of aluminum alloy with an I-type section having tilted flanges. Failure in these beams occurred by local instability of one of the flanges. The measured strains and deflections are being analyzed with the help of compressive stress-strain curves for the flange material which were obtained by the pack method. Failure of the combined-load specimens occurred at a flange stress calculated from the loads which ranged from 34,700 to 36,400 pounds per square inch.

The analysis of the data obtained on the two sheet-stringer panels tested in end compression at the National Bureau of Standards has been completed. Comparison with the results of similar tests at the Navy Model Basin on panels of the same design showed good agreement for the load carried by the sheet at failure. The load carried by stringers at failure was found to be about 10 to 20 percent lower for two of the specimens tested at the Model Basin. This relative loss in strength is probably due to the difference in end restraint, the flat end condition used at the Model Basin providing less restraint against buckling than the casting of the ends in Wood's metal used at the National Bureau of Standards.

The measured strain distribution in the sheet of the two panels tested at the National Bureau of Standards and the measured buckle shape were compared with the deformation calculated from approximate theories developed by S. Timoshenko, by J. M. Frankland, and by K. Marguerre. None of the approximate theories was found to agree accurately with observed deformations. The deflections of the buckled sheet were best described by Timoshenko's theory, the axial strains were about equally well described by all three theories, the transverse strains were best described by Frankland's theory, and the sheet load was best described by Marguerre's theory.

The analysis of the deformation of the stringers in the sheet-stringer panels was confined to a series of plots of deformation against deformation over load in accordance with Southwell's method. If the deformation plotted leads to an instability of the type to which Southwell's relation applies, all points will lie on a straight line with a slope equal to the elastic buckling load. Excellent straight lines could be obtained for some of the stringer twists as measured by the rotation of pointers mounted on the stringer, the slope of the lines being in close agreement with the observed buckling load. The agreement was less satisfactory for plots of other deformations. The lack of general agreement is not surprising, since a proof for the validity of Southwell's method has been given so far only for the column failure of beams under eccentric axial load and under certain combinations of axial and transverse loads.

Eighteen sheet-stringer panels are being fabricated at the Naval Aircraft Factory for the investigation of the effect on the compressive strength of such panels of rivet spacing and spot-spacing. The panels will be 12 and 18 inches long and will consist of three Z-type stringers fastened to the sheet by rivets or spots spaced an amount ranging from ½ to 4 inches. The spacing between stringers, the sheet thickness, and the spacing between rivets or spots will be varied to explore the effect of rivet spacing on both the buckling of the sheet between rivets and on the effective width of the sheet between stringers.

Airplane vibration.—Close cooperation was maintained with the Bureau of Aeronautics of the Navy Department in its program on airplane vibration. The National Bureau of Standards participated actively in a number of conferences at which methods were discussed for recording the readings of vibration pick-ups and of strain pick-ups mounted on various portions of an airplane in flight.

An important part of the program is the development of dynamic-strain pick-ups suitable for attachment to

the structural parts of an airplane. In connection with this work a number of special strain pick-ups have been built by the Sperry Gyroscope Company which embodied a principle of inertia compensation suggested by William M. Bleakney, of the Engineering Mechanics Section of this Bureau. A description of this principle has appeared in the Journal of Research of the National Bureau of Standards for June 1937 under the title "Compensation of Strain Gages of Vibration and Impact," by William M. Bleakney. Three of the experimental pick-ups built by the Sperry Gyroscope Company were tested for compensation and for ruggedness of construction on a device subjecting them to accelerations up to 50 times gravity with negligible strain. Compensation for inertia forces adequate for present applications was obtained on one of these after a number of small adjustments had been made. The calibrations also suggested a number of changes in the design of the gage which would probably improve its operation.

A second type of strain pick-up on which considerable work was done at the Bureau is the strain pick-up of the carbon-resistance type developed by A. V. de-Forest. Static and dynamic calibrations were made on 20 carbon resistance strips, 5 of them of the "granular" type used at the Hamilton Standard Propeller Company, and the remaining 15 of the so-called "Ess-strip" type. A report describing the results of these tests in detail has been forwarded to the Bureau of Aeronautics of the Navy Department. The report gives quantitative results for the effect of frequency, strain amplitude, time under load, and temperature on the calibration of a number of these strain pick-ups.

The best dynamic characteristics were found for the gages of the "Ess-strip" type. These gages showed a resistance amplitude that was nearly proportional to the strain amplitude up to strains of 0.001 (corresponding to stresses of about 10,000 pounds per square inch in aluminum alloy). The calibration factor calculated by dividing the constant of proportionality by the direct-current resistance of the gage was independent of frequency between 30 and 100 cycles per second within ± 10 percent, independent of temperature between $-10°$ C. and 40° C. within ± 10 percent, independent of time for one day within ± 5 percent and for 40 days within ± 9 percent.

The static calibration tests, which were confined to gages of the "Ess-strip" type, gave calibration factors ranging from 40 percent below to 35 percent above the dynamic calibration factors. The effect of temperature variations and of time under load were found to be sufficient to render this type of strain gage very much inferior to accepted gages such as the Tuckerman optical strain gage or the Huggenberger extensometer in those cases where static strains on a large structure are to be measured.

The dynamic calibrations of "Ess-strips," which were made by attaching the gage to a propeller blade and then vibrating this blade in resonance, had indicated the need for a calibrator that would subject the strips to uniform sinusoidal strains of sufficient amplitude and of a frequency that could be varied over a wider range than the restricted number of resonance frequencies (30 to 100 cycles per second) that could be set up in the propeller blades. A device was accordingly designed for calibrating dynamic-strain gages up to 8 inches in length by subjecting them to uniform sinusoidal strains up to 0.001 at frequencies ranging from 10 to 200 cycles per second. This device is now being constructed.

Strength of riveted joints in aluminum alloy.—The investigation described in Technical Note 585 of the National Advisory Committee for Aeronautics has been extended to joints in which combinations of the following alloys were used: rivets, A17ST, 53SW, 53ST, and 24ST; and sheet, 24ST, 24SRT, and Alclad 24ST.

In accordance with the suggestions of manufacturers, tests have been made to determine whether the results previously obtained on 0.25-inch rivets are applicable to rivets of other sizes. Single shear and double shear tests made so far on rivets ranging from $^3/_{32}$ to $^5/_{16}$ inch in diameter indicate that for practical purposes there is no difference between the results obtained on the various sizes. The driving stress required to form a flat head of a given size was found to increase slightly with the diameter of the rivet, but this tendency was not observed for button heads.

Tests to determine the effect of aging upon the driving stress required to form the head, the shearing strength of rivets of the various alloys, and the mechanical properties of rivet wire are being carried out.

To supply information needed by the industry on riveted joints of the flush type, specifications for joints to be made by manufacturers have been prepared and distributed. Several sets of specimens have been received, and these are now being tested. Other flush riveted specimens are being made at this Bureau.

A set of fixtures has been constructed for driving rivets by means of a pneumatic hammer in a manner which minimizes the personal element in the heading process.

Investigation of fatigue resistance of fabricated structural elements of aircraft.—The fatigue test on the rear upper wing beam of a BF2C–1 airplane was followed by a similar test on the front beam of the same wing cell. The test was carried to failure at a nominal stress amplitude of about 5,700 pounds per square inch, as compared to a nominal stress amplitude of about 8,500 pounds per square inch for the first test. After about

2,900,000 cycles one flange parted with a sharp report at a section where a rib attachment had been riveted to the flange. Several other cracks were found in the same flange, and a large crack was found in the web just outside one terminal attachment. Comparison of the stress history with the endurance curve of similar material indicated a stress concentration factor of about 3.7. This is considerably higher than the stress concentration factor of about 3 derived for the first test, and indicates that the fatigue limit of the fabricated structure may be well below one-third the fatigue limit of the material, perhaps as low as a nominal stress of 4,000 pounds per square inch.

Two complete sets of BF2C–1 wings have been supplied by the Navy Department for the fatigue tests. The wing beams have been removed from these wings, and a method of cutting them has been devised which will give eight wing-beam specimens of sufficiently uniform section for the tests. It is planned to test these specimens at different amplitudes of nominal stress in order to obtain a sufficient number of values of stress against cycles to failure to draw a S–N curve for the fabricated wing beam, which may then be compared with the S–N curve of the wing-beam material. The first of these eight specimens is being set up for test in the fatigue machine.

PART II

ORGANIZATION AND GENERAL ACTIVITIES

ORGANIZATION

The National Advisory Committee for Aeronautics was established by act of Congress approved March 3, 1915 (U. S. Code, title 50, sec. 151). The Committee is composed of fifteen members appointed by the President and serving as such without compensation. The law provides that the members shall include two representatives each from the War and Navy Departments and one each from the Smithsonian Institution, the Weather Bureau, and the National Bureau of Standards, together with not more than eight additional persons "who shall be acquainted with the needs of aeronautical science, either civil or military, or skilled in aeronautical engineering or its allied sciences." One of these eight is a representative of the Bureau of Air Commerce of the Department of Commerce. Under the rules and regulations governing the work of the Committee as approved by the President the Chairman and Vice Chairman of the Committee are elected annually. At the meeting held on October 21, 1937, Dr. Joseph S. Ames was reelected Chairman for the ensuing year and Dr. David W. Taylor was reelected Vice Chairman.

Dr. Joseph S. Ames resigned as Chairman of the Executive Committee in April 1937, a position he had filled continuously since October 9, 1919. At the meeting held on April 22, 1937, Dr. Willis Ray Gregg, Chief of the Weather Bureau, was elected to fill out Dr. Ames' unexpired term as Chairman of the Executive Committee. At the meeting held on October 21, 1937, Dr. Gregg was elected Chairman of the Executive Committee for the ensuing year and Dr. William P. MacCracken Vice Chairman of the Executive Committee. Dr. David W. Taylor had served as Vice Chairman of the Executive Committee since that position was created in 1927. He remains Vice Chairman of the main Committee.

During the past year there was one change in the membership of the main Committee. Dr. Fred D. Fagg, Jr., who had succeeded Honorable Eugene L. Vidal as Director of Air Commerce of the Department of Commerce, was, on April 23, 1937, appointed by the President to succeed Mr. Vidal as a member of the National Advisory Committee for Aeronautics.

The executive offices of the Committee, including its offices of aeronautical intelligence and aeronautical inventions, are located in the Navy Building, Washington, D. C., in close proximity to the air organizations of the Army and Navy.

The office of aeronautical intelligence was established in the early part of 1918 as an integral branch of the Committee's activities. Scientific and technical data on aeronautics secured from all parts of the world are classified, catalogued, and disseminated by this office.

To assist in the collection of current scientific and technical information and data, the Committee maintains a technical assistant in Europe with headquarters at the American Embassy in Paris.

CONSIDERATION OF AERONAUTICAL INVENTIONS

By act of Congress approved July 2, 1926, an Aeronautical Patents and Design Board was established consisting of Assistant Secretaries of the Departments of War, Navy, and Commerce. In accordance with that act as amended by the act approved March 3, 1927, the National Advisory Committee for Aeronautics passes upon the merits of aeronautical inventions and designs submitted to any aeronautical division of the Government and submits reports thereon to the Aeronautical Patents and Design Board. That board is authorized, upon the favorable recommendation of the Committee, to "determine whether the use of the design by the Government is desirable or necessary and evaluate the design and fix its worth to the United States in an amount not to exceed $75,000."

During the past year the inventions section received for consideration 1,475 new submissions. It conducted the necessary correspondence and granted interviews as requested by the inventors. Approximately six percent of the new submissions were received through the Aeronautical Patents and Design Board. In those cases reports on the merits of the submissions were made to that board, and in all other cases replies were submitted directly to the inventors.

AERONAUTICAL RESEARCH IN EDUCATIONAL INSTITUTIONS

In continuation of the plan initiated as a result of recommendation of the Federal Aviation Commission, a special allotment of $25,000 was made available from the Committee's funds during the fiscal year 1937 for aeronautical research in educational institutions. Under this allotment eleven contracts were made during the year with five universities and technical schools, for special investigations and reports on the basis of the probable usefulness and value of the information to aeronautics.

Several of the papers prepared under contracts made the preceding year have been published by the Committee, while others have supplied information of value as a basis for further research either at the Committee's laboratory or elsewhere. The papers received under contracts which have been published by the Committee include one technical report and three technical notes. In addition, one paper has been issued in advance confidential form to American manufacturers.

COOPERATION WITH THE AVIATION INDUSTRY

The Committee, in the preparation of its program of research, makes provision for the requirements of the aviation industry as to problems to be investigated, both in connection with design and operation. The aircraft manufacturers and operators bring their problems to the Committee's attention as they arise, either by correspondence or by personal contacts and informal conferences. Advantage is taken by the Committee of every opportunity to obtain suggestions and recommendations from representatives of the industry as to investigations which are of particular importance to them. When the need arises in connection with any particular problem of the industry it is the policy of the Committee to call a special conference, or, as previously stated, to establish a special subcommittee, including in either case representation from the industry.

Realizing that frequently the value of information is greatly enhanced by its prompt availability, every effort is made to place in the hands of the industry at the earliest possible date the results of researches that are of particular interest to commercial aeronautics. It sometimes appears, in the course of an extensive investigation being conducted by the Committee, that the results so far obtained will be of special interest and value to the aircraft industry if made available immediately. In such cases the Committee issues the information in advance confidential form to American manufacturers and the Government services.

Some of the subjects on which results have been released in this manner during the past year are the prevention of ice formation on propellers; the characteristics of related forward camber airfoils, from tests in the variable-density wind tunnel; the characteristics of tapered wings having N. A. C. A. mean lines; the characteristics of tandem air propellers, as investigated by Stanford University under contract with the Committee; wing-fuselage interference, including in the first report a comparison of conventional and airfoil-type fuselage combinations, and in the second report the characteristics of thirty combinations, from tests in the variable-density wind tunnel; transparent plastics for use on aircraft, as investigated by the National Bureau of Standards for the Committee; tricycle-type landing gears, including three phases of the subject—first, accelerations in landing, second, factors affecting the geometrical arrangement; and third, the stability of castering wheels; and the characteristics of tapered wings with ordinary ailerons and partial-span split flaps, as determined in wind-tunnel investigation.

Annual research conference.—As an important aid in keeping in close contact with the problems and needs of the aviation industry, the Committee holds each May at its laboratories at Langley Field an aircraft engineering research conference with representatives of aircraft manufacturers and operators. This conference was initiated in 1926, and has two principal purposes, as follows: First, to enable representatives of the industry to obtain first-hand information on the Committee's research facilities and the results obtained in its investigations; and, second, to afford them an opportunity to present to the Committee their suggestions for investigations to be included in the Committee's research program.

Owing to the large number of those who desired to attend, the conference for the past two years has been held on two days, the same program of discussions and demonstrations being followed both days. The dates of the 1937 conference were May 18 and 20.

Acting under authorization of Dr. Joseph S. Ames, Chairman of the National Advisory Committee for Aeronautics, who was prevented by illness from being present, Honorable Edward P. Warner, a member of the Committee and Chairman of the Committee on Aerodynamics, served as Chairman of the conference on May 18; and on May 20 Dr. Willis Ray Gregg, Chairman of the Executive Committee of the National Advisory Committee for Aeronautics, was Chairman. The Committee was represented on both days by officers and members, and on May 18 also by its Committees on Aerodynamics and Power Plants for Aircraft, and on the 20th by its Committee on Aircraft Structures and Materials and Subcommittee on Structural Loads and Methods of Structural Analysis.

At the morning session each day the principal investigations under way at the laboratory, both in aero-

dynamics and power plants, were explained by the engineers in charge of the work, and charts were exhibited showing some of the results obtained. The guests were then conducted on a tour of inspection of the laboratory and the research equipment was shown in operation.

In the afternoon six simultaneous conferences were held for the discussion of six different subjects, namely, airplane performance and design characteristics, aerodynamic efficiency and interference, cowling and cooling research, aircraft-engine research, seaplanes, and rotorplanes. At these conferences the results of the Committee's researches were presented in further detail, and suggestions were submitted by the representatives of the industry for problems to be added to the Committee's program. Each of these suggestions, according to its nature, was referred to the Committee on Aerodynamics, the Committee on Power Plants for Aircraft, or the Subcommittee on Structural Loads and Methods of Structural Analysis and was considered by that committee in the preparation of the research program being carried on under its cognizance.

SUBCOMMITTEES

The Advisory Committee has organized four main standing technical committees, with subcommittees, for the purpose of supervising its work in their respective fields. The four main technical Committees on Aerodynamics, Power Plants for Aircraft, Aircraft Materials, and Aircraft Structures and their subcommittees supervise and direct the aeronautical research conducted by the Advisory Committee and coordinate the investigations conducted by other agencies.

As previously stated, during the past year there has been a major change in the organization of the Committee's standing technical committees. The Committee on Aircraft Structures and Materials, which was one of the three principal technical committees, and two of its subcommittees, the Subcommittee on Structural Loads and Methods of Structural Analysis and the Subcommittee on Research Program on Monocoque Design, were discharged, and two new standing committees, the Committee on Aircraft Materials and the Committee on Aircraft Structures, were established, each with a status coordinate with that of the Committee on Aerodynamics and the Committee on Power Plants for Aircraft. The Subcommittee on Metals Used in Aircraft and the Subcommittee on Miscellaneous Materials and Accessories were retained as subcommittees of the new Committee on Aircraft Materials.

The work of the standing technical committees and subcommittees has been described in part I.

The organization of the committees and of the standing subcommittees is as follows:

COMMITTEE ON AERODYNAMICS

Hon. Edward P. Warner, Chairman.

Dr. George W. Lewis, National Advisory Committee for Aeronautics, Vice Chairman.

Maj. H. Z. Bogert, Air Corps, United States Army, Matériel Division, Wright Field.

Dr. L. J. Briggs, National Bureau of Standards.

Theophile dePort, Matériel Division, Army Air Corps, Wright Field.

Lt. Comdr. W. S. Diehl, United States Navy.

Dr. H. L. Dryden, National Bureau of Standards.

Lt. Col. O. P. Echols, Air Corps, United States Army, Matériel Division, Wright Field.

Richard C. Gazley, Bureau of Air Commerce, Department of Commerce.

Lt. Comdr. L. M. Grant, United States Navy.

Dr. Willis Ray Gregg, United States Weather Bureau.

Lawrence V. Kerber, Bureau of Air Commerce, Department of Commerce.

Delbert M. Little, United States Weather Bureau.

Elton W. Miller, National Advisory Committee for Aeronautics.

Comdr. F. W. Pennoyer, Jr., United States Navy.

H. J. E. Reid, National Advisory Committee for Aeronautics.

Dr. David W. Taylor.

Dr. A. F. Zahm, Division of Aeronautics, Library of Congress.

SUBCOMMITTEE ON AIRSHIPS

Hon. Edward P. Warner, Chairman.

Starr Truscott, National Advisory Committee for Aeronautics, Vice Chairman.

Dr. Karl Arnstein, Goodyear-Zeppelin Corporation.

Maj. H. Z. Bogert, Air Corps, United States Army, Matériel Division, Wright Field.

Commander Garland Fulton, United States Navy.

Dr. George W. Lewis, National Advisory Committee for Aeronautics (ex officio member).

Ralph H. Upson, Ann Arbor, Mich.

SUBCOMMITTEE ON METEOROLOGICAL PROBLEMS

Dr. Willis Ray Gregg, United States Weather Bureau, Chairman.

Dr. W. J. Humphreys, United States Weather Bureau.

Dr. J. C. Hunsaker, Massachusetts Institute of Technology.

Dr. George W. Lewis, National Advisory Committee for Aeronautics (ex officio member).

Delbert M. Little, United States Weather Bureau.

Dr. Charles F. Marvin.

Lt. Comdr. F. W. Reichelderfer, United States Navy, Naval Air Station, Lakehurst.

Dr. C. G. Rossby, Massachusetts Institute of Technology.

Maj. B. J. Sherry, United States Army, Signal Corps, War Department.

Eugene Sibley, Bureau of Air Commerce, Department of Commerce.

SUBCOMMITTEE ON SEAPLANES

Capt. H. C. Richardson, United States Navy, Chairman.

Maj. H. Z. Bogert, Air Corps, United States Army, Matériel Division, Wright Field.

Theophile dePort, Matériel Division, Army Air Corps, Wright Field.

Lt. Comdr. W. S. Diehl, United States Navy.

Richard C. Gazley, Bureau of Air Commerce, Department of Commerce.

Jack T. Gray, Bureau of Air Commerce, Department of Commerce.

Dr. George W. Lewis, National Advisory Committee for Aeronautics (ex officio member).

Lt. Comdr. A. O. Rule, United States Navy.

Starr Truscott, National Advisory Committee for Aeronautics.

COMMITTEE ON POWER PLANTS FOR AIRCRAFT

Dr. William P. MacCracken, Chairman.

Dr. George W. Lewis, National Advisory Committee for Aeronautics, Vice Chairman.

Lt. Comdr. Rico Botta, United States Navy.

Dr. H. C. Dickinson, National Bureau of Standards.

John H. Geisse, Bureau of Air Commerce, Department of Commerce.

Carlton Kemper, National Advisory Committee for Aeronautics.

Gaylord W. Newton, Bureau of Air Commerce, Department of Commerce.

Maj. E. R. Page, Air Corps, United States Army, Matériel Division, Wright Field.

Prof. C. Fayette Taylor, Massachusetts Institute of Technology.

SUBCOMMITTEE ON AIRCRAFT FUELS AND LUBRICANTS

Dr. H. C. Dickinson, National Bureau of Standards, Chairman.

Lt. Comdr. Rico Botta, United States Navy.

Dr. O. C. Bridgeman, National Bureau of Standards.

Lt. Comdr. James V. Carney, United States Navy.

H. K. Cummings, National Bureau of Standards.

L. S. Hobbs, The Pratt and Whitney Aircraft Company.

Robert V. Kerley, Matériel Division, Army Air Corps, Wright Field.

Dr. George W. Lewis, National Advisory Committee for Aeronautics (ex officio member).

Gaylord W. Newton, Bureau of Air Commerce, Department of Commerce.

Arthur Nutt, Wright Aeronautical Corporation.

Maj. E. R. Page, Air Corps, United States Army, Matériel Division, Wright Field.

Addison M. Rothrock, National Advisory Committee for Aeronautics.

COMMITTEE ON AIRCRAFT MATERIALS

Dr. L. J. Briggs, National Bureau of Standards, Chairman.

Prof. H. L. Whittemore, National Bureau of Standards, Vice Chairman.

Maj. H. Z. Bogert, Air Corps, United States Army, Matériel Division, Wright Field.

S. K. Colby, Aluminum Co. of America.

Lt. Comdr. C. F. Cotton, United States Navy.

Edgar H. Dix, Jr., American Magnesium Corporation.

Warren E. Emley, National Bureau of Standards.

Comdr. Garland Fulton, United States Navy.

Richard C. Gazley, Bureau of Air Commerce, Department of Commerce.

Jack T. Gray, Bureau of Air Commerce, Department of Commerce.

C. H. Helms, National Advisory Committee for Aeronautics.

J. B. Johnson, Matériel Division, Army Air Corps, Wright Field.

Dr. George W. Lewis, National Advisory Committee for Aeronautics (ex officio member).

H. S. Rawdon, National Bureau of Standards.

E. C. Smith, Republic Steel Corporation.

Paul F. Voigt, Jr., Carnegie-Illinois Steel Corporation.

Hon. Edward P. Warner.

SUBCOMMITTEE ON METALS USED IN AIRCRAFT

H. S. Rawdon, National Bureau of Standards, Chairman.

E. H. Dix, Jr., American Magnesium Corporation.

Comdr. Garland Fulton, United States Navy.

J. B. Johnson, Matériel Division, Army Air Corps, Wright Field.

Dr. George W. Lewis, National Advisory Committee for Aeronautics (ex officio member).

E. C. Smith, Republic Steel Corporation.

John Vitol, Bureau of Air Commerce, Department of Commerce.

Prof. H. L. Whittemore, National Bureau of Standards.

SUBCOMMITTEE ON MISCELLANEOUS MATERIALS AND ACCESSORIES

Warren E. Emley, National Bureau of Standards, Chairman.

C. J. Cleary, Matériel Division, Army Air Corps, Wright Field.

John Easton, Bureau of Air Commerce, Department of Commerce.

C. H. Helms, National Advisory Committee for Aeronautics.

E. F. Hickson, National Bureau of Standards.

Dr. George W. Lewis, National Advisory Committee for Aeronautics (ex officio member).

J. E. Sullivan, Bureau of Aeronautics, Navy Department.

G. W. Trayer, Forest Service, Department of Agriculture.

COMMITTEE ON AIRCRAFT STRUCTURES

Dr. L. J. Briggs, National Bureau of Standards, Chairman.

Richard C. Gazley, Bureau of Air Commerce, Department of Commerce.

Lt. Comdr. L. M. Grant, United States Navy.

Maj. C. F. Greene, Air Corps, United States Army, Matériel Division, Wright Field.

Capt. Paul H. Kemmer, Air Corps, United States Army, Matériel Division, Wright Field.

Dr. George W. Lewis, National Advisory Committee for Aeronautics (ex officio member).

Eugene E. Lundquist, National Advisory Committee for Aeronautics.

Lt. Comdr. R. D. MacCart, United States Navy.

Prof. Joseph S. Newell, Massachusetts Institute of Technology.

Dr. Walter Ramberg, National Bureau of Standards.

Richard V. Rhode, National Advisory Committee for Aeronautics.

Edward I. Ryder, Bureau of Air Commerce, Department of Commerce.

R. L. Templin, Aluminum Company of America.

Dr. L. B. Tuckerman, National Bureau of Standards.

Hon. Edward P. Warner.

COMMITTEE ON AIRCRAFT ACCIDENTS

Hon. Edward P. Warner, Chairman.

Lt. J. F. Greenslade, United States Navy.

Maj. E. V. Harbeck, Jr., Air Corps, United States Army.

J. W. Lankford, Bureau of Air Commerce, Department of Commerce.

Dr. George W. Lewis, National Advisory Committee for Aeronautics.

Lt. Comdr. A. O. Rule, United States Navy.

J. T. Shumate, Bureau of Air Commerce, Department of Commerce.

Maj. Lowell H. Smith, Air Corps, United States Army.

COMMITTEE ON AERONAUTICAL INVENTIONS AND DESIGNS

Dr. L. J. Briggs, National Bureau of Standards, Chairman.

Dr. Willis Ray Gregg, United States Weather Bureau.

Capt. S. M. Kraus, United States Navy.

Brig. Gen. A. W. Robins, Air Corps, United States Army. Matériel Division, Wright Field.

Dr. David W. Taylor.

John F. Victory, Secretary.

COMMITTEE ON PUBLICATIONS AND INTELLIGENCE

Dr. Joseph S. Ames, Chairman.

Dr. Willis Ray Gregg, United States Weather Bureau, Vice Chairman.

Miss M. M. Muller, Secretary.

COMMITTEE ON PERSONNEL, BUILDINGS, AND EQUIPMENT

Dr. Joseph S. Ames, Chairman.

Dr. David W. Taylor, Vice Chairman.

Dr. Willis Ray Gregg, United States Weather Bureau.

John F. Victory, Secretary.

TECHNICAL PUBLICATIONS OF THE COMMITTEE

The Committee has four series of publications, namely technical reports, technical notes, technical memorandums, and aircraft circulars.

The technical reports present the results of fundamental research in aeronautics. The technical notes are mimeographed and present the results of short research investigations and the results of studies of specific detail problems which form parts of long investigations. The technical memorandums are mimeographed and contain translations and reproductions of important foreign aeronautical articles. The aircraft circulars are mimeographed and contain descriptions of new types of foreign aircraft.

The following are lists of the publications issued:

LIST OF TECHNICAL REPORTS ISSUED DURING THE PAST YEAR

No.

577. Prechamber Compression-Ignition Engine Performance. By Charles S. Moore and John H. Collins, Jr., N. A. C. A.

578. Flight Measurements of the Dynamic Longitudinal Stability of Several Airplanes and a Correlation of the Measurements with Pilots' Observations of Handling Characteristics. By Hartley A. Soulé, N. A. C. A.

579. A Study of the Two-Control Operation of an Airplane. By Robert T. Jones, N. A. C. A.

580. Heat Transfer to Fuel Sprays Injected into Heated Gases. By Robert F. Selden and Robert C. Spencer, N. A. C. A.

581. Measurements of Intensity and Scale of Wind-Tunnel Turbulence and Their Relation to the Critical Reynolds Number of Spheres. By Hugh L. Dryden, G. B. Schubauer, W. C. Mock, Jr., and H. K. Skramstad, National Bureau of Standards.

582. A Theory for Primary Failure of Straight Centrally Loaded Columns. By Eugene E. Lundquist and Claude M. Fligg, N. A. C. A.

583. The Rolling Friction of Several Airplane Wheels and Tires and the Effect of Rolling Friction on Take-Off. By J. W. Wetmore, N. A. C. A.

584. Strength of Welded Aircraft Joints. By W. C. Brueggeman, National Bureau of Standards.

585. Span Load Distribution for Tapered Wings with Partial-Span Flaps. By H. A. Pearson, N. A. C. A.

586. Airfoil Section Characteristics as Affected by Variations of the Reynolds Number. By Eastman N. Jacobs and Albert Sherman, N. A. C. A.

587. Blower Cooling of Finned Cylinders. By Oscar W. Schey and Herman H. Ellerbrock, Jr., N. A. C. A.

588. Fuel Spray and Flame Formation in a Compression-Ignition Engine Employing Air Flow. By A. M. Rothrock and C. D. Waldron, N. A. C. A.

589. An Analysis of Lateral Stability in Power-Off Flight with Charts for Use in Design. By Charles H. Zimmerman, N. A. C. A.

590. Pressure-Distribution Measurements on an O–2H Airplane in Flight. By H. A. Pearson, N. A. C. A.

591. An Analytical and Experimental Study of the Effect of Periodic Blade Twist on the Thrust, Torque, and Flapping Motion of an Autogiro Rotor. By John B. Wheatley, N. A. C. A.

592. Full-Scale Tests of N. A. C. A. Cowlings. By Theodore Theodorsen, M. J. Brevoort, and George W. Stickle, N. A. C. A.

593. Cooling of Airplane Engines at Low Air Speeds. By Theodore Theodorsen, M. J. Brevoort, and George W. Stickle, N. A. C. A.

594. Characteristics of Six Propellers Including the High-Speed Range. By Theodore Theodorsen, George W. Stickle, and M. J. Brevoort, N. A. C. A.

595. Full-Scale Tests of a New Type N. A. C. A. Nose-Slot Cowling. By Theodore Theodorsen, M. J. Brevoort, George W. Stickle, and M. N. Gough, N. A. C. A.

596. Cooling Tests of a Single-Row Radial Engine with Several N. A. C. A. Cowlings. By M. J. Brevoort, George W. Stickle, and Herman H. Ellerbrock, Jr., N. A. C. A.

597. Air Propellers in Yaw. By E. P. Lesley, George F. Worley, and Stanley Moy, Stanford University.

598. Alternating-Current Equipment for the Measurement of Fluctuations of Air Speed in Turbulent Flow. By W. C. Mock, Jr., National Bureau of Standards.

599. Flight Tests of the Drag and Torque of the Propeller in Terminal-Velocity Dives. By Richard V. Rhode and Henry A. Pearson, N. A. C. A.

600. An Analysis of the Factors That Determine the Periodic Twist of an Autogiro Rotor Blade, with a Comparison of Predicted and Measured Results. By John B. Wheatley, N. A. C. A.

601. Torsion Tests of Tubes. By Ambrose H. Stang, Walter Ramberg, and Goldie Back, National Bureau of Standards.

602. Wind-Tunnel and Flight Tests of Slot-Lip Ailerons. By Joseph A. Shortal, N. A. C. A.

603. Wind-Tunnel Investigation of Wings with Ordinary Ailerons and Full-Span External-Airfoil Flaps. By Robert C. Platt and Joseph A. Shortal, N. A. C. A.

604. Pressure-Distribution Measurements at Large Angles of Pitch on Fins of Different Span-Chord Ratio on a 1/40-Scale Model of the U. S. Airship "Akron." By James G. McHugh, N. A. C. A.

605. Résumé and Analysis of N. A. C. A. Lateral Control Research. By Fred E. Weick and Robert T. Jones, N. A. C. A.
606. Electrical Thermometers for Aircraft. By John B. Peterson and S. H. J. Womack, National Bureau of Standards.
607. Spinning Characteristics of the XN2Y–1 Airplane Obtained from the Spinning Balance and Compared with Results from the Spinning Tunnel and from Flight Tests. By M. J. Bamber and R. O. House, N. A. C. A.
608. Stress Analysis of Beams with Shear Deformation of the Flanges. By Paul Kuhn, N. A. C. A.
609. Experimental Investigation of Wind-Tunnel Interference on the Downwash behind an Airfoil. By Abe Silverstein and S. Katzoff, N. A. C. A.
610. Tests of Related Forward-Camber Airfoils in the Variable-Density Wind Tunnel. By Eastman N. Jacobs, Robert M. Pinkerton, and Harry Greenberg, N. A. C. A.
611. Wind-Tunnel Investigation of Tapered Wings with Ordinary Ailerons and Partial-Span Split Flaps. By Carl J. Wenzinger, N. A. C. A.

LIST OF TECHNICAL NOTES ISSUED DURING THE PAST YEAR

No.

582. Analysis and Model Tests of Autogiro Jump Take-Off. By John B. Wheatley and Carlton Bioletti, N. A. C. A.
583. Mixture Distribution in a Single-Row Radial Engine. By Harold C. Gerrish and Fred Voss, N. A. C. A.
584. Effect of Several Factors on Cooling of a Radial Engine in Flight. By Oscar W. Schey and Benjamin Pinkel, N. A. C. A.
585. Mechanical Properties of Aluminum-Alloy Rivets. By Wm. C. Brueggeman, National Bureau of Standards.
586. The Reduction of Aileron Operating Force by Differential Linkage. By Robert T. Jones and Albert I. Nerken, N. A. C. A.
587. The Forces and Moments on Airplane Engine Mounts. By Philip Donely, N. A. C. A.
588. Strain Measurements on Small Duralumin Box Beams in Bending. By Paul Kuhn, N. A. C. A.
589. Theoretical Span Loading and Moments of Tapered Wings Produced by Aileron Deflection. By H. A. Pearson, N. A. C. A.
590. Hydrodynamic Tests in the N. A. C. A. Tank of a Model of the Hull of the Short Calcutta Flying Boat. By Kenneth E. Ward, N. A. C. A.
591. Full-Scale Span Load Distribution on a Tapered Wing with Split Flaps of Various Spans. By John F. Parsons and Abe Silverstein, N. A. C. A.
592. A Study of the Factors Affecting the Range of Airplanes. By David Biermann, N. A. C. A.
593. Pressure Drop in Tubing in Aircraft Instrument Installations. By W. A. Wildhack, National Bureau of Standards.
594. Tank Tests of Two Models of Flying-Boat Hulls to Determine the Effect of Ventilating the Step. By John R. Dawson, N. A. C. A.
595. Bending Tests of Circular Cylinders of Corrugated Aluminum-Alloy Sheet. By Alfred S. Niles, John C. Buckwalter, and Warren D. Reed, Stanford University.
596. Full-Scale Wind-Tunnel and Flight Tests of a Fairchild 22 Airplane Equipped with a Zap Flap and Zap Ailerons. By C. H. Dearborn and H. A. Soulé, N. A. C. A.
597. Notes on the Calculation of the Minimum Horizontal Tail Surface for Airplanes Equipped with Wing Flaps. By Hartley A. Soulé, N. A. C. A.
598. Wind-Tunnel Tests of a Clark Y Wing with "Maxwell" Leading-Edge Slots. By William E. Gauvain, N. A. C. A.
599. Charts Expressing the Time, Velocity, and Altitude Relations for an Airplane Diving in a Standard Atmosphere. By H. A. Pearson, N. A. C. A.
600. Discharge Characteristics of a Double Injection-Valve Single-Pump Injection System. By Dana W. Lee and E. T. Marsh, N. A. C. A.
601. The Lateral Instability of Deep Rectangular Beams. By C. Dumont and H. N. Hill, Aluminum Company of America.
602. Heat Transfer from Cylinders Having Closely Spaced Fins. By Arnold E. Biermann, N. A. C. A.
603. A Preliminary Study of Flame Propagation in a Spark-Ignition Engine. By A. M. Rothrock and R. C. Spencer, N. A. C. A.
604. Full-Scale Wind-Tunnel and Flight Tests of a Fairchild 22 Airplane Equipped with External-Airfoil Flaps. By Warren D. Reed and William C. Clay, N. A. C. A.
605. Noise from Propellers with Symmetrical Sections at Zero Blade Angle. By A. F. Deming, N. A. C. A.
606. Empirical Corrections to the Span Load Distribution at the Tip. By H. A. Pearson, N. A. C. A.
607. The Behavior of Thin-Wall Monocoque Cylinders Under Torsional Vibration. By Robert E. Pekelsma, University of Michigan.
608. Free-Spinning Wind-Tunnel Tests of a Low-Wing Monoplane with Systematic Changes in Wings and Tails. I—Basic Loading Condition. By Oscar Seidman and A. I. Neihouse, N. A. C. A.
609. Considerations Affecting the Additional Weight Required in Mass Balance of Ailerons. By W. S. Diehl, Bureau of Aeronautics, Navy Department.
610. Effect of Air-Entry Angle on Performance of a 2-Stroke-Cycle Compression-Ignition Engine. By Sherod L. Earle and Francis J. Dutee, N. A. C. A.
611. The Sonic Altimeter for Aircraft. By C. S. Draper, Massachusetts Institute of Technology.
612. Spinning Characteristics of Wings. III—A Rectangular and a Tapered Clark Y Monoplane Wing with Rounded Tips. By M. J. Bamber and R. O. House, N. A. C. A.
613. The Effect of Curvature on the Transition from Laminar to Turbulent Boundary Layer. By Milton Clauser and Francis Clauser, California Institute of Technology.
614. Fuselage-Drag Tests in the Variable-Density Wind Tunnel: Streamline Bodies of Revolution, Fineness Ratio of 5. By Ira H. Abbott, N. A. C. A.
615. Motion of the Two-Control Airplane in Rectilinear Flight after Initial Disturbances with Introduction of Controls Following an Exponential Law. By Alexander Klemin, New York University.

LIST OF TECHNICAL MEMORANDUMS ISSUED DURING THE PAST YEAR

No.

805. General Considerations on the Flow of Compressible Fluids. By L. Prandtl. Paper presented at Volta meeting in Italy, September 30 to October 6, 1935.
806. The Question of Spontaneous Wing Oscillations (Determination of Critical Velocity through Flight-Oscillation Tests). By B. v. Schlippe. From Luftfahrtforschung, February 20, 1936.
807. Torsion and Buckling of Open Sections. By Herbert Wagner. From the 25th anniversary number of the Technische Hochschule, Danzig 1904–1929.

808. High-Speed Wind Tunnels. By J. Ackeret. Paper presented at the fifth convention of the Volta Congress, Italy, September 30 to October 6, 1935.
809. Tests for the Determination of the Stress Condition in Tension Fields. By R. Lahde and H. Wagner. From Luftfahrtforschung, August 20, 1936.
810. Impact of a Vee-Type Seaplane on Water with Reference to Elasticity. By F. Weinig. From Luftfahrtforschung, May 20, 1936.
811. The Impact on Floats or Hulls During Landing as Affected by Bottom Width. By E. Mewes. From Luftfahrtforschung, May 20, 1936.
812. The Horsepower of Aircraft Engines and Their Maximum Frontal Area. By Michel Precoul. From L'Aéronautique, No. 207, August 1936.
813. The Cetene Scale and the Induction Period Preceding the Spontaneous Ignition of Diesel Fuels in Bombs. By M. N. Michailova and M. B. Neumann. From Comptes Rendus (Doklady) de l'Academie des Sciences de l'URSS, Vol. II (XI), No. 4 (90), 1936.
814. Experimental Studies of the Effective Width of Buckled Sheets. By R. Lahde and H. Wagner. From Luftfahrtforschung, July 20, 1936.
815. Automatic Stabilization. By Fr. Haus. From L'Aéronautique, March 1936.
816. The Gyroplane—Its Principles and Its Possibilities. By Louis Breguet. From Journees Techniques Internationales de l'Aéronautique, November 23–27, 1936.
817. The Stress Distribution in Shell Bodies and Wings as an Equilibrium Problem. By H. Wagner. From Luftfahrtforschung, September 20, 1936.
818. Valve-Spring Surge. By Willy Marti. Federal Polytechnic Institute of Zurich. 1935.
819. Experimental Apparatus for the Study of Propellers. By M. Panetti. From Experimental reports by the Aeronautical Laboratory of the Royal Engineering Institute of Turin, series 1.
820. Some Experiments on the Slipstream Effect. By C. Ferrari. From Experimental reports by the Aeronautical Laboratory of the Royal Engineering Institute of Turin, series 2.
821. On the Actual Loads on Airplane Landing Gears. By S. Shiskin. From Report No. 269, of the Central Aero-Hydrodynamical Institute, Moscow, 1936.
822. Turbulent Boundary Layer of an Airfoil. By K. Fediaevsky. From Report No. 282, of the Central Aero-Hydrodynamical Institute, Moscow, 1936.
823. Experimental Investigation of the Problem of Surface Roughness. By H. Schlichting. From Ingenieur-Archiv, February 1936.
824. The Photoelastic Investigation of Three-Dimensional Stress and Strain Conditions. By G. Oppel. From Forschung auf dem Gebiete des Ingenieurwesens, September–October 1936.
825. The Source of Propeller Noise. By W. Ernsthausen. From Luftfahrtforschung, December 20, 1936.
826. The Scale Effect in Towing Tests with Airplane-Float Systems. By Rudolph Schmidt. From Luftfahrtforschung, July 20, 1936.
827. Helicopter Problems. By H. G. Küssner. From Luftfahrtforschung, January 20, 1937.
828. Ground Effect—Theory and Practice. By E. Pistolesi. From Pubblicazioni della R. Scuola d'Ingegneria di Pisa, series 6, July 1935.
829. Method of Curved Models and Its Application to the Study of Curvilinear Flight of Airships. Part I. By G. A. Gourjienko. From Central Aero-Hydrodynamical Institute, Moscow, Report No. 182, 1934.
830. Method of Curved Models and Its Application to the Study of Curvilinear Flight of Airships. Part II. By G. A. Gourjienko. From Central Aero-Hydrodynamical Institute, Moscow, Report No. 182, 1934.
831. Contributions to the Theory of Incomplete Tension Bay. By E. Schapitz. From Luftfarhrtforschung, March 20, 1937.
832. The Critical Velocity of a Body Towed by a Cable from an Airplane. By C. Koning and T. P. DeHaas. From Rijks-Studiedienst voor de Luchtvaart, Amsterdam, Report A 367.
833. The Apparent Width of the Plate in Compression. By Karl Marguerre. From Luftfahrtforschung, March 20, 1937.
834. The Stability of Orthotropic Elliptic Cylinders in Pure Bending. By O. S. Heck. From Luftfahrtforschung, March 20, 1937.
835. Pressure Distribution on a Wing Section with Slotted Flap in Free Flight Tests. By Georg Kiel. From Luftfahrtforschung, February 20, 1937.
836. The Ground Effect on Lifting Propellers. By A. Betz. From Zeitschrift für angewandte Mathematik und Mechanik, April 1937.
837. Charts for Checking the Stability of Plane Systems of Rods. By K. Borkmann. From Luftfarhrtforschung, February 20, 1937.
838. The Strength of Shell Bodies—Theory and Practice. By H. Ebner. From Luftfahrtforschung, March 20, 1937.

LIST OF AIRCRAFT CIRCULARS ISSUED DURING THE PAST YEAR

No.

205. The Hafner A.R.III Gyroplane (British). From Flight, February 18, 1937.
206. Armstrong Whitworth 27 "Ensign" Commercial Airplane (British). An All-Metal High-Wing Monoplane. From Flight, January 7, and April 1, 1937.
207. Baynes Bee Light Airplane (British). A Two-Seat High-Wing Monoplane. From The Aeroplane, March 17, 1937; and Flight, March 11, and March 18, 1937.
208. The Airspeed "Oxford" Training Airplane (British). A Two-Engine Cantilever Monoplane. From The Aeroplane, June 23, and July 28, 1937; and Flight, April 29, and July 1, 1937.

FINANCIAL REPORT

The general appropriation for the National Advisory Committee for Aeronautics for the fiscal year 1937, as contained in the Independent Offices Appropriation Act approved March 19, 1936, was $1,158,850. A supplemental appropriation of $1,367,000 was made available in the First Deficiency Appropriation Act, fiscal year 1936, approved June 22, 1936, for the same purposes specified in the Committee's regular appropriation act for 1936, to continue available until June 30, 1937, and providing for expenditure of not to exceed $1,100,000 for the construction and equipment of an additional wind tunnel (19-foot pressure

tunnel), and not to exceed $267,000 for increasing the length of the seaplane model testing tank and for additional equipment therefor. The total amount available for general expenditure during the fiscal year 1937, therefore, was $2,525,850. The amount expended and obligated was $2,337,638, itemized as follows:

Personal services	$928,337
Supplies and materials	71,788
Communication service	3,053
Travel expenses	14,464
Transportation of things	2,742
Furnishing of electricity	36,258
Repairs and alterations	4,639
Special investigations and reports	80,744
Equipment	381,519
Structures	814,094
Expended and obligated	2,337,638
Unobligated balance	188,212
Total, general appropriation	2,525,850

The appropriation for printing and binding for 1937 was $18,700, of which $18,679 was expended.

The sum of $19,689 was received during the fiscal year 1937 as special deposits to cover the estimated cost of scientific services to be furnished private parties. The total cost of investigations completed for private parties during the fiscal year, amounting to $12,073, was deposited in the Treasury to the credit of Miscellaneous Receipts.

The amount of the regular appropriation for the fiscal year 1938 is $1,259,850, as provided in the Independent Offices Appropriation Act approved June 28, 1937. A supplemental appropriation of $453,000 was made available in the Second Deficiency Appropriation Act, fiscal year 1937, approved May 28, 1937, for the same purposes specified in the Committee's regular appropriation act for 1937, to continue available until June 30, 1938, and providing that $353,000 shall be available only for the construction and equipment of facilities and for the purchase of an airplane of the light metal private type; and providing further, that the unexpended balance of the supplemental appropriation of $1,367,000 for 1937 be continued available until June 30, 1938. That unexpended balance was $186,968. The total amount available for general expenditure during the fiscal year 1938, therefore, is $1,899,818. In addition, the amount of $21,000 was appropriated for printing and binding for the fiscal year 1938.

An allotment of $7,350 was received from the State Department for payments during the fiscal year 1937 to employees stationed abroad, on account of exchange losses due to appreciation of foreign currencies, and of this amount $2,866 was paid during the fiscal year to employees of the Committee stationed in the Paris Office, leaving a balance of $4,484 turned back into the Treasury.

Of the allotment of $2,000 for participation in the Greater Texas and Pan American Exposition, which opened at Dallas, Texas, June 12, 1937, the amount of $404 was expended and obligated as at June 30, 1937.

CONCLUDING STATEMENT

The greatly extended use of aircraft for both military and civil purposes has been reflected in an increased activity on the part of progressive nations in extending their aeronautical research facilities. The demands made upon the Committee by the War, Navy, and Commerce Departments for new information are increasing in number and in difficulty with the increase in the speed and size of aircraft. The Committee fully recognizes its enlarged responsibility to make provision not only to take care of research needs arising from current problems, but also to look well into the future and to anticipate the needs that will arise as a result of the trend toward the construction of much larger landplanes and seaplanes.

The Committee is grateful to the President and to the Congress for the earnest consideration and support that have been given to its needs, and urges the continued support of this most fundamental activity of the Federal Government in connection with aeronautics.

Respectfully submitted,

NATIONAL ADVISORY COMMITTEE
FOR AERONAUTICS,
JOSEPH S. AMES, *Chairman.*

REPORT No. 577

PRECHAMBER COMPRESSION-IGNITION ENGINE PERFORMANCE

By Charles S. Moore and John H. Collins, Jr.

SUMMARY

Single-cylinder compression-ignition engine tests were made to investigate the performance characteristics of the prechamber type of cylinder head. Certain fundamental variables influencing engine performance—clearance distribution, size, shape, and direction of the passage connecting the cylinder and prechamber, shape of prechamber, cylinder clearance, compression ratio, and boosting—were independently tested. Results of motoring and of power tests, including several typical indicator cards, are presented.

Results of the investigation indicate that for maximum performance of this 5- by 7-inch engine at speeds up to 1,500 r. p. m., the compression ratio should be between 15.5 and 17.5 and the prechamber should be as large as possible, disk-shaped, and connected to the cylinder by a single passage. A strong rotational air flow should be created in the prechamber by introducing the passage tangentially. Flaring should be employed on the cylinder end of the passage to spread the issuing gases over the flat piston crown. At 1,500 r. p. m., the injection system should deliver in approximately 20 crankshaft degrees the full-load fuel in the shape of a narrow conical spray with high penetration. This spray should be directed across the disk chamber toward the mouth of the connecting passage. Boosting the inlet-air pressure effectively raises the power output. As the prechamber is inaccessible for scavenging and the lack of clearance under the valves prohibits the use of proper valve timing, the prechamber type of cylinder head is judged to be incapable of developing the high specific output required of aircraft engines.

INTRODUCTION

The general problem in the development of aircraft compression-ignition engines is to obtain complete and properly timed combustion in the engine cylinder at high crankshaft speeds. A prime requirement for complete combustion is that the fuel charge be intimately mixed with the air. Furthermore, combustion must be so controlled that it is completed early in the power stroke without combustion shock. In order to accomplish these requirements, numerous chamber designs and fuel-spray arrangements have been tried by different designers with varying degrees of success. Each has its own relative merits and its own field of usefulness.

The prechamber, which may be classed as an auxiliary-chamber type, has been extensively used. Its popularity is no doubt due to the simplicity of the fuel-spray arrangement which may be used and to the variety of means which may be employed to control the mixing and combustion of the fuel and air. The auxiliary chamber may function as an air reservoir to meter the air to the cylinder, or it may serve as a mixing chamber in which the fuel charge is prepared for combustion before it passes into the cylinder. When combustion starts and is partly completed in the auxiliary chamber, this type becomes the usual precombustion chamber.

For designs in which the auxiliary chamber acts as a prechamber, or mixing chamber, the connecting passage and chamber have two functions to perform: First, the forced air flow is controlled by the size, shape, and direction of the connecting passage, these factors being selected to give the best mixing in the chamber with the least loss by resistance to the flow; and second, the mixing of the fuel and air is controlled by the size, shape, and position of the prechamber, these factors being designed to conserve and utilize the forced air flow as a residual flow. After combustion starts, the passage further functions to meter and direct the partly burned, overrich mixture into the cylinder in such a way that all the cylinder air is reached by the unburned fuel and at such a rate as to control the pressures developed in the cylinder.

As a part of a general research on aircraft-type compression-ignition engines, the Committee has been investigating the performance to be obtained with the prechamber type of cylinder head. Most of the work herein reported has been published as the several investigations were completed; the purpose of the subject report is to include the final and unreported work of the investigation and to combine all the more important results into a single publication.

APPARATUS AND TEST PROCEDURE

TEST ENGINE

The single-cylinder-engine test unit shown in figure 1 was used in this investigation. This figure shows the assembly of equipment at the time the investigation was completed; the original set-up, however, differed only in minor details. The compression-ignition 4-

stroke-cycle engine had a 5-inch bore and 7-inch stroke. Originally a single-cylinder Liberty test engine was used (reference 1), in which the cast-iron head was bolted to a special steel cylinder; the cylinder in turn was bolted to the engine crankcase. Later a more flexible unit was required, and an N. A. C. A. universal engine crankcase (reference 2) and cylinder were substituted for the Liberty crankcase and cylinder. Standard Liberty engine parts were used wherever possible. Fuel, oil, and water temperatures were maintained at 80°, 140°, and 170° F., respectively, during all tests. A 50–75 horsepower electric cradle-type dynamometer measured the torque and absorbed the engine power.

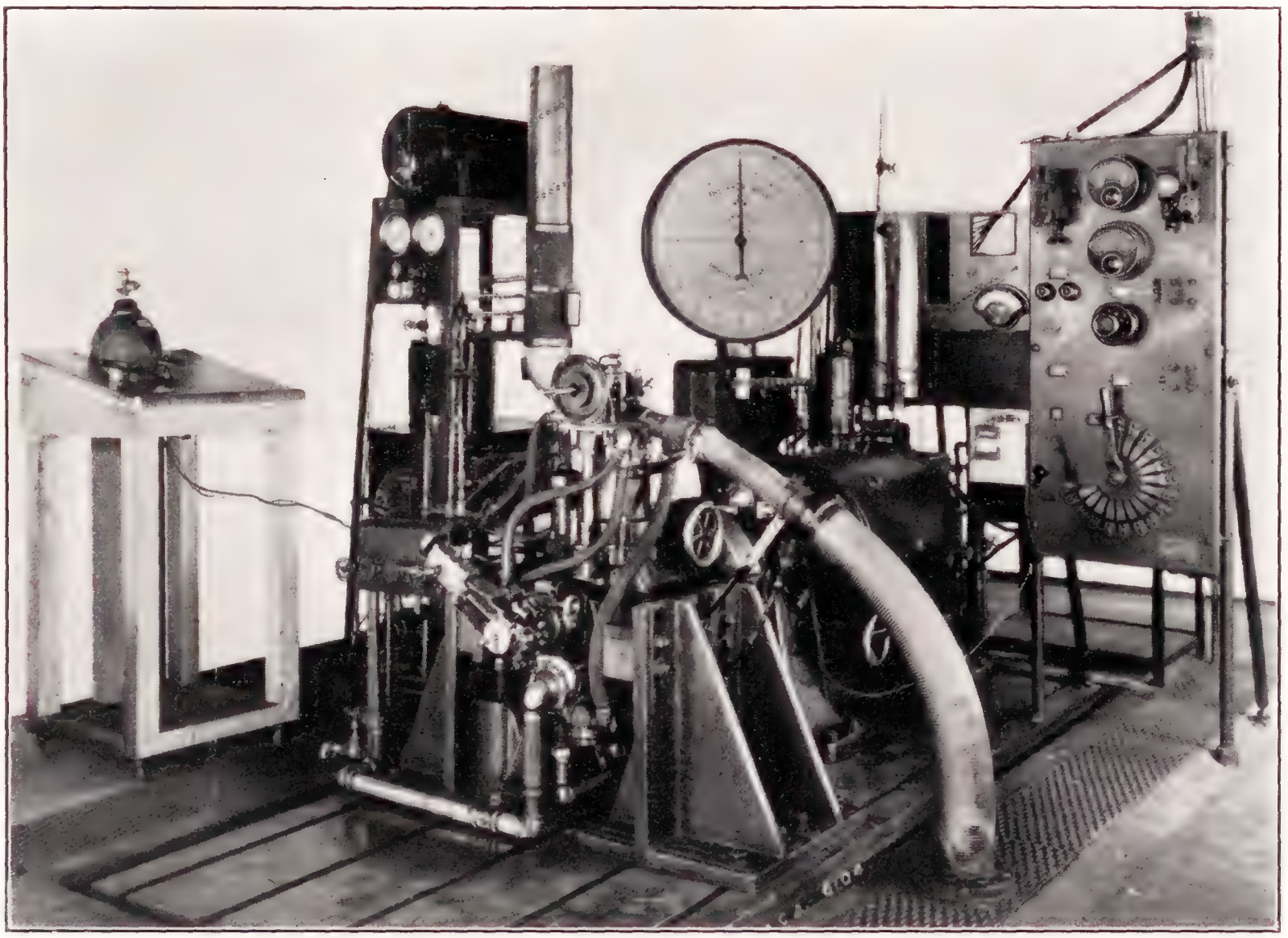

FIGURE 1.—Single-cylinder engine and test equipment.

CYLINDER HEADS

The several cylinder heads used in this investigation will be described in the order of their use. In the first design a pear-shaped auxiliary chamber was cast integrally with the head with a 1-inch-diameter passage connecting the chamber to the cylinder. With a standard high-compression Liberty piston the compression ratio was 9.9. The first combustion-chamber design was altered in order to increase the compression ratio and to create a higher degree of turbulence within the pear-shaped chamber on the compression stroke and within the cylinder on the expansion stroke (fig. 2). The turbulence was generated by locating the $\frac{9}{16}$-inch-diameter passage to produce tangential flow in both the bulb and the cylinder. When the piston was a top center, the ratio of the volume of air in the pear shaped chamber to the volume of air in the cylinder wa approximately 1. Preliminary tests at a compressio ratio of 13.5 were made to determine the effect of pro gressively altering the passage shape.

N. A. C. A. cylinder-head design 7 was made (see fig 3) to permit a wide range of changes in the connectin passage and auxiliary chamber without disturbing othe parts of the head. By the construction and assembl of different chamber parts and adjustments of the universal test engine, this cylinder head was readily adapted to the investigation of a variety of combustion-chamber forms and variables.

AUXILIARY TEST EQUIPMENT

Except for those tests in which the fuel-injection system was the variable, the same injection system was used in all the tests. A speed-reduction and timing mechanism, which operated the pump at camshaft speed, allowed the injection advance angle to be varied while the engine was running by changing the angular relation of the fuel cam with respect to the crankshaft. Varying the duration of the closure of a bypass valve in the constant-stroke pump controlled the quantity of fuel delivered to an automatic fuel-injection valve. A single 0.050-inch-diameter orifice with a length-diameter ratio of 2.5 was used in connection with a plain stem.

The Diesel fuel used in most of the tests had a specific gravity of 0.847 and a viscosity of 41 seconds Saybolt Universal at 80° F. Fuel input was measured by timing electrically the consumption of ½ pound of fuel oil while a synchronized revolution counter recorded the number of engine revolutions. Air consumption was measured by recording the time required for 80 cubic feet to be displaced from a 100-cubic-foot gasometer. Explosion pressures were indicated by the N. A. C. A. balanced-diaphragm valve. Indicator cards were obtained with a Farnboro electric indicator. A stroborama was used to determine the injection periods and injection advance angles. From the indicator cards, the ignition lags and rates of pressure rise were determined. The ignition lag is considered as the time in seconds from the start of injection of the fuel to the start of pressure rise on the card.

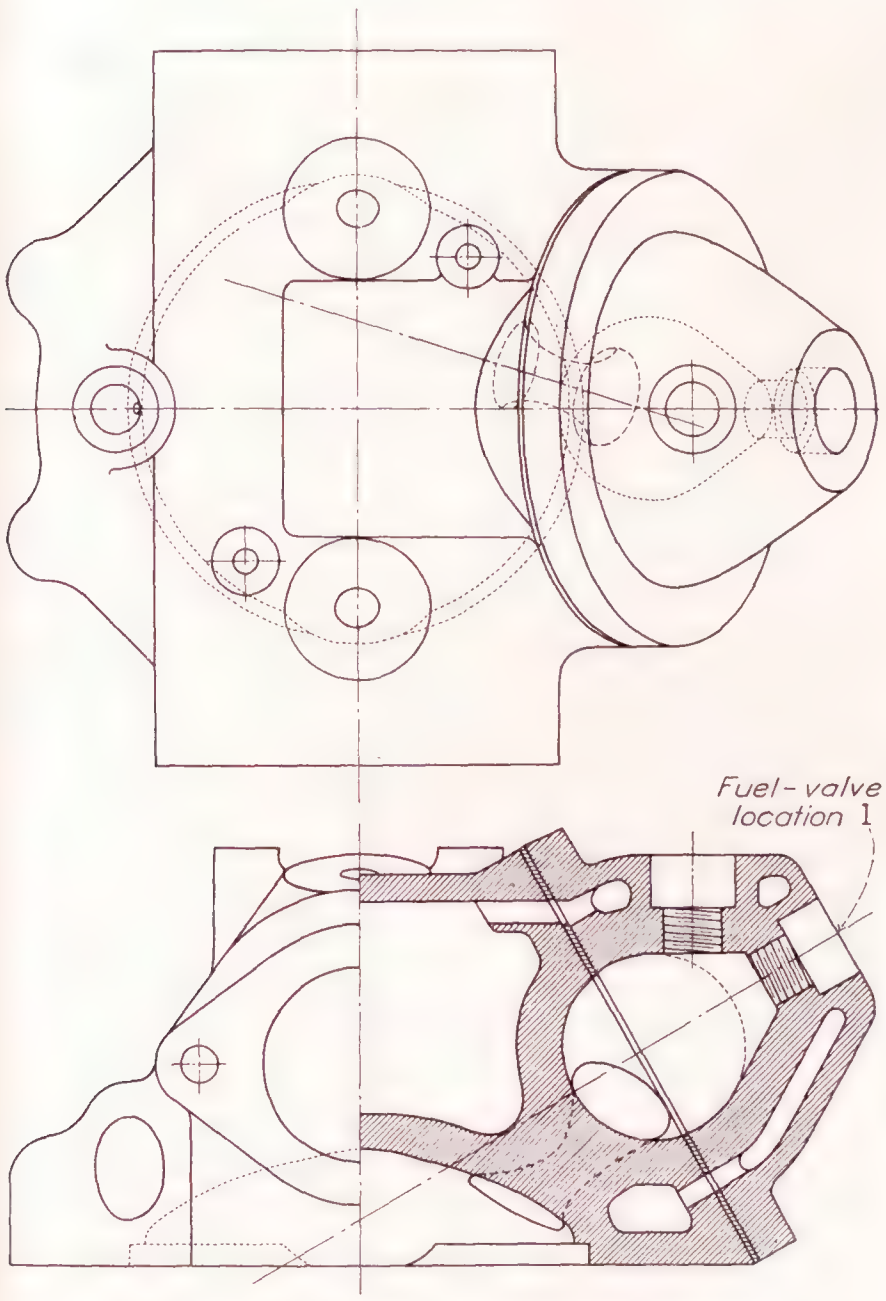

FIGURE 2.—Cylinder-head design showing pear-shaped prechamber.

TEST PROCEDURE

After the preliminary investigation was completed, a more systematic study was undertaken. The most important variables indicated by an analysis of the problem were studied in the following order: clearance distribution between cylinder and chamber, connecting-passage diameter, prechamber shape, cylinder-clearance shape, compression ratio, and boost pressure. Throughout the investigation, only one variable at a time was changed; all other conditions were held constant insofar as was conveniently possible. Although in some cases a dependent factor changed when an attempt was made to change a single variable, in no case was this condition permitted if it was of major importance or if it was economically possible to vary only the single variable. All pieces of apparatus were calibrated at intervals during the tests and corrections were applied to the results. During the testing, the barometric pressure varied from 29.49 to 30.40 inches of mercury; no attempt

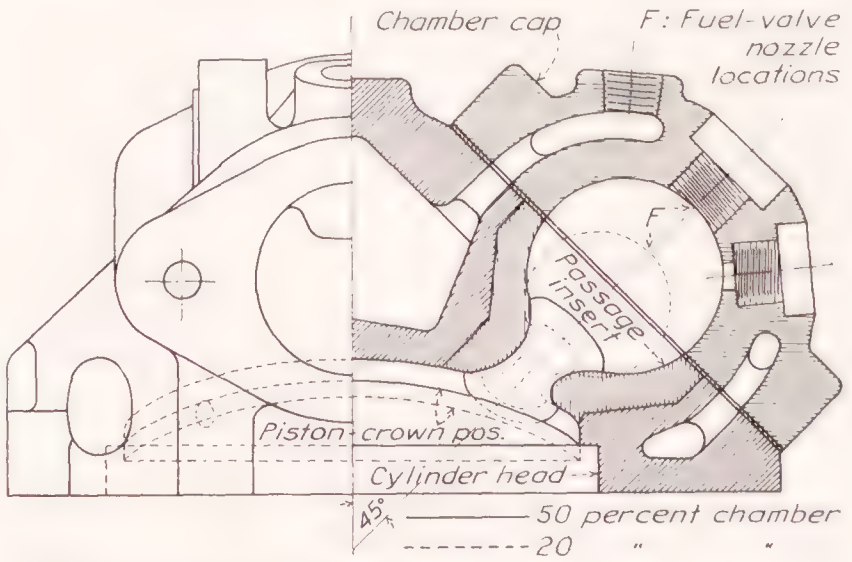

(a) Spherical prechamber with radial passage

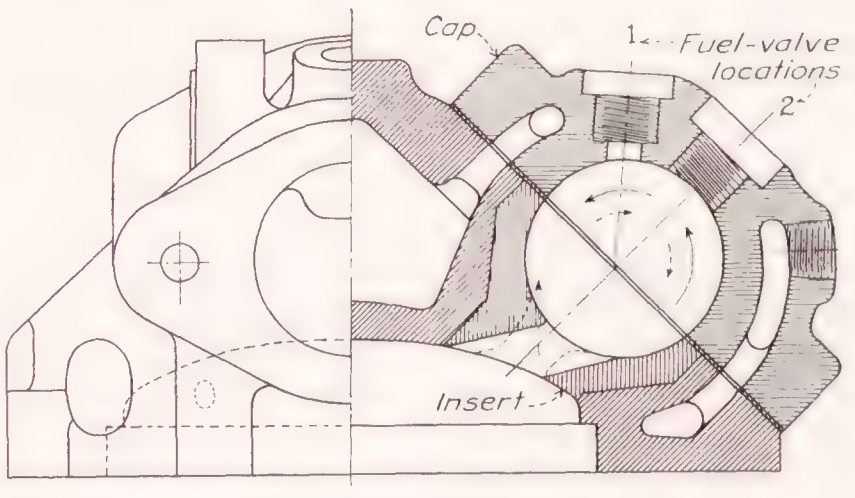

(b) Spherical prechamber with tangential and radial (dotted) passage.

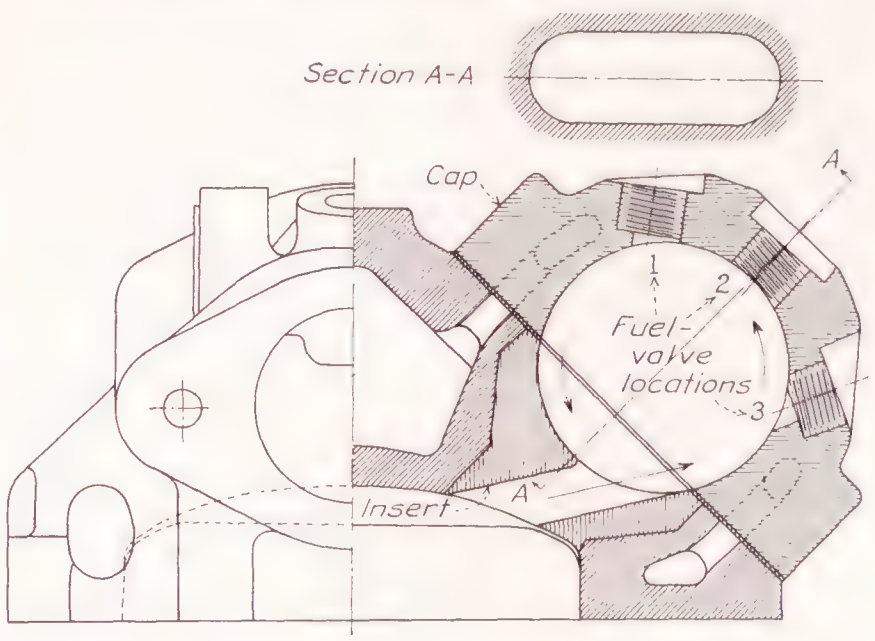

(c) Disk-shaped prechamber.

FIGURE 3.—Cylinder-head designs showing different prechambers.

has been made, however, to correct the data to a standard pressure, temperature, or humidity because there is no generally recognized method of correcting compression-ignition data to standard conditions.

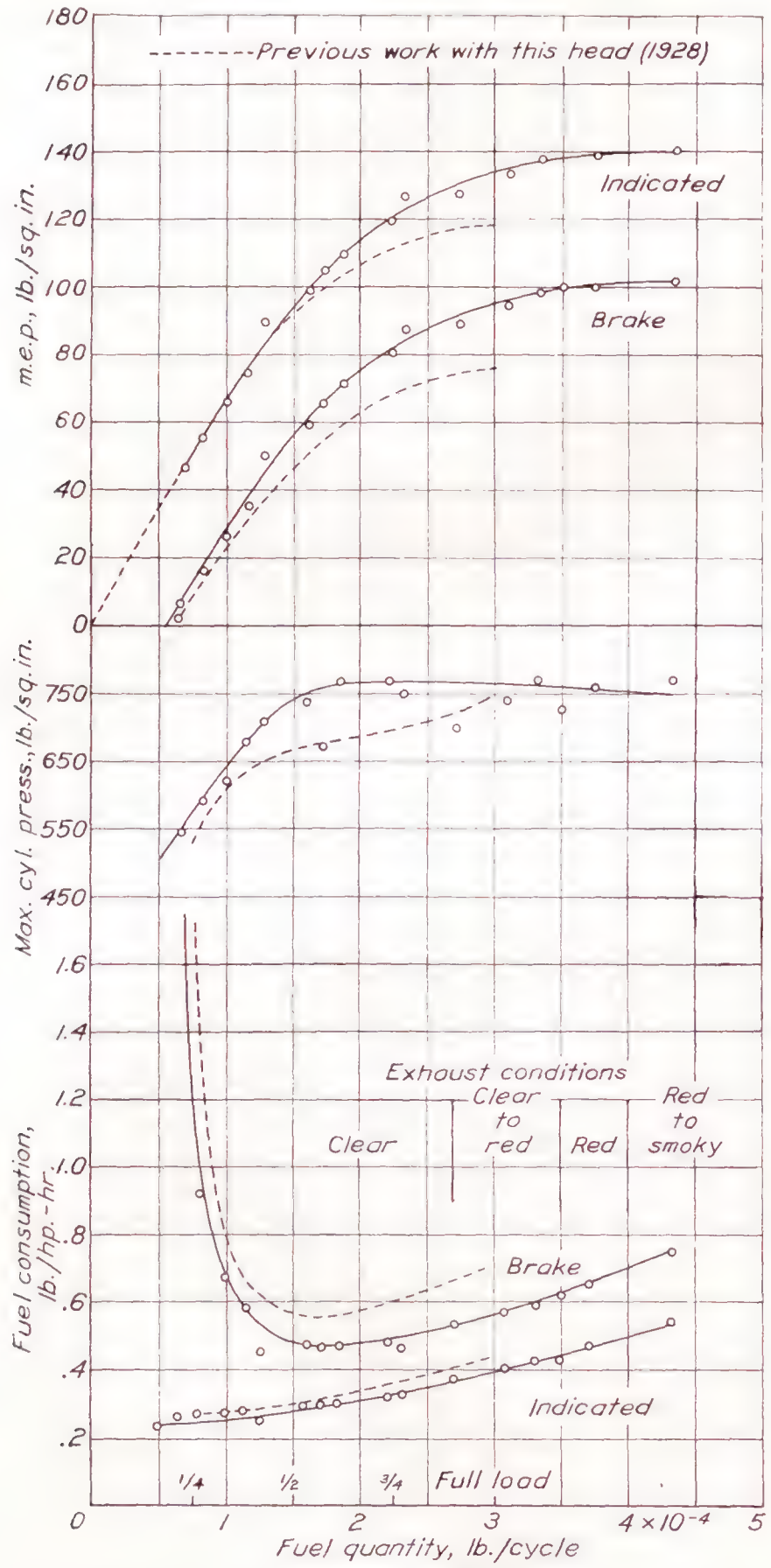

FIGURE 4.—Effect of fuel quantity on engine performance. Engine speed, 1,500 r. p. m.; cylinder head as shown in figure 2; compression ratio, 13.5; N. A. C. A. 7A fuel pump and 13A fuel valve; 0.050-inch nozzle; length-diameter ratio, 2.5.

TESTS AND RESULTS

PRELIMINARY INVESTIGATION

The curves showing the results of the preliminary investigation of the prechamber type of cylinder head are presented in reference 3. Owing to the low compression ratio of 9.9 the engine was difficult to start. Acceptable operation, however, was obtained at 1,80 r. p. m. which, at the time these data were first pub lished, was considered an exceptionally high speed fo compression-ignition engines.

According to the results obtained with the firs cylinder head, the N. A. C. A. combustion chamber (fig. 2) was designed to cause a residual air flow fo mixing the fuel and air (reference 3). This head bot improved the performance and reduced the maximu cylinder pressures A series of tests was made wit this cylinder head, in which the location of the fue nozzle with respect to the walls of the auxiliary chambe was varied. With the fuel valve in location 1, the fue nozzle was extended into the chamber by increment from the flush position to a point 1½ inches from th wall. Different orifices and spray types were tried but no improvement in performance was obtained ove that with the simple spray in the flush position.

With the cylinder head shown in figure 2, the greates improvement in performance (fig. 4) was obtained b shortening the injection period from approximatel 64 to 21 crankshaft degrees, although a small improve ment may have been due to flaring the cylinder end o the connecting passage.

CLEARANCE DISTRIBUTION

As maximum performance was not the first consider ation, the shape of the combustion chamber was no selected for best performance but to permit the study o chamber size without introducing a secondary variable For this reason, the chamber was made spherical to permit varying the allocation of the clearance betwee cylinder and chamber with a minimum change in th shape of the combustion space. The spherical pre chambers plus one-half the connecting passage con tained 20, 35, 50, and 70 percent of the total clearanc at a compression ratio of 13.5. For convenience o reference, these clearance distributions will be called the 20-, 35-, 50-, and 70-percent chambers. Clearanc in the cylinder was formed between the domed cylinde head and the domed piston crown.

The connecting passages were circular in cross sec tion, of constant length-diameter ratio, and were flared at both ends. Each of the four passages was designed to have a cross-sectional area proportional to th prechamber volume. Thus, at the same engine speed for each of the four clearance distributions, the calcu lated air velocities through the passages were the same Passage diameters obtained by this method were $^{23}/_{64}$, $^{15}/_{32}$, $^{9}/_{16}$, and $^{43}/_{64}$ inch for the 20-, 35-, 50-, and 70 percent chambers, respectively. The axis of the passage included the center of the spherical chamber and inter sected the cylinder axis at an angle of 45°.

The injection-advance-angle range from misfiring to allowable knocking was negligibly affected by clearance

distribution. With the fuel valve in the lower hole of the 20-percent chamber the operating range increased from 12° to 27°, but the power decreased and the smoke and flame of the exhaust increased. The injection advance angle of 7° at 1,500 r. p. m. gave a start of pressure rise that varied from T. C. to 3° A. T. C. for all clearance distributions, as determined by inspection of indicator cards.

Table I presents additional data on the engine-operating characteristics.

TABLE I

GENERAL OPERATING CHARACTERISTICS—CLEARANCE DISTRIBUTION

[Engine speed, 1,500 r. p. m.; fuel consumption, 3.0×10^{-4} lb./cycle; 12 percent excess air; cylinder head as shown in fig. 3 (a); compression ratio, 13.5; N. A. C. A. 7A fuel pump and 13A fuel valve; 0.050-inch nozzle; length-diameter ratio, 2.5]

Operating characteristics	20-percent chamber		35-percent chamber		50-percent chamber		70-percent chamber	
Combustion knock	Dull—Regular		Slight—Irregular		Hard—Irregular		Harder—Irregular.	
Injection range, allowable knock to miss	13° B. T. C. to 1° B. T. C		10° B. T. C. to 2° B. T. C		11° B. T. C. to 1° B. T. C		10° B. T. C. to 1° A. T. C.	
Centrifugal spray compared to noncentrifugal spray.	Knock and performance slightly worse for centrifugal spray.		Knock and performance worse for centrifugal spray.		Knock and performance worse for centrifugal spray.		Knock and performance slightly better for centrifugal spray.	
Lower fuel-valve position compared to upper position.	Performance worse for lower position i. a. a. range 27°.		No change		Performance worse for lower position.		Performance worse for lower position.	
Optimum valve-opening pressure, lb./sq. in.	3,500		5,000		5,000		3,500.	
Carbon deposits	Chamber, much	Cylinder, little	Chamber, soot and "cake"	Cylinder, soot	Chamber, soot	Cylinder, soot	Chamber, soft soot	Cylinder, soft soot
Cyclic variation in maximum explosion pressure, lb./sq. in.	300	100	200	100	140	130	90	140

Figure 5 shows that, for the design of prechambers used in these tests, the minimum volume in the chamber for good performance is about 35 percent of the total clearance volume. The inferior performance with the 20-percent chamber cannot be attributed to the deposit of fuel on the walls by the noncentrifugal spray because the centrifugal spray that had insufficient penetration to hit the walls gave slightly worse performance. More power was obtained with the larger chambers because of the greater quantity of air ready for initial combustion. Air in the cylinder, being distributed over the piston crown, cannot be effectively reached by the unburned gasses issuing from the chamber and therefore does not materially assist the combustion process.

The motoring and combustion characteristics are shown in figure 6. The motoring characteristics remain nearly constant as the clearance distribution varies. With the smaller chambers, less air is moved through the passage and the friction mean effective pressure should be less; the decrease in friction mean effective pressure, however, is slight. Maximum indicated compression pressures are slightly higher in the chambers than in the cylinder, probably owing to the method used in measuring the pressures (reference 4).

Figure 6 also shows that clearance distribution does not have an appreciable effect on ignition lag. This result may be expected as the conditions of temperature, pressure, and air speed were held constant during the tests. For all clearance distributions the pressure rises are straight lines and of such high rates that it is impossible to measure them accurately; the numerical values are therefore only approximations. As the chamber proportion increases, the chamber rate tends to decrease and the cylinder rate to increase and then to decrease. The larger chambers containing more air should give a faster rate of pressure rise because the fuel and air mixture would have more nearly the correct proportions for complete combustion. The opposite occurs, however, indicating that the passage size influences the rate of pressure rise, the larger passages of the larger chambers allowing the gases to pass more freely into the cylinder.

Improvement in exhaust conditions that occurs with increase of chamber proportions is caused by the availability of more air for combustion in the auxiliary chamber. Decrease in the rate of improvement with increased allocation of clearance to the chamber of more than 35 percent is due to the combination of spray shape and air flow as used in these combustion-chamber forms. This combination allows a maximum of approximately 35 percent of the fuel to be mixed with air for efficient combustion. The remaining fuel is burned either very late or not at all.

An increase in chamber volume from 20 to 70 percent causes the total heat loss to the cooling water to increase from 21 to 29 percent, owing to the increased quantity of fuel burned in the chamber and also to an increase of approximately 10 percent in the total combustion-chamber surface area (table II). The amount of heat loss from the chamber increases with chamber volume and surface, whereas the amount of heat loss from the head decreases. As the combustion in the chamber increases with increased chamber proportion, the cylinder heat loss decreases.

TABLE II

EFFECT OF CLEARANCE DISTRIBUTION ON HEAT LOSS TO COOLING WATER

[Engine speed, 1,500 r. p. m.; fuel consumption, 3.0 × 10⁻⁴ lb./cycle; 12 percent excess air; cylinder head as shown in fig. 3 (a); compression ratio, 13.5; N. A. C. A. 7A fuel pump and 13A fuel valve; 0.050-inch nozzle; length-diameter ratio, 2.5.]

Chamber volume in percentage of total clearance	Distribution of heat loss to cooling water			Percentage of total heat in fuel
	Cylinder	Head	Chamber cap	
	Percent	*Percent*	*Percent*	
20	50	44	6	21
35	46	34	20	22
50	44	20	36	26
70	43	17	40	29

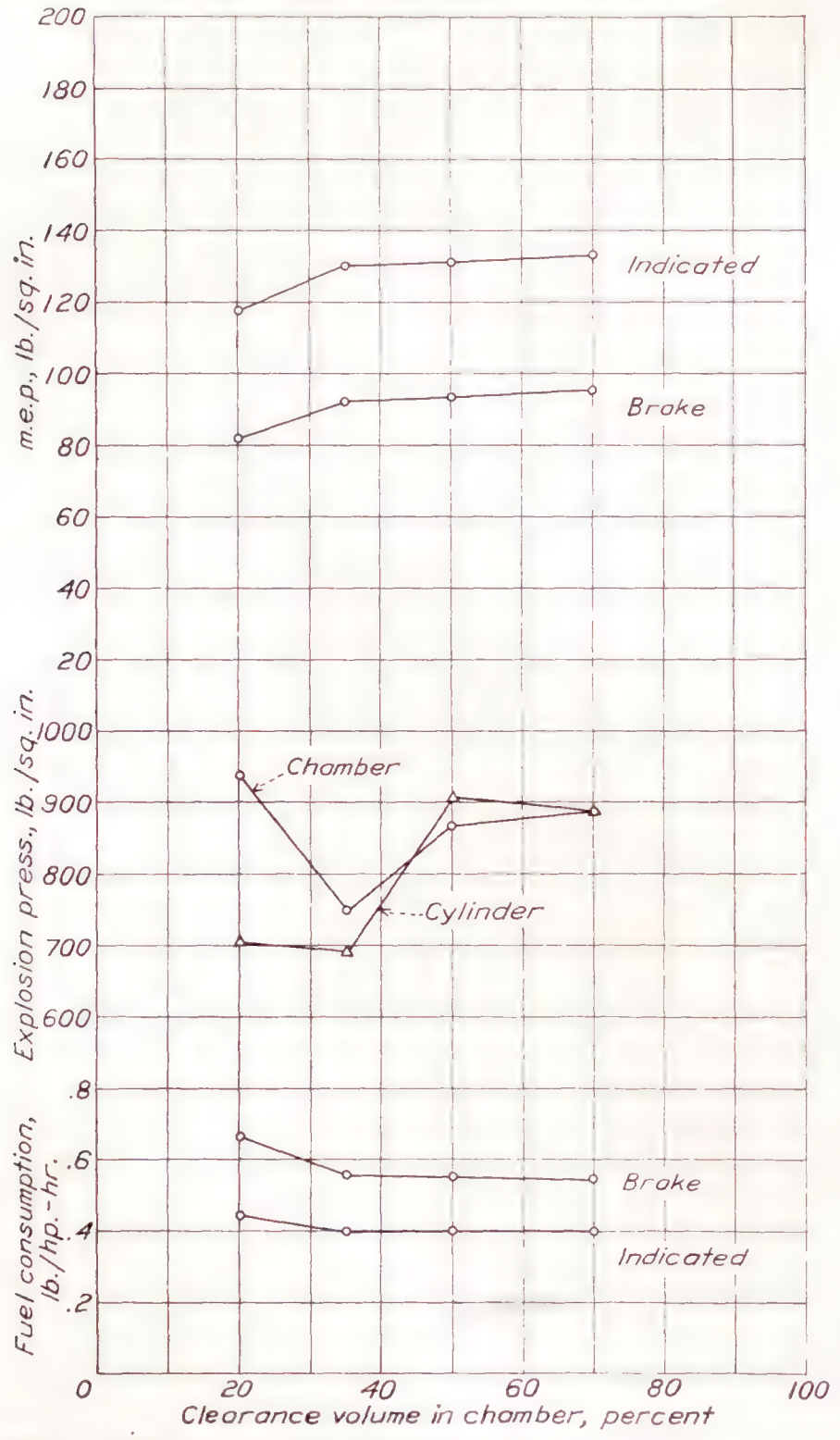

FIGURE 5.—Effect of clearance distribution on engine performance. Engine speed, 1,500 r. p. m.; fuel consumption, 3.0 × 10⁻⁴ lb./cycle; 12 percent excess air; cylinder head as shown in figure 3 (a); compression ratio, 13.5; N. A. C. A. 7A fuel pump and 13A fuel valve; 0.050-inch nozzle; length-diameter ratio, 2.5.

Figure 7 shows the general effect of engine speed and air-flow speed on mean effective pressure and fuel consumption. The trend is nearly the same for all the chambers with the optimum speed, based on maximum i. m. e. p., at 1,200 r. p. m. The larger chambers because of a more intimate mixture of a larger quantity of fuel and air, developed the most power with the best fuel economy. It is believed that the great difference in i. m. e. p. shown by the curves for the 20-percent chamber was caused by insufficient air in the small

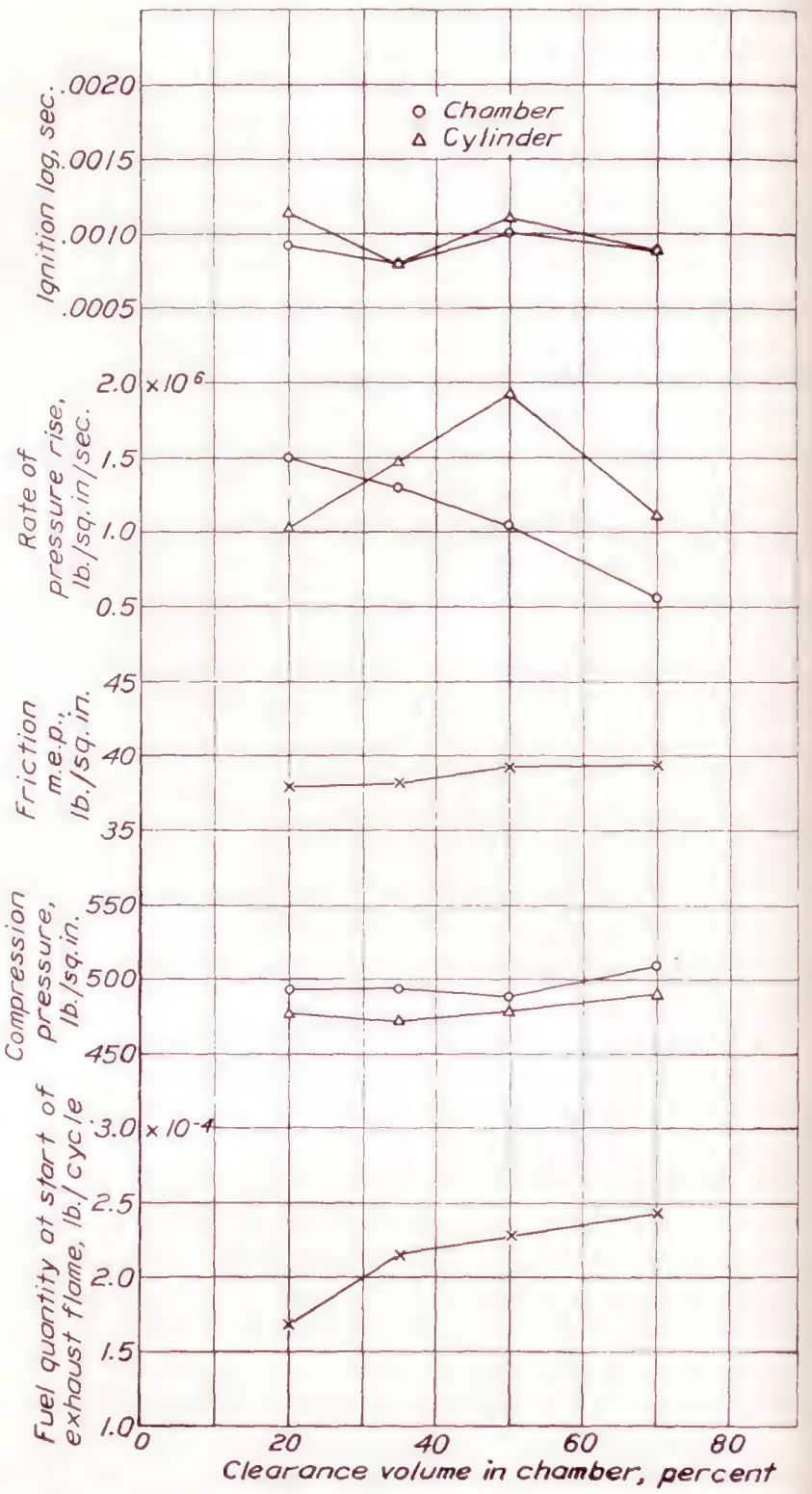

FIGURE 6.—Effect of clearance distribution on motoring and combustion characteristics. Engine speed, 1,500 r. p. m.; cylinder head as shown in figure 3 (a); compression ratio, 13.5; N. A. C. A. 7A fuel pump and 13A fuel valve; 0.050-inch nozzle length-diameter ratio, 2.5; injection advance angle, 7° B. T. C.

chamber. Explosion pressures of all the chambers increase with speed up to 1,200 r. p. m. because of the better mixing of fuel and air and resultant faster burning. As the engine speed increases above 1,200 r. p. m., most of the curves show a tendency to fall off. The smaller chambers with small passage areas confine the pressure, giving high chamber and low cylinder pressures.

The 50-percent chamber was selected as being representative of all the chambers and the effect of speed on combustion characteristics was investigated. Indi-

cator cards from the other three combustion chambers gave trends similar to those shown in figure 8, which is for the 50-percent chamber. As the engine speed increases, the velocity of air flow in the passage in-

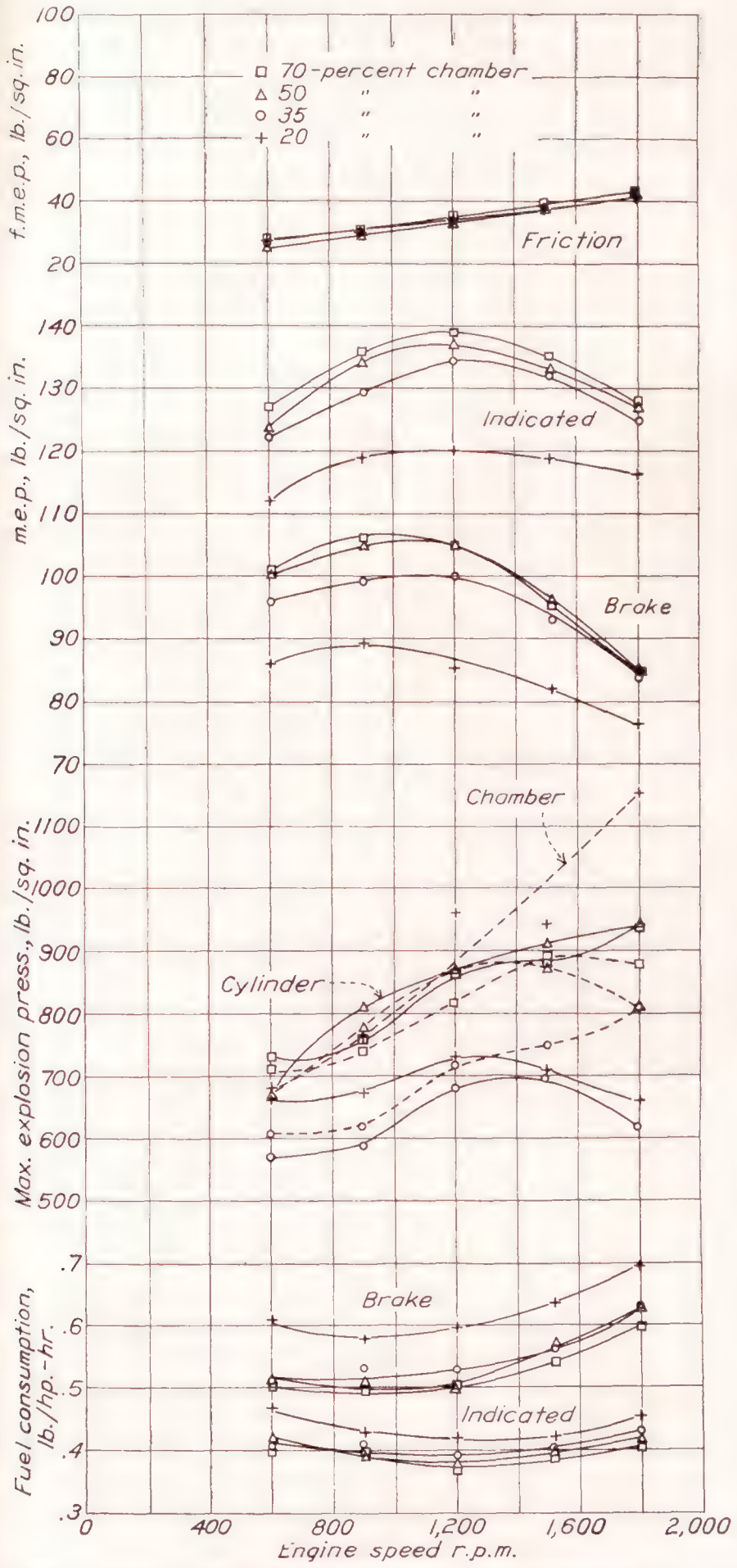

FIGURE 7.—Effect of speed on engine performance. Fuel consumption, 3.0×10^{-4} lb./cycle; 12 percent excess air; cylinder head as shown in figure 3 (a); compression ratio, 13.5; N. A. C. A. 7A fuel pump and 13A fuel valve; 0.050-inch nozzle; length-diameter ratio, 2.5.

creases and the mixing of fuel and air in the chamber is more complete with more rapid combustion and higher rates of pressure rise. Successive engine cycles varied, as the engine sound clearly indicated, so that the points on the Farnboro indicator cards are widely dispersed, especially at the pressure peaks. The rates of pressure rise were obtained by considering the leading points of the card. Apparently, rate of pressure rise and knock do not vary together, inasmuch as the rates of pressure rise were less at the lower speeds and the combustion-knock audibility remained constant.

The starting point of the pressure rise was dependent upon ignition lag and injection advance angle, the latter

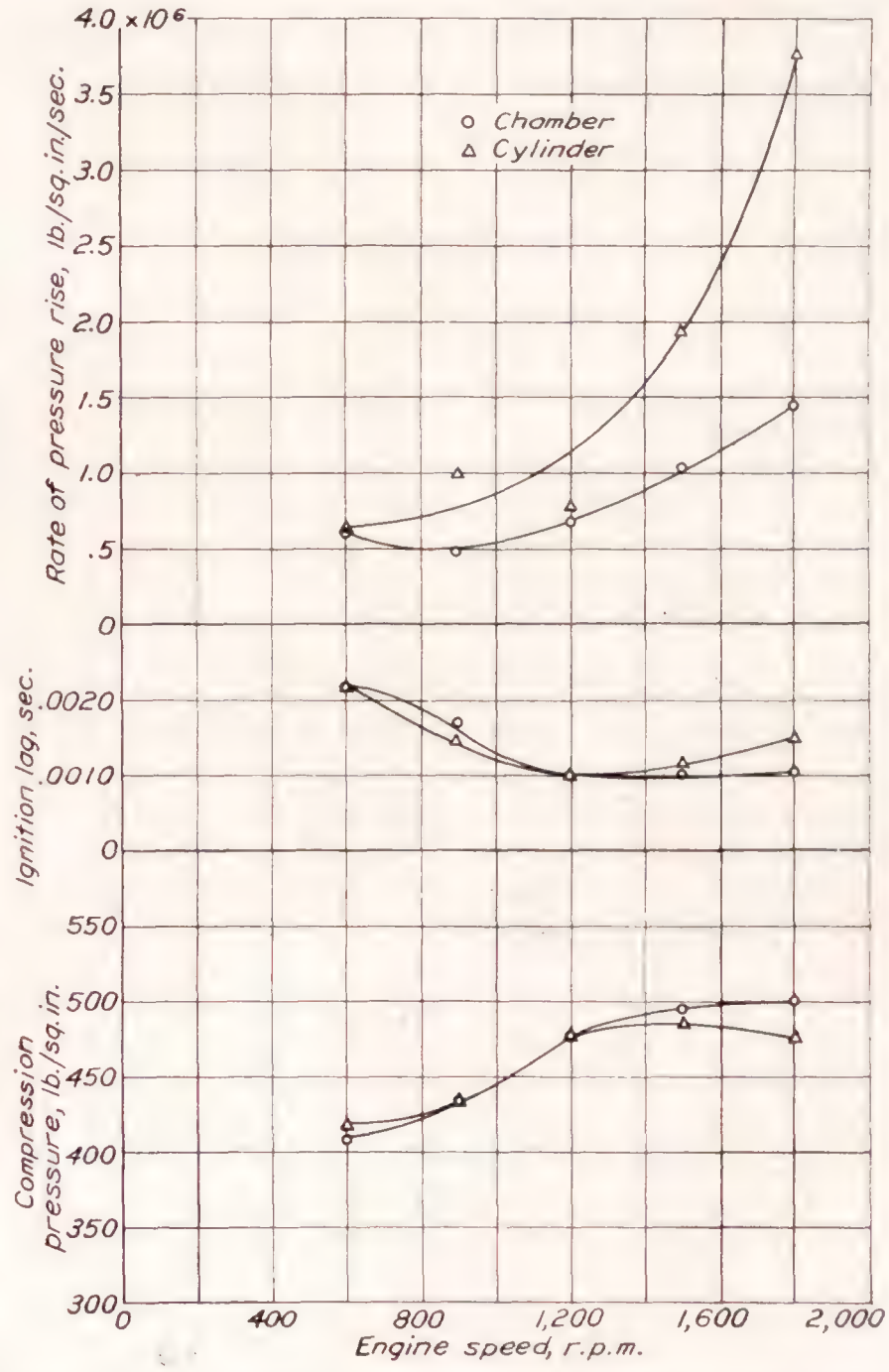

FIGURE 8.—Effect of speed on compression pressure and combustion characteristics. Fuel consumption, 3.0×10^{-4} lb./cycle; 12 percent excess air; cylinder head as shown in figure 3 (a); 50-percent chamber; compression ratio, 13.5; N. A. C. A. 7A fuel pump and 13A fuel valve; 0.050-inch nozzle; length-diameter ratio, 2.5.

being the greatest permitted by allowable knock intensity. The start of pressure rise varied from approximately 10° A. T. C. at 600 r. p. m. to 2° A. T. C. at 1,800 r. p. m. The ignition lag measured in seconds was reduced one-half by an increase in engine speed of from 600 to 1,200 r. p. m., primarily because more heat was brought to the fuel by the higher air-flow speed.

CONNECTING-PASSAGE DIAMETER

In order to investigate the effect of connecting-passage diameter, the 50-percent prechamber was selected and the diameter of the connecting passage was varied. As in former tests, the single passage used was

circular in cross section. This shape was retained because, with a circular passage, there is a minimum change in clearance shape as the cross-sectional area of the passage is increased. A connecting passage considered too small for practical operation was selected and progressively enlarged. (See table III.) The compression ratio varied from 13.2 to 13.7 with change in passage area. Air-flow speeds through the passages of different size used were calculated by the method given in reference 5 and the results are shown in figure 9.

The general operating and combustion characteristics of the engine changed as the diameter of the connecting passage was varied and the data recorded during the tests are shown in table III.

TABLE III

GENERAL OPERATING CHARACTERISTICS—PASSAGE DIAMETER

[Engine speed, 1,500 r. p. m.; fuel consumption, 3.0 × 10^{-4} lb./cycle; 12 percent excess air; cylinder head as shown in fig. 3 (a); compression ratio, 13.5; N. A. C. A. 7A fuel pump and 13A fuel valve; 0.050-inch nozzle; length-diameter ratio, 2.5.]

Passage diameter, in.	Passage area, sq. in.	Idling	Injection range (allowable knock to miss), Crank angle, degrees	Cyclic variation of maximum explosion pressure		Combustion sound intensity and regularity	Carbon deposits	
				Chamber, lb./sq. in.	Cylinder, lb./sq. in.		Chamber	Cylinder
3/16 [1]	0.028	Good	38 B. T. C. to 2 A. T. C.		Small	Quiet, regular	None	Light.
17/64 [1]	.055	do	18 B. T. C. to 2 A. T. C.		do	do	do	Do.
3/8	.110	do	11 B. T. C. to 1 A. T. C.		80	Light knock, regular	Increasing carbon.	Increasing carbon.
29/64	.161	do	11 B. T. C. to 1 A. T. C.	100	100	Medium knock, regular	do	Do.
17/32	.222	do	10 B. T. C. to 1 A. T. C.	120	120	Hard knock, regular	do	Do.
21/32	.338	Fair	11 B. T. C. to 1 A. T. C.	100	160	Dull knock, irregular	do	Do.
3/4	.442	Poor	11 B. T. C. to 1 A. T. C.	120	130	do	do	Do.
1 1/16 [2]	.887	Bad	11 B. T. C. to 5 A. T. C.			Light knock, irregular	do	Do.

[1] Erosion of piston crown prevented complete power tests.
[2] Excess heating of exhaust valve and manifold prevented complete tests.

Motoring characteristics shown in figure 10 indicate that friction increases rapidly when passages of less than 29/64-inch diameter are used. The large effect on friction mean effective pressure in this range is due mostly to passage throttling losses because the mechanical and induction losses remain nearly constant (reference 6). The pressure difference between chamber and cylinder is greater with the smaller passages than with the larger ones, which approach the integral combustion chamber condition and show little pressure difference. Figure 11 is a representative motoring card and shows the lag of chamber pressure behind cylinder pressure. The effect of speed on compression pressures and friction mean effective pressure is shown in figure 12. These curves illustrate the increasing

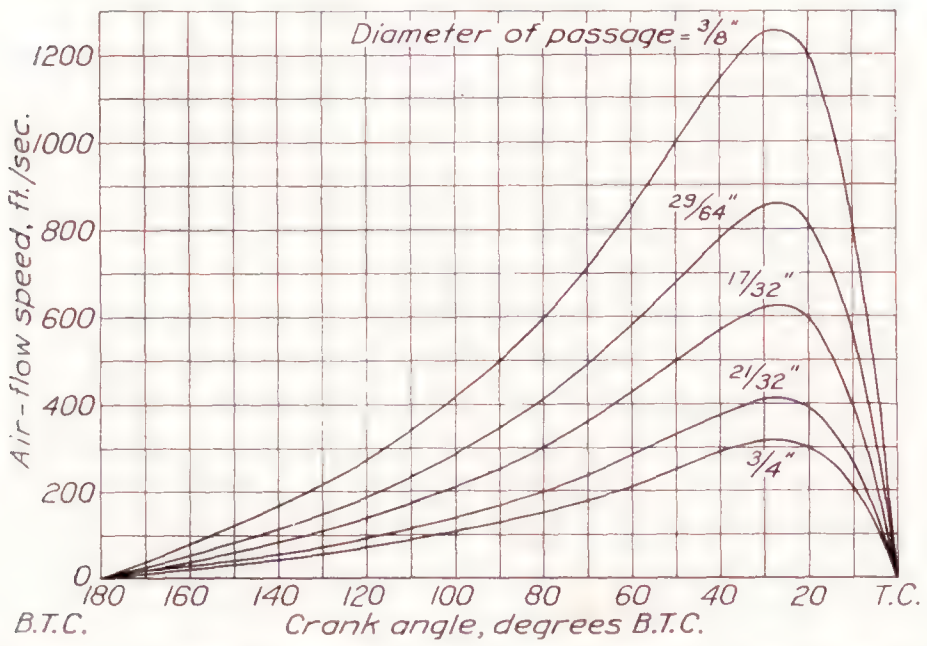

FIGURE 9.—Relationship of air-flow speed to crank position and passage diameter during the compression stroke of a 5- by 7-inch engine with a 12-inch connecting rod. Engine speed, 1,500 r. p. m.; cylinder head as shown in figure 3 (a); 50-percent chamber.

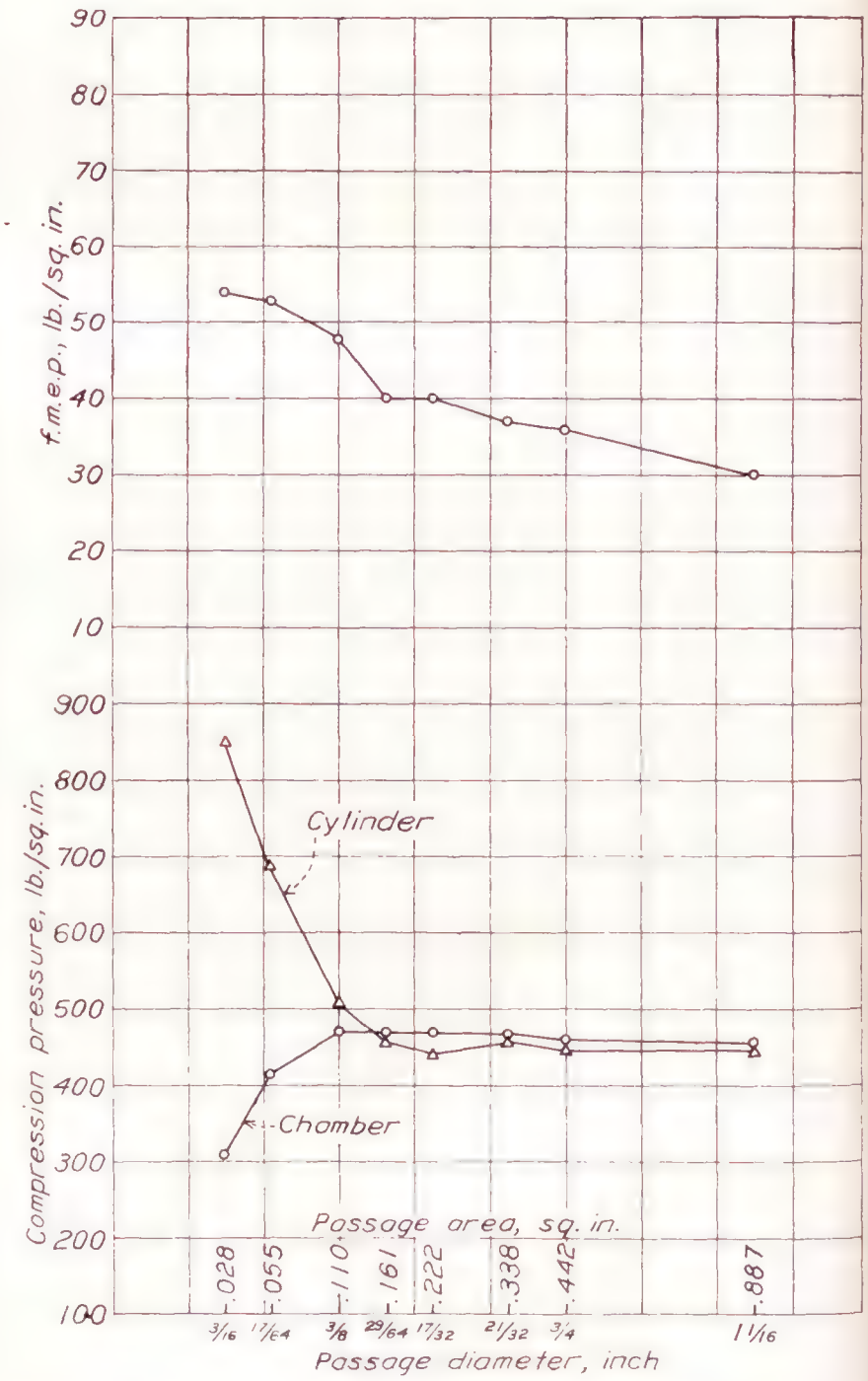

FIGURE 10.—Effect of passage diameter on motoring characteristics. Engine speed, 1,500 r. p. m.; cylinder head as shown in figure 3 (a); compression ratio, 13.5; 50-percent chamber.

effect of the passage area on the different variables as the engine speed is increased.

Figure 13 shows that, for the clearance shape used in these tests, a connecting passage of approximately $^{29}/_{64}$ inch in diameter will give nearly optimum performance over the speed range investigated. Because the airflow velocity through the passage depends on engine speed, the consistent performance over a wide speed range indicates that the longer time available for the preparation of the mixture at low speeds compensates for the lower velocity of the air through the passage and makes good performance with satisfactory engine-operating conditions possible over a wide speed range. In this instance, the criterions for satisfactory engine-operating conditions are moderate cylinder pressures, rates of pressure rise, and combustion sound. At 1,500 r. p. m., while the smallest passage was on test, the pressure in the chamber could not be measured because the engine-operating conditions caused the repeated failure of the pressure-measuring apparatus.

Although the combustion is evidently better at high speed and with small passage diameters, the performance is not the optimum owing to the excessive throttling of the small passages. Throttling becomes less important with decrease in engine speed and the resulting performance curves at 1,000 and 500 r. p. m. are quite flat. In the design of a prechamber, this lack of sensitivity at low engine speeds is therefore advantageous because an optimum passage size for the maximum engine speed can be selected and the performance at lower speeds will not be adversely affected.

Figure 13 shows at 1,500 r. p. m. an increase in ignition lag and a decrease in the rate of pressure rise in both chamber and cylinder as the passage diameter is increased. Increase in ignition lag in the tests of passage sizes ranging from $^{3}/_{8}$-inch to $^{17}/_{32}$-inch diameter was accompanied by an increase in combustion knock; however, for the two larger passages the ignition lag increased slightly, but the combustion knock became less intense. (See knock rating of table III.) In the opinion of some investigators, combustion knock is caused by a high rate of pressure rise. The results of these tests indicate that this condition is not always true because, at a speed of 1,500 r. p. m., the passage giving the highest rate of pressure rise gave the quietest engine operation.

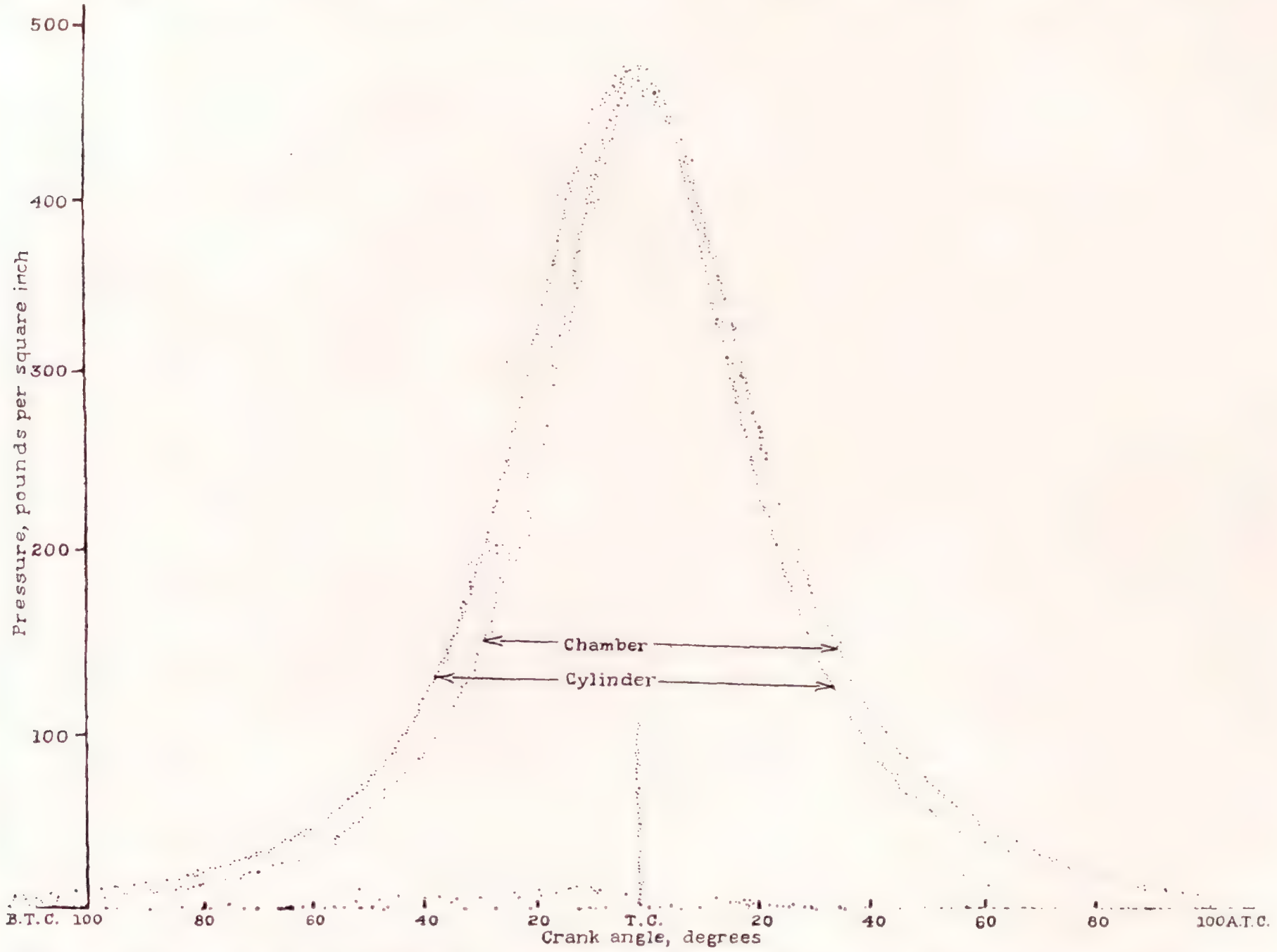

FIGURE 11.—Motoring indicator card. Engine speed, 1,500 r. p. m.; cylinder head as shown in figure 3 (a); passage diameter, 29/64 inch; compression ratio, 13.5.

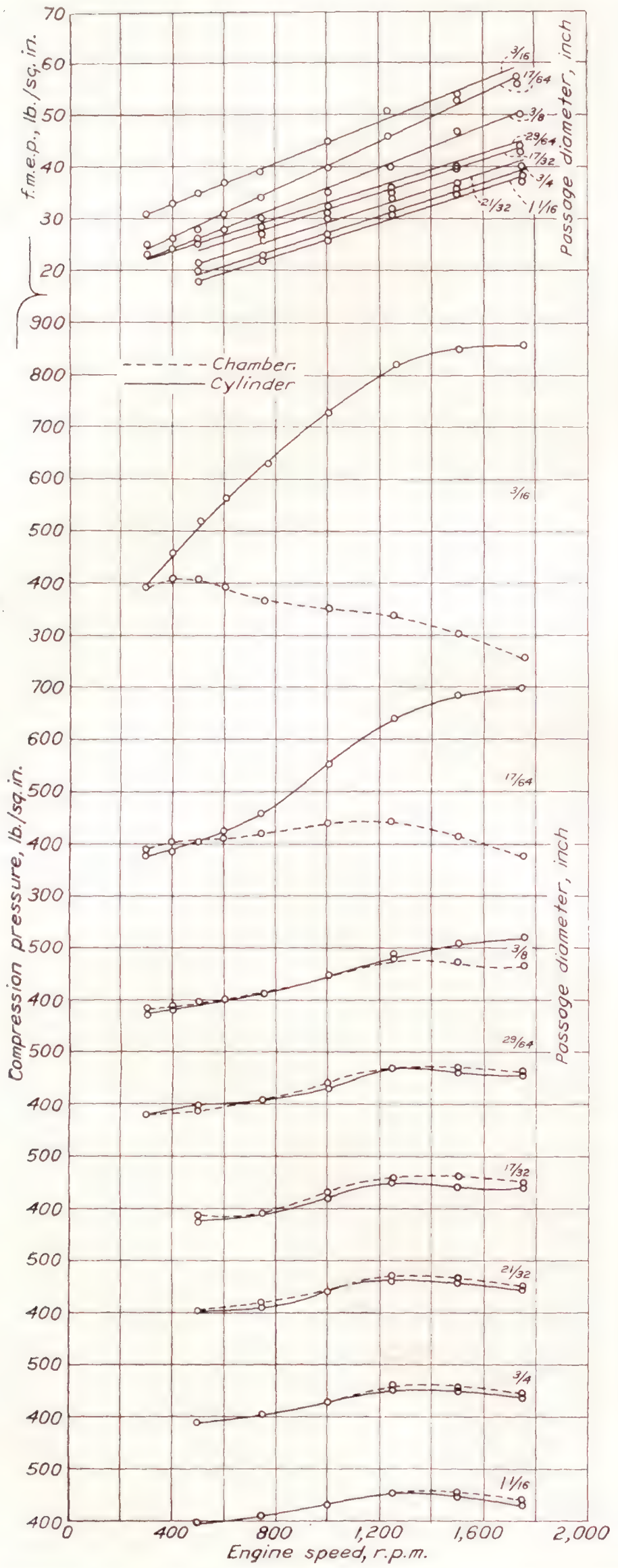

FIGURE 12.—Effect of speed on compression pressures and f. m. e. p. Cylinder head as shown in figure 3 (a); compression ratio, 13.5.

A conclusion drawn from the results of these tests is that combustion knock is more dependent upon ignition lag than upon rate of pressure rise; however, the effect of a small change in either condition is not consistent. The tests made at 1,000 and 500 r. p. m. (fig. 13), owing to the lesser velocities of air flow at these speeds, do not show trends as sharply defined as those shown at 1,500 r. p. m. At each speed, the injection advance angle and rate of fuel injection were held constant for the series of passage diameters tested.

The curves show that some combustion-pressure control can be obtained by means of small passage diameters because with the ⅜-inch-diameter passage the rates of pressure rise are higher in the chamber than in the cylinder. The equivalent data could not be obtained from either of the two smaller passages because, after short power runs, the piston crown was dangerously eroded by the impingement of the concentrated jet of burning gases issuing from the small passage. Small passages, however, do give good mixture control and minimize the effects of irregularities of the fuel-injection system, such as small variations in the start of injection. This effect is shown by the small cyclic variations in cylinder explosion pressure as measured with the balanced-diaphragm pressure indicator. The combustion obtained using the largest passage tested was so slow that the exhaust valve and exhaust manifold became red hot after a few minutes of operation.

Supplementary tests made at maximum allowable advance angle are represented in figure 13 by the points that do not fall on the curves. These runs were made because it was found that the explosion pressures were decreasing with an increase in passage diameter and it was considered advisable to determine whether the best performance could be equaled by advancing the injection and thereby raising the explosion pressures. The results of these tests at maximum allowable advance angle show that, although the maximum explosion pressures were considerably increased, the performance was only slightly improved. The combustion knock under these conditions was much worse than when testing any passage and using optimum injection advance angle.

COMBUSTION-CHAMBER SHAPE

Clearance distribution and connecting-passage diameter were considered the most important variables in the design of a prechamber cylinder head and therefore they were extensively investigated. Several lesser variables that contribute to the performance characteristics of the combustion chamber were also investigated.

The prechamber was kept at 50 percent of the total clearance for most of the tests, and the connecting passage was maintained at 5/16-inch diameter or the equivalent area. Although these proportions are not

the optimum for prechamber design, the sacrifice in performance was sufficiently small to justify their use to maintain continuity throughout the entire investigation.

The passage was brought into the chamber radially and tangentially (fig. 3 (b)) by using inserts designed and constructed to permit such variations. When the tangential passage was used, the direction of the passage to the cylinder was changed by rotating the chamber cap and passage insert as a unit into positions as far as 72° to the right and to the left. The ends of the passage were successively flared to determine the effect of passage flaring.

The effect of prechamber shape was investigated for a limited series of tests. Analysis and test results indicated the advisability of confining the test shapes to volumes of revolution in order to conserve the residual air flow within the chamber. The spherical chamber of the first tests was changed to a disk rounded at the outer edge and arranged vertically so that the plane of the disk was parallel to the axis of the engine cylinder. The connecting passage was introduced tangentially to the disk (fig. 3(c)). Three injection-valve locations were provided as shown, and power tests were made with the fuel valve in each.

The effect of increasing the quantity of air rotated in the prechamber was investigated by changing the volume of a spherical chamber from 50 to 70 percent of the clearance volume. The tangential passage was substituted for the radial passage and comparable tests were made. The approximate direction of the air flow for both the 50- and the 70-percent chambers with radial and tangential passages was indicated by air-flow patterns made by extending a number of copper nibs into the auxiliary chamber from a gasket clamped between the two parts of the chamber, as described in reference 4. In order to take the air-flow patterns, the engine was started from rest, motored up to 1,500 r. p. m. as quickly as possible, and then stopped. The variation in performance when the engine was operated with the fuel valve first in the central and then in the top injection-valve location was determined for both prechambers.

The general operating characteristics of the engine—that is, starting and idling ability, cyclic regularity, and combustion shock—were little affected by any of the changes made during these tests. A change from the Diesel fuel used in previous tests to Auto Diesel fuel greatly reduced the combustion knock, increased the injection-advance-angle range, and decreased the cyclic variation in maximum cylinder pressure from ±75 to ±40 pounds per square inch. Some combustion knock was present in all tests but was not considered serious. The rates of pressure rise in the cylinder and the prechamber were, respectively, 68 and

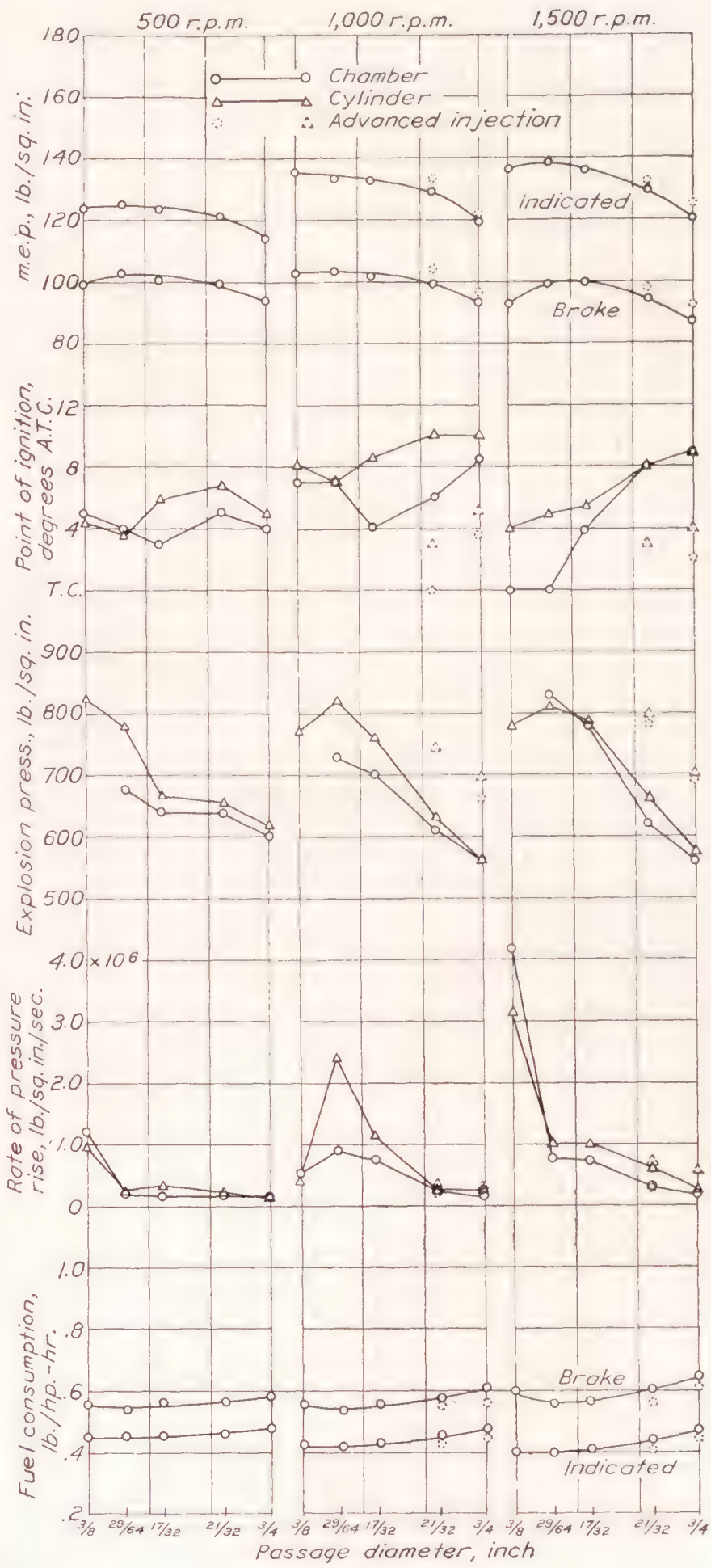

FIGURE 13.—Effect of passage diameter on engine performance. Fuel consumption, 3.25×10^{-4} lb./cycle; no excess air; cylinder head as shown in figure 3 (a); compression ratio, 13.5; N. A. C. A. 7A fuel pump and 13A fuel valve; 0.050-inch nozzle; length-diameter ratio, 2.5; injection advance angle, 11° B. T. C.

45 pounds per square inch per degree at 1,500 r. p. m. with the best combination of variables covered in this report. Rates of pressure rise for previous work, in which the spherical chamber and the original fuel were used, were in the order of 85 and 75 pounds per square

inch per degree at 1,500 r. p. m. for cylinder and chamber, respectively.

The purpose of directing the passage tangentially to the chamber instead of radially was to create a high-velocity, rotational, residual air flow in the auxiliary chamber to improve the fuel and air mixing. Table IV shows the effects of flaring and of changes in the intensity of the rotational air swirls obtained by several combinations of connecting passage. Flaring the passage had very little effect on the performance. Several other methods of spreading the gases over the piston crown were tried, such as an elliptical passage insert and a three-passage insert designed according to the proportional-orifice principle (reference 7). The effect of these changes on the performance was also negligible.

As a rotational swirl was found to be effective in the chamber, it was decided to determine the effect of a swirl in the cylinder. This effect was produced by changing the passage direction in the cylinder. Carbon deposits showed that a swirl was produced, but there was no appreciable improvement in engine performance.

TABLE IV

EFFECT OF PASSAGE DIRECTION AND FLARE ON ENGINE PERFORMANCE

[Fuel consumption, 3.25×10^{-4} lb./cycle; no excess air; cylinder head as shown in fig. 3 (b); compression ratio, 13.5; N. A. C. A. 7A fuel pump and 13A fuel valve; 0.050-inch nozzle; length-diameter ratio, 2.5]

	1,000 r. p. m.					1,500 r. p. m.				
	i. m. e. p., lb./sq. in.	b. m. e. p., lb./sq.in.	Explosion pressure, lb./sq.in.	Fuel consumption		i. m. e. p., lb./sq. in.	b. m. e. p., lb./sq. in.	Explosion pressure, lb./sq. in.	Fuel consumption	
				lb./i.hp.-hr.	lb./b.hp.-hr.				lb./i.hp.-hr.	lb./b.hp.-hr.
RADIAL PASSAGE										
Slight rotational air flow	137	109	795	0.42	0.52	133	98	750	0.42	0.58
Strong rotational air flow	139	111	740	.41	.51	137	102	730	.41	.55
TANGENTIAL PASSAGE										
Strong rotational air flow	141	112	740	0.38	0.48	142	104	720	0.38	0.53
Cylinder end of passage flared	141	112	740	.39	.49	144	106	730	.38	.52
Both ends of passage flared	140	113	800	.39	.49	141	105	770	.40	.54

Table V shows the effect of changing the prechamber shape from a sphere to a disk of equal volume and also the effect of fuel-valve location in the disk chamber. Tangential passages were used in both cases. The disk chamber with tbe injection valve in the central location gave an improvement in i. m. e. p. at 1,500 r. p. m. over the spherical chamber under similar conditions, which can be attributed to the fact that in the disk chamber the low-velocity zones of the spherical chamber were removed and the rotating mass of air was in the zone of the single fuel spray and the connecting passage. This relation of chamber shape and fuel spray evidently resulted in better mixing in the prechamber with the resultant improved performance.

TABLE V

EFFECT OF PRECHAMBER SHAPE AND FUEL-VALVE LOCATION ON ENGINE PERFORMANCE

Fuel consumption, 3.25×10^{-4} lb./cycle; no excess air; cylinder head as shown in figs. 3 (b) and 3 (c); compression ratio, 13.5; N. A. C. A. 7A fuel pump and 13A fuel valve; 0.050-inch nozzle; length-diameter ratio, 2.5]

Fuel-valve location	1,000 r. p. m.										1,500 r. p. m.									
	i. m. e. p., lb./sq. in.		b. m. e. p., lb./sq. in.		Explosion pressure, lb./sq. in.		Fuel consumption				i. m. e. p., lb./sq. in.		b. m. e. p., lb./sq. in.		Explosion pressure, lb./sq. in.		Fuel consumption			
							lb./i. hp.-hr.		lb./b. hp.-hr.								lb./i. hp.-hr.		lb./b. hp.-hr.	
	Flame start	Full load	Flame start	Full load	Flame start	Full load	Flame start	Full load	Flame start	Full load	Flame start	Full load	Flame start	Full load	Flame start	Full load	Flame start	Full load	Flame start	Full load
SPHERICAL CHAMBER (FIG. 3 (b))																				
2	130	140	103	113	800	790	0.36	0.39	0.46	0.48	126	140	91	105	740	760	0.33	0.40	0.45	0.54
DISK CHAMBER (FIG. 3 (c))																				
3	99	124	72	98	780	790	0.40	0.44	0.55	0.56	101	128	66	92	780	760	0.37	0.45	0.57	0.62
2	138	141	111	113	780	780	.38	.41	.47	.50	133	145	98	109	740	740	.35	.38	.48	.51
1	143	147	115	119	780	760	.37	.38	.47	.48	143	149	106	113	740	740	.36	.38	.48	.51

The effect of fuel-valve location is also shown in table V; the great difference in maximum power for the three fuel-valve locations provided in the disk chamber indicates the importance of the position of the fuel spray relative to the air movement. The best performance was obtained with the spray axis from the single-orifice nozzle directed in the same plane with the air flow and at only a small angle from the direction at right angles to the air flow. The spray was also directed toward the connecting passage. The worst performance was obtained with the fuel valve in the lowest position (see fig. 3 (c)) in which the spray was injected counter to the air flow and, with the injection timing used, should have penetrated directly through the passage to the cylinder. The fact that the fuel did penetrate at least to the passage was indicated by carbon formation around the mouth of the passage. This arrangement was made to obtain a rich mixture adjacent to the passage ready to be ejected into the cylinder by the pressure resulting from the combustion in the chamber. The chamber cap was rotated 180° so that the lower valve position was in approximately the same location but the spray was directed, not through the passage, but above the entrance to the passage and at an angle to the air flow, not counter to it. This condition increased the brake mean effective pressure approximately 10 pounds per square inch over that originally obtained with the fuel valve in the lowest position.

An analysis of previous work indicated that the greater the amount of air in motion the better would be the mixing of the fuel and air and, consequently, the better the performance. A tangential passage in conjunction with a chamber that contained a larger percentage of the clearance volume was used to increase the quantity of air in motion. Table VI shows that this analysis was correct for spherical chambers because, with the fuel valve in the central location, the improvement in the performance with increase in chamber volume was greater when a tangential passage was used than when a radial passage was used. Increase in rotational, and probably residual, air-flow velocity due to the tangential passage was sufficient to make an appreciable difference in the performance. The investigation was made with spherical chambers although the maximum performance would be less than with the disk chambers; the indicated trend, however, should be the same for both auxiliary-chamber shapes.

The tangential connecting passage was used because introducing the air tangentially to a volume of revolution assisted in setting up a rotational swirl in the chamber, which should persist after the piston had reached the upper limit of its travel. As this residual air flow was believed to be the cause of the increased power, every attempt was made to intensify and preserve the flow. This theory could not be definitely proved because there are no means available for measuring the velocity of the flow; the predominating direction of the air flow, however, was determined by means of the air-flow patterns. The radial passage to the same chamber also showed rotational air flow but of less intensity and in the opposite direction. This condition was probably caused by the short passage used, which permitted some air from the cylinder to pass directly into the prechamber without being directed by the passage. (See fig. 3 (b).) The passage was as long as the construction of the head would permit.

TABLE VI

EFFECT OF PASSAGE DIRECTION, PRECHAMBER VOLUME, AND FUEL-VALVE LOCATION ON ENGINE PERFORMANCE

Engine speed, 1,500 r. p. m.; fuel consumption, 3.25×10^{-4} lb./cycle; no excess air; cylinder head as shown in fig. 3 (b); compression ratio, 13.5; N. A. C. A. 7A pump and 13A fuel valve; 0.050-inch nozzle; length-diameter ratio, 2.5]

Passage	i. m. e. p., lb./sq. in.		b. m. e. p., lb./sq. in.		Explosion pressure, lb./sq. in.		Fuel consumption			
							lb./i. hp.-hr.		lb./b. hp.-hr.	
	Flame start	Full load	Flame start	Full load	Flame start	Full load	Flame start	Full load	Flame start	Full load
FUEL-VALVE LOCATION 2										
50-percent radial	133	138	98	103	730	720	0.35	0.41	0.48	0.56
50-percent tangential	138	141	103	106	760	760	.33	.40	.46	.52
70-percent radial	133	140	98	104	830	830	.34	.41	.48	.55
70-percent tangential	139	144	104	109	800	790	.36	.38	.48	.51
FUEL-VALVE LOCATION 1										
50-percent radial	131	141	99	109	790	800	0.35	0.41	0.48	0.52
50-percent tangential	131	135	98	102	820	820	.38	.42	.51	.55
70-percent radial	141	147	108	112	880	880	.35	.39	.47	.52
70-percent tangential	132	138	98	104	800	780	.36	.42	.49	.55

As the air flow with either passage is rotational, the differences in performance shown for the different fuel-valve locations (table VI) are more readily understood. It was found that with either passage in the spherical chamber the performance was improved by injecting the fuel at the point "upstream" on the circumference of the chamber. Location 1 was better when using the radial passage and location 2 better when using the tangential passage. (See fig. 3 (b).) In the disk chamber, injecting the fuel near the passage mouth but directly toward the passage gave the worst results.

CYLINDER-CLEARANCE SHAPE

In the tests of clearance distribution and passage size, a domed piston crown was employed. At the conclusion of these tests, the performance with the domed crown was compared with that using first a flat crown, second a dished crown, and third a piston crown with all the cylinder clearance concentrated in front of the connecting passage. Extensive tests were made using this latter type of piston crown, but the performance was inferior to either of the other two piston crowns.

For the sake of convenience in testing, subsequent tests were made using a flat piston crown since there was little difference between the performance of the flat and the domed crown piston.

INJECTION SYSTEMS

The 50-percent disk chamber with the tangential passage was assembled with head 7 at a compression ratio of 13.5 and, using fuel-valve location 1, the injection system was varied to determine the effect on engine performance. Three fuel pumps having widely different characteristics were selected and tested with different fuel-valve assemblies that gave a variety of injection systems. The N. A. C. A. 7A and the commercial fuel pump used were cam-operated and of constant stroke but had different rates of displacement. The third injection pump was the N. A. C. A. 12, a cam-operated plunger type, but one in which injection is caused by the release of pressure stored in a reservoir of correct volume. This pump in combination with the correct valve gives a fast rate of injection and was used to obtain a shorter injection period than that of any of the other pump and valve combinations. The N. A. C. A. 7A fuel pump and the single 0.050-inch-diameter orifice were used to determine the effect of the orifice length-diameter ratio. Results obtained by using multiple orifices to distribute the fuel by injection as well as by air flow were also determined. Tests of a pintle nozzle with two different fuel pumps were included in the injection-system investigation. With the injection system that gave the best engine performance, tests were made to determine the effect of injection advance angle and fuel quantity on engine performance.

In order to improve the inherently poor starting characteristics of this type of combustion chamber, a series of starting tests was made, injecting the fuel directly into the cylinder instead of into the prechamber. An 0.008-inch-diameter orifice nozzle was used with a valve-opening pressure of 2,500 pounds per square inch. The size of the orifice used limited the fuel injected to very small quantities. The engine was motored at gradually increasing speeds until the engine started firing and the speed could be maintained under its own power. For comparison, this procedure was repeated with the same fuel nozzle in the prechamber.

Table VII shows the results of the injection-system tests. The object of these tests was to obtain a fuel spray the characteristics of which best suited the 50-percent vertical-disk chamber and tangential passage, the arrangement that had given the best performance for this size of chamber. Injection period was the only spray characteristic accurately measured because in this type of chamber with its high air-flow speed other characteristics, such as distribution of fuel within the spray and spray cone angle, should not be critical. As shown in the table the optimum performance based on the i. m. e. p. at flame start and full load was obtained using the N. A. C. A. 7A fuel pump, 13A fuel valve, and 0.050-inch nozzle with a length-diameter ratio of 6. Multiple-orifice nozzles were tried but, as they were definitely inferior, the performance is not included.

TABLE VII

EFFECT OF INJECTION SYSTEMS ON ENGINE PERFORMANCE

[Engine speed, 1,500 r. p. m.; fuel consumption, 3.25×10^{-4} lb./cycle; no excess air; cylinder head as shown in fig. 3 (c); compression ratio, 13.5; fuel valve in location 1]

Injection system	i. m. e. p. lb./sq. in.		b. m. e. p. lb./sq. in.		Explosion pressure lb./sq. in.		Fuel consumption				Relation of injection to top center, crank angle, degrees
							lb./i. hp.-hr.		lb./b. hp.-hr.		
	Flame start	Full load	Flame start	Full load	Flame start	Full load	Flame start	Full load	Flame start	Full load	
N. A. C. A. 7A pump:											
13A valve:											
0.050-inch-diameter orifice:											
Length-diameter ratio, 2.5	145	149	109	112	700	700	0.35	0.38	0.48	0.49	7 B. T. C. to 14 A. T. C.
Length-diameter ratio, 4.0	143	148	107	111	710	700	.36	.38	.48	.50	Do.
Length-diameter ratio, 5.0	145	149	108	112	.....	.....	.35	.37	.47	.50	Do.
Length-diameter ratio, 6.0	146	150	109	113	700	700	.35	.37	.48	.49	Do.
0.040-inch-diameter orifice	132	142	95	106	640	630	.35	.40	.49	.53	7 B. T. C. to 15 A. T. C.
0.070-inch-diameter orifice	145	148	108	112	740	730	.36	.38	.48	.49	7 B. T. C. to 12 A. T. C.
Commercial valve; pintle nozzle	141	147	104	110	720	720	.35	.36	.47	.50	7 B. T. C. to 16 A. T. C.
Commercial pump:											
13A valve; 0.050-inch-diameter orifice; 3,500 lb./sq. in. valve-opening pressure.	140	150	103	113	760	740	.33	.38	.46	.50	7 B. T. C. to 14 A. T. C.
Commercial valve; pintle nozzle, 3,500 lb./sq. in. valve-opening pressure.	133	143	98	108	740	790	.35	.39	.48	.51	4 B. T. C. to 20 A. T. C.
N. A. C. A. 12 pump:											
13A valve; 0.050-inch-diameter orifice; 3,500 lb./sq. in. valve-opening pressure.	141	147	104	111	860	870	.34	.38	.47	.50	7 B. T. C. to 27 A. T. C.
17—3/16 F. I. S. valve; 0.059-inch-diameter orifice; 6,000 lb./sq. in. valve-opening pressure.	128	144	92	108	720	720	.35	.39	.48	.52	3 B. T. C. to 7 A. T. C.
17—3/16 F. I. S. valve; 0.051-inch-diameter orifice, 3,500 lb./sq. in. valve-opening pressure.	.....	150	.....	112	.....	730	.....	.38	.....	.50	4 B. T. C. to 11 A. T. C.

Marked improvement in the capability of the engine to start at a temperature of about 70° F. was obtained by injecting the fuel into the cylinder. By the use of a nozzle with a single 0.008-inch-diameter orifice and the injection of only a small percentage of full-load fuel quantity, the engine could be started by motoring the engine at from 200 to 300 r. p. m.; whereas, when the fuel was injected into the chamber with the same nozzle, a speed of 600 to 700 r. p. m. was required. Improvement in starting is due to a higher temperature in the cylinder.

Figure 14 shows the results of the variable-injection-advance-angle tests. These curves are characteristic

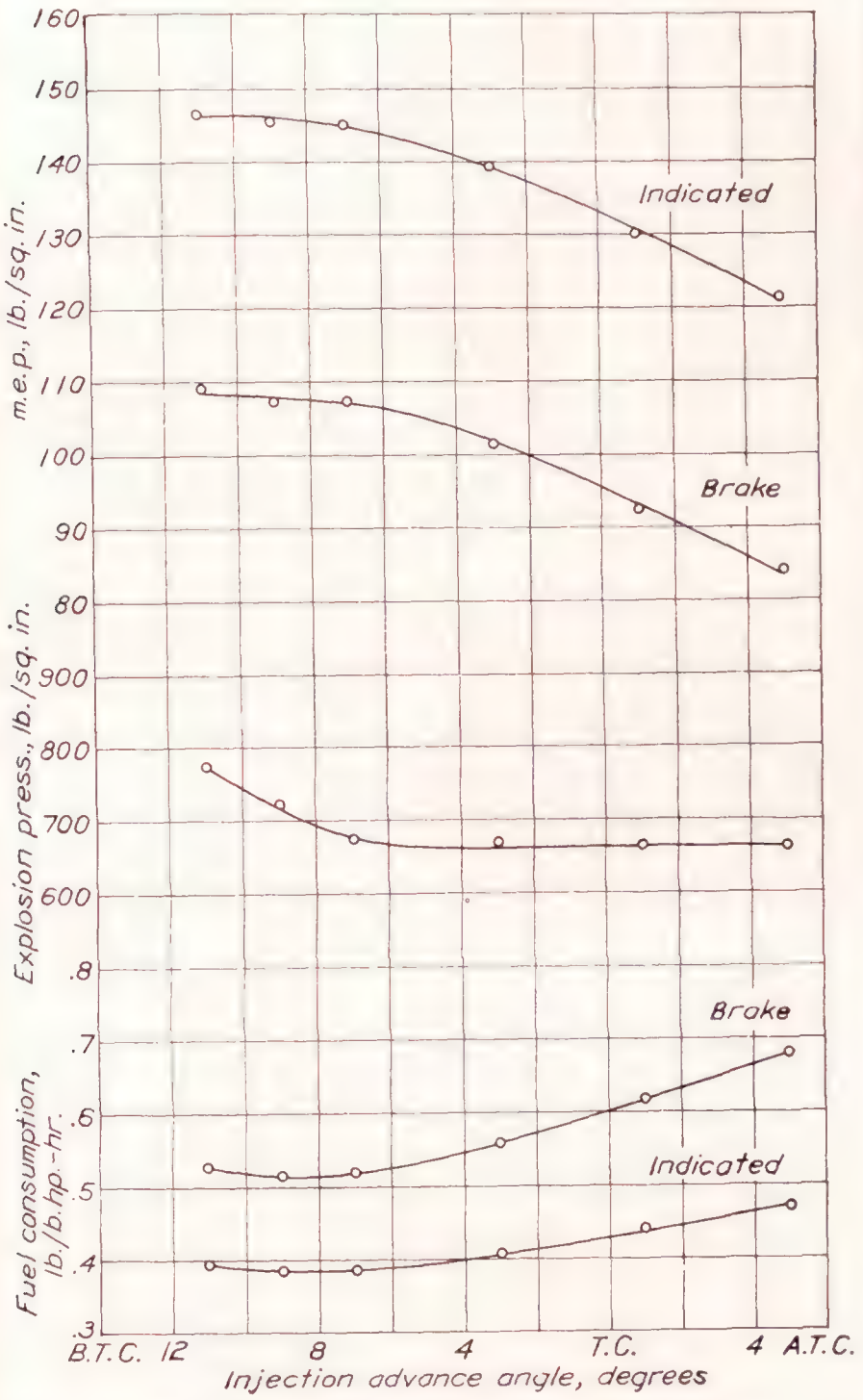

FIGURE 14.—Effect of injection advance angle on engine performance. Engine speed, 1,500 r. p. m.; fuel consumption, 3.0 × 10^{-4} lb./cycle; 12 percent excess air; cylinder head as shown in figure 3 (c); compression ratio, 13.5; N. A. C. A. 7A fuel pump and 13A fuel valve; 0.050-inch nozzle; length-diameter ratio, 2.5.

of the prechamber type of combustion chamber. For these tests the optimum advance angle was 7° before top center because at this point increase in mean effective pressure stopped while increase in maximum cylinder pressure began.

The results of the variable-fuel-quantity test are shown in figure 15. The curve of mean effective pressure against fuel quantity shows the characteristic straight line at small fuel quantities but, for the combustion chamber under test, the curve continues straight to comparatively large fuel quantities. The mean

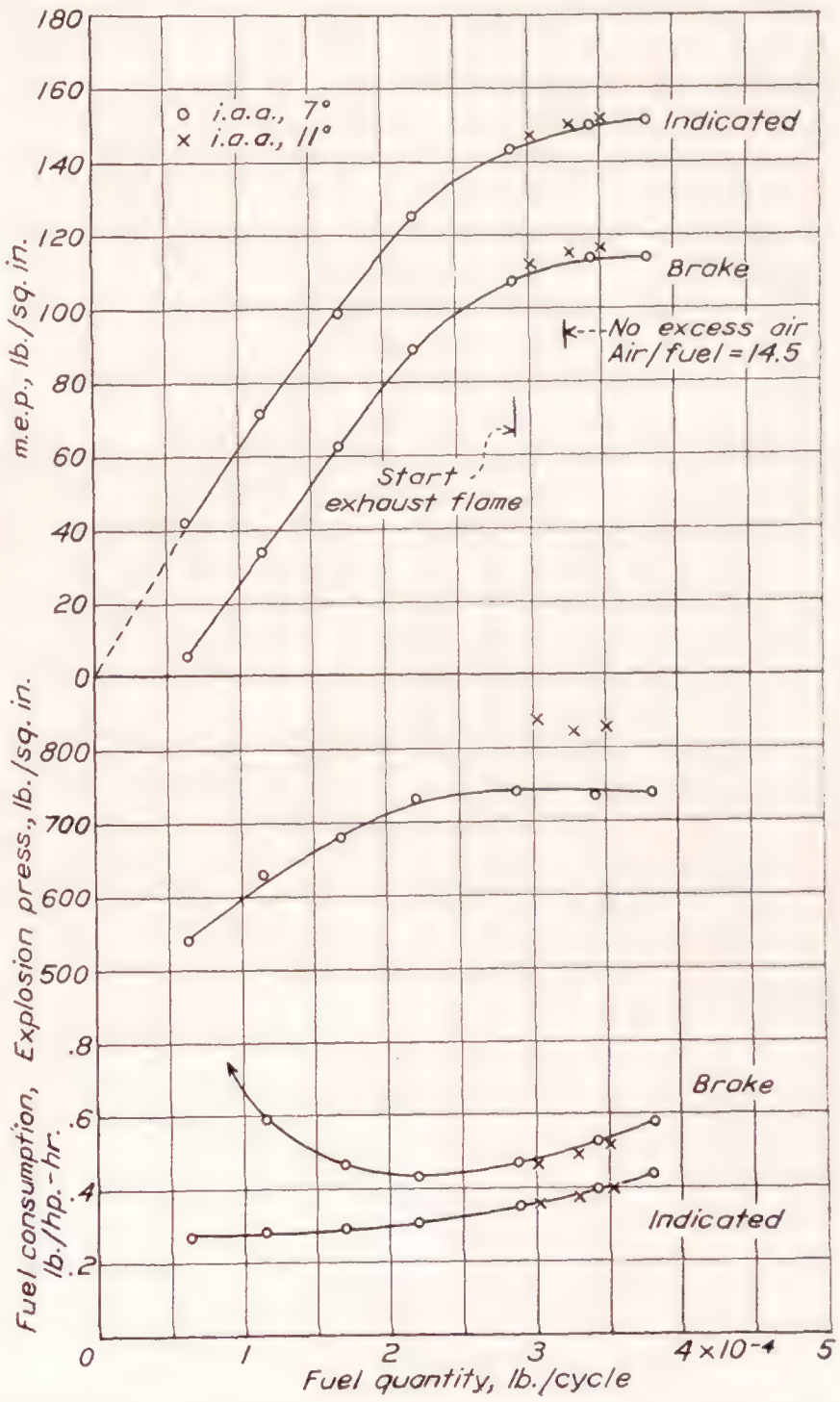

FIGURE 15.—Effect of fuel quantity on engine performance. Engine speed, 1,500 r. p. m.; cylinder head as shown in figure 3 (c); compression ratio, 13.5; N. A. C. A. 7A fuel pump and 13A fuel valve; 0.050-inch nozzle; length-diameter ratio, 6.

effective pressure varies linearly with the quantity of fuel injected up to a fuel quantity of 2.25×10^{-4} pound per cycle (air-fuel ratio approximately 23) but the curve begins to droop at this point; when the fuel quantity is increased to 2.90×10^{-4}, flame appears in the exhaust. With this type of combustion chamber, flame appears in the exhaust before smoke. Both flame and smoke can be seen in the exhaust at full-load fuel quantity.

The points of figure 15 that do not fall on the curve represent the data obtained at a 4° increase of the injection advance angle. It will be noted that the explosion pressure increased out of proportion to the increase in engine performance, and therefore the

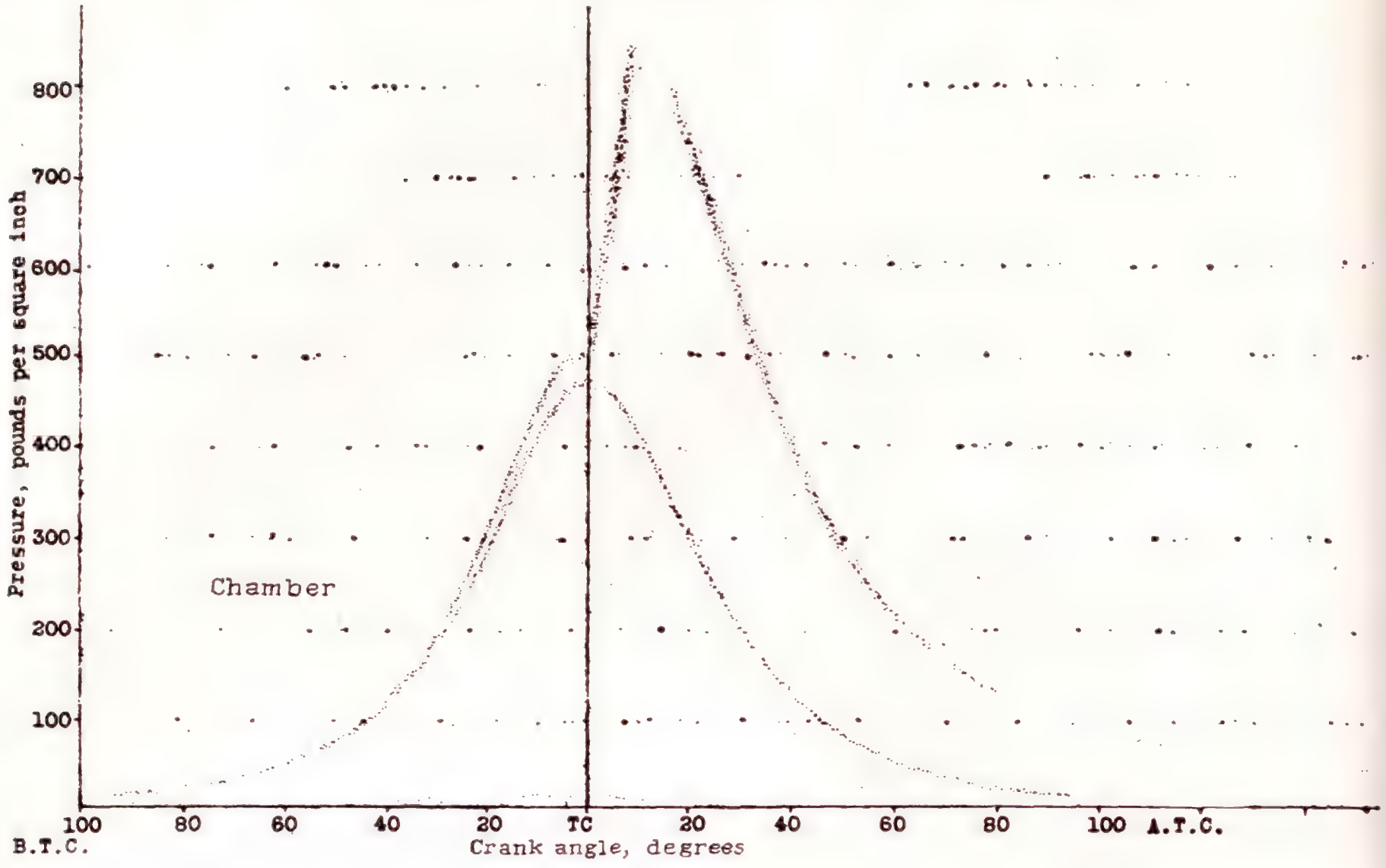

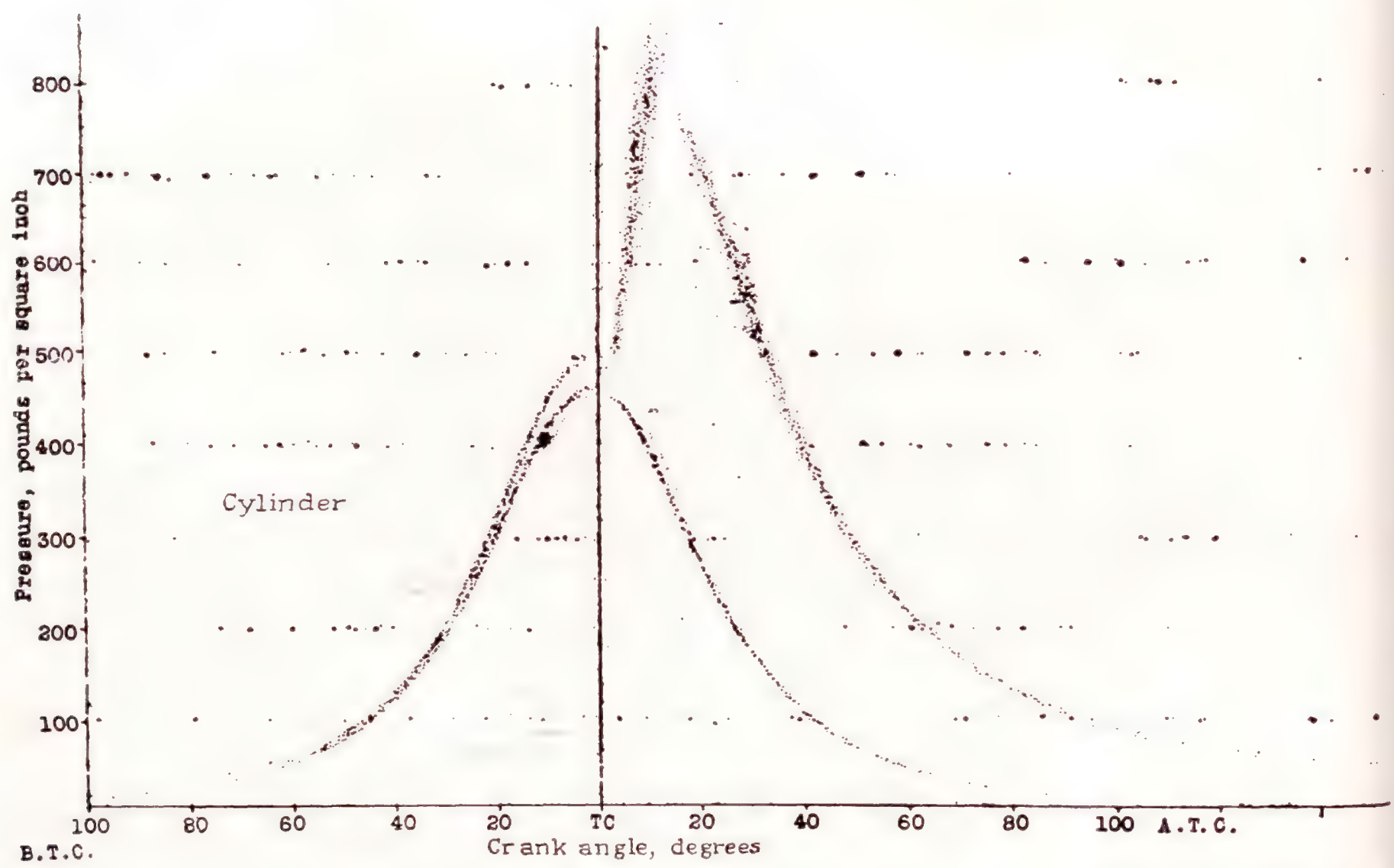

FIGURE 16.—Typical power and motoring indicator cards. Engine speed, 1,500 r. p. m.; fuel consumption, 3.25×10^{-4} lb./cycle; no excess air; cylinder head as shown in figure 3 (c); N. A. C. A. 7A fuel pump and 13A fuel valve; 0.050-inch nozzle; length-diameter ratio, 6; injection advance angle, 7° B. T. C.

injection advance angle was not further increased. In all except these tests the injection advance angle was determined by the combustion sound. In these tests, although the sound of combustion became more intense, the condition was not considered dangerous.

At the full-load fuel quantity during the variable-load run, made with the best combustion-chamber shape and fuel-injection system, indicator cards typical of those obtained from this engine were taken from the chamber and cylinder (fig. 16). The rates of pressure rise determined from the indicator diagrams are 68 and 45 pounds per square inch per degree for the cylinder and prechamber, respectively.

COMPRESSION RATIO

The lack of engine data concerning the influence of compression ratio on engine operation and performance made an investigation of compression ratio desirable (reference 8). An attempt was first made to follow the usual procedure of changing only one variable at a time. After some preliminary tests, however, this procedure was found to be so expensive that it was decided to permit variation of the clearance distribution and to change the compression ratio by raising or lowering the head, i. e., by varying the cylinder-clearance volume. Explosion pressures were kept nearly constant by controlling the injection advance angle.

The results of the tests at different compression ratios are shown in figure 17. The curves have been plotted without correcting for the change in performance due to the increase in relative chamber size, which would amount to about one-half the mean-effective-pressure increase shown at the highest compression ratio. When the chamber size is taken into account, there is still a small but definite trend toward an increase in indicated power with an increase in compression ratio. This trend is in agreement with theoretical analysis, which indicates higher cycle efficiencies at higher compression ratios. The brake performance shows very little change, possibly because the increased cycle efficiency at the higher compression ratios was counteracted by the decreased mechanical efficiency.

Starting and general operating characteristics improved with increasing compression ratio. At the highest compression ratio, the increased compression temperature reduced the ignition lag and caused the combustion knock to soften and practically disappear. As the compression ratio was increased, it was found necessary to reduce the injection advance angle by several degrees in order to hold the cylinder pressure constant throughout the tests. Limitation of maximum cylinder pressure, however, did not result in a loss of power; in fact, short tests at higher cylinder pressures in some cases showed a slight impairment of performance.

Indicator cards taken at each compression ratio illustrated very clearly the decrease in allowable pressure rise as the compression pressure approached the maximum cylinder pressure; the only gain in performance was from the higher cycle efficiency. A decrease in the rate of pressure rise is also shown on the cards, but otherwise they have the same general shape as the cards heretofore presented; therefore they are not included.

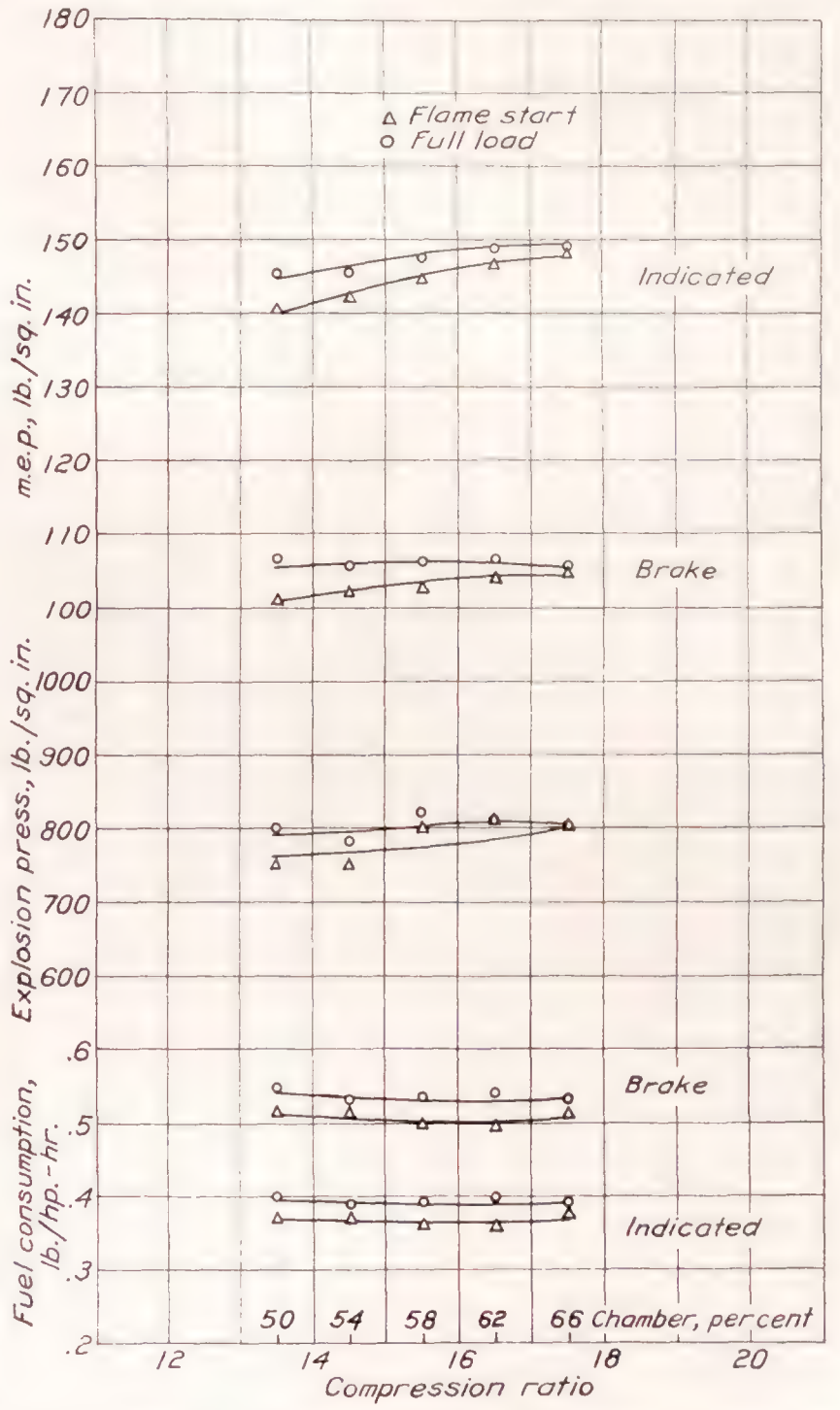

FIGURE 17.—Effect of compression ratio on engine performance. Engine speed, 1,500 r. p. m.; fuel consumption, 3.25×10^{-4} lb./cycle; no excess air; cylinder as shown in figure 3 (c); N. A. C. A. 7A fuel pump and 13A fuel valve; 0.050-inch nozzle; length-diameter ratio, 6.

With the disk chamber, the greatest compression ratio that could be obtained was 17.5. The trend of the curves indicates, however, that there would be no improvement in brake performance at higher compression ratios. Although an optimum compression ratio is not clearly defined, the b. m. e. p. at flame start, the easier starting, and the quieter operation favor the use of a high compression ratio in this type of engine.

BOOSTING OF AIR CHARGES

Boosting tests were conducted on the engine assembled with the optimum combination of variables. For continuity throughout the investigation, the compression

ratio was retained at 13.5. A DePalma supercharger with a 12-cubic-foot surge tank was connected to the engine and variable-load runs made at boost pressures

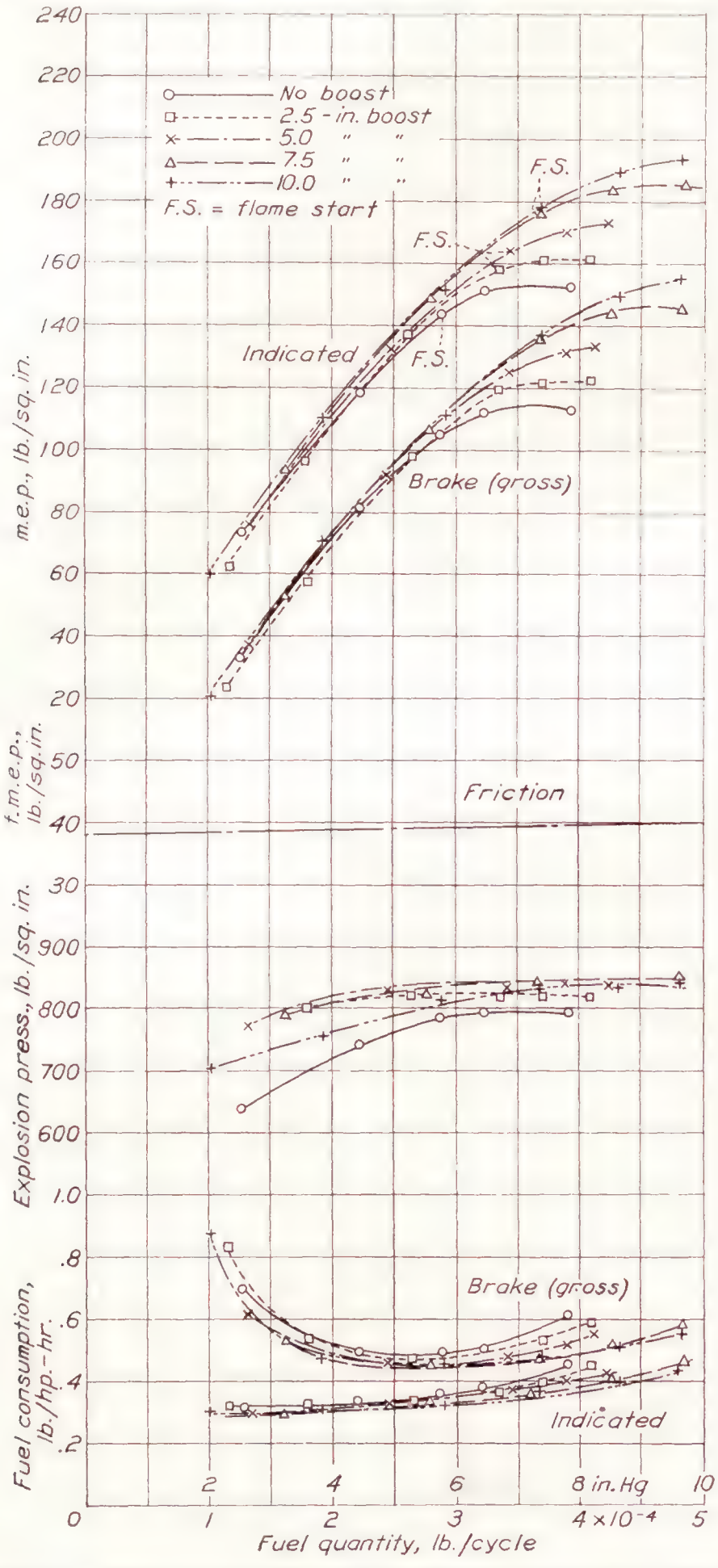

FIGURE 18.—Effect of fuel quantity on engine performance at several boost pressures. Engine speed, 1,500 r. p. m.; cylinder head as shown in figure 3 (c); compression ratio, 13.5; N. A. C. A. 7A fuel pump and 13A fuel valve; 0.050-inch nozzle; length-diameter, 6.

of 0, 2.5, 5, 7.5, and 10 inches of mercury at 900, 1,200, and 1,500 r. p. m. At 1,500 r. p. m. one point was taken at the highest boost pressure obtainable with the supercharger used, about 13½ inches of mercury. Explosion pressures were kept nearly constant by retarding the injection advance angle as the boost pressure was increased. At 1,800 r. p. m. power tests were made at each of the test pressures at the flame-start fuel quantity and at one larger fuel quantity. Friction tests were made by motoring the engine after each power run at the different boost pressures and engine speeds.

The effect of boosting a prechamber type of cylinder head was rather thoroughly investigated because the authors could find no references to previous tests by other investigators. However, only the data at 1,500 r. p. m., which are representative of the entire family of curves, are presented (fig. 18). The m. e. p. curves are quite conventional in shape and, at an air-fuel ratio of 14.5, show a constant increase of from 3 to 4 pounds per square inch per inch of boost pressure.

The objective of holding the explosion pressure constant while the boost pressure was varied during the tests was not exactly accomplished, but the increase in explosion pressure shown was within the limitations of the equipment used. Explosion pressures were controlled by varying the injection advance angle, which was 7° at zero boost pressure and was progressively retarded until at 10 inches of mercury the injection advance angle was only 2°. Since the compression pressure increases with boost pressure and the maximum cylinder pressure was kept constant, the amount of fuel that could be burned at or near top center was decreased by retarding the injection. If it had not been necessary to decrease the injection advance angle, the gain in power with increased boost pressure would have been slightly greater because more fuel could have been burned at or near top center with a resulting greater efficiency. Because of the higher compression pressures with the consequent reduction in ignition lag, however, the power loss was not nearly so great as if the injection advance angle had been reduced the same amount at zero boost pressure.

In view of these facts, it is possible that it might be advantageous to use a compression ratio lower than 13.5 for boosting because the compression pressure would be lower and a greater useful pressure rise could be used. The influence of boost pressure on the combustion shock would permit a lower compression ratio to be used because the combustion shock is diminished with increased inlet pressure, although a lower compression ratio alone would increase it. At the boost pressure of 7.5 inches of mercury, the sound of the engine was very satisfactory at all loads and at each test speed.

An examination of the curves presented herein shows that the friction mean effective pressure, neglecting supercharger friction mean effective pressure, did not decrease with increase in boost pressure. This observation applies for all test speeds. With the integral combustion-chamber type of cylinder head, the friction mean effective pressure, also neglecting the power required by the supercharger, was found to decrease

slightly with increase in boost pressure. This condition did not exist with the type of cylinder head under test, probably because of the increase in pumping loss as the weight of air forced through the connecting passage is increased. At large boost pressures the higher pumping losses more than offset the work done on the piston during the intake stroke, which resulted in a slight increase in friction mean effective pressure.

In these tests the connecting passage was maintained at a fixed diameter, which is probably not the best condition. The ideal way of conducting the tests would have been to determine and use the correct passage size for each boost pressure. The injection period was too long at high boost pressures, as the injection system is designed to deliver, in approximately 20 crankshaft degrees, a fuel quantity of 3.25×10^{-4} pounds per cycle, which is full load at zero boost. The full-load fuel quantity and consequently the injection period, however, increase with boost. At high boost pressures, therefore, the injection period continued too long after top center for efficient combustion. It is believed that the performance at the optimum boost pressure would be improved if the correct passage area and injection period were used; however, the scope of these tests did not include the determination and application of each of these conditions. With this type of combustion chamber improvement in engine performance by scavenging the clearance volume is practically impossible because all the clearance should be in the prechamber away from the valves. Furthermore, owing to lack of mechanical clearance when the piston is on top center, both valves must be closed. This condition is improper for the best exhausting and air charging, which limits the specific output.

CONCLUSIONS

The following specific conclusions are presented:

1. Clearance distribution:

(*a*) For maximum performance the prechamber should be relatively as large as is practicable; however, lower cylinder pressures, less combustion knock, and less heat loss to the cooling water occur with the smaller chamber sizes.

(*b*) The size of the prechamber has a negligible effect on friction mean effective pressure and compression pressures.

(*c*) Variation of clearance distribution only, for a fixed ratio of prechamber volume to connecting passage area, does not sufficiently control combustion or eliminate combustion knock.

2. Connecting-passage diameter:

(*a*) For the engine size and combustion-chamber design used in this investigation, the connecting-passage diameter should be between $^{29}/_{64}$ and $^{17}/_{32}$ inch, or the equivalent area; the i. m. e. p., the fuel economy, and combustion knock at 1,500 r. p. m. favoring the smaller passage size.

(*b*) The size of the connecting passage becomes less critical as the engine speed is decreased. It is therefore possible to select a passage size for maximum operating speed and still have good performance at the lower speeds.

(*c*) The friction mean effective pressure due largely to throttling losses was excessive when a passage diameter of less than $^{29}/_{64}$ inch was employed; however, for a passage diameter equal to $^{29}/_{64}$ inch, the friction mean effective pressure was acceptable and the rate of decrease with increase in passage area became much less.

(*d*) It was impossible to obtain both high performance and combustion-pressure control with any combination of variables tried in this investigation.

The general conclusions are:

From the results of this investigation of the prechamber type of cylinder head, several optimum conditions are evident. For maximum performance of this engine, which has a 5-inch bore and a 7-inch stroke, the compression ratio should be between 15.5 and 17.5, the prechamber should be relatively as large as possible, disk-shaped, and connected to the cylinder clearance by a single passage the area of which is determined by the highest engine speed. Entering the chamber tangentially, the passage should cause a strong rotational air flow and, upon entering the cylinder, should be flared to spread the issuing gases over the piston crown. The injection system should deliver full-load fuel with atmospheric induction in the shape of a narrow conical spray of high penetration requiring approximately 20 crankshaft degrees for injection. This spray should be directed across the disk chamber, with the air flow, toward the mouth of the connecting passage. The spray direction greatly affects the engine performance. Considerable improvement in engine performance and combustion knock can be obtained by boosting.

As all of the clearance should be in the prechamber, proper valve timing and scavenging are prohibited, a condition which limits the specific output.

LANGLEY MEMORIAL AERONAUTICAL LABORATORY,
NATIONAL ADVISORY COMMITTEE FOR AERONAUTICS,
LANGLEY FIELD, VA., *July 7, 1936.*

REFERENCES

1. Reichle, W. A.: Report of One Cylinder Liberty Engine Tests. Serial No. 55, Bur. Aircraft Production, Airplane Eng. Div., McCook Field, Dayton, Ohio, June 10, 1918.
2. Ware, Marsden: Description of the N. A. C. A. Universal Test Engine and Some Test Results. T. R. No. 250, N. A. C. A., 1927.
3. Joachim, William F., and Kemper, Carlton: The Performance of Several Combustion Chambers Designed for Aircraft Oil Engines. T. R. No. 282, N. A. C. A., 1928.

4. Spanogle, J. A., and Moore, C. S.: Performance of a Compression-Ignition Engine with a Precombustion Chamber Having High-Velocity Air Flow. T. N. No. 396, N. A. C. A., 1931.
5. Moore, C. S., and Foster, H. H.: Performance Tests of a Single-Cylinder Compression-Ignition Engine with a Displacer Piston. T. N. No. 518, N. A. C. A., 1935.
6. Moore, Charles S., and Collins, John H., Jr.: Friction of Compression-Ignition Engines. T. N. No. 577, N. A. C. A., 1936.
7. Spanogle, J. A., and Foster, H. H.: Basic Requirements of Fuel-Injection Nozzles for Quiescent Combustion Chambers. T. N. No. 382, N. A. C. A., 1931.
8. Pye, D. R.: The Limits of Compression Ratio in Diesel Engines. R. & M. No. 1365, British A. R. C., 1931.

BIBLIOGRAPHY

Loschge, A.: Vergleichende Druckindizierversuche an einem Luftspeicherund an einem Vorkammerdieselmotor. Auto. tech. Zeitschr., Jahrg. 35, Nr. 23, 10. Dezember, 1932, S. 562–568.

Mehlig, Hans: Die Vorkammergrösse und ihr Einfluss auf das Arbeitsverfahren der Vorkammer-Dieselmaschinen. Auto. tech. Zeitschr., Jahrg. 32, Nr. 32, 20. November, 1929, S. 723–725, und Jahrg. 32, Nr. 34, 10. Dezember 1929, S. 783–785.

Moore, C. S., and Collins, J. H., Jr.: The Effect of Clearance Distribution on the Performance of a Compression-Ignition Engine with a Precombustion Chamber. T. N. No. 433, N. A. C. A., 1932.

Moore, C. S., and Collins, J. H., Jr.: The Effect of Connecting Passage Diameter on the Performance of a Compression-Ignition Engine with a Precombustion Chamber. T. N. No. 436, N. A. C. A., 1932.

Moore, C. S., and Collins, J. H., Jr.: Effect of Combustion-Chamber Shape on the Performance of a Prechamber Compression-Ignition Engine. T. N. No. 514, N. A. C. A., 1934.

Neumann, Kurt: Diesel-Engine Investigations. Ignition Chamber Engines. T. M. No. 589, N. A. C. A., 1930.

Ritz, G.: Beitrag zur Verbrennungstechnik des schnellaufenden Vorkammer-Dieselmotors. Auto. tech. Zeitschr., Jahrg. 36, Nr. 8, 25. April 1933, S. 197–203.

Rühle, Hans: Der Druckverlauf im Zündkammermotor. Zeitschr. f. tech. Physik, Bd., Zehnter Jahrg., Nr. 10, 1929, S. 465–472.

Schlaefke, K.: Vorgänge beim Verdichtungshub von Vorkammer-Dieselmaschinen. Z. V. D. I., Bd. 75, Nr. 33, 15. August 1931, S. 1043–1046.

Schwaiger, K.: Einzelheiten über das Vorkammerverfahren. Auto. tech. Zeitschr., Jahrg. 37, Nr. 16, 25. August 1934, S. 422–424.

REPORT No. 578

FLIGHT MEASUREMENTS OF THE DYNAMIC LONGITUDINAL STABILITY OF SEVERAL AIRPLANES AND A CORRELATION OF THE MEASUREMENTS WITH PILOTS' OBSERVATIONS OF HANDLING CHARACTERISTICS

By Hartley A. Soulé

SUMMARY

The dynamic longitudinal stability characteristics of eight airplanes as defined by the period and damping of the longitudinal oscillations were measured in flight to determine the degree of stability that may be expected in conventional airplanes. An attempt was made to correlate the measured stability with pilots' opinions of the general handling characteristics of the airplanes in order to obtain an indication of the most desirable degree of dynamic stability. The results of the measurements show that the period of oscillation increases with speed. At low speeds a range of periods from 11 to 23 seconds was recorded for the different airplanes. At high speeds the periods ranged from 23 to 64 seconds. The damping showed no definite trend with speed. A general tendency for airplanes that were stable with power off to become unstable with power on was noted. The maximum damping recorded was sufficient to reduce the amplitude of oscillation by one-half in 9 seconds, or approximately one-fourth cycle. The opinions of two pilots concerning the handling characteristics of the airplanes apparently were not influenced by the stability characteristics as defined by the period and damping of the longitudinal oscillations.

INTRODUCTION

The theory of dynamic longitudinal stability of airplanes, although not complete for power-on flight owing to a lack of knowledge of the effect of the propeller slipstream on certain of the stability derivatives, has been developed to the point where it is possible to predict the power-off stability characteristics of an airplane from its dimensions. (See reference 1.) The longitudinal motion of an airplane following a disturbance may consist either of a continuous divergence, i. e., static instability, or of two superimposed oscillations of different periods and damping. In the present case consideration is given only to the oscillatory motion since no statically unstable airplane should be regarded as satisfactory. The periods and damping of both oscillations are given by the theory but, as the short-period oscillation is so heavily damped that there is no probability of instability of the oscillation for conventional airplanes, it is usual to consider the dynamic longitudinal stability characteristics to be defined by the period and damping of only the long-period, or phugoid, oscillation. With the aid of the charts of reference 1, the areas and dimensions of airplanes can be adjusted during design to produce, within limits, any length of the period and magnitude of damping desired for this oscillation. Aside from the desirability of having the airplane stable for all normal-flight conditions, little is known as to the length of the period and the magnitude of the damping that constitute satisfactory stability. Pilots express opinions of an airplane's longitudinal stability in terms of such factors as "stiffness" and of pitching or unsteadiness in flight through rough air, but the relation between these observed characteristics and the degree of stability as defined by the period and damping of the phugoid oscillation is unknown.

In the present tests, the period and damping of the phugoid oscillations of several airplanes were measured and, in addition, the general handling characteristics as related to longitudinal motions were observed. The measurements were made to obtain information on the degree of stability to be expected in conventional airplanes. The observations of the handling characteristics were made to determine whether there is any definite relationship between the stability as defined by period and damping of oscillations and the pilot's impression of handling characteristics. It was hoped that the tests would provide an indication of the degree of dynamic stability desired.

The theory of stability indicates that the period and damping of the phugoid oscillations are affected by engine power and elevator restraint as well as by speed. It was therefore desirable to make the measurements for several conditions. The tests were made with eight single-engine airplanes of different types:

two high-wing monoplanes and six biplanes. The weights ranged from 1,440 to 6,100 pounds and the engine powers from 95 to 575 horsepower. Where feasible, the measurements of period and damping were made for a speed range extending from 10 miles per hour above the minimum speed to the maximum speed in level flight for the following conditions:

1. Elevator fixed with throttle closed.
2. Elevator fixed with full throttle.
3. Elevator free with throttle closed.
4. Elevator free with full throttle.

The handling characteristics of each airplane were rated by each of two test pilots.

APPARATUS AND METHOD

The eight airplanes tested were the Fairchild 22, the Martin XBM–1, the Verville AT, the Martin T4M–1, the Fairchild FC2–W2, the Boeing F4B–2, the Consolidated NY–2, and the Douglas O–2H. The dimensions of these airplanes pertinent to their longitudinal-stability characteristics are given in table I. The weights and center-of-gravity locations given are for the airplanes as flown in the tests and do not represent full-load conditions. The NY–2 airplane has a fixed stabilizer that limited the elevator-free runs to one air speed.

The following procedure was employed in the tests: All runs were made at a mean pressure altitude of approximately 3,000 feet. Steady conditions were first obtained at a given speed. For the elevator-free runs the stabilizer was adjusted to obtain trim at this speed. The oscillations were induced by depressing the nose of the airplane with the elevator until a steady speed of approximately 5 miles per hour above the initial flight speed was obtained. The elevator was then immediately returned to the original setting for the elevator-fixed runs or freed for the elevator-free runs. Adjustable stops were provided for the elevator-fixed runs to assist the pilot in resetting the elevator to the original position and in holding it fixed during the oscillations.

The air speed was used for the determination of the period and damping of the oscillations. The variation of air speed with time was obtained by means of a recording air-speed meter and timer started prior to the start of the oscillations. The record of air speed was obtained for at least two complete cycles of oscillation. The period of the oscillation was, of course, the time between successive peaks on the air-speed record. The damping factor ζ was computed by the equation

$$\zeta=\frac{2}{P}\log_e\frac{V_3-V_2}{V_1-V_2}\quad\text{(from reference 2)}$$

where P is the period in seconds, V_1 and V_3 are the true air speeds in feet per second at successive maximums, and V_2 the air speed at the intervening minimum. The time T required for an oscillation to damp to one-half amplitude was obtained by the equation

$$T=\frac{-0.693}{\zeta}$$

The period and the time to damp to one-half amplitude were plotted as functions of the mean air speed during the oscillation.

RESULTS AND DISCUSSION

The results of the measurements are given in figures 1 to 4. The figures show that the period and the damping vary considerably with speed for a given condition, between different conditions, and among different airplanes. The condition with the elevator fixed with throttle closed (fig. 1) is the only one which is completely covered by the theory at the present time and for which the stability derivatives may be readily computed. For this condition, all the airplanes were stable in the speed ranges covered by the tests. The curves show an almost linear increase of period with the velocity of flight and, with the exception of the results for the O–2H airplane, there is very little difference between the curves for the different airplanes. Longitudinal-stability theory indicates that the period may be approximated by the equation

$$P=0.142(2+a)^{1/2}V$$

where V is the velocity in miles per hour, and a is a variable dependent on the aerodynamic characteristics but which does not change greatly for conventional airplanes. Computations made on the basis of figure 1 show that a constant value of 1.4 for a is satisfactory for approximating the period of conventional airplanes for the speed range of the tests for the power-off elevator fixed condition. The equation would then reduce to

$$P=0.262V$$

The damping is a more critical stability characteristic than the period and, consequently, the damping curves show more dispersion than those for the period. The times for an oscillation to damp to one-half amplitude show a slight general tendency to decrease with increasing velocity. In general, the number of cycles required to damp to one-half amplitude varies inversely as the period.

The effect of power on the stability characteristics is shown by a comparison of the curves of figure 2, for the elevator fixed with full throttle, with the curves of figure 1. The periods of the oscillations are generally longer with full throttle than with the throttle closed. The damping is less, that is, the time required to damp to one-half amplitude is longer. The power effects are greatest at low speeds where the propeller thrust and the ratio of slipstream velocity to forward speed are greatest. All of the airplanes with the exception of the

T4M–1 showed a tendency toward dynamic instability at low speeds with power on. Four airplanes, the O–2H, the F4B–2, the AT, and the NY–2, actually became unstable within the speed range covered by the tests. The instability existed in the form of an increase in the amplitude of the oscillations with time. No case of instability in the form of continuous divergence from steady conditions, corresponding to a positive slope of the pitching-moment curve or static instability, was encountered in the tests.

Figures 3 and 4 present the results for the elevator-free tests. A comparison of figures 1, 2, and 3 shows

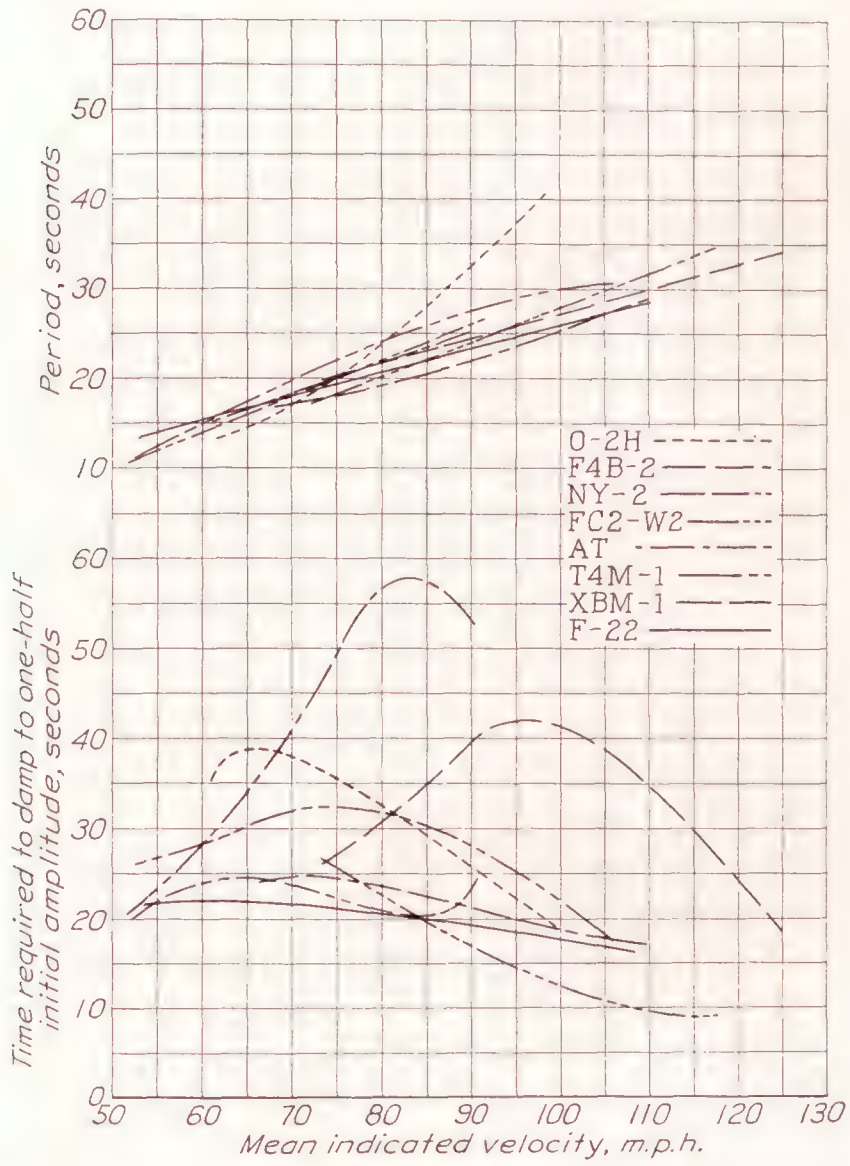

FIGURE 1.—Period and damping of longitudinal oscillations with elevator fixed and power off.

that the stability characteristics are considerably less affected by freeing the elevator than by applying power. The periods are slightly shorter with free elevator than with the elevator fixed. The damping is decreased, but only the results for the O–2H airplane show instability. All the airplanes had statically unbalanced elevators. For elevators equipped with mass balances, as is usual with more modern airplanes, the differences between the elevator-fixed and elevator-free stability would probably be less than that recorded.

For most cases power has the same general effect of decreasing the period and damping with the elevator free as with it fixed. The O–2H airplane is an exception. This airplane with the elevator fixed was stable with the throttle closed and unstable with the throttle open. With elevator free, it was unstable with the throttle closed and stable with the throttle open.

Table II has been prepared to show the test conditions for which instability was recorded for the various airplanes. As will be noted, only the F–22 and the T4M–1 were stable for all test conditions and speeds. The FC2–W2 and the XBM–1 were stable for three of the four test conditions. The F4B–2, AT, and O–2H airplanes were completely stable for only two conditions. The NY–2 airplane was unstable for only one condition but, since this airplane had a fixed stabilizer, the elevator-free runs were made at only one speed.

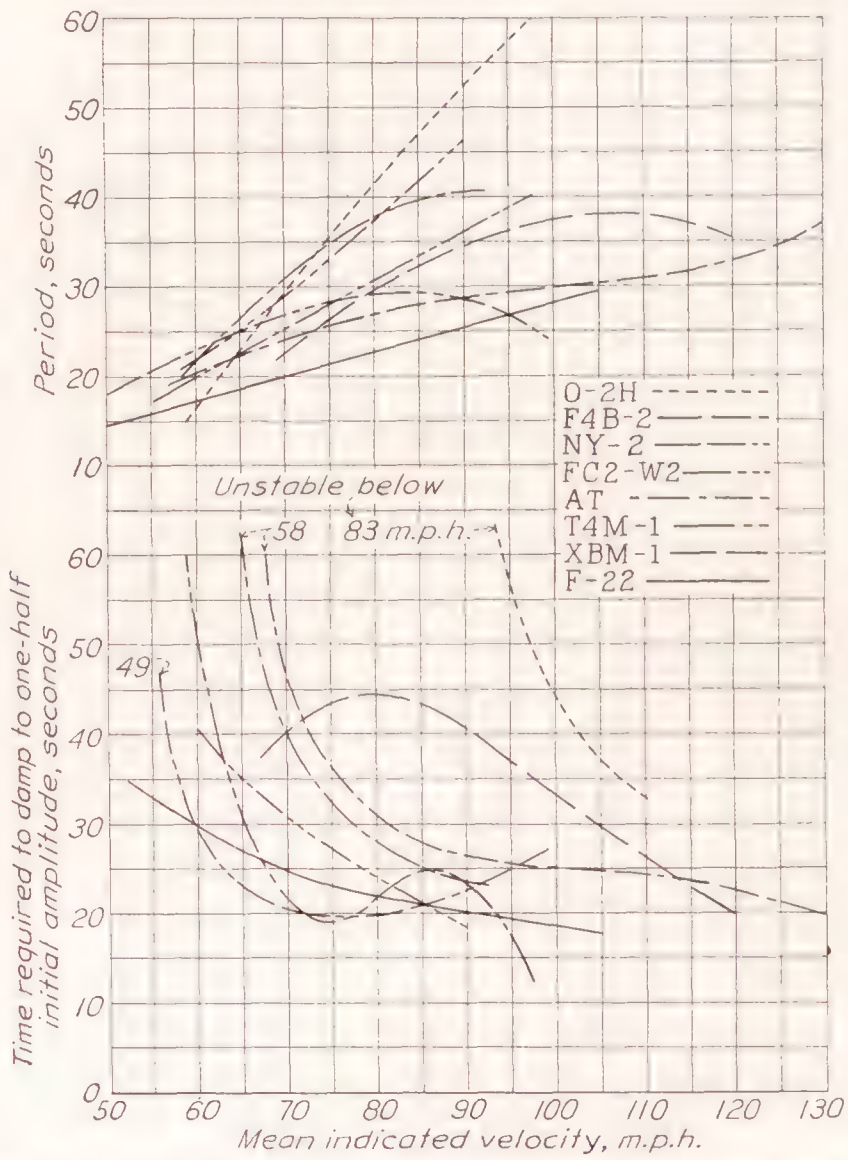

FIGURE 2.—Period and damping of longitudinal oscillations with elevator fixed and power on.

The range for periods of oscillations given by the results for all test conditions extends from 11 seconds, for the F–22 airplane at 60 miles per hour in gliding flight with the elevator free, to 64 seconds, for the O–2H airplane at 102 miles per hour with the elevator fixed and power on. It has been noted previously that, for the power-off elevator-fixed condition, all airplanes except the O–2H had approximately the same period at any given speed. If all test conditions are taken into consideration, however, fairly large variations of the periods at a given speed are noted. At 60 miles per hour, the shortest period is 11 seconds and the longest 23 seconds. At 102 miles per hour, the shortest period is 23 seconds and the longest 64 seconds. It is of

interest to note that for most airplanes and test conditions the maximum period is about 45 seconds.

The times for the oscillation to subside to one-half amplitude vary from infinity for the cases of instability previously discussed to 9 seconds for the FC2–W2 airplane in gliding flight at 118 miles per hour with the elevator fixed. On the basis of the number of cycles, this damping corresponds to a reduction of the amplitude to one-half in approximately one-fourth cycle. The damping shows no definite trend with speed of flight, so ranges at different speeds are of no importance.

Table III shows alphabetical ratings of the airplanes based on measured stability characteristics as compared with pilots' ratings based on observed longitudinal

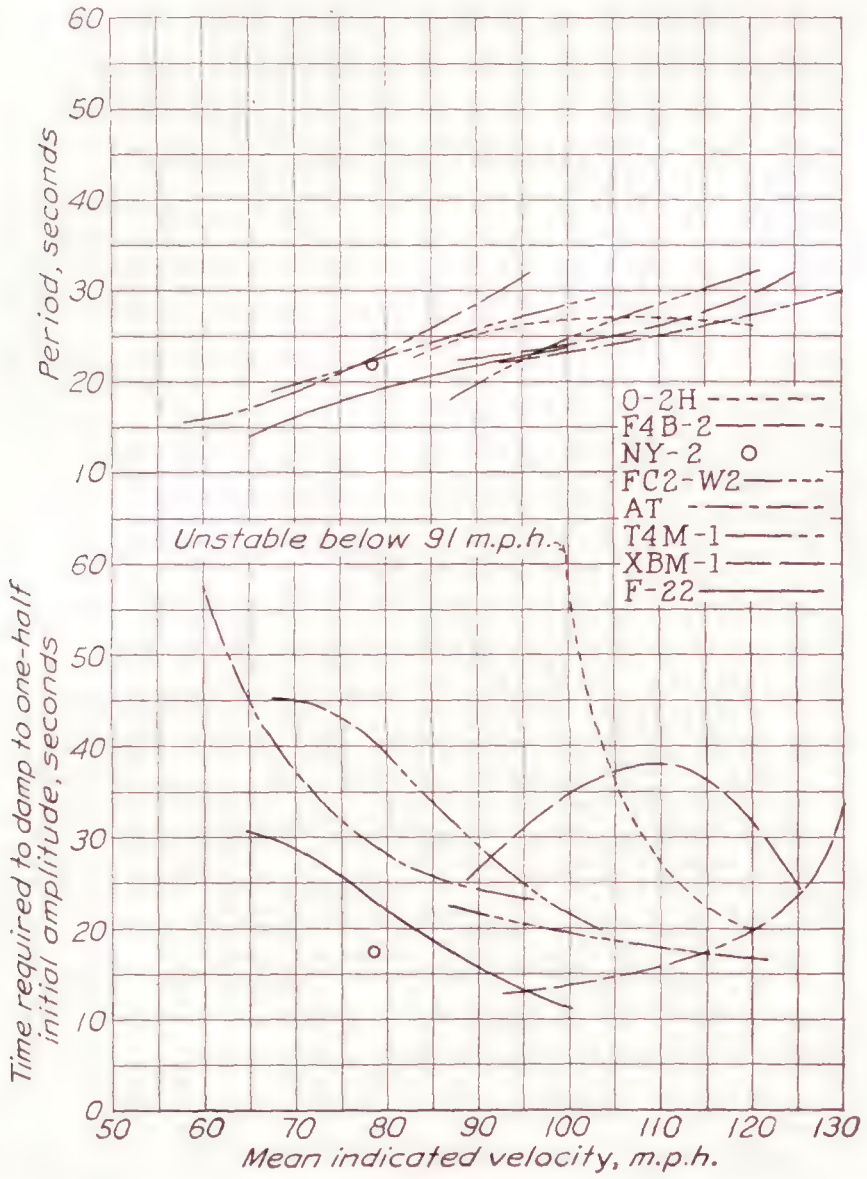

FIGURE 3.—Period and damping of longitudinal oscillations with elevator free and power off.

control and handling qualities. It will be appreciated that any ratings made on the basis of the measurements for comparison with the pilots' ratings can only be approximate and represent average conditions. The ratings for the period given in table III consider the entire speed range. The shortest period is designated A. The periods increase in alphabetical order. The ratings for damping consider primarily the higher portion of the speed range where most flying is done and where most of the airplanes are stable. The greatest damping is designated A.

The magnitude of the elevator forces and movements required for normal operation of an airplane, through their partial dependence on the slope of the pitching-moment curve, are indirectly related to the stability as defined by the period and damping of the longitudinal oscillation. The relationship has resulted in the use of the loosely defined piloting term "stiffness" to describe the combined longitudinal stability and control characteristics. The general usage of the term has made it desirable to make it one of the bases for rating the airplanes, although it is appreciated that the ratings given depend on the interpretation of only two pilots and might be somewhat different from those that would have been obtained had more pilots been consulted. In table III, the stiffest airplane has been designated A.

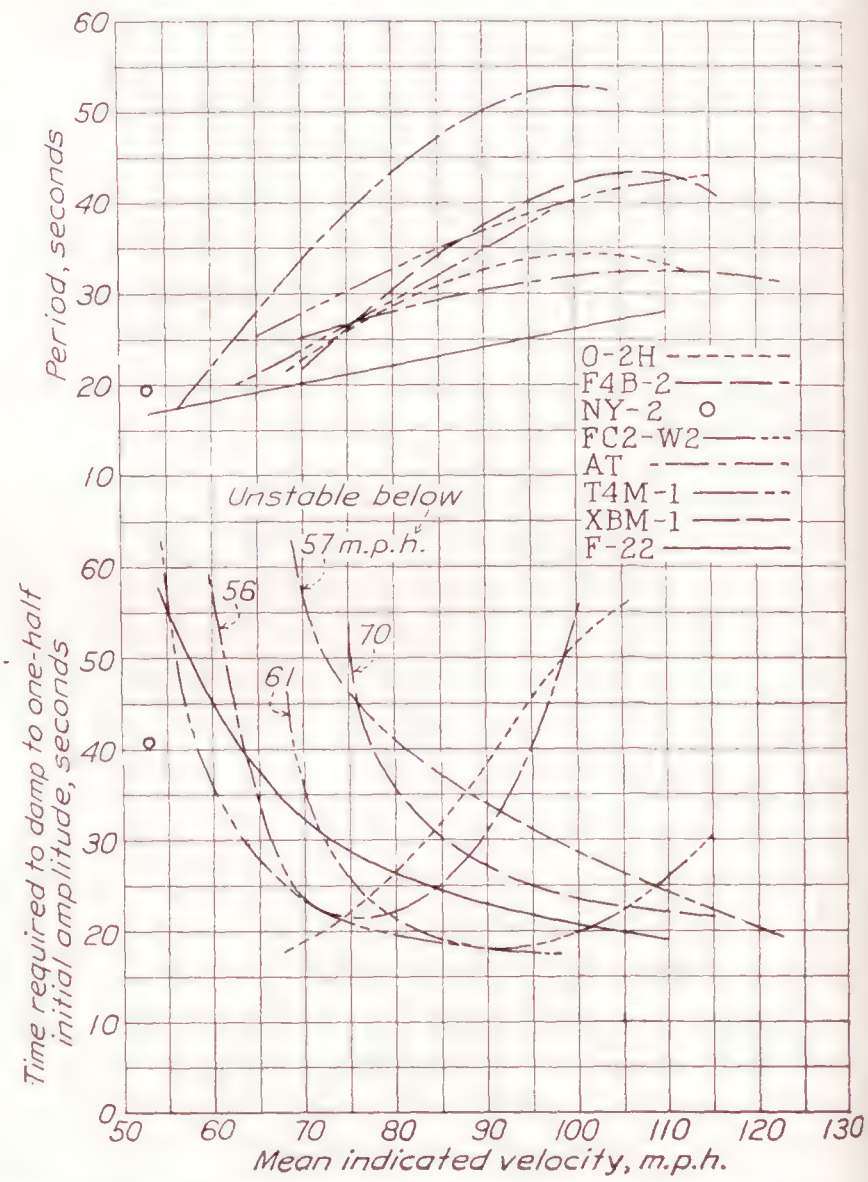

FIGURE 4.—Period and damping of longitudinal oscillations with elevator free and power on.

Because stiffness does include the elevator force and movements, pilots prepared separate ratings on the basis of these two items. The airplane with the heaviest elevator control and the one requiring the greatest elevator movements are designated A. A rating was also prepared on the basis of the amount of pitching occurring during flight in rough air. In this case, A designated the airplane doing the most pitching or being the unsteadiest in flight in rough air.

A comparison of the different ratings prepared by the pilots shows that the ratings for stiffness are almost identical with those for elevator force. Aside from the fact that stiffness is given in four gradations and the elevator force in three, the T4M–1 airplane is the only

one for which there is actual disagreement. This airplane was the largest of the group tested and had a wheel control. The pilots associate heavier forces with a wheel than with stick control and rate airplanes for stiffness accordingly. Apparently, at least for the Committee's pilots, stiffness refers primarily to elevator force with consideration taken of the size of the airplane and type of control. The ratings for elevator movement show that there is a tendency for large elevator forces to be associated with large elevator movements. The ratings for pitching in rough air show no correlation with those for any other item.

In the vibration of springs, the period of oscillation varies in an inverse ratio to the spring stiffness. By analogy the airplane having the shortest period may be considered the stiffest. From the listings on table III, it will be noted that the pilots' ratings for stiffness are in almost direct opposition to the stiffness as indicated by the period. There are too many variables involved to determine the reason for the reverse order for the two ratings, but the conclusions cannot be drawn that this reverse order will occur for all airplanes. The disagreement, however, indicates that elevator forces and period are not closely enough related to the slope of the pitching-moment curve to assume that high forces and a short period will result from a large negative slope to the curve. Neither can the ratings for damping be correlated with the pilots' observations of stiffness. Likewise, there is no apparent correlation between the pilots' ratings for pitching or unsteadiness in rough air and either the measured periods or the damping. It is also of interest to note, in connection with the lack of correlation of the measured dynamic stability characteristics and the characteristics observed by the pilots, that the instability of the oscillations for the power-on conditions for several of the airplanes had no appreciable effect on their flying characteristics and was not noted by the pilots prior to the tests.

It is evident from the foregoing comparisons that the dynamic longitudinal stability characteristics, as defined by the period and damping of the phugoid oscillation, are not apparent to the pilot and, therefore, cannot be taken as an indication of the handling characteristics of airplanes. If the most desirable degree of dynamic stability is to be determined, factors other than the handling characteristics will have to be considered. The reaction of the airplane to rough-air conditions appears to offer a possible basis. The pitching in rough air, from the present tests, does not appear to be related to the phugoid oscillation. It may, however, be related to the short-period oscillation, and this possibility should perhaps be investigated. Fisher (reference 3) shows that the structural loads imposed by gusts are influenced by the stability derivatives.

CONCLUSIONS

1. The period of the phugoid longitudinal oscillations for the eight airplanes tested varied from 11 seconds at low speeds to 64 seconds at high speeds. For the elevator-fixed power-off condition the period for conventional airplanes may be approximated by the equation

$$P=0.262V$$

2. The maximum damping encountered in the tests was sufficient to reduce the amplitude of oscillation to one-half in 9 seconds, or in approximately one-fourth cycle.

3. Four of the eight airplanes were dynamically unstable with power on although all were stable with power off and the elevator fixed and only one was unstable with power off and the elevator free, indicating the importance of the effect of power upon the stability characteristics.

4. The dynamic longitudinal stability of airplanes, as defined by the period and damping of the phugoid oscillation, has no apparent bearing on the factors from which pilots judge the handling characteristics.

LANGLEY MEMORIAL AERONAUTICAL LABORATORY,
NATIONAL ADVISORY COMMITTEE FOR AERONAUTICS,
LANGLEY FIELD, VA., *July 15, 1936.*

REFERENCES

1. Zimmerman, Charles H.: An Analysis of Longitudinal Stability in Power-Off Flight with Charts for Use in Deisgn. T. R. No. 521, N. A. C. A., 1935.
2. Soulé, Hartley A., and Wheatley, John B.: A Comparison between the Theoretical and Measured Longitudinal Stability Characteristics of an Airplane. T. R. No. 442, N. A. C. A., 1932.
3. Fisher, H. R.: The Normal Acceleration Experienced by Aeroplanes Flying through Vertical Air Currents. Part I. The Calculation of the Acceleration Experienced by an Aeroplane Flying through a Given Gust. R. & M. No. 1463, British A. R. C., 1932.

TABLE I

CHARACTERISTICS OF AIRPLANES TESTED

Airplane	Fairchild 22	Martin XBM-1	Verville AT	Martin T4M-1	Fairchild FC2-W2	Boeing F4B-2	Consolidated NY-2	Douglas O-2H
Type	Parasol monoplane	Biplane	Biplane	Biplane	High-wing monoplane	Biplane	Biplane	Biplane
Wing area (sq. ft.)	171	412	242	656	336	236	370	368
Weight (lb.)	1,440	6,100	2,300	5,824	4,510	2,875	2,769	4,960
Engine horsepower	95	575	165	525	450	500	220	400
Wing loading (lb./sq. ft.)	8.4	14.8	9.5	8.9	13.4	12.2	7.5	13.5
Power loading (lb./hp.)	15.2	10.6	13.9	11.1	10.0	5.75	18.2	12.4
Wing dimensions:								
Span upper (ft.)	32.83	41.0	31.0	53.0	50.0	30.0	40.0	40.17
Span lower (ft.)	----------	40.0	31.0	53.0	----------	26.33	40.0	38.67
Chord upper (ft.)	5.5	6.17	4.17	6.58	7.0	5.0	5.0	5.0
Chord lower (ft.)	----------	5.42	4.17	6.58	----------	3.75	5.0	5.0
Gap (ft.)	----------	6.17	5.0	7.5	----------	4.87	4.96	6.0
Stagger (ft.)	----------	2.58	2.13	0	----------	2.67	2.33	1.85
Wing setting (deg.)	1.0	0	0	2.0	2.6	0	2.0	2.0
Airfoil section	N-22	N-22	Clark Y-15	Clark Y-15	Göttingen 387	Boeing 106	Clark Y	Göttingen 398
Mean aerodynamic chord (ft.)	5.50	5.66	4.17	6.58	7.0	4.60	5.00	5.00
Leading edge to leading edge of lower wing: vertical (ft.)	.13	3.60	2.92	4.03	.25	3.30	2.83	3.48
Leading edge to leading edge of lower wing: horizontal (ft.)	0	.92	1.18	0	0	2.05	1.33	.99
Tail dimensions:								
Span (ft.)	10.0	14.0	10.0	18.92	11.6	12.17	12.27	13.92
Stabilizer area (sq. ft.)	15.8	28.4	16.6	54.5	28.6	19.9	17.3	23.8
Elevator area (sq. ft.)	10.4	25.6	13.3	30.0	17.6	17.9	17.6	23.1
Elevator hinge to leading edge of lower wing: vertical (ft.)	−2.0	3.0	2.3	5.5	.7	2.17	4.25	4.06
Elevator hinge to leading edge of lower wing: horizontal (ft.)	14.69	18.20	15.4	24.0	25.34	12.53	18.18	20.71
c. g. location:								
Relative to M. A. C. vertical percent of M. A. C.	−52.3	−35.8	−21.6	−21.7	−29.0	−32.8	−18.2	1.2
Relative to M. A. C. horizontal percent of M. A. C.	28.0	29.7	33.1	30.9	30.6	38.5	28.6	36.6
Relative to thrust axis (ft.)	−.30	−.38	.08	−.40	.83	.12	−.08	1.41

TABLE II

SUMMARY OF DYNAMICALLY STABLE AND UNSTABLE CONDITIONS OF AIRPLANES TESTED

[S, stable; U, unstable]

Airplane	Elevator fixed throttle closed	Elevator fixed full throttle	Elevator free throttle closed	Elevator free full throttle
Fairchild 22	S	S	S	S.
Martin T4M-1	S	S	S	S.
Consolidated NY-2	S	U below 49 m. p. h.	S	S.
Boeing F4B-2	S	U below 58 m. p. h.	S	U below 56 m. p. h.
Verville AT	S	U below 58 m. p. h.	S	U below 57 m. p. h.
Douglas O-2H	S	U below 83 m. p. h.	U below 91 m. p. h.	S.
Fairchild FC2-W2	S	S	S	U below 61 m. p. h.
Martin XBM-1	S	S	S	U below 70 m. p. h.

TABLE III

RATING OF LONGITUDINAL STABILITY AND HANDLING QUALITIES OF AIRPLANES TESTED

Airplane	Observed characteristics				Measured characteristics	
	Stiffness	Factors affecting stiffness			Period	Damping
		Elevator force	Elevator movement	Pitching in rough air		
Fairchild 22	D	C	B	A	A	A
Martin T4M-1	C	A	A	B	B	B
Consolidated NY-2	C	B	B	A	B	B
Boeing F4B-2	D	C	C	C	A	C
Verville AT	C	C	B	B	D	B
Douglas O-2H	A	A	A	A	D	D
Fairchild FC2-W2	B	B	B	B	C	A
Martin XBM-1	A	A	C	D	C	D

A is used to designate airplanes that are stiffest, require the greatest elevator forces and movement, do most pitching in rough air, and have the shortest periods and the greatest damping.

REPORT No. 579

A STUDY OF THE TWO-CONTROL OPERATION OF AN AIRPLANE

By Robert T. Jones

SUMMARY

The two-control operation of a conventional airplane is treated by means of the theory of disturbed motions. The consequences of this method of control are studied with regard to the stability of the airplane in its unconstrained components of motion and the movements set up during turn maneuvers.

It is found that the motion of a conventional airplane is more stable when an arbitrary kinematic constraint is imposed in banking than when such constraint is imposed in yawing. Several hypothetical assumptions of piloting procedure, each of which is considered to represent a component of the actual procedure, are studied. Different means of two-control operation are also discussed and it is concluded that a reliable rolling-moment control that does not give the usual adverse secondary yawing moment should be most satisfactory. Several special modifications intended to make the airplane more suitable for two-control operation are also discussed, and it is found that relatively great weathercock stability (N_v) would be desirable.

INTRODUCTION

A number of flights have been made with airplanes utilizing both the aileron-elevator and the elevator-rudder combinations for two-control operation. Some question exists as to which of these modes of operation is likely to prove the better and also whether either of them is capable of affording the controllability requisite to safety in flight. Such questions must, of course, be eventually decided by experience, no mathematical analysis being sufficiently broad to deal with all aspects of the problem. It is believed, nevertheless, that certain conceptions gained from an analysis of the problem may be useful in furthering development along these lines.

One of the purposes of the present work was to ascertain on theoretical grounds which of the two possible modes of operation was more likely to prove satisfactory. It was also desired to find what changes might be effected in a conventional airplane to make it more suitable for two-control operation.

The analysis of the various dynamical problems that arise makes use of many concepts that are discussed at length in reference 1. The treatment of airplane motion as a problem of dynamics is based primarily on the assumptions of the theory of airplane stability as developed by Bryan and others; for the elucidation of this theory the reader is referred to text books on aeronautics.

MATHEMATICAL TREATMENT OF CONTROLLED MOTION

The motion of an airplane with adequate control about its three axes may, in one sense, be regarded as a purely constrained motion. From this point of view, the act of piloting the airplane must be considered to be the use of the available control means for overcoming the inherent aerodynamic and inertial reactions of the airplane, causing it to follow a more or less definitely constrained motion induced by the controls. The natural oscillation and damping of the free motion of the airplane do not appear, then, in the controlled motion because the pilot has accommodated his use of the available control to the governing of these inherent tendencies. Accordingly the stability or instability of the airplane will be apparent only in the requisite use of the controls to perform a given maneuver.

It has been found by experience that the lateral-stability characteristics of an ordinary airplane are such that it is feasible to abandon one of the direct constraints of the lateral motion in ordinary flight maneuvers. All lateral maneuvers that are to be performed with a minimum of sideslipping or sidewise acceleration require a definite coordination between the banking and yawing motions; it appears that a conventional airplane will naturally tend to fulfill this requisite relation in greater or less degree, on account of the inherent stability, even when one of the lateral controls is abandoned.

Under the conditions of two-control operation the motion of the airplane cannot be considered as an entirely constrained motion. The pilot of such a machine can exercise direct constraint in only one of the three components of lateral movement and must depend on the natural tendencies of the airplane for the requisite coordination of the other motions. In order to show this coordination the airplane need not be entirely stable with all controls released, but it is imperative that there be satisfactory stability in those components in which the machine is unconstrained. Thus, if an

airplane is to be controlled by the ailerons and elevator alone, it must be satisfactorily stable in combined yawing and sideslipping, in which it is free; if control is by rudder and elevator, corresponding stability in combined banking and sideslipping is necessary.

If the controls are considered to impress constraints in those components of motion in which they operate directly, the movements of a two-control airplane may be studied by the method of forced oscillations. Thus, if the airplane controlled by ailerons is caused to follow a definite course in banking, in which it is considered to be constrained, this motion will impress disturbing forces and couples leading indirectly to yawing and sideslipping motions. The yawing and sideslipping motions must, however, be considered to be unconstrained and to be conditioned by the natural stability of the machine as well as by the impressed disturbances.

The disturbing forces or couples impressed in those components in which the airplane is unconstrained are caused by the constrained movements and are considered proportional to them. The factors of proportionality are simply the appropriate stability derivatives of the airplane. Thus, if the machine is constrained to follow a definite sequence of rolling motions by the application of a suitable control moment, a disturbing acceleration in yawing that is proportional to the given rate of rolling at each instant will be impressed, namely:

$$\text{impressed } \frac{dr}{dt}=p\times N_p$$

In order to express the foregoing ideas definitely it will be necessary to resort to mathematical treatment of the motions. It is convenient for this purpose to choose a set of axes rigidly fixed in the airplane at its center of gravity and inclined at the angle of attack α, so that the X axis points into the direction of the relative wind in steady flight at the specified lift coefficient. The following notation and diagram define the quantities used in the subsequent equations.

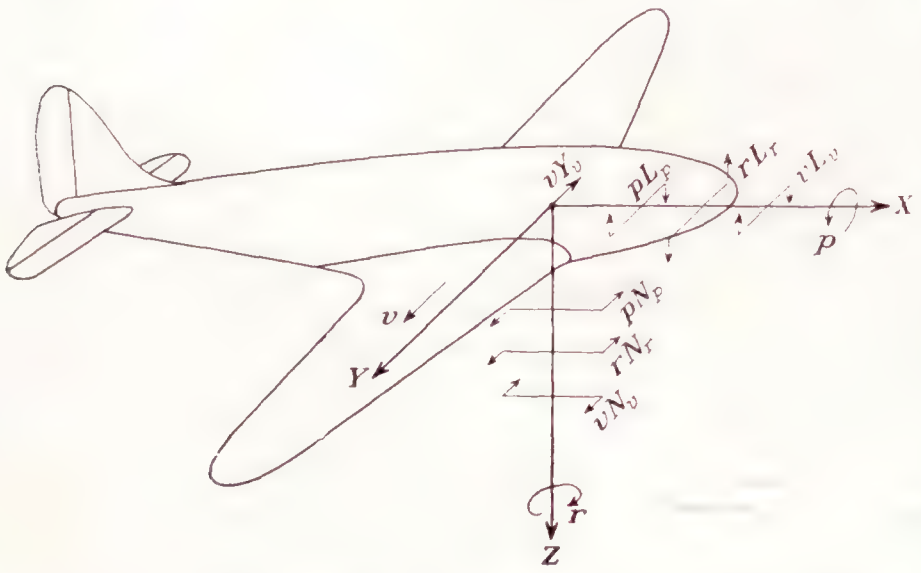

U_0, forward (X-wise) velocity in steady flight.

p, rolling component of angular velocity.

r, yawing component of angular velocity.

v, component of flight velocity along Y axis (sideslip).

φ, angle of bank (relative to gravity).

β, angle of sideslip v/U_0, approximately

δ, angle of rudder or aileron deflection.

Y, force component along the direction of the Y axis.

L, rolling-moment component.

N, yawing-moment component.

$\delta L_\delta=L/mk_X^2$, $\delta N_\delta=N/mk_Z^2$, Control moments per unit moment of inertia of airplane.

Y_v, L_p, L_r, L_v, N_p, N_r, N_v Stability derivatives in terms of unit mass or moment of inertia of airplane, thus:

$$Y_v=\frac{\partial Y}{\partial v}/m$$

$$L_r=\frac{\partial L}{\partial r}/mk_X^2, \text{ etc.}$$

A number of secondary considerations will be neglected in the mathematical analysis of the problems to make the mathematical expressions as simple as possible and because it is not considered important to secure exact numerical results for studying the general problem. For these approximate calculations the lateral and longitudinal motions of the airplane will be considered separable during turning flight. A check of the maximum gyroscopic couples encountered shows that they are negligible for the present study, although it is probable that the longitudinal and lateral oscillations in turning flight can be separated for only a relatively short time after the passing of a disturbance. Another assumption made is that the effect of a component torque applied to the airplane is an angular acceleration about the axis of the torque. In general, the angular acceleration does not have the same axis as the applied torque but in the present case the reference axes chosen lie near the assumed principal axes of inertia, and the difference of moments of inertia taken about various axes is not great. In addition, the flight of the airplane is assumed to be horizontal and the speed not to vary appreciably from the average (U_0) in a given case.

According to the previously outlined treatment, the movement of the airplane in at least one of the lateral coordinates will be modified by a constraint. The complete set of three degrees of freedom is not in this case expressed in the usual three simultaneous equations of motion, for this procedure would imply that each component of the motion was affected by the other two, whereas the present problem calls for an independent expression of one of them. Thus, it is assumed that the available control is sufficiently powerful to force any desired motion in the controlled component. When setting up the equations, this

motion will be considered to be given as a function of the time.

It is important to emphasize in the interpretation of the mathematical analysis the practical significance of the assumptions used. The solution of the equations requires that the complete history of the variation of one of the components of the motion (or the control setting) be known beforehand. This variation is not subsequently altered to accommodate the variation of the other motions as would be the case if an intelligent pilot were at the controls. It may be imagined that the pilot has only one degree of attention. Having fixed on a procedure of rolling the airplane, he concentrates on the execution of this alone, paying no attention to the consequences in yawing or sideslipping. It would be feasible to assume that the pilot concentrated his attention on carrying out a predetermined manipulation of the controls, without regard to any of the motions set up. This assumption is, however, considered to be too far removed from actuality to be of much use in analyzing the problem. It would be of more practical interest to assume that the pilot had sufficient skill to enforce a desired motion in every respect, taking no account of the control manipulations. The control manipulations required could then be calculated and an idea of the degree of skill necessary to attain a perfect result could be derived therefrom.

With two-control operation a perfect coordination of the motions is, of course, not possible. If the pilot enforces complete control over one component of the airplane's motion, he must do so at the expense of control in some other component. The residual component is then considered to be free. In practice the pilot can exercise an indirect influence on all lateral motions with only a single lateral control. Hence, it is possible to assume that a skilled pilot could enforce complete control over the yawing motion even though his available control exerted only rolling moments directly. Then the rolling motion must be considered free and not subject to the pilot's attention although his available control operates directly on this motion. Such an assumption obviously cannot give an accurate description of anything occurring in practice. The same is true in some degree of any other assumed procedure that can be mathematically treated. The actual procedure of a pilot is undoubtedly an indeterminate and variable synthesis of such elementary procedures. The study of a single assumption of this nature is therefore incomplete, constituting simply a part in the analysis of the problem.

In order to illustrate the variety of assumptions that may be treated, four equations, containing movements both of the airplane and of the control surface, will be set down:

$$\left.\begin{aligned}
&\frac{dv}{dt}-g\varphi+rU_0-vY_v &&=0\\
&\frac{dp}{dt}-pL_p-rL_r-vL_v-\delta L_\delta &&=0\\
&\frac{dr}{dt}-pN_p-rN_r-vN_v-\delta N_\delta &&=0\\
&\frac{d\varphi}{dt}-p &&=0
\end{aligned}\right\}(1)$$

These equations are to be satisfied simultaneously and, since there are more variables than equations, one of the variables must be given in terms of the time to effect a solution. Any assumption of the kind considered may be applied by setting one of the variables equal to a function of t. Thus the equations of motion with an arbitrarily prescribed course in rolling are:

$$\left.\begin{aligned}
&\frac{dv}{dt}+rU_0-vY_v &&=g\varphi(t)\\
&-rL_r-vL_v-\delta L_\delta &&=L_pp(t)-\frac{d}{dt}p(t)\\
&\frac{dr}{dt}-rN_r-vN_v-\delta N_\delta &&=N_pp(t)
\end{aligned}\right\}(2)$$

Similarly, if the pilot uses the control to enforce some given motion in yawing, the equations are:

$$\left.\begin{aligned}
&\frac{dv}{dt}-g\varphi-vY_v &&=-U_0r(t)\\
&\frac{dp}{dt}-pL_p-vL_v-\delta L_\delta &&=L_rr(t)\\
&-pN_p-vN_v-\delta N_\delta &&=N_rr(t)-\frac{d}{dt}r(t)\\
&\frac{d\varphi}{dt}-p &&=0
\end{aligned}\right\}(3)$$

Solutions of the foregoing differential equations have the general form

$$v, p, \delta, \text{ or } r=(C_1e^{\lambda_1t}+C_2e^{\lambda_2t}+\ \ldots\ C_ne^{\lambda_nt})+\zeta(t) \qquad (4)$$

This type of solution has two significant components; the part enclosed by parentheses represents the occurrence of the natural oscillations and damping in the resultant motion. If the natural modes of motion are stable, this component will disappear with time and the solution will be represented by $\zeta(t)$. If the impressed disturbance is periodic, the motion will at first be conditioned by the natural period but, if this is damped, will later follow the impressed period in accordance with Herschel's theorem. In these cases the term $\zeta(t)$ may be called the "steady-state solution."

Under the assumed conditions of two-control operation the pilot enforces one component of the motion and relies on the reaction of this motion on the uncontrolled component to induce an appropriate

motion there. As seen in equation (4), this accompanying motion is at first conditioned by the natural oscillations. Obviously for satisfactory two-control operation it is desirable that the natural oscillations in the uncontrolled components quickly die away. It also appears that if any reasonable coordination of the motions is to be obtained the period of the free oscillation must be short compared with the duration of the maneuver.

STABILITY OF A CONVENTIONAL AIRPLANE OPERATED WITH TWO CONTROLS

From the foregoing considerations it is apparent that the airplane must have certain degrees of stability for satisfactory two-control operation. Operation with constraint in yawing calls for stability in combined rolling and sideslipping, whereas operation with rolling constraint requires stability in combined yawing and sideslipping, as indicated by equations (2) and (3). In order to illustrate the degree of stability of a conventional airplane in these motions, data from an assumed average airplane (described in reference 2) have been used and several calculations made for the two cases. The principal characteristics of the assumed airplane are given in the table I.

TABLE I

CHARACTERISTICS OF ASSUMED AVERAGE AIRPLANE

Type	Monoplane, 2-passenger.
Gross weight	1,600 lb.
Wing area	171 sq. ft.
Wing span	32 ft.
mk_X^2	1,216 slug-ft.^{2}
mk_Z^2	1,700 slug-ft.^{2}

Stability derivatives at various lift coefficients:

C_L	L_p	L_r	[a]L_v	N_p	N_r	N_v	Y_v
0.35	−5.44	1.11	−0.0544	−0.207	−0.913	0.0368	−0.172
1.0	−3.23	1.88	−.0415	−.301	−.663	.0231	−.145
[b] 1.8	−2.46	2.51	−.0461	−.310	−.977	.0221	−.224

[a] 5° dihedral.
[b] Flaps down.

STABILITY WHEN CONSTRAINED IN ROLLING

The stability of the motion of the airplane (or of the movement of the control, δ) when the rolling component is arbitrarily constrained may be calculated from the complementary equations of (2):

$$\left.\begin{aligned} \frac{dv}{dt}+rU_0-vY_v &=0 \\ -rL_r-vL_v-\delta L_\delta &=0 \\ \frac{dr}{dt}-rN_r-vN_v-\delta N_\delta &=0 \end{aligned}\right\} \tag{5}$$

The complementary equations express only a part of the complete motion. They show the influence of stability on the manipulations of the control required to enforce the desired constraint in bank as well as the stability of the free yawing and sideslipping oscillations. Whatever rolling motion is assumed, a solution of the complementary equations will appear as a component of the final solution.

The third equation of (5) may be solved for v and the resulting expression substituted into the first equation, etc. The same procedure may be carried out for r or δ; in either case the so-called "auxiliary" equation is:

$$\begin{aligned} &L_\delta[\lambda^2-(N_r+Y_v)\lambda+N_rY_v+U_0N_v] \\ &+N_\delta[L_r\lambda-L_rY_v-U_0L_v]=0 \end{aligned} \tag{6}$$

The equation is conveniently divided into two parts to show the effects of control rolling and yawing moments. If the rolling motion is constrained by a direct rolling-moment control, the second part of the equation (containing N_δ) is eliminated. Since the first polynomial is a quadratic, its roots are:

$$\lambda=\frac{(N_r+Y_v)\pm\sqrt{(N_r+Y_v)^2-4(N_rY_v+N_vU_0)}}{2} \tag{7}$$

If the airplane shows an average degree of weathercock stability ($N_v>0$), the roots will be conjugate complex numbers and the terms

$$C_1e^{\lambda_1 t}+C_2e^{\lambda_2}$$

of equation (4) will represent a damped oscillation. If $\lambda_1=a+ib$ and $\lambda_2=a-ib$, the period of this oscillation is

$$T_1=\frac{2\pi}{b} \tag{8}$$

and the time to damp to one-half amplitude:

$$T_2=-\frac{\log 0.5}{a}=\frac{0.7}{a} \tag{9}$$

provided that a is negative.

Neglecting the first part of equation (6) (containing L_δ) amounts to the assumption that the banking motion is constrained by the application of a rudder control. The solution of this part of the equation alone is:

$$\lambda=Y_v+\frac{U_0L_v}{L_r} \tag{10}$$

The auxiliary equation thus has only one real root and it is negative, indicating stability. The assumption is that a sidewise disturbance (v) causes the pilot to give the airplane a rate of yawing such that

$$rL_r=-vL_v \tag{11}$$

As L_r is positive, this yawing reduces the sideslip and must then itself be reduced in proportion to prevent rolling, thus resulting in a convergence. This control procedure, although stable and nonoscillatory, represents a more artificial assumption than the control of

the rolling motion by direct rolling moments, for here the pilot in order to check a sudden disturbance must move the airplane as a whole with equal suddenness while with direct control he is only called upon to deflect the control surface suddenly.

Although the motion that occurs when the rolling is controlled—either directly by a variable rolling moment alone or indirectly by a yawing moment—is stable, a control device that gives both rolling and yawing moments in combination may cause instability. Inasmuch as conventional ailerons do give secondary yawing moments, this case is of considerable interest. Denoting the ratio:

$$\frac{N_\delta}{L_\delta}=\kappa$$

where each δ denotes aileron deflection, the following resolution of equation (6) is obtained

$$\lambda^2-[(N_r-\kappa L_r)+Y_v]\lambda+(N_r-\kappa L_r)Y_v + U_0(N_v-\kappa L_v)=0 \tag{12}$$

The solution of this equation differs from that of the first component of equation (6) in that the quantities N_v and N_r are replaced by $(N_v-\kappa L_v)$ and $(N_r-\kappa L_r)$, respectively. Thus it is concluded that an effect of a secondary *adverse* yawing moment in an attempted rolling maneuver will be an apparent reduction of both the *weathercock stability* (N_v) and the damping in yawing (N_r).

Calculation shows that the motion becomes unstable when

$$\kappa>\frac{N_r+Y_v}{L_r} \tag{13}$$

or when

$$\kappa>\frac{Y_vN_r+U_0N_v}{Y_vL_r+U_0L_v} \tag{14}$$

in negative magnitude. Such instability would indicate that an arbitrary constraint in rolling (such as attempted level flight) could not be maintained by the ailerons alone.

Conventional ailerons give rise to adverse yawing moments in an amount approximately independent of the speed of flight while the rolling moments and stabilizing factors are much reduced at the lower speeds. The result is that the ratio κ approaches the foregoing undesirable magnitude at the highest lift coefficients. It is therefore considered that ordinary ailerons working on a part of the wing surface that sustains a high lift would not be desirable for two-control operation.

Table II lists the results of calculations of the stability indexes of the average airplane in free yawing and sideslipping motions at several lift coefficients. Since these calculations were to be used later in investigating the motions set up during turning maneuvers, a certain increase in the steady-flight speed at a given lift coefficient was assumed. The increase amounted to 7½ percent and the stability derivatives at each lift coefficient were multiplied by this factor.

TABLE II

INDEXES OF STABILITY OF MOTION WITH CONSTRAINT IN ROLLING

	C_L	Roots of stability equation	Period of oscillation	Time to damp ½
			Seconds	*Seconds*
$\kappa=0$	0.35	$-0.583\pm2.50i$	2.51	1.18
	1.0	$-.435\pm1.51i$	4.16	1.60
	1.8	$-.645\pm1.23i$	5.10	1.08
Adverse yaw $\kappa=-0.15$	1.0	$-.283\pm1.31i$	4.80	2.5
Favorable yaw $\kappa=0.15$	1.0	$-.585\pm1.67i$	3.76	1.2

The combined yawing and sideslipping motion under consideration is, in general, very stable. Further calculations have shown that the stability of the motion when free only in yawing and sideslipping is much greater than the stability of the completely free motion. The oscillations have, in general, a shorter period and greater damping.

STABILITY WHEN CONSTRAINED IN YAWING

Calculation of the stability of the rolling and sideslipping motions when the airplane is constrained in yawing is similar to that given for constraint in banking. Here the complementary equations of (3) are used. The corresponding auxiliary equation is

$$N_\delta[\lambda^3-(L_p+Y_v)\lambda^2+L_pY_v\lambda-gL_v] + L_\delta[-N_p\lambda^2+N_pY_v\lambda-gN_v]=0 \tag{15}$$

The complementary part of the general solution (4) will be of the form

$$p,\ v,\ \text{or}\ \delta=C_1e^{\lambda_1 t}+C_2e^{\lambda_2 t}+C_3e^{\lambda_3 v} \tag{16}$$

since there are now three roots. In case the yawing motion is constrained directly by the application of control yawing moments, only the first part of the equation will be in force. Calculation shows that two of the roots will then be of the conjugate complex type previously discussed and that the third root will be very nearly equal to L_p. Table III gives these roots as calculated for the average airplane under conditions similar to those assumed in table II.

TABLE III

STABILITY OF MOTION OF AVERAGE AIRPLANE WITH CONSTRAINT IN YAWING

C_L	Real root	Complex roots	Period of oscillation	Time to damp ½ (complex roots)
			Seconds	*Seconds*
0.35	−5.90	$-0.064\pm0.562i$	11.2	10.8
1.0	−3.59	$-.019\pm.636i$	9.9	36.6
1.8	−2.67	$-.015\pm.716i$	8.8	46.3

The fact that the auxiliary equation for the case of free rolling and sideslipping motion with yawing control has roots of such widely different magnitude is an indication that the motion may be separated into distinct modes. The large real root (nearly equal to L_p) indicates the sharp damping of an initial rolling motion and is of such magnitude that the wings may be considered to be in a measure constrained against rolling relatively to the air. A possible rolling motion, however, that will not be appreciably damped consists in rolling about an instantaneous center some distance above the center of gravity of the airplane. For rotation of the airplane as a rigid body about this point the rolling moment due to sideslip will balance the damping of the rolling.[1] The height, $\bar{z}_L$, of the instantaneous center above the center of gravity is found from:

$$vL_v=-pL_p$$

where

$$v=-p\bar{z}$$

whence

$$\bar{z}_L=\frac{L_p}{L_v} \tag{17}$$

The mode of motion represented by the small complex roots (table III) thus consists in a swinging oscillation of the airplane about the metacenter $\bar{z}$ as a pendulum suspended from that point. The characteristic roots for the pendulum motion would be

$$\pm\sqrt{-\frac{g}{\bar{z}}}=\pm i\sqrt{\frac{gL_v}{L_p}} \tag{18}$$

which are seen to be approximate roots of equation (15) ($L_\delta=0$).

From these considerations it appears that the two-control airplane constrained in yawing with the rudder would be subject to swinging oscillations of long period and slight damping. If the airplane is given an initial angle of sideslip, it will be restrained against banking directly by the relatively great damping in rolling L_p and the banking that occurs will conform nearly to a rotation of the airplane about the metacenter $\bar{z}_L$. It will be of interest to calculate this height, using the stability derivatives given in table I:

C_L	$z_L=\frac{L_p}{L_v}$
	Feet
0.35	100
1.0	92.5
1.8	53

Physical considerations indicate that the damping of this mode of motion is almost entirely dependent on Y_v; hence, for two-control operation with the rudder, it should be desirable to have a large value of this derivative.

It is possible for the pilot to apply a yawing moment either through the secondary influence of an aileron control or indirectly by rolling the airplane as a whole. If the latter effect were used to constrain the yawing, the resulting motion would be excessively unstable. Thus, in order to prevent a sidewise disturbance from yawing the airplane ($r=0$), the pilot must execute a roll such that the forward wing is depressed ($pN_p=-vN_v$). This roll provides the occasion for an increase of sideslip due to the bank and requires, in turn, more rapid rolling so that the motion diverges quickly. Secondary aileron yawing moments of either sign moderate this instability and the motion may become stable if the yawing moment is favorable.

These considerations indicate that the pilot could not maintain an exact yawing constraint by the use of ailerons alone. On the other hand, this inability is probably not of great importance since the assumption of piloting procedure is obviously artificial and since the former calculations (stability with constraint in rolling) indicated that, if the ailerons were used to hold the wings level, the free yawing oscillations would be short and quickly damped. (See table II.) Thus it appears that, in order to prevent any yawing whatever during a disturbance, the pilot would have to execute a divergent bank whereas if he merely held the wings level the yawing motion might be unnoticeable. The divergent bank consists in a rotation of the airplane about the metacenter

$$\bar{z}_N=\frac{N_p}{N_v} \tag{19}$$

which is now situated below the airplane. The motion is like that of a pendulum placed at this height above its point of support.

TWO-CONTROL OPERATION IN STEADY TURNS

The two-control average airplane, showing stability both in combined yawing and sideslipping (rolling control) and in combined rolling and sideslipping (yawing control), should reach a definite condition of equilibrium with some fixed setting of the lateral control. In general, the equilibrium condition corresponding to a definite rudder or aileron setting will be a steady turn at a definite angle of bank. If the components of rolling and yawing angular acceleration produced by the deflected controls are δL_δ and δN_δ, as before, the equations of lateral equilibrium at a fixed angle of bank may be written:

$$\left.\begin{aligned} g\varphi-rU_0+vY_v &=0\\ rL_r+vL_v+\delta L_\delta&=0\\ rN_r+vN_v+\delta N_\delta&=0 \end{aligned}\right\} \tag{20}$$

In case control is by ailerons giving secondary (adverse or favorable) yawing moments, the term N_δ is replaced by κL_δ; and, in case control is by rudder alone, L_δ is dropped from the equations. In any case it has

[1] This mode of oscillation has been discussed by Lanchester.

to be assumed that the longitudinal control is properly manipulated for maintaining altitude and speed while turning.

Two special conditions of equilibrium are of interest. Solving the equations for the angle of bank

$$\varphi=\frac{(Y_vL_r+L_vU_0)\delta N_\delta-(Y_vN_r+N_vU_0)\delta L_\delta}{g(L_rN_v-L_vN_r)} \tag{21}$$

The necessary condition for the bank angle to be zero with deflected controls is:

$$\frac{1}{\kappa}=\frac{L_\delta}{N_\delta}=\left(\frac{Y_vL_r+L_vU_0}{Y_vN_r+N_vU_0}\right) \tag{22}$$

(See equation (14).)

In case the applied control rolling and yawing moments are in this ratio, the steady state of motion of the airplane will be a flat turn without bank. This limiting ratio may be compared with the ratio of the secondary aileron yawing moments to the rolling moments. If the secondary moment is adverse and exceeds a certain proportion of the rolling moment, an equilibrium condition in which the ailerons do not produce a bank of the airplane becomes possible. In this condition a gradual deflection of the ailerons would merely cause the airplane to assume a yawed attitude, turning slowly under the influence of the side pressure vY_v. Such a condition should be especially avoided in a two-control airplane utilizing aileron operation.

Another simpler condition of equilibrium that is also of interest is the condition for zero rate of yawing with deflected controls. The resolution of the equations in this case is:

$$r=\left(\frac{L_vN_\delta-N_vL_\delta}{L_rN_v-L_vN_r}\right)=0 \tag{23}$$

This is the condition for an ordinary sideslip and the ratio of yawing to rolling moment requisite to this condition is simply

$$\frac{1}{\kappa}=\frac{L_\delta}{N_\delta}=\frac{L_v}{N_v} \tag{24}$$

Obviously it should be considered undesirable to allow the secondary adverse yawing moment of the ailerons to approach this proportion of the rolling moment.

By a similar resolution of the equations another condition, namely,

$$\frac{1}{\kappa}=\frac{L_\delta}{N_\delta}=\frac{L_r}{N_r} \tag{25}$$

is obtained for the case of steady turning without sideslipping. This equilibrium is possible with aileron control alone in the case of secondary adverse yawing moments and furnishes another criterion for the magnitude of these secondary moments. In this case it would be expected that a gradual application of the rolling control would lead to turning at a progressively greater rate with the angle of bank opposite in sense to the applied rolling moment.

The main point of interest in the condition of steady turning with two-control operation is the angle of sideslip incident to the turn at various angles of bank. The resolution of the equations for v results in:

$$v=g\varphi\frac{N_r-\kappa L_r}{\kappa(Y_vL_r+U_0L_v)-(Y_vN_r+U_0N_v)} \tag{26}$$

In the case of rudder control, where $L_\delta=0$ the expression for v reduces to:

$$v=\frac{-g\varphi}{\left(Y_v+U_0\frac{L_v}{L_r}\right)} \tag{27}$$

while in the case of pure rolling-moment control (ailerons giving no secondary yawing moments)

$$v=\frac{-g\varphi}{\left(Y_v+U_0\frac{N_v}{N_r}\right)} \tag{28}$$

Thus the sideslip incident to turning with only rudder control is mainly dependent on the ratio of L_v/L_r while with rolling-moment control the important factor is

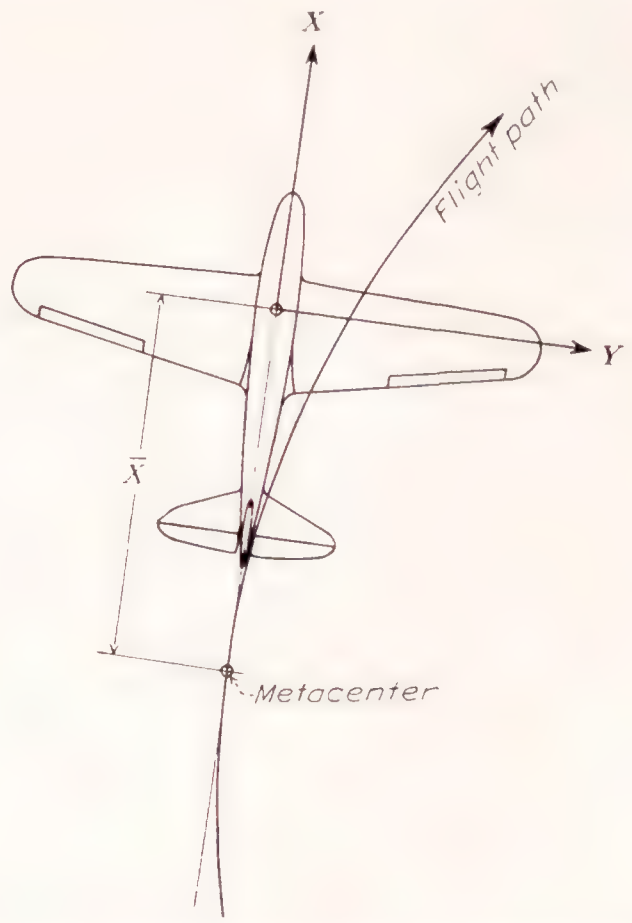

FIGURE 1.—Diagram illustrating combined yawing and sideslipping motion during a steady two-control turn. Metacenter for yawing moment $\bar{x}_N=\frac{N_r}{N_v}$; metacenter for rolling moment $\bar{x}_L=\frac{L_r}{L_v}$.

N_v/N_r. In both cases the sideslip will ordinarily be positive (toward the center of the turn) although the airplane does not necessarily lose altitude on this account.

Figure 1 illustrates the combined sideslipping and yawing of a two-control airplane during a steady turn.

In the case of rudder control the inward sideslip must be such that $vL_v = -rL_r$ to prevent rolling. This combined sideslipping and yawing motion may be ascribed to a rotation of the airplane about some point aft of the center of gravity. If the distance of this point behind the center of gravity is denoted by $\bar{x}_L$

$$r\bar{x}_L L_v = -rL_r$$

or

$$\bar{x}_L = -\frac{L_r}{L_v} \tag{29}$$

for the case of rudder-controlled turns. For rotation of the airplane about this point the rolling moment vanishes, hence the point is a metacenter for the rolling moment. The X axis will be tangent to the flight path at this point in rounding a turn, as shown in figure 1.

Similar considerations apply in the case of operation with a rolling-moment control with fixed rudder. Here the metacenter is for a vanishing yawing moment, the amount of sideslip being that necessary for $vN_v = -rN_r$. The distance of the metacenter aft of the center of gravity is found from

$$r\bar{x}_N N_v = -rN_r$$

or

$$\bar{x}_N = -\frac{N_r}{N_v} \tag{30}$$

An interesting point arises in connection with the relation of the two metacenters ($\bar{x}_L$ and $\bar{x}_N$). For positive rotation of the airplane about a point nearer the center of gravity than $\bar{x}_N$ the residual yawing moment will be negative; hence if the metacenter $\bar{x}_L$ is nearer the center of gravity than $\bar{x}_N$, steady turning with rudder operation will require a positive setting of the rudder, i. e., in a direction to aid the turn. Conversely, if control is by rolling moments, the steady motion will be a rotation about $\bar{x}_N$ and, if the residual rolling moment for rotation about this point is negative ($\bar{x}_L < \bar{x}_N$), the rolling control setting will be positive, also in a sense aiding the turn. Obviously, the condition $\bar{x}_N < \bar{x}_L$ corresponds to *instability* since in this case with either mode of two-control operation the control setting during a steady turn would be one appropriate to recovery from the turn. This condition is analogous to the spiral instability discussed by Lanchester. The following table gives the metacenters $\bar{x}_L$ and $\bar{x}_N$ for the average airplane at various lift coefficients:

C_L	$\bar{x}_L$	$\bar{x}_N$
	Feet	*Feet*
0.35	20	25
1.0	45	29
1.8	55	44

At the lowest speeds ($C_L = 1.0$ and 1.8) $\bar{x}_N$ is less than $\bar{x}_L$, indicating that negative rudder and aileron settings will be required during steady positive turns. Figure 2 shows results of calculations of the control-moment coefficients for equilibrium in turning at

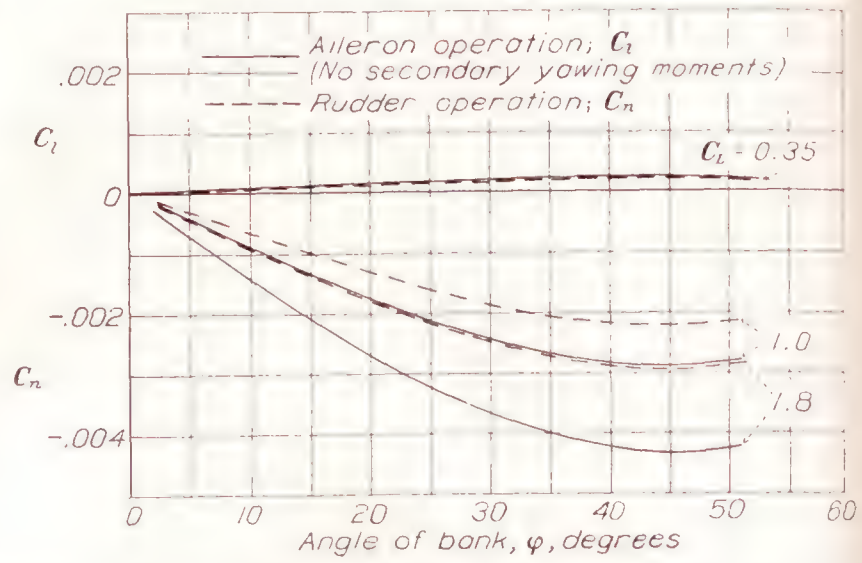

FIGURE 2.—Moment coefficients indicating control settings during steady turns at various angles of bank.

various angles of bank that give an indication of the fixed control settings.

Equilibrium angles of sideslip in steady turning with both modes of two-control operation are shown in figure 3. It is to be noted that the angle of sideslip is not greatly different in steady turning with either type of control and in every case is positive.

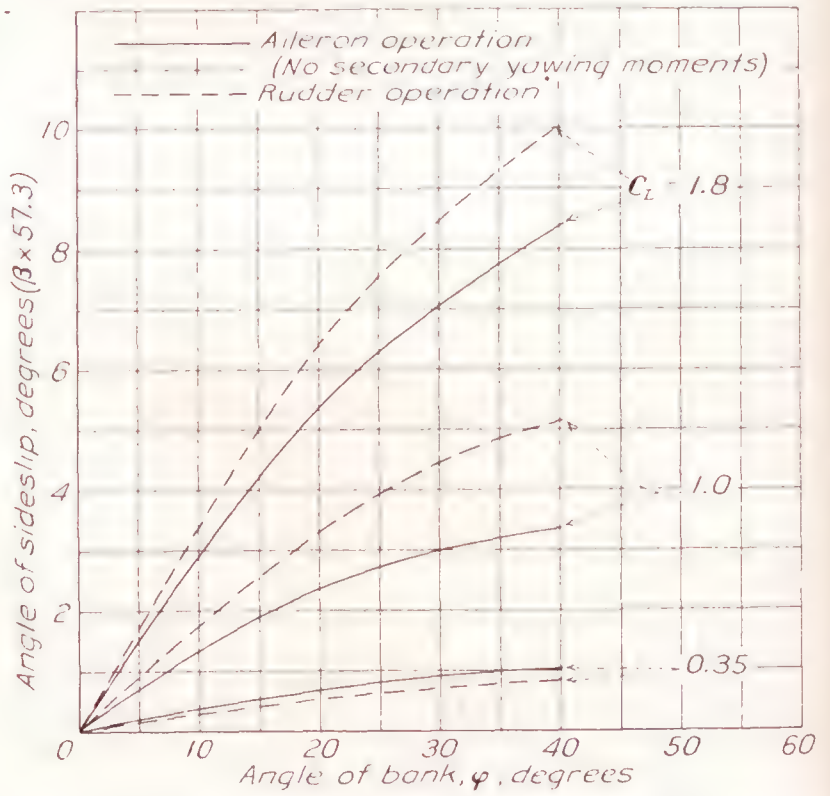

FIGURE 3.—Angles of sideslip during steady turns at various angles of bank with different modes of two-control operation.

The only possibility of outward or negative sideslip during the steady turn occurs when rolling and yawing moments are applied in combination. Such an occurrence is illustrated in figure 4, which shows the effect of secondary aileron yawing moments on the equilibrium during 30° bank turns. At $C_L = 1.0$ the sideslip becomes

negative, or outward, when the ratio N_δ/L_δ exceeds negatively N_τ/L_τ, i. e.:

$$\kappa=\frac{C_n}{C_l}\frac{I_X}{I_Z}=\frac{N_\delta}{L_\delta}>\frac{N_\tau}{L_\tau} \tag{31}$$

(See equation (25).)

Whether or not a given secondary aileron yawing moment will reduce or increase the equilibrium sideslip angle during a steady turn depends on the spiral stability of the airplane, for this characteristic determines the sign of the equilibrium control setting.

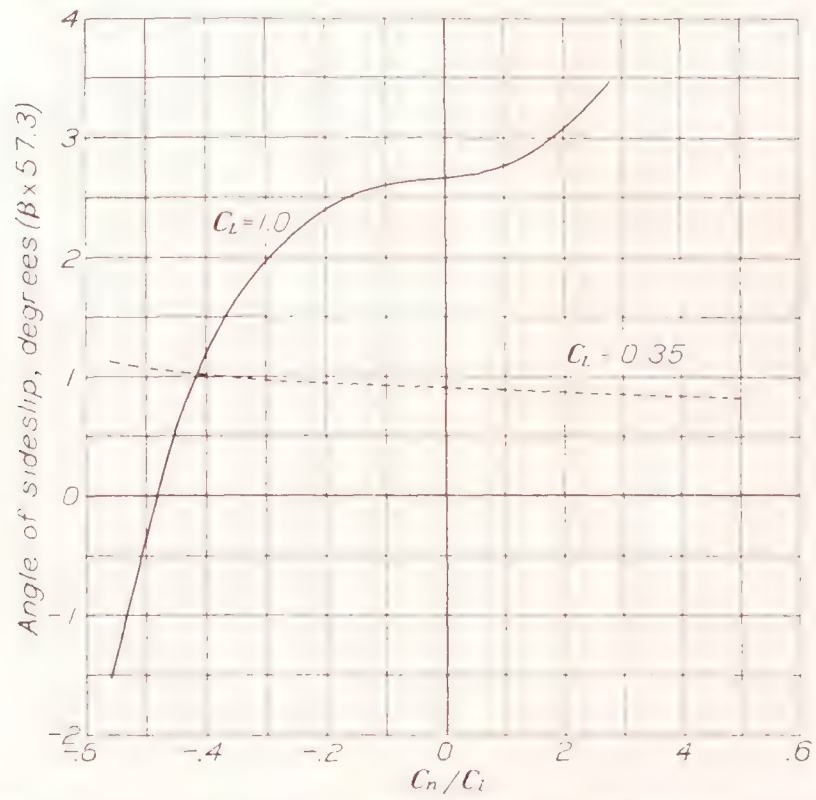

FIGURE 4.—The effect of secondary yawing moments on sideslip during a 30° bank steady turn; two-control operation with ailerons.

Thus, in the case of a spirally unstable machine the aileron setting will be appropriate to recovery from the bank and an adverse yawing moment will act in a positive direction, aiding the turn. In any event, spiral stability, if present, must be considered as a small effect (with conventional airplanes); and the control setting during steady turns is, if positive, almost certain to be small so that secondary moments will have little effect. (See fig. 4, C_L=0.35.)

TWO-CONTROL OPERATION IN UNSTEADY TURNS

The consideration of the equilibrium state is sufficient for the study of conditions during slowly executed maneuvers of sufficient duration for the natural free oscillations of the airplane to die out. In the case of rapid maneuvers performed by more or less quick movements of the control the equilibrium conditions are of secondary importance and the primary consideration is the oscillation and damping of the free motion.

According to the previously outlined treatment, the motions of the two-control airplane set up during unsteady turns will be studied by considering a constraint impressed on the motion in the particular coordinate in which the available control operates. Thus in one case of rudder control a definite sequence of yawing motions appropriate to the turn maneuver under consideration will be assumed. The free rolling motion that the airplane takes up during the maneuver will then be studied and compared with the rolling motion that would be considered appropriate for the execution of the maneuver.

The investigation of unsteady conditions during various maneuvers required that the equations of motion (equations (1) to (3)) be solved for different types and variations of the impressed disturbances. The first step in the procedure consisted in obtaining solutions of the equations for "unit disturbances" substituted into each coordinate of freedom.

The unit disturbance is defined by

$$\left.\begin{aligned} 1(t)&=0 \text{ when } t<0\\ 1(t)&=1 \text{ when } t>0 \end{aligned}\right\} \tag{32}$$

(see reference 3) and is taken to represent a disturbing acceleration of unit magnitude applied instantly at t=0.

The solutions of the equations of motion for this type of disturbance were found by methods described in reference 4. The result thus obtained is analogous

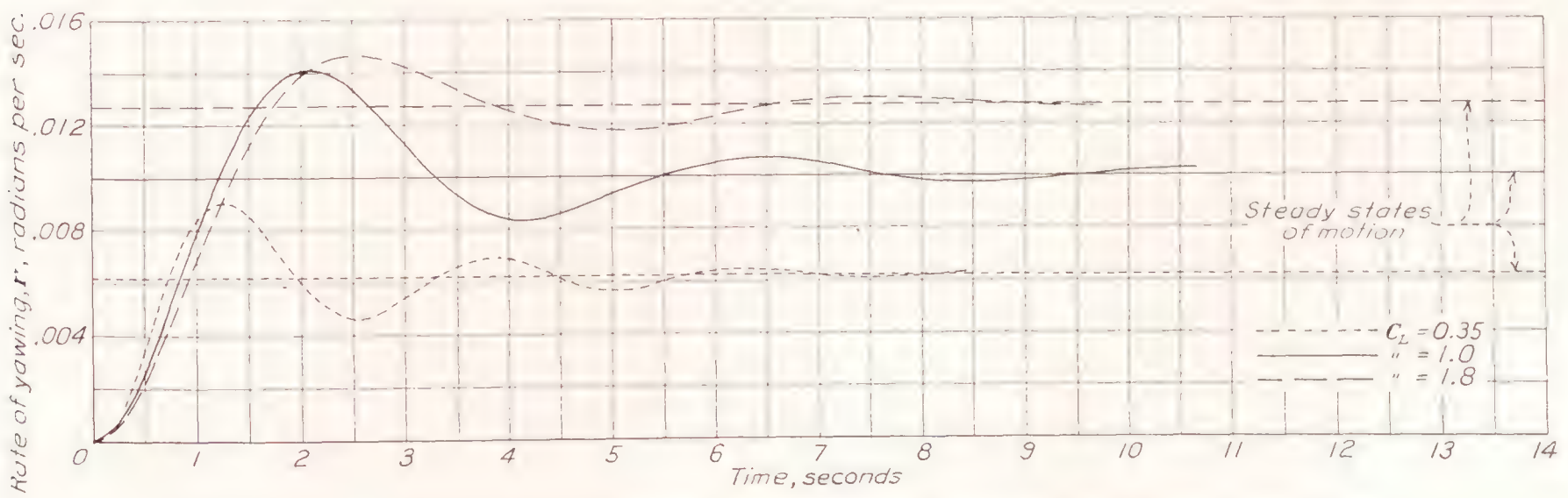

FIGURE 5.—Yawing motion due to unit *side* disturbance; two-control airplane constrained in rolling (aileron operation; κ=0).

to the so-called "indicial admittance" of the electric-circuit theory and was combined with Carson's generalized expansion theorem (see reference 5) to obtain the motion due to the varying forms of disturbance. If $v_1(t)$ is the motion calculated for a unit disturbance $1(t)$, and $v(t)$ is the motion due to a varying disturbance, say $\varphi(t)$ (see equation (2)), then Carson's theorem may be written

$$v(t_n)=v_1(t_n)\varphi(0)+\int_0^{t_n} v_1(t_n-t)\frac{d\varphi}{dt}\,dt \qquad (33)$$

It was found convenient to evaluate this integral graphically.

Figures 5 and 6 show the motions of the two-control airplane constrained in rolling (aileron operation) due to unit disturbances acting in each of the two remaining degrees of freedom. Figure 5 shows the yawing motions resulting from a suddenly impressed sidewise acceleration of 1 foot per second per second. The conditions here may be assumed to represent the effect of an initial and constantly maintained angle of bank of approximately

$$\varphi=\frac{1}{g} \qquad (34)$$

In order to maintain this bank angle without sideslipping, the airplane should immediately acquire a uniform rate of yawing of approximately

$$r=\frac{1}{U_0} \qquad (35)$$

As the curves show, the actual yawing is delayed fo an instant but in each case oscillates about the mea value given by (35). The most favorable condition i that at high speed (C_L=0.35) since the appropriat yawing motion occurs with the least delay and the os cillations are most quickly damped.

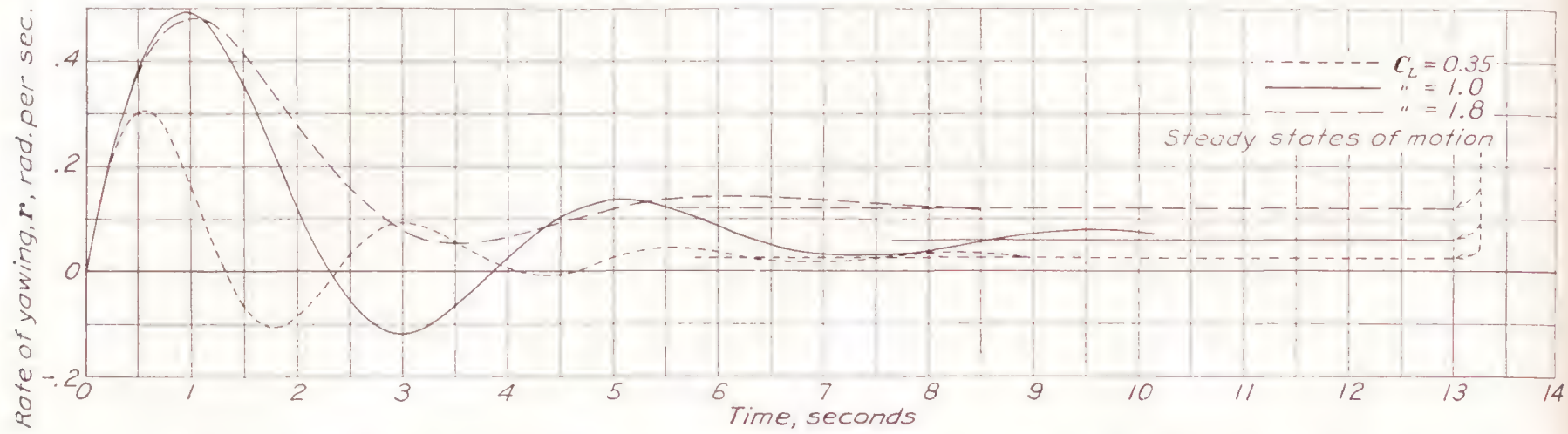

FIGURE 6.—Yawing motion due to unit *yawing* disturbance; two-control airplane constrained in rolling (aileron operation; κ=0).

As stated previously, the unit motions, or motion due to unit disturbances, were utilized in calculatin the effects of varying disturbances assumed during tur maneuvers. Thus the curves given in figure 5 wer used to find the motions due to a varying angle of ban by means of Carson's integral (33). Actually, in con straining the airplane to a definite bank angle as wa assumed, a varying aileron rolling moment has to b applied and, if this moment is accompanied by a

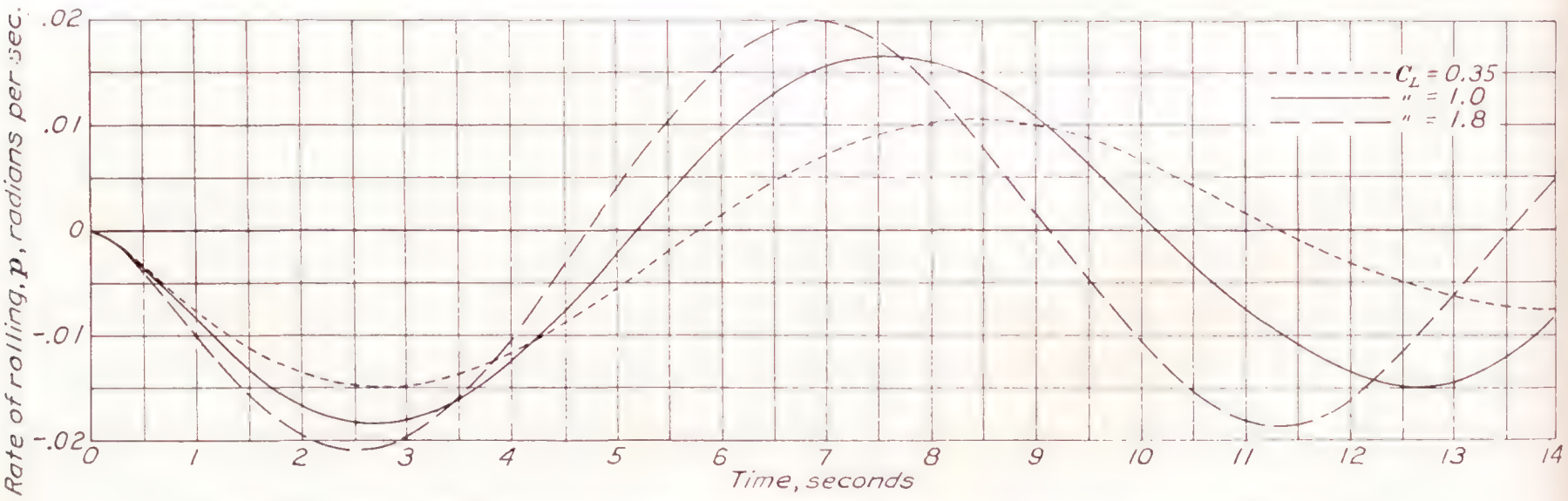

FIGURE 7.—Rolling motion due to unit *side* disturbance; two-control airplane constrained in yawing (rudder operation).

secondary yawing moment, additional disturbances in yawing will be introduced. The rolling motion will also introduce a secondary disturbance in yawing equal to $N_p \times p(t)$. Figure 6 shows the yawing motion produced by a unit disturbance in yawing that was used in calculating the effects of such impressed yawing disturbances. This curve may be considered to represent the yawing motion following the sudden application of a control yawing moment. The final effect of this disturbance is to cause the machine to assume a yawed attitude, turning slowly under the influence of the side force vY_v.

Figures 7 and 8 show the corresponding solutions of the equations of motion (3) for the case of the airplane constrained in yawing by a rudder control. Figure 7

may be taken to represent the rolling motion following an initial bank angle. Presumably the ideal condition would be a rapid diminishing of this bank angle to zero. The integrated areas under the curves shown would then approach a definite value after a few oscillations, which area should be equal to the initial bank angle, namely approximately

$$\varphi=\frac{1}{g} \tag{36}$$

Instead, the airplane continues to roll one way and then the other, executing the pendulum-like oscillations described in the discussion of the stability of this motion. The damping of these oscillations is slight and is most apparent at the lowest lift coefficient, $C_L=0.35$.

Figure 8 is similar to figure 7 except that here the rolling motion is due to a suddenly impressed angular acceleration in rolling. These curves were used in calculating the effect of varying rolling moments impressed indirectly by yawing motion $L_r \times r(t)$. (See equation (3).) Figure 8 is of interest in illustrating the two more or less distinct modes of motion in free rolling and sideslipping. It will be noted that the rolling starts very rapidly (with an initial angular acceleration of one radian per second per second) but soon takes up the slow swinging oscillation. As in the previous case of rolling motion, the steady state finally approached is a definite angle of bank.

The foregoing calculations are of interest in indicating how the different types of two-control airplanes may be expected to respond to attempted maneuvers. The first step in the calculation of an actual complete maneuver is to arrive at a specification for that part of the motion which is assumed to be constrained. It will be of interest to compare the motions executed by the two-control airplane with the most perfect possible coordination of the motions that might be obtained with three-control operation. Obviously, it will be necessary to specify a maneuver that is within the power of the control to produce and it will be desirable to conform the specification to a type of turn likely to be followed in practice. In other respects, it was thought that any smooth curve representing the banking or yawing of the machine up to a definite angle or rate maintained steadily for a short time and followed by a smooth recovery to straight flight would serve the purpose. Figure 9 shows the time history of the ideal three-control turn that was assumed in the subsequent investigation. In most cases the manuever was assumed to be completed in 6.28 seconds and this time is taken to represent about the maximum rapidity with which the maneuver could be performed at the lowest speed using conventional-type controls. Figure 10

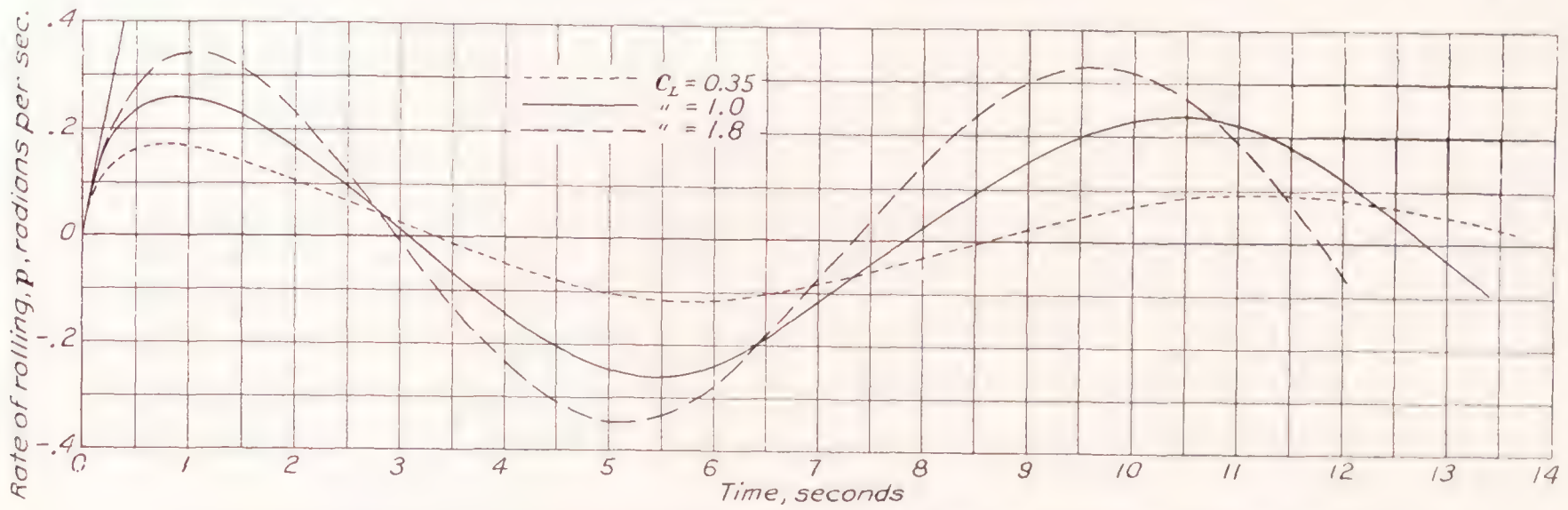

FIGURE 8.—Rolling motion due to unit *rolling* disturbance; two-control airplane constrained in yawing (rudder operation).

shows the control-moment coefficients necessary to constrain the rolling and yawing motions to the specified maneuver with perfect three-control operation. Under the conditions of two-control operation the turns

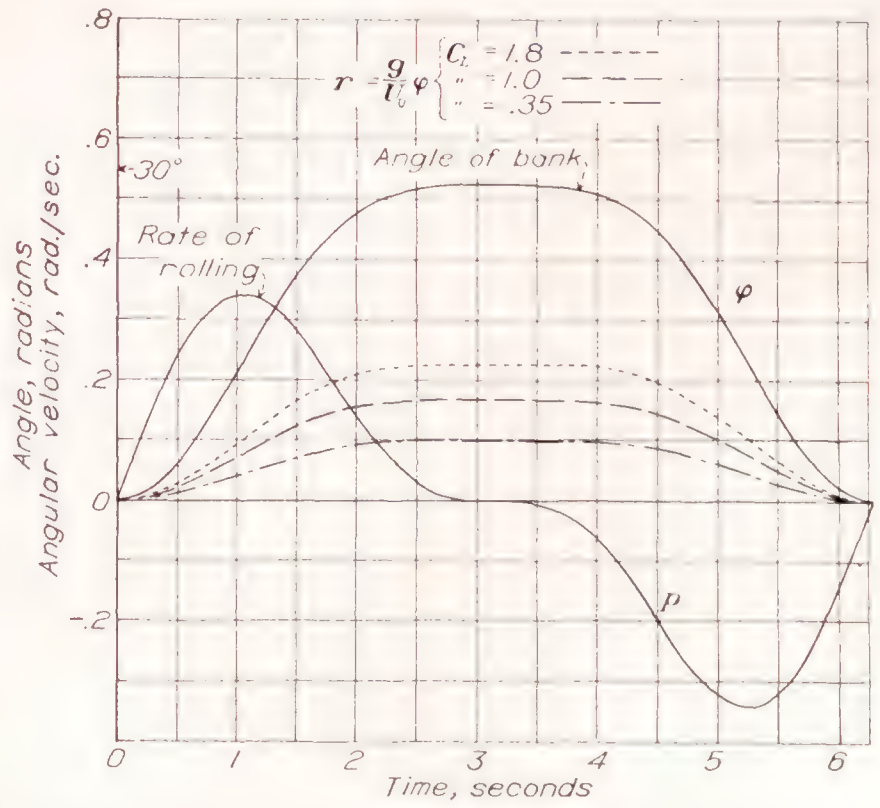

FIGURE 9.—Angle of bank and rates of rolling and yawing specified for 30° bank two-control turn maneuvers.

will not be perfect owing to the sideslipping and it is to be expected that this sideslipping will in some degree modify the control settings.

In the calculations illustrated in figure 11 the banking motion was assumed to be forced to follow the ideal bank by means of a rolling control and the resultant free yawing motions were computed. The reaction of the machine was evidently favorable in this case. This result could have been anticipated from the calcu-

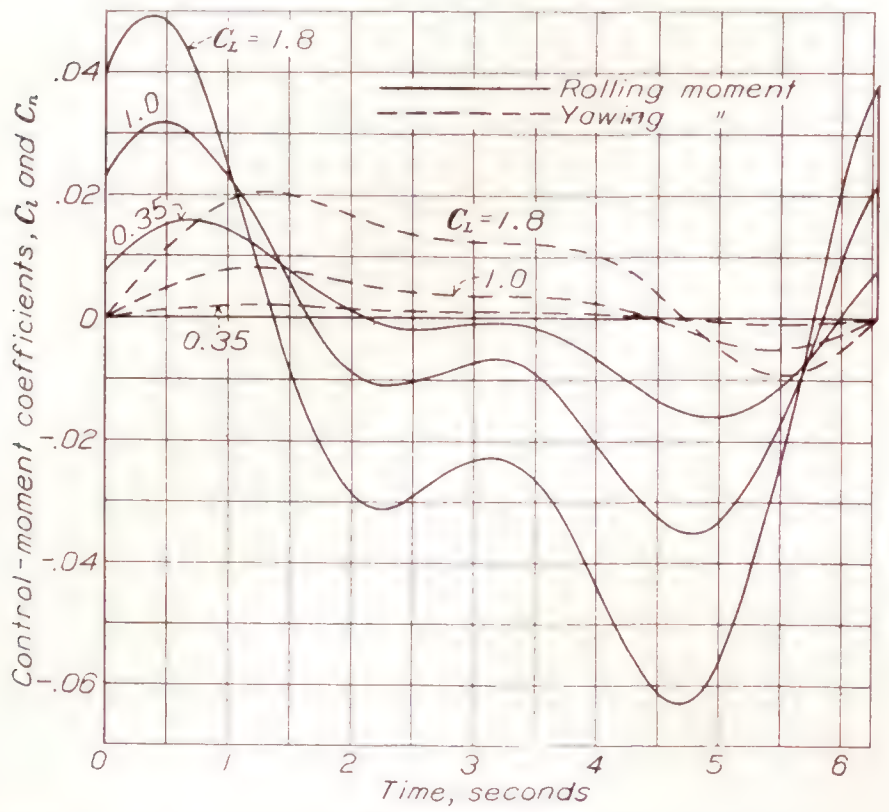

FIGURE 10.—Control-moment coefficients necessary to produce specified manuever with zero sideslip.

lations of stability, which showed that the free yawing motion was of short period and strongly damped.

The curves of figure 11, although indicating the advantage of rolling-moment control, also bring out an imperfection in the coordination of the yawing motion. The rolling motion itself tends to induce an unfavorable

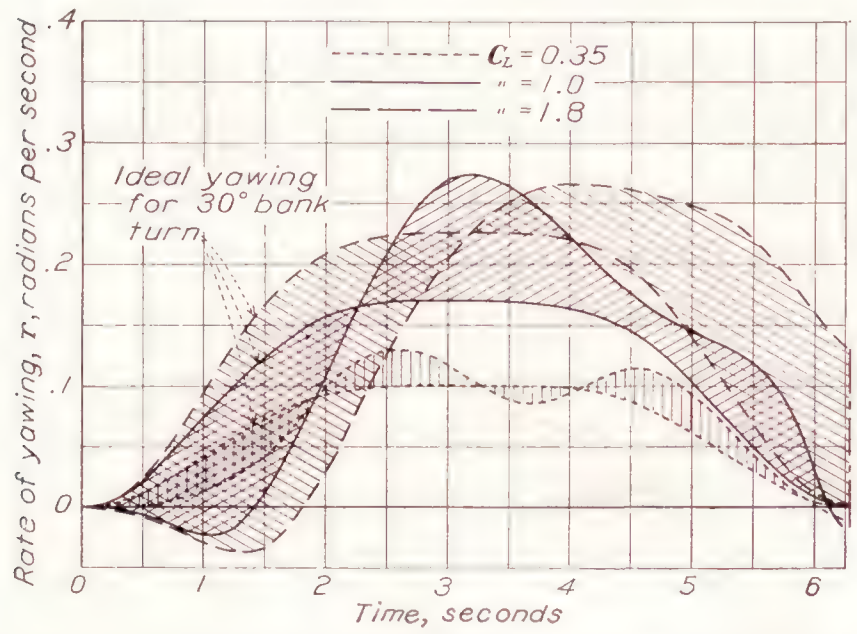

FIGURE 11.—Free yawing motion during 30° bank maneuvers performed with rolling control.

yawing motion at the start of the maneuver due to the adverse sign of N_p. This effect becomes more pronounced at the higher lift coefficients and, in the worst case (C_L=1.8), produces an adverse change in the heading of the machine of 2.0°. The total change in heading produced by the maneuver at this speed is approximately 50°.

From the foregoing considerations, it appeared that a certain amount of favorable secondary aileron yawing moment might be desirable to overcome the adverse yaw caused by the rolling motion at the start of the

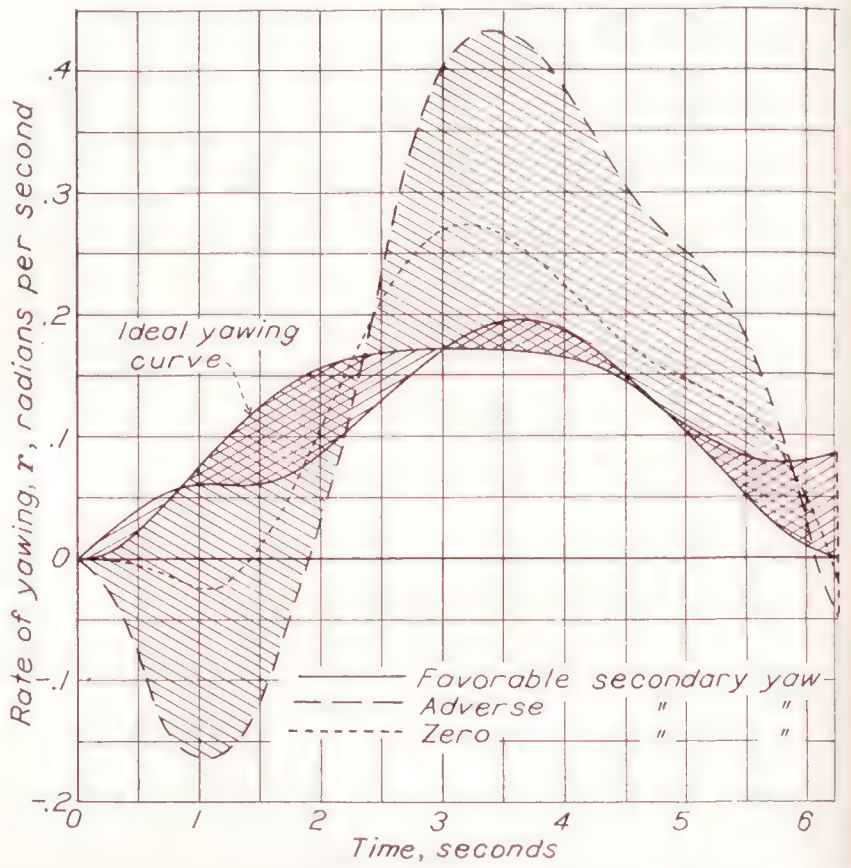

FIGURE 12.—The effect of secondary yawing moments on yawing motions during 30° bank maneuver performed with rolling control; C_L=1.0. C_n=± 0.21C_l (κ=± 0.15).

turn. The effects of secondary yawing moments of both favorable and adverse sign applied in proportion to the control rolling moment are illustrated in figures 12, 13, and 14.

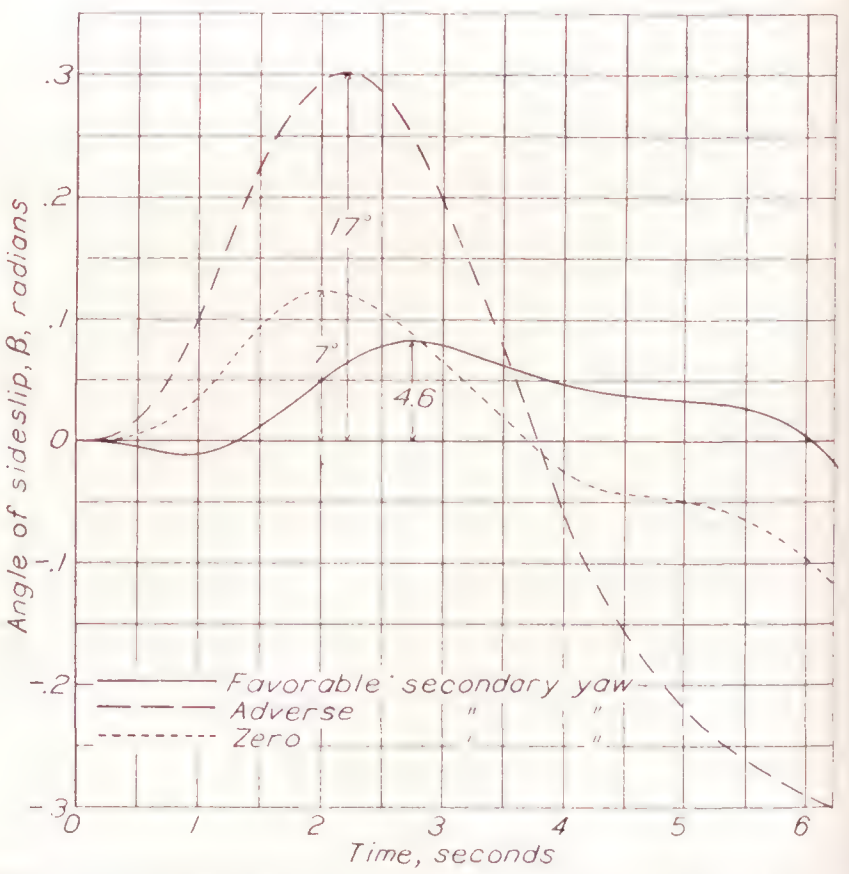

FIGURE 13.—The effect of secondary yawing moments on sideslip during 30° bank maneuver performed with rolling control; C_L=1.0. C_n=±0.21C_l (κ=±0.15).

The curves shown were calculated by equation (2) and take account of the increments of control displacement necessary to accommodate the rolling moments introduced by the yawing and sideslipping oscillations.

The effect of these increments of control displacement is to modify the stability of the yawing and sideslipping motions, an adverse yawing moment reducing the damping and lengthening the period. The results indicate especially the disadvantage of adverse yaw and show that some improvement may be had from a favorable yawing moment.

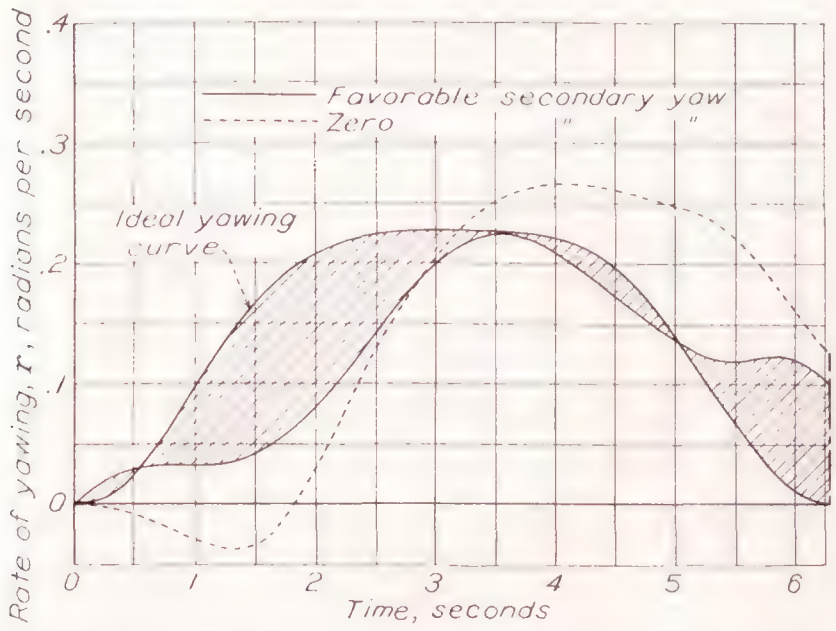

FIGURE 14.—The effect of favorable secondary yawing moment on yawing motion during 30° bank maneuver performed with rolling control; $C_L=1.8$. $C_n=0.21C_l$ ($\kappa=0.15$).

In order to study more closely the possible beneficial effects of a favorable aileron yawing moment, it is of some interest to analyze further the control application into several components. The component that results in modification of the stability through the action of the secondary yawing moment may be considered to be directly favorable to improved coordination of the

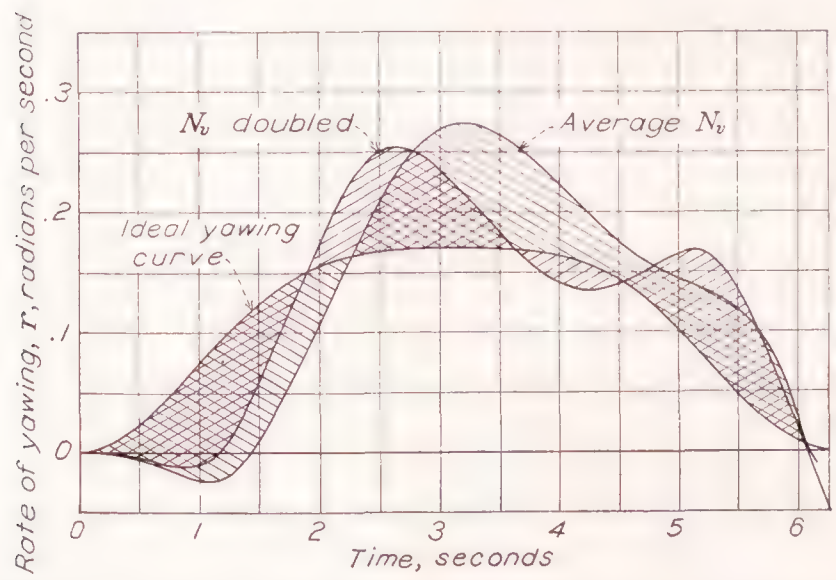

FIGURE 15.—The effect of increased N_v on yawing motion during 30° bank maneuver; aileron operation (no secondary yawing moment); $C_L=1.0$.

yawing motion because it shortens the natural oscillation period and increases the damping. With a given proportion of favorable yawing moment, increasing the dihedral angle should result in further improvement in this respect since the apparent weathercock stability ($N_v-\kappa L_v$) is increased in that way. Another component of the applied rolling control is directed to overcoming the damping of the rolling incident to the maneuver. The secondary yawing disturbance thus introduced is of the same form as pN_p and may be calculated as

$$N_p'=(N_p-\kappa L_p) \tag{37}$$

The condition for perfect coordination of banking and yawing motion during the turn requires that the acceleration in yawing be very nearly proportional to the rate of rolling; namely,

$$\frac{dr}{dt}=\frac{g}{U_0}\times p \tag{38}$$

The component of rolling control directed toward opposing the damping in rolling is applied in this way

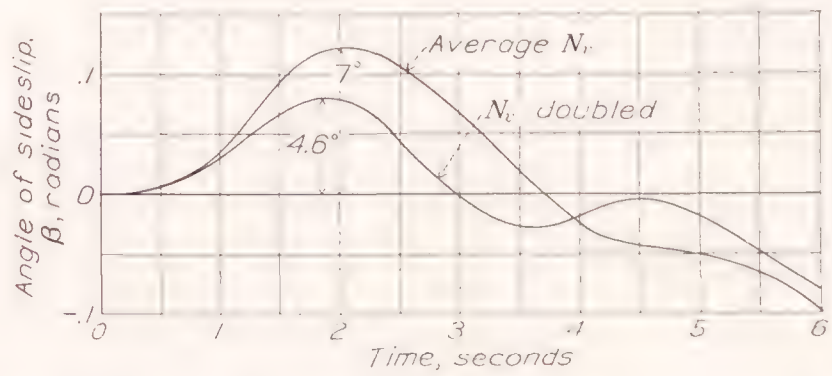

FIGURE 16.—The effect of increased N_v on sideslip during two-control 30° bank maneuver; aileron operation (no secondary yawing moment); $C_L=1.0$.

and it is seen that this component of the secondary favorable yawing moment is properly directed toward improved coordination of the yawing motion. The component of control application necessary to accelerate the rolling motion does not, however, lead to a desirable secondary yawing acceleration since this acceleration is not proportioned to the rolling velocity.

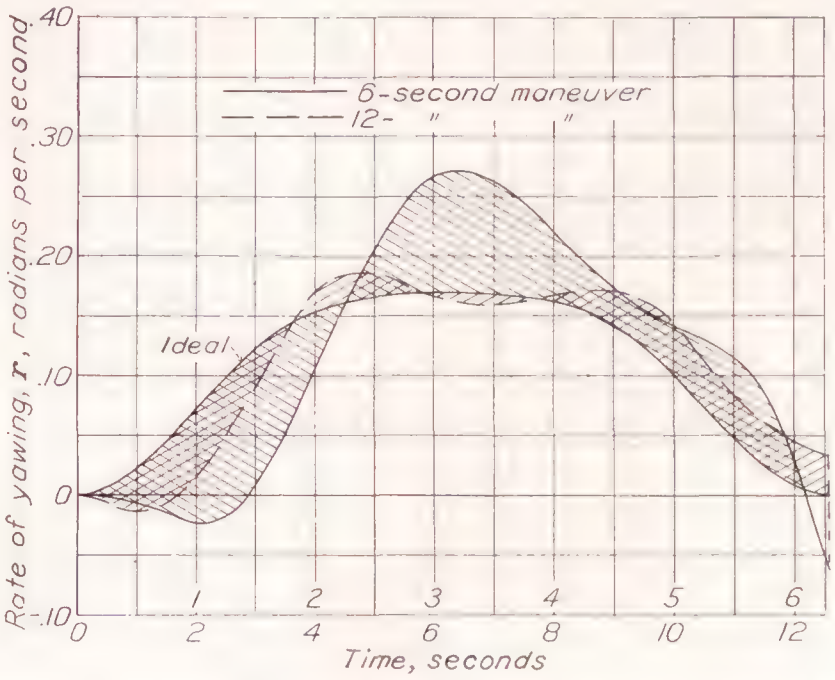

FIGURE 17.—Comparison of yawing motions during maneuvers of different time extents; aileron operation (no secondary yawing moment); $C_L=1.0$.

This component results in the primary disadvantage associated with favorable-yaw ailerons. Quick or irregular movements of the control may lead to pronounced yawing oscillations if the secondary moment is very great.

It appears that a decisive method of improving the aileron-operated two-control airplane would be to

increase the weathercock-stability factor N_v. This method would serve directly to reduce the sideslipping to a minimum both in steady turning and in rapidly executed turn maneuvers. Figure 15 shows the effect of doubling N_v on the yawing motion during the maneuver performed at $C_L=1.0$. This modification of the airplane shortened the natural period of the oscillation and resulted in the yawing action taking place more quickly. The effect on sideslip is shown in figure 16. Although the maneuver ends with about 5° of outward sideslip, this value will be quickly reduced to zero on account of the natural stability of the motion. With different timing of the maneuver it may, of course, be brought to an end with no residual sideslip. The following table shows the effect of arbitrarily increasing N_v on the natural period of the yawing oscillations:

Ratio of N_v to that of average airplane	Period
	Seconds
1	4. 16
2	2. 92
4	2. 05

It is to be noted that an increase in vertical-fin area will increase the derivative N_r as well as N_v and will thus result in greater damping of the motion.

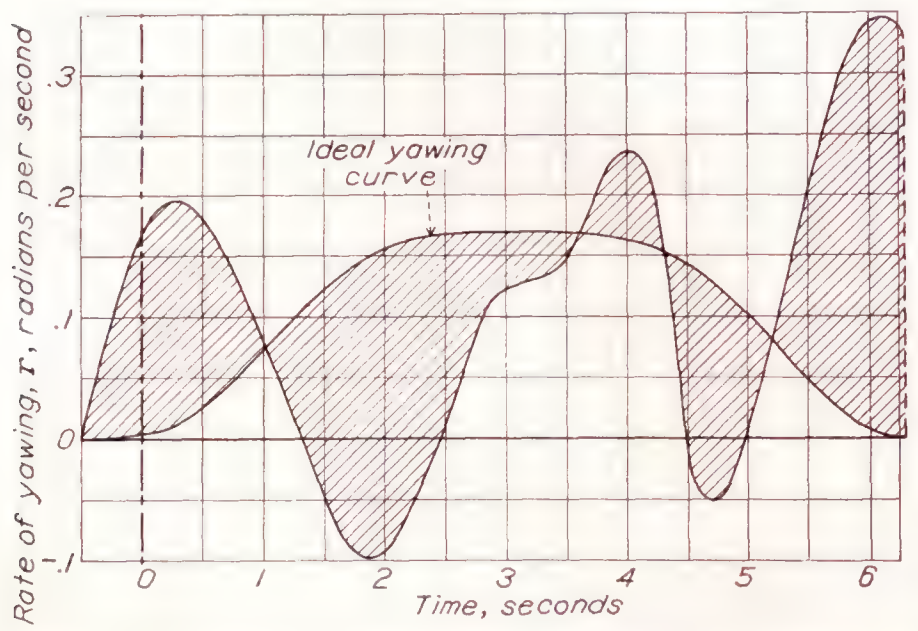

FIGURE 18.—Yawing motion necessary to enforce assumed 30° bank maneuver with rudder operation; $C_L=1.0$.

A certain disadvantage associated with increased N_v is the relatively greater tendency for spiral instability and the consequent necessity for holding the control against the steady turn. It may be expected, however, that this undesirable tendency could be overcome by properly proportioning the dihedral of the wings. The greatest possible effect of increase of vertical-fin area would be to cause the metacenter for yawing moments $\bar{x}_N$ (see discussion of stability) to approach coincidence with the fin; it would then appear necessary to arrange the metacenter for rolling moments ahead of this point in order to accommodate any desired increase of vertical-fin area and secure spiral stability.

Further improvement in the operation of the aileron-controlled machine could be had by decreasing the yawing derivative in rolling N_p. Alteration of this derivative apparently would require fundamental changes in wing design, improvement being in the direction of lower aspect ratio, which might, of course, conflict with other requirements.

As pointed out, the maneuvers assumed in these calculations are considered to be more rapid than usual in

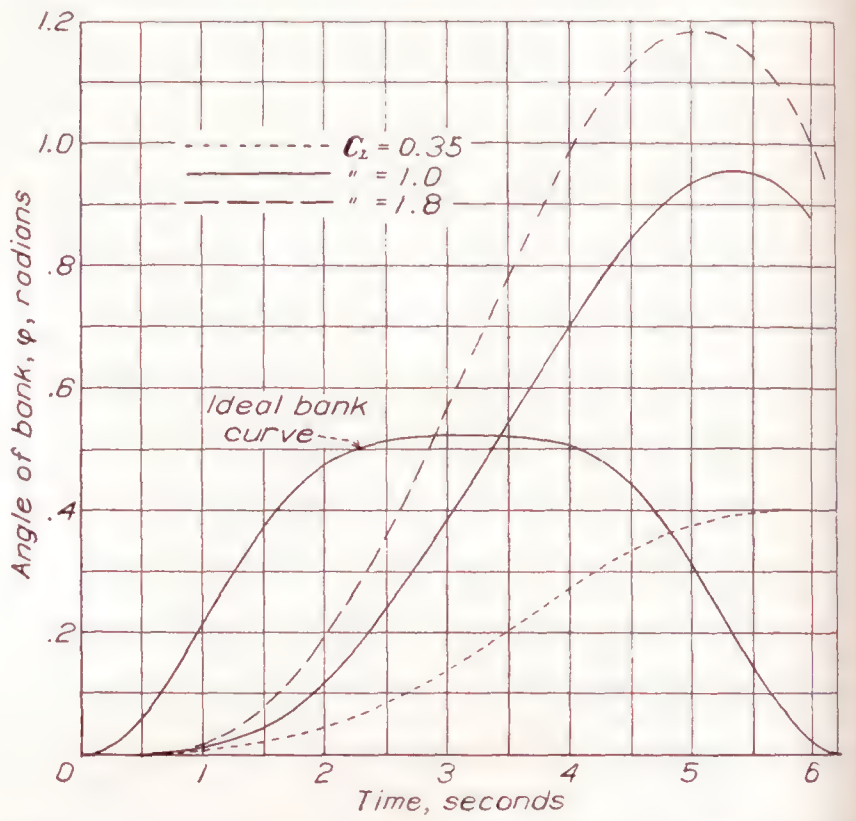

FIGURE 19.—Free angles of bank during turn maneuvers performed with rudder compared with ideal bank curve; yawing constraints for 30° bank maneuver.

normal flight, since they represent the use of a large proportion of the control power ordinarily available at the lower speeds. With slower maneuvers the coordination of the motions of the two-control airplane would be expected to be much better, especially when the duration of the maneuver becomes large relative to the natural period of oscillation of the airplane. Figure 17 shows the result of a calculation in which the duration of the 6.28-second maneuver was doubled.

It is worth noting that the actual deflection of the flight path of an airplane relative to the earth is accomplished much more directly by banking than by steering. Regardless of the sideslipping and coordination of angular motions, any decided acceleration of the path must be brought about by inclination of the lift and is not directly affected to any great extent by rotating the airplane in yaw. Such deflection of the path would be the principal objective in turning to avoid an obstacle. Thus the airplane with rolling-moment control should be capable of avoiding obstacles equally as quickly as a conventional three-control airplane. As is the case with three-control operation, the tendency of a two-control airplane to accelerate downward when banked must be counteracted by a movement of the elevator.

If the airplane is assumed to execute a sharp turn to avoid an obstacle, the primary consideration will thus be the ability to produce a specified bank. Under such

conditions the pilot of the rudder-operated airplane would be expected to make an effort at indirect control of the bank without regard to the coordination of the yawing motion. The question then arises as to what yawing motion would have to be prescribed in the case of the rudder-controlled machine to enforce the desired motion in banking.

Figure 18 shows the yawing motion that results in a bank curve similar to that given in figure 9. It appears that, in order to attain the bank angle as shown, a relatively powerful rudder control would have to be applied about one-half second in advance of the usual start of the turn. Further calculations showed that the prescribed yawing motion could be attained throughout if a rather large amount of rudder control were available. That such an attempt to follow a definite course in banking would require a vigorous use of the rudder is evident from the oscillation of the yawing curve.

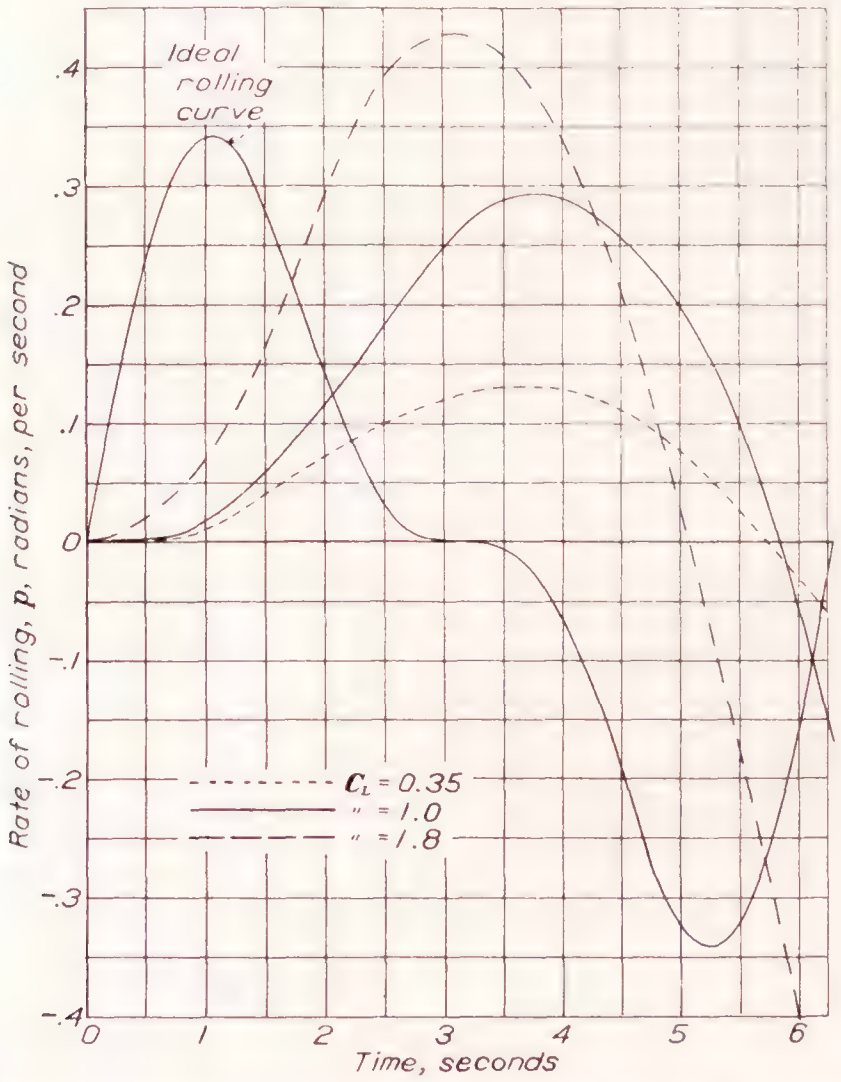

FIGURE 20.—Free rolling motion during turn maneuvers performed with rudder; yawing constraints for 30° bank maneuver.

In the case of two-control operation with a constraint in yawing by means of the rudder, the yawing motions shown in figure 9 were assumed and the resulting free rolling motions were calculated. Figures 19 and 20 show the results of such calculations made at different lift coefficients. The angles of bank and rates of rolling attained are compared with those that would be appropriate to the constrained yawing motion. It is apparent from these and the preceding figures that the two-control airplane operated with the rudder cannot be expected to perform rapid maneuvers of the type considered. The natural reaction of the rolling motion is too slow and the damping is too slight to enable even an approximate coordination of the motions within the short time of duration of the maneuver.

Figure 21 shows the angles of sideslip attained with the various modes of operation considered, summarizing the results of the calculations.

The reasons for the inability of the rudder-controlled airplane to execute rapid turns are: First, that the secondary rolling reaction due to yawing motion is insufficient to overcome the relatively great damping of direct rolling motion; second, that for a rapid turn the rate of rolling required on entry and recovery greatly exceeds the maximum rate of yawing; and third, that the free rolling and sideslipping oscillations set up are not very well damped. The greatest possibility for

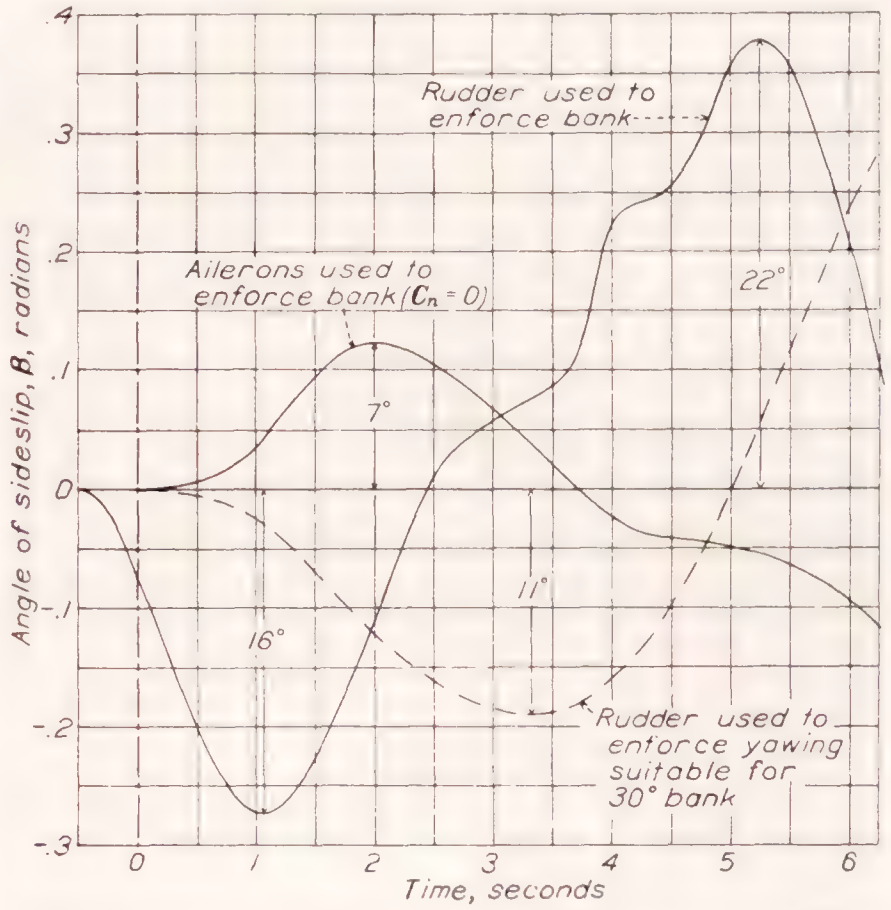

FIGURE 21.—Angles of sideslip during two-control turn maneuvers with different modes of operation; 30° bank turn maneuver.

improvement would appear to be in increasing the derivatives L_v and Y_v. The first (L_v) would call for increased dihedral angle and would serve to shorten the natural period of the rolling and sideslipping motion, while the second (Y_v) would call for increased area of the side projection of the airplane and should improve the damping of the oscillations. The following table shows the effects of changing these derivatives on the natural period and damping of the oscillations at C_L=1.0.

	Ratio of derivative to that of average airplane				
	L_v			Y_v	
	½	1	2	1	2
Time to damp ½, seconds	12.4	36.6	∞	36.6	6.25
Period, seconds	15.3	9.9	7.65	9.9	10.9

CONCLUSION

The lateral motion of a conventional airplane is more stable when constrained in rolling than when constrained in yawing. The stability of the free yawing and sideslipping motion is greater than that of the entirely free motion; the stability of the free rolling and sideslipping is less than that of the entirely free motion.

If a rolling-moment control is used to enforce an arbitrary constraint in banking, the free yawing that results will be approximately coordinated to the bank if the airplane has the average degree of weathercock stability (N_v). The yawing in this case is also approximately adjusted to the speed of flight so that with a given bank maneuver a more rapid rate of yawing is attained at low speed than at high speed, as is desirable. The deviation of the yawing from the ideal is greater, however, at lower speeds and is also greater in quick turns than in more slowly executed ones. If the rolling control were designed to give a moderate favorable yawing moment, the coordination of the motions would be improved. Improvement may also be effected by increasing the weathercock stability. If, however, the aileron control gives the usual proportion of secondary adverse yawing moment, the coordination of the yawing with the banking will be relatively very poor. The motions may then become unstable and uncontrollable in an extreme case at high lift coefficient. These latter statements are particularly applicable to conventional-type ailerons, which are considered as undesirable on this account for use at low flight speed unless compensated by the rudder.

A rudder control may be used to enforce a constraint either directly on the yawing motion or indirectly on the rolling motion provided that the maneuver specified is not too rapid nor the disturbances encountered too severe. In the former case the free banking motion occurs as a series of long oscillations that do not begin to approximate the desired bank until some time after the start of a maneuver or after the passing of a disturbance. During a rapid yawing maneuver the bank that occurs is greater at low flight speed than at high, indicating that the coordination of the centrifugal and the gravitational accelerations is not adapted to the desired variation with flight speed.

Although the coordination of the motions with aileron control grows worse as the flight speed is reduced, the coordination with rudder control improves somewhat at the lower speeds. This effect would be especially apparent if the rudder were applied in such a way as to enforce indirectly a desired banking motion. Such indirect control requires, however, that the rudder be deflected in advance of the desired effect. The yawing that arises when the bank is indirectly controlled with the rudder is a very poor approximation to the ideal yawing and calls for large and irregular control movements.

The amount of sideslipping during *steady* turns is not greatly different with either mode of operation. In either case it appears desirable that the free motion of the airplane show spiral stability so that control settings opposing the turn will not be required.

In general, it is concluded that a reliable rolling-moment control that does not give a secondary adverse yawing moment would afford the most satisfactory means for two-control operation. It appears that a moderate amount of favorable secondary yaw would be desirable although certain disadvantages appear if the proportion is too great.

The disadvantage in two-control operation lies not so much in the imperfection of control of the flight path of the airplane relative to the earth as in the sideslipping and sidewise accelerations that arise through the imperfect coordination of the yawing and banking motions. It appears possible that this tendency may be so reduced by the use of suitable control organs and properly modified stability characteristics as to be unobjectionable.

LANGLEY MEMORIAL AERONAUTICAL LABORATORY,
NATIONAL ADVISORY COMMITTEE FOR AERONAUTICS.
LANGLEY FIELD, VA., *August 12, 1936.*

REFERENCES

1. Routh, E. J.: Advanced Rigid Dynamics, vol. II. The Macmillan Co.,1905.
2. Weick, Fred E., and Jones, Robert T.: The Effect of Lateral Controls in Producing Motion of an Airplane as Computed from Wind-Tunnel Data. T. R. No. 570, N. A. C. A., 1936.
3. Bush, V.: Operational Circuit Analysis. John Wiley and Sons, Inc., 1929, p. 41.
4. Jones, Robert T.: A Simplified Application of the Method of Operators to the Calculation of Disturbed Motions of an Airplane. T. R. No. 560, N. A. C. A., 1936.
5. Carson, J. R.: Electric Circuit Theory and Operational Calculus. McGraw-Hill Book Co., Inc., 1926.

REPORT No. 580

HEAT TRANSFER TO FUEL SPRAYS INJECTED INTO HEATED GASES

By Robert F. Selden and Robert C. Spencer

SUMMARY

A study has been made of the influence of several variables on the pressure decrease accompanying injection of a relatively cool liquid into a heated compressed gas. Indirectly, this pressure decrease and the time rate of change of it are indicative of the total heat transferred as well as of the rate of heat transfer between the gas and the injected liquid. Air, nitrogen, and carbon dioxide were used as ambient gases; Diesel fuel and benzene were the injected liquids. The gas densities and gas-fuel ratios covered approximately the range used in compression-ignition engines. The gas temperatures ranged from 150° C. to 350° C.

Several general conclusions may be drawn from the experimental results: Vaporization begins immediately after the start of injection; the initial rate of heat transfer is a direct function of the initial temperature difference between the gas and the fuel; and the heat transfer is less efficient the greater the injected fuel quantity, even though the total heat transferred is greater.

INTRODUCTION

It is generally recognized that the compression-ignition engine in its present state of development suffers the disadvantage of inefficient utilization of its air charge. Recognizing that the utilization of the air must be partly dependent upon the fuel spray, Lee has conducted a detailed photographic investigation of the exterior characteristics of fuel sprays (reference 1). He has also determined the spatial distribution of the fuel within the spray (reference 2). These spray investigations have been extended by tests with the N. A. C. A. combustion apparatus and the results give an improved insight into the gross physical and chemical processes as they occur in the engine. (See references 3 and 4.)

The ignition lag in compression-ignition engines has been shown to influence the character of the subsequent explosion (references 5 and 6). No entirely satisfactory explanation of this fact has been given, but certain general conclusions can be drawn: In general, the fuel must be heated after injection; the fuel and the air must be mixed; and certain preliminary chemical reactions must take place before the actual ignition can occur. The observed lag is thus a composite of the intervals associated with these processes. It follows that heating the fuel prior to injection cannot reduce the ignition lag indefinitely although some reduction may be accomplished in this manner (reference 7). Rothrock and Waldron have shown that appreciable vaporization follows injection of the fuel into the combustion apparatus (reference 8). The time required for this vaporization to begin was not established but, in view of Wentzel's theoretical analysis of the heating and vaporization of fuel droplets suspended in a heated gas (reference 9), there is every reason to believe that appreciable vaporization occurs in a compression-ignition engine during the ignition-lag period.

The present investigation was undertaken to isolate the heat transfer accompanying the mixing of a fuel spray and the ambient gas in a bomb and to study the influence of several variables on this individual process. The results of this investigation should give an insight into the time required to effect some vaporization since this process necessarily corresponds to a portion of the total heat transfer. Experimentally, heat transfer is not directly measurable in a system of this type; therefore, resort has been had to an indirect approach, namely, the measurement of the change in pressure accompanying the adiabatic exchange of heat between the gas and fuel after injection of the fuel into a bomb. The primary variables were the gas temperature, the gas density, and the gas-fuel ratio. The effects of the nozzle design, the fuel temperature, the kind of fuel, and the character of the ambient gas were less extensively investigated.

Gas densities covering most of the range found in engine practice were used. For mechanical reasons temperatures corresponding to those attained in compression-ignition engines at top center could not be used. The maximum temperature employed was actually somewhat less than that of the gas charge prevailing at the start of injection (references 10 and 11) in compression-ignition engines.

ANALYSIS OF THE PROBLEM

The transfer of heat to a suspended droplet can take place by two mechanisms: conduction and radiation. Except insofar as their boundary conditions are altered, the mass flow of gas, induced by the injection of the liquid fuel, presumably is of little importance with respect to the individual droplets because of their low relative velocity (reference 12). The situation may be

vastly different, however, for the spray considered as a unit, particularly for injection into an engine having induced air flow. Radiation to the surfaces of the droplets takes place to some extent and, whereas the actual magnitude of this exchange is uncertain, the maximum rate for energy transferred in this manner can be estimated for comparative purposes.

For conductive heat transfer there are two controlling resistances: The first is within the droplet itself and the second must be associated with the equivalent of a film surrounding the droplet. The first can be analytically treated but the second presents difficulties. Because of the net transfer of molecules from the droplet surface, the character of this film is not independent of time, as is usually assumed in theoretical treatments. (See references 9, 13, 14, and 15.) In fuel sprays the vapor films about the liquid droplets probably interpenetrate, thus necessitating some consideration of the spray as a whole. Moreover, the fuel is not uniformly distributed within the spray. In view of these difficulties no attempt will be made to establish any mathematical relations for the heat transfer through the film encompassing the droplet.

Heat transfer within a droplet.—Ingersoll and Zobel have published equations pertaining to the internal heating of a rigid sphere suddenly inserted into a fluid possessing a higher temperature (reference 16). These equations may be modified to give, respectively, the instantaneous center temperature t_c and the average temperature t_a of the droplet:

$$t_c=t_i+(t_s-t_i)\left[1-2\left(e^{\frac{-\pi^2h^2t}{R^2}}-e^{\frac{-4\pi^2h^2t}{R^2}}+e^{\frac{-9\pi^2h^2t}{R^2}}-\ldots\right)\right]$$

$$t_a=t_i+(t_s-t_i)\left[1-\frac{6}{\pi^2}\left(e^{\frac{-\pi^2h^2t}{R^2}}+\frac{1}{4}e^{\frac{-4\pi^2h^2t}{R^2}}+\frac{1}{9}e^{\frac{-9\pi^2h^2t}{R^2}}+\ldots\right)\right]$$

where t_s is the temperature of the shell, ° C.
t_i, the initial droplet temperature, ° C.
R, the radius of the shell, centimeters.
t, the immersion time, seconds.
h^2, the thermal diffusivity of the liquid in the droplet.

As applied to liquid droplets these relations do not represent the effects of possible internal convection currents. These currents, if present, would increase the rate of temperature rise as determined by these relations.

It follows from these relations that when h^2 is considered constant, the increase in both the center and average temperature above the initial droplet temperature is a definite fraction of the difference t_s-t_i; thus $t_c-t_i=\alpha\,(t_s-t_i)$ and $t_a-t_i=\beta\,(t_s-t_i)$. The assumption of a constant value of h^2, independent of temperature in the range employed, appears justified for the purpose of qualitative comparisons in view of the uncertainty involved in its estimation. An average value for the range 49° C. to 350° C. can be estimated on the basis of the average values of the thermal conductivity (0.00027 calorie per second per centimeter per degree C., reference 17), the density (0.713 gram per cubic centimeter, reference 18), and the specific heat (0.662 calorie per gram per degree C., reference 19). These values result in $h^2=0.000572$ square centimeter per second.

Values of α and β are given in the following table for several immersion intervals and droplet radii, the largest radius corresponding to the initial average size (reference 20). No actual values of droplet temperatures are given inasmuch as there is no adequate basis on which to estimate their surface temperature. Incidentally, the foregoing relations tacitly assume that the surface temperature is instantaneously attained and thereafter remains constant. This assumption does not greatly invalidate the fact that the increase in the temperature of the droplet, particularly the average temperature as shown by the β values, attains a large fraction of the possible increase in a remarkably short time. Moreover, the smaller the radius the more quickly this fraction approaches unity. As a result of evaporation, the surface temperature does not attain so high a value as it would if all the heat reaching the drop served to heat it. Even so, such evaporation presumably does not alter the establishment of thermal equilibrium within the droplet and hence the α and β quantities still have significance.

HEATING RATES FOR IMMERSED SPHERES

$[t_c-t_i=\alpha(t_s-t_i);\ t_a-t_i=\beta(t_s-t_i)]$

Droplet radius (cm / in.) / Immersion time	0.0015 / .00059		0.0020 / .00079		0.0025 / .00098	
	α	β	α	β	α	β
Second						
0.0001	0.002	0.464	0.000	0.362	0.000	0.296
.0003	.154	.706	.018	.573	.004	.479
.0005	.444	.826	.128	.690	.024	.587
.0007	.658	.895	.296	.771	.092	.666
.0010	.838	.951	.520	.851	.344	.749
.0015	.874	.962	.760	.927	.494	.842
.0020	.986	.996	.882	.964	.674	.900

Radiation from bomb wall.—Some insight into the possible contribution of radiation from the bomb wall to the total heat transfer follows from a consideration of the maximum rate of radiation. If the very questionable assumption is made that the droplets are true black bodies suspended in a space filled with black-body radiation, the net energy transferred in calories per second is given by:

$$\Delta H=1.37\times10^{-4}S\left[\left(\frac{T_1}{100}\right)^4-\left(\frac{T_2}{100}\right)^4\right]$$

(reference 21) where
S is the surface area of the drop.
T_1, the bomb-wall temperature, degrees K.
T_2, the droplet temperature, degrees K.

The extent to which the droplets are not black bodies introduces a factor that reduces this rate. The existence of black-body radiation within the bomb is actually the case prior to injection, but thereafter the radiation within the spray envelope undoubtedly corresponds to a lower temperature than that of the bomb walls. This fact again entails a diminution in the rate indicated by the equation. The area S may be taken as equivalent to that of the number of droplets of average size (reference 20) required for a spray of given weight.

For comparison with the observed rate of heat transfer, expressed in this case in terms of rate of pressure drop, the calculated rate of radiant transfer must be expressed in identical units. Although not indicative of the actual mechanism, this rate can be put in terms of the units in which the experimental data are expressed by considering all the radiant energy as being derived from the ambient gas.

Basic considerations of experimental method.—The observed decrease in pressure accompanied the decrease in temperature of the ambient gas caused by the flow of heat from it to the injected liquid. This process was essentially adiabatic in view of the small rate of heat transfer from the bomb wall. Cragoe's empirical relations (reference 17) for the specific and vaporization heats of oils permit the calculation of the pressure decrease that should accompany the complete vaporization of a given amount of fuel when all the heat is abstracted from the gas phase. When the total heat absorbed by the fuel in vaporizing is equated to that lost by the ambient gas, these relations lead to an expression that can be solved by trial and error to give the final equilibrium temperature:

$$t_f=\frac{NC_vt_i-49.5w}{NC_v+0.333w+0.000444wt_f}$$

where N is the moles of ambient gas.
C_v, the molal specific heat of this gas, taken as constant between t_f and t_i.
t_i, the initial gas temperature, °C.
w, the weight of injected fuel, grams.

It follows at once that the temperature drop (t_i-t_f) should remain constant for a given initial temperature and gas-fuel ratio, i. e., essentially N/w. The corresponding diminutions in the partial pressure of the gas are calculable from the expression

$$P_i-P_f=\frac{P_i(T_i-T_f)}{T_i}$$

in which P_i is the initial pressure, atmospheres.
P_f, the final pressure, atmospheres.
T_i, the initial absolute gas temperature, degrees K.
T_f, the final equilibrium gas temperature, degrees K.

This expression is strictly applicable only to the initial stage of the heat-transfer process when little vapor exists. Later in the process, however, these diminutions should be greater than the experimentally derived maximum values to the extent of the partial pressures of the vapor, these latter being directly proportional to the initial pressure for a given initial temperature and gas-fuel ratio. Thus the calculated actual drop to be expected under these stipulated conditions is in accordance with

$$(P_i-P_f)_{\text{actual}}=P_i\left[\frac{(T_i-T_f)}{T_i}-C\right]$$

where C is a correction factor necessitated by the presence of the fuel vapor. This factor is equal to the partial pressure of the vapor of the injected liquid divided by the initial gas pressure. The partial pressure was obtained from the perfect gas law and the known bomb volume, gas temperature, fuel weight for the particular gas-fuel ratio, and an estimated average molecular weight of 200 (reference 22). It follows from this expression that the pressure drop should be directly proportional to the initial pressure if the fuel derived all its heat from the gas phase under the assumed conditions of constant initial temperature and air-fuel ratio.

Some conception of the rate of heat transfer can also be obtained from the experimental results, particularly for the early part of the process in which the number of moles of gas is essentially invariant. It follows from the perfect gas law that the rate of pressure change is related to the rate of temperature change by

$$\frac{dP}{dt}=\frac{NR}{V}\frac{dT}{dt}$$

wherein R is the gas constant.
V, the volume of the bomb.

Also, the rate of change in the energy content of the gas phase must equal the rate of heat transfer, thus:

$$\frac{dQ}{dt}=C_vN\frac{dT}{dt}$$

If minor variations in C_v and N are neglected, it follows that the rate of heat transfer is proportional to the rate of pressure decrease. For the practical purpose of showing the trends in the present data it is sufficient to use these rates interchangeably as though they were synonymous.

The expression $\frac{dP}{dt}=\frac{NR}{V}\frac{dT}{dt}$ can also be used to compare the relative rates of temperature drop in different gases when the corresponding rates of pressure change are known for a given initial gas temperature, density, and gas-fuel ratio. The initial pressure under such conditions is very nearly proportional to N, hence the ratio of the initial rate of pressure drop to the initial pressure is proportional to the initial rate of temperature drop irrespective of the nature of the gas.

APPARATUS AND METHOD

The experimental method employed in this investigation consisted in photographically recording with a suitable indicator the decrease in pressure following the injection of a definite quantity of liquid into a spherical bomb containing a gas at a known temperature and pressure. With the exception of a few minor modifications this apparatus was essentially as described in reference 23. The present arrangement is shown diagrammatically in figure 1. The essential parts were a bomb, a constant-temperature bath, a fuel-injection system, and an optical-type differential-pressure indicator. The stainless-steel bomb has a volume of 600 cubic centimeters and is provided with openings for the injection valve, the gas inlet and exhaust fittings, and the indicator.

The liquids used in the constant-temperature bath were S. A. E. 30 lubricating oil for the low temperatures and an approximately 1:1 mixture of sodium and potassium nitrates for the high temperatures. The bath temperature was kept within $\pm 2°$ C. of the desired value by an automatic control.

The injection system delivered a single fuel charge of the desired weight upon the release of a trip mechanism. The injection valve was so constructed that fuel could be continuously circulated through it, thereby maintaining a constant fuel temperature of $49° \pm 1.5°$C. Three nozzles were used, all having equivalent orifice areas: A 13-orifice, a 2-impinging-jets, and a single-orifice nozzle with an orifice diameter of 0.050 inch (fig. 2). The fuel weights were varied by changing the injection pressures; the latter varied from about 194 to 600 atmospheres (2,850 to 9,000 pounds per square inch) for each nozzle. The requisite injection pressure for a given fuel quantity was determined just prior to a series of tests at each temperature. The injection period ranged between 0.002 and 0.006 second, depending upon the injection pressure used.

The high-pressure indicator employed in earlier work (references 6, 11, and 23) was altered to record small pressure differences by substituting a thin corrugated phosphor-bronze diaphragm for the heavy steel diaphragm and by providing a gas connection between the sealed chamber above the diaphragm and the bomb proper. The same initial pressure was applied to both sides of the diaphragm but, just before injection, a valve inserted in this connection was closed. This procedure permitted the subsequent pressure difference to actuate the indicator and thus to generate a trace of the pressure-difference variation with time on the film. This valve was opened again immediately after injection in order to minimize the interval within which the diaphragm remained deflected. A spark, recorded as a vertical line on certain records, marked the start of injection. This spark and injection start were synchronized by observing the spray with a neon-tube stroboscope actuated by the switching device on the injection system that ordinarily controlled the spark. The film drum was driven by a synchronous motor to provide the time scale.

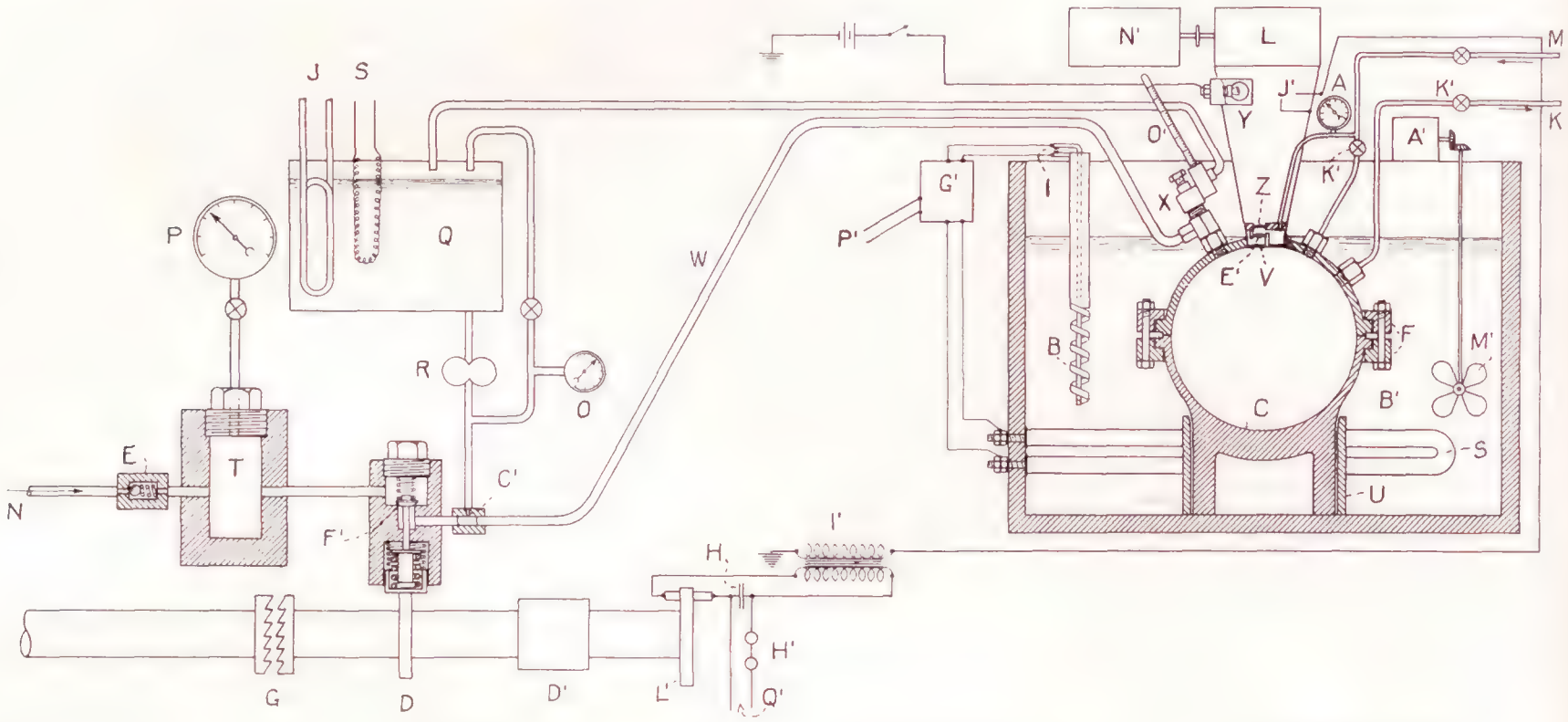

A, air gage.
B, bimetallic strip.
C, bomb.
D, cam.
E, check valve.
F, clamping rings.
G, clutch.
H, condenser, 8 microfarad.
I, contact points.
J, cooling coil.
K, exhaust.
L, film drum.
M, from compressed-gas bottle.
N, from high-pressure pump.
O, fuel-circulating pressure gage.
P, fuel high-pressure gage.
Q, fuel reservoir.
R, gear pump.
S, heating coil.
T, high-pressure reservoir.
U, holder for bomb.
V, indicator diaphragm.
W, injection tube.
X, injection valve.
Y, lamp.
Z, lens.
A′, motor.
B′, oil bath.
C′, orifice, 0.020 inch.
D′, phase-changing gears.
E′, pivoted mirror.
F′, poppet valve.
G′, relay.
H′, resistance lamps.
I′, spark coil.
J′, spark gap.
K′, quick-acting valves.
L′, spark-timing switch.
M′, stirrer.
N′, synchronous motor.
O′, thermometer.
P′, voltage 220 a. c.
Q′, voltage 230 d. c.

FIGURE 1.—Diagrammatic sketch of the apparatus.

Air, nitrogen, and carbon dioxide were used as ambient gases; nitrogen was substituted for air in the tests at the higher temperatures because air permitted auto-ignition of the fuel oil at 230° C. with certain gas-fuel ratios. A few tests were made with carbon dioxide because its physical characteristics were considerably different from the other two gases. The gas densities correspond to 5, 10, 15, and in some tests 20 atmospheres absolute at 100° C. All gases were considered to be ideal when computing the pressures corresponding to the several densities and temperatures. The initial gas temperatures ranged from 150° to 350° C.

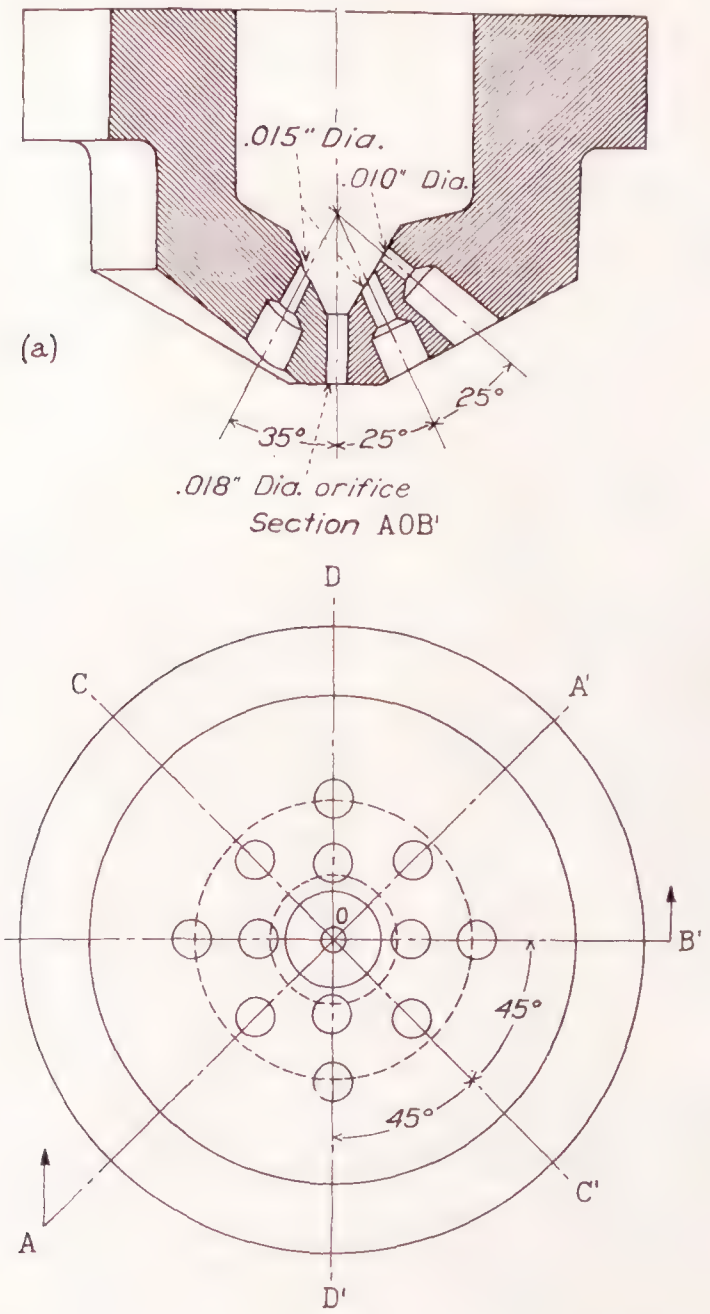

(a) The 13-orifice nozzle; plane DD′ is identical with BB′, and plane CC′ is identical with AA′.

(b) The 2-impinging-jets nozzle.

(c) The single-orifice nozzle.

FIGURE 2.—Diagrammatic sketches of the three nozzles.

Different liquids were injected: An automotive Diesel fuel (Auto Diesel) was investigated most extensively because of its practical importance; benzene, because its critical temperature was within the available temperature range; and water, because of its large heat of vaporization. The water tests were not very extensive and, as they failed to show any interesting dissimilarities, these data have been omitted. The Diesel fuel had a viscosity of 70 and 52 Saybolt seconds Universal at 38° and 99° C. (100° and 210° F.), respectively, and a density of 0.831 gram per cubic centimeter at 15° C. Its A. S. T. M. distillation curve is given in figure 3.

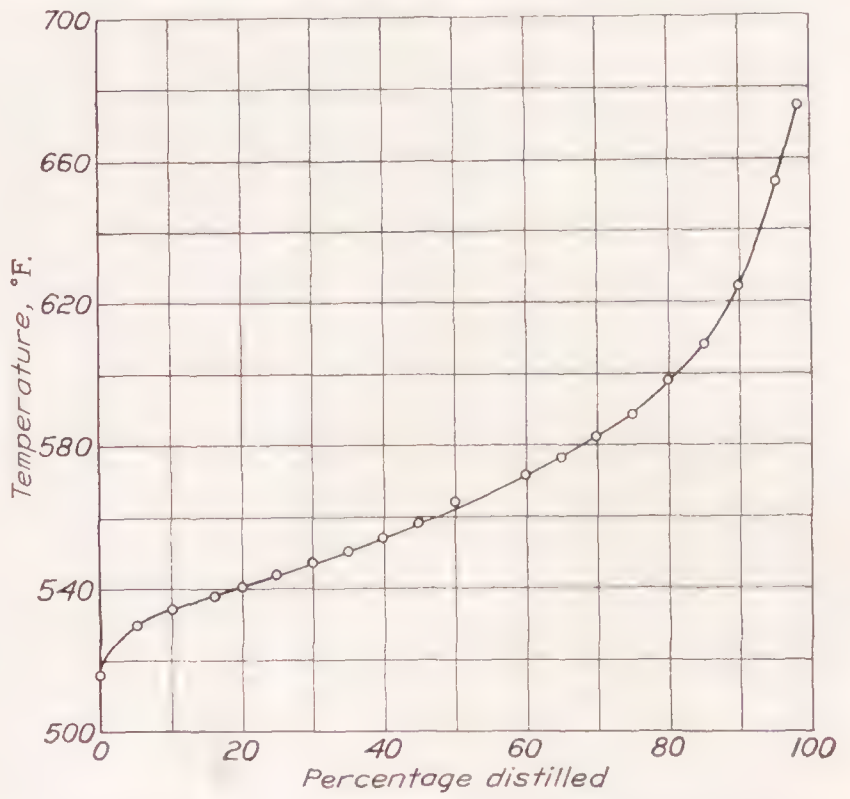

FIGURE 3.—The A. S. T. M. distillation curve for Auto Diesel fuel.

RESULTS

The data derived from the experimental records corresponding to the injection of Diesel fuel are presented in table I. Typical records for an intermediate fuel quantity (0.284 gram) and gas densities of 4.73 and 14.19 grams per liter are reproduced in figure 4. The effect of the nozzle design on the heat transfer to the spray, all other controllable variables being constant, is illustrated by representative records in figure 5.

Results obtained when Diesel fuel was repeatedly injected into a single, individual gas charge are presented in table II. Figure 6 comprises the corresponding records, taken with a gas temperature of 250° C. It is to be noted that these records do not correspond to consecutive injections.

The results obtained with benzene are presented in table III and figure 7. These tests were limited to the smaller weights because of the greater pressure changes per unit weight of liquid.

An inspection of the experimental records reveals two time intervals more or less clearly defined on all the start of injection corresponds, with one exception, to the vertical line appearing on some of the records and is coincident with the A points; i. e., the decrease in the gas pressure began immediately after the first part of the fuel charge entered the bomb. The one exception (record 295, fig. 5) was due to improper synchro-

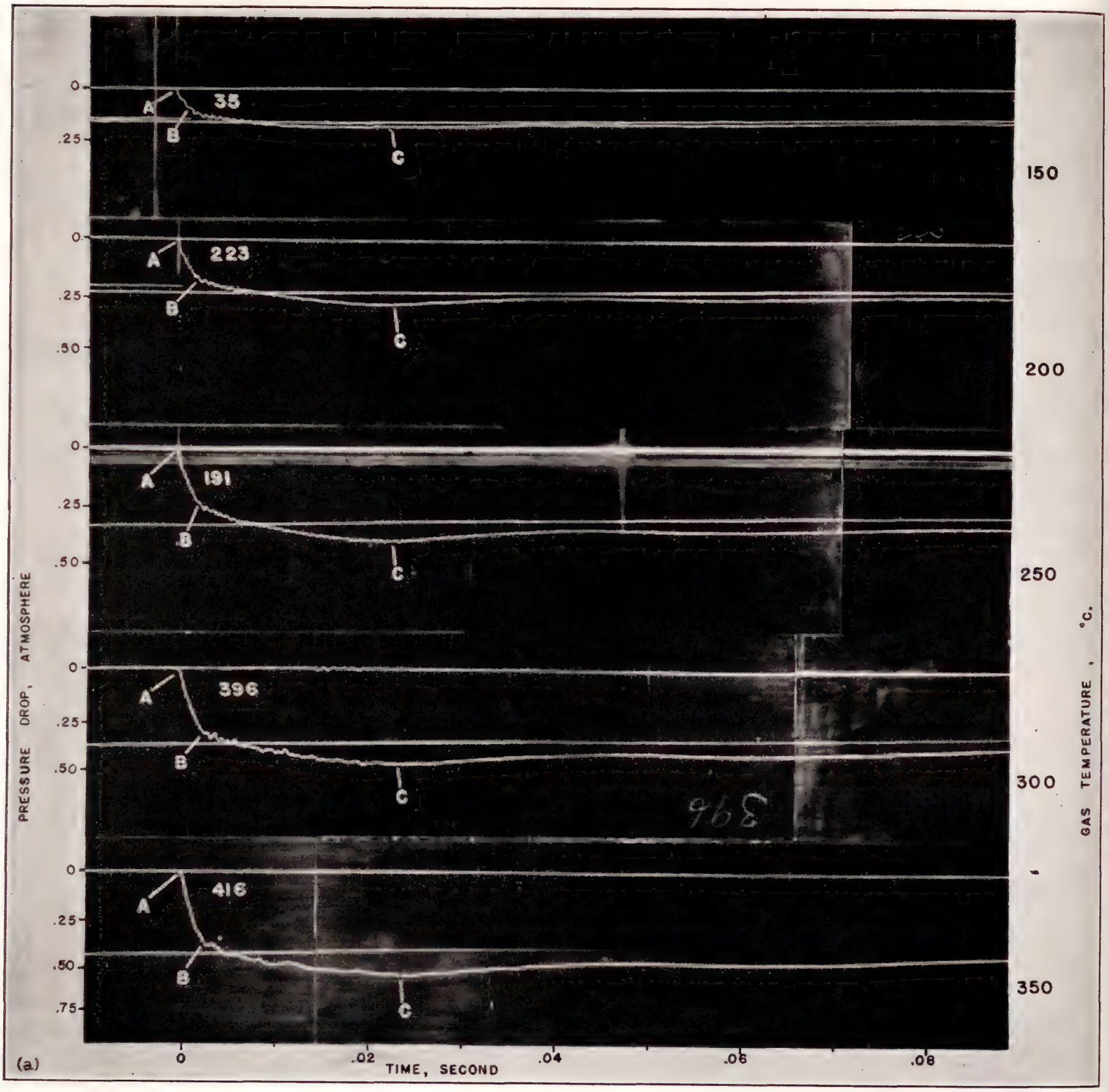

(a) Gas density, 4.73 grams per liter; gas-fuel ratio, 10.

FIGURE 4.—Variation of pressure drop with gas temperature. Diesel fuel; fuel weight, 0.284 gram.

pressure-time curves. Three characteristic points are designated on all the records reproduced: A, the point at which the pressure drop begins; B, the end of the initial pressure drop for which the rate was essentially constant; and C, the minimum pressure point. The nization of the injection start and the timing spark. The A–B interval and the pressure drop associated with it are indicative of processes occurring immediately after the injection starts. This interval is therefore of primary interest with respect to compression-ignition

engines. The whole A–C interval, on the contrary, is of no immediate interest in this respect and corresponds to the period within which heat is being abstracted from the gas phase at a rate greater than the rate of transfer from the bomb wall. The A–C interval is partial pressure of the vaporized fuel. Records representing this condition were not obtained as the relatively low rate of heat transfer from the bomb wall would have necessitated an extended deflection period for the diaphragm.

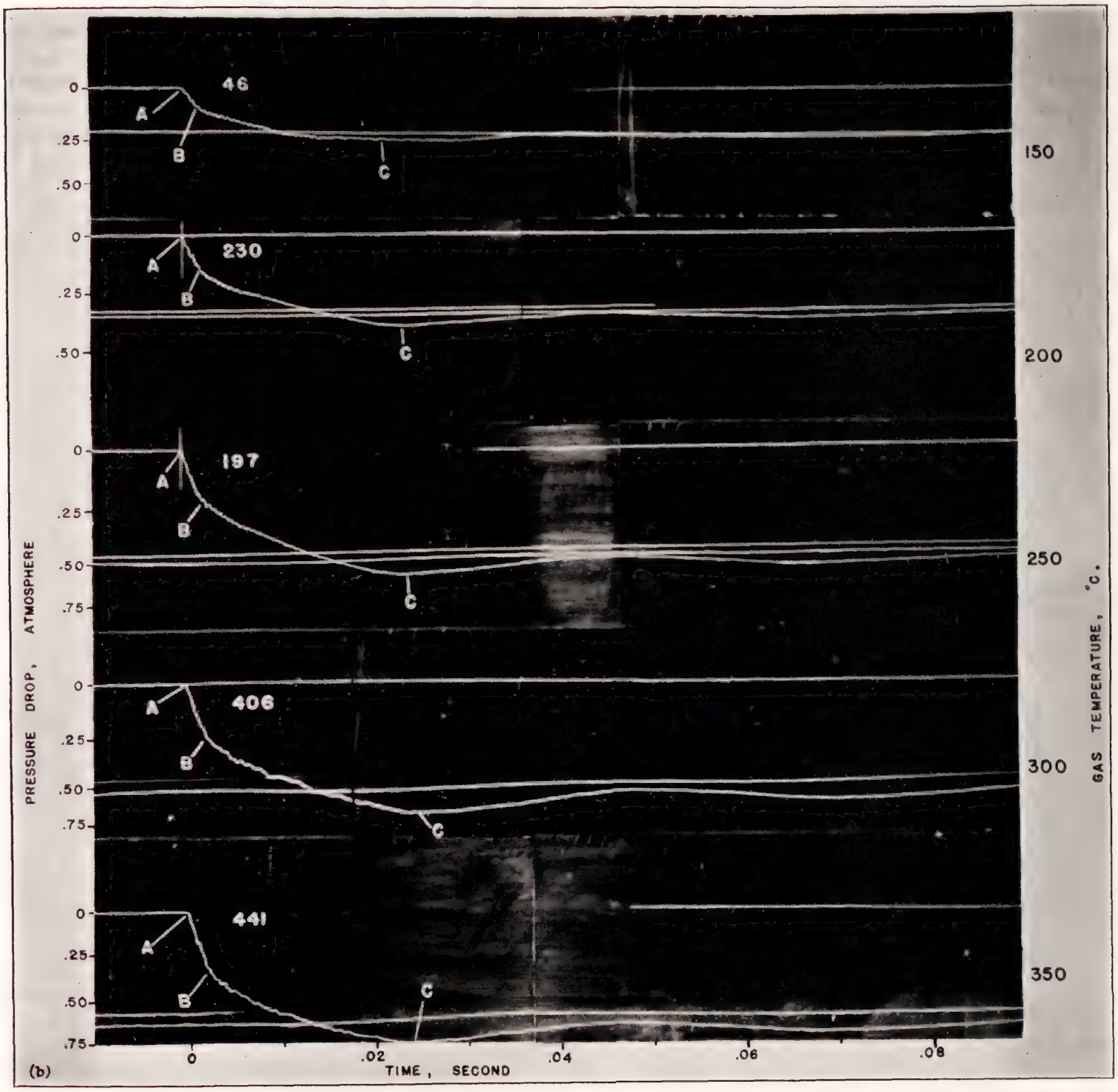

(b) Gas density, 14.19 grams per-liter; gas-fuel ratio, 30.

FIGURE 4.—Continued. Variation of pressure drop with gas temperature, Diesel fuel; fuel weight, 0.0284 gram.

influenced so little by most of the available variables that no theoretical basis for its approximate constancy is at present evident. Eventually, upon reestablishing thermal equilibrium, the pressure should increase beyond its initial value to an extent represented by the

Spray photographs shown in figure 8 illustrate the manner in which sprays from the 13-orifice and the 2-impinging-jets nozzles penetrate air at room temperature and a density of 14.19 grams per liter for an intermediate injection pressure.

PRECISION OF RESULTS

The reproducibility of the experimental results depended upon the nonvariation of the fuel quantity and the indicator calibration. The maximum deviations in the observed data for apparently identical conditions amounted to roughly ±5 percent of the average values. The variation in fuel weights, for apparently identical injection pressures, was approximately the same for all weights and amounted to about ±3.5 percent of the actual weight for the lower injection pressures or to ±1 percent for the higher.

weight, prevented the use of the larger fuel weights. The objectionable feature of the shift arose from the fact that a given deflection before and after a particular test did not correspond to equivalent pressures. A possible error of perhaps ±5 percent may arise in this way; at 350° C. the error is undoubtedly greater.

When the data from the records were evaluated, some personal error was introduced, particularly for the A–B portion of the curve wherein the interval is more or less arbitrary and the distances on the record are often too small to be accurately measured. The magnitude of this uncertainty is shown in figure 9, for which the

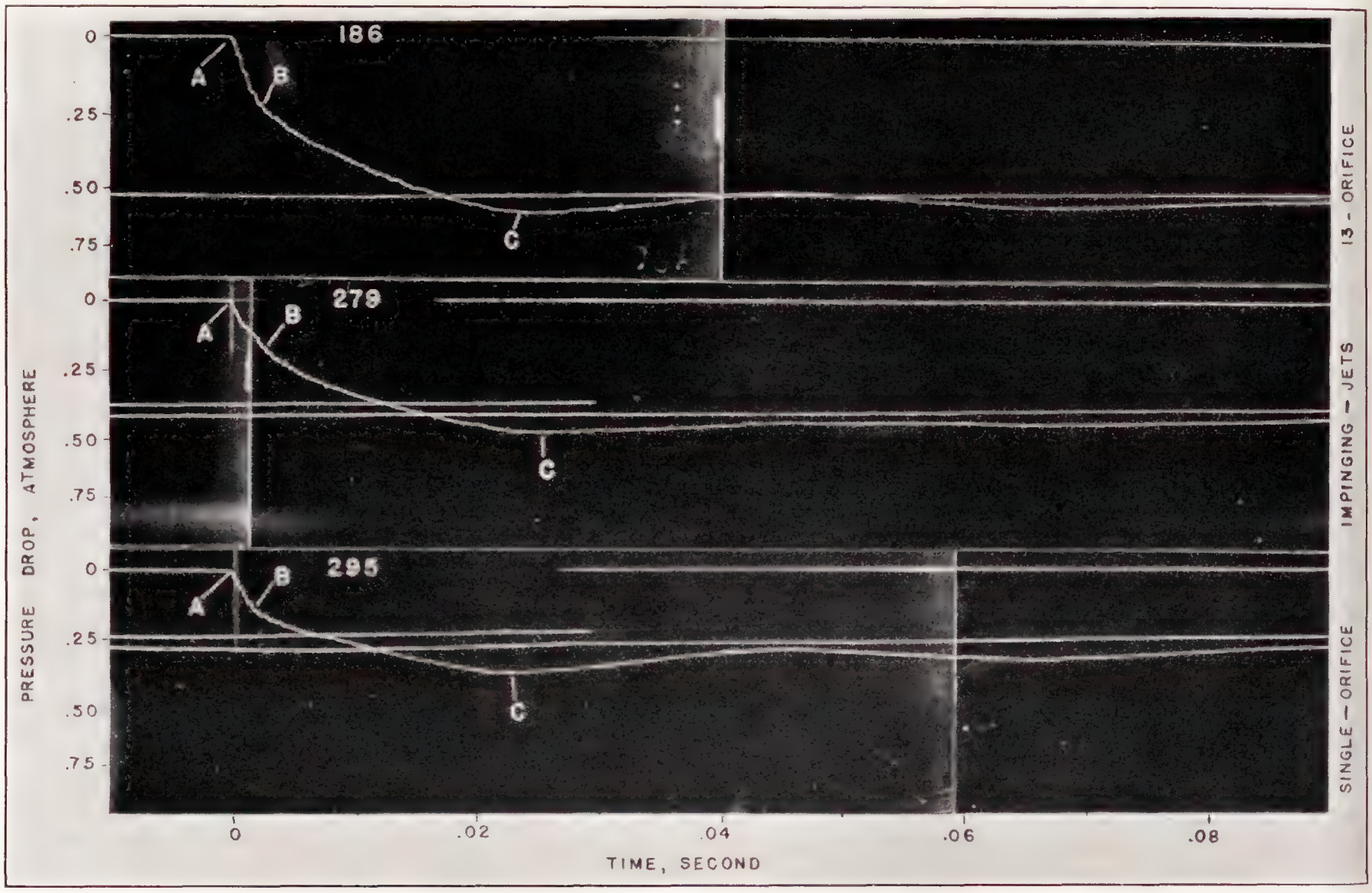

FIGURE 5.—Effect of nozzle design on pressure drop. Diesel fuel; fuel weight, 0.284 gram; gas-fuel ratio, 30; gas density, 14.19 grams per liter; gas temperature, 250° C.

At temperatures of 250° C. and above, the indicator showed a decided tendency to change its zero point as a result of creeping of the diaphragm, particularly during calibration when the deflection period was relatively great. The extent of this shift increased with the amount of deflection, the time of deflection, and the temperature. The deflection interval was diminished as much as possible during calibrations by a quick application and release of the gas pressure. The zero point immediately after deflection was taken as the proper basis for calibration in spite of its tendency in many cases to drift back toward its original position. At 350° C. this restoration was less evident and the shift assumed serious proportions. This fact, together with the increased deflection per unit fuel

data were taken by two observers from the same records. The individual deviations are rather great, but the mean curves seem to fit either set of data equally well. At 150° C. the records were so flat in the neighborhood of the minimum point that C was taken as the center of the flat portion of the curve. For the larger deflections the trace near the minimum point contained a wave of relatively low frequency. An average of the amplitudes of the first cycle was applied as a negative correction to compensate for this wave.

One other point of incidental interest is the change in fuel temperature as a result of the injection process. The passage of the fuel through the nozzle would ordinarily result in a small decrease in temperature on the basis of the Joule-Thomson effect (reference 24), assum-

ing the coefficient to be positive as for certain other hydrocarbons (reference 25). Qualitative experience indicates, however, that the net effect is a temperature increase due to friction in the orifice and the conversion of the kinetic energy of the spray into heat. The

and vaporization. Lee has shown (reference 20) that the degree of subdivision attainable with a hydraulic injection system under operating conditions approaches a practical limit. For the practical range of gas densities and injection pressures, however, it is impossible

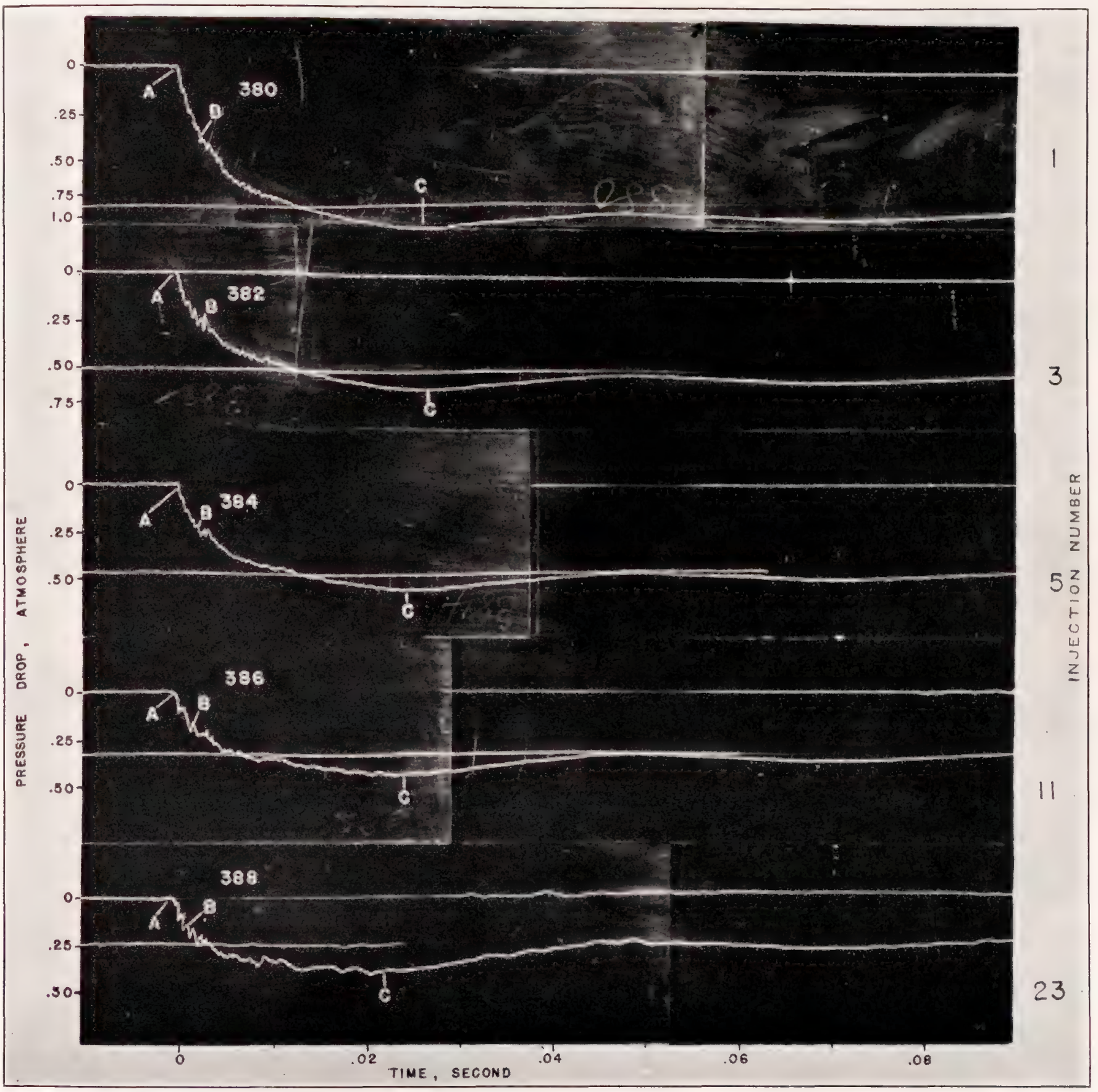

FIGURE 6.—Influence of fuel-vapor concentration, prior to injection, upon pressure drop. Diesel fuel; fuel weight per injection, 0.568 gram; gas density, 10.35 grams per liter; gas temperature, 250° C.

change is believed to be too small to be of any interest in the interpretation of the present results and will therefore be ignored.

DISCUSSION

On the basis of diffusion and heat-transfer concepts the size of a droplet must influence its rate of heating

to vary the distribution of droplet sizes without at the same time varying the rate of spray penetration. This concomitant variation prevents the isolation of any effect that can be associated solely with the distribution of droplet sizes. In the subsequent discussion it is well to bear in mind that the same condition should be true of certain other quantities that may represent an aggregation of variables.

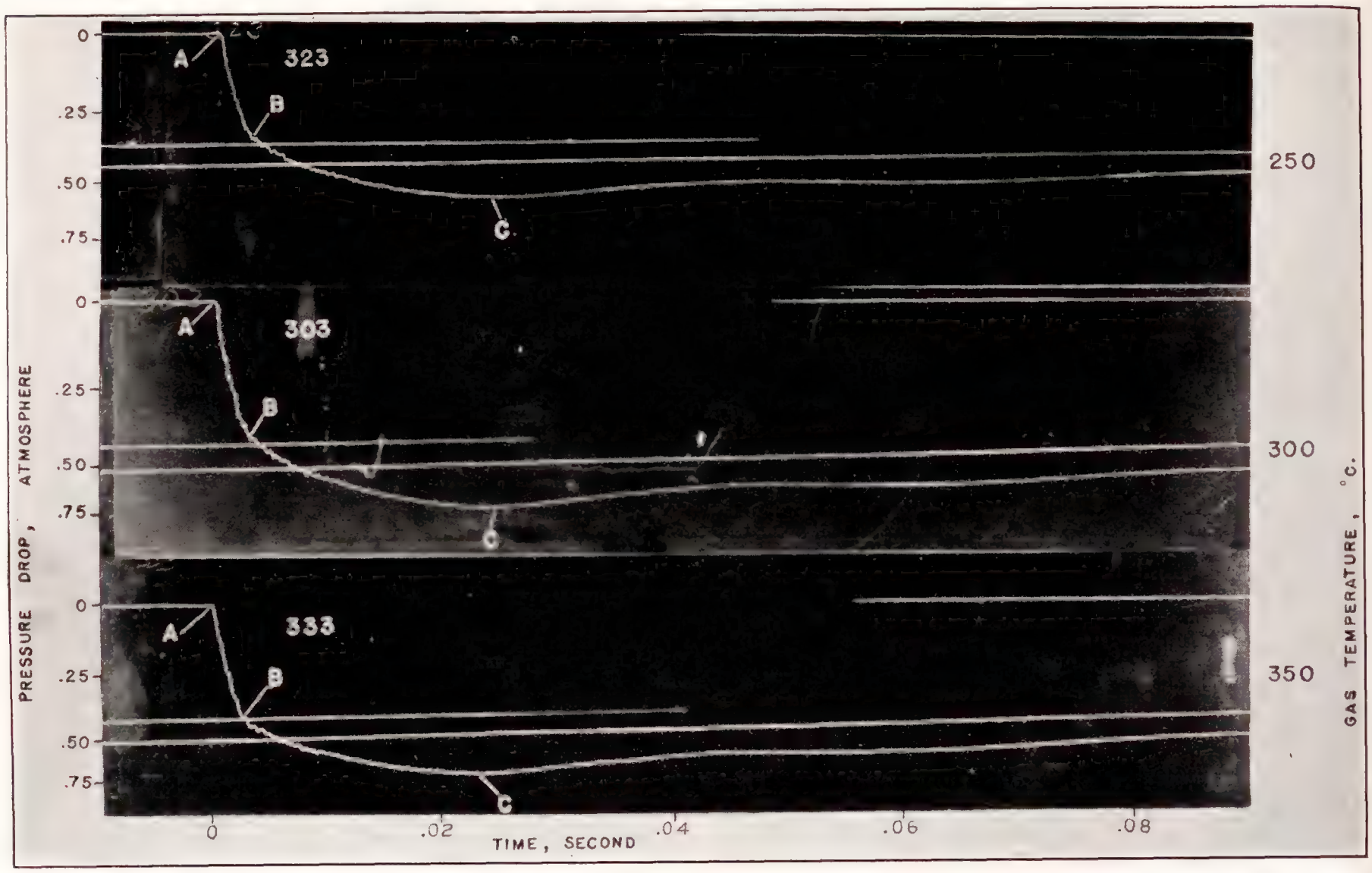

FIGURE 7.—Effect of gas temperature on pressure drop. Benzene as fuel; fuel weight, 0.284 gram; gas-fuel ratio, 10; gas density, 4.73 grams per liter.

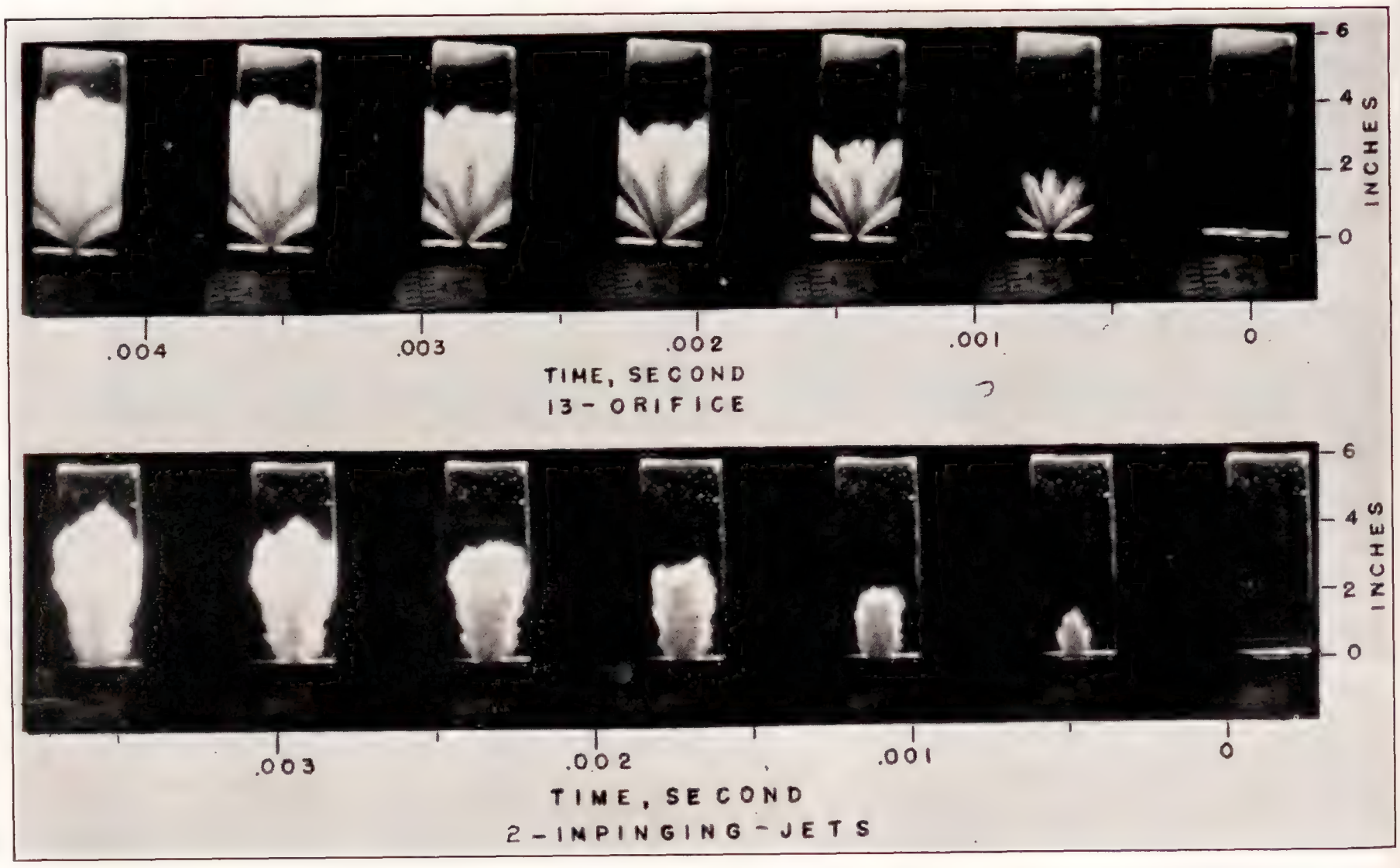

FIGURE 8.—Spray penetration. Gas density, 14.19 grams per liter; injection pressure, 5,800 pounds per square inch.

THE A-B INTERVAL

The A–B intervals correspond to the early part of the spray development for which the rate of heat transfer is essentially constant for a particular record. It is possible that this constancy is in some way associated with the approximately constant initial rate of spray-tip penetration (references 1 and 26). The magnitude of this interval is comparable with the ignition lag in compression-ignition engines. For this reason any conclusions based upon this interval are also applicable to such engines, provided that proper allowances are made for differences in chamber size and air temperature. The photographs shown in figure 8, together with more extensive penetration data (reference 1), show that this interval is essentially equivalent to the time (0.002 to 0.003 second) required by the sprays to traverse a distance of 4 inches, the approximate diameter of the bomb.

This association of the moment of impingement with point B is supported by the fact that the interval decreases as the gas density decreases, i. e., as the penetration increases. (See table I, column 7.) On the contrary, the interval is not appreciably shorter for the single-orifice nozzle in spite of the greater penetration to be expected with it. The period is about the same for carbon dioxide as for nitrogen in contradistinction to the longer A–C interval with carbon dioxide. Increasing the fuel quantity increases the injection period by a maximum factor of 3, yet the interval remains essentially the same. The interval also proved to be independent of the fuel used.

Initial rate of heat transfer.—The magnitude of the initial rate of pressure drop, as shown by the particular pressure-time curve, is representative of the total rate of heat exchange between the gas and the fuel for the early part of the spray. The manner in which this initial rate is influenced by the temperature gradient between the gas and the fuel at two gas densities and several fuel weights is illustrated in figure 9. These initial slopes become more negative, i. e., the initial rate of heat transfer increases, as either the temperature difference or the fuel weight increases. Increasing the gas density decreases the numerical magnitude of the slope for a given fuel quantity but does not greatly alter the temperature dependence of the initial rate of pressure drop of the pressure-time curve: corresponding lines in figure 9 have roughly the same slope.

The increased density evidently decreases the effective transfer area in the early part of the spray as might be expected from the slower rate of spray development shown by the photographs reproduced in reference 1. The decrease cannot be attributed to a lower rate of

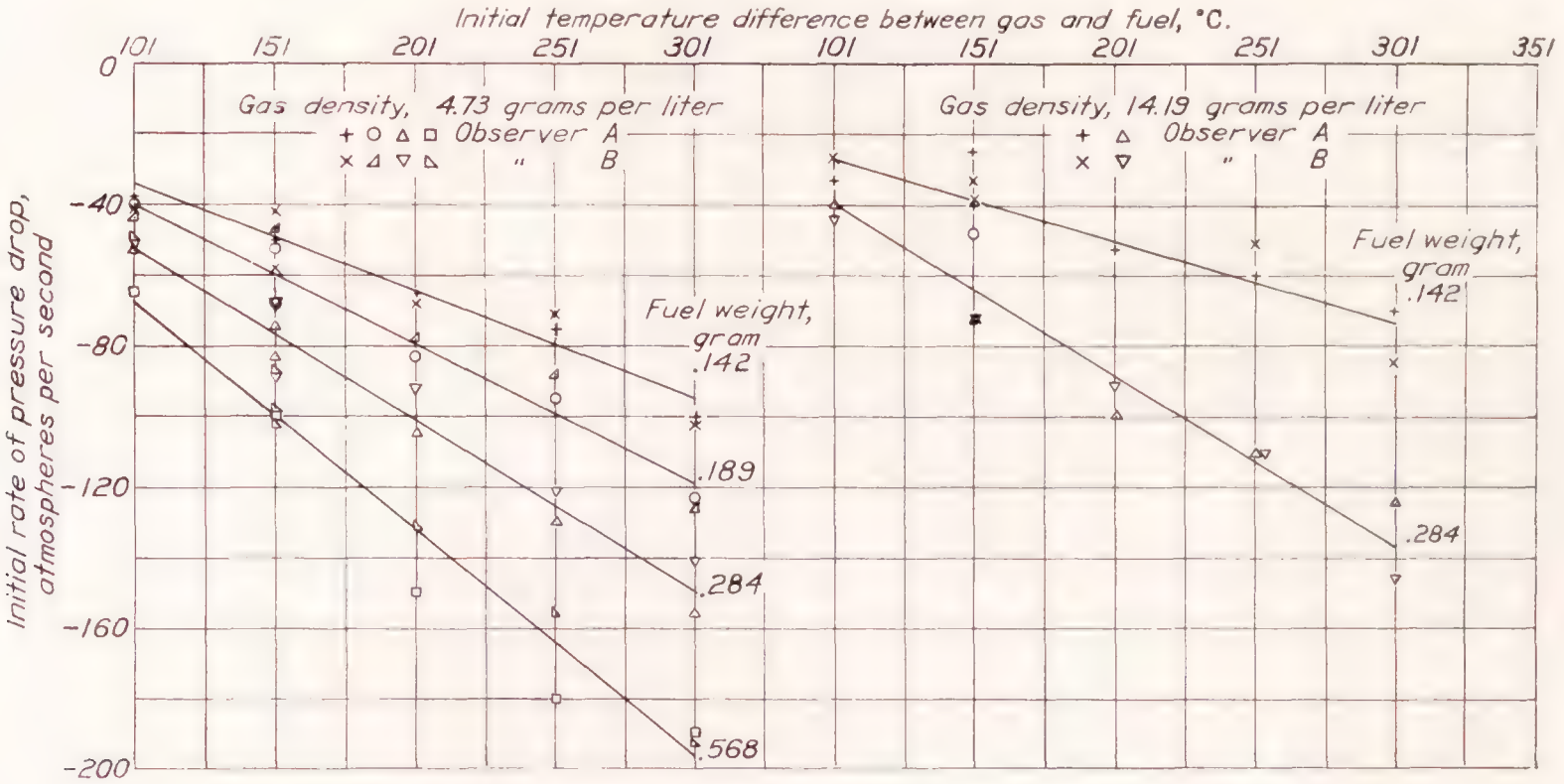

FIGURE 9.—Effect of gas temperature on initial rate of pressure drop at different gas-fuel ratios.

heat transfer per unit area because the coefficient of heat conductivity should be nearly independent of density and the coefficient of heat transfer might be expected to increase with gas density (reference 27). Carbon dioxide gave rise to a greater rate of temperature drop than did nitrogen, even though its rate of pressure drop was smaller. This fact may be demonstrated by dividing the values of the initial slope in column 9 of tables I and III by their respective initial pressures, as outlined earlier in this paper. As the specific heats of nitrogen and carbon dioxide do not differ greatly on a weight basis, carbon dioxide must have given a greater initial rate of heat transfer. Since carbon dioxide has a lower coefficient of heat conductivity, it must give a greater effective heat-transfer area. The slopes for benzene (table III) are slightly greater than for Diesel fuel (table I) owing perhaps to a combination of the differences in the properties (molecular weight, specific heat, heat of vaporization, etc.) of the two fuels.

For the lowest density the impinging-jets nozzle gave a heat-transfer rate similar to the 13-orifice nozzle but at the highest density its rate was substantially less. The single-orifice nozzle gave a smaller rate at all densities. The maximum cylinder pressures obtained with similar nozzles and the N. A. C. A. combustion apparatus show the same trends, indicating that better initial mixing of fuel and air, together with the resulting improvement in heat transfer, occurs with the high-dispersion nozzles (reference 3). No information relevant to the effect of vapor concentration on the ignition lag can be obtained from such an engine study, presumably because all nozzles giving at least moderate fuel dispersion permit the optimum air-vapor mixture somewhere within the spray and thus give approximately the same ignition lag.

The contribution of radiation to the total heat-transfer rate can be shown to be negligible on the basis of the treatment given in an earlier section. If record 418 is considered to be typical of the others, the rate of pressure drop equivalent to the maximum rate of radiation that could occur is only 1 percent of the observed rate. It appears that radiation contributes little toward heating the fuel injected into an engine except for the possibility of unvaporized fuel becoming surrounded by a cloud of radiating combustion products. Even in this case, the conductive heat exchange can be shown to predominate if its rate per degree temperature difference remained constant and independent of the gas temperature to the extent indicated by the data in column 10 of table I.

Effect of temperature on initial heat transfer.—Straight lines seem to agree with the data plotted in figure 9 within the limits of the uncertainty involved and, moreover, such lines are in agreement with a rate of heat transfer directly proportional to the temperature difference. The fact that the lines are straight indicates that the gas temperature has little influence on spray development within the range employed (reference 28), measured in this case by the effective area available for heat transfer. This area appears to be constant for a given density and fuel weight; otherwise a compensating change in the heat-transfer coefficient must be assumed. There is no indication that the slopes of the lines of figure 9, and hence the corresponding heat-transfer coefficients, will assume different values at the higher temperatures attained in an engine. The extrapolation, however, is too great to be of more than qualitative interest. The mass flow of gas inherent in an engine (reference 4) would lead to greater effective transfer areas and thus increase the apparent rate of pressure decrease indicated in this figure.

The ratios of the initial slope values given in column 9 of tables I and III to the respective products of fuel weight and initial fuel-gas temperature difference give a fundamental basis for comparing the relative efficacy of the heat transfer in all cases for a given ambient gas. It follows from such ratios that the rate of heat transfer varies directly with the initial temperature difference, as stated earlier in connection with figure 9. Increasing the weight of Diesel fuel leads to considerable decrease in these values but with benzene the tendency is not so evident. This difference indicates that the effective heat-transfer area is more nearly proportional to the fuel weight for benzene than for Diesel fuel. Again, as with the initial slopes, these ratios are somewhat greater for benzene, but it is not known whether this situation arises from a greater heat requirement or from better spatial distribution of the spray. The latter seems most probable in view of the effect of fuel viscosity on the distribution of fuel within the spray (references 2 and 29).

Fuel vaporization.—The records reproduced in figure 6 show that some evaporation of the fuel occurs during the A–B interval. If all the heat transferred served merely to heat the liquid fuel, it is evident that the initial rate of heat transfer should not decrease as it does in these records. As more and more fuel is injected into the same gas charge, thermal equilibrium being reestablished before each injection, such a condition is approximated as the partial pressure of the vapor and the saturation pressure of the liquid approach one another. Certainly the relatively small molecular concentrations of vapor that produce the diminutions in initial heat-transfer rate evident even after a single injection can only be effective in the observed manner by retarding the evaporation of the fuel. These records show that the heat transferred to the vapor or to the fuel in effecting vaporization represents an appreciable part of the total heat transferred to an ordinary spray during the A–B interval. Rothrock and Waldron (reference 8) have presented conclusive evidence that considerable vaporization does occur in a high-speed engine but the rate, of course, is indeterminate as in the present case. The speed of the engine proved to be influential, presumably for two reasons: differences in mechanical mixing of the spray with the air and certain changes in the thermal boundary conditions of the spray. Photographs in reference 30 of sprays injected into cold and heated air show a distinct decrease in the spray penetration with the hot air. It is quite probable that vaporization of the fuel within the spray envelope contributed to this decrease in addition to the changes in fuel temperature and air viscosity, which were cited in explanation of this phenomenon.

THE A–C INTERVAL

Effectiveness of heat transfer.—Even though the B–C portion of the A–C interval has no particular connection with engine operation, it does present some information of interest on the effectiveness of the heat transfer. This effectiveness is shown most readily by comparing with the actual pressure drop the calculated pressure drop that should take place if all the fuel had vaporized. The nearer the experimental value approaches the calculated value the greater the effective-

ness of the transfer. Calculated and observed pressure changes are plotted against the initial nitrogen (or air) pressure in figure 10 for several temperatures and a gas-fuel ratio of 20.

The disagreement between the calculated and observed pressure drops is very striking and is much too great to be associated with heat transferred from the bomb wall to the gas phase during the A–C interval, as evidenced by the slow rate of pressure rise after point C. A probable explanation is that a good fraction of the fuel struck the wall, deriving most of its heat therefrom. This assumption is supported by earlier observations that a definite pattern of the sprays could be seen on the bomb wall after certain explosion tests (reference 23) and particularly by the photographs in figure 8. At lower gas densities or with the single-orifice nozzle, the penetration should be greater (reference 1) and the time required to traverse the bomb somewhat shorter. In any case the sprays struck the bomb wall long before minimum pressure was attained.

In view of the discrepancy between the calculated and observed pressure changes it is rather surprising that the experimental pressure drops are directly proportional to the initial pressure. There is no particular reason for believing that the vapor left the wall in temperature equilibrium with it; i. e., that this vapor could abstract little or no heat from the gas phase, unless perhaps the mass motion of the gas was too slow to effect the removal of the vapor from the immediate neighborhood of the wall in the interval examined.

The ratio of observed to calculated pressure drop is indicative of the fraction of the total heat contributed by the gas phase. It follows from figure 10 that above 250° C. the fraction of the total heat contributed by the walls became relatively constant at all temperatures for a given density and a gas-fuel ratio of 20, indicating that a constant fraction of the fuel charge struck the wall at temperatures above 250° C., the gas density being almost noninfluential.

The total pressure drop subsequent to injection increases with initial temperature, fuel quantity, and to some extent with initial density, although in the higher range this latter change is not very evident. There is also a slight decrease in this drop (table I, section 7) with a moderate increase in fuel temperature, showing that in this case less total heat is transferred to the portion of the fuel charge that normally absorbs heat from the gas phase. With carbon dioxide as the ambient gas, the drop is less than that for nitrogen, but a consideration of the relative initial pressures shows that the corresponding temperature drops are of the same magnitude. This similarity might be expected because the spray development is about the same for a given density irrespective of the nature of the gas (reference 28) and, on a weight basis, the specific heat of carbon dioxide is not greatly different from that of nitrogen in this temperature range. For a given fuel weight benzene gives a greater drop than does the Diesel fuel, presumably owing to the greater heat required for vaporization. This presumption assumes that the same fraction of the fuel (benzene or Diesel fuel) fails to strike the wall under identical circumstances. The benzene tests also indicate that the surface temperature of the drops is well below the ambient-gas temperature; although the gas temperatures employed were near to or above the critical temperature of benzene, the fact that the A–C interval was about the same for benzene as for Diesel fuel indicates a droplet temperature much below the critical point.

Time to attain minimum pressure.—Small variations of the A–C interval are evident but, because of possible errors, these variations may not be real. In any case the variations cannot be associated with any primary variable. The interval is greatest for carbon dioxide, intermediate for air, and least for nitrogen; it increases with the fuel quantity for the lower but not for the

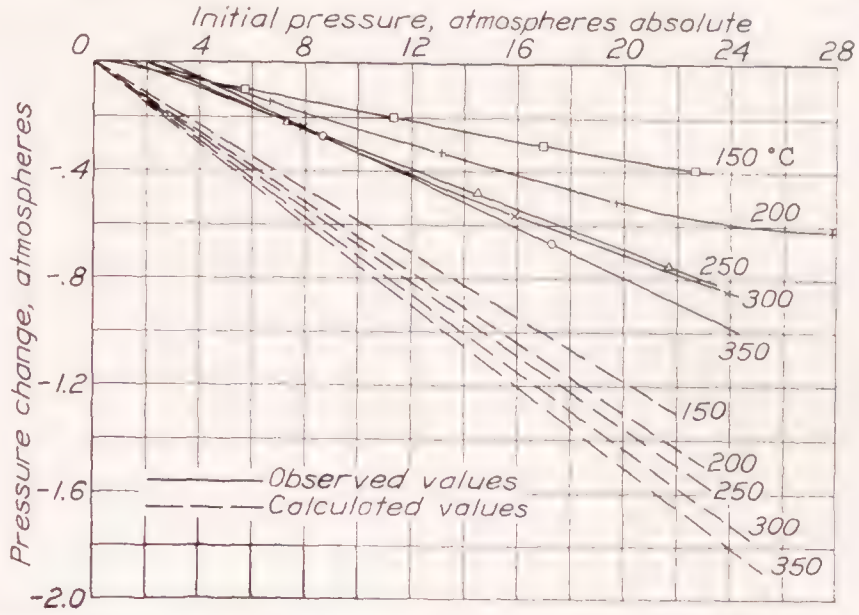

FIGURE 10.—Comparison of calculated and observed pressure drops at various temperatures.

higher weights; and there appears to be a slight increase with gas density. As the total pressure drop increases with an increase in the fuel weight and to some extent with an increase in gas density, it is conceivable that the latter trends arise from an "overshooting" of the true decrease in pressure because of the increased amplitude of the wave evident after point C. The records for benzene, however, fail to show such trends.

In view of the wide variation of the fraction of the fuel that strikes the bomb wall with varying fuel weights and given gas density, the minimum point cannot be logically associated with the moment of complete evaporation of the fuel on the wall. This contention is further substantiated by the failure of benzene to give a shorter interval; its greater volatility should enable it to evaporate more rapidly from the bomb surface. It has previously been shown that nonuniformity of the gas-vapor mixture exists for at least 0.06 second after injection (reference 23). An attempt was made to mix the charge with a 4-blade fan driven at 7,000 r. p. m. but, as the A–C interval corresponded to only two revolutions of the fan, it is not surprising

that the interval was unaltered. Since the rates of heat transfer from the wall and to the fuel are equal at C, it would seem that the interval should depend upon the nonuniformity of the mixture, which in turn should be dependent upon the injected fuel weight and the gas density. Actually, the interval is practically independent of both variables.

CONCLUSIONS

1. The injection of liquid fuel into a heated and compressed gas has furnished data on the initial rate of heat exchange between the ambient gas and the fuel. The actual rates of vaporization were indeterminate, but it is shown that vaporization began immediately after injection started. The same situation must also be true for engines.

2. For given experimental conditions, the initial rate of heat transfer was essentially constant during the time required for the spray to traverse the bomb. This initial rate was found to be proportional to the initial temperature difference between the fuel and the gas. The total heat transferred in engines must be greater owing to the greater initial temperature difference.

3. The initial heat-transfer period was approximately constant (0.0020 ± 0.0005 second) for the 13-orifice, 2-impinging-jets, and single-orifice nozzles tested and also for benzene and Diesel fuel, which have quite different volatilities and viscosities.

4. At the temperatures investigated the transfer of heat by radiation was negligible as compared with that transferred by conduction. This situation must also exist in an engine until the start of flame combustion.

5. The efficacy with which heat transfer took place decreased considerably with increasing fuel quantity at all densities and temperatures investigated.

6. Under all conditions a good fraction of the total heat absorbed after the spray had traversed the bomb must have occurred at the bomb wall.

LANGLEY MEMORIAL AERONAUTICAL LABORATORY,
NATIONAL ADVISORY COMMITTEE FOR AERONAUTICS,
LANGLEY FIELD, VA., *August 25, 1936.*

REFERENCES

1. Lee, Dana W.: A Comparison of Fuel Sprays from Several Types of Injection Nozzles. T. R. No. 520, N. A. C. A., 1935.
2. Lee, Dana W.: Measurements of Fuel Distribution within Sprays for Fuel-Injection Engines. T. R. No. 565, N. A. C. A., 1936.
3. Rothrock, A. M., and Waldron, C. D.: Effect of Nozzle Design on Fuel Spray and Flame Formation in a High-Speed Compression-Ignition Engine. T. R. No. 561, N. A. C. A., 1936.
4. Rothrock, A. M., and Waldron, C. D.: Fuel Spray and Flame Formation in a Compression-Ignition Engine Employing Air Flow. T. R. No. 588, N. A. C. A., 1937.
5. Boerlage, G. D., and van Dyck, W. J. D.: Causes of Detonation in Petrol and Diesel Engines. R. A. S. Jour., Dec. 1934, pp. 953–986.
6. Rothrock, A. M., and Waldron, C. D.: Some Effects of Injection Advance Angle, Engine-Jacket Temperature, and Speed on Combustion in a Compression-Ignition Engine. T. R. No. 525, N. A. C. A., 1935.
7. Gerrish, Harold C., and Ayer, Bruce E.: Influence of Fuel-Oil Temperature on the Combustion in a Prechamber Compression-Ignition Engine. T. N. No. 565, N. A. C. A., 1936.
8. Rothrock, A. M., and Waldron, C. D.: Fuel Vaporization and Its Effect on Combustion in a High-Speed Compression-Ignition Engine. T. R. No. 435, N. A. C. A., 1932.
9. Wentzel, W.: Ignition Process in Diesel Engines. T. M. No. 797, N. A. C. A., 1936.
10. Ellenwood, F. O., Evans, F. C., and Chwang, C. T.: Efficiencies of Otto and Diesel Engines. A. S. M. E. Trans. OGP–50–6, Jan.–April 1928, pp. 1–22.
11. Rothrock, A. M., and Cohn, Mildred: Some Factors Affecting Combustion in an Internal-Combustion Engine. T. R. No. 512, N. A. C. A., 1934.
12. Rothrock, A. M., and Spencer, R. C.: Effect of Moderate Air Flow on the Distribution of Fuel Sprays after Injection Cut-Off. T. R. No. 483, N. A. C. A., 1934.
13. Nusselt, Wilhelm: Wärmeübergang, Diffusion und Verdünstung. Z. f. a. M. M., vol. 10, 1930, pp. 105–121.
14. Fuchs, N.: Über die Verdampfungsgeschwindigkeit kleiner Tröpfchen in einer Gasatmosphäre. Phys. Zeit. Sowjetunion, vol. 6.3, 1934, pp. 224–243.
15. Sherwood, T. K., and Gilliland, E. R.: Diffusion of Vapors through Gas Films. Indus. Eng. Chem., vol. 26, 1934, pp. 1093–1096.
16. Ingersoll, L. R., and Zobel, O. J.: An Introduction to the Mathematical Theory of Heat Conduction. Ginn and Co. 1913, p. 133.
17. Cragoe, C. S.: Thermal Properties of Petroleum Products. Misc. Publication No. 97, Bur. Standards, 1929.
18. National Bureau of Standards: National Standard Petroleum Oil Tables. Circular No. 154, Bur. Standards, 1924, pp. 95–113.
19. Gaucher, L. P.: Specific Heat of Liquid Pure Hydrocarbons and Petroleum Fractions. Indus. Eng. Chem., vol. 27, 1935, pp. 57–64.
20. Lee, Dana W.: The Effect of Nozzle Design and Operating Conditions on the Atomization and Distribution of Fuel Sprays. T. R. No. 425, N. A. C. A., 1932.
21. Walker, William H., Lewis, Warren K., and McAdams, William H.: Principles of Chemical Engineering. McGraw-Hill Book Co., Inc., 1927, p. 162.
22. Watson, K. M., and Nelson, E. F.: Improved Methods for Approximating Critical and Thermal Properties of Petroleum Fractions. Indus. Eng. Chem., vol. 25, 1933, pp. 880–887.
23. Cohn, Mildred, and Spencer, Robert C.: Combustion in a Bomb with a Fuel-Injection System. T. R. No. 544, N. A. C. A., 1935.
24. Lewis, Gilbert Newton, and Randall, Merle: Thermodynamics and the Free Energy of Chemical Substances. McGraw-Hill Book Co., Inc., 1923, p. 68.
25. National Research Council: International Critical Tables vol. V. McGraw-Hill Book Co., Inc., 1929, p. 146.
26. Schweitzer, P. H.: The Penetration of Oil Sprays in Dense Air. Tech. Bull. No. 20, Penn. State Coll., 1934, pp. 108–124.
27. McAdams, William H.: Heat Transmission. McGraw-Hill Book Co., Inc., 1933, pp. 20, 96, 216, and 246.
28. Joachim, W. F., and Beardsley, Edward G.: The Effects of Fuel and Cylinder Gas Densities on the Characteristics of Fuel Sprays for Oil Engines. T. R. No. 281, N. A. C. A., 1927.
29. Lee, Dana W., and Spencer, Robert C.: Photomicrographic Studies of Fuel Sprays. T. R. No. 454, N. A. C. A., 1933.
30. Gelalles, A. G.: Some Effects of Air and Fuel Oil Temperatures on Spray Penetration and Dispersion. T. N. No. 338, N. A. C. A., 1930.

TABLE I

PRESSURE CHANGE ASSOCIATED WITH HEAT TRANSFER TO DIESEL FUEL

1	2		3		4	5	6	7	8	9	10
Record number	Initial gas pressure		Gas density		Gas-fuel ratio	Fuel weight (gram)	Pressure drop (atmosphere)	Interval A to B (second)	Interval A to C (second)	Initial slope (atmospheres per second)	Initial slope per gram per ° C. difference $\left(\frac{\text{atmospheres}}{\text{second gram °C.}}\right)$
	Atmospheres, absolute	Pounds per square inch (gage)	Grams per liter	Pounds per cubic foot							
1. AIR AT 150° C. (302° F.); FUEL TEMPERATURE, 49° C.; 13-ORIFICE NOZZLE											
17	5.67	69	4.73	0.296	20	0.142	0.10	0.0013	0.023	−38	−2.7
34					15	.189	.12	.0015	.023	−40	−2.1
35, 19					10	.284	.15	.0015	.023	−53	−1.8
36, 20					5	.568	.26	.0020	.023	−65	−1.1
37	11.34	152	9.46	.592	40	.142	.12	.0017	.023	−29	−2.0
38					30	.189	.16	.0020	.023	−40	−2.1
39					20	.284	.20	.0020	.023	−50	−1.7
40					15	.378	.25	.0020	.023	−60	−1.6
23, 41					10	.568	.36	.0020	.023	−65	−1.1
44	17.01	235	14.19	.888	60	.142	.12	.0015	.023	−33	−2.3
45					45	.189	.16	.0020	.025	−30	−1.6
46					30	.284	.22	.0020	.025	−40	−1.4
26					20	.426	.30	.0020	.025	−55	−1.3
27					15	.568	.39	.0020	.027	−55	−1.0
50	22.68	319	18.93	1.184	40	.284	.23	.0020	.030	−40	−1.4
49					20	.568	.38	.0020	.027	−50	−.9
2. AIR AT 200° C. (392° F.); FUEL TEMPERATURE, 49° C.; 13-ORIFICE NOZZLE											
73	6.34	79	4.73	0.296	20	0.142	0.15	0.0015	0.023	−47	−2.2
56					15	.189	.18	.0015	.023	−68	−2.4
75					10	.284	.25	.0020	.023	−75	−1.7
76					5	.568	.46	.0015	.023	−100	−1.2
77	12.68	172	9.46	.592	40	.142	.18	.0020	.027	−35	−1.6
78					20	.284	.32	.0020	.027	−70	−1.6
81, 79					15	.378	.41	.0025	.027	−72	−1.3
80					10	.568	.61	.0025	.027	−88	−1.0
82	19.02	265	14.19	.888	60	.142	.18	.0020	.029	−25	−1.2
83					30	.284	.34	.0025	.029	−48	−1.1
84					20	.426	.48	.0025	.029	−60	−.93
85					15	.568	.61	.0025	.030	−72	−.84
86	25.36	358	18.93	1.184	80	.142	.16	.0020	.029	−20	−.93
89					40	.284	.31	.0020	.030	−50	−1.2
88					20	.568	.57	.0020	.030	−65	−.76
3. NITROGEN AT 200° C. (392° F.); FUEL TEMPERATURE, 49° C.; 13-ORIFICE NOZZLE											
202	6.56	82	4.73	0.296	20	0.142	0.14	0.0015	0.023	−50	−2.3
222					15	.189	.17	.0020	.023	−52	−1.8
223					10	.284	.26	.0018	.023	−83	−1.9
205					5	.568	.48	.0025	.023	−88	−1.0
225	13.12	178	9.46	.592	40	.142	.20	.0015	.023	−53	−2.5
207					20	.284	.33	.0020	.023	−80	−1.9
227					15	.378	.45	.0020	.023	−100	−1.8
209					10	.568	.65	.0020	.023	−110	−1.3
211	19.68	275	14.19	.888	60	.142	.21	.0020	.024	−40	−1.9
230					30	.284	.37	.0022	.024	−73	−1.7
213					20	.426	.51	.0025	.023	−88	−1.4
214					15	.568	.67	.0025	.025	−88	−1.0
215	26.24	371	18.93	1.184	80	.142	.18	.0020	.023	−30	−1.4
234					40	.284	.37	.0020	.024	−60	−1.4
235					27	.426	.51	.0025	.023	−72	−1.1
236					20	.568	.63	.0025	.026	−80	−.93
4. NITROGEN AT 250° C. (482° F.); FUEL TEMPERATURE, 49° C.; 13-ORIFICE NOZZLE											
177	7.25	92	4.73	0.296	20	0.142	0.22	0.0015	0.023	−65	−2.3
178					15	.189	.26	.0018	.023	−83	−2.2
191					10	.284	.37	.0020	.023	−115	−2.0
192					5	.568	.69	.0020	.023	−150	−1.3
193, 181	14.50	199	9.46	.592	40	.142	.27	.0018	.024	−55	−1.9
182, 194					20	.284	.48	.0025	.023	−96	−1.7
183, 195					15	.378	.65	.0025	.024	−124	−1.6
184					10	.568		.0025		−140	−1.2
196	21.75	305	14.19	.888	60	.142	.30	.0015	.025	−53	−1.9
197, 186					30	.284	.52	.0020	.024	−100	−1.8
198, 187					20	.426	.75	.0025	.025	−100	−1.2
188					15	.568		.0025		−120	−1.1
5. NITROGEN AT 250° C. (482° F.); FUEL TEMPERATURE, 82° C.; 13-ORIFICE NOZZLE											
255	7.25	92	4.73	0.296	20	0.142	0.20	0.0020	0.023	−60	−2.5
239					15	.189	.23	.0020	.023	−70	−2.2
257					10	.284	.36	.0020	.023	−105	−2.2
241, 258					5	.568	.65	.0020	.023	−140	−1.5
242	14.50	199	9.46	.592	40	.142	.27	.0017	.023	−65	−2.7
260, 243					20	.284	.47	.0022	.023	−100	−2.1
261, 244					15	.378	.60	.0025	.024	−112	−1.8
262, 245					10	.568	.83	.0025	.025	−124	−1.3
246	21.75	305	14.19	.888	60	.142	.27	.0020	.025	−50	−2.1
247, 264					30	.284	.50	.0022	.025	−91	−1.9
265					20	.426	.66	.0025	.025	−104	−1.5
266					15	.568	.86	.0025	.025	−104	−1.1

TABLE I—Continued

PRESSURE CHANGE ASSOCIATED WITH HEAT TRANSFER TO DIESEL FUEL

1	2		3		4	5	6	7	8	9	10
Record number	Initial gas pressure		Gas density		Gas-fuel ratio	Fuel weight (gram)	Pressure drop (atmosphere)	Interval A to B (second)	Interval A to C (second)	Initial slope (atmospheres per second)	Initial slope per gram per ° C. difference $\left(\frac{\text{atmospheres}}{\text{second gram ° C.}}\right)$
	Atmospheres absolute	Pounds per square inch (gage)	Grams per liter	Pounds per cubic foot							
6. NITROGEN AT 300° C. (573° F.); FUEL TEMPERATURE, 49° C.; 13-ORIFICE NOZZLE											
394	7.94	102	4.73	0.296	20	0.142	0.24	0.0020	0.024	−75	−2.1
398					15	.189	.27	.0020	.023	−95	−2.0
396					10	.284	.42	.0020	.023	−130	−1.8
399					5	.568	.86	.0020	.024	−180	−1.3
404	15.88	219	9.46	.592	40	.142	.29	.0017	.025	−82	−2.3
401					20	.284	.56	.0020	.025	−135	−1.9
402					15	.378	.74	.0025	.025	−140	−1.5
403					10	.568		.0025		−160	−1.1
405	23.82	335	14.19	.888	60	.142	.32	.0015	.026	−60	−1.7
406					30	.284	.61	.0020	.026	−110	−1.6
408					22.5	.378	.78	.0025	.026	−112	−1.2
407					20	.426		.0025		−132	−.93
7. NITROGEN AT 350° C. (662° F.); FUEL TEMPERATURE, 49° C.; 13-ORIFICE NOZZLE											
418	8.63	112	4.73	0.296	20	0.142	0.27	0.0017	0.023	−100	−2.3
415					15	.189	.35	.0017	.025	−123	−2.2
416					10	.284	.52	.0020	.024	−156	−1.8
417					5	.568	.92	.0025	.025	−190	−1.1
420	17.26	239	9.46	.592	40	.142	.38	.0018	.025	−94	−2.2
437					30	.189	.47	.0025	.025	−96	−1.7
438					20	.284	.67	.0025	.025	−132	−1.5
439	25.89	366	14.19	.888	60	.142	.40	.0020	.026	−70	−1.6
440					45	.189	.50	.0020	.026	−95	−1.7
441					30	.284	.71	.0025	.025	−124	−1.5
8. NITROGEN AT 250° C. (482° F.); FUEL TEMPERATURE, 49° C.; IMPINGING-JETS NOZZLE											
270	7.25	92	4.73	0.296	20	0.142	0.25	0.0020	0.023	−60	−2.1
271					15	.189	.29	.0020	.023	−80	−2.1
272					10	.284	.37	.0020	.022	−110	−1.9
273					5	.568	.62	.0020	.023	−155	−1.4
274	14.50	199	9.46	.592	40	.142	.28	.0025	.024	−48	−1.7
275					20	.284	.45	.0025	.025	−80	−1.4
276					15	.378	.57	.0025	.024	−100	−1.3
277					10	.568	.74	.0025	.025	−116	−1.0
278	21.75	305	14.19	.888	60	.142	.29	.0022	.024	−41	−1.4
279					30	.284	.44	.0025	.026	−64	−1.1
280					20	.426	.63	.0025	.027	−92	−1.1
281					15	.568	.76	.0025	.027	−100	−.88
9. NITROGEN AT 250° C. (482° F.); FUEL TEMPERATURE, 49° C.; SINGLE-ORIFICE NOZZLE											
286	7.25	92	4.73	0.296	20	0.142	0.10	0.0015	0.023	−33	−1.2
287					15	.189	.15	.0025	.022	−44	−1.2
288					10	.284	.22	.0020	.023	−70	−1.2
289					5	.568	.43	.0020	.020	−110	−.97
290	14.50	199	9.46	.592	40	.142	.16	.0020	.023	−40	−1.4
291					20	.284	.29	.0020	.023	−65	−1.1
292					15	.378	.40	.0020	.022	−95	−1.2
293					10	.568	.53	.0025	.022	−104	−.91
294	21.75	305	14.19	.888	60	.142	.20	.0020	.024	−45	−1.6
295					30	.284	.33	.0020	.023	−65	−1.1
296					20	.426	.51	.0025	.025	−88	−1.0
297					15	.568		.0025		−96	−.84
10. CARBON DIOXIDE AT 200° C. (392° F.); FUEL TEMPRATURE, 49° C.; 13-ORIFICE NOZZLE											
131	4.18	47	4.73	0.296	20	0.142	0.09	0.0012	0.030	−42	−2.0
91					15	.189	.11	.0015	.035	−47	−1.6
114					10	.284	1.6	.0015	.030	−67	−1.6
115					5	.568	3.0	.0015	.030	−80	−.93
95	8.36	108	9.46	.592	40	.142	.11	.0015	.035	−33	−1.5
117					20	.284	.22	.0020	.030	−55	−1.3
97					15	.378	.27	.0020	.030	−60	−1.0
119					10	.568	.41	.0020	.032	−70	−.82
100	12.54	170	14.19	.888	60	.142	.12	.0015	.030	−27	−1.3
121					30	.284	.24	.0020	.035	−50	−1.2
122					20	.426	.34	.0020	.035	−70	−1.1
123					15	.568	.44	.0020	.035	−70	−.82
125	16.72	231	18.93	1.184	80	.142	.12	.0015	.037	−27	−1.3
126					40	.284	.25	.0020	.037	−40	−.93
127					27	.426	.33	.0020	.037	−55	−.85
128					20	.568	.44	.0020	.038	−55	−.64
11. CARBON DIOXIDE AT 250° C. (482° F.); FUEL TEMPERATURE, 49° C.; 13-ORIFICE NOZZLE											
158	4.62	53	4.73	0.296	20	0.142	0.12	0.0015	0.030	−50	−1.7
159					15	.189	.16	.0020	.030	−55	−1.4
160					10	.284	.22	.0015	.030	−100	−1.8
161					5	.568	.44	.0020	.030	−100	−.88
162	9.24	121	9.46	.592	40	.142	.18	.0015	.030	−53	−1.9
163					20	.284	.33	.0020	.031	−90	−1.6
164					15	.378	.44	.0020	.031	−100	−1.3
165					10	.568	.65	.0020	.030	−120	−1.0
166	13.86	189	14.19	.888	60	.142	.21	.0016	.032	−50	−1.7
167					30	.284	.37	.0020	.031	−90	−1.6
168					20	.426	.52	.0020	.031	−100	−1.2
169					15	.568	.68	.0025	.033	−100	−.88
170	18.48	257	18.93	1.184	80	.142	.21	.0015	.033	−40	−1.4
171					40	.284	.39	.0020	.033	−75	−1.3
172					27	.426	.54	.0020	.033	−100	−1.2
173					20	.568	.69	.0020	.035	−100	−.88

TABLE II

EFFECT OF FUEL VAPOR ON PRESSURE CHANGE FOR DIESEL FUEL

1	2		3	4	5	6	7	8	9
Record	Initial gas pressure		Fuel quantity injected (gram)	Injection	Fuel in bomb before injecting (grams)	Pressure drop A to C (atmosphere)	Interval A to B (second)	Interval A to C (second)	Initial slope (atmospheres per second)
	Atmospheres absolute (approx.)	Pounds per square inch (gage)							
NITROGEN AT 250° C. (482° F.); FUEL TEMPERATURE, 49° C.; 13-ORIFICE NOZZLE									
380	15.88	219	0.568	1	0.000	0.94	0.0025	0.025	−156
381			.568	2	.568	.70	.0020	.025	−140
382			.568	3	1.14	.57	.0025	.025	−104
383			.568	4	1.70	.57	.0020	.025	−105
384			.568	5	2.27	.51	.0020	.025	−105
385	to	to	.568	8	3.98	.42	.0025	.025	−80
386			.568	11	5.68	.39	.0020	.025	−90
387			.568	17	9.09	.37	.0020	.025	−90
388			.568	23	12.5	.33	.0020	.023	−90
389	16.57	229	.568	34	18.7	.31	.0020	.023	−80
NITROGEN AT 350° C. (662° F.); FUEL TEMPERATURE, 49° C.; 13-ORIFICE NOZZLE									
446	17.26	239	0.284	1	0.000	0.63	0.0025	0.023	−148
447	to	to	.284	5	1.14	.46	.0022	.024	−95
448			.284	10	2.56	.29	.0025	.025	−56
449	18.68	260	.284	15	3.98	.22	.0020	.024	−55

TABLE III

PRESSURE CHANGE ASSOCIATED WITH HEAT TRANSFER TO BENZENE

1	2		3		4	5	6	7	8	9	10
Record number	Initial gas pressure		Gas density		Gas-fuel ratio	Fuel weight (gram)	Pressure drop (atmosphere)	Interval A to B (second)	Interval A to C (second)	Initial slope (atmospheres per second)	Initial slope per gram per ° C. difference $\left(\frac{\text{atmospheres}}{\text{second-gram ° C.}}\right)$
	Atmospheres absolute	Pounds per square inch (gage)	Grams per liter	Pounds per cubic foot							
1. NITROGEN AT 250° C. (482° F.); FUEL TEMPERATURE, 49° C.; 13-ORIFICE NOZZLE											
315	7.25	92	4.73	0.296	20	0.142	0.30	0.0020	0.025	−85	−3.0
316					15	.189	.35	.0020	.024	−100	−2.6
317, 323					10	.284	.54	.0025	.023	−124	−2.2
318	14.50	199	9.46	.592	40	.142	.33	.0025	.025	−64	−2.2
319					30	.189	.40	.0020	.025	−95	−2.5
320					20	.284	.62	.0025	.024	−124	−2.2
2. NITROGEN AT 300° C. (572° F.); FUEL TEMPERATURE, 49° C-; 13-ORIFICE NOZZLE											
301	7.94	102	4.73	0.296	20	0.142	0.36	0.0020	0.023	−85	−2.4
302					15	.189	.42	.0020	.025	−110	−2.3
303					10	.284	.64	.0025	.024	−144	−2.0
305	15.88	219	9.46	.592	40	.142	.39	.0020	.025	−90	−2.5
306					30	.189	.48	.0025	.024	−92	−1.9
307					20	.284	.76	.0025	.024	−140	−2.0
3. NITROGEN AT 350° C. (662° F.); FUEL TEMPERATURE, 49° C.; 13-ORIFICE NOZZLE											
331	8.63	112	4.73	0.296	20	0.142	0.37	0.0020	0.024	−105	−2.5
332					15	.189	.45	.0025	.024	−112	−2.0
333					10	.284	.69	.0025	.023	−172	−2.0
334	17.26	239	9.46	.592	40	.142	.43	.0025	.024	−92	−2.2
335					30	.189	.56	.0025	.023	−112	−2.0
336					20	.284	.85	.0025	.024	−172	−2.0

REPORT No. 581

MEASUREMENTS OF INTENSITY AND SCALE OF WIND-TUNNEL TURBULENCE AND THEIR RELATION TO THE CRITICAL REYNOLDS NUMBER OF SPHERES

By Hugh L. Dryden, G. B. Schubauer, W. C. Mock, Jr., and H. K. Skramstad

SUMMARY

The investigation of wind-tunnel turbulence, conducted at the National Bureau of Standards with the cooperation and financial assistance of the National Advisory Committee for Aeronautics, has been extended to include a new variable, namely, the scale of the turbulence. This new variable has been studied together with the intensity of the turbulence, and the effect of both on the critical Reynolds Number of spheres has been investigated.

By the use of a modification of the usual hot-wire apparatus incorporating two hot wires suitably connected and mounted so that the cross-stream distance between them may be varied, it has been found possible to determine the correlation between the speed fluctuations existing at the two wires. If u_1 and u_2 are the velocity fluctuations in the direction of the mean speed at the first and second wires, respectively, a correlation coefficient $R(y)$, equal to $\frac{\overline{u_1 u_2}}{\sqrt{\overline{u_1^2}}\sqrt{\overline{u_2^2}}}$ may be found as a function of the separation y. A length characterizing the scale of the turbulence may then be defined by the relation—

$$L=\int_0^\infty R(y)dy$$

The intensity of the turbulence as given by $\frac{\sqrt{\overline{u^2}}}{U}$, where U is the average speed of the stream, and the quantity L were determined by measurements in an air stream made turbulent to various degrees by screens of various mesh. The value of L near the screen was found to be about the same as the wire size of the screen, but increased with distance downstream from the screen. The quantity L may be regarded as a rough measure of the size of the eddies shed by the wires of the screen. The intensity was found to decrease with distance in accordance with the law of decay derived by G. I. Taylor.

Hot-wire measurements of turbulence are in error where the quantity L is of the same order as the length of the wire used. In the present work corrections for the lack of correlation over the entire length of the wires have been made in the measured values of L and $\frac{\sqrt{\overline{u^2}}}{U}$.

With both L and $\frac{\sqrt{\overline{u^2}}}{U}$ known for the stream with the several screens, the critical Reynolds Numbers of spheres were investigated. It was found that the critical Reynolds Number depended on $\frac{D}{L}$, where D is the diameter of the sphere, as well as on $\frac{\sqrt{\overline{u^2}}}{U}$; and that a functional relation between the critical Reynolds Number and $\frac{\sqrt{\overline{u^2}}}{U}\left(\frac{D}{L}\right)^{\frac{1}{5}}$ suggested by G. I. Taylor, was satisfied to within the experimental uncertainty. It is shown that the effect of the size of the sphere that has been observed by other investigators is but a particular manifestation of the foregoing more general relation.

INTRODUCTION

The turbulence of the air stream is generally recognized as a variable of considerable importance in many aerodynamic phenomena, especially those observed in wind tunnels. The drag of an airship model may vary by a factor of 2, the drag of a sphere by a factor of 4, and the maximum lift of an airfoil by a factor of 1.3 in air streams of different turbulence. The determination of turbulence is now a routine matter in many wind tunnels, the most common method being that of determining the value of the Reynolds Number of a sphere for which the drag coefficient is 0.3, the so-called critical Reynolds Number.

The critical Reynolds Number of a sphere is a measure of the aerodynamic effect of turbulence on a particular body and not a direct measurement of the turbulence. A direct measurement of the intensity of the turbulence can be made by means of a hot-wire anemometer suitably compensated for the lag of the wire (reference 1). The intensity of the turbulence is defined as the ratio of the root-mean-square speed fluctuation at a point to the mean speed. The experiments described in reference 1, (fig. 7), show a good correlation between the intensity of the turbulence and the critical Reynolds Numbers of spheres. In subsequent work at the National Bureau of Standards (reference 2) in which various honeycombs were used in the same wind tunnel and the entrance cone was modified, the correlation was not nearly so good.

The existence of a fair correlation was confirmed by Millikan and Klein at the California Institute of Technology (reference 3). These investigators noted that

the critical Reynolds Number of the sphere depended to some extent on the diameter of the sphere, decreasing as the diameter increased.

Since the critical Reynolds Number occurs at lower speeds for larger diameters, it might be supposed that the variation of the critical Reynolds Number with diameter really indicated a variation of the intensity of the turbulence with speed. The direct measurements of the intensity by the hot-wire anemometer show, however, that this explanation cannot be correct. We are thus led to the idea that the scale of the turbulent pattern must be considered. In fact, as early as 1923, Bacon and Reid, in reference 4, predicted an effect of the scale or "grain" of the turbulence and stated that the "effect of scale of turbulence is to control the degree with which true dynamic similarity may be maintained throughout a series of tests with spheres of different size." A study of this subject was begun at the National Bureau of Standards in the fall of 1933.

In order to investigate experimentally the effect of scale of the turbulence as well as its intensity, measurements of the critical Reynolds Number of spheres were made in a stream rendered turbulent by screens of various mesh. The investigation was conducted in the 4½-foot wind tunnel, the screens being placed one at a time completely across the upstream working section of the tunnel. In all, five nearly similar square-mesh screens were used, ranging in size from a 5-inch mesh made of round rods 1 inch in diameter to a ¼-inch mesh with a wire diameter of 0.05 inch. The purpose of the several screens was to vary the scale of the turbulence, it being supposed that the scale would be proportional to the mesh of the screen. It was decided subsequently to measure some dimension characteristic of the fluctuations themselves, and the dimension chosen was that derived from measurements of the correlation between velocity fluctuations at points at varying distances apart transverse to the stream.

Values of the intensity of the turbulence measured by the hot-wire method at different distances downstream from the several screens showed that the turbulence decayed rapidly at first and then more slowly with increasing distance from the screens. Hence in the sphere measurements the intensity of the turbulence produced by any one screen could be varied by varying the distance between the sphere and the screen.

As may be seen from the foregoing discussion, the complete program included several problems, which are treated in the five separate parts of the report as outlined below:

I. The measurement of correlation between velocity fluctuations with modified hot-wire equipment, and the derivation of a length to define the scale of the turbulence, by G. B. Schubauer, W. C. Mock, Jr., and H. K. Skramstad.

II. Measurements of the intensity and rate of decay of turbulence employing the usual type of hot-wire equipment, by G. B. Schubauer, W. C. Mock, Jr., and H. K. Skramstad.

III. The determination of the critical Reynolds Number of spheres under conditions where both the intensity and the scale of the turbulence are known, by Hugh L. Dryden, G. B. Schubauer, and W. C. Mock, Jr.

IV. The mathematical theory pertaining to the correction of the measurements, both of scale and intensity, for lack of complete correlation of the fluctuations over the entire length of the wires, by H. K. Skramstad.

V. Certain subsidiary matters relating to the variation of the correlation coefficient with the frequency characteristics of the measuring apparatus and with azimuth, by Hugh L. Dryden, G. B. Schubauer, and W. C. Mock, Jr.

Throughout the later stages of the work, the staff has been fortunate in being able to discuss by correspondence various aspects of the problem with G. I. Taylor, of Cambridge, England. The discussion of the experimental results is given in terms of his statistical theory of turbulence outlined in reference 5.

I—THE SCALE OF TURBULENCE AS DERIVED FROM MEASUREMENTS OF CORRELATION BETWEEN VELOCITY FLUCTUATIONS

When air flows past guide vanes or straighteners, such as those commonly used in wind tunnels either separately or in the form of a honeycomb, a considerable amount of eddy motion is set up and is carried along with the stream making the flow turbulent. Guide vanes are necessary to prevent large and erratic speed fluctuations, which would exist in the absence of the vanes, as well as to guide the air around turns. It may be assumed as a rough approximation that the eddy size and hence the scale of the turbulence is controlled by some dimension characteristic of the size or the arrangement of the guide vanes. For the case where the guide vanes are arranged in the form of a honeycomb, G. I. Taylor (reference 5) has assumed that the scale of the turbulence is proportional to the size of the cells of the honeycomb.

Figure 1 shows a sketch of the 4-½-foot tunnel used in the present work, in which a honeycomb (B) of 4-inch cells was located at the extreme entrance end and was followed by a contraction in diameter from 10 feet at the honeycomb to 4-½ feet at the working section. Owing to the rather rapid decay of eddy motion, the turbulence always decreases in intensity with distance from its source. In the working section of the present tunnel the intensity of the turbulence was 0.85 percent.[1] The law of eddy decay and the factors governing the scale of the turbulence will be taken up in detail in later sections.

In order to vary the two quantities, intensity and scale, the five screens listed in table I were placed indi-

[1] This is the value corrected for the effect of the length of the wire used in the measurement. The uncorrected value as observed with a wire 8.4 millimeters long was 0.7 percent.

vidually across the upstream working section of the tunnel at the position indicated in figure 1. Figure 2 shows photographs of a small portion of each of the screens, illustrating their relative size and type of construction. It is quite evident that the stream will be rendered turbulent by the eddies shed from a given screen and that the initial size of the eddies, and hence the scale of the turbulence near its point of origin, will be determined by some dimension of the screen. An effort was made to obtain screens of uniform mesh and wire size and to have the five screens as nearly similar to one another as possible. It will be seen by the variations in dimensions shown in table I and by the difference in type of construction shown in figure 2 that neither condition was exactly fulfilled. Since the deviations from the nominal size found by comparing columns 1 and 2 in table I are not outside the average deviations

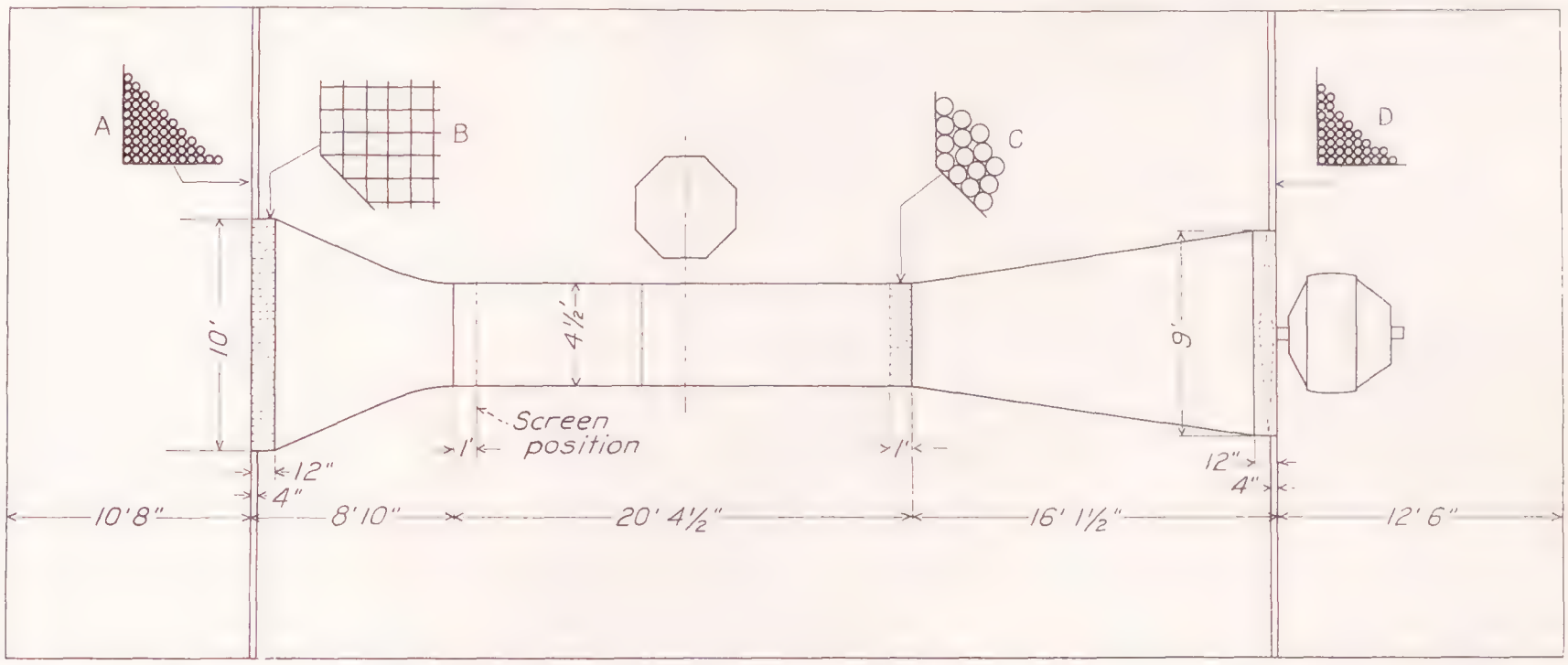

FIGURE 1.—Diagram of the wind tunnel showing position of screens and length of working section. A and D: paper tubes—1 in. diameter, 4 in. long, 3/32 in. wall. B: wooden cells—4 in. square, 12 in. long, 5/16 in. wall. C: metal tubes—3 inch diameter, 12 in. long, 0.025 in. wall.

of the individual meshes from the mean, the nominal mesh size was used as the length characteristic of the screen.

It will appear later that the scale of the turbulence near a screen corresponds more nearly to the wire size than to the mesh size. This fact should not be construed to indicate that the wire size determines the scale since the correspondence depends on the way in which the scale is defined. Since the screens may be regarded as geometrically similar, it is immaterial whether the size of the screen is specified by the wire size or the mesh size.

Immediately downstream from the screens the wakes of the individual wires or rods caused the air speed and the turbulence to vary with position across stream. However at distances greater than 15 mesh lengths the regular pattern of the screen was found to have disappeared, leaving the average speed approximately uniform and the turbulence nearly uniformly distributed. The uniformity of the stream will be discussed at greater length in connection with the sphere measurements in part III.

HOT-WIRE EQUIPMENT USED IN TURBULENCE MEASUREMENTS

A brief description of the essential features of the hot wire and its application to studies of turbulence will suffice here, since full accounts dealing with such equipment may be found in the literature, notably in references 1, 6, and 7. Fundamentally the apparatus consists of a particular type of hot-wire anemometer with an electrically heated wire of such small diameter that the speed fluctuations of the stream in which the wire is placed will cause changes in the wire temperature. The fluctuating voltage drop across the wire, accompanying temperature and resistance changes, would serve as an indication of the speed fluctuations were it not for the failure of the wire to follow the faster fluctuations because of the lag introduced by its thermal capacity. It is however, possible to compensate for this characteristic of the wire by means of an electric network containing an inductance and resistance having the opposite effect. The voltage output of the wire is usually amplified before compensation is introduced, and then the compensated voltage is given additional amplification to enable it to be measured. The indicator used in the present work was a thermal type milliammeter connected to the output of the amplifier. This instrument indicated the mean square of the alternating current output of the amplifier and, with the amplifier calibrated against a known input voltage, the meter reading could be used to calculate the mean square of the compensated voltage fluctuation. In addition, the direct voltage drop across the wire was measured by a potentiometer. All the information necessary for calculating the root-mean-square of the speed fluctuation was thus made available. Details of such calculations are given in reference 1. The factors on which com-

pensation depends and the formula for computing the compensation are given in reference 6.

The amplifier used in the present work was not the one described in reference 7, a new amplifier of a similar type having since been built to make possible the use of an alternating current power supply. The frequency

If the turbulence is isotropic, as it will later be shown to be at a sufficient distance from the source of the disturbance, the fluctuations have equal velocity components in all directions. It is usual, however, to interpret the measured velocity fluctuations as being made up wholly of the component u in the direction of

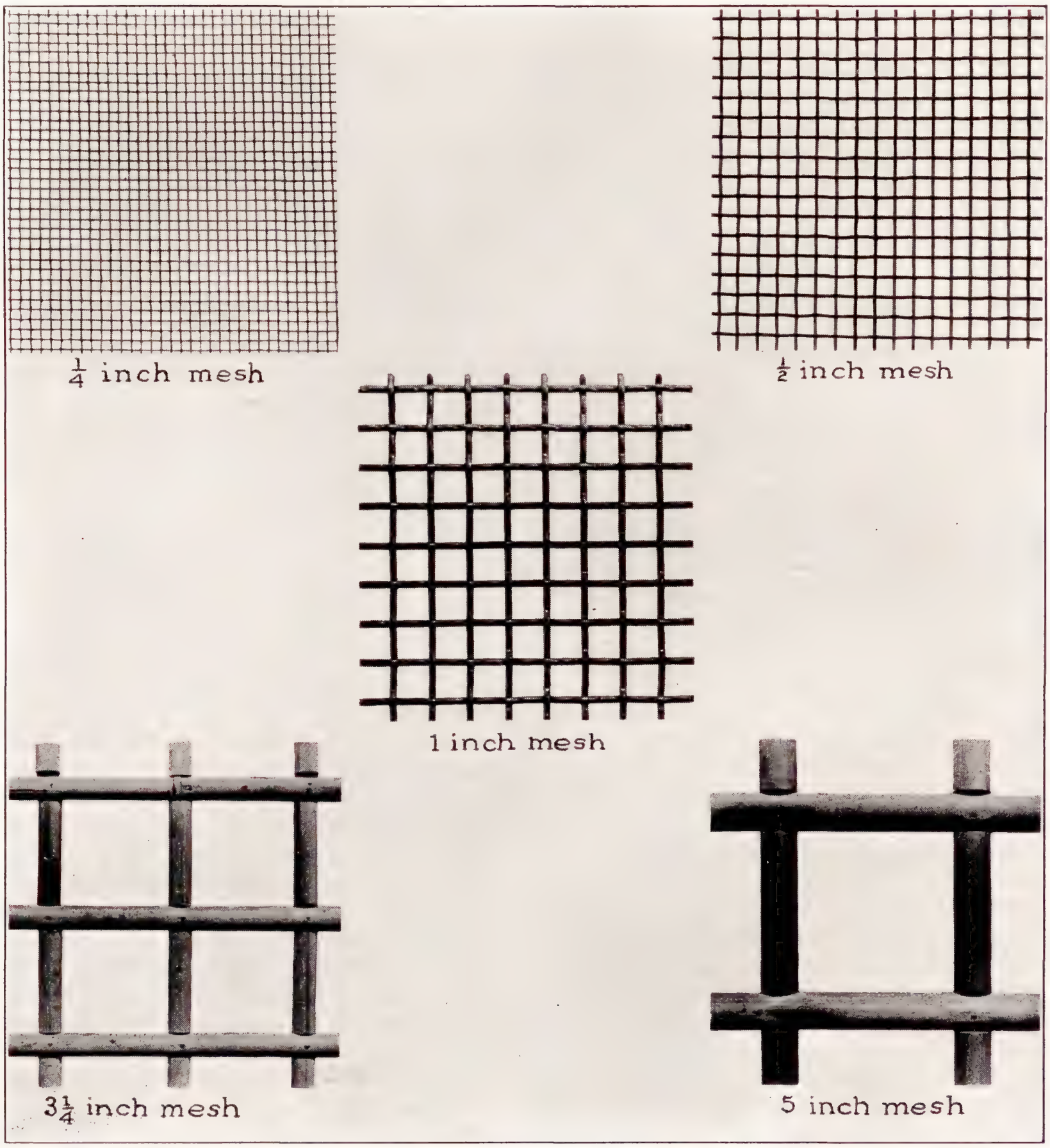

FIGURE 2.—The screens used to produce turbulence showing relative size and type of construction.

characteristics of both the old and the new amplifiers, when combined with the compensating circuit were such as to give satisfactory compensation to all frequencies from a few cycles per second to about 1,000 cycles per second. The platinum wire used in the present work was 0.016 millimeter in diameter; the length was usually 5 millimeters, although some older results are given for which the wire length was 8.4 millimeters.

the mean speed and to neglect entirely the normal component v. The justification for doing so lies in the fact that the v component when superposed on the mean speed has a very much smaller effect on the cooling of the wire than a u component of the same magnitude. The intensity of the turbulence is therefore expressed in terms of $\frac{\sqrt{\overline{u^2}}}{U}$, where $\sqrt{\overline{u^2}}$ is the root-mean-square of the

u component of the fluctuations and U is the average speed. The term "percentage turbulence" is commonly used to denote $100\,\frac{\sqrt{\overline{u^2}}}{U}$.

APPLICATION OF HOT-WIRE EQUIPMENT TO CORRELATION MEASUREMENTS

The determination of the scale of the turbulence involved a procedure closely related to that just described since the length characterizing the scale could best be derived from the distance transverse to the stream over which correlation existed between velocity fluctuations. It was therefore desired to obtain the correlation between the velocity fluctuations at two points separated by known distances across the stream and to express this correlation in terms of the conventional correlation coefficient

$$R=\frac{\overline{u_1u_2}}{\sqrt{\overline{u_1^2}}\sqrt{\overline{u_2^2}}}$$

where u_1 and u_2 are the velocity fluctuations at the points 1 and 2, respectively. The bars signifiy average values. In general, R will be a function $R(y)$ of the separation of the two points, where y is the distance between the points transverse to the stream. It was decided to adopt as a measure of the scale of the turbulence a length L defined as

$$L=\int_0^\infty R(y)dy$$

A length so defined is in accordance with the convention adopted by G. I. Taylor in reference 5.

The experimental problem therefore resolved itself into the determination of the correlation between velocity fluctuations by means of two hot wires. By way of illustrating the method, let us assume two identical wires heated to the same average temperature and placed parallel to one another at a given distance apart. If e_1 and e_2 are the instantaneous values of the fluctuating voltage over the two wires separately, the drop across the two, when they are connected so that their voltages oppose one another, is (e_1-e_2). When the resultant voltage is fed into an amplifier, the indications given by a thermal type milliammeter in the output of the amplifier will be proportional to $\overline{(e_1-e_2)^2}$, where the bar signifies that the meter indicates the average. If compensation is introduced to correct for the attenuation of the higher frequency fluctuations by the wire, then e_1 and e_2 become proportional to u_1 and u_2, the velocity fluctuations at the two wires,[2] and the resultant meter reading will be proportional to $\overline{(u_1-u_2)^2}$.

By the same reasoning it may be seen that a meter reading proportional to $\overline{(u_1+u_2)^2}$ is obtained if the wires are connected so that their voltages add. Figure 3 is a diagram of the electric circuit which shows, in addition to the heating circuits, two sets of potential leads running from the wires to the switch AB by means of which the potentials from the wires may be either added or opposed. If M_a is the meter reading obtained when the voltages are added and M_b is the reading when opposed, then

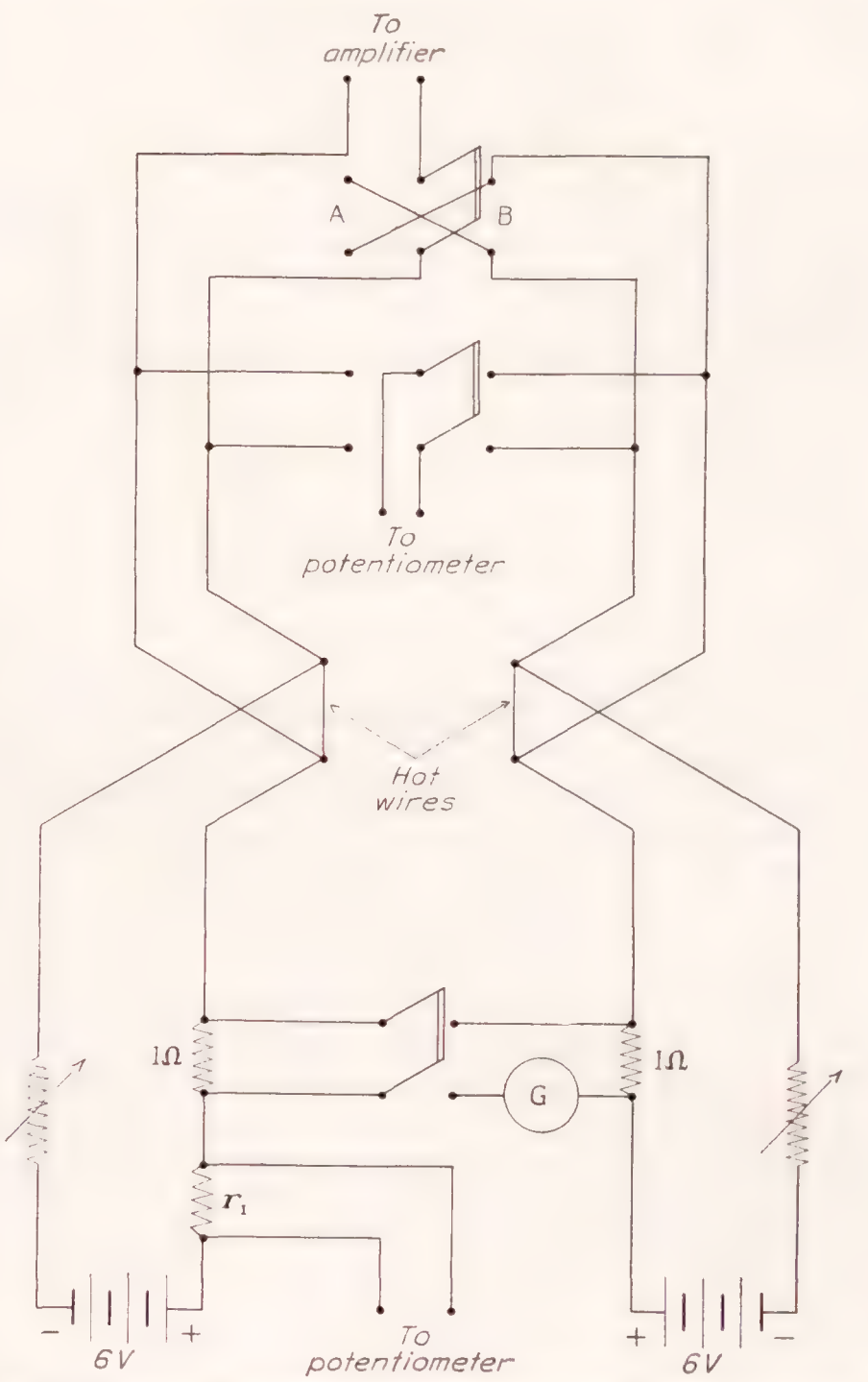

FIGURE 3.—Diagram of the circuit used in the measurement of correlation between velocity fluctuations.

$$M_a=K\overline{(u_1+u_2)^2}=K(\overline{u_1^2}+\overline{u_2^2}+2\overline{u_1u_2}) \quad (1)$$

$$M_b=K\overline{(u_1-u_2)^2}=K(\overline{u_1^2}+\overline{u_2^2}-2\overline{u_1u_2}) \quad (2)$$

where K is simply the constant of proportionality. Forming M_a-M_b and M_a+M_b and dividing

$$\frac{M_a-M_b}{M_a+M_b}=\frac{2\overline{u_1u_2}}{\overline{u_1^2}+\overline{u_2^2}} \quad (3)$$

If the turbulence is uniformly distributed across the stream so that the average square of the fluctuations is the same at wires 1 and 2, then $\overline{u_1^2}=\overline{u_2^2}=\overline{u^2}$, and equation (3) becomes

$$\frac{M_a-M_b}{M_a+M_b}=\frac{\overline{u_1u_2}}{\overline{u^2}} \quad (4)$$

[2] The voltage fluctuations are proportional to the velocity fluctuations only when the latter are small. This condition was closely fulfilled for the conditions of the present experiments.

Under such conditions it is evident that

$$\frac{\overline{u_1u_2}}{\overline{u^2}}=\frac{\overline{u_1u_2}}{\sqrt{\overline{u_1^2}}\sqrt{\overline{u_2^2}}}$$

which is the conventional correlation coefficient. Since, however, it is only possible to measure the average of the fluctuations along wires, the lengths of which in the present case were 5 millimeters, u_1 and u_2 cannot be interpreted as fluctuations at points. Hence the observed correlation coefficient will be denoted by R' as distinguished from R, the coefficient of correlation between the fluctuations at two points.

A little consideration will show that the correlation must depend on the separation of the two wires. For example, if the wires are brought close together so that a disturbance striking the one must strike the other also, u_1 becomes equal to u_2 and R' equal to unity. On the other hand, when the wires are very far apart, the instantaneous u_1 will bear no relation to the instantaneous u_2, and $\overline{u_1u_2}$ and hence R' will equal zero. Values of R' between these two limits may be obtained by taking readings for various separations of the two wires.

An alternative procedure found more convenient than the foregoing one, but less exact if the turbulence is not uniform or conditions are not steady, is to take only meter reading M_b corresponding to various separations of the wires. Denoting by M_b^{∞} the meter reading obtained when the wires are so far apart that no correlation exists, we have by equation (2)

$$M_b^{\infty}=K(\overline{u_1^2}+\overline{u_2^2})$$

Forming the quotient

$$\frac{M_b}{M_b^{\infty}}=\frac{\overline{u_1^2}+\overline{u_2^2}-2\overline{u_1u_2}}{\overline{u_1^2}+\overline{u_2^2}}=1-\frac{2\overline{u_1u_2}}{\overline{u_1^2}+\overline{u_2^2}}$$

and, as before, when $\overline{u_1^2}=\overline{u_2^2}=\overline{u^2}$

$$1-\frac{M_b}{M_b^{\infty}}=\frac{\overline{u_1u_2}}{\overline{u^2}}=R'$$

Obviously M_a could have been used alone in a similar manner but, since M_a does not approach zero for a correlation of unity as does M_b, this method was less sensitive and was never used.

In the wiring diagram of figure 3 the potentiometer and amplifier circuits are omitted since these are standard pieces of equipment. It will be observed that two separate heating circuits are used, the separation of the two circuits being convenient to allow the potential drops across the wires to be either added or opposed. After the current in one of the circuits was set equal to the desired value of 0.2 ampere, as determined by the potentiometer and standard resistance r_1, the current in the other heating circuit was set to the same value by making the drop across the 1 ohm standard resistance in this circuit equal to that across the 1 ohm standard resistance in the other circuit. The potentiometer was also used to measure the voltage drop across each wire. From the voltage drop, the current, and the temperature coefficient of resistance, the temperature of the wire could be computed, a quantity required to compute the compensation resistance.

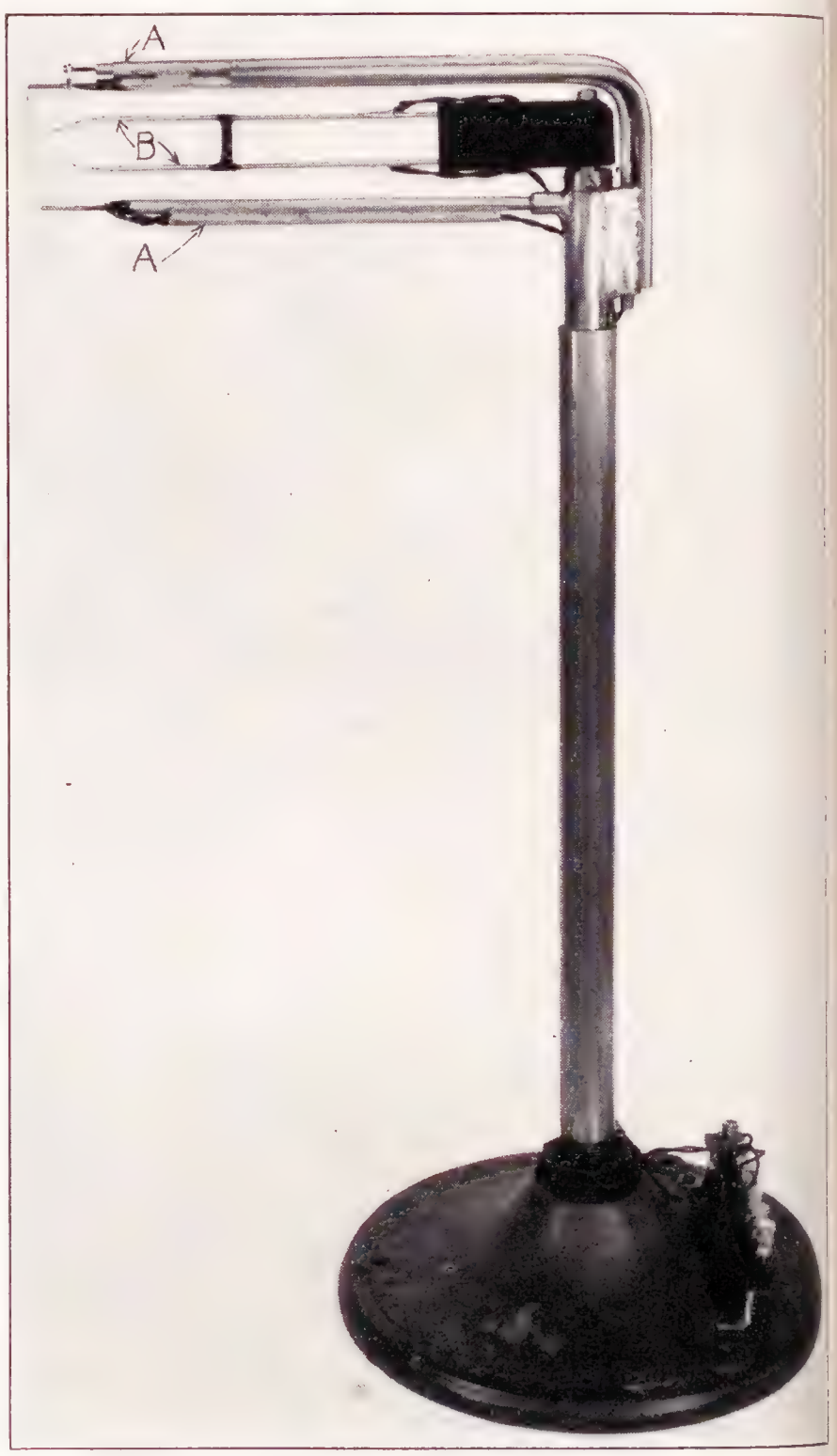

FIGURE 4.—The traversing apparatus used to vary the distance between hot wires in the measurement of correlation between velocity fluctuations.

By means of the traversing apparatus shown in figure 4, the distance between the wires could be varied and R' measured as a function of the distance. The side view of the apparatus clearly shows the two sets of prongs each 1 foot in length from the support to the needle tips to which the wires were attached. The outer set A is fixed rigidly to the vertical supporting member while the inner set B, to permit rotation, is fixed to a vertical shaft running down through the supporting member to the outside of the tunnel. The

movable prongs are slightly shorter than the fixed prongs to allow the movable wire to swing past the fixed wire and thereby permit settings on either side. This clearance was usually no more than a few tenths of a millimeter. Distances were indicated on a linear scale below the tunnel by means of a pointer attached to the vertical shaft carrying the movable prongs. The height of the apparatus was such as to place the wires in the center of the tunnel when in use. The wires were of platinum 0.016 millimeter in diameter and about 5 millimeters long, care being taken to make the lengths of the two as nearly equal as possible. Soft solder was found to be very convenient and quite satisfactory for attaching the wires to the prongs.

The displacement of the movable wire by the swinging motion just described has the disadvantage that the wire moves in an arc of a circle rather than in a straight line and so suffers a downstream displacement as well as a lateral one. This defect increases in importance with the magnitude of the spacing; but, since neglecting the downstream displacement could not introduce an error greater than 2 percent in the measured scale of the turbulence for the greatest spacings encountered, no attempt was made to take it into account.

VARIATION OF CORRELATION WITH DISTANCE

With the apparatus placed at various distances back of the screens listed in table I, traverses were made by taking meter readings for various settings of the movable wire relative to and on either side of the fixed wire. The results obtained are illustrated in figure 5 by the plotted points and the solid curves. The positive and negative branches are the result of taking observations with the movable wire set first to one side and then to the other side of the fixed wire. Among the features to be noted are: first, the order of magnitude of the distance over which correlation exists and, second, the increase in this distance with increasing screen size.

The absence of points at the top of the curves indicates that it was never possible to observe the perfect correlation that must exist in the imaginary case of two coalescing wires. One reason for this difficulty is apparent when it is realized that the wires cannot be brought together without mutual interference. When the movable wire began to enter the wake of the fixed wire, a sharp reduction of correlation was observed. These data are not shown in the figure. Another cause of incomplete correlation near zero is the initial displacement necessary to allow the wires to pass one another. The effect of this displacement will be taken up in greater detail in part V. Another possible cause is a poor matching of the wires; but, as shown by the following example, this feature is not so important as might be supposed. If we reconsider equations (1), (2), and (4) with the response produced by u_1 differing from that produced by u_2 by a factor k, we obtain:

$$M_a=K\overline{(u_1k+u_2)^2}=K(k^2\overline{u_1^2}+\overline{u_2^2}+2k\overline{u_1u_2})$$

$$M_b=K\overline{(u_1k-u_2)^2}=K(k^2\overline{u_1^2}+\overline{u_2^2}-2k\overline{u_1u_2})$$

$$\frac{M_a-M_b}{M_a+M_b}=\frac{2k}{k^2+1}\frac{\overline{u_1u_2}}{\overline{u^2}}$$

where $\overline{u_1^2}=\overline{u_2^2}=\overline{u^2}$. If we suppose k to equal 0.8, then $\frac{2k}{k^2+1}=\frac{1.6}{1.64}=0.976$. In other words, if the two wires differed in length by 20 percent, the final result would be reduced by only 2.4 percent.

As was pointed out earlier, R' is not the correlation between the velocity fluctuations at two points in the stream, but is rather the correlation between the fluctuations over two wires—in this case, over wires 5 millimeters in length. Figure 5 shows that the correlation drops considerably in a distance of 5 millimeters; hence speed fluctuations at points, say at the center of each wire, must be different from those that are found for the average over the whole wire. Qualitatively at least it may be seen that the difference between the observed correlation and that existing between points will depend on the length of the wires and the rapidity with which correlation falls off with distance. In part IV, methods are developed for correcting all hot-wire results, whether of correlation or percentage turbulence, for this lack of complete correlation over the entire length of the wire or wires used. The R curves shown by the broken line in figure 5 were obtained by applying this correction to the R' curves. The R curves therefore represent the variation of correlation with distance between points and are consequently independent of wire length.

To compute R curves from the many observed R' curves, would have proved quite laborious; hence the procedure adopted was to obtain by graphical integration of the R' curves the observed scale of the turbulence L', defined as

$$L'=\int_0^\infty R'(y)dy$$

and then to correct these by dividing by the factor K_2, given in part IV, and so obtain the true scale of the turbulence L, defined as

$$L=\int_0^\infty R(y)dy$$

CHARACTERISTIC LENGTH OR SCALE OF TURBULENCE

In table II are given the values of L' and L expressed as fractions of the mesh size M of the screen that produced the turbulence. A comparison between $\frac{L'}{M}$ and $\frac{L}{M}$ will show the magnitude of the wire-length cor-

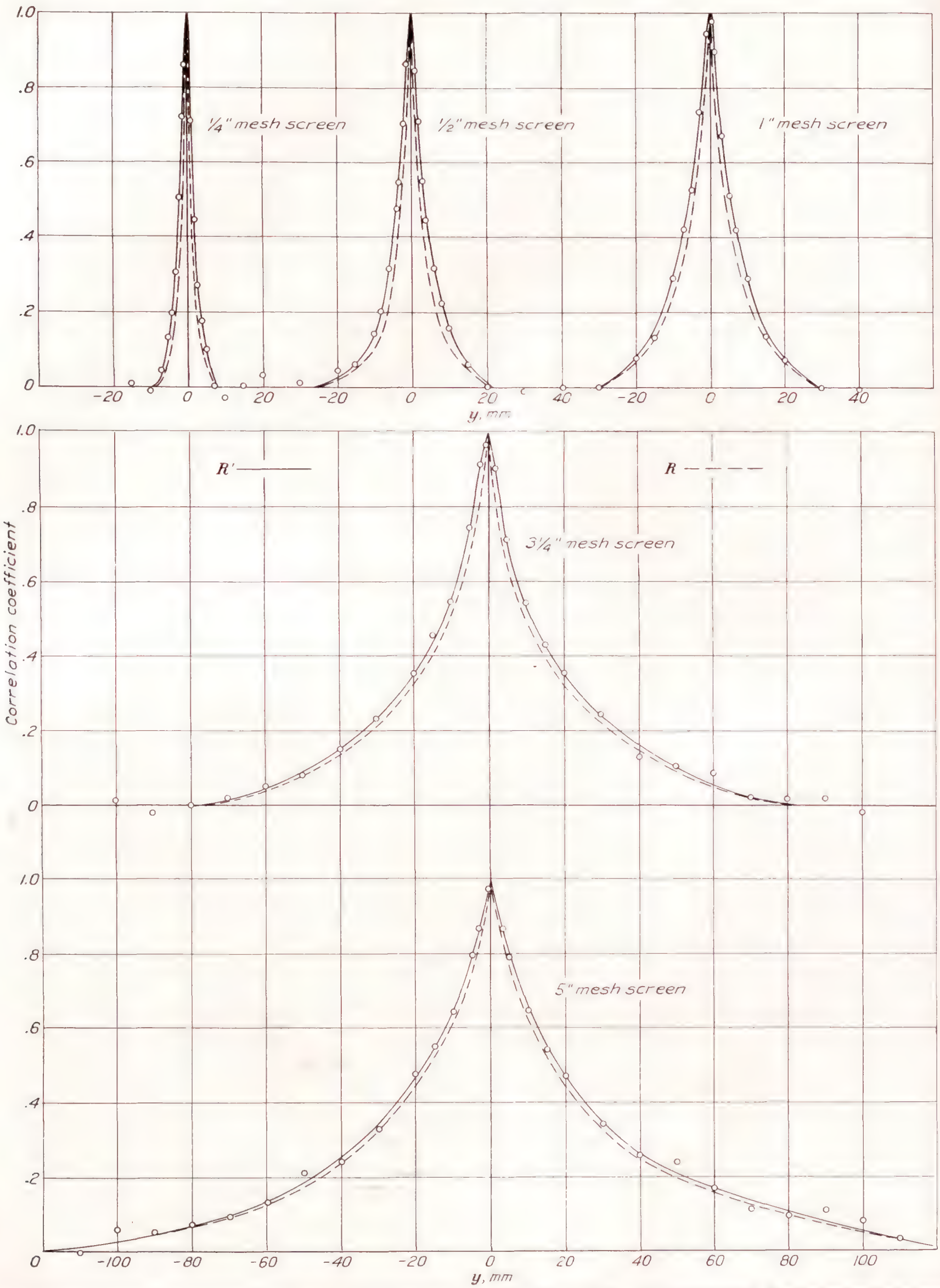

FIGURE 5.—Curves showing variation of correlation coefficient with the cross-stream separation of the hot wires. R' observed curves, R curves resulting when wire-length correction is applied. Observations taken 40 mesh lengths from screens. Wind speed 40 ft./sec.

section. In order to put the results for the several screens on a comparable basis, distances downstream from the screens, as well as L' and L, have been expressed in terms of the mesh of the screens; that is, in terms of $\frac{x}{M}$, where x is distance downstream measured from the screen. It will be apparent that the scale of

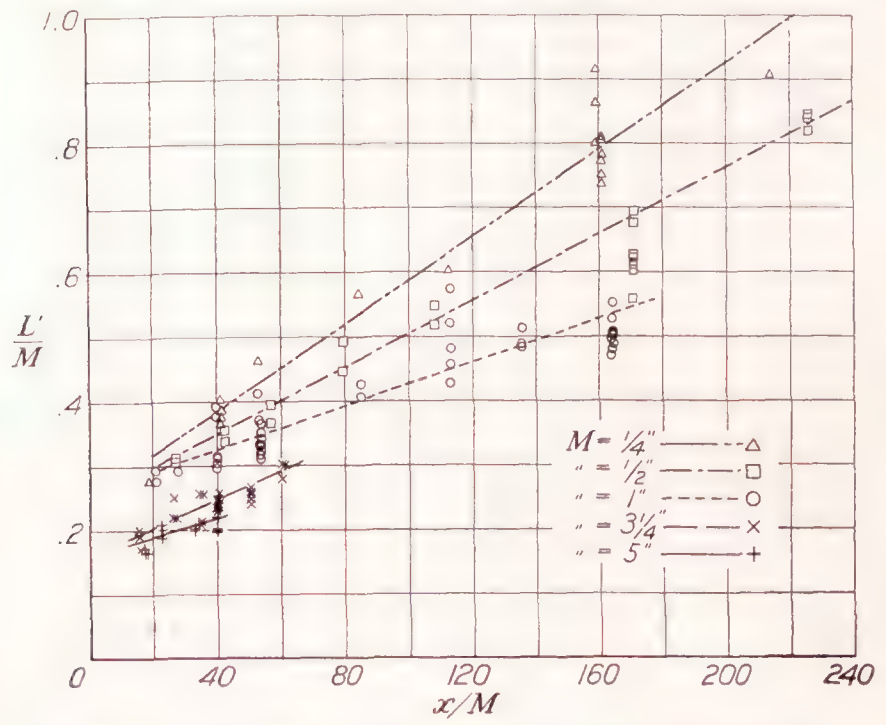

FIGURE 6.—Observed scale of turbulence at several distances from the screens.

$L' = \int_0^\infty R'(y)\,dy$, M=mesh of screen.

the turbulence produced by a given screen is not a constant quantity but increases with distance from the screen. With the exception of the dependence of the scale on the size of the screen and distance from the screen, L appeared to be unaffected by varying conditions of the stream. For example, no effect of air

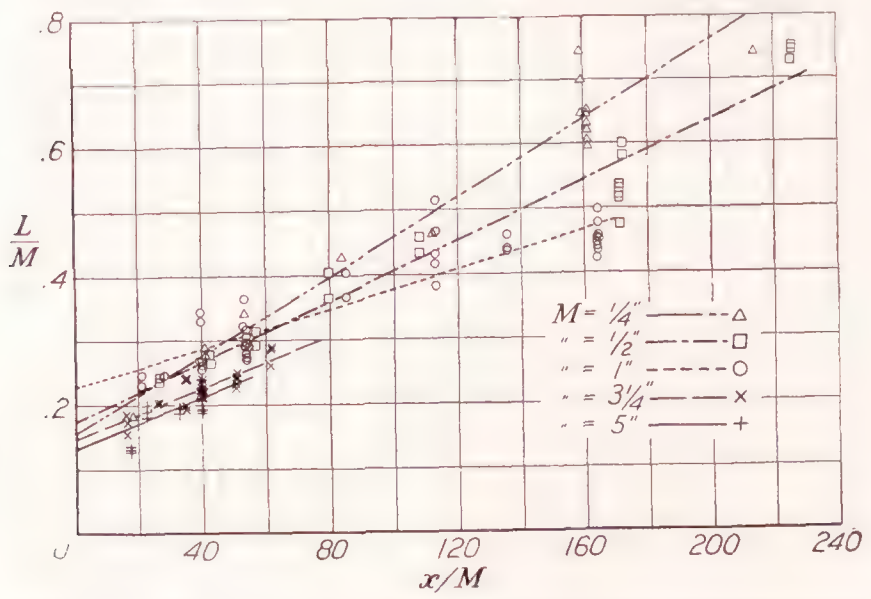

FIGURE 7.—Scale of turbulence corrected for wire length at several distances from the screens. $L = \int_0^\infty R(y)\,dy$, M=mesh of screen.

speed great enough to appear above the experimental variations could be found even though tests were made repeatedly to find an effect; nor did any variation with air temperature appear, even for such variation as from 12° C. to 30° C. Nearly all of the measurements given in the table were made at an air speed of 40 feet per second.

The important facts about L' and L are more clearly shown in figures 6 and 7 where $\frac{L'}{M}$, and $\frac{L}{M}$, respectively are plotted against $\frac{x}{M}$. It may be noted first that the increase with distance is quite marked, and second that the values of $\frac{L'}{M}$ show much more of a systematic change from screen to screen than do values of $\frac{L}{M}$. In fact, values of $\frac{L}{M}$ seem to be grouping close to a single curve. Systematic differences still exist, however, between the results for the several screens in figure 7 and show that the turbulent patterns are not exactly similar. This condition may be due to lack of similarity in the screens or to the residual turbulence produced by the honeycomb in the entrance of the tunnel. Table I and figure 2 show that the screens are similar in regard to major dimensions but different in details of construction. In view of these causes of departure from a single relation, separate curves were put through each set of points.

In figure 6, straight lines were arbitrarily drawn through the points without much consideration as to the appropriate type of curve. The curves of figure 7 were, however, drawn only after considerable study, since it was necessary to know the type of curve representing the relation or relations between $\frac{L}{M}$ and $\frac{x}{M}$ for future applications. Using the method of least squares, relations of the form

$$\frac{L}{M} = a_1 + b_1\frac{x}{M} + c_1\left(\frac{x}{M}\right)^2$$

and

$$\frac{L}{M} = a + b\frac{x}{M}$$

were fitted to the data for each screen separately and to the data for all screens taken together. When the second-degree equation was tried, the coefficient c_1 came out positive for some screens and negative for others, a condition which led to the conclusion that the data could be represented more consistently by the simpler linear relation. Least-square straight lines have therefore been drawn through the points of figure 7. The equations of the separate lines, as well as of a single line fitted to all the data are listed in table III.

Both figures 6 and 7 show a scatter among the points which indicates either a change in the turbulent pattern from time to time or considerable experimental uncertainty. In the worst cases the maximum spread among repeated determinations of $\frac{L}{M}$ for the same screen and the same position reached 30 percent, and in such cases the average deviation from the mean was as great as 10 percent. It will be seen from the curves

that the scatter was less than this for many of the determinations. Extensive study was given to possible causes of these variations, after which it was concluded that the main cause lay in the uncertainty involved in determining the point where the correlation reached zero; that is, where the curves of figure 5 touch the y axis. This uncertainty could be traced to the variations in the meter readings caused by the longer period fluctuations. These variations tended to make the meter difficult to read, especially when the wires were far apart, and to mask the initial changes in the average meter reading accompanying the onset of correlation as the wires were brought together.

The linear law of increase in L should not be regarded as a universal one applying to turbulence regardless of source. Neither should it be regarded as strictly true for the turbulence produced by screens, since there can be little doubt that some residual turbulence from the honeycomb was present in all cases. The important fact here is that under a particular set of conditions the scale of the turbulence for an air stream is given by figure 7; and keeping these conditions the same, the figure may be used to indicate the scale in connection with the investigation of other properties and effects of turbulence, such as those given in subsequent parts of the report.

TAYLOR'S THEORY OF CORRELATION

In reference 8, G. I. Taylor gives the relation

$$R=1-\frac{y^2}{2!\overline{u^2}}\overline{\left(\frac{\partial u}{\partial y}\right)^2}+\frac{y^4}{4!\overline{u^2}}\overline{\left(\frac{\partial^2 u}{\partial y^2}\right)^2}-\cdots\cdots$$
$$(-1)^n\frac{y^{2n}}{(2n)!\overline{u^2}}\overline{\left(\frac{\partial^n u}{\partial y^n}\right)^2} \tag{5}$$

which was deduced from quite general considerations. The assumptions involved are, first, the physical one that $\overline{u^2}$ does not vary with y and, second, a mathematical one that it is possible to differentiate an averaged quantity. Both assumptions appear to be legitimate. From this relation it follows that R must be an even function of y. In reference 5, Taylor has extended his deductions as follows:

In the neighborhood of $y=0$, it is evident that a good approximation of the equation (5) is afforded by

$$R=1-\frac{y^2}{2!\overline{u^2}}\overline{\left(\frac{\partial u}{\partial y}\right)^2} \tag{6}$$

where the terms of y^4 and higher powers have been neglected. Equation (6) should then closely represent the region of the curve of R plotted against y near $y=0$. Solving equation (6) for $\overline{\left(\frac{\partial u}{\partial y}\right)^2}$, we get

$$\overline{\left(\frac{\partial u}{\partial y}\right)^2}=2\overline{u^2}\,Lt_{y\to 0}\left(\frac{1-R}{y^2}\right) \tag{7}$$

It is interesting to examine the curves of figure 5 in the light of the foregoing theory. The restriction imposed by equation (5) that R be an even function of y requires that the curves leave the axis $y=0$ with zero slope. This condition was never found in the observed R' curves, possibly because it was impossible to examine the top of the curves in detail due to their extreme narrowness. A slight rounding is apparent at the apex in all of the R' curves, but this has disappeared with the application of the wire-length correction and is not at all in evidence in the R curves. As seen from figure 21 in part IV, where the difference between the R' and R curves is small, the R curve may be closely represented by

$$R=e^{-\frac{y}{L}} \tag{8}$$

for which the initial slope is $-\frac{1}{L}$. In view of the uncertainties near $R=1$, however, it is quite possible that a sharp change in the slope begins near the origin of y to allow the initial slope of zero as required by equation (5) instead of $-\frac{1}{L}$ given by equation (8).

If R in equation (7) is replaced by $e^{-\frac{y}{L}}$, it may be seen by expansion of the exponential and passing to the limit $y=0$ that $\overline{\left(\frac{\partial u}{\partial y}\right)^2}$ becomes infinite. This condition is obviously impossible since, as will be seen by equation (13), the rate of dissipation of energy in the turbulent motions must then be infinite. It must be concluded therefore that equation (8), although a good approximation on the average, is not correct near $R=1$.

II—MEASUREMENTS OF INTENSITY AND RATE OF DECAY OF TURBULENCE

MEASUREMENTS OF THE INTENSITY BY THE HOT-WIRE METHOD

Using the hot-wire method described in part I, measurements were made of the intensity of the turbulence at various positions back of the screens listed in table I. The single hot wire used in this work was electrically welded to steel needles which formed the tips of a set of fixed supporting prongs.[3] These prongs mounted on a holder, which held the wire near the center of the tunnel and about 18 inches ahead of the supports, took the place of the apparatus shown in figure 4. The rest of the apparatus—omitting, of course, that part required by a second wire—was the same as that used in the correlation measurements. The wire was of platinum 0.016 millimeter in diameter and was about 5 millimeters long for the more recent set of measurements.

In earlier work, before the importance of the wire-length correction was recognized, a wire of about 1

[3] Electrically welding the wire to the prongs is generally found to be superior to soft soldering in the measurement of percentage turbulence because of the necessity of maintaining the calibration of the wire over long periods of time. This requirement was not so stringent in the correlation work since there the properties of the wire and its junctions needed to remain constant only during the time of a traverse.

centimeter length was usually used to gain greater sensitivity than was afforded by a shorter wire. The most recent of such measurements taken with a wire length of 8.4 millimeters, which at the same time apply to the turbulence produced by the screens listed in table I, are given in references 9 and 10. For purposes of comparison, these results are given here in table IV and in figures 8 and 9, along with the more recent results ob-

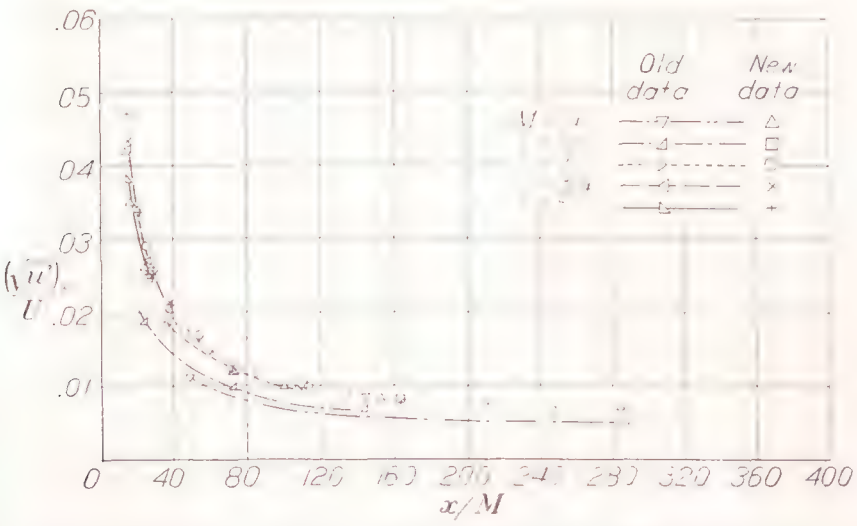

FIGURE 8.—Intensity of turbulence obtained with wires of different length at several distances from the screens. Old data—wire length 8.4 mm. New data—wire length 4.7 mm. (Wire-length correction not applied.) M=mesh of screens.

tained with a wire of length 4.7 millimeters. Both sets of results are plotted with x/M as abscissa in figure 8, without being corrected for the effect of wire length, and in figure 9 with the wire-length correction applied. The uncorrected values are denoted by the subscript w.

It may be noted in figure 8 that the results obtained with the 8.4-millimeter wire show a systematic increase for increasing mesh size for all screens except the 3¼- and 5-inch mesh. The results for the 4.7-millimeter

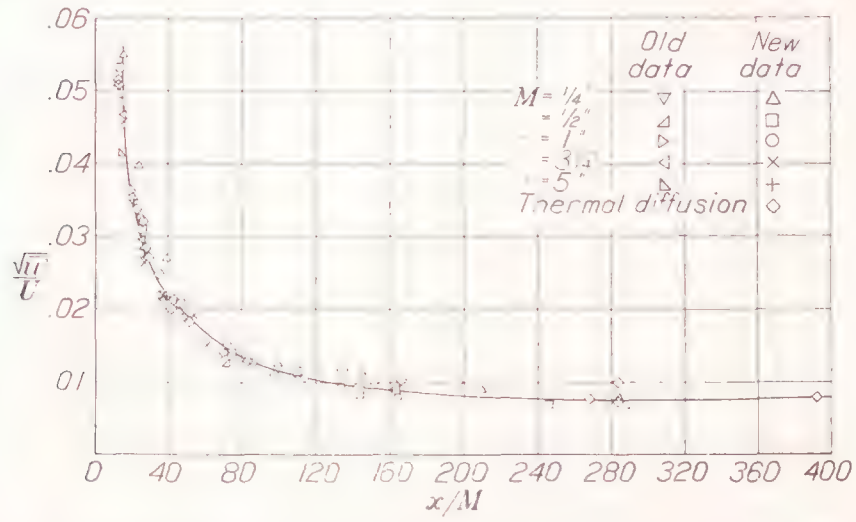

FIGURE 9.—Intensity of turbulence corrected for wire length at several distances from the screens. Old data—wire length 8.4 mm. New data—wire length 4.7 mm. M=mesh of screens.

wire show much less of this tendency and no attempt has been made to draw separate curves through the points. They fall distinctly above the value for the 1-, ½-, and ¼-inch screens obtained with the longer wire but are in fair agreement with the long wire results for the 3¼- and 5-inch mesh screens.

Before the results with the shorter wire were available, the occurrence of the separate curves for the several screens was believed to be due in part at least to an effect of wire length in relation to the scale of the turbulence; but there still remained the possibility of a lack of similarity in the turbulent flow pattern, caused perhaps by some departure from geometrical similarity in the screens themselves. When the results for the shorter wires were obtained, it became certain that the effect of wire length was largely responsible for the systematic differences. By that time the reason for such an effect was understood and the method of correction given in part IV was available. Figure 9 shows the result of applying the corrections. The systematic differences have been greatly reduced and the values for the long and short wires have been brought into agreement. The magnitude of the correction applied to the individual values may be judged from table IV, where both the corrected and uncorrected values are given.

The hot-wire measurements at any given point were always made at a number of wind speeds ranging usually from 20 to 70 feet per second. Throughout this range $\sqrt{\overline{u^2}}/U$ was found to be independent of the speed.

MEASUREMENTS OF THE INTENSITY BY THE THERMAL DIFFUSION METHOD

Figure 9 also shows good agreement between the corrected values of the turbulence obtained by the hot-wire method and those obtained by the method of thermal diffusion. The latter is an independent method of measuring the intensity of the turbulence, the technique of which is described in reference 9. The measurements from which the values given in figure 9 were calculated are also given in this reference for the screens listed in table I. The points for the several screens are not given separate designation since no systematic differences from screen to screen appeared.

Briefly the method of thermal diffusion consists of determining the width of the heated wake at a fixed distance back of a rather long but fine heated wire in the air stream by traversing the wake with a small thermocouple. In the measurements of reference 9 the width of the wake at half the temperature rise at the center of the wake, obtained from the curve of temperature distribution across the wake, was used as a measure of the width. The apparatus was so arranged that the angle subtended at the heating wire for different positions of the thermocouple was obtained; hence the results are given in terms of the angle subtended by the width of the wake at half maximum temperature. After the angle had been corrected for the spreading of the wake caused by the thermal conductivity of the air, it was found that the remaining angle, denoted by α_{turb}, was directly proportional to the turbulence in the stream and independent of the scale. For the conditions obtaining in the experiment it is possible to apply the theory of diffusion by continuous movements given by Taylor in reference 8 to calculate the intensity

of the turbulence from α_{turb} directly.[4] The equations leading to the calculation are given in reference 5 in a form directly applicable to the results of reference 9. These original references should be consulted for details; it suffices to state here that the relation connecting α_{turb} and the intensity of the turbulence is

$$\alpha_{turb}\ (\text{degrees}) = 134.9\frac{\sqrt{\overline{v^2}}}{U}$$

where $\sqrt{\overline{v^2}}$ is the root-mean-square of the cross-stream component of the fluctuation velocity and U is the average speed of the stream.

It will be observed that $\frac{\sqrt{\overline{u^2}}}{U}$ is obtained by the hot-wire method, whereas $\frac{\sqrt{\overline{v^2}}}{U}$ is obtained from thermal diffusion. The fact that $\frac{\sqrt{\overline{u^2}}}{U}$ agrees well with $\frac{\sqrt{\overline{v^2}}}{U}$ in figure 9 indicates that the turbulence must be closely isotropic; that is, that the cross-stream fluctuations are on the average the same as those along the stream. The agreement of the values obtained by these two independent methods also furnishes good evidence that the method of correcting the hot-wire results for wire length is reliable.

No effect of wind speed on the value of α_{turb} could be found throughout the range of speeds investigated, which ranged from 8 to 55 feet per second. The thermal diffusion method then offers additional evidence that the intensity of the turbulence does not vary with wind speed.

THEORY OF DECAY OF TURBULENCE

The usual concept of turbulence is that small fluid masses moving with velocities relative to one another give rise to the observed velocity fluctuations whose root-mean-square value is used as a measure of the intensity of the turbulence. The average distance over which the fluctuations may be regarded as completely correlated will serve as a measure of the average linear dimension of the fluid masses. The average velocity of the masses with respect to the mean velocity may then be identified [5] with $\sqrt{\overline{u^2}}$, the intensity as given by the hot-wire anemometer; and the average linear dimension may be identified with L, the scale as obtained from the area under the correlation curves.

In order to obtain the law of decay of turbulent motions, it is necessary to know the equation of motion of the fluid masses. In the choice of this equation we are guided by the fact that the solution must yield results in accordance with experiment, which are that the rate of decay is a function of $\frac{x}{M}$ and that $\frac{\sqrt{\overline{u^2}}}{U}$ is independent of the average speed U.

Let us assume that the force resisting the motion of the fluid mass is proportional to the product of density by cross-sectional area by the square of its speed relative to the mean flow. If m is the mass of fluid moving with velocity $\sqrt{\overline{u^2}}$, C_1 is the resistance coefficient, and t is the time, the equation of motion is

$$m\frac{d\sqrt{\overline{u^2}}}{dt} + C_1\rho L^2\overline{u^2} = 0 \tag{9}$$

Setting m proportional to ρL^3

$$L\frac{d\sqrt{\overline{u^2}}}{dt} + C_2\overline{u^2} = 0$$

Integrating

$$\frac{1}{(\sqrt{\overline{u^2}})_0} - \frac{1}{\sqrt{\overline{u^2}}} = -C_2\int_0^t \frac{dt}{L}$$

where $(\sqrt{\overline{u^2}})_0$ is the value of $\sqrt{\overline{u^2}}$ at $t=0$. Taking the origin of the turbulence at the screen and x as the distance downstream from the screen, we may set $t=\frac{x}{U}$ where U is the average speed of the stream. When this substitution is made the law of decay becomes

$$\frac{U}{(\sqrt{\overline{u^2}})_0} - \frac{U}{\sqrt{\overline{u^2}}} = -C_2\int_0^x \frac{dx}{L} \tag{10}$$

This equation satisfies the requirement that $\frac{\sqrt{\overline{u^2}}}{U}$ is independent of U if $\frac{(\sqrt{\overline{u^2}})_0}{U}$ is independent of U. We may infer that this last condition is true from the observation that the resistance of any given screen varies approximately as the square of the wind speed and hence that the flow in the immediate vicinity of the screen remains similar at different speeds.

It may be shown that no other resistance law in which the resistance is expressed as a function of the velocity will lead to a law of decay giving $\frac{\sqrt{\overline{u^2}}}{U}$ independent of U.

Taylor derives the law of decay expressed by equation (10) in a somewhat different way. He assumes (reference 5) from the phenomena of turbulent flow in pipes that the average rate of dissipation of energy per unit volume is given by the expression

$$\overline{W} = \frac{C_3\rho(\sqrt{\overline{u^2}})^3}{L} \tag{11}$$

The dissipative stresses within the medium, which act in opposition to the motion of elementary turbulent currents in the manner expressed by equation (9), arise from the action of viscosity in regions where

[4] This calculation is rigorous only when the fluctuation velocity of a particle at the heating wire and that of the same particle after the interval of time required for the particle to reach the thermocouple are perfectly correlated. The distance of 2 inches between the heating wire and the thermocouple, which existed when α_{turb} was measured, was small enough and the time interval consequently short enough to prevent any detectable departure from perfect correlation for all the screens. In fact, no departure from perfect correlation could be detected even at 6 inches. Unfortunately reference 8 was not discovered before the publication of reference 9, and as a result this important calculation was not included.

[5] Actually, $\sqrt{\overline{u^2}}$ is the root-mean-square of the x component of the velocity fluctuations. In the equations to follow, the total velocity of the fluid masses should be used; but since $\overline{u^2}=\overline{v^2}=\overline{w^2}$, the total velocity will differ from the x component only by a numerical factor. This factor will be absorbed along with other factors of proportionality in the constants C_1, C_2, C_3, etc.

velocity gradients exist. In terms of the velocity gradients and the viscosity the rate of dissipation may be expressed by

$$\overline{W}=\mu\left\{2\overline{\left(\frac{\partial u}{\partial x}\right)^2}+2\overline{\left(\frac{\partial v}{\partial y}\right)^2}+2\overline{\left(\frac{\partial w}{\partial z}\right)^2}+\overline{\left(\frac{\partial w}{\partial y}+\frac{\partial v}{\partial z}\right)^2}+\overline{\left(\frac{\partial u}{\partial z}+\frac{\partial w}{\partial x}\right)^2}+\overline{\left(\frac{\partial v}{\partial x}+\frac{\partial u}{\partial y}\right)^2}\right\} \tag{12}$$

where μ is the coefficient of viscosity and u, v, and w are the fluctuation velocities in the x, y, and z directions, respectively. For isotropic turbulence Taylor, in reference 5, has reduced equation (12) to the form

$$\overline{W}=7.5\mu\overline{\left(\frac{\partial u}{\partial y}\right)^2} \tag{13}$$

Two expressions therefore exist for the mean rate of dissipation of turbulent energy: Equation (11) in terms of the fluctuation velocities and the scale, and equation (13) in terms of the velocity gradients due to the fluctuations. As has been pointed out in part I, $\overline{\left(\frac{\partial u}{\partial y}\right)^2}$ determines the shape of the top of the correlation curves near the value of $R=1$, and in principle at least, the dissipation could be determined from equation (13) with the aid of the correlation curves. As has been seen, the correlation curves under the conditions of the present experiments are too narrow at the top to permit the accurate determination of the dissipation in this way.

The turbulent energy content per unit volume of the fluid is $\frac{1}{2}\rho(\overline{u^2}+\overline{v^2}+\overline{w^2})$ or since $\overline{u^2}=\overline{v^2}=\overline{w^2}$, is $\frac{3}{2}\rho\overline{u^2}$. The rate of change of this energy, or the rate of dissipation is therefore

$$\overline{W}=-\frac{3}{2}\rho\frac{d(\overline{u^2})}{dt}=-\frac{3}{2}\rho U\frac{d(\overline{u^2})}{dx} \tag{14}$$

where U is the average speed of the stream and x is distance along the stream. Equating the two expressions for $\overline{W}$ given in equations (11) and (14) and simplifying, we get

$$-\frac{Ud\left(\sqrt{\overline{u^2}}\right)}{\left(\sqrt{\overline{u^2}}\right)^2}=C_4\frac{dx}{L} \tag{15}$$

which is equivalent to equation (10).

Equation (15) may be put in the form

$$-\frac{Ud\left(\sqrt{\overline{u^2}}\right)}{\left(\sqrt{\overline{u^2}}\right)^2}=C_4\frac{d\left(\frac{x}{M}\right)}{\frac{L}{M}} \tag{16}$$

in which $\frac{L}{M}$ may be replaced by $a+b\frac{x}{M}$, given in part I. Substituting and integrating, we get

$$\frac{U}{\sqrt{\overline{u^2}}}-\frac{U}{\left(\sqrt{\overline{u^2}}\right)_0}=\frac{C_5}{b}\log_e\left(1+\frac{b}{a}\frac{x}{M}\right)$$

or changing to $\log_{10}$

$$\frac{U}{\sqrt{\overline{u^2}}}-\frac{U}{\left(\sqrt{\overline{u^2}}\right)_0}=\frac{C_6}{b}\log_{10}\left(1+\frac{b}{a}\frac{x}{M}\right) \tag{17}$$

where $\left(\sqrt{\overline{u^2}}\right)_0$ is the value of $\sqrt{\overline{u^2}}$ at $\frac{x}{M}=0$. The same result would have been obtained from equation (10) had the relation between $\frac{L}{M}$ and $\frac{x}{M}$ been substituted there.

In figure 10 $\frac{U}{\sqrt{\overline{u^2}}}$ has been plotted against $\frac{1}{b}\log_{10}\left(1+\frac{b}{a}\frac{x}{M}\right)$, where a and b have been given the separate

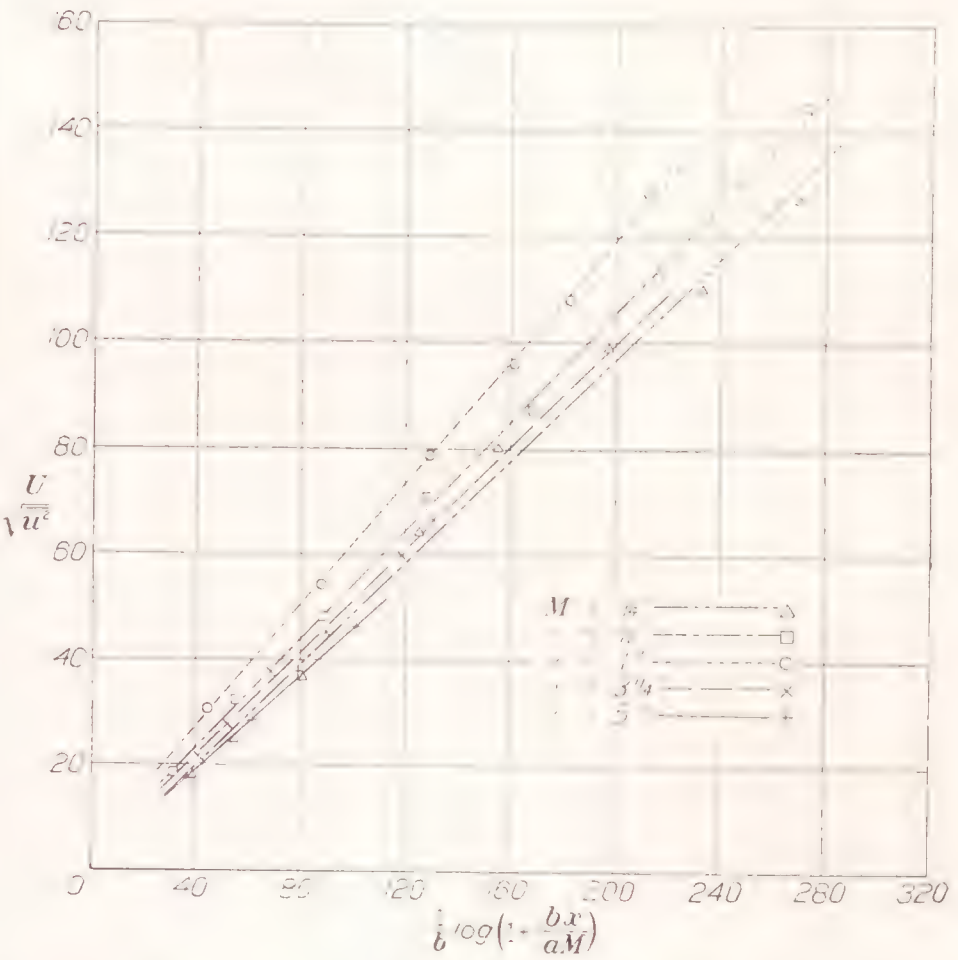

$\frac{1}{b}\log\left(1+\frac{bx}{aM}\right)$

FIGURE 10.—Test of law of decay: $\frac{U}{\sqrt{\overline{u^2}}}-\left(\frac{U}{\sqrt{\overline{u^2}}}\right)_0=\frac{C_6}{b}\log_{10}\left(1+\frac{b}{a}\frac{x}{M}\right)$. Values of a and b are given in table III.

values for the several screens from table III. The plot has been made using only the data for the 4.7-millimeter wire, which is believed to be less subject to error in the wire-length correction than the data for the longer wire. The points are seen to lie along straight lines as well as may be expected from the experimental precision. The separate curves for each screen are due to some extent to the systematic differences from screen to screen in figure 9, not clearly shown by that type of plot, but are to a greater extent due to the separate curves used to represent the relation between $\frac{L}{M}$ and $\frac{x}{M}$ in figure 7; that is, to the different values of a and b. The evidence afforded by figure 10 that equation (17) is of the proper form to represent the decay is to show further that the three experimental facts:

1. $\frac{\sqrt{\overline{u^2}}}{U}$ independent of U

2. A decay of $\frac{\sqrt{\overline{u^2}}}{U}$ given by figure 9

3. An increase of $\frac{L}{M}$ given by figure 7

are all consistent with one another. Having given any two of these conditions, the third must follow.

By least square fitting of the straight lines in figure 10 to the data, the constants $\frac{U}{(\sqrt{\overline{u^2}})_0}$ and C_6 of equation (17) have been evaluated and tabulated in table V. The value of $\frac{U}{(\sqrt{\overline{u^2}})_0}$ is seen to vary considerably from screen to screen, which may be partly due to differences in the geometrical shapes of the screens but more probably to errors involved in the curve fitting. On the other hand, the coefficient C_6, which is closely analogous to a resistance coefficient of the fluid masses, is nearly constant.

To return to a more simple type of representation, we may consider figure 11, where $\frac{U}{\sqrt{\overline{u^2}}}$ has been plotted against $\frac{x}{M}$ for the several screens, along with the theoretical curves given by equation (17) with the constants listed in table V. The new data with the shorter wire from which the constants were evaluated must, of course, fit the curves. The old data obtained with the longer wire and the thermal diffusion data are added to show that they too are not inconsistent with the theory.

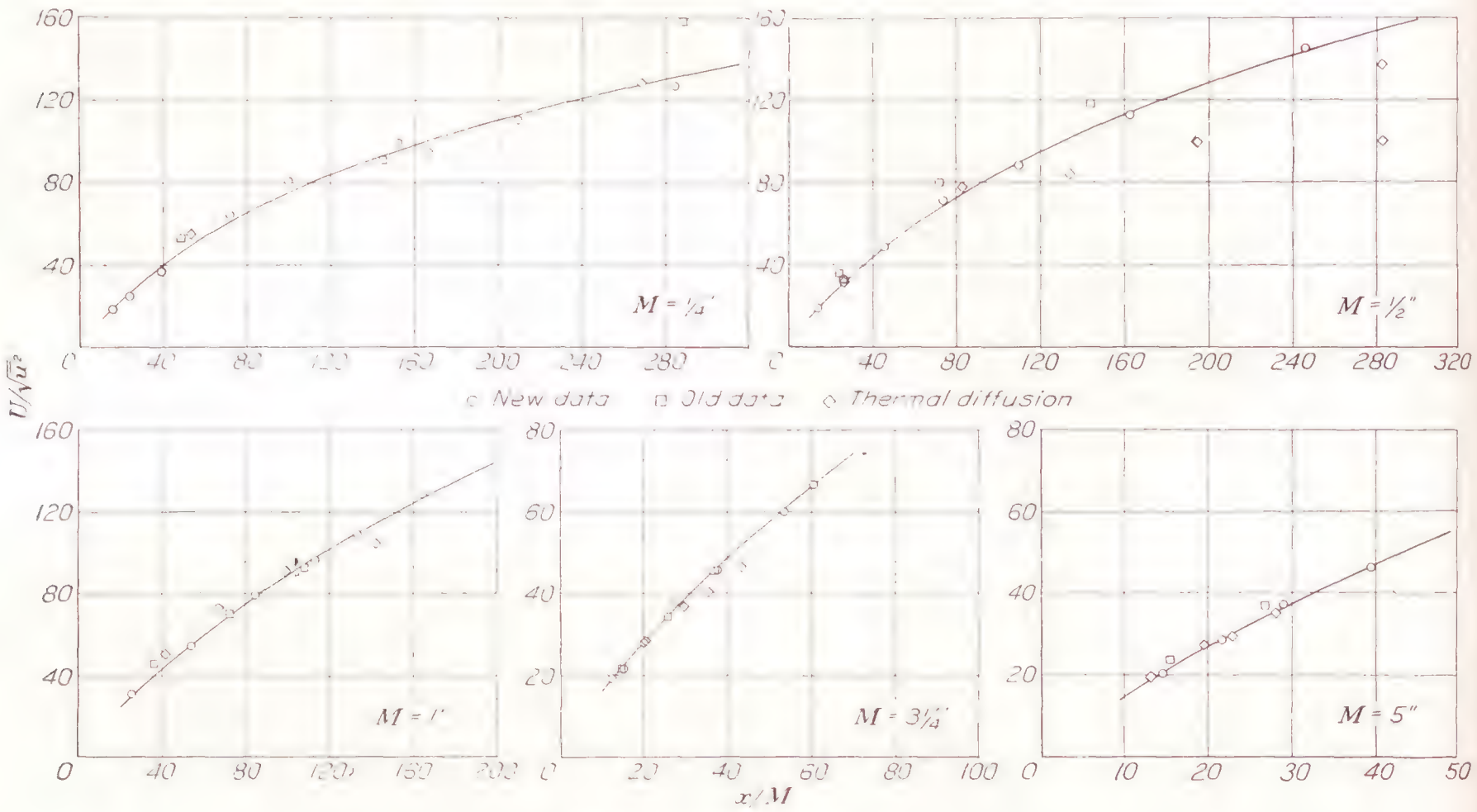

FIGURE 11.—Theoretical decay curves.

III—THE CRITICAL REYNOLDS NUMBER OF SPHERES

The use of a sphere as an indicator of turbulence in wind tunnels was originally proposed by Prandtl (reference 11). If one measures the drag force F on a sphere of diameter D in an air stream of speed U, the air being of density ρ, and viscosity μ, and plots the drag coefficient $C_D = \frac{F}{\frac{\pi}{4}D^2\frac{1}{2}\rho U^2}$ against the Reynolds Number $UD\frac{\rho}{\mu}$, it will be found that at low Reynolds Numbers C_D is approximately constant and equal to about 0.5. At Reynolds Numbers within a range of values dependent on the turbulence of the air stream C_D decreases rapidly to values in the neighborhood of 0.1. Prandtl suggested that "observation of such resistance curves for spheres gives a means of comparing the air streams of different laboratories, with respect to their lesser or greater turbulence." The decrease occurs at higher Reynolds Numbers in streams of lower turbulence.

When a technique had been developed for measuring the intensity of the speed fluctuations by means of the hot-wire anemometer and associated equipment, one of the authors with A. M. Kuethe attempted with some success to calibrate the sphere as a device for measuring the intensity of the turbulence (reference 1). To make the sphere results quantitatively definite, we proposed to define the critical Reynolds Number of a sphere as

the value of the Reynolds Number at which the drag coefficient of the sphere is 0.3.[6] This proposal has been rather generally adopted.

As more data were accumulated in wind tunnels with different honeycomb arrangements (references 2 and 3), the calibration of the sphere in terms of the intensity of the turbulence became more and more unsatisfactory. Millikan and Klein noted that the critical Reynolds Number depended on the diameter of the sphere. It became apparent that a more comprehensive study was needed.

Such a study has been carried out with the cooperation of the National Advisory Committee for Aeronautics. The general plan and the guiding principles have already been stated in the Introduction to this paper. The preceding sections give the methods by which the turbulence was varied, that is, by the use of a series of geometrically similar screens of square mesh. Measurements could be made at various distances from the screens. Data as to the intensity and scale of the turbulence at various distances are given in the preceding sections. The present section describes the measurements of the critical Reynolds Number of spheres and its variation with the intensity and scale of the turbulence.

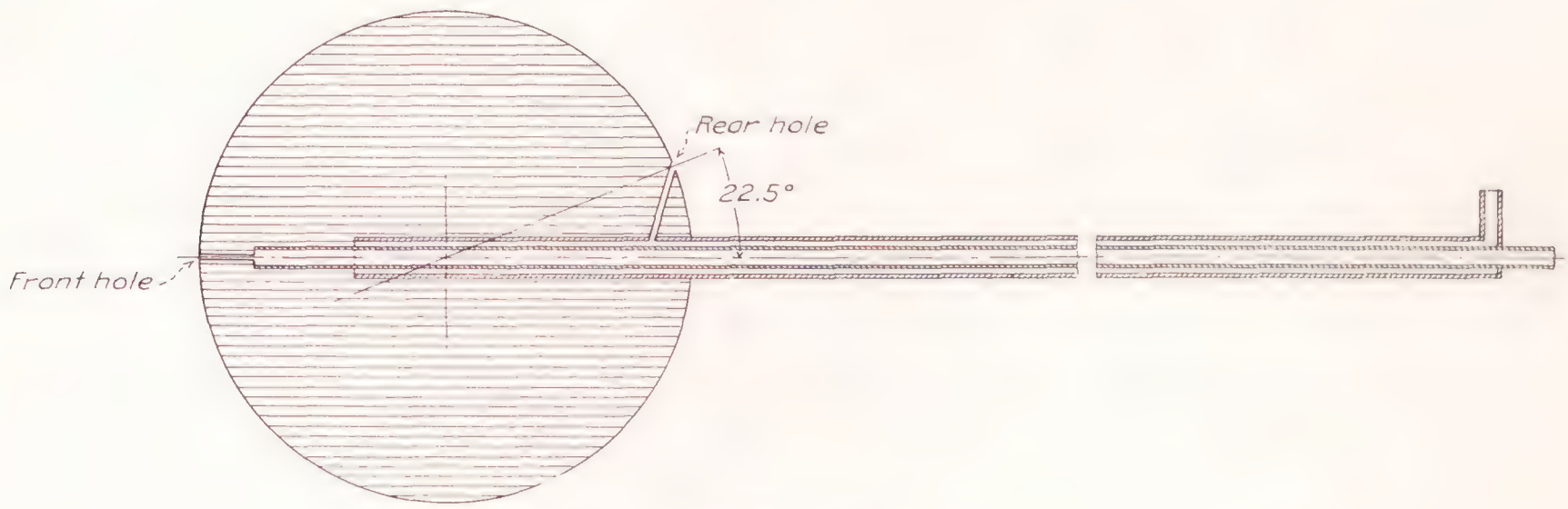

FIGURE 12.—The pressure sphere.

THE PRESSURE SPHERE

The measurement of the resistance of a sphere in wind tunnels of varying size is somewhat inconvenient. The accurate determination of the forces on the supports is time-consuming, and the fact that the balances in normal use are of greatly varying sensitivity in large and small wind tunnels necessitates the construction of a special balance of suitable sensitivity. To simplify the procedure we began in November 1933 the use of a "pressure-sphere" (references 12 and 13). The pressure-sphere is shown diagrammatically in figure 12. It consists of a smooth sphere [7] mounted on a tubular tail spindle. Within the tubular spindle is an inner concentric tube that connects to an impact hole diametrically opposite the spindle. In the hemisphere containing the spindle at an azimuth angle of 157½° from the impact hole, one or more holes are drilled to make connection to the annular space between the tubular spindle and the inner concentric tube. Suitable connecting nipples are provided at the end of the tail spindle.

The differential pressure between the impact hole and the wake can be measured by mounting the pressure-sphere rigidly with the tail spindle parallel to the direction of flow and connecting the nipples to the two sides of a manometer. The downstream holes were not located on the spindle or at the junction of sphere and spindle because we wished to avoid any necessity for controlling the exact geometrical form of the tail spindle.

The results are expressed in terms of a pressure coefficient obtained by dividing the differential pressure given by the pressure-sphere by the velocity pressure. For small Reynolds Numbers the pressure coefficient is approximately 1.4 and for high Reynolds Numbers about 0.9, the rapid decrease from one value to the other occurring at a Reynolds Number dependent on the turbulence of the air stream.

Mr. Robert C. Platt, of the Committee's staff at Langley Field, kindly undertook the comparison of the pressure-sphere results with force measurements for spheres of several sizes. He reported that a value of the pressure coefficient of 1.22 was approximately equivalent to a drag coefficient of 0.3. Hence it was decided to define the critical Reynolds Number of the pressure sphere as the Reynolds Number at which the pressure coefficient is 1.22. It is recognized that the equivalence is not an exact one. The detailed results obtained by Mr. Platt are described in reference 14.

A great advantage of the pressure sphere is the ease with which measurements may be made in flight or on a traveling carriage. Mr. Platt describes measurements of both types, which yield a value of the critical Reynolds Number in turbulence-free air of 385,000.

The pressure-sphere method was independently developed by S. Hoerner (reference 15) at the Deutsche

[6] We did not know at the time that Prandtl had suggested the use of the value 0.36.

[7] We have generally used standard bowling balls, diameter 5 inches or 8.55 inches. The departure of these balls from a spherical form is very small.

Versuchsanstalt für Luftfahrt, with some difference in detail. The rear holes were located in the tail spindle at its junction with the sphere. Pressures are referred to the static pressure of the air stream and hence the DVL pressure coefficients are equal to 1 minus our pressure coefficients. Hoerner used as critical Reynolds Number that for which the pressure at the rear holes was equal to the static pressure, corresponding to a pressure coefficient of 1.00 on our convention. Hence his values of critical Reynolds Number are somewhat higher than ours.

Hoerner also studied the relation between drag coefficient and pressure coefficient. His results on a single sphere in relatively smooth flow indicate that a pressure coefficient of 1.18 on our convention corresponds to a drag coefficient of 0.3, in fair agreement with the value of 1.22 obtained from the more extended measurements of Platt. It must be emphasized, however, that the relations between the values of the critical Reynolds Number as determined by drag measurements and by pressure measurements with different locations of the pressure openings are only approximate, and sufficient work has not been done to determine the influence of turbulence, sphere diameter, and exact location of the rear holes.

MEASUREMENTS WITH SPHERES

Some preliminary studies were made of the reproducibility of the results obtained with several supposedly identical pressure spheres. Three commercial 5-inch bowling balls were used to determine the critical Reynolds Number corresponding to the turbulence in the 3-foot wind tunnel of the National Bureau of Standards. The values obtained were 273,000, 276,000, and 272,000, which agree very well.

The extended series of measurements in the 4½-foot tunnel behind the several screens were made with two spheres, one 5 inches and the other 8.55 inches in diameter. The working distances could not exceed about 15 feet because of the limited length of the working section. In order to avoid large variations in mean speed, the closest distance had to be 15-mesh lengths or greater. Since the spheres are of finite size, extending over a distance of many mesh lengths for the smaller screens, the closest distance was further limited to avoid large changes of turbulence over the sphere. In no case was the closest distance less than 1 foot. The actual working distances, selected somewhat arbitrarily, were 1, 3, and 6 feet for the ¼- and ½-inch screens; 3, 6, and 9 feet for the 1-inch screen; 4, 7, and 10 feet for the 3¼-inch screen; 6 feet 5 inches and 11 feet 2 inches for the 5-inch screen.

The data obtained for the 1-inch screen are plotted in figure 13 for the 5-inch sphere and in figure 14 for the 8.55-inch sphere. The values of the critical Reynolds Number corresponding to the several distances were read from these and similar curves, the critical Reynolds Number being defined as previously explained as the Reynolds Number for which the pressure coefficient is 1.22. The results are given in table VI.

It will be noted that the curves of figures 13 and 14 show abrupt changes of slope at pressure coefficients of 1.1 to 1.15. After some investigation it was discovered that the use of four symmetrically located rear holes instead of a single hole gave curves without breaks, and hence that the breaks were probably due to local asymmetry in the flow about the sphere. Figure 15 shows curves obtained under the same conditions as the curves in figure 14 except that a sphere with four rear holes was used. The values of the critical Reynolds Numbers are unchanged and the breaks are absent.

In order to obtain some idea of the effect of the small departures from a uniform speed distribution, traverses were made with the sphere behind the 5-inch screen that showed the greatest departures. At a distance of 6.4 feet from the screen, the critical Reynolds Number was 107,000 and 109,000 in two runs at the center; 107,000, 2 inches below the center; 108,000, 4 inches below the center; and 109,000, 2 inches above the center. At a distance of 11.2 feet, values of 145,000 and 148,000 were obtained at two positions.

Table VI gives a summary of the pertinent data on the critical Reynolds Number. The values of $\frac{\sqrt{\overline{u^2}}}{U}$ are taken from the least-square lines of figure 10, and the values of L from the least-square lines of figure 7. Figures 16 and 17 show the relation between critical Reynolds Number and $\frac{\sqrt{\overline{u^2}}}{U}$ for the several screens as obtained with the 5 and 8.55 inch spheres, respectively. The points obtained at a distance of 1 foot (encircled in plotting) are not in good agreement with the other observations and the curves have not been extended through them. Evidently 1 foot is too close a working distance for spheres of this size. The observations show a systematic variation from screen to screen and a systematic variation with the diameter of the sphere. The larger the screen mesh, the greater the intensity required to give a specified critical Reynolds Number. The larger the diameter, the smaller the intensity required.

G. I. Taylor suggested in correspondence that the critical Reynolds Number should be a function of the quantity $\frac{\sqrt{\overline{u^2}}}{U}\left(\frac{D}{L}\right)^{\frac{1}{5}}$, where L is the scale of the turbulence. The data plotted in terms of this quantity are shown in figure 18. Except for the measurements made at a distance of 1 foot, the observations for both spheres and all screens lie remarkably well on a single curve, certainly within the observational errors.

The details of the reasoning that led Taylor to this suggestion have been published in reference 16. It may be stated in general terms that the foregoing combination of intensity and scale of turbulence occurs in the expression for the root-mean-square pressure gradient

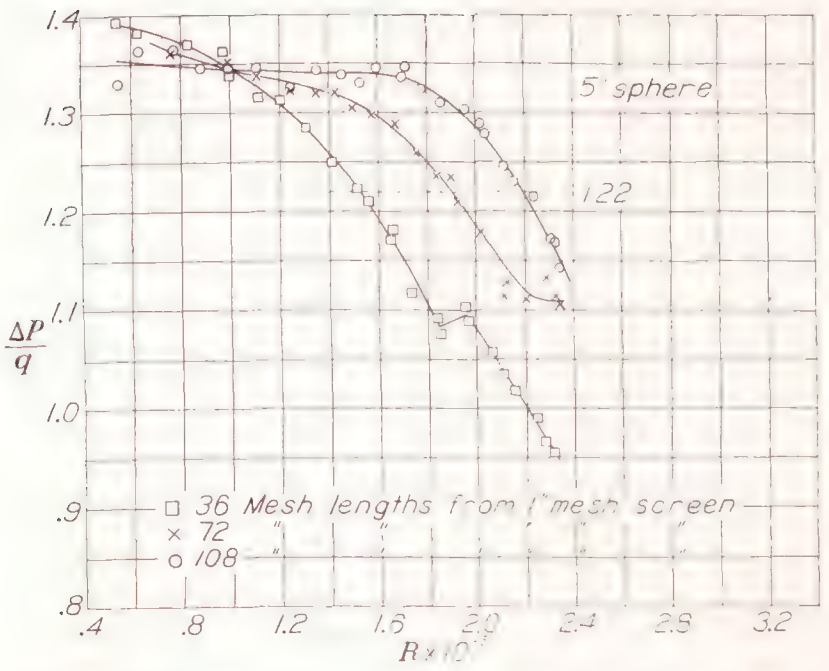

FIGURE 13.—Pressure coefficients for 5-inch sphere behind 1-inch screen.

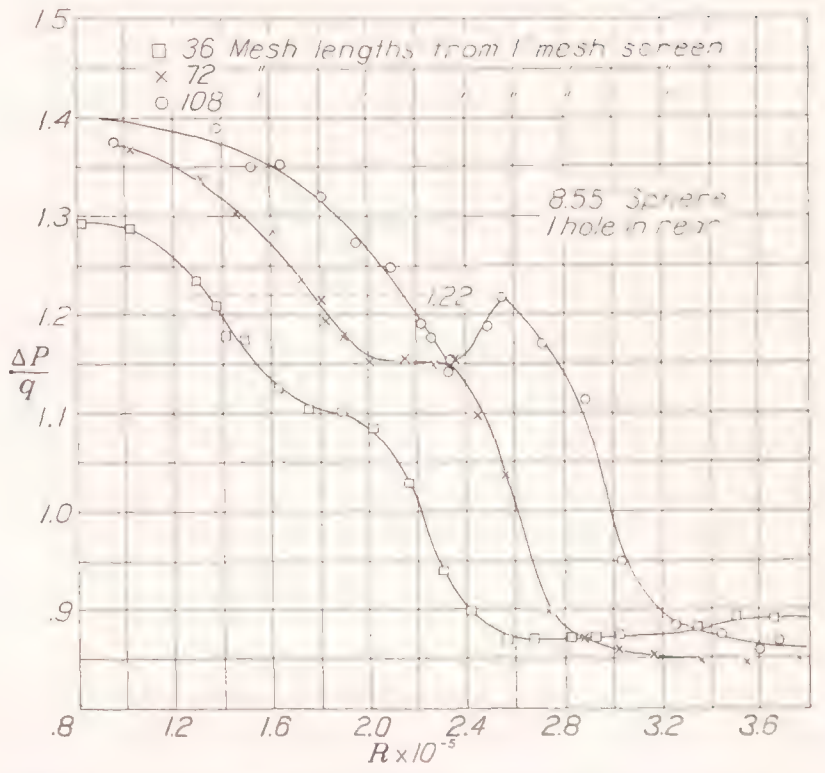

FIGURE 14.—Pressure coefficients for 8.55-inch sphere behind 1-inch screen.

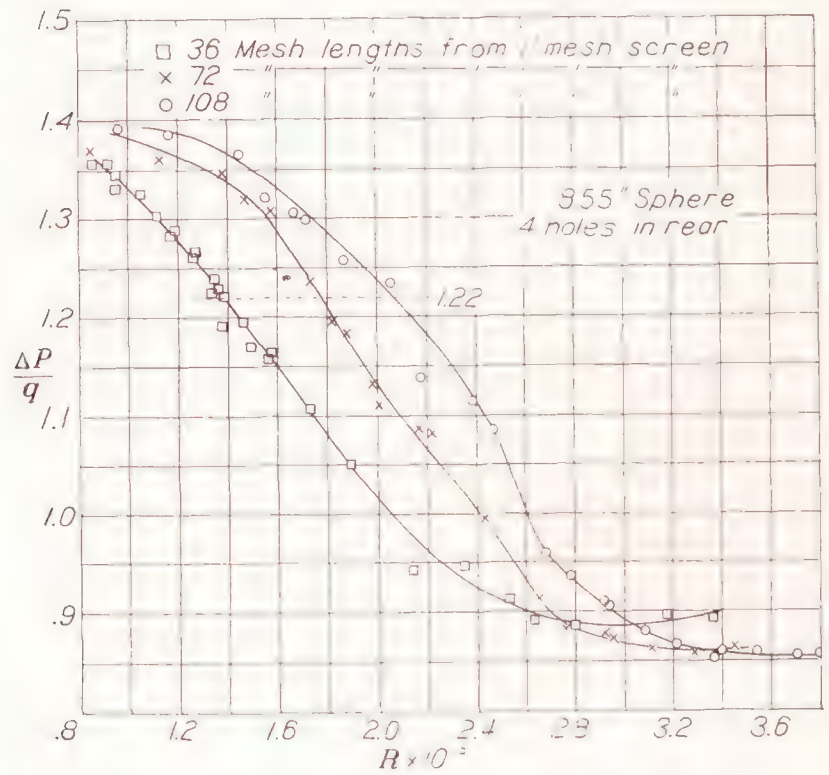

FIGURE 15.—Pressure coefficients for 8.55-inch sphere with four rear holes behind 1-inch screen.

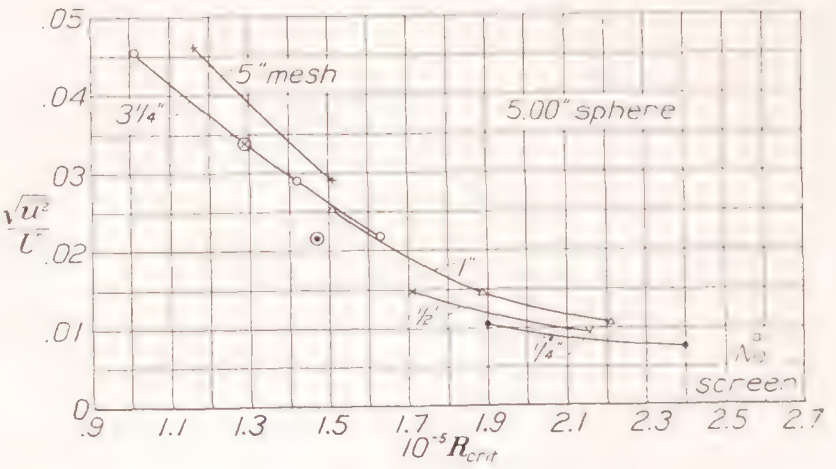

FIGURE 16.—Critical Reynolds Number for 5-inch sphere behind all screens.

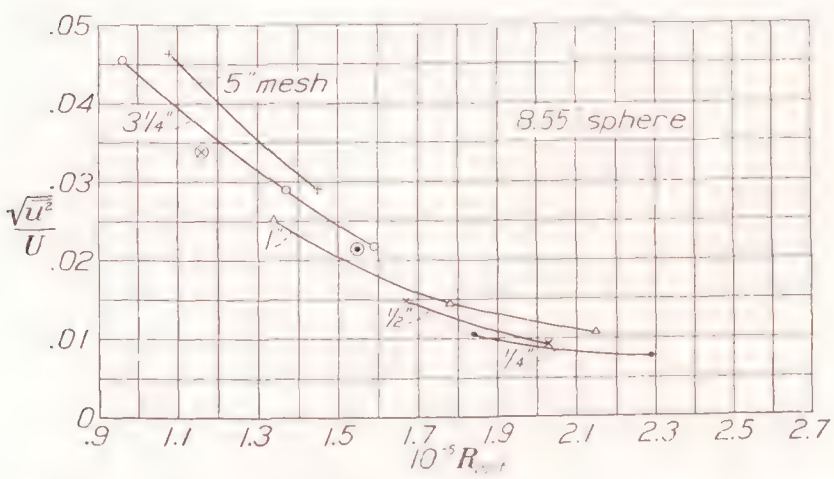

FIGURE 17.—Critical Reynolds Number for 8.55-inch sphere behind all screens.

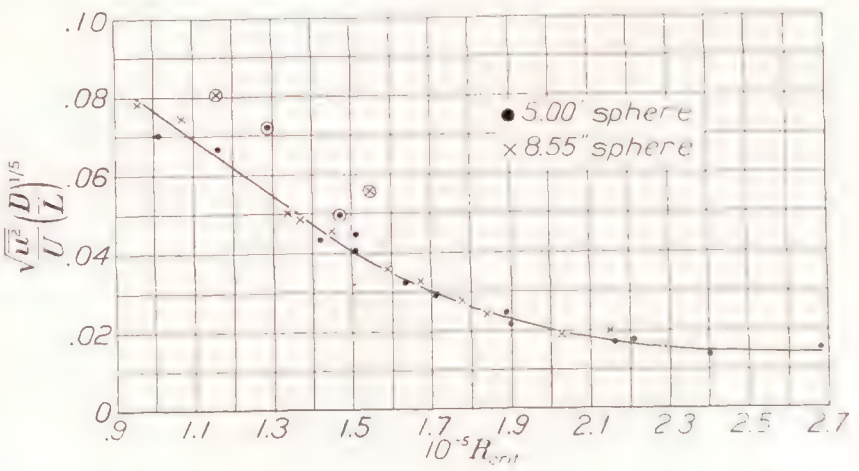

FIGURE 18.—Critical Reynolds Number of spheres as a function of $\frac{\sqrt{u^2}}{U}\left(\frac{D}{L}\right)^{1/5}$.

in the turbulent flow, and that the effect of turbulence is assumed to be that of the pressure gradient on transition.

The wind-tunnel equipment available at the National Bureau of Standards unfortunately does not permit the extension of the curve in figure 18 to a critical Reynolds Number exceeding 270,000. In most of the more recently constructed wind tunnels, values exceeding this value are found. In the large tunnels, the large scale of the turbulence contributes to the high value but, in addition, the intensity is of the order of 0.7 percent or less. The accurate measurement of these small fluctuations is an experimental problem of very considerable difficulty.

DETERMINATION OF AVERAGE VELOCITY PRESSURE

In the production of artificial turbulence in wind tunnels for the purpose of studying the aerodynamic effects of turbulence, it is desired to vary the magnitude of the rapid fluctuations without introducing departures from a uniform distribution in space. Ower and Warden (reference 17) concluded that wire or cord networks were unsuitable because of the introduction of variations in the mean speed produced by the "shadows" of the wires. This general conclusion is somewhat tempered in their detailed discussion by the recognition that the uniformity will depend on the distance from the network at which observations are made and that the uniformity may be satisfactory at distances of the order of 144 wire diameters or 24 mesh lengths. In view of this criticism of networks as sources of turbulence it seems desirable to review the studies that were made behind the screens used in the present series of measurements to determine the degree of uniformity of the mean speed and the average value of the velocity pressure for computing the pressure coefficients of the spheres.

A preliminary series of traverses was made for the purpose of determining the distance at which the pattern of the screen disappeared. For the ¼-, ½-, and 1-inch-mesh screens, a simple impact tube with outside diameter of ⅛ inch and inside diameter of 1/16 inch was used, the static side of the manometer being connected to the wall plate used as a source of reference pressure in the operation of the tunnel. For the larger screens, a standard pitot-static tube was used. Observations were taken at about 24 points along a line parallel to the horizontal wires of the screen and in a horizontal plane passing midway between two wires of the screen. The spacing was 1/16 inch, ⅛ inch, ¼ inch, ½ inch, and 1 inch for the ¼-, ½-, 1-, 3¼-, and 5-inch-mesh screens, respectively. Traverses were made at several distances from about 4 to 20 mesh lengths from the screen. For distances less than 12-mesh lengths, the pressure varied regularly with maxima and minima corresponding to the spacing of the wires of the screen. The curves resemble those shown in reference 17 and are therefore not reproduced in this paper. At distances greater than 12-mesh lengths, there was no regular pattern.

In order to give some idea of the magnitude of the variation, the maximum and mean deviations of the single observations from their arithmetic mean have been computed and are tabulated in table VII. Both quantities are very large close to the screen but rapidly decrease. For distances greater than 12-mesh lengths the gain in uniformity is comparatively small. Hence it was concluded that observations should not in any case be made at distances closer than 12-mesh lengths and, as a precautionary measure, the closest distance used was actually 15-mesh lengths. From table IV, it is seen that the maximum value of $\frac{\sqrt{\overline{u^2}}}{U}$ is accordingly limited to about 0.05.

At the distances for which sphere data had been or were to be obtained, a more extended traverse was made with a standard pitot-static tube. Observations were taken at 12 equidistant points along circles of radii 2, 5, 8, 12, and 18 inches from the tunnel axis, in some cases for three speeds. The maximum and mean deviations of the single observations from their arithmetic mean are also tabulated in table VII for these traverses.

It will be observed that the mean deviations approach different values for the different screens as the distance from the screen is increased: 2.2 percent for the 5-inch screen, about 2.0 percent for the 3¼-inch screen, about 0.5 percent for the 1-inch screen, about 1.0 percent for the ½-inch screen, and about 1.0 percent for the ¼-inch screen. It is probable that these differences reflect corresponding differences in the geometrical accuracy of the spacing of the wires of the screen. The uniformity obtained with the 1-, ½-, and ¼-inch screens is comparable with that obtained in the free stream, the mean deviation of the pressure from the average being 1.0 percent or less, corresponding to 0.5 percent or less in the speed.

The measurements described in this paper extended over a considerable period of time and it was not practicable to install a screen and complete all measurements before removing the screen, because of the necessity of making other tests. The procedure in most of the sphere tests was to determine the ratio of the velocity pressure at the axis of the tunnel to the reference wall plate pressure as a function of the speed: then at one value of the reference pressure to determine the speeds at six points on a circle of 2-inch radius. A faired curve through the points observed in the first run was adjusted as indicated by the ratio of the mean of the six values on the 2-inch circle and the value at the center to the value at the center. For all screens except the 3¼-inch screen, the value adopted did not differ from that given in table VI by as much as the mean deviation given in that table. For one installa-

tion of the 3¼-inch screen, the difference somewhat exceeded the mean deviation.

From a study of the results given later, an error of 1 percent in the determination of the mean velocity pressure produces an average change of $4{,}500 \pm 500$ in the value of the critical Reynolds Number. It is believed that the error in the values used did not in any case exceed the mean deviation given in table VII and was probably less than half that value, which represents the mean deviation over an area much larger than the sphere. The effect of the small departures from a constant speed (as contrasted with an error in the average speed) on the value of the critical Reynolds Number is not known but is probably small for departures of 1 percent or less, as indicated by sphere traverses behind the 5-inch screen previously described.

DISCUSSION

The relationship exhibited in figure 18 shows that a given small percentage change in the intensity of the turbulence produces approximately the same effect as a change of five times as much in the scale of the turbulence. Since the diameter of the sphere enters into the ordinate, the critical Reynolds Number depends on the diameter, but here also it requires a percentage change in diameter approximately five times as great as in the intensity of the turbulence to produce the same effect.

It is of some interest to inquire whether the ratio of the values of the critical Reynolds Number for two air streams depends on the diameter of the sphere used. The ratio will be independent of diameter if and only if the curve of figure 18 is of the form

$$\frac{\sqrt{\overline{u^2}}}{U}\left(\frac{D}{L}\right)^{1/5} = CR^{n}_{crit}$$

It may be seen by plotting on logarithmic paper that the observations do not fit such a curve except over short distances. Hence if the diameter of the sphere is varied through a sufficiently wide range, the ratio of two values as well as the absolute values of the critical Reynolds Number of the sphere for two air streams will depend on the diameter.

The use of spheres of different diameters in the same air stream does not give a separation of the effects of scale and intensity, since each observation when reduced gives only the value of $\frac{\sqrt{\overline{u^2}}}{U}\left(\frac{1}{L}\right)^{1/5}$. If $\frac{\sqrt{\overline{u^2}}}{U}$ is independently measured, it is theoretically possible to determine L but the precision is very poor because of the small slope of the curve of figure 18 and the presence of the fifth root.

In the presentation of the experimental data and the discussion up to this point, we have regarded the sphere as a turbulence-measuring device that was to be calibrated in terms of the intensity and scale of the turbulence. It is also possible to consider the sphere as a typical object of aerodynamic study and the data as the aerodynamic characteristics of the sphere as a function of turbulence. These data may then give some clue as to the effect of turbulence on other bodies in which the phenomenon of separation is involved.

The first conclusion that may be drawn by inference is that some linear dimension corresponding to the diameter of the sphere enters into the turbulence variable. In the case of an airfoil, the ratio of the chord of the airfoil to the scale of the turbulence would be of importance. If, for example, we consider tests on two similar airfoils of different size in the same air stream and at the same Reynolds Number, the maximum lift coefficient may be expected to differ because of the influence of the scale of the turbulence. This result would be analogous to the different drag or pressure coefficients observed at the same Reynolds Number for spheres of different sizes in the same air stream. Because of the fifth root, and the limits on the possible size variation in a given wind tunnel, the effect will be small and perhaps escape detection. But if a sufficient range of variation is made, the effect will be found.

A second inference is that the effect of turbulence on some other body will not necessarily be the same as that on the sphere. The shape of the curve of figure 18 is undoubtedly related to the pressure distribution characteristics of the sphere and the resulting boundary layer thickness. The pressure distribution over an airfoil will be quantitatively different and the relation between turbulence and the Reynolds Number for transition will be different. Hence if the sphere curves for two air streams are considered to differ only by a shift along the Reynolds Number axis, that is, by a turbulence factor formed from the ratio of the two Reynolds Numbers, and if by analogy curves of maximum lift coefficient in these same two air streams are considered to differ only by a similar turbulence factor, the factors cannot be considered the same for spheres and airfoils or even for two different airfoils. Here again the effects may be small and not readily detected. The concept of turbulence factor as previously defined has been found very useful. Because of the small effect of $\frac{D}{L}$ compared with $\frac{\sqrt{\overline{u^2}}}{U}$, the factor has so far proved to be a sufficiently good approximation in engineering practice although, as we have shown here, it is only an approximation.

IV—THE EFFECT OF WIRE LENGTH IN MEASUREMENTS OF INTENSITY AND SCALE OF TURBULENCE BY THE HOT-WIRE METHOD

In the measurements of intensity and scale of turbulence described in parts I and II, hot wires approximately 5 millimeters long were used, the length being sufficiently great so that air velocity fluctuations on one part of the wire are not completely correlated with those on another part. As will be shown, this lack of correlation causes the root-mean-square voltage fluctuation across the wire to be reduced by an amount

that depends upon the rate of falling off of correlation along the wire. This reduction in root-mean-square voltage fluctuation must be taken into account in all measurements of fluctuating velocities by hot-wire anemometers, including its effect on measurements of the intensity of the turbulence and its effect on measurements of the scale of turbulence.

THE EFFECT OF WIRE LENGTH ON INTENSITY MEASUREMENTS

Suppose a hot wire of length l carrying a constant current to be placed in a turbulent air stream perpendicular to the direction of flow, as in the experimental arrangement for measurements of intensity of turbulence. If the fluctuating potential drop across the wire is fed into an amplifier compensated for the thermal lag of the wire, the output voltage, denoted by e, will be directly proportional to the fluctuations of air speed on the hot wire.[8]

For the case of complete correlation of velocity fluctuations at all points of the wire, the fluctuating output voltage will be given by

$$e_1=Kul$$

where u is the fluctuating air velocity, l the length of the wire, and K a constant of proportionality, depending

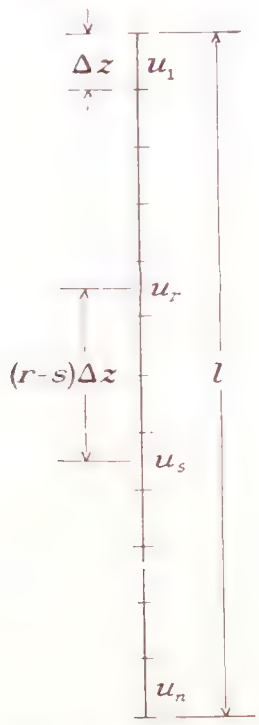

FIGURE 19.—Schematic diagram illustrating nonuniform conditions along the wire as used for measurement of intensity of turbulence.

on the dimensions of the hot wire, its resistivity and temperature coefficient of resistivity, the current through the wire, the mean speed of the air flow, and the amplification.

The output meter on the amplifier (a thermal type milliammeter) gives indications proportional to the mean square of the output voltage, given by

$$\overline{e_1^2}=K^2l^2\overline{u^2} \tag{18}$$

Now consider the case where the velocity fluctuations at various points along the wire are not completely correlated. Let us assume the wire to be divided into n equal segments, each of length Δz, and let the velocity fluctuation of the air passing over any segment be denoted by u_i. (See fig. 19.) For this case the output voltage from the amplifier will be given by

$$e=K\sum_{i=1}^{n}u_i\Delta z$$

and its mean squared value by

$$\begin{aligned}\overline{e^2}&=K^2\Delta z^2\overline{(\Sigma u_1)^2} \qquad (19)\\ &=K^2\Delta z^2[\overline{u_1^2}+\overline{u_2^2}+\overline{u_3^2}+\overline{u_4^2}+\ \ldots\ .+\overline{u_n^2}\\ &\qquad +2\overline{u_1u_2}+2\overline{u_2u_3}+2\overline{u_3u_4}+\ \ldots\ .+2\overline{u_{n-1}u_n}\\ &\qquad +2\overline{u_1u_3}+2\overline{u_2u_4}+\ \ldots\ .+2\overline{u_{n-2}u_n}\\ &\qquad +2\overline{u_1u_4}+\ \ldots\ .+2\overline{u_{n-3}u_n}\\ &\qquad \vdots\\ &\qquad +2\overline{u_1u_n}]\end{aligned}$$

The correlation coefficient R between any two velocity fluctuations, u_r and u_s, is defined as

$$R=\frac{\overline{u_ru_s}}{\sqrt{\overline{u_r^2}}\sqrt{\overline{u_s^2}}}$$

Since the mean square of the velocity fluctuations along the wire is constant

$$\overline{u_r^2}=\overline{u_s^2}=\overline{u^2}$$

$$R=\frac{\overline{u_ru_s}}{\overline{u^2}}$$

Let us assume that the correlation between the velocity fluctuations at any two segments is a function only of the distance between the segments; that is

$$\frac{\overline{u_ru_s}}{\overline{u^2}}=R(\{r-s\}\Delta z)$$

where, as in previous parts of the paper, R followed by a quantity in parentheses means the value of R at a distance equal to that quantity. Thus:

$$\begin{aligned}\overline{u_1u_2}=\overline{u_2u_3}=\ \ldots\ .=\overline{u_{n-1}u_n}&=R(\Delta z)\ \overline{u^2}\\ \overline{u_1u_3}=\overline{u_2u_4}=\ \ldots\ .=\overline{u_{n-2}u_n}&=R(2\Delta z)\overline{u^2}\\ \overline{u_1u_4}=\overline{u_2u_5}=\ \ldots\ .=\overline{u_{n-3}u_n}&=R(3\Delta z)\overline{u^2}\\ &\vdots\\ \overline{u_1u_n}\ \ &=R(\{n-1\}\Delta z)\overline{u^2}\end{aligned}$$

[8] This result is true if the velocity fluctuations are small compared with the mean velocity of flow. (See reference 6.)

Equation (19) thus becomes:

$$\overline{e^2}=K^2\Delta z^2\overline{u^2}\Big[n+2(n-1)R(\Delta z)+2(n-2)R(2\Delta z)+2(n-3)R(3\Delta z)+\ \ldots\ .+2R(\{n-1\}\Delta z)\Big]$$

$$=K^2\overline{u^2}\Big[n\Delta z^2+2n\Delta z\Big\{R(\Delta z)\Delta z+R(2\Delta z)\Delta z+R(3\Delta z)\Delta z+\ \ldots\ .+R(\{n-1\}\Delta z)\Delta z\Big\}$$

$$-2\Big\{\Delta zR(\Delta z)\Delta z+2\Delta zR(2\Delta z)\Delta z+3\Delta zR(3\Delta z)\Delta z+\ \ldots\ .+(n-1)\Delta zR(\{n-1\}\Delta z)\Delta z\Big\}\Big]$$

Now let the number of segments n increase indefinitely, and the length of each segment Δz approach zero, in such a way that the product $n\Delta z$ is always equal to the length of the wire l. Passing to the limit, we have

$$\overline{e^2}=K^2\overline{u^2}\Big[2l\int_0^l R(z)dz-2\int_0^l zR(z)dz\Big]$$

$$=2K^2\overline{u^2}\int_0^l (l-z)R(z)dz \qquad (20)$$

Comparing this expression with equation (18), the effect of the incomplete correlation of velocity fluctuations at different points on the wire is to reduce the mean square fluctuation voltage and thus the meter reading in the ratio K_1^2, given by

$$K_1^2=\frac{\overline{e_1^2}}{\overline{e^2}}=\frac{l^2}{2\int_0^l (l-z)R(z)dz} \qquad (21)$$

In the calculations of intensity of turbulence described in part II, the square root of the output meter reading enters as a multiplying factor. Thus, to obtain the true value for the intensity of turbulence, the calculated values must be multiplied by the factor K_1, given by equation (21). In order to obtain numerical values for K_1, $R(z)$ must be known as a function of z.

THE EFFECT OF WIRE LENGTH ON SCALE MEASUREMENTS

Let us now consider the effect of incomplete correlation of velocity fluctuations at different points of the wire on measurements of the correlation of velocity fluctuations, as described in part I. Suppose two wires A and B, each of length l and carrying a constant current, be placed in a turbulent air stream, parallel to one another, a distance apart y, and in a plane perpendicular to the direction of flow. (See fig. 20.)

Let us assume each wire to be divided into n segments, each of length Δz, and let the velocity fluctuation on any segment of A be denoted by u_i, and of B by v_i. As in the previous discussion, the fluctuating output voltage across each wire will be given by:

$$e_A=K\sum_{i=1}^{n}u_i\Delta z$$

$$e_B=K\sum_{=1}^{n}v_i\Delta z$$

The correlation between the voltage fluctuations e_A and e_B will obviously be a function of y. Let us then define a correlation coefficient $R'(y)$, representing the correlation between the voltage fluctuations of wires A and B, placed a distance y apart. Thus, by definition, $R'(y)$ is given by

$$R'(y)=\frac{\overline{e_A e_B}}{\sqrt{\overline{e_A}^2}\sqrt{\overline{e_B}^2}}$$

Making use of the foregoing equations and of the fact that the mean square of the velocity fluctuations is the same at the two wires, we have:

$$R'(y)=\frac{K^2\Delta z^2\overline{(\Sigma u_i)(\Sigma v_i)}}{K^2\Delta z^2\sqrt{\overline{(\Sigma u_i)^2}}\sqrt{\overline{(\Sigma v_i)^2}}}=\frac{\overline{(\Sigma u_i)(\Sigma v_i)}}{\overline{(\Sigma u_i)^2}} \qquad (22)$$

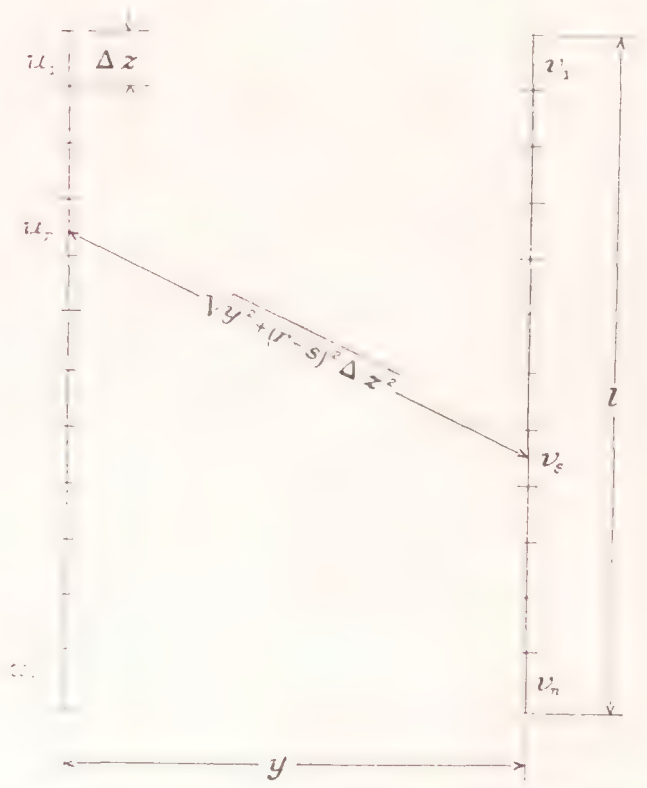

FIGURE 20.—Schematic diagram illustrating nonuniform conditions along two wires as used for measurement of scale of turbulence.

$R'(y)$ may be obtained experimentally as described in part I. Now

$$\begin{aligned}\overline{(\Sigma u_i)(\Sigma v_i)}\Delta z^2=\Delta z^2[&\overline{u_1v_1}+\overline{u_2v_2}+\overline{u_3v_3}+\ \ldots\ .+\overline{u_nv_n}\\&+\overline{u_1v_2}+\overline{u_2v_3}+\ \ldots\ .+\overline{u_{n-1}v_n}\\&+\overline{u_2v_1}+\overline{u_3v_2}+\ \ldots\ .+\overline{u_nv_{n-1}}\\&+\overline{u_1v_3}+\ \ldots\ .+\overline{u_{n-2}v_n}\\&+\overline{u_3v_1}+\ \ldots\ .+\overline{u_nv_{n-2}}\\&\qquad\vdots\\&+\overline{u_1v_n}\\&+\overline{u_nv_1}]\end{aligned}$$

Now let us assume that the correlation of the velocity fluctuations at any segment of A with that at any

segment of B is a function only of the distance between the segments. That is,

$$\frac{\overline{u_r v_s}}{\overline{u^2}} = R(\sqrt{(r-s)^2\Delta z^2 + y^2})$$

Thus:

$$\overline{u_1 v_1} = \overline{u_2 v_2} = \overline{u_3 v_3} = \ldots = \overline{u_n v_n} = R(y)\overline{u^2}$$

$$\overline{u_1 v_2} = \overline{u_2 v_3} = \overline{u_3 v_4} = \ldots = \overline{u_{n-1} v_n}$$

$$= \overline{u_2 v_1} = \overline{u_3 v_2} = u_4 v_3 = \ldots = \overline{u_n v_{n-1}} = R(\sqrt{(\Delta z)^2 + y^2})\overline{u^2}$$

$$\overline{u_1 v_3} = \overline{u_2 v_4} = \overline{u_3 v_5} = \ldots = \overline{u_{n-2} v_n}$$

$$= \overline{u_3 v_1} = \overline{u_4 v_2} = \overline{u_5 v_3} = \ldots = \overline{u_n v_{n-2}} = R(\sqrt{(2\Delta z)^2 + y^2})\overline{u^2}$$

$$\vdots$$

$$\overline{u_1 v_n} = \overline{u_n v_1} = R(\sqrt{(n-1)^2\Delta z^2 + y^2})\overline{u^2}$$

$$\overline{(\Sigma u_i)(\Sigma v_i)}\Delta z^2 = \overline{u^2}\Delta z^2\Big[nR(y) + 2(n-1)R(\sqrt{(\Delta z)^2+y^2}) + 2(n-2)R(\sqrt{(2\Delta z)^2+y^2}) + 2(n-3)R(\sqrt{(3\Delta z)^2+y^2})$$
$$+ \ldots . + 2R(\sqrt{(n-1)^2\Delta z^2 + y^2})\Big]$$
$$= \overline{u^2}\Big[n\Delta z^2 R(y) + 2n\Delta z\Big\{R(\sqrt{\Delta z^2+y^2})\Delta z + R(\sqrt{(2\Delta z)^2+y^2})\Delta z + R(\sqrt{(3\Delta z)^2+y^2})\Delta z + \ldots .$$
$$+ R(\sqrt{(n-1)^2\Delta z^2+y^2})\Delta z\Big\} - 2\Big\{\Delta z R(\sqrt{(\Delta z)^2+y^2})\Delta z + 2\Delta z R(\sqrt{(2\Delta z)^2+y^2})\Delta z + 3\Delta z R(\sqrt{(3\Delta z)^2+y^2})\Delta z +$$
$$\ldots . + (n-1)\Delta z R(\sqrt{(n-1)^2\Delta z^2+y^2})\Delta z\Big|\Big]$$

Now let the number of segments of each wire n increase indefinitely and the length of each segment Δz approach zero in such a way that the product $n\Delta z$ is always equal to the length of each wire, l. Passing to the limit, we have:

$$\overline{(\Sigma u_i)(\Sigma v_i)}\Delta z^2$$

$$= \overline{u^2}\Big[2l\int_0^l R(\sqrt{z^2+y^2})dz - 2\int_0^l zR(\sqrt{z^2+y^2})dz\Big]$$

$$= 2\overline{u^2}\int_0^l (l-z)R(\sqrt{z^2+y^2})dz$$

From equations (19) and (20)

$$\overline{(\Sigma u_i)^2}\Delta z^2 = 2\overline{u^2}\int_0^l (l-z)R(z)dz$$

Thus equation (22) becomes

$$R'(y) = \frac{\int_0^l (l-z)R(\sqrt{z^2+y^2})dz}{\int_0^l (l-z)R(z)dz} \tag{23}$$

The scale of the turbulence L has been defined as the integral

$$L = \int_0^\infty R(y)dy \tag{24}$$

Let us denote by L' the following integral:

$$L' = \int_0^\infty R'(y)dy$$

L' may be determined experimentally as described in Part I, and L may be found by dividing L' by a factor K_2, defined as

$$K_2 = \frac{L'}{L} \tag{25}$$

If $R(y)$ is a known function of y, the integrations expressed in equations (23) and (24) may be performed, and numerical values of K_2 computed.

CALCULATION OF FACTORS FOR APPLICATION TO EXPERIMENTAL RESULTS

It may be seen from equation (23) that the shorter the wires used and the more slowly $R(z)$ varies with z, the more nearly will the right-hand member of this equation approach R(y). Thus curves of $R'(y)$ obtained under conditions where L is much larger than l, resulting either from large scale of the turbulence or the use of short wires, should indicate the character of the function $R(y)$.

In figure 21 are shown observed values of $R'(y)$ representing the average of eight traverses at 200 inches behind the 5-inch-mesh screen where the foregoing conditions are most nearly fulfilled. These points are seen to lie closely to the curve, which is an exponential curve represented by the equation

$$R'(y) = e^{-\frac{y}{L'}}$$

where L' is the uncorrected scale of the turbulence. Since the correction is small, let us assume that $R(y)$ is given by

$$R(y) = e^{-\frac{y}{L}} \tag{26}$$

and determine what form will be taken by $R'(y)$ and what values will be obtained for K_1 and K_2.

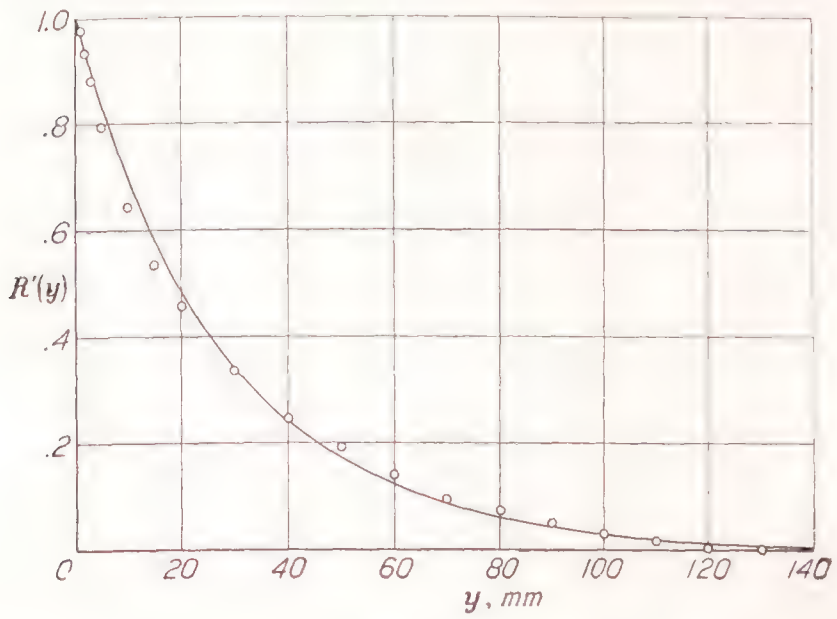

FIGURE 21.—Observed correlation coefficient as a function of y. Points, average of 8 traverses at 200 inches behind 5-inch screen; curve, plot of $R'=e^{-\frac{y}{L'}}$.

Equation (23) becomes

$$R'(y)=\frac{\int_0^l (l-z)e^{-\frac{\sqrt{z^2+y^2}}{L}}dz}{\int_0^l (l-z)e^{-\frac{z}{L}}dz} \tag{27}$$

The factor K_1, given by equation (21) becomes

$$K_1=\frac{l}{\sqrt{2\int_0^l (l-z)e^{-\frac{z}{L}}dz}} \tag{28}$$

and K_2, given by equation (25) becomes

$$K_2=\frac{1}{L}\int_0^\infty R'(y)dy \tag{29}$$

It is convenient to write these equations in non-dimensional form, changing to the new variables

$$r=\frac{y}{l},\ s=\frac{z}{l},\ c=\frac{l}{L}$$

In this notation equation (28) becomes

$$K_1=\frac{1}{\sqrt{2\int_0^1 (1-s)e^{-cs}ds}}=\frac{c}{\sqrt{2(e^{-c}-1+c)}} \tag{30}$$

Equation (27) becomes

$$R'(r)=\frac{\int_0^1 (1-s)e^{-c\sqrt{r^2+s^2}}ds}{\int_0^1 (1-s)e^{-cs}ds}$$

$$=2K_1^2\int_0^1 (1-s)e^{-c\sqrt{r^2+s^2}}ds \tag{31}$$

Equation (31) is not directly integrable but may be evaluated for large values of r by expansion in a power series in s^2 and integrating term by term.

Let

$$f(s^2)=e^{-c\sqrt{r^2+s^2}}$$

Expanding f in powers of s^2, equation (31) becomes

$$R'(r)=2K_1^2\int_0^1 (1-s)\left[f(0)+f'(0)s^2+f''(0)\frac{s^4}{2!}+f'''(0)\frac{s^6}{3!}+\cdots\right]ds$$

$$=K_1^2\left[f(0)+\frac{1}{6}f'(0)+\frac{1}{30}f''(0)+\frac{1}{168}f'''(0)+\cdots\right]$$

Evaluating the terms in this series

$$f(0)=e^{-cr}$$

$$f'(0)=-\frac{ce^{-cr}}{2r}$$

$$f''(0)=+\frac{c(1+cr)e^{-cr}}{4r^3}$$

$$f'''(0)=-\frac{c(3+3cr+c^2r^2)e^{-cr}}{8r^5}$$

Equation (31) then becomes

$$R'(r)=K_1^2e^{-cr}\left[1-\frac{c}{12\,r}+\frac{c(1+cr)}{120\,r^3}-\frac{c\left(1+cr+\frac{c^2r^2}{3}\right)}{448\,r^5}+\cdots\right] \tag{32}$$

The first four terms of this series will give values of $R'(r)$ with sufficient accuracy for $r>1$. For smaller values of r, a series containing positive powers of r must be obtained.

Rewriting equation (31)

$$R'(r)=2K_1^2\left[\int_0^1 e^{-c\sqrt{r^2+s^2}}ds-\int_0^1 s\,e^{-c\sqrt{r^2+s^2}}ds\right]$$

The second integral can be evaluated directly

$$\int_0^1 s\,e^{-c\sqrt{r^2+s^2}}ds=\frac{1}{c^2}\left[e^{-cr}(1+cr)-e^{-c\sqrt{r^2+1}}(1+c\sqrt{r^2+1})\right]$$

The first integral may be evaluated by expanding the integrand in a series of powers of $c\sqrt{r^2+s^2}$.

$$\int_0^1 e^{-c\sqrt{r^2+s^2}}ds=\int_0^1\left[1-c(r^2+s^2)^{1/2}+\frac{c^2}{2!}(r^2+s^2)-\frac{c^3}{3!}(r^2+s^2)^{3/2}+\ldots.\right]ds$$

Let $I_n(r)=\int_0^1 (r^2+s^2)^{n/2}ds$. We then have

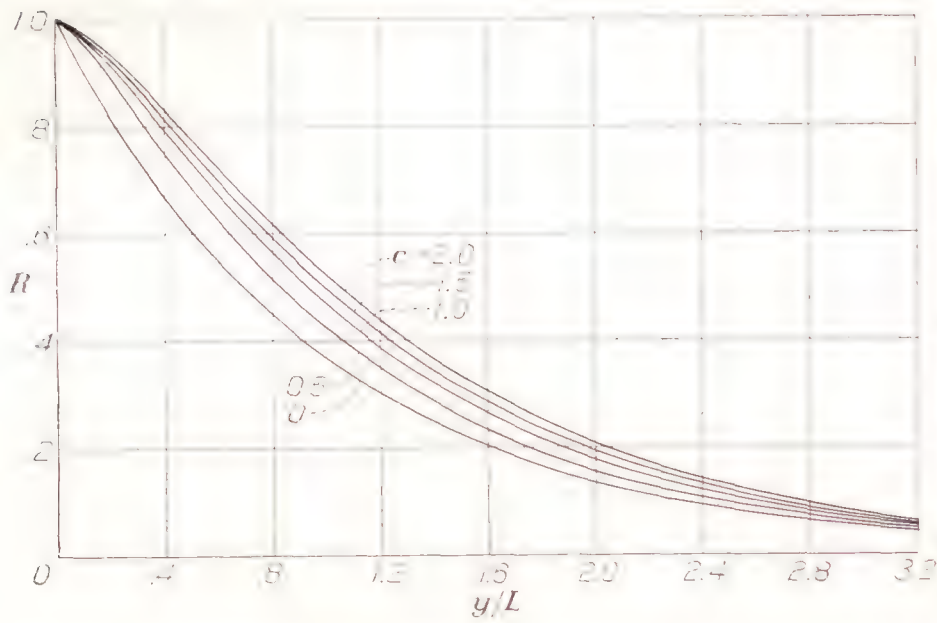

FIGURE 22.—Theoretical values of R and of R' as a function of cr or y/L for various values of c.

$$R'(r)=2K_1^2\left[\frac{e^{-c\sqrt{r^2+1}}}{c^2}(1+c\sqrt{r^2+1})-\frac{e^{-cr}(1+cr)}{c^2}+I_0(r)-cI_1(r)+\frac{c^2}{2!}I_2(r)-\frac{c^3}{3!}I_3(r)+\frac{c^4}{4!}I_4(r)+\ldots.\right] \tag{33}$$

$I_n(r)$ may be computed from the following recurrence formula:

$$I_n(r)=\frac{(r^2+1)^{n/2}}{n+1}+\frac{n}{n+1}r^2I_{n-2}(r)$$

where $I_o(r)=1$

$$I_1(r)=\frac{(r^2+1)^{1/2}}{2}+\frac{r^2}{2}\sinh^{-1}\frac{1}{r}$$

In figure 22 is shown a curve of $R(c=0)$ and of R' as a function of $cr(=y/L)$ for various values of c. It is seen that the effect of the incomplete correlation of velocity fluctuations along the wires is to make the observed correlation too large at large values of r by a factor K_1^2 (see equation 32), and to change the shape of the curve for small values of r.

In figure 23 are shown some experimental curves of $R'(y)$ as a function of y/M for different ratios of the length of the hot wire to the scale of the turbulence, that may be compared to the curves of figure 22. The similarity of these two sets of curves can be noted.

Let us now consider the effect of incomplete correlation of velocity fluctuations along the hot wires on the value of L' obtained by integration of the experimental $R'(y)$ curves. Writing equation (29) in terms of r instead of y

$$K_2=\frac{l}{L}\int_0^\infty R'(r)dr \tag{34}$$

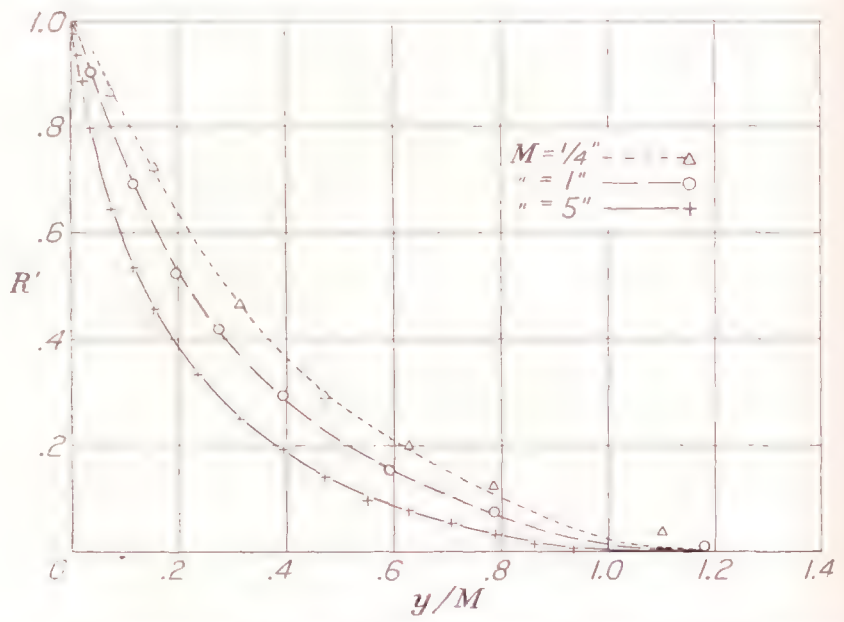

FIGURE 23.—Experimental values of $R'(y)$ for various values of y/M for comparison with figure 22.

This integral may be evaluated by graphical integration of $R'(r)$ calculated from equation (32) and (33), or as follows: Substituting (31) in (34)

$$K_2=2K_1^2c\int_0^\infty\int_0^1(1-s)e^{-c\sqrt{r^2+s^2}}dsdr$$

Transforming this surface integral into polar coordinates, by the transformations

$$r=\rho\cos\theta \qquad s=\rho\sin\theta \qquad dsdr=\rho d\rho d\theta$$

$$K_2=2K_1^2c\int_0^{\pi/2}\int_0^{\csc\theta}(1-\rho\sin\theta)e^{-c\rho}\rho d\rho d\theta$$

Integrating with respect to ρ:

$$K_2=2K_1^2c\int_0^{\pi/2}\left[\frac{1}{c^2}+\frac{e^{-c\csc\theta}}{c^2}+\frac{2\sin\theta e^{-c\csc\theta}}{c^3}-\frac{2\sin\theta}{c^3}\right]d\theta$$

$$K_2=\frac{2K_1^2}{c^2}\left[\frac{\pi}{2}c-2+c\int_0^{\pi/2}e^{-c\csc\theta}\left(1+\frac{2}{c\csc\theta}\right)d\theta\right]$$

Let $J(c)=\int_0^{\pi/2}e^{-c\csc\theta}\left(1+\frac{2}{c\csc\theta}\right)d\theta$

$$K_2=\frac{\frac{\pi}{2}c-2+cJ(c)}{e^{-c}-1+c} \tag{35}$$

The integral $J(c)$ cannot be evaluated directly but may be expanded in an asymptotic series, which will give $J(c)$ for sufficiently large values of c. For small values of c, however, it is most easily evaluated by Simpson's rule.

Table VIII gives values of K_1 and K_2 as a function of $c\left(=\frac{l}{L}\right)$ computed from equations (30) and (35). Curve A of figure 24 shows K_2 plotted as a function of $\frac{l}{L}$. Curve B shows K_2 as a function of $\frac{l}{L'}$, and is obtained from curve A by dividing the abscissa of a given point on A by the ordinate of that point and then plotting that ordinate above the new abscissa obtained. Curve B is used for the correction of the experimental data on correlation of velocity fluctuations. The procedure is as follows: The area under the experimental curves of R' as a function of y is obtained, from which is found L'. The ratio of l, the length of the hot wires, to L' is calculated and from curve B, figure 24, the factor K_2 is found. L' is then divided by K_2 to obtain L.

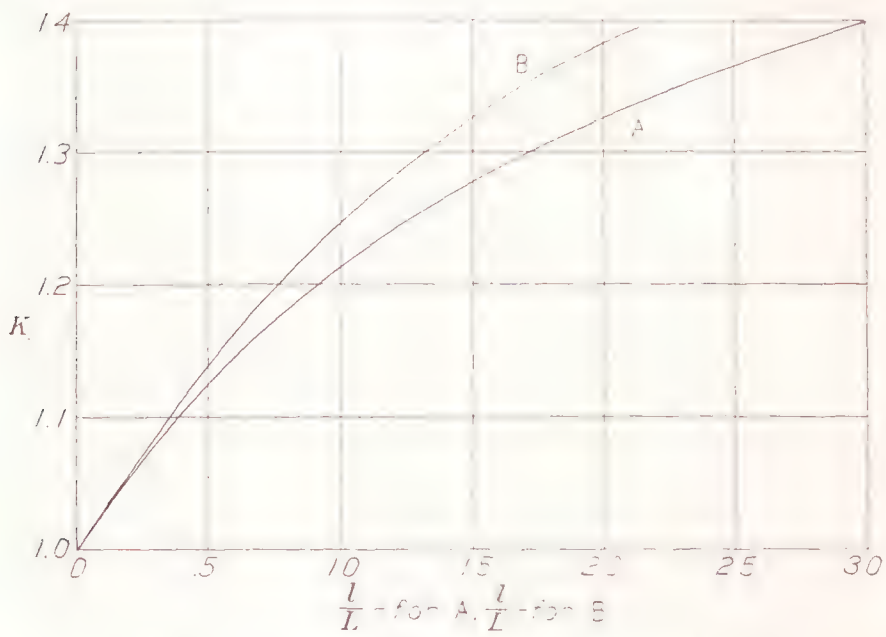

FIGURE 24.—The factor K_2 as a function of l/L and l/L'.

The numerical values obtained for the correction factors K_1 and K_2 depend, of course, on the assumption that R may be represented by equation (26), and thus can be expected to be accurate only in so far as equation (26) represents the true variation of correlation with distance. It is seen from figure 21 that there is a tendency for R or R' to fall off initially more rapidly with distance than the exponential relation until the correlation falls to about 0.3, and then less rapidly, finally falling to zero instead of approaching zero asymptotically.

The correction factors thus computed can be considered only as approximations, and more accurate determination of the variation of the correlation coefficient R with distance, especially for small distances, is needed in order to improve materially their accuracy.

V—VARIATION OF CORRELATION COEFFICIENT WITH FREQUENCY CHARACTERISTICS OF THE MEASURING APPARATUS AND WITH AZIMUTH

In the development of the experimental technique for measuring the scale of the turbulence, certain unexpected phenomena were encountered. These phenomena were studied to only a limited extent, usually only with regard to their bearing on the measurement of the scale of the turbulence as previously defined. The incidental and incomplete studies of these phenomena give additional information as to the characteristics of turbulent flow and since we cannot at present pursue these studies further, the information obtained is placed on record for the benefit of others who may wish to do so.

EFFECT OF COMPENSATION FOR LAG OF WIRE

In our first measurements of the correlation coefficient, no compensation was made for the lag of the wire. We erroneously assumed that, if the two wires were identical in every respect including lag, there would be no effect of the lag on the value of the correlation coefficient. Fortunately, the actual experiment was tried and it was discovered that the introduction of compensation had a very large effect. Two typical comparisons are shown in figure 25. When no compensation was used, the observed correlation coefficient fell off much more slowly with the separation of the wires. As a result, the observed scale L' was much greater. For example, for the 1-inch screen at a distance of 40 mesh lengths, the observed $\frac{L'}{M}$ without compensation was 0.602 as compared with 0.308 obtained with proper compensation, an error of nearly 100 percent. Similarly for the 3¼-inch screen at a distance of 41 mesh lengths, the observed $\frac{L'}{M}$ without compensation was 0.464 as compared with 0.236 obtained with proper compensation. The difference in a number of comparisons at different distances was always greater than 50 percent.

Since the presence or absence of compensation corresponds simply to different frequency characteristics of the measuring apparatus, it was inferred that the results indicated a variation of the correlation coefficient with frequency, the disturbances of lower frequency being correlated over greater distances than the disturbances of higher frequency.

CROSS-STREAM CORRELATION FOR VARIOUS FREQUENCY BANDS

Measurements were made with a set of electric filters to study the correlation for various frequency bands. The compensating circuit was used, so that the results represent, as closely as can be obtained, the variation of the correlation with frequency. The available filters were high- and low-pass filters designed for connection as band-pass filters. The nominal frequency bands were 0–250, 250–500, 500–1500, 1500–3000, and 3000–∞ cycles per second. Ideal filters would give a uniform transmission within the band and no transmission outside the band. The actual characteristics are shown in figure 26. Although extremely good for acoustic measurements, the filters are far from ideal for the present purpose.

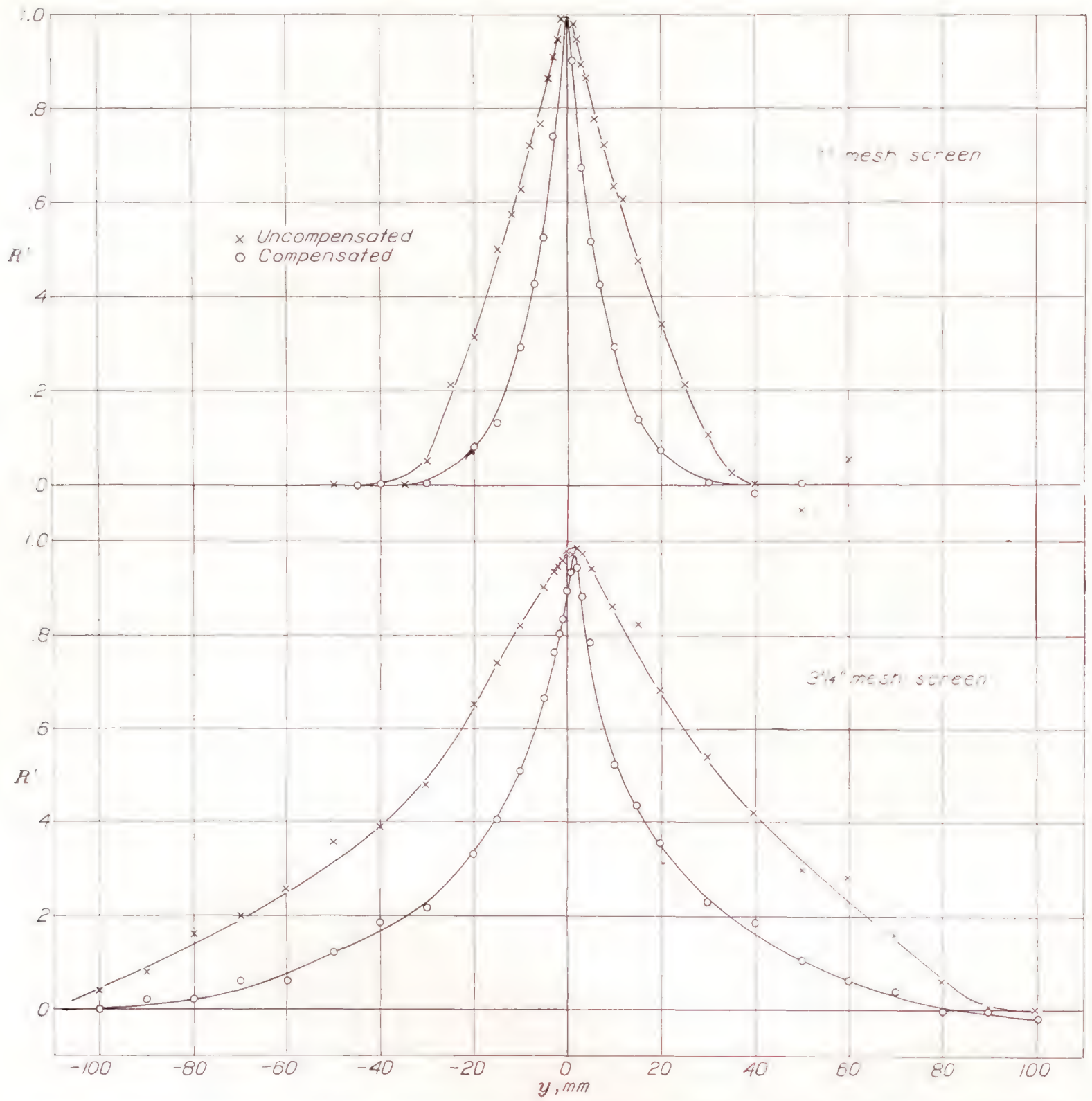

FIGURE 25.—Correlation curves showing effect of compensation. Curves for 1-inch mesh observed at 40 mesh lengths aft. Curves for 3¼-inch mesh observed at 41-mesh lengths aft.

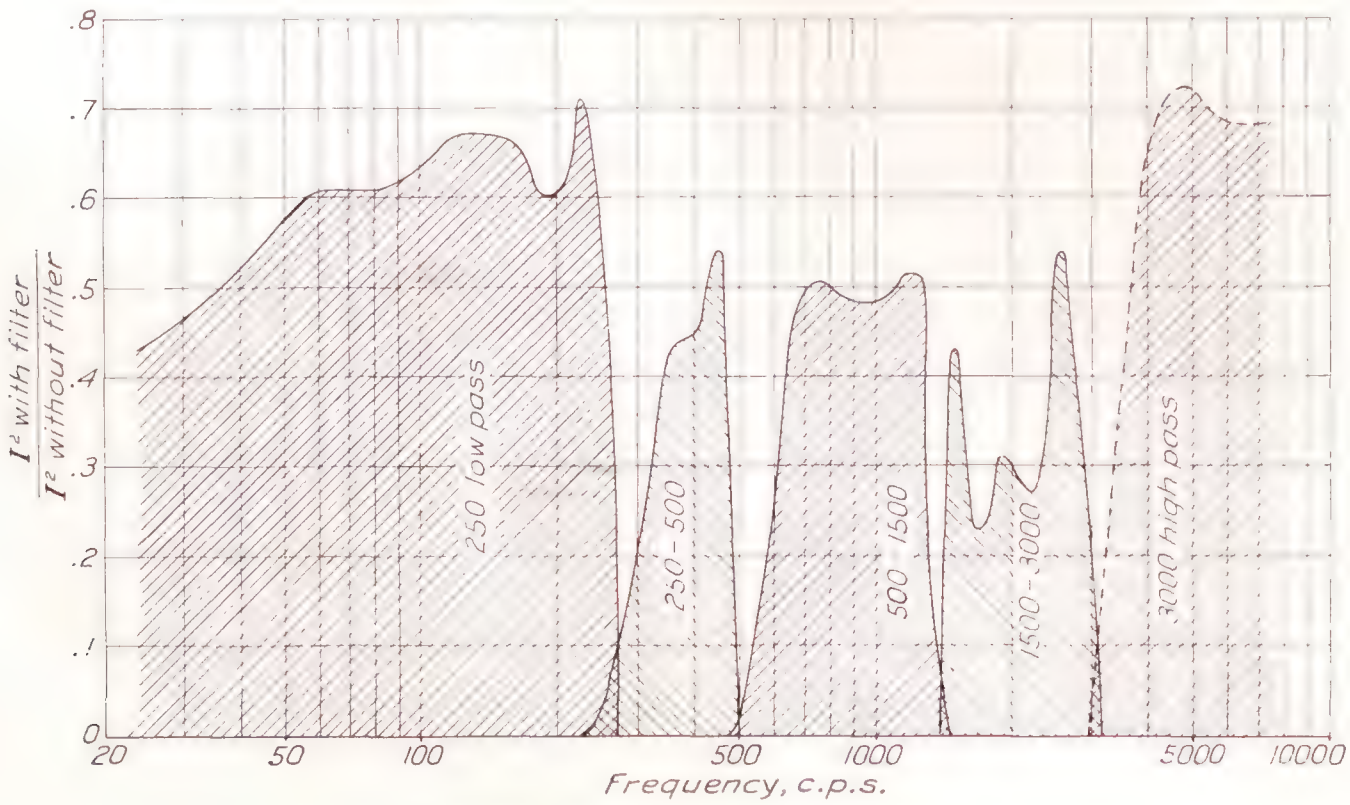

FIGURE 26.—Frequency characteristics of filters.

Measurements of correlation were made at a distance of 40 mesh lengths behind the 1-inch screen at speeds of 20 and 40 feet per second for the bands 0–250, 250–500, 500–1500. The intensity in the two higher bands was so small that satisfactory measurements could not be made. The results are shown in figure 27. The large effect of frequency is obvious. In the 500–1500 band negative correlations are observed, indicating that for frequencies in this band an increase in speed at one wire tends to be associated with a decrease in speed at the other. No attempt was made to correct these observations for the finite length of the wires. Some idea of the magnitude of the effect can be obtained from figure 5. The application of the corrections would not change the general picture.

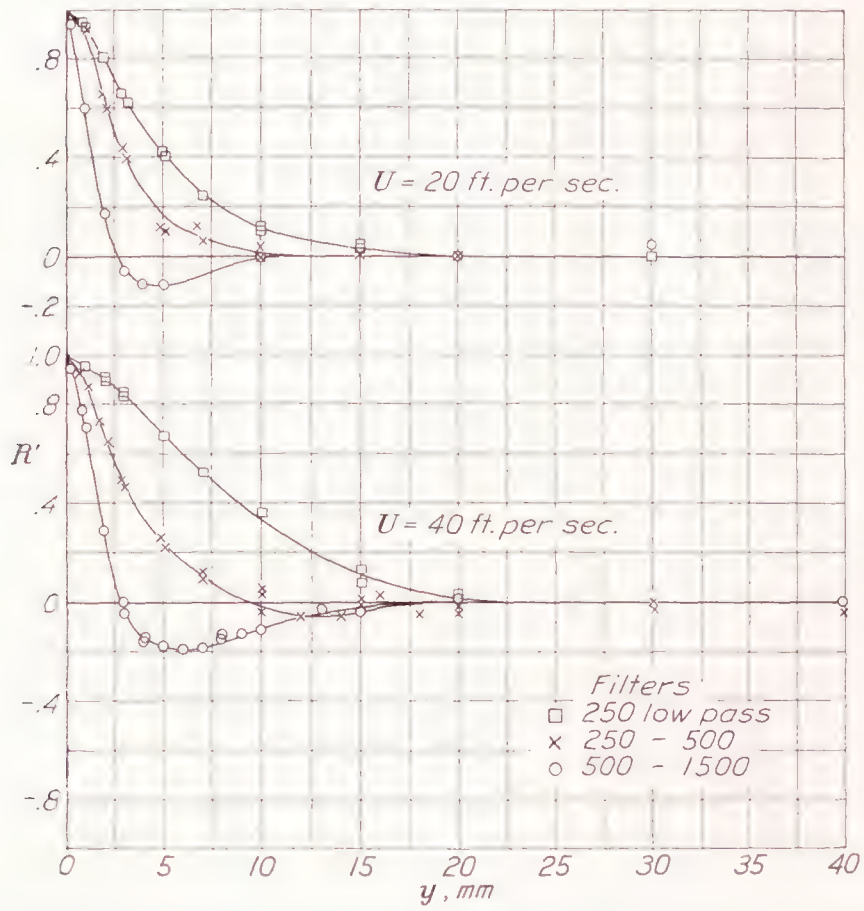

FIGURE 27.—Correlation curves corresponding to several frequency bands. 1-inch screen, 40 mesh lengths aft.

A rough analysis of the distribution of the intensity of the turbulence with frequency was made by means of the filters for a distance of 26 mesh diameters from the 1-inch screen. The results are shown in table IX. The analysis is rough because of the variation of the attenuation of the filters with frequency. Allowance has been made for the differences in average attenuation. The change in the distribution with the change in mean speed is consistent with the assumption that the fluctuations at a point are the result of a pattern of eddy motion in space that is carried along with the mean speed of the stream and changes but little as the mean flow travels a distance of a few centimeters. One may consider the eddy system from the point of view of a stationary observer, in which case it may be described by giving the statistical distribution of intensity with frequency. Or one may consider the system from the point of view of an observer moving with the stream, in which case the system may be described by giving the statistical distribution of intensity with wave length. A wave length λ in the second picture corresponds to a frequency f in the first equal to U/λ, where U is the mean speed. If the statistical distribution of intensity with wave length in space is independent of mean speed, the distribution of intensity with frequency when the pattern is observed at a fixed point is shifted toward higher frequencies as the mean speed is increased. The filter bands are so wide that no complete analysis can be made. It is seen, however, in figure 27, that for a given frequency band the correlation falls off more rapidly with distance at 20 feet per second than at 40 feet per second. The same frequency band corresponds to shorter wave lengths at 20 feet per second than at 40 feet per second. For example, the 250–500 filter used in a stream of mean speed 20 feet per second (610 centimeters per second) selects wave lengths of 1.22 to 2.44 centimeters, whereas in a stream of 40 feet per second (1,220 centimeters per second), the same filter selects wave lengths from 2.44 to 4.88 centimeters. When no filter and no compensation are used, the apparatus weights the various frequencies according to the law $\frac{1}{\sqrt{1+A^2f^2}}$, where f is the frequency and A is a lag constant of the wire. For this condition the correlation falls off less rapidly than for the 0–250 filter.

Experiment shows that, if the apparatus does not weight all frequencies uniformly, the observed correlation curve varies with the mean speed; but, if the frequency compensation is correct, the observed correlation curve is independent of the mean speed. This experimental result is again consistent with the hypothesis that a fixed eddy pattern independent of mean speed is transported past the measuring apparatus at the mean speed. The frequency pattern then varies with the speed. If the apparatus responds uniformly to all frequencies, there will be no effect of mean speed; but, if there is frequency distortion, apparent variations with mean speed will be introduced.

ALONG-STREAM CORRELATION

In order to avoid troublesome constant errors in the measurement of the distance between the two wires of the correlation apparatus, it was decided to allow one wire to travel behind the other with a clearance of a few tenths of a millimeter, so that measurements could be taken on both sides, the zero position being located by the wake disturbance of the upstream wire. This procedure introduces an error whose magnitude was estimated by studying the correlation along the stream direction. Figure 28 gives a comparison between the correlation coefficients transverse and parallel to the stream at 25½ inches behind the 1-inch screen at 40 feet per second. The correlation falls off more slowly along the stream. From these data it may be estimated that the peaks of the correlation curves are somewhat reduced, the maximum being reduced by about 5 percent

when the clearance is 0.3 millimeter and the scale of the turbulence is as small as 5 millimeters. The effect on the determination of the scale of the turbulence is entirely negligible, but this factor adds to the effects of finite wire length and the noise level of the amplifier to make impossible the studies of the curvature near the peak of the curve, which are desired in connection with Taylor's theory.

The effect of frequency characteristics of the measuring apparatus was also studied for the along-stream correlation. The results at 25½ inches behind the 1-inch screen are plotted in figure 29. These curves are very suggestive. We have already stated that the filters select a given band of wave lengths, the 250–500 filter selecting a mean wave length of 1.83 centimeters at 20 feet per second and 3.66 centimeters at 40 feet per second. These values agree remarkably well with the "wave lengths" exhibited by the correlation curves along stream. The high negative correlations indicate a high degree of "coherence", the fluctuation at the

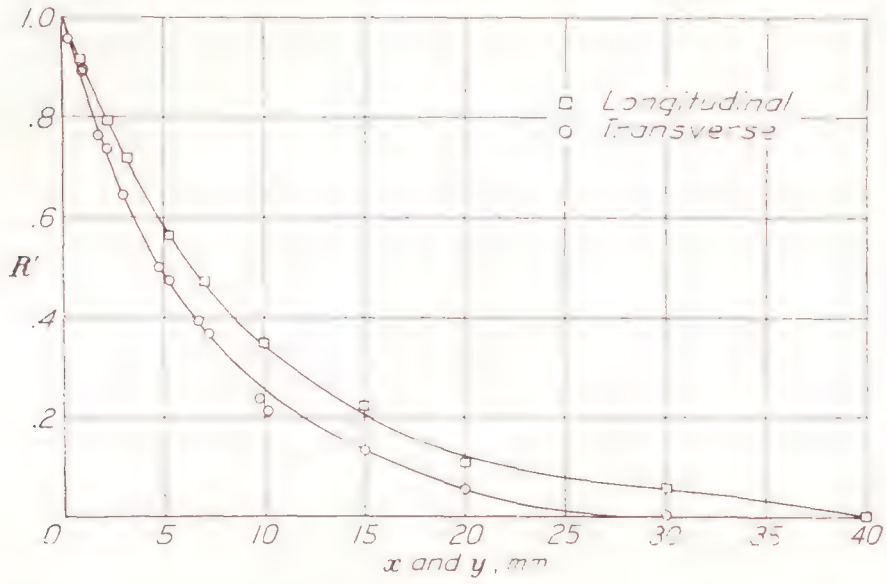

FIGURE 28.—Comparison of transverse and longitudinal correlation. 1-inch-mesh screen, 25-½ mesh lengths aft. Wind speed 40 ft./sec.

upstream wire being repeated a short time later at the downstream wire. It appears probable that if it were possible to make the measurements with a very narrow frequency band, the correlation would vary several times between +1 and −1 as the along-stream separation were increased.

Taylor predicted a relation between the transverse and longitudinal correlation in isotropic turbulence, namely, that the correlation coefficient R varied with the azimuth θ according to the law

$$1-R=(1-R_T)\ (\sin^2\ \theta+\frac{1}{2}\cos^2\ \theta)$$

where R_T is the transverse correlation coefficient.[9]

The longitudinal correlation R_L is then given by the relation

$$2(1-R_L)=(1-R_T)$$

The results of figure 28 do not confirm this relation, since the ratio of $1-R_T'$ to $1-R_L'$ at $y=2$ mm is more nearly 1.4. For smaller or larger values of y, the ratio is less. It does not appear that the correction for finite wire length as computed in part IV would alter this result by more than 10 percent.

In order to study the matter further, the little rotating holder suggested by Taylor (reference 5) was constructed and attention confined to measurements of the ratio. Some results taken with and without the filters

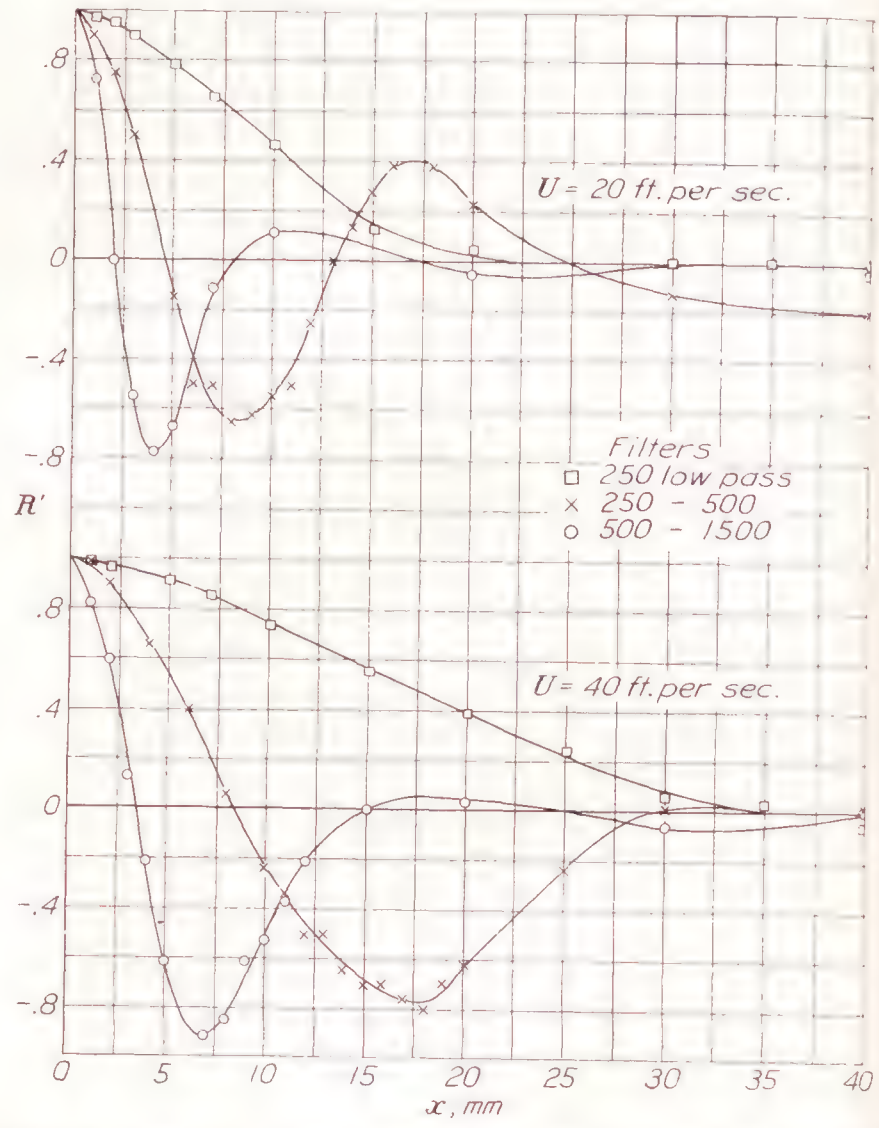

FIGURE 29.—Correlation curves observed along stream corresponding to several frequency bands. 1-inch mesh screen, 25½ inches aft.

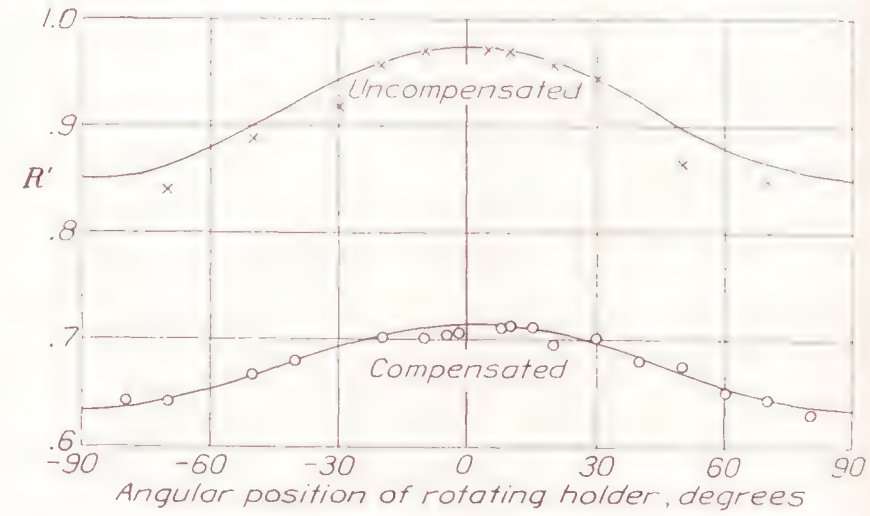

FIGURE 30.—Variation of correlation with azimuth as two wires 5 mm long spaced 9 mm apart are rotated from a position along stream (zero angle) to a position across stream (90° angle).

with wires 2 millimeters apart at 25½ inches behind the 1-inch screen are shown in table X. The ratio varies markedly with frequency and for a given filter with mean speed, as would be expected from figure 29. The value with no filter was about 1.4.

A few measurements with a 9-millimeter spacing of the wires at 38 mesh lengths behind the 3¼-inch screen

[9] In reference 5, the sin and cos of this equation are interchanged.

are shown in figure 30. The curves represent the relation $1-R'=0.150\ (\sin^2\theta+\frac{1}{6}\cos^2\theta)$ for the uncompensated run and $1-R'=0.365\ (\sin^2\theta+\frac{1}{1.28}\cos^2\theta)$ for the compensated run. Here again for the uncompensated run $1-R'$ changes by a factor greater than the theoretical factor 2 between $\theta=0$ and $\theta=90°$ and for the compensated run, less than 2.

This departure from Taylor's theory might be considered an evidence of departure from isotropy but the evidence previously presented as to agreement of values from hot-wire measurements and from measurements of thermal diffusion indicates that such is not the case.

Another possibility is that some systematic experimental error has been overlooked or that the theory of correction for wire length is not based on valid assumptions. The few measurements recorded in this section show that the correlation curves vary with the frequency of the fluctuations considered. Hence the effect of finite wire length is different in different frequency bands, producing a frequency weighting in the apparatus that has been shown to have considerable effect on the observed correlation. The effect would be to suppress the higher frequencies and hence to increase the correlation coefficient at a given separation of the two wires. The magnitude of the increase would be greatest where the scale of the turbulence is least. Such an effect, if of sufficient magnitude, would account for the failure to obtain a single curve of $\frac{L}{M}$ against $\frac{x}{M}$ in figure 7, part I, the curves for small screens being too high. It is also possible that such an effect accounts for the departure of $\frac{1-R_T'}{1-R_L'}$ from the theoretical value 2, since the observed value R_T' would be larger than the true value R_T by a greater amount than R_L' is larger than R_L. The required effects are, however, of such magnitude as to make this explanation seem unreasonable, since the departure from a uniform frequency weighting is small. No adequate theory can be developed without more information as to the variation with frequency. The experimental problem is one of great difficulty since, even if filters of requisite selectivity were available, the further subdivision of the available energy into narrow frequency bands would require still further amplification to make measurements possible.

CONCLUSIONS

The results obtained may be summarized as follows:

1. The scale or "average eddy size" of turbulence may be obtained from the measurement of correlation between speed fluctuations. Such measurements may be made with the same apparatus used to measure the intensity of the turbulence, modified slightly to accommodate two hot wires.

2. A knowledge of the variation of correlation with distance across the stream makes possible a correction of the error introduced in hot-wire results by the lack of complete correlation over the length of the wire. Convenient methods for applying these corrections are presented.

3. Screens are suitable devices for producing turbulence in wind tunnels. The scale of the turbulence is controlled by some dimension of the screen. Since geometrically similar screens were used in the present study, it has not been determined whether mesh or wire size is the controlling factor. The scale of the turbulence produced by a screen increases with distance from the screen.

4. The intensity of the turbulence decreases with distance from the screen, the decay being given by a logarithmic law when the scale of the turbulence increases linearly.

5. The pressure sphere described herein has been found a convenient device for measuring the aerodynamic effect of turbulence. A pressure coefficient of 1.22 corresponds approximately to a drag coefficient of 0.3. Either coefficient will serve to connect a critical Reynolds Number with the effect of turbulence.

6. The critical Reynolds Number of spheres depends on the scale of the turbulence as well as on its intensity. The combined effects may be expressed by

$$R_{crit}=f\left(\frac{\sqrt{\overline{u^2}}}{U}\left[\frac{D}{L}\right]^{1/5}\right)$$

NATIONAL BUREAU OF STANDARDS,
WASHINGTON, D. C., *August 6, 1936.*

REFERENCES

1. Dryden, H. L., and Kuethe, A. M.: Effect of Turbulence in Wind Tunnel Measurements. T. R. No. 342, N. A. C. A., 1930.
2. Dryden, Hugh L.: Reduction of Turbulence in Wind Tunnels. T. R. No. 392, N. A. C. A., 1931.
3. Millikan, C. B., and Klein, A. L.: The Effect of Turbulence. Aircraft Eng., August 1933, pp. 169–174.
4. Bacon, D. L., and Reid, E. G.: The Resistance of Spheres in Wind Tunnels and in Air. T. R. No. 185, N. A. C. A., 1924.
5. Taylor, G. I.: Statistical Theory of Turbulence. Proc. Roy. Soc. of London, series A, vol. 151, no. 873, September 2, 1935, pp. 421–478.
6. Dryden, H. L., and Kuethe, A. M.: The Measurement of Fluctuations of Air Speed by the Hot-Wire Anemometer. T. R. No. 320, N. A. C. A., 1929.
7. Mock, W. C., Jr., and Dryden, H. L.: Improved Apparatus for the Measurement of Fluctuations of Air Speed in Turbulent Flow. T. R. No. 448, N. A. C. A., 1932.
8. Taylor, G. I.: Diffusion by Continuous Movements. Proc. London Math. Soc., vol. 20, August 1921, pp. 196–211.
9. Schubauer, G. B.: A Turbulence Indicator Utilizing the Diffusion of Heat. T. R. No. 524, N. A. C. A., 1935.
10. Schubauer, G. B., and Dryden, H. L.: The Effect of Turbulence on the Drag of Flat Plates. T. R. No. 546, N. A. C. A., 1935.
11. Prandtl, L.: Der Luftwiderstand von Kugeln. Nachr. d. K. Ges. d. Wissensch., Göttingen, Math. phys. Kl., 1914, p. 177.

12. National Advisory Committee for Aeronautics: Twentieth Annual Report, 1934, pp. 16 and 23.
13. Dryden, Hugh L.: Frontiers of Aerodynamics. Jour. Wash. Acad. Sci., vol. 25, March 1935, p. 101.
14. Platt, Robert C.: Turbulence Factors of N. A. C. A. Wind Tunnels as Determined by Sphere Tests. T. R. No. 558, N. A. C. A., 1936.
15. Hoerner, S.: Tests of Spheres with Reference to Reynolds Number, Turbulence, and Surface Roughness. T. M No. 777, N. A. C. A., 1935.
16. Taylor, G. I.: Statistical Theory of Turbulence. Part V. Proc. Roy. Soc. of London, series A, vol. 156, no. 888, August 1936, p. 307.
17. Ower, E., and Warden, R.: Note on the Use of Networks to Introduce Turbulence into a Wind Tunnel. R. & M. No. 1559, British A. R. C., 1934.

TABLE I.—DIMENSIONS OF SCREENS FOR PRODUCING TURBULENCE

Nominal mesh length, inches	Average measured mesh length, inches	Deviation of individual meshes from average, inches		Average measured wire diameter, inches	Material
		Mean	Maximum		
¼	0.248	±0.010	+0.026 / −.023	0.050	Iron wire.
½	.515	.012	+.017 / −.025	.096	Iron wire.
1	1.007	.005	+.015 / −.015	.196	Iron wire.
3¼	3.285	.068	+.163 / −.122	.626	Wooden cylinders.
5	5.016	.021	+.04 / −.04	.976	Wooden cylinders.

TABLE II.—SCALE OF TURBULENCE

$\frac{x}{M}$ Distance from screen in mesh lengths	$\frac{L'}{M}$	$\frac{L}{M}$	$\frac{x}{M}$ Distance from screen in mesh lengths	$\frac{L'}{M}$	$\frac{L}{M}$
¼-inch mesh screen			½-inch mesh screen		
18.5	0.276	0.183	27.0	0.306	0.237
41.0	[a].405	.290	27.0	.311	.240
41.0	[a].375	.269	42.3	.338	.266
41.0	[a].365	.263	42.3	.355	.280
41.0	[a].387	.278	56.7	.395	.315
53.0	.464	.342	56.7	.366	.292
84.0	.566	.429	79.5	.494	.406
112.0	.602	.463	79.5	.445	.366
159.0	.864	.702	108.0	.548	.458
159.0	.916	.745	108.0	.518	.434
159.0	.798	.649	171.0	[a].626	.536
161.0	[a].805	.648	171.0	[a].609	.521
161.0	[a].782	.631	171.0	[a].622	.532
161.0	[a].808	.652	171.0	[a].556	.475
161.0	[a].738	.595	171.0	[a].604	.517
161.0	[a].752	.606	172.0	.695	.601
161.0	[a].770	.621	172.0	.673	.582
211.0	.906	.742	226.0	.842	.746
			226.0	.846	.750
			226.0	.822	.728

TABLE II.—SCALE OF TURBULENCE—Continued

$\frac{x}{M}$ Distance from screen in mesh lengths	$\frac{L'}{M}$	$\frac{L}{M}$
1-inch mesh screen		
21.0	0.293	0.248
21.0	.277	.234
28.0	.291	.246
39.5	.394	.345
39.5	.377	.331
40.0	[a].305	.261
40.0	[a].314	.269
40.0	[a].300	.258
40.0	[a].312	.268
53.0	.413	.363
53.0	.366	.321
53.8	[a].352	.306
53.8	[a].368	.319
53.8	[a].344	.298
53.8	[a].335	.292
53.8	[a].335	.292
53.8	[a].316	.274
53.8	[a].312	.271
53.8	[a].323	.280
85.0	.451	.405
85.0	.406	.365
113.0	.520	.468
113.0	.426	.383
113.0	.574	.516
113.0	.480	.433
113.0	.462	.416
135.5	.512	.461
135.5	.486	.438
135.5	.484	.436
164.0	.496	.446
164.0	.470	.423
164.0	.505	.454
164.3	[a].551	.499
164.3	[a].480	.435
164.3	[a].488	.442
164.3	[a].504	.457
164.3	[a].527	.478
164.3	[a].500	.453

$\frac{x}{M}$ Distance from screen in mesh lengths	$\frac{L'}{M}$	$\frac{L}{M}$
3¼-inch mesh screen		
16.5	[a]0.190	0.175
16.5	[a].202	.187
16.6	.172	.156
26.2	[a].220	.205
26.2	[a].219	.204
26.5	.253	.237
34.6	.257	.241
34.6	.259	.243
34.8	[a].211	.196
34.8	[a].212	.197
39.7	[a].250	.234
39.7	[a].226	.212
40.0	[a].235	.220
40.0	[a].230	.215
40.0	[a].235	.220
40.0	[a].241	.226
40.0	[a].258	.242
50.5	.266	.249
50.5	.242	.226
50.8	[a].258	.242
50.8	[a].261	.245
50.8	[a].248	.233
61.4	[a].303	.287
61.4	[a].303	.287
61.4	[a].281	.266
5-inch mesh screen		
17.1	[a]0.166	0.156
17.1	[a].166	.156
17.1	[a].172	.162
22.7	[a].201	.190
22.7	[a].210	.200
22.7	[a].189	.180
33.0	[a].202	.192
33.0	[a].199	.189
39.9	[a].199	.189
39.9	[a].203	.193
39.9	[a].220	.209
39.9	[a].201	.191
39.9	[a].230	.220
39.9	[a].236	.225
39.9	[a].253	.242
39.9	[a].237	.227

[a] Signifies wires of length 4.75 mm. All other values obtained with wires of length 5.0 mm.

Turbulence in free tunnel 15.5 feet from rear of honeycomb: L'=0.303 inch, L=0.260 inch. No noticeable increase with distance was found, although not thoroughly investigated.

TABLE III.—EQUATIONS FOR CURVES OF FIGURE 7

	a	b
¼-inch mesh	$\frac{L}{M}=0.1559+0.003017\frac{x}{M}$	
½-inch mesh	$\frac{L}{M}=0.1753+0.002307\frac{x}{M}$	
1-inch mesh	$\frac{L}{M}=0.2291+0.001493\frac{x}{M}$	
3¼-inch mesh	$\frac{L}{M}=0.1471+0.002000\frac{x}{M}$	
5-inch mesh	$\frac{L}{M}=0.1316+0.002016\frac{x}{M}$	
All data taken together	$\frac{L}{M}=0.1467+0.002501\frac{x}{M}$	

TABLE IV.—INTENSITY OF TURBULENCE

New Data			Old Data		
$\frac{x}{M}$ Distance from screen in mesh lengths	$\frac{(\sqrt{\overline{u^2}})_w}{U}$ (uncorrected)	$\frac{\sqrt{\overline{u^2}}}{U}$ (corrected)	$\frac{x}{M}$ Distance from screen in mesh lengths	$\frac{(\sqrt{\overline{u^2}})_w}{U}$ (uncorrected)	$\frac{\sqrt{\overline{u^2}}}{U}$ (corrected)
¼-inch-mesh screen					
Length of wire, 4.7 mm			Length of wire, 8.4 mm		
16	0.0350	0.0550	48	0.0111	0.0187
24	.0262	.0397	144	.0080	.0110
39	.0188	.0270	288	.0052	.0063
72	.0118	.0156			
100	.0098	.0124			
152	.0084	.0101			
209	.0078	.0090			
284	.0070	.0079			
½-inch-mesh screen					
Length of wire, 4.7 mm			Length of wire, 8.4 mm		
14	0.0411	0.0531	24	0.0189	0.0276
26	.0246	.0310	72	.0096	.0127
46	.0171	.0208	144	.0069	.0084
74	.0120	.0141			
110	.0100	.0114			
163	.0080	.0089			
246	.0064	.0069			
1-inch-mesh screen					
Length of wire, 4.75 mm			Length of wire, 8.4 mm		
25.3	0.0290	0.0324	36	0.0183	0.0218
54.0	.0168	.0185	72	.0122	.0142
85.3	.0117	.0127	108	.0095	.0109
113.3	.0097	.0104			
133.5	.0086	.0092			
164.5	.0073	.0078			

TABLE IV.—INTENSITY OF TURBULENCE—Continued

New Data			Old Data		
$\frac{x}{M}$ Distance from screen in mesh lengths	$\frac{(\sqrt{\overline{u^2}})_w}{U}$ (uncorrected)	$\frac{(\sqrt{\overline{u^2}}}{U}$ (corrected)	$\frac{x}{M}$ Distance from screen in mesh lengths	$\frac{(\sqrt{\overline{u^2}})_w}{U}$ (uncorrected)	$\frac{\sqrt{\overline{u^2}}}{U}$ (corrected)
3¼-inch-mesh screen					
Length of wire, 4.7 mm			Length of wire, 8.4 mm		
15.5	0.0434	0.0457	14.8	0.0423	0.0464
20.1	.0341	.0358	25.9	.0270	.0293
27.4	.0253	.0265	36.9	.0204	.0220
37.8	.0210	.0219			
53.8	.0161	.0167			
60.8	.0145	.0150			
5-inch-mesh screen					
Length of wire, 4.7 mm			Length of wire, 8.4 mm		
14.6	0.0470	0.0488	15.4	0.0384	0.0414
21.7	.0336	.0348	26.8	.0254	.0269
29.0	.0260	.0269			
39.4	.0210	.0216			

For the free tunnel, 15.5 feet from the rear of the honeycomb, $\frac{(\sqrt{\overline{u^2}})_w}{U}=0.007$ taken with wire 8.4 mm long. The value corrected for wire length is 0.0085. No noticeable change through the length of the working section of the tunnel was found, although not thoroughly investigated.

TABLE V.—CONSTANTS OF EQUATION (17)

Mesh of screen	$\frac{U}{(\sqrt{\overline{u^2}})_0}$	C_6
¼-inch	0.57	0.483
½-inch	2.81	.516
1-inch	4.28	.577
3¼-inch	2.63	.487
5-inch	1.25	.446

TABLE VI.—CRITICAL REYNOLDS NUMBER OF SPHERES

M Mesh of screen, inches	$\frac{x}{M}$ Distance in mesh lengths	$\frac{100\sqrt{u^2}}{U}$ Intensity of of turbulence, percent	L Scale of turbulence, inches	5-inch sphere		8.55-inch sphere	
				R_c Critical Reynolds Number	$\frac{100\sqrt{u^2}}{U}\left(\frac{D}{L}\right)^{1/5}$	R_c Critical Reynolds Number	$\frac{100\sqrt{u^2}}{U}\left(\frac{D}{L}\right)^{1/5}$
5	15.4	4.63	0.813	116,000	6.66	108,000	7.41
5	26.8	2.92	.928	151,000	4.09	145,000	4.55
3.25	14.8	4.55	.574	101,000	7.01	96,000	7.81
3.25	25.9	2.90	.646	142,000	4.37	137,000	4.86
3.25	36.9	2.19	.718	163,000	3.23	159,000	3.59
1	36	2.52	.283	151,000	4.48	134,000	4.98
1	72	1.45	.337	189,000	2.49	178,000	2.77
1	108	1.07	390	221,000	1.78	215,000	1.98
.5	24	3.39	.115	[a] 129,000	7.21	[a] 116,000	8.03
.5	72	1.48	.171	171,000	2.91	167,000	3.24
.5	144	.94	.254	216,000	1.71	203,000	1.90
.25	48	2.16	.075	[a] 147,000	5.00	[a] 155,000	5.57
.25	144	1.07	.148	190,000	2.16	184,000	2.41
.25	288	.76	.256	240,000	1.38	229,000	1.53
None	----------	.85	.260	268,000	1.54	----------	----------

[a] These values were obtained at a distance of 1 foot from the screen. From figures 16, 17, 18, it is evident that these values are not concordant with the others. See text for discussion.

TABLE VII.—DISTRIBUTION OF VELOCITY PRESSURE q BEHIND SCREENS

M mesh of screen, inches	x/M Distance in mesh lengths	Number of stations	Distance between stations, inches	Number of readings	Approximate speed, ft./sec.	Average ratio of q to wall plate pressure	Maximum deviation from average, percent	Mean deviation from average, percent	Regular pattern present
5	4.8	24	1.0	24	65	0.686	17.7	8.6	Yes
	7.2	23	1.0	23	60	.626	9.3	4.2	Yes
	9.6	24	1.0	24	60	.622	7.4	3.3	Yes
	12.0	42	1.0	42	60	.611	6.0	2.9	No
	14.4	23	1.0	23	60	.614	4.6	2.3	No
					80	.618	4.6	2.3	
	16.8	25	1.0	25	60	.612	4.6	2.2	No
	15.4	60	(a)	120	68	.605	6.0	2.2	No
	26.8	60	(a)	120	68	.618	4.7	2.2	No
3.25	3.69	19	0.5	19	65	.689	27.0	14.5	Yes
	5.54	20	.5	20	60	.648	13.8	6.8	Yes
	7.38	45	.5	45	60	.632	11.2	4.6	Yes
	9.23	42	.5	42	60	.620	6.5	2.6	Yes
		34	.5	34	75	.619	7.0	2.7	
	11.07	22	.5	22	60	.614	5.8	3.1	Yes
	12.92	41	.5	41	60	.596	6.0	3.1	No
	14.76	54	(a)	108	50	.601	6.2	2.9	No
					65	.600	6.2	2.3	
					80	.600	6.6	2.6	
	25.83	54	(a)	108	50	.605	4.7	1.7	No
					65	.606	4.7	1.9	
					80	.603	5.1	2.1	
	36.9	54	(a)	108	50	.618	4.1	1.4	No
					65	.617	4.6	1.7	
					80	.615	5.2	1.8	
1.0	4	23	0.125	23	60	b.607	15.6	8.7	Yes
	6	26	.125	26	60	b.680	12.7	5.6	Yes
	8	30	.125	30	60	b.651	7.4	3.5	Yes
	12	28	.125	28	60	b.634	2.4	1.2	No
	16	30	.125	30	60	b.631	2.2	1.3	No
	24	29	.125	29	60	b.627	1.4	1.1	No
	36	72	(a)	143	35	.622	3.2	.8	No
		72		143	70	.620	2.6	.6	
		60		120	80	.615	2.1	.5	
	72	54	(a)	108	35	.636	2.6	.8	No
					70	.633	1.6	.4	
					80	.627	1.3	.4	
	108	54	(a)	108	35	.646	2.1	.7	No
					70	.644	1.3	.4	
					80	.639	1.5	.4	
0.5	6	23	0.125	23	50	b.668	13.8	7.7	Yes
	8	23	.125	23	50	b.637	7.5	4.1	Yes
	10	23	.125	23	50	b.636	4.9	2.1	Yes
	12	23	.125	23	50	b.632	4.1	1.8	Yes
	14	23	.125	23	50	b.631	2.9	1.4	No
	16	23	.125	23	50	b.630	2.8	1.1	No
	24	60	(a)	120	70	.652	4.0	1.3	No
	72	60	(a)	120	70	.644	2.4	1.0	No
	144	60	(a)	120	70	.641	2.8	.9	No
0.25	4	24	0.063	24	55	b.790	66.7	28.1	Yes
	6	23	.063	23	55	b.852	26.6	10.9	Yes
	8	24	.063	24	55	b.678	19.2	9.7	(c)
	12	24	.063	24	55	b.594	7.9	4.1	(c)
	16	24	.063	24	55	b.584	5.1	2.8	(c)
	20	23	.063	23	55	b.586	3.0	1.4	No
	48	60	(a)	120	70	.614	4.8	1.2	No
	144	60	(a)	120	70	.607	4.9	1.2	No
	288	60	(a)	120	70	.604	3.6	1.0	No

[a] For these positions traverses were made at a number (usually 12) equidistant points along circles of radii 2, 5, 8, 12, and 18 inches from the tunnel axis. At other positions the traverse was made along a line which was parallel to the horizontal wires of the screen and in a horizontal plane passing midway between two wires of the screen.

[b] These traverses were made with a small impact tube, the reference pressure being the wall plate static pressure. The values are approximately but not accurately comparable with values of the velocity pressure.

[c] There was evidence of a regular pattern but the pattern did not correspond to the spacing of the wires of the screens.

TABLE VIII.—FACTORS FOR CORRECTING HOT-WIRE RESULTS FOR EFFECT OF WIRE LENGTH

$\frac{l}{L}$	K_1	K_2
0	1.000	1.000
.4	1.067	1.105
.8	1.133	1.182
1.2	1.198	1.241
1.6	1.263	1.289
2.0	1.327	1.327
2.4	1.390	1.359
2.8	1.451	1.384
3.2	1.512	1.406

TABLE IX.—DISTRIBUTION OF INTENSITY WITH FREQUENCY

[Measurements 26 inches behind 1-inch-mesh screen]

Frequency cycles per second	20 ft./sec.	40 ft./sec.
0–250	0.80	0.65
250–500	.14	.16
500–1500	.05	.16
>1500	.01	.03

TABLE X.—VARIATION OF $\frac{1-R_T'}{1-R_L'}$ WITH FREQUENCY

Measurements 25½ inches behind 1-inch screen with wires 5 mm long and 2 mm apart.

Frequency cycles per second	20 ft./sec.	40 ft./sec.
No filter	1.41	1.37
0–250	2.67	4.89
250–500	1.50	2.50
500–1500	.75	1.40
1500–3000	----------	.83
>3000	----------	.70

REPORT No. 582

A THEORY FOR PRIMARY FAILURE OF STRAIGHT CENTRALLY LOADED COLUMNS

By Eugene E. Lundquist and Claude M. Figg

SUMMARY

A theory of primary failure of straight centrally loaded columns is presented. It is assumed that the column cross section and the load are constant throughout the length.

Primary failure is defined as any type of failure in which the cross sections are translated, rotated, or translated and rotated but not distorted in their own planes. In the derivation of the general equation for the critical stress, the cross sections are assumed to rotate about any axis parallel to the column. When the location of the axis of rotation varies from zero to infinity in every direction, all combinations of translation and rotation of the column cross section are obtained.

For illustration, the theory is applied to a column of I *section. The conclusions, however, are generalized to include any column with a cross section symmetrical about its principal axes. It is shown that, for such columns, the theories for bending failure and twisting failure are special cases of this general theory and that primary failure will occur by bending about the axis of minimum moment of inertia or by twisting about the centroid, depending upon which gives the lower critical stress.*

When a column is attached to a skin, the great stiffness of the skin in its own plane causes the axis of rotation to lie in the plane of the skin. When the column cross section is symmetrical about its two principal axes, one of which is normal to the skin, the axis of rotation will be either at the point where the principal axis crosses the skin or at infinity in the plane of the skin, depending upon which location gives the smaller stress.

It is shown how the effective width of skin that may be considered to act with the column and carry the same stress as the column alters the section properties of the column and how the bending stiffness of the skin resists twisting of the column and raises the critical stress. Finally, the effective moduli that apply when the column is stressed above the proportional limit are discussed.

An illustrative problem in the first appendix (A) shows how the theory for primary failure may be used to construct the column curve for a skin-stiffener panel.

Appendix B shows how the theory may be applied to columns of closed section. For closed sections, however, the large torsional rigidity precludes anything but bending failure.

Appendix C contains a derivation of the theoretical equation for the effective modulus of elasticity when the column is stressed above the proportional limit.

INTRODUCTION

In the determination of the compressive strength of sheet and stiffener combinations as employed in stressed-skin structures for aircraft, the strength of the stiffener is a most important factor. When failure occurs by deflection normal to the skin, the accepted column curve for the material applies. (See reference 1.) When failure occurs by deflection of the outstanding portion of the stiffener in a direction parallel to the sheet, however, there is a combined action of bending and twisting in the stiffener that requires for its solution a more general theory for primary failure in columns than has been available heretofore.

Primary failure, as used in this report, is any type of column failure in which the cross sections are translated, rotated, or both translated and rotated but not distorted in their own planes (fig. 1). In keeping with this definition of primary failure, any failure in which the cross sections are distorted in their own planes but not translated or rotated is designated "secondary" or "local" failure. (See fig. 2.) Consideration is given herein only to primary failure.

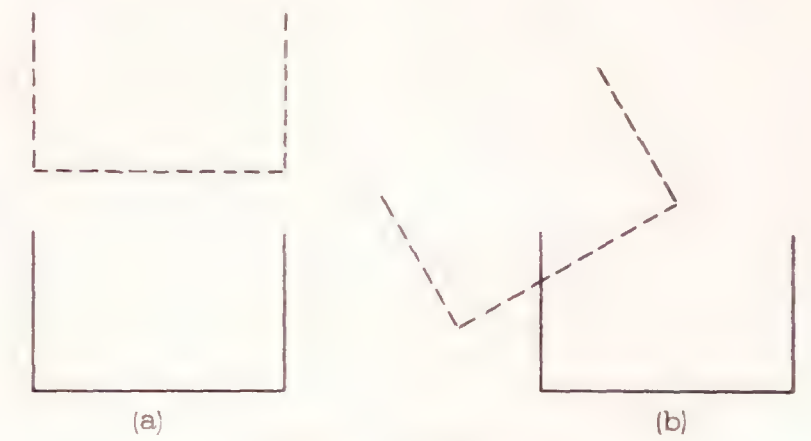

FIGURE 1.—Primary failure.
(a) Translated. (b) Translated and rotated.

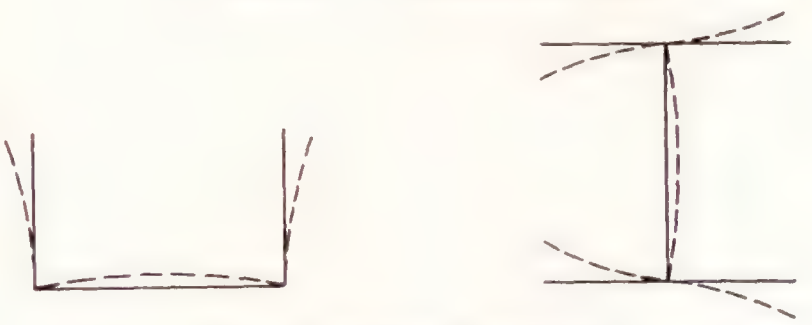

FIGURE 2.—Secondary, or local, failure.

Wagner in reference 2 has presented a theory for torsion-bending failure of open-section columns formed from thin metal. A part of this theory is summarized in reference 3, which also includes the results of tests made to substantiate the theory. In his theory, Wagner considers the cross sections to rotate about an

axis which is parallel to the column and which passes through the center of twist for the section. (See reference 4, p. 194, art. 41, for location of center of twist.) When the column is attached to the skin of a stressed-skin structure, the stiffness of the skin in its own plane and the anchorage of the skin at the sides of the panel are controlling factors in the location of the axis of rotation. If the stiffness of the skin in its own plane is assumed to be infinite, the axis of rotation is forced to lie in the plane of the skin. Rotation of the cross sections about any axis not lying in the plane of the skin would require a movement of the skin in its own plane. Such a movement is prevented by the stiffness of the skin in its own plane and the anchorage of the skin at the sides of the panel. Consequently, for the solution of the skin-stiffener problem the Wagner theory must be extended to include rotation of the cross sections about axes other than the one passing through the center of twist.

The purpose of this report is to present extensions of the Wagner theory, as given in reference 2, to include rotation of the cross sections about any axis parallel to the column. These extensions together with the Wagner theory constitute the general theory of primary failure of straight centrally loaded columns presented in this report. This theory is applicable to any thin-wall metal column of uniform section and contains the Euler theory for bending and the Wagner theory for twisting as special cases. The application of the general theory to columns of open section is illustrated by use of an I section column, both when the column is free and when it is restrained by the attachment of one flange to the skin of a stressed-skin structure. The application of the theory to a design problem involving an open-section column attached to a skin is given in appendix A. The application of the theory to columns of closed section is of less practical importance and is given in appendix B. Appendix C presents the derivation of the theoretical equation for the effective modulus of elasticity when the column is stressed beyond the proportional limit.

THE THEORY OF PRIMARY FAILURE

THE WAGNER EQUATION

The critical compressive load for primary failure of an open-section column that is both straight and centrally loaded when the axis of rotation passes through the shear center, in this report called "center of twist", is given by equation (9) of reference 2, which written with American notation is

$$P_{crit}=\frac{A}{I_p}\left(GJ+\frac{\pi^2}{L_0^2}E\,C_{BT}\right)$$

If both sides of this equation are divided by the cross-sectional area A, the following equation for the critical stress is obtained:

$$f_{crit}=\frac{GJ}{I_p}+\frac{C_{BT}}{I_p}\frac{\pi^2 E}{L_0^2} \tag{1}$$

where

E is the tension-compression modulus of elasticity.

$G=\frac{E}{2(1+\mu)}$, shear modulus of elasticity.

μ, Poisson's ratio for the material.

I_p, polar moment of inertia of the cross section about the axis of rotation.

L_0, effective length of column.

J, torsion constant for the section. The product GJ in torsion problems is analogous to the product EI in bending problems. (See reference 5.)

C_{BT}, torsion-bending constant, dependent upon the location of the axis of rotation and the dimensions of the cross section. A complete discussion of how to evaluate C_{BT} is given in a later section.

In equation (1) the term $\frac{GJ}{I_p}$ is that part of the critical compressive stress caused by the resistance of the column to pure twisting. The term $\frac{C_{BT}}{I_p}\frac{\pi^2 E}{L_0^2}$ is that part of the critical compressive stress caused by the resistance of the column to bending. In the derivation of equation (1) the angular displacement of the cross section about the axis of rotation was found to vary as a half sine wave along the length of the column in the same way that the lateral displacements in an Euler column vary as a half sine wave along the length. Therefore the term $\frac{C_{BT}}{I_p}$ is analogous to $\frac{I}{A}$ in the Euler column formula

$$f_{crit}=\frac{I}{A}\frac{\pi^2 E}{L_0^2} \tag{2}$$

where I is the moment of inertia about a centroidal axis.

In order for a column to fail in the manner shown in figure 3 (a) the end cross sections must be free to rotate about the axis of rotation and there must be no restraint of longitudinal displacements at the ends of the column. Thus, when primary failure occurs in the manner shown in figure 3 (a), the twist per unit length is the same at all stations along the length and the column is said to be in a condition of pure twisting. In a pure twisting failure there are no longitudinal bending stresses, with the result that the second term of equation (1) is zero. The critical stress for a pure twisting failure is therefore given by $\frac{GJ}{I_p}$, which is in agreement with the value given by equation (4a) of reference 6. In order that the second term of equation (1) shall be zero the effective length of the column must be infinite ($L_0=\infty$).

In order for a column to fail in the manner shown in figure 3 (b) the end cross sections must be held

against rotation about the axis of rotation but there must be no restraint of longitudinal displacements at the ends of the column. When primary failure occurs in the manner shown in figure 3 (b), the twist per unit length is variable along the length of the column with rotation about the axis of rotation and when buckling occurs, there must be complete restraint of longitudinal displacements at the ends of the column. Because the end conditions for the type of primary failure shown in figure 3 (c) correspond to built-in ends in an Euler

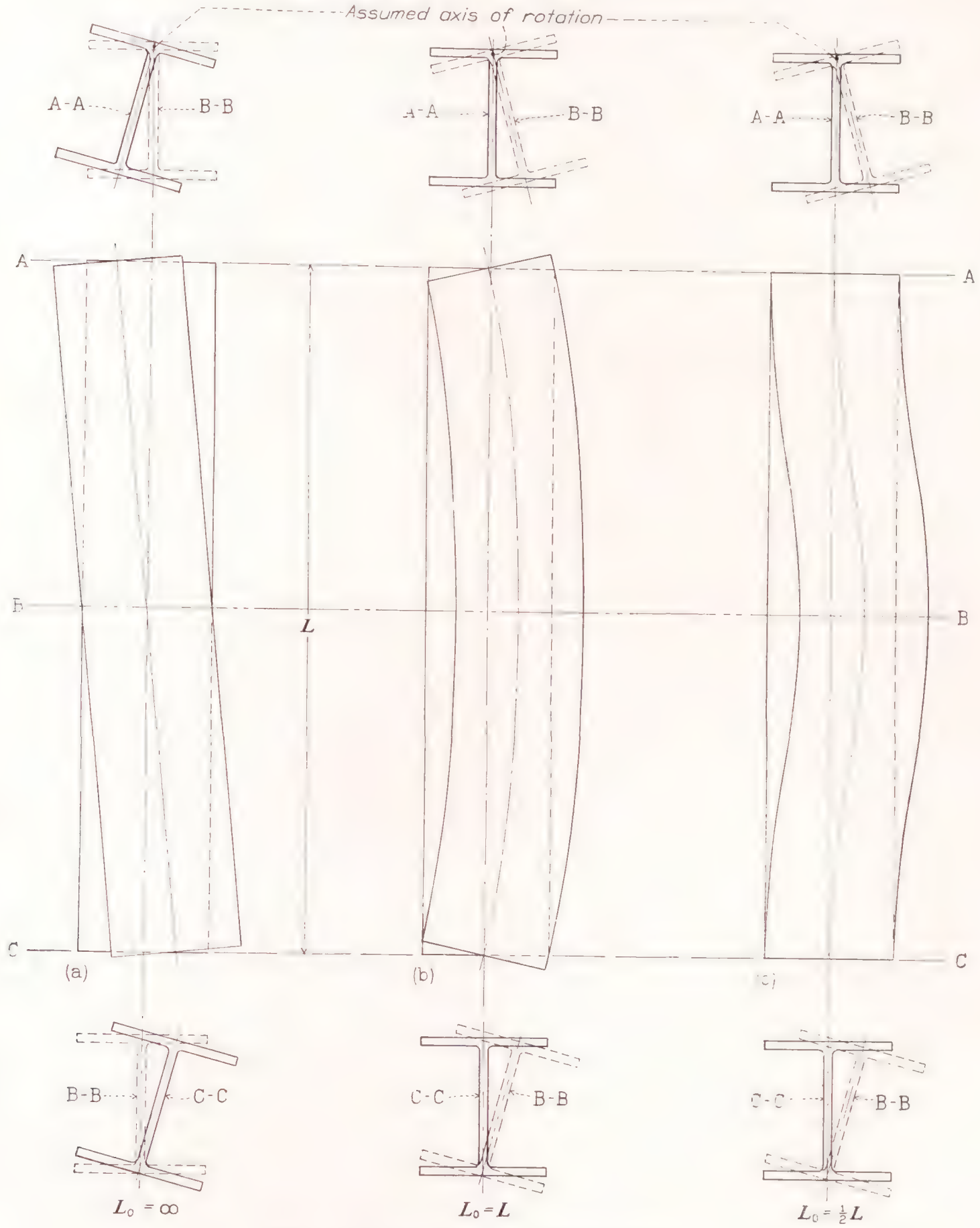

FIGURE 3.—End conditions for different effective lengths, L_0.

$$\sigma_{crit}=\frac{GJ}{I_p}+\frac{C_{BT}}{I_p}\frac{\pi^2 E}{L_0^2}$$

the result that longitudinal bending stresses are present in addition to the shearing stresses of twisting. The end conditions for this case correspond to pin ends in an Euler column with the result that $L_0=L$ in equation (1).

In order for a column to fail in the manner shown in figure 3 (c) the end cross sections must be held against column, $L_0=\frac{L}{2}$ for this case. Similarly, for any degree of restraint against longitudinal displacements of the end cross sections the same effective length applies as for an Euler column with the same condition of end restraint.

GENERALIZATION OF WAGNER THEORY

In the paragraph immediately following equation (2b) on page 6 of reference 2 it is stated, "The longitudinal stresses σ_{bd} should not give a resulting bending moment (since there is no such moment acting on the member). It may easily be shown that this condition may be satisfied if and only if the magnitudes r_u and r_n refer to the shear center; that is, when the section twists about the shear axis, also in the case where longitudinal stresses arise." These statements are correct when there is no moment acting on the member. A general derivation, however, should include a moment acting on the member.

The Wagner theory is therefore based on the assumption that only torque moments are acting on the member at any station x along the column. From this assumption it follows that at failure all but the end cross sections of the column rotate about an axis parallel to the column and passing through the center of twist of the section. When it is assumed that both torque moments and bending moments are acting on the column at any station x, the combined effect is such as to cause the cross sections to rotate about some other axis parallel to the column. In this case equation (1) will give the critical stress provided that C_{BT} and I_p, which depend upon the location of the axis of rotation, are properly evaluated. The Wagner theory, together with this extension of it, of which the purpose is to include rotation of the cross sections about any axis parallel to the column, constitutes a more general theory for primary failure in columns. The development of the general theory is necessary for calculating the column strength of stiffeners attached to skin when failure occurs by deflection of the outstanding portion in a direction parallel to the skin.

EVALUATION OF C_{BT}

The torsion-bending constant C_{BT} is a section property similar to moment of inertia. Like moment of inertia it is dependent upon the axis about which the section property is calculated. Wagner has shown that, in its practical evaluation, C_{BT} may be divided into a major and a minor part, the latter of which may be neglected for most open sections formed of thin metal. In reference 3 it is shown that the major part can be expressed by a simple integral involving certain areas swept by a radius vector. In the evaluation of C_{BT} for some stiffener sections used in aircraft structures, however, the authors of the present report found it expedient to use the basic considerations of displacement from which the simple integral involving swept areas was derived. In this procedure certain concepts, not given in references 2 and 3, were introduced to clarify the method of calculating C_{BT} in the general case.

In order to evaluate C_{BT} by the general method, a portion of the column of length dx is allowed to twist about the axis of rotation an amount such that one end cross section is so displaced that it forms an angle $d\varphi$ with respect to the other end cross section. The longitudinal displacement of any point on the end cross section with respect to a reference plane, normal to the axis of rotation, is proportional to $\frac{d\varphi}{dx}$, the angle of twist per unit length hereinafter designated θ. The reference plane is then located so that the average longitudinal displacement of the elemental areas dA of the end section from this plane is zero; i. e.,

$$\frac{\int D dA}{\int dA}=\frac{\int D dA}{A}=0 \tag{3}$$

where D is the longitudinal displacement from the reference plane of the elemental area dA. Physically the reference plane establishes the neutral axis of the longitudinal bending stresses that result when the end cross section is restrained. The general expression for C_{BT}, which includes both the major and minor parts previously mentioned, is (reference 2, equation (6))

$$C_{BT}=\int u^2 dA \tag{4}$$

where u is the longitudinal displacement, from the reference plane, of the elemental area dA when $\frac{d\varphi}{dx}=\theta=1$.

The general method of evaluating C_{BT} described in the preceding paragraph will now be applied to an I section column with the axis of rotation located at a distance r from the centroid in any direction. Wagner and Pretschner (reference 3) have shown how to compute C_{BT} for an I section when the axis of rotation is at the center of twist, which is at the centroid for the I section. When the axis of rotation has some other location, certain terms must be added to allow for the shift in the axis of rotation. In the derivation of C_{BT} for any location of the axis of rotation, it is convenient to resolve the displacement of the one end cross section (fig. 4 (a)) into two displacements of translation (1 and 2 of fig. 4 (b)) and one displacement of rotation about the center of twist (3 of fig. 4 (b)). The *longitudinal displacements* of the different parts of the cross section caused by the three component displacements of the cross section (fig. 4 (b)) are then added to obtain the total longitudinal displacement. In the following tabulations the longitudinal displacements at the center lines of the web and flanges are given. The algebraic sign of the displacement is positive when a point on the cross section moves in the positive direction of x and negative when it moves in the negative direction of x (figs. 5, 6, and 7). Also note in the expressions for longitudinal displacement (LD–1, 2, 3, etc.) that $\frac{d\varphi}{dx}=\theta$.

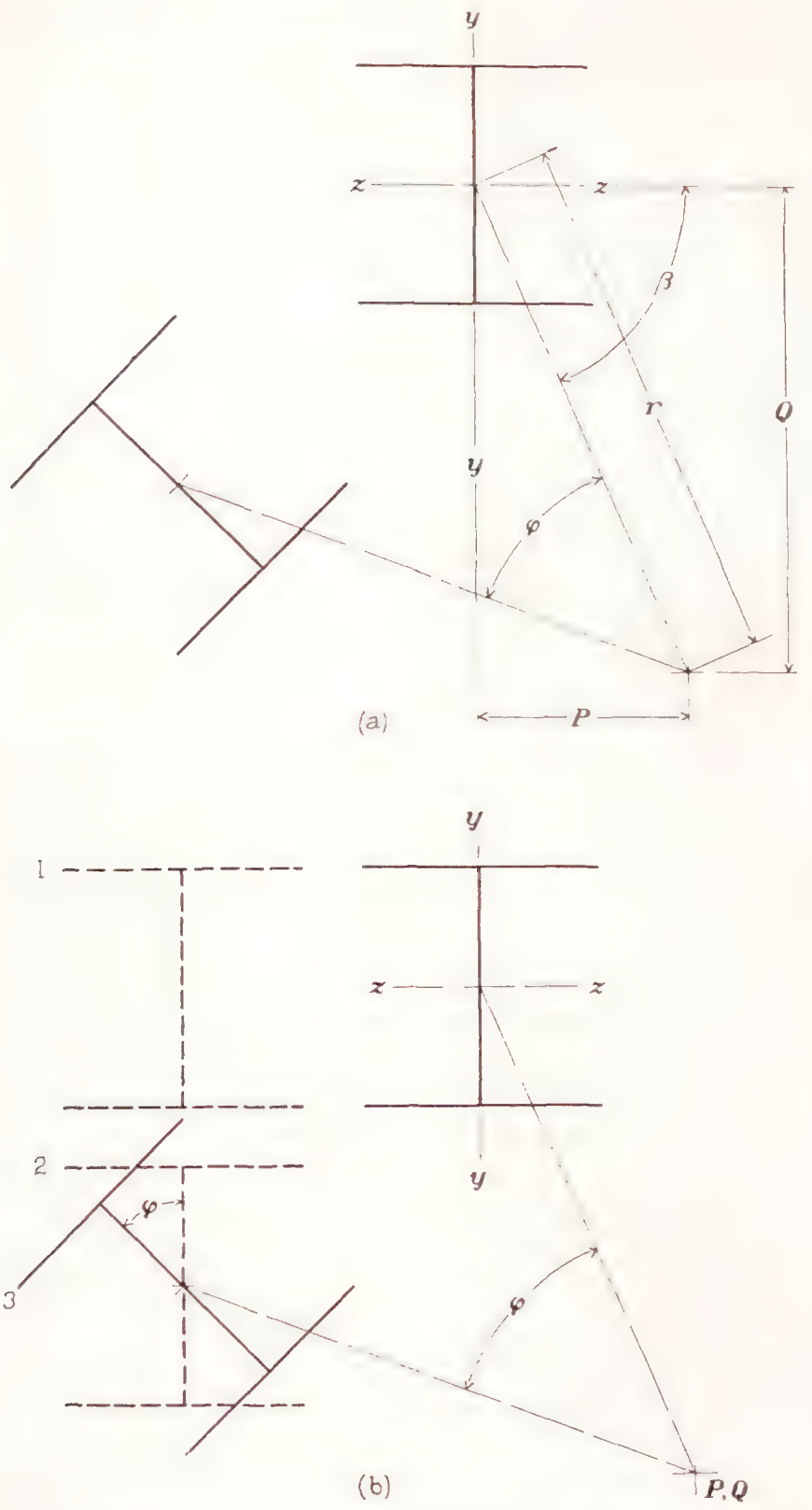

FIGURE 4.—Displacement of one end cross section with respect to the other when rotated about the point *P*, *Q*.

Displacements for rotation about the center of twist (fig. 5).—The longitudinal displacement from the original plane of the end cross section at a distance *s* measured from

$$\left.\begin{array}{ll} \text{B toward A is} & -\theta\frac{h}{2}s \\ \text{B toward C,} & \theta\frac{h}{2}s \\ \text{O toward B,} & 0 \\ \text{O toward B',} & 0 \\ \text{B' toward C',} & -\theta\frac{h}{2}s \\ \text{B' toward A',} & \theta\frac{h}{2}s \end{array}\right\} \text{(LD–1)}$$

Displacements for translation normal to the web (fig. 6).—The longitudinal displacement from the original plane of the end cross section at a distance *s* measured from

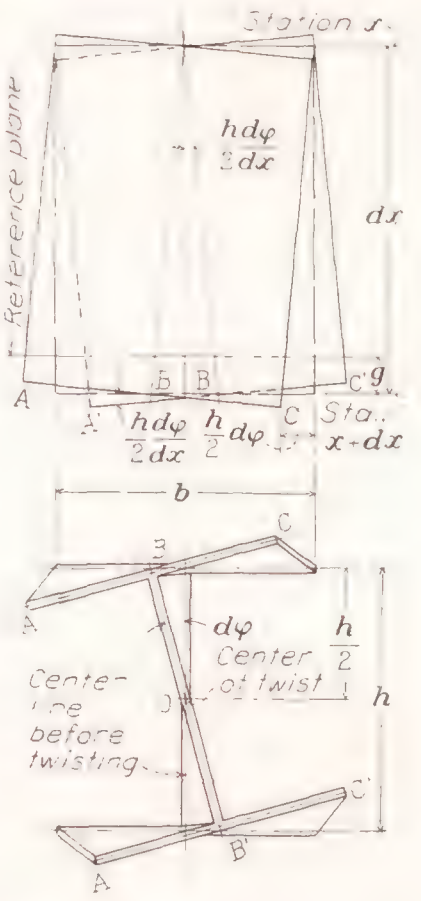

FIGURE 5.—Displacements for rotation about the center of twist.

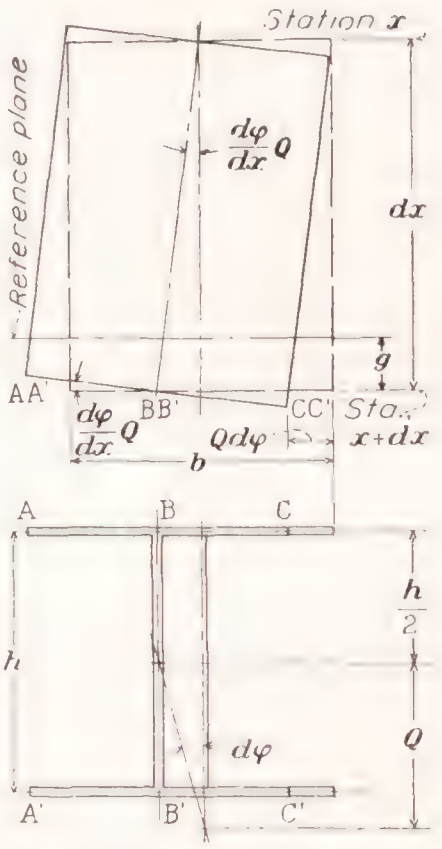

FIGURE 6.—Displacements for translation normal to the web.

$$\left.\begin{array}{ll} \text{B toward A is} & \theta Qs \\ \text{B toward C,} & \theta Qs \\ \text{O toward B,} & 0 \\ \text{O toward B',} & 0 \\ \text{B' toward C',} & \theta Qs \\ \text{B' toward A',} & -\theta Qs \end{array}\right\} \text{(LD–2)}$$

Displacements for translation parallel to the web (fig. 7).—The longitudinal displacements from the original plane of the end cross section at a distance *s* measured from

$$\left.\begin{array}{ll} \text{B toward A is} & \theta P\frac{h}{2} \\ \text{B toward C,} & \theta P\frac{h}{2} \\ \text{O toward B,} & \theta Ps \\ \text{O toward B',} & -\theta Ps \\ \text{B' toward C',} & -\theta P\frac{h}{2} \\ \text{B' toward A',} & -\theta P\frac{h}{2} \end{array}\right\} \text{(LD–3)}$$

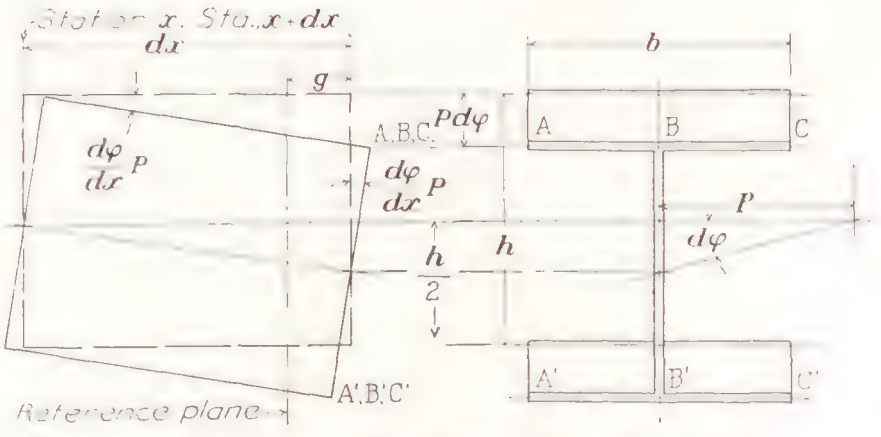

FIGURE 7.—Displacements for translation parallel to the web.

Total displacement for rotation about the point P, Q (figs. 4, 5, 6, and 7).—By addition of the displacements LD–1, LD–2, LD–3, the total longitudinal displacement from the original plane of the end cross section at a distance s measured from

$$\left.\begin{aligned}
&\text{B toward A is } -\theta\left[s\left(\frac{h}{2}+Q\right)-P\frac{h}{2}\right]\\
&\text{B toward C, } \quad \theta\left[s\left(\frac{h}{2}+Q\right)+P\frac{h}{2}\right]\\
&\text{O toward B, } \quad \theta Ps\\
&\text{O toward B', } \quad -\theta Ps\\
&\text{B' toward C', } -\theta\left[s\left(\frac{h}{2}-Q\right)+P\frac{h}{2}\right]\\
&\text{B' toward A', } \quad \theta\left[s\left(\frac{h}{2}-Q\right)-P\frac{h}{2}\right]
\end{aligned}\right\}\text{(LD–4)}$$

Therefore the longitudinal displacement of the end cross section with respect to the reference plane at a distance s measured from

$$\left.\begin{aligned}
&\text{B toward A is } g-\theta\left[s\left(\frac{h}{2}+Q\right)-P\frac{h}{2}\right]\\
&\text{B toward C, } \quad g+\theta\left[s\left(\frac{h}{2}+Q\right)+P\frac{h}{2}\right]\\
&\text{O toward B, } \quad g+\theta Ps\\
&\text{O toward B', } \quad g-\theta Ps\\
&\text{B' toward C', } g-\theta\left[s\left(\frac{h}{2}-Q\right)+P\frac{h}{2}\right]\\
&\text{B' toward A', } g+\theta\left[s\left(\frac{h}{2}-Q\right)-P\frac{h}{2}\right]
\end{aligned}\right\}\text{(LD–5)}$$

Now g, the distance of the reference plane from the original plane of the end cross section, is determined by the conditions of equation (3). The term tds may be substituted for dA because the longitudinal displacements vary linearly across the thickness t_w of the web and t_b of the flanges. Then, if the longitudinal displacement of the center lines (LD–5) is substituted for D, equation (3) becomes, after multiplying by A,

$$\begin{aligned}
0=\int Dtds=&\int_0^{\frac{b}{2}}\left\{g-\theta\left[s\left(\frac{h}{2}+Q\right)-P\frac{h}{2}\right]\right\}t_b ds\\
&+\int_0^{\frac{b}{2}}\left\{g+\theta\left[s\left(\frac{h}{2}+Q\right)+P\frac{h}{2}\right]\right\}t_b ds\\
&+\int_0^{\frac{h}{2}}\left\{g+\theta Ps\right\}t_h ds\\
&+\int_0^{\frac{h}{2}}\left\{g-\theta Ps\right\}t_h ds\\
&+\int_0^{\frac{b}{2}}\left\{g-\theta\left[s\left(\frac{h}{2}-Q\right)+P\frac{h}{2}\right]\right\}t_b ds\\
&+\int_0^{\frac{b}{2}}\left\{g+\theta\left[s\left(\frac{h}{2}-Q\right)-P\frac{h}{2}\right]\right\}t_b ds
\end{aligned}$$

from which

$$g=0 \tag{5}$$

From the symmetry of the I section, it might have been foreseen that $g=0$. The formal proof, however, has been presented to show the method that would be necessary for the determination of g for other sections.

Wagner has shown that for sections formed of thin metal it is convenient to divide C_{BT} into a major part C_B and a minor part C_T so that

$$C_{BT}=C_B+C_T \tag{6}$$

In the major part of C_{BT} the longitudinal displacement is assumed to be uniform across the thickness of the plate and equal to the value at its center line. For the major part, dA in equation (4) is therefore written tds. Hence

$$C_B=\int u^2 tds \tag{7}$$

Substitution of the longitudinal displacements (LD–5) for u in equation (7), with $\theta=1$ and $g=0$, gives for the I section

$$\begin{aligned}
C_B=&\int_0^{\frac{b}{2}}\left[s\left(\frac{h}{2}+Q\right)-P\frac{h}{2}\right]^2 t_b ds\\
&+\int_0^{\frac{b}{2}}\left[s\left(\frac{h}{2}+Q\right)+P\frac{h}{2}\right]^2 t_b ds\\
&+\int_0^{\frac{h}{2}}[Ps]^2 t_h ds\\
&+\int_0^{\frac{h}{2}}[Ps]^2 t_h ds\\
&+\int_0^{\frac{b}{2}}\left[s\left(\frac{h}{2}-Q\right)+P\frac{h}{2}\right]^2 t_b ds\\
&+\int_0^{\frac{b}{2}}\left[s\left(\frac{h}{2}-Q\right)-P\frac{h}{2}\right]^2 t_b ds
\end{aligned}$$

from which

$$C_B=\frac{1}{24}b^3h^2t_b+\left(\frac{h^2bt_b}{2}+\frac{h^3t_h}{12}\right)P^2+\frac{b^3t_b}{6}Q^2 \tag{8}$$

The minor part of C_{BT} is in the nature of a correction to the major part to allow for the variation in longitudinal displacement across the thickness of the web or flange. When the thickness is constant along the web or flange, the general expression for the minor part is (reference 2, equation (6b))

$$C_T=\frac{t^3}{12}\int s^2 ds \tag{9}$$

In order to evaluate $\int s^2 ds$ in this equation, the origin of s must be at the point on the center line of the web

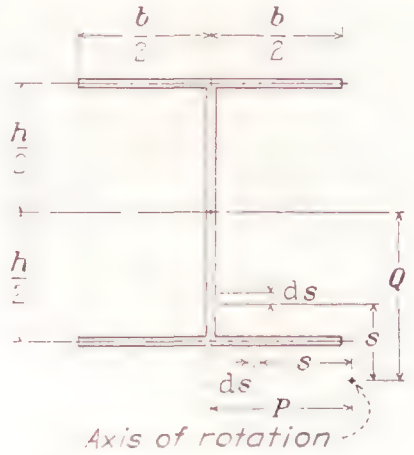

FIGURE 8.—Method of measuring s for evaluation of equation (9).

or flange, extended if necessary, from which a perpendicular may be erected to pass through the axis of rotation. (See fig. 8.) When the thickness varies with

s, t^3 should be placed under the integral sign and equation (9) evaluated by either an analytical or graphical method.

As applied to the I section, equation (9) becomes

$$C_T=2\frac{t_b^3}{12}\int_{P-\frac{b}{2}}^{P+\frac{b}{2}}s^2ds+\frac{t_h^3}{12}\int_{Q-\frac{h}{2}}^{Q+\frac{h}{2}}s^2ds$$

from which

$$C_T=\frac{b^3t_b^3}{72}+\frac{h^3t_h^3}{144}+\frac{bt_b^3}{6}P^2+\frac{ht_h^3}{12}Q^2 \tag{10}$$

When the thicknesses t_b and t_h are small as compared with b and h, respectively, C_T will be very small as compared with C_B and may be neglected in the computation of C_{BT}. Substitution in equation (6) of the values of C_B and C_T, however, as given by equations (8) and (10) gives

$$C_{BT}=\frac{b^3h^2t_b}{24}+\frac{b^3t_b^3}{72}+\frac{h^3t_h^3}{144}+\left(\frac{h^2bt_b}{2}+\frac{h^3t_h}{12}+\frac{bt_b^3}{6}\right)P^2+\left(\frac{b^3t_b}{6}+\frac{ht_h^3}{12}\right)Q^2$$

or

$$C_{BT}=(C_{BT})_{\substack{P=0\\Q=0}}+I_zP^2+I_yQ^2 \tag{11}$$

where I_y and I_z are the moments of inertia of the cross section about the principal axes y and z, respectively, (fig. 4).

CRITICAL STRESS FOR AN I SECTION COLUMN

In order to show the effect of variation in $\frac{b}{h}$ on the critical stress for the I section in a later part of this report, it is convenient to write equation (1) in the following form

$$f_{crit}=KG\frac{t_h^2}{h^2}+K_{BT}\frac{\pi^2Et_h^2}{12L_0^2} \tag{12}$$

where $G\frac{t_h^2}{h^2}$ is the critical compressive stress for a pure twisting failure of the web alone when the axis of rotation is at one edge of the web, that is, the critical compressive stress for a long outstanding flange simply supported at its base. (See reference 7, equation (91).)

$\frac{\pi^2Et_h^2}{12L_0^2}$, the critical compressive stress for the web alone acting as an Euler column.

$K=\frac{h^2}{t_h^2}\frac{J}{I_p}$, $K_{BT}=\frac{12\,C_{BT}}{I_p\,t_h^2}$ constants that vary with the dimensions of the cross section and the location of the axis of rotation.

On the assumption that the torsional stiffness GJ of the I section is equal to the sum of the torsional stiffnesses of the web and flanges (reference 4, p. 76, art. 20) the approximate equation for J is

$$J=\frac{1}{3}ht_h^3+\frac{2}{3}bt_b^3 \tag{13}$$

For any location of the axis of rotation, the value of I_p for the I section is

$$I_p=\frac{1}{12}h^3t_h+\frac{1}{2}h^2bt_b+\frac{1}{6}b^3t_b+(ht_h+2bt_b)(P^2+Q^2) \tag{14}$$

Substitution of the values of J and I_p given by equations (13) and (14) in the equation that defines K gives for the I section

$$K=\frac{4+8\frac{b}{h}\left(\frac{t_b}{t_h}\right)^3}{1+\left[2\frac{b}{h}\frac{t_b}{t_h}\right]\left[3+\left(\frac{b}{h}\right)^2\right]+12\left[1+2\frac{b}{h}\frac{t_b}{t_h}\right]\left[\left(\frac{P}{h}\right)^2+\left(\frac{Q}{h}\right)^2\right]} \tag{15}$$

For the same reason that C_{BT} has been divided into a major part C_B and a minor part C_T (see equation (6)), K_{BT} will likewise be divided into a major part K_B and a minor part K_T so that

$$K_{BT}=K_B+K_T \tag{16}$$

Substitution of the values of C_B and C_T as given by equations (8) and (10) for C_{BT} in the equation that defines K_{BT}, gives for the I section

$$K_B=\frac{6\left(\frac{b}{t_h}\right)^3t_b+12\left(\frac{P}{t_h}\right)^2\left[1+6\frac{b}{h}\frac{t_b}{t_h}\right]+24\left(\frac{b}{h}\right)^3\left(\frac{Q}{t_h}\right)^2t_b}{1+\left[2\frac{b}{h}\frac{t_b}{t_h}\right]\left[3+\left(\frac{b}{h}\right)^2\right]+12\left[1+2\frac{b}{h}\frac{t_b}{t_h}\right]\left[\left(\frac{P}{h}\right)^2+\left(\frac{Q}{h}\right)^2\right]} \tag{17}$$

and

$$K_T=\frac{1+2\left(\frac{b}{h}\right)^3\left(\frac{t_b}{t_h}\right)^3+12\left[2\frac{b}{h}\left(\frac{t_b}{t_h}\right)^3\left(\frac{P}{h}\right)^2+\left(\frac{Q}{h}\right)^2\right]}{1+\left[2\frac{b}{h}\frac{t_b}{t_h}\right]\left[3+\left(\frac{b}{h}\right)^2\right]+12\left[1+2\frac{b}{h}\frac{t_b}{t_h}\right]\left[\left(\frac{P}{h}\right)^2+\left(\frac{Q}{h}\right)^2\right]} \tag{18}$$

DISCUSSION

Location of the axis of rotation for a free column.— When the axis of rotation is located at a distance r from the centroid of a section, the value of $\frac{GJ}{I_p}$ in equation (1) is independent of the direction in which r is measured. Because $\frac{C_{BT}}{I_p}$ is analogous to $\frac{I}{A}$ in the Euler column formula, it seems reasonable to expect that, as the axis of rotation moves around a circle of radius r, $\frac{C_{BT}}{I_p}$ will

vary from a maximum at one of the principal axes to a minimum at the other principal axis. Because I_p is independent of the direction in which r is measured, all the variation in $\frac{C_{BT}}{I_p}$ will occur in C_{BT}. It will now be shown that, for a section symmetrical about each of its two principal axes, C_{BT} is a maximum or minimum when the axis of rotation is on the principal axis about which the moment of inertia is, respectively, maximum or minimum.

It follows from the symmetry of the expressions for longitudinal displacement and the limits of integration that C_{BT} for any section symmetrical about its two principal axes will have the form given by equation (11). From figure 4

$$P=r\cos\beta$$
$$Q=r\sin\beta$$

Substitution of these values in equation (11) gives

$$C_{BT}=(C_{BT})_{\substack{P=0\\Q=0}}+I_z r^2\cos^2\beta+I_y r^2\sin^2\beta$$

The first and second derivatives of C_{BT} with respect to β are, respectively,

$$\frac{dC_{BT}}{d\beta}=r^2(I_y-I_z)\sin 2\beta$$
$$\frac{d^2C_{BT}}{d\beta^2}=2r^2(I_y-I_z)\cos 2\beta$$

The first derivative set equal to zero shows that C_{BT} is either a maximum or minimum when $\beta=0°$, 90°, 180°, or 270°. When $\beta=0°$ or 180°, $\frac{d^2C_{BT}}{d\beta^2}$ is negative provided that $I_y<I_z$, in which case $\beta=0°$ or 180° locates the axis of rotation for $C_{BT_{max.}}$ If $I_y>I_z$, then $\beta=0°$ or 180° locates the axis of rotation for $C_{BT_{min.}}$ Similarly, when $\beta=90°$ or 270°, it may be concluded that C_{BT} is a maximum or minimum when the axis of rotation is on the principal axis about which the moment of inertia is, respectively, maximum or minimum.

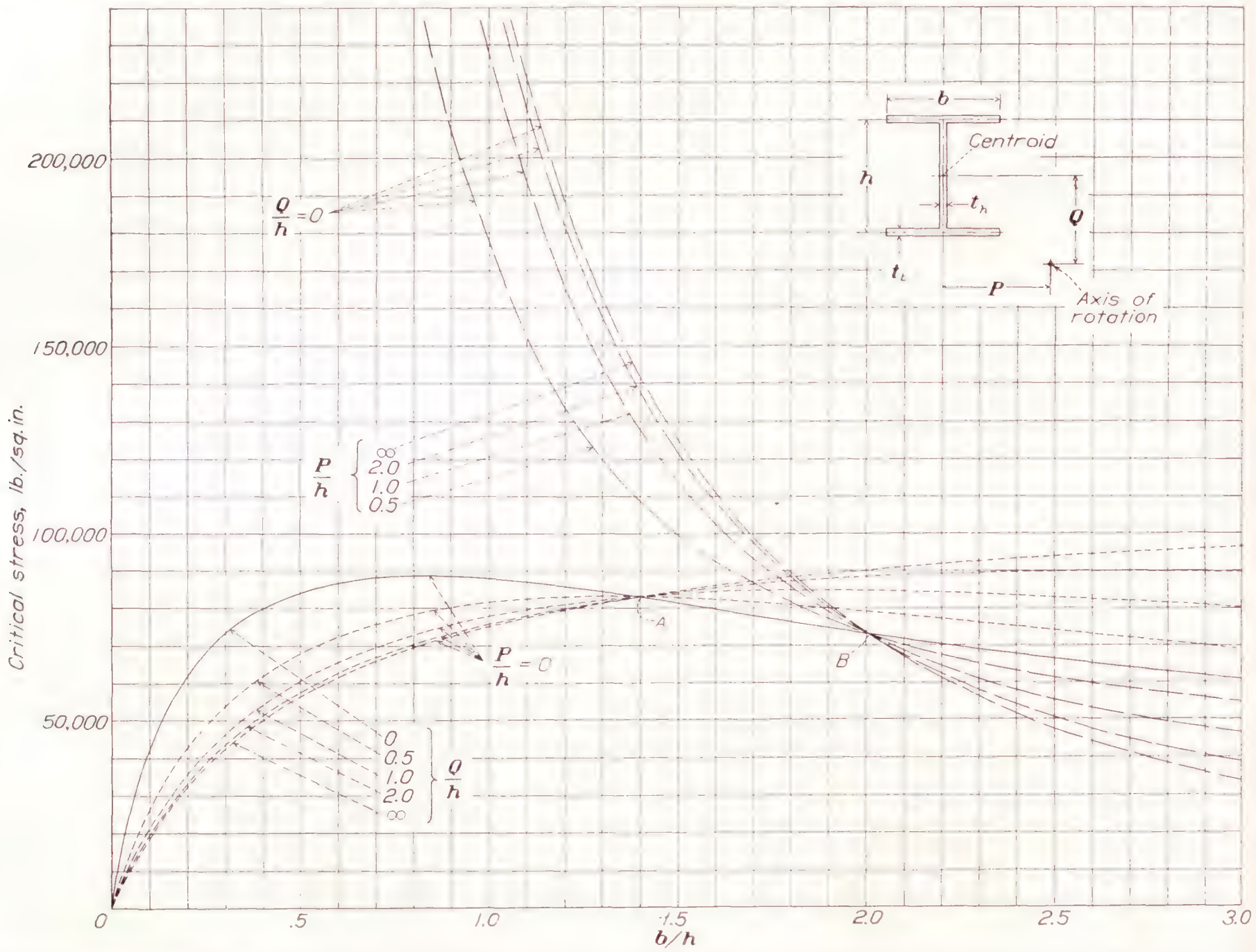

FIGURE 9.—Variation of the critical stress with b/h for different locations of the axis of rotation along the principal axes of an I section column with pin ends. Curves drawn for $b=2$ inches, $t_b=t_h=0.1$ inch, length=17.1 inches, and $E=10^7$ pounds per square inch.

When a free column of symmetrical section with no bending restraint at its ends (pin ends) is of such proportions that it develops a primary failure, the axis of rotation will be either at infinity on one of the principal axes or at the center of twist. Figure 9 illustrates this fact for a family of I section columns by means of curves for critical stress plotted against the ratio $\frac{b}{h}$ for different locations of the axis of ratation along each of the two principal axes. Inspection of figure 9 shows that, for values of $\frac{b}{h}$ between 0 and 1.4, the critical stress is lowest when the axis of rotation is at infinity along the principal axis parallel to the web. For

values of $\frac{b}{h}$ between 1.4 and 2.0, the critical stress is lowest when the axis of rotation is at the center of twist (centroid, for the I section). For values of $\frac{b}{h}$ greater than 2.0, the critical stress is lowest when the axis of rotation is at infinity along the principal axis normal to the web. Had a different set of dimensions been selected for the family of I section columns in figure 9, the crossing points A and B would, in general, have been at different values of $\frac{b}{h}$. Regardless of the dimensions used, however, the lowest critical stress would always be given by one of the three locations of the axis of rotation previously mentioned; i. e., at the center of twist $\left(\frac{P}{h}=0;\ \frac{Q}{h}=0\right)$ or at infinity on either of the two principal axes $\left(\frac{P}{h}=0;\ \frac{Q}{h}=\infty \text{ or } \frac{P}{h}=\infty;\ \frac{Q}{h}=0\right)$.

In figure 9 the critical stresses are, for the most part, greater than the yield point for the present engineering materials having the same value of E as was assumed in the calculation of the curves. ($E=10^7$ pounds per square inch.) This fact does not detract from the conclusions drawn from figure 9 because, when a column is stressed above the proportional limit, equation (1) may be considered to apply with a reduced modulus of elasticity thereby giving a reduced critical stress. The reduced modulus is discussed in a later section of this report.

It will now be proved that *for a free column of* I *section* the axis of rotation will be at infinity along the principal axis parallel to the web provided that

$$\frac{t_h}{t_b}<14.7$$

and

$$\frac{b}{h}<\sqrt[3]{\frac{t_h}{t_b}}$$

Because the axis of rotation might be at the center of twist or at infinity on the principal axis normal to the web (fig. 9), the two following conditions must hold if the axis of rotation is to be at infinity on the principal axis parallel to the web:

$$(f_{crit})_{\substack{P=0\\Q=\infty}}<(f_{crit})_{\substack{P=0\\Q=0}}$$

$$(f_{crit})_{\substack{P=0\\Q=\infty}}<(f_{crit})_{\substack{P=\infty\\Q=0}}$$

The first of these conditions will be satisfied if

$$(f_{crit})_{\substack{P=0\\Q=\infty}}<\left[(f_{crit})-\left(\frac{GJ}{I_p}\right)\right]_{\substack{P=0\\Q=0}}=\left[\frac{C_{BT}}{I_p}\frac{\pi^2E}{L_0^2}\right]_{\substack{P=0\\Q=0}}$$

or if

$$\frac{I_y}{A}\frac{\pi^2E}{L_0^2}<\left[\frac{C_{BT}}{I_p}\frac{\pi^2E}{L_0^2}\right]_{\substack{P=0\\Q=0}}$$

$$\frac{I_y}{A}<\left[\frac{C_{BT}}{I_p}\right]_{\substack{P=0\\Q=0}}$$

$$\frac{\frac{1}{6}b^3t_b}{ht_h+2bt_b}<\frac{\frac{1}{24}h^2b^3t_b}{\frac{1}{12}h^3t_h+\frac{1}{2}h^2bt_b+\frac{1}{6}b^3t_b}$$

from which

$$\frac{b}{h}<\sqrt[3]{\frac{t_h}{t_b}}$$

The second condition will be satisfied if

$$I_y<I_z$$

or if

$$\frac{1}{6}b^3t_b<\frac{1}{12}h^3t_h+\frac{1}{2}h^2bt_b$$

Multiplication of both sides by $\frac{12}{h^3t_b}$ gives

$$2\left(\frac{b}{h}\right)^3<\frac{t_h}{t_b}+6\frac{b}{h}$$

from which

$$\frac{b}{h}<\sqrt[3]{\frac{1}{2}\frac{t_h}{t_b}+3\frac{b}{h}}$$

This condition holds as long as $\frac{b}{h}$ does not become too large. If $\frac{b}{h}$ is as large as $\sqrt[3]{\frac{t_h}{t_b}}$, then the following condition must be satisfied

$$\sqrt[3]{\frac{t_h}{t_b}}<\sqrt[3]{\frac{1}{2}\frac{t_h}{t_b}+3\sqrt[3]{\frac{t_h}{t_b}}}$$

This latter condition will be fulfilled provided that

$$\frac{t_h}{t_b}<14.7 \tag{19}$$

a value of $\frac{t_h}{t_b}$ much larger than will be found in any I section column of practical dimensions. It may therefore be concluded that primary failure in a free column of I section will occur by bending with the neutral axis parallel to the web when

$$\frac{b}{h}<\sqrt[3]{\frac{t_h}{t_b}} \tag{20}$$

When $\frac{b}{h}$ is greater than $\sqrt[3]{\frac{t_h}{t_b}}$ the critical stress for the axis of rotation located at the centroid should be computed and compared with the critical stress for bending about the axis of minimum moment of

inertia. The smaller of these two values will be the stress at which failure occurs.

When the critical stress is to be computed for the axis of rotation at the centroid, the curves given in figures 10 and 11 may be used to determine the values of K and K_B in equation (12).

Proof that bending failure is a special case of the theory presented in this report.—When the axis of rotation is at infinity, equation (1) reduces to the Euler column formula. In this case, I_p and C_{BT} are both infinite. Hence $\frac{GJ}{I_p}=0$ and it remains to be shown that $\frac{C_{BT}}{I_p}=\frac{I}{A}$.

If $\beta=90°$ or 270°

$$\frac{C_{BT}}{I_p}=\frac{I_y}{A}$$

Location of the axis of rotation for a column attached to a skin.—When a column with pin ends is attached to the skin of a stressed-skin structure, the stiffness of the skin in its own plane and the anchorage of the skin at the sides of the panel are controlling factors in the location of the axis of rotation. In this discussion it is assumed that the skin provides only lateral support at its point of attachment to the column. Rotation of the cross sections about any axis not lying in the plane of the skin would therefore require a movement

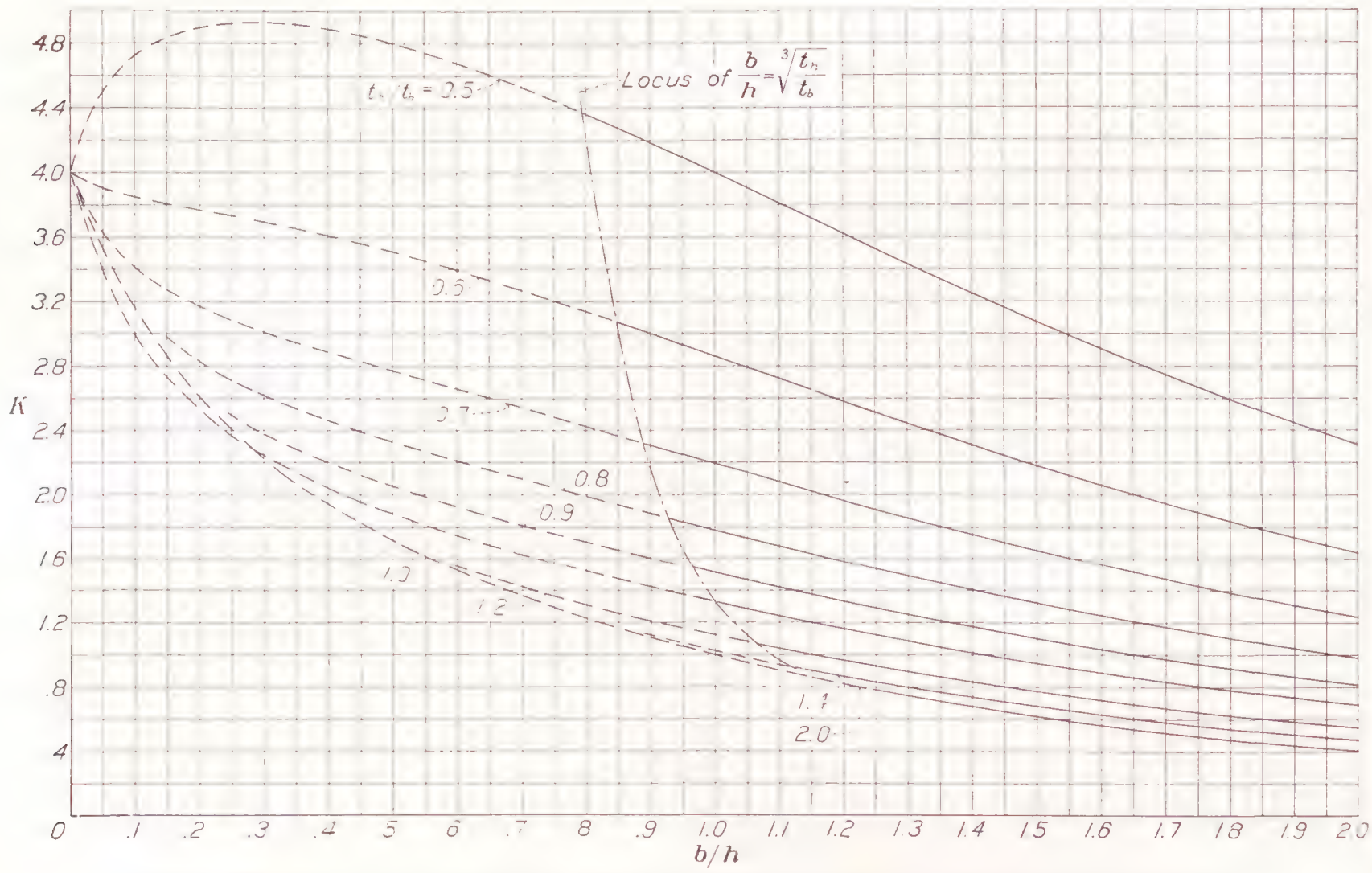

FIGURE 10.—Variation of K with b/h for different values of t_h/t_b when the axis of rotation is at the centroid of an I section column.

Equations (11) and (14) show that as the axis of rotation approaches infinity along a radius r the terms involving both P and Q, if P and Q both approach infinity, become very large in comparison with the remaining terms. Thus, when P and Q become infinite,

$$\frac{C_{BT}}{I_p}=\frac{I_zP^2+I_yQ^2}{A(P^2+Q^2)}$$

or

$$\frac{C_{BT}}{I_p}=\frac{I_z\cos^2\beta+I_y\sin^2\beta}{A}$$

When y and z are the principal axes of the section, $I_z\cos^2\beta+I_y\sin^2\beta$ is the moment of inertia of the cross section about a line that passes through the centroid and the axis of rotation. If $\beta=0°$ or 180°

$$\frac{C_{BT}}{I_p}=\frac{I_z}{A}$$

of the skin in its own plane. The stiffness of the skin in its own plane and the anchorage of the skin at the sides of the panel tend to prevent such a movement and the axis of rotation is forced to lie in the plane of the skin.

For a column the cross section of which is symmetrical about its two principal axes, one of which is normal to the skin, the axis of rotation will lie in the plane of the skin and be either at infinity or at the point where the principal axis crosses the skin. This statement is illustrated in figure 12 in which values of f_{crit} for a family of I section columns having the same dimensions as those of figure 9 are plotted against $\frac{b}{h}$ for different locations of the axis of rotation in the plane of the skin. For simplicity, the skin is assumed to be at the center of one flange. Inspection of figure 12 shows

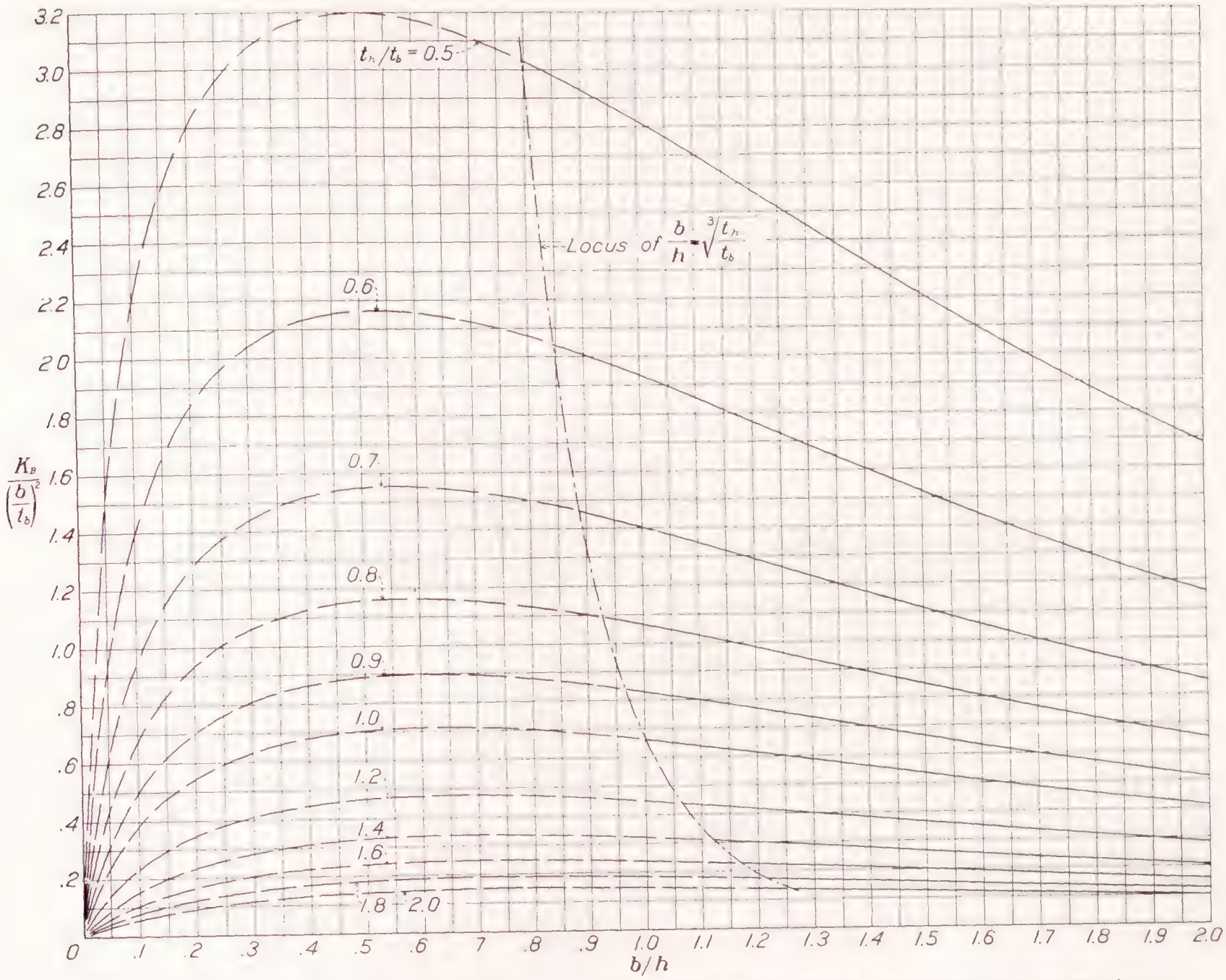

FIGURE 11.—Variation of $K_B/(b/t_b)^2$ with b/h for different values of t_h/t_b when the axis of rotation is at the centroid of an I section column.

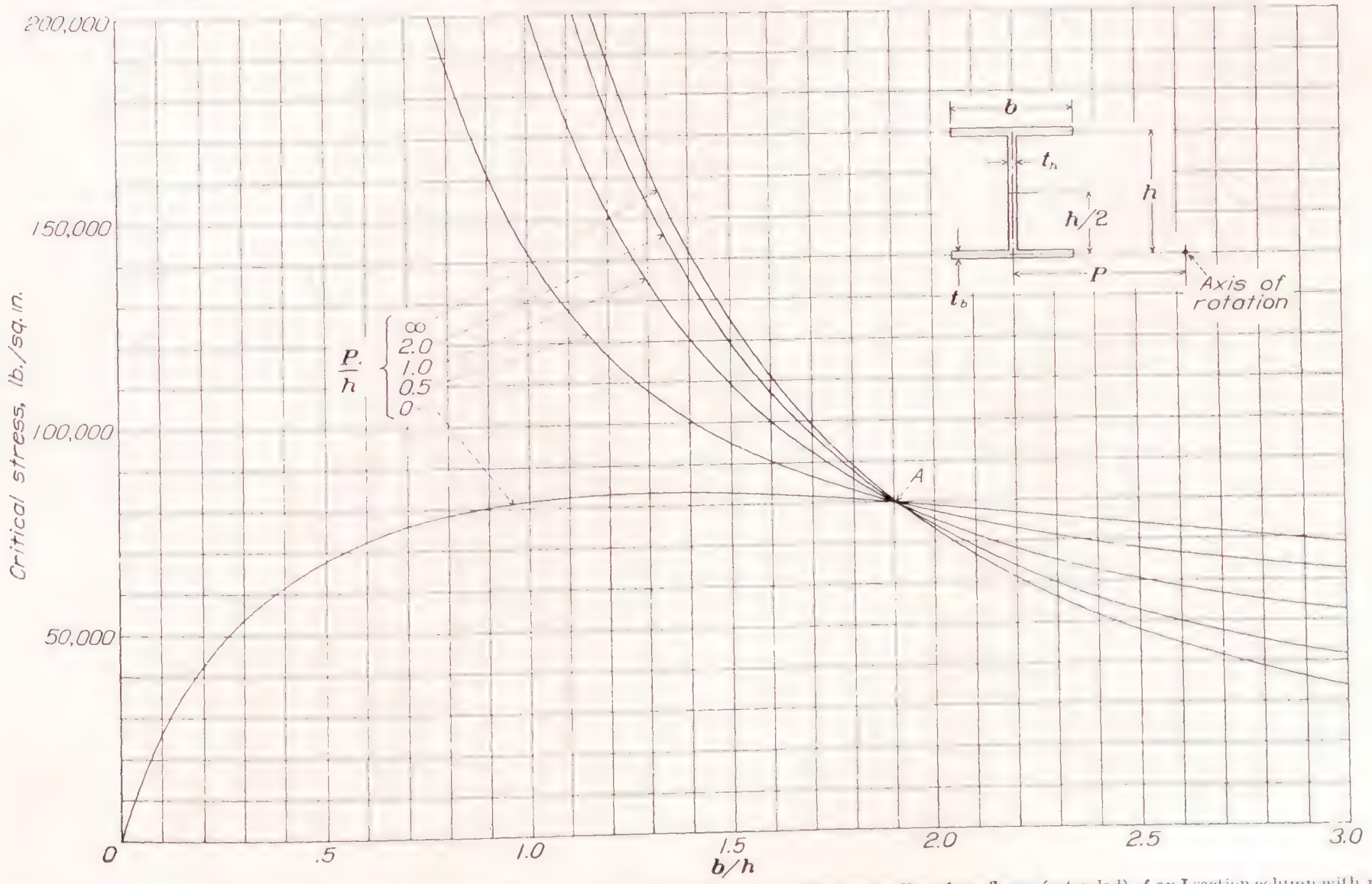

FIGURE 12.—Variation of the critical stress with b/h for different locations of the axis of rotation along the center line of one flange (extended) of an I section column with pin ends. Curves drawn for $b=2$ inches, $t_b=t_h=0.1$ inch, length=17.1 inches, and $E=10^7$ pounds per square inch.

that, for values of $\frac{b}{h}$ between 0 and 1.90, the critical stress is lowest when the axis of rotation is at the web. For values of $\frac{b}{h}$ greater than 1.90, the critical stress is lowest when the axis of rotation is at infinity in the plane of the skin.

As in the case of free columns (fig. 9), the location of the crossing point A in figure 12 will depend upon the particular dimensions selected for the family of columns. Regardless of the dimensions used, the lowest critical stress will always be given by one of the two locations of the axis of rotation previously mentioned; i. e., in the plane of the skin either at infinity $\left(\frac{P}{h}=\infty\right)$ or at the point where the principal axis crosses the skin $\left(\frac{P}{h}=0\right)$. Again, as in figure 9, the necessary use of a reduced modulus at stresses above the proportional limit does not invalidate the conclusions drawn from figure 12.

When a column of I section is attached to a skin, it is not practicable to give a simple criterion by which the location of the axis of rotation may be determined. In view of the fact that the axis of rotation will be either at infinity in the plane of the skin or at the point where the principal axis crosses the skin, the critical stress for these two locations should be computed and the lower value regarded as the failure stress. When the axis of rotation is at infinity in the plane of the skin, the critical stress is given by equation (2) with $I=I_z$. In order to facilitate the computation of f_{crit} when the axis of rotation is at the point where the principal axis crosses the skin, figures 13 and 14 have been prepared from which the values of K and K_B may be obtained for substitution in equation (12).

Effect of the skin in changing the section properties of the column.—In the preceding section it was assumed that the only effect of the skin was to provide lateral support to the column. Inasmuch as the skin is attached to the column, however, it will also carry a part of the compression load on the column and the stress in the skin at its point of attachment will be the same as that in the column. Usually the stiffener spacing in terms of the sheet thickness is such that the skin will buckle between stiffeners and only a small width adjacent to each stiffener will be effective. In reference 1 it is shown that, when failure occurs by bending of the stiffener normal to the skin (axis of rotation at infinity in the plane of the skin), the effective width, which is dependent upon the column stress, may be considered to be a part of the column cross section and is to be included in the computation of section properties.

When the axis of rotation is at the point where the principal axis crosses the skin, twisting of the stiffener about this axis will cause a rotation of the skin near the stiffener. If it is assumed that the effective width of skin rotates with the stiffener, the following increments must be added to J, I_p, and C_{BT} as evaluated for the stiffener when the skin was assumed to provide only lateral support for the stiffener,

$$\Delta J=\frac{1}{3}Ut_s^3 \tag{21}$$

$$\Delta I_p=\frac{1}{12}U^3t_s \tag{22}$$

$$\Delta C_{BT}=\Delta C_T \tag{23}$$

where

$$\Delta C_T=\frac{1}{144}U^3t_s^3 \tag{24}$$

In these equations t_s is the thickness of the skin and U is the effective width of skin that acts with the stiffener, carries the same stress as the stiffener, and is assumed to be continuous across the stiffener and symmetrically located with respect to the web of the I section. The evaluation of U is included in the illustrative problem of appendix A.

Effect of the skin in providing restraint to twisting of the column.—When a column is attached to a skin and the axis of rotation is at a point other than infinity in the plane of the skin, the rotation of the column cross section at failure is resisted by bending of the skin provided that the skin is supported by adjacent stiffeners or other structure. A theoretical analysis of this effect has been reserved for a future report. Only a brief summary of the subject is given herein.

It may be stated that the effect of the bending stiffness of the skin in providing resistance to twisting of the column attached to the skin is such as to increase the critical stress given by equation (1) or (12) by an amount

$$\Delta f_{crit}=\frac{K_1Et_s^3}{6(1-\mu^2)dI_p}\frac{L_0^2}{\pi^2} \tag{25}$$

then

$$f_{crit}=\frac{\overline{G}J}{I_p}+\frac{C_{BT}}{I_p}\frac{\pi^2\overline{E}}{L_0^2}+\frac{K_1Et_s^3}{6(1-\mu^2)dI_p}\frac{L_0^2}{\pi^2} \tag{26}$$

where d is the stiffener spacing.

K_1, a constant depending upon the conditions of support of the skin at the adjacent stiffener or other structure.

It will be noted that in equation (26) $\overline{G}$ and $\overline{E}$ have been substituted for G and E, respectively, in equation (1). The substitution of $\overline{E}$ for E at this time was made to distinguish between the value of E associated with longitudinal stresses in the stiffener and its effective width of sheet and the value of E associated with bending of the skin between stiffeners. The desirability of distinguishing between these two values of E will be explained in a later section of this report in which the evaluation of $\overline{E}$ and $\overline{G}$ is discussed.

If the two ends of the stiffener are held against rotation about the axis of rotation and the end cross sec-

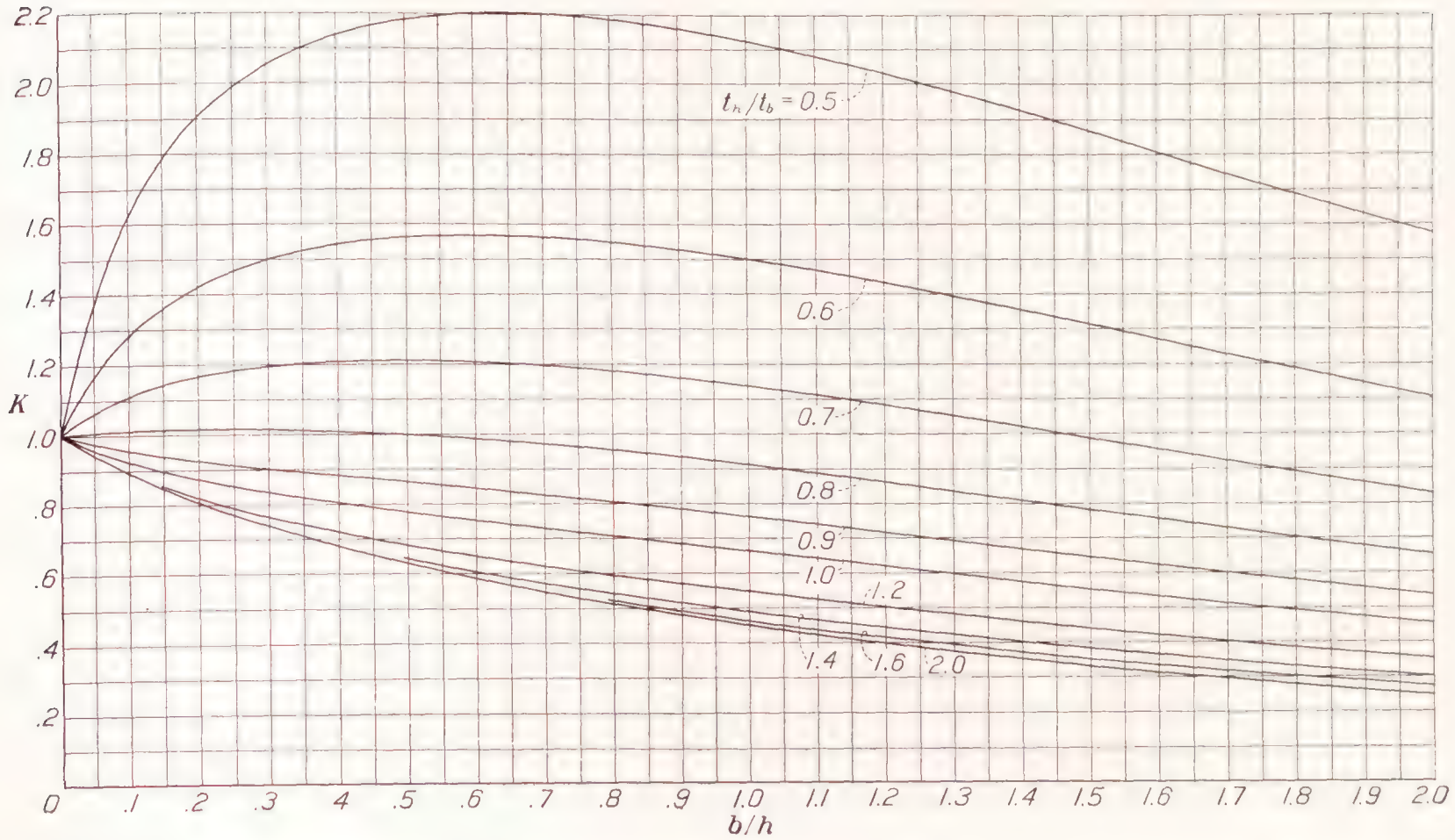

FIGURE 13.—Variation of K with b/h for different values of t_h/t_b when the axis of rotation is at the intersection of the center lines of the web and flange of an I section column

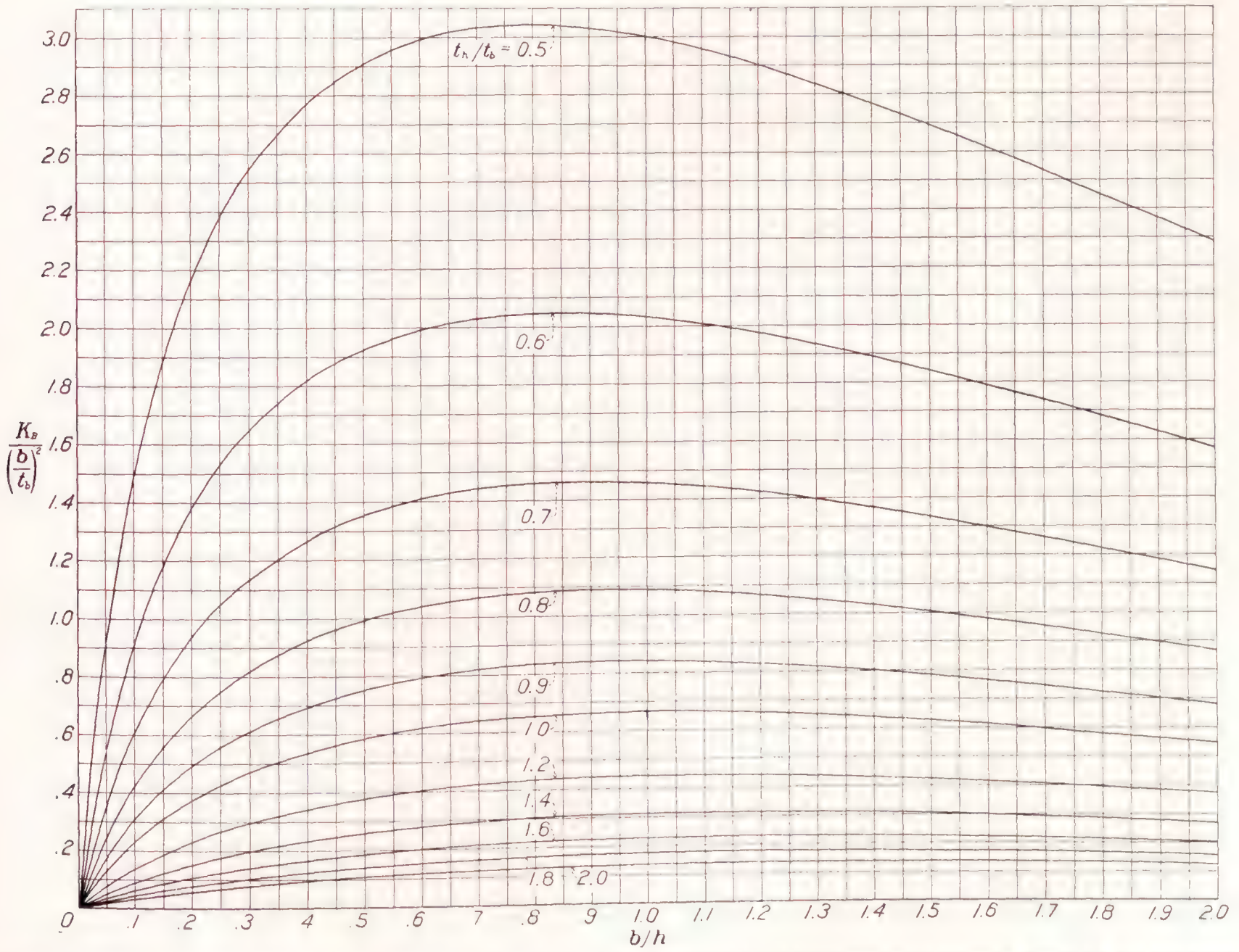

FIGURE 14.—Variation of $K_B/(b/t_b)^2$ with b/h for different values of t_h/t_b when the axis of rotation is at the intersection of the center lines of the web and flange of an I section column.

tions are free to have longitudinal displacements, L_0 cannot exceed the length L. For a skin approaching zero thickness L_0 will be equal to L. (See fig. 3 (b).) In general, however, $L_0=\frac{L}{n}$ where n has integral values ($n=1, 2, 3, 4$, etc.). Thus, when $L_0=\frac{L}{n}$ there will be a particular value of n for each skin-stiffener combination that will cause f_{crit} to be a minimum. A trial calculation should be made with $n=1, 2, 3, 4$, etc. to determine which value of n gives the lowest critical stress. This critical stress should then be compared with that for bending in a plane normal to the skin (reference 1) and the lower of these two stresses regarded as the stress at failure for the stiffener and its effective width of skin.

No information has thus far been given regarding the value of K_1 to be used in equation (26). For a stiffener that has one principal axis normal to the skin and that is also symmetrical about this principal axis, the value of K_1 may be taken from the curve given in figure 15 provided that the total compression load is equally divided among several stiffeners of the same dimensions spaced at equal intervals along the skin. This curve for K_1 was calculated by the energy method (reference 8, p. 584, art. 39) on the following assumptions:

(a) The full width of skin between stiffeners provides resistance to twisting of the stiffener.

(b) The skin is not under edge compression and is therefore flat until twisting of the stiffener occurs.

(c) When the stiffener twists, the skin takes the shape of a circular arc between stiffeners and a sine curve of half wave length L_0 parallel to the stiffeners.

Because the width of the effective skin that acts with the stiffener is small, any error that may result from assumption (a) is likely to be small. Of the three assumptions, (b) is probably the most questionable. Under load the skin is always subjected to edge compression and usually buckling of the skin occurs prior to twisting of the stiffeners. Because L_0 is usually several times the half wave length that forms when the skin alone buckles, any buckling of the skin prior to twisting of the stiffener tends to increase the effective thickness of the skin and hence the resistance of the skin to twisting of the stiffener. The increase in strength caused by the increase in effective thickness of the skin tends to offset any reduction in strength caused by the edge compression. The assumptions made under (c) are the most reasonable that could be made following (a) and (b) without greatly complicating the mathematics of the problem.

Until the curve for K_1 given in figure 15 has been checked by tests, it should be used only as a guide to design. As such, it will point the direction toward a ore efficient proportioning of material between skin and stiffeners. (See appendix A.) In the skin-stiffener combinations that are likely to be used in practice $\frac{L_0}{d}$ will usually be greater than 3. For these cases it will be satisfactory to use $K_1=2$, the asymptote for the curve of figure 15.

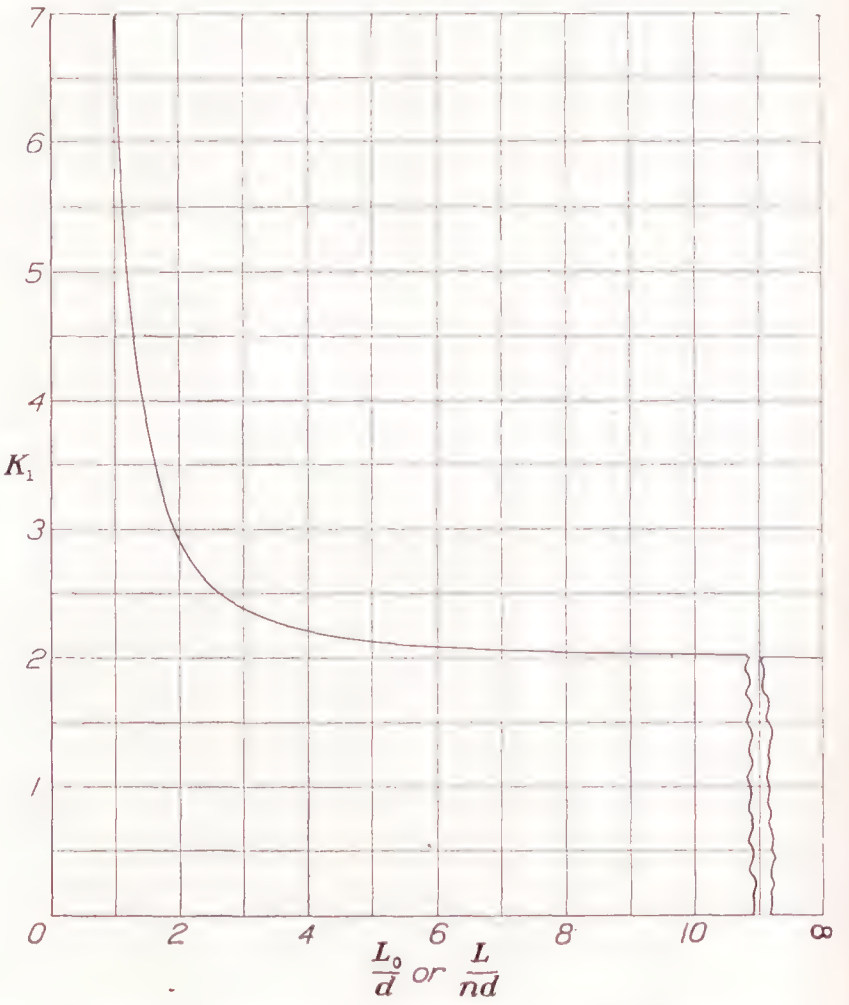

FIGURE 15.—Values of K_1 for use in equations (25) and (26).

$$K_1=\left[2+\frac{\pi^2}{3}\left(\frac{d}{L_0}\right)^2+\frac{\pi^4}{60}\left(\frac{d}{L_0}\right)^4\right]$$

Effective modulus of elasticity.—For columns that fail by bending, the critical stresses depart from the theoretical values given by the Euler formula at low values of the slenderness ratio. Consequently, an empirical straight line or parabolic curve is frequently drawn on the column chart to give the critical stress in this range. Likewise, for the general theory there will be a similar departure of the critical stress from the theoretical values given in this report and empirical curves must be found to give the strength for short lengths.

For a column that fails by bending, the reduced strength at short lengths is explained by the double-modulus theory of column action (reference 8, p. 572, art. 37, and references 9 and 10). This theory follows briefly: When a straight, centrally loaded column is stressed above the proportional limit for the material and deflected, the stress on the concave side increases according to the tangent modulus E' for the material (the slope of the stress-strain curve at the stress concerned) while the stress on the convex side decreases according to Young's modulus E for the material. The critical stress is then given by the Euler formula when an effective modulus $\overline{E}$ is substituted for E. The effective modulus is dependent upon the shape of the

column cross section as well as upon E' and E and is given by the following general expression (references 9 and 10):

$$\overline{E}=\frac{E'I_1+EI_2}{I} \tag{27}$$

where, according to Osgood (reference 9), "I_1 is the moment of inertia about the axis of average stress [zero bending stress, see fig. 16] of the part of the cross-

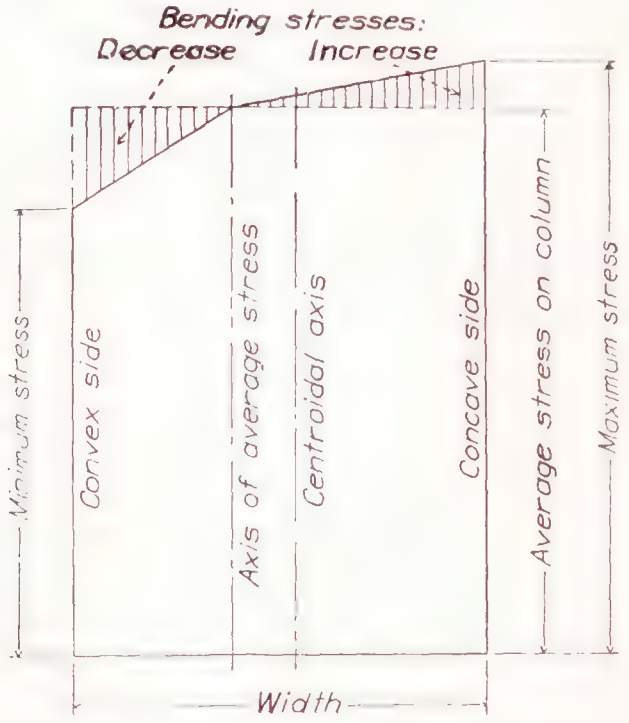

FIGURE 16.—Stress distribution for double-modulus theory.

sectional area which suffers an increase of stress at the instant of failure of the column, I_2 is the moment of inertia about the axis of average stress of the part of the cross-sectional area which suffers a decrease of stress at the instant of failure of the column, and I is the moment of inertia of the total cross-sectional area of the column about the centroidal axis normal to the plane of bending. The position of the axis of average stress is defined by the relation $E'S_1=ES_2$ where S_1 and S_2 are the statical moments about the axis of average stress, respectively, of the two parts of the cross-sectional area just mentioned in connection with I_1 and I_2."

The effective modulus has been evaluated for a number of cross sections. For a rectangular section (reference 4, p. 242, equation (161))

$$\overline{E}=\frac{4EE'}{(\sqrt{E}+\sqrt{E'})^2} \tag{28}$$

from which

$$\frac{\overline{E}}{E}=\frac{4\left(\frac{E'}{E}\right)}{\left(1+\sqrt{\frac{E'}{E}}\right)^2} \tag{29}$$

For an I section with a web of negligible thickness and with bending in the plane of the web (reference 9, equation (4))

$$\overline{E}=\frac{2EE'}{E+E'} \tag{30}$$

from which

$$\frac{\overline{E}}{E}=\frac{2\left(\frac{E'}{E}\right)}{1+\left(\frac{E'}{E}\right)} \tag{31}$$

In the theory for primary failure as herein presented there is a double-modulus action, similar to the double-modulus action in bending, when the column is stressed above the proportional limit for the material. In view of the fact that this double-modulus action is concerned only with longitudinal bending stresses, an effective modulus $\overline{E}$ will be substituted for E in the second term of equations (1) and (12). It is shown theoretically in appendix C that this value of $\overline{E}$ is

$$\overline{E}=\frac{E'C_{BT_1}+EC_{BT_2}}{C_{BT}} \tag{32}$$

where C_{BT_1} is the value obtained from equation (4) when the integration is made over the part of the cross section that suffers an increase of stress at the instant of failure of the column, C_{BT_2} is the value obtained from equation (4) when the integration is made over the part of the cross section that suffers a decrease of stress at the instant of failure of the column, and C_{BT} is the value obtained from equation (4) when the integration is made over the entire cross section as previously outlined. In order to locate the points of average stress (zero bending stress), which define the limits of integration for C_{BT_1} and C_{BT_2}, the reference plane must be so located that

$$E'\int D_1dA+E\int D_2dA=0 \tag{33}$$

where D_1 and D_2 are the longitudinal displacements used in the evaluation of C_{BT_1} and C_{BT_2}, respectively. Physically, equation (33) means that the summation of the forces on the cross section that result from the longitudinal displacements is zero.

When the column is stressed above the proportional limit for the material, the shear modulus G, which is related to E, must be corrected to correspond to the reduced modulus $\overline{E}$ for the column. A theoretical treatment of this problem does not appear to have been published. Bleich (reference 11) used for the effective shear modulus

$$\overline{G}=\sqrt{\tau}G \tag{34}$$

where

$$\tau=\frac{\overline{E}}{E} \tag{35}$$

It was reasoned that the percentage reduction in G was not so great as in E. Because τ is always equal to or less than unity, Bleich selected $\sqrt{\tau}\ G$ as a convenient expression for the effective shear modulus.

After analyzing the results of some 500 tests on angle columns where failure occurred by twisting, Kollbrunner (reference 12) concluded that the effective shear modulus was best given by the equation

$$\overline{G}=\frac{\tau+\sqrt{\tau}}{2}G \tag{36}$$

As this value of $\overline{G}$ is based upon test data, it is recommended that it be used in preference to the value given by equation (34) to express the reduced shear modulus. Thus, when the column is stressed above the proportional limit, the value of $\overline{G}$ given by equation (36) should be substituted for G in the first term of equations (1) and (12).

When the axis of rotation is at infinity on either of the principal axes, equation (32) reduces to equation (27). It can be shown that, when the axis of rotation is at the centroid of an **I** section, the value of $\overline{E}$ is the same as when the axis of rotation is at infinity on the principal axis parallel to the web. For these two locations of the axis of rotation the value of $\overline{E}$ can conservatively be assumed to be the same as that given by equation (28) for the bending of a rectangular cross section. This close agreement is shown in figure 17 where values of $\frac{\overline{E}}{E}$ are plotted against $\frac{E'}{E}$.

When the axis of rotation is at infinity on the principal axis normal to the web of an **I** section, the value of $\overline{E}$ will in all cases lie between that given by equations (28) and (30), as shown in figure 18. It will therefore be conservative to assume that $\overline{E}$ is given by equation (30) for this case.

When the axis of rotation is at the point where the principal axis crosses the skin, the considerations of the double-modulus action result in a lack of symmetry for the **I** section. This lack of symmetry may cause the critical stress to be a minimum when the axis of rotation is slightly shifted in the plane of the skin. Although a study of this condition has not been completed, it appears that the shift of the axis of rotation in the plane of the skin is small, for columns of practical dimension, and that the values of $\overline{E}$ are near those given by equations (28) and (30).

In figure 19 it is shown that the values of $\overline{E}$ as given by equations (28) and (30) are very nearly the same as the values for a thin circular ring or a tube. In view of this fact it appears justifiable for practical use to assume that $\overline{E}$ for the **I** section is the same as $\overline{E}$ for the thin-wall tube in bending. Dr. W. R. Osgood of the National Bureau of Standards suggested that the column curves constructed by the theory of this report be made consistent with the curves now used for tubes, which are determined from column tests, by evaluating $\overline{E}$ according to the following procedure:

1. Assume a series of values for the slenderness ratio $\frac{L_0}{\rho}$.

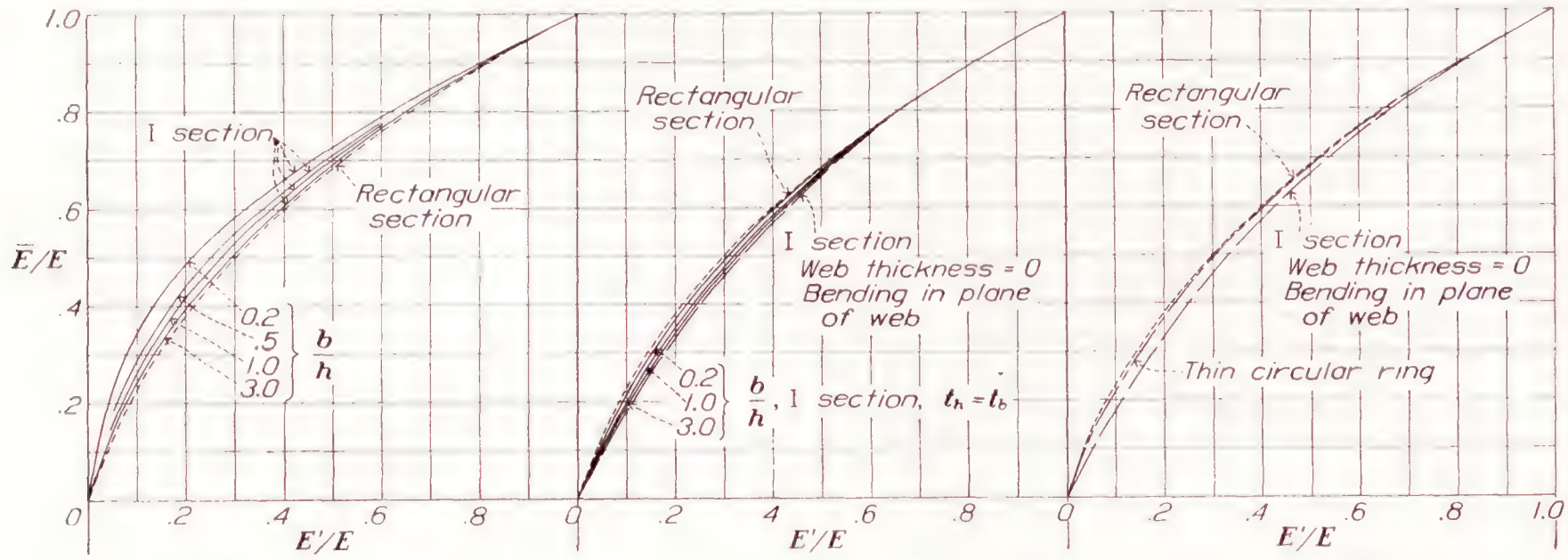

FIGURE 17.—Variation of $\overline{E}/E$ with E'/E for an **I** section column when the axis of rotation is at the centroid or at infinity on the principal axis parallel to the web.

FIGURE 18.—Variation of $\overline{E}/E$ with E'/E for an **I** section column when the axis of rotation is at infinity on the principal axis normal to the web.

FIGURE 19.—Variation of $\overline{E}/E$ with E'/E for a rectangular section, a thin circular ring, and an **I** section in bending.

2. By means of the accepted column curve for tubes of the material under consideration, determine the critical stress f_{crit}.

3. Substitute the assumed values of $\frac{L_0}{\rho}$ and the corresponding values of f_{crit} in the following equation to obtain $\overline{E}$ and plot a curve of f_{crit} against $\overline{E}$:

$$\overline{E}=f_{crit}\frac{1}{\pi^2}\left(\frac{L_0}{\rho}\right)^2 \tag{37}$$

4. Correct this value of $\overline{E}$ for the cross-sectional shape being used (figs. 17 to 19), if desired.

In the construction of a column curve for a particular **I** section, the following procedure should be used:

1. Select the location of the axis of rotation for which the column curve is to be drawn.

2. Assume a series of values of f_{crit}.

3. From the curve of $\overline{E}$ against f_{crit} previously derived, tabulate the values of $\overline{E}$ and $\overline{G}$ that correspond to the assumed values of f_{crit}.

4. Evaluate J, I_p, and C_{BT}.

5. Substitute J, I_p, C_{BT}, the assumed values of f_{crit}, and the corresponding values of $\overline{E}$ and $\overline{G}$ in equation (1) or (12) and solve for the length L_0.

6. The column curve is obtained by plotting the assumed values of f_{crit} against the computed lengths L_0.

If the column is attached to a skin, the values of J, I_p, and C_{BT} calculated under 4 should be increased by the amounts ΔJ, ΔI_p, and ΔC_{BT}, respectively. These values together with the assumed values of f_{crit} and the corresponding values of $\overline{E}$ and $\overline{G}$ are then substituted in equation (26), which is solved for the length L_0. A curve is then drawn by plotting the assumed values of f_{crit} against the computed values of L_0. This curve will be found to have a minimum point at some particular value of L_0. Because $L_0=\frac{L}{n}$, where n is an integral value ($n=1$, 2, 3, 4, etc.), the strength for any particular length L is obtained by choosing such a value of n as will cause the critical stress to be a minimum. (See appendix A.)

CONCLUSIONS

The following conclusions apply when primary column failure is defined as any type of failure in which the cross sections are translated, rotated, or both translated and rotated but not distorted.

1. When primary failure occurs in a pin-end column that is straight and centrally loaded, the general equation for the critical stress is

$$f_{crit}=\frac{\overline{G}J}{I_p}+\frac{C_{BT}}{I_p}\frac{\pi^2\overline{E}}{L_0^2}$$

In the derivation of this equation it is assumed that the cross sections rotate about an axis parallel to the column. The factors I_p and C_{BT} depend upon the location of this axis, which is called the "axis of rotation." The first term $\frac{\overline{G}J}{I_p}$ gives the critical stress for a pure twisting failure about the axis of rotation. The second term $\frac{C_{BT}}{I_p}\frac{\pi^2\overline{E}}{L_0^2}$ is in the nature of a correction for the effect of length caused by longitudinal bending stresses when the end cross sections are held against rotation. All possible combinations of translation and rotation of the column cross section are obtained by letting the location of the axis of rotation vary from zero to infinity in every direction.

2. The theory for primary failure shows that, for a free column with a cross section symmetrical about its two principal axes, the axis of rotation will be at either of the two following locations depending upon which location gives the lower stress:

(a) The center of twist, which is at the centroid of the section.

(b) Infinity on the principal axis about which the moment of inertia is the smaller.

Location (a) gives the condition for twisting failure; location (b), the condition for bending failure.

3. For a pin-end free column of I section symmetrical about its two principal axes the critical stress will be a minimum when the axis of rotation is at infinity on the principal axis parallel to the web, provided that the two following conditions are met:

$$\frac{t_h}{t_b}<14.7$$

and

$$\frac{b}{h}<\sqrt[3]{\frac{t_h}{t_b}}$$

When these conditions are not satisfied, the critical stress should be computed for the axis of rotation located at the centroid and compared with the critical stress for bending about the axis of minimum moment of inertia. The smaller of these two values will then be the stress at which failure occurs.

4. When a column is attached to a skin, the great stiffness of the skin in its own plane causes the axis of rotation to lie in the plane of the skin. When the column cross section is symmetrical about its two principal axes, one of which is normal to the skin, the axis of rotation will be at either of the two following locations depending upon which location gives the smaller stress:

(a) The point where the principal axis crosses the skin.

(b) Infinity in the plane of the skin.

Location (a) gives the condition for twisting failure when the column is attached to a skin; location (b), the condition for bending normal to the skin.

5. When a column is attached to a skin and the axis of rotation is at a point other than infinity in the plane of the skin, the rotation of the cross sections about the axis of rotation is resisted by the bending stiffness of the skin. The effect of this restraint is to increase the critical stress by an amount

$$\Delta f_{crit}=\frac{K_1Et_s^3}{6(1-\mu^2)dI_p}\frac{L^2}{n^2\pi^2}$$

and the critical stress becomes

$$f_{crit}=\frac{\overline{G}J}{I_p}+\frac{C_{BT}}{I_p}\frac{n^2\pi^2\overline{E}}{L^2}+\frac{K_1Et_s^3}{6(1-\mu^2)dI_p}\frac{L^2}{n^2\pi^2}$$

In this equation $n=1$, 2, 3, 4, etc., the number of half waves that develop in the stiffener in the length L. A trial calculation is necessary to determine which value of n gives the lowest critical stress. This critical stress should then be compared with that for bending in a plane normal to the skin and the lower of these two stresses regarded as the stress at failure for the stiffener and its effective width of skin.

6. When the column length is small, there will be a departure of the critical stresses from the theoretical values given by this theory that is similar to the departure from the Euler values in standard column curves. It is because of this fact that the effective moduli $\overline{E}$ and $\overline{G}$ have been substituted for E and G, respectively,

in certain terms of the equations for the critical stress. So long as the column is not stressed above the proportional limit, $\overline{E}$ and $\overline{G}$ are equal to E and G, respectively. Above the proportional limit the substitution of $\overline{E}$ for E follows from the double-modulus theory of bending where

$$\overline{E}=\frac{E'C_{BT_1}+EC_{BT_2}}{C_{BT}}$$

For the evaluation of G, the following empirical expression is recommended:

$$\overline{G}=\frac{\tau+\sqrt{\tau}}{2}G$$

where

$$\tau=\frac{\overline{E}}{E}$$

7. When the axis of rotation of a symmetrical I section column is at the center of twist (centroid) or at infinity on one of the principal axes, the value of $\overline{E}$ is very nearly the same as that for a thin-wall tube of the same material in bending. When the axis of rotation is at the point where the principal axis crosses the skin, the considerations of the double-modulus action result in a lack of symmetry for the I section. This lack of symmetry may cause the critical stress to be a minimum when the axis of rotation is slightly shifted in the plane of the skin. Although a study of this condition has not been completed, it appears that the shift of the axis of rotation in the plane of the skin is small for columns of practical dimensions and that the values of $\overline{E}$ are also near those for a thin-wall tube in bending.

8. The value of $\overline{E}$ varies with the critical stress and should be computed from the accepted column curve for the material by use of the following equation:

$$\overline{E}=f_{crit}\frac{1}{\pi^2}\left(\frac{L_0}{\rho}\right)^2$$

If desired, this value of $\overline{E}$ may be corrected for different cross-sectional shapes.

LANGLEY MEMORIAL AERONAUTICAL LABORATORY,
NATIONAL ADVISORY COMMITTEE FOR AERONAUTICS,
LANGLEY FIELD, VA., *August 17, 1936.*

APPENDIX A

ILLUSTRATIVE PROBLEM

Problem: To construct the column curve for an I section column of 24S-T aluminum-alloy material (E=10,537,000 pounds per square inch), with the dimensions shown in figure 20, used as a stiffener on skin

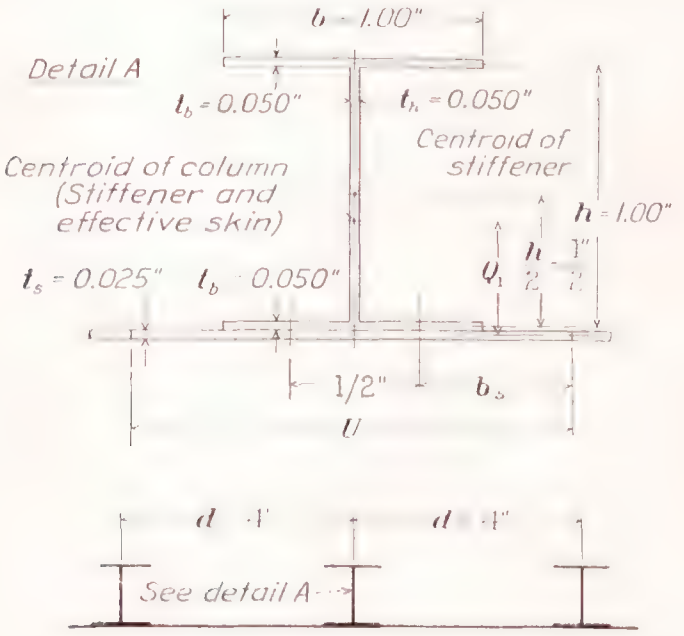

FIGURE 20.—A skin-stiffener combination.

0.025 inch thick. It is assumed that the stiffeners are spaced at 4-inch intervals along the skin and that all stiffeners are equally loaded in compression.

Effective moduli $\overline{E}$ and $\overline{G}$ for 24S-T aluminum alloy.—It is assumed that the pin-end column strength of 24S-T tubes is given by the straight-line equation

$$f_{crit}=58{,}000-527\frac{L_0}{\rho} \tag{38}$$

for values of the slenderness ratio $\frac{L_0}{\rho}$ between 9.5 and 73. Below $\frac{L_0}{\rho}=9.5$ it is assumed that the critical stress is 53,000 pounds per square inch. Above $\frac{L_0}{\rho}=73$ the stress is assumed to be given by the Euler formula

$$f_{crit}=\frac{\pi^2 E}{\left(\frac{L_0}{\rho}\right)^2} \tag{39}$$

The calculations for the effective moduli $\overline{E}$ and $\overline{G}$ are made as follows, the results of which are given in table I:

1. Assume a series of values of $\frac{L_0}{\rho}$

2. Compute f_{crit} from

$$f_{crit}=58{,}000-527\frac{L_0}{\rho} \text{ for } 9.5<\frac{L_0}{\rho}<73$$

$$f_{crit}=\frac{\pi^2 E}{\left(\frac{L_0}{\rho}\right)^2} \qquad \text{for } \frac{L_0}{\rho}>73$$

3. Using the computed values of f_{crit}, compute $\overline{E}$, from

$$\overline{E}=\frac{f_{crit}\left(\frac{L_0}{\rho}\right)^2}{\pi^2} \tag{37}$$

4. Compute τ from

$$\tau=\frac{\overline{E}}{E},\ E=10{,}537{,}000$$

5. Compute $\overline{G}$ from

$$\overline{G}=\left[\frac{\tau+\sqrt{\tau}}{2}\right]G,\ G=0.385E=4{,}057{,}000$$

Effective width of skin that acts with the column.—It is assumed that the column is attached to the skin with two lines of rivets one-half inch apart. The width of the skin between the rivet lines is therefore $20t_s$. The effective width outside the rivet lines is assumed to be given by the von Kármán equation for the effective width with the coefficient of 1.70, established in reference 1

$$2b_s=1.70t_s\sqrt{\frac{E}{f_{crit}}} \tag{40}$$

Professor Joseph S. Newell and Mr. Walter H. Gale in an unpublished report of aircraft materials research at the Massachusetts Institute of Technology for 1931–32 recommend the value of 1.73 for the coefficient in the von Kármán equation.

As the width $20t_s$ between the two rivet lines is less than the smallest value of $2b_s$ given by equation (40) when f_{crit}= 53,000 pounds per square inch, all the material between the two rivet lines must be considered as effective and the total effective width of skin that acts with the column and carries the same stress as the column is

$$U=0.5+2b_s \tag{41}$$

38548—38——12

The effective width of skin is calculated as follows, the results of which are given in table II:

1. Assume a series of values of f_{crit}. (For convenience, use the same values as given in table I.)
2. Compute $2b_s$ by equation (40).
3. Compute U by equation (41).

Axis of rotation at infinity in the plane of the skin for bending failure.—In the report proper it has been shown that, when an **I** section column is attached to a skin, the axis of rotation will be either at infinity in the plane of the skin or at the point where the principal axis crosses the skin. The column curve must therefore be drawn for each location to determine which location gives the lower critical stress.

When the axis of rotation is at infinity in the plane of the skin, the critical stress is given by the Euler formula, equation (2) or (39), with $\overline{E}$ substituted for E. For this case $\frac{I}{A}$, equation (2), is calculated about a centroidal axis parallel to the skin considering the effective area of the skin Ut_s as a part of the column cross section. The calculations for the construction of the column curve are made as follows, the results of which are given in table III:

1. Assume a series of values of f_{crit}. (For convenience use the same values as in table I.)
2. Compute area of effective skin, Ut_s. (For U see table II.) $t_s=0.025$.
3. Compute total area of column cross section, from $A=A_{stiff}+A_U$

where A_{stiff}=area of stiffener=0.15 sq. in.

A_U=area of effective skin=0.025 U

4. Compute the centroid of the column cross section (including the effective skin) and tabulate the distance Q_1 from the center line of the skin to the centroid,

$$Q_1=\frac{A_{stiff}\left(\frac{h}{2}+\frac{t_b+t_s}{2}\right)}{A}=\frac{A_{stiff}\,(0.5375)}{A}\quad\text{(See fig. 20.)}$$

5. Compute the moment of inertia, of the complete column cross section (area A), about the centroidal axis parallel to the skin

$$I=\frac{1}{12}t_h h^3+2bt_b\frac{h^2}{4}+[2bt_b+ht_h]\left[\frac{h}{2}+\frac{t_b+t_s}{2}-Q_1\right]^2+Ut_sQ_1^2$$

$$=0.004167+0.025+0.15\,(0.5375-Q_1)^2+Ut_sQ_1^2$$

6. From table I obtain the values of $\overline{E}$ that correspond to the assumed values of f_{crit}.
7. Compute the lengths L_0 that correspond to the assumed critical stresses by use of the Euler formula where $\overline{E}$ has replaced E,

$$L_0=\pi\sqrt{\frac{I}{A}\frac{\overline{E}}{f_{crit}}}$$

In figure 21 the assumed values of f_{crit} are plotted against the computed values of L_0. For a column with pin ends, $L_0=L$. Hence figure 21 is the column curve for the axis of rotation at infinity in the plane of the skin (bending failure). This direct calculation for obtaining the column curve when failure occurs by bending normal to the skin is preferable to the trial and error procedure recommended in reference 1.

Axis of rotation at the intersection of the center lines of the web and skin—twisting failure.—The calculation for the construction of the column curve when the axis of rotation is at the intersection of the center lines of the web and skin are similar to those for the axis of rotation at infinity in the plane of the skin. The calculations are made as follows; the results are given in table IV.

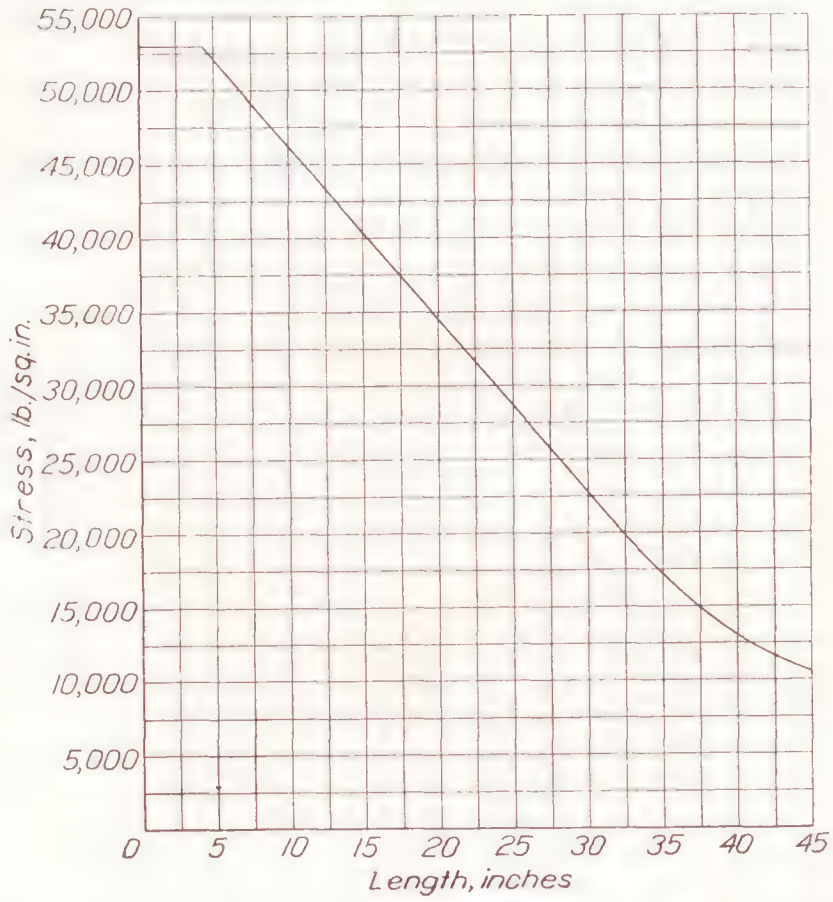

FIGURE 21.—The column curve for bending failure of the skin-stiffener combination shown in figure 20. The axis of rotation is at infinity in the plane of the skin.

1. Assume a series of values for f_{crit}. (For convenience use the same values as in table I.)
2. Compute ΔJ from

$$\Delta J=\frac{1}{3}Ut_s^3 \tag{21}$$

3. Compute J from

$$J=J_{stiff}+\Delta J$$

$$\text{where } J_{stiff}=\frac{1}{3}ht_h^3+\frac{2}{3}bt_b^3 \tag{13}$$

4. Compute ΔI_p from

$$\Delta I_p=\frac{1}{12}U^3t_s \tag{22}$$

5. Compute I_p from

$$I_p=I_{p_{stiff}}+\Delta I_p$$

where

$$I_{p_{stiff}}=\frac{1}{12}h^3t_h+\frac{1}{2}h^2bt_b+\frac{1}{6}b^3t_b+[ht_h+2bt_b]\,[P^2+Q^2] \tag{14}$$

(In the evaluation of equation (14), note that

$$P=0 \text{ and } Q=\frac{h}{2}+\frac{t_b+t_s}{2}=0.5375.)$$

6. Compute ΔC_{BT} from

$$\Delta C_{BT}=\Delta C_T=\frac{1}{144}U^3t_s^3 \tag{24}$$

7. Compute C_{BT} from

$$C_{BT}=C_{BT_{stiff}}+\Delta C_{BT}$$

where

$$C_{BT_{stiff}}=C_B+C_T \tag{6}$$

$$C_B=\frac{1}{24}b^3h^2t_b+\left[\frac{h^2bt_b}{2}+\frac{h^3t_h}{12}\right]P^2+\frac{b^3t_b}{6}Q^2 \tag{8}$$

$$C_T=\frac{b^3t_b^3}{72}+\frac{h^3t_h^3}{144}+\frac{bt_b^3}{6}P^2+\frac{ht_h^3}{12}Q^2 \tag{10}$$

(In the evaluation of equation (6), note that $P=0$ and $Q=0.5375$.)

8. From table I obtain the values of $\overline{E}$ and $\overline{G}$ that correspond to the assumed values of f_{crit}.

9. Solve equation (26) for L_0.

$$L_0=\sqrt{\frac{-\left[\frac{\overline{G}J}{I_p}-f_{crit}\right]\pm\sqrt{\left[\frac{\overline{G}J}{I_p}-f_{crit}\right]^2-4\left[\frac{C_{BT}\pi^2\overline{E}}{I_p}\right]\left[\frac{K_1Et_s^3}{6(1-\mu^2)d\pi^2I_p}\right]}}{\frac{2K_1Et_s^3}{6(1-\mu^2)d\pi^2I_p}}} \tag{42}$$

Evaluate equation (42) using values of J, I_p, C_{BT}, $\overline{G}$, and $\overline{E}$ that correspond to the assumed values of f_{crit}; and

$\mu=0.3$

$E=10{,}537{,}000$ lb. per sq. in.

$d=4$ in.

$t_s=0.025$ in.

$K_1=2$

In figure 22 the assumed values of f_{crit} are plotted against the computed values of L_0. From this figure the column curve for twisting failure is derived in the following manner. Put L_0 equal to $\frac{L}{n}$ and then plot curves of f_{crit} against L for $n=1$, 2, 3, 4, etc. The column curve is then given by the lowest portions of the several curves and is shown by full lines in figure 23.

Column curve for primary failure.—It has been previously shown that primary failure will occur either by bending or by twisting, depending upon which type of failure gives the lower critical stress. The column curves of figures 21 and 23 are therefore combined as shown in figure 24 to obtain the column curve for

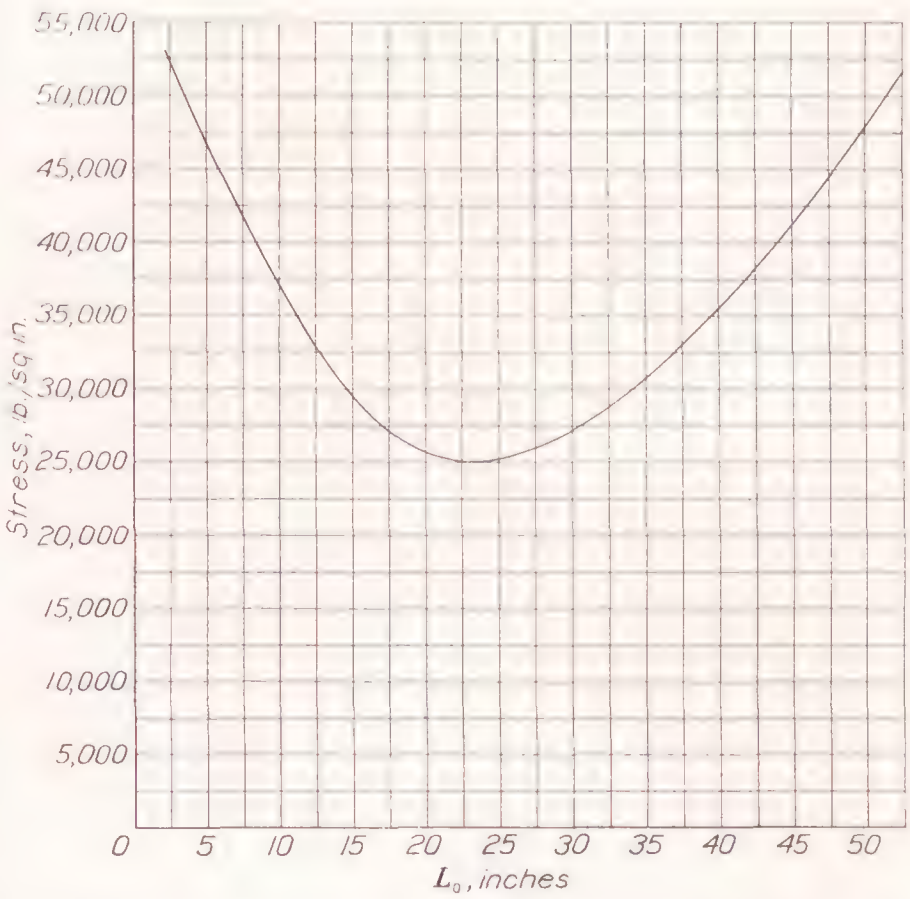

FIGURE 22.—Critical stress plotted against L_0 for twisting failure of the skin-stiffener combination shown in figure 20. The axis of rotation is at the intersection of the center lines of the web and the skin.

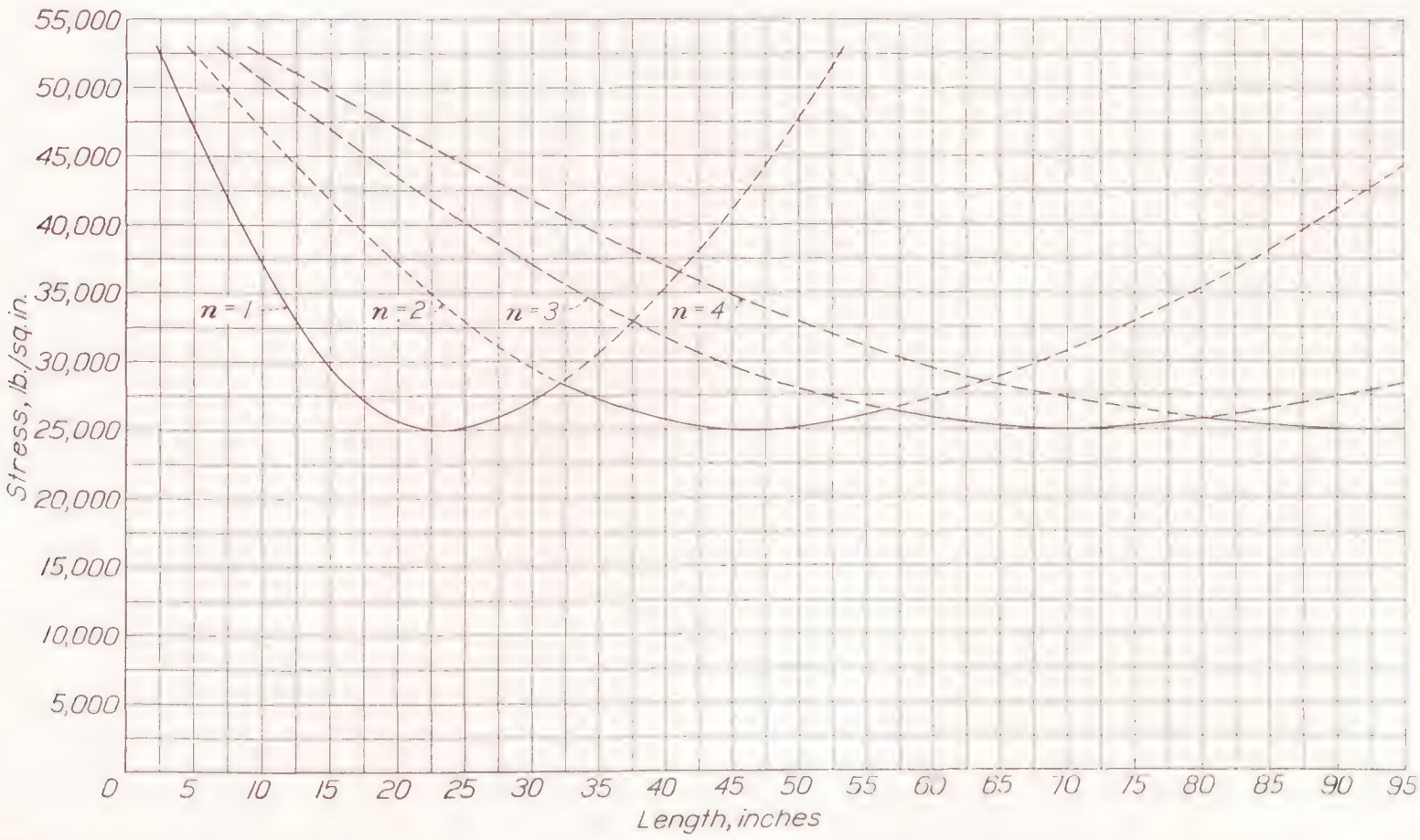

FIGURE 23.—The column curve for twisting failure of the skin-stiffener combination shown in figure 20. The axis of rotation is at the intersection of the web and the skin.

primary failure. It will be noted that, at lengths less than 27.4 inches, failure occurs by twisting; whereas, at lengths greater than 27.4 inches, failure occurs by bending.

Discussion.—In the computed tables for this illustrative problem it will be noted that some of the factors are small and might have been neglected. All of the factors, however, have been included to show their relative numerical values and the method of evaluation. The designer may therefore shorten the calculations here outlined by neglecting the unimportant factors, if desired.

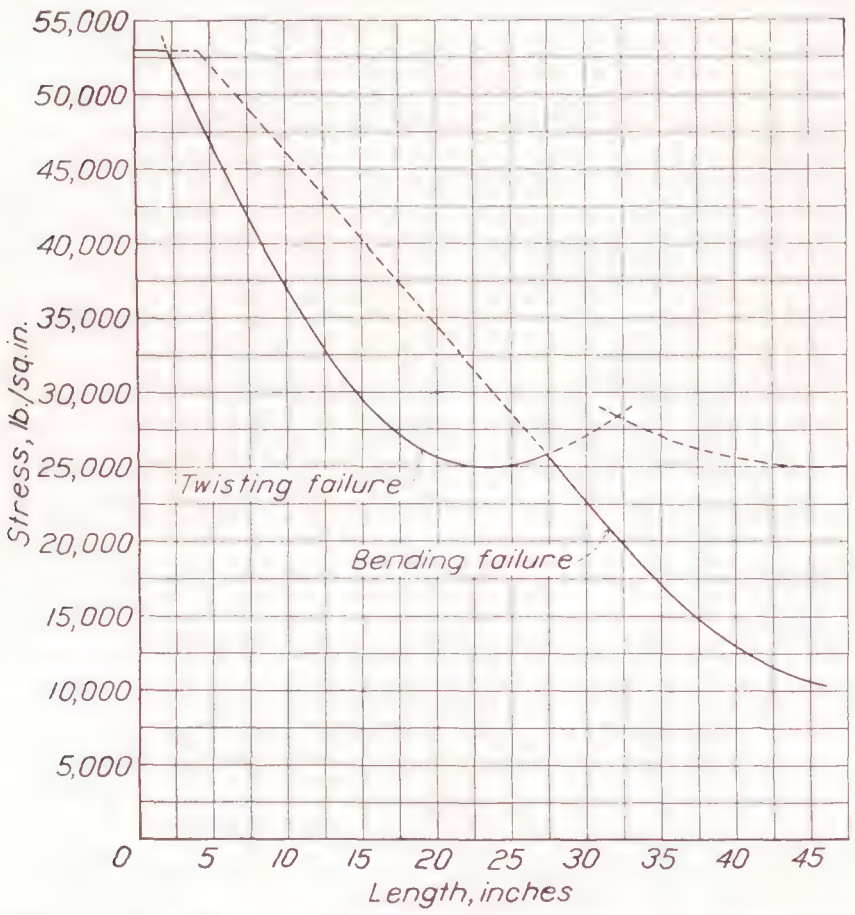

FIGURE 24.—The column curve for primary failure of the skin-stiffener combination shown in figure 20.

In the foregoing calculations for twisting failure it was assumed that $K_1=2$ regardless of the value of $\frac{L_0}{d}$. This value of K_1 was selected because of the possible uncertainty in establishing a more definite value, as discussed in this report. If it had been desired to use the values of K_1 given by the curve of figure 15 rather than the asymptotic value $K_1=2$, the calculation of L_0 would of necessity have been by trial and error because K_1 varies with $\frac{L_0}{d}$.

When a skin-stiffener combination is loaded in compression, buckling will first occur in the skin provided that the stiffener spacing divided by the skin thickness $\frac{d}{t_s}$ is sufficiently large. Because the skin is attached to the stiffeners, the buckling of the skin will twist the stiffeners and form small waves in them, the lengths of which are the same as those in the skin. In this condition the stiffeners are not ready to buckle of themselves but are forced to buckle by the skin. The stiffeners therefore resist buckling of the skin.

Now, if the load on the skin-stiffener combination is increased, the waves in the skin and the corresponding waves in the stiffeners grow larger. Finally a load is reached at which the stiffeners buckle of themselves. The type of buckling that occurs in the stiffeners will be that associated with the lowest critical stress. On the assumption that local buckling does not occur, the stiffeners will either buckle by deflection perpendicular to the skin in the manner of an ordinary column or will twist about an axis in the plane of the skin. If twisting occurs, the skin will resist twisting of the stiffeners. The column curves derived by the methods of this report give the critical stress at which the stiffeners begin to buckle (bend or twist) of themselves. Because the stiffeners are the main strength element in a skin-stiffener combination, it seems quite proper that the strength of the combination should be based on the strength of the stiffeners.

When the stiffeners fail by twisting, it is quite possible that tests will show the ultimate load for a skin-stiffener panel in compression to be greater than the critical load at which twisting begins. The reason for this belief is that when the stiffener twists, the material adjacent to the axis of rotation is not laterally displaced and is therefore capable of further compression. The amount by which the ultimate load will exceed the critical load at which buckling begins is dependent upon a number of factors the consideration of which is beyond the scope of this report.

Until the results of extensive tests made especially to check the theoretical behavior of skin-stiffener combinations in compression become available, the designer should conservatively assume that failure occurs when the buckling load is reached. The methods outlined in this report and illustrated in this appendix may therefore be used to derive column curves for different skin-stiffener combinations. By comparison of the strength-weight ratios the most efficient combination of skin and stiffeners can be selected.

APPENDIX B

APPLICATION OF THE THEORY FOR PRIMARY FAILURE TO A COLUMN OF CLOSED SECTION

Equation (1), which has heretofore been applied to columns of open section, can also be applied to columns of closed section provided that all the factors appearing on the right-hand side of the equality sign can be evaluated. It will be shown how these factors can be evaluated for a thin-wall column of closed rectangular section, symmetrical about its two principal axes. (See fig. 25.)

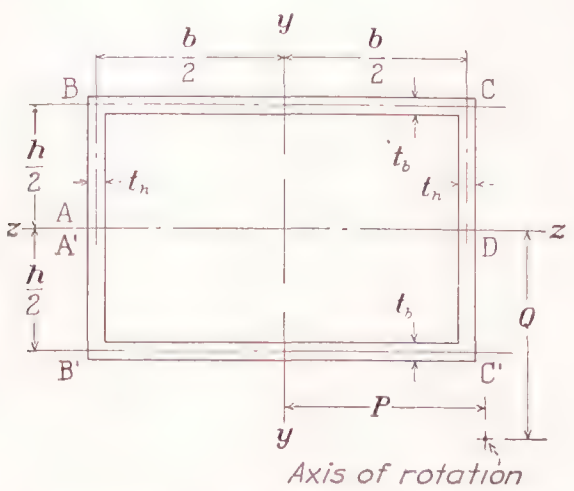

FIGURE 25.—A thin-wall rectangular tube.

Evaluation of GJ/I_p.—Except for J and C_{BT} all of the factors that enter into equation (1) are readily evaluated by standard methods. For the closed section

$$J=\frac{4A^2}{\int\frac{ds}{t}} \tag{43}$$

where A is the area enclosed by the center lines of the wall of the rectangular tube.

ds, differential element of the perimeter.

t, wall thickness of ds.

For a square tube of constant thickness equation (43) becomes

$$J=b^3t$$

Because the square tube is symmetrical about its two principal axes, the critical stress will be a minimum when the axis of rotation for the free column is either at the centroid (center of twist $P=0$, $Q=0$) or at infinity on one of the principal axes. The critical stress when the axis of rotation is at the centroid will be greater than that given by the first term of equation (1) or

$$(f_{crit})_{\substack{P=0\\Q=0}}>\frac{GJ}{I_p}=\frac{0.385Eb^3t}{\frac{4}{3}b^3t}=\frac{3}{4}(0.385E)$$

or, if $E=10^7$ pounds per square inch,

$$(f_{crit})_{\substack{P=0\\Q=0}}>2{,}885{,}000 \text{ pounds per square inch}$$

As this value of the critical stress is much greater than the yield-point stress for any engineering material with $E=10^7$ pounds per square inch, it may be concluded that the large torsional rigidity of a closed section precludes any type of primary failure except bending failure; i. e., axis of rotation at infinity on one of the principal axes.

Evaluation of C_{BT}.—In order to show that C_{BT} can be evaluated for a closed section, the expressions for the longitudinal displacement at the center lines of the wall of the tube will be derived. In view of the conclusion in the preceding paragraph, the value of this work will be more in the possibilities offered in the calculation of the stresses in monocoque shells, such as airplane wings, fuselages, floats, and hulls than in the solution of the column problem.

First, the longitudinal displacements caused by the twisting of the section about its centroid will be determined ($P=0$, $Q=0$ in fig. 25). If the tube is assumed to be slit longitudinally on the z axis at A—A′, the closed section becomes an open section. Now imagine a portion of length dx to be twisted an amount $d\varphi$ about the centroid (center of twist for the closed section). The longitudinal displacements of the points on the end cross section caused by such twisting can then be determined in the same manner as for an open section. These displacements with respect to the original plane of the end cross section are, at a distance s measured from

$$\left.\begin{aligned}
&\text{B toward A,}\quad -\theta\left[\frac{3hb}{4}+\frac{bs}{2}\right]\\
&\text{C toward B,}\quad -\theta\left[\frac{hb}{4}+\frac{hs}{2}\right]\\
&\text{D toward C,}\quad -\theta\left[\frac{bs}{2}\right]\\
&\text{D toward C′,}\quad \theta\left[\frac{bs}{2}\right]\\
&\text{C′ toward B′,}\quad \theta\left[\frac{hb}{4}+\frac{hs}{2}\right]\\
&\text{B′ toward A′,}\quad \theta\left[\frac{3hb}{4}+\frac{bs}{2}\right]
\end{aligned}\right\} \tag{LD—6}$$

The longitudinal displacement of A (just above the slit) is

$$-\theta[hb]$$

and of A′ (just below the slit) is

$$\theta[hb]$$

The longitudinal displacement of A′ with respect to A is therefore

$$\theta[2hb]$$

In order to transform the open section, slit at A—A′, into a closed section, equal and opposite shearing forces F are introduced in the slit to draw A and A′ together. The magnitude of these shearing forces is determined by equating the integral of the shear strain in the section between A and A′ to the longitudinal displacement of A′ with respect to A when the section is slit

$$\int_A^{A'} \frac{F}{tG}\frac{ds}{dx}=\theta[2hb]$$

which becomes for the section shown in figure 25

$$\frac{2F}{G}\frac{1}{dx}\left[\frac{h}{t_h}+\frac{b}{t_b}\right]=\theta[2hb]$$

from which

$$\frac{F}{dx}=\theta\frac{hb}{\frac{h}{t_h}+\frac{b}{t_b}}G \tag{44}$$

The longitudinal displacement with respect to the original plane of the end cross section caused by the shearing force F in the slit is at a distance s measured from

$$\left.\begin{aligned}
&\text{B toward A,} && \frac{F}{dx}\frac{1}{G}\left[\frac{1}{2}\frac{h}{t_h}+\frac{b}{t_b}+\frac{s}{t_h}\right]\\
&\text{C toward B,} && \frac{F}{dx}\frac{1}{G}\left[\frac{1}{2}\frac{h}{t_h}+\frac{s}{t_b}\right]\\
&\text{D toward C,} && \frac{F}{dx}\frac{1}{G}\left[\frac{s}{t_h}\right]\\
&\text{D toward C′,} && -\frac{F}{dx}\frac{1}{G}\left[\frac{s}{t_h}\right]\\
&\text{C′ toward B′,} && -\frac{F}{dx}\frac{1}{G}\left[\frac{1}{2}\frac{h}{t_h}+\frac{s}{t_b}\right]\\
&\text{B′ toward A′,} && -\frac{F}{dx}\frac{1}{G}\left[\frac{1}{2}\frac{h}{t_h}+\frac{b}{t_b}+\frac{s}{t_h}\right]
\end{aligned}\right\}\text{(LD—7)}$$

Adding of these longitudinal displacements to those of (LD—6) and substituting the value of F/dx from equation (44) gives at a distance s measured from

$$\left.\begin{aligned}
&\text{B toward A,} && -\theta\left[\frac{3hb}{4}+\frac{bs}{2}-\frac{hb}{\frac{h}{t_h}+\frac{b}{t_b}}\left(\frac{h}{2t_h}+\frac{b}{t_b}+\frac{s}{t_h}\right)\right]\\
&\text{C toward B,} && -\theta\left[\frac{hb}{4}+\frac{hs}{2}-\frac{hb}{\frac{h}{t_h}+\frac{b}{t_b}}\left(\frac{h}{2t_h}+\frac{s}{t_b}\right)\right]\\
&\text{D toward C,} && -\theta\left[\frac{bs}{2}-\frac{hb}{\frac{h}{t_h}+\frac{b}{t_b}}\left(\frac{s}{t_h}\right)\right]\\
&\text{D toward C′,} && \theta\left[\frac{bs}{2}-\frac{hb}{\frac{h}{t_h}+\frac{b}{t_b}}\left(\frac{s}{t_h}\right)\right]\\
&\text{C′ toward B′,} && \theta\left[\frac{hb}{4}+\frac{hs}{2}-\frac{hb}{\frac{h}{t_h}+\frac{b}{t_b}}\left(\frac{h}{2t_h}+\frac{s}{t_b}\right)\right]\\
&\text{B′ toward A′,} && \theta\left[\frac{3hb}{4}+\frac{bs}{2}-\frac{hb}{\frac{h}{t_h}+\frac{b}{t_b}}\left(\frac{h}{2t_h}+\frac{b}{t_b}+\frac{s}{t_h}\right)\right]
\end{aligned}\right\}\text{(LD–8)}$$

The longitudinal displacements of (LD–8) apply to the closed section of figure 25 when the portion of length dx is twisted an amount $d\varphi$ about the centroid. If the axis of rotation is now shifted from the centroid to the location defined by P and Q, in figure 25, certain terms must be added to (LD–8) that are analogous to the longitudinal displacements of (LD–2) and (LD–3) for the I section. These longitudinal displacements caused by translation are, at a distance s measured from

$$\left.\begin{aligned}
&\text{B toward A,} && \theta\left[P\left(\frac{h}{2}-s\right)-\frac{Qb}{2}\right]\\
&\text{C toward B,} && \theta\left[P\frac{h}{2}+Q\left(\frac{b}{2}-s\right)\right]\\
&\text{D toward C,} && \theta\left[Ps+Q\frac{b}{2}\right]\\
&\text{D toward C′,} && \theta\left[-Ps+Q\frac{b}{2}\right]\\
&\text{C′ toward B′,} && \theta\left[-P\frac{h}{2}+Q\left(\frac{b}{2}-s\right)\right]\\
&\text{B′ toward A′,} && \theta\left[-P\left(\frac{h}{2}-s\right)-Q\frac{b}{2}\right]
\end{aligned}\right\}\text{(LD–9)}$$

Addition of the longitudinal displacements given by equations (LD–8) and (LD–9) give at a distance s measured from

$$\left.\begin{aligned}
&\text{B toward A,}\quad -\theta\left[\frac{3hb}{4}+\frac{bs}{2}-\frac{hb}{\frac{h}{t_h}+\frac{b}{t_b}}\left(\frac{h}{2t_h}+\frac{b}{t_b}+\frac{s}{t_h}\right)-P\left(\frac{h}{2}-s\right)+\frac{Qb}{2}\right]\\
&\text{C toward B,}\quad -\theta\left[\frac{hb}{4}+\frac{hs}{2}-\frac{hb}{\frac{h}{t_h}+\frac{b}{t_b}}\left(\frac{h}{2t_h}+\frac{s}{t_b}\right)-\frac{Ph}{2}-Q\left(\frac{b}{2}-s\right)\right]\\
&\text{D toward C,}\quad -\theta\left[\frac{bs}{2}-\frac{hb}{\frac{h}{t_h}+\frac{b}{t_b}}\left(\frac{s}{t_h}\right)-Ps-\frac{Qb}{2}\right]\\
&\text{D toward C',}\quad \theta\left[\frac{bs}{2}-\frac{hb}{\frac{h}{t_h}+\frac{b}{t_b}}\left(\frac{s}{t_h}\right)-Ps+\frac{Qb}{2}\right]\\
&\text{C' toward B',}\quad \theta\left[\frac{hb}{4}+\frac{hs}{2}-\frac{hb}{\frac{h}{t_h}+\frac{b}{t_b}}\left(\frac{h}{2t_h}+\frac{s}{t_b}\right)-\frac{Ph}{2}+Q\left(\frac{b}{2}-s\right)\right]\\
&\text{B' toward A',}\quad \theta\left[\frac{3hb}{4}+\frac{bs}{2}-\frac{hb}{\frac{h}{t_h}+\frac{b}{t_b}}\left(\frac{h}{2t_h}+\frac{b}{t_b}+\frac{s}{t_h}\right)-P\left(\frac{h}{2}-s\right)-\frac{Qb}{2}\right]
\end{aligned}\right\}\quad\text{(LD–10)}$$

Because the rectangular tube of figure 25 is symmetrical about its two principal axes the reference plane coincides with the original plane of the end cross section. (See derivation of C_{BT} for the I section.) Hence, (LD–10) gives the longitudinal displacements with respect to the reference plane. These longitudinal displacements when substituted for u in equation (7) with $\theta=1$ give the major part of C_{BT}. The minor part of C_{BT} is calculated in the same manner as for an open section.

APPENDIX C

DERIVATION OF THE THEORETICAL VALUE OF THE EFFECTIVE MODULUS $\bar{E}$

If C_{BT_1} is the value obtained from equation (4) when the integration is made over the part of the cross section that suffers an increase of stress at the instant of failure of the column, and E' is the modulus of elasticity for increasing stress, the work done by the increase in compressive stresses is (see equation (3) of reference 2)

$$\frac{1}{2}E'C_{BT_1}\int_0^L(\varphi'')^2dx$$

If C_{BT_2} is the value obtained from equation (4) when the integration is made over the part of the cross section that suffers a decrease of stress at the instant of failure of the column, and E is the modulus of elasticity for decreasing stress, the work done by the decrease in compressive stresses is

$$\frac{1}{2}EC_{BT_2}\int_0^L(\varphi'')^2dx$$

The total work done by the longitudinal bending stresses is therefore

$$\frac{1}{2}(E'C_{BT_1}+EC_{BT_2})\int_0^L(\varphi'')^2dx \qquad \text{(a)}$$

When the modulus of elasticity is the same for increasing stress as for decreasing stress, as it is in the elastic range, the total work done by the longitudinal bending stresses is

$$\frac{1}{2}EC_{BT}\int_0^L(\varphi'')^2dx \qquad \text{(b)}$$

If a modulus $\overline{E}$ is substituted for E in this expression, the total work given by expression (b) can be made to have any desired value depending upon the value assigned to $\overline{E}$. If $\overline{E}$ is allowed to have only such values as will cause the total work given by (b) to equal that given by (a), it is found that

$$\overline{E}=\frac{E'C_{BT_1}+EC_{BT_2}}{C_{BT}}$$

This value of $\overline{E}$ is called the "effective" modulus when the column is loaded above the proportional limit.

The total work done by the longitudinal bending stresses when the column is loaded above the proportional limit is therefore given by the expression

$$\frac{1}{2}\overline{E}C_{BT}\int_0^L(\varphi'')^2dx$$

Thus when the column is loaded above the proportional limit, $\overline{E}$ should be substituted for E in Wagner's equation for the critical stress, i. e., equation (1) of this report.

REFERENCES

1. Lundquist, Eugene E.: Comparison of Three Methods for Calculating the Compressive Strength of Flat and Slightly Curved Sheet and Stiffener Combinations. T. N. No. 455, N. A. C. A., 1933.
2. Wagner, Herbert: Torsion and Buckling of Open Sections. T. M. No. 807, N. A. C. A., 1936.
3. Wagner, H., and Pretschner, W.: Torsion and Buckling of Open Sections. T. M. No. 784, N. A. C. A., 1936.
4. Timoshenko, S.: Strength of Materials, Part I. D. Van Nostrand Co., Inc., 1930.
5. Trayer, George W., and March, H. W.: The Torsion of Members Having Sections Common in Aircraft Construction. T. R. No. 334, N. A. C. A., 1930.
6. Pugsley, A. G.: Torsional Instability in Struts. Aircraft Engineering, vol. IV, no. 43, Sept. 1932, pp. 229–230.
7. Trayer, George W., and March, H. W.: Elastic Instability of Members Having Sections Common in Aircraft Construction. T. R. No. 382, N. A. C. A., 1931.
8. Timoshenko, S.: Strength of Materials, Part II. D. Van Nostrand Co., Inc., 1930.
9. Osgood, William R.: Column Curves and Stress-Strain Diagrams. Research Paper No. 492, Bur. Standards Jour. Res., vol. 9, Oct. 1932, pp. 571–582.
10. Osgood, William R.: The Double-Modulus Theory of Column Action. Civil Engineering, vol. 5, no. 3, Mar. 1935, pp. 173–175.
11. Bleich, Friederich: Theorie und Berechnung der eisernen Brücken. Julius Springer (Berlin), 1924, S. 218–219.
12. Kollbrunner, Curt F.: Das Ausbeulen des auf Druck beanspruchten freistehenden Winkels. Gebr. Leemann & Co. (Zürich & Leipzig), 1935.

TABLE I

EFFECTIVE MODULI $\overline{E}$ AND $\overline{G}$ FOR 24ST ALUMINUM ALLOY

$\frac{L_0}{\rho}$	f_{crit} lb./sq. in.	$\overline{E}$ lb./sq. in.	τ	$\frac{\tau+\sqrt{\tau}}{2}$	$\overline{G}$ lb./sq. in.
9.49	53,000	483,600	0.0459	0.1301	527,600
13.28	51,000	911,300	.0865	.1903	771,900
17.08	49,000	1,453,000	.1379	.2382	966,400
20.87	47,000	2,074,000	.1968	.3203	1,299,000
24.67	45,000	2,775,000	.2633	.3883	1,575,000
28.46	43,000	3,529,000	.3349	.4568	1,853,000
32.26	41,000	4,323,000	.4103	.5254	2,132,000
36.05	39,000	5,135,000	.4874	.5891	2,390,000
39.85	37,000	5,953,000	.5650	.6583	2,671,000
43.64	35,000	6,754,000	.6409	.7208	2,924,000
47.44	33,000	7,525,000	.7141	.7796	3,163,000
51.23	31,000	8,244,000	.7823	.8334	3,381,000
55.03	29,000	8,898,000	.8444	.8817	3,577,000
58.82	27,000	9,465,000	.8982	.9230	3,744,000
60.72	26,000	9,713,000	.9215	.9407	3,817,000
62.62	25,000	9,933,000	.9426	.9568	3,881,000
66.41	23,000	10,278,000	.9754	.9815	3,982,000
70.21	21,000	10,489,000	.9954	.9965	4,043,000
73.00	19,520	10,537,000	1.0000	1.0000	4,057,000
75.00	18,490	10,537,000	1.0000	1.0000	4,057,000
80.00	16,250	10,537,000	1.0000	1.0000	4,057,000
85.00	14,390	10,537,000	1.0000	1.0000	4,057,000
90.00	12,840	10,537,000	1.0000	1.0000	4,057,000
95.00	11,520	10,537,000	1.0000	1.0000	4,057,000
100.00	10,400	10,537,000	1.0000	1.0000	4,057,000

TABLE II

EFFECTIVE WIDTH OF SKIN THAT ACTS WITH THE COLUMN

f_{crit} lb./sq. in.	$2\,b_s$ inches	U inches
53,000	0.599	1.099
51,000	.611	1.111
49,000	.623	1.123
47,000	.636	1.136
45,000	.650	1.150
43,000	.665	1.165
41,000	.681	1.181
39,000	.699	1.199
37,000	.717	1.217
35,000	.737	1.237
33,000	.759	1.259
31,000	.784	1.284
29,000	.810	1.310
27,000	.840	1.340
26,000	.856	1.356
25,000	.873	1.373
23,000	.910	1.410
21,000	.952	1.452
19,520	.988	1.488
18,490	1.015	1.515
16,250	1.082	1.582
14,390	1.150	1.650
12,840	1.218	1.718
11,520	1.285	1.785
10,400	1.353	1.853

TABLE III

CRITICAL STRESS FOR BENDING FAILURE

f_{crit} lb./sq. in.	$U\,t_s$ sq. in.	A sq. in.	Q_1 inch	I in.^{4}	$\overline{E}$ lb./sq. in.	L_0 inches
53,000	0.0275	0.1775	0.4542	0.0359	483,600	4.27
51,000	.0278	.1778	.4535	.0359	911,300	5.97
49,000	.0281	.1781	.4527	.0360	1,453,000	7.69
47,000	.0284	.1784	.4519	.0361	2,074,000	9.38
45,000	.0288	.1788	.4509	.0362	2,775,000	11.09
43,000	.0291	.1791	.4502	.0362	3,529,000	12.80
41,000	.0295	.1795	.4492	.0363	4,323,000	14.51
39,000	.0300	.1800	.4479	.0364	5,135,000	16.21
37,000	.0304	.1804	.4469	.0365	5,953,000	17.92
35,000	.0309	.1809	.4457	.0366	6,754,000	19.62
33,000	.0315	.1815	.4442	.0367	7,525,000	21.33
31,000	.0321	.1821	.4128	.0368	8,244,000	23.03
29,000	.0328	.1828	.4411	.0369	8,898,000	24.73
27,000	.0335	.1835	.4394	.0371	9,465,000	26.44
26,000	.0339	.1839	.4384	.0372	9,713,000	27.29
25,000	.0343	.1843	.4375	.0372	9,933,000	28.15
23,000	.0353	.1853	.4351	.0374	10,278,000	29.84
21,000	.0363	.1863	.4328	.0376	10,489,000	31.55
19,520	.0372	.1872	.4307	.0378	10,537,000	32.79
18,490	.0379	.1879	.4291	.0379	10,537,000	33.68
16,250	.0396	.1896	.4252	.0382	10,537,000	35.91
14,390	.0413	.1913	.4215	.0385	10,537,000	38.15
12,840	.0430	.1930	.4177	.0388	10,537,000	40.36
11,520	.0446	.1946	.4143	.0391	10,537,000	42.60
10,400	.0463	.1963	.4107	.0394	10,537,000	45.80

TABLE IV.—CRITICAL STRESS FOR TWISTING FAILURE

f_{crit} lb./sq. in.	ΔJ in.^{4}	J in.^{4}	ΔI_p in.^{4}	I_p in.^{4}	ΔC_{BT} in.^{6}	[a]C_{BT} in.^{6}	$\overline{G}$ lb./sq. in.	$\overline{E}$ lb./sq. in.	L_0 in.	L_0 in.
53,000	0.0000057	0.0001307	0.00277	0.08360	0.0000001	0.00450	527,600	483,600	53.4	2.2
51,000	.0000058	.0001308	.00286	.08369	.0000001	.00450	771,900	911,300	52.1	3.1
49,000	.0000059	.0001309	.00295	.08379	.0000002	.00450	996,400	1,453,000	50.9	4.0
47,000	.0000059	.0001309	.00366	.08389	.0000002	.00450	1,299,000	2,074,000	49.4	5.0
45,000	.0000060	.0001310	.00317	.08401	.0000002	.00450	1,575,000	2,775,000	48.0	5.9
43,000	.0000061	.0001311	.00330	.08413	.0000002	.00450	1,853,000	3,529,000	46.5	6.9
41,000	.0000062	.0001312	.00343	.08427	.0000002	.00450	2,132,000	4,328,000	44.9	7.9
39,000	.0000062	.0001312	.00359	.08442	.0000002	.00450	2,390,000	5,135,000	43.2	8.9
37,000	.0000063	.0001313	.00376	.08459	.0000002	.00450	2,671,000	5,953,000	41.5	10.0
35,000	.0000064	.0001314	.00395	.08478	.0000002	.00450	2,924,000	6,754,000	39.6	11.2
33,000	.0000066	.0001316	.00416	.08500	.0000002	.00450	3,163,000	7,525,000	37.5	12.5
31,000	.0000067	.0001317	.00441	.08524	.0000002	.00450	3,381,000	8,244,000	35.3	13.9
29,000	.0000068	.0001318	.00468	.08552	.0000002	.00450	3,577,000	8,898,000	32.8	15.5
27,000	.0000070	.0001320	.00501	.08584	.0000003	.00450	3,744,000	9,465,000	29.7	17.7
26,000	.0000071	.0001321	.00519	.08603	.0000003	.00450	3,817,000	9,713,000	27.7	19.2
25,000	.0000072	.0001322	.00539	.08622	.0000003	.00450	3,881,000	9,933,000	23.6	22.8
23,000	.0000073	.0001323	.00584	.08667	.0000003	.00450	3,982,000	10,278,000	Imaginary	

[a] $C_B=0.00449$. $C_T=0.000006$.

REPORT No. 583

THE ROLLING FRICTION OF SEVERAL AIRPLANE WHEELS AND TIRES AND THE EFFECT OF ROLLING FRICTION ON TAKE-OFF

By J. W. Wetmore

SUMMARY

Tests were made to determine the rolling friction of airplane wheels and tires under various conditions of wheel loading, tire inflation pressure, and ground surface. The effect of wheel-bearing type was also investigated. Six pairs of wheels and tires were tested including two sizes of each of the types designated as standard (high pressure), low pressure, and extra low pressure. The results of calculations intended to show the effect of variations in rolling friction on take-off are also presented.

The values of rolling-friction coefficient obtained on a concrete runway varied from 0.009 to 0.035; on firm turf, from 0.023 to 0.054; and on moderately soft turf, where only the high-pressure tires were tested, from 0.064 to 0.077. Of the variables investigated, the ground-surface condition was the most important in its effect on the rolling-friction coefficient. For comparable conditions, both on a concrete surface and on firm turf, the standard wheels and tires offered the least resistance to rolling. Slightly higher values were obtained with the low-pressure wheels and tires, and the extra low-pressure type gave the highest values. The variation in rolling-friction coefficient with wheel loading and inflation pressure was generally quite small. The value of rolling-friction coefficient for wheels equipped with plain bearings was appreciably greater than that for the same wheels provided with roller bearings. The effect on take-off of all the variables, with the exception of ground-surface condition, was sufficiently small to be neglected in rough calculations of take-off performance but should be considered in more accurate work.

INTRODUCTION

In many cases when comparisons have been made between measured and calculated values of the ground-run distance in the take-off of an airplane, the results have shown considerable disagreement. A part of the discrepancy can be attributed to the inadequacy of available information concerning the forces and conditions existing during the take-off. An investigation of the rolling friction of airplane wheels and tires, one of the uncertain factors, was undertaken as a step toward augmenting this information and hence toward improving the reliability of the prediction of take-off performance.

The measurement of the rolling friction was accomplished by recording the pull between a towing vehicle and a loaded trailer equipped with the wheels and tires to be tested. The resistance thus measured included, of course, that due to the wheel bearings as well as that of the tires.

The tires and wheels tested included two sizes of each of the types generally classified as standard (high pressure), low pressure, and extra low pressure. The tests were run at various speeds under several conditions of wheel loading and tire inflation pressure. The ground-surface conditions investigated were concrete, firm turf, and soft turf.

As an indication of the probable effect on take-off of the differences in rolling friction occasioned by the various conditions, calculations were made of the distances required to leave the ground for two hypothetical airplanes of different loading characteristics; for each case several values of rolling-friction coefficient, covering the range determined by the tests, were assumed.

APPARATUS AND METHODS

The trailer used in the tests (fig. 1) was a 2-wheel carriage with provision for interchanging stub axles to accommodate the various wheels. It was capable of carrying up to 3,000 pounds of load in the form of 200-pound lead weights, which, with the weight of the carriage itself, provided a maximum load on the wheels of 3,500 pounds. The carriage was equipped with airplane-type hydraulic shock absorbers to simulate an airplane landing chassis. The axles were so arranged that there was no toe-in of the wheels. A light truck was used as the towing vehicle.

The pull between the truck and the trailer was measured with a dynamometer consisting essentially of a helical spring, the deflection of which, proportional to the force, was recorded by a standard N. A. C. A. instrument of the type ordinarily used to record the position of airplane controls in flight. The force was transmitted from the trailer drawbar to the spring through a cylindrical shaft running in ball-bearing guides that confined the motion of the shaft to an axial direction. All these components were mounted in a

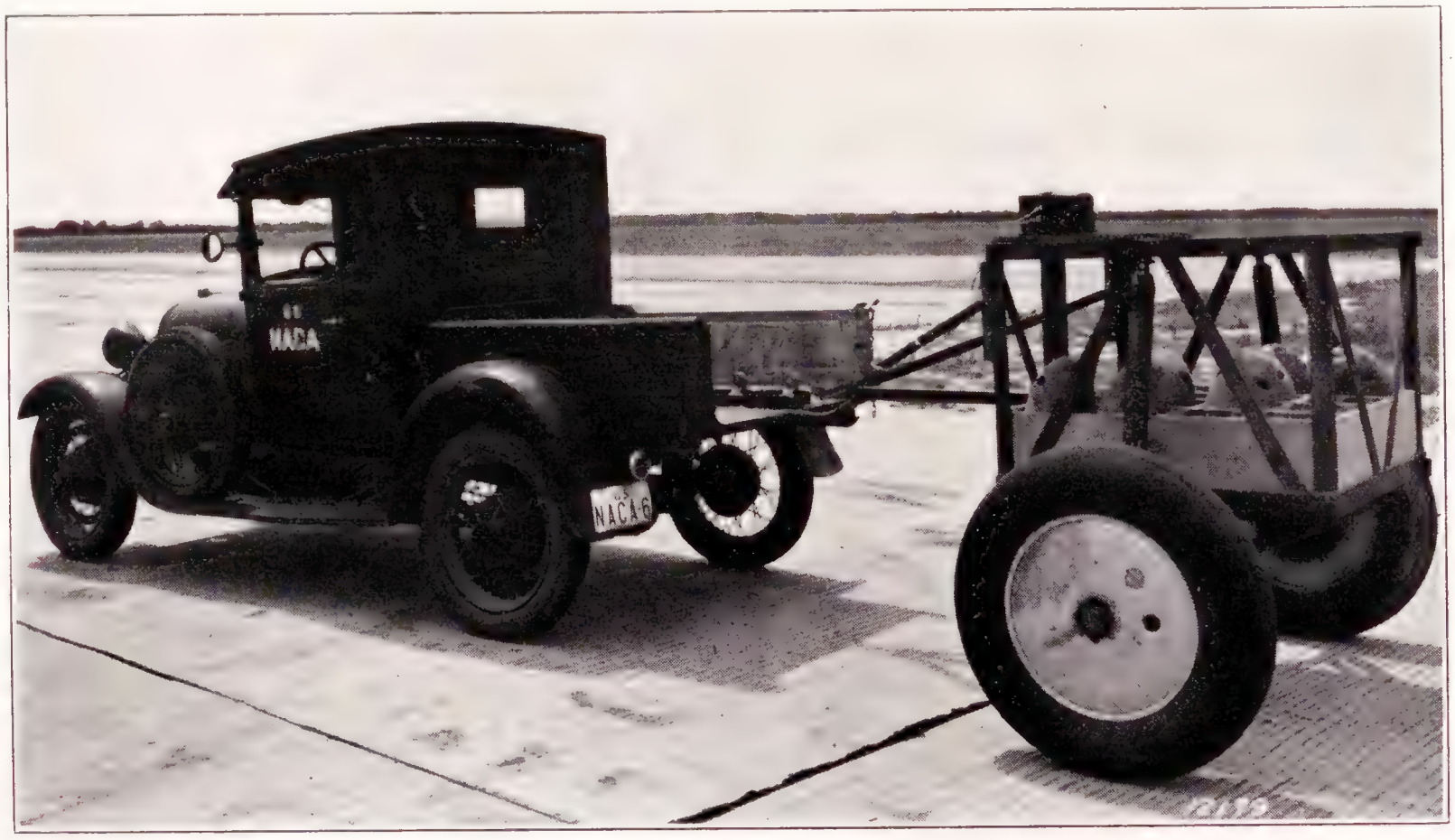

FIGURE 1.—Trailer and test equipment.

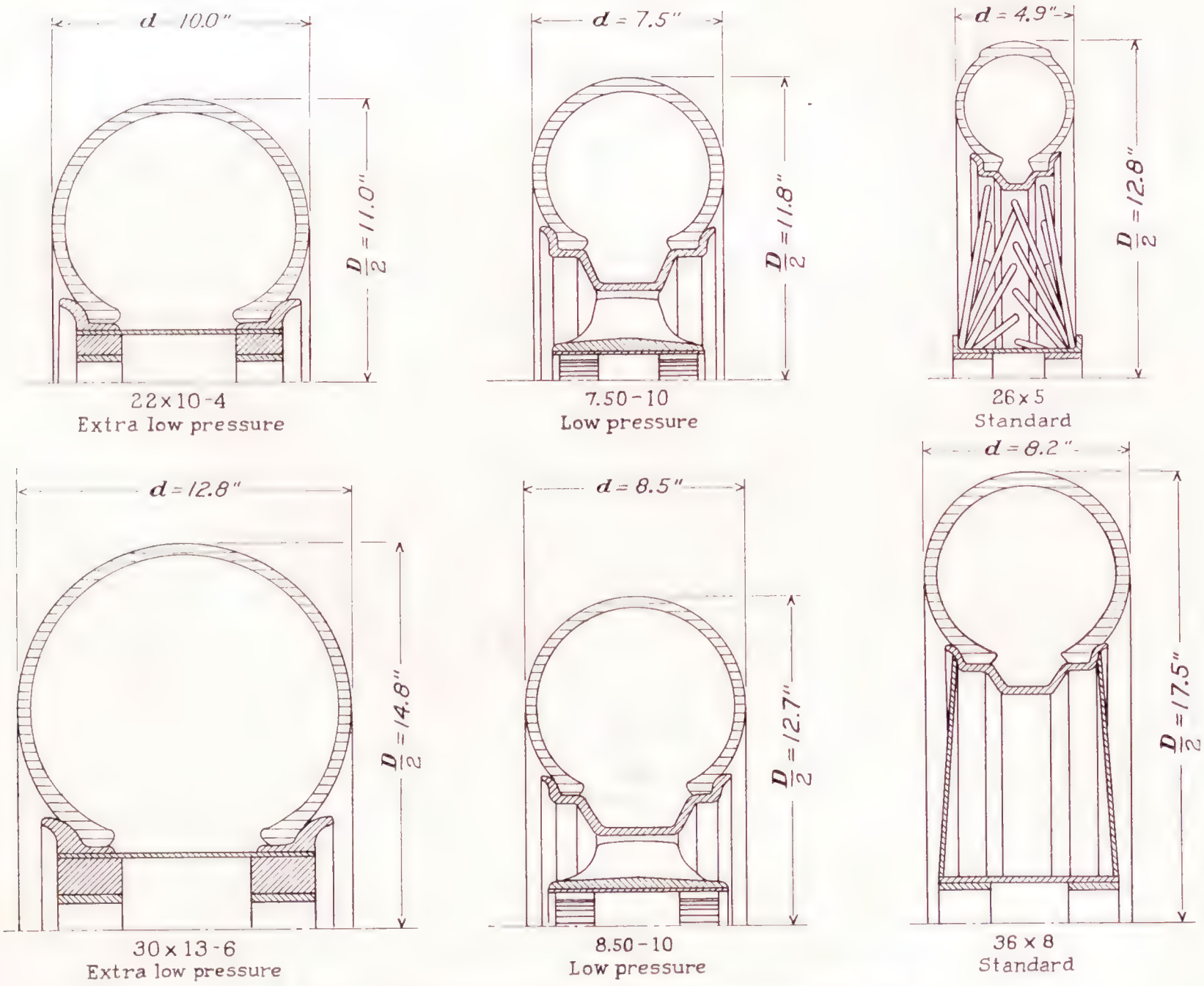

FIGURE 2.—Cross sections and dimensions of the airplane tires and wheels tested.

heavy frame to form a unit which, in turn, was bolted to the bed of the truck.

A standard N. A. C. A. recording inclinometer was mounted on the trailer to determine the horizontal acceleration. A timer was used to synchronize the records of the two recording instruments and also, in conjunction with an electrical-contact mechanism on the front wheel of the truck, to provide a means of evaluating test speeds.

Sketches of the wheels and tires used in the tests are shown in figure 2. The wheels and tires tested included three types: Extra low pressure or airwheels, low pressure, and standard or high pressure. Two sizes of each type were tested. The sizes of extra low pressure tires tested were 22×10–4 and 30×13–6; the recommended tire inflation pressure for both sizes was 12.5 pounds per square inch. The recommended inflation pressure was 20 pounds per square inch for the two sizes of low-pressure tires, 7.50–10 and 8.50–10. The recommended inflation pressure for the 26×5 standard tire was 50 pounds per square inch; for the 36×8 size the recommended pressure was 60 pounds per square inch. All the tires had smooth treads except the 26×5 size, which had a nonskid tread. Static load-deflection curves for all the tires are shown in figure 3.

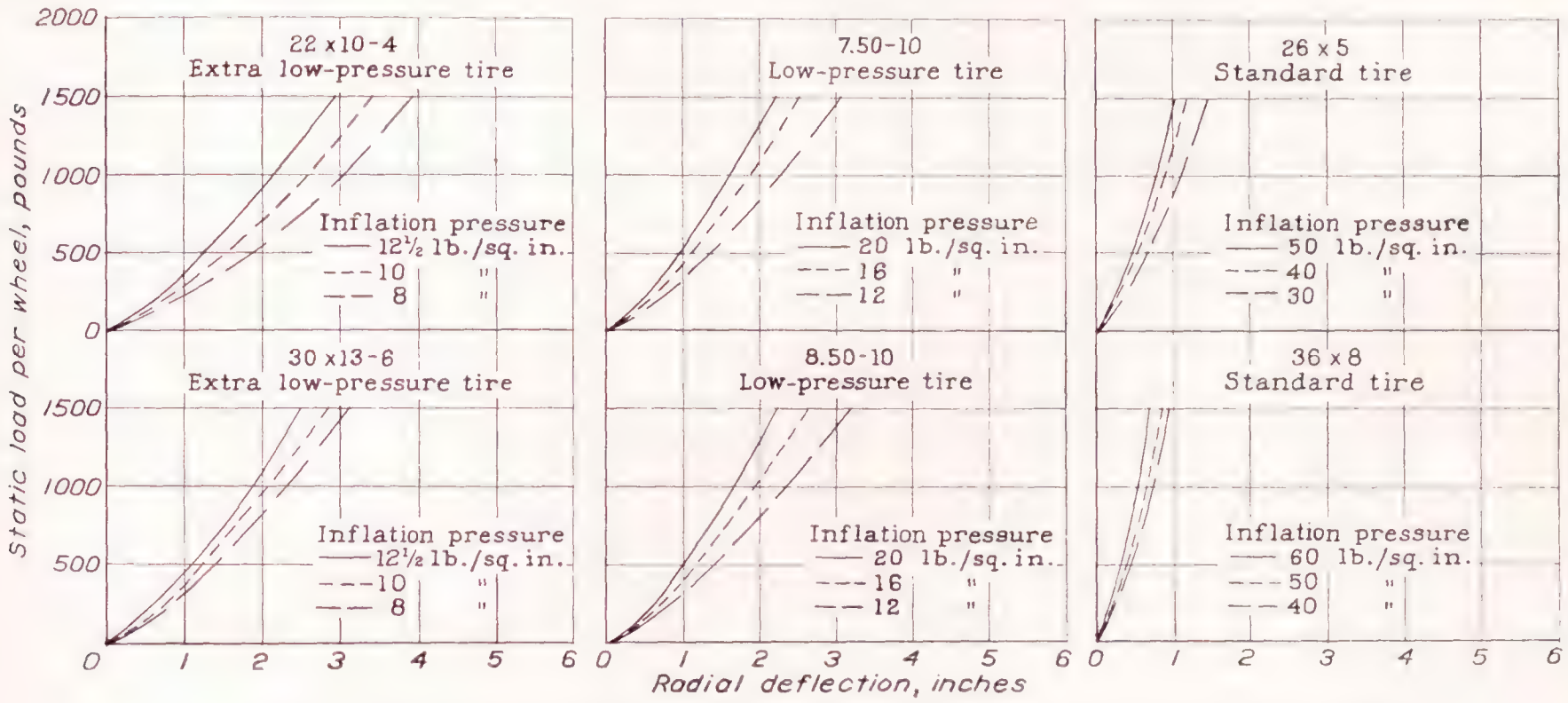

FIGURE 3.—Static load-deflection curves of tires. The highest pressure in each case is the recommended inflation pressure.

The bearings of all the standard and extra low-pressure wheels were of the plain type, i. e., bronze bushings grooved for lubrication and running on steel journals. Both sizes of the low-pressure wheels were equipped with antifriction roller bearings. The tests of the 8.50–10 low-pressure wheels and tires, however, were repeated for two loads with the roller bearings replaced by plain bearings in order to provide an indication of the effect of bearing type.

Each pair of wheels and tires was tested under three loads with the tires inflated to the recommended pressure. The heaviest load in each case was determined either by the recommended maximum static load for the tires or by the capacity of the trailer; the other loads were chosen arbitrarily to provide a convenient range.

With 940 pounds per wheel, a load common to all the test series, the rolling-friction measurements were made at two inflation pressures below and in addition to the recommended value, the lowest pressure being about 50 or 60 percent of the recommended pressure. The 26×5 tires were run only at recommended inflation pressure.

All the foregoing conditions were covered in tests on a concrete runway designed for airplane operations, the surface of which had been scarified to improve its tractional qualities. Tests were likewise run for all conditions on a turf surface of probably average smoothness, having a clay topsoil and covered with fairly thick grass about 6 or 8 inches in height. Most of the tests were made when the surface was very dry and firm, probably representative of the best field condition likely to be encountered. For the tests with varying load on the 26×5 and 36×8 standard wheels and tires, however, the surface was wet and moderately soft so that the truck tires left tracks between one-half and 1 inch in depth, representing fairly unfavorable conditions for normal operation but by no means the worst possible.

The measurements of rolling friction were made for each condition according to the following procedure: 3- or 4-second records were taken at several speeds between 5 and 45 miles per hour on the concrete surface or between 5 and 30 miles per hour on the turf surface, with the speed held as nearly constant as pos-

sible during each run. The value of the mean gross pull P_m between the truck and trailer was determined from the record of dynamometer spring deflection.

Because it was impossible to maintain the speed during the runs sufficiently steady to preclude relatively large errors due to the inertia force of the trailer, the recording inclinometer was used to provide a correction for this force. Before and after each series of runs, several records were taken of the inclinometer angle with the truck and trailer standing on a fairly level surface and heading in various directions so that the average of the readings provided a reference angle θ_0, the angle for no horizontal acceleration. Then the difference between this value and the mean angle θ_m recorded during a run defined the mean direction of the resultant force acting on the inclinometer pendulum relative to the direction of the gravity component, or

$$\theta_m-\theta_0=\tan^{-1}\frac{a_m}{g}$$

where a_m is the mean acceleration in the direction of travel. The mean inertia force P_I was then determined from the relation

$$P_I=W\tan\ (\theta_m-\theta_0)$$

where W is the weight of the loaded trailer.

Owing to the deflection of the truck springs resulting from the drag of the trailer, the attitude angle of the trailer—hence of the inclinometer base—while running differed sufficiently from the static reference angle to cause an appreciable error in the acceleration as determined by the foregoing method. Moreover, a similar effect was caused at higher speeds by a reduction in the deflection of the trailer tires due to centrifugal force. The necessary corrections were found by mounting a second inclinometer between the truck axles where it was not subjected to the described effects and comparing the records of the two instruments for a sufficient number of runs under various conditions to establish a relationship between the correction and the influencing factors. The correction angle θ_c was then the difference between the mean angles recorded by the inclinometer on the truck and the inclinometer on the trailer, and the corrected inertia force became

$$P_I=W\tan\ (\theta_m+\theta_c-\theta_0)$$

The air resistance D of the trailer was determined as the difference between the over-all resistance measured with the trailer covered by a hood and that with the trailer uncovered. The hood consisted of a fabric-covered framework completely enclosing the trailer but entirely free of any mechanical connection with it, being supported by direct connection with the truck and running on skids. The air drag was measured in this manner at several speeds within the range covered by the tests.

The rolling friction or resistance R was evaluated from the test results according to the relation

$$R=P_m-W\tan\ (\theta_m+\theta_c-\theta_0)-D$$

Then the rolling-friction coefficient, the form in which the results are presented, is

$$\mu=\frac{R}{W}$$

PRECISION

The mean gross force was measured by the dynamometer to within ± 1 pound for individual runs. The mean acceleration was determined from the inclinometer records to within ± 0.06 foot per second per second. From this the inertia force is correct to within ± 2 pounds for the lightest load and within ± 6 pounds for the heaviest load. Inasmuch as each of the values presented in the table and the figures was averaged from the results of 18 runs, all but small consistent errors are largely eliminated.

In the case of the tests run on the turf surface, there is a possibility of some lack of uniformity in the condition of the surface between the different series of tests, which was not indicated by its appearance and might introduce an error into the effects attributed to the applied variables. Likewise, inasmuch as the plain bearings used in airplane wheels are of the imperfectly lubricated type and hence of somewhat uncertain frictional characteristics, it is possible that there was some difference in bearing friction between the several wheels equipped with plain bearings so that the differences observed between the over-all friction coefficients of the wheels and tires for similar conditions may not be due solely to tire size and type. These effects are believed, however, to be too small to invalidate the comparisons and conclusions drawn from the results of the tests.

RESULTS

The values of rolling-friction coefficient for all the conditions covered in the tests are presented in table I. Figures 4 and 5 give the results obtained on the concrete runway for all the wheels and tires. Figure 4 shows the effect of wheel load on the rolling-friction coefficient and also the difference between the coefficients with plain and roller bearings as determined on the 8.50–10 low-pressure tires. Figure 5 shows the variation of rolling-friction coefficient with tire inflation pressure for all but the 26×5 tires. The coefficients measured on the turf surface are plotted in figures 6 and 7. Figure 6 shows the variation of the coefficient with wheel load. For the tests of the standard-type wheels and tires, i. e., the 26×5 and 36×8, the surface was wet and fairly soft, whereas for

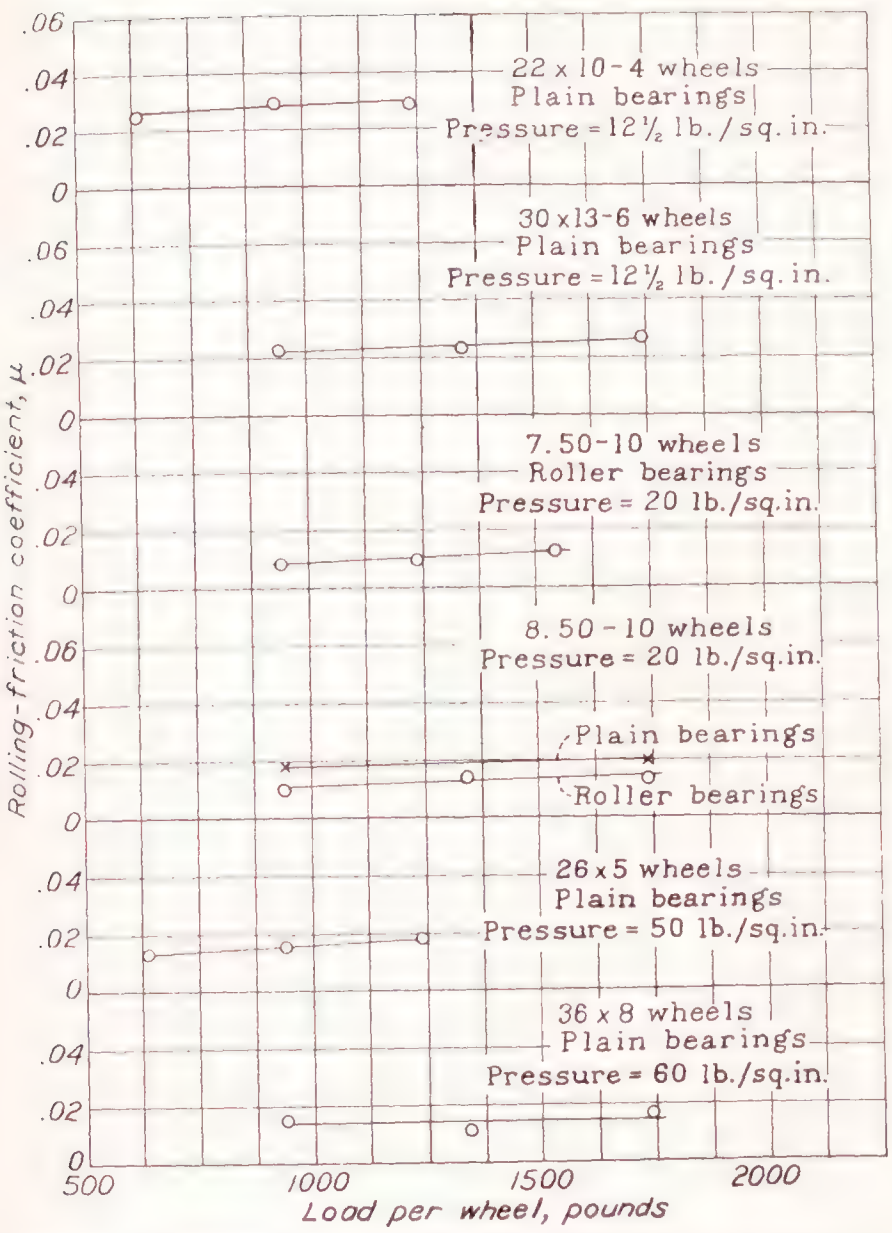

FIGURE 4.—Variation of rolling-friction coefficient with load per wheel; concrete surface; recommended inflation pressure.

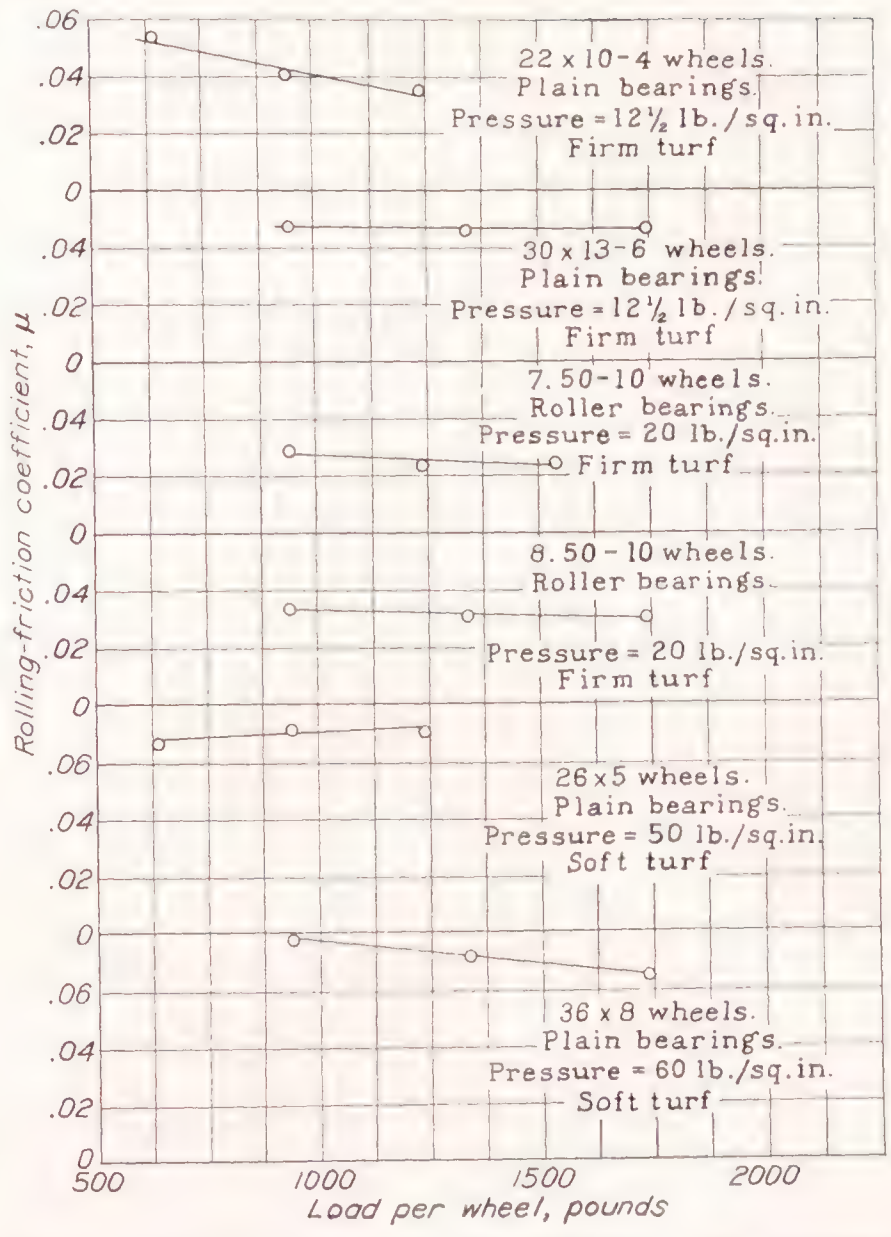

FIGURE 6.—Variation of rolling-friction coefficient with load per wheel; turf surface; recommended inflation pressure.

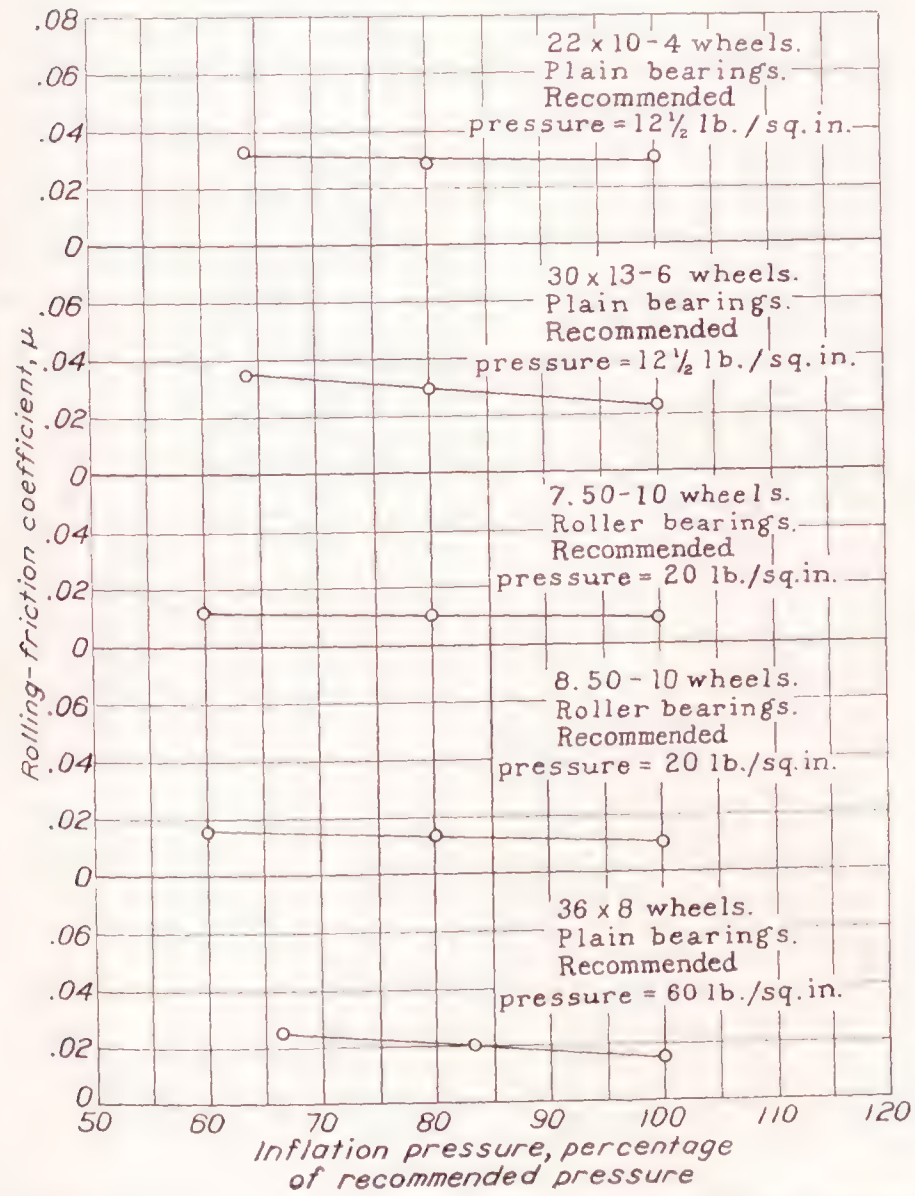

FIGURE 5.—Variation of rolling-friction coefficient with inflation pressure; concrete surface; load per wheel, 940 pounds.

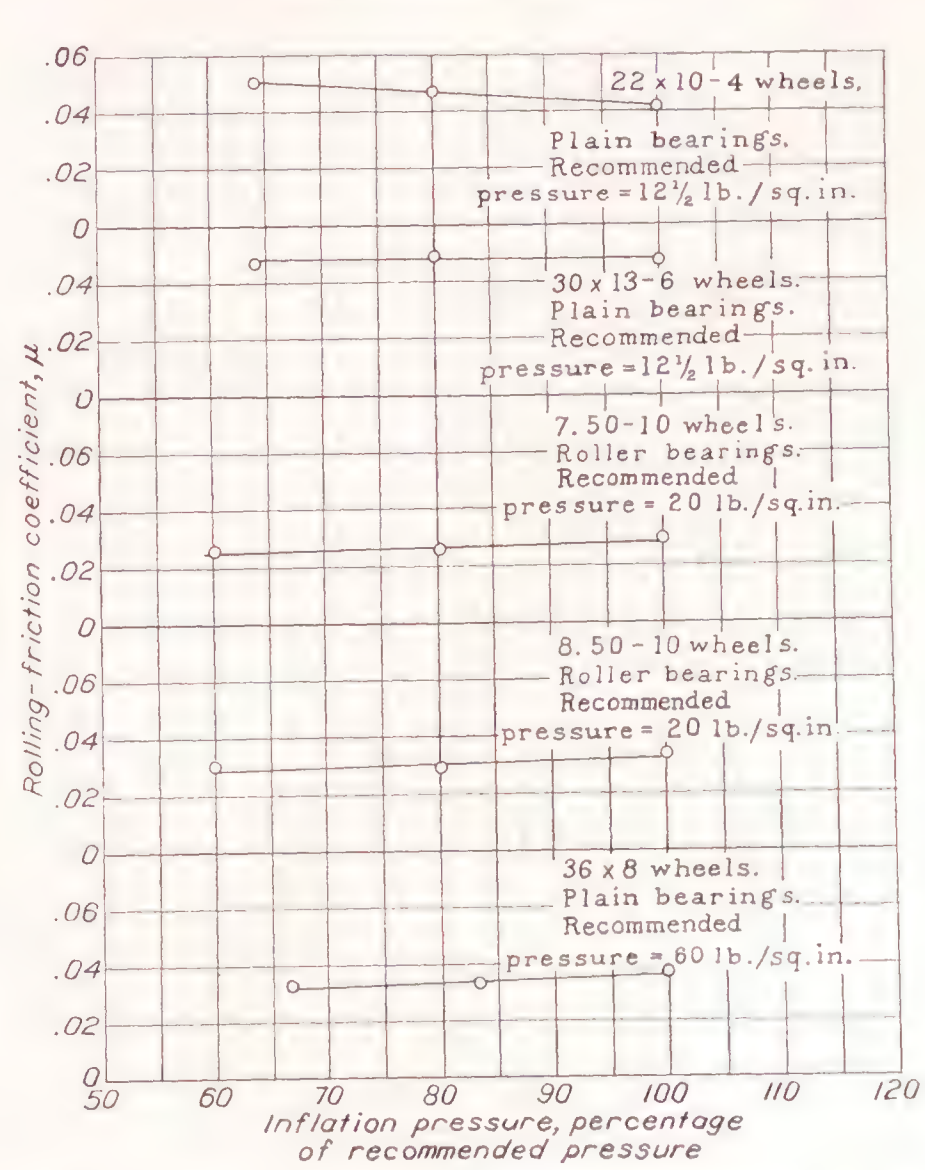

FIGURE 7.—Variation of rolling-friction coefficient with inflation pressure; firm turf surface; load per wheel, 940 pounds.

all the other tires the surface was dry and firm. In figure 7 is shown the variation of rolling-friction coefficient with inflation pressure for all tires except the 26×5 size, the surface being dry and firm in all cases.

As explained before, for each test condition a series of runs was made at different speeds with the intention of determining, if possible, the effect of speed on the rolling-friction coefficient. It is probable, however, that the heat generated by the friction caused a considerable rise in temperature in the tires during a series of runs which, according to the data of reference 1, would result in an appreciable reduction in the rolling friction. Since the runs were made with consecutive increments of speed, the effect of speed would thus be obscured by the temperature effect. The results of the present tests, therefore, do not provide a true indication of the effect of speed and are not so presented. Consideration of these results and of the data presented in reference 1, however, indicates that the effect of speed is probably slight in any case.

Each value of the rolling-friction coefficient given in the table and figures is the average of the several runs made at various speeds and with varying tire temperature, as previously mentioned. The average tire temperature was probably very nearly the same for all conditions with all tires except for those of the standard type. Tests of the standard tires were made in generally cooler weather and, consequently, the values of rolling-friction coefficient are possibly slightly higher relative to the values for the other tires than would be the case had the temperature conditions been comparable. The speed range for the tests on the concrete runway was from 5 to 45 miles per hour, whereas on the turf surface the range was from 5 to 30 miles per hour. The two groups of tests, nevertheless, are sufficiently comparable in view of the probable small effect of speed.

The results of the take-off calculations are shown in figure 8. Values of the take-off ground run were calculated for two hypothetical airplanes, one of moderate loading and the other of high loading. Several values of rolling-friction coefficient covering the range encountered in the tests were assumed for each case. Figure 8 shows the increase in ground run for given rolling-friction coefficients as a percentage of the distance required with no friction plotted against the corresponding coefficients.

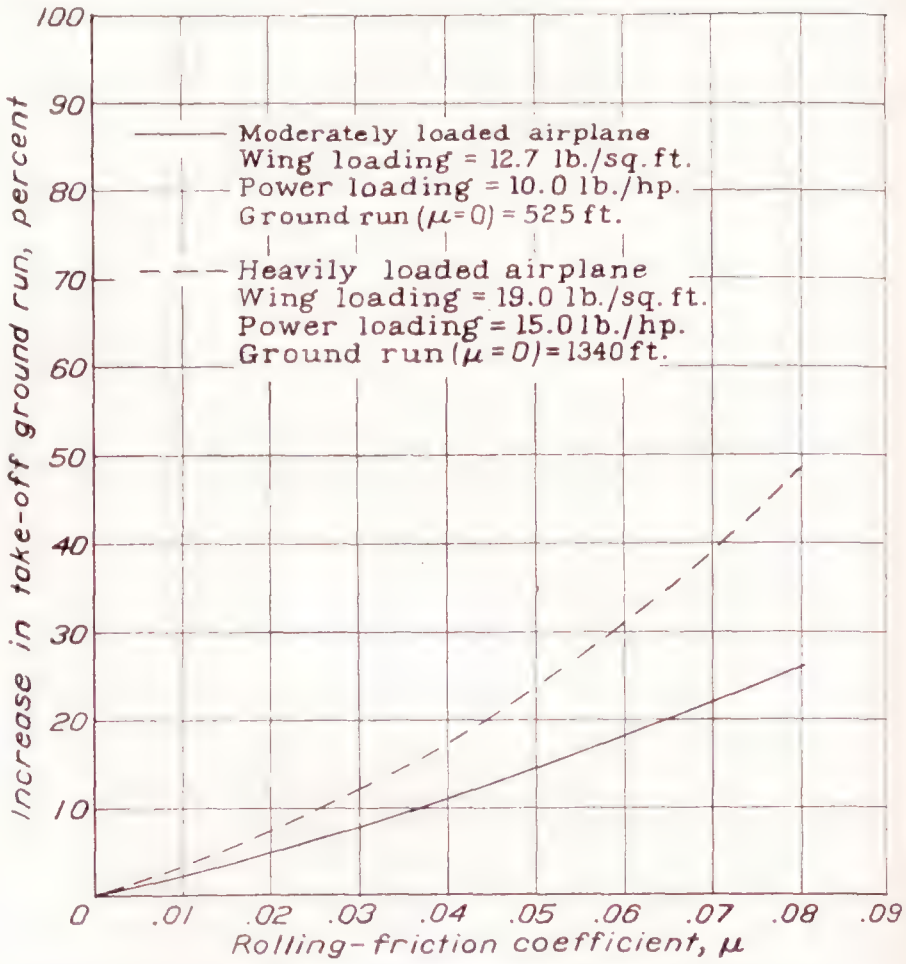

FIGURE 8.—Calculated effect of rolling-friction coefficient on take-off.

DISCUSSION

Rolling-friction coefficients.—On the concrete runway the rolling-friction coefficients obtained ranged from 0.009 to 0.035. The coefficients increased somewhat with increasing load for all wheels and tires, the variation being approximately linear and of similar magnitude for all cases. Likewise, the coefficients increased almost linearly with decreasing inflation pressure, although in this case there were appreciable differences in the magnitude of the variation for the different tires.

The effect of replacing the roller bearings in the 8.50–10 wheels with plain bearings was to increase the over-all rolling-friction coefficient by about 0.007, the increase being sensibly independent of load and representing more than 50 percent of the original values.

Of the three types of wheels and tires tested, the extra low-pressure type gave the highest values of rolling-friction coefficient and the low-pressure type with roller bearings provided the lowest values. The coefficients for the standard wheels and tires were slightly higher than those for the low-pressure type. Increasing the values for the low-pressure tires by the difference in coefficients observed between the values for the plain and roller bearings in order to obtain a fairer comparison would, however, raise the values for these tires somewhat above those for the standard tires. For different sizes of wheels and tires of a given type, the results do not show any consistent relation between tire size and rolling-friction coefficient.

For the tests on the turf surface, there were, of course, factors contributing to the over-all resistance that were not present on the smooth hard surface, such as the energy loss incurred by depressing the grass and earth and also the energy loss to the shock absorbers and tires associated with the unevenness or roughness of the surface.

In general, the values of rolling-friction coefficient derived from the tests on the firm turf surface averaged about twice those obtained on the concrete runway for corresponding conditions, the range of coefficients found being from 0.023 to 0.054. The coefficients

decreased slightly with increasing load for the low-pressure wheels and tires and for the 30×13–6 extra low-pressure wheels and tires. The 22×10–4 extra low-pressure size showed a considerably greater variation in the same sense. The effect of varying load was not determined for the standard-type wheels and tires on the firm turf surface.

Decreasing the inflation pressure resulted in a small reduction in the friction coefficient in the case of the standard and low-pressure tires. The values for the 30×13–6 tires appeared to be very nearly independent of inflation pressure, whereas the 22×10–4 tires showed a fairly large increase in the coefficient with decreasing inflation pressure.

The different types of wheels and tires were in the same order of merit, as regards rolling-friction coefficient, for the firm turf condition as for the concrete runway. In general, the larger tires of each type offered greater resistance to rolling than the smaller size for comparable conditions.

Only the 26×5 and the 36×8 standard-type wheels and tires were tested on the soft turf surface and these only for various loading conditions. The values for this condition were about twice those obtained with the 36×8 wheels and tires on the firm turf surface and were of approximately the same general magnitude for both sets of tires, the coefficients ranging from 0.064 to 0.077. The larger size showed decreasing rolling-friction coefficients with increasing load whereas the values for the smaller tires increased slightly with increasing load.

Effects on take-off.—Some indication of the effects on the take-off ground run that would result from the differences observed in the rolling-friction coefficients corresponding to the various conditions may readily be obtained by cross reference between figure 8 and figures 4 through 7. It may be seen from figure 8 that the effect of rolling friction on the take-off will be much greater for a heavily loaded airplane than for one of moderate loading even when considered, as in the figure, on a percentage basis. For convenience, only the heavily loaded airplane will be considered in this discussion.

Obviously the ground-surface condition is the variable having the greatest effect on the rolling-friction coefficient, and hence on the take-off distance. The distance required to take off on the firm turf would average about 9 percent longer than on the concrete runway, while on the soft turf surface it might be as much as 35 percent longer.

The variation in rolling-friction coefficient on the concrete surface between the highest and lowest loads tested would result in a difference of only 1 or 2 percent in the take-off distance. On the turf surfaces, the effect of varying load on the take-off would likewise be very small in most cases although, for the 36×8 tires on the soft turf surface, the variation in friction coefficient with load is sufficient to cause about 11 percent difference in take-off distance. Inasmuch as the load on the wheels of an airplane is continually decreasing during the take-off ground run, the rolling-friction coefficient will likewise be changing. In most cases, however, this variation can be neglected in take-off calculations without serious error or can be allowed for satisfactorily in any case by assuming a constant value of rolling-friction coefficient corresponding to the load intermediate between the static load and the load at the end of the run prior to the pull-off.

The effect on the take-off of moderate differences in the inflation pressure of a given set of tires would obviously be very small in most cases, probably resulting in a difference of only 1 or 2 percent for as much as 35 or 40 percent underinflation. For the cases showing an unusually large variation of friction coefficient with inflation pressure, the effect might be as high as 6 percent.

Under similar conditions on the concrete runway the take-off distance that would be required with the extra low-pressure tires would be between 4 and 6 percent longer than that with the standard tires. For the low-pressure tires equipped with roller bearings, the take-off distances would be slightly less than with the standard tires, within 2 percent, and with plain bearings about 1 percent greater. The same conclusions apply approximately to the firm turf condition.

In view of the generally small effect on take-off of all the variables with the exception of the ground-surface condition, the assumption of an average rolling-friction coefficient corresponding to a given surface condition should be satisfactory for ordinary routine calculations. Where the greatest possible accuracy is desired in calculating take-off performance, the other factors—type and size of the wheels and tires, wheel load, inflation pressure, and wheel-bearing type—should also be considered.

CONCLUSIONS

1. The values of rolling-friction coefficient obtained on the concrete runway varied from 0.009 to 0.035; on the firm turf surface, from 0.023 to 0.054; and on the soft turf, where only the high-pressure tires were tested, from 0.064 to 0.077.

2. The most important factor affecting the rolling-friction coefficient was the character of the ground surface.

3. For comparable conditions, either on a concrete runway or on firm turf, the standard-type wheels and tires had the lowest values of rolling-friction coefficient; the values for the low-pressure tires were only slightly higher. The highest coefficients were obtained with the extra low-pressure wheels and tires.

4. In general, the variation in rolling-friction coefficient with either wheel load or tire inflation pressure was fairly small.

5. The rolling-friction coefficient was appreciably greater for wheels equipped with plain bearings than for the same wheels having roller bearings.

6. The effect on take-off of all the variables, with the exception of the ground-surface condition, was generally quite small; so that, for ordinary calculations of take-off performance, the assumption of an average value of rolling-friction coefficient corresponding to a given ground-surface condition would probably be satisfactory. Where greater accuracy is desired, however, the other factors, although of less consequence, should nevertheless be considered.

LANGLEY MEMORIAL AERONAUTICAL LABORATORY,
NATIONAL ADVISORY COMMITTEE FOR AERONAUTICS,
LANGLEY FIELD, VA., *September 19, 1936.*

REFERENCE

1. Holt, W. L., and Wormeley, P. L.: Power Losses in Automobile Tires. Tech. Paper No. 213, Bur. Standards, 1922.

TABLE I.—ROLLING-FRICTION COEFFICIENTS

Wheels	Bearings	Load per wheel	Inflation pressure	Static tire deflection	Rolling-friction coefficient, μ		
					Concrete	Firm turf	Soft turf
		Pounds	*lb./sq. in.*	*Inches*			
Extra low pressure:							
22×10–4	Plain	1,240	12.5	2.55	0.029	0.035	
		940	12.5	2.06	.030	.041	
		640	12.5	1.58	.025	.054	
		940	10	2.50	.028	.047	
		940	8	2.92	.033	.050	
30×13–6	do	1,740	12.5	2.82	.027	.046	
		1,340	12.5	2.29	.024	.046	
		940	12.5	1.74	.023	.047	
		940	10	1.96	.029	.049	
		940	8	2.19	.035	.047	
Low pressure:							
7.50–10	Roller	1,540	20	2.26	.013	.025	
		1,240	20	1.90	.010	.023	
		940	20	1.52	.009	.029	
		940	16	1.78	.010	.026	
		940	12	2.18	.012	.026	
8.50–10	do	1,740	20	2.52	.013	.030	
		1,340	20	1.93	.014	.031	
		940	20	1.56	.010	.034	
		940	16	1.83	.013	.029	
		940	12	2.22	.015	.030	
	Plain	1,740	20	2.52	.020		
		940	20	1.56	.018		
Standard:							
26×5	do	1,240	50	.94	.018		0.070
		940	50	.76	.015		.071
		640	50	.58	.013		.066
36×8	do	1,740	60	.80	.017		.064
		1,340	60	.67	.011		.072
		940	60	.53	.015		.077
		940	60	.53		.037	
		940	50	.62	.020	.033	
		940	40	.69	.025	.033	

Report No. 584

STRENGTH OF WELDED AIRCRAFT JOINTS

By W. C. Brueggeman

SUMMARY

The work described in N. A. C. A. Technical Report No. 348 showed that the insertion of gusset plates was the most satisfactory way of strengthening a joint. The additional tests of the present series show that joints of this type could be improved by cutting out the portion of the plate between the intersecting tubes.

T and lattice joints in thin-walled tubing 1½ by 0.020 inch have somewhat lower strengths than joints in tubing of greater wall thickness because of failure by local buckling. In welding the thin-walled tubing, the recently developed "carburizing flux" process was found to be the only method capable of producing joints free from cracks. The "magnetic powder" inspection was used to detect cracks in the joints and flaws in the tubing.

The strengths of chromium-molybdenum T, lattice, and butt joints were materially increased by heat treatment. Butt joints in chromium-molybdenum sheet and tubing welded with low-carbon and chromium-molybdenum welding rod and those welded by the "carburizing flux" process had about the same strength in the "as welded" condition. The chromium-molybdenum and carburizing flux welds were the strongest after heat treatment.

INTRODUCTION

This investigation is a continuation of work started in 1928 at the request of and with the financial assistance of the National Advisory Committee for Aeronautics, and published by the Committee as Technical Report No. 348: Strength of Welded Joints in Tubular Members for Aircraft. It covers additional tests on joints reinforced by inserted gusset plates, tests of joints made with low-carbon and chromium-molybdenum welding rods, and the recently developed "carburizing flux" welds, and new tests made on T joints in which the leg of the T was loaded as a cantilever beam. Tests were also made on joints in thin-walled chromium-molybdenum tubing. Joints were tested in both the heat-treated and "as welded" conditions.

MATERIAL

Steel tubing and sheet of the following materials and sizes were used:

Chromium-molybdenum steel

Tubing—1 inch O. D. (O. D.=outside diameter) by 0.035-inch wall.
1½ inches O. D. by 0.020-inch wall.
1½ inches O. D. by 0.058-inch wall.
1½ inches O. D. by 0.083-inch wall.

Sheet—thickness 0.031, 0.063, 0.125, and 0.188 inch.

Mild-carbon steel

Tubing—1½ by 0.058 inch.

Sheet—thickness 0.063 inch.

The tubing and sheet complied with the following Navy Department specifications:

Chromium-molybdenum steel

Tubing—44T18 [1]

Sheet—47S14a

Mild-carbon steel

Tubing—49T1

Sheet—47S17a

The tensile strengths of the tubes from which the T joints were made are given in table I. Each value is the average strength of two specimens cut from opposite ends of the tube from which the members of the joints were taken. When the joint was heat-treated the tensile specimens were given the same heat treatment. Results of chemical analysis of the materials are given in table II.

TABLE I.—TENSILE STRENGTHS OF MEMBERS OF T JOINTS

Joint No.	Figure	Tensile strength	
		A	*B*
		lb./sq. in.	lb./sq in.
G140	10	107, 500	107, 500
G260	10	109, 600	109, 600
H140	10	148. 100	155, 500
H260	10	152, 500	155, 500
K140	10	85, 900	85, 900
K260	10	83, 300	83, 300
L140	11	134, 900	134, 900
L260	11	130, 100	130, 100
J140	11	129, 400	129, 400
J260	11	125, 800	125, 800
GM140	14	107, 400	102, 600
GM260	14	102, 800	102, 800
GM440	14	107, 400	102, 600
HM140	14	149, 100	161, 400
HM260	14	149, 100	152, 900
KM140	15	81, 300	81, 300
KM260	15	85, 200	85, 200

[1] This specification has been superseded by Navy Department specification 44T18a and supplement 44T18b. The tubing also complied with the new specification.

TABLE II.—CHEMICAL COMPOSITION OF TUBING, SHEET, AND WELDING ROD

Material	Carbon percent	Manganese percent	Phosphorus percent	Sulphur percent	Silicon percent	Chromium percent	Molybdenum percent
Tubing:							
Chromium-molybdenum steel:							
1 inch O. D. by 0.035-inch wall	0.27	0.43	0.01	0.012		0.89	0.20
1½ inch O. D. by 0.020-inch wall	.27	.57	.01	.012		.94	.20
1½ inch O. D. by 0.058-inch wall	.34	.54	.022	.011		1.09	.19
1½ inch O. D. by 0.058-inch wall	.34	.50	.023	.010		1.08	.19
Mild-carbon steel:							
1½ inch O. D. by 0.058-inch wall	.28	.52	.019	.019			
1½ inch O. D. by 0.058-inch wall	.24	.52	.020	.016			
Sheet:							
Chromium-molybdenum steel:							
0.031-inch thickness	.30	.42	.015	.008		.89	.18
0.063-inch thickness	.32	.41	.016	.004		.90	.20
Welding rod: [1]							
1/16-inch diameter, carburizing flux type	.17	1.02	.02	.024	0.38		
1/8-inch diameter, chromium-molybdenum type	.41	.90	.02	.006	.58	1.13	.20

[1] The low-carbon steel welding rod was from the same lot used in the previous investigation. The chemical composition is given in N. A. C. A. Technical Report No. 348, table VII.

PREPARATION OF SPECIMENS

INSPECTION FOR DEFECTS

Method.—Visual inspection of specimens of the previous investigation showed that there were cracks in some of the joints. It was found by experience that it was impossible to detect all of the cracks by visual inspection. Inasmuch as cracks may weaken the joint to an indeterminate extent, it was considered desirable to use a more effective method of inspection.

In 1922 William E. Hoke patented [2] a "method of and means for detecting defects in paramagnetic material" by magnetizing the object "while in proximity to mobile, finely divided paramagnetic material" such as iron filings or powder. A crack lying across the magnetic path presents a relatively high magnetic reluctance. An appreciable difference in magnetic potential thus exists between the two sides of the crack, and if close to the surface there is an external leakage flux between them. When the iron filings are brought into the field of this leakage flux they are attracted to the edges of the crack which is then indicated by an accumulation of the filings. The test may be carried out by immersing the object to be inspected in a fluid bath in which the iron filings are suspended.

In 1927, Roux (reference 1)[3] described a method of testing butt welds in steel plates by producing a magnetic flux in the plate and obtaining a pattern of the leakage flux by sifting iron filings onto a paper placed on the weld. A defective weld having no penetration, for example, has a higher magnetic reluctance than a corresponding portion of the base metal. This is indicated by magnetic leakage from the metal into the air around the defect, causing an accumulation of the powder at the defect. The joint was magnetized by a portable electromagnet with pole pieces which span the weld. By properly interpreting the pattern assumed by the iron filings the operator can often detect the presence of defects.

This method has been used in the United States by Watts (reference 2).

Recently de Forest (reference 3)[4] has developed a technique for inspecting steel and iron for such defects as cracks and other discontinuities. His technique is similar in principle to that of Roux and Watts and consists in suitably magnetizing the object, then sprinkling the magnetic powder onto the surface.

The magnetic powder method appeared to offer a solution to the problem of locating these cracks, and arrangements were therefore made with Professor de Forest to cooperate in the inspection of the joints used in this investigation.

Seams.—Each piece of tubing and sheet was inspected for defects before welding. The apparatus for detection of seams in tubing is shown in figure 1. The tube A was slipped over the copper rod B which was connected to the transformer C. An electric current in the rod produced a circumferential magnetization in the tube. Circumferential magnetization was used because it was believed that any defects originating during the processes of manufacture would probably be longitudinal. A current of from 200 to 300 amperes was found to be satisfactory. D is an ammeter and E is a current transformer for measuring the current. The dust was applied from the shaker F.

Many longitudinal seams were found. Typical indications are shown in figures 2 and 3. The seams were usually less than 1 inch long although some were 4 or 5 inches in length. The seams generally occurred singly, but sometimes in groups of two or more as in figure 2.

---

[2] U. S. Patent No. 1426384, Aug. 22, 1922.

[3] A more complete description of the technique of testing welds by the magnetographic method is given in a paper "Magnetic Testing of Welds", published in the Welding Engineer, vol. 15, no. 2, February 1930, p. 31. This paper was translated from material obtained from the laboratory of La Soudure Autogène Française.

[4] See also U. S. Patent No. 1960898, May 29, 1934.

Where defects were indicated, several of the tubes were sectioned as indicated by the dotted lines in figures 2 and 3, and examined under the microscope. The seams were in approximately a radial direction and varied in depth from about 0.003 to 0.015 inch. They were partially filled with iron oxide. The etched cross section at A, figure 2, shows the surface of the tube and the seam to be decarburized. It is probable that the seams originated during the fabrication of the steel and were caused by surface imperfections being rolled or drawn into the material.

There were seams on the inside as well as the outside of the tubes. It is difficult to inspect the inside surfaces, particularly of long tubes of small diameter. However, deep seams which occurred on the inside could usually be detected by applying the dust on the outside. It is believed that very few of the seams could have been detected visually without the magnetic powder.

Seams were found in the carbon-steel tubing and in two sizes (1½ by 0.058 inch and 1 by 0.035 inch) of chromium-molybdenum steel tubing.

Some of the tubes had grooves on the inside surface as shown at B and C, figure 3. These grooves were visible without using the magnetic powder and apparently were formed when the tube was drawn over a mandrel. When the powder was applied, as in the inspection for seams, the grooves were indicated by longitudinal accumulations of powder extending the full length of the tube as in tubes 5 and 6, figure 3.

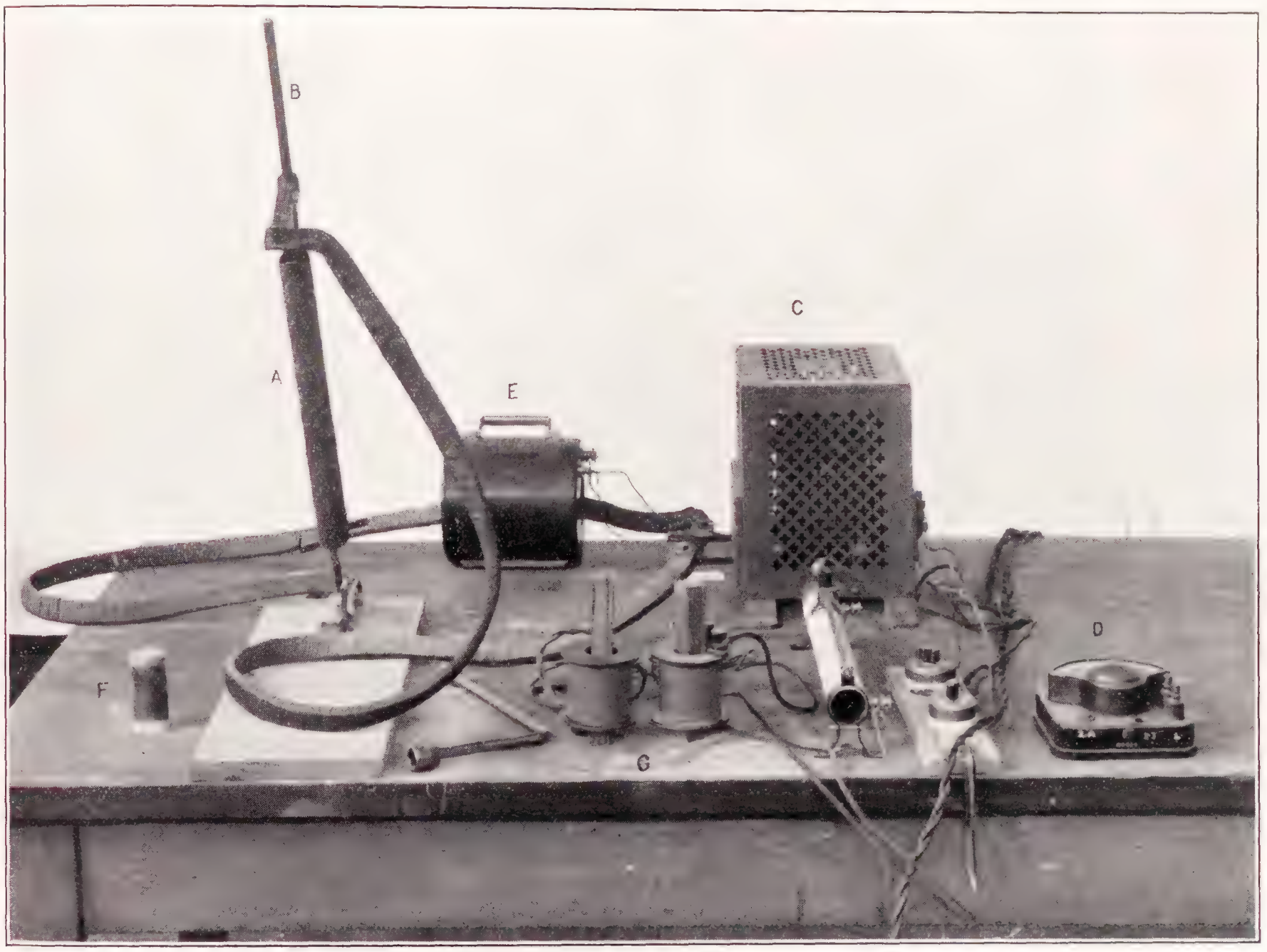

FIGURE 1.—Apparatus for detecting seams in tubing by the magnetic powder method of inspection. The tube A was magnetized by a heavy alternating current produced in the copper rod B by the transformer C. The ammeter D was used with the current transformer E to measure the current. The magnetic powder was applied to the surface of the tube by means of the shaker F. The iron-cored coils G were used when a portable magnetizing apparatus was desired.

The tubes were not rejected because of the presence of seams and grooves. The joints did not rupture at these defects and there was no indication that the strength was lowered under static loading.

The effect of seams and grooves on the torsional and fatigue properties of the tubing was not investigated.

Cracks.—All welded joints were examined for cracks by means of the magnetic powder method. The heat-treated joints were inspected again after heat treatment. The technique was similar to that employed for detecting seams.

The electromagnet shown in figure 4 was used to magnetize the joints. It consists of a solenoid having about

500 turns of No. 18 magnet wire and two steel pole pieces connected by a steel bar. When inspecting joints in tubular members V blocks were used on the ends of the pole pieces. These could be rotated about the axes of the pole pieces. The joint was placed in contact with the V blocks in such a manner that the flux passed through the portion of the joint it was desired to examine. It was sometimes more convenient to use a portable magnetizing apparatus, in which case the two coils F (fig. 1) were used. These are of the same size as the coil shown in figure 4 and are connected in series. Each coil has a laminated iron core about 6 inches long which is placed in contact with the members of the joint. It was necessary to use the coils close together because the magnetic circuit is not so efficient as one in which the core is continuous, as in figure 4. A current of about 1 ampere was found to be satisfactory for both kinds of apparatus.

When inspecting the sheet samples the electromagnet (fig. 4) was used, replacing the V blocks on the pole pieces with flat blocks. No cracks, seams, or other defects were found in the sheets either before or after welding.

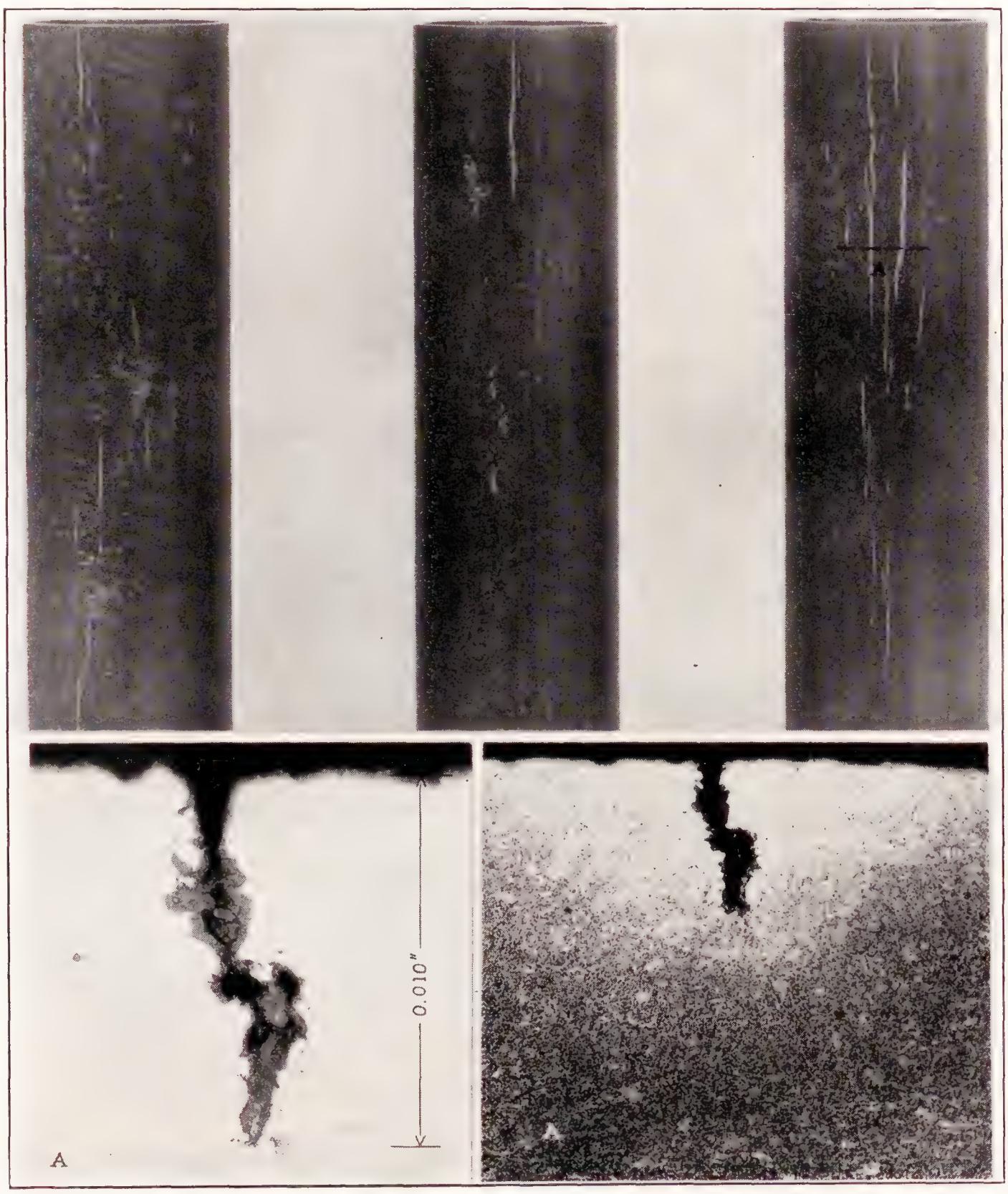

FIGURE 2.—Seams in chromium-molybdenum tubes 1½ inches O. D. by 0.058-inch wall. A microscopic examination was made at the cross section shown by the dotted line. The seam at point A is shown in the photomicrographs (left) in the unetched cross section and at a lower magnification (right) after the cross section had been etched in 1-percent Nital.

Cracks were found in all joints made in thin-walled chromium-molybdenum tubing 1½ by 0.020 inch in which low-carbon welds were made. Figures 5, 6, and 7 show locations of cracks as outlined by the magnetic powder. In the photomicrographs taken at point A,

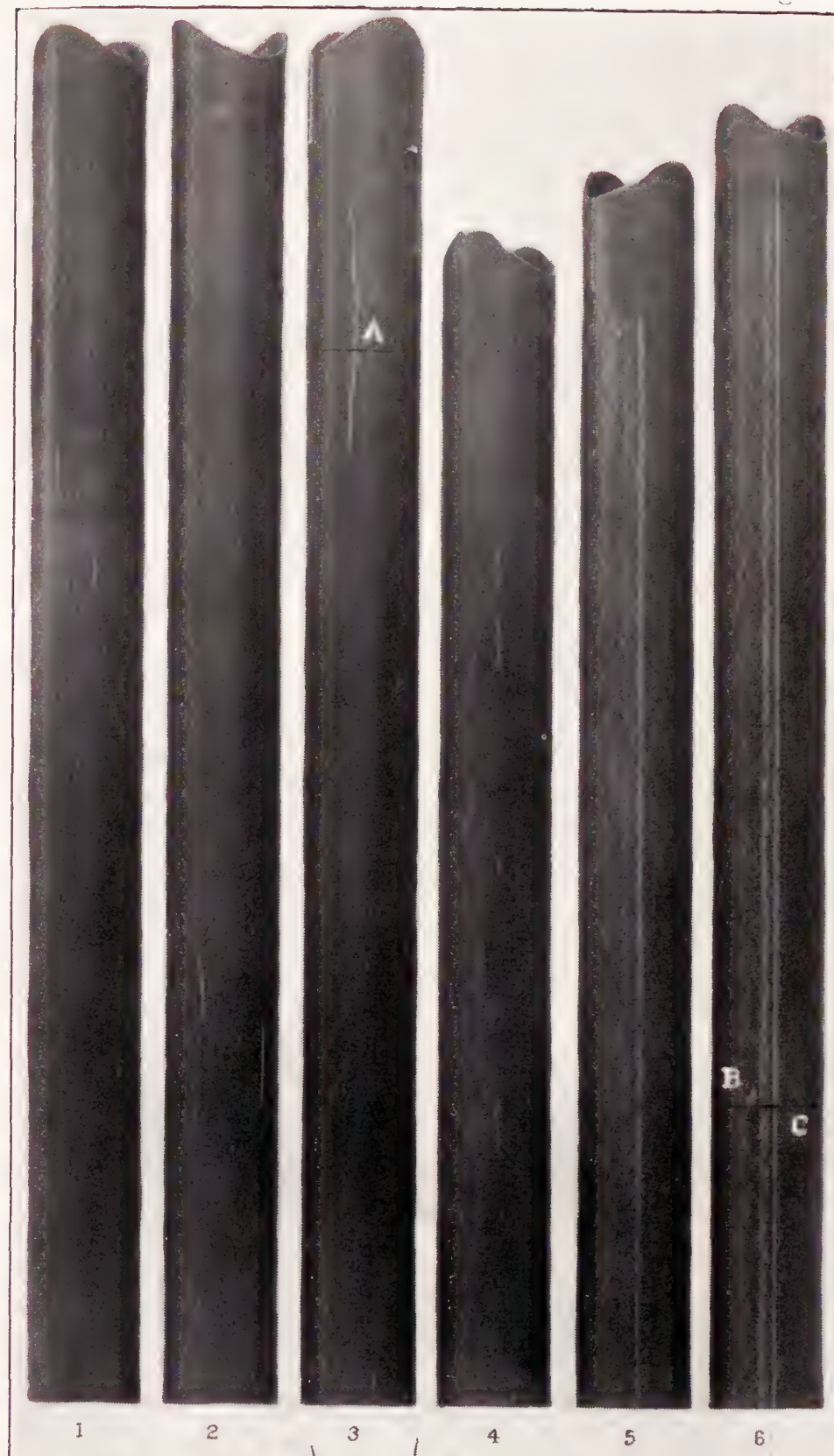

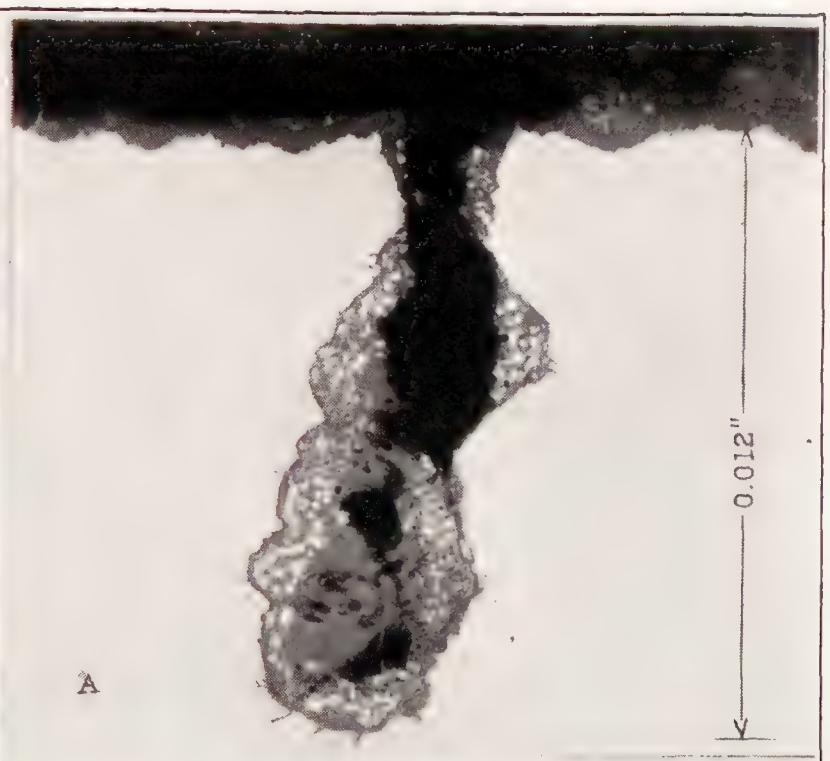

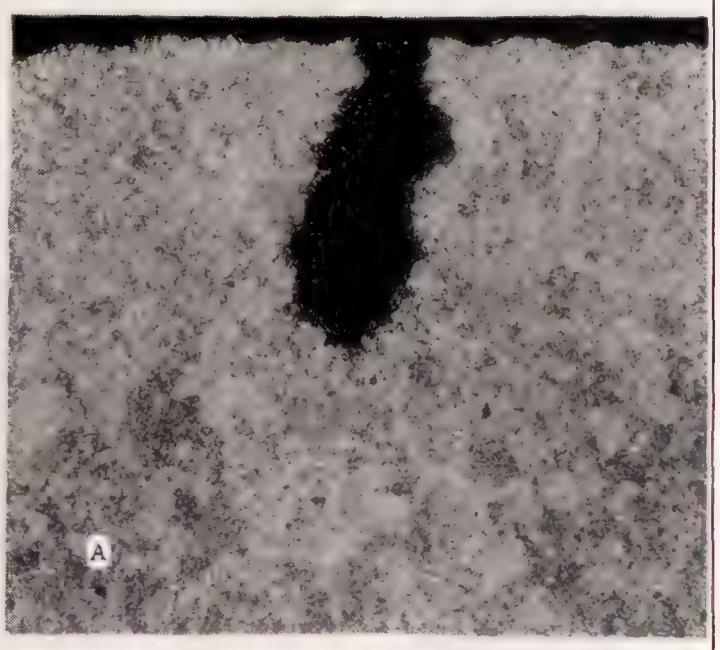

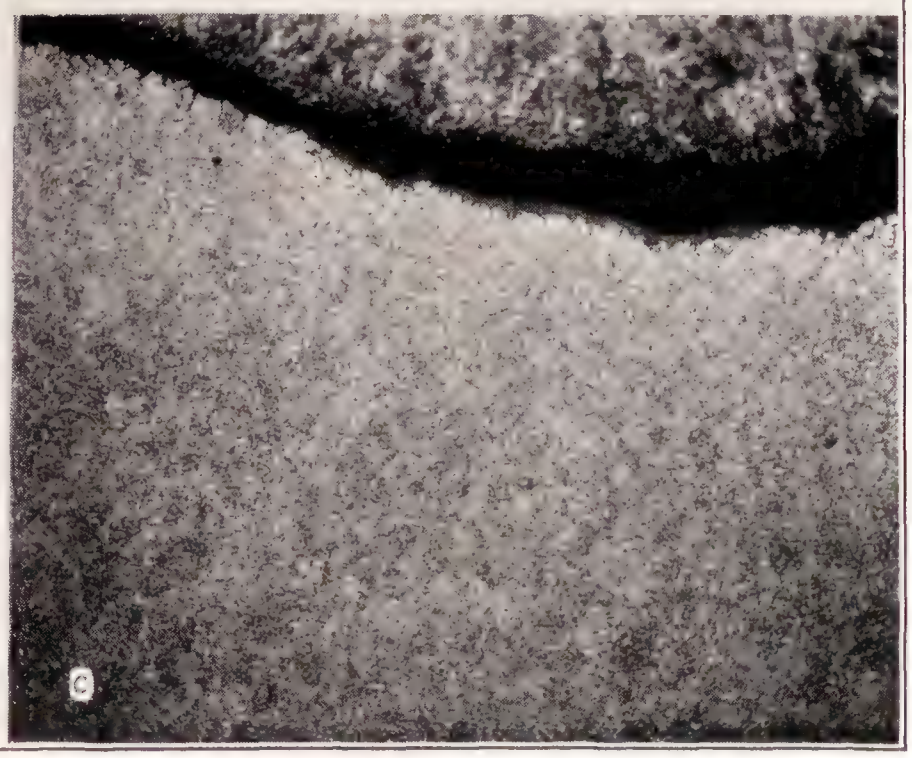

FIGURE 3.—Seams and grooves in other chromium-molybdenum tubes 1½ inches O. D. by 0.058-inch wall. The seam at point A, tube 3, is similar to the one shown in figure 2. The powder accumulations on tubes 5 and 6 are caused by grooves inside the tube as shown in the end view of tube 6. The photomicrograph C shows the cross section adjacent to groove C.

figure 5, there are cracks apparently following the grain boundaries that existed when the steel was in the austenitic state. There were cracks on both the inner and outer surfaces of the tube and one goes completely through the wall. These cracks are partly filled with oxide.

FIGURE 4.—Examining a lattice joint for cracks by the magnetic powder inspection.

The majority of the cracks were less than one-half inch long although in the ⊤ joints shown in figure 7 they extend on one side nearly half the circumference of the tube. The cracks occurred in the base metal of joints in thin-walled tubing made with low-carbon welds, usually about one thirty-second inch from the toe of the fillet, and ran parallel to the fillet.

WELDING

The specimens were welded in the same manner as those of the previous investigation by Mr. J. C. Kushner, of the Keystone Aircraft Corporation. The welding supervisor was H. S. George, research engineer of the Union Carbide and Carbon Research Laboratory. The procedure specifications were prepared for the previous investigation by a Committee on Welding Procedure of the American Bureau of Welding, and are given in N. A. C. A. Technical Report No. 348. The welder complied with the qualification tests of the procedure specifications.

The welding supervisor witnessed all of the welding. In his opinion the joints welded with low-carbon rod complied with the procedure specifications (the specifications had been prepared to apply only to this type of weld).

Four sets of welding equipment were loaned by manufacturers. They are designated as A, B, C, and D, as shown in figure 8. The set used for each joint is indicated at the bottom of the figure showing the test results.

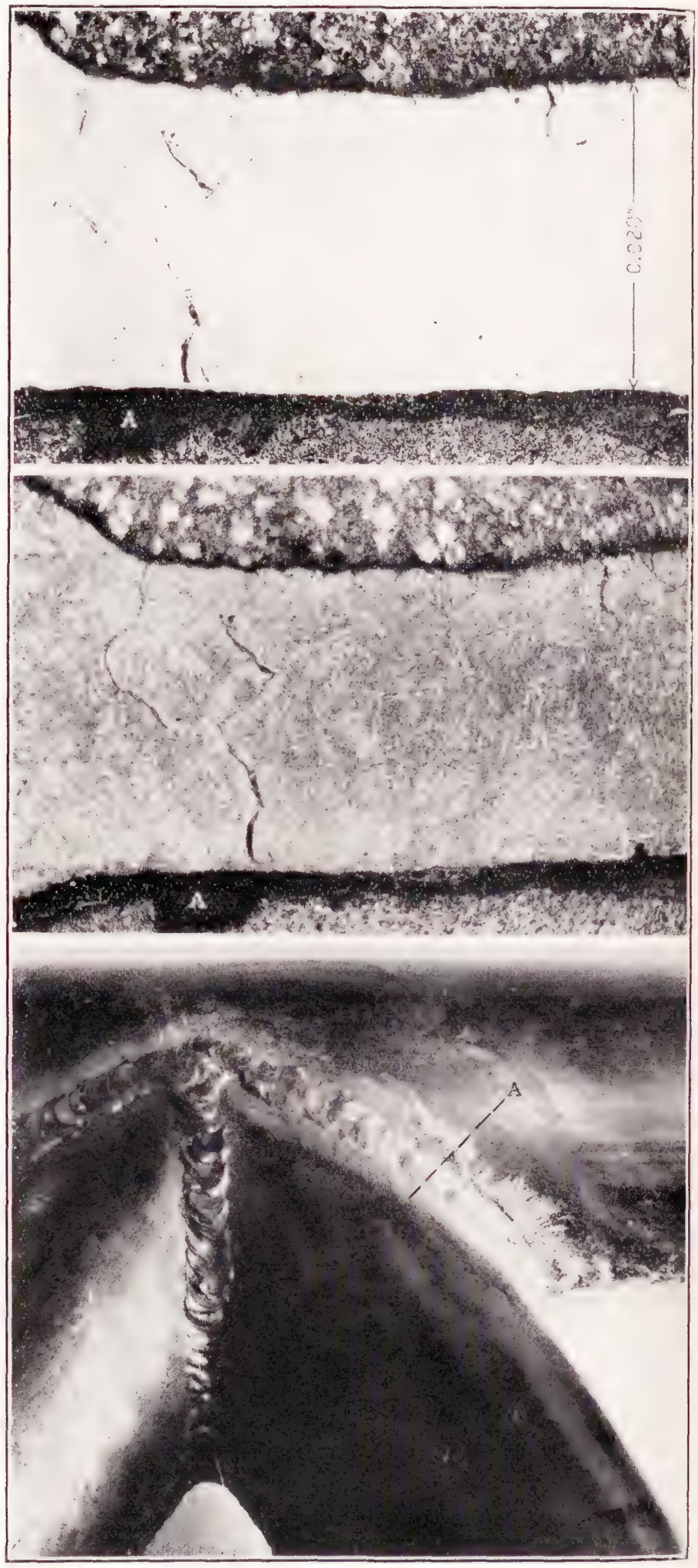

FIGURE 5.—Typical magnetic powder indications of cracks formed during welding in a lattice joint made from thin-walled chromium-molybdenum tubing (1½ inches O. D. by 0.020-inch wall). The photomicrographs taken at point A show the cross section indicated by the dotted line (upper) unetched and (middle) etched in 1-percent Nital. Low-carbon welding rod and a neutral flame were used in welding this joint.

All tubular joints were welded in a suitable jig that held the members in alinement. The time required to complete the weld after the members were set up in the jig was recorded.

It was found impossible to avoid cracks in thin-walled tubing when welding with a low-carbon rod. Several expedients that were tried in attempting to avoid cracks were: Preheating the tubes at the joint before welding by heating to a red heat with the torch; removing all scale adjacent to the weld with emery cloth; minimizing contraction stresses by heating one side of the joint with a torch while welding the other side; using various sizes of beads; exercising care to prevent excessive penetration; trying both forward and backward welding; using small sizes of torch tips and

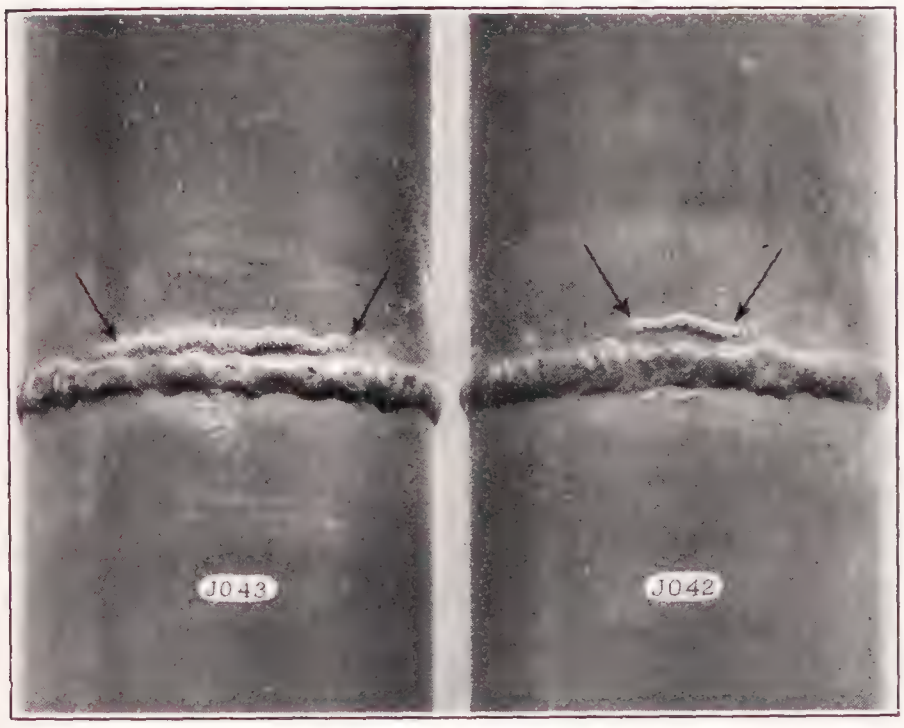

FIGURE 6.—Cracks in butt joints made with thin-walled tubing (1½ inches O. D. by 0.020-inch wall) as indicated in the magnetic powder inspection. These joints were welded with low-carbon rod and a neutral flame.

of welding rod; and, where the end of a tube was welded to the wall of another continuous tube, sawing out the portion of the continuous tube which is covered by the end of the intersecting tube. None of these expedients was successful.

After unsuccessful attempts to weld the thin-walled tubing the welding supervisor suggested that a new welding process recently invented by him might prove successful. This process (reference 4)[5] utilizes the carburized film caused by the absorption of carbon by steel when the latter is heated to a temperature somewhat below its melting point, in a carburizing atmosphere.

The usual type of oxyacetylene torch may be used; the gas flow is adjusted, however, to have an excess of acetylene, producing a carburizing atmosphere. The surface of the base metal when heated to the proper temperature absorbs carbon from this atmosphere. Increasing the carbon content of steel lowers the temperature at which it may be fused; thus a thin liquid film of melted steel is formed on the surface of the base metal at a temperature several hundred degrees lower than the fusion temperature of the base metal itself. The film, which may be recognized by its characteristic wet appearance under the flame, forms ahead of the

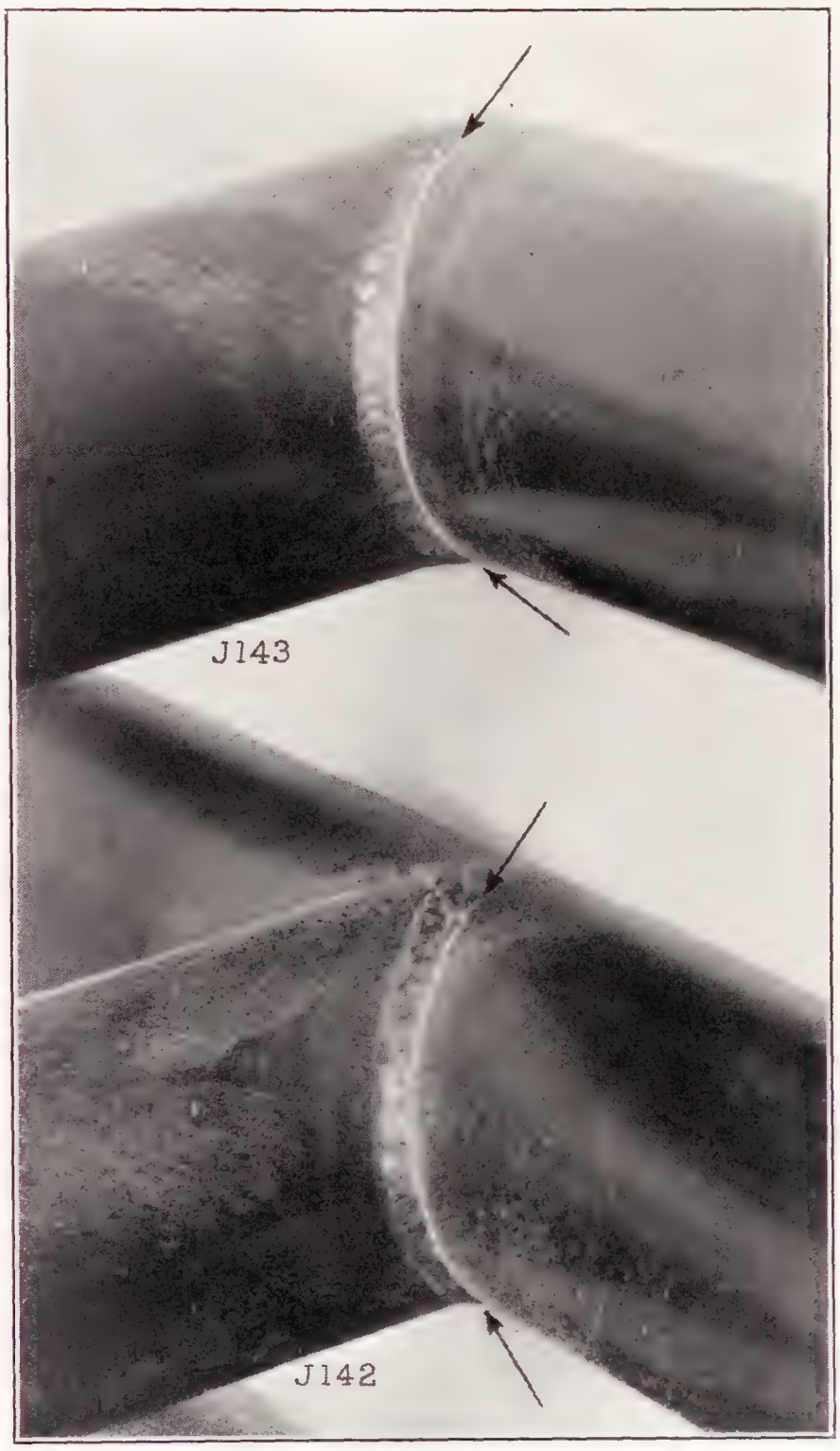

FIGURE 7.—Cracks in T joints made with thin-walled tubing (1½ in. O. D. by 0.020 in. wall) as indicated in the magnetic powder inspection. Low-carbon welding rod and a neutral flame were used in welding these two joints.

advancing melted filler metal and acts as a flux by preventing oxidation and causing intimate union between the base and the filler metals. The fluxing action of this film makes it unnecessary to heat the base metal to its melting point. The technique is somewhat like brazing in this respect, although all of the characteristics of a true weld are attained. A special rod containing carbon, manganese, and silicon as alloying elements in the iron base is used.

[5] See also U. S. Patent No. 1973341, Sept. 11, 1934.

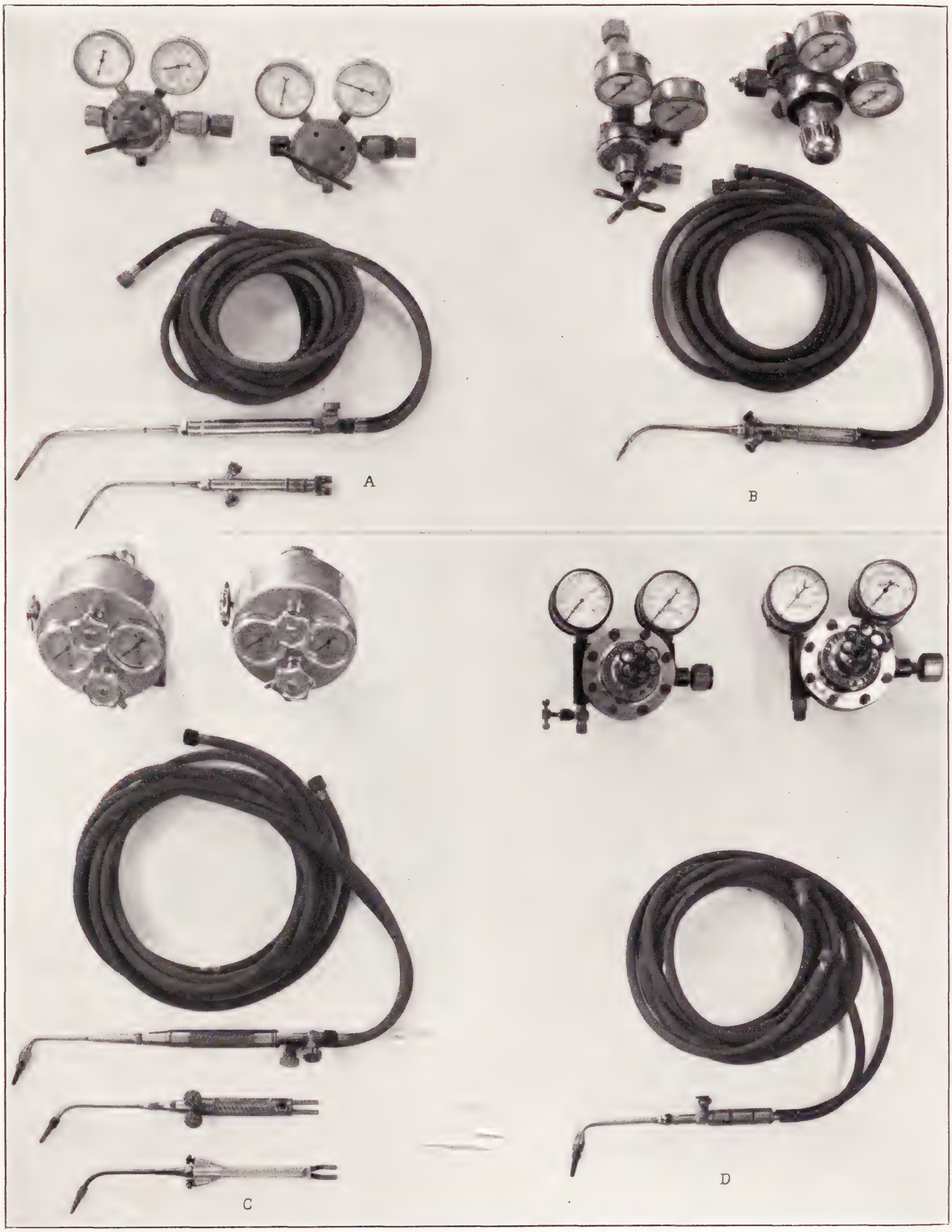

FIGURE 8.—The torches and equipment used. Each set was used to weld about an equal number of specimens.

It was believed that welds made in the thin-walled tubing by this process would be less susceptible to cracking because it would be unnecessary to fuse the base metal. Some preliminary welds were made by the carburizing flux process, and after several days' practice the welder, who had little previous experience with this process, was able to make welds in the thin-walled tubing in which no cracks could be detected.

A series of T, lattice, and butt joints was made in this tubing by the carburizing flux process, using a rod having the chemical composition given in table II. No indications of cracks could be detected by means of the magnetic powder inspection.

A brief description of some special features that were employed in making carburizing flux welds in thin-walled tubing is as follows:

(1) The luminous feather in the welding flame, indicating the amount of acetylene in excess of that required for complete combustion, was maintained at a length of from 2 to 2½ times the length of the inner cone.

(2) Backward welding (see fig. L, N. A. C. A. Technical Report No. 348) was used; that is, the torch was held so that the flame issued in the opposite direction to that of the progressing bead. This was done to retard the rate of cooling of the fillet during the critical interval when the base metal was most susceptible to the formation of heat cracks. It is believed that less oxidation of the unwelded base metal occurs in backward welding and that the base metal is less likely to be overheated. "Forward" welding was used for all tubes having a wall thickness of 0.035 inch or more welded by the carburizing flux process and for all low-carbon welds made by the regular neutral flame technique.

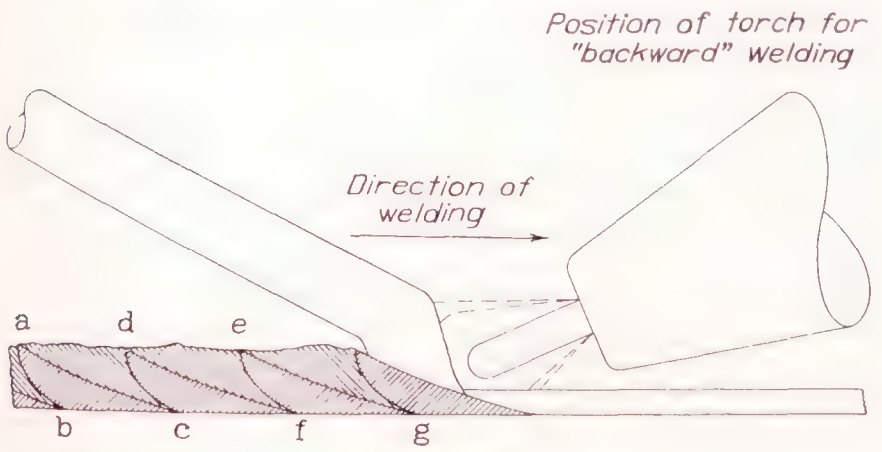

FIGURE 9.—Diagram of bead used in making carburizing flux welds in thin-walled tubing showing how the puddle was made to solidify in increments.

(3) An additional precaution consisted of manipulating the torch so as to confine the melted puddle to as small an area as possible. Instead of maintaining a continuously melted puddle as would be done on heavier base metal the fillet was made to solidify in increments. Starting with a puddle (fig. 9) having a long slope from the top of the fillet a to the point of farthest advance c, the torch was withdrawn until the first puddle had begun to solidify on the bottom (still maintaining the carburizing atmosphere), then more reinforcement a c d was added. After this layer had begun to solidify along the line c d, the next layer d c f was added and so on. The carburized film that was formed on the surface of the overlapping layers as well as on the base metal insured a continuous bead, the layers being welded to each other in the same manner as they were welded to the base metal. Thus the minimum amount of heat was applied to the joint and the length of the puddle, measured in the direction of welding, was kept as short as possible, minimizing the amount of the contraction as the puddles cooled.

Chromium-molybdenum welding rods having the chemical composition given in table II were used to make some of the butt joints that were to be heat-treated after welding.

Henceforth joints welded with low-carbon rod, chromium-molybdenum rod and those welded by the carburizing flux process are termed low-carbon welds, chromium-molybdenum welds, and carburizing flux welds, respectively.

The butt joints in steel sheets were made with reinforcements on each side about equal to half the sheet thickness, making the total thickness of the weld about twice that of the sheet. This type of weld was used to provide a symmetrical specimen and, in the low-carbon welds, to permit the maximum "picking up" of alloying elements from the base metal. Table III gives the average thickness of reinforcement (for both sides) of the butt joints in percentage of the base metal thickness.

TABLE III.—AVERAGE TOTAL THICKNESS OF REINFORCEMENT OF BUTT JOINTS IN PERCENTAGE OF BASE METAL THICKNESS

Type of weld	Sheet thickness, inch				Tube size 1½ by 0.058 inch
	0.031	0.063	0.125	0.188	
Low-carbon, percent	143	126	122	83	113
Carburizing flux, percent	189	121	89	85	124
Chromium-molybdenum, percent	235	100	111	92	----

HEAT TREATMENT

All heat treatment was done by the Division of Metallurgy, National Bureau of Standards. For the normalizing and hardening operations the temperatures given in the chart "Heat treatment and inspection test of aircraft metals—Naval Aircraft Factory", serial no. ML–79L, September 15, 1932, were used.

The lattice and T joints were hardened by heating at 1,600° F. in a gas furnace for 1 hour and quenching in oil. They were tempered at 900° F. for 1 hour and cooled in air. Tensile and compressive specimens of the tubing from which the joints were made were given the same heat treatment.

The butt and cross joints that were heat-treated were hardened by heating at 1,600° F. for 45 minutes and quenching in oil. They were then tempered at 500°, 700°, 900°, and 1,100° F., respectively, for 45 minutes and cooled in air. Specimens that were normalized were held at 1,600° F. for 1 hour and cooled in air. To prevent oxidation a reducing atmosphere was maintained in the furnace for all heating operations above 500° F.

IDENTIFICATION OF T AND LATTICE JOINTS

As in the previous investigation, three specimens were made of each joint. When reference is made to a group of triplicate specimens of the same design a specimen number terminating in a cipher is used, thus, 260; specimens numbered 261, 262, and 263 are the triplicate specimens comprising joints 260. Letters prefixed to the specimen numbers have the following meaning:

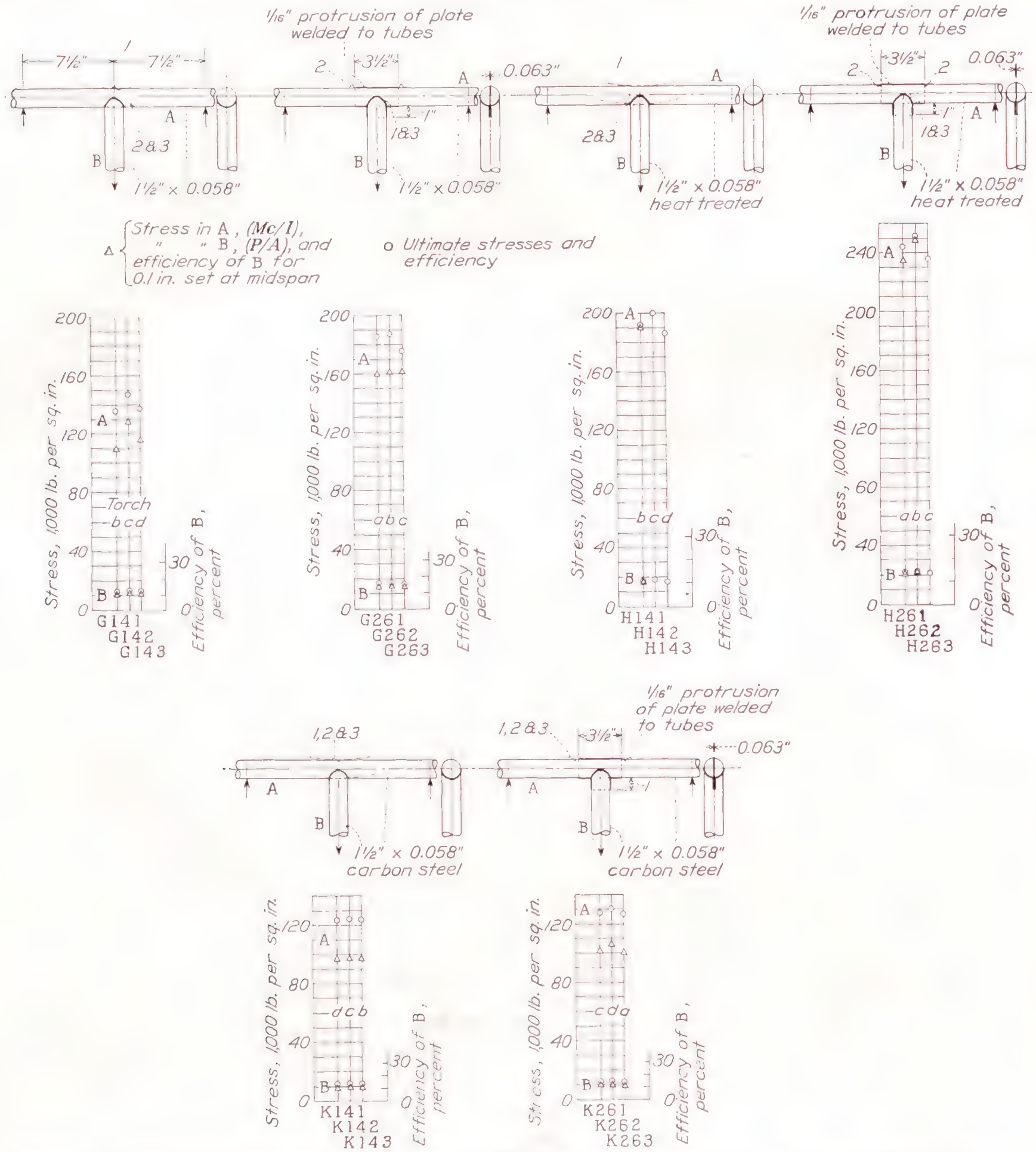

FIGURE 10.—Results of the transverse test of T joints made with chromium-molybdenum steel (upper) and carbon steel (lower) and low-carbon welds. Tube B was loaded in tension with tube A supported at a span of 15 inches. The load producing a permanent set of 0.1 inch at midspan was determined, also the maximum load. The stress Mc/I for tube A was computed for both loads, also the tensile stress and efficiency for tube B.

Letter	Meaning
G	Joint made with 1½ by 0.058-inch chromium-molybdenum tubing and low-carbon weld
H	Joint made with 1½ by 0.058-inch chromium-molybdenum tubing and low-carbon weld, heat-treated after welding
J	Joint made with 1½ by 0.020-inch chromium-molybdenum tubing and low-carbon weld
K	Joint made with 1½ by 0.058-inch carbon-steel tubing and low-carbon weld
L	Joint made with 1½ by 0.020-inch chromium-molybdenum tubing and carburizing flux weld
M	Cantilever loading of T-joint

increasing loads, the load producing a permanent set of 0.1 inch at midspan was determined (loading *I*). As it was believed that a determination of the bending strength of tube A would be more valuable than the results of loading *II* (see p. 25 and fig. 7, N. A. C. A. Technical Report No. 348), in which tube A was supported at the joint and tube B loaded until failure occurred, loading *I* was continued to failure.

Unreinforced T joints, 140, were tested in the heat-treated condition, H140, figure 10.

In an attempt to improve the design of the T joints in the previous investigation, joints 260 were made by inserting a T-shaped gusset plate in slots in the tubes, allowing the edge of the plate to protrude slightly, G260, H260, and K260 (fig. 10).

Carbon-steel joints, K140 and K260 (fig. 10) were tested.

Since the transverse strength of tubing increases with a decrease in the ratio of diameter to wall thickness, in order to investigate joints in tubing having a

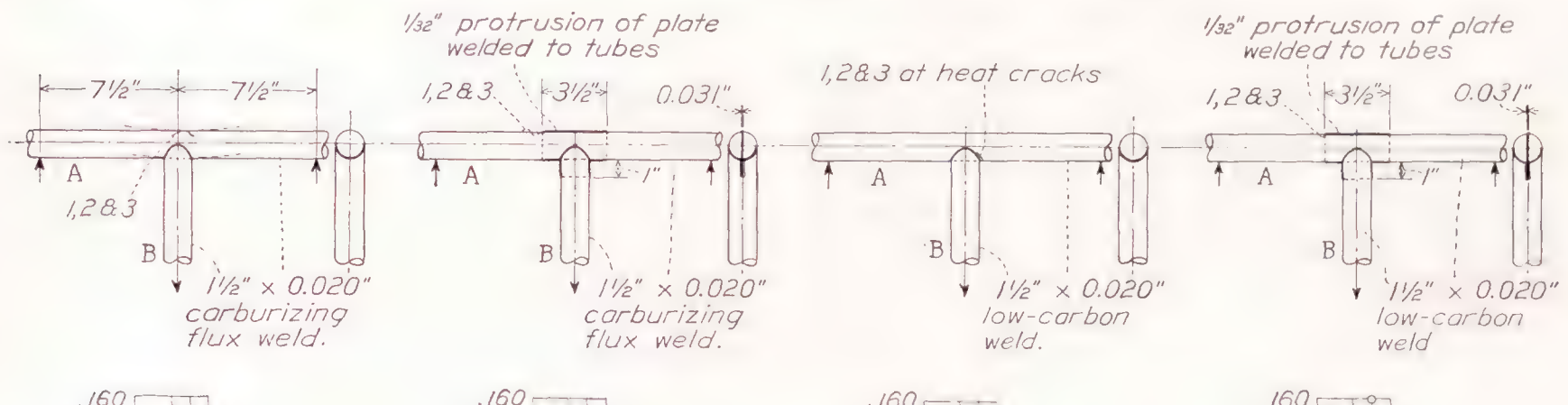

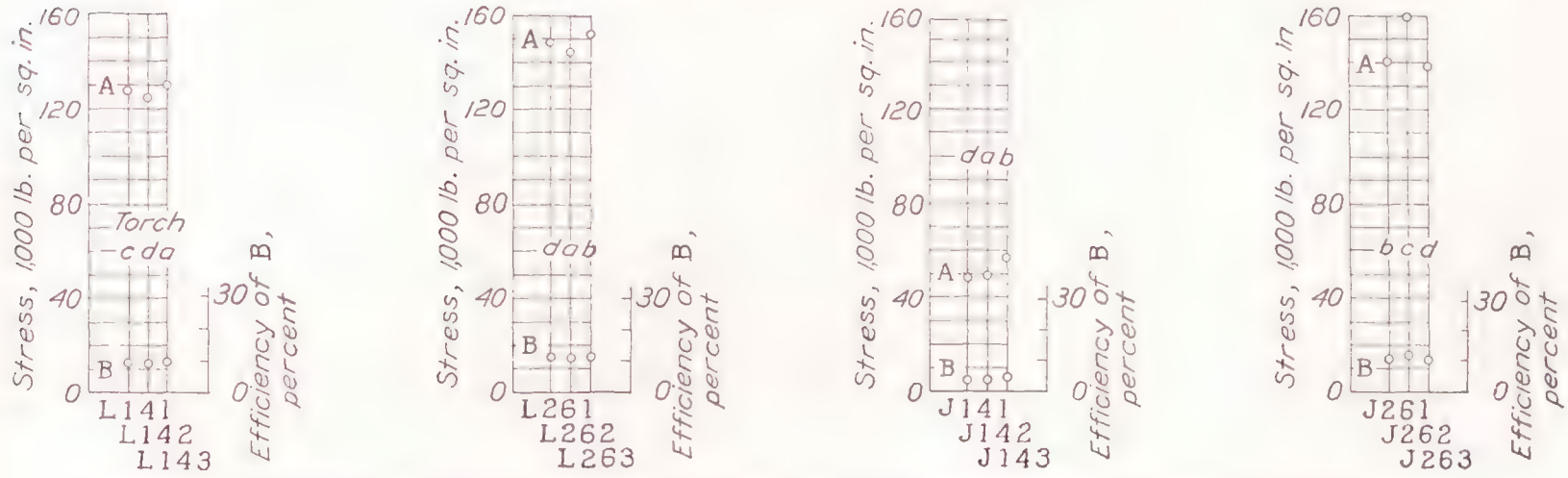

FIGURE 11.—Results of transverse test of T joints made with thin-walled chromium-molybdenum steel tubing.

T JOINTS

TRANSVERSE LOADING

Drawings of the T joints are shown in figures 10 and 11. The method of testing the T joints was changed slightly from the procedure followed in the previous investigation. Tube A was supported on rollers over a span of 10 diameters (15 inches) on the platen of a pendulum hydraulic testing machine (fig. 6, N. A. C. A. Technical Report No. 348). The free end of tube B was gripped in the lower jaws of the machine and load applied. By applying and releasing a succession of greater ratio of diameter to wall thickness than is ordinarily used in aircraft construction, joints J140, J260, L140, and L260 (fig. 11) were included. Chromium-molybdenum tubing 1½ by 0.020 inch was used.

For comparative purposes two nominal stresses in tube A of the T joints were computed, corresponding to loads in B which produced in A a permanent set of 0.1 inch, and failure, respectively. These stresses were computed like moduli of rupture, by dividing the bending moment at midspan by the section modulus of the original tube (that is, the gusset plates, if any, and tube B were neglected); they are plotted in figures 10 and 11.

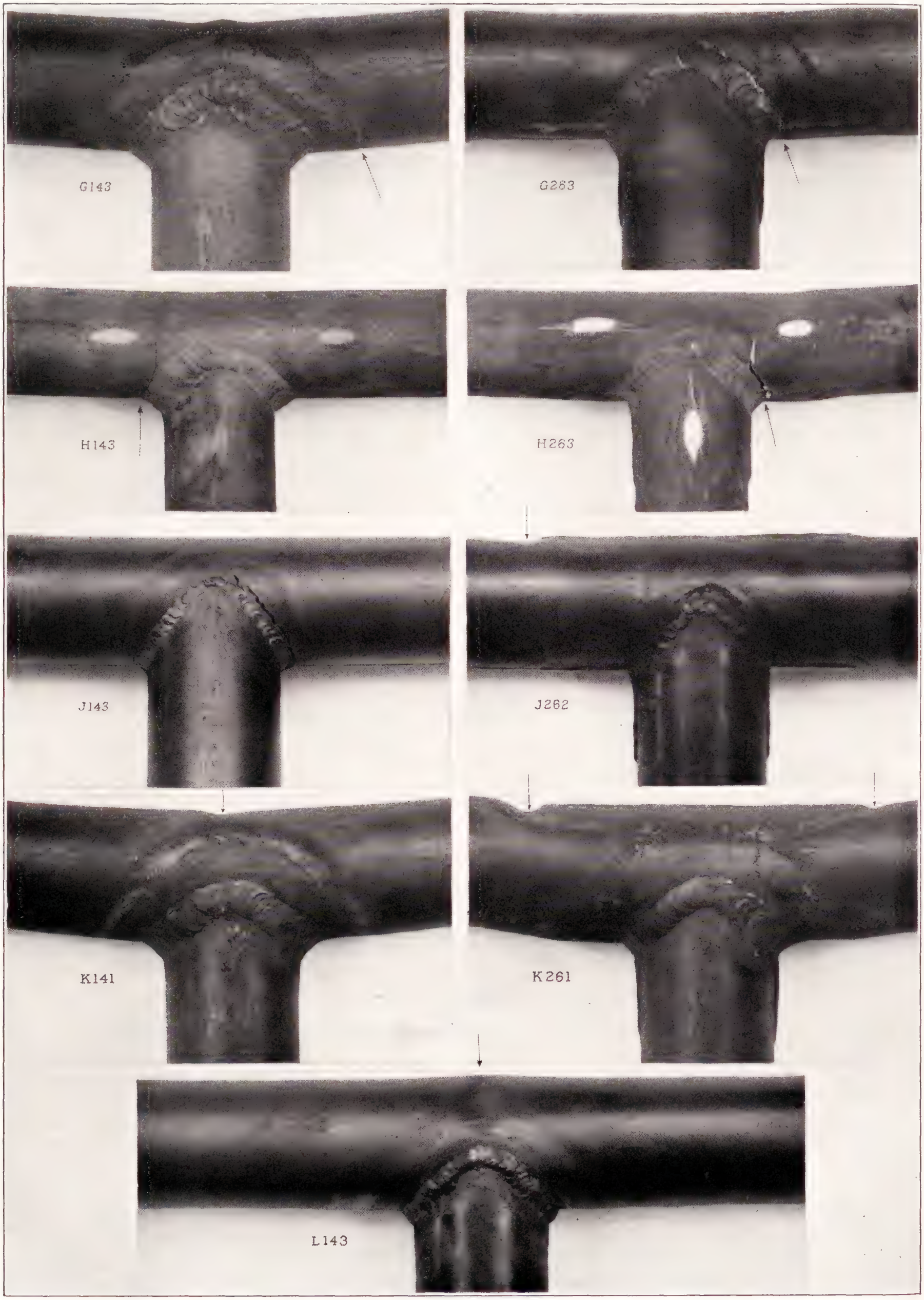

FIGURE 12.—T joints after failure under the transverse loading.

It should be emphasized that while these stresses are a convenient means of comparing the results obtained on different joints of the same size and same size of tubing, the extent to which they could safely be used with other sizes of tubing and different relations of bending moment to shear has not been investigated.

The stresses in tube B at 0.1 inch set and at failure of tube A have been plotted in figures 10 and 11. The ratios of these stresses to the tensile strength of tube B have been denoted the efficiencies of tube B. They indicate the extent to which the strength of the material of tube B has been fully utilized in the joint. The efficiencies are also shown in figures 10 and 11.

Typical failures of T joints under transverse loading are shown in figure 12. The failures are also indicated in figures 10 and 11 by the specimen numbers 1, 2, and 3 at the points of failure. Thus for joints G140, figure 10, the numbers 1, 2, and 3 indicate that specimen G141 failed by buckling and specimens G142 and G143 failed at the bottom of tube A at the locations shown. All the failures at the top of tube A were buckling failures. The failures at other locations were ruptures of either tube A or the weld.

The ratio of the stress for 0.1 inch set to the ultimate stress was much higher for the heat-treated joints than for those which had not been heat-treated. Specimens H142, H143, and H263 failed before the set became 0.1 inch. The strengths of the gusset-reinforced joints G260 under transverse loading were about 31 percent greater than those of the unreinforced joints G140, and the stress which produced a 0.1-inch permanent set in tube A was about 37 percent higher. The heat-treated joints H260 were about 26 percent stronger than the unreinforced heat-treated joints H140.

The carbon-steel joints K140 and K260 had about the same strength. Thus there appears to be little advantage in adding a reinforcing gusset to a carbon-steel T joint.

T joints L140 and L260, figure 11, made with thin-walled tubing by the carburizing flux process, had somewhat lower strengths under transverse loading than joints made from heavier tubing because the thin-walled tubing buckled under lower stresses. There were cracks in joints J140 (see fig. 7), made with low-carbon welds, that greatly lowered the strength of these joints. Cracks were also found in joints J260, made in the same way. The cracks in joints J260 were smaller and did not lie in such a highly stressed portion of the joints as in joints J140. They apparently did not lower the strengths, which were about the same as those of joints L260. All of the joints made with thin-walled tubing failed before developing 0.1-inch set.

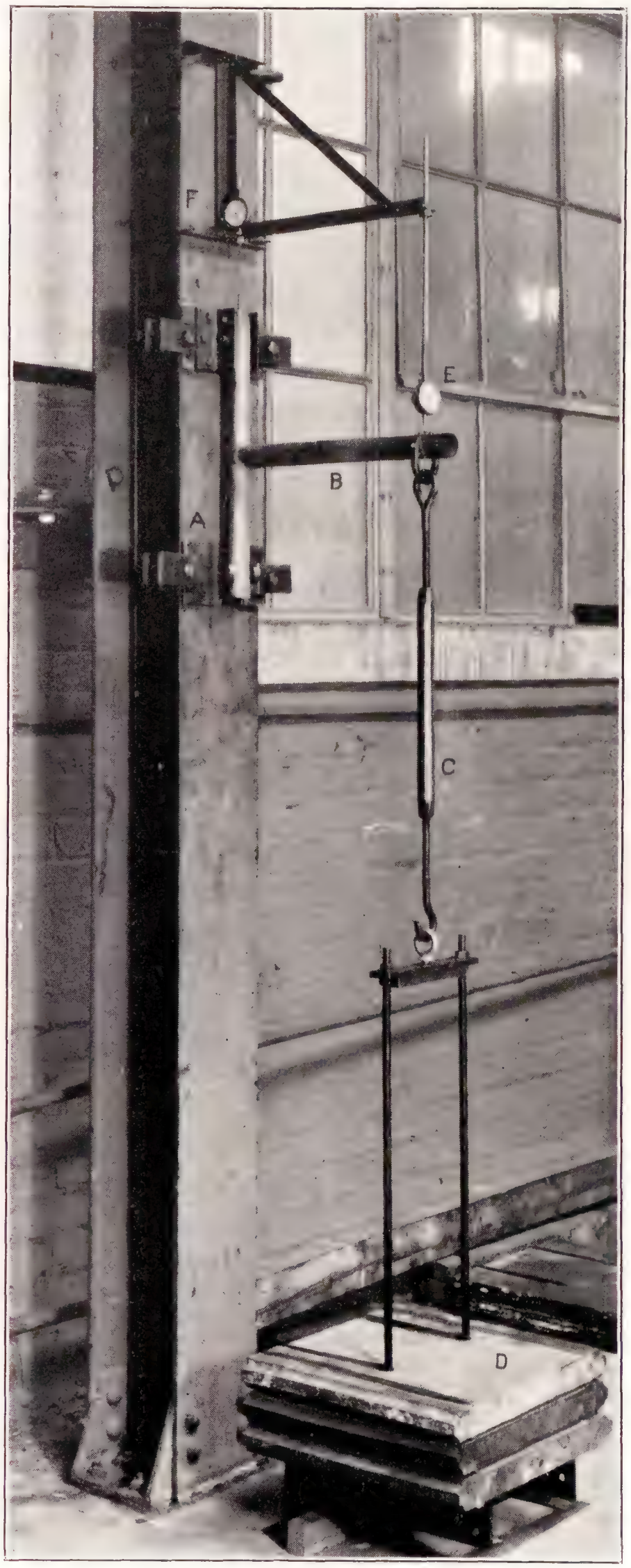

FIGURE 13.—Applying the cantilever leading to a T joint. The weights D were applied by turning the turnbuckle C. The permanent set at E was measured by the dial micrometer.

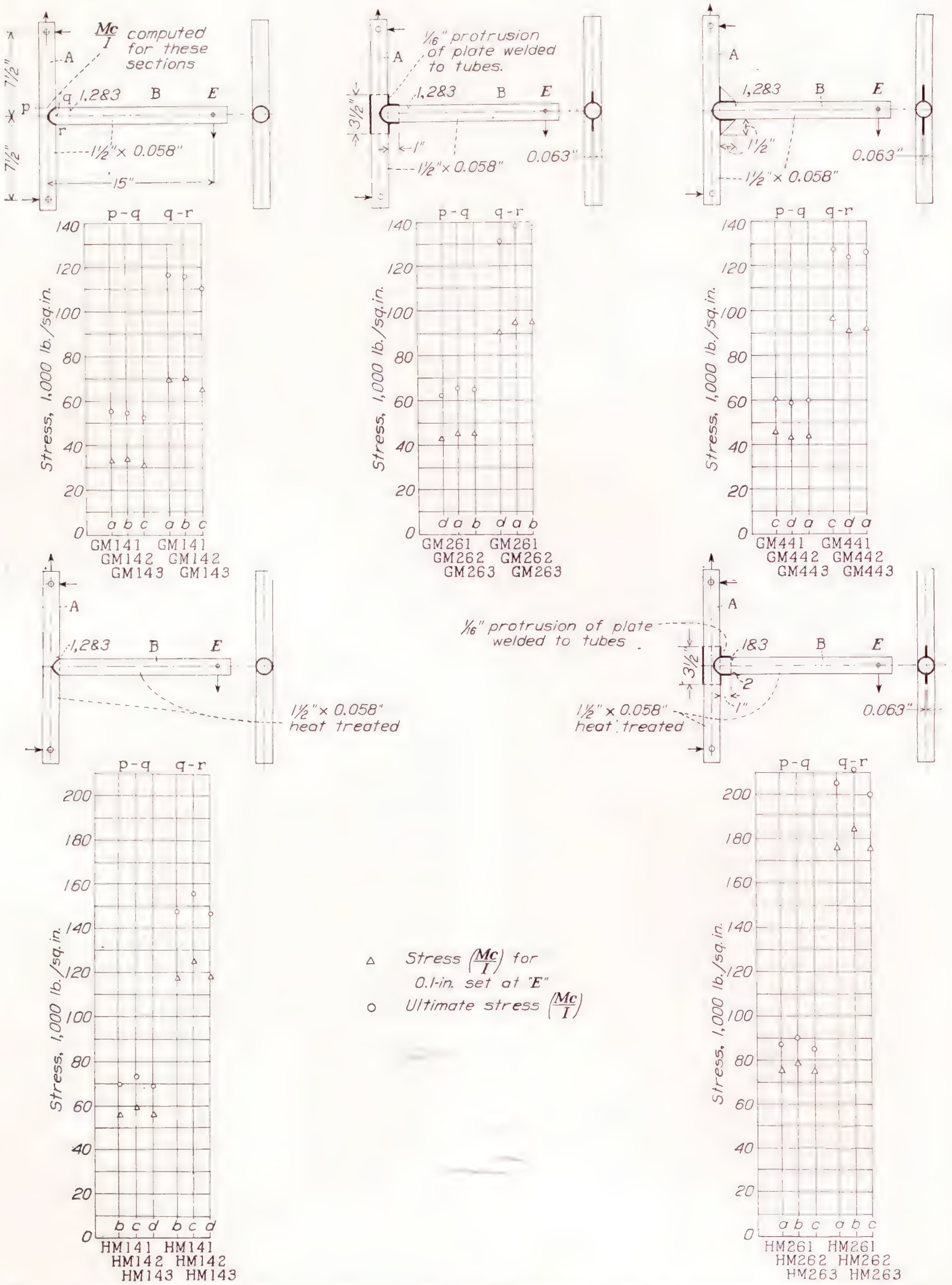

FIGURE 14.—Results of the cantilever test of T joints made with chromium-molybdenum steel and low-carbon welds. The stress Mc/I was computed at section p-q in tube A (see upper left diagram) and at section q-r in tube B for the load producing 0.1 inch permanent set at E and for the maximum load.

CANTILEVER LOADING

It was believed that information regarding the strength of T joints in which the leg of the T was loaded as a cantilever beam would be valuable. Joints were therefore tested as shown in figure 13. Tube A was held in a vertical position between two pins, the upper of which was fixed and the lower was fitted with rollers, allowing movement in a vertical direction. The load was applied by turning the turnbuckle C until the weights D were raised. The dial F measured any movement of the support during loading. No appreciable movement was observed. The pins supporting tube A were spaced 15 inches apart and the length along tube B from the center line of tube A to the point where the load was applied was 15 inches. The load producing 0.1-inch permanent set at the point of loading E was determined, as well as the maximum load. A dial micrometer was used to measure the permanent set.

Figure 14 shows the test results for "cantilever-loaded" T joints made with chromium-molybdenum steel in both "as welded" and heat-treated conditions. Figure 15 shows test results for similar joints made with carbon steel "as welded."

In figures 14 and 15 the stress at section p–q in tube A and at section q–r in tube B has been plotted for the load which produced a permanent set of 0.1 inch at point E. The stress at failure has been plotted also. The stresses were obtained by dividing the bending moment by the section modulus. The guesset plates (if any) were neglected in computing the section modulus. Typical failures are shown in figure 16.

Joints GM260, reinforced by an inserted gusset plate, were about 19 percent stronger than the unreinforced joints GM140. Each failed in tube B where the tube had been annealed during welding.

Joints GM260, reinforced by an inserted gusset plate, were stronger than joints GM440, reinforced by triangular gusset plates.

The unreinforced heat-treated joints HM140 failed by tube B tearing out of the wall of tube A on the upper side. The reinforced heat-treated joints HM260 were about 37 percent stronger than joints HM140 and failed by rupture of tube B at the end of the gusset plate.

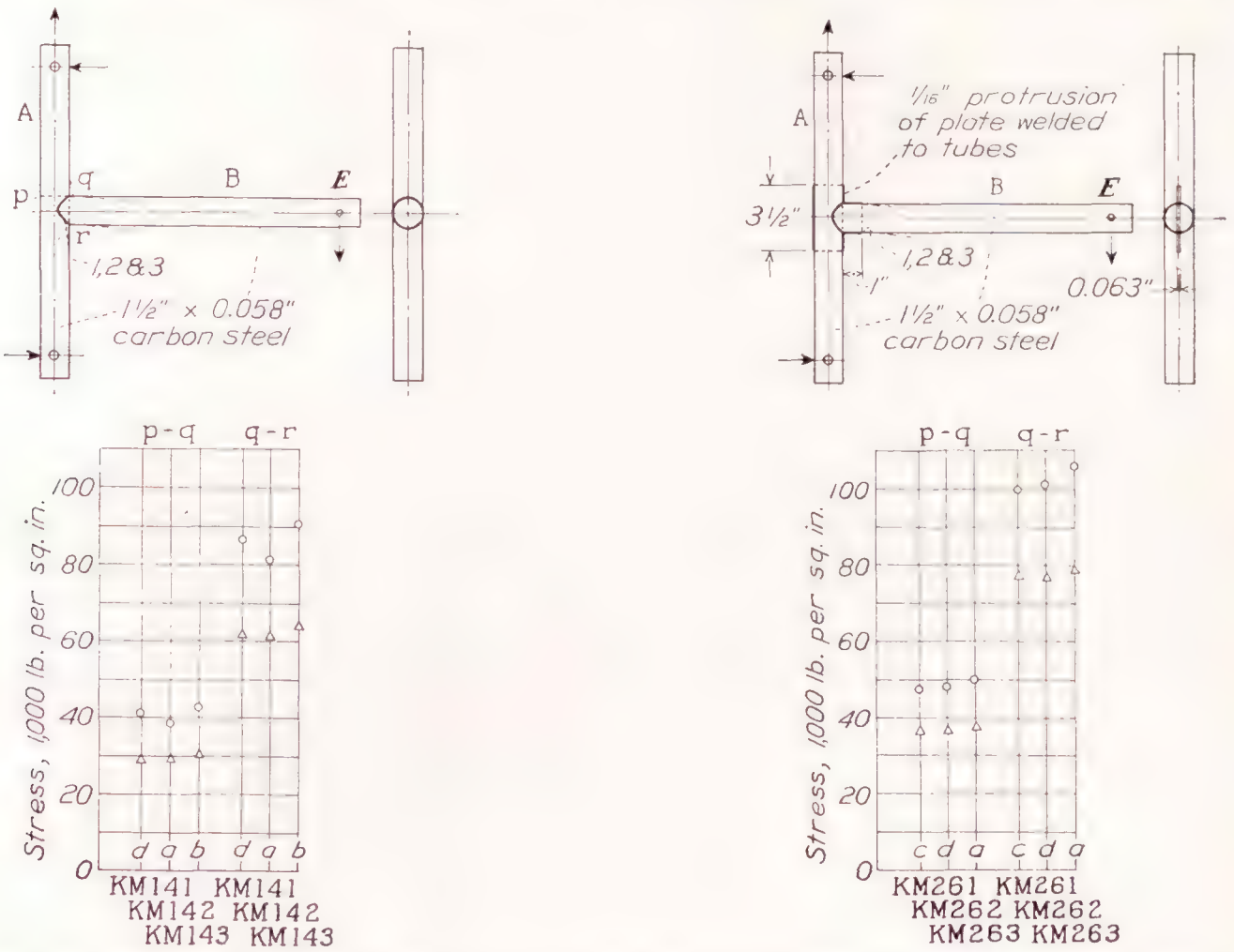

FIGURE 15.—Results of the cantilever test of T joints made with carbon steel and low-carbon welds.

The carbon-steel joints KM140, figure 15, failed by bending of tube B without rupturing or buckling. In joints KM260 tube B buckled on the compression side at the end of the gusset plate.

LATTICE JOINTS

The form of specimen and method of testing used for lattice joints was the same as in the previous investigation. The angle between tubes A and B and between B and C (figs. 17 and 18) was 60°. The ends of tubes A and C were supported on pin bearings in the testing machine as shown in figure 8, N. A. C. A. Technical Report No. 348, and tube B was loaded in tension until the joint failed.

The new type of inserted gusset reinforcement was also used for the lattice joints. Figure 17 shows joints

FIGURE 16.—Cantilever-loaded joints after failure.

G760 made with chromium-molybdenum steel in both "as welded" and heat-treated conditions. Figure 18 shows joints J760 and L760 made in thin-walled chromium-molybdenum tubing, and joints K760 made in carbon-steel tubing.

The unreinforced lattice joints H630, shown in figure 17, were tested in the heat-treated condition. Other joints, L630 and K630, figure 18, were made without reinforcement with thin-walled chromium-molybdenum and carbon-steel tubing, respectively.

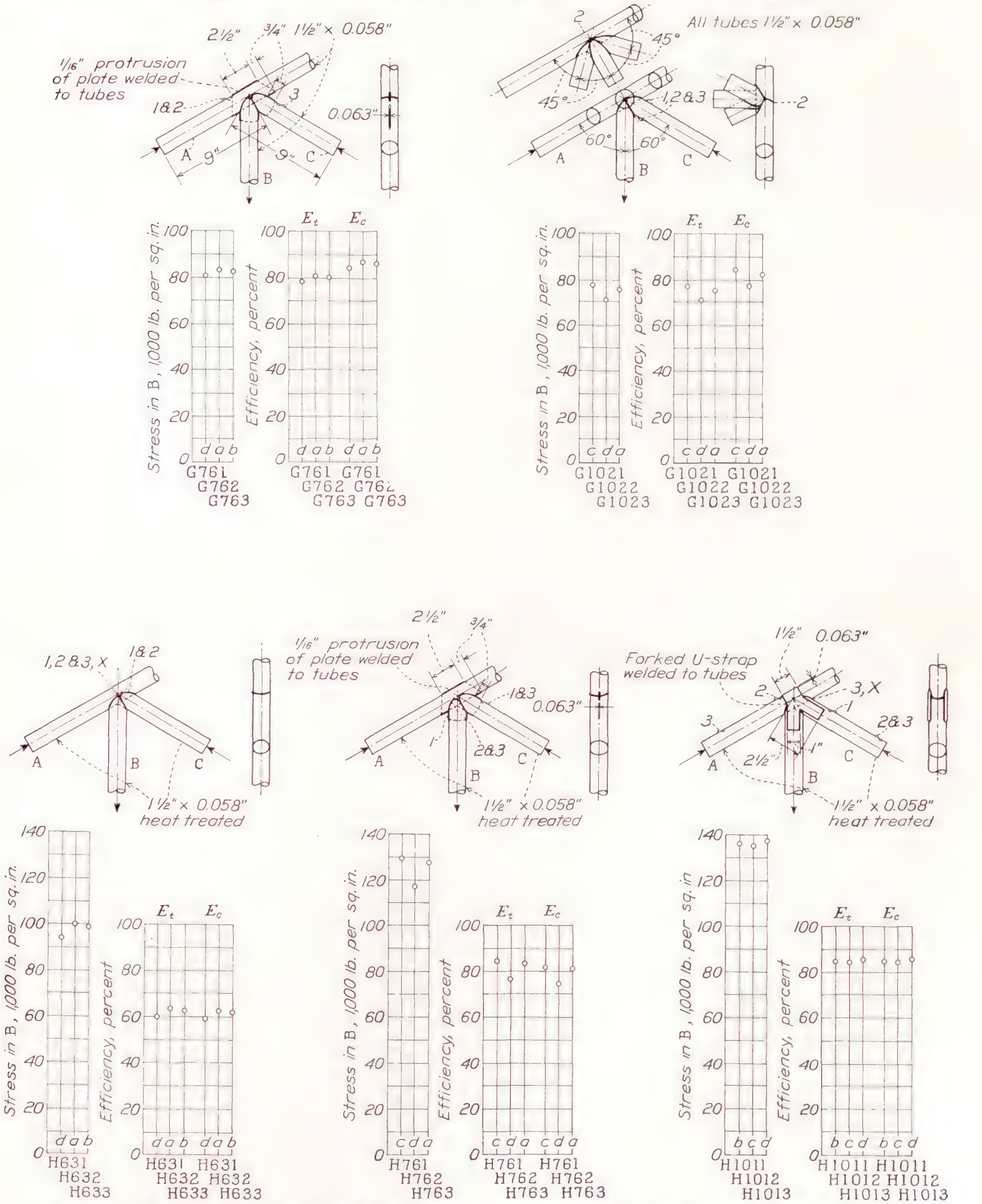

FIGURE 17.—Test results for lattice joints made with chromium-molybdenum steel and low-carbon welds.

To determine the effect upon the strength of the joint of tubes lying in a plane at right angles to the plane of the tubes to which the loads are applied, lattice joints G1020 were made (fig. 17).

The strap-reinforced joints G1010 tested "as welded" in the previous investigation were found to have a high strength. To determine the strength of this type of joint in the heat-treated condition, joints H1010 shown in figure 17, were made.

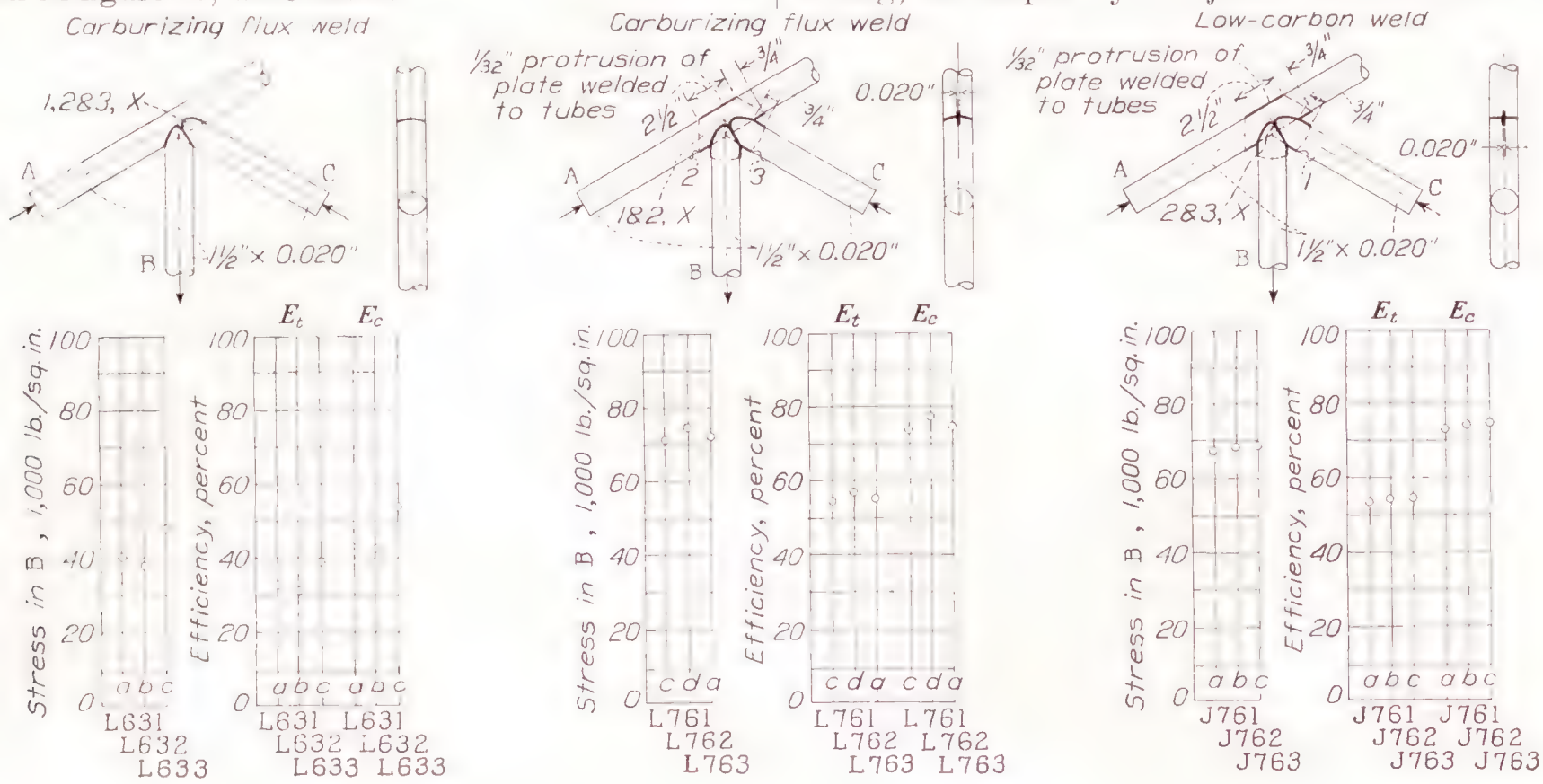

FIGURE 18.—Test results for lattice joints made with carbon-steel tubing and low-carbon welds (lower) and with thin-walled chromium-molybdenum steel tubing (upper).

The results for the lattice joints are plotted in the same manner as in the previous investigation. In figures 17 and 18 the maximum tensile stress in tube B is plotted on the left side of the graphs. The tensile efficiency E_t and the compressive efficiency E_c are plotted on the right side. E_t is the percentage of the tensile strength of tube B developed by the joint and E_c is the percentage of the compressive strength of tubes A and C (both cut from the same length of tubing) developed by the joint. The location of the failure is shown on the drawings. Failure by crushing of the tubes at the joint is indicated by X. Typical failures are shown in figure 19.

Joints G760, figure 17, had about the same strength as joints 750 and 1010 (N. A. C. A. Technical Report

FIGURE 19.—Lattice joints after failure.

No. 348, fig. 27), which were the strongest lattice joints tested in the previous investigation.

The three additional tubes in joints G1020 had a reinforcing effect, as these joints were stronger than joints 630 of the previous investigation.

The strengths of joints 630 were increased by heat treatment, although the tensile and compressive efficiencies were somewhat lowered. Marked increases in the strengths and slight increases in the tensile efficiencies of joints 760 and 1010 were produced by heat treatment. The compressive efficiencies were slightly lowered.

The efficiencies of the joints made from thin-walled tubing, shown in figure 18, were low, especially those of the unreinforced joints L630. Joints J760, for which low-carbon welds were used, have cracks which apparently did not appreciably lower their strengths as their efficiencies were about the same as those of joints L760. The gussets were more effective than in joints made with thicker-walled tubing. The tubes failed by crushing at the joints. The lower strengths of these joints are due to low resistance to lateral crushing or flattening of the thin-walled tubing.

Tensile tests were made of the welded-sheet specimens using either a fluid-support, Bourdon-tube hydraulic machine having dials of 0 to 10,000 pounds, 0 to 50,000 pounds, and 0 to 100,000 pounds capacity or a pendulum hydraulic machine having dials of 0 to 10,000 pounds, 0 to 25,000 pounds, 0 to 50,000 pounds, and 0 to 100,000 pounds capacity.

Templin grips were used for all sheet specimens of which the load did not exceed 10,000 pounds. Specimens having higher strengths were tested in the wedge grips provided with the machine.

Figure 21 shows the four types of fractures of the butt joints for both sheet and tubing. The type of fracture is shown at the top of the diagram in which the test results are plotted. Fractures of type 1 were remote from the weld; type 2 (which occurred for tubular specimens only) in the area where the welding heat had caused a localized annealing effect as shown in figure 17, N. A. C. A. Technical Report No. 348; type 3 at the edge of the weld; and type 4 in the weld. The results for the butt joints in steel sheet are plotted in figures 22 and 23. The strengths of all welds were increased materially by heat treatment, particularly

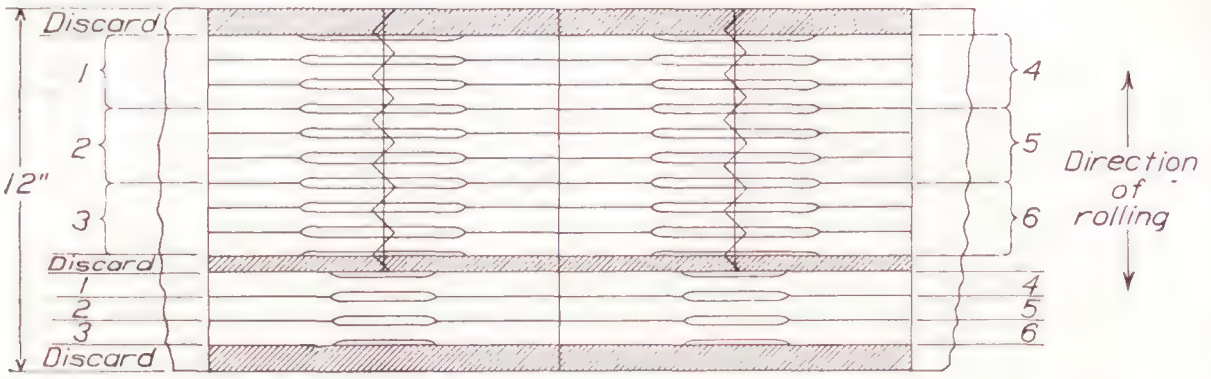

Specimens No.	Heat treatment	
1	None	
2	Normalized	
3	Quenched at 1600° F.	Tempered at 500° F.
4	"	" 700° F.
5	"	" 900° F.
6	"	" 1100° F.

FIGURE 20.—Layout of butt joints and tensile specimens of the base metal in the steel sheets.

The carbon-steel lattice joints, shown in figure 18, had somewhat lower efficiencies than joints made with chromium-molybdenum steel.

BUTT JOINTS

SHEET SPECIMENS

Butt joints were made in chromium-molybdenum sheet and tubing to determine the tensile strengths of heat-treated welds.

Four thicknesses of sheet, 0.031, 0.063, 0.125, and 0.188 inch were used. Open square butt joints were made with the 0.031-inch and 0.063-inch sheets and open 90° single V butt joints with the 0.125-inch and 0.188-inch sheets. All specimens were reinforced on both sides. After welding, tensile specimens were machined from the joints as shown in figure 20. The reduced section was ½ inch wide and 4½ inches long. The weld was at the middle. One series of specimens was made, as shown in figure 20, in each sheet thickness with each of three kinds of welds.

those of the carburizing flux and the chromium-molybdenum welds. There was considerably more scatter in the results of the heat-treated low-carbon welds than in the other types.

In general the full strength of the base metal was realized in the "as welded" and normalized joints in all four sheet thicknesses. Of the joints which were quenched and tempered the carburizing flux welds developed the highest strengths for all tempers in the 0.031-inch sheet thickness. In the other thicknesses the strength of the carburizing flux welds was slightly greater and somewhat more uniform than that of the chromium-molybdenum welds except at the 500° F. temper.

There was some variation in the bead reinforcement (see table III) between specimens of different sheet thicknesses and types of weld. However, none of the chromium-molybdenum welds and only three of the carburizing flux welds (one in the 0.063-inch and two in the 0.188-inch sheet, all quenched and tempered at 500° F.) fractured in the welds, indicating that the

FIGURE 21.—Butt joints in chromium-molybdenum sheet and tubing after failure, illustrating the four types of failure designated in figures 22, 23, 28, 29, and 30.

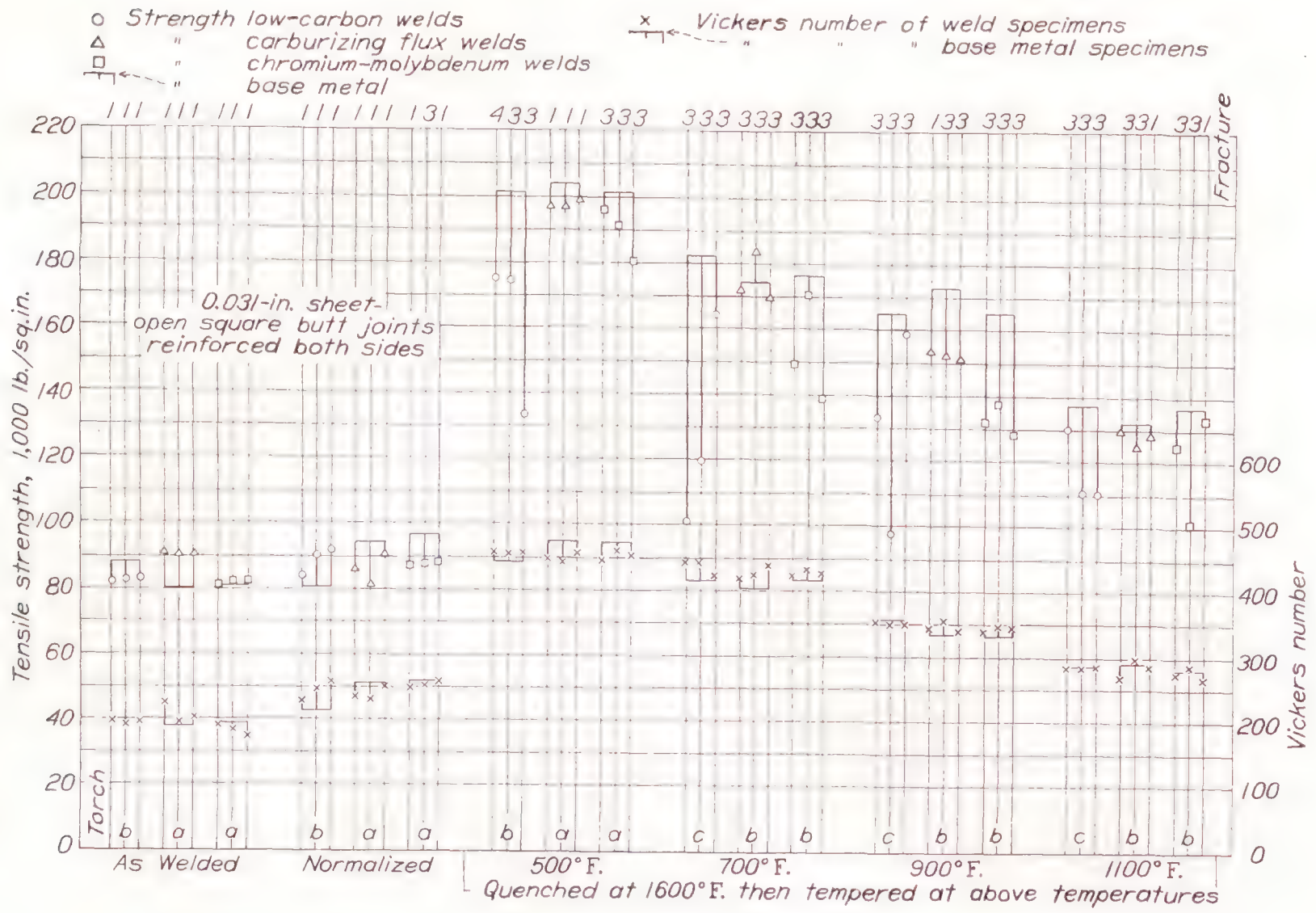

FIGURE 22.—Test results for open square butt joints in 0.031-inch chromium-molybdenum sheet (upper) and in 0.063-inch sheet (lower). Three groups of specimens corresponding to three types of welds were used for each heat treatment. An additional specimen of base metal representing each group of triplicate specimens was heat-treated and tested. The points shown on the graph are the tensile strengths and Vickers numbers of the joints. The corresponding values for the base metal specimens are shown by horizontal lines. The type of fracture of the joints is indicated at the top of the graph; the torch used, at the bottom.

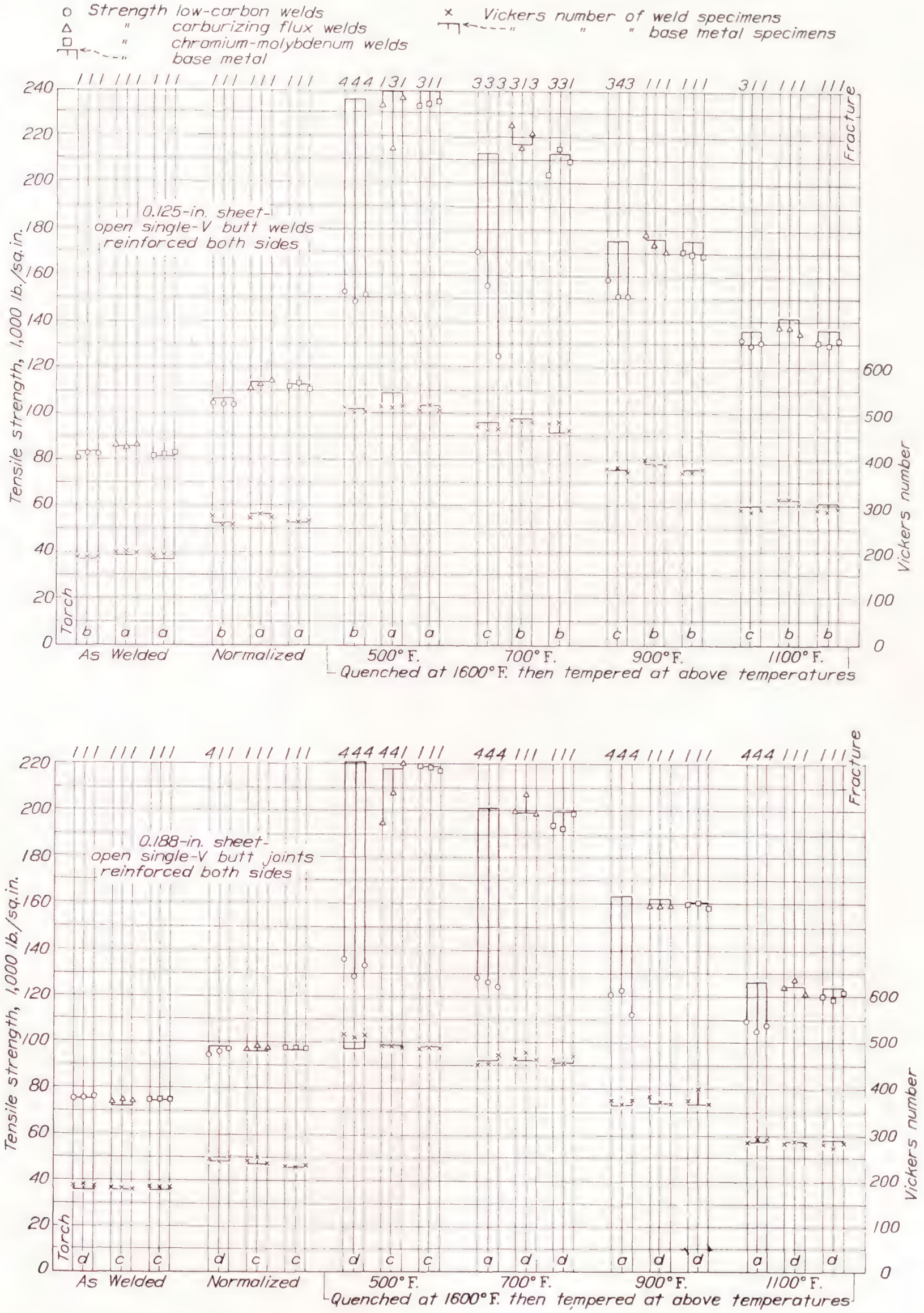

FIGURE 23.—Test results for open single-V butt joints in 0.125-inch chromium-molybdenum sheet (upper) and 0.188-inch sheet (lower).

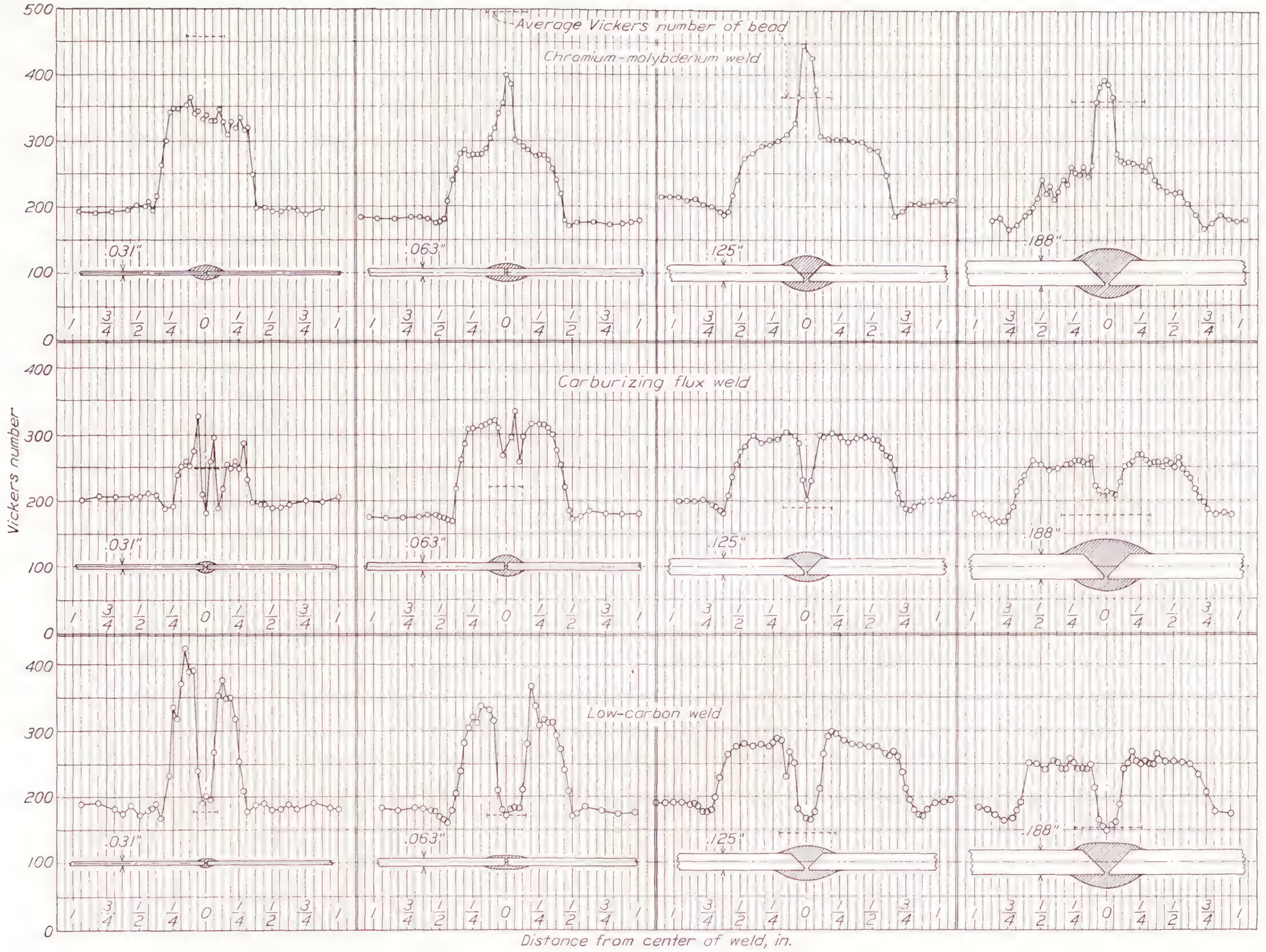

FIGURE 24.—Vickers number of open butt joints in chromium-molybdenum sheet "as welded." The impressions were made on the edge of the specimens.

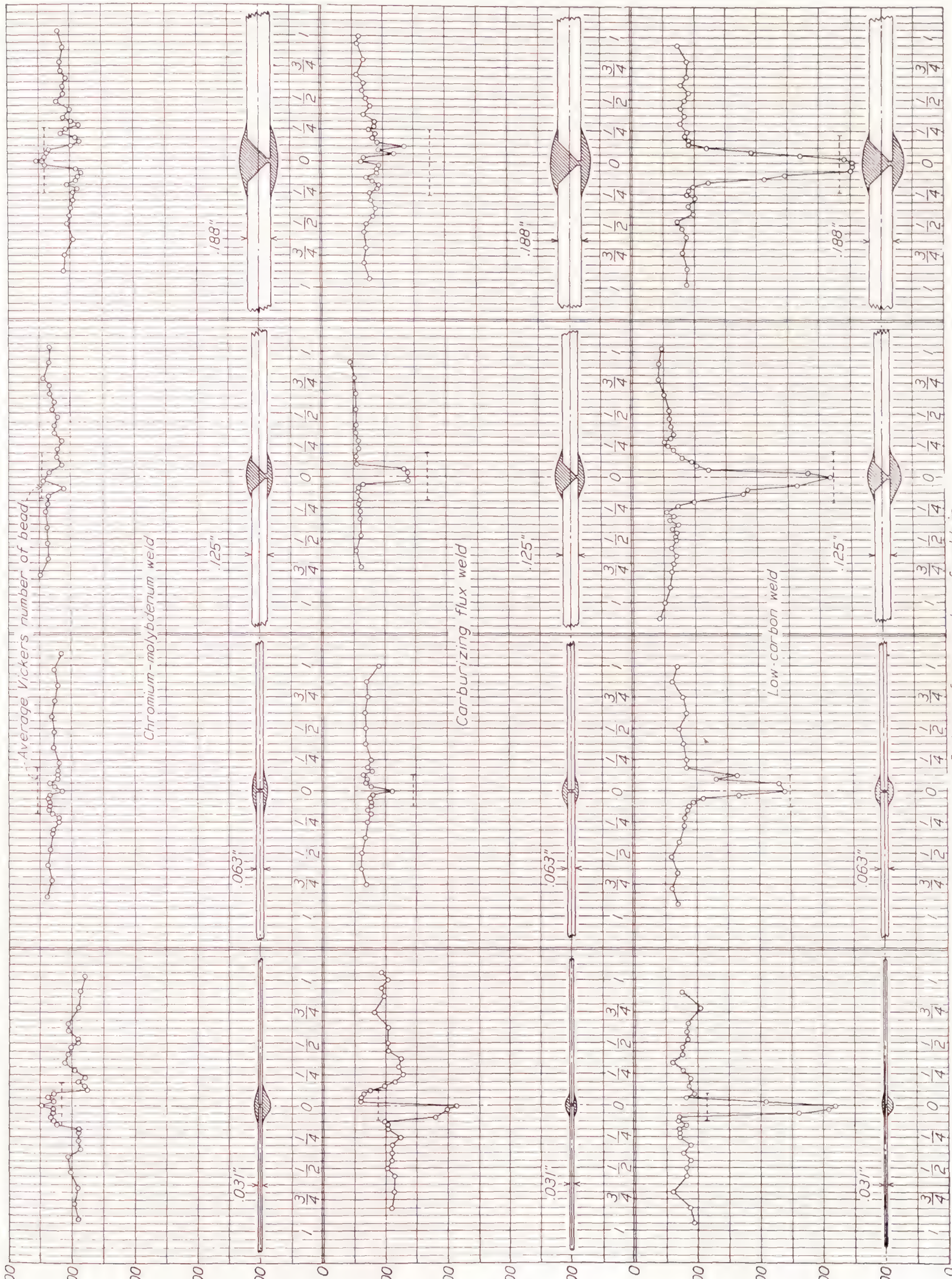

FIGURE 25.—Vickers number of open butt joints in chromium-molybdenum sheet heat-treated after welding by quenching from 1660° F., then tempered at 700° F.

reinforcement was adequate for these welds. Fractures in the weld, type 4, showed a marked reduction in area.

The Vickers explorations shown in figures 24, 25, and 26 were made to study the effect of the heating of the base metal during welding, and the effect of heat treatment after welding. Vickers' impressions were made on the edge of the specimens. The load was varied according to the resistance to indentation and the thickness of the specimen. A 10-kilogram load was generally used for the 0.031-inch specimens. For the thicker specimens the load was 30 kilograms when the Vickers number did not exceed about 250, and 50 kilograms for higher Vickers numbers. One series of impressions was taken along the center line of the edge by advancing the specimens longitudinally by means of a lead screw. These impressions were spaced from one thirty-second to one-fourth inch apart. In addition, impressions were made on the bead at from two to six points (depending on its size) located as close as possible to the edge of the cross section. The averages of these are shown in the figures.

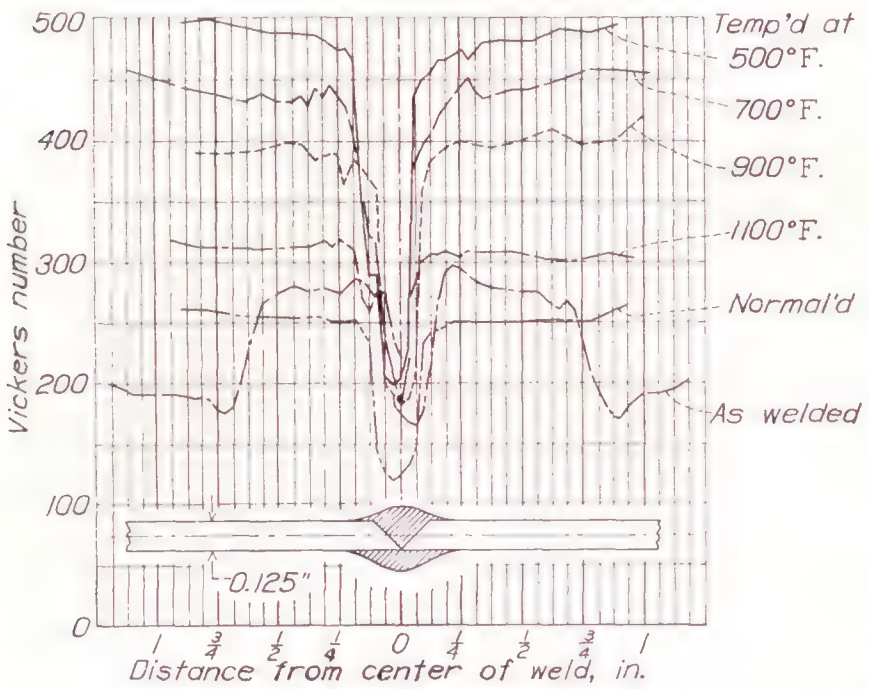

FIGURE 26.—Vickers number of open single-V butt joints in chromium-molybdenum sheet "as welded", normalized and quenched and tempered at several temperatures.

Figure 24 shows that the Vickers number of the weld metal in the "as welded" condition varies with the kind of welding rod used. The welding heat caused hardening of the base metal near the weld in a zone varying in width from about ¼ to ¾ inch on each side of the weld. In this zone the Vickers number was lower in the thicker sheets, probably because of slower cooling of the thicker sheets.

The Vickers number of specimens that had been quenched and tempered at 700° F. are shown in figure 25. The Vickers number of the bead was greatest in the chromium-molybdenum welds and lowest in the low-carbon welds. The thinner sheets in the low-carbon and carburizing flux welds had higher numbers. The Vickers number of the base metal was uniform outside the weld.

Vickers numbers for heat-treated low-carbon welds are shown in figure 26.

TUBULAR SPECIMENS

Four chromium-molybdenum tubes (1½ by 0.058 inch) were laid out, each as shown in figure 27. Low-carbon welds were made in two of the tubes, carburizing flux welds in the other two.

Butt joints were also made in thin-walled tubing 1½ by 0.020 inch and in carbon-steel tubing 1½ by 0.058 inch. These were left "as welded."

The ends of the tubular butt joints were plugged and the specimens were tested in tension using the same apparatus and methods as used for the sheet specimens.

Tubular butt joints (fig. 28) showed more variation in strength than butt joints in sheet. The carburizing flux welds had the highest strengths of any of the quenched and tempered joints. Failure occurred either in the weld or remote from the weld, seldom at the edge. More of the low-carbon welds failed at the edge than in the weld. Those joints that were quenched and tempered showed little difference in strength regardless of tempering temperature.

Results of tests on the thin-walled tubular butt joints are shown in figure 29. All low-carbon welds had cracks (see fig. 7) and failed at these cracks. No cracks were found in the carburizing flux welds. Two of the latter joints failed in the weld, four in the annealed portion of the tube, and one at the edge of the weld. Those failing in the weld had low strengths.

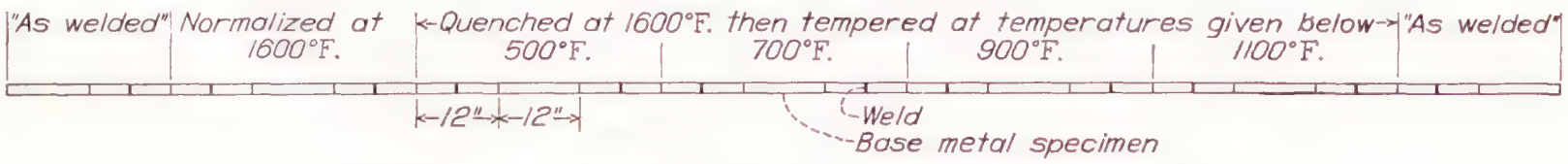

FIGURE 27.—Layout of the tubular butt joints and base metal specimens.

The strengths of the carbon-steel butt joints in 1½ by 0.058-inch tubing are also shown in figure 29.

CROSS JOINTS

Cross joints (shown in fig. 30) were tested to determine the strengths of three types of welds when used to make heat-treated joints in tubes of different thicknesses. These joints consisted of two chromium-molybdenum tubes, 1 by 0.035 inch, lying in the same axis, welded to opposite sides of the wall of a much thicker

tube, 1½ by 0.083 inch. Three types of welds were used: (1) low-carbon welds, (2) carburizing flux welds, and (3) a combination of the first two types in which the welding rod was the same as used for the carburizing flux welds but in which the base metal was fused, using the neutral flame technique of type (1). The 1 by 0.035 inch tubes were laid out as shown in figure 27.

Tensile tests were made in a 100,000-pound pendulum hydraulic testing machine.

The cross joints had the lowest strengths of any of the heat-treated joints. Practically all joints except those tested "as welded" failed at the edge of the weld. There was no significant difference in strength within the range of tempering temperatures used. The low strengths of these joints were probably due to stress concentrations near the weld caused by the sharp changes in cross section. The joints made by the carburizing flux process were slightly stronger than those made with the same rod, and neutral flame technique. The low-carbon welds had the lowest strengths.

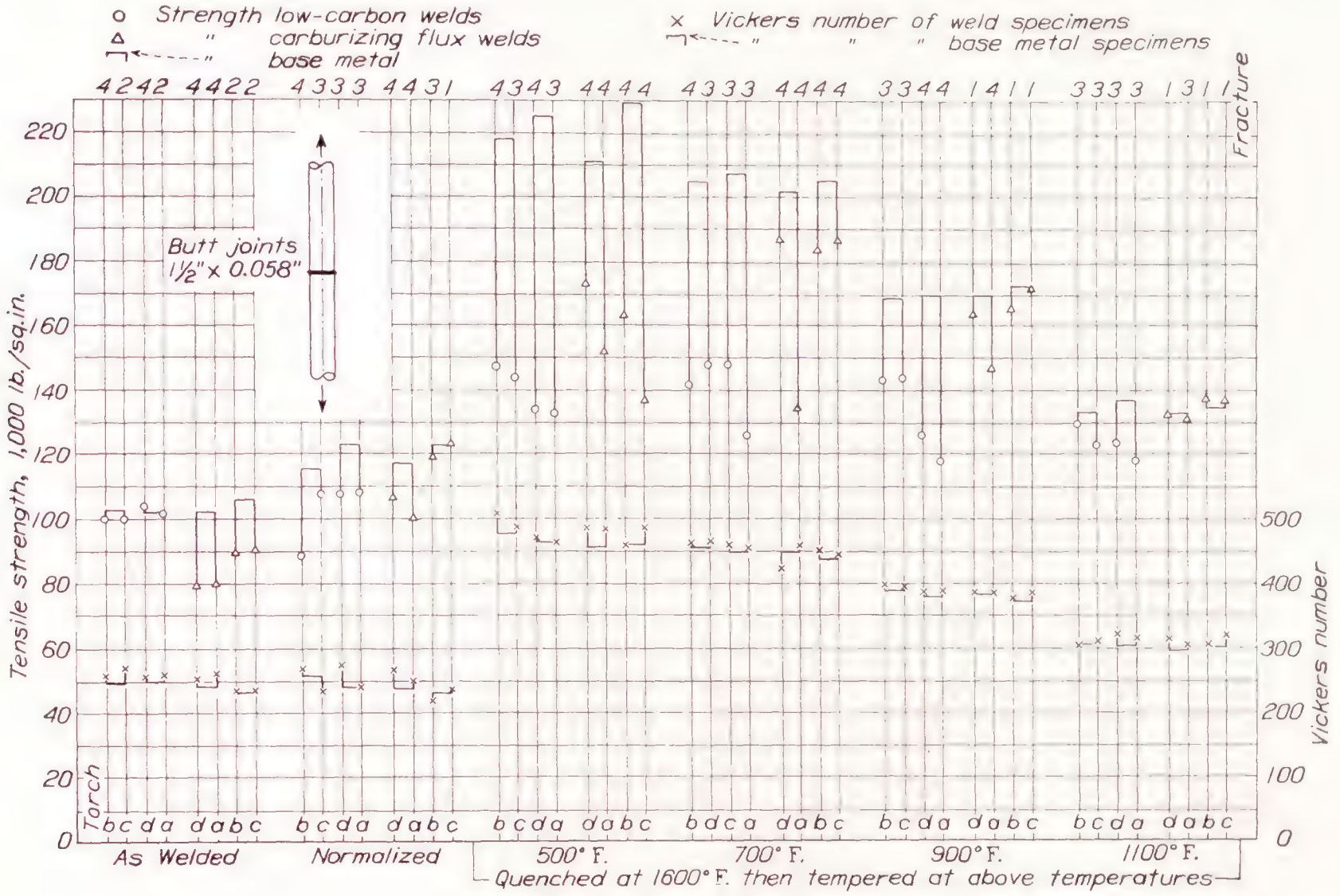

FIGURE 28.—Test results for butt joints in chromium-molybdenum steel tubing 1½ inches O. D. by 0.058-inch wall.

TIME OF WELDING

The time required to machine and weld the joints and the weight of the weld metal and gusset plates are shown in figure 31. The gusset-reinforced joints G260 and G760 required about twice the time to weld as the unreinforced joints 140 and 630 in the previous investigation. As before, no consistent difference in welding speed could be observed for any one torch.

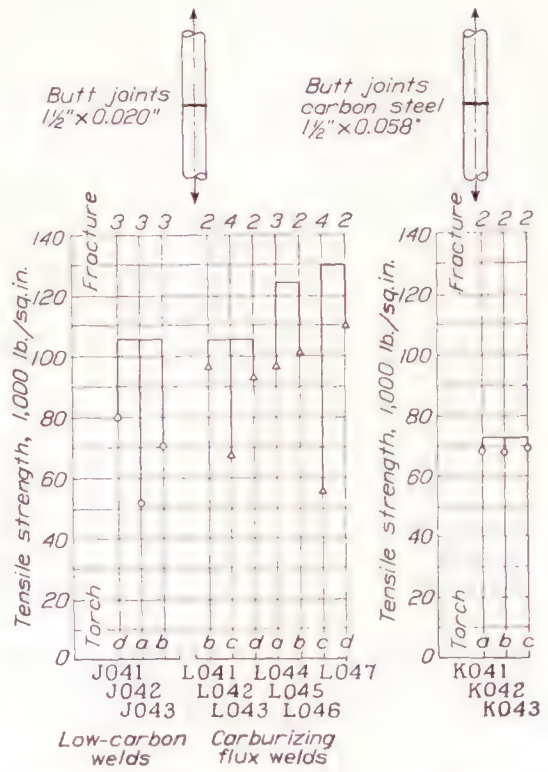

FIGURE 29.—Test results for butt joints in thin-walled chromium-molybdenum steel tubing and in carbon-steel tubing.

MECHANICAL PROPERTIES OF BASE METAL

Tensile tests were made on heat-treated sheet and tubular specimens of the base metal from which the butt and cross joints were made. Stress-strain and

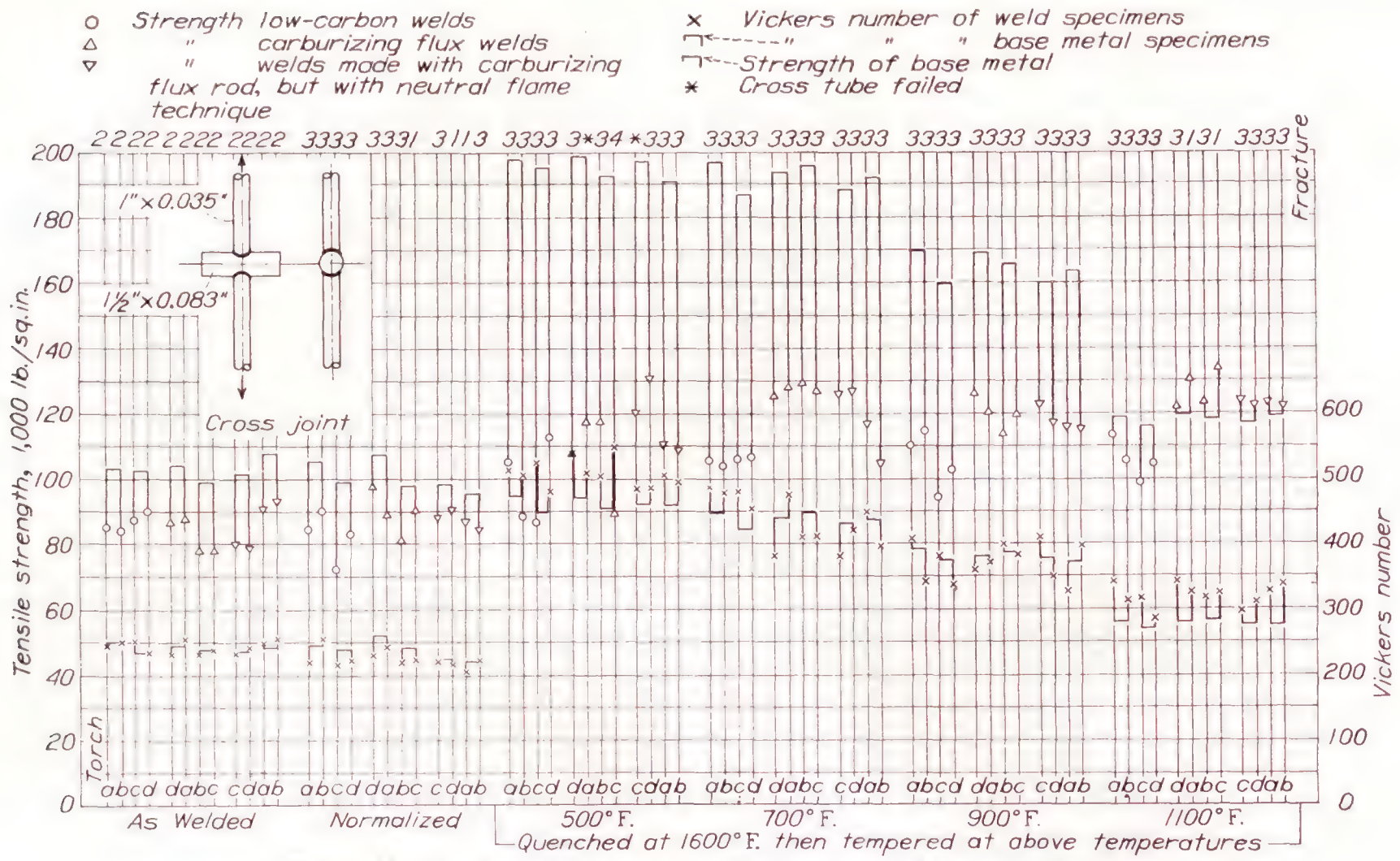

FIGURE 30.—Test results for cross joints in chromium-molybdenum steel tubing.

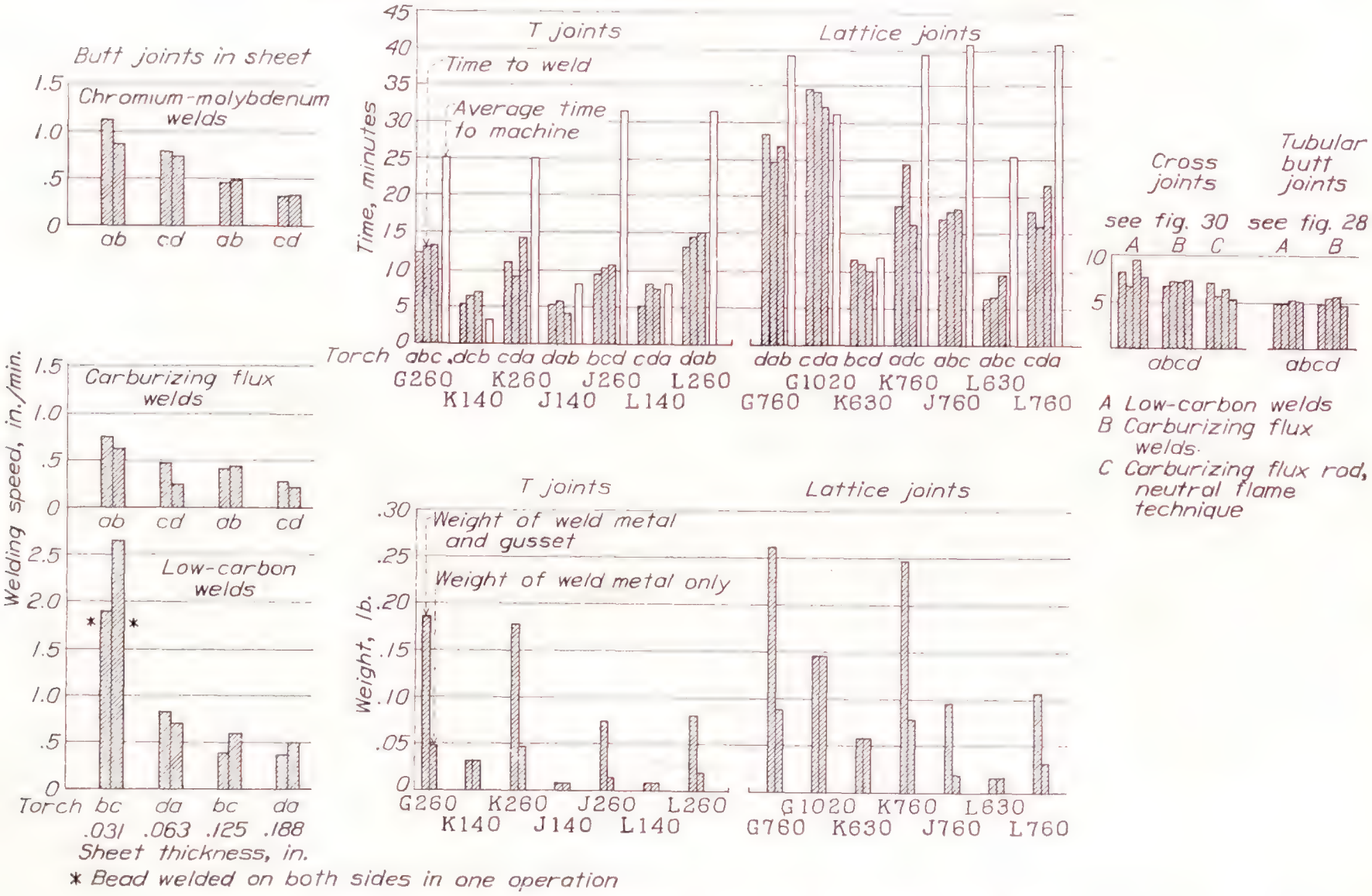

FIGURE 31.—Time required to machine and weld joints; weights of weld metal and reinforcement.

difference curves [5] (fig. 32) were obtained. The mechanical properties are given in figure 33 for tubular specimens and figure 34 for sheet specimens.

The tubes were tested in full section with steel plugs in the ends. For the sheet the American Society for Testing Materials' standard sheet-metal specimen having a 2-inch-gage length and a width of ½ inch was used.

A Ewing extensometer having a 2-inch-gage length was used to measure the strain.

The yield point was determined as required in Navy Department Specification 44T18a, in which it is defined as that stress under which the specimen shows a strain 0.002 inch/inch greater than that computed from the formula

$$\text{Strain (in./in.)} = \frac{\text{stress (lb./sq. in.)}}{30000000}$$

The ⅛-inch sheet specimens had the highest tensile strengths of all quenched and tempered specimens. When tempered at 500° F. the tensile strength was about 238,000 lb./sq. in.

The yield points of the 1 by 0.035-inch tubular specimens were highest when the specimens were tempered at 700° F.

The proportional limits were the most variable of the mechanical properties. The proportional limits of the tubular specimens were highest when the specimens were tempered at either 700° F. or 900° F. The normalized specimens had comparatively low proportional limits.

Young's modulus increased slightly with the tempering temperature for the sheet specimens and for the 1 by 0.035-inch tubular specimens, but not for the 1½ by 0.058-inch tubular specimens.

The elongation in 2 inches increased with the sheet thickness.

The mechanical properties of the heat-treated chromium-molybdenum sheet are in fair agreement with the properties of similar heat-treated sheet tested by F. T. Sisco and D. M. Warner (reference 5).

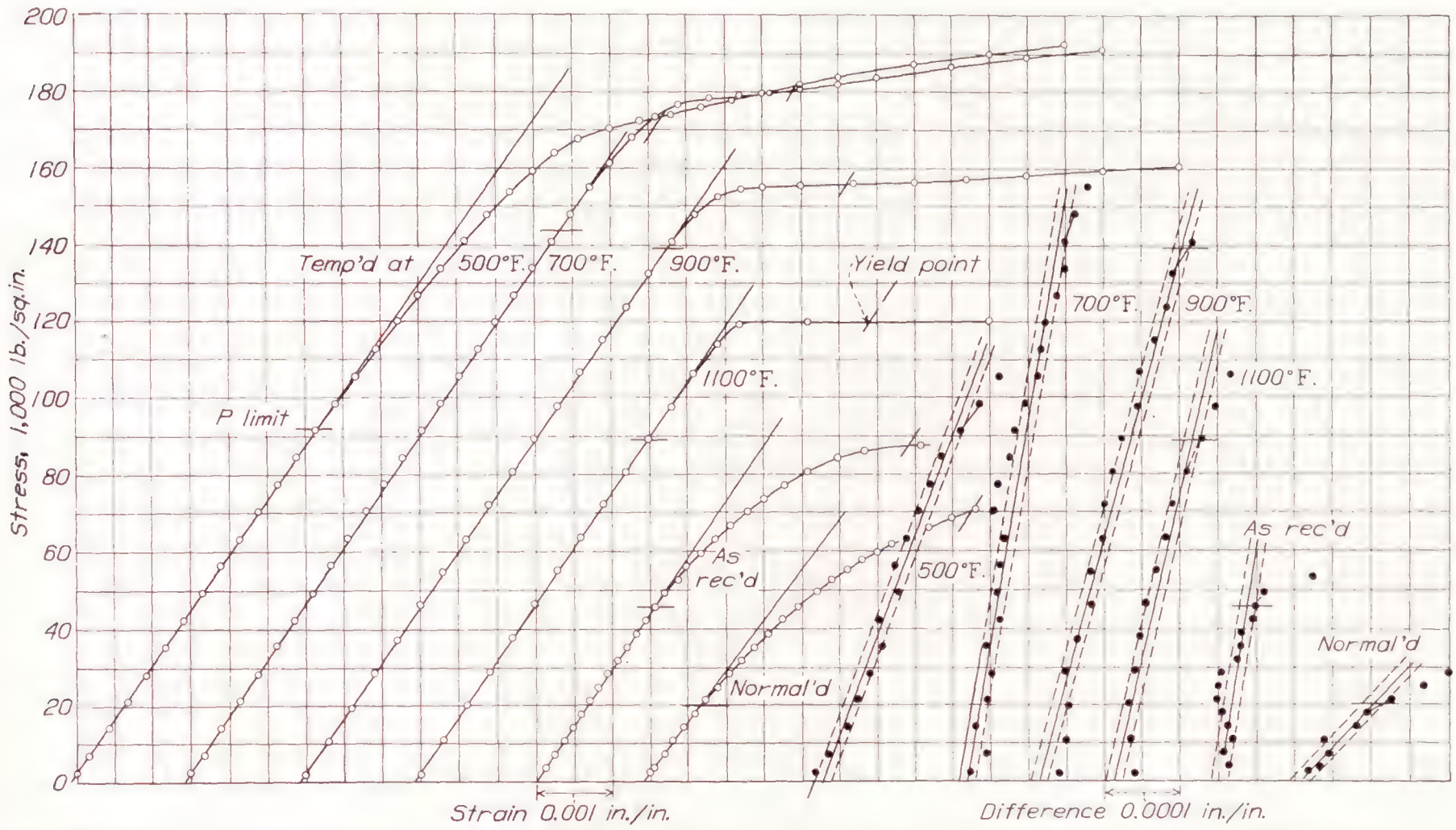

FIGURE 32.—Tensile stress-strain curves for chromium-molybdenum steel tubular specimens 1½ inches O. D. by 0.058-inch wall.

Figure 35 shows the variation of tensile strength with Vickers' number for chromium-molybdenum sheet and tubing.

CONCLUSIONS

1. The magnetic dust-inspection method was quite effective in detecting seams in tubing and cracks in welded joints. This method of inspection could be utilized by manufacturers in the routine examination of steel aircraft materials and welded structures.

2. Based on considerations of strength, weight, welding time, and freedom from cracks, the inserted gusset type of reinforcement used in this investigation for T and lattice joints, is considered to be better than any type tested previously. In increasing the strength of joints this reinforcement was effective for all joints except the carbon-steel T joint under transverse loading.

3. In welding the thin-walled chromium-molybdenum tubing, only the carburizing flux process was

[5] See N. A. C. A. Technical Report No. 348, p. 6; also discussion by L. B. Tuckerman of the Determination and Significance of the Proportional Limit in the Testing of Metals, by R. L. Templin, presented at the Thirty-second Meeting of the American Society for Testing Materials, June 25, 1929.

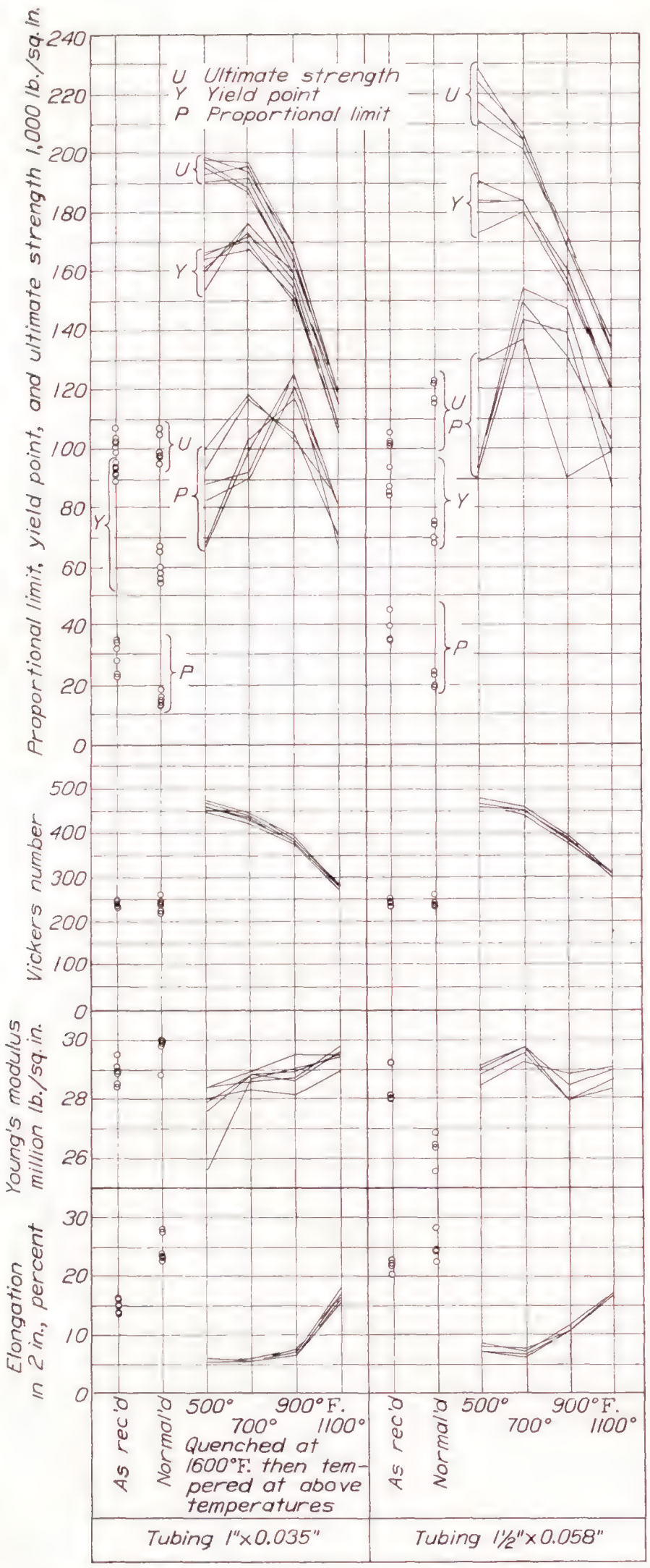

FIGURE 33.—Mechanical properties of two sizes of chromium-molybdenum steel tubing for various heat treatments.

found to produce welds which were free from cracks. T and lattice joints made from this tubing had somewhat lower strengths than joints made from heavier tubing because of failure by local buckling.

4. Normalizing the chromium-molybdenum steel butt joints increased their strengths except in the case of carburizing flux welds in 0.031-inch sheet, which showed a slightly lower strength. Of the sheet specimens heat-treated by hardening and then tempering at various temperatures, the chromium-molybdenum and the carburizing flux welds were approximately equal in strength except in the case of the 0.031-inch sheet which showed a somewhat higher strength for the carburizing flux welds.

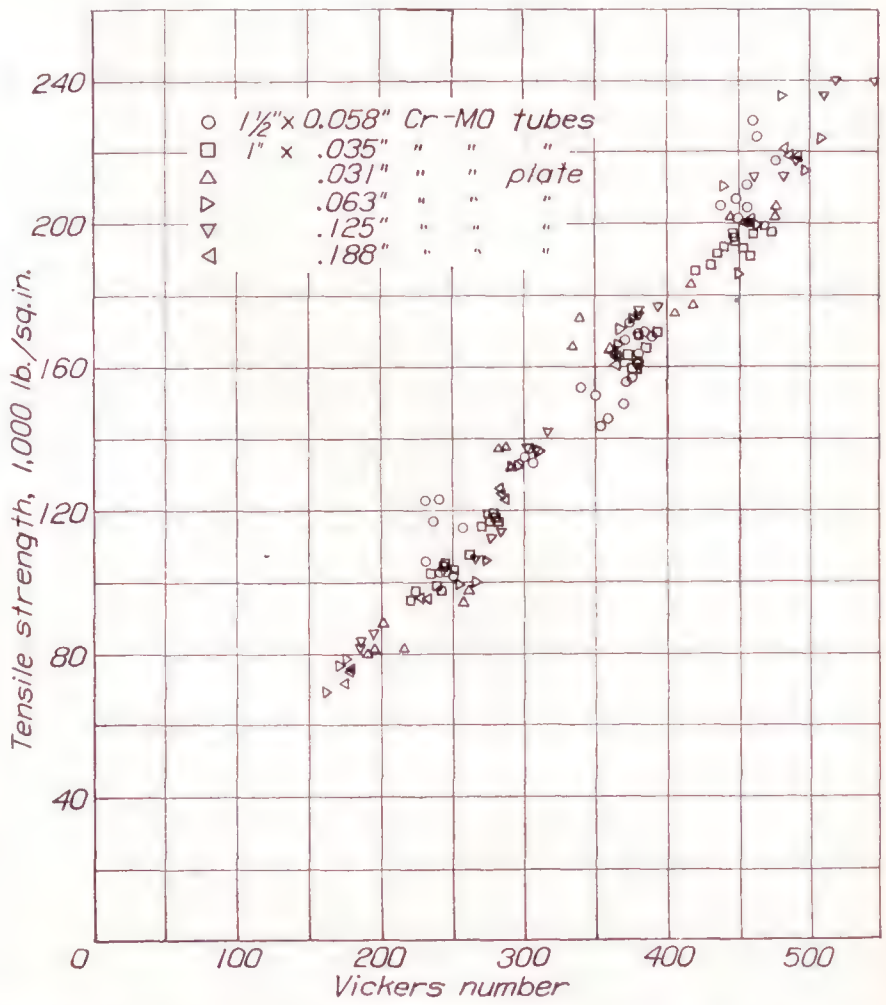

FIGURE 35.—Relation between the Vickers number and the tensile strength for chromium-molybdenum steel sheet and tubing.

5. The strength of the heat-treated butt joints, especially those made with low-carbon welds, was in most cases less uniform than the strength of the base metal. Heat-treated cross joints, in which adjoining tubes had a great difference in diameter and wall thickness, had low strengths compared to the tubular butt joints.

6. As in the first investigation, no consistent difference in strength or speed of welding could be attributed to any one torch.

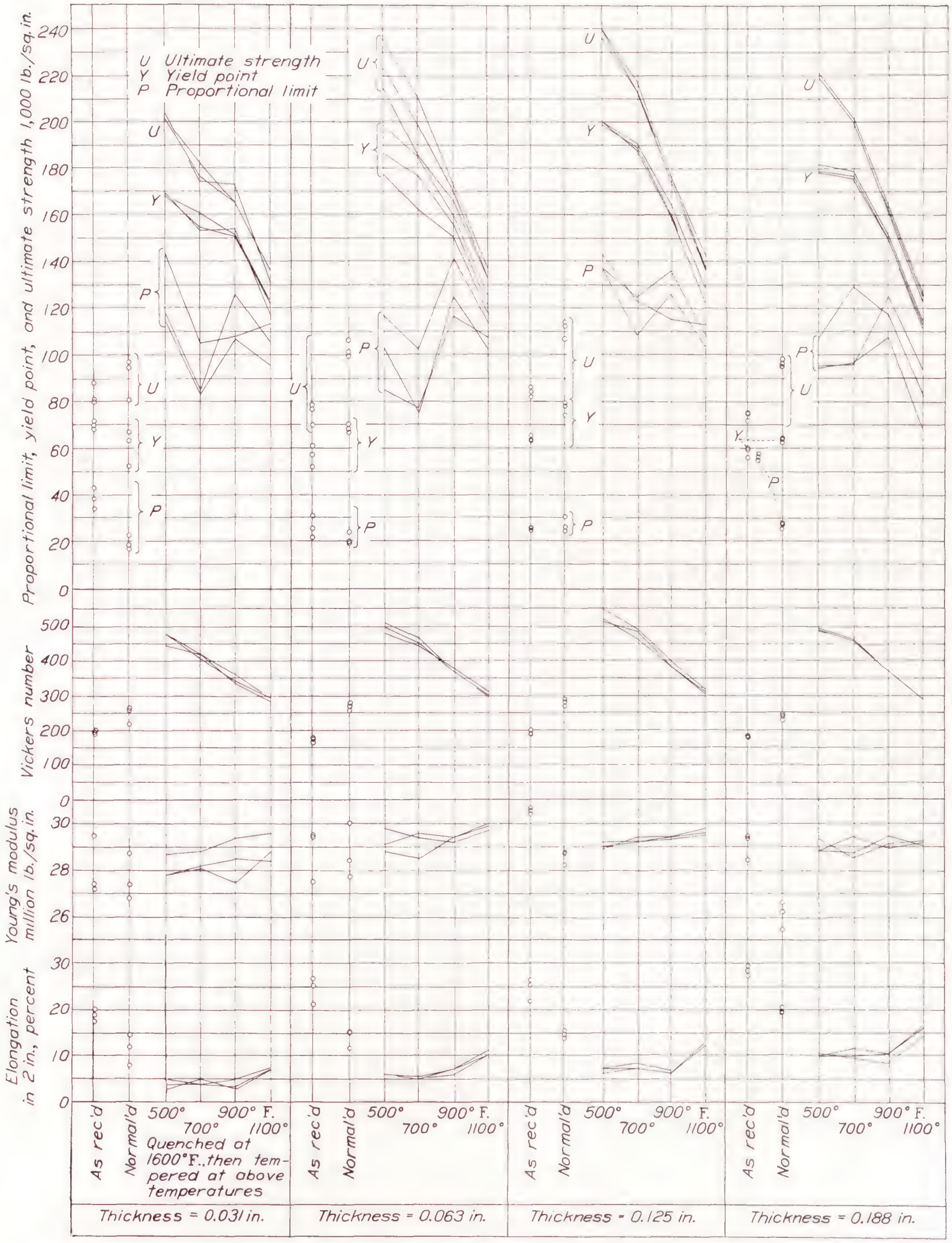

FIGURE 34.—Mechanical properties of four thicknesses of chromium-molybdenum steel sheet for various heat treatments.

ACKNOWLEDGMENTS

Acknowledgment is made to the Air Reduction Sales Co., the Linde Air Products Co., the Torchweld Equipment Co., and the Bastian-Blessing Co. for lending the torches and equipment; to the Linde Air Products Co. for contributing the services of the welding supervisor, Mr. H. S. George, who rendered invaluable assistance during the welding; to the Keystone Aircraft Co. for assistance in obtaining a welder; to Mr. R. M. Fowler, for making chemical analyses of the material; to Messrs. Louis Jordan and H. E. Francis for heat treating some of the welded joints; and to Mr. R. E. Pollard for making a microscopic examination of seams and cracks.

NATIONAL BUREAU OF STANDARDS,
WASHINGTON, D. C., *August 12, 1936.*

REFERENCES

1. Roux, Albert: Contrôle des Soudures par les Spectres Magnétiques. Comptes Rendus de L'Académie des Sciences, vol. 185, October 24, 1927, p. 859.
2. Watts, T. R.: Magnetic Testing of Butt Welds. Jour. of the American Welding Society, vol. 9, no. 9, September 1930, p. 49; also Magnetographic Inspection of Welds. Welding Engineer, vol. 15, no. 10, October 1930, p. 31.
3. de Forest, A. V.: Non-Destructive Tests by the Magnetic Dust Method. Iron Age, vol. 127, no. 20, May 14, 1931, p. 1595.
4. George, H. S.: A New Process for Making Welded Joints. Jour. of the American Welding Society, vol. 11, no. 7, July 1932, p. 22.
5. Sisco, F. T., and Warner, D. M.: Effect of Heat Treatment on the Properties of Chrome-Molybdenum Steel Sheet. Trans. of the American Society for Steel Treating, vol. 14, August 1928, p. 177.

BIBLIOGRAPHY

In addition to the bibliography given in N. A. C. A. Technical Report No. 348, the following technical papers may be of interest:

1. Whittemore, H. L., Crowe, John J., and Moss, H. H.: Procedure Control in Aircraft Welding. Proceedings of the American Society for Testing Materials, vol. 30, Part II, 1930, pp. 140–146.
2. George, H. S.: The Cause and Prevention of Heat Cracks in Aircraft Welding. Mechanical Engineering, vol. 53, no. 6, June 1931, pp. 433–439.
3. Beissner, Hans: Einfluss der Gasschmelzschweissung auf die Biegungsschwingungsfestigkeit von Chrom-Molybdän-Stahlrohren. Z. V. D. I., vol. 75, no. 30, July 25, 1931, pp. 954–956.
4. Rechtlich, von Arved: Grundlagen für die konstruktive Anwendung und Ausführung von Stahlrohrschweissungen im Flugzeugbau. D. V. L. Yearbook, 1931, pp. 379–438.
5. Jansen, P. N., and Speller, T. H.: An Aircraft Manufacturer's Experience with Welding Quality Control. Jour. of the American Welding Society, vol. 12, no. 10, October 1933, pp. 9–13.
6. Müller, J.: Weldability of High-Tensile Steels from Experience in Airplane Construction, with Special Reference to Welding Crack Susceptibility. T. M. No. 779, N. A. C. A., 1935.

REPORT No. 585

SPAN LOAD DISTRIBUTION FOR TAPERED WINGS WITH PARTIAL-SPAN FLAPS

By H. A. Pearson

SUMMARY

Tables are given for determining the load distribution of tapered wings with partial-span flaps placed either at the center or at the wing tips. Seventy-two wing-flap combinations, including two aspect ratios, four taper ratios, and nine flap lengths, are included. The distributions for the flapped wing are divided into two parts, one a zero lift distribution due primarily to the flaps and the other an additional lift distribution due to an angle of attack of the wing as a whole.

Comparisons between theoretical and experimental results for wings indicate that the theory may be used to predict the load distribution with sufficient accuracy for structural purposes.

Simple computing forms are included for determining, by the Lotz method, the theoretical loadings for a combination of any wing with any flap. A discussion of the method is given showing: (1) the effect on the load distribution of increasing the number of harmonics for a wing with partial-span flaps; and (2) the effect of increasing the number of points used across the semispan for a wing of unfair plan form.

INTRODUCTION

A knowledge of the span load distribution over a wing is important not only from structural considerations but also because certain conclusions regarding the behavior of the wing near the stall may be drawn from it. Indirectly, the span load distribution also influences such items relating to performance as the magnitude of the induced drag, the pitching moment of the entire wing about an aerodynamic center, and the angle of zero lift. Because of the importance of span load distribution, numerous methods for computing it have been proposed but, since they are generally lengthy and complicated, they have been little used in practice.

In reference 1 the span loading was given for linearly tapered wings with rounded tips. The results given therein cover a large range of aspect ratios and taper ratios, but they are for the case of a wing in which there is either no twist or only linear twist. Since most airplanes include some sort of high-lift or drag-increasing device covering only part of the span, the wing with an abrupt twist is of particular interest. These high-lift devices, when deflected, may be considered as introducing an effective twist that alters the load distribution along the span. As the actual effective twist depends upon possible combinations of wing angle of attack, flap type, flap deflection, flap span, wing plan form, and the variation of the flap-chord ratio along the span, it is apparent that the resulting load distribution depends upon many variables.

The presence of so many variables precludes the possibility of making either sufficiently extensive theoretical or experimental investigations to provide design charts for the general case. The present report therefore covers only the most commonly used series of wings; i. e., linearly tapered wings with rounded tips having chord distributions like those of reference 1 and equipped with partial-span flaps of constant flap-chord ratio. Comparisons are made of the experimental loadings, taken from reference 2, and the theoretical loadings to give an indication of the differences to be expected when the theory is used. Finally, a method for computing the span loading is included so that those interested will be in a position either to estimate from the results given herein the probable loading for similar cases or, if necessary, actually to make the computations.

Although the present report presents only the span loadings, later reports will deal with the effect of the load distribution on performance and on the behavior of the wing near the stall.

SYMBOLS

b_f, flap span.
b_w, wing span.
S, wing area.
A, aspect ratio, b_w^2/S.
δ_f, flap deflection, positive downward.
V, wind velocity.
ρ, mass density of air.
q, dynamic pressure, $\frac{1}{2}\rho V^2$.
w, induced downflow at a section.
L, lift on wing.
C_L, wing lift coefficient, L/qS.
c_s, chord at plane of symmetry.
c, chord at any section.

α_0, effective angle of attack of any section.

α_a, angle of attack of any section referred to its zero-lift direction.

α_s, angle of attack of section at plane of symmetry referred to its zero-lift direction.

λ, ratio of fictitious tip chord, obtained by extending leading and trailing edges of wing to extreme tip, to the chord at the plane of symmetry.

E, ratio of flap chord to wing chord at any section.

Γ, circulation at a section.

l, section lift (per unit length along span).

c_l, section lift coefficient, l/qc, perpendicular to wind at infinity.

Subscripts:

0, refers to section lift coefficient perpendicular to local relative wind.

b, refers to basic lift ($C_L=0$).

a, refers to additional lift for any C_L.

$a1$, refers to additional lift for $C_L=1.0$.

$c_{l_{max}}$, maximum lift coefficient for any section.

Δc_l, increment in section lift coefficient caused by a flap deflection, δ_f.

c_{d_i}, section induced-drag coefficient.

c_{d_0}, section profile-drag coefficient.

L_a, additional-load parameter, $c_{l_{a1}}\frac{cb}{S}$.

L_b, basic-load parameter, $c_{l_b}\frac{cb}{S\Delta c_l}$.

m, $\frac{dC_L}{d\alpha}$ of entire wing, per radian.

m_0, $\frac{dc_l}{d\alpha_0}$ of any section, per radian.

m_s, $\frac{dc_l}{d\alpha_0}$ of section at plane of symmetry, per radian.

ΔC_L, the part of C_L at a given wing attitude due to any flap deflection.

ΔC_{L_1}, the increment caused by a flap deflection corresponding to a Δc_l of 1.0.

y, variable point along span.

y', fixed point along span.

$\cos\theta$, $\frac{y}{b_w/2}$ (when $y=-b_w/2$, $\theta=0$; when $y=b_w/2$, $\theta=\pi$).

A_n, B_n, C_{2n}, coefficients in Fourier series.

THEORETICAL RESULTS FOR WINGS WITH FLAPS

According to the assumptions upon which wing theory is based, the distribution of lift over the span is a linear function of the angle of attack at each point of the span. Thus it is permissible to compute separately either a zero lift distribution or a distribution due only to the flaps and later to superpose them on appropriate distributions due to an angle of attack of the wing with flaps neutral.

Deflecting flaps on an untwisted wing that previously was at zero lift produces the angle of attack and load distributions shown by the solid lines in figure 1. If the angle of attack of the wing without flaps is reduced so that the area under the dashed load curve is equal to that under the solid curve, their addition will result in a zero-lift curve. It can be seen that the load distribution due to the flap alone (solid curve) does not follow

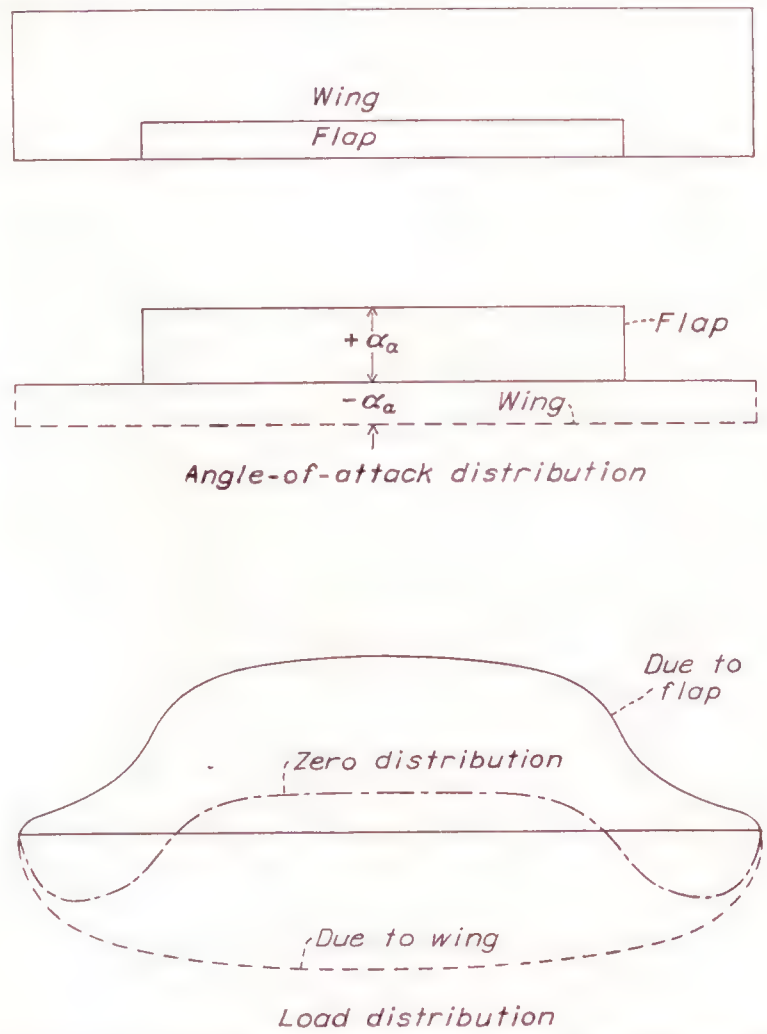

FIGURE 1.—Angle of attack and load distribution for a wing with flaps.

the abrupt angle-of-attack change but, owing to induction, is distributed along the remainder of the span where there is no apparent angle of attack. At these stations there is, however, an effective angle of attack due to the upwash produced by the portion with flaps. Numerically the effective angle of attack at any section is equal to the section c_l divided by the slope of the section lift curve, or it can be given by

$$\alpha_0=\alpha_a-\frac{w}{V} \tag{1}$$

In order to determine the theoretical distribution of the forces and angles for a particular case, it is necessary to obtain a solution of the fundamental formula for induced downflow

$$w=\frac{1}{4}\pi\int_{-\frac{b}{2}}^{\frac{b}{2}}\frac{\frac{d\Gamma}{dy}dy}{y'-y} \tag{2}$$

The graphical and analytical methods for solving this complicated integral tend to be lengthy and none is exact. In the general case where the wing plan

form or angle-of-attack distribution cannot be expressed as simple analytical functions, either the Lotz or Lippisch methods (references 3 and 4) are particularly applicable, although other methods may be used. An adaptation of the Lotz method, which has been used to compute the theoretical load distributions given herein, is given in a later section of this report in a form suitable for routine computation. These load distributions are listed in tables I and II for 72 wing-flap combinations that include two aspect ratios (6 and 10), four taper ratios (1.0, 0.75, 0.50, and 0.25), and nine flap lengths. The flap lengths, expressed as a fraction of the semispan, are:

Flaps at center	Flaps at tip
0.233	0.240
.383	.351
.649	.617
.760	.767
1.000	-----

Table I gives the ordinates of the curves of the additional load distribution at 10 selected spanwise stations in terms of the parameter

$$L_a=c_{l_{a1}}\frac{cb}{S} \tag{3}$$

and table II gives the ordinates for the basic-load distribution in terms of the parameter

$$L_b=c_{l_b}\frac{cb}{S\Delta c_l} \tag{4}$$

The additional-load distribution, given for a wing C_L of 1.0, is independent of wing twist (flap displacement) and maintains the same form throughout the useful range of the lift curve. The basic distributions are zero lift distributions that depend principally on the wing twist.

The values of L_a and L_b were computed by the Lotz method; 10 points across the semispan were used and 10 harmonics of the series were retained. In these computations the slope of the section lift curve was assumed to be equal to 5.67. The odd flap lengths given result from the use of a Fourier series in the solution for the load curves; in the case of a wing with an abrupt twist the discontinuity occurs, mathematically, in the interval including the end of the flap.

Since the parameter L_a has been given for the convenient wing C_L of 1.0, the relation between the additional section lift coefficients c_{l_a} and $c_{l_{a1}}$ becomes

$$c_{l_a}=C_L c_{l_{a1}} \tag{5}$$

The total lift coefficient at each section is

$$c_l=c_{l_b}+C_L c_{l_{a1}} \tag{6}$$

and the lift at a section is

$$l=c_l q c \tag{7}$$

In the application of the results given in tables I and II, interpolation will generally be necessary. For structural purposes a linear interpolation between the different variables is probably justified. The results may also be extrapolated with reasonable accuracy to aspect ratios 4 and 12, although values of L_a may be obtained from reference 1 for aspect ratios from 3 to 20 without the necessity of any extrapolation.

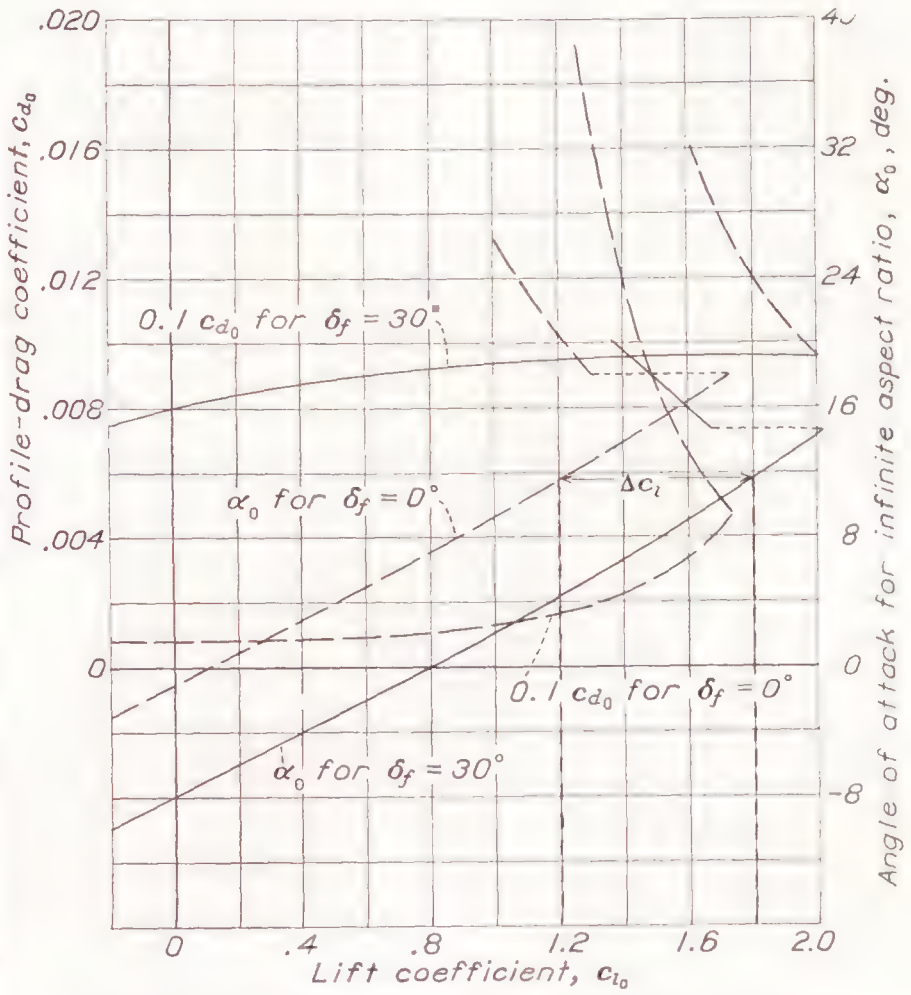

FIGURE 2.—Typical characteristics of a section equipped with a flap.

In order to illustrate the procedure to be followed in the use of the tables, the span loading of a wing with the following characteristics will be found:

$C_L=1.72$
$\lambda=0.625$
$A=6$
$\frac{b_f}{b_w}=0.383.$
$q=57.5$ pounds per square foot
$E=0.20$
$\delta_f=30°$

A table, such as table III, is prepared in which the values of the chord at the various stations are first entered, interpolations are made for taper, etc., and the values of L_a and L_b from tables I and II are entered in columns 3 and 4, respectively. From L_a, the values of $c_{l_{a1}}$ and c_{l_a} are found by the use of equations (3) and (5) and entered in columns 5 and 6.

Before c_{l_b} can be found, however, it is necessary to determine from experimental data the value of Δc_l corresponding to the flap-displacement angle of 30°. This increment is generally found by correcting the results of tests made of a finite wing with full-span flaps of proper type and proper flap-chord ratio to

obtain section characteristics. It is assumed that such section characteristics are available (fig. 2); the value of Δc_l to be used may then readily be found. Theoretically,

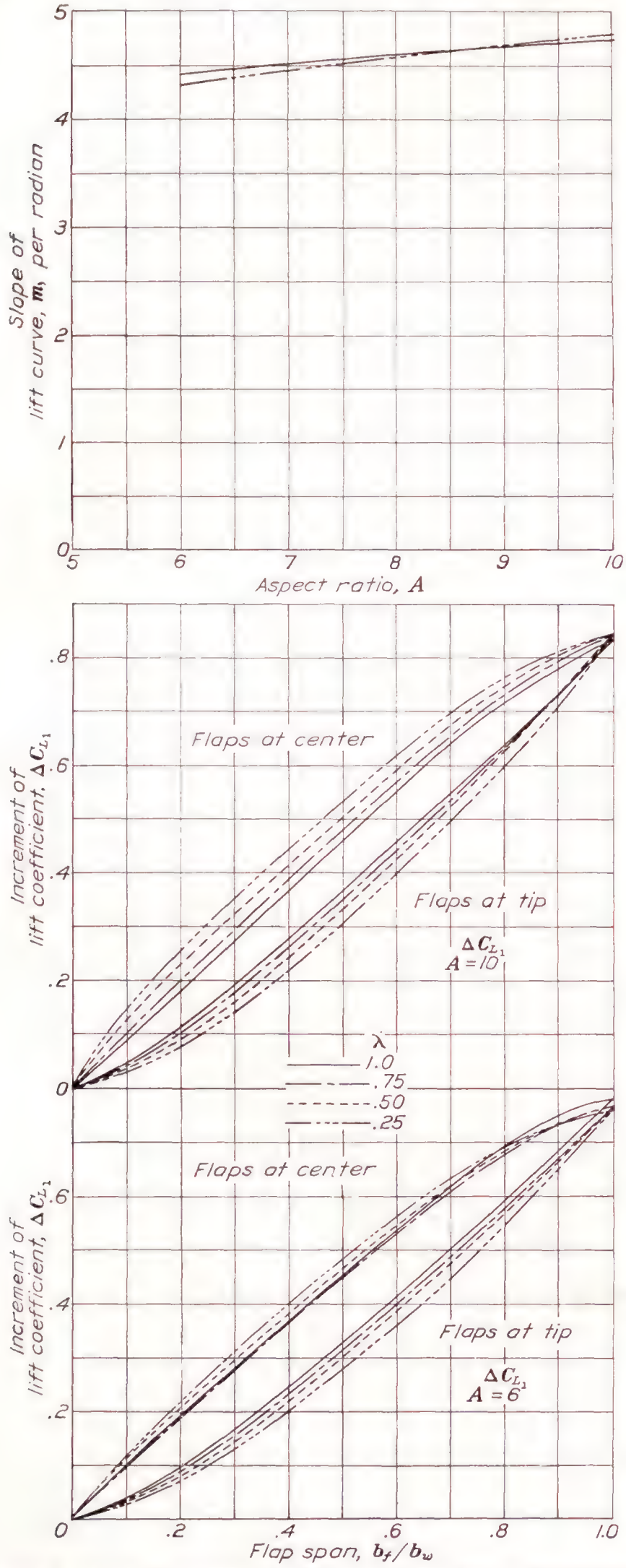

FIGURE 3.—Values of lift increments and lift-curve slopes for wings with partial-span flaps.

the effect of displacing a flap would be to displace the lift curves parallel to each other so that Δc_l would be independent of the effective angle of attack. Experimental results, however, indicate that Δc_l depends on the effective angle of attack and some averaging is thus necessary to determine its value. Since the example is for a high-angle-of-attack condition, the value of Δc_l is arbitrarily taken in this range at an angle corresponding to a c_l of 1.2 for the plain section. By the use of equation (4) together with a value of Δc_l equal to 0.6, from figure 2, the values of c_{l_b} are computed and entered in column 7 of table III. The total section c_l (column 8), from which the load distribution (column 9) is determined, is the sum of columns 6 and 7.

Standard section characteristics for the plain section and the section with a flap are sometimes tabulated instead of being plotted as in figure 2. In such a case the value of Δc_l may be found from the formula

$$\Delta c_l = c_{l_f}\left(1-\frac{a_0}{a_{0_f}}\right)+a_0\left(\alpha_{l_0}-\alpha_{l_{0_f}}\right)$$

where a_0 is the slope of the section lift curve per degree and α_{l_0} the angle of zero lift measured from the chord line in degrees. The subscript f refers to the characteristics with the flap deflected. If desired, the slopes and angles could also be given in radians.

If the induced-drag distribution corresponding to a given load distribution is specifically required, it may be found by the use of the equation

$$c_{d_i}=c_l\left[\left(\frac{C_L-\Delta C_{L_1}\Delta c_l}{m}\right)-\frac{c_l}{m_0}\right] \tag{8}$$

which gives the variation of the section induced-drag coefficient over the portion of the span without flaps, and the equation

$$c_{d_i}=c_l\left[\left(\frac{C_L-\Delta C_{L_1}\Delta c_l}{m}\right)+\left(\frac{\Delta c_l-c_l}{m_0}\right)\right] \tag{9}$$

which holds over the portion of the span with flaps. The increment of wing lift coefficient ΔC_{L_1} and the slope of the lift curve of the finite wing m to be used in these equations are given in figure 3 for the series of wings considered in this report. The value of ΔC_{L_1} (fig. 3) represents the increase in lift coefficient based on the entire wing area due to a flap deflection corresponding to a Δc_l of 1.0. Figure 4 gives typical distributions of $c_l\frac{cb}{S}$ and c_l for various wing-flap combinations corresponding to a Δc_l of 1.0. These distributions are thus directly related to the results given in figure 3.

COMPARISONS OF EXPERIMENTAL AND THEORETICAL RESULTS

Previous comparisons (reference 5) of experimental and theoretical span loadings for a 2:1 tapered U. S. A. airfoil equipped with partial-span flaps of three different lengths indicated a satisfactory agreement. The first conclusion given in reference 5 is: "A satisfactory determination, for all conditions of test, of the span load distribution for an airfoil equipped with a partial-span split flap may be made by applying the Lotz method of

calculating the aerodynamic characteristics of wings. The increments of load due to the deflection of the flap are computed by the Lotz method and added to the span load distribution for the plain airfoil."

Since the publication of reference 5 additional pressure-distribution tests (reference 2) have been made over a rectangular wing having a 0.6-span constant-chord split flap. The wing used was of Clark Y section with a 20-inch chord and a total span of 120 inches. Some of the span-loading curves taken from reference 2 are compared, in figure 5, with corresponding theoretical curves for a wing with square tips.

section the method will be discussed in more detail and a series of computing forms will be given which, it is believed, will make the computations simpler and more direct than if the method of reference 8 were followed.

Outline of theory.—As is customary in aerodynamic theory, the wing is replaced by a single line vortex whose strength at every section along the span is equal to the circulation Γ at that section. The lift per unit length of span is then

$$dL=\rho V\Gamma dy \tag{10}$$

and the problem is to find Γ for any point on a wing of

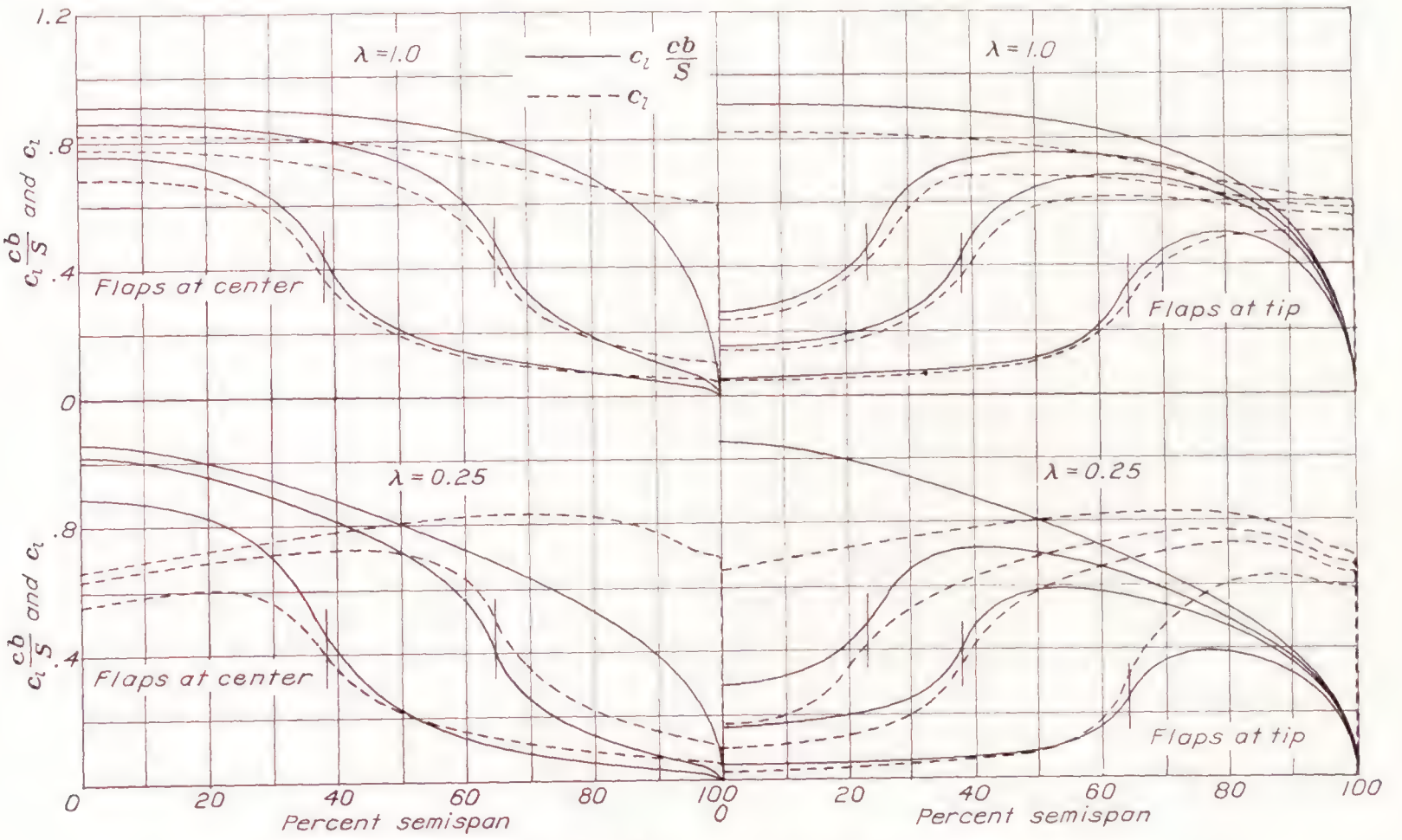

FIGURE 4.—Typical distributions of $c_l \frac{cb}{S}$ and c_l due to a flap deflection. ($\lambda=6$; $\Delta c_l=1.0$.)

Figure 6 shows comparisons of computed and experimental values of ΔC_L for various flap locations. The experimental values of ΔC_L are those given in references 6 and 7 at 8° angle of attack. Reference 6 gives the results of force tests of a rectangular Clark Y wing with partial-span flaps placed at the center and at the wing tips; reference 7 gives similar results for a 5:1 tapered wing. In the comparisons given in figure 6 the experimental results were obtained from tests of wings with straight tips; whereas the computed results are those for wings with rounded tips.

THE LOTZ METHOD FOR CALCULATING THE AERODYNAMIC CHARACTERISTICS OF WINGS

The following method was proposed in 1931 by Miss Lotz (reference 3), who gave the basic theory involved. Shenstone (reference 8) gave a brief discussion of the method and a simple procedure to be used in obtaining the various constants required in the solution. In this

any shape. The relations between Γ, c_l, and α_0 are given by the equations

$$\Gamma=\frac{c_l cV}{2}=\frac{\alpha_0 m_0 cV}{2} \tag{11}$$

where $\alpha_0=\alpha_a-w/V$. Since the induced angle at a particular station y' is

$$\frac{w}{V}=\frac{1}{4\pi V}\int_{-\frac{b}{2}}^{\frac{b}{2}}\frac{\frac{d\Gamma}{dy}}{y'-y}dy \tag{12}$$

the circulation Γ may be expressed by the integral equation

$$\frac{2\Gamma}{m_0 cV}=\alpha_a-\frac{1}{4\pi V}\int_{-\frac{b}{2}}^{\frac{b}{2}}\frac{\frac{d\Gamma}{dy}}{y'-y}dy \tag{13}$$

This equation is to be solved for Γ, and the method used is to replace the circulation by a Fourier series where

$$\Gamma=\frac{c_s m_s V}{2}\Sigma A_n \sin n\theta \tag{14}$$

and hence

$$\frac{2\Gamma}{m_0 c V}=\frac{m_s}{m_0}\frac{c_s}{c}\Sigma A_n \sin n\theta \tag{15}$$

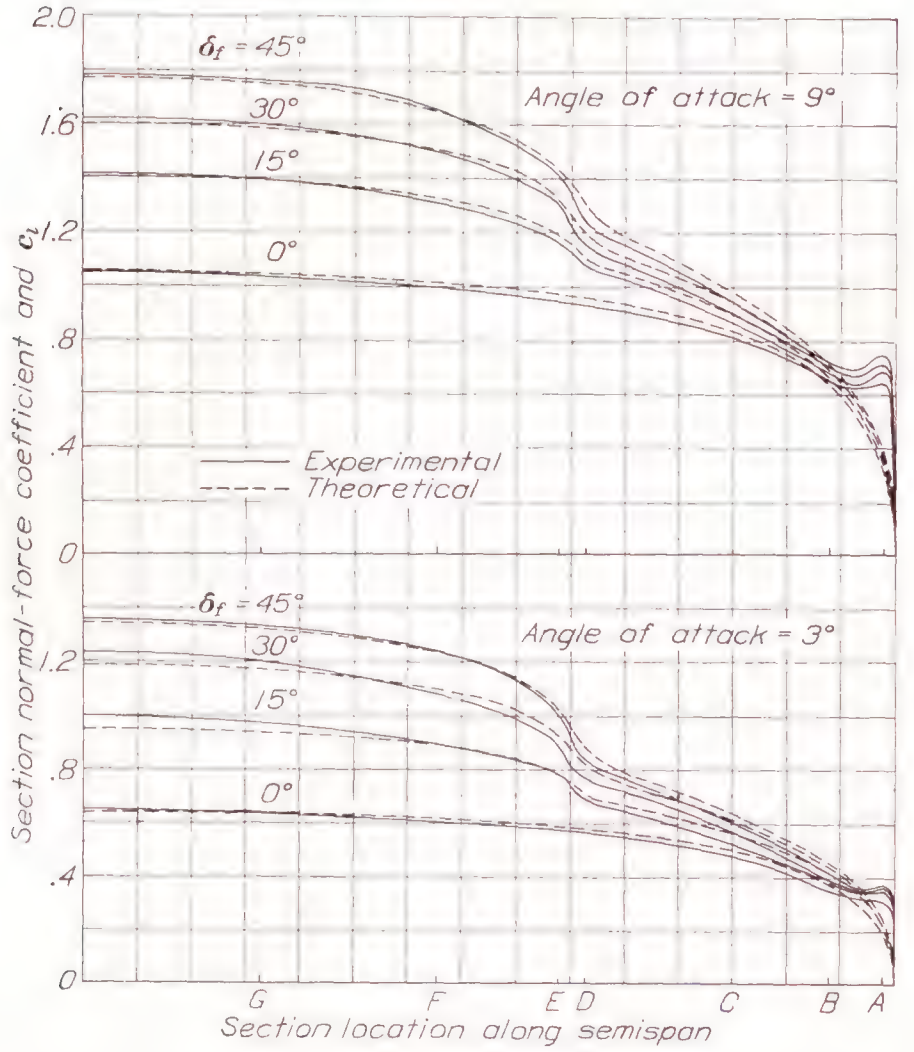

FIGURE 5.—Comparison between experimental and theoretical load distribution for a wing with partial-span flaps. (Data from reference 2; λ=1.0; A=6; square tips.)

As a result of expressing the circulation by the foregoing series, the induced angle becomes

$$\frac{w}{V}=\frac{c_s m_s}{4b}\Sigma n A_n\left(\frac{\sin n\theta}{\sin \theta}\right) \tag{16}$$

By substitution, equation (13) is transformed into

$$\frac{m_s}{m_0}\frac{c_s}{c}\sin\theta\ \Sigma A_n \sin n\theta=\alpha_a \sin\theta-\frac{c_s m_s}{4b}\Sigma n A_n \sin n\theta \tag{17}$$

The new feature introduced by Miss Lotz is to replace $\frac{m_s}{m_0}\frac{c_s}{c}\sin\theta$ and $\alpha_a \sin\theta$ by the two series $\Sigma C_{2n}\cos 2n\theta$ and $\Sigma B_n \sin n\theta$, respectively. As the coefficients in these series are independent of the load distribution, they may be separately computed, and it is possible to increase the accuracy by taking more terms without changing the values of the coefficients already computed. When the wing plan form is symmetrical about the center line, the cosine series contains only even values; whereas, if the angle-of-attack distribution is symmetrical, as it is with flaps, only odd values of n are retained. Equation (17), after the foregoing series have been substituted, becomes

$$\Sigma C_{2n}\cos 2n\theta\ \Sigma A_n \sin n\theta+\frac{c_s m_s}{4b}\Sigma n A_n \sin n\theta=\Sigma B_n \sin n\theta \tag{18}$$

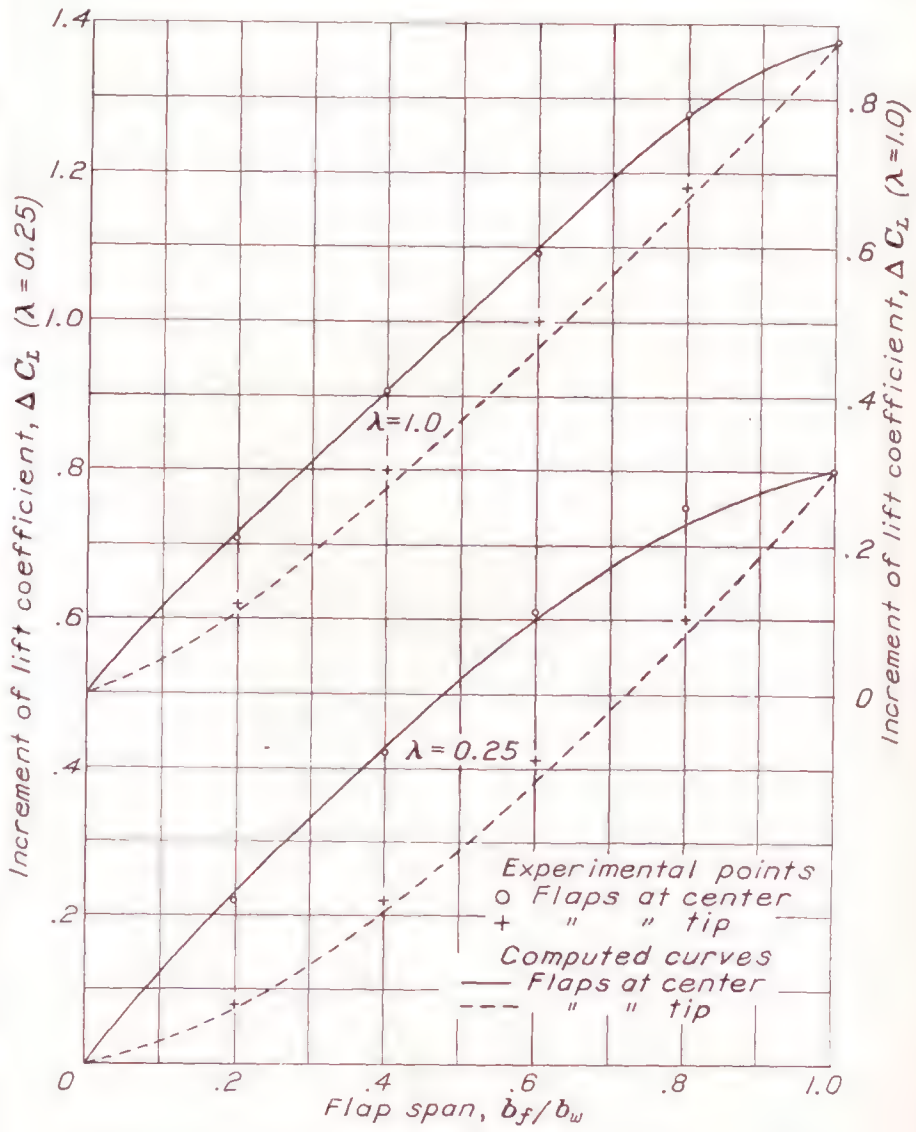

FIGURE 6.—Comparison of experimental and computed values of ΔC_L.

When n is temporarily replaced by the indices k and l, the double series on the left of equation (18) is transformed into

$$\tfrac{1}{2}\sum_k\sum_l A_k C_l[\sin(k+l)\theta+\sin(k-l)\theta]$$

By the substitution of the foregoing series and considerable rearrangement, equation (18) may be expanded into the following form. In its exact form there are an infinite number of equations and terms. For the purpose of calculation, however, the circulation may be computed at a finite number of points with a finite number of equations.

$$
\begin{array}{l}
2P_1A_1+(C_2-C_4)A_3+(C_4-C_6)A_5+(C_6-C_8)A_7+(C_8-C_{10})A_9+(C_{10}-C_{12})A_{11}+(C_{12}-C_{14})A_{13}+(C_{14}-C_{16})A_{15}+(C_{16}-C_{18})A_{17}+(C_{18}-C_{20})A_{19}=2B_1 \\
(C_2-C_4)A_1+2P_3A_3+(C_2-C_8)A_5+(C_4-C_{10})A_7+(C_6-C_{12})A_9+(C_8-C_{14})A_{11}+(C_{10}-C_{16})A_{13}+(C_{12}-C_{18})A_{15}+(C_{14}-C_{20})A_{17}+(C_{16}-C_{22})A_{19}=2B_3 \\
(C_4-C_6)A_1+(C_2-C_8)A_3+2P_5A_5+(C_2-C_{12})A_7+(C_4-C_{14})A_9+(C_5-C_{16})A_{11}+(C_8-C_{18})A_{13}+(C_{10}-C_{20})A_{15}+(C_{12}-C_{22})A_{17}+(C_{14}-C_{24})A_{19}=2B_5 \\
(C_6-C_8)A_1+(C_4-C_{10})A_3+(C_2-C_{12})A_5+2P_7A_7+(C_2-C_{16})A_9+(C_4-C_{18})A_{11}+(C_6-C_{20})A_{13}+(C_8-C_{22})A_{15}+(C_{10}-C_{24})A_{17}+(C_{12}-C_{26})A_{19}=2B_7 \\
(C_8-C_{10})A_1+(C_6-C_{12})A_3+(C_4-C_{14})A_5+(C_2-C_{16})A_7+2P_9A_9+(C_2-C_{20})A_{11}+(C_4-C_{22})A_{13}+(C_6-C_{24})A_{15}+(C_8-C_{26})A_{17}+(C_{10}-C_{28})A_{19}=2B_9 \\
(C_{10}-C_{12})A_1+(C_8-C_{14})A_3+(C_6-C_{16})A_5+(C_4-C_{18})A_7+(C_2-C_{20})A_9+2P_{11}A_{11}+(C_2-C_{24})A_{13}+(C_4-C_{26})A_{15}+(C_6-C_{28})A_{17}+(C_8-C_{30})A_{19}=2B_{11} \\
(C_{12}-C_{14})A_1+(C_{10}-C_{16})A_3+(C_8-C_{18})A_5+(C_6-C_{20})A_7+(C_4-C_{22})A_9+(C_2-C_{24})A_{11}+2P_{13}A_{13}+(C_2-C_{28})A_{15}+(C_4-C_{30})A_{17}+(C_6-C_{32})A_{19}=2B_{13} \\
(C_{14}-C_{16})A_1+(C_{12}-C_{18})A_3+(C_{10}-C_{20})A_5+(C_8-C_{22})A_7+(C_6-C_{24})A_9+(C_4-C_{26})A_{11}+(C_2-C_{28})A_{13}+2P_{15}A_{15}+(C_2-C_{32})A_{17}+(C_4-C_{34})A_{19}=2B_{15} \\
(C_{16}-C_{18})A_1+(C_{14}-C_{20})A_3+(C_{12}-C_{22})A_5+(C_{10}-C_{24})A_7+(C_8-C_{26})A_9+(C_6-C_{28})A_{11}+(C_4-C_{30})A_{13}+(C_2-C_{32})A_{15}+2P_{17}A_{17}+(C_2-C_{36})A_{19}=2B_{17} \\
(C_{18}-C_{20})A_1+(C_{16}-C_{22})A_3+(C_{14}-C_{24})A_5+(C_{12}-C_{26})A_7+(C_{10}-C_{28})A_9+(C_8-C_{30})A_{11}+(C_6-C_{32})A_{13}+(C_4-C_{34})A_{15}+(C_2-C_{36})A_{17}+2P_{19}A_{19}=2B_{19}
\end{array}
\qquad (19)
$$

$$P_n=C_0-\frac{1}{2}C_{2n}+n\frac{c_s m_s}{4b}$$

These equations form a system of normal simultaneous equations, and it will be seen later that in the nth equation the unknown A_n has the greatest coefficient, the others decreasing rather rapidly. Because of this circumstance, the system is most easily solved by a method of successive approximations.

In the first equation, since the value of all the terms is small compared with $P_1 A_1$, an approximation to A_1 is obtained by assuming all terms except A_1 equal to zero. Then in the next equation, since $P_3 A_3$ is large with respect to all terms except $(C_2-C_4) A_1$, which is known, an approximation to A_3 is obtained by assuming the remaining terms equal to zero. Thus by the substitution of the approximated values in the other equations, approximate values of the remaining coefficients are obtained which, when substituted back in the first equation, result in a closer approximation for A_1. A repetition results in closer approximations for all the coefficients. In this way the process can be carried on until the approximations of the coefficients cease to differ. Usually the second approximation is fairly close, and the third may be considered as exact. (See illustrative example.)

Forms for computing B_n and C_{2n} coefficients.—Before the system of simultaneous equations (19) can be solved, the B_n and C_{2n} coefficients must be found. Forms for determining these coefficients are given by plates I to IV, inclusive. Plates I and II are for the case when the circulation is to be determined at 10 points across the semispan and plates III and IV are for 20 points.

It is only necessary to tabulate on each of the forms the values of y_n and y_n' and to follow the steps indicated. The values of y_n are the ordinates for the $\alpha \sin\theta$ curves taken either every 9° or 4½° (starting with the tip as zero), depending upon whether 10 or 20 points are used. The values of y_n' are the ordinates of the $\frac{m_s}{m_0}\frac{c_s}{c}\sin\theta$ curves taken at the same intervals as before. The checks indicated at the bottoms of these forms merely serve as checks of the numerical work performed on that sheet and, if only a few harmonics are to be retained, the arithmetic may be decreased by computing only the coefficients necessary and omitting the checks.

Number of harmonics or points to be retained.—In the series of simultaneous equations given by equation (19) the question naturally arises as to how many equations should be used and how many points across the semispan are required. The system shown is for 10 points, but it may easily be extended to more than 10 points by following the indicated trend. In the case given (equation (19)), the conditions are satisfied at only 10 points when the whole system of equations is solved simultaneously; if the system is cut off, as at A, B, or C, where 4, 5, and 8 harmonics are retained, the circulation may still be found at 10 points but with a greater degree of approximation.

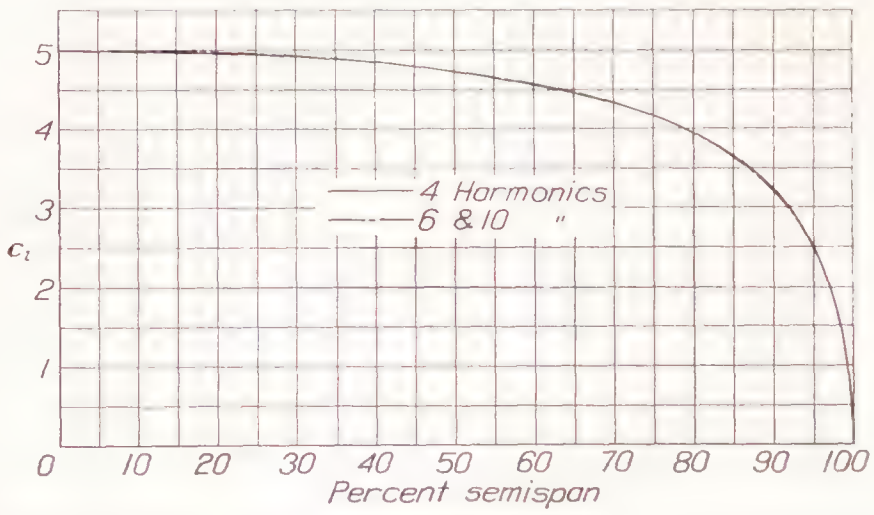

FIGURE 7.—Effect of the number of harmonics on the span of c_l distribution of a wing without flaps. (Angle of attack, α, 1 radian.)

As a criterion for gaging the number of harmonics to be retained, the span c_l distribution has been computed (fig. 7) for an untwisted rectangular wing (straight tips) of aspect ratio 6 at 1 radian angle of attack, using 4, 6, and 10 harmonics. The calculations were repeated (fig. 8) for the same wing with a $\frac{b_f}{b_w}=0.649$ flap extending out from the center. The angle of attack for the portion with flap is 1 radian and that of the remainder of the wing is zero. In both cases 10 points have been used across the semispan. The A_n, or circulation, coefficients from which the distributions of figures 7 and 8 were computed are given in table IV. In figure 9 the distribution has been computed for a wing with double taper. Distributions are given for the case using 10 points

and retaining 4 and 10 harmonics of the series and also for the case with 20 points and 4 harmonics. For convenience the distributions have been computed for an untwisted wing at an angle of attack of 1 radian.

Example.—In order to illustrate the method of calculating the wing characteristics, an example for a wing with partial-span flaps is worked through the forms to determine the B_n and C_{2n} coefficients. The calculations are made for one of the wing shapes given in this report ($\lambda=0.50$, $A=10$, $b_f/b_w=0.489$) at an angle of attack of 1 radian from 0 to 0.489 and 0 from 0.489 to 1.0. The additional types of forms and tables necessary to compute the load distribution for a given case are also included.

Table V is a tabulation of the known geometric quantities of the wing for which the load distribution is desired. Column 1 of this table merely designates the points along the span, the numbers increasing

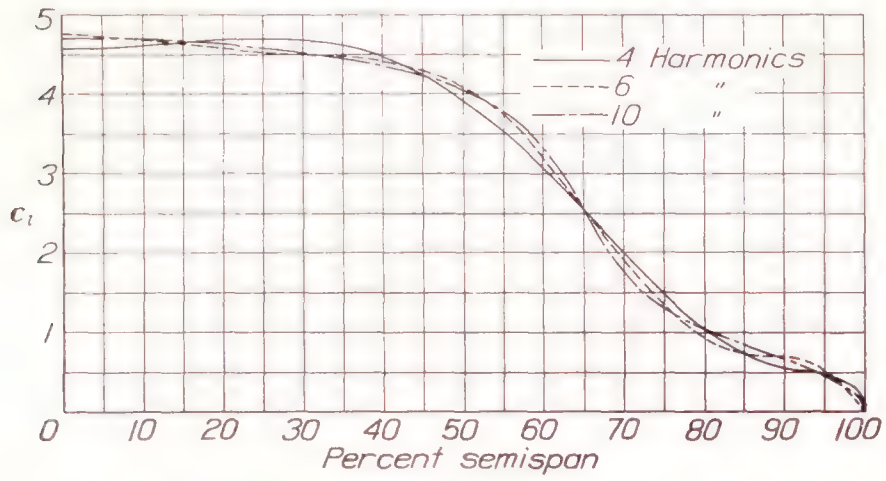

FIGURE 8.—Effect of the number of harmonics on the span c_l distribution of a wing with flaps. (Angle of attack, 1 radian from 0 to 0.649 and 0 from 0.649 to 1.000.)

numerically from the wing tip; column 5 represents the angle of attack measured from zero lift at the points along the span given in column 2. Where an abrupt twist exists, the discontinuity will fall within the portions of the span given in column 2. The final computations, however, will be for the case of a flap whose end lies halfway between these points. Because of this fact a slight discrepancy in length may occur, which can be reduced by increasing the number of points. In the present case only the distribution due to the flaps is found. In order to obtain a complete determination of the distribution at other flap angles and wing angles, it would also be necessary to find the distribution corresponding to the plain wing. For this case the C_{2n} coefficients remain unchanged and $B_1=\alpha_s$, all other B_n values being zero. Column 7 is the slope of the section lift curves along the span which, in this case, is assumed as 5.67. Column 8 is the ratio of the slope of the section at the plane of symmetry to the slopes of the sections at each station. Column 9 is the ratio of the chord at the plane of symmetry to the chord at each section.

The values of columns 6 and 10 (y_n and y_n') are then tabulated as shown in table VI and the instructions of plates I and II, or of plates III and IV as in the present example, are followed until the B_n and C_{2n} coefficients are found. If this method were used and only four harmonics were to be retained, it would be only necessary to compute B_1 to B_7 and C_0 to C_{14} (see A, equation (19)); computing the remaining coefficients would be necessary only to obtain the check.

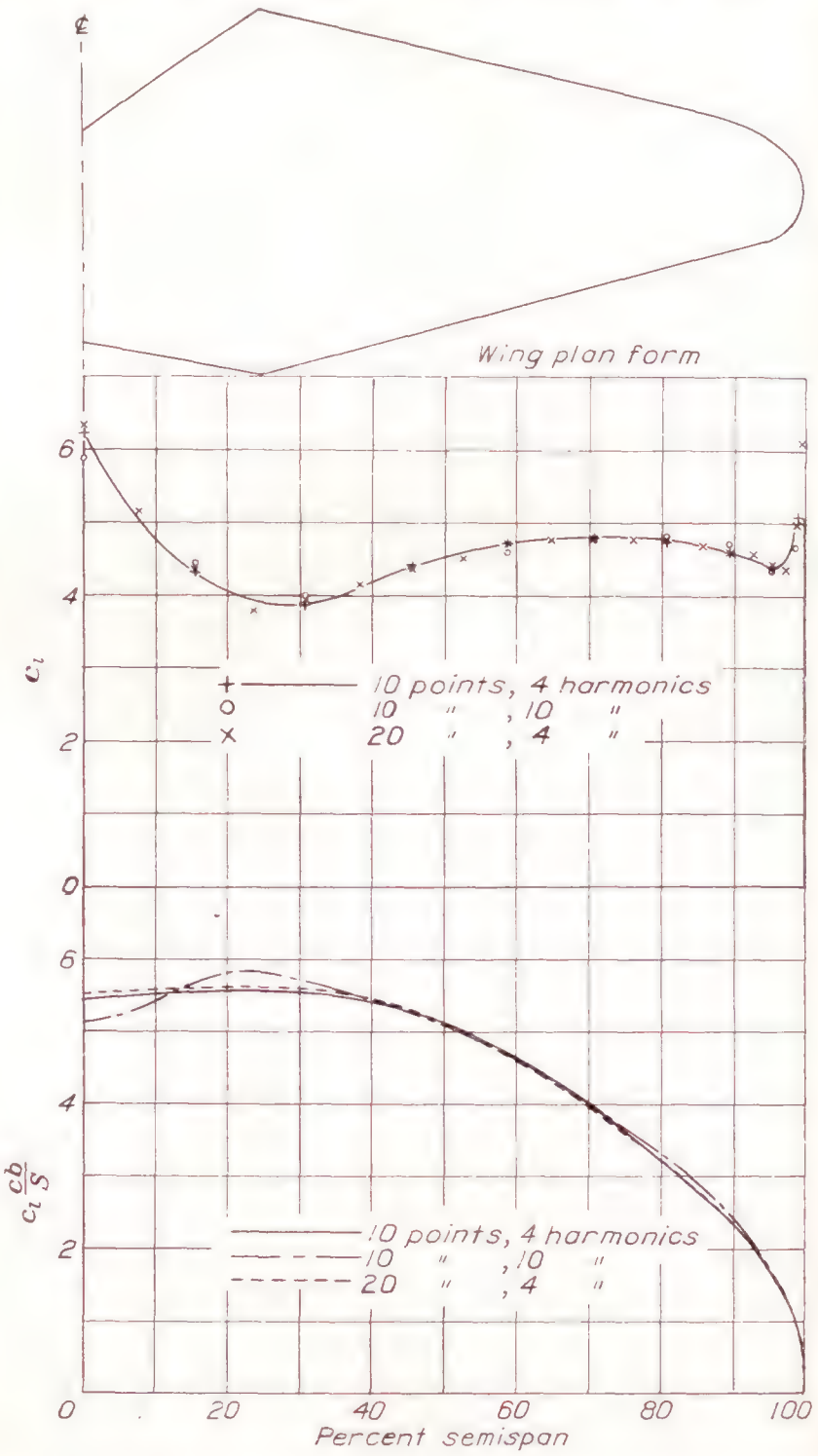

FIGURE 9.—Effect of the number of points and harmonics on the span c_l distribution for a wing with double taper.

A calculating form similar to table VII is then prepared. This form, as given, is complete for the case of 10 harmonics irrespective of the number of points. It will be noted that each major horizontal division represents one of the simultaneous equations occurring in equation (19). In column 1 of table VII are given the operations required to obtain the coefficients and in column 2 are tabulated the values of the coefficients, etc., just found. In column 3 (a) are listed the values of the A_n coefficients when they are known. Since none are known at the start, A_1 is determined as though the others were absent and listed in column 4 (a). The value of A_3 is next approximated in the same way, except that the value of A_1 just found is used as in-

dicated. The same procedure is followed for A_5, A_7, etc., and these values are listed in column 4 (a). After all the A_n's have been approximated in this way, they are written in column 3 (b) and the whole process repeated, using the latest approximated value for each coefficient as it appears. It can be seen that the third approximation shows very little change from the second, indicating that a solution has been obtained. If it is desired to use fewer equations and harmonics, the corresponding computing form can be obtained from the present table VII simply by omitting all computations dealing with the higher harmonics. Thus if four harmonics were retained only portions of the form between the braces would be retained and the computations would proceed as before.

It will be noted, in the present example, that, although the B_n and C_{2n} coefficients were determined for 20 points, it is not necessary that c_l be computed for every point to obtain the final load curve. Even though the computations of the load distribution may be somewhat shortened in this manner, the value of c_l should not be computed at points other than those first selected.

An examination of equation (19) will indicate that, if n harmonics are retained, n values of B and $2n$ values of C are required. Hence, if it were decided to use 10 harmonics and compute the circulation at 10 points, the B_n and C_{2n} values can be determined for 20 points and the process shortened as indicated, or the B_n coefficients could be determined from plate I and the C_{2n} coefficients from plate IV.

After the A_n coefficients have been determined, the c_l values (in the present case $c_l = c_{l_a}$) are found from

$$c_l = \frac{m_s c_s}{c} \Sigma A_n \sin n\theta \tag{20}$$

These computations for c_l are given in table VIII for only 10 points. The wing C_L is found from

$$C_L = \pi A \frac{m_s c_s}{4b} A_1 \tag{21}$$

When this value is known, the distribution at any other C_L is obtained by direct proportion.

If desired, the induced-drag distribution may also be computed by using the A_n coefficients

$$c_{d_i} = c_l \frac{m_s c_s}{4b} \sum \frac{n A_n \sin n\theta}{\sin \theta} \tag{22}$$

as shown in table VIII; however, an easier method would be to compute it at each point from the equation

$$c_{d_i} = c_l \left(\alpha - \frac{c_l}{m_0} \right) \tag{23}$$

DISCUSSION

Although the computed span-loading curves show a qualitative agreement with the experimental wing curves (fig. 5), it is not so good as might be inferred from the results for the 2:1 tapered wing of reference 5. In the present comparison, however, the disagreement at the tip may be somewhat discounted since the square tip on a rectangular wing is known to give a high tip load. Comparisons of experimental and theoretical distributions for plain wings have indicated better agreement either as the tip was rounded or as the value of λ was decreased.

Rib-pressure curves taken from reference 2 (fig. 10) show a drop in positive pressure near the trailing edge for a section just beyond the end of the flap. This loss in lift may partly account for the fact that the experimental distributions give sharper breaks than the corresponding computed curves. An improvement in the

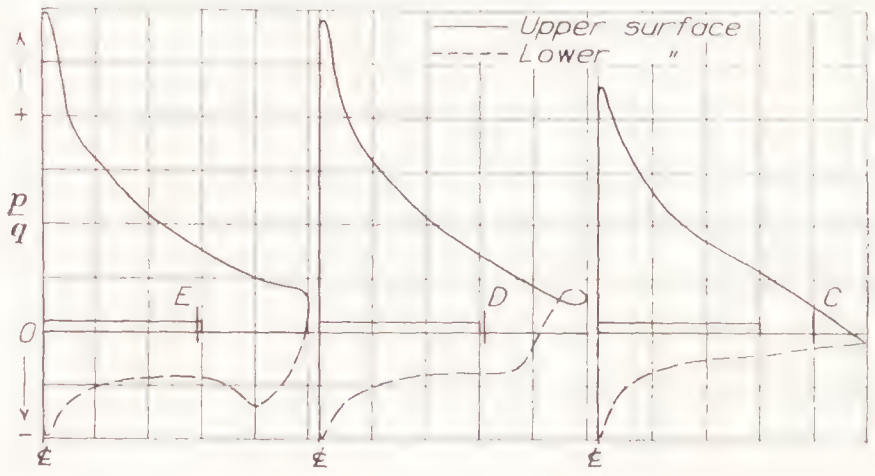

FIGURE 10.—Rib pressure distribution on a Clark Y wing with a partial-span split flap. (Reference 2; $\alpha = 15°$; $\delta_f = 45°$.)

agreement at the end of the flap may also be obtained by using more points and more harmonics in the series for deriving the theoretical distributions.

For the rest of the span the agreement between the computed and experimental curves would have been slightly improved if jet-boundary corrections had been applied to the data of reference 5. This correction, which varies along the wing span, would effect a better agreement in the present case.

The number of harmonics to be used in computing the span loading depends both on the wing plan form and on the type of wing twist. For wings with a continuous taper and twist, four harmonics may be sufficient (fig. 7); whereas, for wings with either a sharp double taper or a discontinuous twist, it may be necessary to increase the number of harmonics and points (figs. 8 and 9), depending, of course, upon the desired accuracy.

Although the data given herein are intended primarily for structural purposes, they may also be useful in relation to the stalling of tapered wings with flaps. When a partial-span flap is deflected, there is an increase in effective angle of attack and in the value of $c_{l_{max}}$ for the sections with the flap; whereas, for the sections beyond the flap, the effective angle of attack is theoretically increased without any increase in the value of $c_{l_{max}}$. Thus, according to lifting-line theory, the tip-stalling tendency of the tapered wing should be augmented by the use of flaps that extend out from the

center, while the center-stalling tendency of the rectangular wing should be increased by flaps at the tips.

Experimental results from reference 2 (fig. 11), however, indicate that the pitching-moment coefficient (or effective camber) of sections considerably beyond the flap are actually increased by a flap deflection. This increase may prevent these outboard sections from stalling as early as would be indicated by the use of lifting-line theory. Furthermore, since theory neglects any transverse flow, any stalling characteristics based upon it may be at best only qualitatively correct. This statement is particularly true of a wing with a partial-span flap, where a relatively large transverse flow exists owing to the abrupt change in lift distribu-

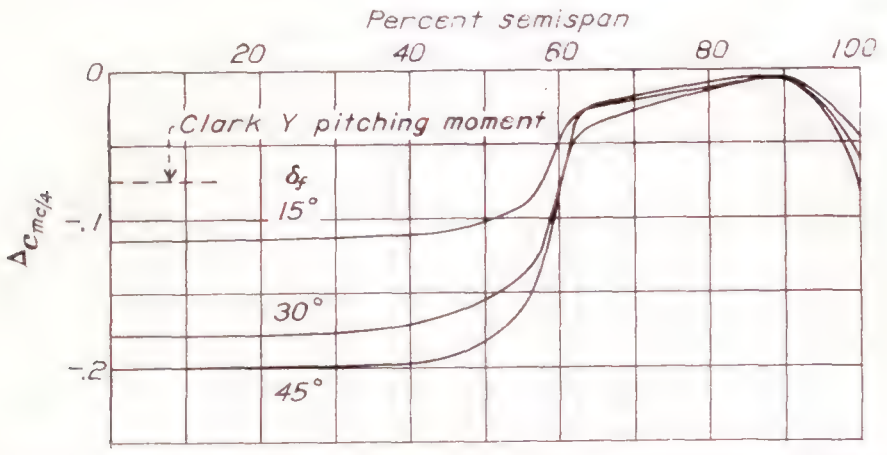

FIGURE 11.—Increment of pitching moment $\Delta_{cmc/4}$ caused by deflecting a 0.6-span split flap on a rectangular Clark Y wing (reference 2).

tion produced by the flap. Lachmann's tests (reference 9), in which the action of wool tufts was observed, seem to indicate that the transverse flow delays the stall of sections immediately adjacent to the flap, thus causing the initial stalling point to move outward away from the flap end.

In regard to the application of the calculations to structural design, fore-and-aft forces as well as vertical forces must be taken into account. An examination of equation (8) indicates that when ΔC_{L_1} Δc_l is equal to C_L (case given by solid lines in fig. 1) the portion of the wing without flaps has its lift vector displaced forward owing to the upflow produced by the flapped part. This forward component may be large enough to cancel the profile drag. Thus, for a wing with flaps at the center, the drag force is concentrated over the flap portion, and there may be an antidrag force over the outer portion of the wing. Hence, in design these conditions should be taken into account in some rational manner.

For structural purposes the c_l values obtained by use of tables I and II, or by computations, may be considered equal to c_{l_0}, the lift coefficient perpendicular to the local relative wind. The values of c_{l_0} and c_{d_0}, which are perpendicular and parallel to the local relative wind, may then be resolved into either chord and beam or any other directions; the fore-and-aft loads are thus obtained without the explicit use of a section induced drag. The angle that the local relative wind makes with the zero-lift direction is obtained by dividing c_{l_0} by m_0. In actual practice a portion of the wing is intercepted by the fuselage so that the actual span load distribution may be modified, depending upon whether or not the fuselage carries its proportionate share of the load. As so few data on fuselage loads are at present available, it may be assumed that for conventional cases the fuselage carries an amount of load equal to the load that would be carried by the wing it displaces.

LANGLEY MEMORIAL AERONAUTICAL LABORATORY,
NATIONAL ADVISORY COMMITTEE FOR AERONAUTICS,
LANGLEY FIELD, VA., *November 21, 1936.*

REFERENCES

1. Anderson, Raymond F.: Determination of the Characteristics of Tapered Wings. T. R. No. 572, N. A. C. A., 1936.
2. Wenzinger, Carl J., and Harris, Thomas A.: Pressure Distribution over a Rectangular Airfoil with a Partial-Span Split Flap. T. R. No. 571, N. A. C. A., 1936.
3. Lotz, Irmgard: Berechnung der Auftriebsverteilung beliebig geformter Flügel. Z. F. M., vol. 22, no. 7, April 14, 1931, S. 189–195.
4. Lippisch, A.: Method for the Determination of the Spanwise Lift Distribution. T. M. No. 778, N. A. C. A., 1935.
5. Parsons, John F.: Span Load Distribution on a Tapered Wing as Affected by Partial-Span Flaps from Tests in the Full-Scale Tunnel. Jour. Aero. Sciences, vol. 3, no. 5, March 1936, pp. 161–164.
6. Wenzinger, Carl J.: The Effect of Partial-Span Split Flaps on the Aerodynamic Characteristics of a Clark Y Wing. T. N. No. 472, N. A. C. A., 1933.
7. Wenzinger, Carl J.: The Effects of Full-Span and Partial-Span Split Flaps on the Aerodynamic Characteristics of a Tapered Wing. T. N. No. 505, N. A. C. A., 1934.
8. Shenstone, B. S.: The Lotz Method for Calculating the Aerodynamic Characteristics of Wings. R. A. S. Jour., vol. XXXVIII, no. 281, May 1934, pp. 432–444.
9. Lachmann, G. V.: Stalling of Tapered Wings. Flight, vol. XXIX, no. 1410, Jan. 2, 1936, pp. 10–13.

PLATE I.—COMPUTING FORM FOR EVALUATING ANGLE COEFFICIENTS, B_n

10 POINTS

y_1 y_2 y_3 y_4 y_5 y_6 y_7 y_8 y_9 $\frac{1}{2}y_{10}$

$y_1+y_3-y_5-y_7+y_9=r_1$ $\quad$ $y_2-y_6+\frac{1}{2}y_{10}=r_2$

Multiply	by					
Sin 9=0.1564	y_1	$-y_7$		$-y_3$	y_9	
Sin 18=0.3090	y_2	y_6		y_6	y_2	
Sin 27=0.4540	y_3	y_1		$-y_9$	$-y_7$	
Sin 36=0.5878	y_4	$-y_8$		y_8	$-y_4$	
Sin 45=0.7071	y_5	y_5	r_1	$-y_5$	y_5	
Sin 54=0.8090	y_6	y_2		y_2	y_6	
Sin 63=0.8910	y_7	$-y_9$		y_1	$-y_3$	
Sin 72=0.9511	y_8	y_4		$-y_4$	$-y_8$	
Sin 81=0.9877	y_9	y_3		y_7	y_1	
Sin 90=1.0000	$\frac{1}{2}y_{10}$	$-\frac{1}{2}y_{10}$	r_2	$-\frac{1}{2}y_{10}$	$\frac{1}{2}y_{10}$	
Sum col. 1						
Sum col. 2						
Col. 1+col. 2	$=5B_1$	$=5B_3$	$=5B_5$	$=5B_7$	$=5B_9$	
Col. 1−col. 2	$=5B_{19}$	$=5B_{17}$	$=5B_{15}$	$=5B_{13}$	$=5B_{11}$	

Check: $B_1-B_3+B_5-B_7+B_9-B_{11}+B_{13}-B_{15}+B_{17}-B_{19}=y_{10}$.
NOTE.—If α_a is constant along the span, $B_1=\alpha_a$ and B_3 to B_{19} are 0.

PLATE II.—COMPUTING FORM FOR EVALUATING PLAN FORM COEFFICIENTS, C_{2n}

10 POINTS

	$\frac{1}{2}y_{10}'$	y_1'	y_2'	y_3'	y_4'	y_5'	v_0	v_1	v_2
		y_4'	y_5'	y_7'	y_6'		r_3	r_4	r_5
Sum	v_0	v_1	v_2	v_3	v_4	r_3	p_0	p_1	p_2
Difference	w_0	w_1	w_2	w_3	w_4		q_0	q_1	q_2

$10\ C_0=p_0+p_1+p_2$
$5\ C_{10}=w_0-w_2+w_4$
$10\ C_{20}=q_0-q_1+q_2$

Multiply	by						
Sin 18=0.3090	w_4	q_2	p_2	$-w_2$	p_1	$-q_1$	
Sin 36=0.5878	w_3			w_1			
Sin 54=0.8090	w_2	q_1	$-p_1$	$-w_4$	$-p_2$	$-q_2$	
Sin 72=0.9511	w_1			$-w_3$			
Sin 90=1.00000	w_0	q_0	p_0	w_0	p_0	q_0	
Sum col. 1							
Sum col. 2		$=5C_4$	$=5C_{10}$		$=5C_8$	$=5C_{12}$	
Col. 1+col. 2	$=5C_2$			$=5C_6$			
Col. 1−col. 2	$=5C_{18}$			$=5C_{14}$			

Check: $C_0+C_2+C_4+C_6+C_8+C_{10}+C_{12}+C_{14}+C_{16}+C_{18}+C_{20}=0$.

PLATE III.—COMPUTING FORM FOR EVALUATING ANGLE COEFFICIENTS, B_n

20 POINTS

y_1 y_2 y_3 y_4 y_5 y_6 y_7 y_8 y_9 y_{10} y_{11} y_{12} y_{13} y_{14} y_{15} y_{16} y_{17} y_{18} y_{19} $\frac{1}{2}y_{20}$

$$y_1+y_7-y_9-y_{15}+y_{17}=r_1$$
$$y_2+y_6-y_{10}-y_{14}+y_{18}=r_2$$
$$y_3+y_5-y_{11}-y_{13}+y_{19}=r_3$$
$$y_4-y_{12}+\tfrac{1}{2}y_{20}=r_4$$

Multiply	by																			
Sin 4.5=0.0785	y_1		y_{13}			y_{17}		y_9		$-y_{11}$		y_3			y_7		$-y_{19}$	
Sin 9.0=0.1564		y_2		$-y_{14}$			$-y_6$		y_{18}		y_{18}		$-y_6$			$-y_{14}$		y_2
Sin 13.5=0.2334	y_3		y_1			$-y_{11}$		y_{13}		$-y_7$		y_9			y_{19}		y_{17}	
Sin 18.0=0.3090		y_4		y_{12}			y_{12}		y_1		$-y_4$		$-y_{12}$			$-y_{12}$		$-y_4$
Sin 22.5=0.3827	y_5		$-y_{15}$		r_1	y_5		$-y_5$		y_{15}		y_{15}		$-r_3$	y_5		$-y_{15}$	
Sin 27.0=0.4540		y_6		y_2			$-y_{18}$		$-y_{14}$		$-y_{14}$		$-y_{18}$			y_2		y_6
Sin 31.5=0.5225	y_7		y_{11}			y_1		$-y_{17}$		y_3		y_{19}			$-y_9$		y_{13}	
Sin 36.0=0.5878		y_8		$-y_{16}$			y_{16}		$-y_8$		y_8		$-y_{16}$			y_{16}		$-y_8$
Sin 40.5=0.6494	y_9		y_9			$-y_7$		y_1		$-y_{19}$		y_{13}			$-y_{17}$		$-y_{11}$	
Sin 45.0=0.7071		y_{10}		y_{10}	r_2		$-y_{10}$		y_{10}		y_{10}		$-y_{10}$	r_2		y_{10}		y_{10}
Sin 49.5=0.7604	y_{11}		$-y_{17}$			y_{13}		y_{19}		y_1		y_7			$-y_3$		y_9	
Sin 54.0=0.8090		y_{12}		y_4			y_4		y_{12}		$-y_{12}$		$-y_4$			$-y_4$		$-y_{12}$
Sin 58.5=0.8526	y_{13}		y_9			$-y_{19}$		y_3		y_{17}		y_1			y_{11}		$-y_7$	
Sin 63.0=0.8910		y_{14}		$-y_{18}$			y_2		$-y_6$		$-y_6$		y_2			$-y_{18}$		y_{14}
Sin 67.5=0.9239	y_{15}		y_5		r_3	y_{15}		$-y_{15}$		$-y_5$		$-y_5$		r_1	y_{15}		y_5	
Sin 72.0=0.9511		y_{16}		y_3			$-y_8$		$-y_{16}$		y_{16}		y_8			$-y_8$		$-y_{16}$
Sin 76.5=0.9724	y_{17}		$-y_{19}$			$-y_9$		$-y_7$		$-y_{13}$		$-y_{11}$			y_1		$-y_3$	
Sin 81.0=0.9877		y_{18}		y_6			y_{14}		y_2		y_2		y_{14}			y_6		y_{18}
Sin 85.5=0.9969	y_{19}		y_7			y_3		y_{11}		y_9		$-y_{17}$			$-y_{13}$		y_1	
Sin 90.0=1.0000		$\frac{1}{2}y_{20}$		$-\frac{1}{2}y_{20}$	r_4		$-\frac{1}{2}y_{20}$		$\frac{1}{2}y_{20}$		$-\frac{1}{2}y_{20}$		$\frac{1}{2}y_{20}$		$-r_4$		$\frac{1}{2}y_{20}$		$-\frac{1}{2}y_{20}$
Sum col. 1																				
Sum col. 2																				
Col. 1+col. 2	$10B_1$		$10B_3$		$10B_5$		$10B_7$		$10B_9$		$10B_{11}$		$10B_{13}$		$10B_{15}$		$10B_{17}$		$10B_{19}$	
Col. 1−col. 2	$10B_{39}$		$10B_{37}$		$10B_{35}$		$10B_{33}$		$10B_{31}$		$10B_{29}$		$10B_{27}$		$10B_{25}$		$10B_{23}$		$10B_{21}$	

Check: $B_1-B_3+B_5-B_7+B_9-\ \ldots\ +\ \ldots\ B_{39}=y_{20}$.

PLATE IV.—COMPUTING FORM FOR EVALUATING PLAN FORM COEFFICIENTS, C_{2n}

20 POINTS

	$\frac{1}{2}y_{20}'$	y_1' y_{19}'	y_2' y_{18}'	y_3' y_{17}'	y_4' y_{16}'	y_5' y_{15}'	y_6' y_{14}'	y_7' y_{13}'	y_8' y_{12}'	y_9' y_{11}'	y_{10}'
Sum	v_0	v_1	v_2	v_3	v_4	v_5	v_6	v_7	v_8	v_9	v_{10}
Difference	w_0	w_1	w_2	w_3	w_4	w_5	w_6	w_7	w_8	w_9	
	v_0	v_1	v_2	v_3	v_4	v_5		p_0	p_1	p_2	
	v_{10}	v_9	v_8	v_7	v_6			p_5	p_4	p_3	
Sum	p_0	p_1	p_2	p_3	p_4	p_5		r_0	r_1	r_2	
Difference	q_0	q_1	q_2	q_3	q_4			s_0	s_1	s_2	

$20\,C_0 = p_0+p_1+p_2+p_3+p_4+p_5$
$10\,C_{10} = \sqrt{2}(w_1-w_3-w_5+w_7+w_9)+w_0-w_4+w_8$
$10\,C_{20} = q_0-q_2+q_4$
$10\,C_{30} = \sqrt{2}(-w_1+w_3+w_5-w_7-w_9)+w_0-w_4+w_8$
$20\,C_{40} = p_0-p_1+p_2-p_3+p_4-p_5$

Multiply	by											
Sin 9=0.1564		w_9				w_3				w_7		w_1				
Sin 18=0.3090	w_8		q_4		$-w_4$		$-q_2$		$-w_4$		w_8		s_2	r_1	$-s_1$	r_2
Sin 27=0.4540		w_7				$-w_9$				w_1		$-w_3$				
Sin 36=0.5878	w_6			q_3	w_2			q_1	$-w_2$		$-w_6$					
Sin 45=0.7071		w_5				$-w_5$				w_5		w_5				
Sin 54=0.8090	w_4		q_2		$-w_8$		$-q_4$		$-w_8$		w_4		s_1	$-r_2$	$-s_2$	$-r_1$
Sin 63=0.8910		w_3				w_1				$-w_9$		$-w_7$				
Sin 72=0.9511	w_2			q_1	$-w_6$			$-q_3$	w_6		$-w_2$					
Sin 81=0.9877		w_1				$-w_7$				$-w_3$		w_9				
Sin 90=1.0000	w_0		q_0		w_0		q_0		w_0		w_0		s_0	r_0	s_0	r_0
Sum col. 1													$10C_8$	$10C_{16}$	$10C_{24}$	$10C_{32}$
Sum col. 2																
Col. 1+col. 2		$10C_2$		$10C_4$		$10C_6$		$10C_{12}$		$10C_{14}$		$10C_{18}$				
Col. 1−col. 2		$10C_{38}$		$10C_{36}$		$10C_{34}$		$10C_{28}$		$10C_{26}$		$10C_{22}$				

Check: $C_0+C_2+C_4 \ldots C_{40}=0$.

TABLE I.—VALUES OF L_a FOR TAPERED WINGS WITH ROUNDED TIPS

$A=6$											$A=10$										
$\frac{y/b}{2}$ / λ	0	0.15	0.30	0.45	0.60	0.70	0.80	0.90	0.95	0.975	0	0.15	0.30	0.45	0.60	0.70	0.80	0.90	0.95	0.975	$\frac{y_1/b}{2}$ / λ
1.00	1.164	1.163	1.144	1.115	1.050	0.987	0.870	0.669	0.485	0.358	1.116	1.111	1.106	1.090	1.052	1.011	0.929	0.757	0.572	0.433	1.00
.75	1.217	1.204	1.167	1.112	1.026	.953	.840	.648	.468	.340	1.194	1.179	1.140	1.089	1.020	.964	.875	.710	.536	.396	.75
.50	1.291	1.263	1.191	1.107	.995	.908	.789	.607	.447	.319	1.292	1.257	1.184	1.093	.982	.903	.800	.648	.492	.367	.50
.25	1.392	1.349	1.243	1.118	.954	.841	.709	.521	.386	.286	1.424	1.368	1.247	1.104	.940	.823	.695	.528	.407	.308	.25

TABLE II.—VALUES OF L_b FOR TAPERED WINGS WITH ROUNDED TIPS

[Values of L_b given for flaps at center. Reverse signs when using for flaps at tips]

Flaps at center	$\frac{b_f}{b_w}$ \ $\frac{y/b}{2}$	$A=6$										$A=10$										$\frac{y/b}{2}$ / $\frac{b_f}{b_w}$	Flaps at tip
		0	0.15	0.30	0.45	0.60	0.70	0.80	0.90	0.95	0.975	0	0.15	0.30	0.45	0.60	0.70	0.80	0.90	0.95	0.975		
		$\lambda=1.00$																					
	0.233	0.400	0.332	−0.002	−0.117	−0.147	−0.155	−0.145	−0.116	−0.085	−0.061	0.487	0.415	−0.023	−0.146	−0.173	−0.181	−0.170	−0.140	−0.107	−0.077	0.767	
	.383	.351	.334	.238	−.112	−.221	−.236	−.227	−.185	−.139	−.100	.423	.405	.305	−.145	−.266	−.283	−.277	−.231	−.175	−.126	.617	
	.649	.192	.189	.169	.133	.006	−.251	−.313	−.275	−.209	−.157	.232	.229	.211	.178	.033	−.317	−.402	−.360	−.280	−.210	.351	
	.760	.110	.109	.106	.093	.060	−.013	−.255	−.289	−.230	−.171	.150	.147	.137	.117	.081	.001	−.340	−.386	−.307	−.227	.240	
		$\lambda=0.75$																					
	0.233	0.406	0.341	−0.004	−0.120	−0.148	−0.154	−0.143	−0.113	−0.083	−0.059	0.509	0.423	−0.027	−0.155	−0.177	−0.181	−0.174	−0.141	−0.107	−0.077	0.767	
	.383	.353	.333	.236	−.114	−.218	−.233	−.222	−.180	−.134	−.096	.433	.414	.301	−.156	−.272	−.283	−.274	−.229	−.174	−.125	.617	
	.649	.192	.186	.164	.125	.006	−.245	−.305	−.266	−.204	−.149	.235	.230	.206	.169	.027	−.314	−.391	−.352	−.275	−.203	.351	
	.760	.118	.114	.104	.084	.046	−.021	−.248	−.273	−.213	−.155	.150	.147	.133	.112	.074	−.001	−.327	−.373	−.298	−.223	.240	
		$\lambda=0.50$																					
	0.233	0.420	0.340	−0.008	−0.124	−0.151	−0.153	−0.141	−0.111	−0.082	−0.059	0.534	0.436	−0.038	−0.167	−0.183	−0.182	−0.169	−0.140	−0.107	−0.077	0.767	
	.383	.360	.335	.227	−.123	−.221	−.230	−.218	−.176	−.134	−.096	.447	.424	.297	−.170	−.277	−.281	−.266	−.224	−.171	−.124	.617	
	.649	.191	.182	.159	.118	.002	−.240	−.295	−.256	−.197	−.146	.234	.226	.198	.159	.021	−.308	−.375	−.332	−.260	−.192	.351	
	.760	.118	.112	.100	.078	.043	−.022	−.240	−.263	−.206	−.150	.148	.141	.126	.103	.065	−.004	−.305	−.352	−.281	−.207	.240	
		$\lambda=0.25$																					
	0.233	0.425	0.342	−0.016	−0.136	−0.154	−0.151	−0.133	−0.106	−0.079	−0.058	0.558	0.445	−0.051	−0.186	−0.191	−0.183	−0.161	−0.129	−0.100	−0.075	0.767	
	.383	.361	.336	.222	−.134	−.225	−.226	−.205	−.164	−.124	−.090	.454	.425	.285	−.193	−.285	−.276	−.247	−.200	−.154	−.113	.617	
	.649	.186	.175	.149	.108	−.006	−.231	−.272	−.234	−.179	−.131	.223	.213	.183	.138	.004	−.266	−.335	−.287	−.228	−.173	.351	
	.760	.109	.104	.092	.070	.035	−.023	−.221	−.237	−.186	−.139	.133	.126	.112	.089	.052	−.009	−.278	−.300	−.241	−.183	.240	

TABLE III.—CALCULATION OF LIFT DISTRIBUTION FOR ILLUSTRATIVE EXAMPLE

[A, 6; b_f/b_w, 0.383; S, 266.7 sq. ft.; b, 40 ft.; λ, 0.625; C_L, 1.72; Δc_l, 0.60; q, 57.5]

1	2	3	4	5	6	7	8	9
Station $y/\frac{b}{2}$	Chord (ft.)	L_a	L_b	$c_{l_{at}}$	c_{l_a}	c_{l_b}	c_l	l (lb.)
0	8.500	1.254	0.356	0.984	1.693	0.168	1.861	91.0
.15	8.022	1.233	.334	1.025	1.762	.167	1.929	89.0
.30	7.544	1.179	.232	1.043	1.794	.123	1.917	83.1
.45	7.066	1.110	−.118	1.047	1.801	−.067	1.734	70.5
.60	6.588	1.010	−.220	1.022	1.758	−.134	1.624	61.6
.70	6.269	.930	−.232	.989	1.700	−.148	1.552	56.0
.80	5.820	.815	−.220	.934	1.607	−.151	1.456	48.7
.90	4.825	.628	−.179	.868	1.492	−.148	1.344	37.3
.95	3.655	.457	−.134	.835	1.435	−.147	1.288	27.1
.975	2.635	.330	−.097	.835	1.435	−.147	1.288	19.5

TABLE IV.—CIRCULATION COEFFICIENTS

[A, 6; λ, 1.0; b_f/b_w, 0.649]

No flaps				Flaps at center			
Coefficient	4 harmonics retained	6 harmonics retained	10 harmonics retained	Coefficient	4 harmonics retained	6 harmonics retained	10 harmonics retained
A_1	0.9280	0.9290	0.9290	A_1	0.6682	0.6684	0.6682
A_3	.1158	.1160	.1161	A_3	−.1825	−.1826	−.1826
A_5	.0251	.0251	.0251	A_5	−.0298	−.0301	−.0300
A_7	.0069	.0072	.0073	A_7	.0588	.0585	.0586
A_9	----------	.0026	.0026	A_9	----------	.0017	.0019
A_{11}	----------	.0011	.0011	A_{11}	----------	−.0286	−.0281
A_{13}	----------	----------	.0005	A_{13}	----------	----------	.0058
A_{15}	----------	----------	.0003	A_{15}	----------	----------	.0168
A_{17}	----------	----------	.0002	A_{17}	----------	----------	−.0083
A_{19}	----------	----------	.0004	A_{19}	----------	----------	−.0104

TABLE V.—GEOMETRIC CHARACTERISTICS OF WING USED IN EXAMPLE

1	2	3	4	5	6	7	8	9	10
A	Fraction of semispan	θ (deg.)	$\sin\theta$	α (rad.)	$\alpha \sin\theta$	m_0 for $b=\infty$	$\frac{m_a}{m_0}$	$\frac{c_a}{c}$	$\frac{m_a c_a}{m_0 c}\sin\theta$
20	0	90	1.0000	1	1.0000	5.67	1.0	1.0000	1.0000
19	.0785	85.5	.9969	1	.9969	5.67	1.0	1.0400	1.0370
18	.1564	81	.9877	1	.9877	5.67	1.0	1.0848	1.0717
17	.2334	76.5	.9724	1	.9724	5.67	1.0	1.1295	1.1030
16	.3090	72	.9511	1	.9511	5.67	1.0	1.1827	1.1252
15	.3827	67.5	.9239	1	.9239	5.67	1.0	1.2386	1.1445
14	.4540	63	.8910	1	.8910	5.67	1.0	1.2937	1.1530
13	.5225	58.5	.8526	0	0	5.67	1.0	1.3555	1.1560
12	.5878	54	.8090	0	0	5.67	1.0	1.4162	1.1455
11	.6494	49.5	.7664	0	0	5.67	1.0	1.4785	1.1245
10	.7071	45	.7071	0	0	5.67	1.0	1.5469	1.0939
9	.7604	40.5	.6494	0	0	5.67	1.0	1.6100	1.0458
8	.8090	36	.5878	0	0	5.67	1.0	1.6793	.9869
7	.8526	31.5	.5225	0	0	5.67	1.0	1.7415	.9100
6	.8910	27	.4540	0	0	5.67	1.0	1.8219	.8272
5	.9239	22.5	.3827	0	0	5.67	1.0	1.9605	.7500
4	.9511	18	.3090	0	0	5.67	1.0	2.2504	.6953
3	.9724	13.5	.2334	0	0	5.67	1.0	2.8280	.6600
2	.9877	9	.1564	0	0	5.67	1.0	4.0742	.6372
1	.9969	4.5	.0785	0	0	5.67	1.0	7.9740	.6260
0	1.0000	0	0	0	0	5.67	1.0	----------	----------

TABLE VI.—COMPUTATION OF ANGLE COEFFICIENTS, B_n

y_1	y_2	y_3	y_4	y_5	y_6	y_7	y_8	y_9	y_{10}	y_{11}	y_{12}	y_{13}	y_{14}	y_{15}	y_{16}	y_{17}	y_{18}	y_{19}	$\frac{1}{2}y_{20}$
0	0	0	0	0	0	0	0	0	0	0	0	0	0.8910	0.9239	0.9511	0.9724	0.9877	0.9969	0.5000

$r_1=0+0-0-0.9239+0.9724=0.0485$
$r_2=0+0-0-0.8910+0.9877=\ .0967$
$r_3=0+0-0-0\quad\ +0.9969=\ .9969$
$r_4=0-0+0.5000\quad\ =\ .5000$

Multiply	by																		
Sin 4.5=0.0785	0		0			0.0763		0		0		0		0		0		−0.0783	
Sin 9 =0.1564		0		−0.1394			0		0.1545		0.1545		0				−0.1394		0
Sin 13.5=0.2334	0		0			0		0		0		0		0		0.2327		.2270	
Sin 18 =0.3090		0		0			0		0		0		0		0		0		0
Sin 22.5=0.3827	0		−0.3536		0.0186		0		0		0.3536		0.3536		−0.3815		0		−.3536
Sin 27 =0.4540		0		0			−0.4484		−.4045		−.4045		−0.4484				0		0
Sin 31.5=0.5225	0		0			0		−0.5081		0		0		.5209			0		0
Sin 36 =0.5878		0		−.5591			.5591		0		0		−.5591					.5591	0
Sin 40.5=0.6494	0		0			0		0		−.6474		0		−.6315			0		
Sin 45 =0.7071		0		0	0.0684		0		0		0		0		0	0.0684		0	0
Sin 49.5=0.7604	0		−.7394			0		.7580		0		0		0			0		0
Sin 54 =0.8090		0		0			0		0		0		0					0	0
Sin 58.5=0.8526	0		0			−.8500		0		.8291		0		0			0		0
Sin 63 =0.8910		.7939		−.8800			0		0		0		0					−.8800	0.7939
Sin 67.5=0.9239	.8536		0		.9210		.8536		−.8536		0		0		.0448		.8536		0
Sin 72 =0.9511		.9046		0			0		−.9046		.9046		0					0	−.9046
Sin 76.5=0.9724	.9456		−.9694			0		0		0		0		0			0		0
Sin 81 =0.9877		.9756		0			.8800		0		0		.8800					0	.9756
Sin 85.5=0.9969	.9938		0			0		0		0		0		−.9694			0		0
Sin 90 =1.0000		.5000		−.5000	.5000		−.5000		.5000		−.5000		.5000		−.5000			.5000	−.5000
Sum col. 1	2.7930		−2.0624		0.9396		0.0799		−0.6037		0.5353		−0.0949		−0.3367		0.4548		−0.2049
Sum col. 2		3.1741		−2.0785		.5684		.4907		−.6546		.1546		.3725		−.4316		.0397	.3649
Col. 1+col. 2	$5.9671=10B_1$		$-4.1409=10B_3$		$1.5080=10B_5$		$0.5706=10B_7$		$-1.2583=10B_9$		$0.6899=10B_{11}$		$0.2776=10B_{13}$		$-0.7683=10B_{15}$		$0.4945=10B_{17}$		$0.1600=10B_{19}$
Col. 1−col. 2	$-.3811=10B_{39}$		$.0161=10B_{37}$		$.3712=10B_{35}$		$-.4108=10B_{33}$		$.0509=10B_{31}$		$.3807=10B_{29}$		$-.4674=10B_{27}$		$.0949=10B_{25}$		$.4151=10B_{23}$		$-.5698=10B_{21}$

Check:

$B_1-B_3+B_5-B_7+B_9-B_{11}+B_{13}-B_{15}+B_{17}-B_{19}+B_{21}-B_{23}+B_{25}-B_{27}+B_{29}-B_{31}+B_{33}-B_{35}+B_{37}-B_{39}=\frac{1}{2}y_{20}$.

$0.5967+0.4141+0.1508-0.0571-0.1258-0.0690+0.0278+0.0768+0.0495-0.0160-0.0570-0.0415+0.0095+0.0467+0.0381-0.0051-0.0411-0.0371+0.0016+0.0381=1.0000$.

COMPUTATION OF PLAN-FORM COEFFICIENTS, C_{2n}

	0.5000	0.6260 1.0370	0.6372 1.0717	0.6600 1.1030	0.6953 1.1252	0.7500 1.1445	0.8272 1.1530	0.9100 1.1560	0.9869 1.1455	1.0458 1.1245	1.0939
Sum	0.5000	1.6630	1.7089	1.7630	1.8205	1.8945	1.9802	2.0660	2.1324	2.1703	1.0939
Difference	−.5000	−.4110	−.4345	−.4430	−.4299	−.3945	−.3258	−.2460	−.1586	−.0787	1.0939

	0.5000 1.0939	1.6630 2.1703	1.7089 2.1324	1.7630 2.0660	1.8205 1.9802	1.8945	1.5939 1.8945	3.8333 3.8007	3.8413 3.8290
Sum	1.5939	3.8333	3.8413	3.8290	3.8007	1.8945	3.4884	7.6340	7.6703
Difference	−.5939	−.5073	−.4235	−.3030	−.1597		−.3006	.0326	.0123

$20C_0=1.5939+3.8333+3.8413+3.8290+3.8007+1.8945=18.7927$
$10C_{10}=1.4142(-0.4110+0.4430+0.3945-0.2460-0.0787)-0.5000+0.4299-0.1586=-0.0847$
$10C_{20}=-0.5939+0.4235-0.1597=-0.3301$
$10C_{30}=1.4142(0.4110-0.4430-0.3945+0.2460+0.0787)-0.5000+0.4299-0.1586=-0.3727$
$20C_{40}=1.5939-3.8333+3.8413-3.8290+3.8007-1.8945=-0.3209$

Multiply	by											
Sin 9=0.1564		−0.0123			−0.0693			−0.0385		−0.0643		
Sin 18=0.3090	−0.0490		−0.0493		0.1328		0.1309		0.1328		−0.0490	0.0038	2.3589	−0.0101	2.3701
Sin 27=0.4540		−.1117				.0357				−.1866		.2011			
Sin 36=0.5878	−.1915			−0.1781	−.2554			−0.2982	.2554		.1915				
Sin 45=0.7071		−.2790				.2790				−.2790		−.2790			
Sin 54=0.8090	−.3478		−.3426		.1283		.1292		.1283		−.3478		.0264	−6.2053	−.0100	−6.1759
Sin 63=0.8910		−.3947				−.3662				.0701		.2192			
Sin 72=0.9511	−.4133			−.4825	.3099			.2882	−.3099		.4133				
Sin 81=0.9877		−.4059				.2430				.4376		−.0777			
Sin 90=1.0000	−.5000		−.5939		−.5000		−.5939		−.5000		−.5000		−.3006	3.4884	−.3006	3.4884
Sum col. 1	−1.5016		−.9858		−.1844		−.3338		−.2934		−.2920		−.2704	−.3580	−.3207	−.3174
Sum col. 2		−1.2036		−.6606		.1222		−.0100		.0036		−.0007	$10C_8$	$10C_{16}$	$10C_{24}$	$10C_{32}$
Col. 1+col. 2	$-2.7052=10C_2$		$-1.6464=10C_4$		$-.0622=10C_6$		$-.3438=10C_{12}$		$-.2898=10C_{14}$		$-.2927=10C_{18}$					
Col. 1−col. 2	$-.2980=10C_{38}$		$-.3252=10C_{36}$		$-.3066=10C_{34}$		$-.3238=10C_{28}$		$-.2970=10C_{26}$		$-.2913=10C_{22}$					

Check: $0.9396-0.2705-0.1646-0.0062-0.0270-0.0085-0.0344-0.0290-0.0358-0.0293-0.0330-0.0291-0.0321-0.0297-0.0324-0.0373-0.0317-0.0307-0.0325-0.0298-0.0160=0$.

TABLE VII.—SOLUTION OF A_n COEFFICIENTS

1	2	3 (a)	3 (b)	3 (c)	4 (a)	4 (b)	4 (c)
$(C_2-C_4)A_3$	−0.1059		−0.2563	−0.2487		0.0271	0.0263
$(C_4-C_6)A_5$	−.1584		.0824	.0823		−.0131	−.0130
$(C_6-C_8)A_7$	.0208		.0182	.0169		.0004	.0004
$(C_8-C_{10})A_9$	−.0185		−.0411	−.0400		.0008	.0007
$(C_{10}-C_{12})A_{11}$	.0259		.0190	.0189		.0005	.0005
$(C_{12}-C_{14})A_{13}$	−.0054		.0092	.0087		0	0
$(C_{14}-C_{16})A_{15}$	.0068		−.0201	−.0197		−.0001	−.0001
$(C_{16}-C_{18})A_{17}$	−.0065		.0117	.0118		−.0001	−.0001
$(C_{18}-C_{20})A_{19}$	.0037		.0032	.0032		0	0
Σ					0	.0155	.0147
$\Sigma/2$					0	.0077	.0073
$B_1-\Sigma/2$	.5967				.5967	.5890	.5894
$A_1=\frac{(B_1-\Sigma/2)}{P_1}$	/1.2667				.4711	.4650	.4653
$(C_2-C_4)A_1$	−0.1059	0.4711	0.4650	0.4653	−0.0499	−0.0492	−0.0493
$(C_2-C_8)A_5$	−.2435		.0824	.0823		−.0201	−.0200
$(C_4-C_{10})A_7$	−.1561		.0182	.0169		−.0028	−.0026
$(C_6-C_{12})A_9$	.0282		−.0411	−.0400		−.0012	−.0011
$(C_8-C_{14})A_{11}$	.0020		.0190	.0189		0	0
$(C_{10}-C_{16})A_{13}$	.0273		.0092	.0087		.0002	.0002
$(C_{12}-C_{18})A_{15}$	−.0051		−.0201	−.0197		.0001	.0001
$(C_{14}-C_{20})A_{17}$	.0040		.0117	.0118		.0001	.0001
$(C_{16}-C_{22})A_{19}$	−.0067		.0032	.0032		0	0
Σ					−.0499	−.0730	−.0726
$\Sigma/2$					−.0249	−.0365	−.0363
$B_3-\Sigma/2$	−.4141				−.3892	−.3776	−.3778
$A_3=\frac{(B_3-\Sigma/2)}{P_3}$	/1.5185				−.2563	−.2487	−.2488
$(C_4-C_6)A_1$	−0.1584	0.4711	0.4650	0.4653	−0.0746	−0.0736	0−.0737
$(C_2-C_8)A_3$	−.2435	−.2563	−.2487	−.2488	.0624	.0606	.0606
$(C_2-C_{12})A_7$	−.2361		.0182	.0169		−.0043	−.0041
$(C_4-C_{14})A_9$	−.1356		−.0411	−.0400		.0056	.0054
$(C_6-C_{16})A_{11}$	.0296		.0190	.0189		.0006	.0006
$(C_8-C_{18})A_{13}$	.0023		.0092	.0087		0	0
$(C_{10}-C_{20})A_{15}$	.0245		−.0201	−.0197		−.0005	−.0005
$(C_{12}-C_{22})A_{17}$	−.0053		.0117	.0118		−.0001	−.0001
$(C_{14}-C_{24})A_{19}$	.0031		.0032	.0032		0	0
Σ					−.0122	−.0117	−.0118
$\Sigma/2$					−.0061	−.0059	−.0059
$B_5-\Sigma/2$	.1508				.1569	.1567	.1567
$A_5=\frac{(B_5-\Sigma/2)}{P_5}$	/1.9035				.0824	.0823	.0823
$(C_6-C_8)A_1$	0.0280	0.4711	0.4650	0.4653	0.0098	0.0097	0.0097
$(C_4-C_{10})A_3$	−.1561	−.2563	−.2487	−.2488	.0400	.0388	.0388
$(C_2-C_{12})A_5$	−.2361	.0824	.0823	.0823	−.0195	−.0194	−.0194
$(C_2-C_{16})A_9$	−.2347		−.0411	−.0400		.0096	.0094
$(C_4-C_{18})A_{11}$	−.1353		.0190	.0189		−.0026	−.0026
$(C_6-C_{20})A_{13}$	.0268		.0092	.0087		.0002	.0002
$(C_8-C_{22})A_{15}$	.0021		−.0201	−.0197	0	0	
$(C_{10}-C_{24})A_{17}$	.0236		.0117	.0118		.0003	.0003
$(C_{12}-C_{26})A_{19}$	−.0047		.0032	.0032	0	0	
Σ					.0303	.0366	.0364
$\Sigma/2$					.0152	.0183	.0182
$B_7-\Sigma/2$	.0571				.0419	.0388	.0389
$A_7=\frac{(B_7-\Sigma/2)}{P_7}$	/2.2977				.0182	.0169	.0169
$(C_8-C_{10})A_1$	−0.0185	0.4711	0.4650	0.4653	−0.0087	−0.0086	−0.0086
$(C_6-C_{12})A_3$	.0282	−.2563	−.2487	−.2488	−.0072	−.0070	−.0070
$(C_4-C_{14})A_5$	−.1356	.0824	.0823	.0823	−.0112	−.0112	−.0112
$(C_2-C_{16})A_7$	−.2347	.0182	.0169	.0169	−.0043	−.0040	−.0040
$(C_2-C_{20})A_{11}$	−.2375		.0190	.0189		−.0045	−.0045
$(C_4-C_{22})A_{13}$	−.1355		.0092	.0087		−.0012	−.0012
$(C_6-C_{24})A_{15}$	.0259		−.0201	−.0197		−.0005	−.0005
$(C_8-C_{26})A_{17}$	.0027		.0117	.0118	0	0	
$(C_{10}-C_{28})A_{19}$	.0239		.0032	.0032		.0001	.0001
Σ					−.0314	−.0369	−.0369
$\Sigma/2$					−.0157	−.0184	−.0184
$B_9-\Sigma/2$	−.1258				−.1101	−.1074	−.1074
$A_9=\frac{(B_9-\Sigma/2)}{P_9}$	/2.6817				−.0411	−.0400	−.0400

1	2	3 (a)	3 (b)	3 (c)	4 (a)	4 (b)	4 (c)
$(C_{10}-C_{12})A_1$	0.0259	0.4711	0.4650	0.4653	0.0122	0.0120	0.0120
$(C_8-C_{14})A_3$	.0020	−.2563	−.2487	−.2488	−.0005	−.0005	−.0005
$(C_6-C_{16})A_5$	.0296	.0824	.0823	.0823	.0024	.0024	.0024
$(C_4-C_{18})A_7$	−.1353	.0182	.0169	.0169	−.0025	−.0023	−.0023
$(C_2-C_{20})A_9$	−.2375	−.0411	−.0400	−.0400	.0098	.0095	.0095
$(C_2-C_{24})A_{13}$	−.2384		.0092	.0087		−.0022	−.0021
$(C_4-C_{26})A_{15}$	−.1349		−.0201	−.0197		.0027	.0027
$(C_6-C_{28})A_{17}$	.0262		.0117	.0118		.0003	.0003
$(C_8-C_{30})A_{19}$	.0103		.0032	.0032		0	0
Σ					.0214	.0219	.0220
$\Sigma/2$					.0107	.0110	.0110
$B_{11}-\Sigma/2$	.0690				.0583	.0580	.0580
$A_{11}=\frac{(B_{11}-\Sigma/2)}{P_{11}}$	/3.0654				.0190	.0189	.0189
$(C_{12}-C_{14})A_1$	−0.0054	0.4711	0.4650	0.4653	−0.0025	−0.0025	−0.0025
$(C_{10}-C_{16})A_3$	.0273	−.2563	−.2487	−.2488	−.0070	−.0068	−.0068
$(C_8-C_{18})A_5$	.0023	.0824	.0823	.0823	.0002	.0002	.0002
$(C_6-C_{20})A_7$	.0268	.0182	.0169	.0169	.0005	.0004	.0004
$(C_4-C_{22})A_9$	−.1355	−.0411	−.0400	−.0400	.0056	.0054	.0054
$(C_2-C_{24})A_{11}$	−.2384	.0190	.0189	.0189	−.0045	−.0045	−.0045
$(C_2-C_{28})A_{15}$	−.2381		−.0201	−.0197		.0048	.0047
$(C_4-C_{30})A_{17}$	−.1273		.0117	.0118		−.0015	−.0015
$(C_6-C_{32})A_{19}$	.0255		.0032	.0032		.0001	.0001
Σ					−.0077	−.0044	−.0045
$\Sigma/2$					−.0039	−.0022	−.0022
$B_{13}-\Sigma/2$	.0278				.0317	.0300	.0300
$A_{13}=\frac{(B_{13}-\Sigma/2)}{P_{13}}$	/3.4496				.0092	.0087	.0087
$(C_{14}-C_{16})A_1$	0.0068	0.4711	0.4650	0.4653	0.0032	0.0032	0.0032
$(C_{12}-C_{18})A_3$	−.0051	−.2563	−.2487	−.2488	.0013	.0013	.0013
$(C_{10}-C_{20})A_5$	.0245	.0824	.0823	.0823	.0020	.0020	.0020
$(C_8-C_{22})A_7$	.0021	.0182	.0169	.0169	0	0	0
$(C_6-C_{24})A_9$	.0259	−.0411	−.0400	−.0400	−.0011	−.0010	−.0010
$(C_4-C_{26})A_{11}$	−.1349	.0190	.0189	.0189	−.0026	−.0026	−.0026
$(C_2-C_{28})A_{13}$	−.2381	.0092	.0087	.0087	−.0022	−.0021	−.0021
$(C_2-C_{32})A_{17}$	−.2388		.0117	.0118		−.0028	−.0028
$(C_4-C_{34})A_{19}$	−.1339		.0032	.0032		−.0004	−.0004
Σ					.0006	−.0024	−.0024
$\Sigma/2$					.0003	−.0012	−.0012
$B_{15}-\Sigma/2$	−.0768				−.0771	−.0756	−.0756
$A_{15}=\frac{(B_{15}-\Sigma/2)}{P_{15}}$	/3.8373				−.0201	−.0197	−.0197
$(C_{16}-C_{18})A_1$	−0.0065	0.4711	0.4650	0.4653	−0.0031	−0.0030	−0.0030
$(C_{14}-C_{20})A_3$	.0040	−.2563	−.2487	−.2488	−.0010	−.0010	−.0010
$(C_{12}-C_{22})A_5$	−.0053	.0824	.0823	.0823	−.0004	−.0004	−.0004
$(C_{10}-C_{24})A_7$	.0236	.0182	.0169	.0169	.0004	.0004	.0004
$(C_8-C_{26})A_9$	.0027	−.0411	−.0400	−.0400	−.0001	−.0001	−.0001
$(C_6-C_{28})A_{11}$	.0262	.0190	.0189	.0189	.0005	.0005	.0005
$(C_4-C_{30})A_{13}$	−.1273	.0092	.0087	.0087	−.0012	−.0011	−.0011
$(C_2-C_{32})A_{15}$	−.2388	−.0201	−.0197	−.0197	.0048	.0047	.0047
$(C_2-C_{36})A_{19}$	−.2380		.0032	.0032		−.0008	−.0008
Σ					−.0001	−.0008	−.0008
$\Sigma/2$					0	−.0004	−.0004
$B_{17}-\Sigma/2$	.0494				.0494	.0498	.0498
$A_{17}=\frac{(B_{17}-\Sigma/2)}{P_{17}}$	/4.2180				.0117	.0118	.0118
$(C_{18}-C_{20})A_1$	0.0037	0.4711	0.4650	0.4653	0.0017	0.0017	0.0017
$(C_{16}-C_{22})A_3$	−.0067	−.2563	−.2487	−.2488	.0017	.0017	.0017
$(C_{14}-C_{24})A_5$	.0031	.0824	.0823	.0823	.0003	.0003	.0003
$(C_{12}-C_{26})A_7$	−.0047	.0182	.0169	.0169	−.0001	−.0001	−.0001
$(C_{10}-C_{28})A_9$	.0239	−.0411	−.0400	−.0400	−.0010	−.0010	−.0010
$(C_8-C_{30})A_{11}$	.0103	.0190	.0189	.0189	.0002	.0002	.0002
$(C_6-C_{32})A_{13}$	.0255	.0092	.0087	.0087	.0002	.0002	.0002
$(C_4-C_{34})A_{15}$	−.1339	−.0201	−.0197	−.0197	.0027	.0026	.0026
$(C_2-C_{36})A_{17}$	−.2380	.0117	.0118	.0118	−.0028	−.0028	−.0028
Σ					.0029	.0028	.0028
$\Sigma/2$					.0015	.0014	.0014
$B_{19}-\Sigma/2$	.0160				.0145	.0146	.0146
$A_{19}=\frac{(B_{19}-\Sigma/2)}{P_{19}}$	/4.6014				.0032	.0032	.0032

TABLE VIII.—COMPUTATION OF LOAD DISTRIBUTIONS

	20	18	16	14	12	10	8	6	4	2
θ, degrees	90	81	72	63	54	45	36	27	18	9
Sin θ	1.0000	0.9877	0.9511	0.8910	0.8090	0.7071	0.5878	0.4540	0.3090	0.1564
Sin 3θ	−1.0000	−.8910	−.5878	−.1564	.3090	.7071	.9511	.9877	.8090	.4540
Sin 5θ	1.0000	.7071	0	−.7071	−1.0000	−.7071	0	.7071	1.0000	.7071
Sin 7θ	−1.0000	−.4540	.5878	.9877	.3090	−.7071	−.9511	−.1564	.8090	.8910
Sin 9θ	1.0000	.1564	−.9511	−.4540	.8090	.7071	−.5878	−.8910	.3090	.9877
Sin 11θ	−1.0000	.1564	.9511	−.4540	−.8090	.7071	.5878	−.8910	−.3090	.9877
Sin 13θ	1.0000	−.4540	−.5878	.9877	−.3090	−.7071	.9511	−.1564	−.8090	.8910
Sin 15θ	−1.0000	.7071	0	−.7071	1.0000	−.7071	0	.7071	−1.0000	.7071
Sin 17θ	1.0000	−.8910	.5878	−.1564	−.3090	.7071	−.9511	.9877	−.8090	.4540
Sin 19θ	−1.0000	.9877	−.9511	.8910	−.8090	.7071	−.5878	.4540	−.3090	.1564
$A_1 \sin \theta$	.4653	.4596	.4425	.4146	.3764	.3290	.2735	.2112	.1438	.0728
$A_3 \sin 3\theta$	.2488	.2217	.1462	.0389	−.0769	−.1759	−.2366	−.2457	−.2013	−.1129
$A_5 \sin 5\theta$	.0823	.0582	0	−.0582	−.0823	−.0582	0	.0582	.0823	.0582
$A_7 \sin 7\theta$	−.0169	−.0077	.0099	.0167	.0052	−.0120	−.0161	−.0026	.0137	.0151
$A_9 \sin 9\theta$	−.0400	−.0063	.0381	.0182	−.0324	−.0283	.0235	.0357	−.0124	−.0396
$A_{11} \sin 11\theta$	−.0189	.0030	.0180	−.0086	−.0153	.0134	.0111	−.0168	−.0058	.0187
$A_{13} \sin 13\theta$	.0087	−.0039	−.0051	.0086	−.0027	−.0061	.0083	−.0014	−.0070	.0077
$A_{15} \sin 15\theta$	.0197	−.0139	0	.0139	−.0197	.0139	0	−.0139	.0197	−.0139
$A_{17} \sin 17\theta$	.0118	−.0105	.0069	−.0018	−.0037	.0084	−.0112	.0117	−.0096	.0054
$A_{19} \sin 19\theta$	−.0032	.0031	−.0030	.0028	−.0026	.0022	−.0019	.0014	−.0010	.0005
$\Sigma A_n \sin n\theta$	.7576	.7033	.6535	.4451	.1460	.0864	.0506	.0378	.0224	.0120
$m_s c_s / c$	5.670	6.152	6.708	7.337	8.029	8.772	9.520	10.331	12.760	23.100
$c_l = m_s c_s / c \times \Sigma()$	4.296	4.327	4.384	3.266	1.172	.7579	.4817	.3905	.2858	.2772
$A_1 \sin \theta$	.4653	.4596	.4425	.4146	.3764	.3290	.2735	.2112	.1438	.0728
$3A_3 \sin 3\theta$	.7463	.6650	.4387	.1167	−.2306	−.5277	−.7098	−.7371	−.6038	−.3388
$5A_5 \sin 5\theta$	.4115	.2910	0	−.2910	−.4115	−.2910	0	.2910	.4115	.2910
$7A_7 \sin 7\theta$	−.1184	−.0538	.0696	.1170	.0366	−.0837	−.1126	−.0185	.0958	.1055
$9A_9 \sin 9\theta$	−.3604	−.0564	.3428	.1636	−.2916	−.2549	.2119	.3212	−.1114	−.3560
$11A_{11} \sin 11\theta$	−.2078	.0325	.1976	−.0943	−.1681	.1469	.1221	−.1851	−.0642	.2052
$13A_{13} \sin 13\theta$	.1130	−.0513	−.0664	.1116	−.0349	−.0799	.1074	−.0177	−.0914	.1007
$15A_{15} \sin 15\theta$	.2957	−.2091	0	.2091	−.2957	.2091	0	−.2091	.2957	−.2091
$17A_{17} \sin 17\theta$	.2009	−.1790	.1181	−.0314	−.0621	.1421	−.1911	.1985	−.1626	.0912
$19A_{19} \sin 19\theta$	−.0602	.0595	−.0573	.0537	−.0487	.0426	−.0354	.0273	−.0186	.0094
$\Sigma n A_n \sin n\theta$	1.4859	.9580	1.4856	.7696	−1.1302	−.3675	−.3340	−.1183	−.1052	−.0281
$m_s c_s / 4b \times \Sigma() / \sin \theta$	.2852	.1839	.2851	.1477	−.2169	−.0705	−.0641	−.0227	−.0202	−.0054
$c_{d_i} = c_l \left[\frac{m_s c_s}{4b} \times \frac{\Sigma()}{\sin \theta} \right]$	1.2252	.7957	1.2499	.4824	−.2542	−.0534	−.0309	−.0089	−.0058	−.0015

REPORT No. 586

AIRFOIL SECTION CHARACTERISTICS AS AFFECTED BY VARIATIONS OF THE REYNOLDS NUMBER

By Eastman N. Jacobs and Albert Sherman

SUMMARY

An investigation of a systematically chosen representative group of related airfoils was made in the N. A. C. A. variable-density wind tunnel over a wide range of the Reynolds Number extending well into the flight range. The tests were made to provide information from which the variations of airfoil section characteristics with changes in the Reynolds Number could be inferred and methods of allowing for these variations in practice could be determined. This work is one phase of an extensive and general airfoil investigation being conducted in the variable-density tunnel and extends the previously published researches concerning airfoil characteristics as affected by variations in airfoil profile determined at a single value of the Reynolds Number.

The object of this report is to provide means for making available as section characteristics at any free-air value of the Reynolds Number the variable-density-tunnel airfoil data previously published. Accordingly, the various corrections involved in deriving more accurate airfoil section characteristics than those heretofore employed are first considered at length and the corrections for turbulence are explained. An appendix is included that covers the results of an investigation of certain consistent errors present in test results from the variable-density tunnel. The origin and nature of scale effects are discussed and the airfoil scale-effect data are analyzed. Finally, methods are given of allowing for scale effects on airfoil section characteristics in practice within ordinary limits of accuracy for the application of variable-density-tunnel airfoil data to flight problems.

INTRODUCTION

When data from a model test are applied to a flight problem, the condition that should be satisfied is that the flows for the two cases be similar. The Reynolds Number, which indicates the ratio of the mass forces to the viscous forces in aerodynamic applications, is ordinarily used as the criterion of similarity. The practical necessity for having the flow about the model aerodynamically similar to the flow about the full-scale object in flight becomes apparent from the fact that aerodynamic coefficients, as a rule, vary with changes in the Reynolds Number. This phenomenon is referred to as "scale effect."

Early investigations of scale effect were made in small atmospheric tunnels at comparatively low values of the Reynolds Number and, for airfoils, covered a range of the Reynolds Number too limited and too remote from the full-scale range to permit reliable extrapolations to flight conditions. Attempts were made to bridge the gap between the two Reynolds Number ranges by making full-scale flight tests for comparison with model tests. These investigations of scale effect, however, proved disappointing owing partly to the difficulty of obtaining good flight tests and to the difficulty of reproducing flight conditions in the model tests and partly to the large unexplored Reynolds Number range between the model and flight tests with consequent uncertainties regarding the continuity of the characteristics over this range. Furthermore, the flight tests could not ordinarily include a sufficiently large range of the Reynolds Number to establish the character of the scale effects for certain of the airfoil characteristics over the full-scale range of the Reynolds Number, which may extend from values as low as a few hundred thousand to thirty million or more.

These limitations of the early investigations were first overcome by the N. A. C. A. through the use of the variable-density tunnel, which was designed to facilitate aerodynamic investigations over the entire range of Reynolds Numbers between the wind tunnel and flight values. Several miscellaneous and commonly used airfoils were investigated for scale effect in the variable-density tunnel during the first years of its operation. The results indicated that important scale effects for some airfoils may be expected above the usual wind-tunnel range and even within the flight range of values of the Reynolds Number. Later, when the N. A. C. A. full-scale tunnel was constructed, airfoil tests therein served to confirm the importance of scale effects occurring in the full-scale range and also provided valuable data for the interpretation of the variable-density-tunnel results, particularly in connection with the effects of the turbulence present in the

variable-density tunnel. The interpretation of the variable-density-tunnel results has consequently been modified to allow for the turbulence on the basis of an "effective Reynolds Number" higher than the test Reynolds Number.

In the meantime, the investigations of airfoils in the variable-density tunnel had been turned to an extensive study of airfoil characteristics as affected by airfoil shape. This phase, which resulted in the development of the well-known N. A. C. A. airfoils, involved the testing of a large number of related airfoils, but these tests were largely confined to one value of the Reynolds Number within the full-scale range. Such a procedure expedited the investigation and provided comparable data for the various airfoils within the full-scale range of the Reynolds Number but, of course, gave no information about scale effects.

As previously stated, the full-scale-tunnel results had provided information regarding the application of the variable-density-tunnel data to flight. Methods were accordingly developed for correcting the data and for presenting them in forms that would facilitate their use as applied to flight problems. Flight problems, however, require airfoil data at various values of the Reynolds Number between values as low as a few hundred thousand in some cases to thirty million or more in others. Obviously the results available from the tests of related airfoils at one value of the Reynolds Number (effective Reynolds Number=8,000,000) are inadequate for the purpose unless they can be corrected to other values of the Reynolds Number. The present investigation was therefore undertaken to study the scale effects for the related airfoil sections primarily with a view to the formulation of general methods for determining scale-effect corrections for any normal airfoil section so that the standard test results from the variable-density tunnel could be applied to flight at any Reynolds Number. For most practical uses it is considered desirable and sufficient to present airfoil test results in the form of tabular values giving certain important aerodynamic characteristics for each *airfoil section*. The primary object of this investigation, therefore, is to give information about the variation of these important airfoil section characteristics with Reynolds Number.

In regard to the scope of the experimental investigation, the Reynolds Number range was chosen as the largest possible in the variable-density tunnel and the airfoil sections were chosen to cover as far as possible the range of shapes commonly employed. Accordingly, groups of related airfoils (fig. 1) were tested to investigate the following variables related to the airfoil-section shape:

Thickness.
Camber.
Thickness and camber.
Thickness shape.
Camber shape.
Sections with high-lift devices.

The testing program was begun in May 1934 and extended several times as it became apparent that additional tests would be desirable. The final tests in the variable-density tunnel were made in September 1935.

TESTS AND MODELS

Descriptions of the variable-density wind tunnel and of the methods of testing are given in reference 1.

The tests herein reported were made for the most part for each airfoil at tank pressures of 1/4, 1/2, 1, 2, 4, 8, 15, and 20 atmospheres, covering a range of test Reynolds Numbers from 40,000 to 3,100,000. The 1/4- and 1/2-atmosphere runs were omitted for many of the airfoils and, in several cases, only the lift-curve peaks were obtained at the lower Reynolds Numbers. Runs at reduced speeds (1/5 and 1/2 the standard value of the dynamic pressure q) at 20 atmospheres were sometimes substituted for the tests at 8 and 15 atmospheres. Several check tests at 8 and 15 atmospheres and results from some earlier investigations have shown that the specific manner of varying the Reynolds Number with respect to speed or density is unimportant when the effects of compressibility are negligible. For all the airfoils, the air in the tunnel was decompressed and the airfoil repolished before running the higher Reynolds Number tests. Tares obtained at corresponding Reynolds Numbers were used in working up the results.

The airfoil models are of metal, usually of duralumin and of standard 5- by 30-inch plan form; the sections employed (see fig. 1), except for the slotted Clark Y, are members of N. A. C. A. airfoil families (references 2 and 3). The slotted Clark Y model is of 36-inch span and 6-inch chord (with the slot closed) and was made to the ordinates given in reference 4. For this airfoil, the coefficients are given as based on the chord and area corresponding to the slot-closed condition. The slat was made of stainless steel and fastened to the main wing in the position reported (reference 4) to result in the highest value of maximum lift coefficient. This model was tested at a much earlier date than the others, and the test data are somewhat less accurate. The main wing of the N. A. C. A. 23012 airfoil with external-airfoil flap is of 30-inch span and 4.167-inch chord. The flap is of stainless steel and is also of N. A. C. A. 23012 section having a chord of 20 percent that of the main airfoil. It was fastened to the main wing in the optimum hinge position reported in reference 5. Data for this airfoil combination are given herein for two angular flap settings: −3°, which corresponds to the minimum-drag condition; and 30°, which corresponds to the maximum-lift condition. The coefficients are given as based on the sums of the main wing and flap chords and areas.

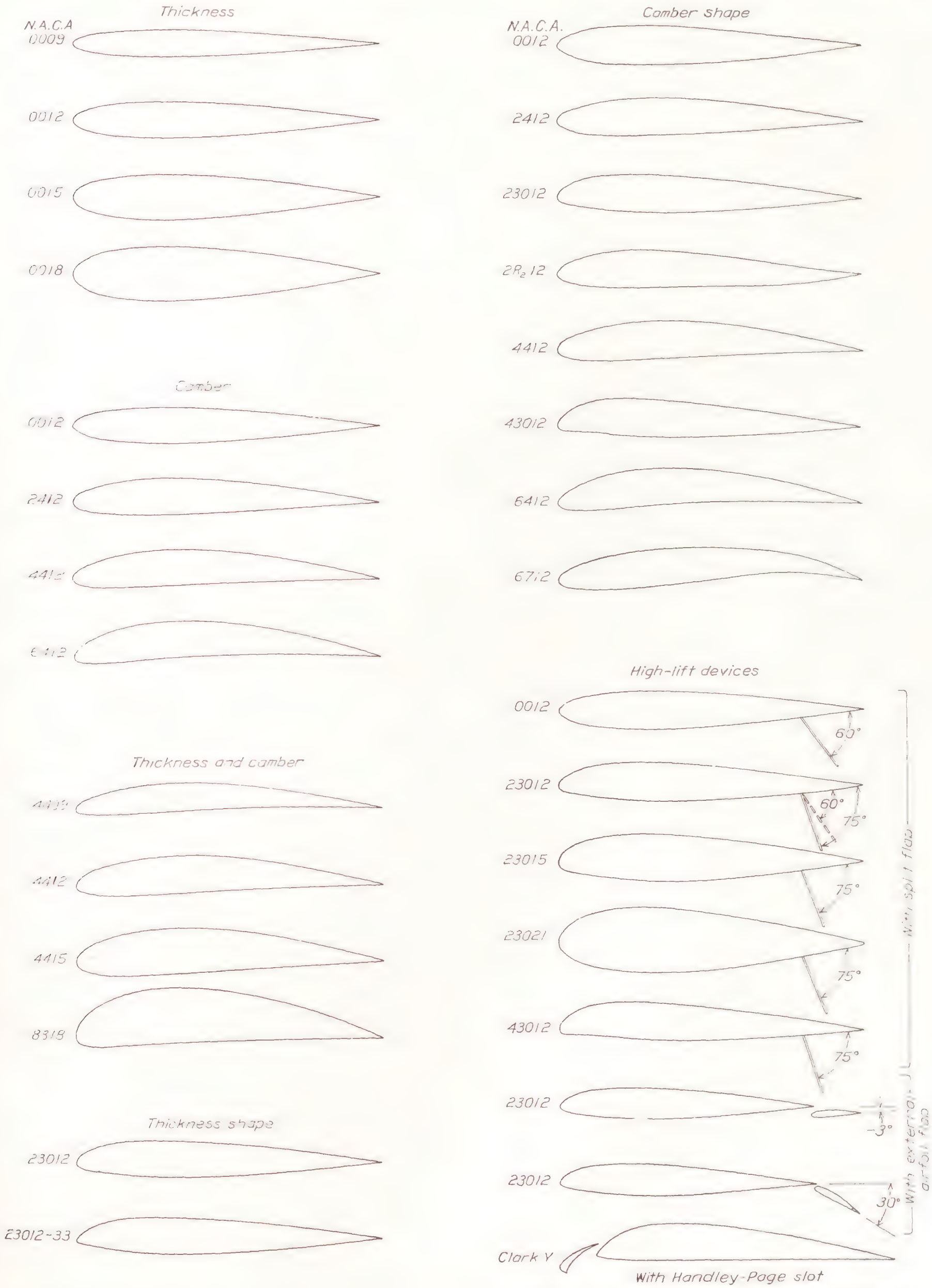

FIGURE 1.—Airfoil sections employed for the scale-effect investigation. The sections, except for the slotted Clark Y, are members of N. A. C. A. airfoil families

ACCURACY

The accuracy of the experimental data of this investigation at the highest Reynolds Number is comparable with that of the standard airfoil test data as discussed in reference 2. The systematic errors of measurement therein mentioned, however, have since been investigated and the results are presented in the appendix to this report. The systematic errors of velocity measurement have hence been eliminated, the errors associated with support deflection have been largely removed, and the errors associated with model roughness have been minimized by giving careful attention to the model surfaces.

The remaining systematic errors are mainly those associated with the interpretation of the wind-tunnel results rather than the direct errors of measurement. These errors are associated, first, with the calculation of airfoil *section* characteristics from the tests of finite-aspect-ratio airfoils and, second, with the correction of the test results to zero turbulence or free-air conditions. Such errors will be more fully treated in the discussion where the methods of correction, including the interpretation of the results as involving the effective Reynolds Number, are considered.

The magnitude of the direct experimental errors, particularly of the accidental errors, increases as the Reynolds Number is reduced. Any variation of the support interference with the Reynolds Number was not taken into account in spite of the fact that the test results tend to indicate that the uncorrected part (see appendix) of the support interference may cease to be negligible at low test Reynolds Numbers. These errors may be judged by a study of the dissymmetry of the test results for positive and negative angles of attack for the symmetrical airfoils and by the scattering of the points representing the experimental data. (See figs. 2 to 24.) Such a study indicates that the results from tests at tank pressures at and above 4 atmospheres (effective Reynolds Numbers above 1,700,000) are of the same order of accuracy as those from the highest Reynolds Number tests. The drag and pitching-moment results for effective Reynolds Numbers below 800,000, however, become relatively inaccurate owing to limitations imposed by the sensitivity of the measuring equipment. In fact, it appears that the accuracy becomes insufficient to define with certainty the shapes of curves representing variations of these quantities with angle of attack or lift coefficient. Hence airfoil characteristics dependent on the shape of such curves, e. g., the optimum lift coefficient and the aerodynamic-center position, are considered unreliable and in most cases are not presented below an effective Reynolds Number of 800,000.

RESULTS

Figures 2 to 24 present the test results corrected after the methods given in reference 1 for approximating infinite-aspect-ratio characteristics. Curves are given (for each airfoil for different test Reynolds Numbers) of lift coefficient C_L against effective angle of attack α_0, and of profile-drag coefficient C_{D_0} and of pitching-moment coefficient about the aerodynamic center $C_{m_{a.c.}}$ against lift coefficient C_L. The x and y coordinates of the aerodynamic center from the airfoil quarter-chord point are also given where the data permit. Although not precisely *section characteristics*, characteristics so corrected have been used heretofore as section characteristics because of the lack of anything more exact.

Further corrections, however, to allow for the effects of wind-tunnel turbulence, airfoil-tip shape, and some of the limitations of the previous corrections based on airfoil theory were developed during the course of this investigation and, when applied, give results representing the most reliable section data now available from the variable-density wind tunnel. These additional corrections and their derivation are fully discussed later in this report. The more exact *section* characteristics have been distinguished by lower-case symbols, e. g., section lift coefficient c_l, section profile-drag coefficient c_{d_0}, section optimum lift coefficient $c_{l_{opt}}$, and section pitching-moment coefficient about the aerodynamic center $c_{m_{a.c.}}$. These values are then considered applicable to flight at the effective Reynolds Number, R_e.

Table I presents, for various Reynolds Numbers, the principal aerodynamic characteristics, in the form of these fully corrected section characteristics, of the airfoils tested. Cross plots of certain of these section characteristics against Reynolds Number are also given for use with the discussion. (See fig. 28 and figs. 32 to 43.)

DISCUSSION

Scale effects, or the variations of aerodynamic coefficients with Reynolds Number, have previously been considered of primary importance only in relation to the interpretation of low-scale test results from atmospheric wind tunnels. It now appears from variable-density and full-scale-tunnel data that important variations of the coefficients must be recognized within the flight range of values of the Reynolds Number, particularly in view of the fact that the flight range is continually being increased.

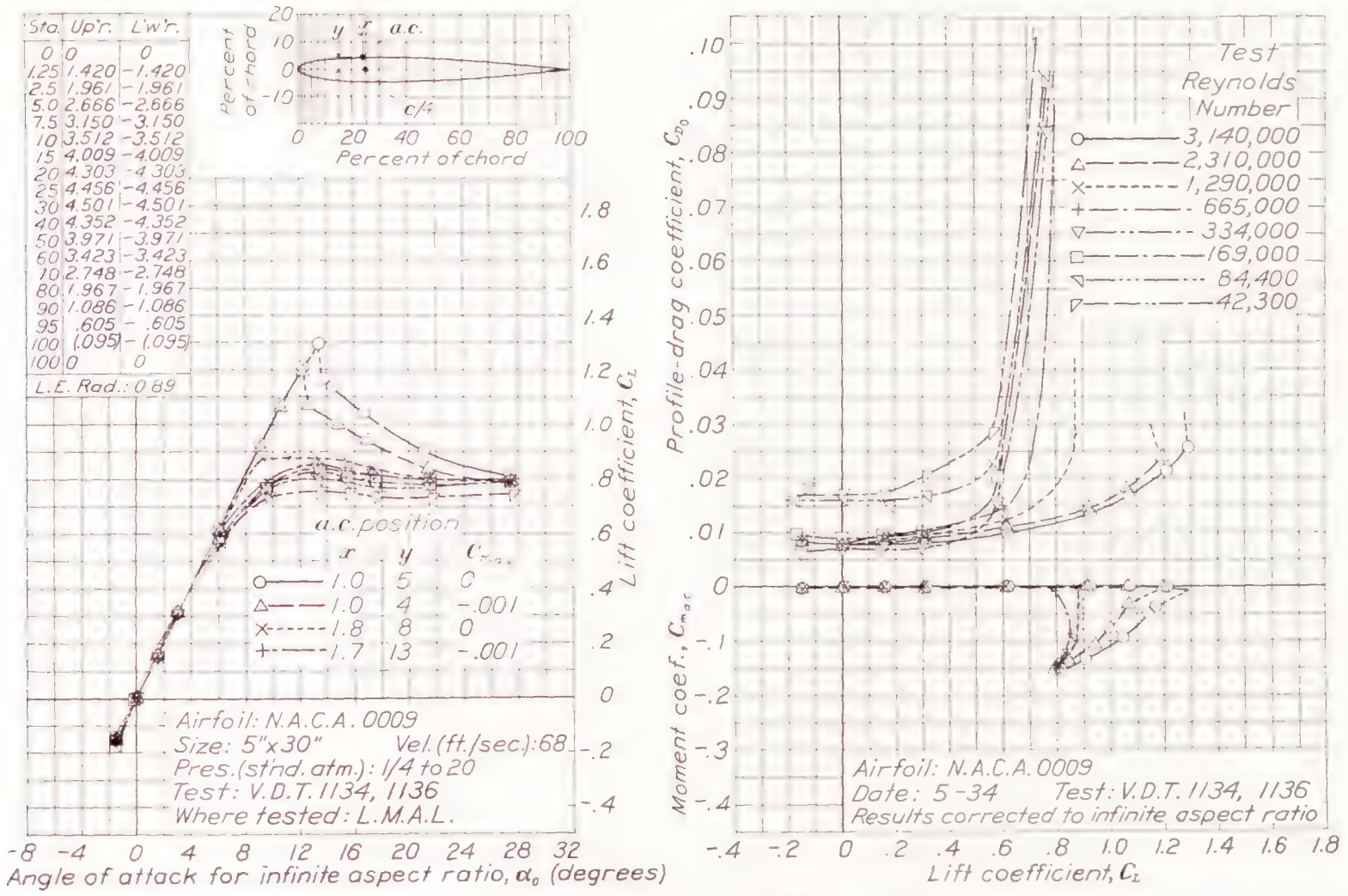

FIGURE 2.—N. A. C. A. 0009.

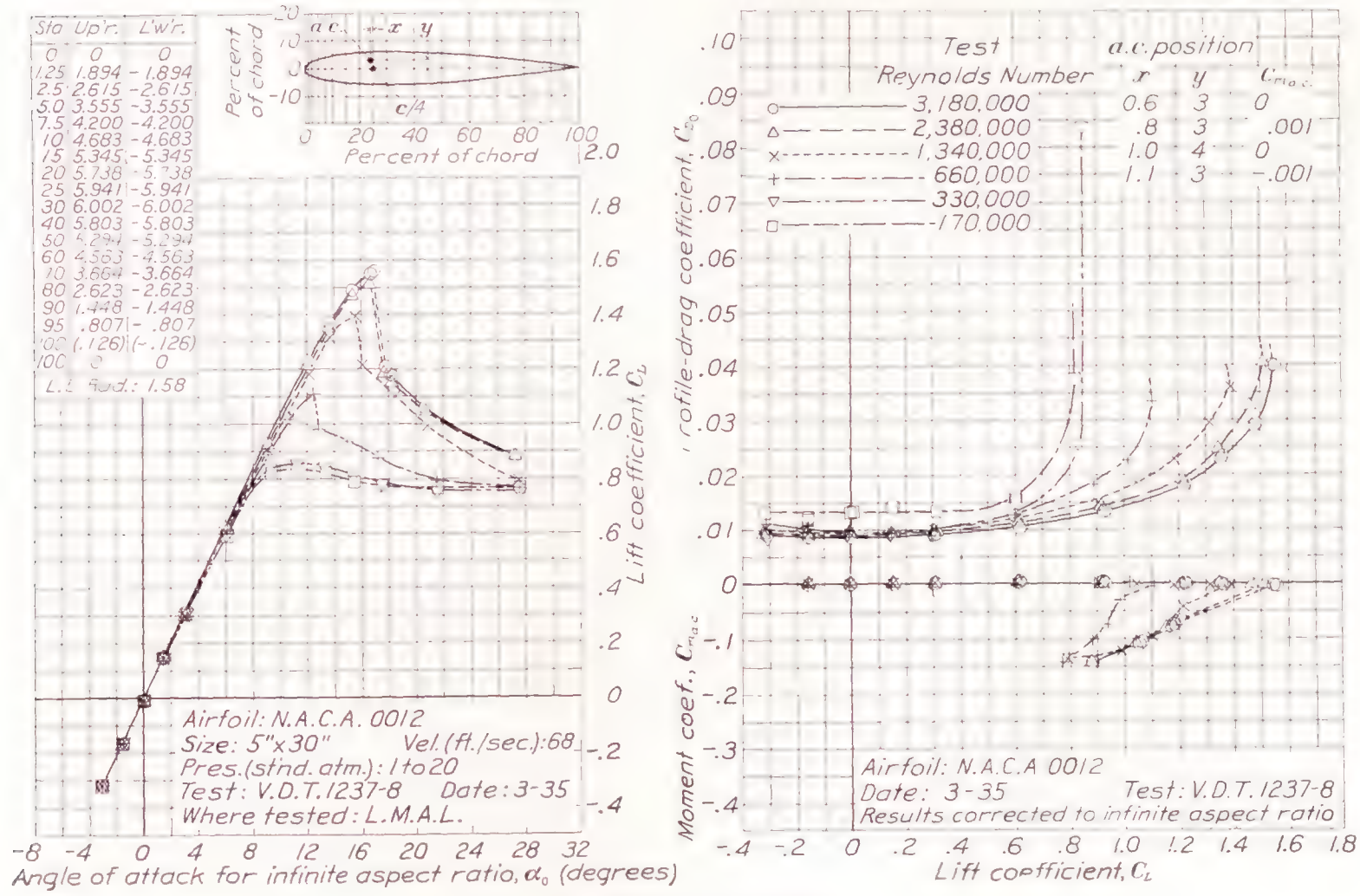

FIGURE 3.—N. A. C. A. 0012.

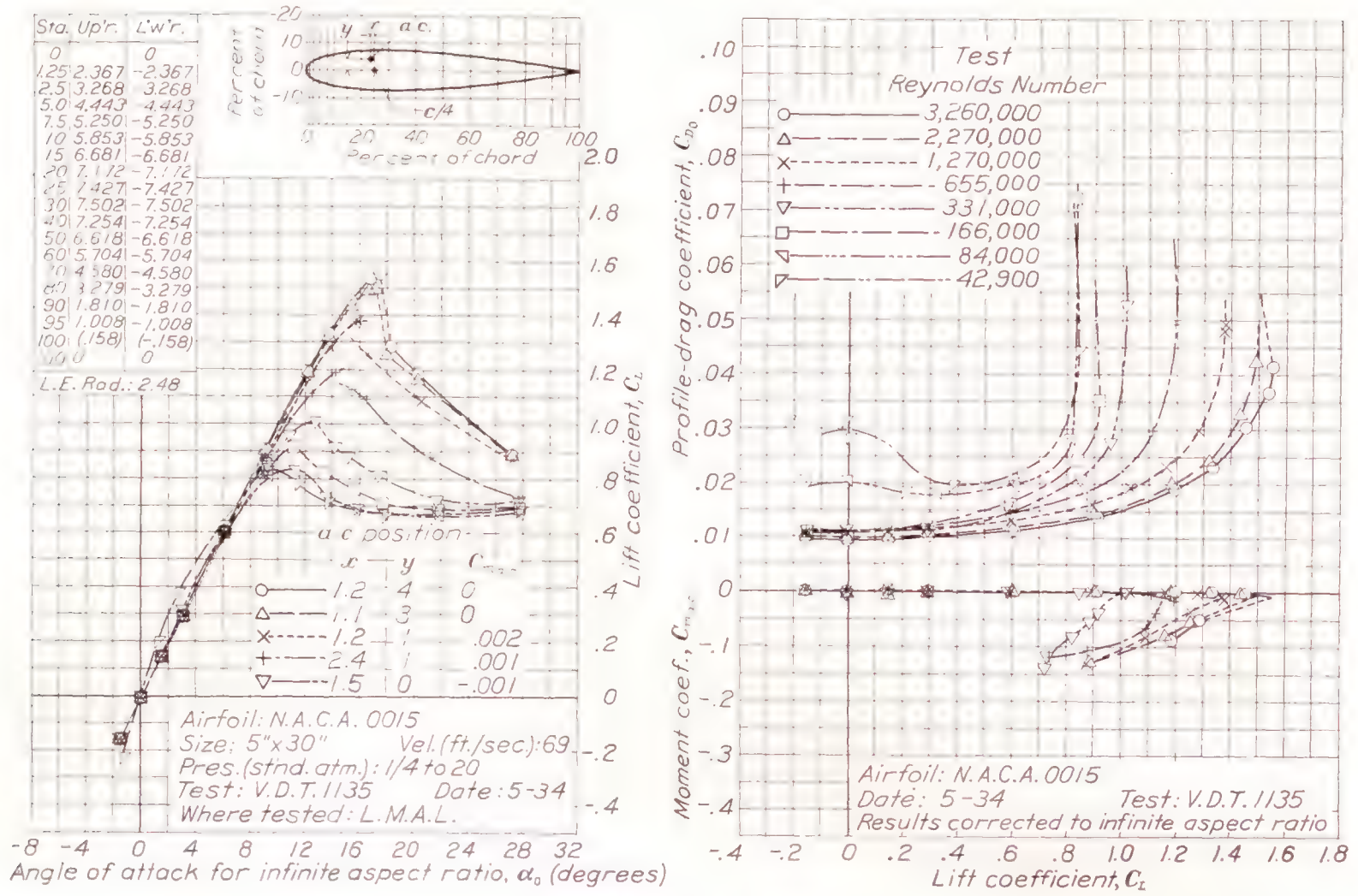

FIGURE 4.—N. A. C. A. 0015.

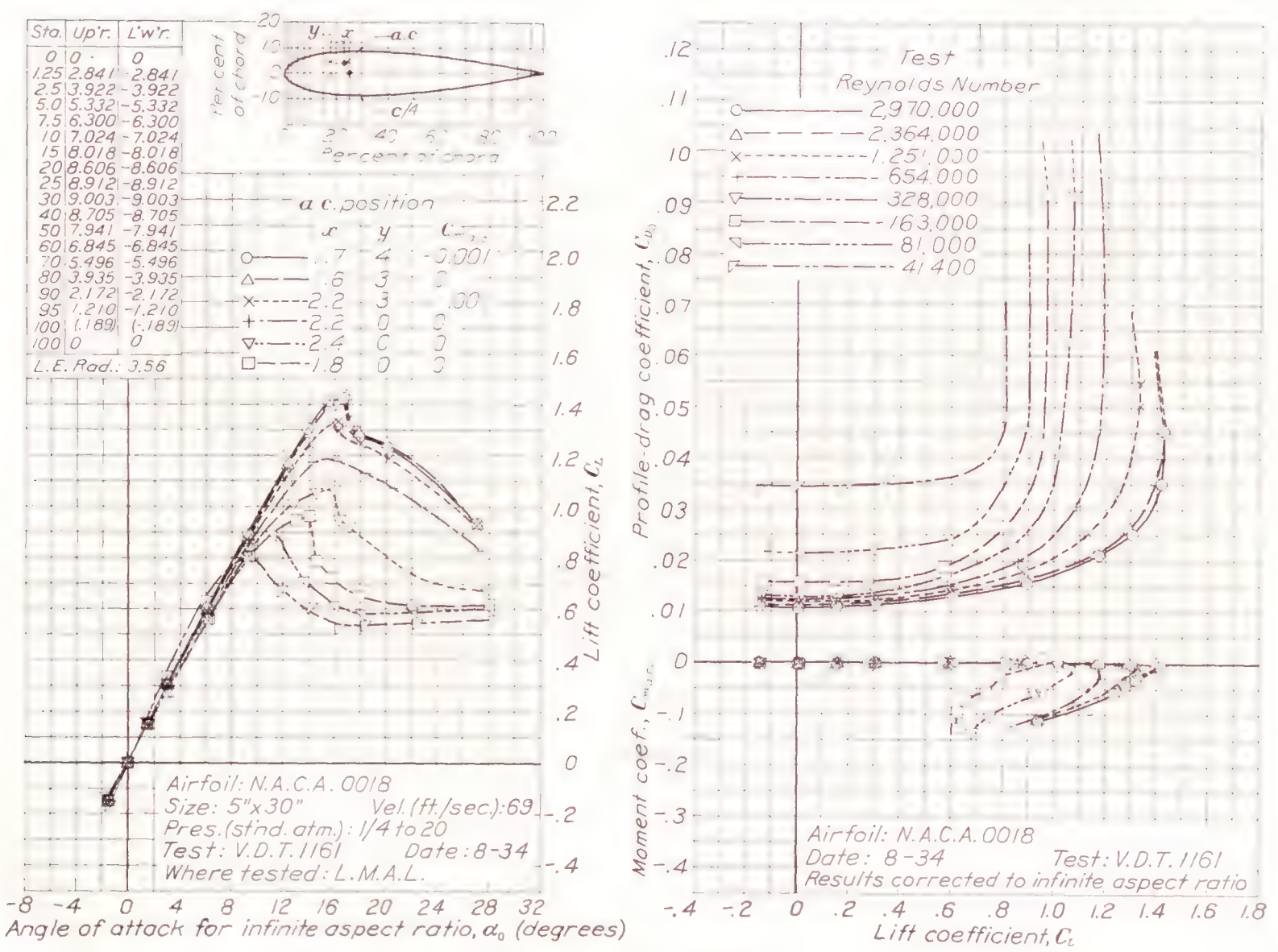

FIGURE 5.—N. A. C. A. 0018.

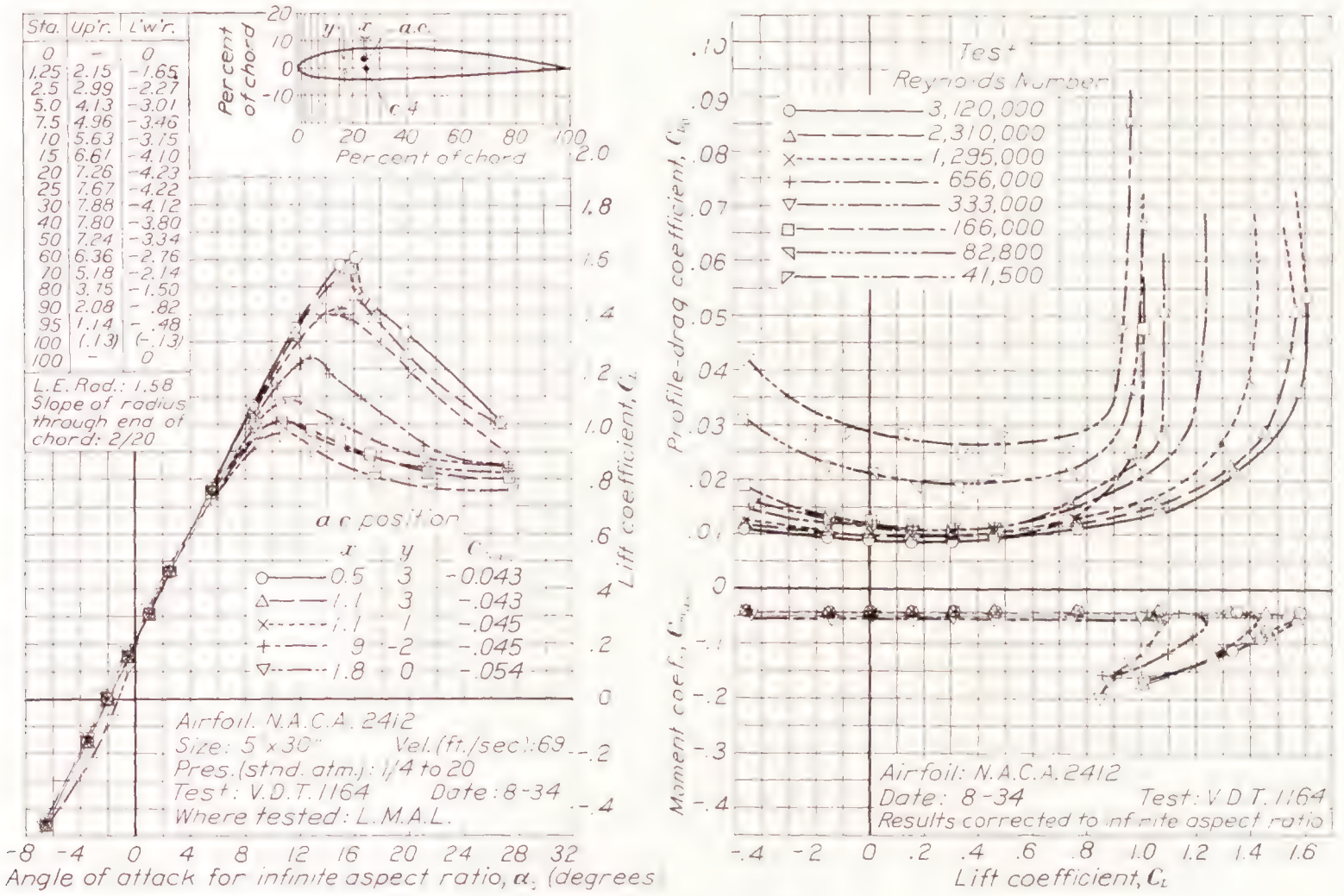

FIGURE 6.—N. A. C. A. 2412.

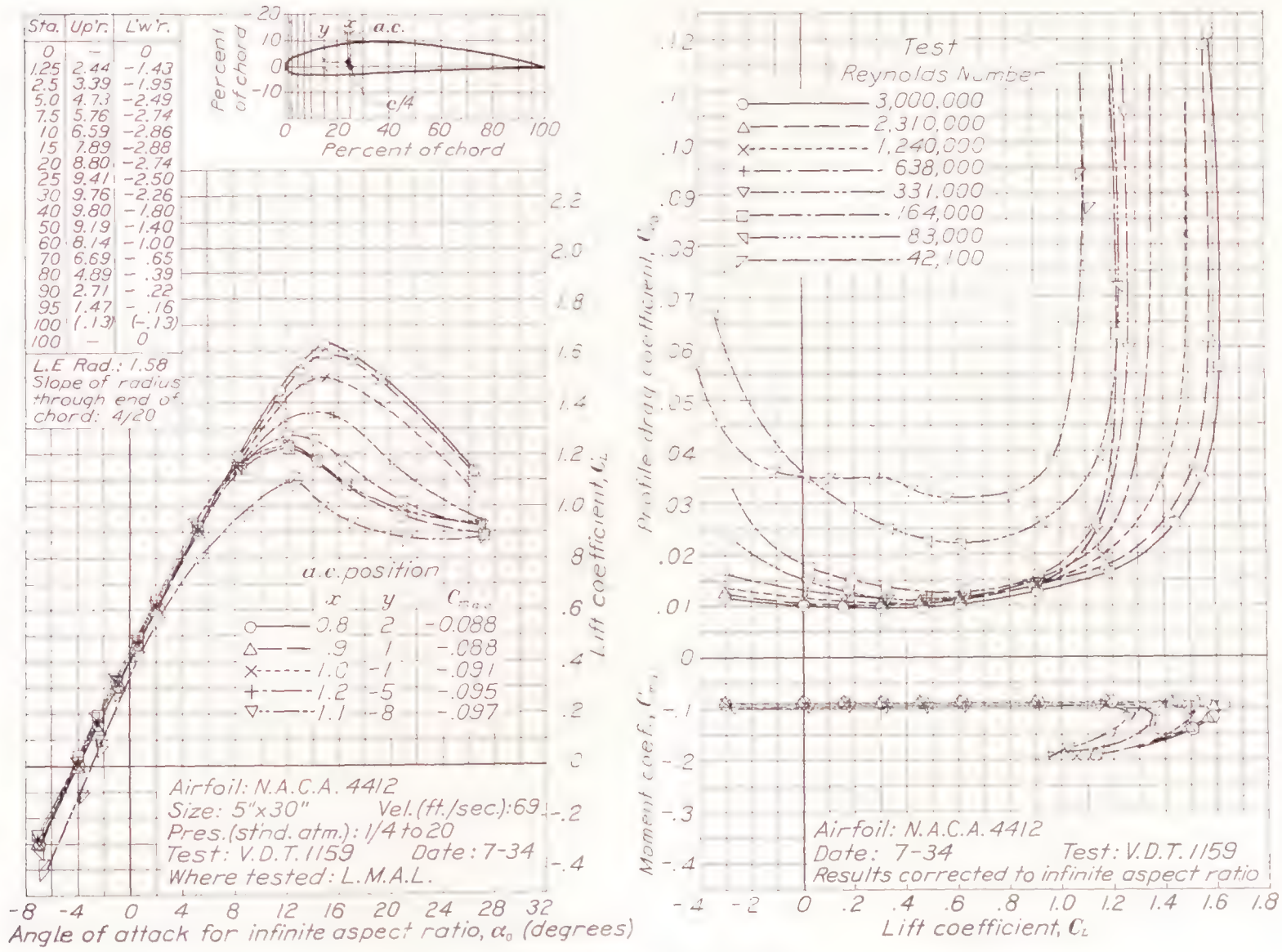

FIGURE 7.—N. A. C. A. 4412.

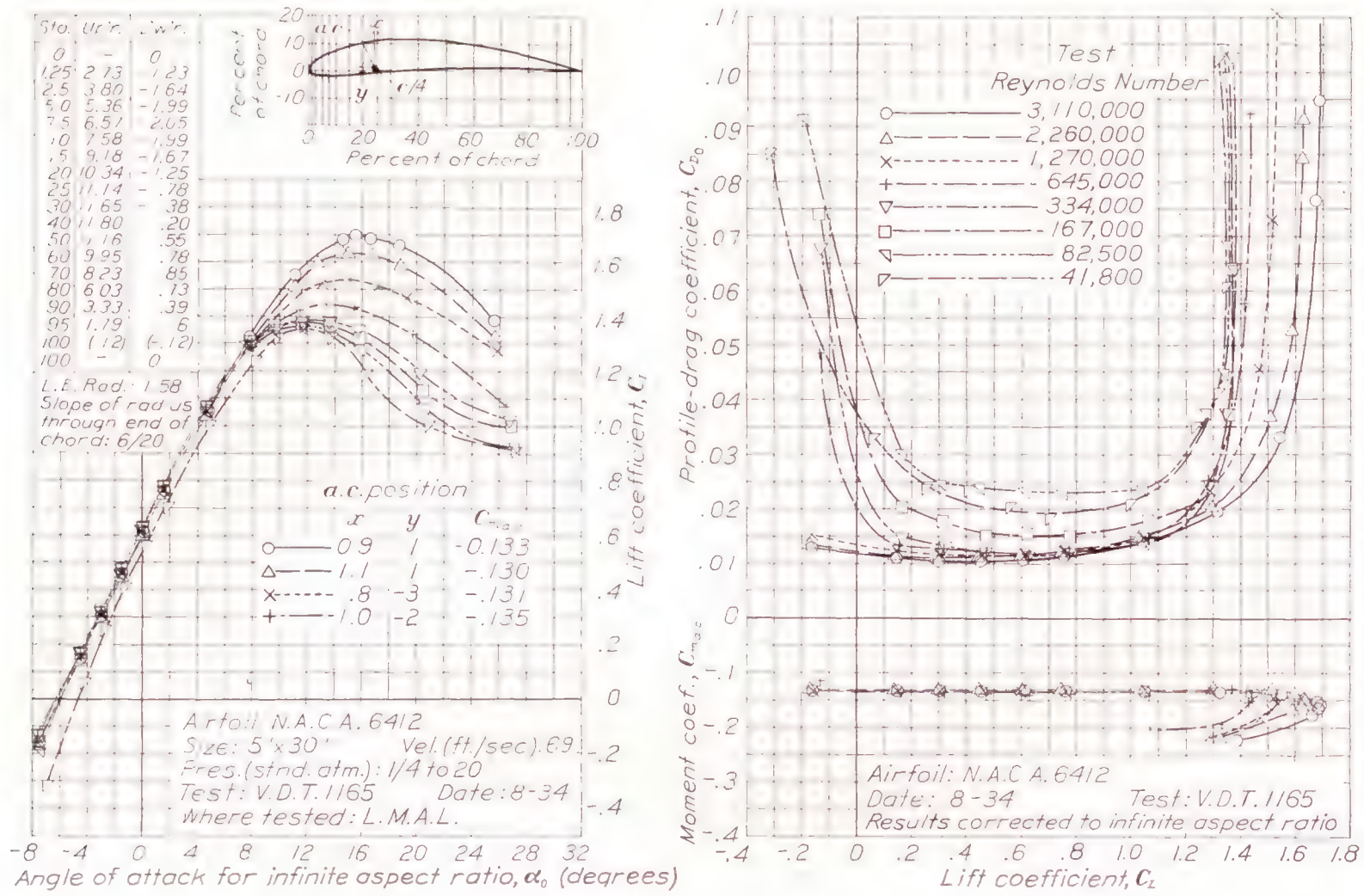

FIGURE 8.—N. A. C. A. 6412.

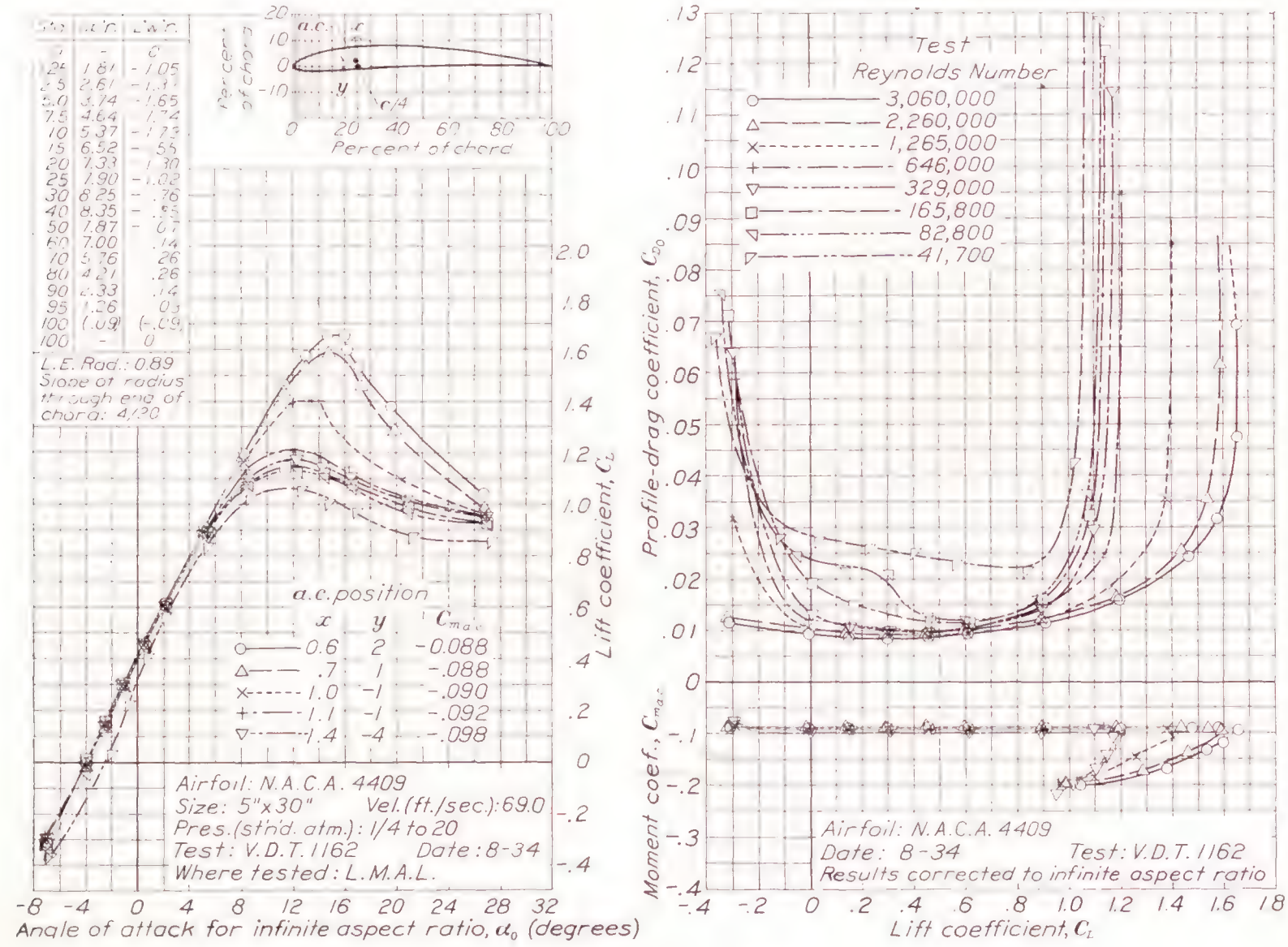

FIGURE 9.—N. A. C. A. 4409.

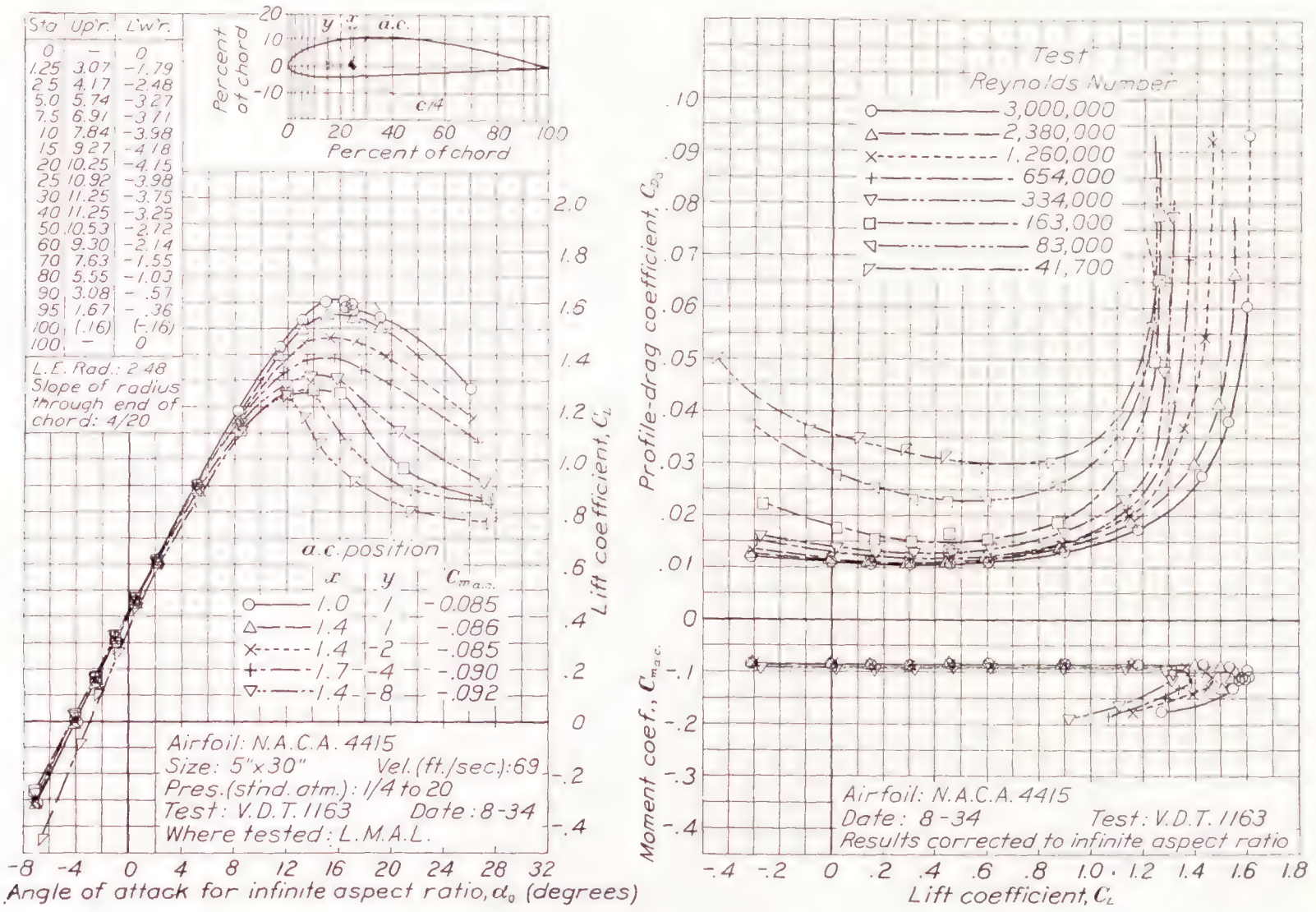

FIGURE 10.—N. A. C. A. 4415.

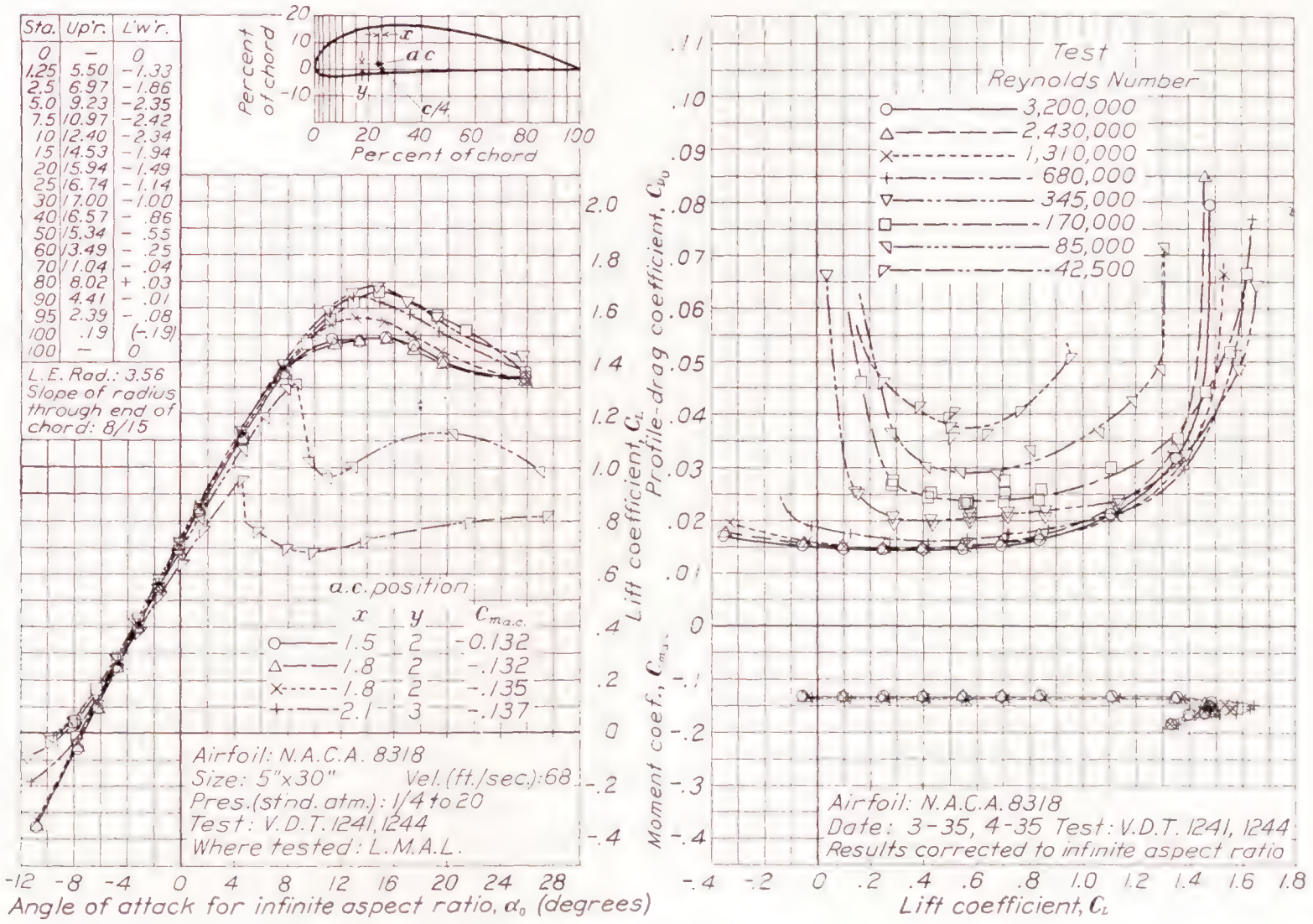

FIGURE 11.—N. A. C. A. 8318.

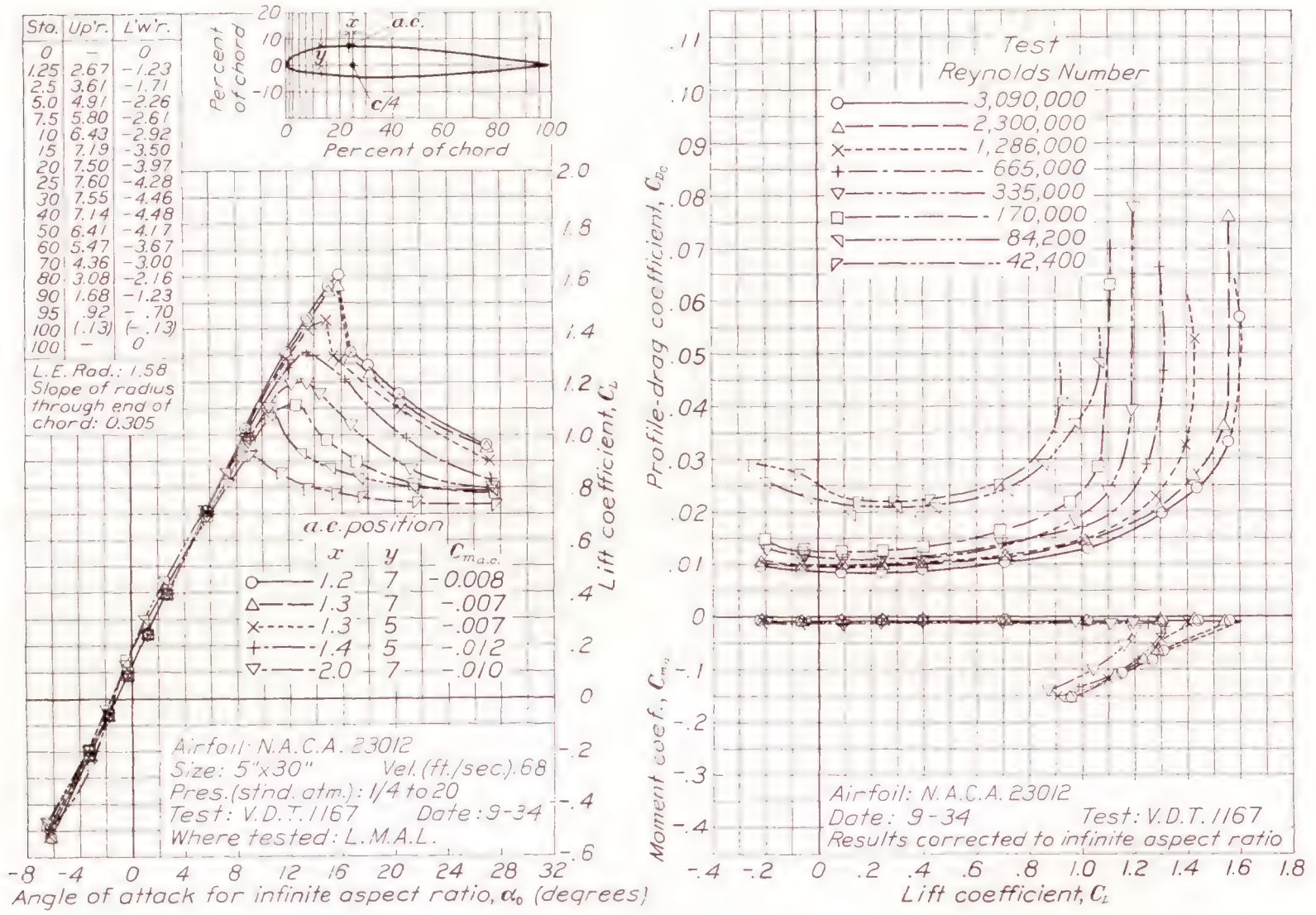

FIGURE 12.—N. A. C. A. 23012.

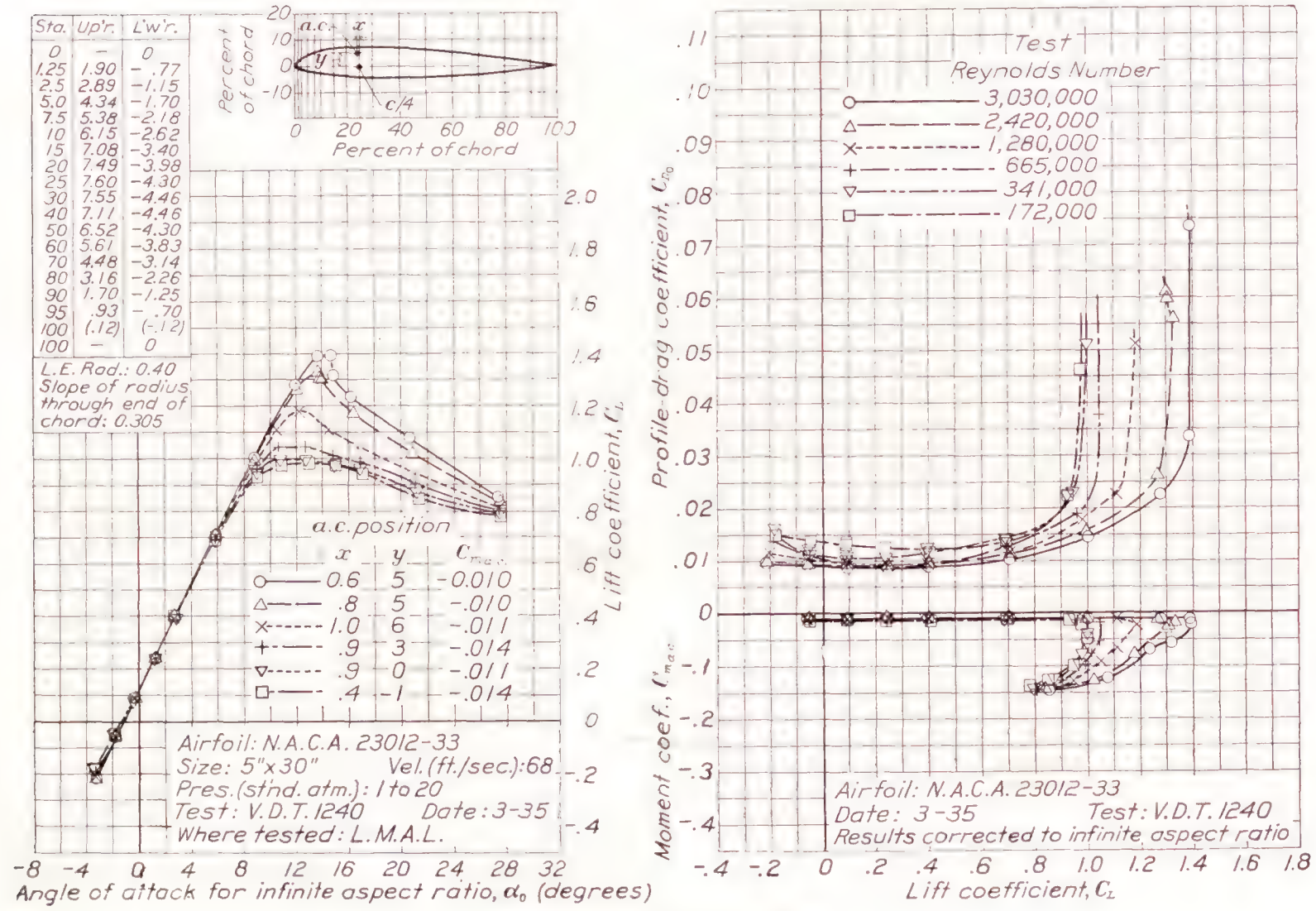

FIGURE 13.—N. A. C. A. 23012-33.

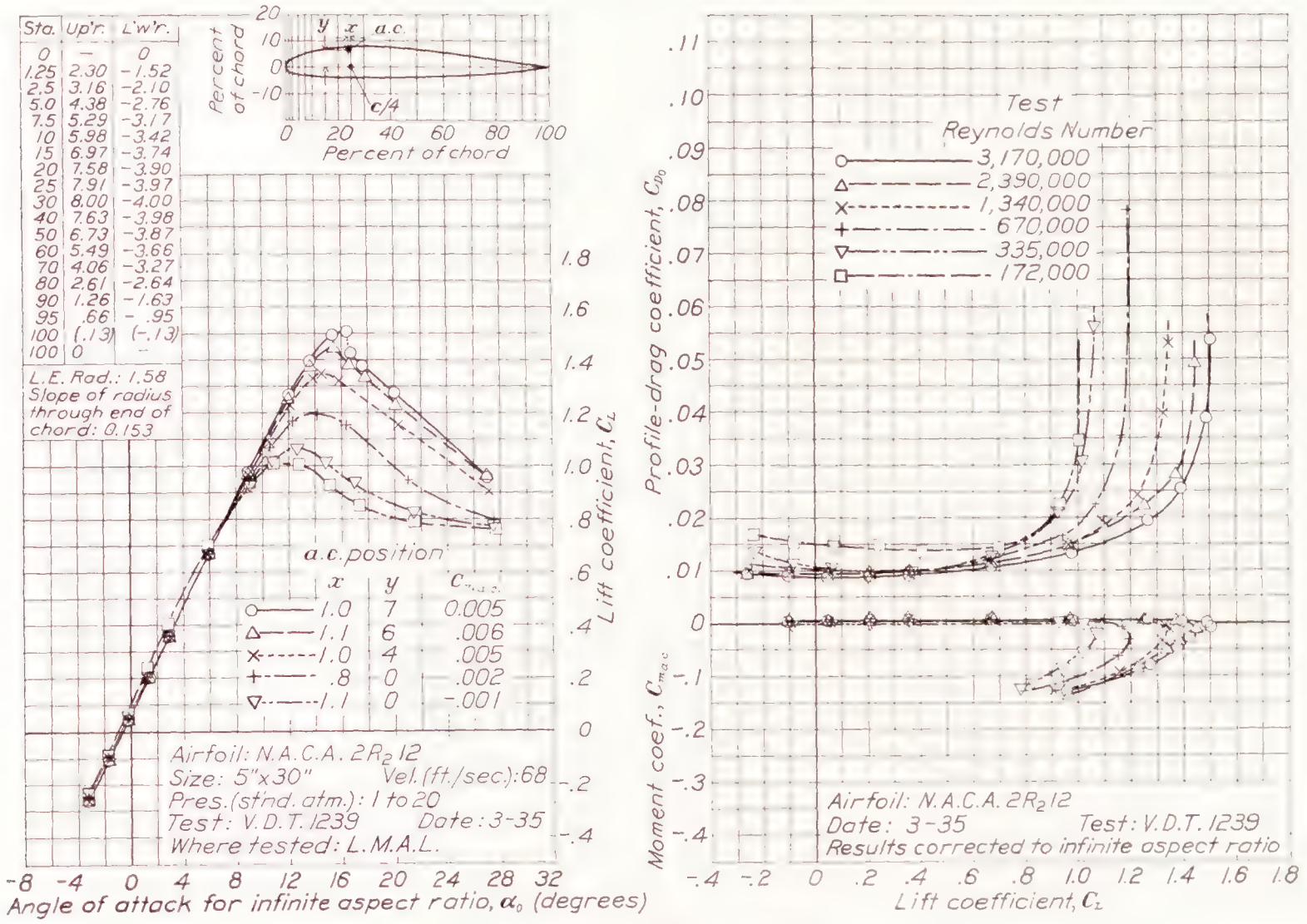

FIGURE 14.—N. A. C. A. 2R212.

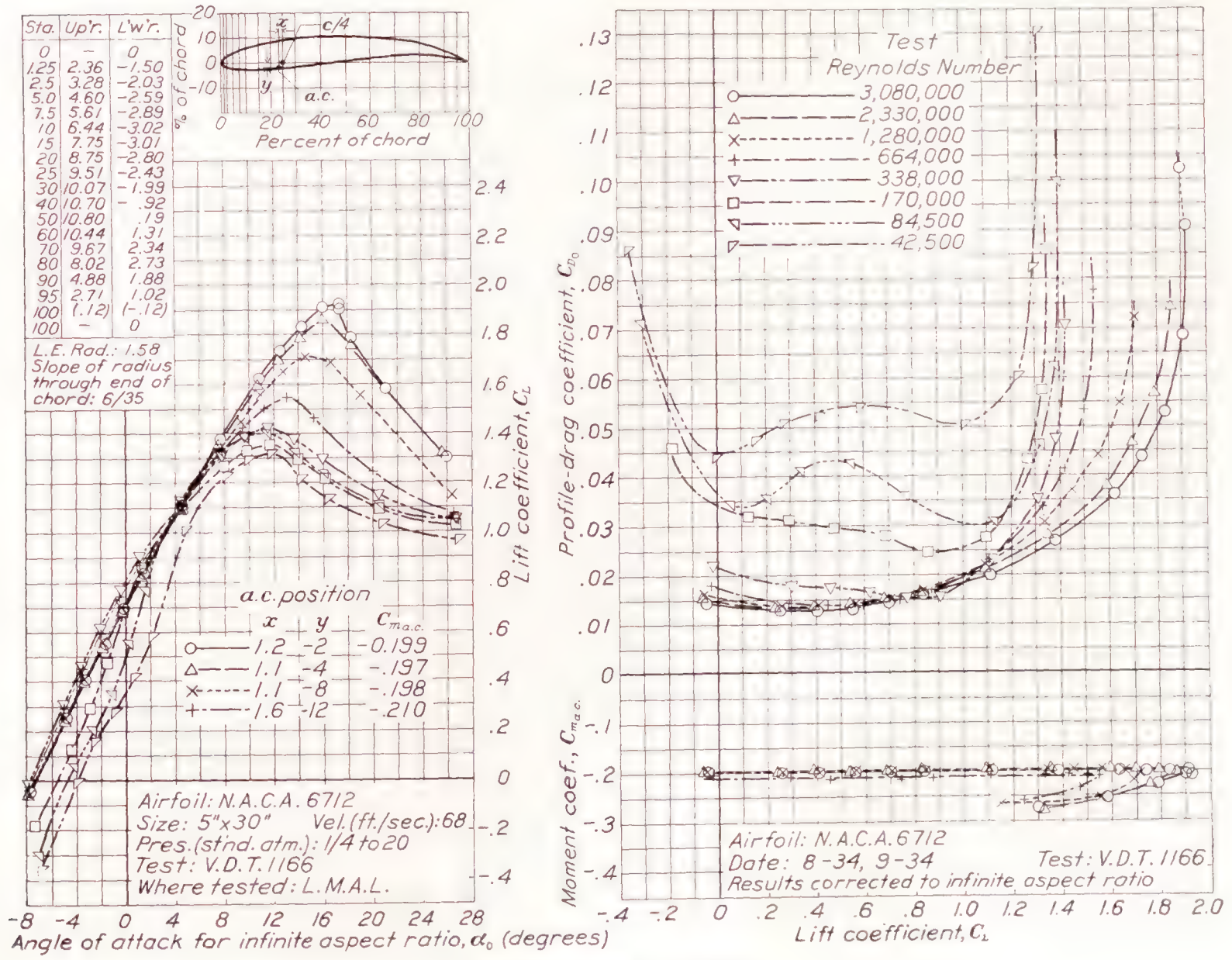

FIGURE 15.—N. A. C. A. 6712.

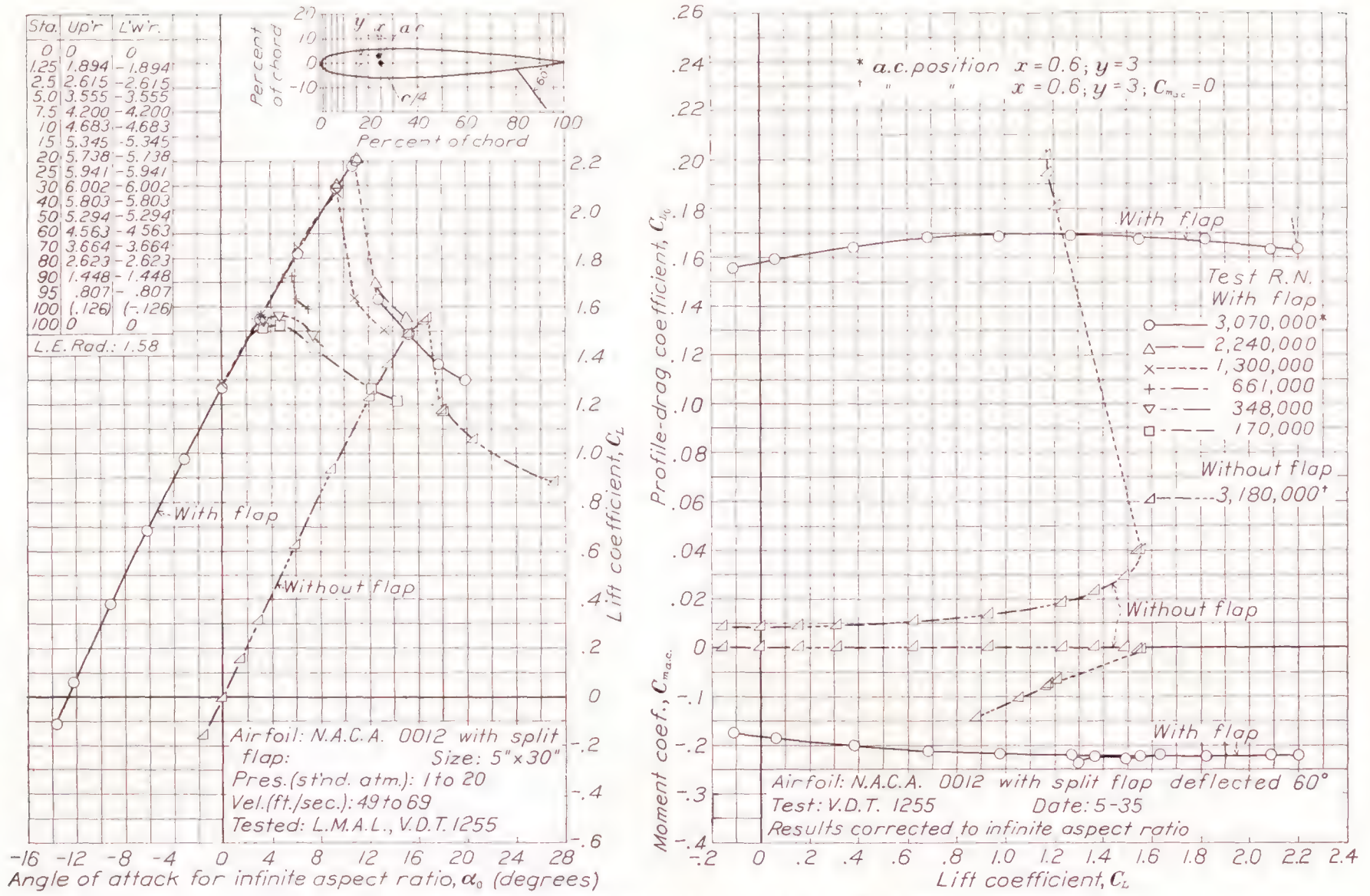

FIGURE 16.—N. A. C. A. 0012 with split flap deflected 60°.

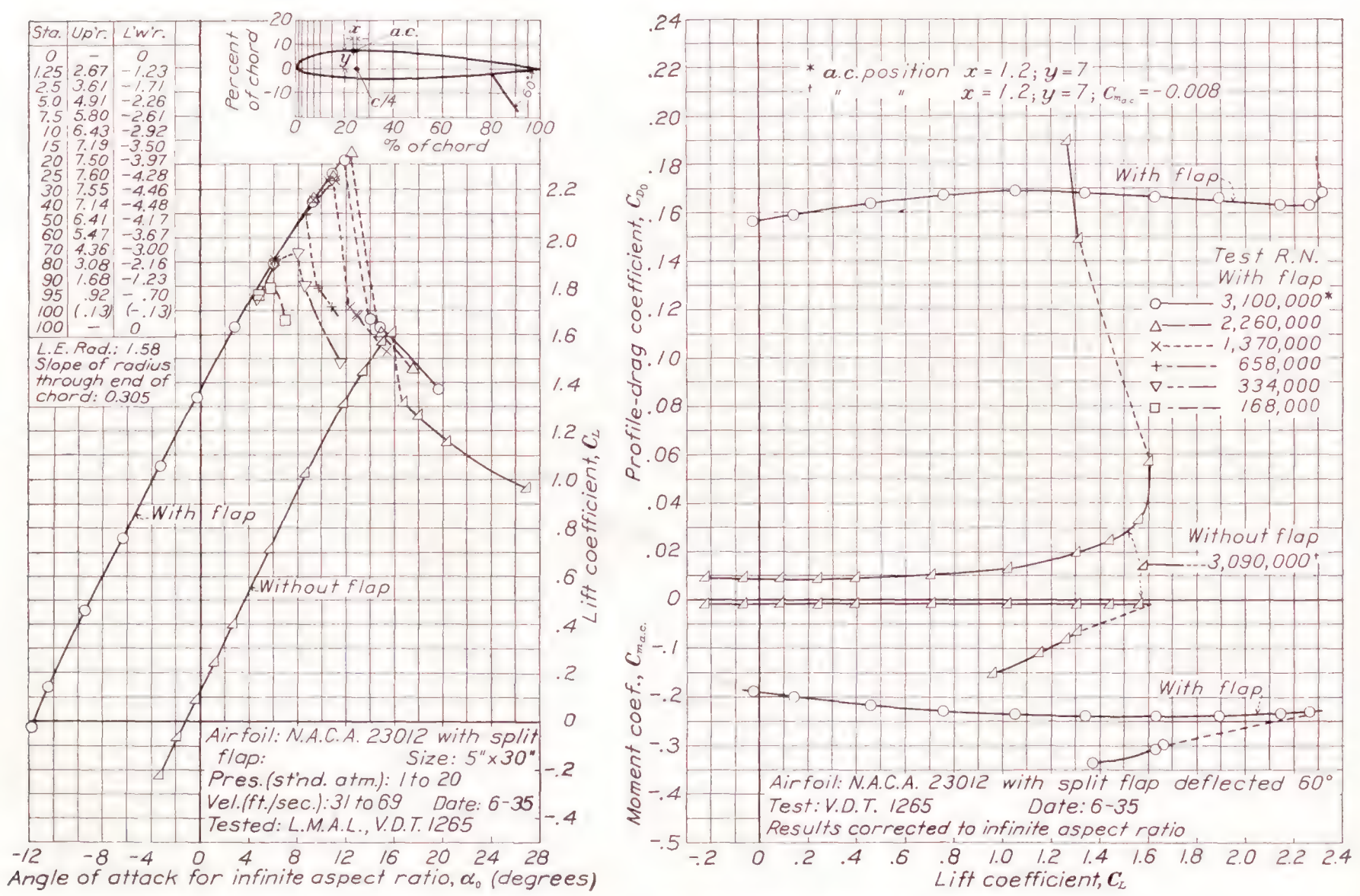

FIGURE 17.—N. A. C. A. 23012 with split flap deflected 60°.

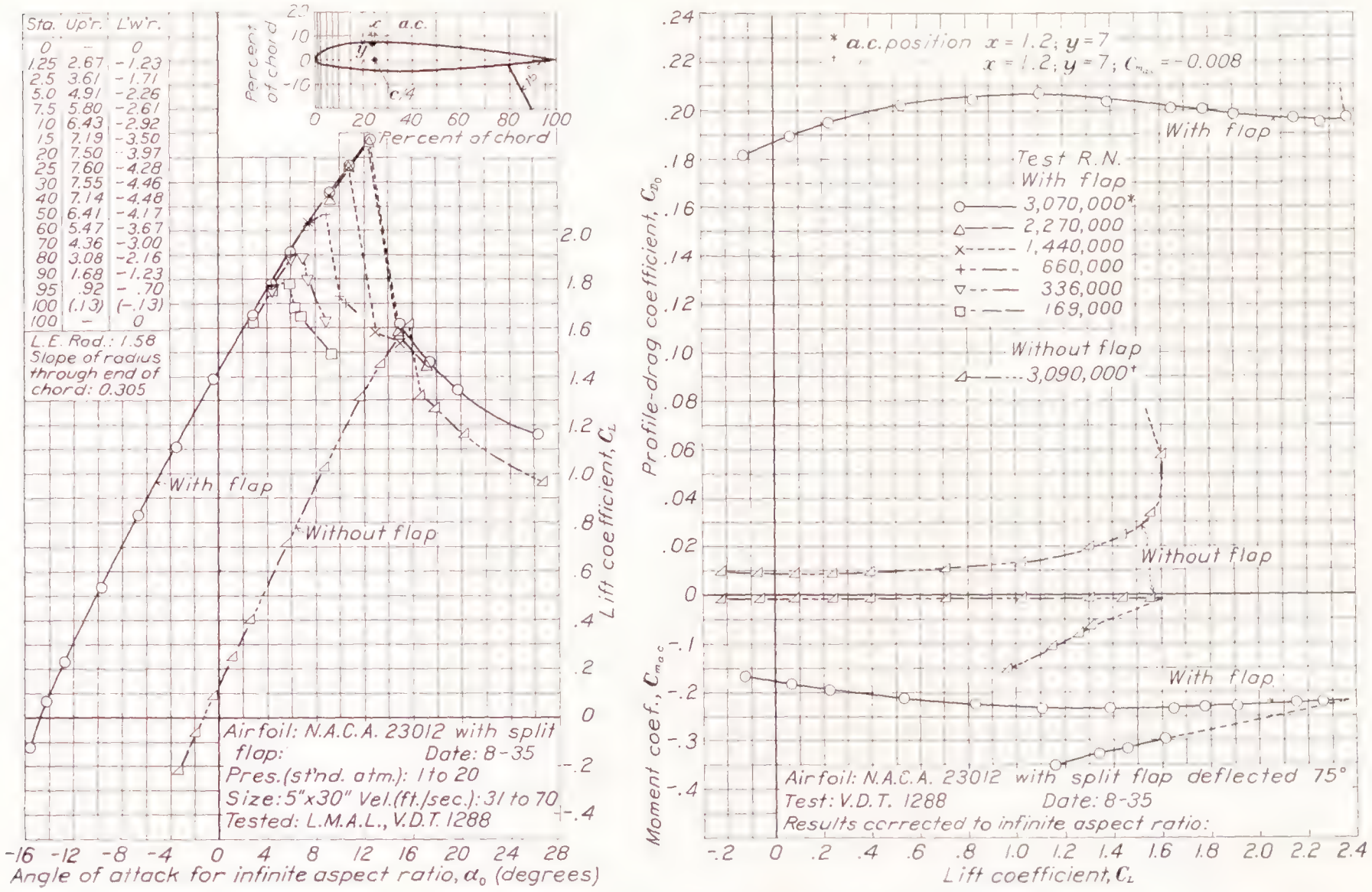

FIGURE 18.—N. A. C. A. 23012 with split flap deflected 75°.

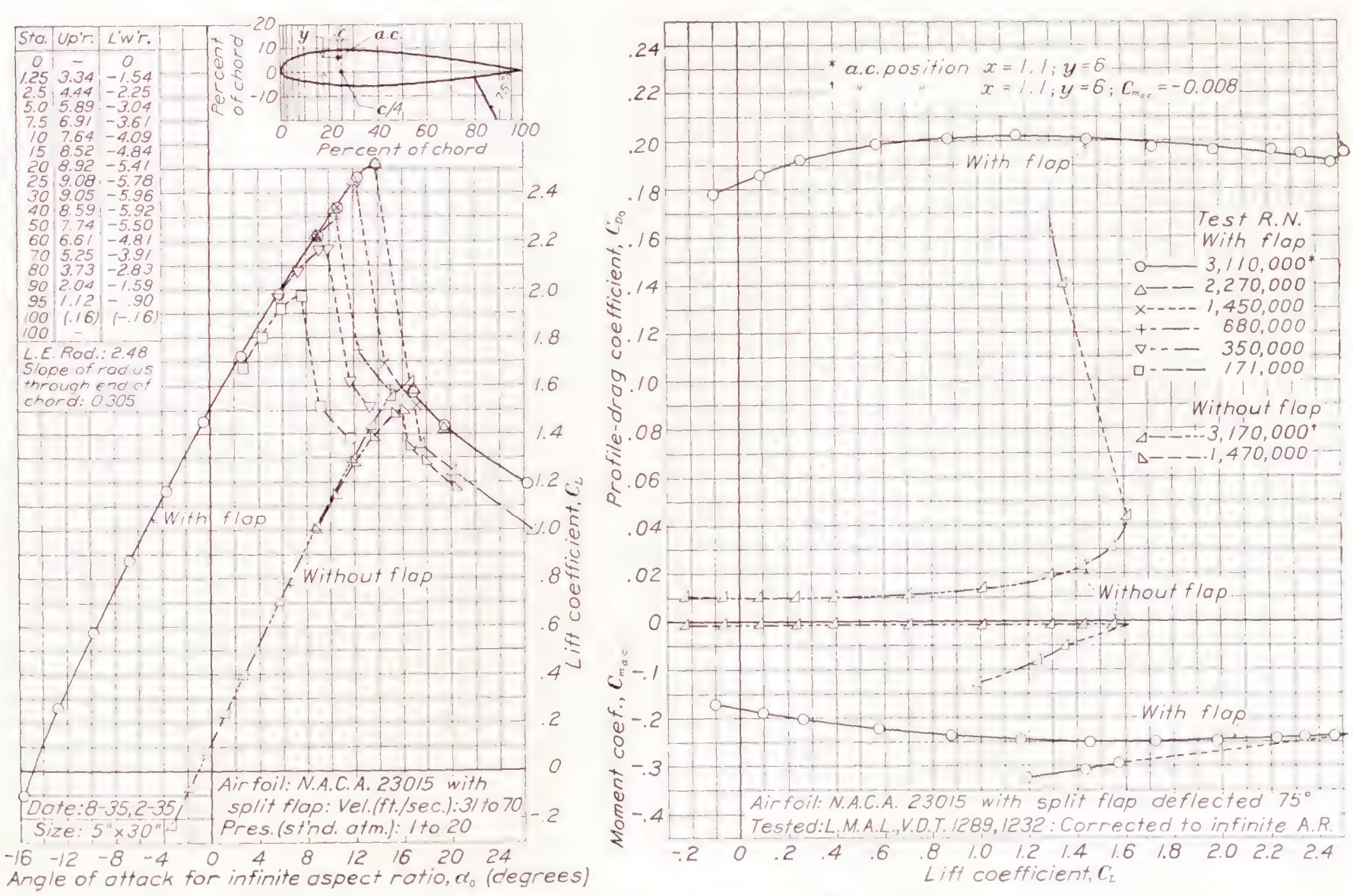

FIGURE 19.—N. A. C. A. 23015 with split flap deflected 75°

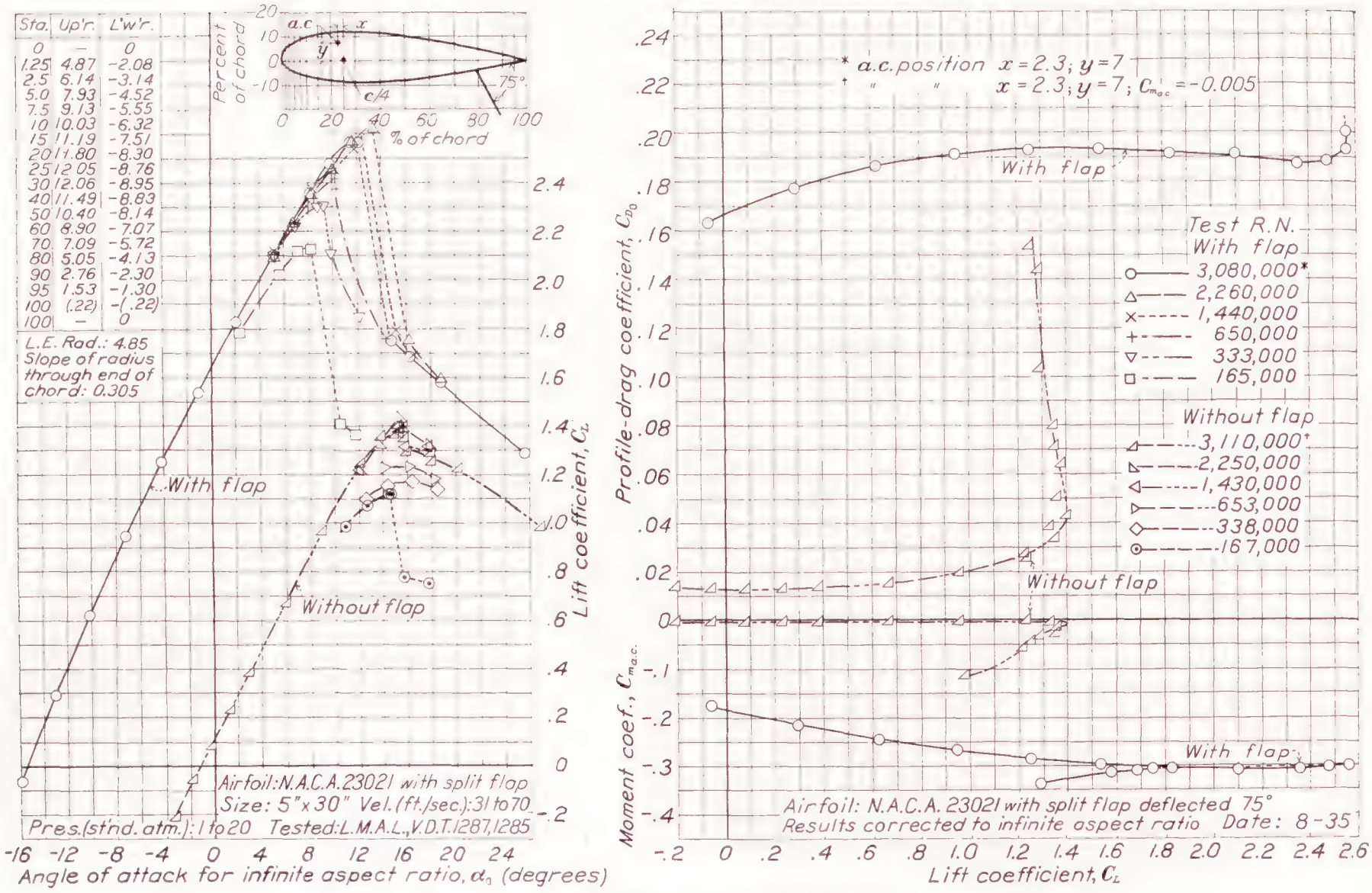

FIGURE 20.—N. A. C. A. 23021 with split flap deflected 75°.

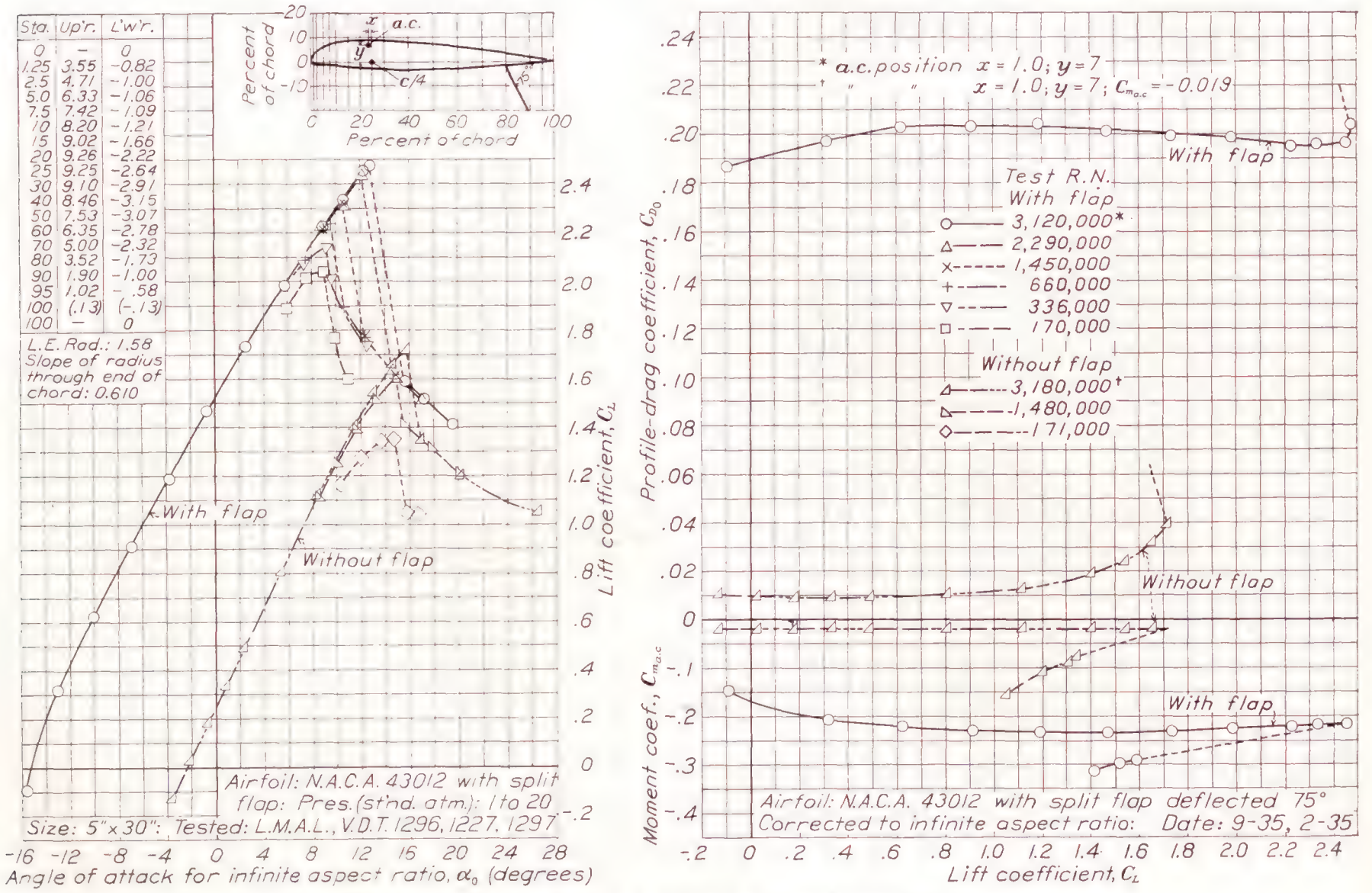

FIGURE 21.—N. A. C. A. 43012 with split flap deflected 75°.

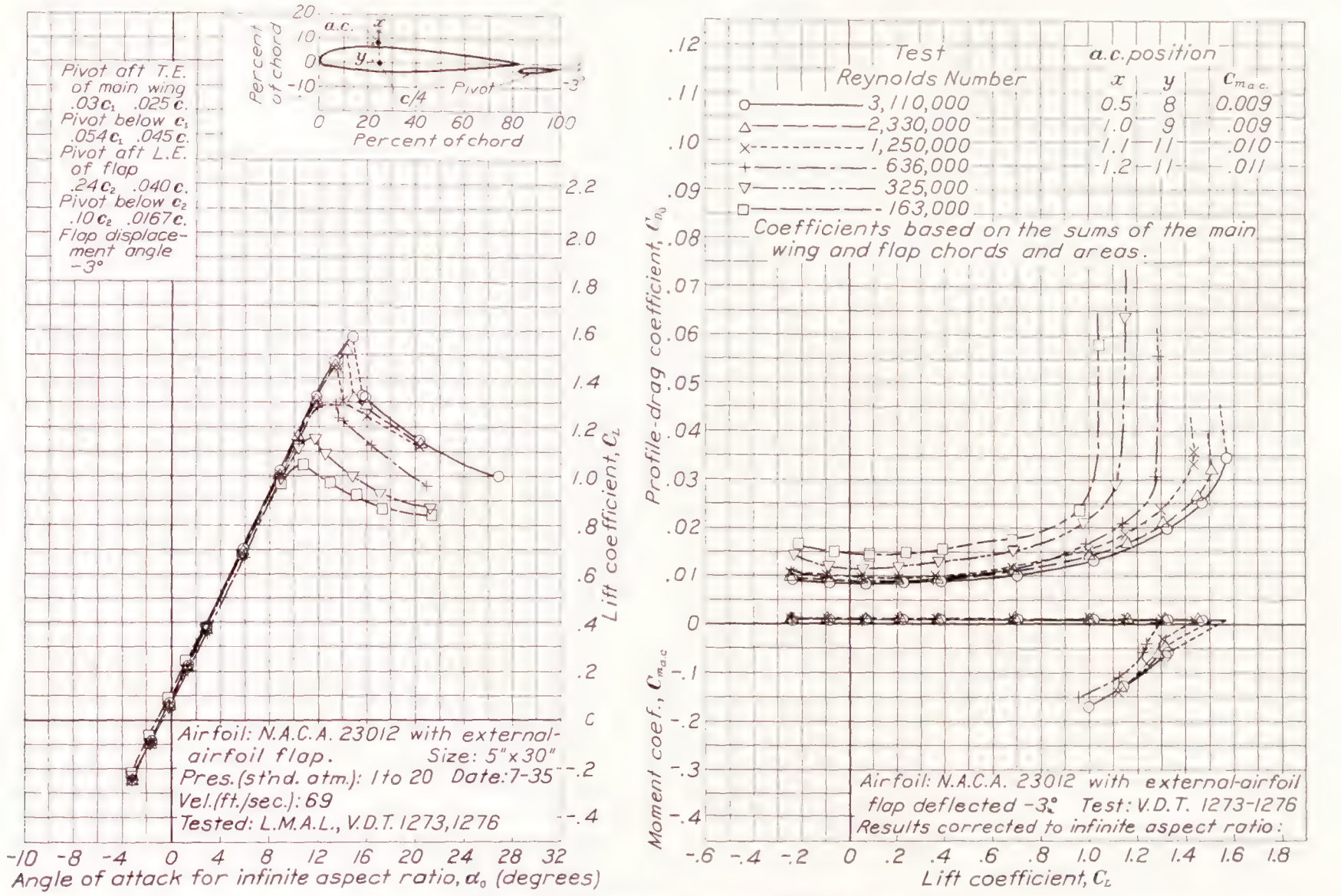

FIGURE 22.—N. A. C. A. 23012 with external-airfoil flap deflected −3°.

Main wing section	N. A. C. A. 23012	Main wing chord, c_1	0.833c	Datum chord, $c=c_1+c_2$.	
Flap section	N. A. C. A. 23012	Flap chord, $c_2=0.2c_1$	.167c		

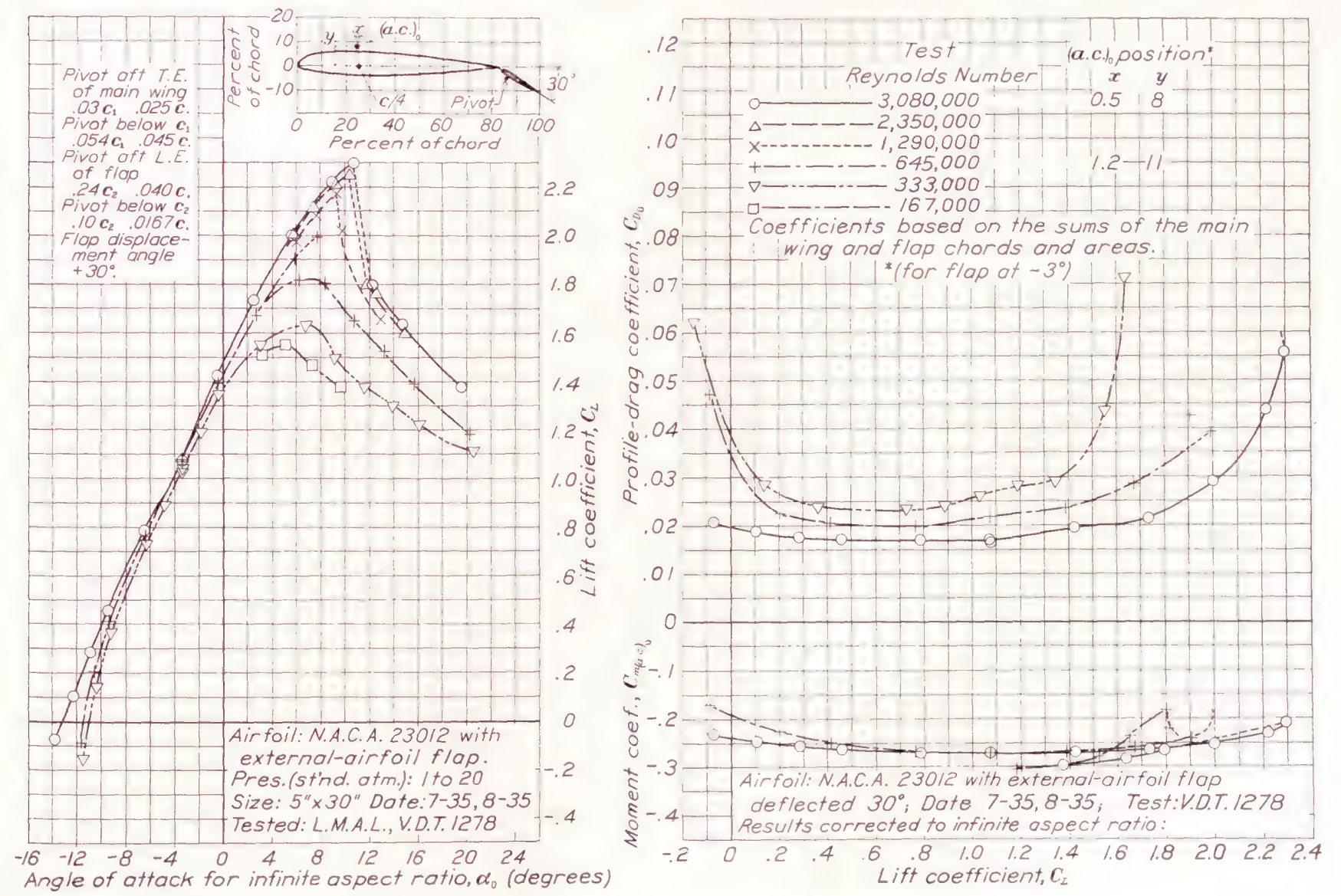

FIGURE 23.—N. A. C. A. 23012 with external-airfoil flap deflected 30°.

Main wing section	N. A. C. A. 23012	Main wing chord, c_1	0.833c	Datum chord, $c=c_1+c_2$.	
Flap section	N. A. C. A. 23012	Flap chord, $c_2=0.2c_1$	.167c		

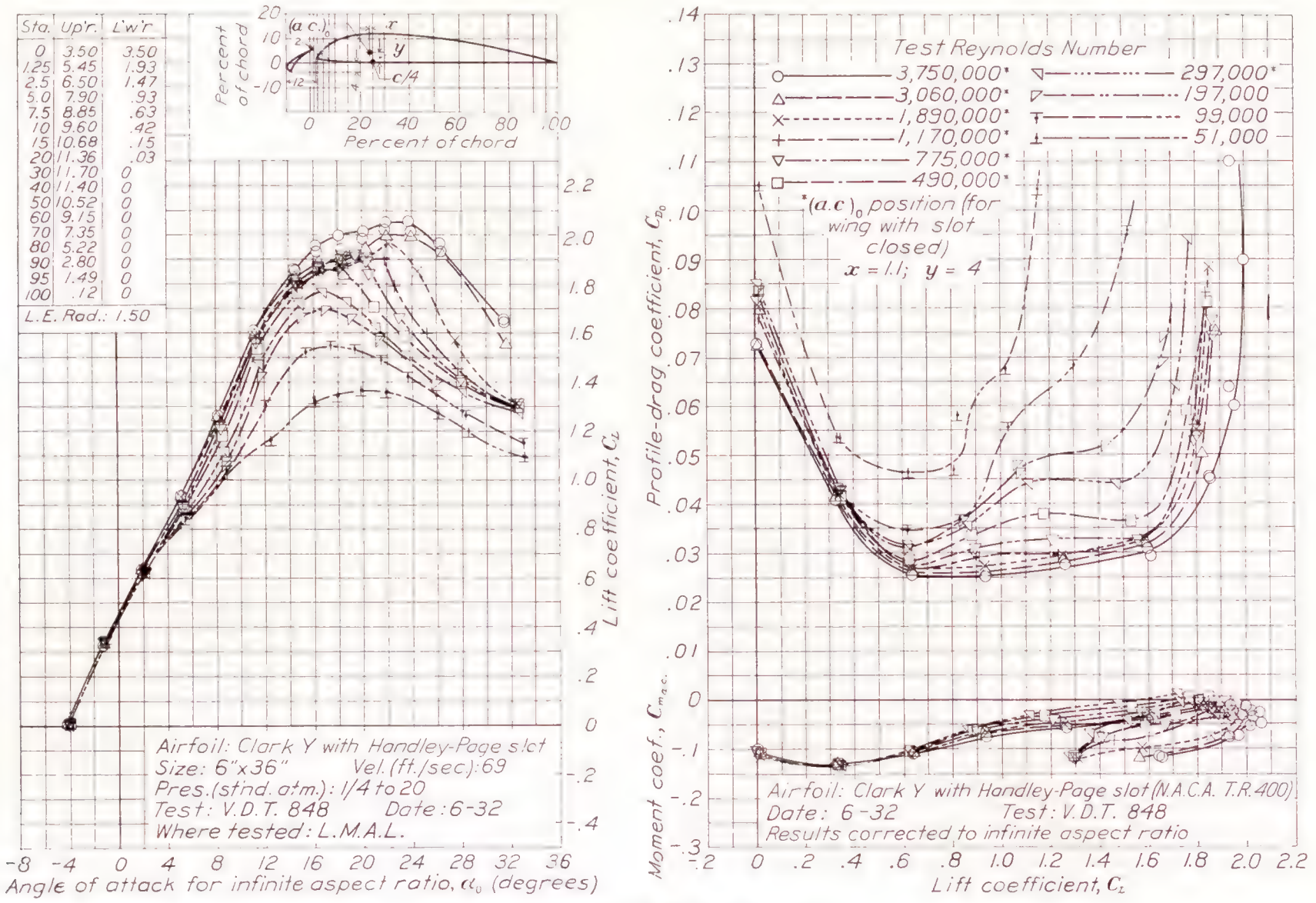

FIGURE 24.—Clark Y with Handley Page slot.

As an example of scale effects within the flight range, figure 25 has been prepared to show how the choice of an airfoil section for maximum aerodynamic efficiency may depend on the flight Reynolds Number at which the airfoil is to be employed. The efficiency is judged by the speed-range index $c_{l_{max}}/c_{d_0}$. Values of $c_{l_{max}}$ were determined for the airfoil sections (N. A. C. A. 230 series) with a deflected 20 percent chord split flap and at a Reynolds Number as indicated on each curve corresponding to the landing condition. The corresponding values of c_{d_0} were taken as the actual profile-drag coefficients associated with a high-speed lift coefficient suitable to an actual speed range of 3.5, but corrected by the methods of this report to the high-speed Reynolds Number (indicated landing Reynolds Number R times 3.5). Four curves were thus derived indicating the variation of speed-range index with section thickness for four values of the landing Reynolds Number: 1, 2, 4, and 8 million, the extremes corresponding to a small airplane and to a conventional transport airplane. The highest value shown, 414, of the speed-range index may appear surprisingly high, but it should be remembered that the corrections to section characteristics and for Reynolds Number, as well as the use of flaps, are all favorable to high values. The important point brought out by figure 25 is that the section thickness corresponding to the maximum aerodynamic efficiency is dependent on the Reynolds Number. The most efficient airfoil for a landing Reynolds Number of 1,000,000, for example, is definitely not the most efficient for a larger airplane landing at a Reynolds Number of 8,000,000. An analysis such as that of the foregoing example or further analyses such as those

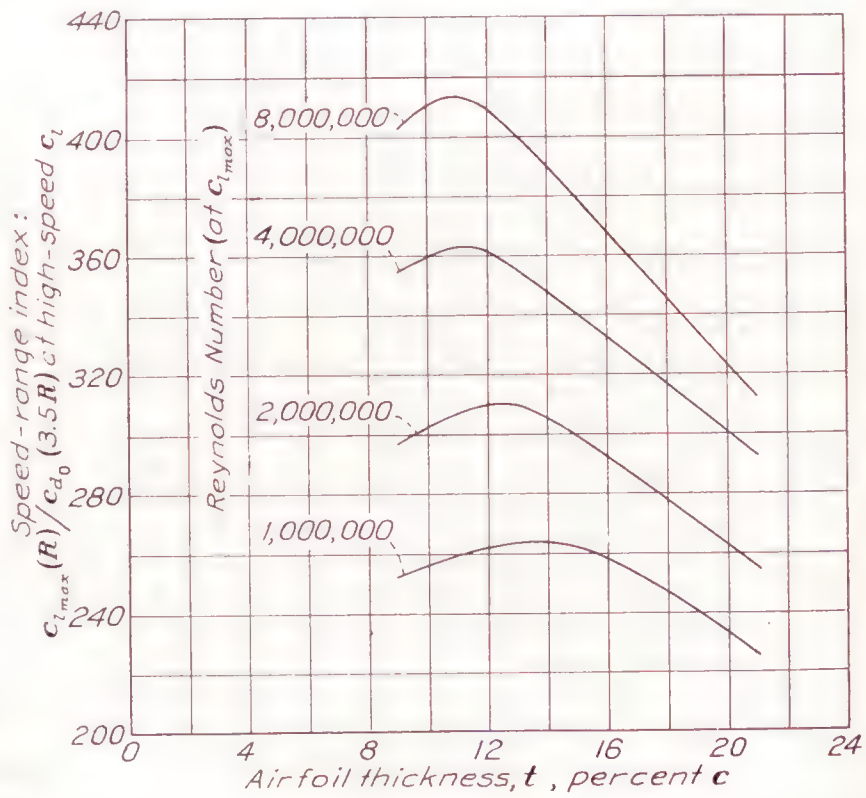

FIGURE 25.—Airfoil speed-range indexes for various Reynolds Numbers. N. A. C. A. 230 series sections; $c_{l_{max}}$ taken for airfoil with 0.20c split flap deflected 75°; c_{d_0} taken for airfoil with flap retracted for a high-speed value of c_l and at 3.5 times the R for the $c_{l_{max}}$.

discussed in reference 8 concerning the determination of the characteristics of wings evidently require a knowledge of the variation of airfoil *section* characteristics with profile shape over the practical range of flight Reynolds Numbers.

DETERMINATION OF *SECTION* CHARACTERISTICS APPLICABLE TO FLIGHT

The present analysis is intended primarily to supply a means of arriving at airfoil *section* characteristics that are applicable to flight at Reynolds Numbers within the practical flight range. This object is best accomplished by applying corrections to the standard airfoil test results from the variable-density tunnel.

The standard airfoil characteristics at large Reynolds Numbers are customarily defined in terms of a few parameters or important airfoil *section* characteristics that may be tabulated for each airfoil section. These important characteristics are:

$c_{l_{max}}$, the section maximum lift coefficient.

a_0, the section lift-curve slope.

α_{l_0}, the angle of zero lift.

$c_{d_{0\,min}}$, the minimum profile-drag coefficient.

$c_{l_{opt}}$, the optimum lift coefficient, or section lift coefficient corresponding to $c_{d_{0\,min}}$.

$c_{m_{a.c.}}$, the pitching-moment coefficient about the section aerodynamic center.

a. c., the aerodynamic center, or point with respect to the airfoil section about which the pitching-moment coefficient tends to remain constant over the range of lift coefficients between zero lift and maximum lift.

Essentially, the general analysis therefore reduces to an analysis of the variation of each of these important section characteristics with Reynolds Number. Before this analysis is begun, however, it will be necessary to consider how values of these *section* characteristics applicable to flight are deduced from the wind-tunnel tests of finite-aspect-ratio airfoils in the comparatively turbulent air stream of the tunnel. The variation of the important *section* characteristics with Reynolds Number will then be considered. Finally, consideration will be given to methods of arriving at complete airfoil characteristics after the important *section* characteristics have been predicted for flight at the desired value of the Reynolds Number.

Correction to infinite aspect ratio.—The derivation of the *section* characteristics from the test results uncorrected for turbulence will be discussed first; the turbulence effects will be considered later. The reduction to *section* characteristics is actually made in three successive approximations. First, the measured characteristics for the rectangular airfoil of aspect ratio 6 are corrected for the usual downflow and induced drag, using appropriate factors that allow at the same time for tunnel-wall interference. These induction factors are based on the usual wing theory as applied to rectangular airfoils. The methods of calculation are presented in reference 1. (Second-order influences have also been investigated; that is, refinement of the tunnel-wall correction to take into account such factors as the load grading and the influence of the tunnel interference on the load grading. (See reference 6.) For the conditions of the standard tunnel test such refinements were found to be unnecessary.) The results thus yield the first approximation characteristics, e. g., the profile-drag coefficient C_{D_0} that has been considered a section characteristic in previous reports (reference 2).

These first-approximation section characteristics are unsatisfactory, first, because the airfoil theory does not represent with sufficient accuracy the flow about the tip portions of rectangular airfoils and, second, because the measured coefficients represent average values for all the sections along the span whereas each section actually operates at a section lift coefficient that may differ markedly from the wing lift coefficient. The second approximation attempts to correct for the shortcomings of the wing theory as applied to rectangular airfoils.

It is well known that pressure-distribution measurements on wings having rectangular tips show humps in the load-distribution curve near the wing tips. These distortions of the load-distribution curve are not represented by the usual wing theory. The failure of the theory is undoubtedly associated with the assumption of plane or two-dimensional flow over the airfoil sections whereas the actual flow near the tips is definitely three-dimensional, there being a marked inflow from the tips on the upper surface and outflow toward the tips on the lower surface. This influence not only affects the induction factors and hence the over-all characteristics of the rectangular wing but also produces local disturbances near the tips that may be expected to affect the average values of the section profile-drag coefficients.

Theoretical load distributions for wings with well-rounded (elliptical) tips agree much more closely with experiment than do the distributions for rectangular-tip wings. Local disturbances near the tips should also be much less pronounced. Test results for rounded-tip wings were therefore employed to evaluate the rectangular-tip effects and hence to arrive at the second approximations. Four wings, having N. A. C. A. 0009, 0012, 0018, and 4412 sections, were employed for the purpose. The normal-wing airfoil sections were employed throughout the rounded-tip portion of the wing but the plan area was reduced elliptically toward each tip beginning at a distance of one chord length from the tip. Section characteristics were derived from tests of these wings in the usual way but using theoretical induction factors appropriate to the modified plan form. These section characteristics when compared

with the first approximation ones from tests of wings with rectangular tips served to determine the second approximations. These values indicated by double primes were given from this analysis in terms of the first approximation values indicated by single primes as follows:

$$C_{L_{max}}'' = 1.03 C_{L_{max}}'$$
$$a_0'' = 0.96 a_0'$$
$$\alpha_0'' = \alpha_0' + 0.39 C_L' \text{ (degrees)}$$
$$C_{D_0}'' = C_{D_0}' + 0.0016 C_L'^2 - \frac{1}{3}(t-6)0.0002 \quad (t \geqq 6)$$

where t is the maximum section thickness in percent chord. In some recent reports on airfoil characteristics (references 3, 5, and 7) these values have been presented as section characteristics except that a small correction has in some cases been applied to the aerodynamic-center positions. This correction is no longer considered justifiable.

These corrections are, of course, entirely empirical. They must be considered as only approximately correct and as being independent of the Reynolds Number. The corrections themselves, however, are small so that they need not be accurately known. All things considered, it is believed that through their use the reliability of the *section* data is definitely improved, at least within the lower part of the range of lift coefficients. For lift coefficients much greater than 1, however, the profile-drag coefficients from the rounded tip and rectangular airfoil tests show discrepancies that increase progressively with lift coefficient and, of course, become very large near the maximum lift coefficient owing to the different maximum-lift values. This difference brings up the necessity for the third approximation. The second approximation values may, however, be considered sufficiently accurate to determine the section profile-drag coefficient c_{d_0} over the lower lift range and also the following important section parameters that are determined largely from the characteristics in the low lift range:

α_{l_0}
a_0
$c_{l_{opt}}$
$c_{d_{0\ min}}$
$c_{m_{a.c.}}$
$a.\ c.$

In this range of the lift coefficient the deviations from the mean of the c_l values along the span have been adequately taken into account. The mean values of c_l and c_{d_0} represent true values as long as the deviations along the span are within a limited range over which the quantities may be considered to vary lineally. Near the maximum lift, however, the deviations become larger and the rates of deviation increase so that the profile drag of the rounded-tip airfoil, for example, is predominantly influenced by the high c_{d_0} values of the central sections which, according to the theory, are operating at c_l values as much as 9 percent higher than the mean value indicated by the wing lift coefficient C_L. Moreover, the actual lift coefficient corresponding to the section stall (in this case the center section) might thus, in accordance with the theory, be taken as 9 percent higher than the measured wing lift coefficient corresponding to the stall.

Several considerations, however, indicate that this 9 percent increase indicated by the simple theory is too large. The simple theory assumes a uniform section lift-curve slope in arriving at the span loading and hence the distribution of the section lift coefficients along the span. Actually on approaching the maximum lift the more heavily loaded sections do not gain lift as fast as the more lightly loaded ones owing to the bending over of the section lift curves near the stall. This effect has also been investigated approximately. The results showed that for commonly used airfoil sections the center lift drops from 9 percent to 5 or 6 percent higher than the mean at the stall of rectangular airfoils with rounded tips. For some unusual sections that have very gradually rounding lift-curve peaks and with little loss of lift beyond the stall, this correction may practically disappear either because the lift virtually equalizes along the span before the stall or because the maximum lift is not reached until most of the sections are actually stalled. Omitting from consideration these sections to which no correction will be applied, the question as to whether or not such a correction should be applied to usual sections was decided by considering how it would affect predictions based on the $c_{l_{max}}$ values.

Maximum-lift measurements had been made for a number of tapered airfoils of various taper ratios and aspect ratios. The same airfoil *section* data presented in this report were applied (taking into account the reduced Reynolds Number of the sections near the tips of highly tapered wings) by the method indicated in reference 8 to predict the maximum lift coefficients of the tapered wings. These predictions appeared somewhat better when the *section* data were obtained on the assumption that the center-section lift coefficient at the stall of the rectangular airfoil with rounded tips is 4 percent higher than the wing lift coefficient. Hence the third approximation as regards the section maximum lift coefficients was obtained by increasing the maximum lift coefficients by 4 percent, although the value of the correction could not be definitely established because it appeared to be of the same order as possible errors in maximum lift measurements and predictions for tapered airfoils. The correction has been applied, however, except in the unusual cases previously mentioned where it obviously was not applicable, by increasing the maximum lift coefficients for the sections

by 4 percent. With the rounded-tip correction this increase makes the total maximum lift coefficient for the *section* 7 percent higher than the measured maximum lift coefficient for the rectangular airfoil of aspect ratio 6.

The correction of the important airfoil section parameters has thus been completed, but the curve of profile-drag coefficient against lift coefficient should now be modified at high lift coefficients owing to the change in $c_{l_{max}}$ and the variation of c_{d_0} along the span. Completely corrected c_{d_0} curves are not presented for the various airfoils in this report. The change resulting from the variation of c_{d_0} along the span has been applied only in a general way in the construction of a generalized c_{d_0} curve. From this curve, values of c_{d_0} at any c_l may be derived in terms of the presented airfoil section parameters. This "generalized section polar" (see fig. 45) was derived from tests of rounded-tip N. A. C. A. 0012 and 4412 airfoils, taking into account the variation of c_{d_0} along the span. For conventional airfoils of medium thickness, c_{d_0} values from this generalized section polar should be more nearly true section characteristics than the C_{D_0} values obtained directly from the test data. This conclusion is particularly important for lift coefficients above 1 where the second approximation correction becomes definitely unreliable and near $c_{l_{max}}$ where the C_{D_0} values are influenced by the variation of c_{d_0} along the span. A reference to figure 26 will show the relation of these successive approximations to the original measurements and to the final results.

Turbulence.—The correction for turbulence is made as in reference 9 by use of the concept of an effective Reynolds Number. Marked scale effects that have been experimentally observed are usually associated with a transition from laminar to turbulent flow in the boundary layer. As examples, consider the more or less sudden increase in the drag coefficient for skin-friction plates and airship models and the drop of the drag coefficient for spheres and cylinders with increasing Reynolds Numbers in the critical range. The latter scale effects are associated with the greater resistance to separation of the turbulent layer. The increase of maximum lift coefficient with Reynolds Number shown by most commonly used airfoils is a similar phenomenon. The drag scale effect for most airfoils, moreover, is at least comparable with the corresponding scale effect for the skin-friction plate.

This transition from laminar to turbulent flow in the boundary layer, as in Reynolds' classic experiments, is primarily a function of the Reynolds Number but, as he showed, the transition is hastened by the presence of unsteadiness or turbulence in the general air stream.

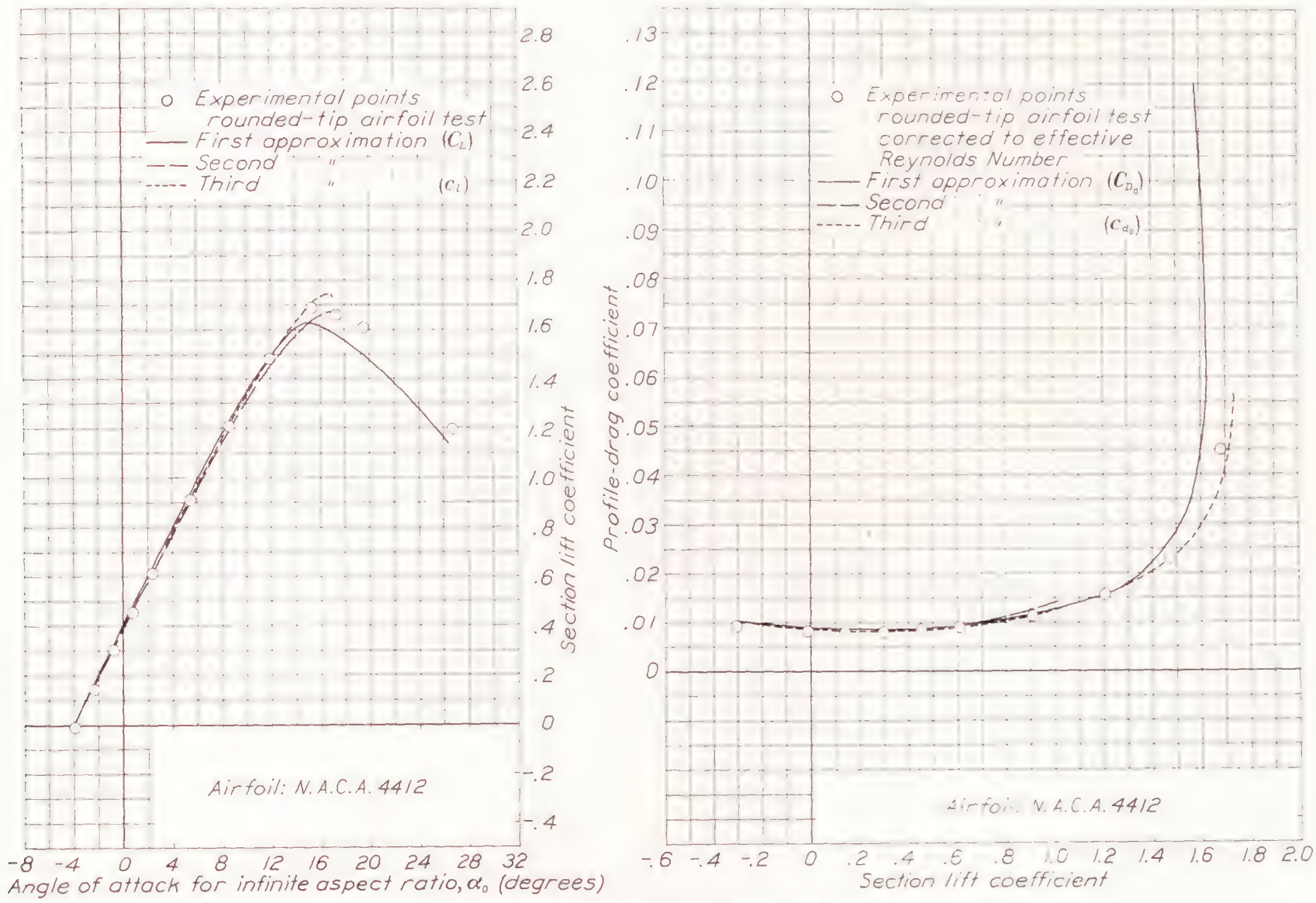

FIGURE 26.—Airfoil section characteristics. Comparison of the various approximations.

Likewise, the transition in the boundary layer is hastened by the turbulence in the air stream of a wind tunnel so that transition occurs at a given point on the model at a lower Reynolds Number in the tunnel than it would in free air. Likewise the associated scale effects that appear in the tunnel tend to correspond with those that would appear in flight at a higher Reynolds Number. This Reynolds Number may therefore be referred to as the "effective Reynolds Number" and is, of course, higher than the actual Reynolds Number of the test.

It appears that the effective Reynolds Number for practical purposes may be obtained by multiplying the test Reynolds Number by a factor referred to as the "turbulence factor." This factor was determined (reference 9) for the variable-density tunnel by a comparison of airfoil tests with tests in the N. A. C. A. full-scale tunnel and hence indirectly with flight. The value 2.64, which was thus obtained after a consideration of sphere tests in the full-scale tunnel and in flight, agrees with a subsequent determination (reference 10) by sphere tests in the variable-density tunnel that were compared directly with corresponding tests in flight.

An effective Reynolds Number is thus determined at which the tunnel results should, in general, be applied to flight. Flight conditions as regards the effects of the transition may then be considered as being approximately reproduced, but it should be remembered that the flow at the lower Reynolds Number cannot exactly reproduce the corresponding flow in flight. Both the laminar and turbulent boundary layers are relatively thicker than those truly corresponding to flight and both boundary layers have higher skin-friction coefficients at the lower Reynolds Number. Nevertheless the most important source of scale effects is taken into account, at least approximately, when the tunnel results are applied to flight at the effective Reynolds Number. The change in skin-friction drag coefficients in passing from the test to the effective Reynolds Number, moreover, is approximately allowed for by deducting a small correction increment from the measured airfoil profile-drag coefficients.

This correction increment was originally employed for tests at high values of the Reynolds Number when the boundary layer on an airfoil is largely turbulent. The correction was therefore estimated as the amount by which the drag coefficient representing the turbulent skin friction on a flat plate would decrease in passing from the test Reynolds Number to the effective Reynolds Number. The values of the increment thus deduced from Prandtl's analysis of the turbulent friction layer, which is substantially in agreement with von Kármán's original derivation, are as follows:

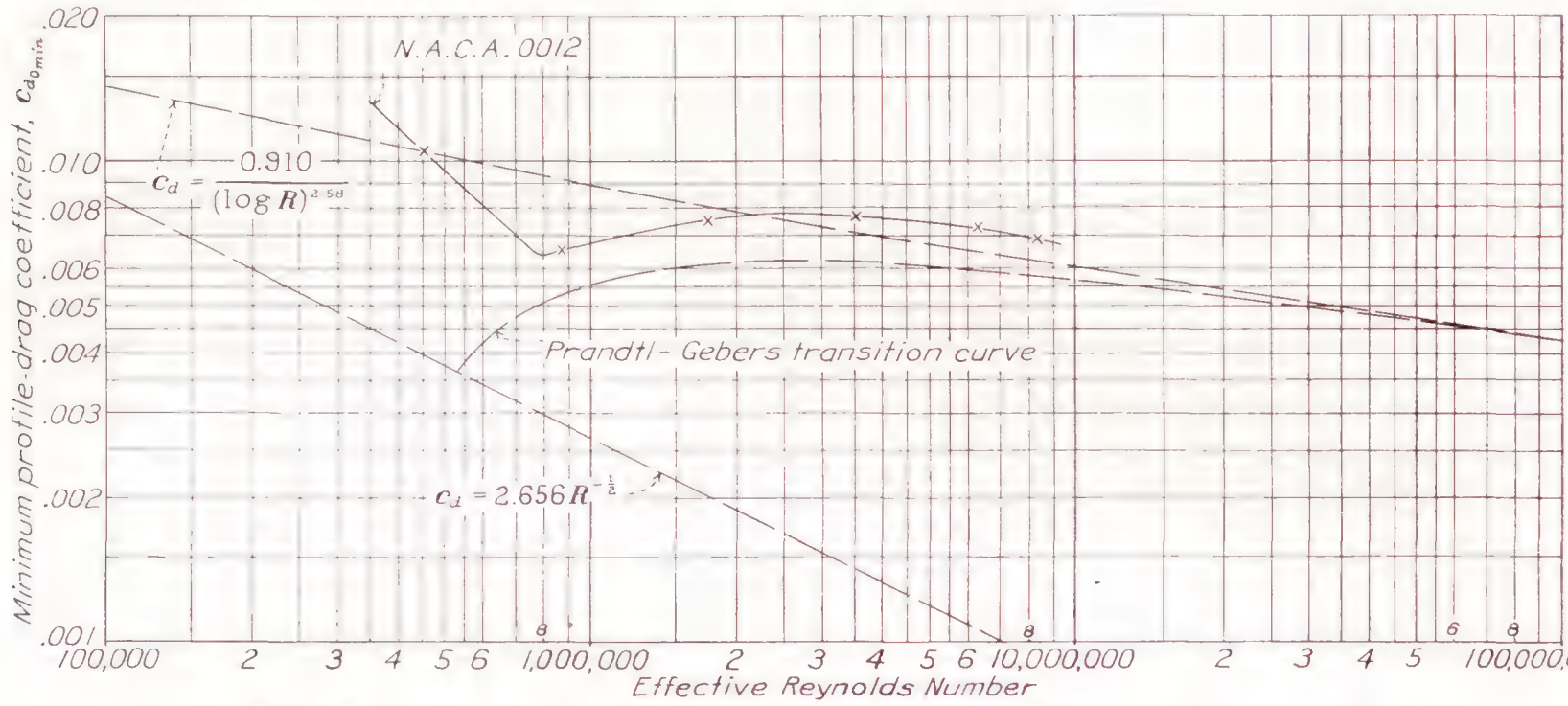

FIGURE 27.—Variation of $c_{d_{0_{min}}}$ with R. Comparison of N. A. C. A. 0012 airfoil with skin-friction plates.

Test Reynolds Number	Effective Reynolds Number	Δc_d
300,000	792,000	0.0020
500,000	1,320,000	.0017
1,000,000	2,640,000	.0014
2,000,000	5,280,000	.0012
3,000,000	7,920,000	.0011

The objection might be raised that the increments Δc_d are based entirely on a turbulent skin-friction layer whereas the boundary layers on airfoils are actually laminar over a considerable part of the forward portion, particularly for the lower values of the Reynolds Number. The Δc_d correction was nevertheless employed over the complete range of Reynolds Numbers for several reasons: primarily for simplicity and consistency, because in the practical flight range the turbulent layer predominates; and secondarily because on most airfoils the boundary layer must be turbulent over a considerable part of the surface at any Reynolds Number sufficiently high to avoid separation. Reference to the corrected minimum-drag results for the N. A. C. A. 0012 section shown in figure 27 may

clarify these statements. Included in the figure are curves representing the variations with Reynolds Number of flat-plate drag coefficients for laminar and turbulent boundary layers and the Prandtl-Gebers transition curve, which represents a computed variation substantially in agreement with Gebers' measurements of the actual variation in drag coefficient for a flat plate towed in water at various Reynolds Numbers. The computed curve is the result of a calculation of the average drag coefficient for the plate when the forward part of the boundary layer is laminar and the after part turbulent and the transition is assumed to take place at a fixed value of the surface-distance Reynolds Number R_x. It is apparent that the airfoil curve tends to parallel the actual flat-plate curve throughout the flight range of values of the Reynolds Number.

In references 11 and 12 corresponding curves were presented for a very thin airfoil section. These results were uncorrected for the turbulence in the tunnel and hence, although they appear to parallel a transition curve like the present corrected results, the transition curve does not correspond to zero turbulence, or flight, but is displaced to the left. The correction increment could have been based on the difference between these two transition curves for flat plates, the one calculated for the tunnel and the other calculated for flight conditions. Such a correction increment would have been slightly different from the one actually employed, particularly in the range of the Reynolds Number below the flight range, owing to larger drag reductions in the laminar part of the boundary layer in passing to the higher Reynolds Number. Both the test results for the N. A. C. A. 0012 (fig. 27) and theoretical calculations for the same airfoil by the method of reference 13 indicate, however, that separation must occur as the Reynolds Number is reduced even in the case of this excellently streamlined form at zero lift. The separation is indicated by the abnormal increase of the drag coefficient shown by the experimental results below a Reynolds Number of 800,000. This separation may at first be a local phenomenon, the flow subsequently changing to turbulent and closing in again downstream from the separation point. In any case it is apparent that the flow will either be to a considerable extent turbulent or will separate so that a correction increment based mainly on a laminar layer would have little significance.

The applied correction increment based on the turbulent layer is thus justifiable as being conservative over the flight range of the Reynolds Number and the influences not considered in its derivation will henceforth be considered as sources of error in the experimental results. Admittedly it would be of interest to give further consideration to the results in the range of Reynolds Number below the usual flight range where the influences of extensive laminar boundary layers and separation are of primary importance, but the relatively poor experimental accuracy of the test data for these low Reynolds Numbers and the lack of practical applications tend to discourage an extensive analysis of the low-scale data.

The accuracy of the final results as applied to flight is best judged from a comparison of the results with those from the N. A. C. A. full-scale tunnel. Such comparisons have been made in references 9 and 10. The agreement for both the maximum lift and minimum drag for the Clark Y is easily within the accuracy of the experiments. For the other airfoil for which a comparison is possible, the N. A. C. A. 23012, the results show similar satisfactory agreement for maximum lift, within 4 percent, and for the drag coefficient at zero lift, within 5 percent. The polar curve of the profile-drag coefficients from the full-scale tunnel, however, tended to show a marked drop for a small range of lift coefficients near that for minimum profile drag. Although the same phenomenon was apparent from the variable-density-tunnel tests, it was less marked. The fact that the minimum drag shown by the full-scale-tunnel test was 17 percent lower than shown by the variable-density-tunnel test thus appears less significant than it otherwise would. Furthermore, it might be expected that this localized dip in the profile-drag curve would tend to disappear at the higher Reynolds Numbers common to flight at low lift cofficients. In spite of the fact that the above-mentioned difference between the results is but slightly outside the limit of *possible* experimental errors, the difference does tend to show how much the turbulence corrections applied to the variable-density-tunnel data may be in error, particularly for a condition like the one considered for which rather extensive laminar boundary layers may be present. Comparatively high velocities over the lifting airfoil as contrasted with the flat plate may also tend to increase the value of the correction increment so that all these considerations are in agreement in indicating that the correction increment applied may be considerably too conservative in some instances, particularly for the lower range of flight Reynolds Numbers.[1] The greatest uncertainty, however, in regard to the application of the drag data to flight is due to the possibility that under certain favorable conditions in flight, corresponding to very smooth surfaces and to practically zero turbulence, the transition may be

[1] Since the writing of this report, the results of comparative experiments made in the less turbulent British C. A. T. on the N. A. C. A. 0012 airfoil have come to the attention of the authors. For the model with the most carefully finished surface, the results do show lower drags over the lower range of flight Reynolds Numbers than the data in this report.

Still more recently the results of tests from England and Germany at moderately large Reynolds Numbers have added further support to the conclusion that the correction increments applied herein are too small. Furthermore, as indicated by the foregoing discussion, the increments should probably increase with the airfoil thickness or drag. For example, better agreement is obtained if, instead of the increment 0.0011 subtracted from the usual large-scale profile-drag results, a correction as a factor applied to the measured profile drag is employed. This factor is 0.85, as similarly determined from the flat plate with completely turbulent boundary layer. Final conclusions, however, must await further information on the transition as it actually occurs in flight.

abnormally delayed. For example, Dryden (reference 14) found very large values of R_x corresponding to transition on a flat plate. The conditions are reminiscent of those of supersaturation in solutions. Following this analogy, it may be impossible to set an upper limit of R above which transition must occur. Unusually low drags would, of course, be associated with the presence of this type of abnormally extensive laminar boundary layer; but, while this possibility should be recognized, it is probable that in most practical applications, conditions such as slight surface irregularities, vibration, or self-induced flow fluctuations will operate against it. The present results may therefore be used in flight calculations as conservative for wings that are not aerodynamically rough.

VARIATION OF IMPORTANT SECTION CHARACTERISTICS WITH REYNOLDS NUMBER

Maximum lift coefficient $c_{l_{max}}$.—The maximum lift coefficient is one of the most important properties of the airfoil section. It largely determines not only the maximum lift coefficient of wings and hence the stalling speed of airplanes but also, for example, influences how and where tapered wings stall and hence the character of the stall in relation to lateral stability and damping in roll. The maximum lift coefficient, moreover, indicates the useful lift range of the section and tends to define the nature of the variation of profile drag with lift. Finally, the maximum lift coefficient is the important aerodynamic characteristic that usually shows the largest scale effects.

It is not surprising to find large variations of $c_{l_{max}}$ with Reynolds Number because $c_{l_{max}}$ is dependent entirely on the boundary-layer behavior, which in turn is directly a function of viscosity as indicated by the value of the Reynolds Number. In other words, potential-flow theory alone is totally incapable of any predictions concerning the value of $c_{l_{max}}$.

The following discussion traces the mechanism of the stall with a view to reaching an understanding of how the stall, and consequently the maximum lift, is affected by variations of the Reynolds Number. Basically, the discussion is concerned mainly with air-flow separation. The pressure distribution over the upper surface of the conventional airfoil section at lift coefficients in the neighborhood of the maximum is characterized by a low-pressure point at a small distance behind the leading edge and by increasing pressures from this point in the direction of flow to the trailing edge. Under these conditions the reduced-energy air in the boundary layer may fail to progress against the pressure gradient. When this air fails to progress along the surface, it accumulates. The accumulating air thereby produces separation of the main flow. The separation, of course, reduces the lift.

Whether or not separation will develop is dependent on the resistance to separation of the boundary layer. The turbulent layer displays much more resistance to separation than the laminar boundary layer. This dependence of separation on the character of the boundary-layer flow was first observed in sphere-drag tests. At low Reynolds Numbers separation of the boundary layer develops near the equator of the sphere. When the boundary layer on the sphere is made turbulent, however, as it is when the Reynolds Number is sufficiently increased, the separation shifts to a position considerably aft.

The occurrence of separation for airfoils, as affected by the transition from laminar to turbulent flow in the boundary layer, is indicated by the scale effects on $c_{l_{max}}$ (fig. 28) for symmetrical sections of varying thickness. For these airfoils at any considerable lift coefficient the low-pressure point on the upper surface tends to occur just behind the nose, on the leading-edge-radius portion of the airfoil. When the boundary layer is laminar behind this point, separation may be expected

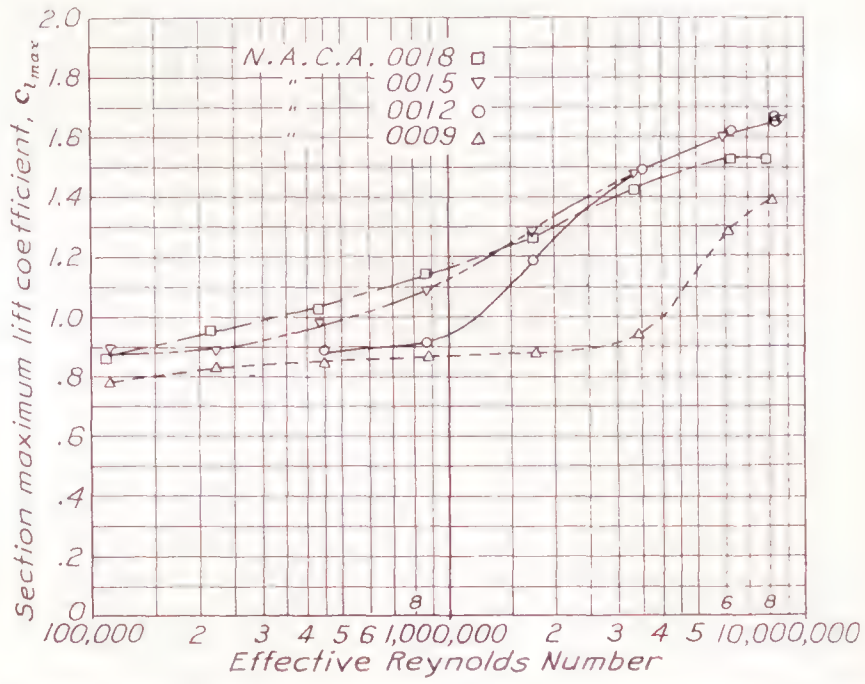

FIGURE 28.—Section maximum lift coefficient, $c_{l_{max}}$. Symmetrical airfoils of varying thickness.

to occur very quickly behind or almost at the low-pressure point owing to the presence of large adverse pressure gradients. In fact, the von Kármán-Millikan method of calculating the incipient separation point for laminar boundary layers (reference 13) has been applied by Millikan to estimate the position of the separation point and also its relation to the transition point as it is assumed to influence the scale effect on the maximum lift coefficient. The number and character of the assumptions involved in such an analysis, however, are such that the results may be expected to yield only qualitative predictions. Elaborate calculations in such cases are of doubtful necessity as indicated by the fact that qualitative predictions, perhaps more reliable, had previously been reached without them. (See references 12, 15, and 16.) Exact methods of calculation are unquestionably desirable but are definitely not a matter for the present but for a time when much more experimental data concerning both separation and transition shall have been secured.

For the present discussion it is sufficient to consider that, if the boundary layer remains laminar, separation will occur very close behind the low-pressure point on the upper surface. Incidentally, the actual separation point is expected, in general, to be forward of the calculated incipient separation point; that is, nearer the low-pressure point. It should not, however, be assumed that the occurrence of separation defines the maximum lift coefficient. For example, at very low Reynolds Numbers, separation on the N. A. C. A. 0012 airfoil occurs even at zero lift, which on this assumption would define zero as the maximum lift. Motion pictures have been made showing the air flow and separation for airfoils at low values of the Reynolds Number. Three photographs from the smoke tunnel are included as figures 29, 30, and 31 to indicate the position and character of the laminar separation for a cambered airfoil. The first two pictures show well-developed separation even at zero angle of attack; the third shows how laminar separation occurs just behind the nose at higher angles of attack.

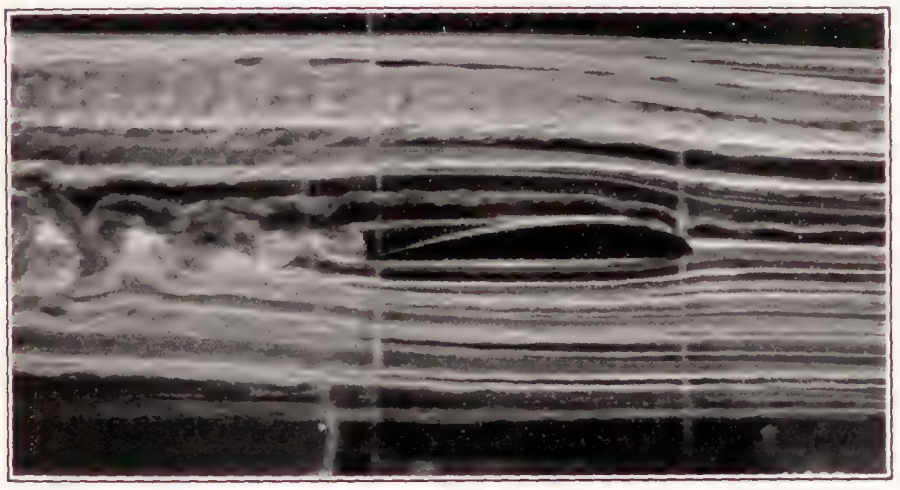

FIGURE 29.—Separation occurring on an airfoil at a low angle of attack.

It is thus apparent that separation of the laminar boundary layer will always be present at a point near the nose at any moderately high lift coefficient if the Reynolds Number is not sufficiently high to make the flow turbulent at that point. This condition certainly exists for the results in figure 28 over the lower range of the Reynolds Number; that is, separation near the nose must have occurred at angles of attack well below that of $c_{l_{max}}$ owing to the very small Reynolds Number associated with the short distance from the nose to the laminar separation point. In this range of R the $c_{l_{max}}$ values are of the order of 0.8 and change little with either R or the section thickness. (See fig. 28.) This value of $c_{l_{max}}$ corresponds approximately to that for a flat plate.

Now consider the character of the flow as the Reynolds Number is increased. The effects are shown very clearly by a comparison of figure 29 and figure 30. Figure 30 corresponds to a higher Reynolds Number and shows turbulence forming at a "transition point" along the separated boundary layer behind the laminar separation point. Incidentally, it should be remembered that the transition point is not really a point but is a more or less extended and fluctuating region in which the laminar layer is progressively changing to the fully

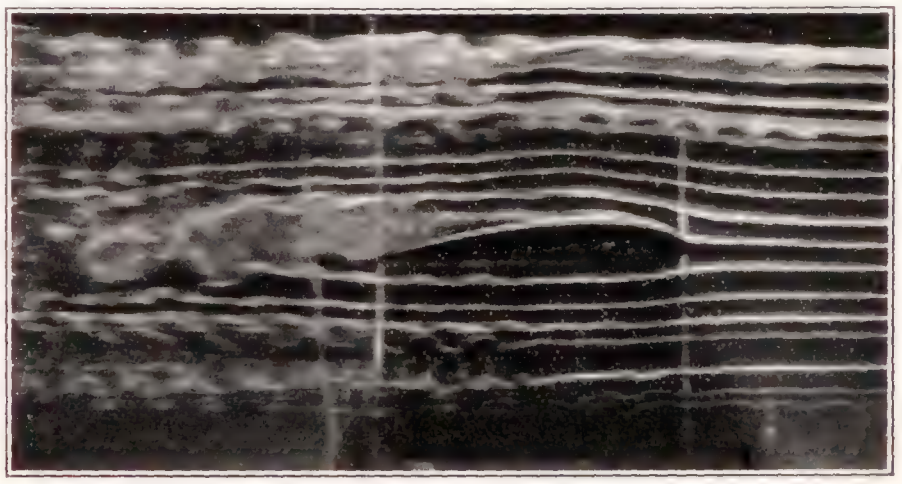

FIGURE 30.—Separation occurring on an airfoil at a low angle of attack (fig. 29) but at an increased Reynolds Number.

developed turbulent layer. This transition region now moves forward toward the separation point as the Reynolds Number is further increased. The formation of turbulence results in a thickening of the boundary layer between the dead air and the overrunning flow until the turbulent mixing extends practically to the airfoil surface. The separated flow may then be considered reestablished. This process would leave a bubble of "dead air" between the separation point and the transition region, the existence of which was predicted several years ago. Subsequently Jones and Farren (reference 17) have actually observed this phenomenon.

As the Reynolds Number is further increased, the transition region progresses toward the leading edge, approaching the region of the laminar separation point. Consider now, for example, the flow about the N. A. C. A. 0012 at a value of R in the neighborhood of R_c, the critical Reynolds Number, where the maximum lift

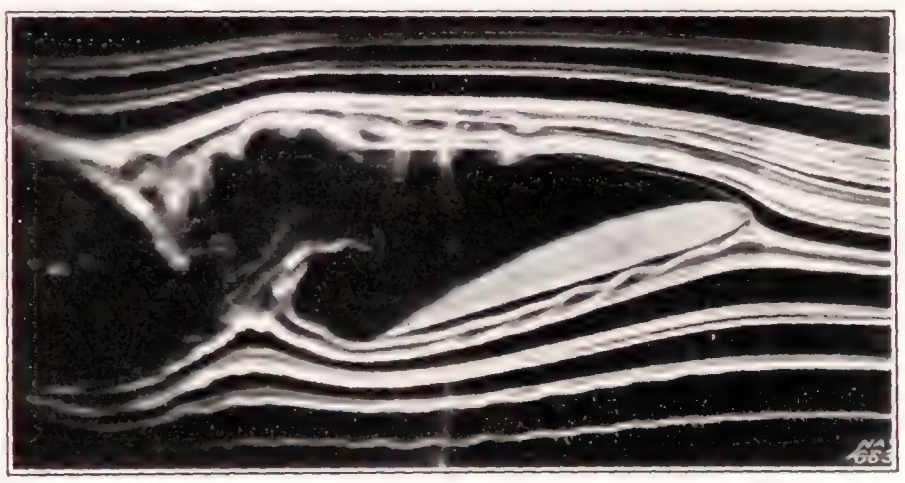

FIGURE 31.—Separation occurring on an airfoil at a high angle of attack.

increases rapidly with R. As shown in figure 28, $c_{l_{max}}$ for the N. A. C. A. 0012 begins to increase rapidly with R at approximately R_c=1,000,000. Consider therefore two flows, one at R_c=1,000,000 just at the attitude of $c_{l_{max}}$, and the other at the same attitude but at a higher

effective Reynolds Number, say 1,750,000. For the former, separation is probably occurring near the low-pressure point, but the turbulence is forming closely enough behind the separation point so that the flow over the upper surface is partly reestablished. An increase of angle of attack fails to increase the lift, however, because the turbulence is forming so late that the local separation and its resulting adverse effect on the thickening or separation of the turbulent layer farther aft prevent a further gain of lift. Now as the Reynolds Number is increased the transition region moves to a position nearer the separation point, the extent of the separated region is reduced and, as shown by reference to figure 3, C_L at the same angle of attack is increased from 0.85 to 1.05 (for the approximately corresponding test Reynolds Numbers of 330,000 and 660,000). Furthermore, the angle of attack may now be increased until C_L reaches 1.1 before the flow following the upper surface fails. The failure now occurs

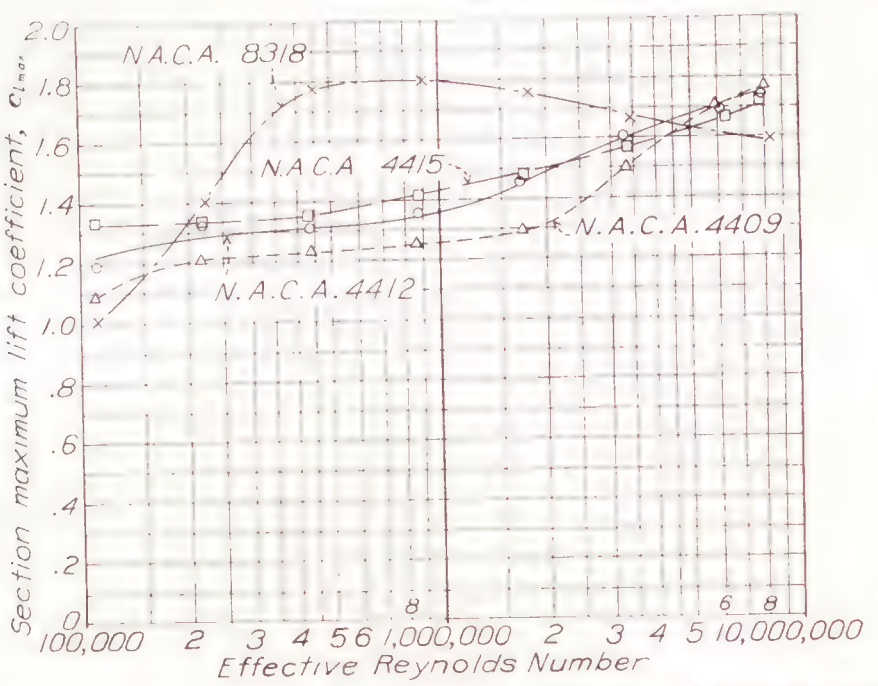

FIGURE 32. Section maximum lift coefficient, $c_{l_{max}}$. Camber and thickness series.

suddenly, causing a break in the lift curve, but again may be delayed by a further increase of the Reynolds Number.

In such cases the scale effect evidently varies with the shape of the nose of the airfoil. If the leading-edge radius is reduced by making the airfoil thinner, the local Reynolds Number for the separation point or the transition region, either R_δ based on boundary-layer thickness or R_x based on the distance along the surface, is reduced with respect to R because the local dimensions near the nose are reduced with respect to the airfoil chord. Higher values of R are therefore required to reach the critical R_x or R_δ values in the neighborhood of the nose. This result is indicated by the higher critical Reynolds Number R_c for the N. A. C. A. 0009 than for the N. A. C. A. 0012, as shown in figure 28. Likewise, the 15 and 18 percent thick airfoils show progressively lower values of R_c than the N. A. C. A. 0012, but the critical range tends to disappear as the thickness is increased.

The range of R is limited by the wind tunnel so that in most instances the scale effect above the critical range could not be determined. It is probable, however, that the highest maximum lift coefficients are reached when the Reynolds Number corresponds to the occurrence of fully developed turbulence practically at the laminar separation point but that this condition occurs above the highest Reynolds Numbers reached except possibly for the thickest airfoil, N. A. C. A. 0018.

High local Reynolds Numbers at the laminar separation point could, however, be reached by employing a thick, highly cambered airfoil. The N. A. C. A. 8318 airfoil was included for this reason. The results (see fig. 32) indicate, as expected, a very low critical Reynolds Number. With increasing Reynolds Number, $c_{l_{max}}$ rises to a maximum at R=900,000 and then falls off slowly. In this instance, at the highest Reynolds Numbers transition probably occurs ahead of any point at which laminar separation could occur. The maxi-

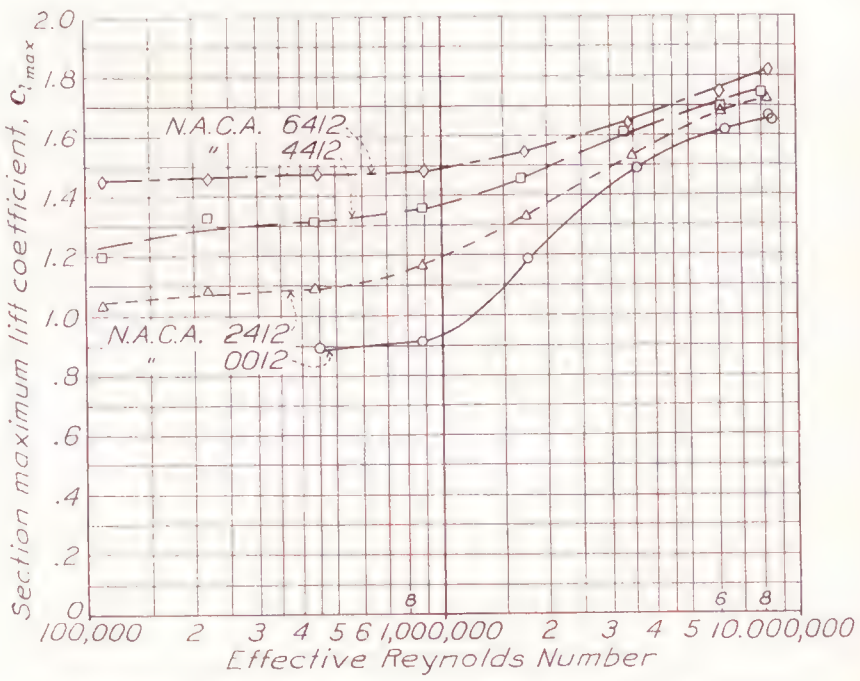

FIGURE 33.—Section maximum lift coefficient, $c_{l_{max}}$. Camber series.

mum lift coefficient must therefore be determined by the behavior of the turbulent layer. The significant conclusion is that $c_{l_{max}}$ then decreases with increasing R. Another significant observation is that under these conditions stalling is progressive as indicated by the rounded lift-curve peaks in figure 11. This type of stalling corresponds to a progressive separation or thickening of the turbulent layer in the region of the trailing edge.

The process of stalling in general is more complex than either of the two distinct processes just discussed. It has been compared by Jones (reference 17) to a contest between laminar separation near the nose and turbulent separation near the trailing edge, one or the other winning and thus producing the stall. Actually it appears from these scale-effect data that, for commonly used airfoils at a high Reynolds Number, the forward separation usually wins but that it is largely conditioned and brought about by the thickening or separation of the turbulent boundary layer near the

trailing edge, which, in turn, may be largely influenced by the local separation near the leading edge. The reasons for these statements will become clear from the consideration of the scale effects for the different types of airfoil.

Consider first the maximum lift of the conventional type of cambered airfoil. Where stalling is determined largely by separation near the leading edge, the maximum lift would be expected to be a function of the curvature near the leading edge and also a function of the mean camber because the effect of the camber is to add a more or less uniformly distributed load along the chord. At some angle of attack above that of zero lift the flow over the nose part of the cambered airfoil approximates that over the nose of the corresponding symmetrical airfoil at zero lift. This correspondence of flows at the leading edges between the symmetrical and cambered airfoils continues as the angles of attack of both are increased. If the stalling were determined largely by the flow near the nose, the two airfoils would stall at the same time, but the lift of the cambered airfoil would be higher than that of the symmetrical airfoil by the amount of the initial lift increment. Reference to figure 33 shows that this expected change of $c_{l_{max}}$ with camber is approximately that shown by the results from tests in the lower range of the Reynolds Number. At high Reynolds Numbers, however, the change of $c_{l_{max}}$ with camber is much smaller than would be expected if the stall were controlled only by conditions near the leading edge. On the other hand, some of the cambered airfoils show a sudden loss in lift at the maximum indicating that separation is occurring near the leading edge but, as the camber is increased, the lift curves become rounded. (See figs. 6, 7, and 8.) For the N. A. C. A. 2412, which shows a sharp break in lift at the maximum but a small gain in $c_{l_{max}}$ due to camber at the high Reynolds Numbers, the boundary-layer thickening or turbulent separation must become pronounced near the trailing edge at the higher Reynolds Numbers before the flow breakdown occurs near the leading edge. This alteration of the flow results in higher angles of attack for a given lift and consequently more severe flow conditions over the nose of the airfoil. These flow conditions, which really originate near the trailing edge, thus bring about the flow breakdown near the leading edge that finally produces the actual stall. It must not, however, be concluded that more gradually rounding lift-curve peaks with increasing R should be the result; actually, the opposite is usually true (e. g., figs. 6, 7, and 8). The explanation is probably that increasing the Reynolds Number reduces the extent of the local separation near the leading edge, which influences the boundary-layer thickening near the trailing edge, at least until the transition region reaches the separation point. That $c_{l_{max}}$ continues to be influenced by the flow conditions near the leading edge, even for highly cambered sections, is shown by the fact that the critical Reynolds Number is little affected by increasing the camber to that of the N. A. C. A. 6412 in spite of the fact that the actual gain in $c_{l_{max}}$ throughout the critical range becomes less for the more highly cambered airfoils. This conclusion is an important one because it can be extended to predict that the critical Reynolds Number will not be affected by flaps and other high-lift devices placed near the trailing edge, which act much like a camber increase.

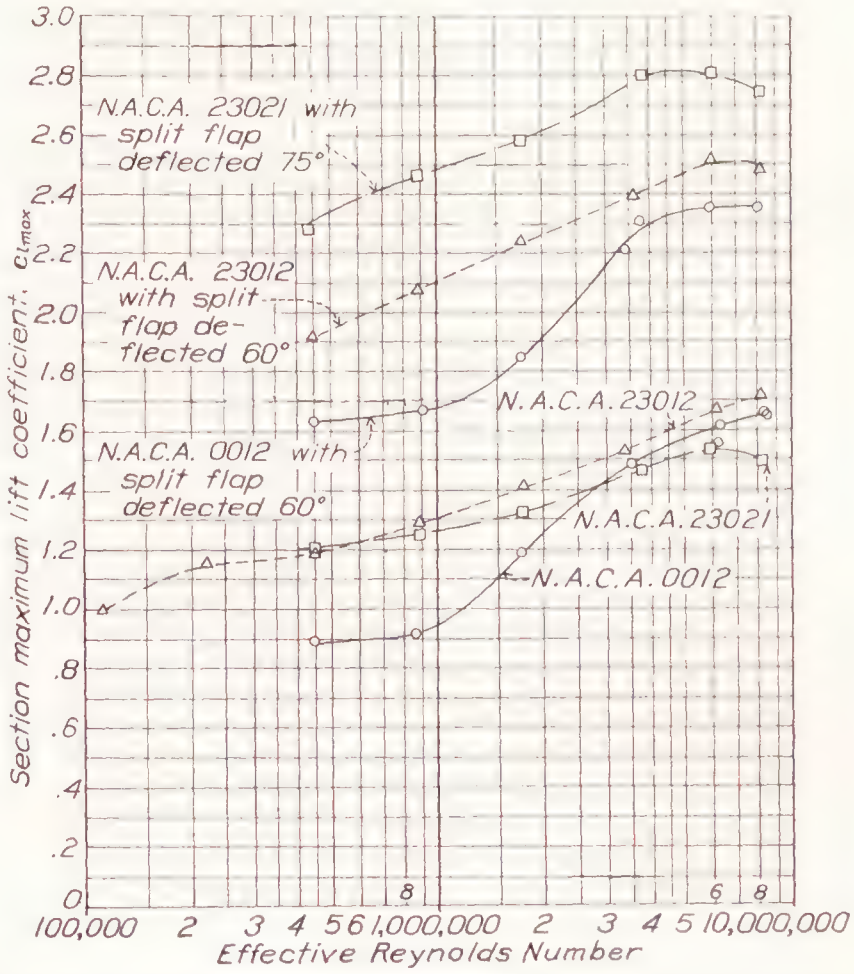

FIGURE 34.—Section maximum lift coefficient, $c_{l_{max}}$. Airfoils with and without flaps.

Reference to figure 34 shows the correctness of this conclusion. It will be noted, moreover, that each scale-effect curve representing an airfoil with a split flap tends to parallel the corresponding curve for the same airfoil without a flap. The split flap thus simply adds an increment to the maximum lift without otherwise changing the character of the scale effect. In this respect the behavior with the flap differs from the behavior with increasing camber. With the split flap, the distribution of pressures over the upper surface is apparently not affected in such a way as to increase the tendency toward trailing-edge stalling, otherwise the scale-effect variations would not be similar with and without the flaps. Incidentally, it is of interest to note that the maximum lift increment due to the split flap is not independent of the airfoil section shape but, for example, increases with the section thickness. (Cf. the N. A. C. A. 230 series, with and without split flaps, table I.)

As regards flaps other than split flaps, recent tests have shown that the maximum lifts attainable are approximately equal for either the ordinary or the split flap. This result might have been expected because the

results of references 18 and 19 had indicated that the flow does not follow the upper surface of an ordinary flap except for small angles of flap deflection. It should therefore make little difference whether or not the upper surface of the flap is deflected with the lower. Furthermore, the same reasoning might be applied to predict the effects of camber, when the mean line is of such a shape that the maximum camber occurs near the trailing edge so that the separation associated with increasing camber is localized in this region. Thus it might have been predicted that the scale effect as shown in figure 35 for the N. A. C. A. 6712 airfoil would be more like that of an airfoil with a split flap than like that of the usual type of cambered airfoil.

Another important conclusion can be deduced from the results in figure 35 showing the scale effects for airfoils having various mean-line shapes. When a mean-line shape like that of the N. A. C. A. 23012 is em-

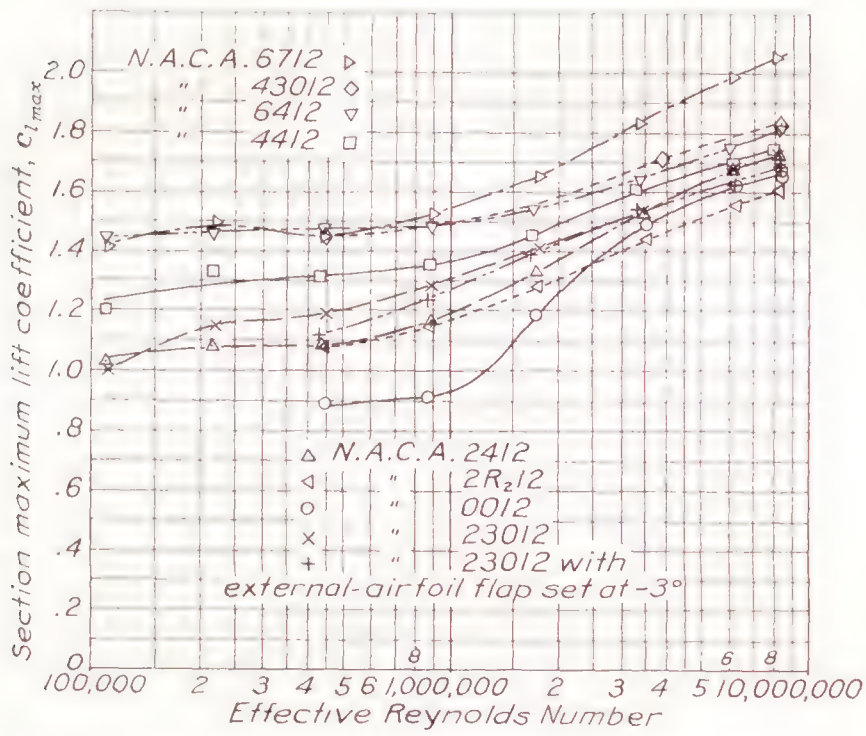

FIGURE 35.—Section maximum lift coefficient, $c_{l_{max}}$. Airfoils with various mean-line shapes.

ployed—that is, one having marked curvature near the nose and a forward camber position—the effect is to alter the conditions of the leading-edge stall. The critical Reynolds Number is thus shifted to the left and the general character of the scale effect becomes more like that of the usual airfoil of 15 instead of 12 percent thickness.

The opposite effect on the nose stall is shown in figure 36 where the critical Reynolds Number is shifted to the right by decreasing the leading-edge radius, that is, by changing from the N. A. C. A. 23012 section to the 23012–33. Thus it appears, in general, that the character of the $c_{l_{max}}$ scale effect, particularly in relation to the value of the critical Reynolds Number, depends mainly on the shape of the airfoil near the leading edge.

The two remaining airfoils not covered by the previous discussion (fig. 37) have slotted high-lift devices. Both the Clark Y airfoil with Handley Page slot and the airfoil with external-airfoil flap show unusual scale effects. The airfoil with Handley Page slot shows an increasing $c_{l_{max}}$ throughout the Reynolds Number range but shows a peculiar change in the character of the stall in the full-scale range near R_e=3,000,000. (See also fig. 24.) The airfoil with the external-airfoil flap shows a break in the scale-effect curve. Two values of $c_{l_{max}}$ were measured for the condition corresponding to R_e=1,700,000 (fig. 23, test R=645,000), one lift curve having a sharp break at the maximum and the other being rounded. It is believed that the change is associated with the action of the slot at the nose of the external-airfoil flap. It is particularly interesting because it represents one of the cases mentioned under the interpretation of the wind-tunnel data for which the failure of the tunnel flow to reproduce exactly at the effective Reynolds Number the corresponding flow in flight becomes of practical importance. A comparison of these tests with tests in the 7- by 10-foot tunnel (reference 5) indicated that such scale effects may be due primarily to the action

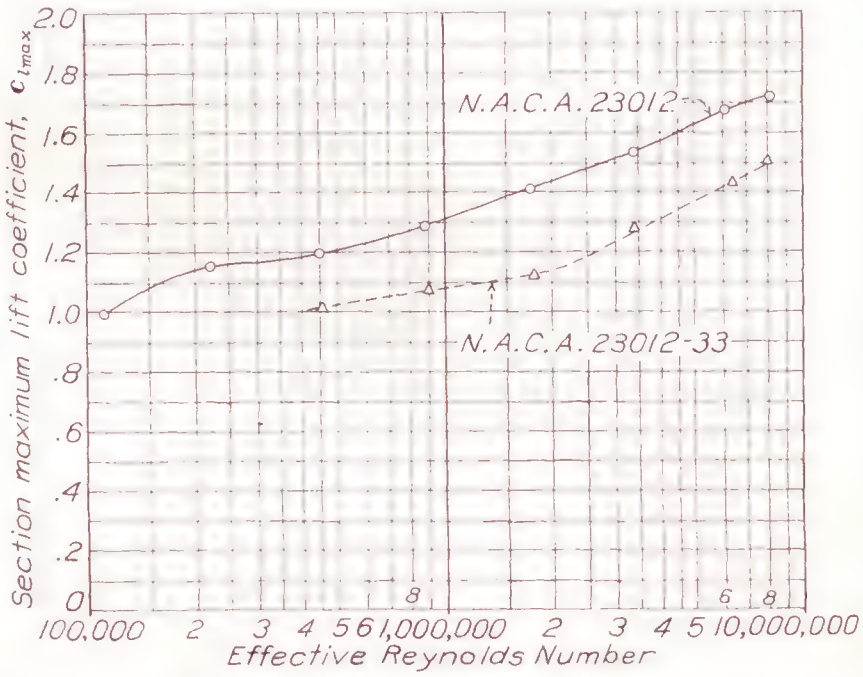

FIGURE 36.—Section maximum lift coefficient, $c_{l_{max}}$. Thickness-shape variation.

of the slot as affected by the boundary-layer thickness relative to the slot width, which is a function of both the test and the effective Reynolds Number, rather than to the transition from laminar to turbulent flow. When interpreted on the basis of the test rather than the effective Reynolds Number as regards the occurrence of the break in the low Reynolds Number range, better agreement with the results from the variable-density tunnel was obtained. On this basis the discontinuity shown in figure 37 as occurring at R_e= 1,700,000 would be expected to occur in flight at a considerably lower Reynolds Number outside the usual flight range.

With regard to $c_{l_{max}}$ scale effects for conventional types of airfoils, it now appears in the light of the preceding discussion that a position has been reached from which the scale effects appear rational and sufficiently regular and systematic so that general scale-effect corrections may be given for such airfoils. This position represents a marked advance. In a later

section of this report such generalized scale-effect corrections for $c_{l_{max}}$ are presented for engineering uses.

Lift variation near $c_{l_{max}}$.—The variation of the lift near the maximum as indicated by the shape of the lift curve is of some importance because it often affects the character of the stall and the corresponding lateral control and stability of the airplane in flight. The character of the stall for the airfoils may be inferred approximately from the preceding discussion of $c_{l_{max}}$ and is indicated by the lift curves in figures 2 to 24. The moderately thick symmetrical airfoils in the critical or flight range of R show sudden losses of lift beyond the maximum. Efficient airfoils of moderate thickness and camber, for example, N. A. C. A. 2412 and 23012, likewise usually show sudden breaks in the lift curve at the maximum for the higher Reynolds Numbers. When the influence of trailing-edge stalling becomes sufficiently marked as it does with airfoils N. A. C. A. 4412 and 6412, the breaks in the lift curves disappear and the lift curve becomes rounded at the maximum. It is interesting to note that breaks occur at comparatively low values of the Reynolds Number for the N. A. C. A. 8318. In this case the breaks appear in the critical range of R, where critical leading-edge stalling occurs, and disappear at higher and lower Reynolds Numbers. (See figs. 11 and 32.)

Lift-curve slope a_0.—The scale effects for a_0 are represented in figure 38. It will be noted that, within the full-scale range, the airfoils show little variation of a_0 with either airfoil shape or with R. In this range most of the airfoils show a slight tendency toward increasing a_0 with R but, for engineering purposes, the variation of a_0 may usually be considered negligible within the flight range. The lift-curve slope, like several of the other section characteristics, begins to display abnormal variations below a Reynolds Number of approximately 800,000. For the lowest values of R the lift curves often became so distorted that lift-curve slopes were not determined. (See figs. 2 to 24.)

Angle of zero lift α_{l_0}.—Scale-effect variations of α_{l_0} are represented in figure 39. The conclusions with respect to this characteristic are almost the same as for the lift-curve slope a_0. Symmetrical airfoils, of course, give $\alpha_{l_0}=0$ at all values of R. The cambered airfoils, in general, show a small decrease in the absolute value of the angle with increasing R above the value at which the variations are abnormal.

Minimum profile-drag coefficient $c_{d_{0min}}$.—The minimum profile-drag coefficient is indicative of the wing drag in high-speed flight and is the other important section characteristic, aside from $c_{l_{max}}$, that shows marked scale-effect variations within the full-scale range which must be taken into account in engineering work.

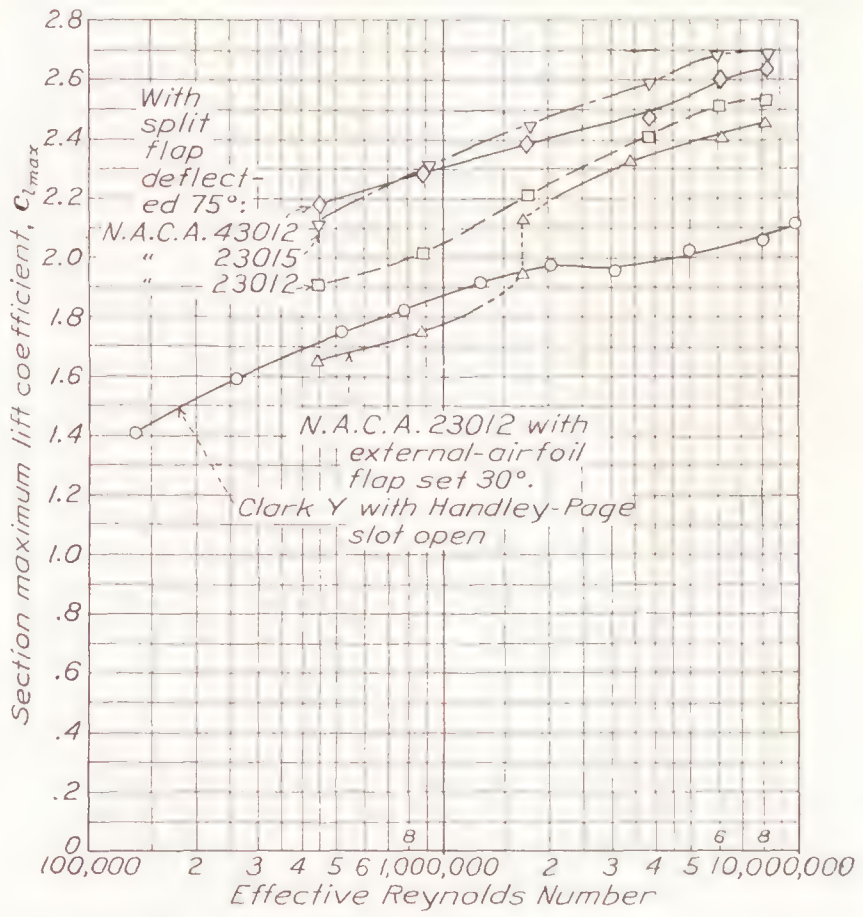

FIGURE 37.—Section maximum lift coefficient, $c_{l_{max}}$. Airfoils with high-lift devices.

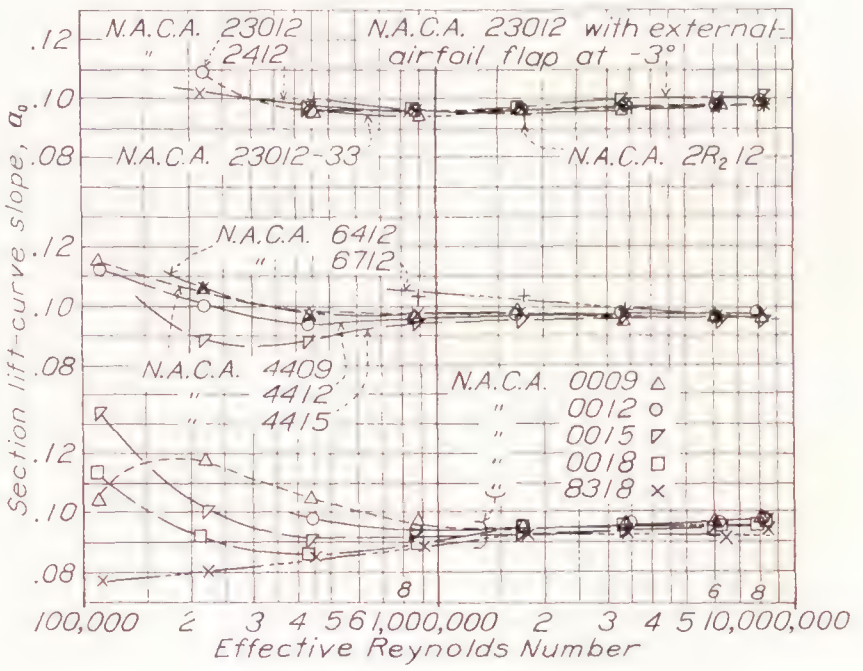

FIGURE 38.—Lift-curve slope, a_0.

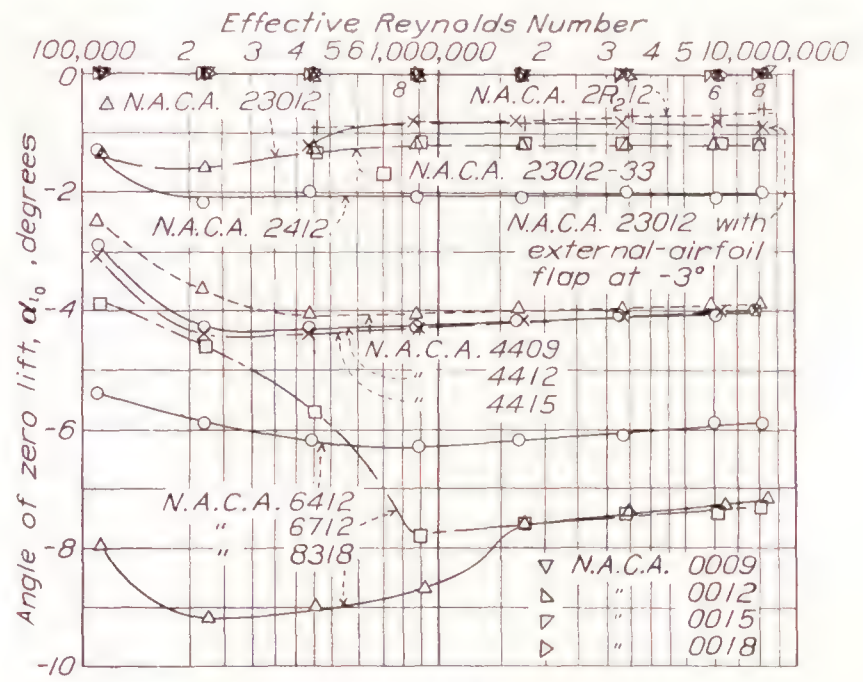

FIGURE 39.—Angle of zero lift, α_{l_0}.

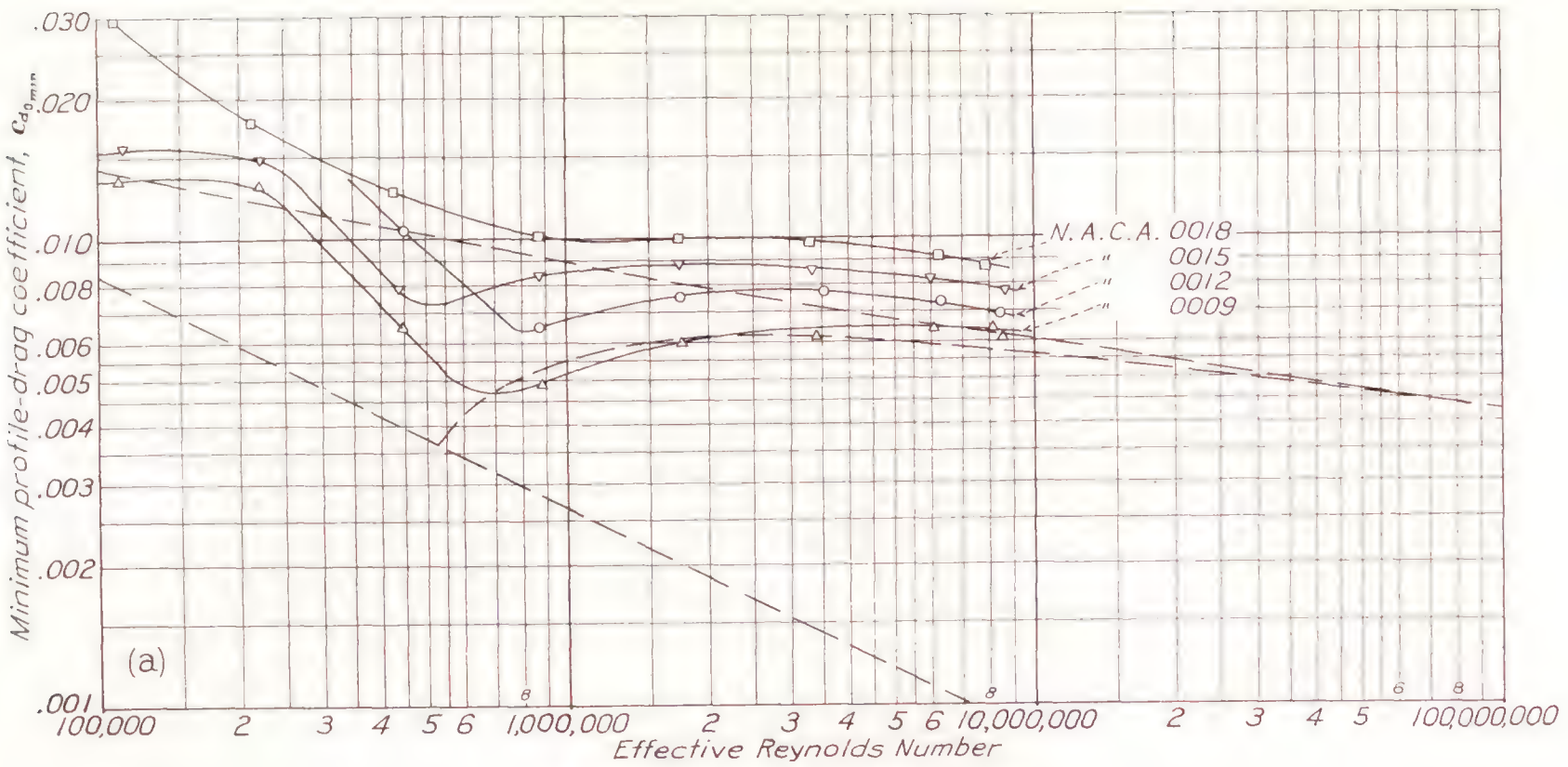

(a) Symmetrical airfoils of varying thickness.

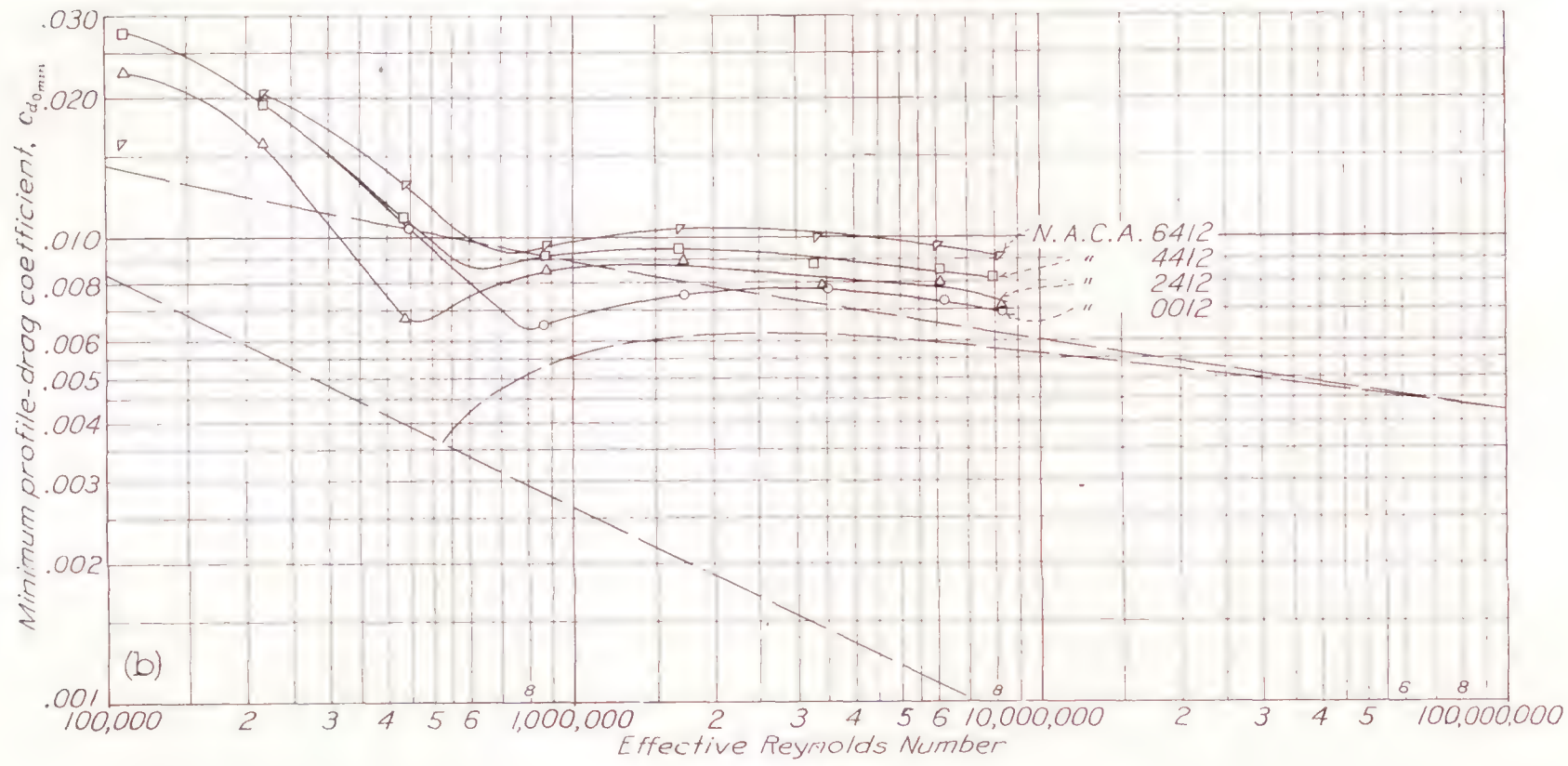

(b) Camber series.

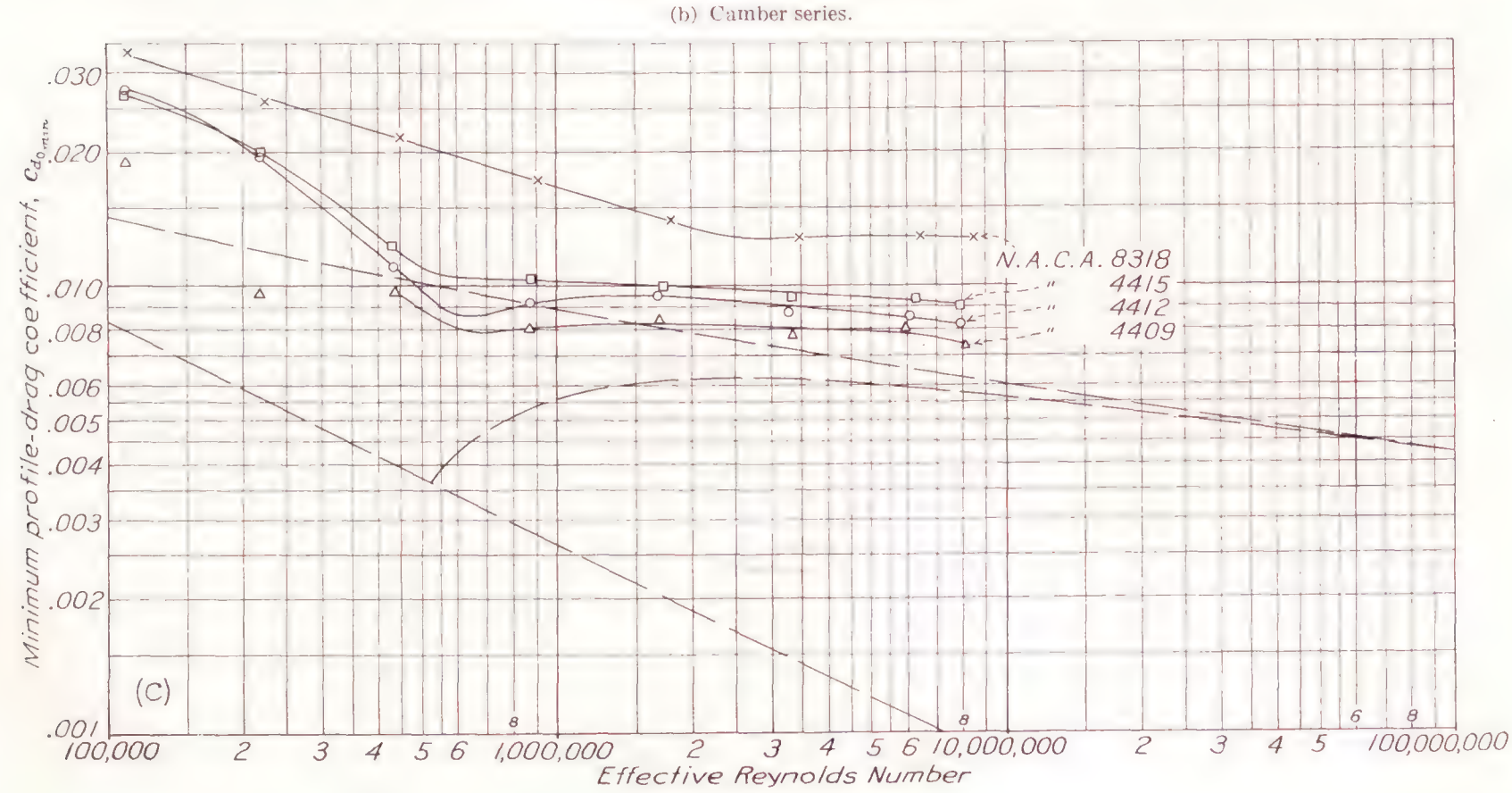

(c) Thickness and camber.

FIGURE 40.—Minimum profile-drag coefficient, $c_{d_{0\ min}}$.

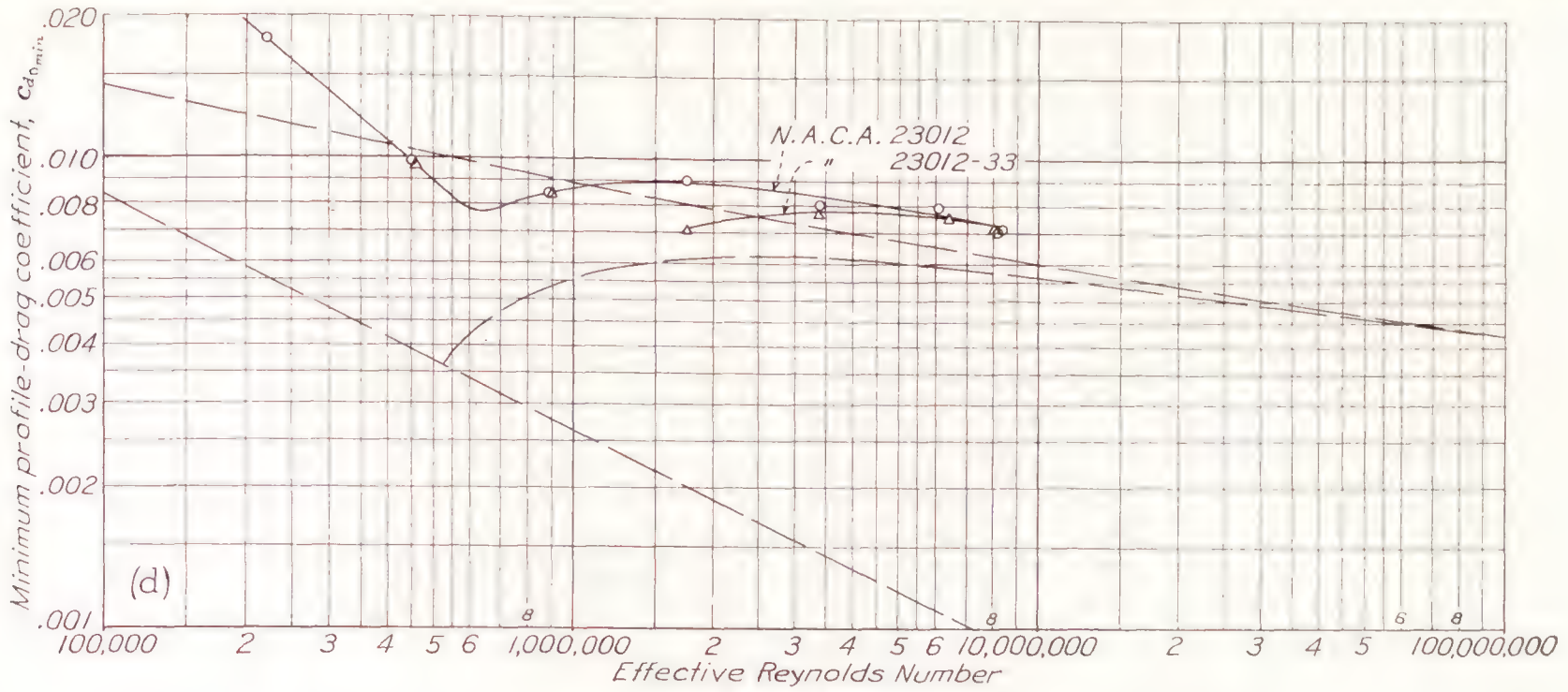

(d) Thickness shape.

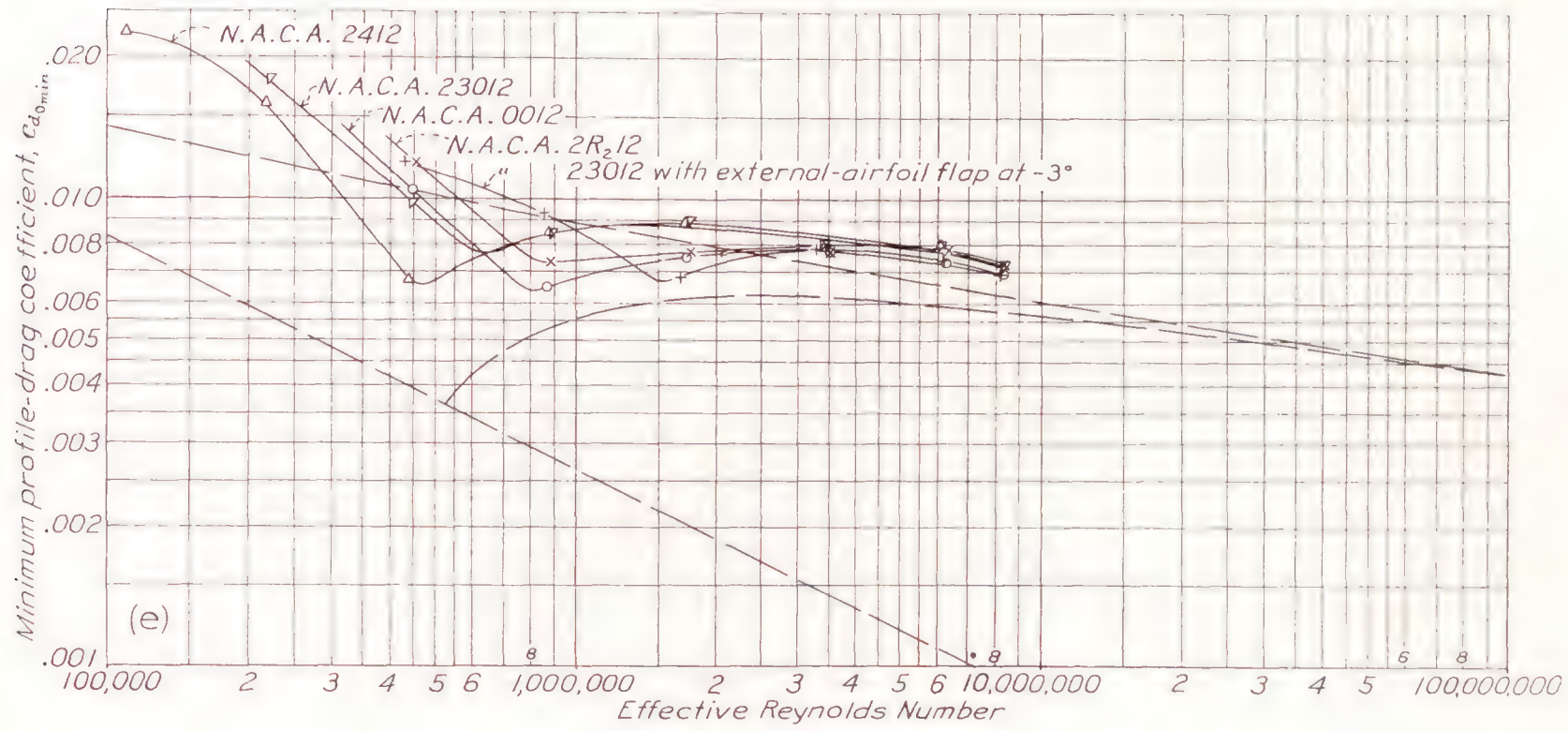

(e) Camber shape.

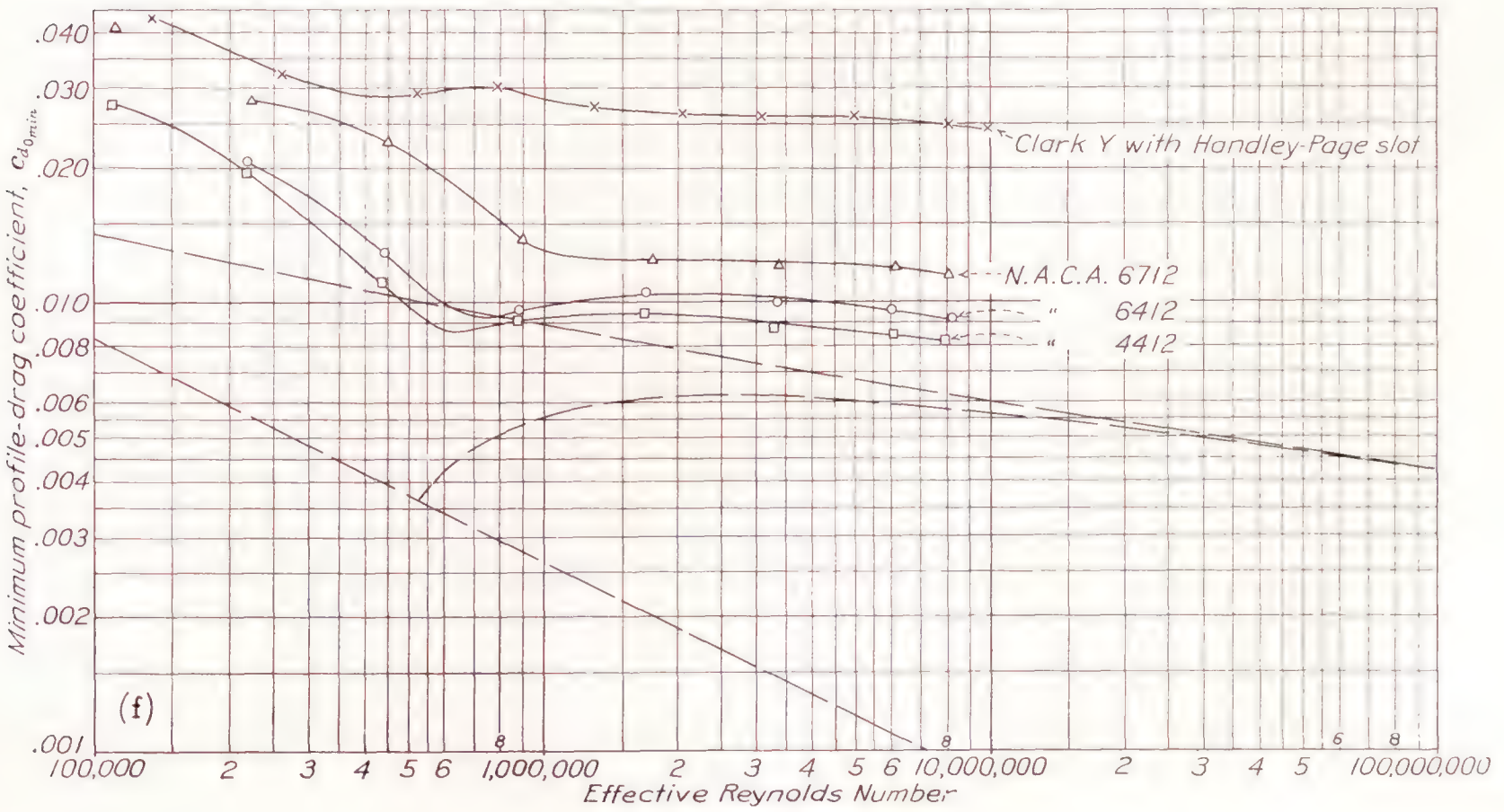

(f) Camber shape.

FIGURE 40 (continued.)—Minimum profile-drag coefficient, $c_{d0\ min.}$

The experimental drag results are presented by means of logarithmic plots with the well-known laminar and turbulent skin-friction curves and the Prandtl-Gebers transition curve shown for comparison. (See figs. 40 (a) to 40 (f).) At the higher Reynolds Numbers a striking similarity exists between the minimum profile-drag coefficients for the airfoils and the transition curve representing the drag coefficient variation with R for a flat plate towed in water. The other striking feature of the drag curves is their departure from regularity at Reynolds Numbers below a certain critical value. This critical value of the Reynolds Number usually lies in the range between 400,000 and 800,000, but a study of the experimental results will show that the critical value itself is irregular, that is, it does not vary systematically with the airfoil shape. The results appear as though two or more drag values were possible within this Reynolds Number range and accidental disturbances determined whether a high or a low value of the drag was measured at a given value of R within this range. One is reminded of Baker's experiments towing airship models in water in a towing basin where measurements could not be repeated until transition was definitely brought about by the use of a cord passing around the model near the nose.

The shape of the scale-effect curve for the N. A. C. A. 0012 airfoil at zero angle of attack (fig. 40 (a)) was studied in the light of boundary-layer calculations. The results indicated that the computed skin-friction drag coefficients to give scale-effect variations in agreement with the measured ones required the presence of rather extensive laminar boundary layers in this critical range of the Reynolds Number. In fact, for the N. A. C. A. 0012 airfoil, the laminar boundary layer was found to have become so extensive when R was reduced to the experimentally determined critical value that a further reduction of R would have required the laminar boundary layer to extend behind the computed laminar separation point, which would have involved at least local separation. It seems evident, therefore, that the increased drag coefficients below the critical range are the result of this condition, which is probably associated with laminar separation and a resulting increase of the pressure or form drag of the section. Fortunately, however, this phenomenon seems to appear below the usual flight range of R.

When designers are concerned with the minimum drag of an airfoil section, it is usually for high-speed or cruising flight, which for modern transport airplanes may correspond to a Reynolds Number of 20,000,000 or more for some of the wing sections. The drag coefficients for the Reynolds Number range above the highest reached in the tunnel are therefore of more interest than those well within the experimental range. Unfortunately, the precision of the measurements permits only an approximate determination of the shape of these scale-effect curves even in the higher experimental range of R so that extrapolations into the higher flight range will necessarily be unreliable. Nevertheless, much engineering work requires a knowledge of airfoil drag coefficients within this range so that the engineer *must* resort to extrapolation. For this purpose the data may be studied in relation to the slopes of the curves for the various airfoils (fig. 40) in the highest range of R reached in the experiments. Such a study indicates that the airfoils, excluding the unusual airfoils N. A. C. A. 8318, N. A. C. A. 6712, and the Clark Y with Handley Page slot, show a decreasing $c_{d_{0\,min}}$ with R that seems, in general, to parallel approximately the corresponding curve for the flat plate. Thus, in general, the slope of the $c_{d_{0\,min}}$ scale-effect curves in the neighborhood of a Reynolds Number of 8,000,000 may be taken as approximately -0.11, which leads to the following extrapolation formula:

$$c_{d_{0\,min}} = \left(c_{d_{0\,min}}\right)_{std}\left(\frac{R_{std}}{R}\right)^{0.11}$$

where the subscript *std* refers to the standard airfoil-test results from the variable-density tunnel corresponding to an effective Reynolds Number of approximately 8,000,000. In such extrapolation formulas, values of the exponent have been used between 1/5, taken from Prandtl's original analysis of the completely turbulent skin-friction layer, and 0.15, which agreed better with experiments with pipes and flat plates at very high values of R and agrees better with von Kármán's recent analysis of the completely turbulent layer in this range of R. It should be emphasized, however, that these comparatively large exponents are not conservative and would be expected to lead to predictions of large-scale drag values much too low, particularly when the extrapolation is made from measurements made in the transition region; for example, in figure 40 (a) measurements in the range between 1,000,000 and 2,000,000 should not be extrapolated by such methods to 20,000,000. Extrapolations from R=8,000,000 using the comparatively low exponent 0.11 are, however, considered reasonably conservative for aerodynamically smooth airfoils.

In regard to profile-drag coefficients at lift coefficients other than the optimum, figure 41 (a) shows the scale effects for c_{d_0} at c_l=0.8 for the symmetrical series of airfoils. The drop in the scale-effect curves in the transition region has disappeared and the two thinner airfoils show evidences of the approaching stall. Curves for members of the camber series of airfoils, N. A. C. A. 0012, 2412, 4412, and 6412 at *zero lift* are shown in figure 41 (b). Here the symmetrical airfoil is operating at its optimum lift and the departure from the optimum for the other airfoils increases with camber. A progressive transition from the $c_{d_{0\,min}}$ type of scale effect to that of figure 41 (a) is apparent. Results (reference 10) from other wind tunnels for the Clark Y airfoil, which is in a sense similar to the N. A. C. A. 4412 but has slightly less camber, are also indicated in figure

41 (b) for comparison. The comparison of the results from the various tunnels should serve to indicate the limitations of accuracy that must be accepted when any of the data are extrapolated to the higher full-scale Reynolds Numbers.

Optimum lift coefficient $c_{l_{opt}}$.—The optimum lift coefficients are presented in figure 42. This characteristic is of importance mainly in relation to c_{d_0} values at other values of c_l. It is not possible, nor essential for this purpose, to evaluate $c_{l_{opt}}$ very accurately. In fact,

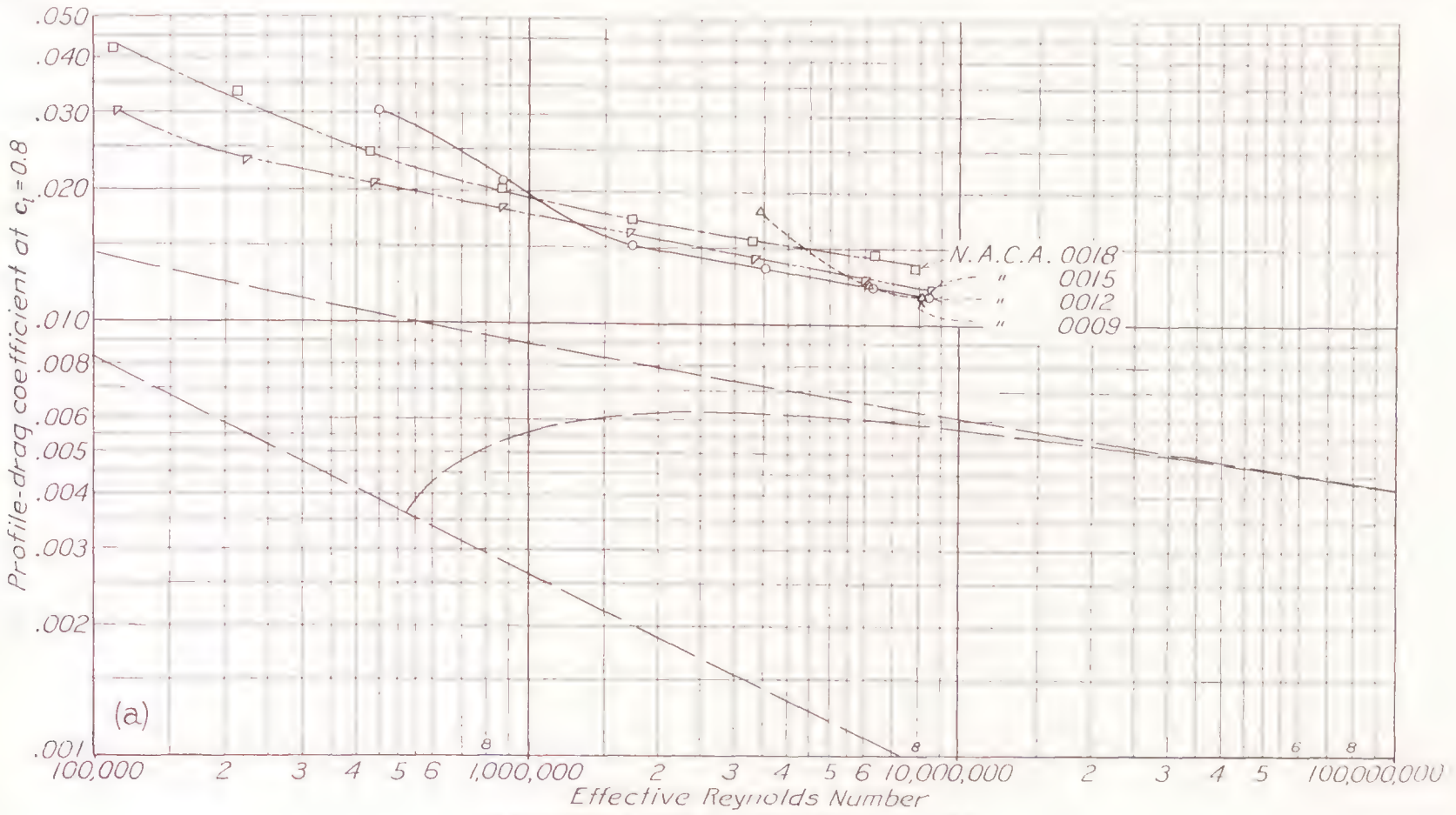

(a) Symmetrical airfoils of varying thickness; c_l=0.8.

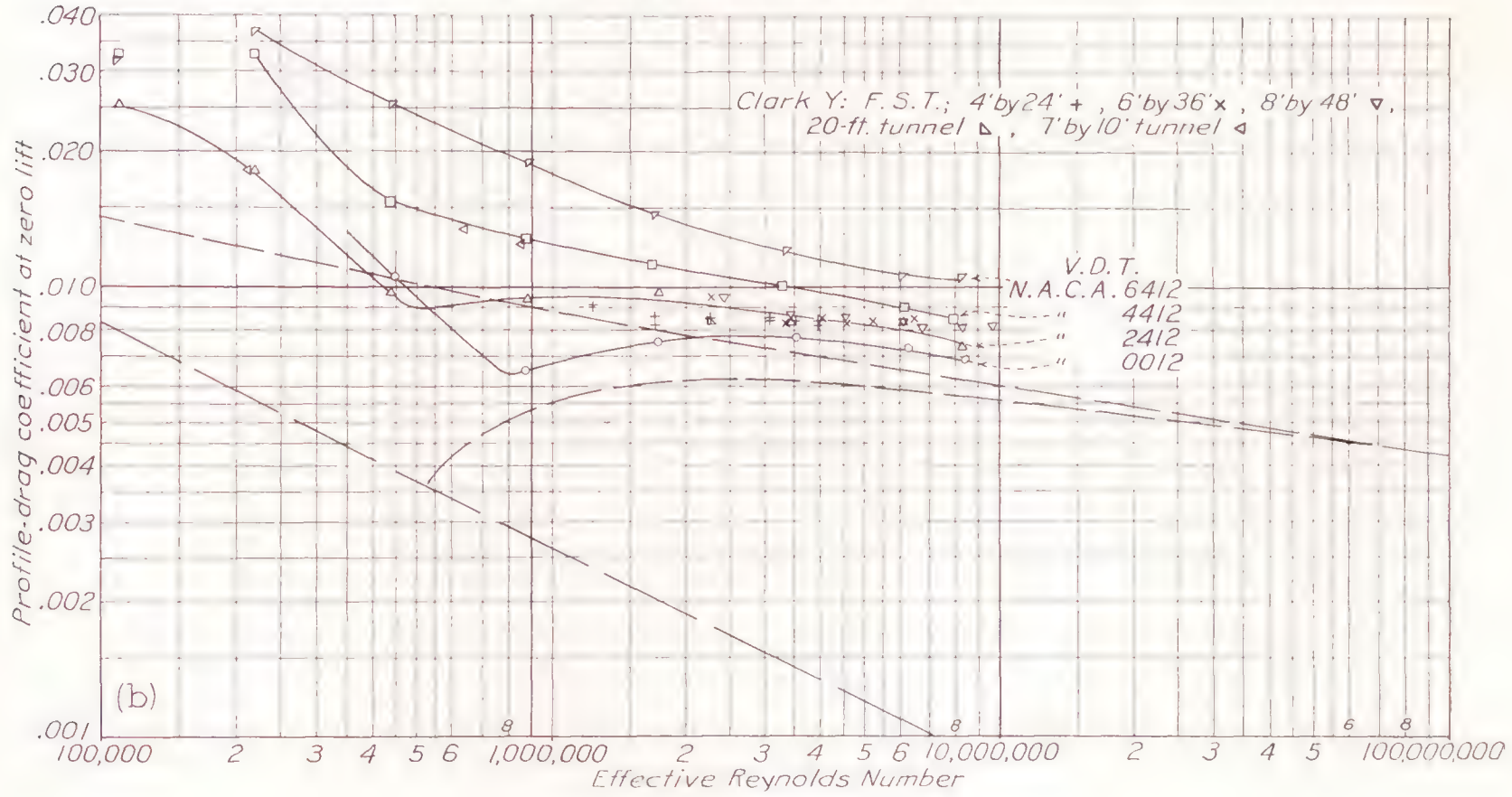

(b) Camber series; c_l=0.

FIGURE 41.—Profile-drag coefficient.

The determination of c_{d_0} values at various lift coefficients in engineering work is best accomplished by a consideration of increments from $c_{d_{0\,min}}$. The method of a "generalized polar" discussed in a later section of this report gives such increments in terms of the departure of c_l from $c_{l_{opt}}$ as compared with the departure of $c_{l_{max}}$ from $c_{l_{opt}}$.

the accuracy of the experimental data is not sufficient to establish the scale-effect variations with certainty. Nevertheless, the results show a definite tendency toward a decreasing $c_{l_{opt}}$ with increasing R. Thus values measured in small atmospheric tunnels may be expected to be too high. Values from the standard airfoil tests in the variable-density tunnel may usually

be taken as approximately correct within the usual full-scale range but may be somewhat too high for the higher flight range of R.

Pitching-moment coefficient $c_{m_{a.c.}}$ and aerodynamic-center position *a. c.*—The values of the pitching-moment coefficient and the aerodynamic-center position establish the pitching-moment characteristics of the airfoil section in the normal operating range between zero lift and the stall. In this range the pitching moment about the aerodynamic-center point may be considered constant for conventional airfoils. The accuracy of the low-scale data did not permit the evaluation of aerodynamic-center positions for values of R much below the flight range, and the variations found in the higher range showed little consistency. Values are indicated in figures 2 to 24 and in table I, but it is not considered advisable in practice to allow for a variation of aerodynamic center with R. The $c_{m_{a.c.}}$ values corresponding to these aerodynamic-center positions are plotted in figure 43. The values are nearly independent of R at high values of R but usually show a tendency to increase numerically as R is reduced toward the lower extremity of the flight range. Thus low-scale tunnel tests may be expected to give pitching moments that are numerically too large.

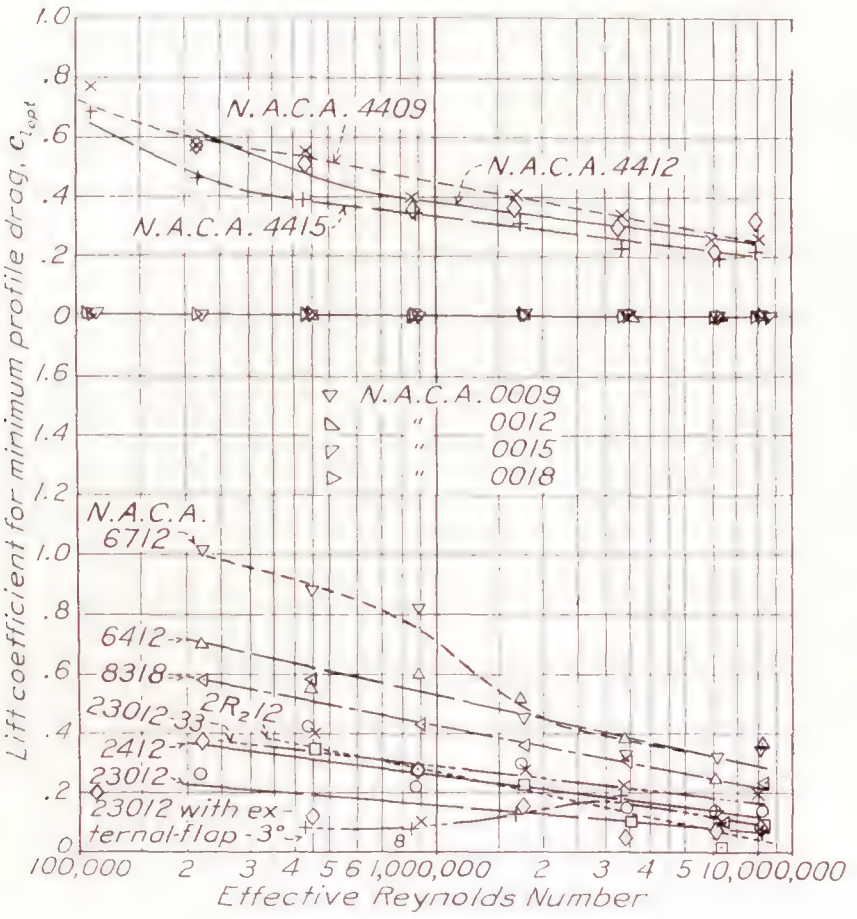

FIGURE 42.—Optimum lift coefficient, $c_{l_{opt}}$.

PREDICTION OF AIRFOIL CHARACTERISTICS AT ANY REYNOLDS NUMBER FOR ENGINEERING USE

In the consideration of methods of predicting wing characteristics, it should be remembered that the scope of this report is confined to the prediction of the *airfoil section* characteristics. Actual *wing* characteristics are obtained from these section characteristics by integrations along the span with suitable allowances for the induced downflow and the corresponding induced drag. Such calculations as applied to tapered wings are fully discussed in reference 8. It remains therefore to predict the airfoil *section* characteristics at any value of the flight Reynolds Number. The preceding discussion has shown that for engineering purposes many of the important airfoil section characteristics may be considered independent of R within the flight range, so that for application to flight at any value of R these characteristics may be taken directly from the tabulated values from the standard airfoil tests in the variable-density tunnel. There remain then the two important *section* characteristics $c_{l_{max}}$ and c_{d_0}, which in general will require correction to the design Reynolds Number before they are employed.

Section maximum lift.—For the prediction of the *section* maximum lift coefficient $c_{l_{max}}$ at values of R other than the R_e value for which they are commonly tabulated, the correction-increment curves of figure 44 have been prepared from the data in this report. In this figure, curves giving the corrections $\Delta c_{l_{max}}$ are grouped in families corresponding to the measured scale-effect variations for various types of airfoils. In general, for normal airfoils the curves in figure 44 marked 0 for types B, C, D, and E correspond to the symmetrical airfoil sections of different thickness and the curves indicated by increasing numbers correspond to airfoil sections of increasing camber.

In practice, the particular curve to be employed for a given airfoil will be indicated in the standard tables of airfoil characteristics such as table II of this report (see also reference 3) under: "Classification, SE."

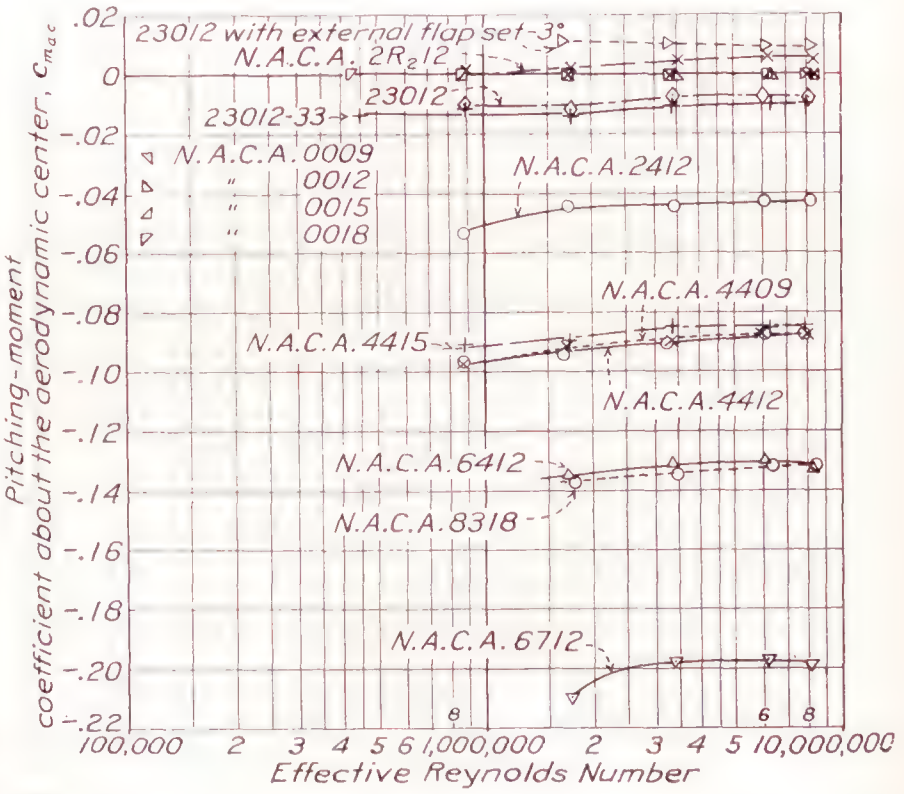

FIGURE 43.—Pitching-moment coefficient about the aerodynamic center, $c_{m_{a.c.}}$.

From the curve thus designated, the correction increment is read at the design Reynolds Number. The required $c_{l_{max}}$ for the section at the particular Reynolds Number is then obtained by adding this increment to the tabulated $c_{l_{max}}$ value.

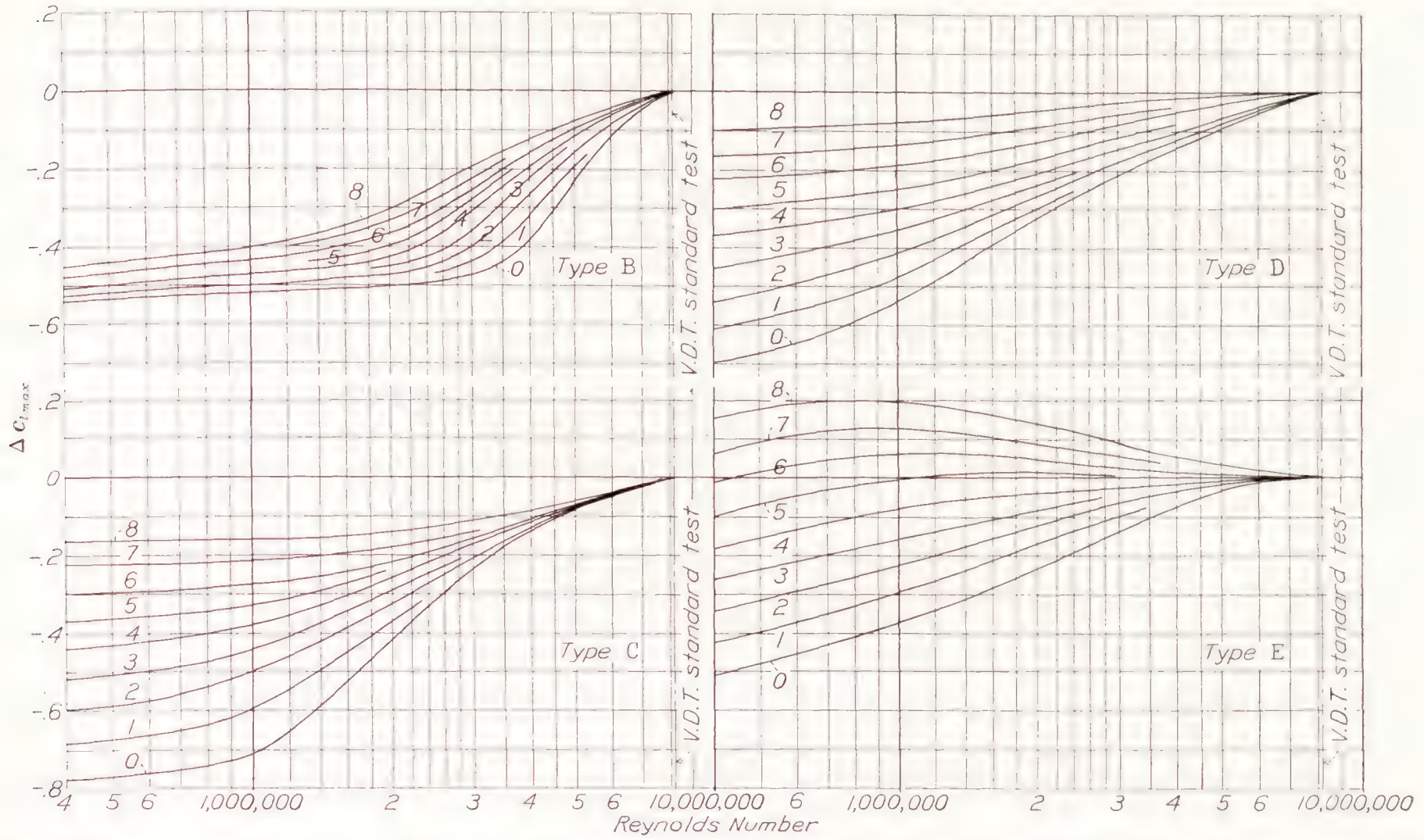

FIGURE 44.—Scale-effect corrections for $c_{l_{max}}$. In order to obtain the section maximum lift coefficient at the desired Reynolds Number, apply to the standard-test value the increment indicated by the curve that corresponds to the scale-effect designation of the airfoil.

Airfoil section drag.—In design work, values of the *section* minimum drag coefficient $c_{d_0\,min}$ for aerodynamically smooth airfoils are first obtained from the tabulated data by means of the extrapolation formula previously given,

$$c_{d_0\,min} = \left(c_{d_0\,min}\right)_{std}\left(\frac{R_{std}}{R}\right)^{0.11}$$

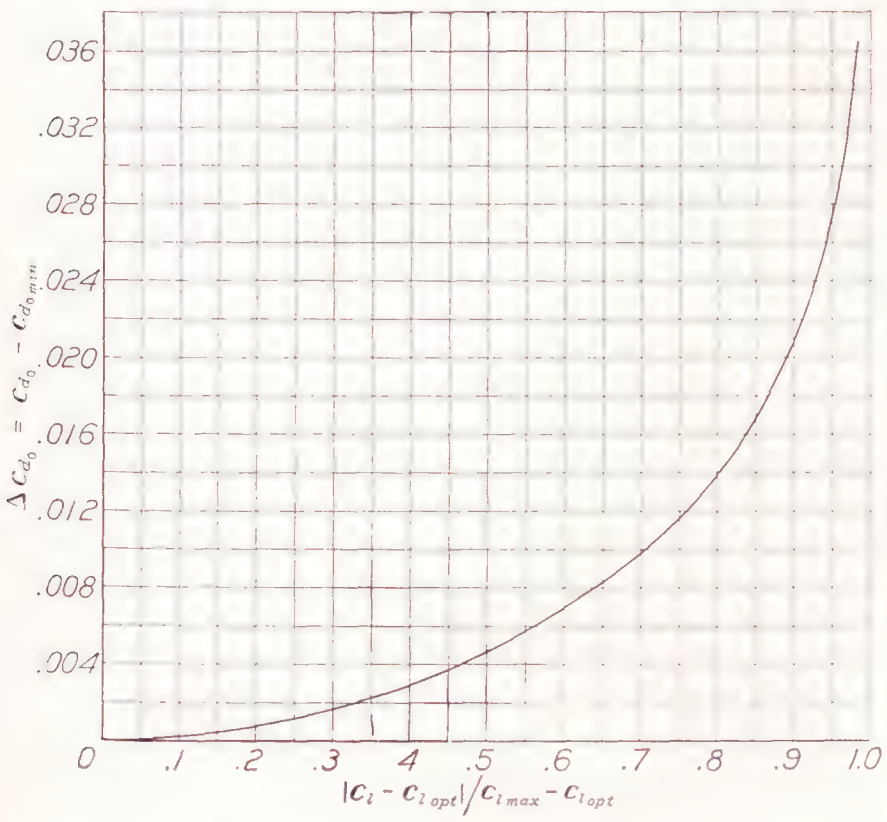

FIGURE 45.—Generalized variation of Δc_{d_0}.

The c_{d_0} values at other lift coefficients may now be obtained from the generalized variation of Δc_{d_0} with $\frac{|c_l - c_{l_{opt}}|}{c_{l_{max}} - c_{l_{opt}}}$ presented in figure 45, where the standard airfoil characteristic table is again employed to find $c_{l_{opt}}$. The $c_{l_{max}}$ value employed should, of course, correspond to the Reynolds Number of the c_{d_0} value being calculated. This procedure may involve the use of $c_{l_{max}}$ values corresponding to very high Reynolds Numbers. These values, however, may be estimated by extrapolating the maximum-lift scale-effect curves, little accuracy being required because c_l will usually be near $c_{l_{opt}}$ and Δc_{d_0} therefore small. A series of Δc_{d_0} values may thus be derived for various lift coefficients and Reynolds Numbers. The corresponding values of c_{d_0} are then obtained by adding these increments to the $c_{d_0\,min}$ value calculated from the preceding extrapolation formula for the corresponding Reynolds Number. In practice, a series of values of c_{d_0} may thus be derived to form a curve of c_{d_0} against c_l along which the Reynolds Number varies with lift coefficient as in flight.

LANGLEY MEMORIAL AERONAUTICAL LABORATORY,
NATIONAL ADVISORY COMMITTEE FOR AERONAUTICS,
LANGLEY FIELD, VA., *June 24, 1936.*

APPENDIX

INVESTIGATION OF CERTAIN CONSISTENT ERRORS PRESENT IN TEST RESULTS FROM THE VARIABLE-DENSITY TUNNEL

By Ira H. Abbott

INTRODUCTION

An investigation has been made to evaluate three corrections that were not applied to the data, obtained in the variable-density wind tunnel, and published in reference 2 and earlier reports. The need for these corrections had been recognized, and possible errors in the data resulting from the lack of these corrections have been listed as consistent errors (reference 2) due to the following effects:

1. Aerodynamic interference of the model supports on the model.

2. Effect of the compressed air on the effective weight of manometer liquids used to measure the dynamic pressure.

3. Combined effects on the measured dynamic pressure of blocking due to the model and to errors in pitot-tube calibration arising from differences in dynamic scale and turbulence between conditions of use in the variable-density tunnel and conditions of calibration. These effects result in errors in the calibration of the static-pressure orifices used to determine the dynamic pressure.

INTERFERENCE OF MODEL SUPPORTS

The model supports used in the variable-density tunnel and the method of determining the tare forces are described in reference 1. The usual tare tests determine the tare forces on the supports including the interference of the model on the supports. In addition, the usual method of determining the balance alinement with respect to the air-flow direction by testing an airfoil erect and inverted includes any interference of the supports on the model that is equivalent to a change in air-flow direction. Earlier attempts to determine any additional interference of the supports on the model were inconclusive except to show that such interference was small.

Two airfoils of moderate thickness were chosen to be used in the present investigation, one being a symmetrical airfoil (N. A. C. A. 0012) and the other an airfoil of moderate camber (N. A. C. A. 4412). Tests were made of each airfoil using three methods of supporting the model. Besides the method using the usual support struts, tests were made with the models mounted on the usual supports with the addition of special wire supports and with the models mounted only on the wire supports. The wire supports consisted of three wires attached to the quarter-chord point of the model at each wing tip and of a sting and angle-of-attack strut so located as to be free from aerodynamic interference with the usual supports. The sting used was symmetrical with respect to the airfoil and was attached near the trailing edge instead of to the lower surface, as is usual.

The tares due to the wire supports were determined from the data obtained from the tests with the models on the usual supports with and without the wire supports. Some difficulty was experienced in obtaining sufficiently accurate tares because of the relatively large drag of the wires as compared with the drag of the model. Sufficient accuracy was obtainable only at the highest value of the test Reynolds Number ordinarily obtained (about 3,000,000). The profile-drag coefficients obtained for the two airfoils are plotted as solid lines in figures 46 and 47, together with data obtained from several tests made with the usual supports over a considerable period of time. The scattering of the points obtained from the tests with the usual supports about the solid line is within the limits of the accidental errors listed in reference 2, showing that there is no support interference within the accuracy of the results at high values of the Reynolds Number.

It is evident that the data obtained can be analyzed in different ways. For example, the data obtained with the models mounted on both the usual supports and the wire supports can be corrected for the usual support tares and compared with the data from tests with the models mounted only on the wire supports. The comparison was made correcting the data for the change in air-flow direction due to the usual supports and failed to show any support interference within the test accuracy.

Analysis of the data to determine the effects of the support interference on the measured pitching-moment coefficients was more difficult. The support wires stretched under the lift and drag loads, necessitating a correction to the measured pitching-moment coefficients, and the method of supporting the model at the wing tips allowed the model itself to deflect under the lift loads much more than when mounted on the usual supports. The correction due to the deflection of the model is difficult to evaluate with certainty because it involves integrations along the span after determination of the span load distribution. Accordingly, the effect of the support interference for the pitching moments

was determined only at zero lift where it was found that the measured pitching-moment coefficient was too large (algebraically) by 0.002. This same correction had been found previously from tests with symmetrical

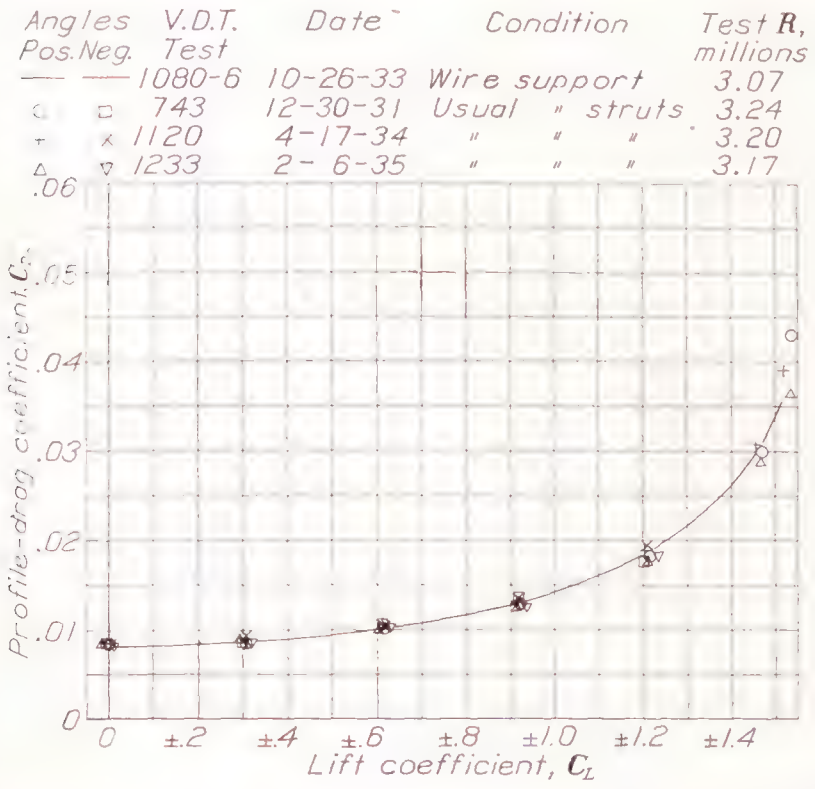

FIGURE 46.—Lift and drag characteristics of the N. A. C. A. 0012 airfoil as determined from tests with the model mounted on the usual support struts and on special wire supports.

airfoils and had been applied so that no new corrections were necessary.

EFFECTIVE WEIGHT OF MANOMETER LIQUIDS

The dynamic pressure is measured by two manometers connected to two sets of calibrated static-pressure orifices as described in reference 1. One manometer is filled with grain alcohol and the other with distilled water, the one filled with alcohol being ordinarily used to hold the dynamic pressure constant throughout a test because it is more easily read than the water manometer. Readings of the water manometer taken during each test serve to check the alcohol manometer and to indicate any change in the specific gravity of the alcohol, which is obtained from time to time by calibrating the alcohol manometer at atmospheric pressure against a head of distilled water.

It is apparent, as has been pointed out by Relf, that when the tank is filled with compressed air the increased density of the air reduces the effective weight of the alcohol or water in the manometers. This effect may be considered as a buoyancy of the air on the liquid and may be computed, but there is no assurance that the effects of other factors such as the amount of air dissolved in the liquid are negligible.

An experimental determination of the effect of the compressed air was made by calibrating the alcohol and water manometers at several tank pressures against a third manometer filled with mercury. The comparatively small buoyancy effect on the mercury was computed and applied to the results as a correction. The effects of other factors on the mercury were considered negligible. In addition to the correction determined in this way, a further small correction was applied to the specific gravity to compensate for the small change in balance calibration with air density due to the buoyancy of the air on the balance counterweights. The net correction at 20 atmospheres tank pressure was found to be 2.0 percent for the alcohol and 1.7 percent for the water, the dynamic pressure as measured being too high. It is planned to replace the manometers by a pressure balance in the near future. Measurements of dynamic pressure will then be independent of specific gravity.

CALIBRATION OF STATIC-PRESSURE ORIFICES

The static-pressure orifices used to measure the dynamic pressure are calibrated by making a velocity survey at the test section, using a calibrated pitot tube (reference 1). The calibration may be in error partly because of differences in dynamic scale and turbulence between conditions of pitot-tube calibration and of use in the variable-density tunnel and also because of possible blocking effects of the model. It is evident that a new method of calibration is necessary to eliminate these uncertainties.

These uncertainties may be largely eliminated by calibrating pitot tubes on an airplane in flight and by calibrating similar pitot tubes, similarly mounted on a model of the airplane in the tunnel. A detailed 1/20-scale model of the FC–2W2 airplane (reference 20) and the airplane itself were available. Three nonswiveling pitot tubes were mounted on the airplane as shown in figure 48. These pitot tubes were 2 inches in diameter

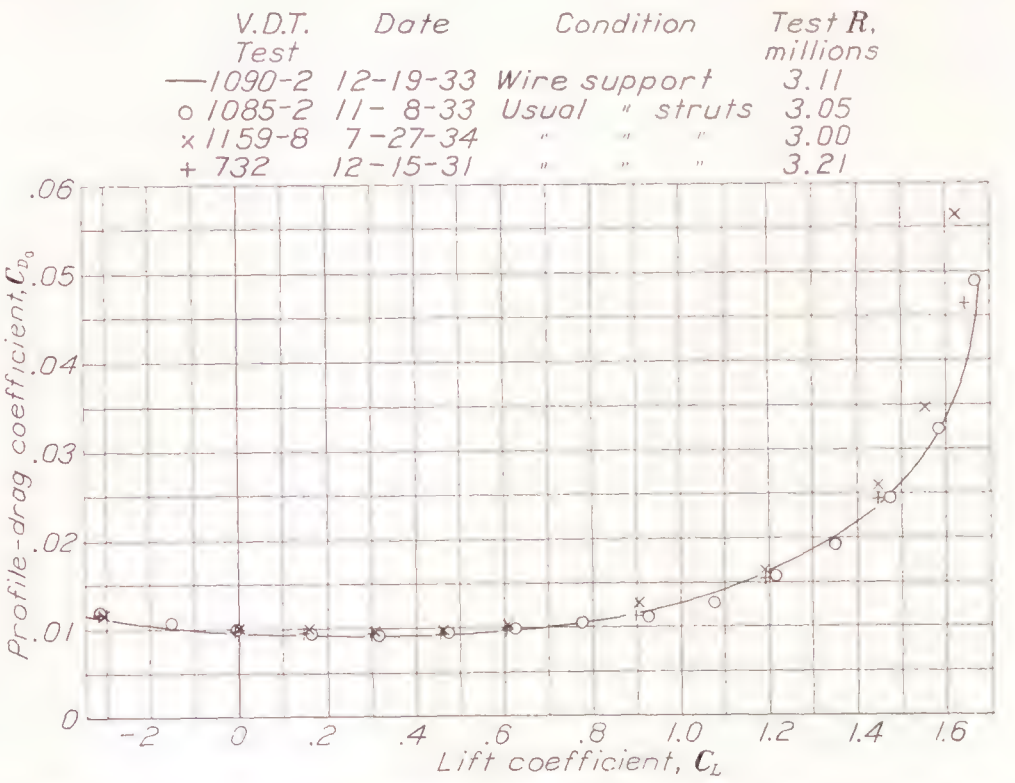

FIGURE 47.—Lift and drag characteristics of the N. A. C. A. 4412 airfoil as determined from tests with the model mounted on the usual support struts and on special wire supports.

with two staggered rows of static-pressure holes. Each row consisted of 12 equally spaced holes 0.22 inch in diameter. The pitot tubes were calibrated in flight against a previously calibrated trailing air-speed head. Three geometrically similar pitot tubes 0.10 inch in diameter were similarly mounted on the model and calibrated in the variable-density tunnel. Great care

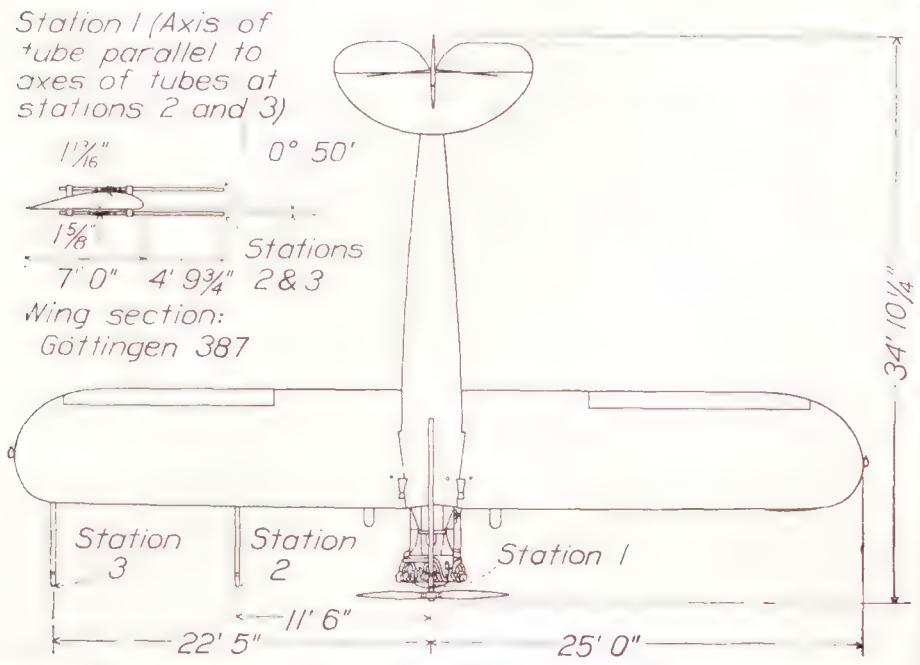

FIGURE 48.—Outline drawing showing location of pitot tubes on the FC–2W2 airplane.

was taken to make the small pitot tubes geometrically similar to the large ones and to mount them in the correct positions on the model.

The pitot tubes were calibrated in the tunnel over an angle-of-attack range from −8° to 14° and over a range of the test Reynolds Number from 1,000,000 to 2,500,000. Tests were made with three tail settings. All pressures were measured by a multiple-tube, photo-recording manometer using a mixture of alcohol and water. Ratios of pressures were obtained directly from ratios of measured deflections and are independent of the specific gravity of the manometer liquid. A test was made with the pitot tubes interchanged as to position on the model to check the accuracy with which they were made. The results checked satisfactorily. Surveys were made upstream from the model with and without the model in place using a bank of 21 small pitot tubes mounted on a strut extending across the tunnel, surveys being made on the vertical center line and 6 and 12 inches to one side of the center line. The data obtained from these surveys are used to check the calibration of the static-pressure orifices from time to time as required. Force tests were also made on the model with and without the pitot tubes in place and with several tail settings.

The results obtained from the calibration of the pitot tubes are presented in figure 49. The data are presented as ratios of the dynamic pressures measured by the pitot tubes to the dynamic pressure as usually obtained from the static-pressure orifices. A fairly consistent variation of the results is shown with changes in Reynolds Number and tail settings. The results obtained from the calibration of the pitot tubes in flight are shown by outlined areas indicating the location of all points obtained.

Comparisons between the tunnel and flight results have been made on the basis of angles of attack, corrected in the case of the tunnel results for the tunnel-

	V.D.T. Test No.	Date	Test Reynolds Number (based on wing chord)	Stabilizer angle	Elevator angle
1	1111-2	3-29-34	1,100,000	3.3°	10°
2	1111-4	3-29-34	2,570,000	3.3°	10°
3	1110-3	3-27-34	2,560,000	3.3°	0°
4	1111-3	3-29-34	2,000,000	3.3°	10°
5	1110-2	3-27-34	1,990,000	3.3°	0°
6	1110-1	3-27-34	1,040,000	3.3°	0°
7	1108-3	3-22-34	2,570,000	0°	0°
8	1107-2	3-20-34	2,000,000	0°	0°
9	1107-1	3-20-34	1,120,000	0°	0°

(3) Outlined areas indicate location of points obtained in flight.
— Corrected calibration in the variable-density tunnel.

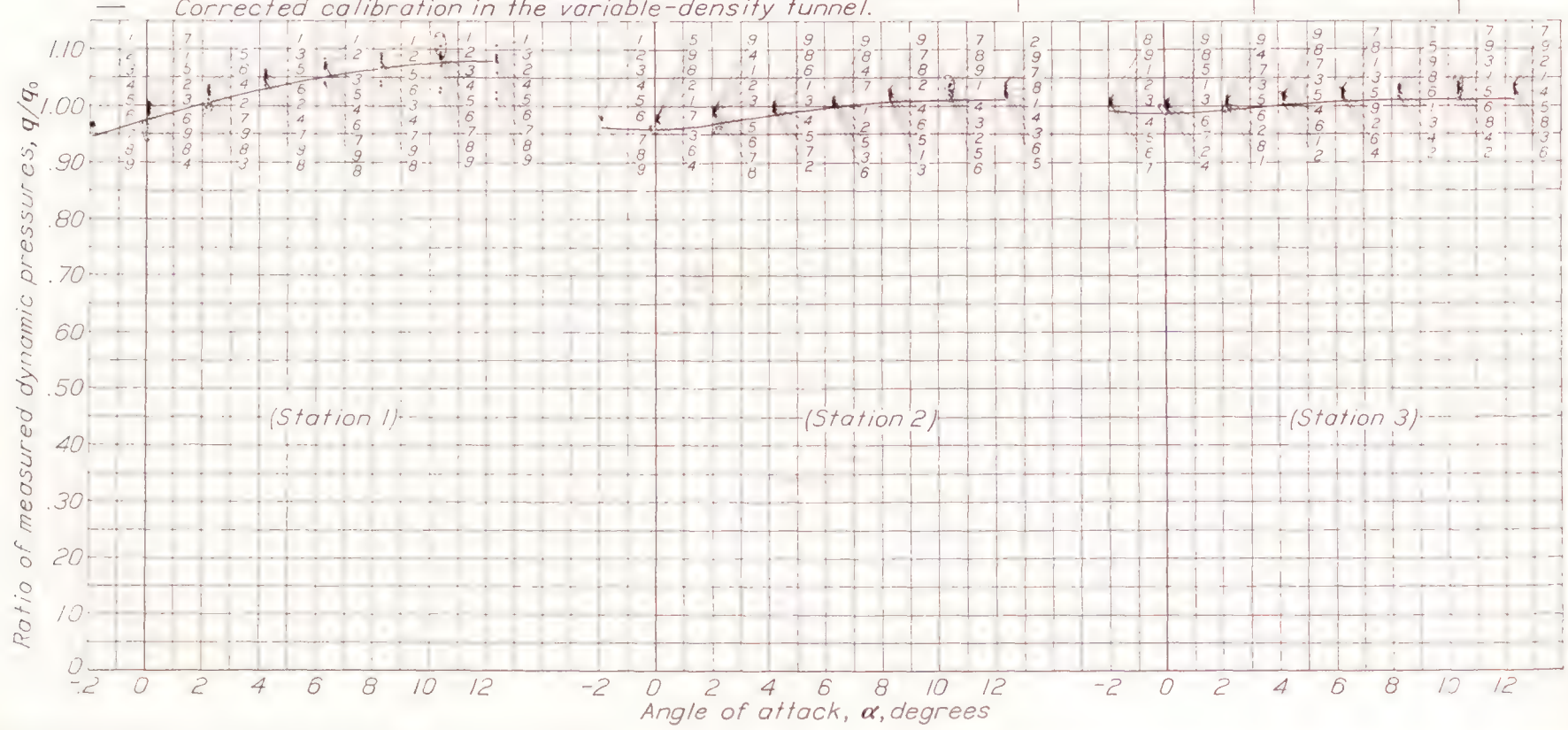

FIGURE 49.—Calibration of pitot tubes mounted on the FC–2W2 airplane in flight and on the FC–2W2 airplane model in the variable-density wind tunnel. Results corrected for tunnel-wall effect.

wall effect. Force tests made in the tunnel and in flight show that this method of comparison is very nearly equivalent to making the comparisons at equal lift coefficients. A value of the ratio q/q_0 was selected from the tunnel data to correspond as well as possible to flight conditions of trim and Reynolds Number for each pitot-tube position at each angle of attack. The values obtained were, in general, higher than the flight values at small angles of attack. Accordingly, the values obtained were reduced by increasing the value of q_0 by 1.5 percent, which is equivalent to a change in the static-pressure-orifice calibration factor from 1.172 to 1.190. The values of the ratio so obtained are plotted on the figure as solid lines, and the values agree reasonably well with the flight data at small

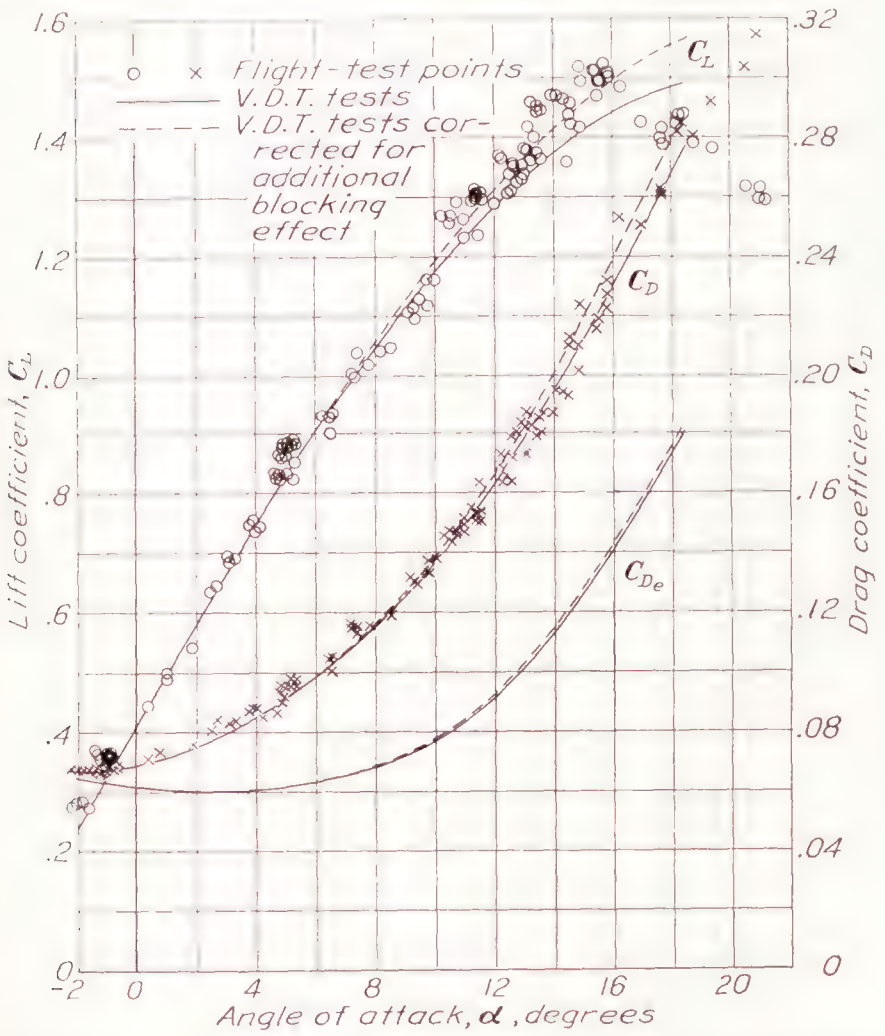

FIGURE 50.—Comparison of data obtained in flight and in the variable-density wind tunnel for the FC-2W2 airplane and model.

angles of attack. A comparison of the tunnel and flight data indicates that a further correction, which may be due to blocking effects, may be desirable at high angles of attack. The airplane model, however, had large drags at high angles of attack as compared with models normally used in the tunnel, making the application of this additional correction questionable for the usual airfoil tests.

The results of the force tests of the model are shown by means of composite curves drawn as solid lines in figure 50. The curves were obtained from the test results by selecting, at each angle of attack, test results to correspond as well as possible with flight conditions of trim and Reynolds Number. The tunnel results have been fully corrected including corrections to the effective Reynolds Number. Data obtained in flight tests (reference 20) are shown on the figure.

Although the model was much more detailed and accurate than is usual in wind-tunnel models, it was not considered before the tests to represent the airplane with sufficient accuracy and detail to give reliable drag results. Therefore too much emphasis should not be given to the good agreement of drag coefficients obtained in flight and in the tunnel. At lift coefficients less than 1.0 the agreement between flight and tunnel data is considered satisfactory. At higher lift coefficients some divergence of the tunnel and flight data is indicated. As previously stated, the results obtained from the pitot-tube calibration showed that an additional correction to the calibration factor of the static-pressure orifice might be desirable at high angles of attack. Such a correction has been determined from figure 49 and applied to the data. The results are plotted as dotted lines in figure 50 and show an improved agreement of the lift coefficients obtained in flight and in the tunnel at high angles of attack.

This additional correction is not ordinarily applied to the data obtained in the variable-density tunnel because it is doubtful whether the correction in most cases would give a better approximation to the actual conditions than no correction. The pitot-tube calibration tests were less accurate at high angles of attack than at low ones and, as previously stated, the drag of the model was larger than is the case for the models usually tested. Another fact indicating that this correction is small is that, up to the point of maximum lift, the lift curves obtained in the tunnel for some airfoils are very nearly straight. Any appreciable correction of this type would result in such lift curves being concave upward.

CONCLUSIONS

1. The results of the investigation show no interference of the model supports on the model for which corrections had not previously been made.

2. The investigation of the effects of compressed air on the effective weight of the manometer liquid showed a 2.0 percent error in the measured dynamic pressure; the dynamic pressure as previously measured was too large.

3. The investigation of the calibration of the static pressure orifices showed an error of 1.5 percent in this calibration; the dynamic pressure as previously measured was too small.

4. The total effect of the investigation is a change in the measured dynamic pressure of 0.5 percent; the dynamic pressure as previously measured was too large. Data previously published (reference 2 and earlier reports) to which these corrections have not been applied may be corrected by changing the coefficients to correspond to a reduction of measured dynamic pressure of 0.5 percent.

REFERENCES

1. Jacobs, Eastman N., and Abbott, Ira H.: The N. A. C. A. Variable-Density Wind Tunnel. T. R. No. 416, N. A. C. A. 1932.
2. Jacobs, Eastman N., Ward, Kenneth E., and Pinkerton, Robert M.: The Characteristics of 78 Related Airfoil Sections from Tests in the Variable-Density Wind Tunnel. T. R. No. 460, N. A. C. A., 1933.
3. Jacobs, Eastman N., and Pinkerton, Robert M.: Tests in the Variable-Density Wind Tunnel of Related Airfoils Having the Maximum Camber Unusually Far Forward. T. R. No. 537, N. A. C. A., 1935.
4. Wenzinger, Carl J., and Shortal, Joseph A.: The Aerodynamic Characteristics of a Slotted Clark Y Wing as Affected by the Auxiliary Airfoil Position. T. R. No. 400, N. A. C. A., 1931.
5. Platt, Robert C., and Abbott, Ira H.: Aerodynamic Characteristics of N. A. C. A. 23012 and 23021 Airfoils with 20-Percent-Chord External-Airfoil Flaps of N. A. C. A. 23012 Section. T. R. No. 573, N. A. C. A., 1936.
6. Millikan, Clark B.: On the Lift Distribution for a Wing of Arbitrary Plan Form in a Circular Wind Tunnel. Publication No. 22, C. I. T., 1932.
7. Jacobs, Eastman N., and Pinkerton, Robert M.: Tests of N. A. C. A. Airfoils in the Variable-Density Wind Tunnel. Series 230. T. N. No. 567, N. A. C. A., 1936.
8. Anderson, R. F.: Determination of the Characteristics of Tapered Wings. T. R. No. 572, N. A. C. A., 1936.
9. Jacobs, Eastman N., and Clay, William C.: Characteristics of the N. A. C. A. 23012 Airfoil from Tests in the Full-Scale and Variable-Density Tunnels. T. R. No. 530, N. A. C. A., 1935.
10. Platt, Robert C.: Turbulence Factors of N. A. C. A. Wind Tunnels as Determined by Sphere Tests. T. R. No. 558, N. A. C. A., 1936.
11. Stack, John: Tests in the Variable-Density Wind Tunnel to Investigate the Effects of Scale and Turbulence on Airfoil Characteristics. T. N. No. 364, N. A. C. A., 1931.
12. Toussaint, A., and Jacobs, E.: Experimental Methods–Wind Tunnels. Vol. III, div. I of Aerodynamic Theory, W. F. Durand, editor, Julius Springer (Berlin), 1935, p. 332.
13. von Kármán, Th., and Millikan, C. B.: On the Theory of Laminary Boundary Layers Involving Separation. T. R. No. 504, N. A. C. A., 1934.
14. Dryden, H. L.: Air Flow in the Boundary Layer Near a Plate. T. R. No. 562, N. A. C. A., 1936.
15. Dryden, H. L., and Kuethe, A. M.: Effect of Turbulence in Wind Tunnel Measurements. T. R. No. 342, N. A. C. A., 1930.
16. Jacobs, Eastman N.: The Aerodynamic Characteristics of Eight Very Thick Airfoils from Tests in the Variable-Density Wind Tunnel. T. R. No. 391, N. A. C. A., 1931.
17. Jones, B. Melvill: Stalling. R. A. S. Jour., vol. XXXVIII, No. 285, Sept. 1934, pp. 753–769.
18. Higgins, George J., and Jacobs, Eastman N.: The Effect of a Flap and Ailerons on the N. A. C. A. –M6 Airfoil Section. T. R. No. 260, N. A. C. A., 1927.
19. Jacobs, Eastman N., and Pinkerton, Robert M.: Pressure Distribution over a Symmetrical Airfoil Section with Trailing Edge Flap. T. R. No. 360, N. A. C. A., 1930.
20. Thompson, F. L., and Keister, P. H.: Lift and Drag Characteristics of a Cabin Monoplane Determined in Flight. T. N. No. 362, N. A. C. A., 1931.

TABLE I

IMPORTANT AIRFOIL SECTION CHARACTERISTICS

N. A. C. A. airfoil	R_c (millions)	α_{l_0} (deg.)	a_0	$c_{l_{max}}$[1]	$c_{l_{opt}}$	$c_{d_{0_{min}}}$	$c_{m_{a.c.}}$	a. c.	
								x (percent c)	y (percent c)
0009	8.470					[2] 0.0061			
	8.290	0	0.098	A1.39	0	.0064	0	1.0	5
	6.100	0	.097	A1.28	0	.0064	0	1.0	4
	3.410	0	.097	D.94	0	.0062	0	1.8	8
	1.760	0	.096	D.88	0	.0060	0	1.7	13
	.882	0	.096	D.86	0	.0049	0		
	.446	0	.105	D.85	0	.0065	0		
	.223	0	.117	D.83	0	.0131	0		
	.112	0	.104	D.78	0	.0135	0		
0012	8.370	0	.099	A1.66	0	.0069	0	.6	3
	8.450	0	.100	A1.65	0	.0069	0	.6	3
	6.280	0	.097	A1.62	0	.0073	0	.8	3
	3.540	0	.097	A1.49	0	.0077	0	1.0	4
	1.740	0	.096	A1.18	0	.0075	0	1.1	3
	.871	0	.094	D.91	0	.0065			
	.449	0	.098	D.89	0	.0105			
0015	8.610	0	.097	A1.66	0	.0077	0	1.2	4
	5.990	0	.096	A1.60	0	.0082	0	1.1	3
	3.350	0	.094	C1.48	0	.0086	0	1.2	1
	1.730	0	.093	C1.28	0	.0088	0	2.4	1
	.874	0	.092	C1.09	0	.0084	0	1.5	0
	.438	0	.091	D.98	0	.0079			
	.222	0	.101	D.89		.0149			
	.113	0	.134	D.90		.0158			
0018	7.840	0	.096	A1.53	0	.0088	0	1.7	4
	6.240	0	.096	A1.53	0	.0092	0	1.6	3
	3.300	0	.096	C1.42	0	.0098	0	2.2	3
	1.730	0	.095	D1.26	0	.0100	0	2.2	0
	.866	0	.090	C1.15	0	.0102	0	2.4	0
	.430	0	.086	A1.03	0	.0127	0	1.8	0
	.214	0	.092	D.96	0	.0179			
	.109	0	.114	D.86	0	.0297			
2412	8.240	−2.0	.098	A1.72	.14	.0071	−.043	.5	3
	6.100	−2.1	.097	A1.68	.14	.0080	−.043	1.1	3
	3.420	−2.0	.098	C1.53	.15	.0079	−.045	1.1	1
	1.730	−2.1	.096	D1.33	.30	.0089	−.045	.9	−2
	.879	−2.1	.096	D1.16	.22	.0085	−.054	1.8	0
	.438	−2.0	.098	D1.08	.42	.0067			
	.218	−2.2	.102	D1.08	.26	.0159			
	.110	−1.3		D1.03		.0227			
23012	8.370					[3] .0071			
	8.160	−1.2	.100	A1.72	.08	.0070	−.008	1.2	7
	6.070	−1.2	.098	A1.67	.08	.0079	−.007	1.3	7
	3.400	−1.2	.098	A1.53	.05	.0080	−.007	1.3	5
	1.760	−1.2	.097	D1.41	.16	.0090	−.012	1.4	5
	.884	−1.2	.096	D1.28	.28	.0084	−.010	2.0	7
	.449	−1.3	.096	D1.19	.12	.0098			
	.221	−1.6	.109	D1.15	.37	.0179			
	.112	−1.4		D1.00	.20	.0182			
23012–33	8.000	−1.2	.097	B1.49	.20	.0071	−.010	.6	5
	6.390	−1.2	.098	A1.42	.10	.0075	−.010	.8	5
	3.380	−1.2	.096	D1.26	.23	.0076	−.011	1.0	6
	1.760	−1.2	.096	D1.12	.28	.0071	−.014	.9	3
	.900	−1.2	.094	D1.07	.10	.0084	−.011	.9	0
	.454	−1.4	.096	D1.01	.40	.0096	−.014	.4	−1
2R$_2$12	8.370	−.6	.098	A1.61	.10	.0073	.005	1.0	7
	6.310	−.7	.097	D1.55	.02	.0078	.006	1.1	6
	3.540	−.7	.097	D1.44	.11	.0077	.005	1.0	4
	1.770	−.8	.095	D1.28	.23	.0077	.002	.8	0
	.884	−.8	.096	D1.14	.28	.0073	−.001	1.1	0
	.454	−.9	.100	D1.08	.35	.0118			
4409	8.080	−3.9	.096	A1.77	.26	.0073	−.088	.6	2
	5.970	−3.9	.096	D1.70	.26	.0080	−.088	.7	1
	3.340	−4.0	.095	C1.50	.34	.0077	−.090	1.0	−1
	1.700	−4.0	.098	D1.29	.41	.0084	−.092	1.1	−1
	.869	−4.1	.096	D1.26	.40	.0080	−.098	1.4	−4
	.438	−4.1	.097	D1.23	.55	.0097			
	.218	−3.7	.105	D1.21	.57	.0096			
	.110	−2.5	.115	D1.09	.77	.0189			
4412	7.920	−4.0	.098	D1.74	.32	.0082	−.088	.8	2
	6.100	−4.1	.096	D1.70	.22	.0085	−.088	.9	1
	3.270	−4.1	.098	D1.61	.30	.0087	−.091	1.0	−1
	1.680	−4.2	.097	D1.46	.37	.0095	−.095	1.2	−5
	.874	−4.3	.096	D1.36	.36	.0091	−.097	1.1	−8
	.433	−4.3	.094	D1.31	.51	.0109			
	.219	−4.3	.100	D1.32	.57	.0194			
	.111	−2.9	.113	D1.20		.0276			
4415	7.920	−4.0	.097	C1.72	.22	.0090	−.085	1.0	1
	6.280	−4.0	.095	D1.66	.20	.0093	−.086	1.4	1
	3.340	−4.1	.096	D1.56	.23	.0094	−.085	1.4	−2
	1.730	−4.2	.095	D1.48	.31	.0099	−.090	1.7	−4
	.882	−4.3	.094	D1.41	.34	.0103	−.092	1.4	−8
	.431	−4.4	.089	D1.35	.39	.0123			
	.219	−4.4	.089	D1.34	.46	.0198			
	.110	−3.1		D1.34	.68	.0269			
6412	8.210	−5.9	.098	D1.82	.37	.0091	−.133	.9	1
	6.020	−5.9	.096	D1.75	.25	.0096	−.130	1.1	1
	3.350	−6.1	.097	D1.64	.38	.0099	−.131	.8	−3
	1.700	−6.2	.097	D1.54	.52	.0104	−.135	1.0	−2
	.882	−6.3	.097	D1.48	.60	.0096			
	.441	−6.2	.097	D1.47	.55	.0129			
	.219	−5.9	.106	D1.46	.70	.0205			
	.110	−5.4		D1.45		.0160			

[1] Type lift-curve peak:

[2] From reference 2.
[3] From reference 7

TABLE I—Continued

IMPORTANT AIRFOIL SECTION CHARACTERISTICS—Continued

N. A. C. A. airfoil	R_c (millions)	α_{l_0} (deg.)	a_0	$c_{l_{max}}$ [1]	$c_{l_{opt}}$	$c_{d_{0\ min}}$	$c_{m_{a.c.}}$	a. c. x (percent c)	a. c. y (percent c)
6712	8.100	−7.3	0.096	[D] 2.05	0.35	0.0115	−0.199	1.2	−2
	6.120	−7.4	.095	[D] 1.99	.32	.0119	−.197	1.1	−4
	3.380	−7.4	.098	[D] 1.83	.33	.0120	−.198	1.1	−8
	1.750	−7.6	.103	[D] 1.65	.45	.0124	−.210	1.6	−12
	.892	−7.8	.103	[D] 1.52	.82	.0138			
	.449	−5.7		[D] 1.45	.88	.0228			
	.222	−4.6		[D] 1.50	1.01	.0283			
	.112	−3.9		[D] 1.41	−.02	.0411			
8318	8.450	−7.2	.095	[D] 1.59	.24	.0127	−.132	1.5	2
	6.420	−7.3	.092		.10	.0128	−.132	1.8	2
	3.460	−7.4	.093	[D] 1.67	.31	.0128	−.135	1.8	2
	1.790	−7.6	.093	[D] 1.76	.36	.0140	−.137	2.1	3
	.911	−8.7	.088	[D] 1.80	.43	.0173			
	.449	−9.0	.085	[D] 1.78	.58	.0215			
	.224	−9.2	.080	[D] 1.40	.58	.0259			
	.112	−8.0	.077	[D] 1.02		.0332			
0012	8.110	[4] −13.1	[5] .091	[A] 2.35		[7] .167	[8] −.220	.6	3
(With split flap at 60°.)	5.910			[A] 2.35					
	3.770			[A] 2.30					
	3.430			[A] 2.21					
	1.740			[A] 1.84					
	.919			[D] 1.67					
	.449			[D] 1.63					
23012	8.180	[4] −14.3	[5] .088	[A] 2.48		[7] .166	[8] −.236	1.2	7
(With split flap at 60°.)	5.970			[A] 2.51					
	3.620 (Average)			[A] 2.39					
	1.740			[A] 2.24					
	.882			[A] 2.07					
	.444			[D] 1.92					
23012	8.100	[4] −15.6	[5] .085	[A] 2.54		[7] .201	[8] −.228	1.2	7
(With split flap at 75°.)	5.990			[A] 2.52					
	3.800			[A] 2.41					
	1.740			[A] 2.21					
	.887			[A] 2.01					
	.446			[A] 1.90					
23015	8.370	−1.1	.098	[A] 1.73	.10	.0081	−.008	1.1	6
	3.880			[C] 1.60					
23015	8.210	[4] −16.2	[5] .086	[A] 2.70		[7] .198	[8] −.245	1.1	6
(With split flap at 75°.)	5.990			[A] 2.69					
	3.830			[A] 2.59					
	1.800			[A] 2.45					
	.924			[A] 2.32					
	.450			[A] 2.11					
23021	8.210	−1.2	.092	[B] 1.50	.07	.0101	−.005	2.3	7
	5.940			[A] 1.54					
	3.770			[A] 1.47					
	1.720			[D] 1.32					
	.892			[D] 1.26					
	.441			[A] 1.20					
23021	8.130	[4] −16.5	[5] .094	[A] 2.74		[7] .191	[8] −.300	2.3	7
(With split flap at 75°.)	5.960			[A] 2.81					
	3.800			[A] 2.79					
	1.720			[A] 2.58					
	.879			[A] 2.46					
	.435			[A] 2.28					
43012	8.390	−2.3	.100	[A] 1.84	.26	.0079	−.019	1.0	7
	3.890			[A] 1.71					
	.449			[A] 1.44					
43012	8.240	[4] −17.3	[5] .082	[A] 2.65		[7] .200	[8] −.225	1.0	7
(With split flap at 75°.)	6.040			[A] 2.60					
	3.830			[A] 2.47					
	1.740			[A] 2.39					
	.887			[A] 2.29					
	.449			[A] 2.18					
23012	8.210	−.9	.101	[A] 1.68	.07	.0069	.009	.5	8
(With 23012 flap 3° up.)	6.150	−.8	.100	[A] 1.62	.15	.0074	.009	1.0	9
	3.300	−.8	.100	[A] 1.54	.19	.0078	.010	1.1	11
	1.680	−.8	.097	[A] 1.39	.13	.0068	.011	1.2	11
	.858	−.8	.096	[D] 1.24	.08	.0093			
	.430	−1.2	.096	[D] 1.12	.08	.0119			
23012	8.140	[4] −13.8	[5] .102	[A] 2.46	.45	.0161	[9] −.260	.5	8
(With 23012 flap set 30°.)	6.200			[A] 2.40					
	3.410			[A] 2.32					
	1.700	[4] −12.5	[5] .103	[6] [C] 2.13	.70	.0184	[9] −.260	1.2	11
	1.700			[6] [D] 1.95					
	.879	[4] −11.9	[5] .102	[D] 1.75	.60	.0218			
	.441			[D] 1.66					
Clark Y [10]	9.900	−4.2	[5] .099	[D] 2.12	.76	.0242			
(With Handley Page slot.)	8.080	−4.3	[5] .099	[D] 2.06	.76	.0248			
	4.990	−4.2	[5] .098	[D] 2.02	.69	.0260			
	3.090	−4.2	[5] .097	[D] 1.96	.62	.0260			
	2.040	−4.1	[5] .096	[D] 1.98	.65	.0264			
	1.290	−4.1	[5] .092	[D] 1.92	.63	.0272			
	.784	−4.1		[D] 1.82	.64	.0301			
	.520	−4.1		[D] 1.75	.63	.0291			
	.261	−4.1		[D] 1.60	.64	.0322			
	.135	−4.3		[D] 1.41	.63	.0431			

[1] See footnote 1, p. 39.

[4] Angle of zero lift determined from linear lift curve approximating experimental lift curve.

[5] Slope of lift curve determined from linear lift curve approximating experimental lift curve.

[6] Discontinuity present in the scale effect.

[7] Value of the drag that applies approximately over the entire useful range of lift coefficients.

[8] $c_{m_{a.c.}}$ is taken about the aerodynamic center of the plain wing and is fairly constant at high lift coefficients.

[9] $c_{m_{a.c.}}$ is taken about the aerodynamic center of the wing with flap neutral and is fairly constant at high lift coefficients.

[10] Not N. A. C. A.

TABLE II

AIRFOIL SECTION CHARACTERISTICS

N. A. C. A. airfoil	Classification			R_c [4] (millions)	Fundamental section characteristics							
	Chord [1]	SE [2]	$C_{L_{max}}$ [3]		$c_{l_{max}}$	α_{l_0} (deg.)	a_0, per degree	$c_{l_{opt}}$	$c_{d_{0\,min}}$	$c_{m\,a.c.}$	a. c. (percent c from c/4)	
											Ahead	Above
0009	A	B	A	8.29	1.39	0	0.098	0	0.0064	0	1.0	5
0012	A	C0	A	8.37	1.66	0	.099	0	.0069	0	.6	3
0015	A	D0	A	8.61	1.66	0	.097	0	.0077	0	1.2	4
0018	A	E0	A	7.84	1.53	0	.096	0	.0088	0	1.7	4
2412	A	C2	A	8.24	1.72	−2.0	.098	.14	.0071	−.043	.5	3
23012	A	D2	A	8.16	1.72	−1.2	.100	.08	.0070	−.008	1.2	7
23012-33	A	B6	B	8.00	1.49	−1.2	.097	.20	.0071	−.010	.6	5
$2R_212$	A	C3	A	8.37	1.61	−.6	.098	.10	.0073	.005	1.0	7
4409	A	B4	A	8.08	1.77	−3.9	.096	.26	.0073	−.088	.6	2
4412	A	C4	D	7.92	1.74	−4.0	.098	.32	.0082	−.088	.8	2
4415	A	D4	C	7.92	1.72	−4.0	.097	.22	.0090	−.085	1.0	1
6412	A	C6	D	8.21	1.82	−5.9	.098	.37	.0091	−.133	.9	1
6712	A	C2	D	8.10	2.05	−7.3	.096	.35	.0115	−.199	1.2	−2
8318	A	E8	D	8.45	1.59	−7.2	.095	.24	.0127	−.132	1.5	2
0012 with split flap at 60°	A	C0	A	8.11	2.35	[5] −13.1	[6] .091		[7] .167	[8] −.220	.6	3
23012 with split flap at 60°	A	D2	A	8.18	2.48	[5] −14.3	[6] .088		[7] .166	[8] −.236	1.2	7
23012 with split flap at 75°	A	D2	A	8.10	2.54	[5] −15.6	[6] .085		[7] .201	[8] −.228	1.2	7
23015	A	D2	A	8.37	1.73	−1.1	.098	.10	.0081	−.008	1.1	6
23015 with split flap at 75°	A	D2	A	8.21	2.70	[5] −16.2	[6] .086		[7] .198	[8] −.245	1.1	6
23021	A	E2	B	8.21	1.50	−1.2	.092	.07	.0101	−.005	2.3	7
23021 with split flap at 75°	A	E2	A	8.13	2.74	[5] −16.5	[6] .094		[7] .191	[8] −.300	2.3	7
43012	A	D4	A	8.39	1.84	−2.3	.100	.26	.0079	−.019	1.0	7
43012 with split flap at 75°	A	D4	A	8.24	2.65	[5] −17.3	[6] .082		[7] .200	[8] −.225	1.0	7
23012 with 23012 flap 3° up	A	D2	A	8.21	1.68	−.9	.101	.07	.0069	.009	.5	8
23012 with 23012 flap set 30°	A		A	8.14	2.46	[5] −13.8	[6] .102	.45	.0161	[9] −.260	.5	8
Clark Y with Handley Page slot [10]	B		D	8.08	2.06	−4.3	[6] .099	.76	.0248			

[1] Type of chord. A refers to a chord defined as a line joining the extremities of the mean line.

[2] Type of scale effect on maximum lift.

[3] Type of lift-curve peak as shown in the sketches below:

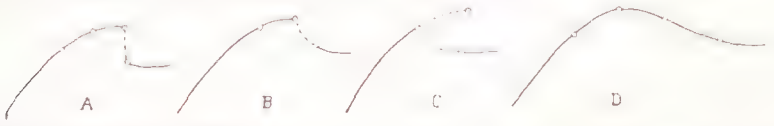

[4] Turbulence factor is 2.64.

[5] Angle of zero lift determined from linear lift curve approximating experimental lift curve.

[6] Slope of lift curve determined from linear lift curve approximating experimental lift curve.

[7] Value of the drag that applies approximately over the entire useful range of lift coefficients.

[8] $c_{m_{a.c.}}$ is taken about the aerodynamic center of the plain wing and is fairly constant at high lift coefficients.

[9] $c_{m_{a.c.}}$ is taken about the aerodynamic center of the wing with flap neutral (−3°) and is fairly constant at high lift coefficients.

[10] Not N. A. C. A.

REPORT No. 587

BLOWER COOLING OF FINNED CYLINDERS

By Oscar W. Schey and Herman H. Ellerbrock, Jr.

SUMMARY

Several electrically heated finned steel cylinders enclosed in jackets were cooled by air from a blower. The effect of the air conditions and fin dimensions on the average surface heat-transfer coefficient q and the power required to force the air around the cylinders were determined. Tests were conducted at air velocities between the fins from 10 to 130 miles per hour and at specific weights of the air varying from 0.046 to 0.074 pound per cubic foot. The fin dimensions of the cylinders covered a range of fin pitches from 0.057 to 0.25 inch, average fin thicknesses from 0.035 to 0.04 inch, and fin widths from 0.67 to 1.22 inches.

The value of q, based on the difference between the cylinder temperature and the inlet-air temperature, varied as the 0.667 power of the weight velocity of the cooling air for cylinders having spaces from 0.077 to 0.21 inch between fins. Below 0.077-inch space the exponent of the curves increased for each successive decrease in space. The value of q was independent of fin width for the range of widths tested and decreased as the space between the fins decreased.

The power required for cooling, neglecting the kinetic energy lost from the exit of the jacket, varied as the 2.69 power of the weight velocity for a given specific weight and inversely as the square of the specific weight for a given weight velocity of the cooling air. For a given weight velocity of the cooling air or a given power and for a fin width of 1.22 inches, the fin space giving the maximum heat transfer was approximately 0.045 inch.

INTRODUCTION

A general investigation is being conducted by the Committee to determine the comparative cooling of cylinders having fins of varying pitch, thickness, and width when tested in a free air stream and when tested with blower cooling. For the conditions in a free air stream the cylinders are tested with and without baffles and, for the conditions in which the blower is used, the cylinders are enclosed in a jacket.

The first report published on the investigation (reference 1) presents the results of extensive tests to determine the heat-transfer coefficients of finned cylinders in a free air stream and a method for calculating the heat dissipated, utilizing these coefficients. The second report (reference 2) includes results showing how the heat-transfer coefficient may be increased by using baffles to direct the air toward the rear of the cylinder.

Tests on nine steel cylinders, herein reported, were conducted to investigate blower cooling. Tests were made on all of the cylinders to determine the effect of velocity and specific weight of the cooling air on the heat transfer and on five of the cylinders to determine the effect of the same factors on power required. The cylinders had fins of varying width and pitch; the range of fin width investigated varied from 0.67 inch to 1.22 inches, the pitch from 0.057 inch to 0.25 inch, and the thickness from 0.035 inch to 0.040 inch.

APPARATUS

TEST CYLINDER

The construction of the test unit is shown in figure 1. This unit, which has been described in detail in preceding reports (references 1 and 3), consists essentially

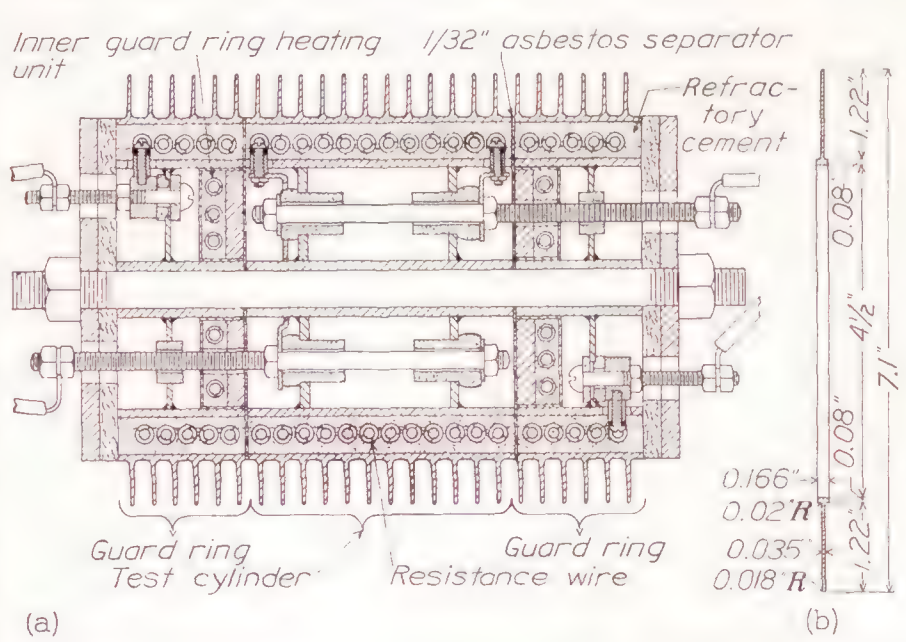

(a) Details of construction. (b) Individual fin section.

FIGURE 1.—Construction of test unit.

of three electrically heated finned cylinders, the central one forming the test section and the ones on each end serving as guard rings to prevent heat losses through the ends. The guard rings are of practically the same construction as the test section except that each ring is only one-half as long as the test section. The heat input to each guard ring and test specimen can be separately controlled by oil-cooled rheostats. A complete wiring diagram of the test set-up is shown in reference 1.

Four of the cylinders were machined from a steel billet so that the fins were integral with the cylinder wall. The other five cylinders were built up of indi-

vidually constructed fins (see fig. 1 (b)) held in place by solder, a method that facilitated the making of cylinders having closely spaced wide fins. With this method of construction the same fins may be used on several cylinders of different pitch by cutting down in successive steps the thickness of the wall section and thus reducing the space between the fins. As the space is reduced, more fins are added so that the same cylinder length is maintained and the same heating unit can be used.

For convenience in referring to the finned cylinders, the designations composed of the fin pitch, width, and thickness adopted in reference 1 are also used in this report. For example, the designation 0.25–0.67–0.04 indicates a finned cylinder having a fin pitch of 0.25 inch, a fin width of 0.67 inch, and an average fin thickness of 0.04 inch. The fin proportions for each of the nine cylinders tested are shown in the following table and in figure 8.

Fin pitch (inch)	Fin width (inches)	Fin thickness (inch)	Fin space (inch)
0.25	1.22	0.04	0.21
.25	.97	.04	.21
.25	.67	.04	.21
.15	.97	.04	.11
.166	1.22	.035	.131
.137	1.22	.035	.102
.112	1.22	.035	.077
.083	1.22	.035	.048
.057	1.22	.035	.022

The diameter of the cylinders at the fin root was 4.66 inches, the length of the test sections 10 inches, and the length of each guard ring 5 inches.

AIR SYSTEM

The quantity of cooling air supplied was measured by sharp-edge orifices placed at each end of a tank. The air system used in testing the 0.25–1.22–0.04, 0.25–0.97–0.04, 0.25–0.67–0.04, and 0.15–0.97–0.04 cylinders, hereinafter designated "series A" tests, is shown diagrammatically in figure 2 (a). A tank was placed in the air duct on each side of the supercharger to reduce the pressure pulsations created by the Roots blower. At the entrance of the jacket there was another tank equipped with a valve for throttling the air when the specific weight was varied.

The cooling air was directed around the cylinder by a jacket placed approximately ⅛ inch from the fin tips, as shown in figure 3 (a). Whenever the outside diameter (fin width) of the test cylinder was reduced, the ⅛-inch clearance at the tips was maintained by using sleeves inside the jacket. The inlet of the jacket was faired and proportioned in such a manner as to reduce as much as possible the breakaway of the air from the walls.

The air system used to test the 0.166–1.22–0.035, 0.137–1.22–0.035, 0.112–1.22–0.035, 0.083–1.22–0.035, and 0.057–1.22–0.035 cylinders, hereinafter designated "series B" tests, is shown diagrammatically in figure 2 (b). The jacket used on these five cylinders was in contact with the fin tips (fig. 3 (b)).

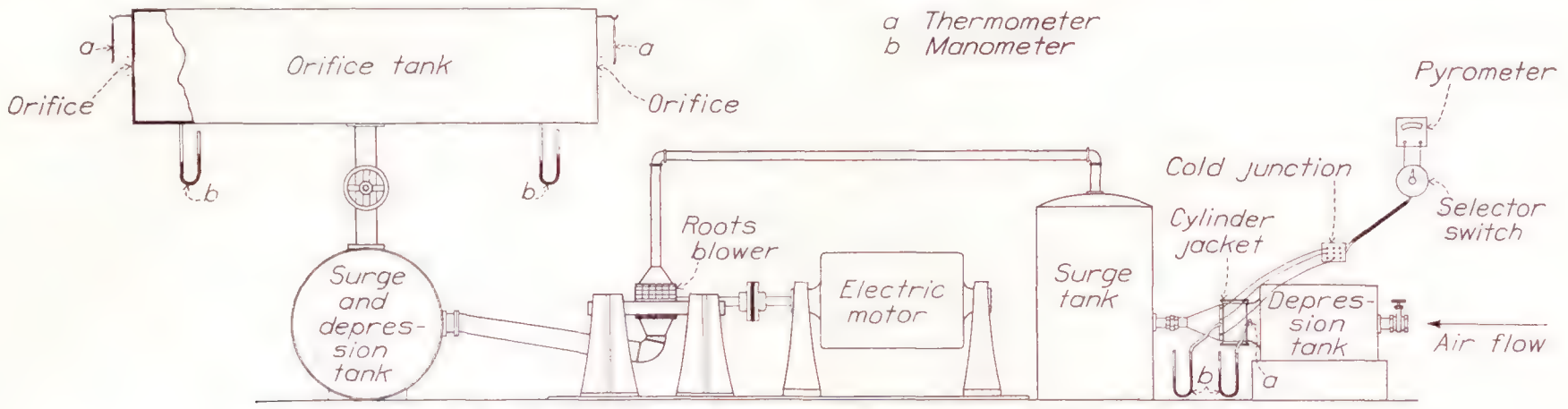

(a) Equipment used to test the 0.25–1.22–0.04, 0.25–0.97–0.04, 0.25–0.67–0.04, and 0.15–0.97–0.04 cylinders.

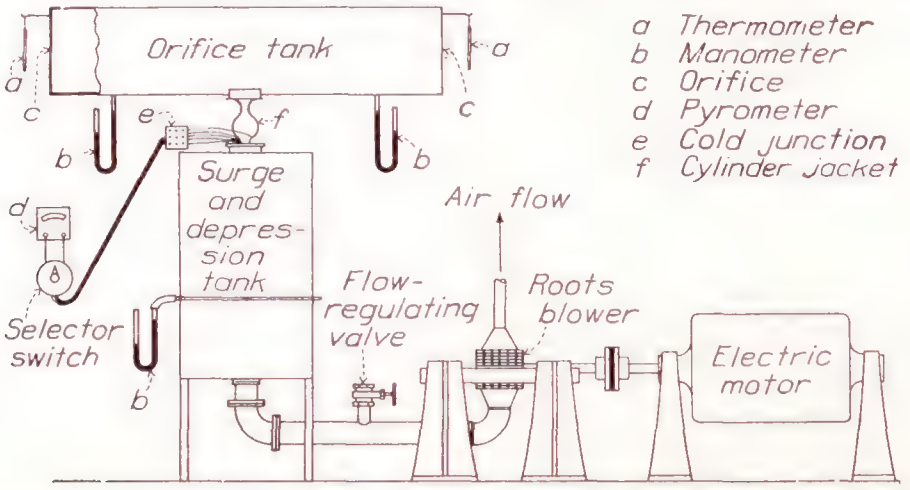

(b) Equipment used to test the 0.166–1.22–0.035, 0.137–1.22–0.035, 0.112–1.22–0.035, 0.083–1.22–0.035, and 0.057–1.22–0.035 cylinders.

FIGURE 2.—Diagrammatic sketch of equipment.

INSTRUMENTS

The cylinder temperatures were measured with 24 iron-constantan thermocouples connected through a selector switch to a portable pyrometer. The thermo-

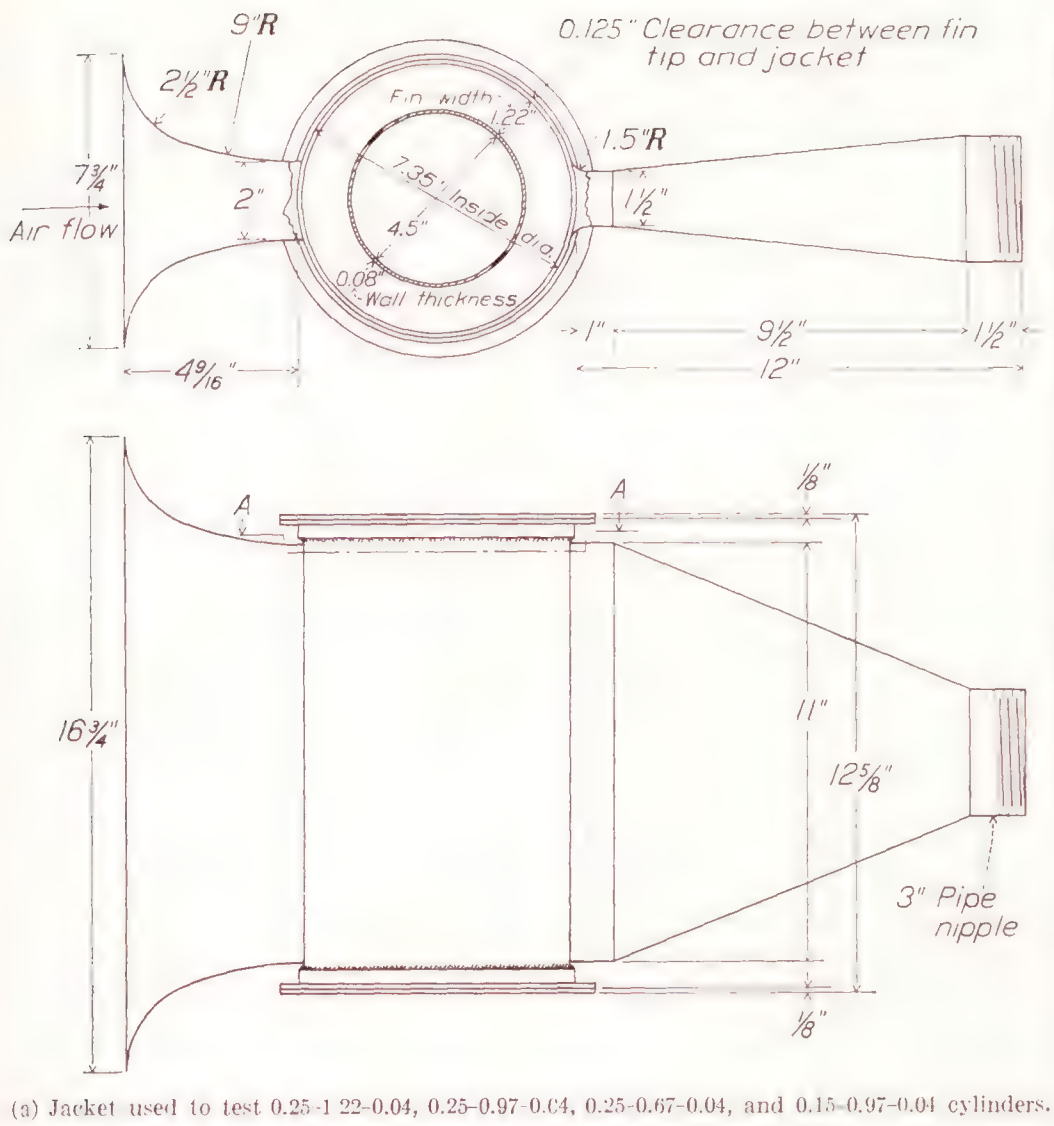

(a) Jacket used to test 0.25-1.22-0.04, 0.25-0.97-0.04, 0.25-0.67-0.04, and 0.15-0.97-0.04 cylinders.

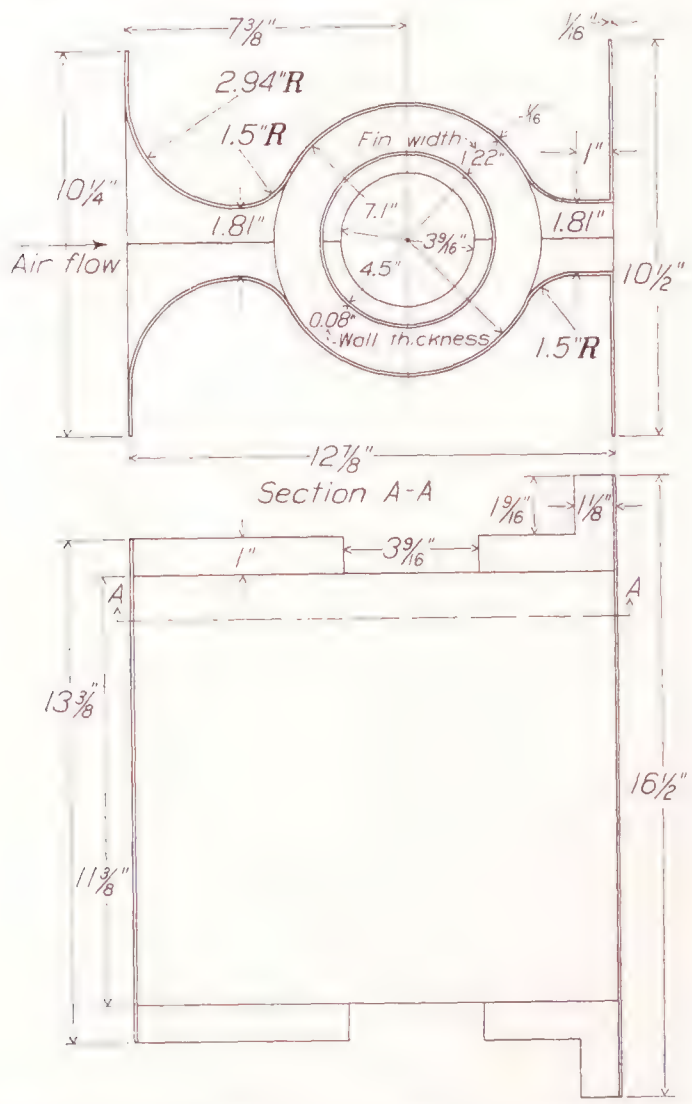

(b) Jacket used to test 0.166-1.22-0.035, 0.137-1.22-0.35, 0.112-1.22-0.035, 0.083-1.22-0.035, and 0.057-1.22-0.035 cylinders.

FIGURE 3.—Sketches of jackets.

couples were made of 0.013-inch-diameter silk-covered enameled wire and were welded to the cooling surface at the points shown in figure 4. Differential thermocouples, which were connected to sensitive galvanometers, were placed on the adjacent surfaces between the guard rings and the test cylinder to facilitate adjusting the heat input to the guard rings so that there would be no heat exchange between the test section and the guard rings. Ammeters and voltmeters were used to measure the electrical power input to the test cylinder and guard rings.

The temperature of the air at the entrance of the jacket was measured with an alcohol ther-

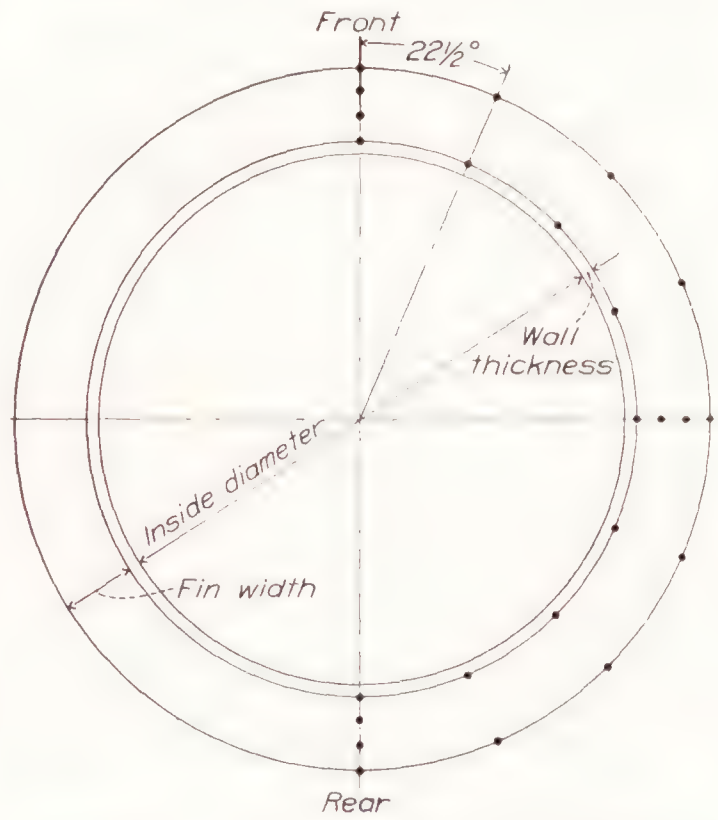

FIGURE 4.—Location of thermocouples on test cylinder.

mometer and at the exit of the jacket with three chromel-constantan thermocouples connected through a selector switch to a low-resistance portable pyrometer. In the series A tests the pressures at the entrance and the exit of the jacket and the pressure drop across the orifice tank were measured with water manometers. In the series B tests the pressure drop across the orifice tank and the pressure in the depression tank were measured with water manometers.

TESTS

Tests were conducted at air velocities from 10 to 130 miles per hour and at specific air weights from 0.046 to 0.074 pound per cubic foot. The recorded data were the electrical power input to the guard rings and test cylinder, the temperature of the air entering the orifice tank, the temperature of air entering and leaving the cool-

ing jacket, the pressure drop across the orifice tank, the pressure at the entrance and exit of the jacket in series A tests, the pressure in the depression tank in series B tests, and the temperatures at the various points on the cooling surface.

The velocity was varied by changing the speed of the blower. The specific air weight was varied in the series A tests by throttling the air at the entrance of the depression tank. The specific weight of the air was not varied in the series B tests.

The heat inputs varied from 83 to 97 B.t.u. per square inch wall area per hour (0.0326 to 0.0381 horsepower per square inch wall area) for the various cylinders; the heat input was approximately constant, however, for any one cylinder.

The series A tests were conducted principally to determine the effect of fin width on heat transfer; those of series B were conducted to determine the effect of fin spacing on heat transfer and power required.

CALCULATIONS

The results were obtained by the following formulas:
Specific weight of the air, $\rho_1 g$:

$$\rho_1 g = \frac{1.325 \times p_1}{460 + T_1} \tag{1}$$

Mean velocity of the air between the fins, V_m:

$$V_m = \frac{W_t}{\rho_1 g} \times \frac{144}{A_{tr}} \tag{2}$$

(The method of calculating W_t is given in reference 4.)
Experimental and calculated heat-transfer coefficients, U_{exp} and U_{cal}:

$$U_{exp} = \frac{Q}{A_b \theta_b} \tag{3}$$

$$U_{cal} = \frac{q}{s+t}\left\{\frac{2}{a}\left(1+\frac{w}{2R_b}\right)\tanh aw' + s\right\} \tag{4}$$

where

$$a = \sqrt{\frac{2q}{kt}}$$

The value of $k=2.17$ for this report.
Equation (4) is derived as equation (13) in reference 1.
Average outlet cooling-air temperature T_2:

The outlet cooling-air temperature is an average of the indicated temperatures of the three thermocouples after corrections have been applied for instrument calibration and cold-junction temperature.
Power required across the test cylinder, P_t:

$$P_t = 0.000893 V_m A_t \{p_1 - (p_2 + 0.00022 V_m^2 \rho_1 g A_t^2 / A_1^2)\} \tag{5}$$

In this formula the specific weight of the air at the inlet of the jacket was used instead of the specific weights at the inlet and outlet as theoretically should be done. The error introduced by this method is small, however, and formula (5) is simpler than the rigorously correct one. It was very difficult to measure the static head at the entrance and exit of the jacket so that in formula (5) p_1 is the total head in the orifice tank (see fig. 2 (a)) and p_2 is the static head in the depression tank. The use of these heads leads to very little error unless there is a vena contracta in the entrance and exit.
Power required to generate the outlet velocity, P_a:

$$P_a = 1.965 \times 10^{-7} A_1 \rho_2 g V_2^3 \tag{6}$$

RESULTS AND DISCUSSION

The problem of blower cooling can be divided into two parts, a study of the heat transfer obtained and of the blower power required for various conditions of operation. The heat transfer for a given case can be calculated when the surface heat-transfer coefficient q of the fins is known, use being made of equation (4). A study will now be made of the dependence of q and the blower power on the fin dimensions, the physical properties of the air, and the air speed. Because a large number of variables are involved, dimensional theory is used in clarifying and simplifying the analysis.

As q depends on the specific weight, viscosity, specific heat, thermal conductivity, velocity of the air, and the various dimensions of the finned cylinder, by dimensional analysis the following expression can be set up (see equation (1), reference 1):

$$q = c_p \rho_1 g V_m f\left(\frac{\rho_1 g V_m D}{\mu}, \frac{\mu c_p}{k_a}, \frac{t}{D}, \frac{w}{D}, \frac{s}{D}\right) \tag{7}$$

With the exception of the specific heat and the conductivity of the air, the blower power depends on the same group of variables and the following relation can be obtained:

$$P_t = \rho_1 g V_m^3 D f\left(\frac{\rho_1 g V_m D}{\mu}, \frac{t}{D}, \frac{w}{D}, \frac{s}{D}\right) \tag{8}$$

where P_t is the power per unit length of cylinder. In this analysis the flow is assumed as two-dimensional, which condition the tests very closely simulated.

EFFECT OF VARIABLES ON q

Weight velocity of the air and fin dimension.—Equation (7) shows that, when all other quantities remain constant, the value of q varies as the weight velocity of the cooling air, $V_m \rho_1 g$. Tests presented herein were performed in which both the velocity and specific weight were independently varied. The values of q obtained from these tests are plotted against weight velocity on logarithmic-coordinate paper in figures 5 and 6. For any one test cylinder a straight line fitted the data fairly well.

The curves of figure 5 for the cylinders having pitches from 0.112 to 0.25 inch, inclusive, have been drawn parallel and have a slope of 0.667. For cylinders with pitches less than 0.112 inch the slope becomes increasingly greater as the pitch is decreased. From the

relation between q and weight velocity shown in figure 5 for cylinders having pitches of 0.112 inch or greater, equation (7) can be modified as follows:

$$q = c_p \rho_1 g V_m \left(\frac{\rho_1 g V_m D}{\mu}\right)^{-0.333} f'\left(\frac{\mu c_p}{k_a}, \frac{t}{D}, \frac{w}{D}, \frac{s}{D}\right) \qquad (9)$$

Below 0.112-inch pitch the exponent —0.333 decreases as the pitch decreases.

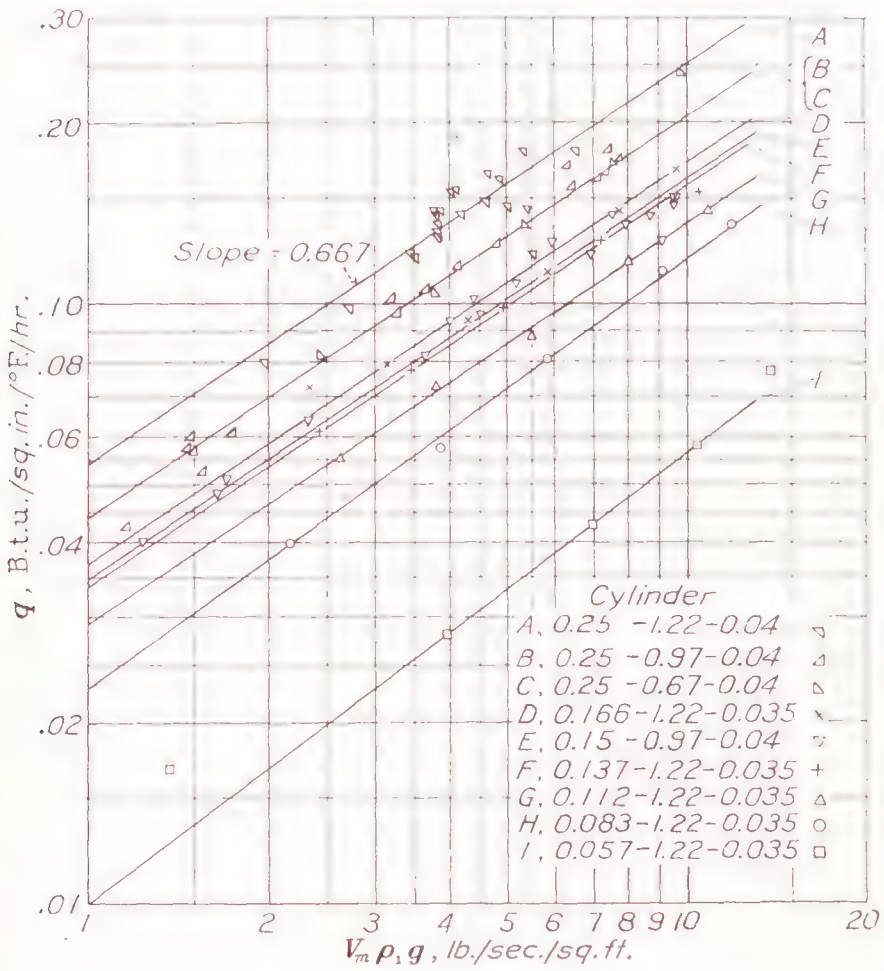

FIGURE 5.—Effect of weight velocity of the cooling air on the average surface heat-transfer coefficients, based on the difference between the cylinder temperature and the inlet-air temperature.

The curves of figure 5 in which the value of q is based on the difference between the inlet-air temperature and the average cylinder temperature show that, when the pitch is decreased, the value of q will decrease even though the weight velocity of the cooling air remains constant. If the values of q are based on the difference between the average cooling-air temperature and the average cylinder temperature, the results will be as shown in figure 6. The outlet-air temperature was calculated from the weight of air flowing over the test cylinder, the heat input to the test cylinder, the specific heat of the air, and the inlet-air temperature. It was found that more than three thermocouples in the outlet of the jacket were necessary to give a correct average temperature. Because the effect of the heating of the air on the value of q is greater at low air speeds than at high air speeds, the slope of the curves in figure 6 is much less than the slope of the curves in figure 5; all the curves in figure 6 have the same slope.

Figure 7 was obtained by cross-plotting figure 5 at a weight velocity of the air of 4 pounds per second per square foot and shows the effect of fin space on q. The surface heat-transfer coefficient varies as the 0.386 power of the fin space from 0.09- to 0.21-inch space. From 0.048- to 0.09-inch space the slope is a little greater than 0.386, and below 0.048 inch q decreases rapidly.

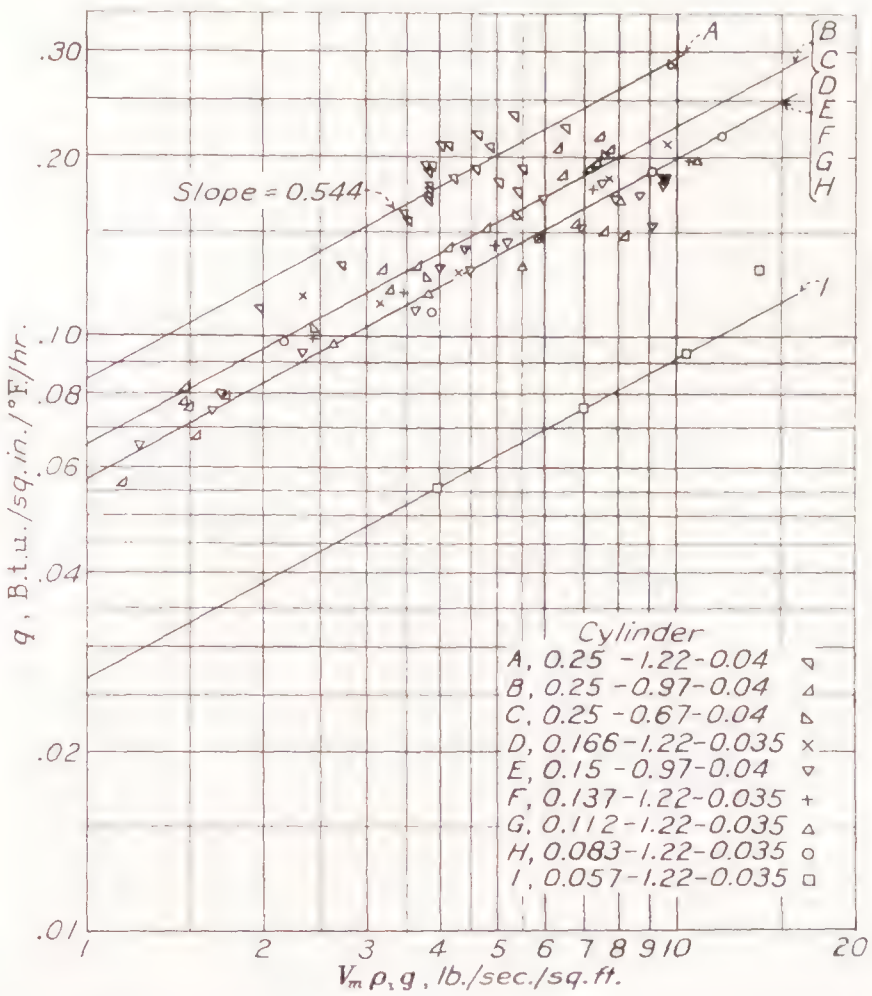

FIGURE 6.—Effect of weight velocity of the cooling air on the average surface heat-transfer coefficients, based on the difference between the cylinder temperature and the average air temperature.

It is interesting to note that the value of q, even when corrected for the heating of the air, is less for cylinders with closely spaced fins than for cylinders with widely

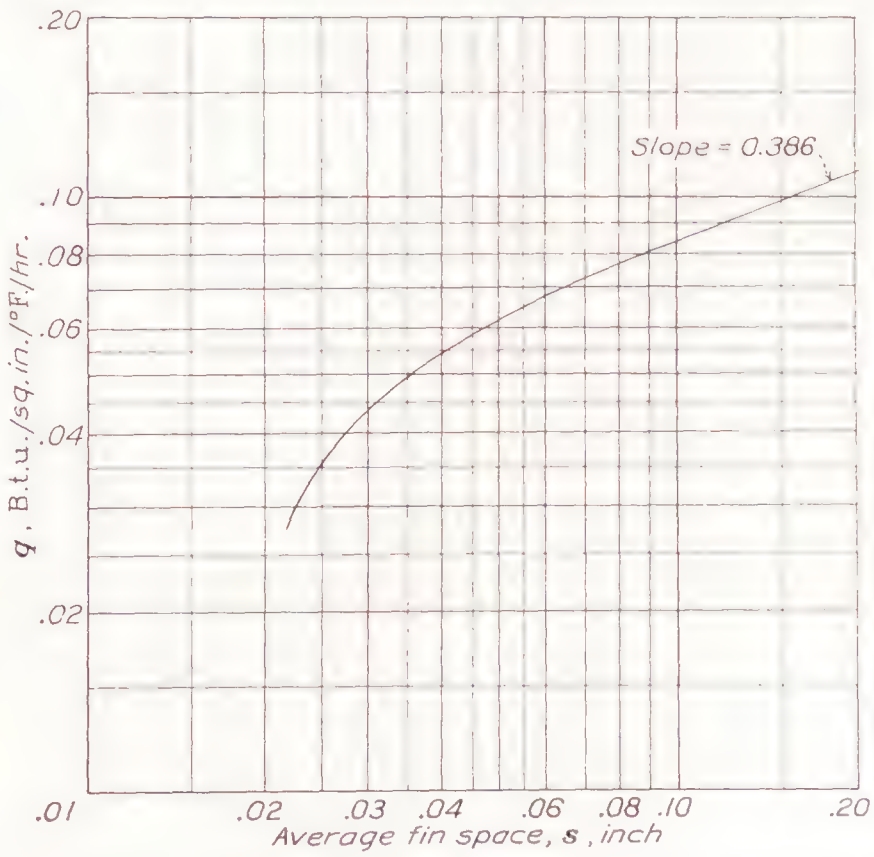

FIGURE 7.—Effect of fin space on the average surface heat-transfer coefficient. Weight velocity 4 pounds per second per square foot.

spaced fins although the average weight velocity between the fins is the same. Recent tests (reference 5) based on a study of air flow between fins indicated that

the cooling was best with a 0.031-inch space between the fins, the minimum used in the air-flow tests. The cooling with closely spaced fins is greatly impaired because the flow pattern between the fins is not so conducive to a high over-all heat-transfer coefficient as the flow pattern for more widely spaced fins.

The test results indicate that fin width had little effect on q for two of the cylinders tested, the 0.25–0.97–0.04 and the 0.25–0.67–0.04. The values of q for the 0.25–1.22–0.04 cylinders are, however, greater than for the other two cylinders.

Previous tests conducted on finned cylinders having pitches of 0.15 and 0.25 inch and mounted in a free air stream indicated that, for fin widths greater than 0.4 inch, the value of q varied little with change in width (reference 1). For the tests herein reported the air was guided around the cylinder and the velocity distribution along the fin width was more uniform than for the cylinder in the free air stream (reference 5). The variation in q with fin width for two cylinders, as expected, was less than in tests on cylinders in a free air stream (reference 1). Because of the unexpected increase in q for the 0.25–1.22–0.04 cylinder, further tests are being made to determine the effect of fin width on q.

The tests on the cylinders in a free air stream also indicated that fin thickness had a minor effect on the value of q and it is reasonable to expect that the same would hold true for cylinders surrounded by a jacket. Therefore, no tests were conducted to determine the effect of fin thickness.

Air temperature.—Although no experiments were made to determine the effect of temperature of the air on q, some idea of the effect can be obtained from equation (9). The quantities u, c_p, k_a, and $\rho_1 g$ depend on the temperature of the air. The effect of $\rho_1 g$ on q has been determined. For the range of temperatures encountered in an ordinary altitude change, however, c_p, uc_p/k_a, and $u^{0.333}$ are practically constant. The heat-transfer coefficient q is therefore affected by temperature of the air only as the latter affects $\rho_1 g$.

EFFECT OF VARIABLES ON U

Weight velocity of the air and fin dimensions.—As the amount of base surface available on a cylinder for finning is limited, a fin design should be selected that gives the maximum value of U—the heat carried away per unit wall area per degree temperature difference between the cylinder wall and the cooling air per hour. Therefore, in the design of fins, the maximum cooling surface consistent with a high value of q must be used to obtain maximum cooling. The calculated values of U shown in figure 8, except for the 0.25–1.22–0.04 cylinder, were determined from equation (4) and from the values of q given in figure 5; the experimental values were computed from test results. The calculated values of U for the 0.25–1.22–0.04 cylinder shown in figure 8 were obtained from equation (4) and from the values of q shown in figure 5 for the 0.25–0.97–0.04 and 0.25–0.67–0.04 cylinders. Values of U calculated from the values of q for the 0.25–1.22–0.04 cylinder in figure 5 did not check the experimental values of U. This discrepancy is a further indication that the experimental values of q for the 0.25–1.22–0.04 cylinder are questionable and that fin width has little effect on q. These curves show that the agreement between the calculated and the experimental values is sufficiently good to justify the use of equation (4) in calculating the heat dissipated by a cylinder enclosed by a jacket.

Figure 9 is a cross plot of the experimental values of U in figure 8 and shows the effect of fin pitch on U at several constant weight velocities of the air for the cylinders with 1.22-inch fin width and 0.035-inch fin thickness. The value of U for these curves is based on the difference between the inlet-air temperature and the average cylinder-wall temperature. The values of U for the 0.112–1.22–0.035 and the 0.137–1.22–0.035 cylinders did not fall on the faired curves as well as the values of U for the other cylinders but were sufficiently close to establish this part of the curve. The calculated values of U for cylinders 0.112–1.22–0.035 and 0.137–1.22–0.035 were very close to the faired curves. The results show that for all weight velocities of the cooling air investigated the maximum heat transfer falls between cylinders of 0.057-inch and 0.083-inch pitch or 0.022-inch to 0.048-inch space. The curves have been dotted between these two values as no data were taken to establish definitely these portions of the curves. The curves show that the heat-transfer coefficient is not sensitive to the number of fins per inch for values on either side of and near the maximum. For example, with 11 or 16 fins per inch the heat-transfer coefficient U is 95 percent of the maximum value, obtained with approximately 13 fins per inch of 0.035 thickness. The fin space giving the maximum value of the heat-transfer coefficient U will vary as the fin thickness is varied and the number of fins per inch will increase as the fin thickness decreases.

The experimental values of U for the curves in figure 10 are based on the difference between the average cylinder-wall temperature and the average air temperature. The difference between the values of U in figures 9 and 10 is caused by the heating of the air. With a fin pitch of 0.05 inch and with a weight velocity of 3 pounds per square foot per second the heat-transfer coefficient is approximately 55 percent higher when based on the average cooling-air temperature; whereas, with a weight velocity of 8 pounds, the coefficient would be approximately 19 percent greater when based on the average cooling-air temperature. Likewise with a fin pitch of 0.15 inch and with a weight velocity of 3 pounds per square foot per second the heat-transfer coefficient would be approximately 29.6 percent greater when based on the average cooling-air temperature; whereas, with a weight velocity of 8, the heat-transfer

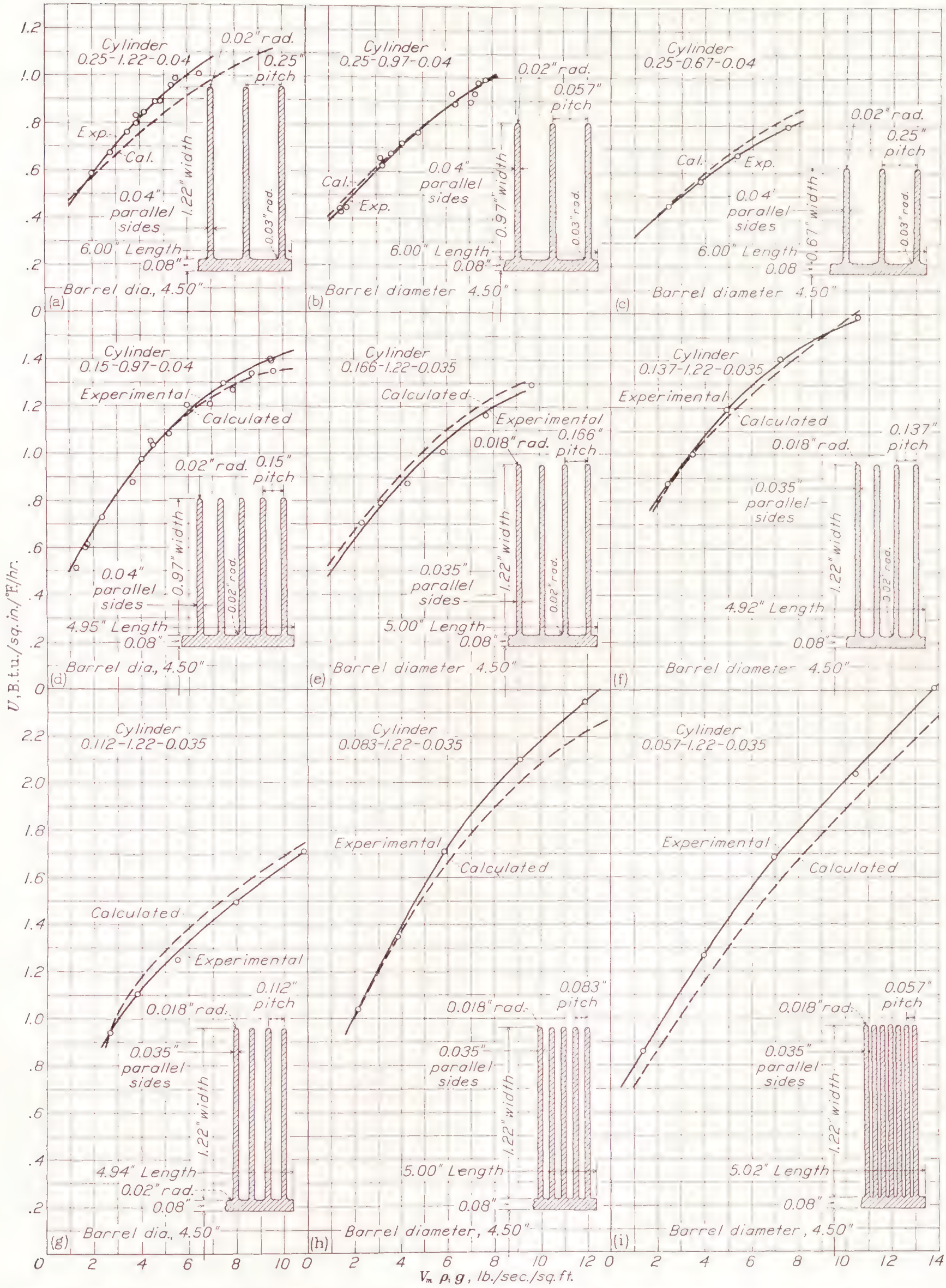

FIGURE 8.—Effect of weight velocity of the cooling air on the average experimental and calculated wall heat-transfer coefficients for the nine test cylinders.

coefficient would be approximately 17.6 percent greater. The curves in figure 10, like those in figure 9, show that the pitch for the maximum heat transfer lies between 0.057 and 0.083 inch.

EFFECT OF VARIABLES ON BLOWER POWER REQUIRED

The blower power required can be divided into two main parts: that required across the cylinder and that required to generate the outlet velocity. For a given test arrangement, the power required to generate the outlet velocity may be reduced a small amount by a properly expanding exit passage.

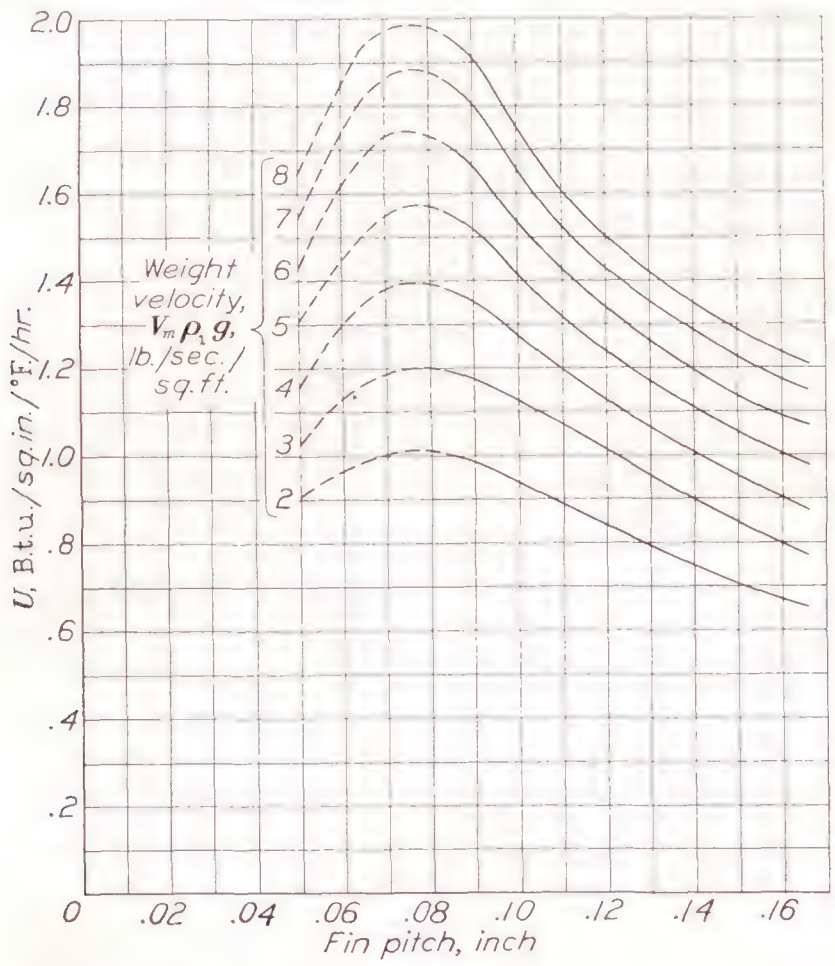

FIGURE 9.—Effect of fin pitch on the average wall heat-transfer coefficient, based on the difference between the cylinder-wall temperature and the inlet-air temperature. Fin width, 1.22 inches; fin thickness, 0.035 inch.

Weight velocity of the air and the fin dimensions.—The effect of weight velocity of the cooling air on power for five of the cylinders tested is shown in figure 11, by plotting $P_t(\rho_1 g)^2/w$ against $V_m\rho_1 g$ on logarithmic paper. The jacket around these cylinders was in contact with the fin tips, as shown in figure 3 (b). From equation (8), $P_t(\rho_1 g)^2$ varies as a function of $V_m\rho_1 g$. The effect of a small variation in the specific weight was eliminated by plotting the results in this form. Also $P_t(\rho_1 g)^2$ was divided by the fin width before plotting as it seemed reasonable to expect the pressure drop to change very little with fin width; the power would therefore vary directly as the fin width.

The slope of the curves in figure 11 shows that $P_t(\rho_1 g)^2/w$ varies as the 2.69 power of the weight velocity of the air. The data seem to show that there is a break in the curves at the lower values of weight velocity, probably caused by a change from turbulent to laminar flow but, as there are not enough points definitely to establish this break, the curves have been dotted at the lower values of weight velocity.

Dryden and Kuethe (reference 6) have shown that for flat plates the friction drag is theoretically proportional to the 1.8 power of the velocity for turbulent flow. Unpublished tests made at the Massachusetts Institute of Technology by R. H. Smith and R. T. Sauerwein show that for various finned plates the drag varied as the velocity to the 1.75 to 1.96 power, depending on the pitch and width of the fins. As the drag is directly proportional to the pressure drop in the present tests and as the power is proportional to the product of the pressure drop and the volume, the power required for friction drag should theoretically vary as the velocity to the 2.8 power, which is very close to what was obtained.

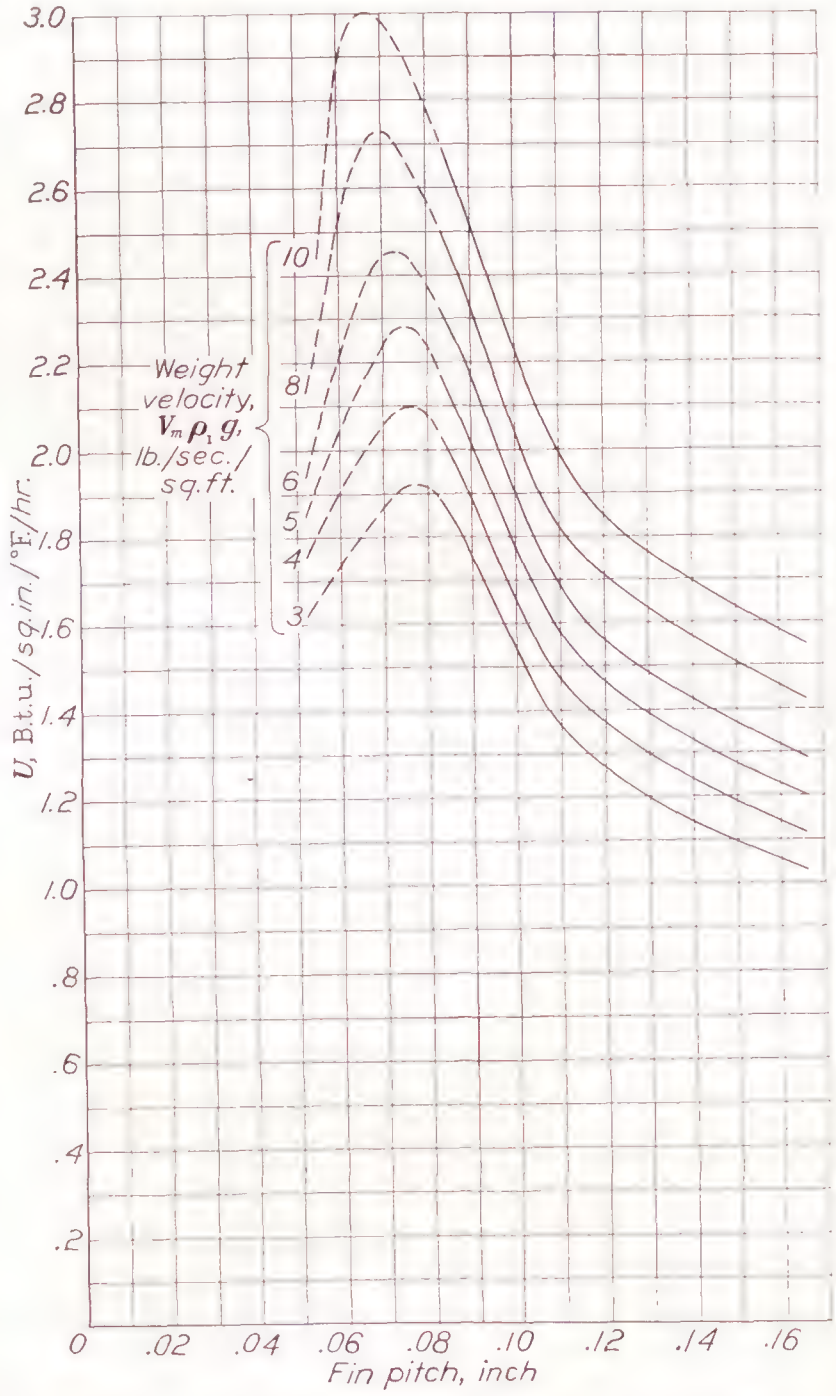

FIGURE 10.—Effect of fin pitch on the average wall heat-transfer coefficient, based on the difference between the cylinder-wall temperature and the average air temperature. Fin width, 1.22 inches; fin thickness, 0.035 inch.

From these results in order to give the observed variation of blower power with specific weight and weight velocity of the air, equation (8) must take the form

$$P_t=\frac{(\rho_1 g V_m)^3}{(\rho_1 g)^2}D\left(\frac{\rho_1 g V_m D}{\mu}\right)^{-0.31} f'\left(\frac{s}{D},\frac{t}{D},\frac{w}{D}\right) \qquad (10)$$

Figure 11 shows that the power required for cooling increases as the space between the fins decreases for the

same weight velocity of the air except for the 0.166 cylinder. The data for the 0.166 cylinder fell on the same curve as the data for the 0.137-inch pitch cylinder. This result was surprising as it was expected that less

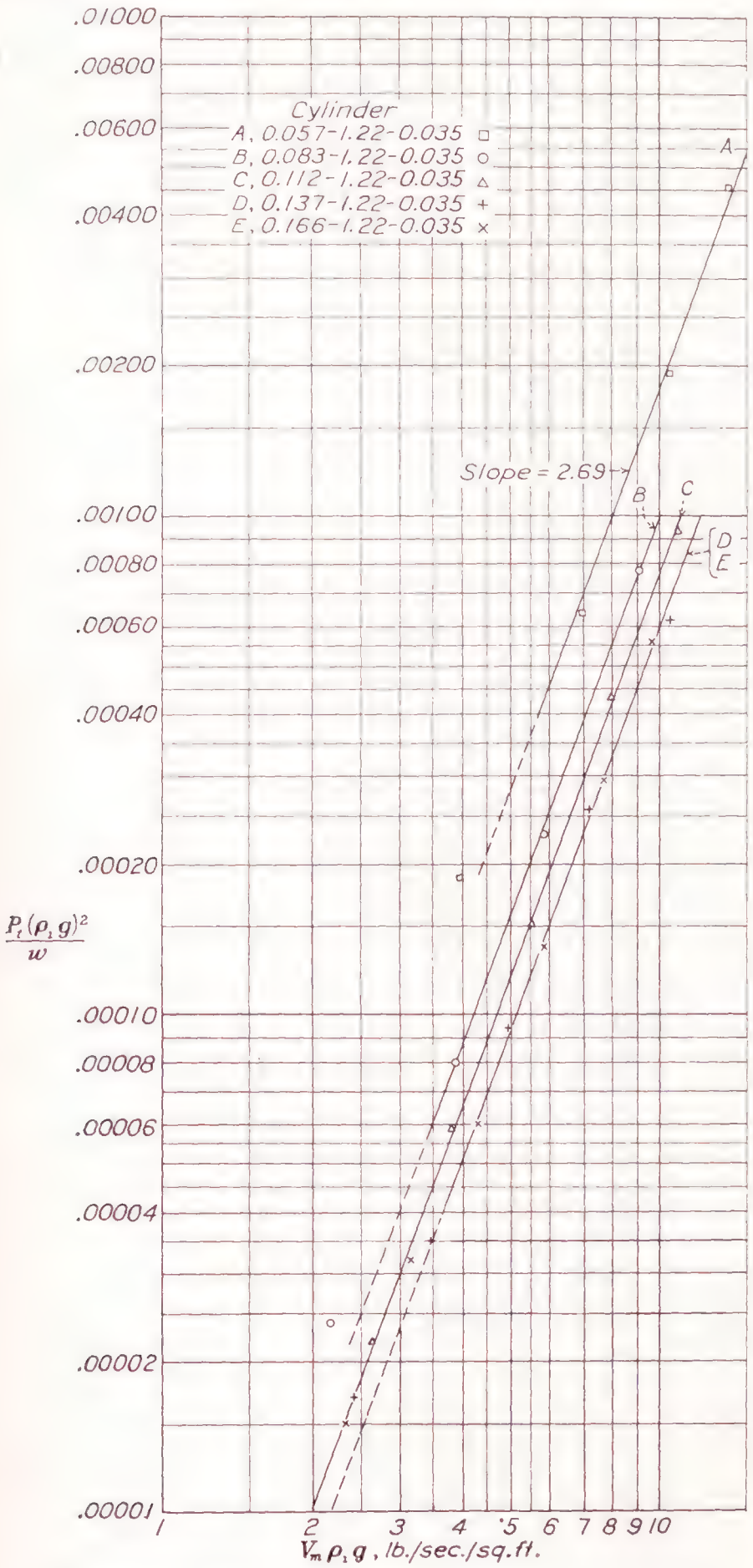

FIGURE 11.—Effect of weight velocity of the cooling air on $P_t(\rho_1 g)^2/w$.

power would be required to force air by more widely spaced fins. An analysis of the pressure drops around cylinders to be presented in a later report shows that power increases as space decreases but for the 0.166- and 0.137-inch pitch cylinders the difference is very small.

Curves of $P_b(\rho_1 g)^2/w$ plotted against weight velocity of the air are shown in figure 12 for the same cylinders as are shown in figure 11, where P_b is the total power loss across the jacket and includes both P_t and the kinetic energy lost at the exit. The total power varied as the 2.61 power of the weight velocity for all the cylinders and increased as the pitch decreased, below 0.112-inch pitch, for a constant weight velocity. The data for the 0.166, 0.137, and 0.112 cylinders are repre-

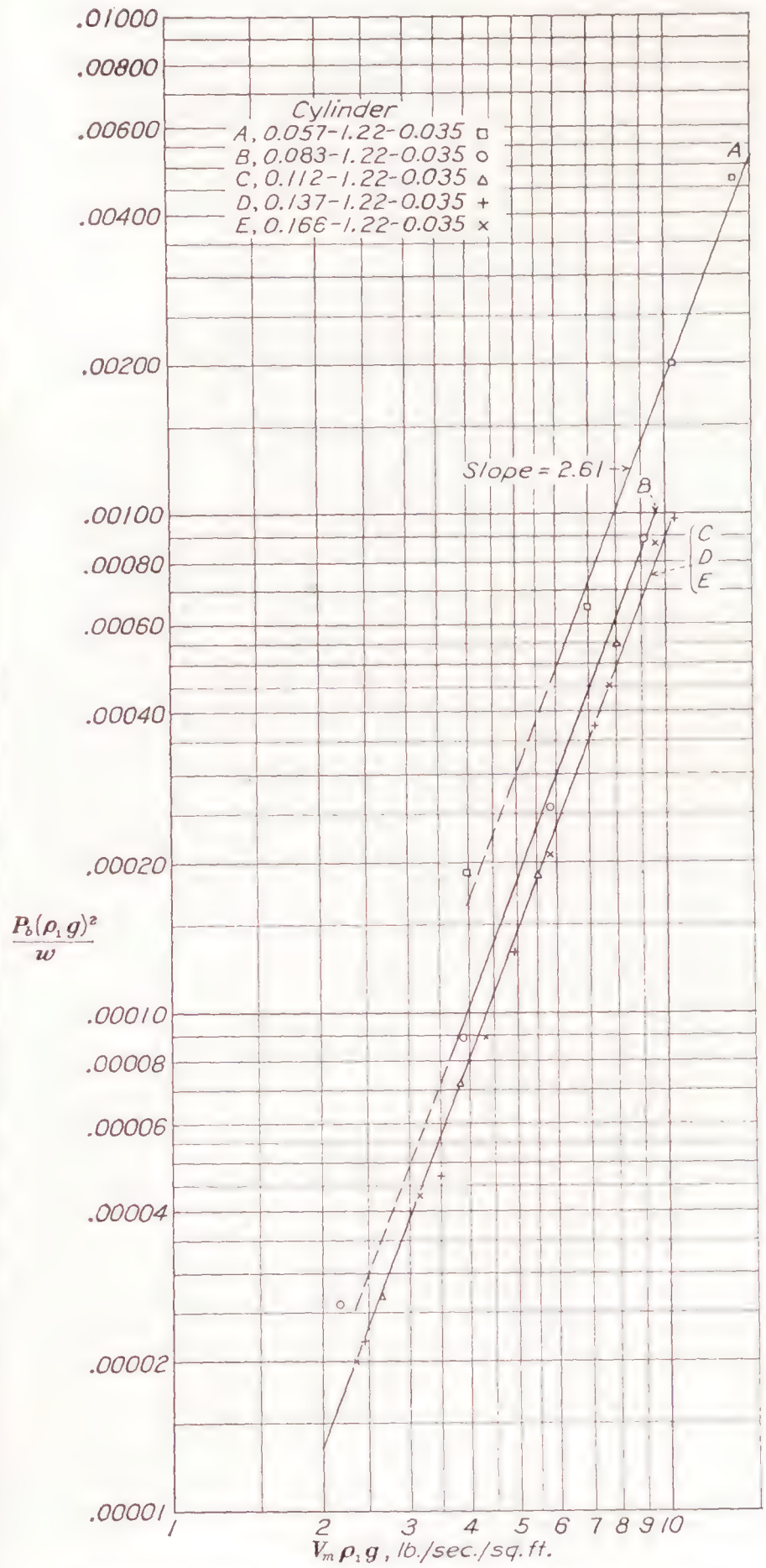

FIGURE 12.—Effect of weight velocity of the cooling air on $P_b(\rho_1 g)^2/w$.

sented by a single curve. It can be shown from figure 11 and the change in loss out the exit for the three cylinders, with a constant jacket exit area and weight velocity over the fins, that the total power required for

the 0.166, the 0.137, and the 0.112 cylinders is approximately constant.

Further tests are being made to determine the effect of fin pitch, width, and Reynolds Number on the power required.

Air temperature.—The temperature of the air affects its specific weight and viscosity. The effect of variation in specific weight on power has been shown. Equation (10) shows that the power varies as the 0.31 power of the viscosity. For the range of temperatures encountered in an ordinary altitude change, the effect of change in viscosity would be small.

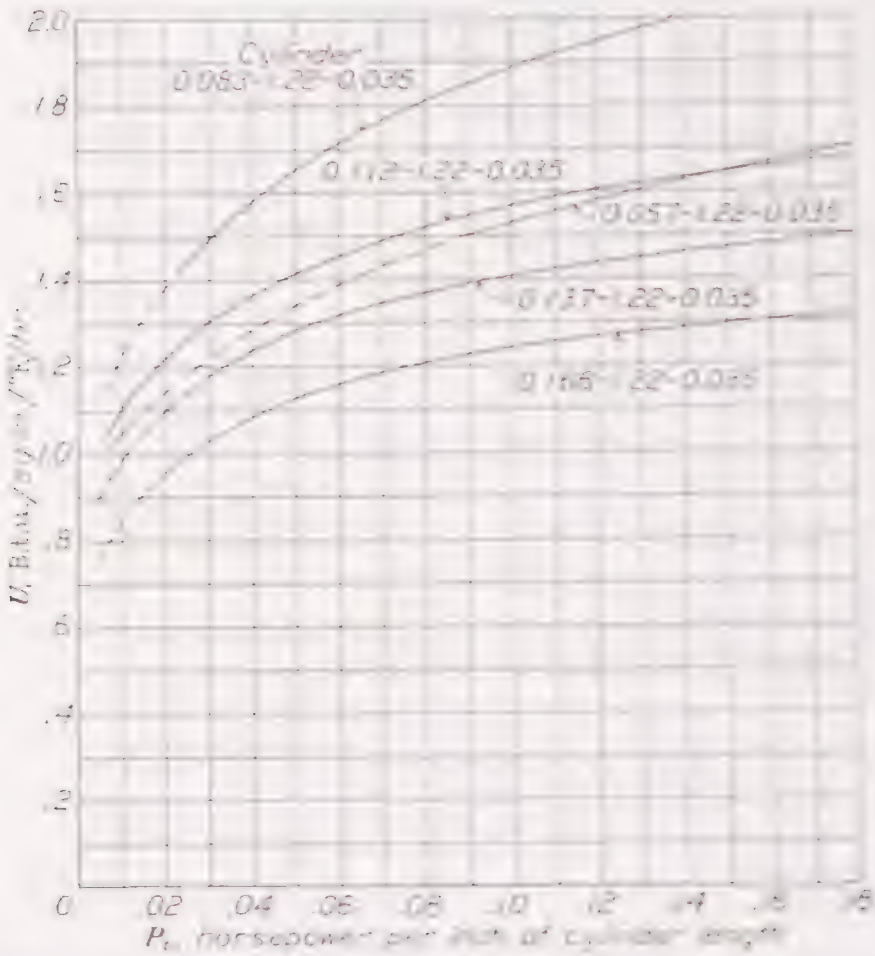

FIGURE 13.—Variation of average wall heat-transfer coefficient with power, P_t. Specific weight of the air, 0.0717 pound per cubic foot.

RELATION BETWEEN HEAT DISSIPATION AND BLOWER POWER

The wall heat-transfer coefficient U is shown plotted against the power P_t in figure 13 for a specific weight of the air of 0.0717 pound per cubic foot. These results were obtained from figures 9 and 11 and indicate that for a given power the heat transfer can be increased by decreasing the pitch up to a limiting value of approximately 0.08 inch; below this pitch the heat transfer decreases as the pitch decreases. Thus, with 0.10 horsepower, U increases from 1.24 B.t.u. per square inch per °F. per hour for the 0.166 cylinder to 1.885 for the 0.083 cylinder, an increase of approximately 52 percent, and then decreases to 1.53 B.t.u. per square inch per °F. per hour for the 0.057 cylinder. With a given horsepower, except for the 0.166-inch pitch, the weight velocity of the air decreases as the fin pitch decreases. This decrease in weight velocity tends to decrease U but decreasing the fin pitch tends to increase U until a limiting value is reached. As the effect of fin pitch predominates, the fin pitch giving maximum heat transfer for a given weight velocity will give maximum heat transfer for a given power.

Figure 14 shows curves similar to figure 13 in which the power lost as kinetic energy in the air leaving the

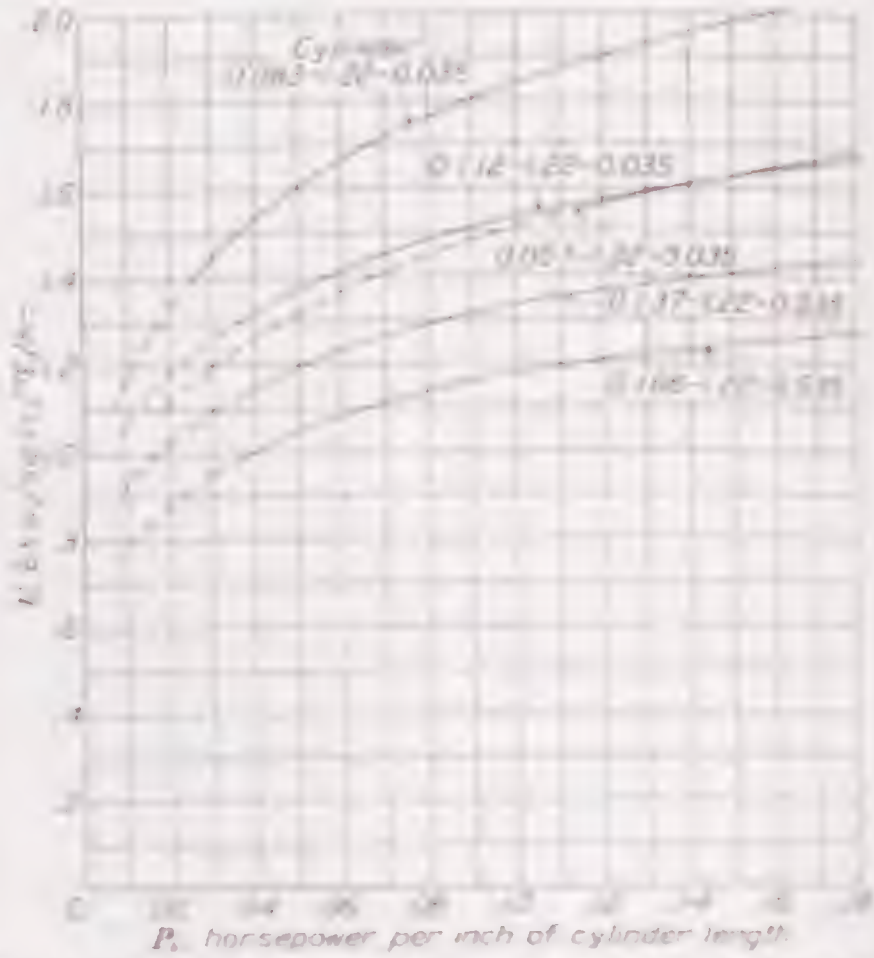

exit passage of the jacket is included in calculating the required power. As previously stated, the power lost at the exit can be somewhat decreased by providing a properly expanding passage. The curves of figure 14

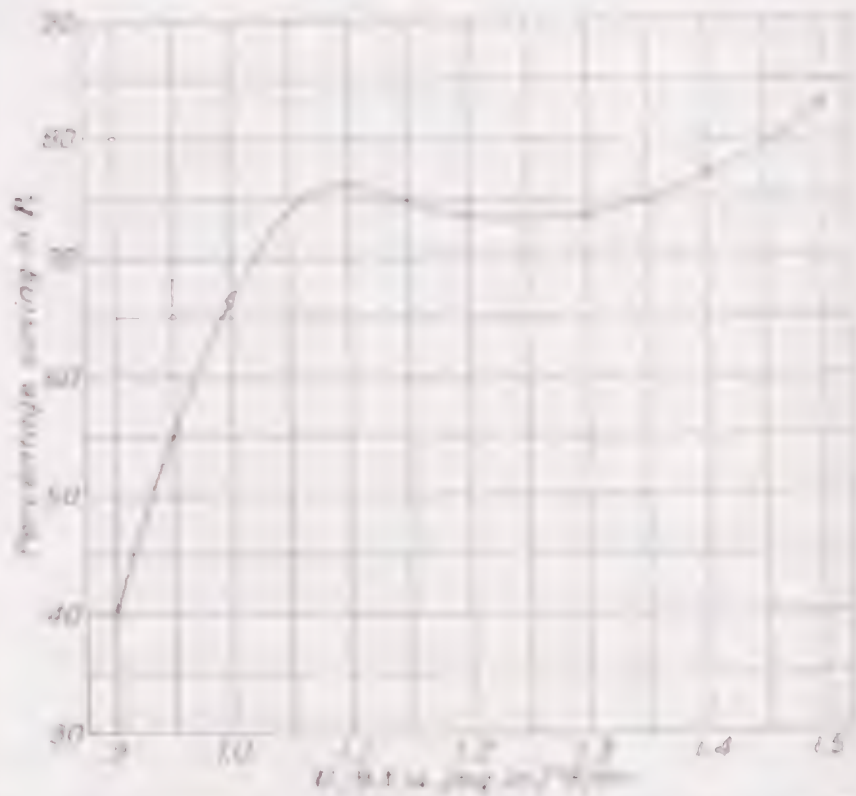

FIGURE 15.—Percentage saving in P_t by using fin pitch of 0.083 inch instead of 0.137 inch.

were obtained from figures 9 and 12 and show the same trends as do those of figure 13.

Figure 15, obtained from figure 13, is a plot of the percentage saving in P_t, the power required for cooling,

through the use of a fin pitch of 0.083 inch instead of 0.137 inch at various values of U. The saving in cooling power is appreciable and, as cylinders used in conventional practice usually have fin pitches greater than 0.137 inch, it might be thought that much is to be gained from a power consideration by decreasing the pitch. The percentage of engine power required for blower cooling of conventional cylinders is, however, a small percentage of the total engine power. Löhner (reference 7) gives a value of 3.5 percent of the brake horsepower required for cooling a multicylinder engine with blowers and 8.3 percent for a single-cylinder engine. It has been found in tests of a single-cylinder engine (reference 8) that the power required for cooling varied from approximately 2.9 to 8.6 percent of the engine power, based on a blower efficiency of 70 percent and a temperature difference of 405° F. at a point between the exhaust valve and the rear spark plug, depending on cylinder and jacket design and engine-operating conditions.

CONCLUSIONS

1. The average surface heat-transfer coefficient q, based on the temperature difference between the cylinder and the inlet air, varied as the 0.667 power of the weight velocity of the cooling air for cylinders with fin spaces from 0.077 to 0.21 inch. Below 0.077 inch the exponent of the curves increased for each successive decrease in space.

2. The average surface heat-transfer coefficient q, based on the temperature difference between the cylinder and the inlet air, was independent of fin width for a range of fin widths from 0.67 inch to 1.22 inches and decreased as the space between the fins decreased. Below approximately 0.048 inch the decrease of q with fin space was very rapid.

3. The average surface heat-transfer coefficient q, based on the difference between the cylinder temperature and the average air temperature, remained constant for a given weight velocity of the air, for fin spaces from 0.048 to 0.131 inch; below approximately 0.048 inch q decreased and above 0.131 inch q increased.

4. The power required to force the air around the cylinder varied directly as the 2.69 power of the weight velocity for a constant specific weight and inversely as the square of the specific weight for a constant weight velocity of the cooling air.

5. For a given power expended in cooling, the heat dissipated from the cylinder could be increased by decreasing the space between the fins to approximately 0.045 inch for a cylinder with fins 1.22 inches wide. Below 0.045 inch space the heat dissipated decreased.

LANGLEY MEMORIAL AERONAUTICAL LABORATORY,
NATIONAL ADVISORY COMMITTEE FOR AERONAUTICS,
LANGLEY FIELD, VA., *November 14, 1936.*

85548—38——19

APPENDIX

SYMBOLS

w, fin width, inches.

w', effective fin width ($w'=w+t/2$).

t, average thickness of fins, inches.

s, average space between adjacent fin surfaces, inches.

p, pitch of fins, $p=s+t$, inches.

D, cylinder diameter at fin root, inches.

R_b, radius from center of cylinder to fin root, inches ($R_b=D/2$).

R_a, average radius from center of cylinder to finned surface, inches ($R_a=R_b+w/2$).

A_b, outside base area of test cylinder, square inches (πDl).

S, total area of heated surface exposed to air stream (including fin area), square inches.

A_t, total area of spaces between fins of the test cylinder per inch of cylinder length, square inches.

A_{tr}, total area of spaces between fins of both the test cylinder and the guard rings, square inches.

A_1, area of outlet of jacket, around test cylinder per inch of cylinder length, square inches.

W_t, total weight of air flowing across test cylinder and guard rings, pounds per second.

p_1, absolute total pressure of the air in the orifice tank, inches Hg.

p_2 absolute static pressure of the air in the depression tank (fig. 2 (b)), inches Hg.

T_1, temperature of the air at the inlet of the jacket, °F.

T_2, average temperature of the air at the outlet of the jacket, °F.

V_m, average velocity of the air across the fins, feet per second.

T_b, average temperature of the root of the fin, °F.

T_m, average temperature of the root of the fin and fins of the test cylinder, °F. (These two quantities, T_b and T_m, were calculated from the test data, as explained in reference 1.)

θ_b, average temperature difference between the root of the fin and the air, °F. ($\theta_b=T_b-T_1$).

θ_m, average temperature difference between the test cylinder and the air, °F. ($\theta_m=T_m-T_1$).

Q, total heat input to test cylinder, B.t.u. per hour.

U, average over-all heat-transfer coefficient, B.t.u. per square inch base area (A_b) per hour, per °F. temperature difference between the cylinder wall and the cooling air (θ_b).

q, average surface heat-transfer coefficient, B.t.u. per square inch total surface area (S) per hour, per °F. temperature difference between the surface and the cooling air (θ_m).

c_p, specific heat of the air at constant pressure, B.t.u. per pound per °F. ($c_p=1.41\ c_v$).

μ, absolute viscosity of the air, pounds per second per foot.

k_a, thermal conductivity of the air, B.t.u. per square foot per °F. through 1 foot per second.

k, thermal conductivity of the metal, B.t.u. per square inch per °F. through 1 inch per hour.

$\rho_1 g$, specific weight of the air at the inlet of the jacket, pounds per cubic foot.

$\rho_2 g$, specific weight of the air at the outlet of the jacket, pounds per cubic foot.

V_2, velocity of the air at the outlet of the jacket, feet per second.

P_t, total horsepower per inch of cylinder length required by test cylinder to overcome losses.

P_a, horsepower required per inch of cylinder length to accelerate outlet air.

P_b, horsepower required per inch of cylinder length to accelerate outlet air and overcome all losses ($P_b=P_a+P_t$).

REFERENCES

1. Biermann, Arnold E., and Pinkel, Benjamin: Heat Transfer from Finned Metal Cylinders in an Air Stream. T. R. No. 488, N. A. C. A., 1934.

2. Schey, Oscar W., and Rollin, Vern G.: The Effect of Baffles on the Temperature Distribution and Heat-Transfer Coefficients of Finned Cylinders. T. R. No. 511, N. A. C. A., 1934.

3. Schey, Oscar W., and Biermann, Arnold E.: Heat Dissipation from a Finned Cylinder at Different Fin-Plane/Air-Stream Angles. T. N. No. 429, N. A. C. A., 1932.

4. Ware, Marsden: Description and Laboratory Tests of a Roots Type Aircraft Engine Supercharger. T. R. No. 230, N. A. C. A., 1926.

5. Brevoort, M. J., and Rollin, Vern G.: Air Flow Around Finned Cylinders. T. R. No. 555, N. A. C. A., 1936.

6. Dryden, H. L., and Keuthe, A. M.: Effect of Turbulence in Wind Tunnel Measurements. T. R. No. 342, N. A. C. A., 1930.

7. Löhner, Kurt: Development of Air-Cooled Engines with Blower Cooling. T. M. No. 725, N. A. C. A., 1933.

8. Schey, Oscar W., and Ellerbrock, Herman H., Jr.: Performance of Air-Cooled Engine Cylinders Using Blower Cooling. T. N. No. 572, N. A. C. A., 1936.

REPORT No. 588

FUEL SPRAY AND FLAME FORMATION IN A COMPRESSION-IGNITION ENGINE EMPLOYING AIR FLOW

By A. M. Rothrock and C. D. Waldron

SUMMARY

The effects of air flow on fuel spray and flame formation in a high-speed compression-ignition engine have been investigated by means of the N. A. C. A. combustion apparatus. The process was studied by examining high-speed motion pictures taken at the rate of 2,200 frames a second. The combustion chamber was of the flat-disk type used in previous experiments with this apparatus. The air flow was produced by a rectangular displacer mounted on top of the engine piston. Three fuel-injection nozzles were tested: a 0.020-inch single-orifice nozzle, a 6-orifice nozzle, and a slit nozzle. The air velocity within the combustion chamber was estimated to reach a value of 425 feet a second.

The results show that in no case was the form of the fuel spray completely destroyed by the air jet although in some cases the direction of the spray was changed and the spray envelope was carried away by the moving air. When the fuel distribution within the combustion chamber was particularly poor, the volume in the chamber reached by the flame was considerably increased by the air flow. When the distribution was reasonably good, there was little change in the distribution of the flame. It was found that the air movement set up during the induction of air through ports in the cylinder liner, under a pressure difference of 26 inches of Hg, could be controlled so as materially to aid the air flow set up during the last portion of the compression stroke.

INTRODUCTION

The distribution of the fuel in the combustion chamber of a compression-ignition engine can be regulated to some extent by the design of the combustion chamber, by the design of the fuel-injection nozzle, and by the use of air flow. The N. A. C. A. has been conducting investigations of all three methods, singly and in combination. Tests have been conducted with single-cylinder engines and with special apparatus, by which data unobtainable on the engine may be procured.

With a special high-speed motion-picture camera operating at speeds from 2,000 to 2,400 frames a second in conjunction with the N. A. C. A. combustion apparatus, investigations have been made of some of the effects of injection advance angle, air-fuel ratio, and nozzle design on the combustion process. (See references 1, 2, and 3.) Data obtained by the N. A. C. A. on the effects of combustion-chamber shape and of air flow on combustion in a single-cylinder compression-ignition engine have been published in references 4 to 8. In order to explain further the results obtained in these tests and to coordinate the researches on the combustion apparatus with the engine tests, a program of tests was originated to study the effect of air movement preceding and during the combustion process. In the present tests it was desirable not only to photograph the fuel spray and flame formation in the combustion chamber of the N. A. C. A. combustion apparatus but also to photograph the air movement.

Any method employed for photographing the air movement must not disturb the normal operation of the apparatus, for by so doing the variables under investigation are changed. This condition immediately eliminates methods using such materials as light metal projections or strings to show the direction of the air flow. The use of aluminum dust or some such material was discarded because of its possible effects on combustion. A partial solution of the problem was found in the use of "schlieren" or "striae" photography (reference 9).

METHODS AND APPARATUS

The N. A. C. A. combustion apparatus has been described in references 1 to 3. A diagrammatic sketch showing the engine cylinder, the combustion chamber,

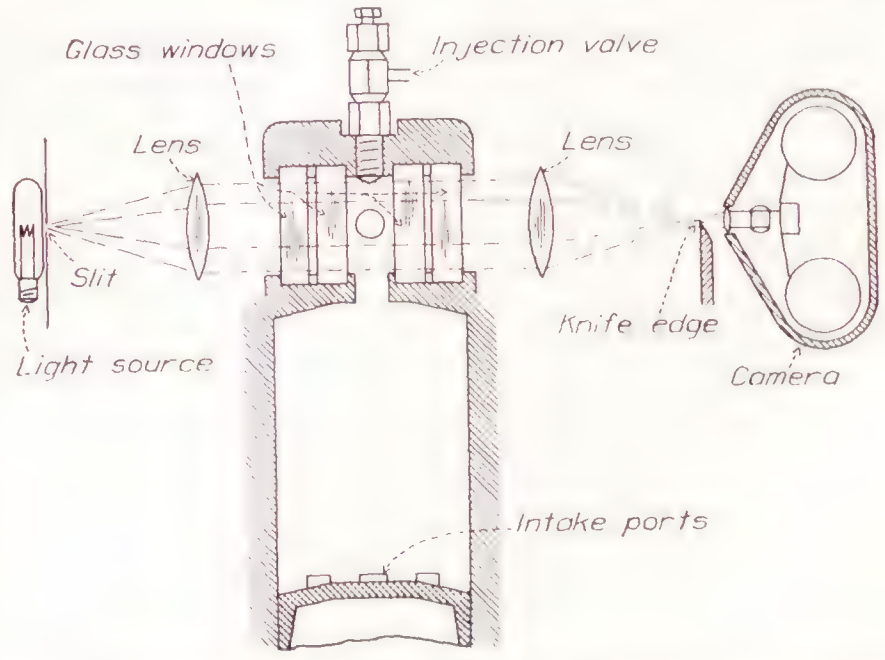

FIGURE 1.—Diagrammatic sketch of the N. A. C. A. combustion apparatus with schlieren equipment.

and the schlieren optical arrangement is shown as figure 1. The air movement, the fuel injection, and the flame spread were photographed through the 2½-inch-diameter glass windows forming the sides of the flat-disk combustion chamber. A 750-watt projection lamp was placed behind the slit as indicated in the diagram. The slit was placed at the focus of the first lens so that parallel light was transmitted through the combustion chamber to the second lens. The knife edge was located at the image of the slit and in such a position that two-thirds of the slit image was intercepted by the knife edge. The image of the combustion chamber was focused on the motion-picture film. Any local change in the index of refraction of the medium between the two lenses caused a deflection in the parallel light rays. This deflection caused the light rays to strike either below or above the original point in the image of the slit. Therefore, a change in the index of refraction of a part of the medium between the lenses resulted in light or dark areas being formed on the motion-picture film in the image of the combustion chamber. Because any air movement in the combustion chamber is accompanied by local changes in the index of refraction of the air, the air movement showed up as light and dark streaks in the image recorded on the photographic film. The image of the fuel-spray silhouette and of the combustion was photographed on the film in the usual manner.

The test procedure was similar to that given in reference 3. No time-pressure records are presented in the present report, although they were taken for each test condition. Such records have been presented in references 1, 2, and 3. As has been previously stated, these records, although giving the general course of the combustion, are not sufficiently accurate to permit close comparisons to be made of the indicated mean effective pressures developed by the engine.

Three fuel-injection nozzles (fig. 2) were tested: a 0.020-inch single-orifice nozzle, a 6-orifice nozzle, and a slit nozzle. These nozzles were chosen from those used in the investigation of the effect of nozzle design on combustion (reference 3). The fuel oil was the same as that used in the tests reported in references 1, 2, and 3.

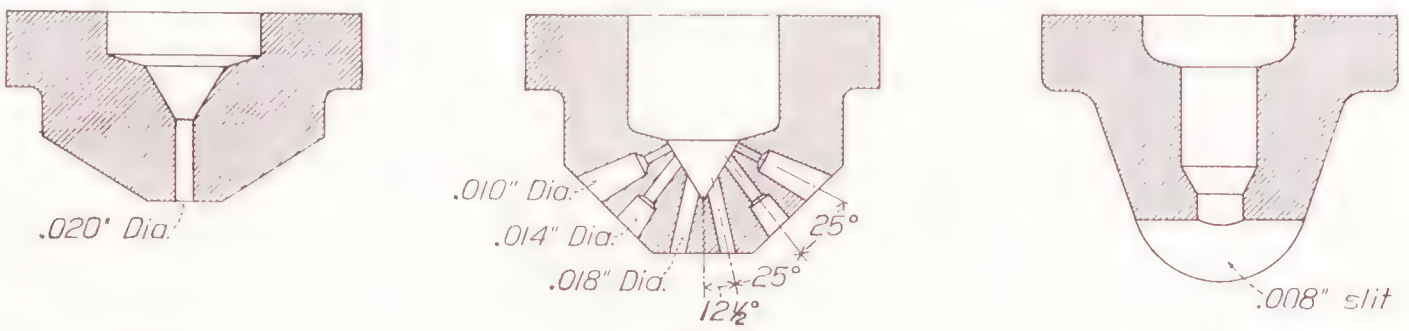

Single orifice. Multiorifice. Slit.

FIGURE 2.—Nozzles tested.

The following test conditions were maintained constant:

Engine bore, inches	5
Engine stroke, do	7
Engine speed, revolutions per minute	1, 500
Engine-jacket coolant temperature (outgoing), °F	150
Engine compression ratio (based on total stroke)	14. 1
Air-fuel ratio (except as otherwise stated)	17
Start of injection, crankshaft degrees B. T. C	15 to 20

A flat-disk combustion chamber was used with a rectangular displacer as adapted by Moore and Foster (references 7 and 8). The displacer was mounted on the engine piston to produce an air flow of high velocity within the combustion chamber. The displacer was arranged so that it could be mounted at either side or directly in the center of the piston, as shown in figure 3. In this manner an air jet could be directed along either or both ends of the combustion chamber. In one test the displacer was removed and a central oval orifice installed in the center of the chamber throat (fig. 3E). The areas between the displacers and the edges of the combustion chamber and of the orifice in combustion chamber E were such that the velocity approximated the value which gave the best performance in the tests presented in reference 7. The velocity of the air as it entered the combustion chambers was estimated accord-

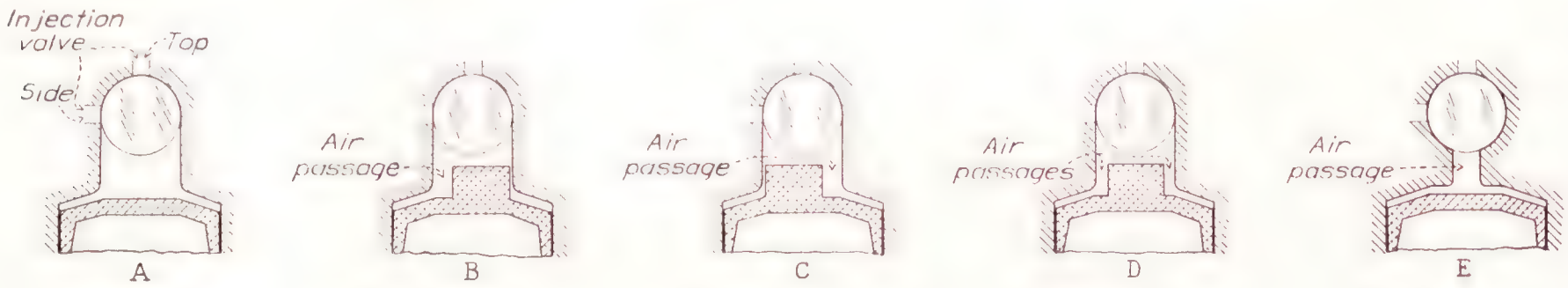

Chamber A Chamber B Chamber C Chamber D Chamber E

FIGURE 3.—Combustion-chamber shapes tested.

ing to the method given in reference 7 and is shown in figure 4 as a function of the crank angle. Combustion chamber A has a width between the glass windows of 0.78 inch and the others a width of 1.01 inches. This variation in width was necessary to maintain a constant compression ratio.

In the tests with the single-orifice nozzle the manifold around the inlet ports of the engine had a single opening in the plane of the combustion-chamber disk on the side in which the injection valve was mounted, and the air entered the cylinder with a definite whirling motion. In the tests with the multiorifice nozzle this manifold was removed so that the air could enter symmetrically with respect to the cylinder. In the tests with the slit-orifice nozzle the same arrangement was used and additional runs were made with the intake ports blocked on first one and then the other side of the cylinder.

RESULTS AND DISCUSSION

The estimated air flow (fig. 4) shows that, as the displacer entered the combustion chamber, the air velocity quickly reached a value of 400 feet a second.

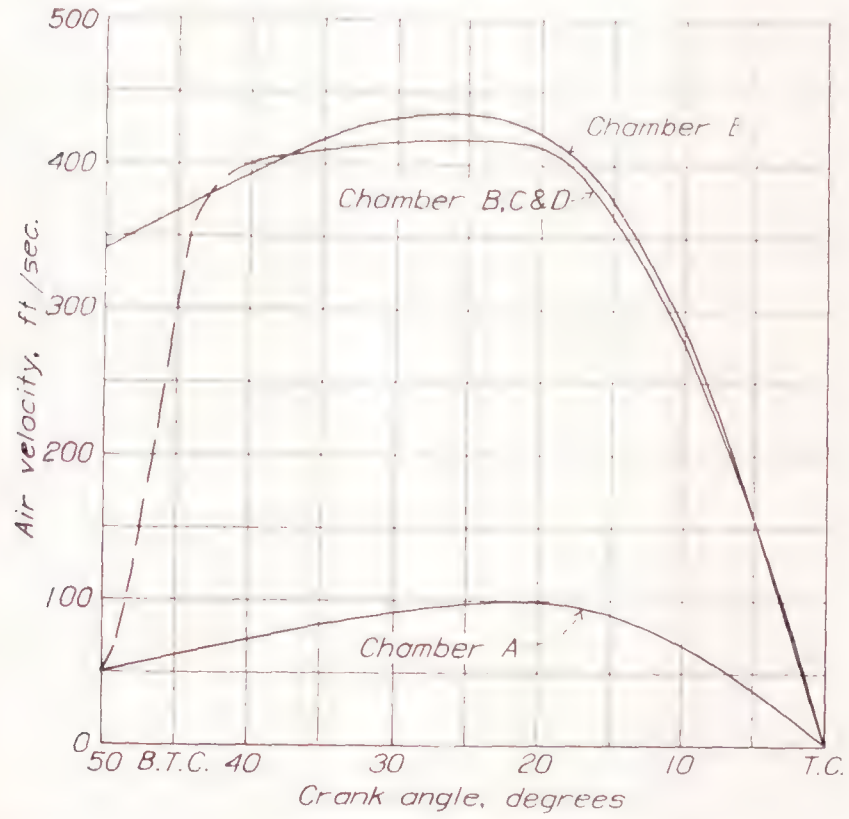

FIGURE 4.—Air velocity through throat connecting displacement volume and combustion chamber.

The rate of velocity increase became successively less and a maximum of 420 feet a second was reached at about 25 crankshaft degrees B. T. C. The velocity then decreased to zero at top center. With combustion chamber E a maximum velocity of 435 feet a second was reached at 33° B. T. C. With combustion chamber A the velocity reached a maximum of 120 feet a second at about the same piston position that the maximum was reached with the displacer. These velocities with the restriction are those estimated for the air as it entered the combustion chamber at the narrowest section. As the air passed from this orifice into the chamber proper there was, of course, a certain amount of expansion of the jet and a certain amount of turbulence was also created. In addition, there was the effect of any air flow produced during the induction of the air through the ports into the displacement volume. The conditions under which the air is inducted are comparable with those existing in a highly supercharged engine because, as was shown in reference 1, the pressure differential between the displacement volume and the intake manifold at the time the piston uncovered the intake ports was approximately 26 inches of Hg.

The photographs showed that two types of air flow might occur in the combustion chamber. The first was

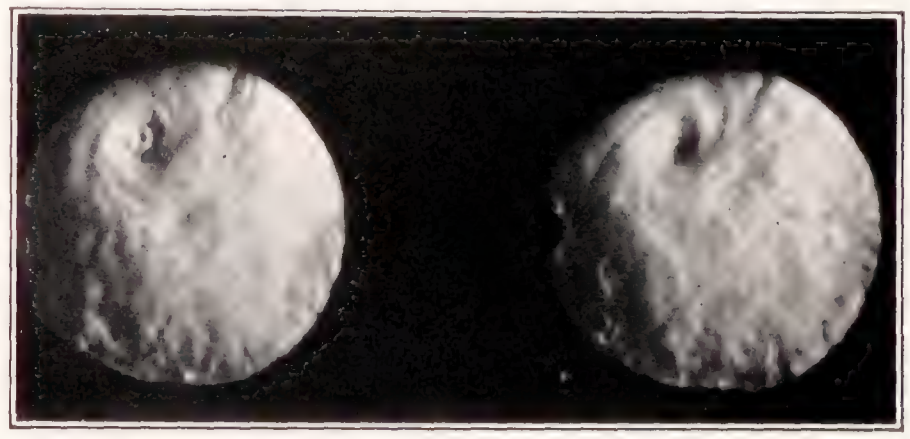

FIGURE 5.—Air vortex in combustion chamber D.

a mass rotation of the air as a whole and the second was the occurrence of a vortex traveling around the combustion chamber. The first type is not visible unless the motion pictures are projected, the individual photographs showing only light and dark areas in the combustion gases. The vortex occurred most often with combustion chamber A. Occasionally a vortex was produced in combustion chamber D (fig. 5). In the photographic prints reproduced in this report, mass movement of the air as a whole is indicated by the deflection of the fuel spray. A description of the flow as visualized when the motion pictures were projected and also as interpreted from the spray shapes is also included. For assistance in the analysis of the results, line drawings of the combustion chambers with arrows indicating the air movement are included with the enlargements from the motion-picture films. The enlargements show the fuel spray from the start of injection and the first three or four photographs of the combustion.

The effect of some air movement on the fuel sprays in combustion chamber A was observed in the results presented in both references 2 and 3. The photographs showed that the spray tips were twisted first to the right and then to the left as the sprays proceeded across the combustion chamber. In the present tests this motion was found to be caused by the vortex (fig. 5) moving around the combustion chamber, generally clockwise in the results reported herein and counterclockwise in the results shown in references 2 and 3. (This difference in directional rotation does not actually occur in the engine. Because of space limitations it was

necessary to reflect the light through 90° in this schlieren set-up. Therefore, results showing clockwise rotation in these photographs correspond to a counterclockwise rotation in the previous results.) The vortex was apparently caused by the air movement set up as the air entered the displacement volume through the inlet ports. It has been shown in reference 3 that this flow caused the flame to predominate on the leeward side of the spray.

Single-orifice nozzle.—With the injection valve mounted in the top (fig. 6 (a)) of combustion chamber A, the single fuel spray penetrated across the visible portion of the chamber. Because of the relationship of the injection-nozzle area to the other injection-system dimensions there was a secondary discharge of the fuel following the first stop of injection. The photographs indicate that this secondary discharge penetrated through the already burning gases. When the injection valve was mounted in the side (fig. 6 (b)) the spray penetrated across the chamber and impinged on the opposite wall. In this case there is visible a slight upward bending of the spray caused by the entering air. Combustion started at the chamber wall. In neither case did the flame spread throughout the chamber. With the injection valve mounted in the side, the motion pictures show that the combustion was followed by a cloud of smoke, which seemed to roll backward from the section of the chamber wall that was struck by the spray core.

The arrows indicate that in one case the general air movement was clockwise and in the other case counterclockwise, but the reason for this apparent occasional reversal of the flow is not known. In no case was it sufficient to have much effect on the fuel spray or flame formation.

Combustion chamber B showed a marked difference from chamber A both in the fuel spray and the flame formation (fig. 7). The motion pictures showed that the rotation of the air caused by the displacer, being in the same direction as that produced during the induction of the air, was in the form of a mass rotation of the air in a clockwise direction as compared with the rotating vortex obtained without the displacer. In the upper half of the visible portion of the chamber the spray is shown blown to the right, and in the lower half to the left. In the seventh photograph of figure 7 (a) (3° B. T. C.) the center of the rotating air is well marked by the spray formation. The flame filled the chamber reasonably well and a decided improvement in mixing over that obtained without the piston displacer is noted. When the injection valve was mounted in the side (fig. 7 (b)), the fuel-spray core was directed upward so that there was little impingement on the opposite wall of the combustion chamber and very little smoke was visible. The downward motion of the air on the right-hand side of the chamber did not have much apparent effect on the spray. Again the cham-

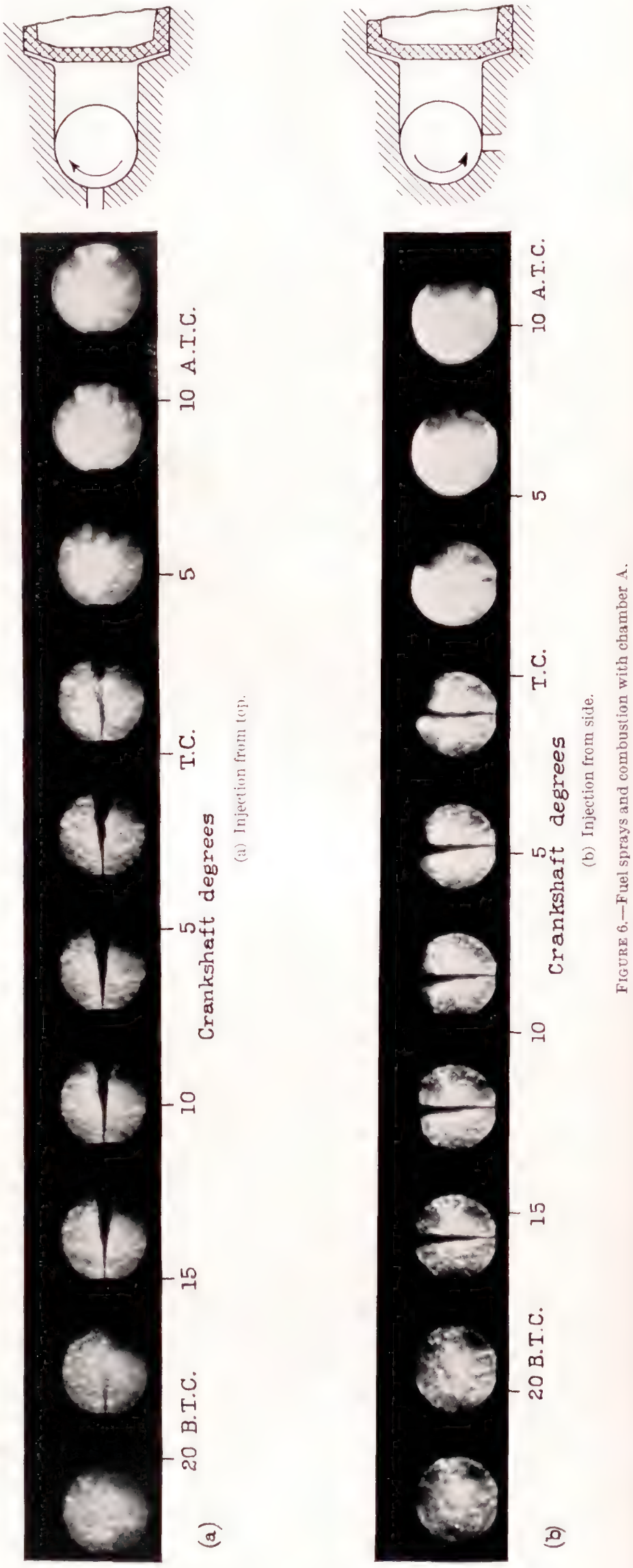

(a) Injection from top.

(b) Injection from side.

FIGURE 6.—Fuel sprays and combustion with chamber A.

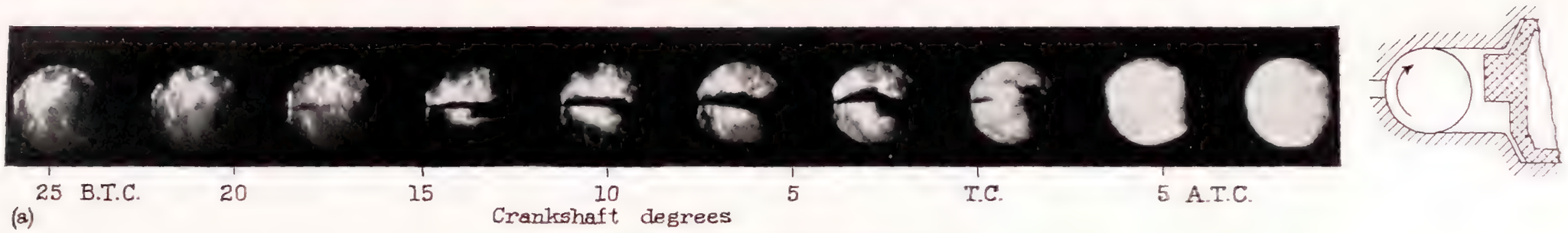

(a) Injection from top of cylinder B.

(b) Injection from side of cylinder B.

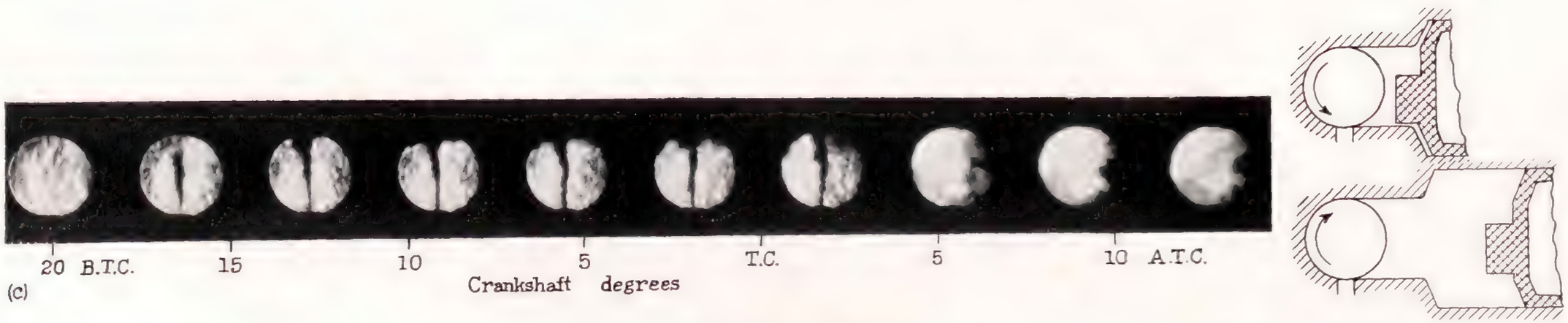

(c) Inection from side of cylinder C.

FIGURE 7.—Fuel spray and combustion with chambers B and C.

ber was fairly well filled with flame. In neither case was the spray core destroyed by the moving air, although the envelope was swept away from the core. The results show that, even in the highly heated air of the combustion chamber, high air velocities do not destroy the core of the spray but nevertheless materially aid in the mixing of the fuel and air.

With combustion chamber C the air rotation produced in the combustion chamber by the displacer was in the opposite direction to that produced by the induction of the air (fig. 7 (c)). The motion pictures show that the air first rotated clockwise and then, as the displacer entered the combustion chamber, the air suddenly changed direction and made a rotation in the counterclockwise direction. As a result of this change of motion, much of the energy of the moving air was lost so that the effect on the fuel spray was considerably less than was the case with combustion chamber B. The spray impinged on the wall of the chamber as it did when no displacer was employed and there was considerable smoke. There is little evidence that with this arrangement the air flow produced beneficial results. The test illustrates the fact that, when designing a combustion chamber to produce a certain type of air flow, extreme care must be taken to insure that the desired results are not nullified by air movements set up by the induction of the air into the displacement volume.

When combustion chamber D was employed (fig. 8), the movement of the air as a whole was hard to distinguish. The rotation of the air before the displacer entered the combustion chamber was still clockwise but it seemed to predominate in the right-hand section of the chamber. With the fuel being sprayed in from the top of the chamber, there was little apparent effect from the air flow. The spray tended to have a somewhat sinuous motion as it penetrated through the combustion air. The flame showed but slightly better distribution than was obtained without the displacer. When the spray was injected from the side, the effect of the air movement was quite noticeable. As the spray first issued from the injection nozzle it was blown upward by the air jet. Its direction was then changed slightly so that it again traveled in a horizontal direction but, as the issuing fuel jet became more dense and the air velocity decreased, the spray core maintained a straight course inclined upward to the horizontal. The downward movement of the air in the center of the chamber is noticeable in the photograph taken at 4° B. T. C. In this frame the spray shows the effects of the air blowing up along the side walls of the chamber and down in the right center. The flame spread throughout most of the visible portion of the chamber but there was still considerable smoke during the expansion stroke.

With combustion chamber E it appeared that the air divided in the center of the chamber, rotating in a clockwise direction in the right half and a counterclockwise

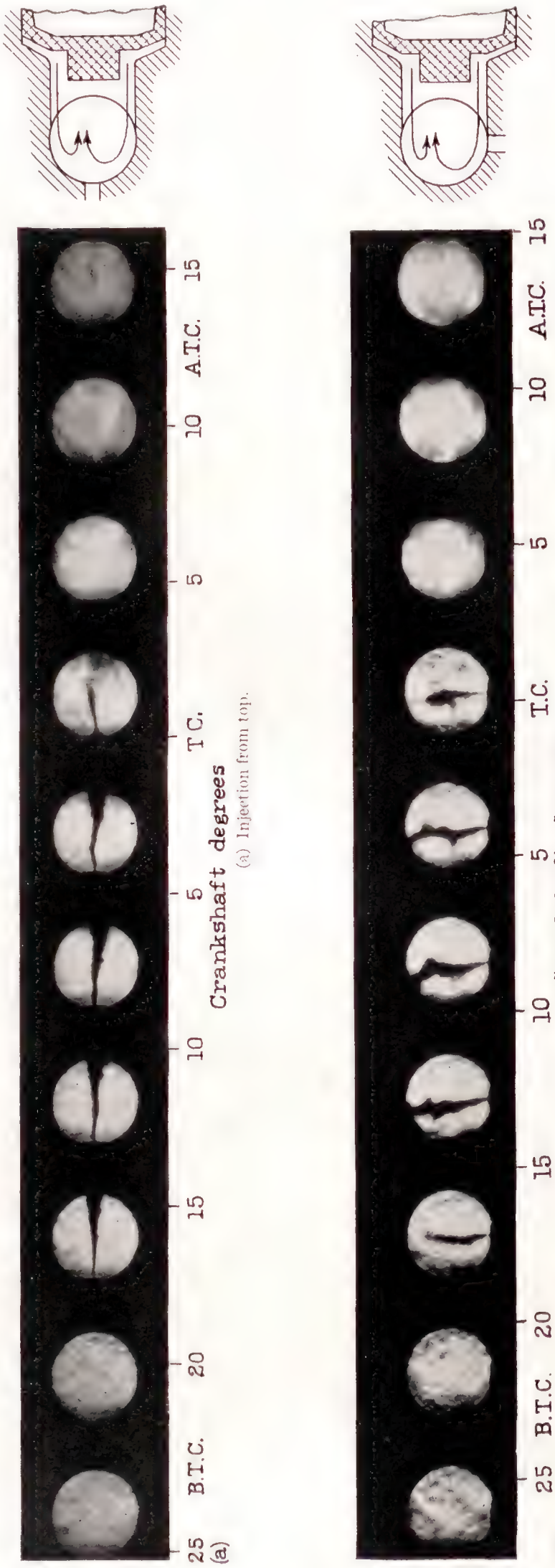

FIGURE 8.—Fuel spray and combustion with chamber D.

85548—38——20

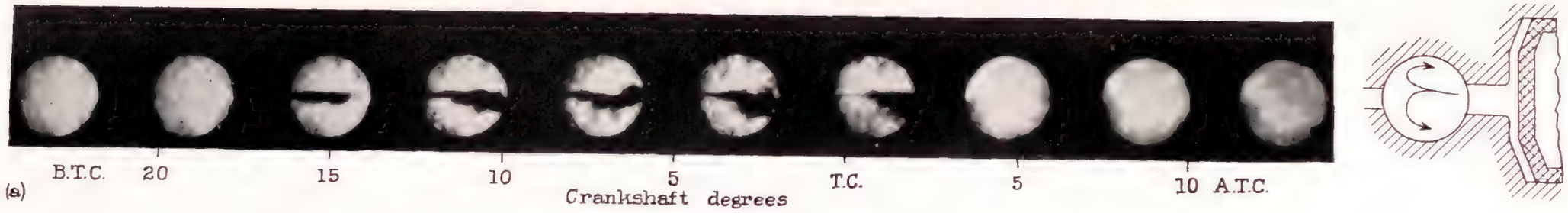

(a) Injection from top.

(b) Injection from side.

FIGURE 9.—Fuel sprays and combustion with chamber E.

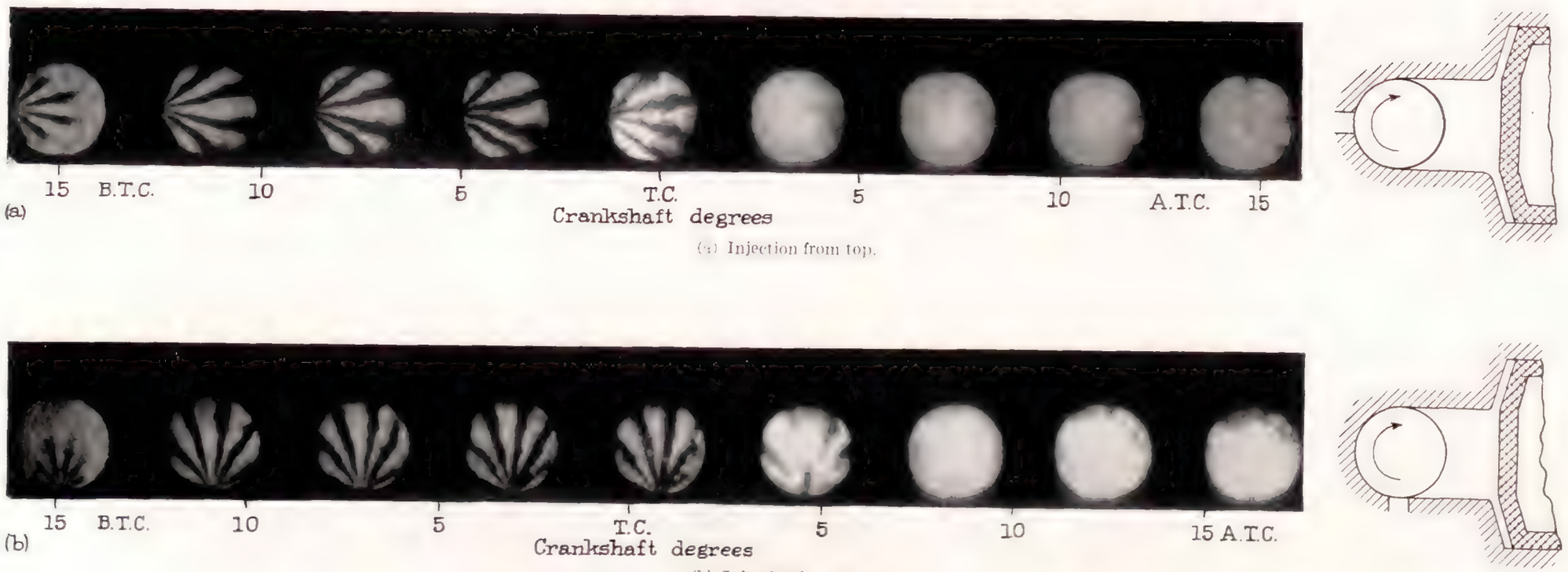

(a) Injection from top.

(b) Injection from side.

FIGURE 10.—Fuel sprays and combustion with multiorifice nozzle and chamber A.

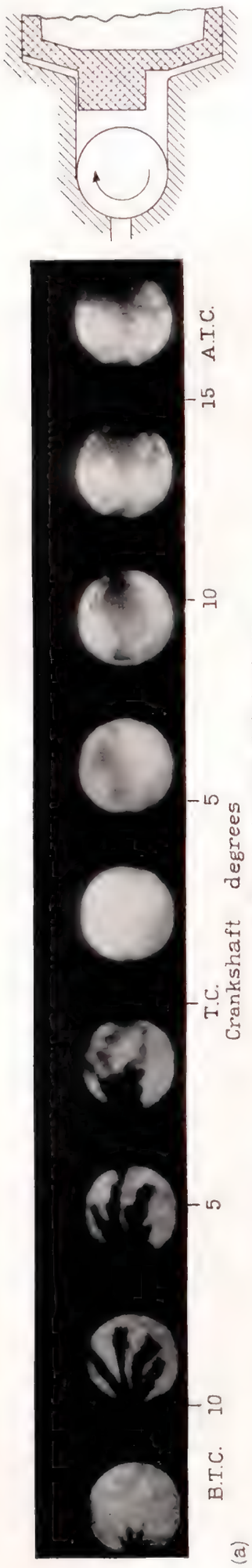

(a) Injection from top; air-fuel ratio, 17.

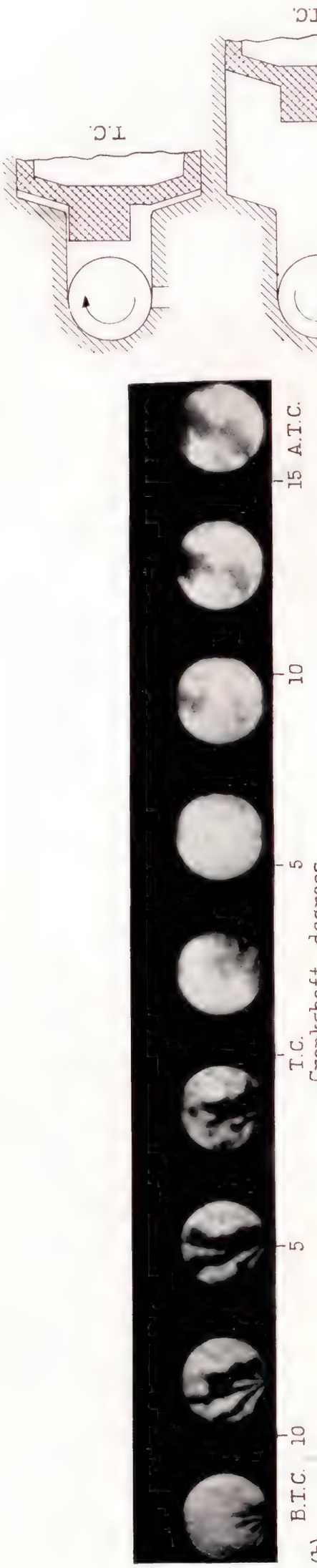

(b) Injection from side; air-fuel ratio, 17.

(c) Injection from side; air-fuel ratio, 33

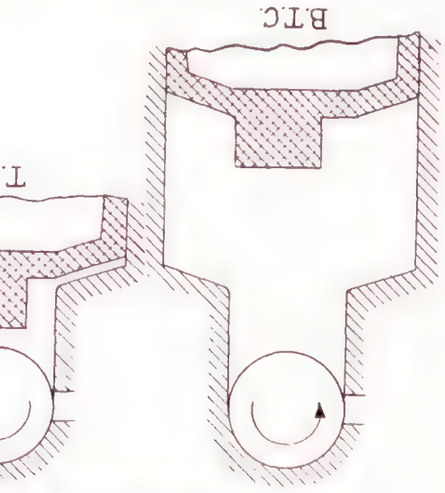

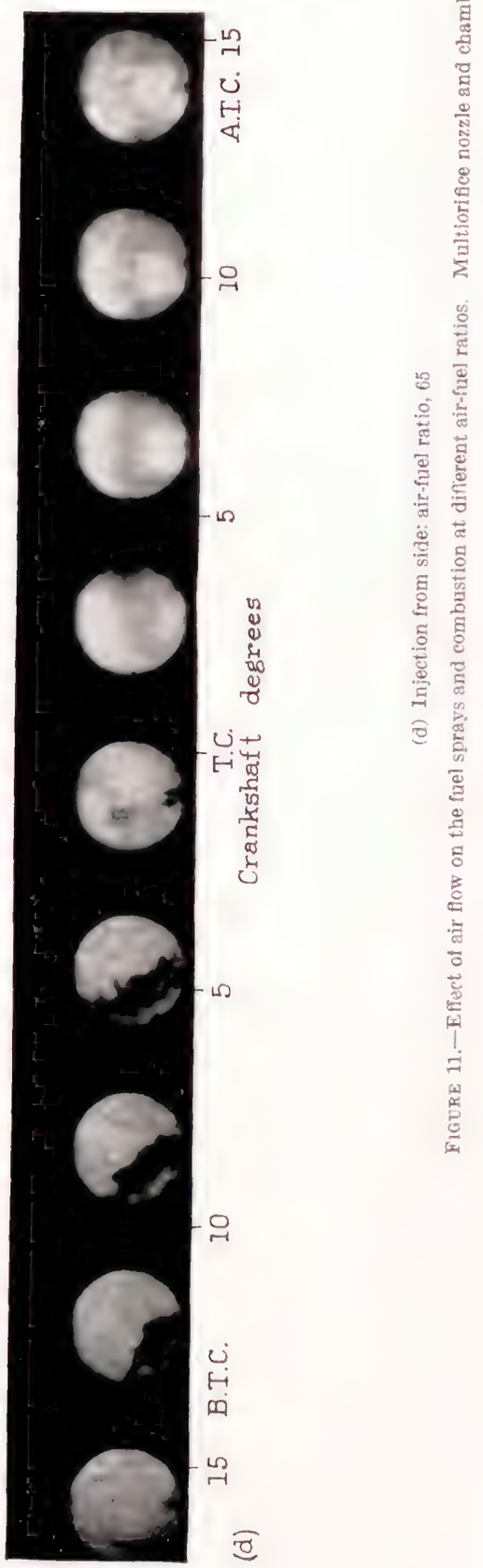

(d) Injection from side: air-fuel ratio, 65

FIGURE 11.—Effect of air flow on the fuel sprays and combustion at different air-fuel ratios. Multiorifice nozzle and chamber B.

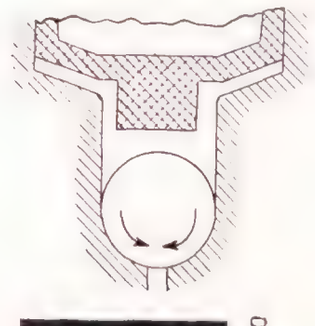

rees

ion from top.

(a) Injection fro

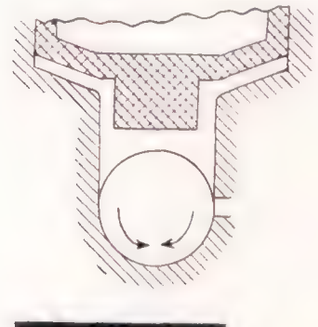

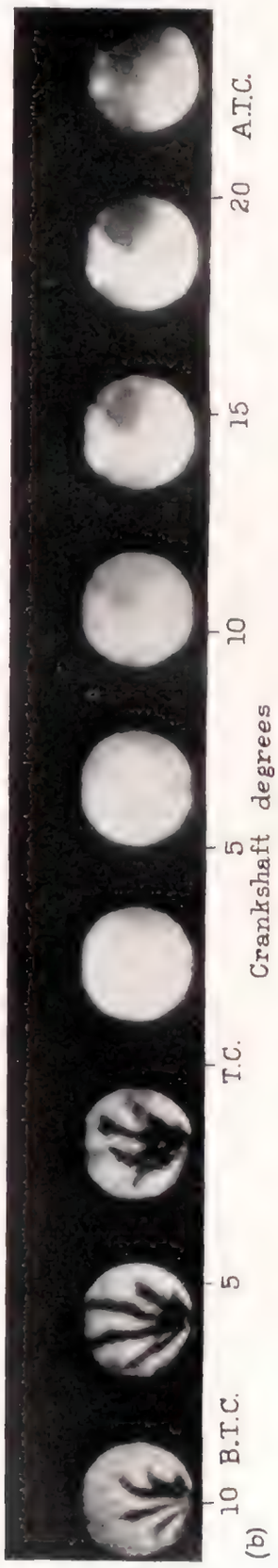

ion from side.

(b) Injection fro

FIGURE 12.—Fuel sprays and combustion with multiorifice nozzle and chamber D.

n with multiorifice nozzle and chamber D.

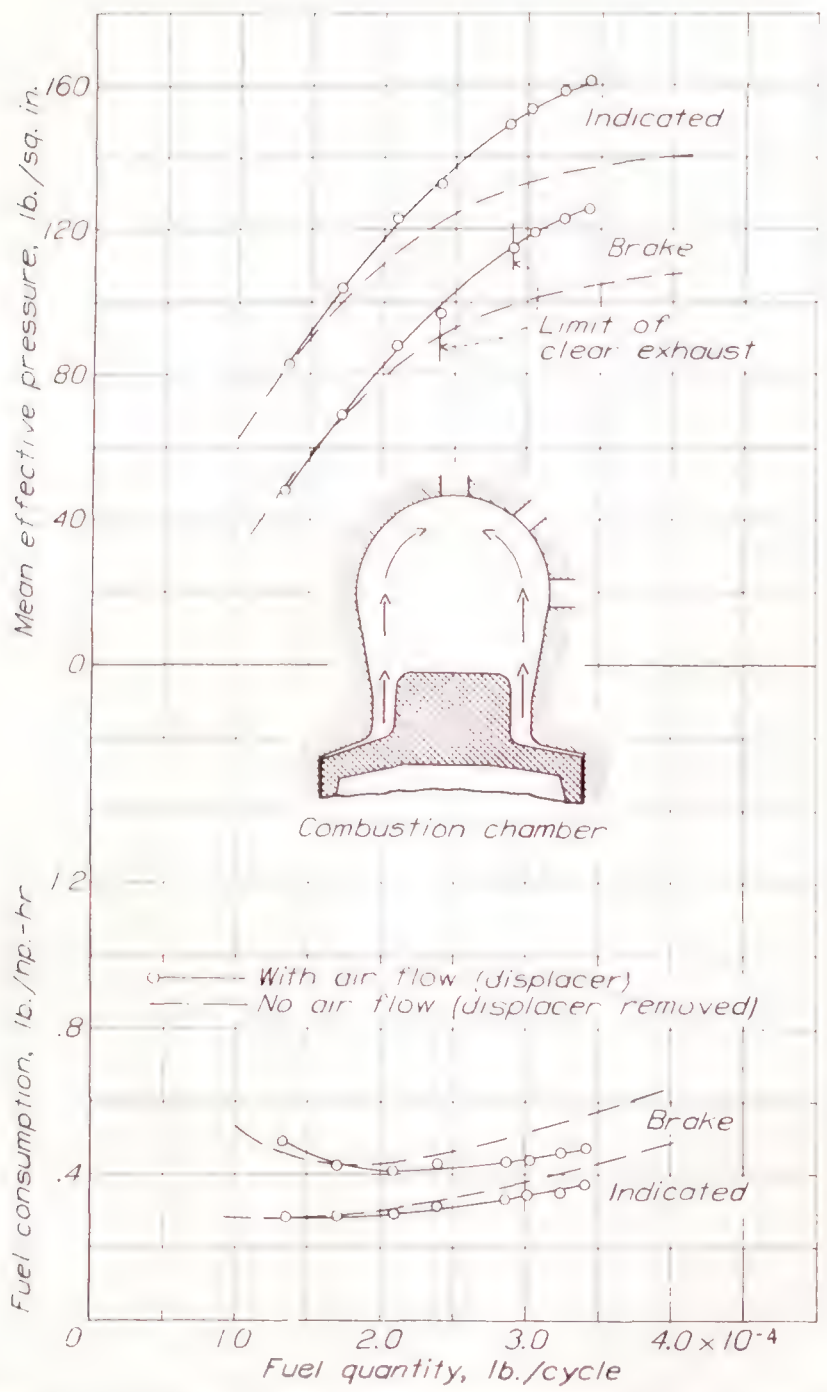

FIGURE 13.—Comparison of performance with and without air flow (reference 7).

direction in the left half (fig. 9). With the injection valve mounted in the top of the spray chamber the spray penetration was decreased by the air jet directed against it. Also the air movement was such that the spray envelope was blown to the left-hand side of the chamber. This deflection is quite noticeable in the photograph obtained 1° A. T. C. The mixing of the fuel and air was not particularly good. The results appeared to be little better than with combustion chamber A. When the injection valve was mounted in the side of the combustion chamber, the spray was deflected upward when it met the incoming air jet about midway across the combustion chamber. The spray impinged on the opposite wall of the chamber and was there blown downward by the air swirl in that half of the chamber. The flame spread to a somewhat greater area than was the case with the spray entering at the top of the chamber, but considerable air was still not reached by the fuel. Again the chamber was partly filled with a dense smoke during the expansion stroke.

Multiorifice nozzle.—The multiorifice nozzle was designed according to the proportionality principle discussed in reference 6. Engine tests (reference 7) have shown that in the type of combustion chamber tested the multiorifice nozzle which gave the best performance with the quiescent combustion chamber also gave the best performance with the same combustion chamber used in conjunction with the displacer piston.

In the tests with the multiorifice nozzle the inlet manifold around the ports was removed. The vortex that appeared when the manifold was in place did not occur so often when the manifold was removed. With the injection valve mounted in the top of chamber A (fig. 10 (a)) the individual sprays penetrated through the highly heated dense air, the side sprays impinging on the combustion-chamber walls. The flame filled the visible portion of the combustion chamber. When the injection valve was mounted in the side of the chamber (fig. 10 (b)), some of the fuel sprays impinged on the opposite wall of the chamber but not with the intensity that accompanied the impingement of the spray from the single 0.020-inch orifice. The two sprays directed toward the entrance throat were definitely deflected upward. The flame again filled the combustion chamber and, although there was some smoke visible on the expansion stroke, it was not so dense as in the case with the single 0.020-inch orifice.

With the nozzle mounted in the top of combustion chamber B (fig. 11 (a)) the sprays from the 0.014- and 0.018-inch orifices on the side of the chamber toward the air jet were deflected to the right by the air movement across the top of the chamber, as they left the nozzle, and to the left nearer the bottom of the chamber because of the upward movement of the air in this portion. The sprays on the other side of the combustion chamber showed less movement although they were somewhat bent. On this side of the chamber the air flow had been decreased because of its greater distance from the displacer passage and also because the air flow had already lost some of its energy in deflecting the first sprays through which it passed.

With the injection nozzle mounted in the side, the effects of the air movement are visible during the entire injection period. The sprays are all deflected upward as they enter the chamber. The envelopes and, in some cases, the spray cores are deflected downward when they reach the opposite side of the chamber.

Projection of the film containing the photographs shown in figure 11 showed that in three cases there was a reversal of rotation of the air flow even though the intake manifold had been removed. The reversal was not so violent, however, as it was with the manifold.

In figures 11 (c) and (d) are shown the results of tests made with air-fuel ratios of 33 and 65, respectively. A comparison of these photographs with those obtained at an air-fuel ratio of 17 shows that, as the fuel quantity was decreased and consequently the energy in the injected spray was decreased, the rotating air turned the fuel jets through a larger angle so that the sprays were forced to the upper left-hand quadrant of the chamber. With the air-fuel ratio of 65 the flame is

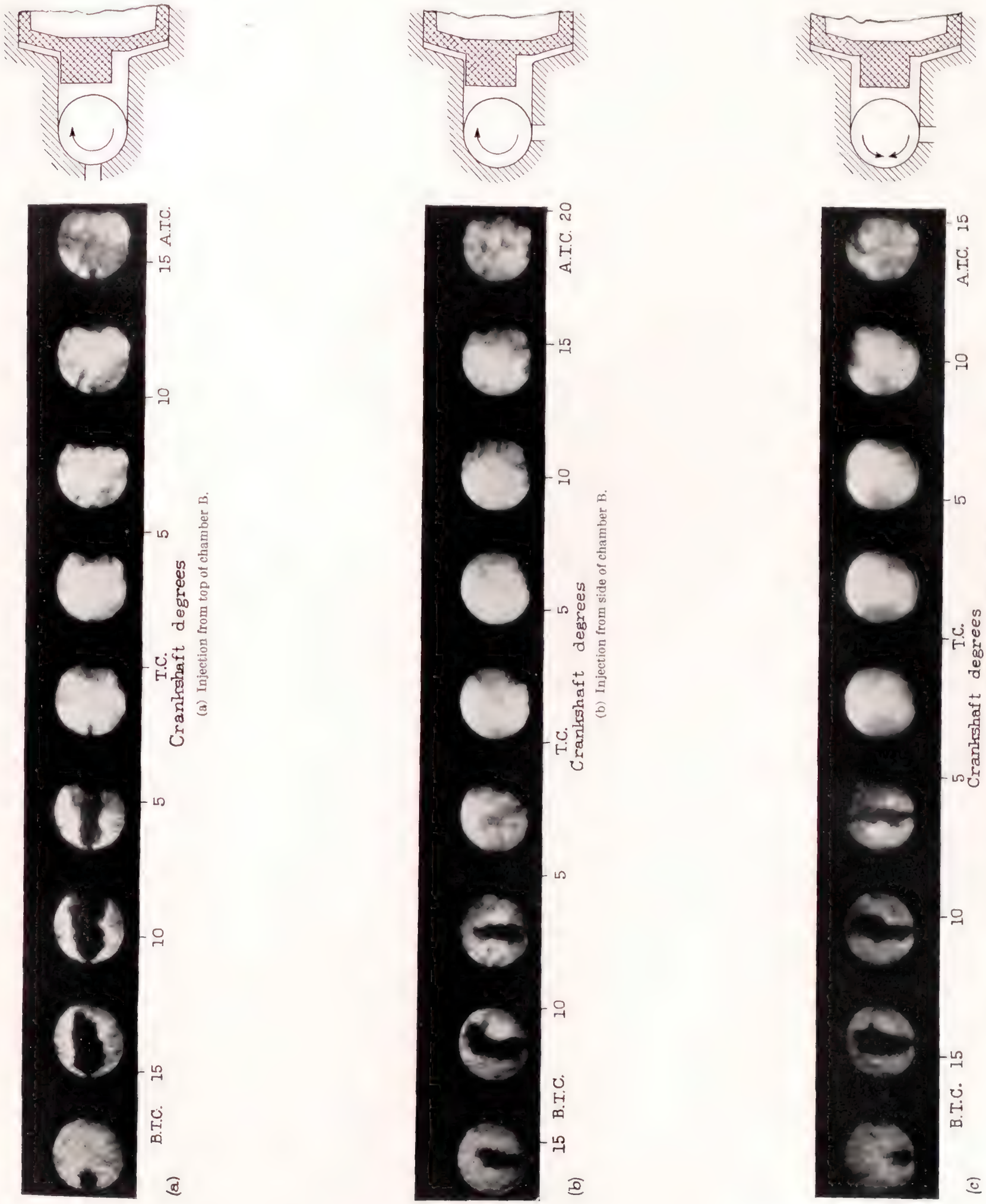

(a) Injection from top of chamber B.

(b) Injection from side of chamber B.

(c) Injection from side of chamber D.

FIGURE 14.—Fuel sprays and combustion with slit nozzle

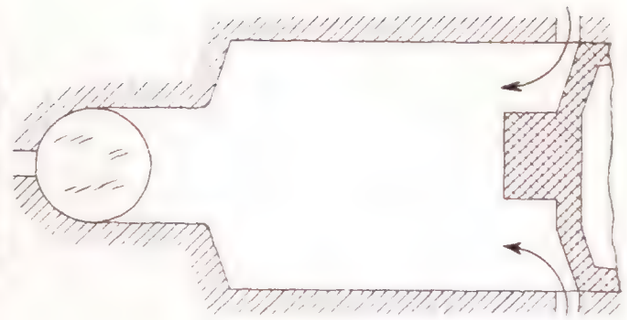

(a) Air flow from both sides.

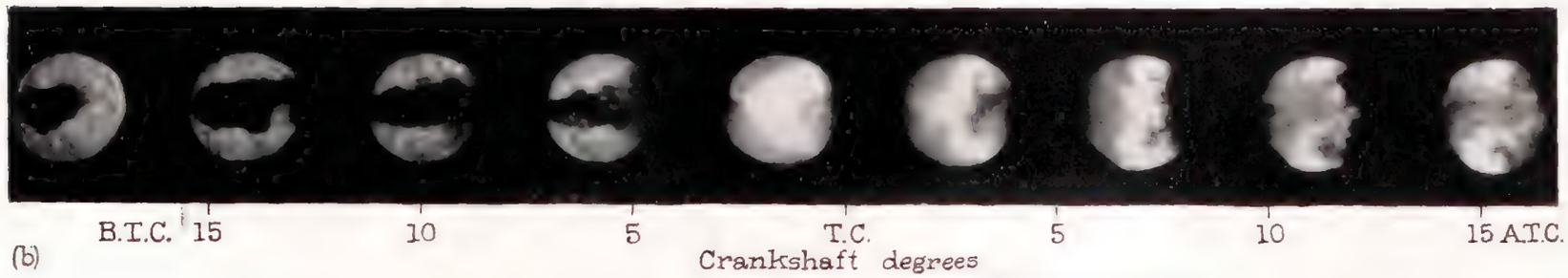

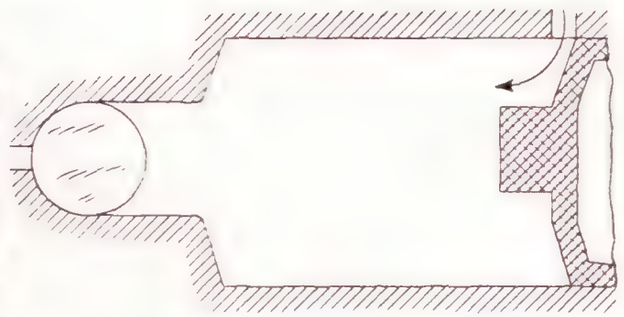

(b) Air flow from right only.

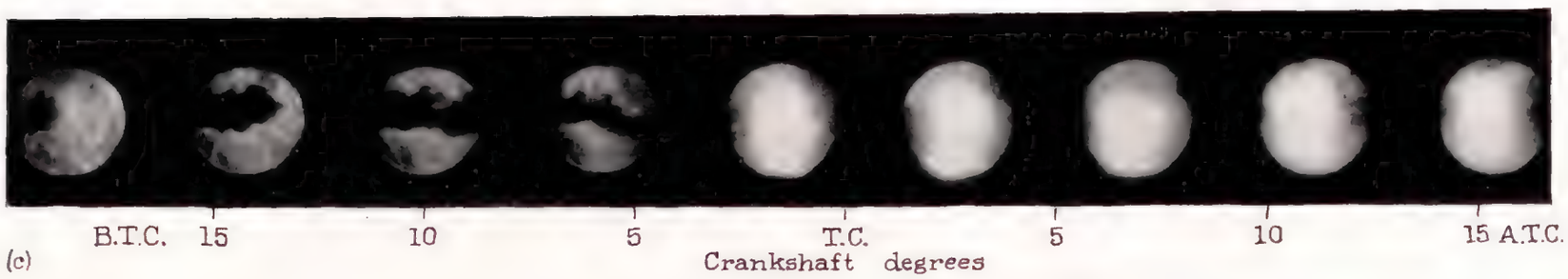

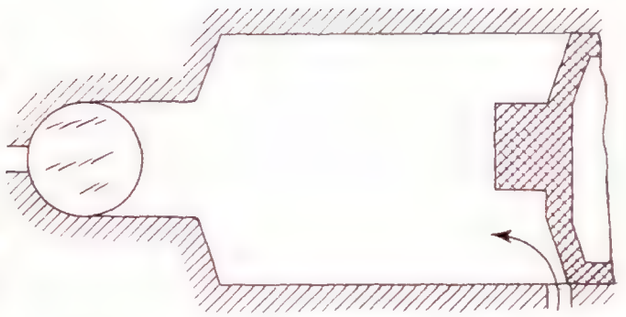

(c) Air flow from left only.

FIGURE 15.—Effect of inlet-port arrangement on fuel spray and flame formation. Slit-orifice nozzle; combustion chamber B; injection from top.

visible in two separate sections. One section extends along the right-hand side of the chamber and the other is in the region surrounding the fuel-injection nozzle. In this case the fuel from the main discharge has apparently been carried to the opposite side of the combustion chamber by the moving air and so forms a stratified charge in this area. The small secondary discharge visible in the photograph taken just before top center was not blown away because of the decrease in the air velocity. The original of this strip of film shows that these two flame areas did not combine. The results therefore prove that, even with high air velocities in the combustion chamber, it is possible to maintain a stratified charge of the fuel and air. For this reason it is believed that in engines employing air flow there should be no difficulty in idling the engine. It is probable that in certain cases where special adapters have been used in the air-induction system to change the air flow for idling conditions, the trouble has not been with the air movement but with the idling characteristics of the fuel-injection system.

The results obtained with combustion chamber D and the multiorifice nozzle are shown in figure 12. With the fuel being injected from the top (fig. 12 (a)) of the chamber, the sprays appeared quite similar to those in chamber A. With the fuel being injected from the side (fig. 12 (b)) of the chamber, the sprays show that there was a clockwise rotation of the air in the left-hand side of the chamber and a counterclockwise rotation in the right-hand side of the chamber. The air flow did not have much directional effect on the fuel sprays as a whole except to concentrate them more in the top of the chamber. Engine tests (fig. 13) reported in reference 7 of a similar combustion chamber have shown that this arrangement gives an appreciable increase in power over the quiescent combustion chamber without the displacer piston.

Slit nozzle.—In the test conducted by Lee of the distribution within different types of fuel sprays (reference 10) it was shown that the distribution within the spray from a slit nozzle was comparatively good but that the dispersion of the spray, that is, the total volume included in the spray, was insufficient and consequently the air-fuel ratio within the spray was too low. The suggestion was made that this type of spray could most beneficially be used with some form of air flow in the combustion chamber. The results in figure 14 show that, even with the air velocities used in the present tests, the energy was insufficient to break up the fuel spray. A comparison of figure 14 with figures 11 and 12 indicates that the spray from the slit-orifice nozzle was less affected than those from the multiorifice nozzle. The conclusion is drawn that because of the large cross-sectional area presented to the air flow the spray from the slit-orifice nozzle tends to damp the air movement to a greater extent than do those from the multiorifice nozzle. With the fuel being injected from the side (fig. 14 (b)) in combustion chamber B, the air-flow effects are more noticeable than is the case when the fuel is injected from the top (fig. 14 (a)).

A direct comparison cannot be made between the results shown in figure 14 and those in figures 7 and 8 because of the difference in the air-intake system. Tests were therefore run with the slit-orifice nozzle in chamber B in which the inlet ports were blocked first on one side and then on the other (fig. 15). At the right of each of the three photographic strips a line drawing shows which inlet ports remained opened and which were closed. The three ports on each side of the engine cylinder are represented by the single opening. Figure 15 (a) shows the results obtained with the ports opened on both sides, the same photographs being shown in figure 14. When the inlet ports on the cylinder side adjacent to the displacer were opened and those on the other side blocked, a counterclockwise rotation of air was produced in the combustion chamber, that is, a rotation opposed to the air movement produced by the displacer. Although this counterclockwise rotation was stopped before the start of the injection of the fuel, a rotation of the air in the opposite direction was not visible and the fuel spray shows no indication of such a reversal. As was the case in the results presented in figure 7 (c), the air flow induced during the induction period opposed that purposely induced during the last part of the compression stroke and nullified its effects. With the air-inlet ports arranged as shown in figure 15 (c), the air swirl produced during the induction period assisted that produced by the piston displacer and the maximum effect of the air flow was obtained.

GENERAL SIGNIFICANCE OF TEST RESULTS

In previous tests (references 3 and 10) it had been concluded that with high-dispersion fuel-injection nozzles the lack of spray penetration must be assisted by air flow. The present tests have shown that with the nozzles now generally employed and with the injection pressures commonly used, it is difficult to obtain a good mixture of the air and fuel even with air flow. The question that naturally follows is: How is the compression-ignition engine to be designed so as to give the power outputs together with the fuel economy inherent in the high compression ratio? It was concluded in reference 3 that the chief obstacle to obtaining this high performance is the slow rate of diffusion of the fuel vapors. The results presented in this report support this conclusion. In the use of air flow to assist diffusion, the air must blow through the fuel jet and continually pick up the vapors from the jet. If the air and the fuel rotate about the chamber as a unit, the mixing of the two is not necessarily improved. It is necessary to have a continual intermixing of the fuel and air taking place within the

combustion chamber. In addition to the controlled air flow, the purpose of which is to destroy the fuel jet, it is desirable and probably necessary to have numerous small eddies throughout the combustion chamber. The production of such an air flow presents a difficult problem, and the development of a method to measure it is probably even more difficult. Whether or not the use of such flow will actually increase the initial rate of heat exchange from the air is questionable. Such an effect has been indicated, however, by the decreased ignition lags in engine tests at this laboratory with the displacer piston. Test results presented by Selden and Spencer (reference 11) have shown that the rate of heat exchange between the injected fuel and the air is not much affected by low air velocities. An extensive discussion of the effects on engine performance of air flow produced by combustion chambers of different design has been presented by Alcock in reference 12.

In both the present tests and those discussed in reference 2 it has been shown that stratification of the charge occurs in the compression-ignition engine; it has not been shown whether or not such stratification is necessary. When spark ignition is employed as in the conventional carburetor engine, it is known that the flame will not propagate across the combustion chamber unless the air-fuel ratio is less than approximately 20. In this case the combustion of each successive portion of the fuel is brought about by the heat from the combustion of the preceding portion of fuel. In the compression-ignition engine, in which the number of ignition sources is infinite, no tests have been conducted to determine to what extent the air-fuel ratio affects the flame spread. Although it is probable that each source of combustion does propagate flame in the normal manner, it is also certain that new sources of ignition are continually being formed. It is therefore believed that, although stratification does occur in the compression-ignition engine, it is not of so much importance at high air-fuel ratios as would be the case in a spark-ignition engine attempting to run on mixtures with an air-fuel ratio greater than necesssary to support flame propagation.

Since the present tests do not show much difference in the appearance of the flame using the multiorifice nozzle with and without the air flow and since those presented in references 7 and 8 show that a considerable improvement in engine performance is gained by the use of air flow under similar conditions, it can be concluded that the chief effect of the air flow in those cases in which the distribution is reasonably good is not on the direction and penetration of the fuel sprays but on the intermixing of the air and fuel by the numerous small eddies. This conclusion is strengthened by the fact that in references 7 and 8 it was shown that the nozzle which gave the best performance with the air flow was the one which gave the best performance in the quiescent combustion chamber.

An examination of the results presented in this report and those presented in references 1 to 3 gives an indication of the rate of diffusion of the fuel vapors but does not indicate the rate of heat exchange between the air and the injected fuel. The test results presented in reference 11 show that the rate of heat exchange is high from the instant injection starts. Tests have been conducted at this laboratory on methods of increasing the effectiveness of this heat exchange, first, by heating the engine jacket (reference 1) and, second, by heating the fuel to a high temperature before injection (reference 13). In neither case was there any appreciable improvement in the engine performance except for a shortening of the ignition lag with its consequent smoother engine operation, indicating that the rate of heat exchange is sufficiently fast under normal operating conditions.

Efforts to improve the atomization of the fuel jet have not shown any marked improvement in engine performance over that obtained with the atomization already realized with the conventional injection systems. In a series of tests conducted at this laboratory (reference 14) a jet of high-velocity air was directed through the fuel spray as it left the injection valve. Tests conducted by the methods described in reference 14 showed that the combination air-fuel injection decreased the mean diameter of the fuel drops and, when the fuel was injected into the atmosphere, it was found that the combination of the air and fuel jet burned with a much fiercer flame than did that of the fuel jet alone. Nevertheless, when the combination air-fuel injection was used in the engine, there was no appreciable gain in engine performance. As a result of these tests it was concluded that the atomization in the conventional hydraulic injection system is sufficient to result in good combustion provided that the fuel is correctly distributed.

Analysis of the results presented in this report, together with those in the references, leads to the conclusion that the factor about which more information should be obtained is the actual air-fuel ratio at each instant throughout the combustion chamber during the injection and combustion period. These ratios are the determining factors that control the performance of the engine. At present it is known that the air-fuel ratio is extremely uneven and that as a result of this unevenness too much of the fuel is burned late on the expansion stroke and, consequently, at a low cycle efficiency. Not only must the combustion efficiency of the engine be improved (by combustion efficiency is meant the percentage of the total fuel injected that is burned between the start of the fuel injection and the completion of the power stroke) but the time at which this burning occurs must also be controlled to a greater extent than is done in present-day designs.

CONCLUSIONS

The analysis of the data on the effect of air flow on fuel spray and flame formation has led to the following conclusions:

1. In the combustion chamber of the compression-ignition engine, air velocities as high as 400 feet a second were not sufficient to destroy the core of a fuel spray from a single round-hole orifice.

2. Air velocities of 400 feet a second were sufficient to change materially the direction and distance of the spray-core penetration and to blow aside the envelopes of sprays from a single round-hole orifice.

3. As the air-fuel ratio was increased the effect of the air flow on the fuel sprays was increased.

4. With fuel-injection nozzles giving poor fuel distribution within the combustion chamber, air flow increased the volume in the combustion chamber reached by flame.

5. With a fuel-injection nozzle giving good distribution, air flow did not result in much change in the spread of the flame although engine tests showed a large increase in performance.

6. High-distribution nozzles such as the slit nozzle did not show much more effect from air flow than did the sprays from round-hole orifices.

7. High-distribution nozzles damped the air flow considerably.

8. When air flow is employed in a combustion chamber, care should be taken that the motion of the air set up during the induction period is not such as to oppose the desired air flow produced at the end of the compression stroke.

LANGLEY MEMORIAL AERONAUTICAL LABORATORY,
NATIONAL ADVISORY COMMITTEE FOR AERONAUTICS,
LANGLEY FIELD, VA., *November 25, 1936.*

REFERENCES

1. Rothrock, A. M., and Waldron, C. D.: Some Effects of Injection Advance Angle, Engine-Jacket Temperature, and Speed on Combustion in a Compression-Ignition Engine. T. R. No. 525, N. A. C. A., 1935.
2. Rothrock, A. M., and Waldron, C. D.: Effects of Air-Fuel Ratio on Fuel Spray and Flame Formation in a Compression-Ignition Engine. T. R. No. 545, N. A. C. A., 1935.
3. Rothrock, A. M., and Waldron, C. D.: Effect of Nozzle Design on Fuel Spray and Flame Formation in a High-Speed Compression-Ignition Engine. T. R. No. 561, N. A. C. A., 1936.
4. Spanogle, J. A., and Whitney, E. G.: A Description and Test Results of a Spark-Ignition and a Compression-Ignition 2-Stroke-Cycle Engine. T. R. No. 495, N. A. C. A., 1934.
5. Moore, C. S., and Collins, J. H., Jr.: Prechamber Compression-Ignition Engine Performance. T. R. No. 577, N. A. C. A., 1936.
6. Foster, H. H.: The Quiescent-Chamber Type Compression-Ignition Engine. T. R. No. 568, N. A. C. A., 1936.
7. Moore, C. S., and Foster, H. H.: Performance Tests of a Single-Cylinder Compression-Ignition Engine with a Displacer Piston. T. N. No. 518, N. A. C. A., 1935.
8. Moore, C. S., and Foster, H. H.: Boosted Performance of a Compression-Ignition Engine with a Displacer Piston. T. N. No. 569, N. A. C. A., 1936.
9. Gawthrop, D. B.: Applications of the Schlieren Method of Photography. Rev. Sci. Instruments, vol. 2, no. 9, Sept. 1931, pp. 522-531.
10. Lee, Dana W.: Measurements of Fuel Distribution within Sprays for Fuel-Injection Engines. T. R. No. 565, N. A. C. A., 1936.
11. Selden, Robert F., and Spencer, Robert C.: Heat Transfer to Fuel Sprays Injected into Heated Gases. T. R. No. 580, N. A. C. A., 1936.
12. Alcock, J. F.: Air Swirl in Oil Engines. Proc. Inst. Mech. Eng. vol. 128, Nov.-Dec. 1934, pp. 123-193.
13. Gerrish, Harold C., and Ayer, Bruce E.: Influence of Fuel-Oil Temperature on the Combustion in a Prechamber Compression-Ignition Engine. T. N. No. 565, N. A. C. A., 1936.
14. National Advisory Committee for Aeronautics: Nineteenth Annual Report, 1933, p. 17.

REPORT No. 589

AN ANALYSIS OF LATERAL STABILITY IN POWER-OFF FLIGHT WITH CHARTS FOR USE IN DESIGN

By Charles H. Zimmerman

SUMMARY

The aerodynamic and mass factors governing lateral stability are discussed and formulas are given for their estimation. Relatively simple relationships between the governing factors and the resulting stability characteristics are presented. A series of charts is included with which approximate stability characteristics may be rapidly estimated.

The effects of the various governing factors upon the stability characteristics are discussed in detail. It is pointed out that much additional research is necessary both to correlate stability characteristics with riding, flying, and handling qualities and to provide suitable data for accurate estimates of those characteristics of an airplane while it is in the design stage.

INTRODUCTION

The lateral stability of airplanes has been the subject of considerable mathematical treatment and many theoretical analyses. (See references.) The main aspects of the problem are therefore well known to students of the subject. Use of the mathematical theory in design is, however, limited by practical difficulties in its application. Determination of numerical values for certain of the aerodynamic quantities is difficult and the results are uncertain. The required calculations are extensive and must be carefully made to avoid erroneous and confusing results.

In this report lateral stability will be discussed and analyzed in a way that, it is believed, will aid in the acquisition of a working knowledge of the subject without long and intensive study. The classical equations have been simplified as much as seems consistent with reasonable accuracy to permit rapid estimation of the stability characteristics. Also included is a series of charts designed to facilitate the rapid estimation of the approximate lateral-stability characteristics of airplanes throughout the normal-flight range. It is hoped that these charts, together with those on longitudinal stability presented in reference 1, will aid in putting the estimation of the complete stability characteristics on a practical basis.

The material is presented in the following order: (1) A discussion of the aerodynamic and mass factors that govern the uncontrolled motion of the airplane together with formulas for estimating these factors; (2) formulas for estimating the stability characteristics of the uncontrolled motion having given the governing factors; (3) charts for the rapid estimation of stability characteristics; (4) a discussion of the effects of the governing factors upon the stability characteristics; (5) comments and suggestions for future study; (6) a brief derivation of the classical stability formulas (appendix I); (7) an accurate semigraphical method for solving biquadratics with a useful approximation based on this method (appendix II); and (8) a list of symbols and their definitions (appendix III).

FACTORS GOVERNING STABILITY

Both theory and experiment indicate that, with certain exceptions, the uncontrolled motion of an airplane can be divided into two independent phases. One phase includes components of the motion that do not displace the plane of symmetry of the airplane from the plane with which it coincides during the steady motion. Stability of this part of the motion is termed "longitudinal stability." The other phase of the complete motion includes all components that do displace the plane of symmetry. This phase of the motion is called "lateral motion" and its stability characteristics, "lateral stability." Although, in the past, reference has frequently been made to directional stability as distinguished from rolling stability (also called "lateral" stability), both theory and experiment indicate that no such division is physically possible for the conventional airplane.

The uncontrolled motion of an airplane quite obviously depends upon the aerodynamic forces and moments arising from any deviation from a steady state together with the inertial forces and moments accompanying the accelerations coupled with the deviations. The lateral motion is zero in steady flight on a straight course. The components of lateral motion in unsteady flight are a linear velocity v along the Y axis (see appendix I and fig. 1) and angular velocities p and r about the X and Z axes, respectively. The forces and moments governing lateral motion therefore arise from the aerodynamic reactions to the

velocities v, p, and r (in the theoretical treatment aerodynamic reactions are assumed to be unaffected by accelerations) and the inertial reactions to the accelerations dv/dt, $g \sin \phi \cos \gamma$, $g \sin \psi \sin \gamma$, dp/dt, and dr/dt, where ϕ is the angle of roll, γ is the angle of the flight path, and ψ is the angle of yaw.

For convenience the components of the reactions referred to the coordinate axes are used rather than the resultant reaction. It appears, then, that a velocity v should result in a side force ΔY, a rolling moment ΔL, and a yawing moment ΔN. Similarly there will be Δ's of Y, L, and N corresponding to the rolling and yawing velocities p and r. The basis for the classical theory of stability is that the algebraic sum of the values of ΔY (for example) for a unit value of v when p and r are zero, for a unit value of p when v and r are zero, and for a unit value of r when v and p are zero is equal to the value of ΔY when the total motion is the resultant of coexisting unit values of v, p, and r. It is further assumed that a reaction ΔY due to a disturb-

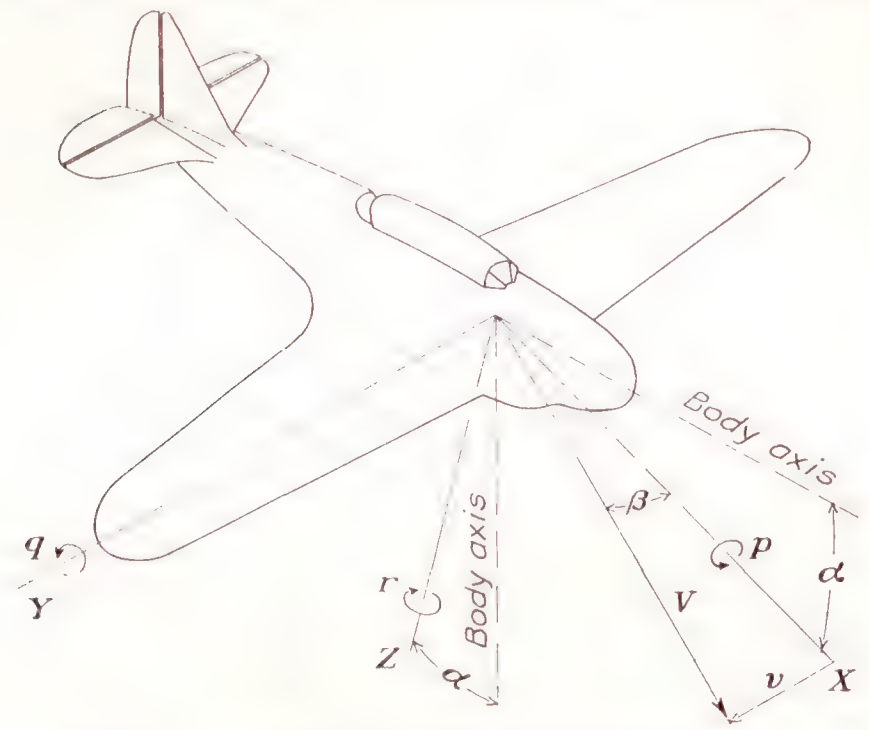

FIGURE 1.—Angular and vertical relationships in flight, power off.

ance of velocity v is directly proportional to the magnitude of v, that is $\Delta Y = v\frac{dY}{dv}$. This assumption is admittedly an approximation but is valid, in general, for small values of the velocities of the disturbance. On this basis the aerodynamic reaction ΔY to a lateral disturbance is

$$\Delta Y = v\frac{dY}{dv} + p\frac{dY}{dp} + r\frac{dY}{dr}$$

and similar expressions exist for ΔL and ΔN.

As a matter of convenience it has been found desirable to express the derivatives dY/dv, dL/dv, etc., in terms of the nondimensional coefficients C_Y, C_l, and C_n where

$$C_Y = \frac{Y}{\frac{1}{2}\rho V^2 S}$$

$$C_l = \frac{L}{\frac{1}{2}\rho V^2 Sb}$$

$$C_n = \frac{N}{\frac{1}{2}\rho V^2 Sb}$$

In order to make the treatment entirely nondimensional, it is convenient to consider the ratios v/V, $pb/2V$, and $rb/2V$ rather than v, p, and r. For small values v/V is equal to β, where β is the angle of sideslip (in radians), and $pb/2V$ is the difference (in radians) between the angle of attack at the center of gravity and the angle of attack at the wing tip. Since the velocity at the wing tip is $V + rb/2$ the value $rb/2V$ is the ratio of the portion of the velocity at the tip due to rotation to the velocity at the center of gravity. Expressed in this way, the lateral-force coefficient due to lateral motion is

$$\Delta C_Y = \beta\frac{dC_Y}{d\beta} + \frac{pb}{2V}\frac{dC_Y}{d\frac{pb}{2V}} + \frac{rb}{2V}\frac{dC_Y}{d\frac{rb}{2V}}$$

and similar expressions exist for ΔC_l and ΔC_n.

Since $dC_Y/d\frac{pb}{2V}$ and $dC_Y/d\frac{rb}{2V}$ are small, they are generally neglected, leaving the following aerodynamic factors to be considered:

1. Those depending on sideslip: $dC_Y/d\beta$, $dC_l/d\beta$, and $dC_n/d\beta$.

2. Those depending on rolling velocity: $dC_l/d\frac{pb}{2V}$ and $dC_n/d\frac{pb}{2V}$.

3. Those depending on yawing velocity: $dC_l/d\frac{rb}{2V}$ and $dC_n/d\frac{rb}{2V}$

In addition to the aerodynamic factors, others that depend on the amount and the distribution of the mass of the airplane must be considered. The important mass factors, expressed nondimensionally, are μ, b/k_X, and b/k_Z. The relative density factor μ is equal to $m/\rho Sb$ and may be considered as being proportional to the ratio of the mass of the airplane to the mass of air influenced by it in traveling one chord length. Under standard conditions $\mu = \frac{13.1(W/S)}{b}$.

AERODYNAMIC FACTORS

Lateral force due to sideslip.—The rate of change of lateral-force coefficient with angle of sideslip $dC_Y/d\beta$ can be accurately determined only by measurement in a wind tunnel. Assuming the wind-tunnel data to have been obtained in terms of angle of yaw ψ in degrees, the value of $dC_Y/d\beta$ is $-57.3\ (dC_Y/d\psi)$, since β is in radians and opposite in sign to ψ. In wind-tunnel practice, cross-wind force rather than lateral force is usually measured. In such cases $dC_Y/d\beta$ can be determined from the relationship

$$\frac{dC_Y}{d\beta} = \frac{dC_c}{d\beta} - C_D \qquad (1)$$

(which follows from the fact that $C_Y = C_c \cos \beta - C_D \sin \beta$).

Diehl gives (reference 2, pp. 254–255) an approximate, empirical value of

$$\frac{dC_c}{d\beta} = -0.12 \frac{bl_1}{S} \tag{2}$$

where l_1 is the over-all length. This formula is useful when wind-tunnel data are not available.

Rolling moment due to sideslip.—The rate of change of rolling-moment coefficient with sideslip $dC_l/d\beta$ must also be measured in a wind tunnel if accurate values are desired. Some systematic research has shown the effect of dihedral and tip shape on the value of $dC_l/d\beta$ for the wing alone (reference 3) but very little is known about the effect of fuselage interference. In certain experiments (data unpublished) a model having a wing with no dihedral mounted in a high-wing position gave a value of $dC_l/d\beta$ corresponding to 5° of positive dihedral for the wing alone. The same model with the wing mounted in a low-wing position gave a very erratic

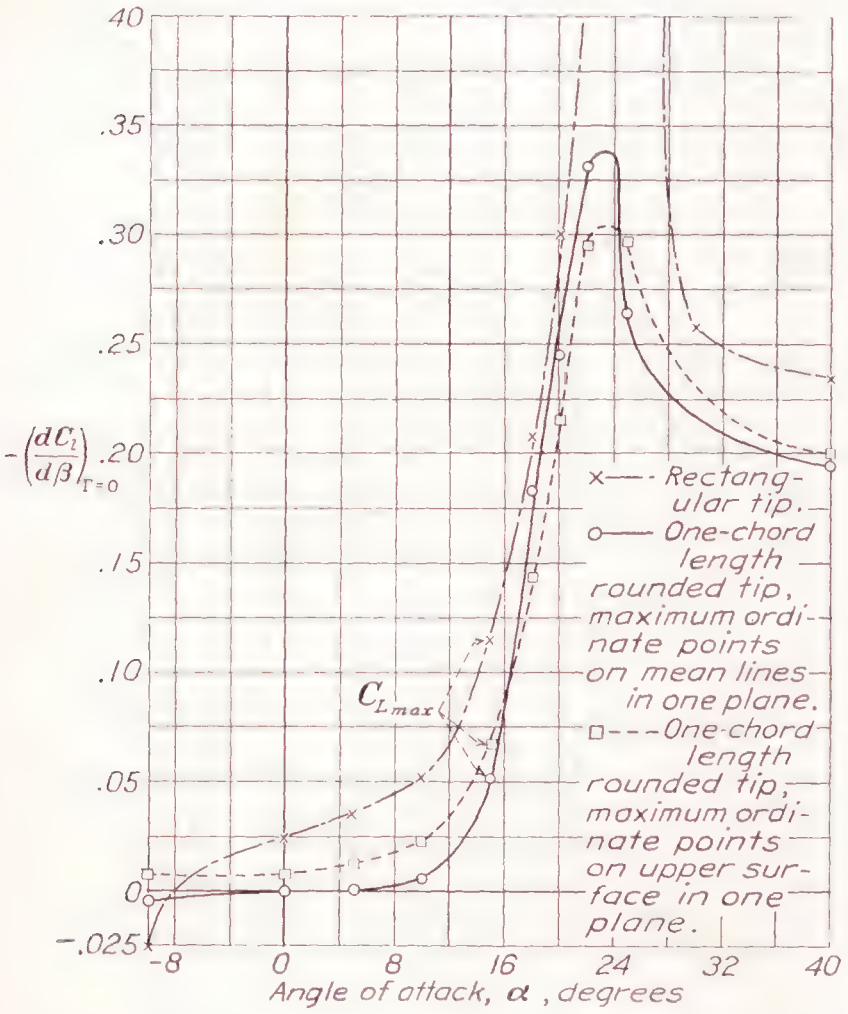

FIGURE 2.—Effect of tip shape on rate of change of rolling-moment coefficient with sideslip.

curve of C_l against β. The slope of this curve indicated zero dihedral effect at zero sideslip. The average dihedral effect up to 30° sideslip corresponded, however, to 4° negative dihedral. These tests were in the nature of preliminary tests and are unconfirmed but give ample evidence of the need for similar additional research.

In the absence of wind-tunnel tests the value of $dC_l/d\beta$ for the wing alone may be computed from the relationship

$$\frac{dC_l}{d\beta} = \left(\frac{dC_l}{d\beta}\right)_{\Gamma=0} + \Gamma(-0.012) \tag{3}$$

where $(dC_l/d\beta)_{\Gamma=0}$ is the value of $dC_l/d\beta$ for the wing without dihedral (see fig. 2) and Γ is the dihedral angle in degrees. This formula was developed from data obtained with wings of aspect ratio 6 and with no taper or sweepback (reference 3). Tapering the wing decreases the effective dihedral but the decrease is somewhat less than would be expected from the geometric proportions because of the tendency of the wing lift to be evenly distributed along the span. Sweepback is equivalent to an increase in dihedral, particularly at high angles of attack, but the effect is negligible for small amounts of sweepback such as are used in conventional airplanes.

The wing, including interference effects, is the chief source of rolling moment due to sideslip and other parts of the airplane can normally be neglected. Vertical-fin area displaced from the longitudinal axis contributes to $dC_l/d\beta$ but the effect is usually small. If, in a particular case, the effect upon the value of $dC_l/d\beta$ is desired for parts having considerable projected side area, it can be computed from the relationship

$$\frac{dC_l}{d\beta} = \frac{S_p}{S} \frac{z_p}{b} \frac{dC_{L_p}}{d\beta} \tag{4}$$

where S_p is the projected side area.

S, the wing area.

z_p, the z coordinate of the center of pressure of projected side area.

C_{L_p}, the absolute coefficient of force on the projected side area.

In this equation $dC_{L_p}/d\beta$ must be estimated, taking into account the shape of the part and the probable interference effects.

Yawing moment due to sideslip.—The change of yawing-moment coefficient with angle of sideslip $dC_n/d\beta$ depends principally upon the fuselage and the vertical-tail area. The contributions of the landing gear, interference effects, etc., are small and can generally be neglected. The contribution of the wings is also small and can be neglected at high or cruising speeds but becomes of increasing importance at slower speeds (reference 3); the effect due to the wing is an increase in $dC_n/d\beta$. The center of pressure upon the fuselage is normally well ahead of the center of gravity so that the moment due to sideslip is such as to increase the sideslip. The magnitude of this unstabilizing tendency varies with the size and shape of the fuselage but, on the average, is equal to about one-third the stabilizing effect of the vertical tail surfaces.

For accurate stability calculations it is necessary that $dC_n/d\beta$ be obtained from wind-tunnel tests at several angles of attack by the use of the relation $dC_n/d\beta = -57.3\, dC_n/d\psi$. The value of $dC_n/d\beta$ can be

calculated approximately from the relation

$$\frac{dC_n}{d\beta}=-\eta_t\frac{l}{b}\frac{S_t}{S}\left(\frac{dC_{L_t}}{d\beta}\right)-K_\beta\frac{S_s l_2}{Sb} \tag{5}$$

where η_t is the tail efficiency.
l, the distance from the center of gravity to the rudder hinge.
l_2, the over-all length of the fuselage.
S_t, the area of the vertical tail surfaces.
C_{L_t}, the absolute coefficient of force on the vertical tail surfaces.
K_β, an empirical constant (reference 2, p. 203).
S_s, the projected side area of the fuselage.

When using equation (5), it is necessary to estimate or assume values of η_t, $dC_{L_t}/d\beta$, and K_β. For modern types of airplane η_t is about 0.80. The slope of the tail-force curve $dC_{L_t}/d\beta$ depends on the aspect ratio of the tail and to a certain extent upon the end-plate effect of the fuselage and the horizontal surfaces. For

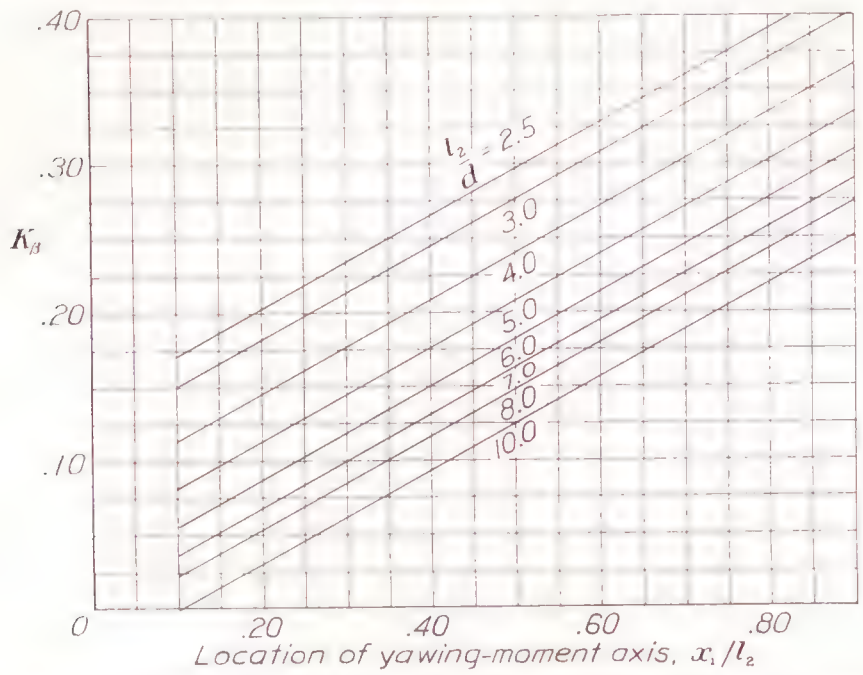

FIGURE 3.—Empirical factor for computing effect of fuselage on rate of change of yawing-moment coefficient with sideslip (from fig. 98, reference 2).

$$K_\beta=\frac{Sb}{S_s l_2}\left(\frac{dC_n}{d\beta}\right)_{\text{fuselage}}$$

conventional arrangements $dC_{L_t}/d\beta=2.2$ is a good average value. Values of K_β as determined by Diehl are given in figure 3. From this figure the value of K_β can be directly determined from the ratio of the distance of the center of gravity back of the nose x_1 to the fuselage length l_2 and the ratio of the maximum fuselage depth d to the fuselage length. In a number of computations made to check the accuracy of formula (5) it was found that the results were generally conservative, i. e., the estimated value of $dC_n/d\beta$ was smaller than the measured value. The difference arose in most cases from the fact that the measured effect of the fuselage was smaller than the estimated effect. The measured effect of the fuselage apparently varies between zero and the effect calculated as $K_\beta\frac{S_s l_2}{Sb}$ depending upon the details of nose shape and fuselage form.

Rolling moment due to rolling.—The rate of change of rolling-moment coefficient with rate of rolling $dC_l/d\frac{pb}{2V}$ arises from the change of angle of attack along the wing. The increment in angle of attack at any spanwise distance y from the center of gravity is py/V (in radian measure), the increment at the tip being $pb/2V$. If a uniform spanwise distribution of lift and drag be assumed, simple integration gives

$$\frac{dC_l}{d\frac{pb}{2V}}=\frac{-(dC_L/d\alpha+C_{D_w})}{6}$$

where C_{D_w} is the drag coefficient of the wing alone. If an elliptical distribution is assumed, integration gives

$$\frac{dC_l}{d\frac{pb}{2V}}=\frac{-(dC_L/d\alpha+C_{D_w})}{8}$$

Actually, measured values of $dC_l/d\frac{pb}{2V}$ are considerably smaller than either formula indicates because of the tendency of the lift to equalize itself along the span during the rotation.

In the absence of data obtained from some such device as a rolling balance, $dC_l/d\frac{pb}{2V}$ can be taken as -0.40 for wing arrangements such as are likely to be used on conventional airplanes. A survey of test results reveals values from -0.35 to -0.47 for plain wings and values as high as -0.50 for wings with tip slots. It would be expected that rounding the tips or tapering the wings would reduce $dC_l/d\frac{pb}{2V}$, and such was found to be the case for the tests reported in reference 3. On the other hand, there is sufficient conflicting evidence to indicate that an attempt to calculate $dC_l/d\frac{pb}{2V}$ taking into account tip shape and taper, is likely to give a result no nearer the true value than is the assumed average, -0.40.

Yawing moment due to rolling.—The rate of change of yawing-moment coefficient with rate of rolling $dC_n/d\frac{pb}{2V}$ arises from the same causes as does $dC_l/d\frac{pb}{2V}$. Simple integration gives for a rectangular-wing force distribution

$$\frac{dC_n}{d\frac{pb}{2V}}=\frac{-\left[C_L-\left(\frac{dC_{D_w}}{d\alpha}\right)\right]}{6}$$

and for an elliptical-wing force distribution gives

$$\frac{dC_n}{d\frac{pb}{2V}}=\frac{-\left[C_L-\left(\frac{dC_{D_w}}{d\alpha}\right)\right]}{8}$$

It will be noticed that the sign of the resulting value of $dC_n/d\frac{pb}{2V}$ indicates that the wing being depressed by the rolling motion is accelerated forward by the resulting yawing moment. The mistake has frequently been made (see reference 4) of assuming that the increase in drag of the wing being depressed would result in a yawing moment retarding that wing, that is, in a positive value of $dC_n/d\frac{pb}{2V}$. This reasoning fails to take into account the forward inclination with increase in angle of attack of the resultant-force vector relative to an axis fixed in the wing.

Wind-tunnel data cannot ordinarily be obtained for $dC_n/d\frac{pb}{2V}$ because there are but few existing balances capable of measuring the yawing moment on a rolling model. It is therefore necessary to rely on estimated values of $dC_n/d\frac{pb}{2V}$. The empirical relationship

$$\frac{dC_n}{d\frac{pb}{2V}}=\frac{-\left(C_L-1.1\frac{dC_{D_w}}{d\alpha}\right)}{8} \tag{6}$$

has been found (reference 5) to give good agreement with measured values below the stall, C_L and $dC_{D_w}/d\alpha$ having been obtained from force tests of the wing alone; but there is need for further experimental data on this factor.

Rolling moment due to yawing.—The rate of change of rolling-moment coefficient with rate of yawing $dC_l/d\frac{rb}{2V}$ results from the difference in velocity between the wing tips, one wing tip having the velocity $V+rb/2$ and the other having the velocity $V-rb/2$. Simple integration gives the value of $dC_l/d\frac{rb}{2V}$ as $C_L/3$ assuming a rectangular distribution of lift or as $C_L/4$ assuming an elliptical distribution. The rolling moment due to yawing is of positive sign since a positive rate of yawing gives a positive rolling moment.

It will ordinarily be impossible to measure $dC_l/d\frac{rb}{2V}$ for a particular design because of lack of equipment. Either special apparatus for oscillating the model or a whirling arm equipped to measure rolling moments is required. In the absence of experimental data, the computed value must be used. Glauert states (reference 6) that

$$\frac{dC_l}{d\frac{rb}{2V}}=\frac{C_L}{4} \tag{7}$$

gives nearly correct values for a rectangular wing. Experimental results for the Bristol Fighter, a biplane with substantially rectangular wings, however, gave $dC_l/d\frac{rb}{2V}$ as nearly $C_L/3$ (reference 7). Measured values from tests of a biplane model reported in reference 8 were approximately equal to $C_L/4$ for three wing combinations. It appears that the assumption that equation (7) gives reasonable values is justified for wings with faired or elliptical tips and slight to moderate taper.

Yawing moment due to yawing.—The rate of change of yawing-moment coefficient due to yawing $dC_n/d\frac{rb}{2V}$ results from the change of velocity along the wing and the change of sideslip velocity along the fuselage and at the tail due to the yawing. On the basis of simple integration the portion of $dC_n/d\frac{rb}{2V}$ due to the wing is $-C_{D_w}/3$ for a rectangular distribution and $-C_{D_w}/4$ for an elliptical distribution. In an extension of work by Wieselsberger, Glauert shows (reference 6) that $dC_n/d\frac{rb}{2V}$ is equal to $-(0.33\ C_{D_0}+0.043\ C_{D_i})$ for a rectangular wing of normal aspect ratio and equal to $-(0.25\ C_{D_0}+0.33\ C_{D_i})$ for an elliptical wing, where C_{D_0} and C_{D_i} are the profile and induced drags, respectively, for the wing alone.

The change in angle of sideslip at the tail due to a yawing velocity r is rl/V. The theoretical value for the vertical tail is

$$\frac{dC_n}{d\frac{rb}{2V}}=-2\eta_t\frac{l^2}{b^2}\frac{S_t}{S}\frac{dC_{L_t}}{d\beta}$$

It will be noted that both the wing and the tail contributions to $dC_n/d\frac{rb}{2V}$ are negative; that is, they are in the sense to oppose the rotation.

It is unfortunate that experimental means of measuring $dC_n/d\frac{rb}{2V}$ are not more commonly available. As will appear later in the report, an accurate knowledge of $dC_n/d\frac{rb}{2V}$ is necessary for reasonable accuracy in estimating stability characteristics. The sparse experimental evidence concerning the value of this factor (see references 7 and 8) indicates that there are, in some cases, large interference effects. For one model tested on a whirling arm the value of $dC_n/d\frac{rb}{2V}$ for the fuselage and tail surfaces combined was only one-third the value for the tail surfaces alone. It is quite evident from such data that computed values can be considered at best

only as rough approximations. With this limitation in mind it appears that the most suitable formula for $dC_n/d\frac{rb}{2V}$ is

$$\frac{dC_n}{d\frac{rb}{2V}}=-\frac{C_{D_w}}{3}-2\eta_t\frac{l^2}{b^2}\frac{S_t}{S}\frac{dC_{L_t}}{d\beta} \tag{8}$$

and that there is no justification for refinements in the formula.

MASS FACTORS

Relative density of airplane and air.—The relative density of the airplane to the air is usually expressed as $\mu=m/\rho Sb$. From this definition μ is $\pi/4$ times the ratio of the mass of the airplane to the mass of air affected by a monoplane wing (on the basis of accepted wing theory) in traveling a distance equal to the mean chord. It thus appears that μ is intimately tied up with the performance characteristics of the airplane.

For standard conditions $\mu=\frac{13.1(W/S)}{b}$. For other conditions μ may be expressed as

$$\frac{13.1(W/S)}{b}\frac{\rho_0}{\rho} \tag{9}$$

where ρ_0 is the standard mass density (0.002378 slug per cubic foot) and ρ is the actual mass density. It appears that μ increases with wing loading and altitude and decreases with span. The numerical value of μ ranges from 2 for large transports to 10 for pursuit airplanes under standard conditions. It appears that large airplanes are dynamically similar to very lightly loaded small airplanes, a transport with a span of 120 feet and wing loading of 25 corresponding to an airplane of 30-foot span with a wing loading of 6.25.

Ratio of wing span to radius of gyration about X axis.—The ratio of the wing span to the radius of gyration about the X axis, b/k_X, has been determined for 15 airplanes (reference 9) and has been found to range from 6.7 to 9.3, with 8.0 as an average value. This ratio can be estimated with sufficient accuracy for stability calculations. For preliminary estimates the average value of 8.0 is satisfactory for conventional types because, as will appear later, stability characteristics are not critically dependent upon the mass distribution.

Ratio of wing span to radius of gyration about Z axis.—The value of the ratio of the wing span to the radius of gyration about the Z axis, b/k_Z, has been found to vary from 5.1 to 6.4, with 5.7 as an average value. As in the case of b/k_X, the average value is satisfactory for most estimates of stability. The value of b/k_Z can be estimated with sufficient accuracy for all stability calculations from a weight analysis of the airplane.

STABILITY DERIVATIVES

In practice it has been found convenient to combine the aerodynamic and mass factors that govern lateral-stability characteristics into stability derivatives. These derivatives take the following forms, one for each of the aerodynamic factors:

$$\begin{aligned}
y_v&=\frac{1}{2}\frac{dC_Y}{d\beta}\\
l_v&=\frac{1}{2}\left(\frac{b}{k_X}\right)^2\frac{dC_l}{d\beta}\\
n_v&=\frac{1}{2}\left(\frac{b}{k_Z}\right)^2\frac{dC_n}{d\beta}\\
l_p&=\frac{1}{4}\left(\frac{b}{k_X}\right)^2\frac{dC_l}{d\frac{pb}{2V}}\\
n_p&=\frac{1}{4}\left(\frac{b}{k_Z}\right)^2\frac{dC_n}{d\frac{pb}{2V}}\\
l_r&=\frac{1}{4}\left(\frac{b}{k_X}\right)^2\frac{dC_l}{d\frac{rb}{2V}}\\
n_r&=\frac{1}{4}\left(\frac{b}{k_Z}\right)^2\frac{dC_n}{d\frac{rb}{2V}}
\end{aligned}$$

Physically these derivatives are, respectively, proportional to the linear or angular acceleration arising from a unit angle of sideslip, a unit rolling velocity as expressed by $pb/2V$, or a unit yawing velocity as expressed by $rb/2V$.

The stability derivatives include all the important factors governing stability characteristics except μ. Since μ occurs only in combination with n_v and l_v and, conversely, since these derivatives occur only in combination with μ, the lateral-stability characteristics can be completely expressed in terms of the seven nondimensional quantities: y_v, μl_v, μn_v, l_p, n_p, l_r, and n_r.

For preliminary estimates it will generally be sufficiently accurate to use the following values for the stability derivatives:

$$\left.\begin{aligned}
y_v&=-0.14\\
l_v&=32\frac{dC_l}{d\beta}\\
n_v&=16\frac{dC_n}{d\beta}\\
l_p&=-6.4\\
n_p&=-0.5\ C_L\\
l_r&=4\ C_L\\
n_r&=8\frac{dC_n}{d\frac{rb}{2V}}
\end{aligned}\right\} \tag{10}$$

A rather small value of y_v has been chosen in order to be conservative. Stability characteristics calculated with this small value of y_v can be readily corrected to correspond to a different y_v, a fact which will be subsequently shown. The derivatives l_p, n_p, and l_r may differ considerably from the foregoing values, particu-

larly at angles of attack above that at which the lift-curve slope begins to decrease. Fortunately the stability characteristics are not greatly affected by moderate variation in these particular factors. If possible, values of $dC_l/d\beta$, $dC_n/d\beta$, and $dC_n/d\frac{rb}{2V}$ should be obtained by actual measurement. There is strong reason for believing that, unless these factors are accurately measured, a false impression of the accuracy of the estimated stability characteristics may be obtained by refinements in estimating the other factors.

FORMULAS FOR ESTIMATING STABILITY CHARACTERISTICS

Stability characteristics about which information is desired.—The preceding portion of this paper has dealt with the various aerodynamic and mass factors that govern stability characteristics. In the following paragraphs these factors will be grouped in relationships which show the effects of the individual factors upon the stability characteristics and from which these characteristics can be quantitatively determined.

Instability can manifest itself either as a continuously increasing divergence from the steady-flight condition or as an oscillation of continuously increasing amplitude about the steady-flight condition. On a logical basis it appears that the questions answered by an estimation of stability characteristics should be: (1) Will there exist a tendency to diverge from the steady-flight condition? (2) Will the oscillations started by a disturbance or by the use of the controls damp out and, if so, how quickly? (3) What will be the period of the lateral oscillations? Approximate relationships to answer these questions have been developed (see appendixes I and II) and are presented in the following pages.

Basis for formulas.—The following formulas are based on the classical theory of small oscillations first applied to airplane dynamics by Bryan and developed and expanded by Bairstow, Wilson, Glauert, and others (references 10 to 13). A brief derivation of the formulas is given in appendix I. The formulas presented represent a first approximation to a semigraphical method of accurately solving the stability biquadratic given by the classical theory. This semigraphical method and the approximation to it are explained in appendix II.

Formulas for predicting a divergence.—Divergence is not possible in the normal-flight range (to which this report is confined) if

$$\mu l_v n_r > \mu n_v l_r \tag{11}$$

and

$$\mu l_v\left(n_p-\frac{C_L}{2}\right)-\mu n_v l_p>0 \tag{12}$$

Failure to meet the first of these conditions results in "spiral divergence," a form of divergence in which the airplane tends to go into a spiral dive. Failure to meet the second condition results in "directional divergence," in which the airplane tends to yaw away from the direction of steady flight.

For purposes of approximate estimation using the values for the derivatives given in equation (10), equations (11) and (12) become

$$4(dC_l/d\beta)\left(dC_n/d\frac{rb}{2V}\right)>C_L(dC_n/d\beta) \tag{13}$$

and

$$-C_L(dC_l/d\beta)+3.2(dC_n/d\beta)>0 \tag{14}$$

If the contributions of the wings, the fuselage, and interference effects upon $dC_n/d\frac{rb}{2V}$ and upon $dC_n/d\beta$ are neglected, equation (13) further simplifies to

$$-dC_l/d\beta>\frac{C_L}{8}\frac{b}{l} \tag{15}$$

This latter equation is, however, an oversimplification for any but the most approximate analyses.

Formulas for estimating the damping of an oscillation.—The number of seconds required for an oscillation to damp to one-half its original amplitude is

$$T=\frac{-0.313\sqrt{\left(\frac{W}{S}\right)\frac{\rho_0}{\rho}C_L}}{\zeta'} \tag{16}$$

where ζ' is the damping coefficient. The time to damp to any other proportion of the original amplitude is given by

$$T_n=T\frac{\log_e n}{-0.693} \tag{17}$$

where n is the desired proportion, such as ¼ or 1/5. To a fairly close approximation (±15 percent)

$$\zeta'=-\frac{1}{2}\left[-y_v+\frac{l_p n_r-l_r n_p}{(-n_r-l_p)}+\frac{\mu n_v(-n_r)}{(-n_r-l_p)^2}+\frac{C_L l_r n_v}{2l_v\left(n_p-\frac{C_L}{2}\right)-2n_v l_p}\right]+\frac{1}{2}\left[\frac{\mu l_v\left(n_p-\frac{C_L}{2}\right)}{(-n_r-l_p)^2}+\frac{C_L l_r n_r}{2l_v\left(n_p-\frac{C_L}{2}\right)-2n_v l_p}\right] \tag{18}$$

In equation (18) the terms in the first pair of brackets are those which make ζ' more negative, i. e., decrease the time required for the oscillation to damp; the terms in the second pair of brackets are those which make ζ' less negative.

If the values from equations (10) are used, equation (18) becomes

$$\zeta' = -0.07 - \frac{25.6\left(-\frac{dC_n}{d\frac{rb}{2V}}\right) + C_L^2}{6.4 + 8\left(-\frac{dC_n}{d\frac{rb}{2V}}\right)} + \frac{16\ C_L\mu\left(-\frac{dC_l}{d\beta}\right) - 64\ \mu\frac{dC_n}{d\beta}\left(\frac{dC_n}{d\frac{rb}{2V}}\right)}{\left[6.4 + 8\left(-\frac{dC_n}{d\frac{rb}{2V}}\right)\right]^2} + \frac{4\left(-\frac{dC_l}{d\beta}\right)\left(-\frac{dC_n}{d\frac{rb}{2V}}\right) - C_L\frac{dC_n}{d\beta}}{2\left(-\frac{dC_l}{d\beta}\right) + \frac{6.4}{C_L}\left(\frac{dC_n}{d\beta}\right)} \tag{19}$$

Since $8\left(-\frac{dC_n}{d\frac{rb}{2V}}\right)$ is small compared with 6.4 a further simplification is obtained by letting $8\left(-\frac{dC_n}{d\frac{rb}{2V}}\right)$, where it appears in the denominator, equal 0.84. On this basis

$$\zeta' = -0.07 - 3.5\left(\frac{dC_n}{d\frac{rb}{2V}}\right) - 0.14\ C_L^2 - 1.2\ \mu\frac{dC_n}{d\beta}\left(-\frac{dC_n}{d\frac{rb}{2V}}\right) + 0.3\ \mu\left(-\frac{dC_l}{d\beta}\right) + \frac{4\left(-\frac{dC_l}{d\beta}\right)\left(-\frac{dC_n}{d\frac{rb}{2V}}\right) - C_L\frac{dC_n}{d\beta}}{2\left(-\frac{dC_l}{d\beta}\right) + \frac{6.4}{C_L}\frac{dC_n}{d\beta}} \tag{20}$$

Formula (20) will lead to fairly large errors if the airplane departs very far from the average. The error is roughly on a percentage basis so that, for small values of damping approaching an undesirable condition, the actual error is small.

Formulas for estimating the period of an oscillation. The period, in seconds, of the lateral oscillation is

$$P = \frac{2.83\sqrt{\left(\frac{W}{S}\right)\frac{\rho_0}{\rho}C_L}}{\psi'} \tag{21}$$

where ψ' is the period coefficient. To a fairly close approximation ψ' is given by

$$\psi' = \sqrt{\frac{\mu l_v\left(n_p - \frac{C_L}{2}\right) - \mu n_v l_p}{(-n_r - l_p)}} \tag{22}$$

substituting the values for the derivatives given in equations (10) and letting $8\left(-dC_n/d\frac{rb}{2V}\right) = 0.84$ gives

$$P = \sqrt{\frac{0.14b}{\left(-\frac{dC_l}{d\beta}\right) + \frac{3.2}{C_L}\frac{dC_n}{d\beta}}} \tag{23}$$

which is correct for the conventional airplane within ±20 percent.

CHARTS FOR ESTIMATING STABILITY CHARACTERISTICS

Explanation of charts.—A series of 22 charts for use in rapid estimation of stability characteristics are given in figures 4 to 25. In these charts the damping and the period of lateral oscillations are given by curves of $T/\sqrt{W/S}$=constant and of $P/\sqrt{W/S}$=constant plotted with $-\mu dC_l/d\beta$ as abscissas and $\mu dC_n/d\beta$ as ordinates. The limits to the region within which both spiral and static directional stability exist are indicated by straight lines representing zero spiral stability and zero directional stability, respectively. The rates of convergence or divergence are not given.

The charts cover values of C_L(0.2 to 2.0) and $dC_n/d\frac{rb}{2V}$ (−0.030 to −0.252) likely to occur in practice with conventional airplanes.

Each chart covers values of $-\mu dC_l/d\beta$ from 0 to 0.5 and of $\mu dC_n/d\beta$ from −0.05 to 0.3. These ranges are sufficiently large for most conventional airplanes. Some extrapolation is permissible in particular cases without much loss of accuracy other than that due to the fundamental weakness of increasing inaccuracy as the damping becomes large.

These charts are based on equations (13), (14), (19), and (23) and are therefore approximations to the same extent as the equations. They are intended principally for use in rapid estimates in design and show fairly accurately the relative effects of changes in C_L, $dC_n/d\frac{rb}{2V}$, $\mu dC_l/d\beta$, and $\mu dC_n/d\beta$. Being based on average values of $dC_Y/d\beta$, $dC_l/d\frac{pb}{2V}$, $dC_n/d\frac{pb}{2V}$, $dC_l/d\frac{rb}{2V}$, b/k_X, and b/k_Z, they cannot be used to determine the effect of changes in these factors. The charts should not be used where very accurate values are desired. On the other hand, there is little justification for using a more accurate method unless measured values of the various aerodynamic factors are available. If $dC_Y/d\beta$ is known to be much larger than −0.28, as, for example, in the case of an airplane with a split flap at a high angle of attack, correction for the damping can be made by the procedure given in the following section.

Method of using charts.—In order to use the charts the following data are needed:

W/S, wing loading.
b, wing span.
C_L, lift coefficient.
$dC_l/d\beta$, rate of change of rolling-moment coefficient with sideslip, per radian.
$dC_n/d\beta$, rate of change of yawing-moment coefficient with sideslip, per radian.
$dC_n/d\frac{rb}{2V}$, rate of change of yawing-moment coefficient with rate of yawing, per unit of $rb/2V$.

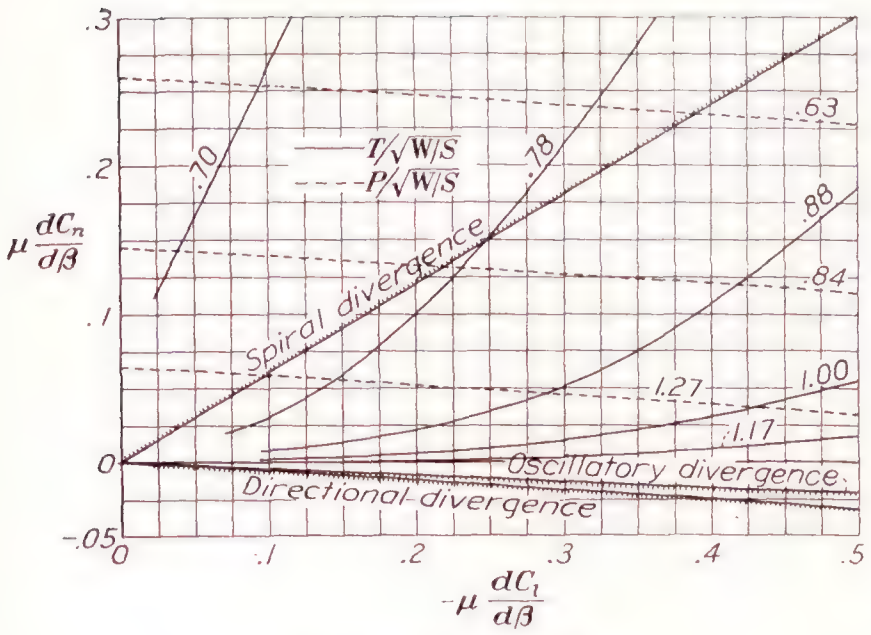

$C_L=0.2 \quad dC_n/d\frac{rb}{2V}=-0.030$

FIGURE 4.

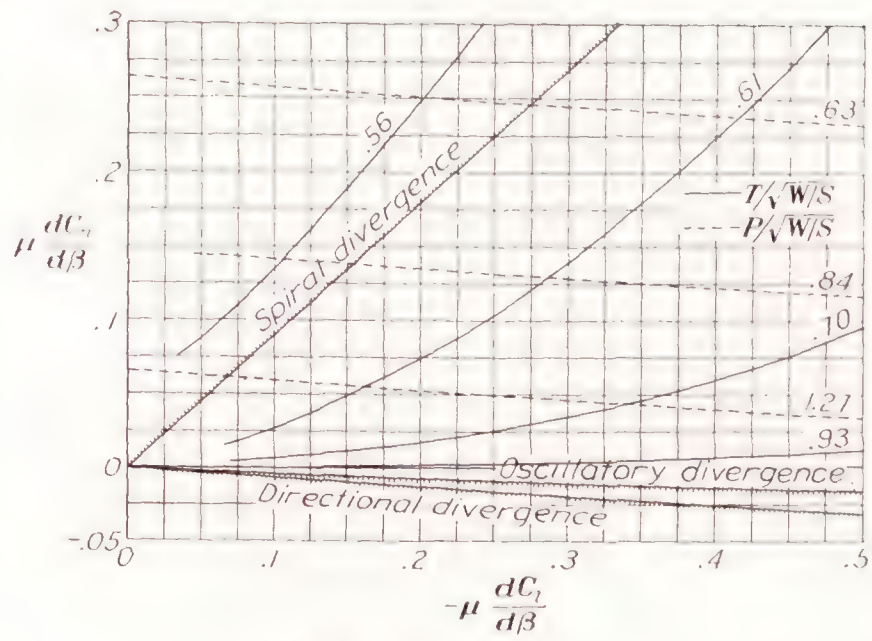

$C_L=0.2 \quad dC_n/d\frac{rb}{2V}=-0.045$

FIGURE 5.

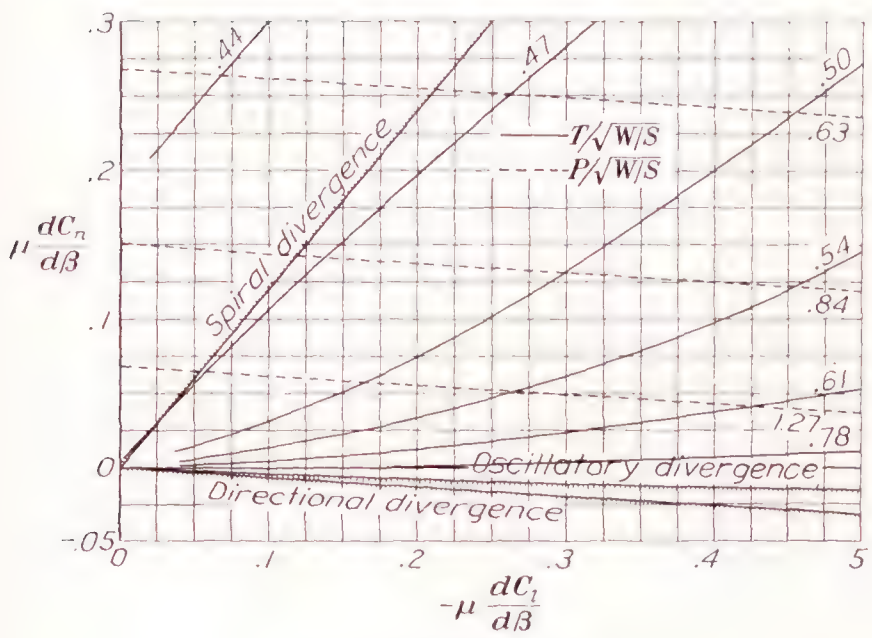

$C_L=0.2 \quad dC_n/d\frac{rb}{2V}=-0.060$

FIGURE 6.

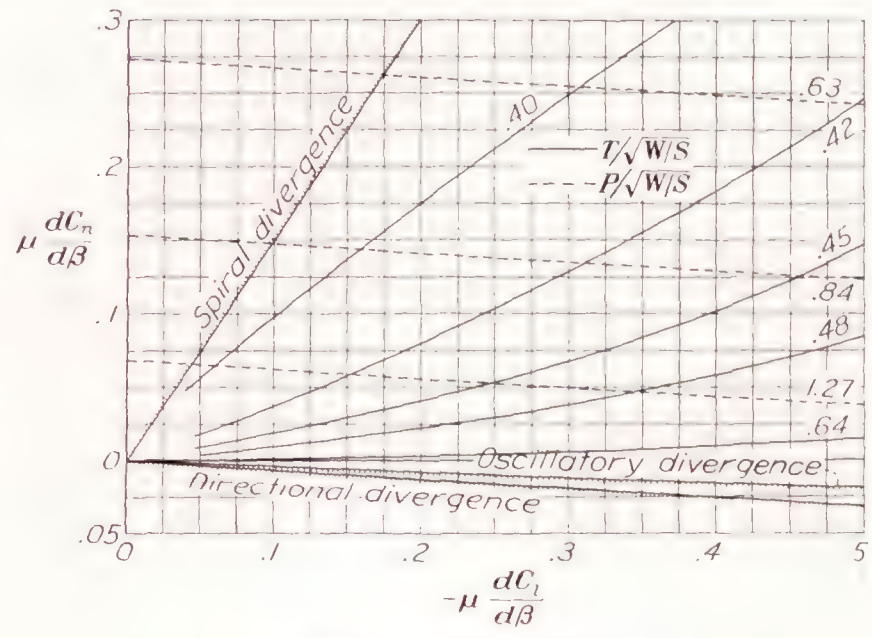

$C_L=0.2 \quad dC_n/d\frac{rb}{2V}=-0.075$

FIGURE 7.

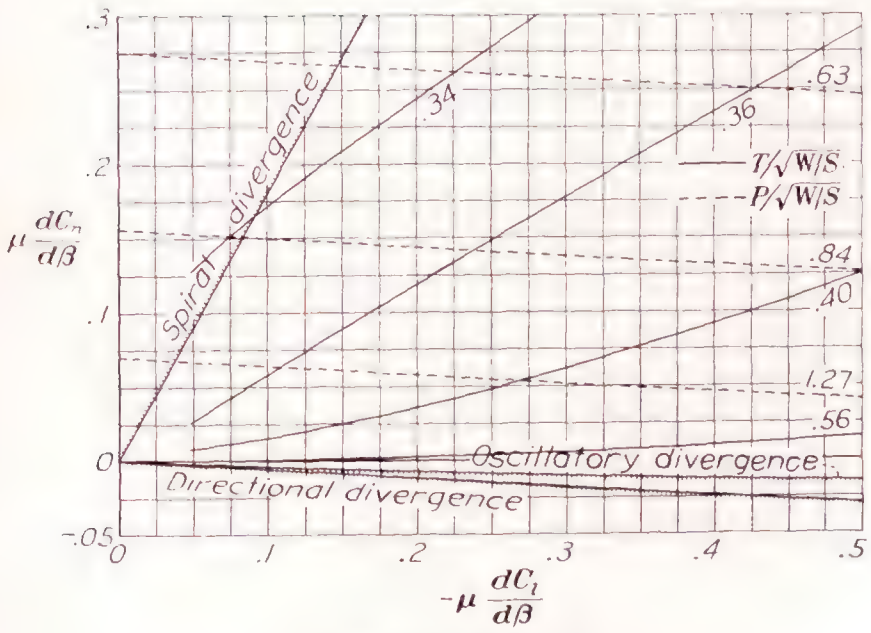

$C_L=0.2 \quad dC_n/d\frac{rb}{2V}=-0.090$

FIGURE 8.

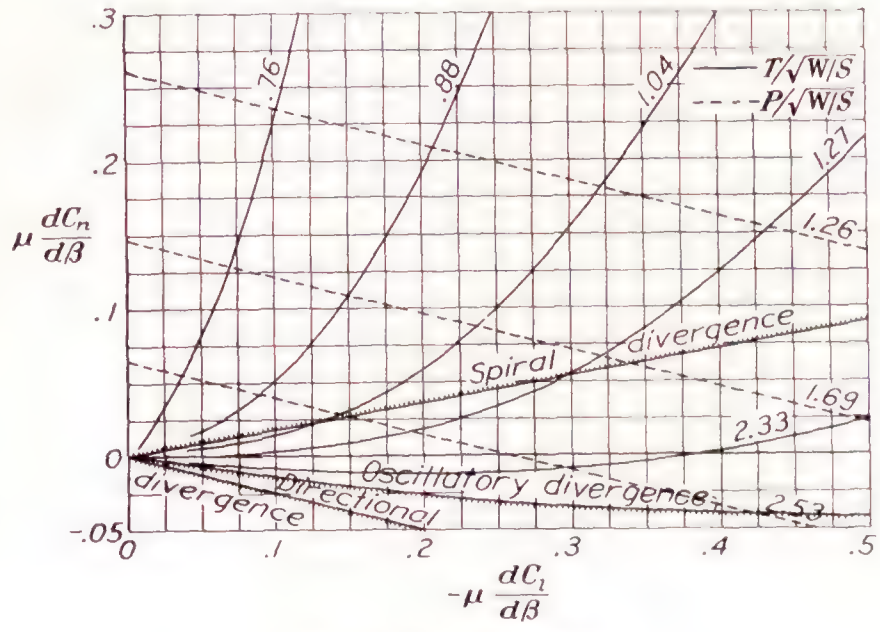

$C_L=0.8 \quad dC_n/d\frac{rb}{2V}=-0.036$

FIGURE 9.

FIGURES 4 to 9.—Lateral-stability charts.

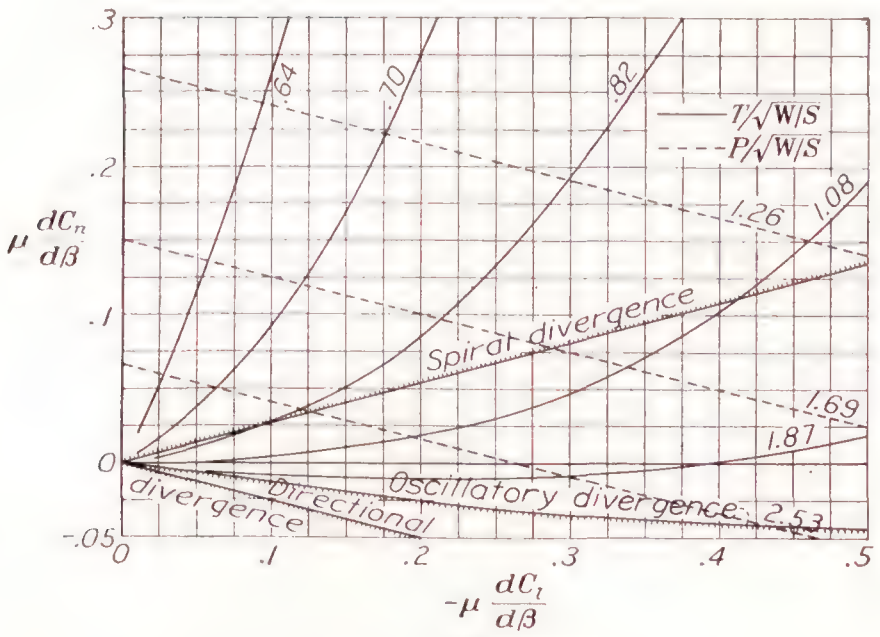

$C_L=0.8$ $dC_n/d\frac{rb}{2V}=-0.054$

FIGURE 10.

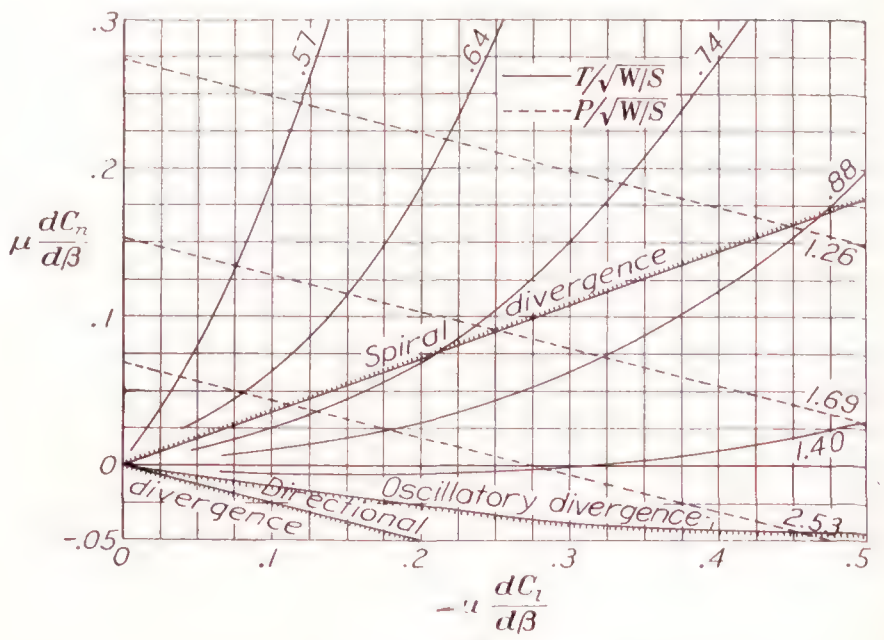

$C_L=0.8$ $dC_n/d\frac{rb}{2V}=-0.072$

FIGURE 11.

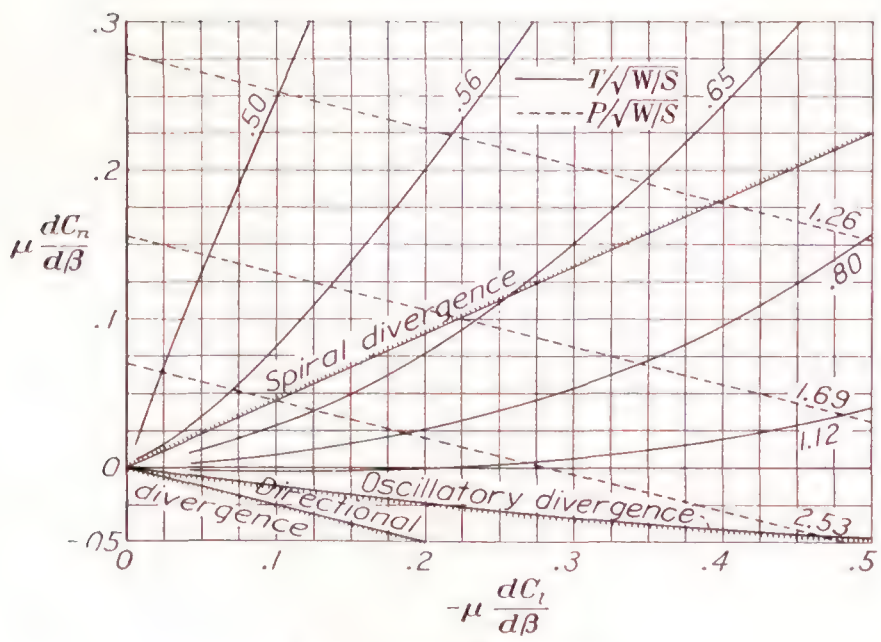

$C_L=0.8$ $dC_n/d\frac{rb}{2V}=-0.090$

FIGURE 12.

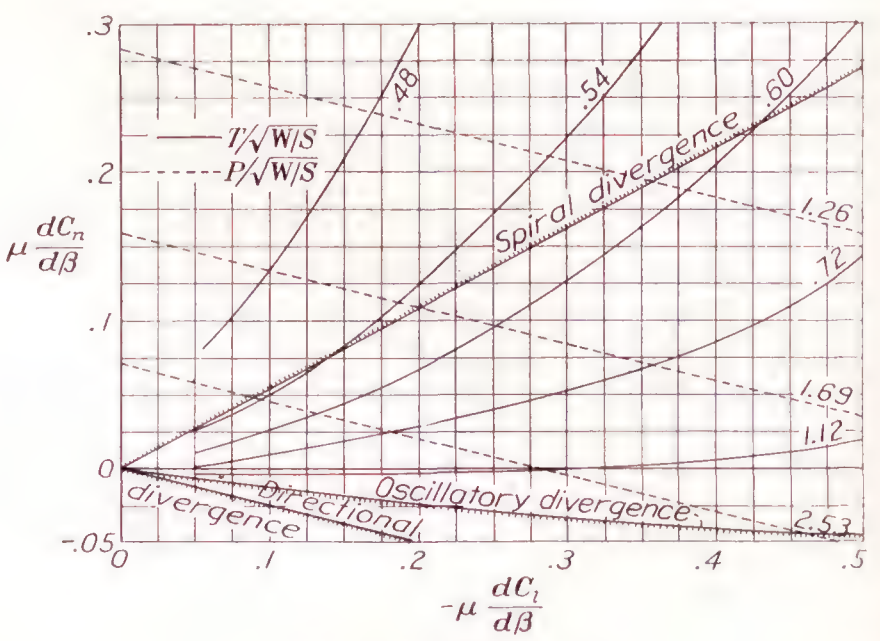

$C_L=0.8$ $dC_n/d\frac{rb}{2V}=-0.108$

FIGURE 13.

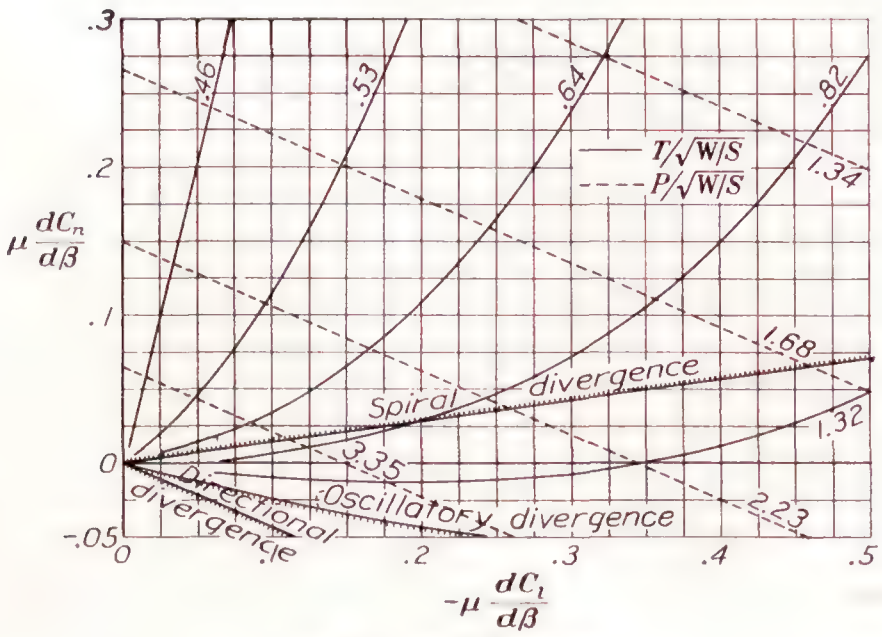

$C_L=1.4$ $dC_n/d\frac{rb}{2V}=-0.050$

FIGURE 14.

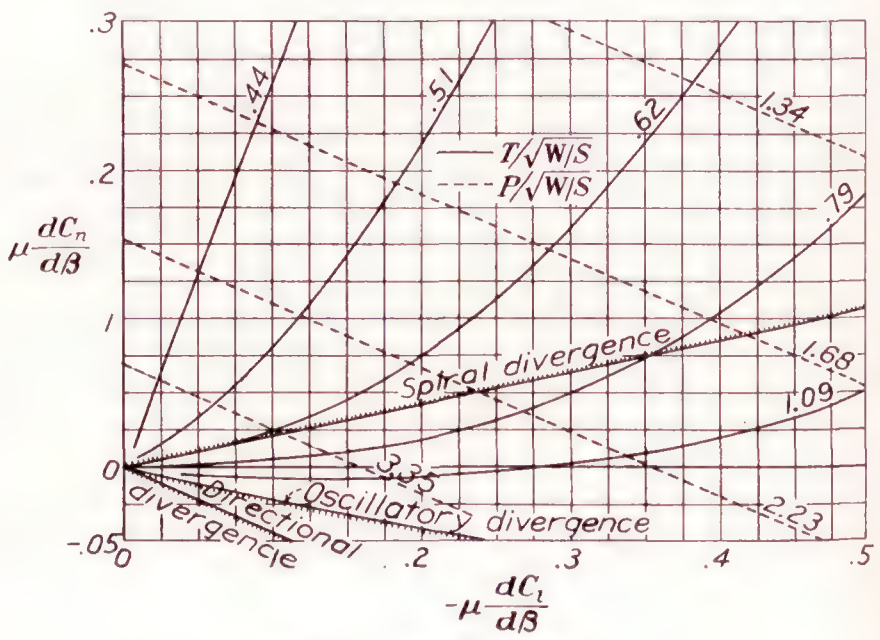

$C_L=1.4$ $dC_n/d\frac{rb}{2V}=-0.075$

FIGURE 15.

FIGURES 10 to 15.—Lateral-stability charts.

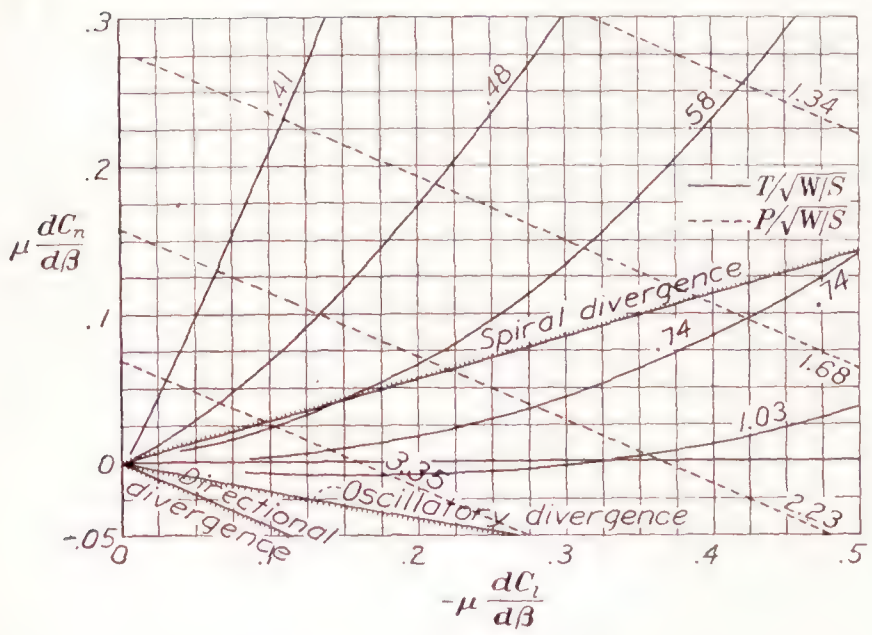

$C_L = 1.4 \quad dC_n/d\frac{rb}{2V} = -0.100$

FIGURE 16.

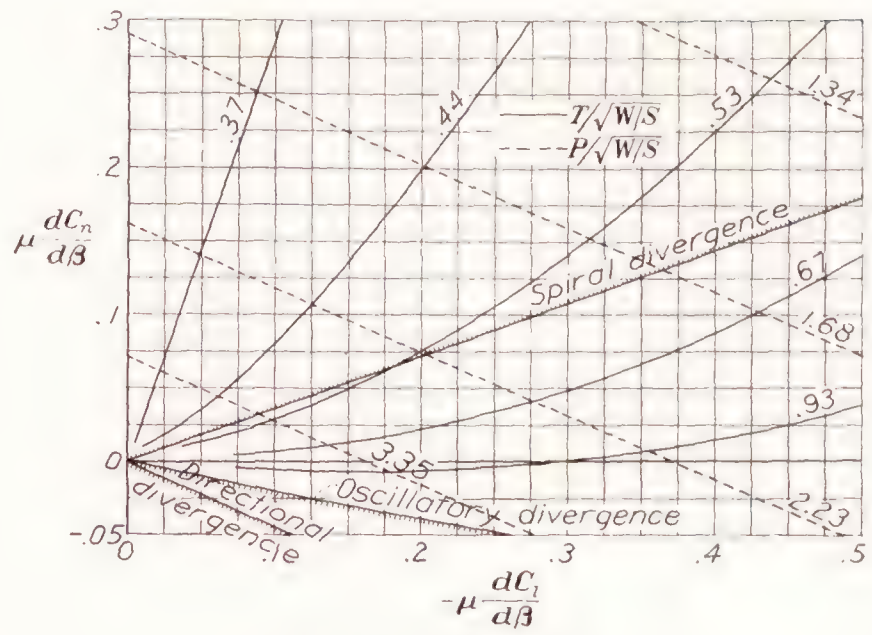

$C_L = 1.4 \quad dC_n/d\frac{rb}{2V} = -0.125$

FIGURE 17.

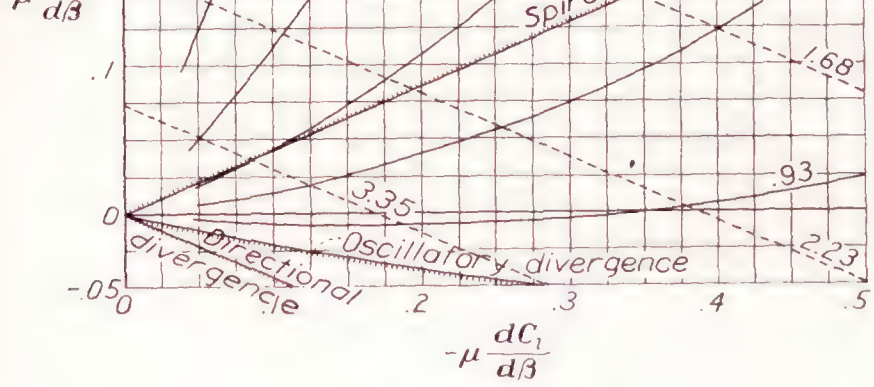

$C_L = 1.4 \quad dC_n/d\frac{rb}{2V} = -0.150$

FIGURE 18.

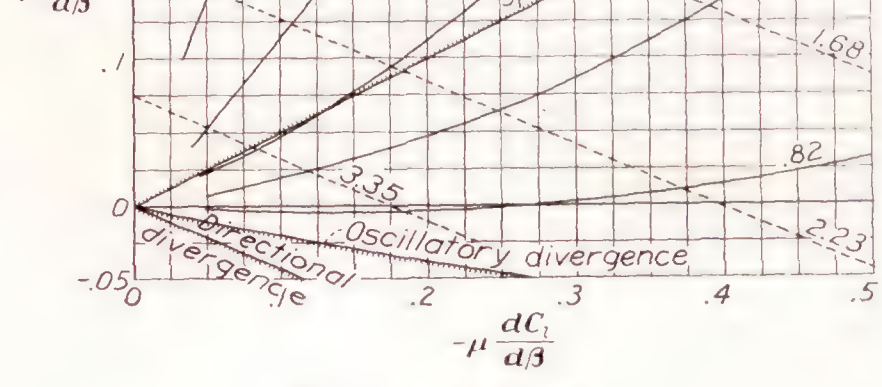

$C_L = 1.4 \quad dC_n/d\frac{rb}{2V} = -0.175$

FIGURE 19.

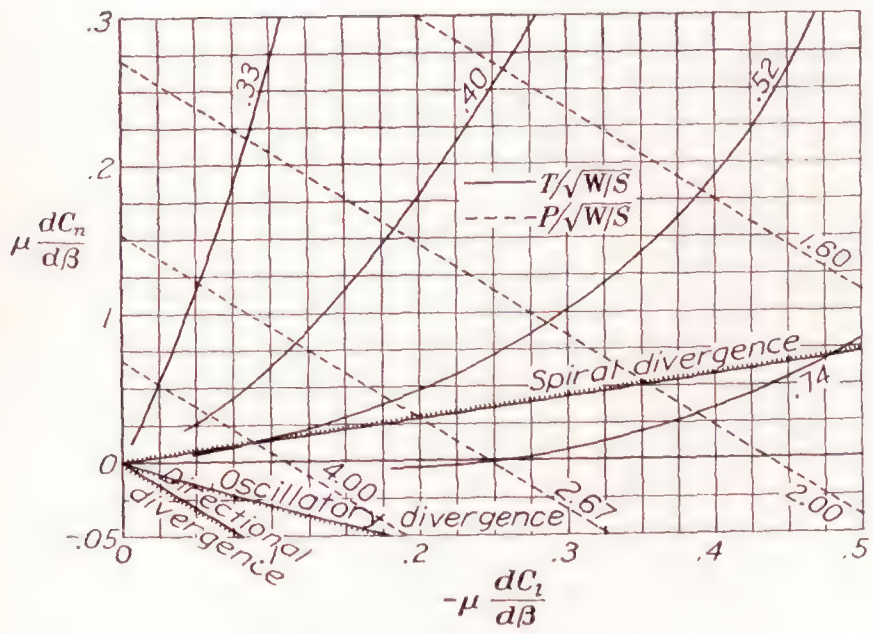

$C_L = 2.0 \quad dC_n/d\frac{rb}{2V} = -0.072$

FIGURE 20.

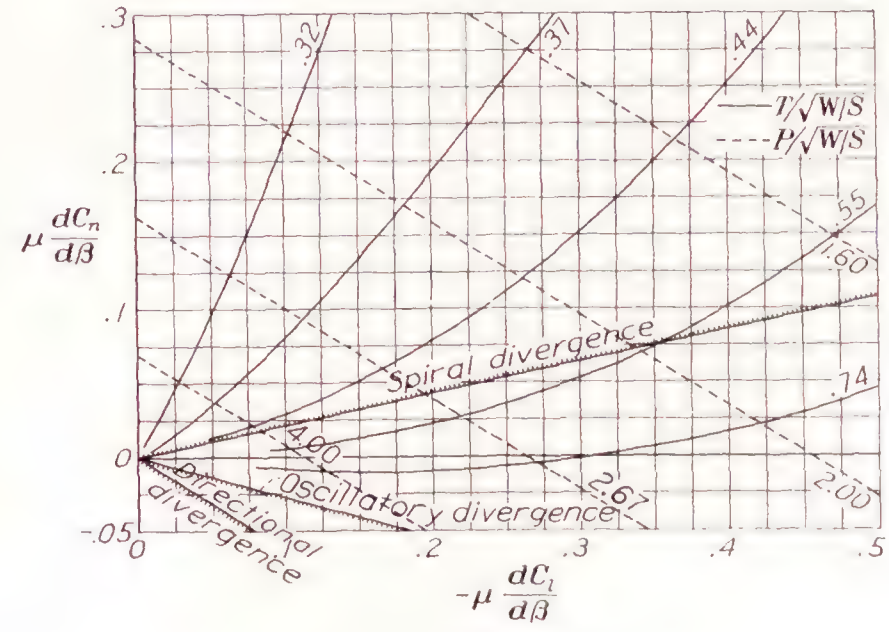

$C_L = 2.0 \quad dC_n/d\frac{rb}{2V} = -0.108$

FIGURE 21.

FIGURES 16 to 21.—Lateral-stability charts.

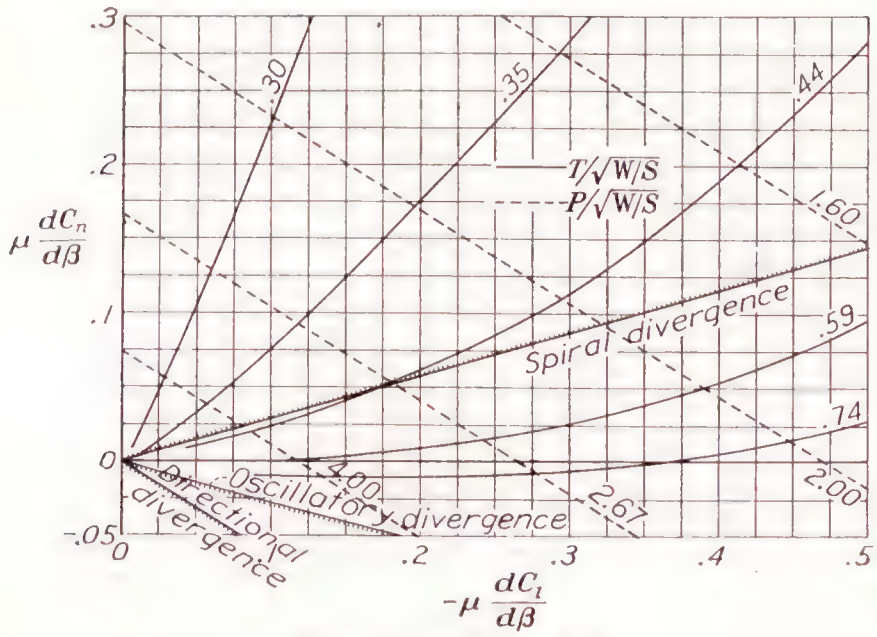

$C_L=2.0$ $dC_n/d\frac{rb}{2V}=-0.144$

FIGURE 22.

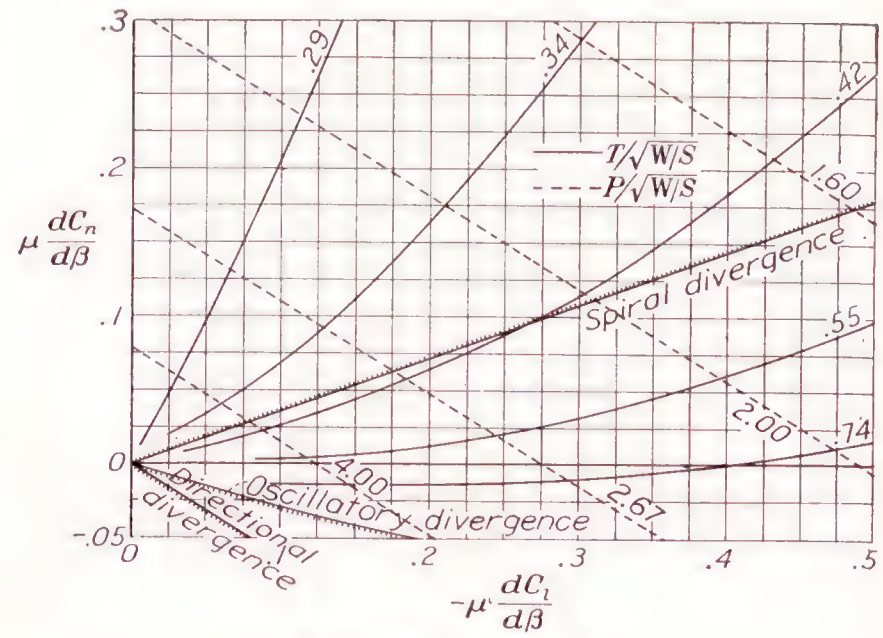

$C_L=2.0$ $dC_n/d\frac{rb}{2V}=-0.180$

FIGURE 23.

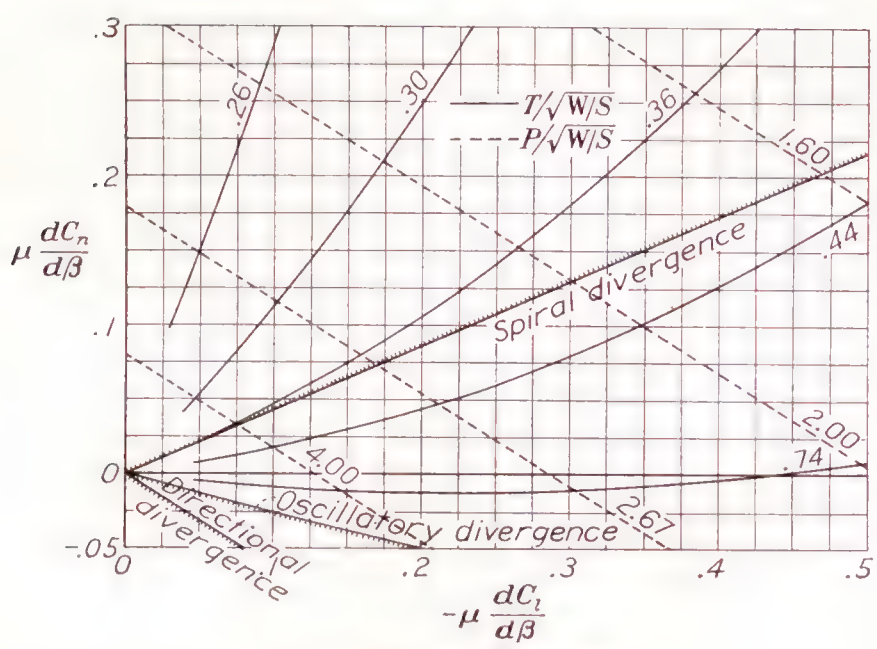

$C_L=2.0$ $dC_n/d\frac{rb}{2V}=-0.216$

FIGURE 24.

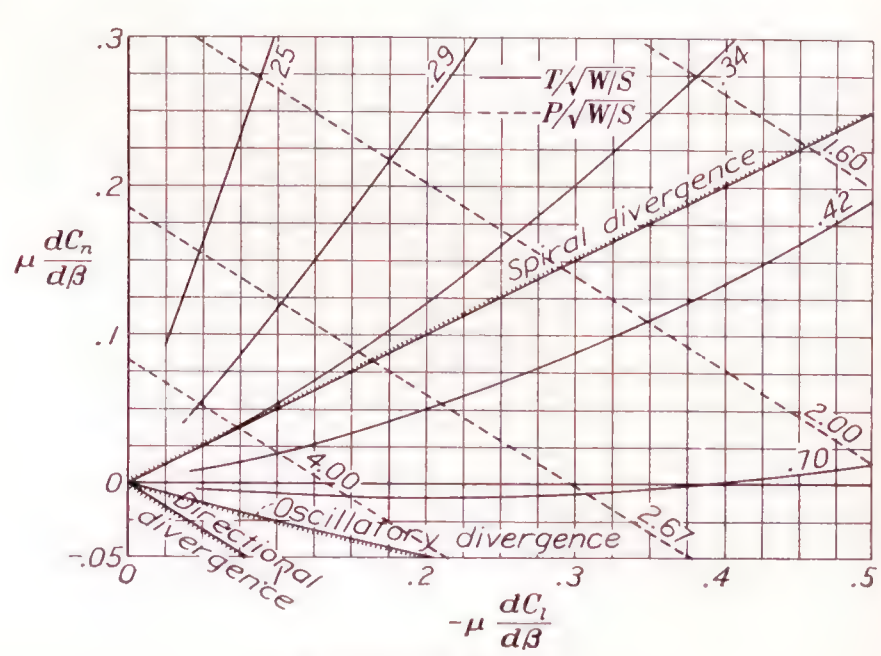

$C_L=2.0$ $dC_n/d\frac{rb}{2V}=-0.252$

FIGURE 25.

FIGURES 22 to 25.—Lateral-stability charts.

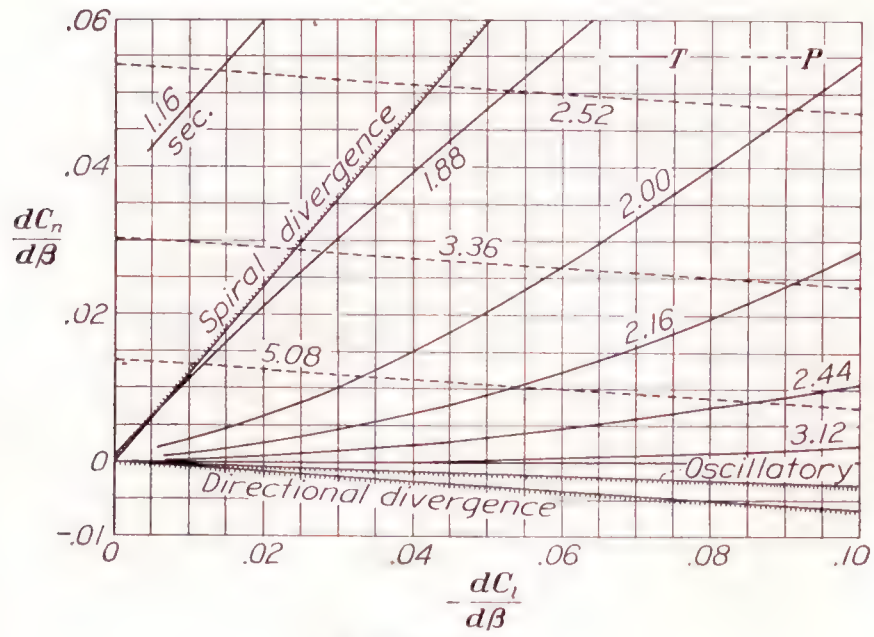

$W/S=16$ lb./sq. ft.
$b=42$ ft. $C_L=0.2$

$dC_n/d\frac{rb}{2V}=-0.060$

FIGURE 26.—Special case of lateral-stability chart

From these data, values of $-\mu dC_l/d\beta$ and $\mu dC_n/d\beta$ can be readily determined since $\mu=\frac{13.1(W/S)}{b}$ (standard conditions).

In general, the value of C_L to represent a particular range of flight conditions can be chosen as 0.2, 0.8, 1.4, or 2.0. It will be necessary in most cases, however, to interpolate between two charts for the value of $dC_n/d\frac{rb}{2V}$. Any point given by $-\mu dC_l/d\beta$, $\mu dC_n/d\beta$ represents a value of $P/\sqrt{W/S}$ and a value of $T/\sqrt{W/S}$. The period and the time to damp to one-half amplitude are readily obtained by multiplying these values by $\sqrt{W/S}$. The location of the point $-\mu dC_l/d\beta$, $\mu dC_n/d\beta$ also indicates whether there will be a tendency to diverge.

The charts are computed for standard conditions. They can be easily applied to a study of stability at altitude by substituting the value $(0.00238/\rho)$ W/S for W/S wherever W/S occurs in the computations.

Correction to a different value of $dC_Y/d\beta$ may be readily made as follows: Compute ζ' for $dC_Y/d\beta=-0.28$, i.e., $y_v=-0.14$, from the relation $\zeta'=\frac{-0.313\sqrt{(W/S)C_L}}{T}$.

Add to this value of ζ' the quantity $\frac{1}{4}(0.28+dC_Y/d\beta)$ to obtain the corrected value of ζ'. Calculate the corrected value of $T/\sqrt{W/S}$ using the corrected value of ζ'.

In cases where a large number of estimates are to be made for a given pair of values of W/S and b, it will sometimes be convenient to convert the charts to read directly in terms of $-dC_l/d\beta$, $dC_n/d\beta$, P, and T. This conversion can readily be accomplished without redrawing the chart by changing the constants. Figure 26 represents figure 6 converted to read directly in the desired quantities for an airplane having $W/S=16$ pounds per square foot and $b=42$ feet.

Example of use of charts.—It is assumed that the lateral-stability characteristics throughout the normal-flight range are desired for a 5,000-pound airplane having a wing loading of 16 pounds per square foot and a span of 42 feet. Values of $dC_n/d\psi$ and $dC_l/d\psi$ are available from wind-tunnel tests. Values of $dC_n/d\frac{rb}{2V}$ must be estimated. The airplane is a modern type with a fairly high top speed and is equipped with split flaps. Flaps were considered to be down at $C_L=2.0$ but up at $C_L=0.2$, 0.8, and 1.4.

The stability characteristics will be estimated for each of the C_L values of 0.2, 0.8, 1.4, and 2.0. Values of $-\mu dC_l/d\beta$ and $\mu dC_n/d\beta$ are determined at each value of C_L from the relationships

$$-\mu dC_l/d\beta=\frac{13.1\times16}{42}\times57.3\times(dC_l/d\psi)$$

and

$$\mu dC_n/d\beta=\frac{13.1\times16}{42}\times57.3\times(-dC_n/d\psi)$$

Values of $dC_n/d\frac{rb}{2V}$ are determined from the relationship

$$dC_n/d\frac{rb}{2V}=-\frac{C_{Dw}}{3}-2\frac{l^2}{b^2}\frac{S_t}{S}\frac{dC_{Lt}}{d\beta}$$

where C_{Dw} is taken from wind-tunnel tests of a similar wing, l/b and S_t/S are dimensional characteristics of the airplane, and $dC_{L_t}/d\beta$ is estimated using the relationship

$$\frac{dC_{L_t}}{d\beta}=\frac{5.5}{1+\frac{2}{b_t^2/S_t}}$$

where b_t is the height of the vertical tail surface. The values of C_{Dw}, $dC_n/d\frac{rb}{2V}$, $-\mu dC_l/d\beta$, and $\mu dC_n/d\beta$ are as follows:

C_L	C_{Dw}	$dC_n/d\frac{rb}{2V}$	$\mu dC_l/d\beta$	$\mu dC_n/d\beta$
0.2	0.008	−0.051	0.20	0.180
.8	.025	−.057	.25	.180
1.4	.070	−.072	.45	.165
2.0	.400	−.182	.55	.130

From the various charts, values of T and P are determined, interpolations and extrapolations being made where necessary. The values of the stability characteristics at each value of C_L follow.

C_L	T (sec.)	P (sec.)	Divergence
0.2	2.1	3.0	None.
.8	3.1	5.5	Spiral.
1.4	3.1	5.8	Do.
2.0	[1] 2.2	6.4	None.

[1] Correction for the increase in $dC_Y/d\beta$ due to the high drag gives the corrected value of T as 1.3 seconds.

EFFECT OF THE GOVERNING FACTORS ON THE STABILITY CHARACTERISTICS

AERODYNAMIC FACTORS

Lateral force due to sideslip.—The lateral force due to sideslip is small, in general, but beneficial in its effect upon stability characteristics. As appears in equation (18), $dC_Y/d\beta$ adds directly to the damping coefficient, $\Delta\zeta'=\frac{1}{4}\Delta dC_Y/d\beta$. For the value of $dC_Y/d\beta=-0.28$, $\Delta\zeta'=-0.07$, which is sufficient to damp the lateral oscillation to one-half amplitude in 8 seconds for an airplane with a wing loading of 16 flying at 176 miles per hour. The effects of $dC_Y/d\beta$ on the period and on the tendency to diverge are negligible.

Rolling moment due to sideslip.—The rate of change of rolling-moment coefficient with sideslip plays a great part in determining the stability characteristics, as is apparent from a glance at the charts of figures 4 to 25. It is necessary for stability that $dC_l/d\beta$ be negative; the term $-dC_l/d\beta$ will be used, as in the charts, for simplicity in discussion.

Increasing $-dC_l/d\beta$ increases the range of values of $dC_n/d\beta$ within which there is no divergence, there being less likelihood of either spiral divergence or directional divergence as $-dC_l/d\beta$ is increased. Increasing $-dC_l/d\beta$ increases the time for an oscillation to damp and shortens the period. These effects are sufficiently small to be of no practical importance at high speeds but are appreciable at low speeds.

Yawing moment due to sideslip.—From the considerations of tendency toward divergence the value of $dC_n/d\beta$ should be small and positive. Too large a positive value of $dC_n/d\beta$ results in spiral divergence. Too large a negative value will lead to undamped lateral oscillations as indicated by the curve of $T/\sqrt{(W/S)}=\infty$ (oscillatory divergence) or to directional divergence. The range of permissible values of $dC_n/d\beta$ is quite narrow for small values of $-dC_l/d\beta$ and $-dC_n/d\frac{rb}{2V}$.

Increasing $dC_n/d\beta$ increases the damping and shortens the period of the lateral oscillations. The effect upon the period is very pronounced, particularly at small values of the lift coefficient corresponding to cruising and high speeds, as is especially apparent in equation (23) where

$$P=\sqrt{\frac{0.14b}{(-dC_l/d\beta)+\frac{3.2}{C_L}dC_n/d\beta}}$$

It appears that for $C_L=0.2$ the effect of $dC_n/d\beta$ upon the period has 16 times the effect of $-dC_l/d\beta$. The effect upon T is less pronounced. It is of interest to note that the theory indicates stability with $dC_n/d\beta$ zero or slightly negative if $dC_Y/d\beta$ and $dC_n/d\frac{rb}{2V}$ are moderate or large.

Rolling moment due to rolling.—Differences in the value of $dC_l/d\frac{pb}{2V}$ of the order of those likely to exist between conventional airplanes in the normal-flight range have but slight effect upon the tendency toward divergence or the oscillatory characteristics. This fact tends to justify the use of an average value for this factor in equations (20) and (23) and in the charts. The small effects occurring are such that increasing $dC_l/d\frac{pb}{2V}$ decreases the time required to damp, in general, and increases the period.

Near the stall $dC_l/d\frac{pb}{2V}$ changes sign and tends to result in violent instability. This report does not deal with stability near the stall, which is amply discussed in references 14, 15, and 16.

Yawing moment due to rolling.—As is the case for $dC_l/d\frac{pb}{2V}$, differences in $dC_n/d\frac{pb}{2V}$ likely to exist in practice have comparatively slight effect upon the stability characteristics below the stall. Increasing $dC_n/d\frac{pb}{2V}$ may either increase or decrease T, depending upon the magnitudes of other quantities, and increases P slightly. Here again the selection of an average value for this factor seems justified. Near the stall $dC_n/d\frac{pb}{2V}$ changes sign and becomes an important factor in producing instability.

Rolling moment due to yawing.—The rolling moment due to yawing is chiefly of importance in connection with the likelihood of spiral divergence. Increasing $dC_l/d\frac{rb}{2V}$ decreases the range of values of $dC_n/d\beta$ for which spiral convergence exists for a given set of values of $-dC_l/d\beta$ and $dC_n/d\frac{rb}{2V}$. Increasing $dC_l/d\frac{rb}{2V}$ generally decreases T but has no noticeable effect upon P or the likelihood of directional divergence.

Yawing moment due to yawing.—Increasing $dC_n/d\frac{rb}{2V}$ increases the permissible range of values of $dC_n/d\beta$ for spiral convergence and decreases the time required for the oscillation to damp to one-half amplitude. It is apparent from equations (20) and (13) and from the charts that an accurate knowledge of $dC_n/d\frac{rb}{2V}$ is essential to accurate calculations of T and of the limiting values of $dC_n/d\beta$ within which spiral convergence exists. On the other hand, $dC_n/d\frac{rb}{2V}$ has only a very slight effect upon the directional convergence or upon the period of the oscillations.

MASS FACTORS

Relative density of airplane to air.—The relative density μ has no effect upon the likelihood of either spiral or directional convergence. Its effect upon the period and damping of the lateral oscillation can best be understood by considering the separate effects of the factors which determine μ, namely W/S, b, and ρ. Since a decrease in ρ has precisely the same effect as an increase in W/S, the effects of altitude are the same as the effects of increasing the wing loading and will therefore not be discussed separately.

The effect of wing loading upon the time required to damp the oscillation to one-half amplitude can best be deduced from equations (16) and (20). From equation (20) it appears that if, for the case at hand $1.2\frac{dC_n}{d\beta}\left(-\frac{dC_n}{d\frac{rb}{2V}}\right)$ is greater than 0.3 $(-dC_l/d\beta)$, then increasing W/S (since μ is proportional to W/S) will make ζ' greater in the negative sense. This will be the case only for very small values of $-dC_l/d\beta$. In general, therefore, increasing W/S will increase T both by decreasing ζ' and by increasing the numerator in the relationship

$$T=\frac{-0.313\sqrt{(W/S)C_L}}{\zeta'}$$

On the other hand, wing loading has no appreciable effect upon the period, at a given C_L, as is apparent from equation (23).

From the charts it appears that, since increasing b decreases $\mu dC_n/d\beta$ and $-\mu dC_l/d\beta$, increasing the span will decrease the time required to damp the oscillations over most of the range of values of the parameters. As pointed out in the preceding paragraph, the effect depends upon the relative magnitudes of $dC_n/d\beta$, $dC_n/d\frac{rb}{2V}$, and $-dC_l/d\beta$. Only in the case of very small values of $-dC_l/d\beta$, will increasing the span increase T. For practical purposes the period of the lateral oscillation is proportional to the square root of the span, as is shown by equation (23).

Ratio of wing span to radius of gyration about X axis.—In the discussion of the effects of changing b it was assumed that the ratios b/k_X and b/k_Z were kept constant. The effects of changing these ratios can be most readily explained on the basis of keeping b constant.

The value of k_X has no effect upon either spiral or directional convergence. Although not readily apparent in equations (18) and (22), increasing k_X results in small increases in T and P. There is, however, no justification for extensive labor to determine k_X accurately in the absence of accurate data on all the aerodynamic factors.

Ratio of wing span to radius of gyration about Z axis.—The effects of increasing k_Z are similar to the effects of increasing k_X. It has a slight but unimportant effect upon directional convergence. Its effect upon the period is greater than the effect of increasing k_X, but not great enough to be of practical importance in most cases.

GENERAL COMMENTS

The present state of knowledge does not justify positive assertions as to the desirability of any given set of stability characteristics. Very little has been done to determine quantitatively the stability characteristics that result in the most satisfactory riding and handling characteristics. Such research (reference 17) has given more or less negative results, at least with respect to the period and the damping of oscillations. It is definitely known, however, that very great instability, such as that at the stall, and very great stability are both undesirable. There is strong reason to believe that any tendency to diverge is undesirable but that, if such a tendency is of small magnitude, it will not seriously inconvenience the pilot.

When the foregoing facts are taken into consideration, it seems desirable that for airplanes designed for most purposes, excepting machines intended as pursuits, fighters, or for acrobatics, there should be no tendency to diverge, oscillations should be moderately to heavily damped, and the period of the oscillations should be as long as practicable. It is believed that such characteristics will require a minimum of effort from the pilot and will result in a maximum of passenger comfort.

Reference to the charts of figures 4 to 25 reveals that these characteristics can be attained only by making $dC_n/d\beta$ small while keeping $dC_n/d\frac{rb}{2V}$ and $dC_Y/d\beta$ large. Some additional advantage is gained by keeping $-dC_l/d\beta$ small, particularly at high angles of attack. Probably the best value of $-dC_l/d\beta$ is from small to moderate, the moderate values giving more pronounced spiral and directional convergence. The best method of keeping $dC_n/d\beta$ small while retaining large values of $dC_n/d\frac{rb}{2V}$ and $dC_Y/d\beta$ appears to be the use of a fuselage giving an unstable yawing moment of rather large magnitude. The unstabilizing effect of the fuselage depends on its length, breadth, the distance of the center of gravity from the nose, and on the shape. The shape of the fuselage, and possibly interference effects, play an important part, which can be determined accurately only by wind-tunnel tests. A large value of l tends to make $dC_n/d\frac{rb}{2V}$ large and a large, deep fuselage tends to give a large value of $dC_Y/d\beta$. The dihedral of the wings can be adjusted to bring $dC_l/d\beta$ to the desired value but here again, with present knowledge, it is necessary to make wind-tunnel tests.

Although control is outside the intended scope of this paper, it should be pointed out that appearance of instability may, under certain circumstances, be brought about by the influence of the controls. The two most common instances are that of directional divergence arising out of an attempt to hold the wings level with conventional ailerons, the rudder being held neutral; and that of increasing or poorly damped oscillations arising out of operation of the rudder in improper phase relationship to the change in attitude of the airplane. The directional divergence is caused by the adverse yaw of the ailerons and can be avoided by reducing the adverse yaw, by increasing $dC_n/d\beta$, or by holding the ailerons neutral and allowing the airplane to roll. The increasing oscillations are most likely to occur when the natural period of the airplane is short and when the rudder is operated in such a manner as to prevent yawing. They can be avoided by holding the rudder neutral or by operating it in such a manner as to produce sideslip opposing the roll, i. e., by trying to hold the wings level rather than by trying to prevent yawing.

38548—38——21

SUGGESTIONS FOR FUTURE STUDY

A systematic correlation of stability characteristics with riding and handling qualities is needed. It is possible that these qualities are more directly related to certain of the governing factors than to the tendency to diverge or to the characteristics of the oscillations; investigations should be conducted with this possibility in mind.

There is need for adequate comparison between computed values and measured values of stability characteristics as a check upon the accuracy and validity of the mathematical treatment.

At present some of the aerodynamic governing factors cannot be estimated with assurance. A great deal of systematic study will be necessary to provide sufficient data for the formulation of satisfactory empirical constants to be used in estimating these factors.

In this report no consideration has been given to the effect of power on the lateral stability. This problem should be the subject of a study sufficiently thorough to reveal the effects of power on the stability derivatives and upon the mathematical treatment necessary to estimate the stability characteristics.

More satisfactory means of measuring the separate aerodynamic factors and also the final stability characteristics of models are necessary for rapid progress.

LANGLEY MEMORIAL AERONAUTICAL LABORATORY,
NATIONAL ADVISORY COMMITTEE FOR AERONAUTICS,
LANGLEY FIELD, VA., *November 17, 1936.*

APPENDIX I

DERIVATION OF FORMULAS

The theory of small oscillations.—The theory of small oscillations was first applied by Bryan to the dynamics of mechanical flight (reference 10). On the assumption that the direction and magnitude of changes in the aerodynamic characteristics due to changes in motion from the steady-flight condition are known, equations of motion in unsteady flight are written for the case of small deviations from the steady condition, one equation for each of the degrees of freedom of the motion. Simultaneous solution of the equations gives values that describe the motion of the airplane after a disturbance.

Assumptions in the application of the theory.—In the application of the theory of small oscillations to quantitative estimations of stability characteristics, a number of assumptions are necessary in order that the mathematics may not be too involved and the computations too extensive for practical applications. The primary assumptions are as follows:

(*a*) The combined aerodynamic effect of two or more components of motion is assumed equal to the algebraic sum of the separate effects of the individual components.

(*b*) The changes in aerodynamic forces and moments due to a deviation are assumed proportional to the deviation, i. e., the slopes $dC_l/d\beta$, $dC_l/d\frac{pb}{2V}$, etc., are assumed to be constants.

(*c*) The lateral motion involving p, q, and r is assumed to be independent of the longitudinal motion, i. e., the machine is assumed to be symmetrical.

(*d*) Secondary effects such as those involving the products of two or more small quantities are neglected.

(*e*) The values of the aerodynamic factors are assumed to be unaffected by the linear and angular accelerations.

Equations of lateral motion.—The equations of lateral motion will be written for the axes shown in figure 1 using the symbols and notation given in appendix III and on the report covers. The X axis is taken in the direction of the relative wind during the steady-flight condition. The axes are assumed fixed in the airplane. During steady flight,

$$\left.\begin{aligned} Y=L=N=0 \\ v=p=r=0 \\ u=V \end{aligned}\right\}$$

After a disturbance,

$$\left.\begin{aligned} r\frac{dY}{dv}+p\frac{dY}{dp}+r\frac{dY}{dr}+W\sin\phi\cos\gamma \\ +W\sin\psi\sin\gamma=m\frac{dv}{dt}+mru \\ r\frac{dL}{dv}+p\frac{dL}{dp}+r\frac{dL}{dr}=mk_x^2\frac{dp}{dt} \\ v\frac{dN}{dv}+p\frac{dN}{dp}+r\frac{dN}{dr}=mk_z^2\frac{dr}{dt} \end{aligned}\right\} \quad (24)$$

$$\left.\begin{aligned} p=d\phi/dt \\ r=d\psi/dt \end{aligned}\right\} \quad (25)$$

It is assumed in these equations that the principal axes of inertia are coincident with the reference axes, which is not true in the general case. A number of supplementary calculations made as part of the study leading up to this report have indicated, however, that to neglect the angularity of the principal axes to the reference axes will not introduce serious error in the normal-flight range and will give slightly conservative results. Consequently, the terms including the product of inertia were omitted to make the equations as simple as possible.

Since dY/dp and dY/dr are small, they are generally neglected. For the small deviations considered, u may be taken equal to the steady-flight velocity V and the sines of the angles of roll and yaw may be replaced by the angles themselves. Since in power-off flight the lift is equal to $W\cos\gamma$ and the lift times the tangent of the angle of glide is equal to $W\sin\gamma$, the first of the foregoing equations will be rewritten,

$$r\frac{dY}{dv}+\phi\times(\text{lift})+\psi\times(\text{lift})\times\tan\gamma=m\frac{dv}{dt}+mrV$$

The equations of equilibrium finally become,

$$\left.\begin{aligned} r\frac{dY}{dv}-m\frac{dv}{dt}+\phi(\text{lift})+\psi(\text{lift})\tan\gamma-\frac{d\psi}{dt}mV=0 \\ v\frac{dL}{dv}+\frac{d\phi}{dt}\frac{dL}{dp}-\frac{d^2\phi}{dt^2}mk_x^2+\frac{d\psi}{dt}\frac{dL}{dr}=0 \\ v\frac{dN}{dv}+\frac{d\phi}{dt}\frac{dN}{dp}+\frac{d\psi}{dt}\frac{dN}{dr}-\frac{d^2\psi}{dt^2}mk_z^2=0 \end{aligned}\right\} \quad (26)$$

Replacing

$$\frac{dY}{dv}\text{ by }\frac{1}{2}\rho V^2S\frac{dC_Y}{dv}$$

$$(\text{Lift})\text{ by }\frac{1}{2}\rho V^2S\,C_L$$

$\frac{dL}{dv}$ by $\frac{1}{2}\rho V^2 S\, b \frac{dC_l}{dv}$, etc.

$\frac{dN}{dv}$ by $\frac{1}{2}\rho V^2 S\, b \frac{dC_n}{dv}$, etc.

$\frac{m}{\rho S b}$ by μ

$\frac{m}{\rho S V}$ by τ

$\frac{dC_Y}{dv}$ by $\frac{1}{V}\frac{dC_Y}{d\beta}$

Writing in determinant form and simplifying gives,

$$\begin{vmatrix} v\ y_v-\tau\frac{dv}{dt} & \frac{C_L}{2}\phi & \frac{C_L}{2}(\tan\gamma)\ \psi-\tau\frac{d\psi}{dt} \\ v\ \mu l_v & l_p\tau\frac{d\phi}{dt}-\tau^2\frac{d^2\phi}{dt^2} & l_r\tau\frac{d\psi}{dt} \\ v\ \mu n_v & n_p\tau\frac{d\phi}{dt} & n_r\tau\frac{d\psi}{dt}-\tau^2\frac{d^2\psi}{dt^2} \end{vmatrix}=0 \qquad (27)$$

where $y_v=\frac{1}{2}\frac{dC_Y}{d\beta}$

$l_v=\frac{1}{2}\left(\frac{b}{k_X}\right)^2\frac{dC_l}{d\beta}$

$n_v=\frac{1}{2}\left(\frac{b}{k_Z}\right)^2\frac{dC_n}{d\beta}$

$l_p=\frac{1}{4}\left(\frac{b}{k_X}\right)^2\frac{dC_l}{d\frac{pb}{2V}}$

$n_p=\frac{1}{4}\left(\frac{b}{k_Z}\right)^2\frac{dC_n}{d\frac{pb}{2V}}$

$l_r=\frac{1}{4}\left(\frac{b}{k_X}\right)^2\frac{dC_l}{d\frac{rb}{2V}}$

$n_r=\frac{1}{4}\left(\frac{b}{k_Z}\right)^2\frac{dC_n}{d\frac{rb}{2V}}$

Substituting $v_0\, e^{\lambda t}$ for v, $\phi_0\, e^{\lambda t}$ for ϕ, etc., and simplifying give

$$\begin{vmatrix} y_v-\tau\lambda & \frac{C_L}{2} & \frac{C_L}{2}\tan\gamma-\tau\lambda \\ \mu l_v & l_p\tau\lambda-\tau^2\lambda^2 & l_r\tau\lambda \\ \mu n_v & n_p\tau\lambda & n_r\tau\lambda-\tau^2\lambda^2 \end{vmatrix}=0 \qquad (28)$$

which can be expressed as

$$A(\lambda')^5+B(\lambda')^4+C(\lambda')^3+D(\lambda')^2+E(\lambda')=0 \qquad (29)$$

where,

$\lambda'=\tau\lambda$

$A=1$

$B=-y_v-n_r-l_p$

$C=l_p n_r-l_r n_p+y_v(l_p+n_r)+\mu n_v$

$D=y_v(l_r n_p-l_p n_r)+\mu l_v\left(n_p-\frac{C_L}{2}\right)-\mu n_v\left(\frac{C_L}{2}\tan\gamma+l_p\right)$

$E=\mu\frac{C_L}{2}(l_v n_r-l_r n_v)+\mu\frac{C_L}{2}\tan\gamma(l_p n_v-l_v n_p)$

The solution $\lambda'=0$ is readily apparent in equation (29) and results from the fact that the airplane has no inherent tendency to return to any fixed compass course, being, as the solution shows, neutrally stable in that respect. This solution, $\lambda'=0$, is generally neglected and the lateral-stability characteristics are considered as those given by the biquadratic

$$A(\lambda')^4+B(\lambda')^3+C(\lambda')^2+D(\lambda')+E=0 \qquad (30)$$

The deviation of each one of the components of the lateral motion varies with time according to the relation,

$$v,\ p,\ \text{or}\ r=C_1e^{\lambda_1 t}+C_2e^{\lambda_2 t}+C_3e^{\lambda_3 t}+C_4e^{\lambda_4 t}$$

where λ_1, λ_2, λ_3, and λ_4 are the four roots of the biquadratic. In lateral motion the constants B, C, D, and E are generally such that there are one pair of real roots and one pair of conjugate complex roots indicating motion of the type,

$$v,\ p,\ \text{or}\ r=C_5e^{\zeta t}(\cos\psi t-C_6)+C_3e^{\lambda_3 t}+C_4e^{\lambda_4 t}$$

where ζ and ψ are the real and imaginary parts, respectively, of the conjugate roots. This motion represents an oscillation superimposed upon two rates of convergence (or divergence). It is evident that for stability ζ, λ_3, and λ_4 must be real and negative so that the values of v, p, and r will reduce to zero. In order that the real parts of the roots shall all be negative it is necessary and sufficient that B, C, D, E, and $(BCD-D^2-B^2E)$ each be positive. In order to determine the rates of convergence and the damping and period of the oscillation, it is necessary to solve the biquadratic. A convenient semigraphical method of solving stability biquadratics was pointed out in reference 1 and is described in detail in appendix II.

APPENDIX II

SOLUTION OF STABILITY BIQUADRATIC

Semigraphical method of solving biquadratics.—The biquadratic

$$\lambda^4+B\lambda^3+C\lambda^2+D\lambda+E=0$$

can be expressed as

$$(\lambda^2+a_1\lambda+b_1)(\lambda^2+a_2\lambda+b_2)=0 \tag{31}$$

from which

$$\left.\begin{aligned}\lambda&=-\frac{a_1}{2}\pm\sqrt{\left(\frac{a_1}{2}\right)^2-b_1}\\ \lambda&=-\frac{a_2}{2}\pm\sqrt{\left(\frac{a_2}{2}\right)^2-b_2}\end{aligned}\right\} \tag{32}$$

are roots of the general equation. It appears that

$$\left.\begin{aligned}B&=a_1+a_2\\ C&=a_1a_2+b_1+b_2\\ D&=a_1b_2+a_2b_1\\ E&=b_1b_2\end{aligned}\right\} \tag{33}$$

Eliminating values of a_2 and b_2,

$$a_1=\frac{B}{2}\pm\sqrt{\left(\frac{B}{2}\right)^2-C+b_1+\frac{E}{b_1}} \tag{34}$$

and

$$a_1=\frac{b_1^2B-b_1D}{b_1^2-E} \tag{35}$$

Note that, if the minus sign in equation (34) is chosen for a_1, the plus sign will correspond to a_2.

Values of a_1 and b_1 that will satisfy these equations separately are plotted on charts having values of a as abscissas and values of b as ordinates. The intersection of the resulting curves represents values of a_1 and b_1 that satisfy both equations. There are two intersections in the general case, one corresponding to a_1 and b_1, the other to a_2 and b_2. Ordinarily it is more convenient to find one of the intersections by plotting and to solve for the remaining values by the use of equations (33).

Figure 27 gives a solution of a typical stability biquadratic and illustrates the use of this semigraphical method. For most cases time can be saved in locating the intersection by letting a_1 equal zero in equation (35), thus determining the intersection of the plot of equation (35) with the b axis. The resulting value of b_1 when substituted in equation (34) will give an approximate value for a_1. The final values can then be determined as accurately as desired by locating the point of intersection of the curves. This method has been applied to several hundred solutions of stability biquadratics in the course of the study leading up to this report and has been found to be very satisfactory, particularly so if systematic changes in factors are being studied.

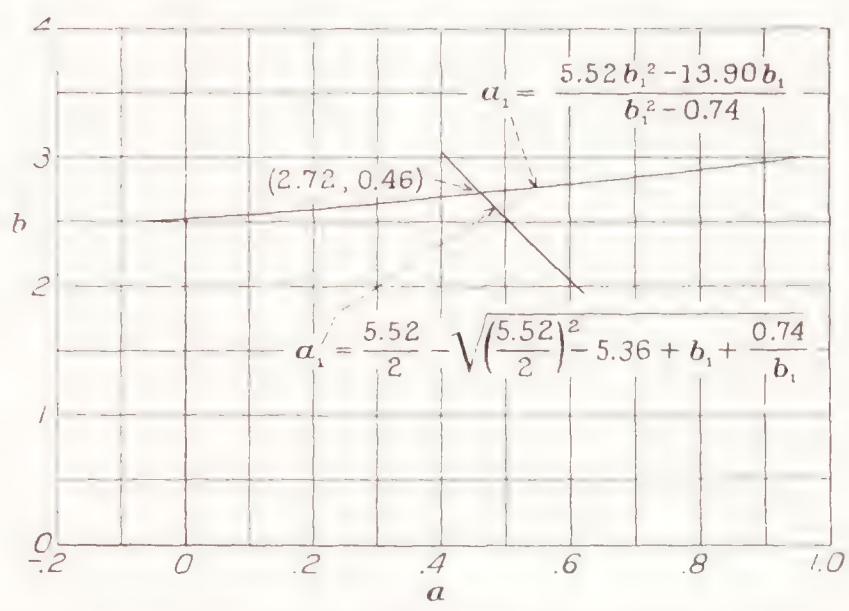

FIGURE 27.—A semigraphical method of solving stability biquadratics. Solution of biquadratic:

$$\lambda^4+5.52\lambda^3+5.36\lambda^2+13.90\lambda+0.74=(\lambda^2+a_1\lambda+b_1)(\lambda^2+a_2\lambda+b_2)=0$$

From intersection of curves

$$a_1=0.46;\ b_1=2.72$$

From equations (33)

$$a_2=5.52-0.46=5.06;\ b_2=0.74/2.72=0.027$$

From $\lambda^2+0.46\lambda+2.72=0$, $\lambda=-0.23\pm i\ 1.6$
From $\lambda^2+5.06\lambda+0.027=0$, $\lambda=-5.05$
$\lambda=-0.01$

Approximate formulas for the damping and the period of the oscillation.—As was stated in the preceding paragraph, an approximate value of b_1 can be found by substituting $a_1=0$ in equation (35) giving

$$b_1=\frac{D}{B} \tag{36}$$

Substitution of this value of b_1 in equation (34) gives the approximate value for a_1 of

$$a_1=\frac{B}{2}\pm\sqrt{\left(\frac{B}{2}\right)^2-C+\frac{D}{B}+\frac{EB}{D}} \tag{37}$$

This latter equation can be further simplified without loss of accuracy by removing the radical and assuming $a_1^2=0$. The resulting equation for a_1 is

$$a_1=\frac{C}{B}-\frac{D}{B^2}-\frac{E}{D} \tag{38}$$

Since

$$\lambda=-\frac{a_1}{2}\pm\sqrt{\left(\frac{a_1}{2}\right)^2-b_1}$$

$$=\zeta'\pm i\psi' \tag{39}$$

$$\zeta'=-\frac{a_1}{2} \tag{40}$$

$$\psi'=\sqrt{-\left(\frac{a_1}{2}\right)^2+b_1}$$

Since $\left(\frac{a_1}{2}\right)^2$ is normally small compared with b_1, it is sufficiently accurate for practical purposes to put

$$\psi'=\sqrt{b_1} \tag{41}$$

From equations (38) and (36),

$$\zeta'=-\frac{1}{2}\left[\frac{C}{B}-\frac{D}{B^2}-\frac{E}{D}\right] \tag{42}$$

$$\psi'=\sqrt{\frac{D}{B}} \tag{43}$$

Supplementary study has indicated that further simplification can be had with but slight loss in accuracy by neglecting values of y_v in the expression for B and D and neglecting tan γ in the expression for D and E giving

$$\left.\begin{aligned} B&=-n_r-l_p\\ C&=l_pn_r-l_rn_p+y_v(l_p+n_r)+\mu n_v\\ D&=\mu l_v\left(n_p-\frac{C_L}{2}\right)-\mu n_vl_p\\ E&=\mu\frac{C_L}{2}(l_vn_r-l_rn_v)\end{aligned}\right\} \tag{44}$$

Substituting these values in equations (42) and (43) and simplifying where possible gives

$$\zeta'=-\frac{1}{2}\left[-y_v+\frac{l_pn_r-l_rn_p}{(-n_r-l_p)}+\frac{\mu n_v(-n_r)}{(-n_r-l_p)^2}+\frac{C_Ll_rn_v}{2l_v\left(n_p-\frac{C_L}{2}\right)-2n_vl_p}\right]$$

$$+\frac{1}{2}\left[\frac{\mu l_v\left(n_p-\frac{C_L}{2}\right)}{(-n_r-l_p)^2}+\frac{C_Ll_vn_r}{2l_v\left(n_p-\frac{C_L}{2}\right)-2n_vl_p}\right] \tag{45}$$

and

$$\psi'=\sqrt{\frac{\mu l_v\left(n_p-\frac{C_L}{2}\right)-\mu n_vl_p}{(-n_r-l_p)}} \tag{46}$$

The time in seconds to damp to one-half amplitude is given by

$$T=\frac{\log_e 0.5}{\zeta}=\frac{-0.693}{\zeta'}\tau$$

(since $\zeta'=\tau\zeta$).

Expressed in more convenient form, this equation becomes

$$T=\frac{-0.313\sqrt{\left(\frac{W}{S}\right)\frac{\rho_0}{\rho}C_L}}{\zeta'} \tag{47}$$

The period in seconds of the lateral oscillation is

$$P=\frac{2\pi}{\psi}=\frac{2\pi\tau}{\psi'}$$

or

$$P=\frac{2.83\sqrt{\left(\frac{W}{S}\right)\frac{\rho_0}{\rho}C_L}}{\psi'} \tag{48}$$

Approximate formulas for the convergence characteristics.—Since a_1 is small, a_2 is approximately equal to B.

Letting $a_2=B$

and $b_2=\frac{EB}{D}$

gives

$$\lambda=-\frac{B}{2}\pm\sqrt{\left(\frac{B}{2}\right)^2-\frac{EB}{D}} \tag{49}$$

as the solution for the pair of the roots of the stability biquadratics corresponding to the convergence characteristics. Since B is always positive and large in the normal-flight range, it appears that this equation represents two convergences if EB/D is positive and less than $(B/2)^2$, a heavily damped oscillation if EB/D is positive and greater than $(B/2)^2$, a divergence and a convergence if EB/D is negative and less than $(B/2)^2$, and two divergences if EB/D is negative and greater than $(B/2)^2$. Instability is therefore possible if either E or D becomes negative. For most cases E is small but may be either positive or negative and D is positive and large. These circumstances give the usual solution of (49) as a large negative root approximately equal to $-B=n_r+l_p$ and a small root approximately equal to $-E/D$.

In the usual case it is desired to know whether or not there will be a divergence rather than to know the rapidity of the convergence. For such a case it is sufficient to know that

$$D>0$$

and

$$E>0$$

By the use of the relationships of equations (44), these conditions are represented by

$$l_v\left(n_p-\frac{C_L}{2}\right)-n_vl_p>0 \tag{50}$$

and

$$l_vn_r>l_rn_v \tag{51}$$

These equations neglect the effects of y_v and tan γ, a procedure that is conservative for power-off flight.

APPENDIX III

SYMBOLS

X, Y, Z, axes of reference fixed in the airplane having the origin at the center of gravity, the X axis in the plane of symmetry and along the relative wind in steady flight, the Y axis perpendicular to the plane of symmetry, and the Z axis in the plane of symmetry and perpendicular to the X axis.

X, Y, Z, forces along the respective axes, X being positive when directed forward, Y positive when directed to the right, and Z positive when directed downward.

L, M, N, moments about the X, Y, and Z axes, respectively, L being positive when it tends to depress the right wing, M positive when it tends to depress the tail, and N positive when it tends to retard the right wing.

u, v, w, components of linear velocity of the airplane along the X, Y, and Z axes, respectively, having the same positive directions as the X, Y, and Z forces.

V, resultant velocity.

p, q, r, components of angular velocity about the X, Y, and Z axes, respectively, having the same positive directions as L, M, and N.

ϕ, θ, ψ, components of angular displacement from a given attitude about the X, Y, and Z axes, respectively.

α, angle between the relative wind on a plane parallel to the plane of symmetry and the wing chord, positive when corresponding to positive rotation θ of the airplane relative to the wind.

β, angle between the relative wind and a plane parallel to the plane of symmetry, equal to $\sin^{-1}\frac{v}{V}$; angle of sideslip in radians.

γ, angle of flight path to horizontal, positive in a climb.

Γ, dihedral angle, degrees.

$C_Y=\frac{Y}{qS}$, coefficient of lateral force.

$C_l=\frac{L}{qSb}$, coefficient of rolling moment.

$C_n=\frac{N}{qSb}$, coefficient of yawing moment.

C_{D_w}, coefficient of drag for the wing alone.

C_{L_p}, coefficient of force on projected side area.

C_{L_t}, coefficient of force on vertical-tail area.

S, wing area.

S_s, projected side area of fuselage.

S_t, vertical-tail area.

S_p, projected side area.

d, maximum depth of fuselage.

y, spanwise distance from plane of symmetry.

x_1, distance from fuselage nose to center of gravity.

l, distance from center of gravity to rudder hinge.

l_1, over-all length.

l_2, over-all length of fuselage.

ρ_0, mass density of air under standard conditions.

ρ, mass density of air under condition of flight.

t, subscript denoting vertical tail surfaces.

b_t, height of vertical tail.

η_t, tail efficiency.

z_p, the Z coordinate of the center of pressure of projected side area.

K_β, empirical factor for estimating $dC_n/d\beta$ for fuselage.

$\mu=\frac{m}{\rho Sb}$, relative density factor.

For standard atmosphere, $\mu=\frac{13.1(W/S)}{b}$.

$\tau=\frac{m}{\rho SV}=\mu\frac{b}{V}$, time conversion factor.

$y_v=\frac{1}{2}\frac{dC_Y}{d\beta}$, nondimensional derivative of lateral force due to sideslip.

$l_v=\frac{1}{2}\left(\frac{b}{k_X}\right)^2\frac{dC_l}{d\beta}$, nondimensional derivative of rolling moment due to sideslip.

$n_v=\frac{1}{2}\left(\frac{b}{k_Z}\right)^2\frac{dC_n}{d\beta}$, nondimensional derivative of yawing moment due to sideslip.

$l_p=\frac{1}{4}\left(\frac{b}{k_X}\right)^2\frac{dC_l}{d\frac{pb}{2V}}$, nondimensional derivative of rolling moment due to rolling.

$n_p=\frac{1}{4}\left(\frac{b}{k_Z}\right)^2\frac{dC_n}{d\frac{pb}{2V}}$, nondimensional derivative of yawing moment due to rolling.

$l_r=\frac{1}{4}\left(\frac{b}{k_X}\right)^2\frac{dC_l}{d\frac{rb}{2V}}$, nondimensional derivative of rolling moment due to yawing.

$n_r=\frac{1}{4}\left(\frac{b}{k_Z}\right)^2\frac{dC_n}{d\frac{rb}{2V}}$, nondimensional derivative of yawing moment due to yawing.

B, C, D, E, coefficients of stability biquadratic.

$\lambda=\frac{\lambda'}{\tau}=\zeta\pm i\psi=\frac{\zeta'}{\tau}\pm i\frac{\psi'}{\tau}$, root of stability equation.

T, time for oscillation to decrease to one-half amplitude, seconds.

$$T=\frac{-0.693}{\zeta'}\times\tau$$

$$=\frac{-0.313\sqrt{(W/S)C_L}}{\zeta'}\text{ (Standard atmosphere).}$$

P, period of oscillation, seconds.

$$P=\frac{2\pi\tau}{\psi'}$$

$$=\frac{2.83\sqrt{(W/S)C_L}}{\psi'}\text{ (Standard atmosphere).}$$

a, b, coefficients of stability quadratic.

REFERENCES

1. Zimmerman, Charles H.: An Analysis of Longitudinal Stability in Power-Off Flight with Charts for Use in Design. T. R. No. 521, N. A. C. A., 1935.
2. Diehl, Walter S.: Engineering Aerodynamics. The Ronald Press Company (revised edition), 1936.
3. Shortal, Joseph A.: Effect of Tip Shape and Dihedral on Lateral-Stability Characteristics. T. R. No. 548, N. A. C. A., 1935.
4. Wilson, Edwin Bidwell: The Variation of Yawing Moment Due to Rolling. T. R. No. 26, N. A. C. A., 1919.
5. Bradfield, F. B.: Lateral Control of Bristol Fighter at Low Speeds. Measurement of Rolling and Yawing Moments of Model Wings, Due to Rolling. R. & M. No. 787, British A. R. C., 1922.
6. Glauert, H.: Calculation of the Rotary Derivatives Due to Yawing for a Monoplane Wing. R. & M. No. 866, British A. R. C., 1923.
7. Halliday, A. S.: Stability Derivatives of the Bristol Fighter. R. & M. No. 1277, British A. R. C., 1930.
8. Halliday, A. S., and Burge, C. H.: Experiments on the Whirling Arm. Yawing and Rolling Moments on the Hornbill and Various Aerofoils Also Pressure Distribution and Flow Tests on R. A. F. 15. R. & M. No. 1642, British A. R. C., 1935.
9. Soulé, Hartley A., and Miller, Marvel P.: The Experimental Determination of the Moments of Inertia of Airplanes. T. R. No. 467, N. A. C. A., 1933.
10. Bryan, G. H.: Stability in Aviation. MacMillan and Co., Ltd. (London), 1911.
11. Bairstow, Leonard: Applied Aerodynamics. Longmans, Green and Co. (London), 1920.
12. Wilson, Edwin Bidwell: Aeronautics. John Wiley and Sons, Inc., 1920.
13. Glauert, H.: A Non-Dimensional Form of the Stability Equations of an Aeroplane. R. & M. No. 1093, British A. R. C., 1927.
14. Weick, Fred E., and Jones, Robert T.: The Effect of Lateral Controls in Producing Motion of an Airplane as Computed from Wind-Tunnel Data. T. R. No. 570, N. A. C. A., 1936.
15. The Stability and Control Panel: The Lateral Control of Stalled Aeroplanes. General Report by the Stability and Control Panel. R. & M. No. 1000, British A. R. C., 1926.
16. Bryant, L. W., Jones, I. M. W., and Pawsey, G. L.: The Lateral Stability of an Aeroplane Beyond the Stall. R. & M. No. 1519, British A. R. C., 1933.
17. Soulé, Hartley A.: Flight Measurements of the Dynamic Longitudinal Stability of Several Airplanes and a Correlation of the Measurements with Pilots' Observations of Handling Characteristics. T. R. No. 578, N. A. C. A., 1936.

REPORT No. 590

PRESSURE-DISTRIBUTION MEASUREMENTS ON AN O–2H AIRPLANE IN FLIGHT

By H. A. Pearson

SUMMARY

Results are given of pressure-distribution measurements made over two different horizontal tail surfaces and the right wing cellule, including the slipstream area, of an observation-type biplane. Measurements were also taken of air speed, control-surface positions, control-stick forces, angular velocities, and accelerations during various abrupt maneuvers. These maneuvers consisted of push-downs and pull-ups from level flight, dive pull-outs, and aileron rolls with various thrust conditions.

The results from the pressure-distribution measurements over the wing cellule are given on charts showing the variation of individual rib coefficients with wing coefficients; the data from the tail-surface pressure-distribution measurements are given mainly as total loads and moments. These data are supplemented by time histories of the measured quantities and isometric views of the rib pressure distributions occurring in abrupt maneuvers.

The results indicate that there is little if any dissymmetry of load on the tail due to slipstream rotation and that the up loads may be as much as the down loads. From the results of the wing investigation it was found that the relative efficiency of the wings depended upon the type of maneuver.

INTRODUCTION

Following the completion of pressure-distribution tests made of a PW–9 pursuit airplane in 1928 (reference 1), similar tests of an observation biplane were requested by the Army Air Corps. The original object of this request was to institute a program that would lead to information on an observation type of airplane corresponding to the information already obtained on the pursuit type. An O–2H airplane was made available. Pressure of other work at the N. A. C. A. laboratories, however, delayed work on the rather extensive installation of apparatus, and flight tests could not be started until 1932.

Although the O–2H airplane was by then an obsolescent type and although the results of other related research projects had led to an improved understanding of many questions concerning external loads and their distribution on airplane structures, it was decided to complete the tests of the O–2H because it was believed that they would constitute a useful set of data with which modern methods of computing loads and load distribution might be compared.

The results are presented in a two-part paper, the first part giving the results of tests made of two tail surfaces and the second the results of an investigation over the right wing cellule and slipstream area.

APPARATUS

Airplane.—The airplane used in these tests (figs. 1 and 2) was a standard Army O–2H observation airplane with the following modifications: (1) The fabric covering on the fuselage from just abaft the engine hood to

FIGURE 1.—The O–2H airplane.

the rear of the observer's cockpit was replaced by thin duralumin sheets that could easily be removed;

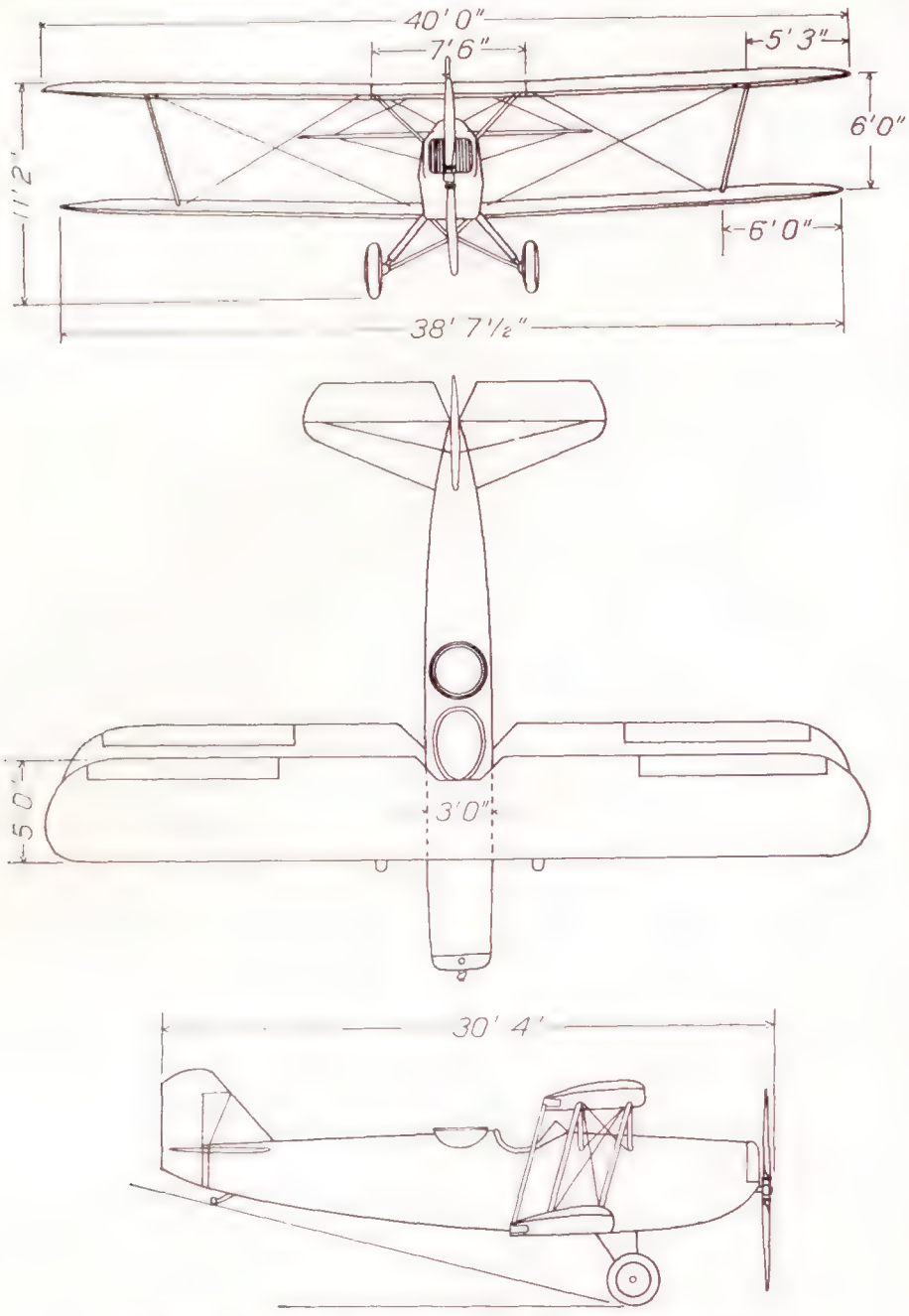

FIGURE 2.—Line drawing and dimensions of the O-2H airplane.

(2) the original 9.5-foot propeller was replaced by a 10.5-foot propeller; and (3) a boom carrying a swiveling pitot head was attached to the interplane struts.

The two horizontal tail surfaces are shown in figures 3 (a) and 3 (b) and the wing surfaces are shown in figure 4. These figures give the location of the pressure points and other pertinent dimensions. Additional data

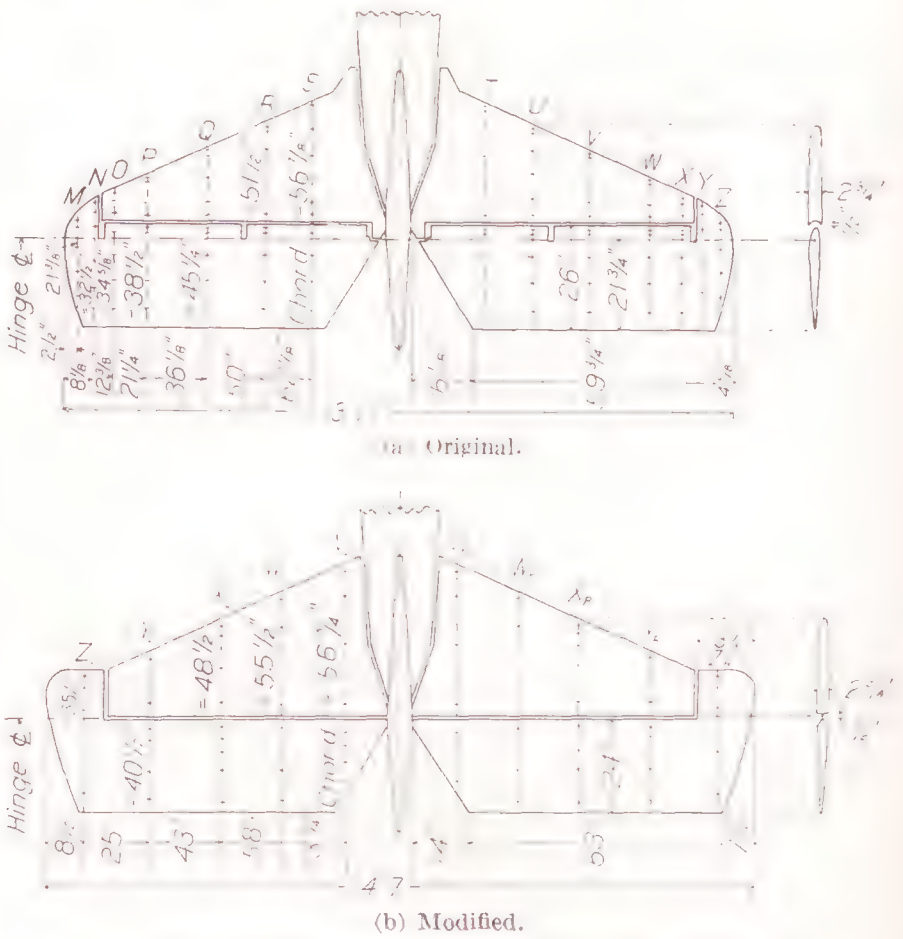

(a) Original.

(b) Modified.

FIGURE 3.—Tail surfaces with pressure-rib and orifice locations.

concerning both the airplane and the various surfaces are given in table I.

Pressure orifices and tubing.—The orifice and tubing installation is much the same as that described in reference 1. For the tail-surface investigation the metal pressure tubes from both the elevator and the stabilizer were brought out in bundles near the fuselage (fig. 5), from which point they were connected by short lengths

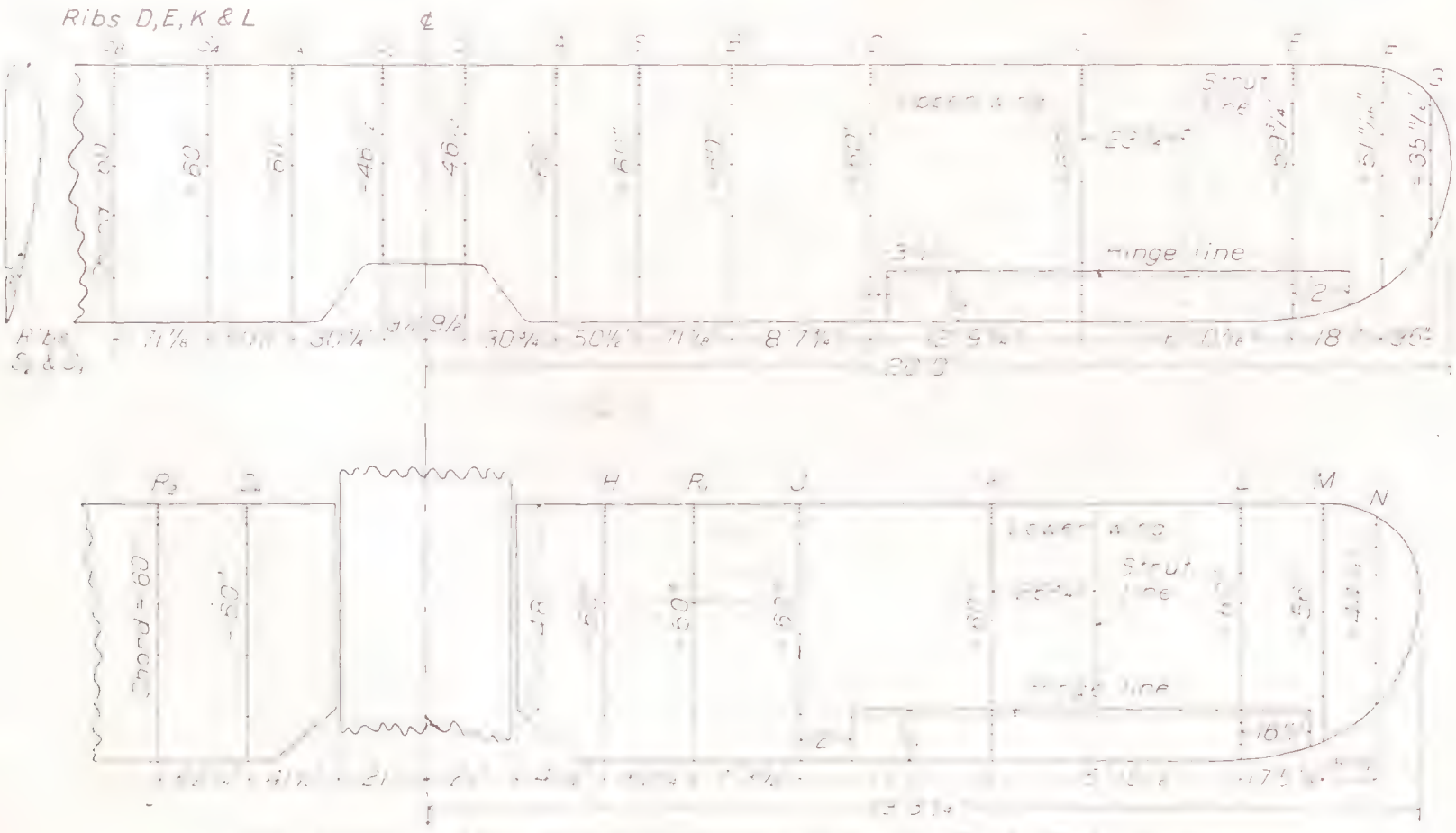

FIGURE 4.—Upper and lower wings of O-2H airplane with pressure-rib and orifice locations.

of rubber tubing to metal tubes leading directly to the manometers. For the wing investigation the tubing from the lower wing was carried through the wing root to the manometers and that from the upper wing was faired around the cabane struts and brought to the manometers. The tubing from the aileron ribs was grouped in small bundles, midway between the pressure ribs, and was connected by short pieces of rubber tubing to metal tubes within the wing.

Instruments.—Each pressure orifice was connected to a pressure cell on either of two N. A. C. A. type 60 multiple recording manometers located in the observer's cockpit midway between the upper and lower longerons. The pressure cells were similar to those of reference 1

FIGURE 5.—Tail-surface tubing installation

but were corrected for temperature effects by the method given in reference 2.

In the tail-surface investigation the load distribution occurring over each tail surface was measured during steady flight, dive pull-outs, and pull-ups from level flight. For the steady-flight condition the following standard N. A. C. A. photographically recording instruments were used: air-speed meter, control-position recorder, control-force recorder, inclinometer, and tachometer. For the pull-ups and pull-outs an accelerometer and a turnmeter, both located near the center of gravity of the airplane, were substituted for the inclinometer and tachometer used in the steady flights. All instruments were synchronized by an N. A. C. A. timer incorporated into their circuit.

In the wing-cellule and slipstream investigations the load distribution was measured in steady flight, push-downs and pull-ups from level flight, dive pull-outs, and aileron rolls. With the exception of an additional accelerometer mounted 18 inches in from the right wing tip for the aileron rolls, the instruments were the same as used for the tail-surface investigation.

I. PRESSURE-DISTRIBUTION TESTS OVER TWO SETS OF HORIZONTAL TAIL SURFACES

METHOD

In the tests made of the modified tail (fig. 3 (b)), resultant pressures were recorded at 74 points. The remaining pressure cells were connected to wing ribs for the purpose of correlating the tail-surface and wing results. Subsequent tests showed this precaution to be unnecessary as the various stabilizer and elevator settings did not measurably affect the pressure distribution on the wing ribs. Consequently, in the series of tests of the original tail (fig. 3 (a)), the full 120 pressure cells were used on the tail alone.

Steady dives.—In order to obtain information on certain flap parameters, tail loads were measured during steady dives with the stabilizer in various settings. For the most part, the effect of the slipstream was minimized by running the tests near zero propeller thrust. Several tests were made, however, with the throttle fully closed and also with the throttle open to a position corresponding to what was considered to be a maximum safe engine speed. The method used to obtain zero thrust was to compute the V/nD for zero propeller thrust from an analysis of full-scale propeller tests. The pilot was then instructed to dive at a certain steady air speed and with a definite engine speed before taking records. Actually, this procedure required that the throttle be slightly opened.

In the tests of the modified tail, the stabilizer settings specified to the pilot were full nose heavy, full tail heavy, and trim.[1] Obviously, when trim was specified, several settings in the range of adjustment were possible depending upon the pilot's "feel" and the altitude at which he trimmed the airplane. This procedure led to complications in the analysis of the data owing to the number of variables involved. Consequently, in the tests of the original tail only three stabilizer settings were used: The two extreme settings and one midway between them.

With the exception noted, the test procedure for the two tail surfaces was the same and consisted of steady glides starting from 120 miles per hour and increasing by increments of roughly 10 miles per hour up to the maximum diving speed considered to be safe. The pressures measured at each point were the algebraic sum of those on the top and bottom of the airfoil surface (resultant pressures), no attempt being made to separate them. Simultaneously with these measurements, air-speed, control-force, control-position, inclinometer, and tachometer records were taken.

[1] "Stabilizer set tail heavy" as used here means that the stabilizer is set so as to make the tail seem heavy. From this definition the meaning of "trim" and "full nose heavy" settings is readily deduced.

The rib pressure-distribution curves for each tail rib were mechanically integrated to obtain the load and the moment of the load about the elevator-hinge center line. The rib loads and moments were then plotted against their span location and these curves, in turn, were integrated for the total load and moment of the tail. These results were then converted to tail load center of pressure with respect to the hinge line and finally to the moment exerted by the tail surfaces about the center of gravity of the airplane. A similar procedure was followed to obtain the load carried by the elevator and its hinge moment. The velocity used in all calculations for normal-force and hinge-moment coefficients was that given by a swiveling air-speed head located on a boom one wing chord length forward of the leading edge of the upper wing (fig. 1).

Pull-ups.—Pressure measurements were taken in abrupt pull-ups from steady level flight throughout the speed range with various stabilizer settings. Several graduated pull-ups from high-speed level flight and several pull-outs from shallow dives were also made. In these miscellaneous tests the stabilizer was set to trim.

In addition to the pressure measurements taken in the pull-up, records were also taken of the air speed, normal acceleration, angular velocity, control position, and control force. In most of the pull-up tests the results were computed from the records for only the time corresponding to the maximum down tail load. For the purpose of showing time histories, however, the results were in some cases computed for an interval that included the initial tail load and the subsequent maximum downward- and upward-acting tail loads.

The method by which total loads and moments were obtained from point pressures is the same as that previously explained.

PRECISION

A number of possible sources of error are present and may be listed as follows:

Individual pressure measurements may be incorrect because of—

(*a*) Orifices not flush with surface.
(*b*) Tube stopped or leaking.
(*c*) Lag in tube and diaphragm.
(*d*) Shrinkage of film.
(*e*) Changed pressure-cell calibrations due to aging and temperature effects.
(*f*) Personal errors in plotting and reading records.
(*g*) Excessive width and haziness of pressure record line due to dust or oil on lens, small rapid pressure fluctuations, or vibration.

Rib loads and moments may be incorrect because of—

(*a*) False individual pressures due to above errors.
(*b*) Errors in plotting.
(*c*) False fairing of curves due to insufficient points.
(*d*) Integration errors.
(*e*) Error introduced by neglecting the foreshortening of the chord line with a control displacement. The resultant pressure at each point was, in all cases, plotted normal to the original chord line.

Sufficient checking was done to insure that errors in the individual pressures arising from sources (*a*) to (*d*) were negligible in these tests. The error due to source (*e*) was minimized by frequent calibrations and the use of temperature-compensated pressure cells. Errors due to (*f*) were practically eliminated by checking at all phases of the work. The largest source of error in the individual pressures is due to the haziness and width of the lines on the pressure records. Generally, the records taken in the dives were better in this respect than those in the pull-ups; also, those farther out on the tail were better than the ones close to the fuselage. The widths of the record lines were in some cases, where the deflections were small, so large as to make it impossible to tell whether a small positive or negative pressure existed. From the foregoing, it is obviously impossible to express the accuracy of the individual pressure on a percentage basis, since it varies with the amount of the local pressure, location of the pressure point, and the type of maneuver. The estimated maximum absolute error in the individual pressures was no more than 3 pounds per square foot for the high-range cells, which, in general, were connected to orifices located near the leading edges and close to the hinge center line. The error in the low-range cells was estimated to be no more than 1 pound per square foot. The low-range cells were connected to orifices located near the middle of the stabilizer ribs and at the trailing edges of the elevator.

The errors in rib loads due to source (*e*) were small in the case of the dives since the elevator displacements rarely exceeded 15°. In the abrupt pull-ups, however, where the elevator may be deflected as much as 30°, the error in the total tail load may be as much as 7 percent. This error does not enter into the elevator loads or moments.

The principal source of error in the rib-load curves is known to be in the fairing of the curves. The magnitude of this error varied with the type of pressure distribution obtained. In the steady dives with the stabilizer in the full nose-heavy setting, the error in the tail load due to fairing is believed to be a minimum and that obtained with the stabilizer in the other extreme position a maximum. In the nose-heavy case the maximum error in the tail load at speeds above 150 miles per hour is probably no more than 25 pounds as compared with 60 pounds for the full tail-heavy position. The maximum down tail loads occurring in the pull-ups

and pull-outs are estimated to be correct to within 50 pounds.

The indicated air-speed measurements are believed to be correct to within 1½ miles per hour as shown by several flights over a measured course. The recorded accelerations are accurate to within 0.2 g and the control-force measurements correct to within 3 pounds. Angular displacements, as given by the control-position recorder, are correct to within ½° and 2° for the stabilizer and elevator, respectively, while angular velocities about the center of gravity were measured to within 0.05 radian per second. Although tachometer readings were taken in the dives, no estimate of their accuracy is needed since it was found that the erratic effect of the various degrees of thrust in the tail-surface pressure-distribution tests did not exceed the effect that might arise from other errors. Consequently, in the following discussion, no discrimination is made regarding the various thrust conditions.

RESULTS AND DISCUSSION

Steady dives.—The variation of the tail moment about the center of gravity with air speed is given in figures 6 and 7 for the modified and original tail surfaces, respectively. From these figures it appears that the moment furnished by the tail, at a given air speed, is considerably affected by the stablizer setting. Since the tail surfaces provide a moment about the center of gravity of the airplane that balances the resultant moment due to all other parts, it would be expected that the moment furnished by the tail would be approximately constant. The tail-moment curves, however (figs. 6 and 7), indicate that, as the stabilizer moves toward the tail-heavy position, the moment becomes smaller and the scattering of the experimental points becomes greater.

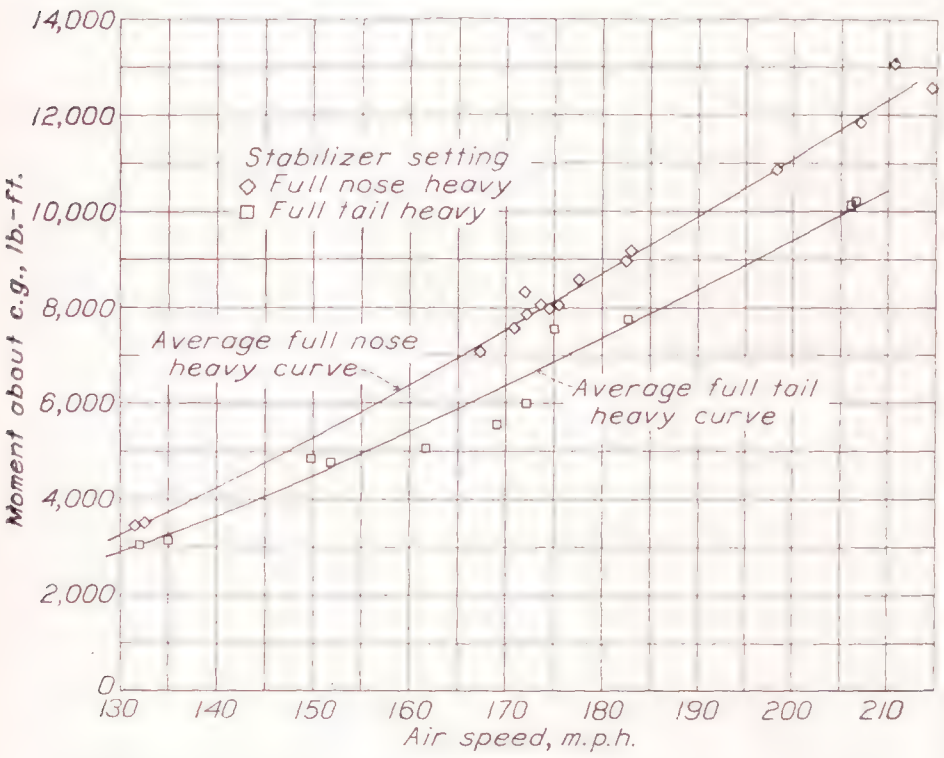

FIGURE 6.—Tail moment about airplane center of gravity (modified tail).

Typical curves for the pressure distribution measured over the tail-surface ribs are given in figures 8 to 12. Figures 8 and 9 are for the modified tail surfaces and figures 10, 11, and 12 are for the original tail. The ordinates of these rib pressure-distribution curves are given in terms of the ratio p/q where p is the local pressure difference and q is the dynamic pressure measured at the air-speed head. A comparison of the results for identical stabilizer settings either in figures 8 and 9 or in figures 10, 11, and 12 shows an increase in peak pressure at the stabilizer leading edge with an increase in air speed. Although this difference in peak pressure is due to the cumulative effect of several factors, such as possible changes in interference, downwash, and elevator angle, it is thought that the greater

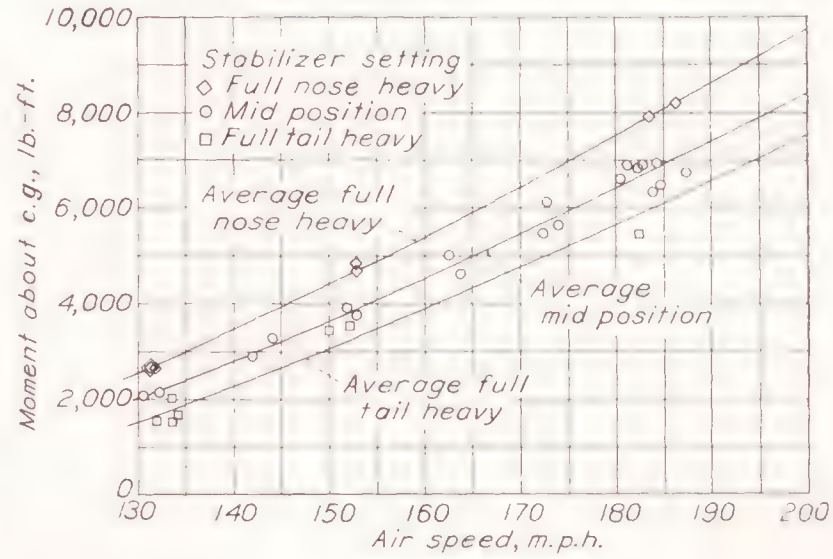

FIGURE 7.—Tail moment about airplane center of gravity (original tail).

structural deflection which occurs at the highest speed would account for a good portion of the variation with air speed. Static tests with a loading corresponding to that of the full tail-heavy setting for the modified tail indicated that at 170 miles per hour the change in stabilizer angle due to this structural deflection was approximately 1°.

The pressure distributions shown over ribs Z_R and Z_L (figs. 8 and 9) seem to indicate that with small elevator deflection the balance portion is of little value in reducing the stick loads. A similar conclusion is inferred in reference 3, in which calculated balance coefficients obtained by the usual methods were not verified by the pilots' observations. The rib-pressure diagrams for the original tail (figs. 10, 11, and 12) show that in the dives the peak pressure on the elevator occurs nearer to the hinge line than to the leading edge; however, in the dives the elevator leading edge seldom projects either above or below the stabilizer surfaces.

The form of the rib-pressure diagrams for the full tail-heavy setting explains the tendency to the wide scattering of the experimental points given in figures 6 and 7 for this setting. Figures 8 to 12 show that for the tail-heavy setting the resultant tail load is the difference between upward- and downward-acting loads, either one of which is larger than the resultant.

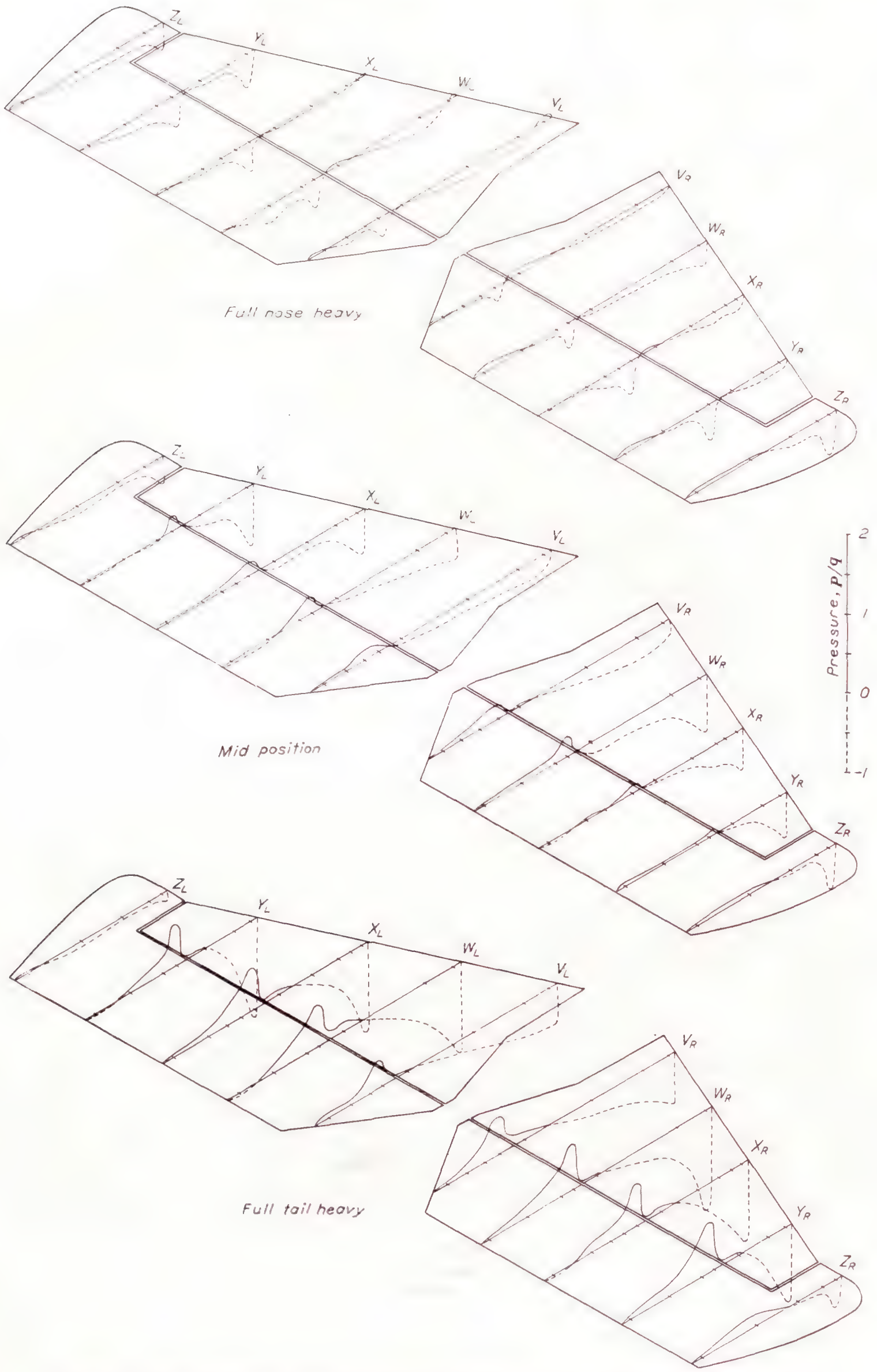

FIGURE 8.—Distribution of resultant pressures on modified tail surfaces for different stabilizer settings at 130 miles per hour.

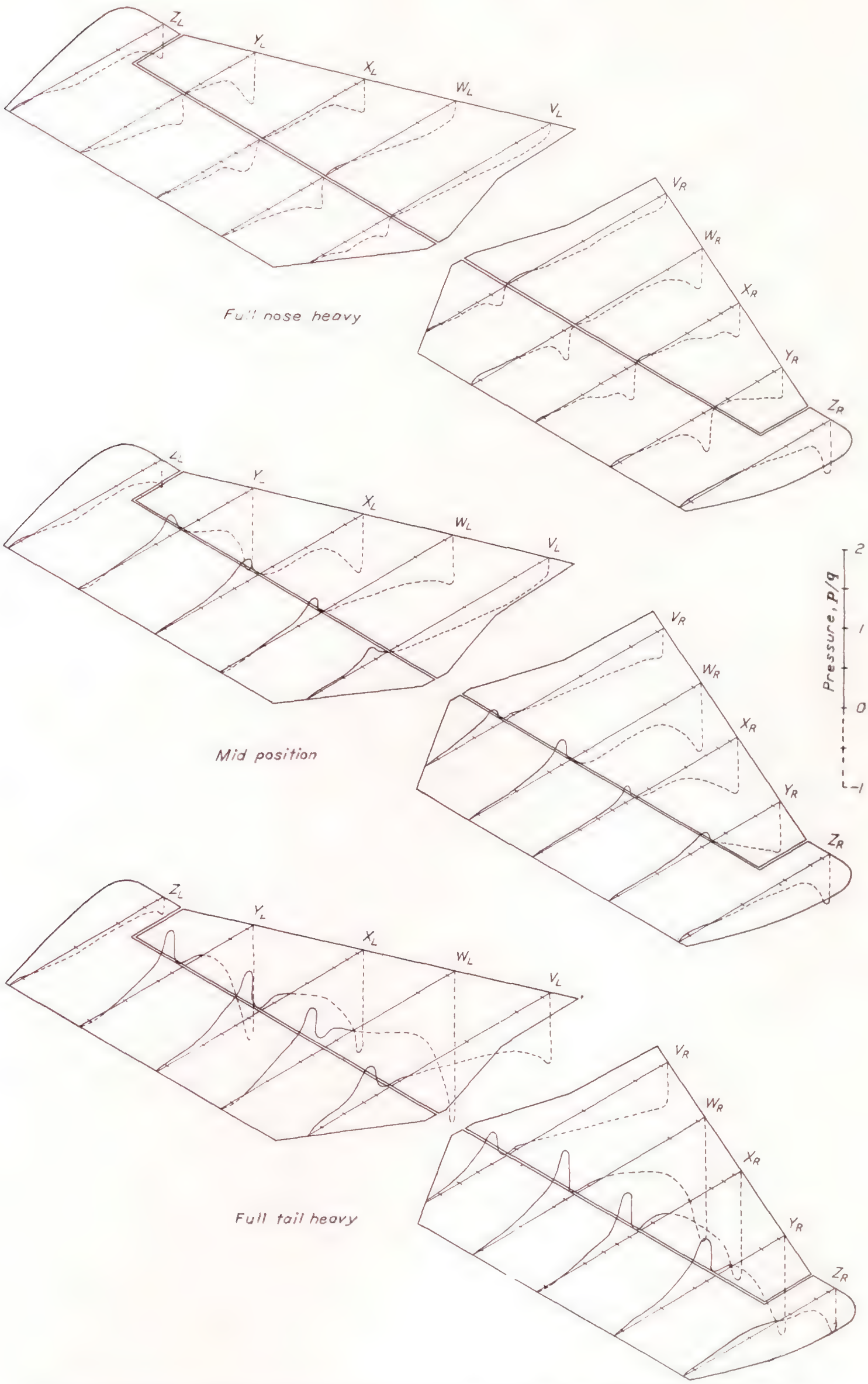

FIGURE 9.—Distribution of resultant pressures on modified tail surfaces for different stabilizer settings at 170 miles per hour.

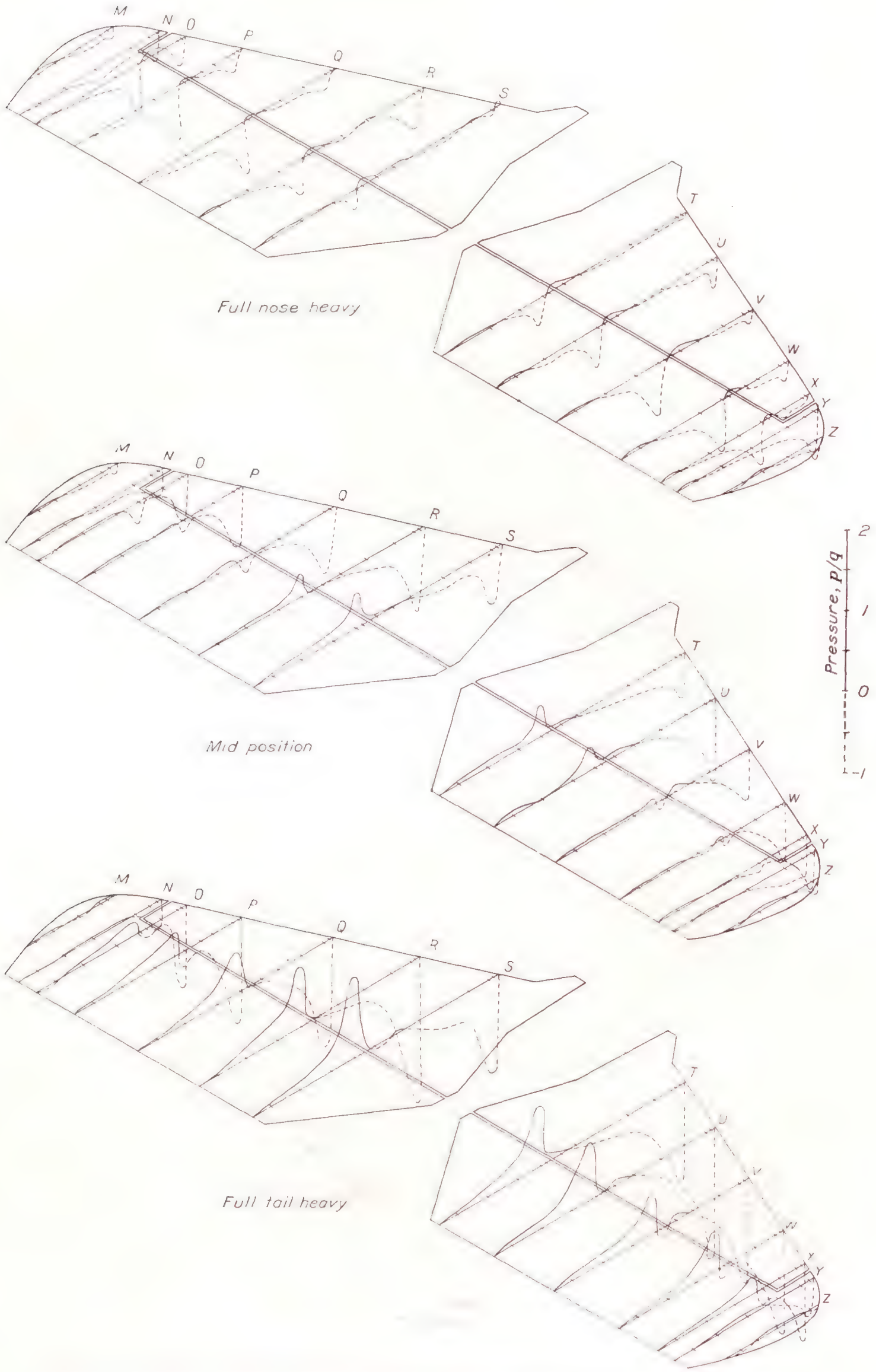

FIGURE 10.—Distribution of resultant pressures on original tail surfaces for different stabilizer settings at 130 miles per hour.

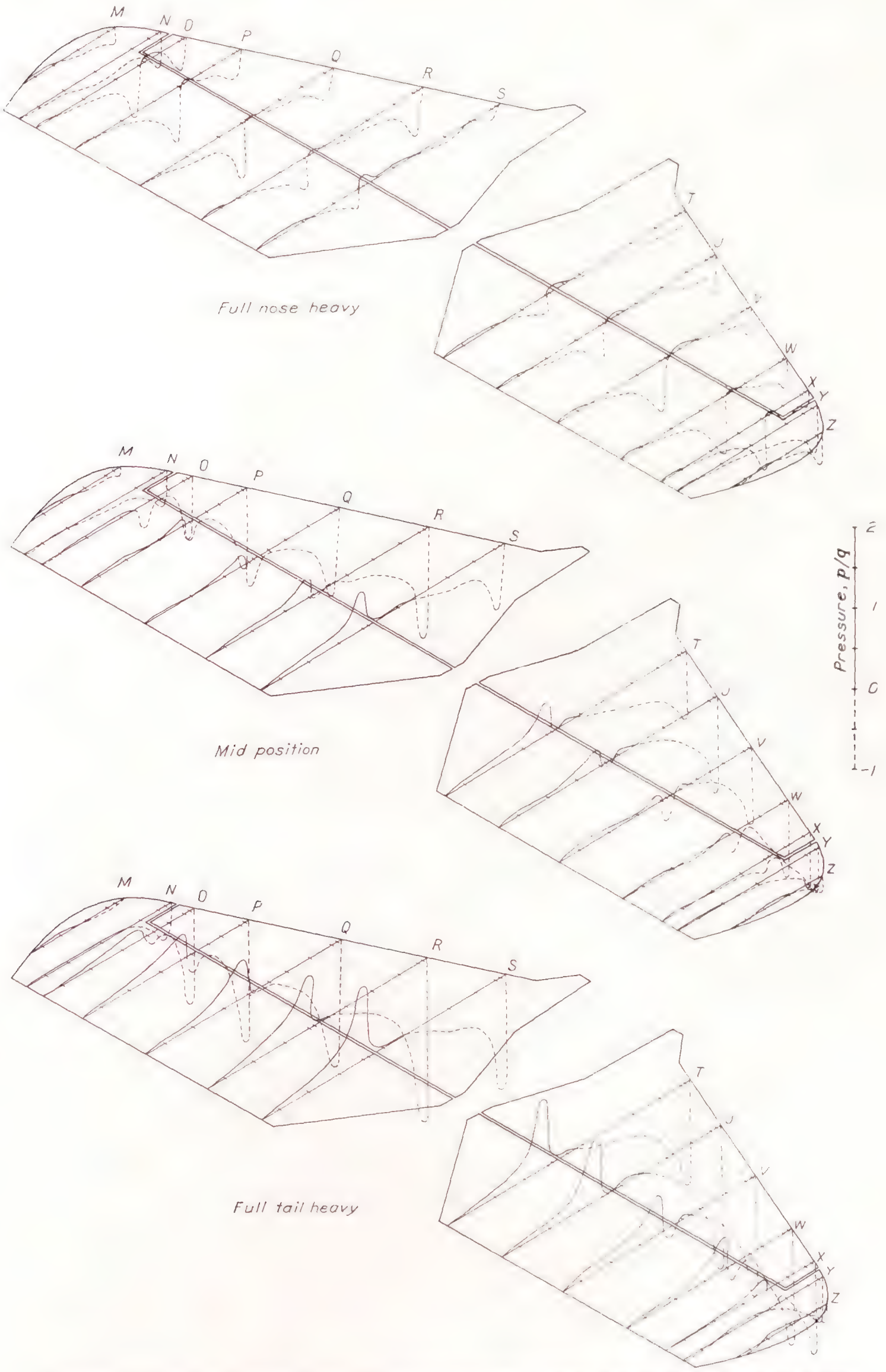

FIGURE 11.—Distribution of resultant pressures on original tail surfaces for different stabilizer settings at 150 miles per hour.

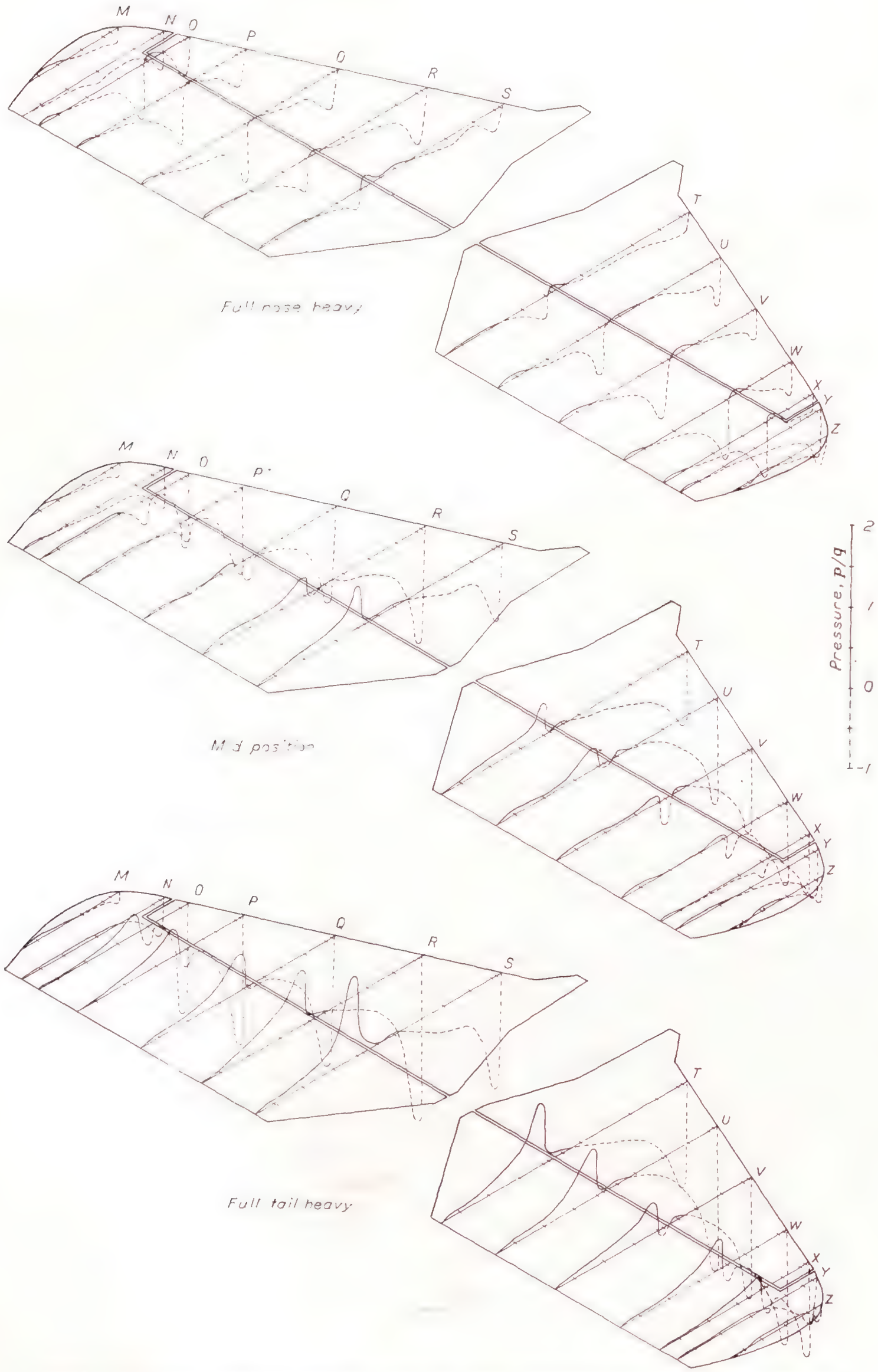

FIGURE 12.—Distribution of resultant pressures on original tail surfaces for different stabilizer settings at 180 miles per hour.

Because of this condition, small inaccuracies in fairing may lead to considerable dispersion in the final results. Aside from the inaccuracy due to fairing, the individual rib loads, and consequently the tail loads, are likely to be low for the full tail-heavy setting owing to the fact that the large down pressures at the leading edge could not be measured. Since the rib-pressure curves for the stabilizer set full nose heavy are not subject to these sources of discrepancy, it is felt that the moment curves for this setting (figs. 6 and 7) are more indicative of the true moment than any of the others.

In order to gain an idea as to how the experimental moment curves for the nose-heavy settings compare with the computed ones, several curves, representing varying degrees of refinement, are given (fig. 13). Curve A is for the case when only the moments of the two wings about their quarter-chord points are taken into account; in curves B the moment about the airplane center of gravity has been computed for the case when the additional moments due to the lift and drag vectors are also included. These vectors were assumed to act at the wing quarter-chord points and their magnitudes were determined from the relative lift distribution between the wings, which was determined in the wing investigation. As the airplane centers of gravity were different (table I) for the two tail-surface investigations, two separate curves were required.

Curves C also include the probable effect of the fuselage on the moment about the center of gravity, assuming that the fuselage exerts a constant moment given by

$$M_f = C_{m_f} q A_f c_f$$

where C_{m_f} is the moment coefficient, 0.01.

A_f, horizontal projected area, 65 square feet.

c_f, fuselage length, 27 feet.

The value of the moment coefficient defined by the foregoing equation was taken to be 0.01 after an analysis of the data contained in reference 4. The final comparisons (curves C and D) could no doubt be improved if it were possible to include the effect of the landing gear and tail surfaces. The moments that they introduced were, however, of opposite sign and tended to cancel.

The span load distribution across the tail for the foregoing rib pressure-distribution plots is given in figure 14. These curves show irregularities that are more or less to be expected owing to the irregular nature of the flow over the tail surfaces and to the comparatively small loads measured in the steady dives. An analysis of the data indicated that, in spite of the irregularity of the loading, the average difference in load between the two halves of the tail was of the order of 3 percent and 5 percent of the total load for the original and modified tail, respectively. Inasmuch as the sides that carried the most load varied between the two tail surfaces, it must be concluded that the difference in load is due to slight differences in rigging rather than to a slipstream effect.

In these tests the elevator moments about the hinge axis were obtained from both the pressure distribution and the control-force-recorder measurements; the results are compared in figure 15 for the original tail. In order to make this comparison between the two hinge moments, however, it was necessary to correct the measurements given by the control-force recorder for the moment exerted by the elevator (because of its unbalanced weight) about the hinge line and for the moment exerted by the unbalanced weight in the stick about its pivot point. Although the magnitude of the friction moment was known, it was impossible to correct for it in the steady dives because its direction was unknown. Even with these corrections the moments given by the control-force recorder were found to be more consistent than those given by pressure-distribution measurements and hence were used for computing hinge-moment coefficients.

The variation of the hinge-moment coefficient with elevator angle is given in figures 16 and 17 for the

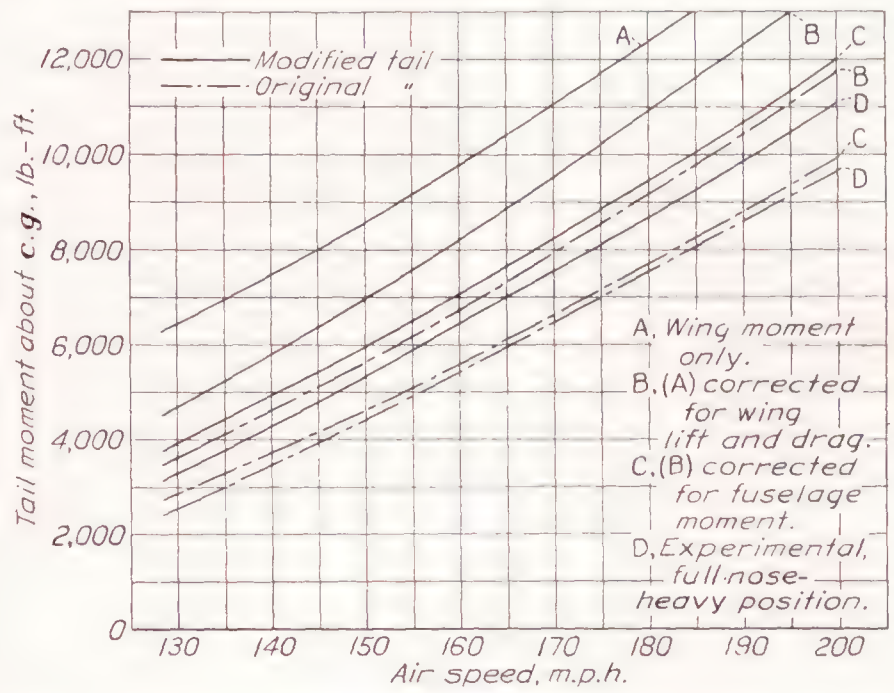

FIGURE 13.—Computed and experimental tail moments about the center of gravity.

modified and original tail surfaces, respectively. These coefficients have been computed from the relation

$$C_{h_e} = \frac{M_e}{q S_e c_e}$$

where M_e is the elevator hinge moment given by the control-force recorder.

c_e, the average elevator chord obtained by dividing the elevator area behind the hinge line by the elevator span.

S_e, the elevator area behind the hinge line.

Although the points for the modified tail (fig. 16) show a fairly close grouping to a common line, those for the original tail (fig. 17) indicate considerable dispersion. Even though the scattering of these points is fairly large, it can be seen that there is a tendency for the points to move upward as the tail normal-force coefficient increases negatively. This shift is in qualitative agreement with the theory for an airfoil with a flap.

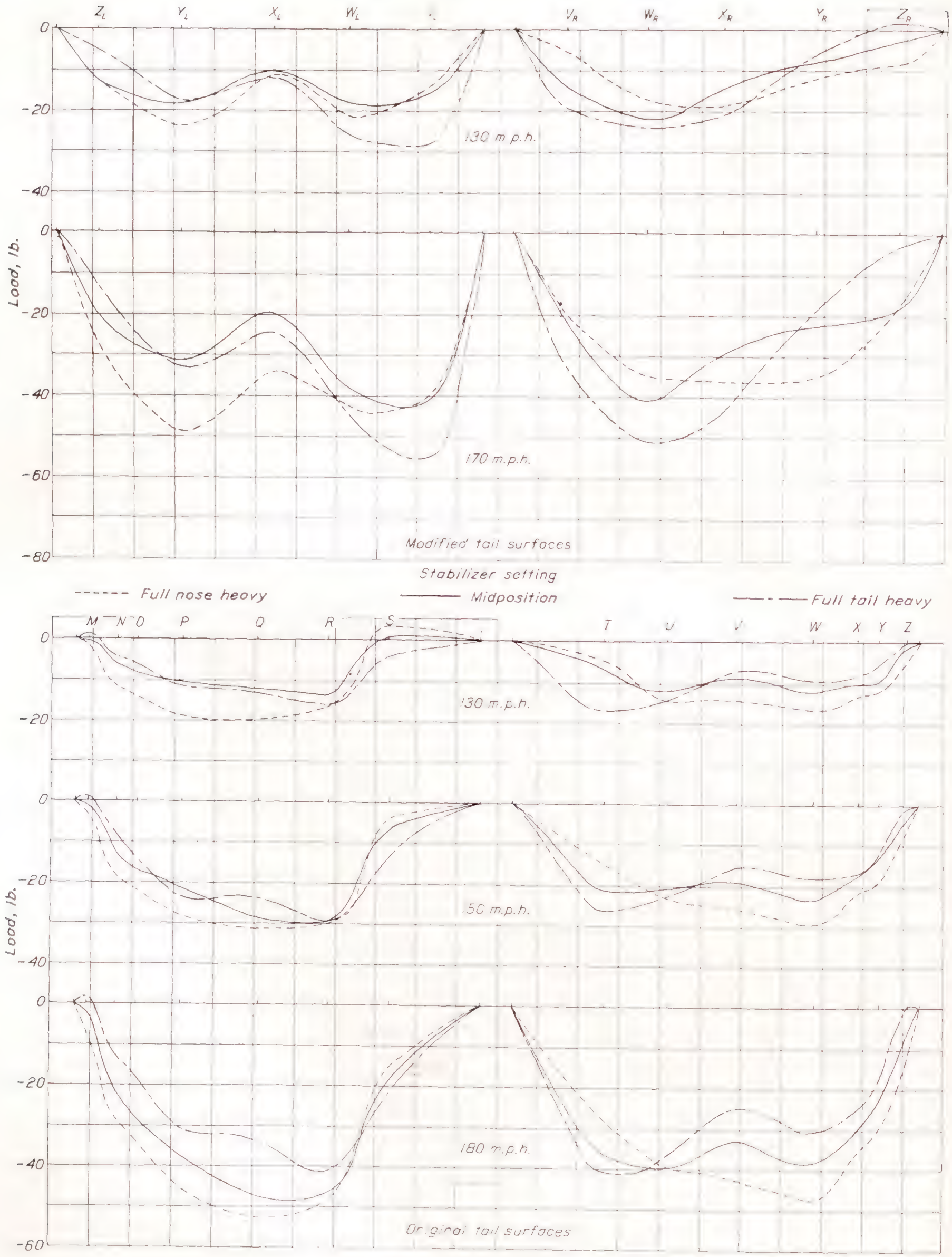

FIGURE 14.—Span load distribution in steady dives.

Pull-ups.—Typical results of the pull-up tests of the original tail are given in figures 18 to 24. Figures 18 and 19 are time histories of the measured quantities in abrupt pull-ups from level flight at various air speeds with the initial stabilizer settings full nose heavy and full tail heavy, respectively. Figure 20 presents time histories of two fairly abrupt pull-outs from dives at approximately 170 miles per hour with the stabilizer trimmed.

The time histories shown in figures 18 and 19 indicate that the maximum down tail loads occurring in the abrupt pull-ups vary with stabilizer setting. At a given air speed the loads with the stabilizer in an initially

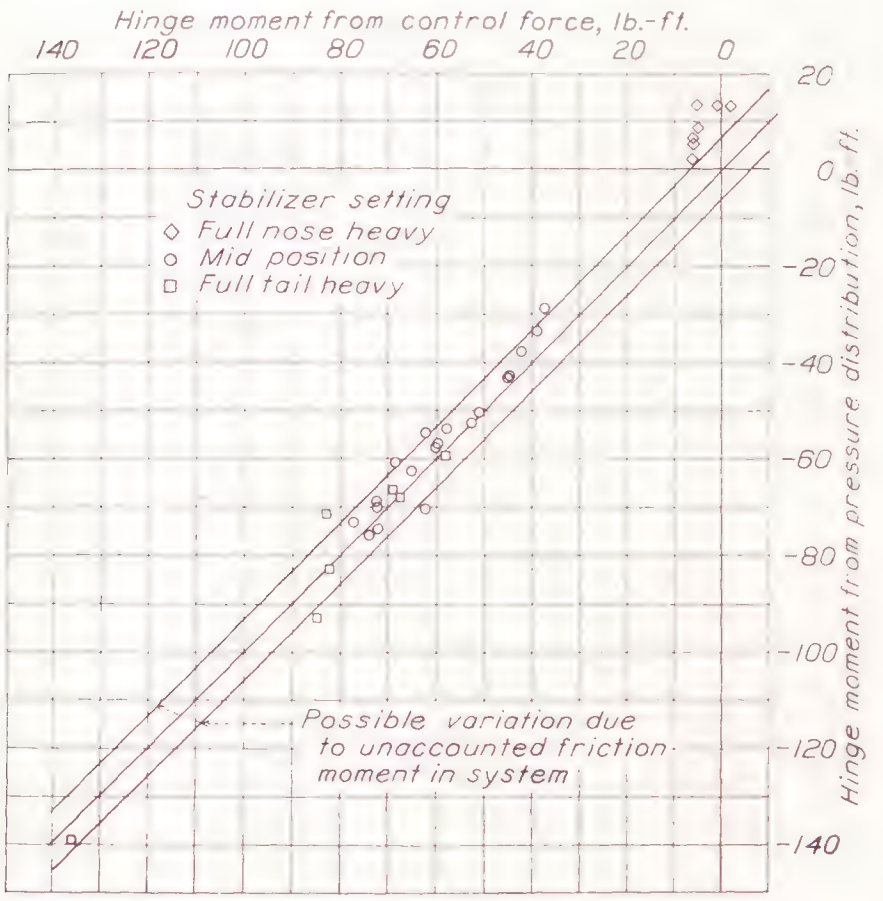

FIGURE 15.—Comparison of elevator hinge moments obtained from pressure-distribution measurements with those obtained from control-force measurements (original tail).

full tail heavy setting are greater than those when the stabilizer is in the other extreme position, but it should be noted that in the nose-heavy setting the total elevator displacements are less. Regardless of stabilizer setting, however, the tail load reaches a maximum with the maximum elevator displacement and before the airplane has had a chance to pitch. The load then quickly decreases and reaches a positive maximum as the airplane gains angular velocity. This positive maximum is generally less than the down load and occurs at about the same time as the maximum acceleration at the center of gravity. In the space of 1.0 second the tail has thus undergone two peak loadings of opposite sign.

The most interesting item occurring in figure 20 is a measured up load greater than the maximum down load. In this run (run 79) it may be observed that the acceleration mounted rapidly toward 6g, where it was abruptly checked when the pilot returned the elevator to neutral. This condition probably occurs quite frequently in airplanes performing acrobatics and the horizontal tail surfaces for such airplanes should consequently be designed to withstand the same load in both directions.

The evolution of the rib pressure distribution occurring in the abrupt pull-ups from level flight at approximately 115 miles per hour is shown in figures 21 and 22. These diagrams correspond to runs 67 and 70 of figures 18 and 19, respectively. Similarly, figure 23 shows the rib pressure distribution occurring in the dive pull-out represented by run 77 of figure 20. It can be seen from these diagrams that with the larger elevator displacements the horn balance performs its

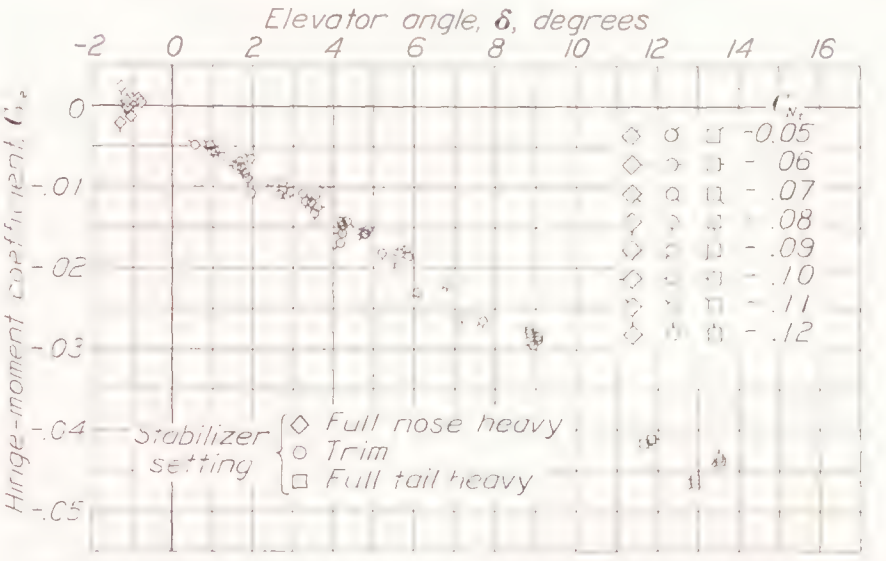

FIGURE 16.—Elevator hinge-moment coefficients with the modified tail.

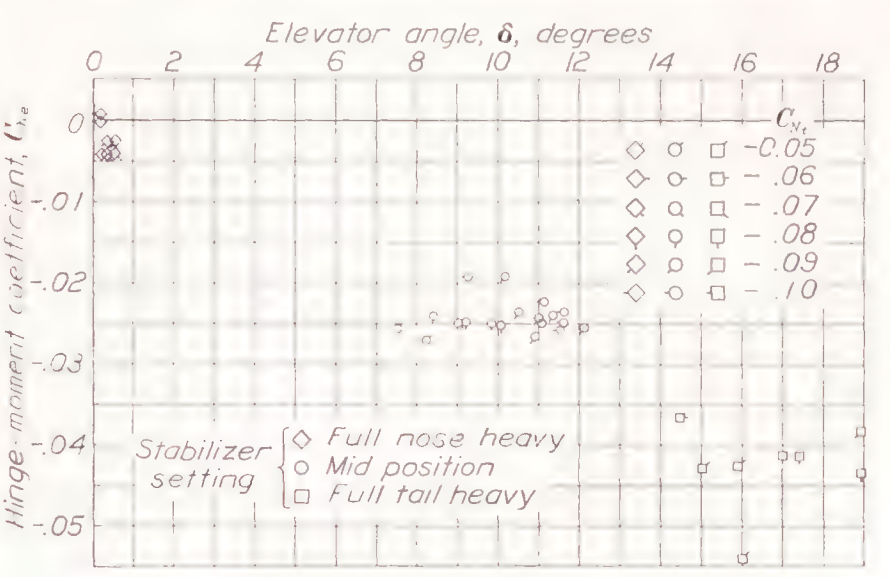

FIGURE 17.—Elevator hinge-moment coefficients with the original tail.

proper function. The Handley Page part of the balance, however, does not contribute so much toward balancing during the first phase of the pull-up as would be expected and during the latter phase it works against balance.

A typical variation of the change in the spanwise load distribution with time is given in figure 24 and corresponds to the results given in figure 22. The shape of the loading curve is more regular than in the steady dives mainly because the larger loads result in larger recorded deflections, which may be read with a greater percentage of accuracy. Another reason for the greater regularity may be that in the pull-up the tail surfaces tend to swing out of the relatively irregular slipstream area.

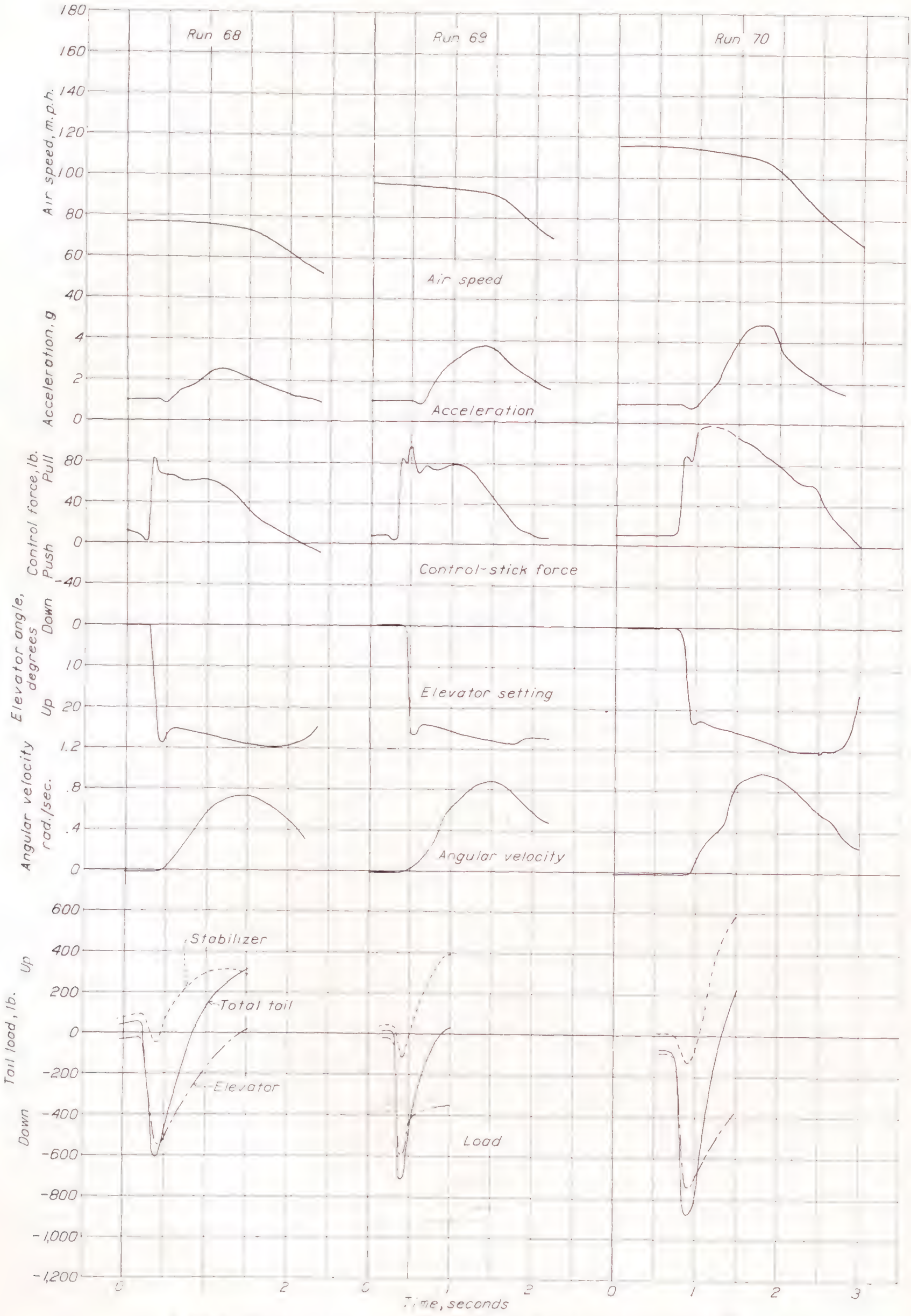

FIGURE 18.—Time history of pull-ups from level flight (stabilizer full nose heavy, original tail).

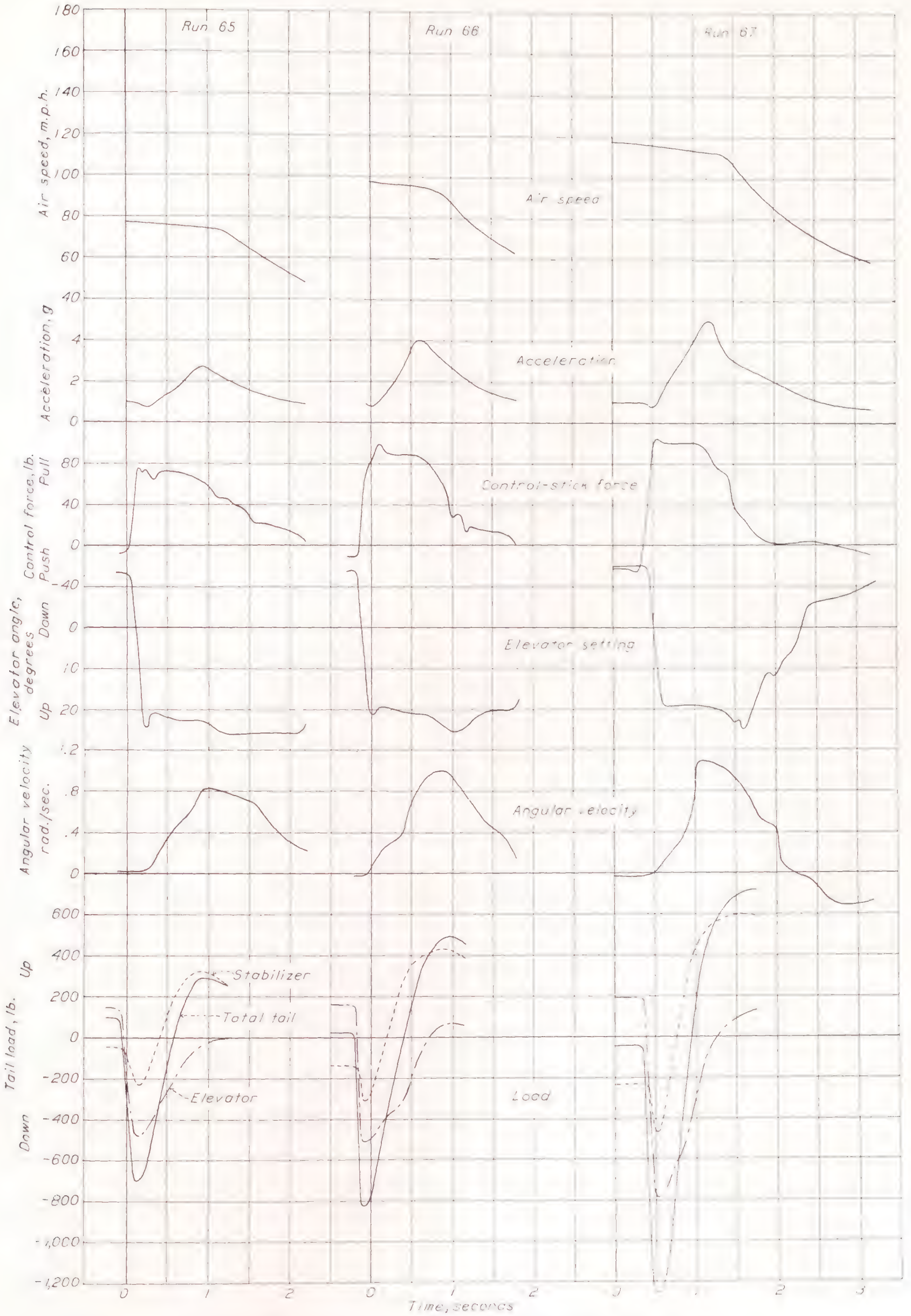

FIGURE 19.—Time history of pull-ups from level flight (stabilizer full tail heavy, original tail).

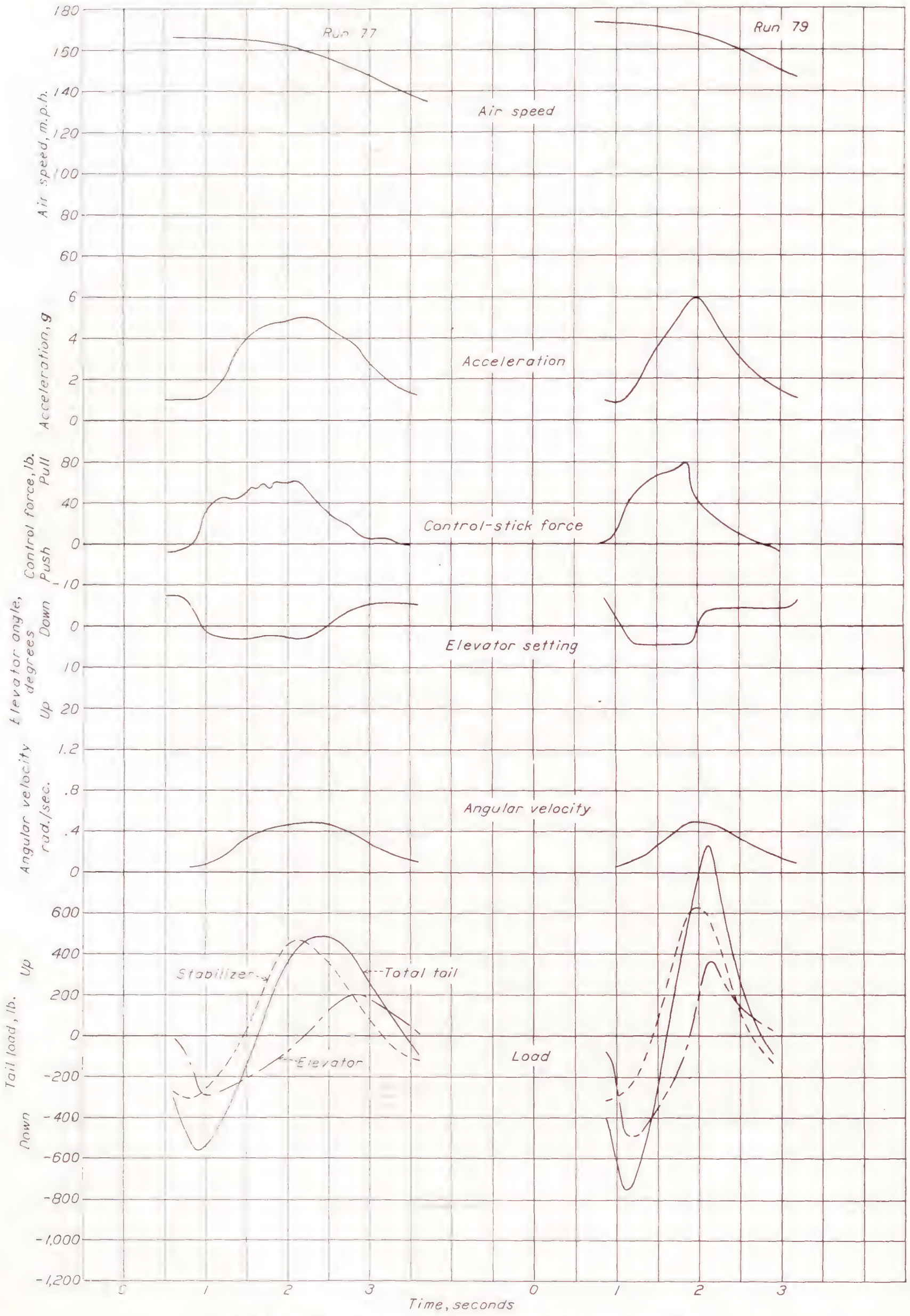

FIGURE 20.—Time history of pull-outs from dives (stabilizer set to trim, original tail).

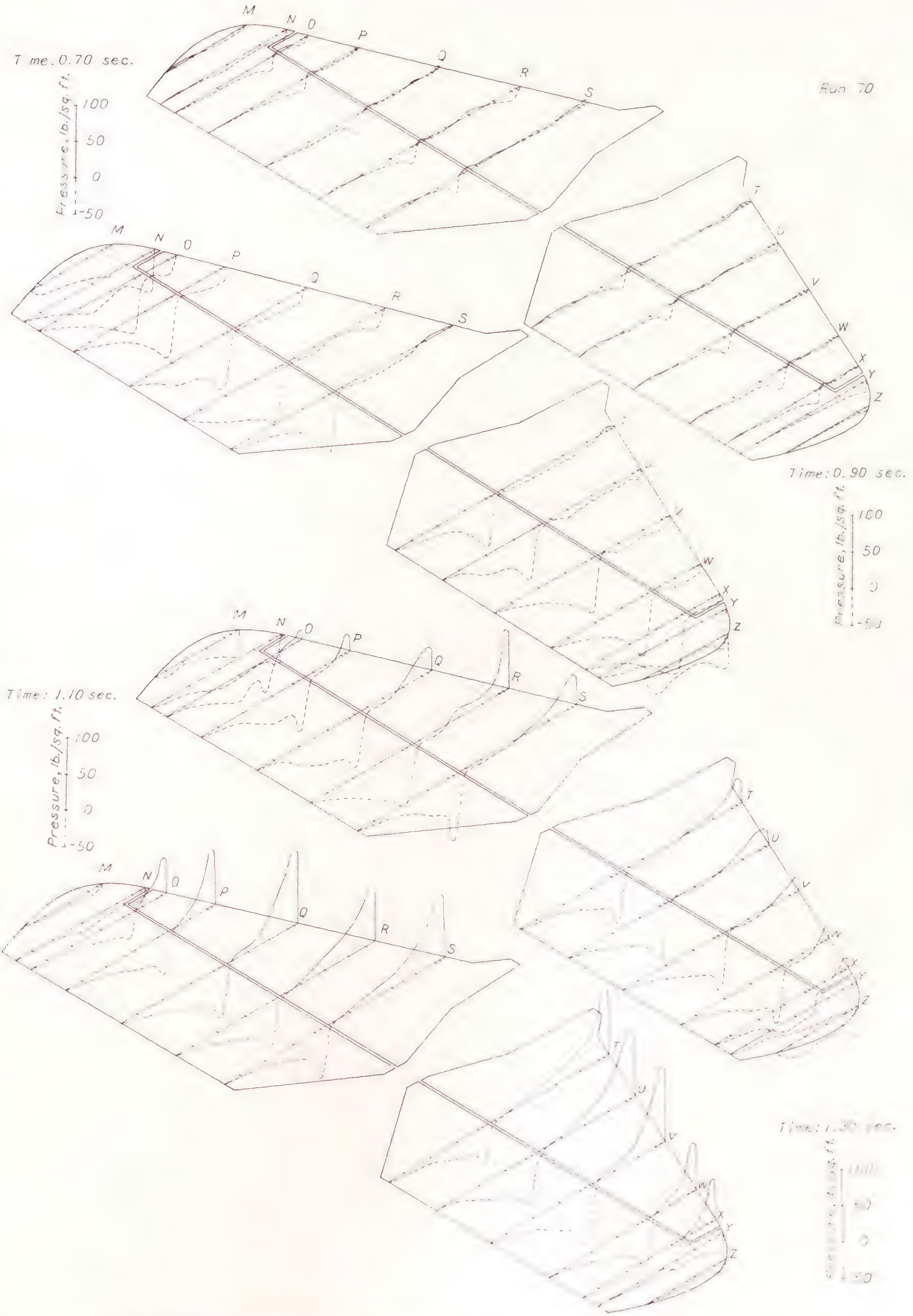

FIGURE 21.—Distribution of resultant pressures at various stages of a pull-up from level flight at 115 miles per hour (stabilizer full nose heavy).

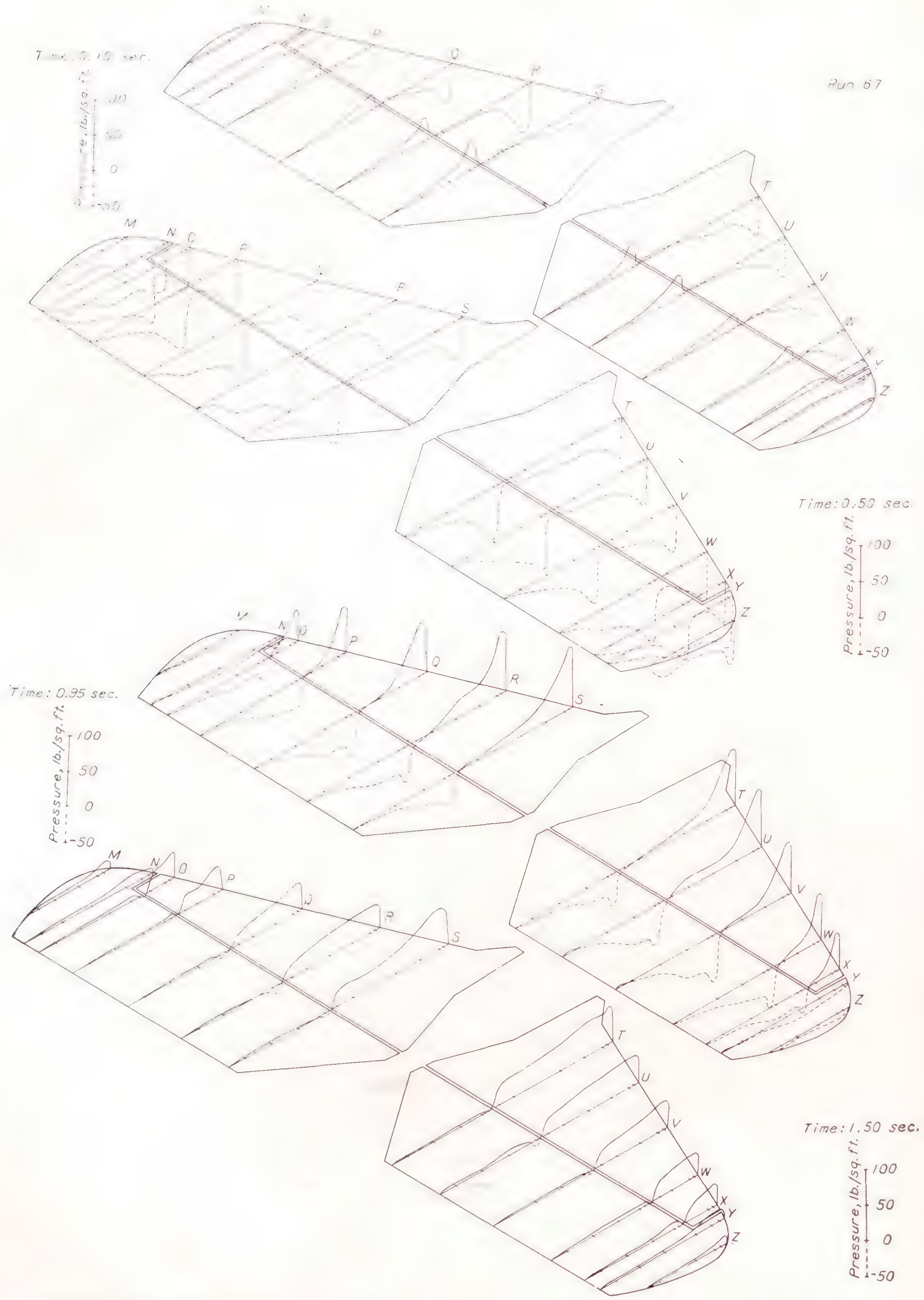

FIGURE 22.—Distribution of resultant pressures at various stages of a pull-up from level flight at 117 miles per hour (stabilizer full tail heavy).

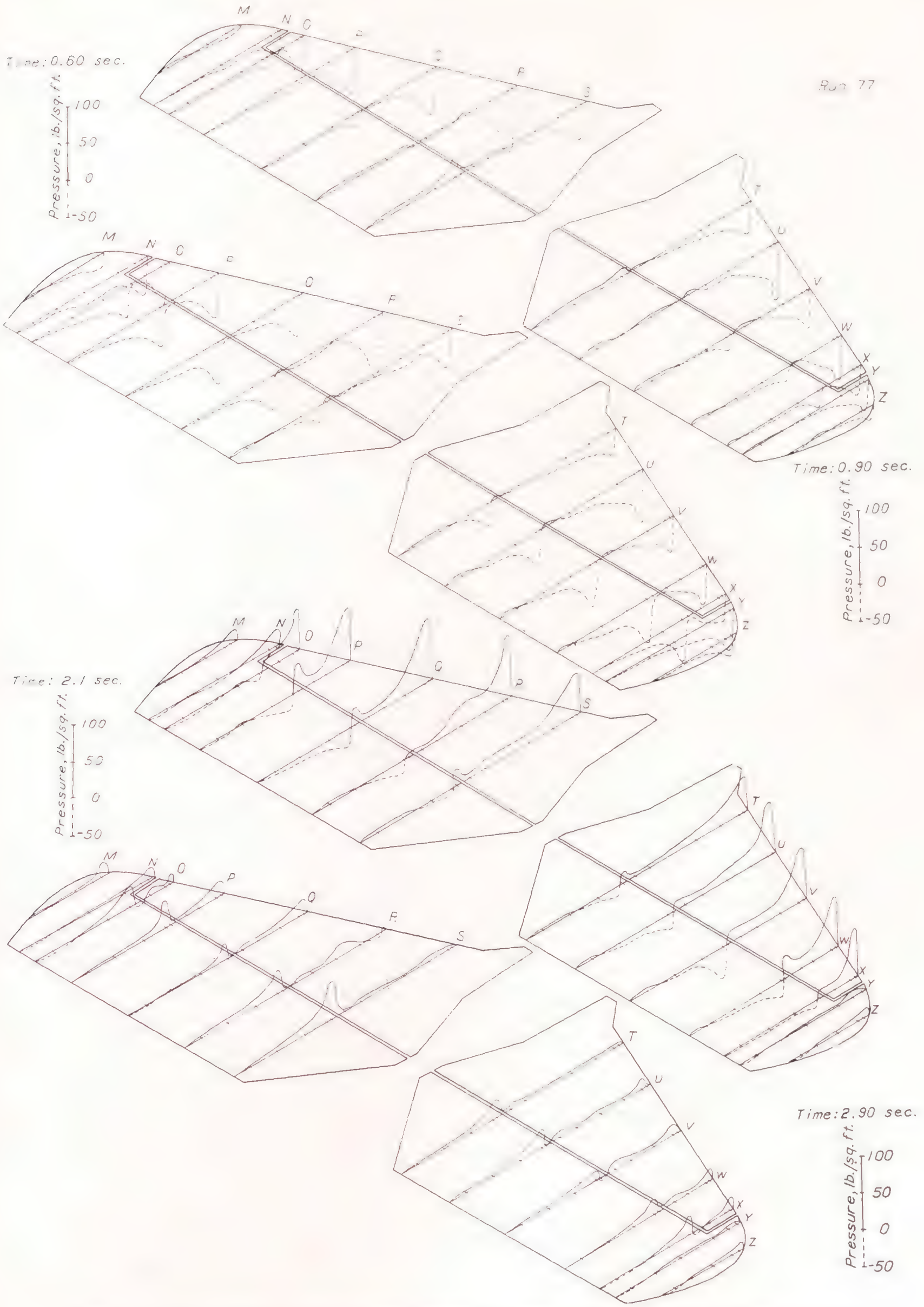

FIGURE 23.—Distribution of resultant pressures at various stages of a pull-out from a dive at 166 miles per hour (stabilizer set to trim).

Although the foregoing figures (figs. 18-24) have given results for the original tail, they also typify those obtained with the modified tail. In figures 25 and 26, however, over-all loads and coefficients are given for both tail surfaces. Figure 25 gives the variation with air speed of the maximum loads measured in abrupt pull-ups from level flight and figure 26 is a plot of the

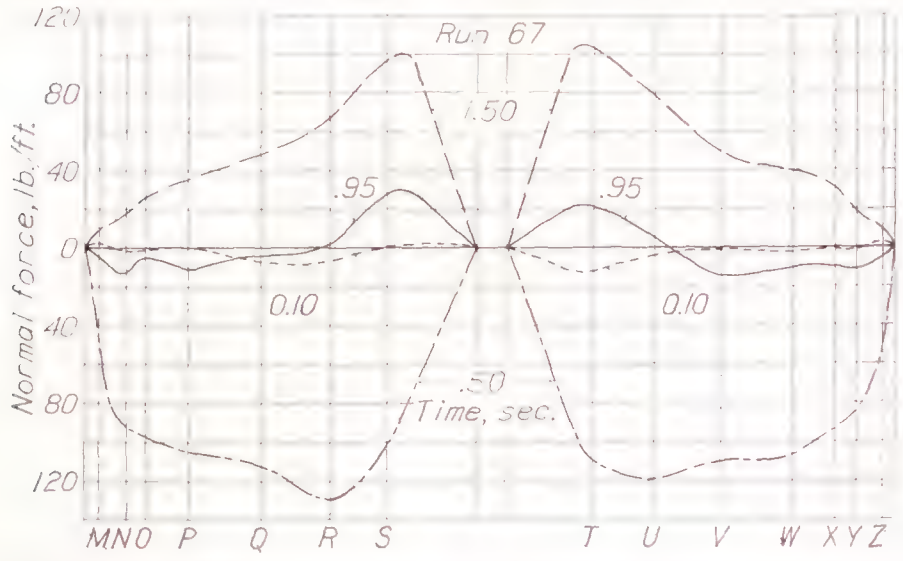

FIGURE 24.—Distribution of normal force along the span of the original tail during a pull-up from level flight at 117 miles per hour (stabilizer full tail heavy).

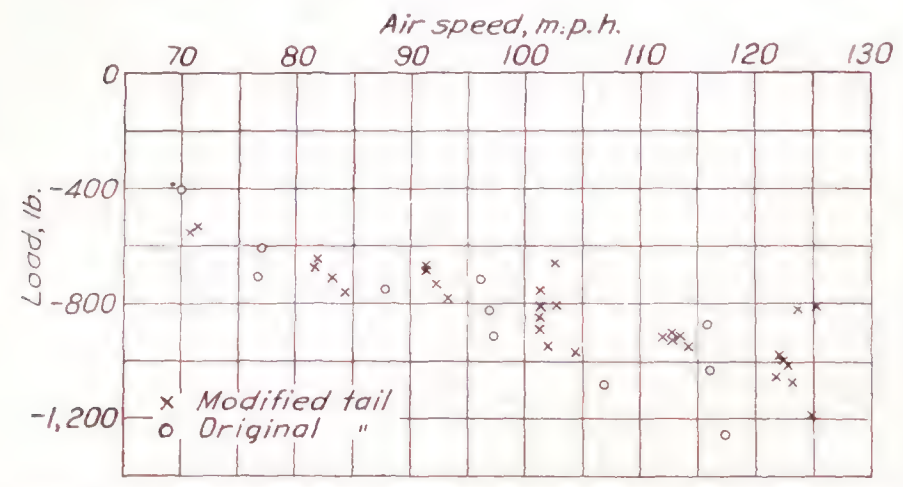

FIGURE 25.—Maximum down tail loads measured in abrupt pull-ups from level flight.

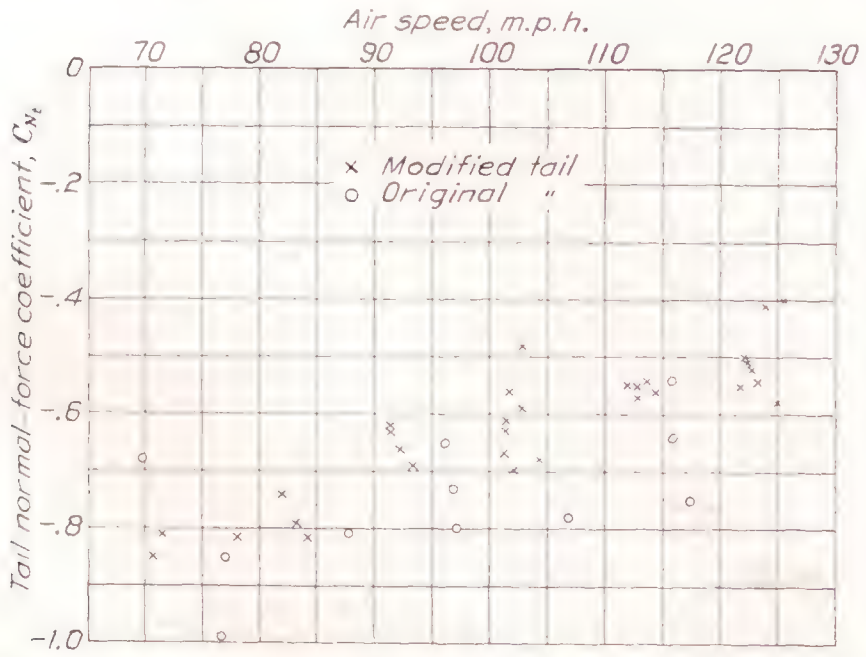

FIGURE 26.—Maximum values of the tail normal-force coefficient measured in abrupt pull-ups from level flight.

corresponding normal-force coefficients, computed from the relation

$$C_{N_t}=\frac{\text{tail load}}{q\,S}$$

where S is the actual tail area including the balances, in square feet. The maximum loads measured are of the same order of magnitude, about 1,200 pounds, for both tail surfaces. For the original tail, however, the maximum unit loading per square foot is higher (26.6 pounds) because of its smaller area. At a given air speed there is a large variation in the maximum loads

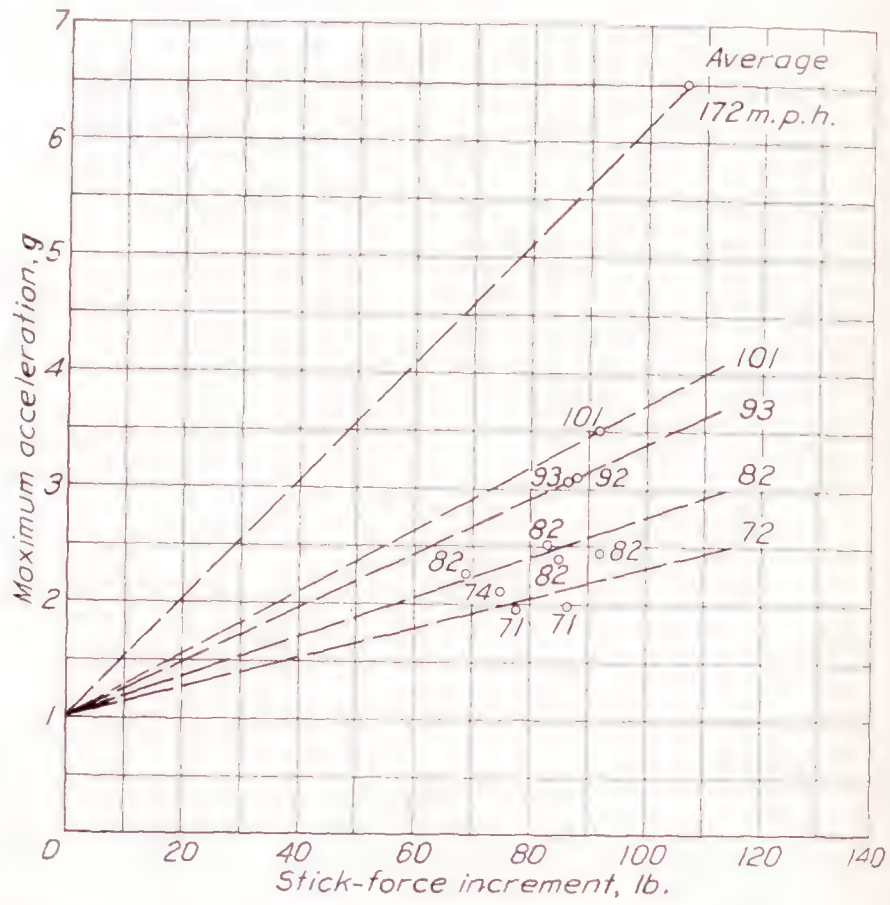

FIGURE 27.—Relation between acceleration and stick-force increment in abrupt pull-ups from level flight (modified tail). Numbers refer to air speed at start of pull-up.

measured that is due to slightly different rates of stick movement and to differences in the applied forces. Differences in the rate of stick movement are difficult

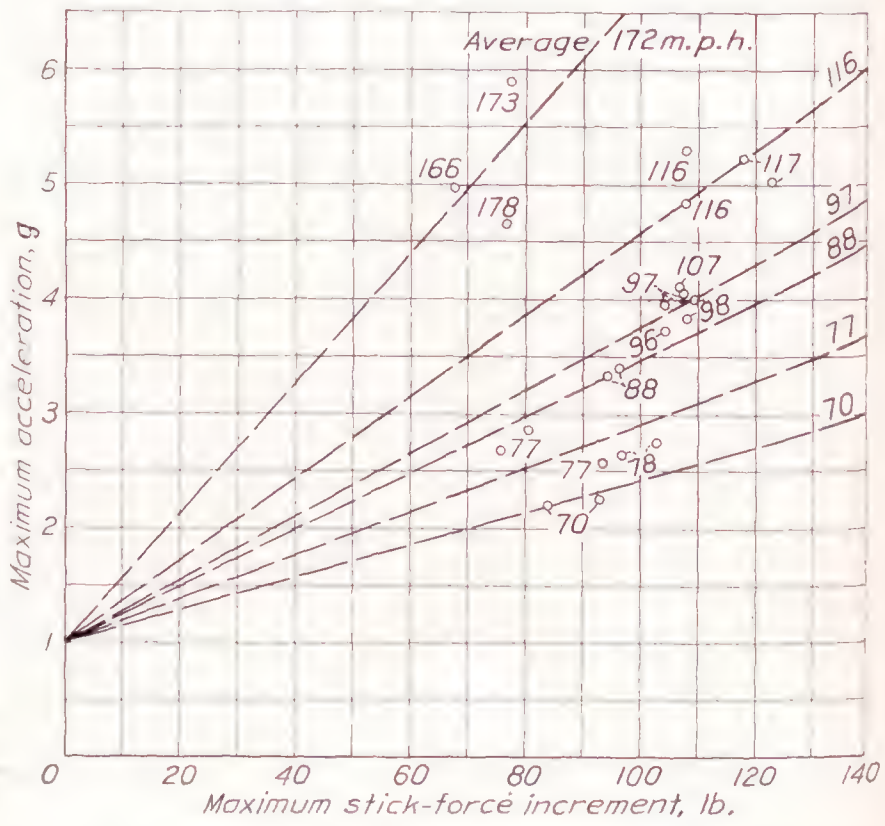

FIGURE 28.—Relation between acceleration and stick-force increment in abrupt pull-ups from level flight (original tail). Numbers refer to air speed at start of pull-up.

to detect because of the steep gradient of the control records.

An average line through the points of figure 25 would indicate that the maximum load obtained in the abrupt pull-ups varies nearly linearly with the air speed instead of as the square and, as a consequence, the normal-force coefficients increase inversely with the air speed.

The variation of the maximum acceleration in the abrupt pull-ups with the increment in stick force is plotted in figures 27 and 28 for the two tail surfaces with each point labeled for the air speed that existed at the start. The increment given is the difference between the maximum force recorded during the pull-up and the initial force on the stick prior to the maneuver. If straight lines are drawn, as indicated, through the average of each group of points for a given air speed and the 0–1g point, it is apparent that the increment of force required to produce a given acceleration increases with a decrease in air speed. Since no graduated pull-ups were made, the relation between acceleration and stick-force increment may not be linear as indicated by the lines in figures 27 and 28.

II. PRESSURE DISTRIBUTION OVER THE RIGHT WING CELLULE AND SLIPSTREAM SECTIONS

METHOD

The tests of the wing cellule were carried out in two parts in order to make the best use of the available pressure cells. In the first section, called the "wing hook-up," pressure measurements were taken on all ribs on the upper wing outboard of, and including, rib S_1 and all ribs, excepting R_1, on the right lower wing (fig. 4). In the next section, called the "slipstream hook-up," pressure measurements were taken on ribs S_1, B, and H, in addition to all the ribs previously omitted. Thus ribs S_1, B, and H furnished a means for tying in the data between the two sections, a procedure simplified by making similar runs with the two arrangements.

The flight tests with each arrangement were divided into three groups consisting of: (1) a series of level-flight runs starting from just above stalling speed and increasing by approximately 10-mile-per-hour increments up to high speed, (2) a series of abrupt pull-ups and push-downs from level flight at the foregoing speeds, and (3) a series of abrupt right and left aileron rolls with rudder neutral at various speeds throughout the speed range. Several shallow dives at about 170 miles per hour were also made with the engine fully throttled.

The method of working up the results was somewhat similar to that employed in the tail-surface tests. For the symmetrical-loading conditions the rib-pressure curves were mechanically integrated to obtain the rib load and the rib moment about the wing leading edge. The rib loads and moments were then converted into coefficient form by the relations

$$(1)\ c_n = n/qc$$

$$(2)\ c_m = m_{l.e.}/qc^2$$

where

c_n is the rib normal-force coefficient.
n, rib load normal to chord, pounds per foot of span.
q, dynamic pressure, pounds per square foot.
$m_{l.e.}$, pitching moment about leading edge, foot-pounds per foot.
c_m, pitching-moment coefficient about leading edge.
c, rib chord, feet.

The rib loads were then plotted against their span location and the resulting curves integrated for total wing load. These loads were converted to individual wing and wing cellule normal-force coefficients from the relations

$$C_{N_U} = \frac{N_U}{qS_U};\quad C_{N_L} = \frac{N_L}{qS_L}$$

and

$$\text{Cellule } C_N = \frac{C_{N_U}S_U + C_{N_L}S_L}{S_U + S_L}$$

where

N_U and N_L are the integrated loads for upper and lower wings, pounds.
S_U and S_L are the upper and lower wing areas, square feet. The lower wing area does not include the part intercepted by the fuselage.

In the aileron rolls, the rib-pressure curves were integrated for both load and moment but the results were not converted into coefficient form.

Since the tie-in rib S_1 on the upper wing was some distance out from the center, it was necessary, in order to obtain the cellule and upper wing normal-force coefficients, to extend the span loadings to the wing center. In the symmetrical-flight conditions they were extending by plotting the values of the normal-force coefficients of the slipstream ribs against that of the tie-in rib. The span load for the upper wing was then continued by means of these intermediate plots together with the appropriate value of the normal-force coefficient for rib S_1. In the aileron rolls, the span loads were continued across the slipstream sections by interpolation between the partial-span load curves for the slipstream section by the use of the values of normal-force coefficients given by the tie-in ribs S_1 and H.

PRECISION

The individual rib pressures in the wing investigation are subject to the same errors listed for the tail pressures. The magnitudes of the different sources of error are the same with the exception of that due to width and haziness of the record lines, which is less for the wing tests. The errors in rib loads due to fairing are also smaller because of the larger number or orifices per rib.

The loads on the individual wings are believed to be correct to within 75 pounds and individual rib loads to within 7 pounds. A good idea of the accuracy of the load results may be obtained by noting the dispersion of the points in figures 33 and 34.

The air speeds in level flight are correct to within 1½ miles per hour. In the push-downs, pull-ups, and rolls, the air-speed head, although measuring the dynamic pressure at the head correctly to within 2 percent, does not record the correct dynamic pressures for calculating coefficients since the speed varies along the span. Control positions and control forces are believed accurate to within 2° and 3 pounds, respectively.

RESULTS AND DISCUSSION

Symmetrical-flight condition.—Results for the symmetrical-flight condition, which includes push-downs, pull-ups, dive pull-outs, and steady flight, are given in figures 29 to 35.

Typical span load and span c_n variations are given in figure 29 for steady flight at air speeds ranging from 58 to 171 miles per hour. The span loadings over the upper wing in level flight (fig. 29 (a)) show comparatively little variation with air speed. At the center the loads tend to be low owing to the center-section cut-out; also, owing to a clockwise rotation of the slipstream, there is a tendency for the loads just to the right of the center line to be lower than those to the left. The load curves for the lower wing show a similar but increased slipstream effect, which is due to the low position of the thrust line. Although the rotation effect is present on the wings, the tests of the tail surfaces indicated that there it had been practically damped out since little dissymmetry of load occurred.

In the throttled dive (fig. 29 (a)) the span loading is much more irregular than in the level-flight condition owing to the fact that a negative thrust is present and that the wing had a slight twist, the effect of a small twist on the load being much more noticeable at the smaller wing lift coefficients. Measurements of the profiles of the extreme tip ribs (G and N) on both wings showed them to be at a smaller effective angle than those farther inboard while ribs F and M were found to be at a higher angle. This twist at the tip was due to the fairing used in forming the rounded portion of the wing, although there may also have been an actual twist of the wing structure in flight.

The curves given by figure 29 (b) indicate that the c_n values at the center tend to be high, even though these sections are effectively washed out with respect to the rest of the wing, because of the tendency for the lift to be maintained across a cut-out. This washout arises from the fact that the ribs in the center section were formed by simply cutting off the trailing edge of a Göttingen 398 airfoil and fairing in the bottom surface, as shown by figure 4.

The distribution of load on the individual wing ribs is given in figure 30 where the local pressures are given in terms of the dynamic pressure at the air-speed head. These distributions, which correspond to some of the previous span-loading curves, are similar to those obtained in other investigations and require no comment as to their shape. It will be noted, however, that the pressures at the leading edge show a peculiar variation, indicating that there the flow is extremely critical.

Although figures 29 and 30 showed typical results for the load distribution, the final averaged results for the symmetrical-flight condition are contained in figures 31 and 32. The results of these figures, which give the variation of rib c_n with individual wing C_N and of rib c_m with rib c_n respectively, were determined from curves similar to those given in figures 33 and 34, which indicate both the average scattering and the number of experimental points used to establish each of the curves given in figures 31 and 32. It will be noted (figs. 31 and 32) that ribs S_2 and S_3 show two distinct curves at the higher lift coefficients. The points that form the second, or dotted, curve occurred in some but not all of the pull-ups. An analysis of the points determining the two curves showed no tendency for one curve to be associated with pull-ups at one end of the speed range or vice versa; also, since these pull-ups were made from power-on flight, a difference in slipstream conditions was not an explanation. The only cause to which this peculiar flow could be attributed was that the flow past the top of the fuselage nose, which incidentally had louvers, was critical to the shutter opening on the radiator.

In these tests the maximum individual wing C_N measured was 1.9 (upper wing); the maximum individual rib c_n values measured were over 2.1 for ribs S_2, S_3, and S_A. These high values are common in abrupt maneuvers and occur if the angular velocity in pitch is sufficiently great to carry the lift past the normal burble angle before the wing stalls.

The relative efficiency of the wings is given in figure 35 where the ratio C_{N_U}/C_{N_L} is plotted against the cellule C_N. These curves were determined from the results of an integration of individual wing-load curves, known wing areas, and an air speed measured one chord length ahead of the upper wing. It is obvious, however, that in a pull-up or push-down the wings are actually traveling at different air speeds owing to the angular velocity in pitch and that the effect, if a single air speed is used, is to change the apparent relative efficiencies between the wings of a biplane. Figure 35 shows three distinct curves, rather than a series of transition curves, because the points determining them were obtained from records that were read near or at the peak loads, which occur practically simultaneously with the maximum angular velocity. If the records had been read at intervening time intervals, a gradual transition from the level-flight to the pull-up curve would have been indicated.

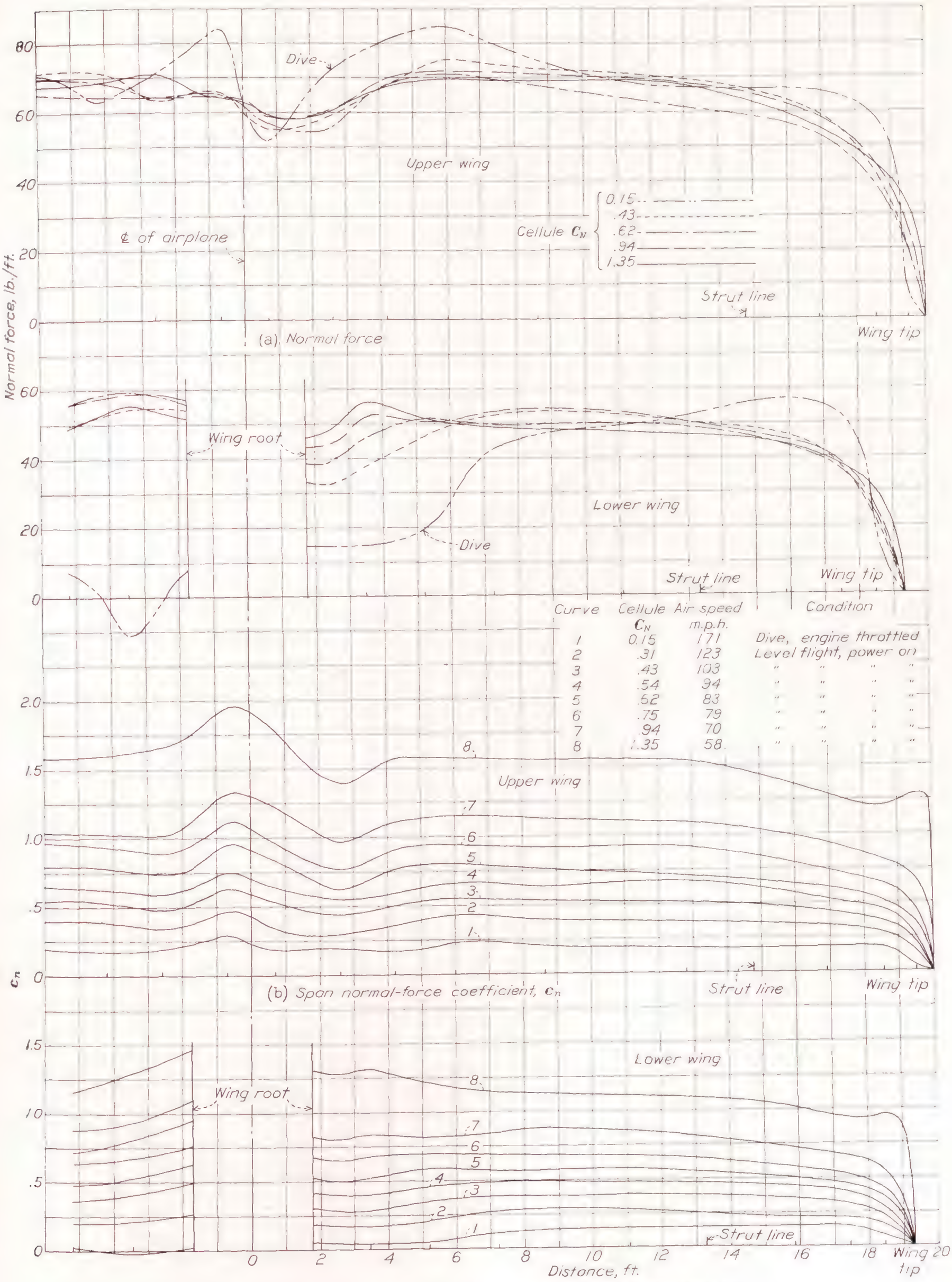

FIGURE 29.—Distribution of normal force and normal-force coefficient along the wing span.

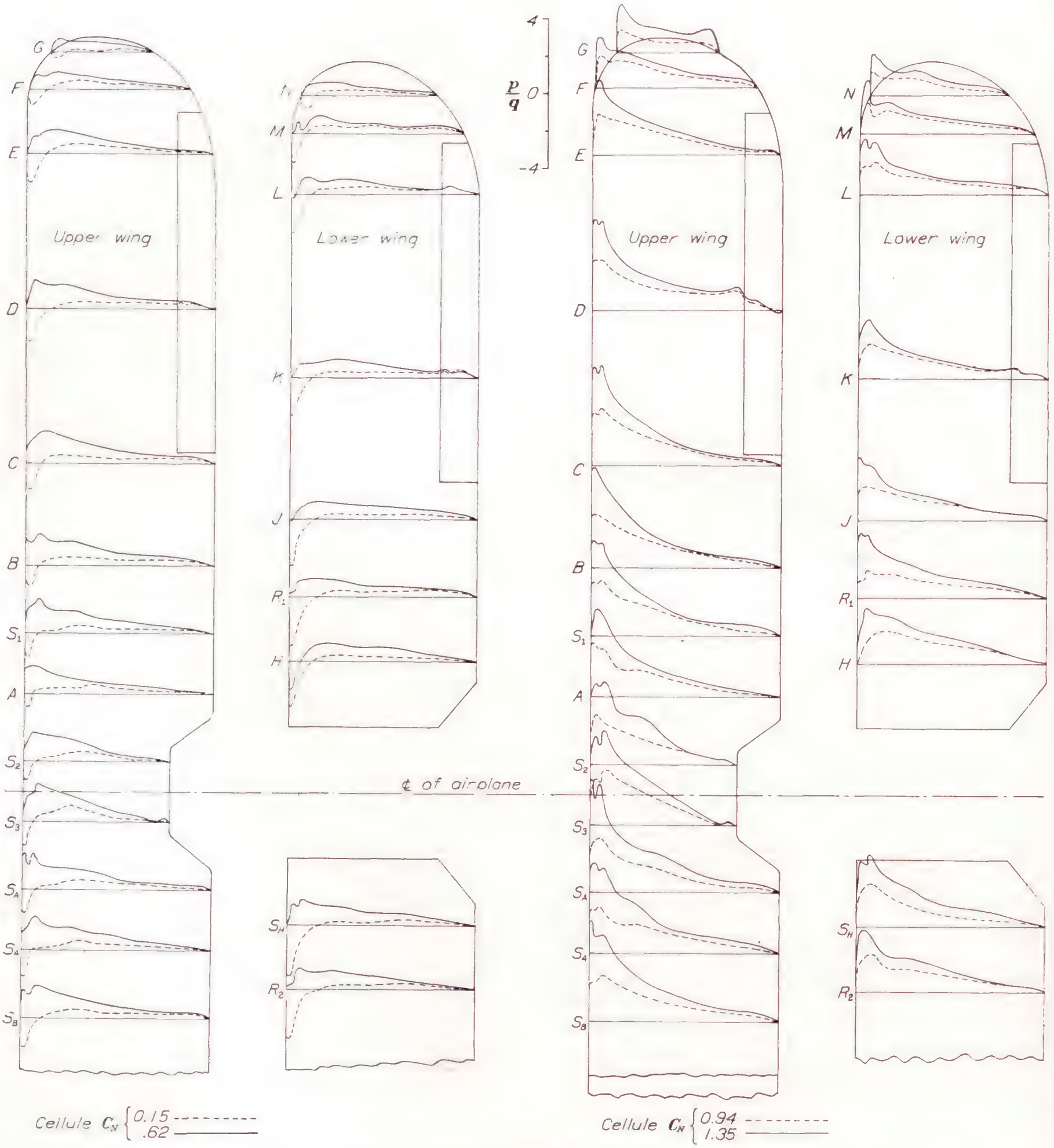

FIGURE 30.—Rib pressure distribution in steady flight.

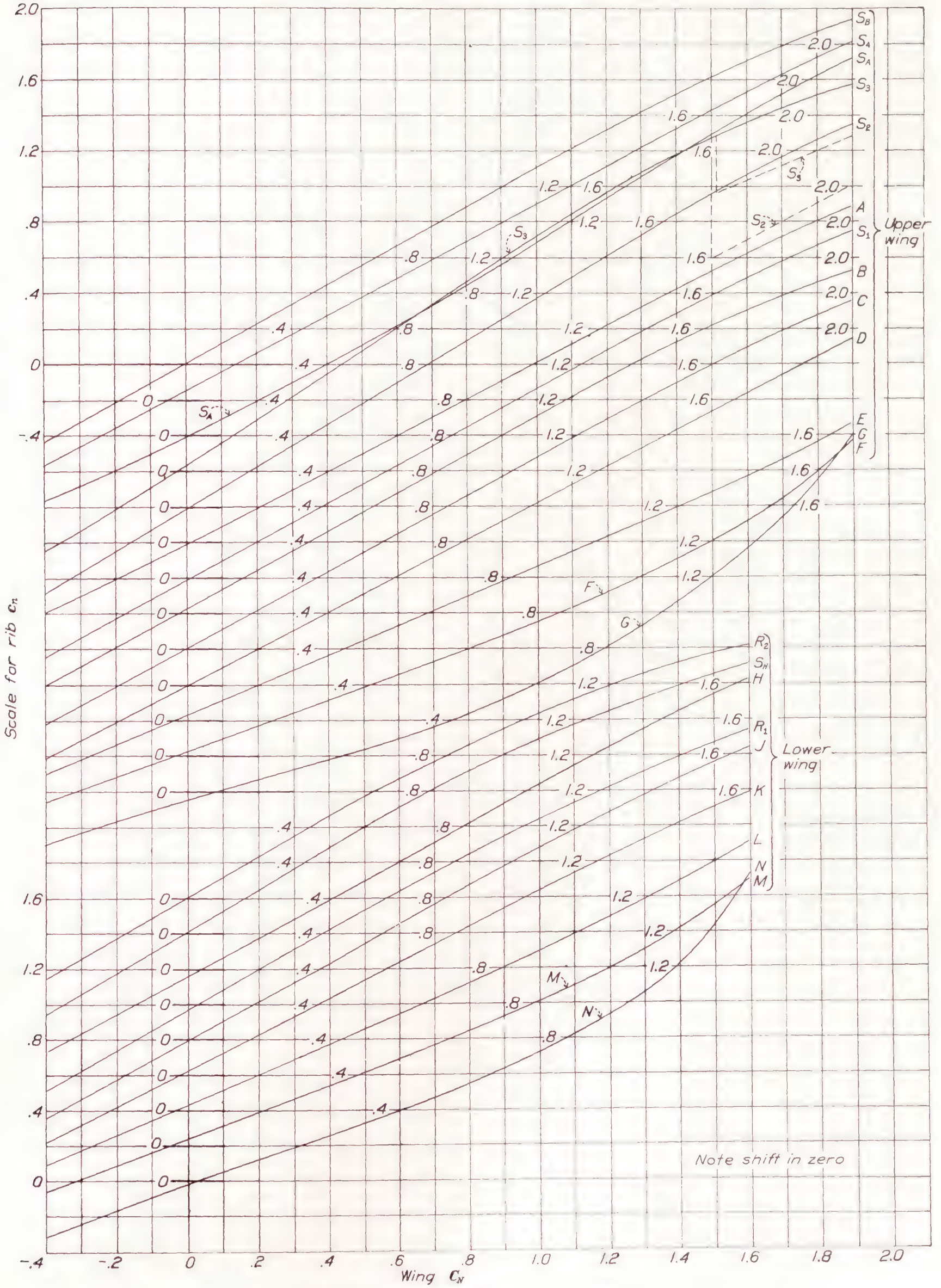

FIGURE 31.—Variation of rib c_n with individual wing C_N.

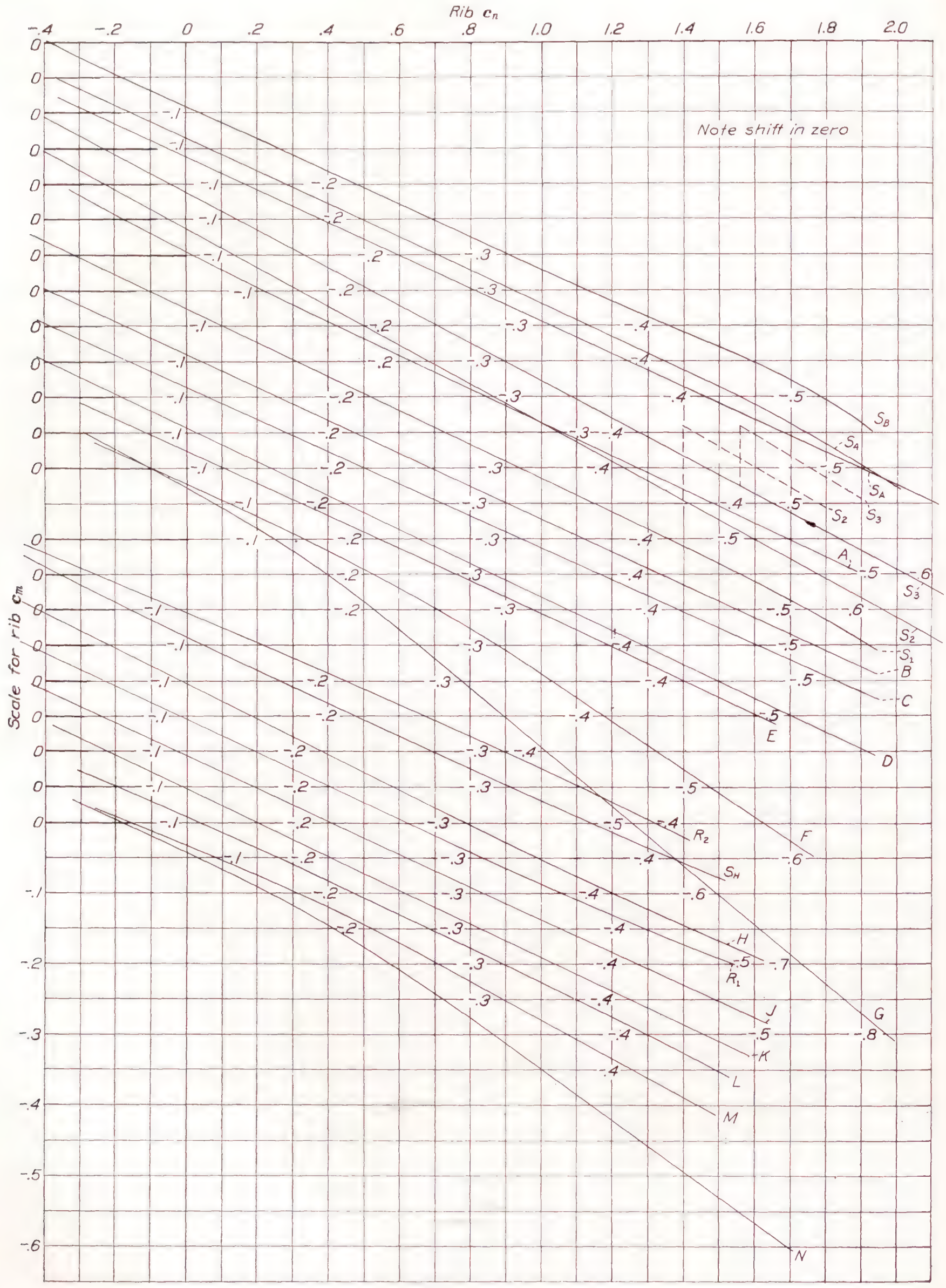

FIGURE 32.—Variation of rib c_m with rib c_n.

In order to reconstruct the span c_n or c_m distributions obtained in the symmetrical-flight conditions a cellule coefficient is first chosen and reference made to figure 35 to find the relative efficiency. With this ratio and the formula

$$\text{Cellule } C_N = \frac{C_{N_U}S_U + C_{N_L}S_L}{S_U + S_L}$$

the individual wing C_N values may be found. Figures 31 and 32 are then referred to for the variation of rib c_n and c_m along the span.

Aileron rolls.—The results of the aileron rolls are given in figures 36 to 41 and in table II. Time histories of the measured quantities are given in figures 36 and 37 for 6 right and 6 left aileron rolls made at various air speeds. Figures 38 to 40 give the variation with time of the span load distribution, rib load distribution, and individual wing load during abrupt right and left aileron rolls at 120 miles per hour. These results, which correspond to runs 43 and 39 (figs. 36 and 37), are typical of those measured at other speeds. The maximum measured air loads on aileron ribs D and K are given in figure 41. The wing rib characteristics,

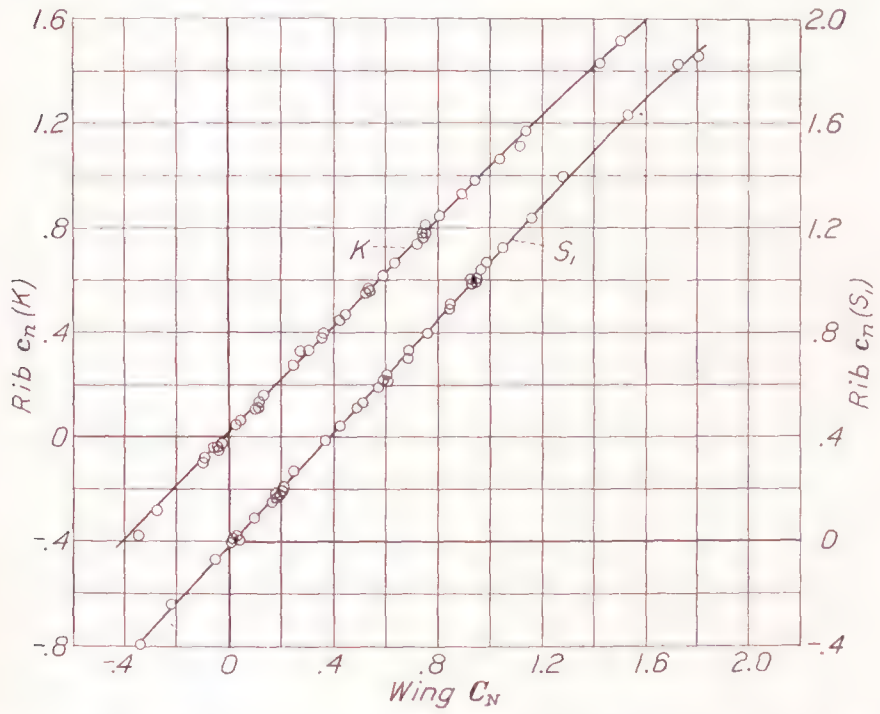

FIGURE 33.—Typical wing rib c_n curves showing scattering of experimental points for ribs S_1 and K.

i. e., rib loads, rib moments about the leading edge, and rib centers of pressure, are tabulated in table II for all the aileron rolls.

The irregularity of the span-load curves in the roll (fig. 38) is due to the combination of an effective twist introduced by deflecting the ailerons and a twist introduced by the subsequent rolling motion. In a left roll, the load on the right wing is first increased owing to the down aileron; then, as the airplane rolls, the load decreases owing to the rolling action and also to the decrease of the component of airplane weight normal to the span. In a right roll, the load on the right wing is first decreased by the aileron action; subsequently it tends to increase as rolling occurs and finally to decrease as the lift component becomes smaller. This variation is indicated both by the time histories of the accelerometer mounted inside the wing near the tip (figs. 36 and 37) and by the results shown in figure 40.

The load distribution over the aileron ribs (fig. 39) indicates that the peak pressure at the leading edge of the aileron is greater during the left aileron roll than during the right. This variation is due to a smaller aileron deflection and is shown in figures 36 and 37. Since the ailerons had no differential action, the smaller deflection is a direct result of piloting technique.

The results shown in figure 41 indicate that the loads measured on aileron ribs D and K tend to increase

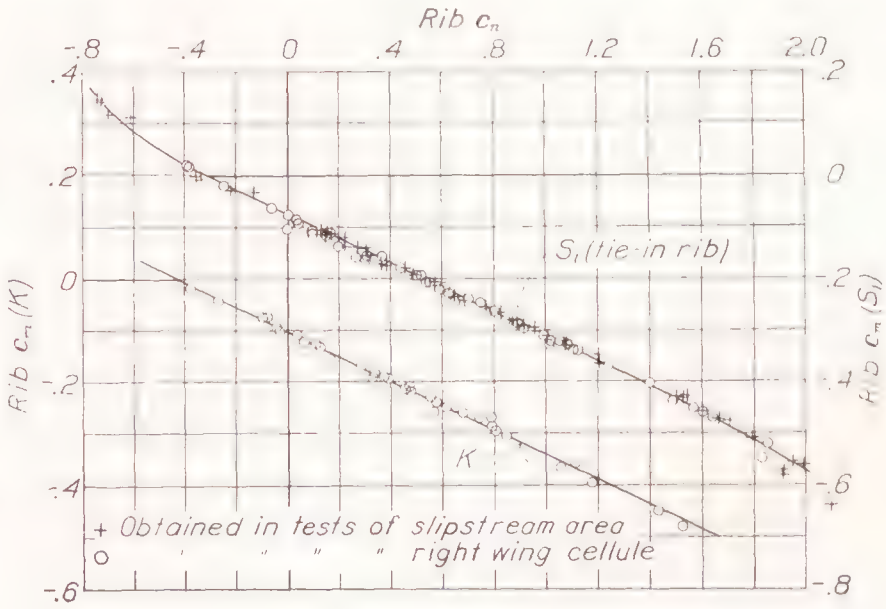

FIGURE 34.—Typical wing rib c_m curves showing scattering of experimental points for ribs S_1 and K.

linearly with initial air speed as did the maximum load on the tail surfaces in the abrupt pull-ups. The load on the upper aileron rib (rib D) is larger than that on the lower aileron rib regardless of the direction of deflection. Since the resultant load on the aileron is upward for zero deflection (fig. 30), the magnitude of the up loads with the aileron down is greater than the corresponding down loads when the aileron is up.

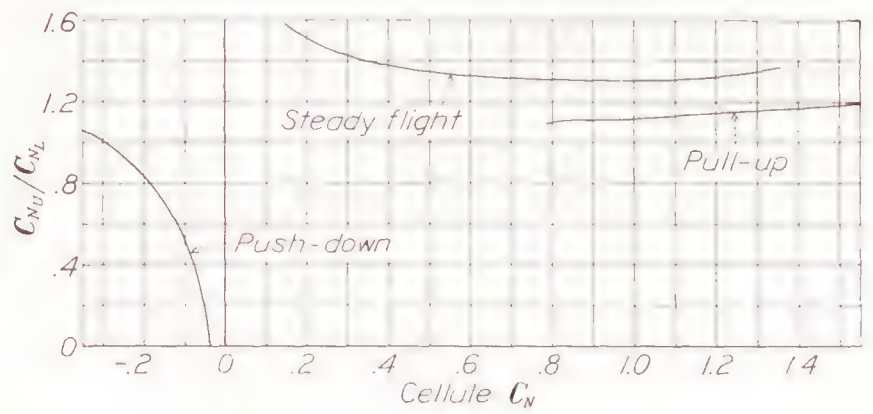

FIGURE 35.—Relative efficiency of upper and lower wings.

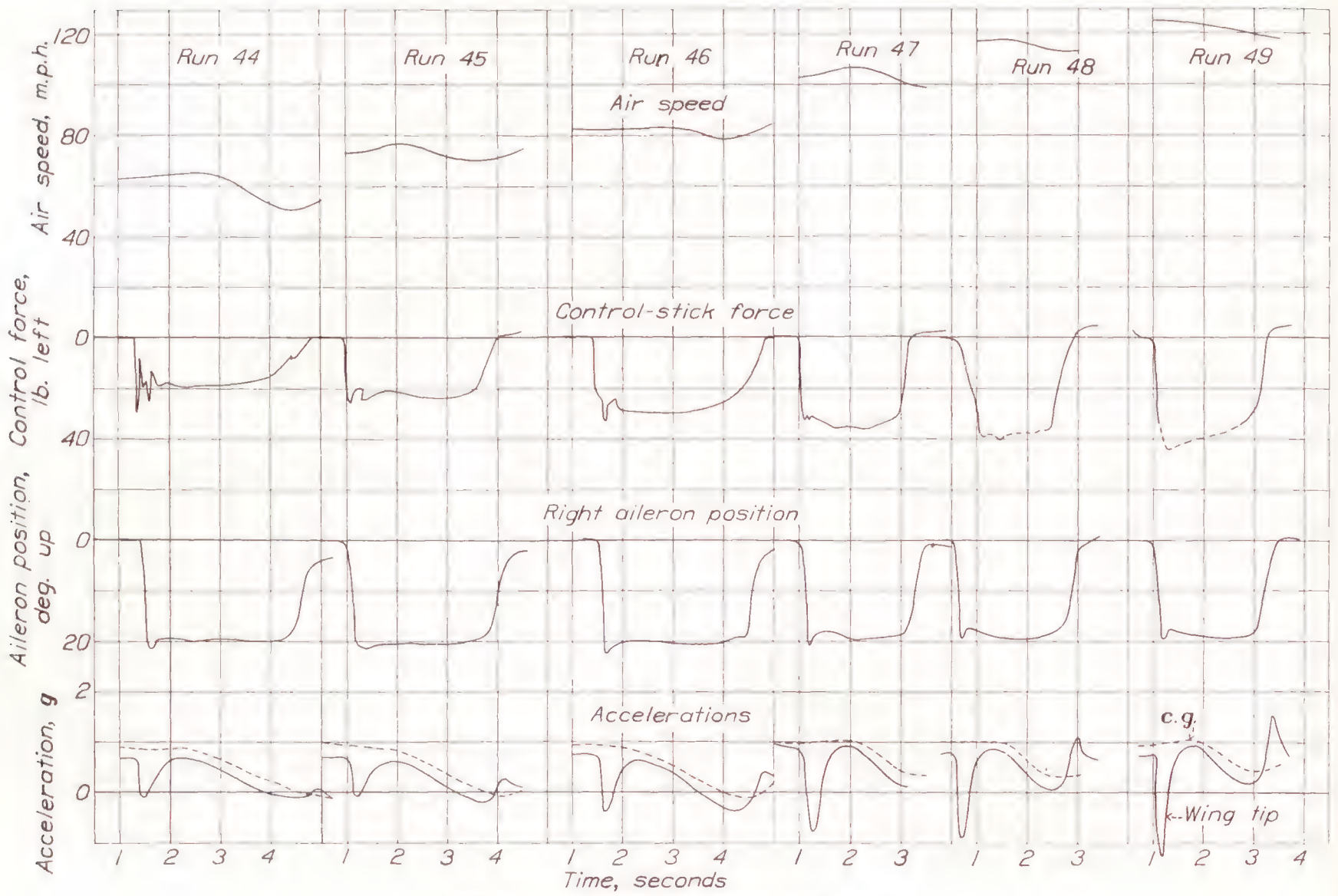

FIGURE 36.—Time histories of six right aileron rolls.

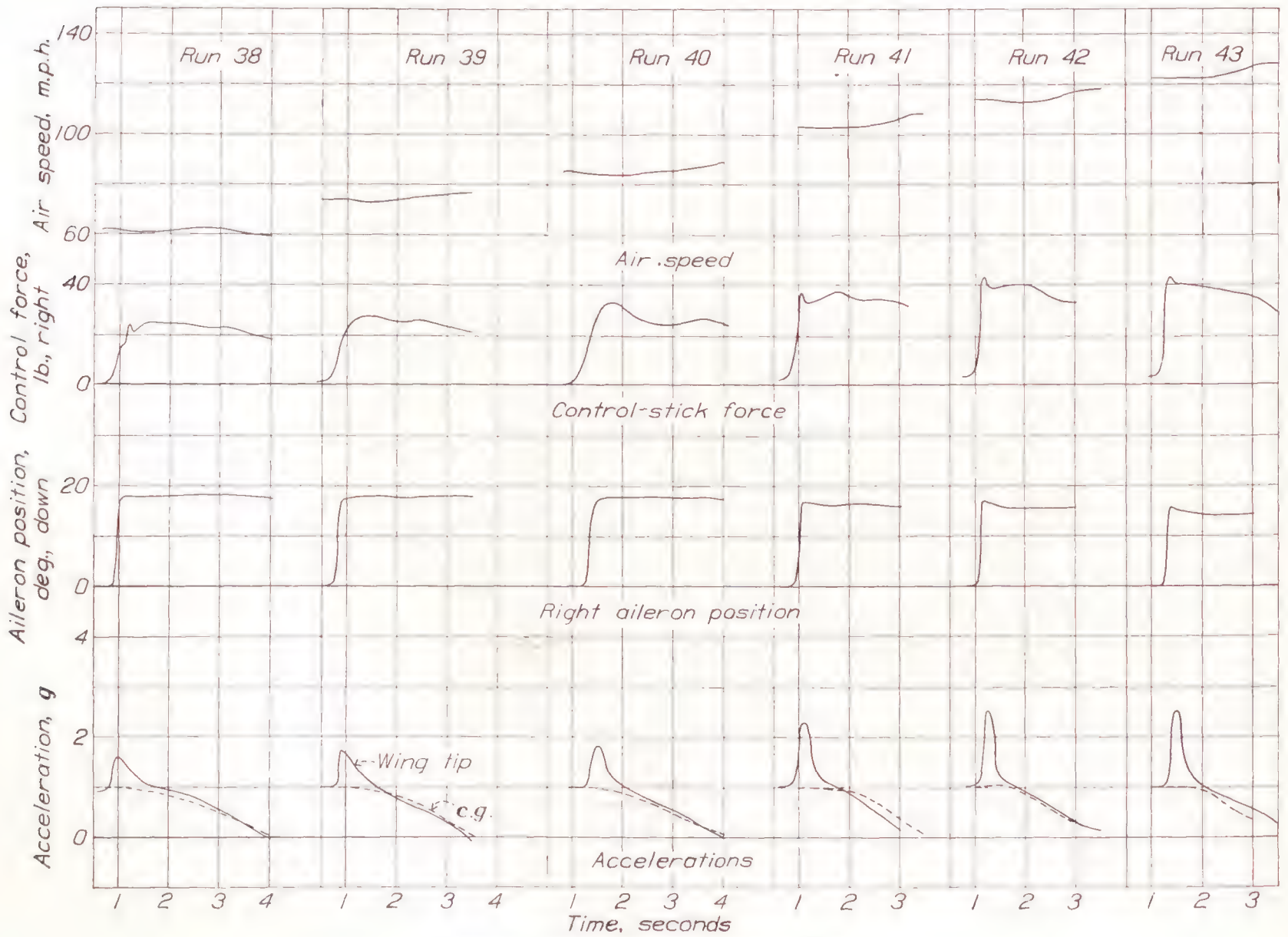

FIGURE 37.—Time histories of six left aileron rolls.

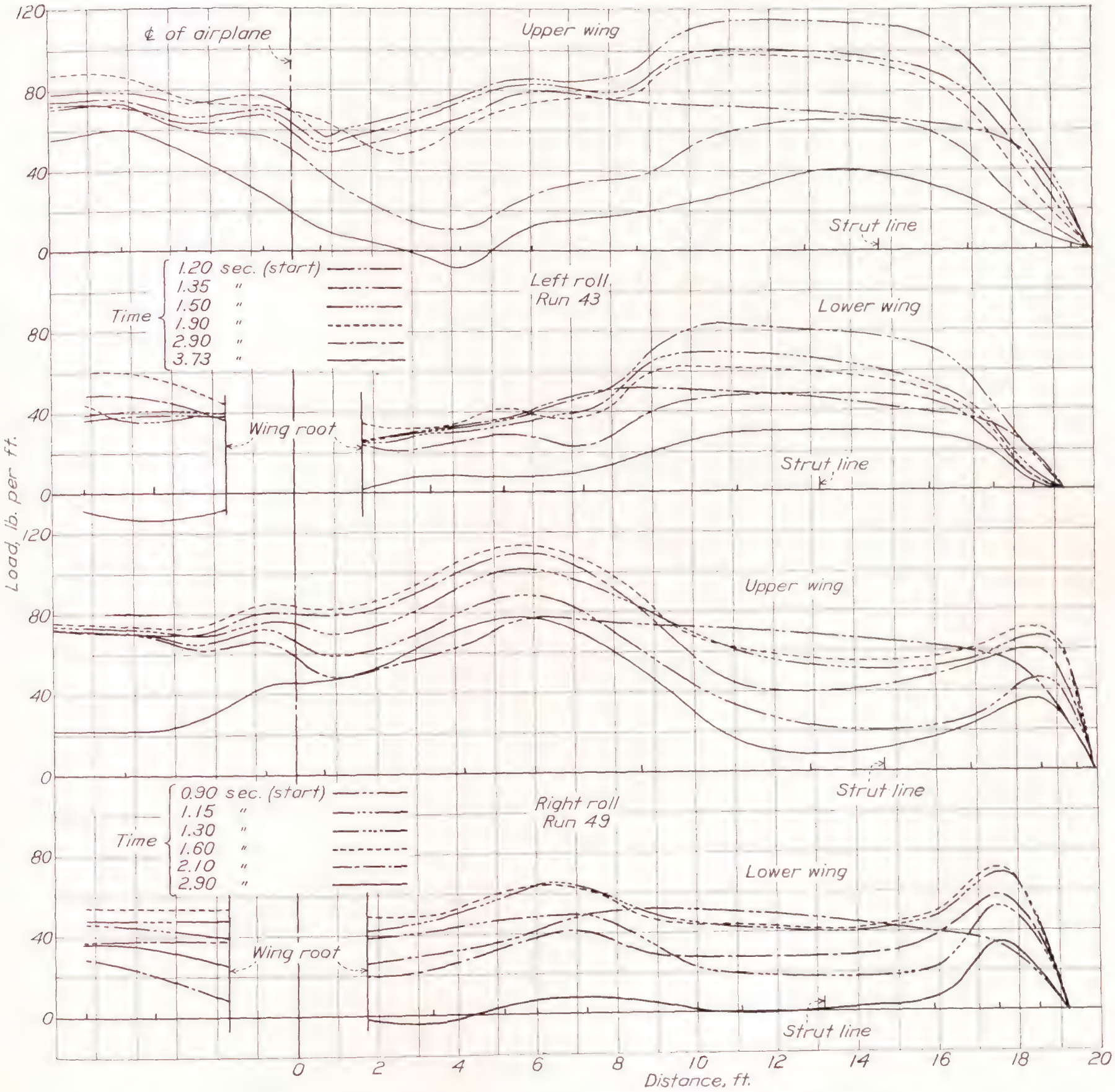

FIGURE 38.—Distribution of normal force along wing span obtained in abrupt aileron rolls at 120 miles per hour.

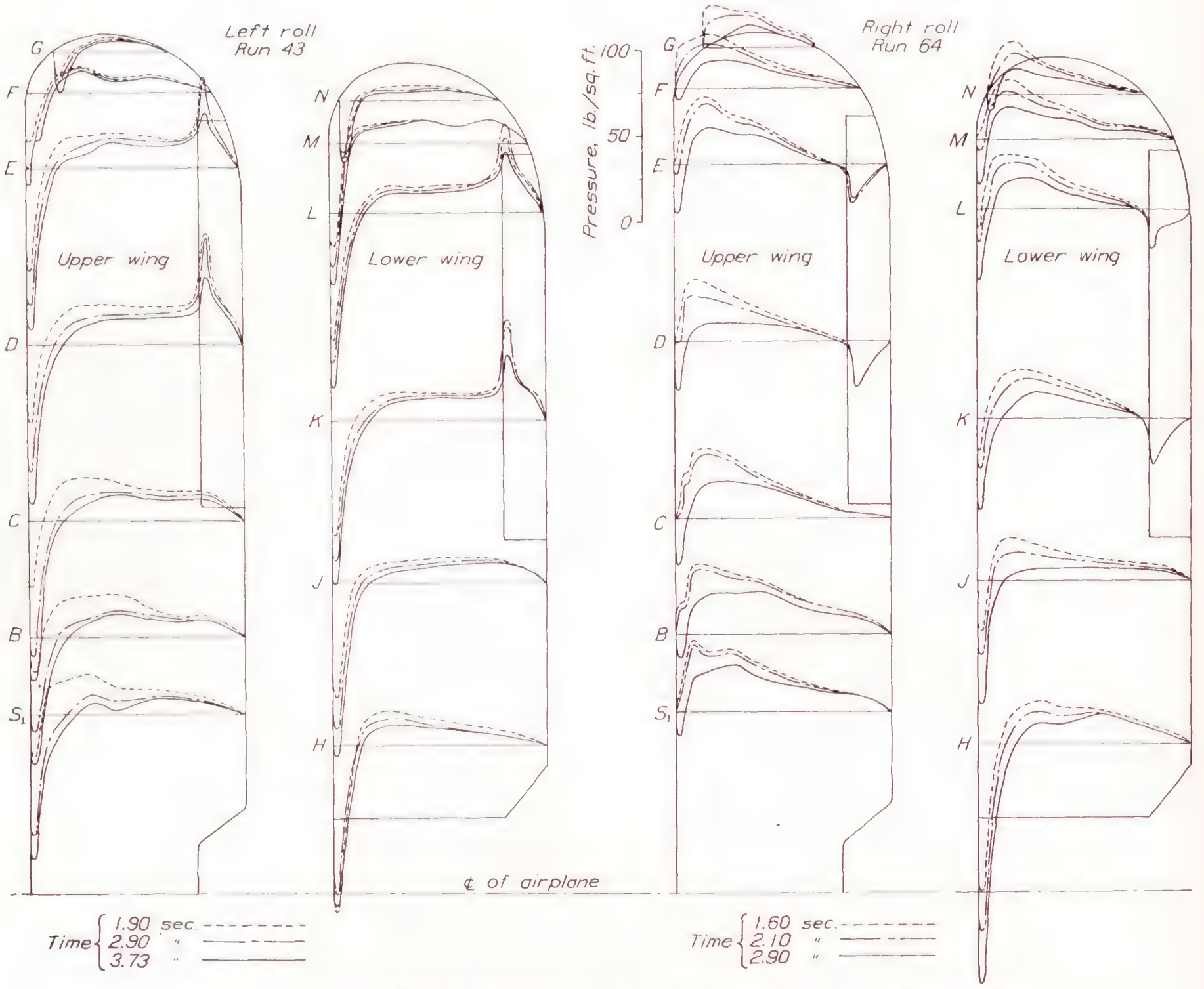

FIGURE 39.—Rib pressure distribution over the upper and lower wings during abrupt aileron rolls at 120 miles per hour.

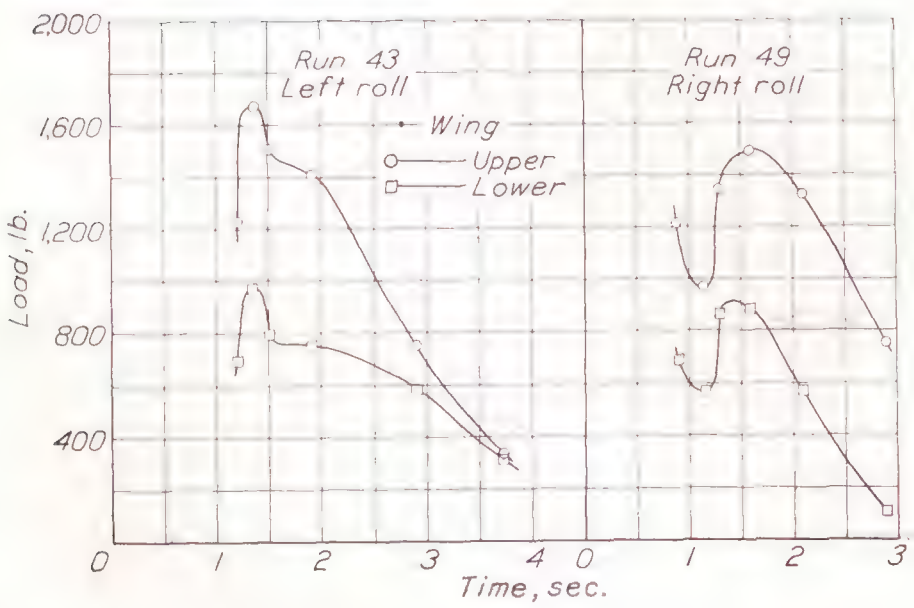

FIGURE 40.—Variation of individual wing loads measured in abrupt aileron rolls at 120 miles per hour.

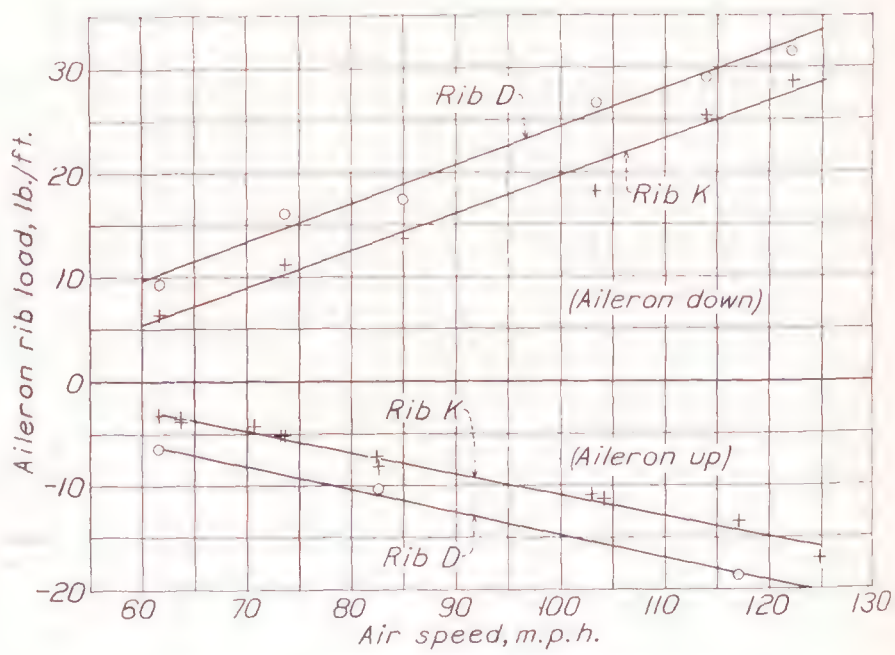

FIGURE 41.—Aileron rib load in abrupt aileron rolls.

CONCLUSIONS

The pressure-distribution tests over the two tail surfaces showed that:

1. Although for large elevator deflections horn-type balances performed their intended function of reducing hinge moments, they actually increased the hinge moment for small deflections.

2. The difference in the load on the two sides of the tail surfaces due to slipstream rotation was of minor importance.

3. The tail moment in the steady dive was calculated with fair accuracy by static-equilibrium equations that took into account the moments exerted by the wing and fuselage.

4. In abrupt pull-ups the maximum up tail loads may be as great as the maximum down tail loads.

5. In abrupt pull-ups the maximum tail normal-force coefficients developed decreased with an increase in air speed.

6. The acceleration produced with a given increment of stick force increased with the initial air speed.

The pressure-distribution tests over the right wing cellule and slipstream area showed that:

1. The effective relative efficiency between biplane wings varied considerably with the type of maneuver.

2. The maximum unsymmetrical load in the abrupt aileron roll occurred as soon as the aileron reached its maximum deflection.

3. The unit loadings on the ailerons of a biplane are affected by the relative efficiency between the wings.

LANGLEY MEMORIAL AERONAUTICAL LABORATORY,
NATIONAL ADVISORY COMMITTEE FOR AERONAUTICS,
LANGLEY FIELD, VA., *December 8, 1936.*

REFERENCES

1. Rhode, Richard V.: The Pressure Distribution over the Wings and Tail Surfaces of a PW–9 Pursuit Airplane in Flight. T. R. No. 364, N. A. C. A., 1930.
2. Theodorsen, Theodore: Investigation of the Diaphragm-Type Pressure Cell. T. R. No. 388, N. A. C. A., 1931.
3. Roche, J. A.: Study of Balanced Rudders. A. C. I. C. No. 586, Matériel Division, Army Air Corps, 1927.
4. Rhode, Richard V., and Lundquist, Eugene E.: Pressure Distribution over the Fuselage of a PW–9 Pursuit Airplane in Flight. T. R. No. 380, N. A. C. A., 1931.

TABLE I

CHARACTERISTICS OF DOUGLAS O–2H AIRPLANE

Engine—Liberty	420 hp. at 1,750 r. p. m.
Airfoil	Göttingen 398
Weight during pressure-distribution measurements of	
Modified tail	4,660 lb.
Original tail	4,736 lb.
Wing cellule	4,708 lb.
Areas:	
Upper wing	190.4 sq. ft.
Lower wing	182.4 sq. ft.
Total	372.8 sq. ft.
Elevator, modified tail (including 2.06-square-foot balance)	27.00 sq. ft.
Stabilizer, modified tail	23.82 sq. ft.
Total horizontal surfaces, modified tail	50.82 sq. ft.
Elevator, original tail (including 4.53-square-foot balance)	25.70 sq. ft.
Stabilizer, original tail	21.24 sq. ft.
Total horizontal surfaces, original tail	46.94 sq. ft.
Rudder, all tests (including 0.93-square-foot balance)	11.81 sq. ft.
Fin, all tests	6.41 sq. ft.
Total vertical tail surfaces	18.22 sq. ft.
c. g. location back of leading edge of lower wing during tests:	
Modified tail	8.20 in.
Original tail	9.55 in.
Wing cellule	6.80 in.
G/c	1.2
Stagger	17° or 22 in.
Dihedral	2°
Decalage	0.
Incidence	2°
Thrust-line location above leading edge of lower wing	2 ft. 1.4 in.
Distance from leading edge of lower wing to center line of tail-hinge axis	20 ft. 3 in.
Tail-hinge location above thrust line	2 ft. 0 in.

TABLE

WING RIB LOADS AND MOMENTS

Rib \ Time, sec.	Run 38 (air speed 62 m. p. h.[1])									Run 39 (air speed 74 m. p. h.[1])									Run 40 (air speed 85 m. p. h.[1])								
	Rib load, lb.			Rib moment, lb.-ft.			c. p. from leading edge, ft.			Rib load, lb.			Rib moment, lb.-ft.			c. p. from leading edge, ft.			Rib load, lb.			Rib moment, lb.-ft.			c. p. from leading edge, ft.		
	1.09	1.90	2.50	1.09	1.90	2.50	1.09	1.90	2.50	0.90	1.90	2.50	0.90	1.90	2.50	0.90	1.90	2.50	1.40	2.09	2.90	1.40	2.09	2.90	1.40	2.09	2.90
S_B	77	77	72	−112	−99	−95	1.45	1.28	1.32	84	69	60	−125	−107	−98	1.49	1.55	1.63	98	83	63	−156	−137	−111	1.59	1.65	1.76
S_4	75	75	70	−109	−97	−93	1.45	1.29	1.33	84	69	62	−126	−108	−99	1.50	1.56	1.60	94	79	62	−144	−125	−105	1.53	1.58	1.69
S_A	81	80	72	−117	−103	−93	1.45	1.29	1.29	82	67	56	−124	−104	−90	1.51	1.55	1.61	89	74	58	−137	−118	−99	1.54	1.60	1.71
S_3	73	73	65	−92	−76	−62	1.26	1.04	.95	75	55	40	−94	−70	−49	1.25	1.27	1.22	82	67	46	−105	−86	−61	1.28	1.28	1.33
S_2	67	67	56	−91	−74	−55	1.36	1.10	.98	64	32	22	−85	−60	−36	1.33	1.87	1.64	68	53	26	−99	−80	−47	1.45	1.51	1.81
A	63	63	54	−88	−74	−63	1.40	1.17	1.17	65	29	16	−93	−66	−38	1.43	2.27	2.37	68	53	26	−116	−92	−91	1.71	1.74	3.50
S_1	72	60	38	−109	−92	−70	1.51	1.53	1.84	73	45	14	−112	−81	−44	1.53	1.80	3.14	70	56	16	−120	−101	−56	1.71	1.80	3.50
B	75	64	44	−117	−103	−77	1.56	1.61	1.75	76	52	21	−120	−96	−58	1.58	1.85	2.76	77	63	24	−137	−116	−71	1.78	1.84	2.96
C	76	63	47	−119	−101	−87	1.57	1.60	1.85	78	54	28	−129	−106	−78	1.65	1.96	2.78	78	65	31	−142	−129	−95	1.82	1.98	3.06
D	80	71	58	−153	−147	−120	1.91	2.07	2.07	92	68	46	−193	−156	−129	2.10	2.30	2.81	94	78	54	−213	−191	−168	2.26	2.45	3.11
E	64	54	42	−126	−112	−89	1.97	2.08	2.12	74	51	32	−158	−125	−103	2.14	2.45	3.22	74	57	38	−175	−153	−132	2.36	2.68	3.47
F	40	32	25	−64	−49	−38	1.60	1.53	1.52	42	26	17	−65	−44	−36	1.55	1.69	2.12	40	29	19	−68	−56	−45	1.70	1.93	2.37
G	22	16	10	−24	−17	−9	1.09	1.06	.90	23	9	6	−22	−9	−4	.96	1.00	.67	19	10	7	−20	−11	−8	1.05	1.10	1.14
R_2	58	42	35	−94	−65	−54	1.62	1.55	1.54	57	38	17	−94	−72	−33	1.65	1.90	1.94	59	51	23	−119	−95	−54	2.02	1.86	2.35
S_H	65	44	37	−102	−69	−55	1.57	1.57	1.49	64	41	15	−102	−77	−28	1.59	1.88	1.87	63	55	20	−125	−99	−53	1.98	1.80	2.65
H	54	55	49	−100	−101	−89	1.85	1.84	1.81	52	44	33	−102	−90	−67	1.96	2.04	2.03	52	43	32	−122	−102	−77	2.35	2.37	2.41
R_1	55	60	53	−98	−112	−101	1.78	1.87	1.91	54	47	36	−101	−97	−86	1.87	2.06	2.39	55	46	31	−120	−103	−91	2.18	2.24	2.94
J	53	51	50	−95	−90	−94	1.79	1.76	1.88	54	46	39	−98	−94	−96	1.81	2.04	2.46	53	49	42	−111	−109	−112	2.09	2.22	2.66
K	51	46	42	−104	−96	−89	2.04	2.09	2.12	63	50	34	−141	−123	−101	2.24	2.46	2.97	65	37	41	−164	−109	−134	2.52	2.95	3.27
L	46	43	40	−97	−92	−86	2.11	2.14	2.15	57	41	34	−129	−106	−100	2.26	2.59	2.94	58	44	37	−142	−128	−127	2.45	2.91	3.43
M	34	31	29	−61	−56	−52	1.79	1.81	1.79	40	28	22	−70	−60	−53	1.75	2.14	2.41	38	29	25	−78	−71	−69	2.05	2.45	2.76
N	18	15	12	−28	−20	−17	1.55	1.33	1.42	22	12	8	−30	−19	−15	1.36	1.58	1.87	19	12	10	−28	−22	−18	1.47	1.83	1.80

Rib \ Time, sec	Run 44 (air speed 63 m. p. h.[1])									Run 45 (air speed 74 m. p. h.[1])									Run 46 (air speed 83 m. p. h.[1])								
	Rib load, lb.			Rib moment, lb.-ft.			c. p. from leading edge, ft.			Rib load, lb.			Rib moment, lb.-ft.			c. p. from leading edge, ft.			Rib load, lb.			Rib moment, lb.-ft.			c. p. from leading edge, ft.		
	1.40	2.10	3.90	1.40	2.10	3.90	1.40	2.10	3.90	1.10	1.90	2.90	1.10	1.90	2.90	1.10	1.90	2.90	1.60	2.15	3.10	1.60	2.15	3.10	1.60	2.15	3.10
S_B	61	66	11	−106	−105	−46	1.74	1.59	4.18	58	63	33	−101	−109	−76	1.74	1.73	2.30	55	63	34	−108	−120	−87	1.96	1.91	2.56
S_4	60	65	12	−104	−103	−47	1.73	1.58	3.92	52	57	28	−86	−94	−61	1.65	1.65	2.18	56	62	34	−105	−116	−82	1.87	1.87	2.41
S_A	67	72	24	−106	−105	−56	1.58	1.46	2.33	61	66	38	−99	−107	−73	1.62	1.62	1.92	58	65	38	−100	−112	−79	1.72	1.72	2.08
S_3	67	71	28	−89	−88	−43	1.33	1.24	1.53	63	68	43	−83	−91	−61	1.32	1.34	1.42	59	66	43	−81	−92	−63	1.37	1.39	1.46
S_2	58	63	28	−85	−84	−36	1.46	1.33	1.29	57	62	41	−83	−91	−61	1.46	1.47	1.49	64	71	50	−96	−107	−76	1.50	1.51	1.52
A	66	70	43	−94	−93	−63	1.42	1.33	1.46	62	67	50	−86	−94	−70	1.39	1.40	1.40	63	70	56	−98	−109	−87	1.55	1.56	1.55
S_1	72	77	43	−106	−105	−72	1.47	1.36	1.67	75	80	59	−114	−121	−95	1.52	1.51	1.61	75	83	64	−122	−133	−109	1.63	1.60	1.70
B	77	81	44	−114	−112	−73	1.48	1.38	1.66	80	84	59	−126	−130	−101	1.57	1.55	1.71	81	88	66	−135	−143	−115	1.67	1.62	1.74
C	64	69	30	−83	−89	−45	1.30	1.29	1.50	66	69	41	−89	−90	−64	1.35	1.30	1.56	64	73	48	−89	−101	−74	1.39	1.38	1.54
D	50	59	13	−43	−53	−6	.86	.90	.46	51	57	21	−40	−48	−11	.78	.84	.52	43	55	21	−28	−42	−8	.65	.76	.38
E	40	49	15	−31	−44	−8	.77	.90	.53	41	48	24	−37	−41	−16	.90	.85	.67	37	52	28	−24	−42	−14	.65	.81	.50
F	40	50	19	−54	−65	−32	1.35	1.30	1.68	40	49	27	−58	−68	−42	1.45	1.39	1.55	39	54	32	−58	−73	−48	1.49	1.35	1.50
G	28	40	17	−30	−47	−20	1.07	1.17	1.18	25	36	20	−28	−41	−24	1.12	1.14	1.20	24	35	22	−25	−40	−26	1.04	1.14	1.18
R_2	60	53	28	−98	−81	−52	1.63	1.53	1.86	65	53	34	−116	−99	−55	1.78	1.86	1.62	63	59	33	−128	−125	−60	2.03	2.12	1.82
S_H	67	60	20	−104	−87	−36	1.55	1.45	1.80	64	51	28	−106	−88	−37	1.66	1.73	1.32	63	59	28	−118	−115	−40	1.87	1.95	1.43
H	56	49	−11	−102	−86	−6	1.82	1.75	−.54	54	42	2	−113	−96	−35	2.09	2.28	17.50	51	47	1	−115	−111	−17	2.26	2.36	17.00
R_1	55	48	−5	−94	−77	−10	1.71	1.60	−2.00	57	45	8	−105	−88	−28	1.84	1.95	3.50	63	58	12	−128	−125	−30	2.03	2.16	2.50
J	46	47	4	−69	−67	−14	1.50	1.42	3.50	49	43	12	−84	−70	−30	1.71	1.63	2.50	47	48	16	−85	−84	−40	1.81	1.75	2.50
K	34	39	4	−30	−37	3	.88	.95	−.75	34	35	9	−34	−30	−3	1.00	.86	.33	29	36	12	−20	−25	−1	.69	.69	.08
L	31	40	5	−22	−32	7	.71	.80	−1.40	28	35	10	−21	−24	4	.75	.69	−.40	27	37	10	−11	−20	−10	.41	.54	1.00
M	40	44	15	−61	−64	−29	1.52	1.45	1.93	38	44	21	−60	−67	−36	1.58	1.52	1.71	39	48	25	−64	−74	−44	1.64	1.54	1.76
N	31	39	12	−38	−47	−17	1.22	1.21	1.42	30	37	17	−34	−44	−22	1.13	1.19	1.29	29	39	20	−33	−47	−26	1.14	1.20	1.30

[1] Denotes air speed at start.

II

DURING AILERON ROLLS

Run 41 (air speed 103 m. p. h.[1])									Run 42 (air speed 114 m. p. h.[1])									Run 43 (air speed 122 m. p. h.[1])									Time sec. / Rib
Rib load, lb.			Rib moment, lb.-ft.			*c. p.* from leading edge, ft.			Rib load, lb.			Rib moment, lb.-ft.			*c. p.* from leading edge, ft.			Rib load, lb.			Rib moment, lb.-ft.			*c. p.* from leading edge, ft.			
1.93	2.92	3.38	1.93	2.92	3.38	1.93	2.92	3.38	1.90	2.92	3.53	1.90	2.92	3.53	1.90	2.92	3.53	1.90	2.90	3.73	1.90	2.90	3.73	1.90	2.90	3.73	
88	57	30	−161	−121	−116	1.83	2.12	3.87	84	60	46	−162	−149	−145	1.93	2.48	3.15	88	71	55	−182	−158	−151	2.07	2.23	2.75	S_B
86	64	35	−154	−135	−134	1.79	2.11	3.83	83	52	49	−151	−142	−140	1.82	2.73	2.86	87	73	60	−176	−155	−150	2.02	2.12	2.50	S_4
74	54	28	−131	−113	−112	1.77	2.09	4.00	72	49	46	−126	−113	−111	1.75	2.31	2.41	75	60	48	−148	−127	−122	1.97	2.12	2.54	S_A
69	38	12	−97	−59	−55	1.41	1.55	4.58	65	38	35	−88	−67	−64	1.35	1.76	1.83	72	58	29	−111	−81	−71	1.54	1.40	2.45	S_3
53	11	−15	−101	−52	−46	1.91	4.73	−3.07	55	17	13	−96	−58	−56	1.74	3.41	4.31	65	40	11	−112	−76	−62	1.72	1.90	5.64	S_2
57	16	−16	−134	−92	−87	2.35	5.75	−5.44	39	3	1	−80	−42	−41	2.05	14.00	41.00	48	18	1	−88	−61	−52	1.83	3.39	52.00	A
49	−11	−22	−114	−49	−41	2.32	−4.45	−1.86	51	−3	−8	−128	−67	−62	2.51	−22.33	−7.75	61	10	−9	−146	−97	−75	2.40	9.70	−8.33	S_1
57	−3	−8	−131	−70	−62	2.30	−23.33	−7.75	60	11	1	−148	−99	−82	2.47	9.00	82.00	74	27	12	−180	−128	−110	2.43	4.74	9.17	B
64	13	0	−158	−109	−94	2.47	8.38	∞	66	19	5	−180	−129	−106	2.73	6.79	21.20	77	36	18	−208	−160	−138	2.70	4.45	7.66	C
85	45	22	−252	−216	−171	2.96	4.80	7.77	85	54	23	−272	−241	−157	3.20	4.46	6.83	96	65	38	−310	−273	−204	3.13	4.20	5.37	D
64	30	14	−203	−173	−141	3.17	5.77	10.07	64	38	18	−225	−199	−150	3.52	5.24	3.33	72	50	26	−250	−227	−177	3.47	4.54	6.81	E
31	13	6	−73	−62	−52	2.36	4.77	8.67	25	10	5	−71	−61	−55	2.84	6.10	11.00	27	17	8	−76	−69	−63	2.82	4.06	7.88	F
10	5	2	−15	−13	−10	1.50	2.60	5.00	8	2	2	−15	−13	−15	1.87	6.50	7.50	10	7	3	−18	−16	−13	1.80	2.29	4.33	G
45	1	−15	−110	−53	−28	2.44	53.00	−1.87	53	12	4	−110	−78	−74	2.07	6.50	18.50	60	49	−9	−150	−120	−79	2.50	2.45	−8.78	R_2
45	−6	−26	−113	−50	−24	2.51	−8.34	−.92	52	11	1	−110	−78	−72	2.12	7.08	72.00	58	47	−14	−142	−115	−80	2.45	2.45	−5.72	S_H
37	15	4	−113	−70	−45	3.05	4.66	11.25	29	12	8	−104	−83	−79	3.58	6.92	9.88	33	21	10	−127	−106	−89	3.85	5.05	8.90	H
41	15	−2	−122	−103	−71	2.98	6.87	−35.50	39	11	5	−128	−111	−107	3.28	10.09	21.40	42	31	8	−152	−133	−120	3.62	4.29	15.00	R_1
41	14	4	−122	−103	−92	2.98	7.35	23.00	35	14	11	−128	−119	−118	3.66	8.50	10.72	38	23	12	−146	−135	−127	3.84	5.87	10.59	J
56	26	19	−197	−166	−158	3.52	6.38	8.31	57	32	17	−226	−202	−154	3.97	6.31	9.06	62	47	30	−250	−241	−198	4.03	5.13	6.60	K
50	32	21	−182	−174	−157	3.64	5.44	1.48	49	34	18	−204	−195	−150	4.16	5.74	8.33	51	47	29	−215	−230	−190	4.22	4.90	6.55	L
30	18	13	−94	−92	−90	3.13	5.11	6.92	26	18	14	−98	−100	−96	3.77	5.55	6.85	31	28	21	−116	−122	−122	3.74	4.35	5.81	M
12	5	2	−26	−24	−24	2.17	4.80	12.00	9	6	1	−29	−30	−25	3.22	5.00	25.00	8	8	4	−31	−31	−28	3.87	3.87	7.00	N

Run 47 (air speed 103 m. p. h.[1])									Run 48 (air speed 117 m. p. h.[1])									Run 49 (air speed 125 m. p. h.[1])									Time sec. / Rib
Rib load, lb.			Rib moment, lb.-ft.			*c. p.* from leading edge, ft.			Rib load, lb.			Rib moment, lb.-ft.			*c. p.* from leading edge, ft.			Rib load, lb.			Rib moment, lb.-ft.			*c. p.* from leading edge, ft.			
1.75	2.50	3.10	1.75	2.50	3.10	1.75	2.50	3.10	1.08	1.92	2.60	1.08	1.92	2.60	1.08	1.92	2.60	1.60	2.10	2.90	1.60	2.10	2.90	1.60	2.10	2.90	
62	46	20	−136	−112	−88	2.20	2.44	4.40	78	66	−1	−181	−164	−125	2.32	2.48	−125.00	76	72	22	−186	−179	−131	2.45	2.49	5.95	S_B
60	44	19	−127	−103	−79	2.12	2.34	4.16	78	66	−3	−171	−154	−115	2.20	2.34	−38.30	75	71	22	−174	−167	−122	2.32	2.35	5.55	S_4
66	50	26	−122	−98	−74	1.85	1.96	2.84	66	54	−3	−152	−135	−95	2.30	2.50	−31.70	73	69	26	−152	−145	−100	2.08	2.10	3.85	S_A
73	57	34	−111	−87	−63	1.52	1.52	1.85	84	72	22	−134	−117	−82	1.59	1.62	3.73	86	82	45	−135	−128	−87	1.57	1.56	1.93	S_3
79	63	41	−121	−97	−73	1.53	1.54	1.78	72	60	33	−119	−102	−71	1.65	1.70	2.15	83	79	46	−137	−130	−89	1.65	1.65	1.93	S_2
88	72	50	−143	−119	−95	1.62	1.65	1.90	87	75	42	−162	−145	−112	1.86	1.93	2.67	91	87	58	−157	−150	−114	1.73	1.72	1.97	A
100	83	61	−169	−146	−121	1.69	1.76	1.98	99	86	54	−183	−166	−137	1.85	1.93	2.54	106	102	72	−199	−191	−155	1.88	1.87	2.15	S_1
106	88	61	−183	−164	−130	1.73	1.87	2.13	108	91	61	−203	−182	−159	1.88	2.00	2.61	115	111	77	−217	−211	−175	1.88	1.90	2.27	B
87	64	41	−121	−104	−81	1.39	1.63	1.98	86	64	37	−135	−116	−103	1.57	1.81	2.79	93	83	52	−147	−134	−107	1.58	1.61	2.06	C
54	29	3	−34	−3	16	.63	.10	−5.33	56	25	7	−42	0	−4	.75	0	.57	59	41	10	−42	−10	9	.71	.24	−.90	D
62	37	17	−49	−24	1	.79	.65	−.06	60	34	19	−47	−16	−23	.78	.47	1.21	62	53	24	−47	−36	−9	.76	.68	.37	E
66	43	26	−96	−68	−51	1.45	1.58	1.96	67	46	26	−99	−76	−62	1.47	1.65	2.38	74	61	37	−111	−96	−68	1.50	1.57	1.83	F
41	27	14	−45	−33	−19	1.10	1.22	1.36	39	26	12	−43	−32	−22	1.10	1.23	1.83	42	35	19	−45	−40	−24	1.07	1.14	1.26	G
76	32	−3	−169	−101	−76	2.22	3.16	−25.33	50	29	9	−149	−121	−118	2.98	4.17	13.10	55	36	29	−169	−136	−128	3.07	3.78	4.41	R_2
74	29	−6	−143	−75	−53	1.93	2.58	−8.84	50	28	5	−137	−101	−90	2.74	3.61	18.00	55	34	21	−157	−124	−100	2.85	3.65	4.77	S_H
51	4	−20	−141	−72	−50	2.76	18.00	−2.50	48	7	−21	−145	−99	−74	3.02	14.10	−3.52	51	23	−3	−161	−129	−99	3.16	5.61	−33.00	H
65	15	−13	−156	−87	−60	2.40	5.80	−4.62	59	20	−12	−156	−110	−85	2.64	5.50	−7.08	62	34	5	−172	−139	−106	2.77	4.09	21.20	R_1
59	21	−1	−117	−67	−43	1.98	3.19	−43.00	59	21	4	−134	−84	−81	2.27	4.00	20.20	63	42	10	−146	−116	−79	2.32	2.76	7.90	J
46	18	−2	−42	−10	8	.91	.55	4.00	43	15	1	−49	−12	−18	1.14	.80	18.00	45	29	1	−51	−24	1	1.13	.83	−1.00	K
49	18	0	−39	2	20	.80	−.11	∞	47	18	1	−37	0	3	.79	0	−3.00	50	38	8	−43	−31	11	.86	.82	−1.37	L
64	39	22	−101	−71	−50	1.58	1.82	2.27	67	43	26	−112	−81	−73	1.67	1.88	2.81	73	59	36	−123	−106	−77	1.69	1.80	2.14	M
45	28	13	−56	−38	−22	1.24	1.35	1.69	45	28	16	−57	−39	−30	1.26	1.39	1.87	51	41	22	−64	−53	−34	1.25	1.29	1.54	N

[1] Denotes air speed at start.

REPORT No. 591

AN ANALYTICAL AND EXPERIMENTAL STUDY OF THE EFFECT OF PERIODIC BLADE TWIST ON THE THRUST, TORQUE, AND FLAPPING MOTION OF AN AUTOGIRO ROTOR

By JOHN B. WHEATLEY

SUMMARY

An analysis is made of the influence on autogiro rotor characteristics of a periodic blade twist that varies with the azimuth position of the rotor blade and the results are compared with experimental data. The analysis expresses the influence of this type of twist upon the thrust, torque, and flapping motion of the rotor. The check against experimental data shows that the periodic twist has a pronounced influence on the flapping motion and that this influence is accurately predicted by the analysis. The influence of the twist upon the thrust and torque could be demonstrated only indirectly, but its importance is indicated.

INTRODUCTION

The resultant of the air forces and the mass reactions on an autogiro rotor blade produces a couple tending to twist the blade unless the chordwise center of gravity of the blade and the center of pressure of the air forces are coincident. This fact has been known for some time, but it has not been generally realized that, except in particular cases, the resultant twist is periodic and is a function of the angular position of the blade in azimuth. The periodic twist may be of a magnitude comparable with or even exceeding the pitch setting of the rotor, which demonstrates the necessity of including it as a factor in the analysis of autogiro-rotor characteristics.

It is the purpose of this paper to present an analysis of the periodic twist and to support the validity of the analysis by a comparison of predicted results with experimental information obtained from flight tests of a direct-control wingless autogiro. The scope of the paper will be limited to a study of the influence of a known periodic twist upon the thrust, flapping motion, and torque of a rotor; the effect of such a twist upon rotor vibrations and stability and the problem of predicting the twist will be treated in a subsequent report.

ANALYSIS

It has been experimentally shown in previously unpublished data that, except in special cases, the air forces acting on a rotor blade cause a twist of the blade and a consequent change in the blade pitch angle. The twist is not constant but is a function of blade azimuth angle because of the variation of the air forces on the blade with this angle. In the following analysis the basic equations expressing the rotor characteristics will be generalized to include the factor of periodic twist. The notation of reference 1 will be used throughout this paper except for minor changes; for convenience, the list of symbols is appended at the end of this section.

The following additional notation is used:

$$r=xR \tag{1}$$

$$dr=Rdx \tag{2}$$

The problem is now the solution of the equations for the autogiro rotor when the pitch angle θ has the form

$$\theta=\theta_0+x\theta_1+x\epsilon_0+x\epsilon_1\cos\psi+x\eta_1\sin\psi+x\epsilon_2\cos 2\psi+x\eta_2\sin 2\psi+\ldots \tag{3}$$

where ϵ_n and η_n are coefficients descriptive of θ.

It will be noted that an assumption is here made concerning the distribution of the twist along the radius; equation (3) shows that a linear distribution, starting from zero at the blade hub, has been used. Actually the twist reaches zero just outboard of the vertical pin and is not, in general, absolutely linear from there to the tip; the assumption used, however, does not introduce a serious error and is considered justified for its simplicity.

It is obvious that the expressions of reference 1 for interference flow v, angle of attack α, blade flapping angle β, and the dynamic equation of flapping are unaltered; they are

$$v=\frac{C_T\Omega R}{2(\lambda^2+\mu^2)^{\frac{1}{2}}} \tag{4}$$

$$\tan\alpha=\frac{\lambda}{\mu}+\frac{C_T}{2\mu(\lambda^2+\mu^2)^{\frac{1}{2}}} \tag{5}$$

$$\beta=a_0-a_1\cos\psi-b_1\sin\psi-a_2\cos 2\psi-b_2\sin 2\psi-\ldots \tag{6}$$

$$I_1\left(\frac{d^2\beta}{dt^2}+\Omega^2\beta\right)=M_T-M_W \tag{7}$$

Using the notation of equation (1), the velocity components at the rotor blade are:

$$\frac{U_T}{\Omega R}=u_T=x+\mu \sin \psi \tag{8}$$

$$\frac{U_P}{\Omega R}=u_P=\lambda+\frac{1}{2}\mu a_1+\left(-\mu a_0+xb_1+\frac{1}{2}\mu a_2\right)\cos \psi$$
$$+\left(-xa_1+\frac{1}{2}\mu b_2\right)\sin \psi+\left(\frac{1}{2}\mu a_1+2xb_2\right)\cos 2\psi$$
$$+\left(\frac{1}{2}\mu b_1-2xa_2\right)\sin 2\psi+\frac{1}{2}\mu a_2 \cos 3\psi+\frac{1}{2}\mu b_2 \sin 3\psi \tag{9}$$

Also

$$u_T{}^2=x^2+\frac{1}{2}\mu^2+2\mu x \sin \psi-\frac{1}{2}\mu^2 \cos 2\psi \tag{10}$$

$$u_T u_P=x\lambda+\frac{1}{4}\mu^2 b_2+\left(-\mu x a_0+b_1\left[x^2+\frac{1}{4}\mu^2\right]-\frac{1}{2}\mu x a_2\right)\cos \psi$$
$$+\left(\mu\lambda-a_1\left[x^2-\frac{1}{4}\mu^2\right]-\frac{1}{2}\mu x b_2\right)\sin \psi$$
$$+(\mu x a_1+2x^2 b_2)\cos 2\psi+\left(-\frac{1}{2}\mu^2 a_0+\mu x b_1-2x^2 a_2\right)\sin 2\psi$$
$$+\left(-\frac{1}{4}\mu^2 b_1+\frac{3}{2}\mu x a_2\right)\cos 3\psi+\left(\frac{1}{4}\mu^2 a_1+\frac{3}{2}\mu x b_2\right)\sin 3\psi$$
$$-\frac{1}{4}\mu^2 b_2 \cos 4\psi+\frac{1}{4}\mu^2 a_2 \sin 4\psi \tag{11}$$

The rotor thrust is calculated upon the assumptions that the elemental force on the blade lies in a plane perpendicular to the blade-span axis and that the force depends only on the velocity in that plane; it is further assumed that u_P is small compared with u_T, so that the angle φ between u_T and the resultant velocity $(u_T{}^2+u_P{}^2)^{\frac{1}{2}}$ may be equated to its sine and tangent. As an approximate allowance for tip loss, it will be assumed that the thrust becomes zero at a radius $x=B$ where it is arbitrarily assumed that $B=1-\frac{c}{2R}$. Then

$$T=\frac{b}{2\pi}\int_0^{2\pi} d\psi \int_0^B \frac{1}{2}\rho c\Omega^2 R^3 u_T{}^2 C_L dx \tag{12}$$

It is further assumed that C_L is a linear function of the blade-element angle of attack α_r, which is, of course, accurate below the stall; then

$$C_L=a\alpha_r \tag{13}$$

$$\alpha_r=\theta+\varphi \tag{14}$$

Errors are introduced by the assumption that $C_L=a\alpha_r$; however, a graphical evaluation of the thrust made without this assumption and using a curve of C_L against α derived from wind-tunnel tests disclosed that the error so introduced was negligible. Another error in the thrust expression exists where u_T is negative; this error can be approximately nullified by the following correction. When u_T is negative, the normal expression for the blade-element angle of attack must be altered to

$$\alpha_r{}'=-\theta-\varphi \tag{15}$$

and equation (15) must be used in the part of the disk bounded by $x=-\mu \sin \psi$ and $x=0$ and by $\psi=\pi$ and $\psi=2\pi$. The expression for the thrust is now, after substituting for C_L, θ, and $\varphi=u_P/u_T$,

$$T=\frac{1}{2}\rho c a\Omega^2 R^3 \frac{b}{2\pi}\int_0^{2\pi} d\psi \int_0^B u_T{}^2(\theta_0+x\theta_1+x\epsilon_0+x\epsilon_1 \cos \psi$$
$$+x\eta_1 \sin \psi+x\epsilon_2 \cos 2\psi+x\eta_2 \sin 2\psi+ \ldots)dx$$
$$+\frac{1}{2}\rho c a\Omega^2 R^3 \frac{b}{2\pi}\int_0^{2\pi} d\psi \int_0^B u_T u_P dx$$
$$-\frac{1}{2}\rho c a\Omega^2 R^3 \frac{b}{\pi}\int_\pi^{2\pi} d\psi \int_0^{-\mu \sin \psi} u_T{}^2(\theta_0+x\theta_1+x\epsilon_0+x\epsilon_1 \cos \psi$$
$$+x\eta_1 \sin \psi+x\epsilon_2 \cos 2\psi+x\eta_2 \sin 2\psi+ \ldots)dx$$
$$-\frac{1}{2}\rho c a\Omega^2 R^3 \frac{b}{\pi}\int_\pi^{2\pi} d\psi \int_0^{-\mu \sin \psi} u_T u_P dx \tag{16}$$

$$T=\frac{1}{2}bc\rho a\Omega^2 R^3\left\{\frac{1}{2}\lambda\left(B^2+\frac{1}{2}\mu^2\right)+\theta_0\left(\frac{1}{3}B^3+\frac{1}{2}\mu^2 B-\frac{4}{9\pi}\mu^3\right)\right.$$
$$+\theta_1\left(\frac{1}{4}B^4+\frac{1}{4}\mu^2 B^2-\frac{1}{32}\mu^4\right)+\frac{1}{8}\mu^3 a_1+\frac{1}{4}\mu^2 b_2 B$$
$$\left.+\epsilon_0\left(\frac{1}{4}B^4+\frac{1}{4}\mu^2 B^2-\frac{1}{32}\mu^4\right)+\frac{1}{3}\mu\eta_1 B^3-\frac{1}{8}\mu^2\epsilon_2 B^2\right\} \tag{17}$$

It has already been shown (reference 1) that a_n and b_n are of the order μ^n; it can similarly be shown that ϵ_n and η_n are of the order μ^n.

The expression for thrust has been integrated upon the assumption, which experience has shown to be valid, that terms of higher order in μ than the fourth are negligible. This same assumption will be used throughout the remainder of this analysis.

The change in thrust caused by twist is

$$\Delta T=\frac{1}{2}bc\rho a\Omega^2 R^3\left\{\epsilon_0\left(\frac{1}{4}B^4+\frac{1}{4}\mu^2 B^2-\frac{1}{32}\mu^4\right)+\frac{1}{3}\mu\eta_1 B^3-\frac{1}{8}\mu^2\epsilon_2 B^2\right\} \tag{18}$$

The thrust moment M_T is, from reference 1,

$$M_T=\int_0^B \frac{1}{2}\rho c a\Omega^2 R^4\{\theta u_T{}^2+u_T u_P\}x dx$$
$$-2\int_0^{-\mu \sin \psi}\frac{1}{2}\rho c a\Omega^2 R^4\{\theta u_T{}^2+u_T u_P\}x dx\Bigg]_\pi^{2\pi} \tag{19}$$

where the second integral is added to thrust moment only in the interval $\psi=\pi$ to $\psi=2\pi$. The integrated value of M_T is

$$\frac{M_T}{\frac{1}{2}\rho c a\Omega^2 R^4}=\left\{\frac{1}{3}\lambda B^3+0.080\mu^3\lambda+\frac{1}{4}\theta_0\left(B^4+\mu^2B^2-\frac{1}{8}\mu^4\right)\right.$$
$$+\theta_1\left(\frac{1}{5}B^5+\frac{1}{6}\mu^2B^3\right)+\frac{1}{8}\mu^2b_2B^2+\epsilon_0\left(\frac{1}{5}B^5+\frac{1}{6}\mu^2B^3\right)$$
$$\left.+\frac{1}{4}\mu\eta_1B^4-\frac{1}{12}\mu^2\epsilon_2B^3\right\}$$
$$+\left\{\frac{1}{2}\mu\lambda B^2-\frac{1}{8}\mu^3\lambda+\frac{2}{3}\mu\theta_0B^3+0.053\mu^4\theta_0+\frac{1}{2}\mu\theta_1B^4\right.$$
$$-a_1\left(\frac{1}{4}B^4-\frac{1}{8}\mu^2B^2\right)-\frac{1}{6}\mu b_2B^3+\frac{1}{2}\mu\epsilon_0B^4$$
$$\left.+\eta_1\left(\frac{1}{5}B^5+\frac{1}{4}\mu^2B^3\right)-\frac{1}{4}\mu\epsilon_2B^4\right\}\sin\psi$$
$$+\left\{-\frac{1}{3}\mu a_0B^3-0.035\mu^4a_0+b_1\left(\frac{1}{4}B^4+\frac{1}{8}\mu^2B^2\right)\right.$$
$$-\frac{1}{6}\mu a_2B^3+\epsilon_1\left(\frac{1}{5}B^5+\frac{1}{12}\mu^2B^3\right)+\frac{1}{4}\mu\eta_2B^4\Big\}\cos\psi$$
$$+\left\{-\frac{1}{4}\mu^2a_0B^2+\frac{1}{24}\mu^4a_0+\frac{1}{3}\mu b_1B^3-\frac{1}{2}a_2B^4+\frac{1}{4}\mu\epsilon_1B^4\right.$$
$$\left.+\eta_2\left(\frac{1}{5}B^5+\frac{1}{6}\mu^2B^3\right)-\frac{1}{4}\mu\epsilon_3B^4\right\}\sin 2\psi$$
$$+\left\{-0.053\mu^3\lambda-\frac{1}{4}\mu^2\theta_0B^2+\frac{1}{32}\mu^4\theta_0-\frac{1}{6}\mu^2\theta_1B^3\right.$$
$$+\frac{1}{3}\mu a_1B^3+\frac{1}{2}b_2B^4-\frac{1}{6}\mu^2\epsilon_0B^3-\frac{1}{4}\mu\eta_1B^4$$
$$\left.+\epsilon_2\left(\frac{1}{5}B^5+\frac{1}{6}\mu^2B^3\right)+\frac{1}{4}\mu\eta_3B^4\right\}\cos 2\psi \tag{20}$$

Equation (7) can now be expanded into

$$I_1\Omega^2(a_0+3a_2\cos 2\psi+3b_2\sin 2\psi)=M_T-M_W \tag{21}$$

The coefficients of the flapping angle β can now be obtained by substituting for M_T in equation (21) and equating the coefficients of similar trigonometric functions; then, letting $\gamma=c\rho aR^4/I_1$

$$a_0=\frac{1}{2}\gamma\left\{\frac{1}{3}\lambda B^3+0.080\mu^3\lambda+\frac{1}{4}\theta_0\left(B^4+\mu^2B^2-\frac{1}{8}\mu^4\right)\right.$$
$$+\theta_1\left(\frac{1}{5}B^5+\frac{1}{6}\mu^2B^3\right)+\frac{1}{8}\mu^2b_2B^2+\epsilon_0\left(\frac{1}{5}B^5+\frac{1}{6}\mu^2B^3\right)$$
$$\left.+\frac{1}{4}\mu\eta_1B^4-\frac{1}{12}\mu^2\epsilon_2B^3\right\}-\frac{M_W}{I_1\Omega^2} \tag{22}$$

$$a_1=\frac{2\mu}{B^4-\frac{1}{2}\mu^2B^2}\left\{\lambda\left(B^2-\frac{1}{4}\mu^2\right)+\theta_0\left(\frac{4}{3}B^3+0.106\mu^3\right)+\theta_1B^4\right.$$
$$\left.-\frac{1}{3}b_2B^3+\epsilon_0B^4+\frac{\eta_1}{\mu}\left(\frac{2}{5}B^5+\frac{1}{2}\mu^2B^3\right)-\frac{1}{2}\epsilon_2B^4\right\} \tag{23}$$

$$b_1=\frac{4\mu}{B^4+\frac{1}{2}\mu^2B^2}\left\{a_0\left(\frac{1}{3}B^3+0.035\mu^3\right)+\frac{1}{6}a_2B^3\right.$$
$$\left.-\frac{\epsilon_1}{\mu}\left(\frac{1}{5}B^5+\frac{1}{12}\mu^2B^3\right)-\frac{1}{4}\eta_2B^4\right\} \tag{24}$$

The expressions for a_2 and b_2 must be expanded in powers of μ before solution is possible; it will be shown later that expansion to the order of μ^2 is sufficient to express the thrust and torque to the order of μ^4. To this order the equations for a_2 and b_2 are

$$\frac{6}{\gamma}b_2+\frac{1}{2}a_2B^4=\mu^2\left\{-\frac{1}{4}a_0B^2+\frac{1}{3}\frac{b_1}{\mu}B^3+\frac{1}{4}\frac{\epsilon_1}{\mu}B^4+\frac{1}{5}\frac{\eta_2}{\mu^2}B^5\right\} \tag{25}$$

$$\frac{6}{\gamma}a_2-\frac{1}{2}b_2B^4=\mu^2\left\{-\frac{1}{4}\theta_0B^2-\frac{1}{6}\theta_1B^3+\frac{1}{3}\frac{a_1}{\mu}B^3-\frac{1}{6}\epsilon_0B^3\right.$$
$$\left.-\frac{1}{4}\frac{\eta_1}{\mu}B^4+\frac{1}{5}\frac{\epsilon_2}{\mu^2}B^5\right\} \tag{26}$$

Equations (25) and (26) may be solved for a_2 and b_2 after substituting for a_0, a_1, and b_1 to the appropriate order of μ; then

$$a_2=\frac{\mu^2\gamma}{\gamma^2B^8+144}\left\{\lambda B\left(16+\frac{7\gamma^2B^8}{108}\right)+\theta_0B^2\left(\frac{46}{3}+\frac{7\gamma^2B^8}{144}\right)\right.$$
$$+\theta_1B^3\left(12+\frac{7\gamma^2B^8}{180}\right)+\epsilon_0B^3\left(12+\frac{7\gamma^2B^8}{180}\right)$$
$$\left.-\frac{1}{30}\frac{\epsilon_1}{\mu}\gamma B^8+\frac{2}{5}\frac{\eta_1}{\mu}B^4+\frac{24}{5}\frac{\epsilon_2}{\mu^2}B^5+\frac{2}{5}\frac{\eta_2}{\mu^2}\gamma B^9\right\} \tag{27}$$

$$b_2=\frac{-\mu^2\gamma^2}{\gamma^2B^8+144}\left\{\frac{5}{9}\lambda B^5+\frac{25}{36}\theta_0B^6+\frac{8}{15}\theta_1B^7+\frac{8}{15}\epsilon_0B^7\right.$$
$$\left.+\frac{2}{5\gamma}\frac{\epsilon_1}{\mu}B^4+\frac{1}{30}\frac{\eta_1}{\mu}B^8+\frac{2}{5}\frac{\epsilon_2}{\mu^2}B^9-\frac{24}{5\gamma}\frac{\eta_2}{\mu^2}B^5\right\} \tag{28}$$

The changes in the expressions for the blade-motion coefficients arising from the twist are:

$$\Delta a_0=\frac{1}{2}\gamma\left\{\epsilon_0\left(\frac{1}{5}B^5+\frac{1}{6}\mu^2B^3\right)+\frac{1}{4}\mu\eta_1B^4-\frac{1}{12}\mu^2\epsilon_2B^3\right\} \tag{29}$$

$$\Delta a_1=\frac{2\mu}{B^4-\frac{1}{2}\mu^2B^2}\left\{\epsilon_0B^4+\frac{\eta_1}{\mu}\left(\frac{2}{5}B^5+\frac{1}{2}\mu^2B^3\right)-\frac{1}{2}\epsilon_2B^4\right\} \tag{30}$$

$$\Delta b_1=\frac{4\mu}{B^4+\frac{1}{2}\mu^2B^2}\left\{\gamma\epsilon_0\left(\frac{1}{30}B^8+\frac{1}{36}\mu^2B^6\right)\right.$$
$$\left.-\frac{\epsilon_1}{\mu}\left(\frac{1}{5}B^5+\frac{1}{12}\mu^2B^3\right)+\frac{1}{24}\mu\gamma\eta_1B^7-\frac{1}{4}\eta_2B^4\right\} \tag{31}$$

$$\Delta a_2=\frac{\mu^2\gamma}{\gamma^2B^8+144}\left\{\epsilon_0B^3\left(12+\frac{7\gamma^2B^8}{180}\right)-\frac{1}{30}\frac{\epsilon_1}{\mu}\gamma B^8+\frac{2}{5}\frac{\eta_1}{\mu}B^4\right.$$
$$\left.+\frac{24}{5}\frac{\epsilon_2}{\mu^2}B^5+\frac{2}{5}\frac{\eta_2}{\mu^2}\gamma B^9\right\} \tag{32}$$

$$\Delta b_2=\frac{-\mu^2\gamma^2}{\gamma^2B^8+144}\left\{\frac{8}{15}\epsilon_0B^7+\frac{2}{5\gamma}\frac{\epsilon_1}{\mu}B^4+\frac{1}{30}\frac{\eta_1}{\mu}B^8\right.$$
$$\left.+\frac{2}{5}\frac{\epsilon_2}{\mu^2}B^9-\frac{24}{5\gamma}\frac{\eta_2}{\mu^2}B^5\right\} \tag{33}$$

The air torque on the rotor blade is the sum of the accelerating torque arising from the lift elements and the decelerating torque arising from the drag elements. It has been assumed that the lift elements are zero between $x=B$ and $x=1$; it is thought reasonable, however, to assume that the drag exists over the entire blade. An average value of the blade-element drag coefficient δ will be used; this value is assumed constant with respect to the angle of attack. The torque Q, which must be zero by hypothesis, since the rotor is in a state of steady rotation, is then

$$Q=0=\frac{b}{2\pi}\int_0^{2\pi}d\psi\int_0^B\frac{1}{2}\rho c\Omega^2R^4u_T^2\varphi C_L x\,dx - \frac{b}{2\pi}\int_0^{2\pi}d\psi\int_0^1\frac{1}{2}\rho c\Omega^2R^4u_T^2\delta x\,dx \tag{34}$$

This expression after substitution for θ, C_L, and μ integrates into

$$\begin{aligned}0=&-\lambda^2\left(\frac{1}{2}B^2-\frac{1}{4}\mu^2\right)+\lambda\left(\frac{1}{3}\theta_0B^3+\frac{2}{9\pi}\mu^3\theta_0+\frac{1}{4}\theta_1B^4+\frac{1}{32}\mu^4\theta_1\right)\\&+\mu\lambda a_1\left(\frac{1}{2}B^2-\frac{3}{8}\mu^2\right)+a_0^2\left(\frac{1}{4}\mu^2B^2-\frac{1}{16}\mu^4\right)-\frac{1}{3}\mu a_0b_1B^3\\&+a_1^2\left(\frac{1}{8}B^4+\frac{3}{16}\mu^2B^2\right)+b_1^2\left(\frac{1}{8}B^4+\frac{1}{16}\mu^2B^2\right)\\&-a_2\left(\frac{1}{4}\mu^2a_0B^2+\frac{1}{6}\mu b_1B^3\right)+\frac{1}{2}a_2^2B^4\\&+b_2\left(\frac{1}{8}\mu^2\theta_0B^2+\frac{1}{12}\mu^2\theta_1B^3+\frac{1}{6}\mu a_1B^3\right)+\frac{1}{2}b_2^2B^4\\&-\frac{\delta}{4a}\left(1+\mu^2-\frac{1}{8}\mu^4\right)+\epsilon_0\left(\frac{1}{4}\lambda B^4+\frac{1}{32}\mu^4\lambda+\frac{1}{12}\mu^2b_2B^3\right)\\&+\frac{1}{2}\epsilon_1\left(-\frac{1}{4}\mu a_0B^4+b_1\left[\frac{1}{5}B^5+\frac{1}{12}\mu^2B^3\right]-\frac{1}{8}\mu a_2B^4\right)\\&+\frac{1}{2}\eta_1\left(\frac{1}{3}\mu\lambda B^3-a_1\left[\frac{1}{5}B^5-\frac{1}{12}\mu^2B^3\right]-\frac{1}{8}\mu b_2B^4\right)\\&+\frac{1}{2}\epsilon_2\left(\frac{1}{4}\mu a_1B^4+\frac{2}{5}b_2B^5\right)\\&+\frac{1}{2}\eta_2\left(-\frac{1}{6}\mu^2a_0B^3+\frac{1}{4}\mu b_1B^4-\frac{2}{5}a_2B^5\right)\end{aligned} \tag{35}$$

Equation (35) is a quadratic in λ with the coefficients of the quadratic dependent upon μ, γ, B, θ_0, θ_1, and the ϵ and η coefficients describing the periodic twist. The evaluation of equation (35) requires the substitution of known values of ϵ and η in the expressions for a_n and b_n. The scope of this study includes only the prediction of the effect of a known twist upon rotor characteristics; consequently, the solution of equation (35) is possible when the drag term $\frac{\delta}{4a}\left(1+\mu^2-\frac{1}{8}\mu^4\right)$ is known.

Examination of equations (17) and (35) shows that the thrust and torque are expressed to the order μ^4 if a_2 and b_2 are expressed to the order μ^2, inasmuch as ϵ_n and η_n are of the order μ^n. This last condition has been analytically proved but will not be included in this paper; the analysis of the ϵ and η coefficients of twist will be the subject of another paper.

LIST OF SYMBOLS

R, blade radius.
b, number of blades.
c, blade chord, feet.
r, radius of blade element.
x, r/R.
θ_0, blade pitch angle at hub, radians.
θ_1, difference between hub and tip pitch angles, radians.
ϵ_n, coefficient of cos $n\psi$ in expression for θ, radians.
η_n, coefficient of sin $n\psi$ in expression for θ, radians.
θ, instantaneous pitch angle, radians.
δ, mean profile-drag coefficient of rotor-blade airfoil section.
ψ, blade azimuth angle measured from down wind in direction of rotation, radians.
v, rotor induced velocity.
Ω, rotor angular velocity, $d\psi/dt$, radians per second.
$\lambda\Omega R$, speed of axial flow through rotor.
$\mu\Omega R$, component of forward speed in plane of disk, equal to $V\cos\alpha$ where V is forward speed, feet per second.
β, blade flapping angle, radians.
a_n, coefficient of cos $n\psi$ in expression for β, radians.
b_n, coefficient of sin $n\psi$ in expression for β, radians.
I_1, mass moment of inertia of rotor blade about horizontal hinge.
α, rotor angle of attack, radians.
M_T, thrust moment about horizontal hinge.
M_W, weight moment of blade about horizontal hinge.
$u_T\Omega R$, velocity component at blade element perpendicular to blade span and parallel to rotor disk.
$u_P\Omega R$, velocity component at blade element perpendicular to blade span and to $u_T\Omega R$.
T, rotor thrust.
$C_T=\frac{T}{\rho\Omega^2\pi R^4}$
Q, rotor torque.
$C_Q=\frac{Q}{\rho\Omega^2\pi R^5}$
a, slope of curve of lift coefficient against angle of attack of blade airfoil section, in radian measure.
$\varphi=\tan^{-1}\frac{u_P}{u_T}$
α_r, blade-element angle of attack, radians.
$\gamma=\frac{c\rho aR^4}{I_1}$, mass constant of rotor blade.
$B=1-\frac{c}{2R}$, factor allowing for tip losses.

EXPERIMENT

Flight tests were made of a Kellett KD–1 autogiro having the following characteristics:

Gross weight, W	2,100 pounds.
Rotor radius, R	20.0 feet.
Number of blades, b	3.
Blade chord, c	1.00 foot.
Blade weight, w_b	61.5 pounds.
Blade-weight moment, M_W	482 pound-feet.
Blade moment of inertia, I_1	175 slug-feet.^{2}
Rotor solidity, $\sigma=\frac{bc}{\pi R}$	0.0478.
Blade mass constant, (sea level) $\gamma=\frac{c\rho a R^4}{I_1}$	12.74.
Blade airfoil section	Göttingen 606.
Pitch setting, θ_0 $(\theta_1=0)$	0.0960 radian.
Airfoil section moment coefficient, $C_{m_{a.c.}}$ (about aerodynamic center)	—0.056.
Blade chordwise center-of-gravity location, c_T (aft of aerodynamic center)	0.038 foot.

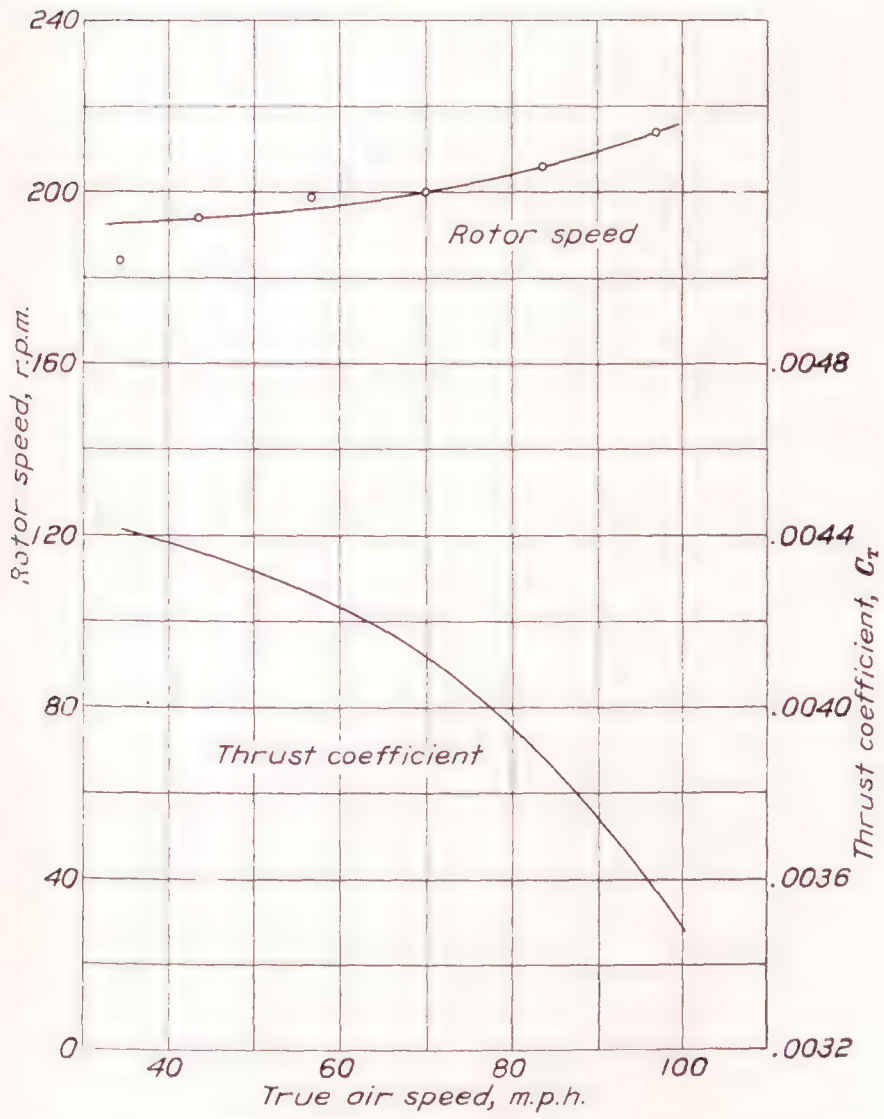

FIGURE 1.—Rotor speed and rotor thrust coefficient of KD–1 autogiro as measured in flight.

The flight tests included the measurement of rotor speed as a function of air speed (fig. 1) from which, since the autogiro had no fixed wing, the thrust coefficient could be calculated. Simultaneous measurements of the blade flapping angle and twist were made with a motion-picture camera mounted on and turning with the rotor hub. The data for twist are shown in figure 2. The flapping-angle data are represented by the experimental

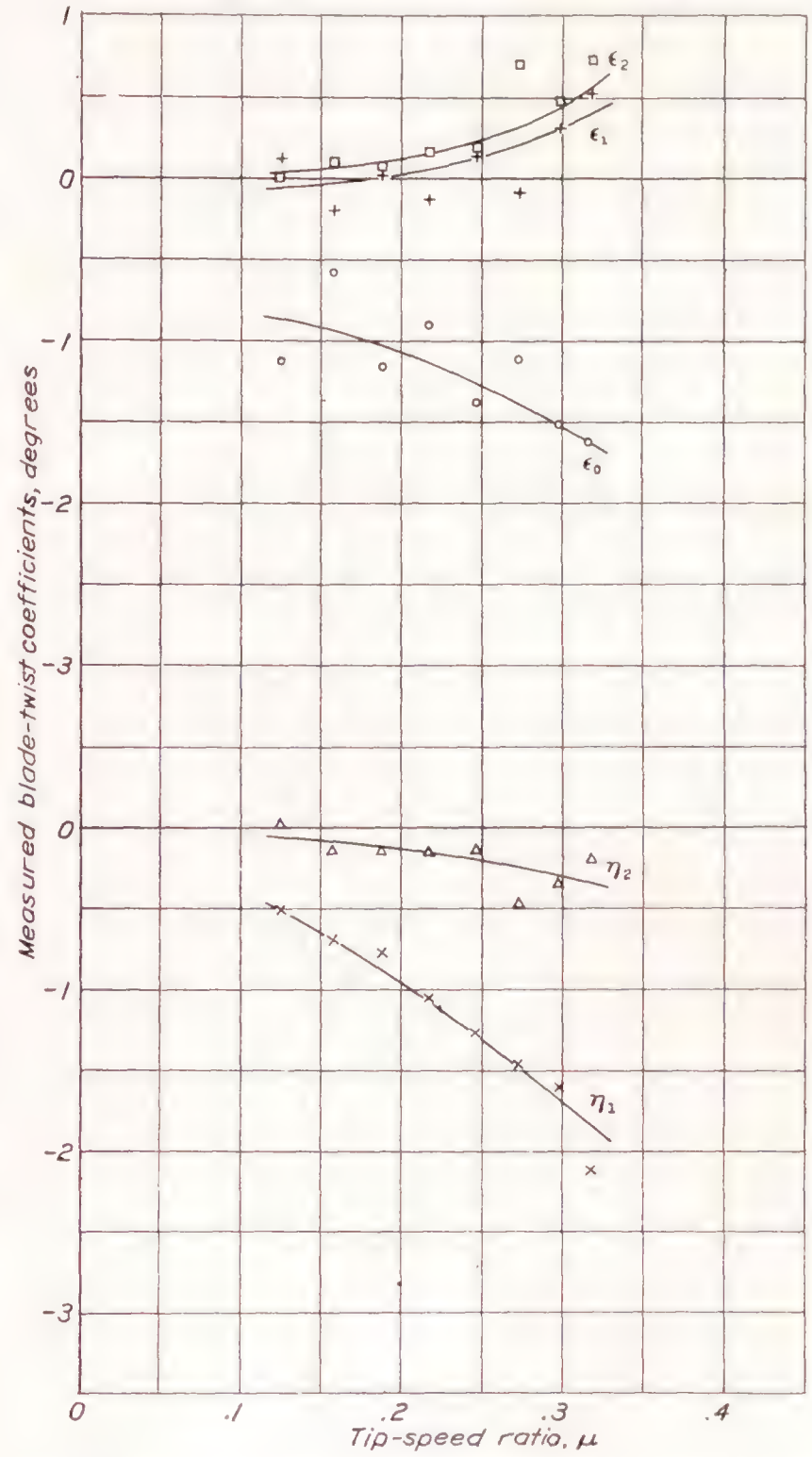

FIGURE 2.—Blade twist coefficients of KD–1 autogiro rotor as measured in flight.

points of figure 3. Both the flapping angle and the twist have been presented as the coefficients a_n, b_n, ϵ_n, and η_n of the expressions used in the previous section to represent β and θ.

The effect of periodic twist upon the thrust coefficient C_T was obtained by calculating the increment in C_T caused by the periodic twist and deducting the increment from the experimental value. The results are shown in figure 4.

In order to check the derived expressions for the effect of periodic twist upon the flapping motion, the inflow factor λ was calculated from the expression for the thrust (equation (17)) in which λ was the only unknown; the calculation was made using the experimental values of the periodic twist, and it was also made on the assumption that all ϵ and η coefficients except ϵ_0

were zero. The two results are shown in figure 5. These values of λ were then used in equations (22), (23), (24), (27), and (28) to calculate the blade flapping coefficients both with and without the effect of the periodic twist; these results are shown in figure 3, together with the measured values of the blade-flapping-angle coefficients. Since the measured values of the periodic twist were obtained from targets placed at 3/4 R, they

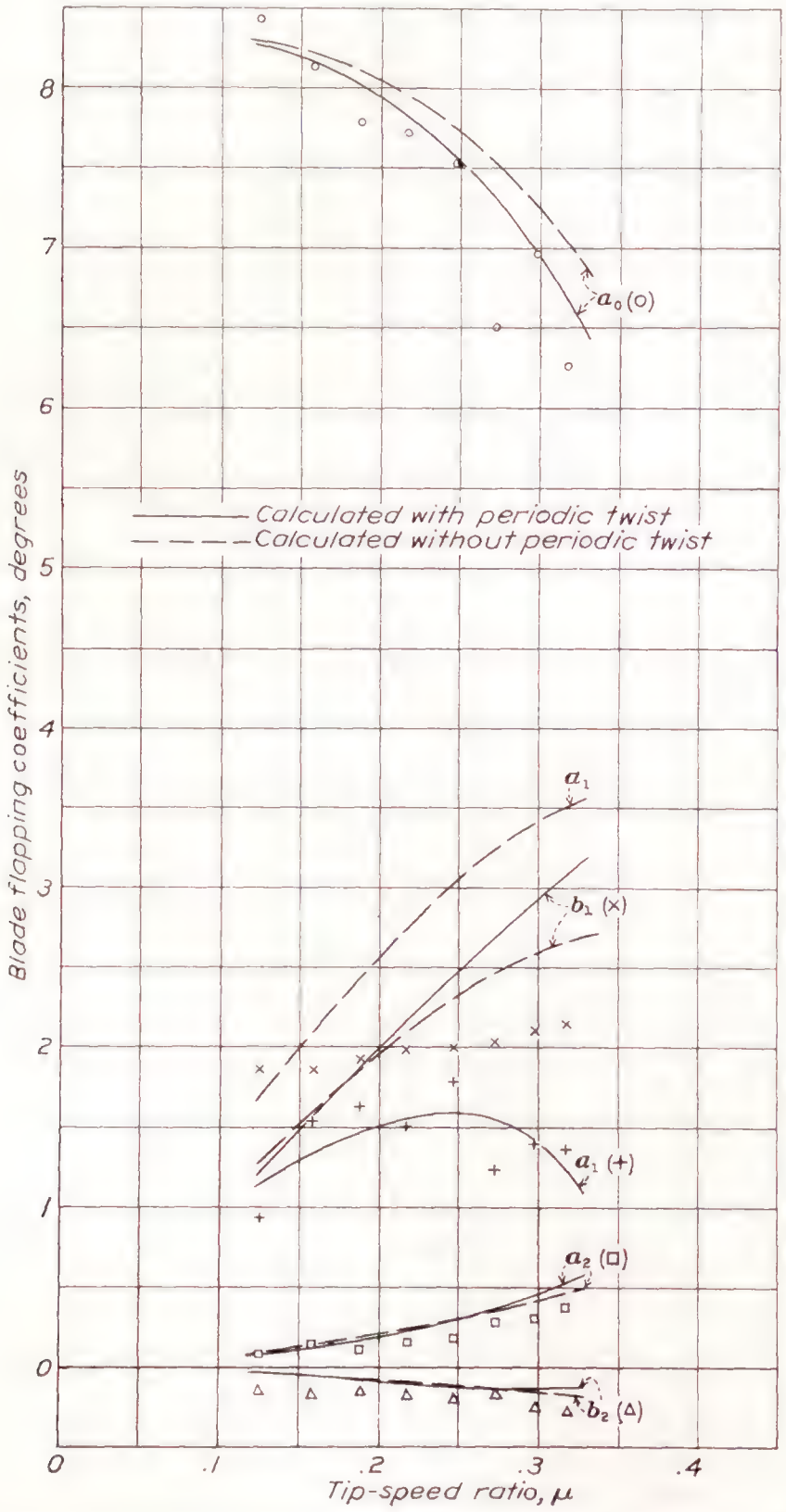

FIGURE 3.—Blade flapping coefficients of KD–1 autogiro rotor as measured in flight and as calculated with and without periodic twist.

were multiplied by 4/3 before insertion in the equations.

The effect of the periodic twist in the torque equation was estimated in the following manner: Known values of λ, a_n, b_n, ϵ_n, η_n, θ_0, and θ_1 were substituted in equation (35); the resultant expression was used to evaluate the remaining unknown term $\frac{\delta}{4a}\left(1+\mu^2-\frac{1}{8}\mu^4\right)$. The calculation was then repeated with the assumption that the periodic twist was zero and that λ rather than the δ term was unknown; the factors a_n, b_n, θ_0, θ_1, and ϵ_0 were assigned the same values in both calculations. The results of these calculations are shown in table I.

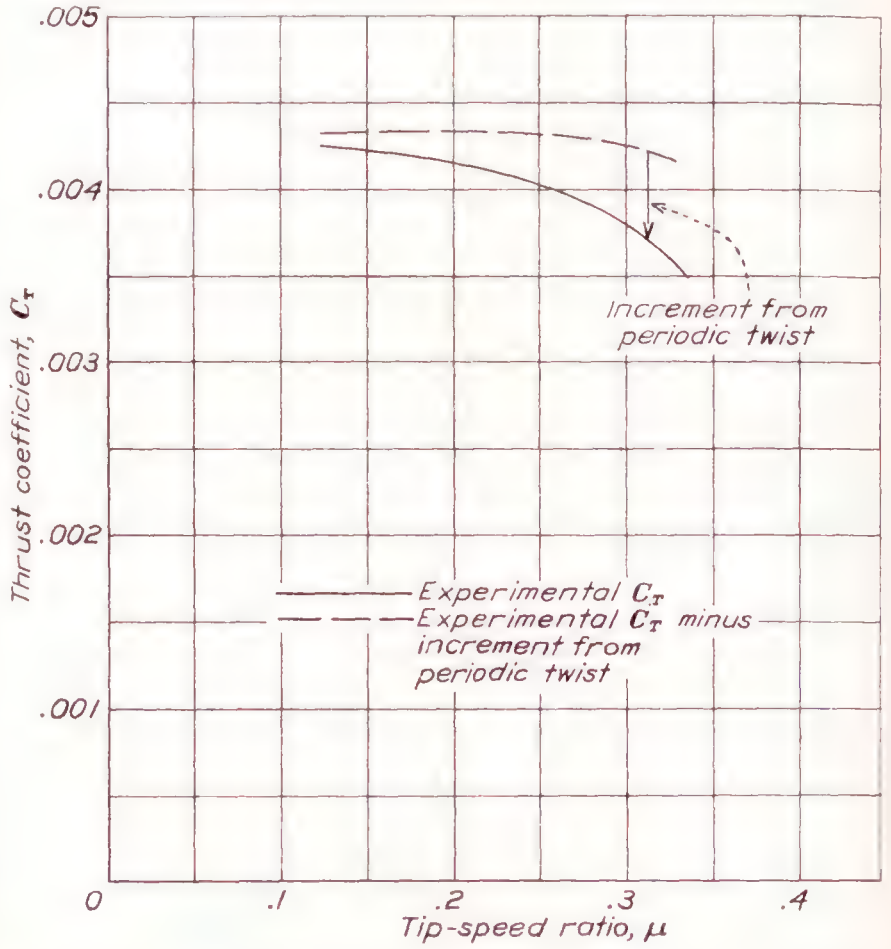

FIGURE 4.—Calculated periodic twist effect on thrust coefficient of KD–1 autogiro.

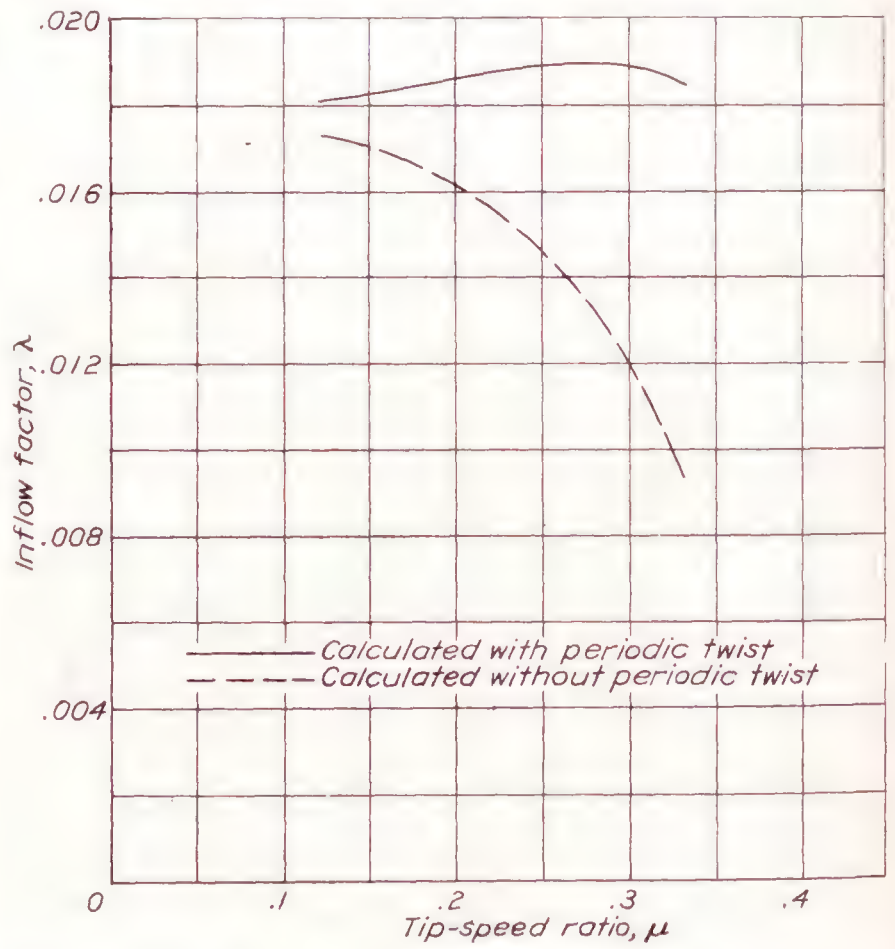

FIGURE 5.—Inflow factor λ of KD–1 autogiro as calculated from thrust coefficient with and without periodic twist effect.

DISCUSSION

The influence of periodic blade twist on the rotor characteristics is illustrated in figures, 3, 4, and 5. The data in figure 3 afford convincing proof not only of the validity of the twist analysis but also of the effect of periodic blade twist upon the rotor characteristics.

The data demonstrate that the type of twist developed in this rotor has a pronounced influence on the coning angle a_0 and on the flapping angle a_1. The influence on the lag angle b_1 and on the second harmonics a_2 and b_2 is considerably smaller. The agreement between the values of a_0 and a_1 calculated from the expressions including the periodic twist and the experimental values is quite good. The calculated values of the lag angle b_1 are in radical disagreement with experiment; this same condition was encountered in previous work (reference 1) and has been partially explained. In the reference it was shown that a variation of the rotor-induced velocity along the chord of the rotor disk had an appreciable effect upon the variation of b_1 with μ; an induced velocity increasing from the leading edge to the trailing edge increases b_1. Since this type of asymmetry exists (reference 2) and varies inversely in magnitude with μ, the evaluation of its influence upon b_1 would improve the qualitative agreement between the calculated and measured values.

Figure 4 illustrates the magnitude of the periodic-twist contribution to the thrust coefficient. A different result was obtained in figure 5 by showing the difference in the values of λ calculated when the periodic twist was considered and when it was neglected.

In table I the calculated influence of periodic twist upon the torque equation and upon the resultant value of λ is shown to be the least in magnitude of the effects studied. The effect is not, however, small enough to be neglected and would be an important factor if it were extrapolated to higher tip-speed ratios.

TABLE 1.—EFFECT OF PERIODIC BLADE TWIST ON TORQUE EQUATION

μ	λ (experimental)	$\frac{\delta}{4a}\left(1+\mu^2-\frac{1}{8}\mu^4\right)$	λ (calculated without periodic twist)
0.15	0.0182	0.000700	0.0177
.20	.0186	.000794	.0175
.25	.0189	.000845	.0171
.30	.0189	.000800	.0161

CONCLUSIONS

1. The effect of periodic twist upon rotor-blade flapping coefficients is satisfactorily predicted by this analysis.

2. The influence of periodic twist upon rotor characteristics as calculated from and checked with available data is an important factor in rotor analysis and can be adequately evaluated by the methods presented.

LANGLEY MEMORIAL AERONAUTICAL LABORATORY,
NATIONAL ADVISORY COMMITTEE FOR AERONAUTICS,
LANGLEY FIELD, VA., *January 28, 1937.*

REFERENCES

1. Wheatley, John B.: An Aerodynamic Analysis of the Autogiro Rotor with a Comparison between Calculated and Experimental Results. T. R. No. 487, N. A. C. A., 1934.
2. Wheatley, John B., and Hood, Manley J.: Full-Scale Wind-Tunnel Tests of a PCA–2 Autogiro Rotor. T. R. No. 515 N. A. C. A., 1935.

REPORT No. 592

FULL-SCALE TESTS OF N. A. C. A. COWLINGS

By Theodore Theodorsen, M. J. Brevoort, and George W. Stickle

SUMMARY

A comprehensive investigation has been carried on with full-scale models in the N. A. C. A. 20-foot wind tunnel, the general purpose of which is to furnish information in regard to the physical functioning of the composite propeller-nacelle unit under all conditions of take-off, taxying, and normal flight. This report deals exclusively with the cowling characteristics under conditions of normal flight and includes the results of tests of numerous combinations of more than a dozen nose cowlings, about a dozen skirts, two propellers, two sizes of nacelle, as well as various types of spinners and other devices.

The optimum shape of a low-drag cowling has been determined. The shape of the leading edge and the contours of the exit passage are the cause of large losses when improperly designed. The importance of providing means for regulating the quantity of cooling air to the minimum that will prevent excessive losses at high speeds has been demonstrated. The N. A. C. A. cowlings show a remarkably high efficiency when considered as a pump for the cooling air. The superiority of a baffled over an unbaffled engine has been verified and it has, furthermore, been shown that tightly fitting baffles are superior to the deflector type.

INTRODUCTION

The general purpose of a cowling has been known for some time. The original tests of N. A. C. A. cowlings are given in reference 1 and later studies in references 2, 3, and 4. The actual design of the engine cowling has, however, been based on a very inadequate scientific knowledge of its functions, owing largely to a lack of conclusive experimental data. The two basic functions of the engine cowlings are: (1) To provide an engine enclosure having minimum air resistance and (2) to act as a pump for the air that is to cool the engine or the radiator.

The cowling is usually designed to fit tightly about the engine unit with a rearward taper gradually faired into a wing or with a slightly expanding section that forms the front portion of a fuselage. The design of the portion ahead of the engine has been quite haphazard and often aerodynamically poor. As the cowling has a leading edge quite similar to that of an airfoil, it must be expected to react aerodynamically in much the same manner. The leading edge being fairly thin, the cowling must be sensitive to the "angle of attack" of the local air flow at the leading edge. This question has, in fact, been considered as a direct consequence of the findings of reference 5, in which an "ideal angle of attack" is defined.

No information has been available until quite recently on the function of the cowling as an air pump.

Since the summer of 1935 the N. A. C. A. has been conducting a very extensive investigation of propellers, nacelles, and cowlings with numerous special devices ncluding a dozen different cowlings with a variety of skirts. Attention is being paid to the mutual interference of the parts and to their effect on engine cooling. This first report comprises the results of the tests of cowlings, nacelles, and spinners under normal-flight conditions.

ANALYSIS OF THE PROBLEM

As previously stated, the two primary functions of the cowling are: (1) To provide an engine enclosure of minimum drag and (2) to pump the cooling air through the engine or the radiator. These functions are distinct because the definite amount of work required to be done on the cooling air is distinctly different from the ordinary aerodynamic drag of the cowling itself. In order to cool the engine, a certain quantity of air Q has to be forced through the engine per second at a certain pressure difference Δp. A related increment is observed in the drag $D-D_0$ at an air speed V. The work done per second is thus $Q\Delta p$ and the work expended exclusively for cooling is $(D-D_0)\ V$, which gives an efficiency of pumping

$$\eta_p=\frac{Q\Delta p}{(D-D_0)\,V}$$

The quantity D_0, which is given considerable significance, is defined as the drag of a closed cowling with major dimensions similar to those of the actual cowling as indicated by the sketch in figure 1. (See also the actual design in fig. 4, nose 19, skirt 5.)

Writing the total drag of the cowling-nacelle unit

$$D=\frac{Q\Delta p}{\eta_p V}+D_0$$

the problem is stated. It is, of course, evident that η_p should be as large and D_0 should be as small as possible.

Thus far the presence of a propeller has been ignored. On first consideration one might be led to believe the propeller to be nonessential in the sense that all conclusions drawn from a test without a propeller might readily be applied. That such a procedure is not permissible will be evident from the results. The main interaction may, however, be fairly well isolated and described. In order to determine the pump efficiency with a propeller, the net efficiency of the propeller-nacelle unit will first be defined as

$$\eta_n = \frac{RV}{P}$$

where R is the thrust of the unit and P the power supplied to the propeller shaft. The value η_n thus includes the useful expenditure to cooling.

As the propeller is a secondary consideration, it will be treated very simply as a disk capable of producing the desired pressure difference or forward thrust. The velocity increase and the contraction of the slipstream

FIGURE 1.—Basic cowling shape for determining minimum drag.

are found to be proportional to the unit disk loading, defined as

$$P_c = \frac{P}{qSV}$$

where q is the dynamic pressure $\frac{1}{2}\rho V^2$ and S is the disk area $\frac{\pi}{4}D^2$.[1]

Any combinations of P, S, and q (or of V) that give fixed values of P_c are therefore essentially similar in geometrical appearance of the flow field. In the study of the effect of the propeller on the cowling, the parameter P_c will frequently be employed, or rather the more convenient expression

$$\frac{1}{\sqrt[3]{P_c}} = V\sqrt[3]{\frac{\frac{\pi}{4}D^2\frac{1}{2}\rho}{P}} = V\sqrt[3]{\frac{\rho S}{2P}}$$

It may be noted that large values of $\frac{1}{\sqrt[3]{P_c}}$ correspond to small contractions and vice versa.

An expression for the pumping efficiency of the cowling for the power tests is obtained by recognizing the fact that part of the apparent loss in aerodynamic efficiency reappears as useful work in cooling the engine. The net efficiency pertaining to a certain installation has been given as η_n, which is experimentally determined for several values of P_c. The mechanical cost of the cooling is determined by employing the closed cowling in figure 1 to obtain a series of points on the net-efficiency curve for this limiting case of no cooling or pumping losses. This particular net efficiency is denoted as η_0. A comparison of these net efficiencies at a value of P_c representing a desired standard condition gives the pump efficiency at P_c as

$$\eta_p = \frac{Q\Delta p}{(\eta_0 - \eta_n)P}$$

Consider for a moment the product $Q\Delta p$. The engine or the radiator permits a rate of flow Q at a pressure difference Δp. For a given engine the pressure drop across the baffles is obviously very nearly proportional to the square of the volume and to the density ρ. A nondimensional quantity can easily be obtained. Let A be the cross-sectional area of the portion of the main air stream in front of the engine, which actually enters the engine as cooling air. (See fig. 21(d).) For a given engine or radiator the volume per unit time AV is proportional to $\sqrt{\Delta p}$; that is, the area is proportional to $\sqrt{\frac{\Delta p}{q}}$. The constant of proportionality may be defined as

$$k = \frac{A}{\sqrt{\frac{\Delta p}{q}}}$$

where k is seen to represent an area. In order to obtain a nondimensional expression, k may be expressed in terms of some representative area, such as the cross-sectional area of the nacelle F. Thus

$$K = \frac{k}{F} = \frac{\frac{A}{F}}{\sqrt{\frac{\Delta p}{q}}} \tag{1}$$

The term K, which shall be termed "the conductivity of the engine," is now a pure number. It is easy to visualize when Δp is equal to q: when the available head is used across the resistance. In this case $K = \frac{A}{F}$ and the conductivity K may be defined as the fraction of the total air column with a cross section equal to that of the nacelle that enters the inside of the cowling when the pressure drop across the resistance is equal to the velocity head q.

The term "conductivity" has been used from time to time in various forms by other authors. It is adopted because of a certain analogy to electrical terminology, as will be discussed later.

The value of $\Delta p/q$ is nearly unity in baffled engines and K normally lies between 0.05 and 0.1. Most of the reported tests were conducted with tightly fitted baffles, in which case the value of K is 0.0424. This value of K is referred to as "standard baffling." Subsequent tests were run with loosely fitting baffles in which K was 0.0909. A final series of tests was made with the baffles removed and K, approximately 0.5.

[1] It is noted that the power supplied to the air stream as thrust is somewhat less than P and that the effective disk area is reduced by the Goldstein effect. (See reference 6.)

The great convenience of having the engine-flow resistance given by a single number can be realized. If the defined quantity K is used to obtain an expression for the quantity of the cooling air

$$Q=K\sqrt{\frac{\Delta p}{q}}\,FV \tag{2}$$

a form is obtained that is particularly convenient inasmuch as a single calibration suffices to determine K for each engine baffle or radiator. The method of calibration will be described later.

Introducing K in the efficiency formulas, there is obtained for the nacelle tests with $D=C_D\,Fq$

$$\eta_p=\frac{K\left(\frac{\Delta p}{q}\right)^{3/2}}{C_D-C_{D_0}} \tag{3}$$

as the final formula for the pump efficiency. Similarly for the propeller tests

$$\eta_p=\frac{K\left(\frac{\Delta p}{q}\right)^{3/2}FVq}{(\eta_0-\eta_n)P}=\frac{K\left(\frac{\Delta p}{q}\right)^{3/2}}{\eta_0-\eta_n}\,\frac{F}{P_cS}$$

or

$$\eta_p=C\frac{\left(\frac{\Delta p}{q}\right)^{3/2}}{\eta_0-\eta_n} \tag{4}$$

where $C=\frac{KF}{SP_c}$. This formula is convenient as K is a constant, as are the disk area S and the nacelle cross-sectional area F. It will later be shown that the value of $\frac{1}{\sqrt[3]{P_c}}=1.8$ has been chosen as a standard of reference.

The influence of the exit area on the flow through the cowling is best explained by reference to figure 2.

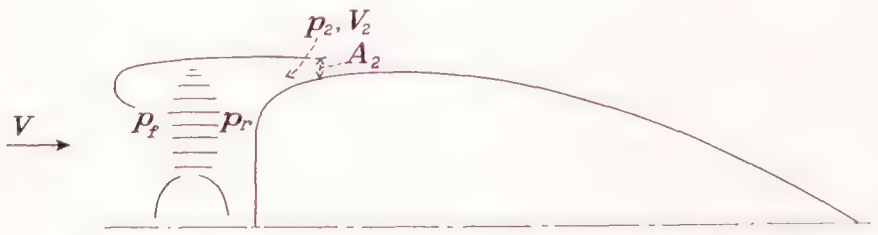

FIGURE 2.—Pressures and velocities for defining conductivity.

Observe that p_2 and V_2 are the pressure and velocity, respectively, in the exit. The static pressure p_2 is practically identical with the static pressure of the outside flow at the slot because the flow line dividing the external and internal fields is nearly straight. The expression for the total available drop is thus

$$\Delta P=\Delta p+\Delta p_2$$

where ΔP is the total head on the front minus the static pressure at the exit. The static pressure at the exit, as will be seen from a number of pressure plots, is usually slightly negative and may in some cases reach a value of $-0.3\ q$. The frontal pressure is fairly close to q on all normal cowlings. The pressure ΔP thus ranges from approximately 1 q to 1.3 q. The right-hand terms of the foregoing equation are the pressure drop across the engine and the pressure to produce the velocity head in the exit. The preceding equation written in nondimensional form is

$$\frac{\Delta P}{q}=\frac{\Delta p}{q}+\frac{\Delta p_2}{q}$$

For the pressure drop across the engine there has already been obtained the relation

$$Q=K\sqrt{\frac{\Delta p}{q}}\,FV$$

or

$$\frac{\Delta p}{q}=\left(\frac{Q}{KFV}\right)^2$$

For the pressure that produces the velocity head in the exit, there is simply

$$\Delta p_2=\frac{1}{2}\rho V_2^2$$

as the internal-friction loss in the passage is considered negligible. Inasmuch as $V_2=\frac{Q}{A_2}$ and $q=\frac{1}{2}\rho V^2$, there may be written

$$\frac{\Delta p_2}{q}=\left(\frac{Q}{A_2V}\right)^2$$

The area of the exit of the slot A_2 may be written in coefficient form as a fraction of the maximum cross-sectional area F, as K_2F. Then

$$\frac{\Delta p_2}{q}=\left(\frac{Q}{K_2FV}\right)^2$$

and for the total pressure drop the final relation [2]

$$\frac{\Delta P}{q}=\left(\frac{Q}{KFV}\right)^2+\left(\frac{Q}{K_2FV}\right)^2=\left(\frac{Q}{FV}\right)^2\left[\frac{1}{K^2}+\frac{1}{K_2^2}\right] \tag{5}$$

representing the case of two resistances in series. The pressure drop $\frac{\Delta P}{q}$ corresponds to the voltage V, the square of the rate of flow $\left(\frac{Q}{FV}\right)^2$ to the current J, and the conductivities K to $\sqrt{C}$.

A few remarks on the foregoing equation of flow regulation may be in order. Restating, the left-hand side is independent of air speed and is equal to slightly more than unity. Even with the use of cowling flaps the increase is only from about 1.1 to 1.3. The associated increase in Q is thus of the order of 10 percent and the increase in cooling is very slight. Indeed, if K is of the usual small value of baffled engines, not much is gained by increasing also the exit conductivity K_2. Representative values of K and K_2 as used in the most efficient and satisfactory installations tested are 0.05 and 0.15, respectively. The pressures across the resistances are therefore $\frac{1}{(0.05)^2}$ and $\frac{1}{(0.15)^2}$, or in the ratio [3] of 9 to 1. Any possible increase in K_2 results in only a negligible increase of Q.

---

[2] Note the electrical analogy, $V=J\left(\frac{1}{C}+\frac{1}{C_1}\right)$.

[3] For constant cooling, this ratio decreases as the air speed increases.

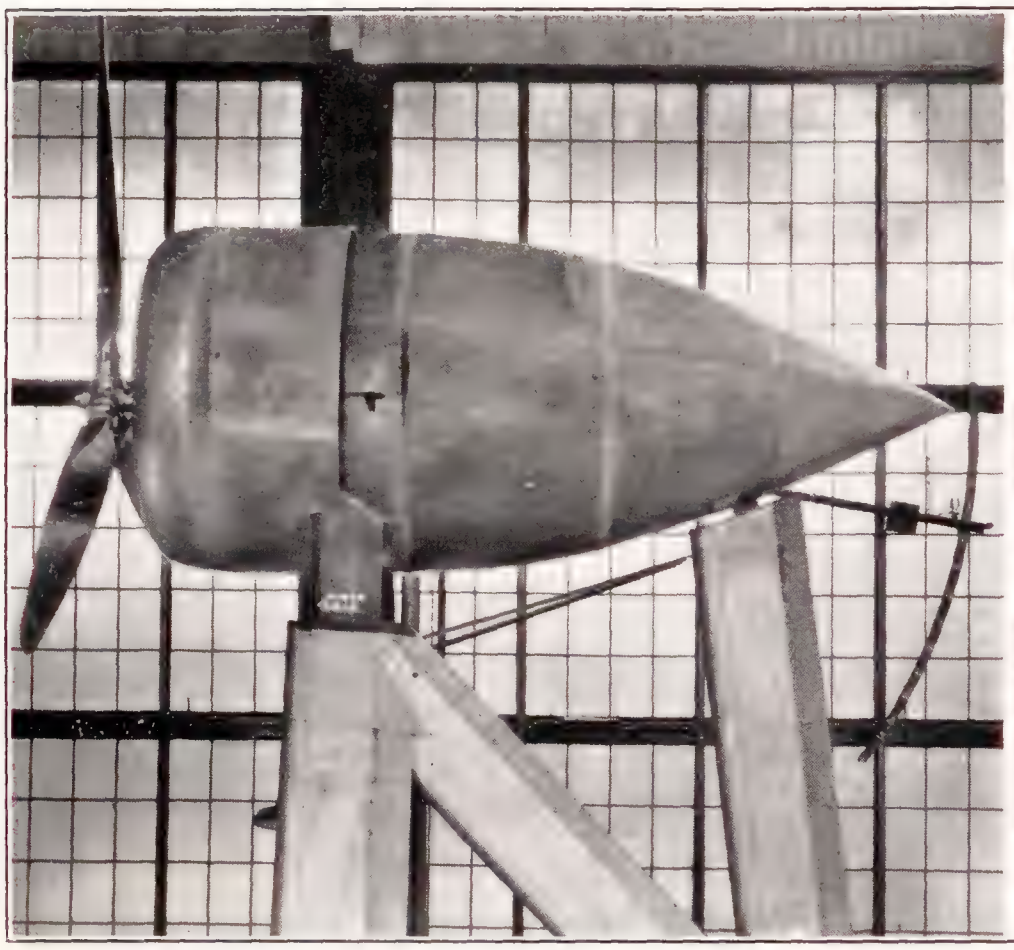

(a) Nacelle 2, nose 7, skirt 6, propeller B, inner cowling 6 (7—6—B—6—0).

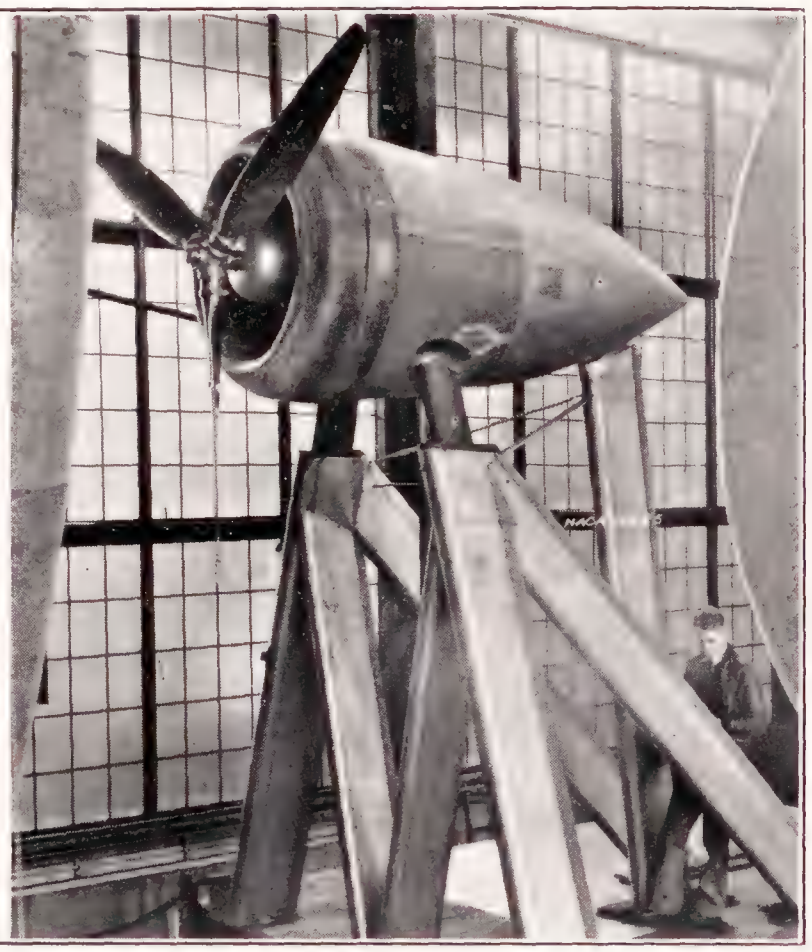

(b) Nacelle 1, nose 7, skirt 5, propeller B, inner cowling 3 (7—5—B—3—0).

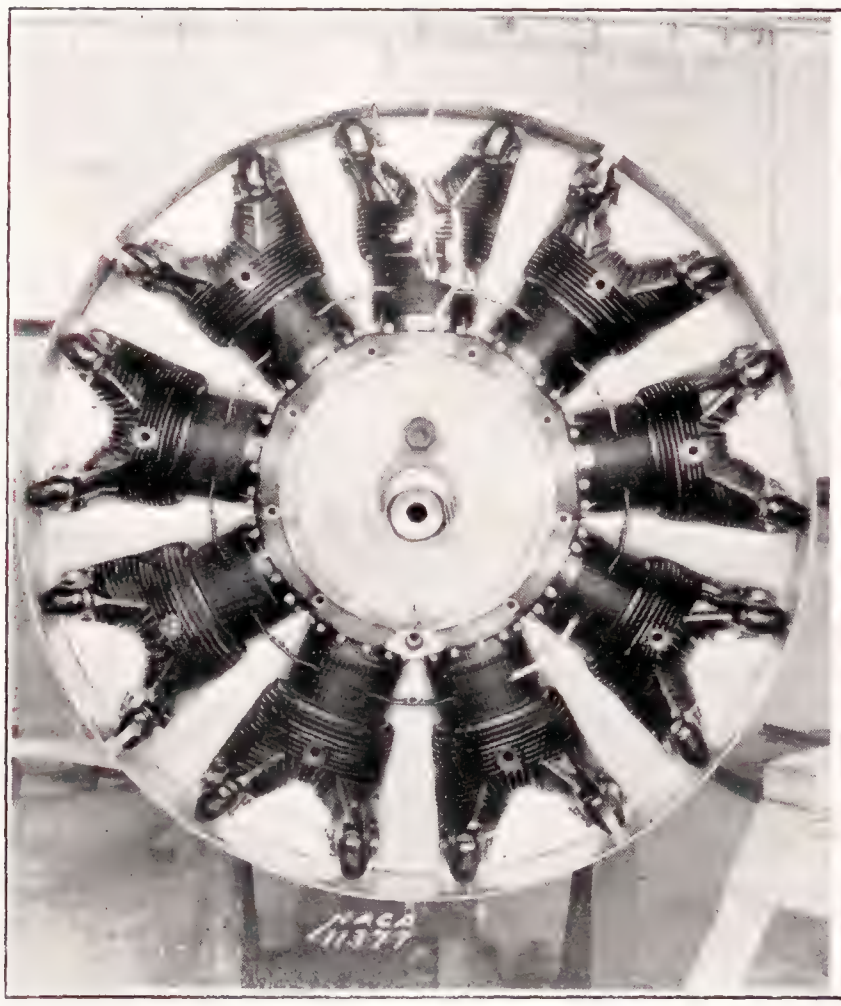

(c) Front view of engine cylinders with baffles and center section of the cowling.

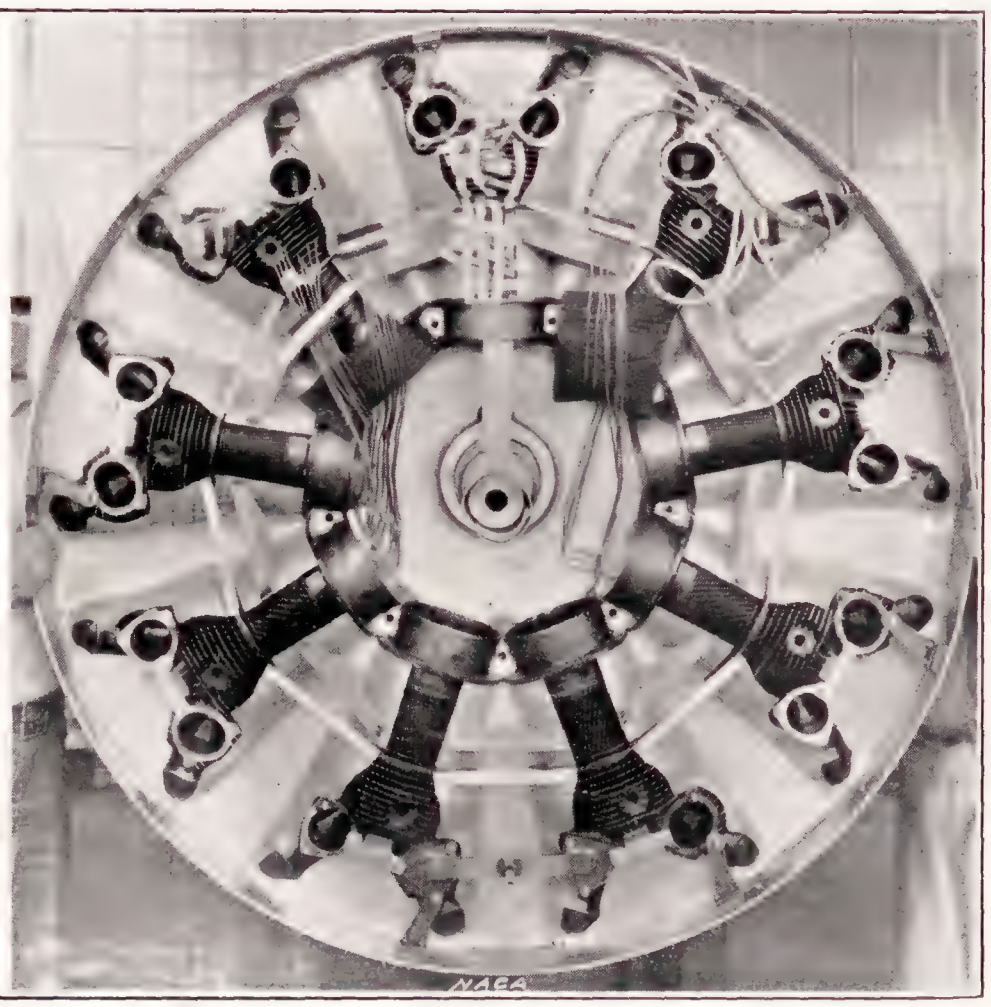

(d) Rear view of engine cylinders with baffles and center section of the cowling.

FIGURE 3.—The test set-up.

The conductivity K completely represents the engine as regards the aerodynamic tests of the nacelle-propeller unit.

The choice of the value of 1.8 is made strictly for the convenience of comparison. Each individual propeller was tested over a complete range of angles of attack. A plot of the net efficiency against $\frac{1}{\sqrt[3]{P_c}}$ shows that the range of $\frac{1}{\sqrt[3]{P_c}}$ extends from 0 to about 3, the net efficiency becoming zero at the latter point. This particular shape of the efficiency curve is, of course, a function of the present test set-up, which consists solely of an engine-nacelle unit. It is obvious that the presence of a wing section or of an entire airplane would change the shape of the entire curve. It is fairly safe to assume, however, that the differences in propellers, cowlings, spinners, etc., would manifest themselves in the same relative manner.

The condition $\frac{1}{\sqrt[3]{P_c}}=1.8$ might be more easily kept in mind as a fixed slipstream contraction; it is used to permit a comparison of the effect of the propeller on the cowling-nacelle unit under equal or similar conditions of flow.[4]

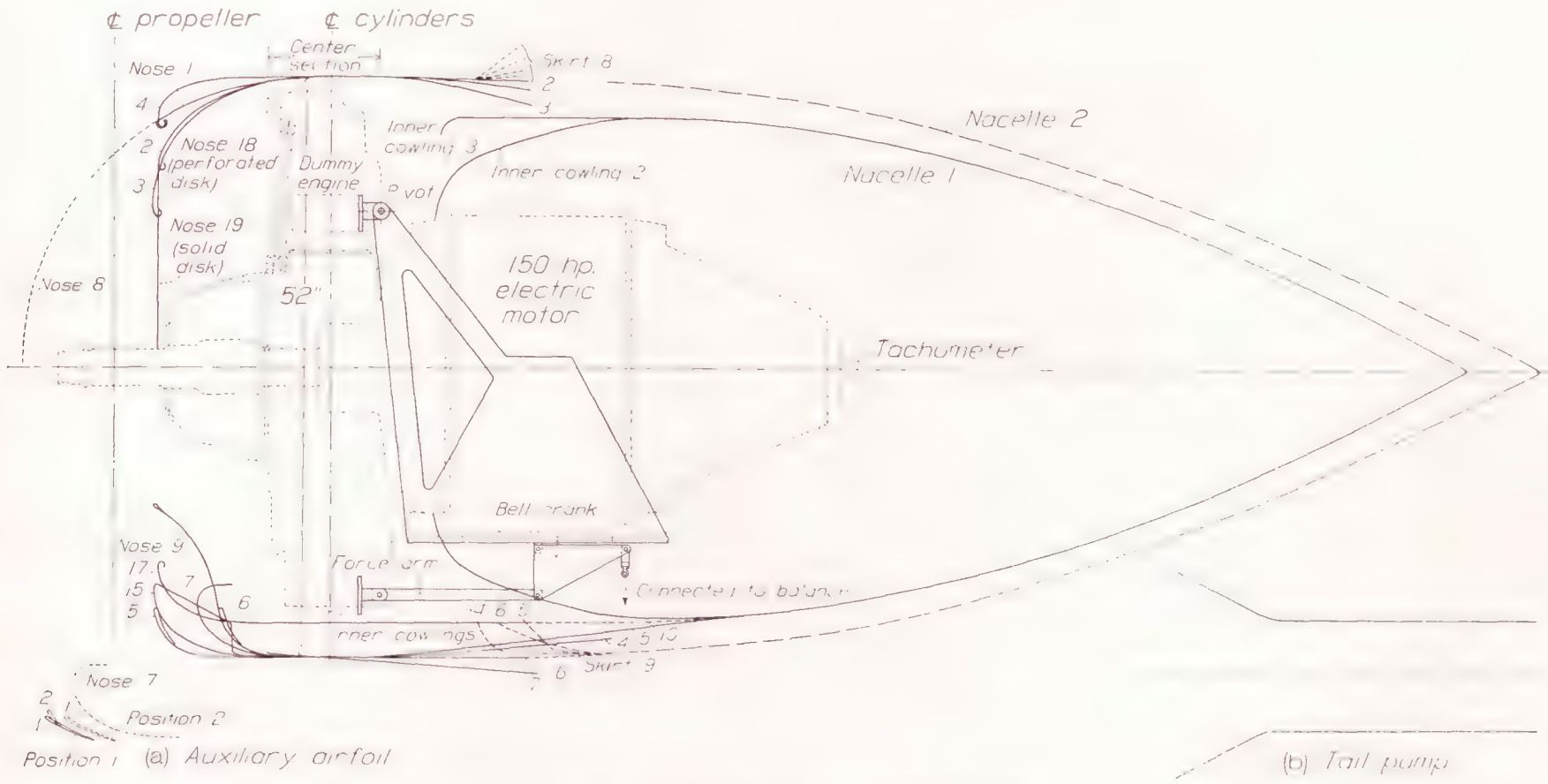

FIGURE 4.—Test model lay-out with cowling shapes.

APPARATUS

The cowling investigation was conducted in the N. A. C. A. 20-foot wind tunnel, which with its standard equipment is described in reference 7. The full-scale cowling model was attached to the standard balance frame by the supports shown in figures 3 (a) and 3 (b). The supports were shielded from the air stream in the regular manner to minimize tare drag. The cowlings were built to enclose a Pratt & Whitney Wasp engine having a maximum diameter of 52 inches. The dummy engine used in the main series of tests consisted of Wasp engine cylinders mounted on the front half of the crankcase (figs. 3 (c) and 3 (d)). The engine was pivoted on an axis at the top (fig. 4) and the force was taken by a bell crank connected to a scale at the bottom. This arrangement permitted the direct determination of the axial force on the engine and the ring-cowling assembly.

A 150-horsepower, 3-phase, wound-rotor induction motor was mounted in the nacelle behind the dummy engine (fig. 4). This motor was calibrated in a special brake test over the entire range of speed and torque. The propeller was mounted in proper relation to the engine by an extension shaft, which replaced the engine shaft. The speed and the power output were controlled by resistance in the rotor circuit. This arrangement permitted a flexibility and accuracy far superior to those obtainable on an engine run on its own power. Another important reason for the electric drive is its dependability. With the complex installation comprised of more than 100 pressure tubes and several dozen thermocouples all over the unit, mechanical repairs would have been cumbersome.

[4] For example, the value $1/\sqrt[3]{P_c}=1.8$ is represented by a 550-horsepower engine and a 10-foot propeller at about 180 miles per hour or by a 200-horsepower engine and an 8-foot propeller at about 150 miles per hour.

The heat transmission through the cylinders was obtained by the employment of a 2-kilowatt electric heater of fixed output mounted inside cylinder 1, which was completely sealed. The measured surface temperatures thus furnished an accurate index of the coefficient of heat transmission, not subject to the multiplicity of errors associated with tests of a gasoline engine. These temperatures will be referred to in the text and tables as "index" temperatures T_i. A short preliminary series was run on an actual engine, a Pratt & Whitney Wasp S1H1–G, baffled in the average manner and run by its own power. Conductivity and temperature distribution were measured in several cases for reference purposes.

Cowlings.—All cowlings used in this investigation are surfaces of revolution about the propeller axis. The various forms are represented by profile lines in figure 4. For convenience, the rear portion enclosing the electric motor will be referred to as the "nacelle." The portion forward of the exit opening will be referred to as the "cowling." The cowling may be considered to consist of three parts: (1) Nose, (2) center section, and (3) skirt. The center section of the cowling is attached permanently to the engine cylinders (figs. 3(c) and 3(d)). The same center section was used throughout all tests with the exception of the single test on the complete cowling 17. The nose and skirt sections were attached to the center section, care being taken to form a continuous smooth line. A photograph of each nose shape tested is reproduced in figure 5.

The original series comprised nose shapes 1, 2, 3, and 4, all being of the same length and general construction. Noses 1 and 4 had the same size of front opening but had very different angles of attack at the leading edge. Nose 5 differed from nose 4 by having the leading edge designed as an airfoil section. Nose 6 was identical with nose 5 except for a shortening of 6 inches in the axial length. Nose 7 was designed with a greater radius of curvature than nose 6, representing a cowling very neutral to the direction of the oncoming air flow. Nose 8, which was built on the basic form of nose 1, represents a completely closed nose used for special purposes. Nose 9 is built on nose 6 with a forward reversed curvature. Nose 15 is especially designed for housing a blower attached to the propeller shaft. Nose 17 is a design to determine the effect of reducing the main diameter of the cowling by placing bumps over the rocker boxes to house them. The

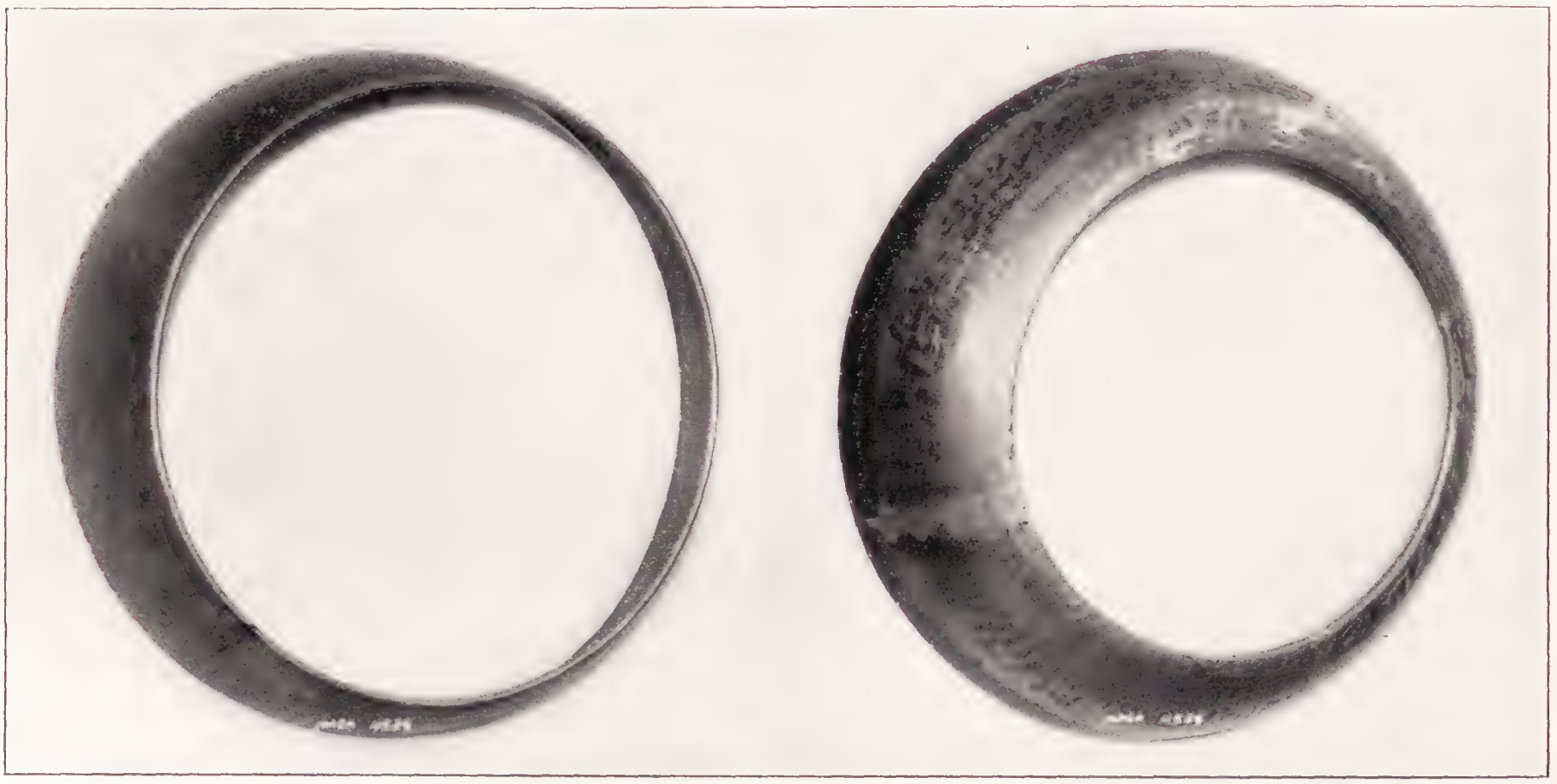

Nose 1 FIGURE 5.—Nose shapes of cowlings tested. Nose 2

basic shape is shown in figure 4 and in figure 5. Nose 18 is a combination of a perforated disk and nose 2. Nose 19 is a combination of a solid plate and nose 2.

The various shapes of skirt section tested are shown in figure 4. Skirts 5, 9, and 10 closed up the rear opening to the cowling. Skirt 8 had flaps of 5-inch chord and 6-inch span turned out in the positions shown in figure 4.

Nacelles.—Nacelles 1 and 2, 44 and 50 inches in diameter, respectively, were used in this investigation. The leading contour of the nacelle formed the inner surface for the cowling slot and is termed "inner cowling." Inner cowlings 2 and 3 were used with nacelle 1; inner cowlings 4, 5, and 6 were used with nacelle 2. These inner cowlings and the nacelles are shown in figure 4.

Baffles.—Baffles of conventional shape were used in this investigation. (See figs. 3(c) and 3(d).) They were in contact with the cylinder barrel fins from the 100° position to the 145° position (see fig. 6) for the standard-baffle condition shown in table I. In order to cover different degrees of baffling in this investigation, the baffles were moved back ½ inch for a few tests. The baffles were removed for several tests, as shown in table I.

Propellers.—Two 10-foot diameter, 3-blade Hamilton Standard adjustable propellers (fig. 7) were used for these tests. Propeller B (Hamilton Standard drawing 1C1–0) has airfoil sections close to the propeller hub. Propeller C (Navy plan form 5868–9) has the round part of the shank carrying farther out on the blade and fairing slowly into an airfoil section. Propeller B_x is the same as propeller B except that the distribution of blade-angle setting beyond the 70-percent radius has been changed. A more complete description of the propellers is given in the associated report on propellers (reference 8).

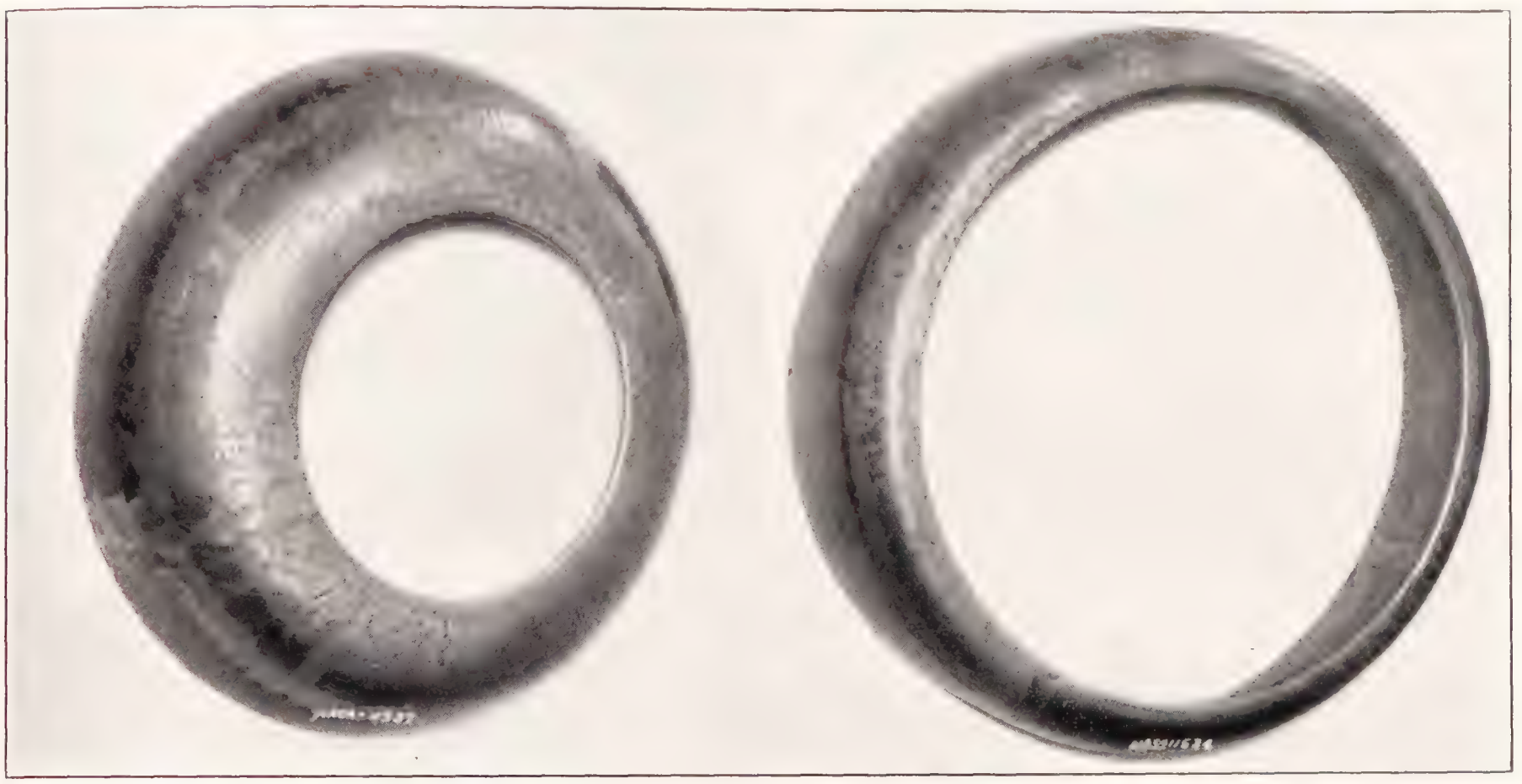

Nose 3 Nose 4

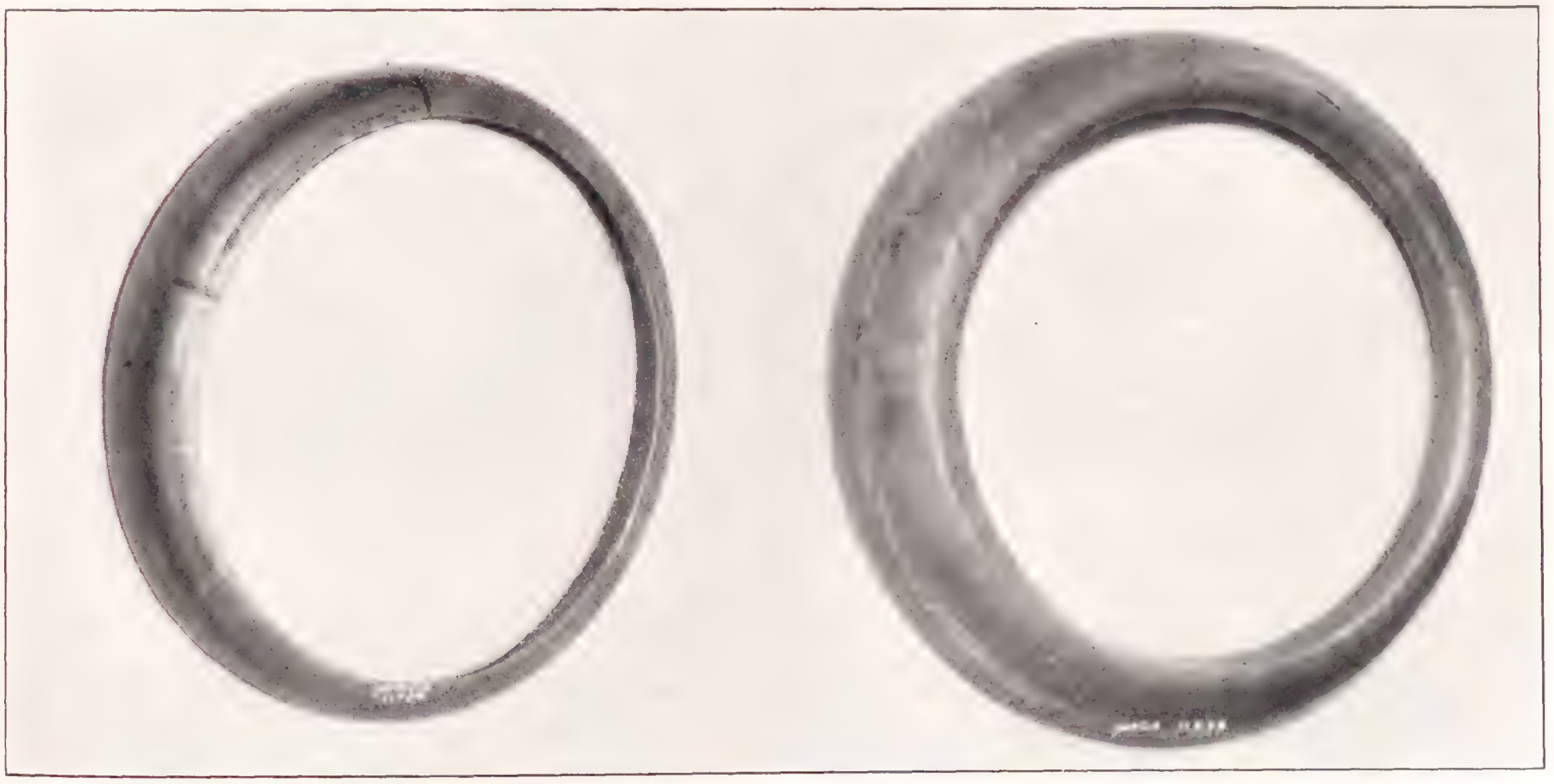

Nose 6 Nose 7

FIGURE 5.—Continued. Nose shapes of cowlings tested.

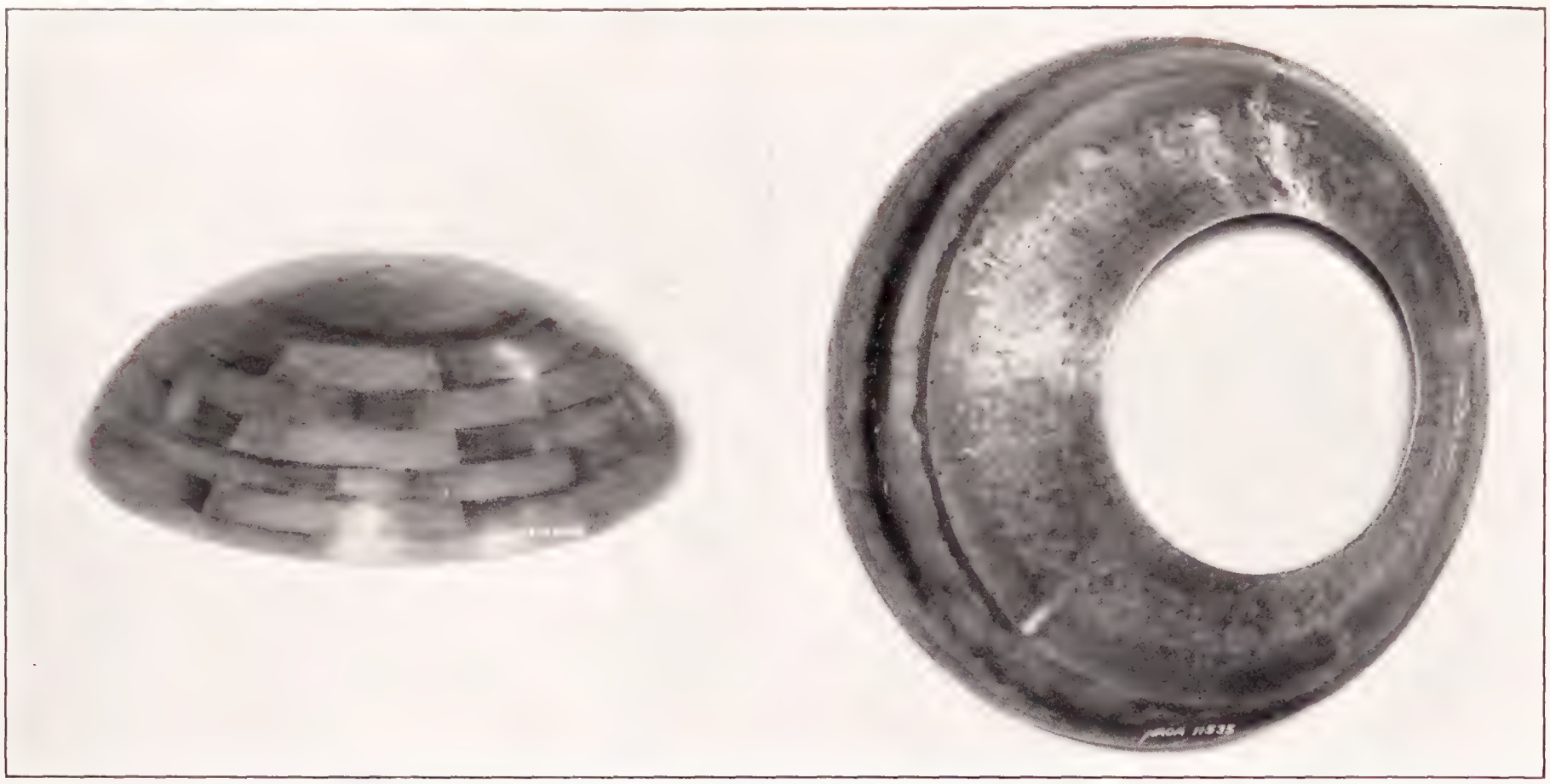

Nose 8 Nose 9

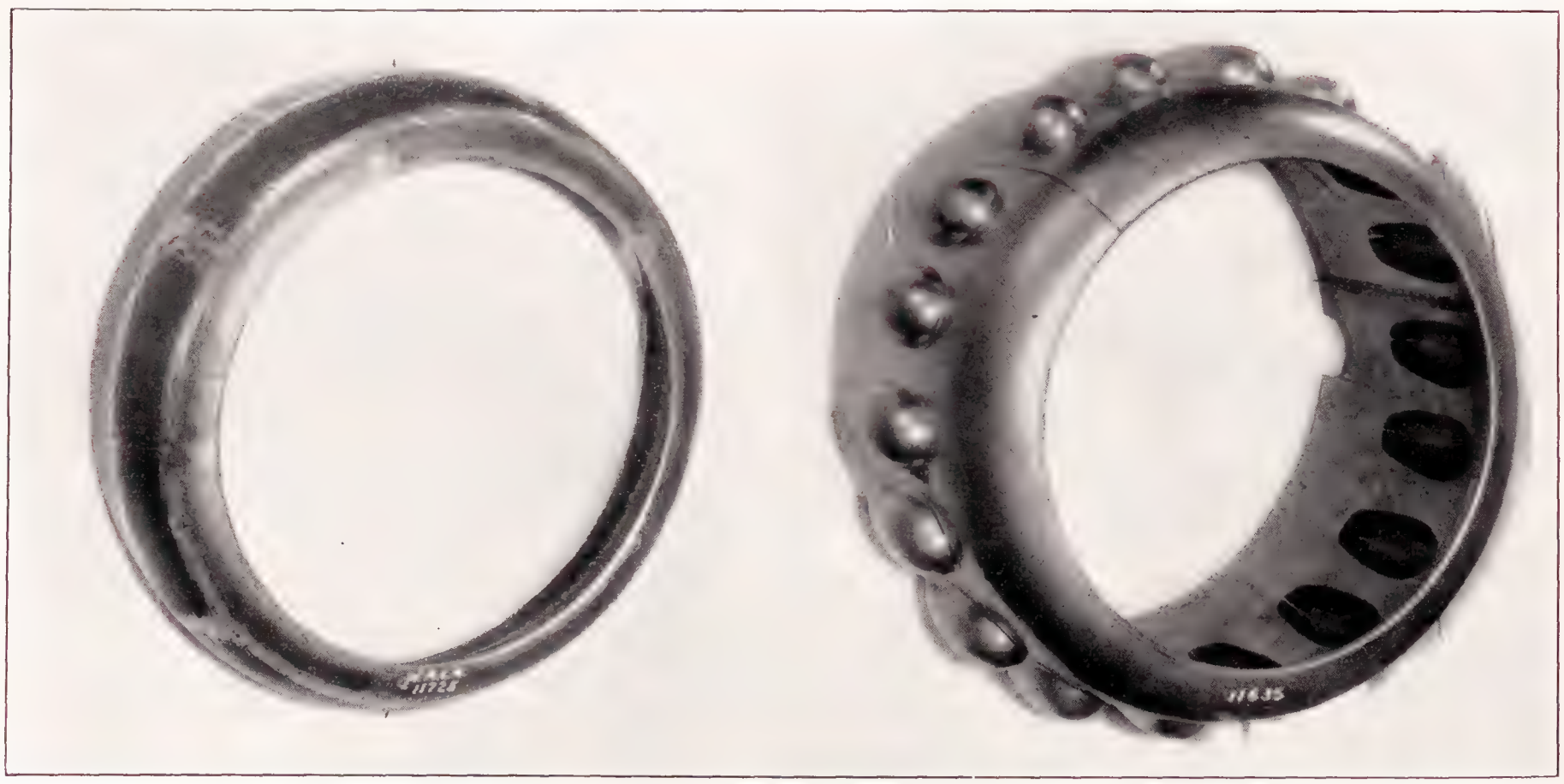

Nose 15 Nose 17

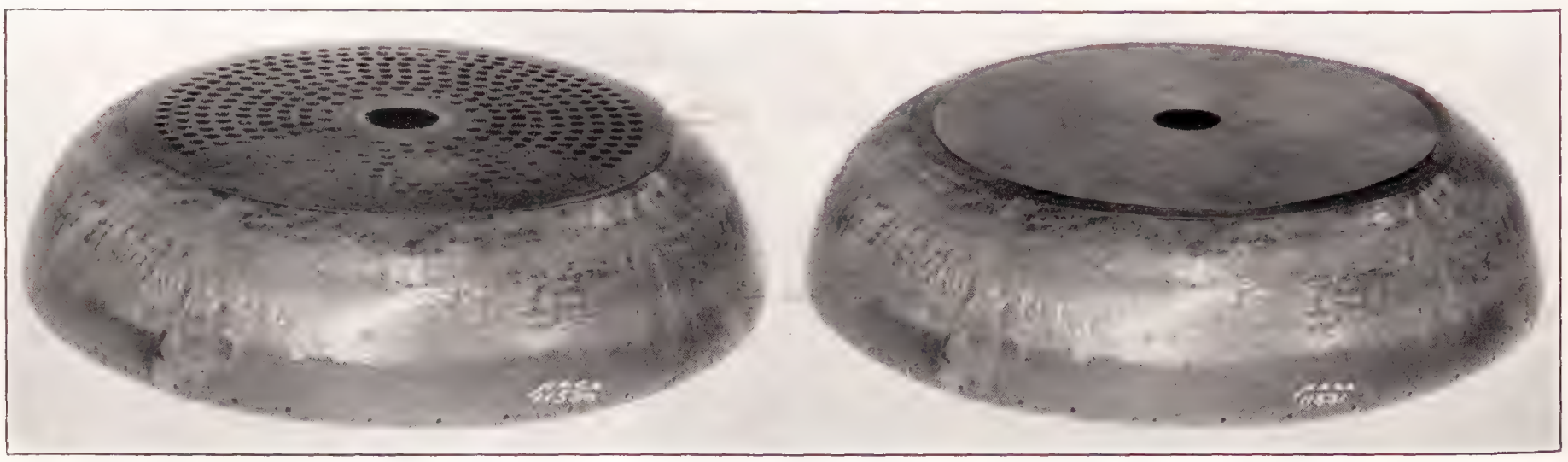

Nose 18 FIGURE 5.—Continued. Nose shapes of cowlings tested. Nose 19

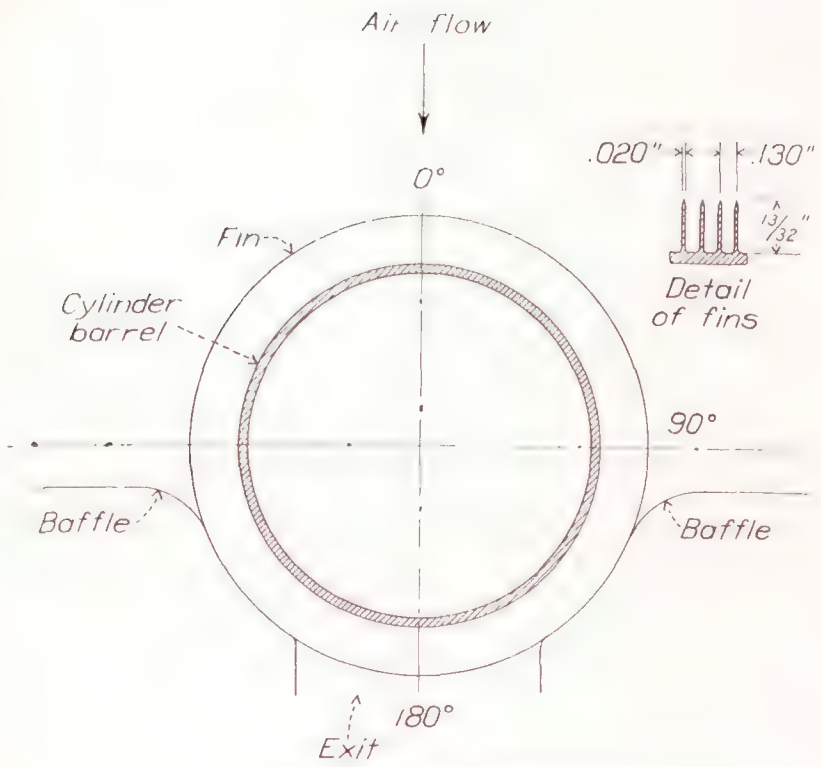

FIGURE 6.—Standard baffle arrangement.

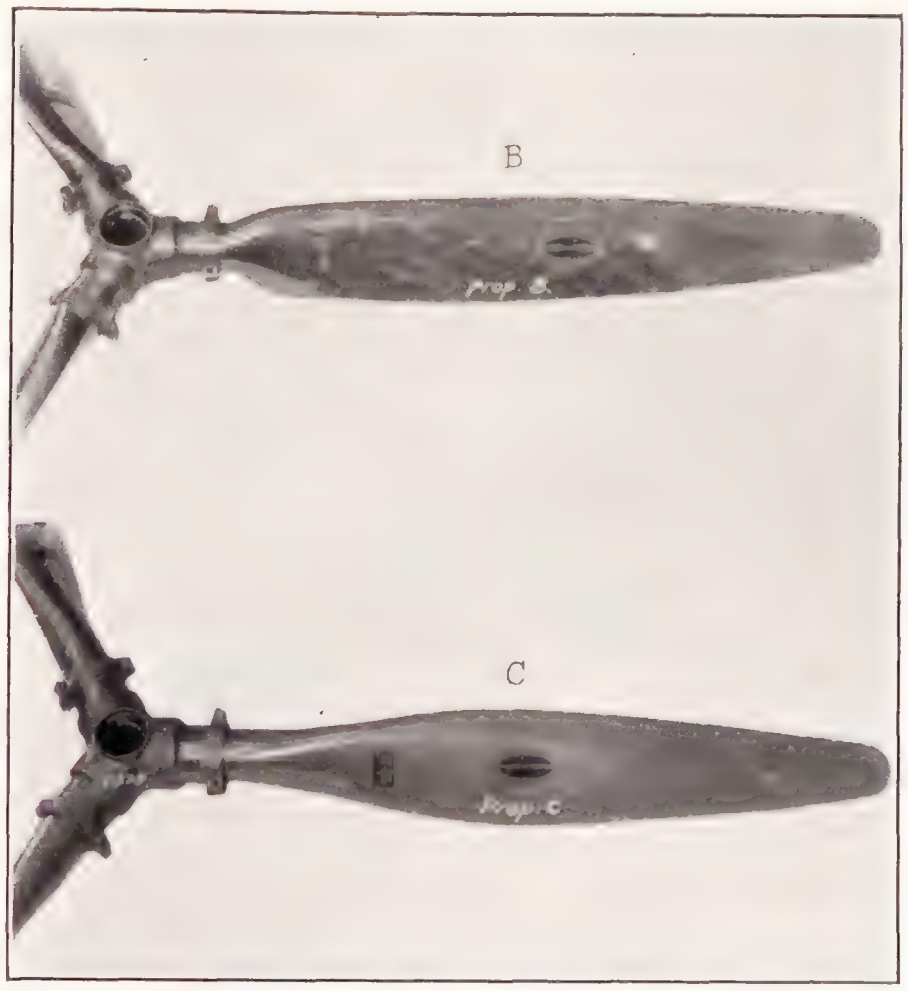

FIGURE 7.—Propellers used for the cowling tests.

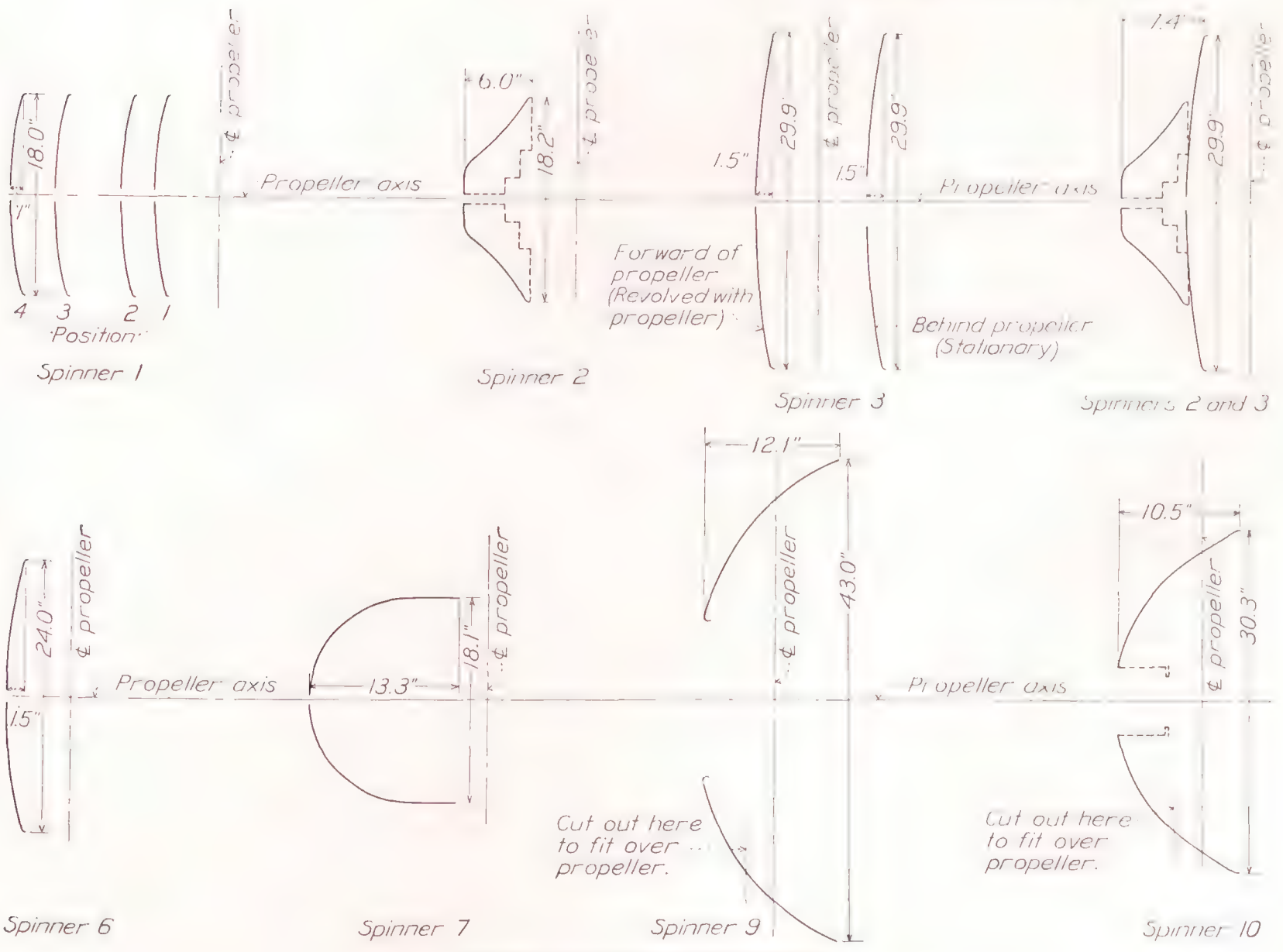

FIGURE 8.—Spinner shapes and positions.

Spinners.—Dimensioned drawings of the spinner shapes and their positions with reference to the plane of the propeller are given in figure 8. (See also fig. 9.) Spinner 9 was the only spinner that admitted air through the center.

Special devices.—Several special devices were tested in order to gain some insight into their effects on the normal arrangement.

1. Auxiliary airfoil: A circular airfoil of the section shown in figure 4(a) was used in combination with

nose 7. Auxiliary airfoil 1 was tried in two positions as shown. Auxiliary airfoil 2 had the same chord as airfoil 1, but the leading edge was turned down as shown in the drawing. It was tried only in position 1.

2. In order to investigate the possibility of discharging the cooling air through the rear of the nacelle, the special design shown in figure 4(b) was tested. Unfortunately, the resistance through the nacelle was too large to permit a sufficient range to be covered.

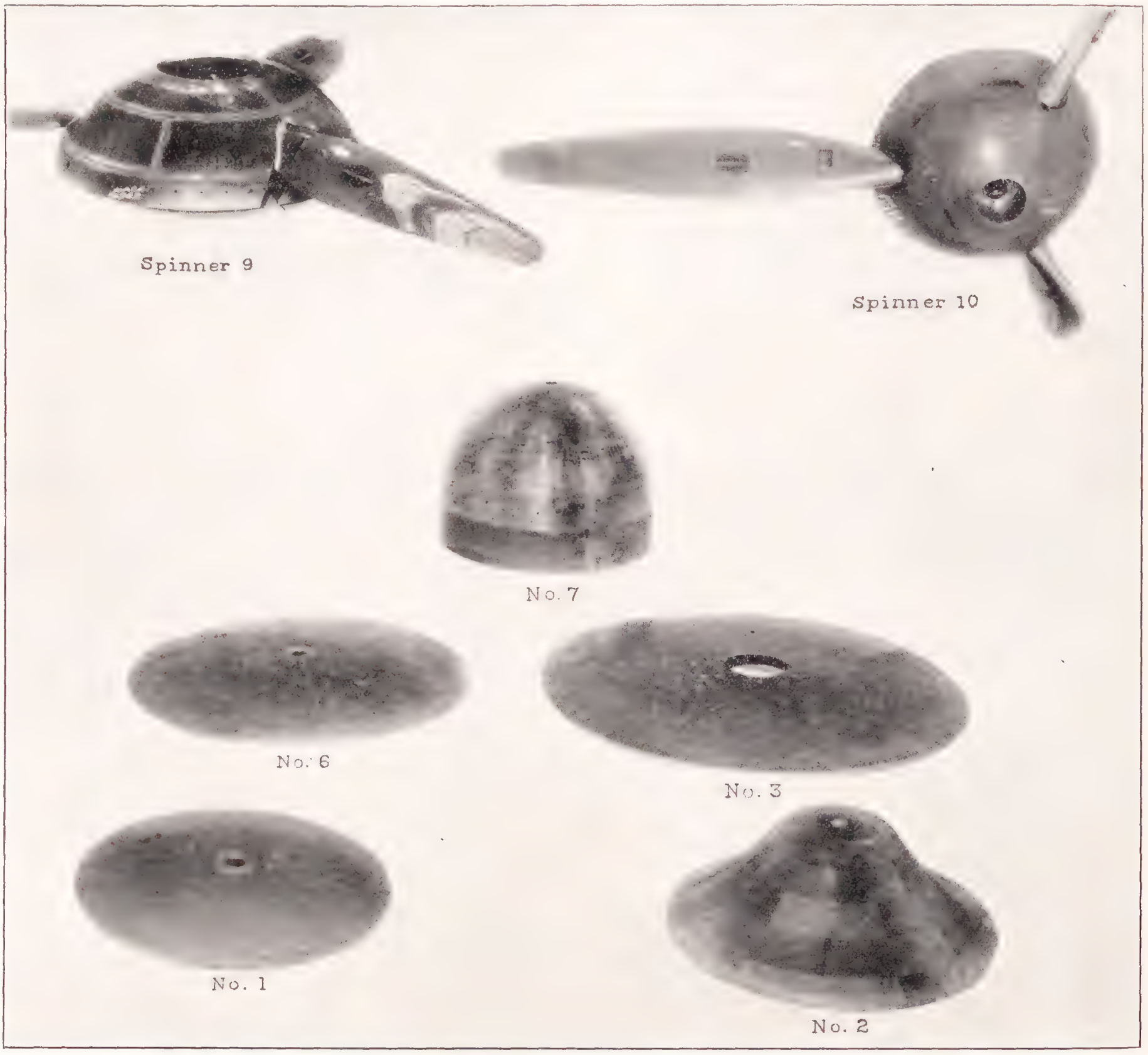

FIGURE 9.—Spinners.

Pressure and temperature apparatus.—Static-pressure orifices were placed over the inner and outer surfaces of the cowling to give a sufficient number of measurements to determine the static pressure at any point on these surfaces. Twelve pitot tubes and twelve static-pressure tubes were placed between the fins on a cylinder to measure the loss in energy as the air flowed around the cylinder. Four pitot tubes and four static-pressure tubes were placed across the exit of the baffles to determine the energy in the air at that place. Sixteen pitot tubes and eight static-pressure tubes were placed in the exit of the skirt to measure the air flow through the engine. Survey tubes were placed at intervals outside the cowling surface to determine the flow condition with different cowling shapes. A survey was made of the air stream at six locations along the axis of the nacelle with each propeller and with no propeller.

Thermocouples were placed at positions around the cylinder corresponding to the positions of the pressure measurements. Hot-wire anemometers were used in the front and the rear of the cylinder to determine the relative cooling obtained in each place.

RESULTS

The top speed actually employed in the tunnel was approximately 100 miles per hour. The V/nD values were, however, extended to depict conditions up to 300 miles per hour at one-third the actual Reynolds Number. The present paper is confined to a report on the results of the aerodynamic properties of cowlings at normal-flight speeds. Several of the tests were also concerned with the cooling properties.

All propellers were actually tested throughout the blade-angle range of 15° to 45° (reference 8). The present report includes only propellers B and C at a blade-angle setting of 25°. The tests were actually extended over the complete range of P_c and it is entirely for convenience that the results of this paper are confined to a representation of a normal cruising condition. All conclusions in regard to the results are definitely identical with those obtainable at any other value of P_c in the cruising range. The conditions obtained in the lower end of the speed range are presented in a separate report (reference 9). The tests, in general, comprised the following measurements:

Drag, or thrust, and the power supplied.
Pressure distribution over nose, skirt, and nacelles.
Pressures in front and rear of engine unit.
Velocities through baffles and skirt opening.
Temperatures of heated-cylinder barrel.

Table I summarizes the condensed results pertaining to the experiments on cowlings under a cruising condition and includes pertinent related information. The subdivisions relate to specific variables. The main division is on the basis of conductivity with secondary divisions for the nacelles, spinners, and other special devices.

Each unit was given a designation made up of five numbers or letters separated by dashes. These numbers refer to the parts of the unit shown in figure 4 and are, in order, nose—skirt—propeller—inner cowling—spinner. Thus 7—2—C—3—7 represents a test made on nose 7, skirt 2, propeller C, inner cowling 3, and spinner 7. A missing part is represented by the number 0. These designations are given in column 1 of table I. Column 2 is the pressure p_f in front of the engine divided by the air-stream velocity head q. Column 3 is the pressure in the rear of the engine p_r divided by q. Column 4 is the difference between columns 2 and 3, or $\Delta p/q$. Column 5 gives the values of the conventional drag coefficient $C_D=D/qF$. Column 6 gives the drag at $q=25.6$ pounds per square foot, which corresponds to a speed of 100 miles an hour at standard conditions, or the thrust at a value of $1/\sqrt[3]{P_c}$ of 1.8 at a q of 25.6 pounds per square foot. Column 7 is the net efficiency of the arrangement at the value of $1/\sqrt[3]{P_c}$ of 1.8. Column 8 presents the pump efficiency. Columns 9 and 10 give the index temperatures at the front and back, respectively, of the barrel of the electrically heated cylinder. The index temperatures are the temperature differences between the cylinder and the air stream.

FORCE MEASUREMENTS

The total drag for the test arrangement 7—2—0—3—0 for a range of q up to 28 pounds per square foot is given in figure 10. In order to have a representative picture in a particular case of the drag distribution of each part of the set-up, the pressure distribution over the whole unit is shown in figure 11(a). The values plotted are the nondimensional pressures p/q measured along the surface of the body. The recorded pressures are plotted on normals to the surface at the point where the orifice was located. Both positive and negative values are plotted on the outside of the body, the appropriate sign being indicated.

Using the same values, secondary plots (fig. 11) give the graphical integration of the axial force with the pressure plotted against the radius. The area under the plots represents the pressure drag of the body. The figures also give the individual contribution of each part, the momentum in the exit slot being included.

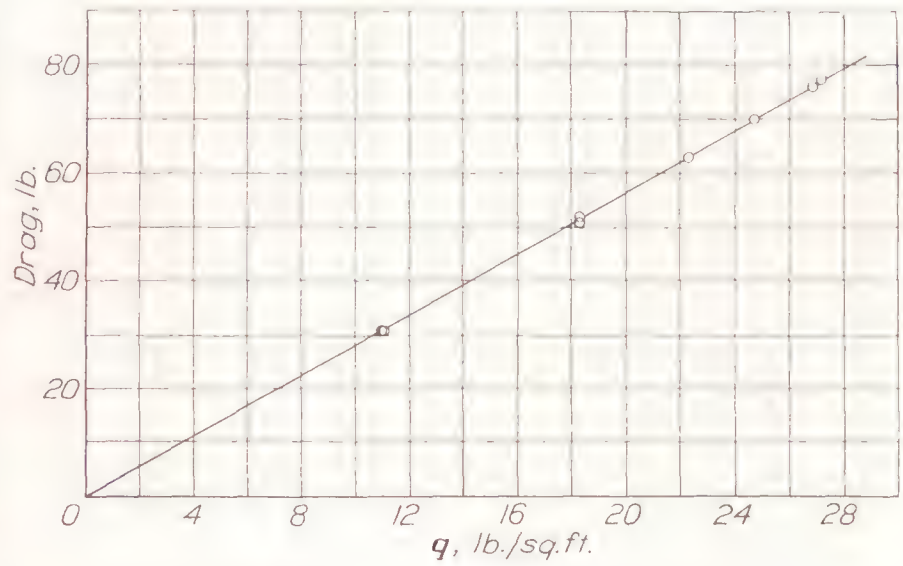

FIGURE 10.—Sample drag curve for test arrangement 7—2—0—3—0.

The actual measured drag for the unit was 72.5 pounds and the value given by the pressure plot is 57 pounds. To the latter value should be added 10 pounds, or more, estimated for the skin friction. The essential point in this comparison is not the closeness of the agreement but the picture obtained of the relative effect of the several parts of the set-up.

The same set-up was tested with propeller B operating (7—2—B—3—0). The conventional curves of propeller thrust coefficient C_T, power coefficient C_P, and propulsive efficiency η are plotted against V/nD in the usual manner (fig. 12(a)). Of more direct concern in the present paper is, however, the curve of net efficiency η_n plotted against the quantity $1/\sqrt[3]{P_c}$ (fig. 12 (b)), both quantities having been defined in the earlier analysis of the problem. As previously mentioned, the values of η_n included in table I were taken from such curves of η_n against $1/\sqrt[3]{P_c}$ for a value of $1/\sqrt[3]{P_c}$ of 1.8.

PRESSURE DISTRIBUTION

As mentioned in the introduction, the drag of an arrangement without the propeller operating is not a safe criterion of performance. This section and table I show how the pressures over the body change with propellers operating in front of the body. Under the cruising condition reported here the effect of the propeller is less marked than in the condition of climb or take-off.

From the distribution of the static pressure over the entire unit as given graphically in figure 11, an impression of the relative importance of the various parts is obtained. A study of a number of similar plots shows that the pressure drag of the rear portion, or nacelle, remains fairly constant, resulting in the important conclusion that the cause of essential differences in the drags of the several arrangements is to be found in the cowling or, more specifically, may be traced back to the nose section. Another cause of large losses may be traced back to an inefficient skirt section. An indirect effect of the nose manifests itself in a variation of the static pressure on the frontal area of the engine, this pressure being always somewhat less than the corresponding total head of the air stream. This pressure on the front of the engine must be measured with considerable care in order to obtain reasonable accuracy in the integrated pressure drag. An error of 0.05 q at a value of q of 25.6 pounds per square foot corresponds to an error of 19 pounds in the pressure drag.

The pressures p_f/q on the front of the engine, taken as an average of several simultaneous measurements over the area, are given in table I. The pressure distribution over a number of individual cowlings is given in figure 13. The pressure distribution over a

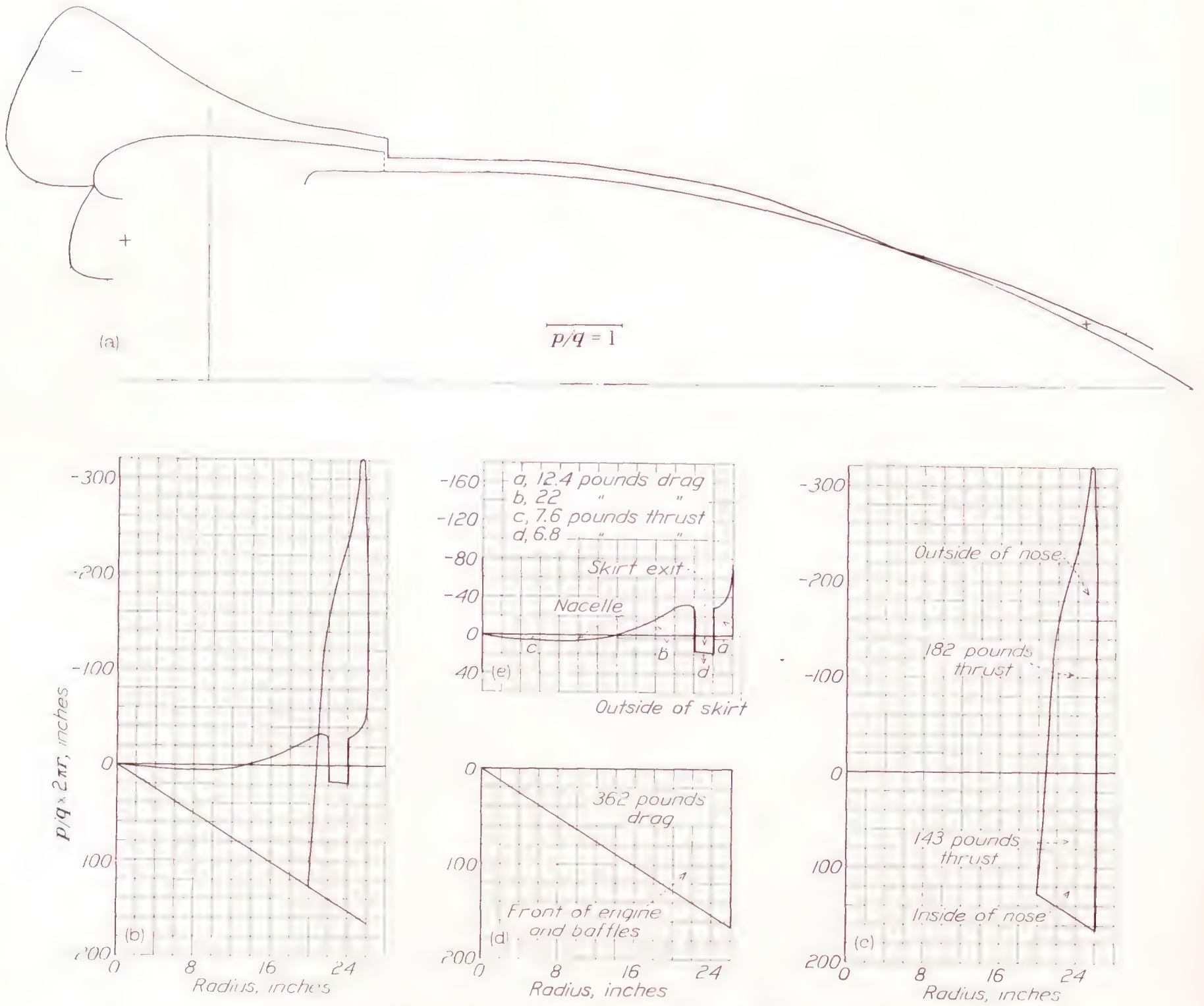

FIGURE 11.—Pressure distribution on the test arrangement 7—2—0—3—0 and the integrated drag from the pressure distribution.

number of skirts tested in conjunction with nose 7 is given in figure 14. The effect of a propeller on the pressure distribution on arrangement 7—2—B—3—0 is given in figure 15 for several air speeds. The greatest value of such pressure plots lies in the possibility of qualitatively distinguishing between desirable and undesirable flow characteristics. It is possible to associate an efficient nose with a smooth distribution of the static pressure. On such a basis one would evidently select nose 2, 3, or 7.

Attention will be called to the fact that care must be taken to obtain the pressure distribution under the correct conditions. Some noses, in particular nose 1, are very critical in regard to the effect of the propeller slipstream. This effect has been referred to in the introduction as an effect of the relative direction of the local air flow with respect to the leading edge or contour of the nose. It is interesting to observe that nose 1, which is unusually inefficient at normal air speeds, approaches a reasonable efficiency at low air speeds.

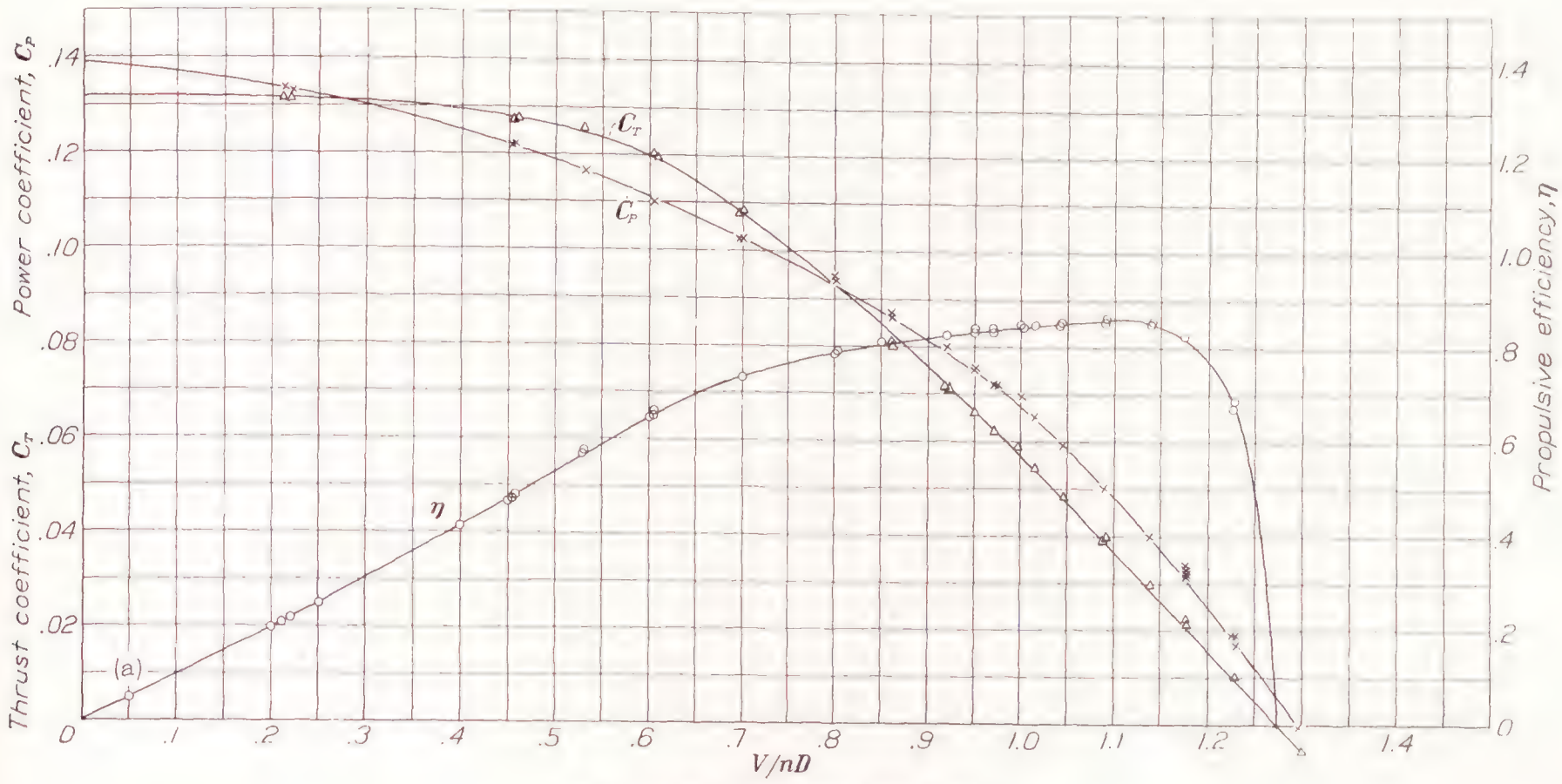

(a) Curves of C_T, C_P, and η against V/nD.

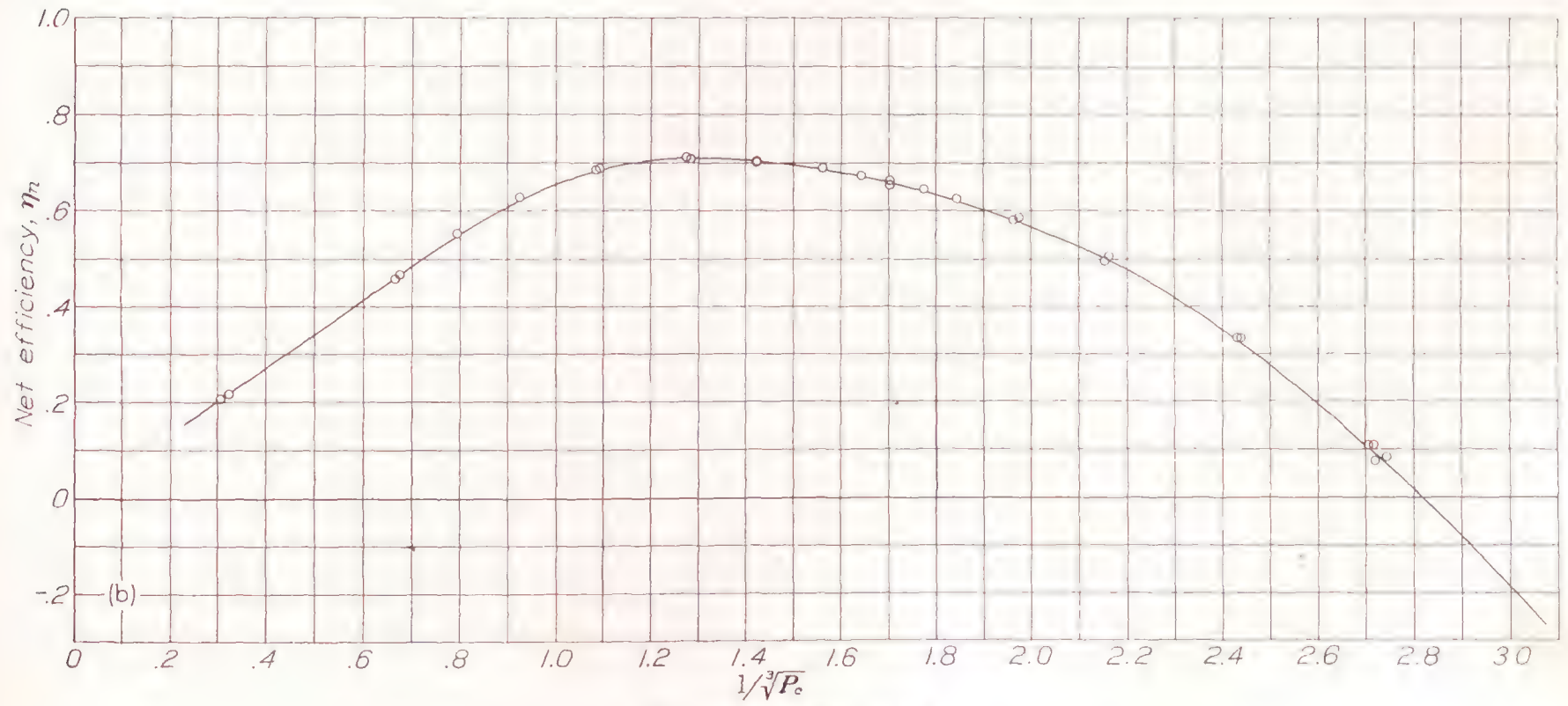

(b) Curves of η_n against $1/\sqrt[3]{P_c}$.

FIGURE 12.—Sample curves. Arrangement 7—2—B—3—0. Blade angle set 25° at 0.75R.

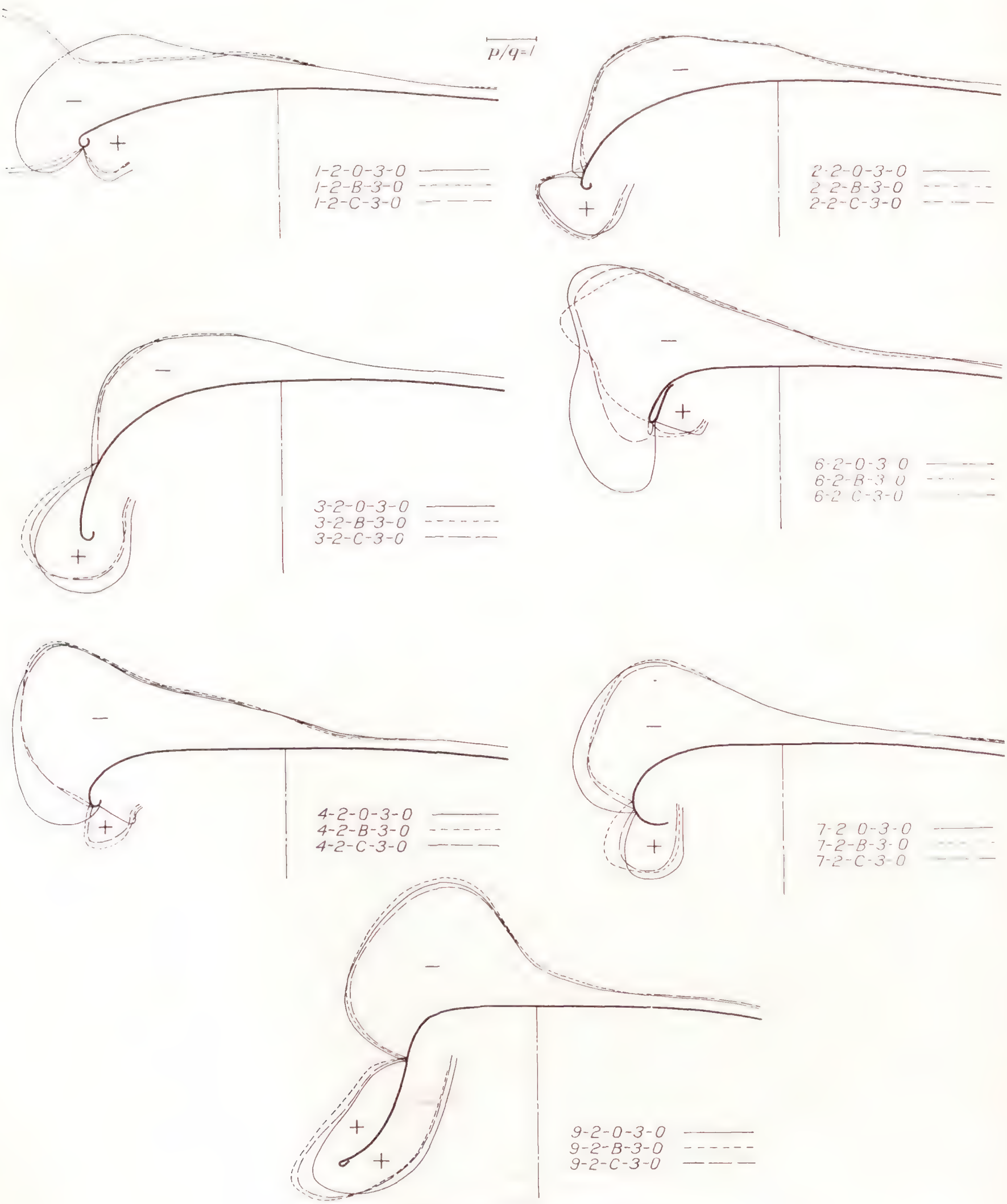

FIGURE 13.—Pressure distribution over various cowling shapes.

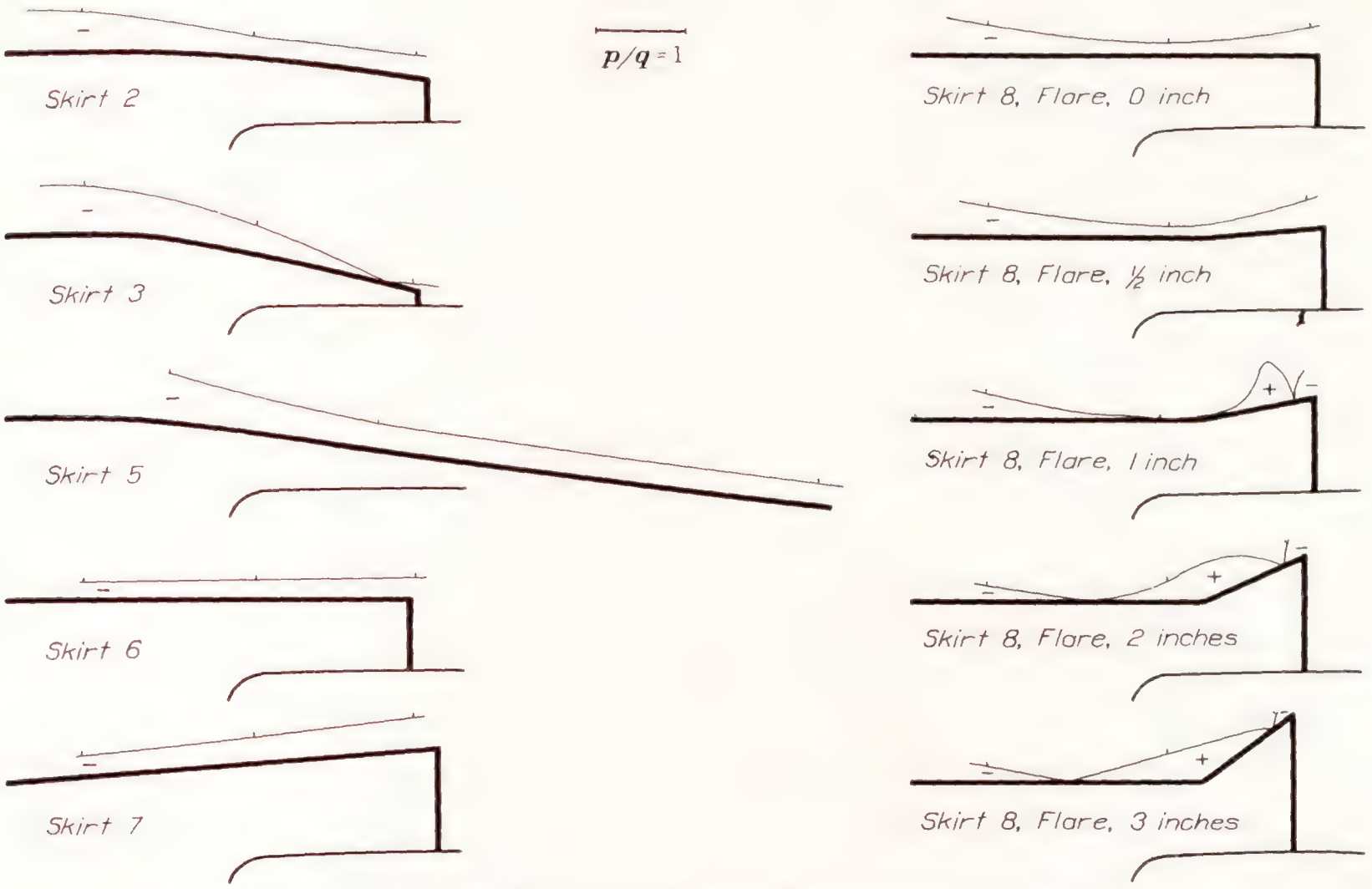

FIGURE 14.—Pressure distribution over the various skirts for test arrangement 7—X—0—3—0.

Curve	Arrangement	Propeller setting	Speed (r.p.m.)	q (lb./sq.ft.)
A	7-2-0-3-0	25° at 0.75R		25.80
B	7-2-B-3-0		648	.64
C	7-2-B-3-0		675	2.94
D	7-2-B-3-0		766	11.32
E	7-2-B-3-0		835	18.15
F	7-2-B-3-0		871	21.80

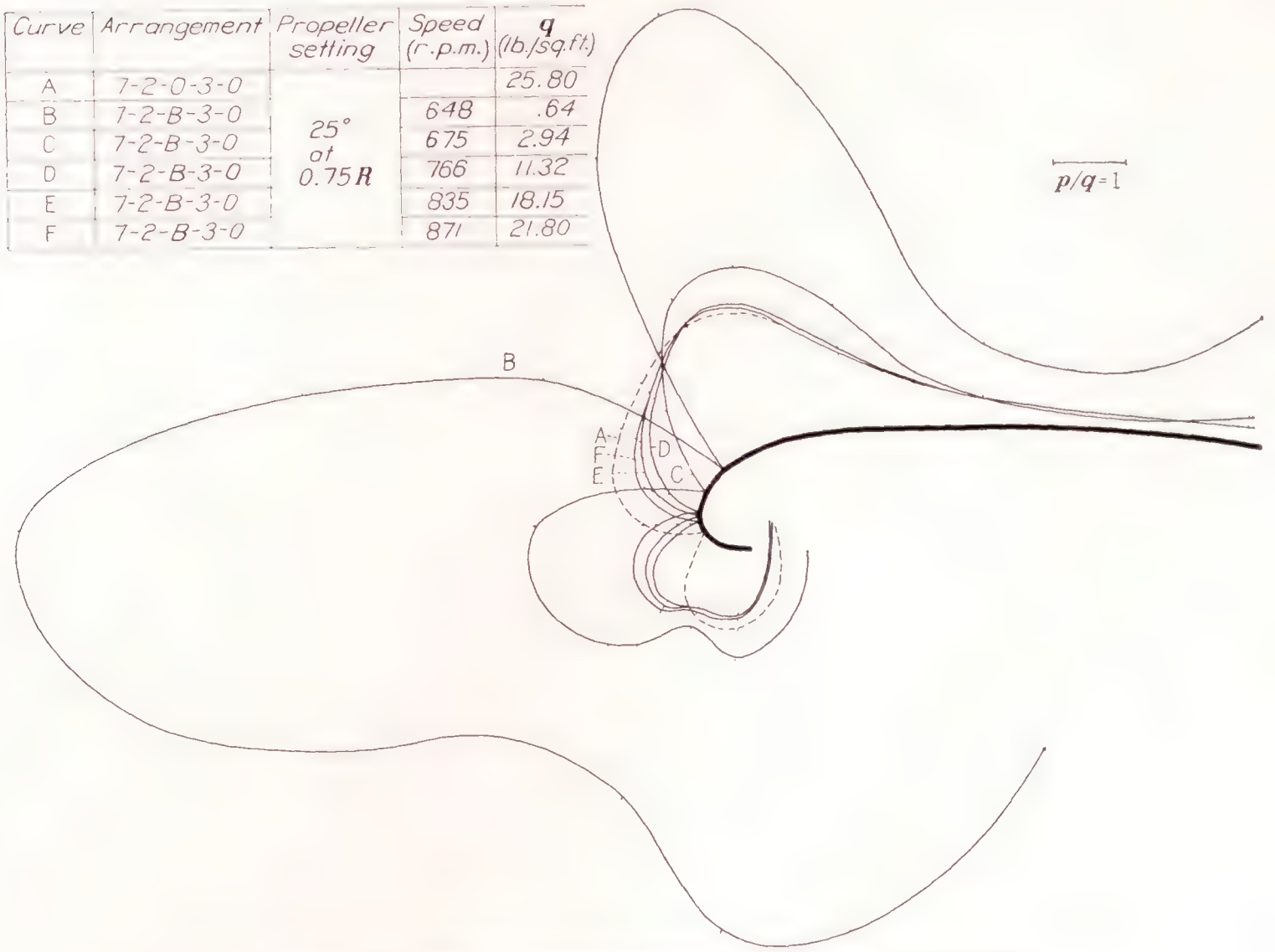

FIGURE 15.—The effect of the propeller on pressure distribution at several air speeds.

Thus with a proper consideration of the effect of Reynolds Number and the propeller slipstream, it is concluded that the pressure distribution is an excellent although somewhat indirect method for evolving an aerodynamically efficient cowling design, the procedure being to adjust the shape repeatedly until the smoothest pressure distribution is reached in whatever range may be desired. Cowling 7 was directly produced as a result of this type of procedure, this cowling being the least critical to changes in operating conditions, combined with high efficiency. The high negative pressure on the nose of the cowling is utilized in the new nose-slot cowling (reference 10) to give a higher pressure drop across the engine for cooling.

CONDUCTIVITY

The physical definition of the term "conductivity" has already been given. Two measurements are needed to determine experimentally this quantity K: the pressure drop $\Delta p/q$ across the resistance and the rate of air flow Q. The value $\Delta p/q$ is obtained directly by a system of pressure tubes placed over the front and the rear areas of the engine unit, the averages being given in table I. The rate of flow is determined by a number of permanent installations for velocity surveys across the exit opening, a total of 24 tubes, 16 impact and 8 static, being used. As previously mentioned, the conductivity is obtained by the formula

$$K=\frac{\frac{Q}{FV}}{\sqrt{\frac{\Delta p}{q}}}$$

It is to be noted that, thus defined, the quantity K is entirely a function of engine-baffle design. That this assertion is strictly true was confirmed by tests of a given baffle arrangement with a variety of different noses and skirts, all resulting substantially in the same value of K. Independence of the Reynolds Number was similarly established by tests over the entire range of air speeds. This independency of the Reynolds Number is explained by the fact that the pressure loss in the baffles consists primarily of the exit loss and is therefore nearly proportional to the square of the velocity.

Three values of conductivity are used in the present investigation:

(1) $K=0.0424$, representing the case of the baffles fitting tightly against the cylinder barrel.

(2) $K=0.0909$, representing the case of the baffles moved back ½ inch, giving a somewhat diverging channel along the back of the cylinder barrel.

(3) $K=$about 0.5, representing the case of an unbaffled engine, the pressure drop being too small to be measured with sufficient accuracy.

The accuracy in determining the values (1) and (2) by the above-described method is within 1 percent.

These conductivities cover the useful range, as the value of the conductivity for an actual engine with commercial type of baffles of satisfactory design had been determined in the preliminary test as $K=0.06$. Deeper fins and more cylinders in parallel, as used in 2-row radials, might increase this value to as much as 0.15.

In regard to the optimum conductivity of the engine-baffle unit, it is to be observed that a minimum quantity of air is necessary to carry away a given quantity of heat. The maximum temperature difference between the air and the cylinder is of the order of 400° F. By the reduction of the quantity of cooling air, a condition is soon reached in which the effect of the reduced temperature difference more than offsets other advantages. A reasonable increase in the temperature of the cooling air on passing through the baffles is of the order of 50° to 60° F. The corresponding air quantity may be considered the minimum and the related conductivity the optimum.

The "apparent conductivity" of the skirt exit openings, defined as A_2/F, is found to be large compared with the conductivity of the engine. The pressure drop through the skirt is therefore small in comparison with the pressure across the engine, except for the narrowest skirt 3. This condition is different for the unbaffled engine. In such an engine the pressure drop is largely used to create velocity in the exit opening. It may, in consequence, be seen from table I that a value of very nearly $1q$ is available for cooling under ordinary conditions.

PUMP EFFICIENCY

It has been shown in the first part of the paper that the pump efficiency is given by formula (3)

$$\eta_p=K\left(\frac{\Delta p}{q}\right)^{3/2}\frac{1}{C_D-C_{D_0}}$$

for the case of the propeller off. Similarly, formula (4)

$$\eta_p=C\frac{\left(\frac{\Delta p}{q}\right)^{3/2}}{\eta_0-\eta}$$

is used for the power tests. The values of C_{D_0} and η_0, which quantities relate to the closed basic contour indicated in figure 1, were determined by tests of the actual shape 19—5—0—3—0 as $C_{D_0}=0.112$, or a drag of 42 pounds at 100 miles per hour, and by tests of the shape 19—5—C—3—0 as $\eta_0=74.2$ percent.

For propellers B and C the values of the constant C, representing KF/SP_c, in formula (4) at the standard value of $1/\sqrt[3]{P_c}$ of 1.8 are 0.046 and 0.099 for the conductivities K of 0.0424 and 0.0909, respectively.

The experimentally determined pump efficiencies are given in table I. These efficiencies are in strict accordance with the definition given in the introductory analysis and in complete agreement with one adopted

in reference 11. The drag obtained on the closed basic cowling shape (fig. 1) is to a certain extent arbitrary, thus permitting efficiencies in excess of unity as may be noted in a few cases. It must be realized that such a definition permits efficiencies in excess of unity, explainable by the fact that some duct arrangements improve the flow to some extent, which condition might

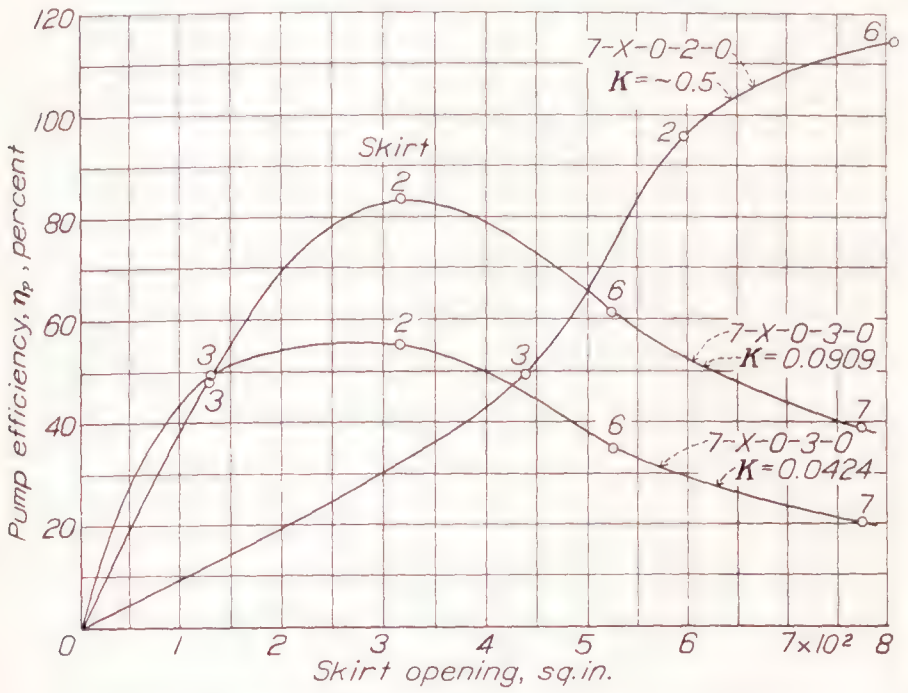

FIGURE 16.—Pump efficiency against skirt exit area for several skirts.

be expected to occur on somewhat inefficient forms, that is, forms with poor streamlining.

The table shows widely varying pump efficiencies from almost zero to more than unity (i. e., 100 percent). Some of the results are reproduced in figures 16, 17, and 18. In figure 16 the pump efficiency is plotted against

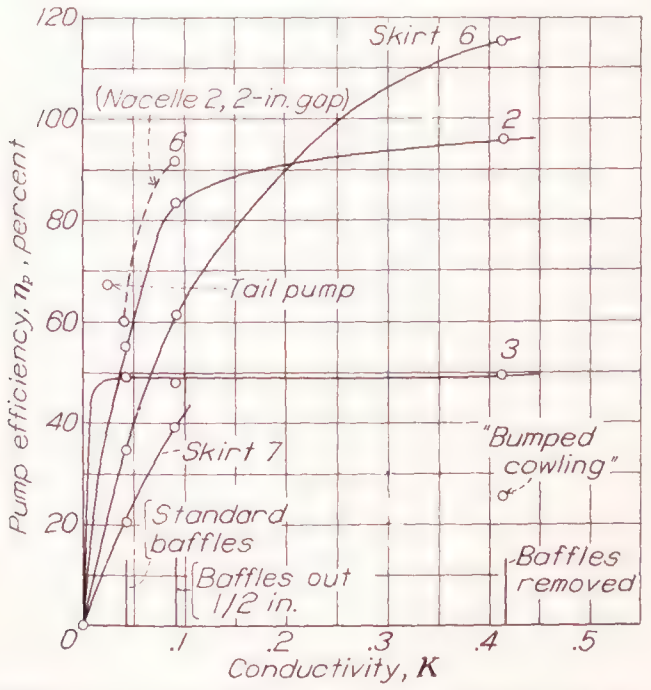

FIGURE 17.—Pump efficiency against conductivity for nose 7. Each curve is for a particular skirt.

the area of the exit opening; each of the three curves relate to a constant conductivity. Note that the peak efficiencies increase with the conductivity and occur at successively larger exit openings. It is to be noted that the pump efficiency depends to a considerable extent on the shape of opening and not only on its cross-sectional area. The curve for each conductivity, therefore, does not necessarily attain the optimum efficiency at each skirt size. This fact is particularly true for the small and the large skirt openings. Notice that skirt 2 yields efficiencies of from 50 to more than 80 percent for normal conductivities of baffled engines, and of 100 percent for the unbaffled engine. As might be expected, the pump efficiency is seen to increase

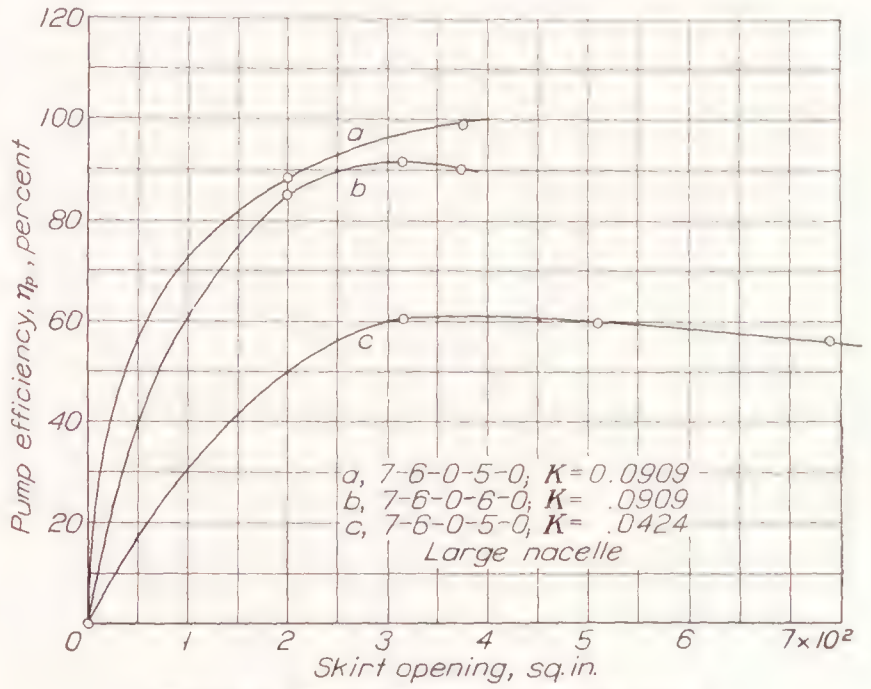

FIGURE 18.—Pump efficiency against skirt exit area.

with increase in flow velocity through the exit opening, indicating that the major loss is of the nature of mixing or impact loss occurring along the nacelle.

Figure 17 is a cross plot of figure 16, the efficiency being plotted against the conductivity, each curve representing a given skirt. Note, in particular, that the

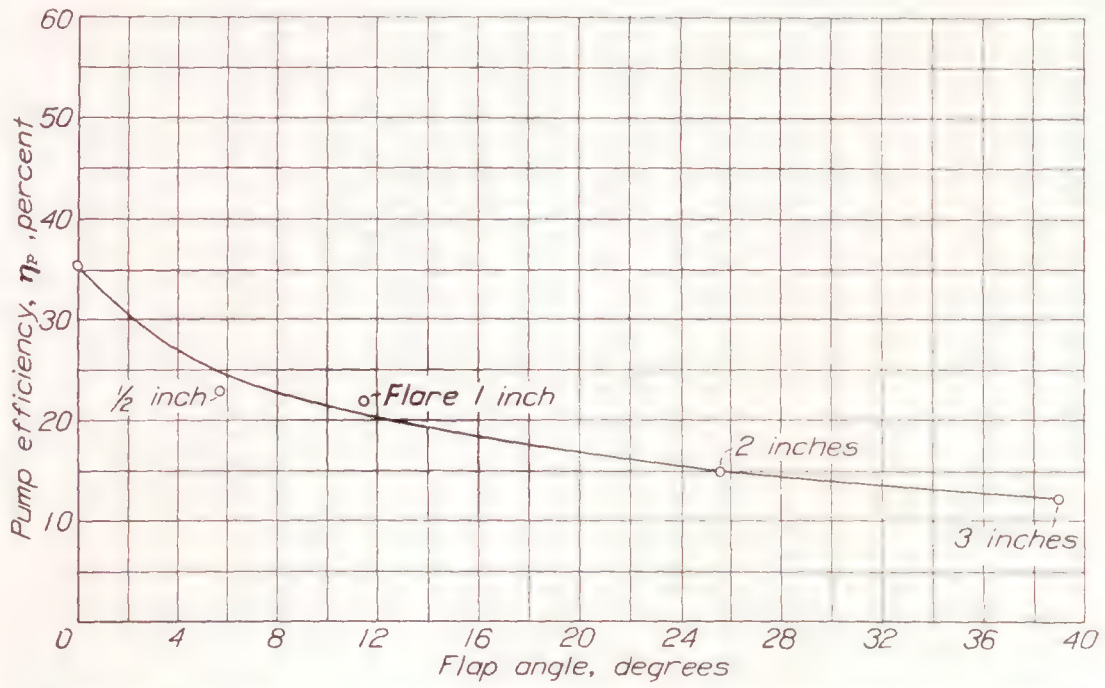

FIGURE 19.—The effect of flaps applied to skirt 8 for test arrangement 7—8—0—3—0; K=0.0424.

smaller skirt openings yield considerably higher efficiencies at the low conductivities corresponding to standard type baffles. The dotted curve obtained on the large nacelle 2 with a small skirt opening, shown in this figure for comparison, gives an efficiency of from 80 to 90 percent in the same range of conductivity, indicating definitely a beneficial influence from the increase in nacelle diameter.

Figure 18 refers to the large nacelle, 2. Note that the efficiencies exceed those from the tests of the small nacelle, all lying in the range from 70 to 100 percent. These tests were obtained with skirt 6, the exit opening being varied by increasing or decreasing the actual length of the skirt. As skirt 6 is cylindrical, the exit area was varied without changing the external contour of the body.

The effect of flaps on the pump efficiency is shown in figure 19, in which the pump efficiency is plotted against the flap angle in degrees. The steep slope of the curve at small angles confirms the importance of careful streamlining in order to attain the highest efficiencies. These tests were obtained on skirt 8, which was successively bent in the shapes indicated in the main drawing (fig. 4). It is of interest to note that the available pressure drop is increased only very slightly by the flaps (table I), the maximum increase amounting to less than 20 percent and associated with a decrease in pump efficiency.

STUDY OF FLOW LINES

In order to gain a quantitative insight into the condition of the flow around and into the cowling, the actual flow lines were determined as shown in figure 20 (the method used will be described in a later paper) and a photographic study of smoke flow was carried out. Figure 21 shows a group of smoke pictures taken with a moving-picture camera. A study of these films in slow motion reveals several interesting details. There seem to exist certain fairly well-defined main flows almost stationary in character. The flow appears, on the whole, extremely turbulent with disturbances of large size. Figure 21(a) shows the flow in front of the engine. Notice the very disturbed flow. The remaining figures 21(b–e) serve to illustrate the direction of the flow lines in front of the engine and the magnitude of the conductivity. The value of the conductivity obtained from the location of the streamline outlining the flow into the cowling is in expected agreement with the calculated value; this particular streamline corresponds very nearly to the smoke line shown in figure 21(d). In figure 21(c) all the smoke flows outside, while in 21(e) all the smoke flows definitely through the cowling. Note the closeness of the smoke nozzle to the axis. These figures also demonstrate the instability of the flow around the nose of a cowling, as the smoke stream oscillates alternately in and out of the cowling.

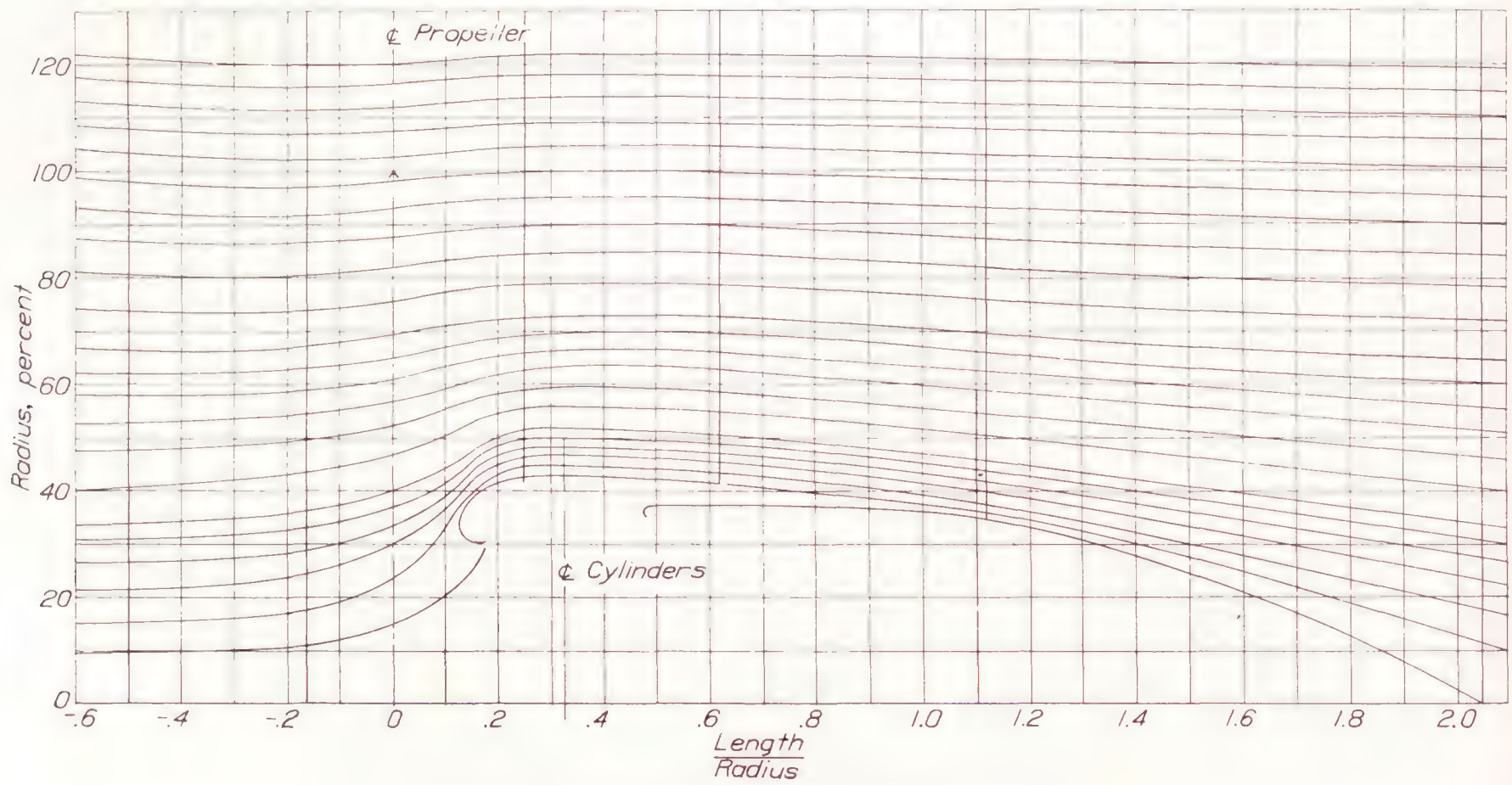

FIGURE 20.—Measured streamlines for test arrangement 7—2—B_x—3—0.

COOLING

The photographic smoke-flow studies show a violent large-grain turbulence in front of the engine. This fact must be kept in mind when analyzing the results of the cooling tests. These results are given in compact form in the main table I. The temperatures given are the temperatures of the front and the back of the cylinder barrel. Figure 22(a) is an example of the actual distribution of the temperature around the electrically heated cylinder, the front being indicated by the 0°. This test refers to the standard baffle arrangement shown in cross section in figure 6. The temperatures plotted are the differences between the cylinder temperature and that of the tunnel air stream. The electric heat input was held constant throughout all tests at 1.75 kilowatts so that the index temperature is a direct measure of the local heat transfer. All heat-transfer tests are taken at a tunnel speed of 100 miles per hour.

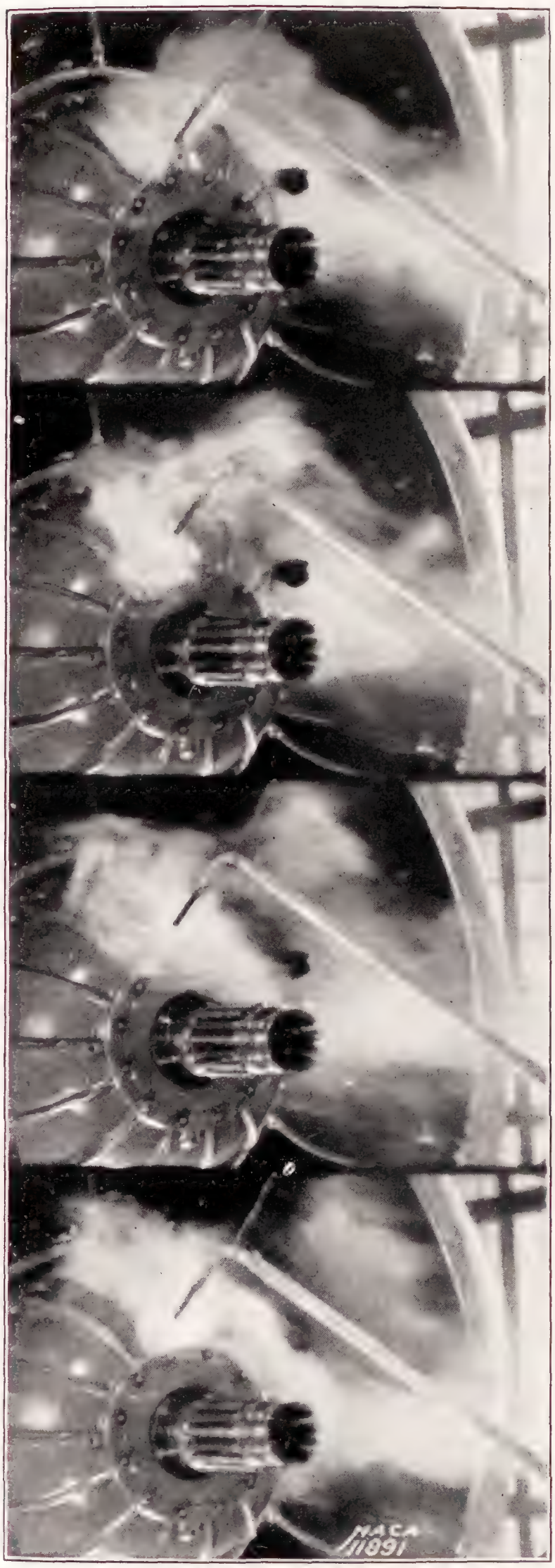

(a) Smoke flow in front of the cowling without the propeller.

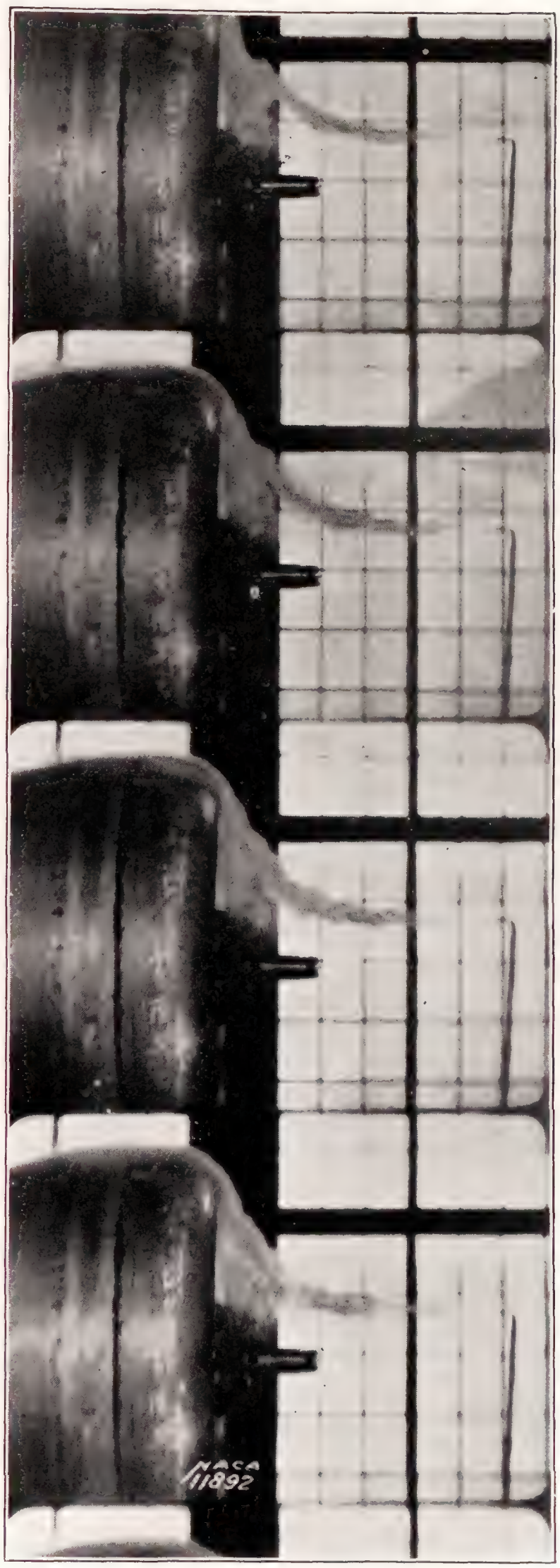

(b) Smoke flow into the cowling without the propeller.

FIGURE 21.—Smoke flow around cowlings.

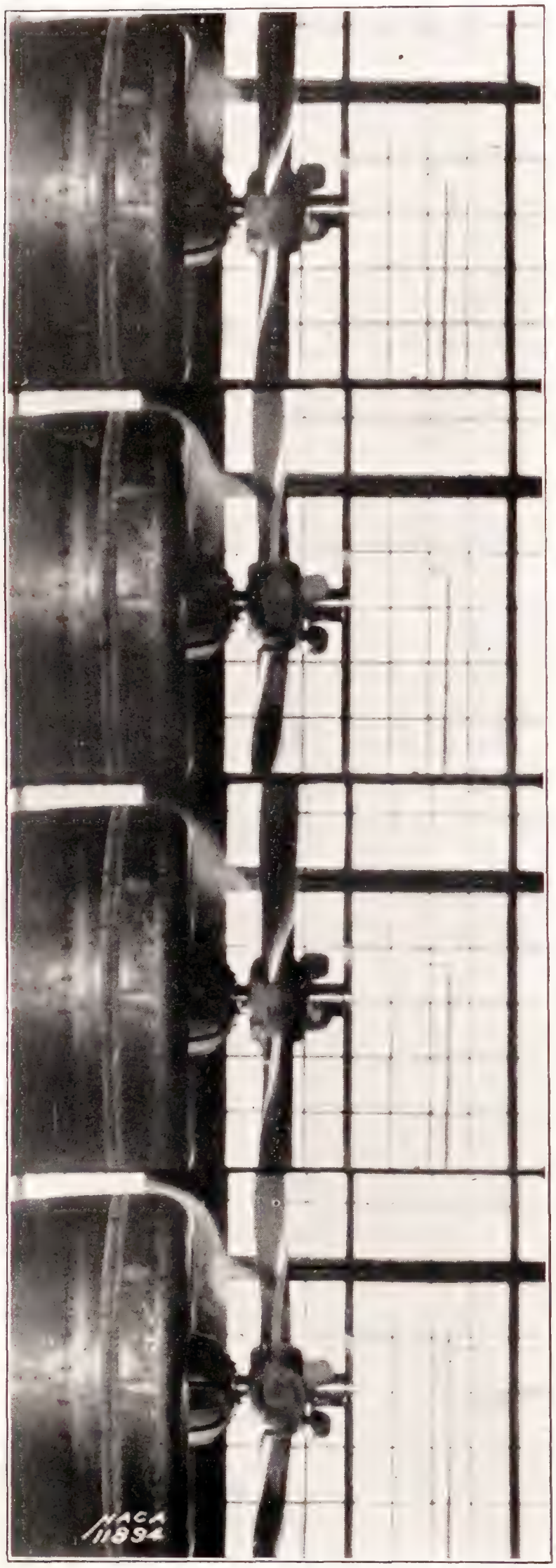

(c) Smoke flow into the cowling outside the streamline with the propeller operating.

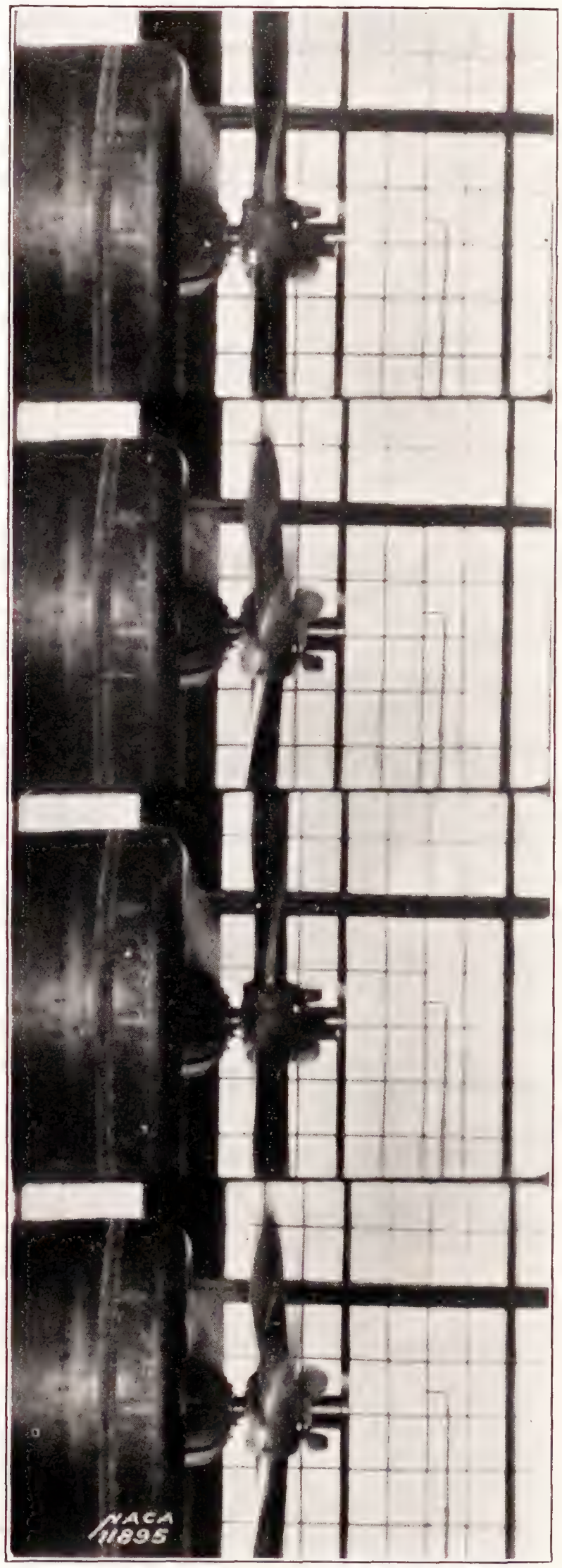

(d) Smoke flow into the cowling with the propeller operating; streamline.

FIGURE 21.—Continued. Smoke flow around cowlings.

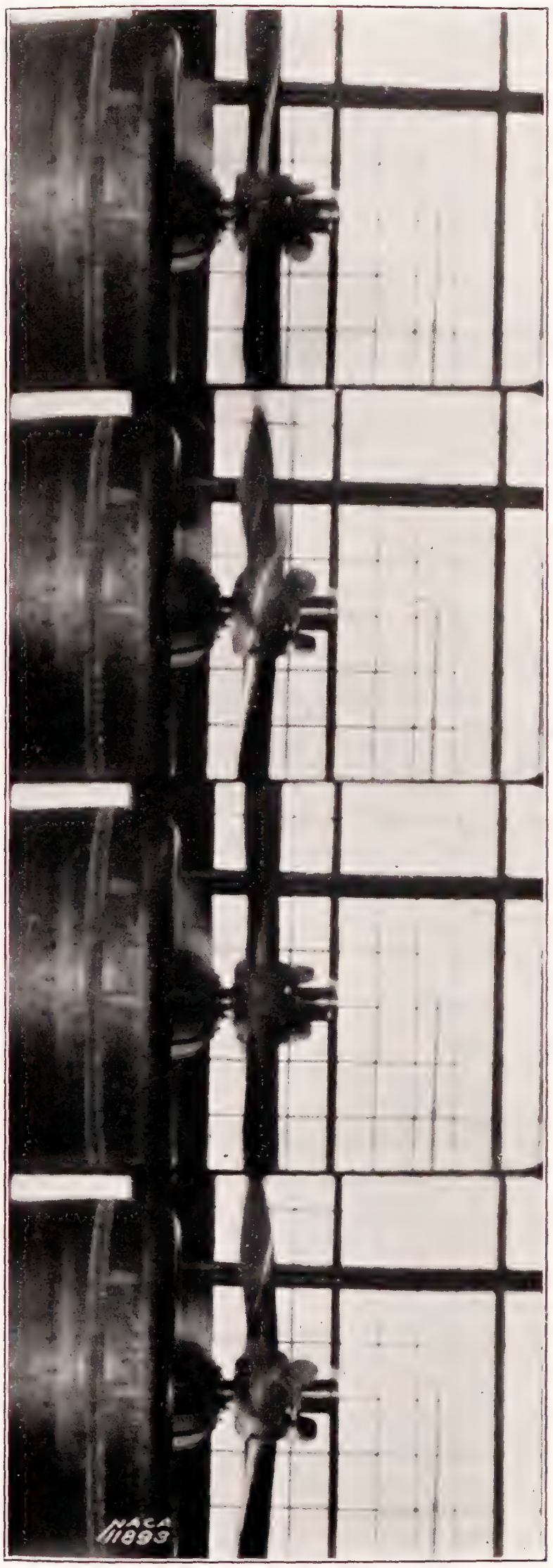

(e) Smoke flow into the cowling inside the streamline with the propeller operating.

FIGURE 21.—Continued. Smoke flow around cowlings.

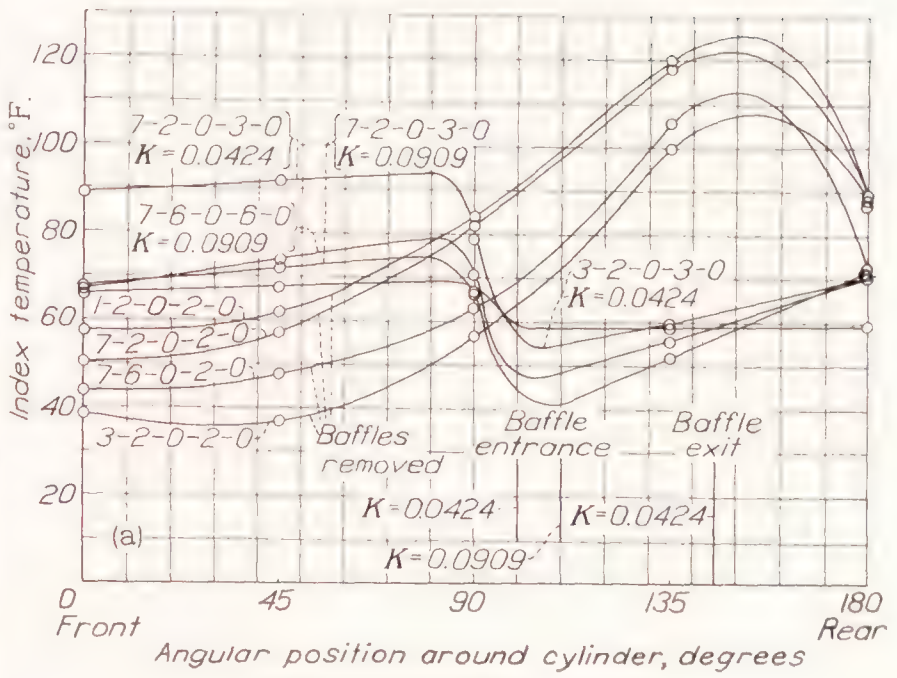

(a) Several cases with no propeller.

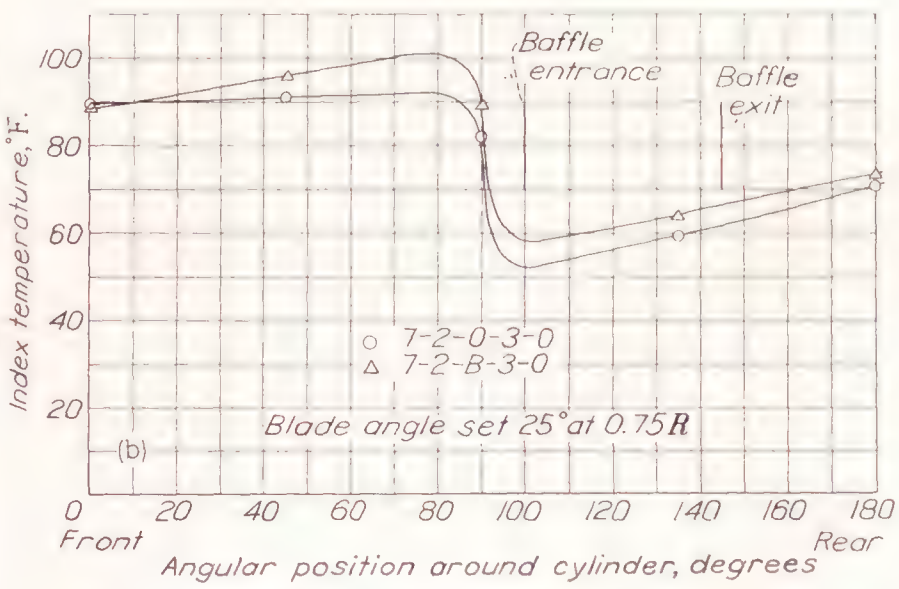

(b) Reference case with no propeller and with propeller B; $K=0.0424$.

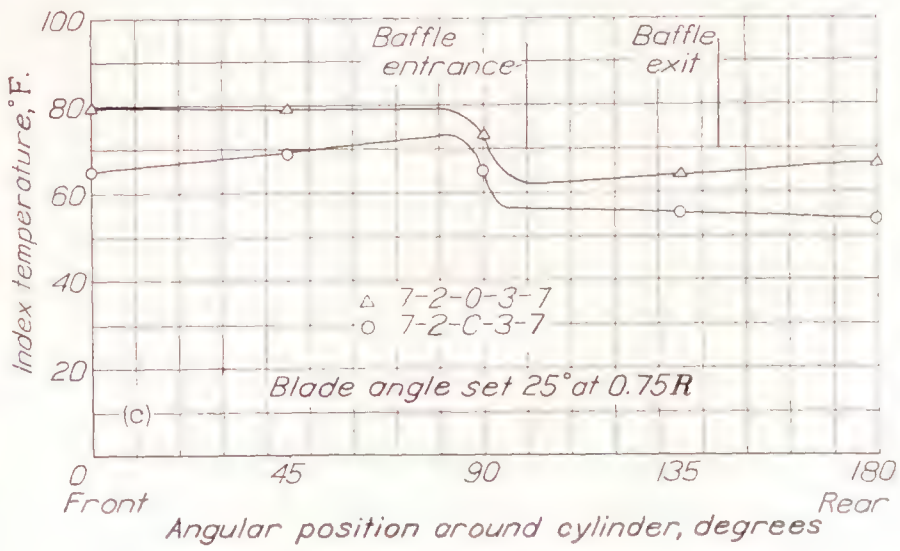

(c) Condition corresponding to most efficient cooling; $K=0.0424$.

FIGURE 22.—Temperature distribution around the electrically heated cylinder.

A reference point for the index temperatures tabulated in table I is obtained by comparing any given case with the temperatures given for the test arrangement 7—2—B—3—0, which copies an actual power run of a similar engine of 550 horsepower tested at the same tunnel velocity of 100 miles per hour and using the same external cowling arrangement. This engine

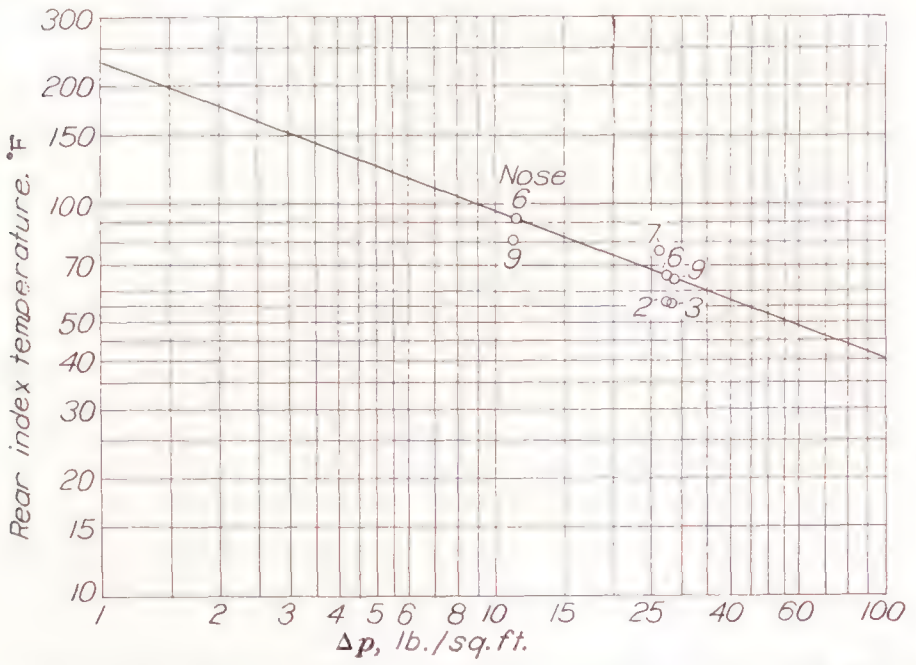

FIGURE 23.—Rear index temperature against Δp for the various noses on skirt 2; $K=0.0424$.

showed a maximum cylinder temperature of 400° F. above that of the air stream. The index temperature of 73° shown in table I for this particular test represents, therefore, exactly the same condition of cooling; that is, a rear temperature of more than 73° may be considered unsatisfactory in the same sense as a temperature in excess of 400° F. above that of the sur-

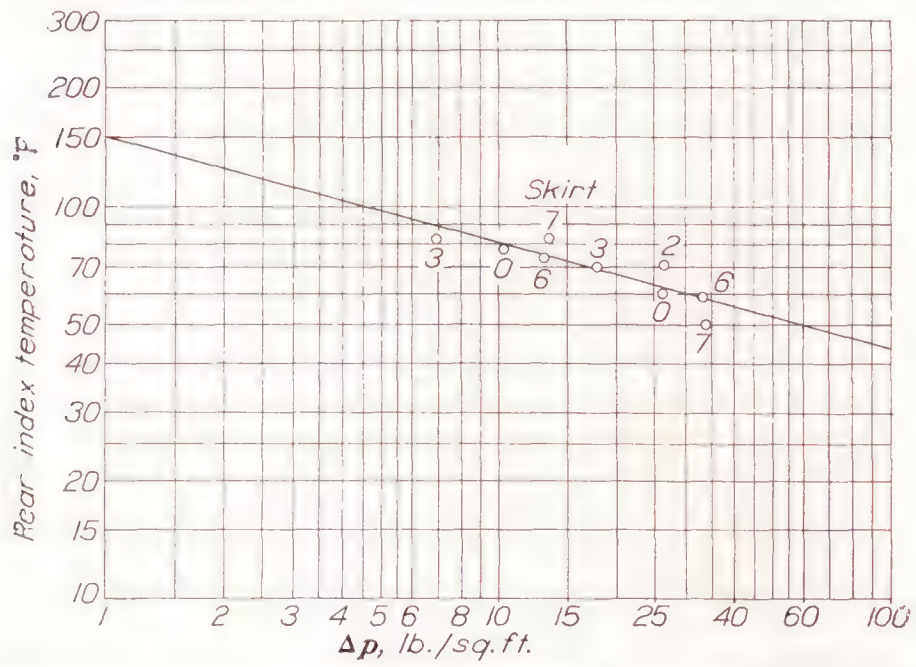

FIGURE 24.—Rear index temperature against Δp for the various skirts for nose 7 with no propeller; $K=0.0424$.

roundings in the actual case. Other plots of temperature distribution around the cylinder barrel are shown in figures 22 (b) and (c). It is to be noted that the condition constituting sufficient cooling on the Pratt & Whitney Wasp S1H1–G might be too conservative. It is entirely possible that a reference temperature of 80° F. or even of 90° F. might represent sufficient cooling on improved designs.

Figures 23, 24, 25, and 26 illustrate the dependency of the rear index temperature on the pressure drop across the engine, plotted on logarithmic scales. The slope of the line that seems to fit the experimental results the closest is -0.31, or $T_i=C\Delta p^{-0.31}$. Figure 23 shows results for the various nose shapes using skirt 2 and no propeller; figure 24, the results for various

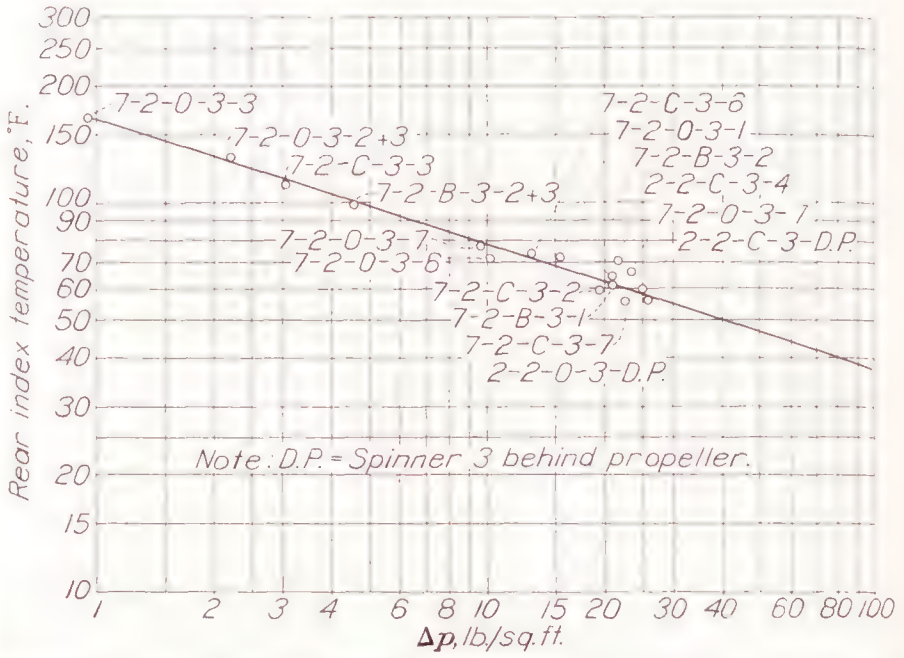

FIGURE 25.—Rear index temperature against Δp for the various spinners on noses 2 and 7 with skirt 2; $K=0.0424$.

skirts in conjunction with nose 7; figure 25 gives the results for a number of combinations of propellers and spinners on noses 2 and 7; and figure 26 shows the results for the conductivity 0.0909 both for the large and the small nacelles. Two main conclusions may be drawn from these results:

(1) That the rear index temperature for a given conductivity depends only on the pressure drop through

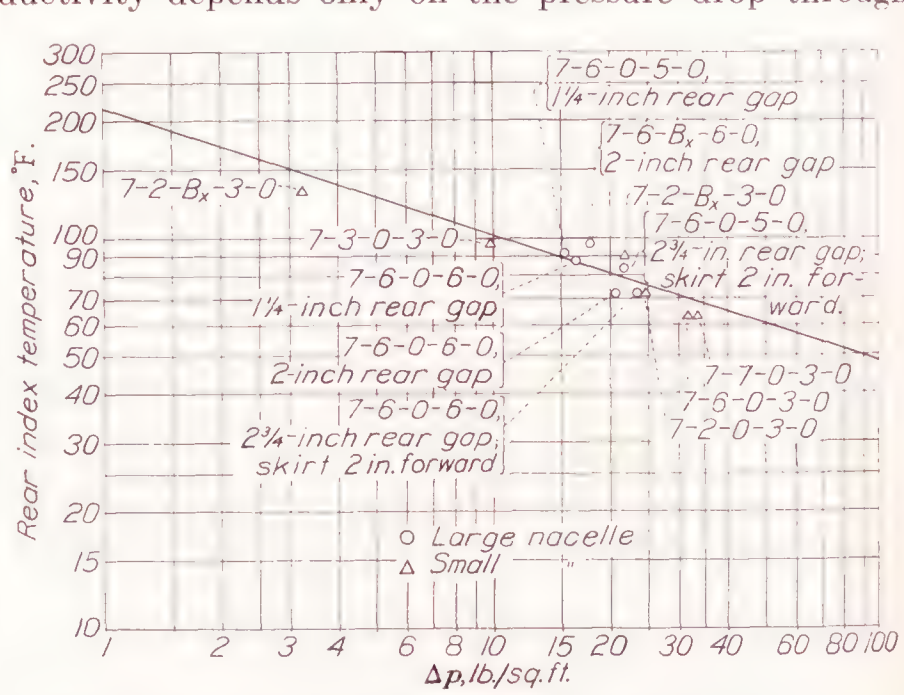

FIGURE 26.—Rear index temperature against Δp for several arrangements; $K=0.0909$.

the baffle. All points lie reasonably close to the average line drawn in the figures.

(2) That the increased conductivity has a detrimental effect on the heat transmission. It is seen by comparing the results in figures 25 and 26 representing the conductivities of 0.0424 and 0.0909, respectively, that the temperature is increased from 78° F. to 102° F. at a given pressure drop of $\Delta p=10$ pounds per square foot.

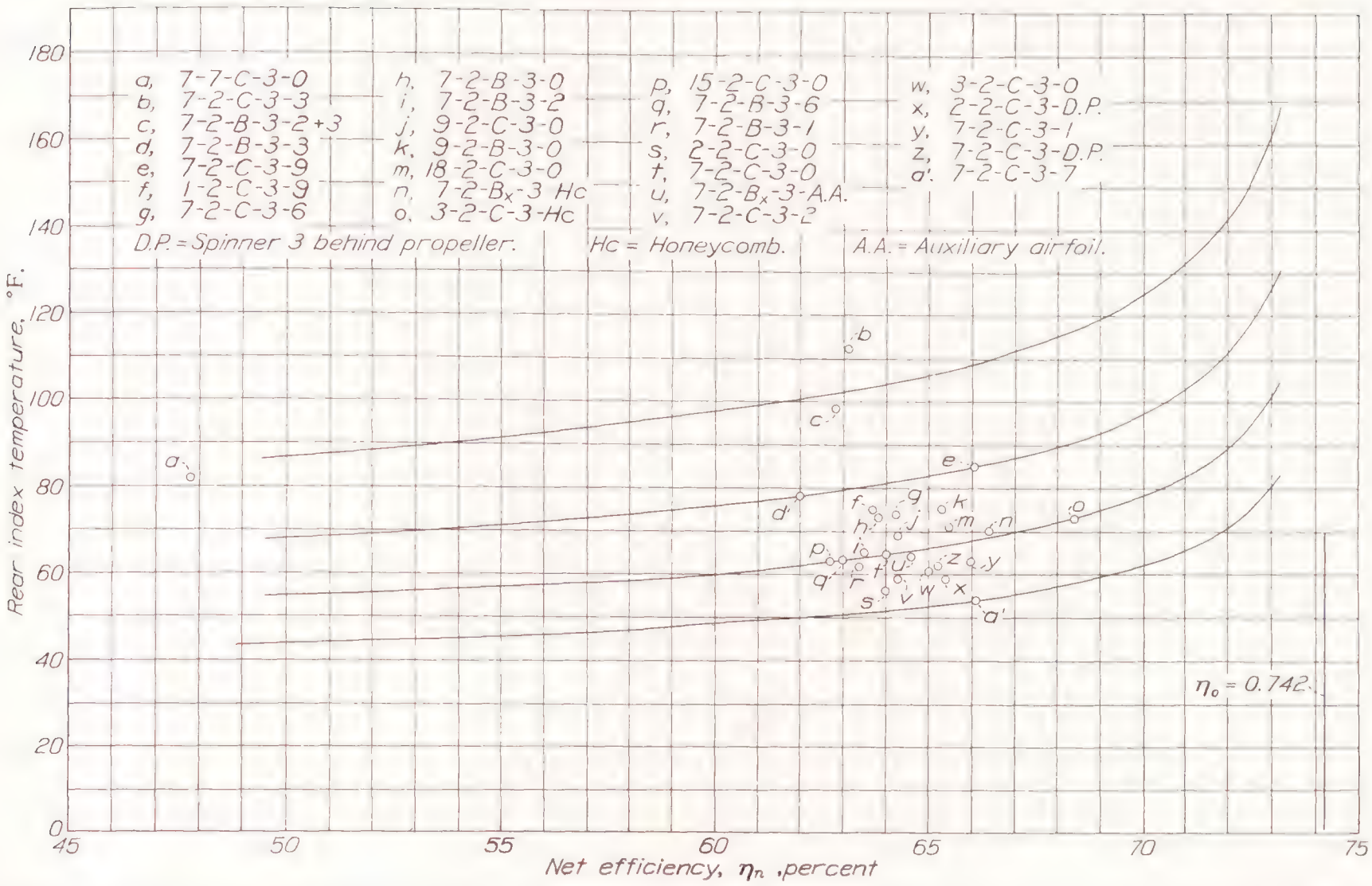

FIGURE 27.—Rear index temperature against η_n for all cases of 0.0424 conductivity with curves designating equal performance in respect to cooling and efficiency.
Small nacelle used.

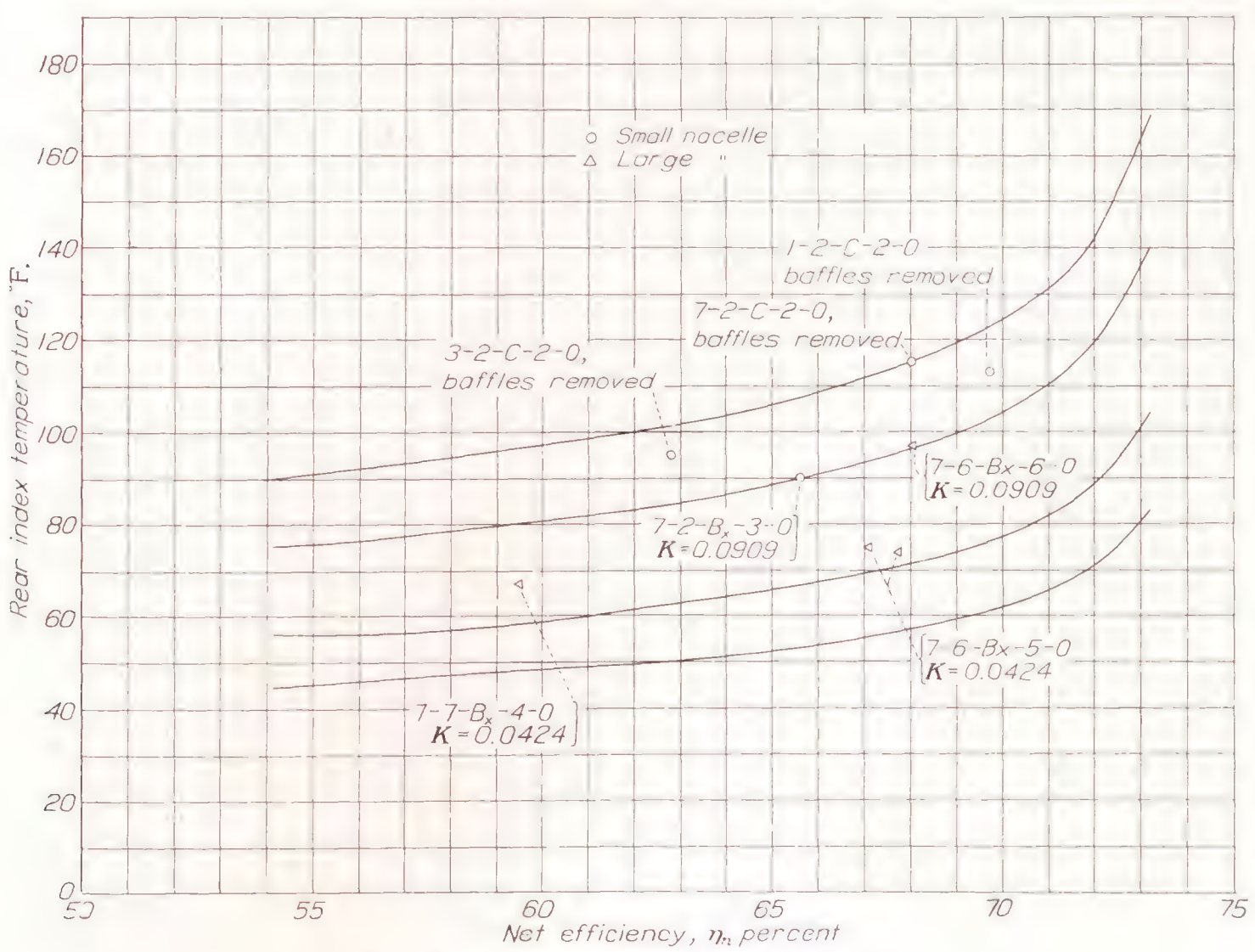

FIGURE 28.—Rear index temperature against net efficiency.

In figures 27 and 28 the index temperature is plotted against the net efficiency η_n, in figure 27 for the standard conductivity $K=0.0424$ and the small nacelle, and in figure 28 for the large conductivity $K=0.0909$ for tests on both the small and large nacelles. These charts give in a compact form the entire results of this investigation. The cost of the cooling is represented by the distance between the particular point η_n and the ordinate representing the ideal efficiency at $\eta_0=74.2$ percent. The temperatures are seen to range from 54° F. to more than 100° F. The curves drawn in the figures are considered to be curves of constant performance. They are obtained by the following reasoning: If overcooling exists in a certain test, there is a possible and permissible gain in the net efficiency, which can be realized by using a narrower skirt. Assuming a constant pump efficiency there exist the following relations:

The index temperature $T_i=\Delta p^{-0.31}$ constant and the work done $\eta_0-\eta=\Delta p^{3/2}$ constant and thus, by elimination of Δp, $T_i=(\eta_0-\eta_n)^{-0.206}$ constant or T_i is nearly proportional to the inverse of $\sqrt[5]{\eta_0-\eta_n}$. Thus it is seen that the change in T_i due to a regulation in the quantity of cooling air can be predicted on the basis of the net efficiency. A given increase in index temperature is thus associated with a definite increase in net efficiency.

Although the rear cylinder temperatures seem to depend in a very regular manner on the pressure drop Δp, the front temperature shows no such relationship. It is rather remarkable that the front portion of the cylinders cools, on the whole, just as well as the baffled portion. The very unstable three-dimensional flow in front of the cowling is obviously very beneficial to the heat transmission. As the present investigation is restricted primarily to the matter of cowling design, only a few remarks will be made here. It is noted (fig. 22(a)) that an unbaffled engine is overcooled on the front and overheated on the rear, demonstrating conclusively the technical value of the baffles. A comparison of figures 22(b) and (c) shows the apparent value of a spinner in improving the frontal heat transmission. A study of the main table I reveals several cases of good front cooling. Spinner 3 appears to show a very low front temperature.

In regard to the cost of the cooling on the front, it is observed in table I that the drag of the basic cowling shape is 42 pounds at 100 miles per hour and that the drag of the better streamline form employing nose 8 is only 32 pounds. It seems necessary to conclude that the difference of 10 pounds represents the cost of the comparatively poor aerodynamic shape of the nose of the conventional type cowling, which, on the other hand, reappears as a beneficial effect in regard to the cooling of the front of the cylinders. It might be expected that the reasonably large spinner might reclaim a certain fraction, at least, of the 10-pound drag loss. The various spinners tested have been described (fig. 9). It is quite interesting to observe that several of these spinners show a large beneficial influence on the front cooling, particularly the flat spinners 1, 3, and 6.

Table II shows the front temperatures obtained on various spinners.

Figure 29 shows the pressure distribution obtained on nose 7 in the presence of three typical spinners. In this group the plot (b) for spinner 7 is of the most interest, owing to the fact that this test represents the most efficient arrangement obtained throughout the entire series. (Cf. fig. 27.) The high net efficiency and the good cooling are in this case definitely attributable to the spinner. The relatively small dimensions of this spinner make possible the practical realization of these gains.

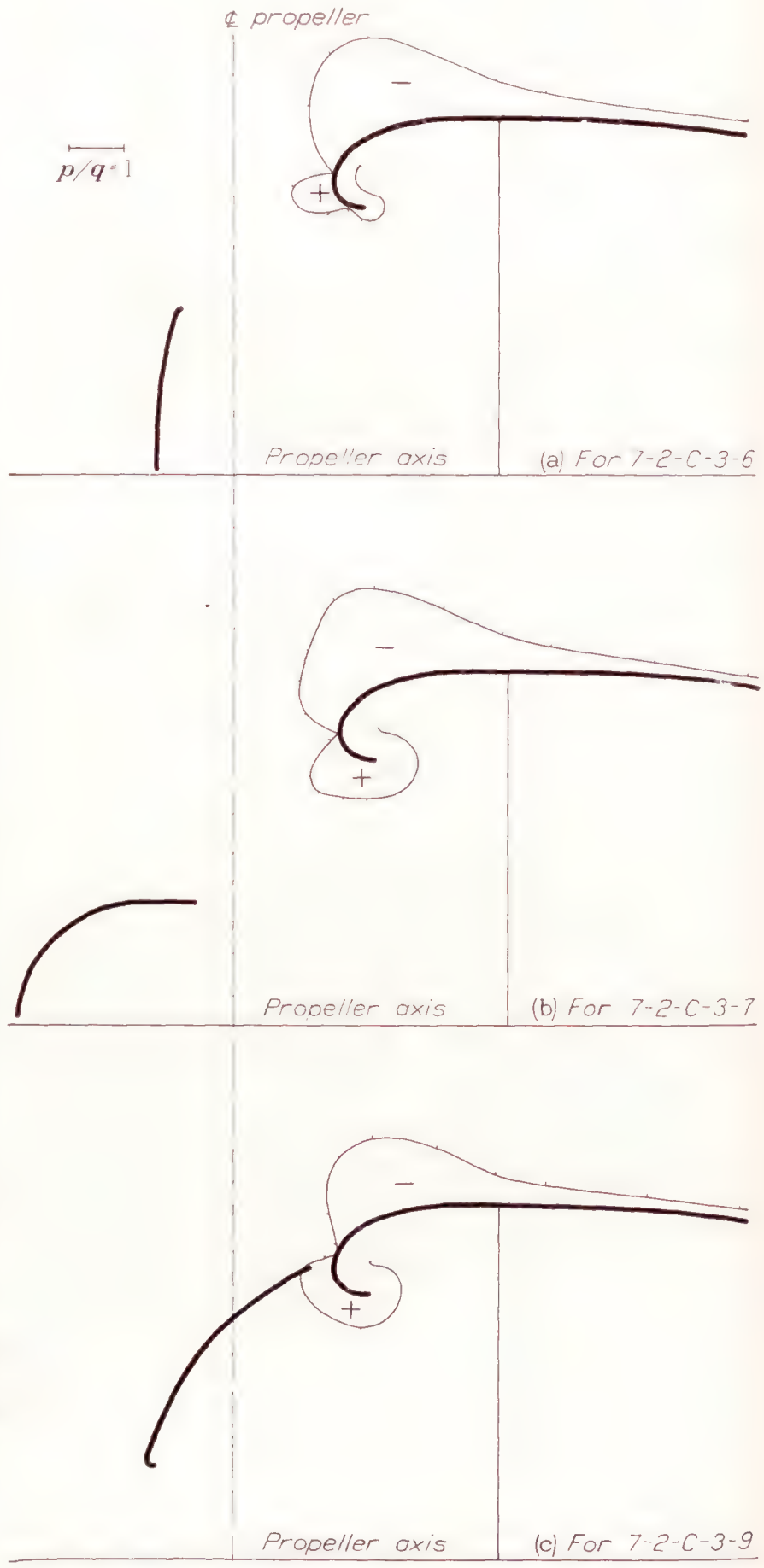

FIGURE 29.—The pressure distribution as affected by several spinners.

There is, finally, another problem that will be touched upon. It concerns the matter of baffle design. The present investigation confined itself to tests on a single baffle as described. Pitot tubes installed between the fins of the cylinder permitted the determination of the energy loss along the flow path. Results obtained in parallel with the temperature curves just presented (in fig. 22) are given for the total pressures in figure 30. Figure 30(a) shows these curves for the two lowest conductivities. It may be seen in figure 6 that the baffle covers about 45°, extending from 100° to 145° for the tightly fitting baffle. It is interesting so observe that only about one-third of the energy lost takes place inside the baffle and two-thirds behind. The baffle transposed rearward one-half inch and forming a diverging channel appears to provide a more efficient design, the exit loss being fairly small. The next figure 30(b) shows several cases with baffles removed. The low pressure in front of the cylinder with nose 3 is rather noticeable. The standard baffle is shown again in figure 30(c). Notice the slight effect of the propeller. Figure 30(d) is of interest as it refers to the test arrangement 7—2—C—3—7, which represents in every respect the best combination discovered in the investigation.

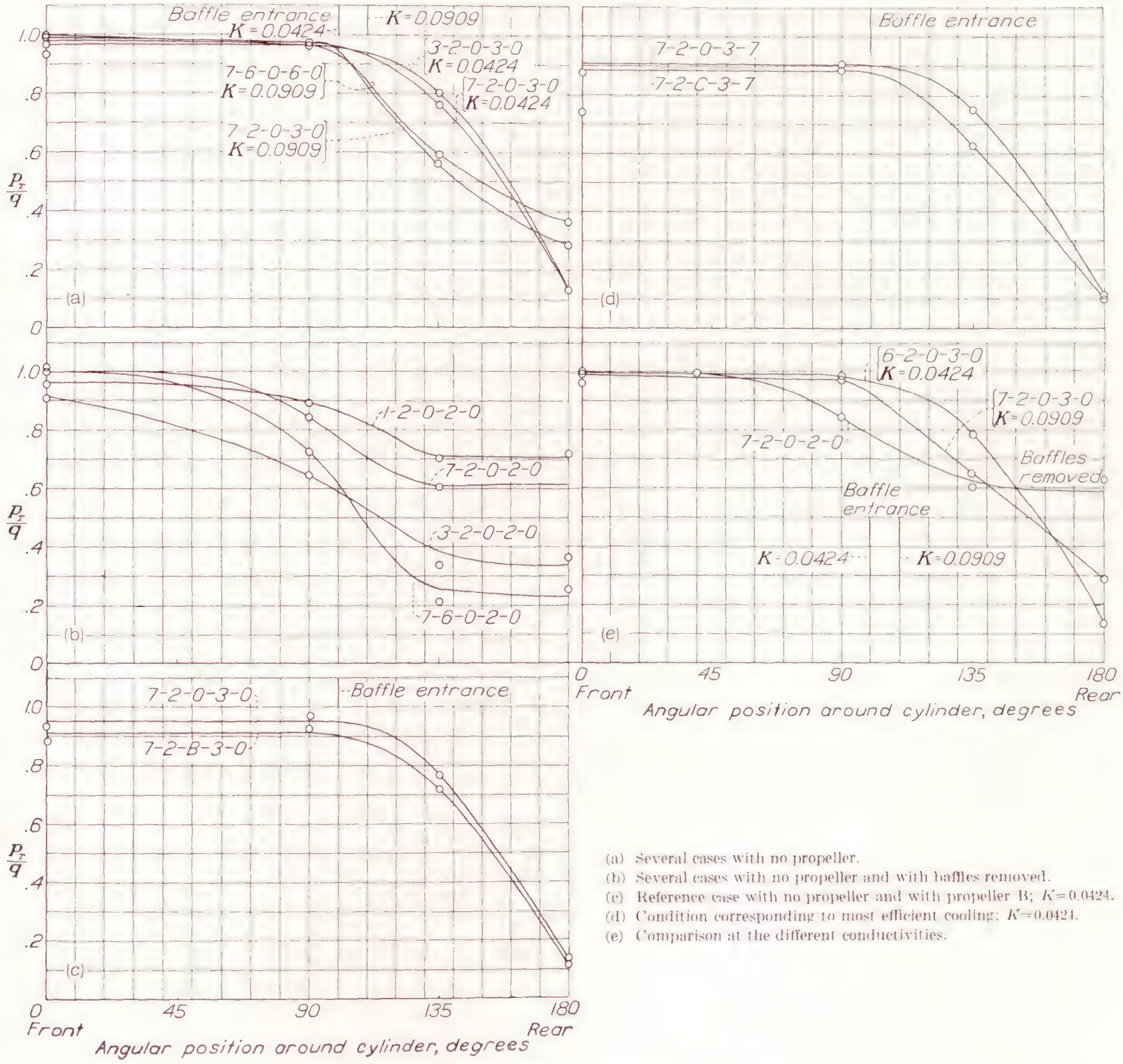

(a) Several cases with no propeller.
(b) Several cases with no propeller and with baffles removed.
(c) Reference case with no propeller and with propeller B; $K=0.0424$.
(d) Condition corresponding to most efficient cooling: $K=0.0424$.
(e) Comparison at the different conductivities.

FIGURE 30.—Total pressure distribution around the cylinder.

GENERAL CONCLUSIONS

1. It has been found that the basic blunt-nose cowling shape of an air-cooled engine has a drag somewhat in excess of that of a more properly streamline shape, such as an airship form. It was shown that the blunt nose is the cause of an instability in the air flow in front of the cowling that sets up a large-scale turbulence. This turbulence accounts for the remarkably good cooling on the front of the engine. The mechanical cost of this particular cooling compares favorably with the pressure cooling obtained on the rear of the engine.

2. The pumping efficiency, the ratio of the internal work done to the work expended by the corresponding increase in drag, has been found to range from almost zero to more than unity. The pump efficiency is largely dependent on the flow velocity and the shape of the exit passage.

3. The leading edge of the cowling should be given a smooth, very rounded form, such as nose 7. The diameter of the cowling inlet nose opening was found to be of little significance, either in regard to drag or in regard to cooling. As a general rule, the larger the opening, the better, care being taken only to provide a proper design of the nose contour. In this connection, it is worth keeping in mind that the flow immediately in front of the cowling is almost radial. A too straight cowling gives rise to a condition of breakdown of the flow at the front edge of the cowling. This effect was demonstrated in the present investigation in the case of cowling 1.

4. It has been found that a smooth contour line for the skirt design is a primary requirement. The rear edge of the skirt should not project into the air stream. The necessary exit opening should be obtained by a retraction of the inner cowling. The design of the inner cowling is less critical.

5. The most obvious method of varying the pressure across the engine is to vary the area of the exit opening. If this increase in area is accompanied by an outward flare of the trailing edge as is accomplished by the use of cowl flaps, a slightly greater increase in the pressure difference can be obtained than that resulting from a simple increase in area.

6. It is obvious from theoretical considerations that in a normal cruising condition the propeller causes only a slight contraction of the streamlines around the nacelle and that therefore no important effects of any kind are to be expected. This effect was amply verified by the test results. The propeller actually shows a blocking effect that gives a slight decrease in cooling. Spinners influence the stability of the flow around the front of the cowling and do, in some cases, improve the over-all performance of the combination. Spinner 7 on cowling 7 showed both an increase in net efficiency and improved cooling. The condition at low air speed is discussed in reference 9.

7. Tests performed on the combination with the larger afterbody showed a consistent increase in performance, demonstrating the importance of a smooth merging of the contour lines of the front and afterbody and the value of a better exposure of the exit opening of the unexpanded and stabler air stream.

8. The main result of the cooling problem studied in this investigation is that a tightly baffled engine is definitely superior in regard to cooling efficiency. The results obtained at the minimum conductivity $K = 0.0424$ are in every respect better than those obtained at the conductivity $K = 0.0909$ or on an unbaffled engine. Another important result is the observation that the inherent large-scale turbulence occurring in front of the cowling accounts for the good cooling on the exposed frontal area of the engine. This effect should, of course, be used to the fullest extent in the design of baffles.

9. It is of interest to note that, although increased conductivity of an engine is beneficial to pump efficiency the detrimental effect on cooling is so much greater that no compromise is possible. In other words, a tightly baffled engine is superior in over-all performance in spite of an inferior pumping efficiency. With a new type of nose-slot cowling greater pump efficiency is obtained at low conductivities.

LANGLEY MEMORIAL AERONAUTICAL LABORATORY,
NATIONAL ADVISORY COMMITTEE FOR AERONAUTICS.
LANGLEY FIELD, VA., *May 18, 1936.*

LIST OF SYMBOLS

p_f, pressure in front of the engine.

p_r, pressure in rear of the engine.

Δp, pressure drop across the engine, $\Delta p = p_f - p_r$.

D, drag of the cowling-nacelle unit.

D_0, drag of a smooth nacelle entirely enclosing the engine.

q, dynamic pressure of the air stream.

ρ, density of the air.

F, frontal area of the engine.

$C_D = \frac{D}{qF}$

$C_{D_0} = \frac{D_0}{qF}$

Q, quantity of the air flowing through the cowling.

V, velocity of the air stream.

$\eta_p = \frac{Q\Delta p}{(D - D_0)V}$, pump efficiency, without propeller.

R, net force on the thrust balance with propeller on.

$T = R + D$, propulsive thrust.

P, power supplied to propeller.

$\eta_n = \frac{RV}{P}$, net efficiency of propeller-nacelle unit.

S, propeller disk area.

$P_c = \frac{P}{qSV}$, unit disk loading.

$\frac{1}{\sqrt{P_c}} = V\sqrt{\frac{\rho S}{2P}}$

η_{n_0}, net propeller-nacelle efficiency obtained on same set-up as used for D_0.

$\eta_p = \frac{Q\Delta p}{(D - D_0)P}$, pump efficiency with propeller operating.

A, area of the free air stream entering the cowling.

$k = \frac{A}{\sqrt{\frac{\Delta p}{q}}}$

$K = \frac{k}{f} = \frac{\frac{A}{F}}{\sqrt{\frac{\Delta p}{q}}}$, conductivity of the engine

$Q = K\sqrt{\frac{\Delta p}{\rho}}FV$

p_2, static pressure at the exit of the slot.

V_2, velocity in the exit of the slot.

Δp_2, pressure drop through exit passage.

A_2, area of exit of the slot.

$\Delta P = \Delta p + \Delta p_2$, total pressure drop across cowling.

K_2, apparent conductivity of the exit slot.

$\frac{\Delta P}{q} = \left(\frac{Q}{FV}\right)^2\left[\frac{1}{K^2} + \frac{1}{K_2^2}\right]$, relation of conductivities of engine and slot exit.

n, revolutions per second of the propeller.

D, diameter of the propeller.

$C_T = \frac{T}{\rho n^2 D^4}$, thrust coefficient.

$C_P = \frac{P}{\rho n^3 D^5}$, power coefficient.

$\frac{V}{nD}$, advance-diameter ratio of the propeller.

$\eta = \frac{TV}{P}$, propulsive efficiency.

T_t, index temperature.

W, work done by the cooling air.

REFERENCES

1. Weick, Fred E.: Drag and Cooling with Various Forms of Cowling for a "Whirlwind" Radial Air-Cooled Engine—I. T. R. No. 313, N. A. C. A., 1929.
2. Weick, Fred E.: Drag and Cooling with Various Forms of Cowling for a "Whirlwind" Radial Air-Cooled Engine—II. T. R. No. 314, N. A. C. A., 1929.
3. Schey, Oscar W., and Biermann, Arnold E.: The Effect of Cowling on Cylinder Temperatures and Performance of a Wright J-5 Engine. T. R. No. 332, N. A. C. A., 1929.
4. McAvoy, William H., Schey, Oscar W., and Young, Alfred W.: The Effect on Airplane Performance of the Factors that Must Be Considered in Applying Low-Drag Cowling to Radial Engines. T. R. No. 414, N. A. C. A., 1932.
5. Theodorsen, Theodore: On the Theory of Wing Sections with Particular Reference to the Lift Distribution. T. R. No. 383, N. A. C. A., 1931.
6. Goldstein, Sydney: On the Vortex Theory of Screw Propellers. Proc. Roy. Soc. (London), Series A, vol. 123, April 6, 1929, pp. 440–465.
7. Weick, Fred E., and Wood, Donald H.: The Twenty-Foot Propeller Research Tunnel of the National Advisory Committee for Aeronautics. T. R. No. 300, N. A. C. A., 1928.
8. Theodorsen, Theodore, Stickle, George W., and Brevoort, M. J.: Characteristics of Six Propellers Including the High-Speed Range. T. R. No. 594, N. A. C. A., 1937.
9. Theodorsen, Theodore, Brevoort, M. J., and Stickle, George W.: Cooling of Airplane Engines at Low Air Speeds. T. R. No. 593, N. A. C. A., 1937.
10. Theodorsen, Theodore, Brevoort, M. J., Stickle, George W., and Gough, M. N.: Full-Scale Tests of a New Type N. A. C. A. Nose-Slot Cowling. T. R. No. 595, N. A. C. A., 1937.
11. Hartshorn, A. S.: Wind Tunnel Investigation of the Cooling of an Air-Jacketed Engine. R. & M. No. 1641, British A. R. C., 1935.

TABLE I.—CONDENSED EXPERIMENTAL RESULTS

1	2	3	4	5	6	7	8	9	10	
Designation of arrangement (Nose — Skirt — Propeller — Inner cowling — Spinner)	p_f/q	p_r/q	(2—3) $\Delta p/q$	C_D (D/qF)	Drag in lb. at q=25.6 lb. per sq. ft., or thrust at $1/\sqrt[3]{P_c}$=1.8 and q=25.6 lb. per sq. ft.	η_n at $1/\sqrt[3]{P_c}$=1.8	η_p	Index temperatures: Front T_f	Index temperatures: Rear T_r	Remarks
NACELLE 1—ZERO AIR										
2— 5—0 —3—0				0.1193	45.0					Closed skirt.
7— 2—0 —3—0	1.00	−0.274	1.274	.1365	51.5					Closed by flat plate at front of cylinders.
7— 3—0 —3—0	1.00	−.071	1.071	.1246	47.0					
7— 6—0 —3—0	1.00	−.417	1.417	.1749	66.0					
7— 7—0 —3—0	1.00	−.442	1.442	245	92.5					
7— 0—0 —3—0	1.00	−.371	1.371	.1516	61.0					
STANDARD BAFFLES—CONDUCTIVITY 0.0424										
0— 2—0 —3—0	1.004	−0.295	1.299	1.182	446.0		0.058			
0— 2—C —3—0	.910	−.230	1.140			−0.075	.068			
1— 2—0 —3—0	1.008	−.062	1.070	.330	124.5		.214			
1— 2—B —3—0	.982	−.050	1.032		206.0	.589	.316			
1— 2—C —3—0	.906	−.059	.965		211.0	.605	.320			
2— 2—0 —3—0	.956	−.048	1.004	.194	73.0		.517	81.7	57.1	
2— 2—B —3—0	.926	−.057	.983		222.0	.636	.421			
2— 2—C —3—0	.883	−.057	.939		223.0	.640	.412	71.6	56.2	
2— 5—0 —3—0				.123	46.4					Zero cooling air.
3— 2—0 —3—0	.973	−.051	1.024	.196	74.0		.521	66.0	57.0	
3— 2—B —3—0	.877	−.061	.939		226.0	.648	.445			
3— 2—C —3—0	.853	−.062	.915		227.0	.650	.438	59.8	60.8	
4— 2—0 —3—0	.989	−.039	1.027	.1935	73.0		.539			
4— 2—B —3—0	1.004	−.032	1.036		214.0	.612	.375			
4— 2—C —3—0	.894	−.045	.944		218.0	.625	.363			
5— 4—0 —2—0	.984	.064	.920	.1755	66.4		.823			Conductivity 0.060. Preliminary test.
6— 2—0 —3—0	.971	−.058	1.030	.2027	76.5		.486	79.3	65.9	
6— 2—B —3—0	.885	−.061	.945		224.0	.642	.423			
6— 2—C —3—0	.868	−.074	.942		220.0	.631	.380			
6— 3—0 —3—0	.962	.345	.616	.1603	60.5		.417	81.8	68.8	
6— 4—0 —2—0	.960	.047	.913	.1755	66.4		.813			Do.
7— 2—0 —3—0	.983	−.046	1.030	.1929	72.5		.551	89.5	70.6	
7— 2—B —3—0	.901	−.053	.954		223.0	.638	.410	88.6	73.0	
7— 2—C —3—0	.871	−.062	.933		223.0	.640	.408	77.2	64.7	
7— 2—B_x —3—0	.888	−.045	.934		226.0	.646	.432			
7— 3—0 —3—0	.946	.358	.588	.1497	56.5		.494	104.6	76.5	
7— 4—0 —2—0	.952	.067	.885	.1772	67.0		.757			Do.
7— 6—0 —3—0	.975	−.218	1.194	.2700	102.0		.349	82.0	59.0	
7— 7—0 —3—0	.967	−.249	1.215	.387	146.0		.205	71.3	50.7	
7— 7—C —3—0	.871	−.312	1.183		167.0	.478		81.0	81.7	
7— 0—0 —3—0	.953	−.261	1.214	.237	89.5		.451	81.5	60.0	
FLAPS										
7— 8—0 —3—0	0.956	−0.222	1.179	0.265	100.0		0.353			
7— 8—C —3—0	.870	−.264	1.133		201.0	0.576	.336			
7— 8—0 —3—0	.980	−.233	1.213	.307	116.0		.289			½-inch flare.
7— 8—C —3—0	.877	−.293	1.170		186.0	.534	.280			Do.
7— 8—0 —3—0	.972	−.242	1.214	.372	140.5		.218			1-inch flare.
7— 8—C —3—0	.874	−.319	1.193		170.0	.486	.235			Do.
7— 8—0 —3—0	.995	−.246	1.241	.506	191.0		.149			2-inch flare.
7— 8—C —3—0	.872	−.289	1.161		108.0	.310	.134			Do.
7— 8—0 —3—0	.980	−.246	1.225	.583	220.0		.122			3-inch flare.
7— 8—C —3—0	.874	−.291	1.165		73.0	.208	.109			Do.
STREAMLINE SHAPE										
8— 3—0 —2—0				0.1007	38.0					Zero cooling air.
8— 5—0 —2—0				.0861	32.5					Do.
9— 2—0 —3—0	0.959	−0.058	1.017	.1987	75.0		0.497	73.0	64.0	
9— 2—B —3—0	.842	−.077	.919		228.0	0.653	.456	74.0	75.0	
9— 2—C —3—0	.836	−.080	.916		224.0	.643	.408	68.0	69.0	
NOSE TO FIT BLOWER										
15— 2—0 —3—0	0.984	−0.031	1.015	0.1975	74.5		0.500	99.0	60.5	
15— 2—C —3—0	.893	−.044	.937		219.0	.627	.364	95.0	63.0	
PERFORATED DISK										
18— 2—0 —3—0	0.793	−0.074	0.867	0.1908	72.0		0.429			
18— 2—B —3—0	.768	−.083	.851		223.0	0.640	.354			
18— 2—C —3—0	.692	−.086	.778		229.0	.655	.365	110.0	71.0	
FLAT DISK										
19— 2—0 —3—0		−0.300		0.1259	47.5					Zero cooling air.
19— 5—0 —3—0				.1115	42.0					Zero cooling air. (C_{D_0}).
19— 5—B —3—0					254.0	0.728				Zero cooling air.
19— 5—C —3—0					259.0	.742				Zero cooling air. (η_0).

TABLE I.—CONDENSED EXPERIMENTAL RESULTS—Continued

1	2	3	4	5	6	7	8	9	10	Remarks
Designation of arrangement: Nose — Skirt — Propeller — Inner cowling — Spinner	p_f/q	p_r/q	(2—3) $\Delta p/q$	C_D (D/qF)	Drag in lb. at q=25.6 lb. per sq. ft., or thrust at $1/\sqrt[3]{P_c}$=1.8 and q=25.6 lb. per sq. ft.	η_n at $1/\sqrt[3]{P_c}$=1.8	η_p	Index temperatures: Front T_f	Index temperatures: Rear T_r	
SPINNERS										
1— 2—0 —3—1	0.598	−0.085	0.683	0.1855	70.0		0.321			Position 1.
1— 2—C —3—1	.674	−.071	.745		215.0	0.617	.237			Do.
1— 2—0 —3—1	.437	−.103	.540	.1841	69.5		.232			Position 2.
1— 2—0 —3—2	.707	−.074	.781	.1975	74.5		.339			
1— 2—C —3—2	.723	−.073	.796		214.0	.612	.252			
1— 2—C —3—9	.743	−.071	.814		222.0	.637	.323	83.0	75.0	
2— 2—0 —3—3	.895	−.062	.957	.1895	71.5		.504	84.0	56.0	Dishpan.
2— 2—C —3—3	.832	−.071	.903		228.0	.654	.452	78.0	59.0	Do.
7— 2—0 —3—1	.481	−.088	.569	.1815	68.5		.256	72.5	66.0	Position 1.
7— 2—B —3—1	.673	−.070	.743		221.0	.634	.272	59.0	62.0	Do.
7— 2—C —3—1	.547	−.087	.634		230.0	.660	.284	65.0	63.0	Do.
7— 2—0 —3—2	.548	−.069	.617	.1815	68.5		.291			
7— 2—B —3—2	.677	−.066	.743		222.0	.635	.275	67.0	65.0	
7— 2—C —3—2	.608	−.034	.692		224.0	.643	.268	62.0	59.0	
7— 2—0 —3—3	−.176	−.210	.034	.1550	58.5		.006	112.0	158.0	
7— 2—B —3—3	−.028	−.178	.150		216.0	.620	.022	50.0	78.0	
7— 2—C —3—3	−.087	−.194	.107		220.0	.631	.015	68.0	112.0	
7— 2—C —3—3	.671	−.082	.753		228.0	.652	.334	82.0	62.0	Dishpan.
7— 2—0 —3—2&3	−.126	−.206	.080	.1510	57.0		.024	87.0	128.0	
7— 2—B —3—2&3	.009	−.177	.186		219.0	.628	.032	65.0	98.0	
7— 2—0 —3—6	.254	−.121	.375	.1722	65.0		.159	69.5	74.0	
7— 2—B —3—6	.431	−.106	.537		220.0	.630	.161	55.0	63.0	
7— 2—C —3—6	.351	−.117	.468		224.0	.642	.148	65.0	74.0	
7— 2—0 —3—7	.778	−.070	.848	.1935	73.0		.400	80.0	67.0	
7— 2—C —3—7	.744	−.065	.809		231.0	.661	.413	65.0	54.0	
7— 2—C —3—9	.199	−.145	.344		231.0	.661	.115	55.0	85.0	
7— 2—C —3—10	.606	−.080	.686		230.0	.658	.313			
SPECIAL DEVICES—HONEYCOMB										
3— 2—0 —3—0	0.864	−0.049	0.913	0.1908	72.0		0.461	63.0	66.0	
3— 2—C —3—0	.775	−.063	.838		239.0	0.684	.609	69.0	73.0	
7— 2—0 —3—0	.871	−.043	.914	.1908	72.0		.464	64.0	65.0	
7— 2—B_x—3—0	.844	−.048	.892		232.0	.664	.495	84.0	70.0	
AUXILIARY AIRFOIL										
7— 2—0 —3—0	0.961	−0.036	0.997	0.2200	83.0		0.386			No. 1 position 1.
7— 2—B_x—3—0	.906	−.039	.945		228.0	0.653	.475			Do.
7— 2—0 —3—0	.965	−.038	1.003	.2320	87.5		.351	86.0	63.0	No. 1 position 2.
7— 2—B_x—3—0	.876	−.045	.921		225.0	.646	.423	82.0	64.0	Do.
7— 2—0 —3—0	.977	−.028	1.005	.2040	77.0		.458			No. 2 position 1.
7— 2—B_x—3—0	.905	−.038	.943		229.0	.657	.493			Do.
TAIL PUMP—CONDUCTIVITY 0.0250										
19— 5—0 —3—0				0.1087	41.0		0			Zero cooling air.
2— 5—0 —3—0	0.928	0.357	0.571	.1272	48.0		.685			
2— 5—B —3—0	.903	.281	.622		242.0	0.693	.270			
NACELLE 1—BAFFLES BACK ½ INCH—CONDUCTIVITY 0.0909										
7— 2—0 —3—0	0.992	0.116	0.876	0.2000	75.5		0.837	68.0	72.0	
7— 2—B_x—3—0	.891	.119	.772		229.0	0.656	.777	80.0	90.0	
7— 3—0 —3—0	.941	.588	.353	.1510	57.0		.480	89.0	98.0	
7— 6—0 —3—0	.999	−.139	1.138	.2910	110.0		.615	59.0	63.0	
7— 7—0 —3—0	.987	−.206	1.193	.4130	156.0		.393	60.0	63.0	
NACELLE 1—BAFFLES REMOVED—CONDUCTIVITY APPROXIMATELY 0.3–0.6										
0— 0—0 —2—0				0.399	150.5					
1— 2—0 —2—0	0.958	0.835	0.123	.1630	61.5			58.0	89.0	
1— 2—C —2—0	.878	.816	.062		243.0	0.697		65.0	113.0	
3— 2—0 —2—0	.909	.428	.481	.2040	77.0			38.5	87.0	
3— 2—C —2—0	.747	.320	.427		219.0	.628		42.0	95.0	
7— 2—0 —2—0	1.015	.768	.247	.1616	61.0			50.0	100.0	
7— 2—C —2—0	.868	.676	.192		237.0	.680		53.0	115.0	
7— 3—0 —2—0	.993	.902	.091	.1325	50.0			76.0	146.0	
7— 6—0 —2—0	.999	.447	.552	.2400	90.5			44.0	72.0	
BUMPED COWLING										
17— 0—0 —2—0	0.916	0.866	0.050	0.1259	47.5					
17— 0—C —2—0	.865	.800	.065		250.0	0.716				
17—10—0 —2—0				.1232	46.5					Nose closed off.
17—10—C —2—0					255.0	.739				Do.

TABLE I.—CONDENSED EXPERIMENTAL RESULTS—Continued

1	2	3	4	5	6	7	8	9	10	
Designation of arrangement (Nose, Skirt, Propeller, Inner cowling, Spinner)	p_f/q	p_r/q	(2−3) $\Delta p/q$	C_D (D/qF)	Drag in lb. at q=25.6 lb. per sq. ft., or thrust at $1/\sqrt[3]{P_c}$=1.8 and q=25.6 lb. per sq. ft.	η_n at $1/\sqrt[3]{P_c}$=1.8	η_p	Index temperatures: Front T_f	Index temperatures: Rear T_r	Remarks
NACELLE 2—STANDARD BAFFLES—CONDUCTIVITY 0.0424										
19— 9—0 —6—0				0.1126	42.5					Zero air.
7— 7—0 —4—0	0.962	−0.205	1.167	.2680	101.0		0.339	80.0	53.0	
7— 7—B_x—4—0	.889	−.256	1.145		208.0	0.595	.384	91.0	67.0	
7— 7—C —4—0	.886	−.241	1.127		205.0	.587	.357			
7— 6—0 —5—0	.967	.082	.885	.1696	64.0		.602	59.0	87.0	1.7-inch opening.
7— 6—B_x—5—0	.878	.075	.803		236.0	.677	.508	98.0	74.0	
7— 6—0 —5—0	.973	.026	.947	.1762	66.5		.597	83.0	57.0	2.5-inch opening.
7— 6—B_x—5—0	.892	.023	.869		234.0	.671	.522	100.0	75.0	
7— 6—0 —5—0	.959	−.029	.988	.1855	70.0		.562			3.9-inch opening.
7— 6—B_x—5—0	.881	−.033	.914		233.0	.668	.543			
7— 0—0 —5—0	.963	−.139	1.102	.2070	78.0		.510			
7— 6—0 —6—0	.982	.028	.954	.1749	66.0		.617			1⅞-inch rear opening.
7— 6—B_x—6—0	.877	.024	.853		237.0	.679	.574			
7— 6—0 —6—0	.993	.147	.846	.1630	61.5		.635			1¼-inch rear opening.
7— 6—B_x—6—0	.885	.134	.751		241.0	.692	.599			
7— 8—0 —6—0	.953	−.282	1.235	.4480	169.0		.172			2-inch flare.
7— 8—B_x—6—0	.872	−.425	1.297		156.0	.447	.230			Do.
7— 9—0 —6—0	.900			.1193	45.0					
7— 9—C —6—0	.890				251.0	.720				
SPINNERS										
7— 9—C —6—1	0.523				249.0	0.713				Position 1.
7— 9—C —6—1	.312				241.0	.691				Position 3.
7— 9—C —6—1	.257				237.0	.679				Position 4.
NACELLE 2—BAFFLES BACK ½ INCH—CONDUCTIVITY 0.0909										
7— 6—0 —5—0	0.983	0.428	0.555	0.1537	58.0		0.885	83.0	92.0	1¼-inch rear gap.
7— 6—0 —5—0	.979	.191	.788	.1755	67.0		.990	77.0	84.0	2¾-inch rear gap.
7— 6—0 —6—0	.980	.394	.586	.1590	60.0		.851	80.0	88.0	1¼-inch rear gap.
7— 6—0 —6—0	.975	.240	.735	.1735	65.5		.919	67.0	72.0	2-inch rear gap.
7— 6—B_x—6—0	.869	.241	.628		238.0	0.681	.804	89.0	97.0	Do.
7— 6—0 —6—0	.986	.151	.835	.1881	71.0		.900	66.0	73.0	2¾-inch rear gap.

TABLE II.—FRONT CYLINDER TEMPERATURES OBTAINED WITH VARIOUS SPINNERS

Designation of arrangement (Nose, Skirt, Propeller, Inner cowling, Spinner)	Front cylinder temperature T_f (°F.)	Ratio of front to rear cylinder temperature $\frac{T_f}{T_r}$	Remarks
1—2—C—3—9	83	1.106	
2—2—0—3—3	84	1.50	Dishpan behind propeller.
2—2—C—3—3	78	1.323	Do.
7—2—0—3—1	72.5	1.098	Position I.
7—2—B—3—1	59	.952	Do.
7—2—C—3—1	65	1.033	Do.
7—2—B—3—2	67	1.032	
7—2—C—3—2	62	1.05	
7—2—0—3—3	112	.709	
7—2—B—3—3	50	.642	
7—2—C—3—3	68	.607	
7—2—C—3—3	82	1.322	Dishpan behind propeller.
7—2—C—3—2 & 3			
7—2—B—3—2 & 3	65	.663	
7—2—0—3—6	69.5	.939	
7—2—B—3—6	55	.873	
7—2—C—3—6	66	.892	
7—2—0—3—7	80	1.193	
7—2—C—3—7	65	1.202	
7—2—C—3—9	55	.647	

REPORT No. 593

COOLING OF AIRPLANE ENGINES AT LOW AIR SPEEDS

By Theodore Theodorsen, M. J. Brevoort, and George W. Stickle

SUMMARY

A comprehensive experimental study has been carried out at full scale in the N. A. C. A. 20-foot wind tunnel, the general purpose of which is to furnish information in regard to the functioning of the power plant and propeller unit under different conditions. This report deals particularly with the problem of the cooling of an airplane engine on the ground. The influence of different nose forms, skirts, flaps, propellers, spinners, and special blowers has been investigated. Among the more interesting results are the demonstration of the comparative inefficiency of adjustable skirt flaps, the detrimental effect of small-diameter front openings of the cowling, and the very beneficial effect of a carefully designed airfoil section near the hub of the propeller. A small axial fan of simple construction was found to give efficient cooling on the ground.

INTRODUCTION

The problem of cooling an airplane engine on the ground obviously presents the greatest difficulty. The velocity head in the slipstream is then a minimum. The engine does not ordinarily develop its maximum horsepower, but the quantity of heat to be disposed of is not much reduced. A certain velocity head and a corresponding pressure drop are generally required to cool the engine satisfactorily. The problem then becomes one of providing a certain pressure drop for cooling on the ground or at a minimum air speed; cooling at higher speeds, of course, follows. Special devices, such as flaps on the skirt or fans in front of the cowling, are sometimes used to improve the cooling on the ground.

It has been shown (reference 1) that the cooling for the cruising condition is almost exclusively a function of air speed, the effect of the propeller slipstream velocity being of little importance. At low air speeds the situation is different; the cooling is largely dependent on the propeller effect. On the ground the cooling depends, of course, entirely on the propeller. The subject of primary interest in this paper is the study of the factors affecting the cooling on the ground.

ANALYSIS OF THE PROBLEM

It was shown in reference 1 that the cooling of an engine is a function of the pressure drop Δp across the cylinder bank. Most of the tests reported in this paper were extended down to the minimum tunnel speed. This minimum tunnel speed corresponds to the effect of the local propeller slipstream on the closed-circuit tunnel and is approximately 20 miles per hour, low enough to permit an extrapolation of results to the condition of zero air speed.

At very low air speeds the effect of the slipstream dominates the situation, the propeller functioning as a low-pressure blower. For the condition of zero air speed, the quantity $\Delta p/n^2$ has been chosen as the characteristic function, this quantity being independent of the revolution speed of the propeller. The square root

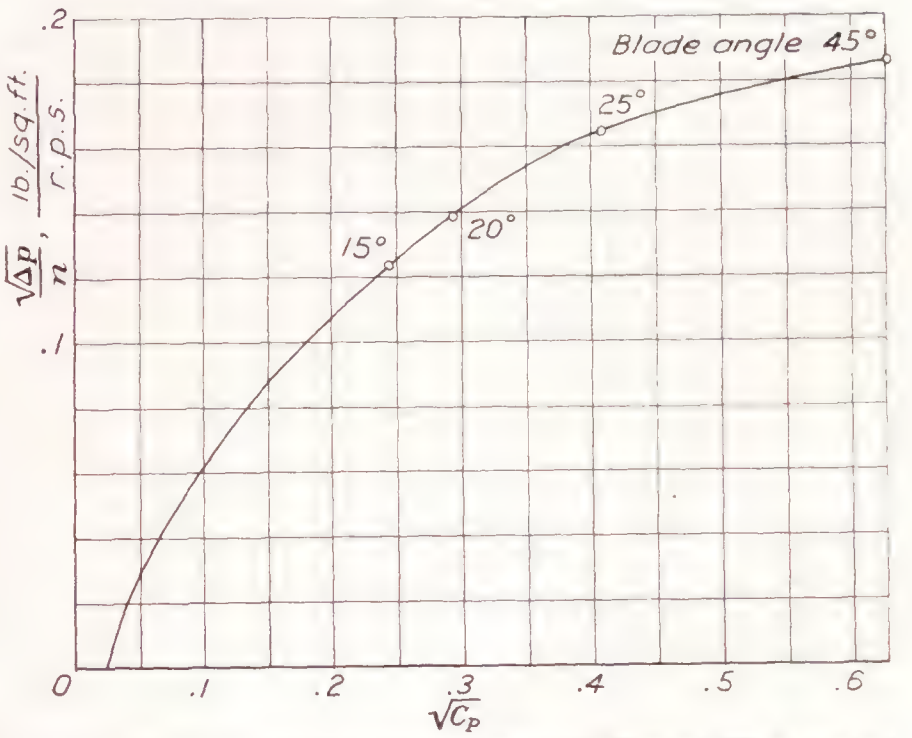

FIGURE 1.—Typical curve showing the dependency of $\sqrt{\Delta p}/n$ on $\sqrt{C_P}$ for $V/nD=0$.

of this quantity is plotted against the advance-diameter ratio V/nD. Plots of this type conveniently picture the relationship between the available pressure and the air speed at any combinations of the other variables and show directly the primary results of the present investigation.

In order to apply the results for the condition of zero air speed, there need be known only the revolution speed n of the propeller at any particular angle of attack. For this purpose it is very convenient to plot the pressure function $\Delta p/n^2$ against the nondimensional power coefficient C_P at zero air speed, defined as

$$C_P=\frac{P}{\rho n^3 D^5}=\frac{2\pi Q}{\rho n^2 D^5}$$

where P is the power and Q the torque of the propeller. A curve of this type is illustrated in figure 1

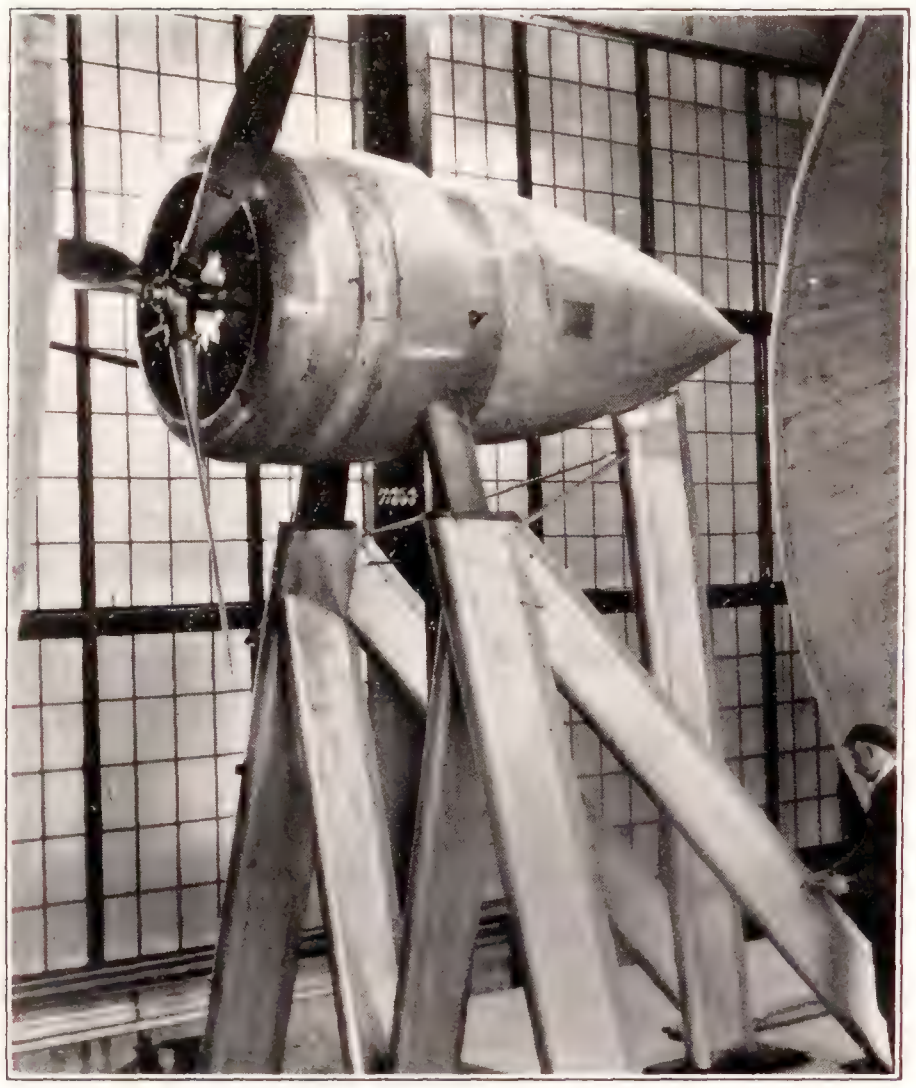

FIGURE 2.—The N. A. C. A. fan installed on the engine.

for a particular propeller over the entire range of blade-angle settings. The ordinate used is actually the square root of the pressure function, or $\sqrt{\Delta p}/n$, and the abscissa is similarly $\sqrt{C_p}$. At a given power and propeller diameter the revolution speed is known at each blade angle and, in consequence, also the value of Δp. The selection of the blade angle producing the highest pressure drop Δp is identical with the selection of the point on the curve having the greatest slope for a straight line drawn from the point to the origin. It is found, in general, that this condition corresponds to that of the maximum speed of the engine and a resulting minimum propeller blade-angle setting. In order to represent the degree of transmissibility of the baffles, a quantity K, designated "conductivity," has been defined in reference 1 as

$$K=\frac{Q}{FV\sqrt{\frac{\Delta p}{q}}}$$

where Q is the quantity of the air passing through the baffles per second.

F, the cross section of the nacelle as a reference area.

q, the velocity head.

and V, the velocity of the air stream.

(a) Lay-out of cowling shapes.
(b) Wright blower.
(c) N.A.C.A. fan.
(d) Spinner 6.
(e) " 10.

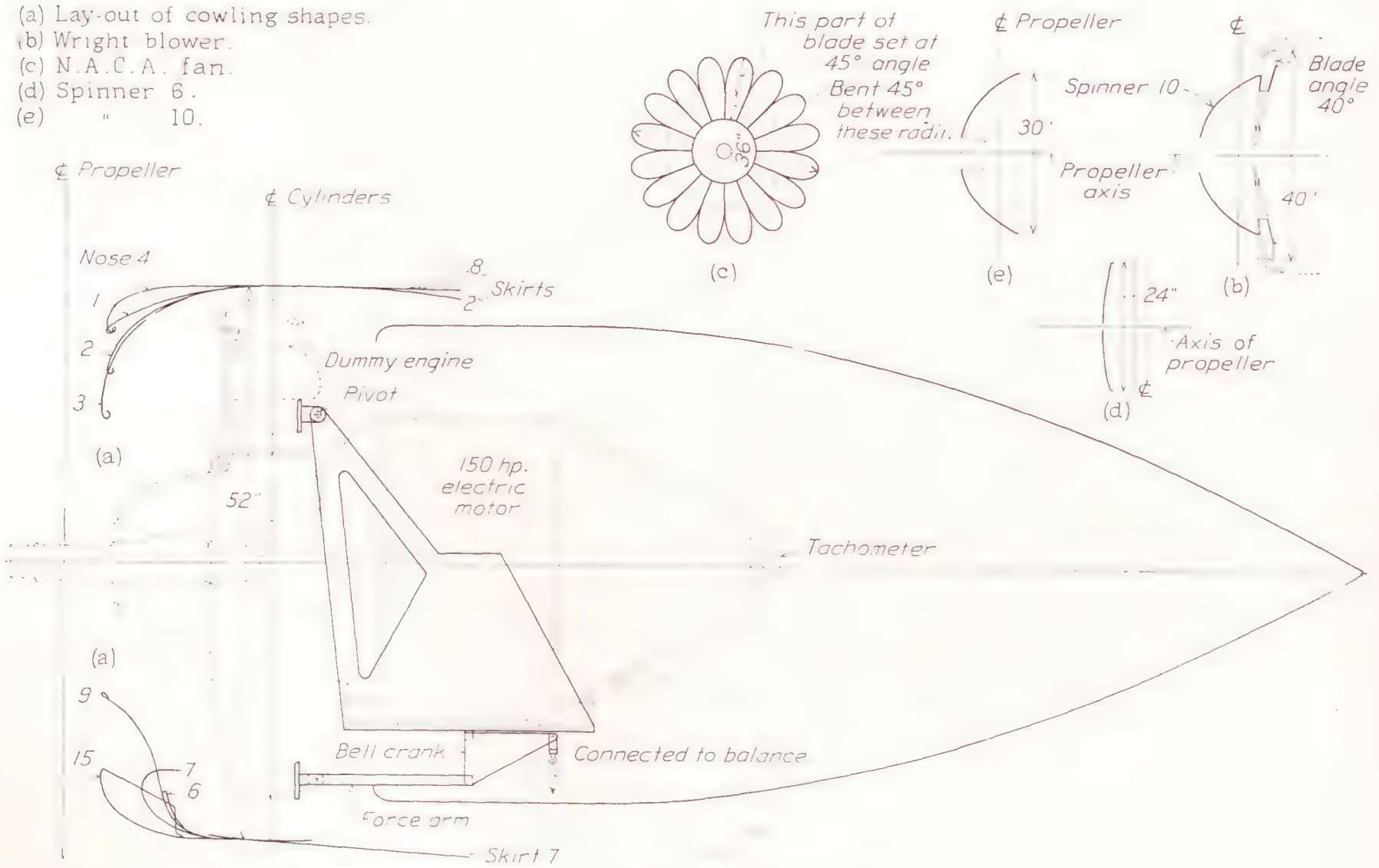

FIGURE 3.—Lay-out of the test arrangements.

DESCRIPTION OF EQUIPMENT

This investigation was conducted in the N. A. C. A. 20-foot tunnel, which, with its equipment, is described in detail in reference 2. The general arrangement of the test model is shown in figure 2. Detailed description of the particular equipment used is given in reference 3. Figure 3 (a) shows the various nose cowlings and skirts employed in the present investigation, together with other equipment used. Figure 3 (b) shows an experimental blower used in conjunction with nose 15 especially designed to house it. Figure 3 (c) shows an axial fan of simple construction hereinafter referred to as the "N. A. C. A. fan." Figure 3 (d) shows a circular flat disk 24 inches in diameter, which was attached to the front of the propeller in some of the following tests and is referred to as "spinner 6." Figure 3 (e) shows a normal type of spinner which was actually an integral part of the experimental blower shown in figure 3 (b) but which was sometimes used separately and designated "spinner 10." Figure 4 is a photograph of the four propellers with the designations employed in this report. The following table is given for reference from the associated propeller report (reference 3). A photograph of the experimental blower is shown in figure 5; the N. A. C. A. fan may be seen just behind the propeller in figure 2.

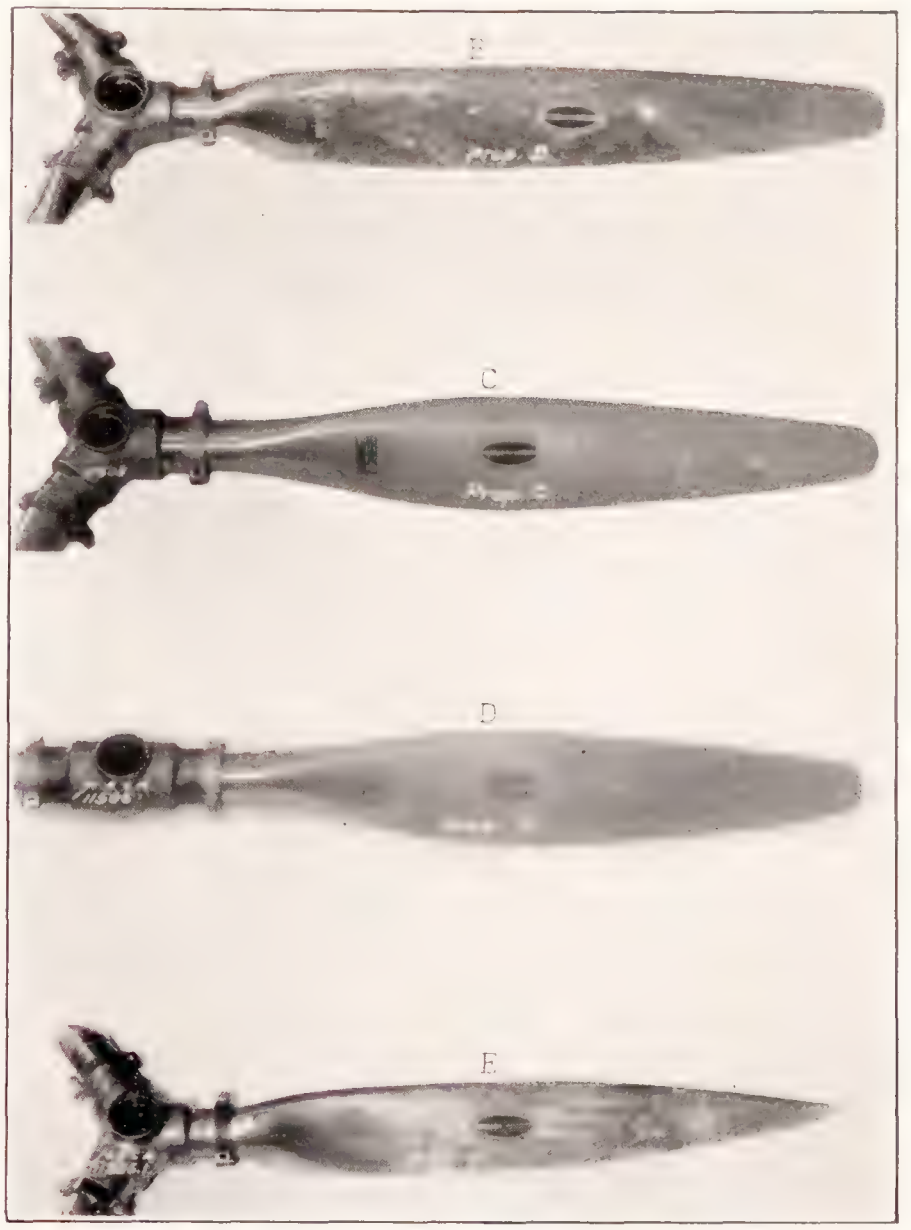

FIGURE 4.—Propellers tested.

PROPELLER DATA

Propeller designation	Drawing	Number of blades	Diameter (feet)	Type	Remarks	Airfoil section
A	Hamilton-Standard 6101-0	3	10.06	Controllable		Clark Y.
B	Hamilton-Standard 1C1-0	3	10.04	Adjustable		Do.
B_x	Hamilton-Standard 1C1-0 (modified)	3	10.04	do	Pitch decreased from the 70 percent radius to the tip.	Do.
C	Navy plan form 5868-9	3	10.02	do		Do.
D	Navy plan form 5868-9	2	10.00	do	Same as C except 2 blades	Do.
E	Navy plan form 3790	3	9.04	do		R. A. F.-6.

RESULTS

Figures 6, 7, 8, and 9 show the basic results of the investigation. Code numbers appear showing different arrangements. For example, arrangement 6–2–B–3–0 indicates that nose 6, skirt 2, propeller B, inner cowling 3, and no spinner were used. The ordinate used is $\sqrt{\Delta p}/n$ and the abscissa is the quantity V/nD, as prescribed in the preceding analysis. The range presented is actually the entire range of flight speed and it is noted that the slipstream effect gradually diminishes as the speed is increased. The curves asymptotically approach straight lines through the origin.

The series given in figure 6 shows, in particular, the effect of the blade-angle setting, the propellers B, B_x, C, D, and E being used on the most neutral cowlings composed of noses 6 or 7 and skirt 2. It is noticed that propeller B, or B_x, which has a good airfoil section near

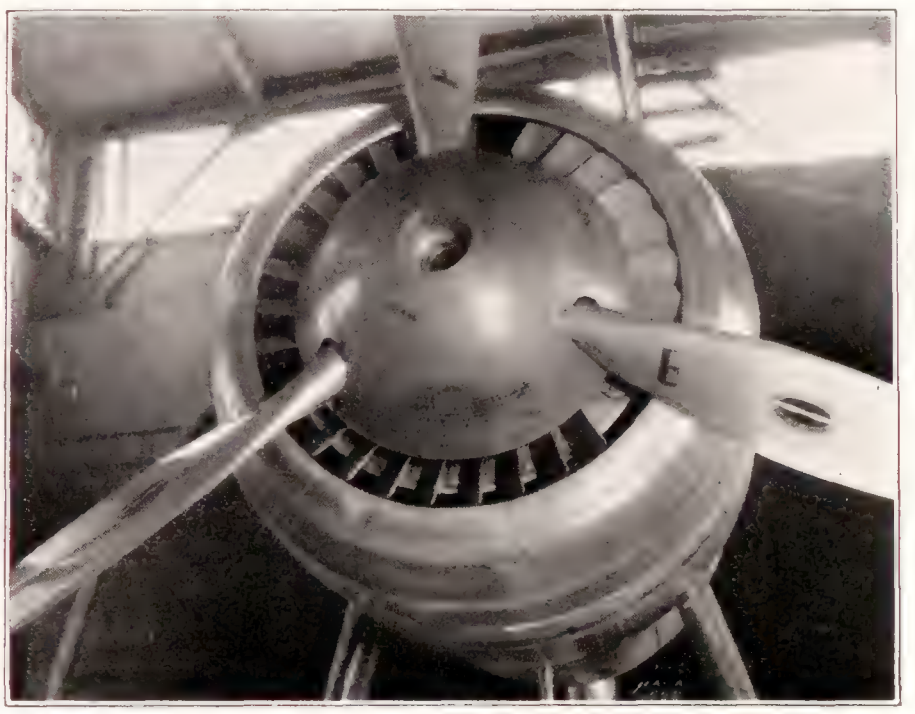

FIGURE 5.—Wright blower with propeller C and spinner 10.

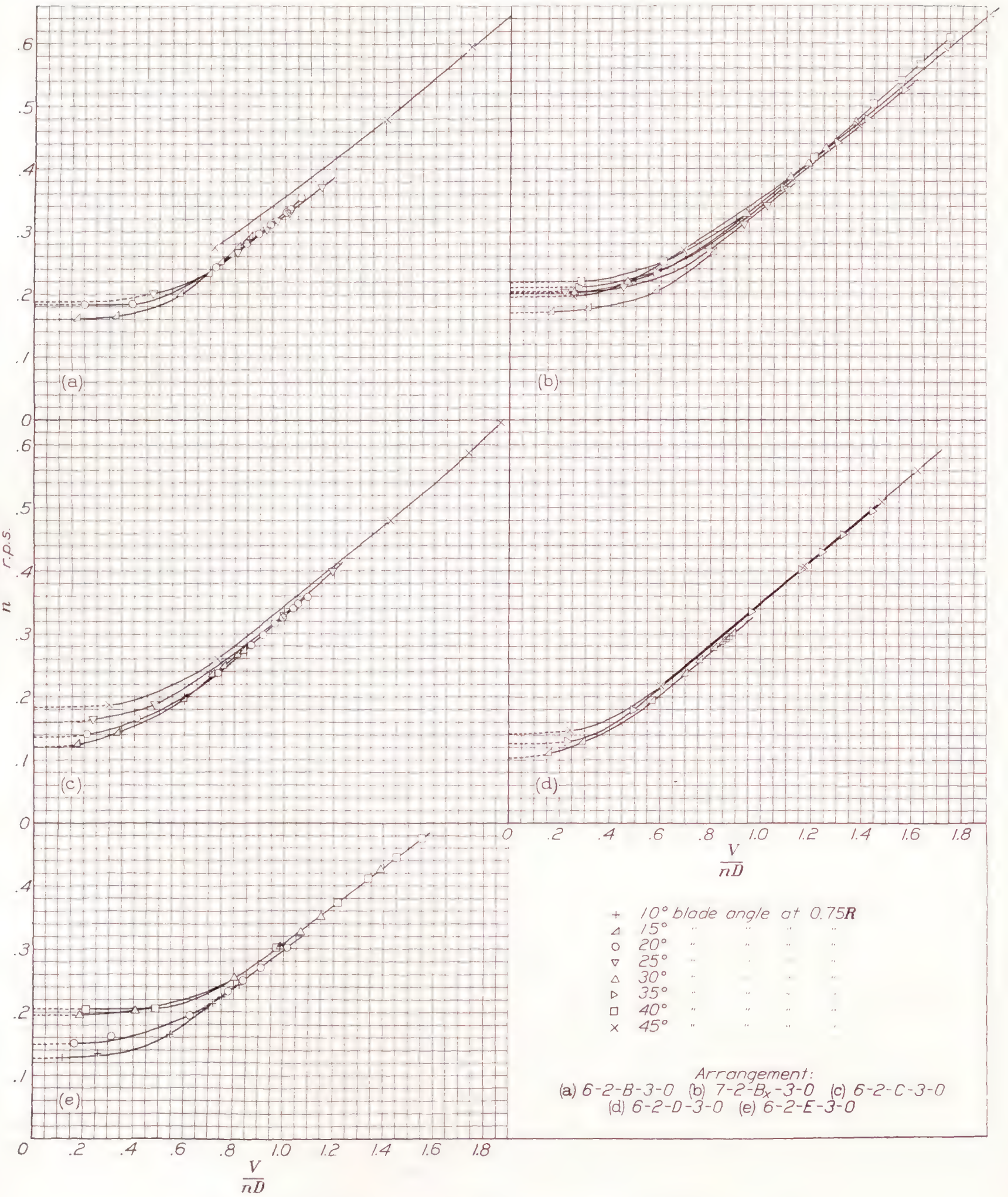

FIGURE 6.—Dependency of $\sqrt{\Delta p}/n$ on V/nD for several propellers at various blade angles.

the hub, is superior to the almost identical propeller C with a round hub section. The three-blade propeller C, and the two-blade propeller D, having identical blade sections, give available pressure drops almost proportional to the number of blades.

The next series (fig. 7) gives the effect of the various noses tested, the propellers used being restricted to B and C at blade angles of 25° and 35°. The result of most immediate interest is the apparent inferior cooling properties of the noses 3 and 9, the available pressure drop Δp being of the order of one-half or less of those obtained on the normal designs. It is further noticed that nose 4, which is characterized by a very flat nose section pointing radially inward, shows without exception the highest available pressure at the ground point. Noses 6 and 7, which are among the best at cruising condition (reference 1), appear, however, to be fairly close to the maximum.

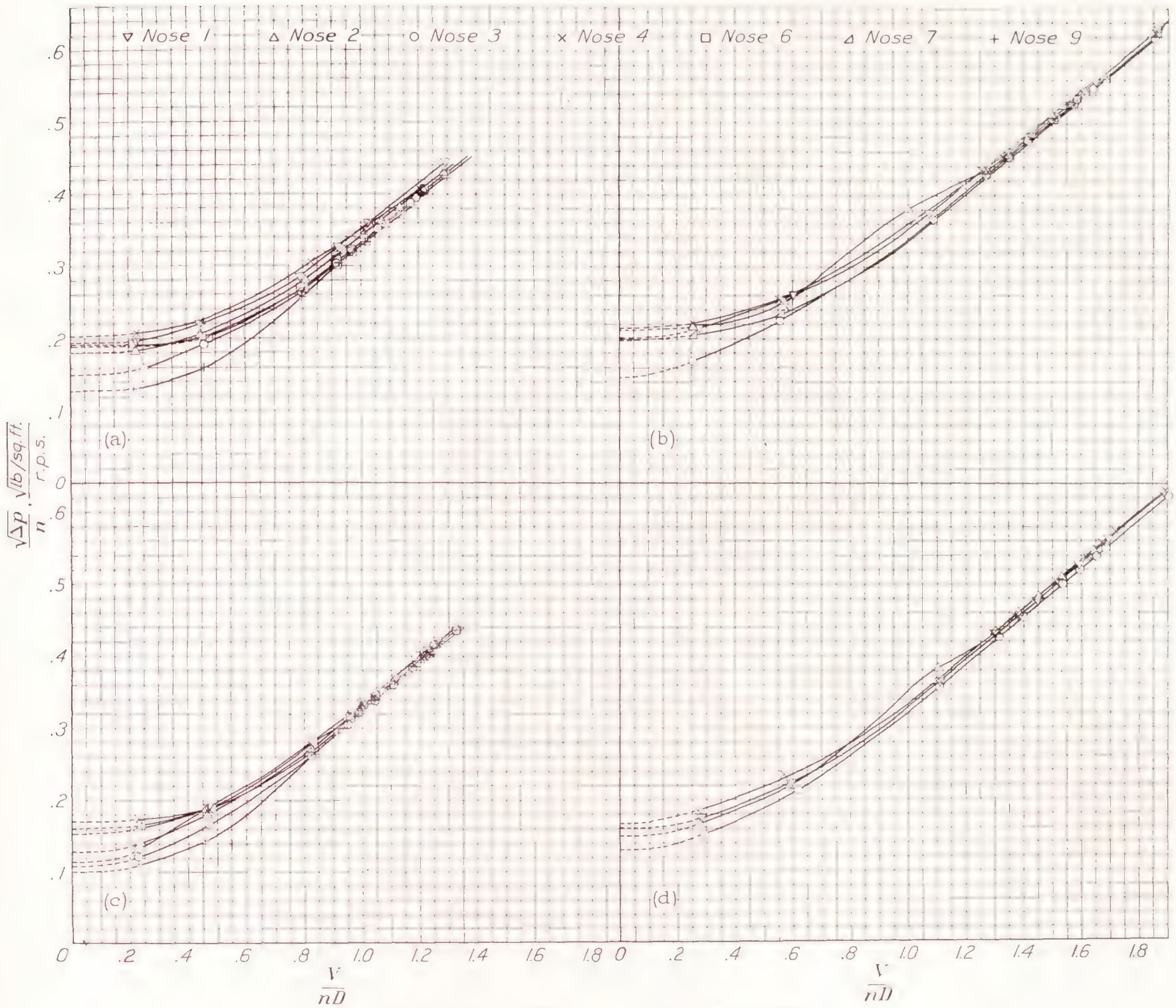

(a) Propeller B set 25°. (b) Propeller B set 35°.
(c) Propeller C set 25°. (d) Propeller C set 35°.

FIGURE 7.—Dependency of $\sqrt{\Delta p}/n$ on V/nD for several nose shapes on different propeller arrangements; skirt 2.

Figure 8 reproduces the experimental results in regard to the much-discussed problem relating to the use of cowling flaps. The flaps used were of normal design, 5 inches long, and were given successive increases in flap angle corresponding to flares of ½, 1, 2, and 3 inches at the rear end. The results show that the gain in available pressure is in the order of 15 percent as compared with the unflared skirt. This result is interesting insofar as it shows the performance of normal short flaps to produce a suction at the slot. In contrast, it is seen that skirts 7 and 8 represent a decided gain over the narrower skirt 2, this latter gain being in the order of 50 percent. Similar results are available for other propellers and blade angles and show substantial agreement.

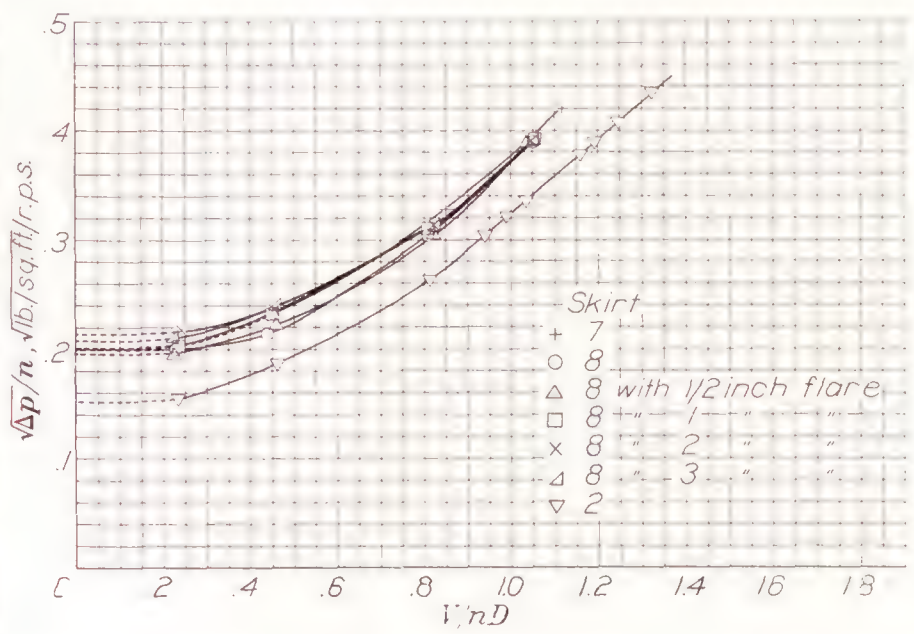

FIGURE 8.—Dependency of $\sqrt{\Delta p}/n$ on V/nD for several skirts with nose 7 and propeller C set 25° at $0.75R$.

Figure 9 shows the results of a related investigation on the effect of fans or blowers, presented for comparison in conjunction with some other typical cases. The most interesting result is the remarkable effectiveness of the very simple N. A. C. A. fan. The Wright blower is seen to be very inefficient, the pressure function remaining below 0.2, and is inferior to the propeller B alone.

Improved cooling on the ground is generally attained at some loss of efficiency at high air speeds. This loss is evident from the associated net-efficiency curves of figure 9. It is noticed that nose 7 with spinner 10, which gives poor cooling on the ground, shows the highest efficiency in flight conditions; whereas the N. A. C. A. fan, being superior for cooling, shows the lowest net efficiency.

The following table shows the pressure constants for the various propeller noses and skirts for the condition of cooling on the ground.

VALUES OF PRESSURE CONSTANT $\frac{\sqrt{\Delta p}}{n}$ AT $\frac{V}{nD}=0$

Blade angle (degs.)		Propeller B				Propeller B_s						Propeller C					Propeller D			Propeller E				Remarks
		15	20	25	35	15	25	30	35	40	45	15	20	25	35	45	15	35	45	10	20	30	40	
Nose	Skirt																							
1	2			0.193	0.201									0.114	0.160									
2	2			.180	.212									.128	.149									
3	2			.150	.146									.108	.129									
4	2			.202	.214									.170	.166									
6	2	0.160	0.183	.188								0.121	0.136	.160		0.184	0.104	0.127	0.142	0.127	0.148	0.195	0.205	
7	2			.190	.198	0.170	0.202	0.204	0.210	0.218	0.195			.152										
9	2			.128										.100										
7	7													0.200										
7	8													.199										
7	8													.195										½-inch flare.
7	8													.201										1-inch flare.
7	8													.214										2-inch flare.
7	8													.208										3-inch flare.
15	2													0.150										
15	2													.195										Spinner 10 and Wright blower.
15	2													.243										N. A. C. A. fan.
7	2													.183										Spinner 10.

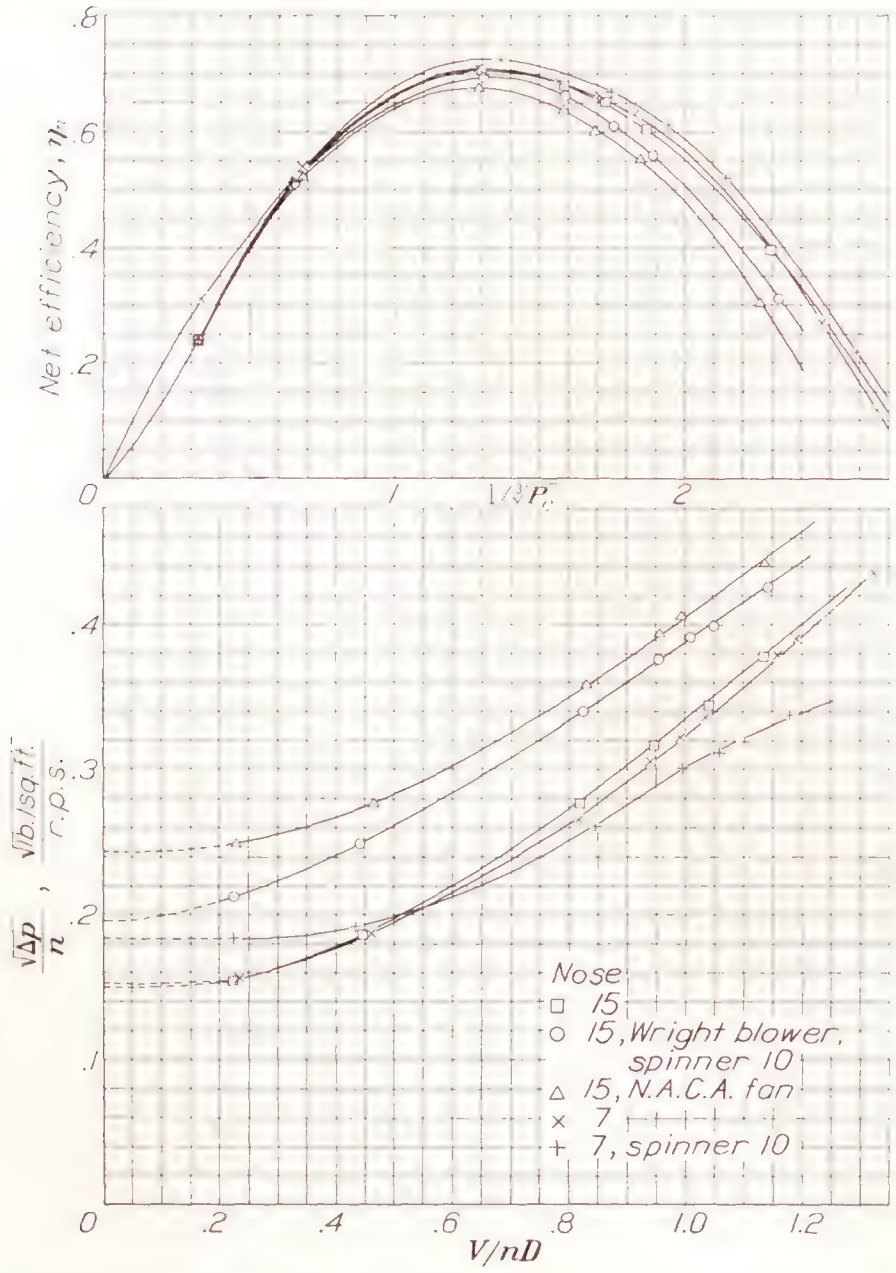

FIGURE 9.—Dependency of $\sqrt{\Delta p}/n$ on V/nD and of η_n on $1/\sqrt[3]{P_c}$ for propeller C set 25° at 0.75R with different test units.

Figure 10 shows the pressure function $\sqrt{\Delta p}/n$ on the ground for the five propellers. As explained in the previous analysis, the slope of a line drawn from any particular point on this curve to the origin is proportional to the square root of the available pressure Δp, the maximum slope giving the greatest available pressure on the ground. It is seen that this point, at which the highest pressure occurs in most cases, corresponds to a blade angle of less than 15°. Assuming a 550-horsepower engine with a 10-foot controllable propeller, the minimum blade angle permissible to prevent excess speed is about 19°, which corresponds to 1,460 r. p. m. of the propeller. The reason for the more effective action of the propellers occurring at low pitch settings lies in the fact that the propeller loading is concentrated more toward the hub. The practical conclusion is that, in order to obtain maximum cooling on the ground, the propeller should be given a minimum blade-angle setting corresponding to maximum engine speed.

Thus far the discussion has dealt entirely with the pressure drop and the factors affecting it. Results of some related tests of temperature measurements that were conducted at the same time will now be presented. It has previously been found (reference 1) that an available pressure drop of 10 pounds per square foot across the engine, if properly used, will provide sufficient cooling in accordance with present-day practice. It was found that a very definite relation between the rear temperature and the pressure drop exists; the front temperature was shown to depend on several

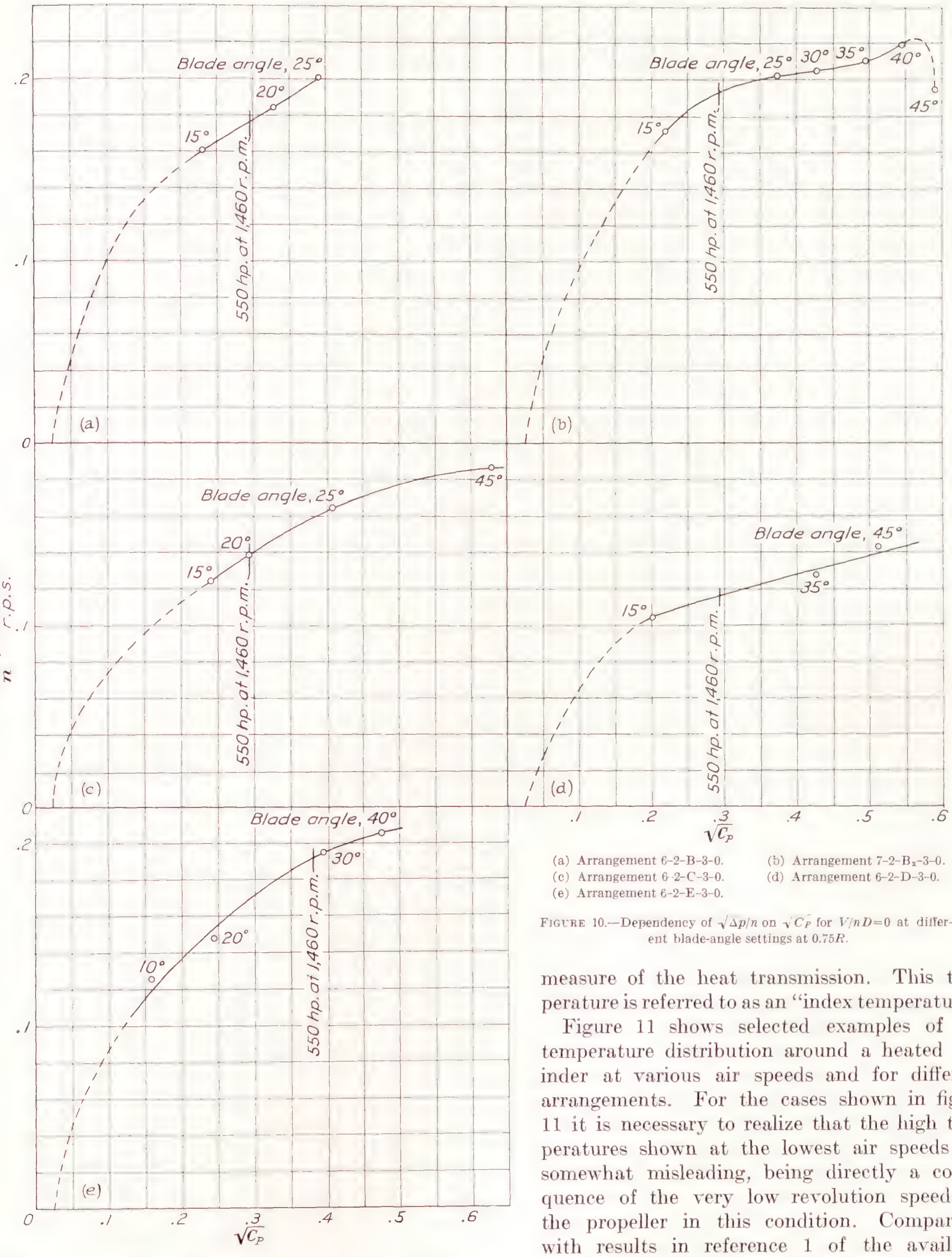

(a) Arrangement 6-2-B-3-0. (b) Arrangement 7-2-B_x-3-0.
(c) Arrangement 6-2-C-3-0. (d) Arrangement 6-2-D-3-0.
(e) Arrangement 6-2-E-3-0.

FIGURE 10.—Dependency of $\sqrt{\Delta p}/n$ on $\sqrt{C_P}$ for $V/nD=0$ at different blade-angle settings at $0.75R$.

other factors. In the present paper, the temperature distribution around the circumference of a cylinder is shown in more detail. The particular cylinder on which the measurements were made contained an electric heater, the output of which was kept constant at 1.75 kilowatts, the temperature thus being a direct measure of the heat transmission. This temperature is referred to as an "index temperature."

Figure 11 shows selected examples of the temperature distribution around a heated cylinder at various air speeds and for different arrangements. For the cases shown in figure 11 it is necessary to realize that the high temperatures shown at the lowest air speeds are somewhat misleading, being directly a consequence of the very low revolution speeds of the propeller in this condition. Comparison with results in reference 1 of the available pressure on the ground and at low speeds indicates that the extrapolated values of the temperatures at zero air speed would not be much in excess of those obtained at the lowest air speed. The revolution speeds employed in the tests were roughly of the order of one-half of those on conventional installations since

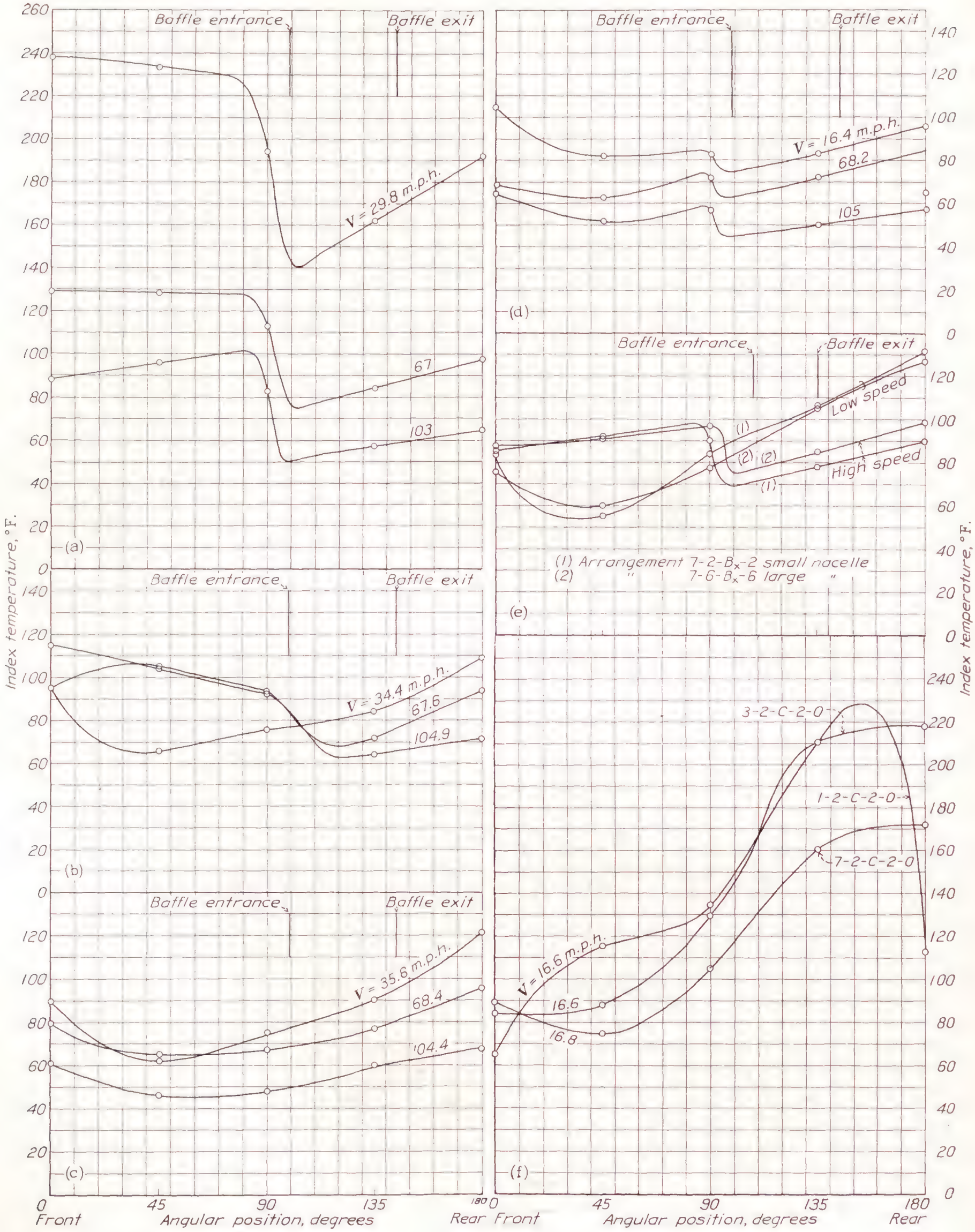

(a) Arrangement 7–2–0–3–0; K=0.0424.
(b) Arrangement 7–2–B–3–0; K=0.0424.
(c) Arrangement 7–2–B–3–6; K=0.0424.
(d) Arrangement 15–2–C–3–10 (Wright blower); K=0.0424.
(e) High and low speed for two arrangements; K=0.0909.
(f) Baffles removed from arrangement of three nose shapes; K=0.3 to 0.6.

FIGURE 11.—Distribution of index temperature around the cylinder for various arrangements.

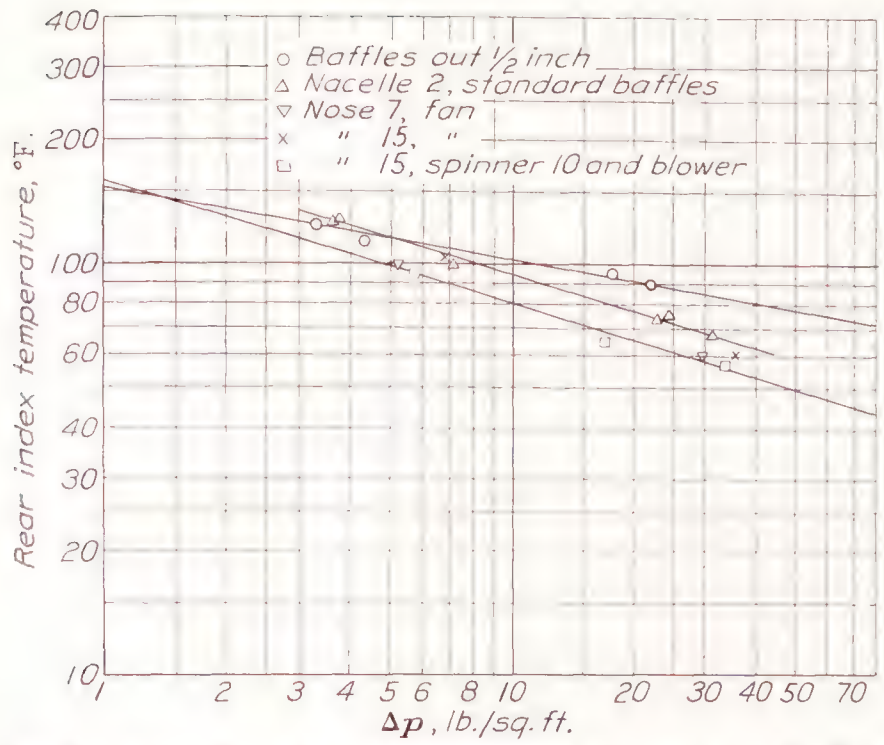

FIGURE 12.—Dependency of index temperature on Δp for several nose shapes, fans, and conductivities.

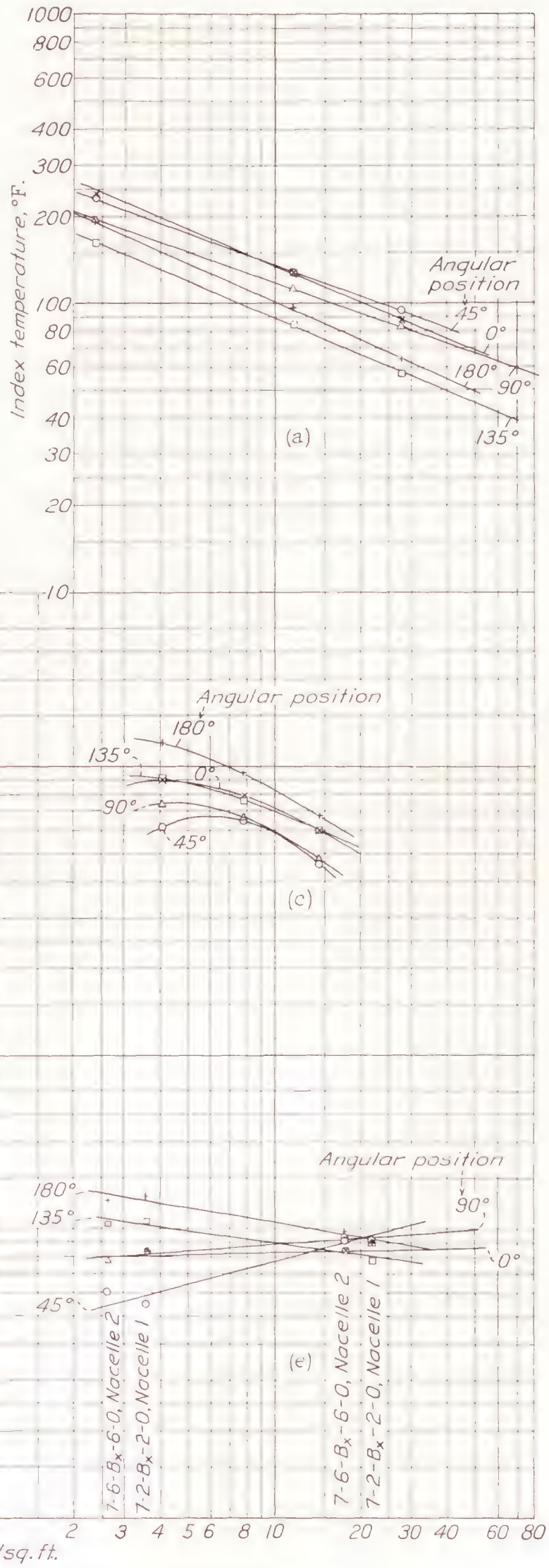

(a) Arrangement 7-2-0-3-0; $K=0.0424$.
(b) Arrangement 7-2-B-3-0; $K=0.0424$.
(c) Arrangement 7-2-B-3-6; $K=0.0424$.
(d) Arrangement 15-2-C-3-10 (Wright blower); $K=0.0424$.
(e) High and low speed for two arrangements; $K=0.0909$.

FIGURE 13.—Dependency of index temperature on Δp for various arrangements.

only about one-eighth of the power was used. As a result, the ground cooling pressure amounted to about one-quarter of actual values and the coefficients of heat transmission to approximately $4^{-0.3}$, or about two-thirds of the values at the proper propeller speed. As a consequence the temperatures measured are about 50 percent in excess of the values that would be obtained for the same heat output at normal propeller speeds. The first four sets of curves of figure 11 are for the standard baffling, $K=0.0424$, all taken on the small nacelle. In figure 11 (a) is shown a case of propeller off; the three curves show three different tunnel speeds. In figure 11 (b) is shown a case with propeller B and in figure 11 (c) a flat spinner has been added. Note the very beneficial effect of the spinner on the front temperatures. In figure 11 (d) the results are given for a special test series on a Wright experimental blower. The next figure, 11 (e), shows the temperature distribution obtained with a larger gap between the cylinder and the baffles; $K=0.0909$ at two air speeds and with both nacelles. Note the large increase in the rear temperatures. Figure 11 (f) shows the distribution for minimum air speed for the case of baffles removed; $K=0.3$ to 0.6.

Figure 12 shows the relationship between the rear temperature and the pressure drop across the cylinder bank as resulting exclusively from the change in the air speed. The slopes of the resultant curves are somewhat inconsistent, lying apparently between -0.2 and -0.3.

Figure 13 is given to indicate the exponents of the temperature-pressure relationship at various angular positions around the cylinder. It is apparent that the frontal temperature is very independent of the pressure drop. Figure 13 (e) shows a particularly irregular result; the heat transmission on the front actually increasing at low tunnel speeds, especially at the 45° position, probably indicating a peculiar flow condition.

GENERAL CONCLUSIONS

1. A blade section of proper airfoil shape near the hub is found to be effective in producing increased cooling on the ground, being far superior to the conventional round shank. The N. A. C. A. fan of very simple construction gave the highest observed available pressure; it appears, however, that this result could be equaled by improving the design of the airfoil section near the hub.

2. Adjustable skirt flaps were found to increase the pressure drop in the order of 15 percent. Flaps are not recommended except for very loosely baffled or unbaffled engines.

3. The design of the nose of a cowling is of some influence in regard to the cooling at the ground point. Noses with a small frontal opening were found to be inferior and are not recommended. A nose design with a radial inward bend of the leading edge (nose 4) was found to be superior to, but only slightly better than, the normal designs (nose 7) recommended for cruising conditions.

4. The charts given in the paper for a number of conventional propellers indicate the most efficient blade-angle setting for obtaining the best cooling at the ground point. The angle is apparently a function only of the permissible maximum engine speed, which was found to correspond to a blade angle of about 20°.

5. No very general conclusion is possible in regard to the temperature distribution. The beneficial influence of a tight baffling has been demonstrated. A flat plate, or spinner, in front of the propeller hub has been demonstrated to improve very effectively the cooling on the front. The apparently inconsistent results often obtained on the cooling of the front of the cylinder seem to indicate that several unknown factors are involved and leave a field for future study.

LANGLEY MEMORIAL AERONAUTICAL LABORATORY,
NATIONAL ADVISORY COMMITTEE FOR AERONAUTICS,
LANGLEY FIELD, VA., *June 2, 1936.*

REFERENCES

1. Theodorsen, Theodore, Brevoort, M. J., and Stickle, George W.: Full-Scale Tests of N. A. C. A. Cowlings. T. R. No. 592, N. A. C. A., 1937.
2. Weick, Fred E., and Wood, Donald H.: The Twenty-Foot Propeller Research Tunnel of the National Advisory Committee for Aernautics. T. R. No. 300, N. A. C. A., 1928.
3. Theodorsen, Theodore, Stickle, George W., and Brevoort, M. J.: Characteristics of Six Propellers Including the High-Speed Range. T. R. No. 594, N. A. C. A., 1937.

REPORT No. 594

CHARACTERISTICS OF SIX PROPELLERS INCLUDING THE HIGH-SPEED RANGE

By Theodore Theodorsen, George W. Stickle, and M. J. Brevoort

SUMMARY

This investigation is part of an extensive experimental study that has been carried out at full scale in the N. A. C. A. 20-foot tunnel, the purpose of which has been to furnish information in regard to the functioning of the propeller-cowling-nacelle unit under all conditions of take-off, climbing, and normal flight. This report presents the results of tests of six propellers in the normal and high-speed flight range and also includes a study of the take-off characteristics. The range of the advance-diameter ratio has been extended far beyond that of earlier full-scale experiments at the Laboratory, blade-angle settings up to 45° being included, which are equivalent to air speeds of more than 300 miles per hour for propellers of normal size and revolution speed. All the propellers were tested in conjunction with a standard nacelle unit equipped with half a dozen representative N. A. C. A. cowlings.

The results show very striking differences in the aerodynamic qualities of the various propellers, particularly in the high-speed range. Also of interest is the fact that the conventional propeller is shown to reach its peak efficiency in a range of 200 to 350 miles per hour and at a blade angle of approximately 35°. The inadequacy of using the propulsive efficiency unconditionally as a figure of merit is shown. This efficiency, defined in conventional manner, is found actually to exceed unity in certain cases, owing to the fact that certain cowlings show a decreased drag in the propeller slipstream. The adoption of some standard nacelle unit is therefore recommended as a basis for the comparative testing of propellers. The experimental results are presented in convenient charts. Charts for practical use in selecting propeller diameters and charts for choosing the optimum blade-angle setting in the take-off range are given in an appendix.

INTRODUCTION

The reported investigation is part of a comprehensive study of cowling-nacelle-propeller combinations (references 1 and 2). The tests were conducted in the N. A. C. A. 20-foot tunnel (reference 3) of full-size commercial propellers over the full range of blade angles up to 45° and over the full range of tunnel speeds up to about 100 miles per hour. Recent rapid increase in the speed of airplanes has produced a need for tests extending to large values of the advance-diameter ratio V/nD. To the knowledge of the authors this is the first time that the effect of the cowling form on the propeller has been systematically investigated and that a series of full-scale propellers has been tested up to 45° blade angle.

It has been mentioned elsewhere (reference 1) that the quantity $P_c = \frac{P}{qSV}$ (where P is the power supplied to the propeller shaft, S the disk area, V the velocity, and q the velocity head of the air stream) represents the contraction of the propeller slipstream. It will be referred to as the "unit disk loading" or "disk-loading coefficient."

The great convenience of using the quantity P_c in comparing the results of tests of various propellers is realized. The ideal efficiency is directly a function of P_c. For a given horsepower and propeller size, P_c is proportional to the inverse of the third power of the air speed. For this reason the various diagrams are based on $1/\sqrt[3]{P_c}$ rather than on P_c, the abscissa thus being proportional to the air speed. The various efficiencies have in several cases been plotted against this quantity. For practical purposes of choosing propeller diameters for given values of the other variables, it is perfectly possible to include curves of constant V/nD and blade-angle setting. All practical values may, however, be obtained directly from the contour charts given in the appendix, which are based on the experimental results of this investigation.

Equal values of P_c actually correspond to similar flow conditions through the propeller disk and around the nacelle. A test to simulate a speed of 300 miles per hour may thus be run at 100 miles per hour tunnel speed with the value of P_c adjusted to give the identical slipstream contraction. This value is obtained by reducing the thrust to 1/9 or the power supplied to the shaft to 1/27 of the actual values at 300 miles per hour. The test is thus actually conducted at a scale or Reynolds Number of 1/3 of the full-scale values. Experience shows, however, that no particular Reynolds Number

effect is expected in this range since the tests are conducted far beyond the usual model range. On the other hand, the reported tests were all conducted at tip speeds far below sound velocity and the results may

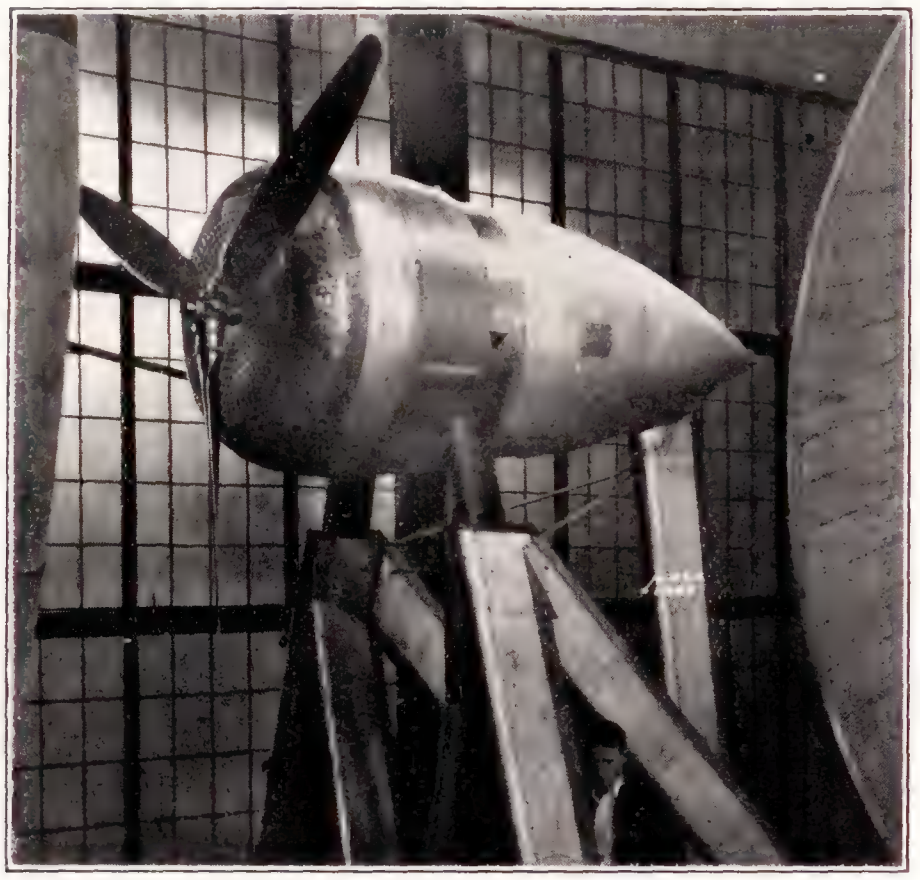

FIGURE 1.—Test model with nose 18 and propeller B mounted on the balance frame in the 20-foot wind tunnel.

be considered free from any effects of the compressibility of the air.

As will be evident from the test results, the propulsive efficiency alone as defined in the usual manner is not a dependable criterion of the efficiency of the propeller tested in conjunction with a nacelle but is quite dependent on the particular nacelle or body used behind the propeller. This efficiency is therefore significant only if the various propellers are tested on the identical nacelle. For this reason a quantity termed the "net efficiency," which relates to the entire propeller-nacelle unit, has been used throughout this report. It is defined as

$$\eta_n = \frac{RV}{P}$$

where R is the net forward thrust of the entire unit as measured on the thrust scale. This quantity is in itself a perfectly arbitrary reference number, depending largely on the relative dimensions of the propeller and the nacelle.

Since the same nacelle has been used throughout the entire test series, it is certain that the combination giving the highest net efficiency under any specified condition is superior to any other combination. The net efficiency may be considered as containing the propulsive efficiency together with the efficiency of the cowling-nacelle.

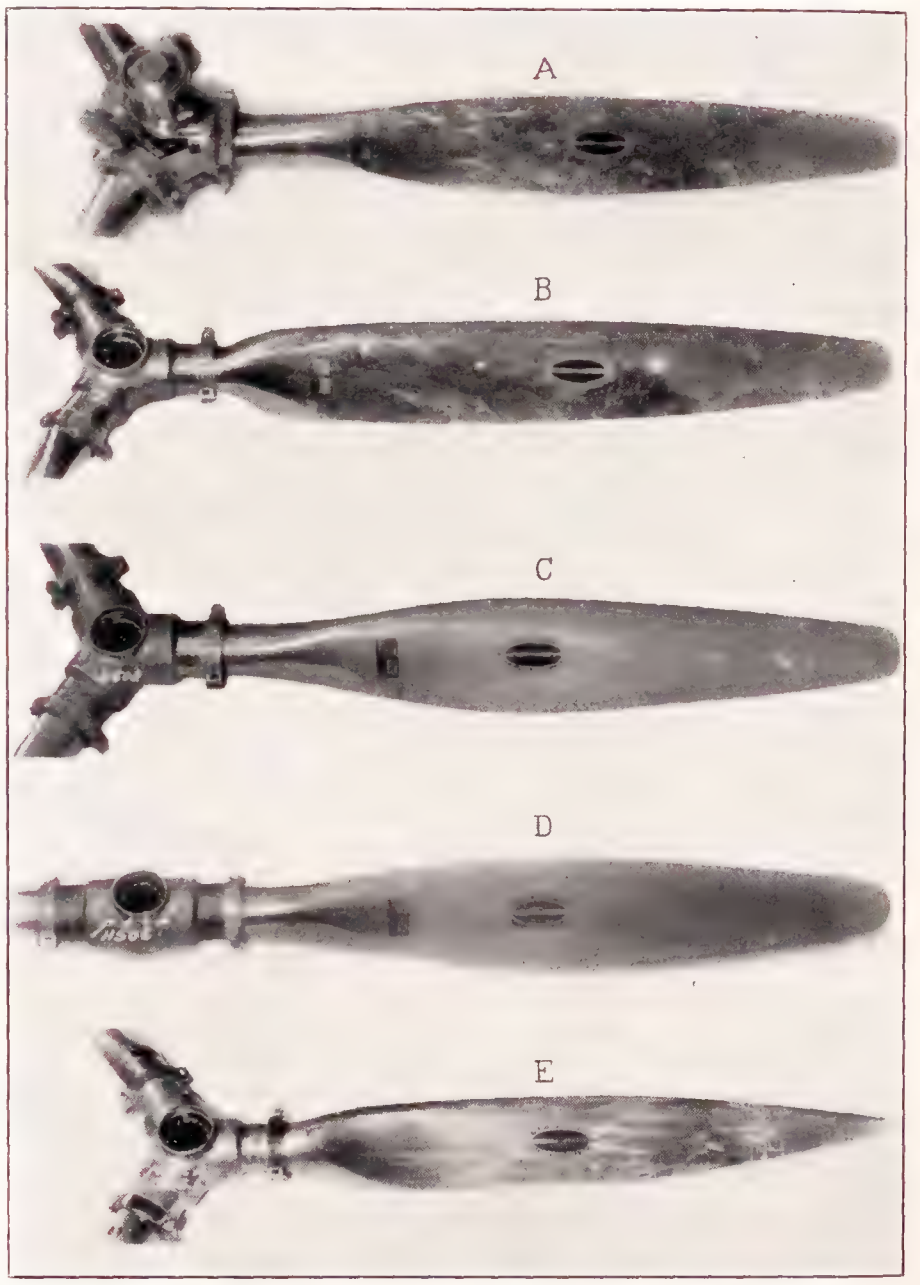

FIGURE 2.—Propellers used in the investigation.

DESCRIPTION OF TESTS

Figure 1 is a photograph of the installation in the 20-foot tunnel used for this investigation. Figure 2 shows the propellers used, the complete details of which are shown in figure 3 and in the following table.

PROPELLERS

Propeller designation	Drawing	Number of blades	Diameter	Type	Remarks	Airfoil section
			Feet			
A	Hamilton-Standard 6101–0	3	10.06	Controllable		Clark Y.
B	Hamilton-Standard 1C1–0	3	10.04	Adjustable	Blade section same as A except near hub	Do.
B_x	Hamilton-Standard 1C1–0 (modified)	3	10.04	do	Blade angle decreased from the 70-percent radius to the tip (fig. 3).	Do.
C	Navy plan form 5868–9	3	10.02	do		Do.
D	Navy plan form 5868–9	2	10.00	do	Same as C except 2 blades	Do
E	Navy plan form 3790	3	9.04	do		R. A. F. 6.

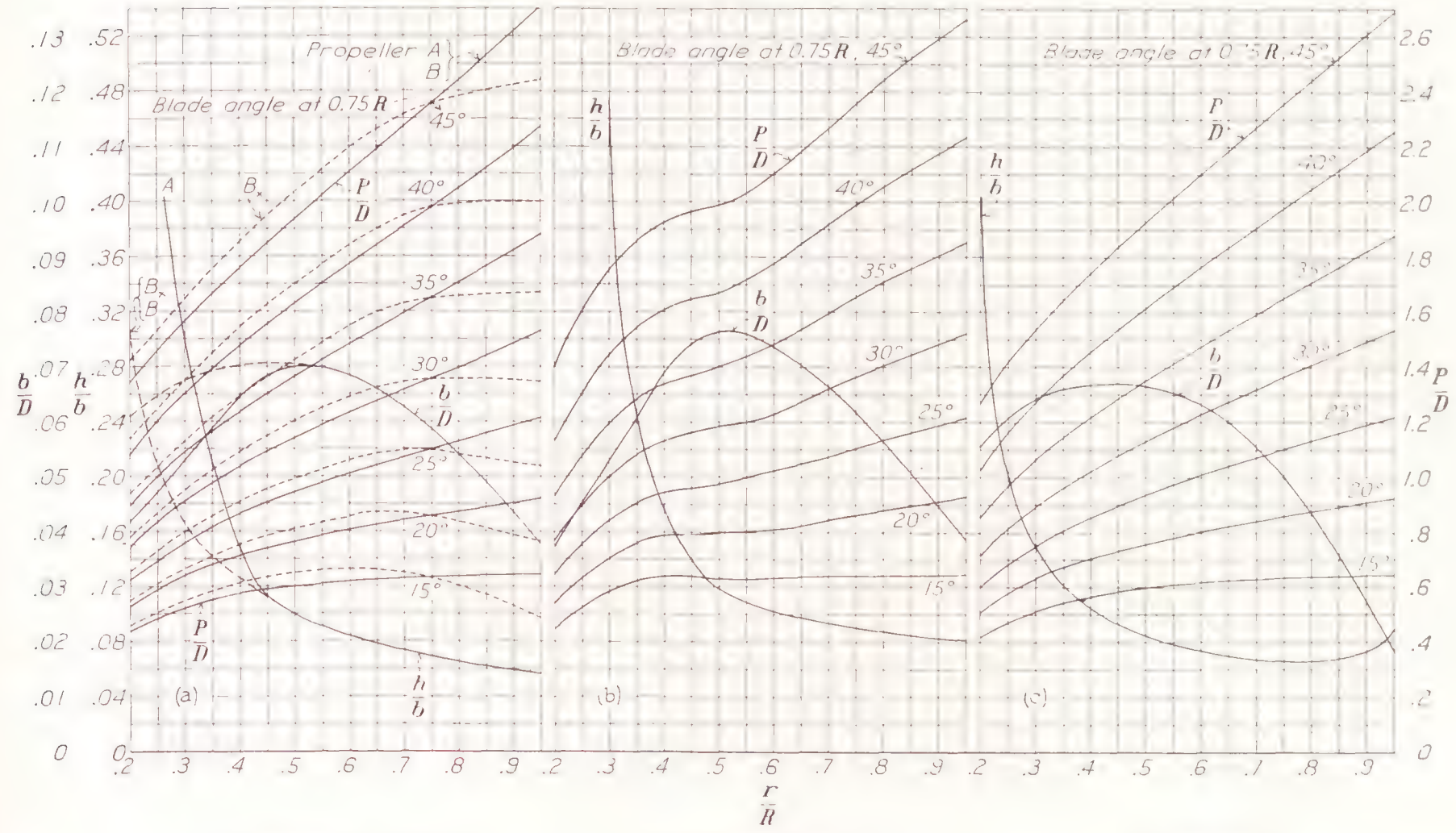

(a) Propellers A, B, and B_x. (b) Propellers C and D. (c) Propeller E.

FIGURE 3.—Blade-form curves for the propellers tested. D, diameter; b, blade width; h, blade thickness; P, pitch; $R=D/2$, radius at tip; r, radius.

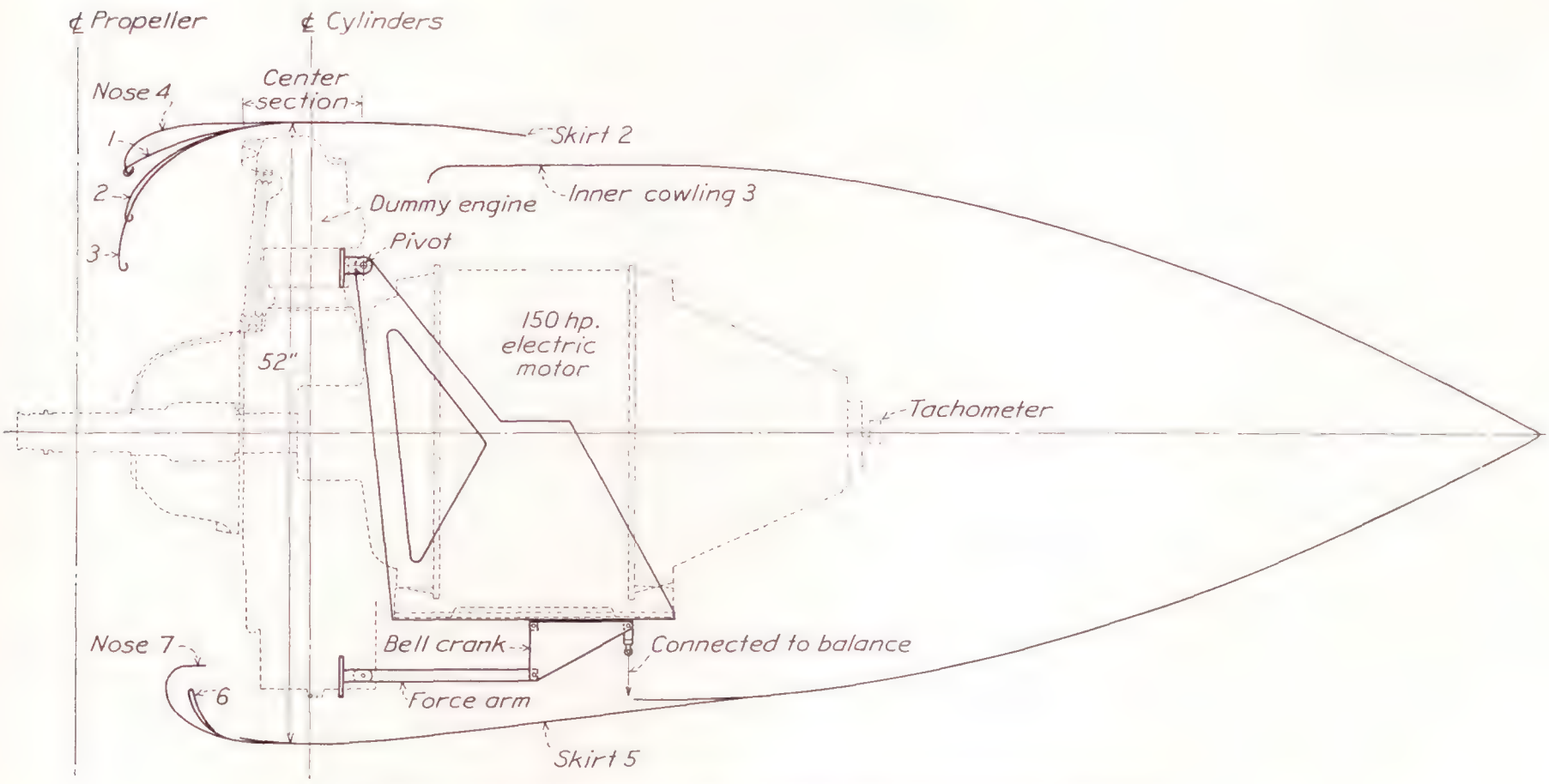

FIGURE 4.—Test arrangement and cowling shapes used in the propeller investigation.

The drawing in figure 4 shows in detail the nacelle unit with the particular noses and skirts used in the propeller tests. Power to the propeller was furnished by a variable-speed electric motor enclosed in the nacelle unit. The propellers were tested up to and including a blade angle of 45° at $0.75R$ and at tunnel speeds up to more than 100 miles per hour.

TEST RESULTS

Figures 5 to 22 show the results of the experimental investigation of six commercial propellers tested in conjunction with a total of six different cowling shapes.[1] Each figure includes the variation with V/nD of the conventional coefficients C_T, C_P, and the propulsive efficiency η, all usually given at several blade-angle settings. The coefficients C_T and C_P are defined as follows:

$$C_T=\frac{T}{\rho n^2 D^4}$$

$$C_P=\frac{P}{\rho n^3 D^5}$$

where ρ is air density and D the propeller diameter.

[1] Owing to special interest in particular propellers, the faired values of C_T, C_P, η, and Cs for propellers B and C with nose 6 and for propeller B_x with nose 7 are presented in tables I, II, and III. It is of interest to note that the values of C_T and C_P at low values of V/nD for the blade angles near 20° and 25° at $0.75R$ do not fair with the values from the other blade angles as well as might be expected. These values check, however, with values from other tests of the same propellers with different test set-ups, indicating an instability of flow for low values of V/nD in this region of blade-angle setting.

The propulsive efficiency η is defined

$$\eta=\frac{TV}{P}$$

where $T=R+D$, R being the reading on the thrust scale under test conditions and D the drag for the corresponding air speed of the nacelle unit measured with the propeller off.

The net efficiency has been given in several cases. The net efficiency is simply defined as

$$\eta_n=\frac{RV}{P}$$

and is a sort of over-all efficiency of the engine-nacelle-propeller unit. This efficiency is plotted against the quantity $1/\sqrt[3]{P_c}$, where P_c is the propeller unit disk loading.

The following table is a key to the numbers of the figures in which are plotted the data of the various combinations tested.

KEY TABLE TO FIGURE NUMBERS

	Curves of C_T, C_P, and η against $\frac{V}{nD}$																																	Propulsive-efficiency envelopes						Net-efficiency envelopes					
Propeller	A	B							B_x						C							D						E							A	B	B_x	C	D	E	A	B	B_x	C	D	E
Blade angle (deg.)	24.1	15	20	25	30	35	40	45	15	25	30	35	40	45	15	20	25	30	35	40	45	15	25	30	35	45	10	20	30	40	All angles																	
Nose																																															
1				5		5												6		6																			30		30			
2				7		7												8		8															23		23			31		31		
3				9		9												10		10															24		24			32		32		
4	13			11	11	11[a]												12		12	12								15						25	25		25			33	33		33		33
6	14	16	16	16	16	16	16	16								17	17	17	17	17	17	17	18	18	18	18	18	19	19	19	19	25	26		26	26	26		34		34	34	34
7				20		20			21	21	21	21	21	21				22		22															27	27	27			35	35	35		
Propulsive efficiency envelopes, all noses tested					28													29																										
Net efficiency envelopes, all noses tested					36													37																										
η_n and η_0 nose 2					38													38																										

[a] 33°.

The original results are given in figures 5 to 22. Figures 23 to 27 give the efficiency envelopes of each of the propellers for five different noses. Figures 28 and 29 give a comparison of propellers B and C with separate efficiency envelopes for each of the noses tested. The drag for the various noses tested is given in reference 1. The net efficiencies are given in figures 30 to 35, and the particular results for propellers B and C in regard to net efficiencies are further given in figures 36 and 37. All the results are strictly comparable in showing the effect of propellers and noses since the same skirt, the same conductivity[2] of the engine, and, as a consequence, the same quantity of cooling air were used in all the tests. Figure 38 shows the net efficiency with no cooling air as obtained with nose 19 and skirt 5.

[2] In order to represent the degree of transmissibility of the baffles, a quantity K, designated "conductivity," has been defined in reference 1 as

$$K=\frac{Q}{FV\sqrt{\frac{\Delta p}{q}}}$$

where

Q is the volume of the air passing through the baffles per second.

F, the cross section of the nacelle as a reference area.

q, the velocity head.

V, the velocity of the air stream.

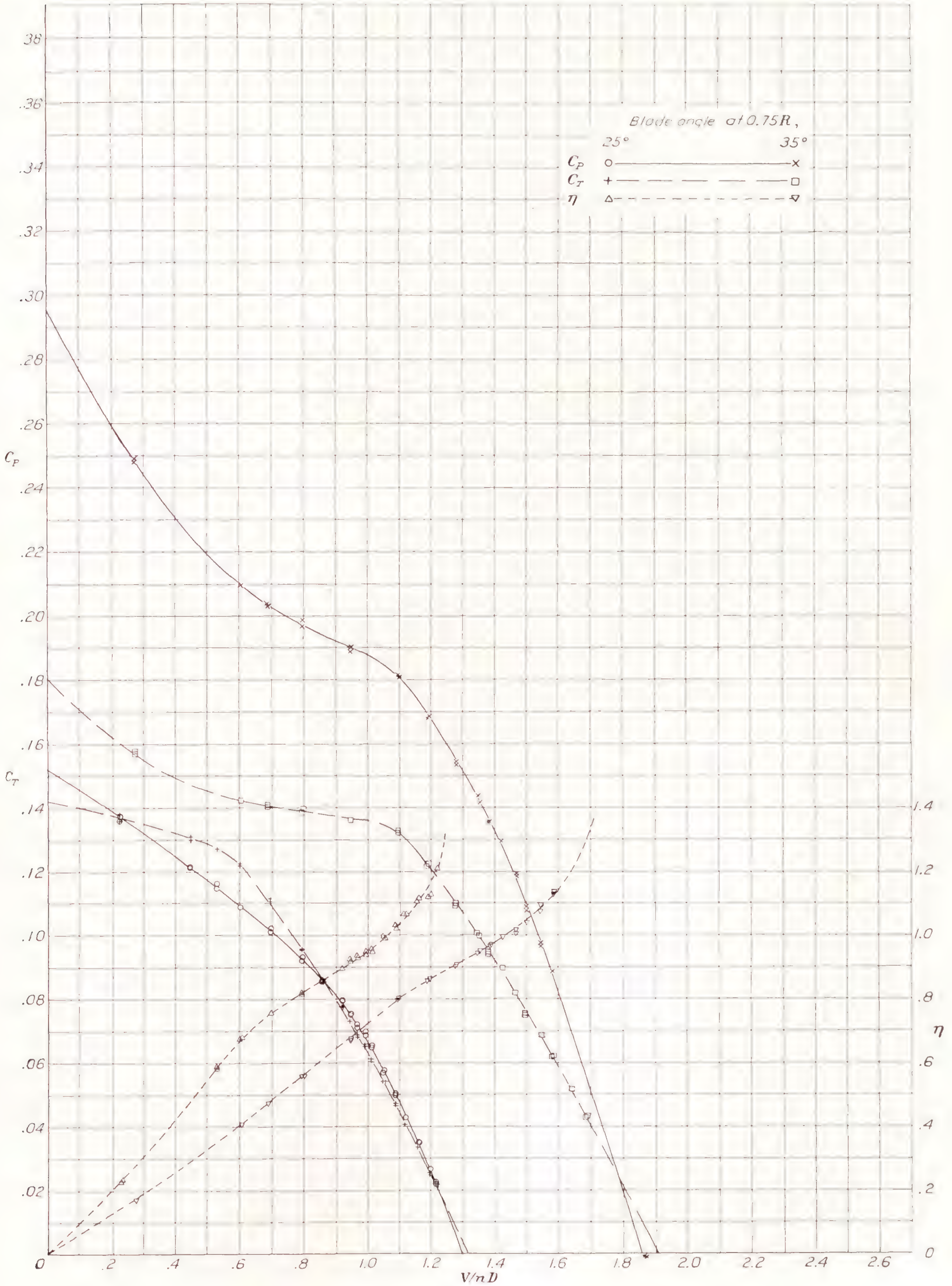

FIGURE 5.—Curves of C_T, C_P, and η against V/nD for nose 1, propeller B.

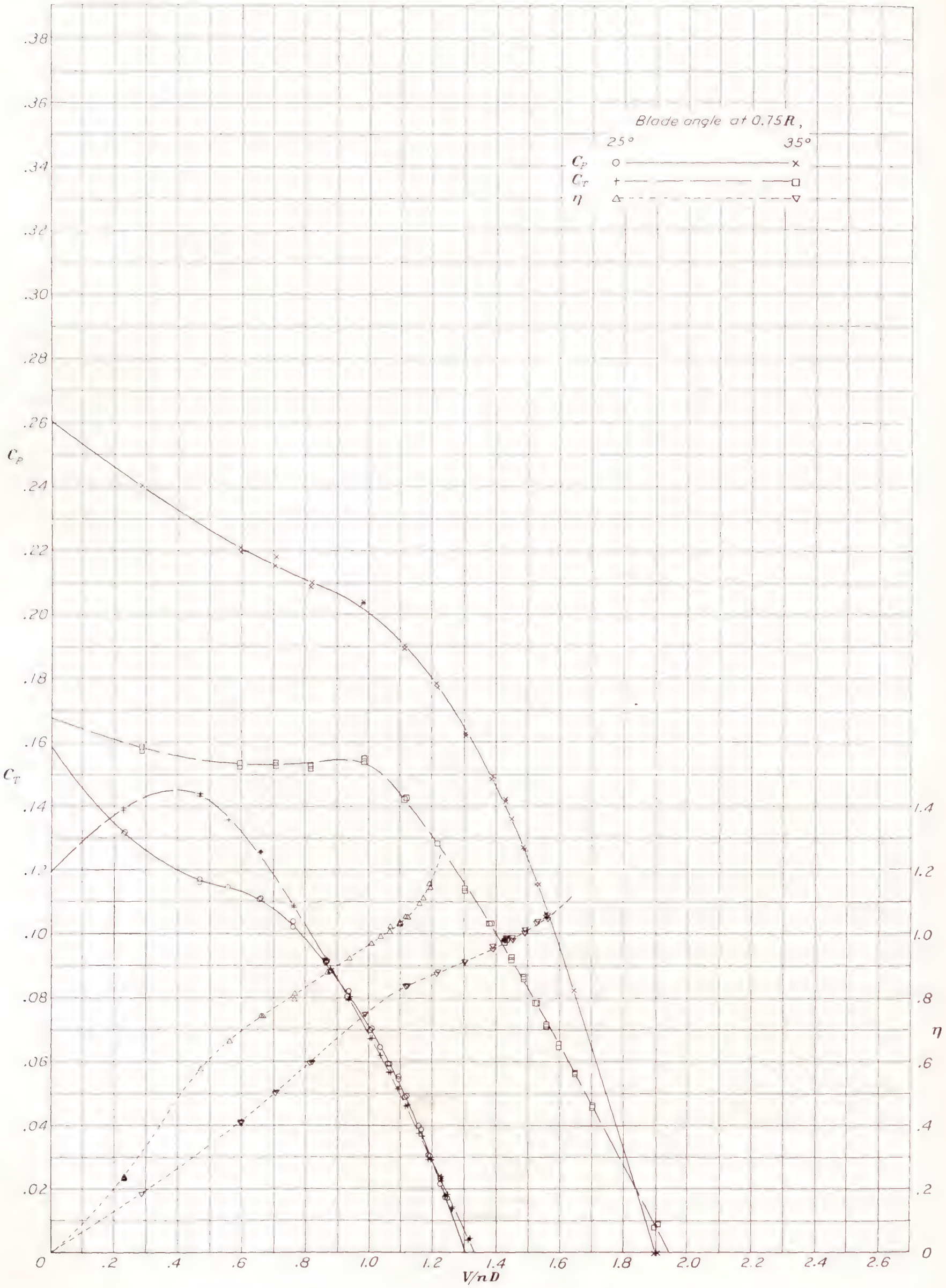

FIGURE 6.—Curves of C_T, C_P, and η against V/nD for nose 1, propeller C.

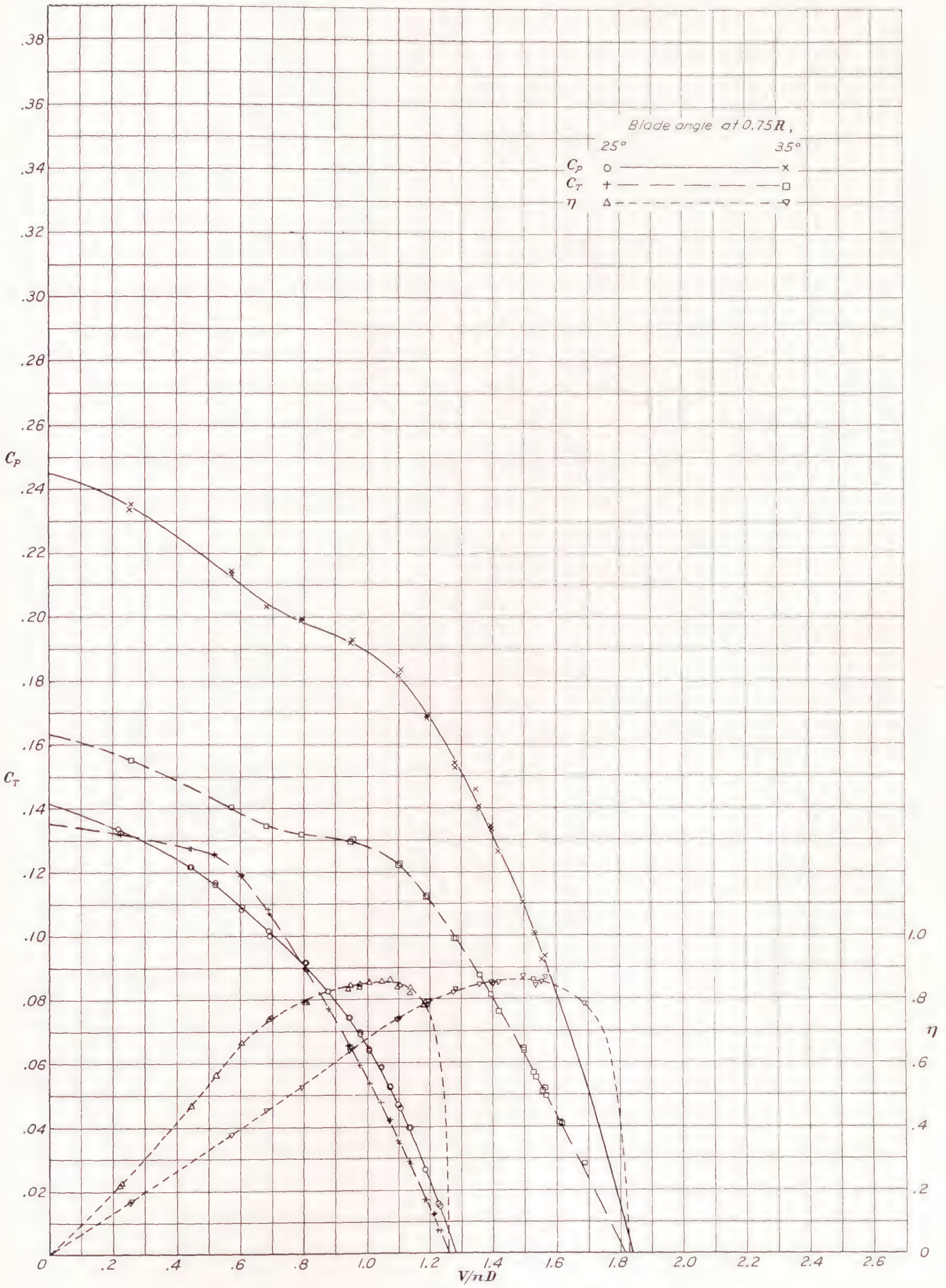

FIGURE 7.—Curves of C_T, C_P, and η against V/nD for nose 2, propeller B.

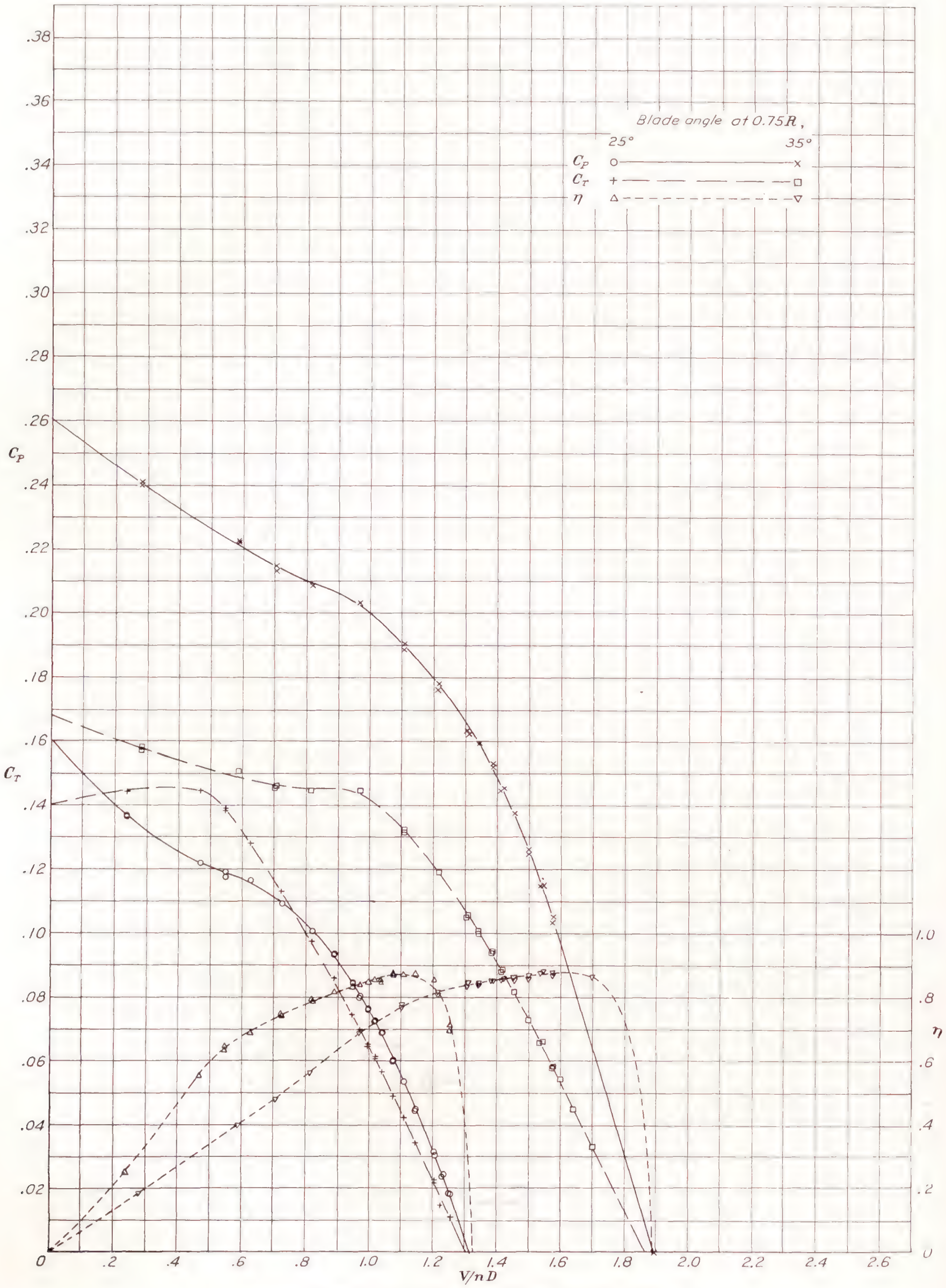

FIGURE 8.—Curves of C_T, C_P, and η against V/nD for nose 2, propeller C.

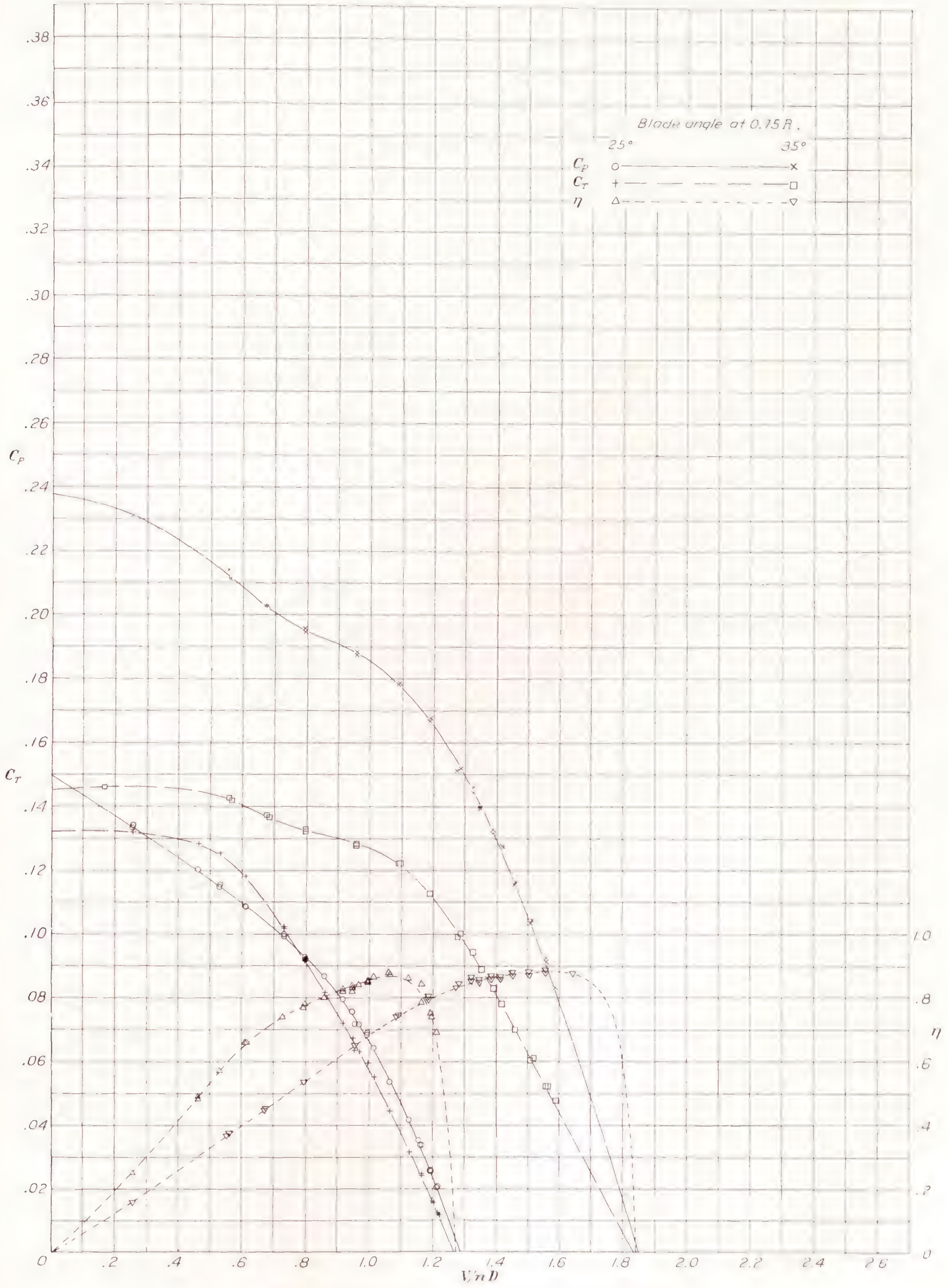

FIGURE 9.—Curves of C_T, C_P, and η against V/nD for nose 3, propeller B.

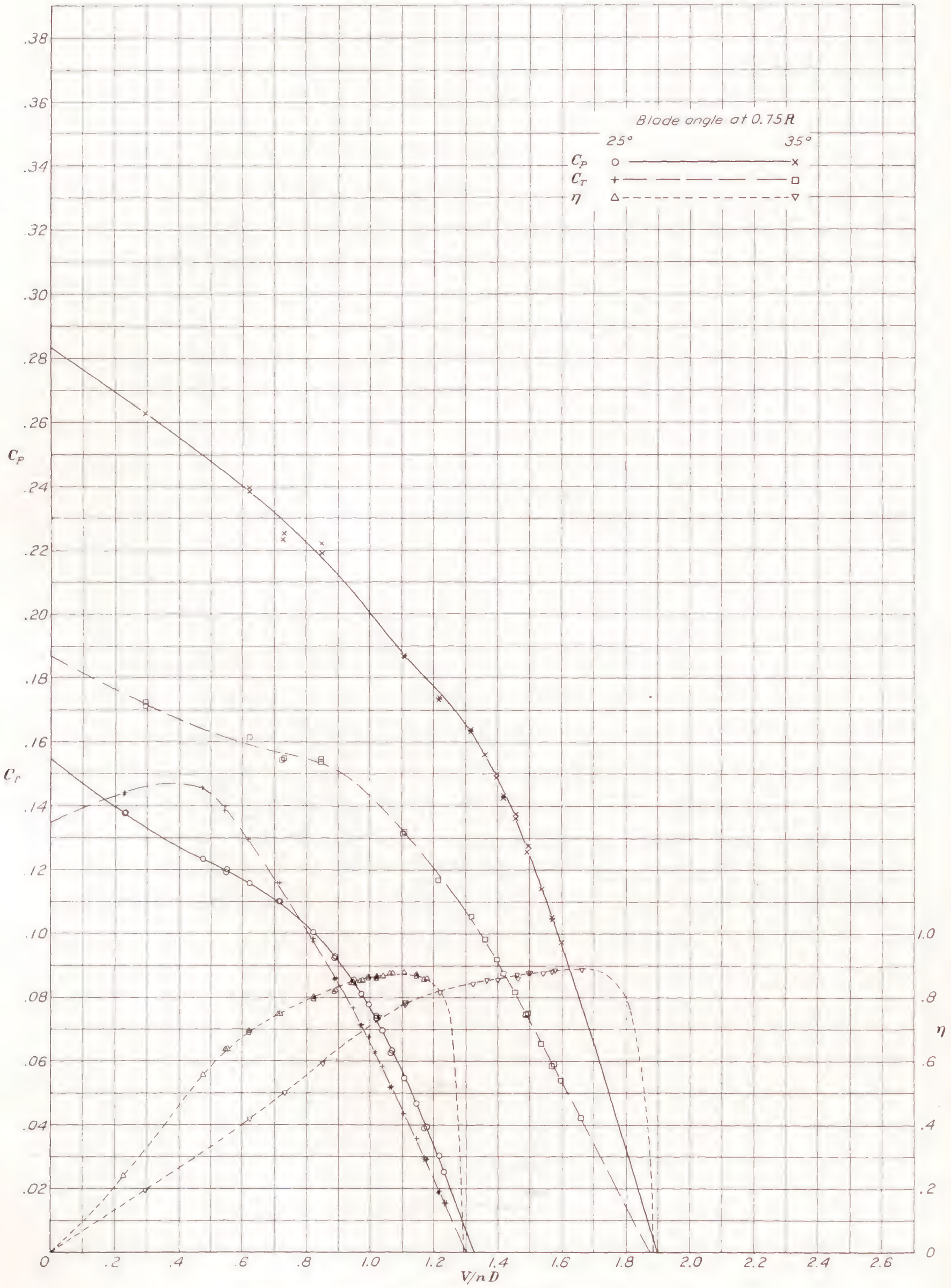

FIGURE 10.—Curves of C_T, C_P, and η against V/nD for nose 3, propeller C.

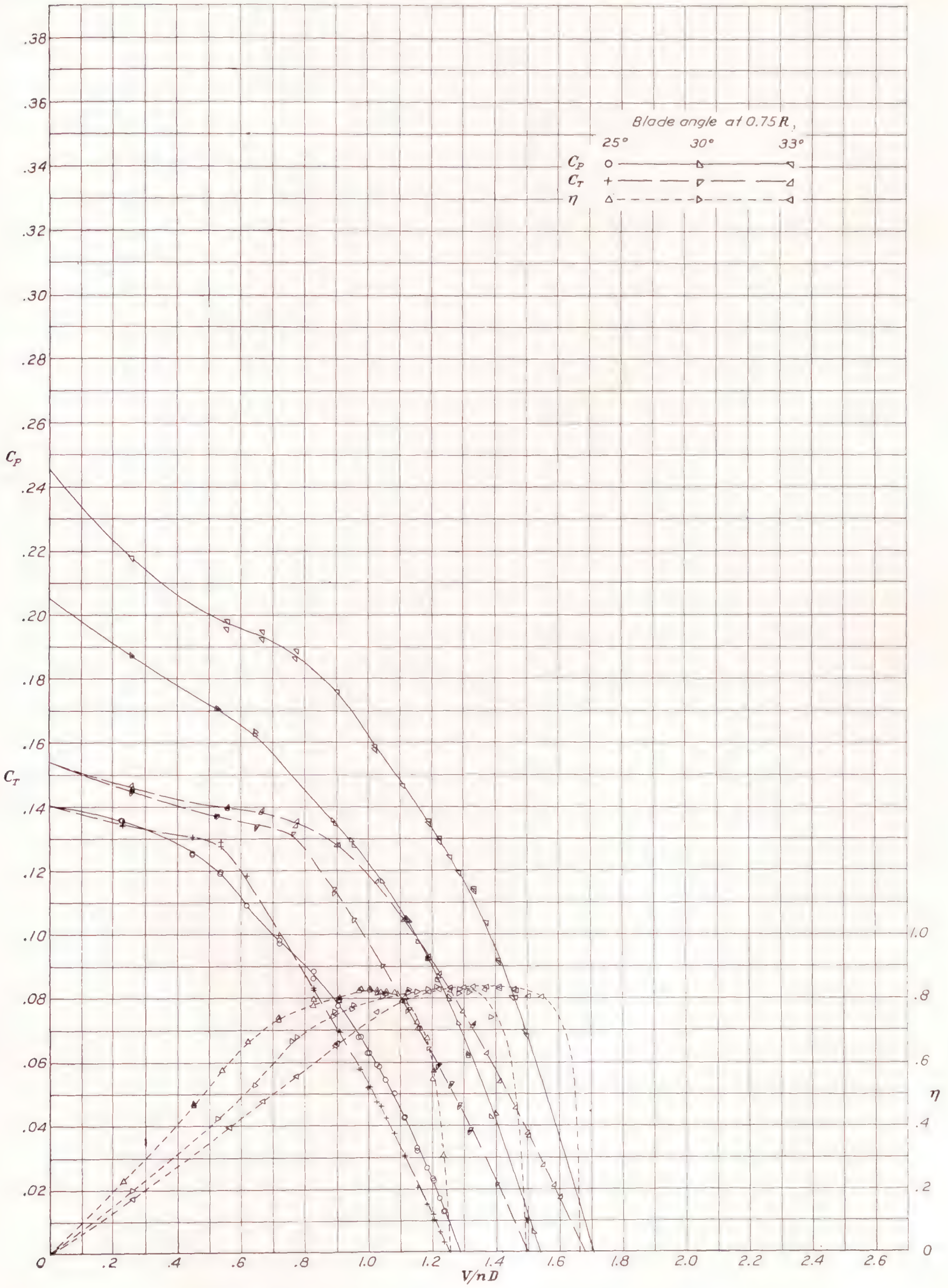

FIGURE 11.—Curves of C_T, C_P, and η against V/nD for nose 4, propeller B.

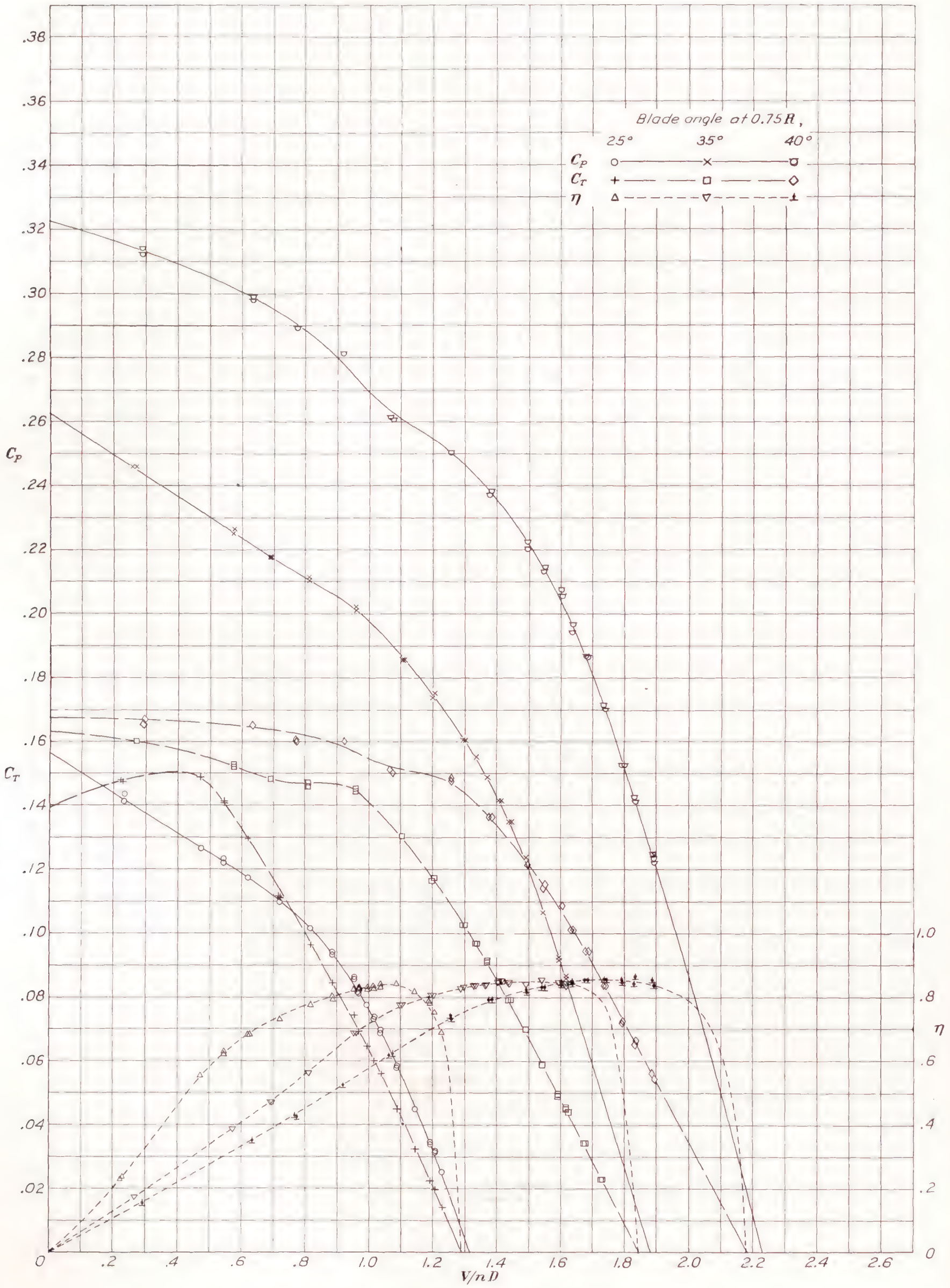

FIGURE 12.—Curves of C_T, C_P, and η against V/nD for nose 4, propeller C.

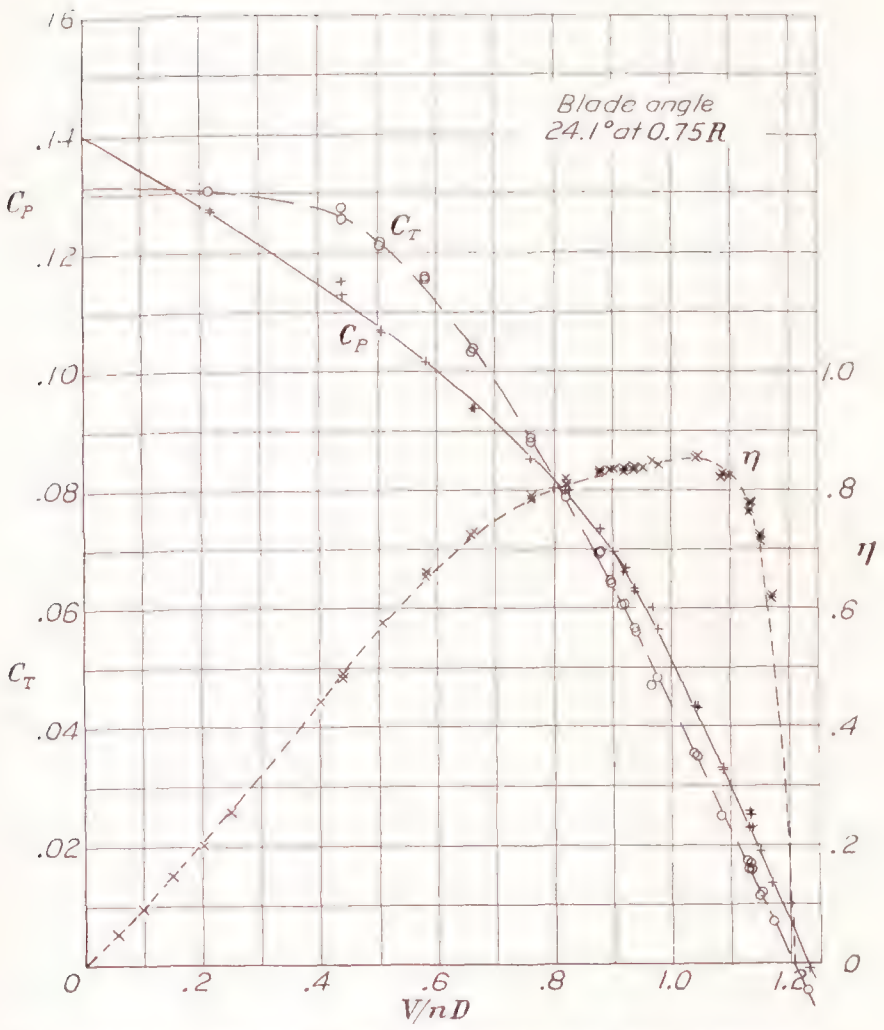

FIGURE 13.—Curves of C_T, C_P, and η against V/nD for nose 4, propeller A.

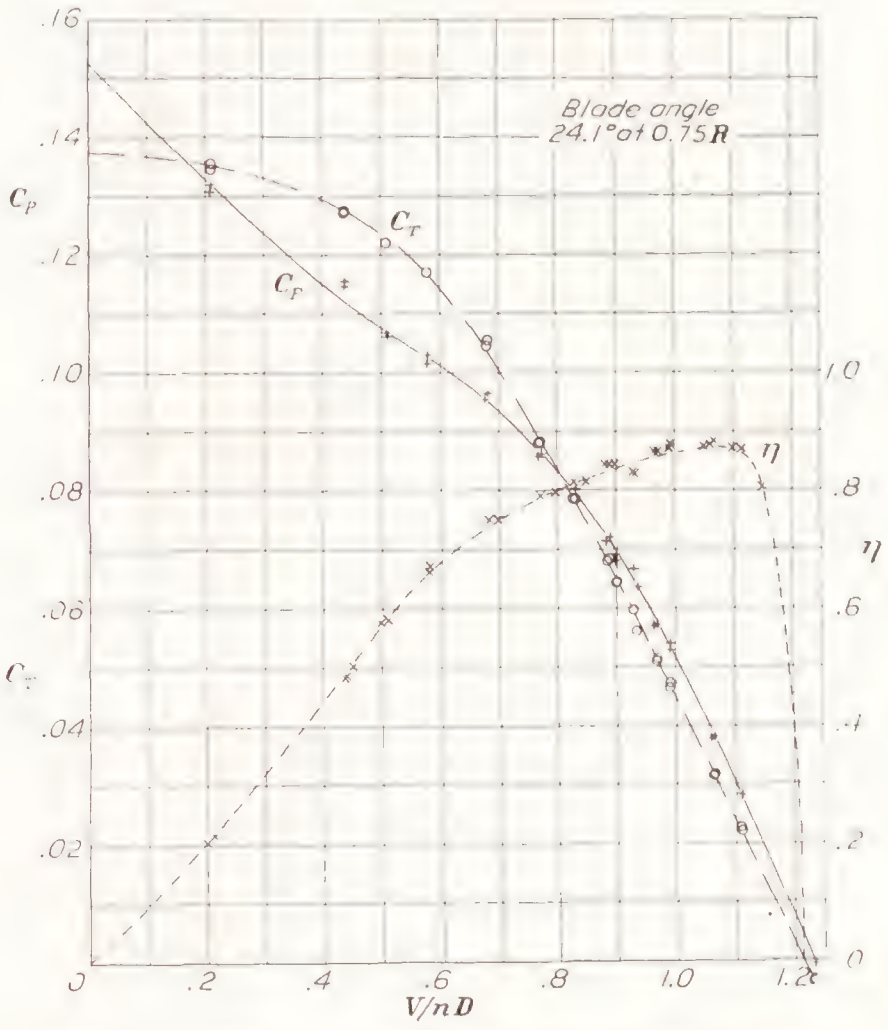

FIGURE 14.—Curves of C_T, C_P, and η against V/nD for nose 6, propeller A.

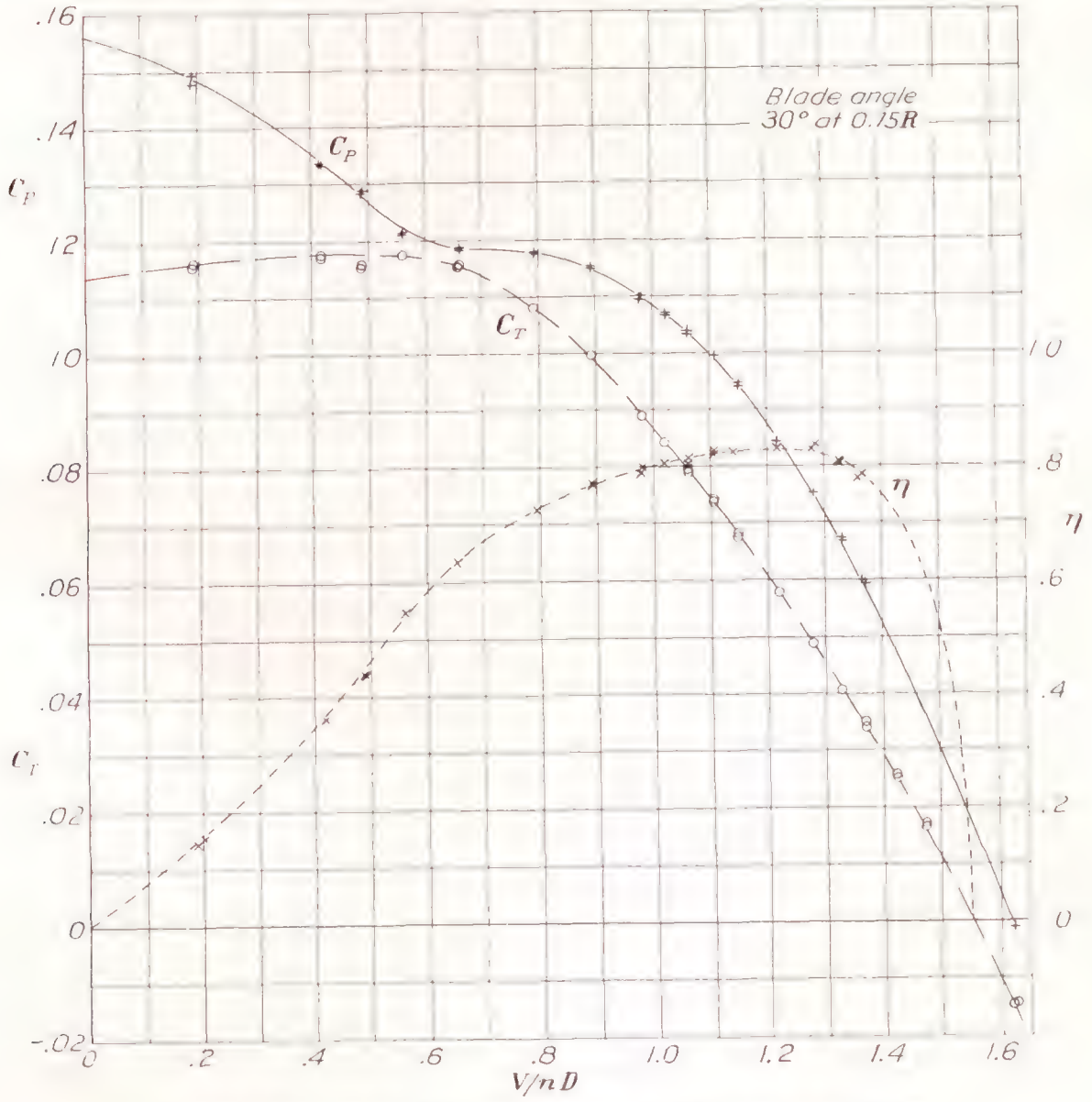

FIGURE 15.—Curves of C_T, C_P, and η against V/nD for nose 4, propeller E.

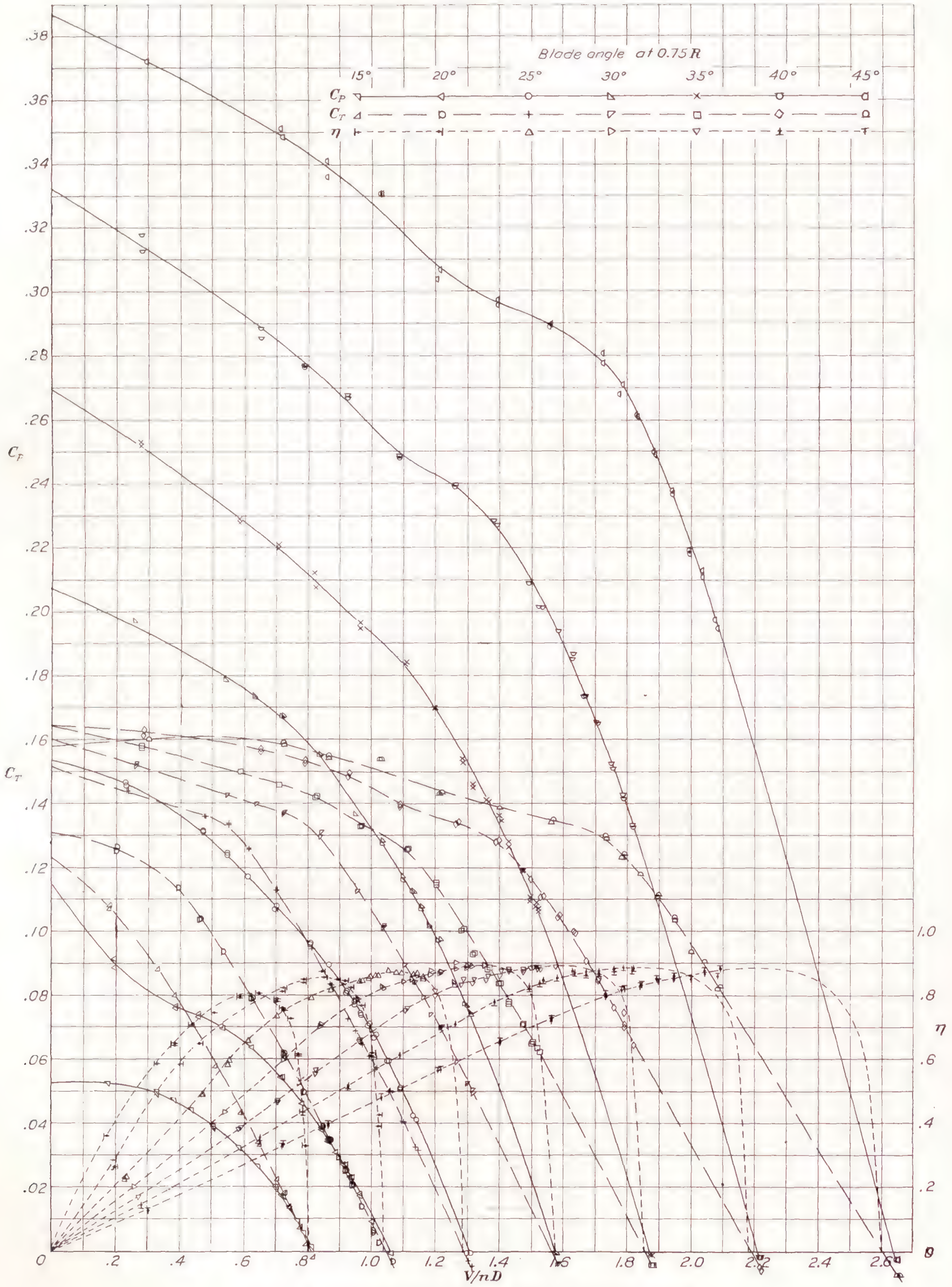

FIGURE 16.—Curves of C_T, C_P, and η against V/nD for nose 6, propeller B.

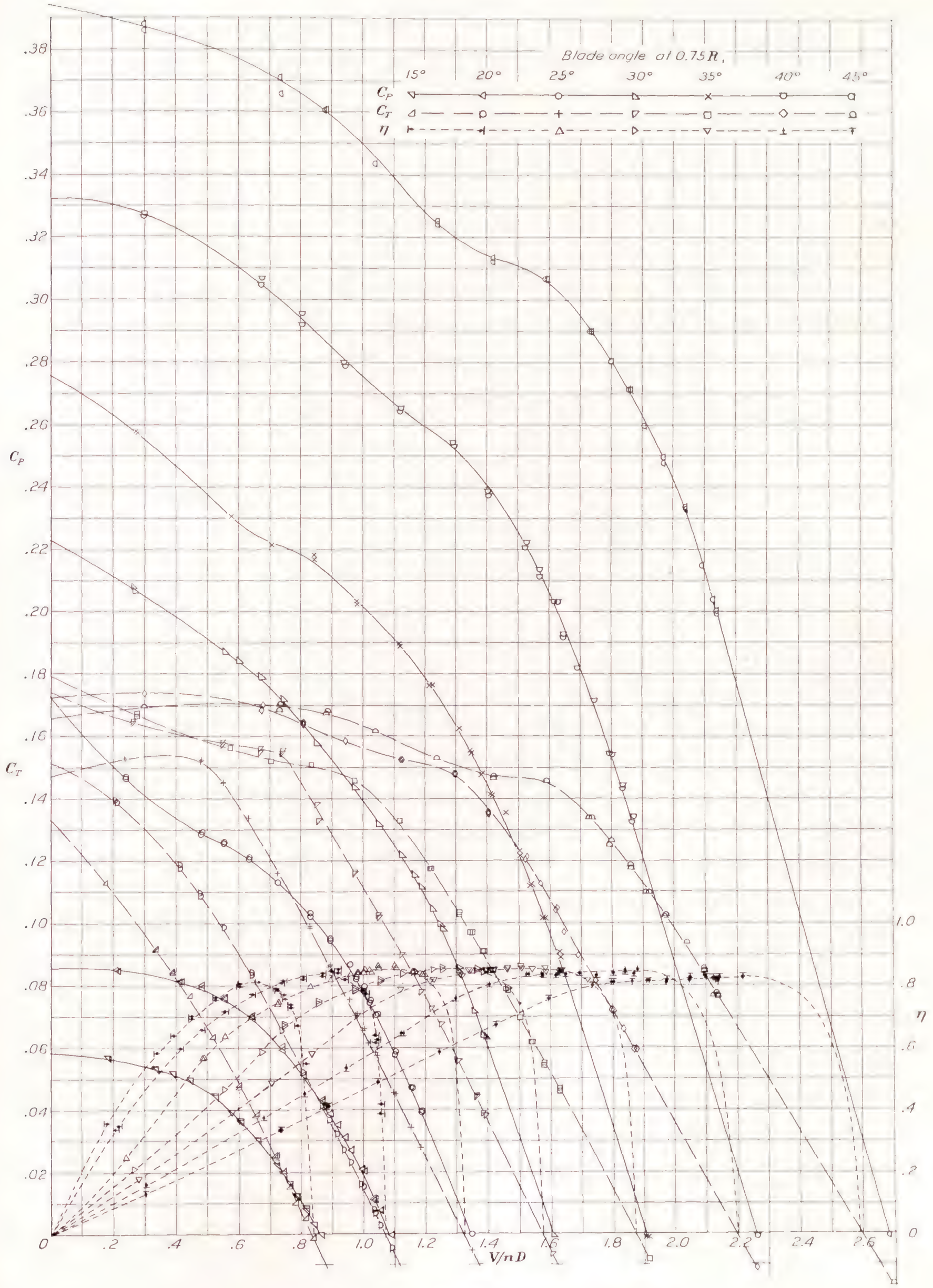

FIGURE 17.—Curves of C_T, C_P, and η against V/nD for nose 6, propeller C.

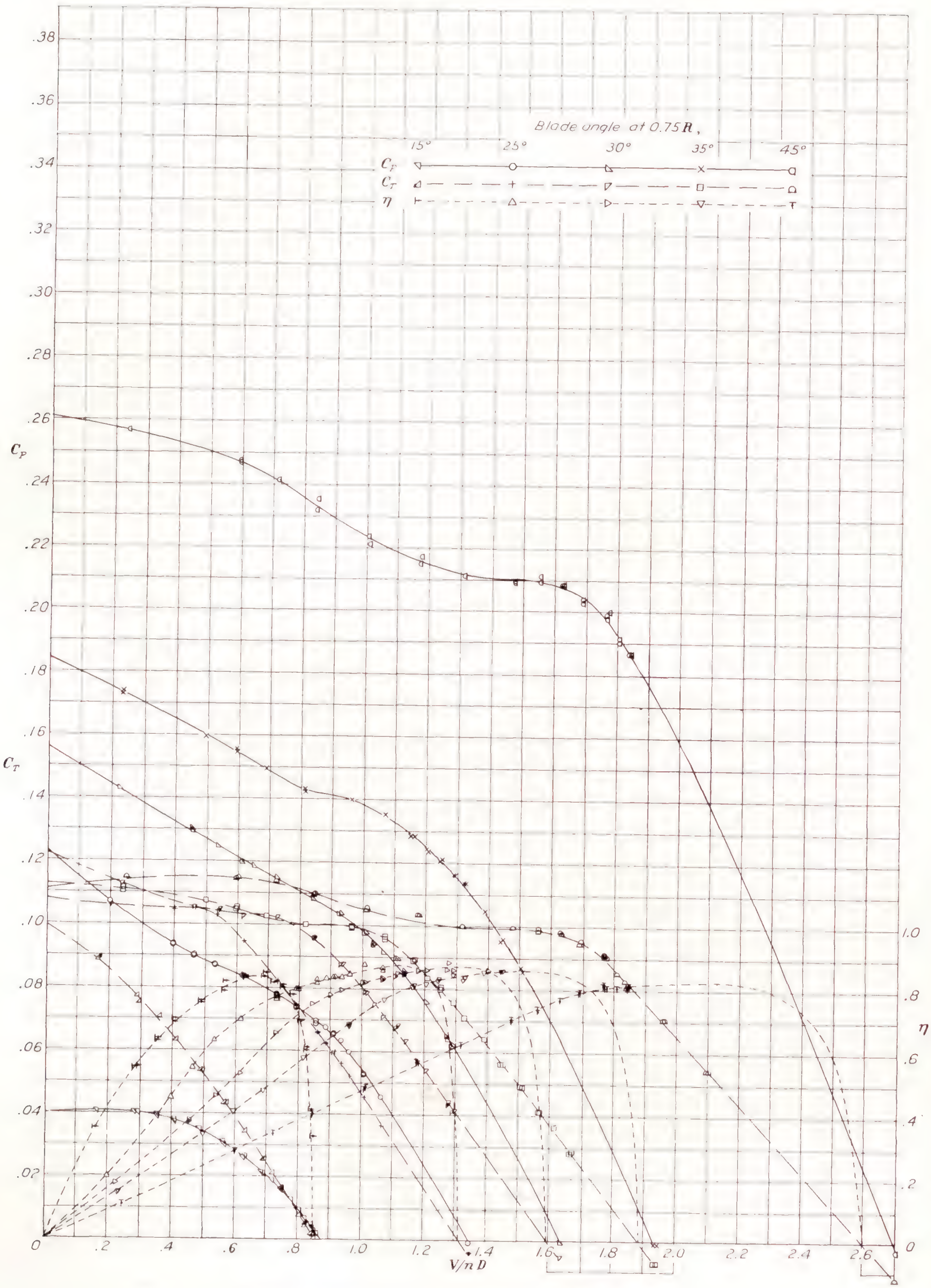

FIGURE 18.—Curves of C_T, C_P, and η against V/nD for nose 6, propeller D.

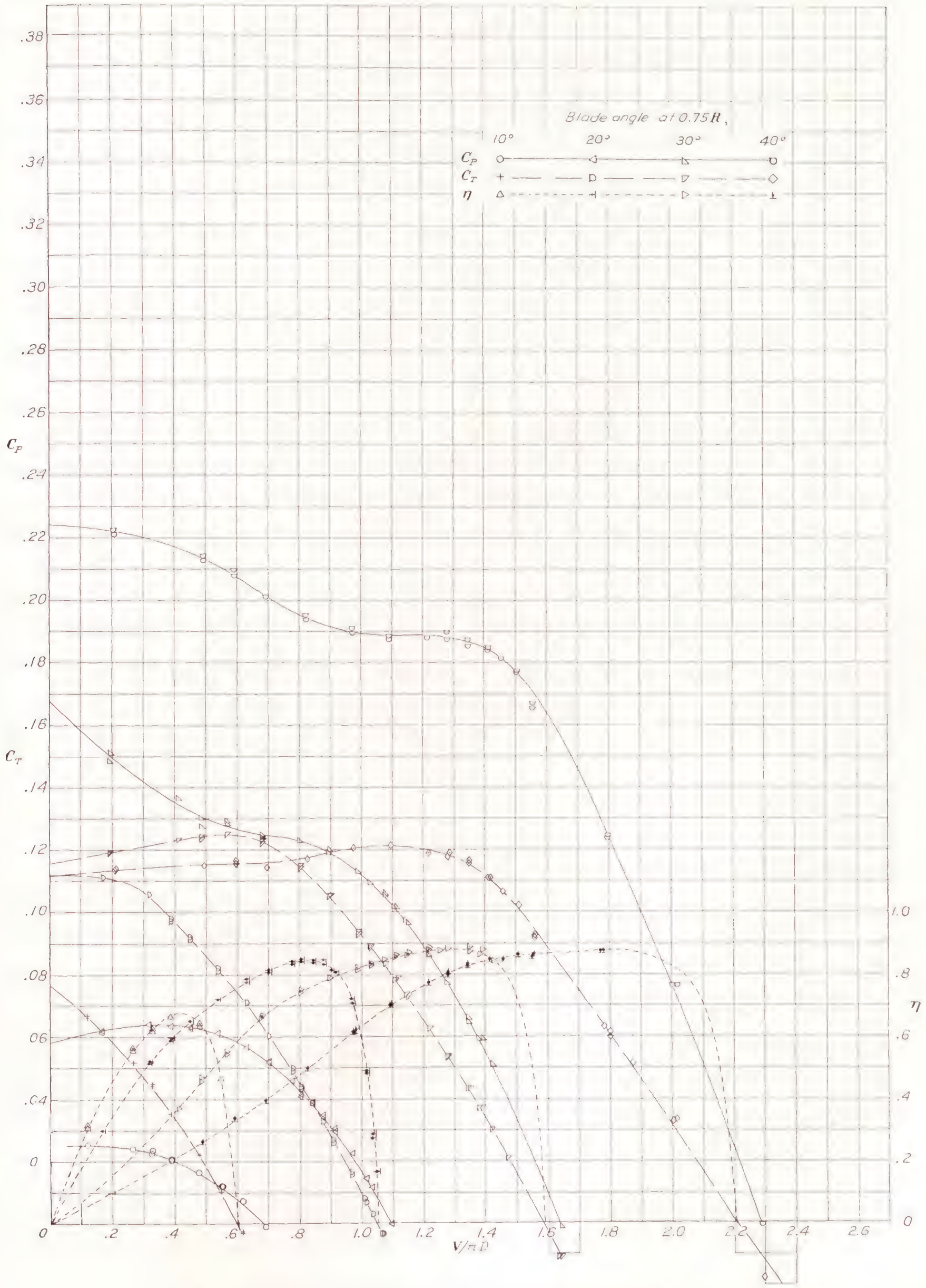

FIGURE 19.—Curves of C_T, C_P, and η against V/nD for nose 6, propeller E

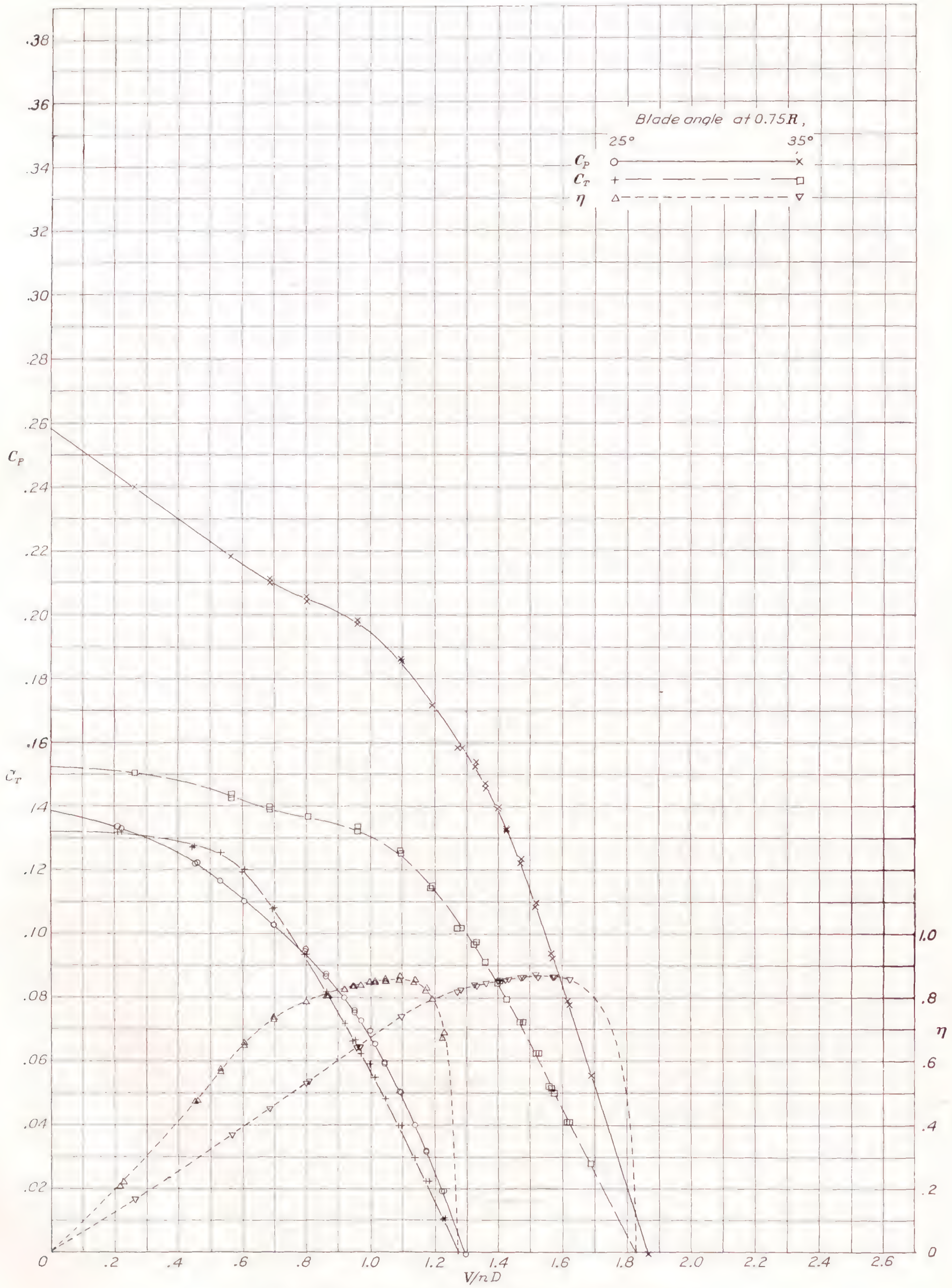

FIGURE 20.—Curves of C_T, C_P, and η against V/nD for nose 7, propeller B

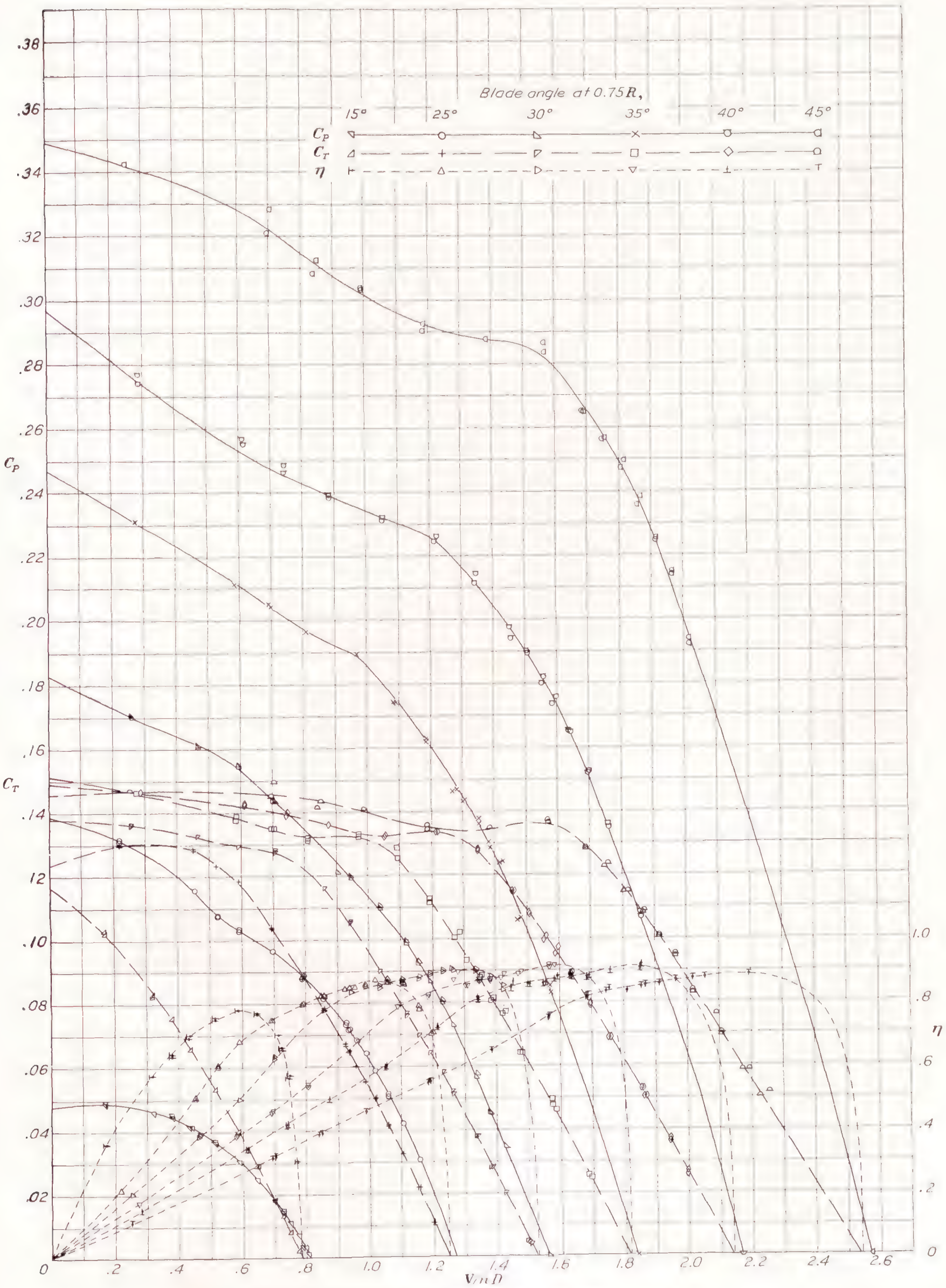

FIGURE 21.—Curves of C_T, C_P, and η against V/nD for nose 7, propeller B_4.

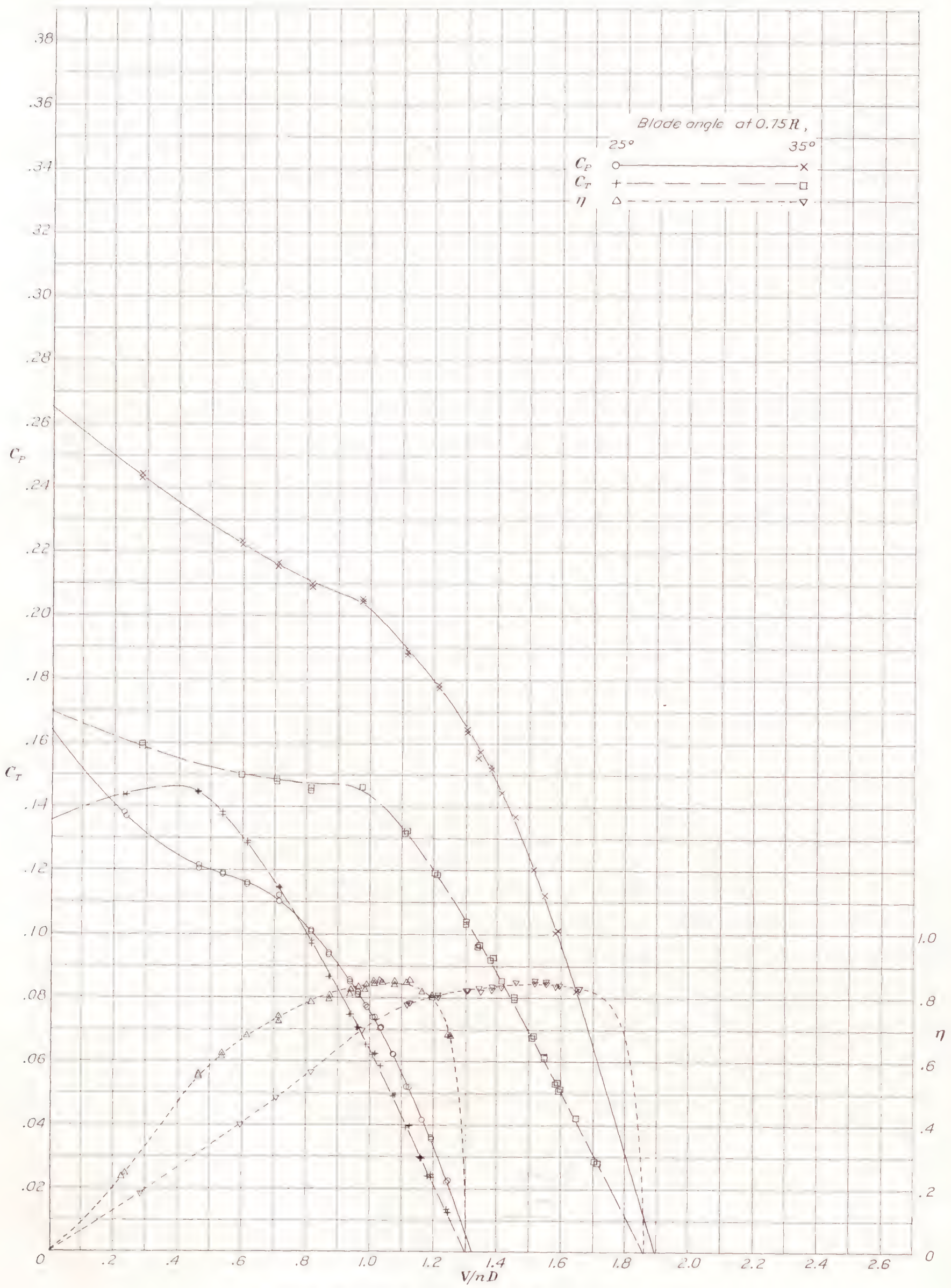

FIGURE 22.—Curves of C_T, C_P, and η against V/nD for nose 7, propeller C.

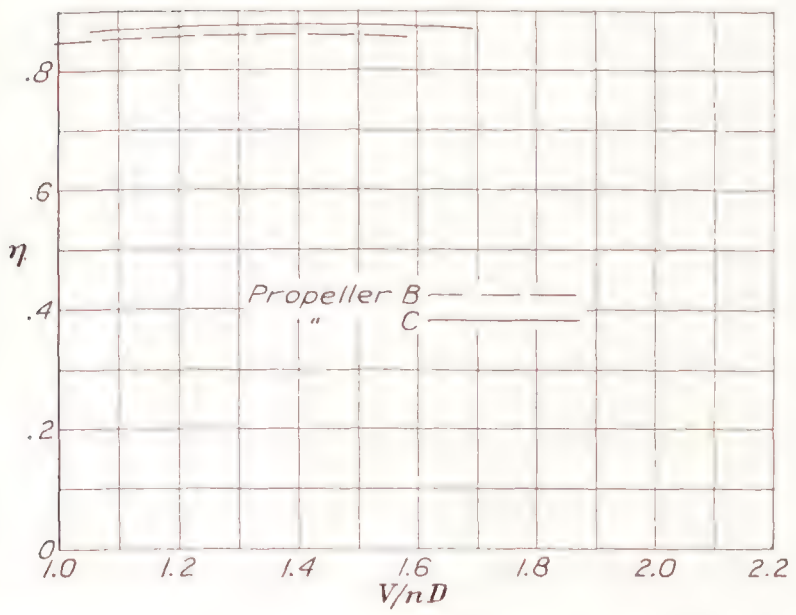

FIGURE 23.—Propulsive-efficiency envelopes against V/nD for propellers B and C on nose 2.

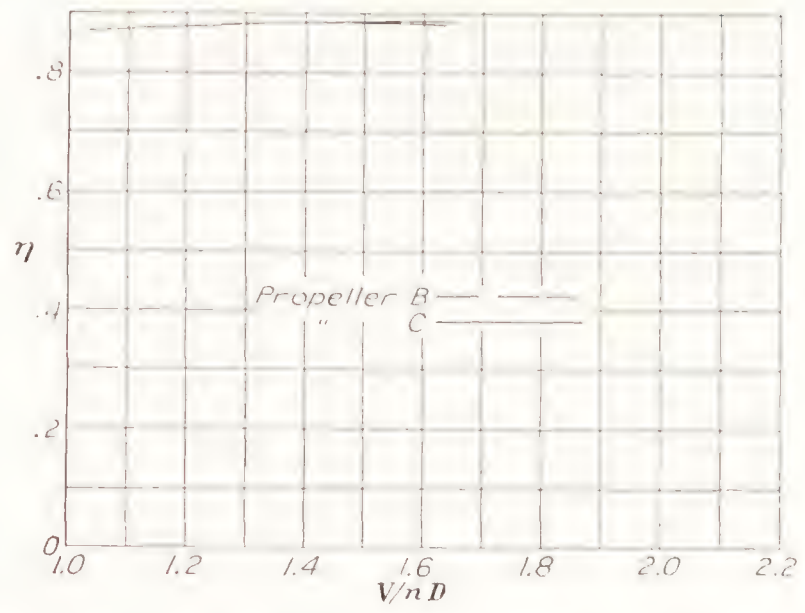

FIGURE 24.—Propulsive-efficiency envelopes against V/nD for propellers B and C on nose 3.

DISCUSSION OF RESULTS

It should be noticed that the propulsive efficiency in figure 5 is greater than 100 percent. The high value of this efficiency is caused by a certain peculiarity in the characteristics of nose 1, which has been pointed out in an earlier report (reference 1). It was shown in reference 1 that the drag of this particular nose decreased substantially with an increase in slipstream velocity owing to the fact that the local angle of attack at the leading edge of the cowling was sufficiently decreased to prevent a marked breakdown that occurred with the propeller off. This effect, which is quite contrary to the expectations of the theory, renders the practical use of the propulsive efficiency rather questionable. In other words, whenever some critical flow conditions exist that may be favorably affected by the propeller slipstream, it is perfectly possible to obtain efficiencies close to or in excess of unity. High efficiencies reported from time to time may easily be explained on this basis. There are, therefore, only two alternatives. One is to adopt a standardized cowling-nacelle shape. Nose 7, described in reference 1, is particularly recommended for this purpose as being unusually neutral to the local flow condition at the nose. The other alternative is to avoid the use of the propulsive efficiency altogether by adopting some other figure of merit relating to the entire cowling-nacelle-

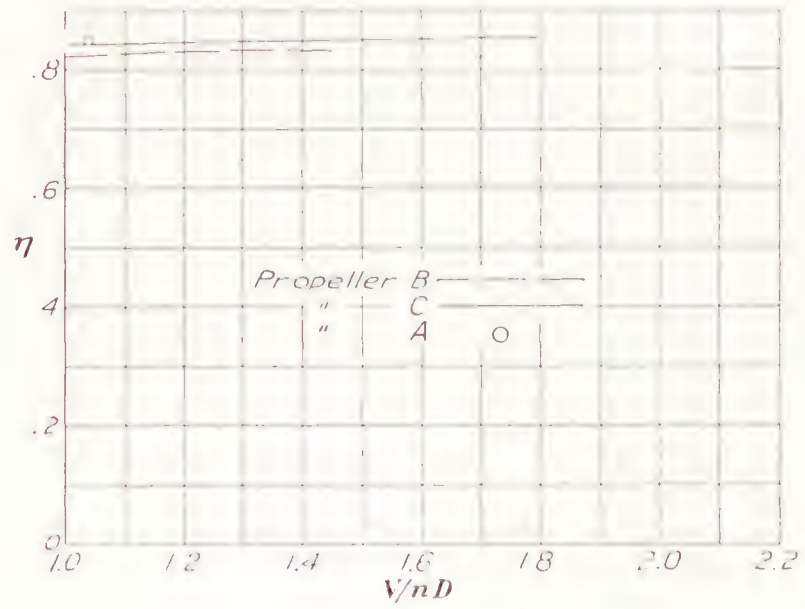

FIGURE 25.—Propulsive-efficiency envelopes against V/nD for propellers A, B, and C on nose 4.

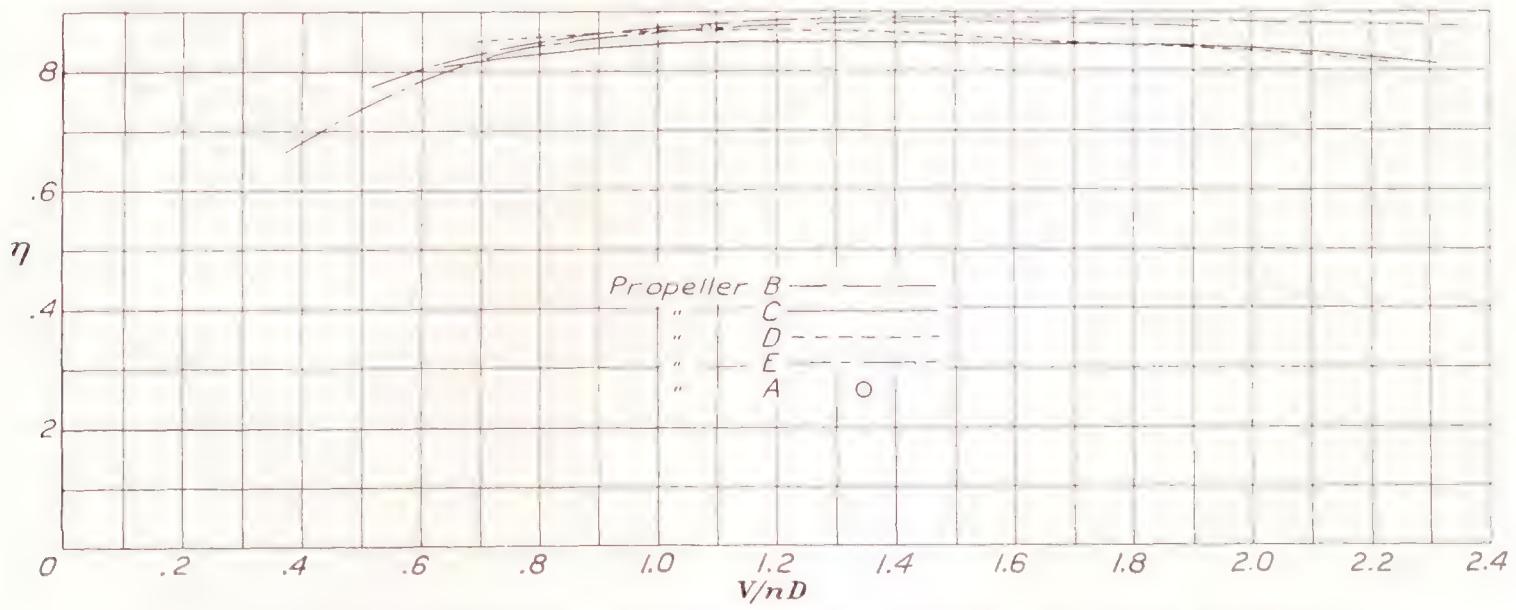

FIGURE 26.—Propulsive-efficiency envelopes against V/nD for propellers A, B, C, D, E on nose 6.

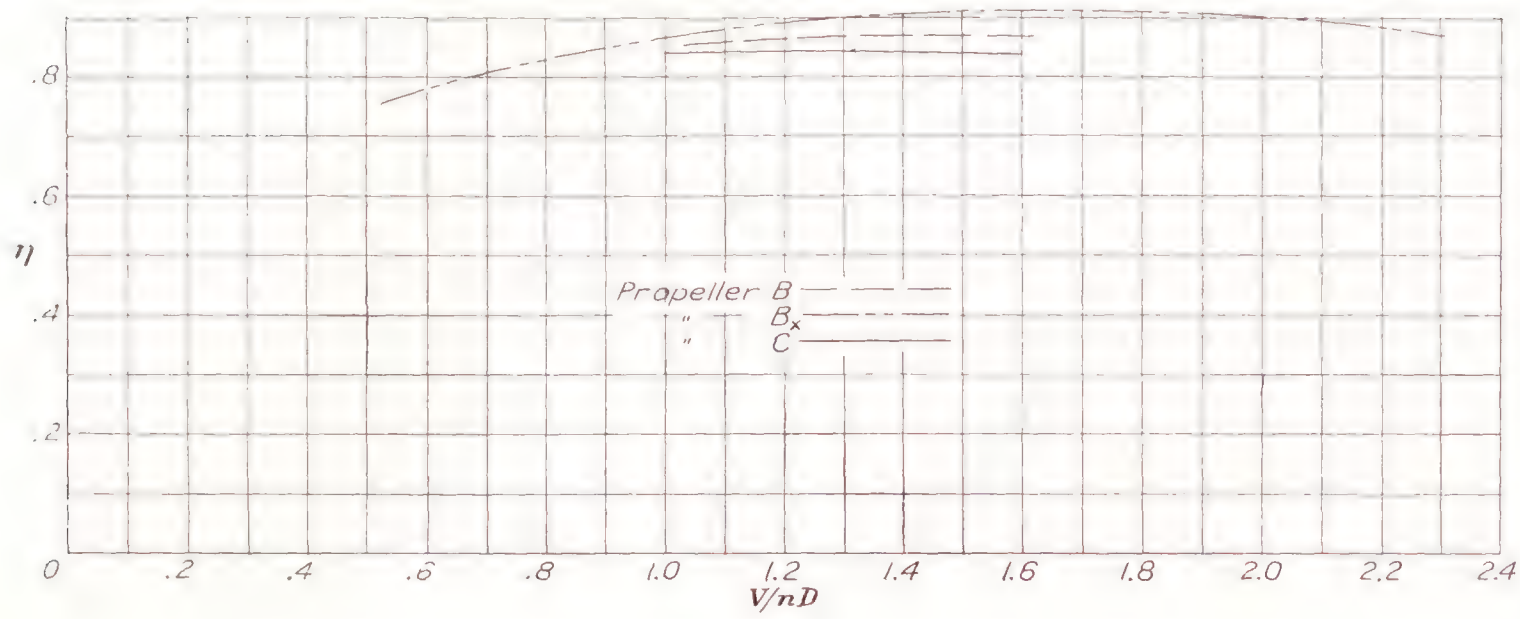

FIGURE 27.—Propulsive-efficiency envelopes against V/nD for propellers B, B_x, and C on nose 7.

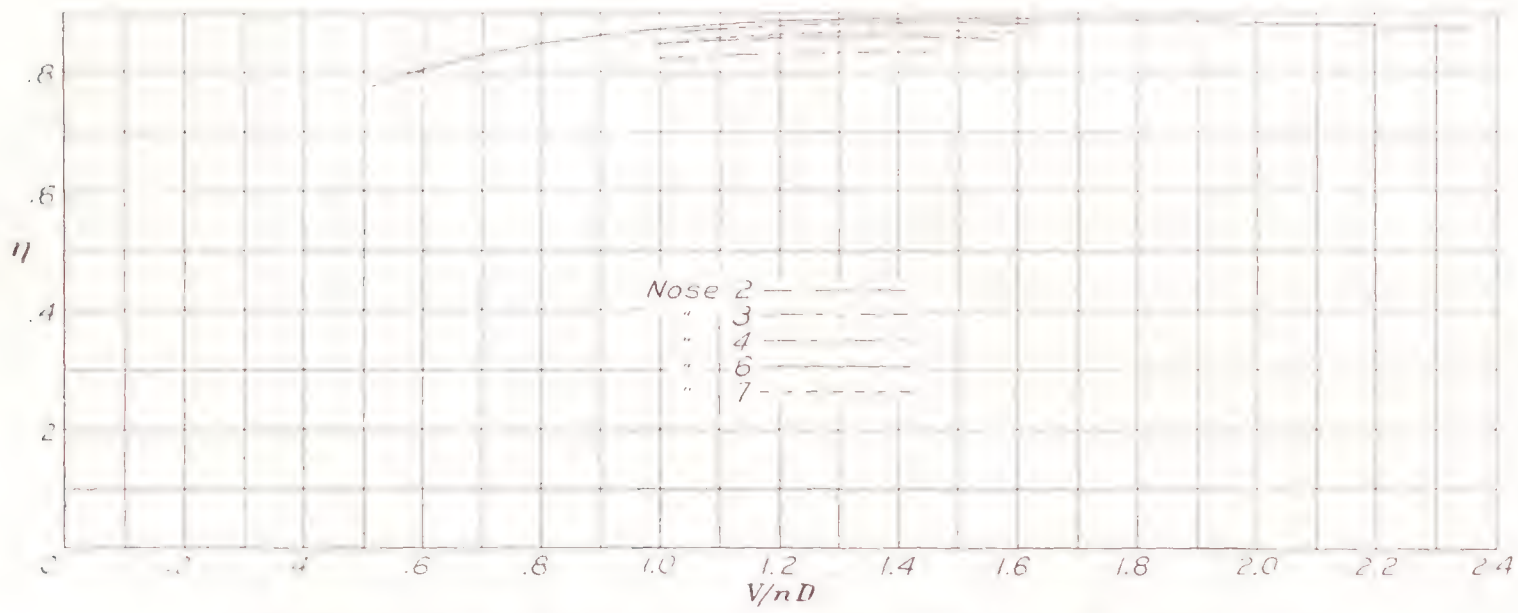

FIGURE 28.—Propulsive-efficiency envelopes against V/nD for noses 2, 3, 4, 6, and 7 with propeller B.

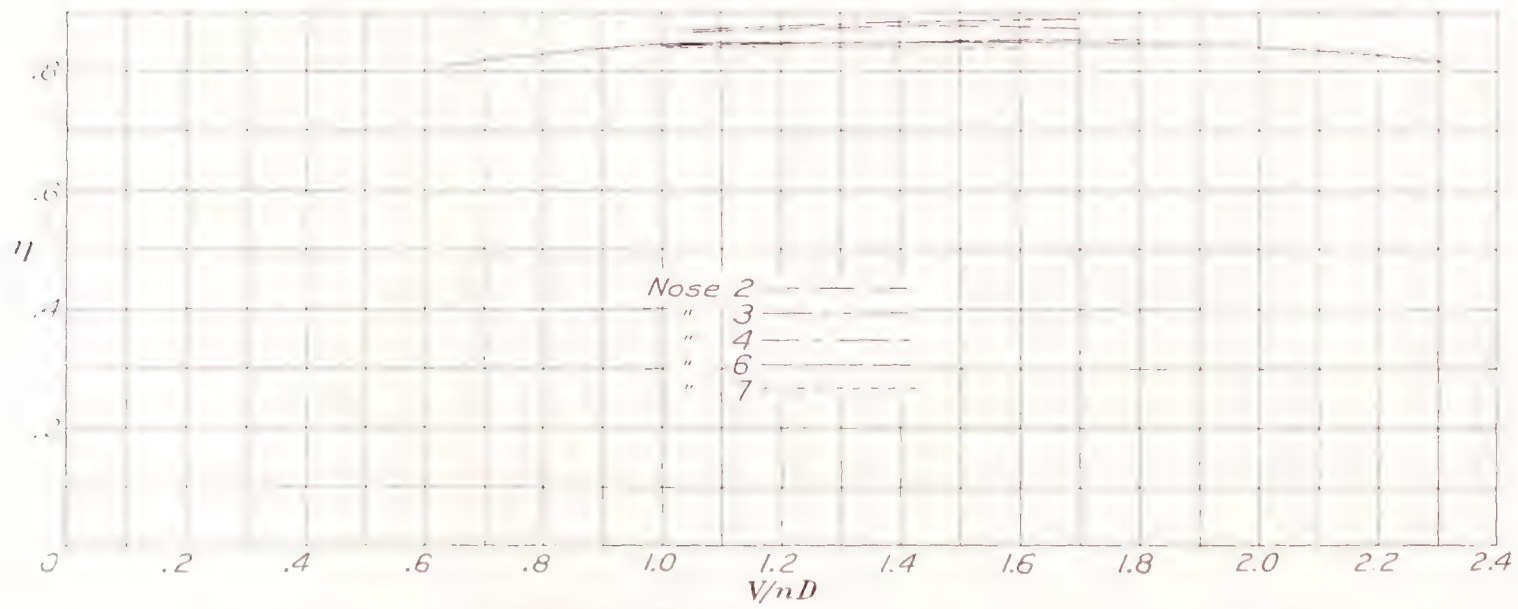

FIGURE 29.—Propulsive-efficiency envelopes against V/nD for noses 2, 3, 4, 6, and 7 with propeller C.

propeller unit. The quantity defined as net efficiency has been used for this purpose. In the present report both these characteristics have been given.

The propulsive efficiencies given in figures 26 and 27 for the most neutral cowlings 6 and 7 show that propeller B_x is definitely superior to the others, exceeding the least efficient propeller by 4 to 6 percent. Figure 28 shows the results for propeller B in conjunction with five different cowlings. It will be seen that cowling 6 is superior, exceeding cowling 3 by 1 percent and cowling 7 by about 2 percent. Figure 29 gives the results of tests of propeller C with the five different noses. In this case noses 3 and 2 exceed the others in efficiency by about 5 percent. The highest of all efficiencies obtained is 91 percent for propeller B_x with nose 7.[3]

[3] If a propeller is operating at tip speeds near the velocity of sound, these efficiencies will, of course, be somewhat reduced by compressibility losses. The compressibility losses may be minimized by using thin propeller tip sections at or near the ideal angle of attack. (See reference 4.) Earlier experiments at the Laboratory (reference 5) have shown that sound velocity may be approached within 10 percent with no loss in efficiency.

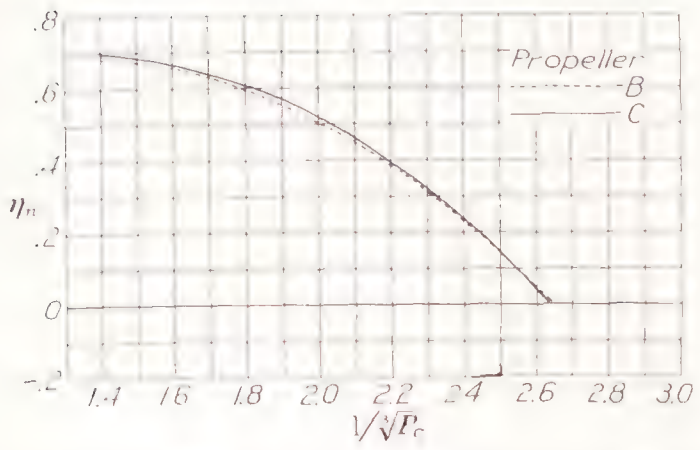

FIGURE 30.—Net-efficiency envelopes against $1/\sqrt[3]{P_c}$ for propellers B and C on nose 1.

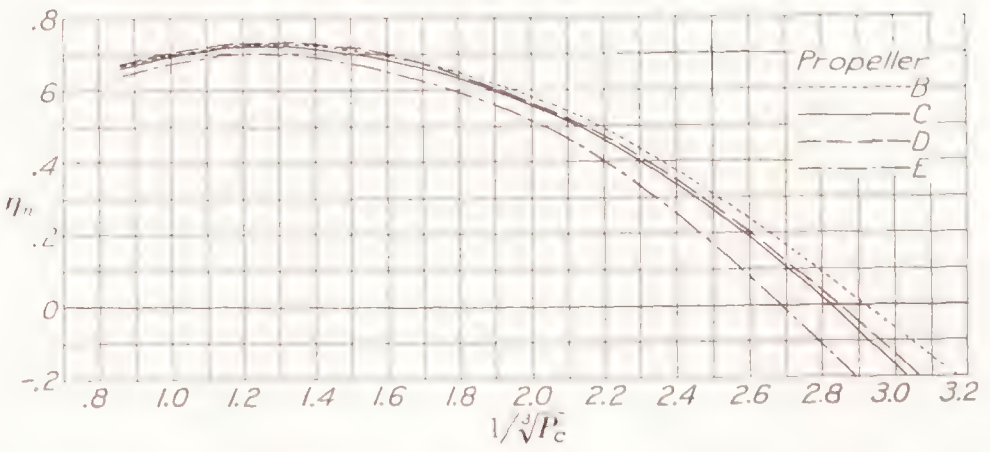

FIGURE 34.—Net-efficiency envelopes against $1/\sqrt[3]{P_c}$ for propellers B, C, D, and E on nose 6.

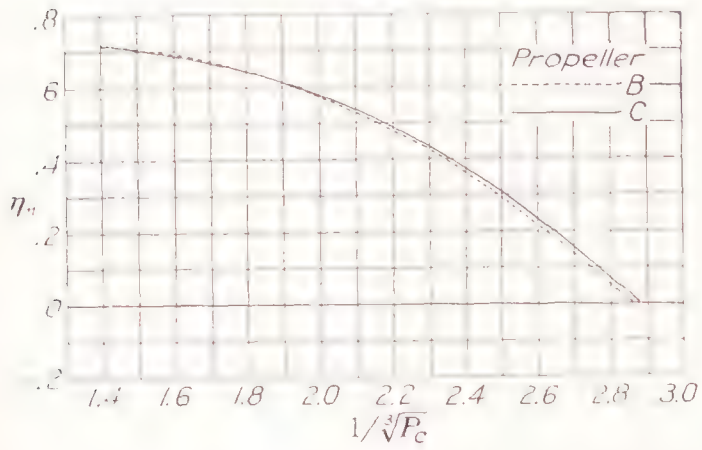

FIGURE 31.—Net-efficiency envelopes against $1/\sqrt[3]{P_c}$ for propellers B and C on nose 2.

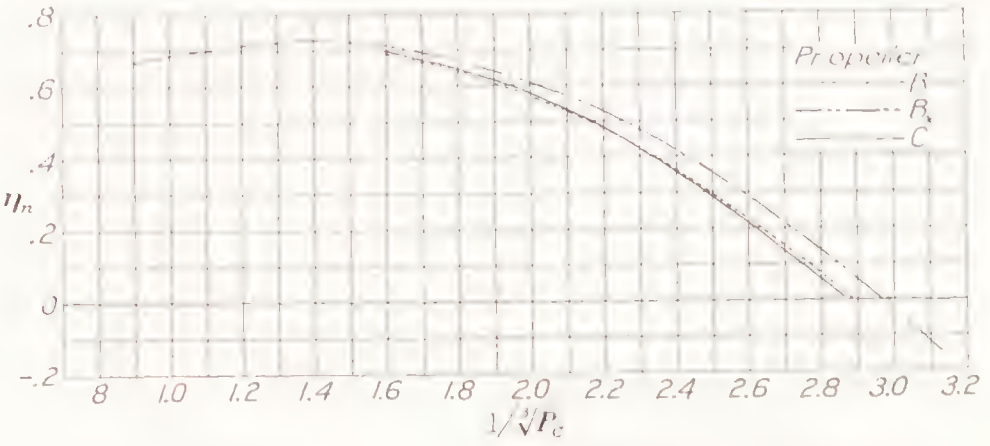

FIGURE 35.—Net-efficiency envelopes against $1/\sqrt[3]{P_c}$ for propellers B, B_2, and C on nose 7.

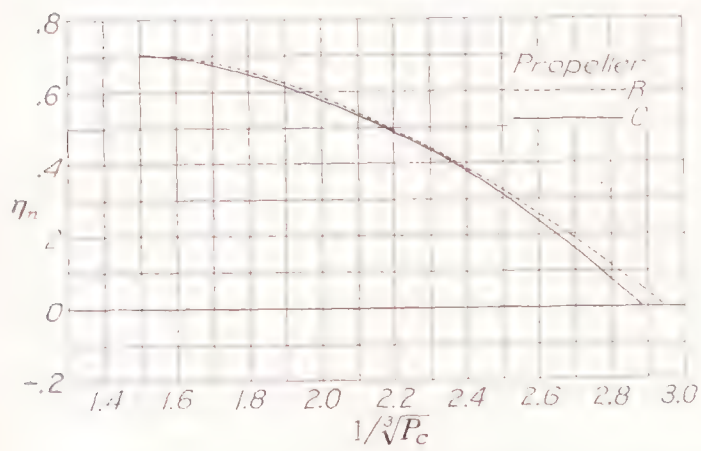

FIGURE 32.—Net-efficiency envelopes against $1/\sqrt[3]{P_c}$ for propellers B and C on nose 3.

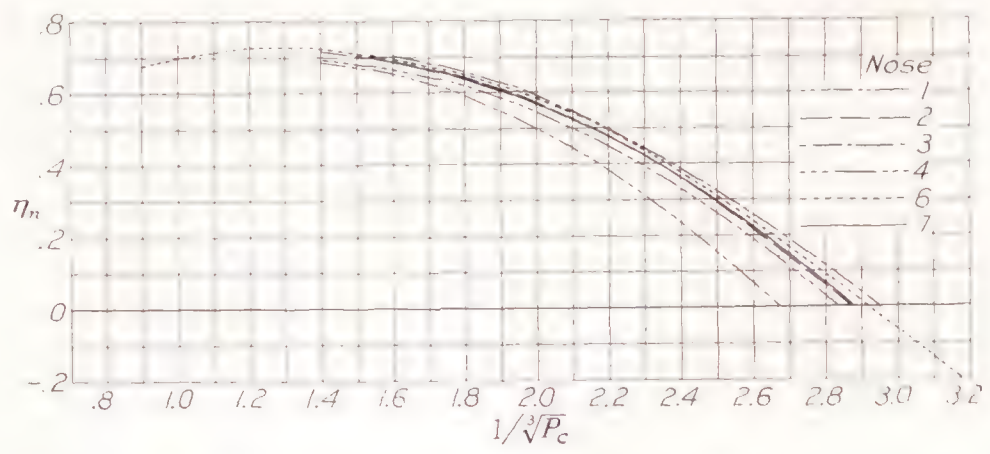

FIGURE 36.—Net-efficiency envelopes against $1/\sqrt[3]{P_c}$ for noses 1, 2, 3, 4, 6, and 7 with propeller B.

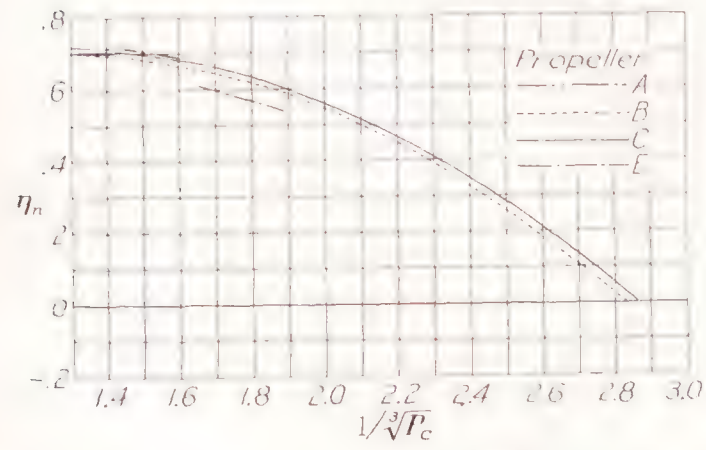

FIGURE 33.—Net-efficiency envelopes against $1/\sqrt[3]{P_c}$ for propellers A, B, C, and E on nose 4.

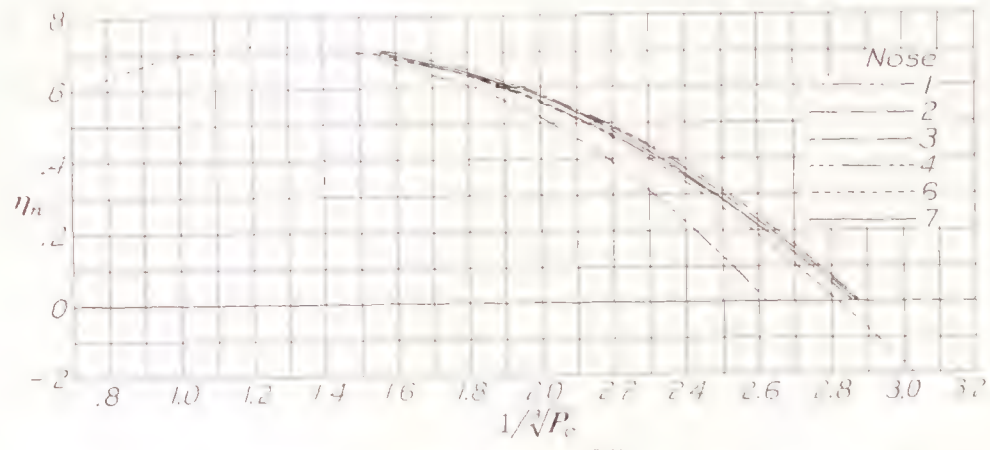

FIGURE 37.—Net-efficiency envelopes against $1/\sqrt[3]{P_c}$ for noses 1, 2, 3, 4, 6, and 7 with propeller C.

Similarly, comparing net efficiencies for the most complete cases, cowlings 6 and 7, as given in figures 34 and 35, respectively, it is again seen that propeller B_x is superior over most of the range. Notice also the marked improvement in the net efficiency of propeller B_x as compared with that of its original form, B. Figure 36 for propeller B shows the superiority of noses 3 and 6 with 7 next. Since nose 3 gives poor cooling at low air speed, it should not be considered on an equal basis. Similar results for propeller C are shown in figure 37. This propeller is again less efficient than propeller B. Notice in both figures the very inferior efficiency of nose 1. Figure 38 has been included to show the cost of the cooling air as obtained by the standard skirt 2.

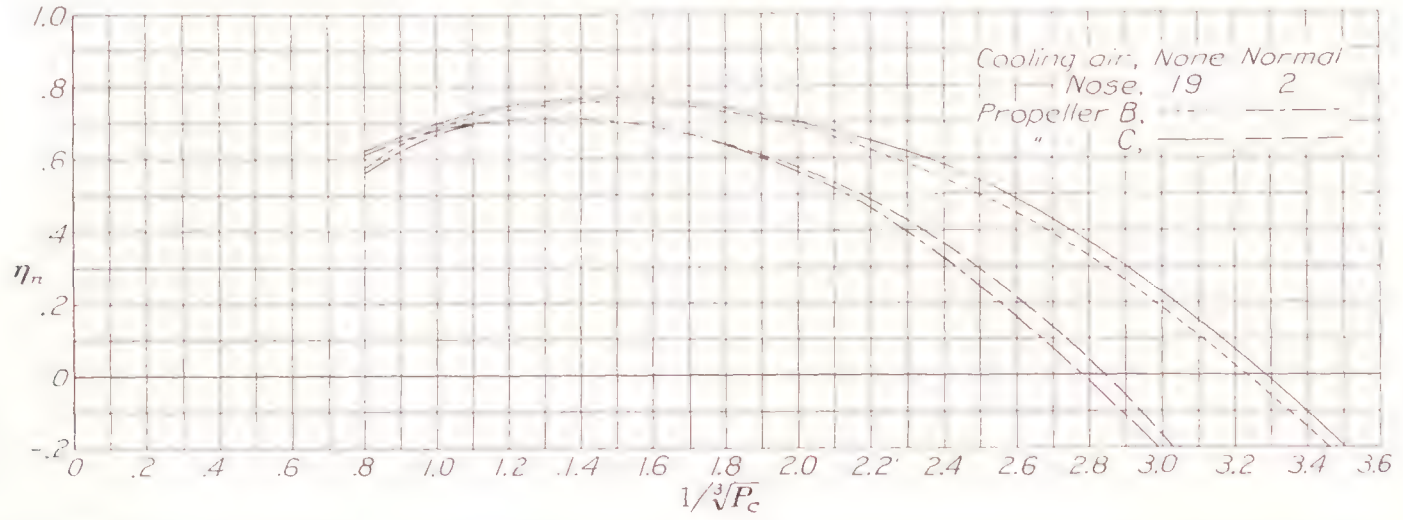

FIGURE 38.—Curves of net efficiency against $1/\sqrt[3]{P_c}$ for propellers B and C set 25° at 0.75R; on nose 19, skirt 5, without cooling air; and on nose 2, skirt 2, with normal cooling air.

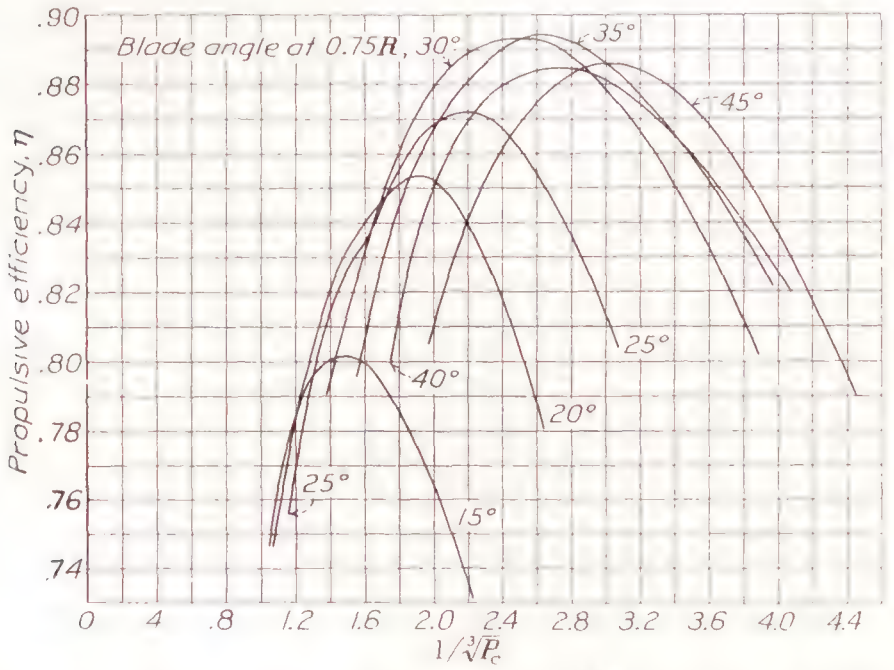

FIGURE 39.—Curves of propulsive efficiency against $1/\sqrt[3]{P_c}$ for propeller B on nose 6.

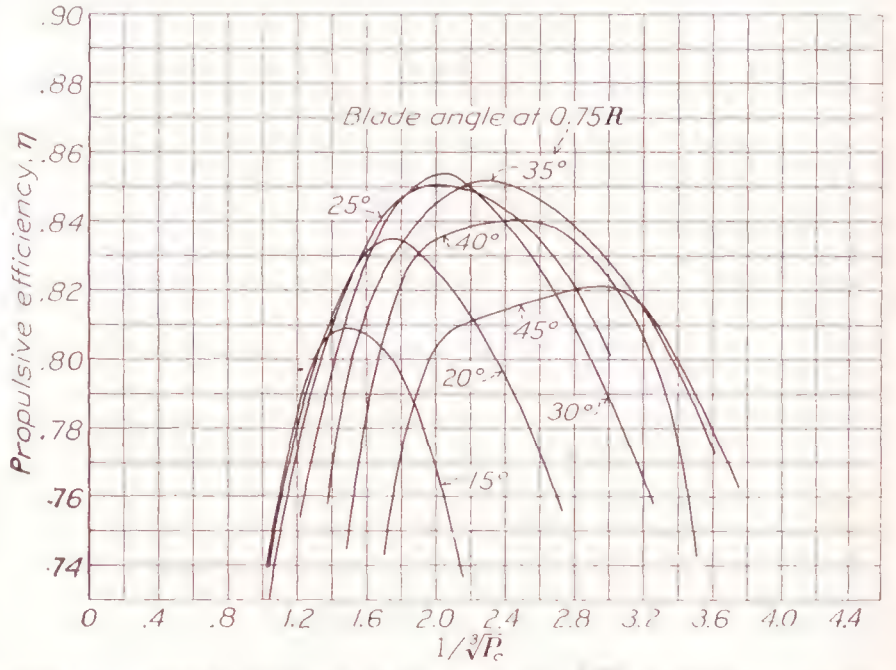

FIGURE 41.—Curves of propulsive efficiency against $1/\sqrt[3]{P_c}$ for propeller C on nose 6

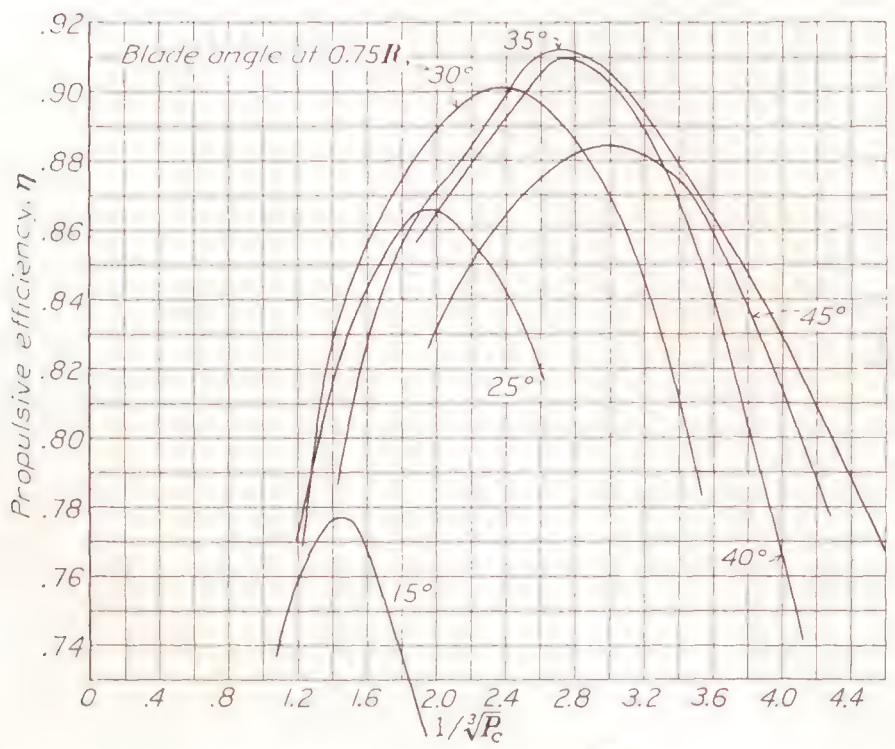

FIGURE 40.—Curves of propulsive efficiency against $1/\sqrt[3]{P_c}$ for propeller B_x on nose 7.

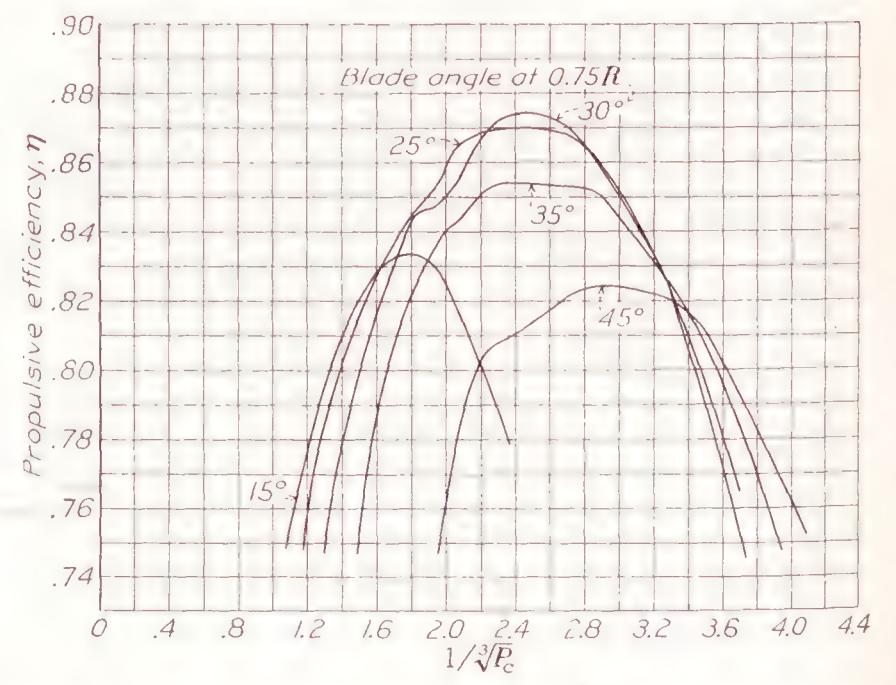

FIGURE 42.—Curves of propulsive efficiency against $1/\sqrt[3]{P_c}$ for propeller D on nose 6.

In figures 39 to 42 the propulsive efficiency η has been plotted against $1/\sqrt[3]{P_c}$ for propellers B, B_x, C, and D. The envelopes for each of the five propellers are shown in figure 43. If the definition of P_c is recalled, it may be noted that with a fixed horsepower and a fixed propeller diameter the abscissa may be considered to represent the air speed. With a 550-horsepower engine and a 10-foot propeller, the abscissa happens to give the air speed in units of almost exactly 100 miles per hour. The propulsive efficiencies are compared at, say, 250 miles per hour. They are: Propeller B_x, 90.9 percent; B, 89.4 percent; the two-blade propeller D, 87.4 percent; and propeller C, 84.9 percent, or a range of 6 percent. At lower speeds the differences are still of concern although less marked. It is of interest to note that the peak efficiencies of all propellers tested is found at a blade angle of approximately 35°.

The chart (fig. 43) is of value in demonstrating the fact that the present commonly used power plant of 550 horsepower in combination with a 10-foot propeller could be used to best advantage in the speed range 220 to 300 miles per hour. A 1,000-horsepower engine used on the same size propeller could be used to greatest advantage at about 25 percent higher speeds or in the range of 270 to 370 miles per hour. In order to make full use of a 1,000-horsepower engine at a speed

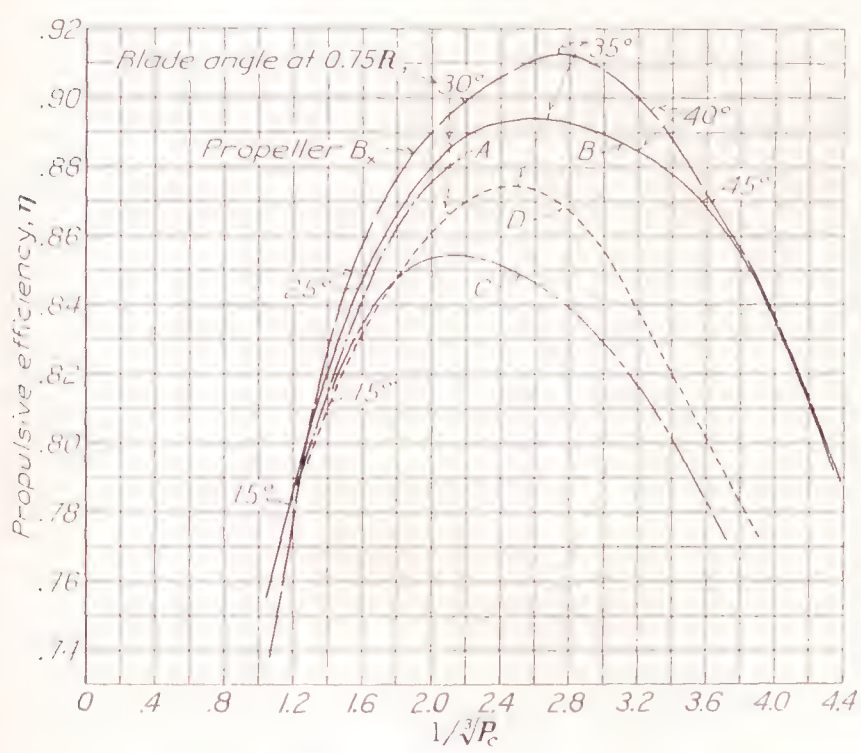

FIGURE 43.—Propulsive-efficiency envelopes against $1/\sqrt[3]{P_c}$ for propellers A, B, B_x, C, and D.

of 200 miles per hour, an impracticably large propeller diameter is required.

It also is of interest to note that the two-blade propeller D, employing the same blades as the three-blade propeller C, reaches a considerably greater peak efficiency. If 550 horsepower are used with both propellers, it is seen that the propulsive efficiencies at the speed of 250 miles per hour are, respectively, 87.4 and 84.9. This is a consequence of the fact that the commonly used propeller sections are altogether too wide. It was found that at the condition of peak efficiency of the propeller, the actual or effective angle of attack amounts to only about 4° to 5°. It can be shown that a narrower blade with a correspondingly higher effective angle would be aerodynamically more efficient Vibration and flutter and other considerations, however, prevent the practical use of such a blade.

Propellers B, C, and D all are designed with a constant blade angle for a setting of 12° at $0.75R$. Propeller B_x has a constant blade angle from $0.60R$ outward for a setting of 30° at $0.75R$. (See fig. 3(a).)

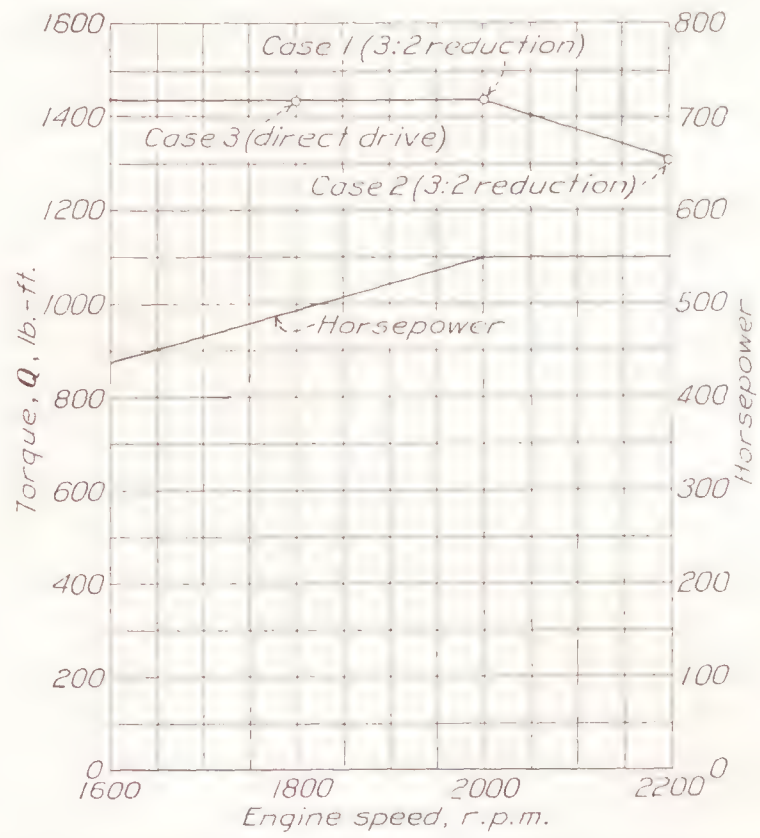

FIGURE 44.—Power and torque characteristics of an actual engine used as an example.

In fact, propeller B_x is identical to propeller B except for this change in blade-angle distribution. The gain of almost 2 percent in efficiency observed in figure 43 demonstrates the importance of employing a design blade angle adjusted to the proper flight condition. Notice also that this gain is not obtained at the expense of decreased efficiency in the lower speed range. Propeller B_x happens to be superior to all the propellers tested over the entire practical flight range.

The results of the tests of propellers B and C in conjunction with six different cowlings (figs. 36 and 37) illustrate the importance of the effect of the cowling. Considering the somewhat fictitious case of the top speed attainable with the present nacelle alone, it is observed in figure 36 that the comparative top speeds range from 267 miles per hour for nose 1 to 295 miles per hour for nose 3. For propeller C (fig. 37) the comparative range is 262 miles to 288 miles. Although the differences between the cowlings of reasonable design are fairly small, the inferiority of a design resembling nose 1 should be kept in mind, this nose being the cause of a speed reduction of almost 10 percent.

TAKE-OFF CHARACTERISTICS

The propeller characteristics at low air speeds may be obtained from the basic test results given in figures 5 to 22. In order to make full use of this information

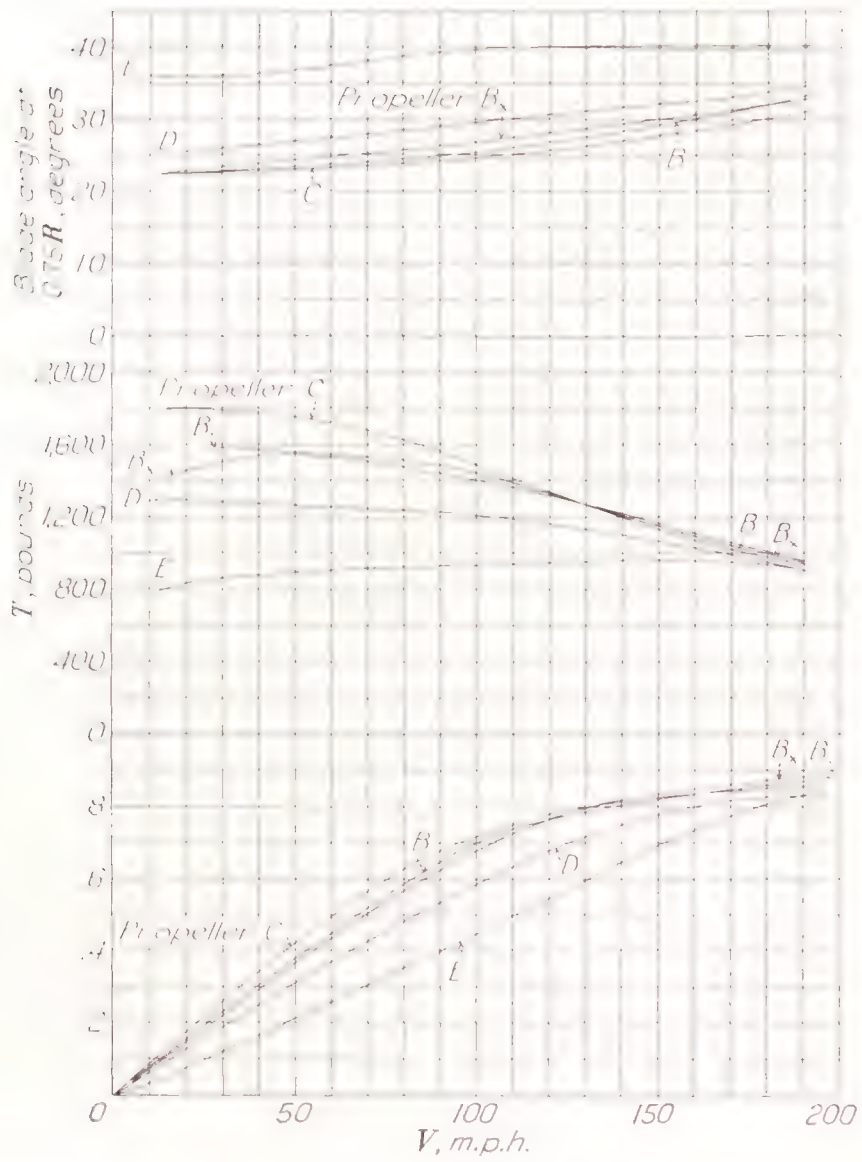

FIGURE 45.—Optimum blade angle and thrust in the take-off range, engine speed 2,000 revolutions per minute, with a 3:2 gear reduction ratio.

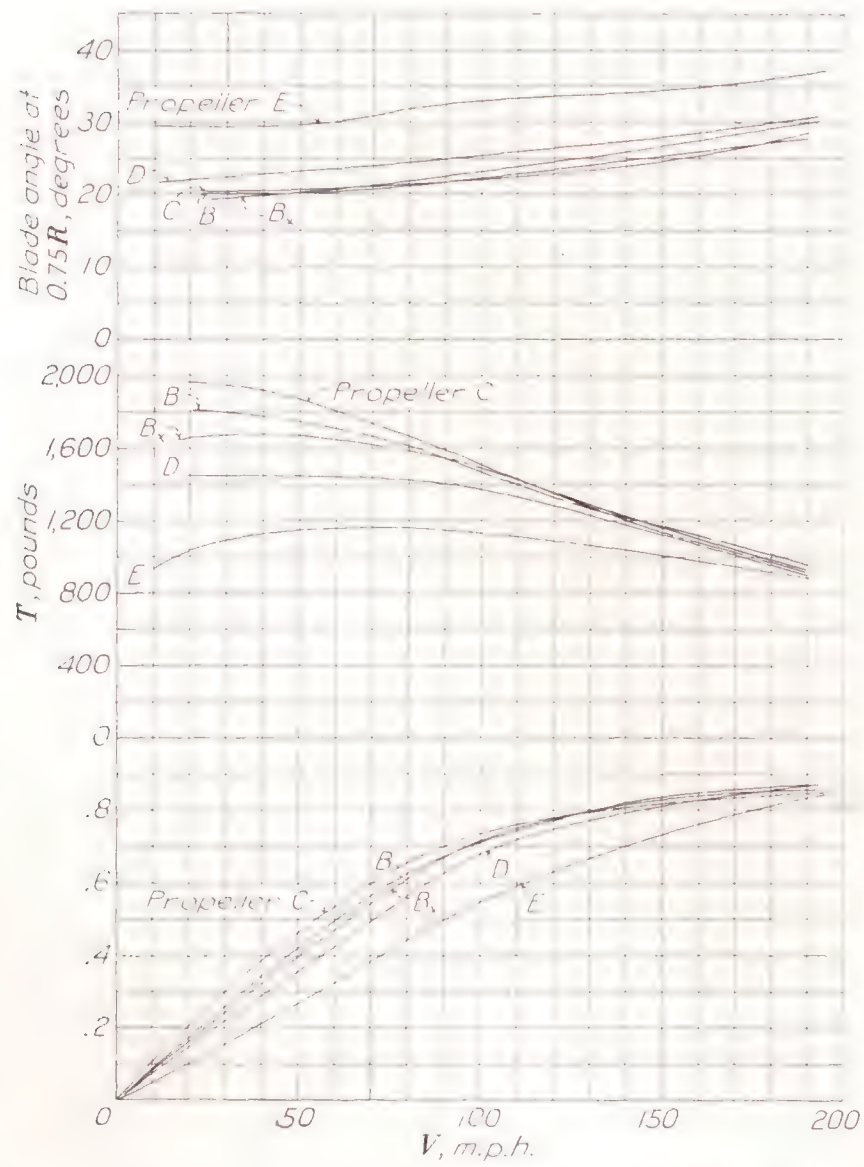

FIGURE 46.—Optimum blade angle and thrust in the take-off range, engine speed 2,200 revolutions per minute with a 3:2 gear reduction ratio.

in calculating the take-off distance for a given set of conditions, however, it is necessary to present the data in a more direct manner. The optimum blade-angle setting corresponding to the maximum available thrust at any particular air speed is of particular interest.

The actual differences in the take-off characteristics will be directly demonstrated by the use of a particular example using engine characteristics as given in figure 44 corresponding to those actually obtained on a 550-horsepower engine. The engine speeds chosen are: 2,000 revolutions per minute and 2,200 revolutions per minute, both with a 3:2 gear reduction ratio; and 1,800 revolutions per minute with direct drive.

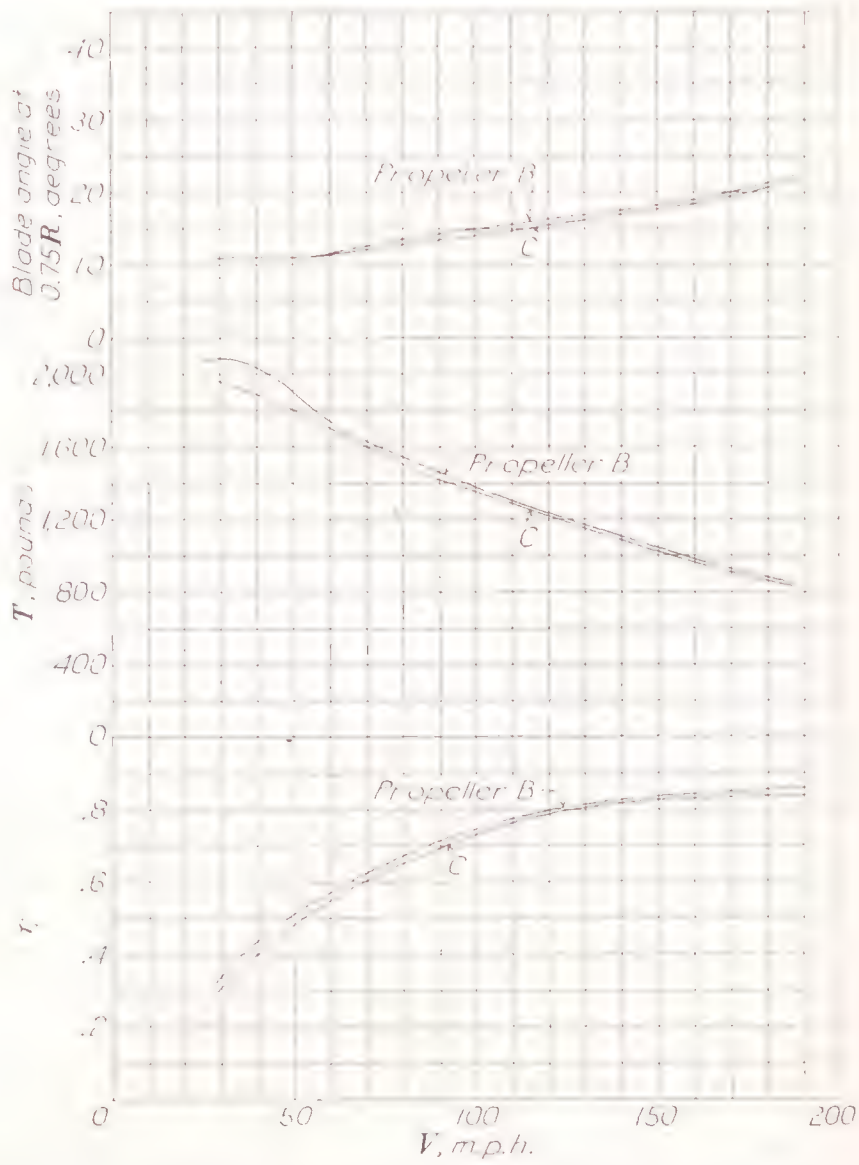

FIGURE 47.—Optimum blade angle and thrust in the take-off range, engine speed 1,800 revolutions per minute with direct drive.

The resulting blade-angle settings and thrusts in the take-off range obtained from charts in the appendix are presented in figures 45, 46, and 47. It is noticed in working through one of these examples that no particular optimum setting is reached; the maximum permissible engine speed is the limiting condition. Notice that propeller C is very superior to B or B_x in regard to take-off, particularly in the lowest speed range.[4] The thrust of the two-blade propeller D is further seen to amount to a little more than two-thirds of that of the corresponding three-blade propeller C. Propeller B_x is noticed to be slightly inferior to propeller

[4] This comparison is valid when propellers of a constant diameter are being compared, as would be the case when the propeller diameter is the limiting design factor. Given a free choice of diameters, the comparisons must be made with a view to the high-speed performance, necessitating an individual study of each case.

B at speeds less than about 100 miles per hour. Notice the inferior thrust values of the 9-foot propeller E. Absorbing the same horsepower, this propeller is relatively overloaded and should not be directly compared. The beneficial influence of increasing the propeller speed may be observed by comparing the results from the three figures.

The results are, of course, strictly true only for the relative dimensions of the propeller and nacelle used in these particular experiments, a larger propeller thus calling for a larger nacelle, and vice versa. It is, however, known that the propulsive efficiency will be affected very little by this variation in relative dimensions. The results may, therefore, be considered valid also for the case of different relative dimensions of the propeller in regard to the nacelle.

As these propellers are fairly representative of commonly used types, it is possible by some exercise of judgment to obtain a fairly reasonable estimate of the take-off characteristics also of any other propellers.

GENERAL CONCLUSIONS

1. Peak efficiency of the propellers tested occurs at a blade-angle setting of approximately 35°. The difference in peak efficiency varies as much as 6 percent, demonstrating the value of selecting a good design, particularly in the high-speed range.

2. The peak propulsive efficiency of the conventionally dimensional units of 9- to 12-foot propellers on 500- to 1,000-horsepower engines has been found to lie in the range of 200 to 350 miles per hour, showing the beneficial influence of higher air speeds on the propeller.

3. A two-blade propeller of the kind tested was found to be superior in efficiency (in the high-speed range) to a three-blade propeller using identical blades, the peak efficiency exceeding that of the three-blade propeller by about 2 percent.

4. A propeller equipped with a controllable hub shows an almost negligible decrease in efficiency as compared with the identical propeller with a standard hub. The difference is of the order of ½ percent, which is close to the limit of test accuracy.

5. In regard to the take-off characteristics, the maximum permissible revolution speed is in all cases found to be the most favorable. The three-blade propeller is superior to the two-blade propeller using the same horsepower, which is to be expected.

LANGLEY MEMORIAL AERONAUTICAL LABORATORY,
NATIONAL ADVISORY COMMITTEE FOR AERONAUTICS,
LANGLEY FIELD, VA., *June 4, 1936.*

LIST OF SYMBOLS

V, velocity of air stream.

n, revolutions per unit time of the propeller.

D, diameter of propeller.

$\frac{V}{nD}$, advance-diameter ratio of the propeller.

P, power supplied to propeller shaft.

S, disk area of propeller.

q, velocity head of air stream, $\frac{1}{2}\rho V^2$.

$P_c=\frac{P}{qSV}$, unit disk loading or disk-loading coefficient.

ρ, air density.

R, net forward thrust of the entire unit as measured on the thrust scale.

$\eta_n=\frac{RV}{P}$, net efficiency.

$T=R+D$, thrust.

D, drag of the nacelle unit for the corresponding air speed measured with the propeller off.

$C_T=\frac{T}{\rho n^2D^4}$, thrust coefficient.

$\frac{1}{\sqrt[3]{P_c}}=V\sqrt[3]{\frac{\rho S}{2P}}$

$C_P=\frac{P}{\rho n^3D^5}$, power coefficient.

$C_Q=\frac{Q}{\rho n^2D^5}$, torque coefficient.

$\eta=\frac{TV}{P}$, propulsive efficiency.

Q, torque of propeller.

$Q_c=\frac{Q}{\rho V^2D^3}$, torque coefficient.

h, thickness of blade section of propeller.

b, width of blade section of propeller.

r, radius to any blade section of propeller.

R, radius of propeller.

β, propeller blade-angle setting at 0.75 R.

P, geometric pitch of propeller.

$C_s=\sqrt[5]{\frac{\rho V^5}{Pn^2}}$, speed-power coefficient.

η_0, net propeller-nacelle efficiency with no cooling air.

APPENDIX

CHARTS FOR SELECTING PROPELLER DIAMETERS

The characteristics of a propeller are given as a relation of three and only three variables; these variables may be given as C_T, C_P, V/nD. For geometrically similar propellers these quantities remain constant. Any other three independent variables may be selected, and the combination of C_s, V/nD, and η is chosen because of certain advantages. Since only three quantities are involved, it is obviously possible to give a complete representation of the characteristics in a single contour chart. Inserting values of the efficiency η against C_s as ordinates and V/nD as abscissas for various blade-angle settings, connecting points of equal efficiencies and points representing given blade angles, *gives a contour map containing all results.* This type of chart is primarily useful in selecting the diameter of a propeller. It is tacitly assumed that the type of propeller has already been chosen and that charts are available. It is interesting to observe that the contour lines map a smoothly shaped peak; no crowding of the lines occurs. In the selection of a propeller diameter this type of chart makes it possible to judge the effect of changes by observing how the representative point moves with respect to the efficiency peak.

Charts I give the results for the three-blade propeller B, the modified version B_x, C, and the two-blade propeller D. The charts are applicable to controllable propellers allowing for 1/2 percent decrease in efficiency by a slight increase in the diameter.

PROCEDURE FOR THE USE OF CONTOUR CHARTS FOR SELECTING PROPELLER DIAMETERS

Given: Horsepower P, revolutions per second n, air speed V, and density ρ.

Calculate:

$$C_s = V\sqrt[5]{\frac{\rho}{Pn^2}}$$

(1) For a controllable-pitch propeller, select the point of maximum efficiency at this value of C_s. (The efficiency envelope is shown by a curve on the chart.) Read off angle setting and V/nD, the latter giving the value of D.[1]

Examples are shown on the particular charts.

(2) For a fixed-pitch propeller the selection of the blade-angle setting is a matter of compromise. It is necessary to choose a blade angle that shows peak efficiency at a somewhat smaller value of C_s than the one calculated for the flight condition. The choice depends on how much efficiency is to be sacrificed at the high-speed condition in order to improve the take-off. It is therefore necessary to resort to the simultaneous use of charts giving the take-off characteristics.

[1] Notice that the blade-angle setting in the charts is the true setting at the operating condition. The results presented are free from compressibility effects and twist of blades due to air loads and the effect of the centrifugal force. The blade twist can be estimated and allowed for.

CHARTS FOR THE TAKE-OFF CONDITION

In the determination of the diameter of a propeller, consideration must be given also to the condition of take-off. It is desirable to know the thrust in order to calculate the take-off distance. For the controllable-pitch propeller, the determination of the minimum blade-angle setting is of interest. For the fixed-pitch propeller, the setting is a matter of balancing the performance at high speed against that at take-off. It will probably be necessary to study two or three blade-angle settings in order to arrive at a specific result. Charts for determining the take-off thrust, based on the results of this investigation, are given in charts II as supplements to charts I already described. These charts, which have been developed along similar lines, show contour curves of constant thrust and constant blade-angle setting against the coordinates V/nD and $1/\sqrt{Q_c} = V\sqrt{\frac{\rho D^3}{Q}}$, the latter quantity representing a torque coefficient; the actual engine torque Q is, as usual, considered to be a constant. Results are given in charts II.

PROCEDURE FOR THE USE OF CHARTS ON TAKE-OFF CHARACTERISTICS

(1) Controllable-pitch propeller.

Given: Engine torque Q, propeller diameter D, revolutions per second n, and air speed V.

Calculate $1/\sqrt{Q_c}$ and V/nD.

Read off from the chart $C_T/C_Q = TD/Q$ and the blade angle. For constant n the whole range of air speed is given by a straight line through this point and the origin. Plot thrust and blade angle against air speed (as in fig. 45, etc.).

(2) Fixed-pitch propeller

Calculate $1/\sqrt{Q_c}$ and V/nD.

Make a choice of blade angle and read from the chart the related values of C_T/C_Q and $1/\sqrt{Q_c}$. Plot thrust against air speed for this blade angle. If the resulting take-off thrust is found to be inadequate, choose a lower blade angle and repeat the procedure; or vice versa.

REFERENCES

1. Theodorsen, Theodore, Brevoort, M. J., and Stickle, George W.: Full-scale Tests of N. A. C. A. Cowlings. T. R. No. 592, N. A. C. A., 1937.
2. Theodorsen, Theodore, Brevoort, M. J., and Stickle, George W.: Cooling of Airplane Engines at Low Air Speeds. T. R. No. 593, N. A. C. A., 1937.
3. Weick, Fred E., and Wood, Donald H.: The Twenty-Foot Propeller Research Tunnel of the National Advisory Committee for Aeronautics. T. R. No. 300, N. A. C. A., 1928.
4. Theodorsen, Theodore: On the Theory of Wing Sections with Particular Reference to the Lift Distribution. T. R. No. 383, N. A. C. A., 1931.
5. Wood, Donald H.: Full-Scale Tests of Metal Propellers at High Tip Speeds. T. R. No. 375, N. A. C. A., 1931.

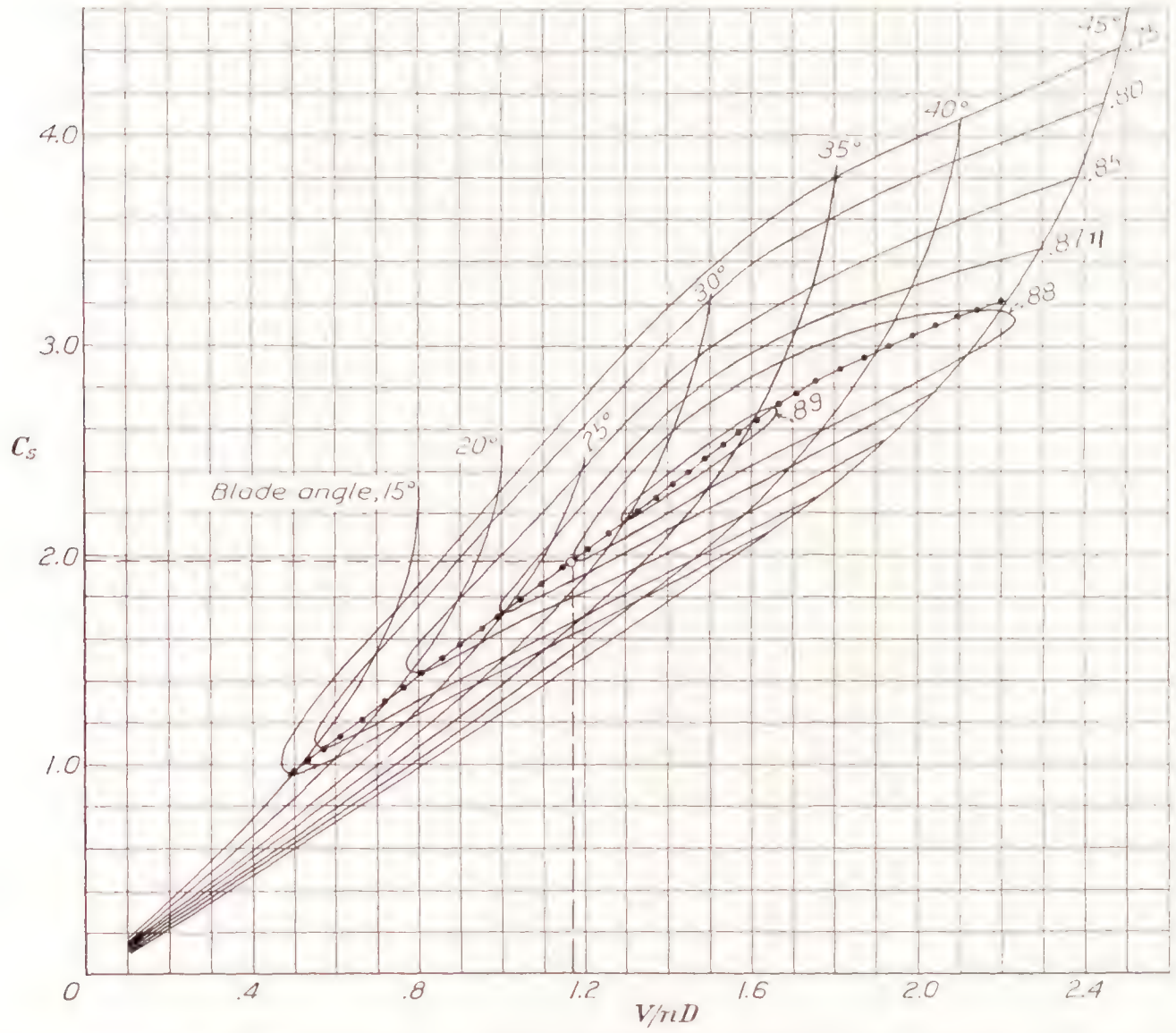

CHART I (a).—Characteristics of three-blade propeller B. Hamilton-Standard 1C1-0. Example (shown by circle)—Given: P=550 horsepower; n=24 revolutions per second; V=200 miles per hour. Result: β=27°; η=0.877; D=10.68 feet.

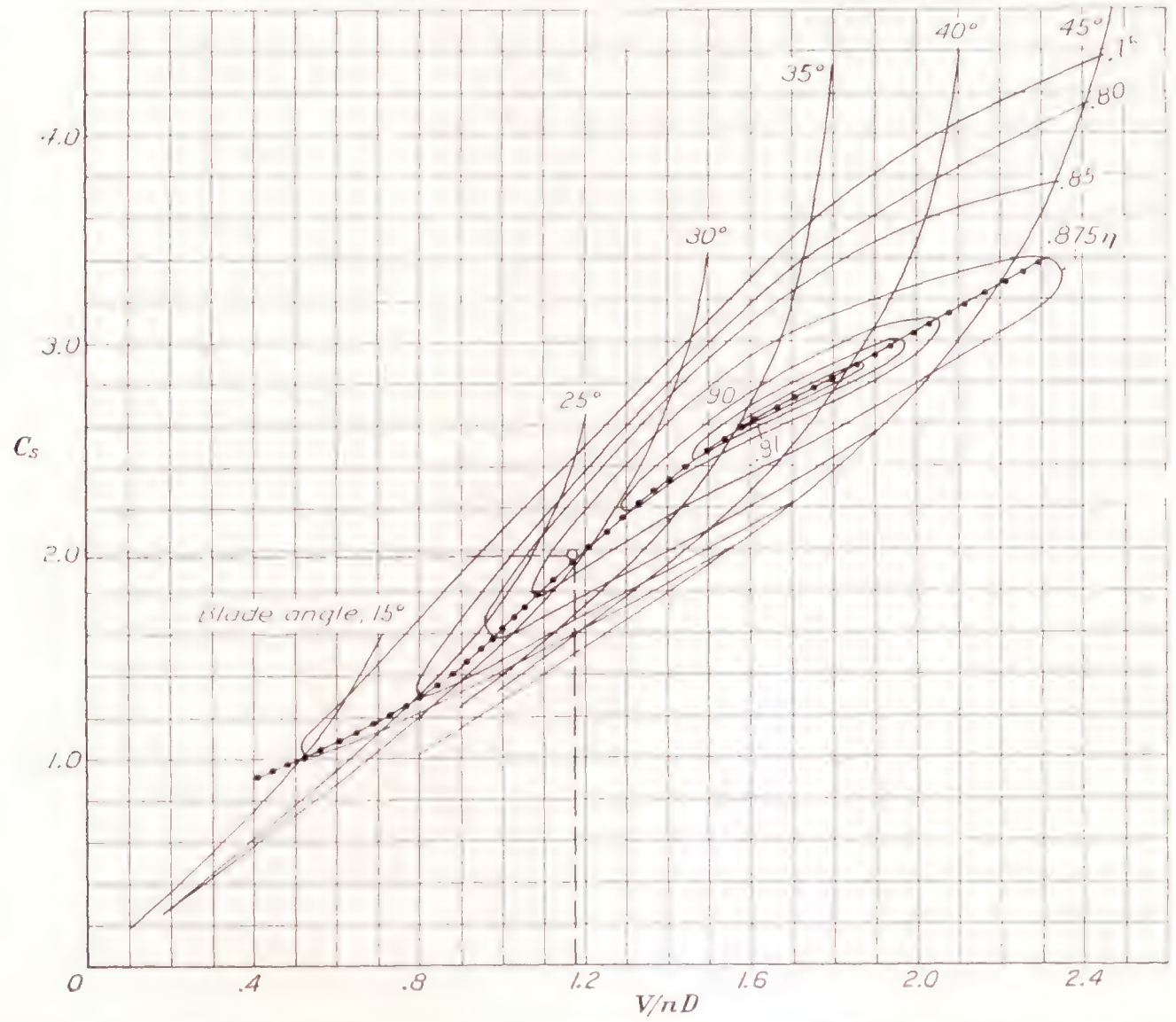

CHART I (b).—Characteristics of three-blade propeller B_x. Hamilton-Standard 1C1-0 (modified). Example (shown by circle)— Given: P=550 horsepower; n=24 revolutions per second; V=200 miles per hour. Result: β=29°; η=0.883; D=10.44 feet.

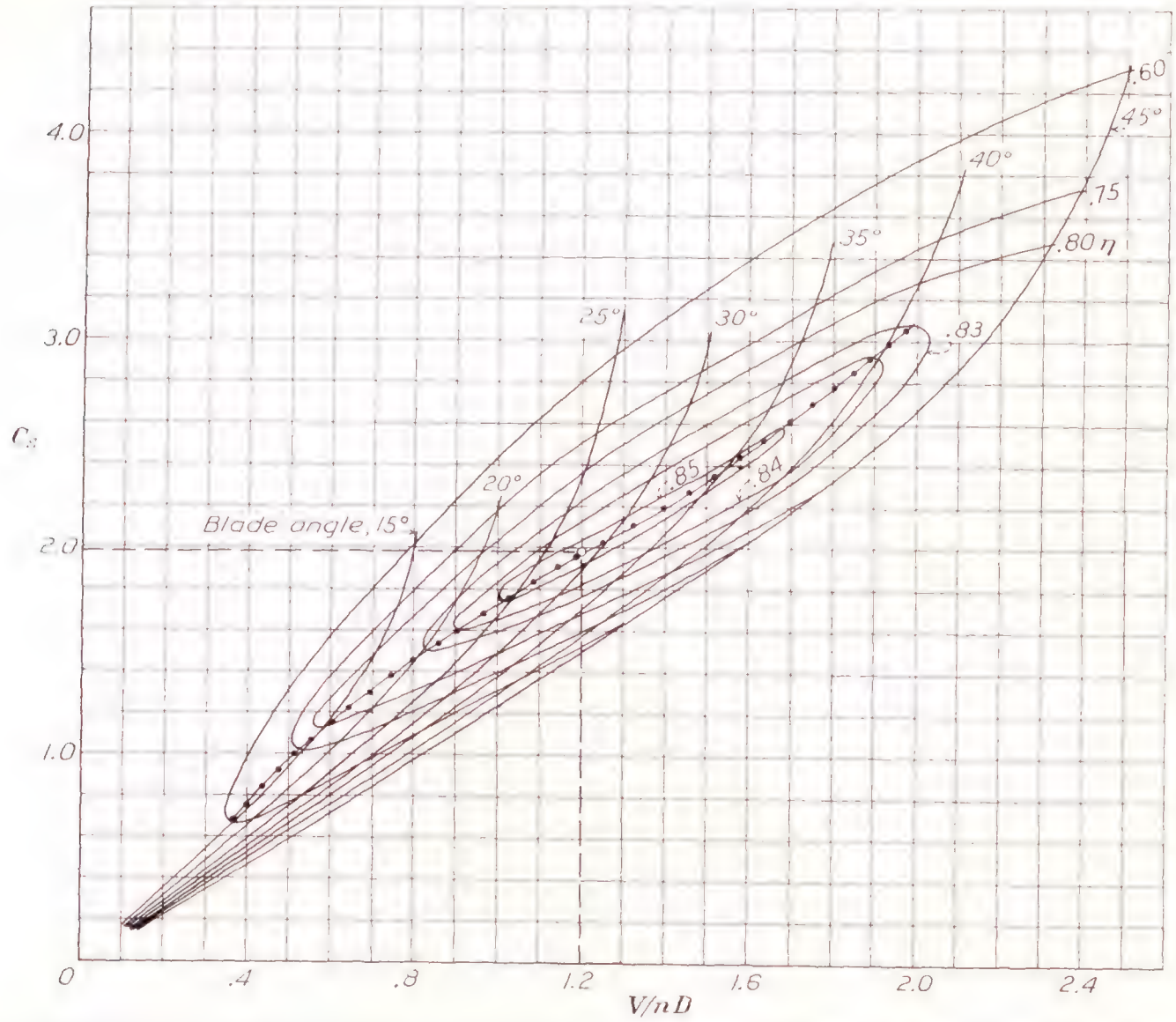

CHART I (c).—Characteristics of three-blade propeller C. Navy plan form 5868-9. Example (shown by circle)—Given: P=550 horsepower; n=24 revolutions per second; V=200 miles per hour. Result: β=28.3°; η=0.855; D=10.18 feet.

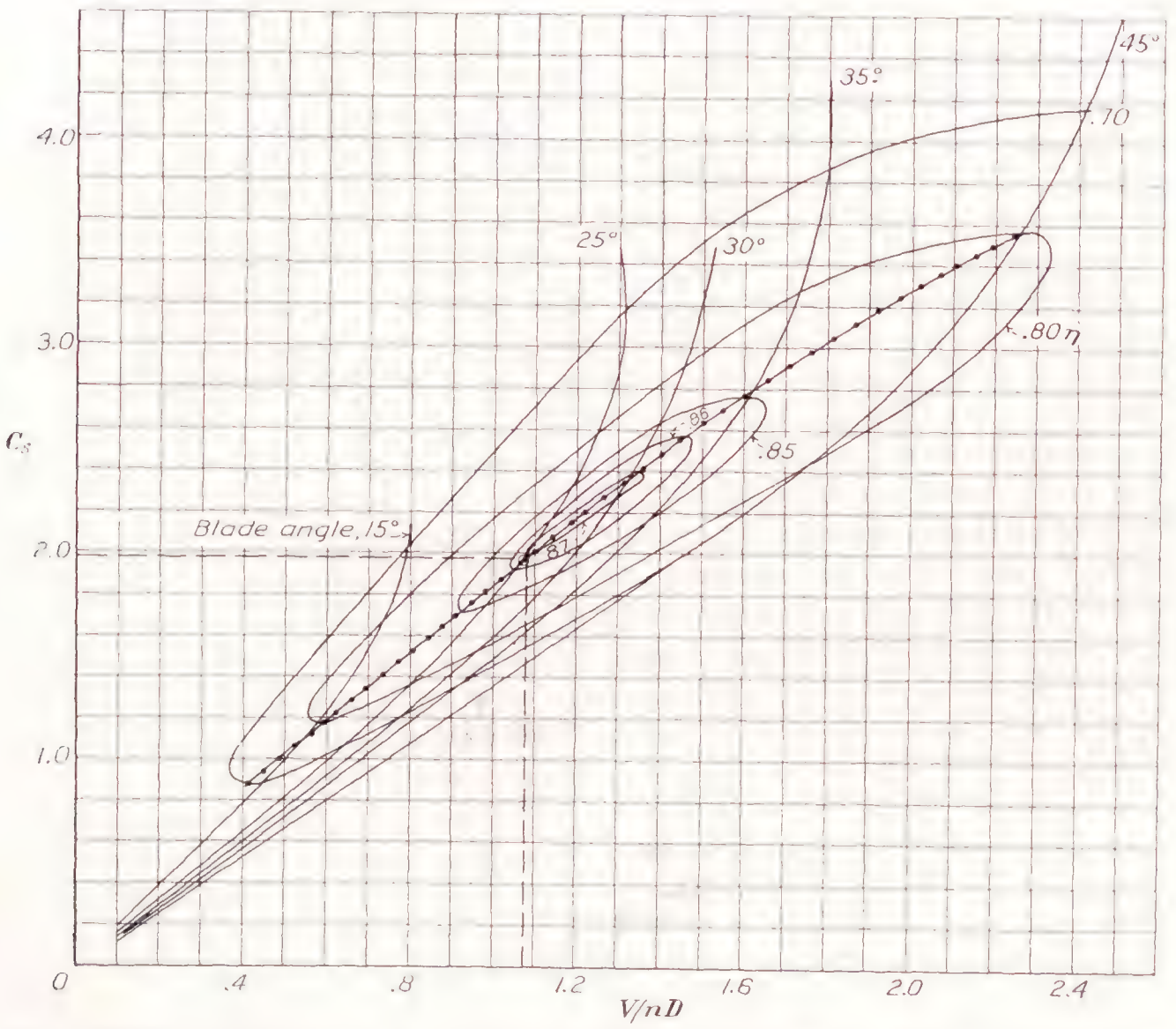

CHART I (d).—Characteristics of two-blade propeller D. Navy plan form 5868-9. Example (shown by circle)—Given: P=550 horsepower; n=24 revolutions per second; V=200 miles per hour. Result: β=25°; η=0.865; D=11.50 feet.

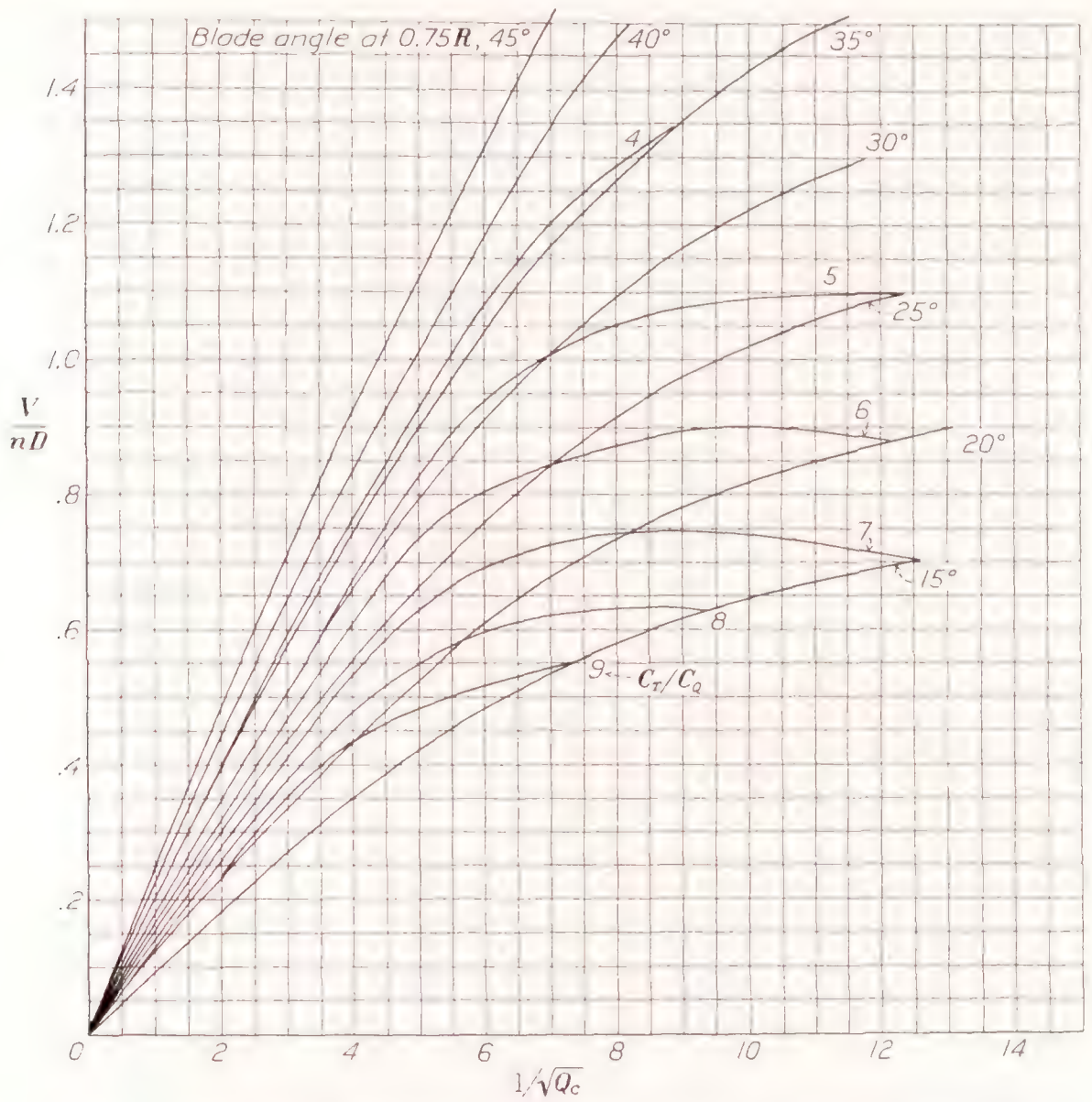

CHART II (a).—Take-off characteristics for three-blade propeller B. Hamilton-Standard 1C1–0.

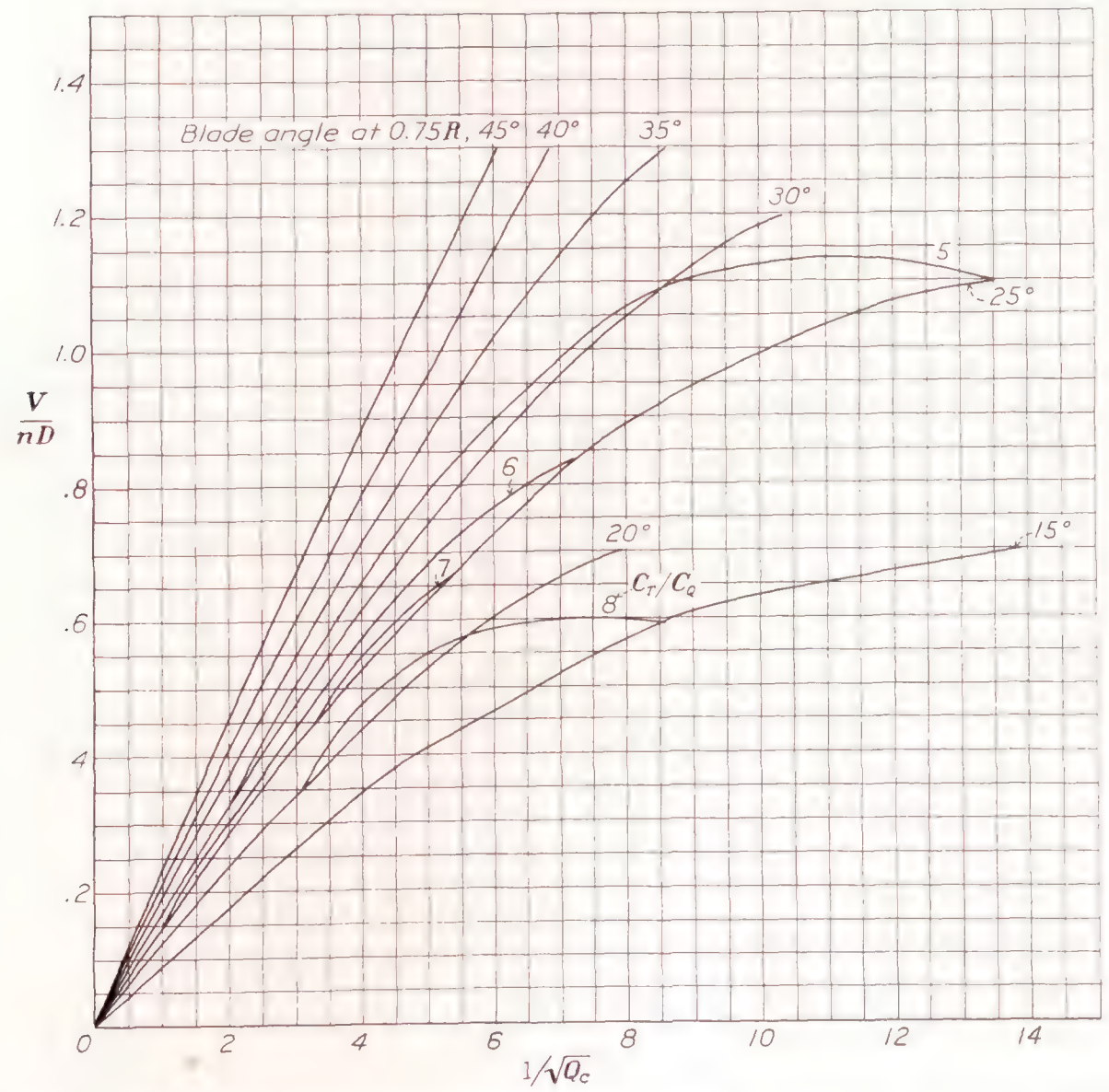

CHART II (b).—Take-off characteristics for three-blade propeller B_x. Hamilton-Standard 1C1–0 (modified).

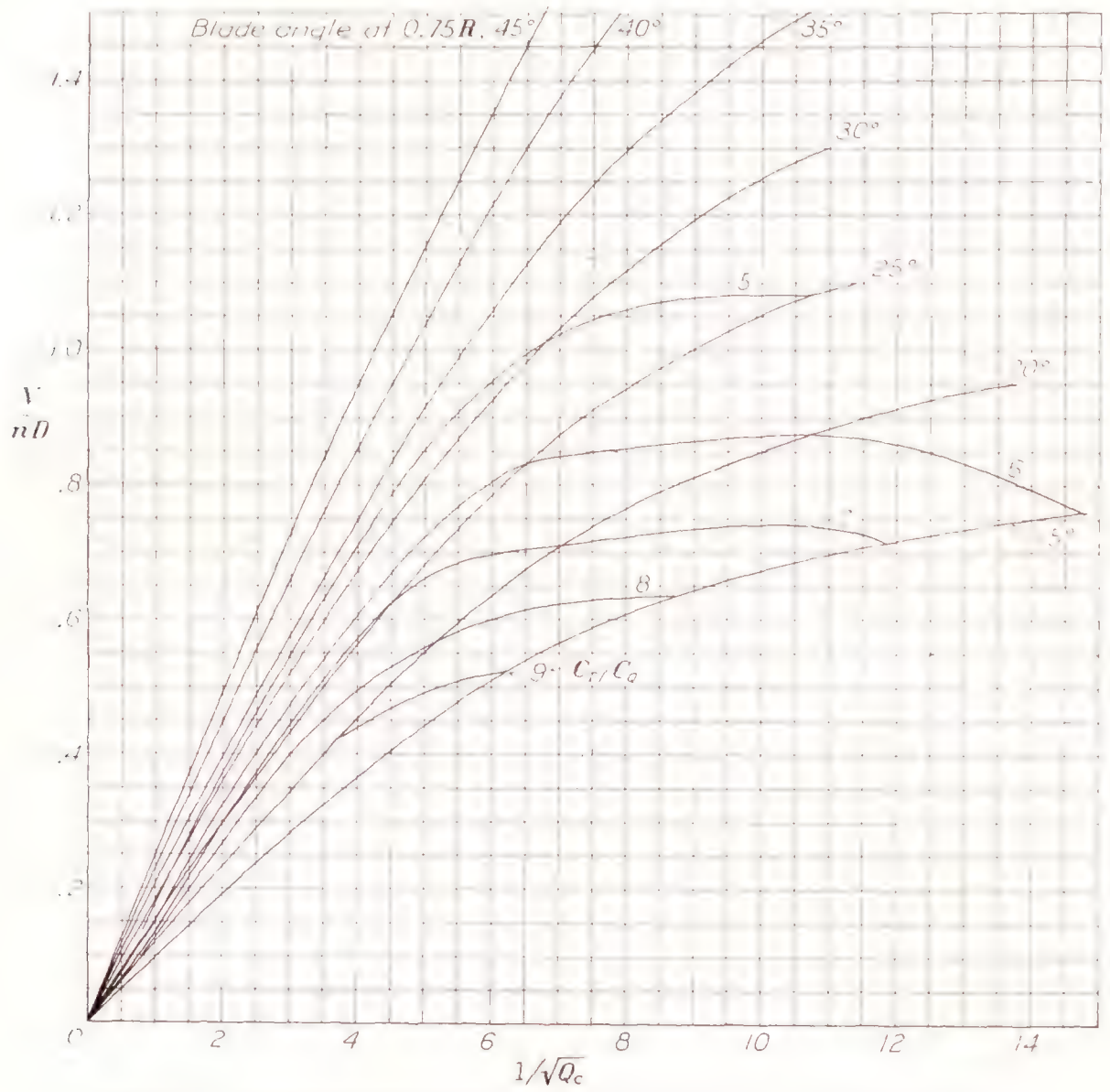

CHART II (c).—Take-off characteristics for three-blade propeller C. Navy plan form 5868–9.

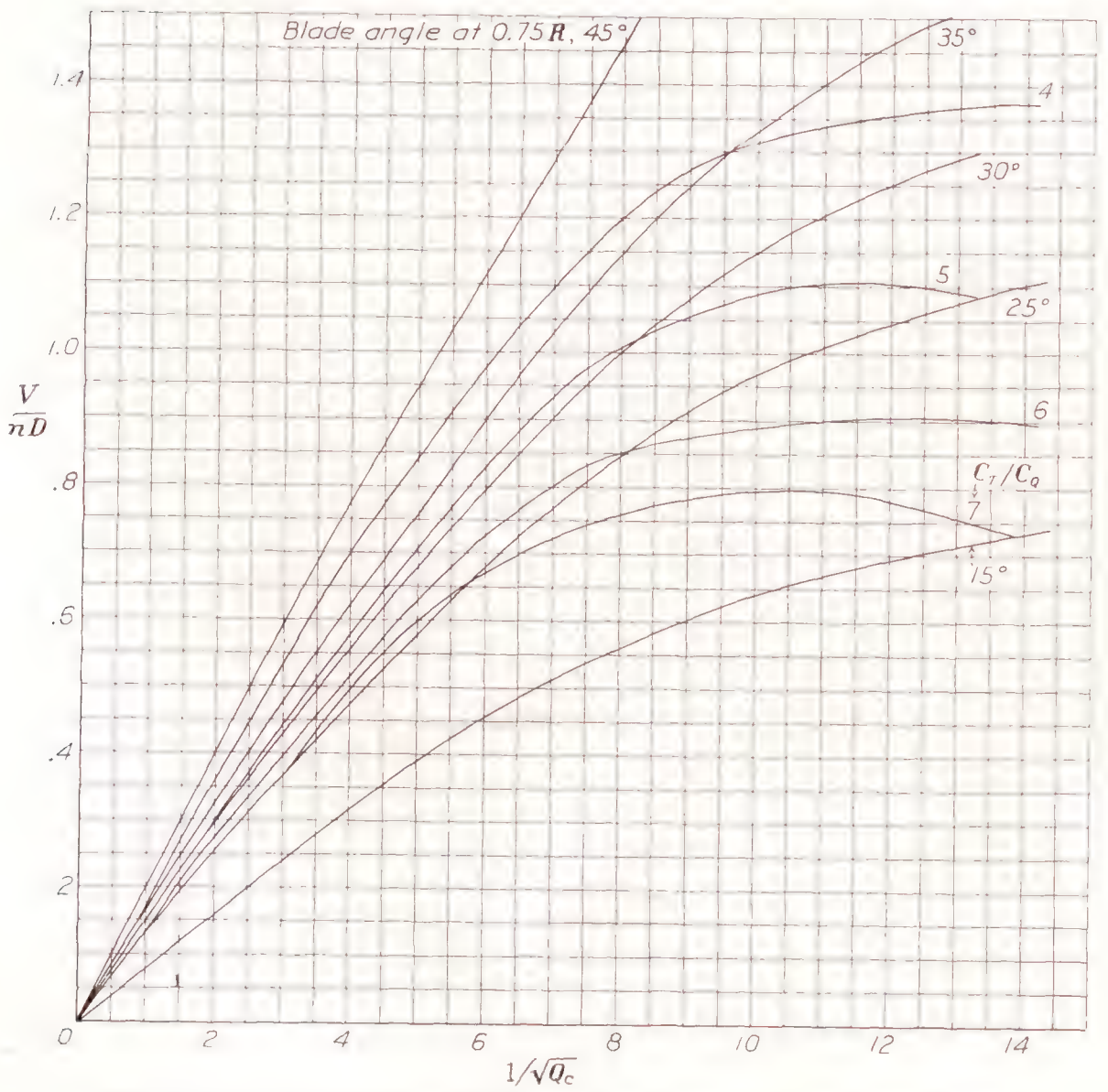

CHART II (d).—Take-off characteristics for two-blade propeller D. Navy plan form 5868–9

TABLE I.—FAIRED VALUES FOR NOSE 6, PROPELLER B

V/nD	Set 15° at 0.75R				Set 20° at 0.75R				Set 25° at 0.75R				Set 30° at 0.75R			
	C_T	C_P	η	C_s	C_T	C_P	η	C_s	C_T	C_P	η	C_s	C_T	C_P	η	C_s
0	0.1230	0.0529	0	0	0.1323	0.1140	0	0	0.1529	0.1563	0	0	0.1598	0.2074	0	0
.05	.1191	.0529	.113	.09	.1299	.1078	.060	.08	.1492	.1522	.049	.07	.1582	.2051	.039	.07
.10	.1150	.0529	.217	.18	.1288	.1009	.128	.16	.1477	.1510	.098	.15	.1566	.2030	.077	.14
.15	.1101	.0527	.314	.27	.1272	.0948	.201	.24	.1459	.1494	.146	.22	.1550	.2007	.116	.21
.20	.1048	.0522	.402	.36	.1253	.0897	.280	.32	.1442	.1474	.196	.29	.1535	.1982	.155	.28
.25	.0988	.0516	.479	.45	.1231	.0851	.362	.41	.1427	.1451	.246	.37	.1519	.1959	.194	.35
.30	.0920	.0505	.546	.54	.1201	.0812	.445	.50	.1411	.1425	.298	.44	.1502	.1933	.233	.42
.35	.0849	.0487	.610	.64	.1169	.0782	.523	.58	.1395	.1397	.350	.52	.1487	.1908	.273	.49
.40	.0770	.0463	.665	.74	.1120	.0760	.590	.67	.1380	.1363	.405	.59	.1470	.1881	.312	.56
.45	.0687	.0432	.715	.84	.1053	.0741	.640	.76	.1365	.1326	.463	.68	.1454	.1853	.353	.63
.50	.0602	.0398	.756	.95	.0982	.0719	.684	.85	.1350	.1285	.525	.76	.1440	.1824	.395	.70
.55	.0512	.0358	.786	1.07	.0907	.0691	.722	.94	.1322	.1238	.588	.84	.1423	.1794	.436	.78
.60	.0417	.0313	.800	1.20	.0827	.0657	.755	1.03	.1272	.1187	.644	.92	.1408	.1761	.480	.85
.65	.0320	.0260	.800	1.35	.0743	.0615	.785	1.13	.1202	.1133	.690	1.01	.1391	.1721	.525	.92
.70	.0223	.0201	.777	1.53	.0656	.0567	.810	1.24	.1125	.1082	.728	1.09	.1377	.1686	.572	1.00
.75	.0124	.0131	.710	1.79	.0565	.0510	.830	1.36	.1044	.1028	.762	1.18	.1357	.1643	.620	1.08
.80	.0016	.0047	.272	2.34	.0472	.0446	.846	1.49	.0960	.0970	.791	1.28	.1326	.1594	.665	1.16
.85					.0377	.0376	.852	1.64	.0870	.0910	.812	1.37	.1275	.1537	.705	1.24
.90					.0282	.0300	.846	1.81	.0788	.0847	.837	1.48	.1207	.1466	.740	1.32
.95					.0182	.0215	.805	2.05	.0688	.0775	.845	1.67	.1135	.1400	.770	1.41
1.00					.0080	.0125	.640	2.42	.0595	.0695	.856	1.71	.1060	.1324	.800	1.50
1.05					.0018	.0020		3.65	.0500	.0600	.874	1.84	.0980	.1250	.823	1.59
1.10									.0400	.0502	.876	2.00	.0896	.1171	.841	1.69
1.15									.0297	.0392	.871	2.20	.0810	.1085	.859	1.80
1.20									.0189	.0275	.825	2.46	.0719	.0990	.870	1.90
1.25									.0080	.0145	.745	2.91	.0624	.0880	.885	2.03
1.30									−.0028	.0015		3.62	.0527	.0769	.891	2.17
1.35													.0430	.0650	.893	2.33
1.40													.0327	.0514	.890	2.54
1.45													.0225	.0380	.858	2.79
1.50													.0124	.0231	.806	3.18
1.55													.0020	.0080	.387	4.07
1.60																
1.65																
1.70																
1.75																
1.80																
1.85																
1.90																
1.95																
2.00																
2.05																
2.10																
2.15																
2.20																
2.25																
2.30																
2.35																
2.40																
2.45																
2.50																
2.55																
2.60																

TABLE I.—FAIRED VALUES FOR NOSE 6, PROPELLER B—Continued

V/nD	Set 35° at 0.75R				Set 40° at 0.75R				Set 45° at 0.75R			
	C_T	C_P	η	C_s	C_T	C_P	η	C_s	C_T	C_P	η	C_s
0	0.1635	0.2695	0	0	0.1643	0.3324	0	0	0.1576	0.3868	0	0
.05	.1629	.2662	.031	.07	.1640	.3291	.025	.06	.1581	.3842	.021	.06
.10	.1617	.2631	.062	.13	.1637	.3260	.050	.13	.1585	.3817	.042	.12
.15	.1606	.2600	.093	.20	.1633	.3228	.076	.19	.1589	.3792	.063	.18
.20	.1593	.2567	.124	.26	.1628	.3197	.102	.25	.1592	.3767	.085	.24
.25	.1583	.2535	.156	.33	.1624	.3164	.128	.32	.1596	.3742	.106	.30
.30	.1570	.2501	.188	.40	.1618	.3132	.155	.38	.1599	.3717	.129	.37
.35	.1557	.2467	.221	.46	.1613	.3100	.182	.44	.1602	.3693	.152	.43
.40	.1543	.2432	.254	.53	.1607	.3067	.210	.51	.1605	.3667	.175	.49
.45	.1530	.2396	.288	.60	.1600	.3033	.238	.57	.1608	.3640	.199	.55
.50	.1517	.2360	.322	.67	.1593	.3000	.266	.64	.1607	.3614	.222	.61
.55	.1502	.2323	.356	.74	.1585	.2963	.294	.70	.1605	.3586	.246	.68
.60	.1490	.2285	.391	.81	.1577	.2927	.323	.77	.1601	.3557	.270	.74
.65	.1475	.2245	.427	.88	.1566	.2890	.352	.83	.1596	.3527	.294	.80
.70	.1462	.2205	.464	.95	.1554	.2853	.381	.90	.1588	.3499	.318	.86
.75	.1445	.2165	.500	1.02	.1542	.2813	.412	.97	.1577	.3466	.341	.93
.80	.1427	.2121	.538	1.09	.1527	.2770	.441	1.03	.1565	.3434	.365	.99
.85	.1405	.2078	.575	1.17	.1510	.2730	.470	1.10	.1550	.3400	.388	1.05
.90	.1375	.2028	.610	1.24	.1492	.2683	.500	1.17	.1538	.3362	.411	1.12
.95	.1345	.1982	.645	1.31	.1470	.2634	.530	1.25	.1522	.3324	.435	1.19
1.00	.1317	.1940	.678	1.39	.1445	.2580	.560	1.31	.1507	.3277	.460	1.25
1.05	.1290	.1895	.715	1.47	.1418	.2530	.589	1.38	.1490	.3232	.484	1.32
1.10	.1255	.1841	.750	1.54	.1392	.2490	.615	1.45	.1475	.3183	.510	1.38
1.15	.1202	.1777	.779	1.62	.1372	.2455	.643	1.52	.1460	.3135	.536	1.45
1.20	.1140	.1700	.804	1.71	.1355	.2428	.670	1.59	.1443	.3088	.560	1.52
1.25	.1067	.1624	.820	1.80	.1340	.2400	.698	1.66	.1428	.3052	.585	1.59
1.30	.0993	.1533	.842	1.89	.1324	.2360	.730	1.74	.1412	.3015	.610	1.65
1.35	.0913	.1440	.855	1.99	.1300	.2310	.760	1.81	.1398	.2990	.631	1.72
1.40	.0830	.1340	.867	2.09	.1267	.2255	.796	1.89	.1385	.2964	.655	1.79
1.45	.0750	.1240	.876	2.20	.1215	.2185	.805	1.96	.1371	.2948	.675	1.85
1.50	.0658	.1117	.884	2.32	.1157	.2103	.825	2.05	.1360	.2925	.698	1.92
1.55	.0570	.0990	.893	2.46	.1090	.2010	.841	2.13	.1348	.2904	.720	1.98
1.60	.0478	.0850	.900	2.62	.1020	.1910	.855	2.23	.1339	.2878	.745	2.05
1.65	.0385	.0712	.892	2.80	.0940	.1790	.866	2.32	.1324	.2845	.767	2.12
1.70	.0288	.0558	.876	3.03	.0858	.1670	.873	2.42	.1303	.2805	.790	2.20
1.75	.0195	.0400	.853	3.33	.0770	.1540	.875	2.54	.1270	.2760	.805	2.27
1.80	.0100	.0237	.760	3.80	.0685	.1400	.881	2.66	.1220	.2690	.816	2.34
1.85	.0007	.0078	.166	4.88	.0595	.1240	.888	2.81	.1160	.2590	.829	2.42
1.90					.0500	.1080	.880	2.96	.1095	.2480	.839	2.51
1.95					.0410	.0915	.874	3.14	.1030	.2353	.855	2.60
2.00					.0320	.0745	.860	3.36	.0950	.2220	.855	2.70
2.05					.0230	.0575	.810	3.63	.0876	.2080	.863	2.80
2.10					.0147	.0400	.771	4.00	.0800	.1920	.874	2.92
2.15					.0058	.0220	.566	4.61	.0714	.1750	.877	3.05
2.20					−.0025	.0038		6.70	.0632	.1580	.880	3.18
2.25									.0550	.1400	.883	3.30
2.30									.0470	.1230	.878	3.50
2.35									.0387	.1050	.867	3.69
2.40									.0305	.0870	.842	3.91
2.45									.0228	.0688	.812	4.18
2.50									.0150	.0505	.742	4.53
2.55									.0070	.0320	.558	4.81
2.60									−.0005	.0140		6.10

TABLE II.—FAIRED VALUES FOR NOSE 7, PROPELLER Bx

V/nD	Set 15° at 0.75R				Set 25° at 0.75R				Set 30° at 0.75R			
	C_T	C_P	η	C_s	C_T	C_P	η	C_s	C_T	C_P	η	C_s
0	0.1167	0.0480	0	0	0.1240	0.1388	0	0	0.1381	0.1828	0	0
.05	.1131	.0483	.117	.09	.1259	.1375	.046	.07	.1380	.1802	.038	.07
.10	.1088	.0485	.224	.18	.1275	.1360	.094	.15	.1378	.1778	.078	.14
.15	.1043	.0485	.323	.27	.1289	.1340	.144	.22	.1373	.1751	.118	.21
.20	.0990	.0482	.411	.37	.1298	.1322	.196	.30	.1370	.1728	.159	.28
.25	.0931	.0478	.487	46	.1304	.1298	.251	.38	.1365	.1705	.200	.36
.30	.0868	.0468	.556	.55	.1307	.1270	.308	.45	.1359	.1681	.242	.43
.35	.0797	.0452	.617	.65	.1305	.1240	.368	.53	.1350	.1660	.284	.50
.40	.0720	.0430	.670	.75	.1300	.1200	.433	.61	.1340	.1638	328	.58
.45	.0640	.0405	.711	.85	.1285	.1155	.501	.69	.1330	.1620	.369	.65
.50	.0555	.0375	.740	.96	.1259	.1100	.572	.78	.1315	.1596	.412	.72
.55	.0467	.0338	.760	1.08	.1222	.1060	.634	.86	.1305	.1570	.457	.80
.60	.0378	.0293	.775	1.21	.1170	.1022	.687	.95	.1295	.1535	.506	.87
.65	.0281	.0240	.761	1.37	.1102	.0993	.722	1.03	.1289	.1487	.564	.95
.70	.0181	.0180	.705	1.56	.1030	.0960	.752	1.12	.1277	.1440	.620	1.03
.75	.0087	.0125	.522	1.80	.0954	.0921	.777	1.21	.1258	.1390	.679	1.11
.80	−.0041	.0021		2.75	.0873	.0877	.796	1.30	.1222	.1343	.728	1.19
.85					.0795	.0825	.819	1.40	.1170	.1292	.770	1.28
.90					.0710	.0761	.840	1.51	.1105	.1240	.802	1.37
.95					.0620	.0692	.850	1.62	.1040	.1187	.832	1.46
1.00					.0530	.0614	.863	1.75	.0960	.1130	.850	1.55
1.05					.0433	.0525	.865	1.89	.0879	.1070	.862	1.64
1.10					.0330	.0425	.854	2.07	.0797	.1008	.870	1.74
1.15					.0225	.0320	.808	2.29	.0713	.0937	.875	1.85
1.20					.0118	.0195	.727	2.64	.0630	.0850	.889	1.96
1.25					.0005	.0065	.096	3.42	.0540	.0750	.900	2.10
1.30									.0447	.0645	.901	2.25
1.35									.0348	.0522	.900	2.43
1.40									.0250	.0400	.875	2.66
1.45									.0150	.0273	.797	2.98
1.50									.0050	.0150	.500	3.47
1.55									−.0050	.0018		5.50
1.60												
1.65												
1.70												
1.75												
1.80												
1.85												
1.90												
1.95												
2.00												
2.05												
2.10												
2.15												
2.20												
2.25												
2.30												
2.35												
2.40												
2.45												
2.50												
2.55												

TABLE II.—FAIRED VALUES FOR NOSE 7, PROPELLER Bx—Continued

V/nD	Set 35° at 0.75R				Set 40° at 0.75R				Set 45° at 0.75R			
	C_T	C_P	η	C_s	C_T	C_P	η	C_s	C_T	C_P	η	C_s
0	0.1515	0.2468	0	0	0.1492	0.2970	0	0	0.1456	0.3490	0	0
.05	.1508	.2440	.031	.07	.1490	.2930	.025	.06	.1460	.3480	.021	.06
.10	.1500	.2410	.062	.13	.1484	.2890	.051	.13	.1462	.3465	.042	.12
.15	.1490	.2381	.094	.20	.1480	.2850	.078	.19	.1465	.3450	.064	.19
.20	.1480	.2351	.126	.27	.1473	.2810	.105	.26	.1468	.3435	.086	.25
.25	.1470	.2292	.160	.34	.1470	.2773	.133	.32	.1470	.3420	.107	.31
.30	.1460	.2263	.194	.41	.1463	.2734	.161	.39	.1470	.3405	.129	.37
.35	.1448	.2233	.227	.47	.1457	.2695	.189	.46	.1470	.3385	.152	.44
.40	.1435	.2202	.260	.54	.1450	.2658	.217	.52	.1470	.3370	.175	.50
.45	.1423	.2170	.295	.61	.1443	.2625	.248	.59	.1470	.3350	.197	.56
.50	.1410	.2140	.330	.68	.1435	.2590	.278	.66	.1470	.3330	221	.62
.55	.1397	.2105	.365	.75	.1429	.2560	.307	.72	.1470	.3308	.244	.69
.60	.1382	.2074	.400	.82	.1420	.2530	.337	.79	.1468	.3283	.268	.75
.65	.1365	.2040	.435	.89	.1410	.2500	.367	.86	.1464	.3255	.292	.81
.70	.1348	.2004	.470	.97	.1400	.2472	.397	.93	.1460	.3220	.318	.88
.75	.1333	.1972	.507	1.04	.1390	.2445	.427	1.00	.1455	.3185	.343	.94
.80	.1325	.1944	545	1.11	.1380	.2420	.456	1.06	.1448	.3148	.368	1.01
.85	.1325	.1920	.586	1.18	.1368	.2400	.485	1.13	.1440	.3110	.394	1.07
.90	.1330	.1897	.630	1.26	.1353	.2378	.512	1.20	.1429	.3075	.418	1.14
.95	.1325	.1855	.679	1.33	.1338	.2356	.545	1.27	.1415	.3043	.441	1.21
1.00	.1315	.1800	.730	1.41	.1328	.2335	.569	1.34	.1401	.3013	.465	1.28
1.05	.1293	.1800	.754	1.48	.1325	.2317	.601	1.41	.1384	.2985	.487	1.34
1.10	.1250	.1740	.791	1.56	.1331	.2300	.637	1.48	.1370	.2960	.510	1.40
1.15	.1181	1670	.813	1.64	.1334	.2282	.671	1.55	.1358	.2938	.532	1.47
1.20	.1110	.1600	.833	1.73	.1335	.2258	.710	1.62	.1350	.2918	.555	1.53
1.25	.1033	.1525	.846	1.82	.1330	.2215	.750	1.69	.1343	.2901	.578	1.60
1.30	.0955	.1445	.853	1.92	.1310	.2163	.787	1.77	.1340	.2889	.603	1.67
1.35	.0870	.1360	.864	2.01	.1270	.2105	.815	1.84	.1343	.2880	.629	1.73
1.40	.0785	.1260	.872	2.12	.1213	.2044	.830	1.92	.1349	.2875	.655	1.80
1.45	.0698	.1147	.881	2.24	.1150	.1976	.844	2.00	.1359	.2870	.686	1.87
1.50	.0610	.1023	.895	2.36	.1086	.1900	.857	2.08	.1365	.2858	.717	1.93
1.55	.0520	.0890	.905	2.51	.1018	.1820	.866	2.18	.1365	.2830	.747	2.00
1.60	.0428	.0745	.918	2.69	.0940	.1730	.870	2.28	.1353	.2783	.777	2.07
1.65	.0333	.0600	.915	2.89	.0864	.1620	.880	2.38	.1324	.2723	.801	2.14
1.70	.0230	.0450	.869	3.16	.0785	.1500	.890	2.48	.1280	.2650	.821	2.22
1.75	.0135	.0290	.814	3.56	.0700	.1367	.896	2.60	.1225	.2575	.832	2.30
1.80	.0040	.0123	.585	4.33	.0620	.1225	.911	2.74	.1167	.2495	.842	2.38
1.85					.0530	.1080	.908	2.89	.1100	.2400	.848	2.46
1.90					.0440	.0930	.900	3.05	.1030	.2282	.858	2.56
1.95					.0350	.0782	.873	3.24	.0950	.2150	.862	2.66
2.00					.0260	.0630	.825	3.48	.0870	.2010	.865	2.76
2.05					.0170	.0465	.749	3.88	.0790	.1853	.874	2.87
2.10					.0078	.0270	.607	4.32	.0713	.1700	.880	2.99
2.15					−.0013	.0060		5.99	.0632	.1535	.886	3.13
2.20									.0554	.1380	.883	3.27
2.25									.0470	.1205	.879	3.44
2.30									.0393	.1040	.870	3.62
2.35									.0310	.0870	.836	3.82
2.40									.0231	.0695	.797	4.09
2.45									.0150	.0500	.735	4.45
2.50									.0070	.0295	.593	5.05
2.55									−.0010	.0095		6.48

TABLE III.—FAIRED VALUES FOR NOSE 6, PROPELLER C

V/nD	Set 15° at 0.75R				Set 20° at 0.75R				Set 25° at 0.75R				Set 30° at 0.75R			
	C_T	C_P	η	C_s	C_T	C_P	η	C_s	C_T	C_P	η	C_s	C_T	C_P	η	C_s
0	0.1322	0.0584	0	0	0.1514	0.0856	0	0	0.1469	0.1742	0	0	0	0	0	0
.05	.1280	.0582	.110	.09	.1492	.0857	.087	.08	.1486	.1668	.045	.07	.1709	.2201	.039	.07
.10	.1224	.0578	.212	.18	.1465	.0858	.170	.16	.1499	.1610	.093	.14	.1692	.2173	.078	.14
.15	.1165	.0572	.306	.27	.1433	.0857	.251	.25	.1510	.1556	.146	.22	.1678	.2144	.117	.20
.20	.1101	.0564	.391	.36	.1397	.0853	.328	.33	.1520	1505	.208	.29	.1662	.2114	.157	.27
.25	.1036	.0555	.467	.45	.1352	.0848	.399	.41	.1529	.1460	.262	37	.1648	.2083	.198	.34
.30	.0968	.0543	.535	.54	.1306	.0840	.467	.49	.1534	.1414	.325	.44	.1635	.2050	.240	.41
.35	.0899	.0530	.593	.63	.1252	.0831	.528	.58	.1538	.1373	.392	.52	.1622	.2017	.282	.48
.40	.0826	.0514	.643	.72	.1193	.0819	.583	.66	.1538	.1338	.460	.60	.1610	.1982	.325	.55
.45	.0752	.0492	.688	.82	.1129	.0804	.632	.75	.1529	.1307	.527	.68	.1599	.1947	.370	.62
.50	.0674	.0461	.732	.93	.1060	.0786	.675	.83	.1505	.1282	.587	.76	.1588	.1910	.414	.70
.55	.0587	.0419	.770	1.04	.0985	0764	.710	.92	.1452	.1258	.635	.84	.1578	.1974	.465	.77
.60	.0495	.0370	.802	1.16	.0905	.0732	.743	1.01	.1378	.1230	.673	.91	.1570	.1840	.512	.84
.65	.0391	.0314	.810	1.30	.0818	.0691	.770	1.11	.1297	.1194	.705	.99	.1562	.1804	.563	.92
.70	.0288	.0252	.800	1.46	.0729	.0643	.793	1.21	.1212	.1155	.735	1.08	.1554	.1761	.617	.99
.75	.0183	.0182	.755	1.67	.0635	.0586	.812	1.32	.1126	.1110	.752	1.16	.1532	.1708	.673	1.07
.80	.0080	.0106	.604	1.99	.0542	.0523	.829	1.44	.1037	.1062	.788	1.25	.1454	.1649	.705	1.15
.85	−.0020	.0025		2.82	.0447	.0455	.835	1.58	.0943	.1003	.800	1.34	.1369	.1589	.733	1.23
.90					.0350	.0380	.828	1.73	.0849	.0940	.813	1.45	.1286	.1528	.760	1.31
.95					.0254	.0298	.810	1.92	.0757	.0868	.829	1.55	.1201	.1461	.781	1.39
1.00					.0153	.0200	.765	2.20	.0662	.0788	.840	1.67	.1117	.1397	.800	1.48
1.05					.0043	.0090	.510	2.69	.0557	.0693	.844	1.79	.1031	.1329	.815	1.57
1.10									.0454	.0586	.852	1.94	.0948	.1256	.830	1.67
1.15									.0350	.0480	.839	2.11	.0862	.1175	.844	1.77
1.20									.0250	.0364	.825	2.33	0770	.1090	.848	1.87
1.25									.0150	.0240	.781	2.64	.0679	.1000	.849	1.98
1.30									.0047	.0118	.518	3.16	.0577	.0881	.851	2.11
1.35													.0472	.0752	.845	2.26
1.40													.0365	.0612	.835	2.45
1.45													.0265	.0470	.818	2.67
1.50													.0159	.0327	.730	2.98
1.55													.0068	.0184	.572	3.45
1.60													−.0047	.0040		4.83
1.65																
1.70																
1.75																
1.80																
1.85																
1.90																
1.95																
2.00																
2.05																
2.10																
2.15																
2.20																
2.25																
2.30																
2.35																
2.40																
2.45																
2.50																
2.55																
2.60																
2.65																

TABLE III.—FAIRED VALUES FOR NOSE 6, PROPELLER C—Continued

V/nD	Set 35° at 0.75R				Set 40° at 0.75R				Set 45° at 0.75R			
	C_T	C_P	η	C_s	C_T	C_P	η	C_s	C_T	C_P	η	C_s
0	0	0	0	0	0	0	0	0	0	0	0	0
.05	.1770	.2728	.033	.06	.1725	.3324	.026	.06	.1663	.3937	.021	.06
.10	.1757	.2699	.065	.13	.1730	.3320	.052	.12	.1670	.3925	.043	.12
.15	.1723	.2665	.097	.20	.1733	.3313	.079	.19	.1677	.3911	.064	.18
.20	.1702	.2630	.130	.26	.1737	.3302	.105	.25	.1682	.3900	.086	.24
.25	.1680	.2592	.162	.33	.1738	.3288	.132	.31	.1687	.3886	.109	.30
.30	.1659	.2552	.195	.39	.1739	.3270	.160	.38	.1692	.3871	.131	.36
.35	.1638	.2510	.228	.46	.1738	.3249	.187	.44	.1697	.3857	.154	.42
.40	.1618	.2467	.262	.53	.1737	.3226	.215	.50	.1700	.3840	.177	.48
.45	.1600	.2422	.297	.60	.1733	.3199	.244	.57	.1702	.3824	.200	.55
.50	.1582	.2377	.335	.67	.1728	.3170	.273	.63	.1704	.3806	.224	.61
.55	.1566	.2330	.370	.74	.1720	.3138	.302	.69	.1705	.3788	.247	.67
.60	.1550	.2283	.407	.81	.1710	.3102	.330	.76	.1704	.3767	.271	.73
.65	.1538	.2245	445	.88	.1699	.3066	.360	.82	.1702	.3743	.295	.79
.70	.1527	.2220	.480	.95	.1684	.3027	.388	.89	.1700	.3720	.320	.85
.75	.1517	.2206	.516	1.02	.1663	.2988	.417	.96	.1694	.3690	.344	.92
.80	.1508	.2186	.552	1.09	.1641	.2945	.445	1.02	.1687	.3660	.369	.98
.85	.1501	.2154	.593	1.16	.1619	.2898	.477	1.09	.1678	.3625	.393	1.04
.90	.1488	.2110	.635	1.23	.1598	.2847	.505	1.16	.1666	.3587	.418	1.10
.95	.1471	.2062	.680	1.30	.1578	.2799	.536	1.23	.1650	.3544	.442	1.17
1.00	.1442	.2015	.715	1.38	.1560	.2755	.568	1.30	.1631	.3498	.467	1.24
1.05	.1393	.1968	.743	1.45	.1545	.2712	.599	1.37	.1609	.3446	.490	1.30
1.10	.1340	.1915	.770	1.53	.1531	.2672	.631	1.43	.1585	.3390	.514	1.37
1.15	.1279	.1858	.791	1.61	.1520	.2632	.665	1.50	.1563	.3333	.540	1.43
1.20	.1210	.1795	.810	1.69	.1511	.2595	.699	1.57	.1542	.3280	.564	1.50
1.25	.1131	.1723	.821	1.78	.1497	.2550	.730	1.64	.1522	.3236	.589	1.57
1.30	.1048	.1644	.828	1.87	.1472	.2519	.761	1.71	.1503	.3199	.611	1.63
1.35	.0962	.1550	.837	1.96	.1427	.2470	.780	1.79	.1488	.3168	.633	1.70
1.40	.0875	.1453	.843	2.06	.1372	.2409	.797	1.86	.1476	.3142	.657	1.77
1.45	.0788	.1345	.848	2.17	.1310	.2340	.811	1.94	.1470	.3127	.681	1.83
1.50	.0700	.1236	.850	2.28	.1240	2262	.822	2.02	.1468	.3110	.708	1.90
1.55	.0611	.1110	.853	2.41	.1160	.2170	.829	2.10	.1460	.3088	.732	1.96
1.60	.0521	.0984	.848	2.54	.1078	.2065	.835	2.19	.1445	.3054	.756	2.03
1.65	.0430	.0843	.842	2.71	.0988	.1950	.836	2.29	.1413	.3010	.775	2.10
1.70	.0340	.0693	.835	2.90	.0900	.1825	.838	2.39	.1370	.2950	.790	2.17
1.75	.0243	.0531	.800	3.15	.0810	.1690	.839	2.49	.1318	.2880	.800	2.25
1.80	.0145	.0365	.715	3.49	.0720	.1540	.840	2 62	.1255	.2800	.806	2.33
1.85	.0048	.0200	.444	4.05	.0630	.1385	.841	2.75	.1191	.2720	.810	2.40
1.90	−.0051	.0031	.....	6.03	.0540	.1230	.835	2.90	.1125	.2636	.811	2.48
1.95	.....	.....	.....	.....	.0450	.1070	.820	3.05	.1056	.2535	.812	2.56
2.00	.....	.....	.....	.....	.0360	.0900	.800	3.24	.0986	.2427	.813	2.66
2.05	.....	.....	.....	.....	.0265	.0720	.754	3.48	.0910	.2293	.814	2.76
2.10	.....	.....	.....	.....	.0175	.0545	.675	3.76	.0830	.2135	.816	2.86
2.15	.....	.....	.....	.....	.0083	.0365	.489	4.16	.0746	.1961	.818	2.98
2.20	.....	.....	.....	.....	−.0008	.0190	.....	4.86	.0663	.1780	.819	3.10
2.25	.....	.....	.....	.....	−.0100	.0010	.....	8.96	.0580	.1595	.820	3.25
2.30	.....	.....	.....	.....	.....	.....	.....	.....	.0500	.1410	.816	3.40
2.35	.....	.....	.....	.....	.....	.....	.....	.....	.0412	.1220	.795	3.58
2.40	.....	.....	.....	.....	.....	.....	.....	.....	.0330	.1040	.762	3.77
2.45	.....	.....	.....	.....	.....	.....	.....	.....	.0242	.0855	.694	4.00
2.50	.....	.....	.....	.....	.....	.....	.....	.....	.0160	.0670	.597	4.26
2.55	.....	.....	.....	.....	.....	.....	.....	.....	.0073	.0485	.383	4.67
2.60	.....	.....	.....	.....	.....	.....	.....	.....	−.0010	.0300	.....	5.24
2.65	.....	.....	.....	.....	.....	.....	.....	.....	−.0095	.0120	.....	6.42

REPORT No. 595

FULL-SCALE TESTS OF A NEW TYPE N. A. C. A. NOSE-SLOT COWLING

By Theodore Theodorsen, M. J. Brevoort, George W. Stickle, and M. N. Gough

SUMMARY

An extended experimental study has been made in regard to the various refinements in the design of engine cowlings as related to the propeller-nacelle unit as a whole, under conditions corresponding to take-off, climb, and normal flight. The tests were all conducted at full scale in the 20-foot wind tunnel. This report presents the results of a novel type of engine cowling, characterized by the fact that the exit opening discharging the cooling air is not, as usual, located behind the engine but at the foremost extremity or nose of the cowling. This type of cowling is inherently capable of producing two to three times the pressure head obtainable with the normal type of cowling because the exit opening is located in a field of considerable negative pressure. Thus identical conditions of cooling can be obtained at correspondingly lower air speeds. In general, the efficiency is found to be high, owing to the fact that higher velocities may be used in the exit opening.

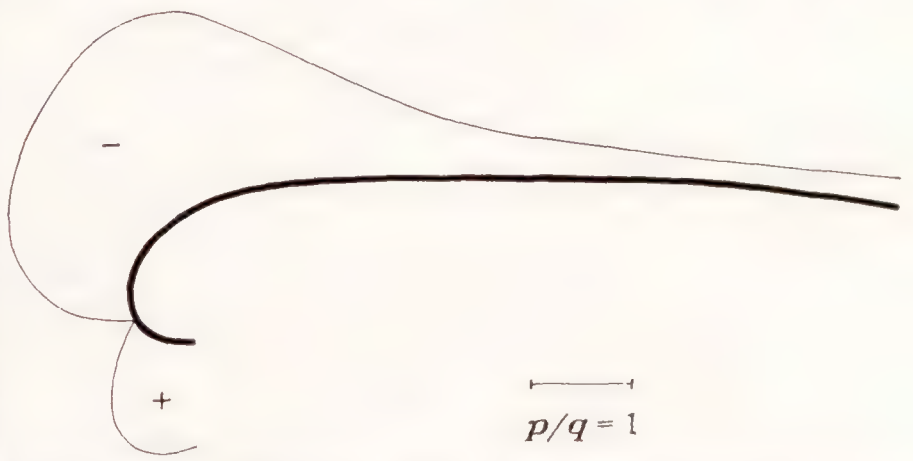

FIGURE 1.—Typical pressure distribution on cowlings. Test arrangement 7-2-0-3-0.

Flight tests of a temporary installation showed promising results.

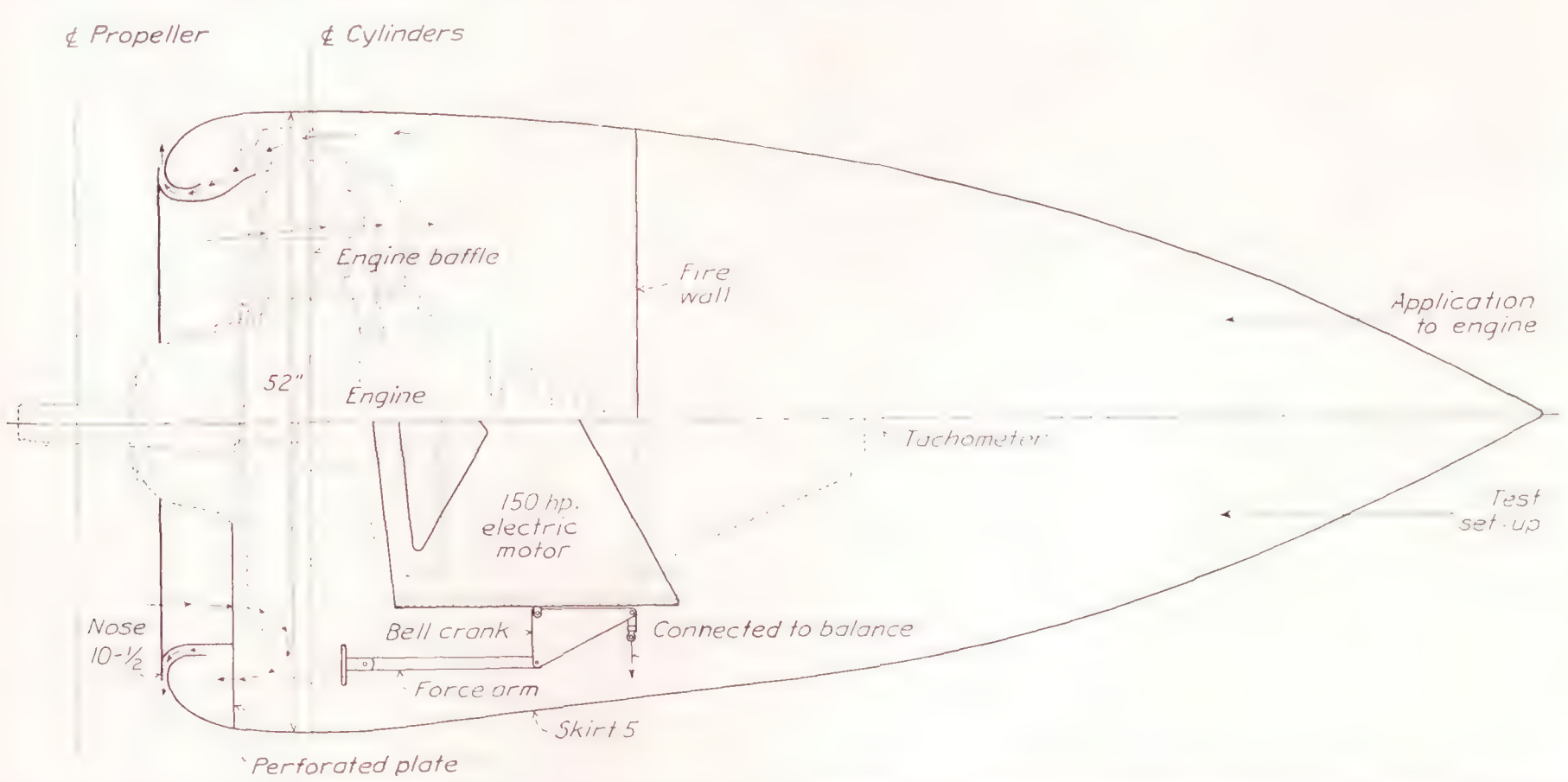

FIGURE 2.—Drawing showing the principle of operation of the nose-slot cowling. The upper half of the drawing shows the practical application; the lower half shows the arrangement of the test installation with nose 10-½.

INTRODUCTION

It has been shown in the report on conventional cowlings (reference 1) that the available pressure head across the engine is very nearly equal to 1 q and that only in very extreme cases, as by the use of skirt flaps, may this value be exceeded by about 20 percent. The pressure-distribution tests reported in the same reference show that a negative pressure of several times the velocity head is available near the nose of the cowling. (See fig. 1.) Since cases may be expected to occur in which a

large pressure drop is desired, a special type of cowling was designed to have the exit opening at or very near the front portion of the cowling in order to make use of this available pressure drop. At first thought, this arrangement might be expected to be inefficient as a fairly large disturbance in the entire boundary layer is normally expected. Peculiarly enough the contrary seemed to be the case, the very first design showing a very high efficiency. The air enters the cowling in the central front opening in the usual manner, passes through the engine baffles, and is then returned across

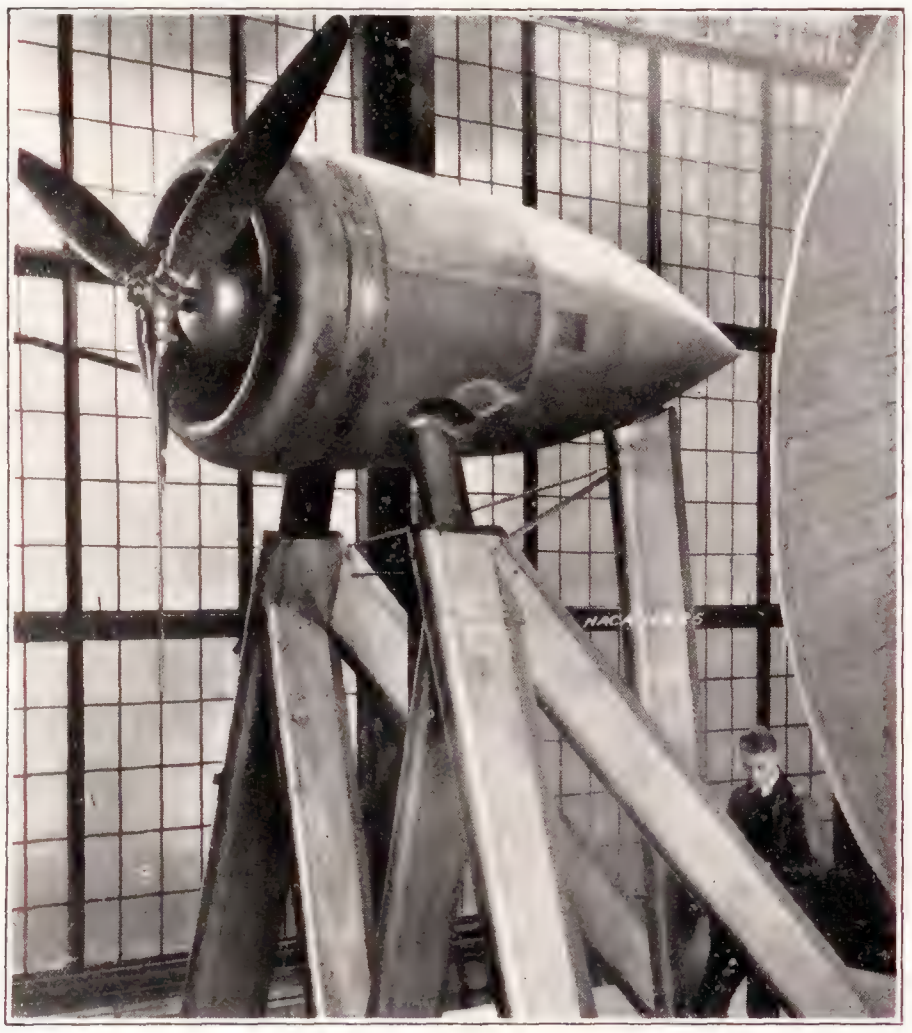

FIGURE 3.—The test installation in the 20-foot wind tunnel.

the top of the cylinders, guided into the nose ring, and discharged through the slot.

DESCRIPTION OF TEST ARRANGEMENT

Figure 2 gives a general idea of the test arrangement; the engine resistance was replaced by a perforated plate just behind the nose ring, as shown in the lower half of the figure. This plate contained several hundred 1-inch holes, any number of which could be closed as desired, thus representing engines of a wide variety of conductivities. Figure 3 is a photograph of the installation with the original nose, which is designated 10–½, the first numeral giving the number of the nose and the second numeral giving the exit opening in inches, as some of these noses were tested with two sizes of exit opening. Figure 4 (a) is a photograph of nose 10–½; figures 4 (b) and 4 (c) show two more designs, 11–1 and 12–1, tested successively. A total of nine cowlings of

(a) Nose 10-½.

(b) Nose 11-1.

(c) Nose 12-1.

FIGURE 4.—Photographs of noses tested.

this type were tested, all of which are shown with the proper designations in the scale drawing (fig. 5). All the cowling nose rings were given the same major dimensions; all were fitted to the same perforated disk comprising the test resistance. The conductivity of this perforated disk could be changed at will between the limits of 0 to 0.09, thus simulating the complete range of actual installations. No heat-transmission tests were conducted in connection with these tests as the requisite information was available from reference 1.

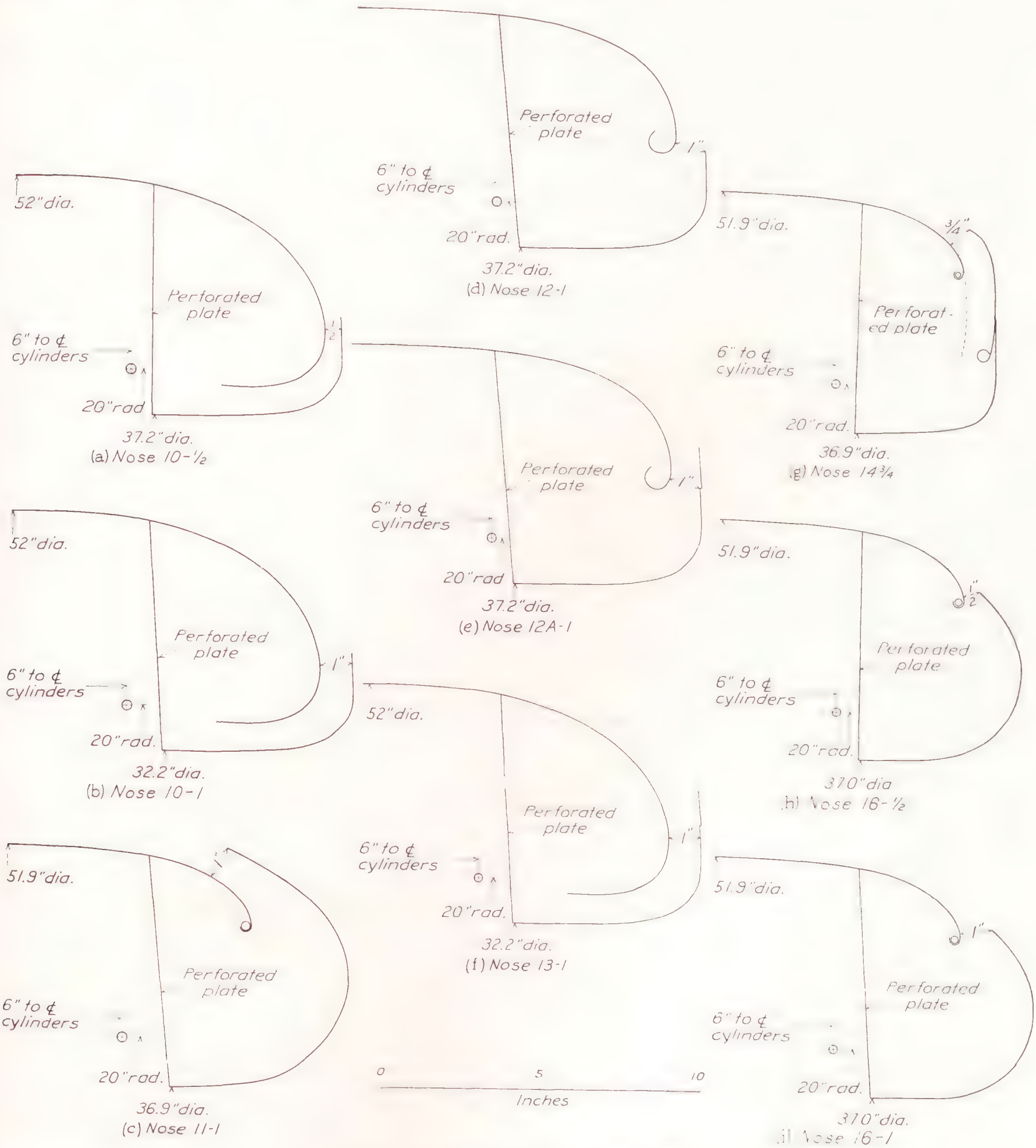

FIGURE 5.—Drawings of the nine nose cowlings tested.

The tests were performed at both high and low air speeds, the low speeds for the purpose of obtaining the cooling from the propeller slipstream alone. The tests were conducted as usual, with the propeller both on and off for the sake of completeness.

DEFINITION OF PARAMETERS USED

The various terms used in the paper will be defined and briefly discussed. These terms are taken from the report on conventional cowlings (reference 1).

(1) Pump efficiency, defined as

$$\eta_p=\frac{Q\Delta p}{(D-D_0)V}$$

where Q is the quantity of air per second which is forced through the resistance.

Δp, the associated pressure drop across the same resistance.

D, the observed drag of the cowling-nacelle unit.

D_0, the drag of a body of identical major dimensions but with the cooling channels closed and the outline faired into a streamline contour.

V, the air speed.

It may thus be seen that $Q\Delta p$ is the useful work done per second and that $(D-D_0)V$ is the work expended. It will be realized from the following that the pump efficiency is a very precise measure of the aerodynamic quality of the design. For the case of the power run, or the propeller on, the pump efficiency is given by the formula

$$\eta_p=\frac{(\Delta p/q)^{3/2}}{\eta_0-\eta}\quad\frac{P_cS}{KF}$$

where the quantities K, F, P_c, S, η_0, and η will be defined under the next headings.

(2) Conductivity, defined as

$$K=\frac{A/F}{\sqrt{\Delta p/q}}=\frac{Q}{\sqrt{\Delta p/q}FV}$$

where F is the maximum cross-sectional area of the nacelle. This quantity gives the inverse of the resistance of the engine to the air flow and is nondimensional.

The apparent conductivity of the exit opening may similarly be represented by a value K_2 which is simply the ratio of the area of the exit opening to that of the maximum cross section of the nacelle, or

$$K_2=\frac{A_2}{F}$$

It has been shown in reference 1 that the following relation exists in regard to the flow through the cowling:

$$\frac{\Delta P}{q}=\left(\frac{Q}{FV}\right)^2\left[\frac{1}{K^2}+\frac{1}{K_2{}^2}\right]$$

where ΔP is equal to the total head of the air entering the cowling minus the static pressure in the region of the exit opening. The former pressure is always found to be very nearly equal to the total head of the air stream. This equation will be referred to as "the equation of flow regulation."

(3) Propeller load factor or disk-loading coefficient, defined as

$$P_c=\frac{P}{qSV}$$

where P is the power supplied to the propeller shaft, and S is the disk area of the propeller. This quantity is in the first order proportional to the contraction of the propeller slipstream (reference 1). Equal values of P_c thus essentially represent geometrically identical flow pictures. In the analysis of the results obtained for various propellers a certain simplicity is achieved in comparing such results at a fixed value of P_c.

(4) Net efficiency, defined as

$$\eta_n=\frac{RV}{P}$$

in the case of the power runs, where R is the thrust of the unit as given by the thrust scale. The net efficiency obtained with the cooling air shut off and the outline faired into a carefully streamline contour is needed to determine the pump efficiency for the case of propeller on and is designated η_0.

(5) In reference 2 the quantity $\Delta p/n^2$ was chosen as a characteristic function to represent the cooling properties of any particular combination of engine cowling and propeller at the condition of zero air speed, representing the case of cooling airplane engines on the ground. The square root of the foregoing quantity, or $\sqrt{\Delta p}/n$, obtained from experimental data, is given as a function of the advance-diameter ratio V/nD. It is realized that the propeller at zero air speed acts very much the same as any other blower in regard to the pressure produced for cooling. The quantity $\Delta p/n^2$ or $\sqrt{\Delta p}/n$ is therefore very nearly a constant for a given propeller at a given blade-angle setting and is independent of the revolution speed of the propeller. It is referred to in the following discussion as the "pressure constant." The speed of the propeller may be considered known from the results of a previous investigation (reference 3).

TEST RESULTS

The test results are shown in condensed form in table I. Column 1 gives the designation of the cowling nose corresponding to those given in figure 5. Column 2 shows the propeller used, the zero standing for propeller off and the B_x and C, for the purpose of the present paper, representing two normal 10-foot propellers (reference 3). The main difference between B_x and C is that B_x has a well-shaped airfoil section extending down close to the hub, whereas C has a round shank. Column 3 shows the apparent conductivity of the exit opening. Column 4 is the conductivity of the test resistance or "engine." Columns 5, 6, and 7 show the pressures (in terms of q) with respect to the test resist-

ance. Column 5 gives values of p_f, the pressures in front of, and column 6 gives values of p_r, the pressures in the rear of the resistance; column 7 gives values of Δp, the pressure difference across the resistance. Column 8 gives the drag in usual coefficient form C_D. Column 9 is given, for convenience, to illustrate the approximate forces involved by giving the drag at 100 miles per hour or, more exactly, at a q of 25.6 pounds per square foot for the drag run; i. e., the forward net

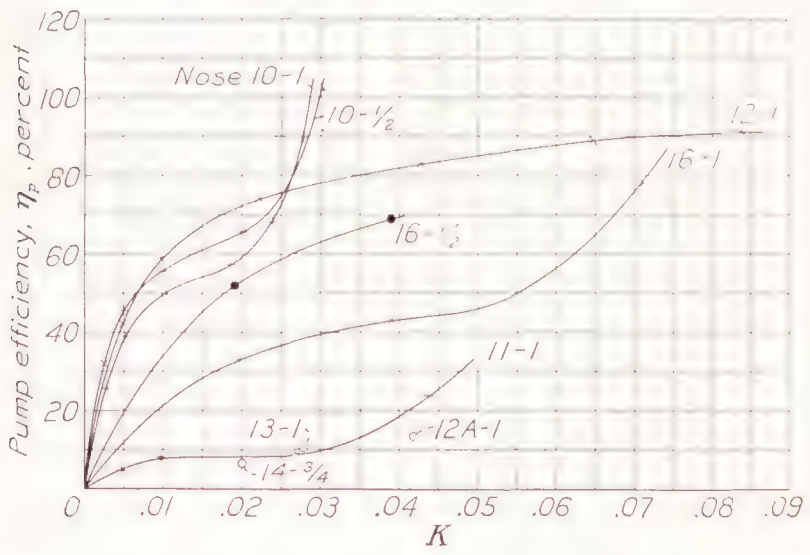

FIGURE 6.—Dependency of pump efficiency on conductivity.

thrust at the same tunnel speed and at a fixed disk loading for the propeller runs. Column 10 gives the net efficiency η_n for the propeller runs, and column 11 the pump efficiency η_p as defined in the preceding section.

In figure 6 the pump efficiency has been plotted against the conductivity for various noses. It was the very successful result on the original nose 10–½ that prompted the study of several other designs, which were later tested. Noses 10, 12, and 16 all tend to reach a 100-percent efficiency at conductivities beyond 0.07 and 0.08. Nose 10 actually exceeds 100-percent pump efficiency even at the low conductivity 0.03.

The reason for the relatively large efficiences obtained with this type of cowling lies in the fact that the velocities in the exit opening more nearly equal those of the external air stream. The beneficial effect of large exit velocities on the pump efficiency has been conclusively demonstrated in reference 1. The reason for the larger exit velocities is due to the fact that a much larger pressure difference is available and that part of this difference may be used in the exit opening, leaving at least the usual pressure drop for cooling.

The noses showing a very low efficiency in figure 6 were designed primarily with the intention of obtaining a large available pressure drop at zero air speed. On the whole, the design was found to be critical, a minor change in the external contour sufficing to drop the efficiency from near 100 percent to a small quantity. It was found that a projecting edge at the slot, such as embodied in cowlings 12, 13, or 14 in figure 5, was very detrimental to the efficiency. It was also noted that the highest efficiency was obtained by locating the outlet in a converging-flow field, as for nose 10, in contrast to the low efficiency obtaining by locating the outlet back of the maximum velocity, as for nose 11.

As is evident from the introduction, the main reason for designing and testing the new nose-slot cowling is the large pressure available for cooling. Figure 7 is a plot of the results in table I giving the available pressure against the engine conductivity, K. It is seen that the available pressure difference created by this type of cowling lies in the region of 2 q and in a few cases even exceeds 2.5 q. The decrease in available pressure with increased conductivity is caused by the fairly small size of the apparent exit conductivities. It may be observed from the equation of flow regulation previously given that a small value of K_2 means that a large part of the pressure difference created by the cowling is used to produce velocity head in the exit opening and the remaining pressure Δp available for cooling is correspondingly reduced. If the pressure available for cooling Δp is added to the velocity head in the slot, it is found that the total, which is ΔP, is of a nearly constant magnitude for any given cowling.

The values K_2 have been inserted for the various noses shown in figure 7. It has been shown in reference 1 that K=0.05 may be considered as the normal value of the conductivity of a well-baffled single-row radial engine. The average available pressure of the nose cowling at this conductivity is seen to approximate 1 q and to reach a maximum of about 1¼ q with nose 16–1. A comparison of the available pressure drops and efficiencies at any desired conductivity with those obtained

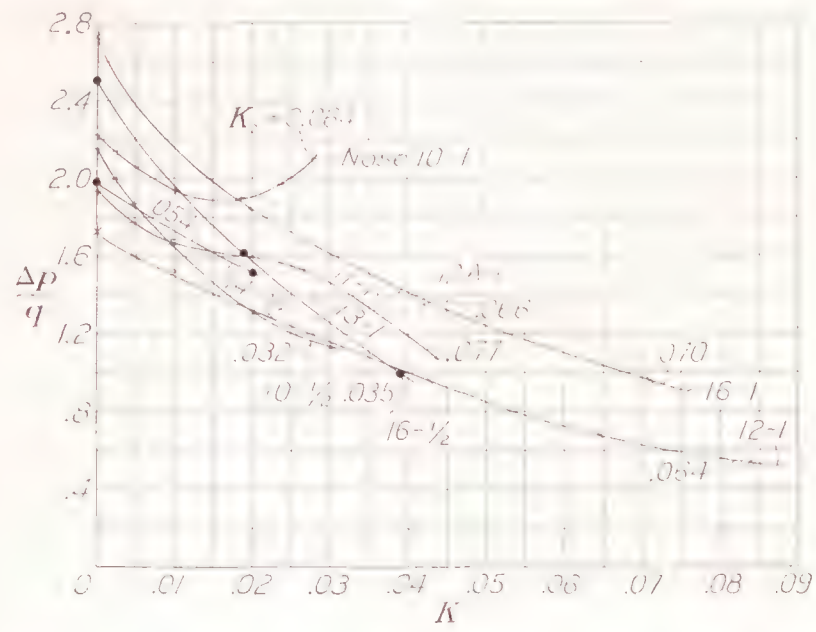

FIGURE 7.—Available pressure differences across the engine plotted against conductivity.

on the regular cowlings (reference 1) shows that the nose-slot cowlings for most conditions are superior; hence, at an available pressure drop across the engine of about 1 q, the efficiencies on some of the nose-slot cowlings approach 100 percent, while in the normal type they were of the order of 60 to 80 percent.

No attempt was made during the present investigation to test nose-slot cowlings with large exit conductivities. Such cowlings should provide a larger pres-

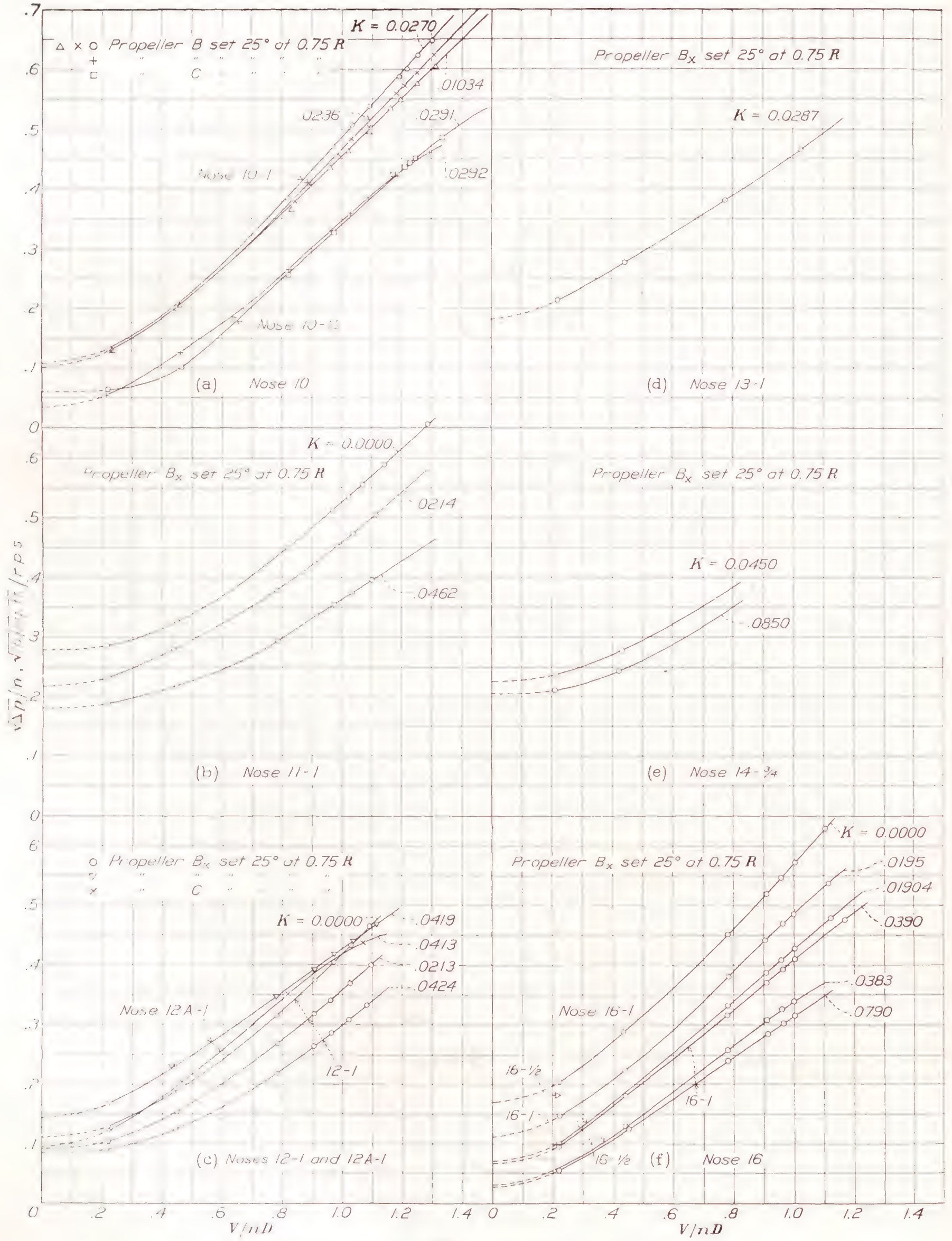

FIGURE 8.—Pressure constants $\sqrt{\Delta p/n}$ against V/nD for the several noses tested.

sure drop for cooling, probably at some expense of pump efficiency. Since the largest pressure drop is

FIGURE 9.—Original cowling installation on the Curtiss BFC–1 airplane.

needed only at low speed, the matter of some efficiency loss is not important. It is perfectly possible to provide means for changing the exit opening during flights.

FIGURE 10.—Close-up of the original cowling on the Curtiss BFC–1 airplane

The experimental results in regard to the pressure drop available for cooling with the propeller slipstream at zero air speed are given in figure 8 for noses 10, 11, 12, 13, 14, and 16. These results will be more fully understood by a study of reference 2, which shows the pressure constant at zero air speed for various normal and special arrangements. Noses 10, 12, and 16 are seen to give very low pressure constants at the ground point. Nose 11 compares favorably with the best results previously obtained on normal cowlings. Noses 13 and 14 also give large available pressures on the ground. It is noticed, in general, that the noses giving high available pressures on the ground are not efficient in the flight condition, and vice versa.

PRELIMINARY FLIGHT TESTS OF THE NEW TYPE N. A. C. A. COWLING ON BFC-1 AIRPLANE

In order that the practical value of the information on the new type of cowling might be demonstrated,

FIGURE 11.—The Curtiss BFC–1 airplane equipped with the nose-slot cowling.

the following flight tests were made with a preliminary cowling installation on the Curtiss BFC–1 airplane.

The Curtiss BFC–1 airplane (fig. 9) has a Wright SGR–1510 twin-row, 14-cylinder, geared engine, completely equipped with pressure baffles and a wide-chord ring cowling (fig. 10). A selective thermocouple installation allowed the determination of temperature for 28 positions on the heads and bases of the 14 cylinders. In this condition a level flight was made for reference purposes at maximum allowable continuous power for a sufficient length of time to allow all temperatures to stabilize. Complete data identifying the flight were recorded.

The new N. A. C. A. nose-slot cowling was then installed as shown in figure 11. This photograph does not show the external oil cooler, as in figure 1, as it had been removed just before the picture was taken. The installation used nose 16–1 (fig. 5) and was arranged as shown in the upper part of figure 2, except for the fact that the internal dividing wall was located between the heads and the cylinder barrel and below the spark plugs. The wall extended back to the second row. The flow is approximately as indicated by arrows in the upper part of figure 2. Close-up photographs of the design are shown in figure 12.

Another change consisted in reversing the pressure baffles on the cylinder heads to suit the reversed flow direction; the baffles on the barrel were redesigned to fit the new installation. Three thermocouples on front cylinders were moved from the rear to the front spark-plug bosses. It should be noted that the location of the exhaust manifold (see fig. 10) could not be changed for these tests and that therefore it was entirely enclosed within the new cowling.

The operation on the ground of the engine with the new nose-slot cowling indicated the absence of excessive heating, which would have prevented flight tests. There was some evidence of unusual local heating, mainly of the rubber connections on the intake manifold. It is appreciated that the completely new arrangement might cause some change in local heating of parts not designed for the type of air flow provided by this cowling. No evidence of overheating appeared. After a cautious take-off and climb, a level flight reproducing the conditions of the one with the original cowling was made. From this flight the following comparison was obtained.

At the same density altitude and with the same power but with a free-air temperature lower by 13° C., the indicated air speed was, within the accuracy of measurement, the same. The oil, both in and out, was 6° C. cooler; the cylinder bases consistently averaged 30° C. cooler; the heads, 35° C. hotter, there being little difference between the front and rear plugs; and the magneto, 30° C. cooler. No difficulties were experienced. The handling characteristics of the airplane, the visibility, the local cockpit heating, and the engine-operating conditions appeared unchanged. Another flight verified the results.

An inspection immediately after the engine was stopped on the ground revealed nothing amiss; the engine accessory or auxiliary compartment and the cowling aft of the cylinders was exceptionally cool. It

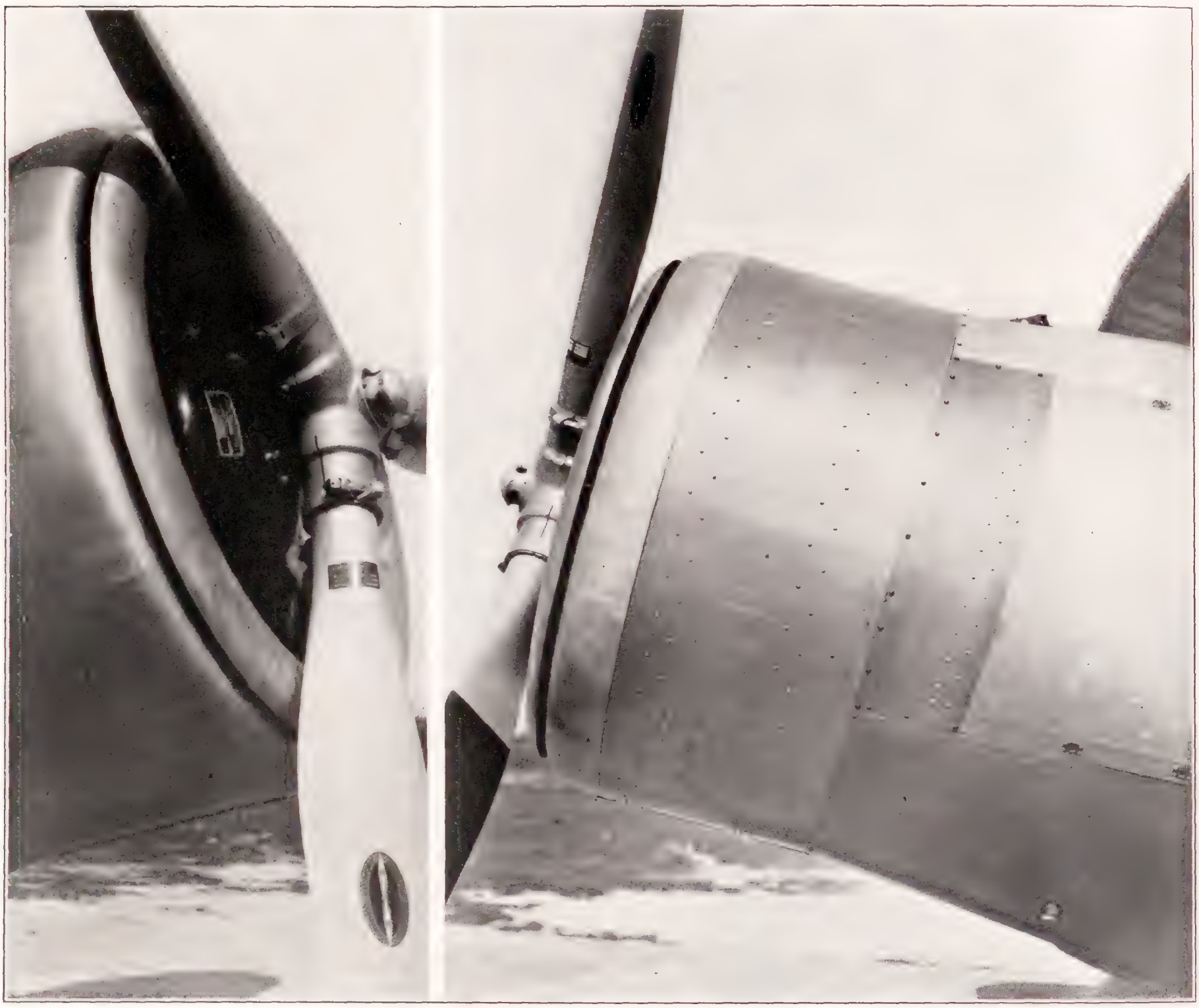

FIGURE 12.—Close-ups of the nose-slot cowling installed on a Curtiss BFC–1 airplane.

was interesting to observe that, as expected, the nose of the cowling was the hottest point.

In view of the fact that the air used to cool the heads contains also the accumulated heat obtained from the exhaust manifold, the results obtained indicate very promising possibilities for considerably improved cooling when the baffling and manifold locations are designed specifically for this type cowling. Possible speed gains are also indicated when the external cowling lines may be incorporated in a new design rather than adapted to an already existing afterbody shape.

GENERAL CONCLUSIONS

1. It has been found that the new type nose-slot cowling produces pressure differences of 2 to 2.5 times the velocity head of the air stream, as compared with 1 velocity head for the normal cowling. This fact is important as regards cooling in climb and at low air speeds.

2. A well-designed nose-slot cowling shows pump efficiencies close to 100 percent, owing to the fact that a smaller fraction of the total available pressure head is needed in the resistance, thus leaving a larger velocity head in the exit opening and reducing the impact or mixing losses that take place as the low-energy cooling air re-enters the main air stream.

3. Nose-slot cowlings designed for high efficiency at normal speed were found to be slightly inferior to normal cowlings in regard to cooling in the propeller slipstream. A specially designed nose-slot cowling for improving the cooling on the ground was found to be inefficient at normal-flight speeds in comparison with normal cowlings. A two-slot design, in which one slot may be closed at will, may therefore be recommended for cases in which good cooling from the propeller slipstream is particularly important.

4. The nose-slot cowling is critical in regard to design. It has been found that the exit opening should be located so as to permit the low-energy air to join the main air stream in a convergent-flow field, that is, ahead of the point of maximum velocity. High efficiency is obtained only by exercising great care in the detail design.

5. Preliminary flight tests gave promising results.

Langley Memorial Aeronautical Laboratory,
National Advisory Committee for Aeronautics,
Langley Field, Va., *June 5, 1936.*

REFERENCES

1. Theodorsen, Theodore, Brevoort, M. J., and Stickle, George W.: Full-Scale Tests of N. A. C. A. Cowlings. T. R. No. 592, N. A. C. A., 1937.
2. Theodorsen, Theodore, Brevoort, M. J., and Stickle, George W.: Cooling of Airplane Engines at Low Air Speeds. T. R. No. 593, N. A. C. A., 1937.
3. Theodorsen, Theodore, Stickle, George W., and Brevoort, M. J.: Characteristics of Six Propellers Including the High-Speed Range. T. R. No. 594, N. A. C. A., 1937.

TABLE I.—CONDENSED TEST RESULTS

1	2	3	4	5	6	7	8	9	10	11
Nose	Propeller	K_2	K	$\frac{p_f}{q}$	$\frac{p_r}{q}$	$\frac{\Delta p}{q}$	C_D	Drag in pounds at q=25.6 pounds/square foot, or thrust at $1/\sqrt[3]{P_c}$= 1.8 and q=25.6 pounds/square foot	η_n	η_p
10–½	0	0.032	0.0000	0.922	−1.250	2.170	0.1287	48.6	------	0.000
10–½	0		.00248	.904	−1.083	1.986	.1330	50.2	------	.318
10–½	0		.00497	.904	−.955	1.860	.1388	52.4	------	.457
10–½	0		.00981	.929	−.756	1.683	.1499	56.6	------	.552
10–½	0		.0200	.926	−.388	1.313	.1573	59.4	------	.652
10–½	0		.0304	.918	−.216	1.135	.1475	55.7	------	1.013
10–½	B		.0292	.881	−.153	1.034	------	250	0.716	1.278
10–½	C		.0291	.854	−.190	1.043	------	247	.708	.998
10–1	0	.064	.0000	.911	−1.313	2.223	.1372	51.8	------	.000
10–1	0		.00267	.930	−1.209	2.140	.1433	54.1	------	.260
10–1	0		.00527	.923	−1.117	2.040	.1510	57.0	------	.386
10–1	0		.01034	.927	−1.010	1.938	.1671	63.1	------	.500
10–1	0		.01862	.926	−.966	1.894	.1965	74.2	------	.568
10–1	0		.0238	.925	−1.058	1.983	.209	78.9	------	.680
10–1	0		.0278	.928	−1.166	2.095	.205	77.6	------	.899
10–1	B		.0270	.891	−1.101	1.992	------	236.0	.676	1.243
10–1	B		.0236	.887	−.955	1.840	------	239.0	.685	1.117
10–1	B		.01034	.901	−.907	1.808	------	242.0	.693	.555
11–1	0	.077	.0000	.925	−1.009	1.935	.299	113.0	------	.000
11–1	B_x		.0000	.913	−1.306	2.220	------	200.0	.573	.000
11–1	0		.00484	.918	−.849	1.768	.342	129.0	------	.0493
11–1	0		.00979	.934	−.731	1.665	.381	144.0	------	.0780
11–1	0		.0267	.943	−.593	1.536	.416	157.0	------	.0865
11–1	B_x		.0214	.923	−.800	1.723	------	166.0	.476	.197
11–1	B_x		.0462	.918	−.172	1.090	------	180.0	.516	.252
11–1	0		.0438	.950	−.114	1.064	.318	120.0	------	.233
12–1	0	.064	.0000	.933	−.794	1.725	.1245	47.0	------	.000
12–1	B_x		.0000	.920	−.561	1.482	------	244.0	.698	.000
12–1	0		.00493	.914	−.681	1.594	.1345	50.8	------	.426
12–1	0		.00998	.910	−.595	1.504	.1427	53.9	------	.584
12–1	0		.0222	.914	−.386	1.301	.1557	58.8	------	.739
12–1	B_x		.0213	.920	−.175	1.095	------	243.0	.696	.574
12–1	0		.0427	.932	−.017	.948	.1589	60.0	------	.827
12–1	0		.0647	.939	.261	.679	.1520	57.4	------	.890
12–1	B_x		.0424	.915	.137	.779	------	242.0	.693	.645
12–1	0		.0839	.933	.397	.536	.1475	55.7	------	.908
12A–1	B_x	.066	.0419	.920	−.613	1.531	------	150.5	.431	.276
12A–1	0		.0419	.957	−.373	1.330	.580	219.0	------	.137
12A–1	C		.0413	.863	−.569	1.433	------	147.0	.42	.240
13–1	0	.066	.0281	.938	−.446	1.384	.575	217.0	------	.099
13–1	B_x		.0287	.913	−.767	1.679	------	143.0	.41	.203
14–¾	0	.054	.0000	.948	−1.038	1.983	.527	199.0	------	.000
14–¾	B_x		.0000	------	------	------	------	------	.44	.000
14–¾	B_x		------	------	------	------	------	112.0	32	------
14–¾	0		.0201	.955	−.563	1.519	.651	246.0	------	.070
14–¾	0		------	------	------	------	.625	236.0	------	------
14–¾	B_x		------	------	------	------	------	105.0	.30	------
16–1	0	.070	.0000	.921	−1.809	2.730	.1324	50.0	------	.000
16–1	B_x		.0000	.897	−1.750	2.645	------	244.0	.700	.000
16–1	B_x		.01950	.894	−1.030	1.923	------	219.0	.627	.490
16–1	0		.01965	.903	−.946	1.848	.263	99.5	------	.325
16–1	0		.0388	.918	−.488	1.408	.263	99.5	------	.427
16–1	B_x		.0390	.893	−.499	1.391	------	216.0	.620	.568
16–1	B_x		.0790	.888	.061	.826	------	226.0	.648	.683
16–1	0		.0711	.908	−.049	.958	.1967	74.3	------	.782
16–½	0	.035	.0000	.890	−1.621	2.513	.1290	48.7	------	.000
16–½	B_x		.01904	.878	−.668	1.547	------	234.0	.671	.557
16–½	0		.01920	.903	−.712	1.614	.1872	70.7	------	.518
16–½	0		.0390	.907	.095	1.000	.1679	63.4	------	.688
16–½	B_x		.0383	.875	−.082	.955	------	235.0	.673	.561

38548—38——30

REPORT No. 596

COOLING TESTS OF A SINGLE-ROW RADIAL ENGINE WITH SEVERAL N. A. C. A. COWLINGS

By M. J. Brevoort, George W. Stickle, and Herman H. Ellerbrock, Jr.

SUMMARY

The cooling of a single-row radial air-cooled engine using several cowling arrangements has been studied in the N. A. C. A. 20-foot wind tunnel. The results show the effect of the propeller and several cowling arrangements on cooling for various values of the indicated horsepower in the climb condition. A table giving comparative performance of the various cowling arrangements is presented. The dependence of temperature on indicated horsepower and pressure drop across the baffles is shown by charts. Other charts show the limiting indicated horsepower against the pressure drop across the engine and the heat dissipated at various values of the indicated horsepower.

INTRODUCTION

A study was made to determine the cooling characteristics and performance of a typical radial air-cooled engine, using several cowling arrangements. The tests were made in the N. A. C. A. 20-foot wind tunnel, which has a maximum speed of 110 miles per hour. With such a maximum speed the tests are obviously confined to the condition of climb. From practical considerations such a range is ideal because, except under very special operating conditions, the problem of cooling is most important during climb. It follows, then, that all conclusions concerning aerodynamic characteristics and efficiency drawn from these tests relate to the condition of climb alone. In tests covering the complete range of take-off, climb, and cruising conditions for several cowlings (references 1 and 2), it was shown that certain cowlings which appear aerodynamically good in climb are poor in the cruising condition.

The results show, for a particular engine, the relationship existing between the cooling and the developed horsepower and the pressure drop across the baffles. It is obvious that the results are, in detail, applicable only to this engine. In the discussion of the results, however, the chief emphasis is laid on general considerations and on the mechanism of cooling. It is believed that, although the details are interesting, the more important aspect of the investigation is the contribution to a clearer picture of the mechanism of cooling.

EQUIPMENT AND TESTS

The engine was mounted in the N. A. C. A. 20-foot wind tunnel (reference 3) as shown in figure 1. The engine is a 9-cylinder radial R–1340 S1H1–G Pratt & Whitney Wasp. The over-all diameter is 51$\frac{7}{16}$ inches. It is rated at 550 horsepower at 2,200 r. p. m. and at 8,000 feet altitude. It has a 3:2 reduction gear, a compression ratio of 6, and is equipped with a geared

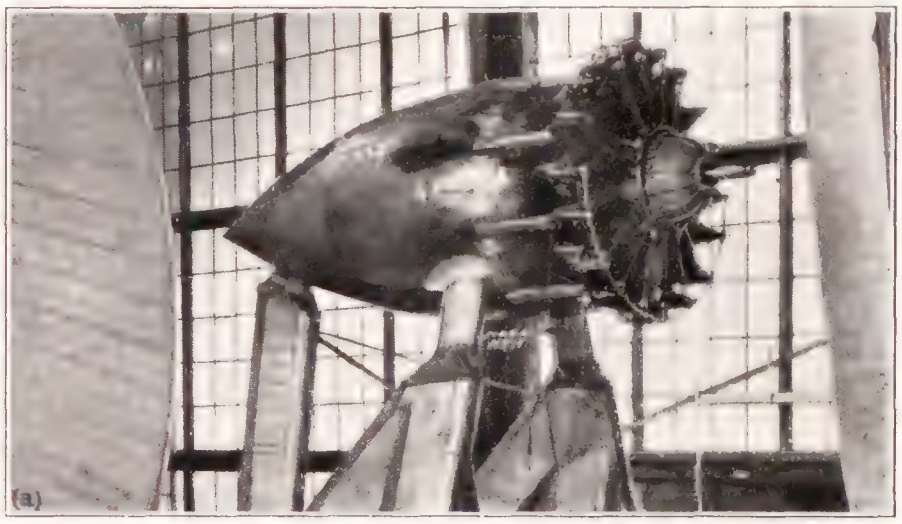

(a) Bare engine.

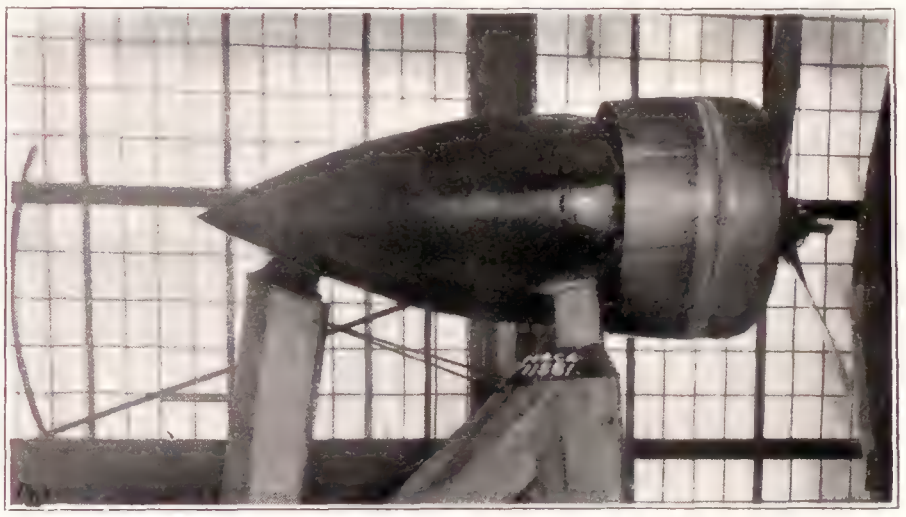

(b) With cowling.

FIGURE 1.—Engine and nacelle set-ups.

centrifugal supercharger that operates at 12 times engine speed. The bore of the cylinders is 5.75 inches and the stroke is 5.75 inches.

The two propellers used are shown in figure 2. Propeller A is a Hamilton Standard controllable propeller of blade form No. 6101–0 and propeller B is a Hamilton Standard adjustable propeller of blade form No. 1C1–0.

Figure 3 is a profile drawing of the engine and nacelle with the various noses, skirts, and inner cowlings used in this study.

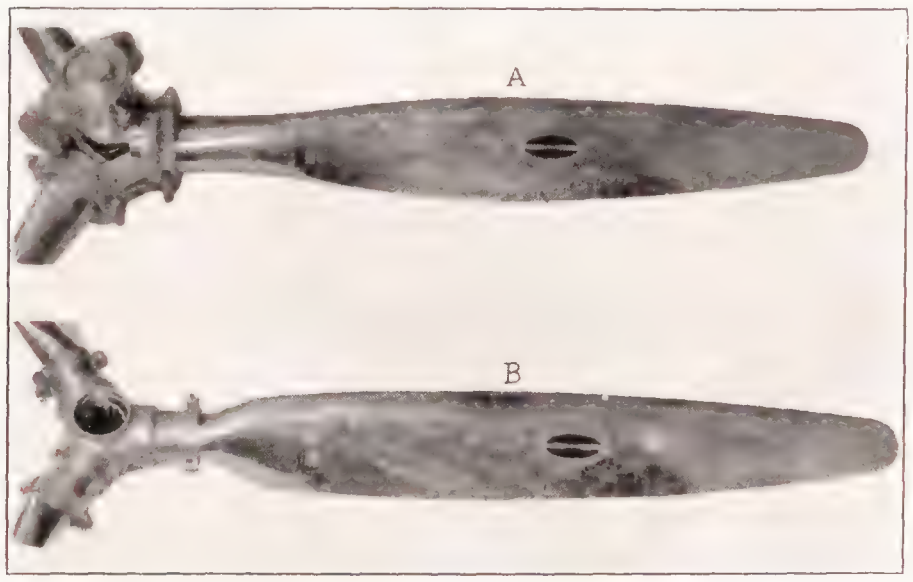

Controllable (A). Adjustable (B).

FIGURE 2.—Propellers used.

Figure 4 shows the arrangement of baffles on the head and barrel of the cylinder. Note that these baffles are not tightly fitting in the sense that they touch the fin tips but that they are comparatively close-fitting baffles.

The temperature of the engine was measured by 24 thermocouples connected to a recording pyrometer. The thermocouples were peened to the head and spot-welded to the barrel of the cylinder. The thermocouple locations on cylinder 3 are shown by figure 5. Thermocouples 1 to 9 were located on cylinders 1 to 9, respectively, at the position indicated for thermocouple 3 in figure 5. Thermocouples 10, 11, 12, and 13 were located on cylinders 1, 3, 5, and 7 at the position shown for thermocouple 11. Thermocouple 24 was located on cylinder 8 at the position of thermocouple 23 on cylinder 3. The remaining thermocouples were located on cylinder 3. Cylinders are numbered counter-clockwise, cylinder 1 being at the top.

Air temperatures in front of and behind the engine, oil-in and oil-out temperatures, and carburetor-air temperatures were measured by shielded resistance thermometers. The oil was cooled by a water radiator located inside the nacelle.

The drop in pressure across the engine was measured by pitot-static tubes located in front of and behind the cylinders. The quantity of air passing through the baffles was measured by pitot-static tubes located in the skirt exit.

The engine power was controlled by varying the manifold pressure. The manifold pressure, engine speed, and air temperature gave the horsepower from a calibration furnished by the manufacturer. The fuel consumption was measured and frequent checks were made on the exhaust-gas analysis from each cylinder.

The routine of an individual test was as follows: The engine speed, the horsepower, and the tunnel speed were adjusted to the desired values. Sufficient time was allowed for all temperatures to become stabilized. All temperatures and pressures were then recorded. This procedure was repeated for various values of engine speed, indicated horsepower, and tunnel speed. Each cowling arrangment was tested in this manner. Ranges of engine speeds from 1,600 to 2,000 r. p. m., power from 300 to 550 horsepower, and air speeds from 80 to 110 miles per hour were covered. Drag tests with propeller off were made.

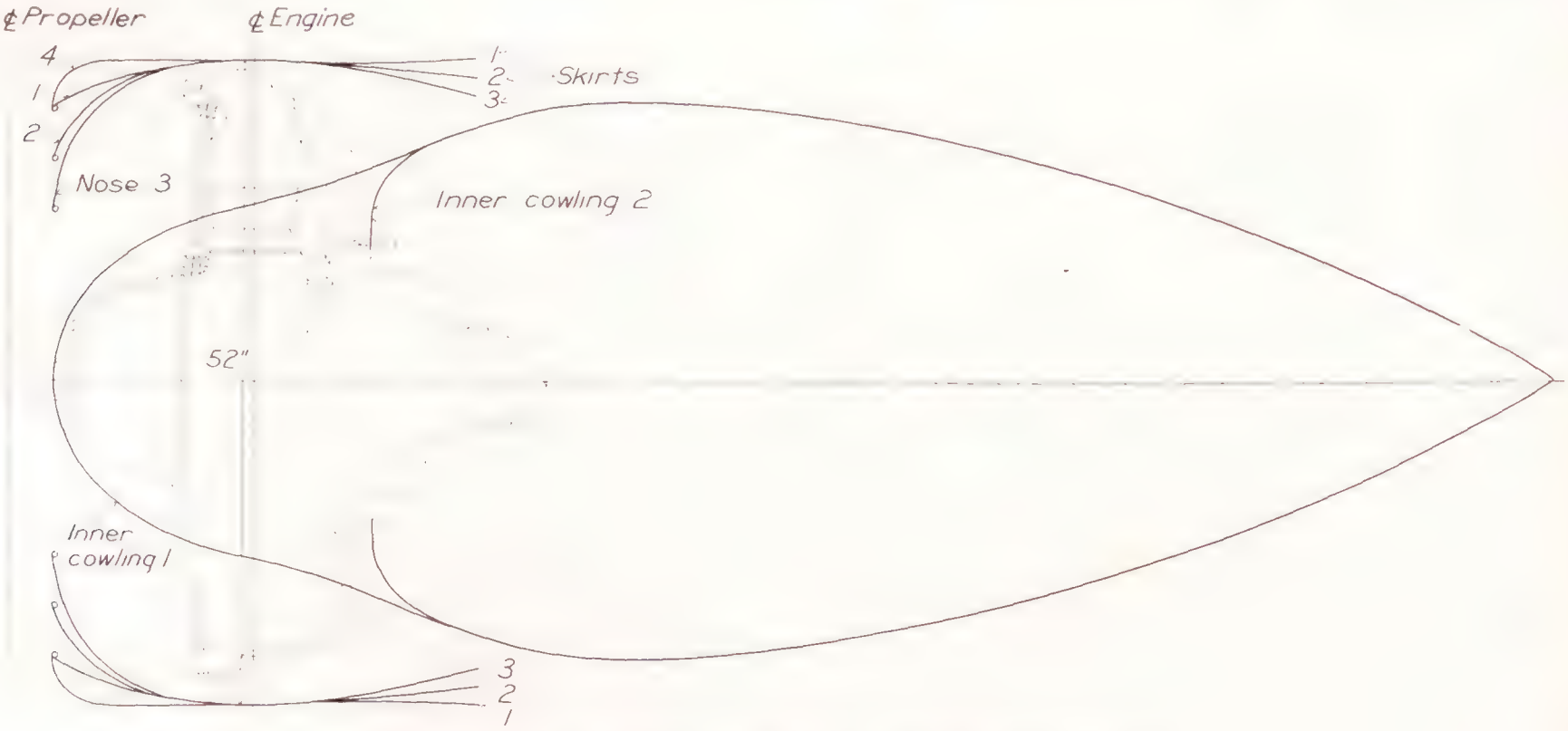

FIGURE 3.—Sketch of cowlings tested. Wasp SIHI-G engine fairing and cowlings.

LIST OF SYMBOLS

Q, quantity of cooling air passing through the engine per second.

Δp, pressure drop across the baffle.

$K=\dfrac{\dfrac{A}{F}}{\sqrt{\dfrac{\Delta p}{q}}}$, conductivity of the engine.

F, cross-sectional area of the engine.
ρ, mass density of the air.
A, area of the free air stream entering the engine.

$q=\frac{1}{2}\rho V^2$, dynamic pressure of the free air stream.

p_f, pressure in front of the cylinder.
p_r, pressure in rear of the cylinder.
V, velocity of the free air stream.

$P_c=\dfrac{P}{qSV}$, propeller disk loading coefficient.

P, power supplied to the propeller.
S, disk area of the propeller.
n, revolutions per second of the propeller.
D, diameter of the propeller.
ΔT, difference between the temperature of a particular point on the cylinder and that of the inlet cooling air.

ANALYSIS OF THE PROBLEM

The useful work done in cooling the engine is $Q\Delta p$, and Q is proportional to $\sqrt{\Delta p}$. The power to cool can then be written as proportional to $(\Delta p)^{3/2}$. It has been shown in reference 1 that

$$\text{Power to cool}=\frac{\sqrt{2}KF(\Delta p)^{3/2}}{\sqrt{\rho}}$$

$$K=\frac{\dfrac{A}{F}}{\sqrt{\dfrac{\Delta p}{q}}}$$

The value $K=0.06$ was constant throughout the investigation. It depends entirely upon the finning and the baffling of the cylinders. The pressure drop Δp is a function of the air-stream velocity and of the cowling and baffle design. It is obvious from the foregoing equation that the selection of the minimum values of K and Δp which will provide adequate cooling is very desirable from the standpoint of aerodynamic efficiency.

Reference 1 has shown that it is practically impossible to develop a Δp of more than $1.3q$ for this general type of cowling. Such a high value, moreover, is attained at very low efficiency.

The problem, then, is to determine under what conditions and how efficiently the modern engine can be cooled with various pressure drops. This study of the climb condition answers a part of that question.

In such a study it is extremely important that only the quantity under consideration be permitted to vary, all other factors remaining constant. This condition is particularly difficult when the tests are made on an actual engine, where variations in air-fuel ratio, car, buretor-air temperature, oil temperature, oil pressure-

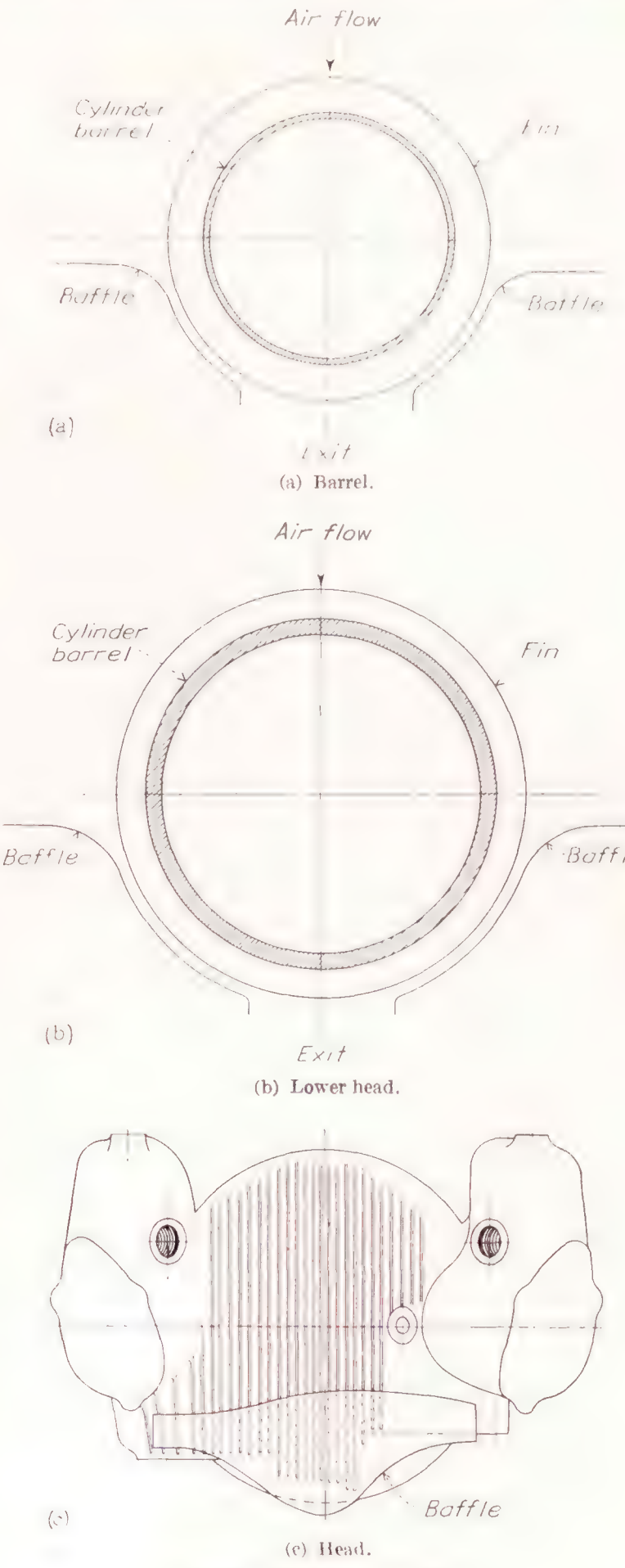

(a) Barrel.

(b) Lower head.

(c) Head.

FIGURE 4.—Baffle arrangement.

and mechanical condition of the engine must be eliminated as far as possible. Tests have shown (reference 4) that a variation of 1.0 in the air-fuel ratio will result in a change of approximately 20° F. in the cylinder temperature. The maximum variation from cylinder

to cylinder was 0.8 of a ratio, which should result in a temperature variation of 16° F. The carburetor-air temperature never varied more than 24° F. for a single cowling test nor more than 58° F. for all the tests. Such variations will, according to unpublished test results, cause temperature variations of 3° F. and 8° F., respectively. The oil temperature and pressure were maintained relatively constant and the spark plugs and mechanical condition of the engine were checked at frequent intervals.

It is believed that the careful control of these variables reduced the variation in results due to undesired

RESULTS

Table I is presented as a short résumé of the results for all the cowlings for a particular horsepower, engine speed, and air speed. Column 1 gives the number of the nose; column 2 gives the number of the skirt; column 3 gives the number of the inner cowling. These three numbers are used, in the same order, to designate the complete cowling. Column 4 gives the measured drag of the engine and nacelle at a dynamic pressure of 25.6 pounds per square foot. Column 5 gives the propeller designation. Column 6 gives the pressure in front of the cylinders divided by the dynamic pressure;

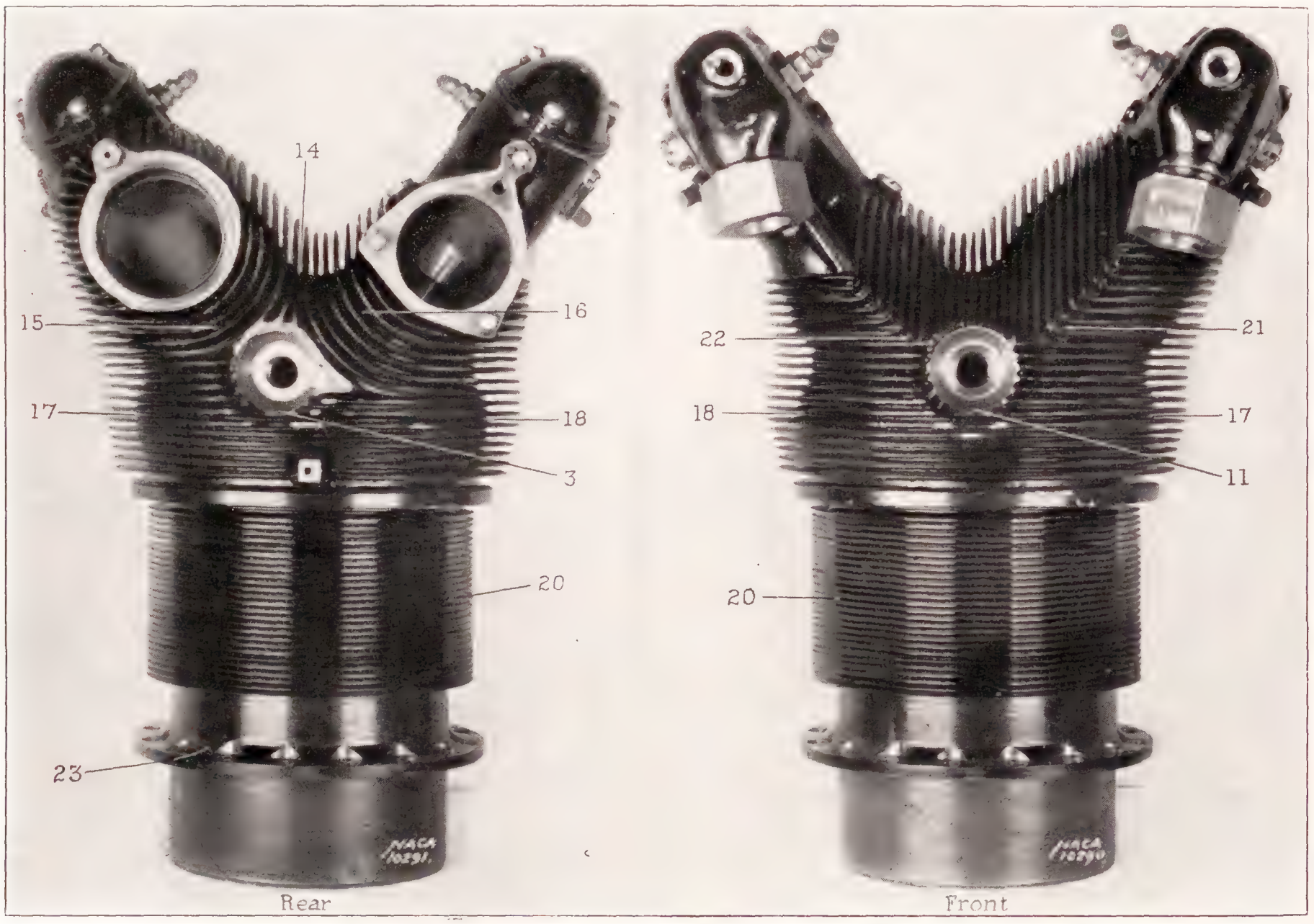

FIGURE 5.—Thermocouple locations on cylinder 3.

causes to a minimum. The air-fuel ratio was checked by exhaust-gas analysis and the fuel consumption was maintained constant at 0.57 lb./b. hp.-hr. by the use of a fuel flow meter. The variations of air-fuel ratio from cylinder to cylinder are characteristic of the engine and check the cylinder-to-cylinder temperature variation reasonably well. Any variation due to carburetor-air temperature or over-all air-fuel ratio affects all cylinders and causes discrepancies resulting in a scattering of the points. This type of variation was relatively small.

Isolated cases of temperatures that appear to be in error by as much as 40° F. will be found but, in general, the temperatures are accurate to $\pm 10°$ F.

column 7 gives the pressure in rear of the cylinders divided by the dynamic pressure; column 8 is the difference between columns 6 and 7, or the pressure drop, in percentage of q, across the baffles. Column 9 is the actual pressure drop across the baffles in pounds per square foot at a dynamic pressure of 25.6 pounds per square foot, which corresponds to 100 miles per hour under standard conditions. Column 10 gives the temperature in front of the cylinder, an average of thermocouples 10 through 13; column 11 gives the temperature in the rear of the cylinder, an average of thermocouples 1 through 9. Throughout the report, all temperatures are given as the difference between the temperature at

a particular point on the cylinder and that of the inlet cooling air. Column 12 gives the net thrust of the engine-propeller-nacelle unit at a value of $1/\sqrt[3]{P_c}=1.12$ and a velocity of 100 miles per hour.

TABLE I

[100 m. p. h.; 425 i. hp.; 1,800 r. p. m.; 380 b. hp.]

1	2	3	4	5	6	7	8	9	10	11	12
Nose	Skirt	Inner cowling	Drag (lb.) at $q=25.6$ lb. per sq. ft.	Propeller	$\frac{p_f}{q}$	$\frac{p_r}{q}$	$\frac{\Delta p}{q}$	Δp (lb. per sq. ft.)	Temperature difference		Net thrust (lb.) for $1/\sqrt[3]{P_c}=1.12$ and $q=25.6$ lb. per sq. ft.
									Front (°F.)	Rear (°F.)	
1	1	1	152.4	Off	1.00	−0.252	1.252	32.0			
1	1	1		A	0.782	−.508	1.290	32.1	273	239	931
1	2	1	117.1	Off	.990	−.091	1.081	27.7			
1	2	1		A	.770	−.083	.853	21.1	293	279	963
1	3	1	106.8	Off	.975	.091	.884	22.6			
1	3	1		A	.849	.227	.622	15.2	292	296	979
2	3	1	53.5	Off	.977	.159	.818	21.3			
2	3	1		A	.824	.271	.553	13.7	275	313	950
2	2	1	69.0	Off	.978	−.068	1.046	26.5			
2	2	1		A	.752	−.114	.866	21.0	265	291	925
2	1	1	110.9	Off	.972	−.280	1.252	31.4			
2	1	1		A	.725	−.512	1.237	29.7	265	267	897
3	1	1	110.5	Off	.868	−.299	1.167	29.8			
3	1	1		A	.560	−.514	1.074	26.0	257	275	916
3	2	1	68.0	Off	.903	−.099	1.002	25.7			
3	2	1		A	.628	−.137	.765	18.8	286	309	942
3	3	1	55.2	Off	.920	.141	.779	20.3			
3	3	1		A	.671	.186	.485	11.8	315	357	937
4	3	1	56.0	Off	.984	.162	.822	21.4			
4	3	1		A	.808	.247	.561	13.7	304	320	947
4	1	1	111.0	Off	1.000	−.273	1.273	32.1			
4	1	1		A	.852	−.519	1.371	32.9	274	268	875
3	1	2	121.5	Off	.913	−.268	1.181	30.5			
3	1	2		A	.628	−.464	1.092	26.8	266	274	906
2	1	2	119.0	Off	.955	−.284	1.239	32.0			
2	1	2		A	.726	−.491	1.217	29.7	265	290	884
1	1	2	150.0	Off	.949	−.288	1.237	31.2			
1	1	2		A	.808	−.480	1.288	32.3	266	241	916
4	1	2	119.2	Off	.945	−.281	1.226	31.5			
4	1	2		A	.836	−.481	1.317	33.2	263	260	870
4	2	2	73.0	Off	.950	−.042	.992	25.5			
4	2	2		A	.810	−.042	.852	20.4	292	296	907

The dependence of the temperature upon the pressure drop is quite apparent. It can also be seen that large pressure drops are very costly in drag. It is evident that, for cases of propeller on, the pressure in front of the cylinder is decreased and that in the rear is exaggerated; that is, a negative pressure behind the cylinder with propeller off becomes more negative with propeller on and a positive pressure becomes more positive. It is well to remember that this effect of the slipstream is of importance only in the low-speed range; it becomes negligible under cruising conditions. Further, except in a few arrangements using skirt 1, which has a wide opening, $\Delta p/q$ is actually higher without the propeller operating. Another point of interest is that the maximum value of $\Delta p/q$ is approximately 1.3 in spite of the high power put into the slipstream.

The net thrust of the engine-propeller-nacelle unit as given in column 12 shows that nose 1 gives the greatest net thrust. It can be seen that this same nose gave the highest drag with the propeller off (column 4). This seemingly contradictory result is caused by the critical flow over the leading edge of nose 1 and is consistent with the results of references 1 and 2. Attention is called to the fact that nose 1 is again inferior in the high-speed range (reference 1). This result brings out the importance of testing cowlings at the operating condition under which best operation is desired.

Table I introduces the type of result derived from the tests. The plan of presentation of the results will be to show by charts the interdependence of the various quantities as the engine power, the air speed, etc., are varied.

Figure 6 shows plots of $\sqrt{\Delta p}/n$ against V/nD for the 10-foot-diameter propeller used. Plots of this type conveniently picture the relationship between the available pressure, the air speed, and the propeller speed. These results are not directly comparable with those presented in reference 2. The present tests were made using a controllable propeller, the blade-angle setting varying throughout the range of V/nD; whereas the tests of references 1 and 2 were made using an adjustable pro-

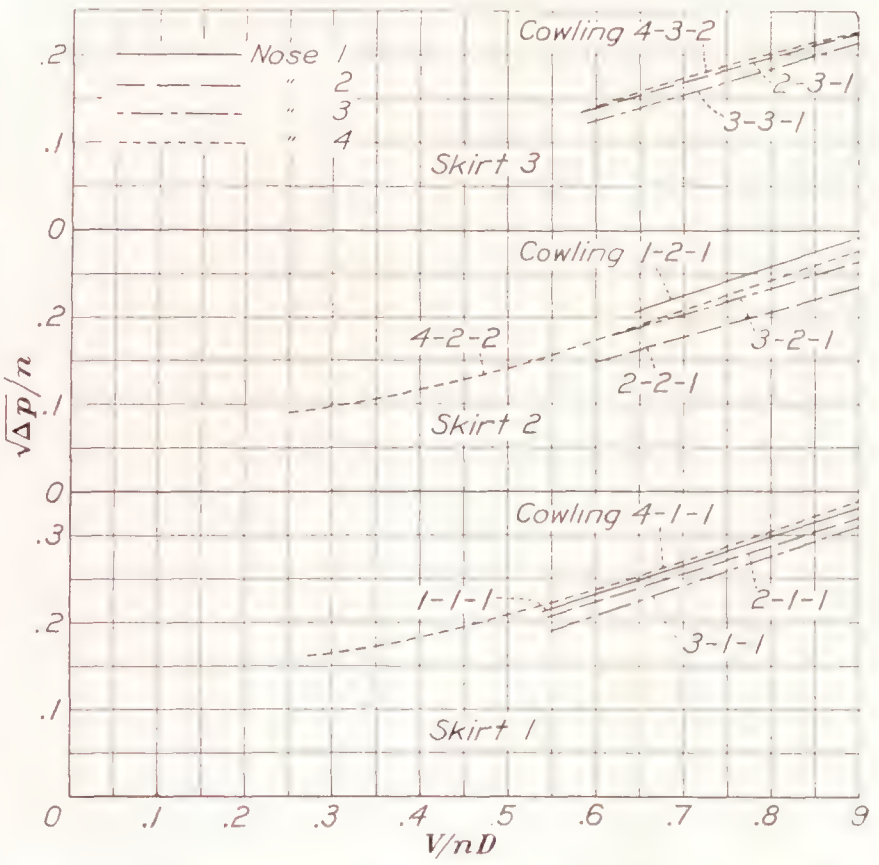

FIGURE 6.—Variation of the pressure constant $\sqrt{\Delta p}/n$ with V/nD and cowling arrangements.

peller, the setting remaining constant throughout the range of V/nD. Figure 7 shows plots of $\sqrt{\Delta p}/n$ against V/nD for the various arrangements, with a dashed line showing the case of propeller off. Such a line is known to pass through the origin and to have a slope of $\sqrt{\Delta p}\,D/V$ so that it can be precisely drawn. It is of interest to show the little-realized fact that a propeller with a large hub and a round blade section near the hub often decreases instead of increasing the Δp obtained without the propeller. One exception is noted, the arrangement 4–1–1, shown in figure 7 (d). Propellers with a good airfoil section near the hub, such as propeller B in figure 7 (d), give an increase in Δp.

Figure 8 shows the temperature difference plotted against the indicated horsepower. The points determining a given line are for a constant Δp. The scattering of the points can be explained by small variations

in Δp. The conditions under which the tests were run are indicated. Although the range is not sufficient to define the slope precisely, lines drawn with a slope of 0.37 are quite consistent with the data. This result is all the more convincing when one considers that the points are taken for several engine speeds. Further, this slope is of the same magnitude as that found by Schey and Pinkel (reference 5) from flight tests on a Pratt & Whitney 1535 supercharged engine. It is recognized that this slope is a function of the baffling, the cylinder finning, and the mechanism of cooling; consequently, it can be used only for the arrangement tested. It is necessary, however, in studying cowling performance to be able to correct for variations in horsepower. The determination of such a slope makes this possible.

Cross plots (fig. 9) of the curves of figure 8, in which the indicated horsepower is plotted against Δp for three temperature differences, give three curves that show the limiting indicated horsepower permissible at various values of Δp. These curves show the advantage, with limited power, of allowing as high a cylinder temperature as possible.

The slope found in figure 8 is used in figure 10, in which the temperature difference divided by the indicated horsepower to the 0.37 power is plotted against

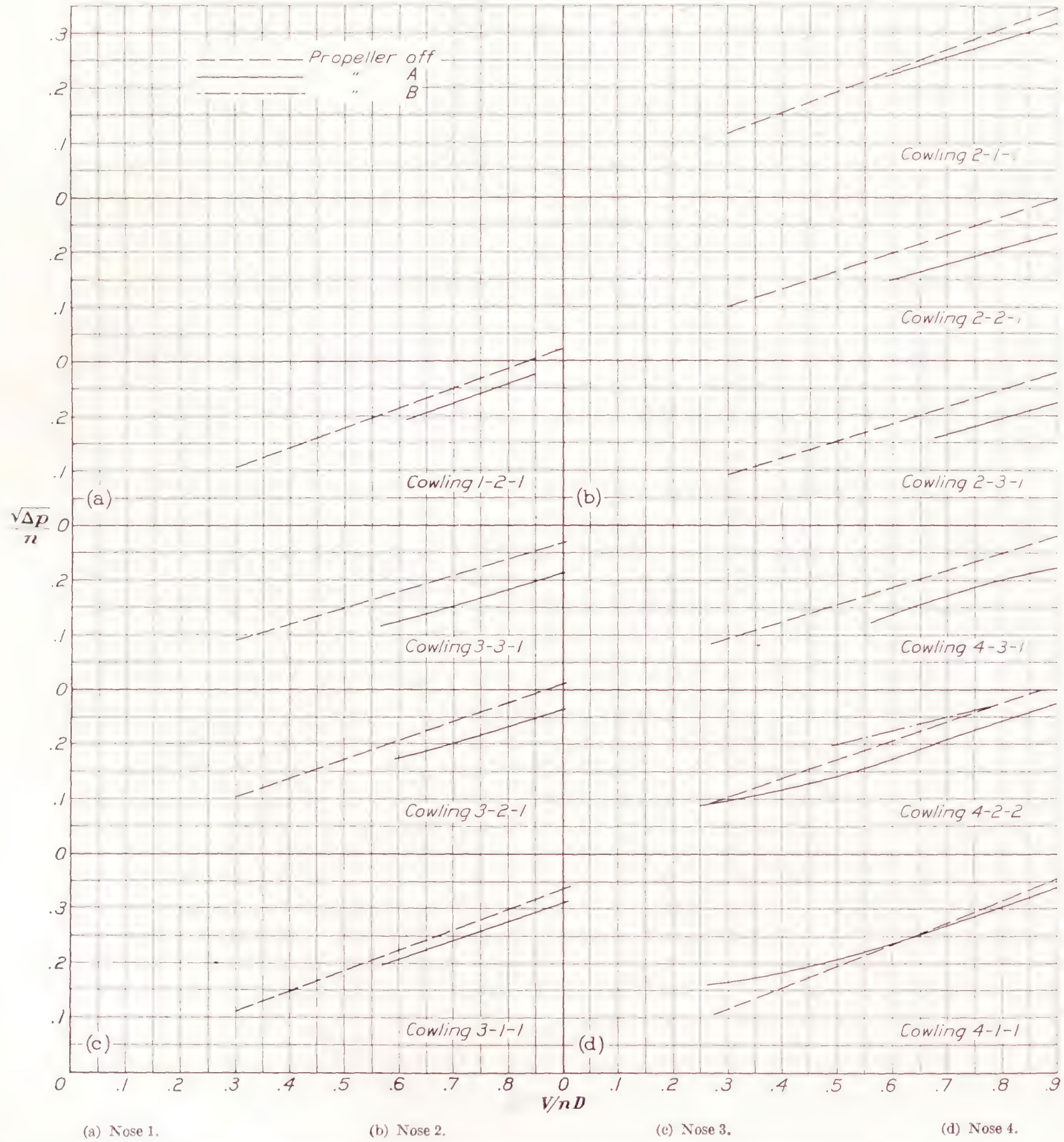

(a) Nose 1. (b) Nose 2. (c) Nose 3. (d) Nose 4.

FIGURE 7.—Comparison of the available pressure drop for the conditions of propeller off and propeller on.

$2\Delta p$. The value $2\Delta p$ is used instead of Δp for convenience in plotting. These curves show reasonable slopes for the dependence of cooling on Δp. The slope may vary from -0.4 to 0, -0.4 resulting from a completely turbulent boundary layer on fins of narrow width. The minimum slope will result when the cooling does not depend upon the velocity flow. Intermediate values of the slope correspond to longer fins (reference 6) and laminar flow in the boundary layer. Thus, when part of the cooling is accomplished by other means than a directed velocity flow of air over the fins, the slope will be less than was expected. This result is particularly true of the front of the cylinder, where there is no directed velocity. The only reason for the existence of a slope is the fact that both turbulence and Δp are functions of the air-stream velocity. It has been shown (reference 1) that the cooling in the front of the cylinder is accomplished by such large-scale turbulence. The consistently lower slopes found for the thermocouples on the front than on the rear of the cylinder in this study confirm this result.

Figure 11 shows plots similar to those of figure 10 for noses 2, 3, and 4. Here again it is noted that the curves for the thermocouples on the front of the cylinder have lower slopes. The wide scattering of the points in some cases for the front thermocouples can possibly be explained as follows: Δp can be varied in two ways, by varying the air-stream velocity and, as a result, the turbulence, or by varying the skirt exit. When Δp is simultaneously varied by both means, it is quite likely to cause considerable scattering.

Figure 12 shows the dependence of ΔT on Δp for several positions on the cylinder at a constant horsepower. The results are shown for both the adjustable and the controllable propellers. The temperatures in the rear show the same dependence on Δp as in the previous charts. The temperatures on the front show a lack of dependence on Δp that cannot be explained.

It has been shown, in the analysis of the problem, that the power required to cool is $\frac{\sqrt{2}KF(\Delta)p^{3/2}}{\sqrt{\rho}}$. It has been calculated for the tests of cowlings 2, 3, and 4 and is shown in figure 13 plotted against the temperature difference. This chart serves to emphasize the well-known fact that a small reduction in temperature is accomplished at a large expenditure of power to cool. It becomes all the more striking when it is remembered that large expenditures of power are, in general, made at relatively low efficiencies. If it is assumed that a rea-

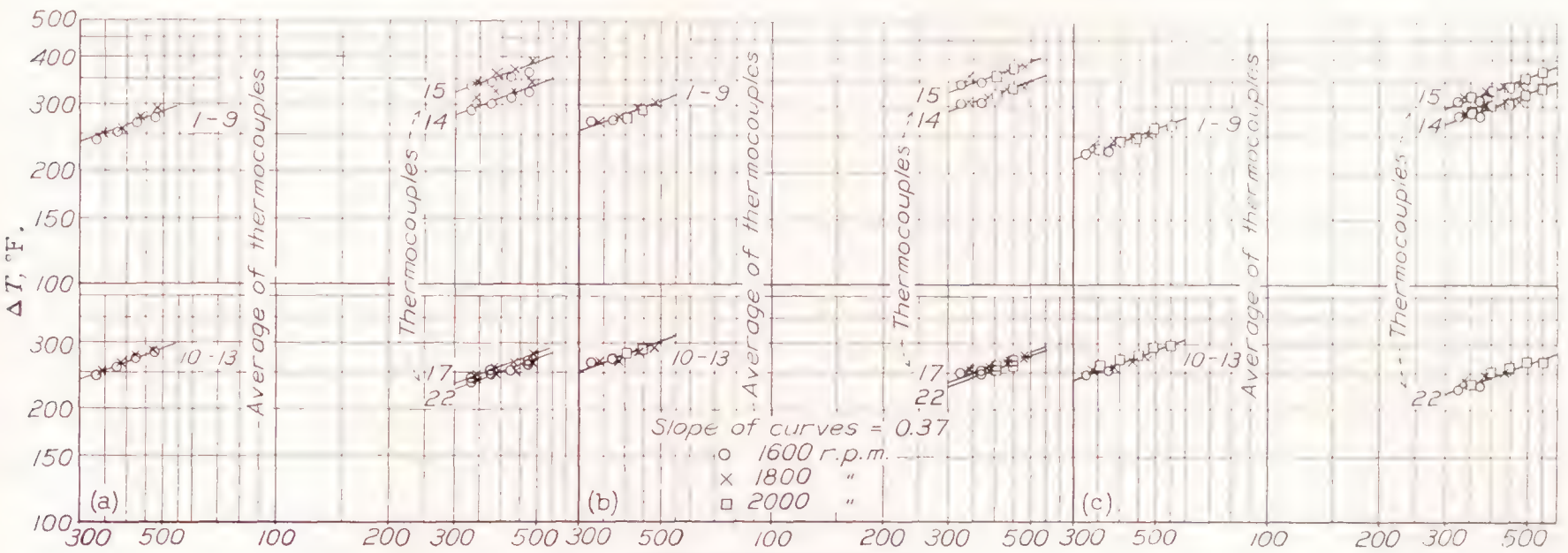

	Cowling	Approximate air speed, m. p. h.	Pressure drop across cylinder Δp, lb./sq. ft.
(a)	1–2–1	80	21.1
(b)	1–3–1	100	14.2
(c)	1–1–2	110	31.8

FIGURE 8.—The effect of indicated horsepower on the cylinder temperature difference. Fuel consumption, 0.57 pound per brake horsepower-hour.

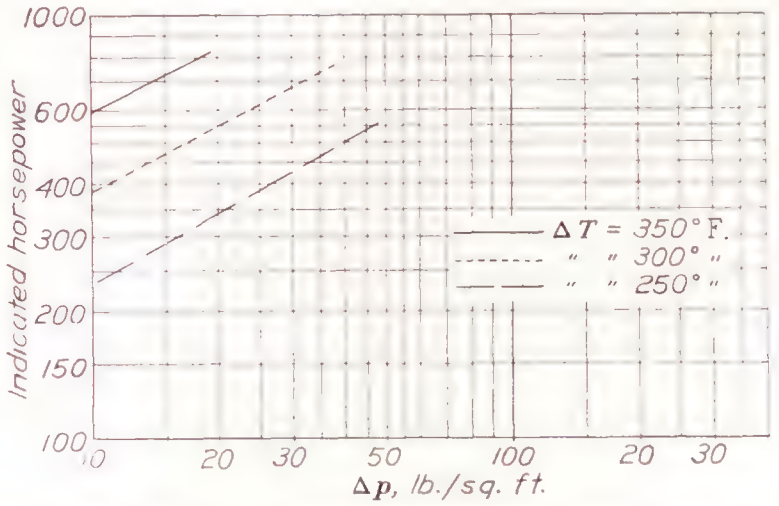

FIGURE 9.—The effect of Δp on the limiting horsepower at several constant temperature differences. Average of thermocouples 1 to 9.

sonable operating temperature involves a temperature difference of 300° F., then it is evident (fig. 13) that the cost in power to cool is from 1 to 1.5 percent of the indicated horsepower.

As a rule, the heat dissipated is not directly discussed in such an analysis. Measurements were made, however, that allow a rough determination of the heat dissipated both to the cooling air and to the oil cooler. Figure 14 shows the amount of heat dissipated to the cooling air for several arrangements, and figure 15 shows the amount dissipated to the oil cooler. The percentage of the indicated horsepower dissipated varies from 40 to 75. It will be noted that the percentage of heat dissipated is relatively higher at lower indicated horsepower.

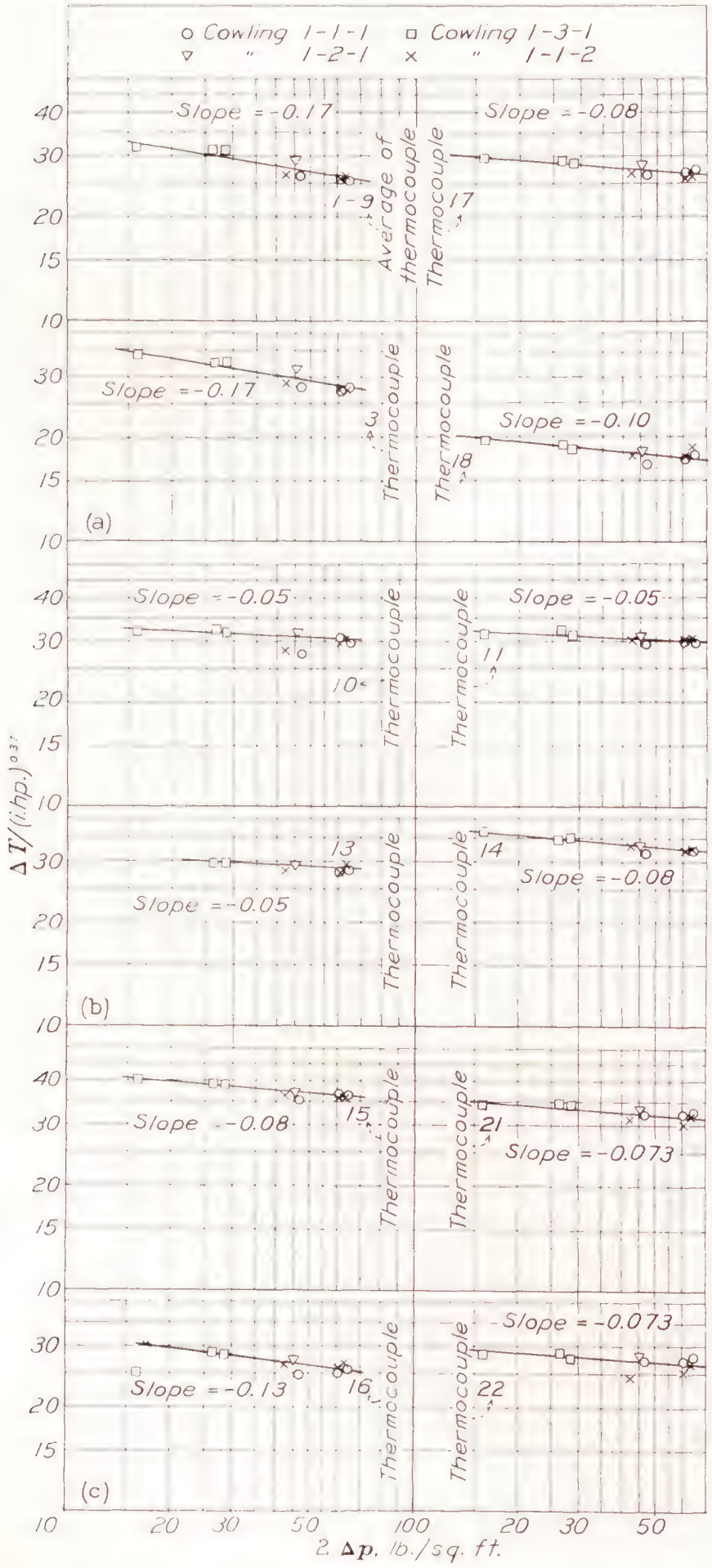

FIGURE 10.—The effect of Δp on $\Delta T/(\text{i. hp.})^{0.37}$ for all cowlings with nose 1

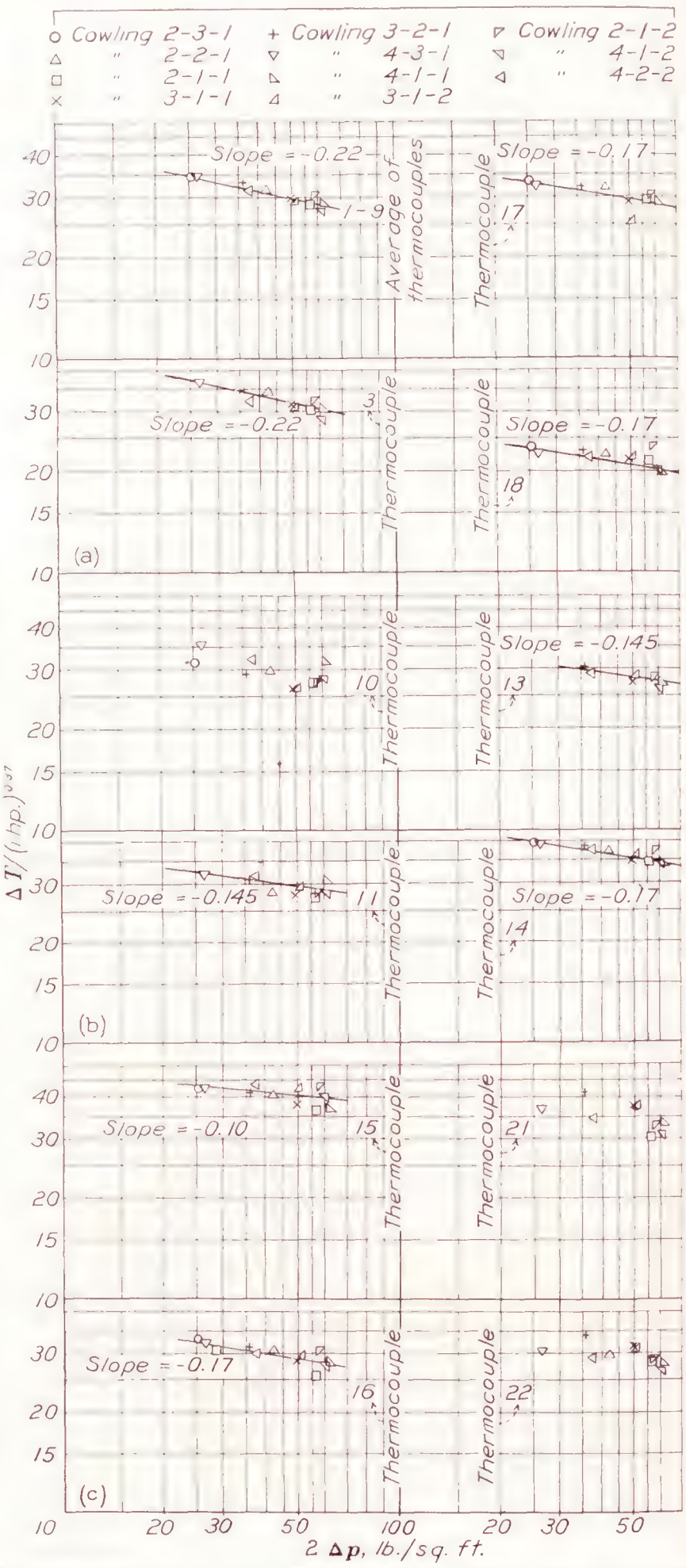

FIGURE 11.—The effect of Δp on $\Delta T/(\text{i. hp.})^{0.37}$ for all cowlings with noses 2, 3, and 4.

DISCUSSION

In the presentation of the results, considerable emphasis has been placed on the fact that the temperatures on the front of the cylinder do not, in general,

depend on Δp but upon large-scale turbulence. Such emphasis is justified by the general misconception that, if the required Δp is developed, the cooling problem has been solved. It is, however, quite possible to develop a desired Δp that will cool the baffled part of the cylinder satisfactorily yet be so deficient in large-scale turbulence on the front of the cylinder that little

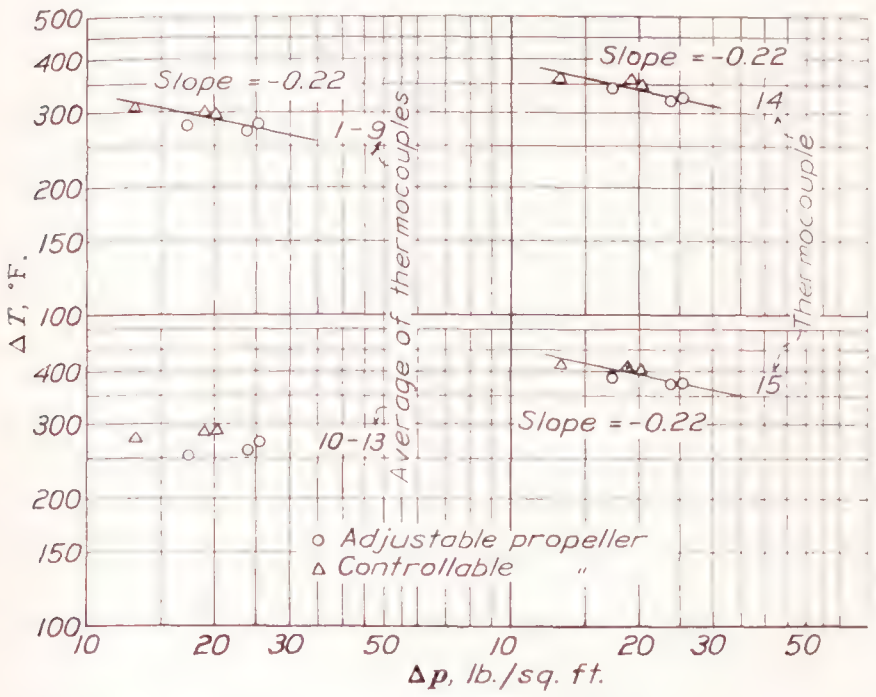

FIGURE 12.—The effect of Δp on temperature difference with adjustable and controllable propellers. Cowling 4-2-2; indicated horsepower, 430; specific fuel consumption, 0.57 pound per brake horsepower-hour; air speed, 80 to 110 miles per hour approximately.

cooling results there. A suction fan behind the engine would furnish just this type of cooling. A blower on the front, connected to the propeller may, or may not, develop the required turbulence for cooling. This turbulence, which is so important in the cooling of the unbaffled front of the cylinder and cylinder head, is of no importance in the cooling of the baffled and rear

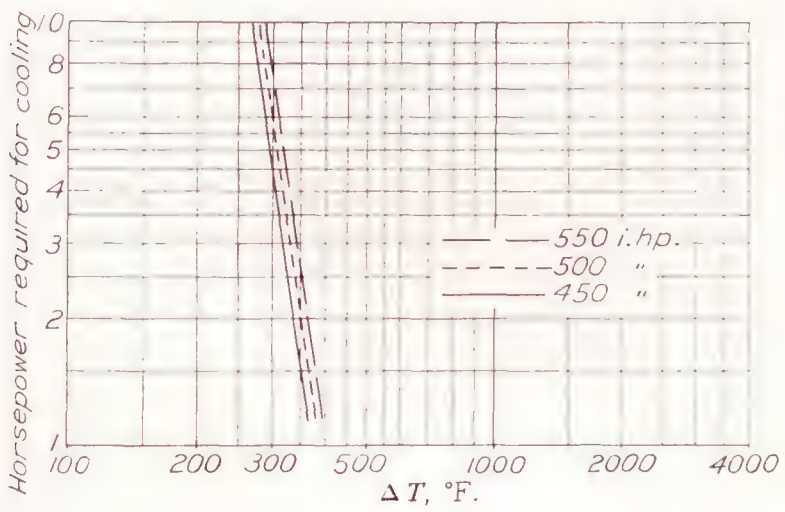

FIGURE 13.—Horsepower required for cooling for various temperature differences at several constant horsepowers. Noses 2, 3, and 4; thermocouples 1 to 9.

parts of the cylinder. Here the only consideration is the development of a value of Δp and, as a result, a velocity flow over the surface of the fins, sufficient to carry away the required amount of heat. The consistency of all the results for rear temperatures bear out this statement. A slope of -0.22 in the plots of Δp against $\frac{\Delta T}{(\text{i.hp.})^{0.37}}$ is found consistently throughout these tests for the baffled part of the cylinder. This slope is somewhat lower than the value given in reference 1. This difference is probably due to the difference in the location of the thermocouples in the two series of

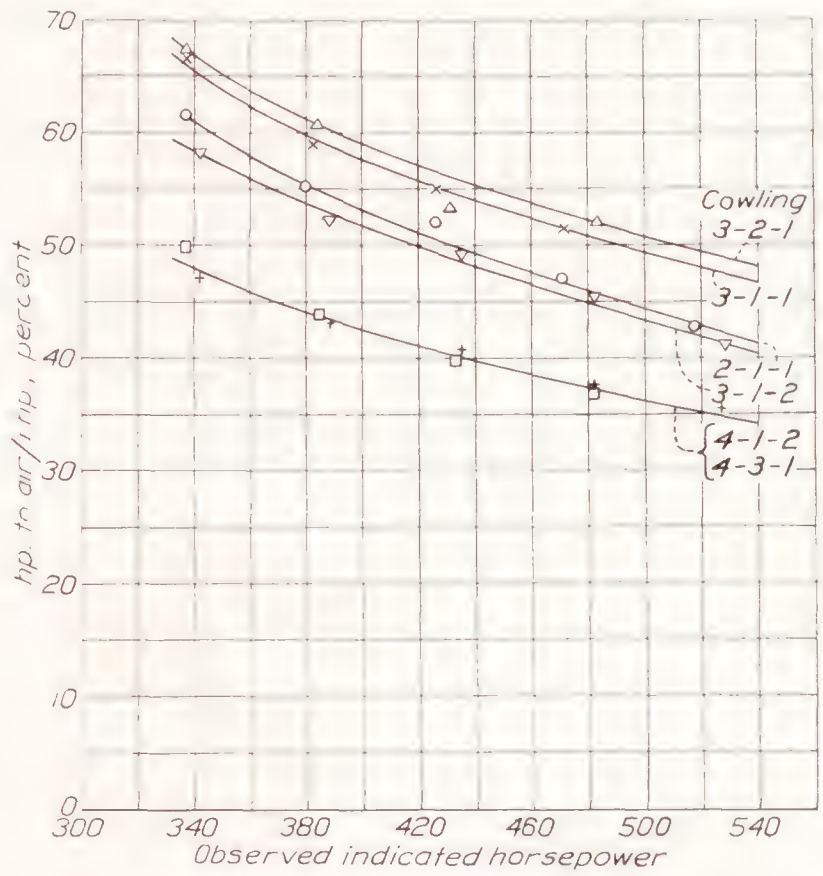

FIGURE 14.—The effect of indicated horsepower on the percentage of heat carried away by the cooling air for various cowling arrangements. Air speed, 100 miles per hour; engine speed, 1,800 r. p. m.

tests. In the former tests the thermocouples were located at the rear of the barrel itself; in the present series of tests the thermocouples were located on the rear spark-plug boss. It is quite possible that there is sufficient difference in the mechanism of cooling due to

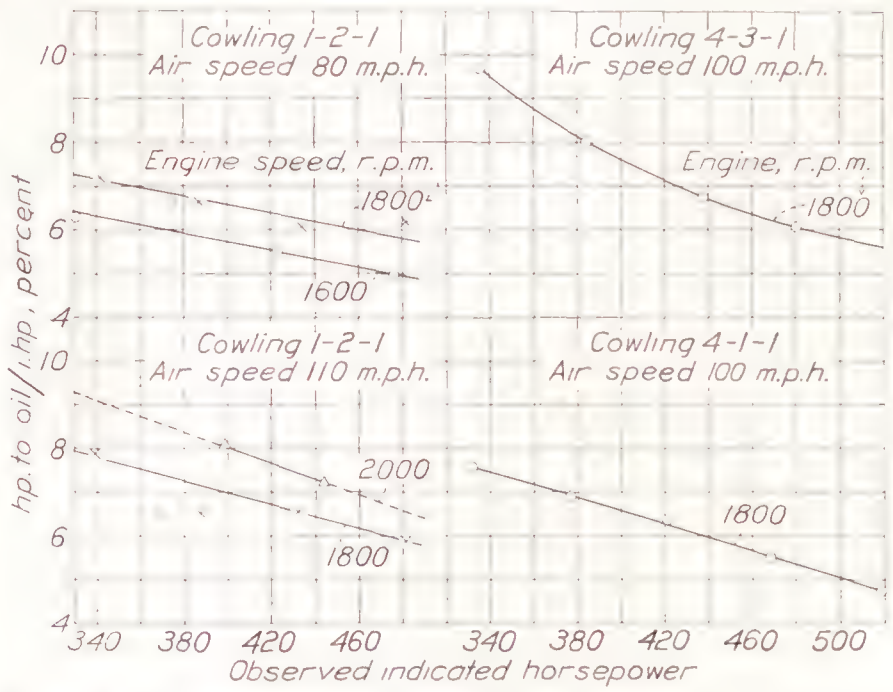

FIGURE 15.—The effect of indicated horsepower on the percentage of heat carried away by the oil for several cowling arrangements.

the finning near the spark-plug boss and the cylinder barrel to account for the difference in slope. It is also conceivable that the temperature of the spark-plug boss is affected less by velocity than that of the fins themselves. If this assumption is correct, the difference is in the right direction.

The effect of the propeller slipstream has also been emphasized in the present report. The misconception is often encountered that the propeller slipstream, regardless of the design of the propeller, increases the Δp available for cooling. References 1 and 2 have shown that, in general, this assumption is untenable. On the contrary, the Δp at a particular slipstream contraction is dependent on the blade-angle distribution, especially near the hub. Moreover, it has been pointed out that by designing for a large blowing action from the blade sections near the hub, a considerable increase in Δp can be realized. The large hub is not believed to contribute directly to the lower Δp. Indirectly, the difficulty encountered in designing a good airfoil section near the axis of the propeller limits the available blowing action.

No effect of engine speed on cooling could be found. With a given indicated horsepower and Δp the engine speed could be varied from 1,600 to 2,200 r. p. m. without any measurable deviation in temperature. It is obvious that, to the extent that Δp was changed, there was a corresponding effect on the rear temperature. It might be expected that the propeller would superimpose some flow that would improve the cooling on the front of the cylinder. No such effect could be found.

The percentage of the indicated horsepower required to cool varied from 1 to 1.5 and is based on the assumption that the Δp is developed at 100 percent efficiency. Reference 1 shows that the efficiency varies with both skirt shape and skirt opening. In the analysis of the problem it has been shown that the useful power expended in cooling is proportional to $(\Delta p)^{3/2}$. It follows, then, that the values of 1 to 1.5 percent of the indicated horsepower apply to a particular Δp or to a particular air speed alone. At higher air speeds, with a given arrangement, a larger Δp will be developed and a correspondingly higher power will be used.

The limiting indicated horsepower at various values of Δp for three values of the temperature was found. Both the percentage of indicated horsepower required to cool and the limiting indicated horsepower, when considered together, bring out clearly the expensiveness of overcooling. The obvious recommendation is to decrease the skirt exit and thus decrease the Δp at high air speeds. It has been shown (reference 1) that by decreasing the skirt exit in the proper manner the exit orifice or pump could be made to act more efficiently. Thus the real cost of cooling will be lower than the corresponding decrease in Δp would indicate. The results presented here show that this engine, when developing 500 horsepower, will cool so that the hottest point (thermocouple 15) does not exceed 400° F. above cooling-air temperature with a Δp of 25 pounds per square foot. It has been shown (reference 1) that by using closer baffling this value can be appreciably reduced.

The amount of heat that must be dissipated to provide adequate cooling was determined. The present value, or any value, is useful only when all engine conditions, such as cylinder size, finning, baffling, temperature distribution on the cylinder surface, compression ratio, air-fuel ratio, and mechanical condition of the engine are reproduced. The relative values of heat dissipated at high and low values of the indicated horsepower are of the most importance. Comparatively, the results should be usable.

CONCLUSIONS

Tests on an R–1340 S1H1–G Pratt & Whitney Wasp engine with several cooling arrangements showed:

1. A pressure drop sufficient for cooling in climb under full power can be developed.
2. The controllable propeller had no beneficial effect on cooling and the adjustable propeller improved the cooling only slightly.
3. Equally good cooling, for a particular pressure drop, resulted from each of the cowlings tested.
4. With a given baffling and finning on the cylinders, the skirt is the controlling factor in cooling in climb.

Langley Memorial Aeronautical Laboratory,
National Advisory Committee for Aeronautics,
Langley Field, Va., *August 20, 1936.*

REFERENCES

1. Theodorsen, Theodore, Brevoort, M. J., and Stickle, George W.: Full-Scale Tests of N. A. C. A. Cowlings. T. R. No. 592, N. A. C. A., 1937.
2. Theodorsen, Theodore, Brevoort, M. J., and Stickle, George W.: Cooling of Airplane Engines at Low Air Speeds. T. R. No. 593, N. A. C. A., 1937.
3. Weick, Fred E., and Wood, Donald H.: The Twenty-Foot Propeller Research Tunnel of the National Advisory Committee for Aeronautics. T. R. No. 300, N. A. C. A., 1928.
4. Gerrish, Harold C., and Voss, Fred: Mixture Distribution in a Single-Row Radial Engine. T. N. No. 583, N. A. C. A., 1936.
5. Schey, Oscar W., and Pinkel, Benjamin: Effect of Several Factors on the Cooling of a Radial Engine in Flight. T. N. No. 584, N. A. C. A., 1936.
6. Schey, Oscar W., and Ellerbrock, Herman H., Jr.: Performance of Air-Cooled Engine Cylinders Using Blower Cooling. T. N. No. 572, N. A. C. A., 1936.

REPORT No. 597

AIR PROPELLERS IN YAW

By E. P. Lesley, George F. Worley, and Stanley Moy

SUMMARY

Tests of a 3-foot model propeller at four pitch settings and at 0°, 10°, 20°, and 30° yaw were made at Stanford University. In addition to the usual propeller coefficients, cross-wind and vertical forces and yawing, pitching, and rolling moments were determined about axes having their origin at the intersection of the blade axis and the axis of rotation.

The tests showed that the maximum efficiency was reduced only slightly for angles of yaw up to 10° but that at 30° yaw the loss in efficiency was about 10 percent. In all cases the cross-wind force was found to be greater than the cross-wind component of the axial thrust. With a yawed propeller an appreciable thrust was found for V/nD for zero thrust at zero yaw. Yawing a propeller was found to induce a pitching moment that increased in magnitude with yaw.

INTRODUCTION

Although airplanes are generally designed so that the propeller axis lies approximately in the direction of normal steady flight, the condition of yaw is found during such maneuvers as curved flight and in flight at high angle of attack. These maneuvers are usually of short duration and, while the effect of yaw from these causes may be, in specific cases, of interest, it is possibly of no great consequence. If, however, propellers are to be yawed in the steady-flight condition, the effects of yaw may be important. Such a condition would arise in the case that a wing engine is placed, for structural or other reasons, with its axis at an angle to the longitudinal axis of the plane.

Air propellers in yaw have been the subject of both theoretical and experimental investigation (references 1 to 5) but further information concerning the quantitative effect of small angles of yaw upon thrust, power, cross-wind force, and efficiency seemed desirable and therefore the present study was undertaken. While the study was made with the propeller axis in the horizontal plane and the angle between the propeller axis and the wind direction is thus called an angle of yaw, the results may be applied as well to angles of pitch since such body interference as was present would have been the same in either case.

APPARATUS AND TESTS

Wind tunnel.—The experimental work was done in the wind tunnel of the Daniel Guggenheim Aeronautical Laboratory of Stanford University. This tunnel is of the open-throat type with a throat diameter of 7½ feet. The maximum wind velocity is about 90 miles per hour.

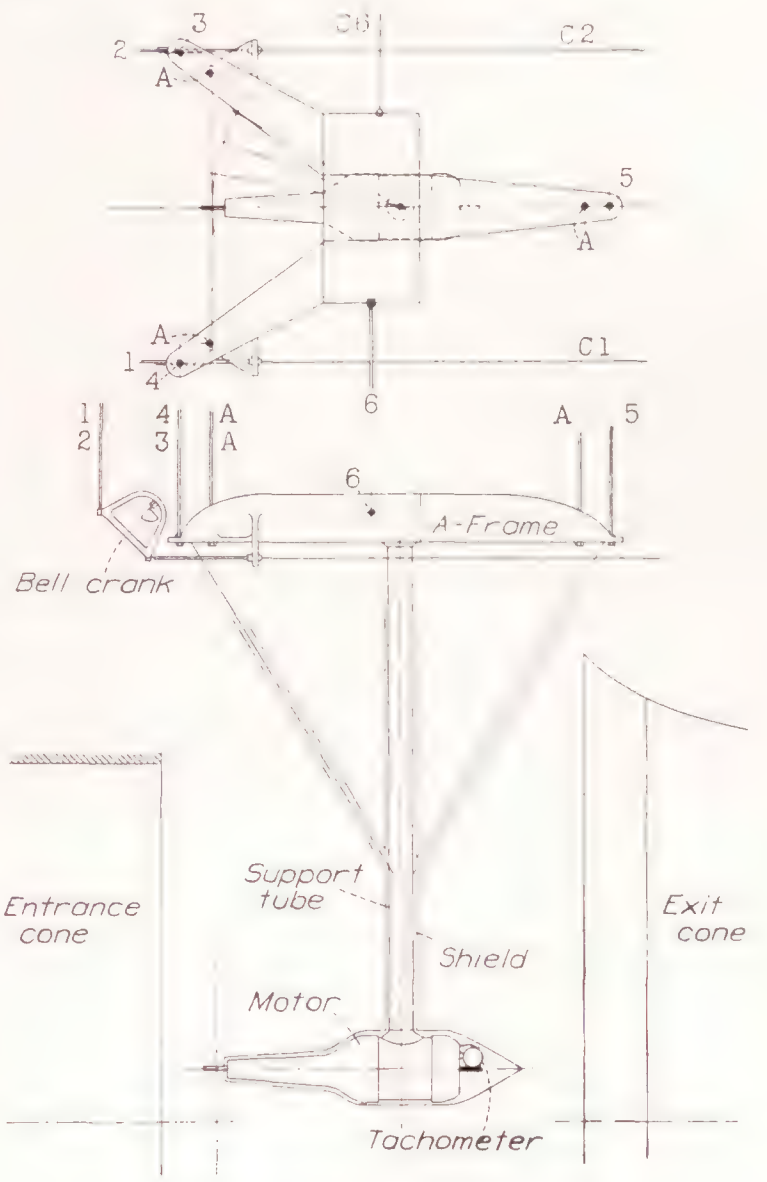

FIGURE 1.—The dynamometer suspension.

Dynamometer.—The propeller dynamometer consists essentially of a six-component balance. A driving motor was rigidly suspended by a steel tube and pylon of steel rods from a platform located above the wind stream. The platform was completely restrained by six electrically operated beam balances.

The general arrangement and appearance of the dynamometer are shown in figures 1, 2, 3, and 4. In

figure 1, numbers 1 to 6 indicate the leads to the restraining beam balances, the balances themselves being similarly numbered in figure 4. As may be seen, the A-frame or platform was restrained in the wind direction by balances 1 and 2, in the vertical direction by balances 3, 4, and 5, and in the cross-wind direction by balance 6. In addition to these restraining or measuring balances, there were three auxiliary beam balances, designated by A in figures 1 and 4, that

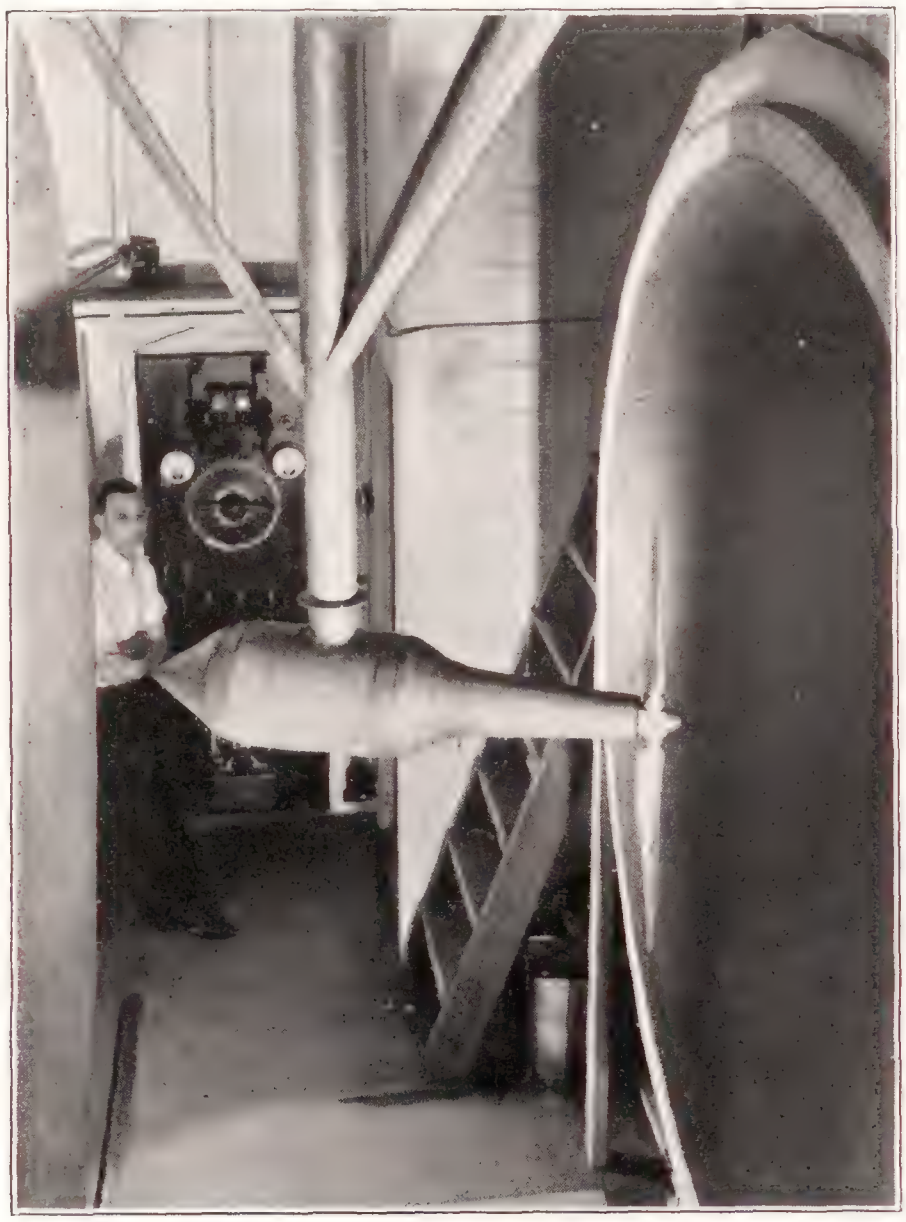

FIGURE 2.—The propeller set-up shown in the yawed position.

carried the dead weight of the platform and suspended motor. The lines labeled C1, C2, and C6 (fig. 1) are leads to counterweights used to give the necessary initial loads on balances 1, 2, and 6.

The forward end-shield of the motor was elongated so that the propeller was well ahead of any considerable wind-stream obstruction. (See figs. 1, 2, and 3.) The distance from the propeller to the center of the supporting tube was two-thirds the propeller diameter. In figures 2 and 3 the motor is shown in the yawed condition. The angle of yaw could be adjusted as desired by a swivel joint provided in the supporting tube.

The motor, and such parts of the suspension as were in the wind stream, were shielded by a sheet-metal cover. Thus only the forces acting on the propeller were communicated to the platform and to the restraining balances. An electric bell gave warning of contact between the motor or its supports and the metal cover.

Propeller.—The propeller used in this investigation was a 3-foot metal right-hand adjustable propeller. It is designated propeller A in reference 6. It has a uniform geometric pitch and a pitch-diameter ratio of 0.7 when the blade angle at 0.75 radius is 16.6°. Four pitch settings were used: 16.6° (uniform pitch), 20.6°, 24.6°, and 28.6°; all pitch settings were measured at the $0.75R$ station.

TESTS

Measurements were made of six components of the air force acting on the propeller, three vertical, two in the wind direction, and one in the cross-wind direction. From these components and the arms of the restraining balances, the rolling, pitching, yawing, and torque moments about axes having their origin at the intersection of the propeller axis and blade axis were com-

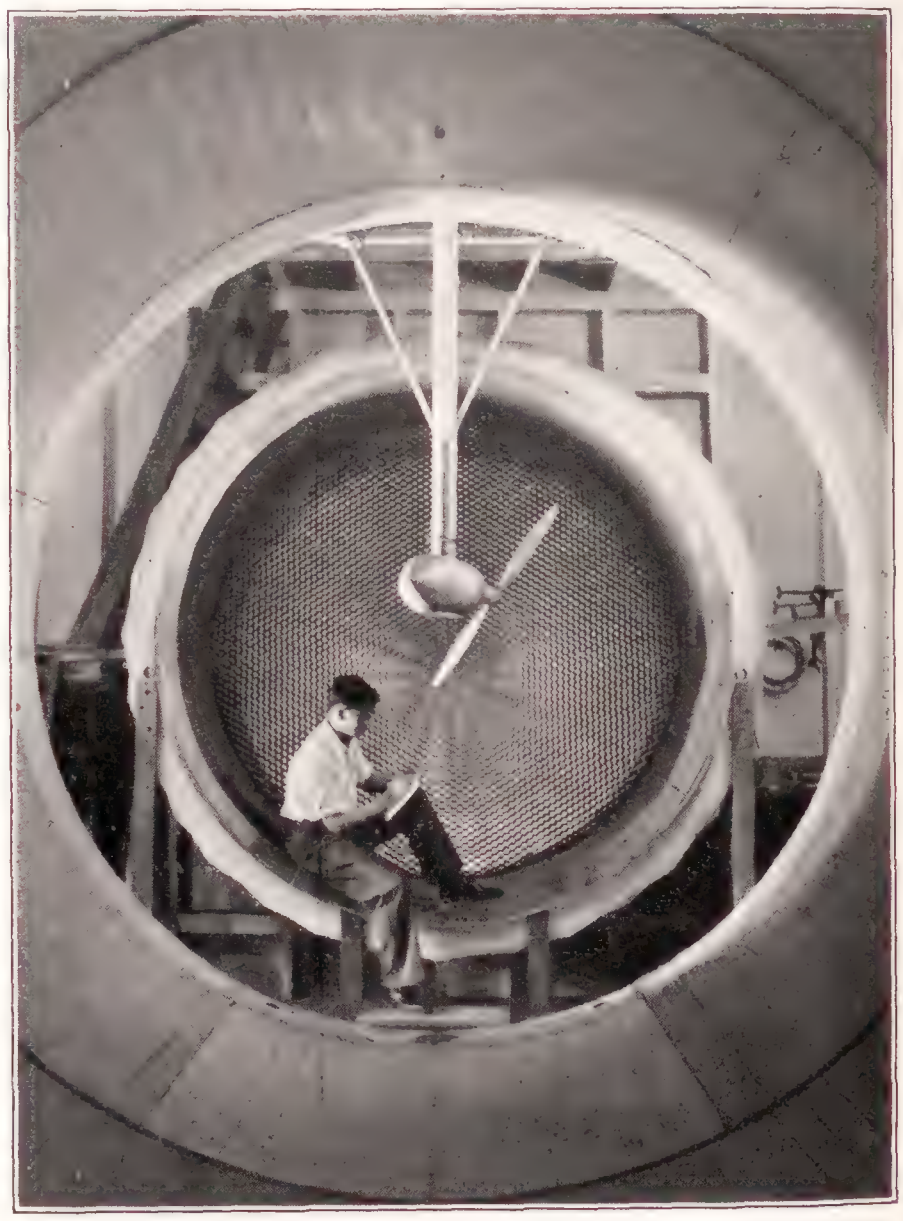

FIGURE 3.—Upstream view of the propeller test set-up.

puted. For each pitch setting of the propeller, tests were made at 0°, 10°, 20°, and 30° yaw.

As the model propeller driving motor was of the constant-speed type (about 1,800 r. p. m.), variations of the parameter V/nD were obtained by increasing the wind velocity in suitable increments. The propeller tip speed therefore remained nearly constant at about 280 feet per second. The Reynolds Number

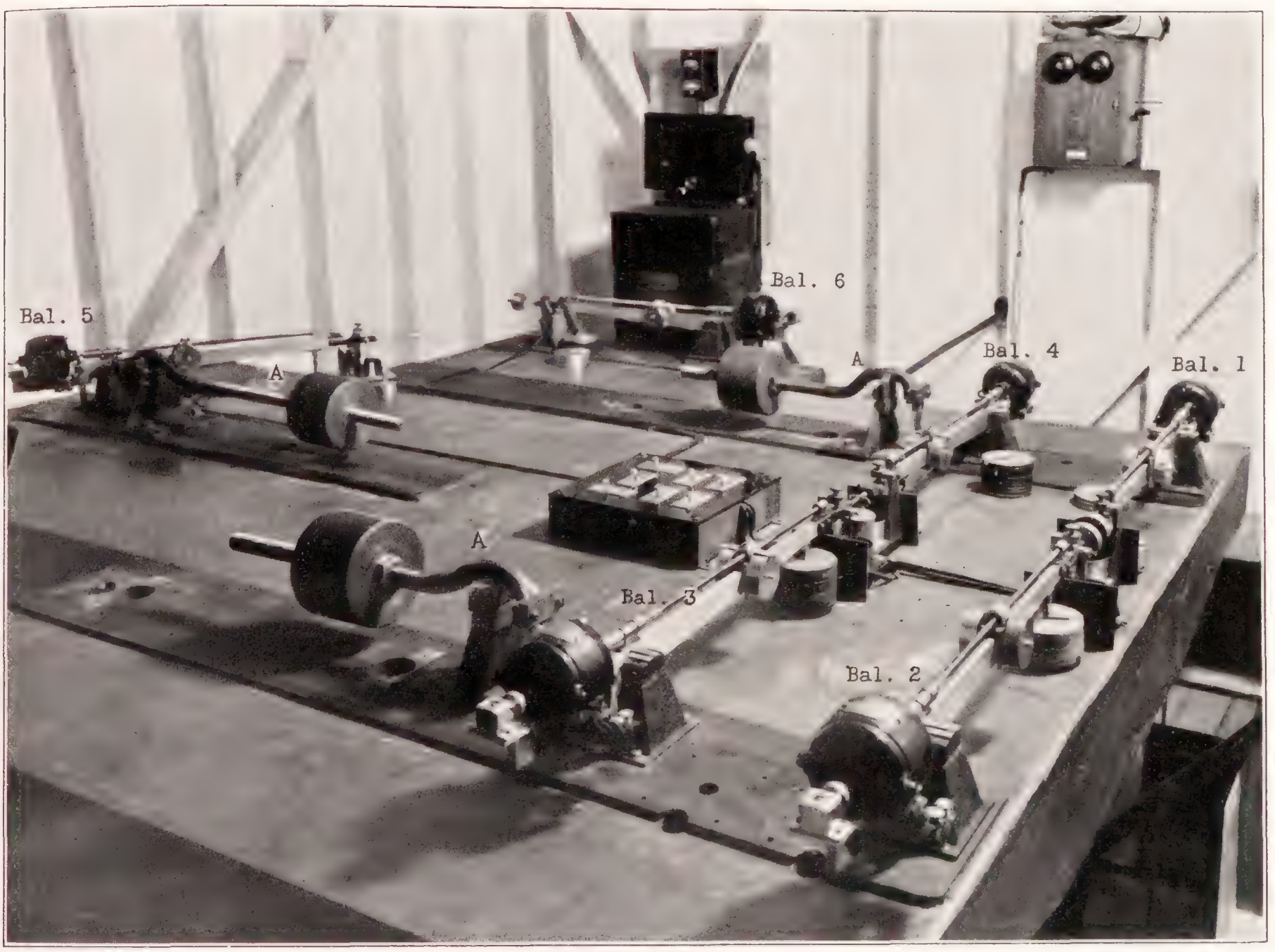

FIGURE 4.—View of the electrical balancing units.

was about 0.1 full scale, assuming the full-scale propeller to be 10 feet in diameter operating at a tip speed of 800 feet per second.

The observed thrust and power are reduced to the usual coefficients

$$C_T = \frac{T}{\rho n^2 D^4}$$

$$C_P = \frac{P}{\rho n^3 D^5}$$

$$\eta = \frac{T \times V}{P} = \frac{C_T}{C_P} \times \frac{V}{nD}$$

$$C_s = \sqrt[5]{\frac{\rho V^5}{P n^2}} = \frac{V}{nD} \sqrt[5]{\frac{1}{C_P}}$$

where

T, thrust of the propeller measured parallel to the axis of the tunnel.
P, motor power.
ρ, mass density of the air.
n, revolutions per unit time.
D, propeller diameter.
V, velocity.

The vertical and cross-wind forces are reduced to coefficients similar to the thrust coefficient,

$$C_{F_z} = \frac{F_z}{\rho n^2 D^4}$$

$$C_{F_y} = \frac{F_y}{\rho n^2 D^4}$$

where

F_z, vertical force.
F_y, cross-wind force.

The moments about the three axes are reduced to coefficients similar in form to the propeller torque coefficient,

$$C_Q = \frac{Q}{\rho n^2 D^5}$$

$$C_l = \frac{L}{\rho n^2 D^5}$$

$$C_m = \frac{M}{\rho n^2 D^5}$$

$$C_n = \frac{N}{\rho n^2 D^5}$$

where

Q, propeller torque.
L, rolling moment.
M, pitching moment
N, yawing moment.

RESULTS AND DISCUSSION

In table I are given the computed values of propeller, force, and moment coefficients for different values of V/nD.

In figure 5 the results of a test with the yaw dynamometer are compared with two earlier tests of the same propeller made in the same wind-tunnel using the Stanford University propeller dynamometer. The tests by Lesley and Reid are reported in reference 6; the tests by Babberger were made in connection with a study of the scale effect on air propellers submitted as a thesis at Stanford University in 1934. The agreement with Babberger's test at 2,000 r. p. m. is excellent, but the thrust and power coefficients derived from the yaw dynamometer test are consistently lower than those observed by Lesley and Reid. The angular

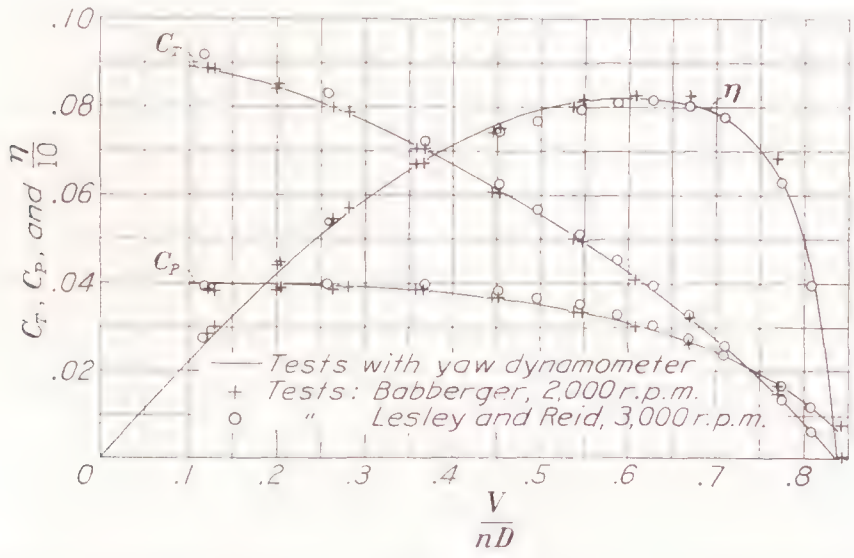

FIGURE 5.—Comparison of data from different tests of the same propeller in the same wind tunnel. Propeller set 16.6° at 0.75R; 0° yaw

velocity in the latter test, however, was about 3,000 r. p. m. and Babberger found that, with this propeller, the thrust and power coefficients increased slightly with angular velocity. Substantial agreement with Babberger's test at 2,000 r. p. m. is regarded as evidence of the accuracy of the yaw dynamometer.

Propeller, vertical-force, and cross-wind-force coefficients are given graphically as functions of V/nD in figures 6 to 21. In figures 22 to 25 efficiency η and V/nD are given as functions of the speed-power ceofficient C_s. The maximum efficiency and V/nD at zero thrust are plotted in figure 26 against the secant of the angle of yaw Ψ. Figure 27 shows the ratio of cross-wind force to thrust for different values of V/nD. In figure 28 this ratio is plotted against the ratio of V/nD to V/nD at zero thrust. Pitching-moment coefficients are given as functions of V/nD in figure 29; yawing-moment, rolling-moment, and torque coefficients are plotted in figures 30, 31, and 32, respectively.

The power coefficient (figs. 6 to 21) is little affected by yaw at low velocities of advance, i. e., at small values of V/nD. At larger values of V/nD the power coefficient increases with each increment of yaw.

The thrust coefficient is decreased by yawing the propeller at low V/nD. This result is to be expected since at $\frac{V}{nD}=0$ the axial thrust would be independent of yaw, and the thrust in the wind direction would be the axial thrust multiplied by the cosine of the angle of yaw. At the larger values of V/nD the thrust coefficient is increased by yaw and the value of V/nD for zero thrust is also increased.

Over the normal working range of a propeller there is thus a decrease in efficiency with yaw, although at the larger values of V/nD, greater than those for maximum efficiency, the efficiency is increased by yaw.

The manner in which efficiency varies with yaw in the normal working range is seen to advantage in figures 22 to 25 in which efficiency is plotted against the speed-power coefficient C_s.

In figure 26 the maximum efficiency for each blade-angle setting is plotted against sec ψ. The resulting parallel straight lines may be expressed by the equation

$$\eta_{max}=\eta_{max_o}-0.6\ (\sec\psi-1)$$

where η_{max_o} is the maximum efficiency at zero yaw.

In figure 26 the V/nD for zero thrust is also plotted against sec ψ. As with η_{max} it is seen that V/nD for zero thrust varies, over the range investigated, directly with sec ψ.

The vertical force coefficient of a propeller in yaw is negligible (it does, however, show an increase with yaw). Although in the graphical representation of figures 6 to 21 this coefficient, as well as the cross-wind force coefficient for zero yaw, appears to have considerable magnitude, it should be noted that the scale to which it is plotted is ten times that used for the thrust coefficient.

The vertical force coefficient, while generally positive, appears in some instances to be negative at low V/nD and to change in sign as higher values of V/nD are reached. It is obvious that, assuming symmetrical flow, the direction of the vertical force would depend on the relation between the direction of propeller rotation and direction of yaw. In these tests the propeller rotation was clockwise when looking upwind and the yaw was positive. Had either been reversed it seems evident that, with symmetrical flow, the sign of the vertical force coefficient would have likewise been changed.

As would be expected, the cross-wind force coefficient shows a marked increase with yaw. The ratio of cross-wind force to thrust is shown for the 28.6° propeller as a function of V/nD in figure 27.

The curves are drawn from points $\frac{F_y}{T}=\tan\psi$ at $\frac{V}{nD}=0$. It is seen that at all values of V/nD greater than zero, F_y/T is greater than tan ψ or that the resultant horizontal force is, except for $\frac{V}{nD}=0$, inclined to the wind direction at an angle greater than the angle of yaw.

The ratio of cross-wind force to thrust as a function of $\frac{V}{nD}\Big/\left(\frac{V}{nD}\right)_0$, where $(V/nD)_0$ is V/nD for zero thrust, is shown for all propellers in figure 28. It is seen that F_y/T increases with propeller pitch setting as well as with yaw.

It may be seen from these results that a propeller with its axis in pitch would develop thrust if operating at V/nD of zero thrust for axis parallel to direction of motion. The thrust under this condition may be of such magnitude that it should be considered in deriving airplane polars from glide tests with propeller running. For example, in glide tests of a VE–7 airplane (see reference 7), the drag coefficient at 15.1° angle of attack was found to be 0.143. From the present tests of propellers in yaw it appears that the thrust exerted by the propeller in the glide test may have been double the amount credited to it and the drag coefficient thus have been 0.148.

Further, in the derivation of the drag of the VE–7 airplane in the power flight tests of reference 7, a quantity T sin B was credited to the propeller as a liftwise force; B is the inclination of the propeller shaft to the wind direction. The present tests show that the credited amount should have been greater.

It may also be seen that the difference between power and thrust coefficients of propellers in the flight and wind-tunnel model tests of reference 7 is qualitatively accounted for by the fact that in flight the propeller axis was at an angle of pitch, while in the wind-tunnel model it was parallel to the wind stream.

The lift developed by a propeller with its axis in pitch is sufficient to account, in considerable degree, for the high lift coefficients apparently developed by an airplane at large angle of attack, power on. Millikan, Russell, and McCoy show (reference 8) an increase in lift coefficient of about 0.2 with power on at 20° angle of attack. Interpolating from these tests in yaw and allowing for the three-blade propeller used by Millikan, Russell, and McCoy, it appears that the liftwise force exerted by the propeller was sufficient to account for more than half of the increase in lift coefficient found.

Pitching-moment coefficients for the propellers in yaw are shown in figure 29 as functions of V/nD. Under the conditions of these tests, the sign of the coefficient depends upon V/nD. It is generally positive at large V/nD and negative at small V/nD. Like the sign of the vertical force coefficient, it is obvious that, assuming symmetrical flow, the sign of the pitching-moment coefficient would also depend upon the relation between the direction of rotation and direction of yaw; a reversal of either would result in reversing the sign of the pitching moment. Since the vertical force is small compared with thrust, a positive pitching moment shows a location of the line of action of thrust below the Y axis and a negative pitching moment a location above the Y axis.

Some verification of the observed change in sign of pitching moment with V/nD may be derived through analysis by simple blade-element theory. For example, it can be shown that for the 24.6° propeller in a vertical position and at 30° yaw, the pitching moments of the 0.75 radius elements are proportional 81 and −14 at V/nD 1.2 and 0.3, respectively. The ratio of these calculated moments is −5.8. The test of this propeller at 30° yaw shows a pitching-moment coefficient of 0.0066 at $V/nD=1.2$ and −0.0018 at $V/nD=0.3$. The ratio of pitching moments in the two cases is thus, for the whole propeller, −3.7.

It is possible that a part of the indicated pitching moment is due to a slight wind-stream asymmetry. Wind-stream surveys, however, revealed not more than 1¼ percent variation of velocity from the mean at the propeller disk, which appears insufficient to account for any considerable proportion of the pitching moment found. It will be noticed that there are insufficient observations to determine definitely the form of the pitching-moment curve in the low V/nD range. As this portion of the curve is of little practical importance, rather arbitrary functions have been drawn that become zero, as they should, at zero V/nD. It seems unlikely that, in the operating range, the magnitude of the pitching moment will be sufficient to affect greatly the stability characteristics of an airplane.

The yawing-moment coefficients, shown for the 16.8° and 28.6° propellers in figure 30, increase slightly with yaw. Even for the 30° yaw tests, however, the magnitude of the yawing moment about the axis chosen is extremely small.

Figures 31 and 32, showing the torque and rolling-moment coefficients for the 28.6° propeller, are of interest because it may be seen that the rolling moment increases more rapidly with yaw than the propeller torque. Although this result is illustrated for only one propeller, computations for the others show similar relations.

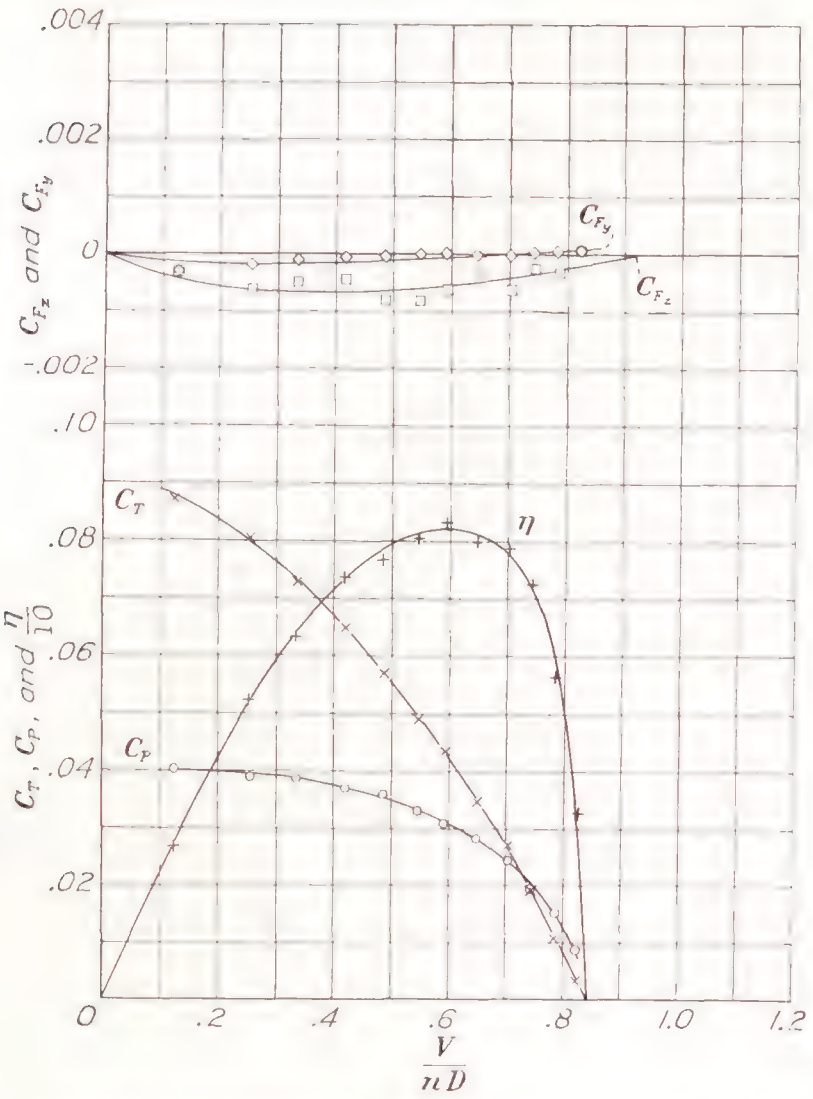

FIGURE 6.—Characteristics of a propeller set 16.6° at 0.75R: 0° yaw.

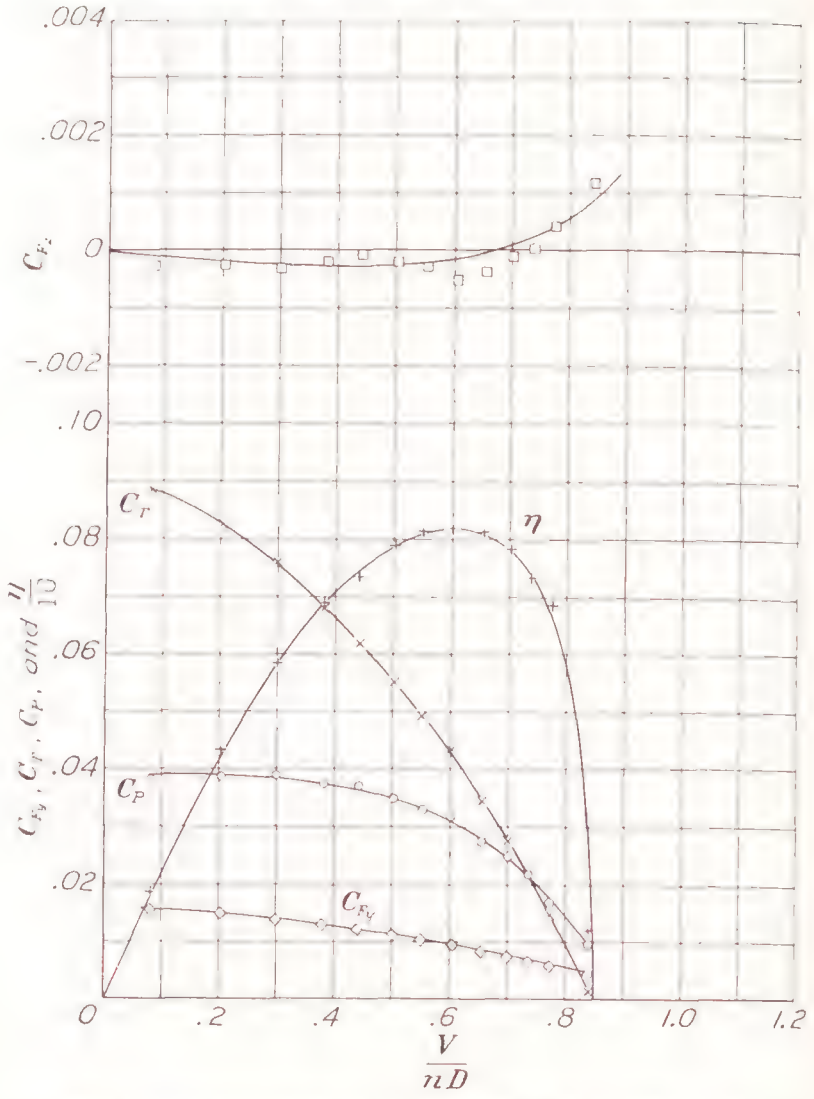

FIGURE 7.—Characteristics of a propeller set 16.6° at 0.75R; 10° yaw.

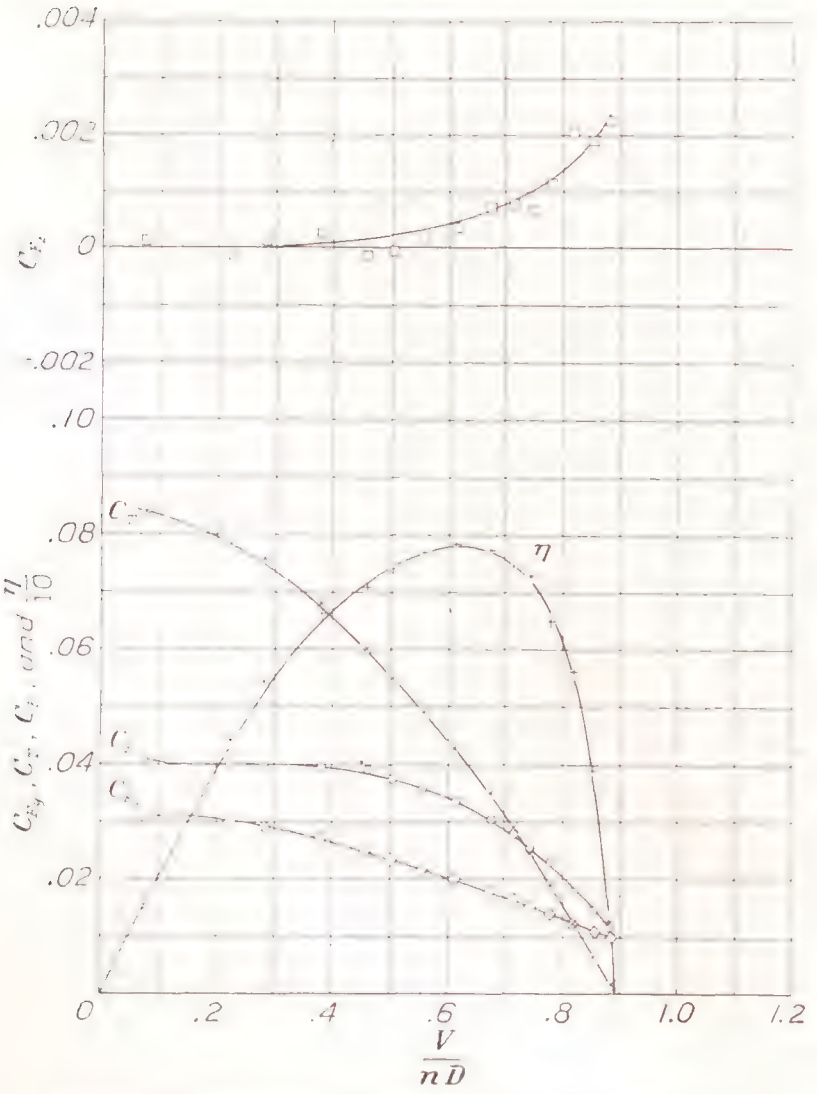

FIGURE 8.—Characteristics of a propeller set 16.6° at 0.75R; 20° yaw.

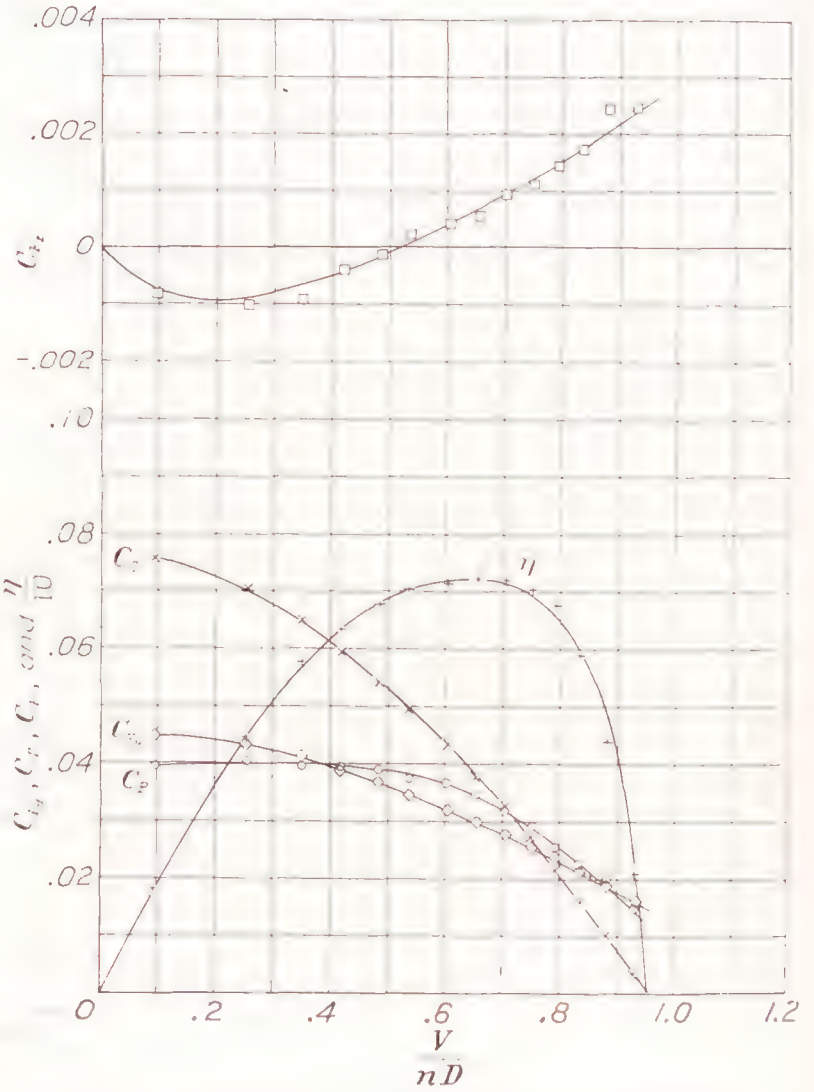

FIGURE 9.—Characteristics of a propeller set 16.6° at 0.75R; 30° yaw.

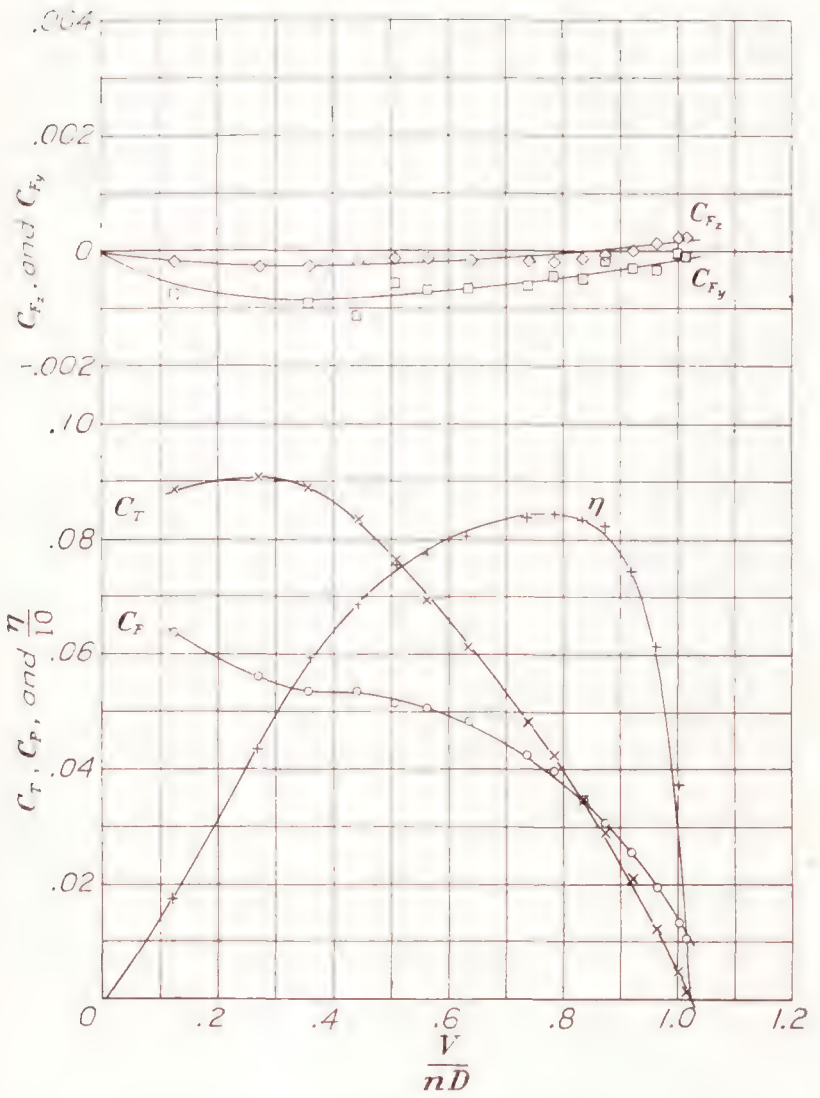

FIGURE 10.—Characteristics of a propeller set 20.6° at 0.75R; 0° yaw.

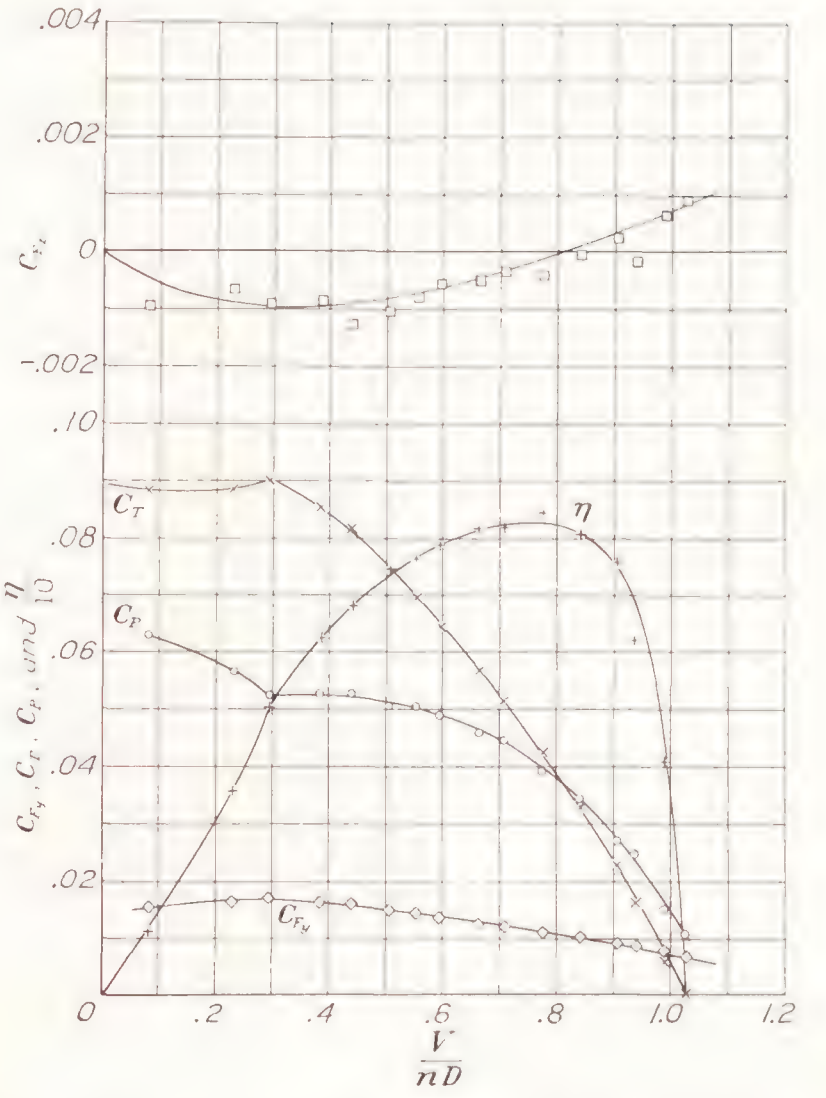

FIGURE 11.—Characteristics of a propeller set 20.6° at 0.75R; 10° yaw.

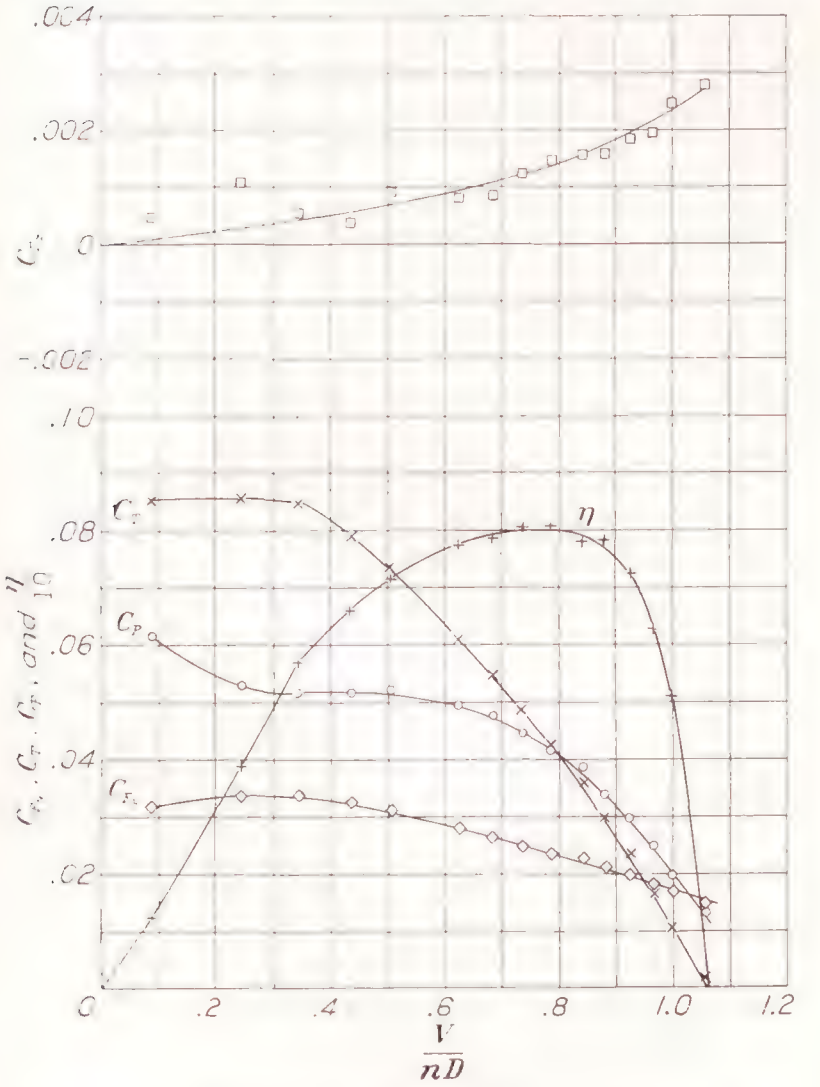

FIGURE 12.—Characteristics of a propeller set 20.6° at 0.75R; 20° yaw.

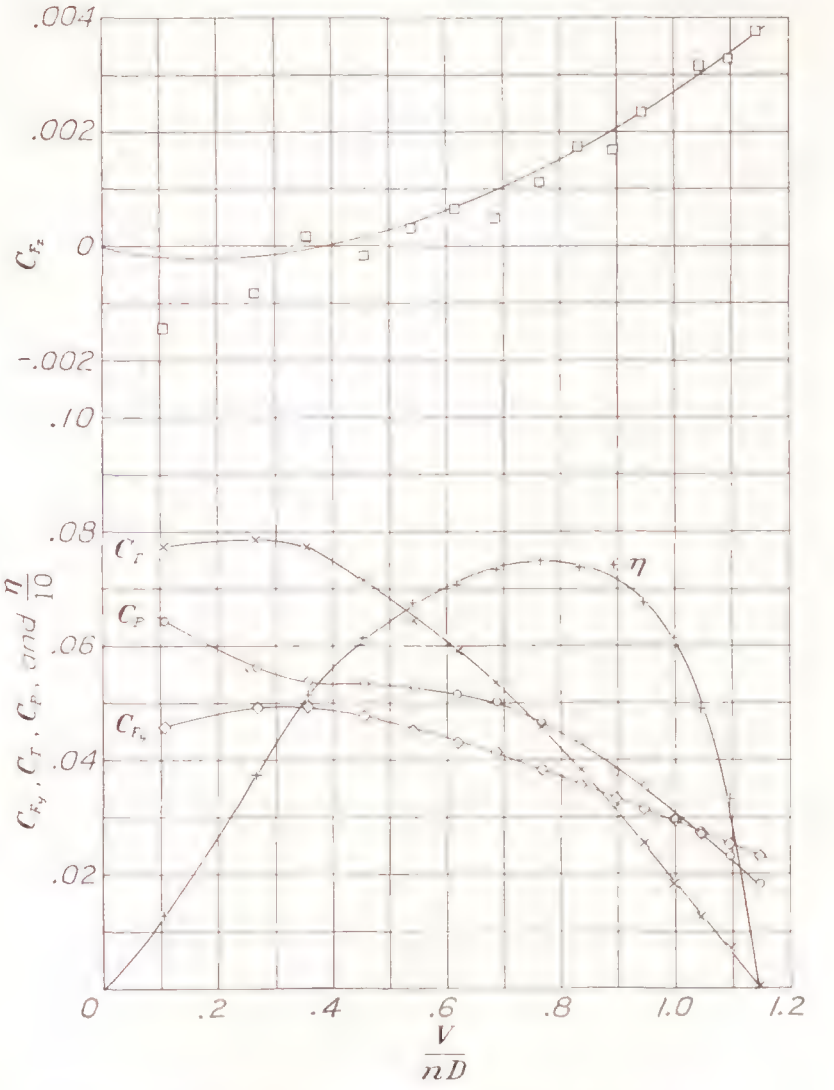

FIGURE 13.—Characteristics of a propeller set 20.6° at 0.75R; 30° yaw.

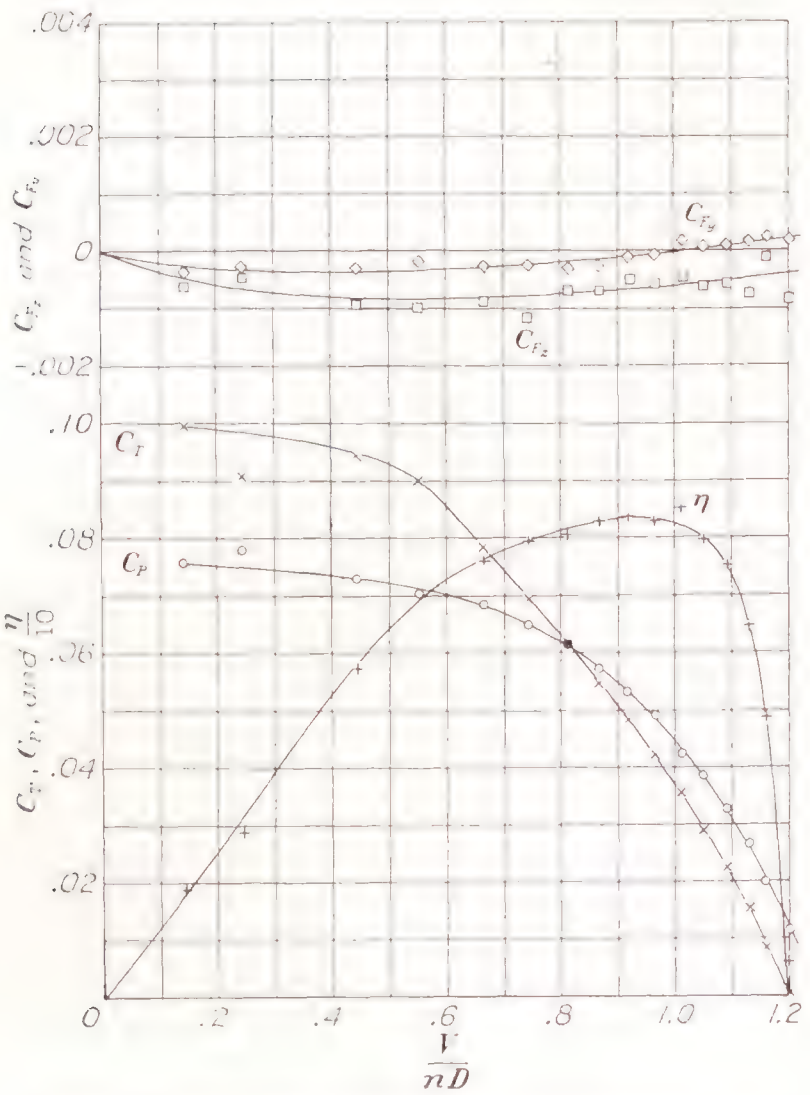

FIGURE 14.—Characteristics of a propeller set 24.6° at 0.75R; 0° yaw.

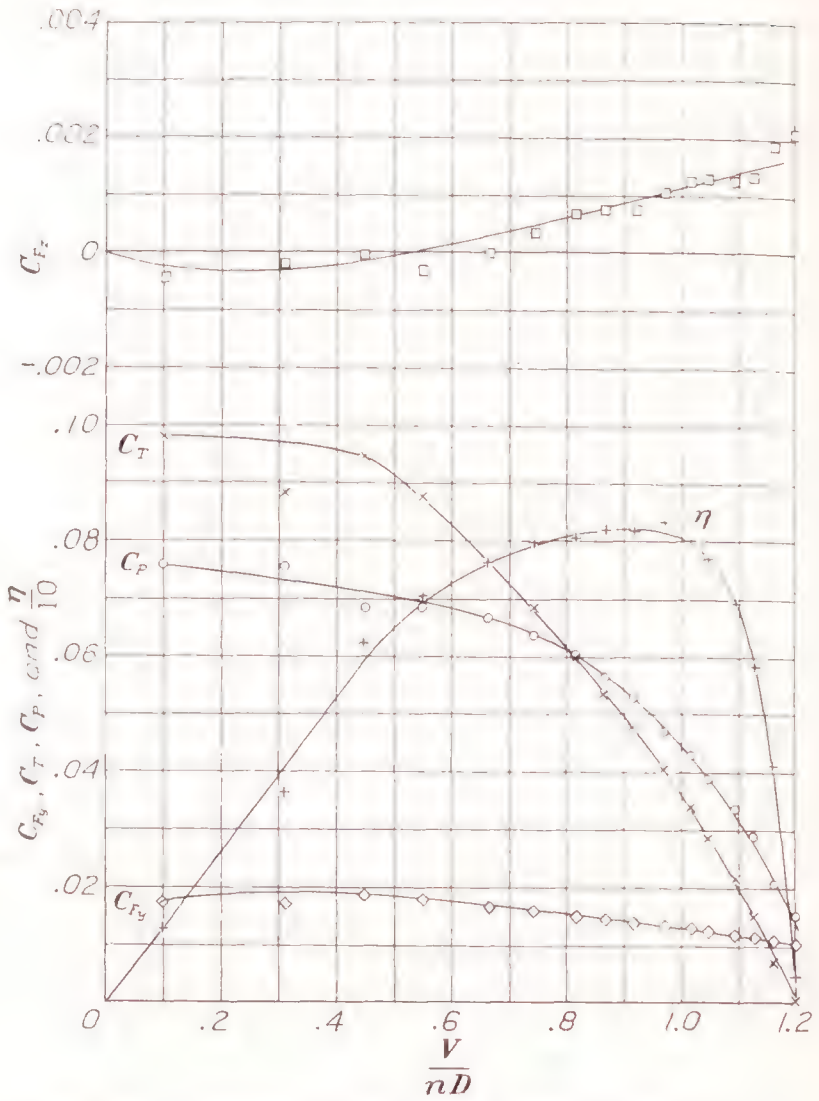

FIGURE 15.—Characteristics of a propeller set 24.6° at 0.75R; 10° yaw.

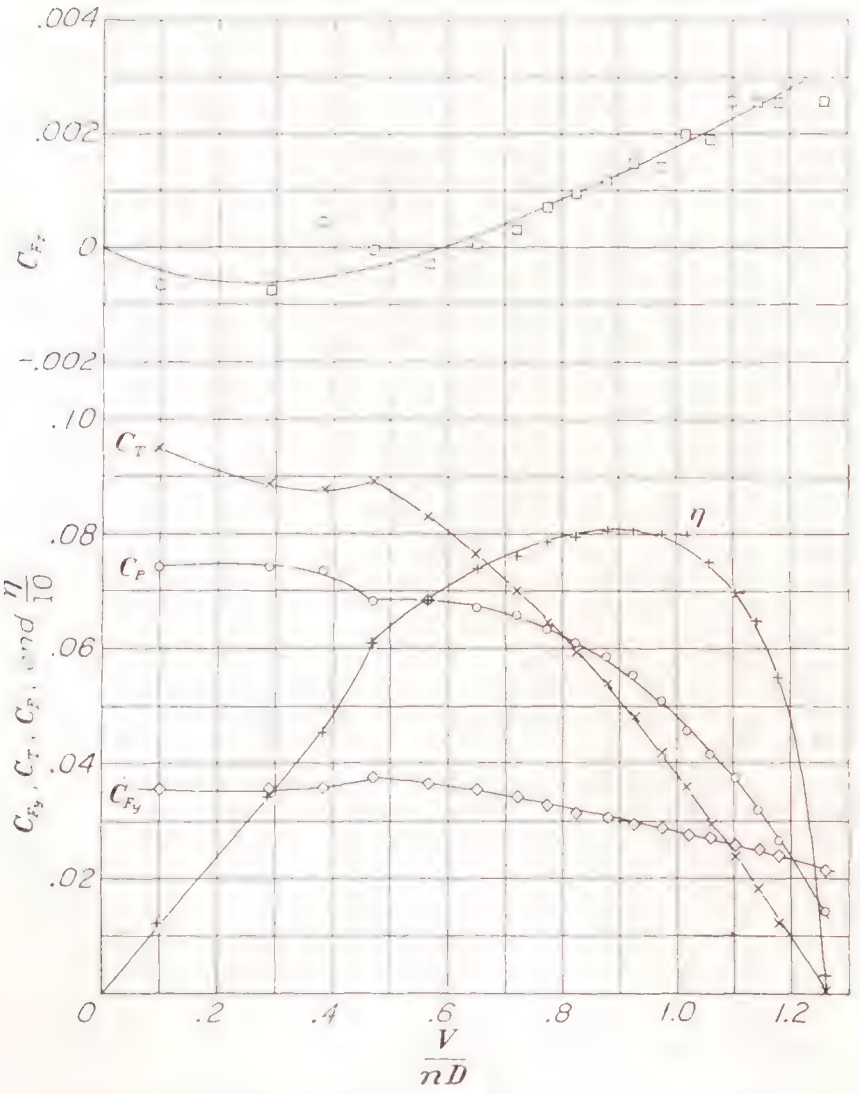

FIGURE 16.—Characteristics of a propeller set 24.6° at 0.75R; 20° yaw.

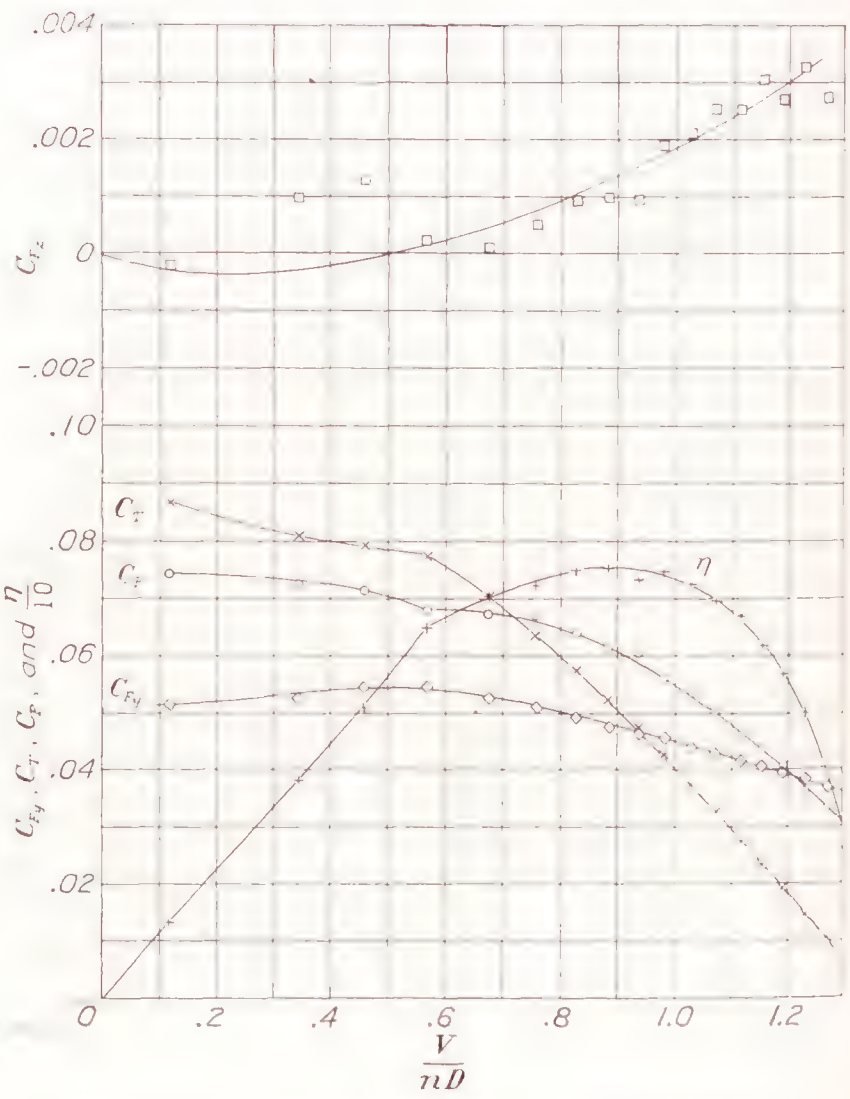

FIGURE 17.—Characteristics of a propeller set 24.6° at 0.75R; 30° yaw.

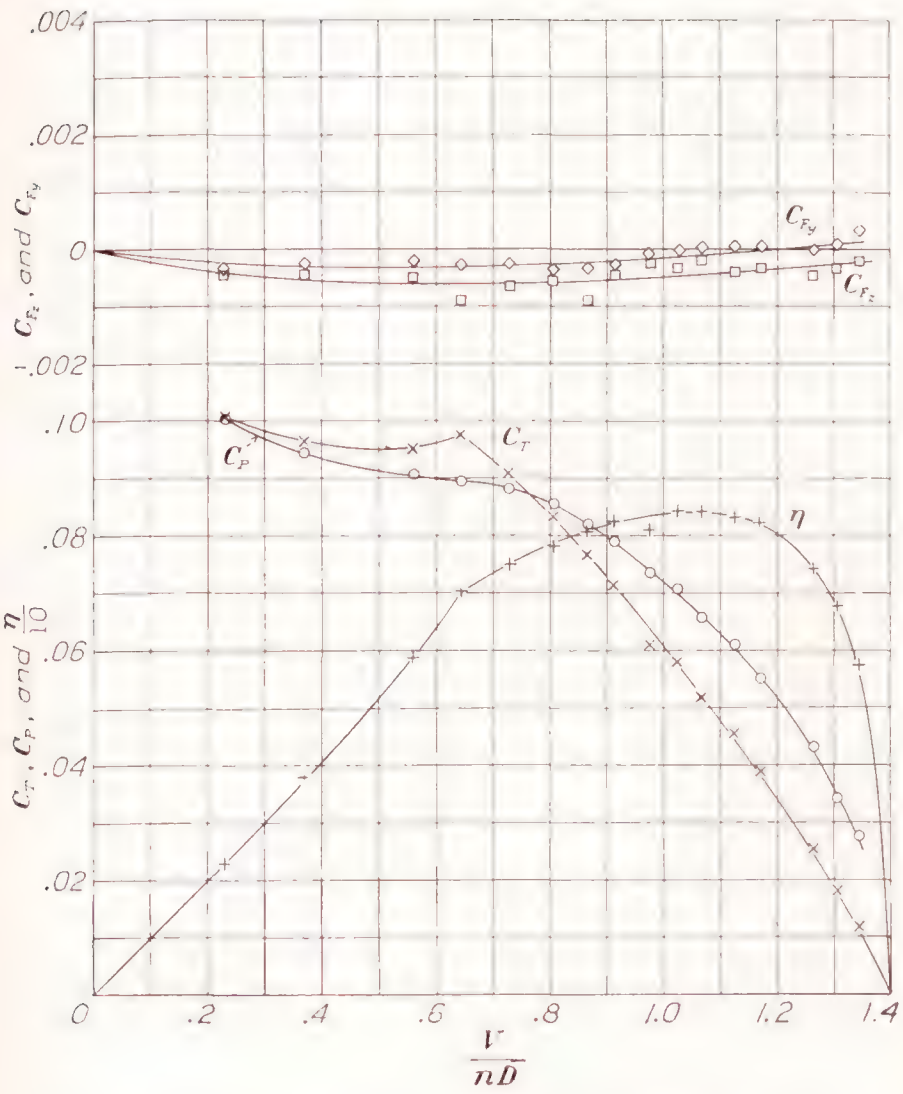

FIGURE 18.—Characteristics of a propeller set 28.6° at 0.75R; 0° yaw

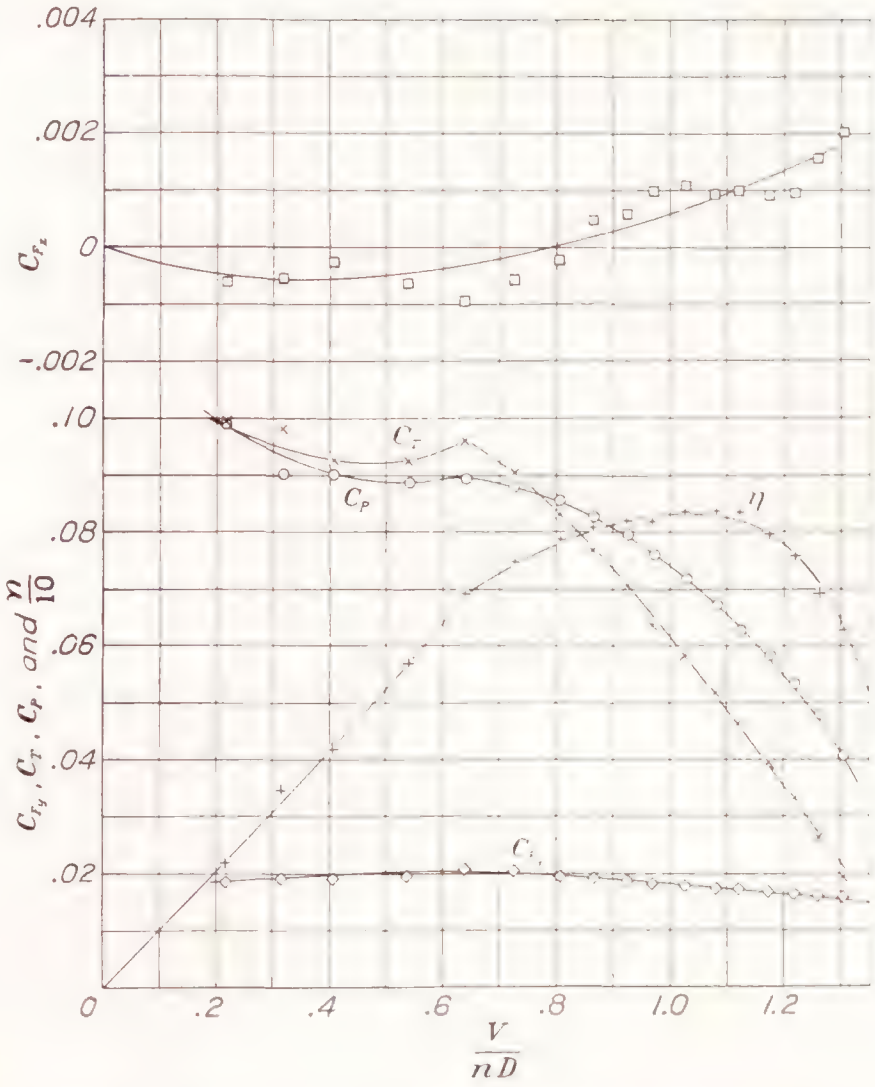

FIGURE 19.—Characteristics of a propeller set 28.6° at 0.75R; 10° yaw.

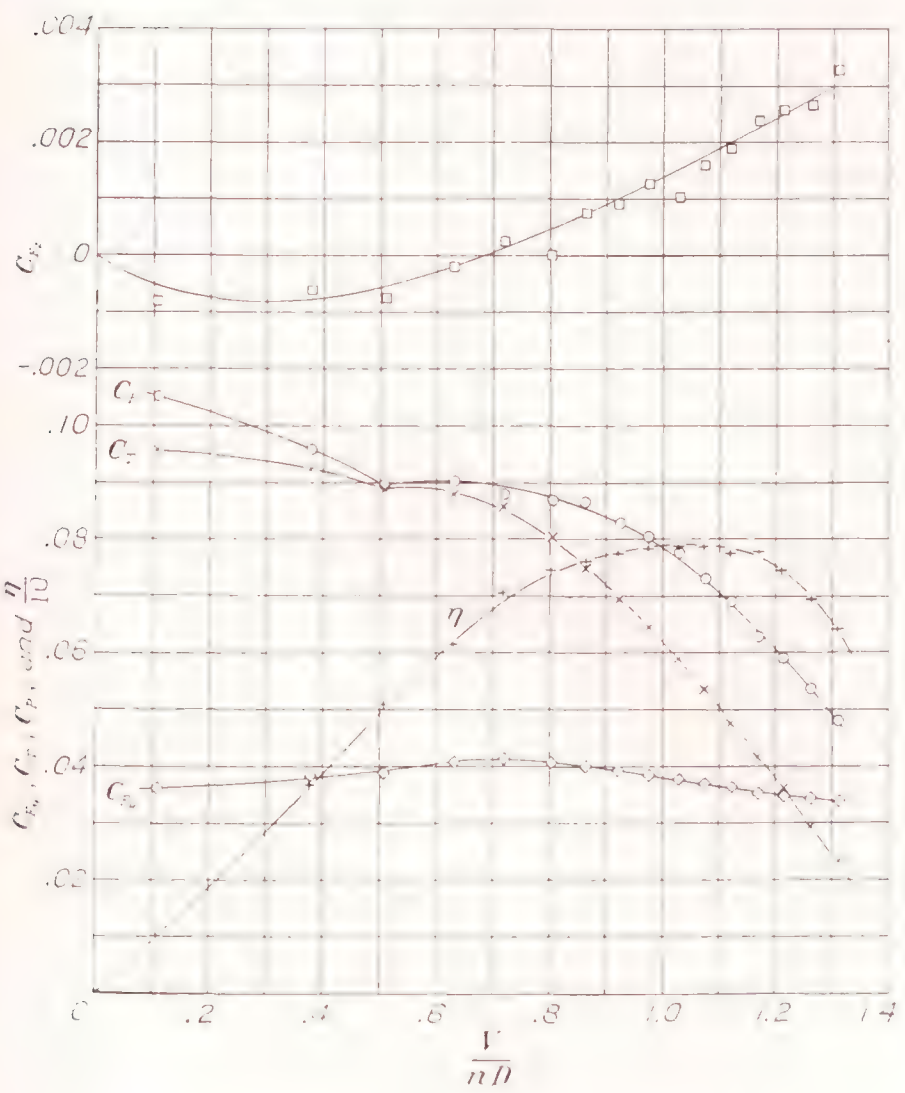

FIGURE 20.—Characteristics of a propeller set 28.6° at 0.75R; 20° yaw.

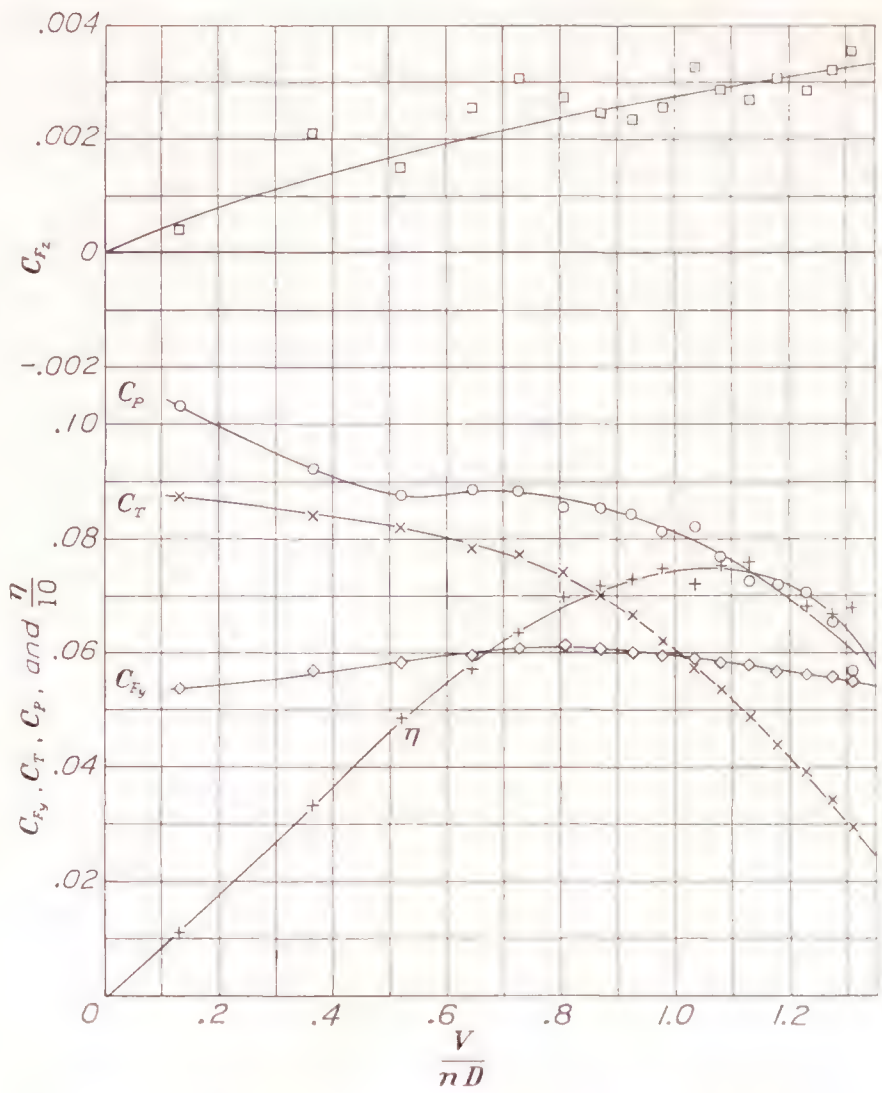

FIGURE 21.—Characteristics of a propeller set 28.6° at 0.75R; 30 °yaw.

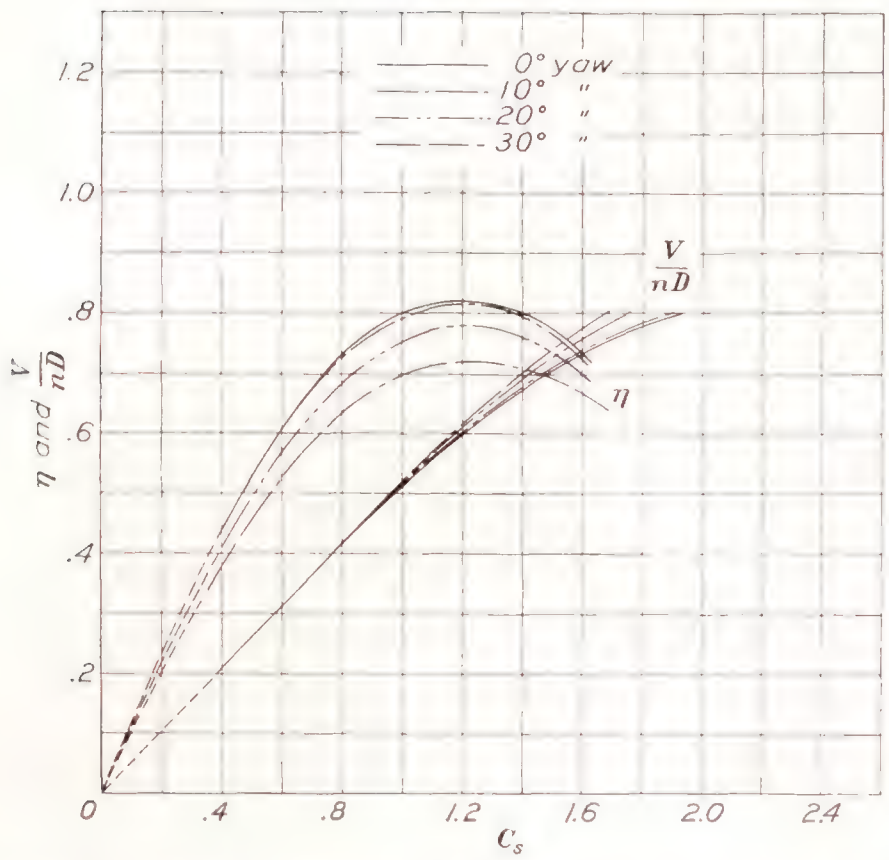

FIGURE 22.—Variation of efficiency and V/nD with speed-power coefficient for a propeller set 16.6° at 0.75R and yawed different amounts.

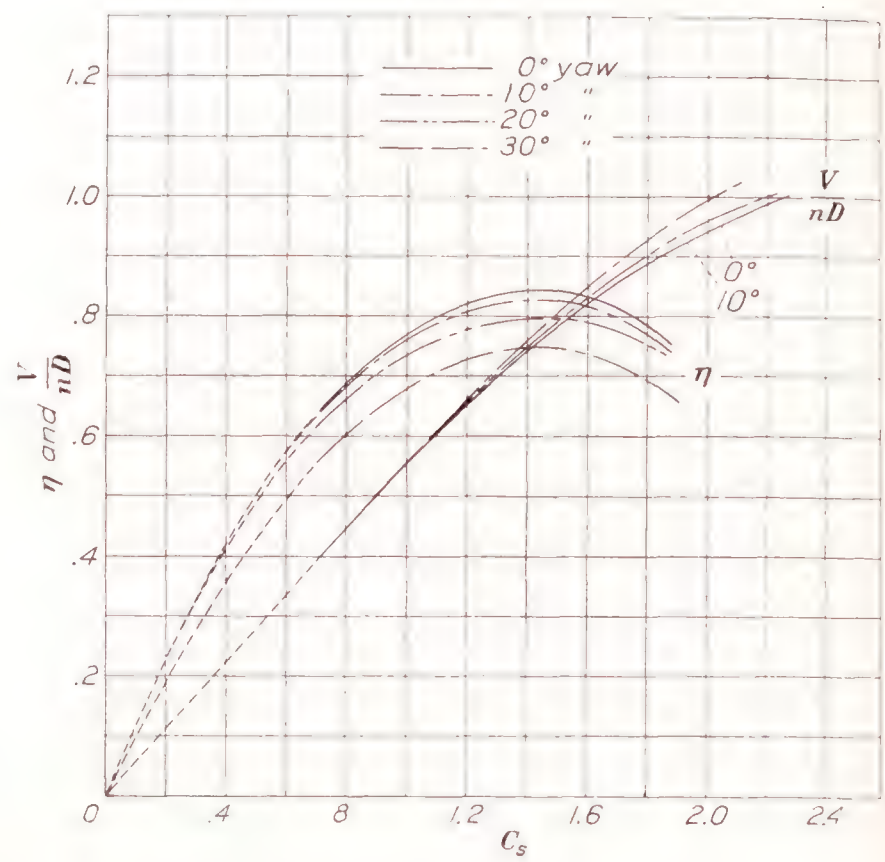

FIGURE 23.—Variation of efficiency and V/nD with speed-power coefficient for propeller set 20.6° at 0.75R and yawed different amounts.

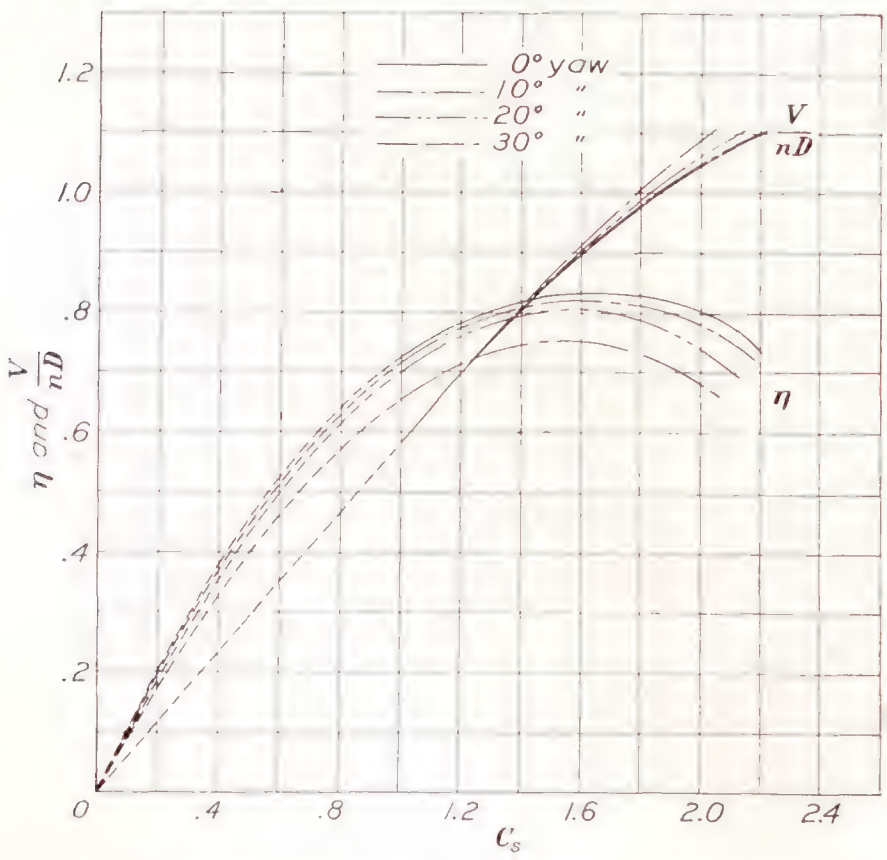

FIGURE 24.—Variation of efficiency and V/nD with speed-power coefficient for a propeller set 24.6° at 0.75R and yawed different amounts.

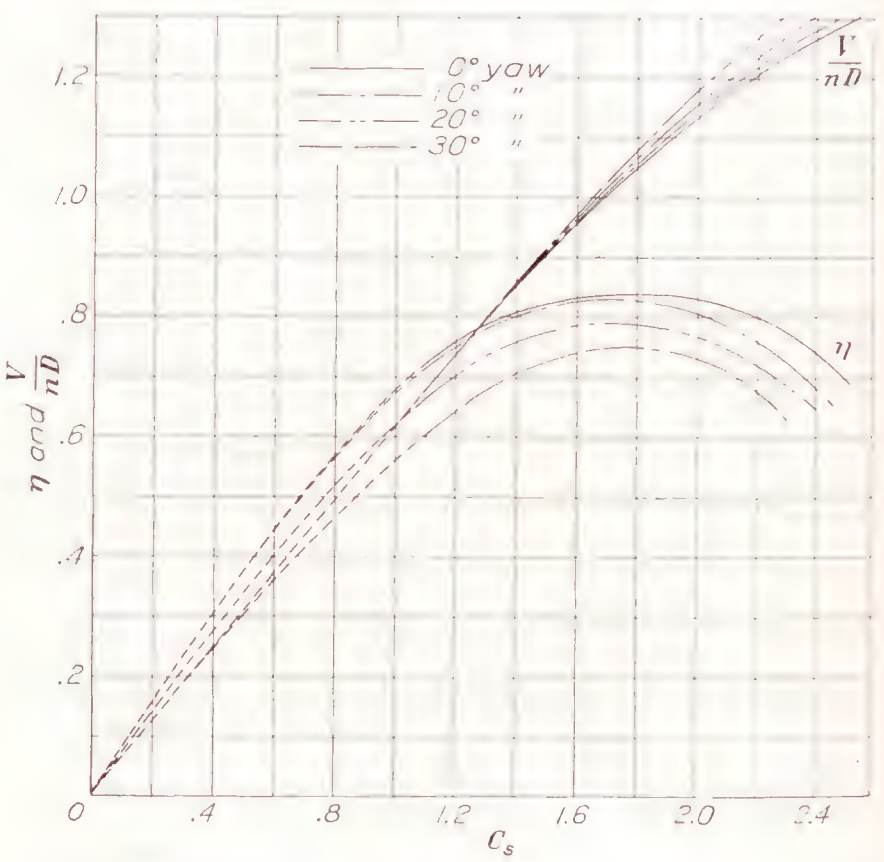

FIGURE 25.—Variation of efficiency and V/nD with speed-power coefficient for a propeller set 28.6° at 0.75R and yawed different amounts.

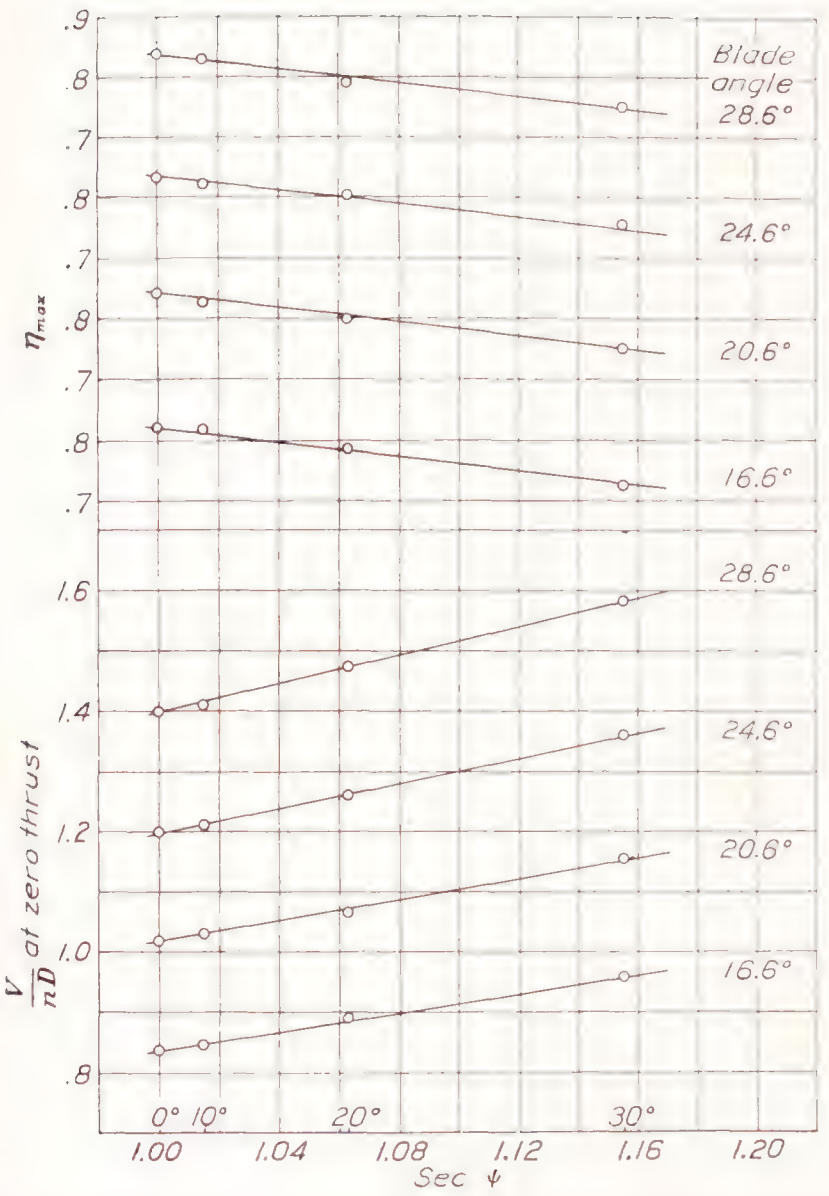

FIGURE 26.—Variation of V/nD at zero thrust and maximum efficiency with sec. ψ for propellers of four different pitch settings at $0.75R$.

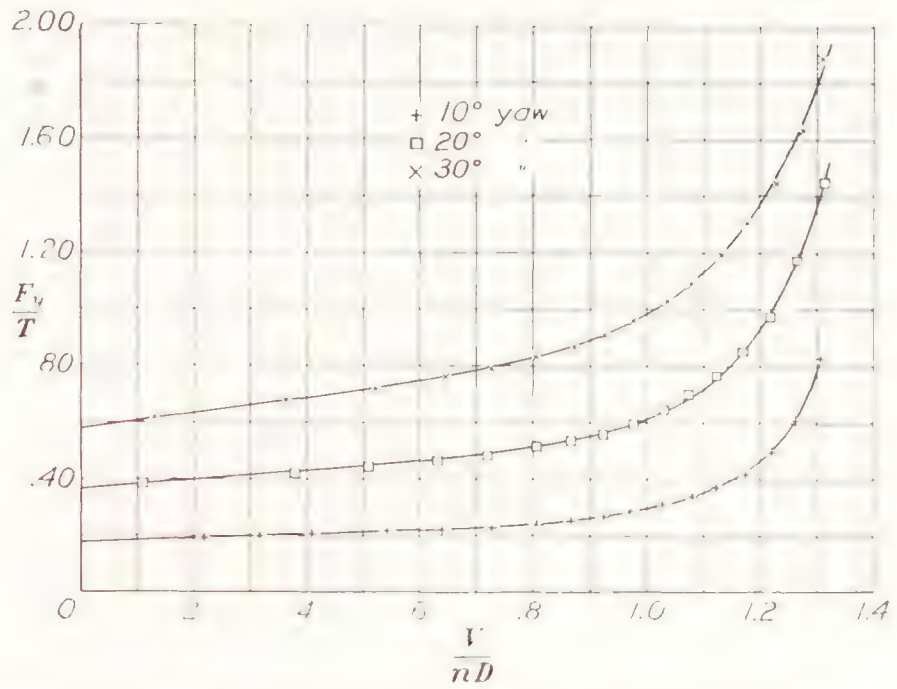

FIGURE 27.—Variation of the ratio of the cross-wind force to the thrust with V/nD for a propeller set 28.6° at $0.75R$.

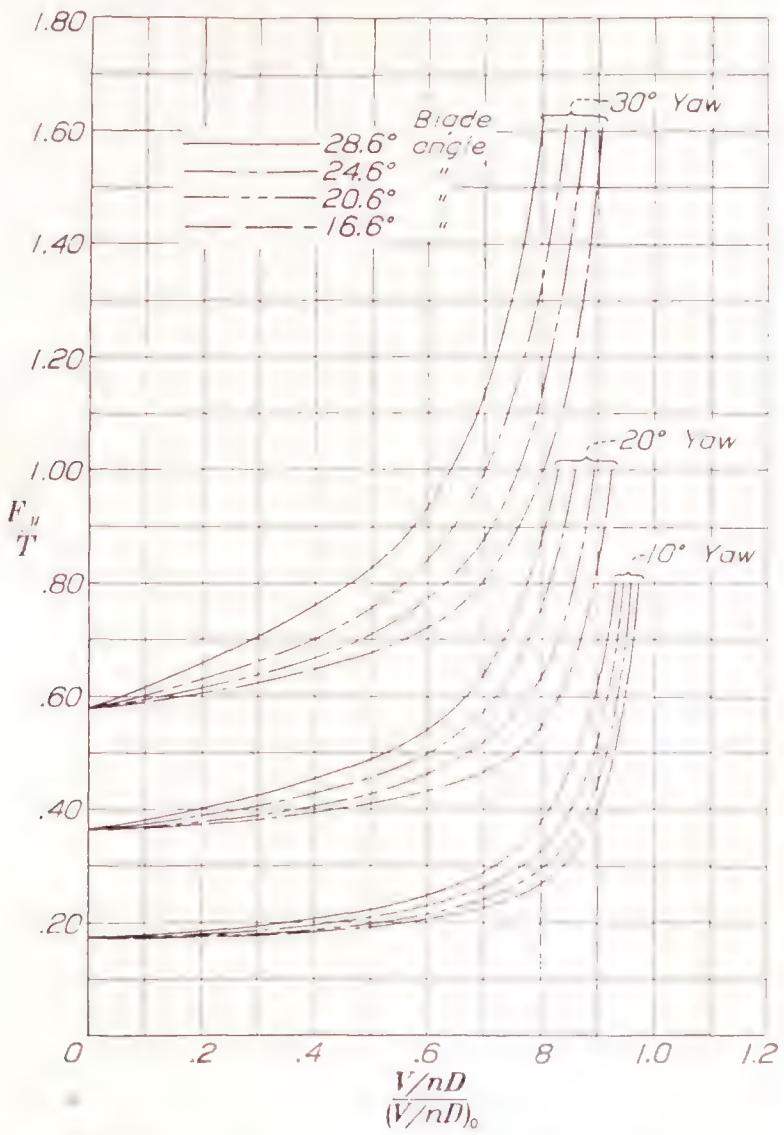

FIGURE 28.—Variation of the ratio of the cross-wind force to thrust with the ratio of V/nD to $(V/nD)_0$ for four pitch settings and three angles of yaw.

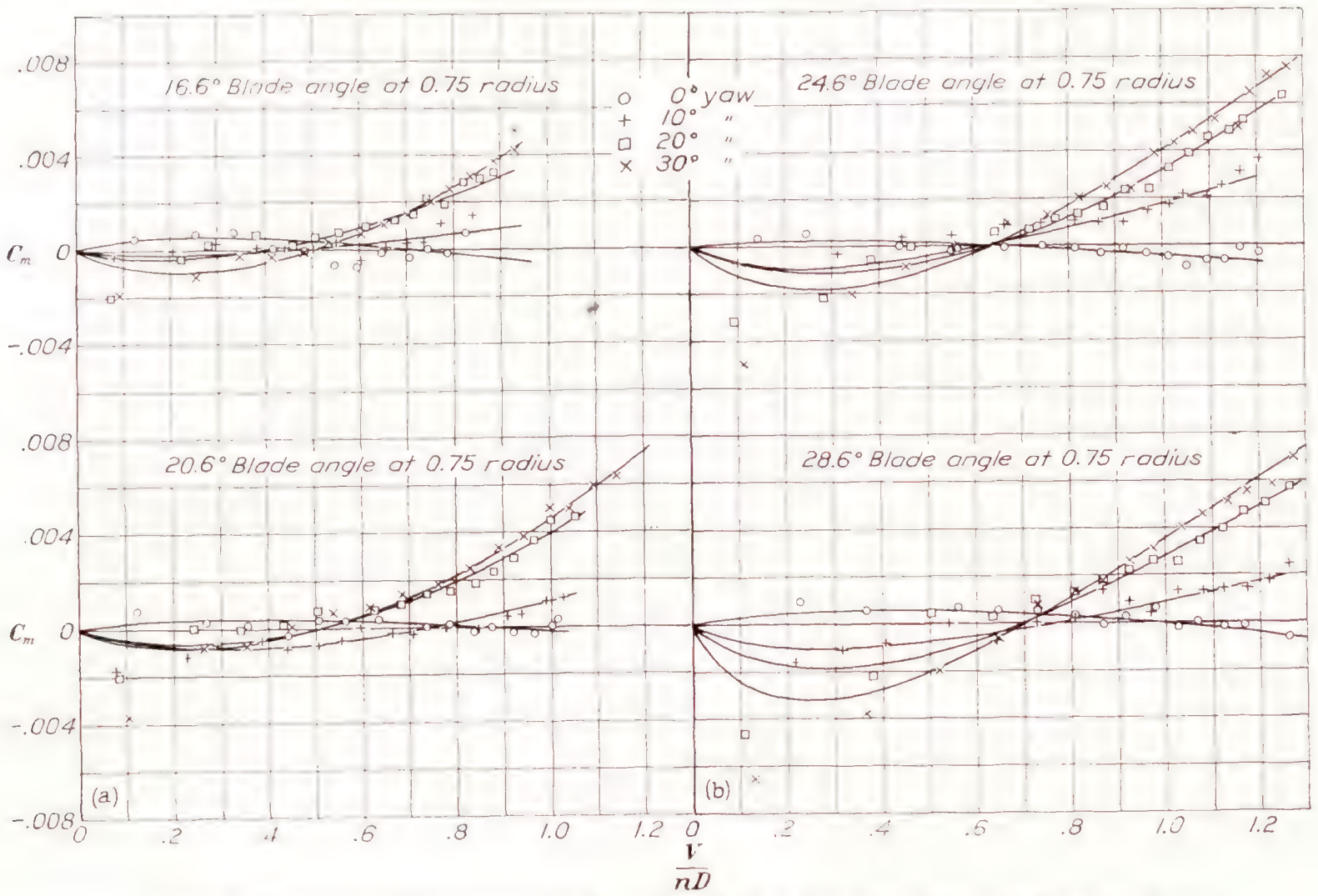

FIGURE 29.—Variation of pitching-moment coefficient with V/nD for four pitch settings and four angles of yaw.

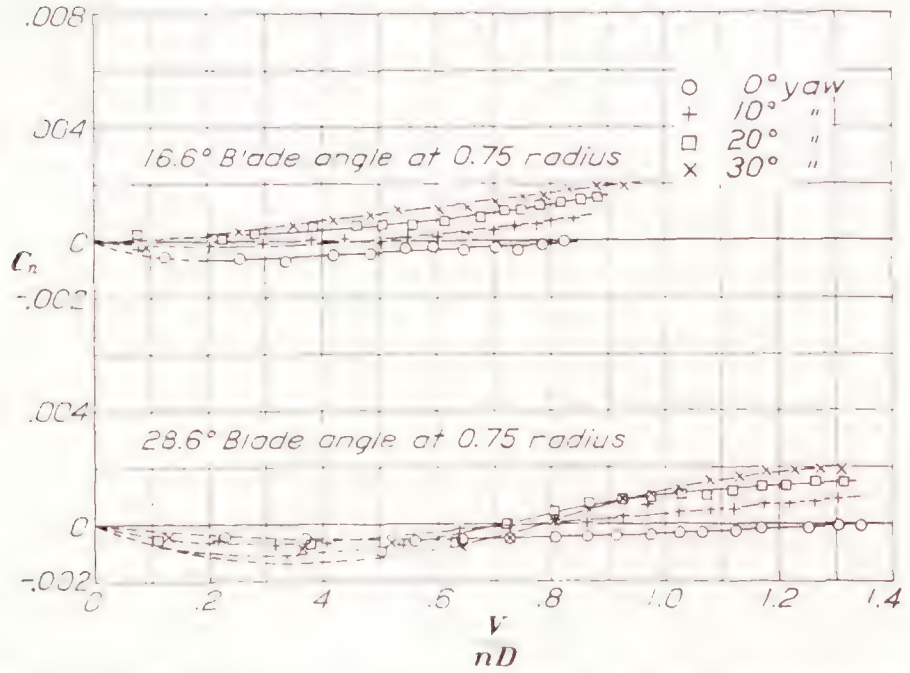

FIGURE 30.—Variation of yawing-moment coefficient with V/nD for two pitch settings and four angles of yaw.

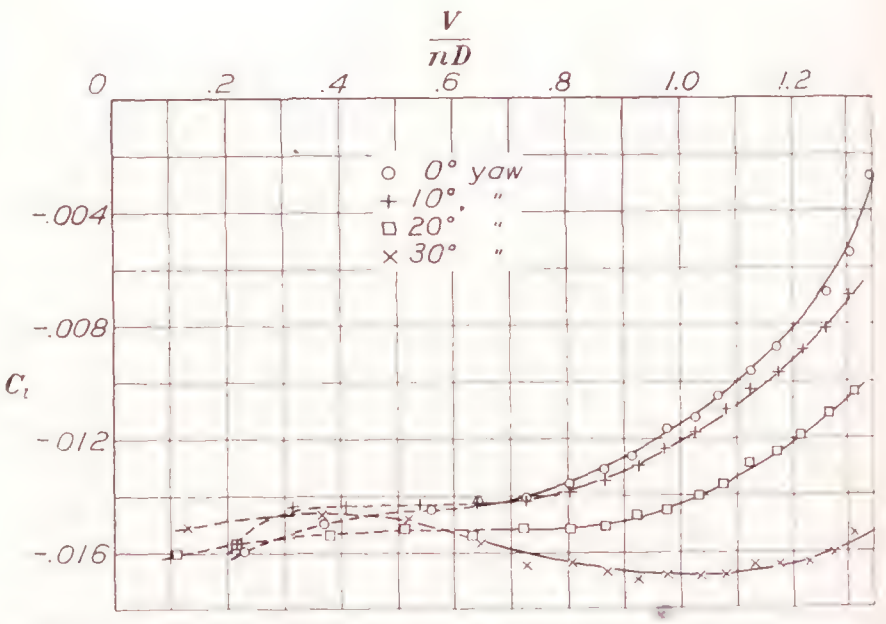

FIGURE 31.—Variation of rolling-moment coefficient with V/nD for a propeller set 28.6° at $0.75R$ for four angles of yaw.

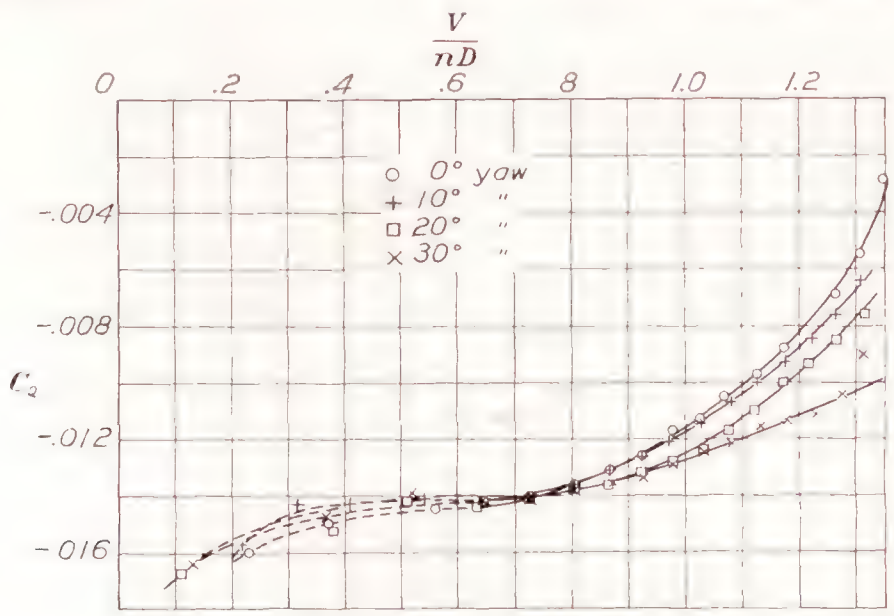

FIGURE 32.—Variation of torque coefficient with V/nD for a propeller set 28.6° at $0.75R$ for four angles of yaw.

CONCLUSIONS

The results of these experiments showed that:

1. Over the normal working range of the propeller, there was a decrease in thrust, an increase in power absorbed, and a decrease in efficiency with yaw. Up to 10° of yaw, the loss in maximum efficiency was not more than 2 percent, but at 30° yaw it became about 10 percent.

2. The cross-wind force was greater than the cross-wind component of the axial thrust. This result indicates that the corresponding lift due to a propeller with its axis in pitch accounts for a larger proportion of the increase of lift coefficients apparent in airplanes at high angles of attack, power on, than would be estimated from the vertical component of the axial thrust.

3. With the yawed propeller, there was an appreciable thrust at V/nD for zero thrust at zero yaw. Consequently, airplane glide tests made with the propeller idling at a V/nD for zero thrust at zero yaw should be corrected for the thrust due to the yawed propeller.

4. Yawing the propeller induced a pitching moment that increased in magnitude with yaw.

DANIEL GUGGENHEIM AERONAUTICAL LABORATORY,
STANFORD UNIVERSITY, CALIFORNIA, *October, 1936.*

REFERENCES

1. Clark, T. W. K.: Effect of Side Wind on a Propeller. R. & M. No. 80, British A. C. A., 1913.
2. Bramwell, F. H., Fage, A., Relf, E. F., and Bryant, L. W.: Experiments on Model Propellers at the National Physical Laboratory. R. & M. No. 123, British A. C. A., 1914.
3. Harris, R. G.: Forces on a Propeller Due to Sideslip. R. & M. No. 427, British A. C. A., 1918.
4. Flachsbart, O., and Kröber, G.: Experimental Investigation of Aircraft Propellers Exposed to Oblique Air Currents. T. M. No. 562, N. A. C. A., 1930.
5. Freeman, Hugh B.: The effect of Small Angles of Yaw and Pitch on the Characteristics of Airplane Propellers. T. R. No. 389, N. A. C. A., 1931.
6. Lesley, E. P., and Reid, Elliott G.: Tests of Five Metal Model Propellers with Various Pitch Distributions in a Free Wind Stream and in Combination with a Model VE–7 Fuselage. T. R. No. 326, N. A. C. A., 1929.
7. Durand, W. F., and Lesley, E. P.: Comparison of Tests on Air Propellers in Flight with Wind Tunnel Model Tests on Similar Forms. T. R. No. 220, N. A. C. A., 1926.
8. Millikan, C. B., Russell, J. S., and McCoy, H. M.: Wind Tunnel Tests on a High Wing Monoplane with Running Propeller. Parts 1 and 2, Jour. Aero. Sciences. vol. 3, no. 3, Jan. 1936, pp. 73–85.

TABLE I

COMPUTED VALUES OF COEFFICIENTS FOR DIFFERENT PITCH SETTINGS AND VARIOUS ANGLES OF YAW

$\frac{V}{nD}$	C_P	C_T	η	C_{Fy}	C_{Fz}	C_m	C_n
16.6° PITCH SETTING, 0° YAW							
0.124	0.0402	0.0873	0.269	−0.00030	−0.00030	0.00047	−0.00055
.254	.0389	.0804	.525	−.00018	−.00061	.00067	−.00061
.335	.0387	.0731	.633	−.00012	−.00049	.00077	−.00069
.419	.0369	.0650	.738	−.00006	−.00043	.00004	−.00049
.484	.0361	.0573	.768	−.00006	−.00079	−.00005	−.00045
.546	.0331	.0489	.807	0	−.00079	−.00055	−.00026
.592	.0310	.0437	.834	0	−.00061	−.00077	−.00022
.648	.0283	.0349	.800	0	−.00030	−.00016	−.00035
.703	.0244	.0274	.790	0	−.00061	−.00037	−.00026
.743	.0200	.0196	.728	.00006	−.00024	.00004	−.00035
.786	.0153	.0110	.565	.00006	−.00030	.00020	−.00018
.822	.0090	.0036	.329	.00006	.00006	.00059	−.00006
16.6° PITCH SETTING, 10° YAW							
0.081	0.0382	0.0884	0.187	0.0155	−0.00024	−0.00023	−0.00030
.203	.0385	.0828	.437	.0150	−.00024	−.00004	−.00020
.297	.0387	.0760	.583	.0140	−.00030	.00026	−.00008
.381	.0376	.0679	.688	.0130	−.00018	.00012	.00006
.441	.0371	.0619	.736	.0121	−.00006	.00012	.00008
.501	.0349	.0549	.788	.0112	−.00018	.00007	−.00006
.551	.0330	.0487	.813	.0103	−.00024	.00036	.00010
.602	.0319	.0434	.819	.0097	−.00048	−.00040	.00008
.656	0276	.0342	.813	.0084	−.00036	.00010	.00032
.700	.0247	.0276	.782	.0076	−.00009	.00030	.00040
.736	.0217	.0216	.733	.0068	.00006	.00032	.00050
.773	.0169	.0149	.682	.0061	.00042	.00111	.00054
.840	.0098	.0014	.120	.0044	.00120	.00148	.00078
16.6° PITCH SETTING, 20° YAW							
0.075	0.0411	0.0841	0.154	0.0308	0.00012	−0.00200	0.00023
.224	.0398	.0784	.441	.0300	−.00012	−.00037	.00012
.283	.0395	.0758	.543	.0291	.00012	.00022	.00026
.381	.0393	.0682	.661	.0273	.00025	.00067	.00047
.460	.0389	.0599	.708	.0248	−.00012	.00021	.00053
.506	.0376	.0549	.739	.0234	−.00006	.00059	.00057
.558	.0357	.0491	.768	.0218	.00018	.00071	.00057
.613	.0334	.0428	.786	.0200	.00037	.00098	.00069
.674	.0304	.0349	.774	.0179	.00073	.00128	.00083
.716	.0279	.0291	.747	.0164	.00079	.00151	.00106
.744	.0252	.0247	.730	.0154	.00067	.00220	.00108
.780	.0228	.0190	.650	.0139	.00116	.00194	.00124
.820	.0178	.0122	.562	.0122	.00207	.00290	.00136
.854	.0147	.0067	.390	.0109	.00195	.00307	.00140
.883	.0115	.0017	.130	.0096	.00225	.00332	.00146
16.6° PITCH SETTING, 30° YAW							
0.095	0.0394	0.0760	0.183	0.0448	−0.00080	−0.00190	−0.00021
.255	.0403	.0704	.446	.0434	−.00099	−.00113	.00035
.350	.0396	.0651	.576	.0413	−.00093	−.00029	.00056
.419	.0393	.0593	.632	.0388	−.00037	−.00031	.00070
.484	.0391	.0545	.675	.0367	−.00012	−.00012	.00088
.536	.0376	.0496	.707	.0345	.00025	.00037	.00111
.603	.0367	.0434	.713	.0320	.00043	.00072	.00111
.654	.0345	.0381	.722	.0298	.00056	.00109	.00117
.703	.0318	.0325	.718	.0276	.00093	.00148	.00136
.751	.0291	.0272	.702	.0255	.00112	.00206	.00159
.792	.0254	.0217	.677	.0235	.00143	.00256	.00155
.834	.0227	.0160	.588	.0211	.00173	.00306	.00175
.882	.0201	.0100	.439	.0188	.00242	.00370	.00192
.930	.0150	.0034	.211	.0162	.00247	.00415	.00185
20.6° PITCH SETTING, 0° YAW							
$\frac{V}{nD}$	C_P	C_T	η	C_{Fy}	C_{Fz}	C_m	
0.124	0.0639	0.0884	0.172	−0.00018	−0.00073	0.00077	
.270	.0561	.0907	.437	−.00024	.00440	.00026	
.359	.0535	.0890	.597	−.00024	−.00091	.00018	
.441	.0534	.0833	.688	−.00018	−.00116	−.00034	
.509	.0515	.0762	.753	−.00012	−.00055	.00034	
.563	.0507	.0697	.774	−.00012	−.00067	.00022	
.634	.0483	.0612	.804	−.00012	−.00067	.00033	
.739	.0425	.0483	.839	−.00018	−.00061	−.00002	
.785	.0398	.0427	.842	−.00018	−.00043	.00014	
.836	.0349	.0350	.838	−.00012	−.00049	−.00020	
.874	.0309	.0291	.823	−.00006	−.00018	−.00004	
.920	.0258	.0210	.749	0	−.00030	−.00024	
.963	.0194	.0124	.616	.00012	−.00042	−.00028	
1.001	.0130	.0049	.377	.00024	−.00006	.00007	
1.015	.0105	.0013	.126	.00024	.00030	.00033	

38548—38——31

TABLE I—Continued

$\frac{V}{nD}$	C_P	C_T	η	C_{Fy}	C_{Fz}	C_m
20.6° PITCH SETTING, 10° YAW						
0.081	0.0632	0.0883	0.113	0.0155	−0.00095	−0.00174
.230	.0568	.0885	.358	.0164	−.00066	−.00120
.294	.0526	.0901	.504	.0170	−.00090	−.00072
.386	.0528	.0855	.625	.0164	−.00084	−.00054
.440	.0528	.0818	.682	.0160	−.00126	−.00092
.507	.0507	.0747	.747	.0150	−.00102	−.00072
.553	.0504	.0694	.762	.0144	−.00078	−.00056
.596	.0489	.0646	.787	.0138	−.00055	.00002
.662	.0460	.0568	.817	.0128	−.00048	−.00024
.708	.0446	.0516	.819	.0122	−.00036	−.00030
.777	.0392	.0426	.844	.0112	−.00042	−.00002
.842	.0344	.0330	.808	.0101	−.00006	−.00002
.906	.0270	.0226	.758	.0091	.00024	.00043
.938	.0245	.0162	.620	.0085	−.00018	.00050
.990	.0150	.0062	.409	.0078	.00066	.00116
1.028	.0107	.0002	.019	.0068	.00090	.00128
20.6° PITCH SETTING, 20° YAW						
0.088	0.0617	0.0854	0.122	0.0317	0.00049	−0.00206
.241	.0529	.0857	.390	.0337	.00109	0
.342	.0519	.0849	.560	.0339	.00054	−.00008
.435	.0518	.0789	.662	.0325	.00037	.00018
.507	.0522	.0735	.714	.0312	.00092	.00071
.623	.0492	.0610	.772	.0279	.00080	.00073
.682	.0471	.0543	.786	.0262	.00086	.00092
.738	.0444	.0485	.806	.0248	.00128	.00141
.786	.0416	.0427	.806	.0235	.00147	.00153
.841	.0386	.0358	.780	.0226	.00159	.00185
.880	.0337	.0299	.780	.0210	.00159	.00235
.925	.0299	.0234	.724	.0197	.00184	.00287
.967	.0248	.0161	.628	.0182	.00197	.00360
1.000	.0198	.0101	.510	.0169	.00249	.00455
1.058	.0131	.0018	.146	.0147	.00276	.00469
20.6° PITCH SETTING, 30° YAW						
0.107	0.0642	0.0772	0.129	0.0460	−0.00143	−0.00376
.267	.0562	.0788	.374	.0493	−.00081	−.00085
.358	.0539	.0772	.513	.0495	.00018	−.00072
.454	.0533	.0718	.612	.0478	−.00018	.00003
.540	.0525	.0654	.673	.0454	.00031	.00066
.618	.0516	.0592	.709	.0432	.00067	.00085
.688	.0502	.0536	.735	.0417	.00050	.00144
.765	.0469	.0460	.750	.0384	.00112	.00188
.831	.0434	.0385	.738	.0359	.00174	.00251
.892	.0378	.0314	.741	.0335	.00169	.00338
.944	.0352	.0253	.678	.0316	.00237	.00379
.998	.0297	.0183	.615	.0293	.00299	.00505
1.044	.0270	.0127	.491	.0275	.00314	.00504
1.096	.0231	.0070	.332	.0257	.00329	.00594
1.147	.0182	.0006	.038	.0232	.00365	.00632
24.6° PITCH SETTING, 0° YAW						
0.143	0.0757	0.0996	0.188	−0.00031	−0.00063	0.00032
.246	.0780	.0909	.287	−.00025	−.00044	.00056
.444	.0730	.0945	.575	−.00024	−.00091	.00004
.552	.0704	.0901	.706	−.00018	−.00098	−.00020
.666	.0685	.0784	.762	−.00025	−.00086	−.00012
.743	.0648	.0693	.794	−.00024	−.00116	−.00004
.811	.0618	.0615	.807	−.00031	−.00068	−.00018
.867	.0572	.0548	.830	−.00025	−.00068	−.00034
.918	.0530	.0482	.835	−.00012	−.00049	−.00012
.964	.0490	.0422	.830	−.00006	−.00055	−.00038
1.012	.0424	.0357	.852	.00018	−.00043	−.00048
1.050	.0386	.0292	.795	.00006	−.00061	−.00090
1.092	.0328	.0226	.752	.00012	−.00055	−.00070
1.131	.0267	.0153	.648	.00018	−.00074	−.00070
1.161	.0200	.0084	.488	.00024	−.00012	−.00015
1.202	.0118	.0006	.061	.00018	−.00085	−.00034
24.6° PITCH SETTING, 10° YAW						
0.099	0.0762	0.0982	0.128	0.0175	−0.00043	−0.00067
.312	.0756	.0881	.364	.0172	−.00018	−.00033
.449	.0683	.0946	.622	.0189	−.00006	.00040
.551	.0686	.0878	.706	.0181	−.00030	.00045
.664	.0665	.0764	.763	.0168	0	.00082
.744	.0637	.0683	.798	.0159	.00037	.00096
.815	.0603	.0597	.807	.0150	.00068	.00104
.867	.0564	.0534	.821	.0145	.00074	.00096
.918	.0530	.0474	.821	.0139	.00074	.00097
.970	.0470	.0404	.834	.0134	.00105	.00145
1.014	.0429	.0339	.801	.0128	.00123	.00176
1.046	.0388	.0286	.772	.0124	.00129	.00211
1.093	.0336	.0214	.696	.0119	.00128	.00208
1.127	.0288	.0149	.583	.0114	.00135	.00256
1.162	.0206	.0073	.412	.0109	.00188	.00311
1.202	.0152	.0006	.047	.0102	.00207	.00363

TABLE I—Continued

$\frac{V}{nD}$	C_P	C_T	η	C_{Fy}	C_{Fz}	C_m
24.6° PITCH SETTING, 20° YAW						
0.094	0.0740	0.0950	0.121	0.0354	−0.00068	−0.00320
.286	.0741	.0885	.342	.0356	−.00074	−.00222
.381	.0734	.0875	.454	.0358	.00043	−.00057
.466	.0682	.0891	.609	.0377	−.00006	−.00002
.562	.0682	.0830	.684	.0365	−.00031	−.00018
.647	.0670	.0765	.738	.0352	.00006	.00053
.717	.0658	.0699	.762	.0339	.00031	.00064
.771	.0632	.0644	.786	.0328	.00068	.00112
.821	.0610	.0592	.797	.0316	.00093	.00132
.874	.0585	.0538	.804	.0306	.00118	.00157
.922	.0553	.0482	.804	.0295	.00149	.00226
.971	.0509	.0418	.798	.0285	.00143	.00232
1.014	.0456	.0359	.798	.0276	.00198	.00328
1.055	.0414	.0295	.752	.0272	.00191	.00387
1.098	.0374	.0238	.699	.0257	.00254	.00458
1.141	.0319	.0181	.648	.0250	.00254	.00487
1.175	.0264	.0124	.552	.0239	.00252	.00531
1.258	.0146	.0004	.031	.0215	.00258	.00632
24.6° PITCH SETTING, 30° YAW						
0.117	0.0742	0.0868	0.137	0.0516	−0.00019	−0.00507
.343	.0724	.0808	.383	.0527	.00099	−.00206
.458	.0713	.0793	.509	.0542	.00130	−.00087
.567	.0678	.0776	.649	.0546	.00025	.00010
.674	.0672	.0703	.705	.0529	.00012	.00097
.757	.0669	.0637	.721	.0510	.00050	.00130
.828	.0638	.0576	.748	.0491	.00093	.00202
.883	.0614	.0522	.751	.0478	.00099	.00249
.937	.0604	.0474	.735	.0466	.00093	.00243
.981	.0561	.0427	.747	.0454	.00193	.00386
1.028	.0534	.0376	.724	.0441	.00212	.00437
1.070	.0501	.0326	.696	.0429	.00255	.00482
1.115	.0462	.0278	.671	.0418	.00256	.00534
1.153	.0438	.0235	.618	.0407	.00301	.00504
1.189	.0408	.0194	.565	.0397	.00273	.00650
1.229	.0362	.0147	.499	.0384	.00328	.00722
1.269	.0331	.0105	.402	.0372	.00272	.00750
1.315	.0289	.0056	.255	.0360	.00340	.00826

28.6° PITCH SETTING, 0° YAW

$\frac{V}{nD}$	C_P	C_T	η	C_{Fy}	C_{Fz}	C_m	C_n	C_l and C_Q
0.229	0.1002	0.1006	0.230	−0.00032	−0.00044	0.00090	−0.00046	−0.0160
.369	.0944	.0965	.377	−.00025	−.00044	.00055	−.00048	−.0150
.560	.0908	.0952	.587	−.00019	−.00051	.00068	−.00056	−.0145
.643	.0894	.0975	.702	−.00025	−.00089	.00055	−.00054	−.0142
.728	.0883	.0909	.750	−.00025	−.00064	.00053	−.00052	−.0141
.806	.0857	.0834	.784	−.00032	−.00057	.00034	−.00043	−.0136
.864	.0821	.0769	.809	−.00032	−.00089	−.00013	−.00046	−.0131
.913	.0792	.0716	.825	−.00025	−.00044	.00030	−.00039	−.0126
.976	.0736	.0612	.812	−.00006	−.00025	.00065	−.00035	−.0117
1.024	.0708	.0582	.842	0	−.00032	−.00023	−.00034	−.0113
1.067	.0658	.0519	.842	.00006	−.00019	.00002	−.00027	−.0105
1.124	.0612	.0455	.836	.00006	−.00038	−.00019	−.00028	−.0097
1.169	.0552	.0390	.826	.00006	−.00032	−.00011	−.00014	−.0088
1.263	.0431	.0254	.744	0	−.00044	−.00061	−.00026	−.0069
1.305	.0343	.0179	.681	.00012	−.00032	−.00042	−.00012	−.0055
1.307	.0343	.0184	.702	.00006	−.00057	−.00080	−.00029	−.0055
1.345	.0276	.0118	.575	.00032	−.00019	−.00038	−.00009	−.0028

28.6° PITCH SETTING, 10° YAW

$\frac{V}{nD}$	C_P	C_T	η	C_{Fy}	C_{Fz}	C_m	C_n	C_l	C_Q
0.218	0.0988	0.0986	0.218	0.0187	−0.00063	−0.00159	−0.00055	−0.0157	−0.0157
.317	.0901	.0981	.345	.0193	−.00056	−.00111	−.00071	−.0144	−.0143
.409	.0901	.0926	.420	.0191	−.00025	−.00082	−.00065	−.0144	−.0143
.541	.0886	.0925	.565	.0198	−.00063	0	−.00078	−.0143	−.0141
.639	.0892	.0960	.688	.0207	−.00095	−.00072	−.00018	−.0143	−.0141
.727	.0877	.0901	.747	.0204	−.00057	.00008	−.00004	−.0142	−.0140
.806	.0854	.0830	.784	.0196	−.00025	.00017	.00011	−.0139	−.0136
.866	.0826	.0768	.805	.0191	.00045	.00145	.00005	−.0135	−.0131
.924	.0796	.0706	.819	.0187	.00057	.00093	.00030	−.0130	−.0127
.970	.0758	.0636	.814	.0182	.00096	.00047	.00066	−.0124	−.0121
1.027	.0716	.0581	.833	.0179	.00108	.00131	.00040	−.0118	−.0114
1.080	.0670	.0518	.835	.0173	.00095	.00135	.00049	−.0110	−.0107
1.122	.0623	.0463	.834	.0171	.00102	.00140	.00049	−.0103	−.0099
1.174	.0583	.0395	.796	.0165	.00089	.00144	.00069	−.0097	−.0093
1.220	.0532	.0330	.757	.0163	.00095	.00182	.00068	−.0089	−.0085
1.263	.0479	.0262	.691	.0161	.00158	.00246	.00079	−.0082	−.0076
1.306	.0404	.0193	.624	.0159	.00202	.00303	.00085	−.0070	−.0064

TABLE I—Continued

28.6° PITCH SETTING, 20° YAW

$\frac{V}{nD}$	C_P	C_T	η	C_{Fy}	C_{Fz}	C_m	C_n	C_l	C_Q
0.110	0.1049	0.0957	0.100	0.0363	−0.00082	−0.00464	−0.00053	−0.0161	−0.0167
.380	.0957	.0924	.367	.0385	−.00063	−.00221	−.00067	−.0154	−.0152
.511	.0894	.0889	.508	.0388	−.00075	.00046	−.00088	−.0152	−.0142
.632	.0902	.0881	.617	.0408	−.00019	.00034	−.00066	−.0154	−.0144
.721	.0879	.0856	.702	.0413	.00025	.00100	−.00002	−.0152	−.0140
.804	.0870	.0803	.742	.0407	0	.00134	.00040	−.0152	−.0138
.865	.0855	.0750	.759	.0400	.00076	.00179	.00072	−.0151	−.0136
.923	.0828	.0696	.776	.0393	.00089	.00226	.00086	−.0147	−.0132
.977	.0805	.0644	.782	.0385	.00127	.00264	.00096	−.0145	−.0128
1.029	.0777	.0591	.783	.0378	.00102	.00258	.00104	−.0140	−.0124
1.076	.0732	.0535	.786	.0371	.00158	.00342	.00099	−.0136	−.0117
1.122	.0689	.0476	.775	.0363	.00190	.00398	.00120	−.0129	−.0110
1.169	.0627	.0418	.779	.0355	.00239	.00469	.00135	−.0125	−.0100
1.215	.0589	.0362	.747	.0352	.00258	.00504	.00138	−.0119	−.0094
1.264	.0536	.0295	.696	.0346	.00264	.00573	.00152	−.0112	−.0085
1.312	.0479	.0234	.641	.0340	.00326	.00832	.00144	−.0104	−.0076

TABLE I—Continued

28.6° PITCH SETTING, 30° YAW

$\frac{V}{nD}$	C_P	C_T	η	C_{Fy}	C_{Fz}	C_m	C_n	C_l	C_Q
0.130	0.1031	0.0874	0.110	0.0536	0.00038	−0.00653	−0.00043	−0.0151	−0.0164
.365	.0922	.0839	.332	.0568	.00212	−.00379	−.00082	−.0147	−.0147
.520	.0875	.0818	.486	.0584	.00149	−.00197	−.00063	−.0148	−.0139
.645	.0884	.0783	.571	.0596	.00256	−.00060	−.00091	−.0157	−.0141
.727	.0882	.0771	.636	.0608	.00307	.00072	−.00052	−.0165	−.0140
.805	.0854	.0739	.697	.0611	.00275	.00135	.00011	−.0164	−.0136
.870	.0853	.0701	.715	.0609	.00245	.00178	.00053	−.0167	−.0136
.924	.0844	.0664	.727	.0601	.00233	.00264	.00086	−.0170	−.0134
.978	.0812	.0620	.747	.0595	.00257	.00318	.00105	−.0168	−.0129
1.034	.0821	.0573	.722	.0590	.00328	.00406	.00128	−.0169	−.0124
1.080	.0766	.0534	.753	.0583	.00284	.00462	.00152	−.0168	−.0122
1.131	.0726	.0488	.760	.0579	.00271	.00515	.00163	−.0164	−.0116
1.178	.0718	.0439	.720	.0570	.00308	.00552	.00180	−.0164	−.0114
1.229	.0706	.0392	.682	.0566	.00285	.00584	.00190	−.0164	−.0112
1.274	.0653	.0343	.669	.0560	.00322	.00696	.00197	−.0161	−.0104
1.310	.0567	.0293	.677	.0551	.00356	.00861	.00193	−.0154	−.0090

REPORT No. 598

ALTERNATING-CURRENT EQUIPMENT FOR THE MEASUREMENT OF FLUCTUATIONS OF AIR SPEED IN TURBULENT FLOW

By W. C. Mock, Jr.

SUMMARY

Recent electrical and mechanical improvements have been made in the equipment developed at the National Bureau of Standards for the measurement of fluctuations of air speed in turbulent flow. Data useful in the design of similar equipment are presented. The design of rectified alternating-current power supplies for such apparatus is treated briefly, and the effect of the power supplies on the performance of the equipment is discussed.

INTRODUCTION

The demand for experimental data on fluctuations of air speed in turbulent air flow still continues, and the hot-wire anemometer remains the tool most frequently used in the attempt to meet this demand. In three earlier papers (references 1, 2, and 3) the development of the equipment used at the National Bureau of Standards has been described in some detail as has also its application to various turbulent-flow investigations. Since the publication of reference 3 further investigations have been conducted (references 4, 5, 6, and 7).

The apparatus described in reference 3 has been extensively changed so that its use is simplified and its performance improved. It was therefore felt desirable to publish a description of the revised equipment and to provide certain design data that might be of use to designers of similar apparatus. The paper first describes the improved equipment now in use at the National Bureau of Standards, gives a brief treatment of the design of power supplies for such apparatus, and discusses the effect of the power supply on the performance of the amplifier.

Recapitulation of the information contained in reference 3 has been avoided as much as possible, so that the entire paper may be considered a continuation of the earlier one. The work was carried out at the National Bureau of Standards with the cooperation and financial support of the National Advisory Committee for Aeronautics.

The author wishes to acknowledge the valuable assistance and advice received from the other members of the staff of the Aerodynamical Physics Section during the design and construction of the apparatus and in the preparation of this paper.

I. THE NEW NATIONAL BUREAU OF STANDARDS EQUIPMENT

As stated in reference 3, the assembly of equipment used for measurement of air-speed fluctuations consists of five parts: (1) the wire itself; (2) a Wheatstone bridge for measurement of the wire resistance at room temperature; (3) an apparatus with suitable switching arrangements for supplying the wire with heating current, measuring the voltage drop across the wire at various air speeds for calibration purposes, and, finally, transferring the fluctuating voltage drop across the wire to the amplifier input; (4) a suitable amplifying system, including the requisite compensation for the amplitude reduction and phase lag of the hot wire; and (5) a final measuring instrument.

Improvement of this equipment has been effected through simplification of operation and maintenance rather than by modification of the basic principle. The major change has been the substitution of rectified alternating-current power supplies for the battery supplies previously used. This and other changes that have been made will be considered separately for each component of the assembly.

Figure 1 is a photograph of the present apparatus; figure 2 is an outline drawing with the various components identified.

HOT WIRES

The hot-wire remains as nearly as possible pure platinum 0.015 mm in diameter and 4 to 8 mm long. Recent investigations (reference 7) indicate the advisability of using short wires; therefore the present hot wires are usually 5 mm or less in length, whereas formerly 8 mm was the usual length. Welding still proves to be the most satisfactory method of attaching the hot wire to its supporting prongs although, when the wire is used in a slack condition, ordinary soft soldering has been fairly satisfactory.

WHEATSTONE BRIDGE

The Wheatstone bridge used for measuring the resistance of the hot wire at room temperature remains unchanged. It is a standard laboratory appliance.

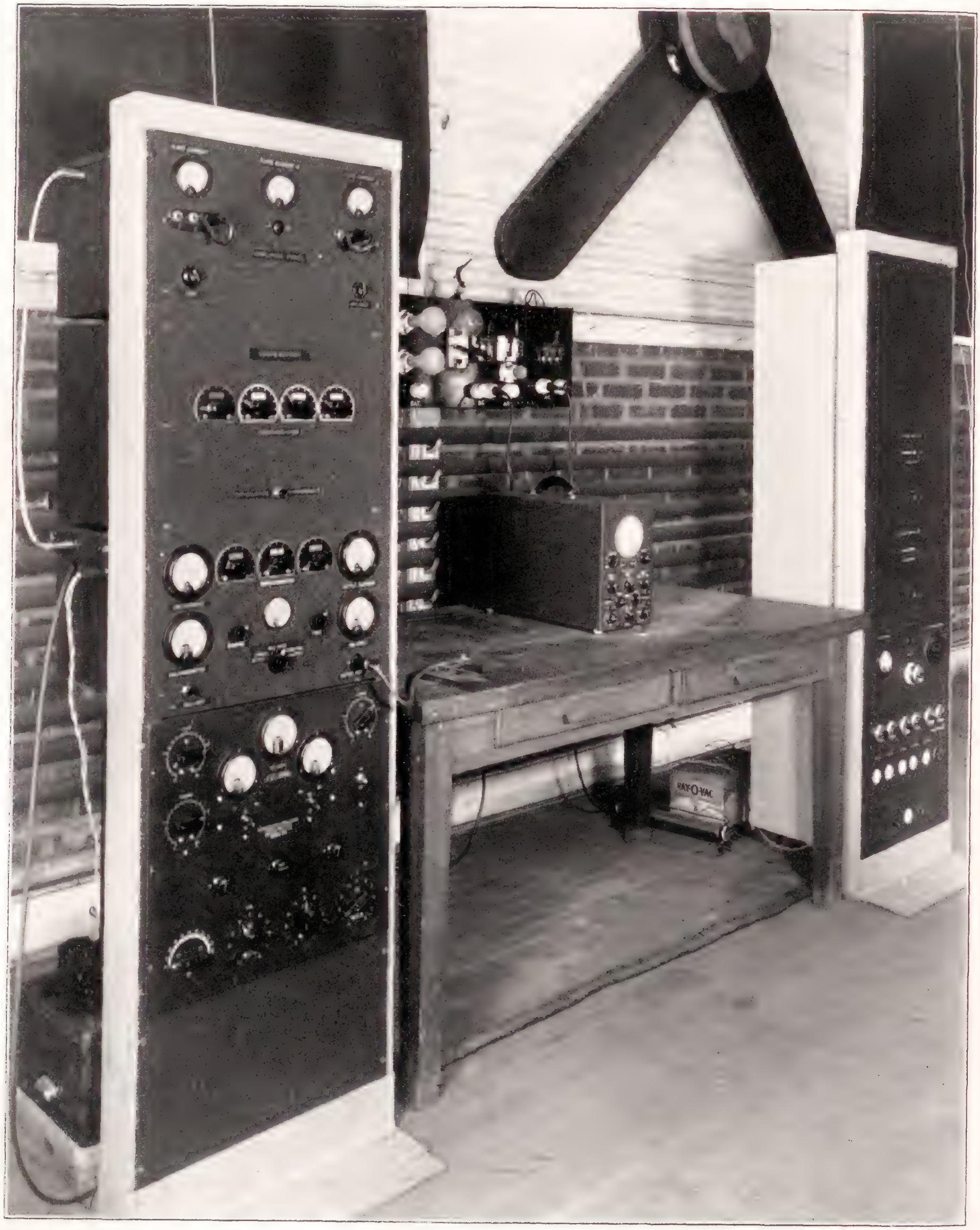

FIGURE 1.—General view of the alternating-current apparatus.

CONTROL EQUIPMENT

The apparatus for supplying and measuring the heating current, measuring the mean voltage drop across the hot-wire, and transferring the fluctuating voltage drop across the hot-wire to the amplifier remains essentially the same as described in references 1, 2, and 3 as far as the electrical circuit is concerned, although its mechanical arrangement has been modified in the interests of ease of manipulation. The only electrical change is the substitution of a two-circuit nonlocking push button for the single-circuit galvanometer key formerly used. This substitution allows the reference battery circuit, as well as the galvanometer circuit, to remain open except when a reading of the galvanometer is to be taken and greatly reduces the drain on the reference battery, making possible the use of standard no. 6 dry cells instead of a storage battery.

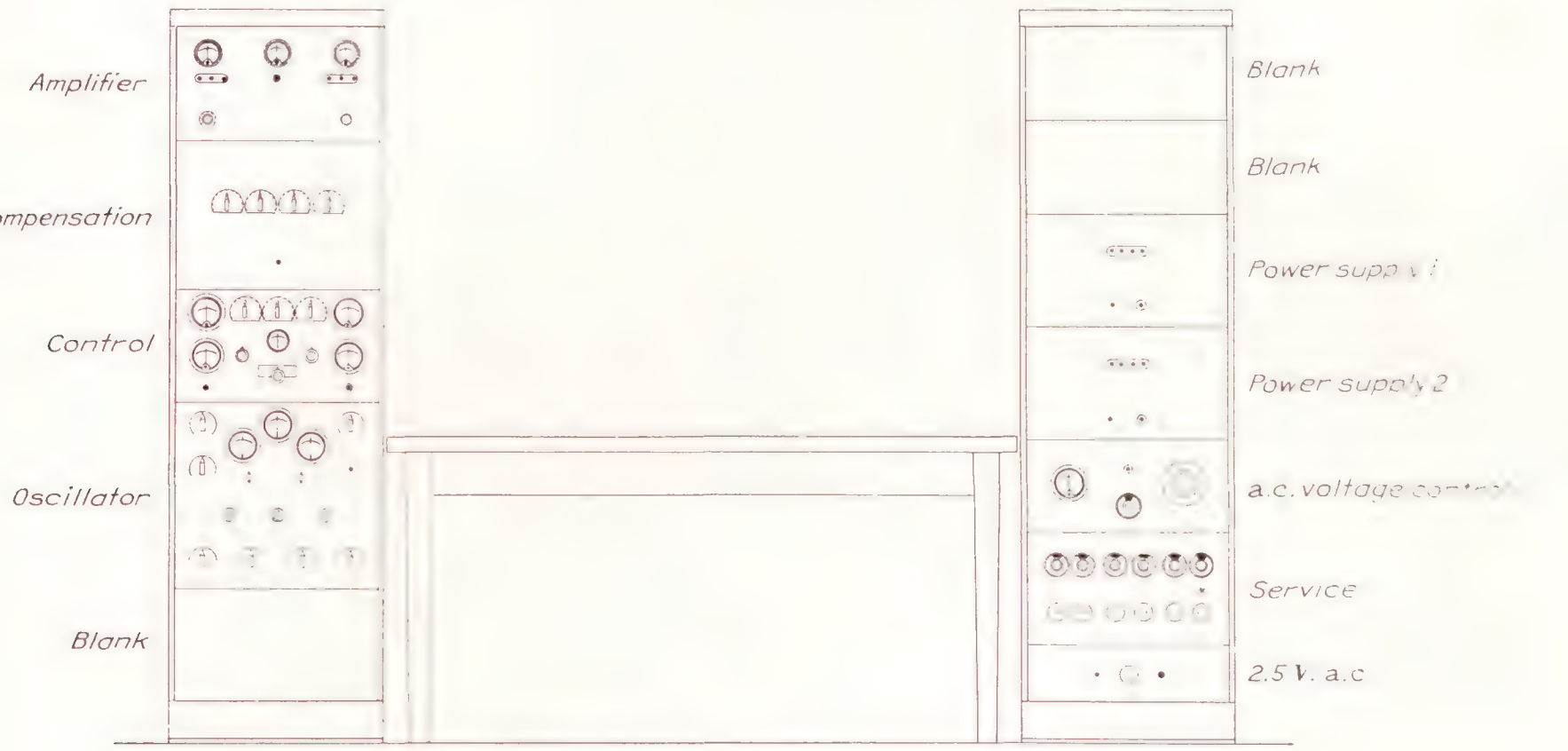

FIGURE 2.—Outline drawing of the alternating-current apparatus.

AMPLIFIER

The fourth unit of the apparatus, the amplifier, has been completely redesigned electrically, as may be seen from the schematic circuit diagram of the entire equipment (fig. 3).

TUBES AND GRID BIAS

For the previously used type 224 tetrode tubes, a type 77 pentode has been substituted in the first stage and type 6C6 pentodes in the second and third stages. These tubes have somewhat superior characteristics to the ones that they replace. The improved characteristics result in considerably increased gain per stage and, because of the pentode construction of the tubes, they are much less critical in regard to screen grid voltage.

Although these pentodes supposedly have nearly identical electrical characteristics, it was found that lowest noise in the first stage and highest amplification in the second and third stages were obtained with the combination shown. It was not determined whether this result was due to inherent differences between the tube types or merely to individual differences between the particular tubes available for trial. In another amplifier a different combination might prove superior. An incidental advantage of the new tubes is that in the first two stages, where the voltage to be amplified is quite low, a satisfactory grid bias may be obtained from a 1.5-volt flashlight-type dry cell inserted in series with the cathode. This arrangement allows the grid resistors to be connected directly to ground, which in turn makes it possible to place the amplification control directly in the grid circuit where it acts also as the grid resistor. The grid bias of the third stage was made adjustable because of the larger input voltages encountered by this tube.

AMPLIFICATION CONTROL

The use of an amplification control is necessary because of the wide range of voltages to be measured. The location of this control in the circuit is dictated by considerations of protection of the tubes from overload and the maintenance of a high ratio of amplified voltage to noise. The noise is an important factor because its magnitude determines the smallest voltage that may be measured, while overloading sets the limit for the largest.

The most important source of noise in an amplifier is the first tube and the circuits associated with it. Noise originating in the tube is caused by irregularities in electron emission from the cathode, which produce fluctuations in the plate current. Associated circuit noise may be due to thermal agitation in the

input circuit or fluctuations in the power-supply voltages. Of these, input circuit noise will be negligible because of the comparatively low input resistance (usually less than 10 ohms), and power-supply voltage fluctuations may be made negligible by proper design, leaving only the tube noise as effective.

Since this noise originates in the plate circuit of the first tube, it is important that full use be made of the amplification of that tube in order that the voltage to be measured may arrive at this point as large as possible relative to the noise originating there. This requirement means that the amplification control must not be placed ahead of the first tube. On the other hand, if the amplification control is not placed in the circuit ahead of the second tube, the large amplification of the first stage may cause overloading of the second or following stages when large values of turbulence are measured.

The amplification control is therefore located between the first and second stages of the amplifier, as in the previous equipment. The present amplifier, however, is different in that this control is in the grid circuit of the second stage rather than in the plate circuit of the first stage. It consists of a resistor of 1,600,000 ohms. The total resistance has taps so located that by switching from one tap to the next the amplification is changed by a factor of 2, the total range of control being 64:1. In the previous equipment this amplification control acted also as the load resistance of the first tube and therefore had in series with it the internal resistance of the plate-voltage source. This source was a bank of lead-acid storage cells, and their very low internal resistance did not greatly affect the calibration of the amplification control. In the case of the present apparatus, however, it was desired to use rectified alternating current for the plate-voltage supply and, because of the much greater internal resistance of this supply, the amplification control was moved to the grid circuit of the second tube.

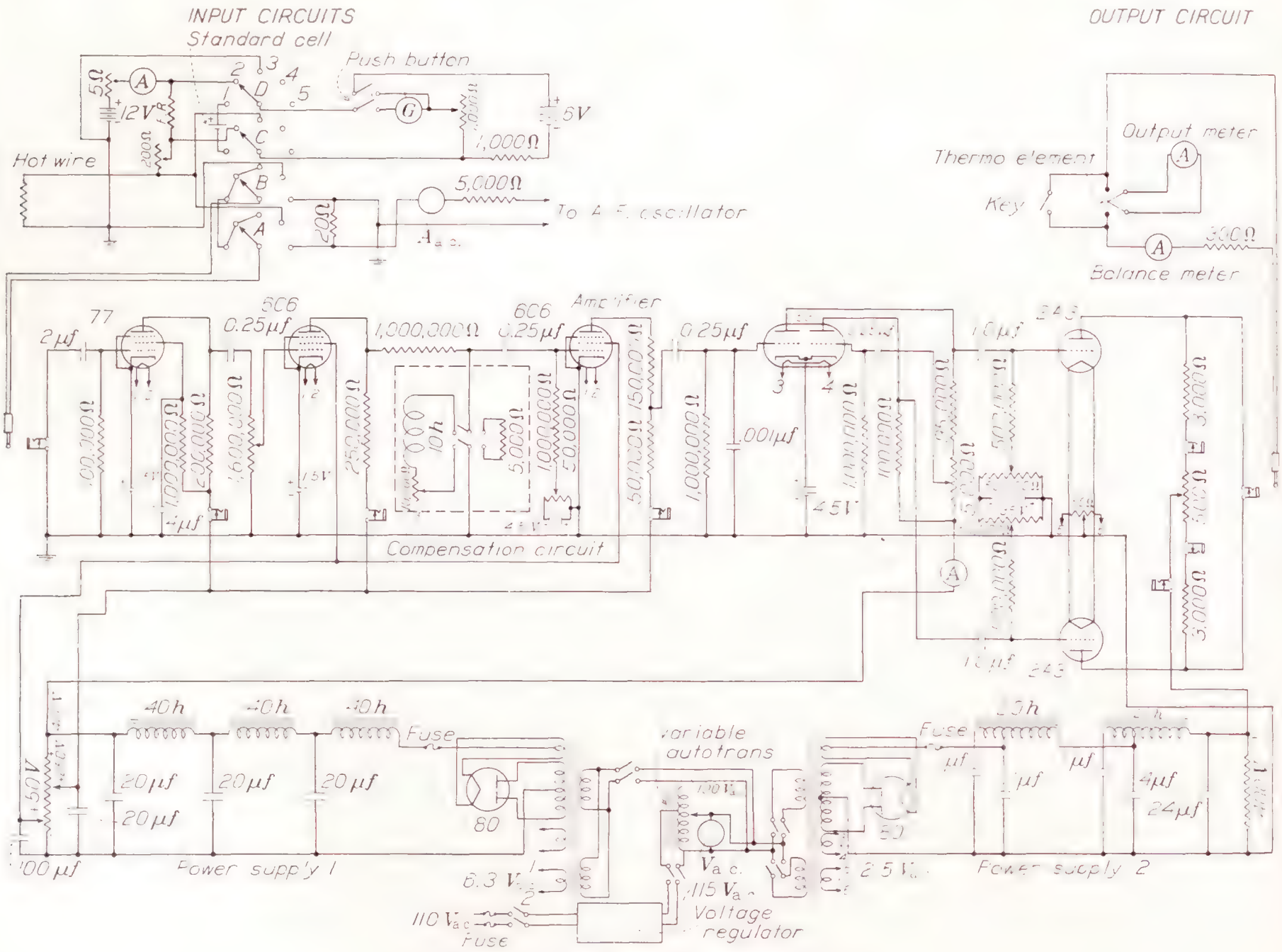

FIGURE 3.—Schematic circuit diagram of the apparatus.

Another advantage of this arrangement is that the possibility of a change in calibration due to unequal heating of the resistors is reduced because no direct plate current flows through the control. Furthermore, as now arranged, the coupling condenser is now always at the lowest possible voltage, which reduces the chance of condenser leakage with its attendant change in grid bias and amplification. As a result of this alteration, the present control changes the gain by a factor of exactly 2 per step.

COMPENSATION CIRCUIT

The only electrical change in the compensation circuit is the return of one terminal to ground rather than to the high-potential end of the plate resistor. This change reduces the direct-current voltage drop across the circuit, with consequent reduction in direct current through the circuit, and the possibility of leakage through the capacitor coupling the circuit to the following tube. It also allows one terminal of the resistor controlling the compensation to be grounded, which somewhat simplifies the mechanical construction.

In the foregoing discussion of the compensation circuit, as well as in the discussion of the amplification control circuit, the importance of reducing coupling capacitor leakage has been stressed. With the large capacitances required, space limitations dictate the use of paper dielectric capacitors that have insulation properties inferior to the more bulky mica dielectric capacitors. Undesirable effects, such as noise and variable amplification that may result from the use of paper coupling condensers, may be reduced by lowering the voltage across them. Any circuit changes, therefore, that will reduce the potential difference across the coupling capacitors will be an improvement.

OUTPUT STAGES

Reference to figure 3 will show that the output stage of the present amplifier differs markedly from the arrangements used in previous equipment. Since it is desired to measure only the alternating-current output from the amplifier, it is necessary to provide some means for keeping the direct plate current of the output tubes from flowing through the measuring instrument.

Three general means to this end exist: first, the use of a transformer to couple the meter to the output tube or tubes; second, the use of a "bucking-out" battery so connected that it supplies across the meter a direct voltage drop equal and opposite to that caused by the direct plate current of the output tube; third, the use of some balanced system, such as that employed in the present equipment, so arranged that the meter is connected across points of equal direct voltage but unequal alternating voltage.

A transformer has the advantages of simplicity and complete elimination of direct current through the meter, but unfortunately it is not possible, at present, to obtain a transformer that will give uniform output over the range of desired frequencies—namely, from less than 5 to over 5,000 cycles per second.

The second system, the use of a bucking potential, has been used in the previous equipment with success. However, it generally requires a battery of some sort, and one of the reasons for construction of the apparatus described herein was to eliminate, as far as possible, all batteries. In addition to the nuisance of battery maintenance, a battery system has the disadvantage of requiring careful adjustment of the operating voltages and currents of the output tube to such values that the direct-current voltage drop across the meter is equal to some voltage that may be conveniently obtained from a dry-cell battery; that is, some multiple of 1.5 volts. Otherwise some form of variable resistance must be incorporated in the circuit so that the bucking voltage may be made equal to the voltage drop across the meter. The use of a resistance for this purpose unavoidably inserts resistance in series with the measuring instrument, with resultant loss in sensitivity and a change in sensitivity with change in "bucking-battery" voltage during the life of the battery.

The third system, the use of a balanced or "push-pull" stage as in the present equipment, eliminates the bucking-battery troubles. It also offers the advantages of greater alternating-current output and independence of balance on tube operating voltages and currents as long as both tubes operate under the same conditions of input voltage and supply voltage. In practice this system is balanced for no direct-current through the meter as follows: The load resistors in the tube plate circuits are first adjusted to the same resistance, and the contact arm of the balance adjusting resistor between them (fig. 3) is set on the midpoint. The plate currents of the two tubes are then made equal to each other, and to the desired value, by means of the independent grid voltage controls. These operations having been performed, the output-meter circuit is attached, and the direct-current balance meter observed. If this meter then shows no current, the balance is correct. If some current is indicated, a slight readjustment of the grid biases should be made. Small unbalances may be corrected by means of the balance adjusting resistor between the plate resistors. A final check on the balance is made by applying an alternating voltage of magnitude just less than that causing overload of the amplifier. If the balance remains correct under this condition, the output stage is in proper adjustment. If the stage becomes unbalanced, dissimilarity of the tubes is indicated, and other tubes must be tried until a matched pair is found. Practically no trouble of this nature has been experienced.

Experiments have shown that the most suitable operating conditions for the output stage of the balanced type differ somewhat from those of the single-tube type. In the instance of the single-tube output amplifier used in the previous amplifier (reference 3), the grid voltage was adjusted so that the tube operated on the straight portion of its curve of grid voltage-plate current characteristic, the "class A" mode of operation, in which the average plate current is constant. With the balanced or "push-pull" type, however, it has been found that best operation is obtained when the adjustment is more nearly that of the "class B" mode, the grid biases being adjusted so that the tubes operate near plate current cut-off. (See fig. 4 (a).)

When so operated, the average plate current is not constant but varies with the applied alternating voltage. The distortion that would result if a single tube were used under these conditions is avoided by the push-pull connection. Attempts to operate the tubes with less grid bias and higher plate current lead to a higher amplification but to a reduced range of input voltages for which a linear relation exists between input voltage and output current. (See fig. 4 (b).) The best bias, depending as it does on the type of tubes used, the plate voltage available, and the load conditions existing, should be determined by trial for each particular installation. For preliminary design purposes the bias may be approximated quite closely by extending the straight portion of the curve of dynamic grid bias-plate current characteristic until it intersects the axis of zero plate current. The grid bias at which this intersection takes place is then that bias which will give the balanced amplifier a linear characteristic over the greatest range of input voltage. This is the adjustment illustrated by figure 4 (a).

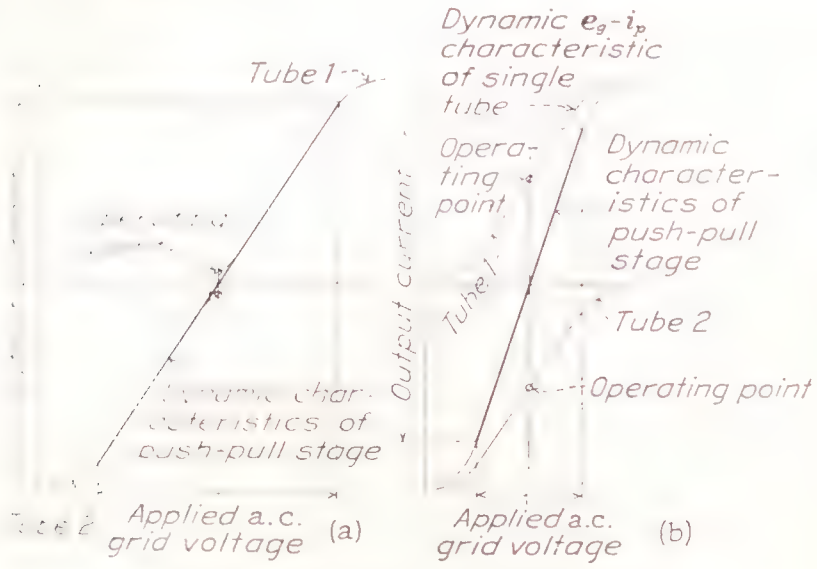

FIGURE 4.—Mode of operation of output amplifier.

In the instance of the balanced output amplifier stage now in use at the National Bureau of Standards, type 2A3 tubes are used because of their very high mutual conductance. This characteristic gives a large change in plate current for a given change in grid voltage. Furthermore, their low plate impedance allows a reasonable match between meter-circuit impedance and tube impedance without the necessity of insertion of excessive resistance in series with the meter in order to avoid distortion. With these tubes and a plate voltage of 400 volts the best operation is obtained when the grid bias is so adjusted that the plate current of each tube is about 5 milliamperes without input voltage. When input voltage is applied the plate current increases, becoming approximately 25 milliamperes per tube at maximum allowable input.

PHASE INVERTER

The use of a balanced output stage introduces an additional problem not encountered in the previous equipment. Because of the manner in which they are connected, the tubes of the balanced amplifier require input voltages exactly equal in magnitude and wave shape, but 180° apart in phase. In an ordinary amplifier these voltages would be obtained by using a coupling transformer having a center-tapped secondary, the grids of the balanced amplifier being connected to the opposite ends of this secondary winding. Since transformers are not usable at the lower frequencies under consideration, recourse must be had to some other method.

One such method that has proved very satisfactory is the use of a phase-inverting tube. This system takes advantage of the fact that the amplified alternating voltage appearing across a resistance load in the plate circuit of a vacuum tube differs 180° in phase from the applied alternating grid voltage that causes it. The circuit is so arranged that the alternating voltage applied to the grid of one of the balanced amplifier tubes is passed through one more stage than that applied to the grid of the other, this additional stage having an amplification of 1:1. Thus the grids of the two balanced amplifier tubes receive voltages 180° apart in phase but equal in magnitude.

A practical circuit of this type is that incorporated in the present amplifier and illustrated by figure 3. For economy of space a type 53 twin-triode tube is used instead of two separate similar tubes. This type 53 tube consists, in effect, of two identical triodes, each having a voltage amplification of about 20. The first of these triodes is inserted directly between the high-gain amplifier and the grid of the upper of the two balanced amplifier tubes. The second receives its input from a voltage-reducing tap on the plate resistor of the first, amplifies this voltage, and applies it to the grid of the lower balanced amplifier tube. The two balanced amplifier tubes thus receive grid voltages that are 180° apart in phase and, when the voltage-reducing tap feeding the second half of the type 53 tube is properly adjusted, are equal in magnitude.

A similar result might be obtained by eliminating the type 53 tube and feeding the grid of one of the balanced amplifiers from a suitably located tap on the plate resistor of the other. This arrangement would, of course, sacrifice the voltage gain of approximately 20 that occurs in the type 53 tube as now used. The choice of method employed thus depends somewhat on the amplification necessary in a given installation.

OUTPUT METER

One of the greatest sources of annoyance in the operation of the older equipment was the frequency with which the highly delicate 0 to 5 milliampere thermoelement alternating-current milliammeter was burned out by momentary overload. The output meter used in the new equipment was designed to overcome this trouble and consists of a 0 to 500 microampere direct-current microammeter operated by a separate heater-type thermoelement. This combination gives a full-scale reading with a current of 25 milliamperes through

the heater of the thermoelement and has a maximum safe current-carrying capacity of 40 milliamperes. In series with the heater, which has a resistance of 10 ohms, is placed a fixed resistance of 300 ohms. The purpose of this resistance is to prevent distortion by making the total resistance of the meter circuit large enough to act as a reasonable load for the output tubes of the amplifier. The exact value of the resistance used is not critical. No difference in performance of the amplifier except a slight loss in over-all sensitivity could be detected when the 300 ohms used was increased to 1,000 ohms. Resistances less than 300 ohms were not tried, as no great increase in sensitivity, or any other benefit, could be expected from their use.

Although the present meter is only one-fifth as sensitive as that employed in the previous equipment and the sensitivity is still further reduced a slight amount by the addition of the series resistance, the amplification of the new amplifier is sufficiently greater than the older one that the actual sensitivity of the equipment from hot wire to meter reading is not decreased. Furthermore, the ruggedness of the meter is so much greater that no trouble whatever from meter burn-out has been experienced in service.

POWER SUPPLY

The apparatus of reference 3 was entirely battery powered, requiring a total of three 6-volt storage batteries, 1,200 small storage cells, three 45-volt dry batteries, and four 4.5-volt dry batteries. The great bulk of this voltage-supply equipment, together with its weight, its comparatively short life, and the almost constant effort required to keep it in good working condition made it highly desirable to use an alternating-current power supply, rectifying and filtering wherever necessary. The new equipment occupies approximately one-tenth the volume of the old plate voltage supply battery alone, weighs somewhat less, has almost unlimited life, and requires little or no attention.

HIGH VOLTAGE

Two separate transformers, rectifiers, and filters are used to supply the high direct-current voltage for plates and screens. One of these sets takes care of the requirements of the high-gain stages and the phase-inverter stage; the other furnishes only plate voltage for the output stage. Both supplies have the same output voltage, namely, 400 volts direct current, but differ in other respects.

The power supply for the high-gain and phase-inverter stages is provided with taps giving 50 volts direct current and 250 volts direct current for screens and high-gain amplifier plates, respectively, as well as the full output of 400 volts for the phase-inverter plates. The filter for this supply consists of three 40-henry 60-milliampere chokes and a total of 180 microfarads of filter capacitance, arranged as shown in figure 3. The rectifier tube used is a type 80 high-vacuum full-wave rectifier.

The power supply for the output stage differs from the above-described supply mainly in the amount of filtering provided. Since the output stage has in itself very little amplification, and particularly because it is not followed by any other amplifier, the filtering necessary to keep the hum at the desired low level is much less than in the case of the high-gain stages. Two 20-henry chokes capable of carrying 200 milliamperes are used in conjunction with 31 microfarads of capacitance arranged as shown in figure 3.

It will be noted that series resonant circuits are employed in this filter as well as the usual pi type low-pass sections. These series circuits are resonant at 120 cycles per second, the main ripple frequency of the rectifier's output wave; and their purpose is to increase the filtering efficiency without the use of large values of capacitance and inductance, particularly the latter.

LOW VOLTAGE

The low voltages necessary for cathode heating in the new equipment are supplied from the 110-volt alternating-current power lines by step-down transformers or windings on the high-voltage transformers, instead of by storage batteries. This change results in a considerable reduction in weight and bulk.

It was thought that excessive hum might be introduced by this change, but tests of the completed amplifier have shown that the total hum, both from this source and from the high-voltage supplies, is too low in magnitude to be measured by the output meter even when maximum amplification is used.

Low voltage, of the order of 50 volts, for the screen grids of the high-gain tubes is obtained from the high-voltage power supply. The method of obtaining screen-grid voltage for the first stage differs from that used in the second and third. The reason for this difference is discussed in the section of this paper dealing with the effect of the power supply on the amplifier characteristics.

The last portion of the power supply proper is the grid bias system. Here dry cells or dry-cell batteries are used as in the previous equipment. The retention of batteries for this purpose is justified because of their long life in such service, their compactness, and their low internal resistance compared with any practical substitute. In almost all cases the drain on the bias batteries in the new equipment has been either completely eliminated or substantially reduced so that greater battery life may be expected than before.

VOLTAGE REGULATION

The use of rectified alternating-current power supplies with amplifiers capable of amplifying very low frequencies leads to unexpected difficulties when the power supply is operated from commercial power lines. In addition to gradual changes of voltage, which are annoying in that they cause corresponding changes in

amplifier sensitivity, such lines usually carry quite rapid voltage fluctuations, caused by switching transients and other load irregularities, which have frequencies high enough to be amplified by the amplifier. Such fluctuations of the line voltage may produce an excessively high and variable noise level, or dangerously large transients in the amplifier. For this reason it has been found necessary to provide voltage regulators between the nominally 115-volt alternating-current line and the power supplies of the amplifier.

Two types of regulation are used. First, a commercial automatic voltage regulator entirely removes the slow changes in line voltage and reduces the transient changes to a low magnitude. Second, a manual control of voltage, in the form of an autotransformer having a practically continuously variable voltage ratio, inserted in the line between the automatic voltage regulator and the power supplies, takes care of voltage changes due to line and power-supply heating and makes possible intentional voltage changes. These two types of voltage regulation almost completely eliminate all line-voltage troubles, making the amplifier independent of line conditions as long as the line voltage remains between the limits of 90 to 130 volts.

MECHANICAL ARRANGEMENT

In the design of the apparatus considerable attention was given to mechanical lay-out. It was desired to have in the completed equipment a tool that might be used with maximum convenience by one operator. At the same time it was necessary to observe certain precautions in the matter of electrical shielding and power-supply location. Ease of repair and maintenance also entered into the problem to a considerable extent. The result of compromise between these sometimes conflicting factors is the apparatus illustrated by figures 1 and 2. Figure 1 is a photograph of the entire equipment as used, including a small cathode-ray oscillograph not properly a part of the assembly. Figure 2 is an outline drawing showing the panel lay-out of the equipment.

Two separate units are used. That on the left in both figures consists of the amplifier and all controls directly associated with it, as well as calibrating and testing equipment. That on the right contains the power-supply equipment and controls.

Both units are assembled on standard steel relay racks taking panels 19 inches in width and multiples of 1¾ inches in height, with a horizontal clearance of 17½ inches between vertical rack members. All apparatus is mounted from its panel, and each individual panel, with its associated apparatus, may be removed as a unit for inspection or repair. The apparatus behind each panel, in the case of the amplifier rack, is fitted with a metal case or dust cover, which also acts as a shield against stray electrical fields in the room. The apparatus on the power-supply rack is covered by one large dust cover supported from the rack itself and removable as a unit. This general method of construction is one that has been widely used in the telephone and other communication fields. It gives compactness with a maximum of accessibility and requires a minimum of floor space.

The amplifier panel carries three direct-current milliammeters, the amplification control switch, and the fine adjustment for balance of the output stage. By means of a plug-and-jack arrangement it is possible to measure the plate current of the various tubes using the three meters provided. Input and output connections to the amplifier are likewise made by means of plugs and jacks.

The arrangement of the amplifier behind the panel is such that all grid and plate leads are very short and each stage is separated from the others by aluminum shields. All grid and plate leads are kept as far as possible from the metal shielding to reduce the loss of amplification at high frequencies. All power-supply leads are run in shielded cables with the shields grounded to the amplifier framework at frequent intervals and are kept well away from the grid and plate leads of the tubes to reduce the possibility of hum pick-up. The input lead to the amplifier is also shielded, and the shielding is grounded, both to reduce pick-up of stray fields in the room and to prevent coupling between input and output circuits of the amplifier. The possibility of such coupling is still further reduced by taking input and output leads from opposite ends of the amplifier.

The compensation-circuit panel carries a four-dial 0–10,000-ohm decade resistance for compensation adjustment, as well as a double-pole, double-throw, locking push-button switch arranged to connect either the compensation circuit or a 5,000-ohm resistor to the amplifier, the resistor being used for amplifier calibration. Behind this panel, supported by a bakelite shelf in a large aluminum box, is the compensating coil. As much space as possible was allowed around the coil in order to prevent excessive reduction of its effective inductance by the metal shield. Attempts to operate with no shielding were unsuccessful because of the stray field pick-up of the large compensation coil. This trouble was experienced in the previous amplifiers also, but to a much lesser extent because of the smaller amplification of that equipment.

Below the compensating-coil panel is that of the potentiometer and control apparatus. Here, conveniently grouped in one spot, are all the controls and meters necessary for routine operation of the equipment with the exception of the compensation adjustment, which is within easy reach on the panel above. The use of an arrangement such as this effects a worth-while saving in time and effort.

The apparatus on the panel is as follows: From left to right in the top row, the alternating-current microammeter indicating the current input from the calibrating oscillator; the three-dial decade 0–1,000-ohm

resistance of the potentiometer for setting the heating current and measuring the mean voltage drop across the wire; and the direct-current microammeter used, in conjunction with a thermoelement, as the output meter. In the next row are the galvanometer for indicating balance in the potentiometer circuit; the coarse adjustment of heating current; a direct-current milliammeter for rough indication of heating current; the fine adjustment of heating current; and the direct-current milliammeter used to indicate balance in the output stage of the amplifier. The bottom row consists of the combined galvanometer and reference-battery key; a five-position, four-gang switch to be described later; and the jack for the output-meter key, which for convenience is attached to a short, two-wire flexible cord.

The above-mentioned five-position, four-gang switch replaces the cumbersome plug-and-jack system employed in the earlier apparatus to control the potentiometer and amplifier input circuits. In the first of the five switch positions the potentiometer and standard cell are so connected that the voltage of the reference battery may be measured. In the second position the potentiometer is connected across a known fixed resistance in the heating-battery circuit so that the current through the hot-wire may either be measured or set to some predetermined value. In the third position of the switch the potentiometer is connected across the hot-wire so that the mean voltage drop may be measured. In the fourth position the hot-wire is connected across the input of the amplifier so that the fluctuating voltage drop may be amplified and measured. Finally, in the fifth position, the amplifier input is connected across a 20-ohm resistor in the oscillator output circuit for calibration and testing purposes. Thus the switch with five settings performs the same functions as the six jacks and three plugs formerly used.

Behind the control panel are mounted the standard cell, the reference battery, and the various fixed and variable resistors associated with the potentiometer circuit and oscillator output circuit, as well as the thermoelement and resistor used in the amplifier output circuit. Shielding between input and output circuits is provided, and all apparatus is contained in an aluminum outer shield with a removable back.

The unit below the control panel is the General Radio type 377B audio-frequency oscillator used for calibration and testing. This oscillator is the one used with the earlier equipment, adapted for rack mounting.

The last unit on the amplifier rack is a blank panel covering space reserved for future expansion.

The power-supply rack carries all power supplies and voltage controls, with the exception of the automatic voltage regulator, which is mounted some distance away so that the amplifier will be less affected by the external field it produces. Starting at the top the first two panels are blanks reserved for future use. The third unit is the power supply for the high-gain and phase-inverter stages of the amplifier. On this panel are mounted an on-off switch controlling the input to the power supply, a red pilot lamp to indicate when the power supply is in operation, and a set of small jacks connected to the various high voltages available at the power-supply output. The main panel of the power supply is ¼-inch cold-rolled steel; this heavy material is used because of the very considerable weight of the power-supply equipment. The component parts, which are of the "bottom connection" type, are mounted on a vertical subpanel about 2 inches behind the main panel and of the same material. The space between main and subpanels is used for the wiring, which is thus protected and hidden.

In order to reduce the external alternating-current field of the power supply, all chokes and transformers are enclosed in very heavy cast cases of high permeability iron alloy and as much of the wiring as possible is confined to the space between main and subpanels or, in the instance of output and input leads, to the interior of the channels forming the vertical members of the rack.

The fourth unit is the power supply for the output stage. This unit differs from the third unit only in the electrical details that have been discussed previously. The mechanical arrangement is identical to that of the other power supply. The fifth unit is the input-voltage control panel, and carries the main alternating-current power switch, a pilot lamp, the manual voltage control autotransformer, and an alternating-current voltmeter that indicates the input voltage to the power supplies. The sixth unit is a service panel carrying several outlets for alternating and direct current, and a battery-charging outlet. The last panel carries a 2.5-volt transformer which supplies heating current for the output stage filaments. On the face of the panel are mounted a switch, a pilot lamp, and an outlet that allows the 2.5 volts alternating current to be used for any purpose.

As mentioned previously, a sheet-iron dust cover encloses the rear of all apparatus on the power-supply rack. This cover also provides some shielding in addition to the iron cases of the individual components of the power supplies. Further shielding is obtained by enclosing all leads connecting the two racks in grounded lead-foil coverings.

PERFORMANCE

The important features of the performance of the complete equipment are summarized by the two curves of figure 5.

In comparison with the performance of the previous equipment (figs. 9 and 11 of reference 3), it is seen that some improvement has been effected in the frequency characteristic of the uncompensated amplifier. The new apparatus maintains its amplification constant to 3,000 cycles per second, whereas the older amplifier started to lose amplification at about 1,600 cycles per second.

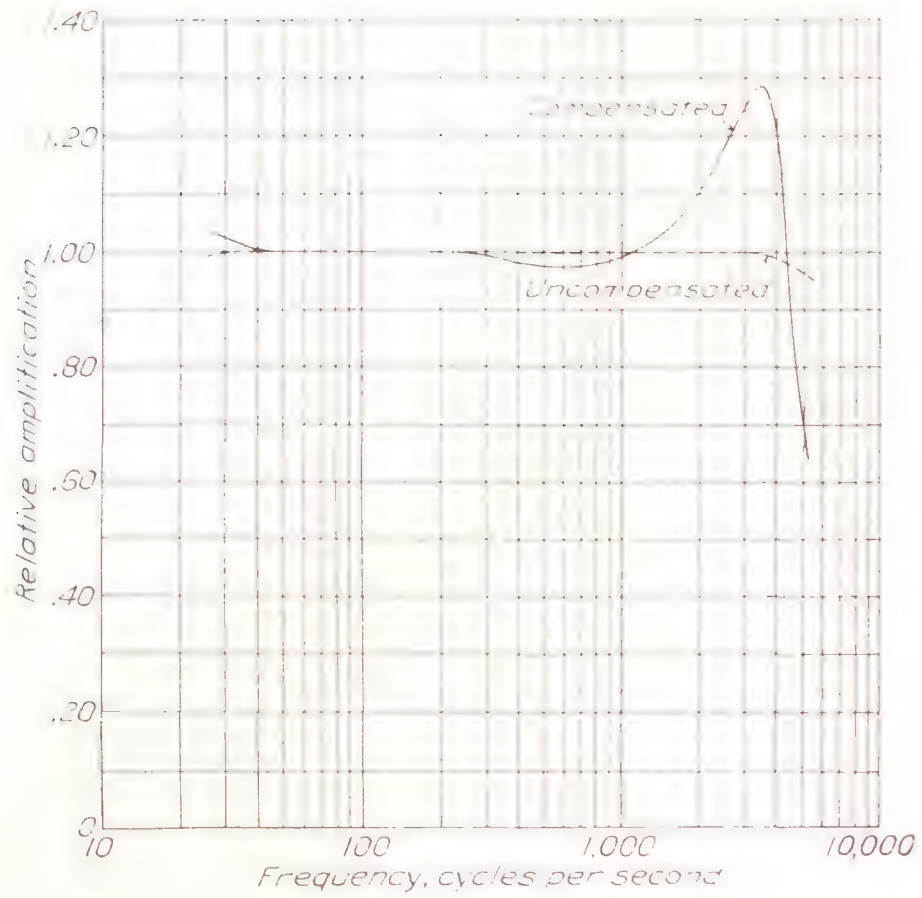

FIGURE 5.—Frequency characteristic of apparatus.

The comparison between the compensated frequency characteristics of the two sets of apparatus is not quite so favorable. Because of the unavoidable decrease in the effective inductance of the compensation coil, caused by proximity to its shielding box, the resonant frequency has been lowered from 4,000 to 3,500 cycles per second. This fact, together with other effects probably due to the use of a power supply having high internal impedance compared with the storage cells formerly used, causes the frequency characteristic to depart from the ideal at a somewhat lower frequency than before. The height of the resonant peak, however, has been reduced and it is felt that the slight sacrifice in frequency-characteristic performance is offset by the increased reliability and usability of the apparatus.

Other features of the performance, not evident from the curves shown, are a sixfold increase in sensitivity, which allows the use of a more rugged meter without loss in effective sensitivity, and an improvement in the constancy of amplification control setting ratios.

II. POWER-SUPPLY DESIGN

In the selection of a power-supply system for an amplifier there is no doubt, from the standpoint of electrical design, that batteries, particularly storage batteries, offer the best results. The cost, the bulk, and the problem of maintaining a battery power supply make it desirable, however, to design an alternating-current operated power supply that will give satisfactory electrical performance.

For cathode heating, alternating current of the proper voltage may be directly applied to the heaters of the indirectly heated cathode type tubes and successful performance obtained even in high amplification amplifiers. In the output stage of the amplifier, directly heated cathode tubes are generally satisfactory. The only precautions necessary are: grounding of the zero potential point of the heater supply circuit, shielding of the supply wires to the tube sockets, the use of some discretion in the placement of these supply wires relative to grid and plate wiring in the amplifier, and the use of magnetically well-shielded transformers located some distance from the amplifier and of ample capacity for the load to which they are connected.

The design of the high-voltage supply is a more complicated matter. It divides itself more or less naturally into two phases. First, the treatment of the problems peculiar to the power supply itself, namely, the provision of sufficient filtering and power capacity. Second, the consideration of the effect that the power supply will have on the characteristics of the amplifier, entirely apart from the possible introduction of hum and noise. These phases will be discussed separately.

FILTER DESIGN

A rectified alternating-current power supply consists, in general, of a transformer to raise the commercial line voltage to the required high voltage, rectifiers to change this high voltage from alternating current to pulsating direct current, and a filter system to remove, as nearly as possible, all these pulsations, leaving only a pure direct current of the desired high voltage.

INDUCTANCE INPUT FILTER

Many types of transformers, rectifiers, and filters may be used in various combinations, but certain combinations are more common than others. Of these the most

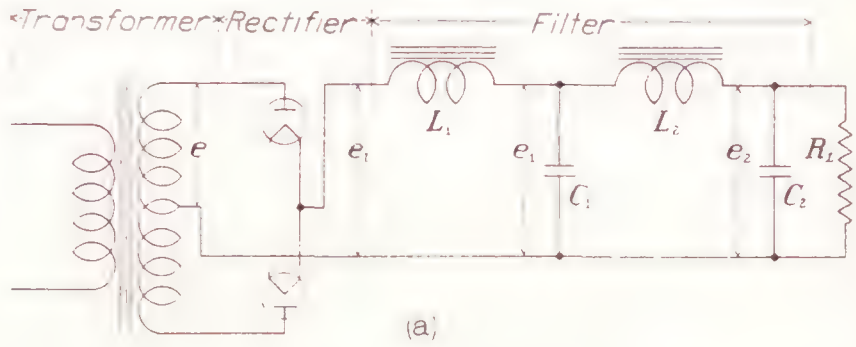

(a) Schematic circuit diagram.

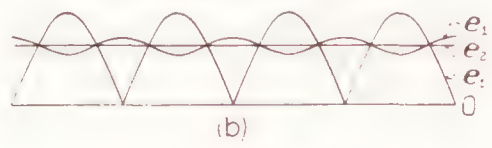

(b) Voltage relations.

FIGURE 6.—The inductance input filter.

common is the single-phase full-wave transformer and rectifier working in conjunction with an inductance input filter. This type is shown in figure 6 (a). The output from the system consists of a series of voltage pulses having twice the frequency of the alternating current supplied to the transformer. Neglecting the minor effects of voltage drop in the rectifiers and transformer leakage reactance, these voltage pulses approximate the shape of arches of sine waves, as shown in figure 6 (b).

If the input inductance of the filter L_1 is made sufficiently large to satisfy the inequality

$$\frac{\omega L_1}{R_L} \geqq \frac{e_{ac}}{e_{dc}}, \tag{1}$$

where ωL_1 is the reactance of L_1 to lowest frequency in rectifier output;
R_L, load resistance into which the filter works;
e_{ac}, amplitude of the lowest frequency component in the rectifier output voltage;
and e_{dc}, direct-current voltage in rectifier output;
a fairly constant input current to the filter will be maintained. Under this condition the voltage across C_1 will fluctuate only slightly about a value equal to the average voltage of the rectifier output pulses (fig. 6 (b)). The action of L_2 and C_2 is to reduce still further the magnitude of the fluctuation. It is possible to reduce the fluctuation components to as small a portion of the total output voltage as may be desired by making L_1, L_2, C_1, and C_2 sufficiently large, or by adding similar sections.

Assuming that the input inductance is large enough to satisfy relation (1), the residual fluctuation components in the filter output may be computed with sufficient accuracy by considering that the output voltage wave, e_i, from the rectifier has the form given by the Fourier series [1]

$$e_i = \frac{2e}{\pi}\left(1 - \frac{2}{3}\cos 2\omega t - \frac{2}{15}\cos 4\omega t - \frac{2}{35}\cos 6\omega t \cdot \cdot \cdot \cdot \cdot - \frac{2}{1-n^2}\cos n\omega t\right), \tag{2}$$

where e is the peak value of alternating-current voltage applied to rectifier,
$\omega = 2\pi f$,
and f is the supply-voltage frequency.

The output wave of the form shown in equation (2) may be applied to the filter under consideration, and the network solved for the value of the components in the filter output by the usual methods for complex networks. This procedure is somewhat laborious, however, and sufficient accuracy may be obtained by means of a simplified computation.

Assuming that the reactance of each series inductance is large compared with the reactance of the preceding and following shunt capacitances and that the reactance of the output capacitance is small compared with the load resistance, the following expression is approximately true,

$$\frac{1}{\omega^{2n}(L_1 L_2 \cdot \cdot \cdot \cdot L_n)(C_1 C_2 \cdot \cdot \cdot \cdot C_n)} = \frac{e_0}{e_i}, \tag{3}$$

where e_i is the magnitude of a given alternating-current component applied to filter;
e_0, magnitude of the same component at the output of the filter;
n, number of sections in the filter;
L_1 to L_n, series inductances;
C_1 to C_n, shunt capacitances;
and f is the frequency of the component under consideration.

For the two-section filter of figure 6 (a) equation (3) becomes

$$\frac{e_0}{e_i} = \frac{1}{\omega^4 L_1 L_2 C_1 C_2}. \tag{4}$$

In the application of the preceding approximate equations the magnitude and frequency of each component of the rectifier output may be substituted in turn, and the resultant magnitude of this component in the output from the filter obtained. In order to simplify this procedure, equation (2), giving the magnitude of the components of the rectifier output, may be written in tabular form as follows, by giving the direct-current output voltage the value 1.00.

TABLE I

VOLTAGE RELATIONS IN SINGLE-PHASE FULL-WAVE RECTIFIERS

Root mean square a. c. voltage applied to each rectifier	1. 11
The d. c. output voltage at rectifier terminals	1. 00
Peak value of lowest frequency a. c. component	0. 667
Peak value of second harmonic of lowest frequency a. c. component	0. 133
Peak value of third harmonic of lowest frequency a. c. component	0. 057
Frequency of lowest frequency a. c. component	$2f$
Frequency of supply voltage	f

In table I it will be noted that the lowest frequency component has a frequency twice that of the supply

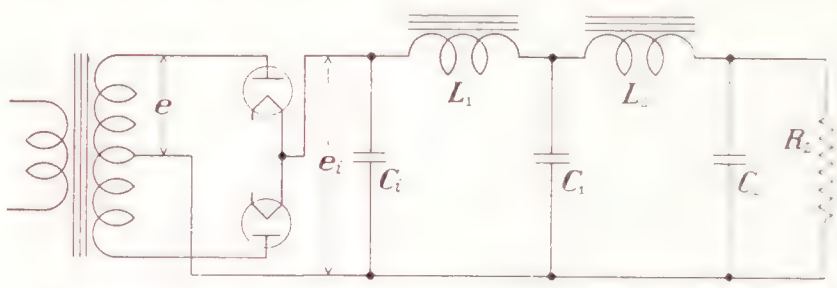

FIGURE 7.—Schematic circuit diagram of capacitance input filter.

voltage. Since in most cases the supply will be from the usual 60 cycles per second lines, this lowest frequency component will have a frequency of 120 cycles per second and the next two higher frequency components will have frequencies of 240 and 360 cycles per second. In view of the fact that the amplitude of the higher frequency components decreases rapidly with increase in order, while the smoothing action of the filter increases as the $2n$ power of the frequency, it is generally sufficient to consider only the lowest frequency component of the rectifier output in computing the filter performance.

CAPACITANCE INPUT FILTER

Another type of rectifier and filter combination often used is the single-phase full-wave rectifier and capacitance input filter, for which a typical schematic circuit diagram is given in figure 7. The advantages of this

[1] This is the Fourier expansion of the half-sine wave shown in fig. 6 (b).

arrangement, in comparison with the inductance input system, are an approximately 25-percent increase in filtering action from a given amount of inductance and capacitance and a considerably higher direct-current output voltage for equal alternating-current inputs to the rectifiers. The disadvantages are the poor voltage regulation of the system under a varying load and the increased load on the rectifier tubes. Neither of these disadvantages is serious when the rectifier and filter are to be used to supply high voltage to a light and constant load, such as that offered by the high-gain stages of a turbulence-measuring amplifier.

The action of a capacitance input filter is somewhat different from that of the inductance input type in respect to the wave form of the voltage applied to the first inductance. In the inductance input filter this voltage depends only on the rectifier, whereas in the capacitance input filter it also depends on the capacitance of the input condenser.

Each time the alternating-current voltage applied to a rectifier anode reaches its peak value, the input condenser C_i charges to this same value. Then, as the alternating-current voltage at the rectifier falls, the condenser discharges into L_1 until the other rectifier anode reaches its peak potential and the condenser is charged again. Since during most of the cycle the condenser is more positive than either rectifier anode, the rectifier current flows for only a short time. During the discharge period of the condenser its voltage drops at a nearly uniform rate because the inductance L_1 tends to draw a constant current. The result of this action is that an approximately saw-tooth voltage wave form is applied to the inductance L_1.

In order to compute the action of the filter under the above-outlined conditions, it is necessary to assume that the impressed wave form has a true saw-tooth shape with a peak amplitude equal to the peak amplitude of the alternating-current voltage applied to the rectifier. This voltage, e_i, can then be considered to be represented by the Fourier series

$$e_i=\frac{e}{1+\frac{\pi}{\omega C_i R_L}}\left\{1+\frac{2}{\omega C_i R_L}\left(\sin \omega t-\frac{1}{2}\sin 2\omega t+\frac{1}{3}\sin 3\omega t-\right.\right.$$
$$\left.\left.\ldots\ldots+\frac{1}{n}\sin n\omega t\right)\right\}, \quad (5)$$

where e is the peak value of alternating-current voltage applied to rectifier;
C_i, input capacitance;
R_L, load resistance;
and f, supply voltage frequency.

The accuracy of the assumptions on which equation (5) is based increases as the voltage variation across C_i decreases, for instance, as C_i and/or L_1 are increased, but in the worst cases likely to be encountered in practice the equation will still give results of sufficient accuracy for most purposes.

It is possible to compute the magnitude of the residual fluctuations in the output voltage from the filter by solving equation (5) for the magnitude of the fluctuation components in the voltage applied to L_1 and then using equation (3) exactly as in the case of the inductance input filter. The fact that the direct-current output from the rectifier and the ratio of the fluctuation components to this direct-current voltage both depend on the magnitudes of C_i and R_L complicates the procedure somewhat by making it impossible to reduce equation (5) to a simple table, as equation (2) was reduced to table I. Equation (5) must be solved using the values of C_i and R_L that apply to the particular problem.

RESONANCE FILTER

A third type of filter to be considered is that in which resonant elements are used. Filters of this type find their greatest application where economy of weight is important, or where considerations of voltage regulation make it desirable to use low-resistance series inductances in the filter circuit. Very low resistance in the series inductance is generally accompanied by low inductance, unless unusually large reactors wound with large wire are used. If the series elements are made parallel resonant at the lowest frequency present in the rectifier output, it is possible to obtain high attenuation to this frequency from comparatively small values of inductance. Alternatively the shunt elements of the filter may be made series resonant to the main fluctuation frequency and a similar effect obtained.

The principal disadvantage of such resonant filter arrangements is that the large attenuation is obtained only at the resonant frequency. The higher frequency fluctuation components are attenuated comparatively little and may reach the output of the filter with large amplitude. A further disadvantage is the fact that the inductance of an iron-core coil, such as a filter reactor, depends on the direct current through the coil. Since this direct current is likely to be variable the inductance may also vary, making it impossible to keep the resonant element resonant at the proper frequency.

For these reasons it is generally best to employ resonant filter elements in conjunction with ordinary series and shunt filter elements so that they do not bear all the burden of filter action. It is also advisable to use series resonant circuits shunted across the filter network, because such circuits carry no direct current and are thus free from the detuning effects of load current changes. The filter used in power supply 2 for the output stage of the amplifier of figure 3 is an example of the combination of series resonant and ordinary filter elements.

If resonant filter elements are combined with ordinary filter elements so that an inductance or capacitance input filter is formed, the resultant network may be solved for the magnitude of the fluctuation components in its output voltage by assuming the input

voltage to have the form given by either equation (2) or equation (5).

If a resonant element forms the filter input the computation becomes more difficult. In general, it will be necessary to determine the shape of the input wave form from an oscillograph record.

CAPACITANCE RESISTANCE FILTER

A fourth type of filter that is occasionally used is one composed of resistance and capacitance elements, instead of inductances and capacitances. The chief application of this type is to power supplies to give fairly high voltage and small current. Its advantages are economy, compactness, and small external field, all of which are due to the fact that no filter inductances are used. Its disadvantages are the need for higher transformer voltages for a given direct-current output voltage and its poor voltage regulation under variable load. Since such filters are not ordinarily used with a variable load, the voltage regulation is not of great importance and it is usually best to use a capacitance input to the filter, thus increasing the direct-current voltage obtainable at the filter input from a given transformer alternating-current voltage. Figure 8 shows such an arrangement.

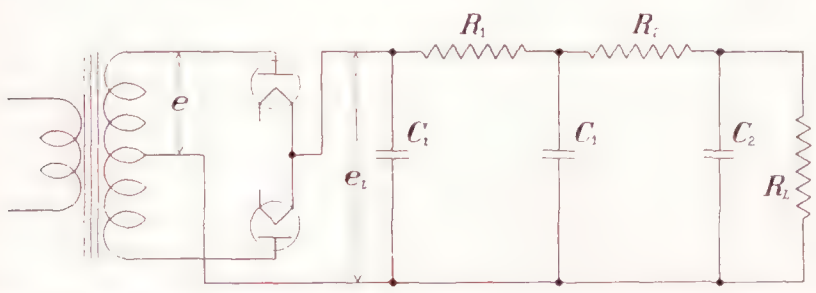

FIGURE 8.—Schematic circuit diagram of capacitance input resistance—capacitance filter.

The computation of the smoothing action of this arrangement may be carried out by assuming the input voltage to have the form given by equation (5) and solving the network, consisting of $R_1\ R_2\ \ldots\ R_n$ and $C_1\ C_2\ \ldots\ C_n$, for the fluctuation components of the output voltage by the usual methods.

Assuming the resistances of $R_1\ R_2$, etc., to be large compared with the reactance of $C_1\ C_2$, etc., it is possible to derive a simplified formula, similar to equation (3), the general form of which will be

$$\frac{e_0}{e_i}=\frac{1}{\omega^n\ (R_1R_2\ \ldots\ R_n)\ (C_1C_2\ \ldots\ C_n)}. \tag{6}$$

In the instance of the two-section filter of figure 8 this equation becomes

$$\frac{e_0}{e_i}=\frac{1}{\omega^2R_1R_2C_1C_2}. \tag{7}$$

FILTER PERFORMANCE

Regardless of the type of filter involved, its suitability for a given purpose depends on the magnitude of fluctuation voltage allowable, which in turn is controlled by the magnitude of the lowest useful amplifier input voltage. In the case of turbulence-measuring equipment, 0.001 volt might be set as the lower limit of the range of voltages to be measured, and it would be desirable to keep the effect of power-supply hum, at the amplifier output, less than $\frac{1}{50}$ the reading produced by this minimum input voltage E_{min}.

The most important point of introduction of hum in the amplifier is in the plate circuit of the first tube, and the voltage introduced here is equal to the hum component of the plate current multiplied by the coupling resistance of the first tube. That is,

$$E_h=IR_c\frac{E_{ac}}{E_{dc}}, \tag{8}$$

where E_h is the hum voltage across R_c due to plate power supply;
I, plate current of first tube;
R_c, coupling resistor of first tube;
E_{ac}, magnitude of principal fluctuation component in plate voltage;
and E_{dc}, the direct-current plate voltage.

Making allowance for possible hum from other sources by the use of the factor 100 instead of 50, and for the fact that the input voltage is amplified by the first tube before it reaches the point where the hum is introduced, the relation between minimum input and maximum allowable hum may be written as

$$E_{h_{max}}\leqq\frac{A_1E_{min}}{100}, \tag{9}$$

where $E_{h_{max}}$ is the maximum allowable hum voltage across R_c,
E_{min}, minimum input voltage,
and A_1, amplification of first stage.

By the use of equations (2) or (5) with (3), (8), and (9) it is possible to determine whether or not an existing rectifier and filter, or a proposed design, will give satisfactory results. As an example of such a determination, consider the power supply for the high amplification stages of the amplifier described in this report.

This power supply has a three-section inductance input filter with an output of 400 volts direct current at 0.016 ampere, working from a full-wave single-phase rectifier. First, the values

L_1=40 henries,
R_L=25,000 (0.016 ampere at 400 volts),
ω =2π (120),
and $\frac{e_{ac}}{e_{dc}}$= 0.667 (from table I),

are found to satisfy relation (1). This result indicates that equation (2) and table I may be safely used to represent the input wave to the filter. From these it is determined that the principal fluctuation frequency of 120 cycles per second (for 60 cycles per second power supply) will have an input peak magnitude of 267 volts.

The ratio of the magnitude of this fluctuation in the filter output to its magnitude in the input will be given from equation (3) by substituting the values L_1, L_2, and $L_3=40$ henries, C_1 and $C_2=0.00002$ farad, $C_3=0.00004$ farad, and $\omega=2\pi$ (120), and is $\frac{e_0}{e_i}=5.35\times10^{-9}$. From this the value 1.43×10^{-6} volts peak is obtained as the magnitude of the principal hum component in the output from the filter. The ratio of this component to the direct-current output is then

$$\frac{e_{ac}}{e_{dc}}=3.75\times10^{-9}.$$

Since a resistance voltage divider is used to reduce the 400-volt direct-current output from the filter to the 250-volt plate voltage for the first tube, the hum component will be reduced by the same ratio as the direct current and the foregoing ratio will remain the same. That is, $\frac{e_{ac}}{e_{dc}}=\frac{E_{ac}}{E_{dc}}$. Substituting this ratio in equation (8), with $I=0.001$ and $R_c=200{,}000$, gives

$E_h=7.15\times10^{-7}$ volts peak, or 5.06×10^{-7} volts r. m. s.,

which is the hum voltage at the output of the first tube.

Substituting this value in equation (9) using $A_1=100$ as the amplification of the first stage, and 0.001 volt as the minimum voltage to be measured, the relation is satisfied and no measurable hum should be expected in the amplifier output. Tests of the completed amplifier verify this conclusion.

In the design of a transformer, rectifier, and filter combination, various factors influence the choice of the components used. In this discussion of the problem, only the full-wave single-phase rectifier will be considered, because this is the most common type.

In connection with the filter, little need be said except that the condensers should be of ample voltage rating for the voltage to be used and that the filter reactors should be capable of maintaining the desired inductance when carrying the direct current required from the filter. Generally, if the direct-current voltage does not exceed 400 volts, electrolytic condensers will be satisfactory and have the advantage of compactness. If the peak voltage encountered by the condenser exceeds 400 volts, as might be the case of an input condenser in a capacitance input filter, it is best to use paper dielectric condensers with continuous service direct-current voltage ratings at least 1.5 times the peak voltage.

The filter reactors chosen should preferably be magnetically shielded by heavy cases of cast-iron alloy. In the selection of the reactors due regard should be given to their resistance, as well as inductance, especially if the filter works into a variable load. Furthermore, it is well to minimize the effect of load variation as much as possible by the use of a fairly low-resistance voltage divider on the filter output, and it is necessary to consider the current drawn by this resistor, as well as the load current to the amplifier, when determining the required current carrying capacity of the reactor.

There is little choice available in the matter of rectifiers. Two general types may be had in the sizes suitable for use in power supplies of the type under discussion, namely, hot cathode mercury vapor rectifiers and high vacuum thermionic rectifiers. Of these types, the first should be avoided, unless its large current capacity and low voltage drop are necessary, because of its tendency to produce high-frequency disturbances. Tubes such as the type 80, 83V, or 5Z3 will prove satisfactory and the choice between them depends only on the voltage and current required from the rectifier filter system.

These high vacuum rectifiers have a large and variable voltage drop, the magnitude of which must be determined from the characteristics published by the manufacturer. It is of importance in the determination of the transformer voltage necessary to produce the required output voltage from the system.

The choice of a transformer for use in a given power supply is based on the direct-current output voltage desired, the power required, and the type of filter to be used. Assuming that an inductance input filter is to be used, the transformer voltage and power capacity can be determined as follows. From table I it is found that the required alternating-current voltage from each end of the secondary winding to the center tap is 1.11 times the direct-current voltage desired, neglecting the voltage drop in the transformer, filter, and rectifier. Therefore, to compute the actual alternating-current voltage required to give the desired direct-current output voltage, it is necessary to determine these neglected voltage drops, add them to the desired direct-current voltage, and multiply by 1.11. In this computation it is usual to neglect the voltage drop in the transformer secondary and the effect of transformer leakage reactance. Both of these factors are small in any good transformer.

If a capacitance input filter is to be used, the required alternating-current voltage may be determined in the same manner as for the inductance input filter case except that the ratio of alternating-current secondary voltage to direct-current output voltage must be determined from equation (5). Once this ratio is known for a given filter and load, the rectifier and filter voltage drop may be added to the desired direct-current output voltage and the required alternating-current voltage on each side of the secondary center tap, computed.

The mechanical lay-out of the power supply is not important. The components, with the exception of the rectifier tube, may be arranged in any manner that is convenient. Provision must be made for ventilation in placing the rectifier tube, and the tube should preferably be mounted vertically. If the tube must be mounted horizontally, it should be so oriented that the filaments do not tend to sag toward the plates.

III. THE EFFECT OF THE POWER SUPPLY ON THE AMPLIFIER

In any multistage amplifying system there is a great difference between the energy levels of the first and last stages and, if even a very small portion of the output energy is allowed to return to the input circuits, the amplification characteristics of the system will be greatly affected. The most frequent medium for such back coupling is the internal resistance of a common power supply, such as illustrated by figure 9. Here it will be noted that the internal impedance Z_c of the power supply is common to all plate circuits, hence any voltage drop e_c across Z_c, caused by the plate current of one tube, will transfer energy to all the other stages in the amplifier. Since the plate current of each stage contributes to the voltage drop e_c, and because energy is transferred to each stage by e_c, the exact mechanism of the action of Z_c on the amplifier is a very complex one. However, Terman has shown (reference 8) that quite accurate results may be obtained by neglecting the interaction between all stages but the first and the last. This procedure is justifiable because the difference in energy level between any other two stages is much smaller than that between the first and last. An analysis of the action of Z_c may be made quite easily on this simplified basis.

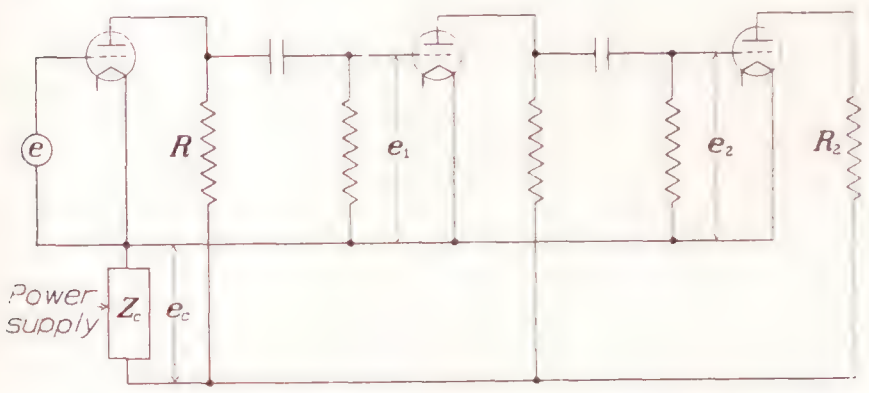

FIGURE 9.—Schematic circuit diagram of multistage amplifier with common plate voltage supply.

If the schematic circuit of figure 9 is redrawn in the form of the approximate equivalent circuit of figure 10, it is seen that the voltage drop across the power-supply impedance, caused by the amplified alternating currents in the last tube is

$$e_c = -\mu_2 e_2 \frac{Z_c}{Z_c + R_2 + r_{p_2}} \qquad (10)$$
$$= e_2 A_c = e_1 A_1 A_c$$

where μ_2 is the amplification factor of last tube;
e_1, a. c. input voltage to second stage;
e_2, a. c. input voltage to last tube;
R_2, load resistance of last tube;
r_{p_2}, internal impedance of last tube;
A_1, amplification between output of first tube and input to last tube;
and

$$A_c = e_c/e_2 = -\mu_2 \frac{Z_c}{Z_c + R_2 + r_{p_2}}.$$

Since the impedance Z_c is generally very small compared with r_p and R, the voltage e_c may be represented as a source of negligible internal impedance in series with the plate circuit of the first tube.

Hence

$$e_1 = e\frac{-\mu R}{R + r_p} + e_c \frac{r_p}{R + r_p}$$

$$= eA - e_1 A_1 A_c \frac{r_p}{R + r_p} \qquad (11)$$

where e is the alternating-current input voltage to the amplifier;
μ, amplification factor of the first tube;
R, load resistance of the first tube;
r_p, internal impedance of the first tube;
and A, amplification of first stage, neglecting the effect of Z_c.

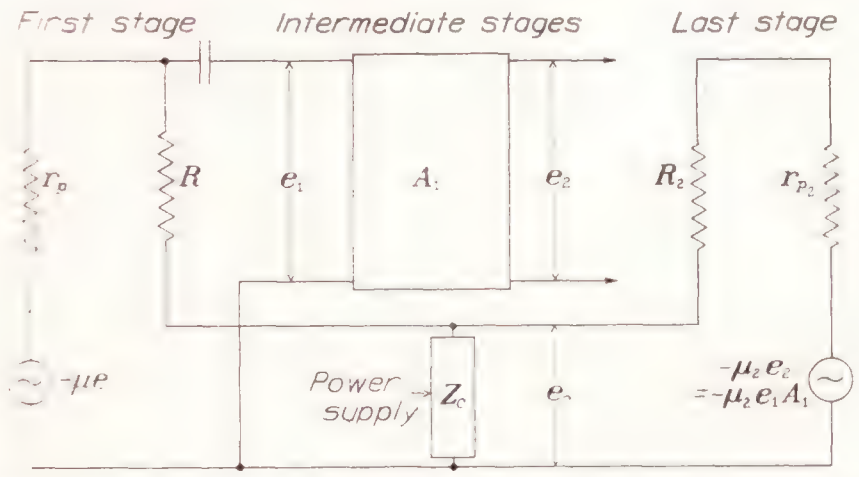

FIGURE 10.—Approximate equivalent circuit of multistage amplifier with common plate voltage supply.

Rearranging equation (11) in the form

$$eA = e_1\left(1 - A_1 A_c \frac{r_p}{R + r_p}\right)$$

or

$$\frac{e_1}{e} = \frac{A}{1 - A_1 A_c \frac{r_p}{R + r_p}}$$

an expression for $\frac{e_1}{e} = A_e$, the effective amplification of the first stage, is obtained. For convenience of analysis this expression may be further rearranged by multiplying the right-hand term of the denominator by A, and by $\frac{r_p + R}{\mu R}$, which is $1/A$. That is,

$$A_e = \frac{e_1}{e} = \frac{A}{1 - A A_1 A_c \frac{r_p}{R + r_p}\frac{R + r_p}{\mu R}}$$

or

$$A_e = \frac{A}{1 - A A_1 A_c \frac{r_p}{\mu R}} \qquad (12)$$

The final result is an expression for A_e, the effective amplification of the first stage, in terms of known or readily measured characteristics of the amplifier. These characteristics, with the exception of μ, R, and r_p are vectors and must be treated accordingly.

In this connection it should be noted tbat A_1 and A will either be very nearly in phase or very nearly 180° out of phase over most of the frequency range of the amplifier. If an odd number of stages is used in the amplifier, the plate currents of the first and last stages will be approximately in phase, and the general effect of Z_c will be an increase in amplification. If the total number of stages is even, a decrease in amplification will occur. In either case the modification of amplification is not likely to be uniform over the frequency range of the amplifier because Z_c will generally be reactive in character and hence will change in magnitude and phase angle as the frequency changes, thus changing A_c and, through A_c, the effective amplification A_e of the first stage.

Three general methods may be employed to eliminate or reduce the effect of Z_c on the amplification. First, Z_c may be entirely eliminated by the use of separate power supplies. Second, its effect may be reduced by making Z_c unimportantly small over the frequency range of the amplifier. Third, filters may be inserted in each plate circuit to reduce the common coupling effect of Z_c.

The first method is, of course, the most satisfactory as far as ease of obtaining the desired result is concerned but has the disadvantage of requiring several power supplies. However, the stages most likely to give trouble are those of the high-gain amplifier, and these stages generally have very modest power requirements. If advantage is taken of this fact and individual power supplies with small low-current high-voltage transformers and resistance capacitance filters are used, it may be possible to provide the required number of power supplies in the available space and without excessive cost. Sometimes it will be found that the desired result may be obtained by providing a separate power supply for only the first stage.

The second method depends for its practicability on the fact that Z_c in most rectified alternating-current power supplies has a predominantly capacitive reactance. It is possible to make the alternating-current voltage drop across Z_c negligible throughout the high- and medium-frequency ranges and well into the low-frequency range of the amplifier by shunting the output terminals of the power supply with suitably large values of capacitance. However, as the frequency is lowered, the effect of Z_c will eventually become very evident, usually as a violent low-frequency oscillation of the amplifier if an odd number of stages is used or, as a marked lack of low-frequency amplification, if the number of stages is even. Because of this difference in the effect with odd and even numbers of stages, slightly different remedies are usually employed in its elimination.

If the number of stages is odd, the usual method of attack is to add enough capacitance across Z_c to cause the frequency at which its effect becomes troublesome to be lower than the lowest frequency that it is desired to amplify. The amplifier is then so arranged, for instance, by reduction of coupling capacitance, that its amplification decreases rapidly for frequencies less than the desired lower limit; that is, in the frequency range where Z_c begins to have an important effect. By a suitable balance of the increase in amplification due to the effect of Z_c against the decrease in amplification introduced into the amplifier to counteract the effect of Z_c, it is often possible to extend the lower limit of useful amplification to a considerably lower frequency than the constants of the amplifier circuit alone would indicate.

If the number of stages is even, the only solution is to add sufficient capacitance to the power-supply output terminals to make Z_c so small that its amplification reducing effect does not become important at the lowest frequency it is desired to amplify. In the case of turbulence-measuring equipment, or any amplifier to be used at very low frequencies, this method requires very large values of capacitance. However, since the output voltage of the power supply is usually not over 400

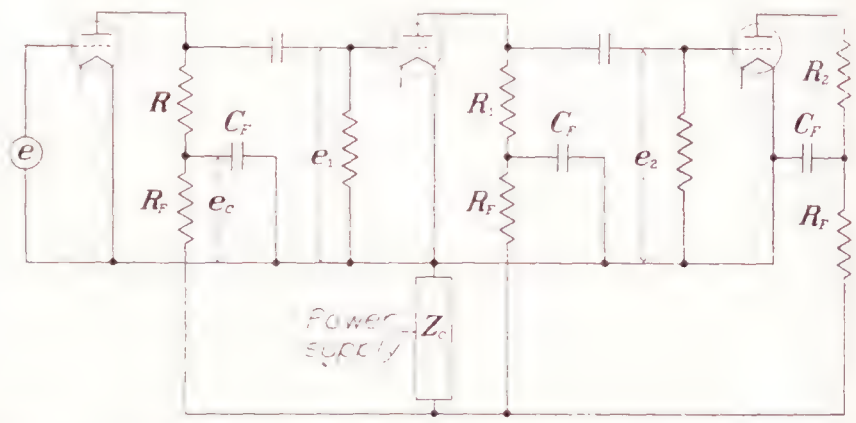

FIGURE 11.—Schematic circuit diagram of multistage amplifier with common plate voltage supply and decoupling filters.

volts, it is generally possible to use electrolytic capacitors and thus obtain large values of capacitance without undue bulk or expense.

Generally, it will be found necessary to provide a separate power supply for the final stage of the system because of the comparatively large drop across Z_c produced by the large alternating-current component in the plate current of this stage. Power supplies for the remaining stages may be provided as convenience or necessity dictate. Usually if an excess of amplification exists in the system, as was the case in the amplifier of figure 3, the desired performance may be obtained most easily by connecting even numbers of stages to the same power supply. If no amplification may be sacrificed, it may be necessary to arrange the circuit so that each power supply serves an odd number of stages.

The third method for eliminating the effect of Z_c, the use of "decoupling filters" is illustrated by figure 11 and by the approximately equivalent circuit of figure 12. This method depends for its operation on the insertion of a resistance R_F in series with each plate circuit, and the use of capacitances C_F connected between the junction of the load resistors R, R_1, R_2, etc., with R_F, and the zero potential side of the circuit.

The function of the capacitors C_F is to provide a low-impedance path to ground for the alternating-current components of the plate current of each tube. The function of the resistors R_F is to insert a high impedance between the bypass circuits and Z_c, the common coupling element of the circuit, thus helping to confine the alternating-current components to the bypasses and to keep them out of Z_c.

The performance of the amplifier power supply combination, when such filters are used, may be estimated by use of equation (12). It is necessary, however, to solve the circuit of figure 12 for an appropriate expression for A_c. If this solution is accomplished, using the same resistance for both resistors R_F and the same capacitance for both capacitors C_F, it is found that

$$A_c=\frac{e_c}{e}=\frac{\mu_2 X_c^2 Z_c}{(r_{p_2}+R_2)(R_F+X_c)^2+Z_c[2(r_{p_2}+R_2)(R_F+X_c)+X_c(2R_F+X_c)+R_F X_c(R+X_c)]} \tag{13}$$

where R_F is the resistance of decoupling filter resistors,

and X_c is the reactance of $C_F=\dfrac{1}{2\pi f C_F}$.

The other symbols have the same significance as in equation (12). If dissimilar resistances are used for the resistors R_F or dissimilar capacitances for capacitors C_F, an equivalent, but more complicated, expression may be derived.

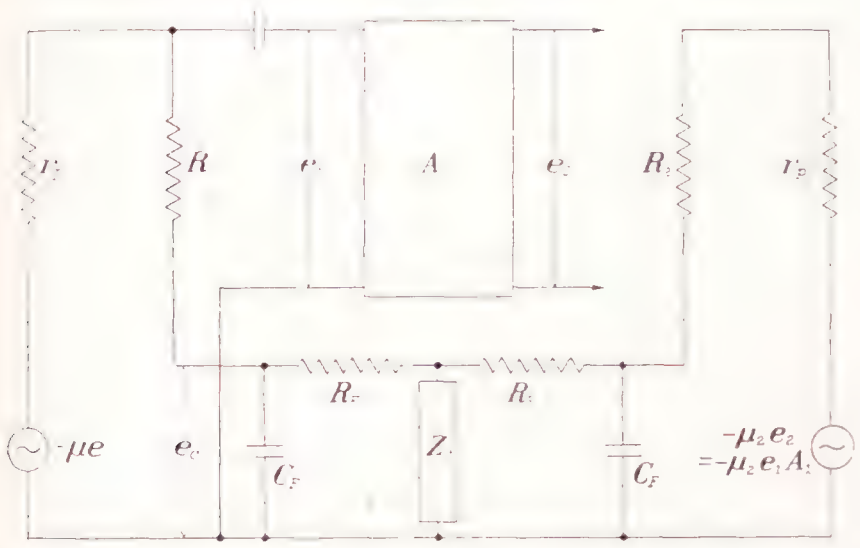

FIGURE 12.—Approximate equivalent circuit of multistage amplifier with common plate voltage supply and "decoupling" filters.

Because the decoupling filter action depends on the maintenance of a high ratio of R_F to X_c, this system also becomes ineffective at very low frequencies, unless large values of capacitance are used at C_F. The system is one that is widely used, however, and, if the output voltage of the power supply is great enough so that high voltage drops in R_F can be tolerated, the filters can be made effective at any reasonable desired low frequency. The usual procedure is first to make the output voltage from the power supply as high as is is economically possible, then to drop this high voltage to that needed for proper operation of the amplifier by making R_F large, and finally to add capacitance at C_F until the desired low-frequency performance is obtained.

If an even number of stages is used in the amplifier, the decoupling filters tend to give somewhat better results than might be indicated by equations (12) and (13), because as the frequency is decreased, X_c increases, and its bypassing action decreases. This result allows R_F to become increasingly a part of the load resistance of the stage concerned, which in turn increases the amplification of that stage, thus tending to offset the decrease in amplification which would normally occur due to the action of Z_c. If an odd number of stages are used, this effect becomes a detriment rather than an advantage because the effect of Z_c is then to increase, rather than to decrease, the amplification.

Of the three described methods for eliminating the common coupling effect of the power supply on a multistage amplifier, the first is undoubtedly the surest and most satisfactory, especially if extremely low frequencies must be amplified. The second method is the simplest, where practicable, and should always be attempted before resort to more complicated systems. The third method is a very useful one, especially where amplification at only moderately low frequencies is necessary.

In the description and analysis of the action of the power supply on the amplifier, as outlined here, it has been assumed that the tubes used were triodes. The results may be extended to multigrid tubes because, in general, the extra elements are at zero potential to the alternating-current components of the voltages being amplified, and the tubes became equivalent triodes.

When the extra element, for example, the screen grid of a pentode or tetrode, must be maintained at some positive direct voltage, it may be connected either to a tap on the plate voltage power supply or to a separate power supply. In either case some impedance will exist between the point of connection and the zero potential side of the circuit and, if several tubes are connected to the same supply, a state very similar to that discussed in connection with the plate power supply will exist. Each tube will then act as a triode composed of the regular control grid, the cathode, and the screen grid acting as an anode and will have a load impedance consisting of the impedance of the screen voltage power supply, which also acts as a common coupling link between tubes.

Fortunately, the conditions will usually be such that the amplification of these accidental triodes will be quite low, and their effect on the main amplifying action of the amplifier will be still lower. The effect may become troublesome, however, and provision for its elimination should always be incorporated in either the amplifier or the power supply. Since the screen voltage required is usually of the order of only 50 volts, conditions are ideal for the application of the decoupling filter method. Excellent decoupling action may be

obtained by dropping the full power supply output voltage down to the required screen voltage through a very high resistance and by using a large bypass capacitance between the screen and the zero potential part of the amplifier circuit. Quite often it will be necessary to use this method only in the first stage of the amplifier, as is the case in the amplifier of figure 3. The remaining stages may usually be supplied with screen voltage from a tap at the proper point on the power supply voltage divider. This tap should be bypassed to the negative terminal of the power supply by a very large capacitance. Because of the low voltage involved, electrolytic condensers are especially suitable for this service.

PRACTICAL DESIGN PROCEDURE

In the design of an amplifier and power-supply combination, due consideration should be given to the factors discussed and every effort be made to arrive at a suitable design before construction. It should not, however, be expected that the completed system will prove to be free from trouble. So many unknown and undeterminable factors are involved in such a highly complex problem as a three or more stage amplifier with two or more power supplies, that the approximations necessary usually fall short of complete validity. In general, the best that may be hoped for is an amplifier that may be made satisfactory by minor changes of circuit constants, rather than by complete reconstruction.

Such an amplifier having been obtained, the procedure to be used in the adjustment of its characteristics is one of the cut-and-try type. Each amplifier is a unique problem and must be treated as such. As an example, the procedure in the case of the amplifier and power, supply system of figure 3 will be considered.

This apparatus was originally intended to consist of three high-amplification stages operating from one power supply and a phase inverter-output stage combination on a separate power supply. Upon completion it was found that the three-stage amplifier had excessive low-frequency amplification and that the phase inverter-output stage combination was unstable. By trial it was found that the instability could be cured by using separate power supplies. With this end in view, the phase inverter was attached to the same power supply as the first three stages and, in addition to curing the trouble in the phase inverter-output stage combination, this change greatly reduced the low-frequency distortion of the first three stages.

Further reduction of the frequency distortion in the first four stages was obtained by changing the screen voltage supply circuit so that the first tube received its screen voltage through a 1-megohm dropping resistor from the 250-volt plate voltage supply, instead of from the 50-volt tap on the power supply voltage divider. It was found necessary to use a paper dielectric condenser for the bypass at the screen grid of the first tube because of the large voltage fluctuations that resulted when an electrolytic condenser, with its more variable leakage resistance, was used. For the 100-microfarad bypass condenser across the 50-volt tap for the screen voltage of the other tubes, electrolytic condensers proved satisfactory.

Tests now indicated that the frequency characteristic of the complete amplifier system was satisfactory, except for a slight loss of amplification at the lower frequencies, but that the over-all amplification was excessive. By a reduction of the amplification at the grid of the fourth stage, thus at the same time producing a reduction of the current through Z_c, it was possible to bring the over-all amplification to the desired level and to improve the frequency characteristic. The final result is illustrated by figure 5.

CONCLUDING REMARKS

It is hoped that the material presented will prove useful to others faced with the problem of designing similar apparatus. No attempt has been made at an exhaustive treatment. The aim, rather, has been to present, under one cover, sufficient data so that a person not particularly familiar with the design of such apparatus may proceed on a sound basis. For additional information the reader should refer to any of the standard works on communication engineering, for instance, reference 8.

National Bureau of Standards,
Washington, D. C., *March 1937*.

REFERENCES

1. Dryden, H. L., and Kuethe, A. M.: The Measurement of Fluctuations of Air Speed by the Hot-Wire Anemometer. T. R. No. 320, N. A. C. A., 1929.
2. Dryden, H. L., and Kuethe, A. M.: Effect of Turbulence in Wind Tunnel Measurements. T. R. No. 342, N. A. C. A., 1930.
3. Mock, W. C., Jr., and Dryden, H. L.: Improved Apparatus for the Measurement of Fluctuations of Air Speed in Turbulent Flow. T. R. No. 448, N. A. C. A., 1932.
4. Schubauer, G. B.: A Turbulence Indicator Utilizing the Diffusion of Heat. T. R. No. 524, N. A. C. A., 1935.
5. Schubauer, G. B., and Dryden, H. L.: The Effect of Turbulence on the Drag of Flat Plates. T. R. No. 546, N. A. C. A., 1935.
6. Dryden, Hugh L.: Air Flow in the Boundary Layer of a Plate. T. R. No. 562, N. A. C. A., 1936.
7. Dryden, Hugh L., Schubauer, G. B., Mock, W. C., Jr., and Skramstad, H. K.: Measurements of Intensity and Scale of Wind-Tunnel Turbulence and Their Relation to the Critical Reynolds Number of Spheres. T. R. No. 581, N. A. C. A., 1937.
8. Terman, F. E.: Radio Engineering. McGraw-Hill Book Co., Inc., 1932.

REPORT No. 599

FLIGHT TESTS OF THE DRAG AND TORQUE OF THE PROPELLER IN TERMINAL-VELOCITY DIVES

By Richard V. Rhode and Henry A. Pearson

SUMMARY

The drag and torque of a controllable propeller at various blade-angle settings, and under various diving conditions, were measured by indirect methods on an F6C–4 airplane in flight. The object of these tests was (1) to provide data on which calculations of the terminal velocity with a throttled engine and the accompanying engine speed could be based and (2) to determine the possibility of utilizing the propeller as an air brake to reduce the terminal velocity.

The data obtained were used in the establishment of propeller charts, on the basis of which the terminal velocity and engine speed could be calculated for airplanes whose characteristics fall within the range of these tests. It was found that the propeller reduced the terminal velocity about 11 percent with the normal blade-angle setting of 19.0° and about 35 percent with a 5.5° setting. Indications were that the terminal velocity could be still further reduced by using even lower blade-angle settings. A method is given for the calculation of the terminal velocity with throttled engine and the engine speed.

INTRODUCTION

In cooperation with the Bureau of Aeronautics, Navy Department, and the Army Air Corps, the National Advisory Committee for Aeronautics has been making a study of rational methods for establishing the structural design conditions for airplanes. In the course of this study, a method was established in 1930 for calculating the terminal velocity of a diving airplane, taking propeller drag into account. The method was based on the results of small-scale propeller tests by Durand and Lesley (references 1 and 2), supplemented by the then unpublished results of a few tests of a 4-foot metal propeller in the N. A. C. A. propeller-research tunnel. Because of insufficient data on torque or power coefficients from these tests, no provision could be included for calculating the engine speed and the method was therefore based on the assumption of such an engine speed, which, for structural-design purposes, was limited to an arbitrary permissible value.

The interest aroused in this work because of the increasing use of the terminal-velocity dive in military tactics led to an extension of the study to determine the feasibility of using the propeller as an air brake to reduce the terminal velocity. As a result, the wind-tunnel tests of the 4-foot propellers were extended to include tests at the lower blade-angle settings and with different propeller-body combinations. At the same time, a program of dive tests to be made of a conventional airplane with a controllable propeller was formulated, the purpose of which was to evaluate the influence of the propeller under full-scale conditions at the high tip speeds associated with a terminal-velocity dive. The present report presents the results of the flight tests in a usable form for the quantitative determination of the influence of the propeller on the terminal velocity and the engine speed.

The flight tests were made in September 1932 by the N. A. C. A. at Langley Field, Va.

APPARATUS AND METHOD

A Navy F6C–4 airplane equipped with a Pratt & Whitney R–1340–CD engine was used in these tests. The pertinent data concerning this airplane are given in table I and a general view is given in figure 1. The propeller used was the Hamilton controllable model described in reference 3. This propeller was not completely adjustable in flight, as it could be set at only two positions, the locations of which depended upon the setting of stop nuts. As delivered, the range of blade-angle settings available was between 13° and 22°, which range was extended down to 5° for these tests by the use of special links. The pitch-changing mechanism consisted of a hydraulic piston and centrifugal weights, which actuated the blades through a system of push-pull rods. The action of the centrifugal weights tended to increase the blade angle; the engine-oil pressure, when acting on the piston, forced the blades to the lower setting.

The airplane was equipped with four synchronized standard N. A. C. A. photographically recording instruments—air-speed meter, tachometer, altimeter, and air-temperature thermometer—and a dive-angle indicator developed especially for these tests.

The diagram of figure 2 shows the simplicity of the dive-angle indicator. Its principal merit lies in the fact that it is not affected by accelerations, as its operation depends upon the reflection of a ray of sunlight onto a frosted-glass scale.

The air-speed head was mounted at the outer strut location on a boom one chord length forward of the leading edge of the wing, in order to reduce the interference on the air-speed measurements to a minimum. The air-speed installation was calibrated over a speed course, and a constant error of 2 percent for speeds between 130 and 150 miles per hour was found. It was assumed that the correction for the diving conditions was also 2 percent.

From data obtained in high-speed level flight the minimum drag coefficient of the airplane was calculated.

FIGURE 1.—The F6C-4 airplane.

The method employed consisted of deducting the calculated induced drag from the total drag, which had been evaluated from the known engine power and the estimated propeller efficiency. On the basis of a study of full-scale propeller-body tests, the propulsive efficiency was estimated in this case to be 75.5 percent.

The main tests consisted of terminal-velocity dives, with the engine fully throttled and with the ignition on, starting at 12,000 feet and continuing to approximately 5,000 feet altitude. The dives were made at various predetermined dive angles to simulate conditions for airplanes of various zero-thrust or "basic" terminal velocities. For each basic terminal velocity, tests were made with propeller blade-angle settings of 5.5°, 9.5°, 14.5°, 19°, and 22.5° at 0.75 radius.

The dive angles at which the tests were made were determined from the relation

$$\sin \gamma = \frac{C_{D_{min}} q S_w}{W}$$

where W, weight of the airplane.

γ, flight-path angle.

$C_{D_{min}}$, minimum drag coefficient of the airplane.

q, dynamic pressure corresponding to the desired zero-thrust or basic terminal velocity.

S_w, wing area.

In order to obtain these dive angles in the flight tests, a curve of the elevation of the sun against time was plotted, and a pointer on the dive-angle indicator was set to indicate the proper dive angle corresponding to the elevation of the sun existing at the instant the dive was to be started. Continuous records of indicated air speed, engine speed, air temperature, and barometric pressure were taken throughout all the dives.

PRECISION

The corrected dynamic pressure measurements at terminal velocity are probably accurate to within 2 percent. During the entry into and accelerated portions of the dive, the precision may be slightly less because of lag in the air-speed system. The tachometer readings are correct to within 30 r. p. m. Barometric pressures were measured to a precision of about 2 percent, and the temperature to about 2° C. The maximum error in the dive angle was about 2° and was caused primarily by the inability of the pilot to maintain the airplane in a steady condition at all times.

RESULTS

The recorded measurements were first plotted as time histories of the quantities measured, to insure proper

evaluation of these quantities at the terminal velocity. A representative time history is shown in figure 3. From curves such as these, the indicated terminal velocities

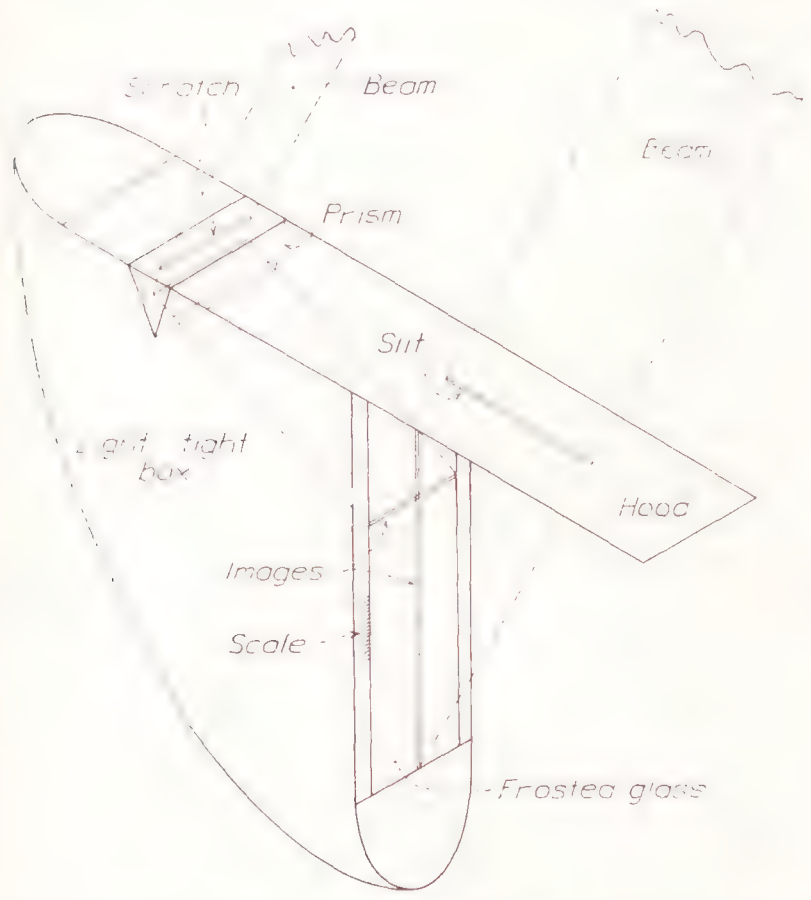

FIGURE 2.—Dive-angle indicator. Prism has blackened surface with horizontal scratch. In operation, pilot heads into the sun so that light through the slit in the hood makes a vertical image on the frosted glass. He then pushes into a dive until the horizontal image reaches a predetermined mark on the scale.

and the accompanying engine speeds were obtained. These quantities were then plotted against the appropriate blade-angle settings for each of the basic terminal velocities, as shown in figure 4. No flight-test points

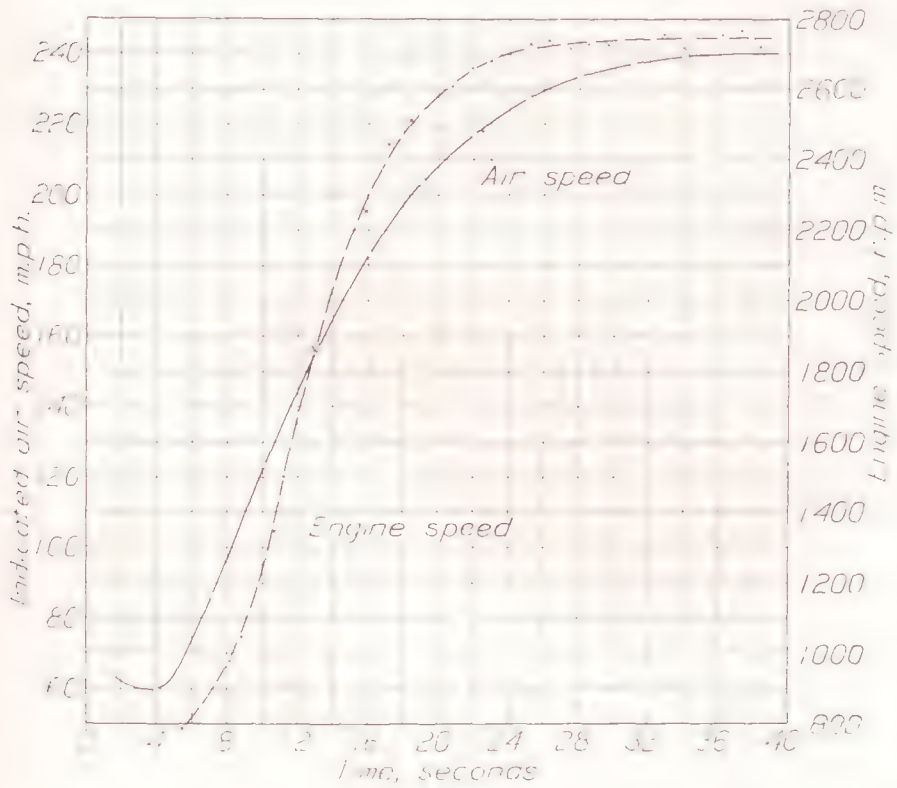

FIGURE 3.—Time history of a vertical dive. Blade-angle setting, 14.5° at 0.75 *R*.

are shown in this figure, as these curves are the results of cross-fairing an intermediate set of curves of the measured values. This cross-fairing was necessitated by the fact that the pilot found it impossible in some cases to dive at exactly the specified time, with the consequence that the angle of dive did not correspond to an integral value of basic terminal velocity. The engine speeds given in figure 4 are those for a standard sea-level density. The engine speed at any other altitude can be obtained by multiplying these values by the square root of the ratio of the sea-level density to the density at altitude. It is assumed that the indicated terminal velocity does not change materially with altitude.

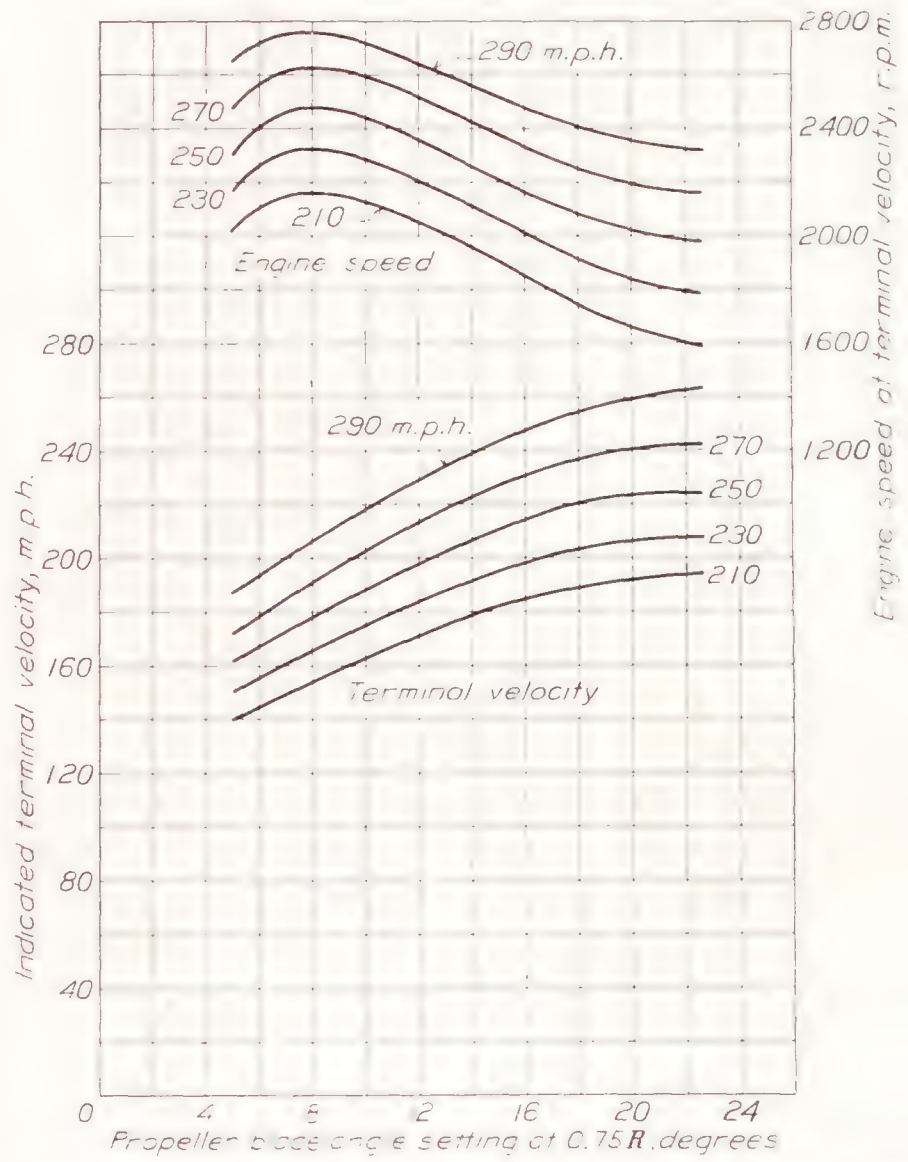

FIGURE 4.—Variation of engine speed and terminal velocity with propeller blade-angle setting for different zero-thrust velocities. The engine speeds are corrected to standard sea-level density. The parameter is zero-thrust terminal velocity.

The variation of air speed with engine speed during a number of dives is shown in figure 5. Two runs, representing the extreme values of the dive angles at which the tests were made, are shown for each blade-angle setting.

DISCUSSION

From figure 4 it can be seen that the terminal velocity decreases with blade-angle setting for the range investigated. Indications are that a further decrease in pitch would lower the limiting velocity still more. However, there is a critical value where a decrease in terminal velocity no longer accompanies a decrease in blade-angle setting, unless power is used to increase the engine speed. This fact is not apparent from the curves of figure 4, as the range of blade-angle settings could not be extended sufficiently low with the propeller used in these tests. The engine speed at terminal velocity increases as the blade angle decreases, down

to about 8°; thereafter, the engine speed decreases with decreasing blade angle.

There is some doubt whether the 22.5° points are correct, since there is a reversal in curvature between the 19.0° and 22.5° settings. Further, on the ground with the stop nuts set for 22.5° the engine speed was not sufficient for the centrifugal force to bring the blades quite against the stops. As the airplane was available for only a limited time, there was no opportunity to

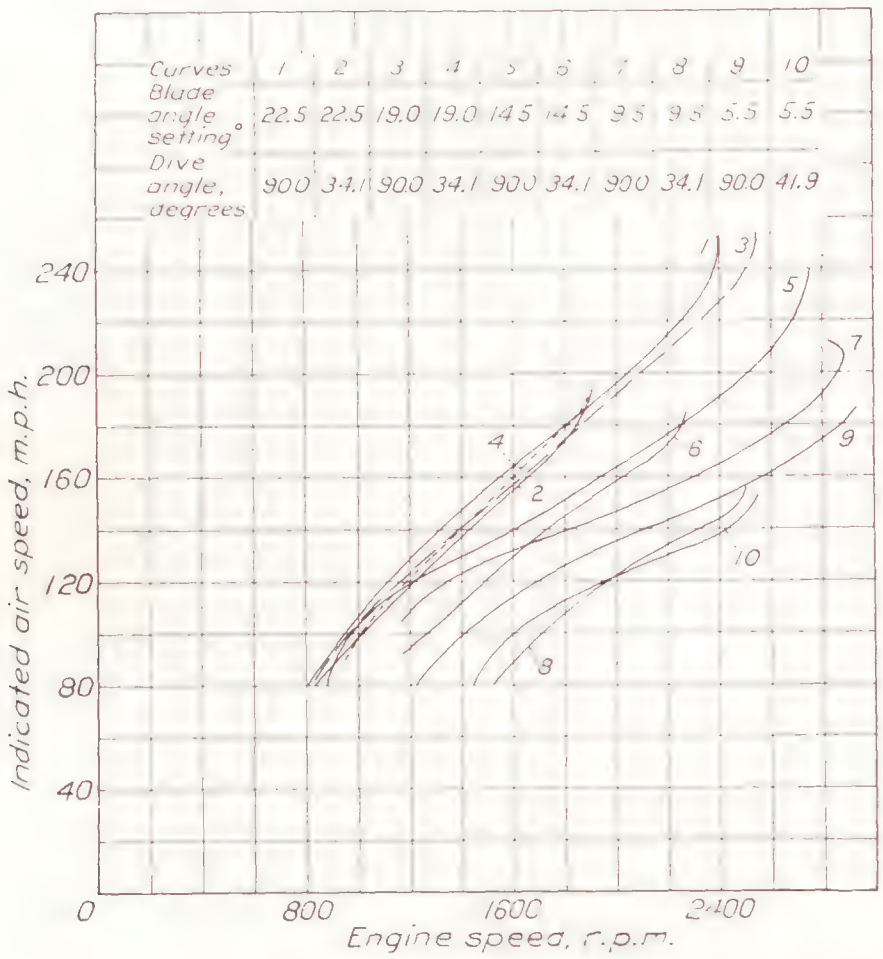

FIGURE 5.—Relation between engine speed and air speed for several dives made with the F6C–4 airplane.

construct the apparatus necessary to determine whether the blades were actually against the stops during the dives.

The significance of the curves in figure 5 is that the value of n/V at which the propeller operates during the major portion of any throttled dive is approximately constant. If the influence of tip speed is neglected, it may be said that the thrust coefficient is also nearly a constant, since the propeller, for a given blade-angle setting, operates at roughly the same value of nD/V. The over-all drag coefficient, which is the sum of the airplane and propeller drag coefficients, is thus approximately constant throughout any dive. This relation suggests that methods for the determination of time-altitude and velocity-altitude relations may be considered sufficiently precise for practical purposes if based on the assumption of a constant drag coefficient, which, of course, should include a proper allowance for the propeller.

DERIVATION OF PROPELLER CHARTS

The coefficients that were found to be most adaptable for reducing propeller data in the negative range are defined as follows:

$$T_c=\frac{T}{\rho V^2D^2}$$

and

$$Q_c=\frac{Q}{\rho V^2D^3}$$

where T is the propeller thrust, lb.
Q, propeller torque, lb.-ft.
D, propeller diameter, ft.
V, air speed, ft. per sec.
ρ, mass density of air, slugs per cu. ft.

These coefficients were computed from the corresponding values of thrust and torque evaluated from the following relations:

$$T=W\sin\gamma-C_{D_{min}}\frac{\rho V^2}{2}S_w$$

$$Q=\frac{550\ \text{f.hp.}}{2\pi n}$$

in which f.hp. is the friction horsepower of the engine and the other symbols have their usual significance.[1]

The experimental thrust and torque coefficients so computed for the 14.5° blade-angle setting are shown plotted against nD/V in figure 6. It will be noted that the points for the various dives made with this setting fall at nearly the same value of nD/V; further, it will be seen that the vertical displacement of the points tends to vary with tip speed. Results for the other blade-angle settings are similar in character to those for the 14.5° setting, but occur at different values of nD/V as indicated by the dashed lines of figure 7, which give the median lines through the test points for different blade-angle settings.

Because of the close grouping of the test points at each blade-angle setting, the establishment of a propeller chart (fig. 7) was necessarily based in part on information from other sources. The method and material used in establishing this chart are explained in the following paragraphs.

The form of the propeller-characteristic curves was determined from the tests by Durand and Lesley and from the unpublished results of the tests made in the

[1] The friction horsepower used in these computations was obtained from a 50-hour endurance test of the Pratt & Whitney "Wasp" aircraft engine. The results are shown in fig. 9. The friction-power characteristics existing under the flight-test conditions may, for a number of reasons, have been at variance with the characteristics determined under the conditions of the engine test. Any such disagreement, of course, results in erroneously derived torque coefficients but, as will be shown later, these errors have a negligible influence on the terminal velocity calculated from the charts and only a small influence on the engine speed.

propeller-research tunnel. The quantitative establishment of the curves involved: (1) determination of the end points on the basis of data from outside sources;

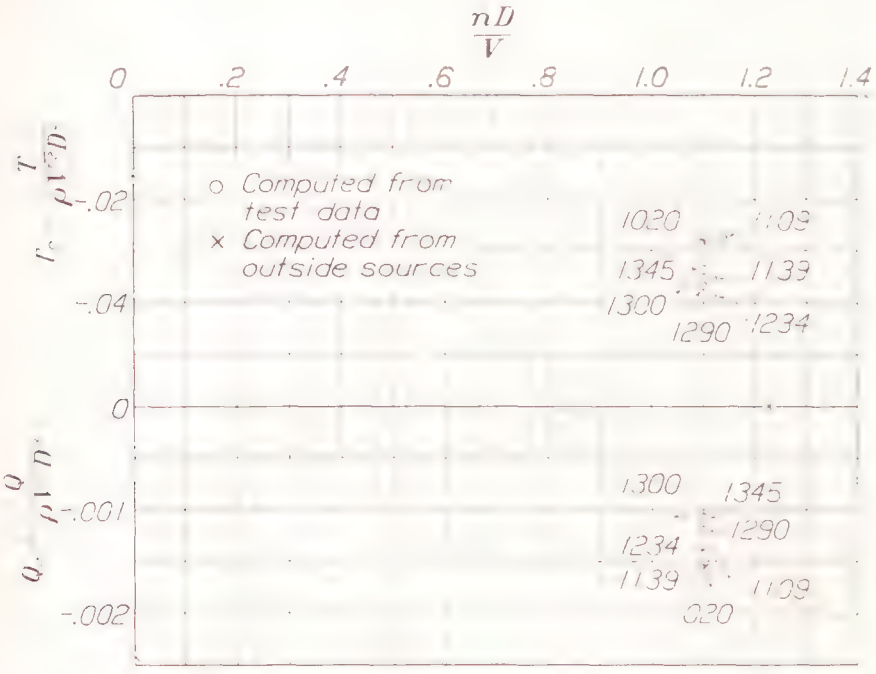

FIGURE 6.—Measured thrust and torque coefficients. Blade-angle setting, 14.5° at 0.75 *R*. All points labeled for tip speed.

(2) fairing of curves through the F6C–4 dive-test points; (3) establishment of tip-speed corrections, which were based largely on the dive-tests results but partly on tests in the propeller-research tunnel (reference 4).

The end points of the T_c curves at zero nD/V were established on the basis of a consideration of Diehl's formula (reference 5), Lock's formula (reference 6), and the data given in reference 7. The quantitative values chosen represent a weighted mean of the data obtained from the three sources. The end points of the Q_c curves at zero nD/V were based entirely on the data of reference 7, which were the only data available.

Values of nD/V at zero T_c and Q_c were partly established by calculations based on the assumption that the aerodynamic characteristics of the blade element at 0.75 radius, considered as an airfoil, represent the action of the propeller as a whole in a condition near zero thrust. For these calculations the angle of zero lift was determined by Munk's method, given in reference 8. Since these points are affected appreciably by interference from the fuselage, consideration was also given to the slopes of the curves of reference 7, with an estimated allowance for fuselage interference, in combination with the requirement that the curves pass through the experimental points from the dive tests.

The propeller-characteristic curves were passed through these end points and through the experimental points (tip speed less than 1,050 feet per second) obtained in the dive tests. As thus drawn, the curves are applicable to cases involving propellers having the proportions of the one used in the dive tests.

In order to make the curves more convenient to apply, they have been corrected to a mean blade-width ratio of 0.1, as presented in figure 7. (Mean blade-width ratio is defined as the ratio of the mean blade

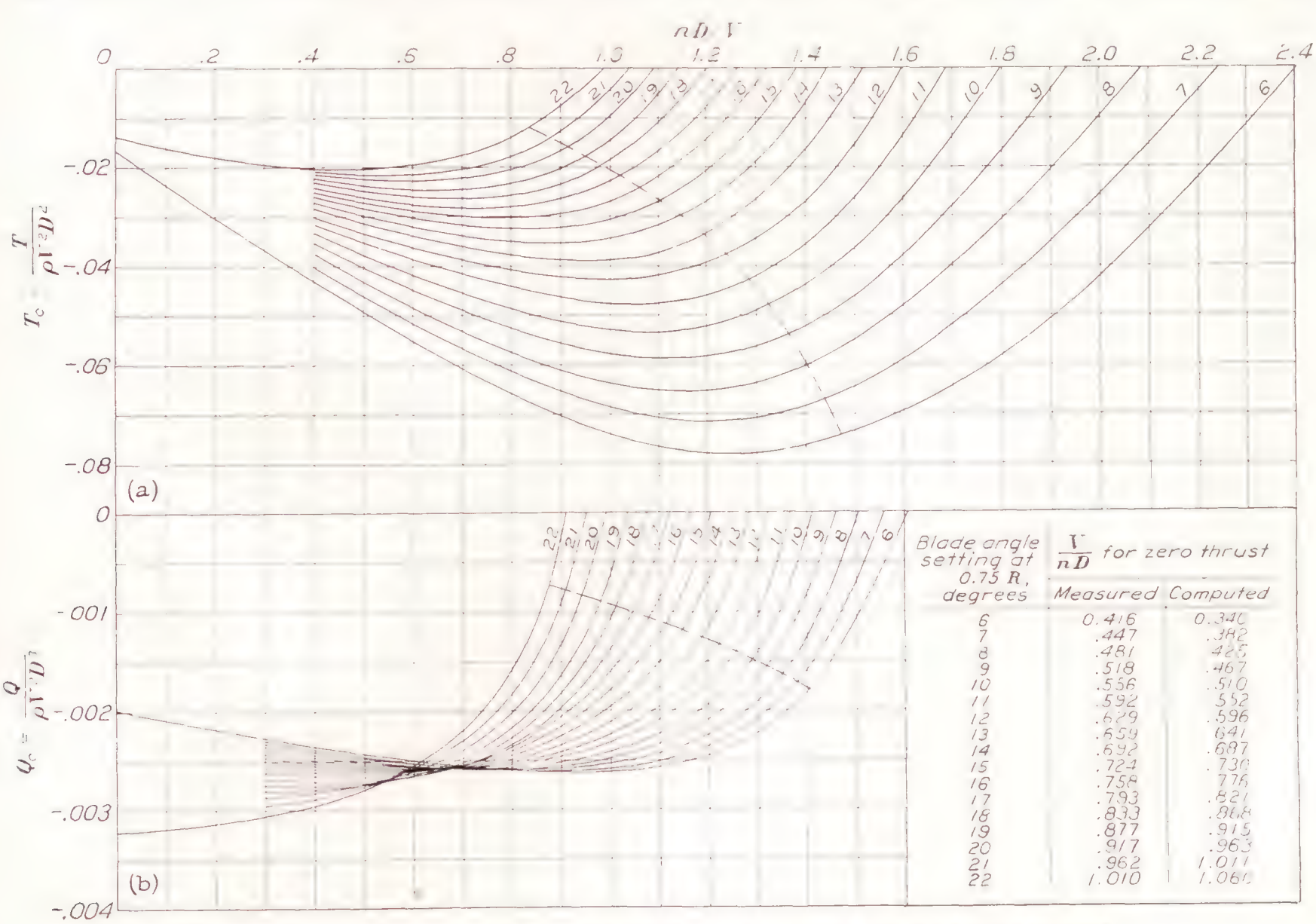

Blade angle setting at 0.75 R, degrees	$\frac{V}{nD}$ for zero thrust	
	Measured	Computed
6	0.416	0.340
7	.447	.382
8	.481	.425
9	.518	.467
10	.556	.510
11	.592	.552
12	.629	.596
13	.659	.641
14	.692	.687
15	.724	.730
16	.758	.776
17	.793	.821
18	.833	.868
19	.877	.915
20	.917	.963
21	.962	1.011
22	1.010	1.061

FIGURE 7.—Propeller characteristics at negative slip for a mean blade-width ratio of 0.1 based on the radius.

width between $0.2R$ and R to R, where R is the radius.) The mean blade-width ratio is a measure of the blade area when the diameter is known. This area must be taken into account in applying a single general set of propeller characteristics to any particular case, in the same manner that the wing area must be taken into account in dealing with wing forces. The coefficients therefore vary directly with the blade area or with the mean blade-width ratio. Since the curves of figure 7 apply to propellers having a mean blade-width ratio of 0.1, the coefficients must be multiplied by the ratio of the actual mean blade-width ratio to 0.1 when using the curves for any other case.

The curves of figure 7 are labeled for blade-angle setting in degrees at $0.75R$ for metal propellers based on either the Clark Y or RAF–6 sections. In order to make the charts more general, values of V/nD for zero thrust are given in two forms, either one of which may be used in lieu of blade-angle setting for selecting the curves in cases involving sections other than the Clark Y or RAF–6. Measured values of V/nD for zero thrust should be used only if the measurements have been made with the proper body interference. Computed values are determined on the basis of a setting determined at the $0.75R$ section and with the zero-lift angle of that section found by Munk's method as given in reference 8.

TIP-SPEED CORRECTION FACTORS

As given in figure 7, the propeller characteristics apply only to cases in which the tip speeds are below the critical value, and they agree well with the flight-test data only for such cases. When the tip speed is above the critical value (approximately 1,050 feet per second), which is the usual case in a dive, the characteristics are different from those given in figure 7. This effect is apparent from figure 6, where the points shift with increasing tip speed. In general, it may be said that there is, for a given propeller and propeller load, a separate set of characteristics for each tip speed above the critical value. The characteristics will, in general, also vary with load at a given tip speed because of variations in the blade deflection with changing load. The characteristics at the higher tip speeds may be determined approximately by introducing conversion factors, which can be used to transform the basic characteristics into those applicable at various tip speeds above the critical value. A method used in determining such conversion factors on the basis of the F6C–4 data follows.

It can be shown qualitatively that as the tip speed increases above the critical value, the value of nD/V for a given value of T_c also increases. Further, it can be shown that at a given value of nD/V the value of Q_c decreases numerically with increasing tip speed above the critical value. These considerations imply that as the tip speed increases above the critical value, the curves of T_c are shifted to the right and the curves of Q_c are shifted upward. The conversion factors evolved are based on these considerations with their numerical values determined by comparing results calculated from the characteristics of figure 7 with the experimental results.

Specifically, the terminal velocities and the engine speeds were calculated for the various dive angles, using as given data the measured weight and the drag coefficient of the airplane, the friction-horsepower curve of the engine, and the propeller characteristics of figure 7. The factors necessary to convert the calculated engine speeds to the experimental values were plotted against tip speed. The mean curve drawn through these points is the conversion curve for nD/V. In a similar manner, conversion factors for

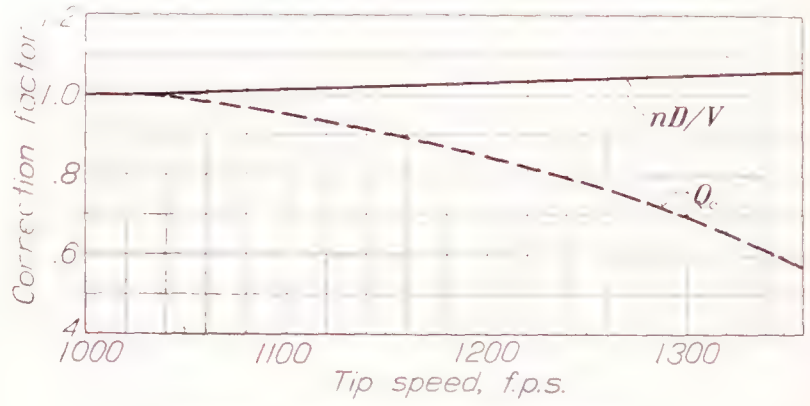

FIGURE 8.—Correction factors for tip speed.

Q_c at the corrected values of nD/V were plotted to give a conversion curve for Q_c. These conversion factors include both the influence of blade deformations with changing load and the influence of tip speed. They are shown in figure 8.

APPLICATION OF CHARTS TO THE CALCULATION OF TERMINAL VELOCITY

PRINCIPLES INVOLVED

The fundamental principles involved in any calculation of terminal velocity where propeller drag is to be taken into account are: (1) At terminal velocity the component of weight along the flight path must equal the total drag; (2) the shaft power of the propeller must equal that absorbed in friction by the engine. Obviously, the point of intersection of the curves of shaft power of the propeller and of power absorbed in friction by the engine, plotted against velocity, meets the conditions required.

Specifically, the following procedure is employed in the calculation of terminal velocity and engine speed:

1. Assume a series of terminal velocities in the interval given by the following formula whose solutions roughly approximate the F6C–4 data:

$$V_{t_{ind}}=K(0.0178\,\theta+0.89\pm0.05)$$

where $V_{t_{ind}}$ is the indicated terminal velocity, in miles per hour.

K, the indicated terminal velocity with zero thrust, in miles per hour.

θ, the difference, in degrees, between the normal high-speed blade-angle setting and that on which the calculations are based. The angle θ is positive when the blade-angle setting under consideration is larger than the normal setting.

2. Compute T_c for the series of assumed velocities from the formula

$$T_c=\frac{W\sin\gamma-C_{D_{min}}\frac{1}{2}\rho V^2S_w}{\rho V^2D^2}$$

3. At the appropriate blade-angle setting obtain from figure 7 the values of nD/V and Q_c corresponding to the computed thrust coefficients.

4. Compute the values of n from the known values of nD/V, D, and V.

5. Compute the propeller torques from the formula

$$Q=Q_c\rho V^2D^5$$

6. Using the computed values of Q and n, compute the shaft horsepower of the propeller from the formula

$$P=\frac{2\pi Qn}{550}$$

7. Plot the results from step 6 against those from step 1.

8. Plot the friction horsepower of the engine against the velocities of step 1.

The curve of power absorbed in friction by the engine against velocity is obtained from a curve of friction horsepower against engine speed using the values of n from step 4. The intersection of the two curves gives the point satisfying the conditions and is the calculated terminal velocity. The speed of the engine can be found by plotting the computed values of n against the assumed velocities and finding n existing at the calculated terminal velocity. The foregoing procedure involves no corrections for tip speed or mean blade-width ratio. The manner in which these corrections are applied is best shown by an illustrative example. A complete series of calculations will not be given but a sample computation using the final calculated terminal velocity for an F6C–4 airplane will be used.

ILLUSTRATIVE EXAMPLE

Given:

Airplane	F6C–4.
Weight (W)	2,830 lb.
Wing area (S_w)	252 sq. ft.
Minimum drag coefficient ($C_{D_{min}}$)	0.0513.
Engine	Pratt & Whitney R–1340–CD.

Friction-horsepower curve (fig. 9)

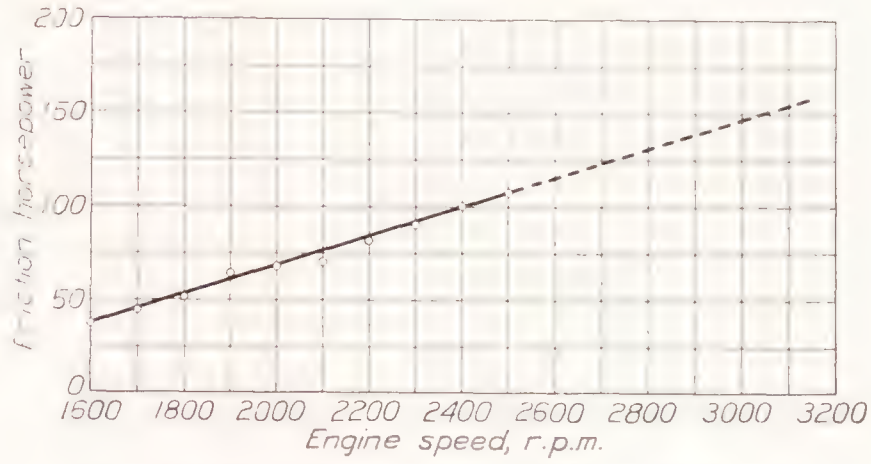

FIGURE 9.—Friction horsepower for P. & W. R–1340–CD engine.

Propeller:

Diameter (D)	9 ft.
Mean blade-width ratio	0.123.
Blade-angle setting at 0.75 R	19.0°.

It is required to find:

1. The indicated terminal velocity in a vertical dive ($\gamma=90°$) at 3,000 ft.
2. The propeller revolution speed at terminal velocity at this altitude.

Assume $V_{t_{ind}}=258.2$ m. p. h.
$=378.9$ f. p. s.
$q=170.6$ lb./sq. ft.

Negative propeller thrust, $T=W\sin\gamma-C_{D_{min}}qS_w$

$$T=2830\times1-0.0513\times170.6\times252=623\text{ lb.}$$

$$T_c=\frac{T}{\rho V^2D^2}=\frac{T}{2qD^2}=\frac{623}{2\times170.6\times81}=0.02252$$

T_c corrected to mean blade-width ratio of 0.1 to allow entry into charts $=\frac{0.1\times0.02252}{0.123}=0.01831$

$\frac{nD}{V}$ at $T_c=0.01831$ for 19.0° $=0.940$ (fig. 7).

$$n=\frac{0.940\times378.9}{9}\times\sqrt{\rho_0/\rho}=41.35\text{ r. p. s.}$$

$\sqrt{\rho_0/\rho}$ at 3,000-foot altitude $=1.045$ (reference 9).

Tip speed $=\sqrt{(\pi Dn)^2+\rho_0/\rho V_{t_{ind}}{}^2}=1{,}235$ f. p. s.

Correction factor for $\frac{nD}{V}=1.038$ (fig. 8).

Correction factor for $Q_c=0.80$ (fig. 8).

Corrected $\frac{(nD)}{V}=\frac{(nD)'}{V}=1.038\times0.940=0.975$.

Corrected $n=n'=1.038\times41.35=42.9$ r. p. s.
(r. p. m.)′ $=60\times42.9=2{,}575$.

Q_c at $\frac{(nD)'}{V}=0.00094$ (fig. 7).

Q_c corrected for tip speed $=0.80\times0.00094=0.000752$.

Q_c corrected to mean blade-width ratio, $0.123=\frac{0.123}{0.1}\times$

$0.000752=0.000925$.

$Q=Q_c\, 2q\, D^3=230$ lb.-ft.

Shaft horsepower of the propeller, $P=\frac{2\pi Qn'}{550}=113.0$.

At a value of n equal to 42.9 r. p. s. and an engine speed of 2,575 r. p. m., the horsepower absorbed in friction by the engine, using the engine friction-horsepower curve, is 113.5. Since the conditions of equilibrium are satisfied, i. e., the total drag equals the weight and the shaft horsepower of the propeller equals that absorbed by the engine, the indicated terminal velocity is 258.2 miles per hour and the engine speed is 2,575 r. p. m.

If, in the preceding example, the problem had been solved for a minimum altitude of 6,000 feet, the values for the indicated terminal velocity would have been 258.0 miles per hour, and the accompanying engine speed, 2,676 r. p. m. The influence of air density on the indicated terminal velocity is seen to be slight, but its influence is appreciable on the engine speed, which varies approximately inversely with the square root of the density.

It has been previously stated that errors in the friction-horsepower curve have but a small influence on the final result. A critical analysis, based on figure 7, of the interrelations of the several variables involved indicates that this statement is true for all reasonable cases. It is perhaps sufficient here, however, to point out that in figure 7 the steepness of the Q_c curves in the neighborhood of the dotted line indicates that fairly large variations of Q_c may occur without greatly affecting the engine speed at given values of D and V. At the same time, small variations in nD/V do not result in as large a change in thrust. Hence, it would be expected that quite large variations in friction horsepower can be taken up by the propeller without greatly affecting either the engine or the airplane speed. As an extreme example, if the friction horsepower of the engine used in the illustrative example is doubled, the terminal velocity is found to be 256 miles per hour and the engine speed about 2,400 r. p. m. These values compare with the original values of 258.2 miles per hour and 2,575 r. p. m., differing by 0.85 percent and 6.8 percent, respectively.

It has been found, in most cases, that the propeller operation in a throttled dive will be defined by characteristics falling close to the dotted lines of figure 7. To operate at greatly lower values of nD/V for any blade-angle setting would require an abnormally small propeller, while to operate at much higher values would require the application of engine power.

COMPARISON OF EXPERIMENTAL AND CALCULATED RESULTS

A comparison between the experimental and calculated results using the tip-speed corrections is made in table II. This comparison merely indicates the degree to which factors other than those included in the method of calculation affect the result. Part of the discrepancies are, however, attributable to experimental error. It will be seen that the percentage error in the terminal velocity is small, the maximum being 4.3 percent, while the average is less than half that value. The average errors in the engine speed are slightly higher, with the maximum error 6.8 percent. As these comparisons cover a wide range of blade-angle settings and dive angles, the agreement is considered to be reasonably good.

Table III includes a comparison between calculated and experimental results for three airplanes on which data were available. The agreement for airplanes A and B is good in regard both to terminal velocity and engine speed. These airplanes were somewhat similar to the F6C–4 airplane in their general features; in particular, the power plants were of the same type and the performances were similar. Hence, a good agreement between the calculated and experimental results on these airplanes was perhaps to be expected.

In the case of airplane C the agreement in terminal velocity is poor although the agreement in engine speed is fair. The experimental results indicate a very slight reduction in terminal velocity due to the propeller, whereas the calculated results indicate a reduction of the same order as those noted for the other airplanes listed. As far as can be determined, there is no unusual feature in airplane C to account for this discrepancy. The airplane minimum drag coefficients as determined from three independent sources agreed within 2 percent. Although the drag coefficient used in the calculations holds for a Reynolds Number corresponding to high-speed level flight and there is evidence that a reduction in drag coefficient with increasing Reynolds Number is to be expected, the influence of such a scale effect should not be felt in this case alone. In other words, the influence of scale effect is implicitly allowed for roughly in the method of calculation because of the empirical nature of the method. There is a possibility that the degree of turbulence in the slipstream with the propeller operating at negative thrust may have a critical effect on the drag of some parts of the structure within the slipstream. At the present state of knowledge it would be practically impossible to take such a phenomenon into account.

It is somewhat difficult, because of the lack of experimental cases, to say whether the method of calculation as presented will generally hold good. It is felt that within the following limitations the method will yield satisfactory results except in cases where unusual or unpredictable influences occur.

LIMITATIONS

1. The propeller-body combination should be approximately similar to that of the F6C–4.

2. Blade-angle settings should not be extrapolated, particularly in the low range.
3. Mean blade-width ratios should not be less than 0.09 nor more than 0.17.
4. The propeller blade sections should be based on either the Clark Y or RAF–6 sections and should be of normal thicknesses.
5. Tip-speed correction factors should not be extrapolated.

RULES OF THUMB

In calculated results for a number of airplanes of widely different characteristics, such as those listed in table III, consistent trends which indicate the feasibility of quick rules have been noted. Thus, the percentage reduction in terminal velocity caused by the propeller in a vertical dive with engine fully throttled and with normal blade-angle setting is given by the equation

$$R \text{ (percent)} = 0.011\ V_{t_0} + 9.7$$

in which V_{t_0} is the terminal velocity (m. p. h.) in a vertical dive with no thrust in standard sea-level conditions of atmosphere.

Engine speed (r. p. m.) is given by the equation

$$N = 15.6\ V_t - \frac{V_t^2}{45}$$

in which V_t is the terminal velocity with the foregoing correction for the propeller effect.

LANGLEY MEMORIAL AERONAUTICAL LABORATORY,
NATIONAL ADVISORY COMMITTEE FOR AERONAUTICS,
LANGLEY FIELD, VA., *August 22, 1933.*

REFERENCES

1. Durand, William F.: Experimental Research on Air Propellers. T. R. No. 14, N. A. C. A., 1917.
2. Durand, William F., and Lesley, E. P.: Experimental Research on Air Propellers, II. T. R. No. 30, N. A. C. A., 1920.
3. Anon.: Hamilton Standard Has Variable Pitch Propeller. The Aviation News (McGraw-Hill Co.), Oct. 18, 1930, p. 6.
4. Wood, Donald H.: Full-Scale Tests of Metal Propellers at High Tip Speeds. T. R. No. 375, N. A. C. A., 1931.
5. Diehl, Walter S.: Engineering Aerodynamics. The Ronald Press Co., 1928, p. 135.
6. Lock, C. N. H., and Bateman, H.: Airscrews at Negative Torque. R. & M. No. 1397, British A. R. C., 1931.
7. Hartman, Edwin P.: Negative Thrust and Torque Characteristics of an Adjustable-Pitch Metal Propeller. T. R. No. 464, N. A. C. A. 1933.
8. Munk, Max M.: The Determination of the Angles of Attack of Zero Lift and of Zero Moment, Based on Munk's Integrals. T. N. No. 122, N. A. C. A. 1923.
9. Diehl, Walter S.: Standard Atmosphere—Tables and Data. T. R. No. 218, N. A. C. A., 1925.

TABLE I

CHARACTERISTICS OF F6C–4 AIRPLANE

Type	Tractor biplane, landplane.
Engine	Pratt & Whitney, R–1340–CD.
Horsepower	450 at 2,100 r. p. m.
Weight (as flown)	2,815 and 2,830 lb.
Principal dimensions:	
Span (upper wing)	31 ft. 6 in.
Span (lower wing)	26 ft.
Length	22 ft. 6 in.
Height	9 ft. 6 in.
Total wing area	252 sq. ft.
Gap	4 ft. $5\frac{5}{16}$ in.
Stagger	3 ft. $2\frac{1}{2}$ in.
$C_{D_{min}}$ (from flight tests)	0.0513

TABLE II

COMPARISON BETWEEN CALCULATED AND CROSS-FAIRED EXPERIMENTAL VALUES

Dive angle (deg.)	Basic terminal velocity (m. p. h.)	Blade-angle setting at 0.75 R (deg.)	Indicated terminal velocity				Engine speed			
			Calculated (m. p. h.)	Experimental (m. p. h.)	Difference (m. p. h.)	Difference (percent)	Calculated (r. p. m.)	Experimental (r. p. m.)	Difference (r. p. m.)	Difference (percent)
90	290	22.5	271.2	263.0	8.2	3.1	2,272	2,320	−48	−2.1
90	290	19.0	258.7	257.0	1.7	.7	2,483	2,385	98	4.1
90	290	14.5	241.4	241.0	.4	.2	2,670	2,540	130	5.1
90	290	9.5	215.4	214.5	.9	.4	2,745	2,730	15	.5
90	290	5.5	195.0	190.0	5.0	2.6	2,713	2,680	33	1.2
59	270	22.5	252.3	242.0	10.3	4.3	2,114	2,160	−46	−2.1
59	270	19.0	240.8	239.5	1.3	.5	2,310	2,225	85	3.8
59	270	14.5	224.2	224.5	−.3	−.1	2,483	2,400	83	3.5
59	270	9.5	200.1	199.5	.6	.3	2,562	2,605	−43	−1.7
59	270	5.5	180.8	175.0	5.8	3.3	2,530	2,520	10	.4
47	250	22.5	233.6	225.0	8.6	3.8	1,953	1,980	−27	−1.4
47	250	19.0	223.1	224.0	−.9	−.4	2,140	2,055	85	4.1
47	250	14.5	207.9	209.0	−1.1	−.5	2,309	2,225	84	3.8
47	250	9.5	185.3	185.0	.3	.2	2,377	2,460	−83	−3.4
47	250	5.5	167.1	164.0	3.1	1.9	2,340	2,360	−20	−.8
38	230	22.5	214.1	208.0	6.1	2.9	1,786	1,780	6	.3
38	230	19.0	204.9	205.5	−.6	−.3	1,954	1,875	79	4.2
38	230	14.5	191.4	193.0	−1.6	−.8	2,117	2,085	32	1.5
38	230	9.5	170.5	172.0	1.5	−.9	2,177	2,295	−118	5.1
38	230	5.5	153.4	153.0	.4	.3	2,124	2,215	−91	−4.1
31.75	210	22.5	196.7	194.0	2.7	1.4	1,640	1,585	55	3.5
31.75	210	19.0	187.8	190.0	−2.2	−1.2	1,785	1,700	85	5.0
31.75	210	14.5	175.6	181.0	−5.4	−3.0	1,930	1,925	5	.3
31.75	210	9.5	156.6	160.0	−3.4	−2.1	1,995	2,140	−145	−6.8
31.75	210	5.5	141.0	142.0	−1.0	.7	1,951	2,060	−109	−5.3

TABLE III

COMPARISON OF CALCULATED AND EXPERIMENTAL RESULTS

Airplane	Engine type and power	Sea-level high speed (m.p.h.)	Propeller diameter (ft.)	Mean blade-width ratio	Blade-angle setting at 0.75 R (deg.)	Dive angle (deg.)	$V_{t_{ind}}$ (sea level) zero thrust (m.p.h.)	$V_{t_{ind}}$ (sea level) closed throttle (m.p.h.)	R.p.m. (sea level) closed throttle	Percentage reduction due to propeller	Experimental $V_{t_{ind}}$ (sea level) closed throttle (m.p.h.)	Experimental r. p. m. (sea level) closed throttle	Percentage error in calculated $V_{t_{ind}}$	Percentage error in calculated r. p. m.
A	P & Ww 450–2,100	140	9	0.1285	17.0	90	288.0	253.3	2,600	12.0	258.0	2,600	−1.8	0
B	P & Ww 450–2,100	160	9	.125	18.0	90	290.5	254.7	2,528	12.3	255.0	[1] 2,500	−.1	1.1
B	P & Ww 450–2,100	160	9	.138	18.0	90	290.5	252.0	2,520	13.2	255.0	[1] 2,500	−1.2	.8
C [2]	P & Wh 575–2,100	131	10	.134	16.0	41	246.3	219.4	2,260	10.9	238.0	2,200	−7.8	2.7
D	Wright R–1510	194	8.5	.166	26.0	90	416.0	361.5	2,720	13.1				
E	Wright R–1820 F1	201	9.5	.129	23.3	90	430.0	371.5	2,775	13.6				

[1] Indicated r. p. m

[2] Calculations made for 4,000 feet.

REPORT No. 600

AN ANALYSIS OF THE FACTORS THAT DETERMINE THE PERIODIC TWIST OF AN AUTOGIRO ROTOR BLADE, WITH A COMPARISON OF PREDICTED AND MEASURED RESULTS

By JOHN B. WHEATLEY

SUMMARY

An analysis is presented of the factors that determine the periodic twist of a rotor blade under the action of the air forces on it. The results of the analysis show that the Fourier coefficients of the twist are linear expressions involving only the tip-speed ratio, the pitch setting, the inflow coefficient, the pitching-moment coefficient of the blade airfoil section, and the physical characteristics of the rotor blade and machine. The validity of the analysis was examined by using it to predict the twist of a rotor whose twist characteristics had previously been measured in flight. The agreement between the calculated and experimental results was satisfactory. An examination of the assumption used in the analysis—that the twist is a linear function of the radius—disclosed that the approximation introduced no appreciable error. From this examination, a formula for the torsional rigidity of the rotor blade was derived.

INTRODUCTION

The development of the wingless direct-control autogiro has been hampered by a number of secondary difficulties. Probably the most troublesome are the avoidance of excessive or unstable center-of-pressure travel in the rotor and the elimination of rotor and control-stick vibrations. The production of a few designs that are satisfactory in these respects has demonstrated that the difficulties are the designer's problem and are not inherent in the direct-control type of rotor; however, the large number of unsuccessful machines is evidence that the basic factors controlling the behavior of the rotor are as yet not clearly understood.

A general survey of the problem indicated that both center-of-pressure travel and rotor vibrations are markedly affected by the periodic twist of the rotor blade arising from the interaction of air forces, elastic forces, and inertia forces during the flapping oscillation. It was accordingly decided that the factors controlling this twist must be understood before any real attack on the initial problems would be fruitful. This paper presents an analysis of periodic blade twist in which the factors controlling the twist are studied. The analysis is supported by a comparison of predicted and measured twist on a direct-control type of autogiro.

ANALYSIS

The motion of an autogiro rotor blade consists chiefly of rotation about the rotor axis, oscillation about the flapping hinge, and oscillation in twist about the blade-span axis. Additional components of the motion are oscillation as a pendulum in the plane of the rotor disk about a second hinge and oscillation in bending in a plane containing the blade span and the rotor axis. Experimental evidence has shown that these additional components have only a second-order influence on the air forces acting on the rotor blade, and they will consequently be neglected in the subsequent discussion.

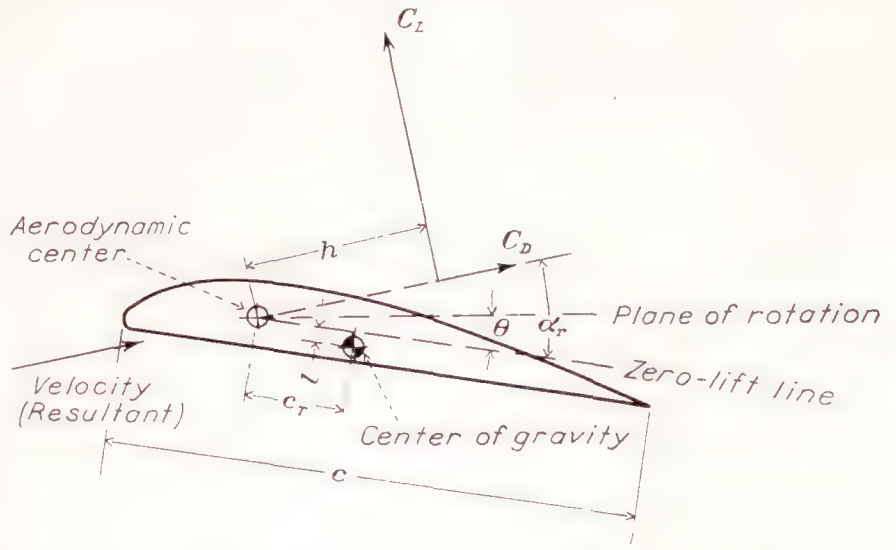

FIGURE 1.—Force diagram of autogiro rotor-blade element.

The coefficients of the air-twisting forces on an element of the autogiro rotor blade are diagrammed in figure 1. In general, the air forces on an airfoil will not pass through the aerodynamic center but will assume such a position that the moment of the air forces expressed in coefficient form is constant about the aerodynamic center. The component of the centrifugal force normal to the blade and the inertia forces of the blade pass through the center of gravity of the blade. Then the moment of the air forces about the center of gravity is the twisting moment on the blade. Let C_M be the moment coefficient of the air forces about the center of gravity; then from figure 1

$$C_M=-C_L\left(\frac{h}{c}-\frac{c_T}{c}\cos\alpha_r+\frac{l}{c}\sin\alpha_r\right)+C_D\left(\frac{c_T}{c}\sin\alpha_r+\frac{l}{c}\cos\alpha_r\right) \quad (1)$$

where the symbols are defined by figure 1; c_T is positive when the center of gravity is farther from the leading edge than the aerodynamic center, and l is positive when the center of gravity is below the aerodynamic center.

From the definition of moment about the aerodynamic center, if h is positive from the aerodynamic center toward the trailing edge,

$$h=\frac{-C_m c}{C_L} \tag{2}$$

where C_m is the coefficient of the moment about the aerodynamic center. Then

$$C_M=C_m+\frac{c_T}{c}(C_L\cos\alpha_r+C_D\sin\alpha_r)-\frac{l}{c}(C_L\sin\alpha_r-C_D\cos\alpha_r) \tag{3}$$

It will be assumed that α_r is sufficiently small that the cosine differs negligibly from unity and the sine can be equated to the angle; also, C_L will be assumed a linear function of the angle of attack. These assumptions do not accurately represent the conditions in the rotor when the resultant velocity is small and the angle of attack high, but the error introduced by them has been found to be small (reference 1). Then

$$C_M=C_m+\alpha_r\frac{c_T}{c}(a+C_D)-\frac{l}{c}(a\alpha_r{}^2-C_D) \tag{4}$$

where a is the lift-curve slope (in radian measure).

The lift-curve slope a at infinite aspect ratio lies between 5.8 and 5.9 for most airfoil sections. Inasmuch as C_D will have actual values varying from 0.009 to 0.03 below the stall, with a weighted average of about 0.015, it is thought unnecessary to use the C_D term in the expression for C_M. In addition, l/c will normally be less than 0.02 and $(a\alpha_r{}^2—C_D)$ will be of the same order of magnitude; the l/c term will consequently be dropped.

From reference 1, if xR be substituted for r, the nondimensional velocity components at the blade element of an autogiro rotor traveling at a speed V equal to $\mu\Omega R/\cos\alpha$ are:

$$u_T=\frac{U_T}{\Omega R}=x+\mu\sin\psi \tag{5}$$

$$\left.\begin{aligned}u_P=\frac{U_P}{\Omega R}=\lambda+\frac{1}{2}\mu a_1+\left(-\mu a_0+xb_1+\frac{1}{2}\mu a_2\right)\cos\psi+\left(-xa_1+\frac{1}{2}\mu b_2\right)\sin\psi+\left(\frac{1}{2}\mu a_1+2xb_2\right)\cos 2\psi\\+\left(\frac{1}{2}\mu b_1-2xa_2\right)\sin 2\psi+\frac{1}{2}\mu a_2\cos 3\psi+\frac{1}{2}\mu b_2\sin 3\psi\end{aligned}\right\} \tag{6}$$

where u_T is the component of the resultant velocity perpendicular to the blade-span axis and to the rotor axis, u_P is the component of the resultant velocity perpendicular to the blade-span axis and to u_T, and ψ is the azimuth angle of the blade from its down-wind position. Also

$$u_T{}^2=x^2+\frac{1}{2}\mu^2+2\mu x\sin\psi-\frac{1}{2}\mu^2\cos 2\psi \tag{7}$$

$$\left.\begin{aligned}u_Tu_P=x\lambda+\frac{1}{4}\mu^2b_2+\left(-\mu xa_0+b_1\left[x^2+\frac{1}{4}\mu^2\right]-\frac{1}{2}\mu xa_2\right)\cos\psi+\left(\mu\lambda-a_1\left[x^2-\frac{1}{4}\mu^2\right]-\frac{1}{2}\mu xb_2\right)\sin\psi\\+\left(\mu xa_1+2x^2b_2\right)\cos 2\psi+\left(-\frac{1}{2}\mu^2a_0+\mu xb_1-2x^2a_2\right)\sin 2\psi+\left(-\frac{1}{4}\mu^2b_1+\frac{3}{2}\mu xa_2\right)\cos 3\psi\\+\left(\frac{1}{4}\mu^2a_1+\frac{3}{2}\mu xb_2\right)\sin 3\psi-\frac{1}{4}\mu^2b_2\cos 4\psi+\frac{1}{4}\mu^2a_2\sin 4\ \psi\end{aligned}\right\} \tag{8}$$

The acute angle β between the blade and the plane perpendicular to the rotor axis is described by the expression

$$\beta=a_0-a_1\cos\psi-b_1\sin\psi-a_2\cos 2\psi-b_2\sin 2\psi-\ldots \tag{9}$$

The notation of reference 1 will be used throughout this analysis; a list of symbols employed and of their definitions is given at the end of this section.

The calculation of the air-twisting moment M_Q at the hub end of the blade will be made on the assumption that the air forces lie in a plane perpendicular to the blade span and depend only upon the resultant velocity in that plane. The angle φ between the resultant velocity and the plane perpendicular to the rotor axis will be assumed equal to its sine and tangent, and to have a cosine of unity. On this basis, the angle of attack of a blade element is

$$\alpha_r=\varphi+\theta=\frac{u_P}{u_T}+\theta \tag{10}$$

where θ is the pitch angle of the blade, measured as the acute angle between the plane perpendicular to the rotor axis and the zero-lift line of the blade airfoil section.

The pitch of the rotor blade will be the sum of the pitch setting and the instantaneous value of the angle of twist to which the blade is deflected by the twisting moment. If the pitch setting is given as $\theta_0+x\theta_1$ and it is assumed that the twist is a linear function of the radius, the pitch angle θ may be expressed in the form

$$\theta=\theta_0+x\theta_1+x\epsilon_0+x\epsilon_1\cos\psi+x\eta_1\sin\psi+x\epsilon_2\cos 2\psi+x\eta_2\sin 2\psi+\ldots \tag{11}$$

The use of a Fourier series in ψ for the angle of twist is justified, as it was for the flapping angle β, by the fact that the twist angle must be a repeated function of ψ. Some question concerning the assumption that the twist is linear along the radius naturally arises; the problem will subequently be examined in more detail.

The air-twisting moment at the blade hub can now be expressed in integral form as

$$M_Q=\int_0^B\frac{1}{2}\rho\Omega^2R^3u_T^2C_Mc^2dx \tag{12}$$

The integration is performed from B to 0 (where B is arbitrarily assigned the value $1-c/2R$) to allow for tip losses. Substituting for C_M from (4)

$$M_Q=\int_0^B\frac{1}{2}\rho\Omega^2R^3c^2u_T^2\left(C_m+a\alpha_r\frac{c_T}{c}\right)dx \tag{13}$$

Expression (10) for a_r can now be used

$$M_Q=\int_0^B\frac{1}{2}\rho\Omega^2R^3c^2u_T^2\left(C_m+a\frac{c_T}{c}\left[\frac{u_P}{u_T}+\theta\right]\right)dx \tag{14}$$

Substitute for θ, u_T^2 and $u_T\,u_P$; then integrate and collect; and

$$\begin{aligned}M_Q=\frac{1}{2}\rho\Omega^2R^3cac_T\Bigg\{&\left(\frac{1}{2}\lambda B^2+\theta_0\left[\frac{1}{3}B^3+\frac{1}{2}\mu^2B\right]+\theta_1\left[\frac{1}{4}B^4+\frac{1}{4}\mu^2B^2\right]+\frac{1}{4}\mu^2b_2B+\epsilon_0\left[\frac{1}{4}B^4+\frac{1}{4}\mu^2B^2\right]+\frac{1}{3}\mu\eta_1B^3-\frac{1}{8}\mu^2\epsilon_2B^2\right.\\
&\left.+\frac{C_mc}{ac_T}\left[\frac{1}{3}B^3+\frac{1}{2}\mu^2B\right]\right)+\left(-\frac{1}{2}\mu a_0B^2+b_1\left[\frac{1}{3}B^3+\frac{1}{4}\mu^2B\right]-\frac{1}{4}\mu a_2B^2+\epsilon_1\left[\frac{1}{4}B^4+\frac{1}{8}\mu^2B^2\right]+\frac{1}{3}\mu\eta_2B^3-\frac{1}{8}\mu^2\epsilon_3B^2\right)\cos\psi\\
&+\left(\mu\lambda B+\mu\theta_0B^2+\frac{2}{3}\mu\theta_1B^3-a_1\left[\frac{1}{3}B^3-\frac{1}{4}\mu^2B\right]-\frac{1}{4}\mu b_2B^2+\frac{2}{3}\mu\epsilon_0B^3+\eta_1\left[\frac{1}{4}B^4+\frac{3}{8}\mu^2B^2\right]\right.\\
&\left.-\frac{1}{3}\mu\epsilon_2B^3-\frac{1}{8}\mu^2\eta_3B^2+\mu\frac{C_mc}{ac_T}B^2\right)\sin\psi+\left(-\frac{1}{2}\mu^2\theta_0B-\frac{1}{4}\mu^2\theta_1B^2+\frac{1}{2}\mu a_1B^2+\frac{2}{3}b_2B^3\right.\\
&\left.-\frac{1}{4}\mu^2\epsilon_0B^2-\frac{1}{3}\mu\eta_1B^3+\epsilon_2\left[\frac{1}{4}B^4+\frac{1}{4}\mu^2B^2\right]+\frac{1}{3}\mu\eta_3B^3-\frac{1}{2}\mu^2\frac{C_mc}{ac_T}B\right)\cos 2\psi\\
&+\left(-\frac{1}{2}\mu^2a_0B+\frac{1}{2}\mu b_1B^2-\frac{2}{3}a_2B^3+\frac{1}{3}\mu\epsilon_1B^3+\eta_2\left[\frac{1}{4}B^4+\frac{1}{4}\mu^2B^2\right]-\frac{1}{3}\mu\epsilon_3B^3\right)\sin 2\psi\\
&+\left(-\frac{1}{4}\mu^2b_1B+\frac{3}{4}\mu a_2B^2-\frac{1}{8}\mu^2\epsilon_1B^2-\frac{1}{3}\mu\eta_2B^3+\epsilon_3\left[\frac{1}{4}B^4+\frac{1}{4}\mu^2B^2\right]\right)\cos 3\psi\\
&+\left(\frac{1}{4}\mu^2a_1B+\frac{3}{4}\mu b_2B^2-\frac{1}{8}\mu^2\eta_1B^2+\frac{1}{3}\mu\epsilon_2B^3+\eta_3\left[\frac{1}{4}B^4+\frac{1}{4}\mu^2B^2\right]\right)\sin 3\psi\Bigg\}\end{aligned} \tag{15}$$

In order to examine the variation of blade twist with radius, it is necessary first to establish an expression for the total air-twisting moment M_{Q_x} outboard of any station x. This moment can be expressed simply as

$$M_{Q_x}=\int_x^B\frac{1}{2}\rho\Omega^2R^3c^2u_T^2\left(C_m+a\frac{c_T}{c}\left[\frac{u_P}{u_T}+\theta\right]\right)dx \tag{16}$$

Substituting as in (14) and integrating

$$\left.\begin{aligned}M_{Q_x}=\frac{1}{2}\rho\Omega^2R^3cac_T\Bigg\{&\left(\mu^2\left[\frac{1}{2}\theta_0+\frac{1}{4}b_2+\frac{1}{2}\frac{C_mc}{ac_T}\right][B-x]+\left[\frac{1}{2}\lambda+\frac{1}{4}\mu^2\theta_1+\frac{1}{4}\mu^2\epsilon_0-\frac{1}{8}\mu^2\epsilon_2\right][B^2-x^2]+\left[\frac{1}{3}\theta_0+\frac{1}{3}\frac{C_mc}{ac_T}+\frac{1}{3}\mu\eta_1\right]\right.\\
&[B^3-x^3]+\left[\frac{1}{4}\theta_1+\frac{1}{4}\epsilon_0\right][B^4-x^4]\Big)+\Big(\frac{1}{4}\mu^2b_1[B-x]+\Big[-\frac{1}{2}\mu a_0-\frac{1}{4}\mu a_2+\frac{1}{8}\mu^2\epsilon_1-\frac{1}{8}\mu^2\epsilon_3\Big][B^2-x^2]\\
&+\left[\frac{1}{3}b_1+\frac{1}{3}\mu\eta_2\right][B^3-x^3]+\frac{1}{4}\epsilon_1[B^4-x^4]\Big)\cos\psi+\Big(\Big[\mu\lambda+\frac{1}{4}\mu^2a_1\Big][B-x]+\mu\Big[\theta_0-\frac{1}{4}b_2+\frac{C_mc}{ac_T}+\frac{3}{8}\mu\eta_1-\frac{1}{8}\mu^2\eta_3\Big]\\
&[B^2-x^2]+\Big[-\frac{1}{3}a_1+\frac{2}{3}\mu\theta_1+\frac{2}{3}\mu\epsilon_0-\frac{1}{3}\mu\epsilon_2\Big][B^3-x^3]+\frac{1}{4}\eta_1[B^4-x^4]\Big)\sin\psi+\Big(\mu^2\Big[-\frac{1}{2}\theta_0-\frac{1}{2}\frac{C_mc}{ac_T}\Big][B-x]\\
&+\Big[-\frac{1}{4}\mu^2\theta_1-\frac{1}{4}\mu^2\epsilon_0+\frac{1}{2}\mu a_1+\frac{1}{4}\mu^2\epsilon_2\Big][B^2-x^2]+\Big[\frac{2}{3}b_2-\frac{1}{3}\mu\eta_1+\frac{1}{3}\mu\eta_3\Big][B^3-x^3]+\frac{1}{4}\epsilon_2[B^4-x^4]\Big)\cos2\psi\\
&+\Big(-\frac{1}{2}\mu^2a_0[B-x]+\Big[\frac{1}{2}\mu b_1+\frac{1}{4}\mu^2\eta_2\Big][B^2-x^2]+\Big[-\frac{2}{3}a_2+\frac{1}{3}\mu\epsilon_1-\frac{1}{3}\mu\epsilon_3\Big][B^3-x^3]+\frac{1}{4}\eta_2[B^4-x^4]\Big)\sin2\psi\\
&+\Big(-\frac{1}{4}\mu^2b_1[B-x]+\Big[\frac{3}{4}\mu a_2-\frac{1}{8}\mu^2\epsilon_1+\frac{1}{4}\mu^2\epsilon_3\Big][B^2-x^2]-\frac{1}{3}\mu\eta_2[B^3-x^3]+\frac{1}{4}\epsilon_3[B^4-x^4]\Big)\cos3\psi\\
&+\Big(\frac{1}{4}\mu^2a_1[B-x]+\Big[\frac{3}{4}\mu b_2-\frac{1}{8}\mu^2\eta_1+\frac{1}{4}\mu^2\eta_3\Big][B^2-x^2]+\frac{1}{3}\mu\epsilon_2[B^3-x^3]+\frac{1}{4}\eta_3[B^4-x^4]\Big)\sin3\psi\Bigg\}\end{aligned}\right\}\tag{17}$$

The torsional deflection of the rotor blade can now be determined. Let G designate a twisting moment that is distributed along the radius in the same manner as M_{Q_x} and is of such magnitude that the blade tip is deflected through 1 radian; then denoting the instantaneous torsional deflection at the tip of the blade by v

$$q\frac{d^2v}{dt^2}+Gv=M_Q \tag{18}$$

where q is the equivalent moment of inertia of the blade about the elastic axis and

$$v=\epsilon_0+\epsilon_1\cos\psi+\eta_1\sin\psi+\epsilon_2\cos2\psi+\eta_2\sin2\psi+\ldots \tag{19}$$

The value of q may be arrived at by considering the problem to be that of the torisonal deflection of a bar connecting two masses having moments of inertia of infinity and zero. The system then has but one degree of freedom and only principal modes of vibration will be assumed existent. Rayleigh's approximation to the exact solution of the problem (reference 2, p. 59), which is sufficiently accurate for use here, is

$$q=\frac{1}{3}il \tag{20}$$

where i is the moment of inertia of the bar per unit length, and l is the length of the bar.

For a particular case, $i=0.0050$, $l=20$, $G=1{,}700$, and $\Omega=21$; then $q=0.0333$ and $\Omega^2q=14.7$. It is seen that 4 Ω^2q and even 9 Ω^2q are quite small in comparison with G; consequently inertia effects on the torsional vibration will be neglected. Then

$$\left.\begin{aligned}&G\{\epsilon_0+\epsilon_1\cos\psi+\eta_1\sin\psi+\epsilon_2\cos2\psi+\eta_2\sin2\psi+\epsilon_3\cos3\psi+\eta_3\sin3\psi\}\\
&=\frac{1}{2}\rho\Omega^2R^3cac_T\Bigg\{\left(\frac{1}{2}\lambda B^2+\theta_0\left[\frac{1}{3}B^3+\frac{1}{2}\mu^2B\right]+\theta_1\left[\frac{1}{4}B^4+\frac{1}{4}\mu^2B^2\right]+\frac{1}{4}\mu^2b_2B+\epsilon_0\left[\frac{1}{4}B^4+\frac{1}{4}\mu^2B^2\right]+\frac{1}{3}\mu\eta_1B^3-\frac{1}{8}\mu^2\epsilon_2B^2\right.\\
&\left.+\frac{C_mc}{ac_T}\left[\frac{1}{3}B^3+\frac{1}{2}\mu^2B\right]\right)+\left(-\frac{1}{2}\mu a_0B^2+b_1\left[\frac{1}{3}B^3+\frac{1}{4}\mu^2B\right]-\frac{1}{4}\mu a_2B^2+\epsilon_1\left[\frac{1}{4}B^4+\frac{1}{8}\mu^2B^2\right]+\frac{1}{3}\mu\eta_2B^3-\frac{1}{8}\mu^2\epsilon_3B^2\right]\cos\psi\\
&+\Big(\mu\lambda B+\mu\theta_0B^2+\frac{2}{3}\mu\theta_1B^3-a_1\Big[\frac{1}{3}B^3-\frac{1}{4}\mu^2B\Big]-\frac{1}{4}\mu b_2B^2+\frac{2}{3}\mu\epsilon_0B^3+\eta_1\Big[\frac{1}{4}B^4+\frac{3}{8}\mu^2B^2\Big]-\frac{1}{3}\mu\epsilon_2B^3-\frac{1}{8}\mu^2\eta_3B^2\\
&+\mu\frac{C_mc}{ac_T}B^2\Big)\sin\psi+\Big(-\frac{1}{2}\mu^2\theta_0B-\frac{1}{4}\mu^2\theta_1B^2+\frac{1}{2}\mu a_1B^2+\frac{2}{3}b_2B^3-\frac{1}{4}\mu^2\epsilon_0B^2-\frac{1}{3}\mu\eta_1B^3+\epsilon_2\Big[\frac{1}{4}B^4+\frac{1}{4}\mu^2B^2\Big]\\
&+\frac{1}{3}\mu\eta_3B^3-\frac{1}{2}\mu^2\frac{C_mc}{ac_T}B\Big)\cos2\psi+\Big(-\frac{1}{2}\mu^2a_0B+\frac{1}{2}\mu b_1B^2-\frac{2}{3}a_2B^3+\frac{1}{3}\mu\epsilon_1B^3+\eta_2\Big[\frac{1}{4}B^4+\frac{1}{4}\mu^2B^2\Big]-\frac{1}{3}\mu\epsilon_3B^3\Big)\sin2\psi\\
&+\Big(-\frac{1}{4}\mu^2b_1B+\frac{3}{4}\mu a_2B^2-\frac{1}{8}\mu^2\epsilon_1B^2-\frac{1}{3}\mu\eta_2B^3+\epsilon_3\Big[\frac{1}{4}B^4+\frac{1}{4}\mu^2B^2\Big]\Big)\cos3\psi\\
&+\Big(\frac{1}{4}\mu^2a_1B+\frac{3}{4}\mu b_2B^2-\frac{1}{8}\mu^2\eta_1B^2+\frac{1}{3}\mu\epsilon_2B^3+\eta_3\Big[\frac{1}{4}B^4+\frac{1}{4}\mu^2B^2\Big]\Big)\sin3\psi\Bigg\}\end{aligned}\right\}\tag{21}$$

The expressions for the thrust and the flapping-motion coefficients have been established in reference 3 for the rotor with varying twist; they are:

$$\left.\begin{aligned} T=\frac{1}{2}bc\rho a\Omega^2R^3\Big\{&\frac{1}{2}\lambda\Big(B^2+\frac{1}{2}\mu^2\Big)+\theta_0\Big(\frac{1}{3}B^3+\frac{1}{2}\mu^2B-\frac{4}{9\pi}\mu^3\Big)+\theta_1\Big(\frac{1}{4}B^4+\frac{1}{4}\mu^2B^2-\frac{1}{32}\mu^4\Big)+\frac{1}{8}\mu^3a_1\\ &+\frac{1}{4}\mu^2b_2B+\epsilon_0\Big(\frac{1}{4}B^4+\frac{1}{4}\mu^2B^2-\frac{1}{32}\mu^4\Big)+\frac{1}{3}\mu\eta_1B^3-\frac{1}{8}\mu^2\epsilon_2B^2\Big\}\end{aligned}\right\}\quad(22)$$

$$\left.\begin{aligned} a_0=\frac{1}{2}\gamma\Big\{&\lambda\Big(\frac{1}{3}B^3+0.080\mu^3\Big)+\theta_0\Big(\frac{1}{4}B^4+\frac{1}{4}\mu^2B^2-\frac{1}{32}\mu^4\Big)+\theta_1\Big(\frac{1}{5}B^5+\frac{1}{6}\mu^2B^3\Big)+\frac{1}{8}\mu^2b_2B^2\\ &+\epsilon_0\Big(\frac{1}{5}B^5+\frac{1}{6}\mu^2B^3\Big)+\frac{1}{4}\mu\eta_1B^4-\frac{1}{12}\mu^2\epsilon_2B^3\Big\}-\frac{M_W}{I_1\Omega^2}\end{aligned}\right\}\quad(23)$$

$$a_1=-\frac{2\mu}{B^4-\frac{1}{2}\mu^2B^2}\Big\{\lambda\Big(B^2-\frac{1}{4}\mu^2\Big)+\theta_0\Big(\frac{4}{3}B^3+0.106\mu^3\Big)+\theta_1B^4-\frac{1}{3}b_2B^3+\epsilon_0B^4+\frac{\eta_1}{\mu}\Big(\frac{2}{5}B^5+\frac{1}{2}\mu^2B^3\Big)-\frac{1}{2}\epsilon_2B^4\Big\}\quad(24)$$

$$b_1=\frac{4\mu}{B^4+\frac{1}{2}\mu^2B^2}\Big\{a_0\Big(\frac{1}{3}B^3+0.035\mu^3\Big)+\frac{1}{6}a_2B^3-\frac{\epsilon_1}{\mu}\Big(\frac{1}{5}B^5+\frac{1}{12}\mu^2B^3\Big)-\frac{1}{4}\eta_2B^4\Big\}\quad(25)$$

$$\left.\begin{aligned} a_2=\frac{\mu^2\gamma}{\gamma^2B^8+144}\Big\{&\lambda B\Big(16+\frac{7\gamma^2B^8}{108}\Big)+\theta_0B^2\Big(\frac{46}{3}+\frac{7\gamma^2B^8}{144}\Big)+\theta_1B^3\Big(12+\frac{7\gamma^2B^8}{180}\Big)+\epsilon_0B^3\Big(12+\frac{7\gamma^2B^8}{180}\Big)\\ &-\frac{1}{30}\frac{\epsilon_1}{\mu}\gamma B^8+\frac{2}{5}\frac{\eta_1}{\mu}B^4+\frac{24}{5}\frac{\epsilon_2}{\mu^2}B^5+\frac{2}{5}\frac{\eta_2}{\mu^2}\gamma B^9\Big\}\end{aligned}\right\}\quad(26)$$

$$b_2=\frac{-\mu^2\gamma^2}{\gamma^2B^8+144}\Big\{\frac{5}{9}\lambda B^5+\frac{25}{36}\theta_0B^6+\frac{8}{15}\theta_1B^7+\frac{8}{15}\epsilon_0B^7+\frac{2}{5\gamma}\frac{\epsilon_1}{\mu}B^4+\frac{1}{30}\frac{\eta_1}{\mu}B^8+\frac{2}{5}\frac{\epsilon_2}{\mu^2}B^9-\frac{24}{5\gamma}\frac{\eta_2}{\mu^2}B^5\Big\}\quad(27)$$

It will be expedient to substitute average values for B and γ in a_2 and b_2; in actuality, B will be but little different from 0.970 for solidities near 0.05, and γ will be between 10 and 18 for present rotor blades. The assumption that B is 0.970 and that γ is 15.0 will accordingly introduce little error. The substitution will be made in such a way that the resultant expressions will be linear, and the coefficients of λ, θ, ϵ, and η will have the same form and exponents as the similar factors already present in the expressions for the twisting moment and the flapping motion. Examination of these equations discloses that the consequent forms for a_2 and b_2 are:

$$\left.\begin{aligned} a_2=&\mu^2\{0.0854\gamma\lambda B+0.0746\gamma\theta_0B^2+0.0588\gamma(\theta_1+\epsilon_0)B^3\}\\ &+\mu\{-0.0184\epsilon_1+0.0012\gamma\eta_1B^4\}+0.0150\gamma\epsilon_2B^5+0.2200\eta_2B\end{aligned}\right\}(28)$$

$$\left.\begin{aligned} b_2=&-\mu^2\{0.306\lambda B^{-3}+0.382\theta_0B^{-2}+0.294(\theta_1+\epsilon_0)B^{-1}\}\\ &-\mu\Big\{\frac{0.2200}{\gamma}\epsilon_1B^{-4}+0.0184\eta_1\Big\}-0.2200\epsilon_2B+\frac{2.650}{\gamma}\eta_2B^{-3}\end{aligned}\right\}(29)$$

Inspection of (26), (27), (28), and (29) shows that substitution for γ^2B^8 has been made in the denominator of (26) and (27), and in the numerator of (26) whenever γ has been raised higher than the first power. The quantity in braces of (27) has been divided by B^8 and the resultant γ^2B^8 outside the braces has been evaluated.

The solution of equation (21) for ϵ and η now will follow, after substituting for the a and b coefficients, by equating the coefficients of identical trigonometric terms in (21). Before this operation is performed, the work may be simplified to some extent by considering the order of accuracy required in the substitution.

It has already been shown (reference 1) that the expressions for the thrust and torque are evaluated to a sufficiently high order of μ (the fourth) if a_0, a_2, and b_2 are expressed to the order μ^2 and a_1 and b_1 to the order μ^3. Reference 3 shows that the same order of accuracy for the thrust and torque will be obtained if ϵ_0 is evaluated to μ^4, ϵ_1 and η_1 to μ^3, and ϵ_2 and η_2 to μ^2. The coefficients ϵ_3 and η_3 do not, to the order of μ^4, influence the thrust and torque. Reference to equation (21) establishes that ϵ_n and η_n are of the order μ^n, a fact that has already been implied by the form of the expressions for a_2 and b_2.

It is seen now that a_1 and b_1 may be expanded in a linear form which is developed only to the μ^3 order and that all terms in a_0 above the order μ^2 may be dropped. Then, substituting for a_2 and b_2,

$$a_0=\frac{1}{6}\gamma\lambda B^3+\gamma\theta_0\Big(\frac{1}{8}B^4+\frac{1}{8}\mu^2B^2\Big)+\gamma(\theta_1+\epsilon_0)\Big(\frac{1}{10}B^5+\frac{1}{12}\mu^2B^3\Big)+\frac{1}{8}\mu\gamma\eta_1B^4\quad(30)$$

$$\left.\begin{aligned} a_1 = {} & \mu\lambda\left(\frac{2}{B^2}+\frac{0.704\mu^2}{B^4}\right)+\mu\theta_0\left(\frac{8}{3B}+\frac{1.588\mu^2}{B^3}\right)+\mu(\theta_1+\epsilon_0)\left(2+\frac{1.196\mu^2}{B^2}\right)+\frac{0.147}{\gamma B^5}\mu^2\epsilon_1+\eta_1\left(\frac{4}{5}B+\frac{1.412\mu^2}{B}\right) \\ & -0.853\mu\epsilon_2-\frac{1.768}{\gamma B^4}\mu\eta_2 \end{aligned}\right\} \tag{31}$$

$$\left.\begin{aligned} b_1 = {} & \mu\gamma\lambda\left(\frac{2}{9}B^2-0.0542\mu^2\right)+\mu\gamma\theta_0\left(\frac{1}{6}B^3+0.1330\mu^2B\right)+\mu\gamma(\theta_1+\epsilon_0)\left(\frac{2}{15}B^4+0.0836\mu^2B^2\right)-\epsilon_1\left(\frac{4}{5}B-0.055\frac{\mu^2}{B}\right) \\ & +0.1676\mu^2\gamma\eta_1B^3+0.0100\mu\gamma\epsilon_2B^4-0.853\mu\eta_2 \end{aligned}\right\} \tag{32}$$

The term $M_W/I_1\Omega^2$ in a_0 has been neglected, since it amounts to 2 percent or less of a_0.

Substitute for a_0, a_1, b_1, a_2, and b_2 in (21); there results a set of linear equations in ϵ and η that can be solved in succession by starting with the highest order. Thus, from the coefficient of cos 3ψ,

$$\left.\begin{aligned} G\epsilon_3 = {} & \frac{1}{2}\rho\Omega^2R^3cac_T\{0.0085\mu^3\gamma\lambda B^3+0.0143\mu^3\gamma\theta_0B^4+0.0108\mu^3\gamma(\theta_1+\epsilon_0)B^5+0.0621\mu^2\epsilon_1B^2+0.0009\mu^2\gamma\eta_1B^6 \\ & +0.0112\mu\gamma\epsilon_2B^7-0.1683\mu\eta_2B^3\} \end{aligned}\right\} \tag{33}$$

From sin 3ψ

$$G\eta_3 = \frac{1}{2}\rho\Omega^2R^3cac_T\left\{0.271\frac{\mu^3}{B}\lambda+0.381\mu^3\theta_0+0.280\mu^3(\theta_1+\epsilon_0)B-\frac{0.1650}{\gamma B^2}\mu^2\epsilon_1+0.0612\mu^2\eta_1B^2+0.1683\mu\epsilon_2B^3+\frac{1.988}{\gamma B}\mu\eta_2\right\} \tag{34}$$

From cos 2ψ, retaining only terms in μ^2 or lower,

$$\left.\begin{aligned} G\epsilon_2 = {} & \frac{1}{2}\rho\Omega^2R^3cac_T\left\{0.796\mu^2\lambda+0.578\mu^2\theta_0B+0.554\mu^2(\theta_1+\epsilon_0)B^2-\frac{0.147}{\gamma B}\mu\epsilon_1+0.055\mu\eta_1B^3+0.1033\epsilon_2B^4+\frac{1.768}{\gamma}\eta_2\right. \\ & \left.-\frac{1}{2}\mu^2\frac{C_m}{ac_T}B\right\} \end{aligned}\right\} \tag{35}$$

From sin 2ψ,

$$\left.\begin{aligned} G\eta_2 = {} & \frac{1}{2}\rho\Omega^2R^3cac_T\{-0.0291\mu^2\gamma\lambda B^4-0.0290\mu^2\gamma\theta_0B^5-0.0225\mu^2\gamma(\theta_1+\epsilon_0)B^6-0.0544\mu\epsilon_1B^3-0.0008\mu\gamma\eta_1B^7 \\ & -0.0100\gamma\epsilon_2B^8+0.1033\eta_2B^4\} \end{aligned}\right\} \tag{36}$$

From cos ψ, retaining all terms up to μ^4,

$$\left.\begin{aligned} G\epsilon_1 = {} & \frac{1}{2}\rho\Omega^2R^3cac_T\left\{-\mu\gamma\lambda\left(\frac{1}{108}B^5-0.0161\mu^2B^3\right)-\mu\gamma\theta_0\left(\frac{1}{144}B^6-0.0049\mu^2B^4\right)-\mu\gamma(\theta_1+\epsilon_0)\left(\frac{1}{180}B^7-0.0048\mu^2B^5\right)\right. \\ & \left.-\epsilon_1\left(\frac{1}{60}B^4-0.073\mu^2B^2\right)-0.0069\mu^2\gamma\eta_1B^6-0.0005\mu\gamma\epsilon_2B^7-0.0057\mu\eta_2B^3\right\} \end{aligned}\right\} \tag{37}$$

From sin ψ,

$$\left.\begin{aligned} G\eta_1 = {} & \frac{1}{2}\rho\Omega^2R^3cac_T\left\{\mu\lambda\left(\frac{1}{3}B+0.341\frac{\mu^2}{B}\right)+\mu\theta_0\left(\frac{1}{9}B^2+0.233\mu^2\right)+0.175\mu^3(\theta_1+\epsilon_0)B+\frac{0.006}{\gamma B_2}\mu^2\epsilon_1+\eta_1\left(\frac{1}{60}B^4-0.008\mu^2B^2\right)\right. \\ & \left.+0.006\ \mu\epsilon_2B^3-\frac{0.073}{\gamma B}\mu\eta_2+\mu\frac{C_mc}{ac_T}B^2\right\} \end{aligned}\right\} \tag{38}$$

From the constant term

$$\left.\begin{aligned} G\epsilon_0 = {} & \frac{1}{2}\rho\Omega^2R^3cac_T\left\{\frac{1}{2}\lambda B^2+\theta_0\left(\frac{1}{3}B^3+\frac{1}{2}\mu^2B\right)+\theta_1\left(\frac{1}{4}B^4+\frac{1}{4}\mu^2B^2\right)+\frac{1}{4}\mu^2b_2B+\epsilon_0\left(\frac{1}{4}B^4+\frac{1}{4}\mu^2B^2\right)+\frac{1}{3}\mu\eta_1B^3-\frac{1}{8}\mu^2\epsilon_2B^2\right. \\ & \left.+\frac{1}{2}\rho\Omega^2R^3c^2C_m\left(\frac{1}{3}B^3+\frac{1}{2}\mu^2B\right)\right\} \end{aligned}\right\} \tag{39}$$

Comparison with (22) shows that the first part of (39) differs only by insignificant terms from the thrust multiplied by $cc_T/\sigma\pi R$, or, since σ is $bc/\pi R$,

$$G\epsilon_0=\frac{Tc_T}{b}+\frac{1}{2}\rho\Omega^2R^3c^2C_m\left(\frac{1}{3}B^3+\frac{1}{2}\mu^2B\right) \tag{40}$$

Let $\rho ca\Omega^2R^3c_T/2G$ be put equal to A; then after substituting from (35), (36), (37), and (38) for ϵ_2, η_2, ϵ_1, and η_1 and neglecting insignificant terms, the final expressions for the twist coefficients are obtained:

$$\epsilon_0=\frac{Tc_T}{bG}+A\frac{C_mc}{ac_T}\left(\frac{1}{3}B^3+\frac{1}{2}\mu^2B\right) \tag{41}$$

$$\left.\begin{aligned}\epsilon_1=&-\mu\gamma A\left\{\lambda\left(\frac{1}{108}B^5-0.0161\mu^2B^3\right)+\theta_0\left(\frac{1}{144}B^6-0.0049\mu^2B^4\right)+\left(\theta_1+\epsilon_0\right)\left(\frac{1}{180}B^7-0.0048\mu^2B^5\right)\right\}\\&+\mu^3\gamma A^2\left\{0.0021\lambda B^7+0.0007\theta_0B^8-0.0002\left(\theta_1+\epsilon_0\right)B^9+0.0071\frac{C_mc}{ac_T}B^8\right\}\end{aligned}\right\} \tag{42}$$

$$\left.\begin{aligned}\eta_1=&\mu A\left\{\lambda\left(\frac{1}{3}B+0.341\frac{\mu^2}{B}\right)+\theta_0\left(\frac{1}{9}B^2+0.233\mu^2\right)+0.175\mu^2\left(\theta_1+\epsilon_0\right)B+\frac{C_mc}{ac_T}B^2\right\}\\&+\mu^3A^2\left\{0.007\lambda B^3+0.006\theta_0B^4+0.005\left(\theta_1+\epsilon_0\right)B^5-0.003\frac{C_mc}{ac_T}B^4\right\}\end{aligned}\right\} \tag{43}$$

$$\left.\begin{aligned}\epsilon_2=&\mu^2A\left\{0.796\lambda+0.578\theta_0B+0.554\left(\theta_1+\epsilon_0\right)B^2-\frac{1}{2}\frac{C_mc}{ac_T}B\right\}\\&-\mu^2A^2\left\{0.032\lambda B^4+0.044\theta_0B^5+0.039\left(\theta_1+\epsilon_0\right)B^6-0.055\frac{C_mc}{ac_T}B^5\right\}\end{aligned}\right\} \tag{44}$$

$$\left.\begin{aligned}\eta_2=&-\mu^2\gamma A\left\{0.0291\lambda B^4+0.0290\theta_0B^5+0.0225\left(\theta_1+\epsilon_0\right)B^6\right\}\\&-\mu^2\gamma A^2\left\{0.0078\lambda B^8+0.0057\theta_0B^9+0.0052\left(\theta_1+\epsilon_0\right)B^{10}-0.0050\frac{C_mc}{ac_T}B^9\right\}\end{aligned}\right\} \tag{45}$$

$$\left.\begin{aligned}\epsilon_3=&\mu^3\gamma A\left\{0.0085\lambda B^3+0.0143\theta_0B^4+0.0108\left(\theta_1+\epsilon_0\right)B^5\right\}\\&+\mu^3\gamma A^2\left\{0.0135\lambda B^7+0.0111\theta_0B^8+0.0097\left(\theta_1+\epsilon_0\right)B^9-0.0047\frac{C_mc}{ac_T}B^8\right\}\end{aligned}\right\} \tag{46}$$

$$\left.\begin{aligned}\eta_3=&\mu^3A\left\{\frac{0.271}{B}\lambda+0.381\theta_0+0.280\left(\theta_1+\epsilon_0\right)B\right\}\\&+\mu^3A^2\left\{0.098\lambda B^3+0.048\theta_0B^4+0.049\left(\theta_1+\epsilon_0\right)B^5-0.023\frac{C_mc}{ac_T}B^4\right\}\end{aligned}\right\} \tag{47}$$

The expressions for the twist coefficients disclose that only ϵ_0, η_1, and ϵ_2 involve the factor $A\frac{C_mc}{ac_T}$, which reduces to $\frac{1}{2G}\rho c^2\Omega^2R^3C_m$ and is independent of c_T. The rest of the coefficients—ϵ_1, η_2, ϵ_3, and η_3, and parts of ϵ_0, η_1, and ϵ_2—are proportional to A and consequently to c_T. Thus if c_T is zero, only ϵ_0, η_1, and ϵ_2 differ from zero, and then only if C_m is not zero. Exclusive of the moment arising from C_m, the factor A represents in nondimensional form the ratio of the moment of the air forces to the torsional rigidity of the rotor blade.

The probable magnitude and range of values of A can be estimated. The rigidity G will be proportional to the polar moment of inertia of the blade spar and inversely proportional to the length of the blade. The moment of inertia of the spar will be proportional to the fourth power of the blade thickness. Then

$$G\propto\frac{c^4t^4}{R} \tag{48}$$

where t is the blade thickness divided by the chord.

The numerator of A can be examined by the following considerations. In the design of a rotor the pitch setting chosen is almost invariably the one that results in the highest efficiency. The rotor speed is then adapted to varying maximum speeds by adjusting the solidity. The rotor disk loading is fixed between fairly

narrow boundaries by the requirement of good low-speed performance. For a given pitch setting, C_T/σ (ratio of thrust coefficient to solidity) is constant and $C_T\rho\Omega^2R^2$ is equal to the disk loading. Thus, $\sigma\rho\Omega^2R^2$ will be almost constant. Now, from (48) and this discussion,

$$A\propto\frac{R^3c_T}{bc^4t^4} \tag{49}$$

Or, from $c=\frac{\sigma\pi R}{b}$,

$$A\propto\frac{b^2c_T}{R\sigma^4t^4} \tag{50}$$

It has been found that a value of A of 0.600 is associated with a rotor that has a radius of 20 feet, a chord of 1.00 foot, a blade thickness ratio of 0.175, and c_T equal to 0.038 foot. It seems unlikely that R/ct will increase by more than 25 percent above the value given here of 114; assuming this increase, and an increase in c_T/c from 0.038 to an upper limit of 0.06, A would become approximately 1.90. The lower limit is obviously zero, since c_T/c may become zero. It will be found that normal designs will result in a value of A of less than unity and that the given value of 0.600 is larger than the average.

LIST OF SYMBOLS

R, blade radius.
b, number of blades.
c, blade chord.
c_T, distance between aerodynamic center and center of gravity of rotor-blade element.
r, radius of blade element.
x, r/R.
θ_0, blade pitch angle at hub, radians.
θ_1, difference between hub and tip pitch angles, radians.
ϵ_n, coefficient of cos $n\psi$ in expression for θ, radians.
η_n, coefficient of sin $n\psi$ in expression for θ, radians.
θ, instantaneous pitch angle, radians.
ψ, blade azimuth angle measured from down wind in direction of rotation, radians.
Ω, rotor angular velocity, $d\psi/dt$, radians per second.
$\lambda\Omega R$, speed of axial flow through rotor.
$\mu\Omega R$, component of forward speed in plane of disk, equal to $V\cos\alpha$, where V is forward speed, feet per second.
β, blade flapping angle, radians.
a_n, coefficient of cos $n\psi$ in expression for β, radians.
b_n, coefficient of sin $n\psi$ in expression for β, radians.
I_1, mass moment of inertia of rotor blade about rotor hinge.
α, rotor angle of attack, radians.
C_m, pitching-moment coefficient of rotor-blade airfoil section.
M_T, thrust moment about horizontal hinge.
M_W, weight moment of blade about horizontal hinge.
$u_T\Omega R$, velocity component at blade element perpendicular to blade span and parallel to rotor disk.
$u_P\Omega R$, velocity component at blade element perpendicular to blade span and to $u_T\Omega R$.
T, rotor thrust.
$C_T=T/\rho\Omega^2\pi R^4$
a, slope of curve of lift coefficient against angle of attack of blade airfoil section, in radian measure.

$\varphi=\tan^{-1}\frac{u_P}{u_T}$

α_r, blade-element angle of attack, radians.

$\gamma=\frac{c\rho aR^4}{I_1}$, mass constant of rotor blade.

$B=1-\frac{c}{2R}$, factor allowing for tip losses.

G, torsional rigidity of rotor blade, ft.-lb. per radian.

FLIGHT TESTS AND CALCULATIONS

Data for investigating the validity of the analysis were obtained in flight tests of a Kellett KD–1 direct-control wingless autògiro. The physical characteristics of the machine and its rotor are given in table I. Measurements were made in a steady glide of the air speed, the rotor speed, and the blade motion. The air speed was obtained with a trailing pitot-static head and an N. A. C. A. air-speed recorder; the rotor speed was observed with a calibrated rotoscope; and the blade motion was photographed with a motion-picture camera mounted on and turning with the rotor hub. The photographs obtained with the motion-picture camera established the blade flapping motion and, in addition, the instantaneous twist at the rotor radius of the markers on the blade.

TABLE I.—PHYSICAL CHARACTERISTICS OF KD–1 AUTOGIRO

Gross weight, W	2,100 pounds.
Rotor radius, R	20.0 feet.
Blade weight, w_b	61.5 pounds.
Blade-weight moment, M_W	482 pound-feet.
Blade moment of inertia, I_1	175 slug-feet^2.
Blade chord, c	1.00 foot.
Chordwise location of blade center of gravity from leading edge	0.280 foot.
Chordwise location of aerodynamic center from leading edge	0.242 foot.
Number of blades, b	3.
Rotor solidity, σ	0.0478.
Blade airfoil section	Göttingen 606.
Blade pitch setting (constant), θ_0	0.0960 radian.
Airfoil section moment coefficient, C_m (about aerodynamic center)	−0.056.
Blade torsional rigidity constant, G	1,700 pound-feet.

In order to investigate the validity of the analysis, the flight-test data were used in two ways. The analysis was checked directly by predicting the blade twist at 0.75 R from the physical constants of the rotor and the value of the inflow coefficient λ. The factor λ was calculated from the experimental thrust coefficient by the substitution of known values in the expression for the thrust coefficient given in the analysis. A further examination of the analysis was made by substituting the experimental values of the inflow factor, the blade-motion coefficients, and the twist coefficients at one tip-speed ratio in the equation expressing the twisting moment as a function of the radius. The resultant twist deflection for a blade of constant rigidity followed directly and could be qualitatively compared with the basic assumption of a linear variation of twist with radius.

RESULTS AND DISCUSSION

Measured values of rotor speed and thrust coefficient are shown in figure 2, and derived values of the inflow factor λ are given in table II. The experimental blade-motion coefficients are presented in figure 3.

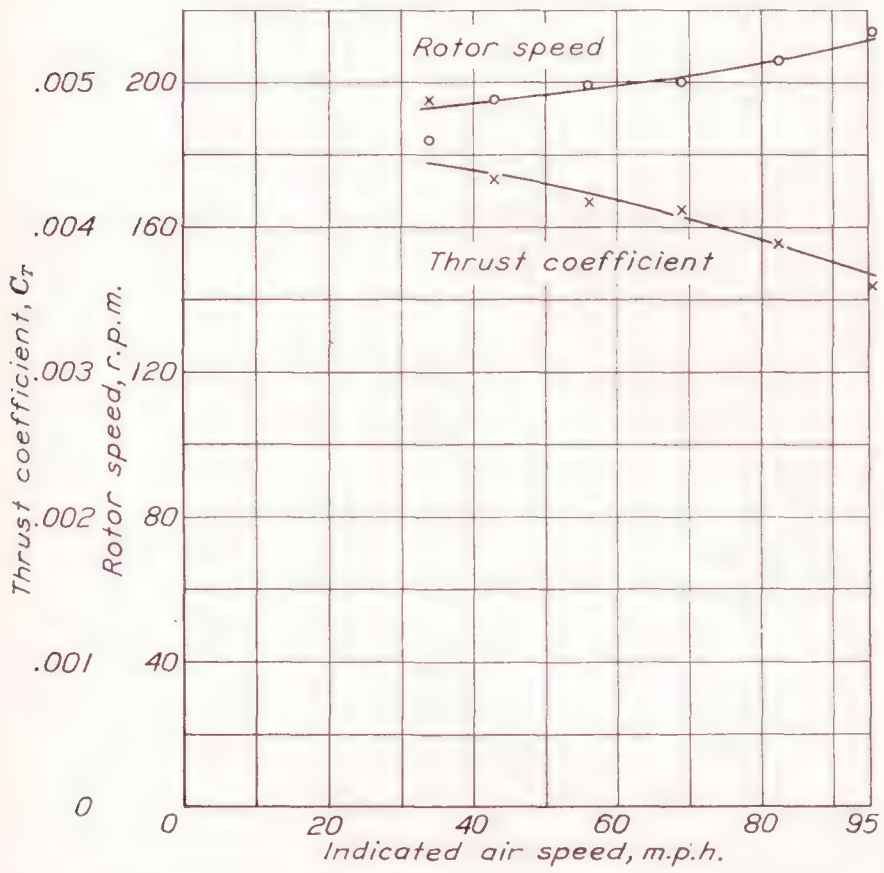

FIGURE 2.—Rotor speed and thrust coefficient of KD-1 autogiro rotor as measured in flight; ρ=0.00231 slug/cu. ft.

TABLE II.—DERIVED VALUES OF INFLOW FACTOR λ

μ	λ	μ	λ	μ	λ
0.125	0.0214	0.200	0.0209	0.275	0.0191
.150	.0213	.225	.0204	.300	.0185
.175	.0212	.250	.0197	.325	.0179

The twist coefficients shown in figure 4 represent a comparison of the experimental points with the calculated values for the radius at which the measurements were made. The agreement of theory with experiment is satisfactory, and strikingly so for η_1, the largest coefficient. The calculated ϵ_0 is consistently smaller than the measured value, but a reasonable explanation of the disagreement will be given later. Unfortunately, the experimental results for ϵ_1 and ϵ_2 are badly dispersed; the mean of the points is not appreciably different, however, from the predicted values.

The variation of twisting moment and twist angle with radius is illustrated in figures 5 and 6. The

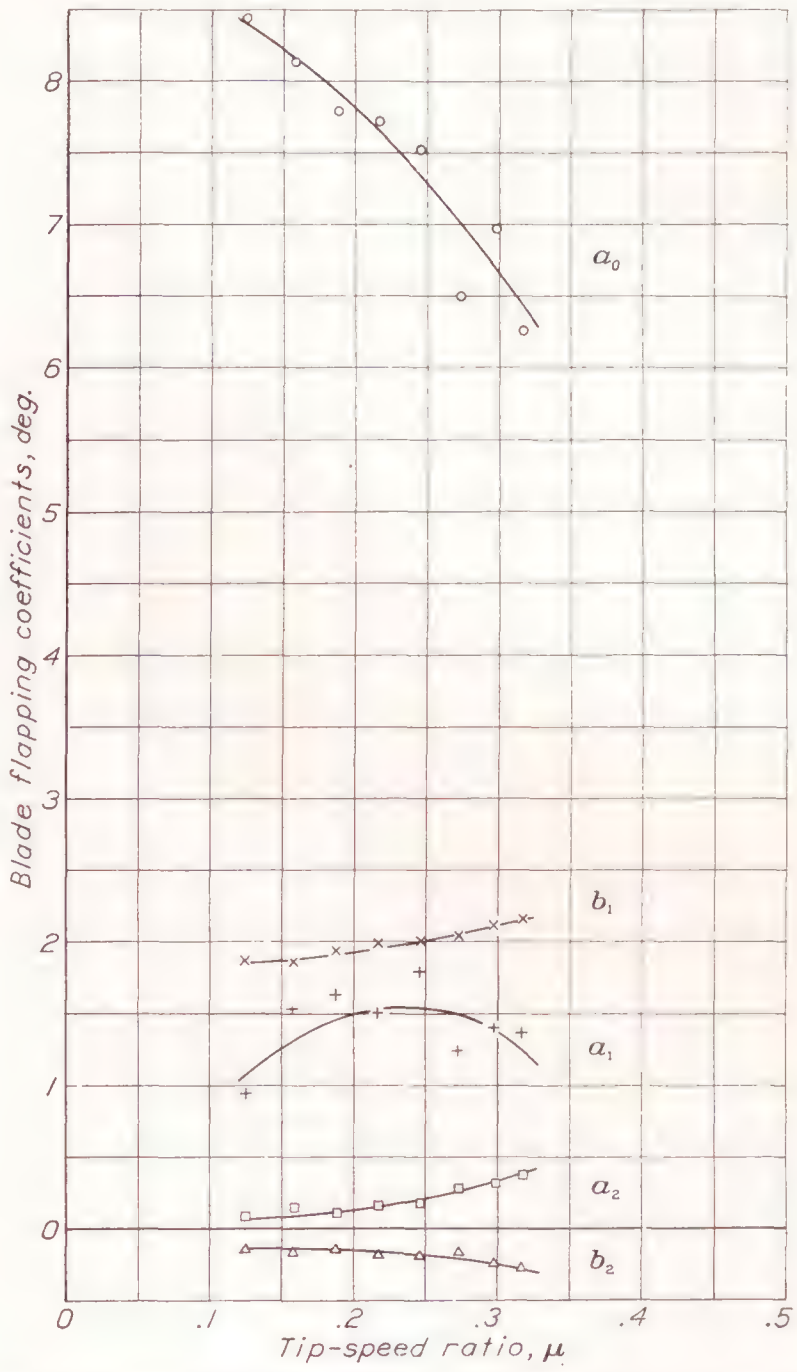

FIGURE 3.—Flapping motion coefficients of KD-1 autogiro rotor as measured in flight.

twisting moment at the hub for each component of the twist has been considered unity; the blade rigidity from x=0 to x=0.05 has been considered infinite as an approximation to the high rigidity inboard of the vertical pin; and the rigidity outboard of x=0.05 was chosen to make ϵ_0 unity at x=1.00. Examination of the figures discloses that ϵ_0 attains a larger value at x=0.75 for the same twisting moment at the hub than any of the remaining components of twist. This result can be considered a partial explanation of the underestimation of ϵ_0 in figure 4. The curves in figures 5 and 6 further indicate that the assumption of linear twist is a reasonably accurate approximation to the actual variation.

The curves in figures 5 and 6 suggest that it would be erroneous to calculate the torsional rigidity from

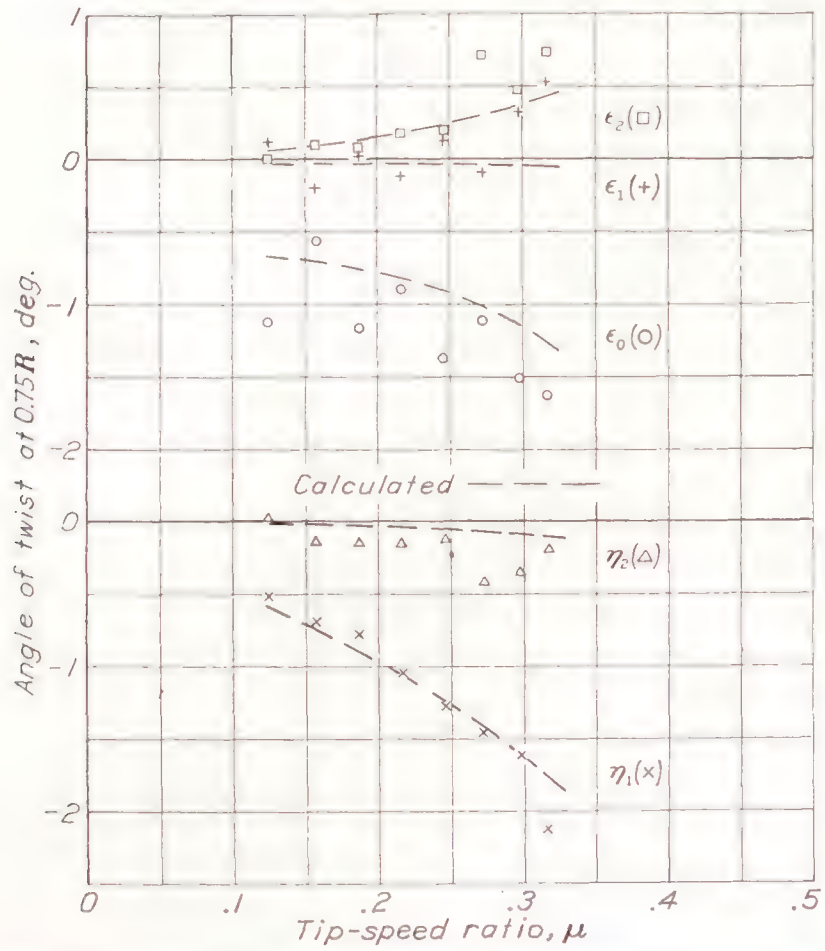

FIGURE 4.—Measured and calculated twist coefficients of KD-1 autogiro rotor.

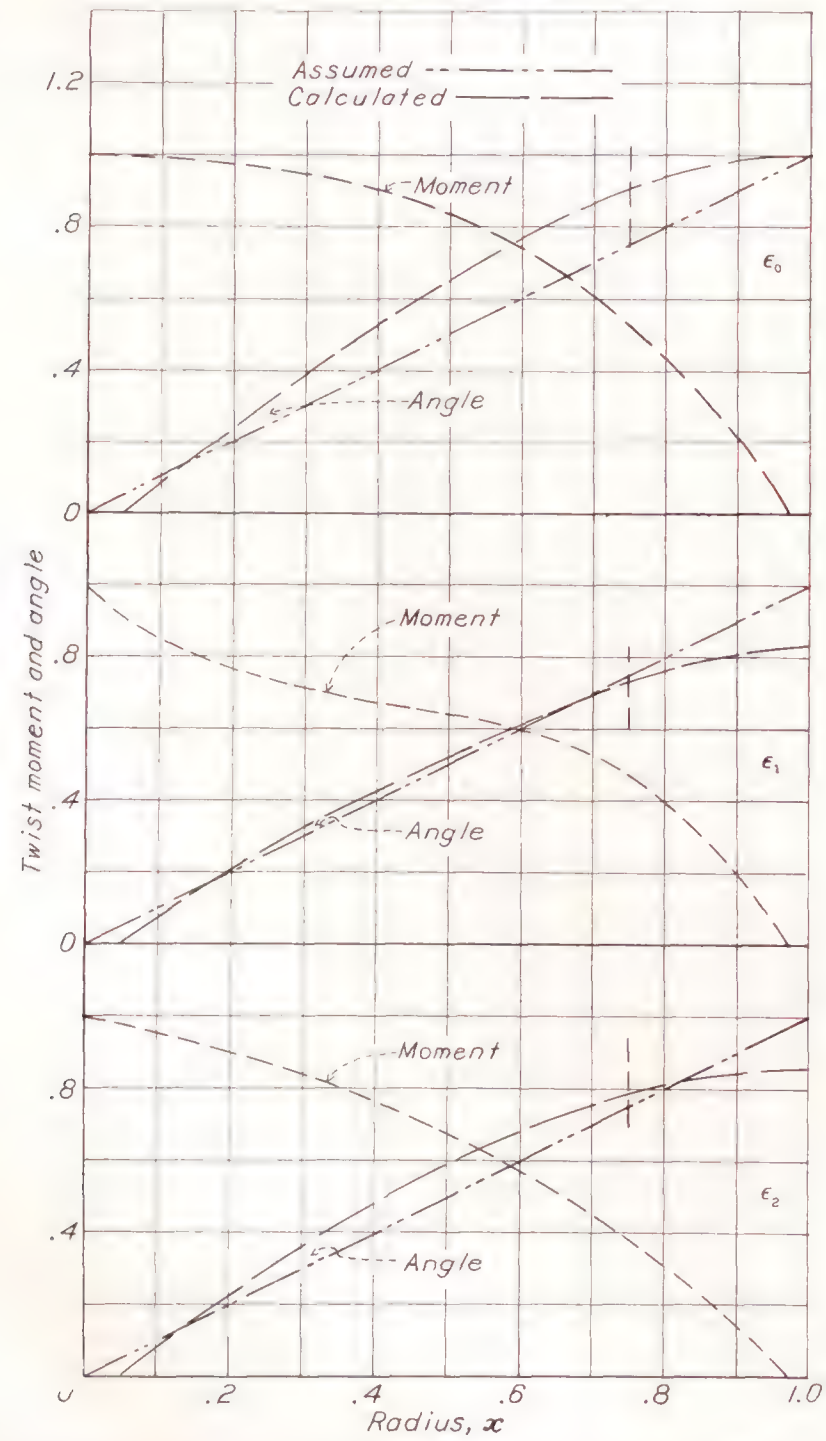

FIGURE 5.—Radial distribution of twisting moment and twist angle of KD-1 autogiro rotor; cos $n\psi$ components; μ=0.325.

the twist produced by a constant moment along the blade. Instead, it is recommended that a moment be assumed which has a value G at the blade root and varies with the radius according to the expression (B^2-x^2). The definition of G suggested is that it be the moment at the hub, distributed as indicated, which will produce a twist of 0.80 radian at 0.75 R. Thus, if I_p is the polar moment of inertia of the blade cross

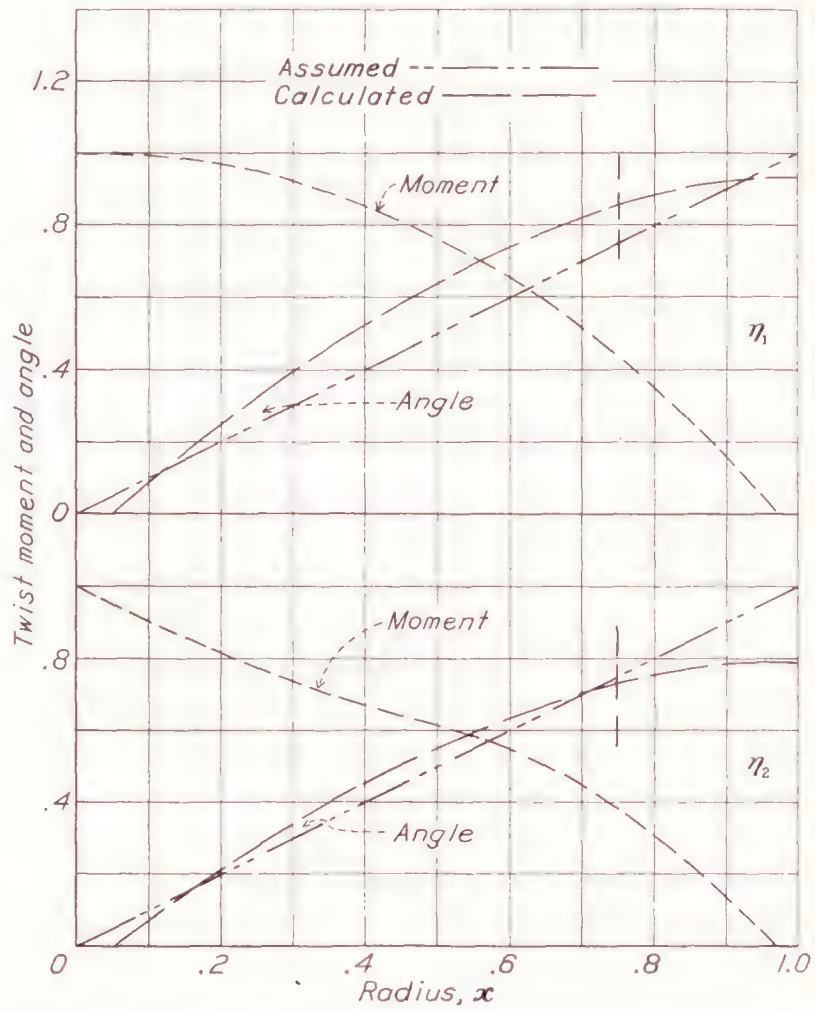

FIGURE 6.—Radial distribution of twisting moment and twist angle of KD-1 autogiro rotor; sin $n\psi$ components; μ=0.325.

section, R the radius (blade length), and E_s the modulus of elasticity in shear,

$$G=\frac{64}{585}\frac{E_sI_p}{R}$$

where G is in pound-feet.

E_s is in pounds per square inch.

I_p is in inches^4.

R is in inches.

The value of 0.80 rather than 0.75 radian for the determination of G appears to result in a curve that is better approximated by a straight-line distribution to 1 radian at the tip, as evidenced in figures 5 and 6.

The merit of the analysis made in this paper depends upon the accuracy and facility with which it may be used to predict the twist of a rotor blade before the rotor itself has passed the drawing-board stage of design. The use of the analysis in this manner is not obvious since at first it appears that the rotor speed is required in order to calculate the twist; whereas the calculation of the rotor speeds can be made only after the twist, and consequently the thrust coefficient, is known. In one sense this objection is valid but in another the difficulty mentioned is not insurmountable. Assume a rotor design in which the known factors are

the blade moment coefficient, the distance between the aerodynamic center and the center of gravity, the radius, the chord, the torsional rigidity, and the design maximum speed. Because of the variation of rotor efficiency with tip-speed ratio, it is mandatory that at maximum speed the tip-speed ratio shall be between 0.40 and 0.45. When the tip-speed ratio for design maximum speed is chosen, the tip speed is fixed. The twist coefficients ϵ_0, η_1, and ϵ_2, which depend principally upon C_m, can now be found with satisfactory accuracy by using the values of pitch setting and inflow coefficient λ that would be assigned to the rotor if the twist were zero. For a given airfoil section there is a mean lift coefficient which results in maximum efficiency and which fixes the ratio C_T/σ; the values of λ and the pitch setting corresponding to this mean lift coefficient should be used. The coefficients ϵ_0, η_1, and ϵ_2 now are known and fixed, and their effect upon C_T/σ can be evaluated. The desired value of C_T/σ is now attained by adjusting the pitch setting to offset the effect of twist, and all design requirements have been met. A final check of the twist coefficients using the final values of λ and the pitch setting can be made but, since C_m dominates the only coefficients that influence C_T/σ, it is found that only in exceptional and peculiar designs will the twist coefficients be affected.

CONCLUSIONS

1. The assumption that the twist of a rotor blade varies linearly with the radius is a satisfactory approximation to actual conditions.

2. The analysis of blade twist predicted without important error the twist of a rotor used as an example.

3. The torsional rigidity of the rotor blade should be calculated on the basis that the twisting moment varies with radius as (B^2-x^2).

LANGLEY MEMORIAL AERONAUTICAL LABORATORY,
NATIONAL ADVISORY COMMITTEE FOR AERONAUTICS,
LANGLEY FIELD, VA., *April 14, 1937.*

REFERENCES

1. Wheatley, John B.: An Aerodynamic Analysis of the Autogiro Rotor with a Comparison between Calculated and Experimental Results. T. R. No. 487, N. A. C. A., 1934.
2. Timoshenko, S.: Vibration Problems in Engineering. D. Van Nostrand Co., Inc., 1928, p. 59.
3. Wheatley, John B.: An Analytical and Experimental Study of the Effect of Periodic Blade Twist on the Thrust, Torque, and Flapping Motion of an Autogiro Rotor. T. R. No. 591, N. A. C. A., 1937.

REPORT No. 601

TORSION TESTS OF TUBES

By Ambrose H. Stang, Walter Ramberg, and Goldie Back

SUMMARY

Torsion tests of 63 chromium-molybdenum steel tubes and 102 17ST aluminum-alloy tubes of various sizes and lengths were made to study the dependence of the torsional strength on both the dimensions of the tube and the physical properties of the tube material. Three types of failure were found to be important for sizes of tubes frequently used in aircraft construction: (1) failure by plastic shear, in which the tube material reached its yield strength before the critical torque was reached; (2) failure by elastic two-lobe buckling, which depended only on the elastic properties of the tube material and the dimensions of the tube; and (3) failure by a combination of (1) and (2), that is, by buckling taking place after some yielding of the tube material.

An adequate theory exists for explaining failure by (1) or (2). Most of the tubes failed by the combined failure (3), for which a theoretical solution seems unattainable at this time. An analysis of the data showed that the torsional strength of these tubes could be expressed by an empirical formula involving only the tensile properties of the tube material in addition to the dimensions of the tube. Design charts were computed from this empirical formula and a number of examples were worked out to facilitate the application of the charts.

INTRODUCTION

Thin-wall tubes are commonly used in airplanes to transmit torques to the ailerons and other control surfaces. It is well known that the maximum fiber stress in torsion that a thin-wall tube will support depends on the ratio (t/D) of its wall thickness to its diameter. Tests have been made (references 1, 2, 3, and 4) to determine the relationship between torsional strength and t/D ratio for tubes of various materials, but the available data resulting from these tests were insufficient to lead to general conclusions or even to determine a fairly accurate design formula for a given material.

It seemed desirable, therefore, to carry out a series of tests with a sufficiently large number of tubes of various lengths and t/D ratios and, if possible, of several materials to supply such data. The present report describes the results of torsion tests of 63 chromium-molybdenum steel tubes and 102 tubes of 17ST aluminum alloy. These tests were made at the National Bureau of Standards with the cooperation of the Bureau of Aeronautics, Navy Department, and the National Advisory Committee for Aeronautics.

APPARATUS AND TESTS

TUBES

The lengths L of the steel tubes ranged from 19 to 60 inches, outside diameters D from ¾ to 2½ inches, thicknesses t from 0.03 to 0.125 inch, t/D ratios from 0.0134 to 0.0840, and L/D ratios from 7.6 to 80.0. The aluminum-alloy tubes were cut in lengths of 20 and 60 inches; their outside diameters ranged from 1 to 2 inches, their wall thicknesses from 0.019 to 0.221 inch, their t/D ratios from 0.0101 to 0.1192, and L/D ratios from 10.0 to 60.2.

The first five lengths (A_0, B_0, C_0, D_0, E_0) of chromium-molybdenum steel tubes used in the tests were purchased under Army Specification 57–180–2A; the other tubes (F_0 to V_0) were bought under Navy Department Specification 44T18. Table I shows that the tensile properties required by these specifications are the same. Somewhat higher properties are required by the more recent Navy Department Specification 44T18a, which is included in table I for the sake of completeness.

TABLE I.—MECHANICAL SPECIFICATION FOR CHROMIUM-MOLYBDENUM STEEL TUBES

Specification	Tensile strength (minimum) (lb./sq. in.)	Yield strength (minimum) (offset 0.2 percent) (lb./sq. in.)	Elongation in 2 inches (minimum) (percent)
Army 57–180–2A	95,000	60,000	10
Navy 44T18	95,000	60,000	10
Navy 44T18a	95,000	75,000	10

The aluminum-alloy tubes were contributed by the Aluminum Company of America. They were manufactured to satisfy Navy Department Specification 44T21. The mechanical properties listed in this specification are given in table II.

TABLE II.—MECHANICAL SPECIFICATION FOR HEAT-TREATED ALUMINUM-ALLOY TUBES

Specification	Nominal outside diameter (in.)	Tensile strength (minimum) (lb./sq. in.)	Yield strength (minimum) (offset 0.2 percent) (lb./sq. in.)	Elongation in 2 inches (minimum) (percent)
Navy 44T21	¼ to 1	55,000	40,000	16
	Over 1 to 1½	55,000	40,000	14
	Over 1½ to 4	55,000	40,000	12

The chemical composition of a few of the steel tubes was determined and the Vickers hardness numbers and tensile properties of each length of tube were obtained before carrying out the torsion tests.

Table III gives the results of analyses made by the Chemistry Division of the National Bureau of Standards on five of the steel tubes selected at random.

TABLE III.—PERCENTAGE OF CHEMICAL ELEMENTS PRESENT IN CHROMIUM-MOLYBDENUM STEEL TUBES

Specimen	Carbon	Manganese	Phosphorus	Sulphur	Chromium	Molybdenum
D	0.34	0.54	0.022	0.011	1.09	0.19
K	.30	.49	.022	.009	.86	.18
N	.31	.59	.029	.013	1.11	.24
O	.39	.49	.021	.013	.86	.23
S	.32	.53	.023	.015	.97	.23

No such analyses were made of the aluminum-alloy tubes, but the nominal composition furnished by the manufacturer is given in table IV.

TABLE IV.—NOMINAL CHEMICAL COMPOSITION OF 17ST TUBES AS GIVEN BY MANUFACTURER, PERCENTAGE

Copper	4.0
Manganese	.5
Magnesium	.5
Aluminum	95.0

Vickers hardness tests were made at both ends of each tube. The results for the chromium-molybdenum steel tubes are given in table V and those for the aluminum-alloy tubes in table VI. For the steel tubes the Vickers numbers varied from 204 to 311. The average variation for a single tube was less than 5 percent and in only one case (tube 0_0, 13.2 percent) did it exceed 10 percent. The Vickers numbers for the aluminum-alloy tubes varied from 125 to 142, the maximum variation for a single tube being less than 2½ percent.

The dimensions of the chromium-molybdenum steel specimens used in the torsion tests are included in table VII and those of the 17ST aluminum-alloy specimens, in table VIII, together with data obtained from the torsion tests.

TENSILE TESTS

Tensile tests were made on specimens 19 to 20 inches long cut from each length of tubing. The specimens were fitted with plugs similar to those described in Navy Department specification 44T18 and were held in V-type jaws attached to the two heads of the testing machine. A hydraulic machine of 100,000-pound capacity was used to test all except one of the chromium-molybdenum steel tubes; this one specimen was tested in a machine of the lever type because its diameter of 2½ inches was too large for the jaws provided with the hydraulic machine. All the aluminum-alloy tensile specimens were tested in lever-type machines of 2,000-, 50,000-, and 100,000-pound capacity. All of the steel specimens except A_0, D_0, and E_0 were prestressed in tension to about 30,000 pounds per square inch. The prestressing served to seat the strain gages and to cold-work the material sufficiently in the low-stress range to obtain from it an approximately straight stress-strain curve, from which the Young's modulus of the material could be derived. The aluminum-alloy tubes had already been prestressed at the factory and only enough load was put on the specimen before test to seat the strain gages securely.

Tensile strains on the steel tubes were measured with a Ewing extensometer using a 2-inch gage length (smallest scale division 0.0001 in./in.) for specimens 1½ inches in diameter or less, and with a Huggenberger extensometer using a 1-inch gage length (smallest scale division 0.00015 in./in.) for tubes of larger diameter. Tuckerman optical strain gages with a 2-inch gage length were used for all aluminum-alloy tubes. The smallest scale division on the vernier of this gage corresponds to a strain increment of 0.000002 in./in.

The strain gages on each of the tensile specimens were placed 8 to 9 inches, or 4 to 9 diameters, away from the jaws gripping both ends of the specimen. A study of the stress distribution in a $2.5\times0.032\times36$ inch tube of chromium-molybdenum steel held between V-type jaws making contact at opposite pairs of points 60° apart had shown that the average of the strains at two ends of any diameter in a cross section removed 3 diameters or more from the ends gave the same value within the error of observation. At a cross section 1½ diameters from any pair of jaws the average strains varied ±6 percent about an average stress of 15,000 pounds per square inch and through ±2.6 percent about an average stress of 27,000 pounds per square inch. From these observations it was concluded that the average strains as measured in the present series of specimens from 4 to 9 diameters from the jaws were correct within the error of observation. The contact points of the jaws in these specimens were more than 60° apart except for some of the 1-inch tubes for which they were a little closer; in the latter case, however, the gages were about 8 diameters away from the jaws.

From each stress-strain curve the yield strength was determined as the stress at which the strain was 0.002 in./in. in excess of the elastic strain with an assumed Young's modulus of 30×10^6 pounds per square inch for the chromium-molybdenum steel tubes and a modulus of 10×10^6 pounds per square inch for the aluminum-alloy tubes. The values are given in table V for the steel tubes and in table VI for the aluminum-alloy tubes. It is seen that the yield strength of the steel

tubes varied from 67,700 to 110,000 and that of the aluminum-alloy tubes, from 44,300 to 50,000 pounds per square inch.

Young's modulus E was obtained by plotting against stress σ the difference $\Delta\epsilon$ between the observed strain and that computed from an assumed modulus E_0 of 30×10^6 pounds per square inch in the case of the steel tubes and a modulus of 10×10^6 pounds per square inch in the case of the aluminum-alloy tubes and by measuring the slope $\Delta\epsilon/\sigma$ of the straight line giving the best fit to the plotted points. The true modulus E is then computed from this slope using the simple relation

$$\frac{1}{E}=\frac{1}{E_0}+\frac{\Delta\epsilon}{\sigma} \qquad (1)$$

Tables V and VI show that the Young's modulus for the steel tubes ranged from 27.3 to 30.2×10^6 pounds per square inch and that for the aluminum-alloy tubes varied from 9.79 to 10.81×10^6 pounds per square inch. In both groups the range of variation was close to 10 percent.

Elongations over a 2-inch gage length were determined by means of dividers; they varied from 11.5 to 32 percent for the steel tubes (table V) and from 17 to 34 percent for the aluminum-alloy tubes (table VI). The specimens that broke at the jaws were not considered in obtaining these limits.

Tables V and VI also give the tensile strength of each specimen. This value ranged from 88,400 to 132,900 pounds per square inch for the steel tubes and from 62,800 to 67,000 pounds per square inch for the aluminum-alloy tubes.

Examination of the stress-strain curves for the steel specimens showed that the material could be divided into two groups with markedly different stress-strain curves. For the greater number of steel tubes the curves were nearly straight until near the yield stress, where they bent fairly sharply. In these specimens the ratio of tensile strength to yield strength varied from 1.03 to about 1.18. Three of these curves (for specimens H_0, R_0, K_0) are shown in figure 1(a). For other specimens, however, the slope of the curves decreased gradually with no sharp bend. For these specimens the ratio of tensile strength to yield strength was much higher, ranging from 1.37 to 1.63. Figure 1(a) also gives three of these curves (for specimens I_0, V_0, N_0). In each of these groups there existed a rough association between different tensile properties. Low tensile strength, high yield strength, low elongation, low ratio of tensile strength to yield strength tend to occur together and high tensile strength is associated with low yield strength, high elongation, etc. However, no quantitative relation could be found between the results for materials in the two groups.

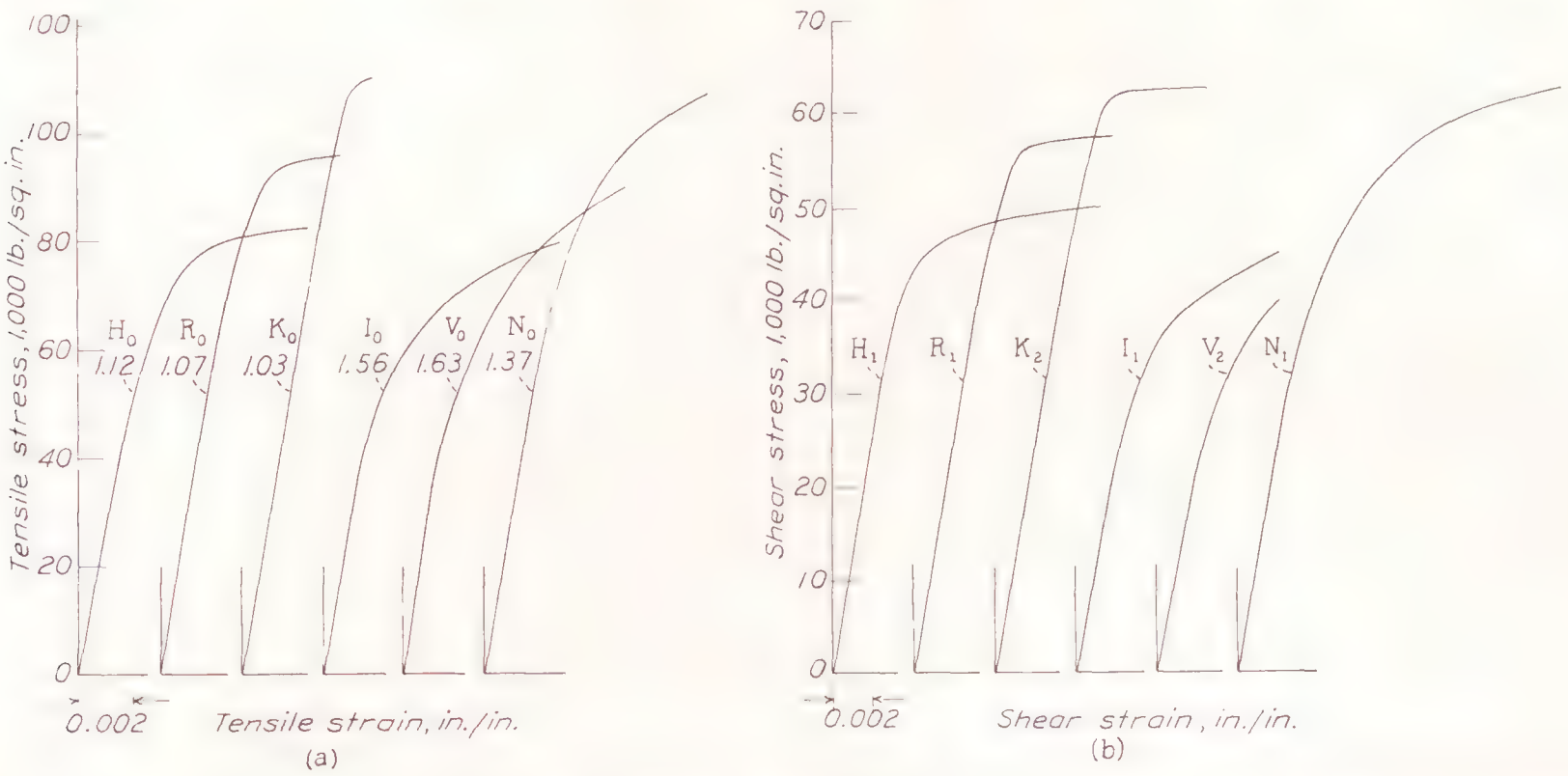

FIGURE 1.—Stress-strain curves of chromium-molybdenum steel tubes. Tensile specimens H_0, R_0, K_0, with sharp knee near the yield strength were cut from the same three lengths of tubing as shear specimens H_1, R_1, K_2, respectively; similarly tensile specimens, I_0, V_0, N_0, with relatively rounded knee near the yield strength, were cut from the same three lengths as shear specimens I_1, V_2, N_1, respectively. The ratio of tensile strength to yield strength in tension is shown as a number on each tensile stress-strain curve.

Not nearly so marked a differentiation into two groups was apparent for the aluminum-alloy tubes. The ratio of tensile strength to yield strength varied through a much smaller range, namely, from 1.27 to 1.49. Figure 2(a) shows three specimens with a relatively sharp knee near the yield stress (P_0, J_0, M_0) and three with a relatively rounded knee (U_0, s_0, x_0). There was again a rough tendency for low tensile strength to occur together with high yield strength, low elongation and low ratio of tensile strength to yield strength.

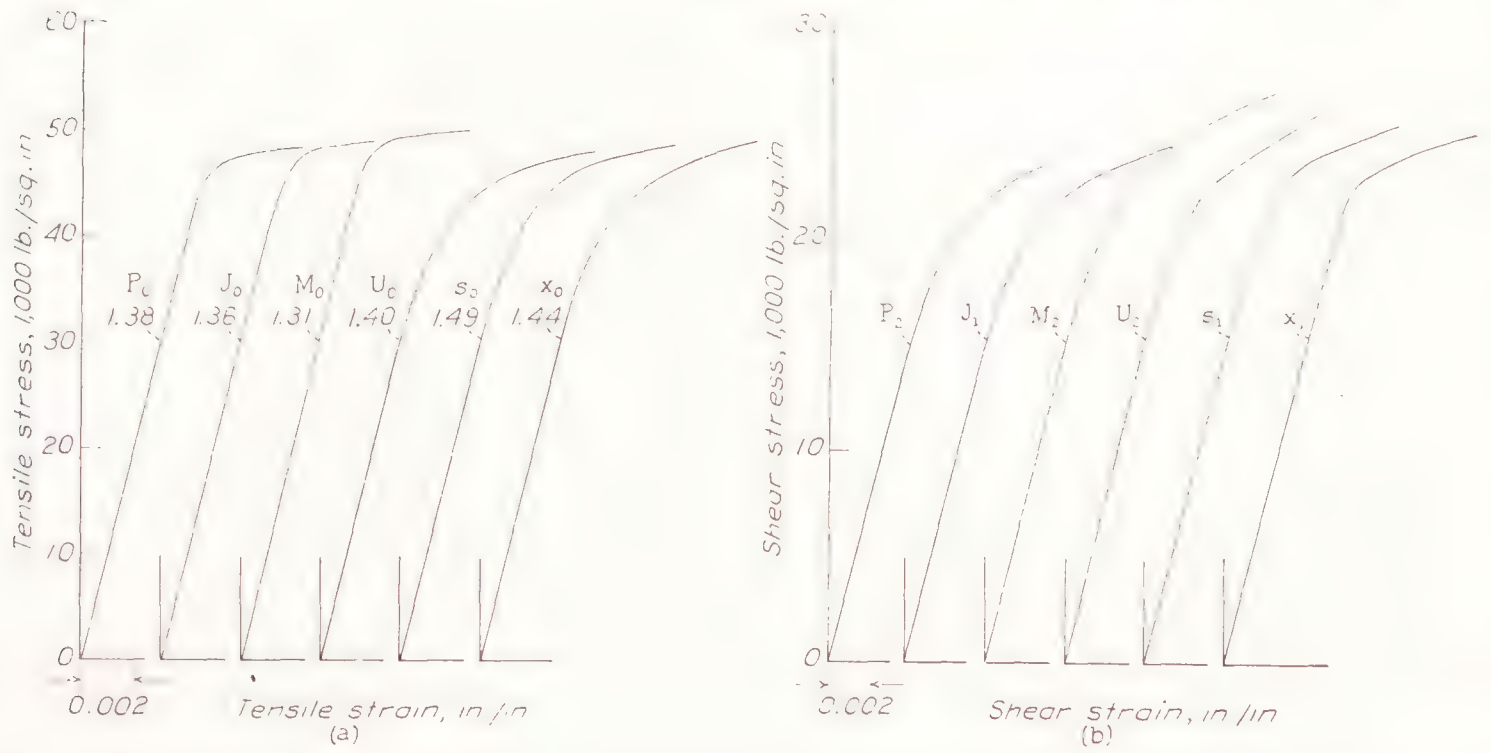

FIGURE 2.—Stress-strain curves of 17ST aluminum-alloy tubes. Tensile specimens P_0, J_0, M_0, with relatively sharp knee near the yield strength were cut from the same three lengths of tubing as shear specimens P_2, J_1, M_2, respectively; similarly tensile specimens U_0, S_0, X_0, with relatively rounded knee near the yield strength were cut from the same three lengths as shear specimens U_2, S_1, X_1, respectively. The ratio of tensile strength to yield strength in tension is shown as a number on each tensile stress-strain curve.

TORSION TESTS

Figure 3 shows the method of mounting the specimen for test in the torsion machine. The ends of the tube were reinforced by two steel plugs of proper diameter and were then clamped solidly between wedge-shaped jaws A; they were free to move in an axial direction throughout the test. Specimens not over 20 inches in length were tested in the 13,000 pound-inch pendulum-type machine shown in figure 3 and the longer tubes were tested in a 60,000 pound-inch lever-type machine.

The method of measuring the angle of twist under load is also shown in figure 3. The fixture consists of two rings B fastened to the specimen at points 25

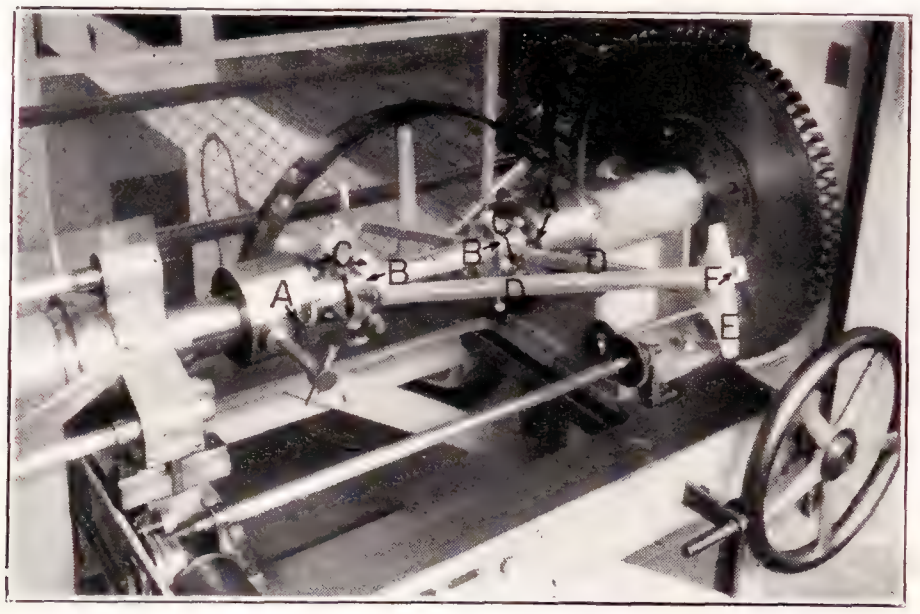

FIGURE 3.—Torsion testing machine with 17ST aluminum-alloy tube in position after test to failure.

centimeters (9.84 inches) apart by three screws C. Each ring carries a pair of aluminum radial arms D, one pair carrying the scales E and the other the pointers F. Readings were taken on both scales and averages were used to compensate for any effect due to bending of the tube under load.

CALCULATION OF SHEAR STRESSES

The torsion tests give the relation between the torque M transmitted by the tube and the angle of twist per unit length θ produced by that torque. The stress-strain curves in shear were computed from these torque-twist curves in the following manner.

The relation between the shear stress τ and the torque M in a twisted circular tube is given by the equation:

$$M(\theta)=2\pi\int_{r_1}^{r_2}\tau r^2 dr \tag{2}$$

where r is the radial distance from the axis of the tube.

r_1, radius of the inner wall.

r_2, radius of the outer wall.

τ, shear stress at a distance r from the axis.

The relation between this shear stress and the shear strain $\gamma=r\theta$,

$$\tau=f(\gamma)=f(r\theta) \tag{3}$$

may be found by substituting (3) in (2) and differentiating both sides with respect to θ. (See reference 5, p. 128.) This gives the differential equation:

$$r_2^3 f(r_2\theta)-r_1^3 f(r_1\theta)=\frac{1}{2\pi}\left(\theta\frac{dM}{d\theta}+3M\right) \tag{4}$$

where $r_2\theta$, $r_1\theta$ are the shear strains at the outside and the inside wall of the tube, respectively. All quantities in this equation are given by the dimensions of the tube and the torque-twist curve except the stresses $f(r_2\theta)$ and $f(r_1\theta)$. The stress $f(r_2\theta)$ can, therefore, be calculated from equation (4) provided $f(r_1\theta)$ is known; this suggests a method of step-by-step solution beginning with the end of the elastic range in which $f(r_1\theta)$ is known. Practically, this method of computation is laborious and is not warranted by the accuracy of the data for tubes as thin as those tested in the present

investigation. It is entirely sufficient in these cases to use approximate methods based upon arbitrary simplifying assumptions.

A number of such methods have been used, all of them serving the purpose equally well. For this investigation the method chosen was to calculate the stress and strain in the mean fiber:

$$\bar{r}=\tfrac{1}{2}(r_1+r_2)=\frac{D-t}{2}$$

on the assumption that both stresses and strains increase linearly with distance from the axis of the tube, as they do in the elastic case. This calculation gave

$$\left.\begin{aligned}\tau&=\frac{M\bar{r}}{I_p}=\frac{2M}{\pi D^2 t}\,\frac{1}{1-2\frac{t}{D}+2\left(\frac{t}{D}\right)^2}\\ \gamma&=\theta\bar{r}=\frac{\theta D}{2}\left(1-\frac{t}{D}\right)\end{aligned}\right\}\qquad(5)$$

where $D=2r_2$ is the outside diameter of the tube and $t=r_2-r_1$ is its wall thickness. Even for the thickest tubes tested $\left(\frac{t}{D}=0.1192\right)$ the stresses so calculated could not differ by more than 14 percent from any stress existing in the wall. The stresses at the mean fiber calculated from (5) could not be in error by more than 1.5 percent for tubes up to $\frac{t}{D}=0.12$. This value is the percentage difference in the mean fiber stress for a given twisting moment M calculated, on the one hand, by the extreme assumption of elastic twist corresponding to the first equation (5) and, on the other hand, by the extreme assumption of pure plastic shear (uniform shearing stress throughout).

Figures 1(b) and 2(b) show a number of stress-strain curves in shear derived from the moment-twist curve, with the help of (5).

The accuracy of the approximation (5) is brought out further by a comparison of exact and approximate analyses for a relatively thick $\left(\frac{t}{D}=0.0562\right)$ steel tube and for one of the thickest aluminum-alloy tubes $\left(\frac{t}{D}=0.1192\right)$. The exact and the approximate stress-strain curves for these two tubes are shown in figures 4 and 5. In each figure the two curves coincide within 1 percent for the most part and differ at no point by more than 2 percent. Their yield strengths in shear defined by the intersection of the sloping line with the stress-strain curve agree within a fraction of 1 percent.

The yield strengths obtained from the torsion tests with the help of equation (5) are listed in table VII for the steel tubes and in table VIII for the aluminum-alloy tubes.

Figure 6 shows four chromium-molybdenum steel tubes and four 17ST aluminum-alloy tubes after completion of the torsion test. The twist gages D (fig. 3) were kept on the tubes until they failed either with a loud snap by two-lobe buckling (specimens P_1, B_1 fig. 6) or until the knee of the torque-twist curve had been well passed. In the latter case the torque increased slowly with increasing twist beyond the point at which the gages had been removed, until failure occurred either by gradual two-lobe buckling (Q_1, J_1), by helical

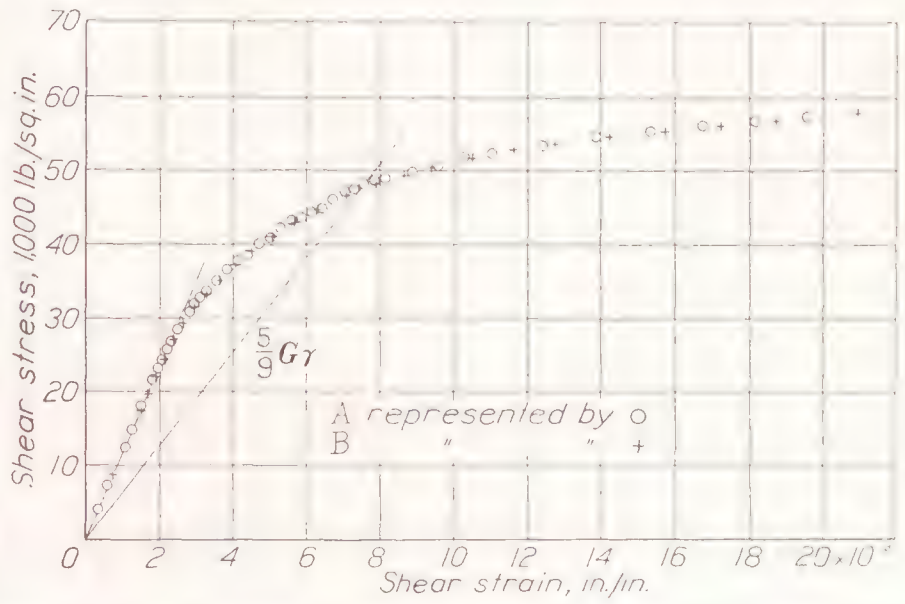

FIGURE 4.—Shear stress-strain curve for specimen J_1 (chromium-molybdenum, $t/D=0.0562$) calculated from torque-twist curve.

A. Approximate method: Assume linear stress distribution across section as in elastic case, calculate stresses and strains at mean fiber from

$$\tau=\frac{2M}{\pi t D^2}\,\frac{1}{1-2\frac{t}{D}+2\frac{t^2}{D^2}}$$

$$\gamma=\frac{\theta D}{2}\left(1-\frac{t}{D}\right)$$

B. Exact method: Solve the recursion formula

$$\frac{\tau D\theta}{2}=\left(\frac{2}{D}\right)^3\left\{\frac{1}{2\pi}\left[\theta\frac{dM}{d\theta}+3M\right]+\left(\frac{D-2t}{2}\right)^3\tau\left(\frac{D-2t}{2}\right)^n\right\}.$$

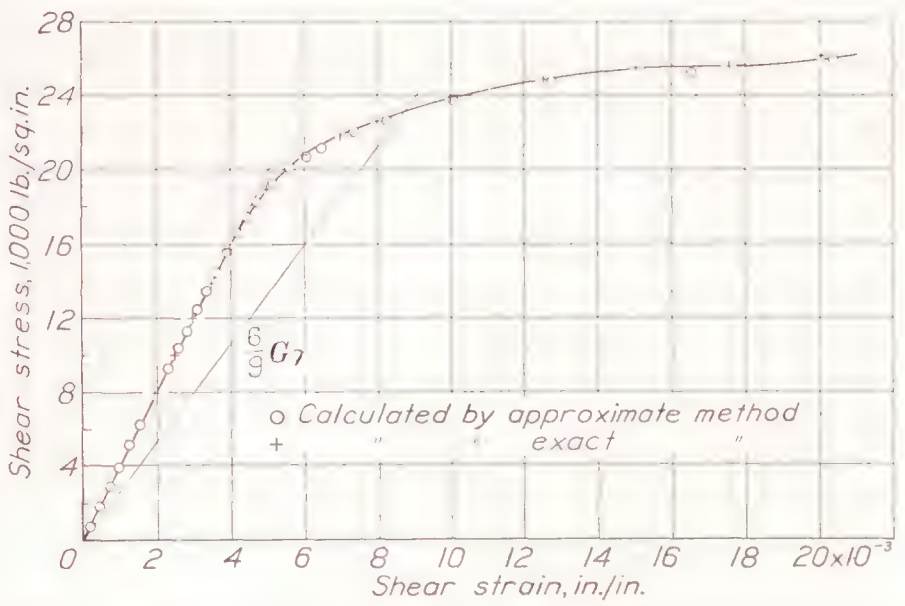

FIGURE 5.—Shear stress-strain curve for specimen Aa_1 (17ST, $t/D=0.1192$) calculated from torque-twist curve.

deformation of the axis of the tube (L_5, S_2) or, as in the case of some of the aluminum-alloy tubes, by a sudden fracture (T_1); specimen J_5 (fig. 6) would probably have failed by fracture if it had not developed a slight two-lobe buckle after twisting plastically through a large angle.

ANALYSIS OF RESULTS

DISCUSSION OF TYPES OF FAILURE

Observation of the failure of thin circular tubes in torsion has shown that three different limiting types of failure are of particular significance in engineering design:

1. Two-lobe buckling of the tube wall.
2. Helical deformation of the axis of the tube.
3. Plastic yielding of the material.

The first two types are caused by elastic instability of the twisted tube and do not necessarily involve permanent deformation of the material. They have been treated theoretically by Schwerin (reference 6).

Schwerin's formulas for the buckling strength of long tubes may be written in terms of the ratio t/D of wall thickness to outside diameter in the following form:

1. For two-lobe buckling

$$\tau=\frac{0.656E}{1-\mu^2}\left(\frac{t}{D}\right)^{3/2}\left(1+2.4\frac{t}{D}+\cdots\right) \tag{6}$$

where τ is the critical shear stress at the mean fiber; E, Young's modulus; and μ, Poisson's ratio of the material. Terms involving $\left(\frac{t}{D}\right)^2$ are neglected in the parentheses since they are small for tubes in which such elastic failure can take place.

2. For buckling of the axis of the tube into a helix Schwerin derived the formula

$$\tau=\frac{\pi E}{1-\mu}\frac{D}{L}\left(1-\frac{t}{D}+\frac{1}{3}\frac{t^2}{D^2}\cdots\right) \tag{7}$$

where L is the length of the tube.

3. If plastic yielding is assumed to progress under a constant and uniformly distributed stress in shear:

$$\tau=\text{constant} \tag{8}$$

the value of the constant being equal to the stress at which the stress-strain curve in shear becomes horizontal.

The conditions of perfect symmetry and homogeneity on which equations (6) and (7) are based are not realized in practice. Nor will the conditions underlying (8), i. e., yielding under constant stress independent of strain, be true for most materials. The equations (6), (7), and (8) represent, therefore, only approximations of practical cases. The degree of approximation for the cases of elastic buckling has been investigated fully in an excellent paper by L. H. Donnell. (See reference 7.) Donnell found that the experimental value of critical shear stress for tubes was roughly 75 percent of the calculated critical stress.

Although equations (6), (7), and (8) are only rough approximations of practical cases, they give a general idea of the effect of different variables upon the torsional strength and upon the type of failure. If they were accurate representations of the behavior of tubes, the stress at failure and the type of failure could be predicted by computations of τ in each of the equations

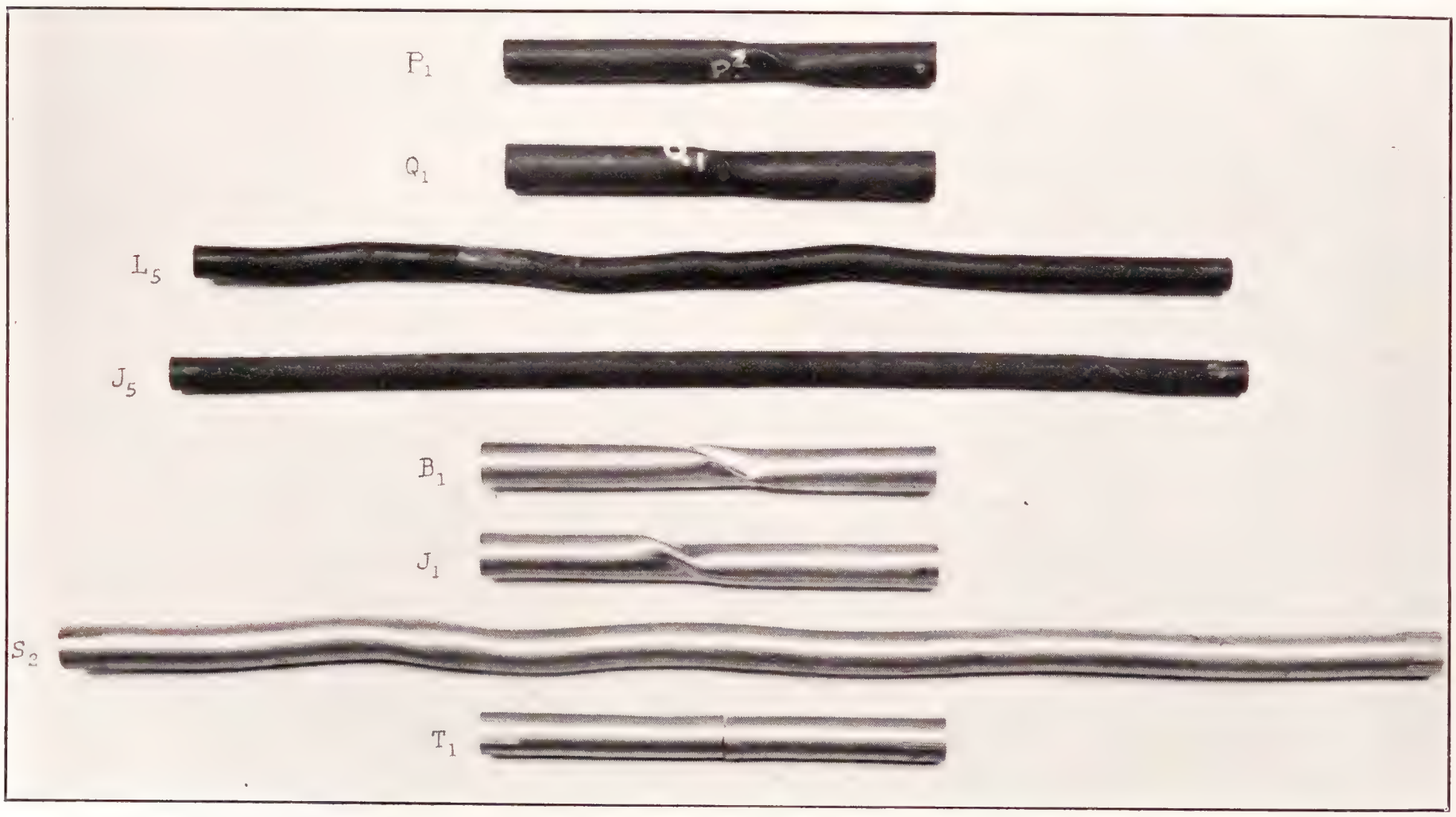

FIGURE 6.—Appearance of four chromium-molybdenum steel tubes (P_1, Q_1, L_5, J_5) and four 17ST aluminum-alloy tubes (B_1, J_1, S_2, T_1) after completion of torsion test. P_1, B_1 failed by sudden two-lobe buckling; Q_1, J_1 failed by gradual two-lobe buckling; L_5, S_2 failed by helical deformation of the axis; T_1 failed by fracture; J_5 twisted plastically through a large angle and then failed by a slight two-lobe buckle.

(6), (7), and (8). The conditions at failure would be those for which τ is smallest. An analysis of this sort was made for all the tubes tested. Young's modulus E and Poisson's ratio μ were taken equal to the average value given in (12) and (13) on page (11) below. The values of μ, E, t, D, and L being known, the critical shear stresses given by equations (6) and (7) were calculated.

The resulting tabulation of values of τ as given by equations (6) and (7) always showed higher values for helical twisting than for two-lobe buckling. The value of τ for two-lobe buckling lay above the yield strength in shear for 55 out of the 63 steel tubes and for 90 out of the 102 aluminum-alloy tubes. The yield strength in shear was taken as the stress at which the secant modulus of the stress-strain curve in shear was $\frac{5}{8}$ times the initial modulus for the steel tubes and $\frac{6}{8}$ times the initial modulus for the aluminum-alloy tubes. More information concerning the factors $\frac{5}{8}$ and $\frac{6}{8}$ is given later.

For the remaining 8 of the steel tubes and for 3 of the aluminum-alloy tubes the theoretical shear stress for two-lobe buckling lay between that at which the secant modulus of the stress-strain curve in shear deviated by 2 percent from its initial value and the yield strength in shear as just defined. For the remaining 9 of the aluminum-alloy tubes it lay below the stress at which the secant modulus deviated 2 percent from its initial value.

It would not be correct to conclude from this analysis that the shear stress had passed beyond the yield strength in most of the tubes tested before failure took place. That statement would be true only if the critical shear stress for two-lobe buckling could be calculated from (6) up to the yield stress in shear. The critical shear stress is considerably lower than that given by (6) if the stress-strain curve deviates gradually from Hooke's law in approaching the yield strength. However, the analysis did show that considerable yielding must have preceded failure in all but 8 of the steel tubes and all but 12 of the aluminum-alloy tubes. For only 9 of the aluminum-alloy tubes did the analysis predict failure by elastic two-lobe buckling.

It is noteworthy that none of the tubes fell into the category of failure by helical twisting. This result does not exclude this type of failure as a practical possibility. It only indicates that none of the tubes used in the present investigation (maximum length/diameter ratio, $L/D = 80$) were sufficiently long to deform into a helix before failing either by two-lobe buckling or by plastic failure.

Inspection of the tubes after failure (see fig. 6 and tables VII and VIII) indicated that helical twisting did actually occur in some of the thick-wall long tubes and also that in the majority of the tubes the final failure was one of two-lobe buckling. The observed helical failures and also many of the two-lobe failures must have occurred after the yield strength of the material had been reached; i. e., they must be considered as a consequence of the yielding of the material rather than the primary cause of failure.

The conclusion that helical failure, with its dependence on length, must have been secondary is confirmed by a comparison of the shear stress at failure for the 60-inch tubes with that for the 20-inch tubes as given in tables VII and VIII. Only the tubes failing elastically show a consistent tendency toward lower strengths with increase in length. However, this tendency does not indicate the occurrence of helical failure even for the tubes failing elastically. The lowering in strength of the elastic tubes may be explained by the effect of length on the stress producing two-lobe buckling.

If plastic failure and two-lobe failure alone controlled the strength of the tubes, it should be possible to describe the strength of these tubes in terms of the variables determining these types of failure. The maximum median-fiber shear stress in the plastic failure of a thin tube depends primarily on the ultimate strength in shear of the material. In a tube that buckles elastically the maximum median-fiber shear stress will, according to equation (6), vary with the ratio t/D. In the intermediate case of plastic buckling both t/D and the shape of the stress-strain curve in shear beyond the proportional limit are important factors.

No simple relation was found to describe accurately the stress-strain curves of the tubes in shear beyond the proportional limit. An approximate idea of the stress-strain curve may be obtained from a knowledge of both the yield strength in shear τ_{yield} and the ultimate strength in shear τ_{ult}. The ratio of ultimate strength in shear to yield strength in shear may be taken as a measure of the rise in the stress-strain curve beyond the yield point. If this ratio is close to 1.0, the stress-strain curve beyond the yield point will be nearly horizontal while a ratio of 1.4 indicates a considerable rise in stress beyond the yield point; in one case the stress-strain curve will have a sharp knee near the yield point while in the other that knee will be well rounded.

RELATION BETWEEN STRESS-STRAIN CURVES IN SHEAR AND STRESS-STRAIN CURVES IN TENSION

There is still one difficulty in choosing τ_{yield}, τ_{ult} as the two variables that, in addition to the variable t/D, affect the strength of the present group of steel and aluminum-alloy tubes. Neither of these quantities is ordinarily known and both can be determined from torsion tests only when the specimen has sufficiently thick walls so that failure occurs by yielding without any buckling. The properties of the material that are generally known are the yield strength in tension, σ_{yield}, and the ultimate strength in tension, σ_{ult}. It would be possible to substitute these two tensile properties for the two shear properties of the material if a simple relation of sufficient accuracy could be found connecting the two sets of properties.

The existence of such a relation, particularly for the chromium-molybdenum steel tubes, is indicated by the

similarity in shape of stress-strain curves in tension and in shear of specimens cut from the same tube (see figs. 1 and 2.) Theoretical considerations (reference 5, p. 204) indicate that the stress-strain curve in shear may be computed from the stress-strain curve in tension by simply multiplying tensile strains by 1.5 and dividing tensile stresses by $\sqrt{3}$.

The applicability of this relation to the steel tubes was tested by using it to compute for several tubes the stress-strain curves in shear from their tensile stress-strain curves. The measured stress-strain curves in shear and those calculated from the tension tests were found to agree fairly well over their entire range. In most cases it was noticed, however, that the calculated stress-strain curve lay a small distance to the right of the observed curve. A closer degree of coincidence could have been obtained by choosing a value less than 1.5 for the factor by which tensile strains must be multiplied to obtain shear strains. This deviation from the theoretical values is not surprising, since the

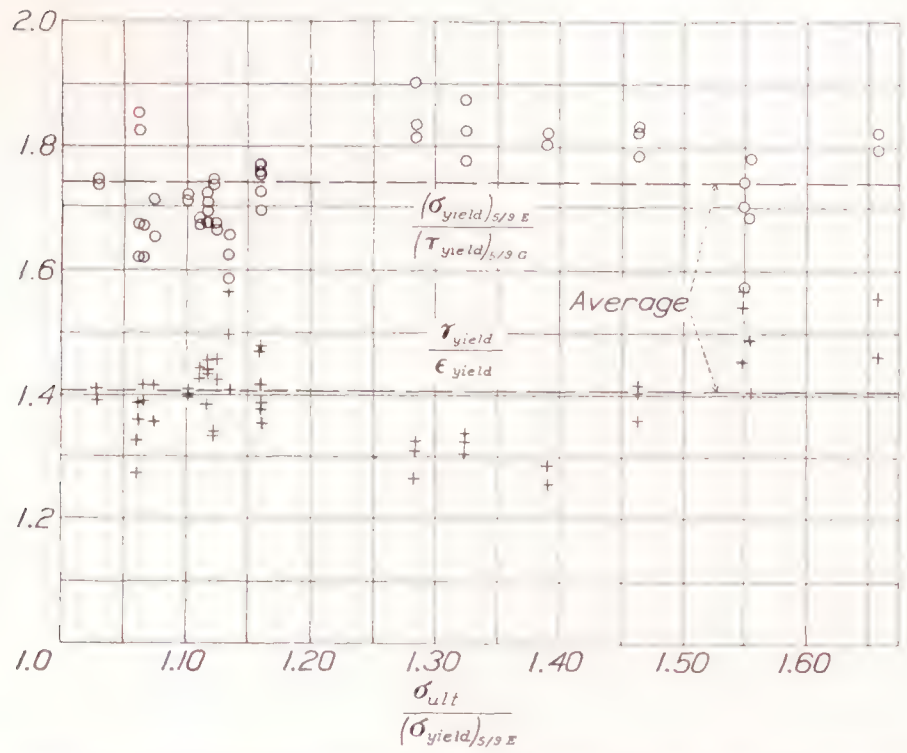

FIGURE 7.—Ratios of yield strengths and yield strains in shear and in tension for chromium-molybdenum steel tubes.

theoretical ratios $\sqrt{3}$ and 1.5 have a sound basis only for an idealized stress-strain curve with an infinitely sharp knee at the yield point and no rise in stress beyond that point. For the same reason one would expect the foregoing ratios not to hold for the aluminum-alloy tubes in which the ratio of ultimate strength to yield strength was not 1, but lay between 1.3 and 1.5.

An estimate of the optimum "factors of affinity" σ/τ and γ/ϵ connecting stress-strain curves in tension and in shear was obtained by plotting the ratios of yield stresses and yield strains $\frac{\sigma_{yield}}{\tau_{yield}}, \frac{\gamma_{yield}}{\epsilon_{yield}}$ for each one of the tubes tested using $\frac{\sigma_{ult}}{\sigma_{yield}}$ as abscissa to bring out the variation of the two ratios of affinity with the change in shape of the stress-strain curve beyond the yield strength. (See fig. 7 for steel tubes and fig. 8 for aluminum-alloy tubes.)

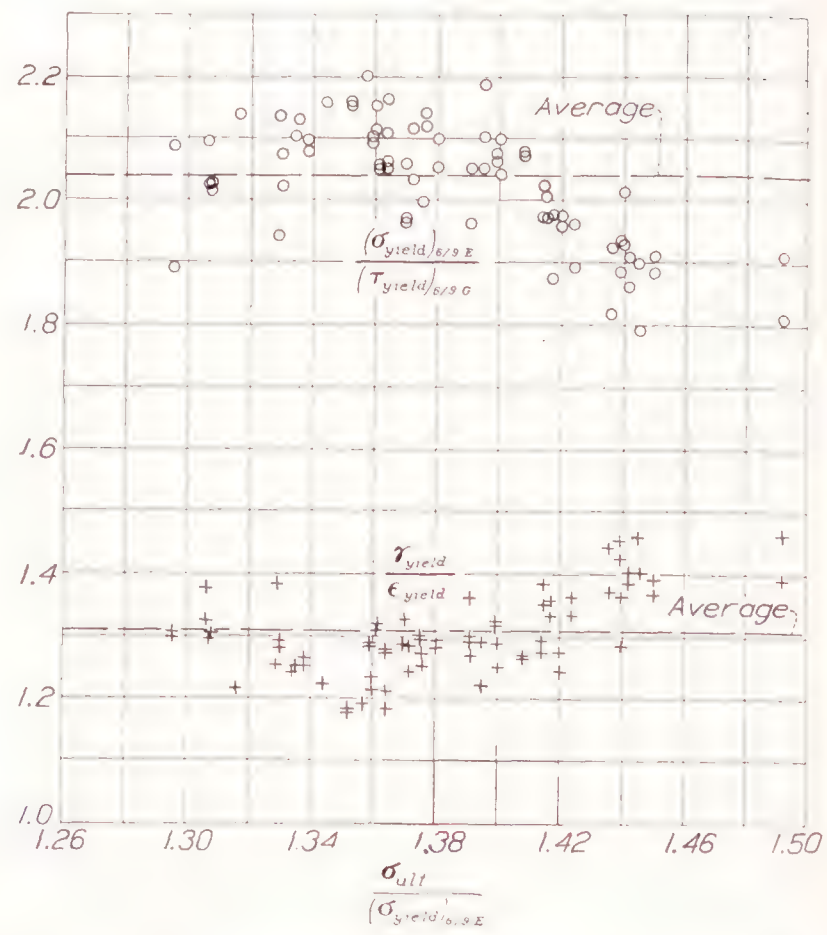

FIGURE 8.—Ratios of yield strengths and yield strains in shear and in tension for 17ST aluminum-alloy tubes.

The yield strength used in these computations was taken as that stress on the stress-strain curve at which the secant modulus was $\frac{5}{9}$ the elastic modulus for the steel tubes and the stress at which it was $\frac{6}{9}$ of the elastic modulus for the aluminum-alloy tubes. The factors $\frac{5}{9}$ and $\frac{6}{9}$ were chosen to give the same value for the tensile yield strength of material just passing Navy Specifications 44T18a and 44T21 (tables I and II) as the yield strength laid down in these specifications (0.2 percent offset), provided the material has a Young's modulus of 30×10^6 pounds per square inch for the steel tubes and one of 10×10^6 pounds per square inch for the aluminum-alloy tubes. The tensile yield strengths computed upon both definitions are listed in tables V and VI. The averages at the bottom of these tables show that the $\frac{5}{9}$ E yield strength is 2 percent higher, on the average, for the chromium-molybdenum steel tubes and that the $\frac{6}{9}$ E yield strength agrees, on the average, within a fraction of 1 percent with the 0.2 percent offset yield strength for the aluminum-alloy tubes. The chief advantage of the $\frac{5}{9}$ E and $\frac{6}{9}$ E yield strengths over the 0.2 percent yield strength is that it will bring the elastic portion of the stress-strain curves in tension into coincidence with the elastic portion of the stress-strain curves in shear if the ordinates and abscissas of the tensile stress-strain curve are multiplied by the factors $\frac{\tau_{yield}}{\sigma_{yield}}, \frac{\gamma_{yield}}{\epsilon_{yield}}$, respectively.

For the steel tubes (fig. 7) the ratio $\frac{\sigma_{yield}}{\tau_{yield}}$ scattered within ±11 percent about an average value of 1.73 while the ratio $\frac{\gamma_{yield}}{\epsilon_{yield}}$ scattered through the same percentage range about an average value of 1.41. There

is a systematic deviation from these average values that becomes a maximum for tubes having $\frac{\sigma_{ult}}{\sigma_{yield}}=1.3$ approximately. The theoretical affinity ratios $\sqrt{3}$ and 1.5 are fair approximations for the stress-strain curves approaching the idealized shape $\frac{\sigma_{ult}}{\sigma_{yield}}=1.0$. For the aluminum-alloy tubes (fig. 8) the picture is quite different; the ratio $\frac{\sigma_{ult}}{\sigma_{yield}}$ lies between 1.3 and 1.5. It is not surprising, therefore, that the average affinity ratios are nowhere near the theoretical values $\sqrt{3}$ and 1.5; they are closer to 2 and 1.3. The maximum scatter to each side of these average values is of the order of ±11 percent.

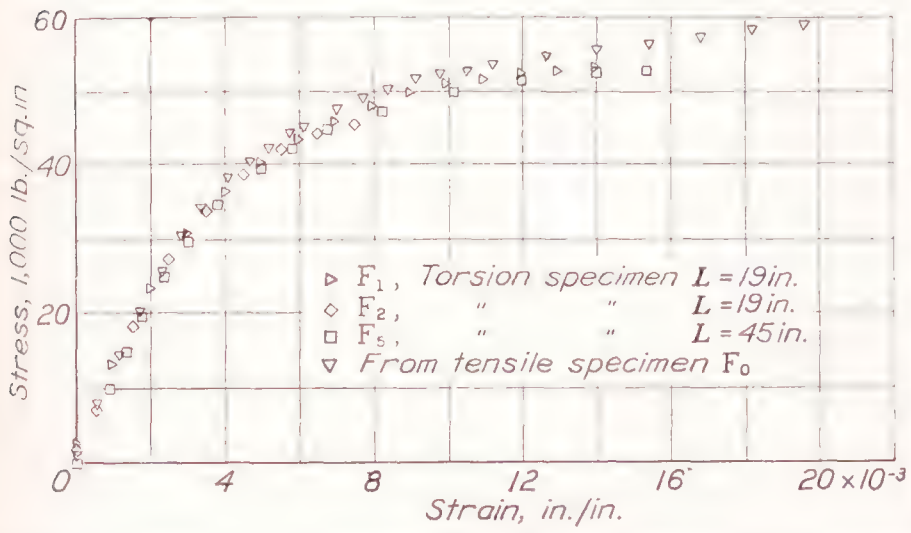

FIGURE 9.—Comparison of stress-strain curves in shear of chromium-molybdenum steel tubes F_0 (1.38 × 0.038 in.) with curve obtained from tensile stress-strain curve by multiplying stresses by $1/\sqrt{3}$ and strains by 1.4.

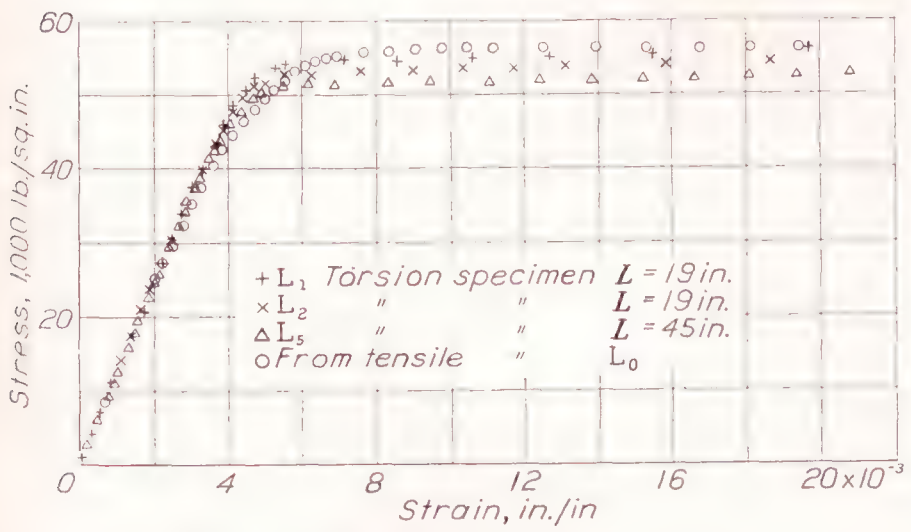

FIGURE 10.—Comparison of stress-strain curves in shear of chromium-molybdenum steel tubes L_0 (1.5 × 0.12 in.) with curve obtained from tensile stress-strain curve by multiplying stresses by $1/\sqrt{3}$ and strains by 1.4.

The usefulness of these approximate affinity relations in predicting the shear stress-strain curve from the tensile stress-strain curve is brought out by figures 9 and 10 for a group of steel tubes and by figures 11 and 12 for a group of aluminum-alloy tubes. These figures show the stress-strain curves in shear as computed from those in tension by multiplying tensile strains by 1.4 for the steel tubes and by 1.3 for the aluminum-alloy tubes and dividing the tensile stresses by $\sqrt{3}$ and 2, respectively. The stress-strain curves in shear as obtained directly from the torque-twist curves are shown for comparison. The calculated curves approached those obtained from the test data satisfactorily; i. e., within the limits of variations of the different torsion tests, except in the neighborhood of the knee, where the stresses deviated as much as 15 percent for the aluminum-alloy tubes M_1, M_2, M_0 (fig. 11). The greater deviation from affinity for the aluminum-alloy tubes as compared with the steel tubes is also brought out by a comparison of figure 2 with figure 1.

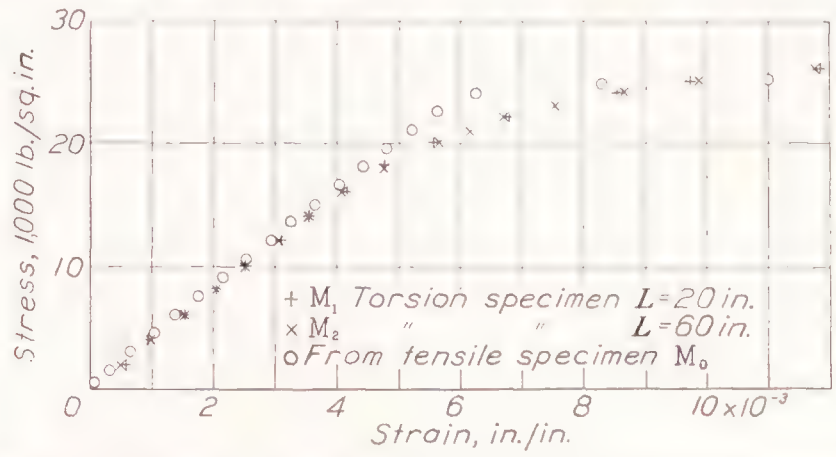

FIGURE 11.—Comparison of stress-strain curves in shear of 17ST aluminum-alloy tubes M_0 (2×0.11 in.) with curve obtained from tensile stress-strain curve by multiplying stresses by 0.5 and strains by 1.3.

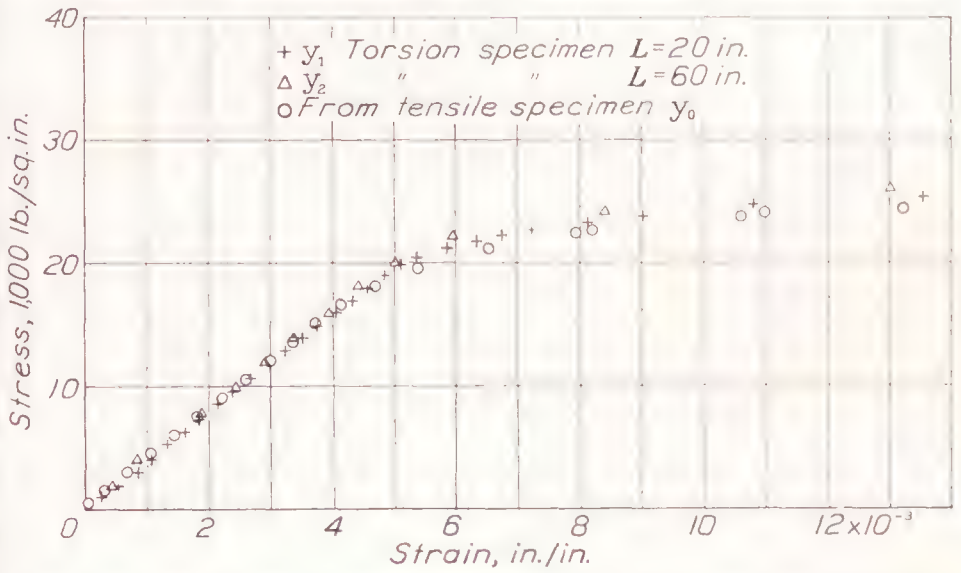

FIGURE 12.—Comparison of stress-strain curves in shear of 17ST aluminum-alloy tubes y_0 (1×0.09 in.) with curve obtained from tensile stress-strain curve by multiplying stresses by 0.5 and strains by 1.3.

VARIATION OF STRENGTH OF TUBES WITH DIMENSIONS AND PHYSICAL PROPERTIES

Variation of stresses at failure.—It has been stated that the tubes tested failed either by plastic torsion, two-lobe buckling, or a failure intermediate between these and that the strength of the tube should therefore depend on the variables determining these three types of failure. For a tube of given metal, i. e., given elastic constants, the length of which is in the range where its effect is negligible, these variables are the wall thickness over diameter ratio t/D, and at least two variables describing the plastic properties in shear of the tube material; e. g., the yield point in shear, τ_{yield} and the ultimate strength in shear, τ_{ult}. In the previous section it was shown that the shear properties and tensile properties of the tube material were roughly affine. The last two variables may therefore be replaced by the corresponding tensile properties, i. e., σ_{yield} and σ_{ult}. In general, then, one would expect that

the maximum shearing stress of the tubes would follow a relation of the type:

$$\tau_{max}=f\left(\frac{t}{D},\ \sigma_{yield},\ \sigma_{ult}\right) \tag{9}$$

It is necessary to reduce the number of independent variables from 3 to 2 in order to represent the results as a family of curves on a sheet of paper. This reduction may be accomplished by trying various relations between τ_{max} and one of the independent variables and then choosing the one that gives the most consistent behavior for the experimental points. After a number of trials the most consistent behavior for the steel tubes was found by plotting:

$$\frac{\sqrt{3}\tau_{max}}{\sigma_{yield}}=f\left(\frac{t}{D},\frac{\sigma_{ult}}{\sigma_{yield}}\right) \tag{10}$$

The factor $\sqrt{3}$ was chosen to make the ordinates close to 1 for most of the tubes.

For the aluminum-alloy tubes it appeared preferable to plot:

$$2\frac{\tau_{max}}{\sigma_{ult}}=f\left(\frac{t}{D},\frac{\sigma_{ult}}{\sigma_{yield}}\right) \tag{11}$$

The corresponding plots using t/D as abscissa and the term on the left as ordinate are shown in figures 13 and 14 for the two groups of tubes. The points for the steel tubes (fig. 13) show a large scatter throughout the range tested. This result would be expected from the considerable variation in the ratio $\frac{\sigma_{ult}}{\sigma_{yield}}$ and the values of σ_{ult} itself (table V). The points for the aluminum-alloy tubes (fig. 14) fall close to a common curve except for the very thin tubes, which failed by elastic buckling. Figure 14 clearly shows a segregation into the three types of failure that were observed; i. e., failure by elastic two-lobe buckling on the extreme left, failure by a combination of yielding in shear and buckling in the middle, failure in pure shear on the extreme right. The two extreme types of failure are understood fairly well. The theoretical shearing stress at failure for a long tube failing elastically is given by equation (6); for tubes of finite length, it can either be derived from Schwerin's theory (reference 6) or it can be read off directly from the curves computed by Donnell (reference 7). (The three curves shown for elastic two-lobe buckling in figs. 13 and 14 correspond to minimum, average, and maximum values of σ_{yield} and σ_{ult}, respectively, as measured for the tubes tested.)

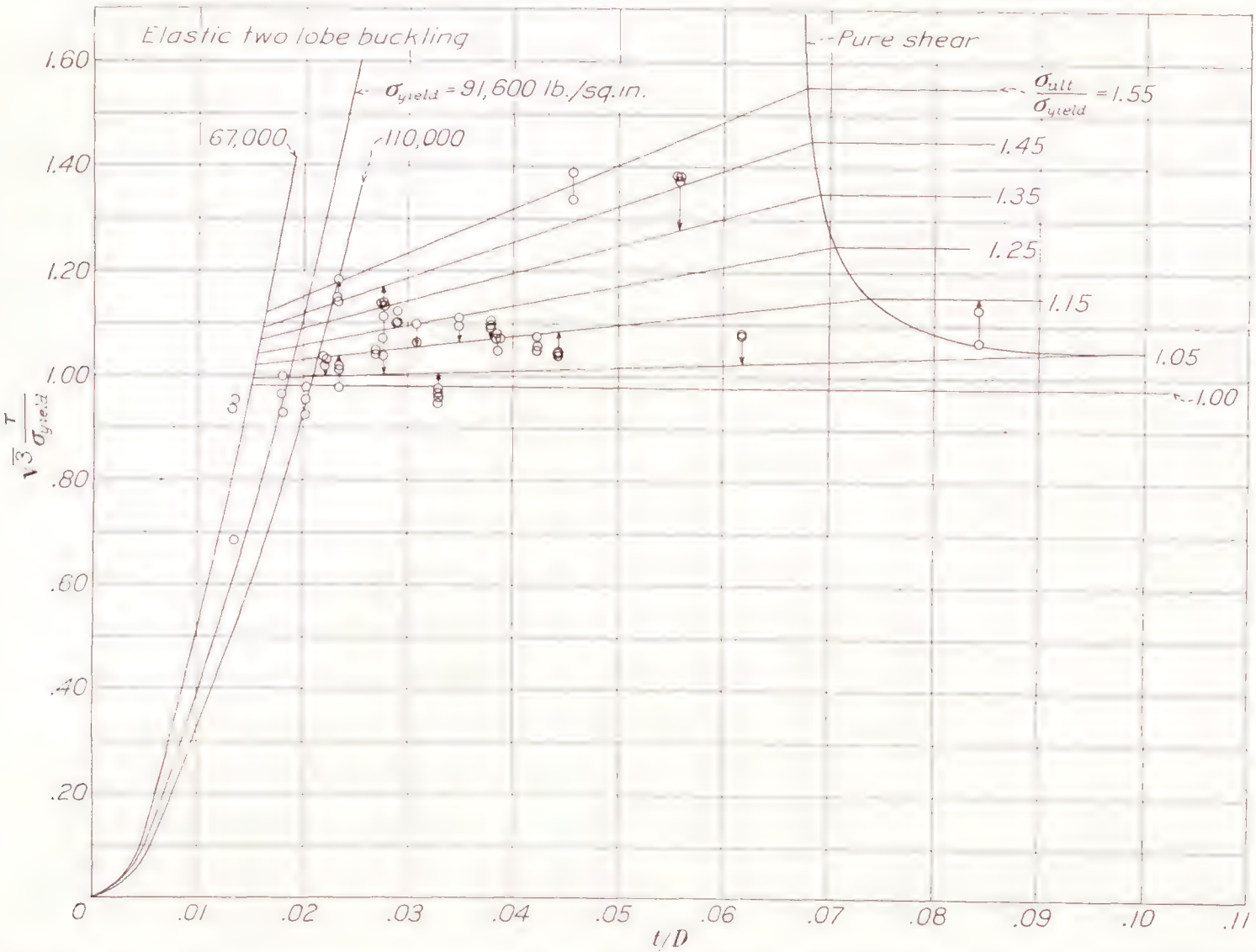

FIGURE 13.—Variation of ratio of shear stress at failure to tensile yield strength with t/D for chromium-molybdenum steel tubes. Straight lines in central region calculated from:

$$\sqrt{3}\frac{\tau}{\sigma_{yield}}=15.27\frac{t}{D}\left(\frac{\sigma_{ult}}{\sigma_{yield}}-1\right)+0.981.$$

Figures 13 and 14 show that no more than 7 of the steel tubes and no more than 20 of the aluminum-alloy tubes can be considered as having failed by elastic buckling; this number includes the tubes lying in the transition region between elastic failure and combined failure as well as those definitely to the left of it. The

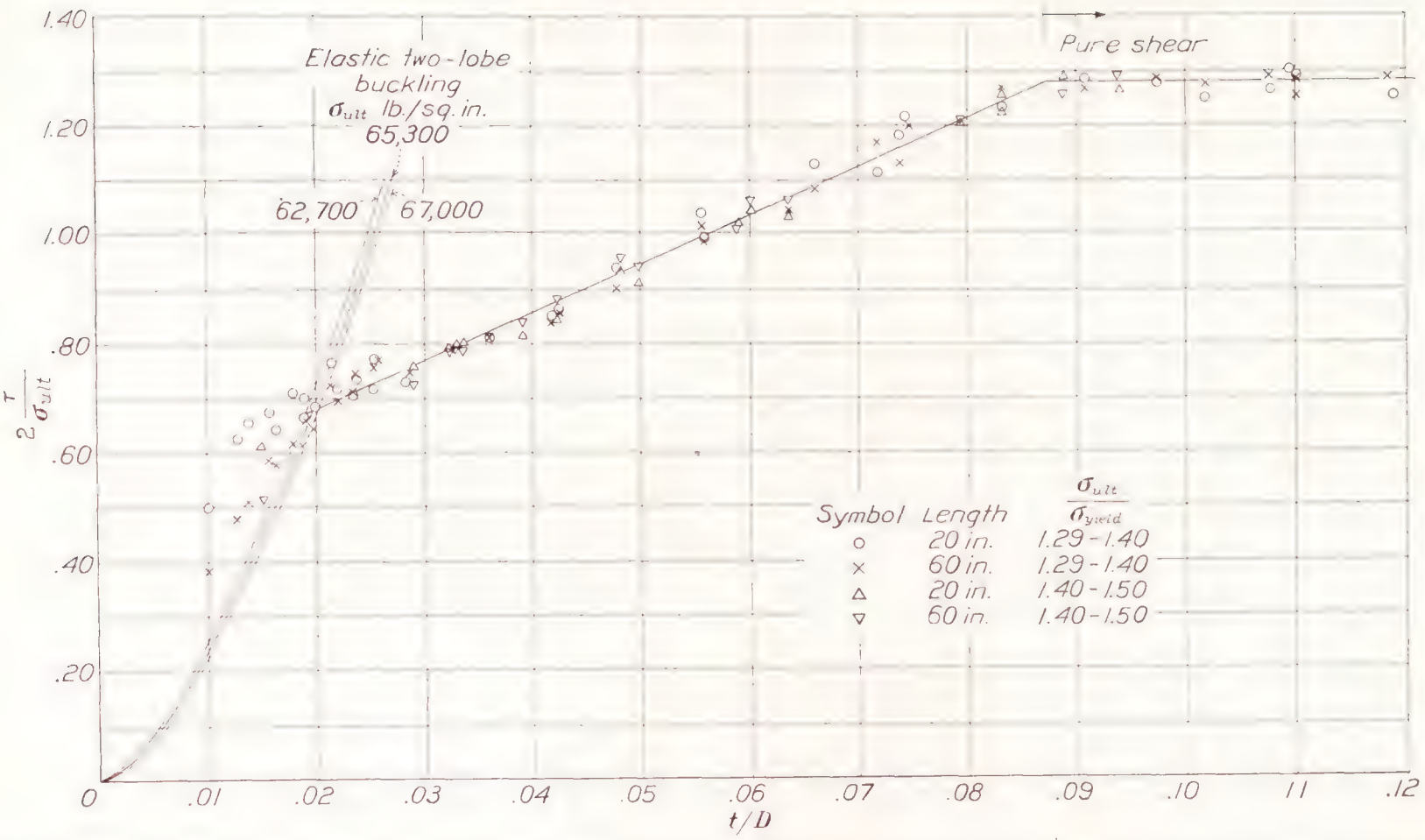

FIGURE 14.—Variation of ratio of shear stress at failure to tensile strength with t/D for 17ST aluminum-alloy tubes. Straight line in central region calculated from:

$$2\frac{\tau}{\sigma_{ult}}=8.96\frac{t}{D}+0.501.$$

approximate analysis in an earlier section of this paper had predicted that 8 of the steel tubes and 11 of the aluminum-alloy tubes should have fallen into this category. The agreement, though not close, is sufficient considering the uncertainty of the assumptions made, especially those relative to the limit above which combined failure must be expected.

In every case of elastic buckling the long tubes failed at a lower stress than the short ones, the difference exceeding 30 percent in some cases. Schwerin's formula for long tubes (equation (6)) is not sufficient, therefore, to describe the strength of the short tubes failing elastically. An adequate comparison with the theory must include the effect of length as considered in general by Schwerin (reference 6) and in detail by Donnell (reference 7). Donnell has shown that the effect of length L, thickness t, and diameter D on the strength in torsion of an elastic tube may be represented on a single curve by plotting

$$B=\sqrt{1-\mu^2}\frac{\tau}{E}\frac{L}{t}$$

as a function of

$$J=\frac{1}{\sqrt{1-\mu^2}}\frac{L^2t}{D^3}$$

Figure 15 shows the curves derived by Donnell for tubes with hinged edges and with clamped edges together with Schwerin's curve for infinitely long tubes. The individual points represent the observed values of $B=f(J)$ computed from the observed shear stress at failure and the dimensions of the tube and the following elastic constants: for chromium-molybdenum steel tubes,

E=28,600,000 pounds per square inch, μ=0.235, (12)

for 17ST aluminum-alloy tubes,

E=10,430,000 pounds per square inch, μ=0.319. (13)

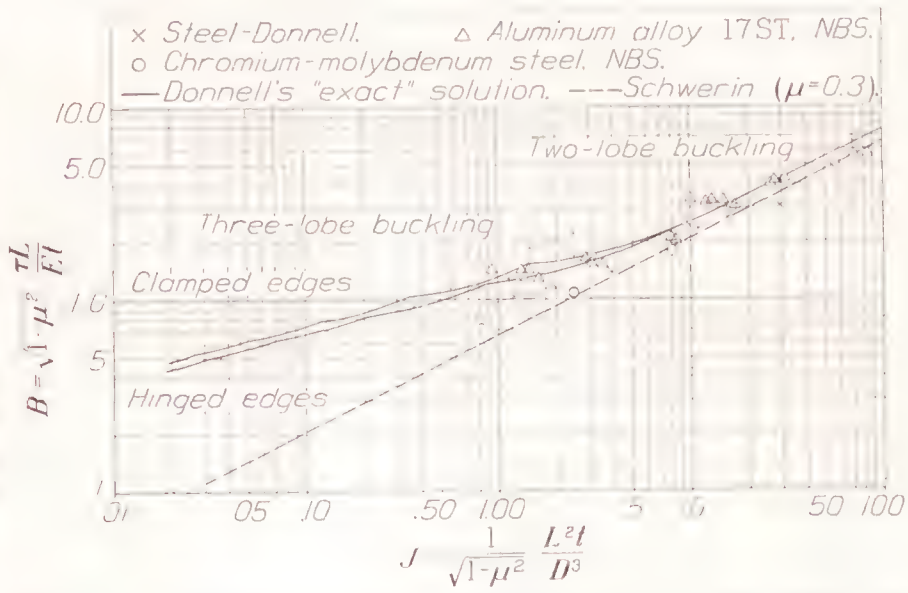

FIGURE 15.—Comparison of observed shear stress at failure of tubes that failed by elastic buckling with theoretical values given by Donnell and Schwerin.

The Young's moduli represent average values of the modulus measured in the tension test (tables V and VI). The values for Poisson's ratio represent an average of values calculated for each size of tube from the well-known relation $\mu=\frac{E}{2G}-1$. This relation is strictly true only for perfectly isotropic material obeying Hooke's Law. The relatively low value of μ for the steel tubes may be due partly to lack of isotropy of the material. It did not seem worth while to investigate this in view of the small effect of a change in μ on the critical stress of a thin tube as given by figure 15. The

points for the steel tubes are scattered over the same region as those obtained by Donnell in tests on steel tubes buckling with two lobes (crosses); they are on the average about 25 percent below the curve for a tube with hinged edges. The points for the aluminum-alloy tubes are somewhat higher, scattering through a range of about ±25 percent about the curve with hinged edges. A few points fell into the border region between two-lobe and three-lobe failure. Examination of the corresponding tubes indicated a failure which may have started with three lobes but which ended with two lobes as the deformation increased. No definite reason can be assigned for the greater strengths of the aluminum-alloy tubes; possibly the closer tolerances within which the tubes are manufactured permit them to develop more nearly the full theoretical strength of the ideal tube. All of the tubes except one showed strengths greater than that given by Schwerin's formula for infinitely long tubes. Donnell's curve for hinged edges may, therefore, be taken as a fair estimate of the probable strength of the tubes failing elastically while Schwerin's formula may be used to give a lower limit of their strength.

Failure in plastic shear may be expected when the shear stress reaches a value equal to the ultimate shear strength, τ_{ult}, of the material. In the case of the steel tubes (fig. 13) this assumption leads to a family of horizontal straight lines having the ordinate

$$\frac{\sqrt{3}\tau}{\sigma_{yield}}=\frac{\sqrt{3}\tau_{ult}}{\sigma_{ult}}\frac{\sigma_{ult}}{\sigma_{yield}}$$

Only 2 of the 63 steel tubes tested fell into the region of failure in pure shear. These two were insufficient to establish a value for the ratio τ_{ult}/σ_{ult}. In the absence of adequate test data it was decided to assume this ratio to be the same as that of the yield strengths:

$$\tau_{ult}=\frac{1}{\sqrt{3}}\sigma_{ult}=0.577\ \sigma_{ult} \tag{14}$$

This assumption is believed to be conservative since the corresponding ratio of ultimate stresses for the aluminum-alloy tubes was found to be about 10 percent higher; i. e., 0.64. Converting equation (14) into the ordinates used in figure 13 gives the family of horizontal lines:

$$\sqrt{3}\frac{\tau_{ult}}{\sigma_{yield}}=\frac{\sigma_{ult}}{\sigma_{yield}}$$

In the case of the aluminum-alloy tubes (fig. 14) 18 of the points fall into the region of plastic shear. They scatter about a common horizontal line with the ordinate

$$2\frac{\tau}{\sigma_{ult}}=1.28 \tag{15}$$

For the aluminum-alloy tubes, therefore, the ultimate strength in plastic shear is about 64 percent of the ultimate strength in tension.

It is seen, after drawing the curves corresponding to elastic failure for a long tube as given by equation (6) and the horizontal straight lines corresponding to failure by plastic shear, that most of the points fall into the intermediate region. For the aluminum-alloy tubes the individual points seem to fall about a common straight line increasing with the t/D ratio. The points for the steel tubes in figure 13 show too great a scatter to suggest the type of variation with t/D at a glance; however, it appears, after segregating the points into groups with nearly constant ratio $\sigma_{ult}/\sigma_{yield}$ that a linear increase with t/D is the simplest variation that gives an approximate fit. It remains to find an empirical relation between the stress ratio at failure and the ratio $\sigma_{ult}/\sigma_{yield}$. A number of formulas were tried and the best fit was obtained with a formula of the type:

$$\frac{\sqrt{3}\tau}{\sigma_{yield}}=a\frac{t}{D}\left(\frac{\sigma_{ult}}{\sigma_{yield}}-1\right)+b \tag{16}$$

where a and b are constants. Evaluating these constants by least squares gave $a=15.27$ and $b=0.981$ so that the stress ratio at failure of the chromium-molybdenum steel tubes buckling plastically may be expressed by the empirical formula:

$$\frac{\sqrt{3}\tau}{\sigma_{yield}}=15.27\frac{t}{D}\left(\frac{\sigma_{ult}}{\sigma_{yield}}-1\right)+0.981,\ \begin{pmatrix}0.02<\frac{t}{D}<0.07\\ (L/D\leq 80).\end{pmatrix} \tag{17}$$

The stress ratios calculated from this formula are plotted against the observed stress ratios in figure 16. The points scatter about 5 percent to either side of the line of exact agreement. The corresponding empirical formula for the plastic buckling of the aluminum-alloy tubes was also evaluated with the help of least squares; it may be written as:

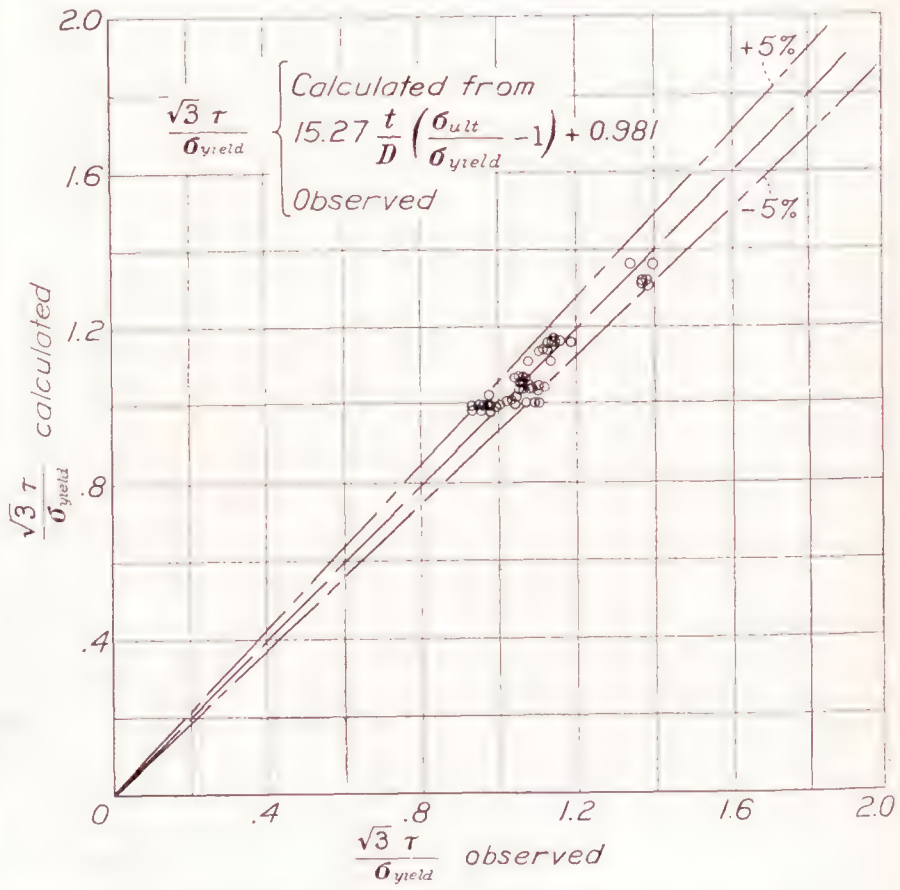

FIGURE 16.—Comparison of calculated and observed stress ratios for chromium-molybdenum steel tubes.

$$\frac{\tau}{\sigma_{ult}}=4.48\frac{t}{D}+0.2506,\left(0.022<\frac{t}{D}<0.085,\frac{L}{D}\leq 60\right). \quad (18)$$

The lower limit of $\frac{t}{D}=0.022$ corresponds to the cut-off of the empirical formula by Schwerin's curve for long tubes. Data on torsion tests of short tubes kindly

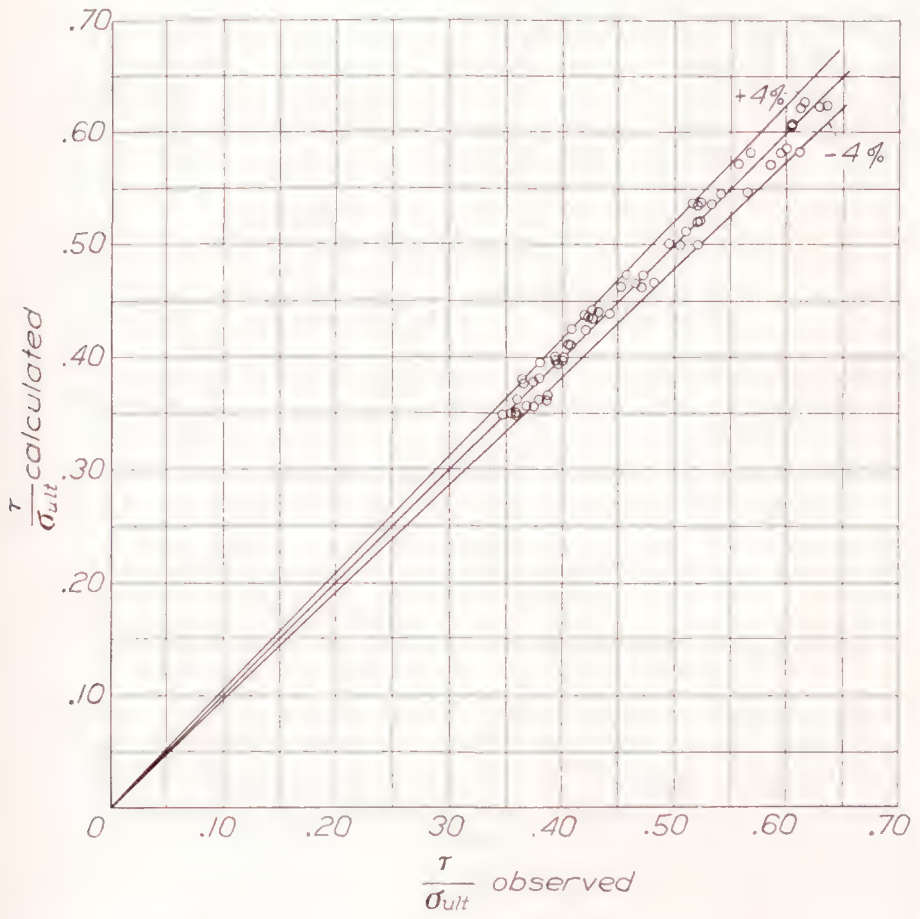

FIGURE 17.—Comparison of calculated and observed stress ratios for 17ST aluminum-alloy tubes:

$$\frac{\tau}{\sigma_{ult}}=4.48\frac{t}{D}+0.2506$$

for, $0.022<\frac{t}{D}<0.085$.

supplied by the Aluminum Company of America indicate that the cut-off for short tubes can be moved to smaller values of $\frac{t}{D}$. The tests made by the Aluminum Company of America (Physical Test Report No. 31–40) on 13 17ST tubes having a $\frac{t}{D}$ ratio ranging from 0.0095 to 0.02 and an $\frac{L}{D}=4.8$, indicate that the straight line (18) may be extended to the left down to $\frac{t}{D}=0.09$ at which point it is cut off by Donnell's curve (see fig. 15) for $\frac{L}{D}=4.8$. Tests on 23 further tubes with $\frac{L}{D}=7$ and with $\frac{t}{D}$ ranging from 0.018 to 0.099 were found to scatter uniformly about the straight lines given by (18) and (15). The stress ratios calculated from formula (18) are compared with the observed stress ratios in figure 17. The individual points scatter about 4 percent to either side of the line of exact agreement.

Design charts for twisting moment producing failure.—Designers are usually more interested in expressing the torsional strength of a tube in terms of torque at failure rather than in terms of the mean fiber stress τ at failure. The value of τ had originally been derived from M by relation (5), so that τ and M are connected by the formula:

$$M=\frac{\pi D^3}{2}\frac{t}{D}\left(1-\frac{2t}{D}+2\left(\frac{t}{D}\right)^2\right)\tau \quad (19)$$

Formulas for M for the three types of failure may be obtained from equation (19) by substituting for τ the value obtained from Donnell's work (fig. 15) for the case of elastic failure, from equations (17) and (18) for the case of combined failure, and from equations (14) and (15) for the case of plastic failure.

Elastic failure by two-lobe buckling depends, according to Donnell, on the length as well as on the wall-thickness ratio t/D of the tube. For long tubes (fig. 15) the length effect is small, however, and the actual strength of the tube will be only a few percent greater than that given by Schwerin's formula (6) in which the length does not enter.

Substituting equations (6), (17), (14), and (12) in equation (19) gives the following formulas for the twisting torque at failure of the chromium-molybdenum steel tubes: two-lobe buckling failure of a long tube:

$$\frac{M}{D^3\sigma_{yield}}=\frac{3.11\times 10^7}{\sigma_{yield}}\left(\frac{t}{D}\right)^{5/2}\left(1+0.4\frac{t}{D}\right) \quad (20)$$
$$\left(0\leq\frac{t}{D}\leq 0.024\right)$$

combined plastic failure and buckling:

$$\frac{M}{D^3\sigma_{yield}}=0.908\left(\frac{t}{D}\right)\left(1-2\frac{t}{D}+2\frac{t^2}{D^2}\right)\left[15.27\frac{t}{D}\left(\frac{\sigma_{ult}}{\sigma_{yield}}-1\right)+0.981\right],\left(0.015>\frac{t}{D}>0.092\right) \quad (21)$$

failure in pure shear:

$$\frac{M}{D^3\sigma_{yield}}=0.908\frac{t}{D}\left(1-2\frac{t}{D}+2\frac{t^2}{D^2}\right)\frac{\sigma_{ult}}{\sigma_{yield}} \quad (22)$$
$$\left(0.068<\frac{t}{D}<0.100\right)$$

The ranges of t/D for which each one of these formulas holds overlap because the boundary between the different types of failure depends on σ_{yield} and σ_{ult} in addition to t/D. The proper type of formula to use in any given case is the one that gives the lowest twisting moment M. In the special case of a material for which $\sigma_{ult}=\sigma_{yield}$, it is seen that combined failure according to equation (21) should always occur in preference to failure in pure shear, the torque for combined failure being about 2 percent less than that for pure shear. Actually the 2 percent variation is not significant; the experimental scatter of points would produce an uncertainty of this

order in the fitting of the empirical relation (17) by least squares. For material having a stress-strain curve such that $\sigma_{ult}=\sigma_{yield}$ equations (21) and (22) should coincide since a tube of such material would not be able to carry more than the yield stress in torsion of the material.

The equations (20), (21), and (22) cannot be expressed in Cartesian coordinates as a single curve or even as a family of curves because they contain the four variables $\frac{M}{D^3\sigma_{yield}}$, $\frac{t}{D}$, $\frac{\sigma_{ult}}{\sigma_{yield}}$, and σ_{yield}. In order to show them as a single curve in a nomographic chart connecting the first three variables, σ_{yield} must be expressed as a function of $\frac{\sigma_{ult}}{\sigma_{yield}}$ of a type form;

$$\sigma_{yield}=\frac{1}{c_0\left(\frac{\sigma_{ult}}{\sigma_{yield}}-1\right)+c_1} \tag{23}$$

which converts equation (20) into the same type form as equation (21). Evaluating c_0 and c_1 to give the best fit to the observed values of the tensile yield strengths plotted as a function of $\frac{\sigma_{ult}}{\sigma_{yield}}$ gave the following relation for (23):

$$\sigma_{yield}=\frac{10^6}{6.62\left(\frac{\sigma_{ult}}{\sigma_{yield}}-1\right)+9.79}. \tag{24}$$

Figure 18 shows the nomogram that was derived from equations (21) and (22) after substituting equation (24) in (20). Two examples illustrate the use of this nomogram.

1. Find the wall thickness of a 2-inch chromium-molybdenum steel tube 4 feet long that will fail when subjected to a torque of 2,500 lb.-ft. The tensile yield strength of the tube material is 80,000 pounds per square inch and its tensile ultimate strength is 100,000 pounds per square inch.

Answer. The tube falls within the range of dimensions and properties of those tested so that figure 18 may be applied to compute its wall thickness.

$$\frac{\sigma_{ult}}{\sigma_{yield}}=\frac{100000}{80000}=1.25$$

$$\frac{M}{D^3\sigma_{yield}}=\frac{2500\times12}{2^3(80000)}=0.0469$$

Connecting these points on the nomogram (dotted line, fig. 18) gives:

$$\frac{t}{D}=0.0487,\ t=2\times0.0487=0.0974 \text{ inch.}$$

Failure by combined plastic shear and buckling may be expected.

2. Find the wall thickness of a 1½-inch chromium-molybdenum steel tube 5 feet long that will fail when subjected to a torque of 600 lb.-ft. The tensile yield strength of the tube material is 75,000 pounds per square inch and its tensile ultimate strength is 95,000 pounds per square inch.

Answer. The tube falls within the range of dimensions and properties of those tested so that figure 18 may be applied to compute it.

$$\frac{\sigma_{ult}}{\sigma_{yield}}=\frac{95,000}{75,000}=1.267$$

$$\frac{M}{D^3\sigma_{yield}}=\frac{600\times12}{1.5^3\times75,000}=0.0284$$

Connecting these points on the nomogram (dotted line, fig. 18) gives two intersections as follows:

$$\frac{t}{D}=0.0229,\ \frac{t}{D}=0.0302.$$

The first value corresponds to two-lobe buckling as a long tube and the second, to combined failure. A heavier tube is required to resist combined failure than to resist buckling; hence combined failure is more likely to occur. The wall thickness must be chosen as

$$t=1.5\times0.0302=0.0453 \text{ inch.}$$

Frequently material is required to satisfy certain specifications for minimum yield strength and tensile strength.

Design curves for such material may easily be derived either from equations (20), (21), and (22) or from figure 18 by the substitution of the specified values of σ_{ult} and σ_{yield}. Figure 19 shows a design chart for determining the size of chromium-molybdenum steel tubes 19 to 60 inches in length that just meet the minimum requirements of Navy Specifications 44T18 and 44T18a (table I).

The material of the tube specified in problem 2 just meets Navy Specification 44T18a. The curve of figure 19 can, therefore, be applied directly to solve problem 2.

$$\frac{M}{D^3}=\frac{600\times12}{1.5^3}=\frac{7,200}{3.375}=2,130 \text{ lb./sq. in.}$$

The ordinate $\frac{M}{D^3}=2,130$ intersects curve B at $\frac{t}{D}=0.03$.

A vertical through the point of intersection extending into the lower half of the chart intersects the inclined line for $D=1.5$ inch at a value of $t=0.045$ inch. This solution coincides with the one obtained from the nomogram of figure 18.

Design charts for the aluminum-alloy tubes may be obtained by substituting the expressions for critical stress given by equations (6), (18), and (15) into equation (19). If, in addition, the values given in equation (13) for the elastic constants E and μ are substituted, the following three equations are obtained for the torque at failure.

For elastic two-lobe buckling of a long tube according to Schwerin:

$$\frac{M}{D^3\sigma_{ult}}=\frac{1.2\times10^7}{\sigma_{ult}}\left(\frac{t}{D}\right)^{5/2}\left(1+0.4\frac{t}{D}\right),\ \left(0<\frac{t}{D}<0.02\right), \tag{25}$$

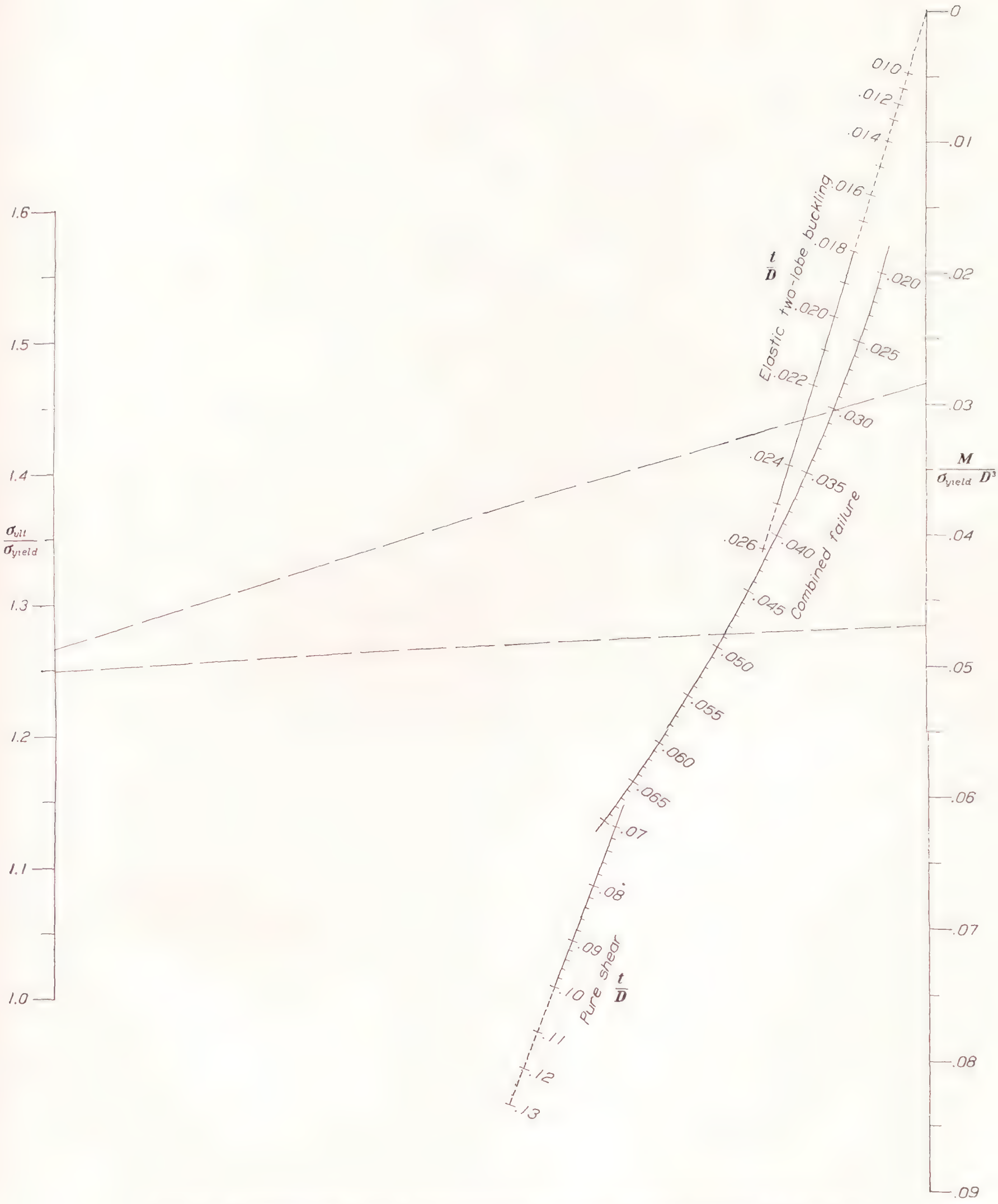

FIGURE 18.—Nomographic design chart for torsional strength of chromium-molybdenum steel tubes 19–60 inches long.

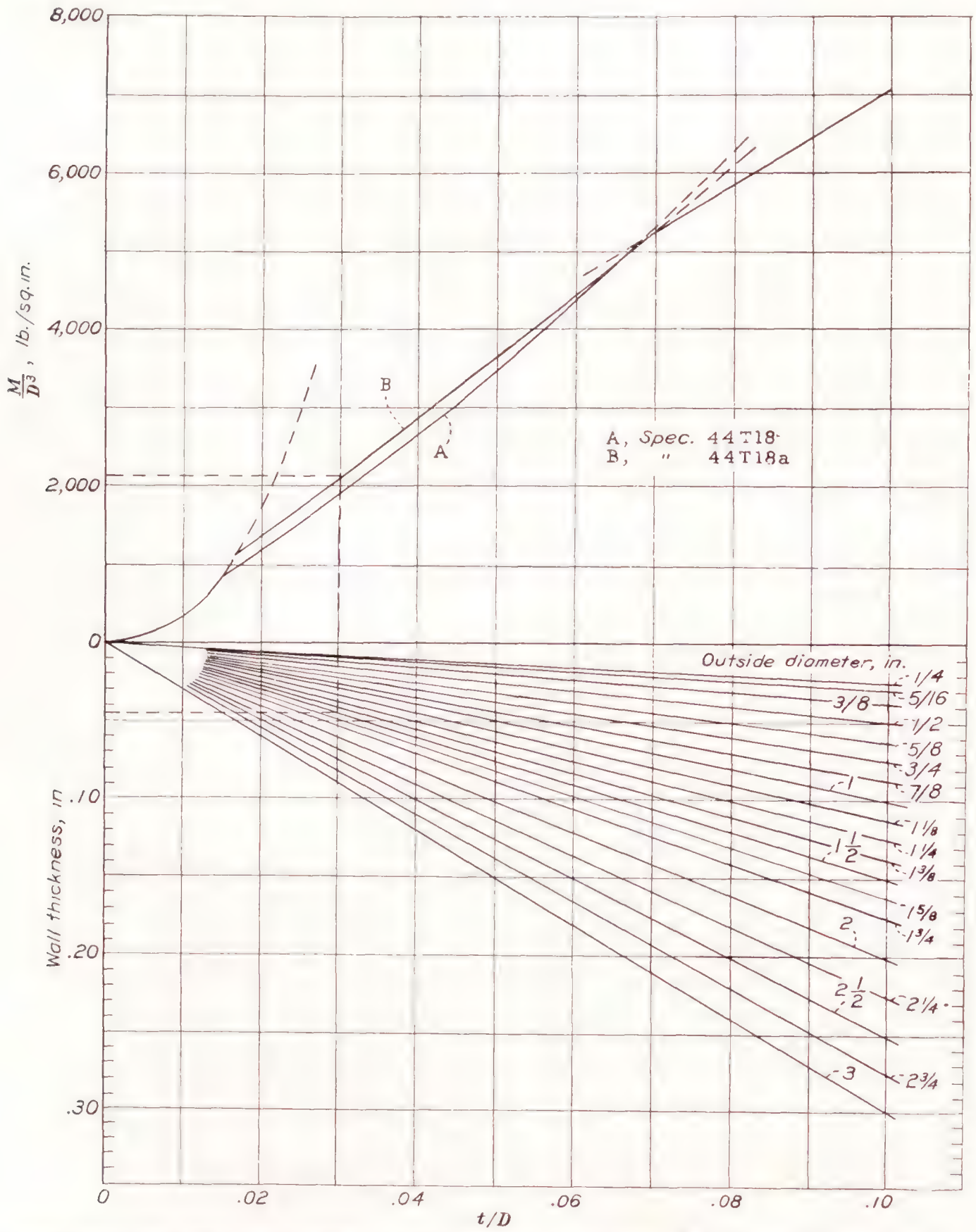

FIGURE 19.—Design chart for torsional strength of chromium-molybdenum steel tubes 19–60 inches long satisfying Navy Specification 44T18 (σ_{ult}=95,000 lb./sq. in., σ_{yield}=60,000 lb./sq. in.) and Navy Specification 44T18a (σ_{ult}=95,000 lb./sq. in., σ_{yield}=75,000 lb./sq. in.).

for combined plastic failure and two-lobe buckling:

$$\frac{M}{D^3\sigma_{ult}}=0.394\left(\frac{t}{D}\right)\left(1+15.9\frac{t}{D}-33.7\frac{t^2}{D^2}\right),$$

$$\left(0.02<\frac{t}{D}<0.088\right), \tag{26}$$

for failure in pure shear:

$$\frac{M}{D^3\sigma_{ult}}=1.005\left(\frac{t}{D}\right)\left(1-2\frac{t}{D}+2\frac{t^2}{D^2}\right),$$

$$\left(0.088<\frac{t}{D}<0.12\right). \tag{27}$$

The strength of the aluminum-alloy tubes can, accordingly, be described with the help of the three variables $\frac{M}{D^3\sigma_{ult}}$, σ_{ult}, and $\frac{t}{D}$. Only the two variables $\frac{M}{D^3\sigma_{ult}}$ and $\frac{t}{D}$ are needed if curves of (25) are plotted for given values of σ_{ult} as in figure 14. This procedure results in figure 20. A simple example will illustrate the use of these curves.

Find the wall thickness of a 2-inch 17ST aluminum-alloy tube 5 feet long that will fail when subjected to a torque of 2,000 lb.-ft. The tensile strength of the tube material is 68,000 pounds per square inch.

Answer.—The tube falls within the range of dimensions and properties of those tested so that figure 20 may be applied to compute it.

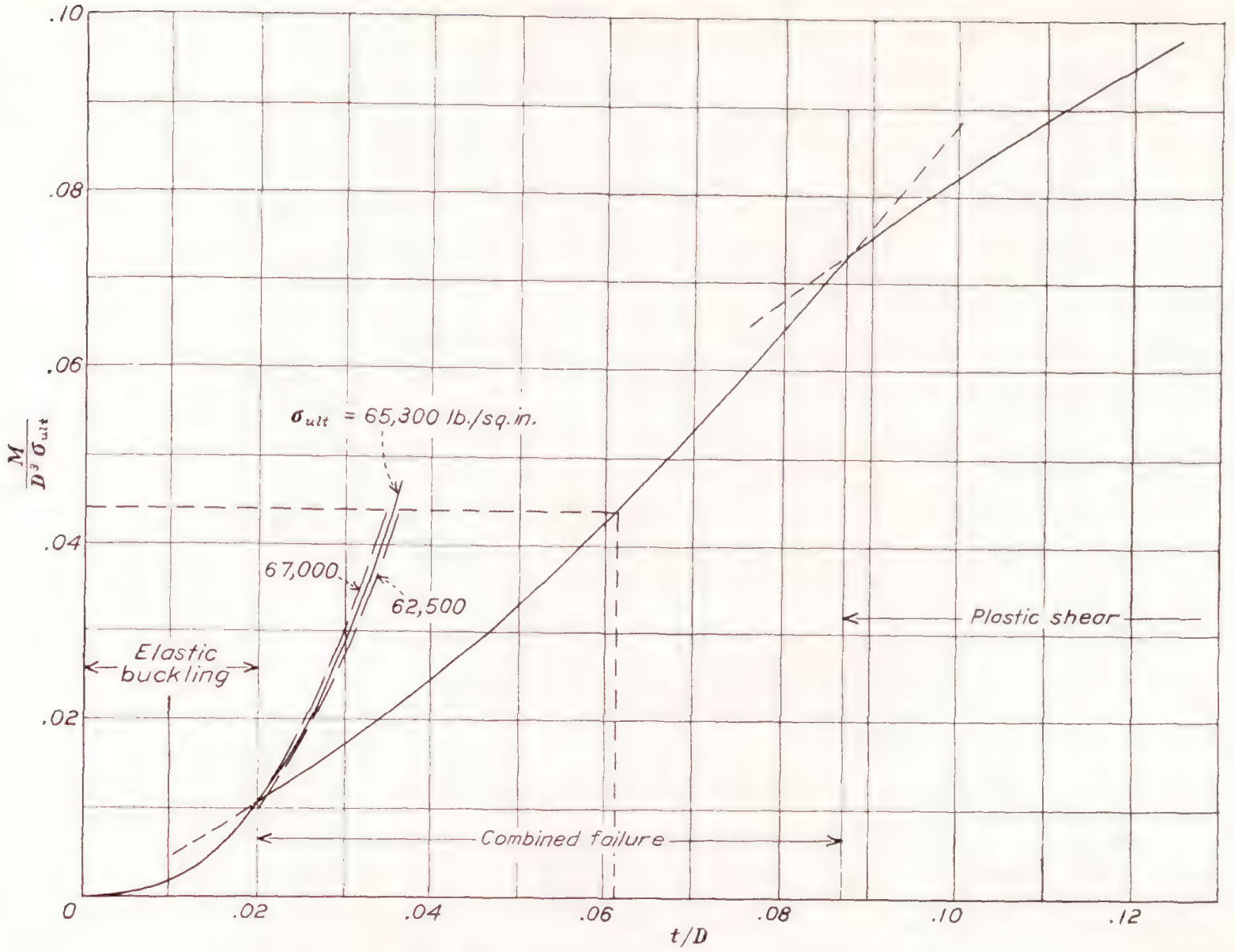

FIGURE 20.—Design chart for torsional strength of 17ST aluminum-alloy tubes.

$$\frac{M}{D^3\sigma_{ult}}=\frac{2{,}000\times12}{2^3\times68{,}000}=0.0441$$

According to figure 20, this corresponds to

$$\frac{t}{D}=0.061,\ t=0.061\times2=0.122 \text{ inch.}$$

The wall thickness of the tube that may be expected to fail under about 2,000 lb.-ft. torque would be 0.122 inch.

A design chart similar to figure 19 may be derived from figure 20 for aluminum-alloy material required to satisfy certain specifications for minimum tensile strength. Figure 21 shows such a chart for 17ST tubing complying with Navy Specification 44T21 (table II); the upper half of the figure was constructed from figure 20 by substituting 55,000 pounds per square inch for σ_{ult}, while the lower half is a set of straight lines corresponding to commercially available diameters of 17ST tubing. The following example illustrates the use of figure 21.

Find the wall thickness of a 2-inch 17ST aluminum-alloy tube 5 feet long that will fail when subjected to a torque of 1,000 lb.-ft. The material of the tube shall just meet Navy Specification 44T21.

The tube falls within the range of dimensions and properties of those tested so that figure 21 may be applied to compute it.

$$\frac{M}{D^3}=\frac{1000\times12}{2^3}=1{,}500$$

It is seen that by following the dotted line in figure 21 that this value corresponds to a wall thickness of t=0.086 inch in a tube 2 inches in diameter.

NATIONAL BUREAU OF STANDARDS,
WASHINGTON, D. C., *February 1937.*

REFERENCES

1. Otey, N. S.: Torsional Strength of Nickel Steel and Duralumin Tubing as Affected by the Ratio of Diameter to Gage Thickness. T. N. No. 189, N. A. C. A., 1924.
2. The Allowable Stress in Tubes Subjected to Torsion. A. C. I. C. No. 641, Matériel Division, Army Air Corps, 1929.
3. Templin, R. L., and Moore, R. L.: Specimens for Torsion Tests of Metals. A. S. T. M. Proc., Part II, 30, 1930, pp. 534–543.
4. Fuller, Forrest B.: The Torsional Strength of Solid and Hollow Cylindrical Sections of Heat-Treated Alloy Steel. Jour. Aero. Sci., vol. III, no. 7, May 1936, pp. 248–251.
5. Nadai, A.: Plasticity. McGraw-Hill Book Co., Inc., 1931.
6. Schwerin, E.: Die Torsionsstabilität des dünnwandigen Rohres. Z. f. a. M. M., vol. V, no. 3, June 1925, pp. 235–243.
7. Donnell, L. H.: Stability of Thin-Walled Tubes Under Torsion. T. R. No. 479, N. A. C. A., 1933.

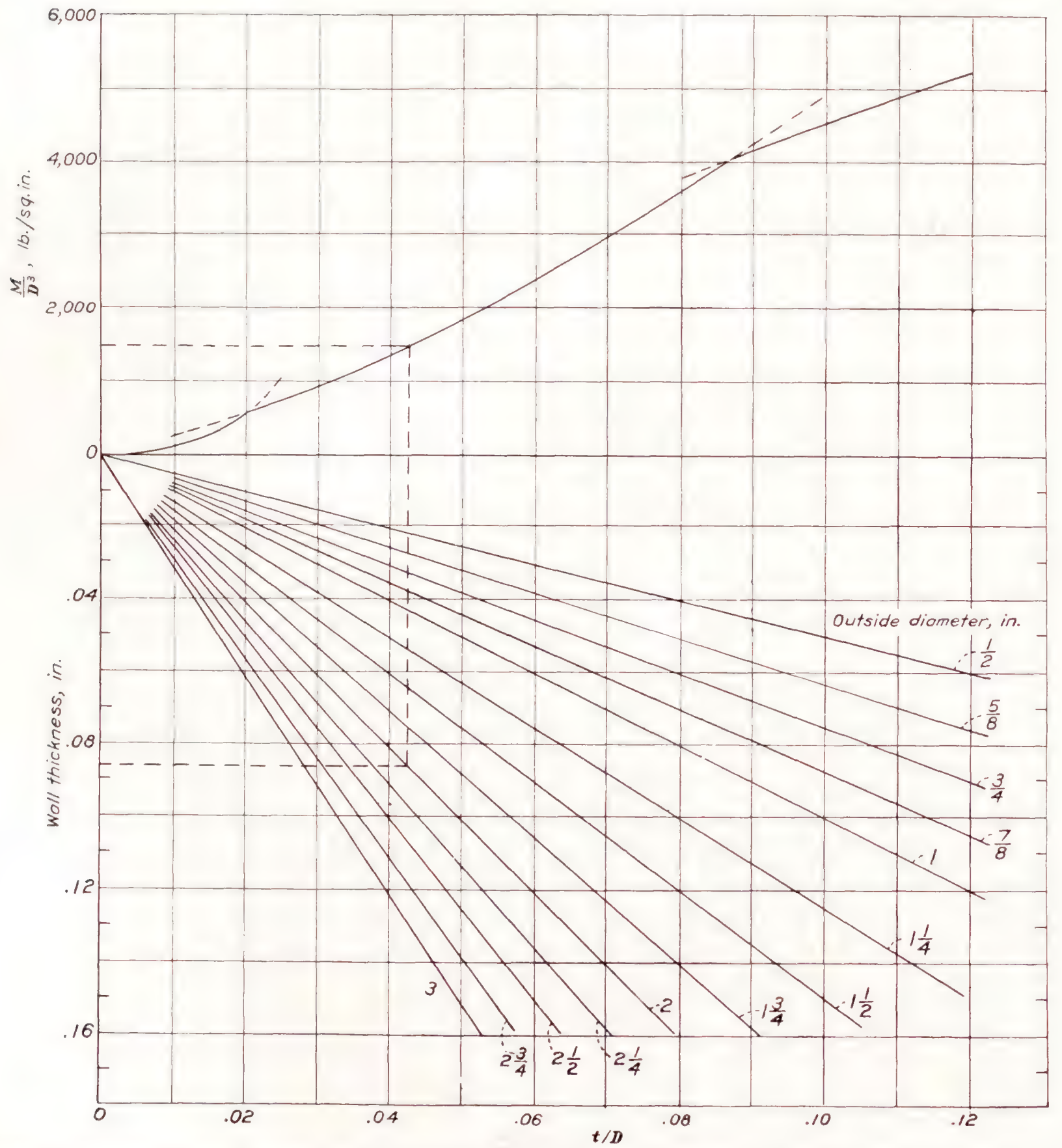

FIGURE 21.—Design chart for torsional strength of 17ST aluminum-alloy tubes 19–60 inches long satisfying Navy Specification 44T21 (σ_{ult}=55,000 lb./sq. in.).

TABLE V.—TENSILE AND HARDNESS PROPERTIES OF CHROMIUM-MOLYBDENUM STEEL TUBES

Specimen	Nominal size (in.)	Yield strength 0.002 [a] (lb./sq. in.)	Yield strength 5/9 *E* (lb./sq. in.)	Tensile strength (lb./sq. in.)	Elongation in 2 inches (percent)	Vickers numbers [b] Left end	Vickers numbers [b] Right end	Young's modulus (lb./sq. in.)	Tensile strength / Yield strength
A_0	¾×0.028	84,000	84,300	97,400	23.0	209	224	29.9×10⁶	[c] 1.16
B_0	1 × .035	89,000	91,000	101,000	18.0	216	214	28.8	1.14
C_0	1⅛× .049	93,000	93,500	102,500	12.5	224	213	29.0	1.10
D_0	1½× .058	99,000	100,000	110,700	18.5	249	240	29.1	1.12
E_0	2 × .065	108,000	109,500	114,800	18.5	264	253	28.7	1.06
F_0	1⅜× .035	81,000	84,000	118,700	17.2	263	264	28.8	1.46
G_0	1½× .035	69,200	69,000	107,300	28.5	260	260	29.0	1.55
H_0	1½× .049	78,600	79,400	88,400	17.0	214	204	28.5	1.12
I_0	1½× .065	67,700	67,700	105,300	32.0	206	214	28.6	1.56
J_0	1½× .083	82,200	85,500	114,300	24.0	262	263	28.8	1.39
K_0	1½× .095	110,000	110,500	113,300	16.8	243	242	28.8	1.03
L_0	1½× .120	96,000	97,000	106,700	26.0	236	232	28.5	1.11
M_0	1⅝× .049	90,500	91,100	96,600	16.0	241	266	27.3	1.07
N_0	1¾× .049	96,800	103,600	132,900	19.0	296	311	27.6	1.37
O_0	1⅝× .035	93,000	93,300	100,300	14.0	240	274	27.5	1.08
P_0	1¾× .035	105,000	105,300	109,700	16.0	283	262	27.6	1.04
Q_0	2 × .035	99,100	101,000	109,200	11.5	264	245	27.6	1.10
R_0	1⅛× .035	95,200	95,900	101,700	14.0	254	248	29.0	1.07
S_0	1¼× .035	87,800	88,200	98,200	16.0	252	239	28.4	1.12
T_0	1½× .035	93,800	95,500	107.400	17.0	245	232	28.2	1.14
U_0	1½× .049	103,800	105,300	122,000	15.0	272	270	28.8	1.18
V_0	2½× .032	75,000	73,000	122,500	24.0	281	270	30.2	1.63
Average (22 specimens)		90,800	92,900	108,200	18.8	249	247	28.6	1.208

[a] Stress at which strain exceeds $\frac{\text{stress}}{30\times10^6}$ by 0.002, in./in.
[b] Vickers numbers for 10-kg weight.
[c] Based on 0.002 yield strength.

TABLE VI.—TENSILE AND HARDNESS PROPERTIES OF 17ST ALUMINUM-ALLOY TUBES

Specimen	Nominal size (in.)	Yield strength 0.002 [a] (lb./sq. in.)	Yield strength 2/3 *E* (lb./sq. in.)	Tensile strength (lb./sq. in.)	Elongation in 2 inches (percent)	Vickers numbers [b] Left end	Vickers numbers [b] Right end	Young's modulus (lb./sq. in.)	Tensile strength / Yield strength
l_0	1 ×0.018	46,600	46,700	63,400	24.0	127	125	10.27×10⁶	[c] 1.36
m_0	1 × .020	47,200	47,300	63,600	22.0	134	133	10.18	1.34
n_0	1 × .022	48,900	49,000	65,400	25.0	134	134	10.13	1.34
o_0	1 × .025	49,000	49,100	65,200	24.0	133	133	10.34	1.33
p_0	1 × .028	46,400	46,400	64,800	25.0	134	136	10.43	1.40
q_0	1 × .032	45,300	45,400	65,400	17.0	134	135	10.31	1.44
s_0	1 × .042	46,500	46,500	65,900	24.0	137	134	10.41	1.42
t_0	1 × .049	46,600	46,600	66,300	27.0	135	135	10.34	1.42
u_0	1 × .058	45,600	45,500	66,000	27.0	137	135	10.48	1.45
v_0	1 × .065	44,300	44,100	65,800	29.0	135	135	10.48	1.49
w_0	1 × .072	45,800	45,600	65,900	29.0	135	134	10.54	1.44
x_0	1 × .083	45,500	45,500	65,300	29.0	135	135	10.37	1.44
y_0	1 × .095	45,300	45,300	65,300	28.0	137	137	10.35	1.44
z_0	1 × .109	47,400	47,400	65,000	28.0	137	138	10.46	1.37
Aa_0	1 × .120	47,400	47,300	65,800	28.0	140	140	10.56	1.39
U_0	1½× .022	46,900	47,100	65,900	18.0	134	132	10.30	1.40
V_0	1½× .025	47,300	47,400	64,200	21.0	136	137	10.42	1.36
W_0	1½× .028	49,400	49,500	67,000	25.0	137	137	10.51	1.35
X_0	1½× .032	48,000	48,100	65,600	25.5	135	134	10.05	1.36
Y_0	1½× .035	50,200	50,300	66,200	27.0	142	142	10.40	1.32
Z_0	1½× .042	47,200	47,300	66,200	23.5	134	137	10.35	1.40
a_0	1½× .049	46,600	46,600	65,900	27.0	135	135	10.17	1.41
b_0	1½× .058	45,800	45,700	65,800	31.0	137	135	10.66	1.44
c_0	1½× .065	46,400	46,400	64,000	28.0	134	131	10.41	1.38
d_0	1½× .072	44,400	44,500	63,200	28.0	140	138	9.79	1.42
e_0	1½× .083	46,500	46,600	63,900	28.0	136	137	10.29	1.37
f_0	1½× .095	47,200	47,200	65,200	25.5	138	138	10.46	1.38
g_0	1½× .109	49,700	49,800	66,200	25.0	137	135	10.36	1.33
h_0	1½× .120	47,600	47,600	67,000	30.0	137	138	10.59	1.41
i_0	1½× .134	47,500	47,500	66,600	30.0	136	137	10.48	1.40
j_0	1½× .148	47,900	47,900	66,400	31.0	135	136	10.59	1.39
k_0	1½× .165	47,400	47,300	66,100	31.0	138	139	10.77	1.40
A_0	2 × .022	47,400	47,400	63,800	[d] 16.5	133	132	10.48	1.35
B_0	2 × .025	49,400	49,400	62,800	[d] 10.0	134	132	10.65	1.27
C_0	2 × .028	48,400	48,500	64,700	[d] 11.0	134	134	10.49	1.33
D_0	2 × .032	48,300	48,400	64,500	23.0	132	131	10.38	1.33
E_0	2 × .035	48,900	49,000	65,400	24.0	134	131	10.50	1.33
F_0	2 × .042	49,600	49,500	64,100	23.0	135	132	10.75	1.30
G_0	2 × .049	50,000	49,900	65,200	22.5	134	133	10.75	1.31
I_0	2 × .065	46,100	46,000	65,100	30.0	134	131	10.61	1.42
J_0	2 × .072	48,600	48,700	66,200	27.0	136	133	10.32	1.36
K_0	2 × .083	47,400	47,200	66,000	29.0	134	134	10.81	1.40
L_0	2 × .095	47,900	47,800	65,100	30.0	133	133	10.73	1.36
M_0	2 × .109	49,700	49,800	65,100	29.0	133	134	10.40	1.31
N_0	2 × .120	46,700	46,700	65,800	29.0	134	133	10.53	1.41
O_0	2 × .134	47,100	47,100	64,000	28.0	133	131	10.56	1.36
P_0	2 × .148	48,000	48,000	66,000	28.0	133	134	10.29	1.38
Q_0	2 × .165	48.800	48,900	65,400	30.0	137	134	10.37	1.34
R_0	2 × .180	48,500	48,500	65,600	31.0	137	134	10.12	1.35
S_0	2 × .203	48,000	48,000	66,100	30.0	135	135	10.64	1.38
T_0	2 × .220	48,300	48,300	65,900	34.0	133	133	10.46	1.36
Average (51 specimens)		47,470	47,480	65,320	26.0	135	134	10.43	1.377

[a] Stress at which strain exceeds $\frac{\text{stress}}{10\times10^6}$ by 0.002 in./in.
[b] Vickers number for 10-kg weight.
[c] Based on 2/3 *E* yield strength.
[d] Broke at end of plug.

TABLE VII.—RESULTS OF TORSION TESTS OF CHROMIUM-MOLYBDENUM STEEL TUBES

Specimen	Length L (in.)	Outside diameter D (in.)	Thickness t (in.)	L/D	t/D	Yield strength in shear by 5/9 G method (lb./sq. in.)	Mean fiber shear stress at failure (lb./sq. in.)	Shear modulus (lb./sq. in.)	Final type of failure [a]
A_1	19	0.750	0.0304	25.3	0.04055	48,600	50,600	11.55×10^6	2 lobes.
A_2	19	.750	.0303	25.3	.04040	47,900	50,400	11.50	Do.
A_5	60	.751	.0302	79.9	.04020	49,500	51,100	12.05	Do.
B_1	19	1.001	.0381	19.0	.03807	54,900	57,000	11.55	Do.
B_2	19	1.001	.0380	19.0	.03795	56,000	57,300	11.80	Do.
B_3	19	1.001	.0380	19.0	.03795	57,400	57,700	11.36	Do.
C_1	19	1.128	.0479	16.9	.04245	54,300	56,400	11.80	Do.
C_2	19	1.127	.0480	16.9	.04255	54,400	56,700	11.86	Do.
C_6	60	1.127	.0480	53.2	.04255	54,500	57,700	11.86	Do.
D_1	19	1.503	.0580	12.6	.03860	59,800	61,500	11.75	Do.
D_2	19	1.503	.0580	12.6	.03860	59,700	61,800	11.75	Do.
D_3	19	1.503	.0581	12.6	.03866	58,000	61,400	11.97	Do.
D_4	19	1.503	.0581	12.6	.03866	59,000	60,800	11.70	Do.
D_5	48	1.503	.0581	31.9	.03866	58,500	59,800	11.52	Do.
E_1	19	2.004	.0652	9.5	.03255	60,100	60,900	11.30	Do.
E_2	19	2.004	.0652	9.5	.03255	57,500	59,100	11.62	Do.
E_3	19	2.004	.0653	9.5	.03258	60,000	60,300	11.45	Do.
E_5	48	2.005	.0652	24.0	.03255	59,100	59,900	11.52	Do.
F_1	19	1.377	.0382	13.8	.02775	47,000	53,400	11.08	Do.
F_2	19	1.377	.0382	13.8	.02775	45,300	53,300	11.23	Do.
F_5	45	1.385	.0381	32.7	.02753	46,100	53,000	11.30	Do.
G_1	19	1.498	.0349	12.7	.02330	39,500	46,000	11.17	Do.
G_2	19	1.499	.0349	12.7	.02326	40,500	45,900	10.86	Do.
G_5	45	1.498	.0349	30.1	.02330	43,800	47,200	11.83	Do.
H_1	19	1.510	.0528	12.6	.03500	47,700	50,500	11.76	Do.
H_2	19	1.511	.0527	12.6	.03486	47,400	49,800	11.42	Do.
I_1	19	1.510	.0685	12.6	.04540	40,000	54,300	11.42	Do.
I_2	19	1.510	.0687	12.6	.04550	38,000	52,200	11.42	Do.
J_1	19	1.503	.0845	12.6	.0562	47,000	65,700	11.90	Do.
J_2	19	1.503	.0845	12.6	.0562	47,100	65,500	11.83	Do.
J_5	47	1.503	.0845	31.4	.0562	47,500	65,100	11.32	Do.
K_1	19	1.502	.0926	12.6	.0617	63,500	68,600	11.90	Do.
K_2	19	1.503	.0925	12.6	.0616	63,100	68,800	11.73	Do.
L_1	19	1.500	.1259	12.7	.0840	54,500	62,900	12.00	Do.
L_2	19	1.499	.1258	12.7	.0840	53,000	61,000	12.05	Do.
L_5	45	1.500	.1258	30.2	.0839	51,500	59,400	11.30	Helix.
M_1	19	1.630	.0495	11.6	.03035	54,500	55,800	11.55	2 lobes.
M_2	19	1.631	.0495	11.6	.03033	54,500	57,400	11.72	Do.
N_1	19	1.753	.0509	10.8	.02905	56,300	62,600	11.26	Do.
N_2	19	1.752	.0509	10.8	.02907	57,000	61,700	11.26	Do.
N_5	45	1.752	.0507	26.1	.02895	54,300	61,500	11.33	Do.
O_1	19	1.626	.0359	11.7	.02206	54,500	54,600	11.60	Do.
O_2	19	1.625	.0358	11.7	.02202	----------	55,400	11.72	Do.
O_3	60	1.628	.0357	35.8	.02196	[b] 56,600	56,000	11.55	Do.
P_1	19	1.751	.0356	10.8	.02030	----------	59,000	11.62	Do.
P_2	19	1.752	.0354	10.8	.02022	----------	57,900	12.23	Do.
P_3	60	1.751	.0354	34.2	.02022	----------	56,000	11.65	Do.
Q_1	19	2.005	.0361	9.5	.01801	----------	56,400	11.30	Do.
Q_3	60	1.998	.0360	30.0	.01801	----------	53,100	11.10	Do.
R_1	19	1.124	.0316	16.9	.02815	[b] 57,200	57,000	11.55	Do.
R_2	19	1.124	.0317	16.9	.02822	[b] 59,100	58,900	11.83	Do.
R_3	60	1.124	.0317	53.4	.02822	----------	61,000	11.69	Do.
S_1	19	1.250	.0338	15.2	.02706	52,500	53,000	11.83	Do.
S_2	19	1.251	.0338	15.2	.02700	52,800	52,800	11.70	Do.
T_1	19	1.503	.0352	12.6	.02342	55,000	55,200	11.73	Do.
T_2	19	1.503	.0352	12.6	.02342	54,800	54,900	11.66	Do.
T_3	60	1.503	.0352	39.9	.02342	----------	52,900	11.60	Do.
U_1	19	1.506	.0501	12.6	.03339	59,000	61,700	11.76	Do.
U_2	19	1.506	.0501	12.6	.03330	59,100	61,600	11.50	Do.
U_3	60	1.506	.0501	39.8	.03330	59,600	61,900	11.80	Do.
V_1	19	2.506	.0341	7.6	.01364	41,100	41,300	11.16	Do.
V_2	19	2.506	.0336	7.6	.01340	40,500	40,500	10.80	Do.
V_3	60	2.504	.0340	24.0	.01358	----------	29,500	10.45	Do.
Average (63 specimens)						52,780	56,550	11.57	

[a] Type of failure as indicated by inspection of tube after removal from test fixture.
[b] Extrapolated value.

TABLE VIII.—RESULTS OF TORSION TESTS OF 17ST ALUMINUM-ALLOY TUBES

Specimen	Length L (in.)	Outside diameter D (in.)	Thickness t (in.)	L/D	t/D	Yield strength 2/3 G (lb./sq. in.)	Mean fiber shear stress at failure (lb./sq. in.)	Shear modulus (lb./sq. in.)	Final type of failure [a]
l_1	20	0.9997	0.0188	20.0	0.01880		21,000	3.86×10^6	2 lobes.
l_2	60	1.0005	.0187	60.0	.01869		19,400	3.86	Do.
m_1	20	.9994	.0199	20.0	.01991	21,900	21,900	3.89	Do.
m_2	60	1.0003	.0198	60.0	.01979		20,500	3.89	Do.
n_1	20	1.0024	.0224	19.9	.02235	23,000	23,100	3.86	Do.
n_2	60	1.0021	.0224	59.8	.02235		23,400	3.86	Do.
o_1	20	1.0016	.0252	19.9	.02516	23,000	23,400	3.88	Do.
o_2	60	1,0017	.0257	59.8	.02566		25,200	3.88	Do.
p_1	20	1.0002	.0283	20.0	.02829	21,200	23,600	3.92	Do.
p_2	60	1.0006	.0285	60.0	.02848	22,600	24,200	4.00	Do.
q_1	20	1.0028	.0324	19.9	.03231	22,500	24,900	4.00	Do.
q_2	60	1.0024	.0325	59.8	.03242	23,500	26,000	3.92	Do.
s_1	20	1.0031	.0422	19.9	.04207	23,500	27,900	3.96	Do.
s_2	60	1.0018	.0423	59.8	.04222	24,800	29,200	4.08	Do.
t_1	20	1.0007	.0498	20.0	.04977	23,700	30,400	4.00	Do.
t_2	60	1.0013	.0498	59.9	.04974	24,600	31,300	4.05	Do.
u_1	20	1.0020	.0590	20.0	.05888	23,800	33,700	3.97	Do.
u_2	60	1.0027	.0588	59.8	.05864	24,100	33,700	3.97	Do.
v_1	20	1.0020	.0637	20.0	.06357	23,000	34,000	3.95	Do.
v_2	60	1.0024	.0637	59.8	.06355	24,300	35,200	3.94	Do.
w_1	20	1.0006	.0718	20.0	.07176	24,000	36,800	4.00	Do.
w_2	60	1.0004	.0717	60.0	.07167	25,400	38,600	4.00	Do.
x_1	20	.9994	.0832	20.0	.08325	23,600	40,000	3.97	Helix and 2 lobes.
x_2	60	.9998	.0832	60.0	.08322	25,000	41,200	3.97	Do.
y_1	20	.9975	.0938	20.0	.09403	23,700	41,400	3.97	Helix.
y_2	60	.9984	.0942	60.1	.09435	24,300	42,400	3.97	Helix and 2 lobes.
z_1	20	.9965	.1076	20.1	.10797	23,000	41,100	3.99	Helix.
z_2	60	.9971	.1074	60.2	.10771	24,000	41,900	3.99	Do.
Aa_1	20	1.0001	.1192	20.0	.11919	23,000	41,300	3.97	Do.
Aa_2	60	1.0005	.1188	60.0	.11874	24,100	42,400	3.97	Do.
U_1	20	1.4955	.0224	13.4	.01498		20,100	3.96	2 lobes.
U_2	60	1.5000	.0227	40.0	.01513		16,900	3.96	Do.
V_1	20	1.4996	.0244	13.3	.01627		20,700	3.94	Do.
V_2	60	1.5003	.0244	40.0	.01626		18,500	3.94	Do.
W_1	20	1.5066	.0285	13.3	.01892		23,500	4.00	Do.
W_2	60	1.5055	.0285	39.9	.01893		22,000	3.94	Do.
X_1	20	1.5035	.0330	13.3	.02195	22,800	23,600	3.96	Do.
X_2	60	1.5033	.0330	39.9	.02195	22,200	22,800	3.96	Do.
Y_1	20	1.4997	.0354	13.3	.02360	23,500	24,400	3.97	Do.
Y_2	60	1.5018	.0354	39.9	.02357		24,800	3.97	Do.
Z_1	20	1.5017	.0436	13.3	.02903	22,500	25,100	3.88	Do.
Z_2	60	1.5022	.0435	39.9	.02896	23,100	24,100	3.93	Do.
a_1	20	1.5001	.0491	13.3	.03273	23,000	26,400	3.92	Do.
a_2	60	1.5006	.0497	40.0	.03312	23,600	26,100	3.97	Do.
b_1	20	1.5031	.0585	13.3	.03892	23,600	27,000	3.94	Do.
b_2	60	1.5035	.0585	39.9	.03891	24,200	27,700	3.94	Do.
c_1	20	1.4995	.0634	13.3	.04228	22,100	27,700	3.95	Do.
c_2	60	1.5000	.0636	40.0	.04240	22,600	27,400	3.97	Do.
d_1	20	1.4988	.0719	13.4	.04797	22,500	29,600	3.97	Do.
d_2	60	1.4980	.0721	40.1	.04813	23,200	30,500	3.99	Do.
e_1	20	1.5002	.0837	13.3	.05579	22,000	31,900	3.94	Do.
e_2	60	1.5007	.0837	40.0	.05577	22,900	31,700	3.98	Do.
f_1	20	1.5019	.0956	13.3	.06365	22,400	33,900	3.93	Do.
f_2	60	1.5015	.0955	39.9	.06360	23,000	34,000	3.93	Do.
g_1	20	1.5004	.1107	13.3	.07378	24,000	39,300	3.95	Do.
g_2	60	1.4996	.1107	40.0	.07382	24,600	37,700	3.97	Helix and 2 lobes.
h_1	20	1.4988	.1192	13.4	.07953	23,300	40,600	4.02	2 lobes.
h_2	60	1.4992	.1195	40.0	.07971	23,400	40,600	4.00	Helix and 2 lobes.
i_1	20	1.5020	.1337	13.3	.08901	23,500	42,900	3.97	Do.
i_2	60	1.5014	.1337	39.9	.08905	23,700	41,900	4.00	Do.
j_1	20	1.4991	.1461	13.3	.09746	23,500	42,700	3.96	Fracture—slight helix.
j_2	60	1.4997	.1466	40.0	.09775	23,800	42,800	3.98	Helix.
k_1	20	1.5010	.1658	13.3	.11046	23,000	42,700	3.97	Do.
k_2	60	1.5010	.1659	39.9	.11053	22,900	41,500	3.93	Do.
A_1	20	2.0035	.0202	10.0	.01008		16,000	3.86	2 lobes.
A_2	60	2.0029	.0202	30.0	.01009		12,200	3.86	Do.
B_1	20	2.0058	.0255	10.0	.01271		19,700	3.95	Do.
B_2	60	2.0037	.0254	30.0	.01268		15,000	3.95	Do.
C_1	20	2.0047	.0274	10.0	.01367		21,200	3.97	Do.
C_2	60	2.0048	.0274	29.9	.01367		16,500	3.97	Do.
D_1	20	2.0061	.0314	10.0	.01565		21,800	3.95	Do.
D_2	60	2.0044	.0315	29.9	.01572		19,000	3.95	Do.
E_1	20	2.0054	.0359	10.0	.01790	23,300	23,300	3.95	Do.
E_2	60	2.0033	.0361	29.9	.01802		20,200	3.95	Do.
F_1	20	2.0020	.0426	10.0	.02128	23,700	24,600	3.99	Do.
F_2	60	2.0020	.0426	29.9	.02128		23,200	3.99	Do.
G_1	20	2.0053	.0509	10.0	.02538	23,800	25,100	3.97	Do.
G_2	60	2.0035	.0510	29.9	.02546	24,600	24,700	3.97	Do.
I_1	20	2.0010	.0668	10.0	.03338	22,900	26,100	3.92	Do.
I_2	60	1.9998	.0670	30.0	.03350	23,300	25,700	3.92	Do.
J_1	20	1.9988	.0716	10.0	.03582	22,600	26,900	3.95	Do.
J_2	60	1.9988	.0716	30.0	.03582	23,000	27,000	3.95	Do.
K_1	20	2.0012	.0833	10.0	.04162	22,700	28,100	3.97	Do.
K_2	60	2.0013	.0838	30.0	.04187	22,800	27,700	3.97	Do.
L_1	20	2.0012	.0952	10.0	.04757	23,200	30,700	3.98	Do.
L_2	60	2.0009	.0952	30.0	.04758	23,300	29,500	3.98	Do.
M_1	20	2.0002	.1110	10.0	.05549	24,700	33,900	3.97	Do.
M_2	60	1.9988	.1109	30.0	.05548	24,600	33,200	3.97	Do.
N_1	20	2.0027	.1206	10.0	.06022	22,500	35,000	4.01	Do.
N_2	60	2.0026	.1209	29.9	.06037	22,500	34,400	4.01	Do.
O_1	20	1.9952	.1316	10.0	.06596	22,400	36,700	3.96	Do.
O_2	60	1.9988	.1326	30.0	.06634	22,500	34,700	3.96	Do.
P_1	20	2.0027	.1487	10.0	.07425	24,000	40,200	3.99	Helix and 2 lobes.
P_2	60	2.0027	.1496	29.9	.07470	24,000	39,600	3.99	Helix.
Q_1	20	1.9974	.1662	10.0	.08321	23,500	41,600	3.97	2 lobes.
Q_2	60	1.9971	.1654	30.0	.08282	23,300	40,300	3.97	Helix.
R_1	20	1.9980	.1816	10.0	.09089	22,500	42,200	3.99	2 lobes.
R_2	60	1.9978	.1816	30.0	.09090	22,500	41,500	3.99	Helix and 2 lobes.
S_1	20	2.0018	.2039	10.0	.10186	22,600	41,400	3.97	Fracture, slight helix.
S_2	60	2.0027	.2040	29.9	.10186	22,400	42,200	3.97	Helix.
T_1	20	1.9994	.2196	10.0	.10983	23,500	43,000	4.00	Fracture.
T_2	60	1.9989	.2206	30.0	.11036	23,400	42,400	4.00	Helix.
Average (102 specimens)						23,310	30,380	3.96	

[a] Type of failure as indicated by inspection of tube after removal from test fixture.

REPORT No. 602

WIND-TUNNEL AND FLIGHT TESTS OF SLOT-LIP AILERONS

By Joseph A. Shortal

SUMMARY

The slot-lip ailerons developed by the N. A. C. A. consist of a flap-type spoiler with an adjoining continuously open slot. The ailerons were developed in an investigation of the delayed response, or lag, of spoiler-type lateral controls. Tests of these slot-lip ailerons were made on wing models in the 7- by 10-foot wind tunnel, on a Fairchild 22 airplane in the full-scale wind tunnel and in flight, and on the Weick W1–A airplane in flight.

The tests showed that, although the slot-lip ailerons did not have the lag normally associated with plain spoilers, they were rather slow in developing the full amount of rolling moment and therefore imparted a sluggish motion to the roll of the airplane. The tests in the full-scale tunnel showed that the drag due to the open slot was excessive, but later tests in the 7- by 10-foot tunnel revealed that this drag could be somewhat reduced by modifying the slot shape.

In spite of their disadvantages, the N. A. C. A. slot-lip ailerons exhibited certain characteristics that are desirable for airplanes in which safety and simplicity of operation are considered of greater importance than high performance and a great degree of maneuverability. The slot-lip ailerons permit the use of a full-span flap; the slot may extend the angle-of-attack range with stability in roll; and the ratios of yawing moment to rolling moment are such as to be particularly satisfactory for the two-control operation of an airplane.

INTRODUCTION

Since the high wing loadings of many modern airplanes have necessitated the use of landing flaps to reduce the landing speed, considerable interest has been displayed in lateral-control devices with which a flap covering the entire wing span can be used. The spoiler type of control, located near the midchord, permits the free use of the trailing edge of the wing for full-span flaps. Wind-tunnel tests (reference 1) of wing models indicated that spoilers had desirable control characteristics, but flight tests (reference 2) revealed considerable lag between the control movement and the beginning of the wing motion in the desired direction. The slot-lip aileron, which consists of a spoiler with an adjoining continuously open slot, has been developed during the attempt to find a control device with the desirable characteristics of the spoiler and without its undesirable lag.

This lag, or the delay of the response motion of the airplane after a control movement, with various spoilers and spoiler-aileron combinations, was measured in the flight tests of reference 2. It was noticed that the pilots failed to detect any lag less than 0.10 second. This value, in seconds, seems to be an upper limit to the lag and is of particular interest. In the interpretation of model tests and the application of the results to airplanes, it seems that the lag should be expressed as the distance in wing chord lengths traveled by the airplane after the control is moved. With the lag expressed in this nondimensional form, the lag in seconds may be computed for a particular airplane and speed and compared with the 0.10-second limit, although this time limit may depend upon the reaction of the pilot and may vary with different pilots.

Another characteristic possessed by lateral-control devices is that of "sluggishness." The control may cause the wing to move in the desired direction immediately, but the moment produced by the control may not reach its maximum until the wing has traveled a considerable distance. As a result, the airplane motion will appear rather sluggish. It seems that all control devices are sluggish to a certain extent because the change in lift is not effected immediately. In the present report, sluggishness is defined as the distance in chords traveled by the airplane from the time the control is deflected until the maximum moment is produced. At the start of the investigation the upper allowable limit of sluggishness was not known but the tests have indicated that the control was satisfactory if the maximum moment was produced before the tested airplane traveled four chord lengths. This value is by no means fixed as it may be masked by such factors as the moment of inertia of the airplane and the indirect rolling moment induced by yawing motions.

The complete wind-tunnel and flight tests that have been made by the N. A. C. A. to determine the practicability of slot-lip ailerons are reported herein. The investigation was divided into the following phases:

1. An investigation in the 7- by 10-foot wind tunnel of the lag characteristics of spoilers and slot-lip ailerons. (See reference 3.)

2. The measurement in the 7- by 10-foot wind tunnel of the lateral-control and stability characteristics of a wing model equipped with slot-lip ailerons in several chordwise locations.

3. The determination of the effect of slot-lip ailerons on the lift and drag of a model wing and of an airplane.

4. A study in the 7- by 10-foot wind tunnel of the effect of various slot shapes on the wing section drag with a large-chord wing.

5. Flight tests of an airplane equipped with slot-lip ailerons.

6. An analysis of the wind-tunnel and flight results to obtain a quantitative comparison of the response characteristics of slot-lip and ordinary ailerons.

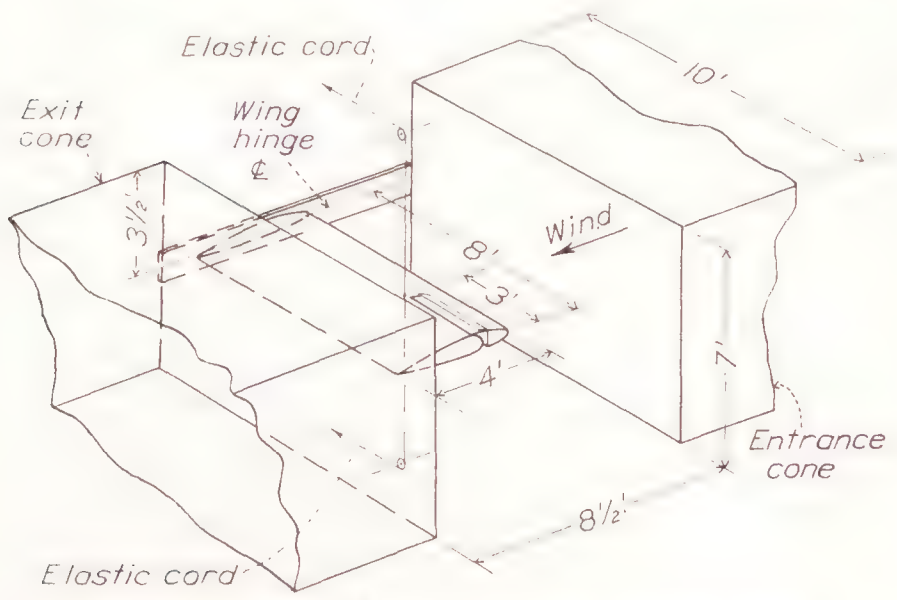

FIGURE 1.—Diagram of the lag set-up in the 7- by 10-foot tunnel.

LAG INVESTIGATION

The lag investigation was conducted in the open-jet 7- by 10-foot wind tunnel (reference 4). A Clark Y–15 wing of 4-foot chord and 8-foot span was hinged at one end to the side of the tunnel as shown in figure 1. The set-up thus simulated a 16-foot wing with one of the tunnel vertical boundaries as an imaginary plane of symmetry. The wing was restrained in roll by long elastic cords but was free to move to a new position of equilibrium when a moment was applied by a control device located at the free wing tip. A continuous record of the control motion and the wing motion was obtained by a recording instrument developed for flight tests. The tests consisted of deflecting the ailerons various amounts and recording the wing motion. The tunnel was operated at an air speed of 80 miles per hour for 0° angle of attack and at 40 miles per hour for 15° angle of attack. The corresponding wing lift coefficients were approximately 0.25 and 1.00.

RETRACTABLE SPOILERS

The retractable spoilers consisted of curved plates that slid in and out of the wing as indicated in figure 2. The spoiler chord and location are given as fractions of the wing chord c_w. The spoilers were of $0.10c_w$ chord and were tested successively at different locations between $0.15c_w$ and $0.83c_w$. Reference 2 had revealed that a retractable spoiler located $0.15c_w$ had considerable lag and reference 5, that a retractable spoiler located $0.83c_w$ was satisfactory. The tests reported in reference 6 indicated that the $0.30c_w$ location should give the optimum rolling and yawing moments. It was considered advisable, therefore, to investigate the variation of lag with spoiler location for the entire chordwise range. Some of the results are plotted in figure 2.

The results from some typical lag records are plotted in figure 3. It will be noticed that the retractable spoiler at $0.15c_w$ caused the wing to roll initially in the wrong direction before rolling in the desired direction. Included in the same figure for comparison is a response curve obtained with a flat plate attached to the trailing edge of the wing and deflected as an aileron; this curve is taken as representative of ordinary aileron action. The considerable difference in the response of the wing to these two devices is quite evident.

The results of figure 2 having indicated satisfactory response time with a spoiler at $0.83c_w$, tests were made to determine the effect of a split flap on the spoiler response. The curves of figure 4 show the time

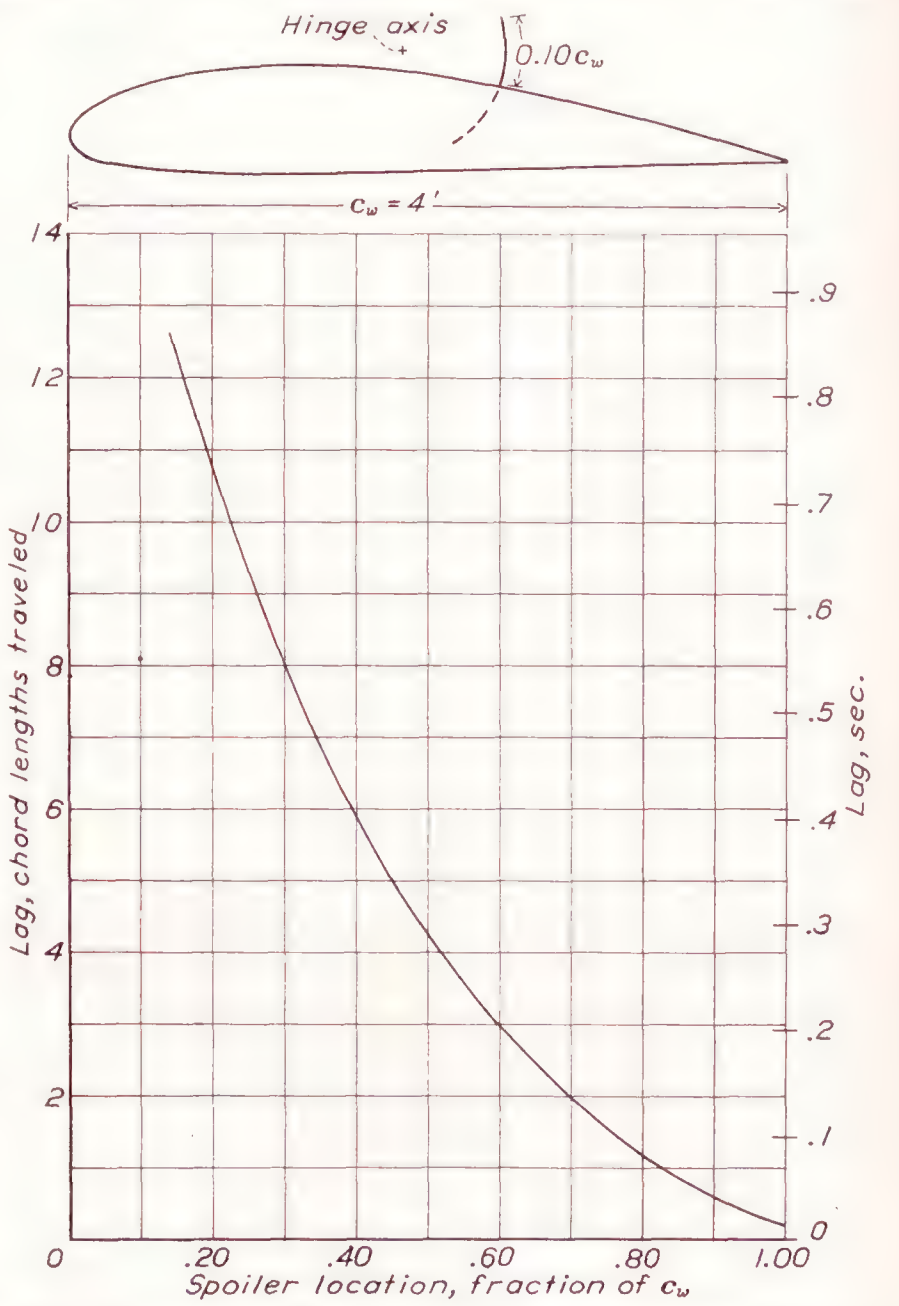

FIGURE 2.—Effect of spoiler location on lag. The 7- by 10-foot tunnel; C_L, 1.0; air speed, 40 m. p. h.

histories with and without a split flap deflected 60° and indicate greater lag with the flap deflected.

Inasmuch as satisfactory operation had been obtained in flight with combinations of ailerons and spoilers, it was considered of interest to measure the lag obtained

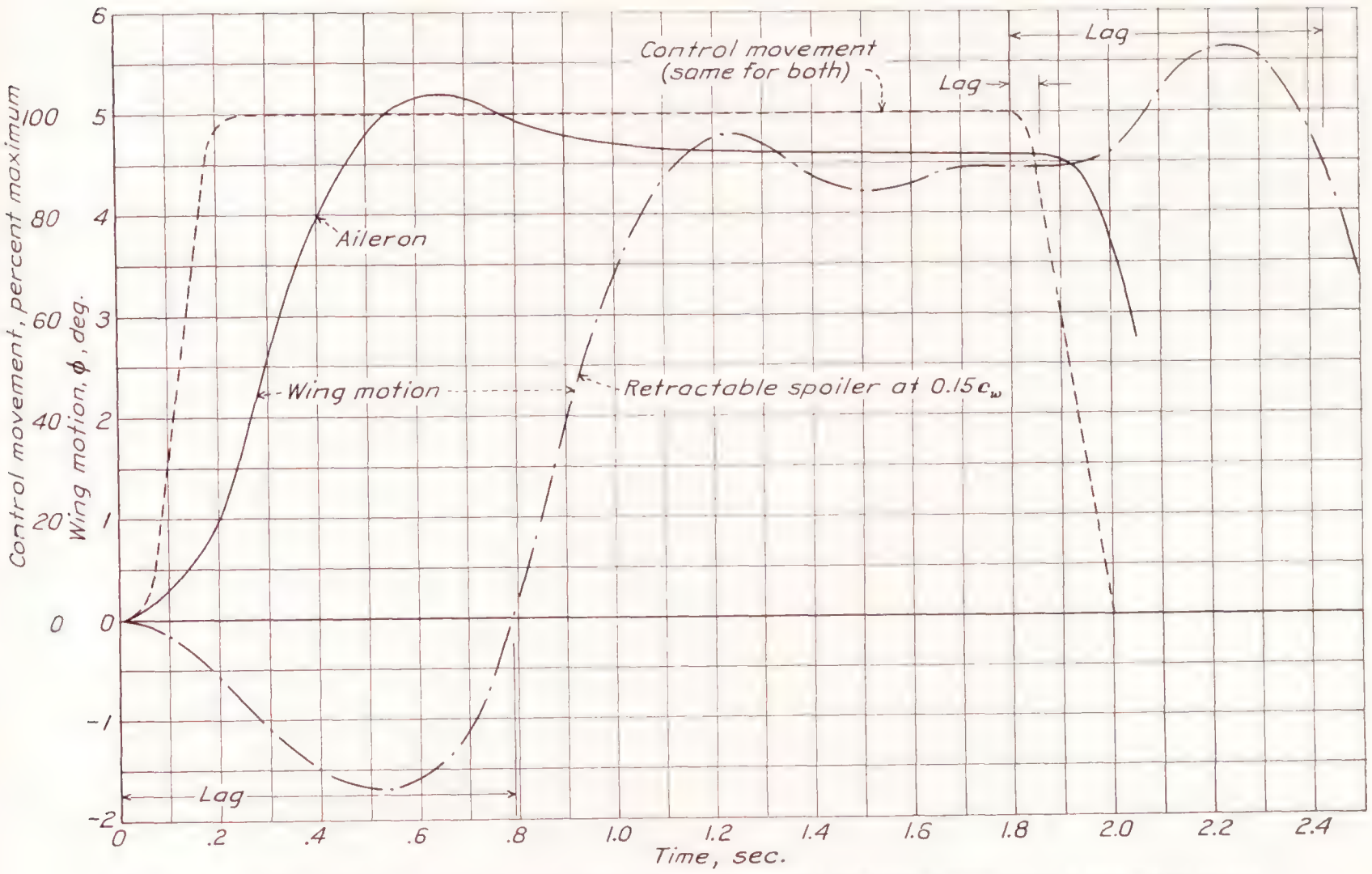

FIGURE 3.—Time history of wing motion with retractable spoiler at 0.15c_w. The 7- by 10-foot tunnel; C_L, 1.0; air speed, 40 m. p. h.

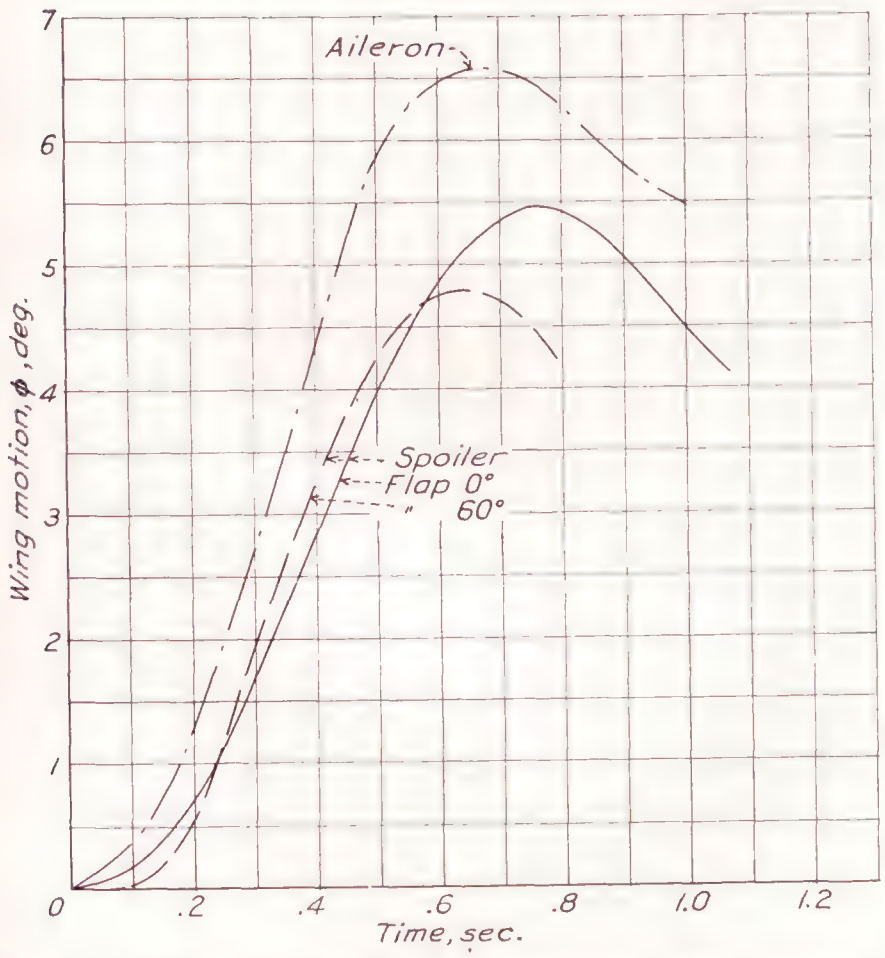

FIGURE 4.—Time histories of wing motion with retractable spoiler at 0.83c_w and with a split flap. The 7- by 10-foot tunnel; C_L, 1.0; air speed, 40 m. p. h.

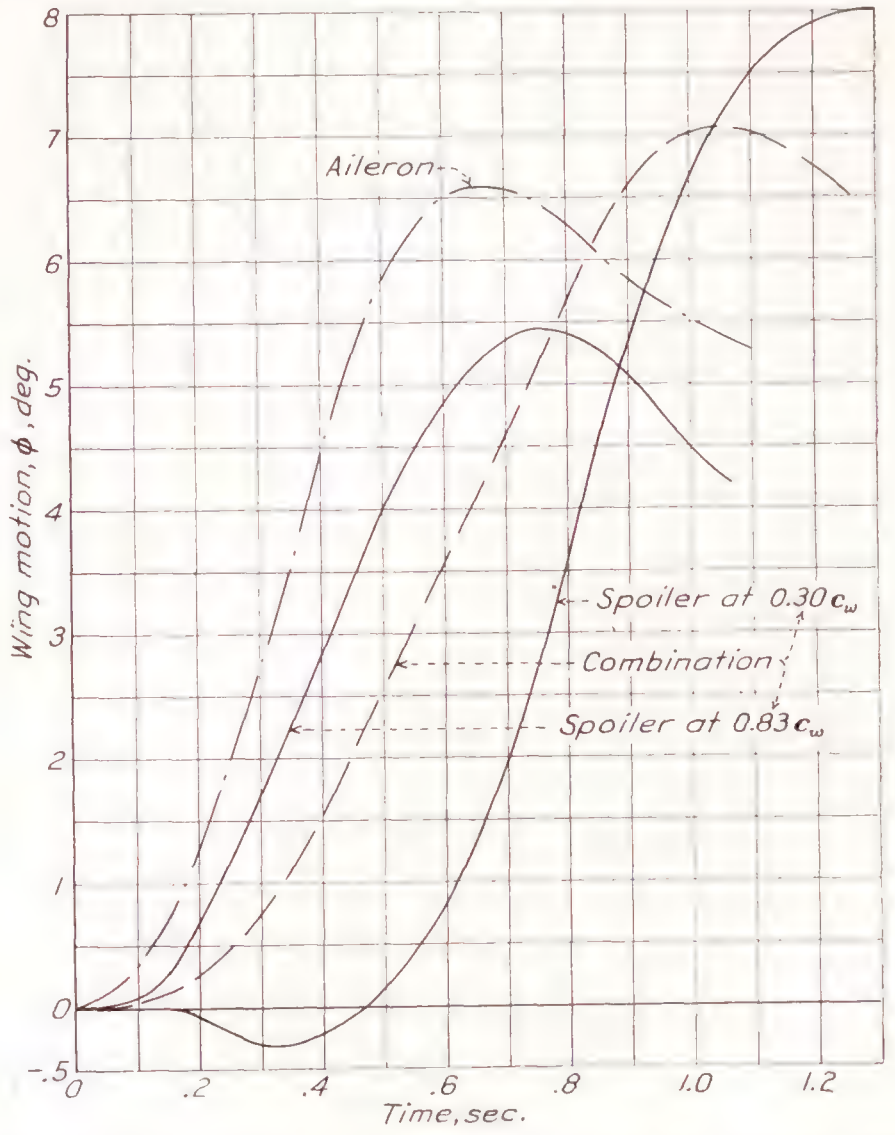

FIGURE 5.—Time histories of wing motion with combinations of spoilers. The 7- by 10-foot tunnel; C_L, 1.0; air speed, 40 m. p. h.

with a combination of two retractable spoilers. A representative time history is given in figure 5. The addition of the $0.83c_w$ spoiler counteracted the lag of

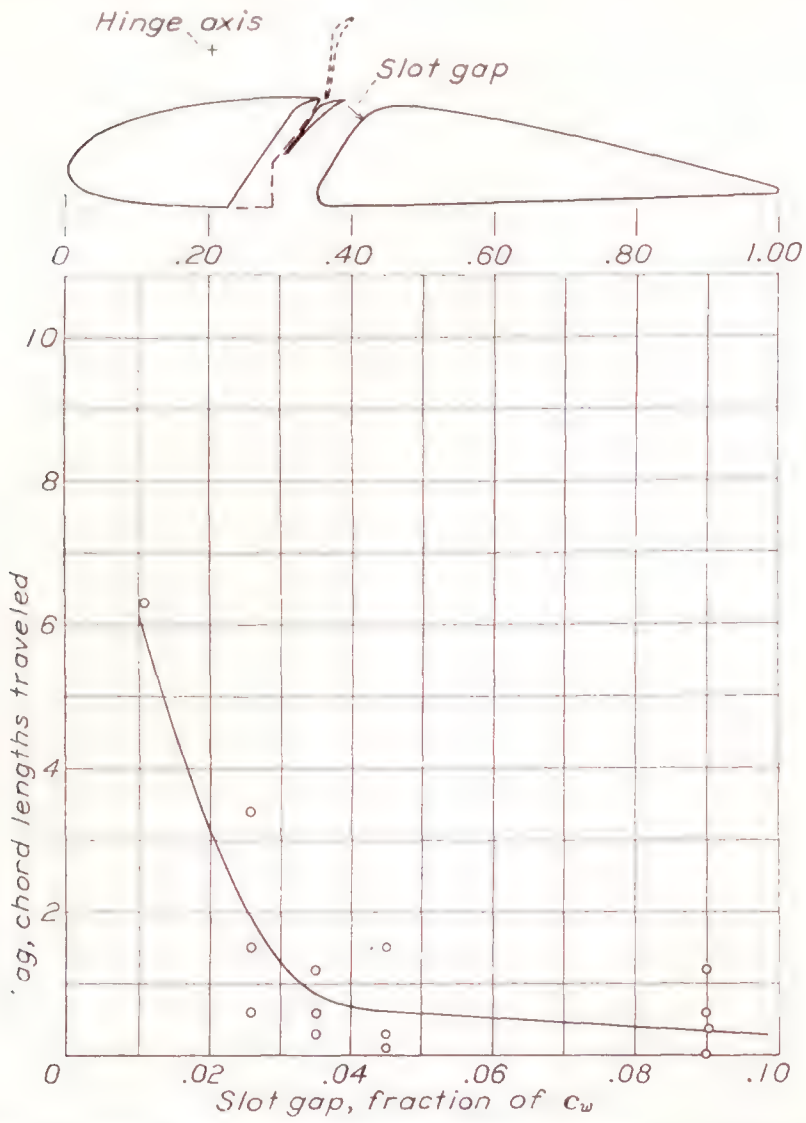

FIGURE 6.—Effect of slot size on lag of retractable spoiler and slot at $0.30c_w$. The 7- by 10-foot tunnel; C_L, 1.0; air speed, 40 m. p. h.

the $0.30c_w$ spoiler, but the response of the combination was not so rapid as that of the rearward one alone nor of the ordinary aileron.

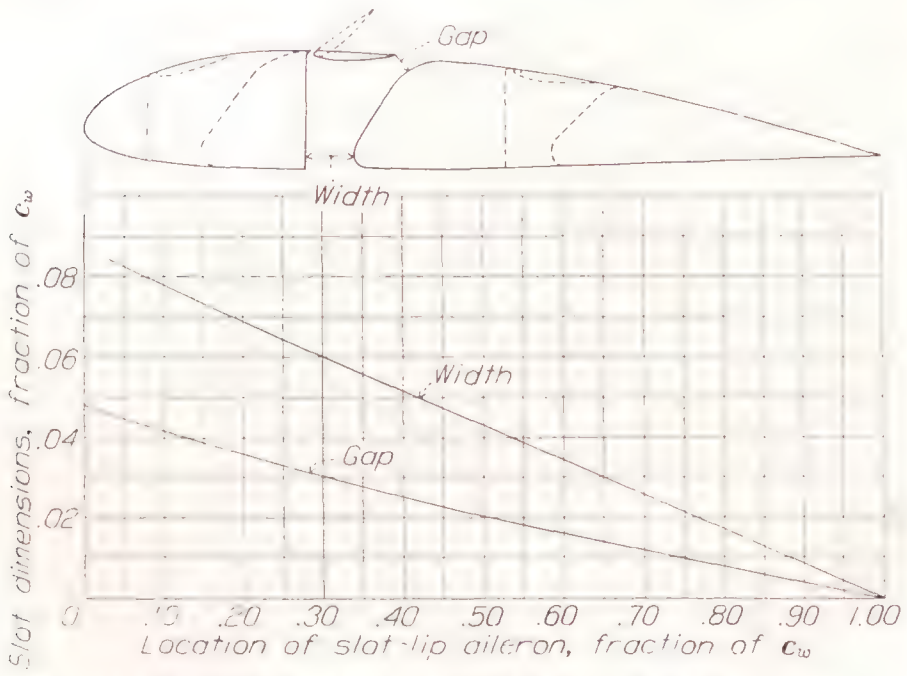

FIGURE 7.—Diagram of the slot-lip ailerons tested in the lag investigation.

It was believed that a slot adjoining the spoiler would relieve the low pressure existing behind the spoiler when it is first deflected. Lag measurements were made of several widths of slot behind a retractable spoiler located near $0.30c_w$. As shown in figure 6, a slot with an upper gap of about $0.035c_w$ reduced the lag from about 8 chord lengths to less than 1 chord length travel. The lower opening of the slot was later reduced to about $0.06c_w$ and to the shape shown by the dashed line without altering the response characteristics.

SLOT-LIP AILERONS

Although the retractable spoilers with a slot would probably give satisfactory control, the device appears structurally undesirable. A simpler arrangement consisting of a slot with the upper portion, or lip, hinged for control was given more consideration. This hinged lip was designated a "slot-lip aileron." Tests were made of various combinations of sizes for the upper and lower slot openings and with the aileron hinge-axis located

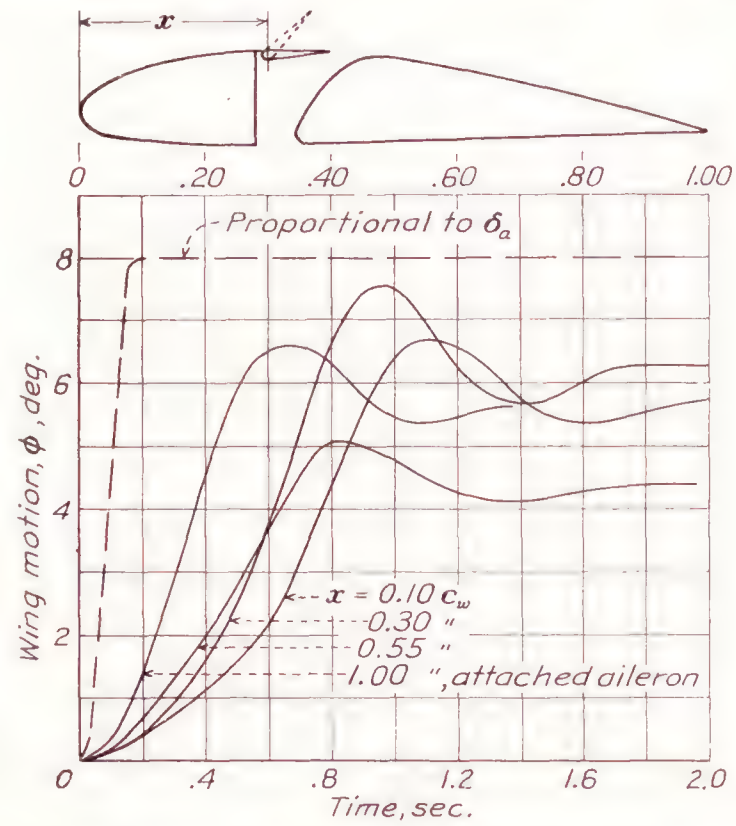

FIGURE 8.—Time histories of wing motion with slot-lip ailerons in various fore-and-aft locations. The 7- by 10-foot tunnel; C_L, 1.0; air speed, 40 m. p. h.

$0.10c_w$, $0.30c_w$, and $0.55c_w$ back from the leading edge. The slot sizes required to obtain an immediate response following control movement were determined for each location and the results are shown in figure 7. The particular shape used was similar to that of a previously developed low-drag slot. (See reference 7.) The chord, c_a, of the slot-lip aileron was $0.10c_w$.

The wing motions obtained with the final slots for each location of the slot-lip ailerons are compared with the aileron curve in figure 8. The curves show immediate response in all cases although the final motion builds up differently in each case.

The effect of the slot is clearly shown in figure 9 by the time histories of the wing motion. With the slot closed at the bottom, the wing moved in the wrong direction as before with a lag of about 0.5 second. With the upper slot opening sealed so that there was no slot with the aileron neutral but a considerable opening with the aileron deflected, the lag was reduced to about 0.3 second but was still unsatisfactorily large.

With the final slot-lip ailerons showing satisfactory lag characteristics, the hinge moments were measured. Some modification of the aileron and slot was necessary to obtain a curve of hinge moment against deflection,

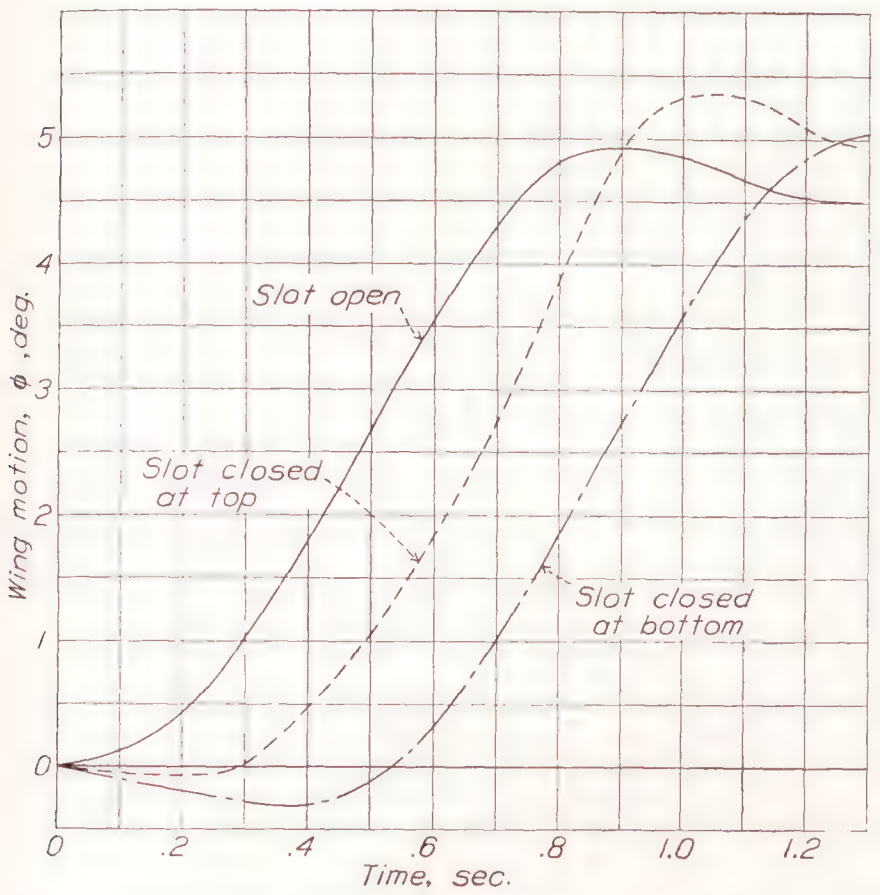

FIGURE 9.—Time histories of wing motion with slot-lip ailerons at 0.30c_w, showing effect of the slot. The 7- by 10-foot tunnel; C_L, 1.0; air speed, 40 m. p. h.

which showed that the arrangement was not overbalanced at the start of control movement. The arrangements tested are reported in more detail in reference 3. The final hinge-moment curves are given in figure 10 at lift coefficients of 0.25 and 1.0. The hinge-moment tests were made with the wing used in the lag tests and at an air speed of 60 miles per hour. The hinge moments are given in the form of absolute coefficients C_h based on the aileron chord c_a and area S_a back of the hinge,

$$C_h = \frac{\text{hinge moment}}{qc_aS_a}$$

ROLLING- AND YAWING-MOMENT TESTS

The lag investigation of slot-lip ailerons indicated the possibilities of their providing improved lateral control. A wing that had been used in the investigation reported in reference 8 was fitted with slot-lip ailerons and the rolling and yawing moments produced by these ailerons were measured. The effect of the slot-lip ailerons on lateral control, on lateral stability, and on lift and drag was determined with and without a split flap.

APPARATUS AND TESTS

The model was mounted on the 6-component balance of the open-throat 7- by 10-foot tunnel. (See reference 4.) The three force and the three moment components can be read independently and simultaneously in the form of coefficients for a standard-size model. The force-test tripod may be replaced by a special mounting that permits the model to rotate

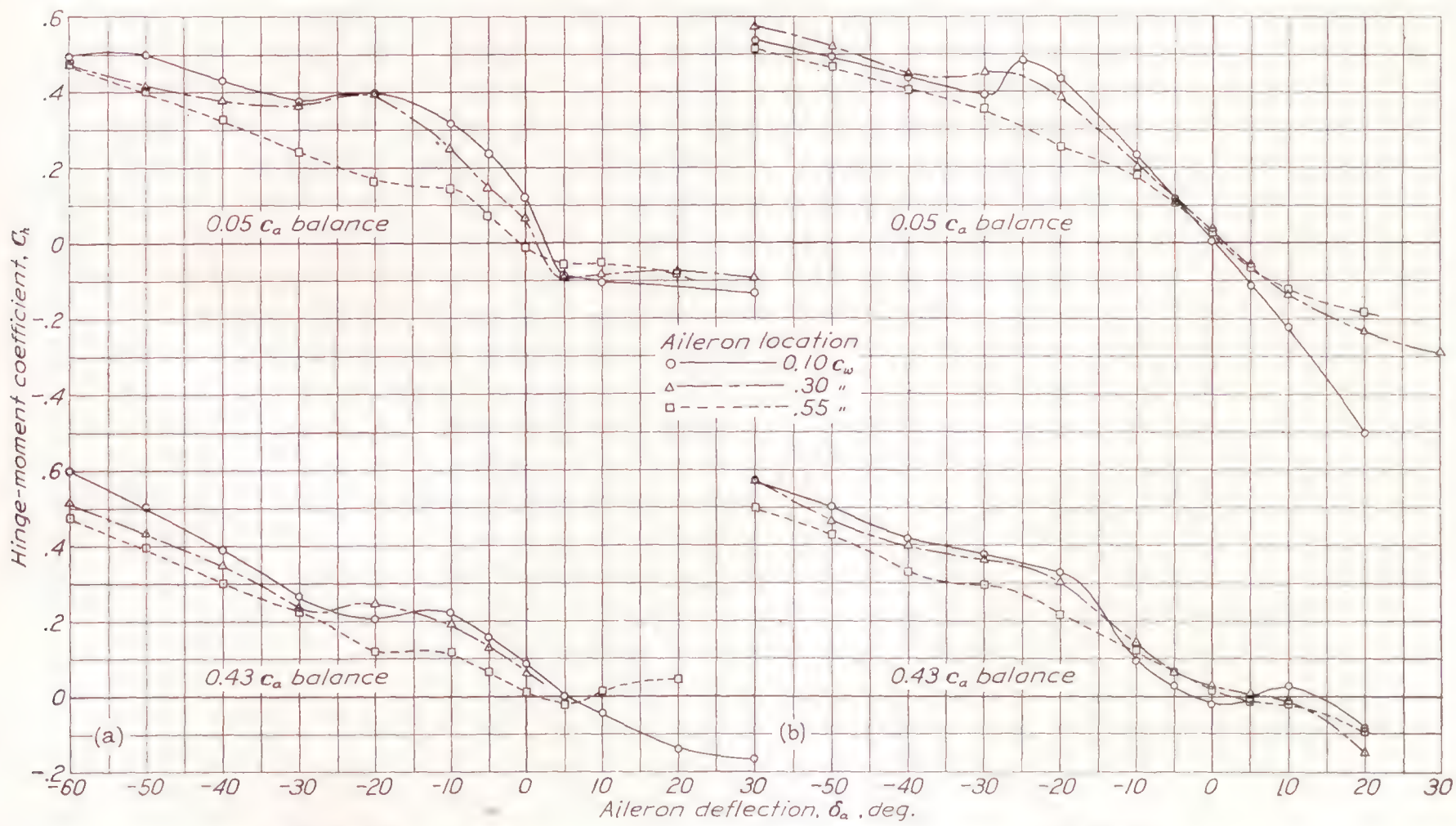

(a) C_L=0.25. (b) C_L=1.0.

FIGURE 10.—Hinge-moment coefficients of slot-lip ailerons on the 4- by 8-foot wing in the 7- by 10-foot tunnel.

about the longitudinal wind axis passing through the midspan quarter-chord point. This apparatus is mounted on the balance and the rolling-moment coefficients are read directly during forced rotation tests.

The model used in this part of the investigation was the one with large rounded tips used for the tests reported in reference 8. A Clark Y wing section was maintained throughout the span with no washout. The basic chord of the wing was 10.66 inches, the span was 60 inches, and the aspect ratio 6.0. A diagram of

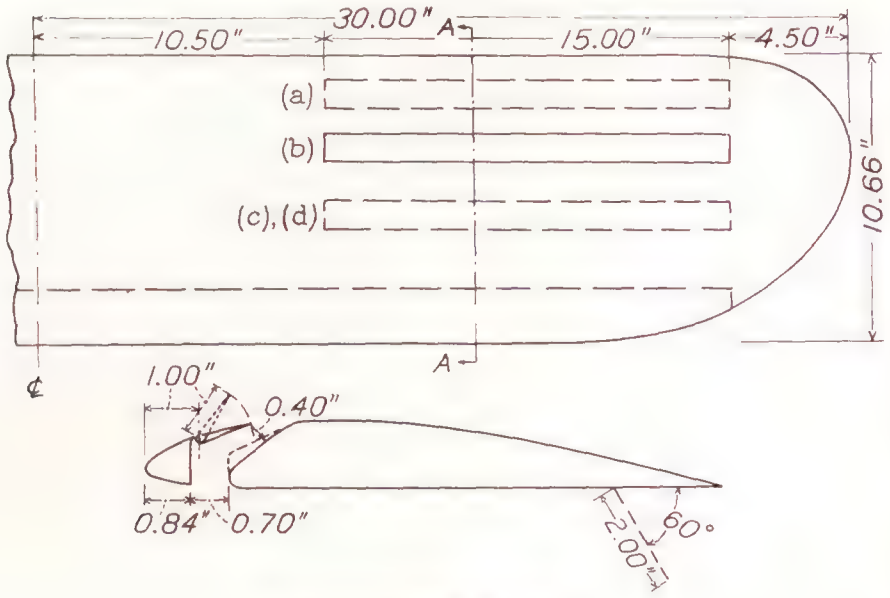

(a) Slot-lip aileron at 0.10 c_w.

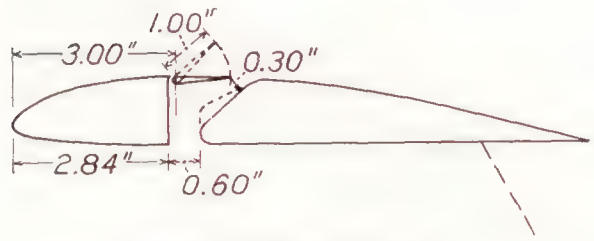

(b) Slot-lip aileron at 0.30 c_w.

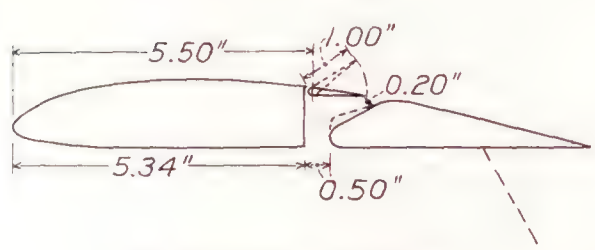

(c) Slot-lip aileron at 0.55 c_w.

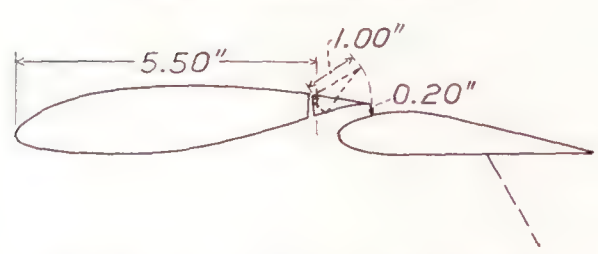

(d) Slot-lip aileron at 0.55 c_w with special slot.

FIGURE 11.—Diagram of the Clark Y wing with slot-lip ailerons tested in the 7- by 10-foot tunnel.

the wing showing the ailerons and flap tested is given in figure 11. The split flap consisted of a sheet-steel strip screwed to the wing at an angle of 60°. The slot-lip ailerons were formed of brass with their upper surfaces conforming to the upper contour of the wing. The slot sizes and shapes were determined from the lag investigation. The modifications to the slots shown by dashed lines were found necessary during the tests and were made with wooden strips screwed to the wing. The slot shape shown as (d) was designed to reduce the drag of the slot by having the slot formed between two airfoil-shape sections.

The standard test procedure was followed at a dynamic pressure of 16.37 pounds per square foot corresponding to an air speed of 80 miles per hour at standard density. The Reynolds Number of the tests was 609,000, based on the average wing chord of 10 inches.

The lift, the drag, and the pitching moment were measured with the ailerons neutral; the rolling and the yawing moments were measured with the ailerons deflected various amounts. Tests were repeated with the split flap deflected 60°. Some of the tests were repeated with the wing yawed to determine the control characteristics while sideslipping. Rotation tests were made with the ailerons neutral when located in all positions along the wing chord to determine the effect of the slots on damping in roll. Rotation tests were then made with the ailerons deflected when located $0.10c_w$ from the leading edge to determine the effect of the deflected control on the damping.

RESULTS

The results are given in figures 12 to 18. The coefficients are obtained directly from the balance and refer to the wind (or tunnel) axes. The results as given have not been corrected for tunnel effects.

The results of the rotation tests are given in the form

of a damping coefficient $\frac{dC_l'}{d\left(\frac{p'b}{2V}\right)}$ obtained from an aver-

age of the results of rotation tests in both directions at a rate of $\frac{p'b}{2V}=0.05$, where p' is the angular velocity in roll and V is the air speed.

Ailerons neutral.—The curves of lift and drag with flap and ailerons neutral are given in figure 12 (a) and with flap deflected 60° in figure 12 (b). The shape of the lift curves with flap neutral is somewhat affected by the slots. The forward slot locations are more effective than the rearward locations in delaying the stall over the adjacent portion of the wing span. This fact is revealed more clearly by the curves of damping in roll in the same figures, which show that damping is maintained to a higher angle of attack with the forward slots than with the rearward slots. The drag due to the slot-lip ailerons will later be discussed in more detail in connection with tests made at a larger value of the Reynolds Number.

The effect of the slots on the manner in which the wing stalled was studied by air-flow surveys with a fine

silk thread attached to a thin sting. The effectiveness of the forwardly located slots is clearly shown in figure 13. The slot-lip ailerons were located in three different positions with the flap neutral and deflected 60°, and the wing was at an angle of attack of 22° (about 6° past maximum lift). The stalled area of the wing is shown by the shaded areas.

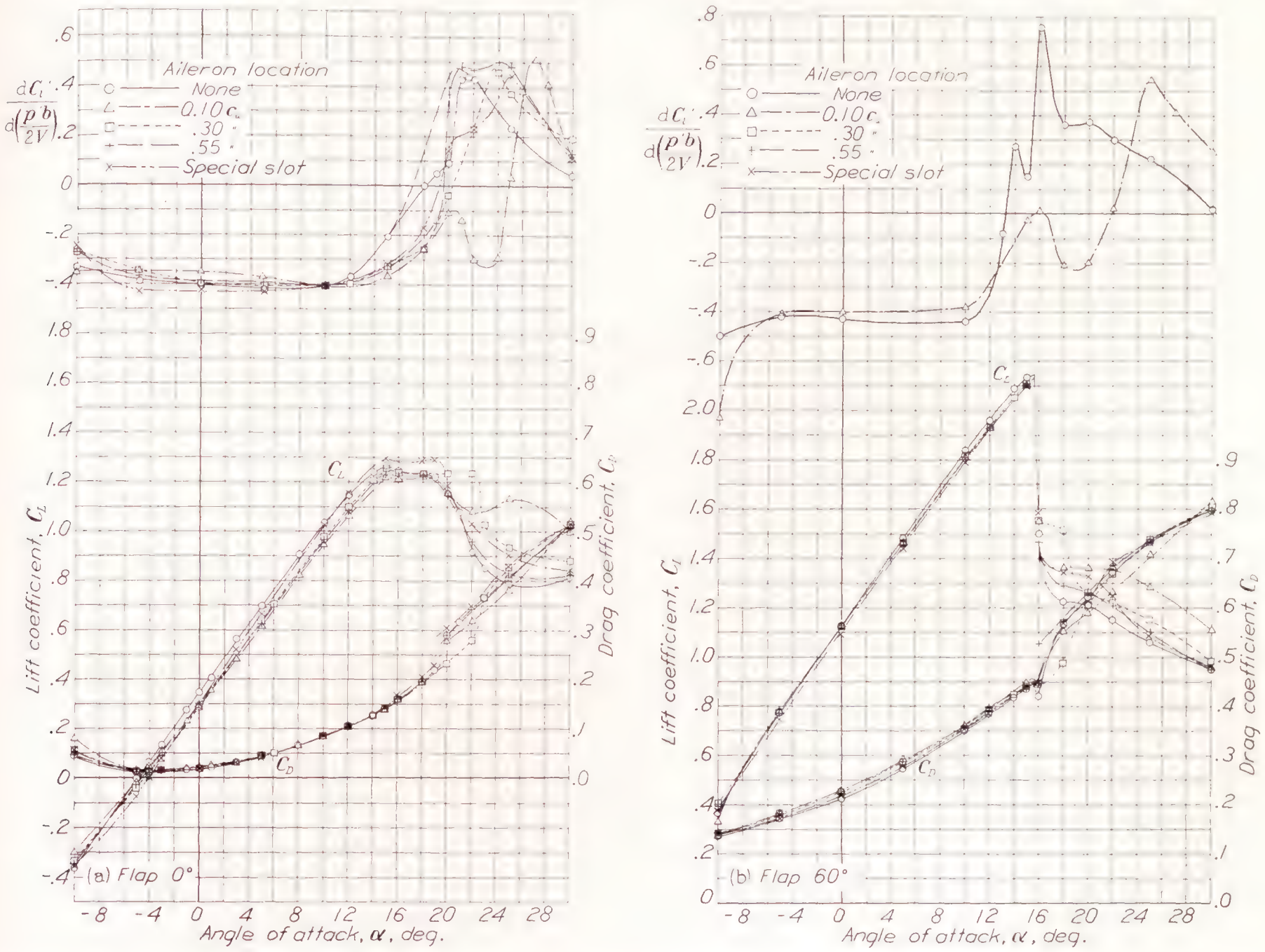

FIGURE 12.—Effect of slot-lip ailerons on lift, drag, and rate of change of rolling-moment coefficient with rate of rotation $\frac{dC_l'}{d\frac{p'b}{2V}}$. Ailerons neutral; 7- by 10-foot tunnel.

Effect of slot shape on control.—The slots first used with the slot-lip ailerons in the present tests were similar to the ones used in the lag investigation but were later modified as shown by the dashed lines in figure 11. The rolling- and yawing-moment coefficients obtained with the original and modified slots with the slot-lip ailerons located at 0.10, 0.30, and $0.55c_w$ from the leading edge are given in figure 18(a) with the right aileron deflected up 40° and the left aileron deflected down 12°, flap 0°. The rolling moments with the modified slot were superior to those with the original slot in most cases. Consequently, complete data have been given only for the tests with the modified slots. The effect of a more drastic change in slot shape was determined from tests of the slot-lip aileron shown in figure 11(d). In this case the slot was formed between two airfoil-shape sections, an arrangement that, it was believed, would result in reduced drag. A comparison of the relative control effectiveness of this aileron and of the modified slot-lip aileron of figure 11(c)

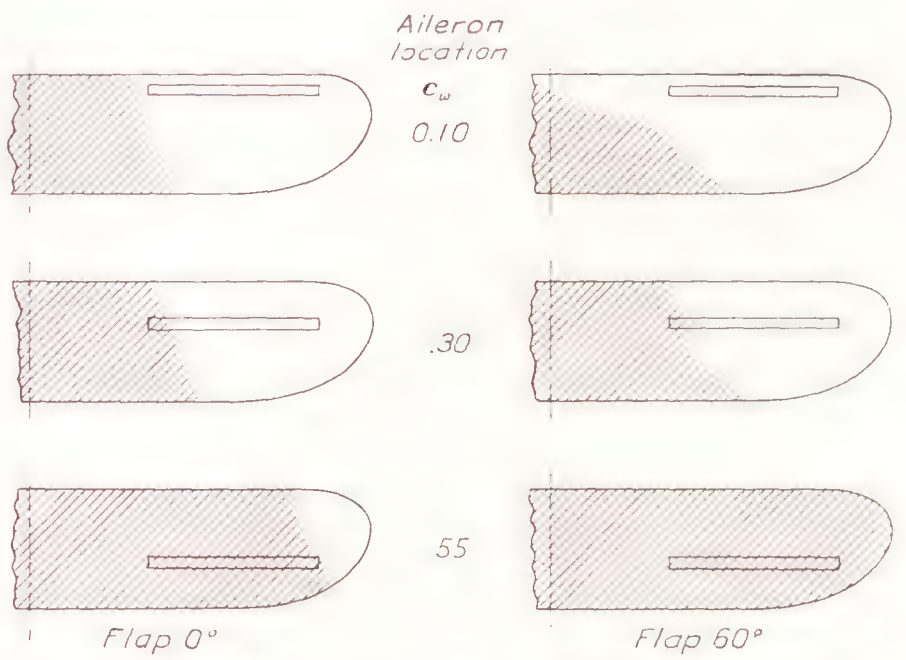

FIGURE 13.—Effect of slot-lip ailerons on air flow above the stall. (Shaded area is stalled.) Ailerons neutral; α, 22°.

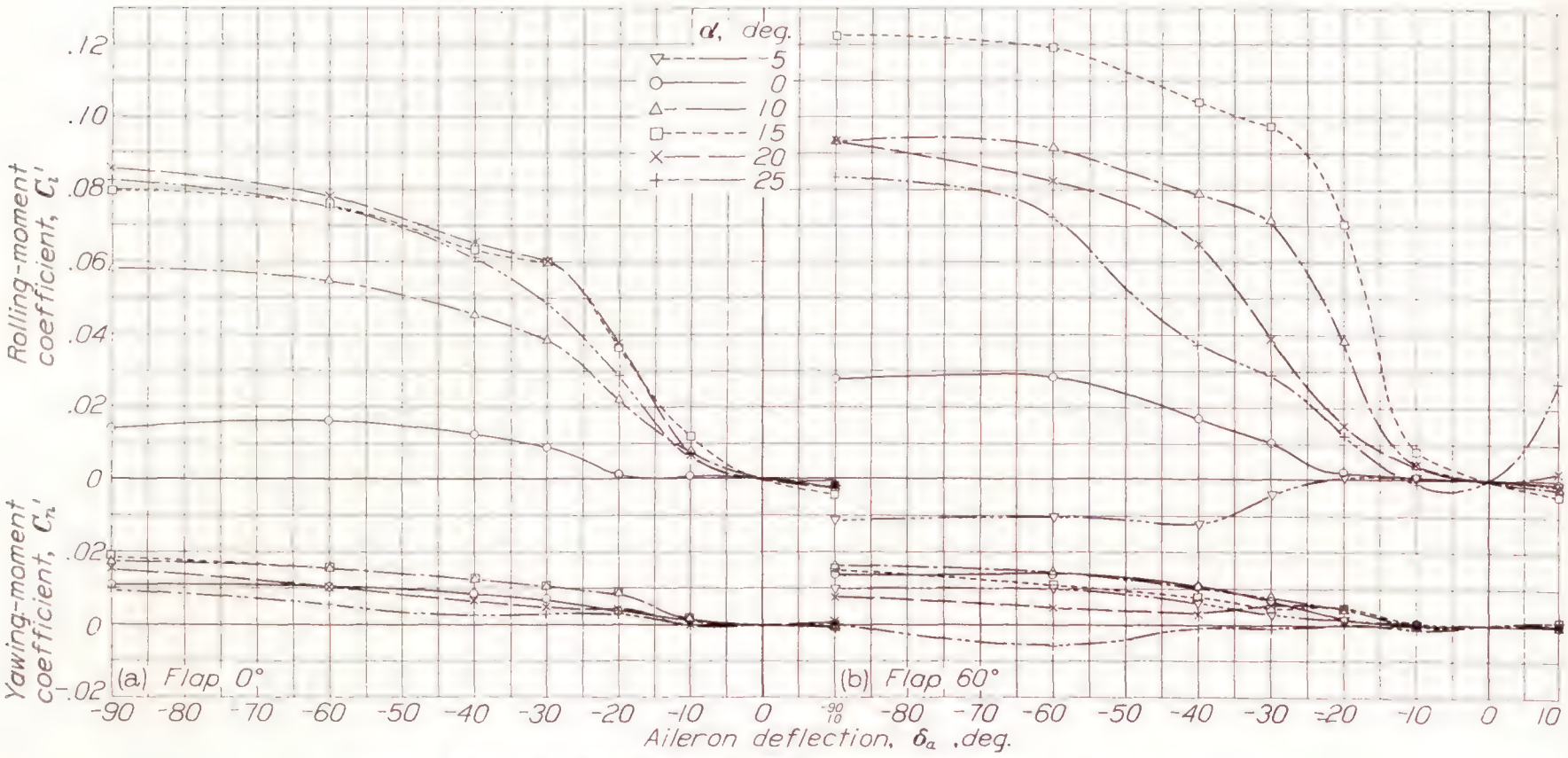

FIGURE 14.—Rolling- and yawing-moment coefficients due to slot-lip ailerons at $0.10c_w$.

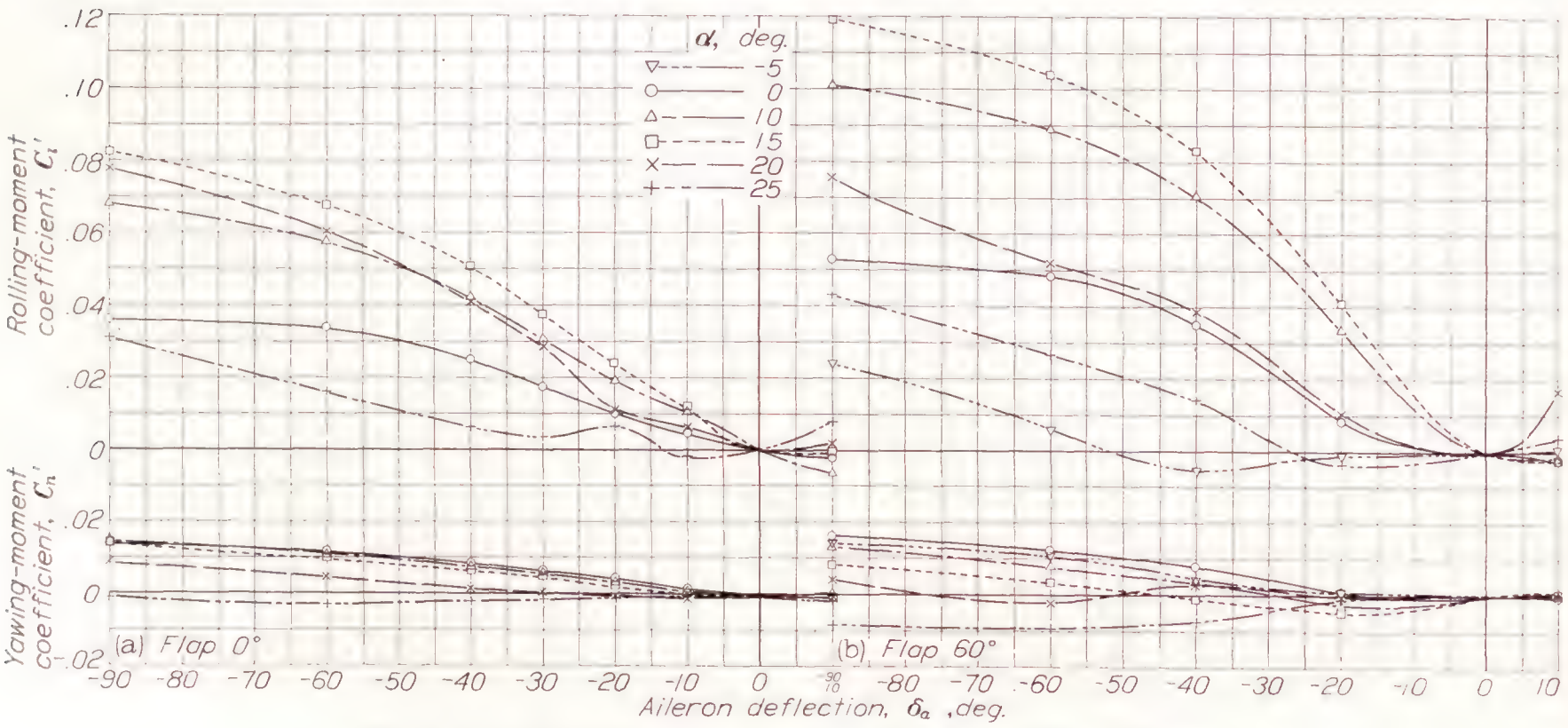

FIGURE 15.—Rolling- and yawing-moment coefficients due to slot-lip ailerons at $0.30c_w$.

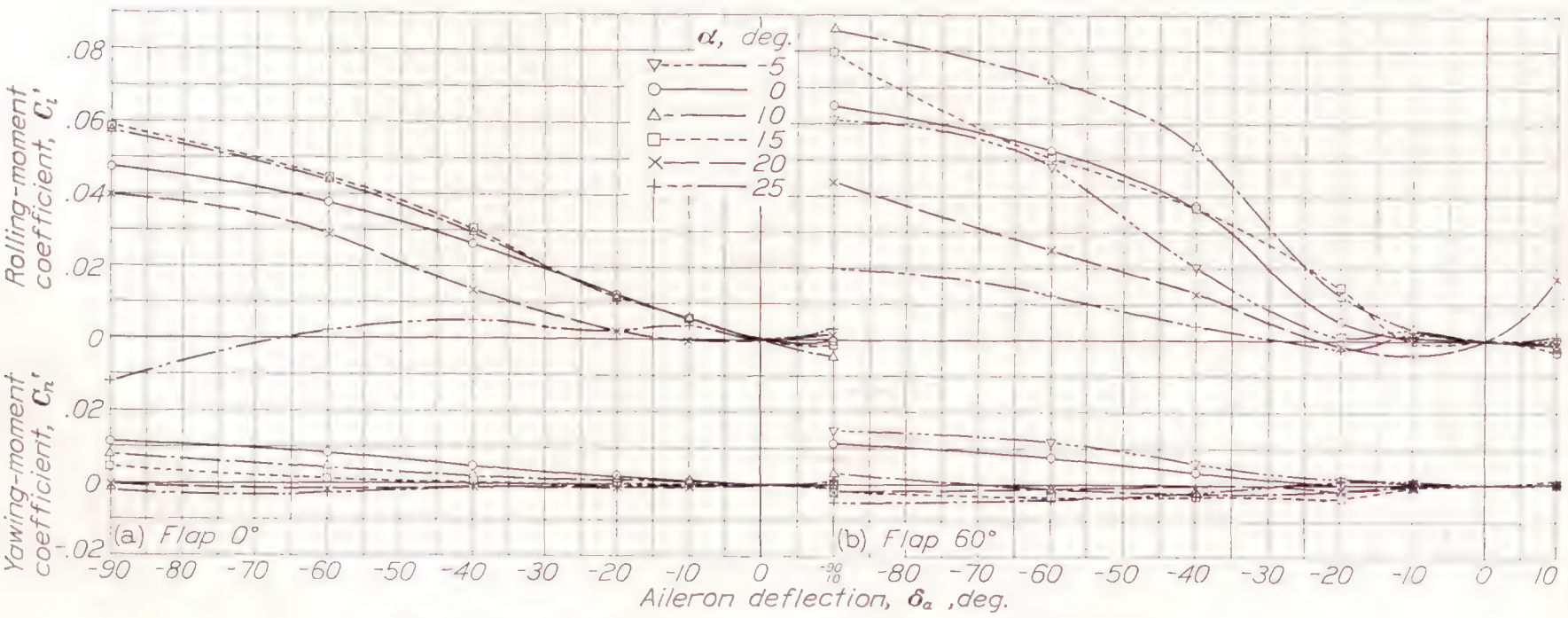

FIGURE 16.—Rolling- and yawing-moment coefficients due to slot-lip ailerons at $0.55c_w$.

may be made from figures 16(a) and 17(a). Although the aileron with the special slot gave higher rolling moments above 20° deflection, the variation of this moment with aileron deflection was not uniform. With the flap deflected, the difference between the two

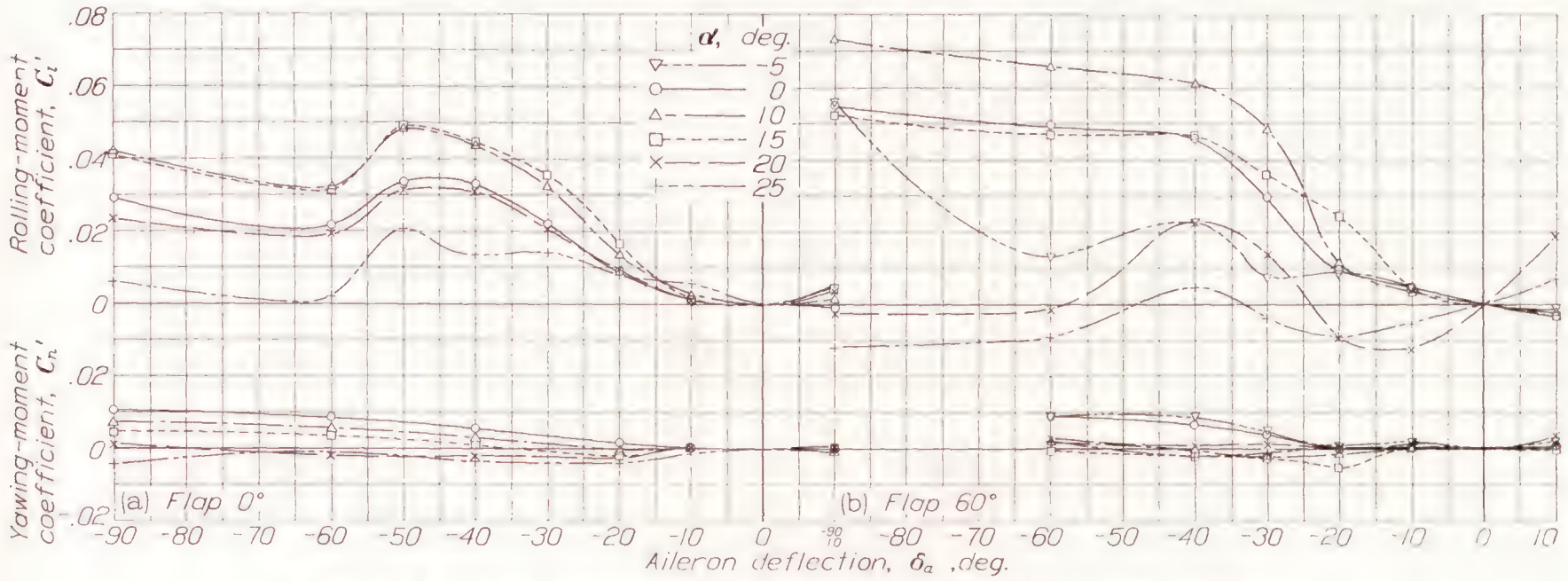

FIGURE 17.—Rolling- and yawing-moment coefficients due to slot-lip ailerons at $0.55c_w$ with special slot.

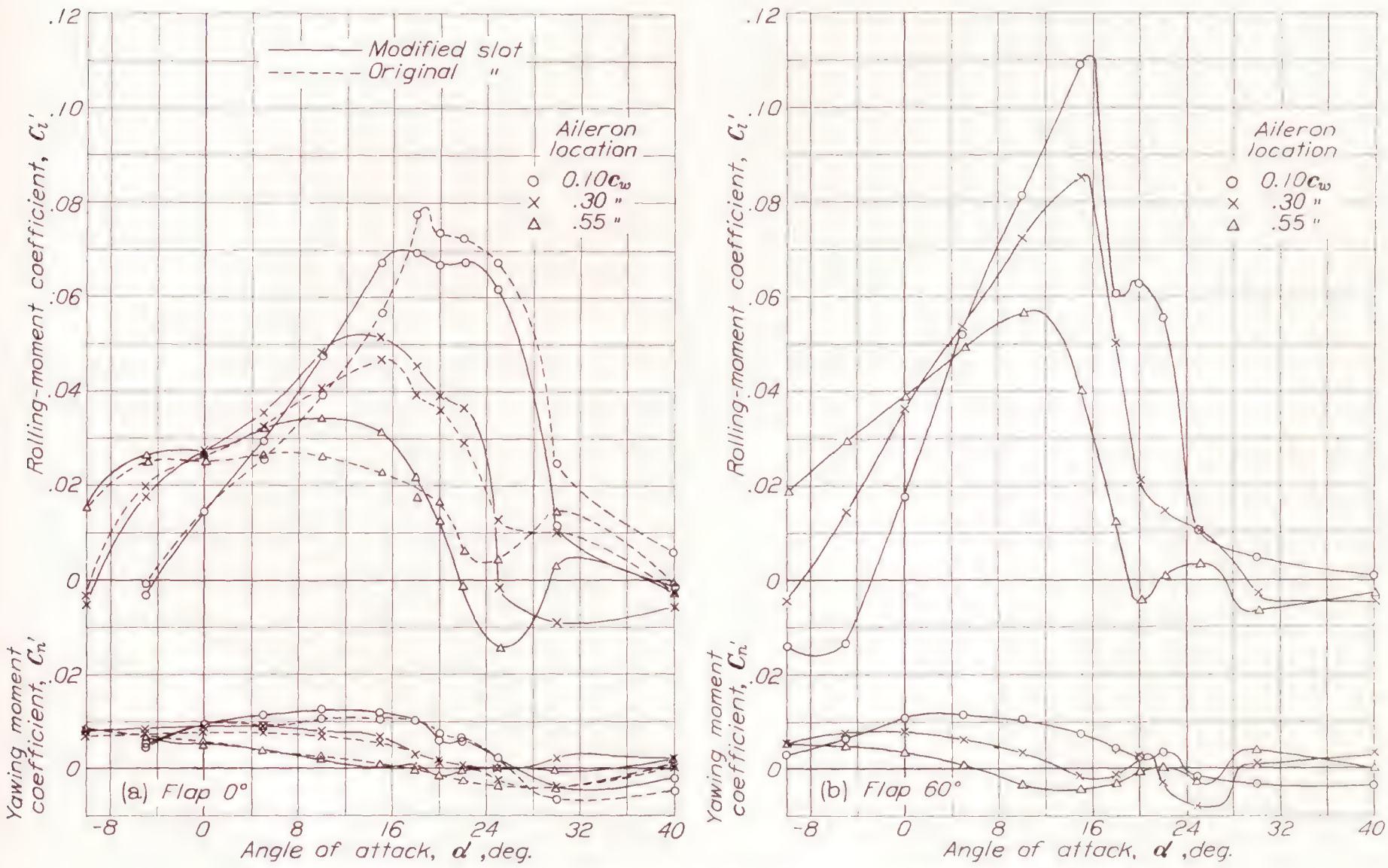

FIGURE 18.—Effect of slot-lip aileron location on rolling- and yawing-moment coefficients, δ_a up 40°, down 12°.

slot shapes was even greater, as may be seen by comparing figures 16(b) and 17(b).

Comparison of slot-lip ailerons and spoilers.—A direct comparison between slot-lip ailerons and plain spoilers was made by testing the slot-lip ailerons in certain conditions with the slot both open and completely sealed. The results are given in figure 19 and show the effect of the slot on the rolling- and yawing-moment coefficients. The ailerons as spoilers were deflected upward 60° in all cases and were located at 0.10, 0.30, and $0.55c_w$. With the slots open the rolling moments are appreciably higher below the stall but are definitely lower above the stall. The yawing-moment coefficients are lower with the slots open.

Effect of slot-lip aileron deflection.—For a satisfactory control device it is desirable that the curve of rolling moment against control deflection have no discontinuities. Owing to the importance of this requirement, the results of all the slot-lip ailerons tested in this part

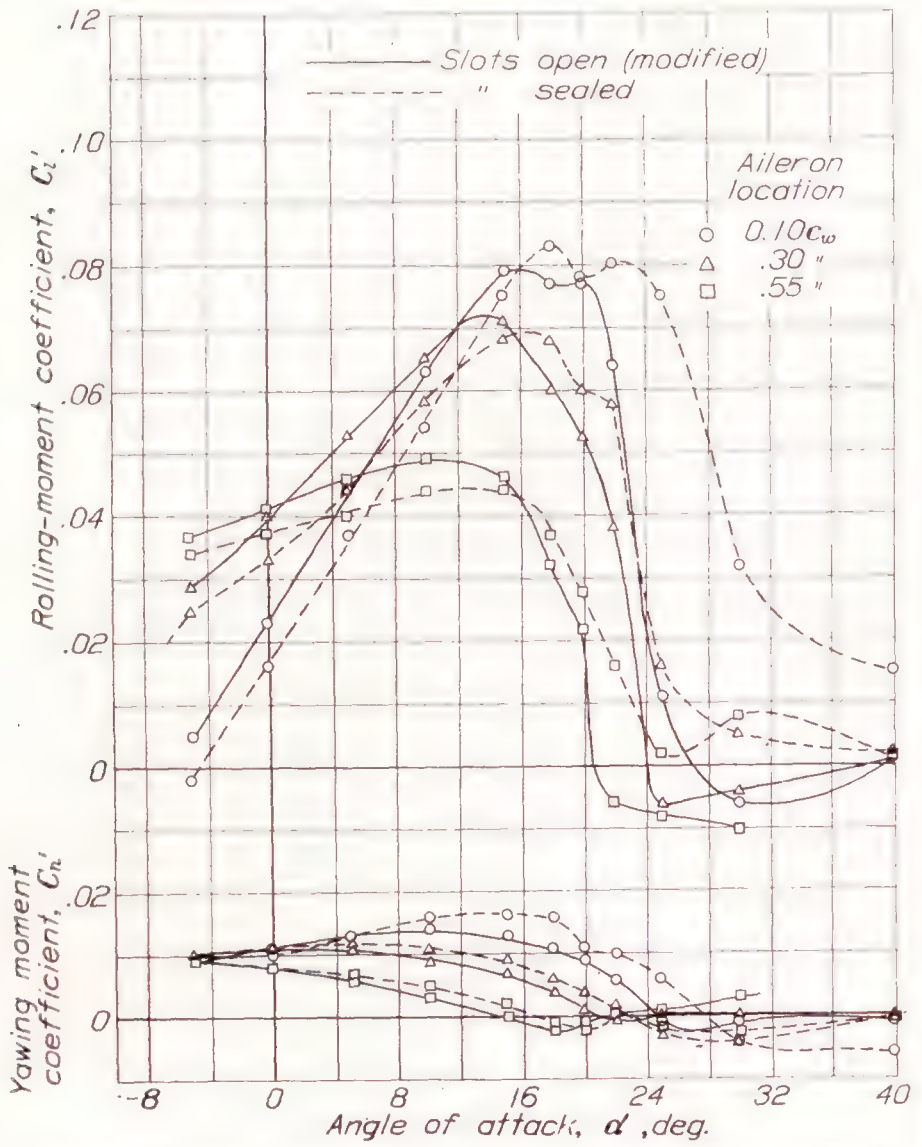

FIGURE 19.—Effect of slot-lip aileron location on rolling- and yawing-moment coefficients, δ_a up 60°; flap, 0°.

of the investigation have been plotted against aileron deflection in figures 14 to 17. With the slot-lip ailerons at the $0.10c_w$ location, the rolling moments are relatively low at 10° aileron deflection, particularly with the flap deflected. With the ailerons at either $0.30c_w$ or $0.55c_w$, however, the moments vary uniformly with aileron deflection except with the flap deflected and the aileron at $0.55c_w$. With the special slot, the rolling moments are low at 10° and 20° deflection but rise to rather high values beyond 30° deflection. In most of the cases given, the rolling moments with the slot-lip aileron deflected downward are opposite in sign to the moments with the ailerons deflected upward. This characteristic allows the use of a differential aileron linkage with some control obtained from the downwardly deflected aileron.

Effect of flap deflection.—With the split flap deflected 60°, the rolling moments produced by the slot-lip ailerons were considerably higher at a given angle of attack than with the flap neutral. Rolling- and yawing-moment coefficients are given in figure 18(b) for the slot-lip ailerons located at the three locations tested with aileron deflection of 40° up, 12° down, with the split flap deflected 60°. Large rolling moments were given by the ailerons at the $0.10c_w$ location at angles of attack near the stall, but these moments rapidly diminish as the angle of attack is reduced.

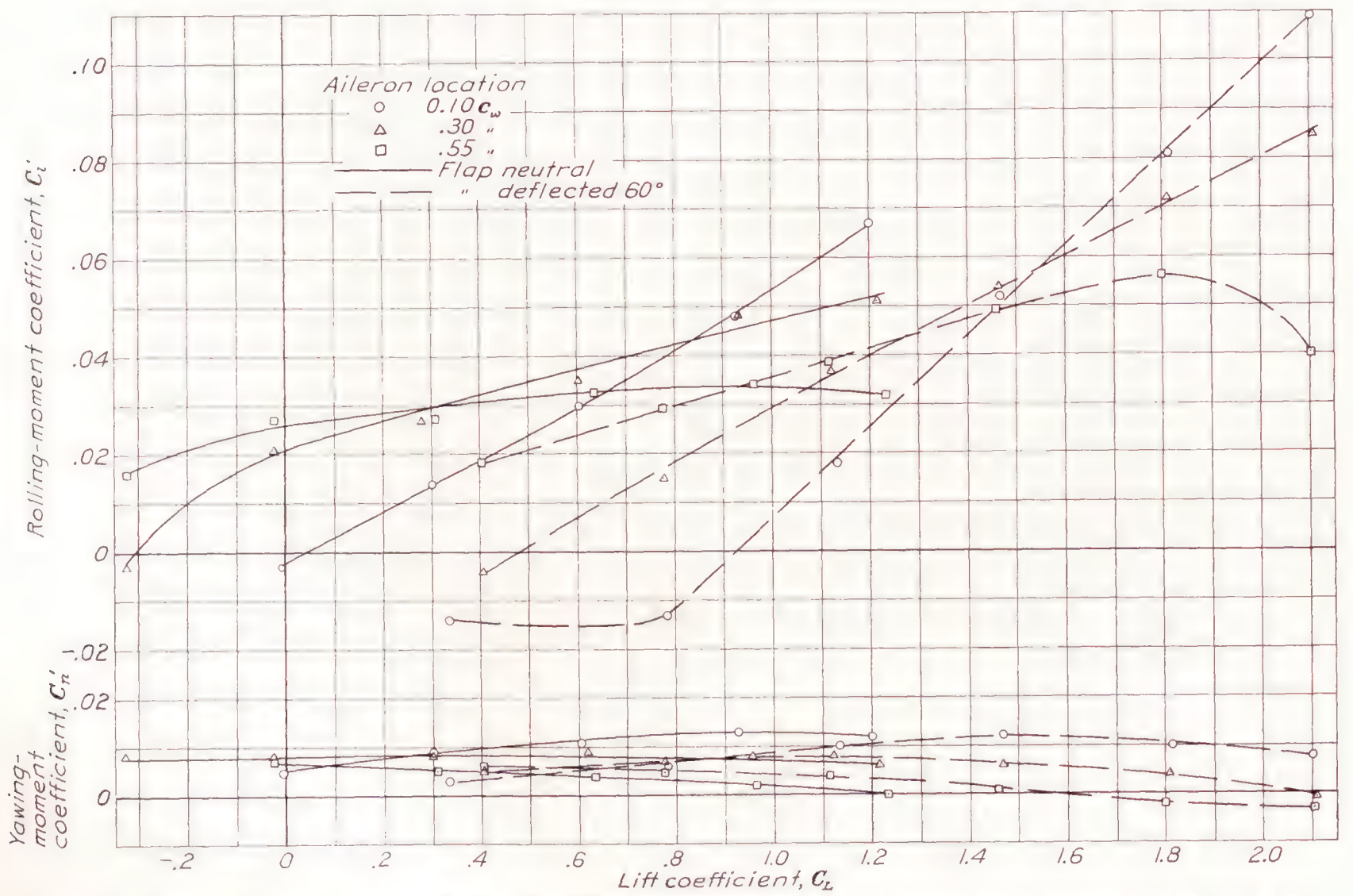

FIGURE 20.—Variation of rolling- and yawing-moment coefficients with lift coefficient for slot-lip ailerons in various locations, δ_a up 40°, down 12°.

A more conclusive comparison of the moments obtained with and without a flap may be made from figure 20 with C_n' and C_l' plotted against C_L. With the flap deflected 60° the rolling moments reached zero at higher values of lift coefficient than with the flap retracted. These values of lift coefficient at which the rolling-moment coefficients vanish are given in figure 21 for various aileron deflections. This characteristic limits the forward location of the ailerons because it is necessary to have control maintained to the highest speed at which the airplane will be flown with the flap deflected. If the corresponding lift coefficient is 0.5, the slot-lip aileron cannot be located farther forward than $0.30c_w$ and still give control.

Effect of deflected ailerons on damping in roll.—With a wing rotating about the longitudinal axis, the downgoing wing is at a higher angle of attack than the center of the wing. If the curve of aileron rolling

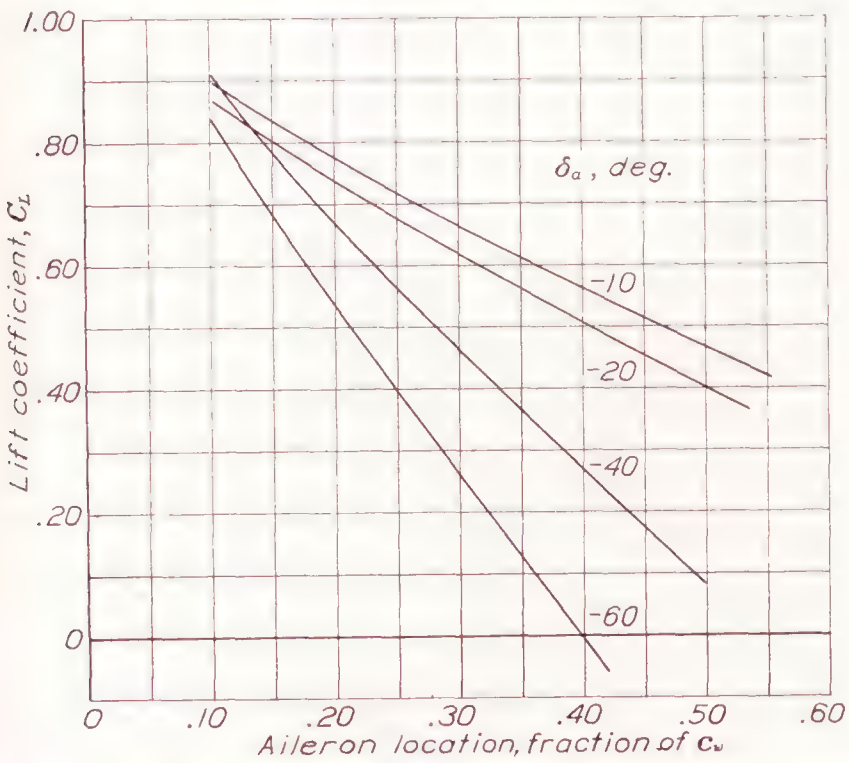

FIGURE 21.—Lift coefficients at which rolling-moment coefficient vanishes when flap is deflected 60°.

moment against angle of attack has a positive slope, the rolling moments obtained with the wing rotating should be higher than those measured in static tests. This increase in rolling effectiveness may be expressed as a reduction in damping in roll. The reduction in damping was checked by rotation tests made with slot-lip ailerons at $0.10c_w$, deflected 40° up, 10° down, and with the split flap both neutral and deflected. The measured values and an approximate curve for the values for the intermediate locations have been included in figure 22.

Choice of slot-lip aileron location.—In the discussion of slot-lip aileron location, it has been shown that the rolling moments are highest at angles of attack near the stall with the forward location. With the aileron in this location, control is not available at high speed with a flap deflected. Control under these conditions is only possible with the location at least as far from the leading edge as $0.30c_w$. Another interesting consideration is the yawing moment accompanying the rolling moment. With ordinary ailerons the induced yawing moment contributes practically the entire yawing moment and the coefficient C_{n_i} is obtained from

$$C_{n_i}=0.20\ C_L C_l'$$

for a rectangular wing of aspect ratio 6 with equal up-and-down aileron deflection. (See reference 9.) In

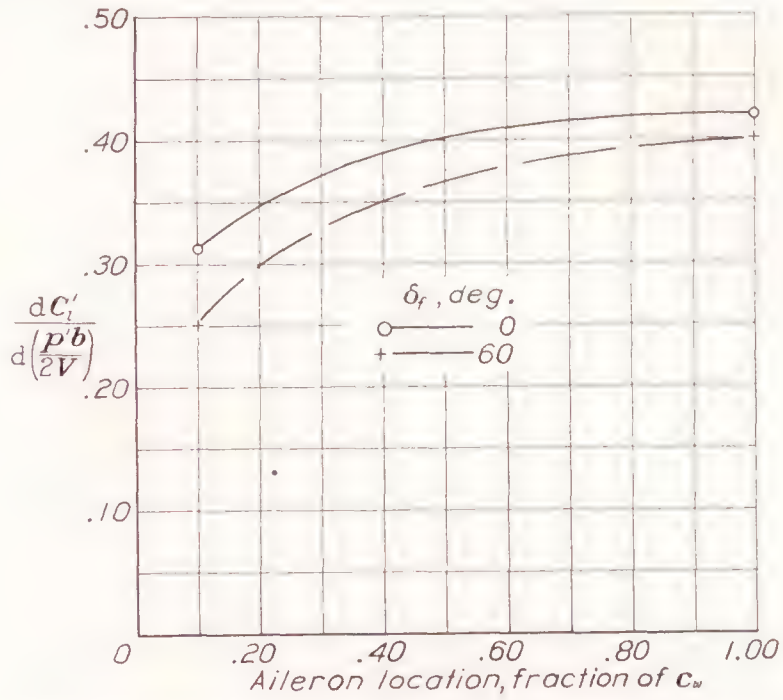

FIGURE 22.—Effect of slot-lip aileron location on damping in roll, δ_a up 40°.

figure 23 are plotted the ratios of yawing moments to rolling moments for the slot-lip ailerons in the three tested positions. Included in the same figure is the theoretical ratio for equal up-and-down deflection of ordinary ailerons. It will be seen that the slot-lip ailerons produced a large profile yawing moment of the same sign as the rolling moment, which was reduced by

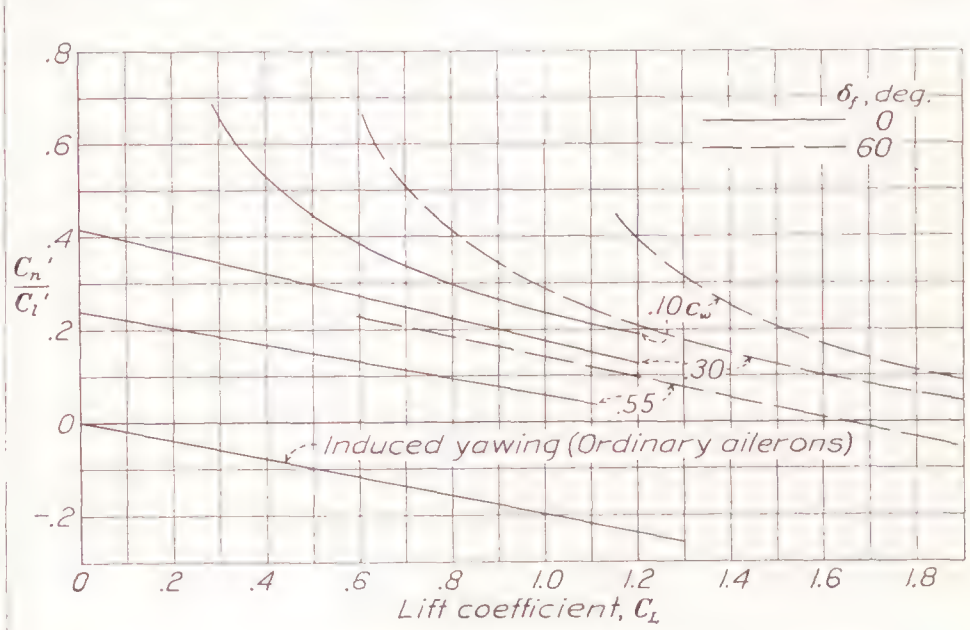

FIGURE 23.—Ratios of yawing moment to rolling moment for slot-lip ailerons.

the induced yawing moment until, at high lift coefficients with the flap down, the yawing moment was negative or adverse with the slot-lip aileron in the rearward location. It appears from reference 10 that, for two-control operation of an airplane, an aileron giving rolling moments accompanied by yawing moments of the same sign (favorable) and about one-fifth the magnitude seems to be the most desirable, although the rate

of application of the control and the airplane characteristics influence the desirable ratio. With the slot-lip aileron at $0.30c_w$, the ratio of C_n'/C_l' varies from about 0.05 at maximum lift with the flap deflected to about 0.40 at high speed, flaps neutral. With the aileron in the $0.55c_w$ location, the ratio becomes negative at the landing condition, whereas at the $0.10c_w$ location the ratio becomes excessively large at high speed. Consideration of lateral stability dictates a forward location; the lowest drag is obtained with the rearward location. The $0.30c_w$ location would seem to be the most desirable for a slot-lip aileron used as the sole means of lateral control, except for the effect of the slots on the drag of the wing.

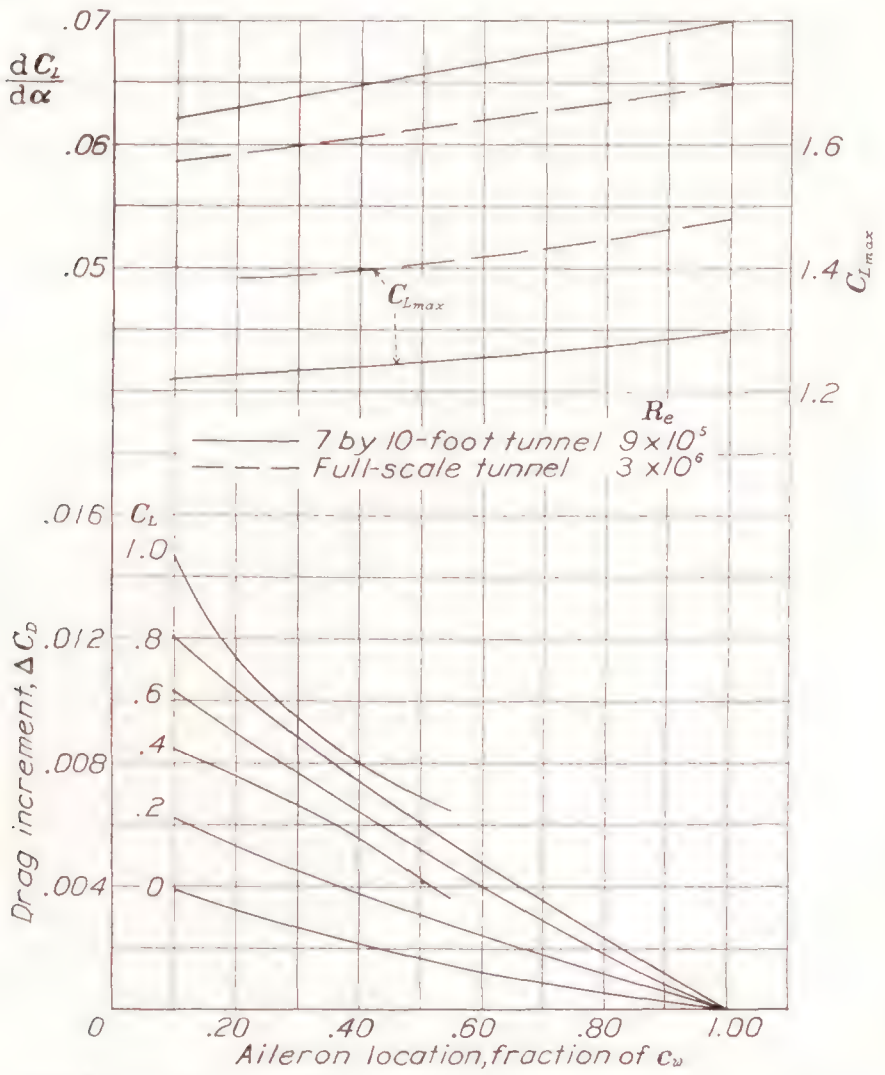

FIGURE 24.—Effect of slot-lip aileron location on ΔC_D, $dC_L/d\alpha$, and $C_{l\,max}$.

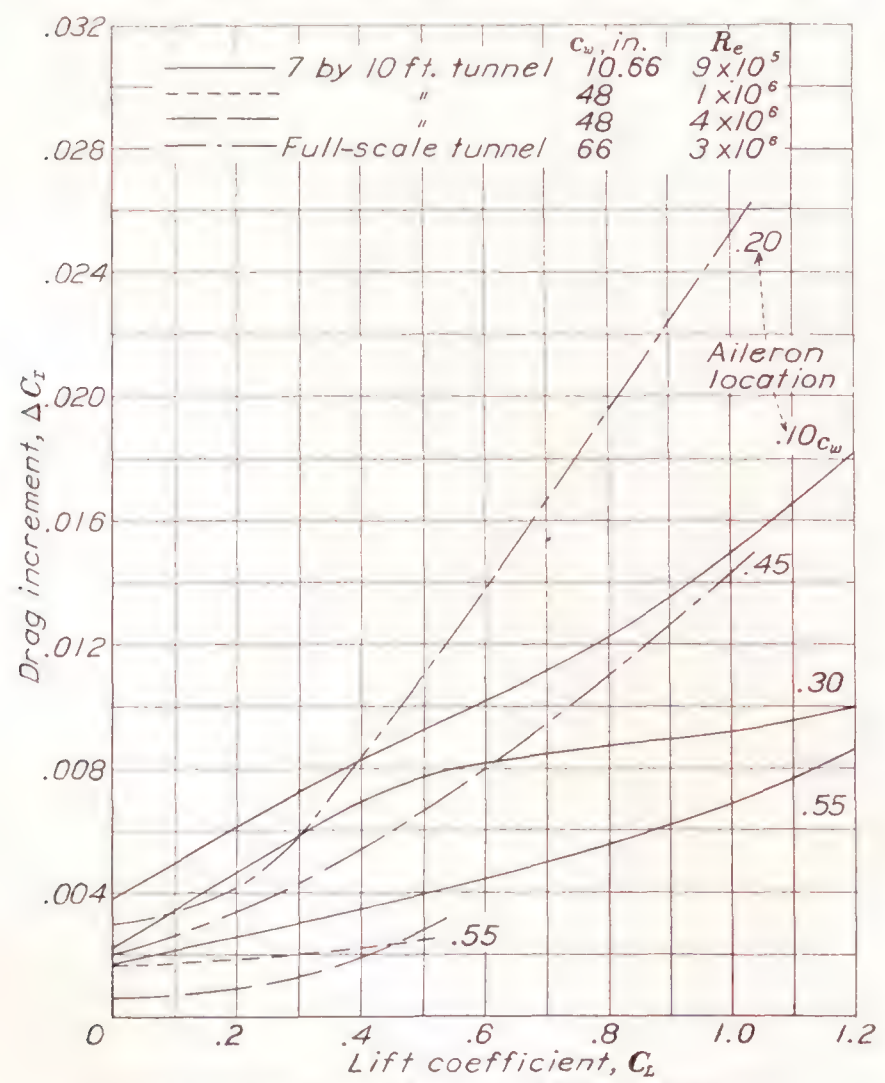

FIGURE 25.—Increments of drag due to 0.50 $b/2$ slot-lip ailerons.

LIFT AND DRAG EFFECTS DUE TO SLOT-LIP AILERONS

The effect of slot-lip ailerons on the lift and the drag is of particular importance for high-performance airplanes. Previous tests have shown that at low angles of attack practically all slots reduce the lift and increase the drag. It has also been shown that a given size of slot has less drag when located rearward on the wing than when located forward. In the present investigation the slots were made as narrow as possible without causing lag. Because the effect of the slots on the drag was large, considerable attention was given to its measurement and to means for reducing it. The effect of the slots on the drag was determined with slot-lip ailerons on a small-scale wing model in the 7- by 10-foot tunnel and on an actual airplane in the full-scale tunnel. The airplane was equipped with slot-lip ailerons in two locations, one ($0.20c_w$) selected for its control and stability characteristics and the other ($0.45c_w$) selected for its smaller effect on lift and drag.

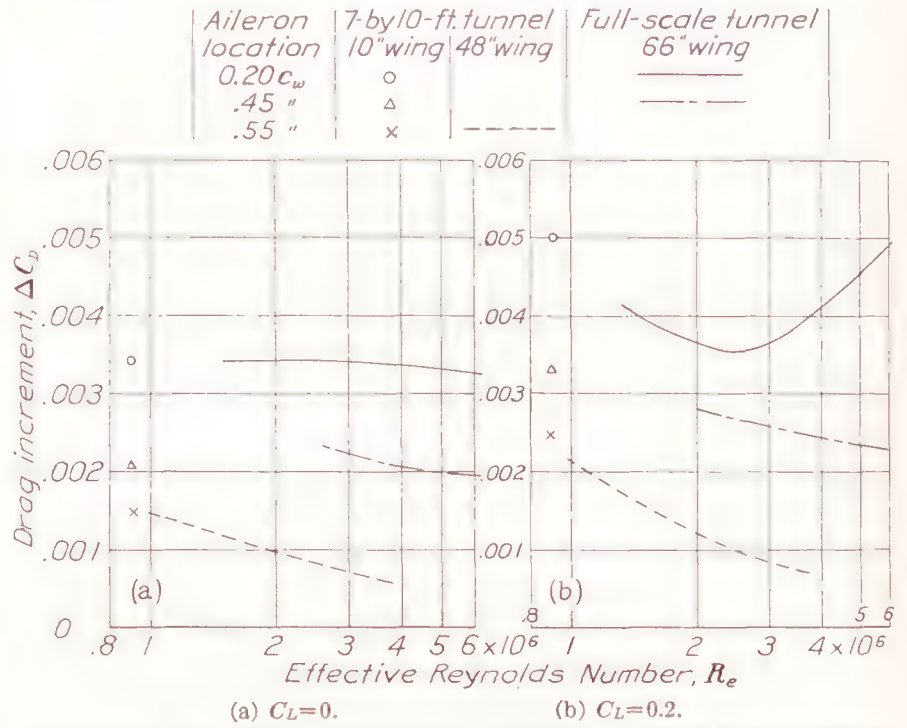

(a) C_L=0. (b) C_L=0.2.

FIGURE 26.—Scale effect on increment of drag due to 0.50 $b/2$ slot-lip ailerons.

TESTS IN THE 7- BY 10-FOOT TUNNEL

The tests of the small model in the 7- by 10-foot tunnel mentioned in the last section are interesting because they indicate certain trends. It would, however, be misleading to attempt to predict the performance of an airplane from the low-scale tests. The values of increments of drag due to the slot-lip ailerons have been computed for the slot-lip ailerons in the three locations tested from polar curves plotted from

the data given in figures 12(a) and 12(b) and from additional check tests. The average values of ΔC_D are given in figures 24, 25, and 26 and are compared with values from other tests at large values of the Reynolds

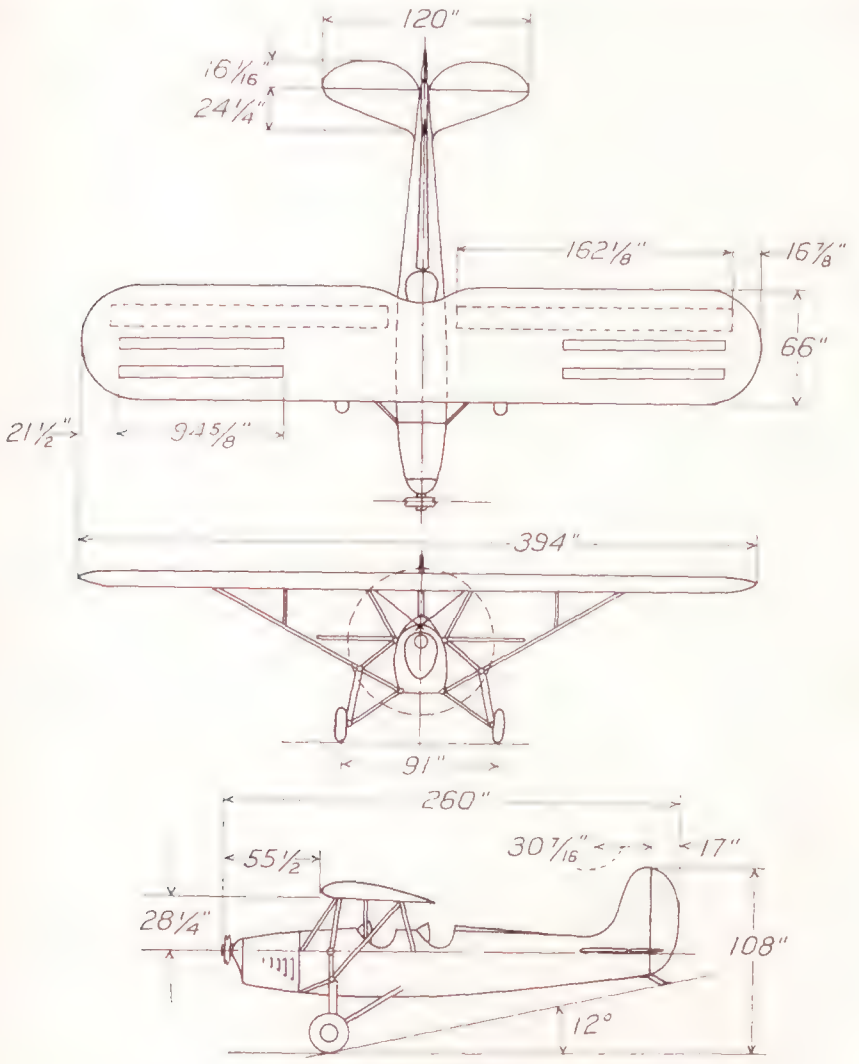

(a) Complete airplane.

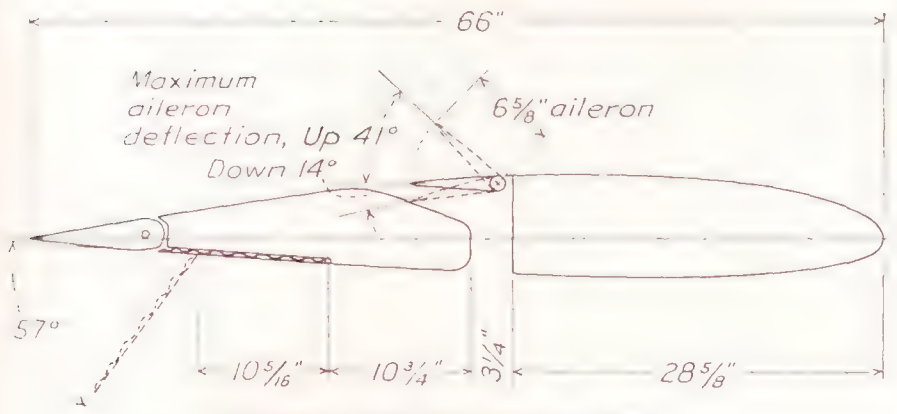

(b) Section with slot-lip aileron at $0.45c_w$.

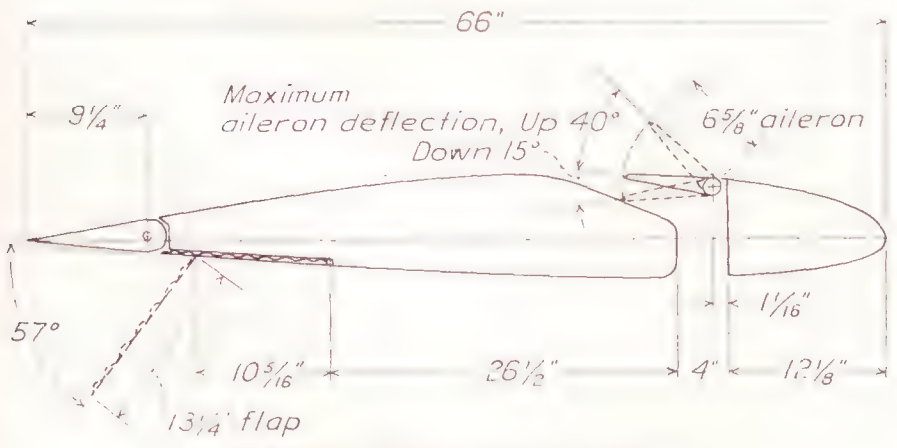

(c) Section with slot-lip aileron at $0.20c_w$.

FIGURE 27.—Fairchild 22 airplane with slot-lip ailerons. The N. A. C. A. 2412 wing section.

Number. The Reynolds Numbers given are the effective Reynolds Number determined for each tunnel from reference 11. The effects of slot-lip aileron location on the slope of the lift curve $dC_L/d\alpha$ and on maximum lift are shown in figure 24 and compared with values from tests in the full-scale tunnel. Because of the different test aspect ratios and different Reynolds Numbers, the actual values do not agree but the reductions in the values due to the slots are comparable. The values at the $1.00c_w$ location are taken from the case with no slot or aileron.

TESTS IN THE FULL-SCALE TUNNEL

In order to determine the practicability of slot-lip ailerons from actual flight tests and to determine their drag at large scale, tests were made of a Fairchild 22 airplane equipped with a wing modified to permit the installation of slot-lip ailerons with their hinge axes at either 0.20 or $0.45c_w$ positions. The F–22 airplane is a two-place, externally braced, parasol-type mono-

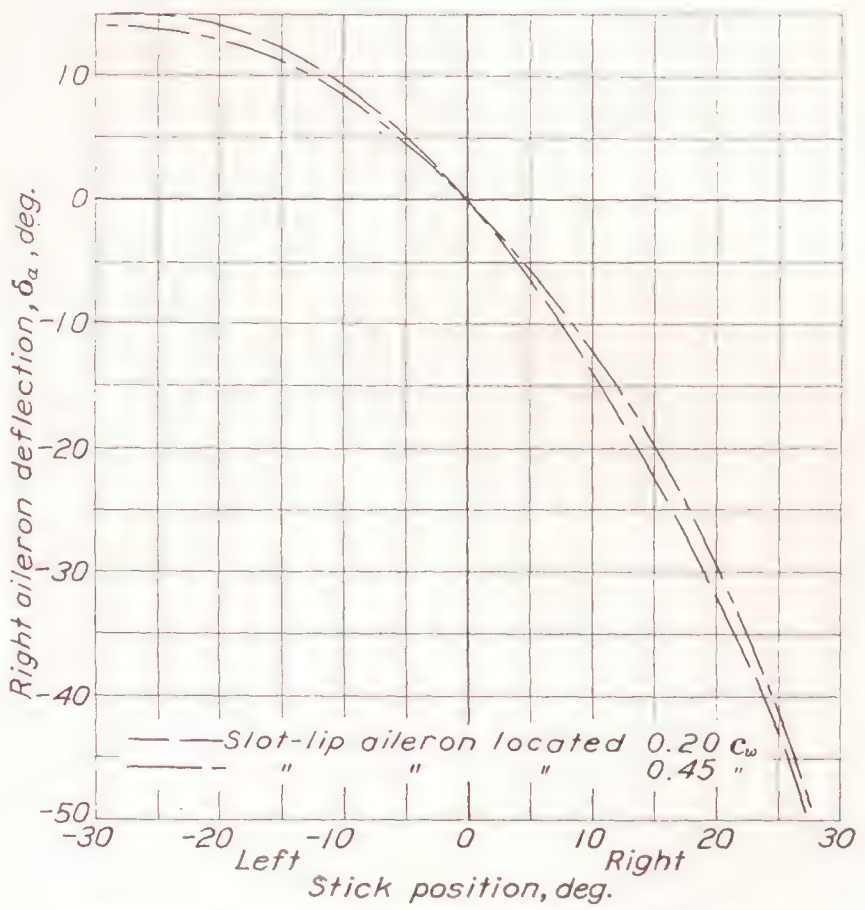

FIGURE 28.—Slot-lip aileron deflections for Fairchild 22 airplane.

plane. A three-view drawing of the airplane as tested in flight is shown in figure 27(a). Section drawings of the wing showing the slot-lip ailerons in the two positions on the N. A. C. A. 2412 wing used are shown in figure 27(b) and (c). The allowable aileron motions are shown in figure 28 for both positions. In the tests in the full-scale tunnel the wing was mounted on a slightly different fuselage for convenience.

The airplane with the horizontal tail surfaces and propeller removed was mounted on the balance in the full-scale tunnel as shown by figure 29. A description of the wind tunnel and balances is given in reference 12. The ailerons were locked in their neutral position and lift, drag, and pitching moments were measured with the slot-lip ailerons first in the $0.20c_w$ location, then in the $0.45c_w$ location, and finally without the slot-lip ailerons. When the slot was not in use, the openings

were covered with metal plates shaped to conform to the wing profile. A photograph (fig. 30) shows the

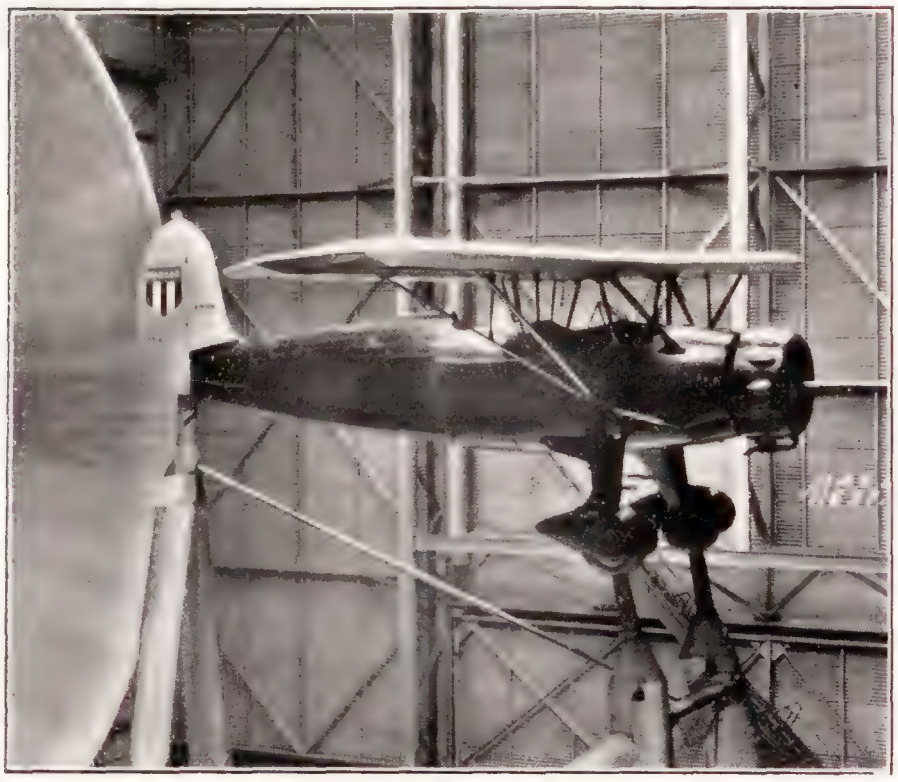

FIGURE 29.—The Fairchild 22 airplane with slot-lip ailerons mounted for test in the full-scale tunnel.

FIGURE 30.—View of the Fairchild 22 airplane wing showing details of slot.

wing with the slot open in the $0.45c_w$ position and with the front position slot covered by a metal plate. The tests were made with the flap both neutral and deflected and covered a range of angles of attack from −8° to 24° at a tunnel air speed of about 56 miles per hour. Scale-effect tests to determine the minimum drag were made over a speed range from 30 to 120 miles per hour with the flap neutral.

All the results have been corrected for tare and wind-tunnel effects. The lift, the drag, and the pitching-moment coefficients are plotted in figure 31 against angle of attack. The effect of the slot-lip ailerons on the lift is clearly shown: The maximum lift and

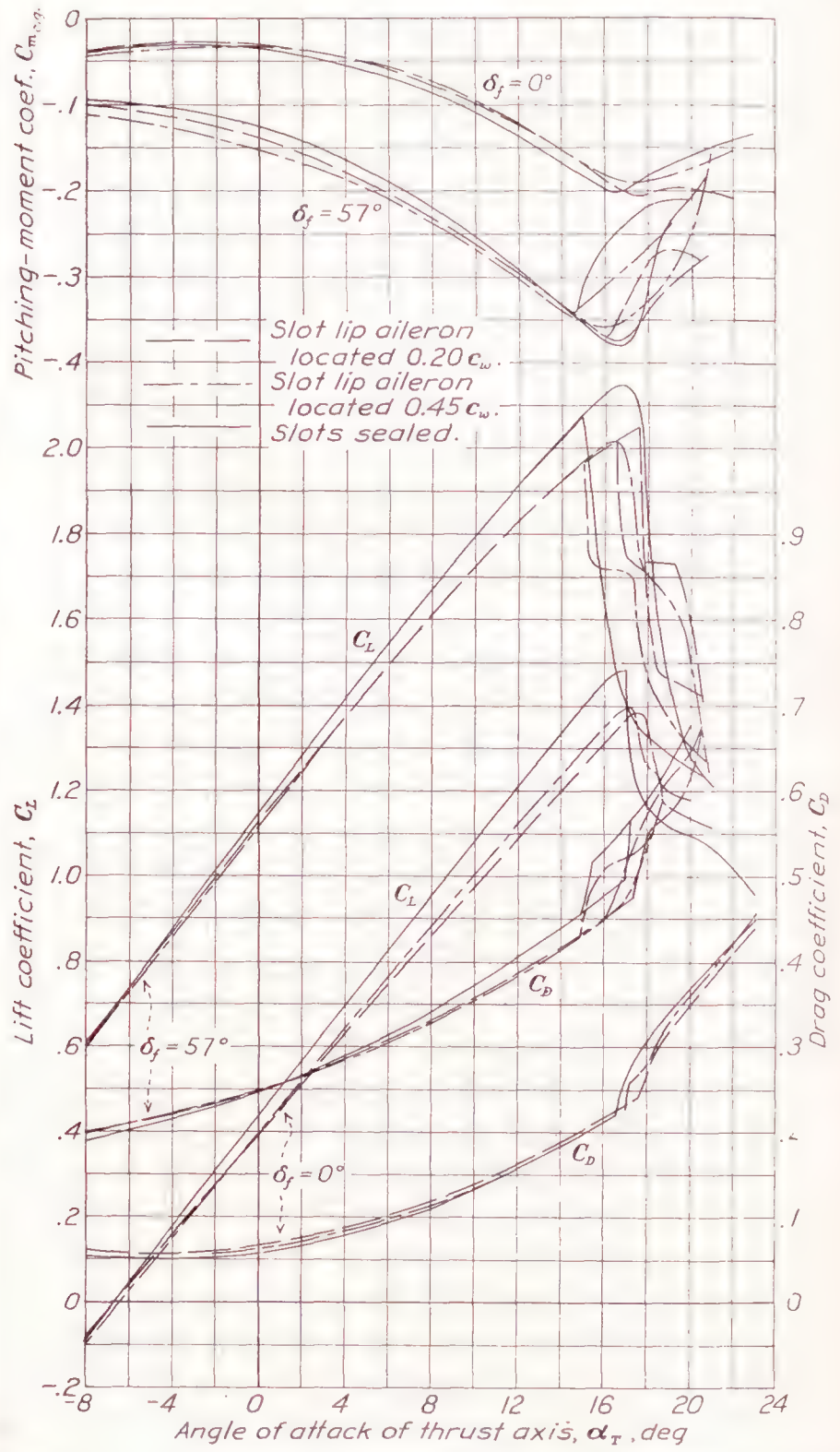

FIGURE 31.—Lift, drag, and pitching-moment coefficients of the Fairchild 22 airplane with slot-lip ailerons. The full-scale tunnel; air speed, 56 m. p. h.; propeller and horizontal tail surfaces removed; angle of wing setting, 4.4°.

the slope of the lift curve are reduced, but the stall is somewhat delayed, as in the wing model tests. The pitching-moment coefficients are only slightly affected by the slot-lip ailerons. The effect of the flap on the pitching moments is not conclusive since the horizontal

tail surface was not in place and the additional downwash at a given angle of attack with the flap deflected would, no doubt, reduce the difference between the results with flap neutral and flap deflected.

The effect of the slot-lip ailerons on drag is clearly shown in figure 32, which is a plot of drag increment

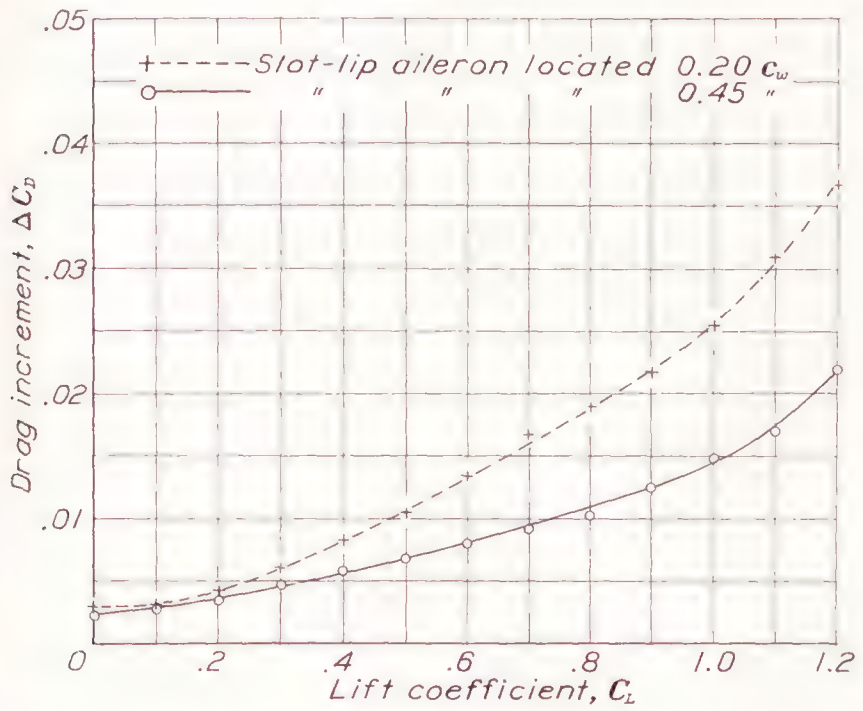

FIGURE 32.—Increase in drag due to slot-lip ailerons on the Fairchild 22 airplane in the full-scale tunnel. Air speed, 56 m. p. h.

ΔC_D against lift coefficient for the slot-lip ailerons in the two locations. With the particular shape of slot used the drag increment increases appreciably with lift coefficient. The effect of air speed on the drag coefficient is shown in figure 33(a) for minimum drag and in figure 33(b) for drag at a lift coefficient of 0.2. The effect of air speed or effective Reynolds Number on the drag increment is shown in figure 26. The scale effect is much greater at high lift coefficients than at the minimum drag attitude. The points of figure 26 taken from interpolated results of small-scale tests agree fairly well with the large-scale tests. Figure 25, however, shows poor agreement between large-scale and small-scale tests at lift coefficients above 0.2.

The effect of the slot-lip ailerons as tested in the full-scale tunnel on the Fairchild 22 airplane is more clearly shown by computing the estimated performance of the airplane. The following table gives the estimated power-on performance characteristics based on the tunnel results.

ESTIMATED PERFORMANCE OF F–22 AIRPLANE WITH SLOT–LIP AILERONS IN TWO LOCATIONS

Slot location	V_{min} (m. p. h.)		V_{max} $\delta_f = 0°$ (m. p. h.)	Maximum rate of climb (ft./min.)	Maximum angle of climb (deg.)
	$\delta_f = 0°$	$\delta_f = 56°$			
0.20c_w	53.08	43.75	122.6	625.0	4.7
0.45c_w	52.91	44.12	125.0	675.0	5.7
No slot	51.37	42.75	129.4	772.5	6.3

SLOT-DRAG INVESTIGATION

An investigation of the drag of slots used with slot-lip ailerons was conducted in the 7- by 10-foot wind tunnel. A wing of N. A. C. A. 23012 section with a chord of

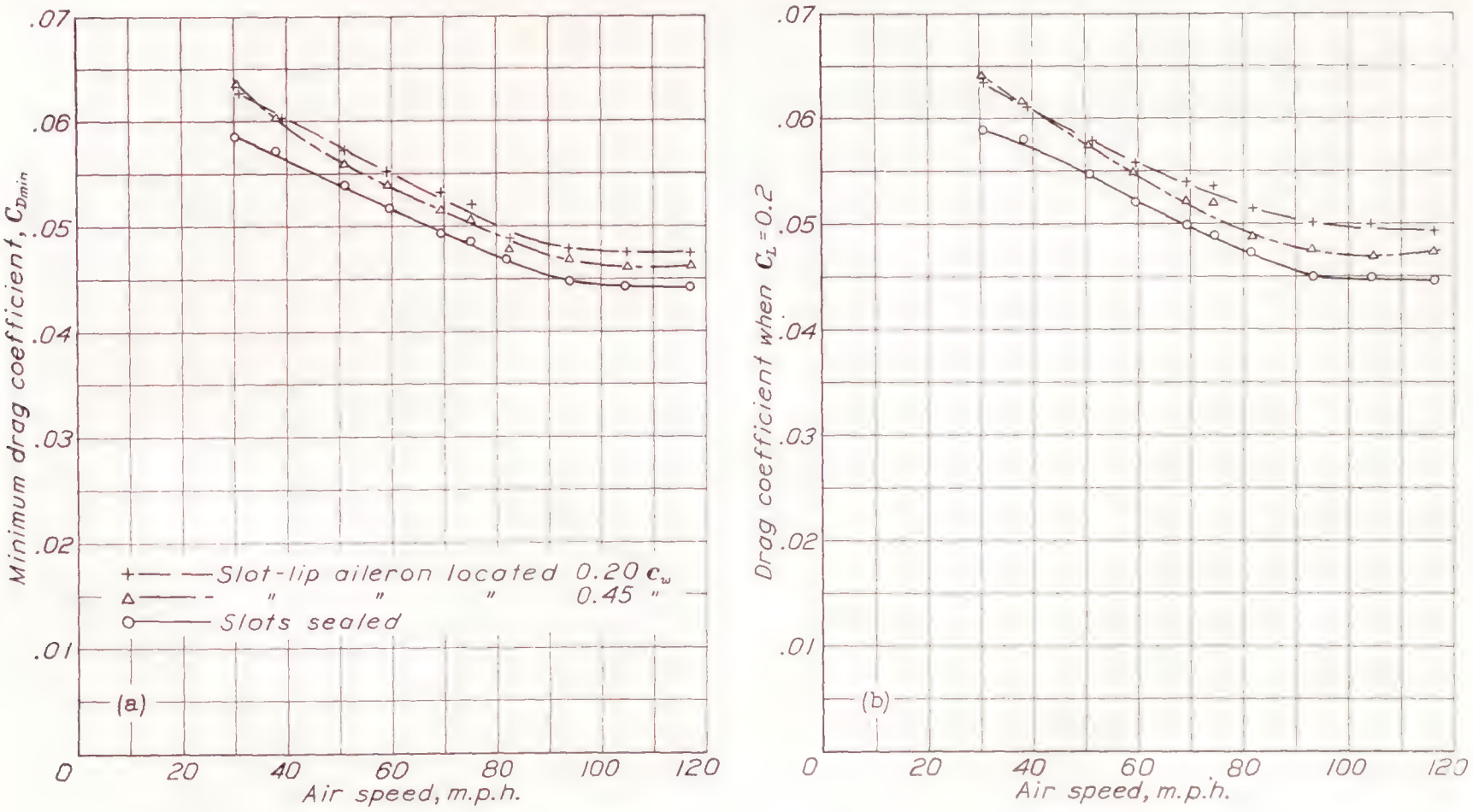

(a) $C_{D_{min}}$. (b) C_D at C_L=0.2.

FIGURE 33.—Scale effect on drag coefficients of Fairchild 22 airplane with slot-lip ailerons tested in the full-scale tunnel.

4 feet and a span of 8 feet was mounted on the regular balance between end planes that spanned the jet vertically as shown in figure 34. With an air speed of 80 miles per hour, the effective Reynolds Number was high enough to overlap the Reynolds Number of the tests

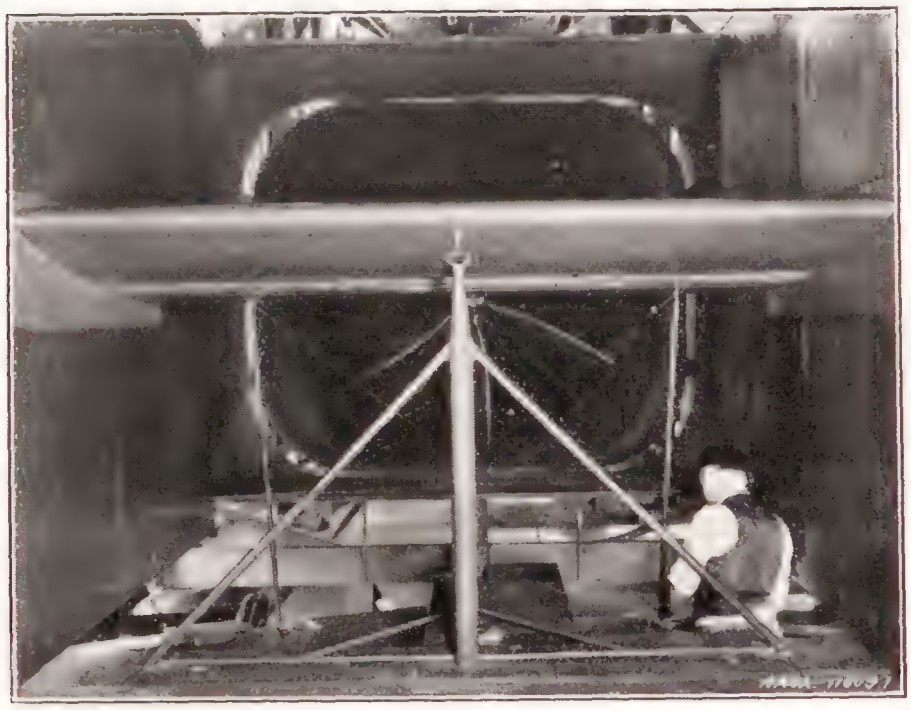

FIGURE 34.—The N. A. C. A. 23012 wing of 4-foot chord and 8-foot span with slots at $0.55c_w$ mounted between end planes in the 7- by 10-foot tunnel.

in the full-scale tunnel. The full-span slots were all located about $0.55c_w$.

Tests were made of the wing with no slots, with slot-lip ailerons of the type previously tested, and with several modifications. The lift, the drag, and the pitching-moment coefficients were obtained at an air speed of 80 miles per hour for all slots and at air speeds of 20, 40, and 60 miles per hour for certain conditions.

The results of the plain-wing tests at 80 miles per hour corrected for tunnel effects are plotted in figure 35. The values of the drag coefficient were corrected for tares and for static-pressure gradient by the usual methods and for deflection of the tunnel air stream by the following equation from reference 13:

$$\Delta C_{D_i}=0.25\frac{c}{h}C_L^2$$

where c/h is the ratio of the wing chord to the height of the jet. With the corrections applied, the profile drag of the plain wing agrees with values obtained in the variable-density tunnel at the same effective Reynolds Number. The accuracy of the equation in correcting for the air-stream deflection depends on the nature of the spillage of air from the open test section of the tunnel. In the 7- by 10-foot tunnel the exit cone is of the same size as the entrance cone and part of the deflected air stream at high lift coefficients flows below the exit cone. In such a condition the theoretical corrections do not hold. The theoretical correction for angle of attack was insufficient to correct the results to infinite aspect ratio, so an arbitrary correction was applied to give a lift-curve slope of $dC_L/d\alpha_0$ of 0.101. The pitching-moment coefficient at zero lift C_{m_0} agreed with the results from tests in the variable-density tunnel, but the aerodynamic-center location was slightly ahead of the location found in the variable-density tunnel although it agreed with previous tests in the 7- by 10-foot tunnel of the same airfoil section. The errors due to tunnel effects are eliminated by presenting the results of the tests with various slots mainly in terms of variation from the plain-wing tests.

The type of slot used with the previously tested slot-lip ailerons was tested first for comparison. (See fig. 11(c).) The increments of drag obtained have been plotted in figures 25 and 26 for comparison with the previous tests. The increments as given are one-half the measured increments for comparison with the other one-half span slots. It will be seen (fig. 26) that the increments agree with the previous tests in the 7- by 10-foot tunnel at low values of the Reynolds Number at values of the lift coefficient of 0 and 0.2. There appears to be a large favorable scale effect for the slot location tested as compared with the tests of the more forward locations in the full-scale tunnel. A direct comparison is given in figure 25 of the drag increments from partial-span slots. Differences in the low-scale tests, which agree at zero lift but do not agree at other lifts, are partly due to the additional induced drag accompanying the distorted span load distribution of the lift. In addition, the scale effect at high lift coefficients differs from that at low lift coefficients. For this reason, the low-scale tests are of little value in predicting the drag at high lift coefficients.

The results of the present tests are given in table I, which shows: A diagram of each slot tested; increments

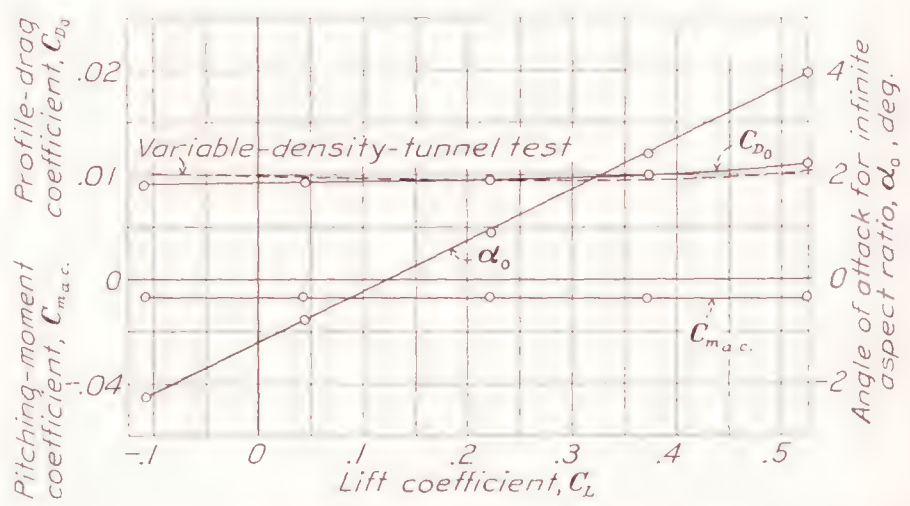

FIGURE 35.—Aerodynamic characteristics of the 4- by 8-foot wing of N. A. C. A. 23012 section mounted between end planes in the 7- by 10-foot tunnel. Effective Reynolds Number, 4,090,000; aerodynamic-center location: ahead of quarter-chord point $0.030c_w$, above chord $0.084c_w$.

of profile drag at $C_L=0$, 0.2, 0.4, and 0.5; slope of the lift curve $dC_L/d\alpha_0$; shift of the angle of attack of zero lift, $\Delta\alpha_{L_0}$; pitching-moment coefficient at zero lift, C_{m_0}; and the approximate aerodynamic-center location in the fraction of c_w from the quarter-chord point of the wing. The values in the table are from the tests at 80 miles per hour. Only a few arrangements will be discussed.

The original slot 1 gave a rather low increment of drag (ΔC_D=0.0013) at zero lift but gave a high increment (ΔC_D=0.0052) at C_L=0.5. With the surface in the rear of the slot reduced in thickness to allow smoother air flow, as in slot 5, the drag coefficient at C_L=0.5 increased to 0.0084 without appreciably affecting the drag at C_L=0. The rounding of the slot entrance so as to offer less resistance to the air, as in slot 11, reduced the drag coefficient at C_L=0.5 to 0.0034 but increased that at C_L=0 to 0.0038. It seemed, therefore, that the sharp-edge entry was desirable for high-speed conditions and further attempts were made to reduce the drag at C_L=0.5. Since the blunt shape of slot 1 gave less drag than the pointed shape of slot 4, slots 12 and 15 were tested, in which the lower opening was variable in size and the rear face was extremely blunt. Then the slot was filled in, as in 16, and the small opening ahead of the slot-lip aileron was sealed, as in slot 18; the drag increments were reduced to 0.0033, which is a substantial reduction from the original value of 0.0052 at C_L=0.5. If the slot size can be reduced as in slot 21, the drag coefficient is reduced to 0.0028. With the slot sealed on the bottom, as in slot 14, the drag increment was only 0.0011; and when sealed only at the top, as in slot 20, the drag increment was only 0.0008. With either surface sealed, however, the lateral control obtained with the slot-lip aileron was no longer satisfactory because of lag. It therefore seems that, although an appreciable reduction in drag due to the original form of the slot-lip ailerons is obtainable, the drag increments would still be considered excessive for high-performance airplanes.

FLIGHT TESTS

After the wind-tunnel tests had indicated that the slot-lip ailerons should give satisfactory lateral control, it seemed desirable to obtain flight tests of the device. The pilots' reactions to the aileron control as well as instrument records of the airplane motion produced by the ailerons were obtained. The airplane as tested in flight with the slot-lip ailerons deflected in the $0.45c_w$ location is shown in figure 36. Four conditions were investigated:

The hinge axis located at $0.20c_w$, flap neutral.
The hinge axis located at $0.20c_w$, flap deflected.
The hinge axis located at $0.45c_w$, flap deflected.
The hinge axis located at $0.45c_w$, flap neutral.

METHODS

The flight tests consisted of three phases. First, the angular velocity in roll and yaw and the control position were recorded on high-speed film during a maneuver in which the ailerons were fully deflected to determine the response. Second, somewhat slower records were obtained with the controls fully deflected at different air speeds. Third, the control obtained with partial aileron deflection at a given air speed was determined. In addition, the force required to deflect the ailerons under different conditions was measured. Graphical differentiation of the angular-velocity records gave the angular acceleration produced.

RESULTS

Time histories showing the response of the airplane to the moment produced by the slot-lip ailerons in the $0.20c_w$ location are given in figure 37(a) with the flap both neutral and deflected. It will be seen that the wing starts to roll in the desired direction immediately but is decidedly slow in attaining maximum angular acceleration. Similar records with the ailerons in the $0.45c_w$ location are shown in figure 37(b). With the ailerons in the rearward location, the maximum acceleration is attained sooner than with them in the forward location.

The effect of aileron deflection on angular velocity and acceleration in roll and in yaw is shown in figure 38.

FIGURE 36.—The Fairchild 22 airplane with slot-lip ailerons as tested in flight.

For satisfactory operation the motions produced by control deflection should not depart excessively from a linear variation with deflection. With the flap neutral this characteristic is obtained, but with the flap deflected the control may be too weak for low aileron deflections.

The variation of control effectiveness with air speed is shown in figure 39. Normally, the angular velocity and acceleration decrease with air speed but, with the slot-lip aileron in the forward location with the flap deflected, the velocity and acceleration decrease with an increase of air speed. In fact, this characteristic seems to be one that limits the forward location of the slot-lip aileron. The slot-lip aileron should be so located as to give good control up to the highest speed flown with flap down. Reference to figure 21 will show the lift coefficient at which control vanishes for various aileron deflections and locations as determined from the wind-tunnel tests.

The stick forces required for maximum deflection of the slot-lip ailerons are given in the following table. The pilots considered all the forces rather heavy and the force of 19.8 pounds excessive with the flap deflected and the aileron in the forward location.

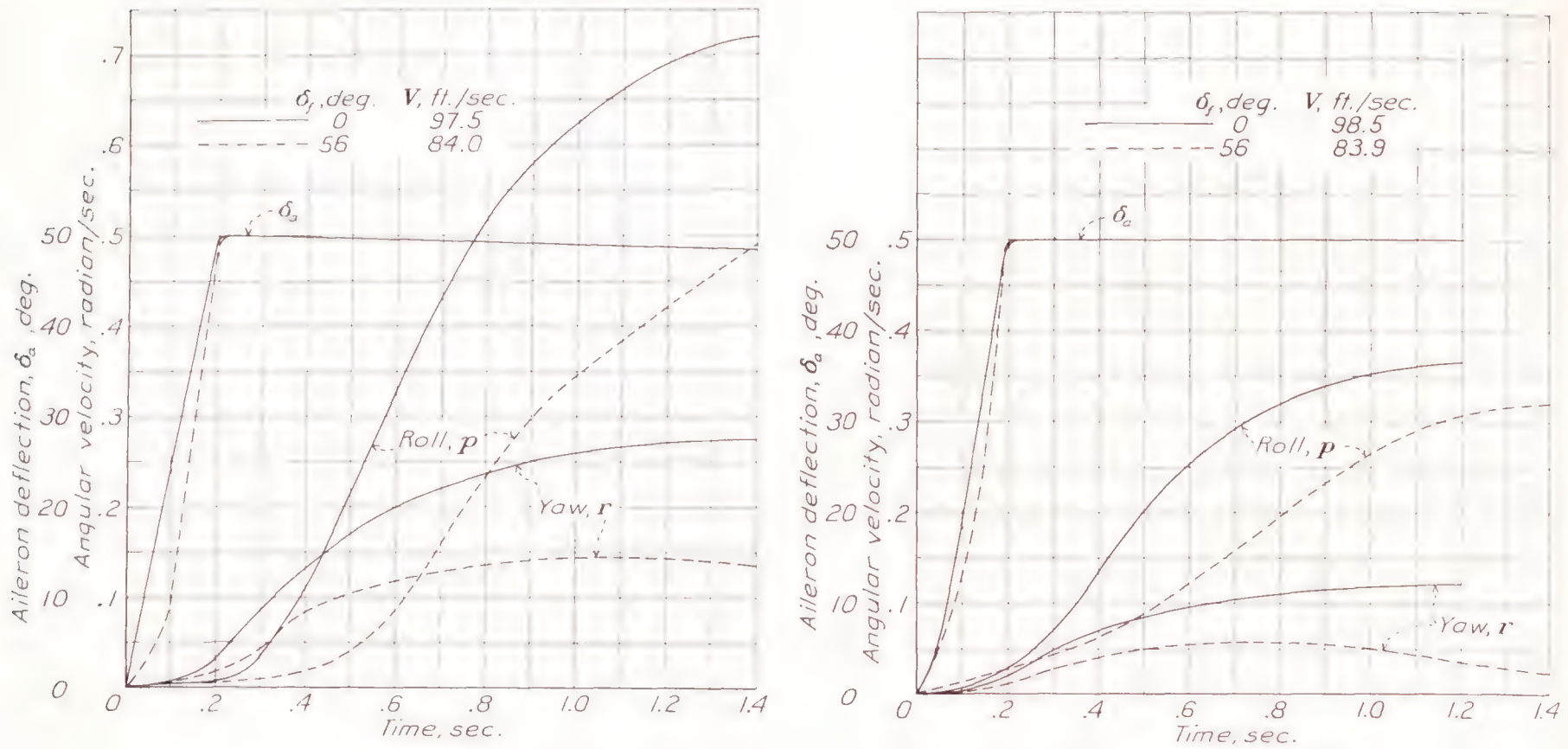

(a) Slot-lip ailerons at $0.20c_w$.

(b) Slot-lip ailerons at $0.45c_w$.

FIGURE 37.—Time history of airplane motion with slot-lip ailerons on the Fairchild 22 airplane.

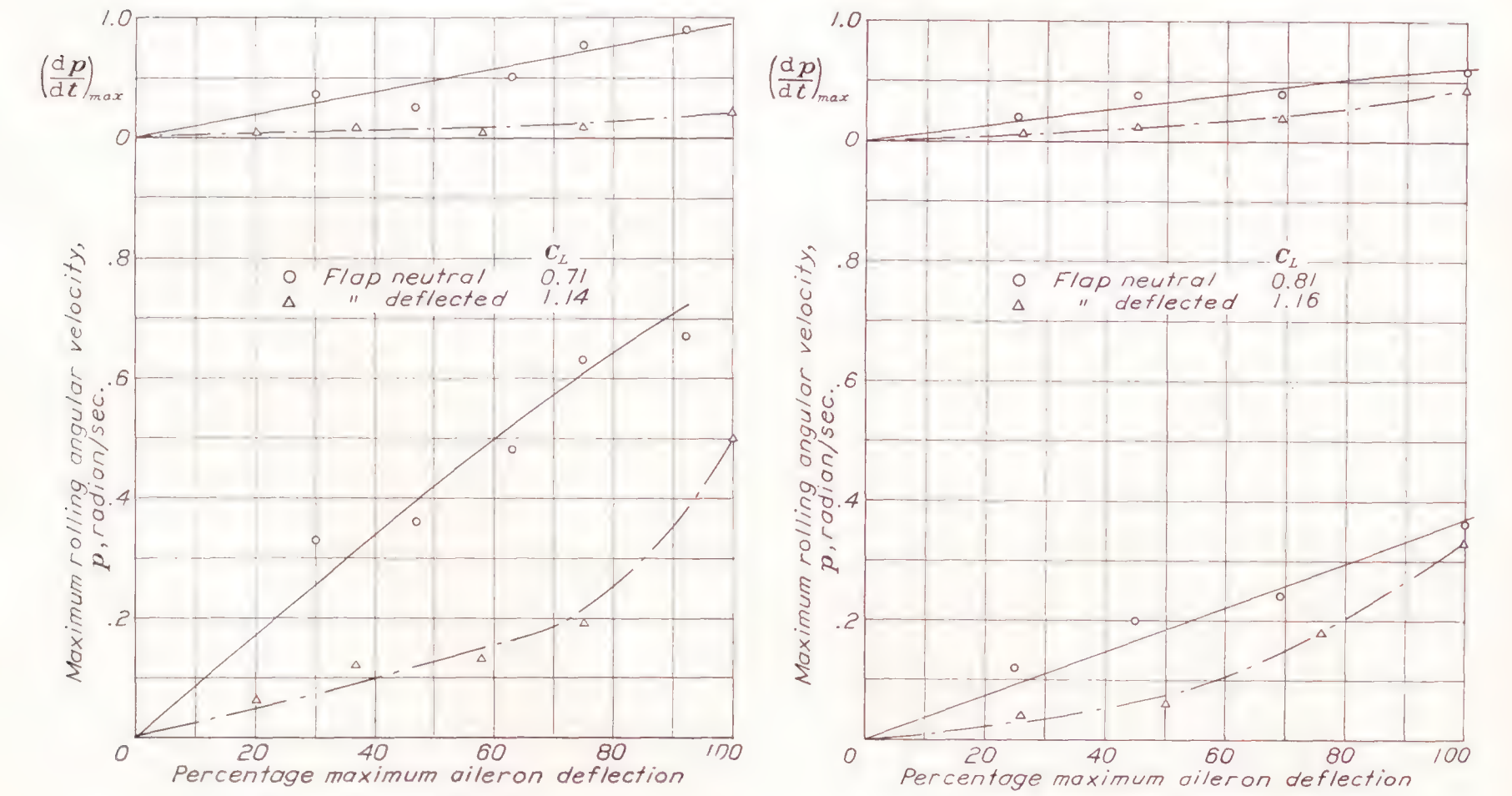

(a) Slot-lip ailerons at $0.20c_w$.

(b) Slot-lip ailerons at $0.45c_w$.

FIGURE 38.—Variation of maximum rolling angular velocity and acceleration with aileron deflection for slot-lip ailerons on the Fairchild 22 airplane.

Aileron location	Flap condition	Air speed (ft./sec.)	Stick force (lb.)
$0.20c_w$	Neutral	88	8.4
$0.20c_w$	do	132	10.8
$0.20c_w$	Deflected	71	14.5
$0.20c_w$	do	108	19.8
$0.45c_w$	Neutral	79	6.4
$0.45c_w$	do	131	12.0
$0.45c_w$	Deflected	64	8.3
$0.45c_w$	do	83	8.8

The pilots reported that the control action was weak for all flight conditions with the slot-lip ailerons and that the sluggishness was definitely objectionable for both locations, although less so at the rearward location. With the flaps deflected, the sluggishness was worse than with them neutral. The actual magnitude of the sluggishness for the different conditions has been computed and is discussed in the next section.

ANALYSIS OF RESULTS

LAG AND SLUGGISHNESS

In the present analysis of wind-tunnel and flight tests in which dynamic lift is produced, an attempt has been made to determine the sluggishness produced by certain control devices. In the case of slot-lip ailerons it is conceivable that the sluggishness might be greater than with ordinary ailerons because the vortices shed from the slot-lip ailerons located at midchord act on the wing for a longer time. In addition, the wing travels a greater distance before the final flow pattern, involving separation over certain regions, is established.

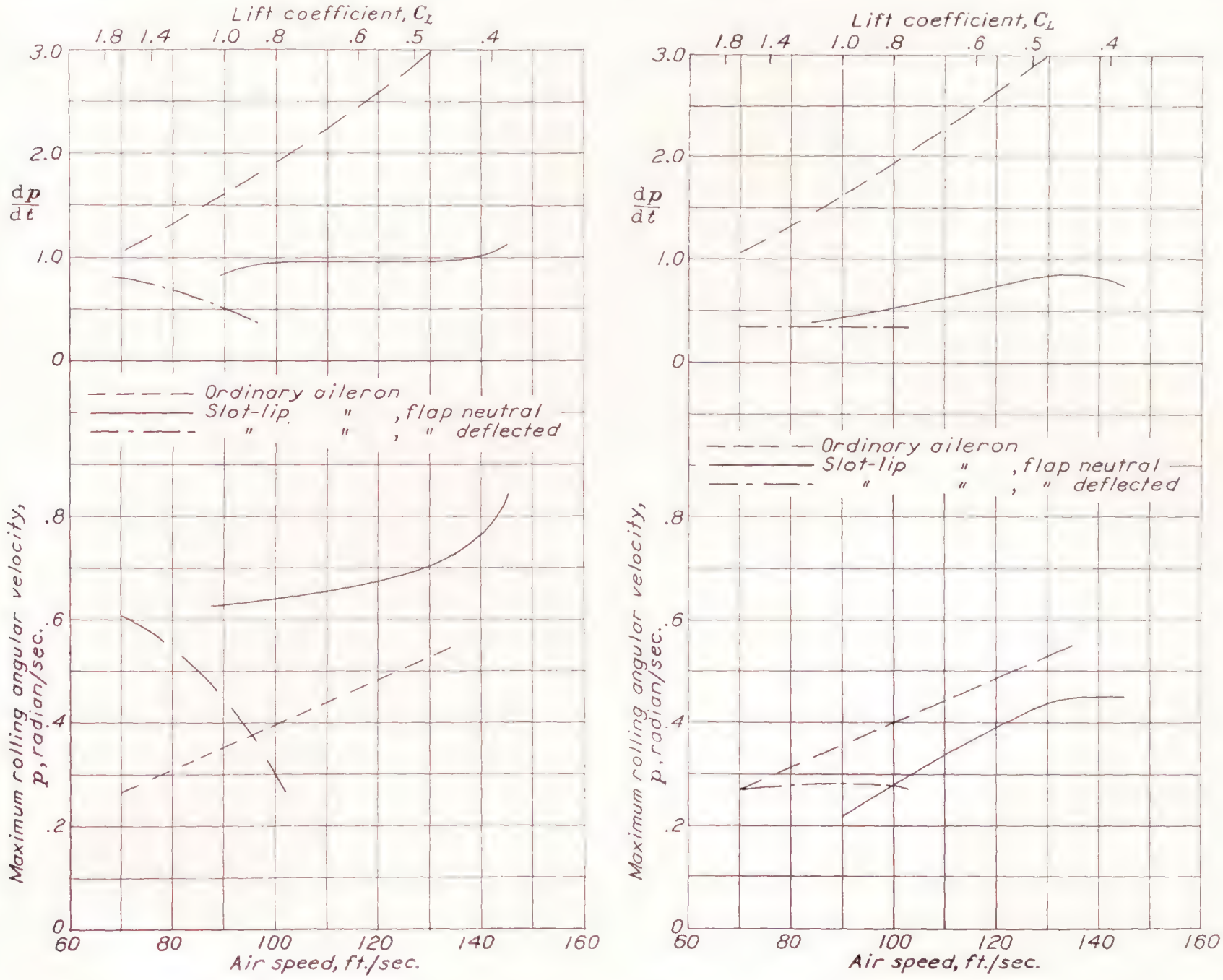

(a) Slot-lip aileron at $0.20c_w$. (b) Slot-lip aileron at $0.45c_w$.

FIGURE 39.—Variation of maximum rolling angular velocity and acceleration with air speed for slot-lip ailerons on the Fairchild 22 airplane.

Wind-tunnel tests.—In the wind-tunnel tests of the lag investigation a half-span wing was restrained in roll by an elastic cord but was free to roll to a new position of equilibrium after a rolling moment was applied by certain control devices. (See fig. 1.) The equation of motion of the wing thus restrained and acted upon may be expressed by

$$\frac{dp}{dt}=L_0+pL_p+\phi L_\phi \qquad (1)$$

where dp/dt is the rolling angular acceleration.

L_o, the applied rolling moment.

pL_p, the damping moment that depends on the angular velocity in roll, p.

and ϕL_ϕ, the restraining moment due to the elastic cords that depends on the angular deflection ϕ. The coefficients L_p and L_ϕ contain I_X, the moment of inertia about the axis of rotation, so that L_0 is expressed as acceleration. The variations with time of the angular deflection ϕ and of the control deflection δ_a were simultaneously recorded on the same film. The values of the angular velocity p were determined by graphical differentiation of the ϕ curves and the angular accelerations dp/dt were determined by graphical differentiation of the p curves. The analysis consisted of determining values of L_0 from the determined values of ϕ, p, and dp/dt by equation (1) and comparing the values with those expected from the particular aileron deflections. A typical curve of δ_a and of ϕ against time is shown in figure 40 with the computed values of p and dp/dt for the wing motion due to a slot-lip aileron located $0.30c_w$ from the leading edge.

The values of L_0 computed for the case shown in figure 40 and the component parts of the moment are

shown in figure 41. The static moment, L, curve has been included as a function of control deflection, assuming the maximum static moment equal to the

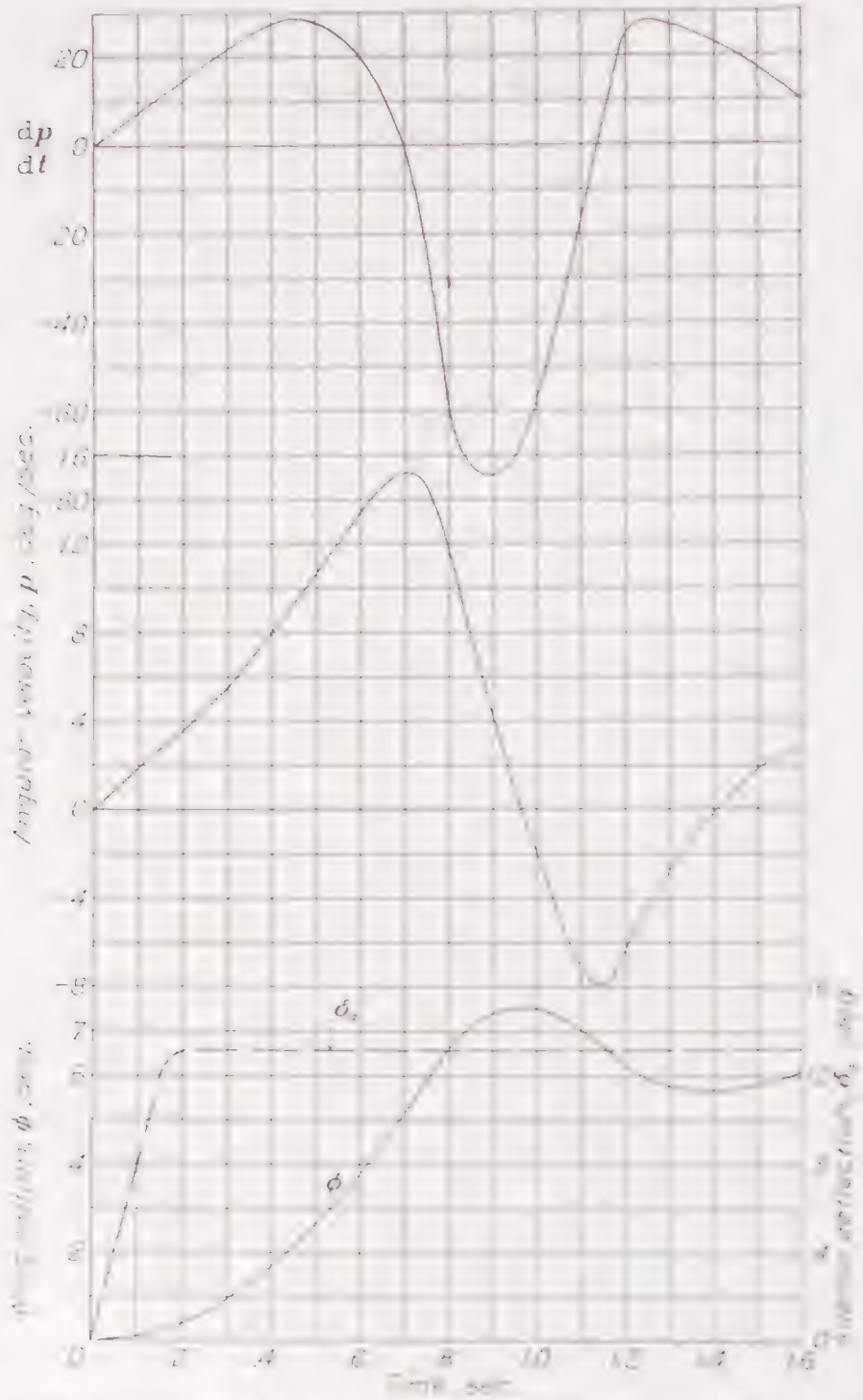

FIGURE 40.—Time history of motion of wing with slot-lip ailerons at $0.30c_w$. The 7 by 10-foot tunnel.

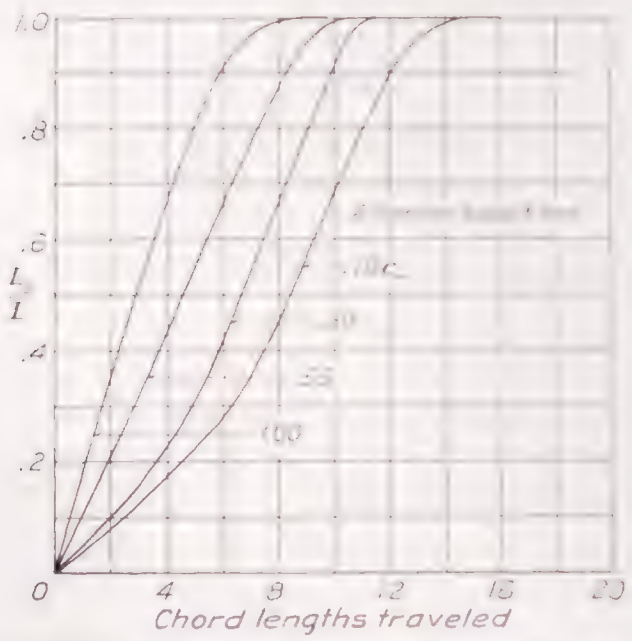

FIGURE 42.—Ratios of effective moment to static moment for various slot-lip ailerons in the 7- by 10-foot tunnel.

maximum value of L_0. Dividing L_0 by the static moment at any instant gives a measure of the sluggishness. Because the sluggishness varies directly as the

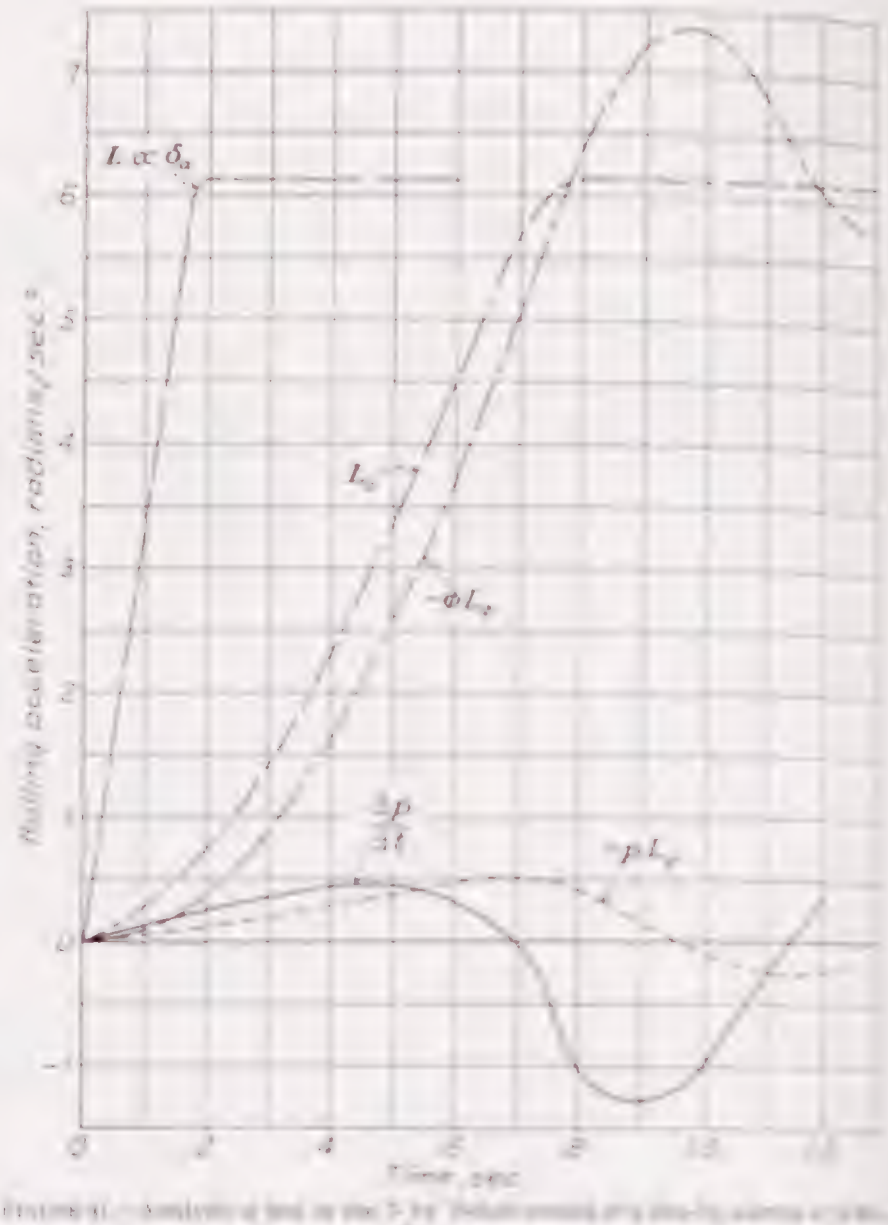

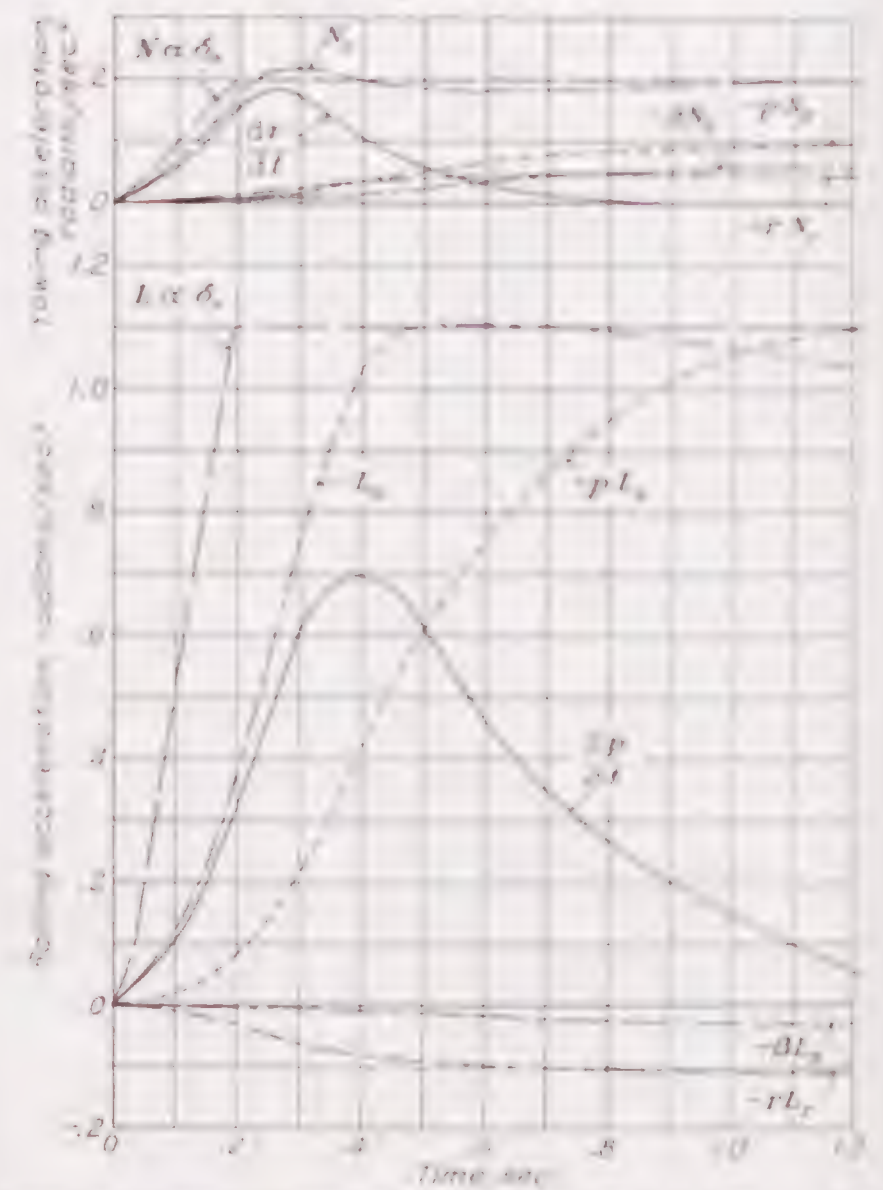

FIGURE 43.—Analysis of aileron control with slot-lip aileron at $0.43c_w$. δ_r, 0°; C_L, 0.827; air speed, 98.5 ft./sec.; flight test.

$$N_0=\frac{dr'}{dt}-r'N_{r'}-p'N_{p'}-\beta N_\beta \qquad L_0=\frac{dp'}{dt}-p'L_{p'}-r'L_{r'}-\beta L_\beta$$

wing chord and inversely as the air speed, the values of time have been converted to the nondimensional form of distance traveled in terms of chord lengths by multiplying by V/c. The sluggishness in terms of L_0/L was computed for slot-lip ailerons in several locations and for an attached aileron as shown in figure 42.

Flight tests.—The method used in analyzing the flight tests was essentially the same as the one used with the wind-tunnel tests. Flight records of simultaneous values of rolling and yawing angular velocities and of the control deflection were obtained. The angular accelerations were graphically determined and, from computed values of the resistance coefficients or derivatives, the moment acting on the airplane at each instant was derived. The derivatives L_p, L_r, L_β, N_p, N_r, and N_β of the equations of motion

$$\frac{dp}{dt}=L_0+pL_p+rL_r+\beta L_\beta \text{ (rolling)} \qquad (2)$$

$$\frac{dr}{dt}=N_0+pN_p+rN_r+\beta N_\beta \text{ (yawing)} \qquad (3)$$

were determined for the particular cases as in reference 14, considering the effects on the derivatives of the slot-lip ailerons and of the flap. The derivatives contain the proper values of I_x and I_z so that L_0 and N_0 are expressed as accelerations.

The values of dp/dt and dr/dt were determined by graphical differentiation of the curves of p and r.

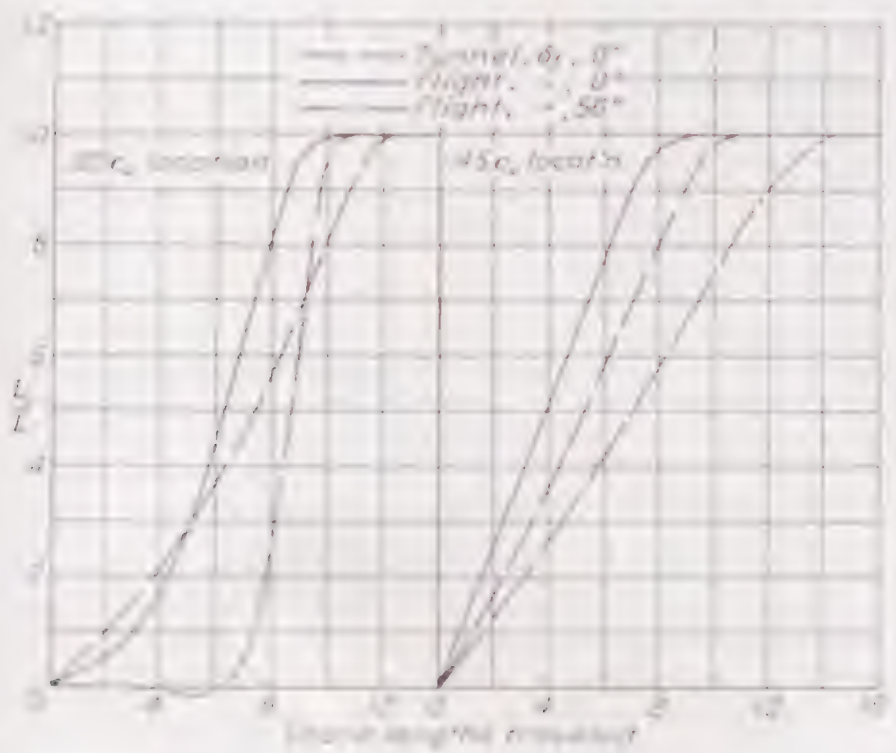

FIGURE 44.—Comparison of flight and tunnel measurements of sluggishness of slot-lip ailerons.

The values of the angle of sideslip β were determined by summing the outward sideslip due to centrifugal force and the inward sideslip due to the banked attitude. With positive r, the outward acceleration due to centrifugal force is

$$-\frac{dv}{dt}=Vr$$

Integrating,

$$\left(\frac{v}{V}\right)_0=-\int r\,dt$$

The inward acceleration is

$$\frac{dv}{dt}=g\sin\phi=g\phi$$

where ϕ is the angle of bank. Integrating,

$$v=g\int\phi dt$$

or

$$\left(\frac{v}{V}\right)_1=\frac{g}{V}\int\phi dt$$

Then the angle of sideslip is

$$\beta=\left(\frac{v}{V}\right)_0+\left(\frac{v}{V}\right)_1=-\int r\,dt+\frac{g}{V}\int\phi dt$$

The values of $\int r\,dt$ and $\int\phi dt$ were determined by graphical integration.

The values of L_0 and N_0 were determined from equations (2) and (3). The interrelation of the various

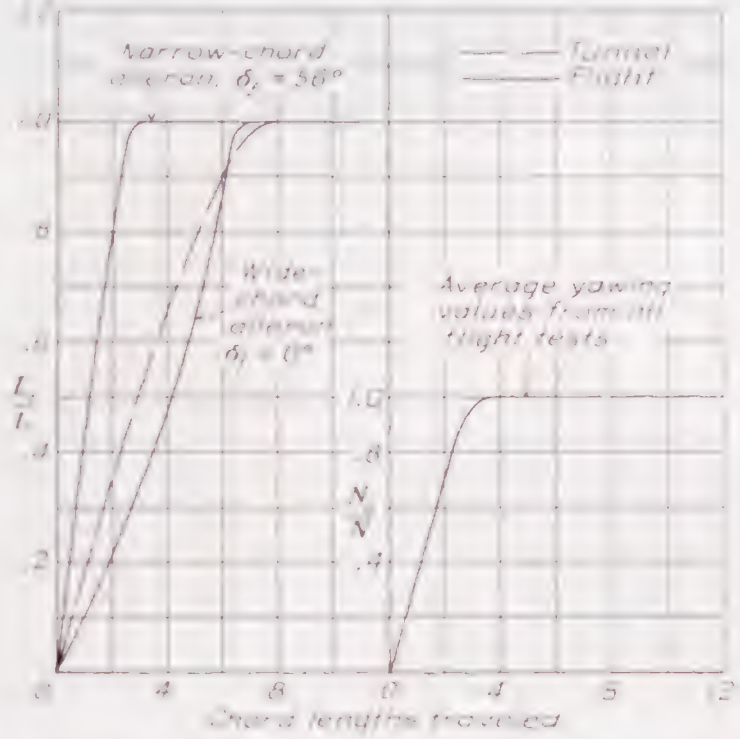

FIGURE 45.—Comparison of flight and tunnel measurements of sluggishness of ordinary ailerons.

components for a typical case of a slot-lip aileron on the F–22 airplane is shown in figure 43. All the values are given in terms of acceleration. The values of L and N are given in proportion to the aileron deflection with maximum values equal to the maximum values of L_0 and N_0. A measure of the sluggishness was taken as the ratios of L_0/L and N_0/N. The outlined procedure was followed in analyzing the flight records for the cases listed in the following table for the F–22 airplane.

Aileron	Location	δ_f (deg.)	C_L	V (ft./sec.)	$\frac{p_2}{2V}$ (sec.)
Slot-lip	0.30c_w	0	0.87	97.5	5.5
Do	0.20c_w	56	1.15	84.0	5.5
Do	0.40c_w	0	.83	98.5	5.5
Do	0.15c_w	56	1.14	84.0	5.5
Narrow, ordinary	T. E.	0	1.00	87.0	5.5
Do	T. E.	56	1.75	66.7	5.5
Wide, ordinary	0.40c_w	0	1.10	95.0	4.5

The ratios of L_0/L have been determined for each tabulated case and are plotted in figures 44 and 45. For comparison, the corresponding values found by interpolation from the wind-tunnel tests have been included in the same figures. The wind-tunnel tests, however, were made only with the flap neutral.

DISCUSSION

With the ordinary ailerons (fig. 45) the full static rolling moment was reached, for the average case, after the airplane had traveled about 4 chord lengths. In the case of the wide-chord ailerons with the flap down, the full moment was not produced until about 7 chord lengths had been traveled; with the narrow aileron, flap neutral, substantially instantaneous response was obtained. The accuracy of the method used in determining the sluggishness depends largely upon the accuracy with which the flight records of aileron motion and airplane motion can be synchronized. The difference between the two extremes and the average of between 3 and 4 chord lengths might easily be attributed to errors in interpreting the flight records. As the response to all the ordinary ailerons tested was satisfactory to the pilots, it follows that any device which gives a moment that is uniformly produced and with the maximum in about 4 chord lengths distance is satisfactory on this airplane. The wind-tunnel tests of the ordinary aileron showed greater sluggishness than did the flight tests.

FIGURE 46.—The W1–A airplane with slot-lip ailerons and slotted flaps.

With the slot-lip ailerons at $0.20c_w$ location (fig. 44) the rolling moment is built up in a nonuniform manner, the maximum being reached in about 10 chord lengths. With the flap deflected, the moment actually lags for 6 chord lengths, the rolling motion of the airplane being indirectly produced by the positive yawing moment due to the ailerons. The wind-tunnel test gave a more uniform curve but with the maximum reached at 12 chord lengths. The sluggishness of these ailerons is considered excessive for the F–22 airplane. With the slot-lip ailerons at $0.45c_w$, the moments built up uniformly to a maximum in 8 chord lengths with flap 0° and in 14 chord lengths with flap deflected. The tunnel test showed a maximum in about 10 chord lengths with flap neutral. As in the case of the ordinary ailerons, the wind-tunnel tests showed greater sluggishness than the flight tests. The sluggishness in flight with the slot-lip aileron, flap neutral, was not appreciably greater than that with the wide-chord ordinary aileron, flap deflected.

The yawing moments, as shown in figure 45, reach their maximum fairly rapidly in all cases and may be considered practically instantaneous.

The results of this analysis agree qualitatively with the pilots' reports of the action of the slot-lip ailerons on the F–22 airplane. The pilots reported that the slot-lip ailerons in either location were more sluggish than ordinary ailerons and were worse with flap deflected than with flap neutral. The $0.45c_w$ location was, however, better than the $0.20c_w$ location. In addition to being sluggish, the aileron action was reported to be very weak. In an effort to find an explanation of this weak action, the moments determined in the analysis have been converted to coefficient form and are given in the following table with corresponding coefficients obtained by interpolation from the wind-tunnel force tests.

Aileron location	Flap deflection	Tunnel			Flight			
	δ_f (deg.)	C_l'	C_n'	δ_a (deg.)	C_l'	C_n'	δ_a for C_l' (deg.)	δ_a for C_n' (deg.)
$0.20c_w$	0	0.0475	0.0105	−40	0.0388	0.0084	−33	−31
$0.20c_w$	56	.0310	.0085	−40	.0199	.0082	−29	−39
$0.45c_w$	0	.0410	.0050	−40	.0239	.0032	−25	−32
$0.45c_w$	56	.0385	.0050	−40	.0219	.0033	−31	−32

The coefficients in flight are seen to be considerably lower than the wind-tunnel values. One reasonable explanation of this difference is that the ailerons in flight may not have been deflected the indicated 40° because of structural flexure. In the last two columns are given the necessary aileron deflections corresponding to the moments produced. The effective deflection was only about 32°.

Another determination of the sluggishness of slot-lip ailerons has been made possible by recent tests of the W1–A airplane made by the N. A. C. A. for the Bureau of Air Commerce. The W1–A airplane (fig. 46) has slot-lip ailerons located $0.30c_w$. (See fig. 47.) With the stable three-wheel landing gear, the large dihedral angle of the wings, and the slot-lip aileron so located as

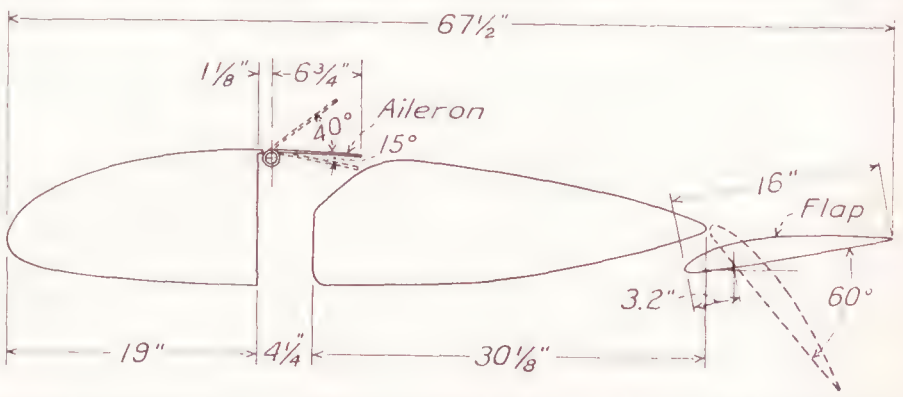

FIGURE 47.—Section of the W1–A airplane wing showing details of slot-lip aileron and slotted flap.

to give a good ratio of yawing moment to rolling moment, it was believed that the airplane could be flown satisfactorily with adequate directional as well as lateral control by means of the slot-lip ailerons alone. The pilots reported that a good degree of control was obtained with the slot-lip ailerons with neither lag nor sluggishness in their action. Successful flights were later made with the rudder locked neutral, leaving only the slot-lip ailerons

for both directional and lateral control. The control was

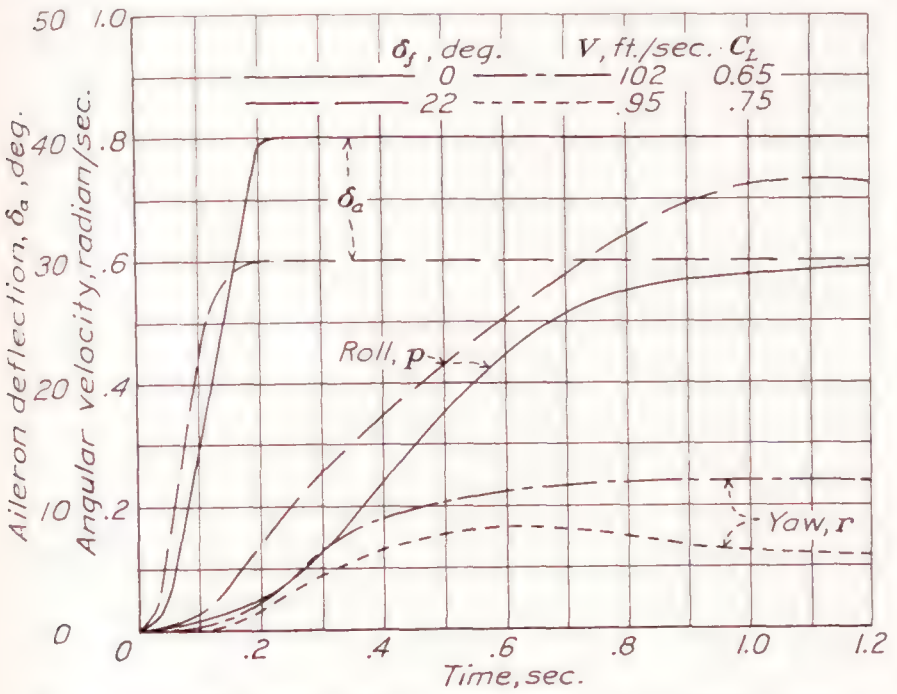

FIGURE 48.—Time history of W1–A airplane motion due to slot-lip ailerons.

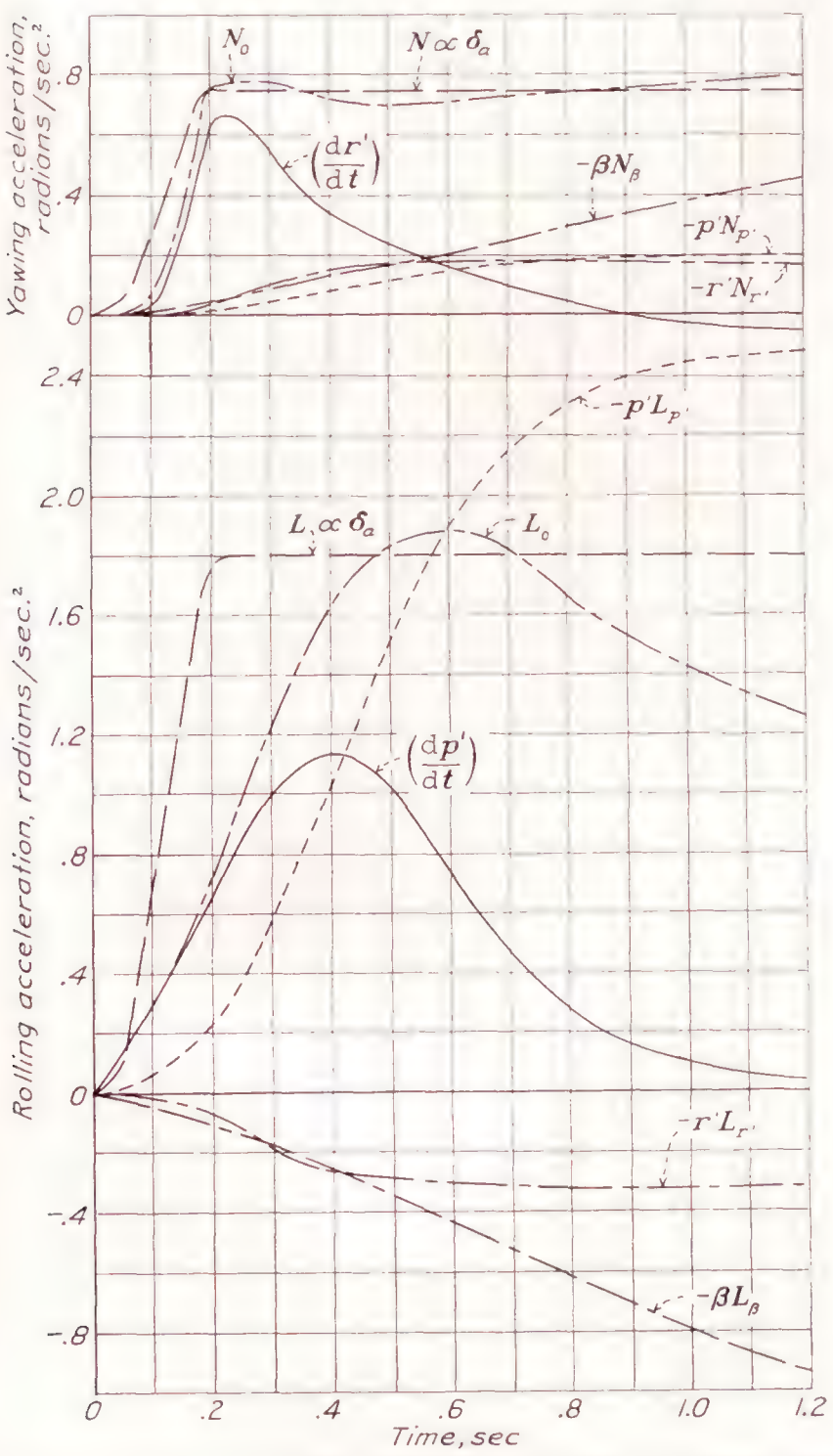

FIGURE 49.—Analysis of flight test of W1-A airplane with slot-lip ailerons at $0.30c_w$. δ_f, 0°; C_L, 0.55.

$$N_0=\frac{dr'}{dt}-r'N_{r'}-p'N_{p'}-\beta N_\beta \qquad L_0=\frac{dp'}{dt}-p'L_{p'}-r'L_{r'}-\beta L_\beta$$

equally good with the slotted flap deflected for landing.

Inasmuch as these results seemed to be in disagreement with the results of the tests of the F–22 airplane, detailed records of the airplane motion following a deflection of the slot-lip ailerons were made and are given in figure 48. An analysis of the motions has been made using estimated resistance derivatives and moments of inertia for the W1–A airplane. The results of the analysis are given in figure 49. It will be readily seen that an appreciable part of the rolling angular velocity was indirectly obtained from the large favorable yawing moment, as evidenced by the large values of βL_β. As in the previous analysis of the F–22 tests, the values of L_0/L and N_0/N were computed and are given in figure 50 with the flap both neutral and deflected. Comparison with figure 44 shows that the curve for L_0/L with the flap neutral lies between the curves from the F–22 tests of slot-lip ailerons located at $0.20c_w$ and $0.45c_w$. It therefore

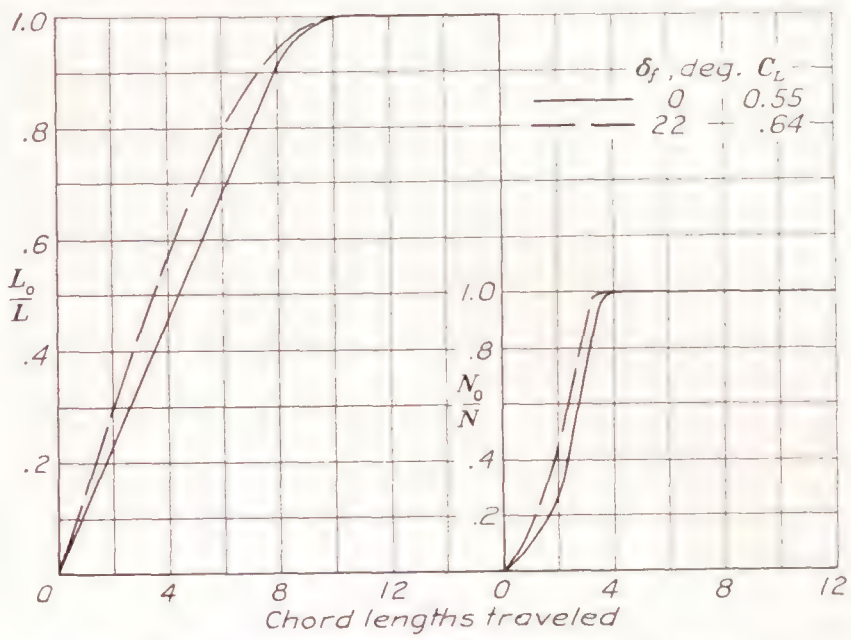

FIGURE 50.—Sluggishness of slot-lip ailerons on W1–A airplane.

seems that the apparent discrepancy between the results of the F–22 tests and the W1–A tests is explained by the large dihedral of the W1–A, which indirectly contributed a large proportion of the roll.

With the special slotted flap of the W1–A deflected 22½°, the sluggishness was appreciably less than that for the F–22 with the split flap deflected 56°. In fact, with the W1–A airplane, the sluggishness was slightly less with the flap deflected than with it retracted. It seems, therefore, that the sluggishness may be critically affected by the particular type of flap used.

CONCLUSIONS

1. For airplanes similar to the ones tested, the lag with single retractable spoilers or ailerons varies with the position along the wing chord from a negligible value near the trailing edge to nearly 1 second for a position near the leading edge. Unless the device is located within 20 percent of the wing chord from the trailing edge, the lag will be objectionably large (more than 0.10 second).

2. With a proper combination of spoiler and slot, such as the N. A. C. A. slot-lip aileron, the lag with

spoiler at any location may be reduced to a negligible value although the sluggishness may be excessive. This sluggishness may be in the order of 4 chord lengths distance traveled by the airplane for ordinary ailerons located at the trailing edge and about 12 chord lengths for slot-lip ailerons located near the leading edge of the wing.

3. The added airplane drag with slot-lip ailerons is considered excessive for high-performance airplanes, being in the order of 10 percent of the wing drag at high speed and about 35 percent of the wing profile drag in the climbing attitude.

4. One advantage of the slots as used for the slot-lip ailerons lies in the extension of the usable angle-of-attack range of an airplane by delaying the stall of the outer portions of the wing and thus maintaining damping in roll. This effect becomes of small importance when the slot is located farther back than 50 percent of the wing chord.

5. For airplanes in which increased safety and simplicity of control is of more importance than high speed, high rate of climb, and high maneuverability, the slot-lip ailerons located between 30 and 40 percent of the wing chord might be desirable, particularly when used on an airplane having considerable dihedral.

LANGLEY MEMORIAL AERONAUTICAL LABORATORY,
NATIONAL ADVISORY COMMITTEE FOR AERONAUTICS,
LANGLEY FIELD, VA., *June 11, 1937.*

REFERENCES

1. Weick, Fred E., and Shortal, Joseph A.: Wind-Tunnel Research Comparing Lateral Control Devices, Particularly at High Angles of Attack. V—Spoilers and Ailerons on Rectangular Wings. T. R. No. 439, N. A. C. A., 1932.
2. Weick, Fred E., Soulé, Hartley A., and Gough, Melvin N.: A Flight Investigation of the Lateral Control Characteristics of Short, Wide Ailerons and Various Spoilers, with Different Amounts of Wing Dihedral. T. R. No. 494, N. A. C. A., 1934.
3. Weick, Fred E., and Shortal, Joseph A.: Development of the N. A. C. A. Slot-Lip Aileron. T. N. No. 547, N. A. C. A., 1935.
4. Harris, Thomas A.: The 7 by 10 Foot Wind Tunnel of the National Advisory Committee for Aeronautics. T. R. No. 412, N. A. C. A., 1931.
5. Soulé, H. A., and McAvoy, W. H.: Flight Investigation of Lateral Control Devices for Use with Full-Span Flaps. T. R. No. 517, N. A. C. A., 1935.
6. Shortal, J. A.: Effect of Retractable-Spoiler Location on Rolling- and Yawing-Moment Coefficients. T. N. No. 499, N. A. C. A., 1934.
7. Weick, Fred E., and Wenzinger, Carl J.: The Characteristics of a Clark Y Wing Model Equipped with Several Forms of Low-Drag Fixed Slots. T. R. No. 407, N. A. C. A., 1932.
8. Weick, Fred E., and Shortal, Joseph A.: Wind-Tunnel Research Comparing Lateral Control Devices, Particularly at High Angles of Attack. VIII. Straight and Skewed Ailerons on Wings with Rounded Tips. T. N. No. 445, N. A. C. A., 1933.
9. Pearson, H. A.: Theoretical Span Loading and Moments of Tapered Wings Produced by Aileron Deflection. T. N. No. 589, N. A. C. A., 1937.
10. Jones, Robert T.: A Study of the Two-Control Operation of an Airplane. T. R. No. 579, N. A. C. A., 1936.
11. Platt, Robert C.: Turbulence Factors of N. A. C. A. Wind Tunnels as Determined by Sphere Tests. T. R. No. 558, N. A. C. A., 1936.
12. De France, Smith J.: The N. A. C. A. Full-Scale Wind Tunnel. T. R. No. 459, N. A. C. A., 1933.
13. Glauert, H.: Wind Tunnel Interference on Wings, Bodies, and Airscrews. R. & M. No. 1566, British A. R. C., 1933.
14. Weick, Fred E., and Jones, Robert T.: The Effect of Lateral Controls in Producing Motion of an Airplane as Computed from Wind-Tunnel Data. T. R. No. 570, N. A. C. A., 1936.

TABLE I

SUMMARY OF DRAG INVESTIGATION OF VARIOUS SLOTS IN A 4- BY 8-FOOT N. A. C. A. 23012 WING IN THE 7- BY 10-FOOT WIND TUNNEL

[Air speed, 80 m. p. h.]

Slot designation	ΔC_D for C_L=				$\frac{dC_L}{d\alpha_0}$	$\Delta\alpha_{L_0}$	C_{m_0}	a. c.[1]
	0	0.2	0.4	0.5				
	0	0	0	0	0.101	0	−0.007	0.030
1	.0013	.0014	.0034	.0052	.091	0	−.007	.030
2	.0014	.0016	.0038	.0052	.091	0	−.007	.030
3	.0018	.0026	.0064	.0085	.086	0	−.008	.034
4	.0014	.0023	.0071	.0078	.084	−.1	−.007	.034
5	.0016	0019	.0060	.0084	.084	−.1	−.007	.034
6	.0018	.0023	.0061	.0090	.084	−.1	−.007	.034
7	.0018	.0026	.0056	.0093	.084	−.1	−.007	.034
8	.0020	.0018	.0055	.0071	.086	0	−.008	.034
9	.0043	.0058	.0068	.0068	.095	.8	−.007	.015
10	.0041	.0045	.0050	.0053	.101	.9	−.007	.000
11	.0038	.0038	.0037	.0034	.103	.9	−.011	.000
12	.0015	.0020	.0041	.0053	.086	0	−.007	.040
13	.0015	.0013	.0028	.0042	.092	0	−.008	.032
14	.0011	.0008	.0008	.0011	.100	−.1	−.008	.028
15	.0012	.0016	.0037	.0050	.086	0	−.007	.040
16	.0016	.0015	.0030	.0040	.090	−.1	−.009	.036
17	.0015	.0019	.0035	.0055	.092	−.1	−.008	.036
18	.0016	.0013	.0022	.0033	.092	−.1	−.009	.036
19	.0014	.0013	.0025	.0036	.103	−.1	−.008	.036
20	.0012	.0008	.0008	.0008	.092	−.1	−.008	.026
21	.0012	.0010	0023	.0028	.095	−.1	−.008	.034

[1] Values are approximate aerodynamic-center location in fractions of c_w ahead of wing quarter-chord point.

REPORT No. 603

WIND-TUNNEL INVESTIGATION OF WINGS WITH ORDINARY AILERONS AND FULL-SPAN EXTERNAL-AIRFOIL FLAPS

By Robert C. Platt and Joseph A. Shortal

SUMMARY

An investigation was carried out in the N. A. C. A. 7- by 10-foot wind tunnel of an N. A. C. A. 23012 airfoil equipped, first, with a full-span N. A. C. A. 23012 external-airfoil flap having a chord 0.20 of the main airfoil chord and with a full-span aileron with a chord 0.12 of the main airfoil chord on the trailing edge of the main airfoil and equipped, second, with a 0.30-chord full-span N. A. C. A. 23012 external-airfoil flap and a 0.13-chord full-span aileron. The results are arranged in three groups, the first two of which deal with the airfoil characteristics of the two airfoil-flap combinations and with the lateral-control characteristics of the airfoil-flap-aileron combinations. The third group of tests deals with several means for balancing ailerons mounted on a special large-chord N. A. C. A. 23012 airfoil model with and without a 0.20-chord N. A. C. A. 23012 external-airfoil flap. The tests included an ordinary aileron, a curtained-nose balance, a Frise balance, and a tab.

The results obtained for the 0.30 c_w flap verify the conclusion made from previous tests of the 0.20 c_w flap combination, namely, that external-airfoil flaps applied to the N. A. C. A. 230 airfoil sections give characteristics more favorable to speed range, to low power requirements in flight at high lift coefficients, and to low flap-operating moments than do other types of flap in general use. The ailerons can produce large rolling moments with relatively small adverse yawing moments in flight conditions ranging from high speed to minimum speed. The nose balance and Frise balance were ineffective in reducing the stick forces required for a given control effectiveness, but the use of tabs in combination with a differential aileron motion provided a means of obtaining desirable stick forces throughout the flight range. The aerodynamic advantages of this aileron-flap combination appear to outweigh probable design difficulties.

INTRODUCTION

Improvement of airplane speed range and performance by the use of trailing-edge high-lift devices has been hampered by the necessary compromise between obtaining the highest possible maximum lift coefficient and the necessity of providing at least a minimum of lateral control. The usual compromise has involved the use of flaps over the central portion of the span with ailerons attached to the tip portion. This procedure results not only in the direct loss of possible maximum lift over the unflapped area but may lead to an additional hazard resulting from the tendency of partial-span flaps of the conventional type to reduce, in some cases, the degree of stability and control near the stall. It is therefore generally recognized that the development of a lateral-control arrangement that can be used in combination with a full-span flap offers definite possibilities for improvements in speed range and safety.

In most of the numerous attempts that have been made to devise such an arrangement (for example, references 1, 2, and 3) unforeseen difficulties have practically canceled the anticipated improvement. In some cases reductions of maximum lift or increases in minimum drag have had to be accepted in order to obtain the minimum acceptable lateral control; the mechanical complications or operational difficulties of other arrangements have prevented their satisfactory application. At present no combination that makes full use of the capabilities of high-lift devices and provides satisfactory lateral control has found general application to airplane design.

The investigation reported herein dealt with an arrangement that, on preliminary study, indicated possibilities of meeting the foregoing requirements. The arrangement consisted of a main airfoil on the trailing edge of which were an external-airfoil flap and ailerons forming the lip of the slot between the main airfoil and the flap. This combination logically results from an attempt to combine the desirable characteristics of the slot-lip ailerons described in reference 3 with those of the external-airfoil flaps described in reference 4. These ailerons being structurally similar to ordinary ailerons, relatively complicated mechanical and structural arrangements are avoided and the main airfoil contour is left unbroken when the ailerons are undeflected, thus making available the full capabilities of external-airfoil flaps for speed-range improvement and reduction of power requirements in low-speed flight.

This wind-tunnel investigation was divided into three general phases:

1. Measurement of the lift, drag, and pitching-moment characteristics and the flap hinge moments of an N. A. C. A. 23012 airfoil with N. A. C. A. 23012

external-airfoil flaps having chords (c_f) that are 0.20 and 0.30 of the main airfoil chord (c_w).

2. In addition to the characteristics measured in the first phase, the measurement of the rolling- and yawing-moment characteristics of the foregoing combinations provided with ailerons having chords (c_a) of 0.12 and 0.13 of the main airfoil chord and deflected various amounts. (The aileron chord was made 10 percent of the over-all airfoil chord in each case to permit the results to be directly compared with the data of reference 3.)

3. Measurement of aileron hinge moments and lift and drag increments of a wide-chord N. A. C. A. 23012 airfoil with and without a 0.20 c_w external-airfoil flap. Various types of aileron balance were tested.

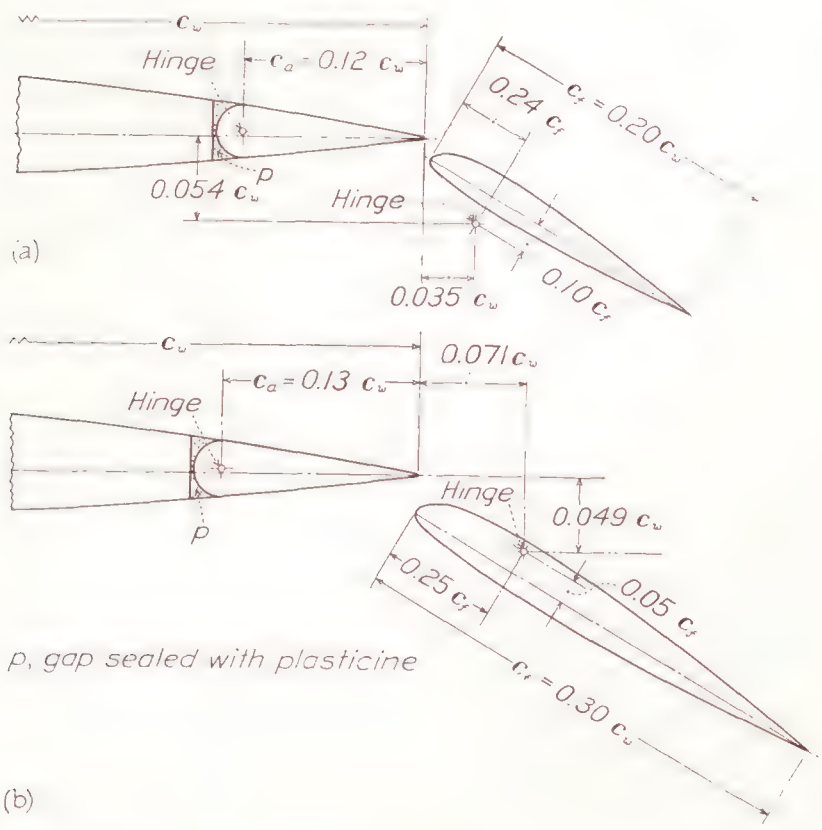

(a) N. A. C. A. 23012 airfoil with 0.20 c_w N. A. C. A. 23012 external-airfoil flap and 0.12 c_w ordinary ailerons.

(b) N. A. C. A. 23012 airfoil with 0.30 c_w N. A. C. A. 23012 external-airfoil flap and 0.13 c_w ordinary ailerons.

FIGURE 1.—Ailerons and flaps tested.

The results obtained have been studied with the purpose of clarifying the fundamental phenomena involved in the operation of the general type of device tested. They further provide the information necessary for comparison of the particular arrangement tested with other devices intended to accomplish the same purpose. Certain difficulties that may be encountered in flight applications of the device are pointed out and some investigation of methods of overcoming these difficulties is discussed.

APPARATUS AND METHODS

The investigation was carried out in the N. A. C. A. 7- by 10-foot open-throat wind tunnel (reference 5). The models used in the first phase of the investigation consisted of the following:

(1) A rectangular N. A. C. A. 23012 airfoil of 10-inch chord and 60-inch span, constructed of laminated mahogany.

(2) One 2-inch-chord and one 3-inch-chord duralumin N. A. C. A. 23012 airfoil, each having a span of 60 inches. These small airfoils served as flaps.

The tests of the combination using the 2-inch-chord flap are described in reference 4; the data have been included in this report for completeness. Exactly similar methods were adopted for the tests of the combination using the 3-inch-chord flap; surveys were made to determine the effect of flap position and angle, a desirable flap-hinge-axis location was selected from contours similar to those in reference 4, and force tests were made to determine the characteristics of the finally selected arrangement at various flap angles. In order to avoid section inaccuracies during the final force tests, these tests were completed before ailerons were built into the trailing edge of the main airfoil.

For the second phase of the investigation the trailing edge of the main airfoil was cut off and ailerons extending across the full 60-inch span of the airfoil were installed. For the tests with the 2-inch flap the chord of the ailerons (back of the hinge) was 1.2 inches; for the tests with the 3-inch flap it was 1.3 inches. The 1.2-inch-chord ailerons were made of the wooden section taken from the trailing edge of the main airfoil but difficulty in maintaining accurate settings of these ailerons indicated the desirability of using duralumin for the wider-chord ailerons. The settings of the 1.3-inch ailerons were probably somewhat more accurate than those of the 1.2-inch ailerons for this reason. Figure 1 shows pertinent details of the models used. Figure 2 is a photograph of the model with the 2-inch flap and 1.2-inch ailerons. If the details relating to the ailerons are disregarded, the figures show the condition of the models in the first phase of the investigation.

A series of tests in which angle of attack, aileron deflection, and flap angle were varied over the useful

FIGURE 2.—Model N. A. C. A. 23012 airfoil with 0.20 c_w N. A. C A. 23012 external-airfoil flap and 0.12 c_w ordinary aileron.

ranges was made for each wing-flap-aileron combination. The deflection of one half-span aileron was varied from the selected maximum up to the maximum down deflection. The effect of moving both ailerons simultaneously may be obtained by the addition of the effects produced by one aileron deflected to each of the assumed settings, due account being taken of the signs of moments and deflections. This method of obtaining rolling, yawing, and hinge moments of ailerons deflected in various ways from the data for one aileron is explained in detail in reference 2.

All tests involved in the first two phases were conducted according to standard force-test procedure in the 7- by 10-foot tunnel (reference 5). The dynamic pressure in the jet was maintained at 16.37 pounds per square foot corresponding to a speed of 80 miles per hour in standard air. The test Reynolds Number was 730,000 for the model with the 0.20 c_w flap and 790,000 for the model with the 0.30 c_w flap. The flow conditions correspond approximately to those that would exist in free air at Reynolds Numbers of 1,000,000 and 1,100,000 respectively (reference 6).

Hinge moments of the flaps and ailerons were measured in the usual manner. A calibrated torque rod, attached to the surface under test and shielded from the air stream, was turned by a pointer mounted next to a graduated disk outside the jet. The difference of the pointer deflections required to bring the surface to the required deflection with the wind off and on was read from the disk. This difference is proportional to the aerodynamic moment about the hinge; the magnitude of the hinge moment follows directly from the known calibration of the rod.

The third phase of the investigation arose as the result of analysis of the data already obtained, which indicated that the ailerons would require excessive operating moments under certain conditions. It was therefore considered desirable to investigate the effectiveness of several methods of obtaining aileron balance. In order to reproduce ailerons of practical sizes with satisfactory accuracy, a special wide-chord model was constructed to be mounted between end planes. Although such an expedient does not reproduce full-scale conditions, practical aileron details, such as clearances and hinges, can be reproduced. As will subsequently be noted, leaks ahead of the aileron hinge resulting from clearance between the wing and the aileron have an appreciable effect on aileron characteristics and the clearance should therefore be accurately controlled.

The wide-chord model consisted of a rectangular N. A. C. A. 23012 airfoil having a chord of 4 feet and a span of 8 feet, equipped with an aileron of 31-inch span and 5.76-inch chord back of the hinge, located centrally along the span. The tests included the types of ailerons shown in figure 3: An ordinary aileron, an aileron with a nose balance shielded by curtains, an aileron with a Frise nose, and an aileron with a tab. An N. A. C. A. 23012 external-airfoil flap of 9.6-inch chord and 8-foot span was provided. The section of this model as tested was an accurate enlargement of that used for the standard-size model tested with the 0.20 c_w external-airfoil flap and 0.12 c_w ailerons. The model, complete with aileron and flap, was mounted between large end planes in the jet of the 7- by 10-foot tunnel. (See fig. 4.)

The regular force-test support, with two special struts for angle-of-attack adjustment, was used to permit measurement of the forces on the model. The aileron hinge moments were measured by a torque-rod and graduated-disk arrangement similar to that used for the standard-size model. Values of lift and drag increments due to aileron deflection and the variation of aileron hinge moment with deflection were measured

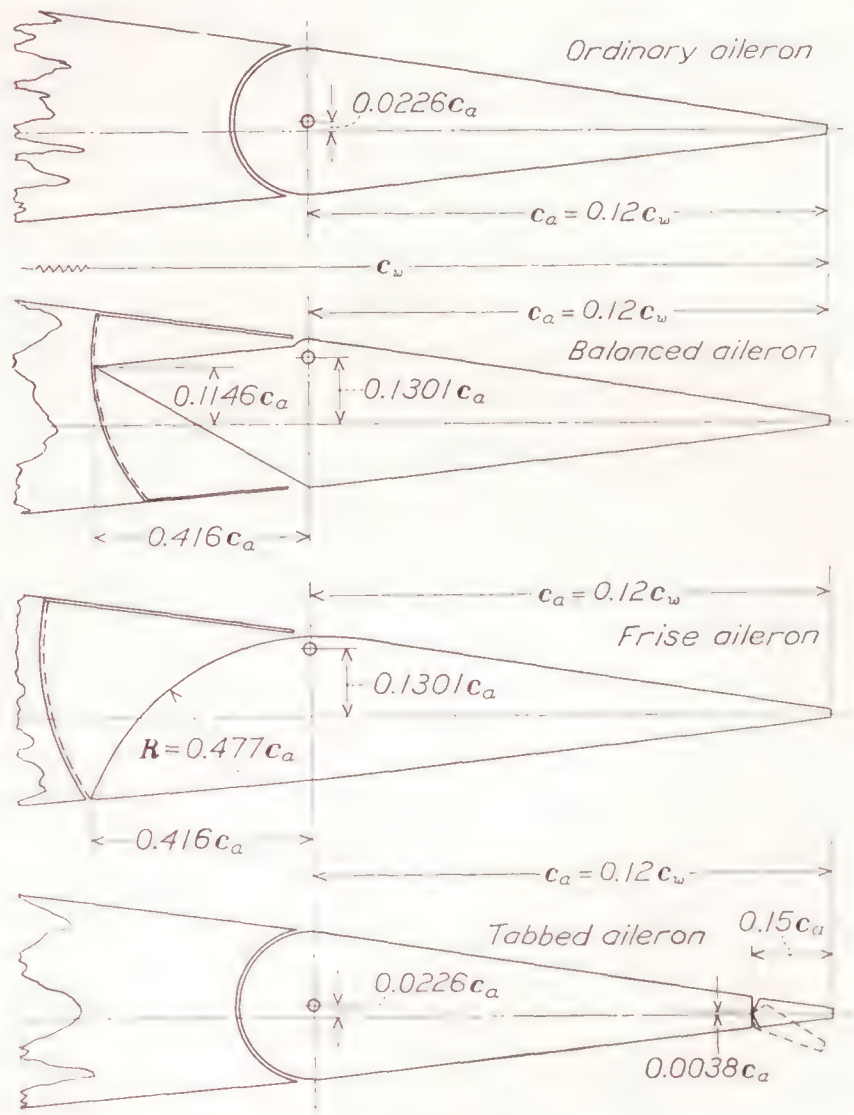

FIGURE 3.—Various balanced ailerons tested on the wide-chord N. A. C. A. 23012 airfoil with and without a 0.20 c_w N. A. C. A. 23012 external-airfoil flap.

at several angles of attack and flap angles. The tests were repeated with the flap removed to determine the effectiveness of the balancing means for narrow-chord ordinary ailerons mounted on a plain wing.

The tests of the wide-chord model were made, in general, at a dynamic pressure of 4.093 pounds per square foot, corresponding to an air speed of 40 miles per hour in standard air. The reduced speed was used to avoid placing excessive loads on the balance parts used as the model support. The effective Reynolds Number in this case was of the order of 5,000,000 but it should not be considered so accurate an index of flow similarity as is usually the case in wind-tunnel testing.

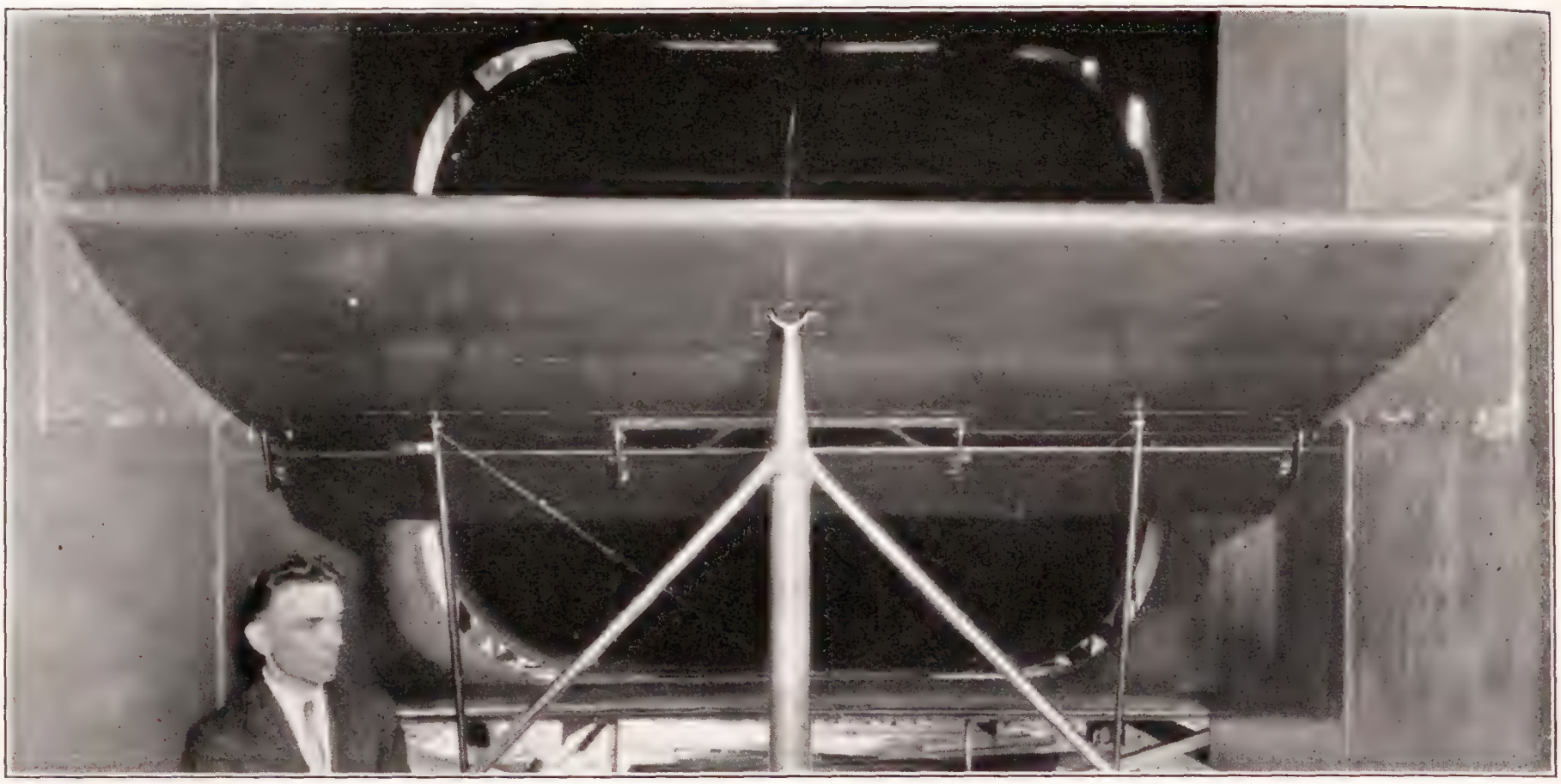

FIGURE 4.—The 4- by 8-foot model of the N. A. C. A. 23012 airfoil with an external-airfoil flap and an ordinary aileron, mounted between end planes in the 7- by 10-foot wind tunnel.

RESULTS

Application of results.—The precision of standard force tests in the 7- by 10-foot tunnel is discussed in references 2 and 5. The results as corrected are considered applicable to flight conditions with normal engineering accuracy at the previously stated values of the effective Reynolds Number. These values are too small to be directly usable in most cases but, with the aid of reference 7, a number of the characteristics of the present airfoils may be inferred for larger values of the Reynolds Number.

The conditions under which the ailerons on the wide-chord airfoil were tested were far removed from those for which theoretical wind-tunnel corrections may be applied; they therefore do not appear susceptible of accurate interpretation in terms of fundamental parameters. The ideal conditions in this respect were disregarded in favor of obtaining a reasonably accurate reproduction of the full-size ailerons themselves, including the end effects, to facilitate accurate comparison of the various ailerons tested. Consequently, any application to flight characteristics must be considered qualitative in nature. For comparison of the ailerons among themselves, however, the accuracy is probably much better than that usually obtained in standard small-scale tests, owing to the relatively large magnitude of the forces acting on the large model. The effectiveness of the data subsequently presented in showing consistent differences between the ailerons serves as an indication of the accuracy with which the values were measured.

Presentation and analysis of results.—The data obtained in the tests have been reduced to nondimensional coefficient form and are presented in a series of standard plots. The usual N. A. C. A. absolute coefficients are used throughout, except for a few symbols that have not been standardized. In the computation of the standard airfoil coefficients, the nominal area has been taken as the sum of the individual areas of the nonretracting surfaces (see references 2 and 4); the chord lengths have been similarly treated. The nonstandard coefficients are:

C_{n_i}, induced yawing-moment coefficient.

C_{n_0}, profile yawing-moment coefficient.

C_h, hinge-moment coefficient based on the dimensions of the surface whose hinge moment is being measured. $\left(\text{Thus, } C_{h_f}=\frac{H_f}{c_f S_f q}\right)$

ΔC_L, the increment of lift coefficient produced by a specified deflection of the aileron on the wide-chord model.

ΔC_D, the increment of drag corresponding to ΔC_L.

δ, angular deflection of the chord line of an auxiliary surface from the chord line of the surface to which it is attached, having the same sign convention as angle of attack.

The following subscripts serve to identify the various parts of the complete wing model:

w, of the main airfoil.

f, of the flap.

a, of the aileron.

t, of the tab.

The results of the first phase of the investigation consist entirely of lift, drag, pitching-moment, and flap hinge-moment data relating to the two high-lift arrangements tested. Data for the plain N. A. C. A. 23012 airfoil used as the basic airfoil are shown in figure 5 together with data from another airfoil of the same section. The data for the basic airfoil equipped with a 0.20 c_w N. A. C. A. 23012 external-airfoil flap deflected through various angles appear in figures 6 to 9.

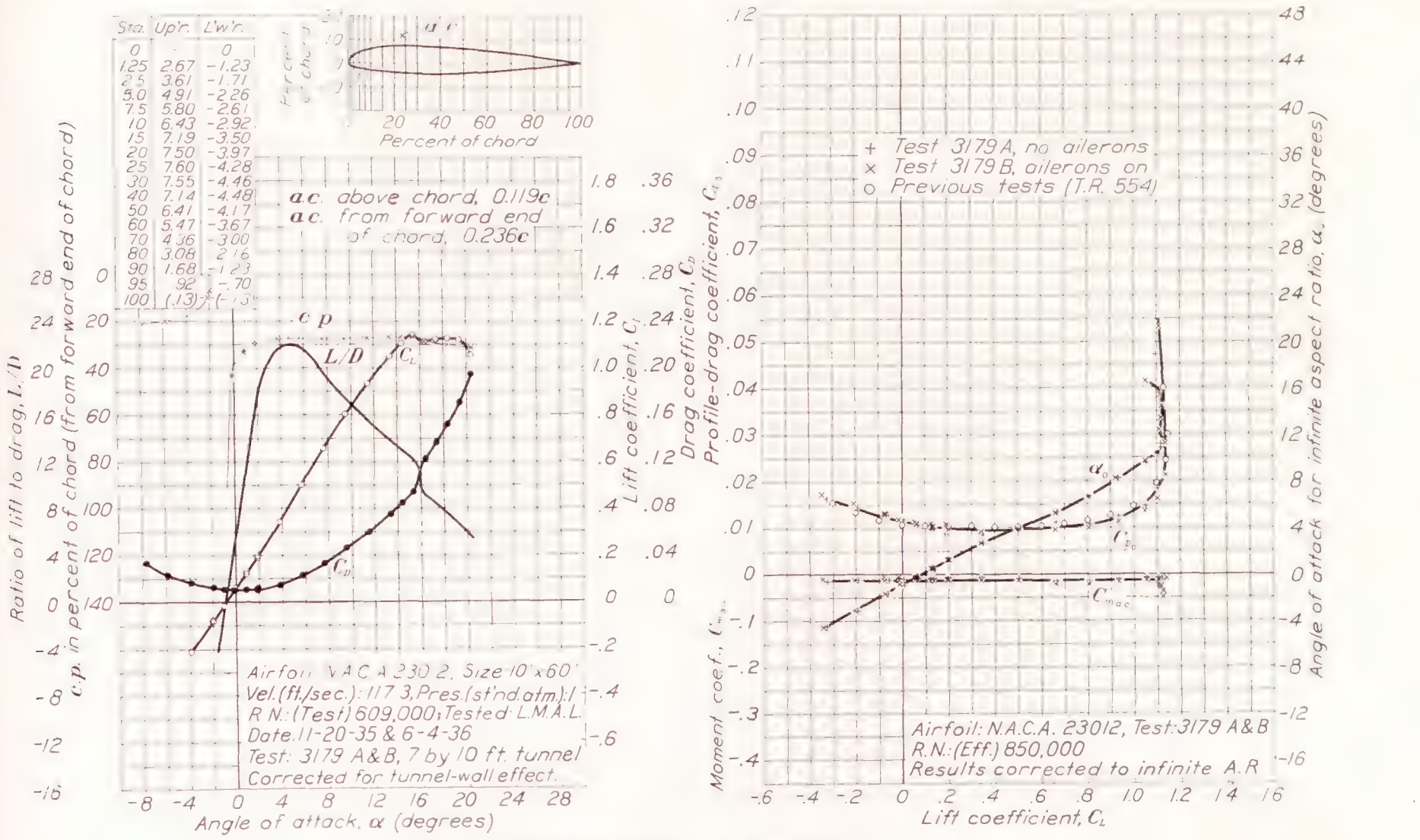

FIGURE 5.—The N. A. C. A. 23012 airfoil.

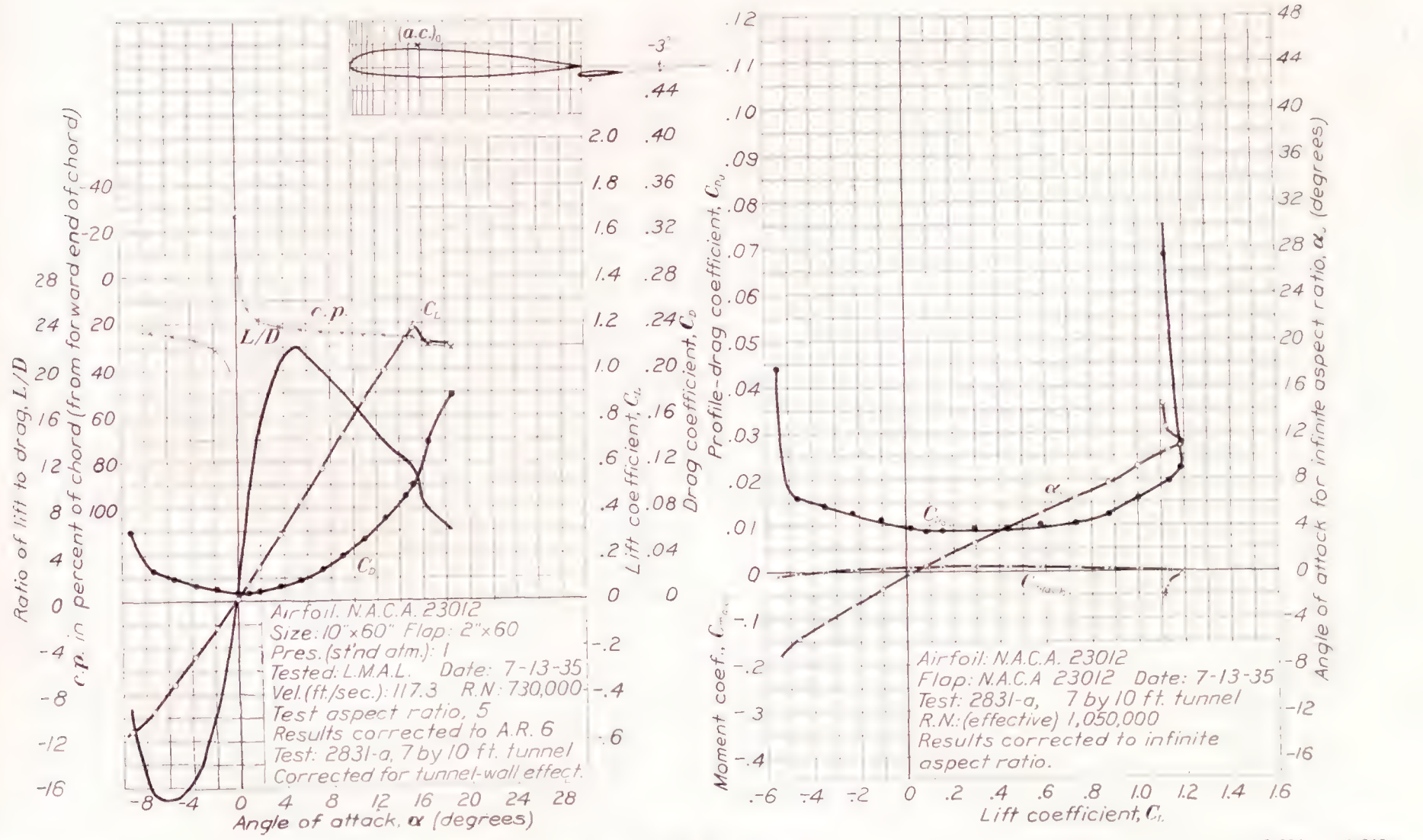

Main wing section	N. A. C. A. 23012	
Flap section	N. A. C. A. 23012	
Main wing chord, c_w	0.833 c	
Flap chord, c_f	0.20 c_w	.1667 c
Datum chord, $c=c_w+c_f$.		
Pivot aft of trailing edge of c_w	.032 c_w	.0266 c
Pivot below c_w	0.054 c_w	0.045 c
Pivot aft of flap leading edge	.25 c_f	.0417 c
Pivot below c_f	.10 c_f	.0167 c
Flap displacement angle		−3°
$(a.c.)_0$ from leading edge		.245 c
$(a.c.)_0$ above main wing chord		.08 c

FIGURE 6.—The N. A. C. A. 23012 airfoil with 0.20 c_w N. A. C. A. external-airfoil flap. Flap angle, −3°. (See reference 4.)

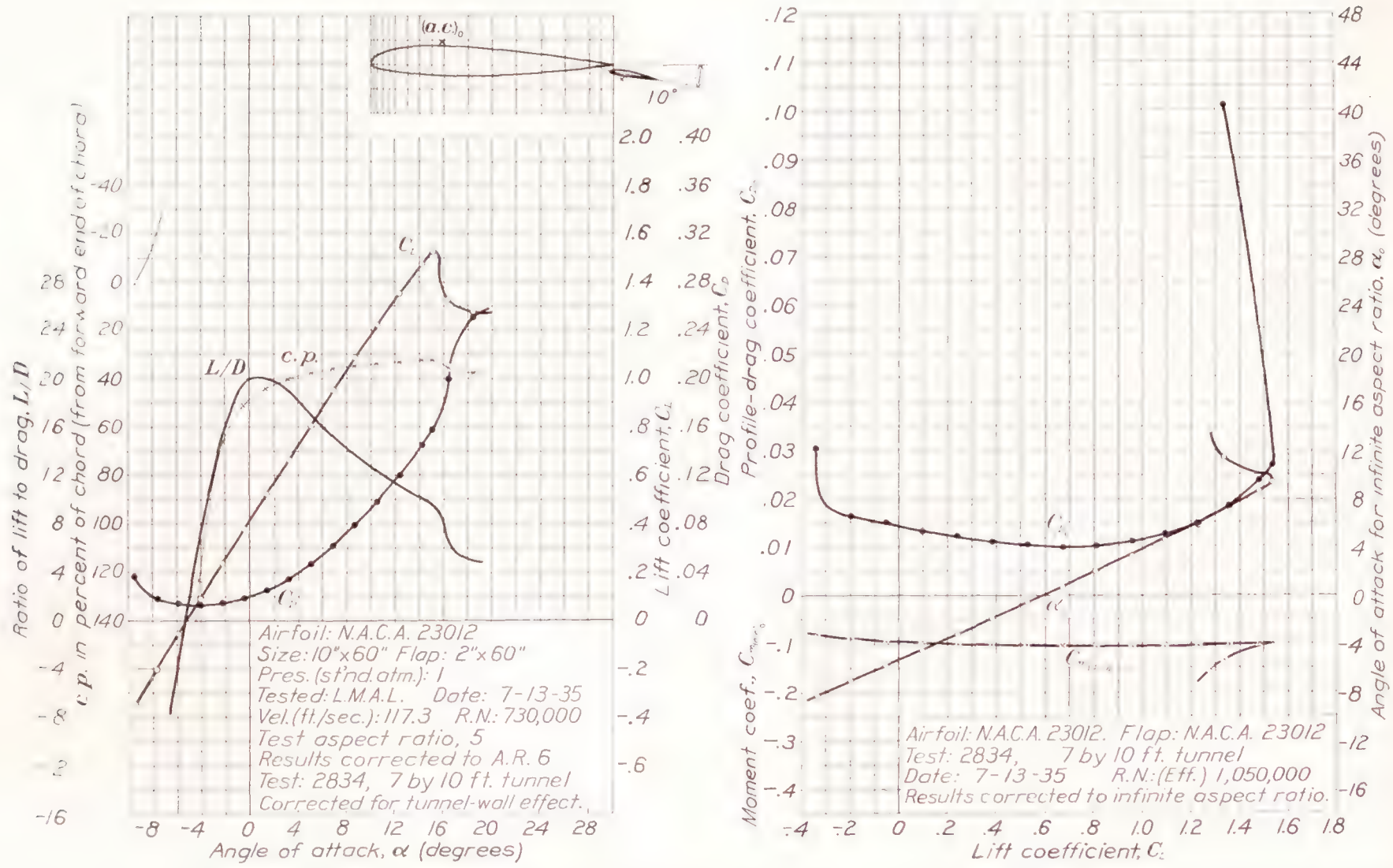

FIGURE 7.—The N. A. C. A. 23012 airfoil with 0.20 c_w N. A. C. A. external-airfoil flap. Flap angle, 10°. The airfoil is the same as used for test 2831-a (fig. 6), except the flap setting. The value of $C_{m_{(a.c.)_0}}$ is computed about the aerodynamic center used for test 2831-a. (See reference 4.)

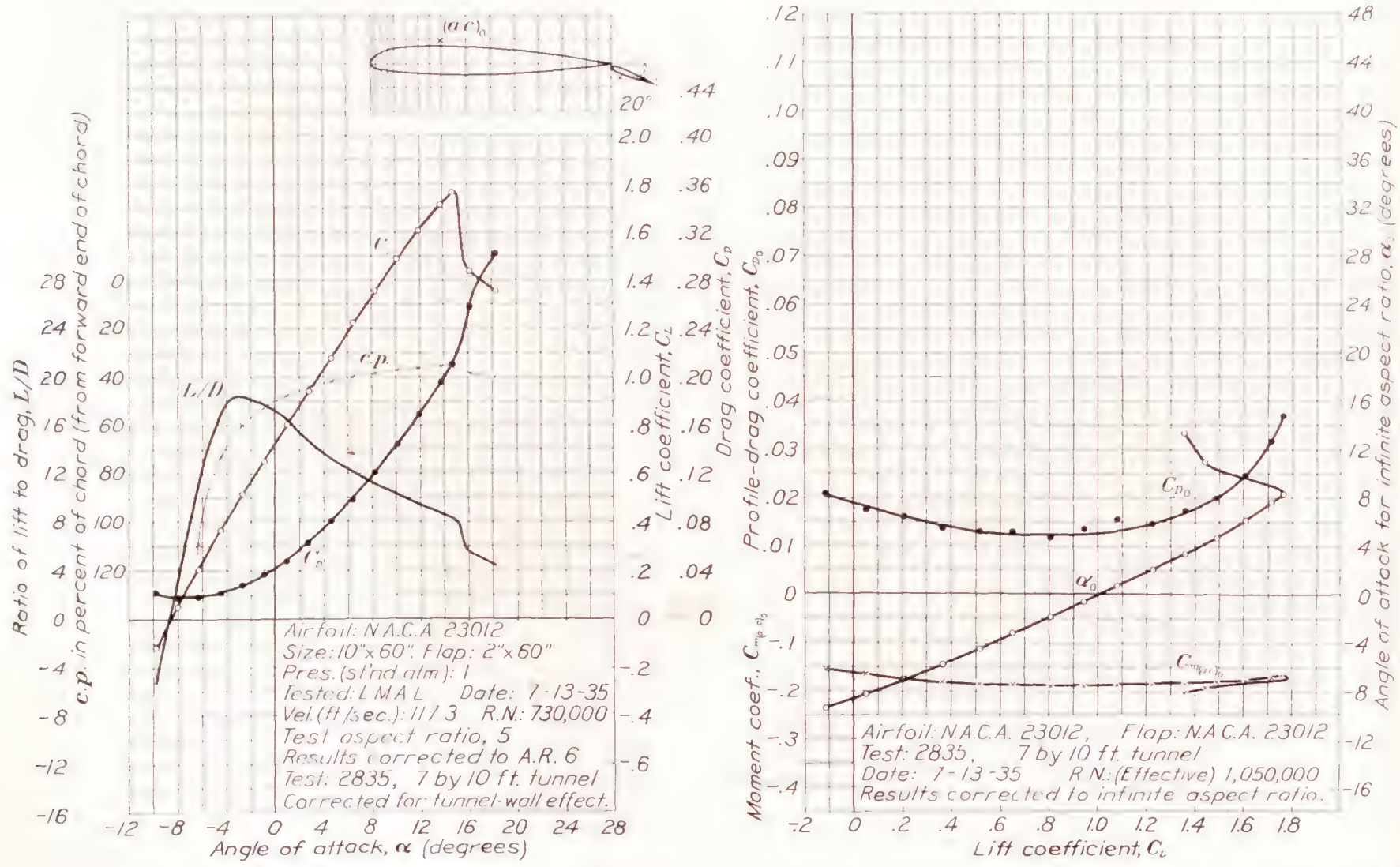

FIGURE 8.—The N. A. C. A. 23012 airfoil with 0.20 c_w N. A. C. A. 23012 external-airfoil flap. Flap angle 20°. The airfoil is the same as used for test 2831-a (fig. 6), except the flap setting. The value of $C_{m_{(a.c.)_0}}$ is computed about the aerodynamic center used for test 2831-a. (See reference 4.)

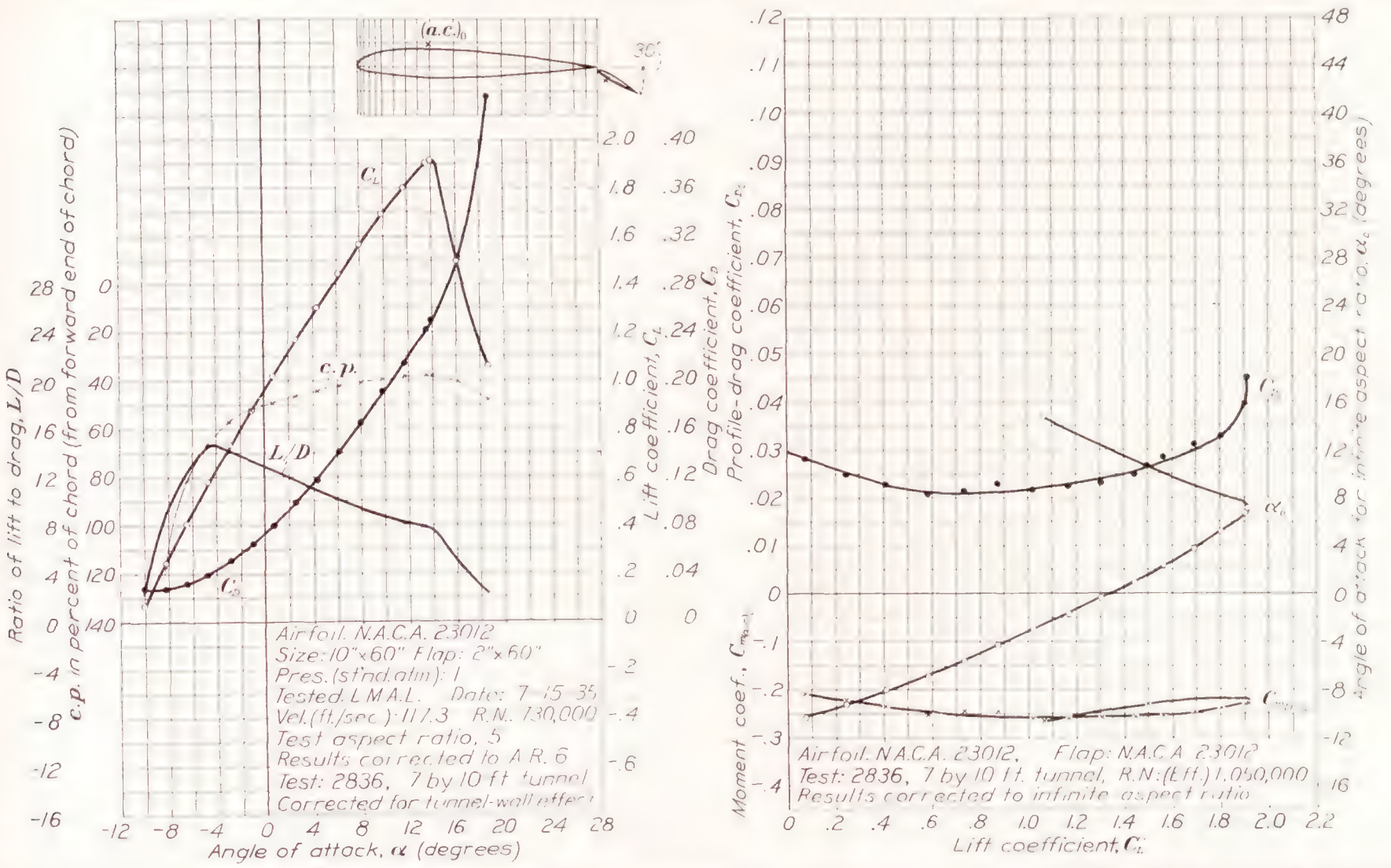

FIGURE 9.—The N. A. C. A. 23012 airfoil with 0.20 c_w N. A. C. A. 23012 external-airfoil flap. Flap angle, 30°. The airfoil is the same as used for test 2831-a (fig 6), except the flap setting. The value of $C_{m_{(a.c.)_0}}$ is computed about the aerodynamic center used for test 2831-a. (See reference 4.)

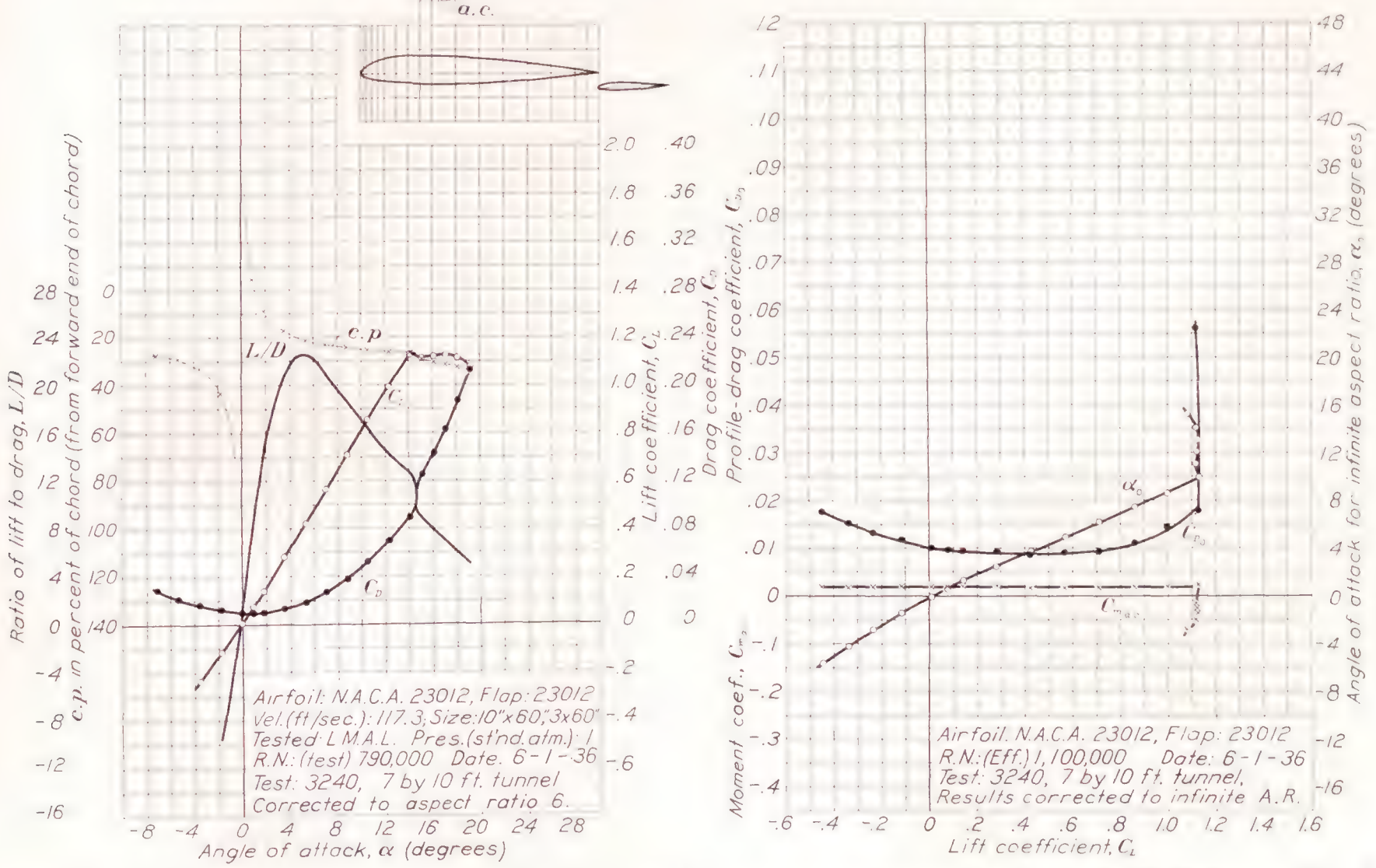

Main wing section	N. A. C. A. 23012	Pivot aft of trailing edge of c_w	0.071 c_w 0.0546 c
Flap section	N. A. C. A. 23012	Pivot below c_w	.049 c_w .0377 c
Over-all wing chord, $c=c_w+c_f$.		Pivot aft of flap leading edge	.25 c_f .0577 c
Main wing chord, c_w	0.769 c	Flap displacement angle	−2°
Flap chord, c_f	0.30 c_w .231 c	$a.c.$ from leading edge	.246 c
Datum chord, $c=c_w+c_f$.		$a.c.$ above main wing chord	.260 c

FIGURE 10.—The N. A. C. A. 23012 airfoil with 0.30 c_w N. A. C. A. 23012 external-airfoil flap. Flap angle, −2°.

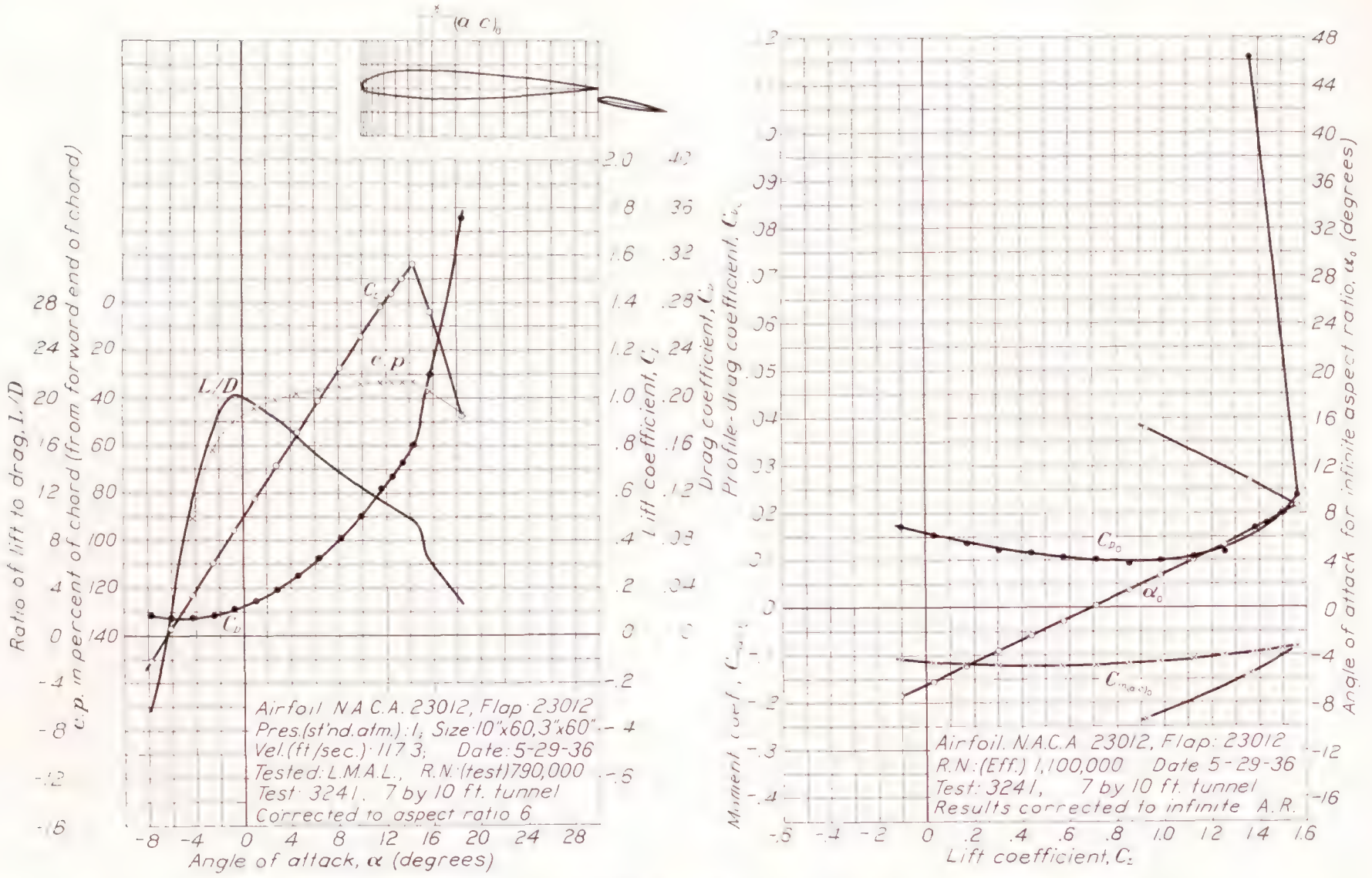

FIGURE 11.—The N. A. C. A. 23012 airfoil with 0.30 c_w N. A. C. A. 23012 external-airfoil flap. Flap angle, 10°. The airfoil is the same as used for test 3240 (fig. 10), except the flap setting. The value of $C_{m_{(a.c.)_0}}$ is computed about the aerodynamic center used for test 3240

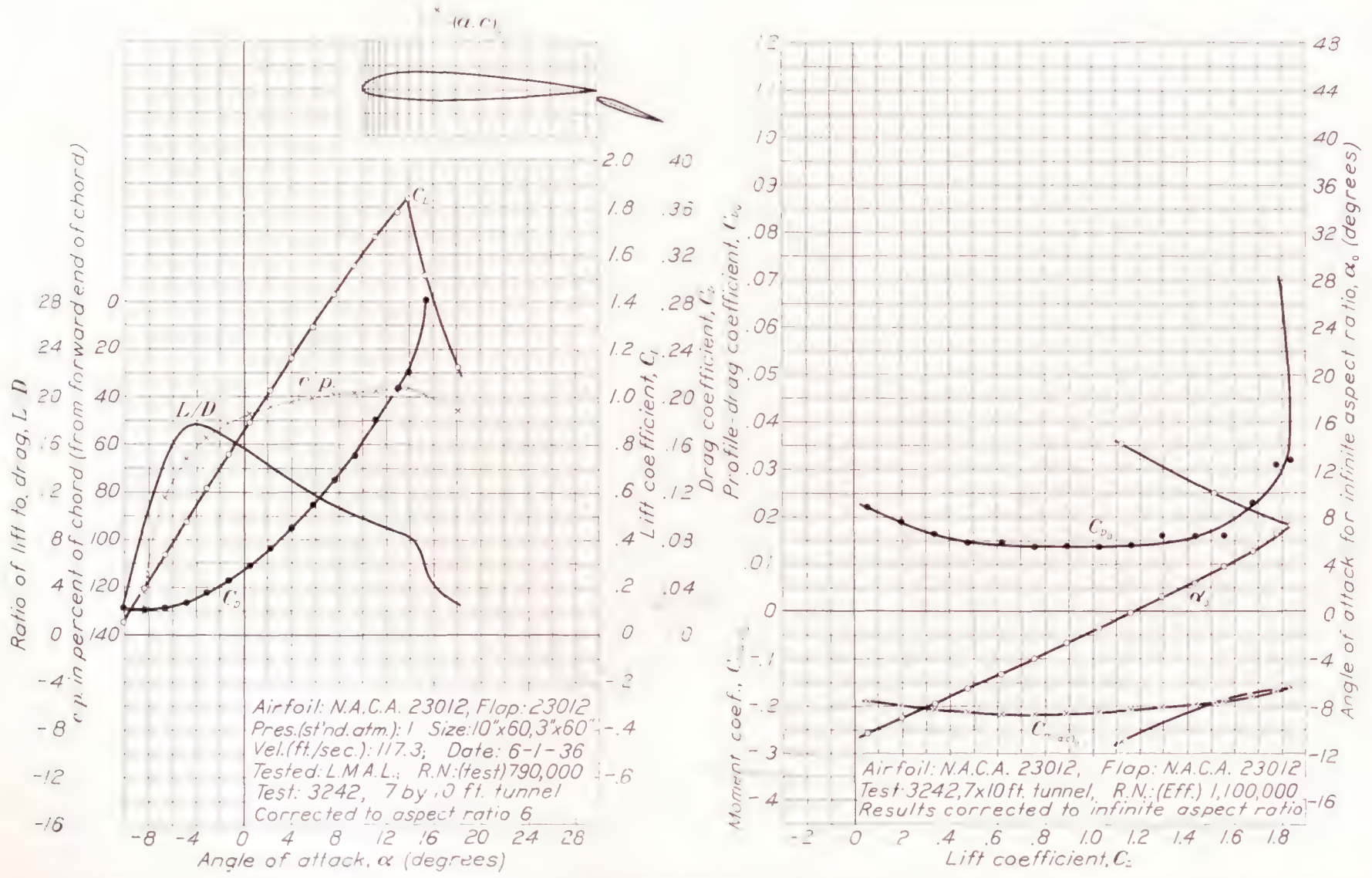

FIGURE 12.—The N. A. C. A. 23012 airfoil with 0.30 c_w N. A. C. A. 23012 external-airfoil flap. Flap angle, 20°. The airfoil is the same as used for test 3240 (fig. 10), except the flap setting. The value of $C_{m_{(a.c.)_0}}$ is computed about the aerodynamic center used for test 3240.

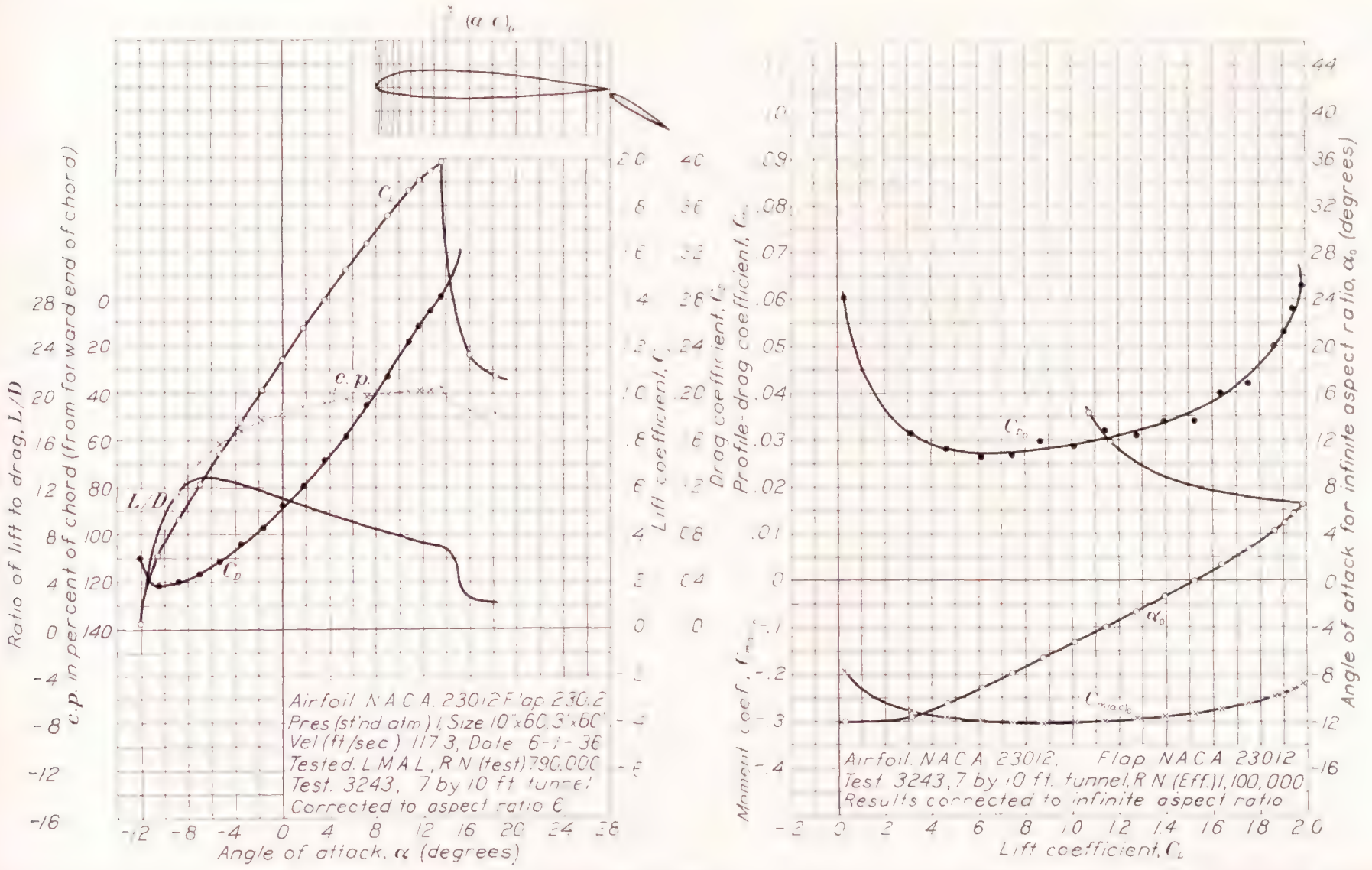

FIGURE 13.—The N. A. C. A. 23012 airfoil with 0.30 c_w N. A. C. A. 23012 external-airfoil flap. Flap angle, 30°. The airfoil is the same as used for test 3240 (fig. 10), except the flap setting. The value of $C_{m_{(a.c.)_0}}$ is computed about the aerodynamic center used for test 3240.

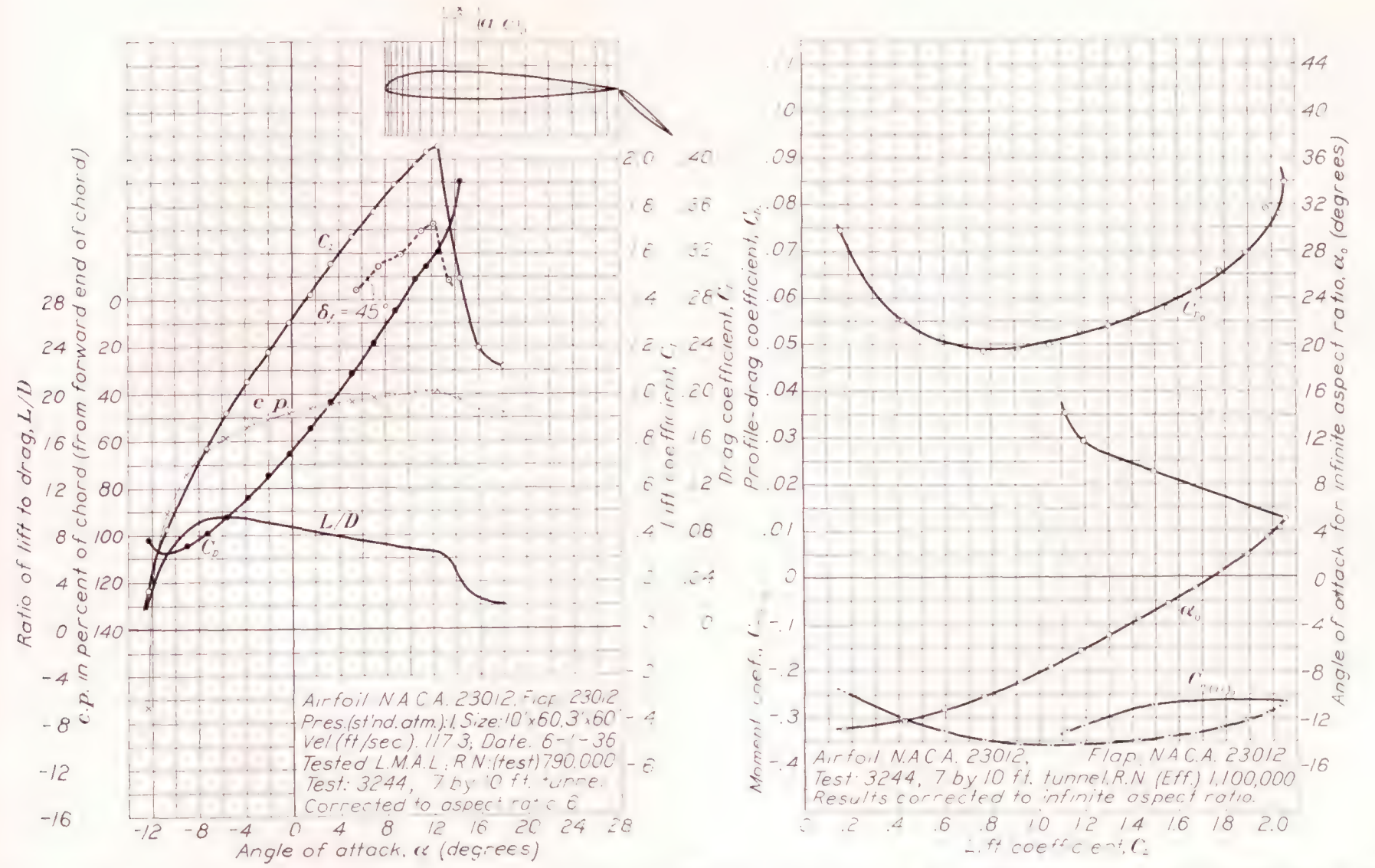

FIGURE 14.—The N. A. C. A. 23012 airfoil with 0.30 c_w N. A. C. A. 23012 external-airfoil flap. Flap angle, 40°. The airfoil is the same as used for test 3240 (fig. 10), except the flap setting. The value of $C_{m_{(a.c.)_0}}$ is computed about the aerodynamic center used for test 3240.

The data for the basic airfoil equipped with a 0.30 c_w external-airfoil flap of N. A. C. A. 23012 section appear in figures 10 to 14. The variation of flap hinge-moment coefficient with flap angle and angle of attack for each flap is shown in figure 15. It will be noted that the geometric aspect ratios of the model with the 0.20 c_w and 0.30 c_w flaps were 5.0 and 4.61, respectively. For purposes of comparison the data have been corrected in the usual manner (reference 2) for jet-boundary and planform effects and are presented in the standard airfoil plots for aspect ratios of 6 and infinity. Likewise, the angles of attack shown for the flap hinge-moment coefficient plots (fig. 15) refer to the conditions for a wing of aspect ratio 6 in an infinite jet.

coefficients is neglected, the plotted values are directly comparable with those obtained in previous lateral-control investigations in the 7- by 10-foot tunnel. The magnitude of the jet-boundary correction of yawing moment is normally small, and the present results may, therefore, be roughly compared with data obtained in previous investigations without correction. For accurate comparison of yawing-moment data, however, previous results should be corrected for the effect of the jet boundaries on induced yawing moment by the method given in the appendix.

The data in the figures have been selected from cross-fairings against angle of attack in such a way as to show the lateral-control characteristics at angles of attack

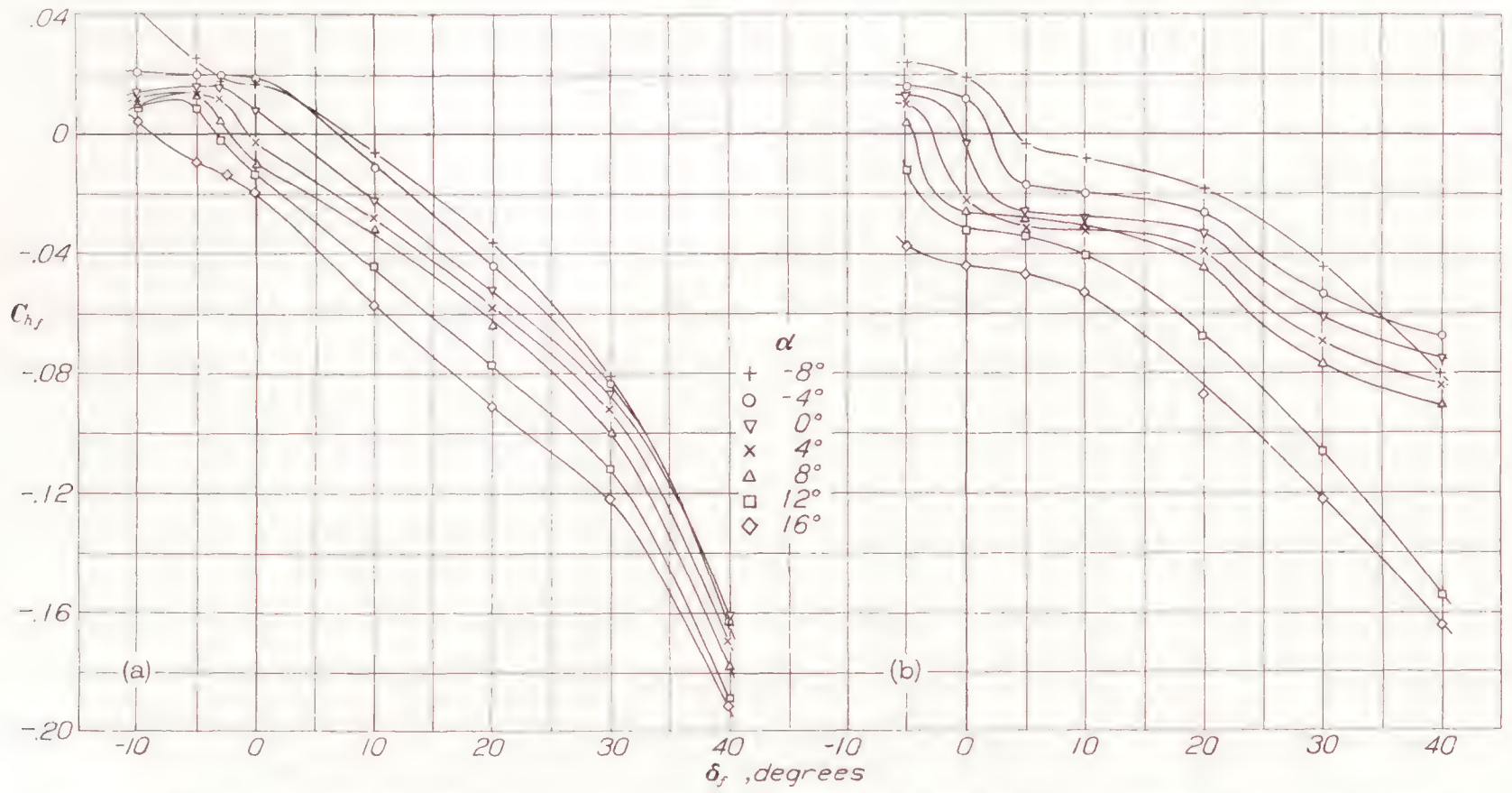

(a) The N. A. C. A. 23012 airfoil with 0.20 c_w external-airfoil flap. (b) The N. A. C. A. 23012 airfoil with 0.30 c_w external-airfoil flap.

FIGURE 15.—Variation of flap hinge-moment coefficient with flap deflection, at several angles of attack.

The results of the second phase of the investigation consist of rolling-moment, yawing-moment, and hinge-moment coefficients, presented as functions of angular deflection of the right aileron, the left aileron being held neutral. The data for the basic model equipped with the 0.20 c_w external-airfoil flap and the 0.12 c_w ailerons appear in figures 16 to 19; those for the model with the 0.30 c_w external-airfoil flap and 0.13 c_w ailerons in figures 20 to 23. For purposes of comparison the rolling- and yawing-moment coefficients have been corrected for jet-boundary and aspect-ratio effects so that the data as presented are representative of conditions existing on a model of aspect ratio 6 in an infinite jet. The method employed in making the corrections is explained in an appendix to this report. Since the effect of jet boundaries on measured rolling-moment

corresponding to lift coefficients of 0.2, 0.7, 1.2, and 1.8 with the ailerons neutral. The variation of lift coefficient with aileron deflection at a given angle of attack was neglected. The lift coefficients were selected as representative of certain flight conditions: high speed, maximum rate of climb, steep climb and approach glide, and flight immediately before landing and after take-off.

The plots of yawing-moment coefficient against rolling-moment coefficient may be regarded as analogous to polar curves of lift and drag. As indicated in the appendix, the theoretical induced yawing-moment coefficients are shown in the figures. By this artifice the figures are made to show the induced and profile parts into which the measured yawing moment may be divided.

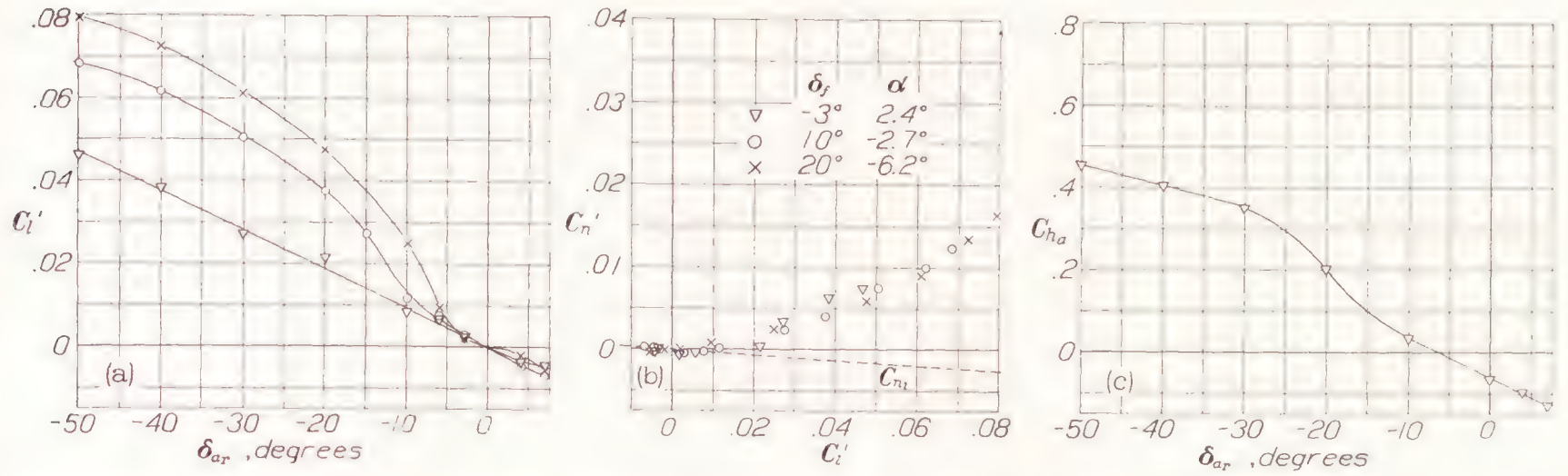

(a) Variation of rolling-moment coefficient with deflection of right aileron. Left aileron, 0°.

(b) Variation of yawing-moment coefficient with rolling-moment coefficient.

(c) Variation of aileron hinge-moment coefficient with aileron deflection.

FIGURE 16.—Rolling-, yawing-, and hinge-moment coefficients of N. A. C. A. 23012 airfoil with 0.12 c_w ordinary aileron and 0.20 c_w external-airfoil flap. $C_L=0.2$.

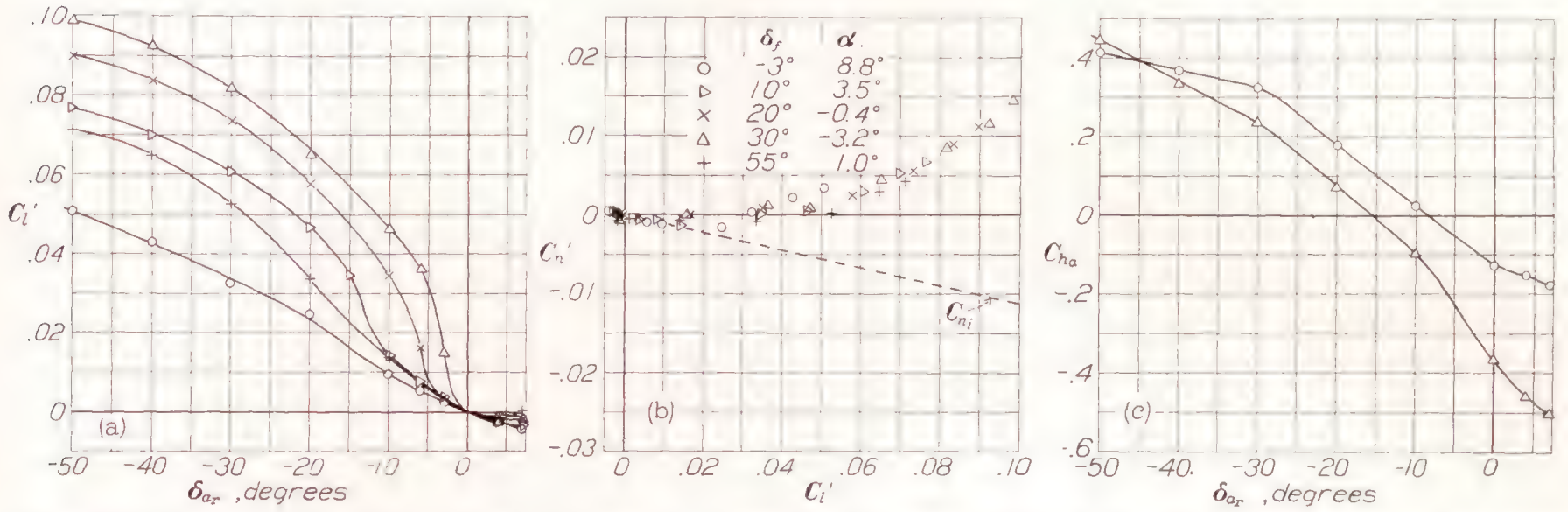

(a) Variation of rolling-moment coefficient with deflection of right aileron. Left aileron, 0°.

(b) Variation of yawing-moment coefficient with rolling-moment coefficient.

(c) Variation of aileron hinge-moment coefficient with aileron deflection.

FIGURE 17.—Rolling-, yawing-, and hinge-moment coefficients of N. A. C. A. 23012 airfoil with 0.12 c_w ordinary aileron and 0.20 c_w external-airfoil flap. $C_L=0.7$.

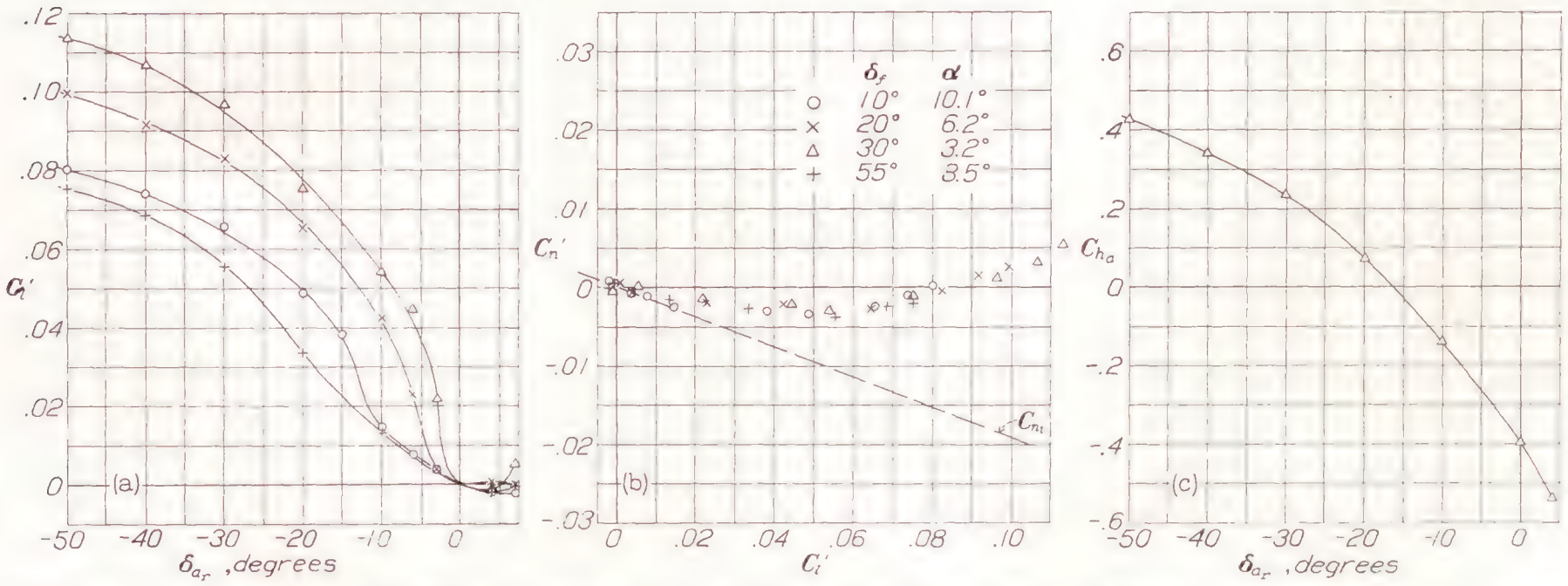

(a) Variation of rolling-moment coefficient with deflection of right aileron. Left aileron, 0°.

(b) Variation of yawing-moment coefficient with rolling-moment coefficient.

(c) Variation of aileron hinge-moment coefficient with aileron deflection.

FIGURE 18.—Rolling-, yawing-, and hinge-moment coefficients of N. A. C. A. 23012 airfoil with 0.12 c_w ordinary aileron and 0.20 c_w external-airfoil flap. $C_L=1.2$.

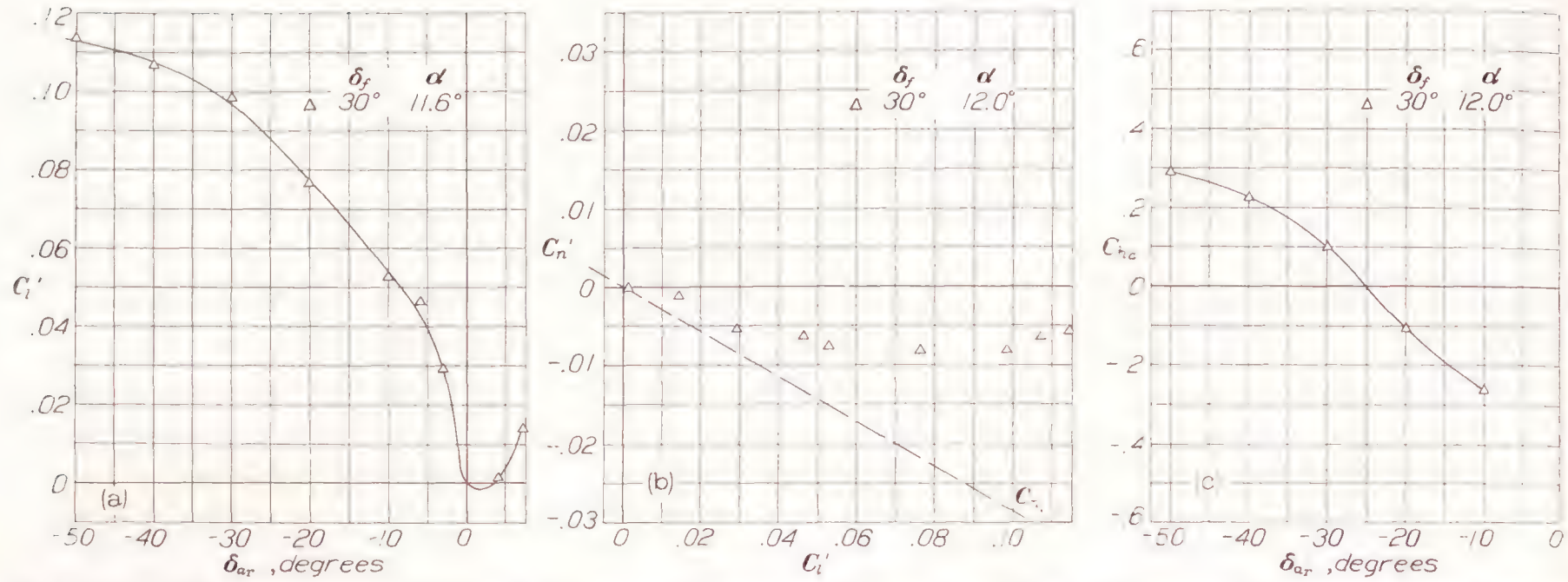

(a) Variation of rolling-moment coefficient with deflection of right aileron. Left aileron, 0°.

(b) Variation of yawing-moment coefficient with rolling-moment coefficient.

(c) Variation of aileron hinge-moment coefficient with aileron deflection.

FIGURE 19.—Rolling-, yawing-, and hinge-moment coefficients of N. A. C. A. 23012 airfoil with 0.12 c_w ordinary aileron and 0.20 c_w external-airfoil flap. C_L=1.8.

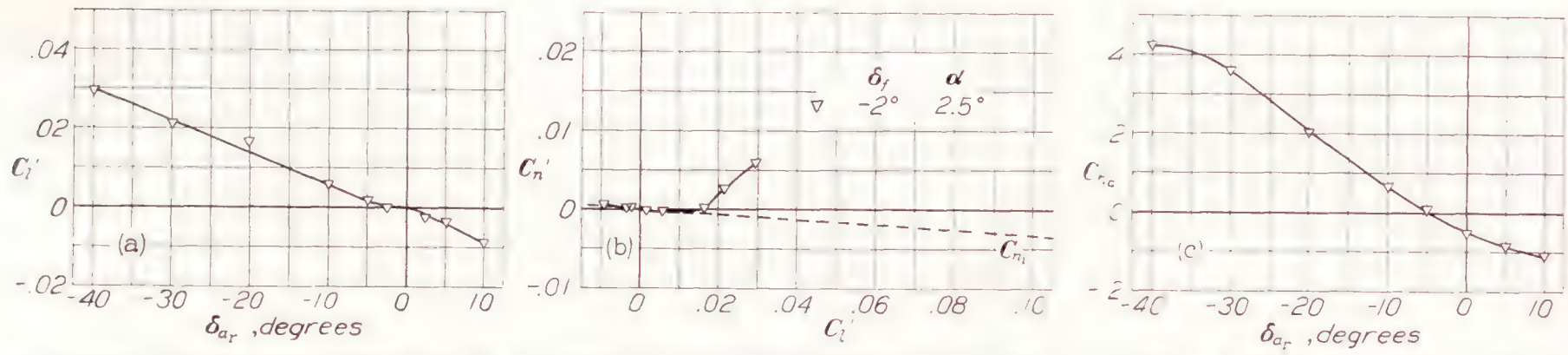

(a) Variation of rolling-moment coefficient with deflection of right aileron. Left aileron, 0°.

(b) Variation of yawing-moment coefficient with rolling-moment coefficient.

(c) Variation of aileron hinge-moment coefficient with aileron deflection.

FIGURE 20.—Rolling-, yawing-, and hinge-moment coefficients of N. A. C. A. 23012 airfoil with 0.13 c_w ordinary aileron and 0.30 c_w external-airfoil flap. C_L=0.2.

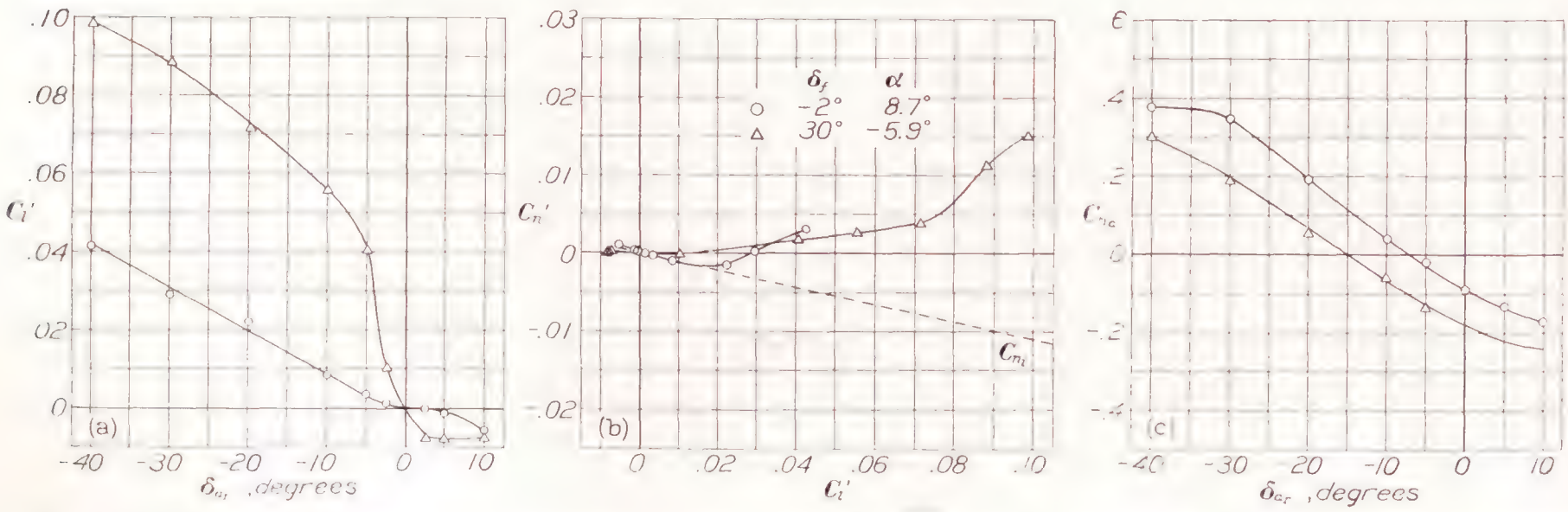

(a) Variation of rolling-moment coefficient with deflection of right aileron. Left aileron, 0°.

(b) Variation of yawing-moment coefficient with rolling-moment coefficient.

(c) Variation of aileron hinge-moment coefficient with aileron deflection.

FIGURE 21.—Rolling-, yawing-, and hinge-moment coefficients of N. A. C. A. 23012 airfoil with 0.13 c_w ordinary aileron and 0.30 c_w external-airfoil flap. C_L=0.7.

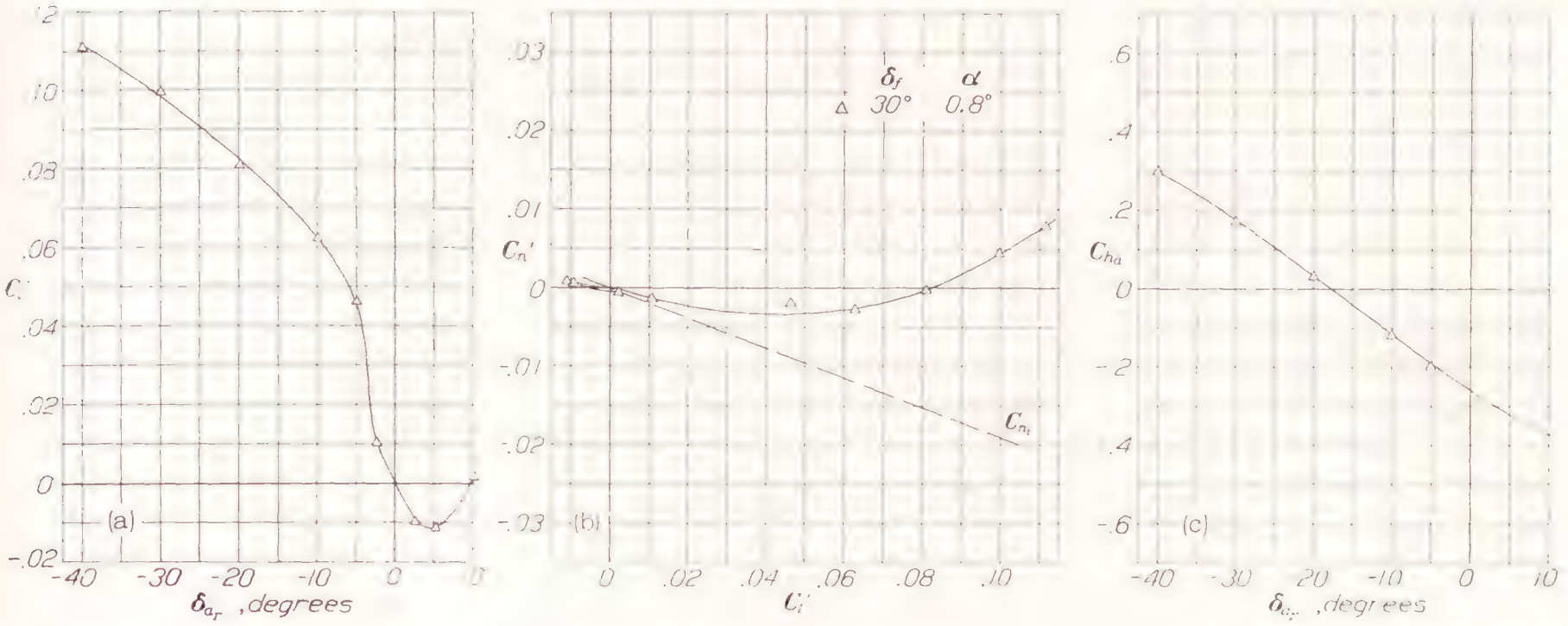

(a) Variation of rolling-moment coefficient with deflection of right aileron. Left aileron, 0°.

(b) Variation of yawing-moment coefficient with rolling-moment coefficient.

(c) Variation of aileron hinge-moment coefficient with aileron deflection.

FIGURE 22.—Rolling-, yawing-, and hinge-moment coefficients of N. A. C. A. 23012 airfoil with 0.13 c_w ordinary aileron and 0.30 c_w external-airfoil flap. $C_L=1.2$.

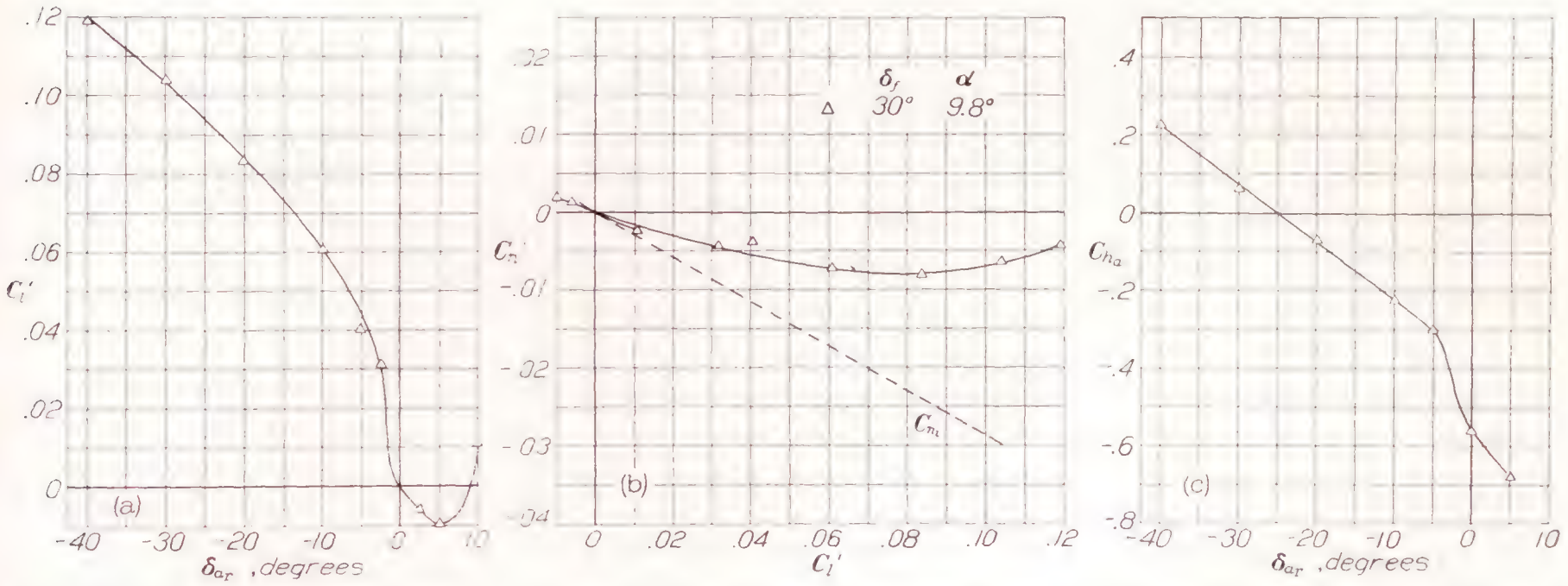

(a) Variation of rolling-moment coefficient with deflection of right aileron. Left aileron, 0°.

(b) Variation of yawing-moment coefficient with rolling-moment coefficient.

(c) Variation of aileron hinge-moment coefficient with aileron deflection.

FIGURE 23.—Rolling-, yawing-, and hinge-moment coefficients of N. A. C. A. 23012 airfoil with 0.13 c_w ordinary aileron and 0.30 c_w external-airfoil flap. $C_L=1.8$.

The data obtained in the third phase of the investigation are given in figures 24 to 31. The measured values of lift and drag have been reduced to the form of the lift and drag increments that result from a given deflection of the aileron under test. The lift increment produced by a deflected aileron on an airplane wing is the direct source of the rolling moment obtained; the drag increment likewise produces a corresponding yawing moment. Thus, under comparable conditions of wing lift coefficient and flap setting, the rolling and yawing moments that one of the ailerons under test would produce on an airplane wing are directly proportional to the measured lift and drag increments. The factor of proportionality varies with wing plan form but, for a given plan form, the factor remains constant regardless of aileron deflection. The curves of lift increment against aileron deflection and drag increment against lift increment are therefore analogous in form to the rolling- and yawing-moment data previously presented. Absolute values of hinge moment as a function of aileron deflection are also given—these values are directly comparable with the data obtained for the standard model.

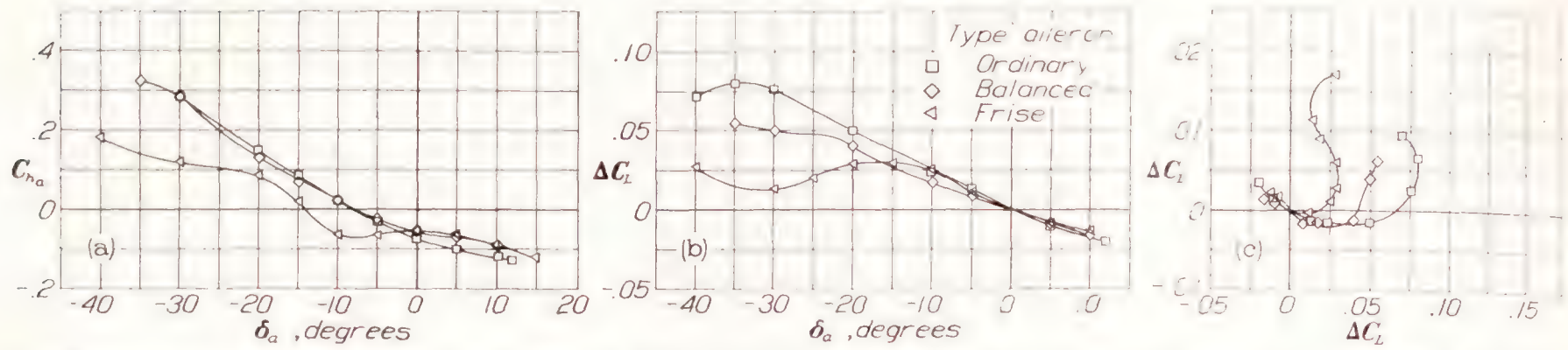

(a) Variation of aileron hinge-moment coefficient with aileron deflection.

(b) Variation of lift-coefficient increment with aileron deflection.

(c) Variation of drag-coefficient increment with lift-coefficient increment.

FIGURE 24.—Characteristics of various balanced ailerons on N. A. C. A. 23012 airfoil with 0.20 c_w external-airfoil flap set at −3°. C_L=0.2.

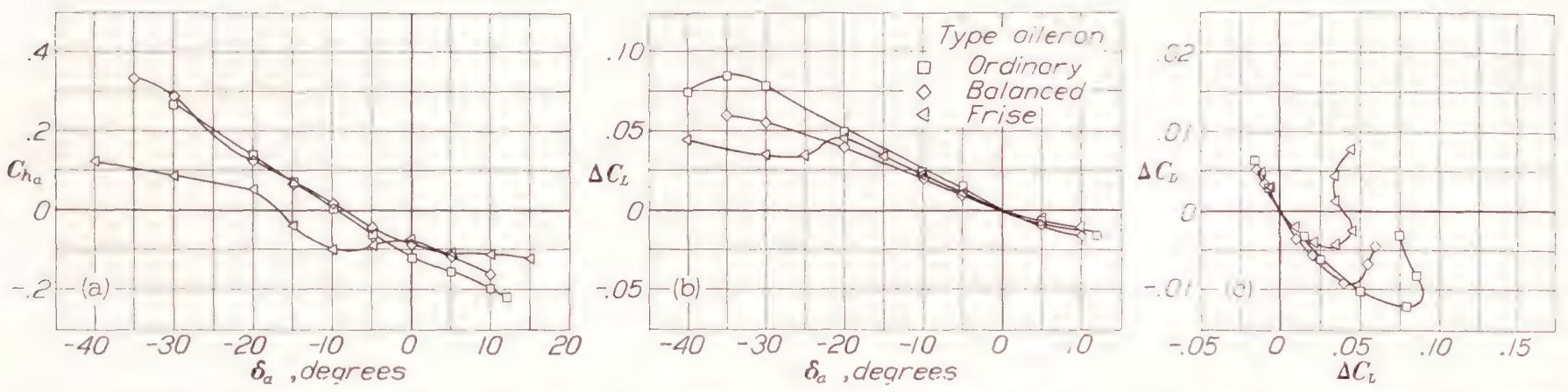

(a) Variation of aileron hinge-moment coefficient with aileron deflection.

(b) Variation of lift-coefficient increment with aileron deflection.

(c) Variation of drag-coefficient increment with lift-coefficient increment.

FIGURE 25.—Characteristics of various balanced ailerons on N. A. C. A. 23012 airfoil with 0.20 c_w external-airfoil flap set at −3°. C_L=0.7.

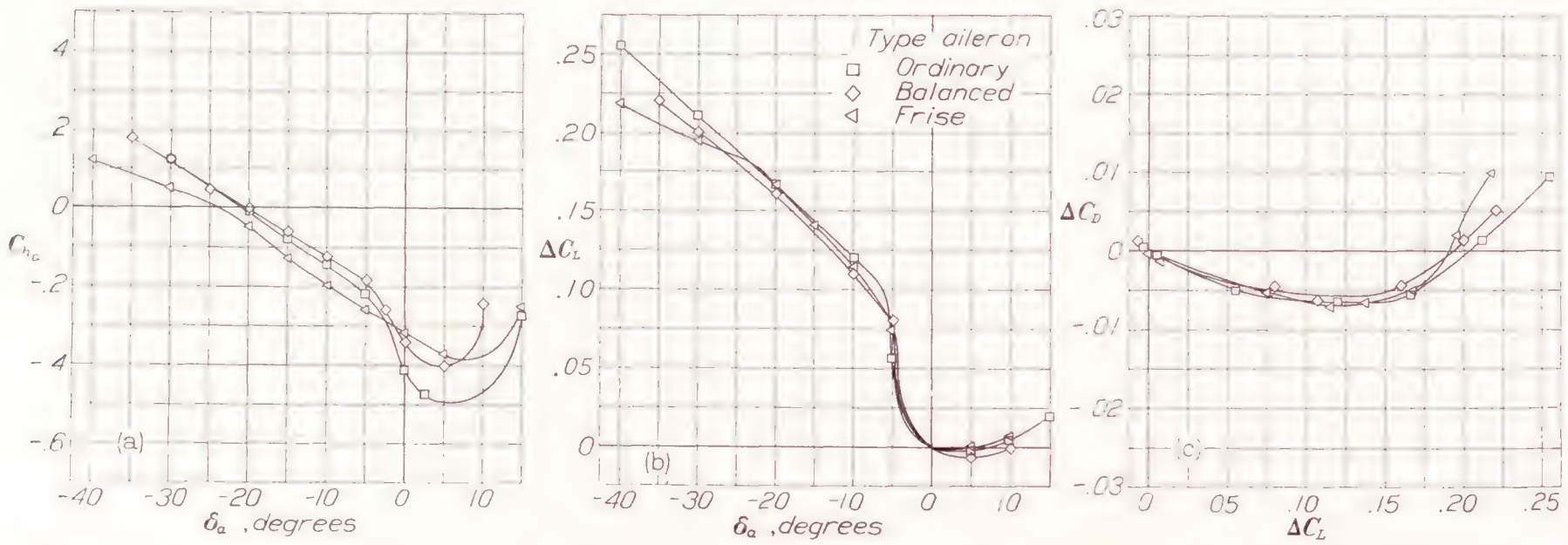

(a) Variation of aileron hinge-moment coefficient with aileron deflection.

(b) Variation of lift-coefficient increment with aileron deflection.

(c) Variation of drag-coefficient increment with lift-coefficient increment.

FIGURE 26.—Characteristics of various balanced ailerons on N. A. C. A. 23012 airfoil with 0.20 c_w external-airfoil flap set at 25°. C_L=0.7.

The data for the wide-chord model with the flap and each of the first three ailerons tested (that is, the plain aileron, the balanced aileron, and the Frise aileron) have been cross-faired to obtain the values of the variables at the same values of lift coefficient that were used for the previous figures and are plotted in figures 24 to 27. Similar data for the model with the same three ailerons but without the flap are shown in figures 28 and 29.

No lift and drag measurements were made of the model with the tabbed aileron because it could be assumed that the aileron lift and drag increments at small constant tab deflections were the same as those for the ordinary aileron without a tab. Experience coincides with flap theory in justifying this assumption for the unstalled lift range although it cannot be expected to hold at lift coefficients very near the stall.

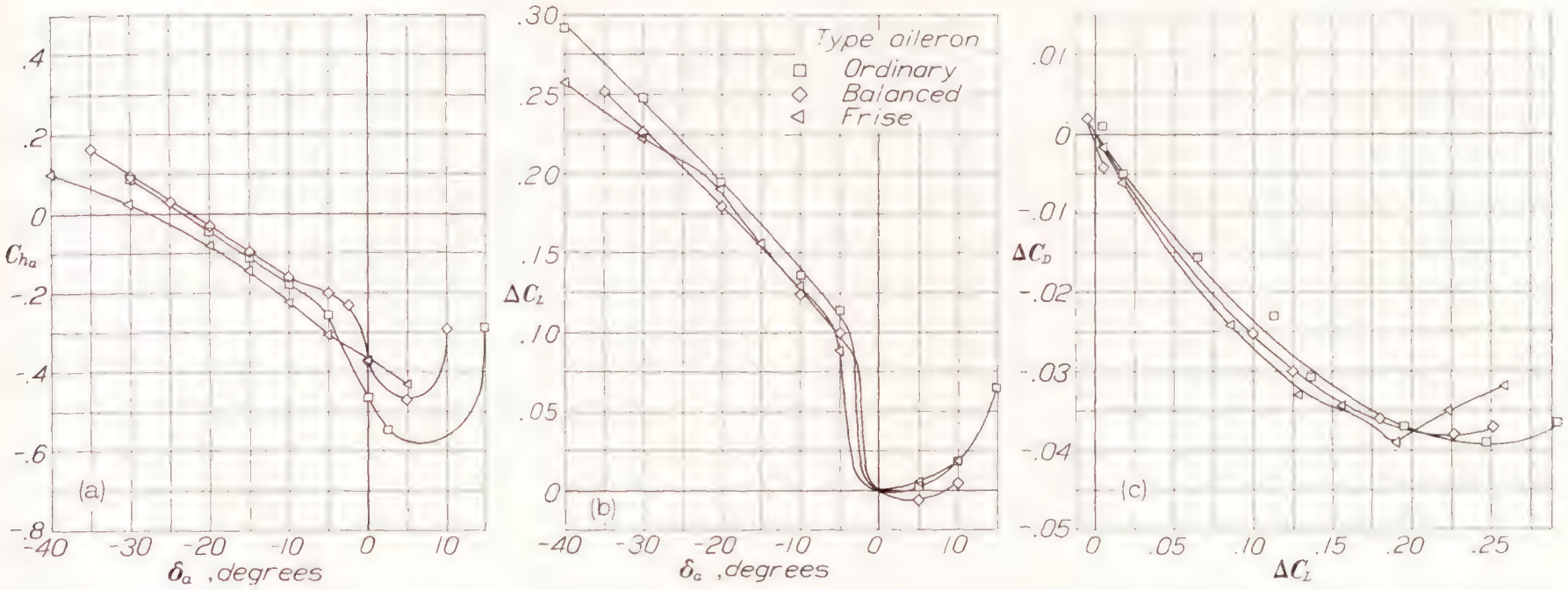

(a) Variation of aileron hinge-moment coefficient with aileron deflection.

(b) Variation of lift-coefficient increment with aileron deflection.

(c) Variation of drag-coefficient increment with lift-coefficient increment.

FIGURE 27.—Characteristics of various balanced ailerons on N. A. C. A. 23012 airfoil with 0.20 c_a external-airfoil flap set at 25°. C_L=1.2.

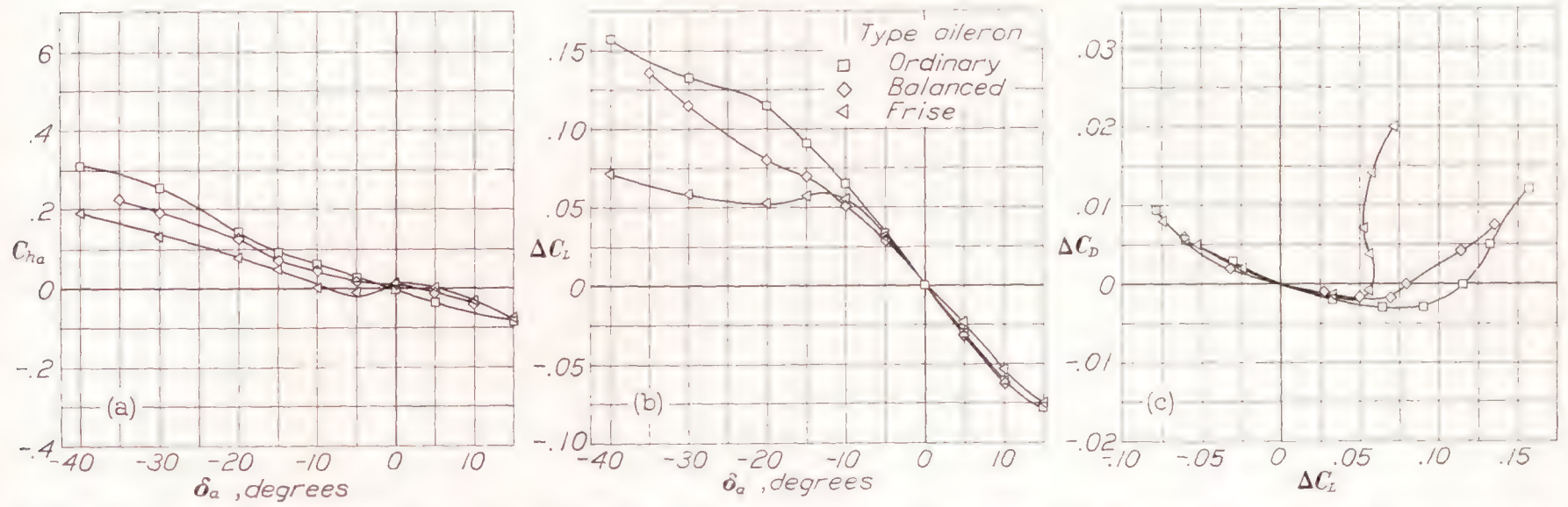

(a) Variation of aileron hinge-moment coefficient with aileron deflection.

(b) Variation of lift-coefficient increment with aileron deflection.

(c) Variation of drag-coefficient increment with lift-coefficient increment.

FIGURE 28.—Characteristics of various balanced ailerons on N. A. C. A. 23012 airfoil. C_L=0.2.

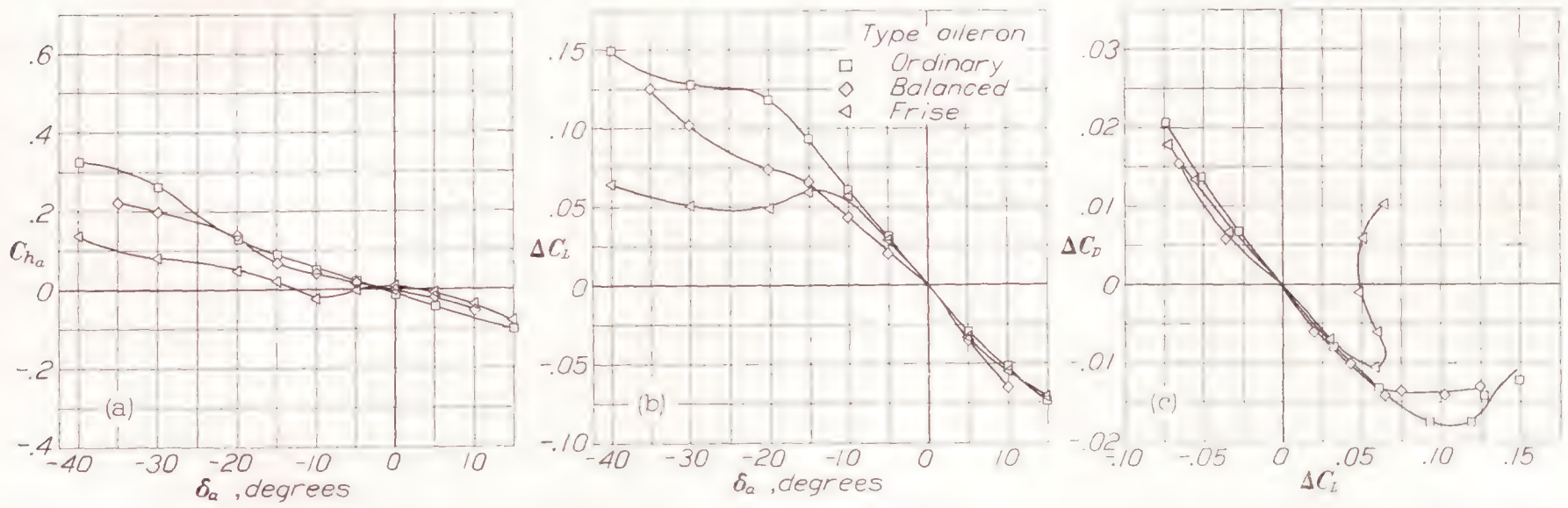

(a) Variation of aileron hinge-moment coefficient with aileron deflection.

(b) Variation of lift-coefficient increment with aileron deflection.

(c) Variation of drag-coefficient increment with lift-coefficient increment.

FIGURE 29.—Characteristics of various balanced ailerons on N. A. C. A. 23012 airfoil. C_L=0.7.

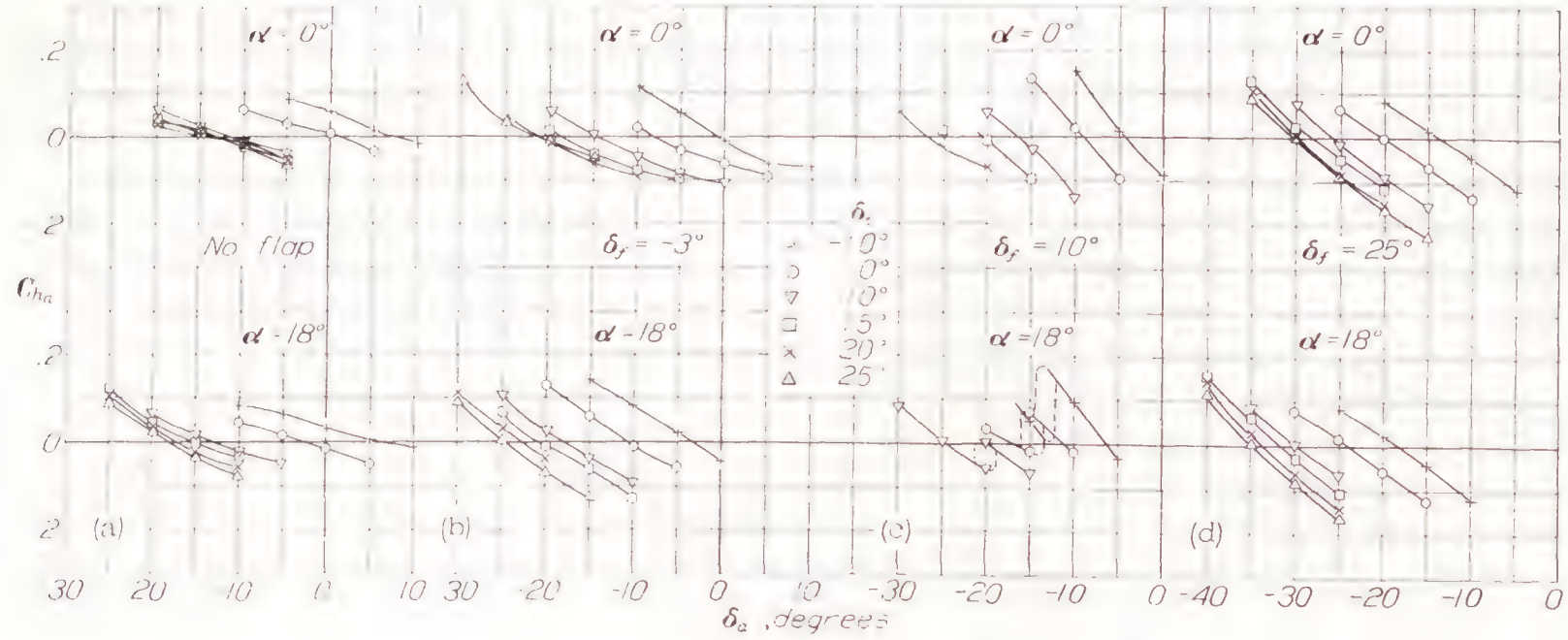

FIGURE 30.—Hinge-moment coefficients of a 0.12 c_w ordinary aileron with 0.15 c_a tab, mounted on an N. A. C. A. 23012 airfoil with and without a 0.20 c_w external-airfoil flap.

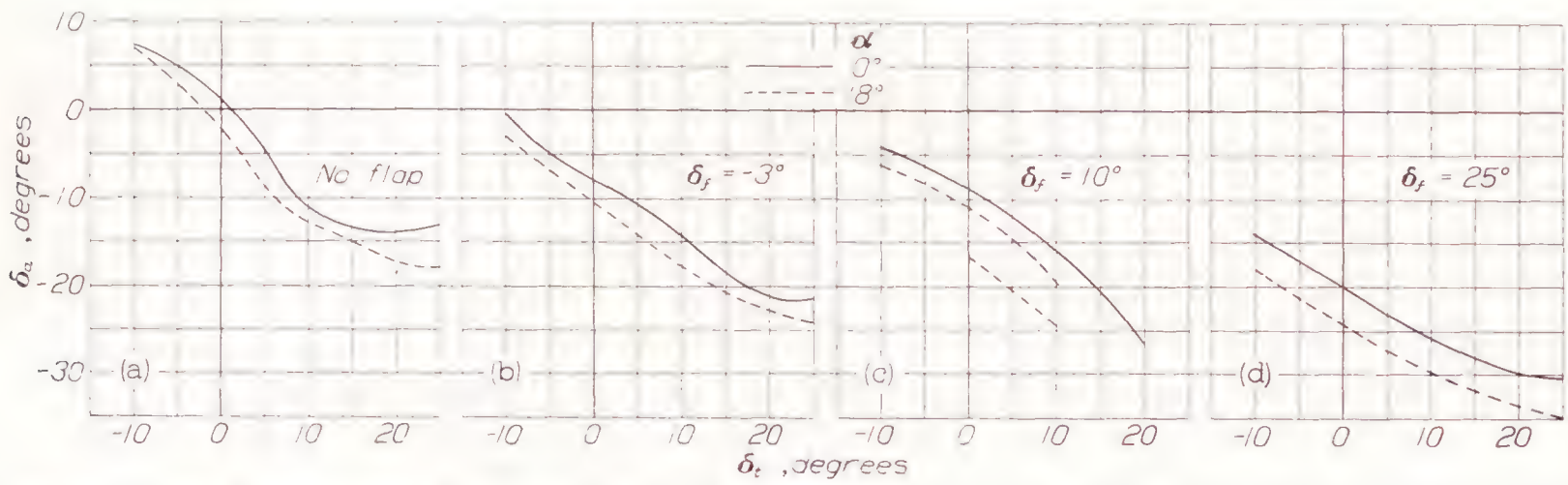

FIGURE 31.—Variation of aileron floating angle with tab deflection; 0.12 c_w ordinary aileron on an N. A. C. A. 23012 airfoil with and without a 0.20 c_w external-airfoil flap.

An unconventional method, subsequently explained, of using the tab to obtain aileron balance dictated the method adopted for presenting the data for the model with the tabbed aileron. In figure 30 the variation of aileron hinge-moment coefficient with aileron deflection is shown for a series of tab deflections at several conditions of angle of attack and flap angle. Figure 31 has been replotted from the data of figure 30 to show the variation of aileron floating angle with tab angle, the data for the model both with and without the flap being included. A drag test made at an air speed of 80 miles per hour with the aileron neutral, the flap both removed and set at the high-speed angle, and the model set at 0° angle of attack indicated that very small drag increments would result from a 20° deflection of the tab. The maximum increment of section profile-drag coefficient obtained was 0.0002, which lies within the limits of accuracy of the test.

DISCUSSION

As previously noted, the present investigation in one of its phases extended the investigation of the N. A. C. A. 23012 airfoil equipped with the N. A. C. A. 23012 external-airfoil flaps (reference 4) to include a flap having a 0.30 c_w chord. The methods used in selecting a desirable location of the flap-hinge axis and in obtaining and presenting the results directly paralleled those described in reference 4. Further, the data considered most significant for the airfoil with the 0.20 c_w flap have been transferred directly into this report for purposes of unity and completeness.

The discussion in reference 4 sets forth certain advantages of the external-airfoil type of wing-flap combination, principally in connection with its ability to produce high lift coefficients with relatively small increases of profile-drag coefficient. Figure 32 indicates the relative value of the 0.20 c_w and 0.30 c_w flaps in producing this effect. The curves are "envelope polars," obtained by fairing an envelope around the polar curves for various settings of the flap. The envelope polars thus show the minimum section profile-drag coefficient that can be obtained at any lift coefficient of which the wing-flap combination is capable. The graph demonstrates that the characteristics of the 0.30 c_w flap arrangement are at least as good as those of the 0.20 c_w flap arrangement and may be slightly better in certain particulars other than the maximum lift coefficient, in which the 0.30 c_w flap is definitely superior.

The better rounding of the polar for the 0.30 c_w flap, which gives it a slightly lower drag in the lift range normally used in take-off and simultaneously would permit a steeper gliding angle to be obtained at lift coefficients near the maximum, is believed to result from the different positioning of the hinge relative to the flap. The use of a hinge location for the 0.20 c_w flap similar to that for the 0.30 c_w might give a polar of more nearly similar shape. The effect on the maximum lift and minimum drag coefficients should not be adverse. No direct experimental evidence on this point was obtained, but comparison of the contour charts when they were used for selection of the hinge axis of the 0.30 c_w flap indicated the possibility.

It may be inferred from the observed variation of lift coefficient with flap angle and angle of attack that an airfoil and an external-airfoil flap act mutually to suppress the tendency of the flow to separate from their upper surfaces and thus delay stalling until a high lift coefficient is reached. An important phase of this action lies in the effect of the slot in producing a considerably higher speed of flow past the trailing edge of the airfoil than would exist with the flap absent. It therefore appears that ailerons placed on the trailing edge of an airfoil equipped with an external-airfoil flap are located in an especially effective position as compared with those located on a plain airfoil. On an ordinary airfoil it is known that the flow passes the trailing edge with little more than the free-stream velocity; in addition, the aileron may suffer from separation at angles somewhat below the stall. Under comparable conditions with the flap in action, it is apparent that the flow past the aileron has been accelerated and that the tendency to separation in this region has been suppressed. It therefore appears that such an aileron is in an excellent location for producing relatively large rolling-moment coefficients when the combination is developing a high lift coefficient. Reference to the flap-load data of reference 4 further shows that the flap carries very small forces when it is set for high speed: As a first approximation with the flap thus set the main airfoil may be considered an independent airfoil without appendages. It can then be inferred that deflection of the flap from the high-speed to the maximum-lift angle should cause a progressive increase in the effectiveness of the ailerons.

The foregoing considerations serve to clarify in part the variation of rolling-moment coefficient with flap deflection shown in figures 16 to 23. It is evident that as the flap is deflected the ailerons do gain considerably in effectiveness at a given lift coefficient of the wing-flap combination. The data reveal an additional simultaneous effect that serves further to improve the aileron effectiveness. As the aileron is deflected upward it bends the flow upward and reduces the lift. At the same time the size of the slot is considerably increased and the flow, tending to follow the lower surface of the aileron, encounters the flap at an increased angle of attack. At a certain point in the aileron travel the slot effectiveness has been reduced and the angle of attack of the flap sufficiently increased to cause the flap to stall, resulting in a further reduction in lift and increase in drag.

Inspection of figures 16 to 23 shows that this effect occurs at smaller aileron deflections as the flap approaches the maximum-lift angle, where the slot size is most critical. In figure 17, for example, the sharp rise in the rolling-moment curve, which is associated with the stalling of the flap, occurs at an aileron deflection of about 12° up when the flap is down 10°, at 5° up when the flap is down 20°, and so on. It is evident that this effect, which further increases the rolling moment and also reduces the adverse yawing moment, likewise comes into action progressively as the flap is deflected from the high-speed to the high-lift condition. When the flap has passed the maximum lift angle (see fig. 17, $\delta_f=55°$), the sudden increase of rolling moment

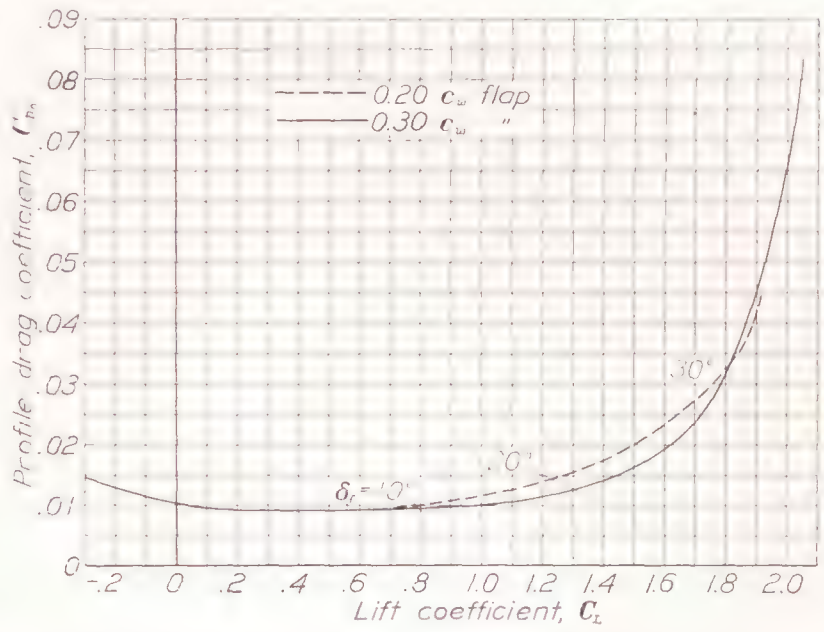

FIGURE 32.—Envelope polars for N. A. C. A. 23012 airfoil with 0.20 c_w and 0.30 c_w external-airfoil flaps. Effective Reynolds Number, approximately 1,000,000.

fails to appear because the flap is already stalled with the aileron neutral.

In connection with the effect of the stalling of the flap, it is noteworthy that the total lift of the flap is not lost, a low pressure is still maintained over the flap upper surface, and its effect in suppressing separation from the main airfoil is still active. Figure 14 shows the effect of deflecting the flap beyond its angle for maximum lift ($\delta_f=40°$ for the 0.30 c_w flap), in which case the flap stalled at a low angle of attack of the combination. Here the maximum lift coefficient was reduced approximately 0.3 by the stalling of the flap. As the maximum increase of $C_{L_{max}}$ produced by the flap in this case is 0.9, it is clear that about two-thirds of the flap effect remains after the flap has stalled. At still larger deflections the slot is completely ineffective, and it can be seen that the external-airfoil flap is then equivalent to a split or Zap flap with a small gap between it and the wing.

Thus far the discussion has tended to bring out considerations favorable to combinations of airfoils, external-airfoil flaps, and ailerons. Certain undesirable consequences of the foregoing considerations must also be recognized. It has been pointed out that ailerons of a given size on a wing with external-airfoil flaps can produce more rolling moment than normal ailerons of the same size on a plain wing. For application to airplane design it might be concluded that satisfactory control could be obtained with smaller ailerons by using them in combination with an external-airfoil flap. Such a conclusion is modified, however, by another important factor: The data (figs. 16 and 17) show that the effect of the flap is not active near the stalling lift coefficient with the flap at the high-speed angle; thus, ailerons of reduced area would be relatively weak in this condition.

The location of the aileron in relatively high-speed flow clearly must lead to increases of hinge moment as well as of rolling moment. Comparison of the lift increment per unit hinge moment of the present ailerons (fig. 24) with that for ordinary ailerons (fig. 28) indicates that with the flap in the high-speed setting the present ailerons are inferior. Since a large part of airplane operation would involve use of the ailerons with the flap at the high-speed setting, it seems desirable that the hinge moments of these ailerons be reduced to values comparable with those of ordinary ailerons for a given rolling moment. These considerations, which were first apparent when the tests of the standard model were compared with generally known characteristics of ordinary ailerons, led directly to the tests of the various balanced ailerons on the wide-chord model.

A study of some unpublished pressure-distribution data for airfoils with external-airfoil flaps suggested that a balance extending ahead of the aileron nose might serve to reduce the aileron hinge moments. Such a balance normally adds an appreciable amount of drag, but the provision of "curtains" covering most of the gap should eliminate the drag increment and still permit the pressures to act on the balance area. The arrangement finally selected, designated the "balanced aileron" in figure 3, was provided with such a balance and could be deflected between a 40° up and 15° down angle without encountering the curtains. Ordinary and Frise ailerons were included to provide a direct comparison with the tests on the standard model and with the action of a balance now in general use.

A slight reduction of hinge moment per unit deflection was obtained from the balanced aileron, but the lift increment per unit deflection likewise decreased from that obtained with the ordinary aileron, resulting in no actual improvement. The loss of lift increment suggests that there was more leakage between the balance nose and the airfoil than existed in the case of the plain aileron. This loss might be regained by the use of some system for sealing the clearance and some advantages thereby obtained. The present results, however, suggest that this form of balance does not merit general application at the present time though further development might render it very useful for wings either with or without external-airfoil flaps.

The data obtained for the Frise aileron clearly illustrate its action. As the aileron is deflected upward the nose drops into the flow below the wing, and the aileron "digs in," giving a mild degree of overbalance. As the nose becomes well extended, the upper surface of the aileron is vented to the lower; the resulting flow between the lower and upper surfaces markedly reduced the effectiveness of the ailerons. Simultaneously, the drag is increased by the disturbance to the flow, which would produce a favorable yawing moment such as has generally been observed in the use of Frise ailerons. In spite of the favorable effect on yawing moment, the Frise ailerons do not appear to be of appreciable interest in the present connection on account of their effect in reducing the maximum available rolling moment and in having a tendency to overbalance in the initial stages of deflection.

Another method of reducing stick forces involves the use of a differential linkage for aileron operation. (See references 2 and 8.) The differential linkage interacts with any tendency of the ailerons to float up from neutral to produce a reduction in the stability of the complete aileron system. In the tests reported in reference 2 certain cases were found where the stability became negative, i. e., the system was actually overbalanced. In this case the action is readily visualized: The downgoing aileron reaches its maximum travel, with the drive crank at dead center, before the upgoing aileron has reached its natural upfloating angle. Thus, the upgoing aileron is trying to deflect itself still farther when the downgoing aileron can no longer exert a restoring moment; the aerodynamic forces thus tend to move the stick away from its neutral position. When the upfloating angle of the ailerons is known, a differential can be selected that will interact with the upfloating tendency to produce a lesser reduction of stability than that previously described. The stick forces are thus reduced without producing overbalance by a proper coordination of the differential linkage with the aileron floating angle and the slope of the curve of hinge moment with deflection.

Jones and Nerken (reference 8) have investigated the properties of differential linkages and give formulas and charts for the proper coordination of the important factors. They have further suggested, in the case of ailerons having a large variation of floating angle with angle of attack, the use of a tab mounted on each aileron to bias the aileron floating angle to a desirable value. In the case of the present type of aileron, this suggestion appears to be especially useful, since other considerations militate against complete freedom of

the designer in selecting a differential linkage suited purely to the aileron characteristics. As the floating angle of these ailerons varies with angle of attack and flap angle, it would be desirable to have the differential vary accordingly. This arrangement would not be feasible, and the tab is therefore used to provide the desired floating angle and thus avoid the necessity for a varying differential. The desirability of preventing the trailing edge of the downgoing aileron from passing the leading edge of the flap indicates a linkage that would reach dead center at a small downward aileron deflection. This result, in turn, indicates that the upgoing aileron deflection will not be large when the downgoing aileron reaches dead center and that large upfloating angles (over 20°, for example) will tend to produce overbalance.

It is evident from the data for the standard model (figs. 16 to 24) and from the foregoing discussion that the ailerons operated by a differential linkage (which apparently is vital to their successful application) would be abnormally heavy in high-speed flight and might become overbalanced in low-speed flight with the flap down. The data of figure 31 show, however, that throughout the normal-flight range the size of tab tested is capable of bringing the aileron upfloating angle within the desired range (15° to 20°).

It should be noted that in this application both tabs are deflected the same amount in the same direction and the tab deflection (with respect to the aileron chord line) remains constant for a given setting of the flap regardless of aileron deflection. It is apparent that this is a highly unconventional application of a tab—the tab merely serves to bias the aileron floating angle and is not used to produce a moment about the aileron hinge opposing the aileron hinge moment, which is the normal use of tabs. The method presented in reference 8, together with the data of figure 31, provides a means of designing a lateral-control system having low stick forces and using the ailerons with the external-airfoil flap in the high-speed and high-lift settings.

In the intermediate range of flap settings (for which hinge moments were measured only on the tabbed aileron) an additional difficulty in connection with the use of the present ailerons became apparent. The data for the tabbed aileron with the flap deflected 10° (fig. 30 (c)) show that "hysteresis" appears in the variation of aileron hinge moment with deflection. This effect is attributed to the phenomenon of flap stalling: As the aileron moves away from the flap, the flow leaves the flap upper surface, relieving the aileron hinge moment and then, as the aileron returns, the flow is restored at a different deflection, producing the observed hysteresis. The appearance of the phenomenon with the tab neutral indicates that it would appear equally on an untabbed aileron although no tests were made of the untabbed ailerons with the flap in the intermediate angle range. The data in figure 30 (c) for the tab 0°, flap 10° down, indicate the range in which the hysteresis appears to be near 15° up aileron deflection, corresponding approximately to the aileron deflection at which the sharp rise of rolling moment took place (see fig. 18 (a), $\delta_f = 10°$) in the tests of the standard model. It is anticipated that this discontinuous action, which might affect the rolling moment as well as the stick force, would be very disconcerting to a pilot. Although no further investigation was undertaken at the time, it is possible that scale effects and the use of a gradually stalling airfoil section for the flap might tend to smooth out the discontinuity.

Certain immediate possibilities of overcoming the difficulty may deserve mention. Use of the flap in only the high-speed and maximum-lift settings with a rapid change between them should permit the pilot to avoid the range in which the hysteresis appears. On very large airplanes in which the ailerons might be power-driven and no aileron "feel" would reach the pilot's control, the aileron deflection would be susceptible of accurate control without reference to the stick forces. In this case, the hysteresis should not be an appreciable disadvantage. This consideration also suggests the use of an irreversible operating mechanism for smaller airplanes, in which case the hysteresis might be noticeable but should not tend to produce disconcerting movements of the airplane. Such an arrangement should also tend to suppress aileron flutter, some tendency to which was noticed in the tests when the aileron trailing edge closely approached the flap leading edge.

CONCLUDING REMARKS

The data obtained in the present investigation indicate the following generalizations. An N. A. C. A. 23012 airfoil equipped with a 0.30 c_w N. A. C. A. 23012 external-airfoil flap, like the similar combination with a 0.20 c_w flap, gave characteristics favorable to speed range, to low power requirements in flight at high lift coefficients, and to low flap-operating moments. The aerodynamic qualities of the combination make it especially suitable for the application of ailerons mounted on the trailing edge of the main airfoil, providing a means of lateral control consistent with the use of full-span external-airfoil flaps. This possibility gives the external-airfoil flap an advantage in speed-range capabilities over such flaps as the ordinary and simple split types, which, when used with ordinary ailerons, sacrifice part of their span for the provision of lateral control.

The results from the narrow-chord long-span ailerons here investigated indicated large rolling-moment coefficients at lift coefficients corresponding to flight conditions ranging from high speed to minimum speed. The adverse yawing moments tended to be somewhat less than those of ordinary ailerons giving the same rolling moment. In general, they agree with Munk's formula for induced yawing moment at low values of the rolling moment; as the rolling moment is increased, they tend to become more favorable.

Three definite difficulties to be anticipated in the application of the combination of ailerons with external-airfoil flaps are indicated. First, the ailerons are relatively weak in producing rolling moment when the wing is near the stalling angle of attack with the flap in the high-speed setting. Second, the variation of aileron hinge moment with angle of attack and flap setting is such as to cause relatively large stick forces in the high-speed range and to cause overbalance near the stall with the flap in the high-lift setting. Third, a discontinuity of hinge moment, and possibly of rolling moment, occurs as the ailerons are deflected with the flap in the intermediate-angle range. The investigation indicated that nose balances and Frise balances were ineffective in reducing the stick forces required for a given control effectiveness in the high-speed condition. The use of a tab to bias the aileron floating angle together with a differential aileron motion provides a means of obtaining reduced stick forces in the high-speed condition and of avoiding overbalance in the high-lift condition. Further research and application to experimental designs should serve to determine the importance of the anticipated difficulties in actual use and should establish more clearly the merit of the combination of ailerons and external-airfoil flaps for airplane-design application.

LANGLEY MEMORIAL AERONAUTICAL LABORATORY,
NATIONAL ADVISORY COMMITTEE FOR AERONAUTICS,
LANGLEY FIELD, VA., *March 12, 1937.*

APPENDIX

EFFECT OF JET BOUNDARIES AND ASPECT RATIO ON MEASURED ROLLING- AND YAWING-MOMENT COEFFICIENTS

As previously noted in the text, the use of standard airfoils for tests of airfoils with external-airfoil flaps in the 7- by 10-foot tunnel led to the use of geometric aspect ratios of 5.0 and 4.61 for the combinations tested in the present investigation. Although main airfoils of larger aspect ratio could have been constructed, considerations of model deflection, comparison of plain-airfoil test data, and economy dictated the method adopted. It was recognized, however, that the variation of lift-curve slope and of induced drag with aspect ratio would result in measured rolling- and yawing-moment coefficients not directly comparable with data from tests of airfoils of aspect ratio 6. Corrections based on present knowledge of induced-flow phenomena were therefore devised to permit such comparisons.

CORRECTION OF ROLLING-MOMENT COEFFICIENT

Pearson (reference 9) has carried out a general solution of the lift distribution for wings with ailerons, from which he obtained an equation for the rolling moment

$$L=2qb^2(k\delta)F_2$$

where q is the dynamic pressure.

b, the wing span.

δ, the aileron deflection.

and F_2, a factor (presented in chart form) depending on plan form, aspect ratio, and ratio of total aileron span to total wing span.

The factor k is a section characteristic for an airfoil with a flap or aileron and is equal to the change of angle of attack equivalent to a given aileron deflection divided by the given aileron deflection. This value may also be expressed as the ratio of the section lift-curve slopes $\frac{dc_l}{d\delta}\Big/\frac{dc_l}{d\alpha_0}$. (The lower-case letters represent airfoil section characteristics; thus c_l is the section lift coefficient, C_L the wing lift coefficient, and C_l the wing rolling-moment coefficient.) The equation thus represents the total rolling moment as the rolling moment to be expected from the change of airfoil section when the aileron is deflected, reduced by a factor to allow for the induced rolling moment resulting from wing plan-form effect.

Computing the rolling-moment coefficient from Pearson's formula, the equation

$$C_l=2A(k\delta)F_2$$

is obtained, where A is the aspect ratio. By the use of this relation and the designation of the values appropriate to two different aspect ratios as subscript A_1 and subscript A_2, it is possible to obtain a factor for the rolling-moment coefficient measured for a wing of $A=A_1$ to express the rolling-moment coefficient for a wing of $A=A_2$ under otherwise identical conditions, as follows:

$$C_{l_{A_2}}=C_{l_{A_1}}\times\frac{A_2F_{2_{A_2}}}{A_1F_{2_{A_1}}}\times\frac{(k\delta)_{A_2}}{(k\delta)_{A_1}}$$

But it has been pointed out that k depends only on the airfoil section characteristics and therefore does not change with A. Thus, at a given value of aileron deflection

$$(k\delta)_{A_1}=(k\delta)_{A_2}$$

and

$$C_{l_{A_2}}=C_{l_{A_1}}\times\frac{A_2F_{2_{A_2}}}{A_1F_{2_{A_1}}}$$

Factors for the particular values of A in question were calculated from the formula using values of F_2 obtained from the reference and cross-plotted against A. The final correction formulas used were as follows: for the airfoil with the 0.20 c_w flap and 0.12 c_w ailerons

$$C_{l_{A=6}}=1.08\ C_{l_m}$$

and for the airfoil with the 0.30 c_w flap and 0.13 c_w ailerons

$$C_{l_{A=5}}=1.12\ C_{l_m}$$

The subscript m signifies the value measured in the wind tunnel.

The error produced by the jet boundaries in the measured rolling-moment coefficient has been estimated from the formula of reference 10; it amounts to less than 1 percent of the measured coefficient and is conservative for prediction of flight rolling moments. This correction is consequently considered negligible.

CORRECTION OF YAWING-MOMENT COEFFICIENT

Munk (reference 11) expressed the induced yawing-moment coefficient of a wing with ailerons having equal up-and-down deflections as

$$C_{n_i}=-\frac{3C_l'}{\pi A}\times C_L$$

(It should be noted that there is a disagreement of sign with the original published formula; the sign has been changed to agree with the standard N. A. C. A. sign convention for moments.) This formula may be used to compute the change of C_{n_i} resulting from a given change of aspect ratio; this computation is directly

analogous to the well-known one for the change of induced drag coefficient with aspect ratio.

The jet-boundary effect on the induced yawing-moment coefficient results from the change in local wind direction (α_{i_t}, the standard angle-of-attack correction) with respect to the model resulting from the limited extent of the air stream. Through this effect the rolling-moment vector is rotated through the angle α_{i_t}, resulting in a component in the yawing-moment direction

$$C_{n_{i_t}}=\alpha_{i_t}\times C_l$$

The jet-boundary correction factor for the 7- by 10-foot tunnel is equal to 0.165 in the formula $\alpha_{i_t}=\delta_\alpha\frac{S}{C}C_L$. (See reference 2.)

The total induced yawing-moment coefficient of a model in the 7- by 10-foot tunnel may then be expressed as

$$C_{n_i}=-\left[\frac{3C_{l_m}}{\pi A_m}\times C_L\right]-\left[0.165\frac{S}{C}\times C_{l_m}\times C_L\right]$$

or

$$C_{n_i}=-C_{l_m}\times C_L\left(\frac{3}{\pi A_m}+0.165\frac{S}{C}\right)$$

The profile yawing-moment coefficient is then

$$C_{n_0}=C_{n_m}+C_{l_m}\times C_L\left(\frac{3}{\pi A_m}+0.165\frac{S}{C}\right)$$

For $A=6$

$$C_{n_i}=-C_{l_{A=6}}\times C_L\times\frac{3}{6\pi}$$

but

$$C_{l_{A=6}}=\beta C_{l_m}$$

where

$$\beta=\frac{A_2F_{2_{A_2}}}{A_1F_{2_{A_1}}}$$

the rolling-moment coefficient correction factor previously developed. Thus for $A=6$

$$C_{n_{i_{A=6}}}=-C_{l_m}\times C_L\times\frac{3\beta}{6\pi}$$

and since

$$C_{n_{A=6}}=C_{n_0}-C_{n_{i_{A=6}}}$$

$$C_{n_{A=6}}=C_{n_m}+C_{l_m}\times C_L\left(0.165\frac{S}{C}+\frac{3}{\pi A_m}-\frac{3\beta}{6\pi}\right)$$

Inserting appropriate values the following correction formulas were derived. For the airfoil with the 0.20 c_w flap and 0.12 c_w ailerons

$$C_{n_{A=6}}=C_{n_m}+0.0309\times C_{l_m}\times C_L$$

For the airfoil with the 0.30 c_w flap and 0.13 c_w ailerons

$$C_{n_{A=6}}=C_{n_m}+0.0418\times C_{l_m}\times C_L$$

In conclusion it should be noted that the foregoing corrections, which have been applied to all the rolling- and yawing-moment coefficients presented in this report, include the standard assumptions of induced flow and jet-boundary correction theory. They should therefore be regarded as first approximations rather than as rigorous expressions of the corrections that should be applied.

REFERENCES

1. Soulé, H. A., and McAvoy, W. H.: Flight Investigation of Lateral Control Devices for Use with Full-Span Flaps. T. R. No. 517, N. A. C. A., 1935.
2. Platt, Robert C.: Aerodynamic Characteristics of Wings with Cambered External-Airfoil Flaps, Including Lateral Control with a Full-Span Flap. T. R. No. 541, N. A. C. A., 1935.
3. Shortal, Joseph A.: Wind-Tunnel and Flight Tests of Slot-Lip Ailerons. T. R. No. 602, N. A. C. A., 1937.
4. Platt, Robert C., and Abbott, Ira H.: Aerodynamic Characteristics of N. A. C. A. 23012 and 23021 Airfoils with 20-Percent-Chord External-Airfoil Flaps of N. A. C. A. 23012 Section. T. R. No. 573, N. A. C. A., 1936.
5. Harris, Thomas A.: The 7 by 10 Foot Wind Tunnel of the National Advisory Committee for Aeronautics. T. R. No. 412, N. A. C. A., 1931.
6. Platt, Robert C.: Turbulence Factors of N. A. C. A. Wind Tunnels as Determined by Sphere Tests. T. R. No. 558, N. A. C. A., 1936.
7. Jacobs, Eastman N., and Sherman, Albert.: Airfoil Section Characteristics as Affected by Variations of the Reynolds Number. T. R. No. 586, N. A. C. A., 1937.
8. Jones, Robert T., and Nerken, Albert I.: The Reduction of Aileron Operating Force by Differential Linkage. T. N. No. 586, N. A. C. A., 1936.
9. Pearson, H. A.: Theoretical Span Loading and Moments of Tapered Wings Produced by Aileron Deflection. T. N. No. 589, N. A. C. A., 1937.
10. Biot, M.: Korrecktur für das Quermoment von Tragflügeln bei Untersuchungen im Windkanal mit Kreisquerschnitt. Z. F. M., 24. Jahrgang, Nr. 15, 14. August 1933, S. 410–411.
11. Munk, Max M.: A New Relation between the Induced Yawing Moment and the Rolling Moment of an Airfoil in Straight Motion. T. R. No. 197, N. A. C. A., 1924.

REPORT No. 604

PRESSURE-DISTRIBUTION MEASUREMENTS AT LARGE ANGLES OF PITCH ON FINS OF DIFFERENT SPAN-CHORD RATIO ON A 1/40-SCALE MODEL OF THE U. S. AIRSHIP "AKRON"

By James G. McHugh

SUMMARY

Pressure-distribution measurements on a 1/40-scale model of the U. S. airship "Akron" were conducted in the N. A. C. A. 20-foot wind tunnel.

The measurements were made on the starboard fin of each of four sets of horizontal tail surfaces, all of approximately the same area but differing in span-chord ratio, for five angles of pitch varying from 11.6° to 34°, for four elevator angles, and at air speeds ranging from 56 to 77 miles per hour. Pressures were also measured at 13 stations along the rear half of the port side of the hull at one elevator setting for the same five angles of pitch and at an air speed of approximately 91 miles per hour.

The maximum pressures recorded on the leading edge of the fins, for pitch angles up to 20°, were approximately the same for all fins tested regardless of span-chord ratio. At angles of pitch above 20° the maximum fin pressures increased with decreasing span-chord ratio. A negative pressure of 13 times the dynamic pressure of the undisturbed air stream was measured on the fin of lowest span-chord ratio at a pitch angle of 34°. The pitching moment contributed by the after portion of the hull increased with pitch until, at the maximum angles tested, it was approximately equal to the moment contributed by the fins. The normal force on the fin and the moment of forces about the fin root were determined. The results indicate that, ignoring the effect on drag, it would be advantageous from structural considerations to use a fin of lower span-chord ratio than that used on the "Akron."

INTRODUCTION

The task of obtaining load measurements on a full-scale airship in free flight is difficult and, consequently, only a small amount of reliable flight data on airship loads is available. Many wind-tunnel tests of scale models have been made but, since the scale of an airship model for wind-tunnel tests must of necessity be very small, the results obtained are in some cases of questionable value.

The results of previous pressure-distribution measurements on the hull and fins of a relatively large (1/40-scale) model of the U. S. airship *Akron* fitted with fins of the type used on the full-scale airship and tested at angles of pitch from 0° to 18° are presented in reference 1. Although such a range of angles of pitch would not be exceeded under normal operating conditions, it appears possible that much larger angles of pitch might be encountered in severe gusts. No

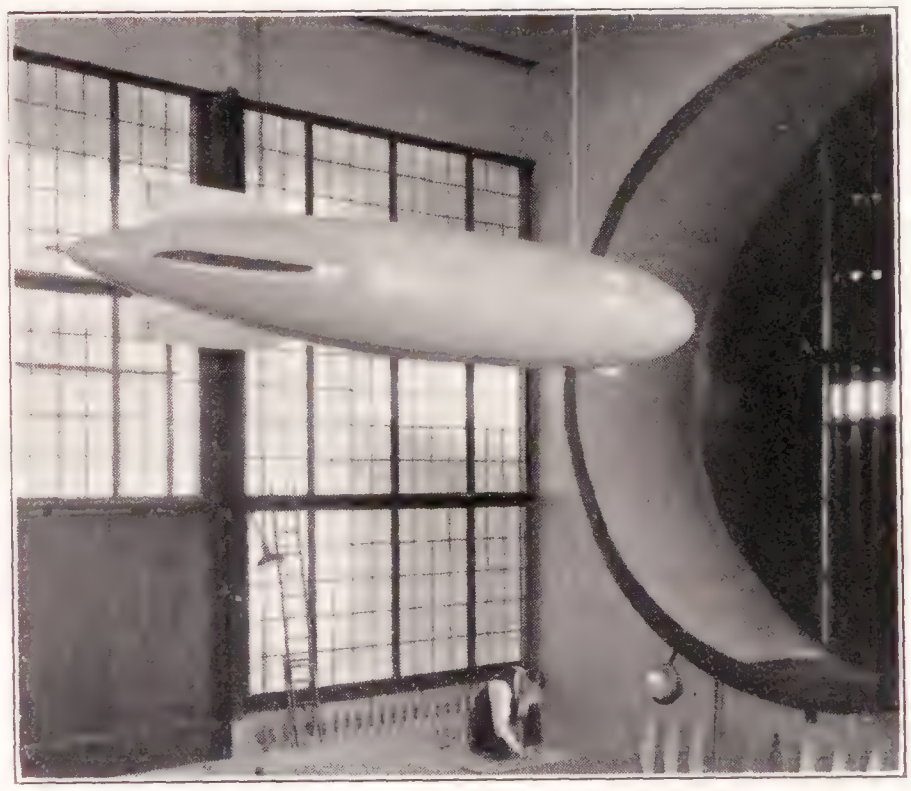

FIGURE. 1—The 1/40-scale model of the *Akron* mounted in the 20-foot wind tunnel.

information concerning the magnitude of fin loads and pressures encountered at larger pitch angles has been available, but the results of reference 1 indicated that a high concentration of load near the tip would be obtained.

At the request of the Bureau of Aeronautics, Navy Department, the investigation herein reported was made to obtain information concerning loads at high angles of pitch and to determine good fin proportions. The 1/40-scale airship model used in the investigation reported in reference 1 was tested through a range of pitch angles from 12° to 34° with the object of determining: (1) The effect of span-chord ratio on the aerodynamic forces acting on the fins of airships; (2) the effect of slots between the fin and the hull on pressure distribution over the fin; and (3) the effect of changes

in fin span-chord ratio on pressure distribution over the hull.

It is believed that the relatively large scale of the model here used, the high pitch angles included, and the fact that simultaneous measurements of pressure were made on both surfaces of an entire fin greatly enhance the value of these results.

APPARATUS AND TESTS

The airship model used in these tests is described in detail in reference 1. The method of mounting it in the wind tunnel is shown in figure 1 and is essentially as described in reference 2, with the exception that for these tests the model was suspended 3½ feet above the center line of the tunnel. The tests were made in the N. A. C. A. 20-foot wind tunnel (reference 3).

In order to determine the effect of different fins on the pressure distribution over the rear part of the hull, 162 pressure orifices distributed among 13 stations on the port side of the model were used. The location of the stations and the distribution of the orifices around the hull are shown in figure 2. Principal dimensions of the hull and fins are given in table I.

The fins were of laminated wood. Pressure orifices were installed by splitting the fins at their plane of symmetry, drilling small holes at the point where pressures were to be measured, inserting short lengths of 1/32-inch (inside diameter) copper tubing therein until they protruded a minute distance beyond the outer surface of the fin, and then, after alining the free ends of the copper tubes in such manner that they protruded through the inboard edge, gluing the two halves of the fin together. The ends of the copper tubing projecting through the fin surfaces were ground flush, thereby forming a smooth pressure orifice.

Four sets of horizontal tail surfaces, designated Mark II fin, fin 3, fin 3–A, and fin 4 (figs. 3 to 7), all of approximately the same area but of different span-chord ratios, were tested. The Mark II fin was the type used on the *Akron*. Fins 3 and 4 were basically similar but their span-chord ratios were changed by cutting areas off the inboard edge and adding an equivalent area at the forward part of the fin in such manner that the position of the elevator axis, the edge shape, and the radius of the tip plan form remained constant for all fins. Fin 3–A was similar to fin 3 except for a change in the plan form of the forward part of the fin. An additional type of fin was obtained by altering the Mark II fin so as to form a slot between the inboard edge of the fin and the hull of the ship. Two slot widths (⅜ inch and ¾ inch) were used. The longitudinal location of the slot on the fin, which corresponded to a location between frame 0 and frame 17. 5 of the full-scale airship, is shown by dotted lines in figure 3. Figure 8 shows the fin with slot mounted for tests.

Pressure orifices were installed in pairs on fins Mark II, 3, and 4. One orifice of each pair opened on the upper surface and the other, on the lower surface of the fin. In the case of fin 3–A, pressure orifices were installed only on the upper surface. On all the

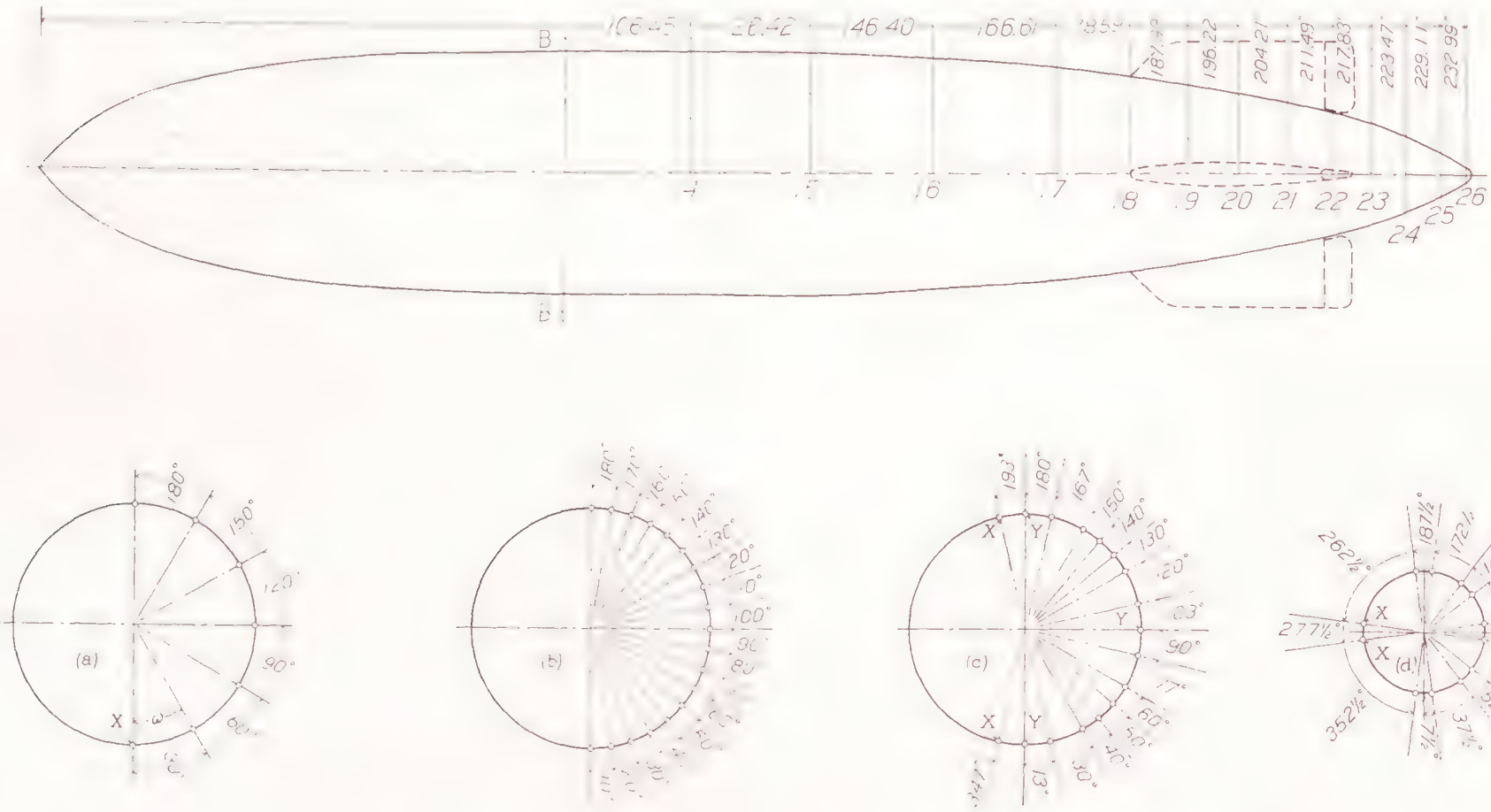

(a) Typical sections in direction B–B at stations 14 and 16 showing radial locations of orifices in hull. Orifice marked X at station 16 only.

(b) Typical sections in direction B–B at stations 15 and 17 showing radial locations of orifices in hull.

(c) Typical sections in direction B–B at stations 18, 19, 20, and 21 showing radial locations of orifices in hull. Two orifices marked X at stations 18, 20, and 21 only. Three orifices marked Y at station 18 only.

(d) Typical sections in direction B–B at stations 22, 23, 24, 25, and 26 showing radial locations of orifices in hull. Two orifices marked X at stations 22 and 23 only.

FIGURE 2.—Locations of orifices for the pressure measurement on a 1/40-scale model of the *Akron*.

fins the pressure orifices were located to facilitate fairing of the pressure diagram; the locations are shown in figures 3 to 6.

Two multiple-tube photographic recording manometers, each composed of a circular bank of 100 glass tubes, were mounted on pivots inside the model and were free to swing about a horizontal axis at right angles to the longitudinal axis of the ship, thus allowing the manometers to remain level for any angle of pitch. The manometers were electrically operated by remote control from the test chamber floor. Photostat paper was automatically drawn around the outer circumference of the bank of tubes, and exposure was made by flashing a lamp at the center of the bank of tubes.

Two simultaneous records, one for each manometer, gave for one pitch angle a complete diagram of the pressure distribution over both surfaces of a fin. Two sets of pressure measurements were made at each pitch angle and an average of the two records was used in plotting the pressure diagram. In order to provide a reference line on the pressure records, six of the glass tubes spaced equidistantly around the manometer were connected to the reference pressure, which for these tests was the static pressure in the test chamber.

With the exception of the Mark II fin, which was tested with and without elevator counterbalances, all fins were tested without counterbalances. In all cases the control car was installed on the hull of the model. All pressure-distribution measurements were made on the starboard fin and for all fins tested the vertical fins were of the Mark II type with rudder neutral and the airship at 0° yaw.

The tests herein reported are listed in the following table:

PRESSURE MEASUREMENTS ON HULL

Fin	Elevator angle (deg.)	Nominal pitch angle (deg.)	Approximate velocity (m. p. h.)
Mark II	20	12, 18, 24, 30, 36	91
3	20	12, 18, 24, 30, 36	91
4	20	12, 18, 24, 30, 36	91

PRESSURE MEASUREMENTS ON FINS

[No pressure-distribution measurements were taken on the elevators]

Fin	Elevator angle (deg.)	Nominal pitch angle (deg.)	Approximate velocity (m. p. h.)
Mark II [1]	0, 10, 20	12, 18, 24, 30, 36	69
Mark II	20	18, 30	77
Mark II, ⅜-inch slot	20	12, 18, 24, 30	77
Mark II, ¾-inch slot	20	12, 18, 24, 30	77
3	−15, 0, 10, 20	12, 18, 24, 30, 36	74
3-A	−15, 0, 10, 20	12, 18, 24, 30, 36	56
4	−15, 0, 10, 20	12, 18, 24, 30, 36	56

[1] With counterbalances.

ACCURACY

The sources of error that affect the pressure-distribution measurements are:

(1) Errors in measurements of the manometer deflection.

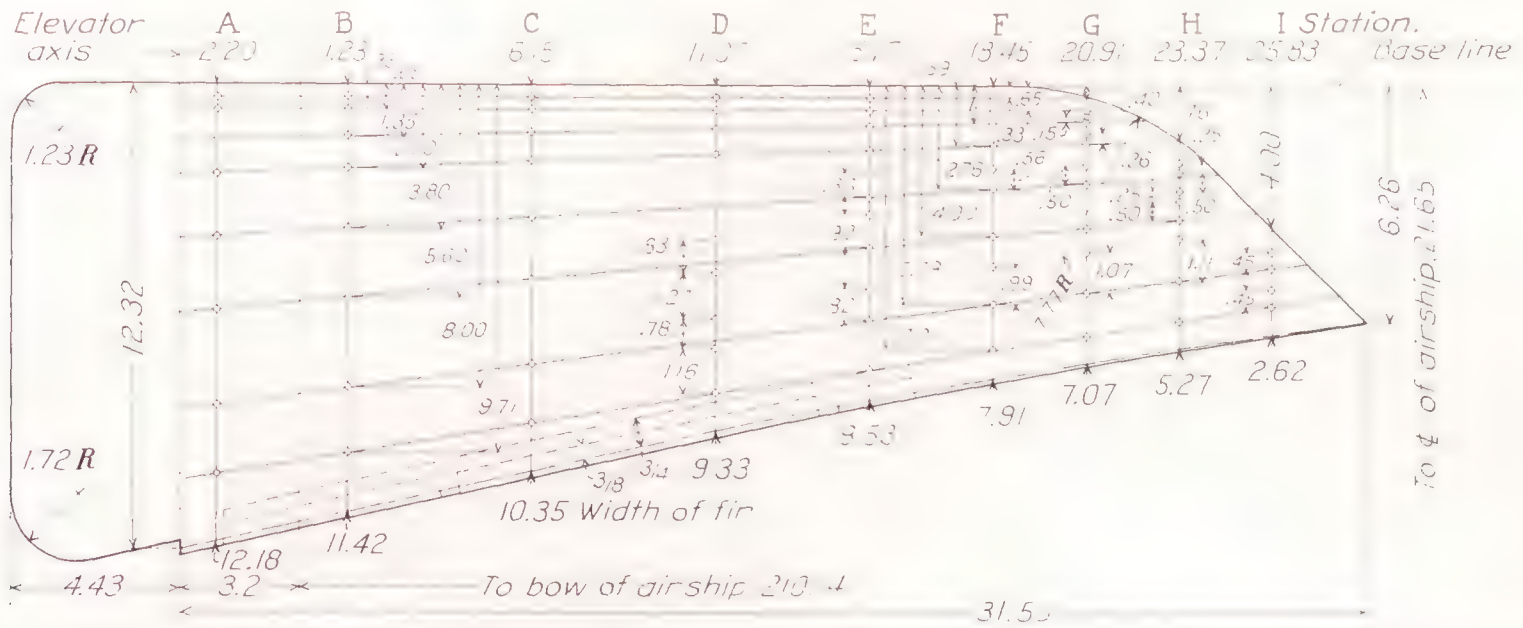

FIGURE 3.—Dimensions and orifice locations. Mark II fin; 1/40-scale model of the *Akron;* slot locations are shown in dotted lines; all dimensions given in inches.

(2) Oscillation of the manometers.

(3) Fluctuation in velocity and direction of the air stream.

(4) Shrinkage of the photostat paper.

The error due to (1) is considered to be small. The errors due to (1), (2), and (3) are of the order of ±2 percent for low pitch angles. At high pitch angles the error is considerably greater, as shown by comparison of check tests. The errors from (4) were found, in general, to be less than 1 percent for all cases.

RESULTS

The great amount of data derived from these tests makes it impractical to present them in their entirety. Consequently, only the portion required for the final analysis of the results is presented.

Final results of the pressure measurements are presented in terms of dynamic pressure q of the air stream. All pressures are referred to the test-chamber pressure, and no correction has been made for the difference between the static pressure in the air stream and the reference pressure. Application of this correction would have no effect on the integrated values of normal force on the fins. Pressures were measured on both the upper and lower surfaces of the fins (except for fin

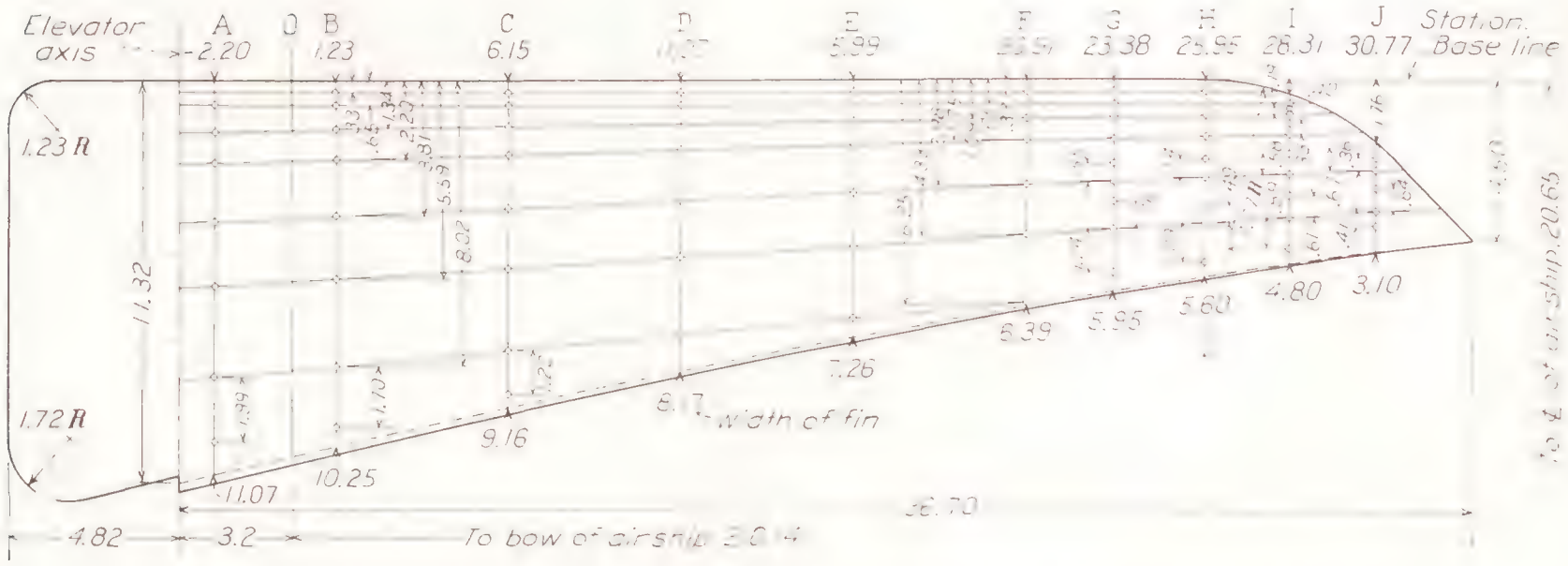

FIGURE 4.—Dimensions and orifice locations. Fin 3; 1/40-scale model of the *Akron;* all dimensions given in inches.

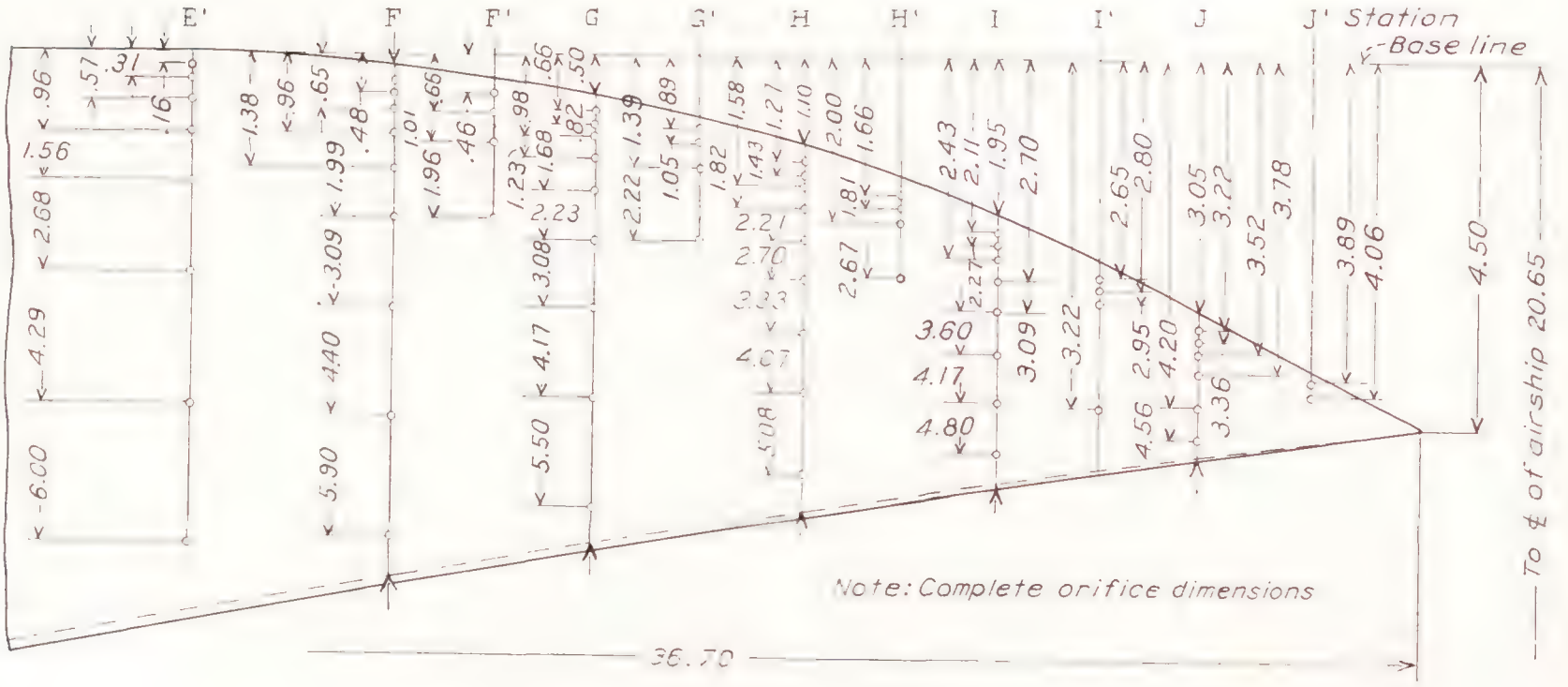

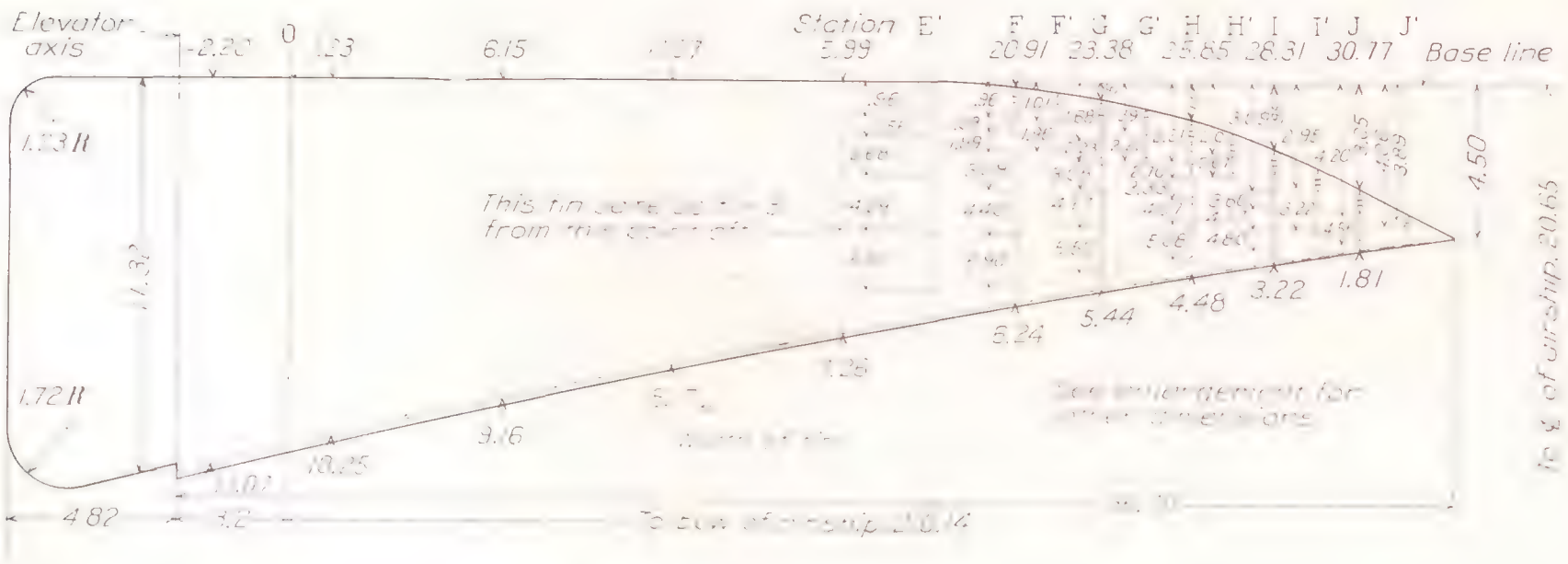

FIGURE 5.—Dimensions and orifice locations. Fin 3-A; 1/40-scale model of the *Akron;* all dimensions given in inches.

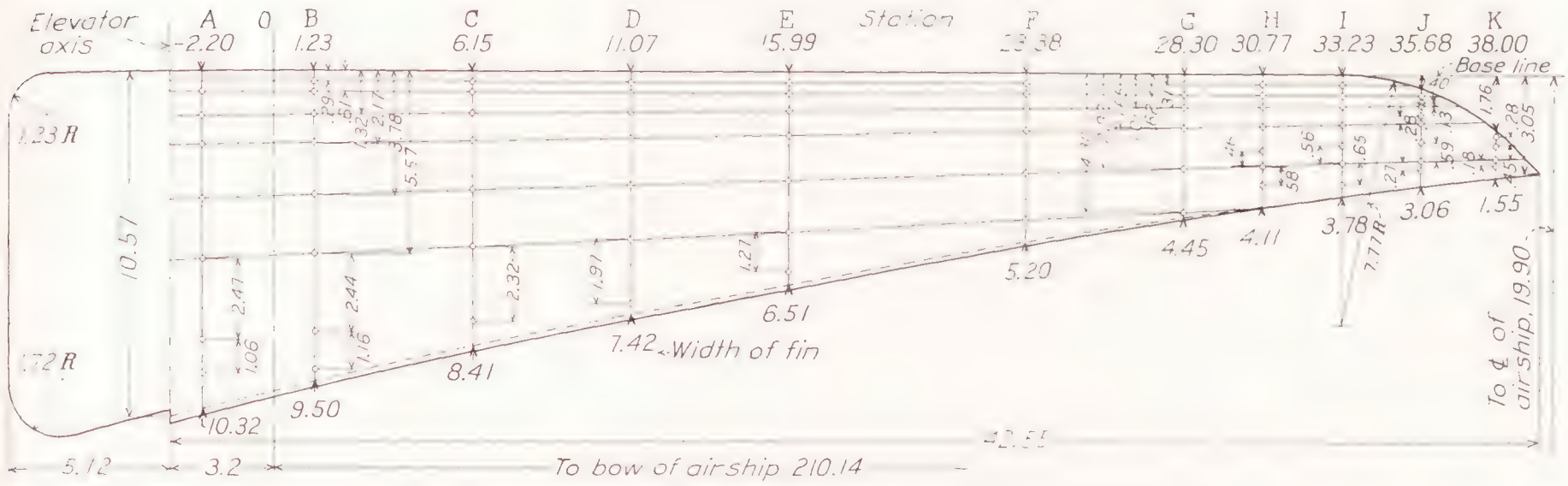

FIGURE 6.—Dimensions and orifice locations. Fin 4; 1/40-scale model of the *Akron;* all dimensions given in inches.

FIGURE 7.—The fins on which pressure-distribution measurements were made.

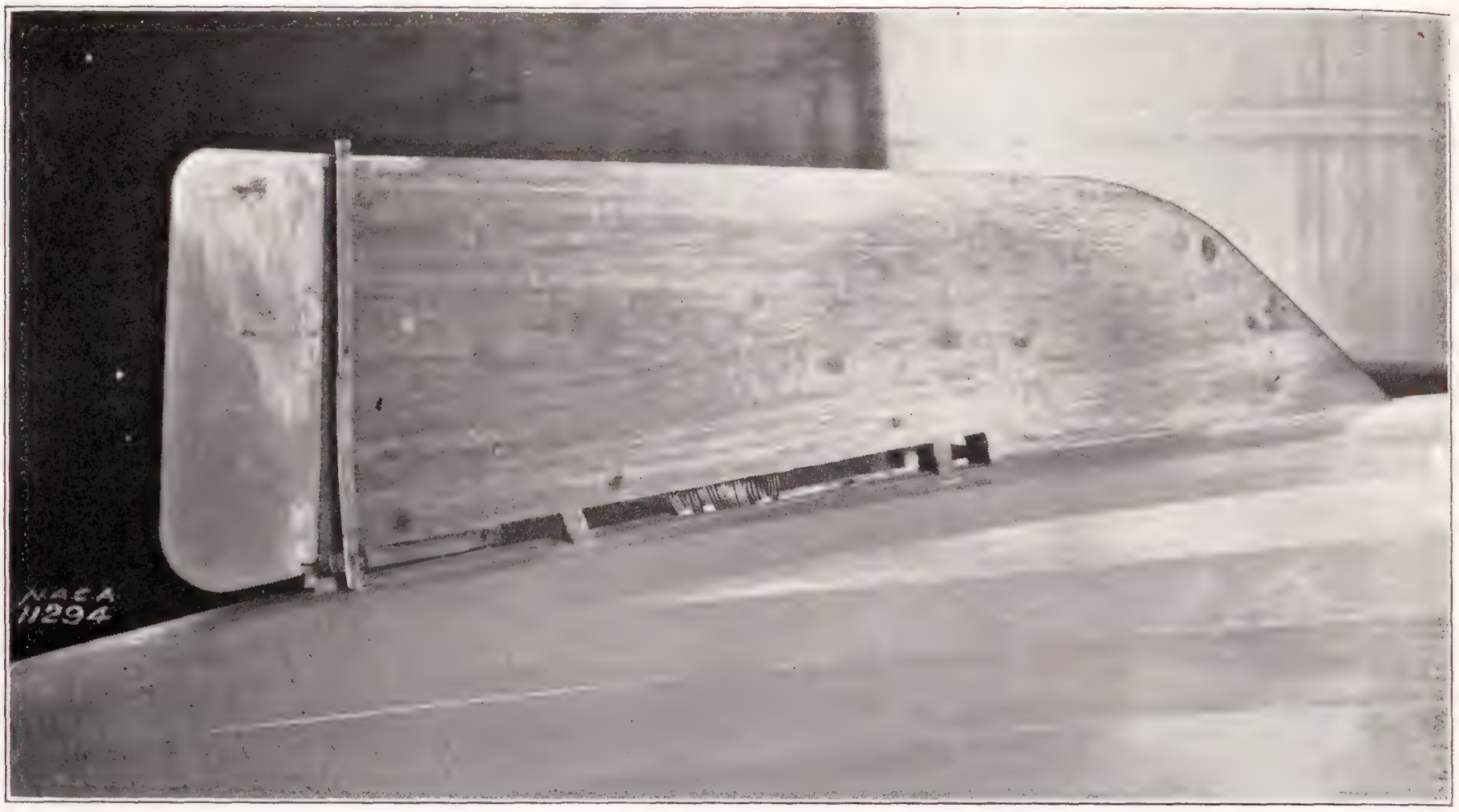

FIGURE 8.—Mark II fin with ¾-inch slot, mounted for tests.

3–A) and the effect of the static-pressure correction would be to shift the position of the pressure diagram without causing any change in the included area. The influence of the static-pressure correction on the point pressures would have been small. A static-pressure survey of the tunnel, made in the absence of the model, showed that the maximum difference between the static pressure in the test chamber and the static

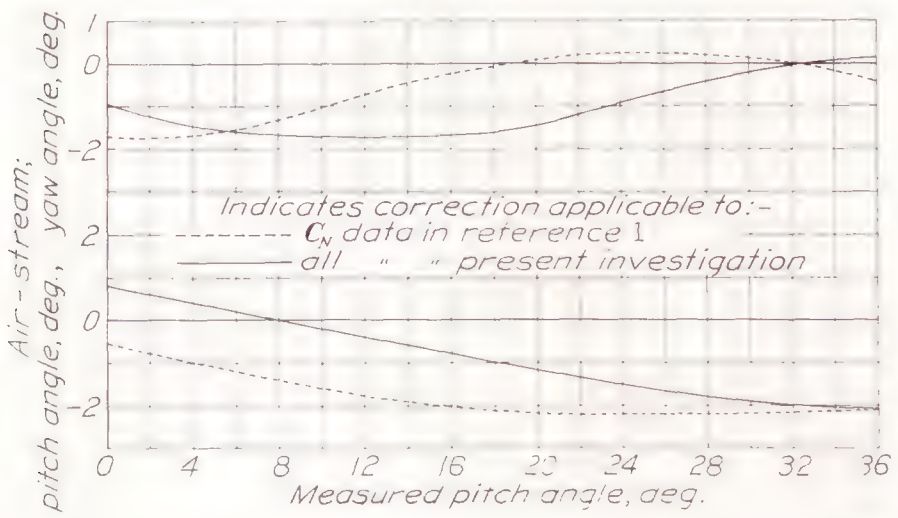

FIGURE 9.—Variation of air-stream angle in region of starboard fin with measured pitch of model.

pressure in the region of the air stream through which pressure measurements were made was of the order of 0.005 q.

A preliminary comparison of the results of these tests with those reported in reference 1 showed poor agreement. Since the only essential difference in the set-ups was the location of the model above the center line of the air stream, 3½ feet for the present tests and 1 foot for the tests reported in reference 1, the lack of agreement was thought to be due to the fact that the flow characteristics of the air stream were different at the two model locations. A stream-angle survey of the air stream confirmed this belief. Figure 9 shows the variation with pitch of the model of the stream angles at the tail of the model. The results have been corrected to take account of the pitch angle in the air stream. No correction has been made to take account of the yaw angle in the air stream.

It is desired to call attention at this time to the fact that the pressures on the upper surfaces of the fins were much greater than had been anticipated. Consequently, at high pitch angles, for the first of the tests made, some of the negative pressures near the tip of the fin were so great that the liquid in the manometer tubes rose above the height of the photostat paper on which the magnitude of the pressures was to be recorded, and consequently no determination could be made of the maximum pressures. In cases where only a few pressures were indeterminate, judgment was used in fairing in the pressure diagrams. In cases where several pressures were indeterminate, the tests in question were repeated at a lower air speed. Eventually all efforts to obtain tests at a high air speed were abandoned and, during the latter part of the program, tests were made at an air speed low enough to insure that all pressures obtained would be recorded on the photostat paper.

In certain cases at high pitch angles where check readings were taken at intervals of approximately 1

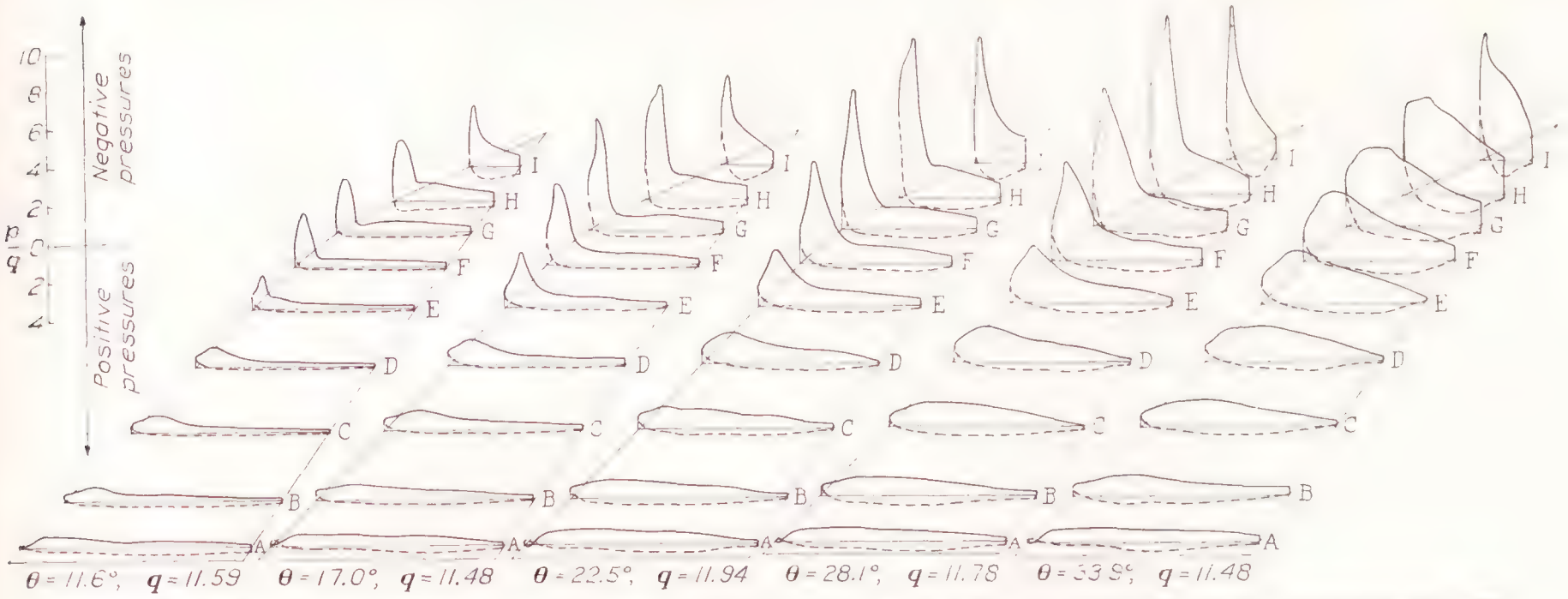

FIGURE 10.- Pressure distribution on horizontal fin of the 1/40-scale model of the *Akron* at various pitch angles. Mark II fin (with counterbalances); $\delta_e = 20°$.

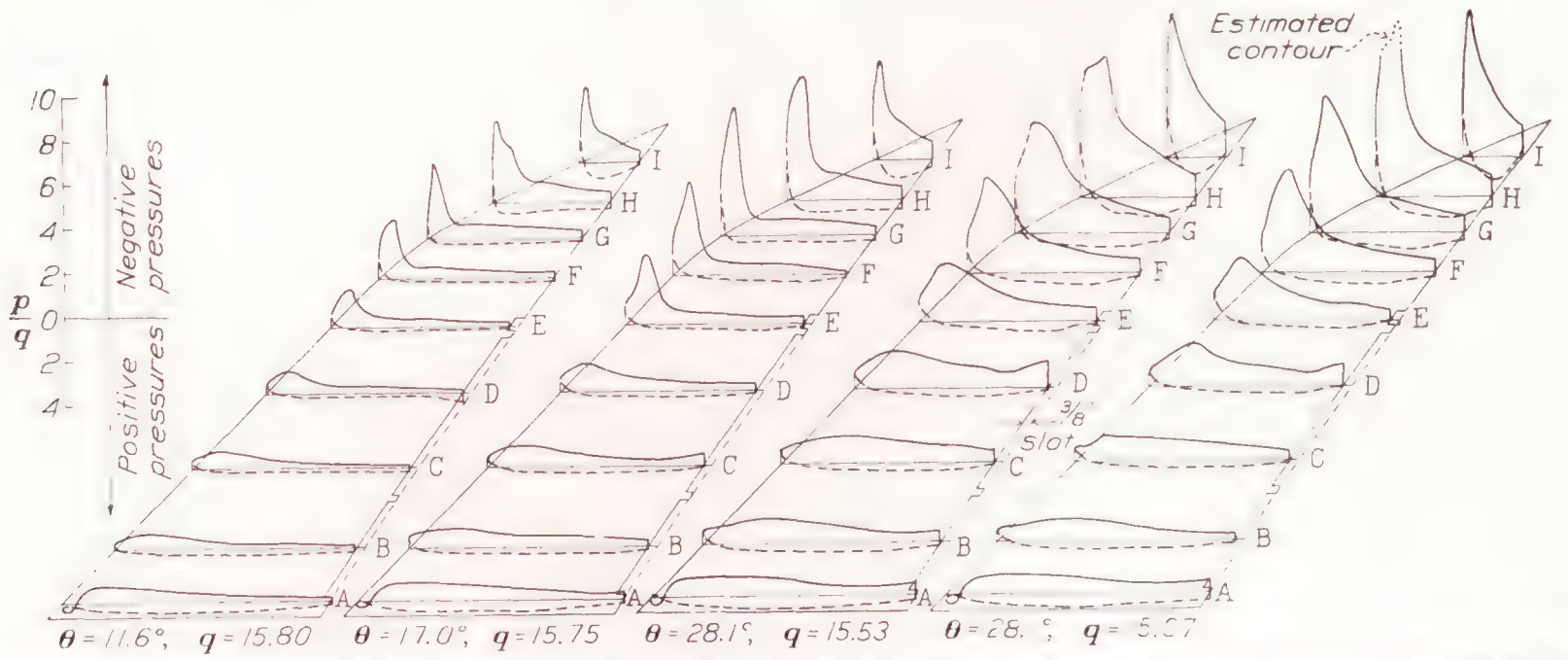

FIGURE 11.- Pressure distribution on horizontal fin of the 1/40-scale model of the *Akron* at various pitch angles. Mark II fin (counterbalances removed); 3/8-inch slot; $\delta_e = 20°$.

minute, a great difference in pressures was recorded. This difference indicated that at extremely high pitch angles (θ=22° to 34°) the forces on the model were fluctuating rapidly, probably owing to instability of the air flow. At times the model was observed to undergo violent spasmodic quivers. This motion was probably due in part to the fluctuation of aerodynamic forces on the tail of the model

Definitions of the terms used in this report follow:

θ, pitch angle.

δ_e, elevator angle.

ω, hull orifice location, measured from keel in degrees.

C_N, $\dfrac{\text{normal force on fins}}{qS}$

q, dynamic pressure ($1/2\ \rho V^2$).

ρ, mass density of the air.

V, air speed.

S, area of fin.

Fin span-chord ratio, $\dfrac{(\text{maximum span of fin})^2}{\text{area of fin}}$

p, observed point pressure.

PRESSURE-DISTRIBUTION MEASUREMENTS ON THE FINS

The magnitude of the maximum pressures and the manner in which the pressure varies over all the fins are illustrated in figures 10 to 15. Large-scale pressure plots of p/q against fin width were made and the pressure diagrams thus formed were graphically integrated to determine the normal force per unit length at each station along the fin. Similarly, the spanwise location of the center of pressure at each longitudinal station on the fin was determined. The values of the normal force per unit length of fin and the moment of that force about the fin root are given in tables II to VII for each station on the fin at which pressure-distribution measurements were made. In order to show the variation of normal force on the fin, there are included, for the various fins tested, typical plots of normal force per unit length against length of fin for the condition of $\delta_e = 20°$ (figs. 16 to 22). Also included, for the same fins and elevator positions, are charts showing the variation along the fin chord of the moment of the forces on the fin about the fin root (figs. 23 to 27).

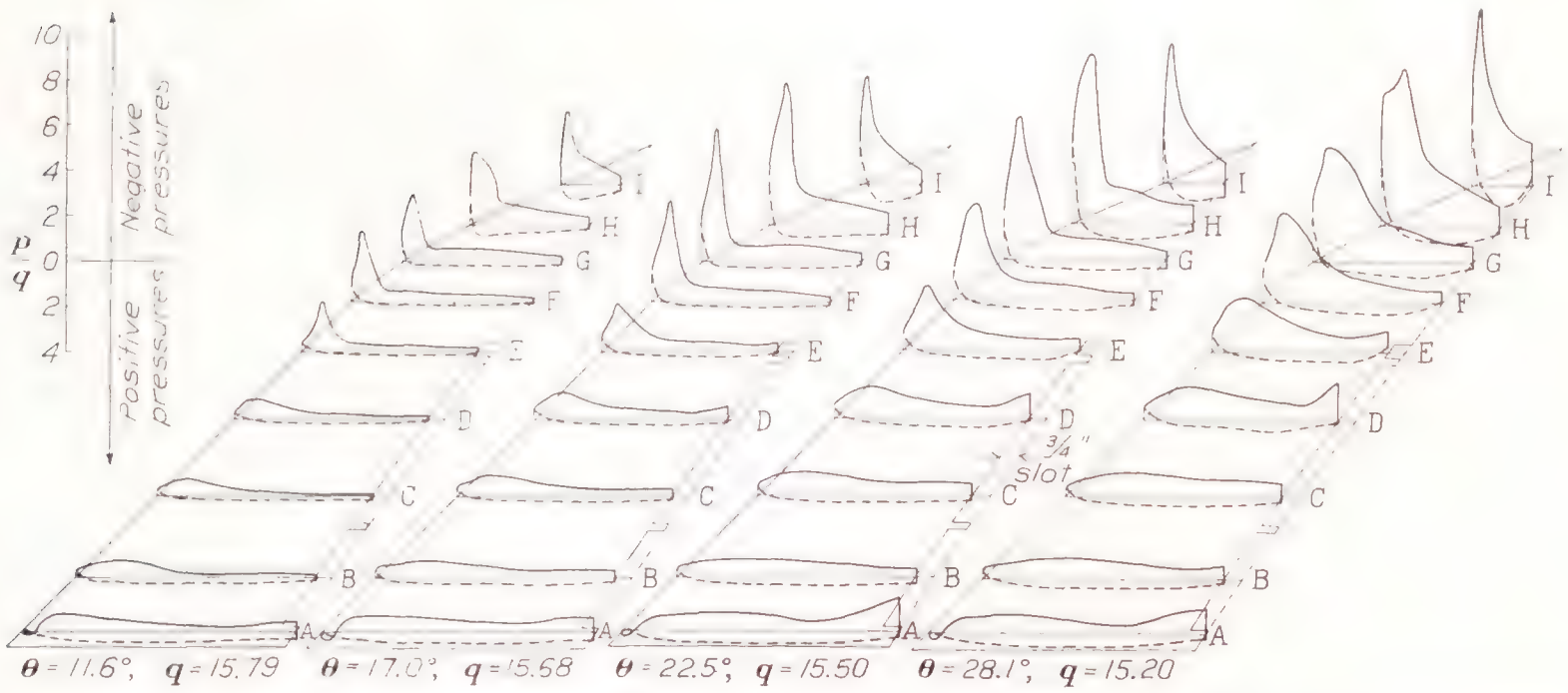

FIGURE 12.—Pressure distribution on horizontal fin of the 1/40-scale model of the *Akron* at various pitch angles. Mark II fin (counterbalances removed); 3/4-inch slot; $\delta_e = 20°$.

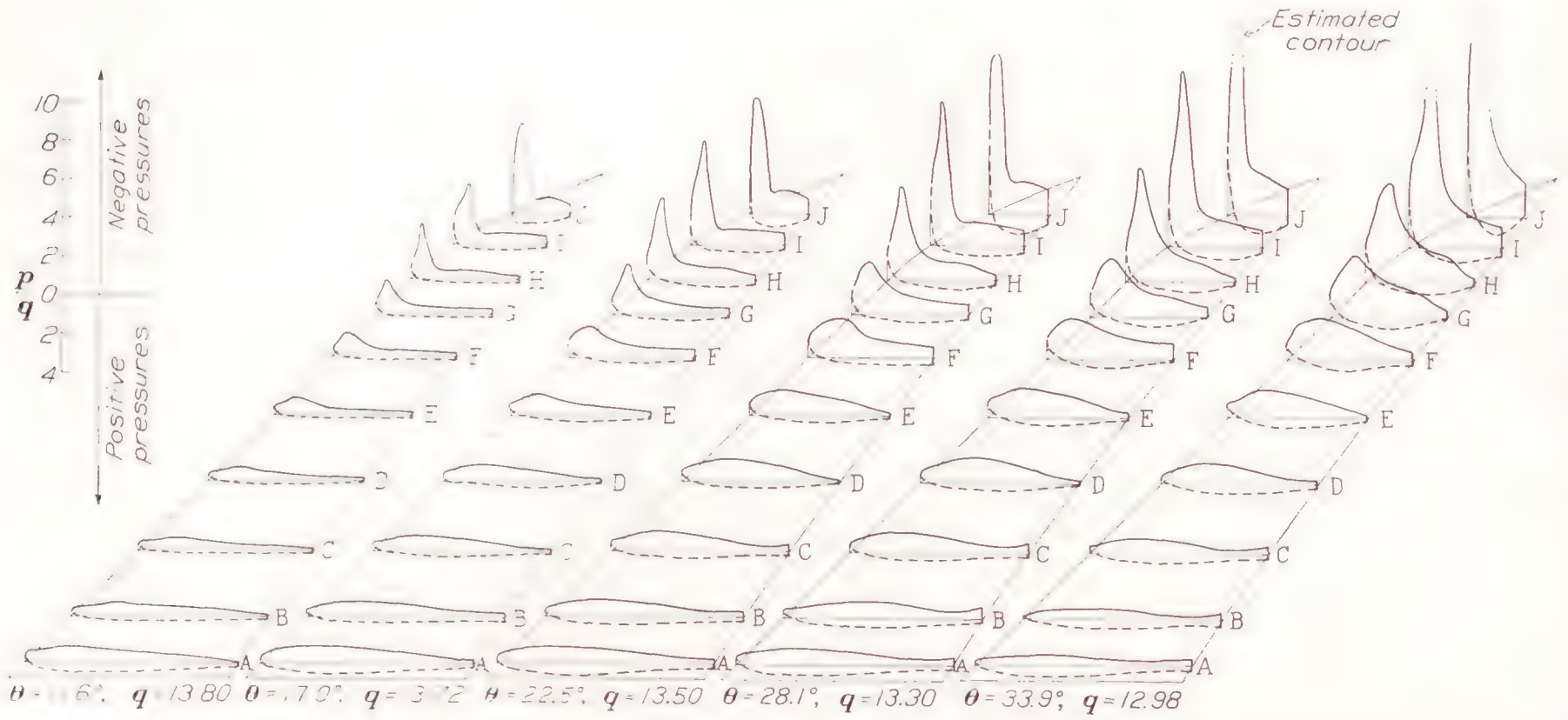

FIGURE 13.—Pressure distribution on horizontal fin of the 1/40-scale model of the *Akron* at various pitch angles. Fin 3; $\delta_e = 20°$.

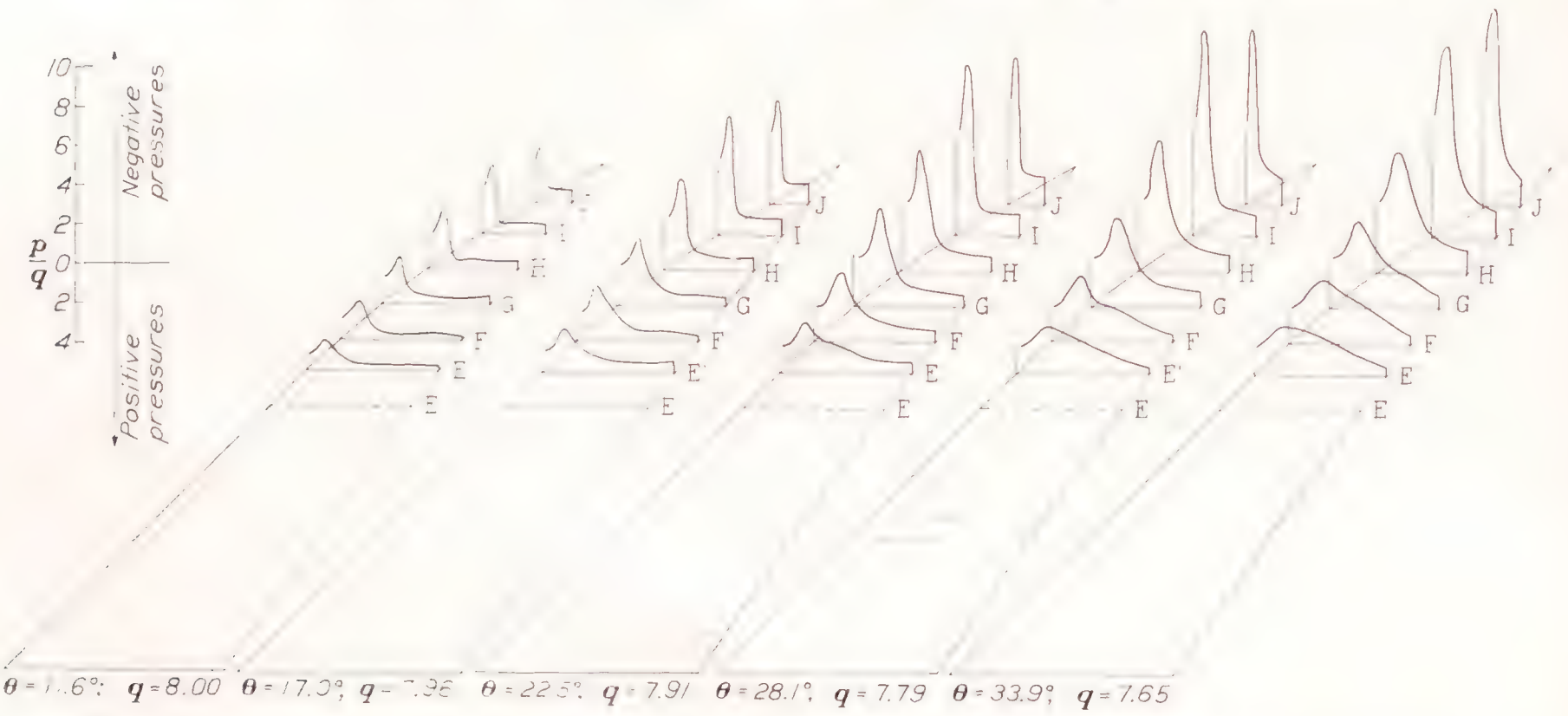

FIGURE 14.—Pressure distribution on upper surface of horizontal fin of the 1/40-scale model of the *Akron* at various pitch angles. Fin 3–A; $\delta_e = 20°$.

Curves showing the variation of normal-force coefficient with pitch angle for various elevator settings are given for the three types of fin tested in figures 28, 29, and 30. Figure 28 also compares the results of these tests of the Mark II fin with those reported in reference 1.

The chordwise location of the center of pressure on the fin was determined from the plots of normal force per unit length against fin length. Values of (normal force)/q and the location of the center of pressure of fin forces are presented in table VIII.

the projected distance of that point on the horizontal radius of the section. The area of the pressure diagram thus formed gave the transverse force per unit length at the particular station in question.

The integrated values of f from station 14 aft were plotted against distance from the bow of the model. The effect at six angles of pitch of different fins on the transverse force on the hull is shown in figures 34, 35, and 36. There are tabulated in table IX: (1) the total transverse force over the rear portion of the hull, which was obtained from graphical integration of the

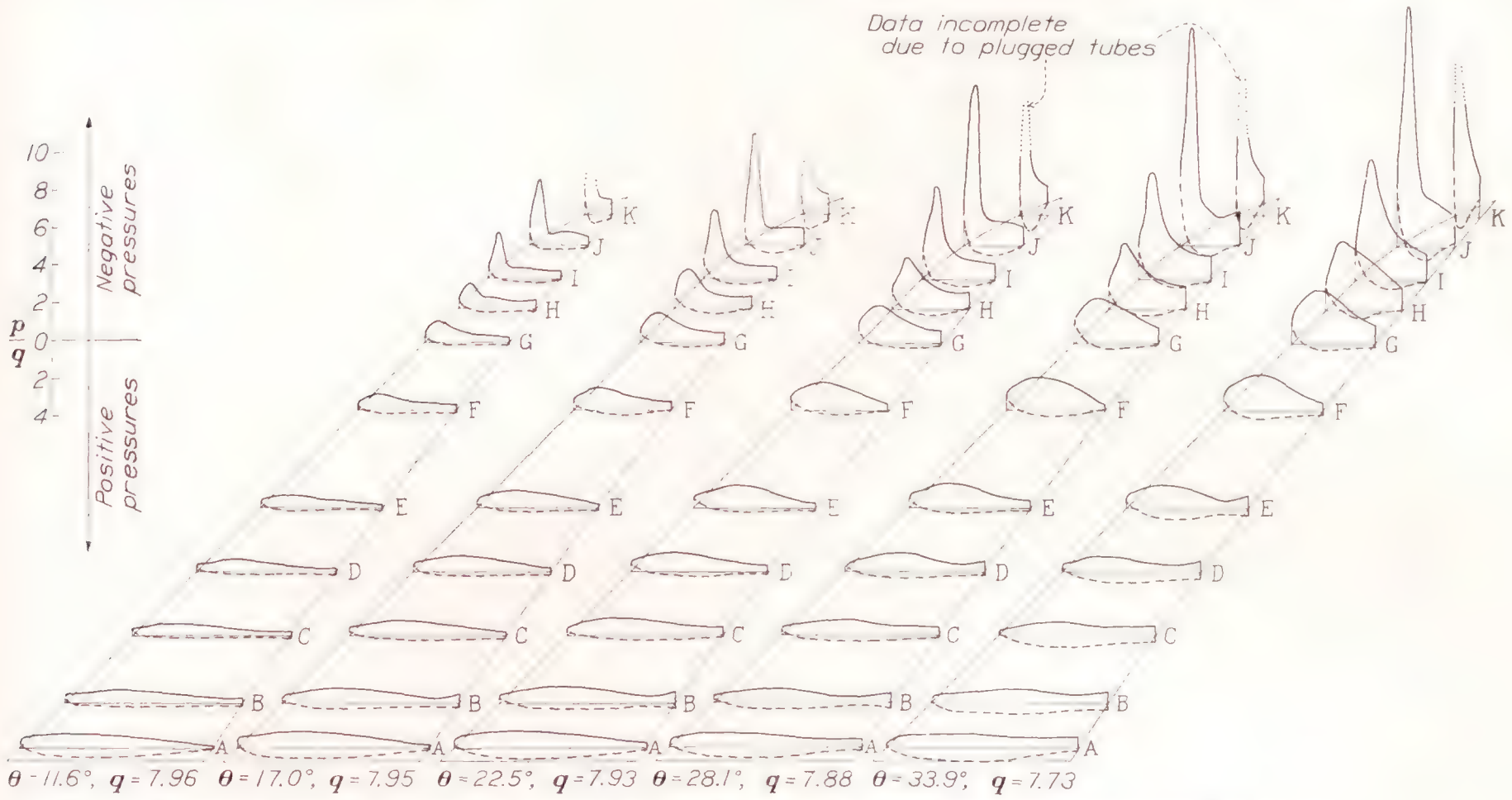

FIGURE 15.—Pressure distribution on horizontal fin of the 1/40-scale model of the *Akron* at various pitch angles. Fin 4; $\delta_e = 20°$.

Figures 31, 32, and 33 show the variation with pitch angle of the maximum point pressure at each station at which pressure-distribution measurements were made.

PRESSURE-DISTRIBUTION MEASUREMENTS ON THE HULL

The value of the transverse force per unit length at any station on the hull is given by the expression

$$f = \frac{dF}{dx} = \int_0^{2\pi} pr \cos \omega d\omega$$

where F is the total transverse force per unit length.

x, the distance from the nose of the hull measured along the longitudinal axis.

r, the radius of the hull.

p, the pressure on the section at a point whose angular distance from the keel is ω.

A graphical solution of this equation was obtained by plotting the pressure at each point on the hull against

areas under the curves shown in figures 34, 35, and 36; (2) the moment about the center of buoyancy of the transverse forces on the rear portion of the hull; (3) the normal force on the various fins that were used on the model when the hull pressures were measured; (4) the moment of the fin force about the center of buoyancy; and (5) the total moment of the combined hull and fin forces about the center of buoyancy.

Figure 37 shows the effects of the different fins on the moment, about the center of buoyancy, of the transverse aerodynamic forces acting on the fins and on the rear portion of the hull.

In order to facilitate the application of model test results to a full-scale airship, there is included in table X the location of the structural frames on the *Akron* and their corresponding location on the 1/40-scale model.

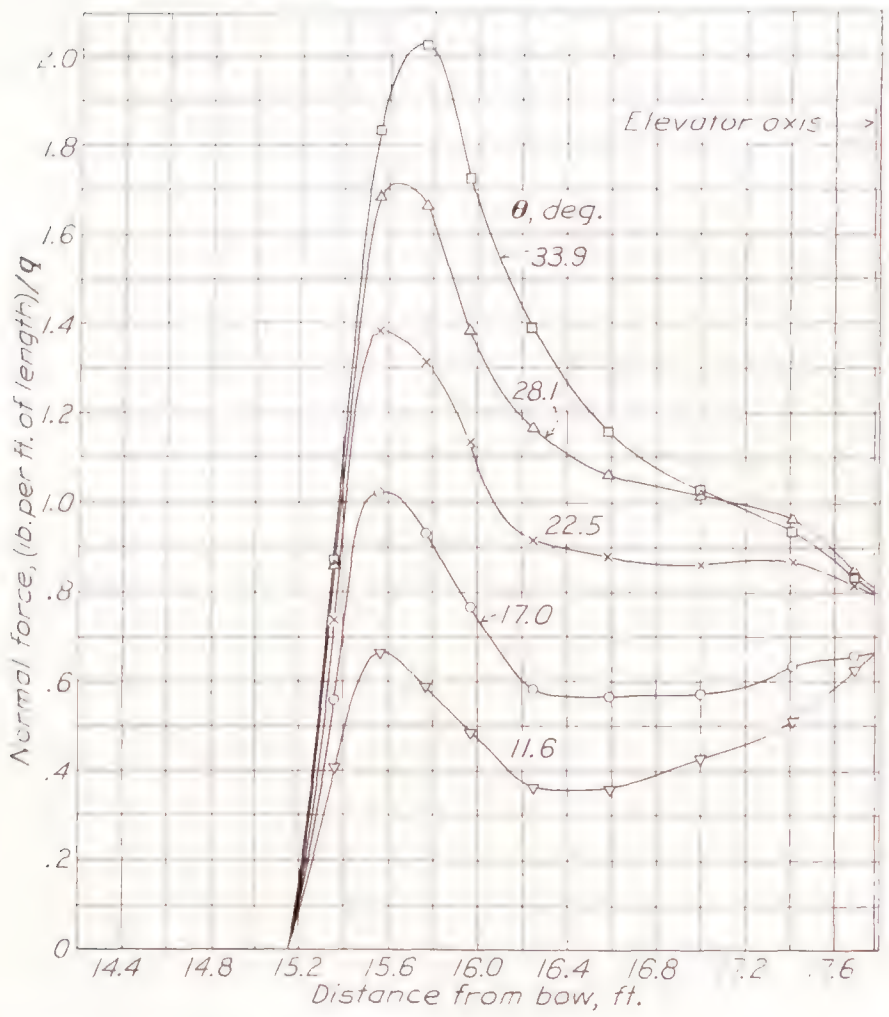

FIGURE 16.—Normal force per unit length on fin of the 1/40-scale model of the *Akron*. Mark II fin (with counterbalances); $\delta_e = 20°$.

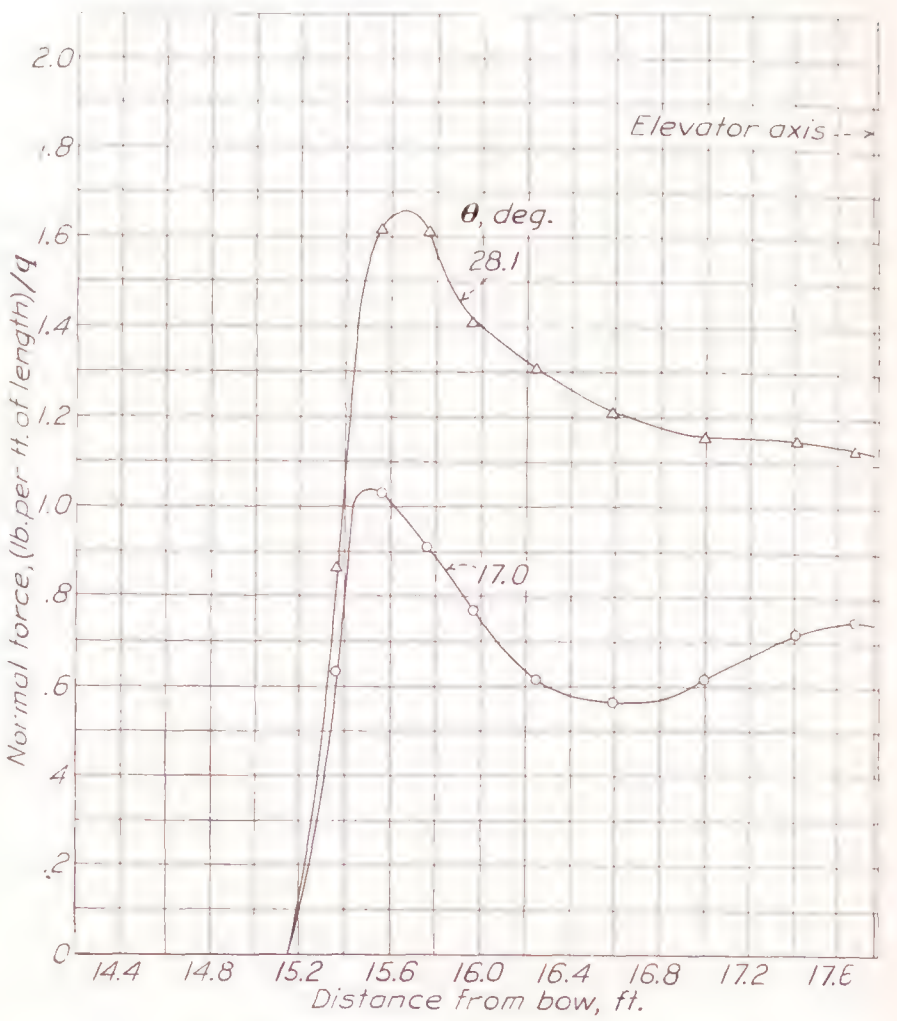

FIGURE 17.—Normal force per unit length on fin of the 1/40-scale model of the *Akron*. Mark II fin (counterbalances removed); $\delta_e = 20°$.

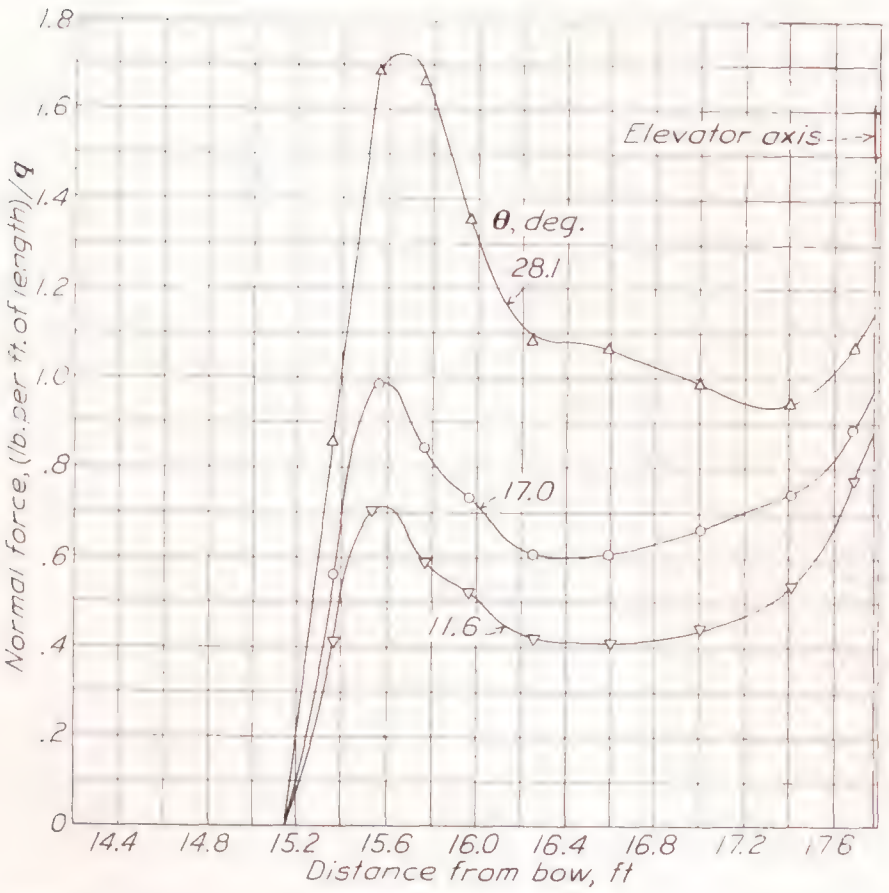

FIGURE 18.—Normal force per unit length on fin of the 1/40-scale model of the *Akron*. Mark II fin (counterbalances removed); 3/8-inch slot; $\delta_e = 20°$.

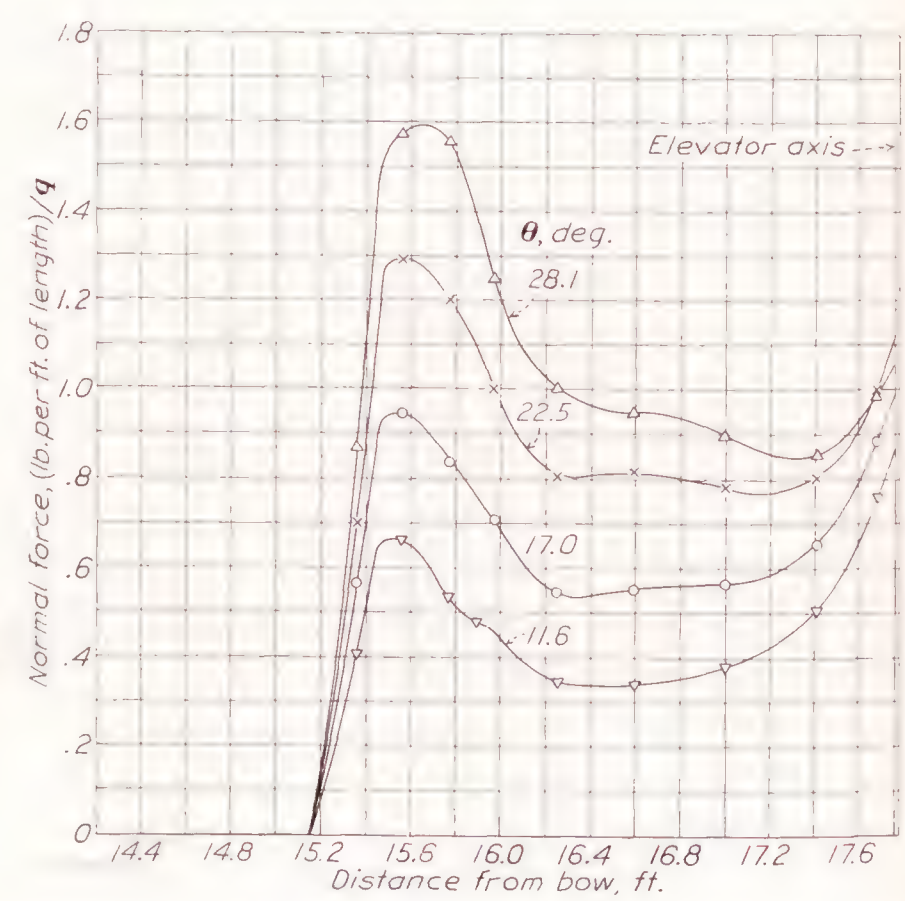

FIGURE 19.—Normal force per unit length on fin of the 1/40-scale model of the *Akron*. Mark II fin (counterbalances removed); 3/4-inch slot; $\delta_e = 20°$.

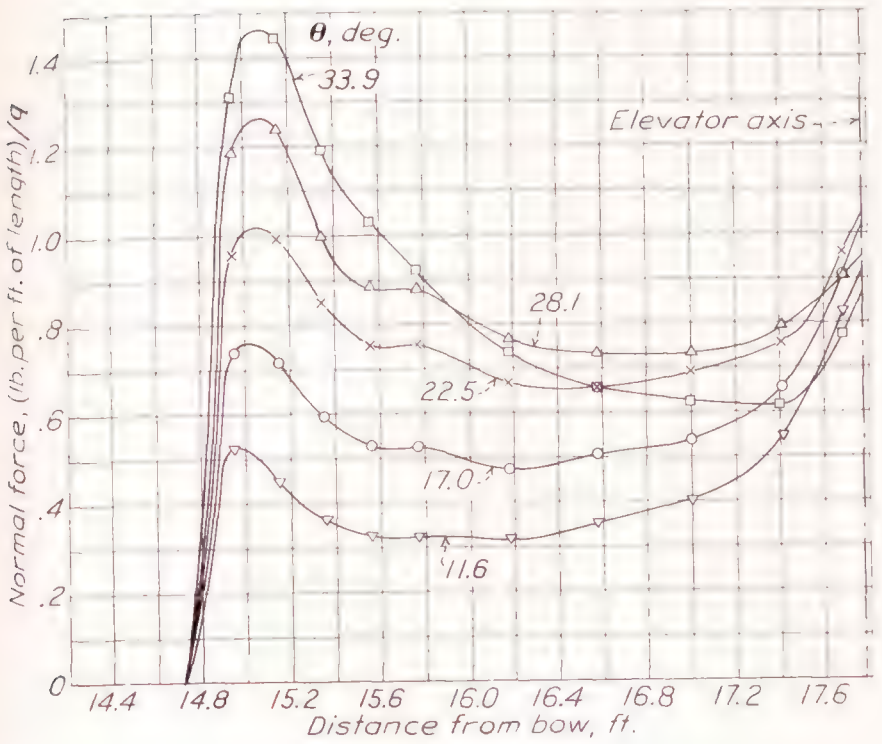

FIGURE 20.—Normal force per unit length on fin of the 1/40-scale model of the *Akron*. Fin 3; $\delta_e=20°$.

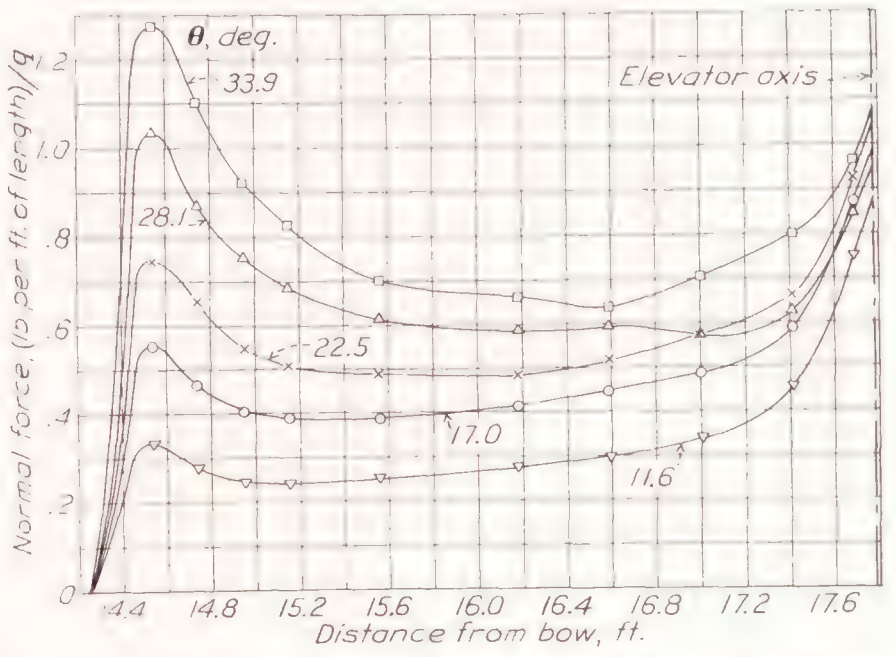

FIGURE 21.—Normal force per unit length on fin of the 1/40-scale model of the *Akron*. Fin 4; $\delta_e=20°$.

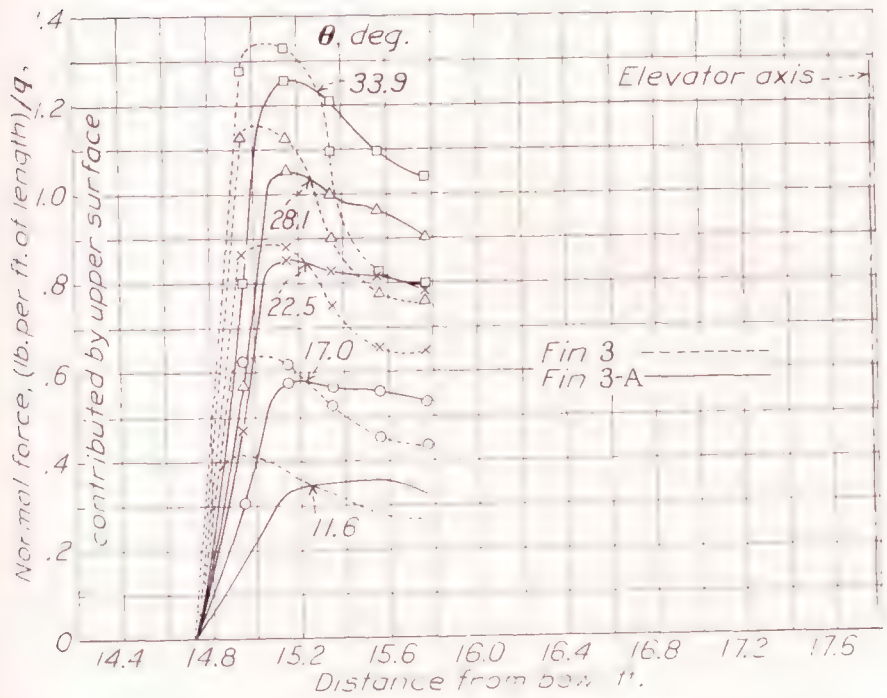

FIGURE 22.—Comparison of normal force per unit length contributed by upper surfaces of fin 3 and fin 3-A of the 1/40-scale model of the *Akron*; $\delta_e=20°$. NOTE.—Pressures on lower surface not measured. Reference pressure is static pressure in test chamber.

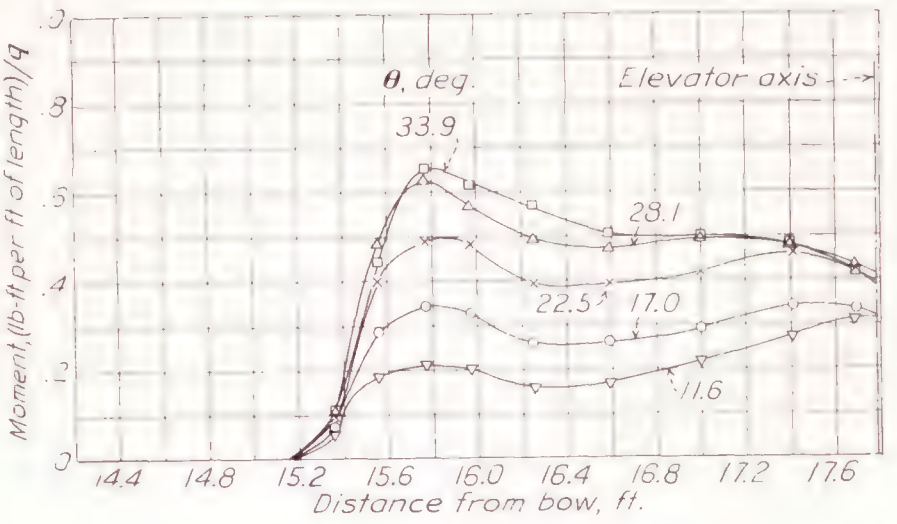

FIGURE 23.—Moment of forces on fin about fin root of the 1/40-scale model of the *Akron*. Mark II fin (with counterbalances); $\delta_e=20°$.

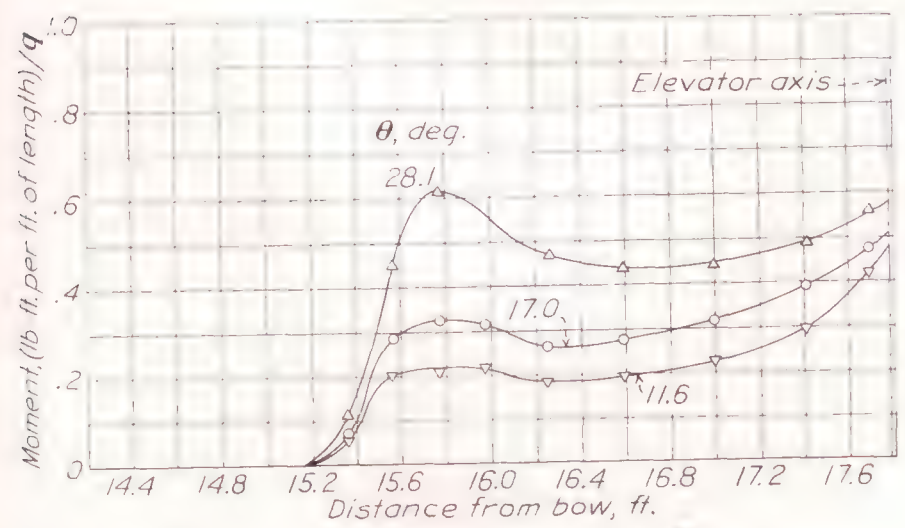

FIGURE 24.—Moment of forces on fin about fin root of the 1/40-scale model of the *Akron*. Mark II fin (counterbalances removed); 3/8-inch slot; $\delta_e=20°$.

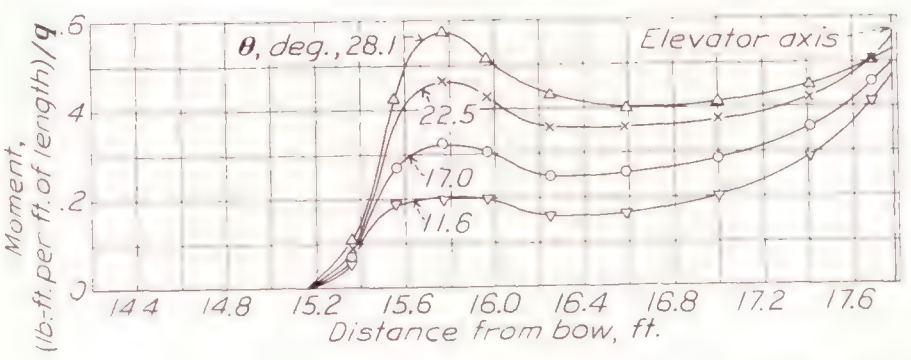

FIGURE 25.—Moment of forces on fin about fin root of the 1/40-scale model of the *Akron*. Mark II fin (counterbalances removed); 3/4-inch slot; $\delta_e=20°$.

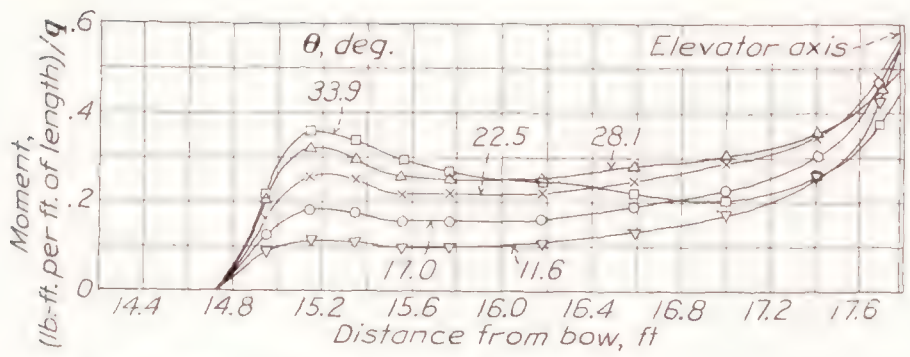

FIGURE 26.—Moment of forces on fin about fin root of the ¼₀-scale model of the *Akron*. Fin 3; δ_e=20°.

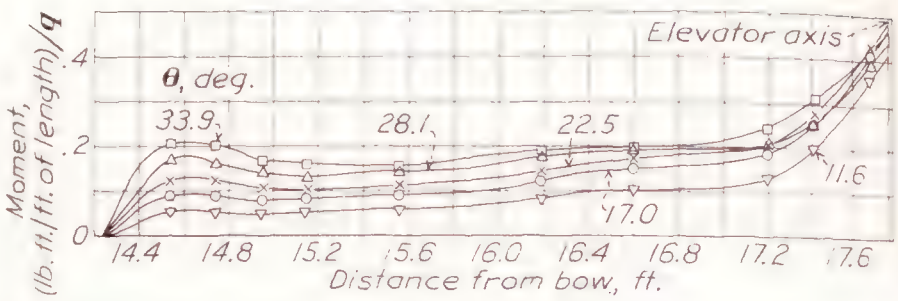

FIGURE 27.—Moment of forces on fin about fin root of the ¼₀-scale model of the *Akron*. Fin 4; δ_e=20°.

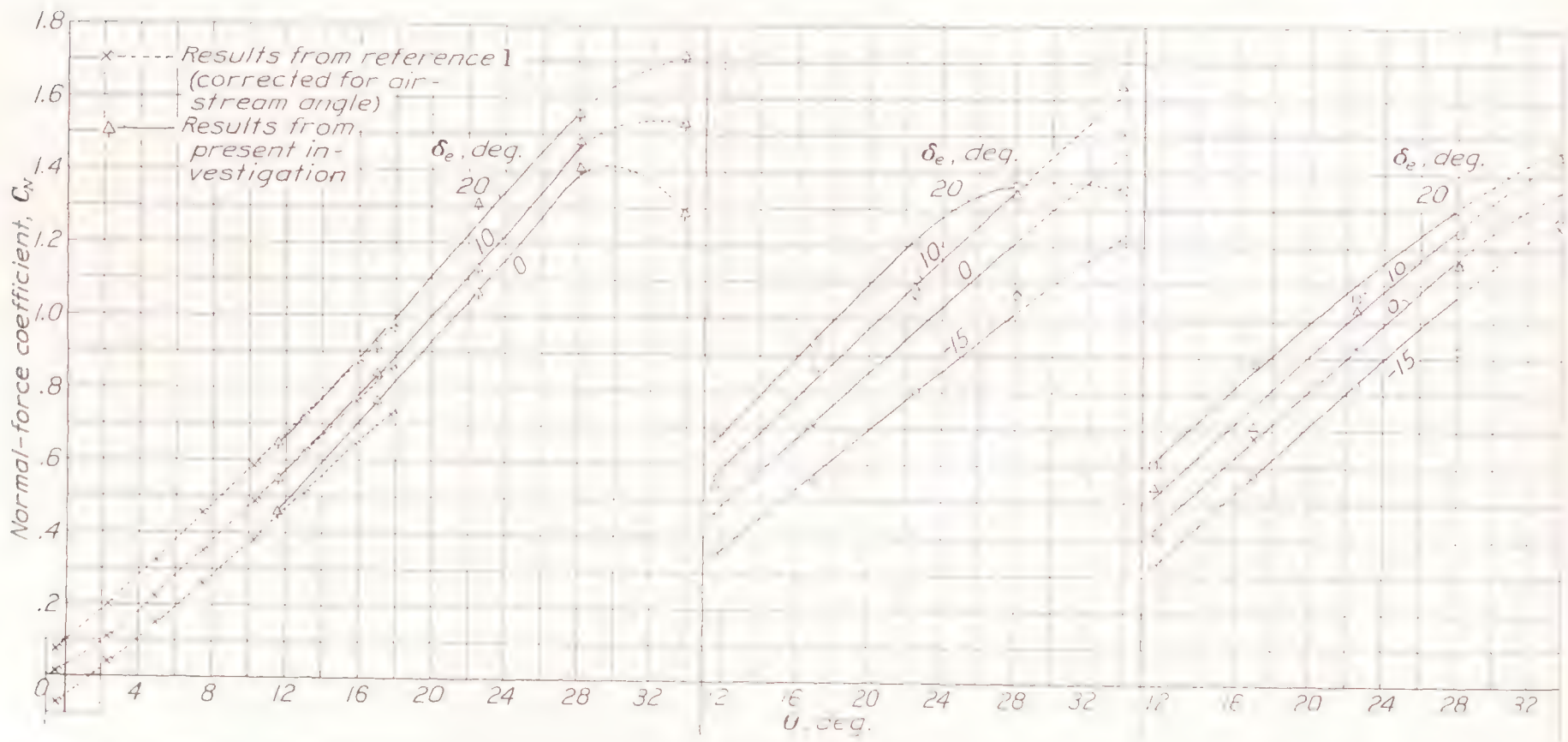

FIGURE 28.—Normal-force coefficients for horizontal fin surfaces on the ¼₀-scale model of the *Akron*. Mark II fin (with counterbalances).

FIGURE 29.—Normal-force coefficients for horizontal fin surfaces on the ¼₀-scale model of the *Akron*. Fin 3.

FIGURE 30.—Normal-force coefficients for horizontal fin surfaces on the ¼₀-scale model of the *Akron*. Fin 4.

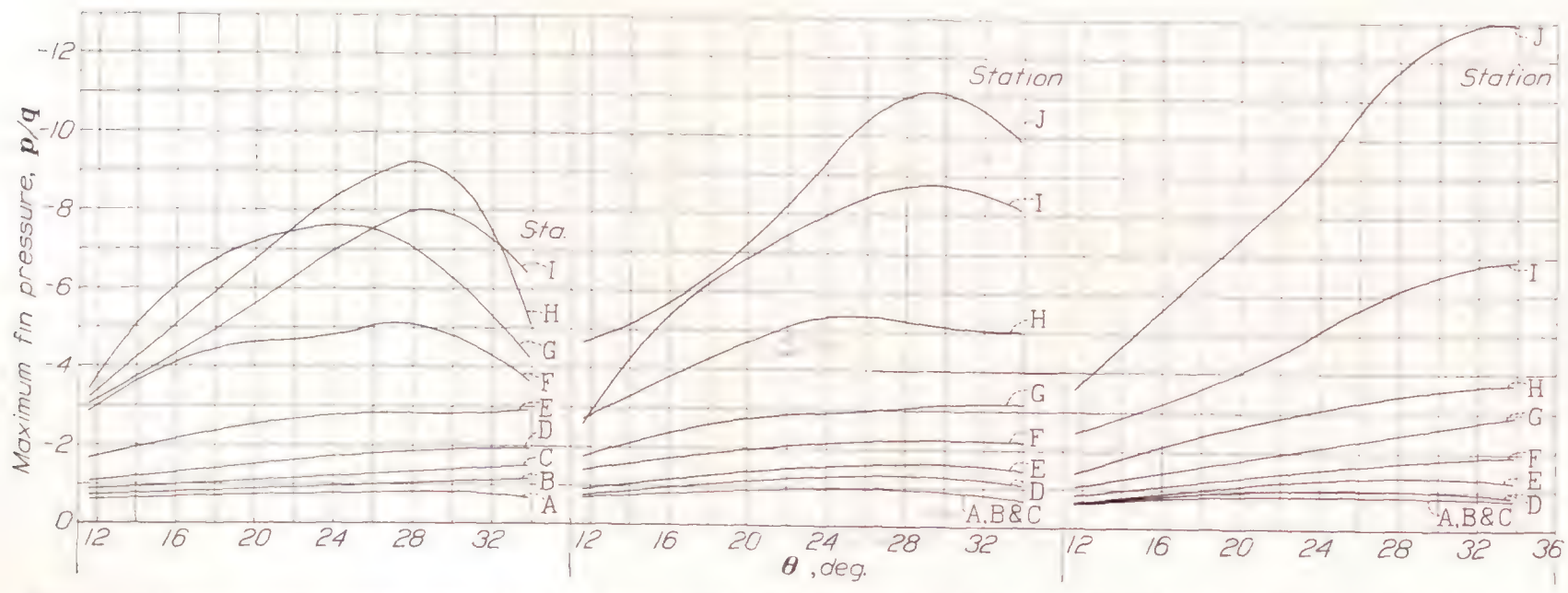

FIGURE 31.—Variation of maximum fin pressure with pitch angle. The ¼₀-scale model of the *Akron*; Mark II fin (with counterbalances); δ_e=20°.

FIGURE 32. Variation of maximum fin pressure with pitch angle. The ¼₀-scale model of the *Akron*; Fin 3; δ_e=20°.

FIGURE 33.—Variation of maximum fin pressure with pitch angle. The ¼₀-scale model of the *Akron*; Fin 4; δ_e=20°.

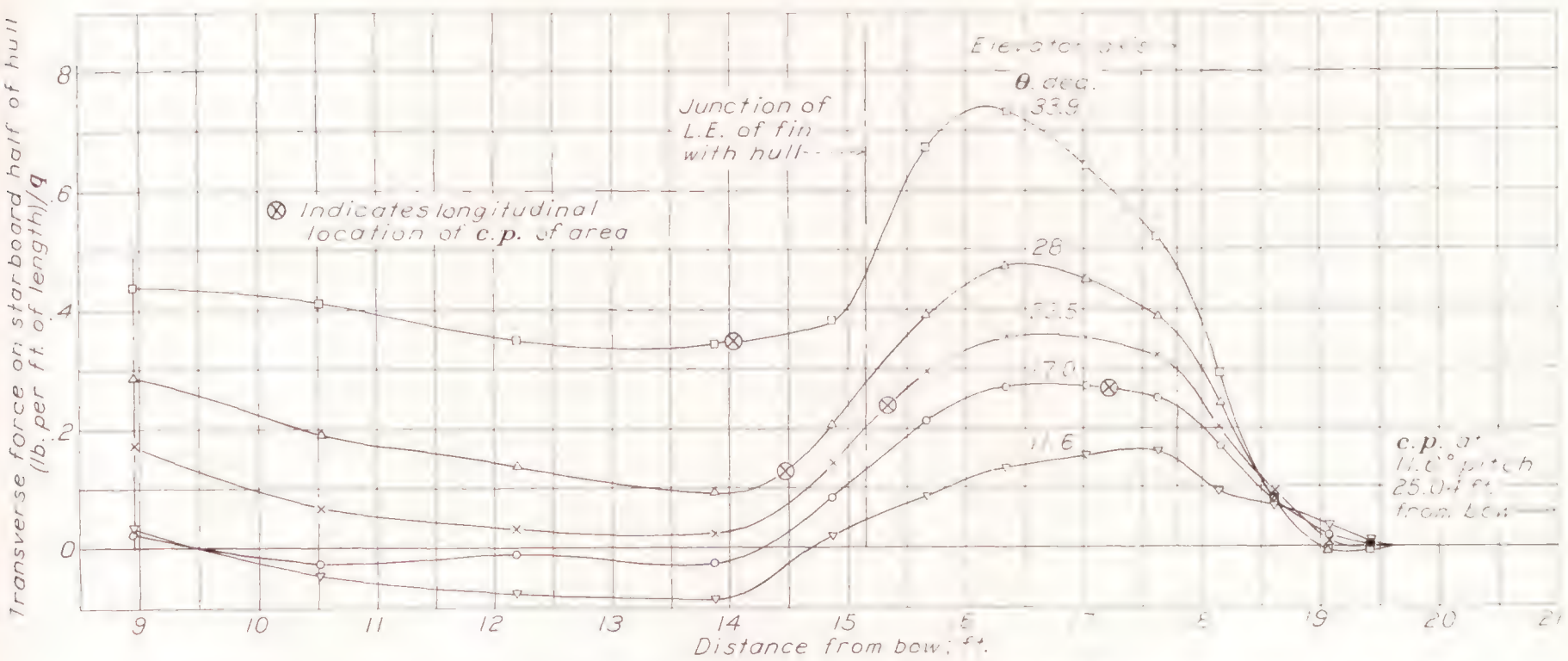

FIGURE 34.—Transverse force per unit length on the hull of the 1/40-scale model of the *Akron*. Mark II fin (counterbalances removed); $\delta_e = 20°$.

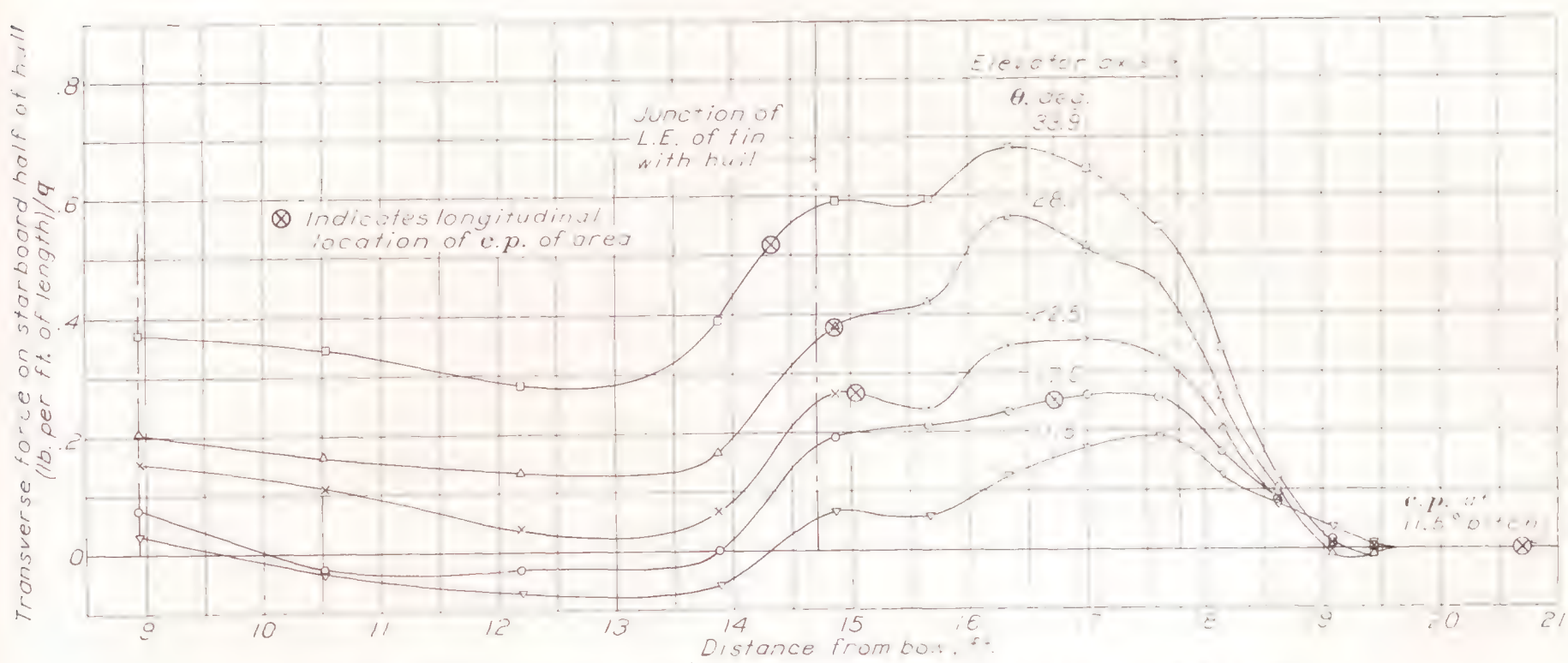

FIGURE 35.—Transverse force per unit length on the hull of the 1/40-scale model of the *Akron*. Fin 3; $\delta_e = 20°$.

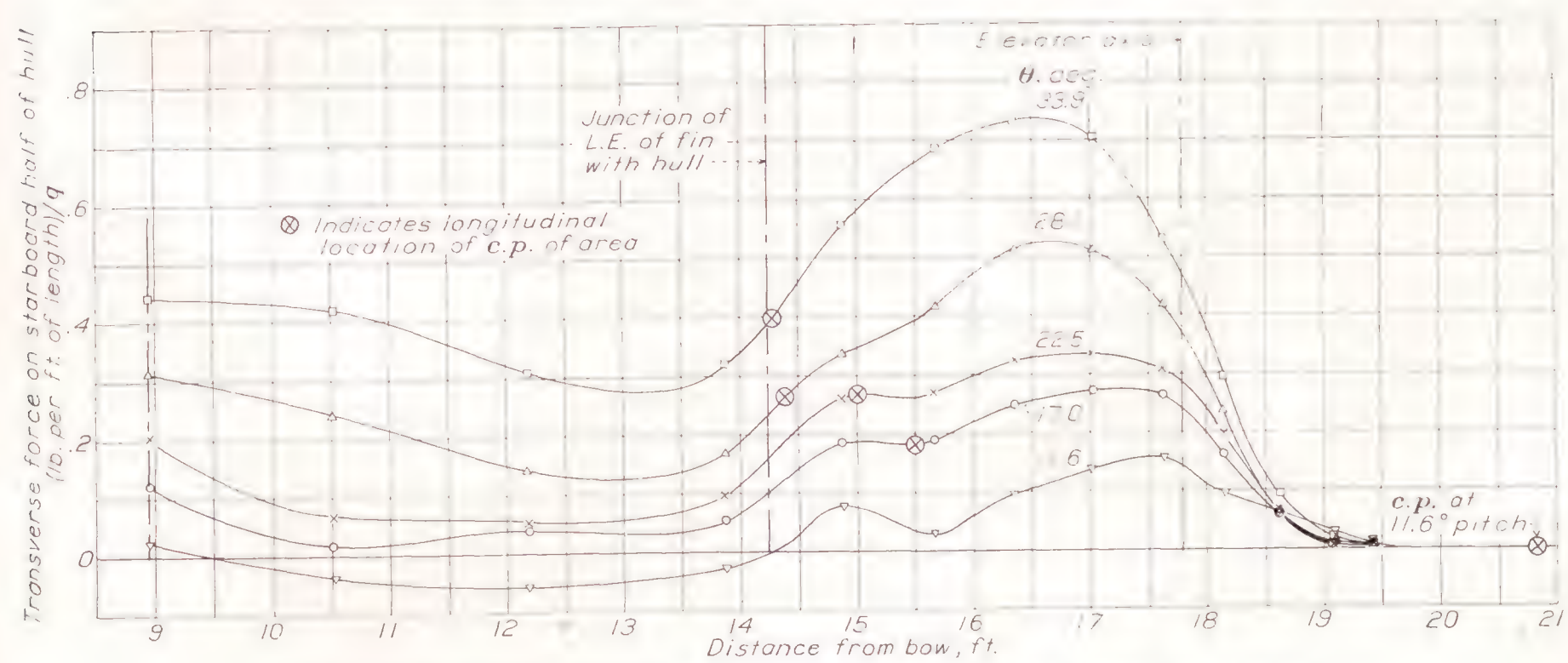

FIGURE 36.—Transverse force per unit length on the hull of the 1/40-scale model of the *Akron*. Fin 4; $\delta_e = 20°$.

DISCUSSION

The results of these tests confirm the conclusions of reference 1 concerning the presence of very large pressures near the leading edge of airship fins. Figures 31, 32, and 33 show that the maximum pressure recorded ($p/q=-13.0$) was obtained at the tip section of fin 4, at the 34° pitch angle. At the same pitch angle the maximum value of p/q obtained on fin 3 was −9.9, and the maximum for the Mark II fin was −6.4. Inspection of figures 31, 32, and 33 also reveals that, although the maximum values of p/q continued to increase on fin 4

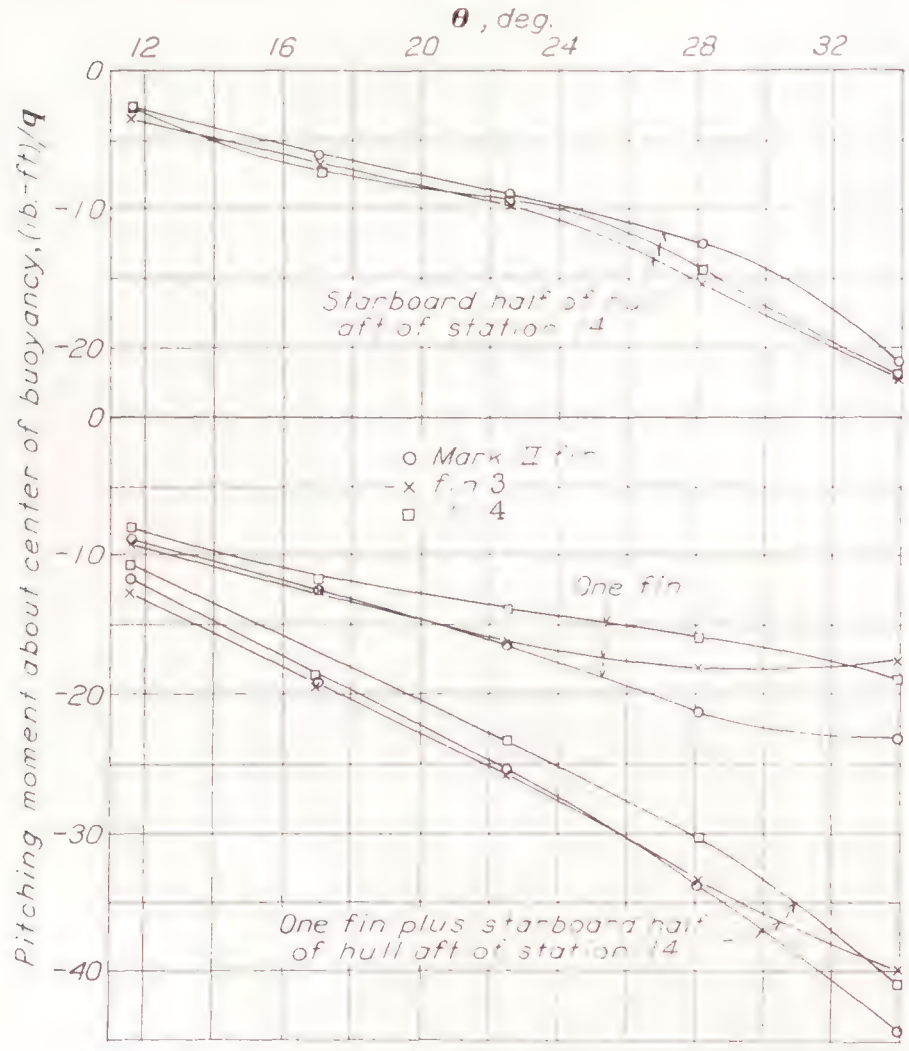

FIGURE 37.—Comparison of pitching moments acting on the 1/40-scale model of the *Akron* when fitted with different horizontal fins; $\delta_e=20°$. (Forces on elevators neglected.)

up to the maximum angle at which tests were run, the values of p/q obtained on fin 3 reached their maximum value of −11.1 at $\theta=29°$ and on the Mark II fin the maximum value (−9.2) occurred at $\theta=28°$. It is of further interest to note that, although at the highest angles of pitch at which tests were made the greatest pressure recorded was that obtained on fin 4, the maximum pressures obtained for all pitch angles below 20° were approximately the same for all fins.

Attention is called to the fact that the pressures cited were obtained from faired curves and that, since the peak pressure would not necessarily occur directly at the points at which the orifices were located and since the slope of the pressure diagram changes from a very large positive value to a very large negative value in the vicinity of the maximum pressure, it is conceivable that greater pressures occurred than those given.

The effect of slots between the hull and fins on the location of the spanwise center of pressure was determined from large-scale pressure diagrams of the type shown in figures 10, 11, and 12. It was observed that neither the ⅜-inch slot nor the ¾-inch slot had much effect at pitch angles below 17°. At higher pitch angles the effect of either slot was to increase the negative pressure at the fin root, thus shifting the center of pressure inboard. The shift was small, however, and was greater for the ⅜-inch slot than for the ¾-inch slot. The maximum movement of center of pressure observed occurred on station D and at $\theta=30°$ where the movement amounted to about 4 percent of the span of the fin at that station. A comparison of figures 18 and 19 with figure 17 in conjunction with table VIII reveals that at the 17° pitch angle, except for an increase in normal force in the vicinity of the elevator axis, neither slot had an appreciable effect on the normal force or its chordwise distribution on the fin. At higher angles of pitch large fluctuations in forces occurred and the precision of the test results is not considered good enough to draw definite conclusions concerning the effect of the slots. The effect, however, is considered to be small.

Figures 16 to 22 show that fins of low span-chord ratio have a more nearly uniform load distribution along their chord than does the Mark II type of fin, and therefore from structural considerations, provided the effectiveness as shown later is equal, the low span-chord ratio is preferable.

The variation with span-chord ratio of the fin normal-force coefficients can be determined from an inspection of figures 28, 29, and 30. The coefficients for the Mark II fin are, in general, greater than for either of the other fins. At high angles of pitch the coefficients for the Mark II fin begin to decrease with further increase in angle of pitch. The shapes of the curves for the other two fins are not so clearly defined because of erratic results at large angles of pitch.

It is interesting to note from inspection of figures 28, 29, and 30 that the slope of the curves of C_N against θ decreases as the span-chord ratio of the fins decreases. This decrease is in accordance with the principle that the decrease in span-chord ratio decreases the effective aspect ratio of the tail.

It has previously been pointed out in this report that original comparison of these test results did not check the results of reference 2 and that the discrepancy disappeared to a large extent when corrections were made to take account of the air-stream-angle variation in the wind tunnel. Figure 28, which shows values of C_N obtained in these tests and corresponding values of C_N from reference 1 plotted against corrected pitch angle (fig. 9), compares the two sets of data. It is to be noted that agreement is, in general, satisfactory.

The data obtained in these tests indicate that the plan form of the forward part of the fin is an important item in fin design. Figure 22 shows a comparison of the forces acting on the upper surfaces of the tips of fins 3 and 3–A. Pressures were not measured on the lower surface of fin 3–A and it is therefore impossible

to compare the total forces on the two fins. It is believed, however, that a comparison of the forces registered on the upper surfaces shows the relative merits of the two different plan forms. Inspection of figure 22 leads to the conclusion that the effect of modifying the fin tip was to decrease the forces over the forward portion of the fin, presumably because of the decreased fin area forward, and to increase the forces in the region between the elevator axis and the fin tip, thus in effect shifting the center of pressure toward the elevator axis. The peaks of the pressure diagrams occur farther inboard on fin 3–A (fig. 14) than they do on fin 3 (fig. 13); also, the magnitude of the pressures near the fin root is greater on fin 3–A.

A comparison of the chordwise force distribution curves shown in figure 16 with similar curves in figure 17 leads to the conclusion that for the condition of $\delta_e=20°$ the effect of the elevator counterbalances is to decrease the normal force on the rear part of the fin.

The chief criterion in the selection of tail surfaces for airships is the ability of the surfaces to give adequate stability and control. In view of the fact that a large proportion of the stabilizing force obtained with fins is due to the influence of the fins on pressural forces on the hull, it is at once evident that the measurements of forces acting on the fins alone do not give sufficient information for the selection of the most efficient fin. The magnitude of the pressural forces from station 14 aft on the port half of the hull when fitted with the Mark II fin and with fins 3 and 4 is shown in figures 34, 35, and 36, respectively.

The moment about the center of buoyancy of the forces represented by the area under the curves shown in figures 34, 35, and 36 is shown as a function of angle of pitch in figure 37. It is believed that, since pressure-distribution measurements were made on all of that portion of the hull over which the fins appear appreciably to influence the hull forces, the curves of pitching moment against angle of pitch (fig. 37) present a valid comparison of the relative stability characteristics of the airship when fitted with the various fins tested. Attention is called to the fact that, since the pressure-distribution measurements from which this chart is derived were made at but one elevator deflection ($\delta_e=20°$), a complete analysis is impossible. It is believed, however, that the same relative effects as here shown would obtain for other elevator deflections.

Inspection of figure 37 indicates that at extremely high pitch angles ($\theta=34°$) the pitching moment about the center of buoyancy due to pressural forces on the rear half of the hull is approximately equal to the corresponding moment due to the forces on the fins themselves. From the curves in the lower part of figure 37 it is to be seen that, except at angles of pitch greater than 26°, the stabilizing moment obtained when the airship is fitted with the Mark II fin is very nearly equal to the stabilizing moment obtained with fin 3. At angles of pitch greater than 26° the Mark II fin is somewhat superior. With the exception of a slight superiority over fin 3 at extremely high pitch angles, fin 4 is inferior to both of the other fins.

It is desired to point out that, although the narrow fins appear to compare quite favorably with the Mark II fins, the results here shown are not conclusive in that they do not show the effect of the various fins on drag. It is possible that, if the drag of the different fins could be compared on the basis of either equal lift or equal moment coefficients, the fins of low span-chord ratio would show up to disadvantage.

38548—38——39

CONCLUSIONS

1. At angles of pitch below about 20° the maximum pressure measured was approximately the same for all fins, regardless of span-chord ratio.

2. At angles of pitch above 20° the maximum fin pressures increase with decreasing span-chord ratio, the highest pressure recorded ($p/q=-13.0$) being that obtained on fin 4 at a pitch angle of 34°.

3. Slots between the hull and fins, of the type here tested, had but little effect on either maximum fin pressures or the position of the center of pressure of fin forces.

4. The plan form of the forward portion of the fin is a critical factor influencing the pressure distribution on the fin.

5. The pitching moment about the center of buoyancy contributed by the rear half of the hull increases with pitch until at an angle of 33° it is approximately equal to the moment contributed by the fins.

6. At any given angle of pitch up to 26° the restoring moment of the model when fitted with the Mark II fin was slightly less than that obtained with fin 3 and appreciably greater than that obtained with fin 4.

7. Neglecting the effect on drag, it appears that fin 3, owing to its relatively low bending moment about the fin root, has certain structural advantages over the Mark II fin.

Langley Memorial Aeronautical Laboratory,
National Advisory Committee for Aeronautics,
Langley Field, Va., *April 4, 1937.*

REFERENCES

1. Freeman, Hugh B.: Pressure-Distribution Measurements on the Hull and Fins of a 1/40-Scale Model of the U. S. Airship *Akron.* T. R. No. 443, N. A. C. A., 1932.
2. Freeman, Hugh B.: Force Measurements on a 1/40-Scale Model of the U. S. Airship *Akron.* T. R. No. 432, N. A. C. A., 1932.
3. Weick, Fred E., and Wood, Donald H.: The Twenty-Foot Propeller Research Tunnel of the National Advisory Committee for Aeronautics. T. R. No. 300, N. A. C. A., 1928.

TABLE I

DIMENSIONS OF THE 1/40-SCALE MODEL "AKRON"

[Length, 19.62 ft.; volume, 115.00 cu. ft.; location of elevator axis, $(x/L)=0.9059$; center of buoyancy, $(x/L)=0.464$.]

Distance from bow / length $\frac{x}{L}$	Radius (circumscribed circle) (in.)	Distance from bow / length $\frac{x}{L}$	Radius (circumscribed circle) (in.)
0.00	0.00	0.50	19.80
.02	4.95	.55	19.59
.05	9.96	.60	19.12
.10	14.20	.65	18.46
.15	16.65	.70	17.50
.20	18.39	.75	16.15
.25	19.12	.80	14.44
.30	19.61	.85	12.29
.35	19.85	.90	9.61
.40	19.90	.95	6.52
.45	19.90	1.00	.00

Fin	Area of one fin (without elevator) (sq. ft.)	Area of elevator (sq. ft.)	Area of elevator counterbalance (sq. ft.)	Elevator chord (ft.)	Maximum chord of fin (ft.)	Maximum span of fin (ft.)	Fin span-chord ratio $\frac{(\text{maximum span of fin})^2}{(\text{area of fin})}$
Mark II	1.850	0.356	0.110	0.396	2.63	1.028	0.570
3	1.858	.356	.....	.402	3.06	.943	.479
3-A	1.775	.356	.....	.402	3.06	.943	.500
4	1.838	.356	.....	.427	3.55	.880	.421

TABLE II

NORMAL FORCE PER UNIT LENGTH OF FIN AND MOMENT OF NORMAL FORCE ABOUT FIN ROOT OF 1/40-SCALE MODEL "AKRON"

MARK II FIN (WITH COUNTERBALANCES)

Station	Distance from bow (ft.)	δ_e (deg.)	Normal force (lb. per ft. length) /q					Moment (ft.-lb. per ft. length) /q				
			θ (deg.)					θ (deg.)				
			11.6	17.0	22.5	28.1	33.9	11.6	17.0	22.5	28.1	33.9
Elevator axis	17.78	0	0.160	0.241	0.295	0.336	0.286	0.106	0.160	0.179	0.204	0.170
A	17.69		.195	.302	.361	.424	.325	.120	.185	.214	.253	.185
B	17.41		.253	.425	.527	.666	.412	.146	.242	.296	.380	.233
C	17.00		.254	.470	.635	.855	.545	.140	.246	.325	.430	.293
D	16.59		.276	.492	.716	1.005	.745	.110	.230	.324	.448	.358
E	16.25		.341	.565	.815	1.135	1.105	.157	.250	.351	.484	.475
F	15.97		.415	.715	1.013	1.391	1.546	.176	.305	.430	.565	.593
G	15.77		.502	.850	1.255	1.673	1.835	.184	.320	.480	.623	.625
H	15.56		.610	.945	1.312	1.665	1.755	.170	.266	.375	.467	.440
I	15.36		.361	.531	.710	.885	.980	.050	.067	.095	.118	.122
Tip of fin	15.15		.000	.000	.000	.000	.000	.000	.000	.000	.000	.000
Elevator axis	17.78	10	0.429	0.486	0.522	0.590	0.573	0.231	0.260	0.280	0.310	0.286
A	17.69		.420	.496	.553	.655	.603	.230	.268	.305	.353	.313
B	17.41		.383	.515	.635	.808	.694	.217	.284	.354	.447	.375
C	17.00		.345	.536	.710	.944	.827	.181	.274	.356	.463	.417
D	16.59		.322	.543	.755	1.033	.985	.153	.255	.340	.459	.442
E	16.25		.364	.574	.823	1.155	1.225	.161	.255	.360	.566	.515
F	15.97		.431	.740	1.046	1.380	1.614	.183	.308	.445	.565	.620
G	15.77		.515	.844	1.224	1.645	1.975	.192	.320	.470	.622	.670
H	15.56		.632	.973	1.335	1.655	1.885	.178	.276	.385	.475	.465
I	15.36		.366	.535	.702	.866	1.005	.146	.070	.092	.118	.125
Tip of fin	15.15		.000	.000	.000	.000	.000	.000	.000	.000	.000	.000
Elevator axis	17.78	20	0.660	0.665	0.794	0.810	0.800	0.312	0.320	0.395	0.412	0.388
A	17.69		.623	.656	.815	.845	.833	.312	.335	.415	.435	.420
B	17.41		.512	.634	.867	.965	.935	.276	.340	.460	.477	.480
C	17.00		.427	.571	.860	1.015	1.028	.220	.290	.418	.491	.500
D	16.59		.362	.567	.880	1.060	1.158	.171	.261	.391	.474	.507
E	16.25		.363	.581	.916	1.165	1.390	.160	.260	.395	.495	.565
F	15.97		.485	.763	1.133	1.380	1.725	.201	.325	.481	.568	.620
G	15.77		.585	.930	1.315	1.665	2.025	.210	.340	.486	.622	.648
H	15.56		.661	1.019	1.383	1.680	1.833	.185	.285	.400	.482	.445
I	15.36		.406	.557	.735	.855	.870	.052	.073	.095	.110	.110
Tip of fin	15.15		.000	.000	.000	.000	.000	.000	.000	.000	.000	.000

TABLE III

NORMAL FORCE PER UNIT LENGTH OF FIN ON 1/40-SCALE MODEL "AKRON"

MARK II FIN (COUNTERBALANCES REMOVED)

Station	Distance from bow (ft.)	δ_e (deg.)	Normal force (lb. per ft. length)/q				
			θ (deg.)				
			11.6	17.0	22.5	28.1	33.9
Elevator axis	17.78	20		0.740		1.122	
A	17.69			.744		1.130	
B	17.41			.713		1.147	
C	17.00			.612		1.156	
D	16.59			.564		1.213	
E	16.25			.615		1.306	
F	15.97			.768		1.415	
G	15.77			.908		1.612	
H	15.56			1.030		1.620	
I	15.36			.620		.860	
Tip of fin	15.15			.000		.000	

TABLE IV

NORMAL FORCE PER UNIT LENGTH OF FIN AND MOMENT OF NORMAL FORCE ABOUT FIN ROOT OF 1/40-SCALE MODEL "AKRON"

MARK II FIN, 3/8-INCH SLOT (COUNTERBALANCES REMOVED)

Station	Distance from bow (ft.)	δ_e (deg.)	Normal force (lb. per ft. length)/q					Moment (lb.-ft. per ft. length)/q				
			θ (deg.)					θ (deg.)				
			11.6	17.0	22.5	28.1	33.9	11.6	17.0	22.5	28.1	33.9
Elevator axis	17.78	20	0.875	0.971		1.143		0.475	0.508		0.575	
A	17.69		.774	.888		1.075		.418	.474		.560	
B	17.41		.535	.743		.945		.295	.393		.490	
C	17.00		.437	.664		.990		.224	.318		.442	
D	16.59		.410	.608		1.065		.193	.276		.435	
E	16.25		.420	.608		1.090		.184	.263		.462	
F	15.97		.520	.732		1.360		.216	.314		.565	
G	15.77		.590	.843		1.660		.219	.323		.610	
H	15.56		.712	.988		1.700		.202	.283		.450	
I	15.36		.413	.562		.860		.055	.071		.113	
Tip of fin	15.15		.000	.000		.000		.000	.000		.000	

TABLE V

NORMAL FORCE PER UNIT LENGTH OF FIN AND MOMENT OF NORMAL FORCE ABOUT FIN ROOT OF 1/40-SCALE MODEL "AKRON"

MARK II FIN, 3/4-INCH SLOT (COUNTERBALANCES REMOVED)

Station	Distance from bow (ft.)	δ_e (deg.)	Normal force (lb. per ft. length)/q					Moment (lb.-ft. per ft. length)/q				
			θ (deg.)					θ (deg.)				
			11.6	17.0	22.5	28.1	33.9	11.6	17.0	22.5	28.1	33.9
Elevator axis	17.78	20	0.875	0.986	1.116	1.055		0.467	0.495	0.555	0.525	
A	17.69		.754	.885	1.002	.985		.413	.450	.506	.500	
B	17.41		.505	.658	.808	.855		.288	.354	.421	.445	
C	17.00		.380	.565	.782	.909		.200	.285	.370	.410	
D	16.59		.339	.550	.810	.950		.164	.253	.358	.402	
E	16.25		.345	.545	.810	1.005		.160	.250	.360	.430	
F	15.97		.459	.706	1.002	1.250		.196	.304	.428	.515	
G	15.77		.530	.841	1.203	1.560		.200	.320	.460	.575	
H	15.56		.661	.944	1.293	1.575		.183	.268	.370	.425	
I	15.36		.404	.565	.700	.870		.053	.070	.088	.110	
Tip of fin	15.15		.000	.000	.000	.000		.000	.000	.000	.000	

TABLE VI

NORMAL FORCE PER UNIT LENGTH OF FIN AND MOMENT OF NORMAL FORCE ABOUT FIN ROOT OF 1/40-SCALE MODEL "AKRON"

FIN 3

Station	Distance from bow (ft.)	δ_e (deg.)	Normal force (lb. per ft. length)/q					Moment (lb.-ft. per ft. length)/q				
			θ (deg.)					θ (deg.)				
			11.6	17.0	22.5	28.1	33.9	11.6	17.0	22.5	28.1	33.9
Elevator axis	17.78	−15	−0.280	−0.300	−0.233	−0.147	−0.008	−0.115	−0.089	−0.057	−0.020	0.011
A	17.69		−.140	−.160	−.077	.022	.100	−.036	−.016	.002	.036	.068
B	17.41		.108	.142	.234	.304	.365	.066	.092	.128	.157	.170
C	17.00		.173	.285	.396	.493	.494	.084	.133	.180	.218	.208
D	16.59		.221	.345	.476	.603	.565	.090	.133	.187	.230	.222
E	16.18		224	.365	.526	.685	.696	.080	.130	.179	.228	.240
F	15.77		.260	.425	.626	.825	.936	.081	.135	.181	.243	.278
G	15.56		.278	.478	.665	.926	1.115	.088	.145	.196	.266	.312
H	15.35		.335	.558	.755	1.066	1.296	.100	.166	.224	.304	.363
I	15.15		.435	.675	.715	1.265	1.563	.110	.175	.238	.322	.370
J	14.95		.450	.700	.943	1.195	1.372	.075	.117	.166	.204	.220
Tip of fin	14.72		.000	.000	.000	.000	.000	.000	.000	.000	.000	.000
Elevator axis	17.78	0	0.176	0.245	0.322	0.270	0.378	0.106	0.158	0.198	0.160	0.210
A	17.69		.200	.275	.383	.303	.443	.116	.160	.210	.161	.225
B	17.41		.264	.335	.494	.373	.591	.130	.165	.235	.180	.262
C	17.00		.263	.370	.565	.475	.719	.120	.163	.246	.203	.290
D	16.59		.243	.392	.610	.546	.804	.094	.150	.233	.210	.296
E	16.18		.266	.390	.633	.593	.910	.084	.134	.208	.200	.292
F	15.77		.288	.443	.715	.776	1.065	.089	.133	.203	.221	.304
G	15.56		.298	.482	.736	.875	1.160	.093	.143	.216	.256	.324
H	15.35		.351	.570	.814	1.008	1.305	.104	.168	.242	.300	.363
I	15.15		.455	.743	1.026	1.256	1.504	.113	.190	.263	.318	.360
J	14.95		.468	.736	1.045	1.247	1.545	.086	.120	.175	.208	.240
Tip of fin	14.72		.000	.000	.000	.000	.000	.000	.000	.000	.000	.000
Elevator axis	17.78	10	0.514	0.665	0.690	0.700	0.738	0.290	0.353	0.373	0.374	0.390
A	17.69		.473	.605	.656	.677	.735	.254	.323	.345	.348	.365
B	17.41		.375	.506	.585	.663	.765	.182	.244	.280	.304	.336
C	17.00		.316	.484	.582	.708	.863	.137	.206	.250	.300	.343
D	16.59		.294	.473	.592	.742	.906	.114	.180	.228	.280	.337
E	16.18		.276	.464	.627	.774	.983	.100	.157	.210	.257	.313
F	15.77		.287	.504	.675	.867	1.127	.090	.155	.200	.254	.321
G	15.56		.288	.540	.706	.930	1.125	.090	.164	.206	.265	.336
H	15.35		.347	.624	.805	1.063	1.275	.106	.183	.235	.307	.358
I	15.15		.446	.746	.975	1.263	1.504	.113	.190	.256	.325	.368
J	14.95		.480	.755	1.020	1.203	1.500	.074	.125	.175	.205	.245
Tip of fin	14.72		.000	.000	.000	.000	.000	.000	.000	.000	.000	.000
Elevator axis	17.78	20	0.916	1.020	1.043	0.947	0.867	0.542	0.550	0.568	0.494	0.445
A	17.69		.822	.910	.955	.905	.775	.428	.467	.486	.452	.375
B	17.41		.543	.656	.756	.792	.615	.255	.304	.347	.356	.260
C	17.00		.404	.538	.688	.732	.626	.170	.226	.288	.302	.205
D	16.59		.352	.504	.655	.730	.655	.135	.190	.246	.280	.220
E	16.18		.318	.473	.667	.765	.735	.110	.160	.220	.253	.245
F	15.77		.323	.522	.753	.874	.918	.100	.108	.220	.250	.268
G	15.56		.326	.525	.756	.880	1.030	.100	.108	.218	.257	.296
H	15.35		.362	.592	.850	.994	1.192	.110	.126	.250	.295	.338
I	15.15		.445	.715	.995	1.235	1.443	.111	.134	.255	.320	.355
J	14.95		.525	.737	.955	1.185	1.313	.088	.126	.161	.204	.215
Tip of fin	14.72		.000	.000	.000	.000	.000	.000	.000	.000	.000	.000

TABLE VII

NORMAL FORCE PER UNIT LENGTH OF FIN AND MOMENT OF NORMAL FORCE ABOUT FIN ROOT OF 1/40-SCALE MODEL "AKRON"

FIN 4

Station	Distance from bow (ft.)	δ_e (deg.)	Normal force (lb. per ft. length)/q					Moment (lb.-ft. per ft. length)/q				
			θ (deg.)					θ (deg.)				
			11.6	17.0	22.5	28.1	33.9	11.6	17.0	22.5	28.1	33.9
Elevator axis	17.78	−15	−0.195	−0.167	−0.062	−0.100	0.000	−0.073	−0.047	0.000	−0.010	0.025
A	17.69		−.119	−.056	.030	.014	.161	−.038	.000	.040	.025	.093
B	17.41		.057	.190	.280	.240	.534	.039	.095	.130	.108	.225
C	17.00		.148	.295	.405	.290	.745	.065	.122	.156	.120	.265
D	16.59		.213	.330	.430	.422	.785	.073	.110	.148	.142	.244
E	16.18		.214	.335	.444	.495	.705	.067	.098	.134	.150	.195
F	15.56		.214	.336	.468	.559	.675	.051	.080	.110	.135	.157
G	15.15		.210	.340	.516	.655	.720	.047	.070	.104	.130	.140
H	14.95		.227	.357	.565	.740	.748	.044	.074	.108	.140	.140
I	14.74		.262	.415	.654	.870	.875	.048	.083	.125	.164	.164
J	14.54		.305	.512	.755	.992	1.035	.049	.084	.120	.160	.174
K	14.35		.135	.203	.275	.333	.385	.020	.031	.041	.075	.100
Tip of fin	14.23		.000	.000	.000	.000	.000	.000	.000	.000	.000	.000
Elevator axis	17.78	0	0.210	0.305	0.388	0.357	0.370	0.123	0.160	0.203	0.190	0.181
A	17.69		.196	.295	.390	.410	.394	.104	.150	.192	.202	.185
B	17.41		.180	.306	.413	.516	.495	.084	.141	.180	.212	.208
C	17.00		214	.356	.475	.565	.695	.088	.140	.180	.204	.233
D	16.59		.218	.367	.495	.592	.635	.077	.123	.165	.192	.207
E	16.18		.213	.360	.480	.602	.618	.063	.104	.140	.175	.178
F	15.56		.220	.355	.481	.606	.612	.051	.081	.110	.142	.142
G	15.15		.212	.355	.504	.660	.735	.043	.072	.102	.130	.140
H	14.95		.226	.375	.535	.712	.790	.043	.076	.105	.135	.146
I	14.74		.263	.434	.650	.820	.915	.051	.083	.122	.152	.168
J	14.54		.324	.509	.747	.965	1.084	.050	.085	.125	.161	.184
K	14.35		.160	.205	.248	.370	.508	.017	.036	.053	.092	.114
Tip of fin	14.23		.000	.000	.000	.000	.000	.000	.000	.000	.000	.000
Elevator axis	17.78	10	0.550	0.650	0.738	0.602	0.620	0.255	0.305	0.350	0.268	0.300
A	17.69		.453	.560	.655	.545	.637	.227	.270	.313	.260	.295
B	17.41		.322	.400	.540	.453	.695	.147	.175	.232	.232	.287
C	17.00		.275	.361	.525	.572	.793	.110	.143	.200	.216	.275
D	16.59		.277	.373	.522	.523	.775	.100	.130	.172	.170	.234
E	16.18		.287	.338	.483	.521	.735	.088	.100	.143	.152	.208
F	15.56		.265	.325	.494	.572	.714	.058	.072	.114	.135	.165
G	15.15		.240	.344	.533	.670	.742	.050	.072	.108	.130	.145
H	14.95		.245	.374	.558	.736	.735	.050	.075	.108	.133	.145
I	14.74		.274	.418	.667	.870	.924	.052	.079	.125	.162	.170
J	14.54		.326	.492	.744	1.008	1.106	.053	.080	.120	.169	.185
K	14.35		.160	.230	.470	.620	.815	.021	.035	.052	.070	.086
Tip of fin	14.23		.000	.000	.000	.000	.000	.000	.000	.000	.000	.000
Elevator axis	17.78	20	0.878	0.990	1.050	0.950	1.082	0.412	0.470	0.485	0.440	0.467
A	17.69		.746	.874	.922	.845	.963	.355	.410	.430	.392	.425
B	17.41		.453	.588	.662	.625	.800	.197	.253	.276	.256	.310
C	17.00		.338	.487	.575	.575	.705	.130	.185	.206	.205	.245
D	16.59		.296	.450	.514	.590	.635	.103	.150	.170	.190	.200
E	16.18		.272	.415	.484	.584	.660	.085	.122	.145	.176	.190
F	15.56		.249	.389	.485	.613	.700	.060	.090	.112	.145	.158
G	15.15		.240	.390	.505	.684	.825	.052	.084	.102	.133	.162
H	14.95		.244	.407	.546	.750	.925	.048	.081	.108	.140	.168
I	14.74		.278	.464	.652	.867	1.100	.053	.090	.125	.162	.202
J	14.54		.332	.555	.743	1.033	1.275	.054	.090	.125	.172	.205
K	14.35		.125	.170	.213	.260	.365	.018	.037	.055	.071	.118
Tip of fin	14.23		.000	.000	.000	.000	.000	.000	.000	.000	.000	.000

TABLE VIII

VALUES OF $\frac{\text{NORMAL FORCE}}{q}$ AND DISTANCES OF CENTER OF PRESSURE OF FIN FORCES FROM ELEVATOR AXIS FOR VARIOUS FINS TESTED ON 1/40-SCALE MODEL "AKRON"

[Values of $\frac{\text{normal force}}{q}$ are for one fin only]

δ_e (deg.)	θ (deg.)	Normal force (lb.)/q						Distance of center of pressure from elevator axis (ft.)					
		Mark II fin (with counterbalances)	Mark II fin (counterbalances removed)	Mark II fin (3/8-in. slot)	Mark II fin (3/4-in. slot)	Fin 3	Fin 4	Mark II fin (with counterbalances)	Mark II fin (counterbalances removed)	Mark II fin (3/8-in. slot)	Mark II fin (3/4-in. slot)	Fin 3	Fin 4
−15	11.6					0.65	0.61					1.96	2.15
	17.0					1.05	1.06					1.94	2.01
	22.5					1.50	1.52					1.87	2.01
	28.1					2.00	1.70					1.87	2.17
	33.9					2.27	2.39					1.91	1.88
0	11.6	0.84				.87	.77	1.47				1.64	1.82
	17.0	1.42				1.31	1.25	1.44				1.70	1.81
	22.5	1.96				1.96	1.71	1.47				1.68	1.83
	28.1	2.60				2.01	2.14	1.47				1.83	1.88
	33.9	2.37				2.80	2.32	1.60				1.76	1.91
10	11.6	1.02				1.01	1.00	1.33				1.49	1.63
	17.0	1.56				1.60	1.31	1.38				1.55	1.69
	22.5	2.09				2.03	1.89	1.41				1.60	1.76
	28.1	2.74				2.50	2.12	1.41				1.65	1.92
	33.9	2.85				3.05	2.68	1.48				1.67	1.82
20	11.6	1.20		1.29	1.16	1.25	1.11	1.25		1.23	1.23	1.34	1.45
	17.0	1.70	1.77	1.80	1.68	1.74	1.63	1.34	1.30	1.25	1.28	1.44	1.56
	22.5	2.24			2.27	2.25	1.96	1.34			1.31	1.51	1.64
	28.1	2.88	3.15	2.89	2.67	2.53	2.28	1.36	1.30	1.34	1.36	1.57	1.79
	33.9	3.18				2.52	2.73	1.40				1.70	1.81

TABLE IX

NORMAL FORCE ON FINS AND HULL AND PITCHING MOMENT ABOUT CENTER OF BUOYANCY OF FINS AND AFTER PART OF HULL OF 1/40-SCALE MODEL "AKRON"

[Values are for one fin and starboard half of hull aft of station 14; $\delta_e = 20°$.]

Fin	θ (deg.)	$\frac{\text{Transverse force}}{q}$ on hull $\left(\frac{\text{lb.}}{q}\right)$	$\frac{M_{c.b.}}{q}$ of forces on hull $\left(\frac{\text{ft.-lb.}}{q}\right)$	$\frac{\text{Normal force}}{q}$ on fin $\left(\frac{\text{lb.}}{q}\right)$	$\frac{M_{c.b.}}{q}$ of force on fin $\left(\frac{\text{ft.-lb}}{q}\right)$	$\frac{\text{Transverse force}}{q}$ on hull plus $\frac{\text{Normal force}}{q}$ on fin $\left(\frac{\text{lb.}}{q}\right)$	$\frac{M_{c.b.}}{q}$ of forces on hull and fin $\left(\frac{\text{ft.-lb.}}{q}\right)$
Mark II (with counterbalances)	11.6	0.17	−2.7	1.20	−8.9	1.37	−11.6
	17.0	.78	−6.3	1.70	−12.5	2.48	−18.8
	22.5	1.44	−9.0	2.24	−16.4	3.68	−25.4
	28.1	2.33	−12.5	2.88	−21.1	5.21	−33.6
	33.9	4.25	−21.0	3.18	−23.1	7.43	−44.1
3	11.6	.30	−3.6	1.25	−9.2	1.55	−12.8
	17.0	.89	−6.8	1.74	−12.6	2.63	−19.4
	22.5	1.65	−9.8	2.25	−16.1	3.90	−25.9
	28.1	2.65	−15.3	2.53	−18.0	5.18	−33.3
	33.9	4.21	−22.1	2.51	−17.5	6.72	−39.6
4	11.6	.23	−2.7	1.11	−8.0	1.34	−10.7
	17.0	1.14	−7.3	1.63	−11.6	2.77	−18.9
	22.5	1.63	−9.6	1.96	−13.8	3.59	−23.4
	28.1	2.73	−14.4	2.28	−15.7	5.01	−30.1
	33.9	4.35	−22.0	2.73	−18.8	7.08	−40.8

TABLE X

LOCATION OF STRUCTURAL FRAMES ON U. S. AIRSHIP "AKRON" AND THEIR CORRESPONDING LOCATION ON A 1/40-SCALE MODEL

Ring location from 0 station (full-scale) (meters)	Ring location from bow (1/40-scale model) (feet)	Ring location from 0 station (full-scale) (meters)	Ring location from bow (1/40-scale model) (feet)
0	17.51	125.0	7.26
17.5	16.08	147.5	5.41
35.0	14.64	170.0	3.57
57.5	12.80	187.5	2.13
80.0	10.95	198.75	1.21
102.5	9.10	210.75	.23

REPORT No. 605

RÉSUMÉ AND ANALYSIS OF N. A. C. A. LATERAL CONTROL RESEARCH

By Fred E. Weick and Robert T. Jones

SUMMARY

An analysis of the principal results of recent N. A. C. A. lateral control research is made by utilizing the experience and progress gained during the course of the investigation. Two things are considered of primary importance in judging the effectiveness of different control devices: The (calculated) banking and yawing motion of a typical small airplane caused by a deflection of the control, and the stick force required to produce this deflection. The report includes a table in which a number of different lateral control devices are compared on these bases.

Experience gained while testing various devices in flight with a Fairchild 22 airplane indicated that, following a sudden deflection of the control at low speed, an angle of bank of 15° in 1 second represented a satisfactory minimum degree of effectiveness for this size of airplane. Some devices capable of giving this degree of control were, however, considered to be not entirely satisfactory on account of sluggishness in starting the motion. Devices located near the trailing edge of the wings had no detectable sluggishness. Lateral control forces considered desirable by the test pilots varied from 2 to 8 pounds; 15 pounds was considered excessive.

Test flights demonstrated that satisfactory lateral control at high angles of attack depends as much on the retention of stability as on aileron effectiveness.

The aerodynamic characteristics of plain sealed ailerons could be accurately predicted by a modification of the aerodynamic theory utilizing the results of experiments with sealed flaps. Straight narrow-chord sealed ailerons covering 60 to 80 percent of the semispan represented about the most efficient arrangement of plain unbalanced ailerons from considerations of operating force. The stick force of plain ailerons can be effectively reduced by the use of a differential linkage in conjunction with a small fixed tab arranged to press the ailerons upward.

INTRODUCTION

In 1931 the Committee started a systematic wind-tunnel investigation of lateral control with special reference to the improvement of control at low air speeds and at high angles of attack. Many different ailerons and other lateral control devices have been subjected to the same systematic investigation in the 7- by 10-foot wind tunnel. (See reference 1.) The devices that seemed most promising were tested in flight (references 2 and 3). In many cases, however, devices that produced what seemed to be satisfactory rolling moments and favorable yawing moments did not give satisfactory control.

An analytical study of control effectiveness was therefore made (reference 4) taking into account a number of secondary factors, including the yawing moments produced by the controls, the effect of the controls on the damping in rolling, the lateral-stability derivatives of the airplane, the moments of inertia, and the time required for the control moments to become established after the deflection of the surfaces. The computations consisted of step-by-step solutions of the equations of rolling and yawing motion for the conditions following a deflection of the controls. The results of these computations based on aerodynamic data obtained from wind-tunnel tests of wings incorporating various devices agreed satisfactorily with the results measured in flight for widely different forms of control, such as ailerons and spoilers.

The study of conditions above the stall indicated that satisfactory control could not be expected without some provision to maintain the damping in rolling and that a dangerous type of instability would arise if the damping were insufficient. Since damping in rolling depends on an increase in the lift of the airfoil with increasing angle of attack, it follows that, in order to obtain satisfactory lateral control, the outer or tip portions of the wing, which govern the rolling moments, must remain unstalled. If damping in rolling is retained, it is practically insured that control moments will be retained as well.

The progress of the investigation has thus led to a more accurate interpretation of the results of the wind-tunnel tests. In the present paper the experience gained during the course of the investigation is made the basis of a revised method of comparison of lateral control devices. Wind-tunnel measurements of control and stability factors (reference 1) are utilized in computations to show the banking and yawing motions that would be produced by the controls acting on a small typical airplane. These computations follow the method of analysis given in reference 4. In section I of the report the new basis of comparison is explained and

a number of the devices that were tested in reference 1 are analyzed and compared. The principal items of comparison are collected into a table. Section II presents an analysis of the rolling, yawing, and hinge moments of plain flap-type ailerons and deals with the application of these data in the design of control systems.

I. COMPARISON OF LATERAL CONTROL DEVICES

REVISED BASIS OF COMPARISON

AIRPLANE USED IN COMPARISON

The procedure adopted in the lateral control investigation has comprised a wind-tunnel test program followed by flight tests of the different devices on the Fairchild 22 airplane. Not all of the devices tested in reference 1 have been tried in flight, however, and the present report may be considered an analytical extension of the flight-test procedure that was applied to some of the devices. The procedure employed to test lateral controls in flight is simulated by means of computation. Thus, the comparative criterions used herein are based on application of the devices to a hypothetical Fairchild 22 type of airplane, which is the type used in the flight tests.

The Fairchild 22 airplane was necessarily somewhat modified for each different flight test and wings of different moment of inertia, plan form, and section were used in some cases. The wing of the hypothetical airplane assumed in the computations represents an average of the tested wings. Furthermore, since the characteristic ratios of dimensions (tail length, tail area, radii of gyration about various axes, etc.) used agree very closely with statistical averages of these quantities, the assumed airplane may be considered to embody average stability characteristics. The principal characteristics of the assumed airplane are as follows:

Weight, W	1,600 lb.
Wing span, b	32 ft.
Wing area, S	171 sq. ft.
Wing loading, W/S	9.4 lb. per sq. ft.
Area of fin and rudder	10.8 sq. ft.
Tail length	14.6 ft.
I_X	1,216 slug-ft.^{2}
I_Z	1,700 slug-ft.^{2}

ROLLING ACTION

It is recognized that different types of airplanes require different amounts of control. At the start of the wind-tunnel investigation of lateral control devices (reference 1) a rolling criterion ($RC=C_l/C_L$) representing a conservative lower limit of rolling control for all types was assumed. The assumed satisfactory value of the rolling criterion was 0.075, which corresponds to a lateral movement of the center of pressure of 7.5 percent of the wing span. Recent experience indicates that this value is likely to be ample for any condition of flight that might be encountered and is therefore a desirable value to attain. Where a compromise must be made between the rolling moment and some other characteristic of the control system, particularly the control force, a decidedly lower value of the rolling criterion may be used. It appears that a value possibly as low as half the original one may be found reasonably satisfactory for practically all conditions of flight with nonacrobatic airplanes.

The criterion of rolling control used in the present analysis is the angle of bank attained in 1 second following a sudden deflection of the control. This criterion shows the actual amount of motion produced and depends on both the acceleration at the start and the final rate of roll. It includes the effect of yawing moment given by the control as well as the stability characteristics and moments of inertia of the airplane. The values of the criterion are found by computation and as such are applicable only to the particular type of airplane (F–22) that has been assumed.

Experience gained in flight tests of the Fairchild 22 airplane with various lateral control devices indicated a minimum satisfactory amount of rolling control corresponding to about 15° of bank in 1 second. (See fig. 1.) Ailerons capable of giving this amount of bank

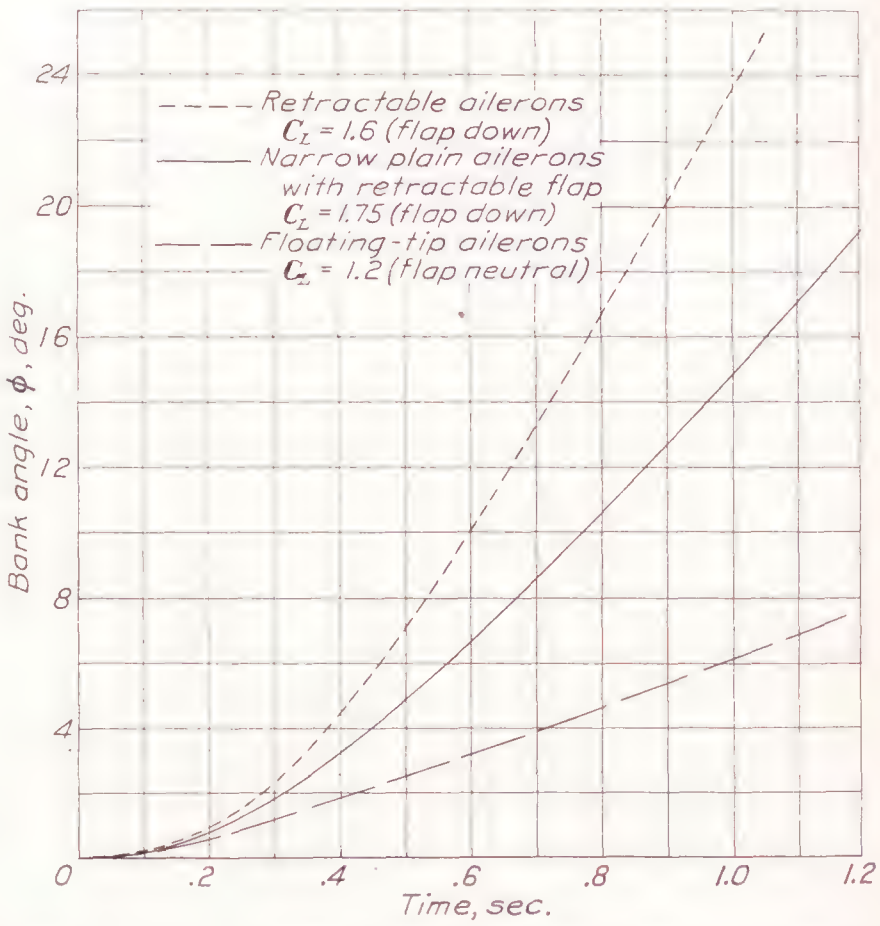

FIGURE 1.—Banking of Fairchild 22 airplane after sudden deflection of lateral control devices at low speed. (The narrow plain ailerons and the retractable ailerons were considered to give a satisfactory amount of control; the floating-tip ailerons were reported as weak.)

at low speed have been found reasonably satisfactory in practice with this type of airplane. Owing to the present general use of high-lift flaps on airplane wings, the size and deflection of ailerons are usually determined by the low-speed condition of flight with the flaps deflected. For comparative computations, in the present report, a lift coefficient of $C_L=1.8$ is assumed as representative of the low-speed condition of flight with

flaps. The sizes or deflections of the lateral controls are selected in each case to give an angle of bank of 15° in 1 second at C_L=1.8.

In addition to providing a sufficient amount of banking motion, two further desirable characteristics of the rolling action are: (1) The response of the airplane in roll to any movement of the lateral control surface should be immediate, any noticeable delay or hesitation in the action being objectionable; and (2) the action should be so graduated that the acceleration and maximum rate of roll increase smoothly and regularly as the stick deflection is increased. Conventional ailerons or similar lateral control devices located near the trailing edge of the wing easily meet these requirements and show, in analyses of motions recorded in flight, practically instantaneous response of rolling acceleration to control-surface movement. From 0.1 to 0.2 second is ordinarily required to deflect the surfaces and, during this interval, the rolling acceleration apparently keeps pace, although only a slight amount of rolling motion is accumulated by the time of full deflection. Comparison shows that good synchronization of the calculated motion with the flight records was obtained when the assumed full deflection was taken at the instant the actual deflection reached half its ultimate value. This assumption was used in the computations for plain ailerons and other devices that gave no indication of sluggish response characteristics.

CONTROL FORCE

During the course of the lateral control investigation it became apparent that the force required to move the controls is of extreme importance in obtaining satisfactory lateral control. As shown by the flight tests of references 2 and 3, an airplane that requires a light control force is likely to seem more controllable to a pilot than one that requires a heavy control force, even though with full deflection the heavier control may be considerably more powerful than the lighter one. It seems desirable to have the control force as light as possible and yet to maintain the feeling of a definite neutral position. This characteristic is especially important in the aileron control since the effort expended in moving the stick sidewise is relatively greater than for other control movements. (See reference 5.) Correlation of test-flight reports and control-force records indicates that the forces required to operate the ailerons should not exceed about 8 pounds in order to be considered desirable. A lower limit of stick force of about 2 pounds at full deflection is apparently considered essential so that there may be a noticeably regulated increase of force with deflection. Friction of the control mechanism plays an increasingly important part as the operating force is reduced and should in no case be great enough to mask the "feel" of the control. It is probable that with sufficiently little friction a force not greatly in excess of 2 pounds would be considered most desirable. A force of 15 pounds is to be considered excessive.

As previously stated, the size or maximum deflection of the control devices compared in this paper have been selected to give an angle of bank of 15° in 1 second following full deflection and considering the average airplane fitted with a high-lift flap and flying at a lift coefficient of 1.8. The ailerons are compared (see table I) on the basis of the stick force required to attain this angle of bank of 15° in 1 second at lift coefficients of 0.35, 1.0, and 1.8, which compose the usual flight range. The lift coefficient of 0.35 represents the conditions of high-speed and cruising flight. The lift coefficient of 1.0 is considered to represent two conditions, the first being that of low-speed flight without a flap, such as is used in an approach to a landing with an unflapped airplane, and the second being one with a flap fully deflected, which represents as high a speed as is usually attained in that condition. The value C_L=1.8 can be obtained only with the flap deflected and represents the low-speed flight condition with the high-lift device in use. When representative values of this nature are used, it is necessary to examine the complete original data to show that the critical values are representative of conditions throughout the flight range. Such an examination has been made for the comparisons of the present report.

The stick force for a 15° bank in 1 second is used as the basis of comparison at all flight speeds and lift coefficients even though the conventional ailerons will produce a decidedly greater bank in 1 second at higher speeds. The 15° value is taken throughout because it is considered to represent the maximum control likely to be used in ordinary flight at any speed and is therefore of greater interest as a basis for stick forces required than the maximum possible deflection, as long as the force at maximum deflection does not approach the strength of the pilot.

The data for some of the ailerons were obtained with plain unflapped wings with which a lift coefficient of 1.8 could not be attained and, in order to have all the lateral control devices on a comparable basis whether mounted on flapped or unflapped wings, their sizes and maximum deflections were selected to give essentially the same rolling effect as the others at a lift coefficient of 1.0. The analysis showed that conventional ailerons which give an angle of bank of 15° in 1 second on a flapped wing at a lift coefficient of 1.8 could, when fully deflected, give an angle of bank of 22.5° with the flap retracted at a lift coefficient of 1.0. The ailerons on the unflapped wings were therefore selected to be capable of giving 22.5° bank in 1 second at a lift coefficient of 1.0, but the values of the stick forces required were computed for partial deflections giving a 15° bank in 1 second at lift coefficients of both 1.0 and 0.35. The first aileron of table I is of the conventional unbalanced flap type on a rectangular wing of aspect ratio 6. It has a chord 0.25 c_w and a span 0.40 $b/2$ and has equal

up-and-down linkage. It will be noted that, for an airplane equipped with these ailerons, the stick force computed for a 15° bank in 1 second at the cruising-flight condition is 4.7 pounds with aileron deflections of only ±3.4°. At a lift coefficient of 1.0, representing the low-speed flight condition for the unflapped wing, the same amount of control was obtained with a stick force of 3.6 pounds and aileron deflections of ±7.4°. All the stick forces are given for an assumed aileron linkage such that at the maximum deflection the control stick, which has a length of 20 inches on the Fairchild 22 airplane and is so assumed for the average airplane, is deflected 25° from neutral. The maximum aileron deflection is 11.2° and is the deflection required to produce a bank of 22.5° in 1 second at C_L=1.0. Here the ailerons are not being taxed to their fullest extent.

The maximum amount of control specified in a design has a predominating effect on the operating force. Figure 2 shows a calculated example of the variation of

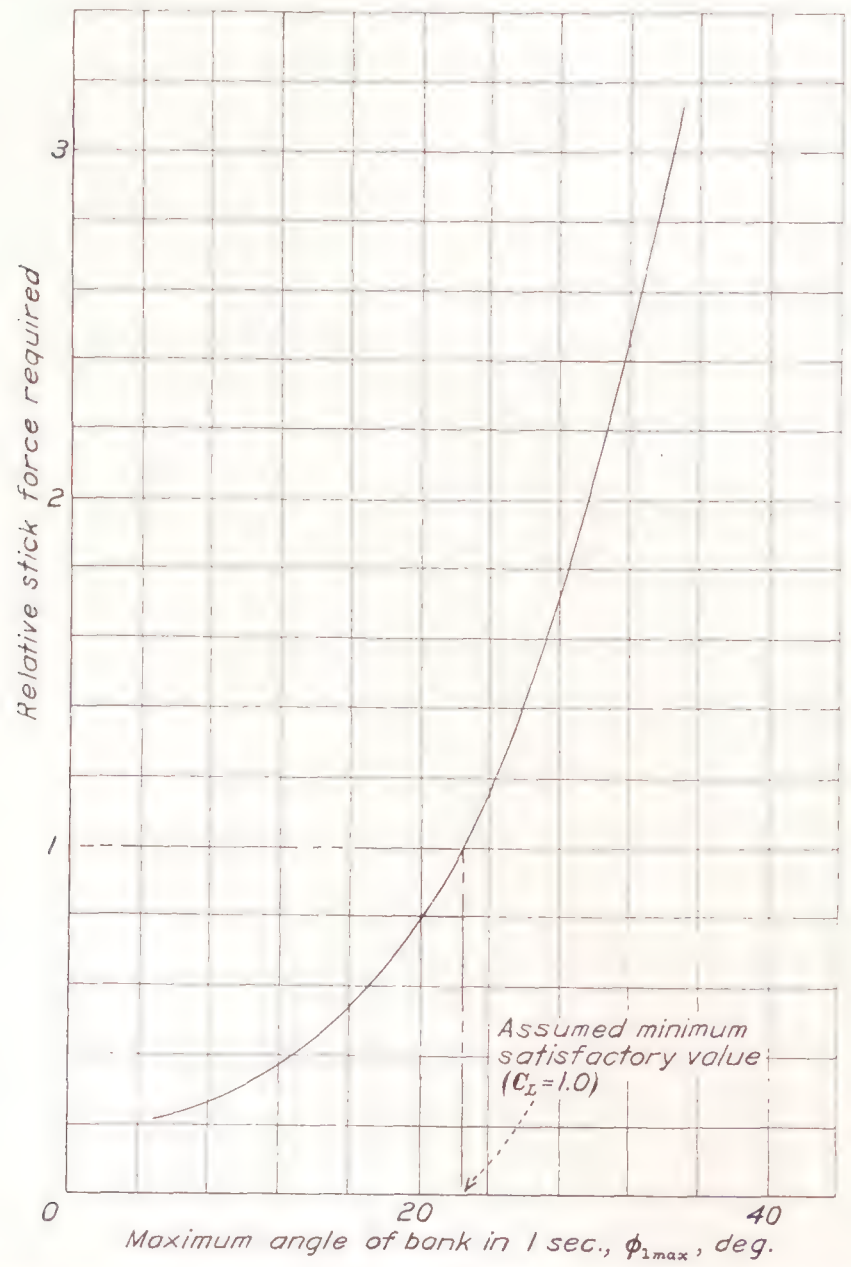

FIGURE 2.—Relation between stick force and maximum amount of control obtained. Fairchild 22 type airplane; 0.80 $\frac{b}{2}$ sealed ailerons deflected ±20°; aileron chord varied.

operating force with specified control in which it was assumed that ailerons with equal up-and-down motion and the most efficient length and deflection (±20°) were used in each case. The rate of increase of operating force with amount of control depends on the manner in which the increase of control is obtained, as will be more fully developed in a later section.

YAWING MOTION AND SIDESLIP

The effect of the yawing moment produced by the ailerons is considered in two ways. First, the secondary effect of yaw on the rolling motions is inherently included in the computed banking effectiveness. Thus, the bank in 1 second is that produced by the ailerons without aid from the rudder. If it is assumed that a sufficiently powerful rudder were used in such a way as to prevent sideslip, a given aileron device would, in general, produce a somewhat greater banking effect. This assumption is not used here, however, and the deflections of the control surfaces given in table I are those required to produce the specified angle of bank in 1 second with the particular combination of rolling and yawing moments produced by the aileron in question.

The second effect considered is the sideslip produced by the sudden use of the aileron control for banking. In flight the rudder is used to avoid sideslipping and the amount of rudder action necessary for this purpose is in direct proportion to the sideslip incurred by the ailerons alone.

The angle of sideslip accompanying a 15° bank in 1 second following the sudden displacement of the lateral controls is also given in table I. The first aileron listed, it will be noted, produces a sideslip of 7° at C_L=1.0 and of 3° at C_L=0.35 when the rudder is not used to correct for this condition.

LATERAL STABILITY

In the ordinary unstalled-flight range the effects of the lateral-stability factors on the lateral control obtained are included in the computations of the angle of bank reached in unit time. The angle of bank ϕ_1 is the angle that would be produced by the control operating on the average airplane. The effect of a given control on an airplane of greatly different lateral-stability characteristics might, of course, be considerably different than indicated in this case.

One of the most important factors in the interaction of lateral stability and control below the stall is the effect of the secondary yawing moment induced by the control and an allowance for this effect should be made in the proportioning of the airplane for lateral stability. Modifications that tend to increase spiral stability in free flight (namely, reduced vertical-fin area and increased dihedral) tend to render the airplane uncontrollable under the action of ailerons giving adverse yawing moment. The degree of "weathercock" stability should be sufficient to restore the airplane from a yawed attitude when the wings are held level by use of the ailerons. For safety in this respect the ratio of adverse yawing to rolling moment given by the ailerons should not be allowed to approach the ratio of yawing to rolling moments that naturally act on the airplane either

in pure sideslipping or pure yawing motion. (See reference 6.)

One of the lateral-stability factors, the damping in rolling, has been shown by the analysis in reference 4 to have a critical effect on the controllability obtained, satisfactory lateral control requiring that positive damping exist. Since the damping in rolling depends on a positive slope of the lift curve, the damping exists only at angles of attack of the outer portions of the wing that are below the maximum lift coefficient. While some semblance to control may be obtained at angles of attack above the stall if controls giving favorable yawing moments as well as sufficiently powerful rolling moments are used, the instability associated with uneven stalling and autorotation is so violent that it is necessary for the pilot to use the controls continually to keep the airplane near the desired attitude. If sufficiently rapid rolling is once started, either by the controls themselves or as the result of gusty air, it cannot be stopped. The angle of attack at which the damping in rolling becomes zero and above which autorotation takes place ($\alpha_{L_p=0}$) is used herein as an indication of the limit of the flight attitude above which satisfactory lateral control cannot be obtained. This value was given in the reports of reference 1 for both the angle of attack at which autorotation was selfstarting and the angle of attack at which the damping became zero when the wing was rotating at the rate $pb/2V=0.05$, a value representative of the rolling likely to be caused by gusty air. The latter value of α has ordinarily been found to be about 1° lower than the former value and, being therefore more decisive, is used in the present report. The difference between the angle of attack for zero damping and the angle of attack for the maximum lift coefficient of the entire wing $(\alpha_{L_p=0}-\alpha_{C_{L_{max}}})$ has been tabulated under Lateral Stability to show whether the maximum lift coefficient can be expected to be reached in flight before satisfactory lateral control is lost. It will be noted that for ailerons 3 and 4 the wing loses its damping in roll at an angle of attack 1° higher than that at which the maximum lift coefficient is reached. Thus, as far as the stability is concerned, lateral control should be possible throughout the entire unstalled-flight range, including the angle of attack for maximum lift coefficient.

WING PERFORMANCE CHARACTERISTICS

The same criterions used throughout the reports of reference 1 to show the relative performance characteristics of the wings are used in the present report and are tabulated in the last three columns of table I. The maximum lift coefficient $C_{L_{max}}$ is given as an indication of the wing area required for a desired minimum speed. The ratio $C_{L_{max}}/C_{D_{min}}$ is an indication of the speed range and, for a given minimum speed, shows the relative effects of the wings on the maximum speed attainable. The ratio L/D taken at a value of the lift coefficient $C_L=0.70$ is an indication of relative merit in climbing flight. In a series of performance computations made for airplanes of different wing loadings and power loadings and with both plain and slotted wings, this criterion was found to be satisfactory throughout the entire range. It should be noted that the comparative values used in the present report are based on tests made in the 7- by 10-foot atmospheric wind tunnel and hence do not coincide in absolute value with results of tests made at different Reynolds Numbers.

APPLICATION TO AIRPLANES OF DIFFERENT SIZES AND LOADINGS

Because the flight experience that led to the specification of a satisfactory degree of control was restricted to the Fairchild 22 type of airplane, there is some doubt about the application of this experience to other types and especially to large or very small airplanes. The Fairchild 22 type of airplane, of course, serves as well as any other when different aileron devices are simply compared among themselves. The principles governing the extension of the computations of motion to geometrically similar airplanes of different sizes and loadings are well known and can be applied here, but this extension of the computations does not definitely answer the question as to what constitutes a satisfactory degree of control for large (or very small) airplanes.

According to the principles of dynamical similarity, large or small similar airplanes of the same wing loading would show the same linear rise and fall of the wing tips $\left(\frac{\phi_1 b}{2}\right)$ during a 1-second banking motion. Large and small airplanes do actually show a tendency toward similarity in important dimensions and size of control surfaces, and it seems logical to assume that a given value of the vertical distance described by the wing tips within 1 second following a sudden control deflection that represents a satisfactory amount of control for the Fairchild 22 airplane should be satisfactory for any size of airplane.

For similar airplanes the linear distance described by the wing tips in banking $\left(\frac{\phi_1 b}{2}\right)$ is independent of the size. Figure 3 shows this distance plotted against wing loading and gives the separate effects of rolling and yawing moments of coefficient 0.01 at different lift coefficients. The banking effect of any combination of rolling and yawing moment may be found by superposition, i. e.,

$$\frac{\phi_1 b}{2}=\frac{C_l}{0.01}\left(\frac{\phi_1 b}{2}\right)_{C_l=0.01}+\frac{C_n}{0.01}\left(\frac{\phi_1 b}{2}\right)_{C_n=0.01} \qquad (1)$$

The ordinates of the figure give directly the circumferential displacement of the wing tip in feet for a unit of 0.01 rolling- or yawing-moment coefficient. It is important to note that the banking effects of rolling and yawing moments can be separately considered and later added in any desired proportion to obtain the total combined effect.

The computations show that, in general, smaller values of the control-moment coefficients are required to produce a given wing-tip displacement in a unit of time for the more heavily loaded airplanes. Another point of interest in connection with the secondary adverse yawing moments produced by conventional-type controls is that these moments are more effective in hindering the control with lightly loaded airplanes than with heavily loaded ones. Note that in the usual case the banking effect of the yawing moment is to be deducted in equation (1) since this moment is usually adverse and therefore negative.

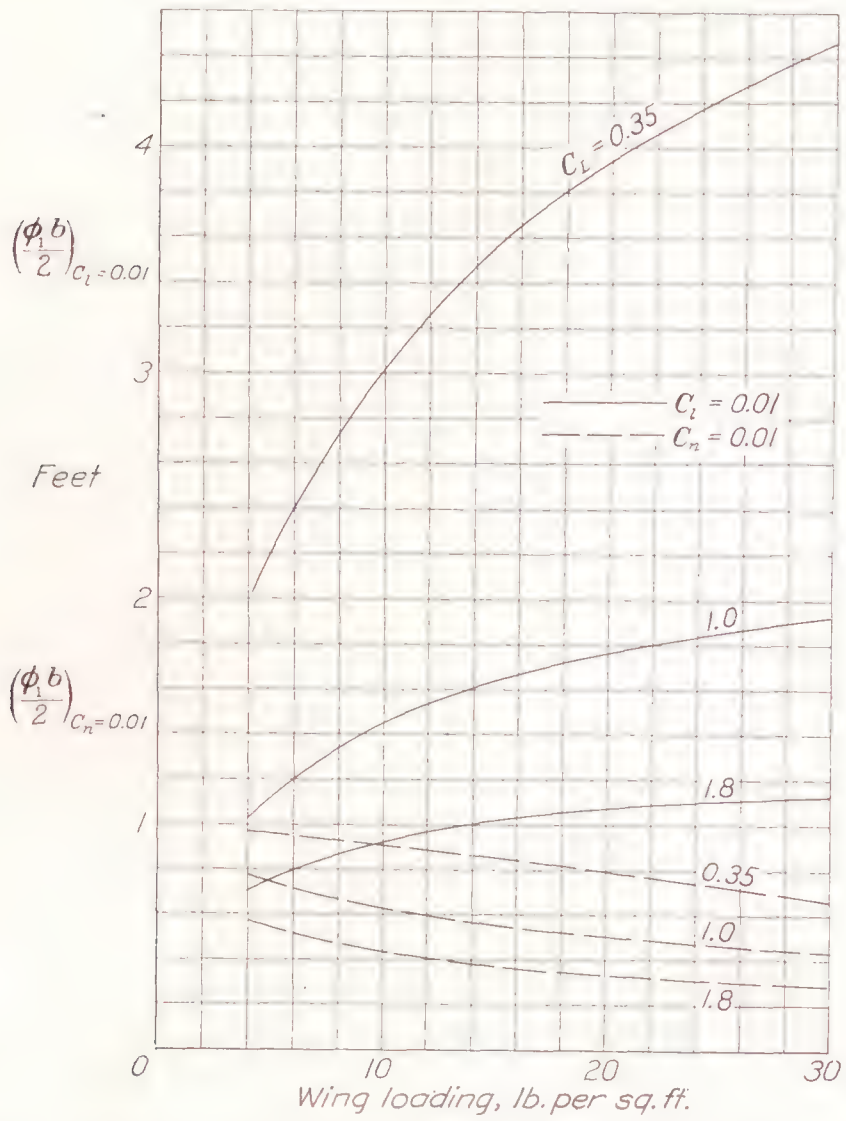

FIGURE 3.—Wing-tip displacement produced in 1 second by suddenly applied rolling and yawing moments for different wing loadings and flight speeds.

$$\frac{\phi_1 b}{2} = \frac{C_l}{0.01}\left(\frac{\phi_1 b}{2}\right)_{c_l=0.01} + \frac{C_n}{0.01}\left(\frac{\phi_1 b}{2}\right)_{c_n=0.01}$$

The variation of control force with size and loading of the airplane may be determined from general rules as in the case of the variation of the amount of rolling motion. As shown by figure 3, heavily loaded airplanes require smaller control-moment coefficients for a comparable amount of control than do lightly loaded airplanes. In general, a heavily loaded airplane that is otherwise similar to a lightly loaded one will have smaller control surfaces. On the other hand, the heavily loaded airplane will fly at a higher speed so that the dynamic pressure will be greater. Figure 4 shows a calculated example of the variation of stick force with wing loading at a given lift coefficient and for a given maximum amount of control. Here, as in figure 2, the most efficient combination of size and deflection is assumed for each point. Figure 4 shows that the stick force required to obtain a given angle of bank in 1 second is practically the same for all wing loadings up to 10 pounds per square foot but that it increases somewhat as the wing loading increases further.

With moderately large airplanes, somewhat higher stick forces are apparently tolerated by pilots without serious objection. With extremely large airplanes, however, the operating force becomes too great to be satisfactorily overcome by the pilot and either servo controls or auxiliary power is required. With auxiliary power, the pilot might presumably operate a valve or easily deflected controller governing a special power source that deflected the control surfaces. Under such conditions the magnitude and variation of the hinge moments would be relatively less important and the maximum deflection of the control surfaces would very likely be determined by the maximum rolling and yawing moments they could produce rather than by the hinge moments and the resultant deflecting force required. Although some indication of the relative performance of the various lateral control devices compared in this report can be obtained from the data as given, it would be desirable to reanalyze the original data given in references 1, 7, 8, 9, and 10 if a comparison on the basis of ailerons operated by auxiliary power were desired.

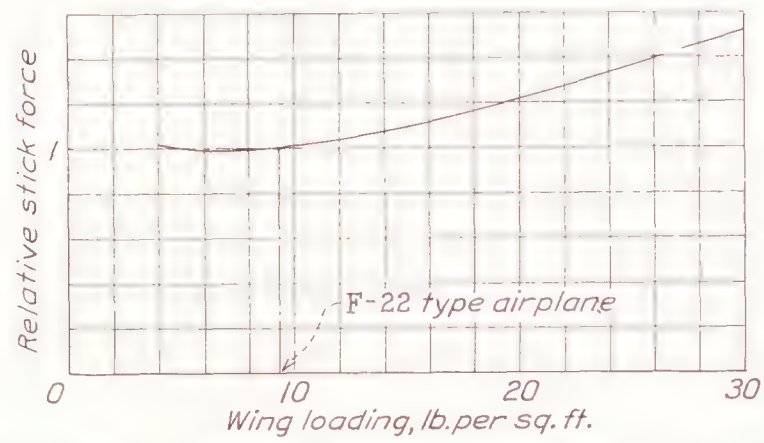

FIGURE 4.—Relation between the wing loading and the stick force required for a given amount of control ($\phi_{1_{max}}=22.5°$; $C_L=1.0$).

COMPARISONS OF VARIOUS DEVICES

PLAIN AILERONS

Effect of aileron and wing plan form.—The tests of reference 1, part I, were made with rectangular wings having ailerons of three different proportions: 0.25 c_w by 0.40 $b/2$ (which were taken as the standard for comparison throughout the series), 0.15 c_w by 0.60 $b/2$, and 0.40 c_w by 0.30 $b/2$. These sizes were selected to give approximately equal rolling moments with the same angular deflection. These ailerons are numbered 2, 3, and 4, respectively, in table I. With equal up-and-down deflection, the stick force is much larger for the short, wide ailerons than for the long, narrow ones and is, in each case, slightly less for the low-speed condition than for high speed. If a suitable differential linkage is employed, the stick forces at the low-speed

condition, where the wide ailerons have the advantage of a large floating angle, are quite low for all three sizes of aileron. At the high-speed condition, however, the 0.40 c_w by 0.30 $b/2$ aileron requires a rather high stick force, even with the best differential.

The sideslip incurred by an angle of bank of 15° in 1 second is not greatly different for the different aileron plan forms either with or without differential linkages. The values are slightly lower at C_L=1.0 with the differential linkages than with the equal up-and-down, and with the 0.25 c_w by 0.40 $b/2$ plan form than with either of the others.

It is possible by methods to be described in section II to compute an optimum size of the aileron, i. e., the size giving the desired amount of control with the least stick force. The effect of varying the aileron span and chord is shown in figure 5, the chord for each span value being

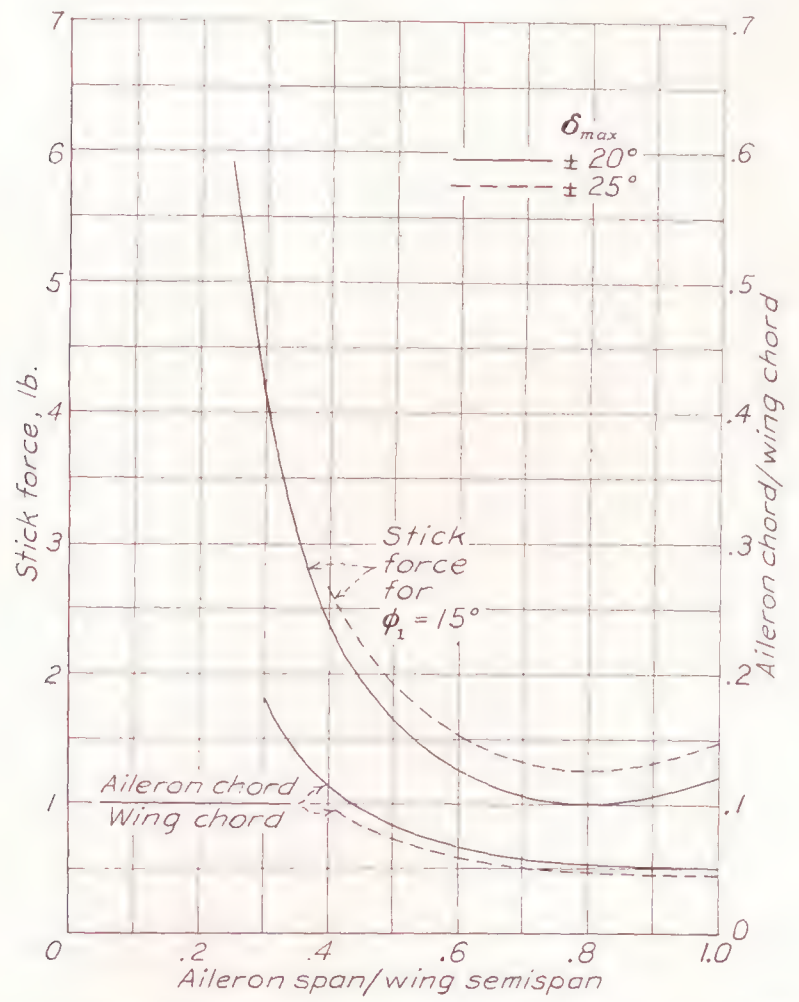

FIGURE 5.—Variation of stick force with aileron span. Aileron chord proportioned to give $\phi_{1_{max}}$=22.5° with maximum deflection of ±25° and ±20°; rectangular wing; average airplane; C_L=1.0; sealed ailerons.

the smallest that will give an angle of bank of 15° in 1 second with the assumed average airplane. From this figure it is apparent that with equal up-and-down deflection an aileron span of 80 percent of the wing semispan will give the lowest stick force, but the variation is small for ailerons between 60 percent and 100 percent of the wing semispan. Other computations not shown lead to the same conclusion for ailerons having differential linkages.

The relations of aileron chord and span, considering especially that the hinge moment increases with the square of the chord while the rolling moment increases only as the square root of the chord, are such that lower stick forces are obtained with narrower chords. The narrower ailerons require greater deflections and the reduction in chord size is limited by the fact that deflections greater than about ±20° are inefficient. Marked separation of the air flow takes place at about this angle of deflection on all the conventional flap-type ailerons tested and, as shown by the typical curves of figure 6, the rolling-moment coefficients increase at a lower rate beyond 20° deflection. If it is attempted to

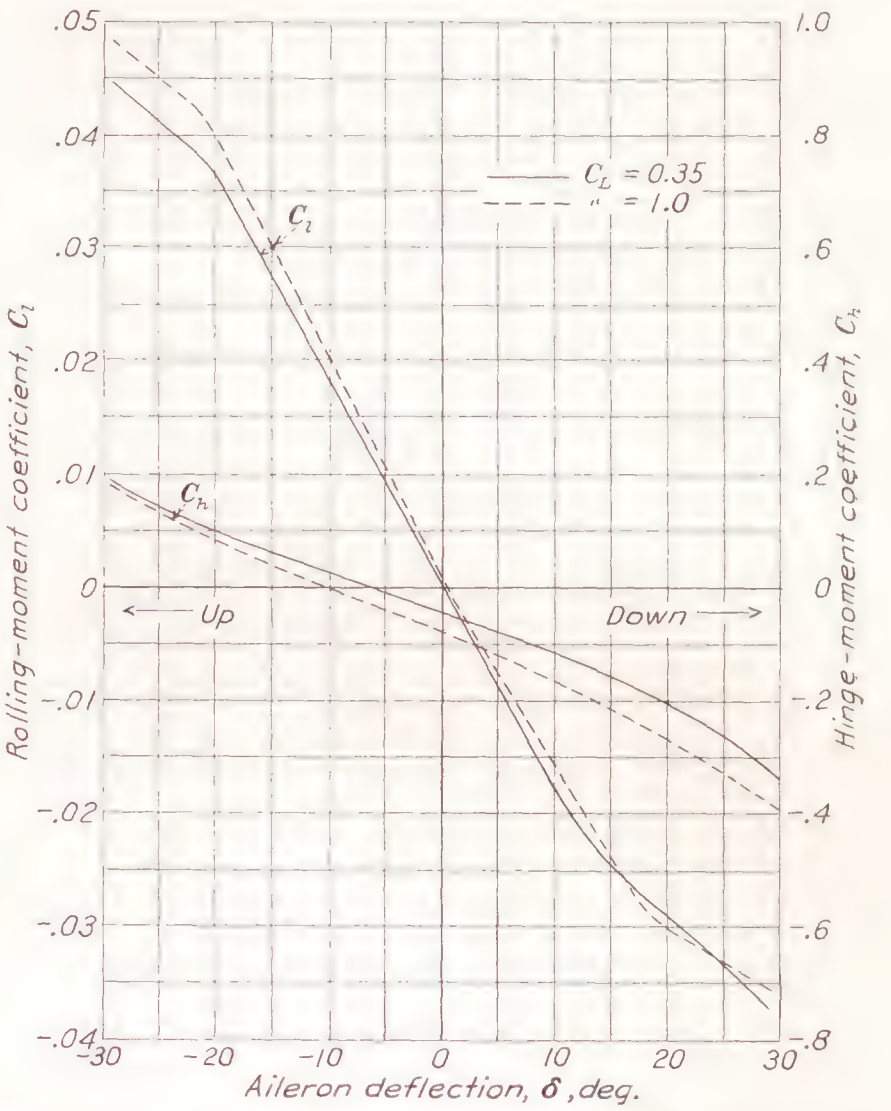

FIGURE 6.—Typical rolling- and hinge-moment coefficient curves for plain ailerons.

reduce further the chord of the aileron by extending the deflection beyond this break, the stick force will be higher because of the loss in mechanical advantage. Figure 5 illustrates this point, for when an aileron deflection of ±25° is assumed, narrower ailerons are required but the stick force is larger for all aileron spans than with a deflection of ±20°.

Aileron 5 (table I) represents the narrowest sealed aileron covering 80 percent of the wing semispan that gives the required control with a deflection of ±20°. The aileron chord in this case is only 5.3 percent of the wing chord, and the stick forces are lower than for any of the previous ailerons. If a differential motion is used, a somewhat wider aileron is required. With narrow ailerons the floating angle is very small, and a tab is required to make the ailerons float at a sufficiently high angle that the differential linkage will be effective in reducing the stick force. (See reference 11.) Aileron 6 of table I is the smallest one covering 80 percent of the semispan that will give the required

amount of control with a differential motion and with suitable aileron tabs. The assumed tab covers the entire trailing edge of the ailerons, has a chord 1.5 percent of the wing chord, and is permanently bent downward 14°. For this case the entire aileron chord including the tab is 7.8 percent of the wing chord and the stick force is only 0.5 pound for the high-speed condition and 0.1 for low speed.

These values of stick force are lower than are considered desirable for the Fairchild 22 airplane but are interesting in showing the possibility of obtaining a satisfactorily low stick force in larger and heavier airplanes. For small airplanes, one satisfactory method of increasing the stick force to the value desired would be to use greater up travel than 20° with differential ailerons, thus getting into the range of inefficient stick force although obtaining the advantage of slightly smaller adverse yawing moments.

In many practical cases the chord of the aileron varies along the span. Inasmuch as the hinge moment varies as the square of the chord and the control effectiveness only about as the square root of the chord of an aileron element, the stick force required to give a certain amount of control is inherently greater if the chord of the aileron varies appreciably along the span. This relation is true in spite of the fact that the portion of the aileron nearer the tip of the wing has a greater lever arm, which suggests that it might be advantageous to increase the chord of the aileron as the wing tip is approached. Thus, it is possible to state as a general rule that to obtain the lowest stick force, ailerons should have an essentially constant chord over their entire span.[1]

On wings having rounded tips it is sometimes the practice to use ailerons having skewed hinge axes like aileron 7 in table I. This aileron corresponds in span, area, and gap to the 0.25 c_w by 0.40 $b/2$ aileron 2, but the stick force is decidedly higher for the skewed ailerons on account of the variation of the aileron chord along the span.

Ailerons 8 and 9 of table I are of tapered plan form and are mounted on tapered wings. In the computations of the rolling effect with the tapered wings the reduction in the moments of inertia due to the taper are taken into account. For example, for the wing with 5:1 taper, the value of I_X was changed from 1,216 slug-feet^2 for the original average airplane to 860, and the value of I_Z from 1,700 to 1,400 slug-feet^2. The lateral-stability derivatives were also changed to take account of the taper. (See reference 4.)

A comparison of ailerons 8 and 9 with aileron 1, which has the same relative chord size but is attached to a rectangular wing, shows that the stick force becomes lower as the taper of the wing is increased. The sideslip or adverse yawing effect is also smaller with the tapered wings than with the rectangular. The lateral-stability factor, damping in roll, is reduced to zero at an angle of attack 3° below the stall with the 5:1 tapered wing, indicating that the airplane could not be safely maintained at the maximum lift condition in flight.

The ailerons on tapered wings dealt with up to this point have had chords that were the same percentage of the wing chord at each position along the span, the ailerons tapering with the wings. It has been stated that the lowest stick force would be obtained with constant-chord ailerons. Computations have been made comparing the straight or constant-chord ailerons on a tapered wing with the ailerons that taper with the wing, and the results are shown in figure 7. The straight

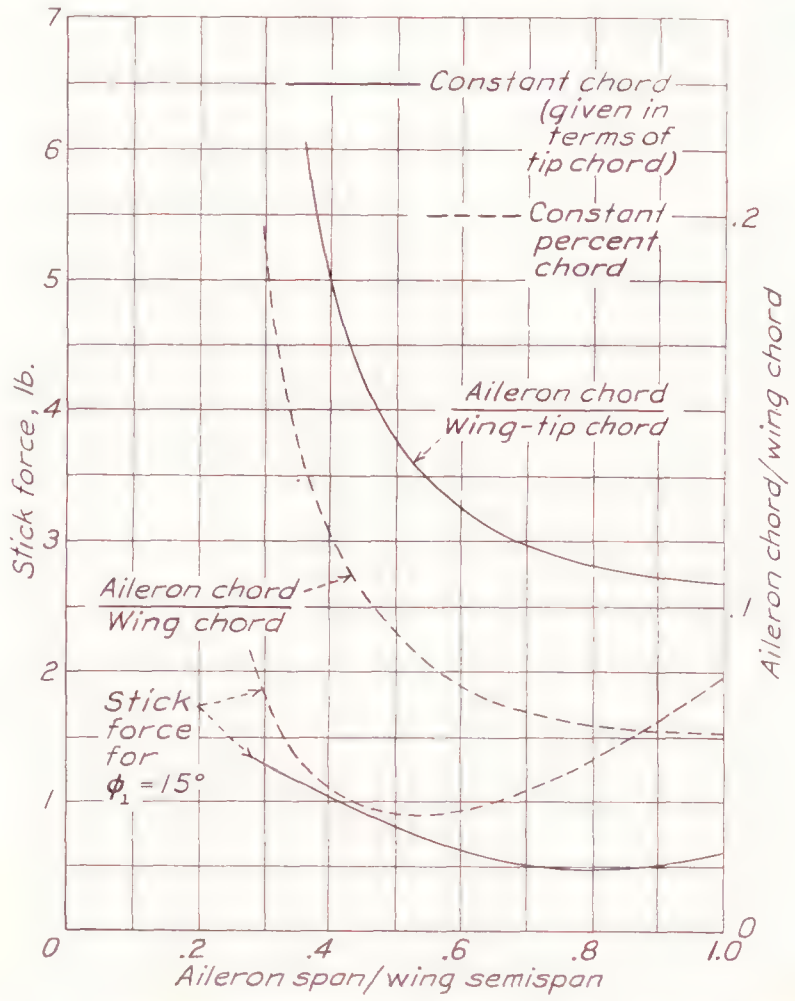

FIGURE 7.—Variation of stick force with aileron span and chord for straight and tapered ailerons on 5:1 tapered wing. Aileron chord proportioned to give $\phi_{1_{max}}$ = 22.5° with maximum deflections of ±20°; C_L = 1.0; sealed ailerons.

or constant-chord ailerons require lower stick forces for any given aileron span. It is interesting to note that with tapered ailerons the aileron span giving the lowest stick force is about half the wing semispan; whereas with constant-chord ailerons the best aileron span is 80 percent of the wing semispan, as it is in the case of rectangular wings. Ailerons 10 and 11 are the optimum sizes for the tapered and straight ailerons, respectively, on a 5:1 tapered wing. With equal up-and-down deflections, the stick forces for the straight ailerons are about half those for the tapered. In either case the stick forces could be nearly counterbalanced by means of a suitable differential linkage and tab, as will be developed more fully in section II.

Effect of hinge gap.—Wind-tunnel tests have shown that even a slight gap between ordinary unbalanced ailerons and the wing upon which they are mounted

[1] The greatest taper mathematically compatible with a minimum stick force is ess than about 3 percent of the aileron chord.

causes a relatively large loss in rolling moment. This loss for unbalanced flaps having a gap of one thirty-second inch on a wing of 10-inch chord was found to be approximately 30 percent. The hinge moment is also reduced by the gap but to a much lesser extent and the resultant stick force for a given amount of lateral control is greater because a larger aileron deflection is required, which necessitates a linkage having a poorer mechanical advantage. The effect on the stick force is shown in table I by a comparison of the values for aileron 2, which has a gap, with those for aileron 1, which is sealed.

BALANCED AILERONS

Balanced ailerons of the Frise and Handley Page types are widely used at the present time, the particular forms of aerodynamic balance incorporated in these ailerons giving improved yawing moments as well as reduced hinge moments. Good results are obtained with proper designs but the exact shape of these ailerons has a critical effect on the rolling and hinge moments, and each different installation is likely to require considerable individual development. Figure 8 shows typical curves of rolling and hinge-moment coefficients for Frise type ailerons. The rolling-moment coefficient for the example shown increases less rapidly with deflection after an upward angle of 7° to 10° has been reached, which is considerably lower than the 20° critical deflection for plain unbalanced ailerons (fig. 6). Thus, it is uneconomical with respect to stick force to use large up deflections and, owing to the smaller maximum deflections, larger ailerons are required for efficiency than when ailerons of the plain unbalanced sealed type are used. The break in the curve of rolling-moment coefficient against deflection is associated in the case of the Frise and Handley Page types of aileron with the downward projection of the nose of the aileron and the resultant breaking away of the flow from the under side of the aileron. This effect can be reduced or possibly eliminated by using a raised-nose portion.

The Frise and Handley Page types of aileron have gaps between the aileron and the wing, and the effectiveness of the ailerons cannot be assumed equal to that of smoothly sealed flaps.

The hinge-moment curves as shown in figure 8 have very low and even negative slopes at places, and extreme differential linkage cannot be used because overbalance would occur with medium or small deflections of the up aileron. Because the hinge-moment curves are far from straight, it is more difficult to select suitable differential linkages for ailerons of this type than for plain unbalanced ailerons. Satisfactory linkages have often been obtained in practice, however, and there are many excellent examples in which a nice balance of conditions has been obtained with satisfactory control and light stick forces.

Ailerons 12 and 13 are examples of the Frise type. A comparison of aileron 12 with the same size of plain unbalanced but sealed ailerons shows that the stick forces at the low-speed condition are about the same for both types of aileron, both with equal up-and-down and with differential motion. At the high-speed condition the Frise ailerons have somewhat lower stick forces than they have for the same control at low speed. It is worthy of note that, although the deflections are small in both cases, the Frise ailerons are apparently not greatly oversized for, in their case, substantially greater deflections would be inefficient. The plain ailerons, on the other hand, have maximum deflections well under the limiting 20° value and are decidedly oversized, considering the amount of control specified.

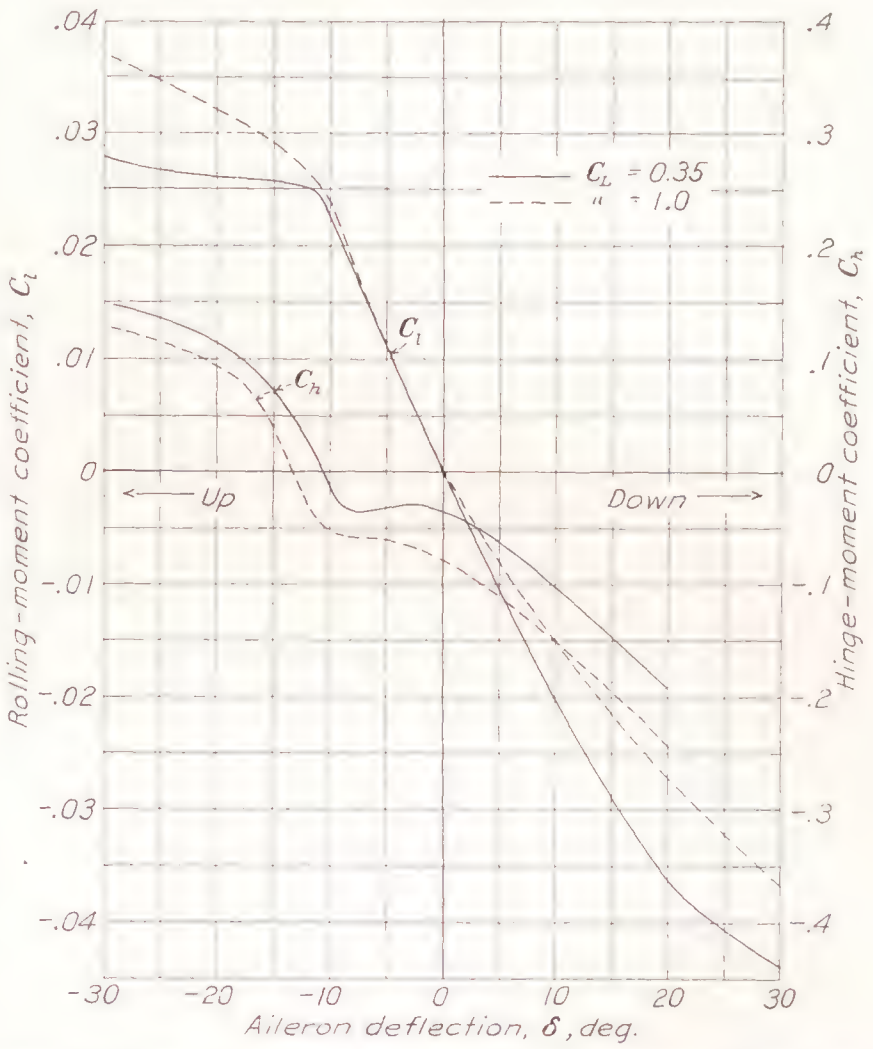

FIGURE 8.—Typical rolling- and hinge-moment coefficient curves for Frise ailerons.

If a fixed tab is used to trim the ailerons upward, lower values of stick force can be obtained with the plain unbalanced ailerons (reference 11). The tab will not give the same improvement with the Frise ailerons because of the varying slopes of the hinge-moment curves.

The 0.40 c_w by 0.30 $b/2$ Frise aileron 13 has a different sectional form than aileron 12 in that the nose portion is raised, and this aileron gives smoother curves of rolling and hinge-moment coefficients. The Frise aileron with the raised nose shows no improvement in yawing effect over the plain unbalanced ailerons of the same size, but the 0.25 c_w by 0.40 $b/2$ Frise aileron, which has the more typical Frise sharp nose, gives a slight improvement in this respect.

The drag of all commonly used forms of Frise and Handley Page ailerons is sufficiently great to be considered a serious disadvantage in connection with

modern high-performance airplanes. For this reason, the development of a type of aerodynamic balance that does not add to the drag is desirable.

FLOATING-TIP AILERONS

Conventional ailerons operating on a lifting portion of the wing suffer several fundamental disadvantages. First, the production of rolling moment by a lifting wing gives rise to the adverse yawing moment; and, second, the loss of lift at the stall is accompanied by a loss of effectiveness of the ailerons. It has become apparent during the investigation, however, that the stall of the wing or, at any rate, of the outer portions of the wing, is accompanied by such a loss of stability that it is hardly an advantage to retain aileron rolling moments in this condition.

In the case of floating-tip ailerons, control is secured by surfaces that contribute no lift. This arrangement avoids both the adverse yawing moment of ordinary ailerons and the loss of rolling moment associated with stalling of the main wing; but it increases the drag of the airplane and adds to the over-all dimensions. If the airplane is designed to fulfill certain performance specifications, such as landing speed, climb, ceiling, etc., the floating-tip ailerons cannot be considered an integral part of the main wing as they do not contribute effectively to the area or span so far as induced drag and lift are concerned.

A number of floating-tip aileron devices were tested in the course of the investigation of reference 1. Apparently the most usable of these are the tip ailerons on the 5:1 tapered wing. Two methods of comparison have been followed. In one case (aileron 14) the ailerons were included within the over-all dimensions of the 5:1 tapered-wing average airplane. The values given in the table for this case (short wing) were based directly on the results of tests made in the 7- by 10-foot wind tunnel (reference 1, part XI). The criterions show the effect of reduced area and span of the lifting portion of the wing as a reduction of the climb and maximum lift.

In order to take account of the effect of simply adding a tip aileron to a normal-size wing, further calculations were made. In this case (aileron 15) it was assumed that the over-all span of the average airplane was increased by the additional span of the tip ailerons; hence, the aspect ratio of the lifting portion of the wing remained the same. The added span of the wing, although it contributed practically no lift and hardly modified other stability characteristics of the airplane, considerably increased the damping in rolling. This fact was accounted for in the computations, data on damping of the tested 5:1 tapered wing with floating-tip ailerons included in the original plan form being extrapolated for this purpose. It would be natural to assume that the floating-tip ailerons would be just as effective as the main portion of the wing in contributing damping. The tests showed, however, that the damping of the 5:1 tapered wing with floating tips was only 85 percent of that with the tips rigid.

The rolling moments produced by floating-tip ailerons can be predicted with good accuracy by the conventional aileron theory. The induced yawing moments correspond to those given by plain ailerons with an extreme uprigging or negative droop corresponding to the neutral floating positions of the tip ailerons. Ordinarily, the tip ailerons, on account of the local upwash at the end of the rigid wing, float at a negative angle of attack relative to the mean direction of flight and hence give slight favorable induced yawing moments with respect to the wind axes. The yawing and hinge moments used in table I for the long-wing airplane (aileron 15) were predicted from the results of the wind-tunnel tests on the short 5:1 tapered wing.

The tabulated results of the computations show that the stick forces required for satisfactory control are reasonably low in the case of the short 5:1 tapered wing. It will be noted that only relatively small deflections of these ailerons are required for control, a fact that can be attributed partly to the reduced damping in rolling shown by this wing. On the other hand with the long wing, when the tip ailerons were added to the regular wing span, the damping in rolling and moment of inertia were increased and, hence, larger stick forces were required to produce the given bank. The same hinge-axis location, and hence the same degree of balance of the ailerons, were assumed in both cases. It will be noted that about the same force was required to produce 15° bank at high and low lift coefficients.

Although the floating-tip ailerons give small favorable yawing moments, it will be noted that their use results in some inward sideslip during the 15° bank. The rolling motion of the wing induces a small adverse yawing effect as is indicated by the adverse sign of the yawing moment due to rolling. This cause combined with the inward acceleration due to gravity is sufficient to bring about the inward sideslip in spite of the favorable yawing moment of the floating ailerons.

It has often been suggested that tip ailerons be trimmed by tabs so as to float downward and give some lift. Such an arrangement should improve the performance characteristics but would void the advantage of these ailerons in giving favorable yawing moments. If the tip ailerons were trimmed so as to produce as much lift as the adjacent rigid portion of the wing, it is to be expected that they would show the same proportion of adverse yawing moment to rolling moment as do conventional ailerons.

At stalling angles of attack for the main wing the floating tips remain unstalled. Hence, they should be expected to aid in preventing the loss of damping in rolling at or near the stall. The only floating aileron device that effectively prevented the loss of damping in rolling in the wind-tunnel experiments was the long nar-

row aileron attached to a rectangular wing. (See reference 1, part XI.) In this particular case the performance characteristics were so poor that the device as tested could not be considered practical for application.

As noted in table I, the lateral-stability characteristics of the 5:1 tapered wing with the floating-tip ailerons are almost as bad as those on the conventional rigid 5:1 wing and are somewhat worse than those of the rigid rectangular wing. Inasmuch as the damping in rolling is lost at an angle of attack 2° below the angle for maximum lift, the airplane could not be safely maintained in flight above this angle even though the ailerons continue to give undiminished rolling moments. Flight tests of floating-tip ailerons on a tapered wing fitted to a Fairchild 22 airplane support this conclusion.

Wind-tunnel results with floating-tip ailerons showed a smaller adverse effect on the performance characteristics of the 5:1 tapered wing than on any of those tested. The effect of reducing the span and area of the rigid portion of a given wing is shown by the comparison of the performance criterions of the short 5:1 tapered wing, having an over-all aspect ratio of 6, with those tabulated for the conventional rigid 5:1 tapered wing, having the same over-all span and area. Here the maximum speed of the airplane will be hardly affected while the climb and maximum lift will be reduced, as indicated. Simply adding the tip portions to the normal-size wing will increase the parasite drag at high speed but, as shown by the tabulated criterions for this case, will probably slightly improve the climb.

SPOILERS

Spoilers in the form of small flaps or projections raised from the upper surface of the wing have presented attractive possibilities as lateral control devices because they give positive or favorable yawing moments and large rolling moments at the high angles of attack through the stall. (See fig. 9.) As spoilers giving apparently satisfactory rolling and yawing moments had been developed in the 7- by 10-foot wind-tunnel investigation (reference 1, part V), they were tested in flight on a Fairchild 22 airplane (reference 2). When the spoilers were first tried in flight, the pilots noticed that the airplane apparently did not react until the control stick had been given a medium amount of deflection, after which the rolling velocity suddenly built up to a much higher value than had been experienced with any previously tested control system. This characteristic made it impossible to perform smooth maneuvers requiring the coordination of the spoilers with the elevator or rudder and led to overcontrolling when an attempt was made to keep the wings level in gusty air. Closer inspection of the spoiler action, however, disclosed that for any spoiler movement there was actually an appreciable delay between the movement of the spoiler itself and the start of the desired rotation in roll of the airplane. In order to substantiate the pilot's findings, records were made of the rotation of the airplane in roll immediately following a movement of the stick and a specimen

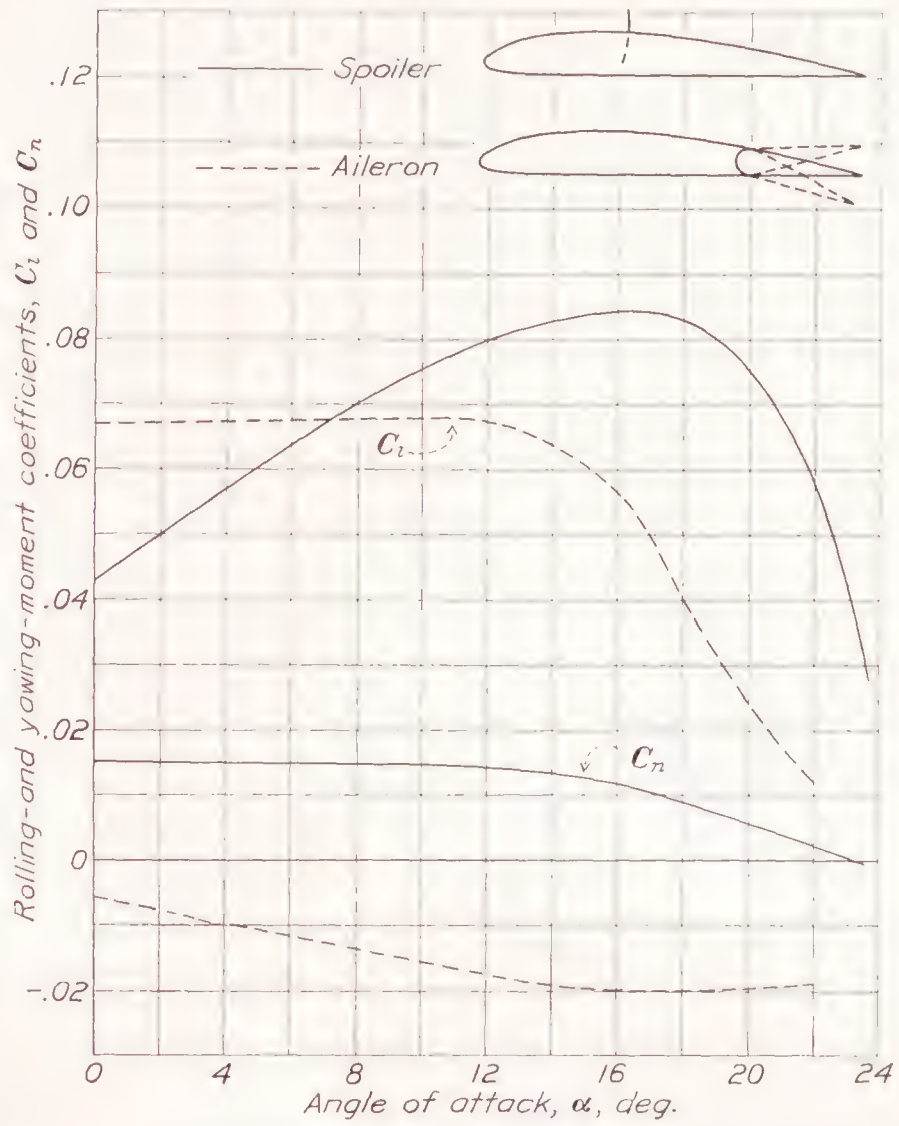

FIGURE 9.—Comparison of rolling- and yawing-moment coefficients obtained with ailerons and spoilers.

time history of the motion is shown in figure 10, together with similar information for other lateral con-

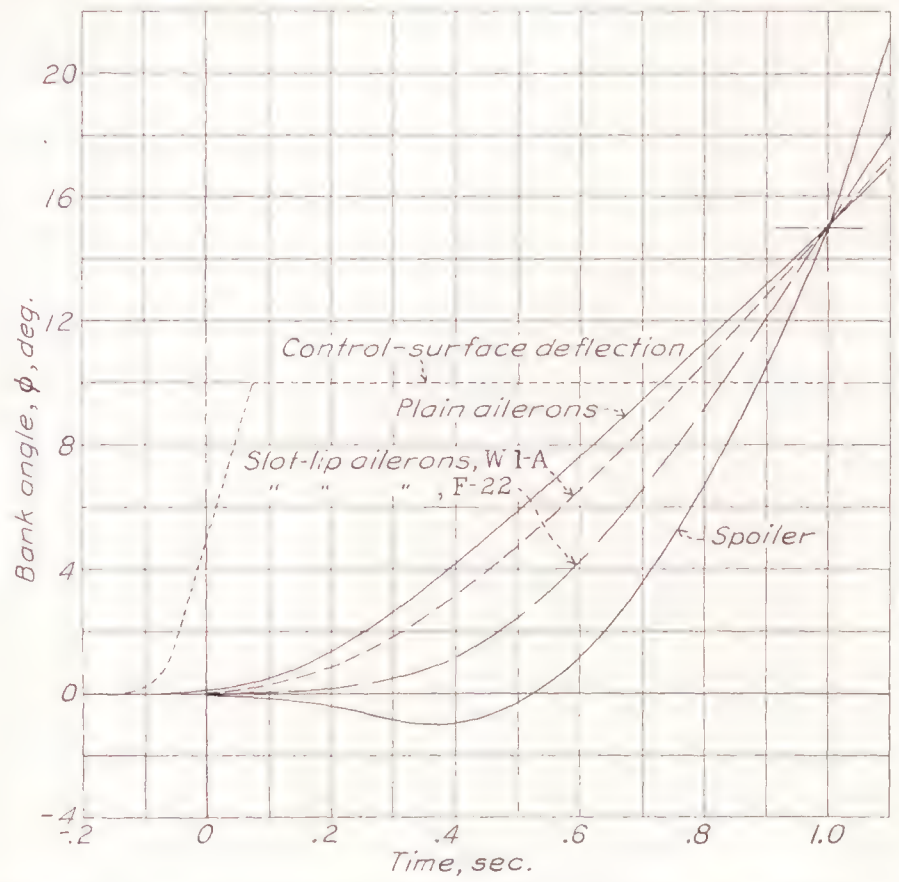

FIGURE 10.—Bank curves derived from flight records illustrating response characteristics of various lateral control devices.

trol devices including conventional ailerons. The records showed that the delay before rotation started

in the desired direction was of the order of half a second. This lag seems surprisingly short to have much effect on the control obtained with spoilers, but apparently it is sufficient to prohibit the use of the spoilers close to the ground because of the danger of overcontrolling.

The lag of spoilers was then studied by means of a special hinged wing model of 4-foot chord mounted in the 7- by 10-foot wind tunnel (reference 12). This installation reproduced the conditions encountered in the flight tests. The tests with spoilers located in different positions along the chord of the wing showed that the lag was relatively large with the spoilers near the leading edge and became less after the spoiler was moved to the rear until it was zero for normal trailing-edge flap-type ailerons.

The spoiler located near the rear of the wing was found to act with a negligible amount of lag (less than one-tenth second could not be detected by the pilots) and seemed to give some promise of making a satisfactory lateral control device. Flight tests were therefore made of a retractable spoiler located 83 percent of the wing chord back of the leading edge which, because of its rearward position, was referred to as a "retractable" aileron. The aileron was made in the form of a plate curved in a circular arc to form a segment of a cylinder and was moved in and out through a slit in the upper surface of the wing and about an axis at the center of the cylinder. This arrangement produced no aerodynamic hinge moment and was found to operate satisfactorily in flight on a Fairchild 22 airplane (reference 3). The retractable aileron mounted on the assumed average airplane is number 16 in table I. The stick-force characteristic (zero force) is not the most desirable but could be brought up to a desired value either by the addition of a spring in the aileron linkage or by an off-center location of the hinge axis of the aileron. A large amount of control is available from ailerons of this type and the yawing characteristics are more satisfactory than those of conventional ailerons.

Combinations of conventional ailerons with spoilers located ahead of them and deflected simultaneously showed some promise in the wind-tunnel investigation (reference 1, part V) and were found to give satisfactory control free from lag when tested in flight on the Fairchild 22 airplane (reference 2). With the spoiler deflected in front of the aileron, the floating angle of the aileron is raised and, if properly developed, certain combinations seem very promising in regard to both yawing effect and stick force. Estimated characteristics of one such combination are given in table I, aileron 17.

Another possible combination that has been tested and may deserve further development is one in which two spoilers are located in tandem and deflected simultaneously. The tests with this arrangement (reference 12) showed that the lag of the combination was no greater than that for the rear spoiler alone, whereas the final rolling moment was the same as for the front one when used without a flap. Later tests indicate that spoilers located on the forward portion of the wing may be rendered ineffective by the action of a split flap. One other point has not yet been completely determined, namely, whether the rolling motion would get under way with sufficient acceleration immediately after the start. This point will be dealt with further in the next section on slot-lip ailerons.

SLOT-LIP AILERONS

Means for the elimination of the lag of spoilers were investigated in the 7- by 10-foot tunnel and it was found that the lag could be eliminated by providing a slot or passage through the wing back of the spoiler. This investigation has resulted in the development of what have been termed the "slot-lip" ailerons (references 8 and 12). The slot-lip aileron is a combination of a spoiler-type flap located on the upper surface of the wing and a continuously opened slot, the flap forming the upper portion or lip of the slot. The computed control performances for two arrangements of slot-lip ailerons in different positions along the chord of the wing are listed 18 and 19 in table I.

The slot-lip ailerons satisfactorily eliminate or reduce to a negligible value the actual lag intervening before the wing starts moving in the desired direction, and they give a very high maximum rate of rolling; but the rolling nevertheless increased less rapidly immediately after the start of the motion than with conventional trailing-edge flap-type ailerons. This condition is illustrated in figure 10, which includes curves from flight records of slot-lip ailerons on the Fairchild 22 airplane and slot-lip ailerons on the W1–A airplane. It will be noticed that with the W1–A the rate of roll increases nearly as rapidly as with conventional ailerons but with the Fairchild 22 the action was considerably more sluggish. The differences in the behavior of these two airplanes have been studied (reference 8) and it has been concluded that the superior response characteristics shown by the W1–A are due in large measure to the relatively great dihedral (5°) and to the smaller moments of inertia of this airplane. The secondary yawing action of the slot-lip ailerons is favorable, hence the dihedral effect increases the rolling action. Other differences favorable to improved response of the W1–A are: (1) The more rearward location of the aileron (0.30 c_w compared with 0.20 c_w tested on the Fairchild 22) and (2) the slightly greater size of the slot.

The lateral control with the slot-lip ailerons on the W1–A seemed satisfactory to the pilots, but on the Fairchild 22 it was found to be too sluggish and to give somewhat the same feeling as a slight amount of lag. This comparison, aided by several others of a pertinent nature, indicates that an additional point must be

covered in a specification for a completely satisfactory lateral control dealing with the acceleration or rate at which the rolling increases during the first half second or so following the actual start. It may be stated in simple quantitative terms, applying to the conditions for the assumed average airplane, that the angle of bank one-half second after a sudden deflection of the controls should be at least one-third the angle of bank reached at 1 second. Thus, if a bank of 15° is reached in 1 second, at least 5° of this should be attained in the first half second.[2]

The sluggishness of the slot-lip ailerons is a great handicap in the method of comparison of control effectiveness used in the present report, in which a certain angle of bank must be obtained in a time of 1 second. Even though these ailerons give a high final rate of roll, excessively great deflections are required to attain an angle of bank of 15° in 1 second at a lift coefficient of 1.8, and the stick forces are excessively high. This particular disadvantage might be overcome by the use of a suitable aerodynamic balance but, even so, the sluggishness of the slot-lip ailerons might prevent them from being considered satisfactory if it were of the magnitude found on the Fairchild 22 instead of that found on the W1–A.

The sideslip accompanying a 15° bank in 1 second is negligible with the 0.55 c_w slot-lip ailerons in the usual flight range with unflapped wings. With more forward locations the yawing moment becomes decidedly positive, resulting in outward sideslip. Because of the action of the slots at high angles of attack, the damping in rolling is retained to an angle of attack beyond that for maximum lift coefficient and, for this reason, it should not be difficult to design an airplane incorporating these ailerons in such a manner that lateral control and stability would be reasonably satisfactory at all angles of attack that could be maintained in flight. The continuously open slot, however, results in a high drag, which reduces the high-speed and climbing performance to a noticeable extent. The drag is less for the rear positions of the slot-lip ailerons and a special investigation has been made in the 7- by 10-foot tunnel to develop slots with reduced drags. Some success has been attained but, considering the best results to date, these ailerons do not seem suitable for modern high-performance airplanes.

LATERAL CONTROL WITH HIGH-LIFT FLAPS

Since the inception of the research program of reference 1, wing flaps have come into very general use and have further complicated the problem of lateral control. In steady flight ordinary ailerons give rolling moments that vary almost inversely with the lift coefficient; hence, wings equipped with high-lift devices require relatively large control surfaces. The installation of an effective flap then becomes more difficult.

Another problem introduced by the use of high-lift devices concerns the adverse yawing moment of the ailerons. The ratio of induced yawing to rolling moment increases (adversely) in direct proportion to the lift coefficient. Furthermore, the effect of a given yawing moment on the rolling control is usually greater with flaps in use on account of the increased dihedral effect due to the flap. Thus it appears almost necessary to use some device that causes large changes of profile drag resulting in a favorable component of yawing moment or to use wings with washout at the tip portions (partial-span flaps) so that the induced yawing moment is reduced. Many of the devices developed in reference 1 for use with full-span flaps show satisfactory yawing moments on account of the profile-drag increments caused. Comparisons of a number of the most promising devices have been made and are listed in section B of table I.

Plain ailerons on wings with partial-span flaps.—On account of the general use of partial-span split flaps with ordinary ailerons, some tests of this arrangement were made in the 7- by 10-foot wind tunnel (reference 7). The tests were made with tapered wings because they represent the most efficient application of the arrangement and are most used in practice. The most interesting result of these tests was the small loss of maximum lift coefficient entailed by the substitution of ailerons for the tip portions of the flap, particularly in the case of ailerons 21 and 23 as listed in table I, where only 30 percent of the semispan was used for the aileron portion. The indicated reduction amounted to less than 10 percent of the maximum lift shown by the same tapered wings with full-span split flaps. The reduction was about the same for the two taper ratios tried. It will be noted that the 5:1 tapered wing gave more efficient control as regards stick forces under all conditions. In each case the stick force is slightly less for the longer ailerons, although of course the wings with shorter ailerons showed better performance characteristics. Both sizes of ailerons on the 5:1 tapered wings showed a marked diminution of effectiveness above about 10° angle of attack, presumably due to flow separation at the tip portions.

The deflection of the partial-span flap introduces a large relative washout of the aileron portions so that at a given over-all lift coefficient the ratio of yawing to rolling moments is less with flap down than with flap neutral. It will be noted that the tabulated values of sideslip remain about the same at $C_L=1.8$ as at $C_L=1.0$. The sideslip at $C_L=1.0$ would have been appreciably less than indicated if a flap-down condition had been assumed here.

Although the lateral-stability characteristics of the highly tapered wing are unfavorable, there are indica-

[2] As mentioned previously, in order to simplify the computations and to make possible a comparison with flight records, the starting time has been arbitrarily taken s the instant at which the control surfaces reached half their final deflection.

tions that the use of a partial-span flap may not aggravate the instability in every case. The results of the aileron tests, as well as visual observations of the flow by means of tufts, show that the effect of the upwash at the tips introduced by lowering the flap may be compensated by a strong spanwise flow, which inhibits the stalling of these portions. The indications are that the angle of attack for autorotational instability would be about the same with the flaps as without for the wings tested, although rolling experiments were not tried.

Plain ailerons with retractable flap.—A plain aileron with a split flap retracting ahead of it was developed as a means of control with a full-span flap. This device has been tested in flight with a modified Fairchild 22 airplane and is one of the few lateral control systems incorporating full-span flaps that has proved entirely satisfactory in flight (reference 3). This device is so designed that the retracted flap does not interfere with the ailerons in any way and hence the control characteristics with flap neutral are those of plain ailerons. With the flap deflected, however, the characteristics are similar to those of the upper-surface ailerons tested in the 7- by 10-foot wind tunnel (reference 1, part XII).

Although the deflected flap is in such a position as to shield the under surface of the ailerons entirely, it was observed in the tests that the ailerons in this condition were nearly as effective as conventional ailerons with unsealed gaps. The effectiveness of downward deflection, however, falls off rapidly at an angle of about 8°.

The rolling-moment characteristics of the plain ailerons with retractable flaps are such as to favor a differential motion, since the upgoing aileron is more effective than the downgoing one at high lift coefficients. The hinge-moment characteristics are, however, distinctly unfavorable for this mode of operation inasmuch as the ailerons show a downward floating tendency with the flap down. Relatively large deflections of the ailerons are required to meet the control requirements at low speed on account of the shielding effect of the flap, and consequently a relatively high gearing ratio of ailerons to control stick is needed. The result is that the stick forces required for the specified banking control are somewhat higher than those for conventional ailerons throughout the flight range. These forces (see aileron 24, table I) are well within the desirable range for the Fairchild 22 airplane, although they indicate undesirably high values for larger airplanes.

The yawing action of these ailerons is about the same as that of the conventional ailerons with partial-span flaps. Although the induced yawing moment of the ailerons with the full-span flap is greater than that with the partial-span flap, the ailerons cause larger compensating changes of profile drag.

Several possible means of improving the control-force characteristics of these devices suggested themselves. The device listed next in table I (aileron 25) shows the calculated effects of such improvements. First, the span of the aileron was increased to what has previously been found the most efficient value and the chord of the aileron was reduced as much as seemed practical. Second, it was assumed that a trailing-edge tab (0.02 c_w bent down 15°) was attached to the aileron so as to avoid the downward-floating tendency. It was assumed that lowering the flap caused the same change in floating angle with the tab as without. Since the deflection of the flap caused a large change in the floating position of the aileron, it was desirable to change the balancing characteristics of the differential with flap deflection. Consequently, it was assumed that the differential cranks were rotated into new positions as the flap was deflected. The resulting stick forces tabulated give an indication of the improvement that might be effected by such development of the device.

Retractable ailerons (spoilers).—Tests of spoilers (reference 12) showed that for locations behind about 80 percent of the wing chord the lag in rolling action would probably be negligible. Flight tests were subsequently made of a Fairchild 22 airplane equipped with a curved-plate spoiler that moved edgewise into and out of the wing through a narrow slit in the upper surface at 83 percent of the airfoil chord. This plate was arranged to rotate about a hinge at the center of curvature, so that the air pressure (being normal to the plate) caused no resultant hinge moment. The test airplane incorporated a full-span split flap and, inasmuch as the downward motion of the spoiler took place entirely within the wing, the flap and spoiler did not interfere.

The flight tests showed very promising results, although the feature of zero hinge moment was not found especially desirable. Angular-velocity and control-position records taken simultaneously in flight showed no definite lag or sluggishness in the response to control movements. (See reference 3.) The devices as tested (0.15 c_w by 0.50 $b/2$) were somewhat larger than necessary to give the assumed satisfactory degree of control. As is indicated in the table, a maximum deflection causing a 7.4 percent c_w projection of the spoiler should be sufficient for control in the flap-down condition.

An important advantage of the retractable ailerons (aside from their advantage in permitting the use of a full-span flap) is that they give small favorable yawing moments throughout the greater portion of the flight range. At high lift coefficients with the flap in use, however, small adverse yawing moments result. (See reference 13.)

Although the deflected spoiler causes quite an increase of profile drag, it is not expected that the incidental deflections required for control in normal flight would appreciably affect the performance. The performance criterions listed are, of course, for undeflected controls.

External-airfoil flap-type ailerons.—The external-airfoil (Junkers or Wragg) type flap has been studied as a possible means for improving the take-off and

ceiling characteristics of airplanes in addition to providing the high-lift features of ordinary and split flaps. As this device showed promise of improved performance, several methods of securing lateral control with such a flap have been studied.

A simple method of providing lateral control with full-span external-airfoil flaps is to move the flaps themselves independently as ailerons. (See reference 10.) Thus the ailerons are used simultaneously as a high-lift device and to provide rolling moments without sacrificing a special part of the wing span. In order to employ these flaps to their best advantage, it is necessary to deflect them downward over the entire wing span, thereby avoiding excessive induced drag. The action of the flaps deflected downward as ailerons is similar to the action of ordinary ailerons with droop. The external-airfoil flaps show a superiority over ordinary flaps for this purpose, however, in that they retain their lift-changing effectiveness at greater downward deflections (in excess of 20°).

Aileron 27 in the table is an arrangement of these flaps whereby the entire span is deflected downward 20° and the semispan portions are moved differentially from this downward position to provide rolling control.

This arrangement was tested in flight with the Fairchild 22 airplane and was found to give unsatisfactory yawing characteristics, although the rolling moments seemed to be ample. The computations made for the average airplane indicated an adverse sideslip of 10° accompanying a 15° bank at low speed with the flaps down.

A possible way of improving the adverse-yaw characteristics of these devices is to make use of the effect of washout. This method was used in the case of aileron 28, where the flap was considered to extend unbroken over the middle portion of the wing with the parts of the flap used as ailerons covering the outer 50 percent of the semispan portions. Wind-tunnel tests (reference 10) showed that, with the inner portion down 30° and the outer, or aileron, portions down only 10°, the performance criterions were about the same as with the whole flap down 20°. This change reduced the yawing effect considerably, as shown by the table, although the sideslip is still somewhat worse than is the case with most of the other devices.

When the stick forces and deflections for these two arrangements are compared, it will be noted that the deflection required with the full semispan aileron is almost as great as that required when only half the flap is used for control. This fact is partly accounted for by the difference in yawing effects.

In the low-speed conditions (C_L=1.8) the ailerons are lowered 20° in one case and 10° in the other and the effective floating angles are thereby increased by these amounts. This fact introduces a difficulty into the design of a suitable differential linkage. A linkage designed to accommodate the floating tendency with flaps neutral will overbalance when the flaps are deflected. In the computations it was assumed that the additional floating tendency was neutralized by a long spring that came into action as the flaps were lowered.

The external-airfoil flaps permit high lift coefficients to be attained without excessive profile drag. The advantage over a split flap begins to be apparent at lift coefficients in excess of 0.7, aiding the take-off and the low-speed climb but hardly affecting the maximum rate of climb. Hence, in this particular case, the performance criterions listed in table I do not fully indicate the differences to be expected with these devices.

Ailerons with external-airfoil flaps.—A logical extension of the development of the slot-lip aileron has led to a device in which the aileron forms the lip of the slot between an ordinary external-airfoil-type flap and the main wing. (See aileron 29, table I.) This arrangement avoids the excessive drag entailed by other forms of slot and, on account of the rearward position of the aileron, should give good response characteristics (except, possibly, under certain conditions noted later).

The device as tested (see reference 9) comprised an aileron 0.12 c_w wide and $b/2$ long. The tests showed that, in general, the effectiveness of the aileron was reduced by the presence of the flap, in accordance with the theoretical consideration that any change in slope of the wing section ahead of the trailing edge is less effective than a corresponding change at the trailing edge itself. When the flap is lowered, however, an upward deflection of the aileron apparently causes separation of flow over the flap, thus greatly reducing the lift and developing a large rolling moment. With the flap down 30° this change occurs at the beginning of the aileron deflection, while at intermediate flap deflections the change occurs at greater up aileron angles. This more or less sudden change of conditions, in addition to giving a large increase of rolling moment, also caused a reduction or a reversal of hinge moment; hence, the device may be impracticable for use at intermediate flap settings. (See reference 9.)

In the device as shown in table I the downward deflection of the aileron is limited by the presence of the flap nose to a maximum of about 7°, and it is consequently necessary to use a differential movement. Change of setting of the flap has a pronounced effect on the floating angle of the aileron. With the flap set at 30° a differential giving no more than 7° downward deflection of the aileron will be overbalanced by this floating tendency. In the computation it was assumed that a spring tending to turn each aileron downward (with a torque of 8.7 foot-pounds acting at the aileron hinge) was brought into action by lowering the flap. With the flap neutral the floating angle of the aileron is too small for satisfactory balance, although wind-tunnel tests showed that it could be effectively increased by a tab. Consequently, the device was assumed to incor-

porate such a tab (0.018 c_w, down 5°) and the spring tension was adjusted to accommodate the effect of the tab with flap down.

The resulting stick forces, together with the deflections required for control, appear in the table. It will be noted that the greatest deflection required is that at $C_L=1.0$. In this condition the aileron does not produce the previously discussed change in flow over the flap. At $C_L=1.8$ the deflection required is small because a small upward movement of the aileron in the flap-down condition produces a large rolling moment. The yawing effect is adverse but is not excessive.

The performance characteristics of this wing (with the N. A. C. A. 23012 airfoil flap) are somewhat better than those of the two wings previously considered, which had flaps of Clark Y section.

II. ANALYSIS OF CONVENTIONAL FLAP-TYPE AILERONS

The practical advantages of plain ailerons are well known and, since they are universally used in more or less modified form, the following section is devoted to an analysis of factors involved in their design.

One of the conclusions of the lateral control investigation has been that no decisive benefit was to be gained from a device that continued to give rolling moments when the major outer portions of the wings were stalled. If stalling of the aileron portions of the wing is prohibited, plain ailerons or other devices located near the trailing edge of the wing will retain their effectiveness.

If the loss of rolling effect on a stalled wing is discounted, it appears that the primary disadvantage to be associated with plain ailerons is their adverse yawing effect. For this reason the yawing action of plain ailerons will be rather fully analyzed.

ROLLING MOMENT

For the purpose of calculating the coefficients of rolling and yawing moment, the effect of a deflected aileron may be ascribed to a change of angle of attack of the wing sections comprising the aileron portions. Thus, the localized effect of the deflected aileron is measured by the change in the angle of zero lift. This change is proportional to the angle of deflection of the aileron for deflections below about ±20° and the factor of proportionality (denoted by $\Delta\alpha/\Delta\delta$) depends on the chord of the aileron. Thus, the plain flap-type aileron is considered merely as a device for changing the angle of attack. The section lift increment is not used to characterize the effect of the flap because this increment cannot, in general, be specified, being dependent on the plan form of the wing. The effective change in angle of attack per unit change of flap deflection is, however, theoretically independent of the aspect ratio and the plan form.

Figure 11 summarizes the results of a number of wind-tunnel experiments with plain flaps (references 14, 15, and 16) and shows the measure of flap effectiveness ($\Delta\alpha/\Delta\delta$) as a function of the relative flap chord. A curve predicted by wing-section theory (reference 17) is also shown for comparison. The surprisingly powerful effect of a narrow flap should be noted. Thus, deflecting a 0.20 c_w flap is about half as effective as deflecting the entire wing section.

Since the effective angle of attack of a wing section is a linear function of the camber (reference 17), the curve of figure 11 may be used to predict the effect of a multiply hinged flap, such as an aileron equipped with a balancing tab. The combined effect of a succession of bends along the wing section may be found by calculating the separate effects of each bend and adding them. Thus the effect of a 0.20 c_w aileron equipped with a 0.05 c_w tab is (using values from fig. 11)

$$\Delta\alpha=0.51\delta_a+0.21\delta_t \tag{2}$$

where δ_a is the deflection of the aileron with respect to the wing and δ_t is the deflection of the tab with respect to the aileron. This simple relation should not be expected to apply beyond ±20° deflection and, in the case of very narrow tabs, beyond about ±15°

Deflected ailerons thus cause, in effect, a discontinuous change of angle of attack across the wing span. The lift change caused by the ailerons cannot be discontinuous, however, because of the natural equalization of pressure along the span. Ailerons covering only a portion of the span influence the lift at every spanwise point and this effect appears to be satisfactorily predicted by the airfoil theory. Calculations of the effects of ailerons based on this theory have been made, the most extensive series being reported in reference 18. Figure 12 shows the rolling-moment coefficient C_l caused by a 1° difference in angle of attack of various right and left portions of a rectangular wing of aspect ratio 6. The abscissa of this diagram represents a semispan of the wing with the midspan point at the origin and the tip at the point 1.0. The ordinate gives directly the rolling- (or yawing-) moment coefficient due to a unit change of angle of attack extending from the point indicated on the abscissa out to the tip. The rolling effect of two ailerons is twice as great as that of a single one and hence the difference of the increments of equivalent angle of attack, as indicated, should be used. The rolling moment is not appreciably changed by differential deflection.

The curves give the values predicted by the theory and the points indicate values obtained in various experiments as noted on the figure. The wing-section characteristic $\Delta\alpha/\Delta\delta$ of the devices tested was determined from figure 11.

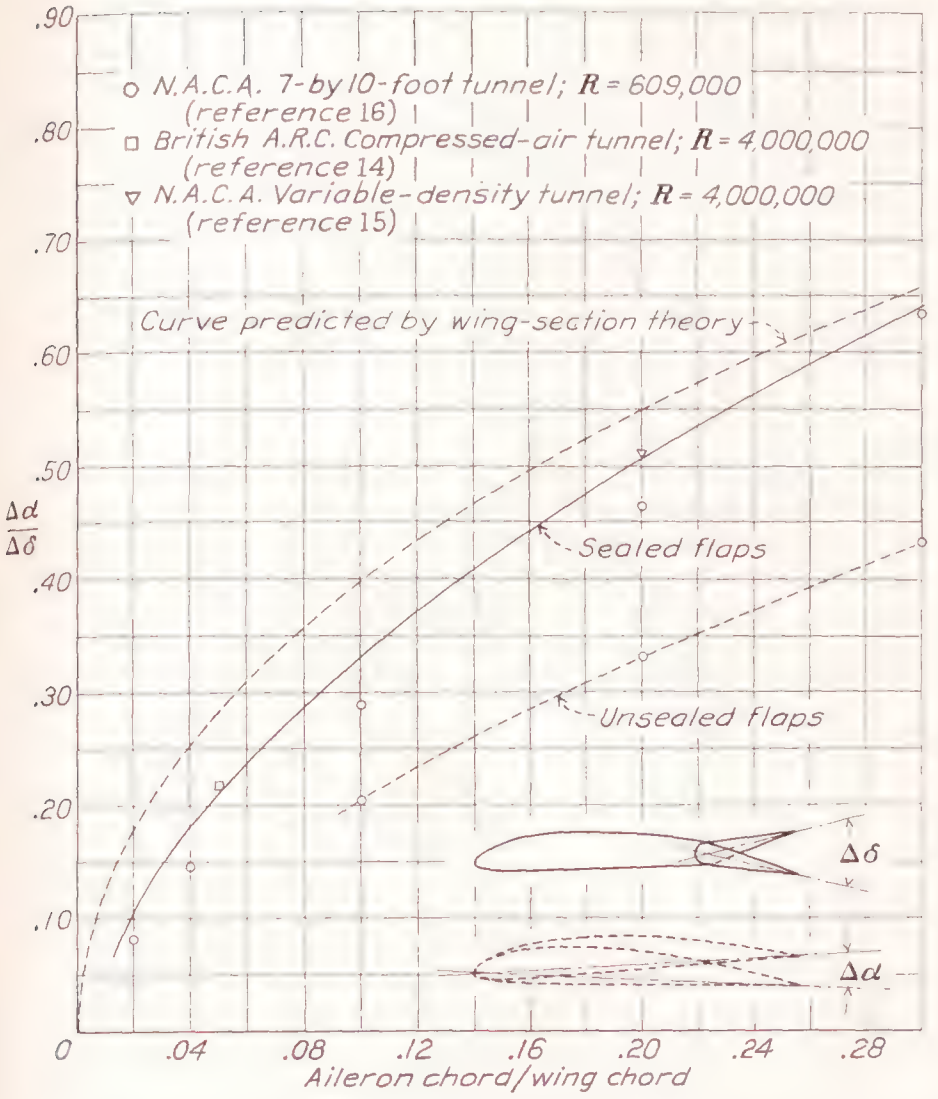

FIGURE 11.—Change of effective angle of attack of a wing section per unit change of flap angle. Plain flaps of various chords at small deflections; $\delta < \pm 20°$.

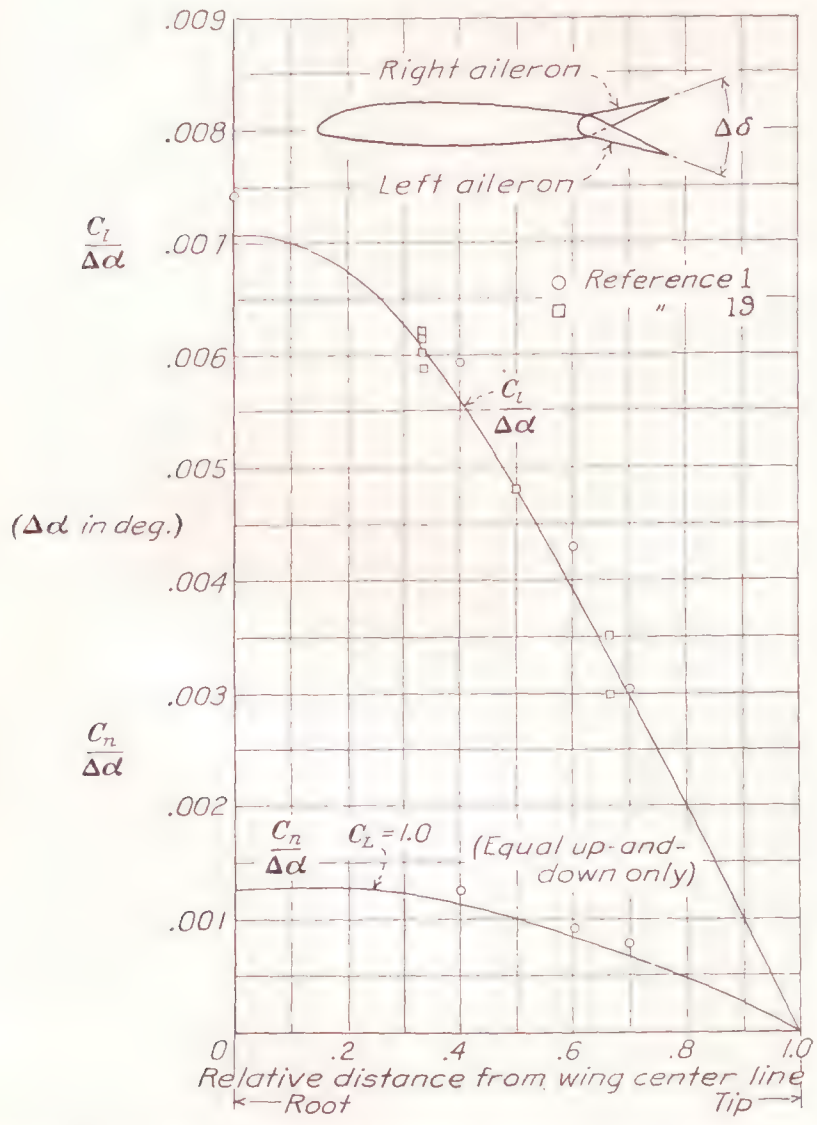

FIGURE 12.—Variation of rolling- and yawing-moment coefficients with aileron span and a comparison of theoretical and experimental values. Rectangular wings; $b^2/S=6$; $\Delta\delta < \pm 20°$.

The rolling-moment characteristics of the plain 0.25 c_w by 0.40 $b/2$ sealed ailerons (aileron 1 of table I) were calculated with the aid of figures 11 and 12. Reference to figure 11 shows that the equivalent change in angle of attack produced by a 0.25 c_w sealed flap is 57.5 percent of the angle of deflection of the flap. Thus, a deflection of $\pm 7.4°$ (see table I) is equivalent to a change in angle of attack of

$$0.575 \times 7.4° = 4.26° \tag{3}$$

or a difference of angle of the right and left aileron portions of 8.52°. According to figure 12 the rolling-moment coefficient per degree of this difference for a 0.40 $b/2$ aileron portion extending to the wing tip is 0.0039; hence, the coefficient predicted is

$$C_l = 8.52 \times 0.0039 = 0.0332 \tag{4}$$

Working charts for predicting the rolling moment of plain ailerons of any size on monoplane wings of various aspect ratios and different degrees of taper are given in figure 13. In order to use these charts it is necessary to ascertain from figure 11 the section characteristic $\Delta\alpha/\Delta\delta$, which is a function of the relative chord of the aileron. The charts may be used for differential ailerons merely by taking the difference of angle of attack of the right and left aileron portions. The theoretical rolling moment is independent of any initial washout of the wing sections along the span; hence, the rolling-moment curves are applicable to wings with partial-span flaps. The charts cannot be used with devices that change the slope of the lift curve nor for excessive deflections that introduce disturbed air flow. In this connection it appears that a deflection of plain ailerons involving disruption of the air flow is inefficient from considerations of stick force.

It will be noted that two sets of curves are given for tapered wings. The solid lines apply to ailerons that are not tapered with the wing, i. e., ailerons of constant actual chord. For this type the change of equivalent angle of attack should be calculated on the basis of the wing-tip chord (whether or not the aileron extends to the wing tip). The long-dash curves are for the particular case in which the aileron chord is a constant proportion of the wing chord along the span, in which case the change of equivalent angle of attack does not vary along the aileron portion. The additive effect of an element of aileron covering any spanwise portion of the wing may be determined from the increment of the $C_l/\Delta\alpha$ curve over that portion. Although the curves of figure 13 show increasing rolling-moment coefficients with increased aspect ratios of the wings, the control requirement (rolling-moment coefficient for a given banking effect) also increases with aspect ratio and, on account of the damping, in nearly the same way as does the coefficient. (See reference 4.) In general, it may be said that the relative proportions of the ailerons

should not be reduced on account of increased aspect ratio.

YAWING MOMENT

Yawing moment with equal up-and-down deflection.—The results of experiments indicate that the primary source of adverse yawing moment given by plain ailerons at small deflections is the theoretical, or induced, yawing moment. The production of rolling moment results in an induced twisting flow analogous to the downwash in direct lift. The yawing moment arises from the resultant inclination of the supporting lift vectors along the span. If the wing is supporting no lift, the production of rolling moment by equal and opposite lift increments on the two wing halves will not result in a yawing moment because the lift increment vectors are all inclined backward by the induction, resulting in a drag. Hence, only the interaction of an initial lift and a rolling moment give rise to an induced yawing moment.

A more specific treatment of this theory is given in reference 18. The formula for yawing moment that results for equal up-and-down deflections is

$$C_n = KC_L \times C_l \tag{5}$$

where K is a factor dependent on the aspect ratio and the plan form of the wing, and to some extent, on the spanwise position of the aileron. It is interesting to note that with a given equal up-and-down aileron deflection the induced yawing *moment* is the same throughout the speed range, while the rolling moments and the stabilizing factors are greatly reduced at the lower speeds.

Figure 12 gives a comparison of theoretical and experimental values of $\frac{C_n/\Delta\alpha}{C_L}$ for a rectangular wing of

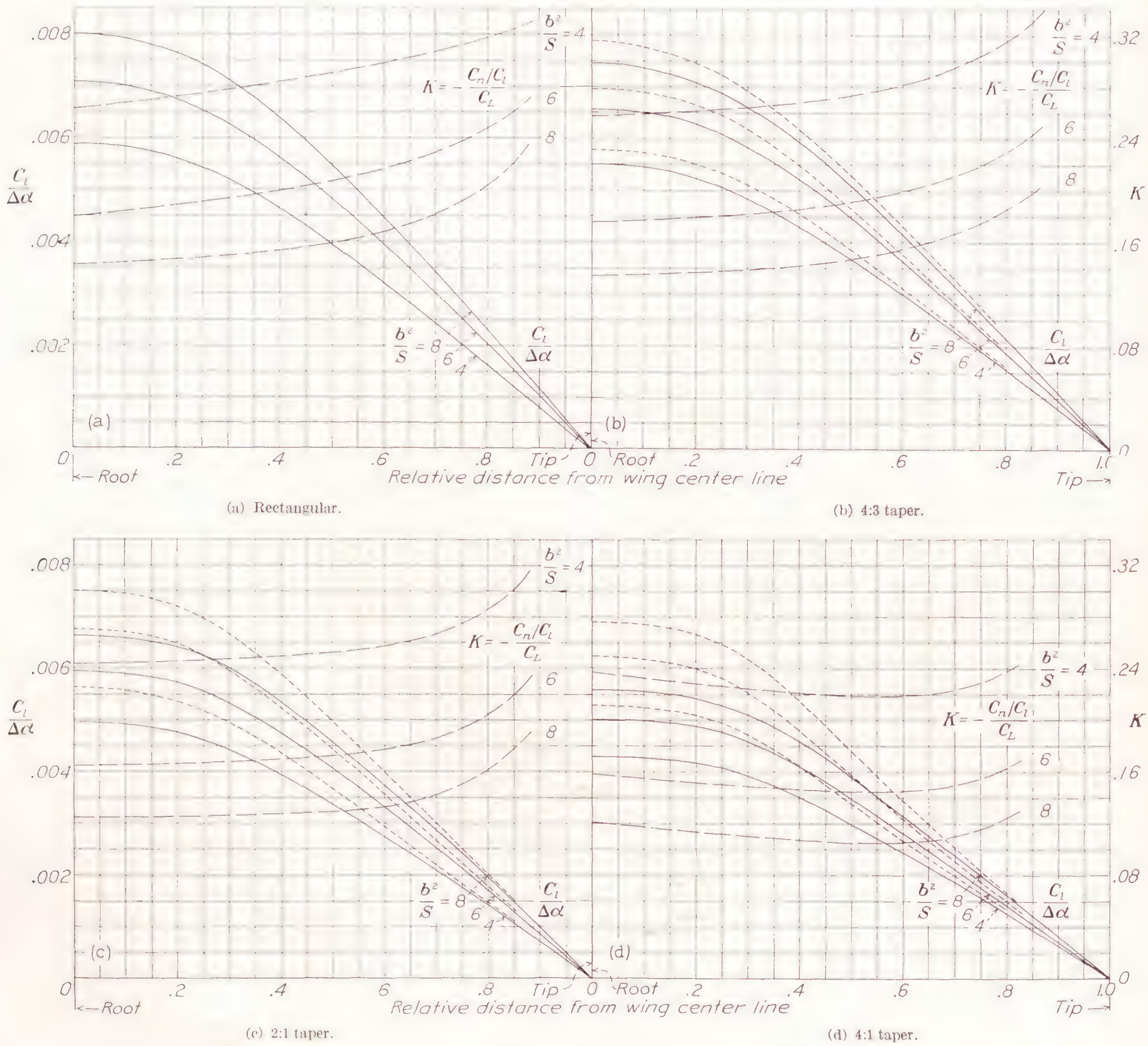

(a) Rectangular.

(b) 4:3 taper.

(c) 2:1 taper.

(d) 4:1 taper.

FIGURE 13.—Charts for calculation of rolling and yawing moments of plain ailerons, showing the effects of span and spanwise location of ailerons with straight and tapered wings.

aspect ratio 6. Deviation from the theory is to be expected at excessive deflections of ordinary ailerons and with special types of devices, since important changes of profile drag may be introduced. If complete wing section data are available, however, the profile-drag part of the yawing moment may be readily estimated.

As in the case of rolling moment, the yawing moment of an aileron at any spanwise position may be calculated by taking the difference of ordinates at abscissas corresponding to the ends of the aileron. Unlike the rolling moment, however, the yawing moment of differential ailerons is not the same as that of ailerons with equal deflections. In the general charts given in figure 13 the ratio of yawing to rolling moments at $C_L = 1.0$ is given rather than $C_n/\Delta\alpha$. In this case the differences between two points cannot be used directly to give the yawing moment of an aileron extending between these two points. The yawing moment caused by an aileron ending inboard of the tip may be found, however, by taking the difference of the yawing moments given by two ailerons, one extending from the inboard end of the actual aileron to the wing tip and the other extending from the outboard end to the tip. The straight and tapered ailerons should give yawing moments in practically the same ratio to the rolling moment; hence, only a single set of values of $K = -\frac{C_n/C_l}{C_L}$ is given.

Referring again to the 0.25 c_w by 0.40 $b/2$ plain aileron (aileron 1) of table I, it is found that the ratio of yawing- to rolling-moment coefficients for this case is

$$\frac{C_n}{C_l} = -0.216 \tag{6}$$

at $C_L = 1.0$. (See fig. 13.) At the deflection given the rolling-moment coefficient previously found is

$$C_l = 0.0332 \tag{7}$$

Hence, the yawing-moment coefficient at $C_L = 1.0$ is

$$C_n = -0.216 \times 0.0332 = -0.0072 \tag{8}$$

The values of both yawing- and rolling-moment coefficients for these ailerons having been obtained, it is now possible to calculate their rolling effectiveness by means of figure 3. The wing loading of the average airplane assumed in table I is 9.4 pounds per square foot; hence, at $C_L = 1.0$ the banking effect of a rolling moment of coefficient 0.01 acting for 1 second is

$$\left(\frac{\phi_1 b}{2}\right)_{C_l = 0.01} = 1.42 \text{ feet} \tag{9}$$

and for a rolling-moment coefficient of 0.0332

$$\frac{\phi_1 b}{2} = 1.42 \times 3.32 = 4.7 \text{ feet} \tag{10}$$

The effect of the yawing moment of coefficient -0.0072 is calculated in the same way, i. e.,

$$\frac{\phi_1 b}{2} = -0.72 \times 0.65 = -0.47 \text{ foot} \tag{11}$$

The effect of these rolling and yawing moments applied simultaneously is

$$\frac{\phi_1 b}{2} = 4.7 - 0.47 = 4.23 \text{ feet} \tag{12}$$

Thus, deflecting the ailerons suddenly to $\pm 7.4°$ causes a 4.23-foot displacement of the wing tips in 1 second. The angle of bank for the average airplane ($b/2 = 16$ feet) is

$$\phi_1 = \frac{\frac{\phi_1 b}{2}}{\frac{b}{2}} \times 57.3 = 15° \tag{13}$$

as appears in the table.

Yawing moment with differential deflection or droop.—The effect of an unequal movement of the ailerons may be taken into account by considering an equivalent equal up-and-down deflection from a mean upward position of the ailerons. Thus, deflections of 15° up and 5° down may be considered as equivalent to 10° equal up-and-down from a mean position 5° up. Inasmuch as a differential deflection of the ailerons changes the mean lift of the wing, figure 13 cannot be used without correction to calculate the yawing moment due to unequal deflection. As was brought out in the preceding discussion, the yawing moment is caused by the interaction of the wing lift and the induced flow caused by the rolling moment. Hence, the yawing moment incident to a given rolling moment depends on the distribution of the basic or symmetrical part of the lift. The basic lift distribution upon which the yawing moment depends is, then, the distribution for a wing with both ailerons raised. The adverse yawing moment will, in this case, be reduced because of the lessened lift over the tip portions. For the conditions following sudden aileron deflections the average upward movement of both ailerons will entail an actual reduction for a short time of the lift of the wing without correspondingly increasing either the flight speed or the angle of attack. The conditions will, of course, be different for steady flight with ailerons held over. For practical purposes it is sufficient to calculate an increment of C_n/C_l due to the increment of lift produced by the symmetrical droop or uprigging of both ailerons. This increment would be the yawing moment incident to a unit rolling moment when the entire lift of the airfoil was due to the droop of the ailerons. The ratio of yawing to rolling moment thus found will be a constant additive contribution to equation (5) at all lift coefficients.

Figure 14 shows the reduction of the ratio of adverse yawing to rolling moment in terms of the reduction of

over-all lift coefficient for a rectangular wing of aspect ratio 6. The experimental points indicated were derived by taking the differences of yawing moment measured with equal up-and-down deflections and up-only deflections and dividing these differences by the measured reduction in total lift coefficient caused by the up-only deflection.

If C_L is the lift of the wing with ailerons undeflected and $\Delta\alpha_m$ is the equivalent angle of washout of the

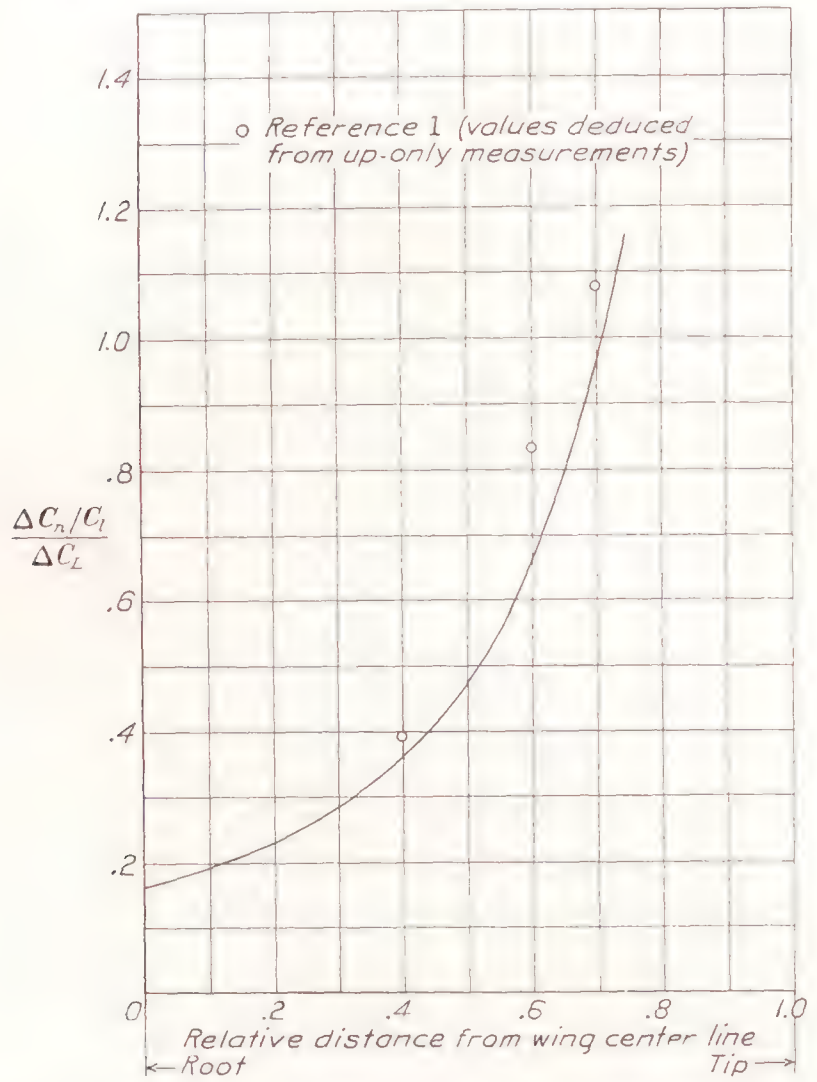

FIGURE 14.—Increment of induced yawing moment due to differential deflection of ailerons; ΔC_L is the reduction of lift coefficient due to differential deflection. Rectangular wing; $b^2/S=6$.

aileron portions introduced by the unequal aileron deflections, then

$$\Delta\frac{C_n}{C_l}=\kappa\Delta\alpha_m \tag{14}$$

since the reduction of lift is proportional to $\Delta\alpha_m$. The factor κ, like the factor K, depends on the wing plan form and the relative length of the aileron portion.

Figure 15 shows theoretical values of κ for wings of aspect ratio 6 and various plan forms. It should be remembered that C_L as used in equation (14) is the lift coefficient with ailerons undeflected. Correction of the values given in figure 15 for wings of different aspect ratio may be made by considering that κ is very nearly inversely proportional to the aspect ratio.

It is evident that the foregoing remarks apply equally as well to wings having washout at the tips or to wings with partial-span flaps. For wings with partial-span flaps $\Delta\alpha_m$ is simply the reduction of the effective angle of attack at the tips due to removal of the tip portions of the flap. It should be remembered that droop of the outer portions (negative $\Delta\alpha_m$) increases the adverse (negative) yawing moment while washout (positive $\Delta\alpha_m$) decreases it.

The increment of yawing moment due to the sum of two distributions of droop or washout is equal to the sum of the increments associated with each separate distribution. This property may be used to compute quite accurately, though not exactly, the yawing

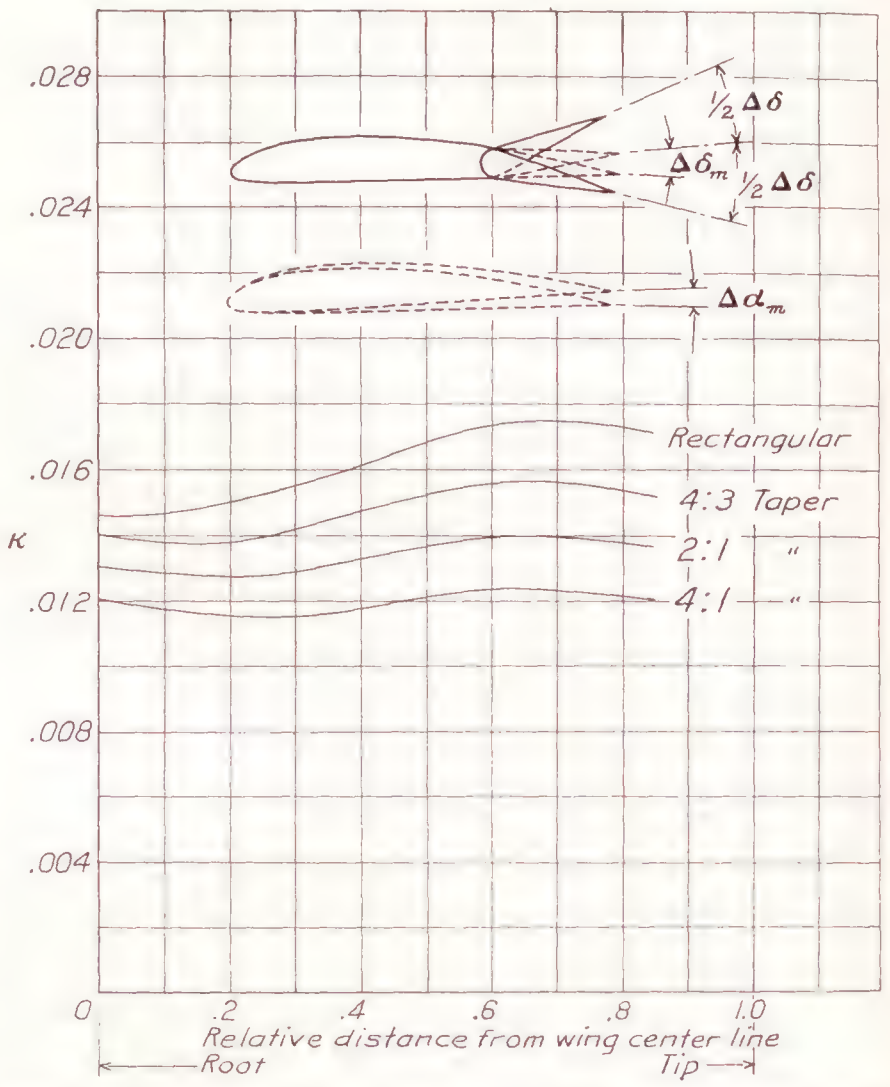

FIGURE 15.—Ratios for calculating additional induced yawing moments of differential ailerons or ailerons on wings with washout; $b^2/S=6$; $\Delta\alpha_m$ is in degrees

$$(1+\Delta)\frac{C_n}{C_l}=-KC_L+\kappa\Delta\alpha_m$$

moment of differential ailerons that end inboard of the wing tip.

CONTROL FORCES

Hinge moment.—The available experimental data indicate that the hinge-moment coefficient C_h of an ordinary aileron can be treated with sufficient accuracy as a characteristic of the wing section, that is, as a characteristic independent of the plan form of the aileron or the wing. An average experimental value for the slope of the hinge-moment curve against deflection is

$$\frac{dC_h}{d\delta}=-0.0085 \text{ per degree} \tag{15}$$

for sealed ailerons of chord c_a and span b_a, where

$$C_h=\frac{\text{hinge moment of aileron element}}{qc_a^2b_a}$$

Thus, the actual hinge moment at a given deflection varies as the aileron span and as the square of the aileron chord.

Strictly speaking, the hinge moment of a deflected flap should be calculated in two parts. The primary part arises from that component of the distributed pressure change which does not contribute to the lift of the airfoil section. Since no lift is involved, this component is independent of the aspect ratio. The second component of the hinge moment, proportional to the lift change, is subject to the ordinary aspect-ratio correction. The correction is, however, small except for wide flaps.

Some additional considerations arise in the application of aileron hinge moments to the calculation of control force. The angular travel and the length of the control stick (or radius of the control wheel) are limited in practice. Thus, ailerons requiring large deflections must be geared to the control stick or wheel in a high ratio. In the case of the average airplane the total circumferential movement of the end of the control stick was assumed to be 0.73 foot in the case of each of the control devices. This value corresponds to a $\pm 25°$ deflection of a 20-inch stick corresponding to that available in the Fairchild 22 airplane.

If reference is made to the tabulated results for aileron 1, it is seen that the total deflection necessary to insure the assumed satisfactory degree of control ($\phi_1 = 22.5°$ at $C_L = 1.0$, in this case) is $\pm 11.2°$. The work of deflecting ailerons of chord c_a and span b_a is

$$\frac{dC_h}{d\delta}\delta\frac{\delta}{57.3}qc_a^2b_a = -0.0085\times\frac{11.2\times 11.2}{57.3}$$
$$\times 9.4\times(0.25\times 5.3)^2\times 0.4\times 16$$
$$= 1.97 \text{ foot-pounds} \qquad (16)$$

The control force is equal to twice the total work divided by the linear travel of the end of the stick, or

$$\text{Stick force} = \frac{3.94}{0.73} = 5.4 \text{ pounds} \qquad (17)$$

The stick force at the partial deflection required for $\phi_1 = 15°$ is

$$2.31\times\frac{\delta 15°}{\delta 22.5°} = 2.31\times\frac{7.4°}{11.2°} = 3.6 \text{ pounds} \qquad (18)$$

These simple relations apply, of course, only to linear variation of the hinge moment and to nondifferential gearing.

Differential linkages.—It appears that a differential linkage can, when properly designed, be a very effective means of reducing the operating force of flap-type ailerons (reference 11). The reduction of operating force is accomplished by taking advantage of the upfloating tendency of the ailerons. With differential linkage the ailerons on opposite tips of the wing begin to move at different rates immediately after they are deflected from neutral, the downgoing aileron moving more slowly than the upgoing one. The upgoing aileron thus has the greater mechanical advantage at the control-stick connection. It is evident that the reduced upward pressure of the upgoing aileron is partly compensated by its increased mechanical advantage and that the increased upward pressure on the downgoing aileron is also partly compensated by its reduced mechanical advantage. At a certain deflection the downgoing aileron reaches dead center and, regardless of its aerodynamic pressure, cannot contribute to the stick force; if the upgoing aileron is then at the floating angle (i. e., angle of zero hinge moment), the stick force will be zero.

Ordinary ailerons show nearly straight-line hinge-moment curves $\left(\frac{dC_h}{d\delta} = -0.0085\right)$ and in this case the balancing effect of a given differential linkage depends only on the upfloating angle. A formula for a differential motion that gives zero operating force over a range of deflections may be obtained by writing the expression for the work of deflection of the ailerons and equating it to zero at every point.

$$\delta_d = \sqrt{(\delta_{uf}+\delta_u)^2 - 2\delta_u^2} - \delta_{uf} \qquad (19)$$

where δ_u and δ_d are the upward and downward deflections of the ailerons and δ_{uf} is the floating angle measured upward from the neutral position. A practical limitation of this formula is reached when $d\delta_d/d\delta_u$ approaches -1, for then both ailerons begin to move in the same direction and at the same rate.

It should be appreciated that a differential designed in accordance with equation (19) will give complete balance at the specified floating angle. It is, however, considered desirable not to eliminate completely the control force at any flight condition, as the pilots' feel of the control would be taken away. This condition can be avoided by designing the linkage for a fictitious floating angle somewhat higher than the maximum actually reached in flight. If $\Delta\delta_{uf}$ is the difference between the floating angle at which the differential gives complete balance and the actual floating angle of the aileron in the given flight condition, the resultant stick coefficient C_{h_s} will be

$$\frac{\text{Stick moment}}{qc_a^2b_a} = C_{h_s} = \Delta\delta_{uf}\frac{dC_h}{d\delta}\left(\frac{d\delta_u}{d\theta}+\frac{d\delta_d}{d\theta}\right) \qquad (20)$$

where θ is the angular deflection of the control stick.

In any given case the stick force can be balanced out at only one angle of attack and, in general, the balancing effect diminishes as the angle of attack is reduced. Hence, if the stick force is made to become zero at an angle of attack above maximum lift, overbalance of the control in normal flight will be avoided.

A more or less complicated mechanical linkage that would give aileron movements approximating equation (19) could be devised. The ordinary simple linkage consisting of two properly set cranks connected by a rod can, however, be arranged to give the desired motion with close approximation, and such an arrangement will be given primary consideration.

Such a simple linkage can be made to satisfy two conditions for a minimum stick force. Figure 16 shows a type of stick-force curve that satisfies two very simple criterions. First, the slope of the curve is zero at the beginning of the deflection and, second, the resultant stick force is zero at a stick deflection corresponding to the floating angle of the up aileron. As was stated earlier, the latter condition is satisfied by arranging for the downgoing aileron to reach dead center when the upgoing aileron reaches the floating angle. Figure 17 shows geometrical arrangements of linkages that satisfy these two criterions for a minimum stick force. If the spacing of the crank centers is known in terms of the crank radius, the figure gives directly the neutral settings of the two cranks. The differential thus chosen will give what amounts to complete balance at the specified floating angle. The maximum downward

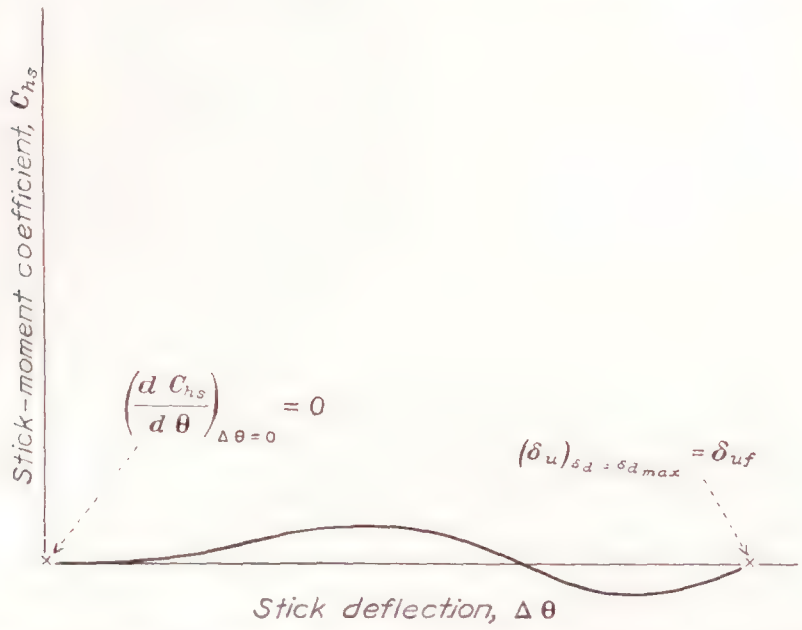

FIGURE 16.—Type of curve that satisfies simple criterions for minimum stick force.

travel of the aileron is shown in each case and it is to be noted that, if the maximum deflection of the upgoing aileron exceeds the assumed floating angle, the downgoing aileron will pass dead center and return toward neutral.

Since the floating tendency of a given aileron has a primary influence on the design of the differential linkage, it will be necessary to devote some study to this aileron characteristic. It appears that the floating angle of a plain flap-type aileron can be attributed to two effects: (1) a hinge moment proportional to the angle of attack of the wing, this moment being greater for large flap chords but independent of the shape of the wing section; and (2) a hinge moment attributed to the camber of the wing section, which remains constant as the angle of attack is changed. This second moment is primarily influenced by the camber of the aileron portion itself and is greatly affected by small changes at the extreme trailing edge. Thus, a small fixed tab can be used to introduce a large constant floating moment.

Figure 18 shows the variation of floating angle with flap chord and lift coefficient for the Clark Y wing section. The floating angles shown were indirectly computed from floating moments that were found by integration of pressure-distribution diagrams for a smooth wing (reference 20) and hence correspond to smoothly sealed flaps.

For the comparisons given in table I, infinite linkages ($R=0$ in fig. 17) were assumed to simplify the computations of control force. In most cases of differential ailerons listed, several trial computations of stick force were made to ascertain the optimum differential arrangement. These trial computations included the

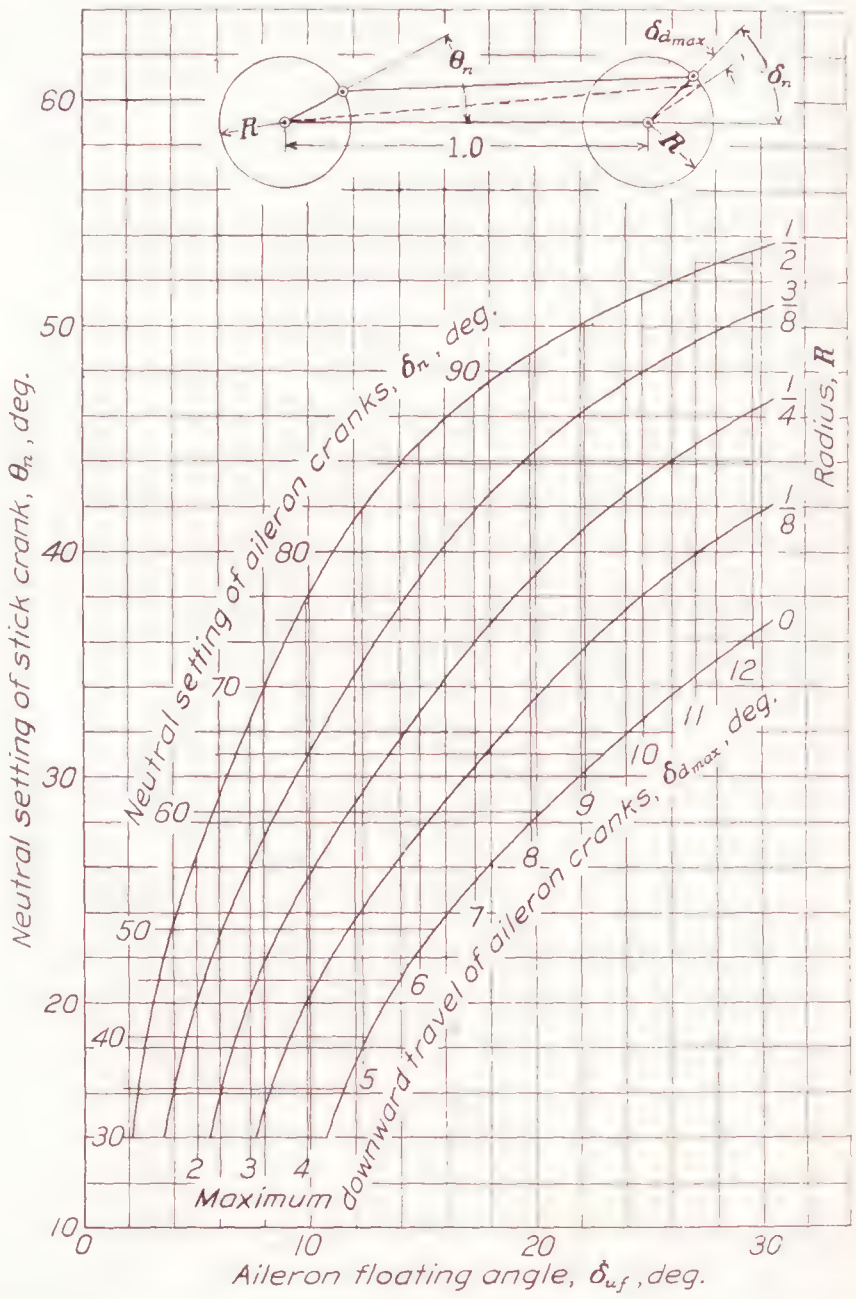

FIGURE 17.—Specifications of simple differential linkages that satisfy criterions for minimum stick force.

$\left(\frac{dC_{h_s}}{d\theta}\right)_{\theta=\theta_n}=0$; $(\delta_u)_{\delta_d=\delta_{d\,max}}=\delta_{uf}$

determination of the curve of stick force against deflection to insure that no reversals of slope of the stick-force curve occurred at any point.

Aileron 1 may be used to illustrate the use of figure 17 in the selection of a differential. Assuming that the greatest possible reduction in stick force is desired, a floating angle only slightly higher than the maximum shown by figure 18 will be assumed. On the assumption that it is permissible to allow the control force to become zero at $C_L=1.25$ ($\delta_{uf}=11°$), the differential chosen by means of the chart will have neutral settings of $\theta_n=15°$ and $\delta_n=30°$, approximately. As indicated by figure 17, the maximum downward deflection obtain-

able with this arrangement will be about 4½° and this angle will be reached when the upgoing aileron reaches 11° deflection. For greater deflections the downgoing aileron will return, reaching neutral when the up aileron is at 22°.

Effect of a fixed tab used in conjunction with a differential linkage.—Figure 18 shows that the floating angles of plain ailerons are reduced as the lift coefficient is reduced. It is on this account that the balancing effect of the differential diminishes. The stick forces tabulated for the differentially linked aileron 1 show this effect as an increase of stick force at high speed. It is possible to introduce a large constant floating moment by means of a properly formed fixed tab. The effect of such a tab is to increase the floating angle at all flight speeds by a constant amount so that the per-

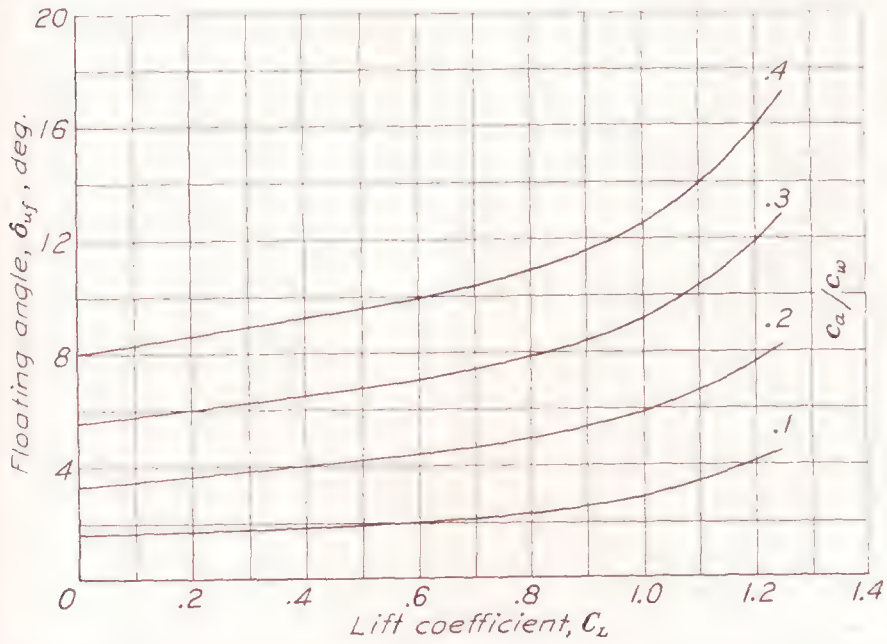

FIGURE 18.—Floating angles of sealed flaps of various chords on a Clark Y wing as computed from pressure-distribution data (reference 20).

centage variation with flight speed is reduced. This effect is especially pronounced in the case of very narrow ailerons, which do not show a very great variation of floating angle with angle of attack.

Furthermore, the maximum floating angle shown by very narrow ailerons is not great enough to permit the use of a differential to the best advantage. Thus, if the floating angle is considerably smaller than the maximum upward deflection required to produce sufficient control, the stick force may rise considerably after this point is reached on account of the return of the downgoing aileron and the consequent extra deflection required of the upgoing aileron. Advantageous use of a differential in such cases can be accomplished by incorporating a fixed tab (or a small amount of camber) arranged to trim both ailerons upward. In order to secure satisfactory results with a tab, a reasonably smooth inset type with a sealed juncture should be used. Attached tabs or tabs set at large angles ($\delta_t > \pm 15°$) have been found to cause an adverse increase in the slope of the hinge-moment curve.

Figure 19 shows the summarized results of experiments with tabs made in the 7- by 10-foot wind tunnel

As was stated before, the tab produces an essentially constant change in floating angle. The variation of floating angle with angle of attack can be found from figure 18. Figure 19 gives the change of aileron floating angle with tab deflection. (See references 9 and 21.) The experiments indicated that this ratio depended primarily on the ratio of tab chord to aileron chord independently of the chord of the aileron, although this relation can not be expected to apply as the aileron chord is indefinitely increased. At the Reynolds Number of the tests the tabs began to lose effectiveness when

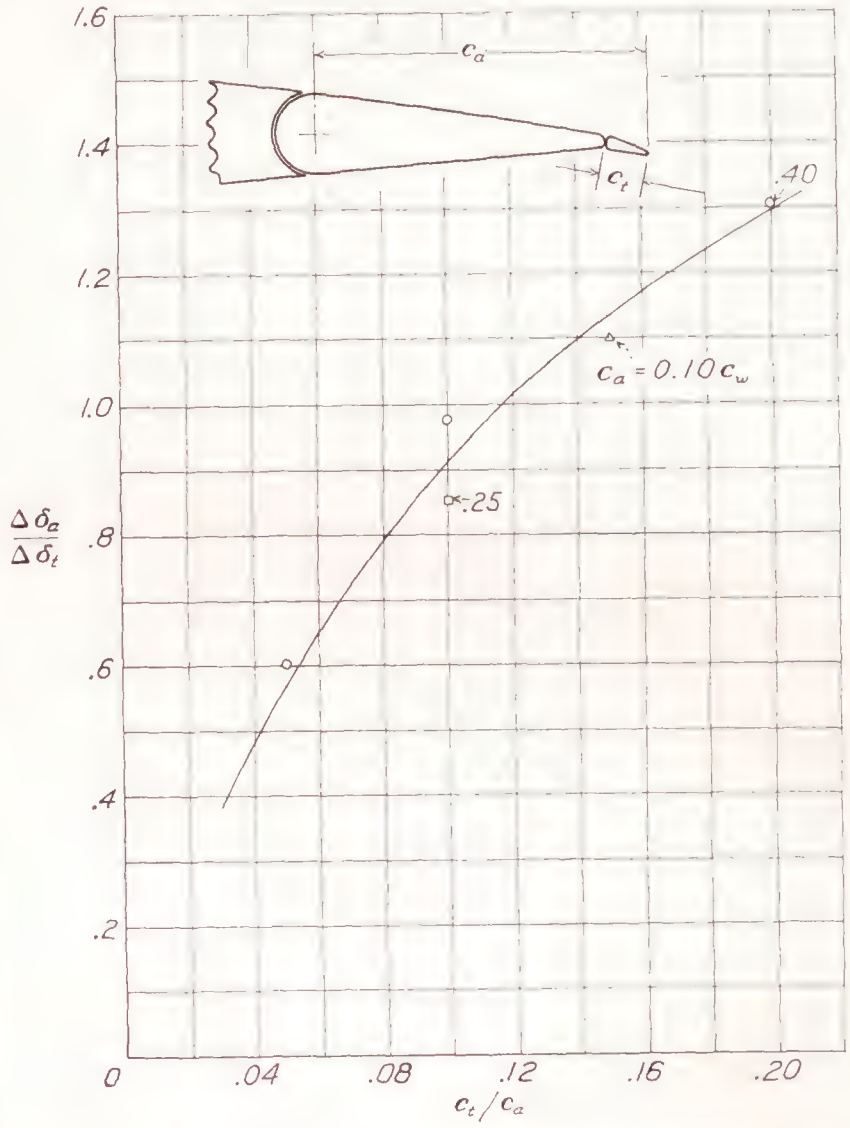

FIGURE 19.—Effect of inset tabs on aileron floating angles (references 9 and 21); $\delta_t < \pm 15°$.

deflected past 15°; hence, the ratios given should be considered applicable to tab deflections not exceeding this angle. Figure 19 may also be used to estimate the balancing effect of a movable tab.

It appears from figure 19 that a very large floating angle can be obtained by the use of a relatively small inset tab and deflection. Thus, the floating angle can very easily be altered to suit a given set of conditions. It has been pointed out that it is desirable to have the floating angle at least as large as the maximum upward deflection required for control so that the stick-force curve will lie reasonably near the minimum throughout the range. The smaller the percentage variation of floating angle with angle of attack, the smaller will be the variation of the actual stick force with flight speed. It would therefore appear desirable to trim the ailerons up as far as possible by means of a tab. On the other

hand, inasmuch as the deflected tab is made an inherent part of the airfoil camber, the size and deflection of the tab cannot be indefinitely increased without adversely affecting the pitching-moment and drag characteristics of the airfoil.

Reference to figure 19 shows that a 0.10 c_a (2½ percent c_w) tab deflected downward 10° will change the floating angles of aileron 1 by approximately 9°, raising the maximum floating angle to about 20°. This tab on the average airplane would be only 1.6 inches wide and the deflection of 10° would displace the trailing edge of the wing section by only one-third inch and would consequently not be expected to make a noticeable change in the drag or the pitching moment of the wing as a whole. The differential linkage giving complete balance at $\alpha=15°$ with this floating angle can be found from figure 17. The neutral settings of the cranks are

$$\theta_n=28°,\ \delta_n=59° \tag{21}$$

The maximum downward deflection found on the chart is about 8°, but in this case the aileron is not required to reach this deflection (20° up and 8° down) to produce a sufficient bank. Reference to figure 18 shows that the reduction in floating angle between $C_L=1.25$ (maximum) and $C_L=1.0$ is 2.5° so that, with the tab assumed, the floating angle at $\alpha=10°$ ($C_L=1.0$) will be

$$20°-2.5°=17.5° \tag{22}$$

Similarly, the new floating angle at $\alpha=0°$ ($C_L=0.35$) will be

$$20°-4.8°=15.2° \tag{23}$$

These values indicate that the balancing effect of the differential will not be greatly reduced at the higher speeds. Table I gives the actual stick forces as computed at these lift coefficients and indicates the reduction possible with a tab. An even better degree and range of balance could be attained with narrower ailerons on account of the smaller variation of floating angle with angle of attack.

CONCLUDING REMARKS

The provision of control rolling moments at high angles of attack or beyond the stall is not sufficient to secure control in flight at these angles unless the damping in rolling is retained. This requirement necessitates that at least the tip portions of the wing remain unstalled; hence, it cannot be considered a decided advantage to retain control rolling moments far above the stall with conventional wings.

The flight-testing experience gained throughout the course of the lateral control investigation has led to more or less definitely quantitative ideas regarding the desired effectiveness of the lateral control and the desirable variation of the control forces in normal flight.

From considerations of operating force required for a given amount of control, plain narrow sealed ailerons with deflections limited to 20° seem about the most efficient. Very great taper, or change of aileron chord along the span, leads to inefficiency whether used with a straight or a tapered wing. A differential linkage can be so designed as to reduce considerably the operating force of ordinary unbalanced ailerons, especially if a small fixed tab is used to increase the floating angle.

Several devices, notably the plain ailerons with flap retracting ahead, and the retractable aileron or spoiler located at 0.80 c_w have been developed and proved in flight to be suitable for use with full-span flaps. It was found, however, that the maximum lift of a tapered wing with split flaps was reduced less than 10 percent by the removal of the outer 0.30 $b/2$ portions of the flap, so that a conventional aileron could be used over that portion of the wing without great loss.

Aerodynamic theory can be successfully applied to the calculation of rolling and yawing moments of plain ailerons provided that experimental section characteristics are used in the computation of the local changes in angle of attack along the wing span caused by the ailerons. Further calculations involving the airplane stability characteristics can be applied to the prediction of the actual resultant motions caused by a given deflection of the control, thus giving a measure of effectiveness in controlling the movements of the airplane.

LANGLEY MEMORIAL AERONAUTICAL LABORATORY,
NATIONAL ADVISORY COMMITTEE FOR AERONAUTICS,
LANGLEY FIELD, VA., *April 20, 1937.*

REFERENCES

1. Wind-Tunnel Research Comparing Lateral Control Devices, Particularly at High Angles of Attack.
   I. Ordinary Ailerons on Rectangular Wings, by Fred E. Weick and Carl J. Wenzinger. T. R. No. 419, N. A. C. A., 1932.
   II. Slotted Ailerons and Frise Ailerons, by Fred E. Weick and Richard W. Noyes. T. R. No. 422, N. A. C. A., 1932.
   III. Ordinary Ailerons Rigged up 10° When Neutral, by Fred E. Weick and Carl J. Wenzinger. T. R. No. 423, N. A. C. A., 1932.
   IV. Floating Tip Ailerons on Rectangular Wings, by Fred E. Weick and Thomas A. Harris. T. R. No. 424, N. A. C. A., 1932.
   V. Spoilers and Ailerons on Rectangular Wings, by Fred E. Weick and Joseph A. Shortal. T. R. No. 439, N. A. C. A., 1932.
   VI. Skewed Ailerons on Rectangular Wings, by Fred E. Weick and Thomas A. Harris. T. R. No. 444, N. A. C. A., 1932.
   VII. Handley Page Tip and Full-Span Slots with Ailerons and Spoilers, by Fred E. Weick and Carl J. Wenzinger. T. N. No. 443, N. A. C. A., 1933.

VIII. Straight and Skewed Ailerons on Wings with Rounded Tips, by Fred E. Weick and Joseph A. Shortal. T. N. No. 445, N. A. C. A., 1933.

IX. Tapered Wings with Ordinary Ailerons, by Fred E. Weick and Carl J. Wenzinger. T. N. No. 449, N. A. C. A., 1933.

X. Various Control Devices on a Wing with a Fixed Auxiliary Airfoil, by Fred E. Weick and Richard W. Noyes. T. N. No. 451, N. A. C. A., 1933.

XI. Various Floating Tip Ailerons on Both Rectangular and Tapered Wings, by Fred E. Weick and Thomas A. Harris. T. N. No. 458, N. A. C. A., 1933.

XII. Upper-Surface Ailerons on Wings with Split Flaps, by Fred E. Weick and Carl J. Wenzinger. T. R. No. 499, N. A. C. A., 1934.

XIII. Auxiliary Airfoils Used as External Ailerons, by Fred E. Weick and Richard W. Noyes. T. R. No. 510, N. A. C. A., 1935.

2 Weick, Fred E., Soulé, Hartley A., and Gough, Melvin N.: A Flight Investigation of the Lateral Control Characteristics of Short Wide Ailerons and Various Spoilers with Different Amounts of Wing Dihedral. T. R. No. 494, N. A. C. A., 1934.

3. Soulé, H. A., and McAvoy, W. H.: Flight Investigation of Lateral Control Devices for Use with Full-Span Flaps. T. R. No. 517, N. A. C. A., 1935.

4. Weick, Fred E., and Jones, Robert T.: The Effect of Lateral Controls in Producing Motion of an Airplane, as Computed from Wind-Tunnel Data. T. R. No. 570, N. A. C. A., 1936.

5. Gough, M. N., and Beard, A. P.: Limitations of the Pilot in Applying Forces to Airplane Controls. T. N. No. 550, N. A. C. A., 1936.

6. Jones, Robert T.: A Study of the Two-Control Operation of an Airplane. T. R. No. 579, N. A. C. A., 1936.

7. Wenzinger, Carl J.: Wind-Tunnel Investigation of Tapered Wings with Ordinary Ailerons and Partial-Span Split Flaps. T. R. No. 611, N. A. C. A., 1937.

8. Shortal, J. A.: Wind-Tunnel and Flight Investigation of Slot-Lip Ailerons. T. R. No. 602, N. A. C. A., 1937.

9. Platt, Robert C., and Shortal, J. A.: Wind-Tunnel Investigation of Wings with Ordinary Ailerons and Full-Span External-Airfoil Flaps. T. R. No. 603, N. A. C. A., 1937.

10. Platt, Robert C.: Aerodynamic Characteristics of Wings with Cambered External-Airfoil Flaps, Including Lateral Control with a Full-Span Flap. T. R. No. 541, N. A. C. A., 1935.

11. Jones, Robert T., and Nerken, Albert I.: The Reduction of Aileron Operating Forces by Differential Linkage. T. N. No. 586, N. A. C. A., 1936.

12. Weick, Fred E., and Shortal, Joseph A.: Development of the N. A. C. A., Slot-Lip Aileron. T. N. No. 547, N. A. C. A., 1935.

13. Shortal, J. A.: Effect of Retractable-Spoiler Location on Rolling- and Yawing-Moment Coefficients. T. N. No. 499, N. A. C. A., 1934.

14. Williams, D. H., and Brown, A. F.: Experiments on a Small-Chord Flap on a Clark YH Aerofoil in the Compressed Air Tunnel. R. & M. No. 1681, British A. R. C., 1936.

15. Higgins, George J., and Jacobs, Eastman N.: The Effect of a Flap and Ailerons on the N. A. C. A.—M6 Airfoil Section. T. R. No. 260, N. A. C. A., 1927.

16. Wenzinger, Carl J.: Wind-Tunnel Investigation of Ordinary and Split Flaps on Airfoils of Different Profile. T. R. No. 554, N. A. C. A., 1936.

17. Munk, Max M.: Elements of the Wing Section Theory and of the Wing Theory. T. R. No. 191, N. A. C. A., 1924.

18. Pearson, H. A.: Theoretical Span Loading and Moments of Tapered Wings Produced by Aileron Deflection. T. N. No. 589, N. A. C. A., 1937.

19. Heald, R. H., and Strother, D. H.: Effect of Variation of Chord and Span of Ailerons on Rolling and Yawing Moments in Level Flight. T. R. No. 298, N. A. C. A., 1928.

20. Wenzinger, Carl J., and Harris, Thomas A.: Pressure Distribution over a Rectangular Airfoil with a Partial-Span Split Flap. T. R. No. 571, N. A. C. A., 1936.

21. Harris, Thomas A.: Reduction of Hinge Moments of Airplane Control Surfaces by Tabs. T. R. No 528, N. A. C. A., 1935.

TABLE I (A).—COMPARISON OF VARIOUS LATERAL CONTROL DEVICES

Device	Criterion	Linkage	Control forces and aileron deflections to produce specified bank in 1 second				Maximum deflection (degrees)	Sideslip with 15° bank in 1 second (degrees)		Lateral stability	Performance		
			$\phi_1=15°$										
			$C_L=0.35$		$C_L=1.0$								
			Stick force (lb.)	Aileron angles (degrees)	Stick force (lb.)	Aileron angles (degrees)	$\phi_1=22.5°$ $C_L=1.0$	$C_L=0.35$	$C_L=1.0$	$\alpha_{L_p=0}$ minus $\alpha_{C_{L_{max}}}$ (degrees)	Maximum lift $C_{L_{max}}$	Speed range $\frac{C_{L_{max}}}{C_{D_{min}}}$	Climb $\frac{L}{D}$ at $C_L=0.7$
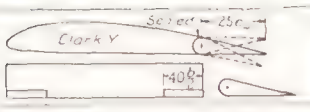	1. Plain ailerons sealed [a] $0.25c_w \times 0.40\frac{b}{2}$.	Equal	4.7	±3.4	3.6	±7.4	±11.2	3	7				
		Diff.	2.1	3.9×2.7	1.1	11.0×4.1	20.0×2.0	3	7				
		Diff. with tab.	.9	3.7×3.0	.3	9.0×6.0	14.0×7.7	3	7				
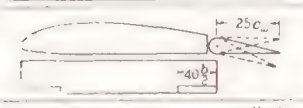	2. Plain ailerons $0.25c_w \times 0.40\frac{b}{2}$.	Equal	6.4	±3.8	5.6	±9.4	±14.5	3	8	0	1.27	91	18.7
		Diff.	2.6	4.5×3.0	1.6	11.0×4.8	18.0×5.0	3	7	0	1.27	91	18.7
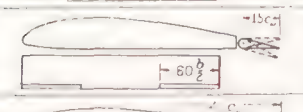	3. Plain ailerons $0.15c_w \times 0.60\frac{b}{2}$.	Equal	3.2	±3.8	2.6	±7.9	±13.0	4	8	1	1.22	85	18.5
		Diff.	2.5	4.5×3.0	1.2	11.0×4.8	23.0×4.0	4	8	1	1.22	85	18.5
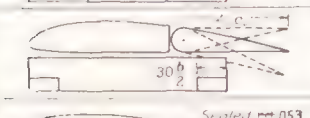	4. Plain ailerons $0.40c_w \times 0.30\frac{b}{2}$.	Equal	14.0	±4.2	11.0	±9.0	±14.0	4	9	1	1.25	87	18.2
		Diff.	7.0	4.8×3.5	2.0	12.0×7.0	18.0×8.0	4	8	1	1.25	87	18.2
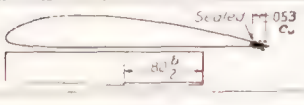	5. Optimum plain sealed ailerons [a] $0.053c_w \times 0.80\frac{b}{2}$.	Equal	1.4	±6.1	1.0	±13.0	±20.0	3	7				
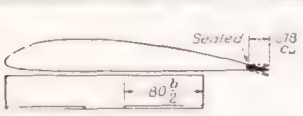	6. Optimum differential sealed ailerons [a] $0.078c_w \times 0.80\frac{b}{2}$; $0.015c_w$ fixed tab, down 14°.	Diff.	0.5	4.5×3.6	0.1	12.0×7.4	20.0×8.6	3	7				
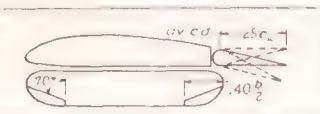	7. Skewed ailerons. Rounded tip wing [b] $0.25c_w \times 0.40\frac{b}{2}$; 20° skew.	Equal	10.0	±4.8	9.2	±12.0	±18.0	5	8	2	1.26	87	18.5
		Diff.	5.2	6.1×3.8	4.7	16.0×5.0	27.0×3.2	4	7	2	1.26	87	18.5
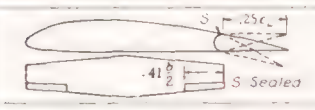	8. Tapered ailerons 5:3 tapered wing $0.25c_w \times 0.41\frac{b}{2}$.	Equal	4.0	±3.0	3.7	±7.5	±11.6	3	7		1.88	125	19.5
		Diff.	2.4	3.4×2.6	1.5	8.4×4.8	15.0×5.6	3	7		1.88	125	19.5
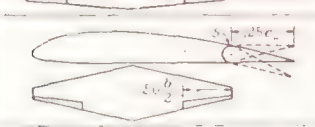	9. Tapered ailerons 5:1 tapered wing $0.25c_w \times 0.50\frac{b}{2}$.	Equal	2.4	±2.8	2.2	±7.4	±11.7	3	6	−3	1.81	129	18.2
		Diff.	1.4	3.1×2.5	1.2	8.2×6.0	13.0×7.8	3	6	−3	1.81	129	18.2
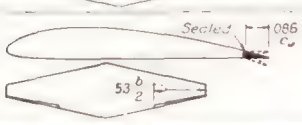	10. Optimum tapered sealed ailerons 5:1 tapered wing [a] $0.086c_w \times 0.53\frac{b}{2}$.	Equal	1.4	±7.3	0.9	±14.5	±20.0	3	6				
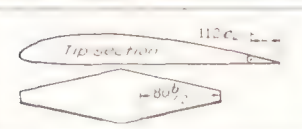	11. Optimum straight sealed ailerons 5:1 tapered wing [a] $0.112c_w$ (at tip)$\times 0.80\frac{b}{2}$.	Equal	0.8	±6.8	0.5	±13.5	±20.0	3	6				
	12. Frise ailerons $0.25c_w \times 0.40\frac{b}{2}$.	Equal	3.2	±2.6	3.8	±7.5	±14.5	3	7	0	1.28	85.0	18.5
		Diff.	1.8	2.6×2.5	1.1	8.0×7.0	18.0×12.0	3	6	0	1.28	85.0	18.5
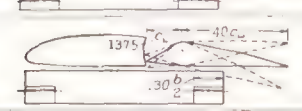	13. Frise ailerons (modified) $0.40c_w \times 0.30\frac{b}{2}$.	Equal	5.1	±4.2	8.1	±10.0	±14.3	5	9				
		Diff.	1.7	4.3×4.0	2.3	11.0×8.5	16.0×11.0	5	8				
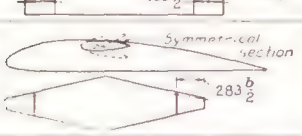	14. Floating-tip ailerons 5:1 tapered wing $1.06c_w \times 0.283\frac{b}{2}$.	Equal	2.5	4.8	2.2	8.6	13.0	2	2	−2	1.18	91.0	12.6
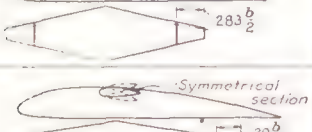	15. Floating-tip ailerons 5:1 tapered special wing [a] $1.00c_w \times 0.20\frac{b}{2}$.	Equal	4.8	7.4	4.9	15.8	25.0	1	2		1.27	84.0	19.5
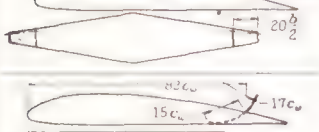	16. Retractable ailerons $0.15c_w \times 0.50\frac{b}{2}$.	Up only	0	0.925c_w [f]	0	0.062c_w [f]	0.074c_w [f]	1	4		1.27	91.0	18.1
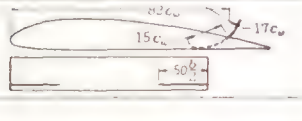	17. Ailerons and spoiler: [a,d] Ailerons $0.25c_w \times 0.40\frac{b}{2}$. Spoiler $0.07c_w \times 0.40\frac{b}{2}$.	Equal	2.3	±2.0	1.2	±4.4	±6.5	3	4	0	1.27	91.4	18.7
		Diff.	1.4	2.4×2.2	.2	6.0×4.4	9.6×5.6	3	4	0	1.27	91.4	18.7
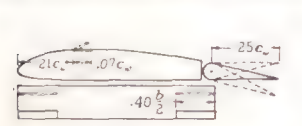	18. Slot-lip ailerons [d] $0.30c_w$ location $0.10c_w \times 0.50\frac{b}{2}$.	Unbalanced.	32.0	23.0×14.6	18.0	55.0×0	55.0×0	−5	−2	4	1.22	75.0	15.0
		Balanced.	29.0	23.0×14.0	16.0	55.0×0	55.0×0	−5	−2	4	1.22	75.0	15.0
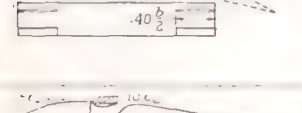	19. Slot-lip ailerons [d] $0.55c_w$ location $0.10c_w \times 0.50\frac{b}{2}$.	Unbalanced.	12.0	19.0×12.0	9.3	43.0×3.0	47.0×6	−1	2	4	1.23	83.0	16.0
		Balanced.	8.5	19.0×12.0	8.5	43.0×3.0	47.0×0	−1	2	4	1.23	83.0	16.0

[a] Computed or estimated results.
[b] Hinge moments computed or estimated.
[d] Device may not give satisfactory response characteristics.
[f] Deflection given in percentage of wing chord.

TABLE I (B).—COMPARISON OF VARIOUS LATERAL CONTROL DEVICES

Device / Criterion	Linkage	Control force and aileron deflection to produce specified bank in 1 second, $\phi_1=15°$: $C_L=0.35$ Stick force (lb.)	$C_L=0.35$ Aileron angles (degrees)	$C_L=1.0$ Stick force (lb.)	$C_L=1.0$ Aileron angles (degrees)	$C_L=1.8$ Stick force (lb.)	$C_L=1.8$ Aileron angles (degrees)	Sideslip with 15° bank in 1 second (degrees): C_L=0.35	C_L=1.0	C_L=1.8	Performance: Maximum lift $C_{l_{max}}$	Speed range $\frac{C_{L_{max}}}{C_{D_{min}}}$	Climb $\frac{L}{D}$ at $C_L=0.7$
20. Tapered ailerons, sealed. 5:3 tapered wing. Partial-span split flap: Ailerons $0.25c_w\times0.41\frac{b}{2}$. Flap $0.15c_w\times0.59\frac{b}{2}$.	Equal	4.0	±3.0	3.7	±7.5	3.5	±12.0	3	7	8	1.88	125	19.5
	Diff.	2.4	3.4×2.6	1.5	8.4×4.8	.8	15.0×5.6	3	7	7	1.88	125	19.5
21. Tapered ailerons, sealed. 5:3 tapered wing. Partial-span split flap: Ailerons $0.25c_w\times0.30\frac{b}{2}$. Flap $0.15c_w\times0.70\frac{b}{2}$.	Equal	4.0	±4.3	3.6	±9.6	4.5	±16.0	3	7	8	1.97	130	19.5
	Diff.	2.1	5.0×3.6	1.1	13.0×5.1	1.3	25.0×1.5	3	6	6	1.97	130	19.5
22. Tapered ailerons, sealed. 5:1 tapered wing. Partial-span split flap: [c] Ailerons $0.25c_w\times0.50\frac{b}{2}$. Flap $0.15c_w\times0.50\frac{b}{2}$.	Equal	2.4	±2.8	2.2	±7.4	1.9	±11.7	3	6	6	1.81	129	18.2
	Diff.	1.4	3.1×2.5	1.2	8.2×6.0	.1	13.0×7.8	3	6	6	1.81	129	18.2
23. Tapered ailerons, sealed. 5:1 tapered wing. Partial-span split flap: Ailerons $0.25c_w\times0.30\frac{b}{2}$. Flap $0.15c_w\times0.70\frac{b}{2}$.	Equal	2.4	±4.2	2.5	±12.0	2.8	±20.0	2	6	6	1.97	141	18.2
	Diff.	1.5	4.5×3.6	1.4	14.0×18.0	1.5	26.0×10.0	2	5	5	1.97	141	18.2
24. Plain ailerons. Retractable flap: Ailerons $0.15c_w\times0.60\frac{b}{2}$. Flap $0.15c_w\times1.00\frac{b}{2}$.	Equal	6.2	±3.8	4.7	±7.8	6.7	±25 0	4	8	8	2.05	143	18.5
	Diff.	5.7	4.0×3.5	3.7	8.7×7.1	5.4	28.0×11.0	4	8	7	2.05	143	18.5
25. Plain sealed ailerons. Retractable flap: [a] Ailerons $0.116c_w\times0.80\frac{b}{2}$. Flap $0.15c_w\times1.00\frac{b}{2}$.	Diff. with tab.	1.4	3.4×4.2	0.9	8.4×6.6	2.7	35 0×0.6	3	8	6	2.05	143	18.5
26. Retractable ailerons. Split flap: Ailerons $0.15c_w\times0.50\frac{b}{2}$. Flap $0.20c_w\times1.00\frac{b}{2}$.	Up only.	0	$0.025c_w$[f]	0	$0.062c_w$[f]	0	$0.074c_w$[f]	1	4	6	2.19	149	18.1
27. External-airfoil flaps [e] $0.20c_w\times1.00\frac{b}{2}$.	Diff.	5.5	3.2×3.0	3.1	6.0×5.5	0.2	13.0×11.0	3	7	10	1.83	172	18.7
28. External-airfoil flap ailerons [e] $0.20c_w\times0.50\frac{b}{2}$.	Diff.	0.9	3.7×3.7	0.8	7.6×7.3	0.3	16.0×9.2	3	7	8	1.80	172	18.7
29. Slot-lip ailerons. External-airfoil flap [e, d] Ailerons $0.12c_w\times1.00\frac{b}{2}$. Flap $0.20c_w\times1.00\frac{b}{2}$.	Diff. with tab.	2.4	10.0×6.0	2.3	25.0×6.5	1.4	14.0×6.8	3	6	7	1.92	202	19.0

[a] Computed or estimated results.
[c] C_L slightly below 1.8.
[d] Device may not give satisfactory response characteristics.
[e] Spring mechanism assumed to avoid overbalance with flap down.
[f] Deflection given in percentage of wing chord.

REPORT No. 606

ELECTRICAL THERMOMETERS FOR AIRCRAFT

By John B. Peterson and S. H. J. Womack

SUMMARY

Electrical thermometers commonly used on aircraft are the thermoelectric type for measuring engine-cylinder temperatures, the resistance type for measuring air temperatures, and the superheat meters of the thermoelectric and resistance types for use on airships. These instruments are described and their advantages and disadvantages enumerated. Methods of testing these instruments and the performance to be expected from each are discussed. The field testing of engine-cylinder thermometers is treated in detail.

INTRODUCTION

On aircraft a knowledge of the temperature of the engine is valuable (1) as an indication of trouble and (2) as an aid in normal operation. An indication of abnormal temperature of the engine cylinder, lubricating oil, or cooling liquid may forewarn of impending failure. Where temperature controls are provided, the temperature of the engine may be maintained at values for which the operation of the engine is most efficient.

A knowledge of the air temperature is essential in flight testing and as a warning of the possibility of ice formation. One of the most important quantities measured in airplane and balloon flights made to obtain meteorological data is the air temperature.

On airships both the air temperature and the difference between the air and lifting-gas temperatures are commonly measured. These data are vital factors in airship navigation.

When measuring temperatures on aircraft, it is obvious that the indicator must in most cases be at a distance from the point of measurement. Electrical thermometers, being inherently suitable for distant indication, are widely used. As an exception, vapor-pressure thermometers are commonly used to measure the temperature of the cooling water or lubricating oil of aircraft engines (reference 1).

Both thermoelectric and resistance types of electrical thermometers are used on aircraft. The choice between the two types of instruments lies principally in the accuracy required. An accuracy of 10° C. is sufficient in the measurement of engine temperatures whereas an accuracy of 1° C. is desired in the measurement of air temperatures. The thermoelectric type is used, to the exclusion of other types, for the indication of the temperature of air-cooled engine cylinders. This type is particularly suitable for this use because (1) the required accuracy can be obtained by using a single thermocouple with a relatively rugged moving-coil instrument, and (2) the thermocouple element is more easily connected thermally to the engine cylinder than any other type. The resistance thermometer is used when a more accurate determination of temperature over a shorter range is desired, as in the measurement of air temperatures.

Superheat meters for airships may be either of the thermoelectric or resistance type. A number of factors must be considered in choosing between the two types. These are discussed in the section on these instruments.

The instruments described in this report include (1) the thermoelectric-type engine-cylinder thermometer, (2) a resistance-type thermometer for measurement of air temperatures, (3) the thermoelectric and the resistance types of superheat meters, and (4) a tester for testing engine-cylinder thermometers. All of these instruments with the exception of the first have been developed at the National Bureau of Standards for use of the Bureau of Aeronautics, Navy Department. The National Advisory Committee for Aeronautics furnished the financial assistance necessary for the preparation of this report.

Where testing methods are described in detail in this report, the methods are those followed at the National Bureau of Standards in testing instruments purchased by the Bureau of Aeronautics, Navy Department.

ENGINE-CYLINDER THERMOMETERS

The thermoelectric circuit.—A diagram of the electrical circuit of an engine-cylinder thermometer with a copper-constantan thermocouple is shown in figure 1. Figure 2 is a diagram of the electrical circuit of a thermometer using several iron-constantan thermocouples with a selector switch. The comparative advantages

and disadvantages of different thermoelectric materials will be discussed later.

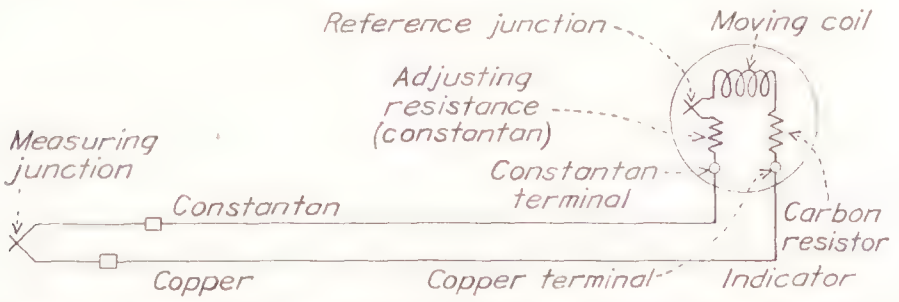

FIGURE 1.—Diagram of the electrical circuit of an engine-cylinder thermometer with a copper-constantan thermocouple.

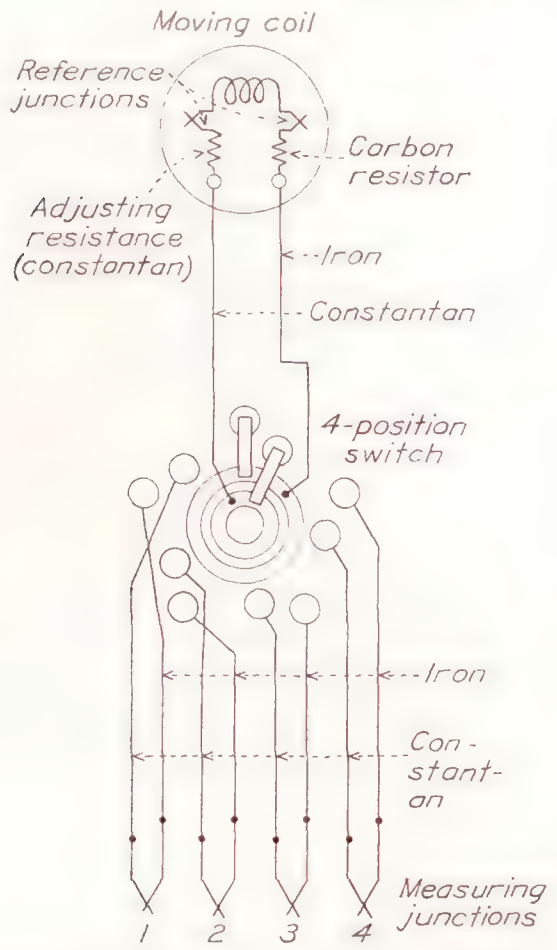

FIGURE 2.—Diagram of the electrical circuit of an engine-clyinder thermometer with a four-position selector switch and iron-constantan thermocouples.

The final design of the circuit is a compromise between many conflicting requirements. The energy available to operate the indicator is limited to the output of the single thermocouple. It follows that a sensitive indicator should be used; yet for operation on an airplane the indicator should have a high torque. The use of a stronger permanent magnet offers advantages in this respect but the difficulties of shielding the instrument so that it will not affect the magnetic compass are increased. The increased weight of a larger magnet is also objectionable.

Thermocouples and leads.—The choice of the most suitable combination of thermoelectric materials depends on several factors:

1. The thermoelectric power (dE/dT) should be high.
2. The mechanical strength after repeated heating and cooling should be good.
3. There should be high resistance to corrosion.
4. The thermal conductivity of the material should be low, so as not to conduct heat away from the part, the temperature of which is being measured.
5. The electrical resistance should be low.
6. The temperature coefficient of electrical resistance should be low.
7. A uniform supply of the material should be obtainable.

A comparison of these seven characteristics for several combinations of thermoelectric materials is given in table I. The first three combinations are at present used in measuring aircraft engine cylinder temperatures, and for the fourth, chromel P-constantan is proposed.

It should be pointed out that the change in resistance per °C., given in table I applies only to the resistance of the leads, which is usually about 0.1 of the total resistance of the circuit.

TABLE I.—PROPERTIES OF THERMOELECTRIC MATERIALS

	dE[1]/dT	Electrical resistance [2]	Change in resistance per degree centigrade [3]	Relative thermal conductivity [4]	Mechanical strength	Resistance to corrosion	Uniformity of supply
Copper	49.5	.074	.012	100	Poor	Fair	Excellent.
Constantan				6	Good	Good	Fair.
Chromel P	40.7	.147	.096	5	do	do	do.
Alumel				7	do	do	Good.
Iron	55.2	.087	.094	18	do	Poor	Fair.
Constantan				6	do	Good	do.
Chromel P	70.1	.176	.024	5	do	do	Good.
Constantan				6	do	do	Fair.

[1] Average microvolts per degree centigrade in the range 0 to 300° C.
[2] Ohms per foot of no. 14 duplex lead, at 20° C., based on the following resistances of the materials in ohms per foot of no. 14 wire: Copper, 0.002525; constantan, 0.0719; chromel P, 0.104; alumel, 0.0433; iron, 0.0149.
[3] Average change in resistance per degree centigrade for the range 20 to −30° C. expressed as a percentage of the resistance at 20° C.
[4] Thermal conductivity of copper = 100.

TABLE II.—AVERAGE TEMPERATURE-E. M. F. CHARACTERISTICS OF THERMOCOUPLES

[Reference 2 is the source of data for chromel-alumel and copper constantan in the range −20 to 50° C. The data for higher temperatures for chromel-alumel were obtained from reference 3, and for copper constantan from reference 4. The iron-constantan and chromel P-constantan curves are from unpublished data on file in the Pyrometry Section of the National Bureau of Standards.]

Temperature		Electromotive force, millivolts			
°C.	°F.	Copper-constantan	Chromel P-alumel	Iron-constantan	Chromel P-constantan
−20	−4	−0.75	−0.77	−1.03	−1.14
−15	5	−.57	−.58	−.77	−.86
−10	14	−.38	−.39	−.52	−.58
−5	23	−.19	−.20	−.26	−.29
0	32	0	0	0	0
5	41	.19	.20	.26	.29
10	50	.39	.40	.52	.59
15	59	.59	.60	.78	.89
20	68	.79	.80	1.05	1.19
25	77	.99	1.00	1.31	1.49
30	86	1.19	1.20	1.58	1.79
35	95	1.40	1.40	1.85	2.10
40	104	1.61	1.61	2.12	2.41
45	113	1.82	1.81	2.38	2.72
50	122	2.03	2.02	2.66	3.04
100	212	4.28	4.10	5.40	6.32
150	302	6.70	6.13	8.19	9.79
200	392	9.28	8.13	10.99	13.42
250	482	12.01	10.15	13.79	17.18
300	572	14.86	12.21	16.56	21.03
350	662	17.82	14.29	19.32	24.96
400	752	----	16.39	22.07	28.94
450	842	----	18.50	24.82	32.96
500	932	----	20.64	27.58	37.00
550	1,022	----	22.77	30.39	41.05

Average temperature-e. m. f. relations for thermocouples of four combinations of materials are given in table II. The data for the lower temperatures are given at short intervals for convenience in applying corrections for the reference junction temperature or in calculations dealing with the range of compensators.

FIGURE 3.—Thermocouples of the gasket and rivet types and a pair of leads.

A photograph of two types of thermocouple is shown in figure 3. This particular equipment was constructed according to specifications of the Bureau of Aeronautics, Navy Department. The gasket-type thermocouple is mounted in place of the regular spark-plug gasket. The rivet-type thermocouple is inserted in a drilled hole, ⅛ inch in diameter and in depth, and a steel pin concentric with the rivet is driven down to expand the copper to hold the rivet securely in place. The thermocouple wires are welded to the gasket or rivet head.

The United States Army has standardized on 2-ohm iron-constantan thermocouples and the Navy, on 2-ohm copper-constantan thermocouples; engine manufacturers install 3-ohm iron-constantan thermocouples in commercial airplanes. These resistance values include both the resistances of the leads and thermocouples.

Thermocouple leads are made in lengths to fit any installation requirement. In order to make leads of different lengths interchangeable, the cross-sectional area of the stranded wire is varied directly as the length so that all leads will have the same resistance. The leads are composed of two insulated conductors, of the same materials as the thermocouple, laid parallel, covered over-all with braid and saturated with flame- and moisture-resistant lacquer.

Selector switches.—When the temperatures of two or more points are to be measured with the same indicator, a selector switch of the required number of positions, a switch lead, and additional thermocouples are required. The switch lead and switch contact resistances are made low so as not appreciably to affect the indicated temperature. (See fig. 2 for a diagram of a 4-position and fig. 4 for a photograph of a 4-position and an 18-position rotary selector switch.) It is necessary that these switches be of the 2-pole type to avoid

FIGURE 4.—Rotary selector switches for connecting an indicator to any one of a number of thermocouples.

stray voltages that might cause erroneous indications if one side of all the thermocouples remained permanently connected to the indicator.

The electrical indicator.—A face view of two electrical indicators is shown in figure 5. Both instruments are inclosed in Army-Navy standard cases of 2¾ inch dial

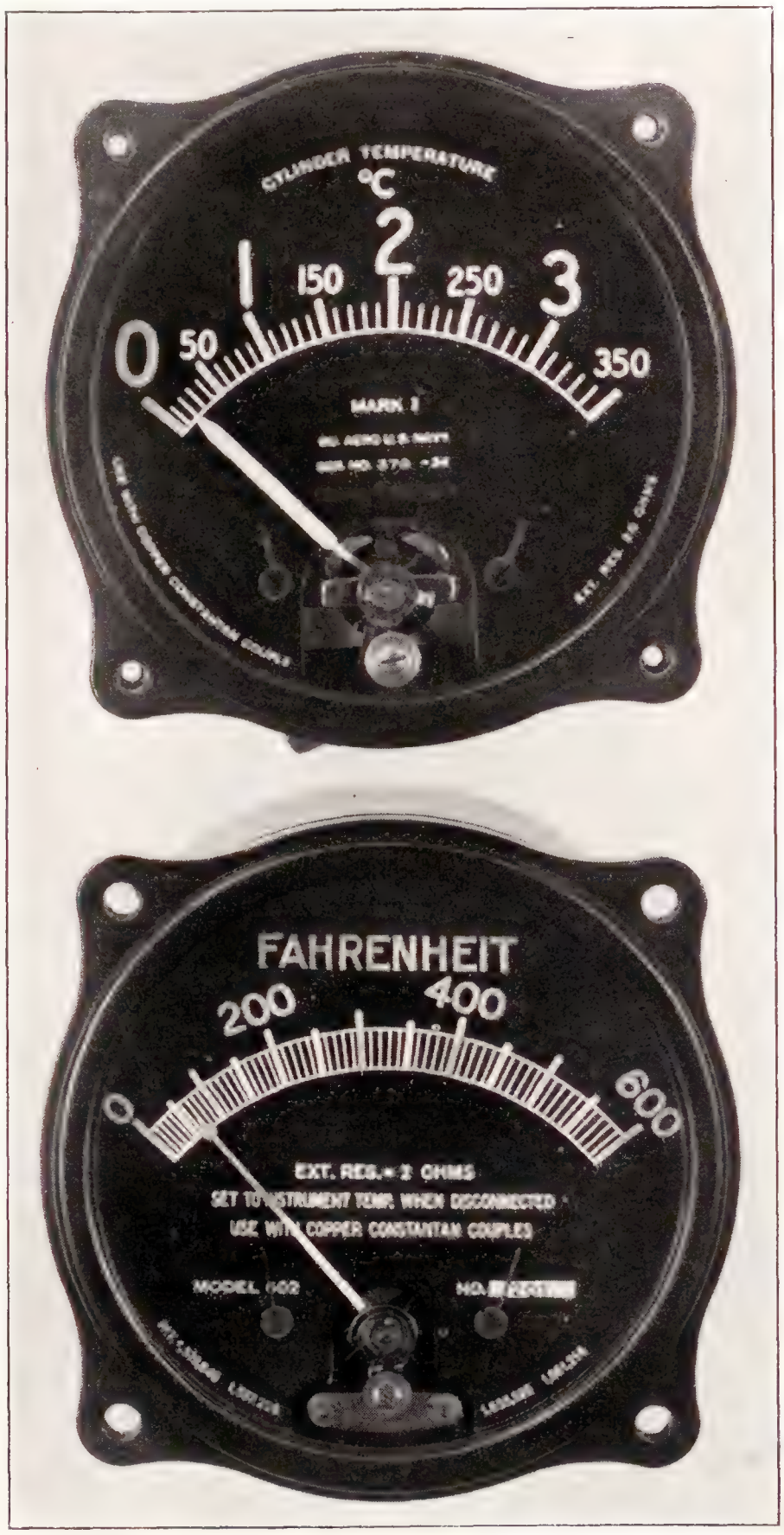

FIGURE 5.—Two engine-cylinder thermometer indicators.

diameter. Attached to the rear of the cases are terminals for connecting the thermocouple leads.

Because of the excessive vibration sometimes encountered on airplane instrument panels, the pivots which carry the moving coil of these indicators have been made blunter than those ordinarily used in electrical instruments. On airplanes there is always enough vibration to overcome the slight friction caused by the blunt pivots. These blunt pivots are known as "airplane pivots."

The electrical indicator must be magnetically shielded to reduce the effect of the permenant magnet on a magnetic compass. A soft-iron cup covers the sides and rear of the instrument and the front is shielded by a soft-iron dial. The shielding adds undesirable weight to an instrument already quite heavy because of the permanent magnet. The weights of indicators range from 1 to 1¾ pounds.

Reference-junction compensation.—Compensation for the temperature of the reference junction is accomplished by a small bimetallic spiral, which controls the position of the outside end of one of the hairsprings. This construction is shown in figure 6. The proper

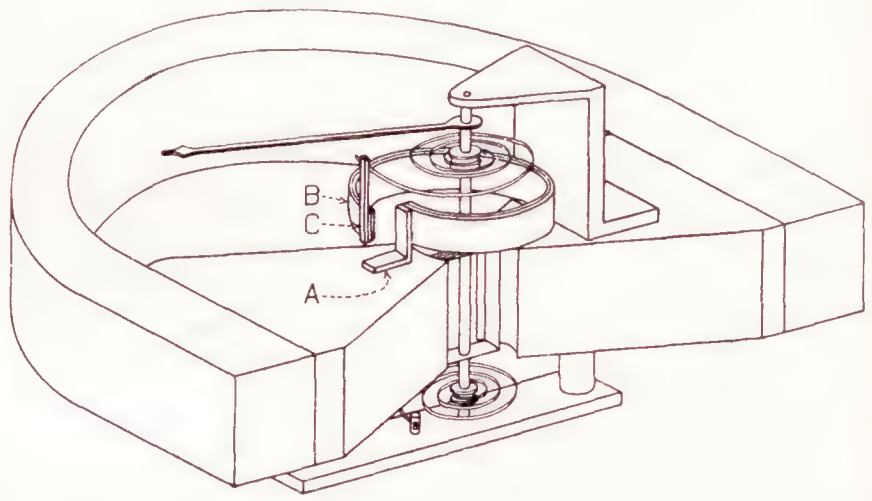

FIGURE 6.—Electrical indicator showing the Bristol reference junction compensator. B is the bimetallic spiral one end of which is fastened to the pole piece at A and the other to the hairspring at C.

action of the compensator is to cause the indicator, when there is no current in the moving coil, to indicate the ambient temperature. The bimetallic compensator and the reference junction should be placed closely together so that their temperatures will be the same. This requirement necessitates that the indicator terminal posts be constructed of the thermoelectric materials, so that there will be no intermediate junctions outside the instrument case. Furthermore, the rates of heating and cooling of the bimetallic compensator and reference junction should correspond, so that their temperatures will be the same for rapidly changing ambient temperatures.

It has become the general practice to connect a carbon resistor of negative temperature coefficient in series with the moving coil of the indicator, to compensate for the positive temperature coefficient of resistance of the copper in the moving coil.

Tests and performance of indicators.—The errors in indication of thermoelectric thermometers may be directly determined by immersing the measuring junction in a liquid bath and comparing the readings at a number of points with those of a calibrated thermometer. In practice, however, a more convenient method of determining the errors of engine cylinder thermome-

ters in use by the Bureau of Aeronautics is to test the indicator, leads, and thermocouple separately.

The Bureau of Aeronautics does not specify the resistance of the indicator, except that it shall be not less than 12 ohms at a temperature of 20° C. Since it is specified that the indication shall be correct when connected to a 2-ohm copper-constantan thermocouple, an exact specification of the resistance would be superfluous and would unnecessarily increase the cost of the instrument.

The scale errors of a millivoltmeter type indicator at room temperature are conveniently determined in the laboratory by connecting the indicator to a standard thermocouple (standard as regards temperature-e. m. f. relation and resistance) and then introducing into the circuit a voltage corresponding to that developed by the measuring junction at a given temperature. This junction is kept at a constant known temperature by placing it in an ice bath. The reading of the instrument

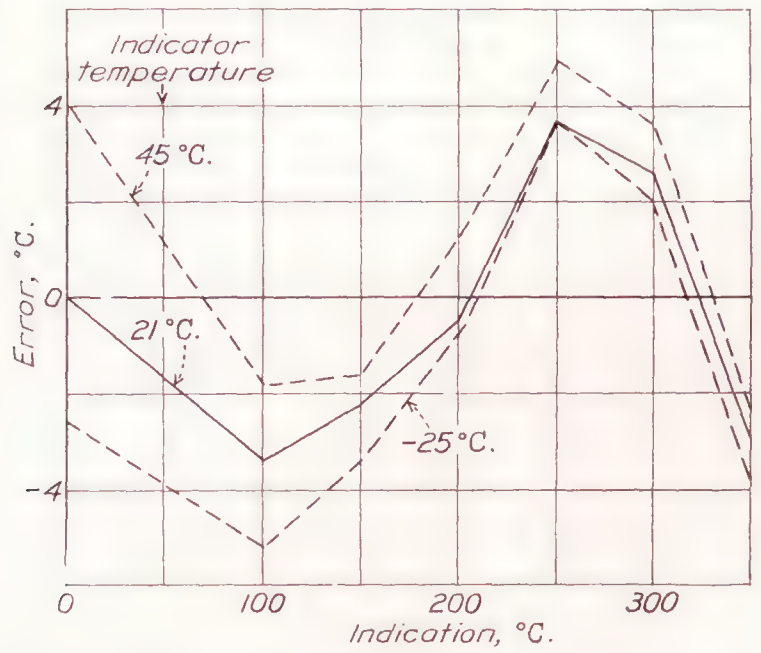

FIGURE 7.—Engine-cylinder thermometer errors for different indicator temperatures. The curves show the average of the errors of five indicators.

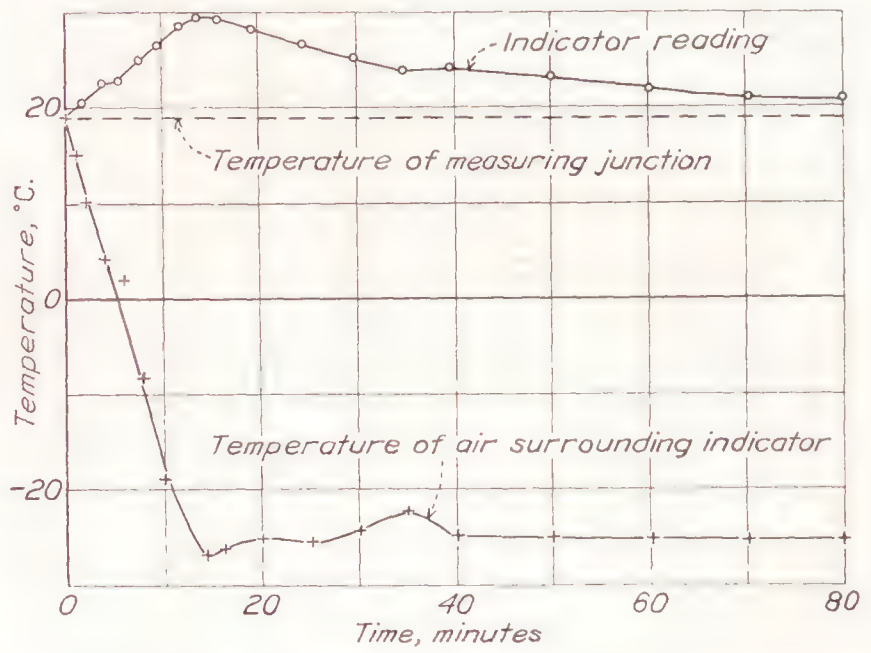

FIGURE 8.—The results of a temperature lag test on an indicator equipped with a bimetallic reference junction compensator.

minus the temperature corresponding to the applied voltage gives the scale error.

Tests similar to the test described are made with the indicator at temperatures of −25 and 45° C. to test the operation of the reference junction compensator and to determine the over-all effect of temperature on the scale error.

The average scale errors of five instruments at three temperatures have been plotted in figure 7. These instruments were equipped with bimetallic compensators and series carbon resistors of negative temperature coefficient. Besides affecting the reference junction and its compensator, a change in indicator temperature also affects the stiffness of the hair springs, the strength of the permanent magnet, and the resistance of the moving coil. The data in figure 7 show that for these instruments the bimetallic spiral overcompensates for the temperature of the reference junction, while the carbon resistor undercompensates for the change in resistance of the copper coil. The combination is adjusted so that the temperature error for the most important part of the scale, 200 to 350° C., is very small.

Figure 8 shows the results of a test to determine the change in reading of an indicator produced by a rapidly changing ambient temperature. The indicator is mounted in a chamber, the temperature of which is uniform and controllable, and connected to a thermocouple immersed in a liquid bath at room temperature. The pointer of the indicator is set to indicate the temperature of the bath. The temperature of the chamber in which the indicator is mounted is reduced from room temperature to approximately −25° C. at a rate of approximately 5° C. per minute. The indicator should continue to indicate the constant temperature of the measuring junction in the liquid bath. Assuming that the bimetallic compensator has been properly adjusted and that the resistance of the carbon resistor has been properly selected so that the indication finally reaches the bath temperature, the deviation of the indication from the bath temperature, as the temperature of the instrument is changed, is due to one or more of the following causes: (1) Improper placing of the reference junction with reference to the compensator; (2) uneven rates of heating and cooling of reference junction and compensator; (3) uneven rates of heating and cooling of the carbon resistor and copper coil; and (4) differences in temperature between the two ends of the carbon resistor.

The effect of vibration on the performance of the indicator is determined by subjecting the indicator to a vibration such that each point on the instrument case describes, in a plane inclined 45° to the horizontal, a circle of $\frac{1}{32}$-inch diameter. During this test the indicator is in the normal, face-vertical position. A description of the vibration machine on which this test is performed is given in reference 1. A voltage of specified value, which is normally sufficient to keep the pointer at approximately half of full-scale deflection, is introduced into the indicator circuit. The total

resistance in the indicator circuit is made equal to that existing in service, so as to obtain the same damping. The frequency of vibration is changed from 1,000 to 2,500 cycles per minute by steps, at each of which the average position of the pointer and the amplitude of oscillation is observed. The results of such a test are plotted in figure 9.

The cumulative effect of continuous vibration on the indicator is determined by subjecting it for periods up to 50 hours to vibrations at 1,800 vibrations per minute, maintaining the supply voltage as previously explained. Scale-error tests are made before and after vibrating, to determine the effect of vibration.

The effect of the indicator on the reading of a standard-type aircraft compass is determined by placing the indicator in various positions about the compass. The horizontal intensity of the magnetic field about the compass should be equal to 0.18 gauss for this test. The indicator shielding is considered satisfactory when, at a distance of 8 inches between the center of the indicator and the center of the compass, the change in compass reading is not more than 4°.

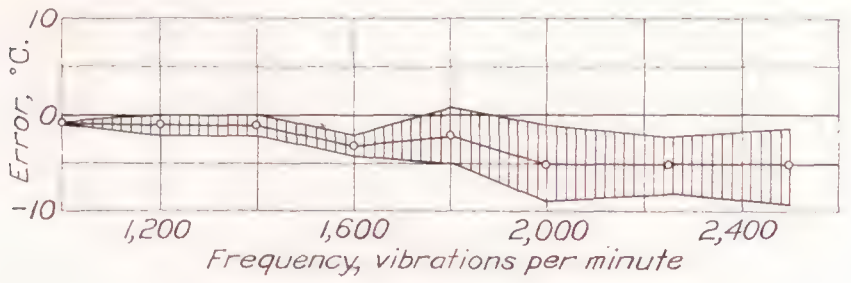

FIGURE 9.—Error in average position and amplitude of oscillation of pointer of typical engine cylinder thermometer when subjected to vibration.

Testing thermocouple material.—Thermocouple materials are tested at certain fixed points on the temperature scale. The melting point of ice (0° C.), the normal boiling point of water (100° C.), the freezing point of tin (231.9° C.), and the freezing point of lead (327.3° C.) are convenient points in the range of engine-cylinder thermometers. The methods used are described in detail by Roeser and Wensel in reference 2.

Some difficulties are experienced in testing short thermocouples, such as those illustrated in figure 3. If the longer wires necessary to connect the thermocouple to the potentiometer have not exactly the same thermoelectric properties as the wire of which the thermocouple is constructed, intermediate junctions are formed, the temperatures of which may be much higher than room temperature, owing to heat conduction along the short length of the thermocouple. Approximate corrections may be made for the temperatures of the intermediate junctions if these temperatures are measured by auxiliary thermocouples soldered onto the intermediate junctions. An easier and more accurate method, however, is to test sample thermocouples made of longer lengths of wire, from each batch of wire purchased.

The thermoelectric characteristics of the leads is found by joining the pair at one end to form a measuring junction. The e. m. f.'s developed for measuring junction temperature elevations of 50 and 100° C are measured directly on a potentiometer.

The Navy Department, Bureau of Aeronautics, specifications allow a deviation of approximately ±1 percent from the e. m. f. of the standard temperature-e. m. f. relation for copper-constantan thermocouples and ±2 percent for the leads. For interchangeability the resistances of thermocouples and leads should be uniform.

Engine-cylinder thermometer tester.—An instrument used in the field for testing copper-constantan thermoelectric type engine cylinder thermometers is shown in figure 10. Figure 11 is a diagram of the electrical con-

FIGURE 10.—Tester for copper-constantan thermoelectric thermometers.

nections of the tester. This tester was built according to the design and specifications of the Bureau of Aeronautics. The tester is designed for testing the calibration of the indicator and for checking roughly the resistance of the leads and the thermocouples.

When testing an indicator, it is connected by means of the 1-ohm copper-constantan clip leads furnished with the tester to the binding posts marked "Indicator test" (fig. 10). Since the resistance between the terminals marked "Indicator test" plus the resistance of the 1-ohm leads is exactly equal to the resistance of a Navy standard 2-ohm thermocouple and leads, indicators of any resistance are properly tested.

If there is a change in indication of the indicator when the circuit is completed and with the tester current off, it is due to a difference in temperature between the reference junction in the indicator and the measuring junction in the tester. If this change in reading exceeds 10° C., time should be allowed for the tester and indicator to come to the same temperature. When the limit of 10° C., is not exceeded, the error obtained in the comparison test ordinarily will not be more than 2° C. When proceeding with the test, the pointers of both the indicator and the milliammeter of the tester are set to the measuring junction temperature as indicated by the mercury thermometer on the tester.

The tester is designed for testing only one indicator at a time. The connection of two or more indicators in parallel will lead to erroneous results.

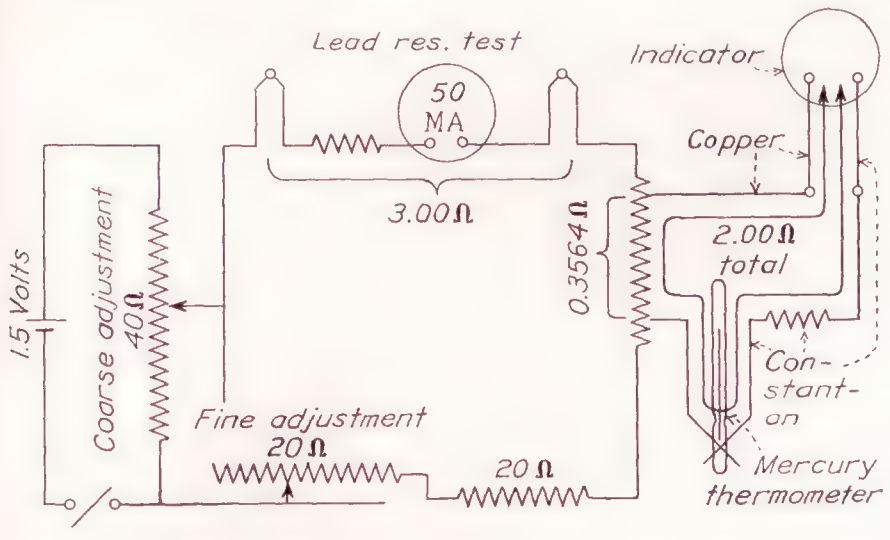

FIGURE 11.—Diagram of electrical connections of tester for copper-constantan thermoelectric thermometers.

RESISTANCE THERMOMETER

For the measurement of air temperatures on aircraft, thermometers of the resistance type are especially suitable on account of their features of remote indication and short-time lag. The temperature-sensitive element may be located in places or at distances impossible or impracticable for liquid-in-glass or bimetal thermometers. Although a resistance thermometer may be made to indicate over the range from —70 to 100° C., no thermometer of the liquid or vapor-pressure type that will operate satisfactorily over this range is known. The winding of the resistance element may be so made that the time lag in air is very much shorter than that of temperature elements of other types. One indicator may be used to indicate successively the temperature of a number of resistance elements by using a selector switch.

The resistance thermometer described in this report was originally designed and constructed for use in the flight testing of airplanes. Instruments of this type have also been used for the indication of air temperature on lighter-than-air ships of the United States Navy, on the National Geographic Society-Army Air Corps stratosphere balloons, and for the determination of temperature of the mixture in gasoline engine intake manifolds.

Indicator.—The instrument is essentially an unbalanced Wheatstone bridge arrangement, as shown schematically in figure 12. Figures 13 and 14 are, respectively, a front view and an inside rear view of the indicator unit. The electrical instrument is a Weston Model 269 milliammeter, giving a full-scale deflection on 3 milliamperes and having a resistance of approximately 35 ohms. The moving coil of the milliammeter is mounted on airplane pivots. If the double amplitude of vibration of the airplane member to which the instrument is fastened exceeds 0.005 inch, shock-absorbing means should be provided to reduce the instrument vibration to or below this value. The zero, or open-circuit, position of the pointer is approximately one-fourth of the length of the scale, from the left, as shown in figure 13. The calibration of the scale is approximately linear.

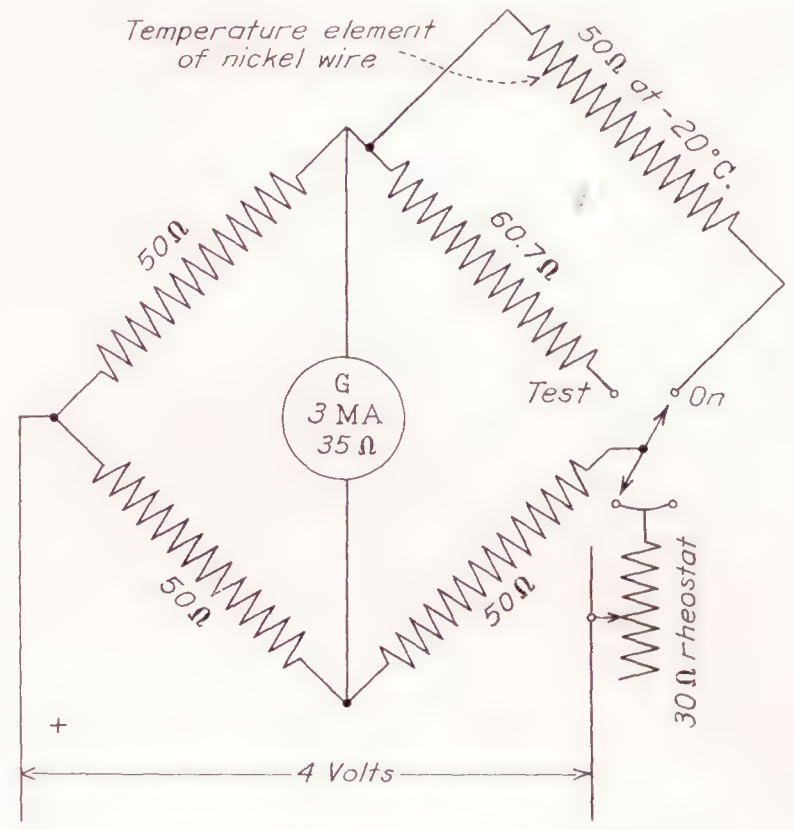

FIGURE 12.—Schematic diagram of resistance thermometer.

The bakelite case built around the electrical instrument (fig. 13) houses the 30-ohm rheostat, the switch, and the separable terminals carrying leads to the electrical supply and to the temperature element. The fixed manganin resistances of the bridge are mounted inside the electrical instrument case. The weight of the indicator unit is approximately 2¾ pounds.

For accurate indications it is necessary that the switch be turned occasionally to the test position and the rheo-

stat adjusted to cause the indicator pointer to stand at the test point (20° C. on fig. 13). When in the test position the switch substitutes a fixed resistance for the temperature element. The value of this fixed resistance is equal to that of the temperature element when it is at the temperature of the test point. Adjusting the rheostat varies the voltage impressed on the bridge. Proper adjustment compensates, exactly at the test point, for variations in the supply voltage and for temperature variations in the resistance of the copper in the moving coil of the electrical instrument. It is obvious that the indications at the balance point (−20° C. in fig. 13) are also free of errors due to these causes. Assuming that the proper voltage adjustment has been made, the errors due to these causes at points on the scale other than at the test and balance points will be negligible.

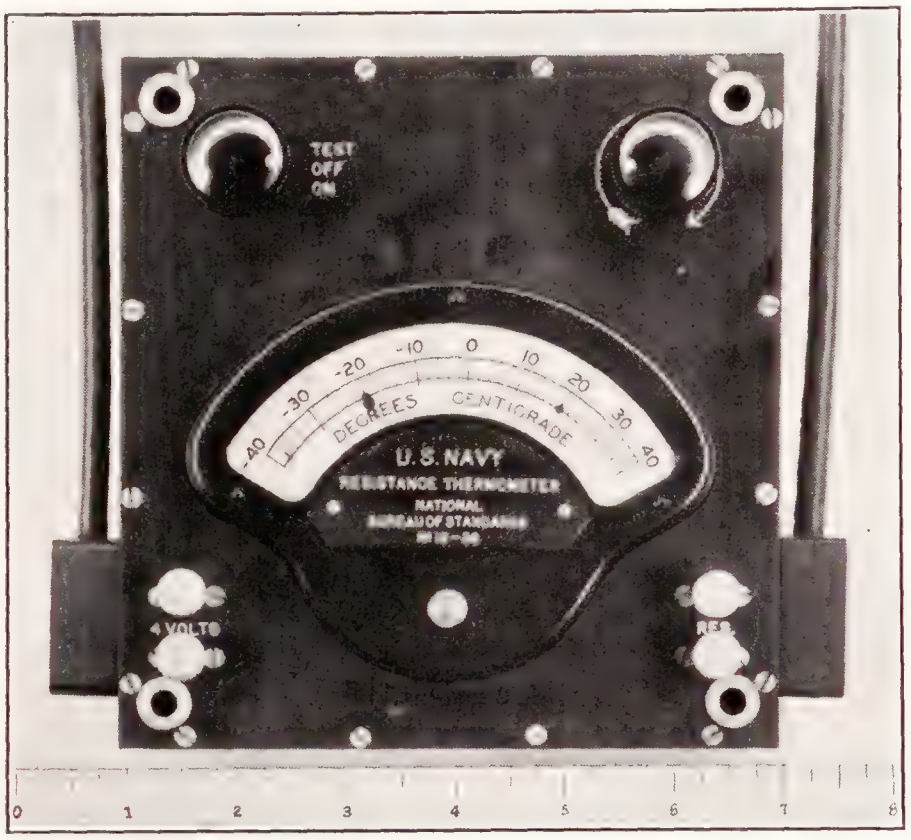

FIGURE 13.—Resistance-thermometer indicator.

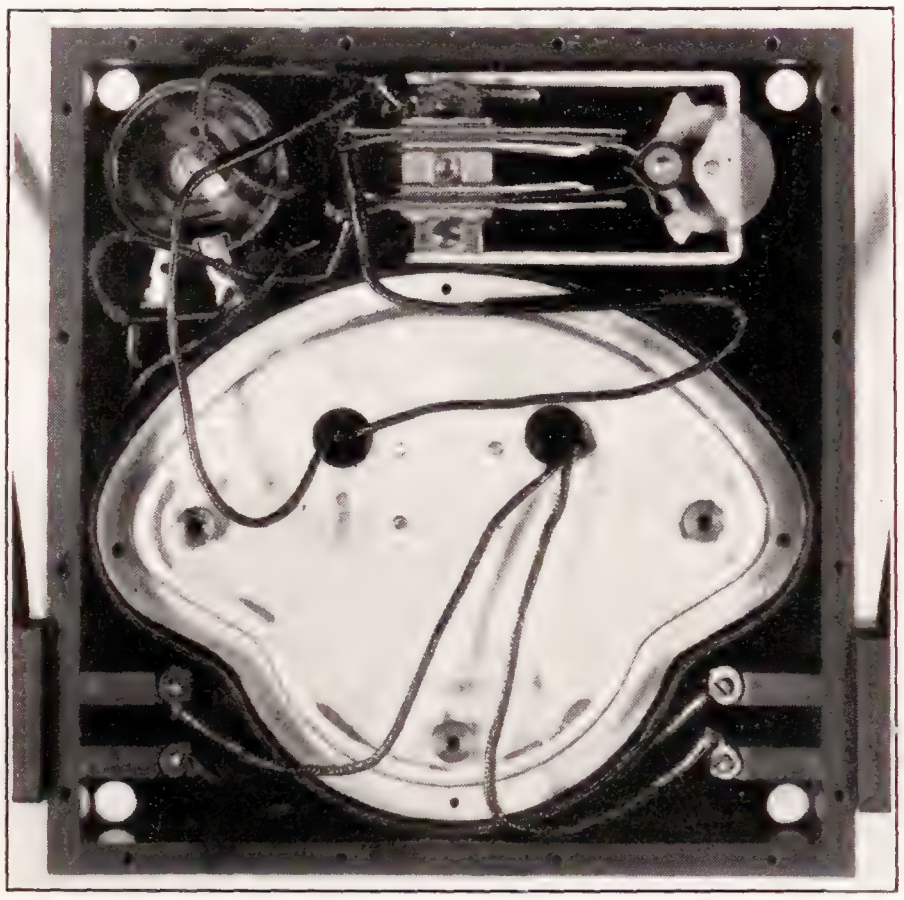

FIGURE 14.—Rear inside view of resistance-thermometer indicator.

Temperature element.—Details of a temperature sensitive element designed for strut mounting on an airplane are shown in figure 15. The temperature sensitive part is a single layer of no. 34 gage single silk-covered nickel wire wound on a bakelite tube of approximately $\frac{1}{64}$-inch wall thickness. The wire is held onto the tube and protected from moisture by several coats of bakelite varnish. The construction of the bakelite base is clearly shown. The connections between the nickel wires from the element and the copper lead wires are inside the base. The outside nickel-plated tube, which has a diameter of 1 inch and a length of $2\frac{3}{4}$ inches, serves to protect the element from the direct rays of the sun.

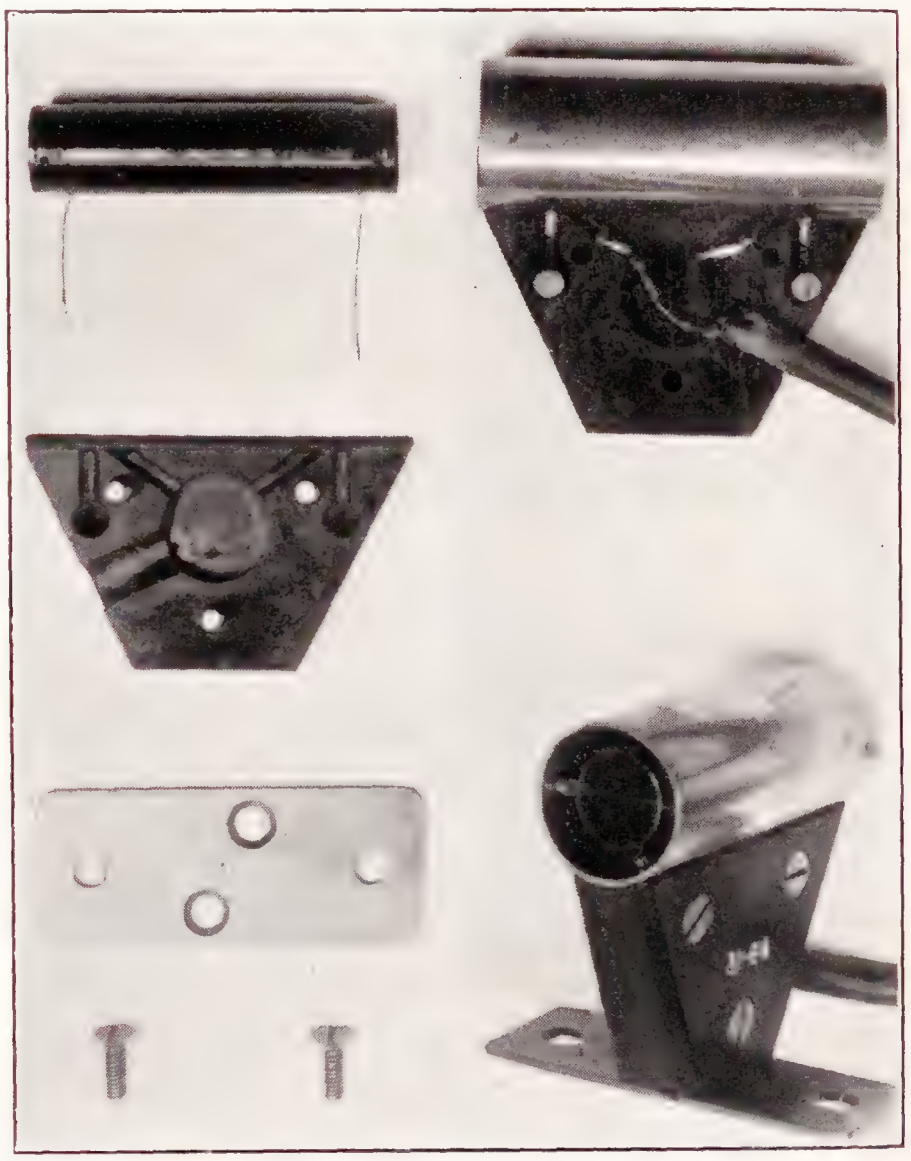

FIGURE 15.—A resistance-thermometer temperature element.

The element should be mounted where its temperature will not be affected by the heat from the engine exhaust. When possible, the leads from the temperature element to the indicator are installed inside the airplane wing covering at the factory. When necessary to make an installation on a finished airplane, a flat duplex lead $\frac{1}{16}$ inch thick and $\frac{5}{8}$ inch wide is sometimes used. This flat lead is held under a strip of fabric attached by dope to the airplane strut or wing.

Driver-Harris Grade A nickel wire has been used in the construction of the temperature elements. It has been found that all the wire from any one spool has approximately the same resistivity and temperature coefficient of resistivity. The resistance R of elements made in the last three years at the National Bureau of Standards (all from one spool) may be expressed by the following equation:

$$R=55.22\ (1+4.85T\times 10^{-3}+6T^{2}\times 10^{-6}) \qquad (1)$$

in which T is the temperature of the element in degrees centigrade. The data used for determining the constants of this equation were obtained by a null bridge method, a temperature element of the usual construction being one arm of the bridge. The temperature element was installed in a temperature chamber in front of a fan giving an air current of approximately 17 miles per hour. The electric current in the temperature element was approximately the same as that in the temperature element of circuit shown in figure 12. The temperature of the air in the chamber was held constant by hand regulation, holding the null indicator on zero. The values of the several constant temperatures were determined from an accurately calibrated copper-constantan thermocouple element installed just ahead of the resistance element. The temperature range of —70 to 40° C. was covered in this calibration. The best curve of the form of equation (1) was then fitted to the observed points. Wire from several spools of Driver-Harris Grade A nickel wire has been tested and found to have appreciably different temperature coefficients.

All resistance elements with the exception of those used on the stratosphere flights have been adjusted to a resistance of 60.7 ohms at a temperature of 20° C. The resistance at —20° C. is 50 ohms. These specified resistances include the resistance of copper lead wires to the element. These leads may be made of no. 16 gage wire, 10 or 20 feet long, the resistance of the two wires being of the order of 0.1 ohm. In use, the difference in temperature between the element and the lead wire is small; since the temperature coefficient of copper is approximately the same as that of the nickel wire used, the error introduced by using the copper lead is considered negligible. If the element and the leads with which it was adjusted are considered as a unit, the units are interchangeable.

Stratosphere instrument.—Resistance thermometers with several special features were constructed for use on the National Geographic Society-United States Army stratosphere balloon flights (reference 5). Figures 16 and 17 are photographs of the indicator and the temperature element. The indicator has a range of —70 to 40° C. The indicator face was photographed during the flights at 90-second intervals. A black scale with white graduations and pointer was used because it has been found that clearer photographic records are thus obtained. Since the knob used to switch from the "on" position to the "test" position in the course of adjusting the voltage did not appear in the photograph it was necessary to install an auxiliary indicator, which may be seen at the upper left-hand corner.

Without special precautions the lag in the temperature element of this instrument would have been prohibitive because at the highest altitude reached the air density was only 5 percent of standard sea-level density and there was practically no movement of the balloon relative to the air. As may be seen in figure 17, the wire of the temperature element was wound on an open frame so that practically the entire surface of the wire was

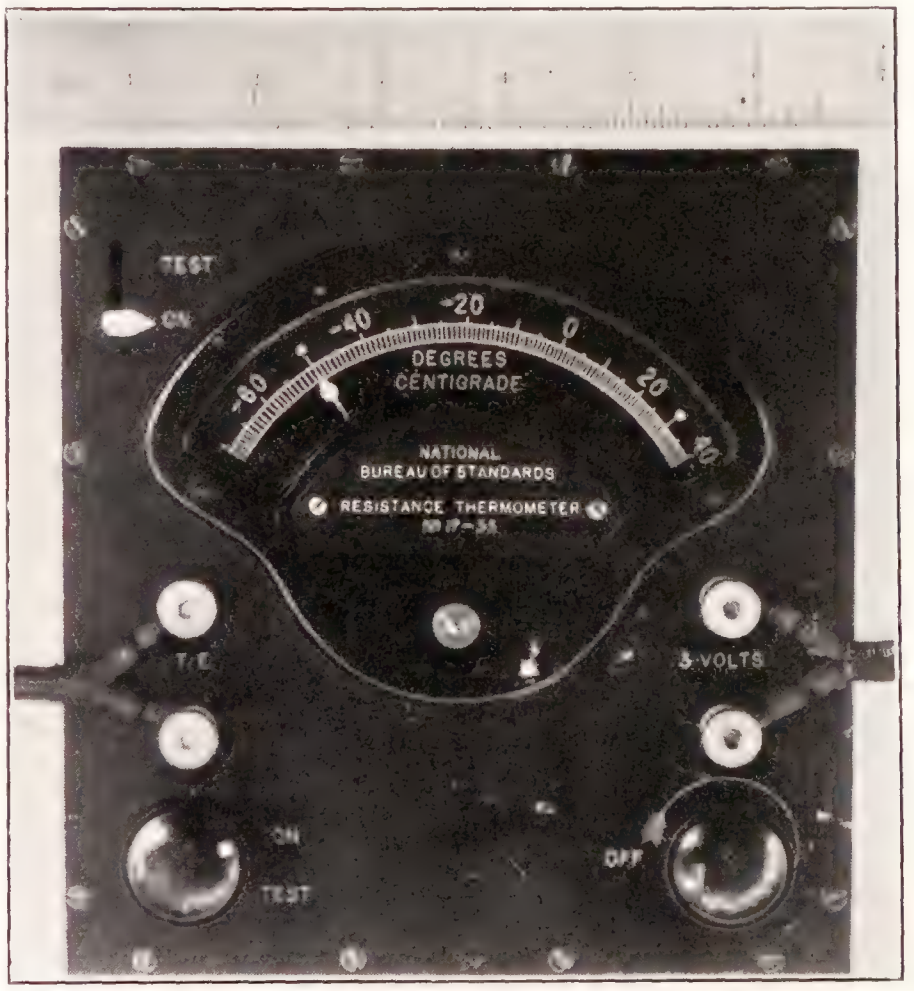

FIGURE 16.—Resistance-thermometer indicator constructed for stratosphere balloon flights.

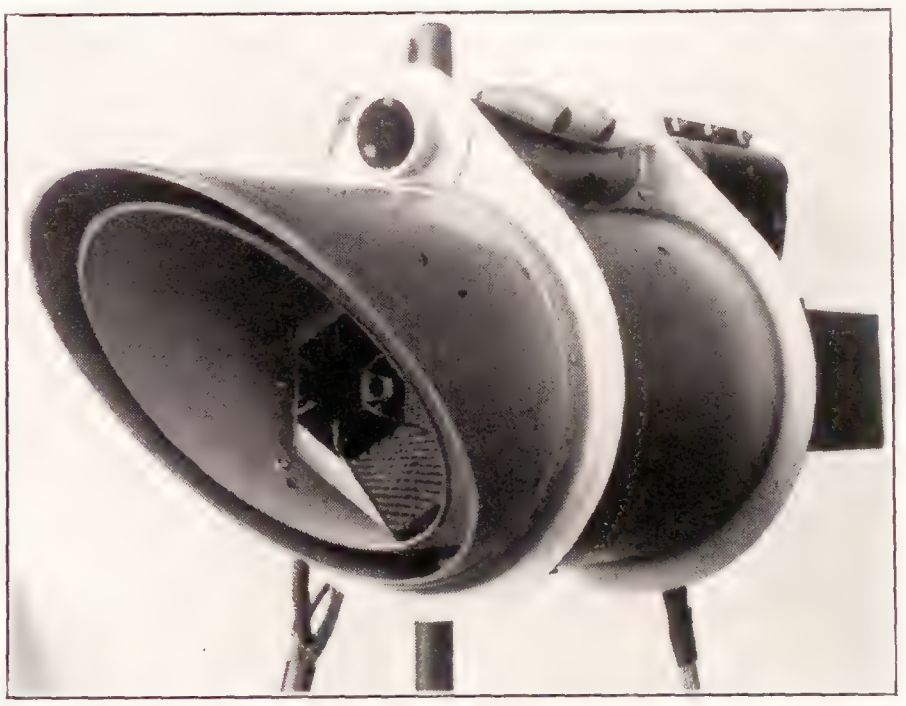

FIGURE 17.—Temperature element of resistance thermometer used on stratosphere flight. This element is ventilated by an electric fan.

exposed to the air. The element was shielded from the direct rays of the sun by two coaxial fiber tubes, the outer of which was 6 inches in diameter. Ventilation was secured by a fan operated by a small electric motor that drew air through the tube.

Time lag.—A detailed discussion of the time lag of thermometers is given by Harper (reference 6). Henrickson (reference 7) describes experimental methods and apparatus for the determination of time-lag constants and gives values of the time-lag constants for various aircraft thermometers.

A convenient method for determining the time-lag constant of air thermometers is to raise the temperature of the element to approximately 60° C. and then suddenly to place it in an air stream at room temperature, measuring with a stop watch the time required for a change in indication between two convenient points on the scale. The time-lag constant λ, in seconds, is defined by the equation,

$$\lambda = \frac{t}{\log_e \frac{T_1 - T_0}{T_2 - T_0}} \tag{2}$$

where T_0 is the temperature of the air stream, T_1 the indication when timing is started, T_2 the indication when timing is stopped, and t the time in seconds for the indication to change from T_1 to T_2.

Tests at air speeds of 30 to 60 miles per hour indicate that approximately, the time lag varies inversely as the air speed V.

$$\lambda_0 = \frac{L}{V} \tag{3}$$

where λ_0 is the value of the time-lag constant at the air density ρ_0 and L is a constant, characteristic of the temperature element. Koning discusses this relation in reference 8. It is evident that at very low air speeds, under a mile or two per hour, convection currents in the air become predominant so that formula (3) does not apply. The value of λ remains finite when $V=0$. However, for airplane speeds the convection constant may be neglected.

Smolar (reference 9) gives the variation of λ with air density as

$$\lambda = \lambda_0 \sqrt{\frac{\rho_0}{\rho}} \tag{4}$$

Combining equations (3) and (4)

$$\lambda = \frac{L}{V} \sqrt{\frac{\rho_0}{\rho}} \tag{5}$$

Since the true air speed V may be expressed as a function of the pitot-static indicated air speed V_i,

$$V = V_i \sqrt{\frac{\rho_0}{\rho}} \tag{6}$$

it follows that,

$$\lambda = \frac{L}{V_i} \tag{7}$$

This equation gives λ as a function of the indicated air speed, independent of air density.

If V_i is expressed in miles per hour and λ in seconds, L for the resistance element illustrated in figure 15 is equal to approximately 160. At an indicated air speed of 100 miles per hour, λ is 1.6 seconds.

It is of interest to review two physical conceptions of the time-lag constant λ. First, assume that the temperature is changing at a rate which has remained constant for some time (fig. 18). The indication T

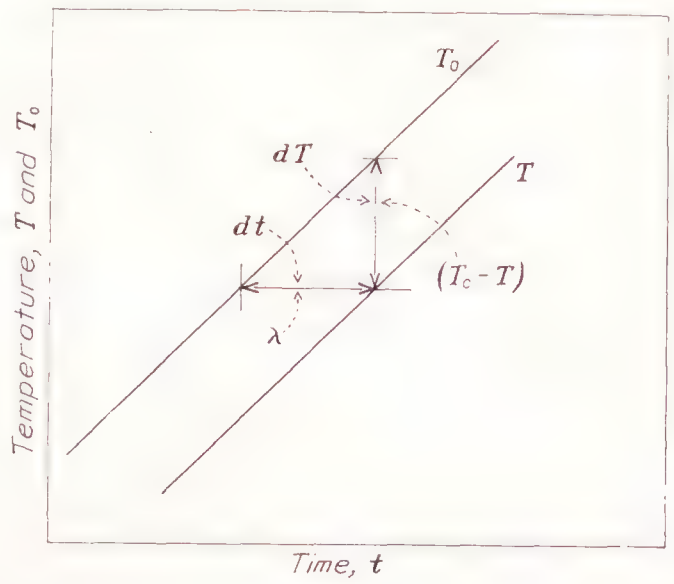

FIGURE 18.—Graphical illustration of time lag of a thermometer in a medium, the temperature T_0 of which is varying at a constant rate. The thermometer indication is T, the time-lag constant is λ, and the temperature lag is T_0-T.

of the thermometer will lag behind the actual temperature T_0, indicating the temperature that existed λ seconds earlier. The lag in temperature indication, T_0-T (in degrees) is the product of the time-lag constant (in seconds) by the rate of change in temperature (in degrees per second). Second, assume that the temperature element is suddenly taken from air at one temperature and placed into air at a different temperature. After λ seconds the indication will still have $1/e(=0.37)$ times the total temperature difference to go before the new temperature is accurately indicated. The value of e, the base of the natural logarithm system, is approximately 2.72. The variation in indication with time is given by equation (2) when T_1 is the indication at time $t=0$ and the indication T_2 at time t.

Temperature rise due to I^2R loss.—Equation (2) was derived on the assumption that Newton's law of cooling holds for the resistance element; that is, that the rate of heat transfer to or from the element is directly proportional to the difference in temperature between the element and the surrounding air. This law may be expressed by

$$M\frac{dT}{dt} = k(T - T_0) \tag{8}$$

where M is the heat capacity of the element and k is a factor of proportionality. In equation (2), M/k was set equal to the single constant λ, the time-lag constant for the element.

If there is an I^2R loss in the element maintaining the element at a constant temperature above that of the air, the rate at which heat is lost must equal the rate

at which it is supplied, that is

$$I^2R=k(T-T)_0 \tag{9}$$

or with $k=M/\lambda$,

$$I^2R=\frac{M}{\lambda}(T-T_0) \tag{10}$$

The temperature rise due to the heating is then

$$T-T_0=\frac{\lambda}{M}I^2R \tag{11}$$

where I is the current and R is the resistance of the element.

The I^2R loss in the element, calculated from the data given in figure 12, is equal to approximately 0.05 watt. The value of M, calculated from the dimensions, densities, and specific heats of the parts, is equal to 3.3 watt-seconds per degree centigrade. Then, for the element illustrated in figure 15,

$$T-T_0=\frac{0.05}{3.3}\lambda=0.015\lambda \tag{12}$$

or, from equation (7),

$$T-T_0=0.015\frac{L}{V_1} \tag{13}$$

The observed value of the time lag of the element in still air with the axis of the tube vertical is 115 seconds. Substituting this value in equation (12), the I^2R temperature rise is equal to 1.7° C. From equation (13) the rise at 50 miles per hour is equal to 0.05° C. Both the time lag and the I^2R temperature rise decrease rapidly with increasing air speed.

Speed correction.—The results of flight tests on high-speed airplanes indicate that thermometers exposed in the air stream give increasing readings with increasing air speed, the air temperature remaining constant. The correction C independent of the air density, when expressed as a function of the indicated air speed, is

$$C=-SV_i^2 \tag{14}$$

where S is a constant, characteristic of the element, and V_i is the pitot-static indicated air speed. If V_i is expressed in miles per hour and C in degrees centigrade, S for the element illustrated in figure 15 is equal to approximately 80×10^{-6}. At an indicated air speed of 200 miles per hour, the correction amounts to 3.2° C. and should be subtracted from the observed readings. This speed error, which is common to all types of thermometers, is discussed in reference 8.

Laboratory tests and performance.—Resistance thermometers are tested for scale errors in an air bath. The temperature element is placed in a chamber in which a fan provides a positive flow of air past the element. The temperature of the air around the element is held constant within narrow limits for several minutes before each reading. This temperature is measured by a calibrated thermocouple placed close to the resistance element. The scale errors, as determined by this method, do not ordinarily exceed 0.5° C.

The method of determining the time-lag constant of the instrument has been discussed.

The effect of change in temperature of the indicator is eliminated for all practical purposes when the voltage is properly adjusted at any given indicator temperature.

SUPERHEAT METERS

The term "superheat" as used in relation to lighter-than-air craft is defined as the temperature of the lifting gas minus the temperature of the outside air. The importance of a knowledge of superheat is evident when the dependence of the lift of a balloon or airship on this temperature difference is considered. The additional lift due to positive superheat is equal to the weight of the air that is forced out of the envelope by the increase in temperature. Strother and Eaton (reference 10) discuss the effect of superheat on the lift of an airship.

The superheat may be determined by separately measuring the outside air temperature and the gas temperature, but it is more convenient, and usually more accurate, to read this temperature difference directly on a superheat meter. Two general types of superheat meters have been constructed at the National Bureau of Standards for use on United States Navy airships, the thermoelectric type and the resistance type. Each type will be described.

Thermoelectric type superheat meter.—The essential details of thermoelectric type superheat meter installation using copper-constantan couples are shown in figure 19. By the use of a selector switch, both forward and after readings are obtained on the same indicator. The indicator is a Weston model 440 galvanometer of 3.5 ohms resistance, giving full-scale deflection on 132×10^{-6} amperes. A photograph of the parts of an instrument for indication of aft superheat only is given in figure 20.

Excessive temperature lag at the junctions is avoided by joining 6-inch lengths of no. 24 gage copper and constantan wires to the no. 16 gage copper and constantan wires and forming the actual junctions by joining the smaller wires. It is essential that the air junction be protected from the direct rays of the sun.

Calculation of errors.—Fortunately the two largest errors in a superheat meter of the thermoelectric type can be made approximately to cancel each other, by proper proportioning of the copper resistance and constantan resistance of which the circuit is composed. These errors are due to (1) the increase in thermoelectric power dE/dT with increase in air temperature and (2) the increase in resistance of copper in the circuit with increase in air temperature. The compensation is based on the assumption that the galvanometer lead wires and air junction are at the same temperature. If the installation cannot be arranged so that this condition is approximately realized, the errors may amount to as much as 5 percent.

(1) The e. m. f.-temperature relation for a Leeds & Northrup copper-constantan thermocouple as derived from test results obtained at the National Bureau of Standards between the temperatures of −20 and 120° F. may be expressed as follows:

$$E=21.4\,T_2(1+0.00058\,T_2)-21.4\,T_1(1+0.00058\,T_1) \quad (15)$$

where E is the e. m. f. in microvolts and T_1 and T_2 are the temperatures of the air and gas junctions, respectively, in degrees Fahrenheit, above a base temperature of 50° F. A base temperature of 50° F., rather than 0° F., is chosen because the higher temperature is nearer the middle of the operating range of the instrument and nearer the temperature at which the instrument is calibrated. Substituting ΔT for (T_2-T_1), this equation may be written as follows:

$$E=21.4\,\Delta T[1+0.00058\,(2\,T_1+\Delta T)] \quad (16)$$

It should be noted that ΔT is the superheat when the thermocouples form part of a superheat meter. It is seen that E is a function of the air-junction temperature T_1 as well as of the superheat ΔT.

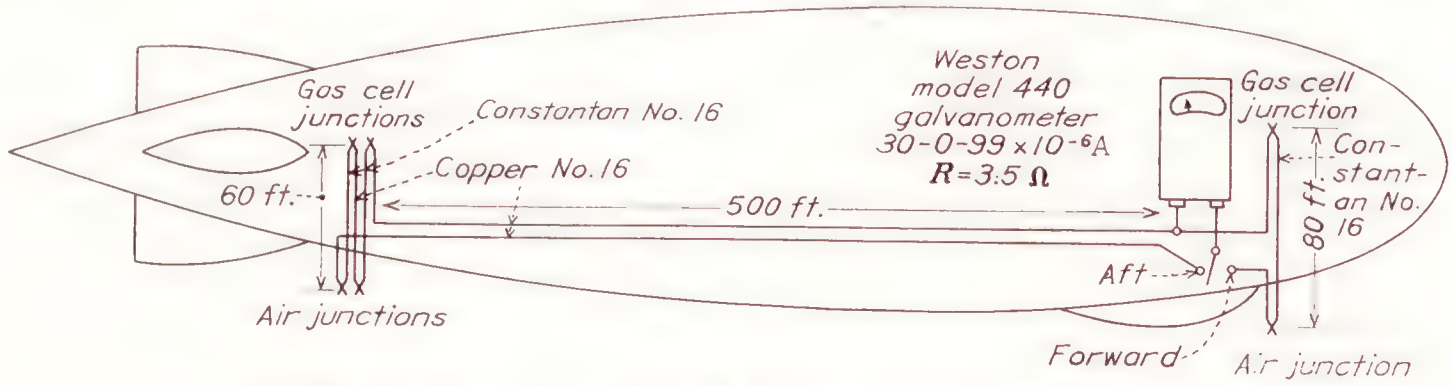

Resistance of aft circuit:	Ohms
Galvanometer	3.50
1,120 feet no. 16 copper	4.48
Added copper	2.42
Total copper	10.40
120 feet no. 16 constantan	8.88
Added constantan	.72
Total constantan	9.60
Total resistance	20.00

Resistance of forward circuit:	Ohms
Galvanometer	3.50
80 feet no. 16 copper	.32
Added copper	.26
Total copper	4.08
80 feet no. 16 constantan	5.92
Total resistance	10.00

FIGURE 19.—Details of a superheat meter for indicating, on a single indicator, the superheat in the forward and after gas cells.

FIGURE 20.—A thermoelectric-type superheat meter, complete with air element (A), gas-cell element (B), and connecting wire (C and D). This instrument was installed in an after cell on the U. S. S. *Los Angeles*.

(2) The resistance of the circuit is

$$R=R_{50}\,(1+N\,\alpha\,T_1) \quad (17)$$

where R is the resistance when the entire circuit is at a temperature T_1 °F. above 50° F., in ohms; R_{50}, is the resistance of the circuit at 50° F., in ohms; N, the ratio of the resistance of the copper in the circuit to the total resistance of the circuit; and $\alpha=0.00222$ per degree Fahrenheit, the temperature coefficient of resistance of copper, at 50° F. The temperature coefficient of resistance of the constantan is assumed to be zero.

The indication is also affected in opposite directions by changes in the temperature of the hairsprings and permanent magnet of the galvanometer. These two effects combined may be called the temperature coefficient of the instrument as an ammeter. It averages +0.0001 per degree Fahrenheit for several instruments which have been tested. Since no definite information, except that the value is small, is available on the value of this coefficient for the Weston Model 440 galvanometer, the value will be assumed to be zero.

The galvanometer current I, in microamperes, as determined from equations (16) and (17) is

$$I=\frac{E}{R}=\frac{21.4\Delta T[1+0.00058(2T_1+\Delta T)]}{R_{50}(1+0.00222NT_1)} \quad (18)$$

If $T_1=0$,

$$I=\frac{21.4\Delta T(1+0.00058\Delta T)}{R_{50}} \quad (19)$$

The instrument scale is constructed according to equation (19). Equation (18) indicates that the calibration is not independent of T_1. However, if

$$N=\frac{2\times 0.00058}{0.00222}=0.52 \qquad (20)$$

the indication, neglecting second-order terms, is correct for all values of T_1. Thus the resistance of the circuit should consist of 52 percent copper and 48 percent constantan. The errors for rather large departures from this ratio are not serious, but there is no reason why the ratio cannot be at least approximated. The requirement is not inconsistent with the practice of selecting a galvanometer that has a resistance equal to that of the external circuit, since the galvanometer resistance is all copper and the resistance external to the galvanometer is mainly constantan.

It is possible to proportion the copper and the constantan in the aft circuit of the instrument outlined in figure 19, so that $N=0.52$ and the error in indication is zero. For the forward instrument the optimum ratio could not be conveniently attained (without the use of larger lead wires). For it, $N=0.41$; and the error in indication is -1 percent of the indication for an air temperature of 90° F. and $+1$ percent for an air temperature of 10° F.

Resistance-type superheat meter.—A resistance-type superheat meter has several advantages over the thermoelectric-type instrument, mainly the possibility of using a more rugged electrical instrument.

The schematic diagram of the essentials of a superheat meter of the resistance type is shown in figure 21. The temperature elements, e and f, are made of no. 34 gage Driver-Harris Grade A nickel wire and have a resistance of 30 ohms at a temperature of 0° F. The temperature coefficient of resistance of this wire has been determined as described in the section on resistance thermometers. The resistance of the 30-ohm elements is

$$R=30(1+2.82T\times 10^{-3}+2T^2\times 10^{-6}) \qquad (21)$$

in which T is the temperature in degrees Fahrenheit.

TABLE III.—RESULTS OF TESTS TO DETERMINE THE BEST COMBINATION OF RESISTANCES FOR THE RESISTANCE TYPE SUPERHEAT METER

Air temperature (°F.)	Superheat (°F.)	Errors, °F., produced by using resistance values as designated in fig. 21				
		$a=b=500$ $c=770\Omega$	$a=b=1500$ $c=200\Omega$	$a=b=1800$ $c=150\Omega$	$a=b=2000$ $c=124\Omega$	$a=b=4000$ $c=0\Omega$
−46.3	0	0	0	0	0	0
	13.6	−.3	−.3	0	−.1	.7
	27.0	−.5	−.4	−.2	−.2	1.2
	40.3	−.7	−.8	−.4	−.2	1.2
0	−13.3	.1	0	0	0	−.3
	0	0	0	0	0	0
	13.2	−.1	−.1	−.2	0	0
	26.3	−.3	−.3	.1	−.1	.2
	39.3	−.4	−.2	−.1	−.1	.1
39.2	−13.0	0	−.1	0	0	0
	0	0	0	0	0	0
	12.8	.1	.1	.2	.1	0
	25.5	.3	.2	.1	.2	−.2
	38.1	.4	.3	.3	.3	−.5
77.3	−12.6	−.2	.2	−.1	−1	.4
	0	0	0	0	0	0
	12.5	.3	0	−.1	0	−.5
	24.9	.4	.1	.1	−.1	−1.1
	37.1	.8	.2	.1	−.1	−.8

The circuit shown in figure 21 was established with dial resistance boxes, setting the resistances e and f to correspond to various temperatures. The resistance c in series with the galvanometer was adjusted on each trial to make the range of the superheat meter −15 to 45° F. The errors determined by this method and reported in table III show that for certain ratios of the resistance arms the errors are reduced to negligible values. It appears from the table that 2,000 ohms each in the arms a and b, offers the best combination.

Table III shows that the resistance ratios are not critical, three of the five trials all showing negligible errors. Low resistances at a and b cause negative errors at low air temperatures and positive errors at high air temperatures; while high resistances at these places cause errors of the opposite sign. The tests were made with a Weston Model 301 instrument having a resistance of approximately 60 ohms and a range of 50–0–150 microamperes. The proposed range of the superheat meter is −15 to 45° F. The circuit was designed for use on

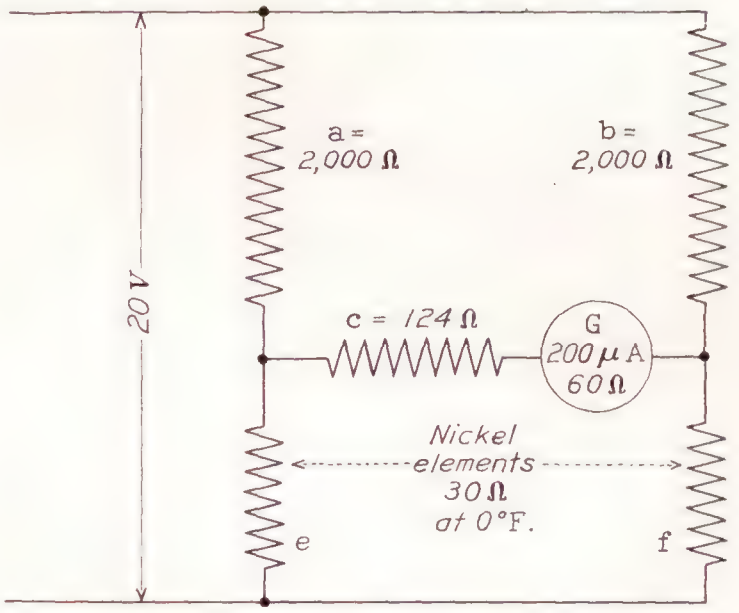

FIGURE 21.—The basic circuit of a resistance-type superheat meter. The fixed resistances of the bridge are a and b; the air and gas elements are e and f.

a 20- to 24-volt battery supply. If designed for 110 volts, with a corresponding increase in resistance, and decrease of current in the temperature sensitive elements, there would be the advantage of relatively less voltage drop in the long leads sometimes required.

Two superheat meters of the resistance type, which have been constructed at the National Bureau of Standards for the U. S. Navy, are shown in figures 22 and 23. The instruments are essentially the same except that one has space provided inside the instrument for a 22½ volt radio B battery while the other must be supplied with current from an external source.

Figure 24 is a diagram of connections applicable to both instruments. The connections are fundamentally the same as shown in figure 21 with the addition of two manganin resistances and a triple-pole double-throw switch arranged for checking the supply voltage. When the switch is in the "test" position, the temperature elements in the bridge circuit are replaced by two

FIGURE 22.—Resistance-type superheat meter with self-contained battery.

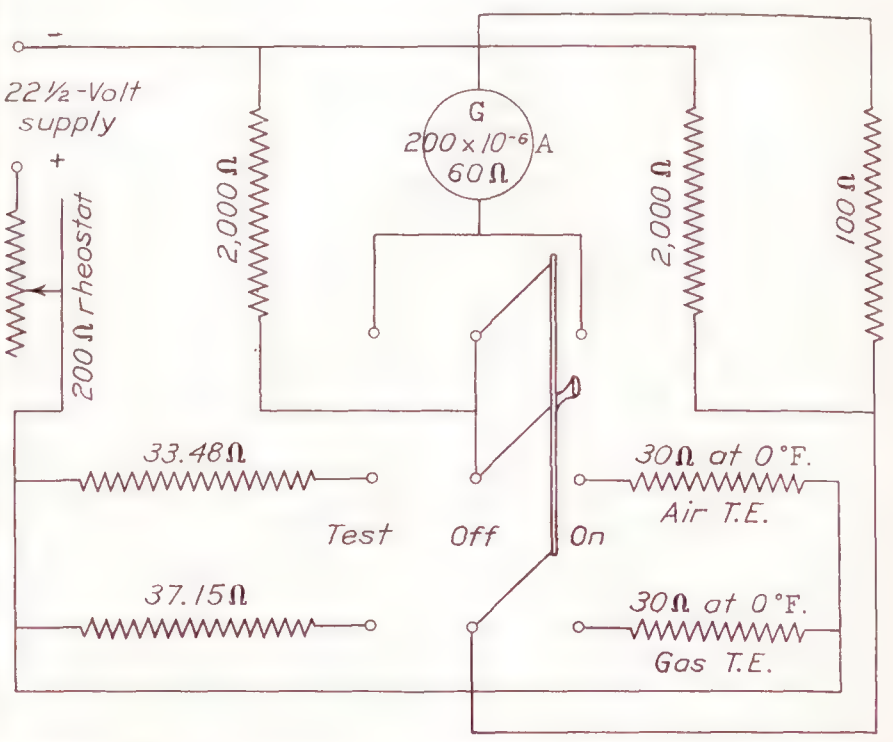

FIGURE 24.—Diagram of connections for a superheat meter of the resistance type.

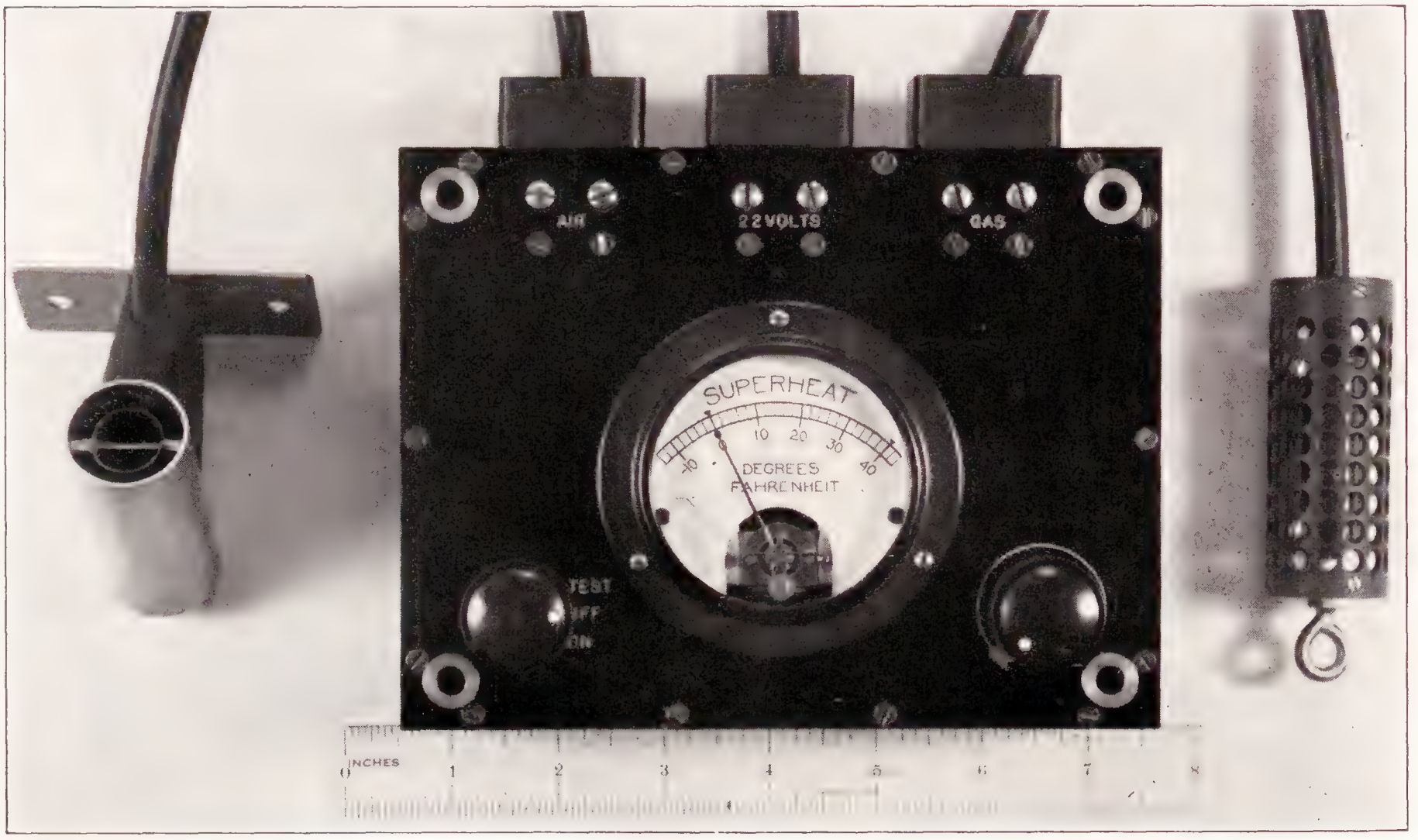

FIGURE 23.—Resistance-type superheat meter with air- and gas-cell elements.

manganin resistances of 33.48 ohms and 37.15 ohms. These values are the resistances of the 30-ohm elements at temperatures of 40 and 80° F., respectively. The 40° F. resistance was selected for the low-value checking resistance because 40° F. is near the average temperature of the air in which an airship operates. The indicator pointer should be adjusted to stand on the zero mark with current off. The rheostat serves to adjust the supply voltage so that the pointer stands on the 40° F. superheat mark when the switch is in the test position. The reference marks at 0 and 40° F. superheat can be seen on the scales of both instruments (figs. 22 and 23).

It should be noted that the indication at zero superheat is independent of battery voltage and that the percentage error at other indications is equal to the percentage variation from the correct voltage adjustment. Adjustment for battery voltage, as described, serves to compensate for the effect of variations in the temperature of the indicator. This fact is obvious when it is noted that the indicator is adjusted to indicate correctly at 40° F. superheat regardless of the resistance of the galvanometer circuit.

The construction of the temperature elements is similar to that described for the resistance thermometer. A photograph of the gas-temperature element is shown in figure 23. The gas-cell element is mounted coaxially with a perforated bakelite outer shell. It is designed to be suspended in the gas cell the superheat of which is to be measured.

FIGURE 25.—A potentiometer temperature indicator.

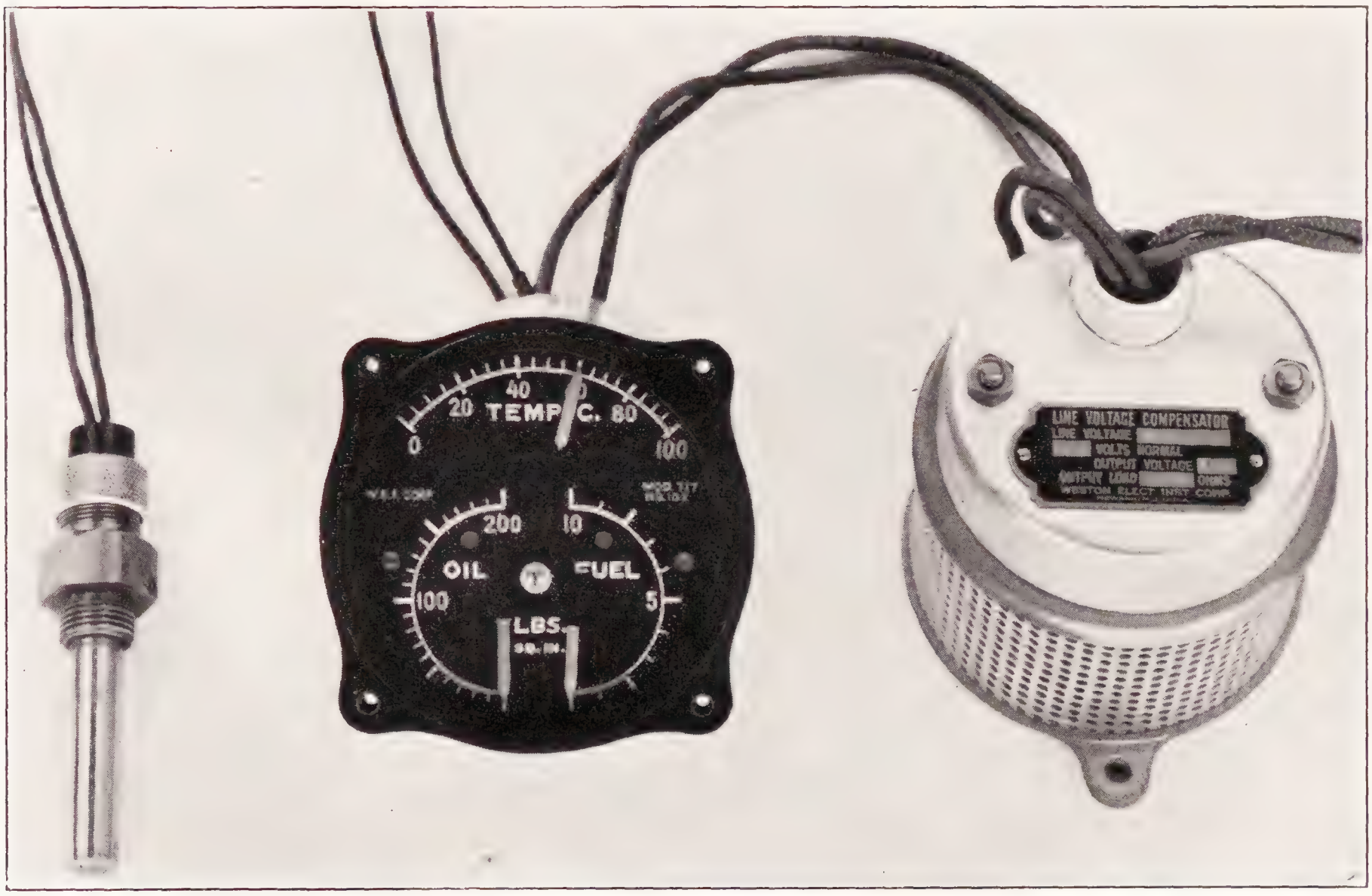

FIGURE 26.—Engine gage unit incorporating a resistance-type oil-temperature indicator.

The length of the copper wires between the indicator and the gas-cell element are usually longer than those between the indicator and the air element and their resistance may be an appreciable part of 30 ohms, but the temperature coefficient of copper is practically the same as that of nickel and if most of the wire is inside the envelope at an average temperature not appreciably different from that of the gas-cell element, the error caused by the lead wires will be negligible.

OTHER INSTRUMENTS

Not all types of electrical thermometers in use on aircraft today are described in this report. Among the types not described, a potentiometer indicator made

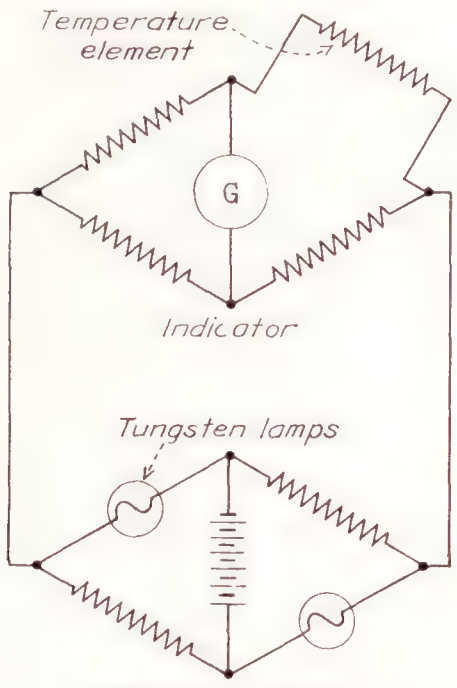

FIGURE 27.—Diagram of connections of resistance-type thermometer with a voltage regulator.

by the Lewis Engineering Company might be mentioned. A photograph of this instrument is shown in figure 25. This instrument may be used as a standard for testing thermoelectric indicators in the field and may be used as the indicator on large aircraft, where the saving in weight of leads, effected by the use of the potentiometer instrument, may be enough to warrant the use of the heavier indicating apparatus.

The Weston Electrical Instrument Corporation has developed a resistance thermometer of a range suitable for measuring radiator cooling liquid or oil temperature. It is of the unbalanced Wheatstone bridge type. A photograph of the instrument, built into an engine gage unit, is shown in figure 26. Figure 27 is a diagram of connections, showing the details of the voltage regulator that compensates for variations in battery voltage.

The General Electric Company has used a crossed-coil ohmmeter type instrument as the indicator in a resistance thermometer. An instrument of this type was used on the National Geographic-Army Air Corps stratosphere flight; it had a temperature element similar to that shown in figure 17.

NATIONAL BUREAU OF STANDARDS,
WASHINGTON, D. C., *December 15, 1936.*

REFERENCES AND BIBLIOGRAPHY

1. Sontag, Harcourt, and Brombacher, W. G.: Aircraft Power-Plant Instruments. T. R. No. 466, N. A. C. A., 1933.
2. Roeser, Wm. F., and Wensel, H. T.: Methods of Testing Thermocouples and Thermocouple Materials. Bur. Standards Jour. Res., vol. 14, no. 3, March 1935, p. 247.
3. Roeser, Wm. F., Dahl, A. I., and Gowens, G. J.: Standard Tables for Chromel-Alumel Thermocouples. Bur. Standards Jour. Res., vol. 14, no. 3, March 1935, p. 239.
4. National Research Council: International Critical Tables, vol. V. McGraw-Hill Book Co., Inc., 1929, p. 58.
5. Stevens, Albert W.: The Scientific Results of the World-Record Strastosphere Flight. The National Geographic Magazine, vol. LXIX, no. 5, May 1936, p. 693.
6. Harper, D. R.: Thermometric Lag. Bur. Standards Bul., vol. 8, no. 4, 1912, p. 659.
7. Henrickson, H. B.: Thermometric Lag of Aircraft Thermometers, Thermographs and Barographs. Bur. Standards Jour. Res., vol. 5, no. 3, September 1930, p. 695.
8. Koning, C.: The Indication of Thermometers in Moving Air. Report no. A322 De Ingenieur (Amsterdam) 1932, no. 45.
9. Smolar, Vaclav: Determination de la Temperature de l'Air Pendant les essais en vol. Aero. Res. Inst., Prague, Czechoslovakia, vol. 6, no. 18, 1932, p. 37. (With French Abstract.)
10. Strother, D. H. and Eaton, H. N.: A Superheat Meter or Differential Thermometer for Airships. Tech. Paper No. 359, Bur. Standards, 1927.

Geyer, Wilhelm: A Bridge for Measurement of Temperature Difference with Electric Resistance Thermometers. Archiv für Elektrotechnik, vol. XXV, no. 7, July 15, 1931, p. 476.

REPORT No. 607

SPINNING CHARACTERISTICS OF THE XN2Y–1 AIRPLANE OBTAINED FROM THE SPINNING BALANCE AND COMPARED WITH RESULTS FROM THE SPINNING TUNNEL AND FROM FLIGHT TESTS

By M. J. Bamber and R. O. House

SUMMARY

A 1/10-scale model of the XN2Y–1 airplane was tested in the N. A. C. A. 5-foot vertical wind tunnel and the six components of the forces and moments were measured. The model was tested in 17 attitudes in which the full-scale airplane had been observed to spin, in order to determine the effects of scale, tunnel, and interference. In addition, a series of tests was made to cover the range of angles of attack, angles of sideslip, rates of rotation, and control settings likely to be encountered by a spinning airplane. The data were used to estimate the probable attitudes in steady spins of an airplane in flight and of a model in the free-spinning tunnel.

The estimated attitudes of steady spin were compared with attitudes measured in flight and in the spinning tunnel. The results indicate that corrections for certain scale and tunnel effects are necessary to estimate full-scale spinning attitudes from model results.

INTRODUCTION

General methods for the theoretical analysis of airplane spinning characteristics have been available for some time. These methods might be used by designers to predict the spinning characteristics of proposed airplane designs if the necessary aerodynamic data were known.

In order to provide these data, the N. A. C. A. is conducting investigations to determine the aerodynamic forces and moments on airplane models and on the various parts of airplane models in spinning attitudes. This report gives a comparison of the results obtained for a model on the spinning balance with those for the airplane in full-scale spins and for a model in the free-spinning tunnel. The XN2Y–1 is the first airplane to be tested for comparative purposes in these three ways. The flight tests are reported in references 1 and 2, the results from the free-spinning tunnel in reference 3, and those from the spinning balance are given in this report. Flight and spinning-balance results have been compared for two other airplanes. (See references 4 and 5.)

The present report gives the aerodynamic forces and moments acting on the XN2Y–1 airplane model for the range of probable spinning attitudes with various rudder, elevator, and aileron deflections and in 17 specific attitudes in which the full-scale airplane had been observed to spin. These forces and moments are also given for parts of the model for the 17 flight attitudes. An analysis of the data and a discussion of the results of the analysis with respect to flight results and to model tests in the free-spinning tunnel are included.

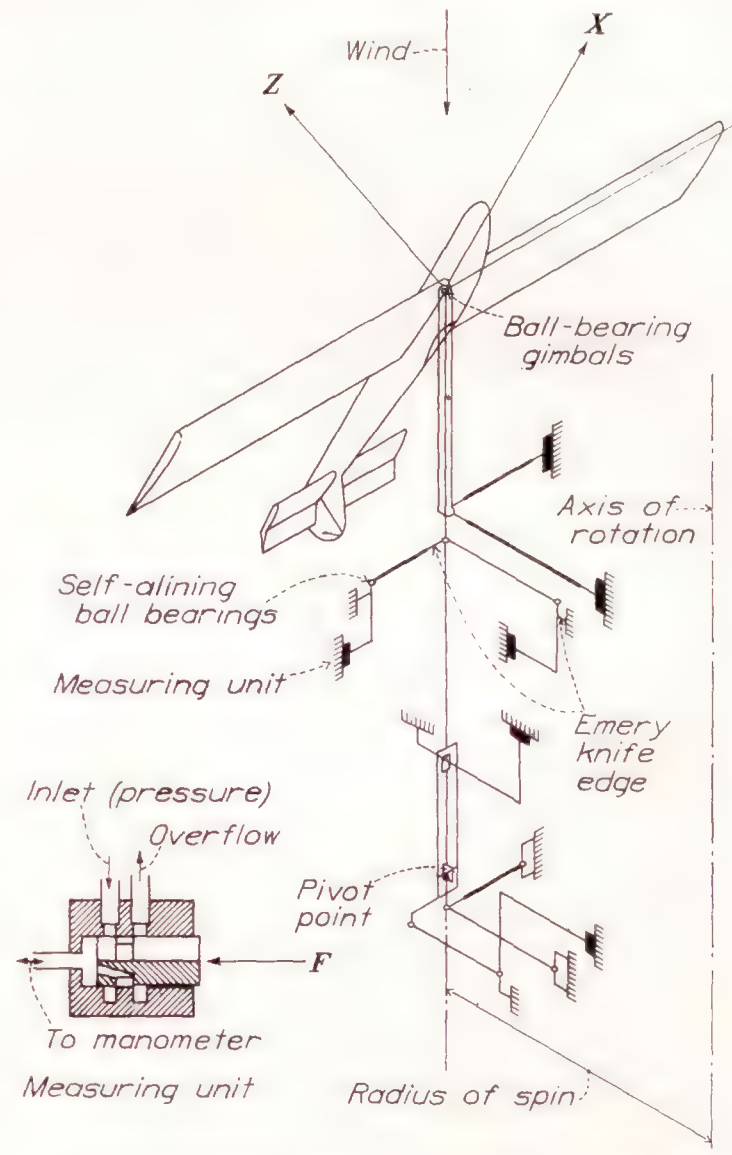

FIGURE 1.– Line diagram of spinning-balance force system.

APPARATUS AND MODELS

The tests were made in the N. A. C. A. 5-foot vertical open-jet wind tunnel described in reference 6.

The 6-component balance, as described in reference 4, was altered to give more accurate results and to allow for more rapid testing. The balance force system, as modified to give more accurate readings, is shown in figure 1. A sleeve to which the model is attached was installed over the upper end of the vertical spindle, is fastened to the spindle by a ball-bearing gimbal joint

at the upper end, and is held in position by linkages to two measuring units at its lower end. This arrangement allows the rolling and pitching moments (earth axes) to be measured directly instead of being the small algebraic sum of two and three relatively large measurements. Consequently, much greater accuracy may be obtained with the same variations in balance readings so that fewer repeat tests are necessary.

This alteration and the direct-indicating force-measuring system that was installed have reduced the time required to obtain data. The force-measuring system consists of an oil pump and six mercury manometers outside the tunnel, seven slip joints on the lower end of the turntable shaft, and six measuring units on the balance head. Each measuring unit consists of a grooved piston and cylinder and is shown by the small sketch in figure 1.

The principle of operation is that the force (see F in fig. 1) applied to the piston is balanced by oil pressure in the cylinder. The grooves in the cylinder and in the piston act as balanced valves, allowing oil to flow into or out of the cylinder, depending on the location of the piston in the cylinder. The oil pressure acting on the piston in the closed end of the cylinder is transmitted through a slip joint and is indicated by the mercury manometer.

One oil-pressure line from the pump and one overflow line connect to all six measuring units. Each unit is connected through a slip joint to a mercury manometer; each manometer is provided with a shut-off valve; and all the valves are operated at the same time so that all the readings are made simultaneously.

The model, a 1/10-scale reproduction of the XN2Y-1 airplane, was made from dimensions obtained from the airplane as used for tests in reference 2. Figure 2 shows it mounted on the balance in the tunnel. The model differed from the airplane principally in that it had no propeller, the struts were round rods, and the fuselage and the trailing-edge center section of the upper wing were cut away for attachment to the balance. The model also differed from the airplane, as tested in reference 1, in that the airplane had the fin offset and the fabric sagged between the ribs. The wings, fuselage, wheels, and stabilizer of the model were of mahogany, the struts of 3/32-inch brass rod, and the fin, rudder, and elevator of duralumin. The wings and the fuselage mounted separately are shown in figures 3 and 4. A small streamline fuselage section was used to attach the wings to the balance. The tolerances allowed for the construction were: Wing profile, ± 0.003 inch; fuselage cross section, ± 0.005 inch; tail surfaces, ± 0.003 inch; other dimensions generally, ± 0.01 inch; and angular relationships, $\pm 0.1°$.

TESTS

Tests were made at 40°, 50°, 60°, and 70° angle of attack. At each angle of attack tests were made at $-10°$, 0°, 5°, and 15° angle of sideslip. At each angle of attack at each angle of sideslip, tests were made with values of $\Omega b/2V$ of 0.35, 0.50, 0.75, and 1.00. For each attitude tests were made with the elevator up, rudder with spin; elevator neutral, rudder neutral; and elevator down, rudder against the spin. For each attitude with elevator up, rudder with the spin, except zero sideslip, tests were made with ailerons with and against the spin. Tests were made with elevator up, ailerons neutral, and rudder positions of 40°, 25°, 17°, 8°, and 0° with the spin at $\alpha=60°$, $\Omega b/2V=0.75$, $\beta=0°$ and 15°; and at $\alpha=50°$, $\Omega b/2V=0.50$, and $\beta=5°$ and $-10°$.

The control-surface angles for the various settings were:

Elevator up	elevators 23° 41′ up.
Elevator down	elevators 25° down.
Rudder with	rudder 40° to aid the rotation.
Rudder against	rudder 40° to oppose the rotation.
Aileron with	ailerons displaced to increase the rolling.
Aileron against	ailerons displaced to oppose the rolling.

Aileron deflections were 25° up and 15° down, both ailerons being deflected in each case.

The radius of the spin for each attitude was computed from an equilibrium of centrifugal and aerodynamic forces. The normal weight of the airplane was used and the aerodynamic forces were obtained from the data in reference 7. The resultant force on the airplane was assumed to be perpendicular to the XY plane.

Tests were also made in 17 specific attitudes obtained from measurements of full-scale spins. Table I gives the attitudes and control positions.

TABLE I.—AIRPLANE ATTITUDES AS TESTED ON THE SPINNING BALANCE

[Tests 44L through 109L from reference 1. Tests 29F through 36 from reference 2. All values have been given proper signs for right spins. Right and left spins given in references 1 and 2. In a right spin inward sideslip is positive.]

Flight test	α (deg.)	β (deg.)	$\frac{\Omega b}{2V}$	δ_r (deg.)	δ_e (deg.) (min.)	δ_a (deg.)	Radius (ft.)
44L	53.1	−0.8	0.554	−40	−25 30	0	2.60
52L	50.1	1.0	.453	−40	−25 30	0	3.70
77L	70.7	9.0	.838	−40	−25 30	0	1.30
84L	69.1	7.4	.970	−40	−25 30	0	.60
107L	57.0	10.8	.753	−40	−25 30	With	1.70
109L	65.5	9.8	.853	−40	−25 30	Against	.94
29F	60.7	13.7	.593	−40	−23 50	0	1.60
29G	60.4	13.0	.622	−40	−23 50	0	1.60
20	50.6	4.3	.598	−40	26 35	0	2.00
30	52.4	1.0	.535	−40	26 35	0	2.30
33	40.2	4.4	.534	0	−23 50	0	2.70
31	48.6	−1.9	.390	−17	−23 50	0	3.50
32C	47.0	.9	.437	−4	−23 50	0	3.90
34B	44.4	.4	.414	−4	−23 50	0	4.00
27B	43.0	3.9	.411	−8	−23 50	0	4.70
35	57.4	9.7	.523	−18	−23 50	0	2.20
36	50.9	.6	.393	−40	26 35	0	2.30

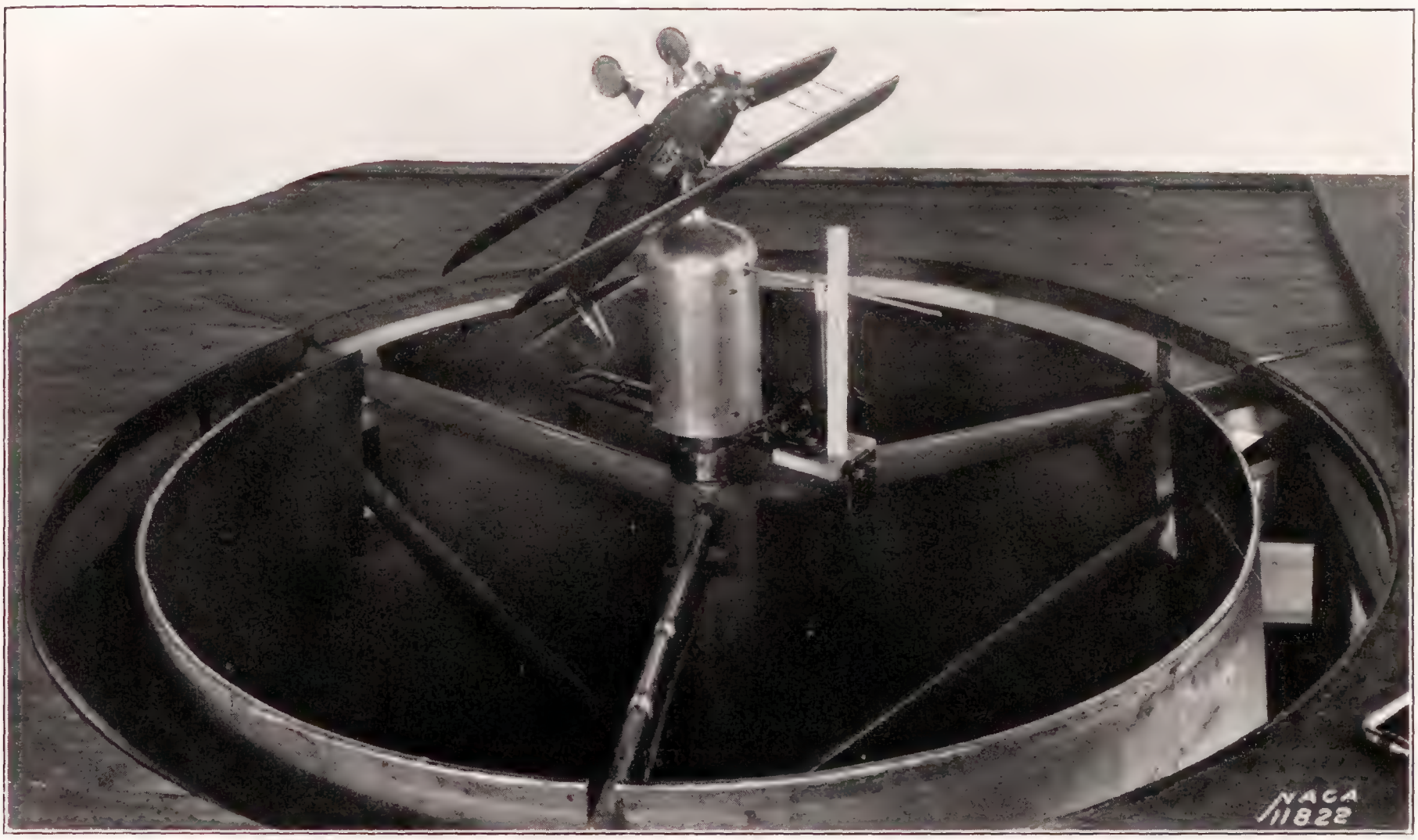

FIGURE 2.—The XN2Y–1 airplane model mounted on the spinning balance.

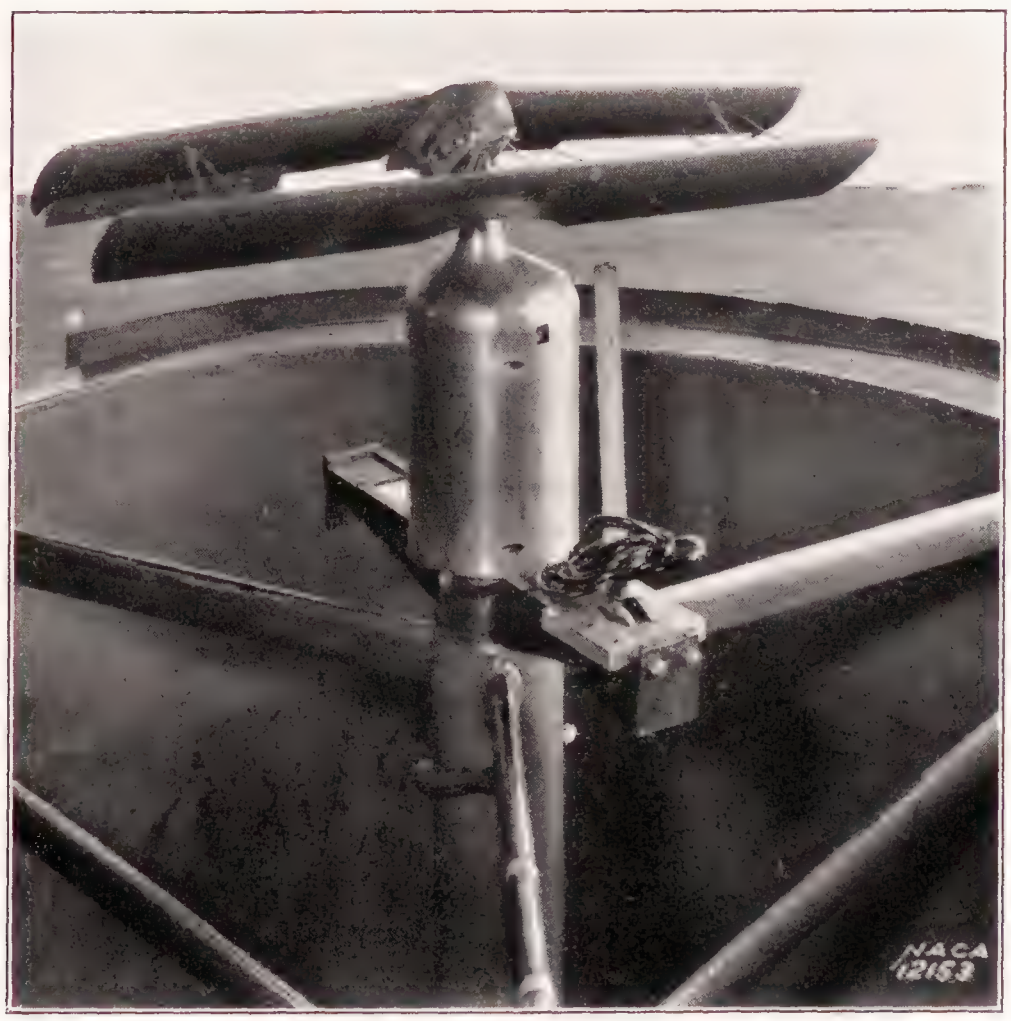

FIGURE 3.—Wings of the XN2Y–1 airplane model mounted on the spinning balance.

FIGURE 4.—The XN2Y–1 airplane model, with wings removed, mounted on the spinning balance.

The model was not changed for the test corresponding to those given in reference 1, in which the airplane had the fin offset and the original wing profile on which the fabric sagged between the ribs. For each test the controls were set the same as for the flight spins. In each attitude tests were made with the model complete, with the fin and rudder removed, with the wings removed, and with the wings alone. (See figs. 3 and 4.)

In order to insure consistency of results, repeat tests were made for each condition until individual balance readings were found to agree within a specified limit or until a sufficient number of readings had been made to form a fair average. In each case an average of the results obtained was used to obtain the coefficients. The air speeds for the tests varied between 43 and 75 feet per second and covered a range of test Reynolds Numbers from about 100,000 to 175,000. Early tests on the spinning balance indicated no scale effects over this speed range (reference 4). The lower air speeds were used with the larger values of $\Omega b/2V$ because of the necessarily high rate of rotation.

SYMBOLS

α, angle of attack at center of gravity.

$\beta=\sin^{-1}\frac{v}{V}$, angle of sideslip at the center of gravity.

V, resultant linear velocity of the center of gravity.

v, linear velocity along the Y airplane axis, positive when the airplane is sideslipping to the right.

Ω, resultant angular velocity (radians per second).

δ_a, aileron deflection.

δ_e, elevator deflection.

δ_r, rudder deflection.

σ, angle between the vertical and the helix described by the center of gravity of the airplane.

b, span of wing.

S, area of wing.

$q=1/2\ \rho V^2$, dynamic pressure.

ρ, air density.

X, longitudinal force acting along the X airplane axis, positive forward.

Y, lateral force acting along the Y airplane axis, positive to the right.

Z, normal force acting along the Z airplane axis, positive downward.

L, rolling moment acting about the X airplane axis, positive when it tends to lower the right wing.

M, pitching moment acting about the Y airplane axis, positive when it tends to increase the angle of attack.

N, yawing moment acting about the Z airplane axis, positive when it tends to turn the airplane to the right.

Forces and moments with double primes (e. g., X'') are in the earth system of axes where Z'' is positive downward and X'' is along the radius of the spin, positive toward the center of the spin.

Coefficients of forces are obtained by dividing the force by qS.

Coefficients of moments are obtained by dividing the moment by qbS.

$\mu=\frac{m}{\rho Sb}$, relative density of airplane to air. Under standard conditions, $\mu=13.1\ W/Sb$.

$m=W/g$, mass.

k_X, k_Y, k_Z, radii of gyration of the airplane about the X, Y, and Z airplane axes, respectively.

$\frac{b^2}{k_Z^2-k_X^2}=\frac{Wb^2}{g(C-A)}$, pitching-moment inertia parameter.

$\frac{k_Z^2-k_Y^2}{k_Z^2-k_X^2}=\frac{C-B}{C-A}$, rolling-moment and yawing-moment inertia parameter.

$A=mk_X^2$, moment of inertia about the X airplane axis.

$B=mk_Y^2$, moment of inertia about the Y airplane axis.

$C=mk_Z^2$, moment of inertia about the Z airplane axis.

RESULTS

Results of the measurements have been reduced to the following coefficient forms, which are standard except that of the pitching moment, for which the coefficient is based on the span of the wing:

$$C_X=\frac{X}{qS} \qquad C_Y=\frac{Y}{qS} \qquad C_Z=\frac{Z}{qS}$$

$$C_l=\frac{L}{qbS} \qquad C_m=\frac{M}{qbS} \qquad C_n=\frac{N}{qbS}$$

Pitching-moment coefficients can be referred to the chord of the wing by multiplying the values given by 7.47. All values of the coefficients are given with proper signs for right-hand spins. The values of the coefficients for the series of tests are given in figures 5 to 9. Variations of C_l, C_m, and C_n with β, $\Omega b/2V$, and control settings for some characteristic cases are shown in figures 10 to 22.

The differences between the coefficients of flight and model results (flight minus model) are given in figures 23 to 26. The values of C_n for parts of the airplane (reference 2) and of the model are given in figure 27. The values of $\sqrt{C_{X''}^2+C_{Y''}^2}$ (or $C_{X''}$) C_l, C_m, and C_n for the airplane and for the model, and the values obtained by adding the coefficients of the wings tested separately to those of the model with the wings removed, are given in figures 28 to 31.

The data given are believed to be correct for the model under the conditions of the tests within the following limits:

C_Z, ± 0.02	C_m, ± 0.002
C_l, ± 0.001	C_n, ± 0.001

No corrections have been made for tunnel-wall, blocking, or scale effects. The interference caused by the balance parts would appear to be large, especially at 40° angle of attack where the tail surfaces were very near the balance, as is shown by figure 2. Interference effects, however, are not obvious in the results given in figures 23 to 31.

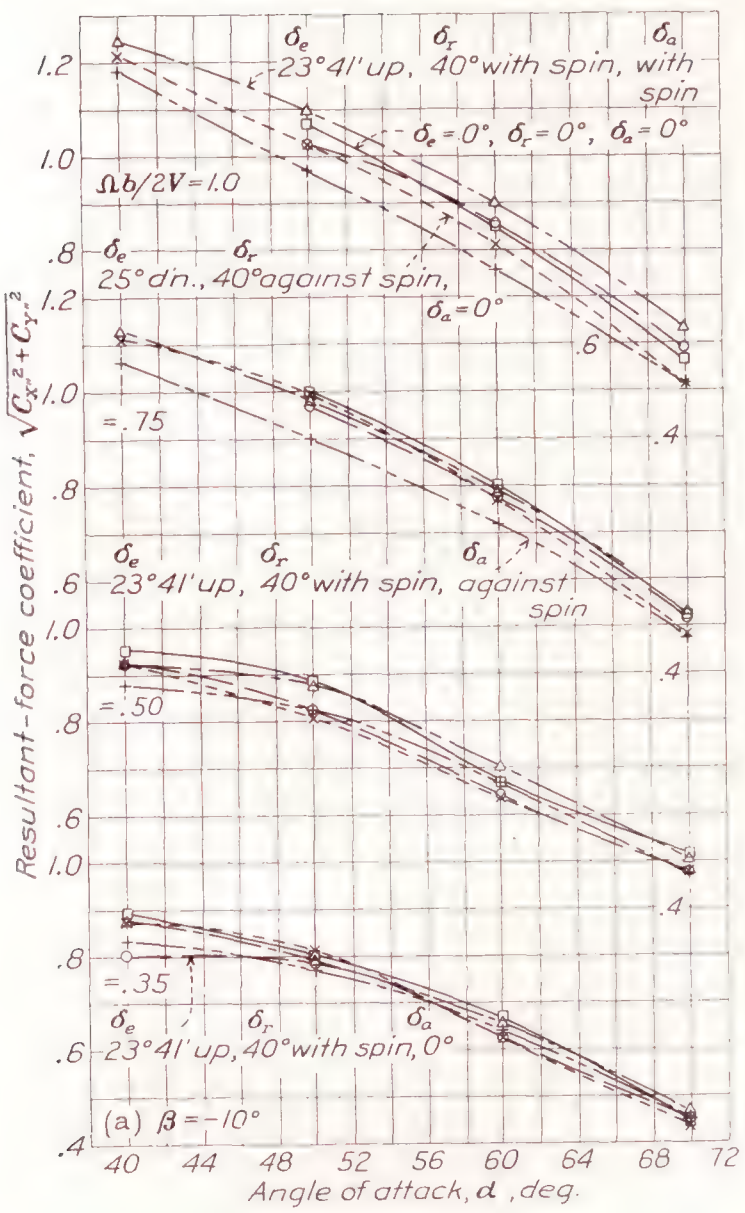

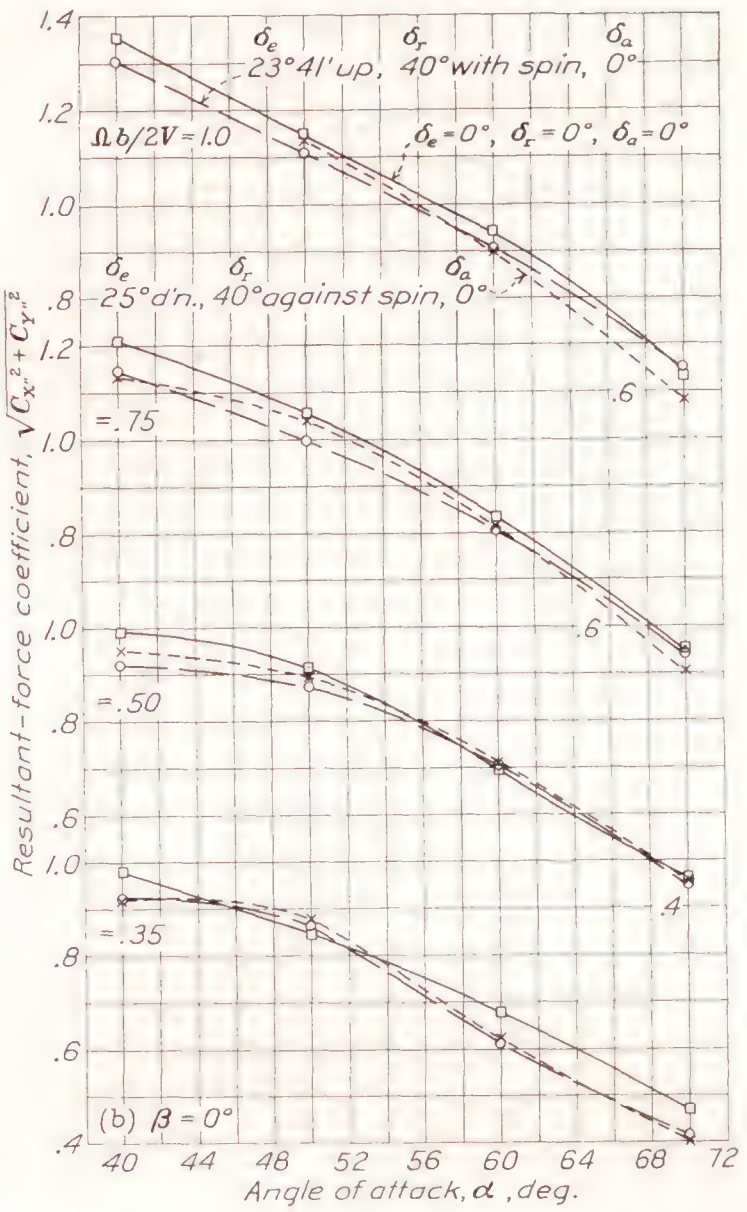

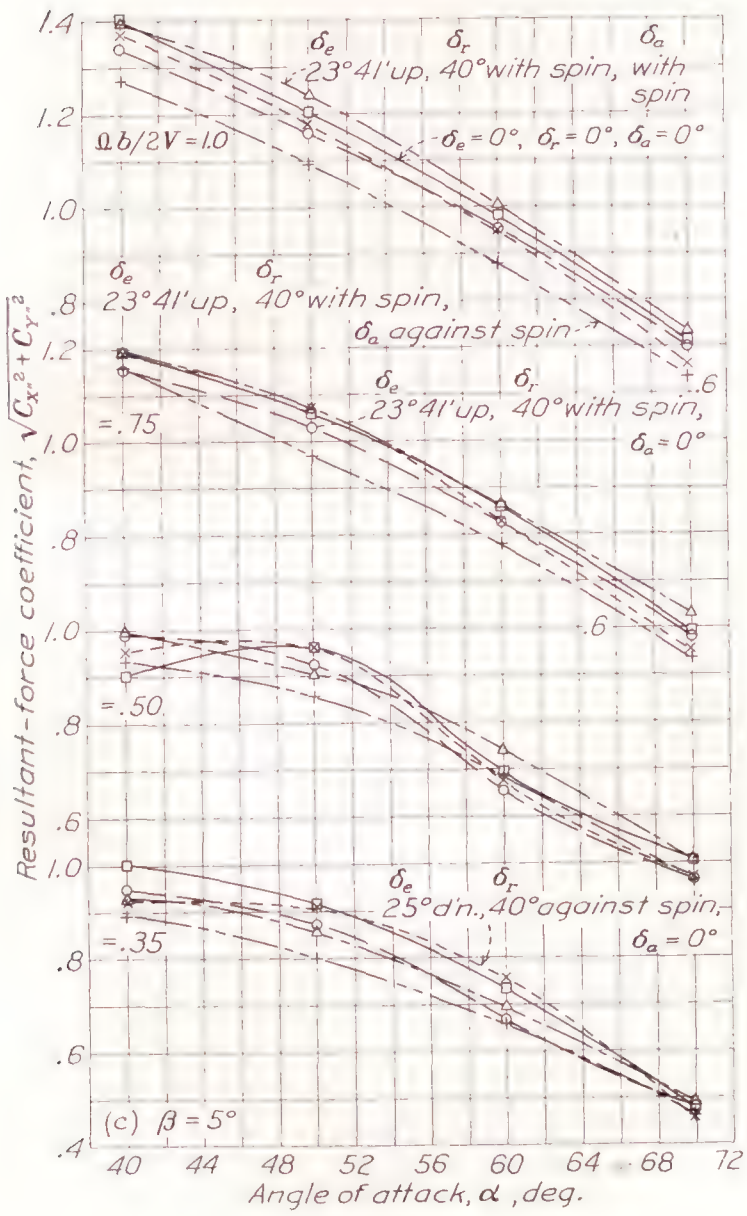

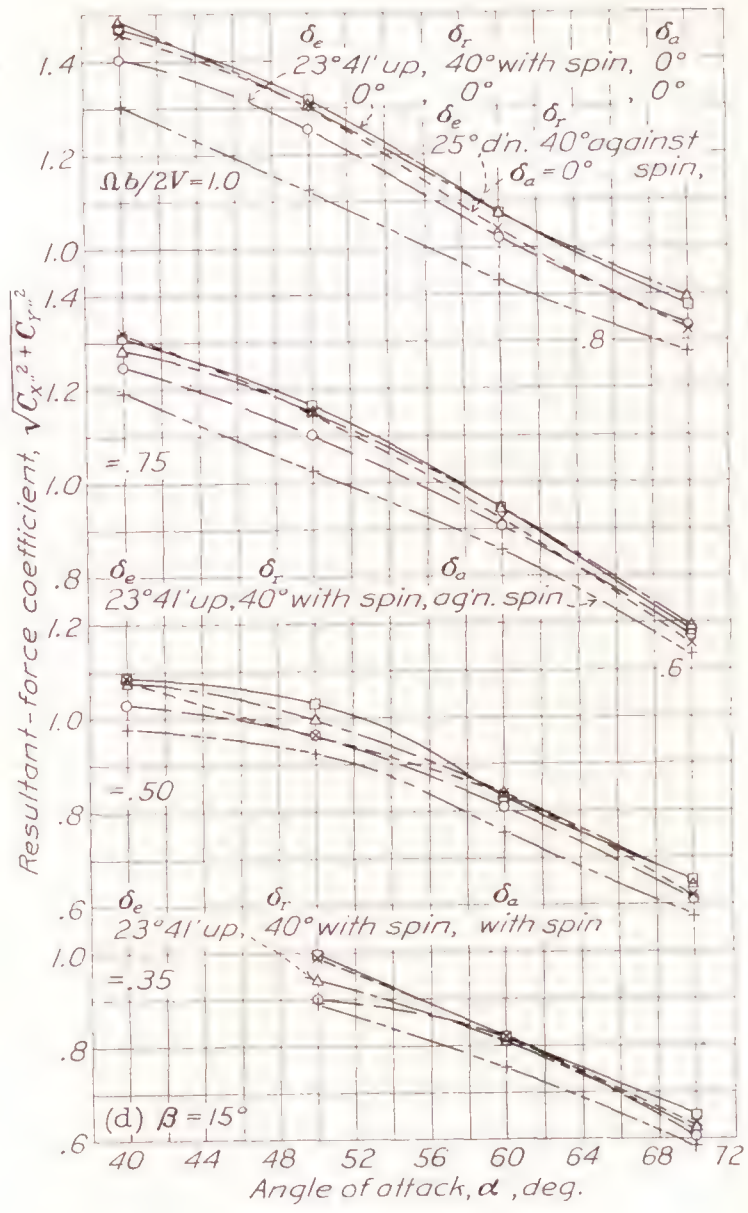

FIGURE 5.--Variation of resultant-force coefficient $\sqrt{C_{X''}^2+C_{Y''}^2}$, horizontal plane (earth axes), with angle of attack.

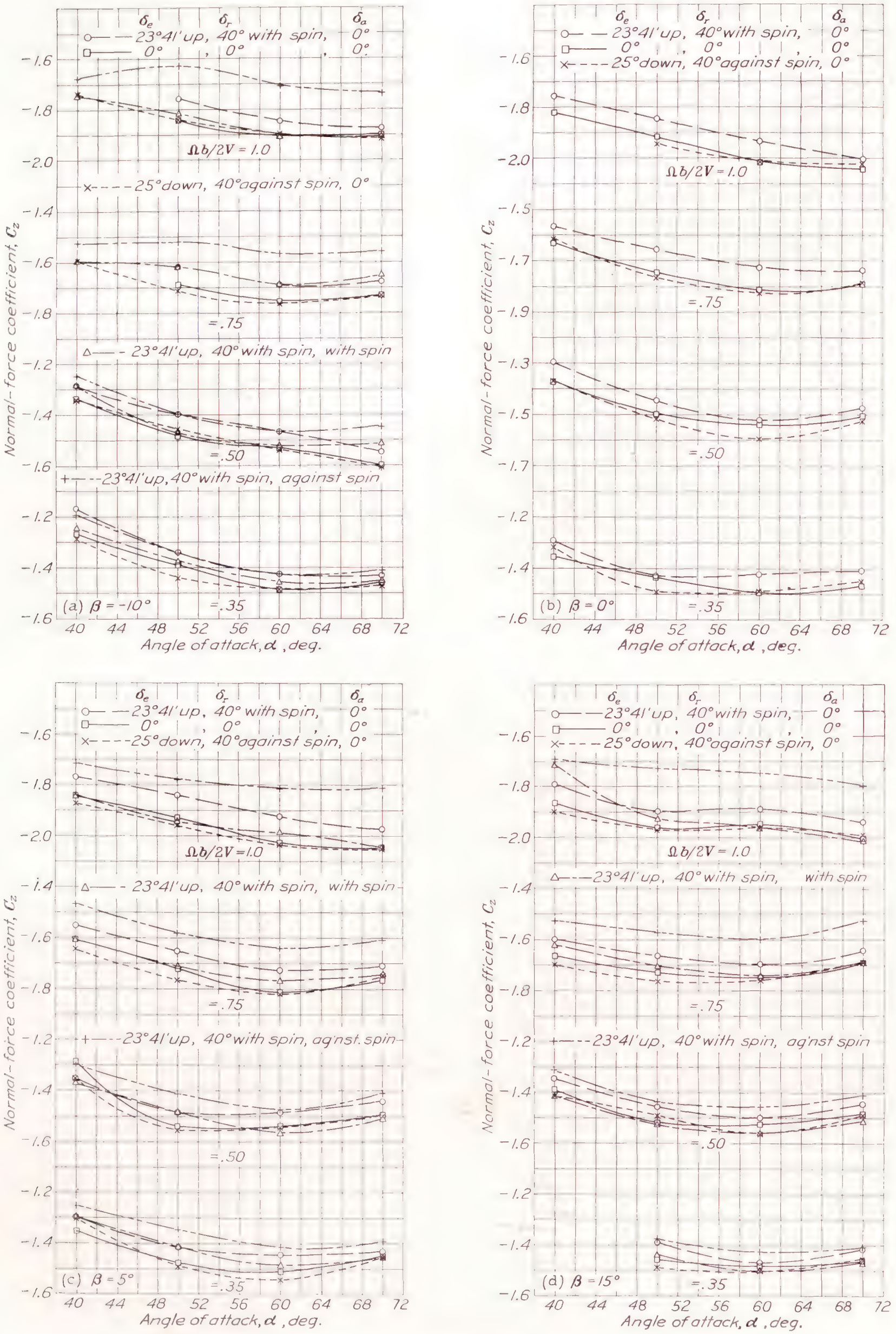

FIGURE 6.—Variation of normal-force coefficient C_Z (body axes) with angle of attack.

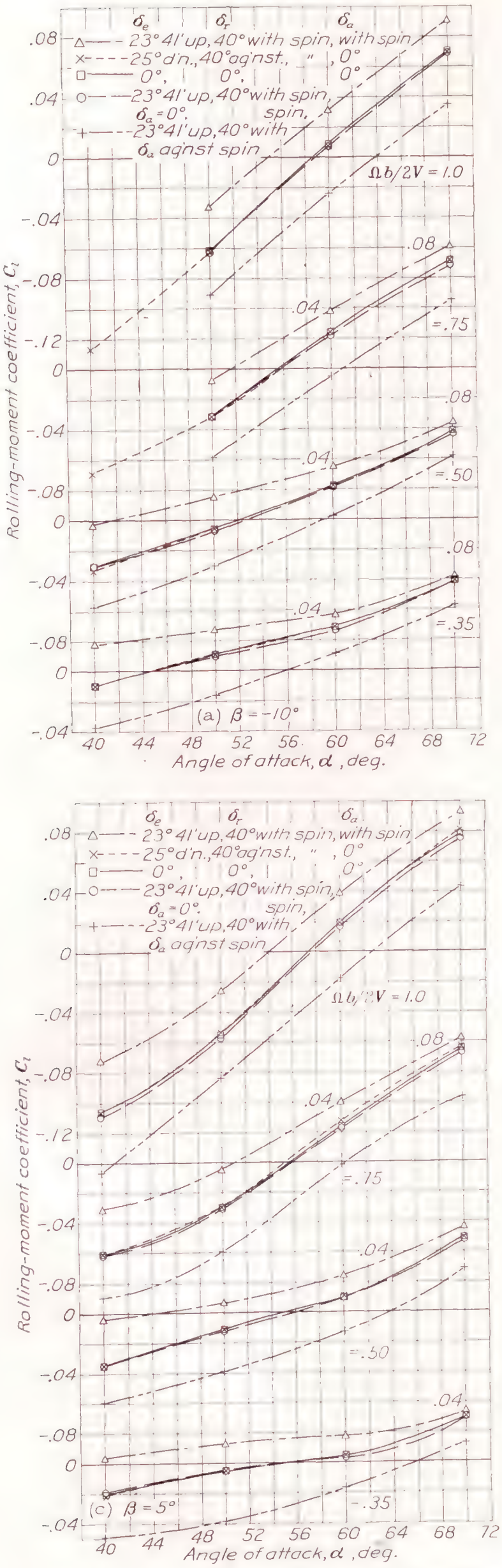

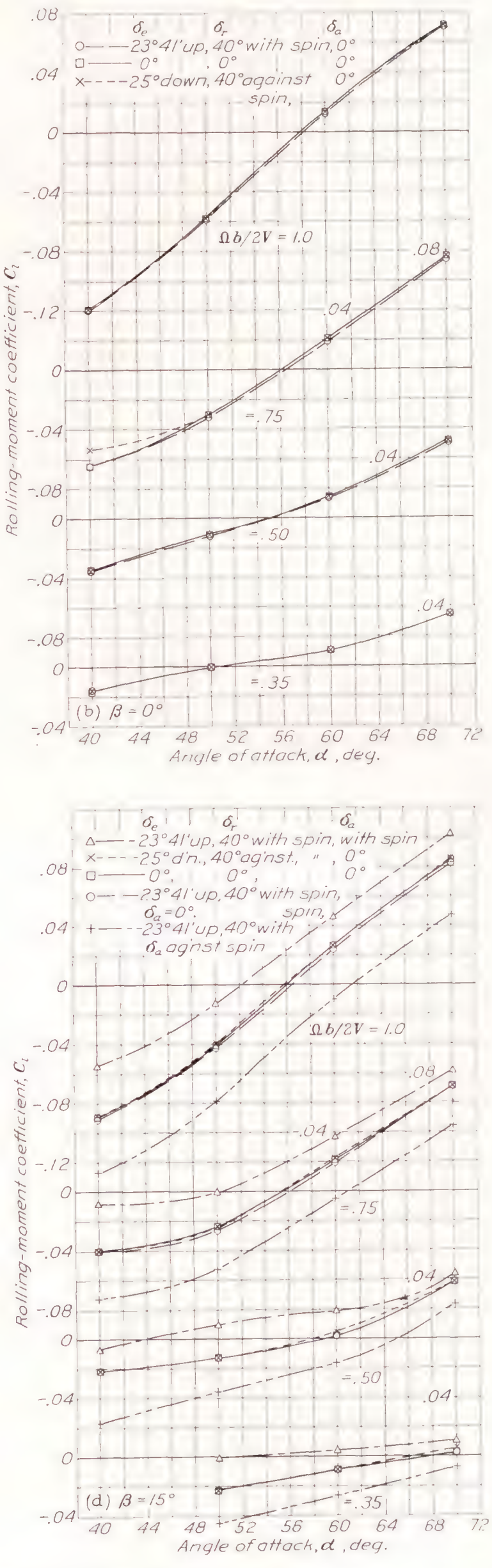

FIGURE 7.—Variation of rolling-moment coefficient C_l (body axes) with angle of attack.

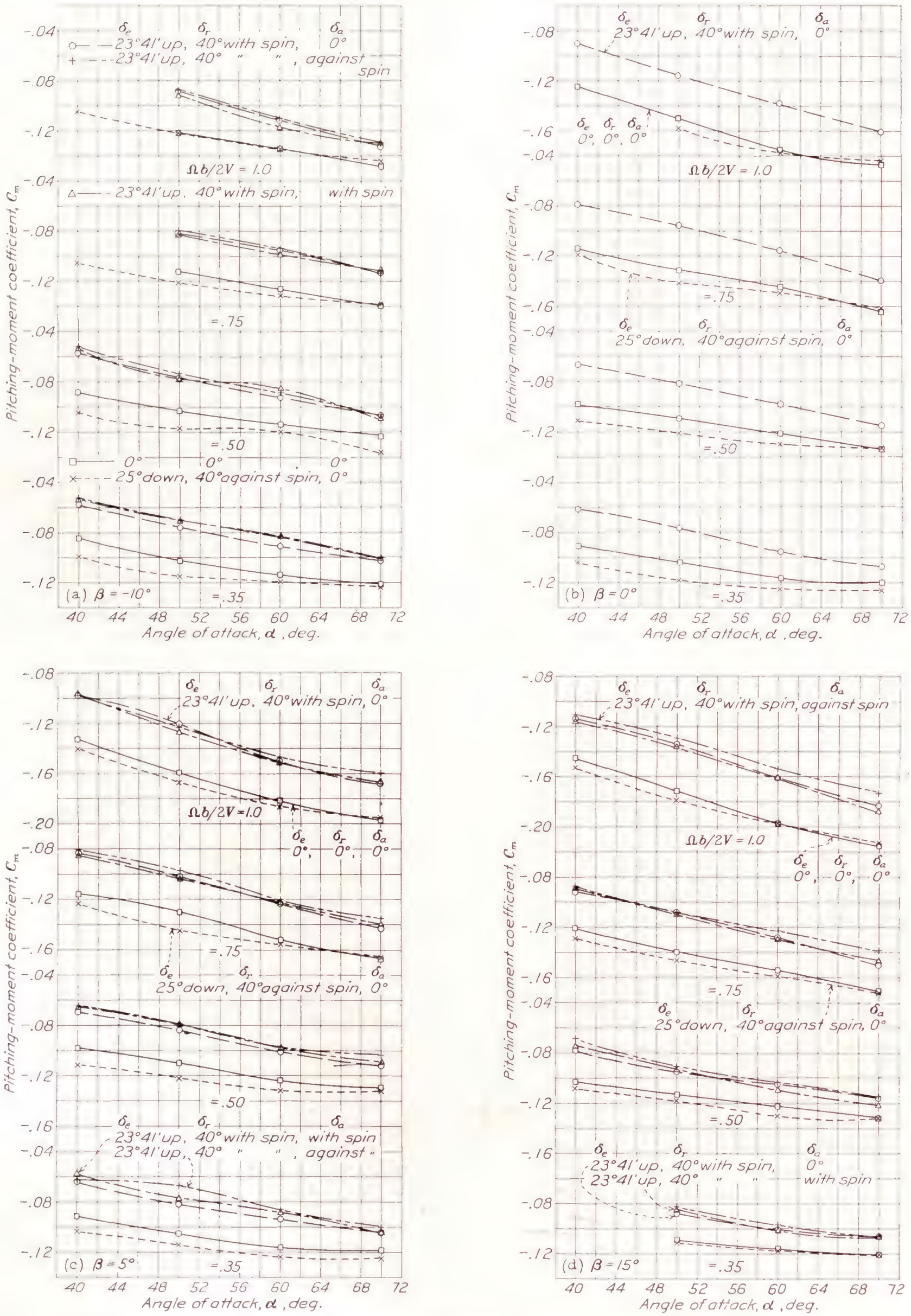

FIGURE 8.—Variation of pitching-moment coefficient C_m (body axes) with angle of attack.

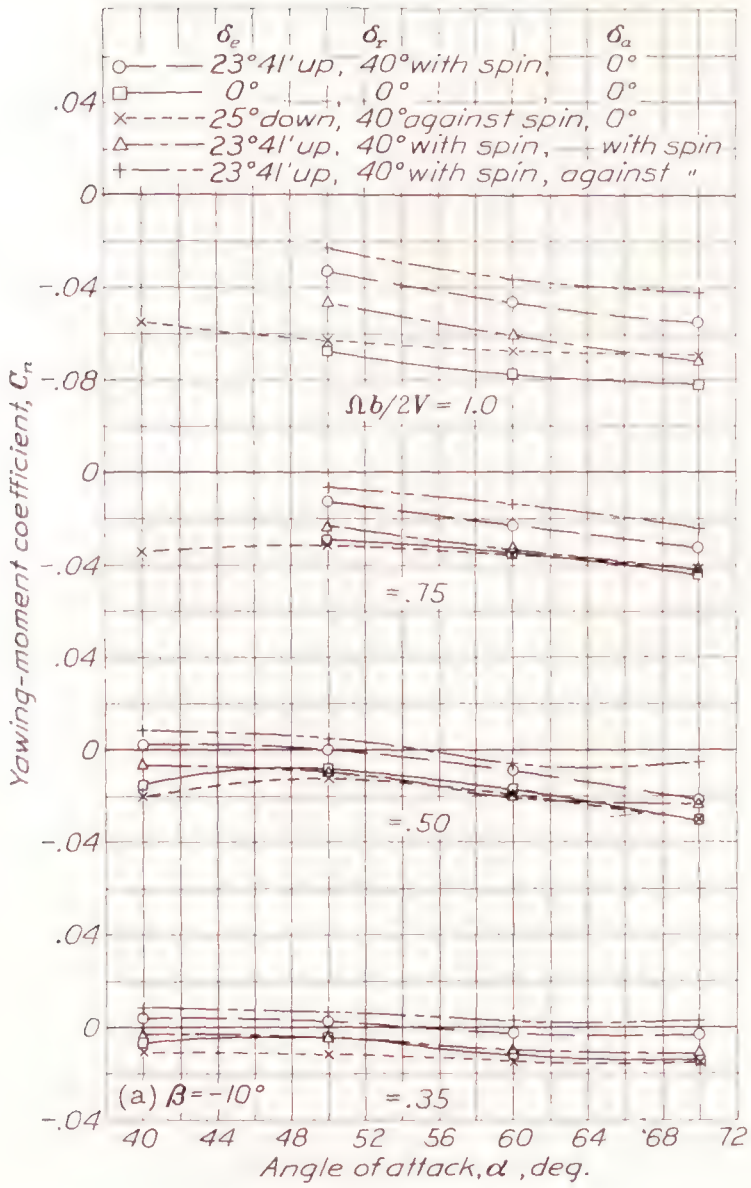

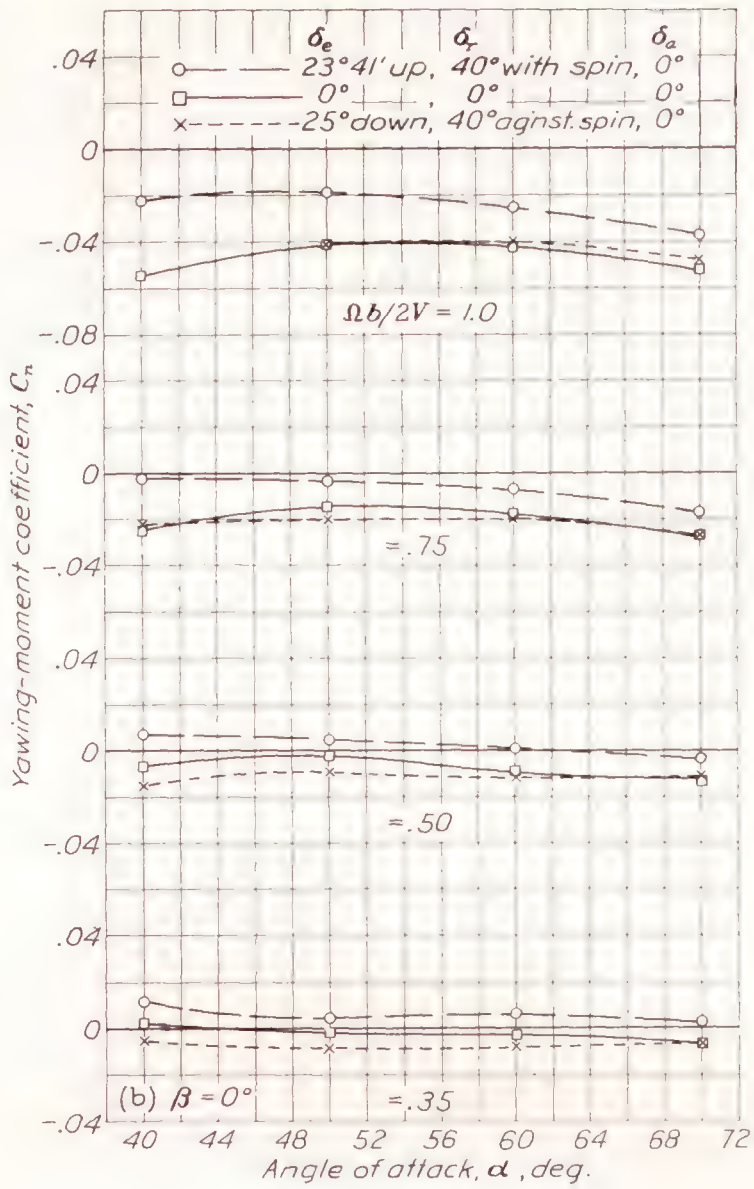

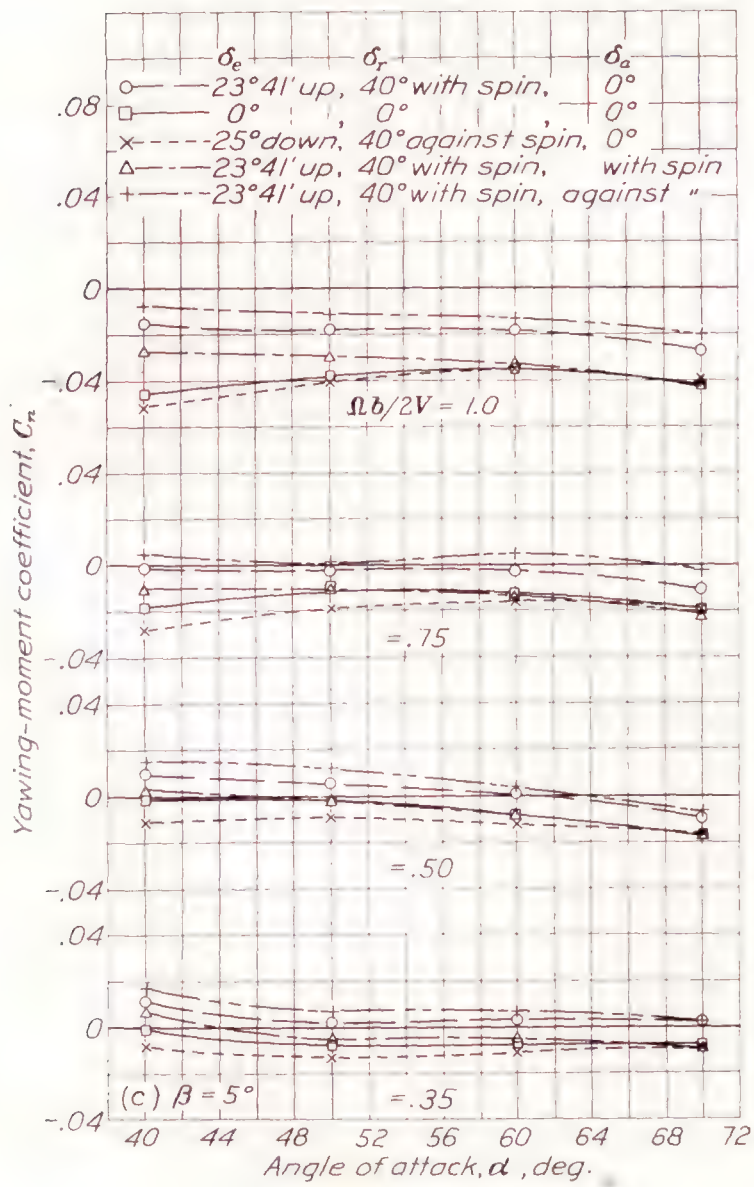

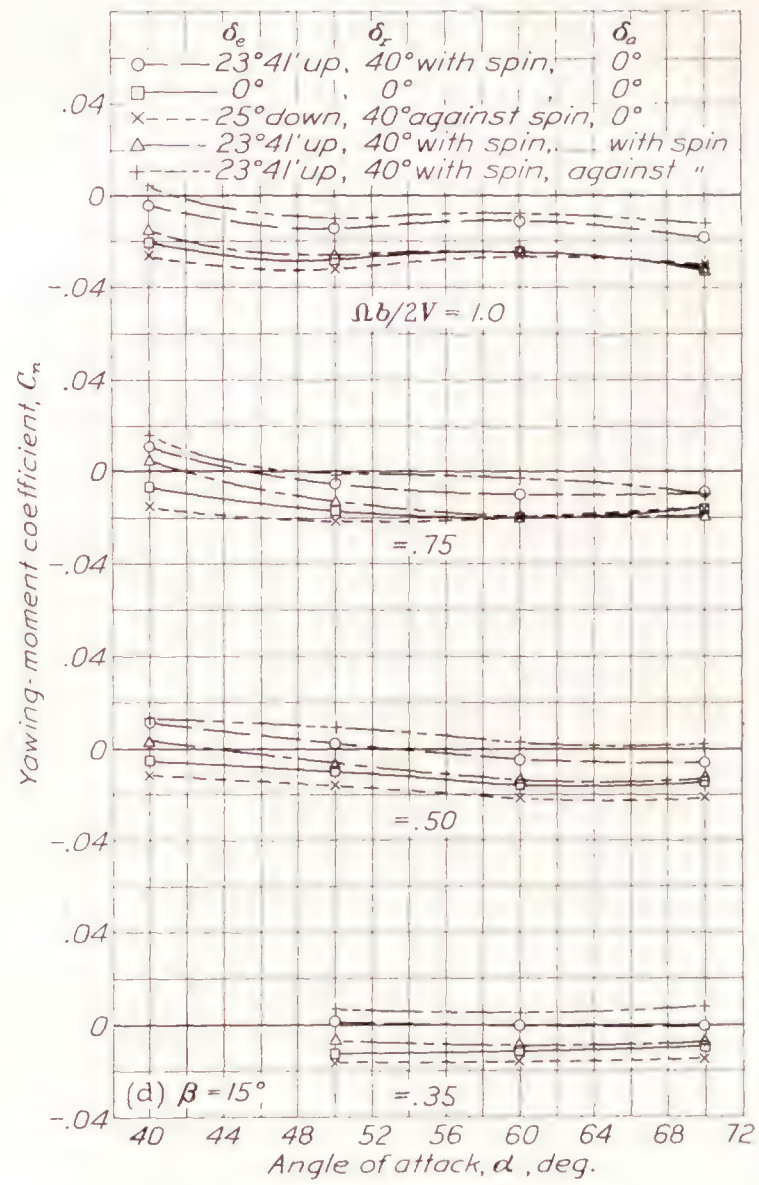

FIGURE 9.—Variation of yawing-moment coefficient C_n (body axes) with angle of attack.

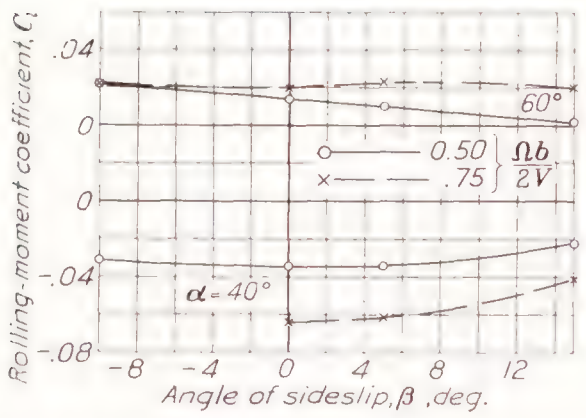

FIGURE 10.—Variation of rolling-moment coefficient C_l (body axes) with angle of sideslip. $\delta_a=0°$; $\delta_e=23°41'$ up; $\delta_r=40°$ with spin.

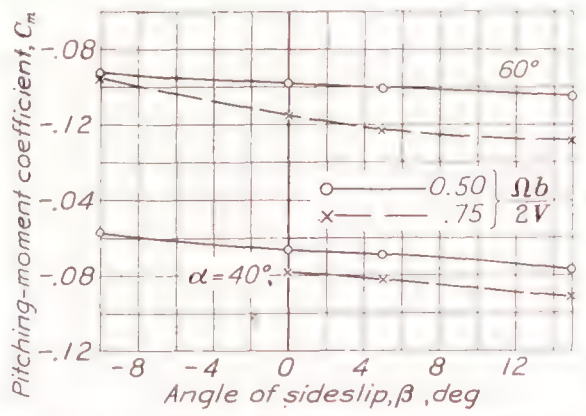

FIGURE 11.—Variation of pitching-moment coefficient C_m (body axes) with angle of sideslip. $\delta_a=0°$; $\delta_e=23°41'$ up; $\delta_r=40°$ with spin.

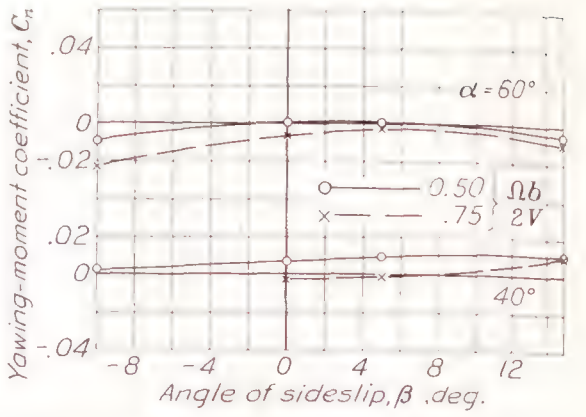

FIGURE 12.—Variation of yawing-moment coefficient C_n (body axes) with angle of sideslip. $\delta_a=0°$; $\delta_e=23°41'$ up; $\delta_r=40°$ with spin.

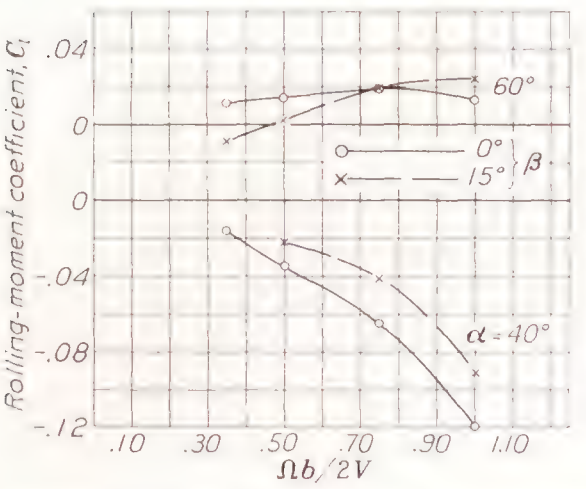

FIGURE 13.—Variation of rolling-moment coefficient C_l (body axes) with $\Omega b/2V$. $\delta_a=0°$; $\delta_e=23°41'$ up; $\delta_r=40°$ with spin.

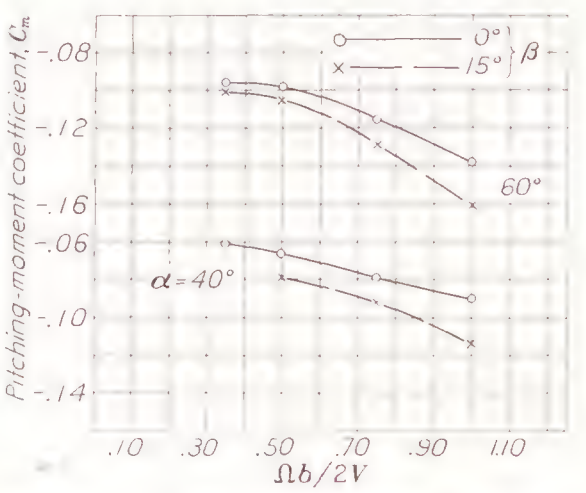

FIGURE 14.—Variation of pitching-moment coefficient C_m (body axes) with $\Omega b/2V$. $\delta_a=0°$; $\delta_e=23°41'$ up; $\delta_r=40°$ with spin.

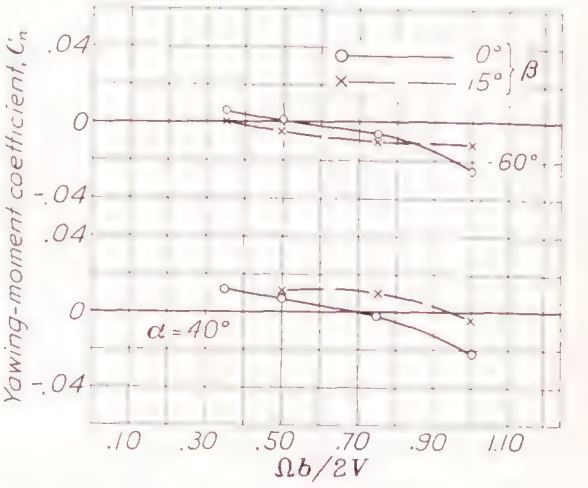

FIGURE 15.—Variation of yawing-moment coefficient C_n (body axes) with $\Omega b/2V$. $\delta_a=0°$; $\delta_e=23°41'$ up; $\delta_r=40°$ with spin.

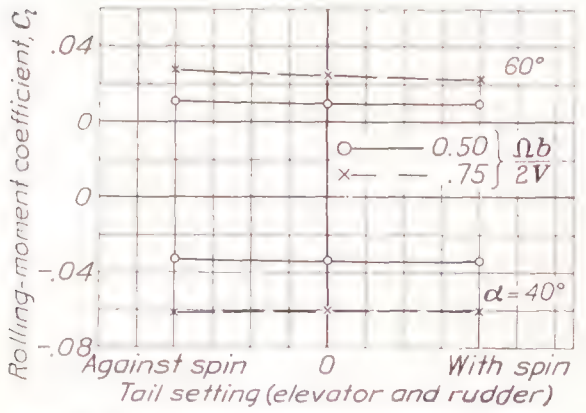

FIGURE 16.—Variation of rolling-moment coefficient C_l (body axes) with tail setting. $\beta=5°$; $\delta_a=0°$.

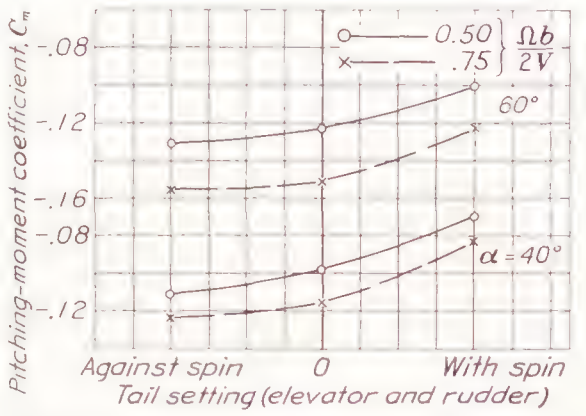

FIGURE 17.—Variation of pitching-moment coefficient C_m (body axes) with tail setting. $\beta=5°$; $\delta_a=0°$.

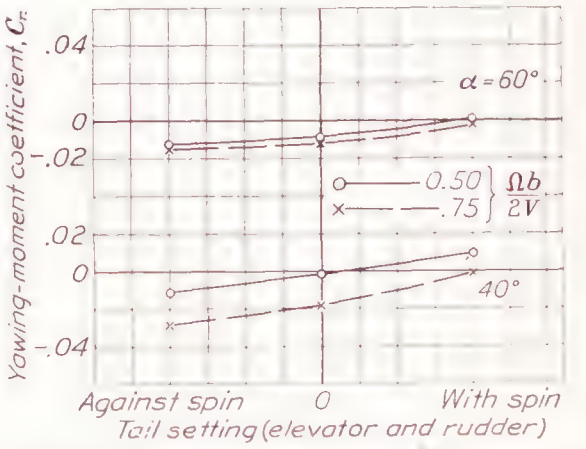

FIGURE 18.—Variation of yawing-moment coefficient C_n (body axes) with tail setting. $\beta=5°$; $\delta_a=0°$.

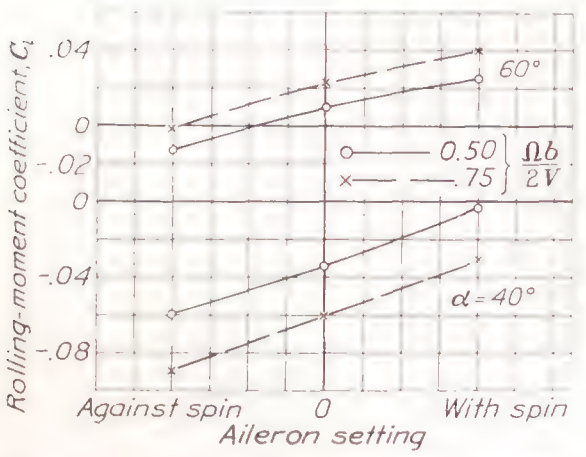

FIGURE 19.—Variation of rolling-moment coefficient C_l (body axes) with aileron setting. $\beta=5°$; $\delta_e=23°41'$ up; $\delta_r=40°$ with spin.

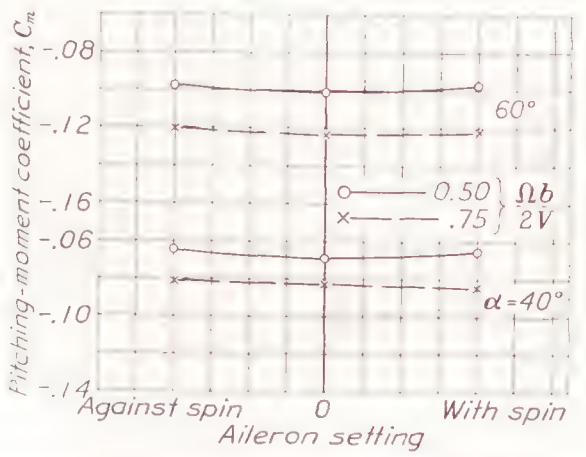

FIGURE 20.—Variation of pitching-moment coefficient C_m (body axes) with aileron setting. $\beta=5°$; $\delta_e=23°41'$ up; $\delta_r=40°$ with spin.

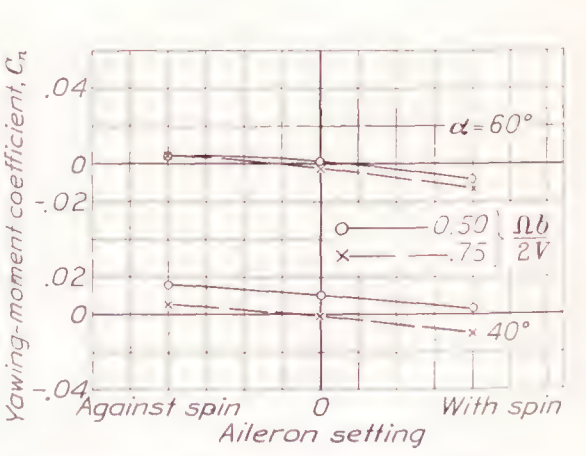

FIGURE 21.—Variation of yawing-moment coefficient C_n (body axes) with aileron setting. $\beta=5°$; $\delta_e=23°41'$ up; $\delta_r=40°$ with spin.

DISCUSSION OF DATA

General series of tests.—The values of $\sqrt{C_{X''}^2+C_{Y''}^2}$ (fig. 5) are given because they were used in the analysis. The values of C_X and C_Y are not given because they are small and are probably of no importance for any analysis of the data.

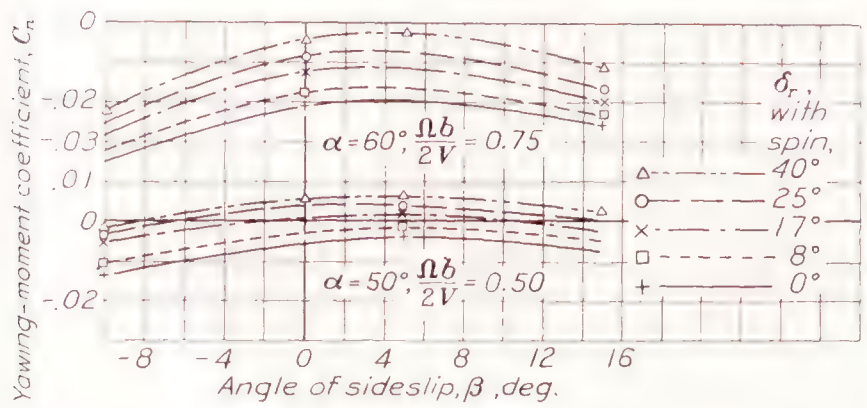

FIGURE 22.—Variation of yawing-moment coefficient C_n (body axes) with rudder setting. $\delta_a=0°$; $\delta_e=23°41'$ up.

Comparison of coefficients from model and flight results.—The difference in the coefficients in the horizontal plane (fig. 23) is irregular but shows a general tendency to be slightly negative (model results smaller than flight).

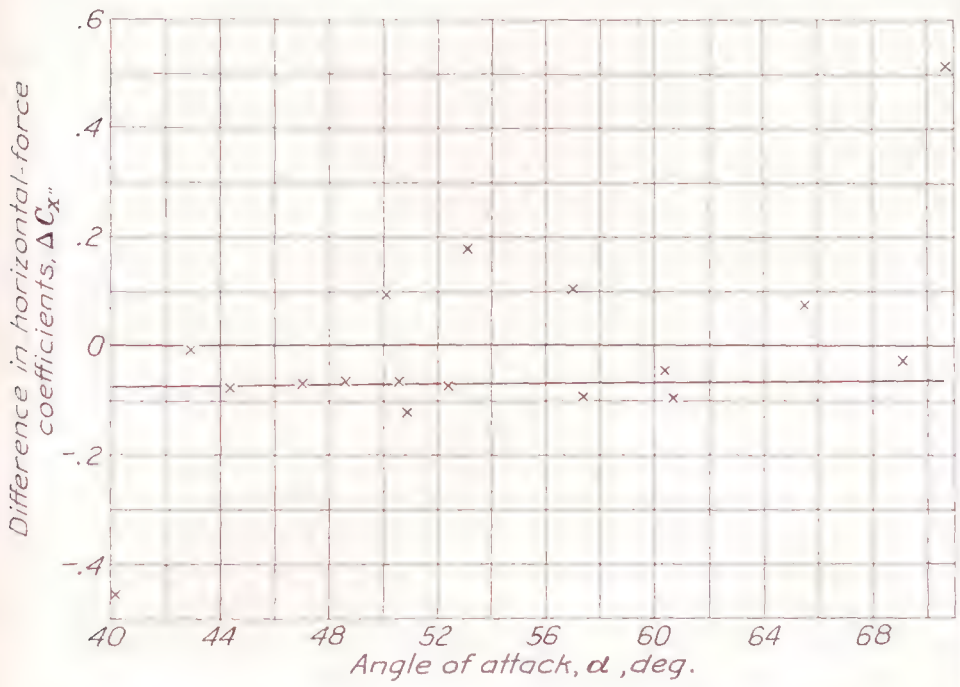

FIGURE 23.—Variation of difference in horizontal-force coefficients of airplane and model $\Delta C_{X''}$ (earth axes) with angle of attack.

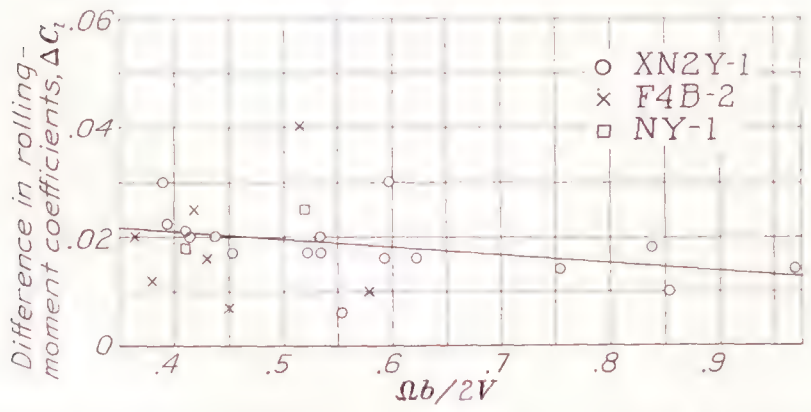

FIGURE 24.—Variation of difference in rolling-moment coefficients of airplane and model ΔC_l (body axes) with $\Omega b/2V$.

The difference in the rolling-moment coefficients ΔC_l shows no general tendency to vary with α or β but shows a slight tendency to decrease as $\Omega b/2V$ is increased (fig. 24). The average value is 0.02, the same as that found for the NY–1 and F4B–2 airplanes (references 4 and 5). The individual values of ΔC_l for the NY–1 and F4B–2 airplanes are given in figure 24.

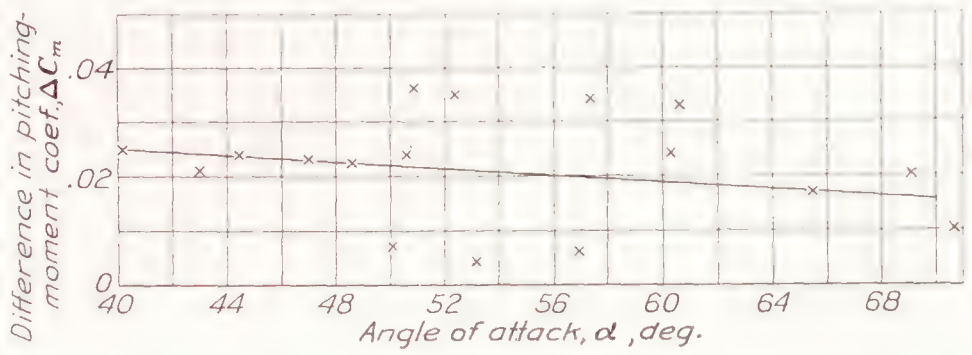

FIGURE 25.—Variation of difference in pitching-moment coefficients of airplane and model ΔC_m (body axes) with angle of attack.

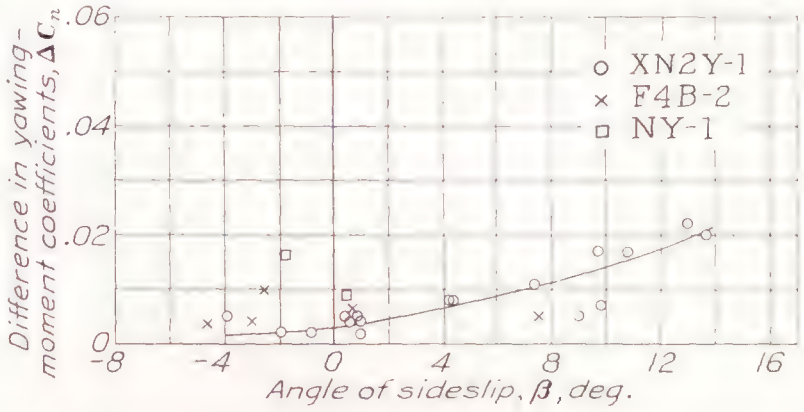

FIGURE 26.—Variation of difference in yawing-moment coefficients of airplane and model ΔC_n (body axes) with angle of sideslip.

The difference in pitching-moment coefficients ΔC_m shows no general variation with β or $\Omega b/2V$ but shows a slight tendency to decrease as α is increased (fig. 25). The average value of the difference is 0.02. The values of ΔC_m from the results obtained with the F4B–2 and the NY–1 airplanes are not sufficiently accurate for comparison.

The difference in yawing-moment coefficients ΔC_n shows no consistent variation with α or $\Omega b/2V$ but increases as β is increased (fig. 26). The difference is about 0.005 at slightly negative values of β, increasing to 0.02 at 13° sideslip. The values for the NY–1 and F4B–2 airplanes are included for comparison.

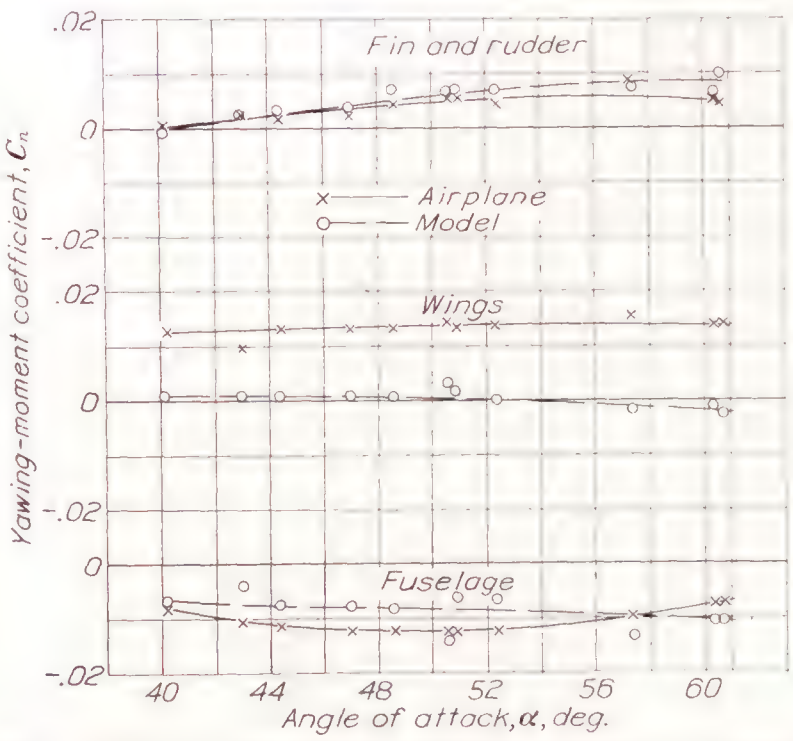

FIGURE 27.—Variation of yawing-moment coefficient C_n of parts of the airplane and parts of the model with angle of attack. (Full-scale results from reference 2.)

The values of C_n for the fin and rudder were obtained from the difference in the results obtained from the tests of the complete model and of the model with the fin and the rudder removed. The difference between flight results (reference 2) and model results changes from zero at 40° angle of attack to 0.003 at 60° (fig. 27). The values of C_n for the model wings with the struts and the attachment to the balance are about zero, while those for the airplane wings are about 0.013. Undoubtedly this difference is largely due to scale effects, which may normally be expected. The values of C_n for the model fuselage were obtained from the results of tests with the wings removed from the model

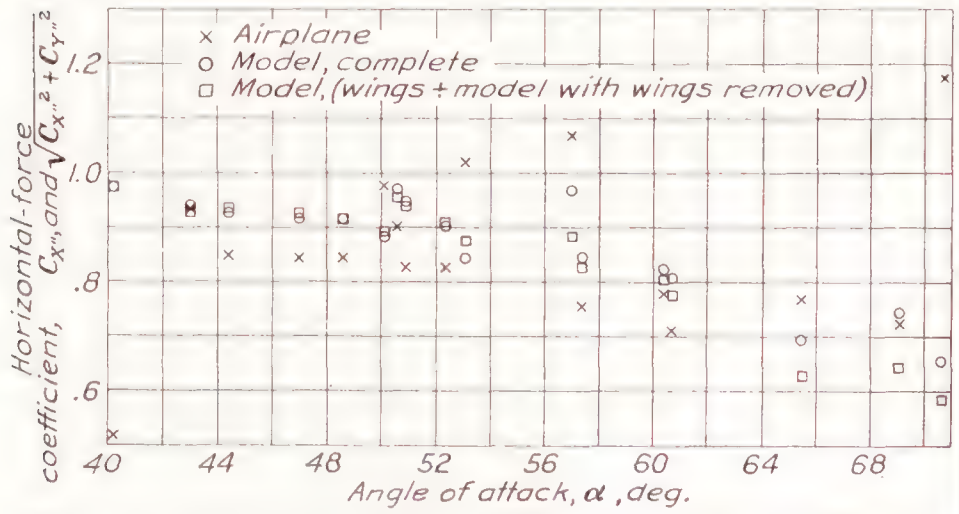

FIGURE 28.—Variation of horizontal-force coefficient $C_{X''}$ (earth axes) of airplane and of resultant-force coefficient $\sqrt{C_{X''^2}+C_{Y''^2}}$ (earth axes) of the model with angle of attack.

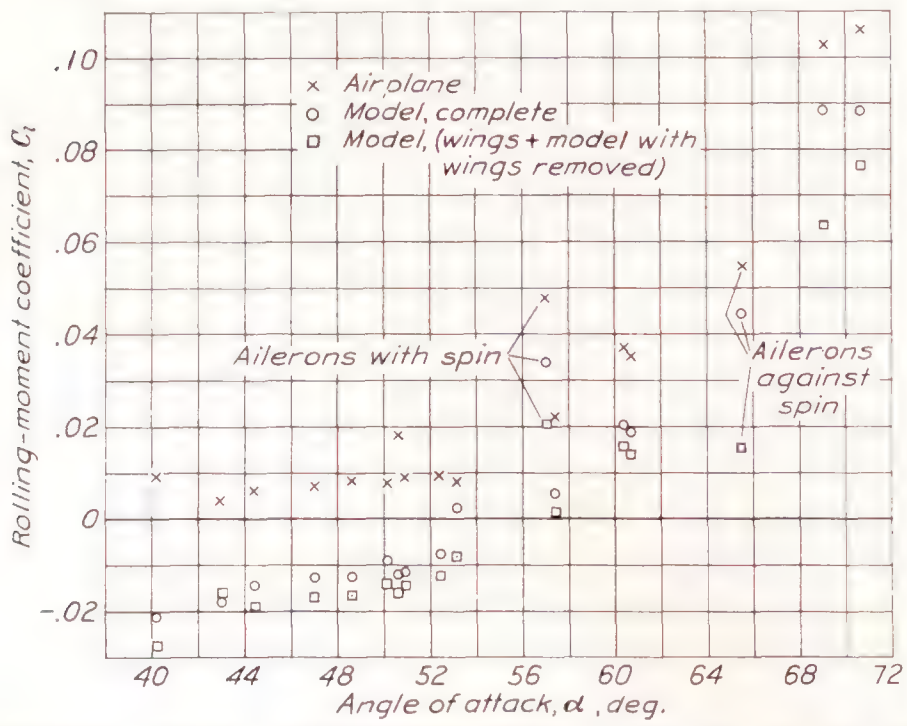

FIGURE 29.—Variation of rolling-moment coefficient C_l (body axes) of airplane and model with angle of attack.

minus the values obtained for the fin and rudder and are about the same as those obtained in flight at 40° and 55° angle of attack. Below 58° the values for the model are more positive and, above 58°, they are more negative than those obtained in flight.

The yawing moments for parts of the airplane were obtained in flight from pressure-distribution measurements on the important fuselage and tail-surface areas; the measurements included the interference of all parts of the airplane. The spinning-balance results were measured without the interference of some parts. This difference in method of measurement should give some difference other than that due to scale effects in the results and was intended to determine the scale and interference effects so that data for individual parts of models might be combined to give the characteristics of the complete model or airplane. The results of this part of the investigation are not sufficiently complete to draw definite conclusions because only one airplane is represented. It does, however, give some indication of the magnitude of the scale and interference effects that may be expected.

The interference effects caused by testing the wings alone and the model with wings removed for all the

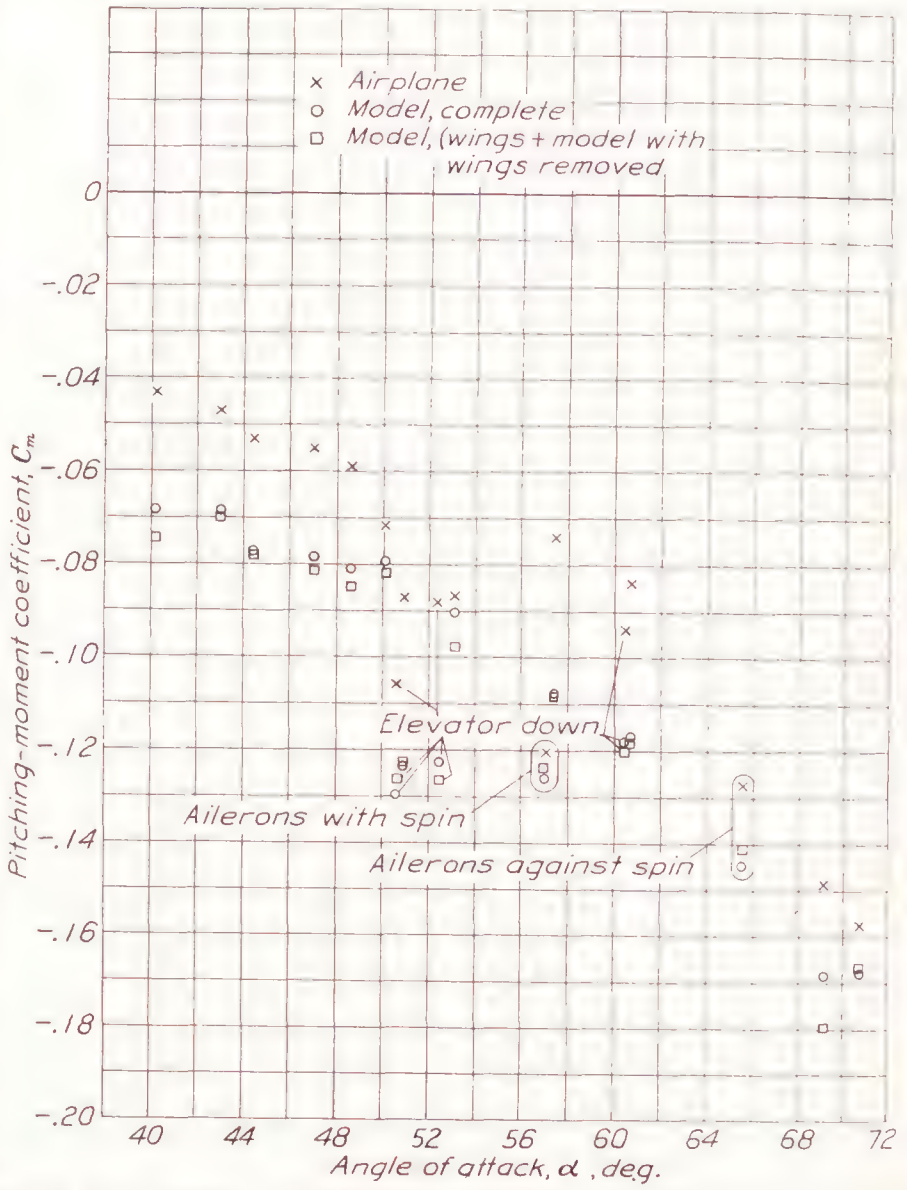

FIGURE 30.—Variation of pitching-moment coefficient C_m (body axes) of airplane and model with angle of attack.

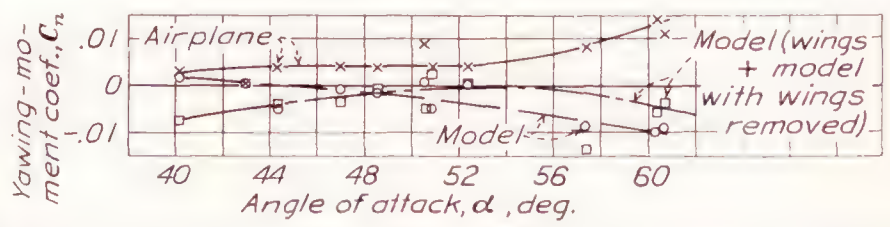

FIGURE 31.—Variation of yawing-moment coefficient C_n (body axes) of airplane and model with angle of attack.

coefficients, together with the values obtained for the airplane, are given in figures 28 to 31. At the higher angles of attack the values of $\sqrt{C_{X''^2}+C_{Y''^2}}$ for the complete model show a tendency to be greater than for the sum of the parts (fig. 28). The values of C_l for the complete model are generally more positive, by about 0.005, than the sum of the parts (fig. 29). The interference effect on C_m is small (fig. 30). The values of C_n for the sum of the parts are more negative than the values for the complete model below 49° angle of attack; above 49° the effect is reversed (fig. 31).

ANALYSIS OF DATA

DERIVATION OF EQUATIONS USED IN COMPUTING THE SPINNING ATTITUDE FROM SPINNING-BALANCE DATA

Since the necessary condition for a steady spin is that the aerodynamic forces and moments must exactly oppose the weight, centrifugal force, and inertia moments of the airplane, the following relations may be written.

(Because the resultant force on an airplane is not necessarily perpendicular to the XY plane of the airplane, as it was assumed to be in the computation of the attitudes, the computed azimuth setting of the model on the balance had the effect of rotating the resultant-force vector in the horizontal plane so that $C_{Y''}$ was not zero. Since $C_{Y''}$ must be zero in a steady spin and the resultant force in the horizontal plane must be exactly opposed by the centrifugal force, the resultant-force coefficient $\sqrt{C_{X''}^2+C_{Y''}^2}$ is used instead of $C_{X''}$ as might normally be expected.)

$$1/2\rho V^2 S C_{Z''}=mg \tag{1}$$

$$1/2\rho V^2 S\sqrt{C_{X''}^2+C_{Y''}^2}=m\Omega^2 R \tag{2}$$

$$1/2\rho V^2 SbC_m=1/2\Omega^2(A-C)\sin 2\alpha\cos^2(\sigma+\beta) \text{ nearly} \tag{3}$$

$$1/2\rho V^2 SbC_l=\Omega^2(C-B)\sin\alpha\sin(\sigma+\beta)\cos(\sigma+\beta) \text{ nearly} \tag{4}$$

$$1/2\rho V^2 SbC_n=\Omega^2(B-A)\cos\alpha\cos(\sigma+\beta)\sin(\sigma+\beta) \text{ nearly} \tag{5}$$

where σ is the angle between the vertical and the helix described by the center of gravity of the airplane. Relation (3) may be rewritten as

$$\frac{\Omega b}{2V}=\sqrt{\frac{-C_m}{4\mu\sin 2\alpha\cos^2(\sigma+\beta)}\times\left(\frac{b^2}{k_Z^2-k_X^2}\right)} \tag{6}$$

where $\mu=\dfrac{m}{\rho Sb}$ and $\left(\dfrac{b^2}{k_Z^2-k_X^2}\right)=\dfrac{Wb^2}{g(C-A)}$

Dividing relation (4) by (3) gives

$$C_l=-C_m\frac{k_Z^2-k_Y^2}{k_Z^2-k_X^2}\frac{\tan(\sigma+\beta)}{\cos\alpha} \tag{7}$$

where $\dfrac{k_Z^2-k_Y^2}{k_Z^2-k_X^2}=\dfrac{C-B}{C-A}$

Dividing relation (5) by (4) gives

$$C_n=C_l\cot\alpha\left(\frac{k_Y^2-k_X^2}{k_Z^2-k_Y^2}\right) \tag{8}$$

where $\left(\dfrac{k_Y^2-k_X^2}{k_Z^2-k_Y^2}\right)=\dfrac{B-A}{C-B}$

$$\sin\sigma=\frac{\Omega R}{V} \text{ from definition} \tag{9}$$

$$\sin\sigma=\frac{\sqrt{C_{X''}^2+C_{Y''}^2}}{4\mu\dfrac{\Omega b}{2V}} \text{ from (2) and (9)} \tag{10}$$

COMPUTED SPINNING EQUILIBRIUM

1. The value of σ is obtained for each test condition by using equation (10).

2. The value of $\Omega b/2V$ required for balance of the aerodynamic and inertia pitching moments is computed from equation (6) for each test condition, C_m being increased by 0.02 for reasons given in the text. These computed values of $\Omega b/2V$ and the values used in testing the model were plotted against C_m. (See fig. 32.) The intersection of these curves gives the equilibrium values of $\Omega b/2V$ and C_m for each angle of attack at each angle of sideslip tested.

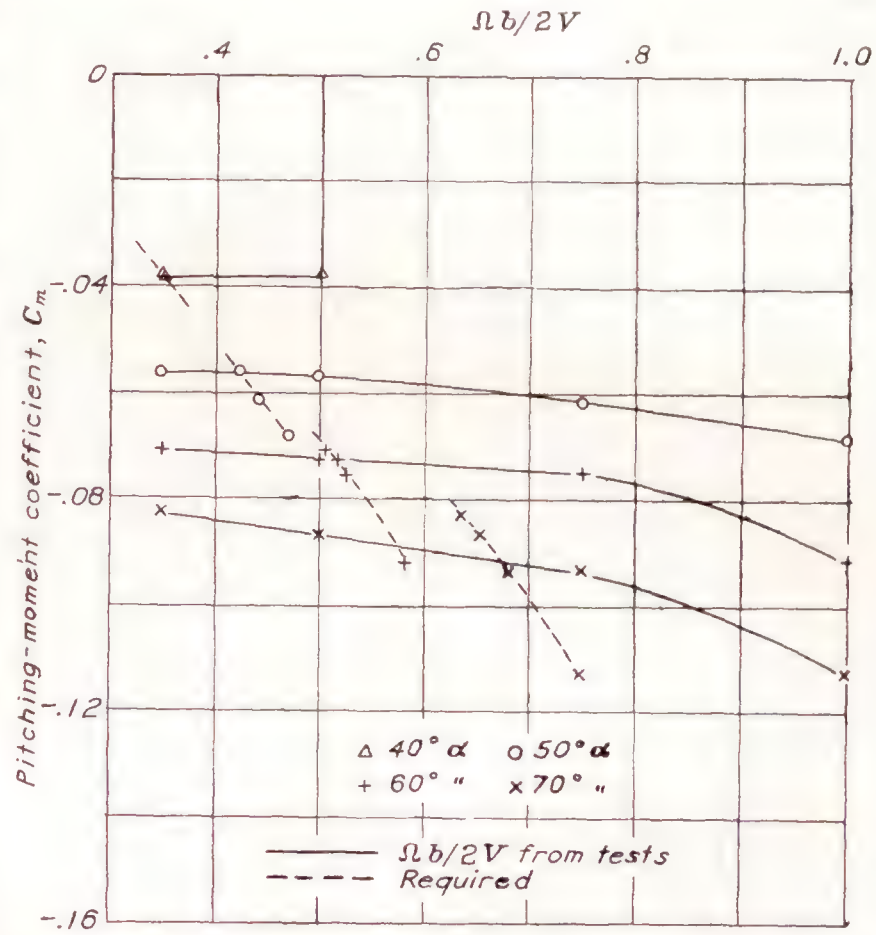

FIGURE 32.—Variation of pitching-moment coefficient C_m (body axes) with $\Omega b/2V$ (Value of $\Omega b/2V$ from tests.) $\beta=-10°$.

3. The value of the rolling moment required for equilibrium with the inertia moment is found from equation (7) by using the values of C_m and σ that gave a balance of pitching moments (par. 2). These rolling moments, and those from the test data, increased by 0.02, are plotted against β for each angle of attack in figure 33. Intersection of these curves gives values of β and C_l for spinning equilibrium at each angle of attack tested.

4. The values of the aerodynamic yawing moment required for equilibrium are obtained from equation (8) by using the value of C_l found from paragraph 3,

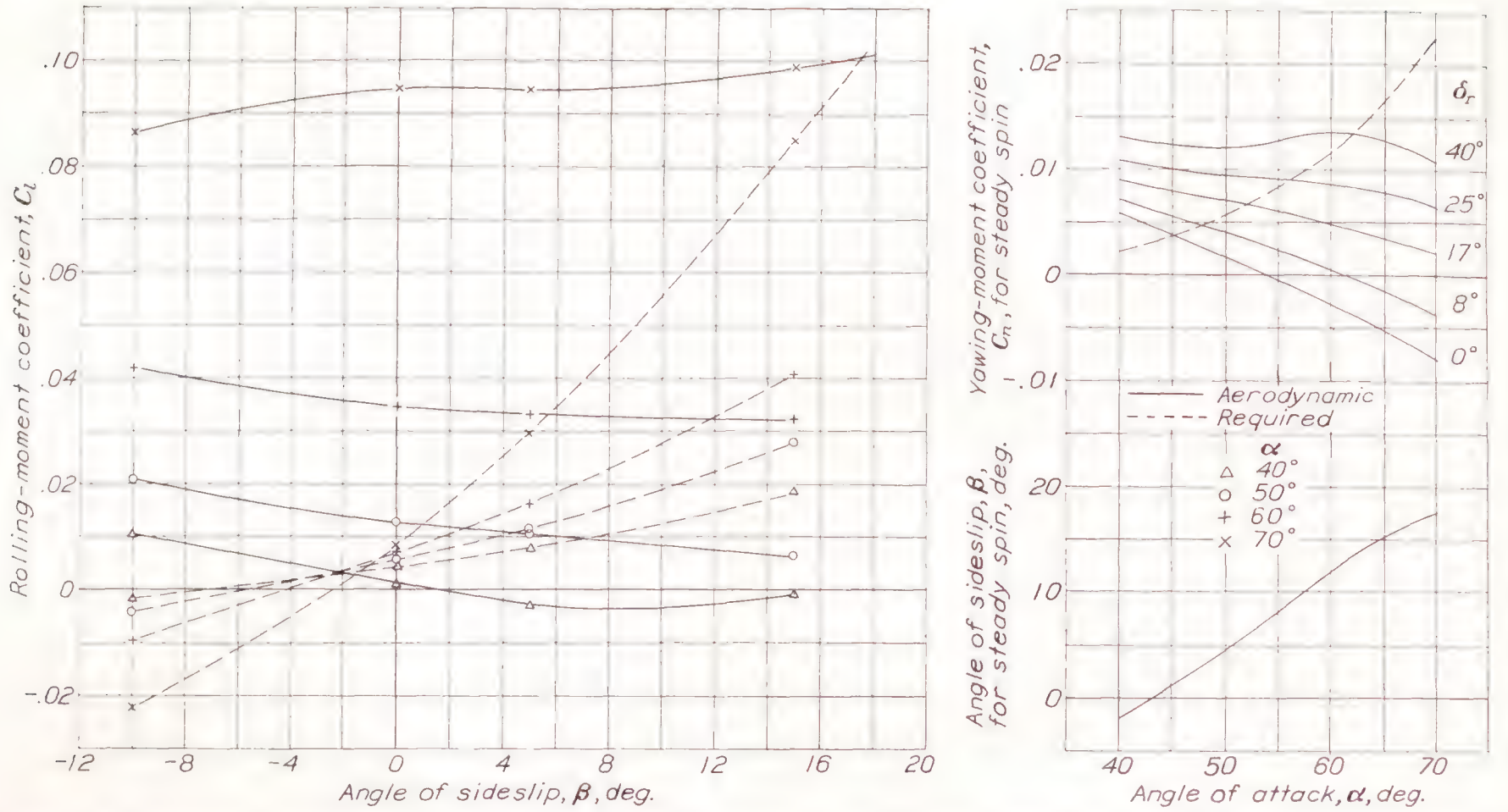

FIGURE 33.—Sample chart showing method of determining angle of sideslip and angle of attack necessary for equilibrium in spins. δ_a=23°41′ up; δ_r=40° with spin; μ=4.74; $\frac{k_Z^2-k_Y^2}{k_Z^2-k_X^2}$=0.616; $\frac{b^2}{k_Z^2-k_X^2}$=59.3.

and those obtained from the data (changed according to fig. 26 for full-scale) at corresponding conditions are plotted against angle of attack (fig. 33). Equilibrium in a spin is indicated where these curves intersect.

5. The value of $\Omega b/2V$ for the attitude found by the method of paragraph 4 is determined in the following way: Plot the aerodynamic rolling moments required, computed for each angle of attack from paragraph 3, against $\Omega b/2V$, from which the value of $\Omega b/2V$ for each angle of attack can be found, since the value of C_l for equilibrium has been obtained in paragraph 3. (Fig. 34 is a sample chart.) Plot these values of $\Omega b/2V$ against α and, since the value of α of the spin is known from paragraph 4, the value of $\Omega b/2V$ for the indicated spin is obtained.

This method of analysis is essentially the same as that given in reference 8, modified for use with the data from the complete model instead of from only the wing.

INDEPENDENT VARIABLES USED IN COMPUTATIONS

Computations for estimations of spin characteristics were made for assumed characteristics of the airplane for comparison with flight results, and are tabulated in table II.

Table III gives the assumed airplane characteristics that were used to estimate spins for a comparison with the results from the free-spinning tunnel. A model made to the same dimensions as the model tested on the spinning balance and with these same parameters was tested in the free-spinning tunnel.

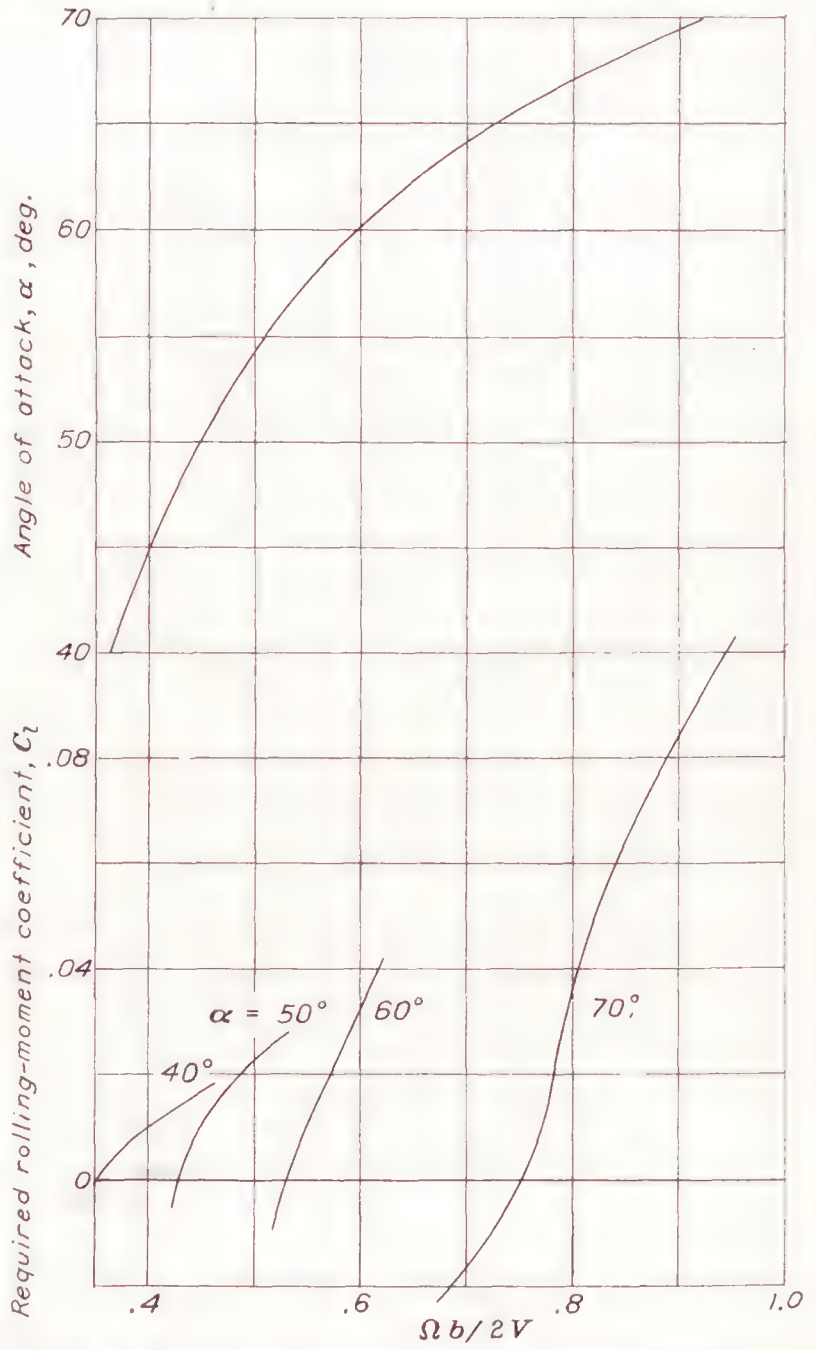

FIGURE 34.—Sample chart showing method of determining $\Omega b/2V$ of spin.

TABLE II.—AIRPLANE PARAMETERS

μ	$\frac{b^2}{k_Z^2-k_X^2}$	$\frac{k_Z^2-k_Y^2}{k_Z^2-k_X^2}$	δ_a (deg.)	δ_e[1] (deg.) (min.)	δ_r[2] (deg.)
2.5	70	1.00	0	−23 41	−40
4.5	70	1.00	0	−23 41	−40
7.5	70	1.00	0	−23 41	−40
10.0	70	1.00	0	−23 41	−40
4.5	50	1.00	0	−23 41	−40
4.5	90	1.00	0	−23 41	−40
4.5	110	1.00	0	−23 41	−40
4.5	70	.50	0	−23 41	−40
4.5	70	1.50	0	−23 41	−40
4.5	70	2.00	0	−23 41	−40
4.5	70	2.50	0	−23 41	−40
4.5	70	1.00	[3] Against	−23 41	−40
4.5	70	2.00	Against	−23 41	−40
4.5	70	1.00	[4] With	−23 41	−40
4.5	70	2.00	With	−23 41	−40
4.74	59.30	.616	0	−23 41	−40
[5] 3.91	60.90	.718	0	−23 41	−40
4.74	73.73	2.0	0	25 0	40
4.74	73.73	2.5	0	25 0	40
4.74	73.73	2.0	0	0 0	0
4.74	73.73	2.5	0	0 0	0
7.5	70	2.0	0	0 0	0
7.5	70	1.0	0	0 0	0
7 5	70	2.0	0	25 0	40
7.5	70	1.0	0	25 0	40

[1] Positive when elevators are down.
[2] Positive in a right spin when rudder is against spin.
[3] Right aileron up 25°, left aileron down 15°.
[4] Left aileron up 25°, right aileron down 15°.
[5] Corresponds to flight tests 38L, 40L, and 41L of reference 1.

TABLE III.—SPIN-TUNNEL PARAMETERS

μ	$\frac{b^2}{k_Z^2-k_X^2}$	$\frac{k_Z^2-k_Y^2}{k_Z^2-k_X^2}$	δ_a (deg.)	δ_e (deg.) (min.)	δ_r (deg.)
4.80	62.00	0.558	0	−23 41	−40
4.90	63.00	.853	0	−23 41	−40
5.00	64.49	1.147	0	−23 41	−40
5.09	65.76	1.440	0	−23 41	−40
5.19	67.03	1.734	0	−23 41	−40
6.16	79.55	.558	0	−23 41	−40
7.52	97.13	.558	0	−23 41	−40
7.52	97.13	.558	0	0 0	0
7.52	97.13	.558	0	25 0	40
7.52	97.13	1.734	0	0 0	0
7.52	97.13	1.734	0	25 0	40

Under standard conditions at sea level for this airplane, values of μ of 2.5 and 10 correspond to wing loadings of 5.36 and 21.46 pounds per square foot, respectively. The variables used were chosen to cover the range for all wing loadings and moments of inertia likely to be used with an airplane of this type and included some specific values used in flight and in the free-spinning tunnel.

The results of the analyses are given in figures 35 to 40. Each analysis, with $\delta_e=23°41'$ up, was computed, in addition to $\delta_r=40°$ with, for rudder settings of 25°, 17°, 8°, and 0° by using the values of C_n given in figure 22 and by assuming that the only effect of moving the rudder from 40° with the spin was to change C_n and that the value of $\Omega b/2V$ was 0.75 at $\alpha=60°$ and 0.50 at $\alpha=50°$. These assumptions are only approximate because C_n changes considerably with $\Omega b/2V$ (see fig. 15) and C_m changes with rudder movement. The results are included because they indicate the general effects of rudder deflections.

ARBITRARY CORRECTIONS TO SPINNING-BALANCE DATA USED IN MAKING THE ANALYSIS

Full-scale.—Previous investigations (references 4 and 5) and figures 23 to 26 indicate that it is necessary to correct spinning-balance data when estimating spins. No correction to $C_{X''}$ is considered necessary because $\Delta C_{X''}$ is a small percentage of $C_{X''}$ and rather large values of $\Delta C_{X''}$ would make but small differences in estimating spins. The average value of 0.02 has been added to C_l and C_m because ΔC_l and ΔC_m show only slight tendencies to vary with α, β, or $\Omega b/2V$, and the individual points are scattered. All C_n values were changed by the amount indicated by the curve (fig. 26) for this analysis because the curve of ΔC_n against β is well defined and the differences are sufficiently large to cause large angle-of-attack differences in the estimated spin.

Free-spinning tunnel.—If the differences between spinning-balance and flight results were all due to scale effect, then steady spins estimated from uncorrected balance data should agree with those obtained in the free-spinning tunnel. However, the values of $\Omega b/2V$ obtained from tests in flight and in the free-spinning tunnel (references 2 and 3) are very nearly the same and, since C_m determines to a large extent the curve of $\Omega b/2V$ against α (fig. 34), a correction of 0.02 was applied to C_m for all estimations of spins used for comparison with the results from the free-spinning tunnel.

DISCUSSION OF RESULTS OF ANALYSIS

ESTIMATED FULL-SCALE ATTITUDES

Increasing μ increases the angle of attack, makes the sideslip more positive, and increases the values of $\Omega b/2V$ when the rudder is 25° or more with the spin (fig. 35). In general, it appears that increased wing loadings and higher altitudes would make the spin flatter and recoveries slower and more difficult.

Increasing the pitching-moment inertia parameter $b^2/(k_Z^2-k_X^2)$ (decreasing $C-A$) generally decreases the angle of attack, makes the sideslip more outward (negative in a right spin), and does not appreciably change $\Omega b/2V$ (fig. 36). The effect on time for recovery of changing $b^2/(k_Z^2-k_X^2)$ would probably be small.

Increasing the rolling- and yawing-moment inertia parameter $(k_Z^2-k_Y^2)/(k_Z^2-k_X^2)$, i. e., moving weight from the center of gravity out along the wings (fig. 37), increases the angle of attack and $\Omega b/2V$ and makes the sideslip more nearly zero. Increasing this parameter would apparently make the airplane spin faster and flatter with recoveries probably slower and more difficult.

This analysis indicates that a large value of μ and a large value of $(k_Z^2-k_Y^2)/(k_Z^2-k_X^3)$ would make the airplane spin at high angles of attack and very fast. It was thought that large values of these parameters might produce spins with the controls neutral or against the spin. Accordingly, analyses were made with $\mu=7.5$, $b^2/(k_Z^2-k_X^2)=70$, $(k_Z^2-k_Y^2)/(k_Z^2-k_X^2)=1.0$ and 2.0, and tail surfaces both neutral and against the spin; but in no case was a spin indicated. Approximately the same conditions were tried in the free-spinning tunnel with the same results.

Moving the rudder, with elevators up, any amount from full with the spin to neutral in all cases reduces the angle of attack and $\Omega b/2V$ and makes the sideslip more outward.

Equilibrium was impossible in every case in a spin analyzed with elevator and rudder neutral or both against the spin. Moving the ailerons from against the spin to with the spin (fig. 38) decreases the angle of attack and decreases $\Omega b/2V$ with elevators up and rudder full with the spin. With other rudder settings this effect is reduced and, with $\delta_r=0°$ and $(k_Z^2-k_Y^2)/(k_Z^2-k_X^2)=2.0$, the angle of attack and $\Omega b/2V$ are increased. Ailerons moved from against the spin to with the spin generally tend to increase the sideslip and make the values more nearly the same for all rudder settings.

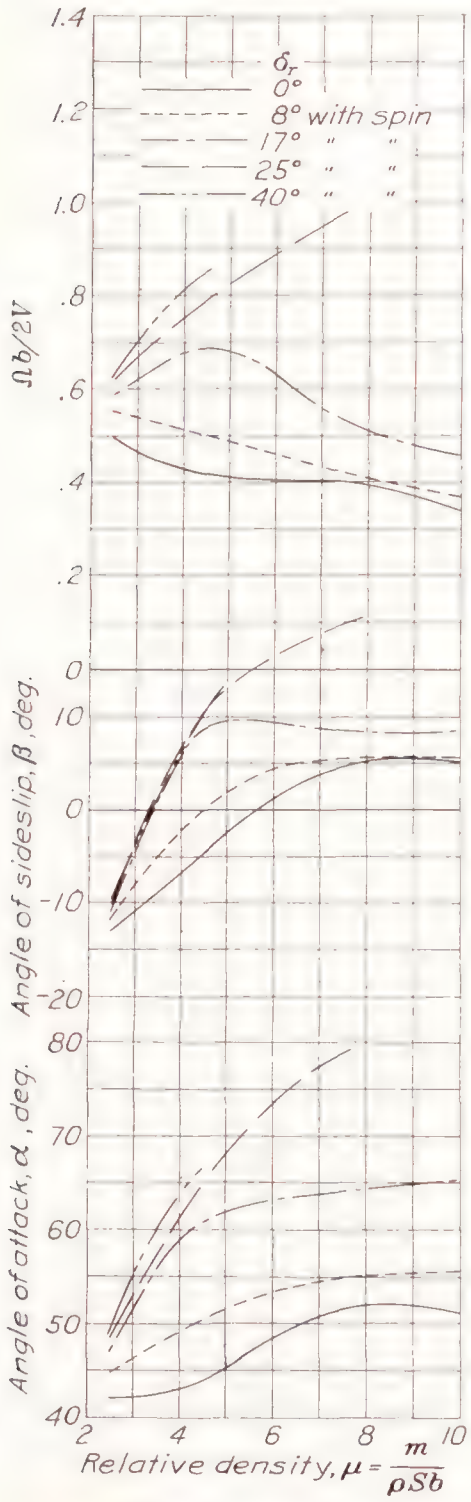

FIGURE 35.—Variation of estimated values of angle of attack, angle of sideslip, and $\Omega b/2V$ with relative density of airplane. $\delta_a=0°$; $\delta_e=23°41'$ up; $\frac{k_Z^2-k_Y^2}{k_Z^2-k_X^2}=1.0$; $\frac{b^2}{k_Z^2-k_X^2}=70$.

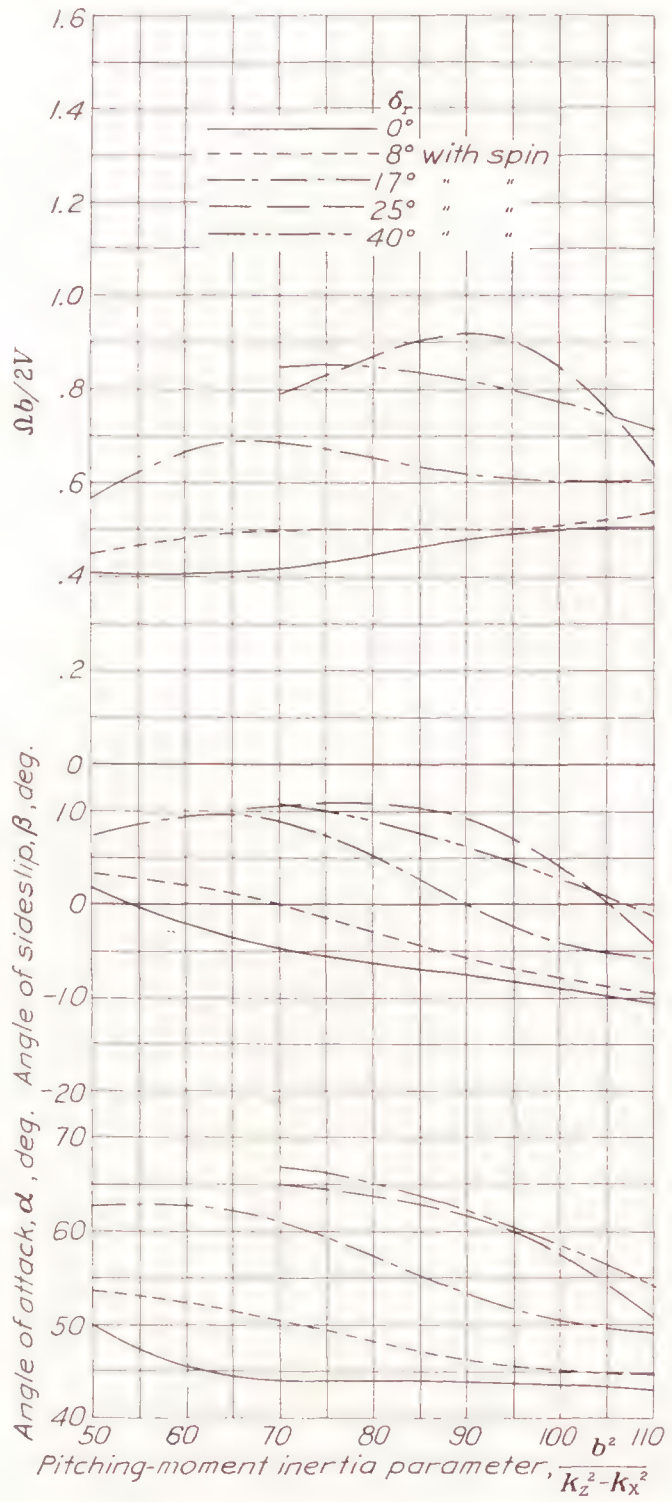

FIGURE 36.—Variation of estimated values of angle of attack, angle of sideslip, and $\Omega b/2V$ with pitching-moment inertia parameter $\frac{b^2}{k_Z^2-k_X^2}$. $\delta_a=0°$; $\delta_e=23°41'$ up; $\mu=4.5$; $\frac{k_Z^2-k_Y^2}{k_Z^2-k_X^2}=1.0$.

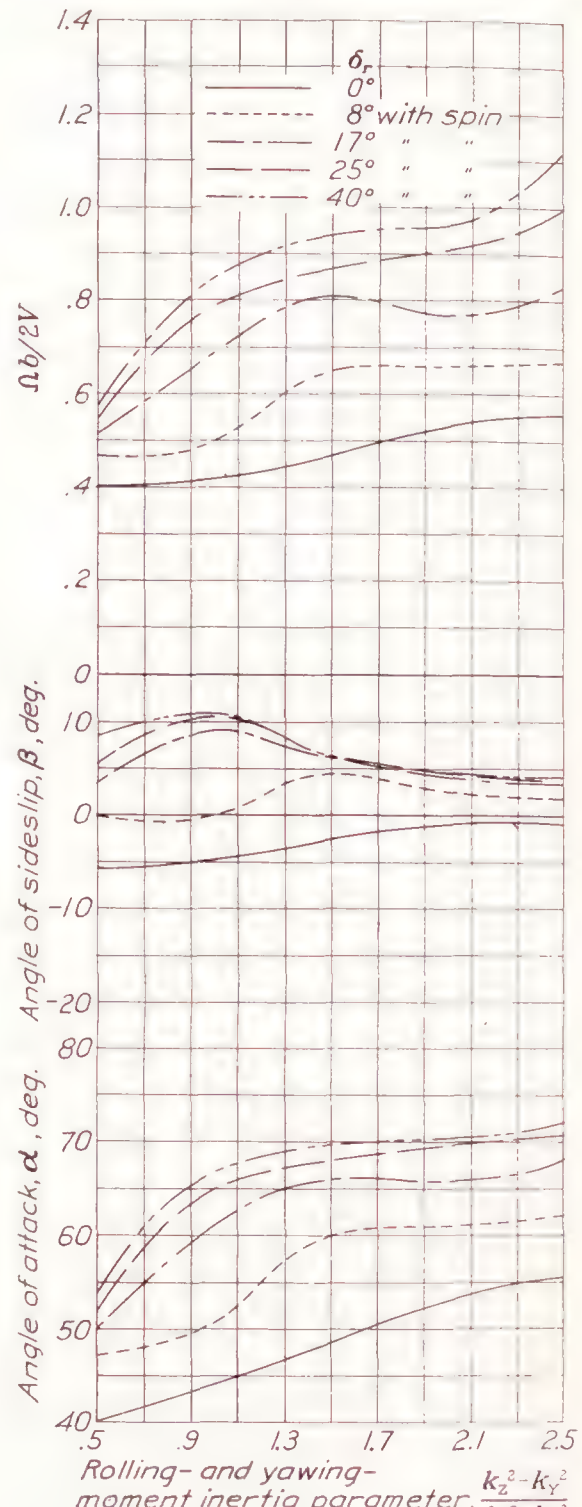

FIGURE 37.—Variation of estimated values of angle of attack, angle of sideslip, and $\Omega b/2V$ with rolling- and yawing-moment inertia parameter $\frac{k_Z^2-k_Y^2}{k_Z^2-k_X^2}$. $\delta_a=0°$; $\delta_e=23°41'$ up; $\mu=4.5$; $\frac{b^2}{k_Z^2-k_X^2}=70$.

COMPARISON WITH FULL-SCALE RESULTS

An analysis for estimation of spins was made for some flight conditions given in reference 1. The results of this analysis are shown in figure 39. The estimated spins agree very well with flight results when $(k_Z^2-k_Y^2)/(k_Z^2-k_X^2)$ is equal to 1.4. For other values of this parameter the disagreement between the results is considerable. When $(k_Z^2-k_Y^2)/(k_Z^2-k_X^2)$ is equal to 0.718, the only condition flight-tested both to the right and left, the flight results are generally greater or less than those obtained from analysis, depending upon whether the airplane was spun to the right or to the left. There is no doubt but that part of this difference is due to dissymmetry of the airplane used in the flight tests. The results of the one test with wing-tip ballast show considerably different aerodynamic characteristics than do the results of the tests without ballast (reference 2); this discrepancy, however, may be due to the changing of the period of vibration of the wings by the ballast, thus affecting the rolling and yawing moments. At the beginning of these tests on the spinning balance it was found that, under certain conditions,

the rolling moment (for earth axes) could be varied as much as 100 percent by changing the tension of a spring attached to the rolling-moment arm in the balance. When the rigidity of the wings with respect to the fuselage was increased, this variation in moment with spring tension completely disappeared. There can be little doubt that this variation was aerodynamic because the balance was carefully checked and a corresponding condition has been observed in which the setting of zero is very questionable, as previously explained, and therefore will not be discussed.

The angle of sideslip for rudder settings of 40° and 17° with the spin is generally within the limits of error (a degree or so) of the results obtained in the free-spinning tunnel.

The values of C_n are usually 0.001 to 0.003 too low to give the angle of attack obtained from the free-spinning tunnel. This difference indicates that the results from

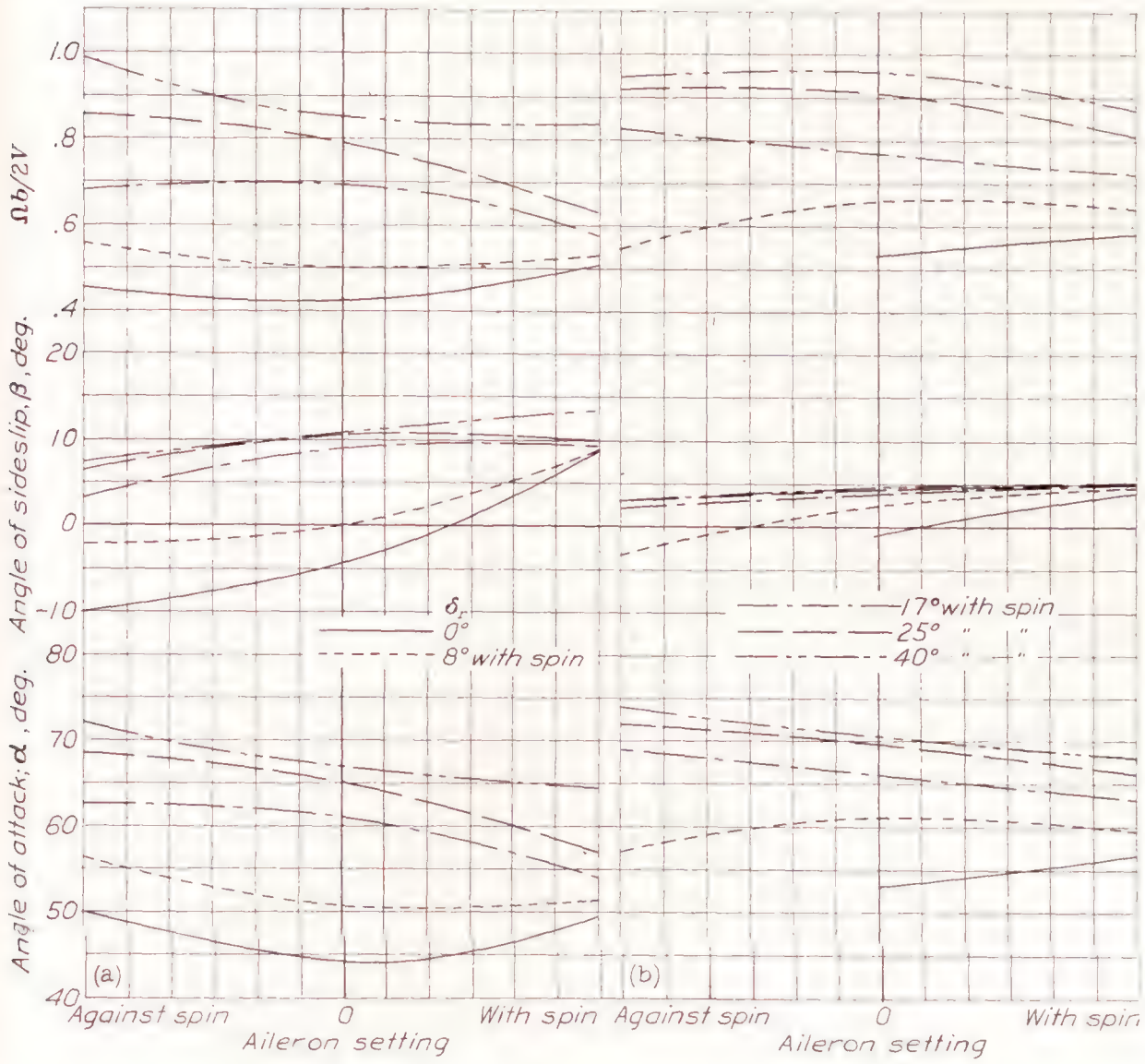

(a) $\frac{k_Z^2-k_Y^2}{k_Z^2-k_X^2}=1.0$. (b) $\frac{k_Z^2-k_Y^2}{k_Z^2-k_X^2}=2.0$.

FIGURE 38.—Variation of estimated values of angle of attack, angle of sideslip, and $\Omega b/2V$ with aileron setting. $\delta_e=23°41'$ up; $\mu=4.5$; $\frac{b^2}{k_Z^2-k_X^2}=70$.

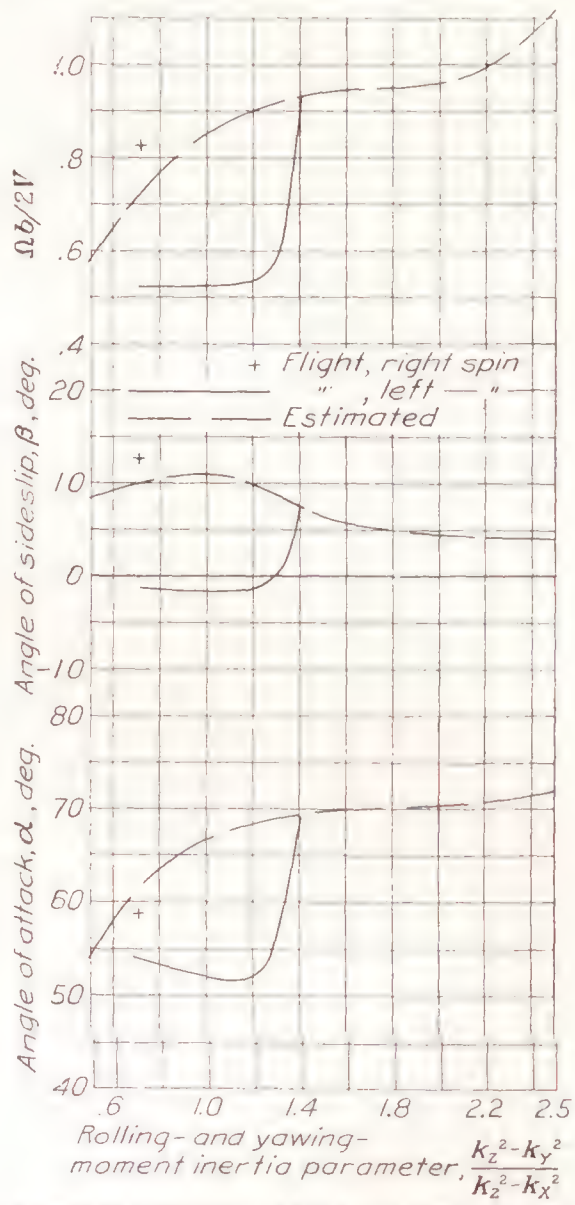

FIGURE 39.—Variation of flight and estimated values of angle of attack, angle of sideslip, and $\Omega b/2V$ with rolling- and yawing-moment inertia parameter $\frac{k_Z^2-k_Y^2}{k_Z^2-k_X^2}$. $\delta_a=0°$; $\delta_r=23°41'$ up; $\delta_r=40°$ with spin $\mu=4.5$; $\frac{b^2}{k_Z^2-k_X^2}=70$.

tail surfaces and wings of a model vibrated during routine tests in another wind tunnel.

COMPARISON WITH RESULTS FROM THE FREE-SPINNING TUNNEL

The results of the analysis and results of tests from the free-spinning tunnel are given in figure 40. The estimated values of β, $\Omega b/2V$, and C_n necessary for equilibrium in a steady spin are plotted against the angle of attack; the values obtained from the free-spinning tunnel were obtained from reference 3 and from unpublished data. The results agree fairly well except below 40° angle of attack, in which range the model could not be tested on the spinning balance because of interference with the balance. The extrapolation of the spinning-balance data for the rudder the free-spinning tunnel are slightly more positive than those obtained from the spinning balance; however, this discrepancy may be an indication that the correction of 0.02 to the pitching moment was not large enough, since increasing the value of the correction reduces the difference.

The fact that the values of $\Omega b/2V$ are usually slightly lower than those obtained from the free-spinning tunnel also indicates that a correction to C_m of the order of 0.021 or 0.022 would have given slightly better agreement for both $\Omega b/2V$ and C_n.

The agreement between spins as estimated from results obtained from the spinning balance and from those obtained from the free-spinning tunnel is generally well within the limits of error except for the necessary correction to C_m.

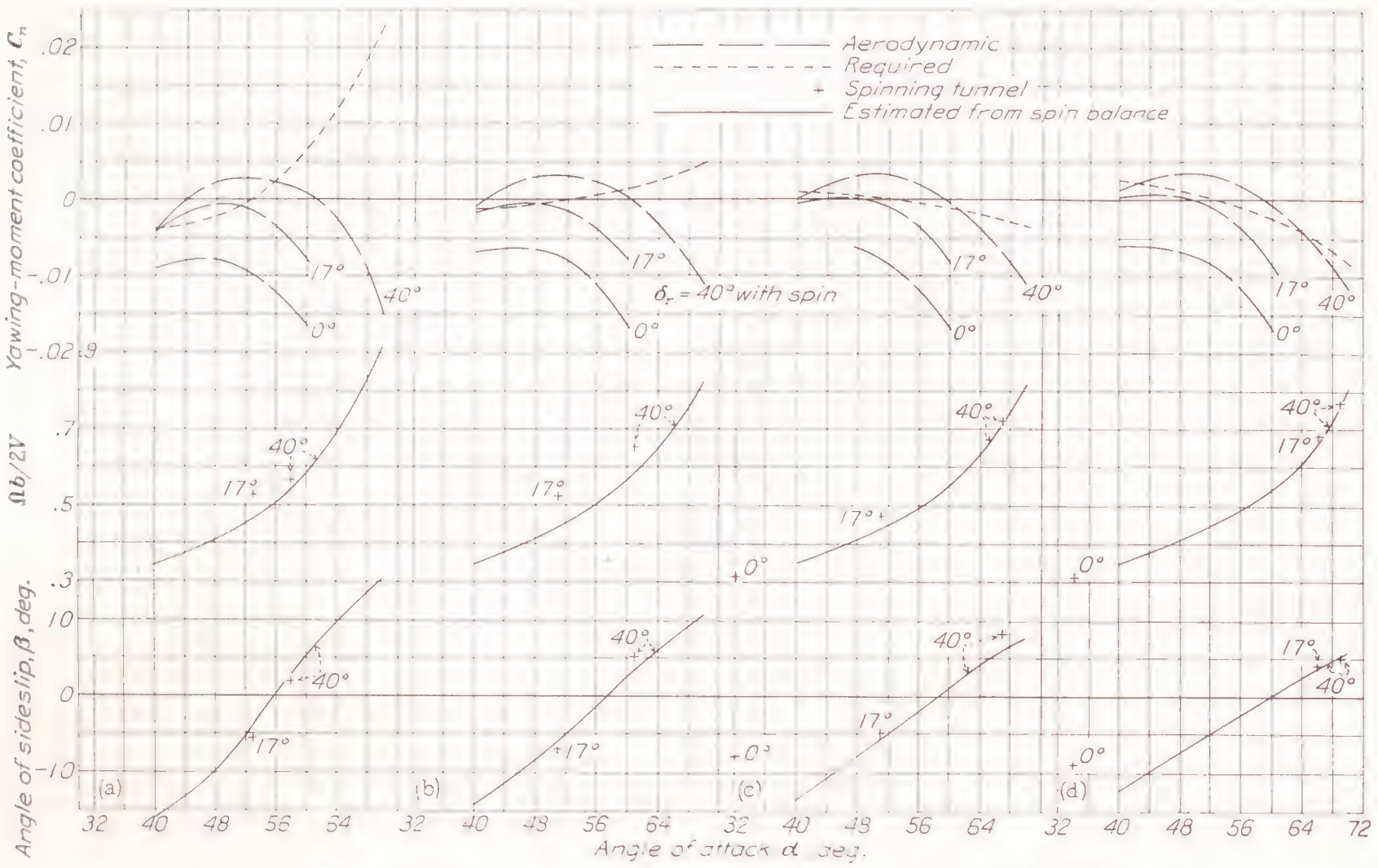

(a) $\mu=4.8$; $\frac{b^2}{k_Z^2-k_X^2}=62$; $\frac{k_Z^2-k_Y^2}{k_Z^2-k_X^2}=0.558$.

(b) $\mu=4.9$; $\frac{b^2}{k_Z^2-k_X^2}=63.3$; $\frac{k_Z^2-k_Y^2}{k_Z^2-k_X^2}=0.853$.

(c) $\mu=5.0$; $\frac{b^2}{k_Z^2-k_X^2}=64.49$; $\frac{k_Z^2-k_Y^2}{k_Z^2-k_X^2}=1.147$.

(d) $\mu=5.09$; $\frac{b^2}{k_Z^2-k_X^2}=65.76$; $\frac{k_Z^2-k_Y^2}{k_Z^2-k_X^2}=1.44$.

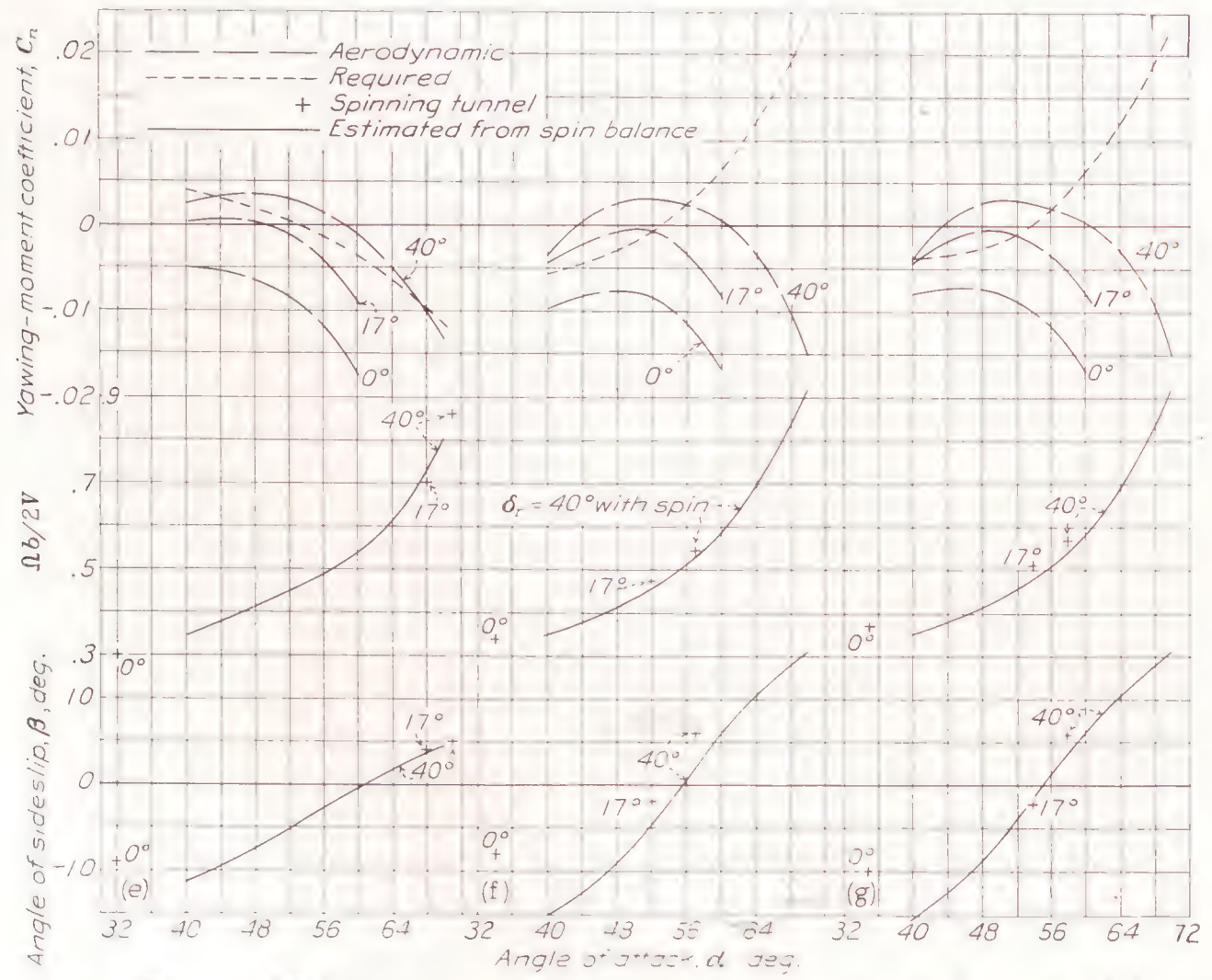

(e) $\mu=5.19$; $\frac{b^2}{k_Z^2-k_X^2}=67.03$; $\frac{k_Z^2-k_Y^2}{k_Z^2-k_X^2}=1.734$.

(f) $\mu=6.16$; $\frac{b^2}{k_Z^2-k_X^2}=79.55$; $\frac{k_Z^2-k_Y^2}{k_Z^2-k_X^2}=0.558$.

(g) $\mu=7.52$; $\frac{b^2}{k_Z^2-k_X^2}=97.13$; $\frac{k_Z^2-k_Y^2}{k_Z^2-k_X^2}=0.558$.

FIGURE 40.—Variation of angle of sideslip, yawing-moment coefficient, and $\Omega b/2V$ with angle of attack. $\delta_a=0°$; $\delta_e=23°41'$ up.

COMPARISON OF SPINS OBTAINED IN THE FREE-SPINNING TUNNEL WITH THOSE OBTAINED IN FLIGHT AS INDICATED BY THE SPINNING-BALANCE DATA

The comparison of spins in flight and in the free-spinning tunnel is based on the necessary corrections to the data obtained from the spinning balance to give agreement with results from flight and from the free-spinning tunnel.

The differences in $C_{X''}$ (force coefficient in the horizontal plane) and in C_m are not large enough to have an appreciable effect on the results. The effect of changes in $C_{X''}$ have been shown in references 7 and 8 and the changes in C_m have been discussed in this report.

If an arbitrary constant of 0.02 could be added to the C_l for tests in the free-spinning tunnel, the sideslip of the model and the airplane should be about the same. The differences in yawing moments are but slightly less than those given in figure 26. In the comparison of spins, however, the difference in yawing moment required caused by the difference in sideslip between the model and the airplane must be considered.

The effect of sideslip on the yawing moment required is reflected as a change in C_l in equation (8):

$$C_n = C_l \cot \alpha \left(\frac{B-A}{C-B}\right)$$

For the model of the XN2Y–1 airplane, C_l would always be about 0.02 less than for the full-scale airplane because the aerodynamic rolling moment does not change much with β. (See fig. 33.) If $(B—A)$ is positive, the value of C_n required for the model will always be less than for the airplane, which gives (in the analysis) the same effect as adding an increment to the aerodynamic yawing moment available. The result of this counteracting effect is that the model may spin at the same angle of attack and recover in much the same manner as the airplane. When $(B—A)$ is negative, this effect will be reversed and greater discrepancies between model and airplane spins may be expected. Also, the aerodynamic yawing moment may be considerably different because of the difference in sideslip between the model and the airplane, since the yawing-moment coefficient varies with angle of sideslip. (See figs. 12 and 22.) The inference from these comparisons is that the free-spinning tunnel will, for certain airplanes, give reasonable indications of the behavior of the airplane in the spin but in other cases the behavior of the model and of the airplane may be considerably different.

CONCLUSIONS

1. Scale effects on models, and tunnel and oscillation effects on the spinning-balance results, make it difficult to estimate the equilibrium attitude in a full-scale spin.

2. For the XN2Y–1 airplane the differences in C_l and C_n between full-scale and spinning-balance results agree with the differences found for two other airplanes previously tested. No comparisons of C_m can be made with previous results because of the inaccuracy of this value in the earlier tests.

3. An average difference of 0.02 was found in C_l and C_m between flight results and spinning-balance results. The differences in C_n were found to increase with β as β became more positive (more inward sideslip in a right spin). The value of C_n was found to be about 0.005 at slightly negative values of sideslip, increasing to 0.02 at 13° positive sideslip.

4. Good agreement for steady-spinning attitudes between results from the free-spinning tunnel and estimations of spins from spinning-balance data can be obtained by adding 0.02 to the values of the pitching-moment coefficients measured with the spinning balance.

5. This investigation indicates that good agreement in the attitude for steady spins between results from full-scale tests and those from the free-spinning tunnel can be obtained by adding 0.02 to the model rolling-moment coefficient and an increment that depends on the angle of sideslip to the model yawing-moment coefficient.

LANGLEY MEMORIAL AERONAUTICAL LABORATORY,
NATIONAL ADVISORY COMMITTEE FOR AERONAUTICS,
LANGLEY FIELD, VA., *April 16, 1937.*

REFERENCES

1. Scudder, N. F.: A Flight Investigation of the Effect of Mass Distribution and Control Setting on the Spinning of the XN2Y–1 Airplane. T. R. No. 484, N. A. C. A., 1934.
2. Scudder, N. F.: The Forces and Moments Acting on Parts of the XN2Y–1 Airplane During Spins. T. R. No. 559, N. A. C. A., 1936.
3. Zimmerman, C. H.: Preliminary Tests in the N. A. C. A. Free-Spinning Wind Tunnel. T. R. No. 557, N. A. C. A., 1936.
4. Bamber, M. J., and Zimmerman, C. H.: The Aerodynamic Forces and Moments Exerted on a Spinning Model of the NY–1 Airplane as Measured by the Spinning Balance. T. R. No. 456, N. A. C. A., 1933.
5. Bamber, M. J., and Zimmerman, C. H.: The Aerodynamic Forces and Moments on a Spinning Model of the F4B–2 Airplane as Measured by the Spinning Balance. T. N. No. 517, N. A. C. A., 1935.
6. Wenzinger, Carl J., and Harris, Thomas A.: The Vertical Wind Tunnel of the National Advisory Committee for Aeronautics. T. R. No. 387, N. A. C. A., 1931.
7. Bamber, M. J.: Spinning Characteristics of Wings. II–Rectangular Clark Y Biplane Cellule: 25 Percent Stagger; 0° Decalage; Gap/Chord 1.0. T. N. No. 526, N. A. C. A., 1935.
8. Bamber, M. J., and Zimmerman, C. H.: Spinning Characteristics of Wings. I–Rectangular Clark Y Monoplane Wing T. R. No. 519, N. A. C. A., 1935.

REPORT No. 608

STRESS ANALYSIS OF BEAMS WITH SHEAR DEFORMATION OF THE FLANGES

By Paul Kuhn

SUMMARY

The fundamental action of shear deformation of the flanges is discussed on the basis of simplifying assumptions. The theory is developed to the point of giving analytical solutions for simple cases of beams and of skin-stringer panels under axial load. Strain-gage tests on a tension panel and on a beam corresponding to these simple cases are described and the results are compared with analytical results. For wing beams, an approximate method of applying the theory is given. As an alternative, the construction of a mechanical analyzer is advocated.

INTRODUCTION

The so-called "semimonocoque" type of construction, which has been favored by aircraft designers for some time, presents serious difficulties in stress analysis. Static tests have proved that the bending action of such a structure is not always described with sufficient accuracy by the standard engineering formulas based on the assumption that plane cross sections remain plane. It will be necessary, therefore, to devise new working theories for the action of semimonocoque beams under bending loads.

In order to arrive at reasonably rapid methods of stress analysis, it is necessary to make rather sweeping assumptions. It is obvious that the range of applicability of any such method is limited. The present paper concerns itself with beams typical in general form of one class of beams used in airplane construction, that is, with *fairly shallow, wide beams, having flat covers, symmetrical about the center line, with two shear webs and with bulkheads that offer no appreciable resistance to deformation out of their planes.*

Briefly, the action of such a beam under loads applied at the shear webs is as follows: The transverse shear is taken up by the shear webs. The flanges attached to these shear webs furnish part of the longitudinal stresses required to balance the external bending moment. The strains set up by these stresses induce shear stresses in the skin which, in turn, cause longitudinal stresses in the intermediate stringers attached to the skin until sufficient longitudinal stresses exist at any section to balance the external bending moment.

If the skin between stringers did not deform under the action of the shear stresses, the standard beam formulas would apply. The thin sheet, however, has very little shear stiffness and suffers large deformations under load. As a result, the first intermediate stringer next to a shear web carries a smaller stress than the flange of the shear web, the next intermediate stringer carries less stress than the first one, and so on to the center stringer, which carries the smallest stress. This phenomenon of the interdependence between stringer stresses and shear deformations forms the subject of the present paper.

Apparently Dr. Younger was the first person in this country to give serious attention to this subject. In reference 1 he gives a formula for the efficiency of a box beam with walls of uniform thickness, which may be considered as the limiting case of very many extremely small stringers. Nothing more on the subject was published until two experimental studies appeared in 1936. Reference 2, dealing with the case of a skin-stringer panel in edge compression, includes a theoretical solution for a particular case. Reference 3 deals with a box beam in pure bending, a problem identical with the one treated in reference 2. In both studies the stringer stresses experimentally obtained were used to compute efficiency factors for the shear stiffness of the sheet.

The most important practical problem is the inverse of the problem dealt with in references 2 and 3; namely, given the shear stiffness, to calculate the stringer stresses. The problem is difficult and complex. In order to arrive at any solution, it has been necessary to use a very much simplified concept of the action of the structure, as suggested in references 1 and 2. On the basis of this simplified concept, the analytical solutions for a few very simple cases of axially loaded panels and of beams are derived in this paper. For other cases, it will be shown that a trial-and-error method of solution is feasible.

The analytical solutions as well as the trial-and-error method apply only to very elementary cases, namely, to three-stringer panels under axial load and to beams with a single longitudinal stringer attached at the center line of the cover sheet. It has been considered worth while to devote considerable space to the discussion of these elementary cases for the following reasons:

1. The study of these simple cases greatly facilitates the understanding of the fundamental principles. (It is very strongly urged that anyone desiring to use the

proposed method of analysis work, by the trial-and-error method, at least one example each of a panel under axial load and of a beam.)

2. The simple cases afford a very convenient way of experimentally checking the validity of the assumptions made. Strain-gage tests made for this purpose on a tension panel and on a beam are described in this paper.

3. The solutions obtained for beams with a single longitudinal can be used as checks on the degree of approximation attainable with the "constant-stress method" proposed later for analyzing actual wing beams.

An additional reason for the lengthy discussion will only be mentioned in passing. Under certain conditions, a beam with a single longitudinal stringer may give useful approximations of the stresses in a beam with many stringers. Such a simplified substitute beam makes it possible to obtain some rough ideas on the influence of bulkheads, an influence that was neglected in the present discussion.

Two methods are proposed for winglike structures. One method is the construction of a mechanical analyzer permitting a solution that is "exact" within the assumptions made. The other method is based on the assumption that the structure is so dimensioned as to approach the ideal design of constant flange stress along the span. For this ideal case, the analytical solution can be obtained. The actual case will have deviations from the ideal case, which are termed "faults." These faults are minimized as much as possible by applying corrections, and the stresses caused by the corrections are superposed on the stresses of the ideal case.

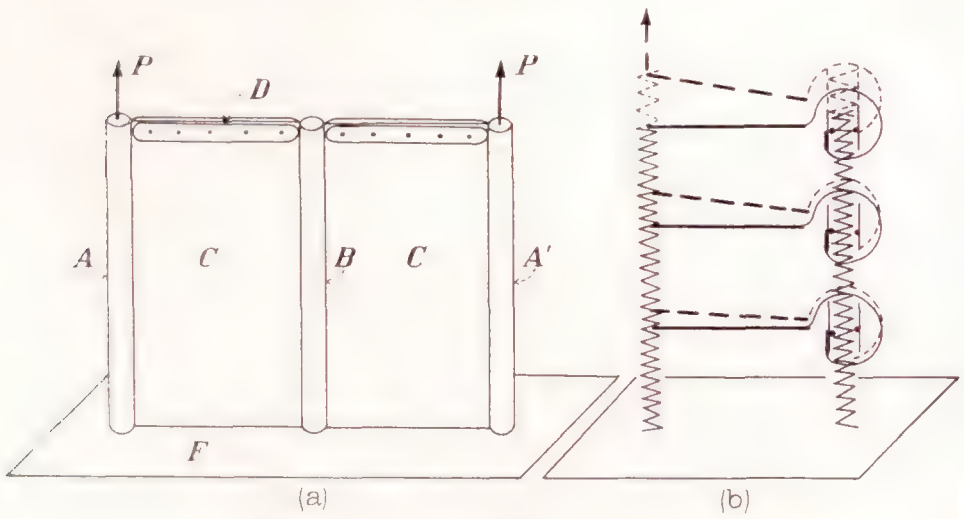

(a) Axially loaded panel subjected to shear deformation.
(b) Mechanical model.

FIGURE 1.—Three-stringer panel.

SYMMETRICAL THREE-STRINGER PANEL UNDER AXIAL LOAD

FUNDAMENTAL CONSIDERATIONS

The simplest possible structure in which shear deformation must be taken into account is shown in figure 1 (a). Two stringers, A and A', of equal section, are connected to an intermediate stringer B by means of a thin sheet C. The upper edge of this sheet is reinforced by bars D. The stringers and the sheet are attached to a foundation F.

The important phases of the elastic action of this structure may be visualized with the help of the mechanical model sketched in figure 1 (b). This model represents one-half the structure, which is permissible because the structure is symmetrical. Helical springs represent the stringers A and B and their elastic resistance to longitudinal deformation. Coil springs represent the elastic resistance of the sheet to shear deformation. It is assumed that the stringers carry only longitudinal stresses and that the sheet carries only shear stresses. For the mechanical model it is assumed that guides prevent any deflection of the springs other than that for which they are designed.

The stresses resulting from the load P are shown qualitatively in figure 2. At the top of stringer A the

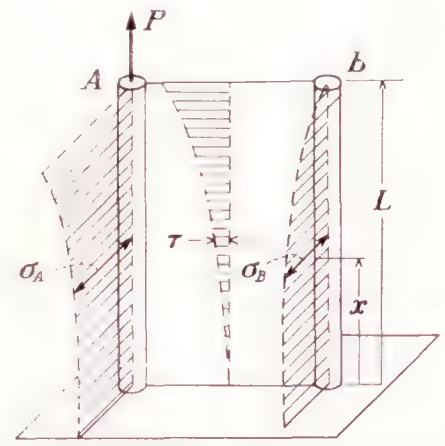

FIGURE 2.—Notation for axially loaded panels.

stress is $\sigma_A = P/A_A$, at the top of stringer B it is $\sigma_B = 0$. The shear stresses τ acting on the sheet gradually take the load out of stringer A and transfer it to stringer B. If the panel has sufficient length and if the sheet has sufficient shear stiffness, the stresses σ_A and σ_B will be very nearly equal at the root.

EQUATIONS OF THE PROBLEM

The equations governing the problem under the simplifying assumptions can be very easily set up. Figure 3 shows a strip of length dx cut from the panel

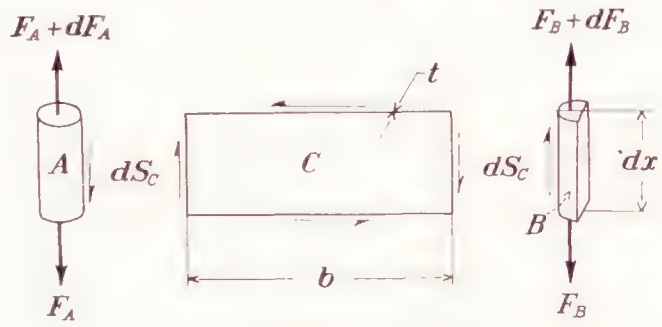

FIGURE 3.—Element of panel.

and separated into its component parts. The equation of equilibrium gives

$$dF_A = dS_C = -dF_B \tag{1}$$

(See list of symbols, appendix A.)

It should be noted that these equations are written for the structure as shown in figures 1 (b), 2, and 3, which is one-half the original structure in figure 1 (a), so that A_B is one-half the area of stringer B as shown in figure 1 (a). The sign convention used throughout this paper is that tensile forces and stresses are positive and

that shear forces and stresses in the sheet are positive when caused by positive stresses in the loaded stringer A (or in the flange F in the case of beams).

The elastic deformation of the structure is shown in figure 4. Two corresponding points 1 and 2 are displaced to new positions 1′ and 2′. The total displacements are given by

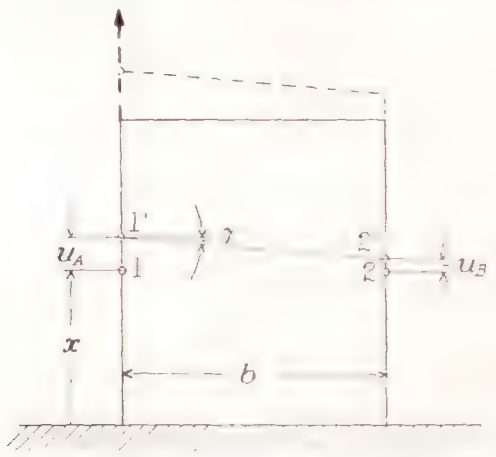

FIGURE 4.—Elastic deformation of panel.

$$u_A=\int^x \frac{\sigma_A}{E}dx \text{ and } u_B=\int^x \frac{\sigma_B}{E}dx$$

The shear strain is given by

$$\gamma=\frac{u_A-u_B}{b}$$

and since

$$\gamma=\frac{\tau}{G_e}$$

where G_e is the effective shear modulus, these relations may be combined into

$$\frac{\tau bE}{G_e}=\int_0^x \sigma_A dx-\int_0^x \sigma_B dx$$

The last equation may be written

$$d\tau=\frac{G_e}{Eb}(\sigma_A-\sigma_B)dx \qquad (2)$$

Equations (1) and (2) may be combined into a differential equation (see appendix B) which, together with the boundary conditions, defines the problem completely. If there are more stringers, a system of simultaneous differential equations results.

SOLUTION OF THE EQUATIONS

For the fundamental case of a symmetrical three-stringer panel of constant cross section, the analytical solutions are given in appendix B for two cases: The panel attached to a rigid foundation and loaded at the free end, and the panel free in space strained by displacing the ends of the stringers a known amount. Combining the two solutions makes it possible to calculate loaded panels attached to an elastically yielding foundation.

For the analysis of three-stringer panels in which the stringer areas and the shear stiffness of the sheet vary along the axis, a trial-and-error method has been found feasible.

The recommended procedure for the trial-and-error method is as follows:

Divide the length L of the specimen into a suitable number of bays. Tabulate the average values of t, A_A, and A_B for each bay.

Assume values for the increment of shear ΔS_C in each bay. According to equation (1)

$$\Delta F_A=-\Delta F_B=\Delta S_C$$

With the assumed values of ΔF_A and ΔF_B and the known values $F_A=P$ and $F_B=0$ at the end of the panel, calculate for all stations along the length of the panel the forces in the stringers and then the stresses in the stringers. From these values calculate the shear stresses and the shear forces in the sheet. The method of tabulation is shown in table I. In this example, the values of A_A, A_B, and t are constant and need not be tabulated.

The calculated values of ΔS_C will not, in general, agree with the originally assumed values. Change the assumed values and repeat the entire process until a satisfactory agreement is reached between the assumed values of ΔS_C and the calculated ones.

In the choice of the first set of values for ΔS_C, the analyst must be guided by previous experience. The only condition known at the outset is

$$S_C<\frac{P A_B}{A_A+A_B}$$

because this is the maximum possible force that would be transmitted to stringer B only if the shear deformation were reduced to zero.

The most difficult step, and the one upon which the success of the method hinges, is to compare the calculated ΔS_C curve with the assumed one and, on the basis of this comparison, to derive a new curve modified in such a way that the repetition of the entire calculation will yield a calculated ΔS_C curve that agrees with the assumed one. No general rule can be given concerning the method beyond stating that decreasing the assumed ΔS_C values at any point will raise the calculated ones and vice versa. Some practice is necessary to develop the skill required for this step. Five trials should be sufficient, in general, to obtain an agreement to 1 or 2 percent for five or six bays unless the variations of areas are extreme.

It should be emphasized that the method is a trial-and-error one and not a method of successive approximation, i. e., the calculated ΔS_C curve cannot be used as the assumed curve for the next cycle.

EFFECTIVE SHEAR STIFFNESS AND EFFECTIVE STRINGER AREAS

Two quantities must be determined before an analysis can be started—the effective shear stiffnesses and the effective stringer areas.

The shear stiffness of a flat sheet is equal to the shear modulus G of the material. If the sheet buckles into a diagonal-tension field and the edge members are rigid, the shear stiffness is the theoretical shear stiffness of a diagonal-tension field $G_e=\frac{5}{8}G$ (for duralumin or steel).

The condition of a pure diagonal-tension field is not reached, however, until the buckling shear stress has been considerably exceeded. Consequently, values intermediate between G and $\frac{5}{8}G$ will occur at stresses not too greatly in excess of the buckling stress (i. e., 3 to 5 times), provided that the edge members are sufficiently stiff. If the edge members are not sufficiently stiff or well braced to take the transverse component of the diagonal tension and particularly if the sheet carries edge compression in addition to shear, the shear stiffness may drop to very low values. Values as low as $G_e = 0.1G$ have been reported (reference 3); although the numerical accuracy of this particular analysis has been questioned, it serves at least as a useful indication of what may be expected, remembering that this test was stopped long before reaching the ultimate load. Quantitative information on this subject is scarce. Fortunately, as will be shown later, the shear stiffness need not be very accurately known to obtain reasonable accuracy in the stringer stresses.

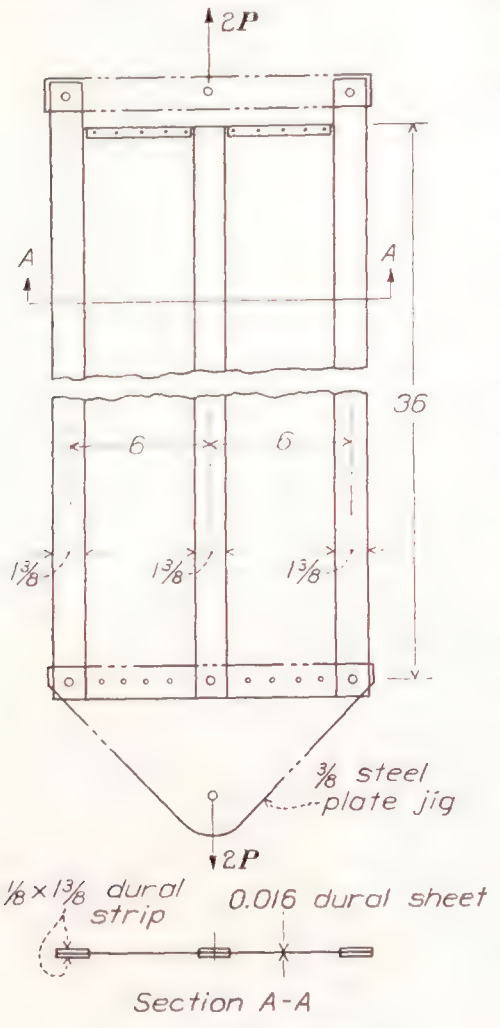

FIGURE 5.—Test panel.

It is clear that the sheet will not only act as a shear member in accordance with the theory but will also assist in carrying longitudinal stresses. The following assumptions have been used:

1. For a sheet carrying tension in addition to shear, it was assumed that the sheet is fully effective in tension; i. e., the sheet up to a line halfway between the stringers is added to the stringer proper when computing the cross-sectional area of the stringer. This assumption is obviously somewhat unsafe and should be modified when the stringer stresses are high.

2. For a sheet carrying compression in addition to the shear, von Kármán's formula for effective width was used in the form

$$2w = 1.9\sqrt{\frac{E}{\sigma}}t$$

where w is the effective width (on one side of the stringer) and σ the stress in the stringer. This formula is probably always conservative in the range in question.

COMPARISON BETWEEN TEST AND CALCULATED RESULTS

In order to check the validity of the method thus far developed, a test specimen was built to represent a structure corresponding to figure 1 (a). A sketch of the actual test specimen is shown in figure 5. Pin-end steel bars (not shown in the figure) spaced 3 inches apart were used to separate the edge stringers from the central stringer and to take up the transverse component of the diagonal-tension field that developed under load. In each bay between these bars, the strains in the stringers were measured with 2-inch Tuckerman strain gages on both sides of the specimen. This precaution proved necessary because the stresses on the two sides differed so much at some stations that readings on only one side would have been almost useless.

The load was increased from zero to the maximum of 4,800 pounds in five steps. With a very few minor exceptions, the points for any one gage fell on straight lines. For each station, the results obtained on the front and the back of the specimen were averaged and the average values are plotted in figure 6.

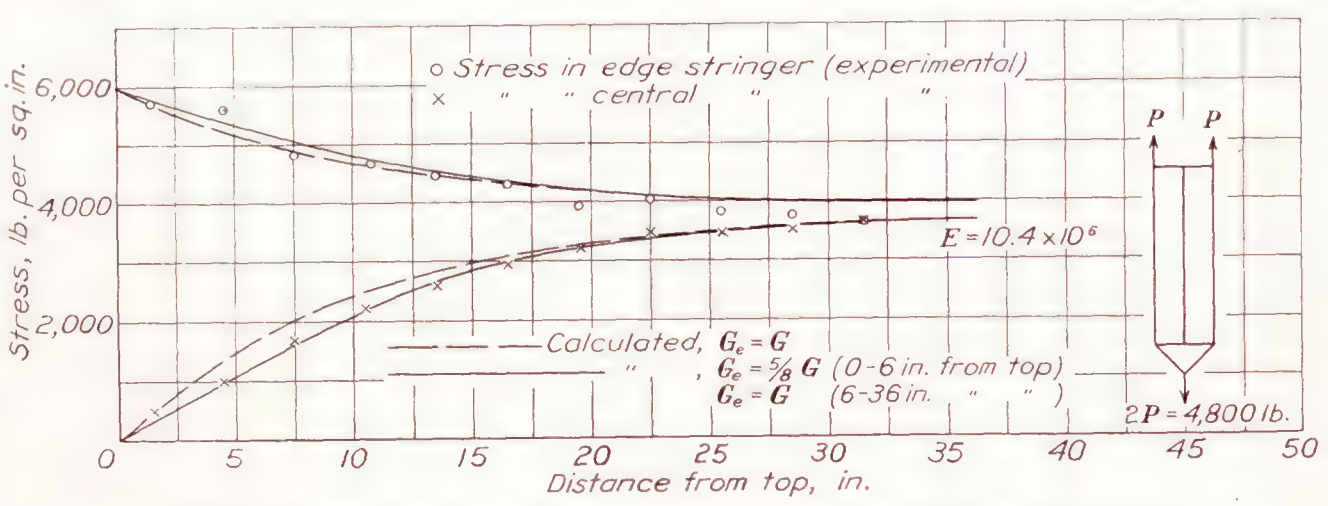

FIGURE 6.—Comparisons between calculated and experimental results for tension test panel.

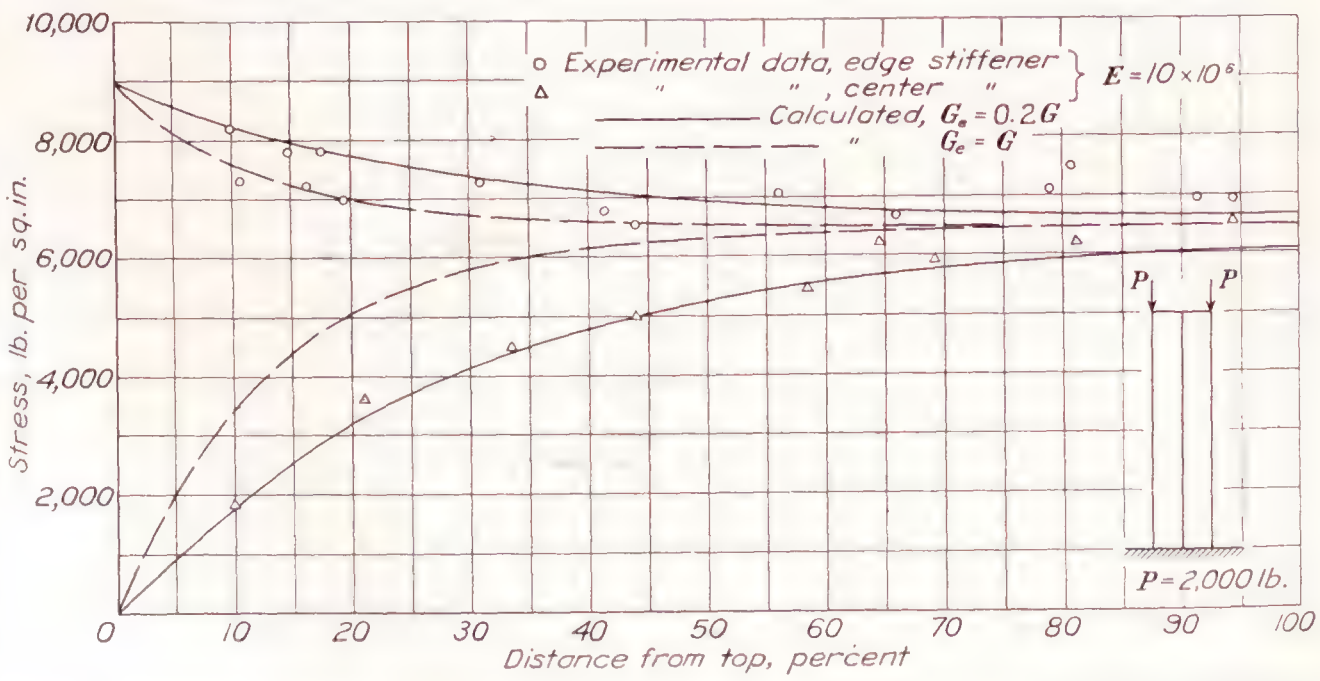

FIGURE 7.—Comparison between calculated and experimental results for compression test panel. (Data from reference 2.)

The calculations were made for the two different assumptions of the shear stiffness indicated on the figure. The second assumption of $G_e=\frac{5}{8}G$ in the top part was based on the experimentally observed fact that one well-developed diagonal-tension fold showed in the top of the panel on each side, in agreement with the calculation showing that at the maximum load the shear stress in this region was about six times the buckling stress.

The second assumption gives perfect agreement between calculated and test results for the stress in the central stringer. The agreement is not quite so good on the edge stringer, the discrepancy occurring chiefly at the root. Several explanations of the discrepancy may be offered. An error of several percent may be caused by an error in the value of E assumed to convert strain readings to stress readings. The simple theory used may break down to some extent near the root and, finally, jig deflection may cause errors. The steel triangle used on the lower end is not a rigid foundation, and a slight elastic deformation of this steel triangle under the edge stringers would relieve the edge stringers of some load and throw it into the sheet and possibly into the central stringer. A deformation of about 0.0003 inch would be sufficient to make the calculated stringer stresses equal at the jig end. Undoubtedly the assumptions of effective areas, effective shear stiffness, and jig deflection could be varied within their possible limits to give a much better agreement with the experimental points.

A similar analysis was made for the panel tested in compression as described in reference 2. The results are shown in figure 7. It will be noted that fair agreement with the experimental points is obtained by assuming that the effective shear stiffness is only 0.2 the shear modulus, in marked contrast to the tension panel. The curves calculated with $G_e=G$ are also given to show the extent to which possible variations in G_e affect the stringer stresses.

BEAMS WITH ONE LONGITUDINAL

BEAM OF CONSTANT DEPTH

The simplest case of a beam subjected to shear deformation of the flange is shown in figure 8. For simplicity of the sketch the flange material on the side not under consideration is assumed to be concentrated at the shear web. This assumption does not influence the analysis when the cover is flat.

For convenience of discussion, the material concentrated at the top of the shear web will be referred to as the "flange" throughout this paper, while the stringer attached to the cover sheet will be referred to as the "longitudinal."

It is again assumed that the longitudinal is cut along the line of symmetry (fig. 8 (b)). The force acting on this halved longitudinal is denoted by F_L, the force on the (tension) flange by F_F. The shear force in the web

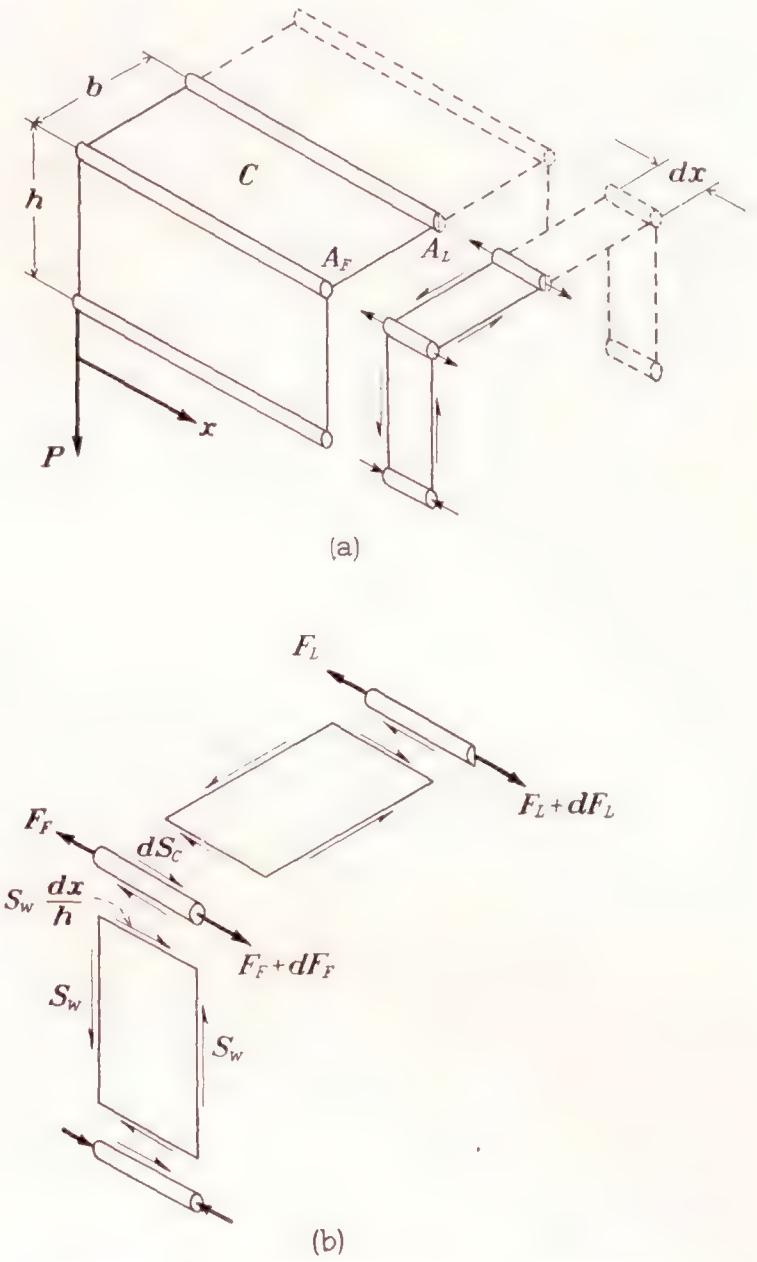

FIGURE 8.—Beam with flat cover and one longitudinal.

is denoted by S_W; the shear force in the cover sheet, by S_C.

The governing equations are

$$dF_F=S_W\frac{dx}{h}-dS_C \tag{3a}$$

$$-dF_L=dS_C \tag{3b}$$

$$d\tau=-\frac{G_e}{Eb}(\sigma_F-\sigma_L)\,dx \tag{3c}$$

with the auxiliary equations

$$\sigma_F=\frac{F_F}{A_F};\ \sigma_L=\frac{F_L}{A_L};\ S_W=P;\ dS_C=\tau t dx$$

The solution of the resulting differential equation is given in appendix B, Case 3 (*a*).

COMPARISON BETWEEN TEST AND CALCULATED RESULTS

The test panel that had been used in the previously described tension test was slightly modified and attached to two duralumin I-beams to form an open

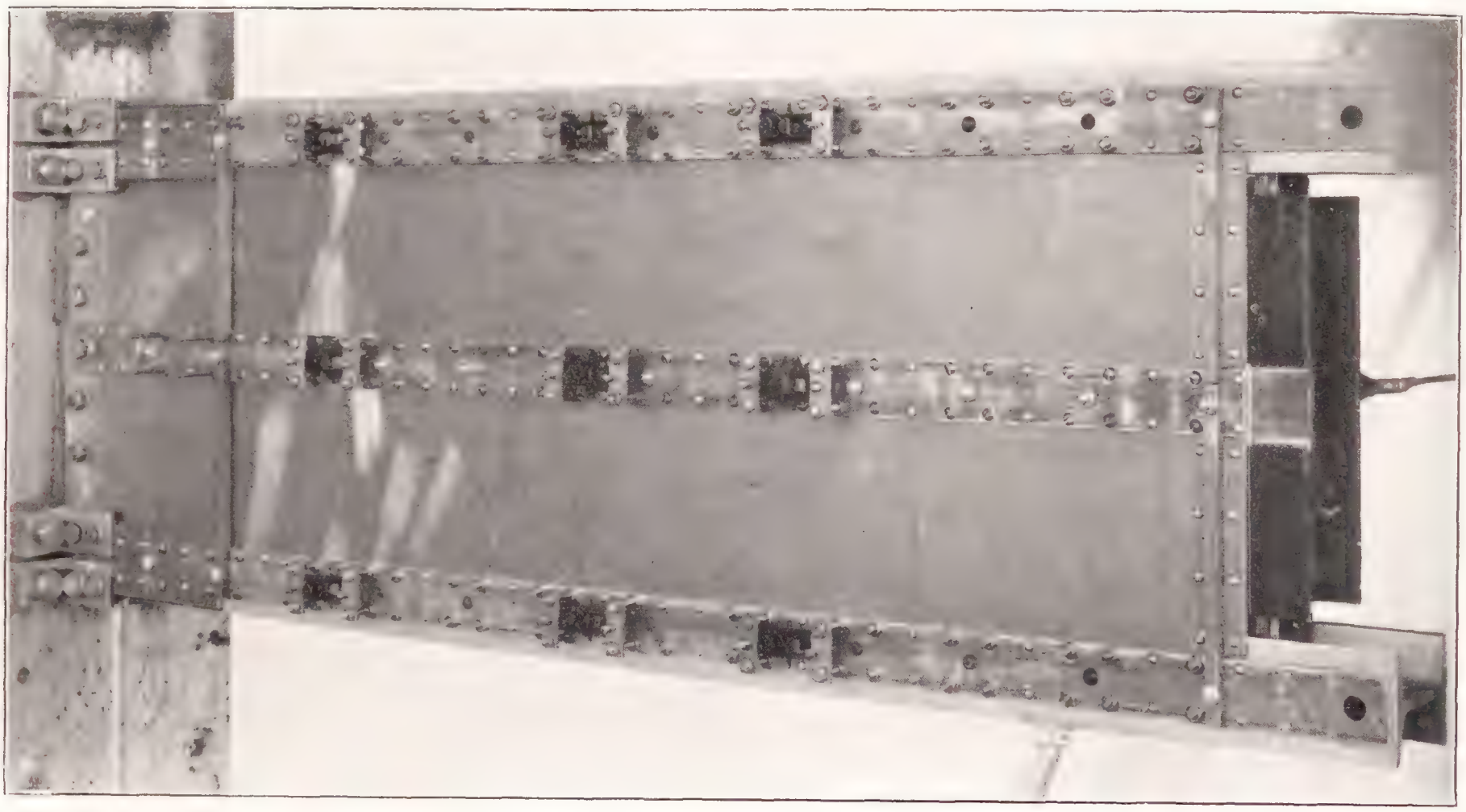

(a) Closed side.

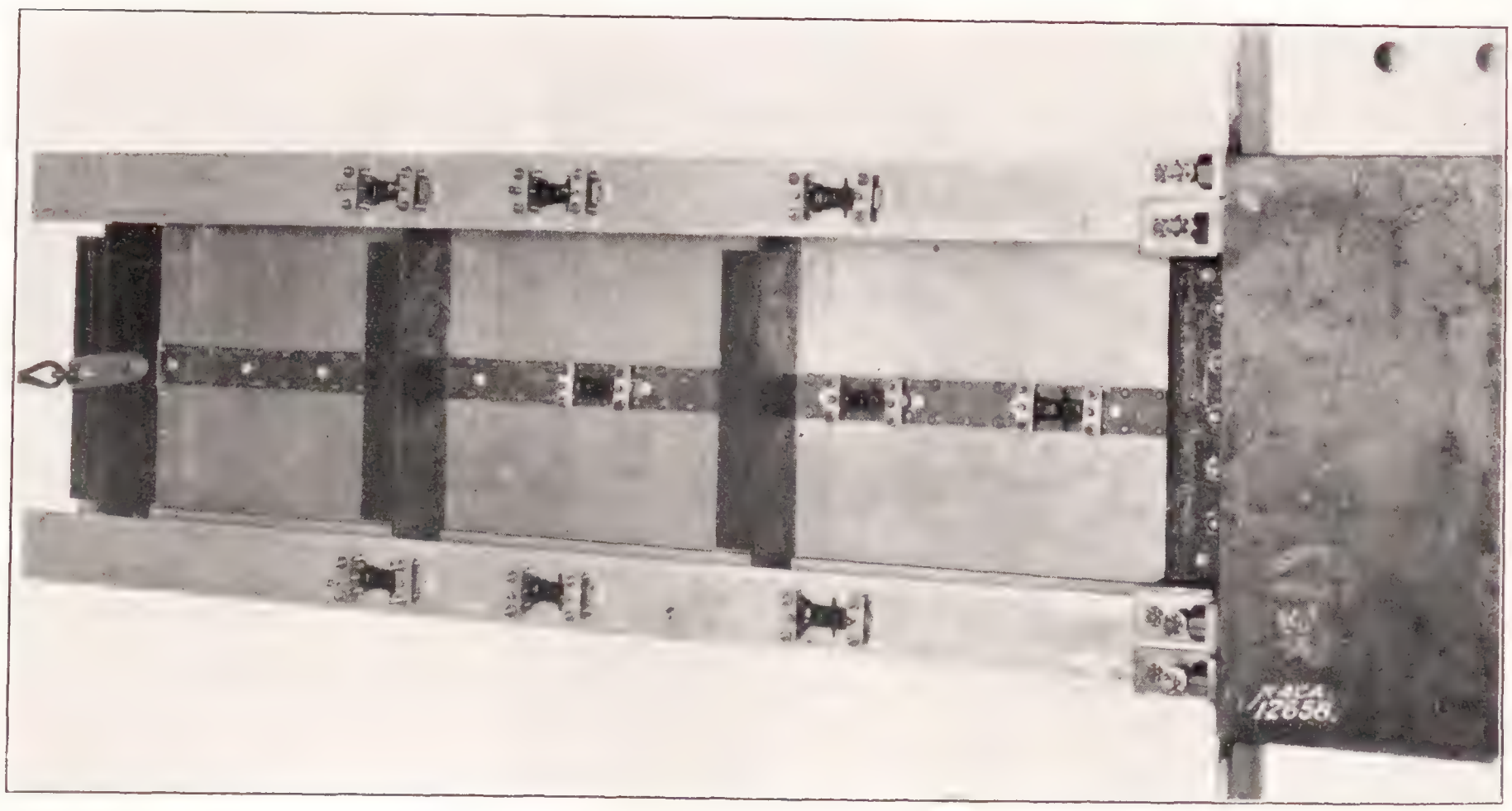

(b) Open side.

FIGURE 9.—View of test beam, showing strain gages.

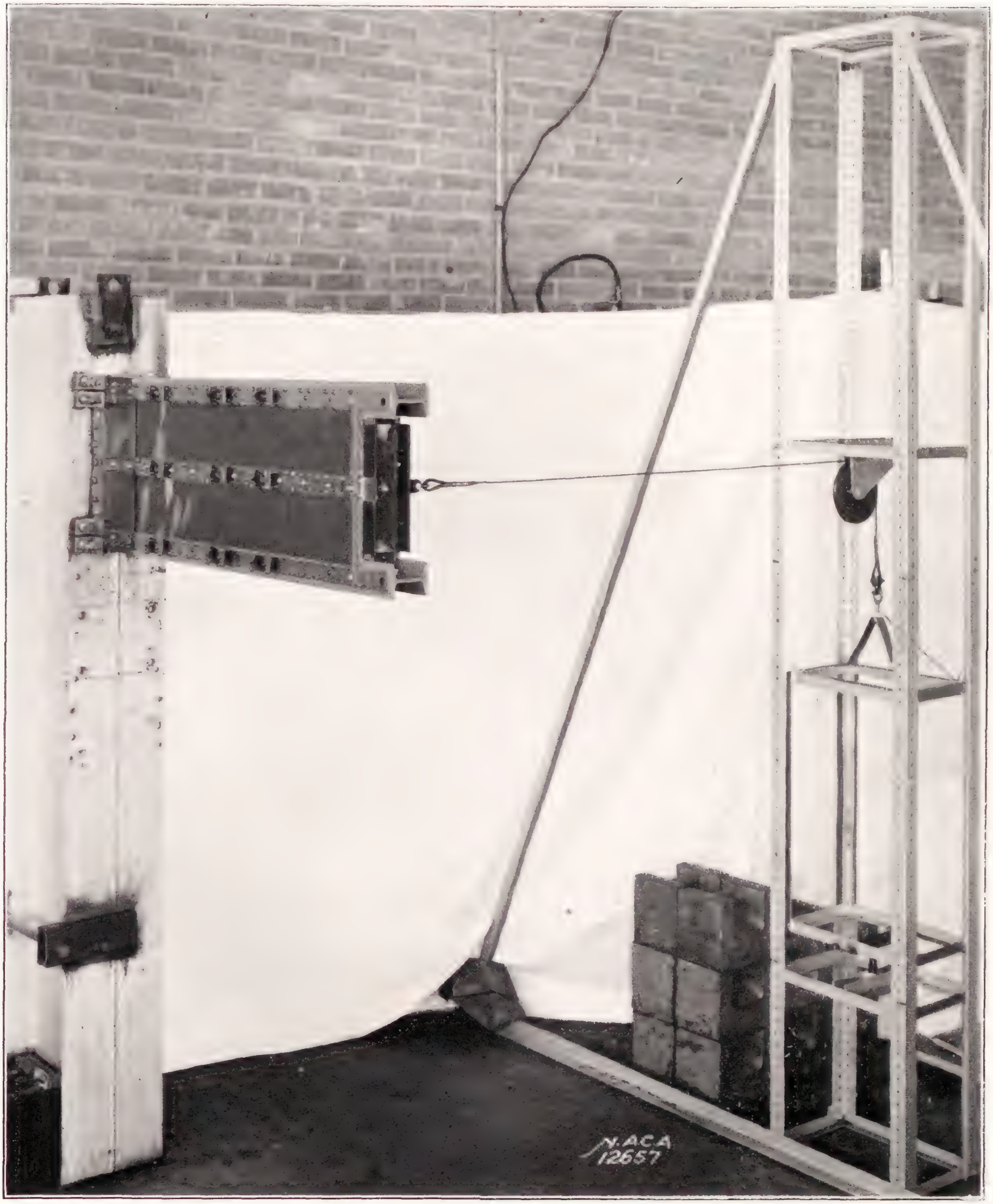

FIGURE 10.—Set-up for testing beams.

box beam. Figure 9 shows photographs of the beam with the strain gages in place for a test run; figure 10 shows the test set-up. The cross section of this beam is shown in figure 11.

It should be noted that the cover sheet and the longitudinal were not attached to the bulkheads except at the root. The flange material of the I-beams (including the cover strips riveted to them and the sheet material effective in tension) was replaced, for the purpose of analysis, by equivalent concentrated flanges with a centroidal distance of 2.80 inches (effective depth h of beam, fig. 8 (a)). The calculated stresses are therefore valid for the flange centroids. For comparison with the measured stresses, the calculated flange stresses were corrected to the outside fiber stresses

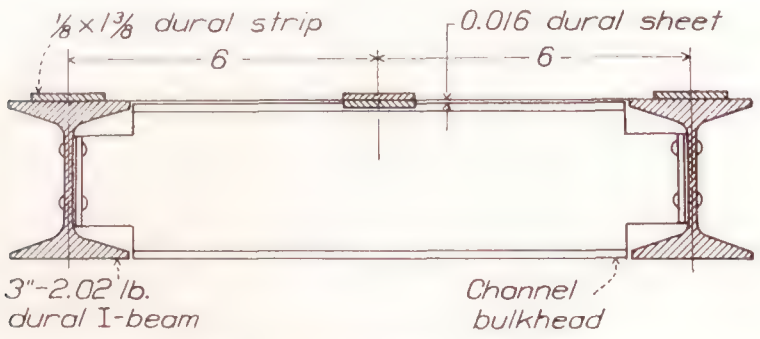

FIGURE 11.—Cross section of test beam.

under the assumption that plane cross sections remain plane for the I-beams with cover strips.

Figure 12 shows the experimental points, the curves calculated for three different assumptions of the shear stiffness, and the stresses calculated by the ordinary bending theory. It can be seen that the experimental points group fairly well about the curve for $G_e = \frac{5}{8} G$, particularly when this curve is corrected for an estimated jig deflection by the formula in appendix B, case 2. Close to the root, however, discrepancies are again observed as in the case of the tension panel. The high flange stress at the station nearest the root may perhaps be explained by nonlinear stress distribution in the I-beams caused by the method of attaching them to the jig, which was not designed for this test. The reduction in shear stiffness of the sheet as compared with the stiffness developed by the same sheet in the tension panel can be ascribed to numerous initial buckles present in the beam but not in the tension panel.

Inspection of figure 12 shows that very large variations of shear stiffness have only a relatively small influence on the bending stresses. This result is due to the fact that, even when the shear stiffness increases to infinity, the bending stresses never exceed a finite limiting value. In many actual structures, the shear stiffness provided is sufficiently large to permit the limiting stress to be approached within a few percent. Practically speaking, this fact means that the shear stiffness need not be very accurately known to obtain the necessary accuracy in the bending stresses.

BEAM OF VARIABLE DEPTH

In a beam with variable depth, the only change in the equations is introduced by the fact that the vertical components of the flange forces balance part of the applied shear, so that the shear in the web now becomes

$$S_W = S_a - \frac{M}{h} (\tan \beta + \tan \gamma) \qquad (5)$$

where β and γ are the angles of inclination of the tension flange and of the compression flange.

The analytical solution for a special case of a beam with variable depth is given in appendix B as Case 3 (b).

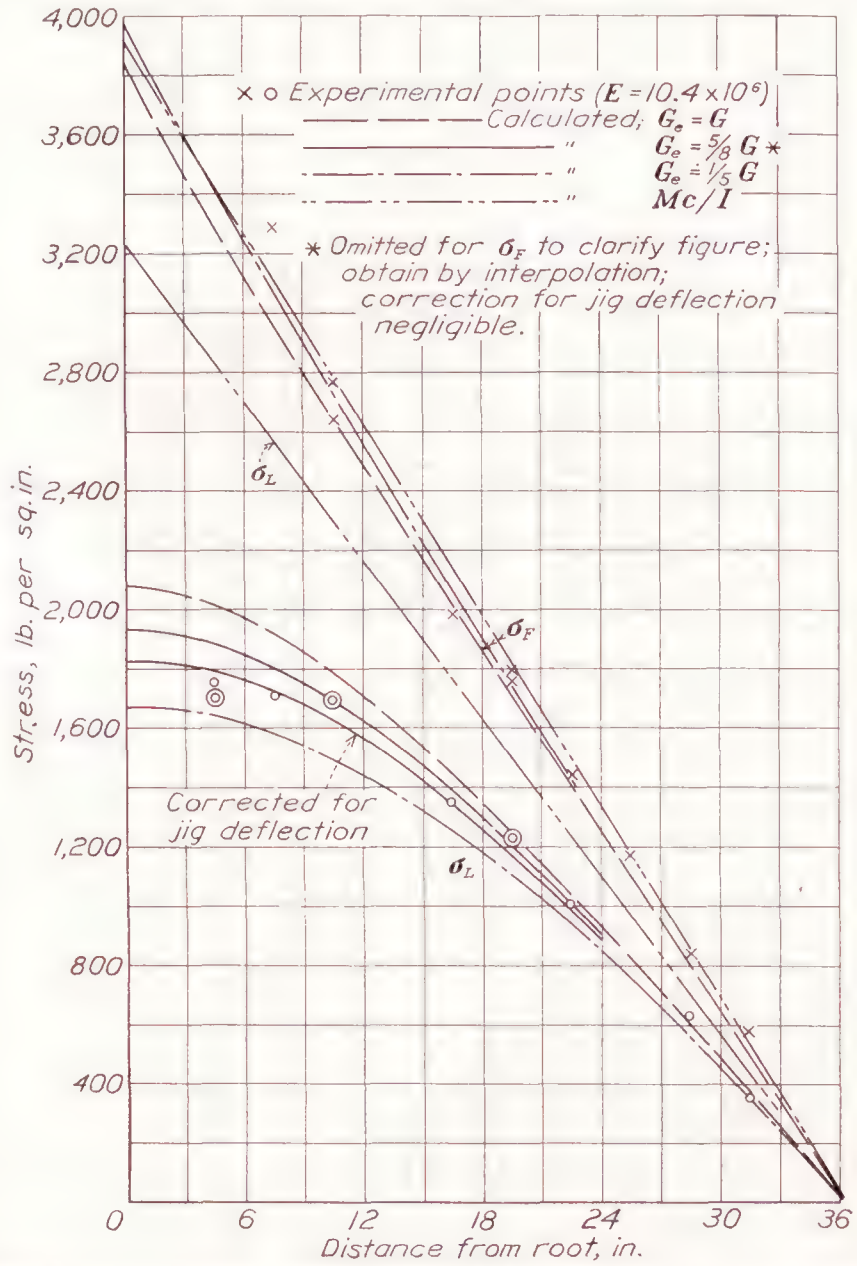

FIGURE 12.—Comparison between calculated and experimental results for test beam.

CONSTANT-STRESS SOLUTION FOR BEAMS WITH ONE LONGITUDINAL

The analytical solutions presented thus far, together with the trial-and-error method, are reasonably adequate for dealing with beams having one longitudinal. There appears to be but slight possibility, however, of extending these solutions to the practical cases of beams with a number of longitudinals. An approximate method will now be developed that can be extended to such beams. The method will first be developed for a beam with a single longitudinal because comparisons can be made with the exact solution to gain some idea of the reliability of the approximate method.

The approximate method is based on the following reasoning. It is the aim of the designer to dimension the structure so that the stress in it is uniform for the given loading. For several reasons this ideal is never reached, but there is usually an effort made to taper the dimensions so as to approach the dimensions of the ideal design. Now the solution for constant stress along the span can be very easily obtained. It is possible, therefore, to consider the actual condition as a superposition upon the ideal case, which can be calculated exactly, of some additional disturbing cases or "faults." These faults can be calculated only approximately, but if they are of minor importance compared with the ideal case, the resulting error of the total solution will be small.

The detailed development of the method is as follows: The fundamental equation

$$d\tau=\frac{G_e}{Eb}(\sigma_F-\sigma_L)dx \tag{6}$$

can be integrated once, if σ_F and σ_L are constant as assumed, to give

$$\tau_x=\frac{(\sigma_F-\sigma_L)}{Eb}\int_0^x G_e dx=\frac{(\sigma_F-\sigma_L)x\overline{G}_x}{Eb} \tag{7}$$

where $\overline{G}_x$ is the shear stiffness averaged over the distance $x=0$ to $x=x$, and the x origin is taken at the root. Integrated again to give the total shear force in the cover sheet

$$S_C=\int_0^L \tau_x t dx=K_1(\sigma_F-\sigma_L) \tag{8}$$

For example, if G_e and t are constant along the span,

$$K_1=\frac{G_e t L^2}{2Eb}$$

Equation (8) furnishes one relation between σ_F and σ_L. One more relation is needed to complete the solution. There are infinitely many conditions from which to choose this relation. At any station along the span, the internal bending moment should equal the external bending moment. The root section has been chosen because in a number of trials it always proved, by far, to be the best choice. Equating the internal and external moment (applied at the root) gives the relation

$$(\sigma_F A_{F_0}+\sigma_L A_{L_0})h_0=M_{a_0} \tag{9}$$

Now remembering that

$$S_C=\sigma_L A_{L_0}$$

equations (8) and (9) can be solved for the bending stresses

$$\sigma_L=\frac{M_0 K_1}{h_0[A_{F_0}A_{L_0}+K_1(A_{F_0}+A_{L_0})]} \tag{10a}$$

$$\sigma_F=\frac{M_0(A_{L_0}+K_1)}{h_0[A_{F_0}A_{L_0}+K_1(A_{F_0}+A_{L_0})]} \tag{10b}$$

Substituting equations (10a) and (10b) into equation (7) gives

$$\tau=\frac{x\overline{G}_x M_0}{Ebh_0\left[A_{F_0}+K_1\left(1+\frac{A_{F_0}}{A_{L_0}}\right)\right]} \tag{10c}$$

Equations (10a), (10b), and (10c) constitute the "pure constant-stress solution" for a beam with a single longitudinal.

The internal bending moment at any station along the span can now be calculated

$$M_{int}=(\sigma_F A_F+\sigma_L A_L)h$$

and, in general, this internal moment will not be equal to the applied moment M_a. This difference constitutes the first fault of the constant-stress solution and will be called the "moment fault."

In order to remove this fault, additional (corrective) bending moments must be added, which are at any station

$$M'=M_a-M_{int}$$

the prime denoting corrective moments. The stresses caused by these corrective moments must be computed and added to the stresses of the pure constant-stress solution.

The method of computing the stresses caused by the corrective moments will be approximate and arbitrary as thus far no exact solutions of this problem have been found. The following method was chosen because the underlying assumption is the most obvious one and because the method is very convenient, eliminating the necessity of computing the internal moments, the corrective moments, and the corrective stresses separately.

From equations (10a) and (10b) it follows that the ratio

$$\left(\frac{\sigma_F}{\sigma_L}\right)_0=r_0=\left(1+\frac{A_{L_0}}{K_1}\right) \tag{11}$$

The assumption is now made that this ratio remains constant ($r=r_0$) along the span and that it holds not only for the stresses caused by the "ideal" moments but also for the stresses caused by the corrective moments. Under this assumption, the direct stresses at any station are given by

$$\sigma_F=\frac{M_a}{hA_F\left(1+\frac{A_L}{rA_F}\right)} \tag{12a}$$

$$\sigma_L=\frac{M_a}{hA_L\left(1+\frac{rA_F}{A_L}\right)} \tag{12b}$$

From these stresses the shear stresses are obtained by using the fundamental relation (2) and integrating from the root toward the tip

$$\tau=\int_0^x \frac{G_e}{Eb}(\sigma_F-\sigma_L)dx \tag{12c}$$

The moment fault has now been removed; that is, the internal moments equal the applied moments when the stresses as given by equations (12a) and (12b) exist in

the flange and in the longitudinal. But equation (12c) follows directly from equations (12a) and (12b) and the stresses given by (12a) and (12c) will not, in general, fulfill the fundamental equation (3a) of equilibrium of the flange element. Equation (3a) requires that, for

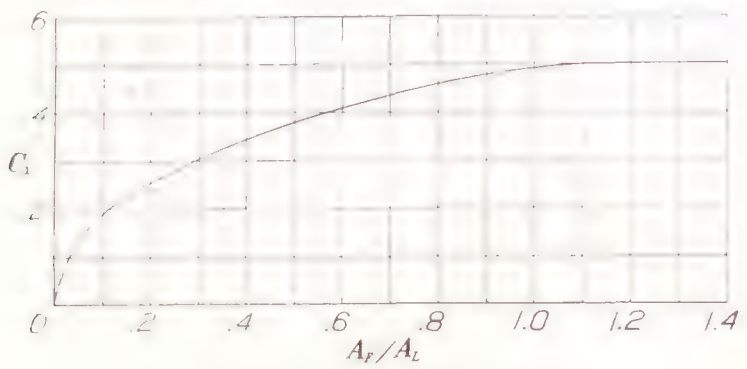

FIGURE 13.—Correction factor, C_1.

equilibrium of the flange element, the increment of shear force in the cover should be

$$\Delta S_{CS}=\frac{S_W}{h}\Delta x-\Delta F_F \tag{13}$$

where the additional subscript S denotes the increment required for static equilibrium. The increment of shear force actually developed is

$$\Delta S_{CE}=\tau t\Delta x \tag{14}$$

where the subcript E refers to the fact that this increment is provided by the elastic deformations of the flange and the longitudinal. Failure of the shear-force increments given by equations (13) and (14) to be identical constitutes the second fault of the constant-stress solution, the so-called "shear fault."

Static equilibrium for the flange elements would be restored if corrective shear-force increments were introduced equal to the differences of these two sets of shear-force increments

$$\Delta S_C'=\Delta S_{CS}-\Delta S_{CE} \tag{15}$$

where the prime again denotes a correction. The corrective shear force S_C' at any station is obtained by integrating from the tip to the desired station, the force being zero at the tip. The corrections to be added to the stresses would then be given by

$$\sigma_F'=\frac{S_C'}{A_F} \qquad \sigma_L'=\frac{-S_C'}{A_L} \qquad \tau'=\frac{\Delta S_C'}{t\Delta x}$$

(Care must be taken in determining the signs of the corrective stresses. The safest method is to compare their direction with the direction of the stresses given by the pure constant-stress solution.)

Introducing these corrective stresses would restore static equilibrium but would again upset the basic elastic relation given by equation (6). A compromise must therefore be made by using only a fraction C_1 of the correction

$$\sigma_F'=C_1\frac{S_C'}{A_F} \qquad \sigma_L'=-C_1\frac{S_C'}{A_L} \qquad \tau'=C_1\frac{\Delta S_C'}{t\Delta x} \tag{16}$$

These stress corrections are added to the stresses obtained from equations (12a), (12b), and (12c) to obtain the final corrected stresses $\sigma_{F_{corr}}$, $\sigma_{L_{corr}}$, and τ_{corr}.

Values of C_1 may be established by comparing a number of exact solutions with the corresponding constant-stress solutions; an averaged curve is shown in figure 13.

In order to gain some idea of the range of applicability of the constant-stress solution, a series of related beams was calculated. The characteristics of three of these beams are given in table II. The first set of calculations was made by using the analytical solutions given in appendix B for beam A and by using the trial-and-error method for beams B and C. The second set of calculations was made by using the constant-stress solution as described. The results of the calculations are shown in figures 14 to 16.

For beam B, the stresses given by the pure constant-stress solution are also shown. Beam B is a constant-stress beam when analyzed by the ordinary bending theory and has zero moment fault. The complete analysis for this beam is given as an example in appendix C.

It is to be expected that, in general, there will be smaller differences between the constant-stress solution and the exact solution for beams with small moment fault than for beams with large moment fault. This expectation is borne out by the results. Beam B,

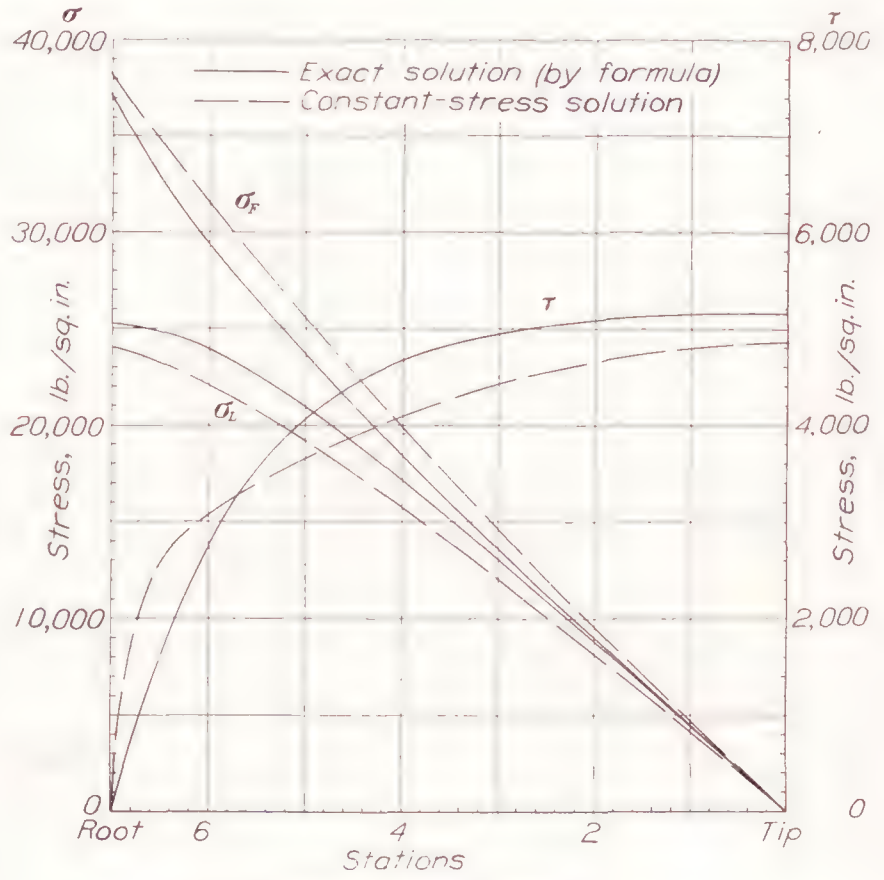

FIGURE 14.—Stresses in beam A.

which comes close to the ideal case, shows smaller differences than beam A, which is further from the ideal case because the areas A_F and A_L are constant along the span. Beam C, which corresponds to an actual case, as far as variation of A_F, A_L, t, and h along

the span is concerned, shows also good agreement for the bending stresses. The agreement is not quite so good for the shear stresses.

Considering all the factors involved, it seems safe to assume that the constant-stress solution will give satisfactory results in practical cases for the maximum stresses, provided that the correction introduced by the shear fault is not larger than about 20 percent of the stress given by the pure constant-stress solution.

BEAMS WITH MANY LONGITUDINALS

YOUNGER'S SOLUTION

Actual wing structures are built as box beams with many longitudinals, and the depth of the beam as well as all cross-sectional areas varies along the span.

The first attempt at obtaining a solution for a multistringer beam was made by Younger (reference 4). He considered the limiting case of infinitely many longitudinals (i. e., a plate cover as shown in fig. 17) and assumed the box to be of constant section; for the distribution of the bending moments he assumed a cosine law.

Younger's solution and its extension to arbitrary moment curves are given in appendix B. It should be noted that this solution does not fulfill the equation of equilibrium for the flange element (the differential

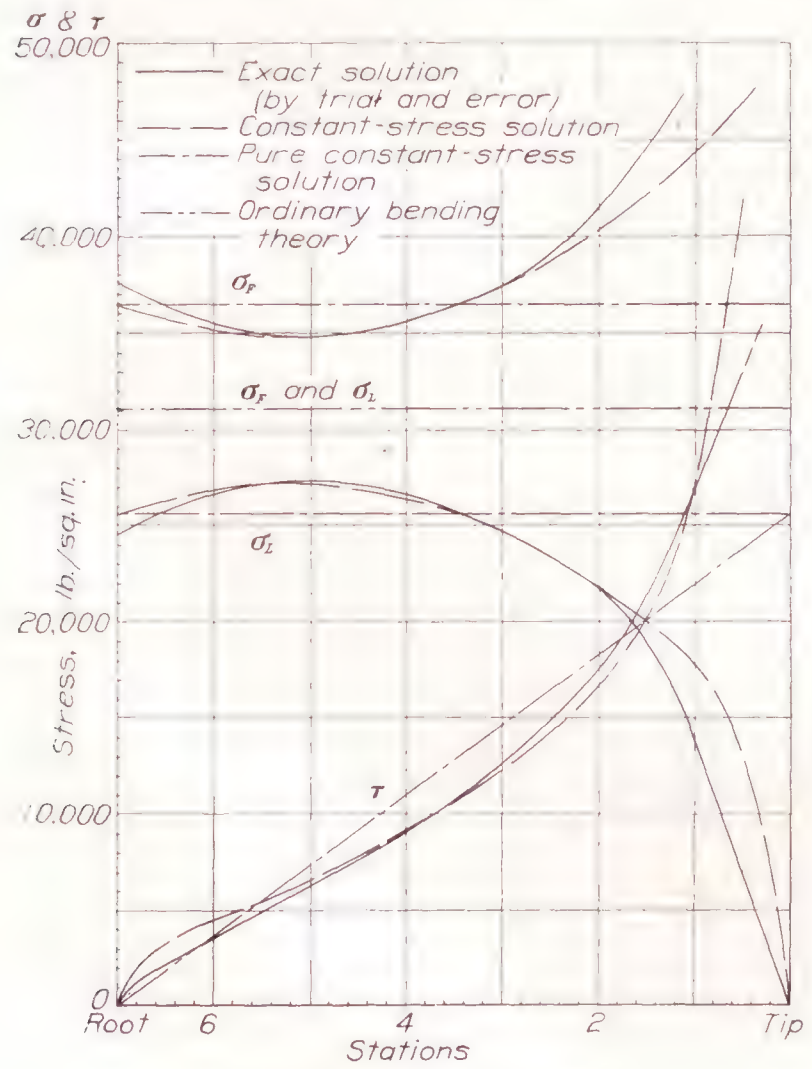

FIGURE 15.—Stresses in beam *B*.

equation does not hold along the flange) so that a shear-fault correction is necessary, as discussed in connection with the constant-stress solution for the beam with a single longitudinal.

CONSTANT-STRESS SOLUTION

The usefulness of Younger's solution is so limited by the assumption of constant cross section along the

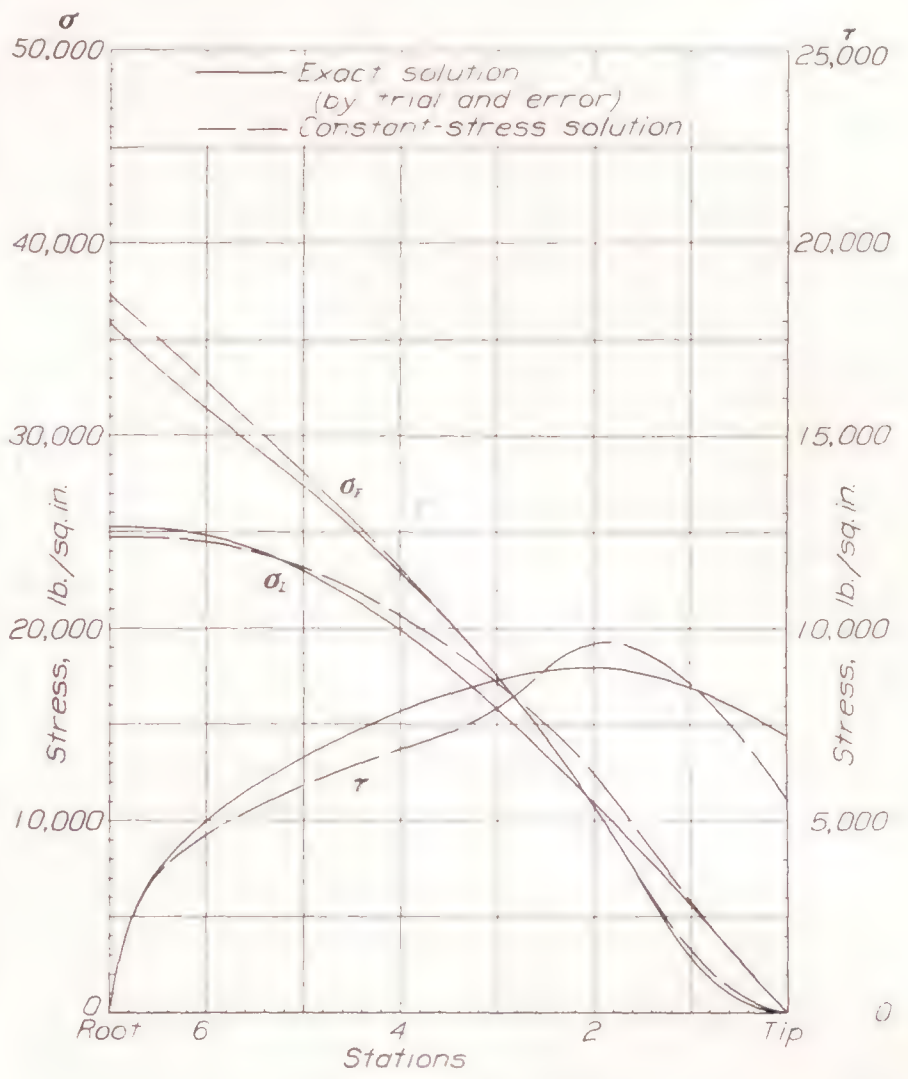

FIGURE 16.—Stresses in beam *C*.

span that a more general method appeared desirable. The constant-stress solution was developed to fill this need of practical stress analysis.

The principles of the constant-stress solution have been discussed in detail for beams with a single longitudinal. The extension of the solution to beams with many longitudinals is given in appendix B. The practical procedure of applying it is essentially identical with the procedure outlined for beams with a single longitudinal. The constant K_2 is computed and used to compute the constant K_3 for the root section, using equation (B–27). The stresses at a number of stations along the span are then obtained by the formula

$$\sigma=\frac{M\cosh K_3 y}{h\left(A_F\cosh K_3 b+\frac{A_L}{K_3 b}\sinh K_3 b\right)} \tag{17}$$

where y varies from $y=0$ for the center line of the beam to $y=b$ for the flange. The shear stress in the cover sheet next to the flange is obtained by integrating from the root outward the expression

$$\left(\frac{d\tau}{dx}\right)_F=\frac{G_e}{E}\sigma_F K_3\tanh K_3 b \tag{18}$$

where σ_F is obtained from equation (17) by setting $y=b$. Equation (18) is obtained from equations (B–20) and (B–25).

The increments of corrective shear force are obtained by using equations (13), (14), and (15). After the integration of (15) in from the tip to obtain the corrective shear force S_C', the correction to the flange stress is calculated by the first expression of (16); the correction to the shear stress is calculated by the last expression of (16).

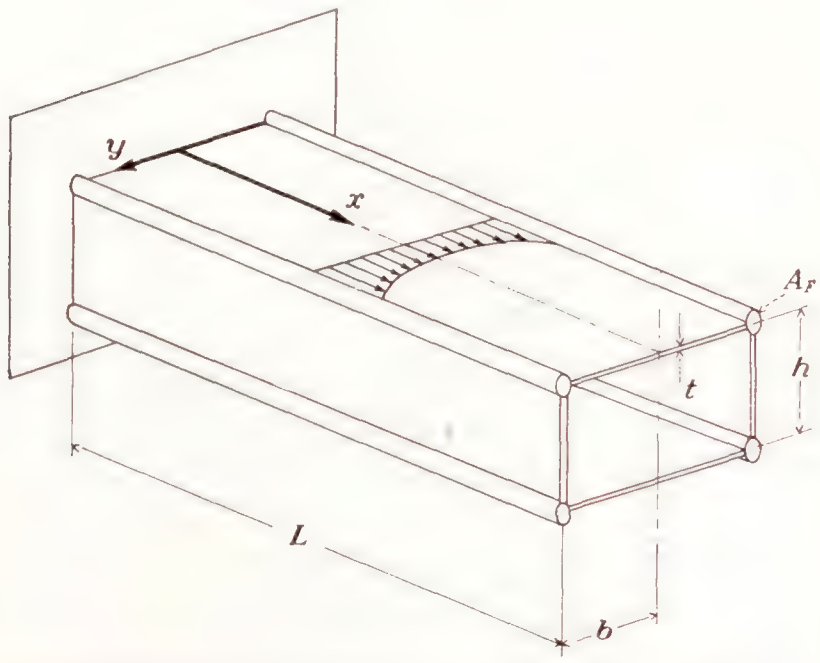

FIGURE 17.—Notation used for beams with orthotropic cover plates.

The calculation of the correction to the stress σ_L is somewhat more complicated because it varies along the chord. The total force on all longitudinals, using equation (17), is given by

$$F_L=\int_0^b \sigma \frac{A_L}{b}dy=\frac{A_L}{K_3 b}\sigma_{CL}\sinh K_3 b \tag{19}$$

where σ_{CL} denotes the stress at the center line of the beam obtained from equation (17) by setting $y=0$. In accordance with (16), only a part of the corrective shear force is applied so that the corrected total force on the longitudinals is

$$F_{L_{corr}}=F_L-C_1 S_C' \tag{20}$$

Assume now that the corrected stresses in the longitudinals are distributed chordwise according to the law

$$\sigma_{corr}=\sigma_{CL_{corr}}\cosh Yy \tag{21}$$

The unknown Y can be found from the equation

$$\frac{\tanh Yb}{Yb}=\frac{F_{L_{corr}}}{A_L\sigma_{F_{corr}}} \tag{22}$$

which is based on the premise that

$$\sigma_{L_{corr}}=\sigma_{F_{corr}}$$

for $y=b$. After Y has been found, the corrected stress at the center line is found from

$$\sigma_{CL_{corr}}=\sigma_{F_{corr}}\operatorname{sech} Yb$$

and equation (21) can then be used to calculate the stresses at intermediate values of y. The right-hand side of equation (22) is the ratio of the average stress in the longitudinals to the stress in the flange. In general, this ratio will be less than unity; however, figure 16 shows that for a beam with a single longitudinal the stress in the longitudinal may be larger than the stress in the flange over a part of the span, and similarly the right-hand side of equation (22) sometimes may exceed unity. In such a case, equations (21) and (22) may be replaced by

$$\sigma_{corr}=\sigma_{CL_{corr}}(2-\cosh Yy) \tag{21a}$$

$$\frac{\left(2-\frac{\sinh Yb}{Yb}\right)}{(2-\cosh Yb)}=\frac{F_{L_{corr}}}{A_L\sigma_{F_{corr}}} \tag{22a}$$

After Y has been found, the corrected stress at the center line is found from

$$\sigma_{CL_{corr}}=\frac{\sigma_{F_{corr}}}{(2-\cosh Yb)}$$

and equation (21a) can then be used to calculate the stresses at intermediate values of y.

The solution of equations (22) and (22a) can be effected by inspection of tables. For practical purposes it should be sufficient to use the curve given on figure 18.

As examples, beams A and B were analyzed under the assumption that longitudinals with the total cross-sectional area A_L are distributed uniformly along the chord. The results are shown in figures 19 and 20. It will be seen that the stress at the center line of the beam is very low. If all longitudinals are of the same cross section, they must be designed to the stress in the first longitudinal adjacent to the flange. Consequently,

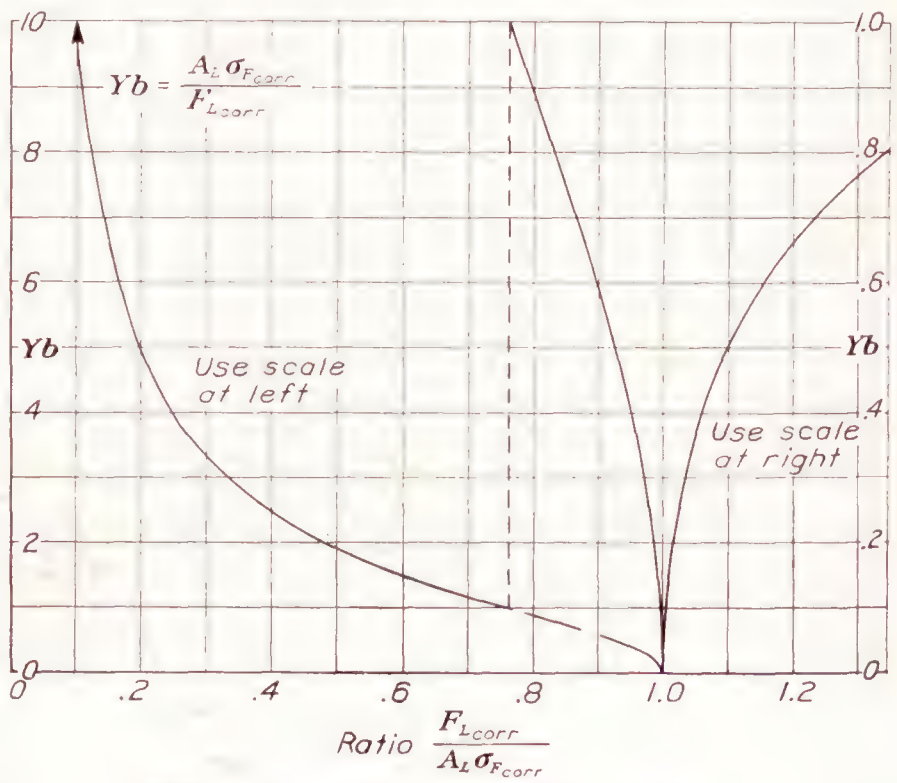

FIGURE 18.—Graph for auxiliary parameter Yb.

the longitudinals near the center line are very ineffectively used. In this connection, attention might be called to the fact that the longitudinals need not be of the same cross-sectional area along the chord. The

assumption of A_L being uniformly distributed may be fulfilled, for instance, by using longitudinals of large cross-sectional area but widely spaced near the flange and longitudinals of small cross-sectional area but closely spaced near the center line. Although such an arrangement would not increase the over-all structural efficiency, it might under certain conditions offer manufacturing advantages.

MECHANICAL ANALYZER

The constant-stress solution is always approximate. When the moment and shear corrections are large, doubts may arise as to whether the solution is sufficiently accurate. It might be advantageous to construct a mechanical analyzer to deal with such cases. One possibility for such an analyzer would be actually to build units representing the mechanical model sketched in figure 1 (b). The springs might be cantilever springs, so that their stiffnesses could be varied by changing their lengths. Each unit would represent one bay of the trial-and-error method of solution and would have one spring to represent the stringer stiffness and one spring to represent the shear stiffness of the sheet attached to one side of the stiffener.

The chief difficulty in the design of such an analyzer would probably be in reducing the friction between the units and the guides necessary to aline them. A fairly large number of units would be necessary to represent a wing cover, which would mean a fairly expensive instrument. This disadvantage is counterbalanced by

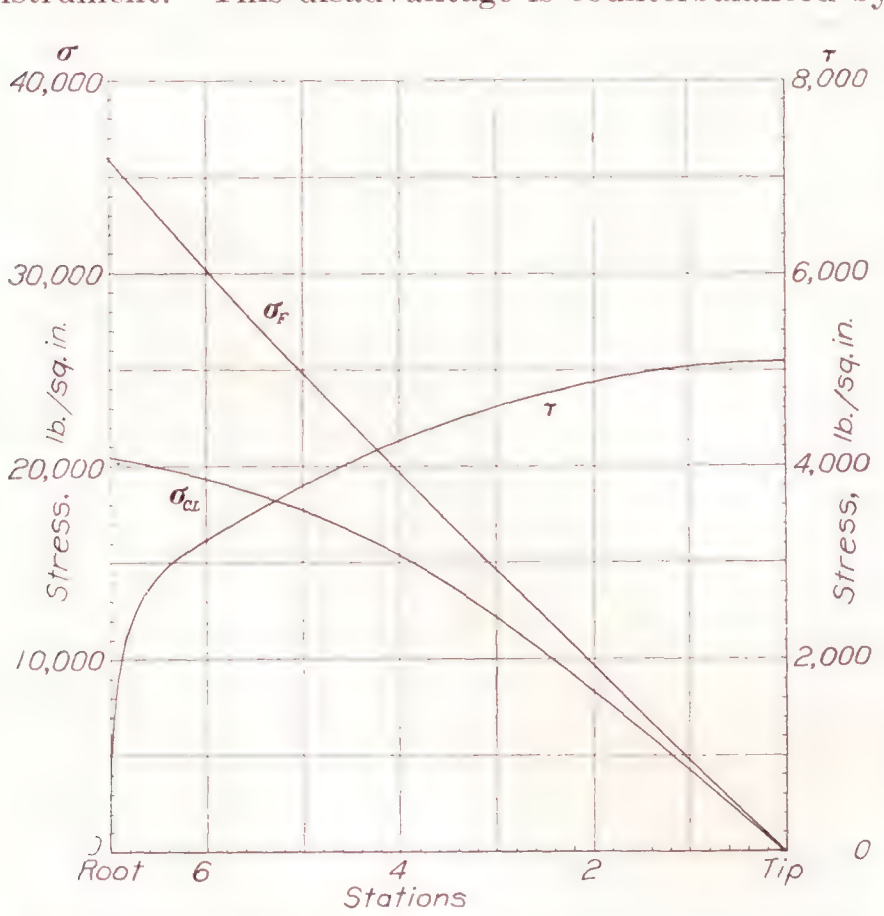

FIGURE 19.—Stresses in beam A with A_L uniformly distributed along chord.

the possibility that the instrument would offer in a comparatively short time quite an exact analysis, including the effects of bulkheads and of yielding supports. The main errors in this solution would be those caused by the finite length of bays.

CONCLUSION

The art of stress-analyzing shell structures is of recent origin, and any methods of analysis proposed must go through a process of trial and development.

Development of the method of shear-deformation analysis is desirable in several directions; e. g., exact

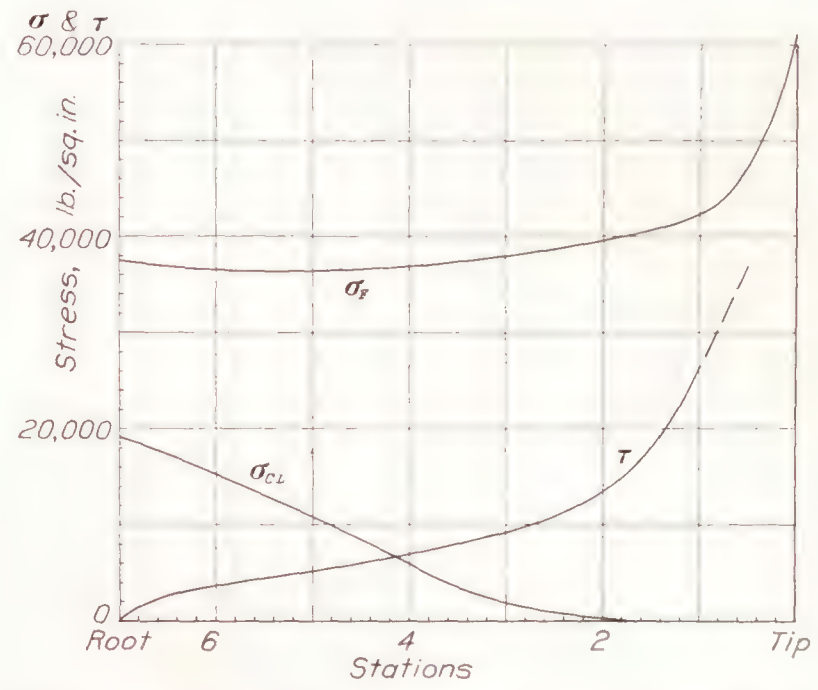

FIGURE 20.—Stresses in beam B with A_L uniformly distributed along chord.

solutions should be found to replace the constant-stress solution and methods should be devised to calculate the influence of bulkheads.

Rough approximate calculations on bulkhead effect can be made by assuming that all the longitudinals are relocated at the center line of the beam. For beams with a single longitudinal, the effect of bulkheads can be calculated. A series of systematic comparisons between the extended solution of Younger and Case 3 (a) of appendix B indicates that for a certain range the single-longitudinal assumption may yield acceptable approximations when used in conjunction with suitable correction factors. The comparisons are not given, however, because they might be misleading in view of the shear fault of Younger's solution. Calculations made thus far indicate that in practical cases the effect of the bulkheads is very small.

It should be emphasized that analyzing shell structures is an art rather than a science. The arithmetic of analyzing highly redundant structures can be reduced to manageable proportions only by making assumptions that will be valid only within a certain range. This fact leads to the unfortunate, but inevitable, conclusion that the analysis of such structures cannot be made entirely by handbook and formula but must be guided by engineering judgment.

LANGLEY MEMORIAL AERONAUTICAL LABORATORY,
NATIONAL ADVISORY COMMITTEE FOR AERONAUTICS,
LANGLEY FIELD, VA., *June 3, 1937.*

APPENDIX A

LIST OF SYMBOLS

A, cross-sectional area (sq. in.).
E, Young's modulus (lb. per sq. in.).
F, internal force (lb.).
G, shear modulus (lb. per sq. in.).
K, constant.
L, length of panel or beam (in.).
M, bending moment (in.-lb.).
P, external load (lb.).
S, shear force (lb.).
b, spacing of stringers (in.). (See figs. 3 and 4.)
b, half width of beam (in.). (See fig. 8.)
c, camber of cover (in.).
h, depth of beam (in.).
t, thickness of cover sheet (in.).
u, displacement of point (in.). (See fig. 4.)
w, running load (lb. per in.).
γ, shear strain.
σ, direct (normal) stress (lb. per sq. in.).
τ, shear stress (lb. per sq. in.).

Subscripts have the following significance:

A, loaded stringer A shown in figures 1, 2, 21, and 22.
B, unloaded stringer B shown in figures 1, 2, 21, and 22.
C, cover sheet.
F, flange of beam.
L, longitudinal of beam.
W, shear web.
a, applied shears and bending moments.
e, effective.
0, root section.
c, compression.
t, tension.
int, internal.
corr, corrected.
S, static equilibrium.
E, elastic equilibrium.
CL, center line.

APPENDIX B

SOLUTIONS OF DIFFERENTIAL EQUATIONS FOR SYMMETRICAL STRUCTURES OF CONSTANT CROSS SECTION

SIGN CONVENTIONS

Forces and stresses in stringers are positive when tensile. Shear forces and stresses in the sheet are positive when caused by positive stresses and strains in the loaded stringer A in the case of axially loaded panels or in the flange F in the case of beams.

CASE 1—THREE-STRINGER PANEL ON RIGID FOUNDATION WITH AXIAL LOAD

The two possible cases shown in figures 21(a) and 21(b) can be mathematically treated by taking one-half the panel, as shown in figure 21(c), which also

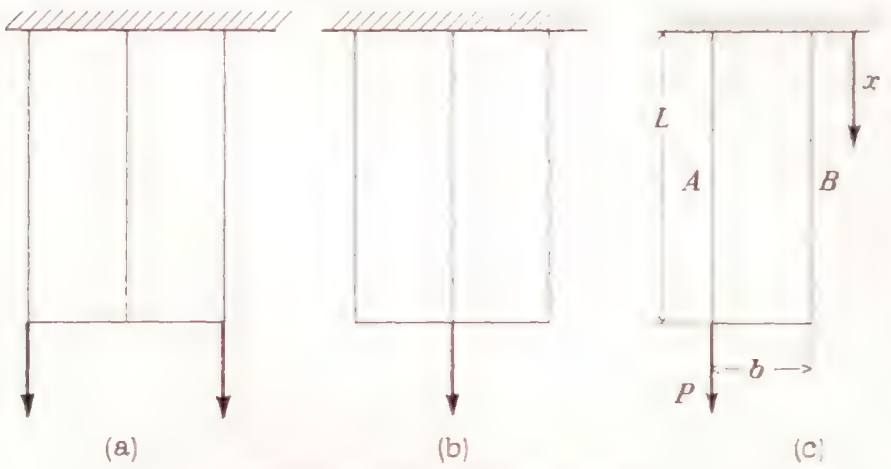

FIGURE 21.—Axially loaded panels.

gives the notation to be used. The derivation of the fundamental equations is given in the main body of this paper. Slightly modified for the purpose of deriving the basic differential equation, these equations are

$$\sigma_A' = \frac{\tau t}{A_A} \text{ and } \sigma_B' = -\frac{\tau t}{A_B} \tag{B–1}$$

$$\tau' = \frac{G_e}{Eb}(\sigma_A - \sigma_B) \tag{B–2}$$

where the primes denote differentiation with respect to x.

Differentiating equation (B–2) again and substituting into the result from equation (B–1),

$$\tau'' - \tau \frac{G_e t}{Eb}\left(\frac{1}{A_A} + \frac{1}{A_B}\right) = 0 \tag{B–3}$$

The boundary conditions are

$$\left.\begin{aligned} &\text{at} \quad x=0\ ,\ \tau=0 \\ &\text{at} \quad x=L\ ,\ \sigma_A=\frac{P}{A_A} \text{ and } \sigma_B=0 \end{aligned}\right\} \tag{B–4}$$

The result is

$$\left.\begin{aligned} \tau &= \frac{P}{A_A}\frac{G_e}{EbK}\frac{\sinh Kx}{\cosh KL} \\ \sigma_B &= \frac{P}{(A_A+A_B)}\left(1-\frac{\cosh Kx}{\cosh KL}\right) \\ \sigma_A &= \frac{P}{A_A}-\frac{A_B}{A_A}\sigma_B \end{aligned}\right\} \tag{B–5}$$

where

$$K^2 = \frac{G_e t}{Eb}\left(\frac{1}{A_A}+\frac{1}{A_B}\right) \tag{B–6}$$

In reference 2 the formula

$$f_b = \frac{2P}{A_7}\left[\frac{\cosh px - \tanh pL \sinh px}{4} - 1\right]$$

where

$$p^2 = \frac{25}{2}\frac{G_e t}{A_7 h E}$$

is given for the special case where the area of the edge stiffener is twice the area of the central stiffener. Taking account of the differences in notation and coordinate systems used, this result agrees with the general formula given under (B–5).

It should be noted that the final formulas (B–5) become invalid when either t or G_e approaches zero because in these cases the equation (B–3) becomes invalid. The solution for such cases is obtained by using the fundamental equations (B–1) and (B–2) directly.

An analogous procedure must be used for Cases 2 and 3.

CASE 2—THREE-STRINGER PANEL STRAINED BY MOTION OF SUPPORTS

The differential equation for the case of figure 22 is

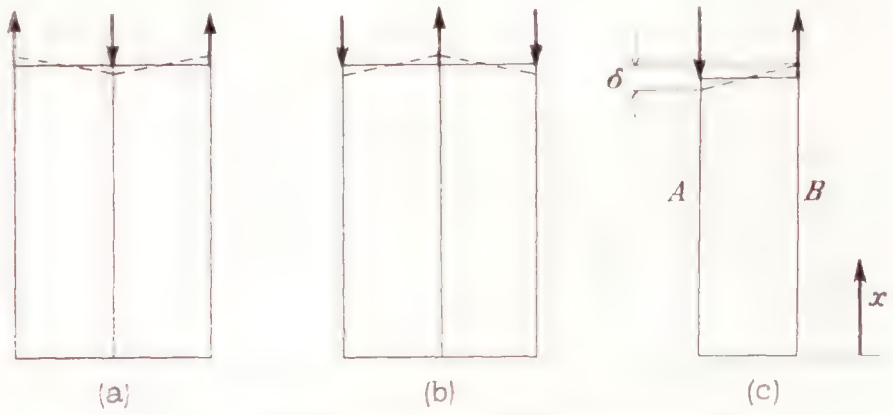

FIGURE 22.—Panels strained by motion of supports.

the same as for Case 1. The boundary conditions are now:

$$\left.\begin{aligned} &\text{at} \quad x=0\ ,\ \sigma_A=0 \text{ and } \sigma_B=0 \\ &\text{at} \quad x=L\ ,\ \tau=\frac{\delta}{b}G_e=\tau_0 \end{aligned}\right\} \tag{B–7}$$

The result is

$$\left.\begin{aligned} \tau &= \tau_0\frac{\cosh Kx}{\cosh KL} \\ \sigma_A &= -\tau_0\frac{t}{KA_A}\frac{\sinh Kx}{\cosh KL} \\ \sigma_B &= \tau_0\frac{t}{KA_B}\frac{\sinh Kx}{\cosh KL} \end{aligned}\right\} \tag{B–8}$$

where K has the same meaning as in (B–6).

CASE 3—CANTILEVER BEAM WITH ONE STRINGER

(*a*) Uniform depth, concentrated load at tip.
(*b*) Depth decreasing lineally to zero, uniformly distributed load.

Figure 8 shows the notation used for both cases. (Note that the x origin is at the tip.) The fundamental equations are for Case 3 (*a*)

$$\left.\begin{aligned} \sigma_F' A_F &= \frac{P}{h} - \tau t \\ \sigma_L' A_L &= \tau t \\ \tau' &= -\frac{G_e}{Eb}(\sigma_F - \sigma_L) \end{aligned}\right\} \quad \text{(B–9)}$$

which gives the differential equation

$$\tau'' - \tau \frac{G_e t}{Eb}\left(\frac{1}{A_F}+\frac{1}{A_L}\right)+\frac{PG_e}{A_F Ebh}=0 \quad \text{(B–10)}$$

The boundary conditions are

$$\left.\begin{aligned} &\text{at} \quad x=0,\ \sigma_F=0, \text{ and } \sigma_L=0 \\ &\text{at} \quad x=L,\ \tau=0 \end{aligned}\right\} \quad \text{(B–11)}$$

The result is

$$\left.\begin{aligned} \tau &= \frac{P}{th\left(1+\frac{A_F}{A_L}\right)}\left(1-\frac{\cosh Kx}{\cosh KL}\right) \\ \sigma_L &= \frac{P}{h(A_L+A_F)}\left(x-\frac{\sinh Kx}{K\cosh KL}\right) \\ \sigma_F &= \frac{1}{A_F}\left(\frac{M_x}{h_x}-\sigma_L A_L\right) \end{aligned}\right\} \quad \text{(B–12)}$$

where K has again the same meaning as in (B–6) with A_F and A_L substituted for A_A and A_B.

In Case 3 (*b*), $wL/2$ is substituted for P; h in this case is the depth at the root.

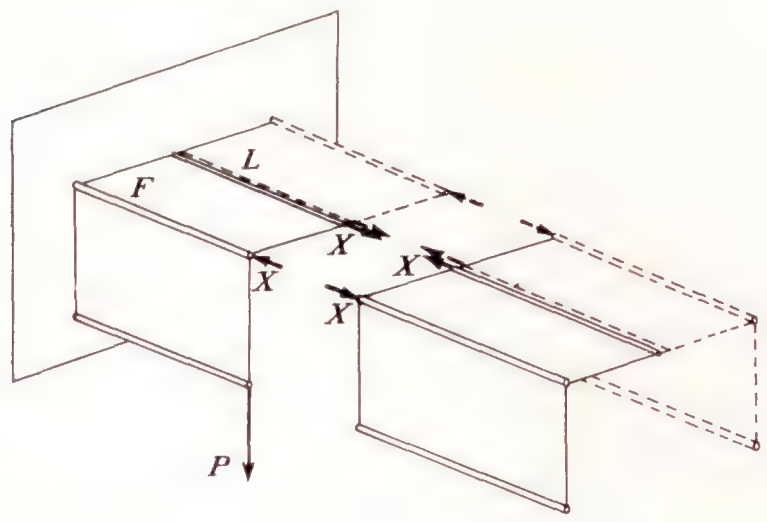

FIGURE 23.—Cantilever beam with concentrated load not at tip.

The case of a beam loaded by a concentrated load not at the tip is a simple problem in indeterminate structures. The beam is cut just outboard of the load (fig. 23) and the stresses in the cantilever part are calculated (Case 3 (*a*)). From these stressss, the distortion of the beam section at the cut; i. e., the relative displacement of the tips of the flange F and the longitudinal L, can be calculated. A system of forces X is then applied to equalize the distortion of the cantilever tip and of the inboard end of the "overhang," utilizing the formulas of Case 2.

CASE 4—CANTILEVER BEAM WITH ORTHOTROPIC COVER PLATE

Younger's solution for a beam of constant section.—The beam and the coordinate system used are shown in figure 17. *It should be noted that the x direction is opposite to that used in Cases 3 and 4.*

Under the assumptions that the transverse stresses and strains are negligible (Poisson's ratio equal to zero), and that G_e is independent of E, the differential equation of the cover is

$$\frac{\partial^2 u}{\partial y^2}+\frac{E}{G_e}\frac{\partial^2 u}{\partial x^2}=0 \quad \text{(B–13)}$$

where u is the displacement of any point on the cover in the x direction.

The boundary conditions are

$$\left.\begin{aligned} &\text{at} \quad x=0, \quad u=0 \text{ and } \frac{\partial u}{\partial y}=0 \\ &\qquad x=L, \frac{\partial u}{\partial x}=0 \\ &\qquad y=0, \frac{\partial u}{\partial y}=0 \end{aligned}\right\} \quad \text{(B–14)}$$

This equation was established by Younger (reference 4, pp. 36–47). For the solution he assumed that the external bending moment (on the whole beam) is given by

$$M=M_0 \cos\frac{\pi x}{2L} \quad \text{(B–15)}$$

and obtained for the longitudinal stress in the cover

$$\left.\begin{aligned} \sigma &= \frac{M_0 \cosh\frac{\pi y}{2KL}\cos\frac{\pi x}{2L}}{2h\left(A_F\cosh\frac{\pi b}{2KL}+\frac{A_L}{b}\frac{2KL}{\pi}\sinh\frac{\pi b}{2KL}\right)} \\ \text{and for the shear stress} \\ \tau &= \frac{M_0 G}{hE}\frac{\sinh\frac{\pi y}{2KL}\sin\frac{\pi x}{2L}}{2KA_F\cosh\frac{\pi b}{2KL}+\frac{4K^2tL}{\pi}\sinh\frac{\pi b}{2KL}} \end{aligned}\right\} \quad \text{(B–16)}$$

where K is defined by

$$K^2=\frac{G_e}{E} \quad \text{(B–17)}$$

Extension of Younger's solution.—Younger's solution can be somewhat extended. The external bending moment can be represented by a superposition of several terms:

$$M=M_1\cos\frac{\pi x}{2L}+M_3\cos\frac{3\pi x}{2L}+M_5\cos\frac{5\pi x}{2L} + \ldots + M_m\cos\frac{m\pi x}{2L} \quad \text{(B–18)}$$

where the m's are odd integers.

The values $M_1 \ldots M_m$ are chosen so that the sum of the terms equals the given external bending moment at m points other than the tip, where it is assumed that $M=0$. In order to make comparisons with Case 3, the bending moment caused by a tip load was expressed by

$$M=PL\left(0.821\cos\frac{\pi x}{2L}+0.101\cos\frac{3\pi x}{2L}+0.045\cos\frac{5\pi x}{2L}+0.033\cos\frac{7\pi x}{2L}\right) \tag{B–19}$$

The stresses corresponding to the mth term are given by

$$\left.\begin{aligned}\sigma_m&=\frac{M_m\cosh\frac{m\pi y}{2KL}\cos\frac{m\pi x}{2L}}{2h\left(A_F\cosh\frac{m\pi b}{2KL}+\frac{A_L}{b}\frac{2KL}{m\pi}\sinh\frac{m\pi b}{2KL}\right)}\\ \tau_m&=\frac{M_m}{h}\frac{G_e}{E}\frac{\sinh\frac{m\pi y}{2KL}\sin\frac{m\pi x}{2L}}{\left(2KA_F\cosh\frac{m\pi b}{2KL}+\frac{A_L4K^2L}{bm\pi}\sinh\frac{m\pi b}{2KL}\right)}\end{aligned}\right\}\text{(B–16a)}$$

The assumptions of Poisson's ratio being zero and G being independent of E are, strictly speaking, incompatible. The physical picture conforming to these assumptions is not a plate but a system of stringers carrying only longitudinal stresses tied together by a sheet carrying only shear stresses. This picture is realized very nearly in practice by a skin-stringer cover, the only difference being that the total cross-sectional area of the stringers is not necessarily equal to the area of the sheet, as in the case of the plain cover sheet. All the equations written for the plain cover sheet apply, therefore, to the skin-stringer cover if only (B–17) is replaced by

$$K^2=R\frac{G_e}{E} \tag{B–17a}$$

where R is the ratio of sheet area to area of longitudinals.

Constant-stress solution.—The coordinate system is that shown in figure 17. Under the assumption that σ=constant for each longitudinal, the fundamental relation

$$\frac{d\tau}{dx}=\frac{G_e\Delta\sigma}{E\Delta y} \tag{B–20}$$

can be integrated once to give

$$\tau_x=\frac{\Delta\sigma}{E\Delta y}\int_0^x G_e dx=\frac{x\Delta\sigma}{E\Delta y}\overline{G}_x \tag{B–21}$$

where $\overline{G}_x$ is the shear stiffness averaged over the distance $x=0$ to $x=x$. Integrating again

$$S_C=\int_0^L \tau_x t dx=\int_0^L \frac{x}{E}\frac{\Delta\sigma}{\Delta y}\overline{G}_x t dx$$

In any given case this integration can be performed and the result is

$$S_C=K_2\frac{\Delta\sigma}{\Delta y} \tag{B–22}$$

where

$$K_2=\int_0^L\frac{x}{E}\overline{G}_x t dx$$

Now

$$S_C=\int_0^y \sigma\frac{A_L}{b}dy$$

(see fig. 24) or

$$\frac{dS_C}{dy}=\sigma\frac{A_L}{b} \tag{B–23}$$

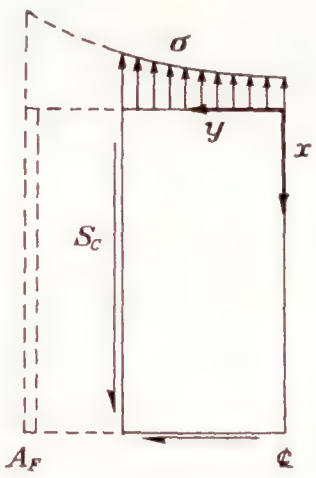

FIGURE 24.—Free-body diagram of cover plate.

Differentiating (B–22) and equating to (B–23)

$$\frac{d^2\sigma}{dy^2}-\sigma\frac{A_L}{bK_2}=0 \tag{B–24}$$

assuming that K_2 is independent of y.

The boundary conditions are

(1) at $y=0$, $\tau=0$ for any x. Therefore $\frac{d\sigma}{dy}=0$

(2) at any desired reference station R, the internal moment equals the external moment M_R.

The solution is

$$\sigma=\frac{M_R\cosh K_3 y}{h_R\left(A_F\cosh K_3 b+\frac{A_L}{bK_3}\sinh K_3 b\right)} \tag{B–25}$$

$$\tau=\sigma\frac{\overline{G}_x}{E}K_3 x\tanh K_3 y \tag{B–26}$$

where K_3 is defined by

$$K_3^2=\frac{A_L}{bK_2}=\frac{A_L}{b\int_0^L\frac{x}{E}\overline{G}_x t dx} \tag{B–27}$$

It may be noted that if G_e and t are not varied along the span, the constant K_3 is identical with the corresponding constant of Younger's solution except for a 10 percent difference in the numerical factor, namely, $\sqrt{2}$ against $\pi/2$.

APPENDIX C

ANALYSIS OF BEAM B

The dimensions and the loading of the beam are shown in table II.

ORDINARY BENDING THEORY

$$\sigma_F = \sigma_L = \sigma = \frac{M}{h(A_F + A_L)} = \frac{2{,}800{,}000}{24(1.875 + 1.875)}$$

31,100 lb. per sq. in.

CONSTANT-STRESS SOLUTION

Since G_e is assumed constant along the span, $\overline{G}_x = G_e$ and, from equation (7),

$$\tau_x = (\sigma_F - \sigma_L)\frac{xG_e}{Eb}$$

From equation (8)

$$S_C = \int_0^L (\sigma_F - \sigma_L)\frac{xG_e}{Eb} t_0 \left(1 - \frac{x}{L}\right) dx$$

$$= (\sigma_F - \sigma_L)\frac{G_e t_0}{Eb}\int_0^L x\left(1 - \frac{x}{L}\right) dx$$

$$= (\sigma_F - \sigma_L)\frac{0.2 \times 0.040}{24}\int_0^{280} x\left(1 - \frac{x}{280}\right) dx$$

$$= 4.35(\sigma_F - \sigma_L)$$

$$K_1 = 4.35$$

From equation (10a)

$$\sigma_L = \frac{2{,}800{,}000 \times 4.35}{24[1.875 \times 1.875 + 4.35(1.875 + 1.875)]}$$

$$= 25{,}550 \text{ lb. per sq. in.}$$

From equation (10b)

$$\sigma_F = \frac{2{,}800{,}000(1.875 + 4.35)}{24[1.875 \times 1.875 + 4.35(1.875 + 1.875)]}$$

$$= 36{,}500 \text{ lb. per sq. in.}$$

Substituting in equation (7) for the shear stress at the tip

$$\tau_{max} = (36{,}500 - 25{,}550)\frac{280 \times 0.2}{24} = 25{,}560 \text{ lb. per sq. in.}$$

The calculation of the shear correction is shown in table III.

TRIAL-AND-ERROR SOLUTION

Take $\Delta x = 40$ in.

$$\frac{S_W \Delta x}{I} = \frac{wxL\Delta x}{2h_0 x} = \frac{wL}{2h_0}\Delta x = \frac{71.4 \times 280 \times 40}{2 \times 24} = 16{,}670 \text{ lb.}$$

$$\Delta F_F = 16{,}670 - \Delta S_C$$

$$\Delta\tau = \frac{G_e \Delta x}{Eb}(\sigma_F - \sigma_L) = \frac{0.2 \times 40}{24}(\sigma_F - \sigma_L) = 0.333(\sigma_F - \sigma_L)$$

A typical cycle of the calculation is shown in table IV.

REFERENCES

1. Younger, John E.: Miscellaneous Collected Airplane Structural Design Data, Formulas, and Methods. A. C. I. C. No. 644, Matériel Division, Army Air Corps, 1930.
2. White, Roland J., and Antz, Hans M.: Tests on the Stress Distribution in Reinforced Panels. Jour. Aero. Sci., vol. 3, no. 6, April 1936, pp. 209–212.
3. Lovett, B. B. C., and Rodee, W. F.: Transfer of Stress from Main Beams to Intermediate Stiffeners in Metal Sheet Covered Box Beams. Jour. Aero. Sci., vol. 3, no. 12, Oct. 1936, pp. 426–430.
4. Younger, John E.: Metal Wing Construction, Part II—Mathematical Investigations. A. C. T. R. ser. no. 3288, Matériel Division, Army Air Corps, 1930.

TABLE I.—ANALYSIS OF TENSION PANEL WITH SHEAR DEFORMATION

$A_A=0.403$
$A_B=0.220$
$t=0.016$
$b=4.60$

$L=36$
$\Delta x=6$
$F_A=2,400-\Sigma\Delta Sc$
$\sigma_A=\frac{F_A}{A_A}=\frac{F_A}{0.403}$

$F_B=\Sigma\Delta Sc$
$\sigma_B=\frac{F_B}{A_B}=\frac{F_B}{0.220}$
$G_e/E=0.4$

$\Delta\tau=\frac{G_e\Delta x}{Eb}(\sigma_A-\sigma_B)=0.522\ (\sigma_A-\sigma_B)$
$\tau=\Sigma\Delta\tau$
$\Delta Sc=\tau t\Delta x=0.096\ \tau$

Station	By trial-and-error method									By formula [1]		
	ΔSc (lb.)	F_A (lb.)	σ_A (lb./sq. in.)	F_B (lb.)	σ_B (lb./sq. in.)	$\sigma_A-\sigma_B$ (lb./sq. in.)	$\Delta\tau$ (lb./sq. in.)	τ (lb./sq. in.)	ΔSc (lb.)	σ_A (lb./sq. in.)	σ_B (lb./sq. in.)	τ (lb./sq. in.)
0		2,400	5,960	0	0					5,960	0	5,230
	376							3,887	373			
1		2,024	5,020	376	1,708	3,312	1,730			5,022	1,717	2,885
	210							2,157	214			
2		1,814	4,500	586	2,662	1,838	960			4,502	2,670	1,584
	112							1,197	115			
3		1,702	4,224	698	3,170	1,054	550			4,220	3,186	856
	60							647	62			
4		1,642	4,075	758	3,444	631	329			4,070	3,461	442
	29							318	30			
5		1,613	4,005	787	3,575	430	224			3,996	3,595	187
	9							94	9			
6		1,604	3,980	796	3,618	362	189			3,968	3,630	0

[1] Appendix B, Case 1.

TABLE II.—CHARACTERISTICS OF BEAMS

The beams are assumed to be half beams as shown in fig. 8 (a).
All beams:

$h=24$ in. at root.
$h=0$ at tip.
$G_e/E=0.2$.
$b=24$ in.
$L=280$ in.
$W=71.4$ lb./in.

Beam	$A_F=A_L$ (sq. in.)		t (in.)		c
	Root	Tip	Root	Tip	
A	1.875	1.875	0.040	0.040	0.
B	1.875	0	.040	.000	0.
C	1.880	.470	.040	.010	0.

TABLE III.—CALCULATION OF SHEAR-FAULT CORRECTION FOR BEAM B

$\Delta x=40$
$F_F=\sigma_F A_F=36,500A_F$
$\Delta Sc_S=Sw\frac{\Delta x}{h}-\Delta F$

$\tau=25,560\frac{x}{L}$
$\Delta Sc_E=\tau t\Delta x$
$\Delta Sc'=\Delta Sc_S-\Delta Sc_E$

$\sigma_F'=0.5\frac{Sc'}{A_F}$
$\sigma_L'=-0.5\frac{Sc'}{A_L}$
$\sigma_{F_{corr}}=36,500+\sigma_F'$

$\sigma_{L_{corr}}=25,550+\sigma_L'$
$\tau'=0.5\frac{\Delta Sc'}{t\Delta x}$
$\tau_{corr}=\tau+\tau'$

Station	x from root (in.)	$A_F=A_L$ (sq. in.)	h (in.)	t (in.)	$Sw\frac{\Delta x}{h}$	F_F (lb.)	ΔF (lb.)	ΔSc_S (lb.)	τ (lb./sq. in.)	ΔSc_E (lb.)	$\Delta Sc'$ (lb.)	Sc' (lb.)	σ_F' (lb./sq. in.)	σ_L' (lb./sq. in.)	$\sigma_{F_{corr}}$ (lb./sq. in.)	$\sigma_{L_{corr}}$ (lb./sq. in.)	τ' (lb./sq. in.)	τ_{corr} (lb./sq. in.)
0																		
	260	0.134	1.71	0.00286	16,660		9,800	6,860	23,740	2,720	4,140						18,100	41,840
1		.268				9,800						4,140	7,720	−7,720	44,220	17,840		
	220	.402	5.14	.00857	16,660		9,800	6,860	20,080	6,880	−20						−30	20,050
2		.536				19,600						4,120	3,840	−3,840	40,340	21,720		
	180	.669	5.86	.0143	16,660		9,800	6,860	16,440	9,400	−2,540						−2,220	14,220
3		.804				29,400						1,580	980	−980	37,480	24,580		
	140	.937	12.00	.0200	16,660		9,800	6,860	12,780	16,220	−3,360						−2,100	10,680
4		1.072				39,200						−1,780	−830	830	35,670	26,390		
	100	1.205	15.42	.0257	16,660		9,800	6,860	9,130	9,400	−2,540						−1,230	7,900
5		1.340				49,000						−4,320	−1,610	1,610	34,890	27,170		
	60	1.473	18.87	.0314	16,660		9,800	6,860	5,480	6,880	−20						−10	5,470
6		1.608				58,800						−4,340	−1,350	1,350	35,150	26,910		
	20	1.740	22.28	.0371	16,660		9,800	6,860	1,826	2,710	4,150						1,400	3,226
7		1.875				68,600						−190	−50	50	36,450	25,610		

TABLE IV.—TRIAL-AND-ERROR SOLUTION FOR BEAM B

Station	x from root (in.)	$A_F=A_L$ (sq. in.)	$t\Delta x$	ΔSc (lb.)	F_L (lb.)	σ_L (lb./sq. in.)	ΔF_F (lb.)	F_F (lb.)	σ_F (lb./sq. in.)	$\sigma_F-\sigma_L$ (lb./sq. in.)	$\Delta\tau$ (lb./sq. in.)	τ (lb./sq. in.)	ΔSc (lb.)
0					0	0		0	0	0			
	280	0					12,940					32,896	3,755
1	260		0.1142	3,730	3,730	13,920		12,940	48,280	34,360	11,453		
	240	.268					9,230					21,443	7,340
2	220		.3426	7,440	11,170	21,740		22,170	41,400	19,660	6,553		
	200	.536					7,990					14,890	8,500
3	180		.571	8,680	19,850	24,700		30,160	37,560	12,860	4,267		
	160	.804					8,000					10,623	8,490
4	140		.799	8,670	28,520	26,620		38,160	35,600	8,980	2,993		
	120	1.072					8,600					7,630	7,840
5	100		1.028	8,070	36,590	27,300		46,760	34,880	7,580	2,527		
	80	1.340					10,310					5,103	6,400
6	60		1.255	6,360	42,950	26,760		57,070	35,470	8,770	2,923		
	40	1.608					13,540					2,180	3,240
7	20		1.485	3,130	46,080	24,560		70,610	37,640	13,080	4,360		
	0	1.875											

REPORT No. 609

EXPERIMENTAL INVESTIGATION OF WIND-TUNNEL INTERFERENCE ON THE DOWNWASH BEHIND AN AIRFOIL

By Abe Silverstein and S. Katzoff

SUMMARY

The interference of the wind-tunnel boundaries on the downwash behind an airfoil has been experimentally investigated and the results have been compared with the available theoretical results for open-throat wind tunnels. As in previous studies, the simplified theoretical treatment that assumes the test section to be an infinite free jet has been shown to be satisfactory at the lifing line. The experimental results, however, show that this assumption may lead to erroneous conclusions regarding the corrections to be applied to the downwash in the region behind the airfoil where the tail surfaces are normally located. The results of a theory based on the more accurate concept of the open-jet wind tunnel as a finite length of free jet provided with a closed exit passage are in good qualitative agreement with the experimental results.

INTRODUCTION

A comprehensive theoretical treatment of wind-tunnel interference exists at present. The theory includes all the major effects attributable to the limited boundaries of the air stream and provides stream-angle corrections both at the airfoil and in the region behind the airfoil. Experimental verification of this theory has, in general, been satisfactory, although mainly confined to the corrections at the lifting line of the airfoil. The present investigation is concerned with the interference in the region behind the wing, a problem of importance in the testing of airplanes or airplane models, since the induced boundary effects at the wing and at the tail surfaces are usually different. A particular purpose of the present investigation was to provide correction factors for airplane test data obtained in the N. A. C. A. full-scale wind tunnel.

The theory of wind-tunnel interference on the downwash at the tail surfaces has been given in references 1, 2, and 3. Reference 3 also contains an evaluation of the correction factors for square and rectangular tunnels. These studies have indicated that the effect in the region of the tail surfaces is of the order of twice that at the wing. The work is based, however, on the assumption that the air stream is of infinite length. This assumption is permissible for a closed wind tunnel but is very questionable for an open tunnel because the actual open test section is usually only about one tunnel diameter long. The boundary condition for free jets, namely, uniformity of pressure over the surface of the jet, thus applies over only a short section; the boundary condition for closed tunnels, zero velocity normal to the surface, applies in front of and behind the open section. The disturbing effect of the exit cone is clear since, upon entering it, any inclination of the free jet induced by the lift on the wing must be so reduced that the air will follow more nearly the horizontal flow direction in the closed tube (fig. 1). From some recent boundary-

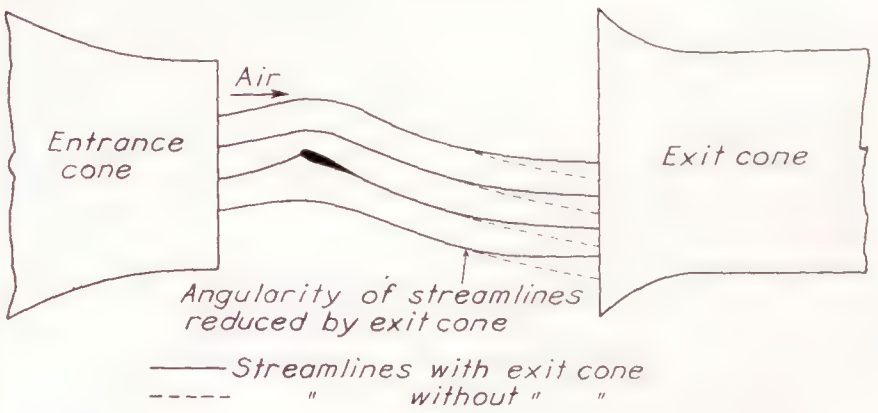

FIGURE 1.—Effect of exit cone on downwash behind an airfoil.

interference calculations (reference 4) for a circular open tunnel of finite length, it was concluded that the assumption of an infinitely long open jet would lead to very serious error in the region of the tail plane but to very little error at the wing. The results from reference 4 are reproduced in figure 2.

Conditions were particularly favorable for experimental investigation of the downwash corrections in the N. A. C. A. full-scale wind tunnel, as a $\frac{1}{15}$-scale model of the tunnel was available. The procedure consisted in measuring the downwash angles behind small airfoils in the model tunnel and comparing them with the measured downwash angles behind the same airfoils in the full-scale wind tunnel. The full-scale wind tunnel is so large in comparison with the airfoils that the boundary interference is negligible. The correction factors thus obtained should be directly applicable to downwash data obtained behind large airfoils in the full-scale tunnel for there is little reason to expect an appreciable scale effect on the induced-velocity distribution. The

free-stream downwash data obtained from the measurements in the full-scale tunnel with the small airfoils should be valuable as standards for comparison with similar measurements in other tunnels. By a comparison, such as was made in the present work, the boundary-interference factors may be derived.

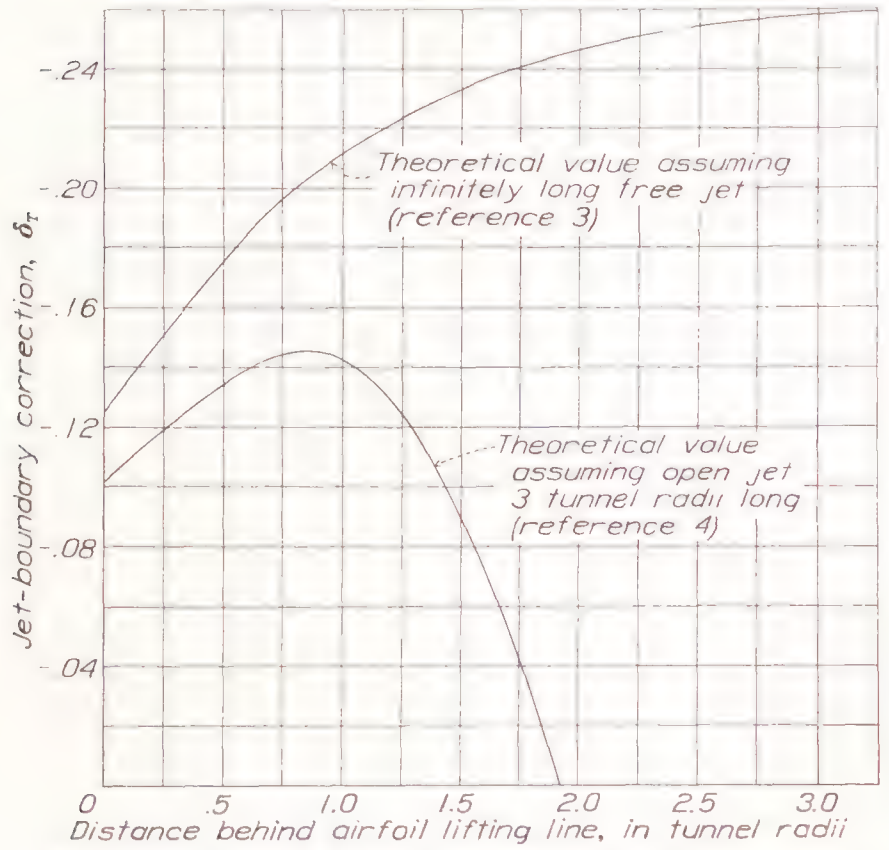

FIGURE 2.—Theoretical jet-boundary corrections for finite and infinite jets.

MODEL-TUNNEL TESTS

Apparatus.—The model tunnel used in these tests is a $\frac{1}{15}$-scale replica of the N. A. C. A. full-scale wind tunnel. A complete description of the small tunnel and its equipment is given in reference 5. A wire balance was devised to measure the lift on the airfoils. The models were suspended from an overhead platform scale, and counterweights were provided below to maintain tension in the system. The angle of attack was changed by an adjustable quadrant on the scale platform.

The tests were made with two rectangular Clark Y airfoils, one with a 5-inch chord and a 30-inch span and the other with a 10-inch chord and a 30-inch span. The 5-inch-chord airfoil in the 2- by 4-foot jet of the model tunnel corresponds in the 30- by 60-foot jet of the full-scale wind tunnel to a 6.25- by 37.50-foot airfoil, which represents the average size of the airfoils tested in the large tunnel. The 10-inch-chord airfoil was chosen to exaggerate the effects investigated and the results from the measurements made with it are, perhaps, of greater academic than practical value. The airfoils were constructed of laminated mahogany, varnished and then polished to a smooth surface.

The downwash angles were measured by means of a calibrated yaw head consisting of two total-head tubes, each inclined at a 42° angle with the horizontal to form a Y with an 84° included angle. The inclination of the air stream was indicated by the pressure difference p between the two prongs of the Y and was measured by means of an alcohol manometer. The yaw head was calibrated in terms of the dynamic pressure q of the air stream, and the stream angle in degrees was obtained from a calibration chart showing p/q against ϵ, the angle of downwash. For measurements of dynamic pressure a small Prandtl-type pitot head was used.

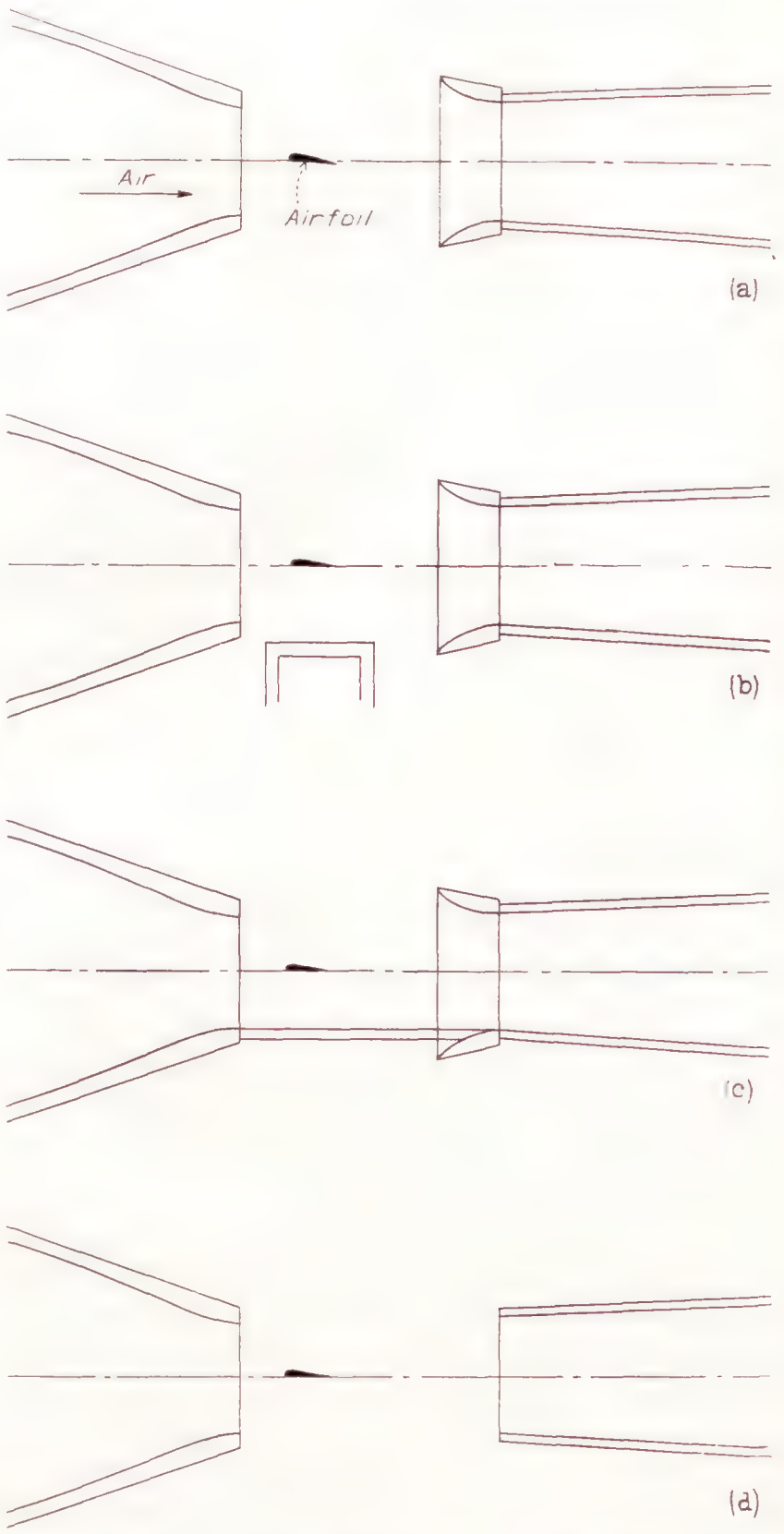

FIGURE 3.—The four test conditions of the model tunnel.
(a) Normal tunnel.
(b) Tunnel with balance house.
(c) Tunnel with ground board.
(d) Tunnel with exit-cone flare removed.

Tests.—Test data were obtained with the model tunnel in four different conditions (fig. 3) as follows:

1. Normal tunnel condition.

2. Normal tunnel condition with a model balance house to simulate the balance house of the full-scale tunnel.

3. Normal tunnel condition with a ground board 32 inches wide extending between the lower surfaces of the entrance and exit cones.

4. Flare removed from the exit cone, increasing the length of the open jet from 44 to 56 inches.

Conditions 1 to 3 simulate possible operating conditions of the full-scale tunnel; condition 4 was studied to determine whether increasing the length of the open section would appreciably affect the downwash at the tail. Tests were made for each of the four tunnel conditions with the 10- by 30-inch airfoil; only conditions 1 and 2 were studied with the 5- by 30-inch airfoil.

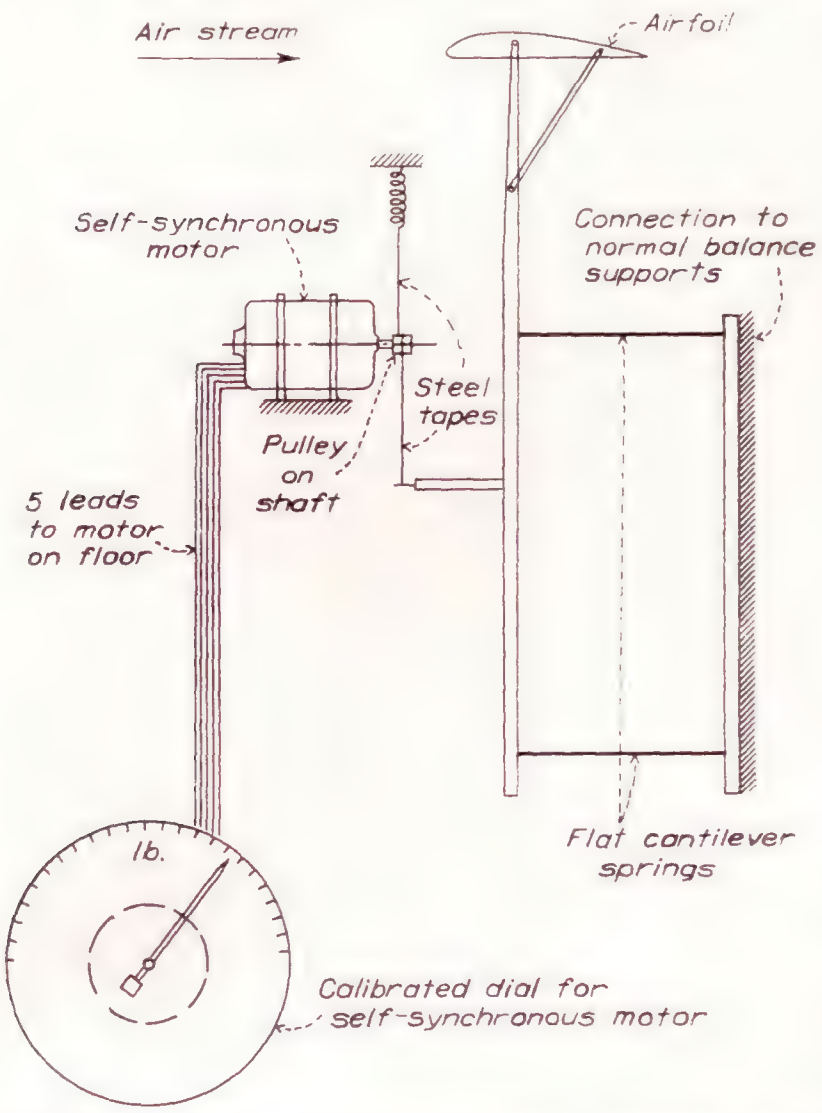

FIGURE 4.—Diagram of self-synchronous motor balance for small-airfoil tests in the full-scale tunnel.

For all the test conditions the air-stream angles in the tunnel at all the stations were obtained with the airfoils removed from the jet. The actual downwash angles were then taken as differences between the air-stream angles with the airfoil present and removed. Downwash surveys were made at three lift coefficients for each airfoil. The lift forces were measured in all cases over a range of angles of attack that included the angles of zero and maximum lift. The downwash surveys were limited to the plane of symmetry of the wing since tail surfaces do not normally extend a great distance on either side of this plane. Measurements were made between 4 inches above and 9 inches below the longitudinal axis through the quarter-chord point of the airfoils, at 1.0 and 1.65 chord lengths back of the trailing edge for the larger airfoil, and at 1, 2, and 3 chord lengths back of the trailing edge for the smaller airfoil. An air speed of about 60 miles per hour was used for all the tests.

FULL-SCALE WIND-TUNNEL TESTS

Apparatus.—Free-air data (free of tunnel-boundary interference effects) for the airfoils were obtained by tests in the full-scale tunnel (reference 6). Owing to the small forces encountered in measuring the lift, it was necessary to construct a special balance, a schematic diagram of which is shown in figure 4. The airfoil was supported on the balance by means of a forked

FIGURE 5.—The experimental set-up in the full-scale tunnel.

frame, this frame being supported in turn on a pair of flat cantilever springs. Vertical forces on the balance deflect the cantilever springs and the motion is converted into rotation of one of a pair of small self-synchronous motors by means of a thin strip of spring steel attached to its shaft. Remote recording of this motion was obtained on the complementary self-synchronous motor, placed in the balance house below the jet. By means of a calibrated dial and a pointer attached to the motor shaft, the lift forces on the airfoils could be observed directly. Effective damping was obtained by means of an oil dashpot. The entire balance was enclosed in a streamline fairing and

attached to one of the normal balance supports (fig. 5). Downwash angles and dynamic pressures were measured with the same instruments used in the model-tunnel tests. These instruments were attached to the survey apparatus in the tunnel (reference 6).

Tests.—Preliminary measurements in the full-scale wind tunnel, with the airfoil removed, consisted of surveys of air-stream angle and dynamic pressure and the determination of tare lift forces on the balance. For each airfoil, the lift forces were measured over the range of angles of attack between zero and maximum lift, and the downwash angles were measured for three lift coefficients. As in the model-tunnel tests, surveys were made only in the plane of symmetry of the airfoil. A slightly larger area was surveyed in

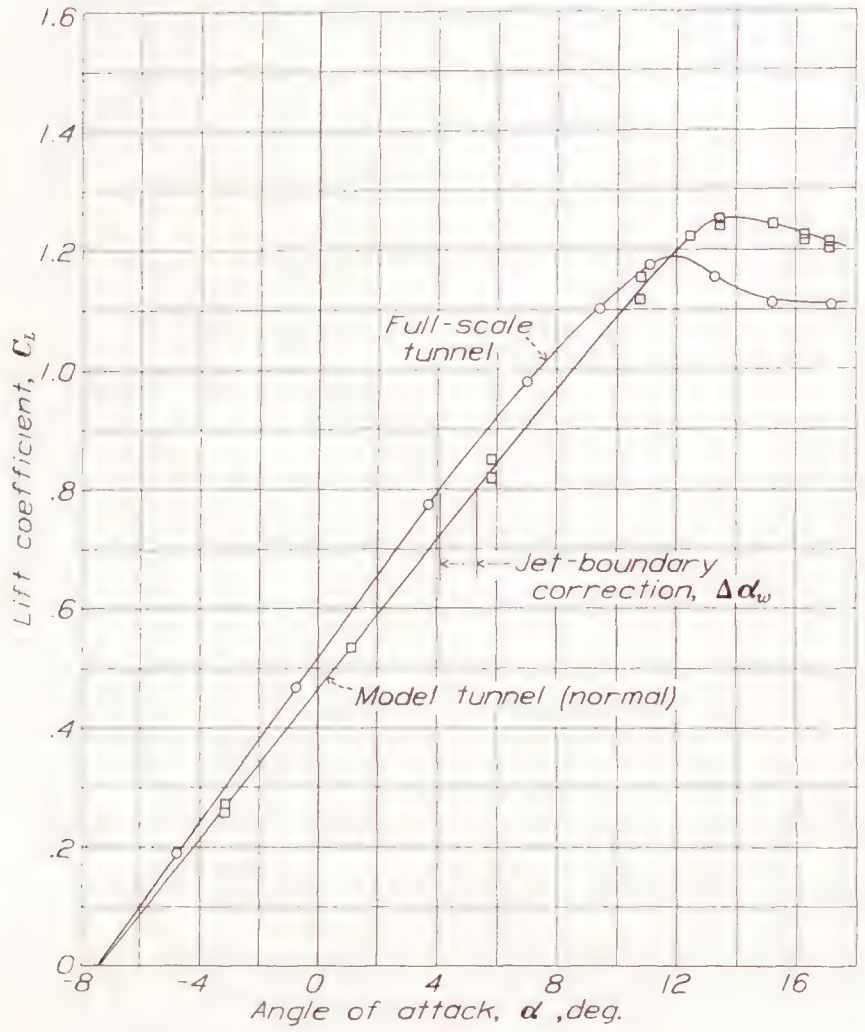

FIGURE 6.—Comparison of lift curves for the 5- by 30-inch airfoil in the normal model tunnel and in the full-scale tunnel.

the full-scale tunnel than in the model tunnel. Downwash measurements were made between 8 inches above and 12 inches below the longitudinal axis, from 1 to 5 chord lengths back of the quarter-chord point for the smaller airfoil, and from 1 to 4 chord lengths back for the larger airfoil.

RESULTS

Representative experimental data are plotted in figures 6 to 9. The final derived jet-boundary corrections are given in figures 10 to 13, in which is plotted the coefficient δ_T used in the usual boundary-correction formula

$$\Delta\alpha = 57.3\ \delta_T \frac{S}{C} C_L$$

in which S and C are the areas of the airfoil and jet cross section, respectively, and $\Delta\alpha$ is the induced downwash angle in degrees due to the influence of the boundaries. The coefficient δ_T represents the total jet-boundary effect rather than the increase in the correction over that at the wing; i. e., $\delta_T = \delta_w + \delta_A$, in which δ_w is the correction factor for the wing and δ_A is the additional factor for the tail. Accordingly, in the application of the results, it must be remembered that, if the angle of attack of the airplane has already been corrected for the jet-boundary effect at the wing, the correction factor for the tail will be only the difference between the δ_T values at the tail and at the wing.

The tunnel-boundary effects at the airfoils were obtained directly from the lift curves (fig. 6) as the difference between the full-scale and model-tunnel angles of attack at a particular lift coefficient. Figures 7, 8, and 9 illustrate some intermediate steps in the derivation of the boundary-interference corrections behind the airfoil. Figure 7 comprises contour maps of the downwash measured in the full-scale tunnel; figures 8 and 9 compare plots of the downwash measured in the model tunnel and in the full-scale tunnel.

The corrections were primarily obtained for application to tests performed in the full-scale wind tunnel and are accordingly plotted against distance downstream in full-scale dimensions (figs. 10 to 13). Points are shown that correspond to each of the two airfoils at each of two lift coefficients. These points are not actual experimental values but were obtained after some interpolation, as the measurements in the two tunnels were made at slightly different lift coefficients and at slightly different positions back of the wing. For comparison with the theoretical values calculated for an infinitely long open jet, the corrections of reference 3 are included with the experimental data (figs. 10, 11, and 13).

The scattering of the experimental points on some of the curves is very noticeable. Although theoretical reasons exist for expecting that the four cases would not exactly check, they appear insufficient to explain the observed amount of variation. The experimental error may possibly have exceeded the estimated value of 0.15°.

DISCUSSION

The results of greatest interest are those for the normal tunnel (fig. 10). It is seen that, whereas the correction at the wing has the theoretical value, the corrections on the longitudinal axis back of the wing not only do not approach twice that at the wing, as given by the theory, but actually decrease rapidly after the first 20 feet behind the wing (about 3 chord lengths). This effect is due to the exit cone. It is therefore apparent that the conception of the open jet as one of infinite length may lead to gross error in applying corrections at the tail surfaces. The curves show a marked resemblance to the one theoretically obtained considering the jet to be of finite length. (See fig. 2 taken from reference 4.)

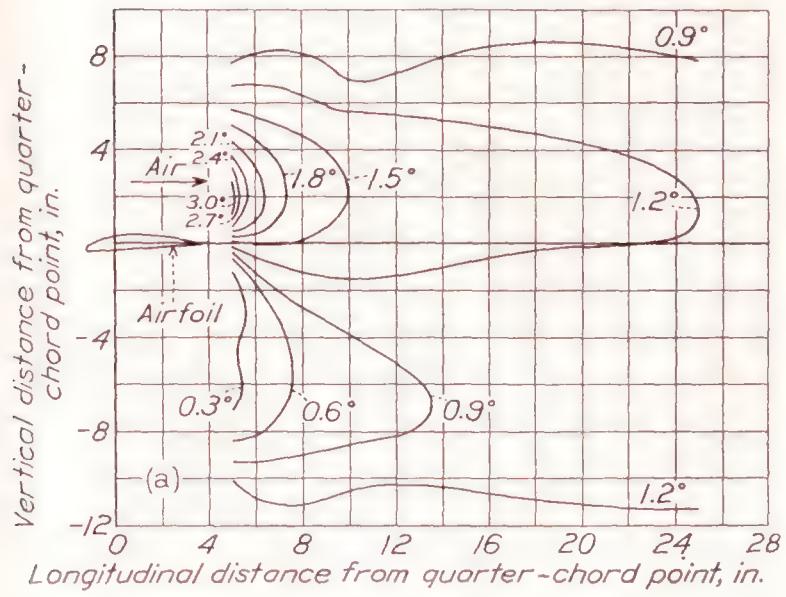

(a) 5- by 30-inch airfoil; α, −3.8°; C_L, 0.25.

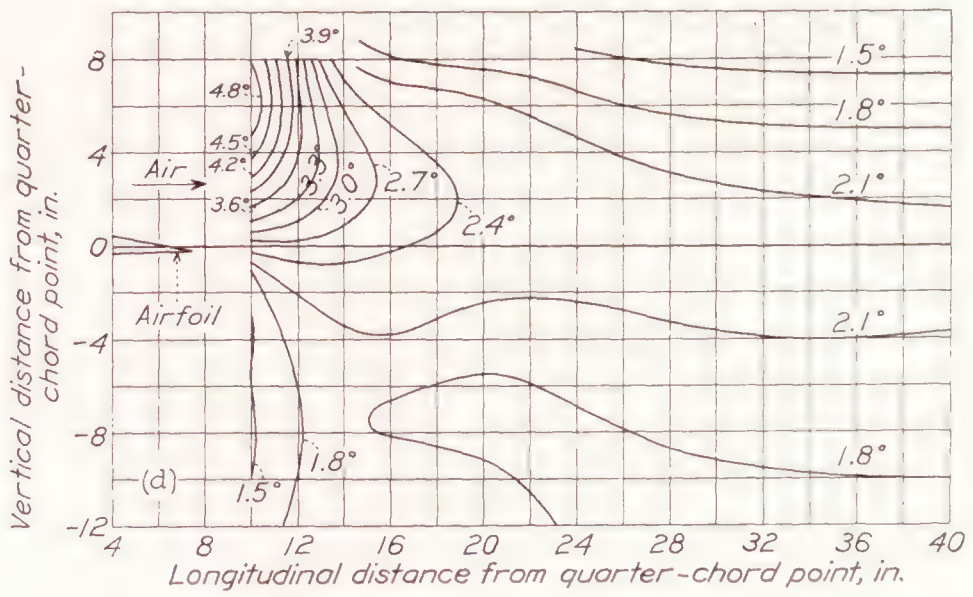

(d) 10- by 30-inch airfoil; α, −1.8°; C_L, 0.21.

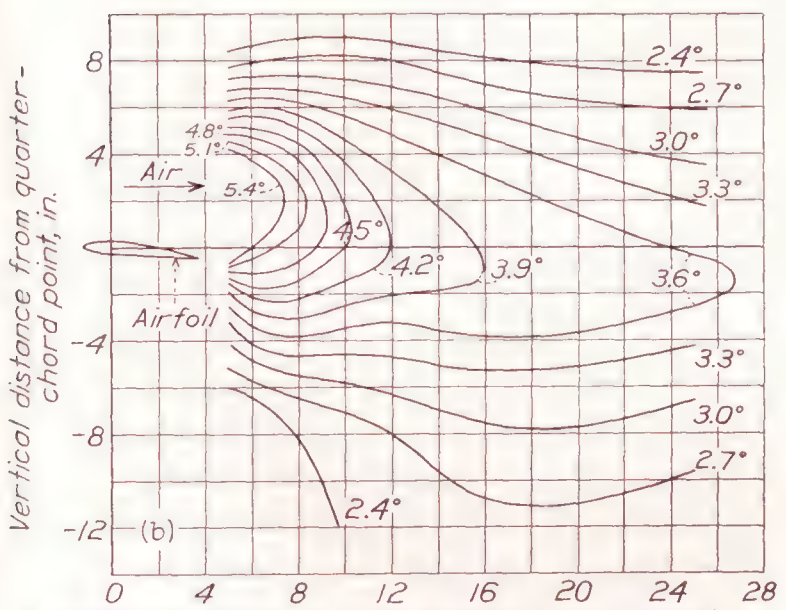

(b) 5- by 30-inch airfoil; α, 3.2°; C_L, 0.74.

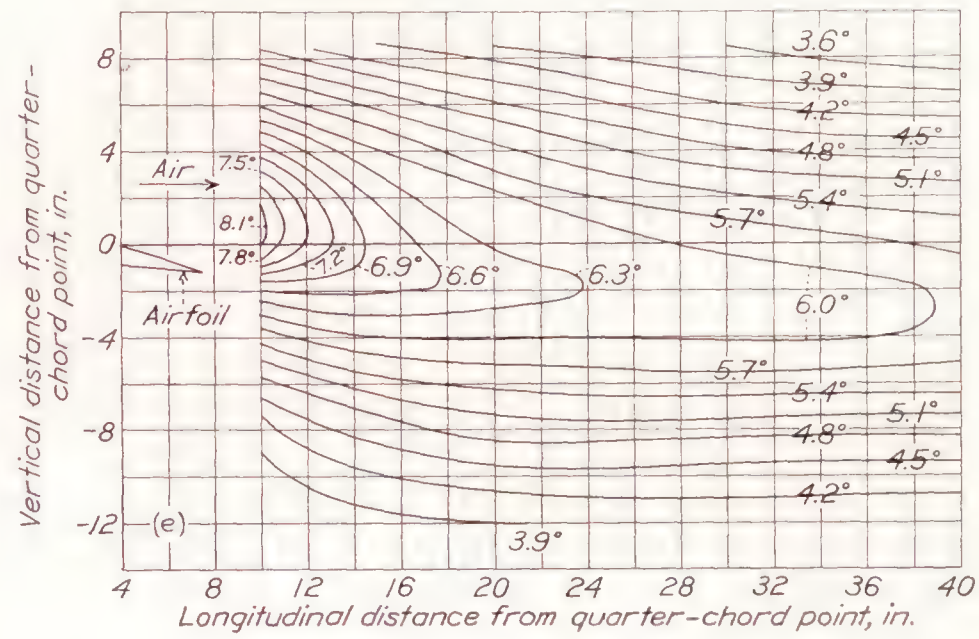

(e)10- by 30-inch airfoil; α, 5.0°; C_L, 0.59.

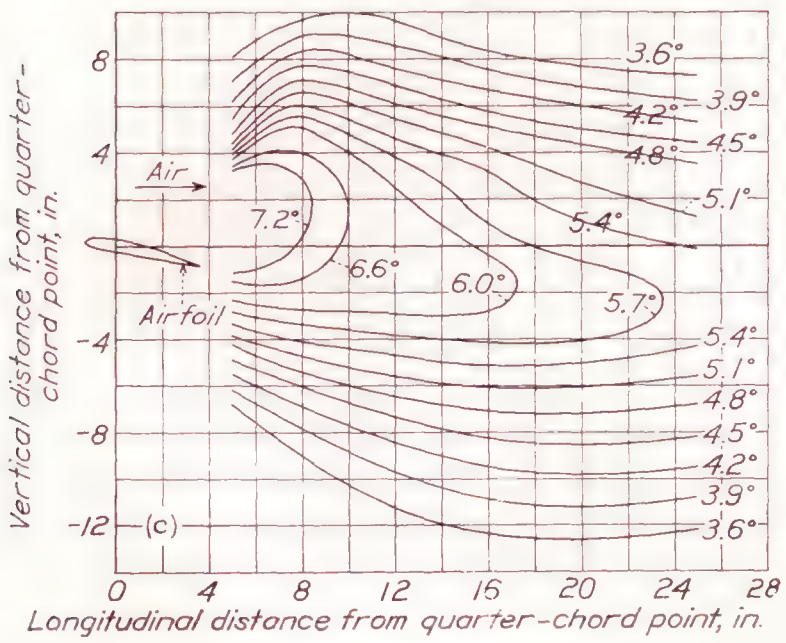

(c) 5- by 30-inch airfoil; α, 9.2°; C_L, 1.09.

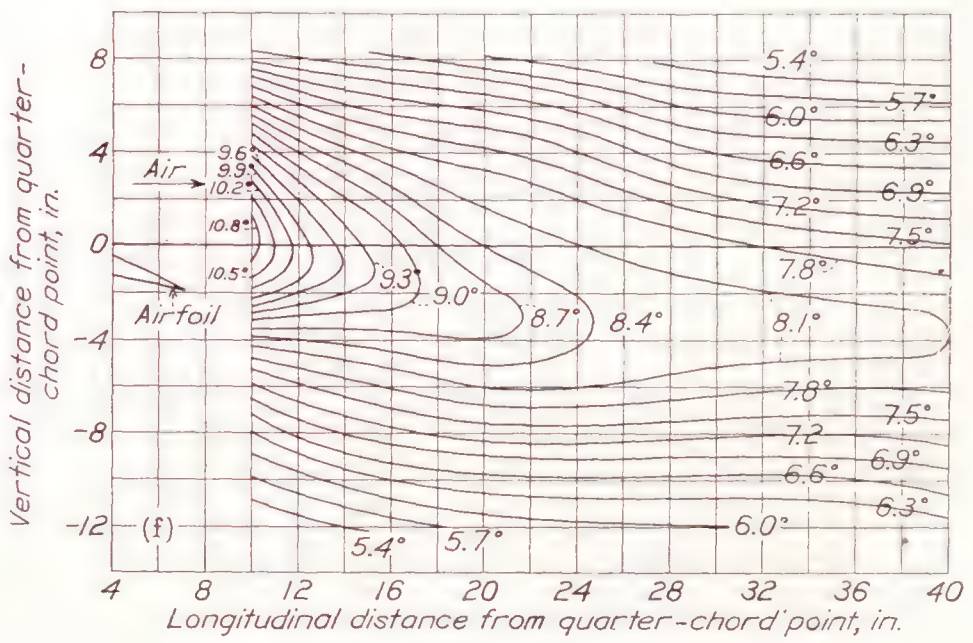

(f) 10- by 30-inch airfoil; α, 11.2° ; C_L, 0.91

FIGURE 7.—Downwash-angle contour lines from surveys in the full-scale wind tunnel on two airfoils of Clark Y section.

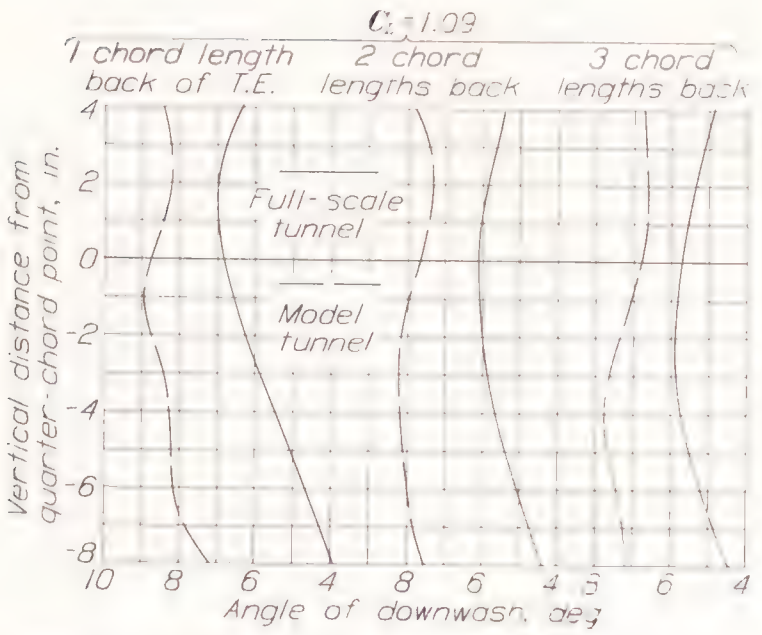

FIGURE 8.—Comparison of model and full-scale tunnel downwash; 5- by 30-inch airfoil; normal model tunnel.

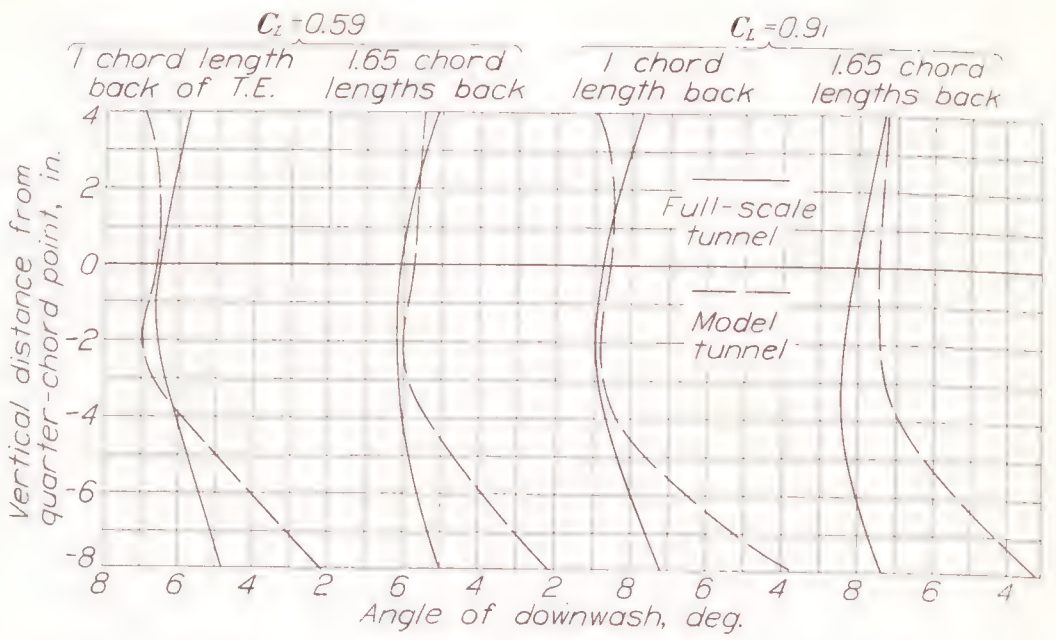

FIGURE 9.—Comparison of model and full-scale tunnel downwash; 10- by 30-inch airfoil; ground board in model tunnel.

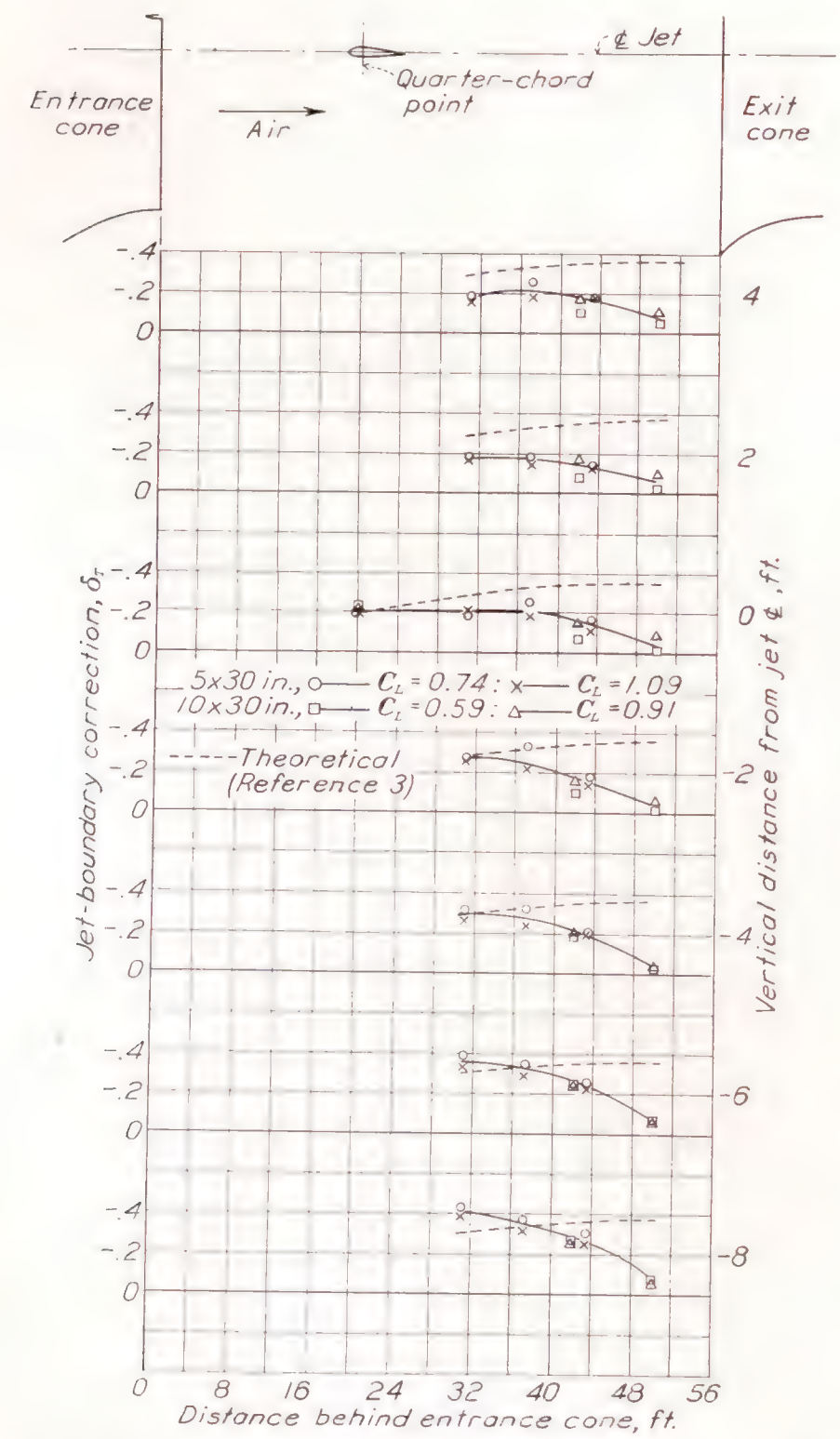

FIGURE 10.—Jet-boundary correction against distance behind entrance cone; tunnel normal.

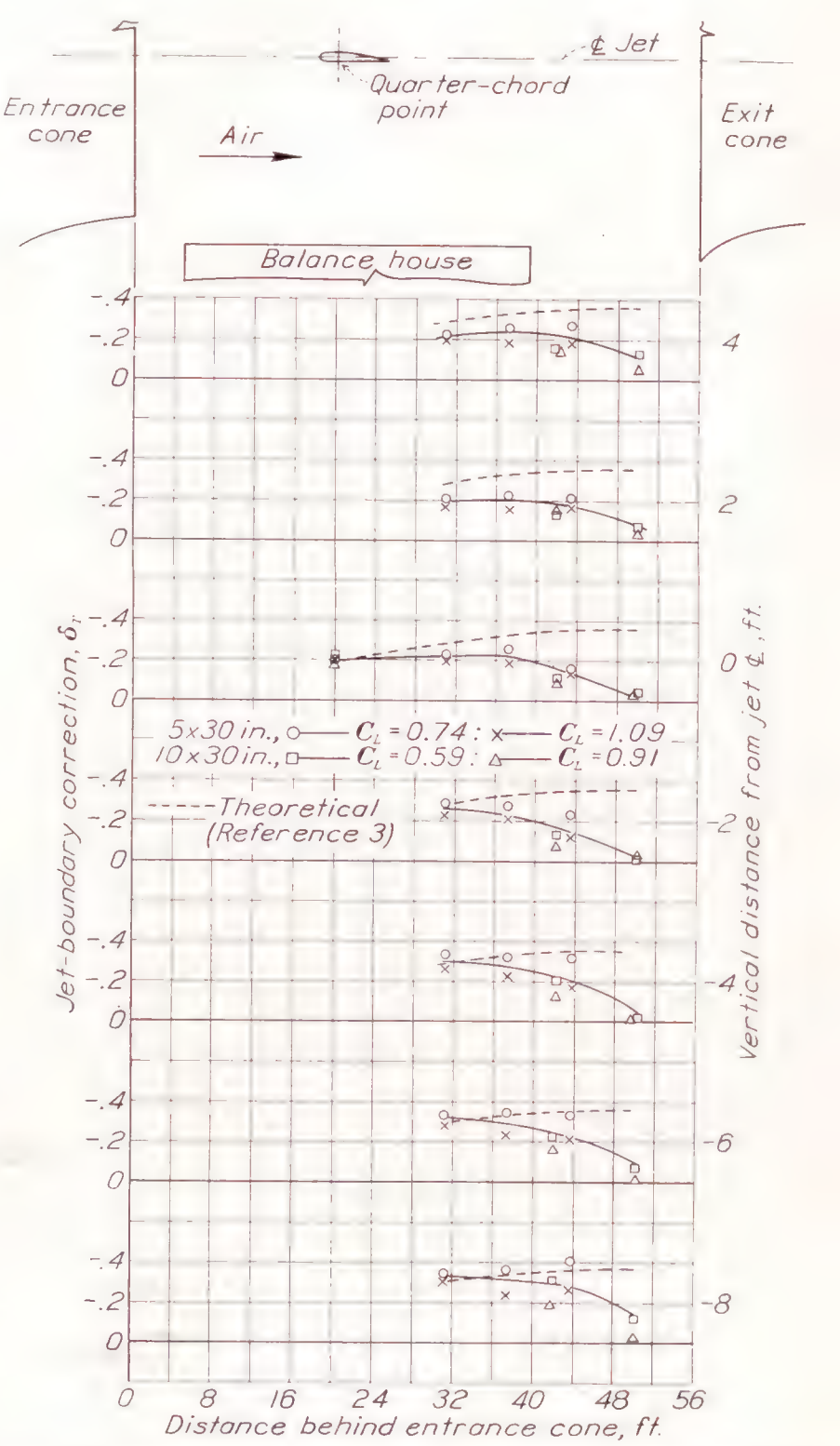

FIGURE 11.—Jet-boundary correction against distance behind entrance cone; tunnel with balance house.

The differences between the experimental and theoretical values are least in the region 4 to 8 feet below and 12 to 20 feet behind the wing. For a high-wing monoplane the tail is in this region at high lift coefficients; so in this case the theoretically calculated effect, assuming an infinitely long section, will not usually be in error by as much as 1°. For low-wing or midwing monoplanes the tails will lie relatively higher and somewhat above this region. For these cases it may be sufficiently accurate to assume that the correction is uniform over the entire airplane and equal to the theoretically calculated effect at the wing.

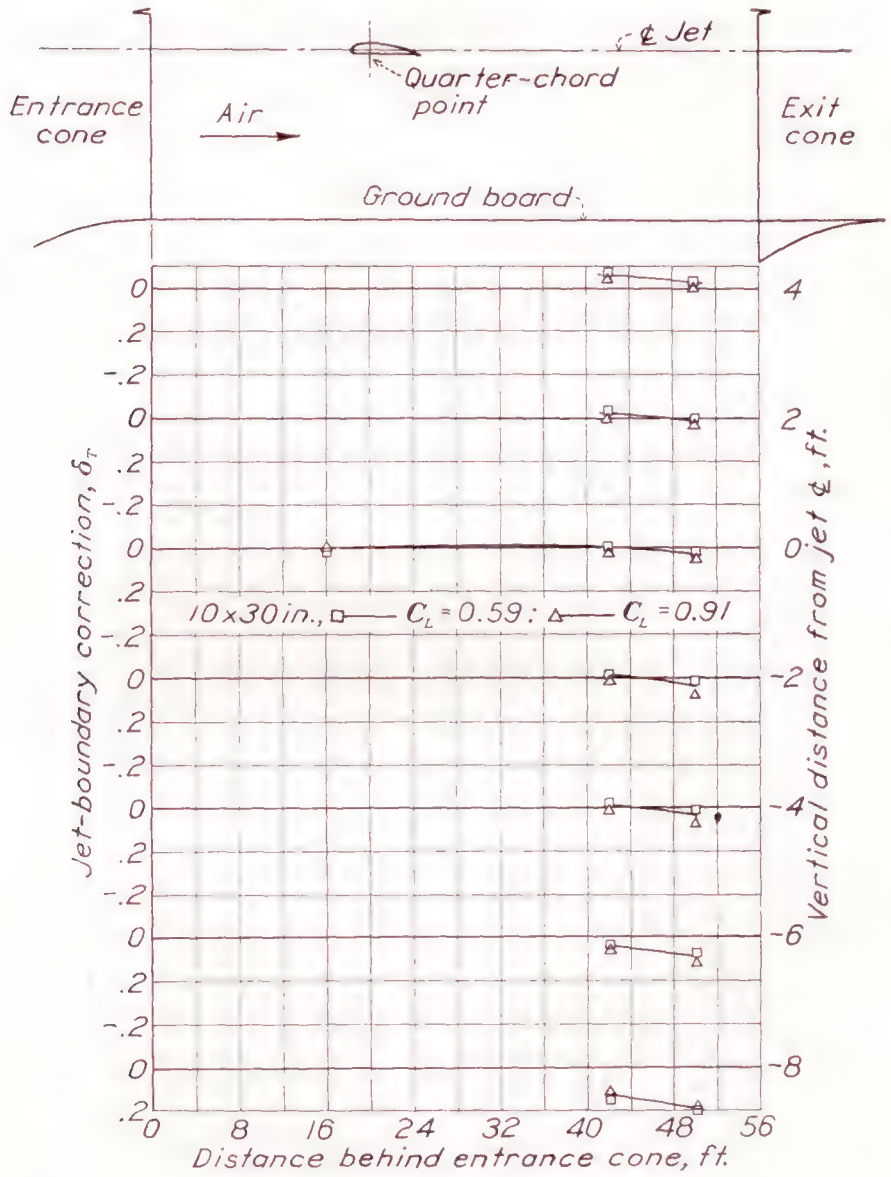

FIGURE 12.—Jet-boundary correction against distance behind entrance cone; tunnel with ground board.

Removal of the exit cone causes somewhat closer approach of the experimental to the theoretical results (fig. 13); it is clear, therefore, that the proximity of the closed section forming the exit cone of the jet contributes considerable inaccuracy to the results of a theory that assumes an infinitely long free jet.

The downwash results when the ground board was used (fig. 12) are, on the other hand, in agreement with the results of the theoretical treatment for an infinitely long jet with bottom boundary. For a long 2:1 rectangular jet, which is open on three sides and closed at the bottom, the theory predicts relatively small

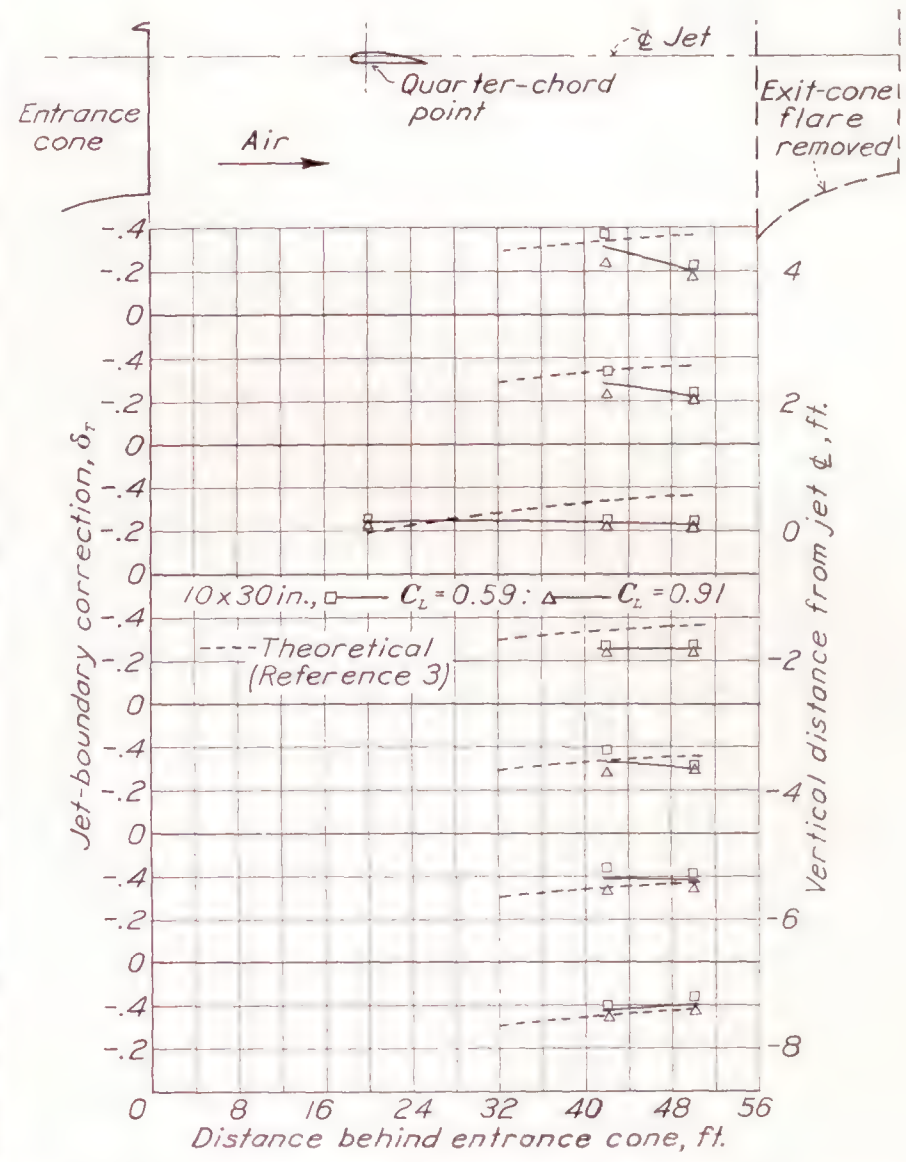

FIGURE 13.—Jet-boundary correction against distance behind entrance cone; tunnel with exit-cone flare removed.

A point of interest is that the observed jet-boundary effect is not symmetrical with respect to the horizontal center plane of the tunnel. This dissymmetry is probably due to the fact that the trailing vortices do not extend straight back from the wing but are inclined downward, owing to the downwash. No theoretical treatment has yet taken this feature into account, although the calculations for a wing placed below the center line should be somewhat comparable and they do indicate the same type of dissymmetry in the downwash. (See fig. 25 of reference 3.)

The results with the model balance house in place (fig. 11) are, as expected, about the same as those without it, except possibly in that portion of the jet closest to it.

tunnel-wall corrections in the region of the axis. The experimental results verified this prediction, although the agreement is somewhat fortuitous since (1) the jet is not quite rectangular, (2) it is not infinitely long, and (3) the ground board did not extend across the entire width. The lift curves were practically the same as those obtained in the full-scale tunnel, as were the downwash angles in the region of the tunnel axis. Near the ground board, however, the deviation from the free-stream downwash becomes very large, owing to the fact that the inclination of the stream must approach zero at the board.

In all the model-tunnel experiments, the lifting line, assumed to be located at the quarter-chord point of the airfoil, was placed 16 inches back of the entrance

cone on the horizontal center line. The results are then strictly applicable to the full-scale tunnel only when the airplane wing is 20 feet behind the entrance cone and on the horizontal center line. This location is approximately the usual one of the wings tested in the tunnel.

The boundary corrections for other wind tunnels may be found by using the downwash contours of figure 7, which are for free-stream conditions. By a comparison of the data obtained in the full-scale wind tunnel with those obtained in other tunnels behind similar airfoils at the same lift coefficients, the boundary-interference corrections may be directly obtained. This method assumes that the scale effects on the downwash contour map and on the jet-boundary effect are negligible.

CONCLUSIONS

1. For an open-jet wind tunnel the boundary corrections at the wing itself may be predicted from the simplified theory, which assumes the jet to be of infinite length; however, the theory gives erroneous results downstream. In the region of the tail surfaces, the jet-boundary corrections are less than those predicted by the simplified theory but are in good qualitative agreement with the results of a theory that considers the jet to be of finite length.

2. For the case of an open rectangular tunnel with ground board, the experiments substantiate the theoretical prediction that in such a tunnel there is relatively little jet-boundary effect either at the wing or at the tail.

3. With special reference to the full-scale wind tunnel, the experiments show that the presence of the balance house below the jet has no appreciable effect on the corrections. Removal of the exit bell improved the agreement between the experimental downwash and that predicted by the simplified theory.

LANGLEY MEMORIAL AERONAUTICAL LABORATORY,
NATIONAL ADVISORY COMMITTEE FOR AERONAUTICS,
LANGLEY FIELD, VA., *June 4, 1937.*

REFERENCES

1. Glauert, H., and Hartshorn, A. S.: The Interference of Wind Channel Walls on the Downwash Angle and the Tailsetting to Trim. R. & M. No. 947, British A. R. C., 1925.
2. Lotz, Irmgard: Correction of Downwash in Wind Tunnels of Circular and Elliptic Sections. T. M. No. 801, N. A. C. A., 1936.
3. Silverstein, Abe, and White, James A.: Wind-Tunnel Interference with Particular Reference to Off-Center Positions of the Wing and to the Downwash at the Tail. T. R. No. 547, N. A. C. A., 1935.
4. Weinig, F.: Der Strahleinfluss bei offenen Windkanälen. Luftfahrtforschung, Bd. 13, Nr. 7, 20. Juli 1936, S. 210–213.
5. Theodorsen, Theodore, and Silverstein, Abe: Experimental Verification of the Theory of Wind-Tunnel Boundary Interference. T. R. No. 478, N. A. C. A., 1934.
6. DeFrance, Smith J.: The N. A. C. A. Full-Scale Wind Tunnel. T. R. No. 459, N. A. C. A., 1933.

REPORT No. 610

TESTS OF RELATED FORWARD-CAMBER AIRFOILS IN THE VARIABLE-DENSITY WIND TUNNEL

By Eastman N. Jacobs, Robert M. Pinkerton, and Harry Greenberg

SUMMARY

A recent investigation of numerous related airfoils indicated that positions of camber forward of the usual location resulted in an increase of the maximum lift. As an extension of this investigation, a series of forward-camber airfoils has been developed, the members of which show airfoil characteristics superior to those of the airfoils previously investigated.

The primary object of the report is to present fully corrected results for airfoils in the useful range of shapes. With the data thus made available, an airplane designer may intelligently choose the best possible airfoil-section shape for a given application and may predict to a reasonable degree the aerodynamic characteristics to be expected in flight from the section shape chosen.

For airfoils of moderate thickness, the optimum camber position was found to correspond to that of the N. A. C. A. 23012 section. A discussion is included concerning the choice of the best thickness and camber for full-scale applications depending on specific design conditions. Data to assist in the choice of the optimum section for a design using split flaps were obtained by testing some of the better sections with trailing-edge split flaps.

INTRODUCTION

The well-known airfoil-section investigations in the N. A. C. A. variable-density wind tunnel have been directed toward studies of the effects of variations of airfoil-section shape. Such studies are intended to determine the range within which the best possible section shapes for any given application will generally be found. With the data thus made available, an airplane designer may intelligently choose the best possible airfoil-section shape for a given application and may predict to a reasonable degree the aerodynamic characteristics to be expected in flight from the section shape chosen.

The first investigation of this series (reference 1) gave comparable data from the standard large Reynolds Number tests in the variable-density tunnel, which were considered as representative within the flight range, for related airfoils covering section-shape variations in the neighborhood of commonly used airfoils. A subsequent investigation (references 2 and 3), covered by this report, deals with airfoil sections differing from those commonly used in that the camber occurs farther forward, i. e., nearer the leading edge. The desirability of this shape characteristic was indicated by the first investigation.

After the mean-line shape designated 230 had been found to be near the optimum (reference 2), an airfoil having the N. A. C. A. 23012 section was tested in the N. A. C. A. full-scale tunnel to verify the superiority of its characteristics over those of commonly used airfoils (reference 4). This and other tests (references 5 and 6) in the full-scale tunnel also provided valuable data on which to base an interpretation of the variable-density-tunnel data as applied to flight. In addition, a selected group of the related airfoils has been tested over a wide range of values of the Reynolds Number. The results of this investigation (reference 6) provided the information needed to apply the standard variable-density-tunnel airfoil data to flight at any particular value of the flight Reynolds Number.

Aside from the presentation of the important section characteristics fully corrected for application to flight at the standard value of the Reynolds Number (effective Reynolds Number approximately 8,000,000) for all the forward-camber series of airfoils tested, one object of the present report is to consider possible improvements of the N. A. C. A. 23012 section. This possibility was investigated by an analysis of test results for a number of airfoils, the shape of which varied systematically from the N. A. C. A. 23012. Finally, several airfoils within the most useful range of shapes were investigated to provide data for the various airfoils that may be chosen as most efficient in particular applications.

The airfoils developed in the variable-density-tunnel investigations have been designated by numbers having four or more digits. As explained in reference 1, the maximum ordinate of the mean line is called the "camber" and the position of the maximum ordinate is called the "position of the camber." The airfoils reported in reference 1 were designated by a number having four digits. The first digit indicated the camber in percent of chord; the second, the shape of the mean line as indicated by the position of the camber in tenths of the chord from the leading edge; and the last two, the maximum thickness in percent of the chord. The extension of the investigation to the forward-camber airfoils presented herein (including the airfoils in references 2 and 3) necessitated an extension of the designation numbers to cover the new mean-line shapes. As before, the first digit indicates the relative magnitude of the camber; but the second has been replaced by a pair of digits, which together indicate the mean-line shape for which position of camber is one of the parameters; and the last two, as before, indicate the thickness of the airfoil section. The camber, the mean-line shape designation, the corresponding values of camber, and the position of camber for these forward-camber airfoils are given in the following table.

Camber designation (first digit) / Mean-line shape designation (second and third digits)	10	20	30	40	50
Position of camber, percent of chord	5	10	15	20	25
	(Actual camber in percent of chord)				
2	1.1	1.5	1.8	2.1	2.3
3	---	2.3	2.8	3.1	---
4	---	3.1	3.7	4.2	---
6	---	4.6	5.5	6.2	---

The table thus indicates, for example, that the N. A. C. A. 230 – – airfoil has the camber 1.8 percent of the chord at 0.15c behind the leading edge.

The airfoils designated by both the four and the five digit numbers have only one form of thickness variation. Changes in the form of the thickness variation made by altering the leading-edge radius and the position of maximum thickness (see reference 7) have been designated by appending two additional digits separated by a dash from the basic airfoil designation. The first of these two digits indicates the relative magnitude of the leading-edge radius and the second indicates the position of the maximum thickness in tenths of the chord from the leading edge. The significance of the leading-edge radius designation is given below:

0 designates sharp leading edge.
3 designates one-fourth normal leading-edge radius.
6 designates normal leading-edge radius.
9 designates three or more times normal leading-edge radius.

The complete system of airfoil designation is illustrated by the following examples: The N. A. C. A. 2212 (reference 1) has a camber of 2 percent of the chord at 0.2 of the chord from the leading edge and a thickness of 12 percent of the chord. The N. A. C. A. 0012 (reference 1) is a symmetrical airfoil having a thickness of 12 percent of the chord. The N. A. C. A. 24012 (reference 2) has a camber of approximately 2 percent of the chord (actually 2.1 of the chord, see table I) at 0.2 of the chord from the leading edge and a thickness of 12 percent of the chord. It will be noted that the N. A. C. A. 2212 and the N. A. C. A. 24012 have practically the same camber, camber position, and thickness; however, the shapes of the mean-camber lines, designated by the digit 2 in one case and 40 in the other, are entirely different. Finally the N. A. C. A. 0012–64 is a symmetrical airfoil having a normal leading-edge radius and the maximum thickness at 0.4 of the chord from the leading edge. The N. A. C. A. 24012–33 has the same mean line and thickness as the N. A. C. A. 24012 but has a leading-edge radius one-fourth the normal and the maximum thickness at 0.3 of the chord from the leading edge.

The scope of the present investigation is best indicated by figure 1, which gives the profiles of the airfoils tested. Of the airfoils of 12 percent thickness there are included a group of increasing camber: 00, 230, 330, 430, and 630; a group of varying camber position: 210, 220, 230, 240, and 250; and some variations of camber position for airfoils more highly cambered than the 230 series. From the results of these tests, the camber position corresponding to the series 230, 430, and 630 appeared to be best, so that in most cases variations of section thickness are included only for these mean-line shapes and for the symmetrical airfoils. Some variations of thickness distribution are included, and also some of the more interesting airfoils with a high-lift device consisting of a 20-percent-chord full-span split flap.

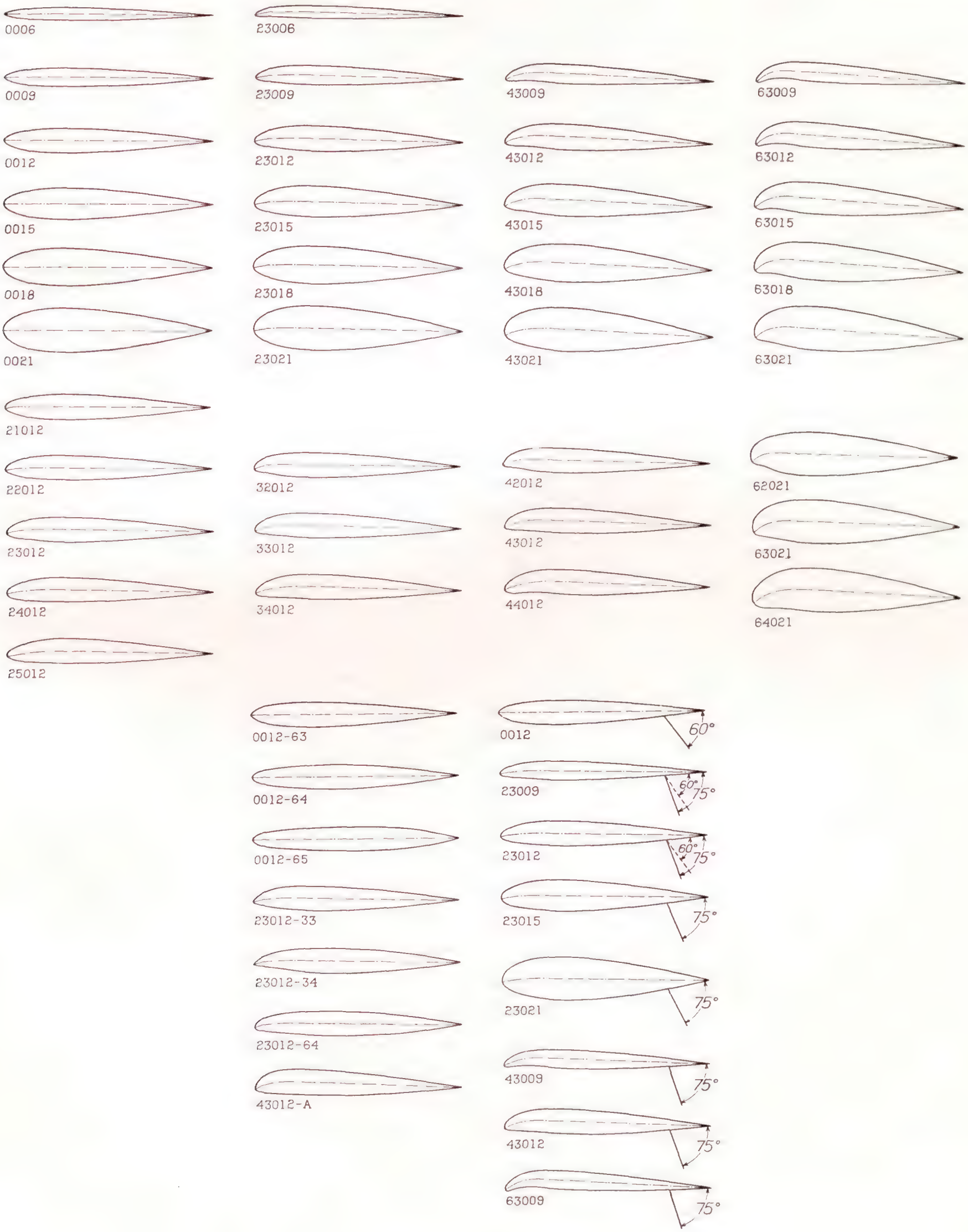

FIGURE 1.—N. A. C. A. airfoil profiles.

DESCRIPTION OF AIRFOILS

The thickness variations of the airfoils are given in references 1 and 7. The cambered airfoils have mean lines of the form given in reference 2. Profiles of all the airfoils presented herein are shown in figure 1.

The models are of 5-inch chord and 30-inch span, of rectangular plan form, and are constructed of duralumin as explained in reference 8.

APPARATUS AND METHOD

The variable-density wind tunnel, in which the tests were made, is described in reference 8. Routine measurements of the lift, drag, and pitching moment were made at an effective Reynolds Number of approximately 8,000,000 (tank pressure 20 atmospheres). In addition, for most of the airfoils, measurements of lift in the neighborhood of maximum lift were made at an effective Reynolds Number of approximately 3,800,000, obtained by running at reduced speed with a tank pressure of 20 atmospheres.

The discussion of precision in reference 1 points out certain errors in the velocity measurements due to a change in the apparent density of the manometer fluid with a change in the tank pressure from atmospheric and to the "blocking effect" of the model in the tunnel. These errors have since been investigated (see the appendix of reference 6) and have been eliminated by correcting the manometer settings used in fixing the tunnel air speed. Other errors mentioned in reference 1 have been somewhat reduced.

RESULTS

The data are presented (figs. 2 to 51) in a manner that is a slight modification of the standard graphic form used in previous reports. The left-hand portion of the plot presents the test data in the usual standard form for rectangular airfoils of aspect ratio 6. Included also are the airfoil profile, the table of ordinates,

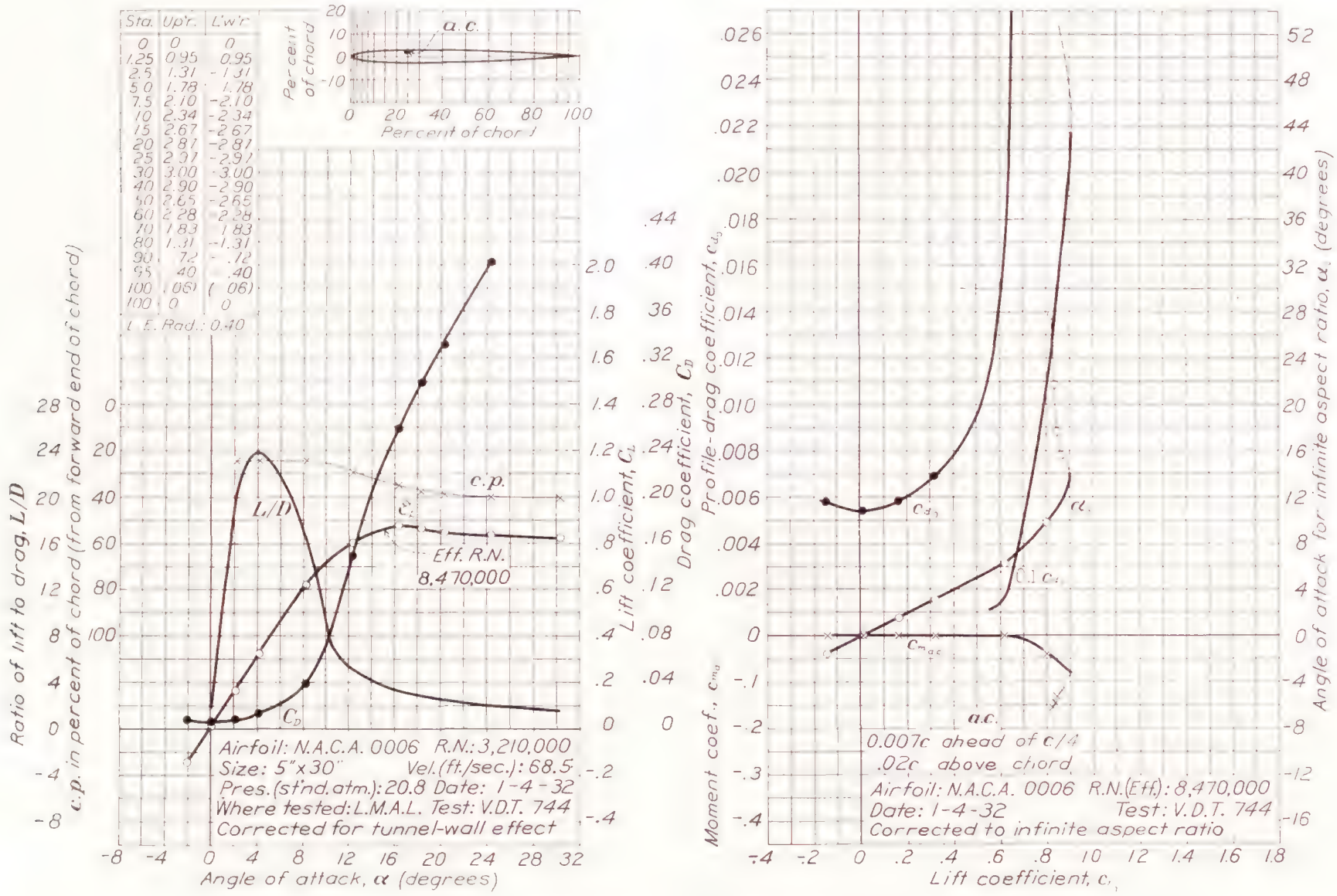

FIGURE 2.—N. A. C. A. 0006 airfoil.

and a portion of the lift curve in the neighborhood of maximum lift obtained at a reduced Reynolds Number. The right-hand portion of the plot presents the section characteristics derived from the experimental data and fully corrected for turbulence and tip effects, as explained in reference 6.

In addition to the graphic form of presentation, the most important characteristics, fully corrected, are presented for each section in table I. The three columns on classification are explained in references 6 and 9.

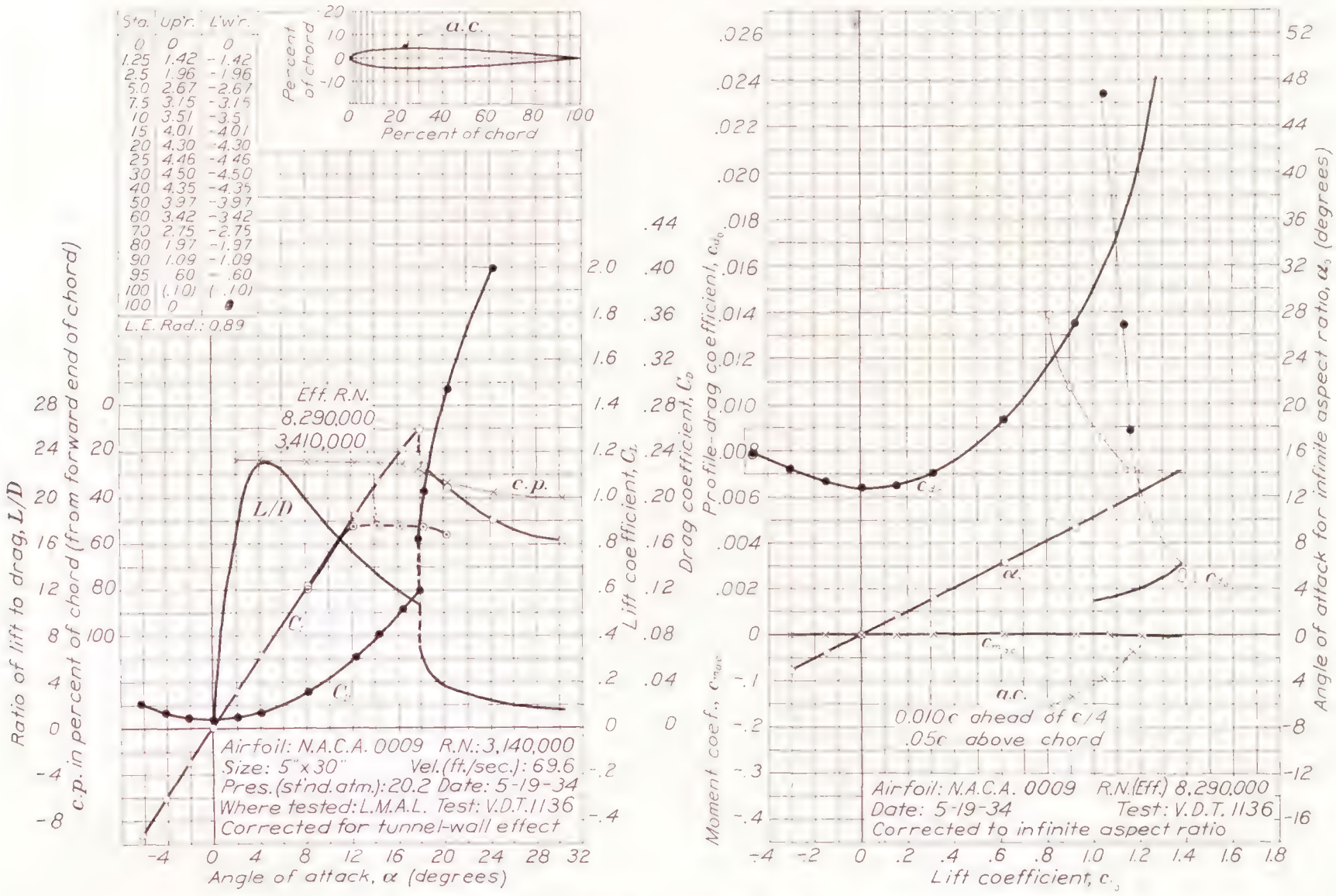

FIGURE 3.—N. A. C. A. 0009 airfoil.

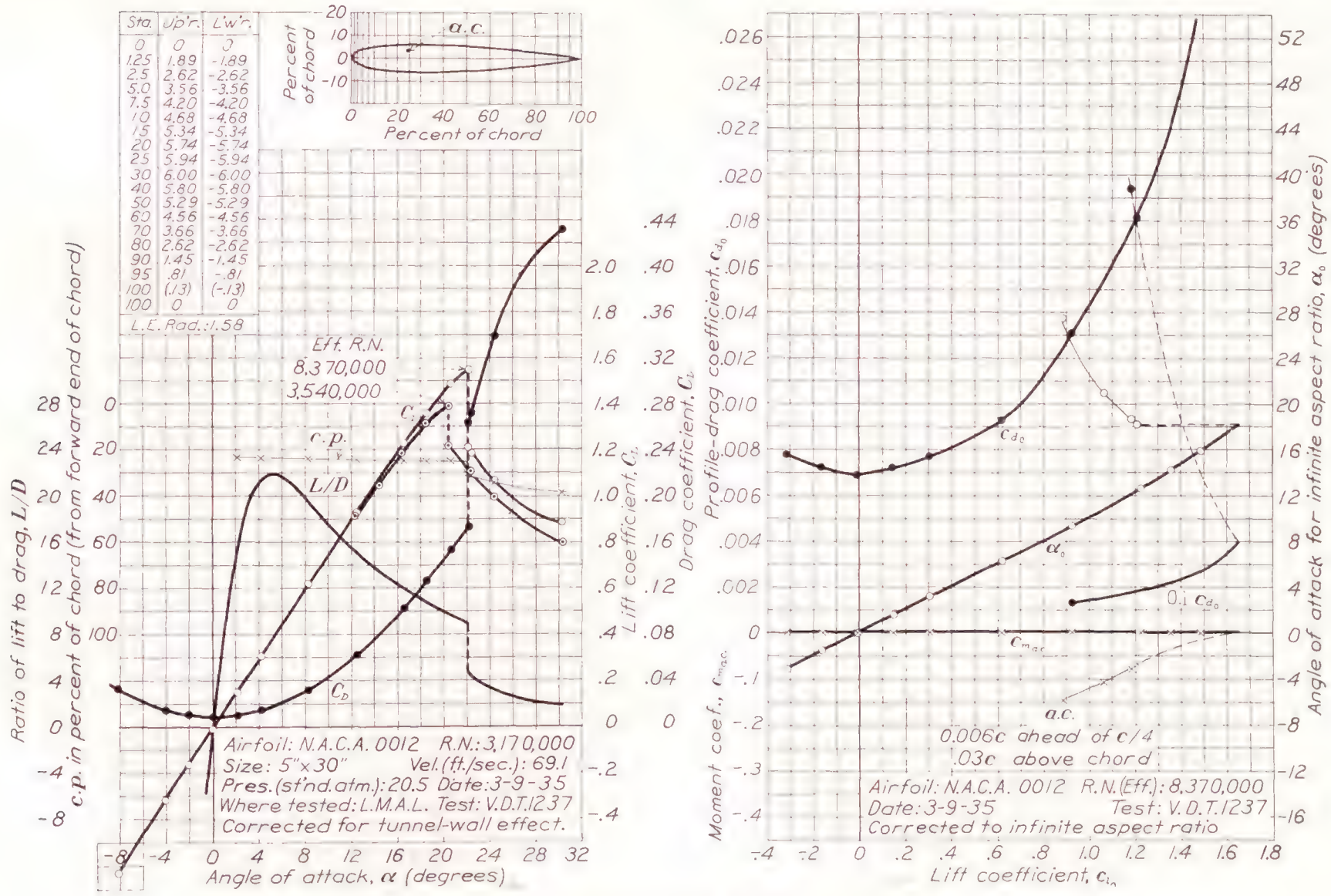

FIGURE 4.—N. A. C. A. 0012 airfoil.

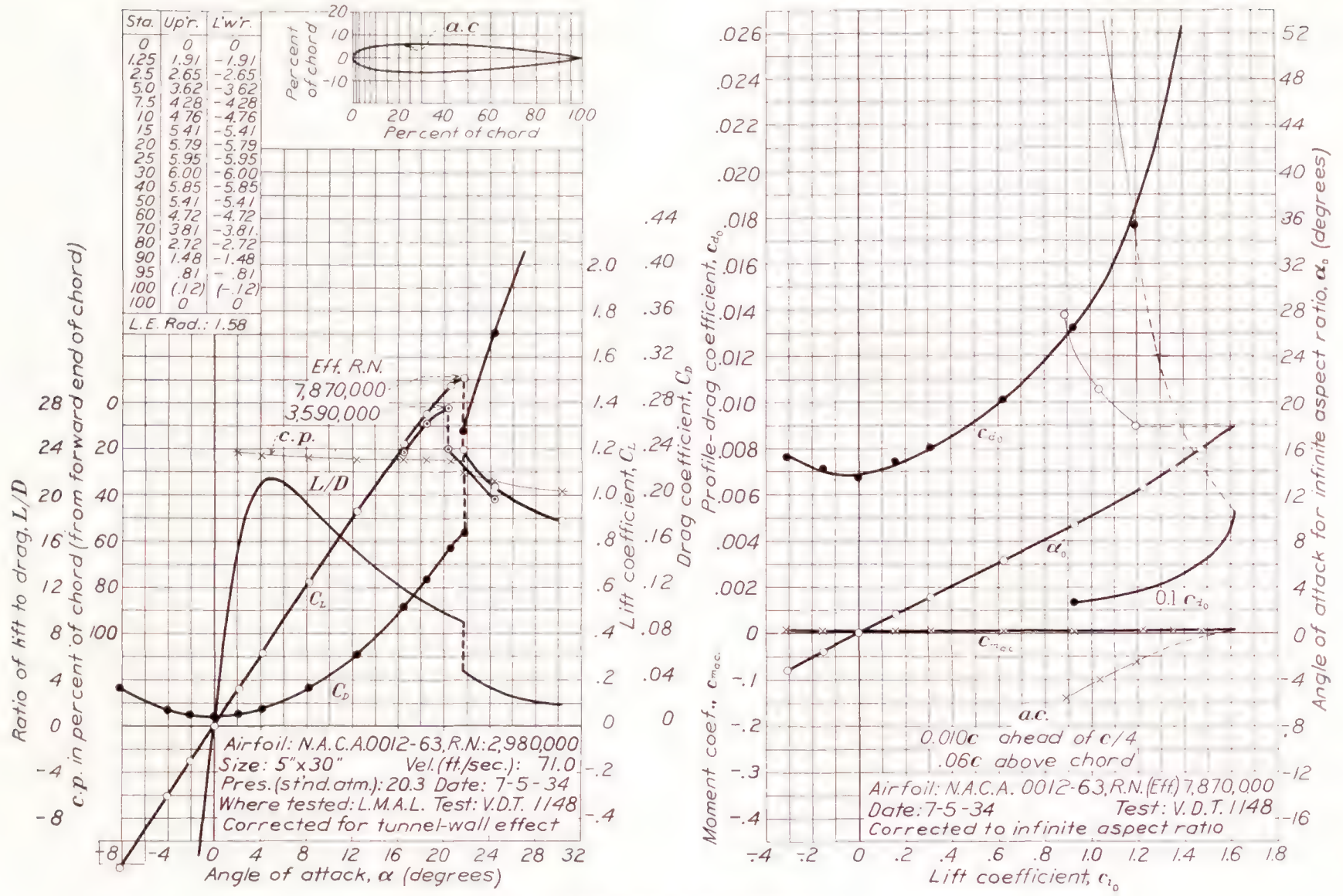

FIGURE 5.—N. A. C. A. 0012-63 airfoil.

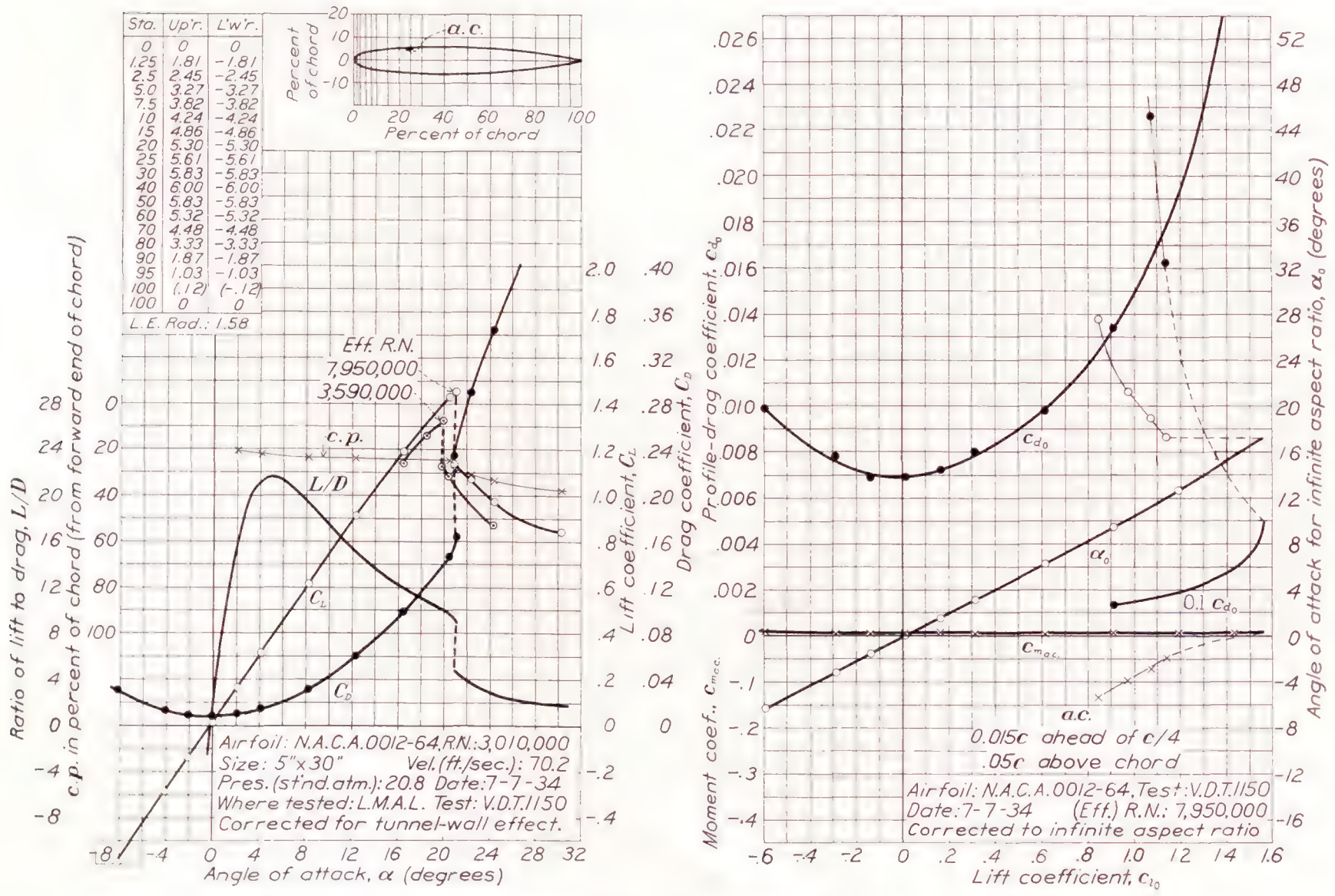

FIGURE 6.—N. A. C. A. 0012-64 airfoil.

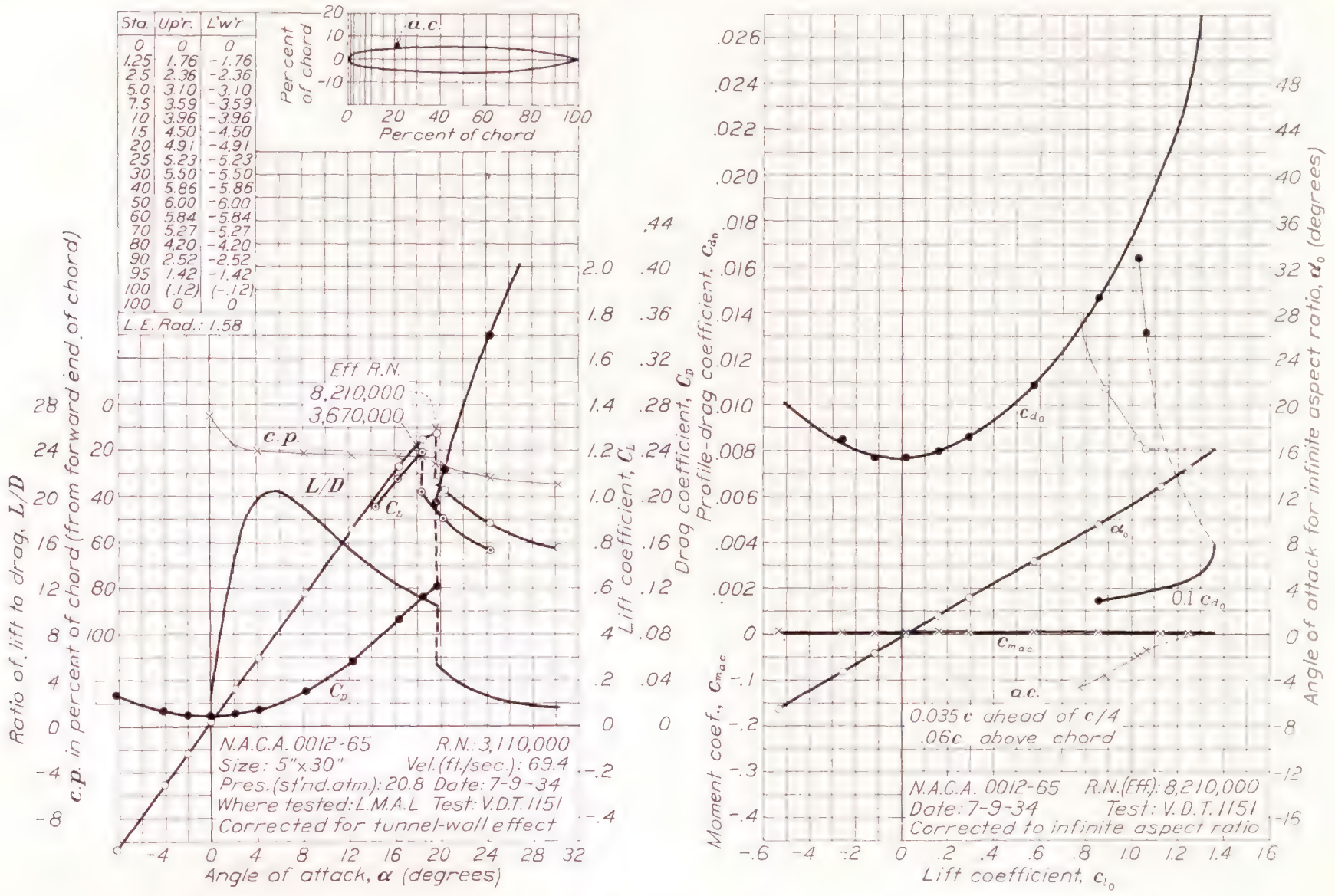

FIGURE 7.—N. A. C. A. 0012-65 airfoil.

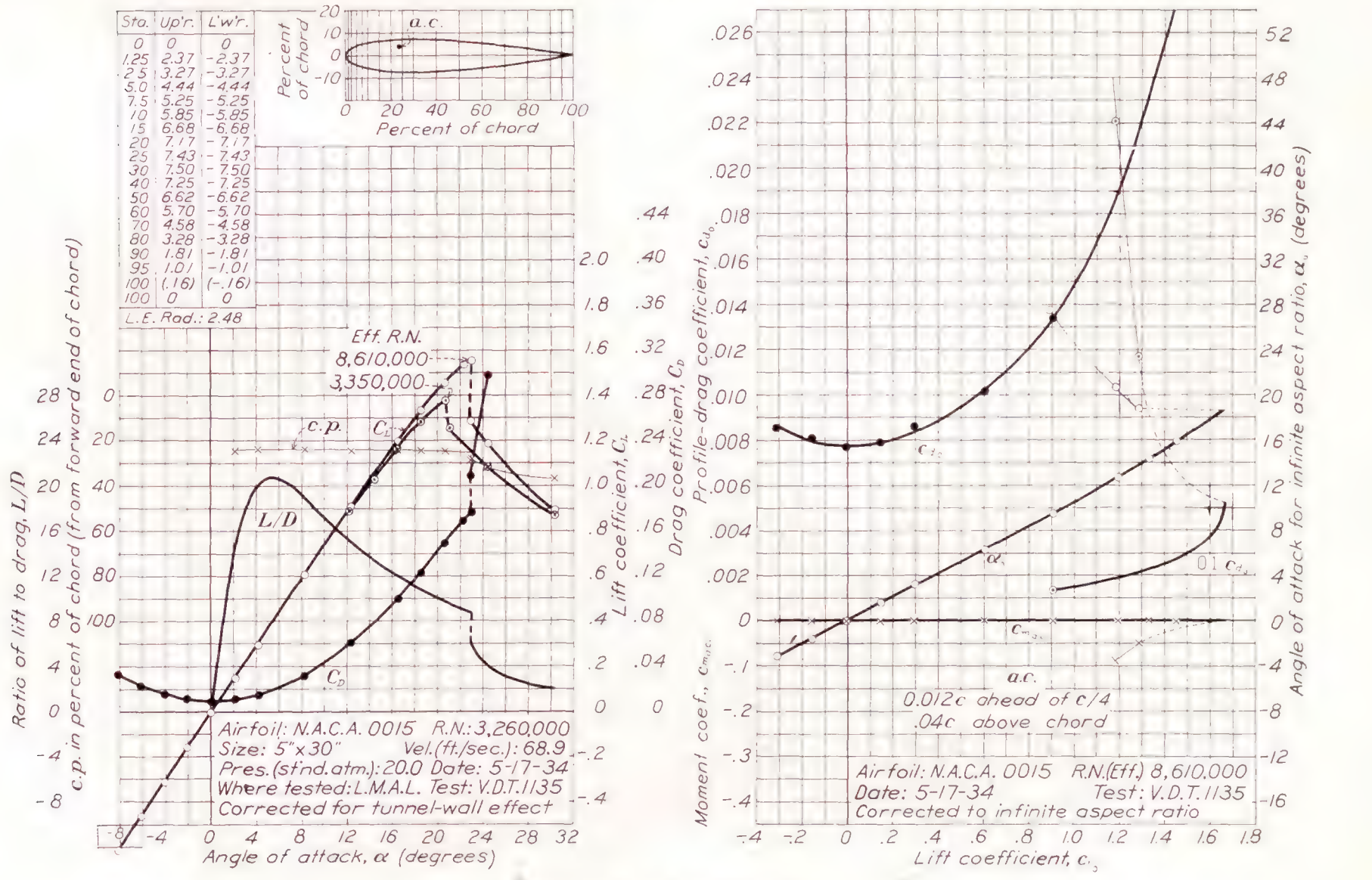

FIGURE 8.—N. A. C. A. 0015 airfoil.

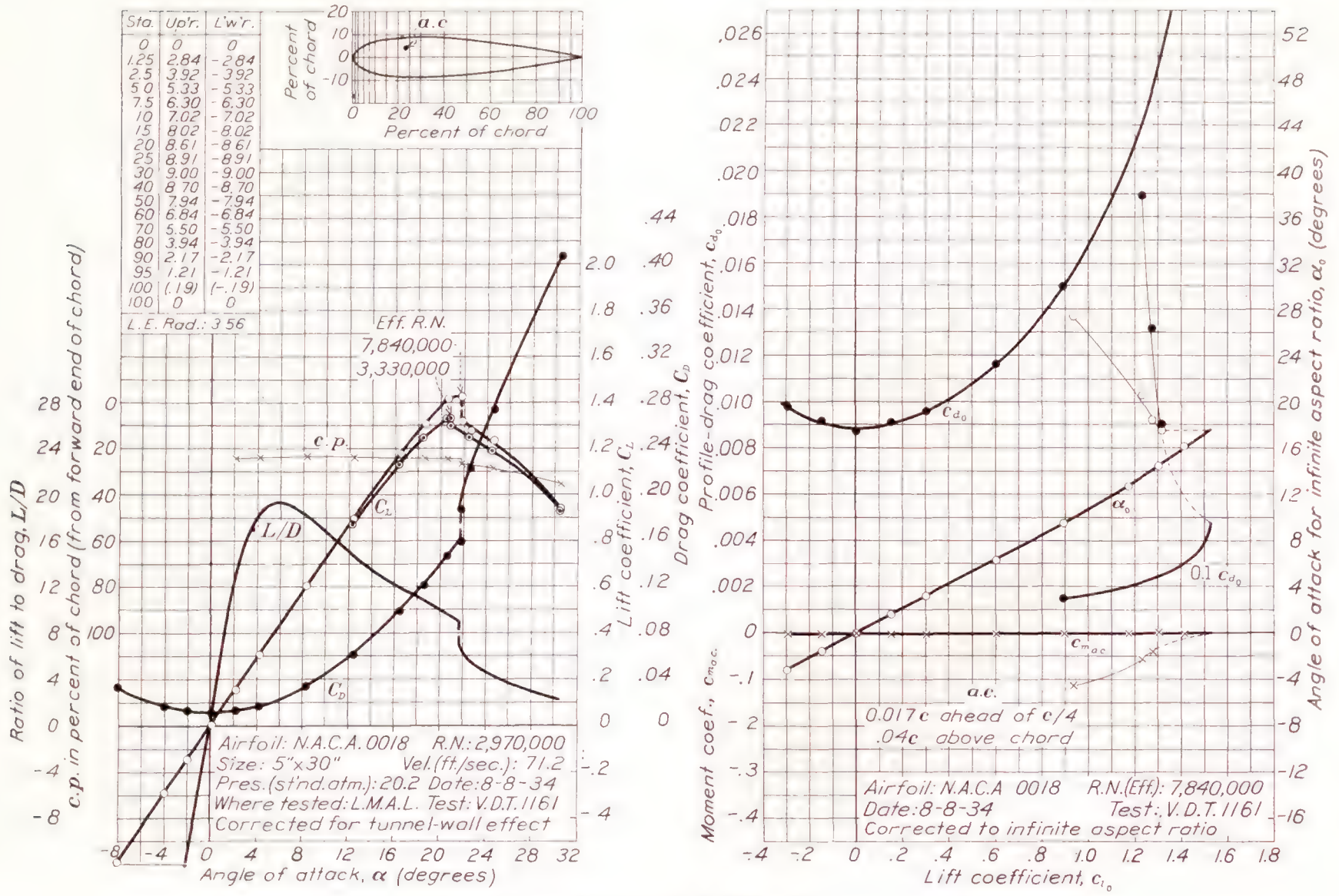

FIGURE 9.—N. A. C. A. 0018 airfoil.

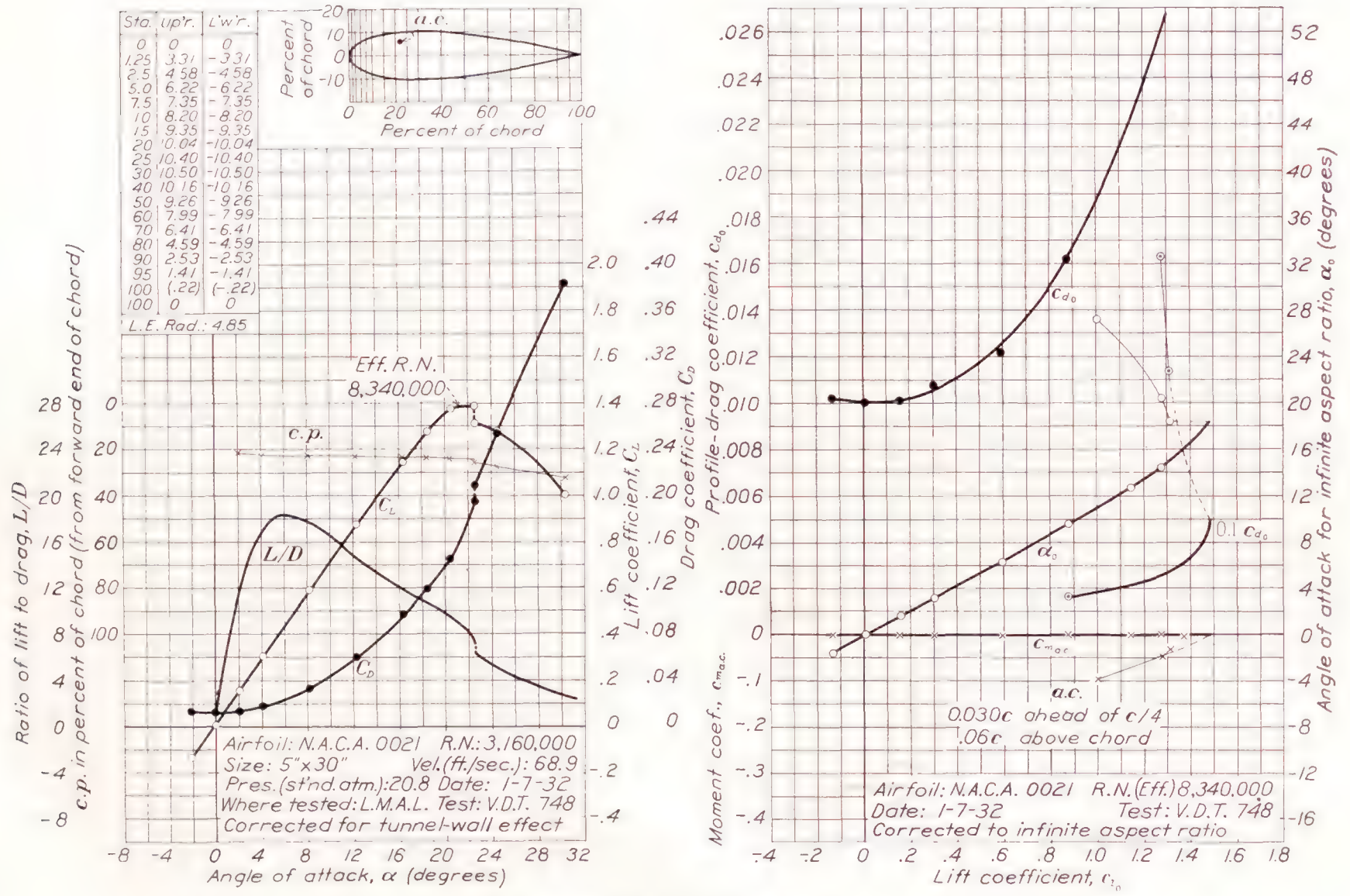

FIGURE 10.—N. A. C. A. 0021 airfoil.

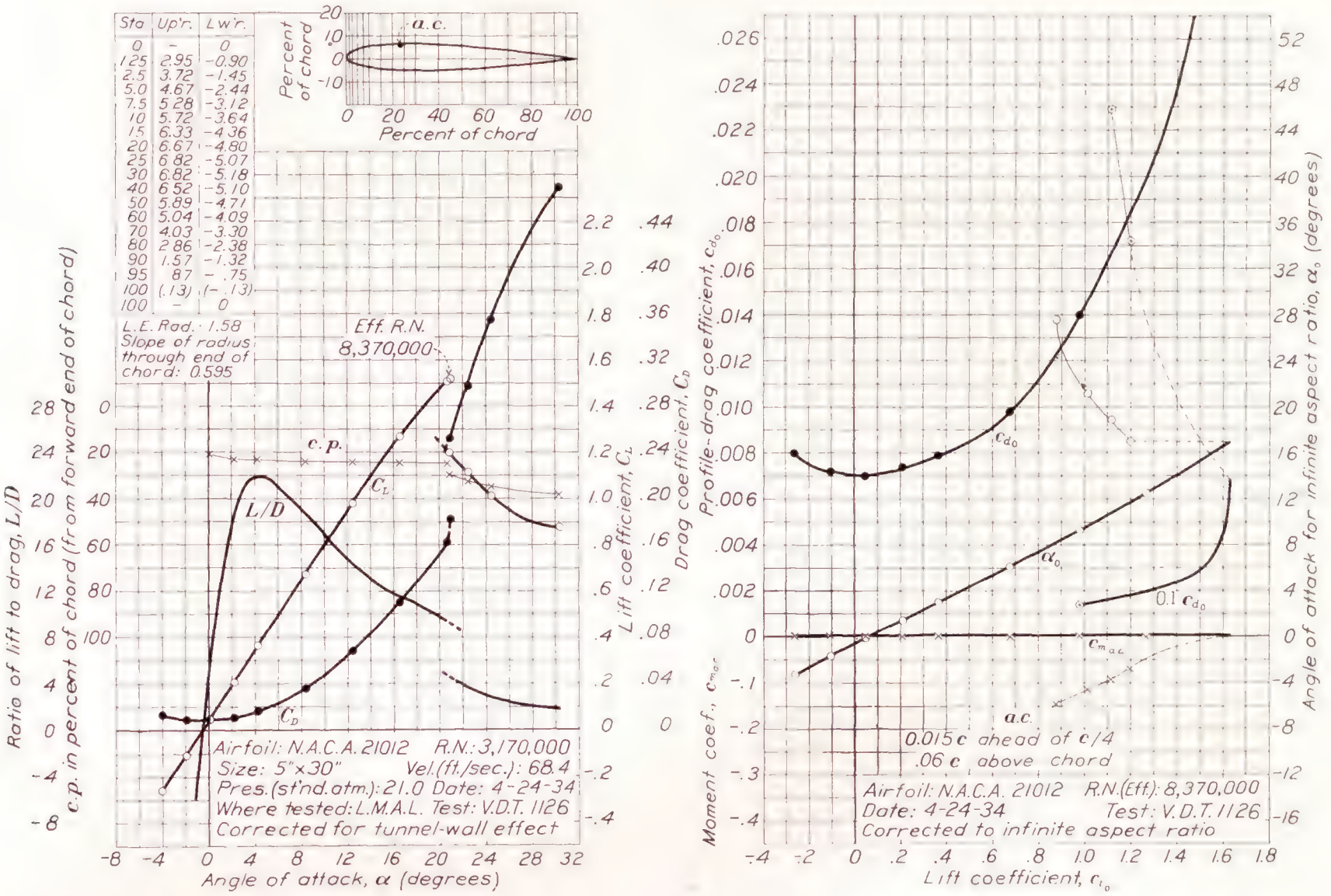

FIGURE 11.—N. A. C. A. 21012 airfoil.

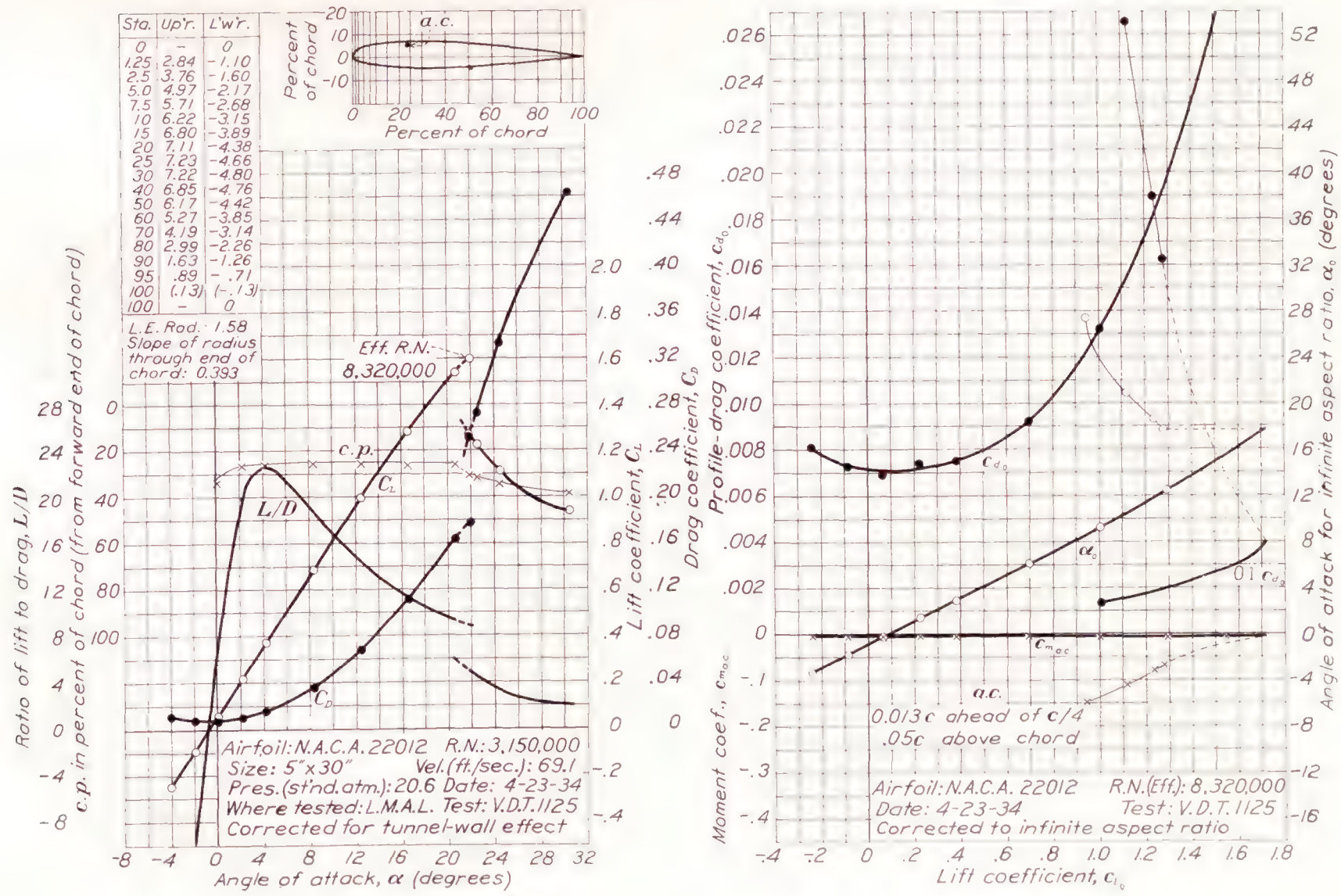

FIGURE 12.—N. A. C. A. 22012 airfoil.

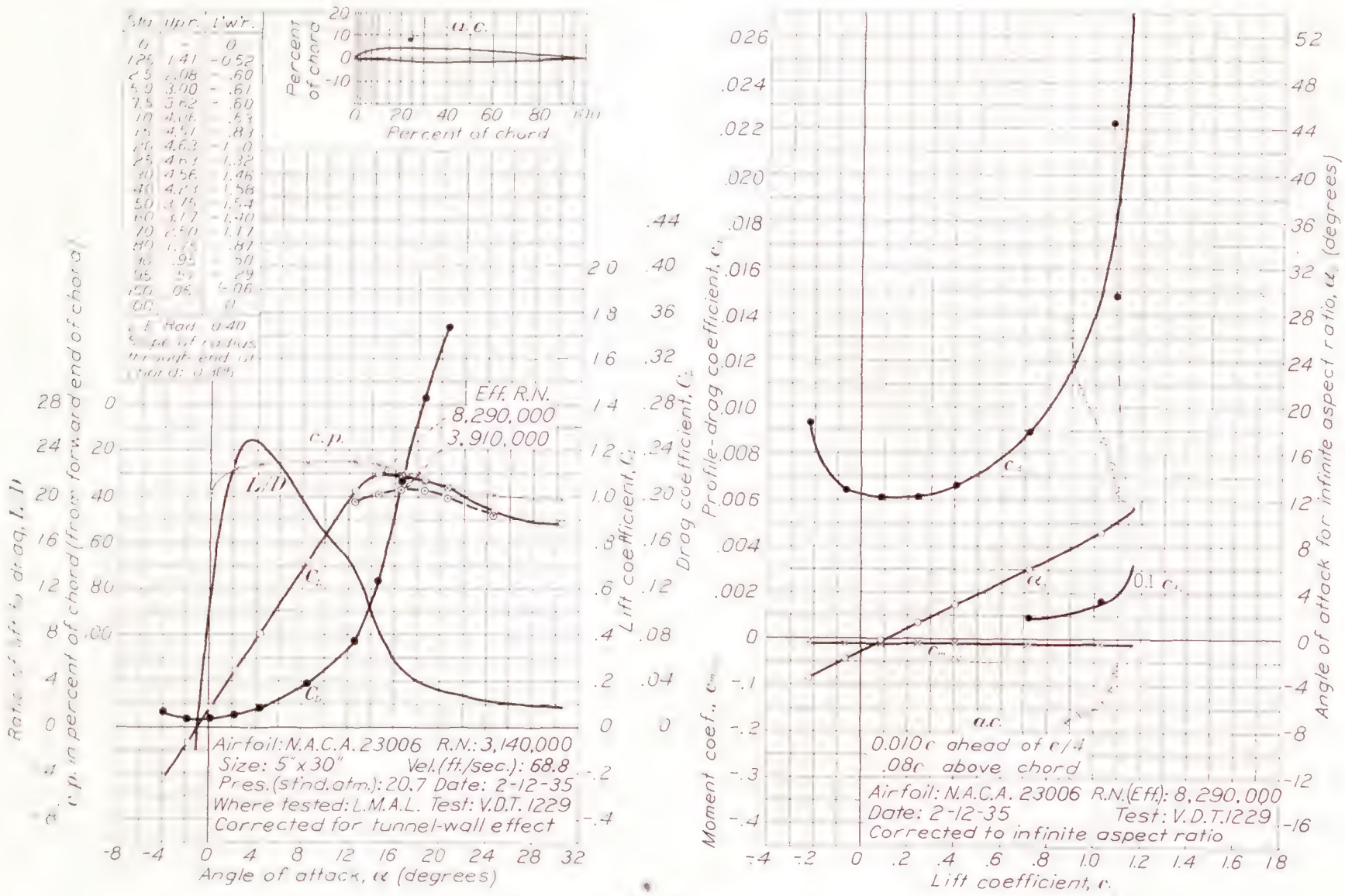

FIGURE 13.—N. A. C. A. 23006 airfoil.

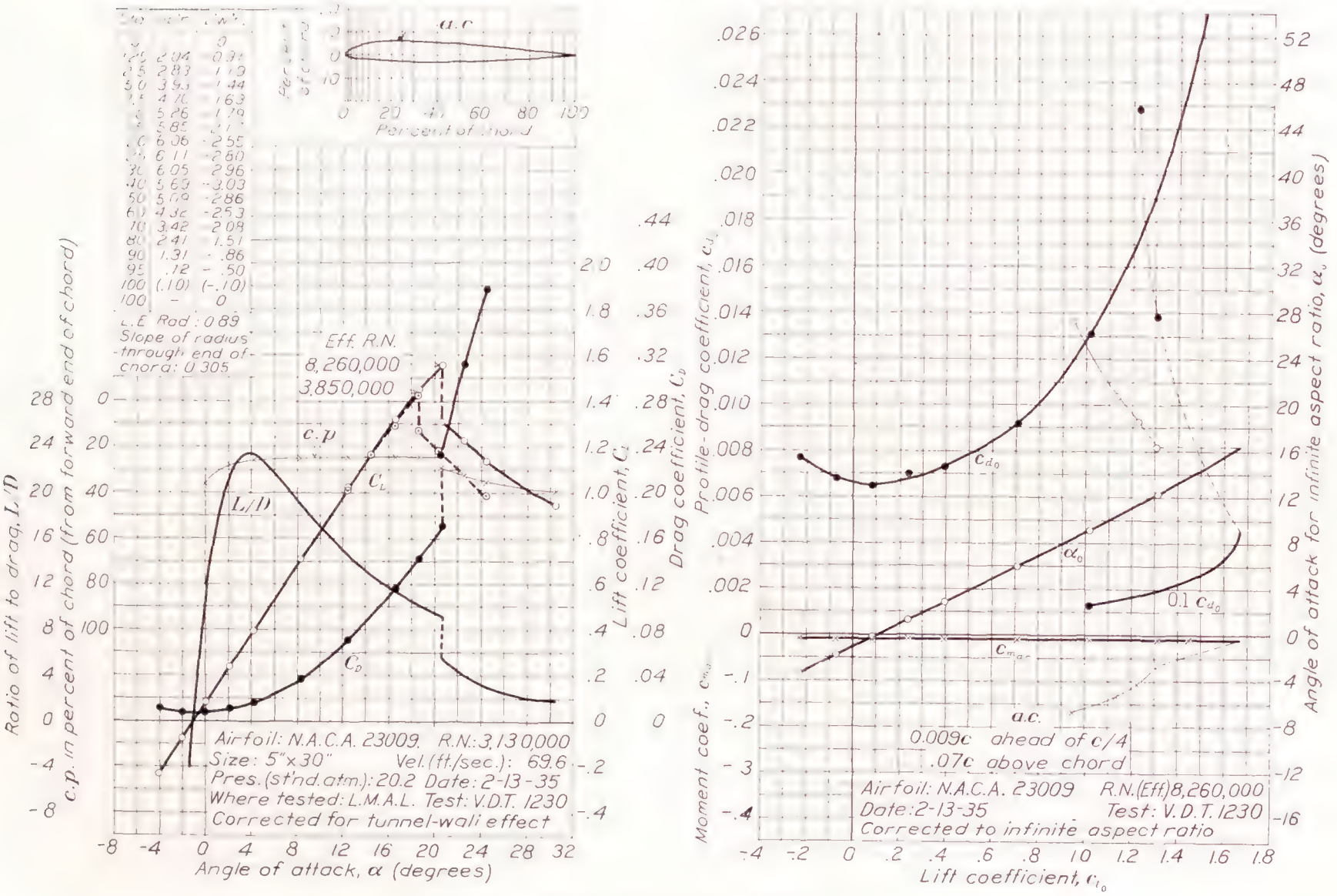

FIGURE 14.—N. A. C. A. 23009 airfoil.

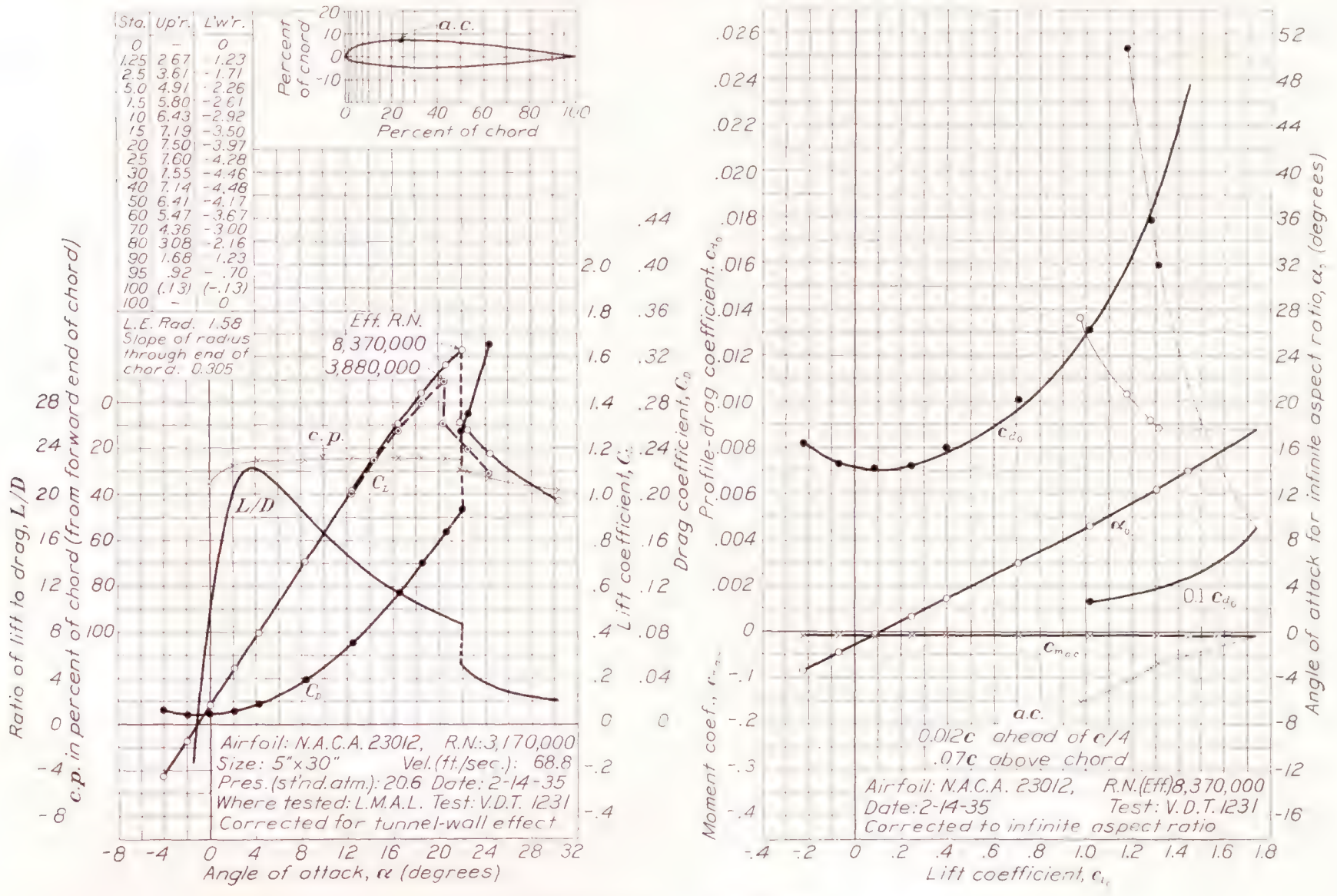

FIGURE 15.—N. A. C. A. 23012 airfoil.

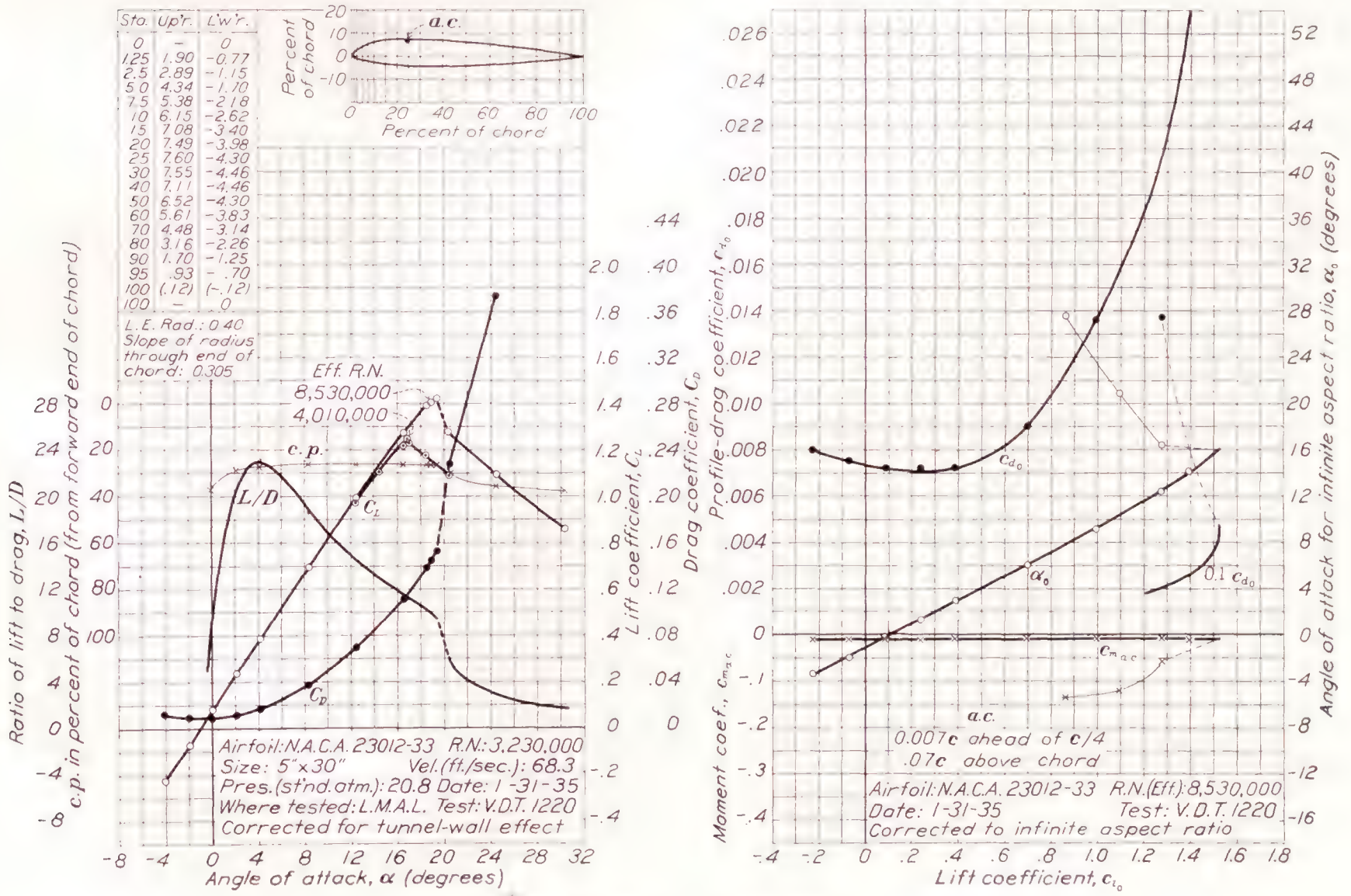

FIGURE 16.—N. A. C. A. 23012-33 airfoil.

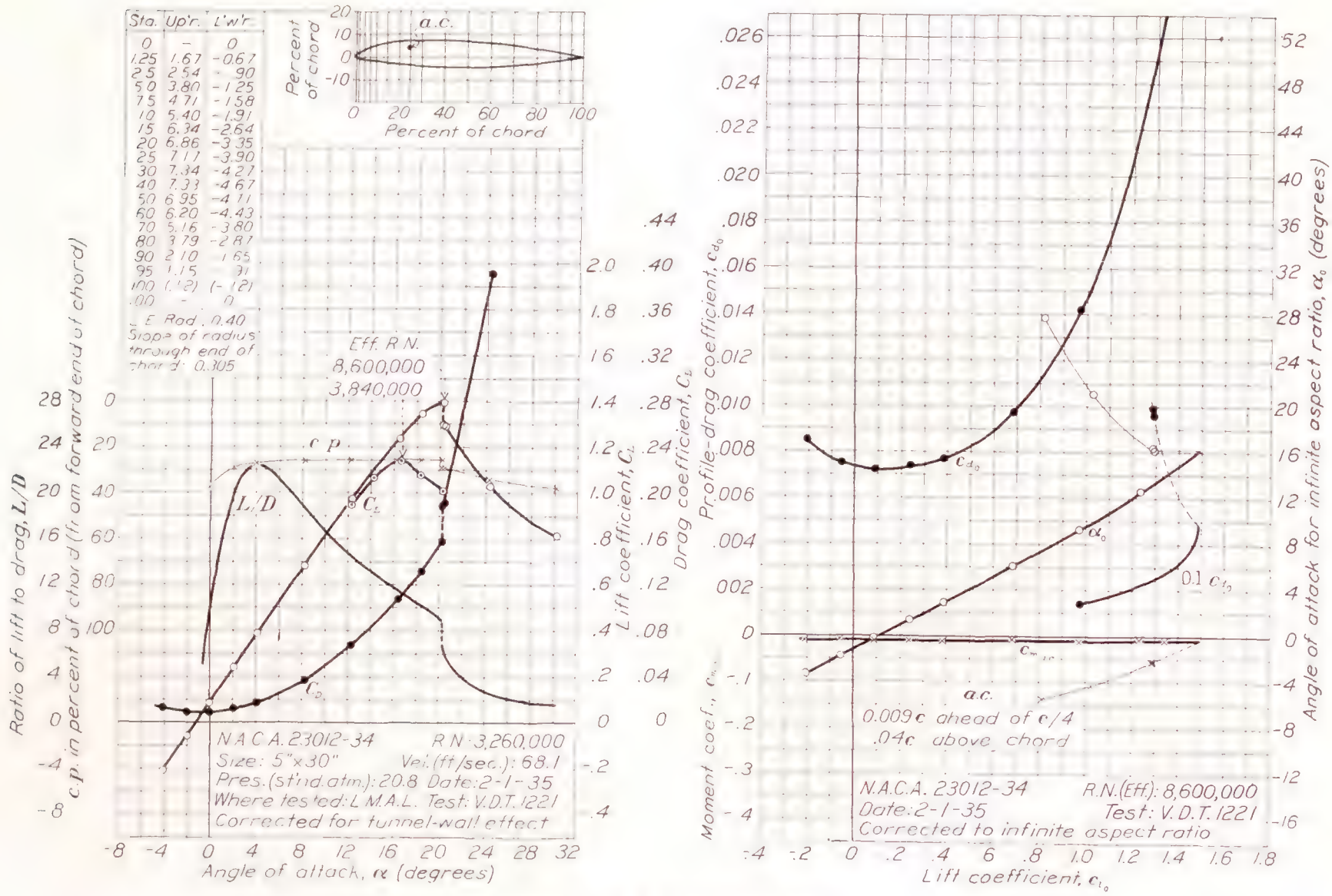

FIGURE 17.—N. A. C. A. 23012-34 airfoil.

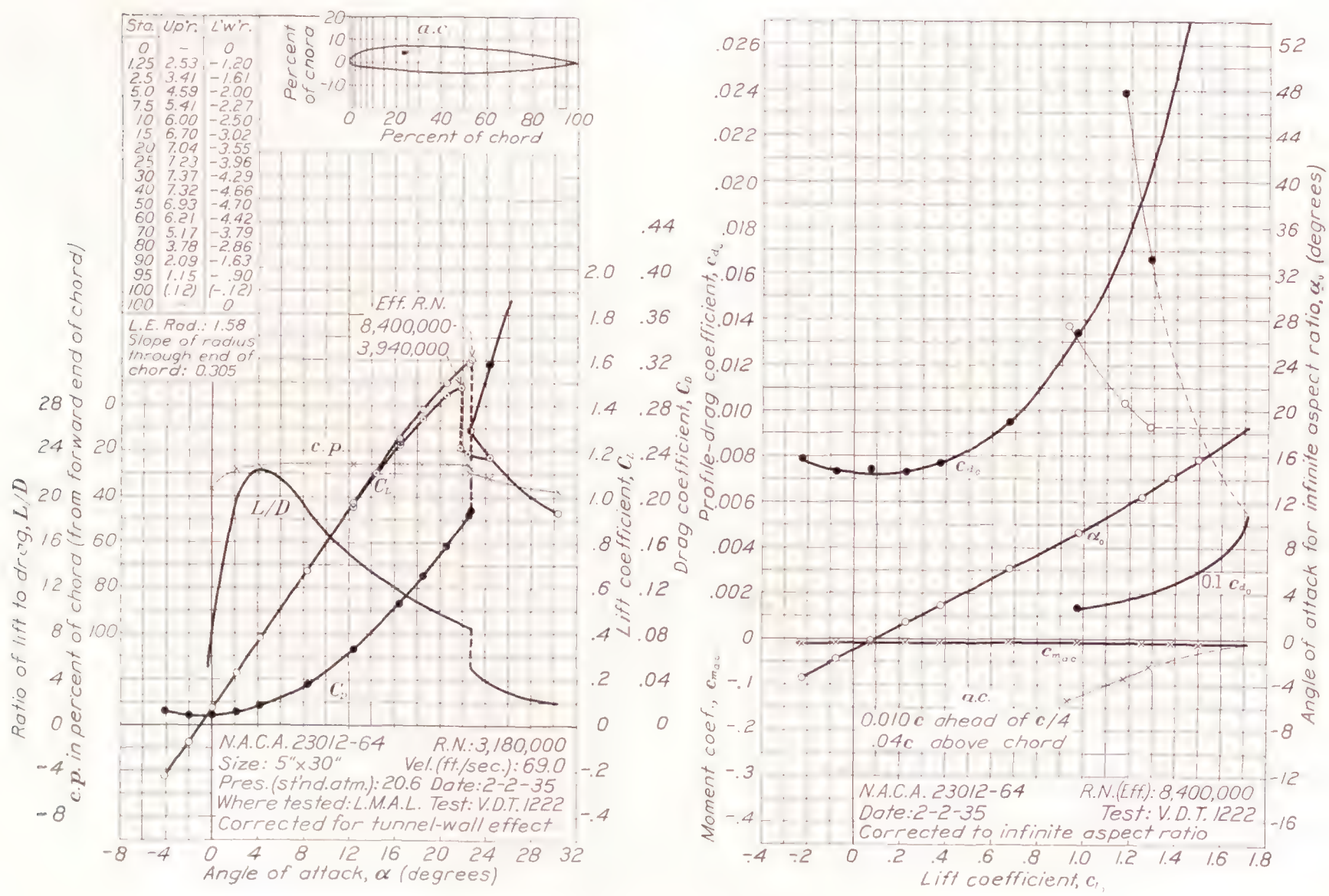

FIGURE 18.—N. A. C. A. 23012-64 airfoil.

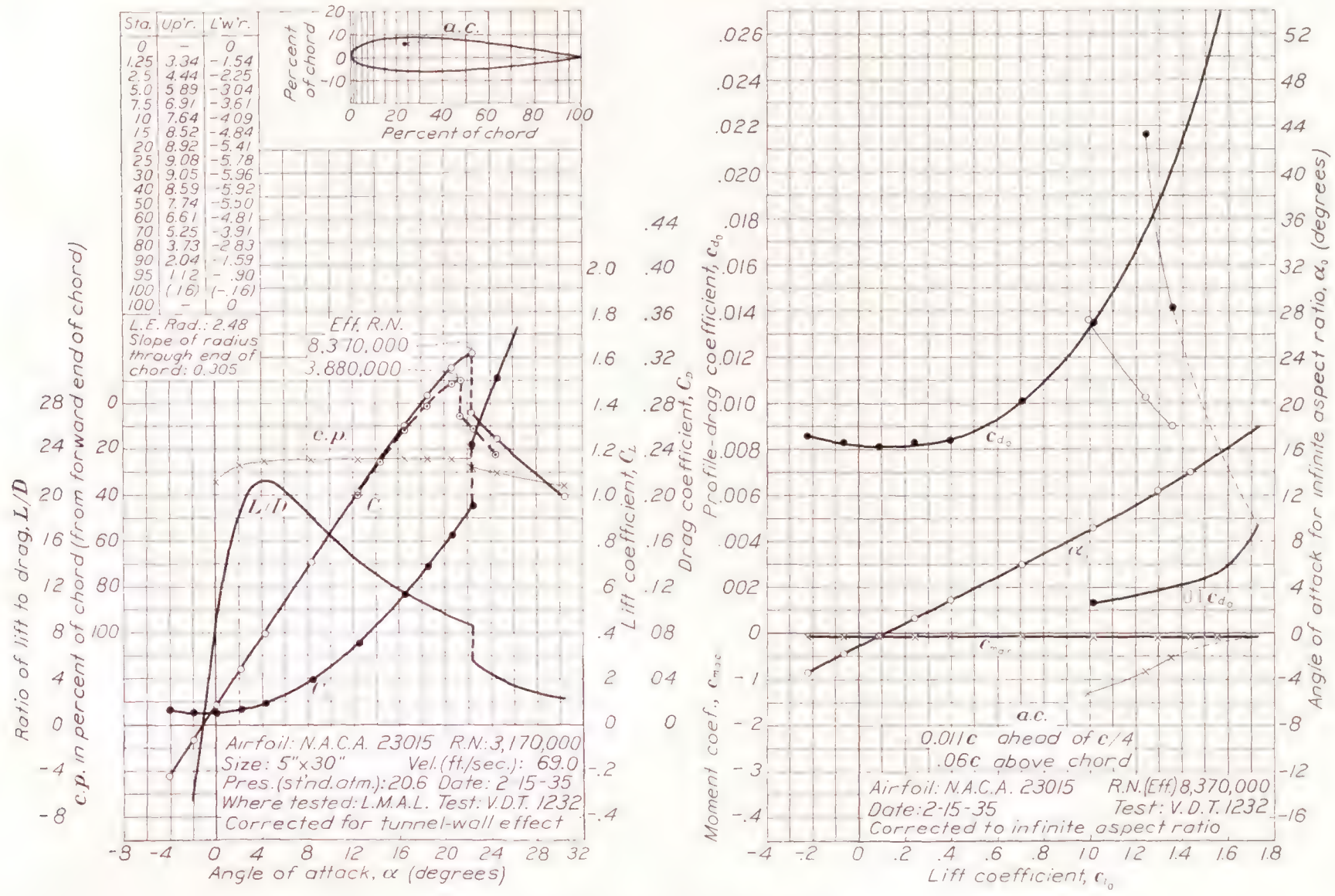

FIGURE 19.—N. A. C. A. 23015 airfoil.

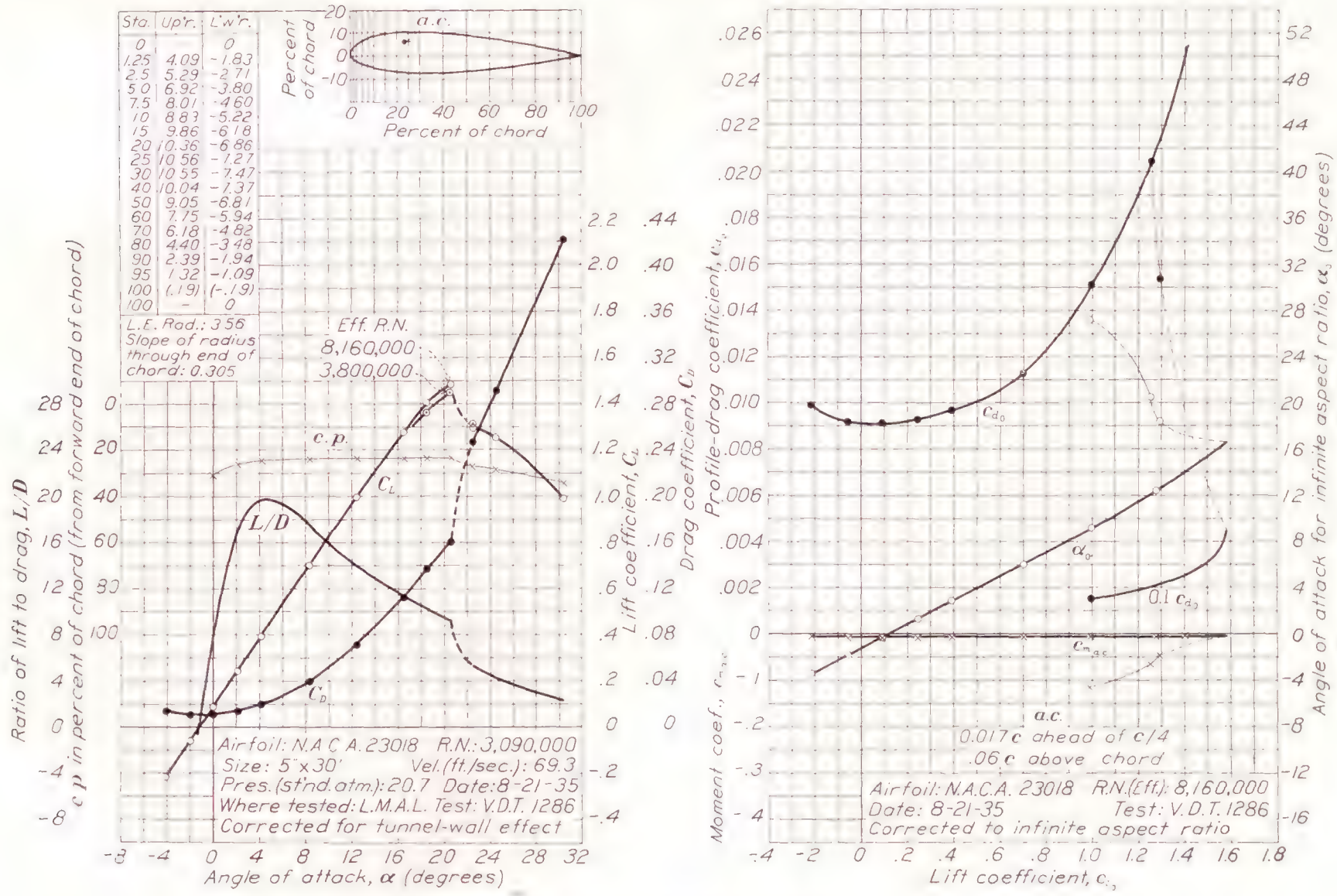

FIGURE 20.—N. A. C. A. 23018 airfoil.

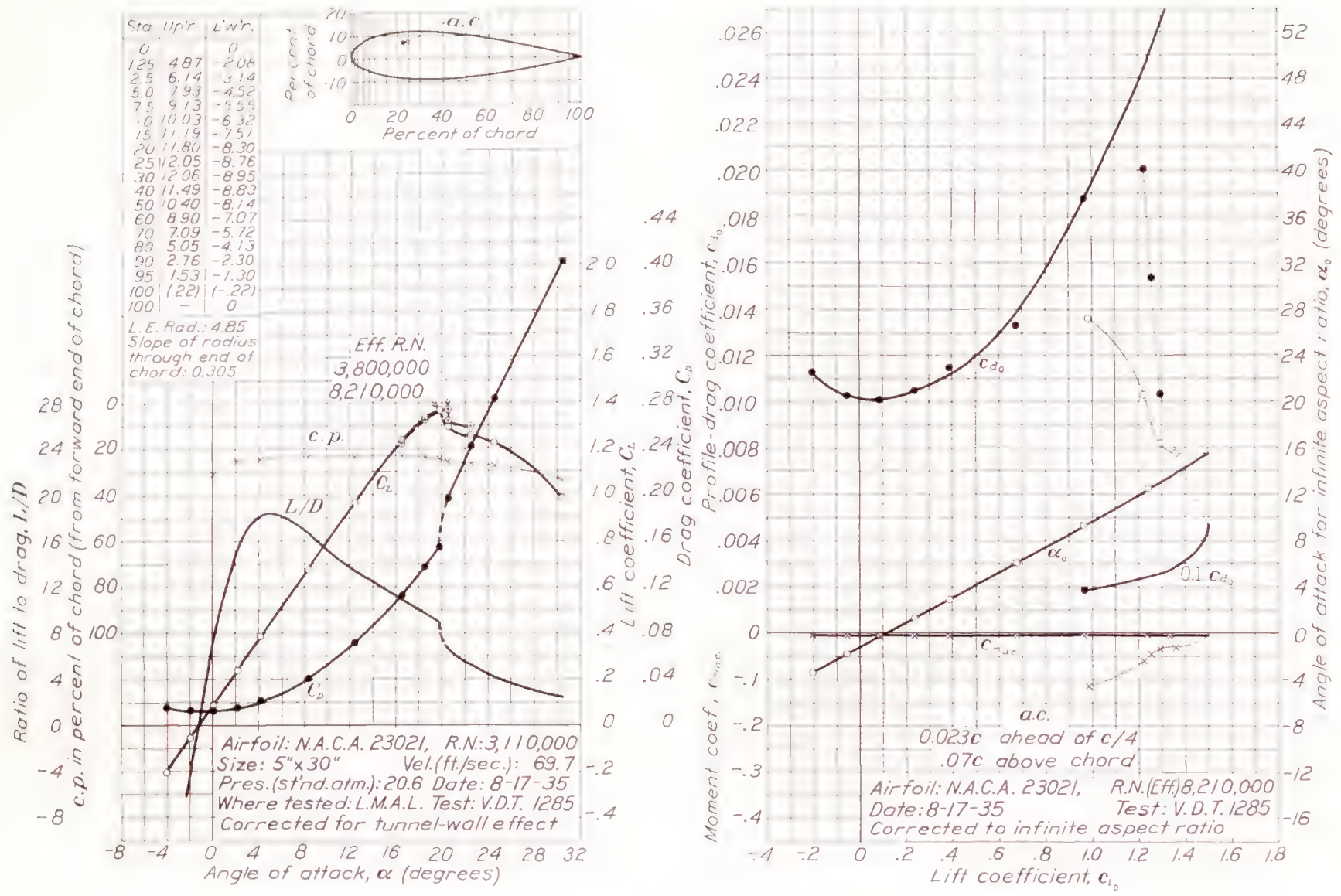

FIGURE 21.—N. A. C. A. 23021 airfoil.

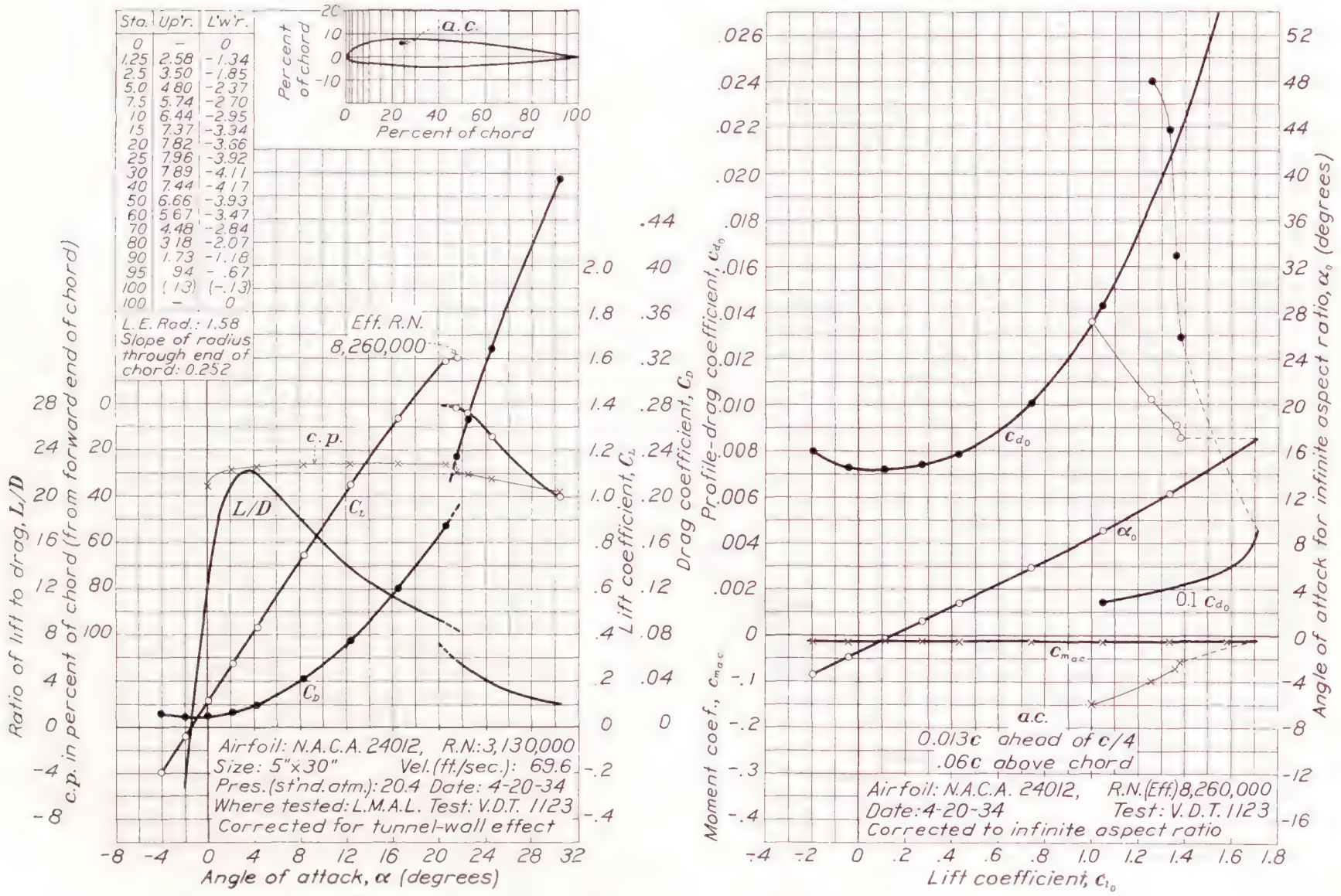

FIGURE 22.—N. A. C. A. 24012 airfoil.

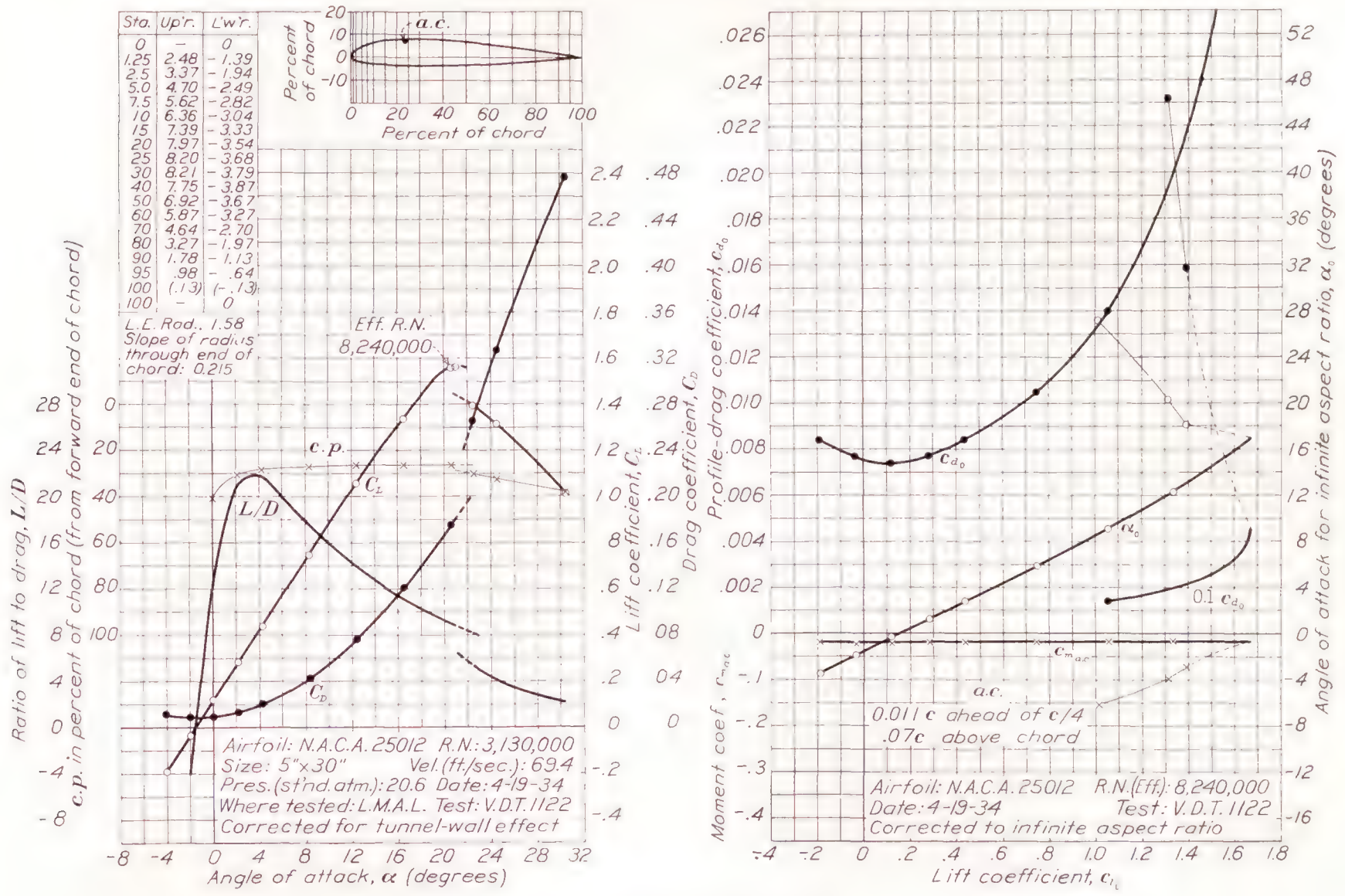

FIGURE 23.—N. A. C. A. 25012 airfoil.

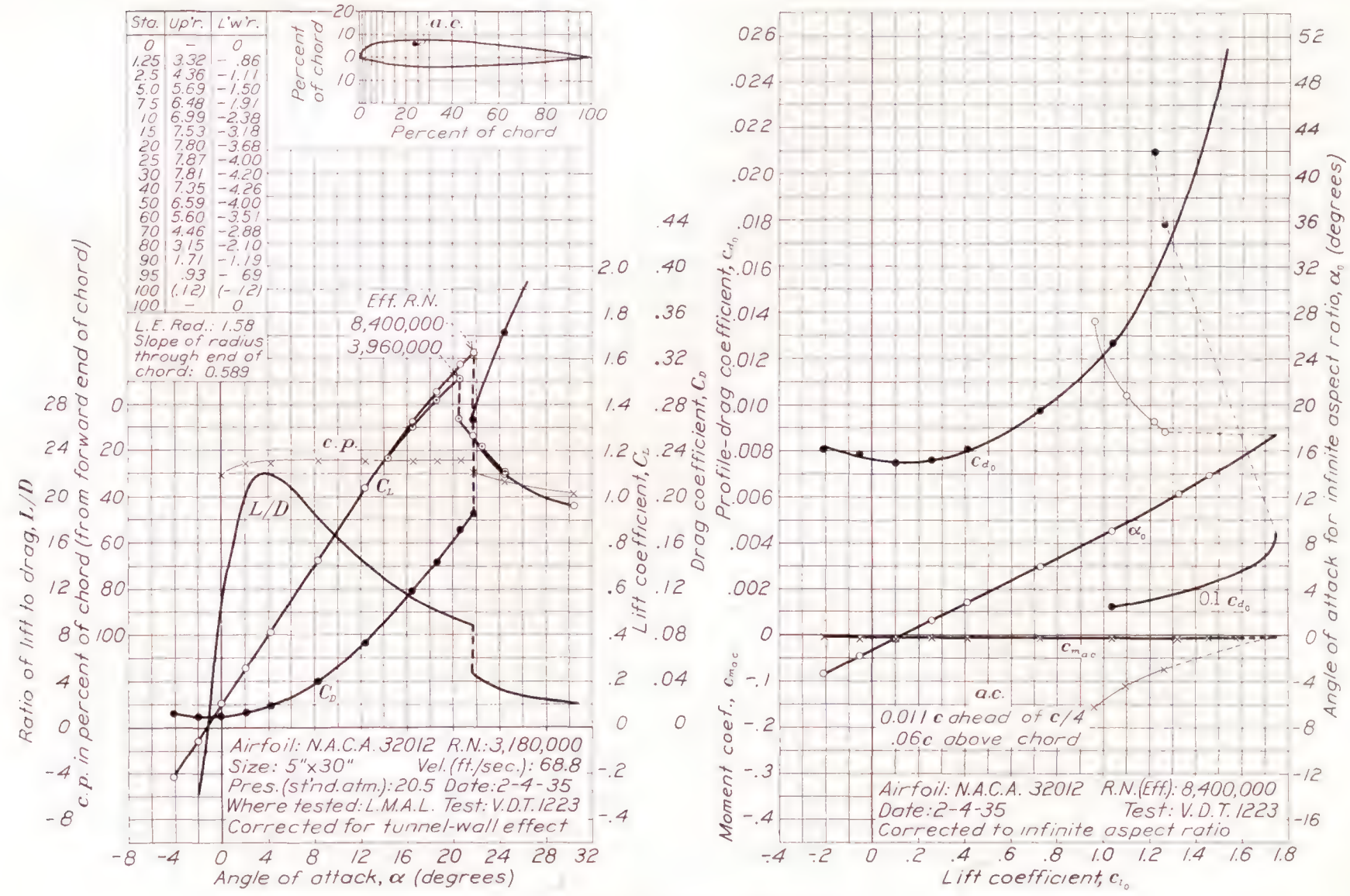

FIGURE 24.—N. A. C. A. 32012 airfoil.

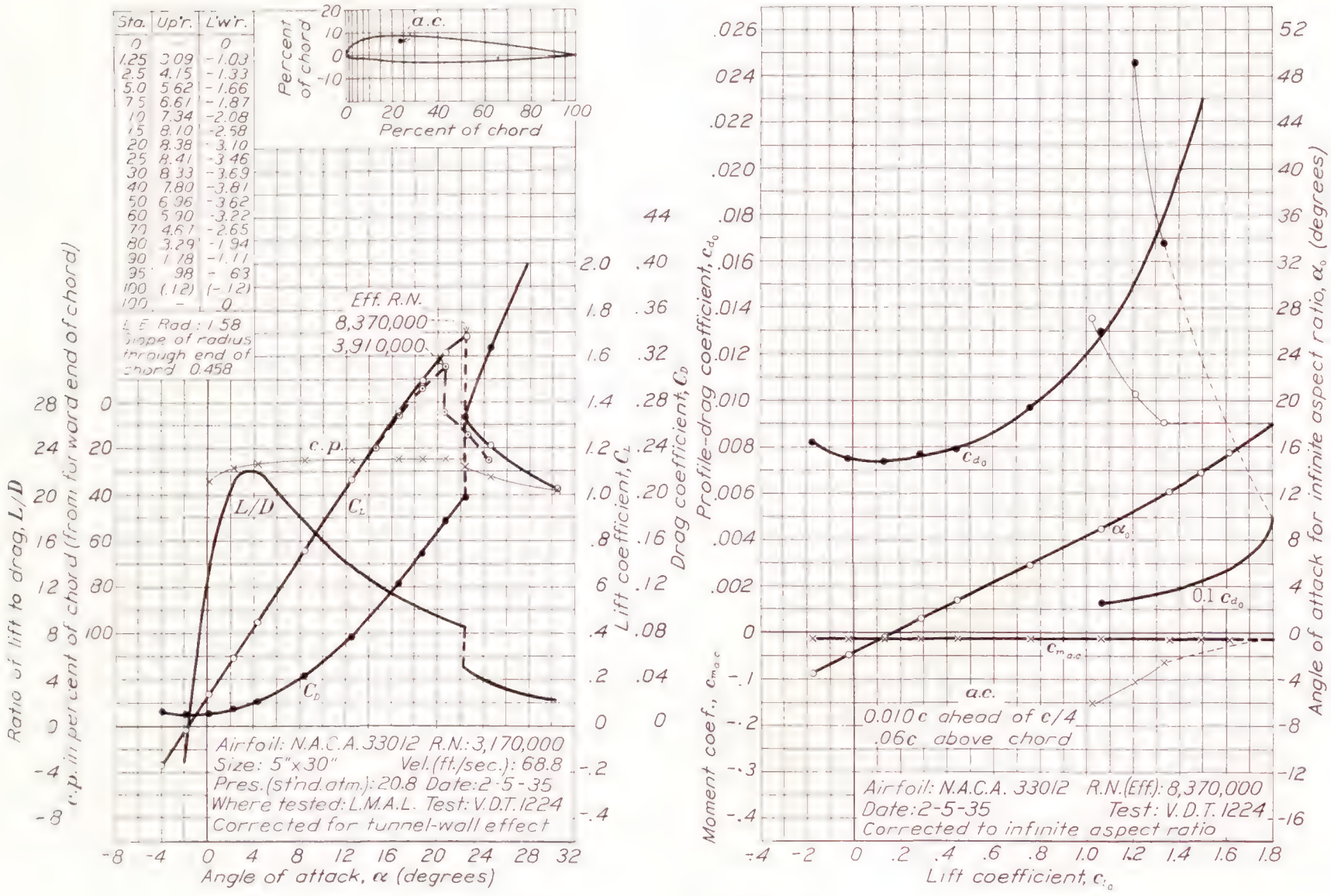

FIGURE 25.—N. A. C. A. 33012 airfoil.

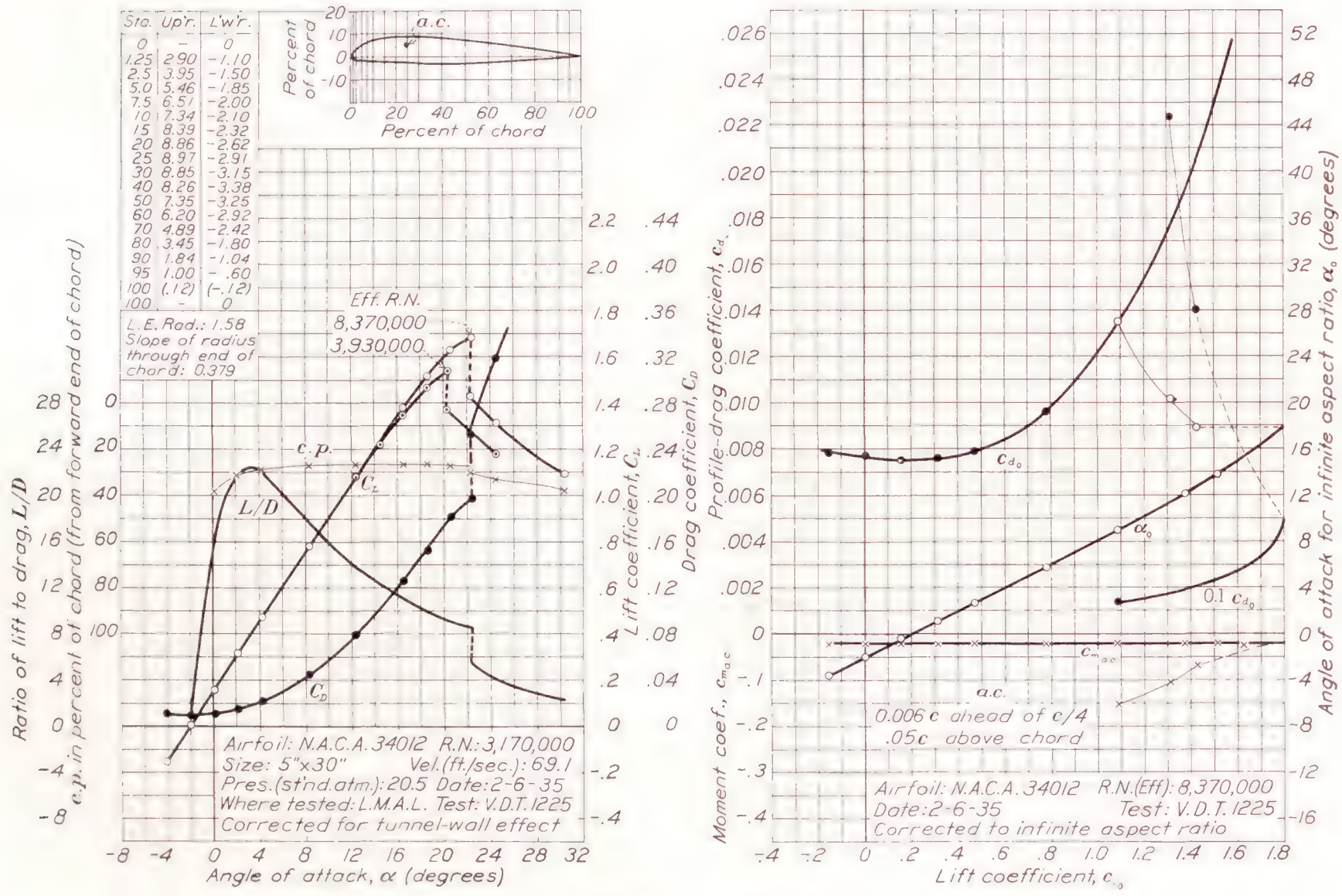

FIGURE 26.—N. A. C. A. 34012 airfoil.

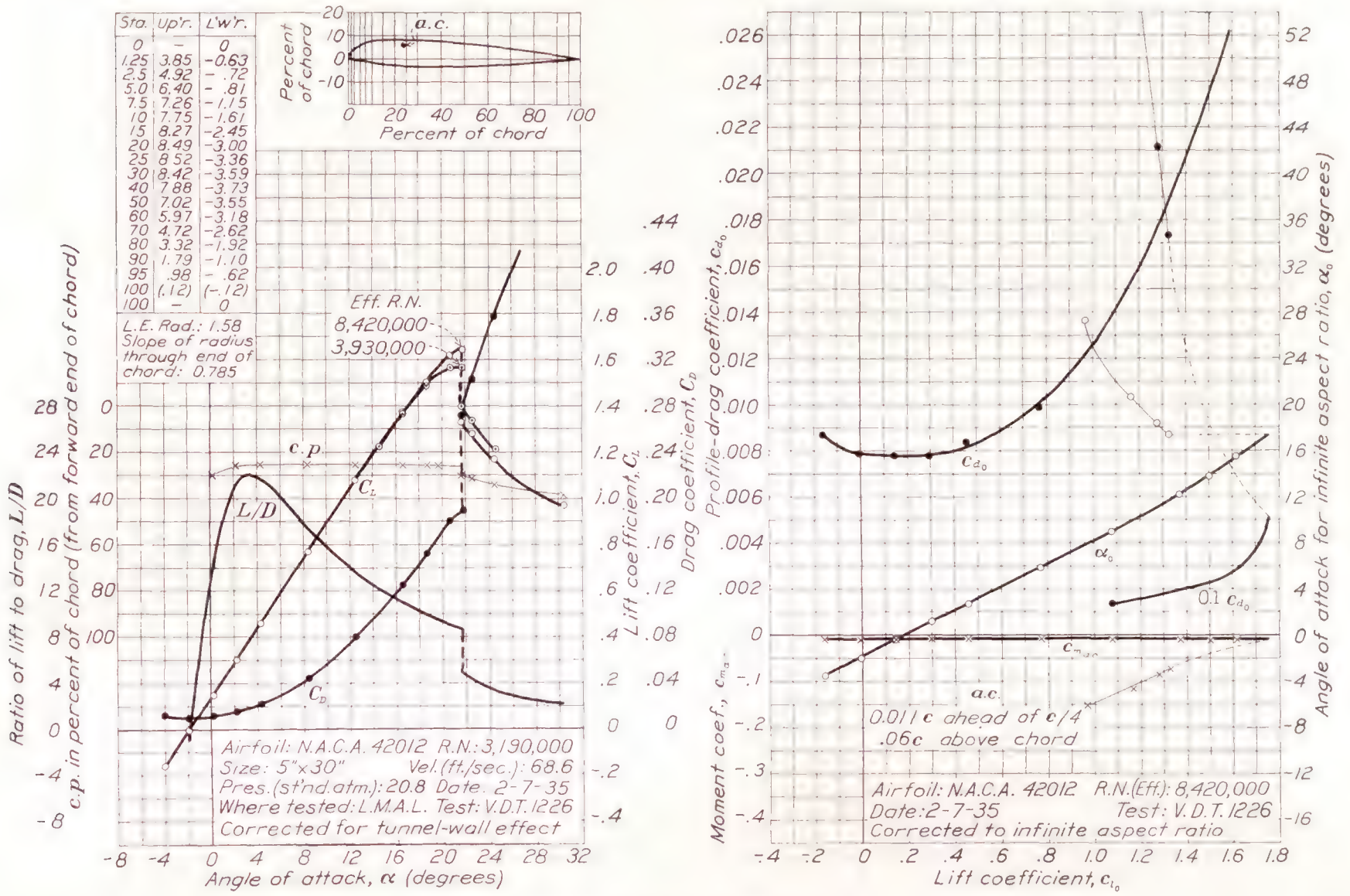

FIGURE 27.—N. A. C. A. 42012 airfoil.

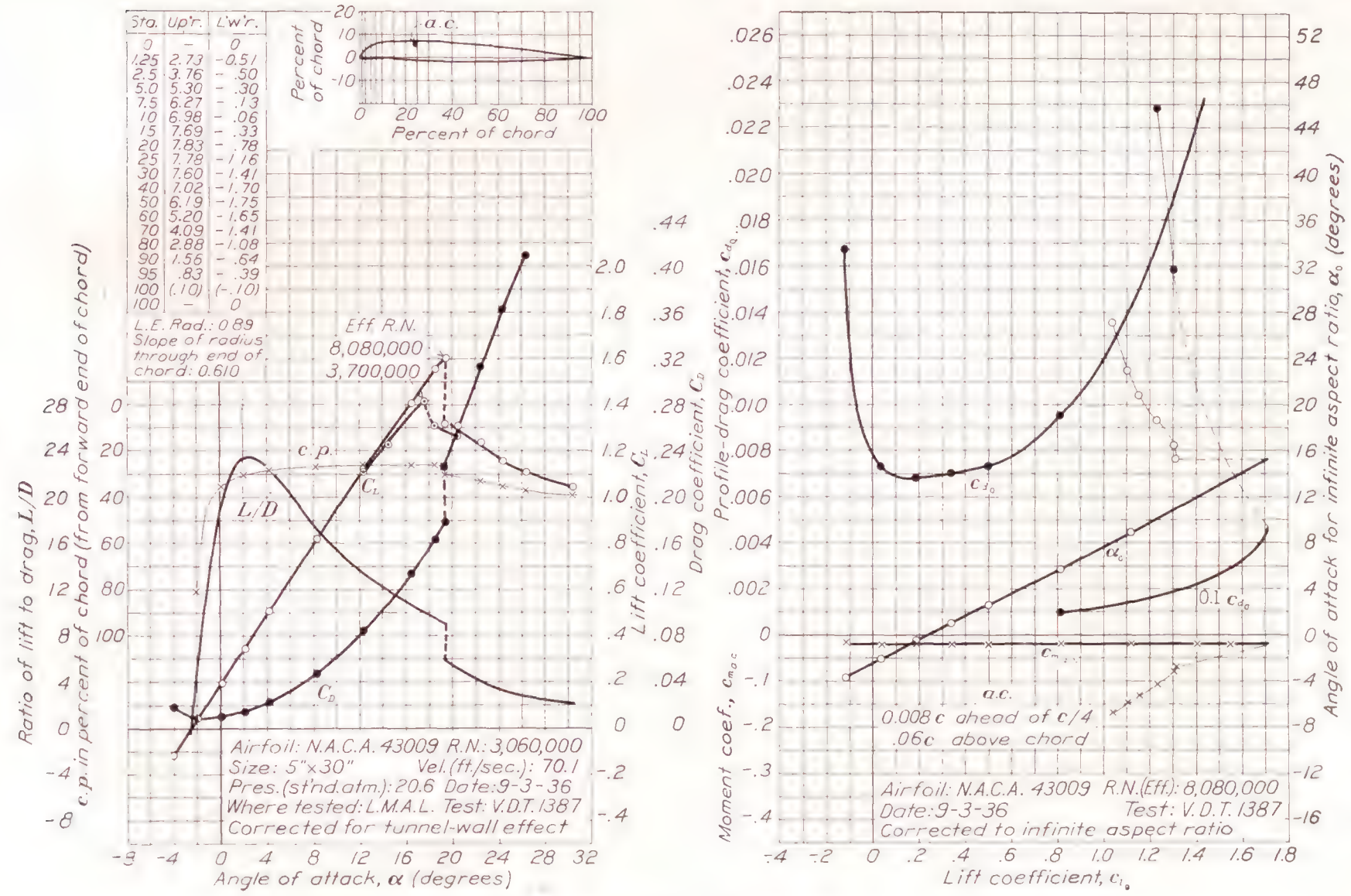

FIGURE 28.—N. A. C. A. 43009 airfoil.

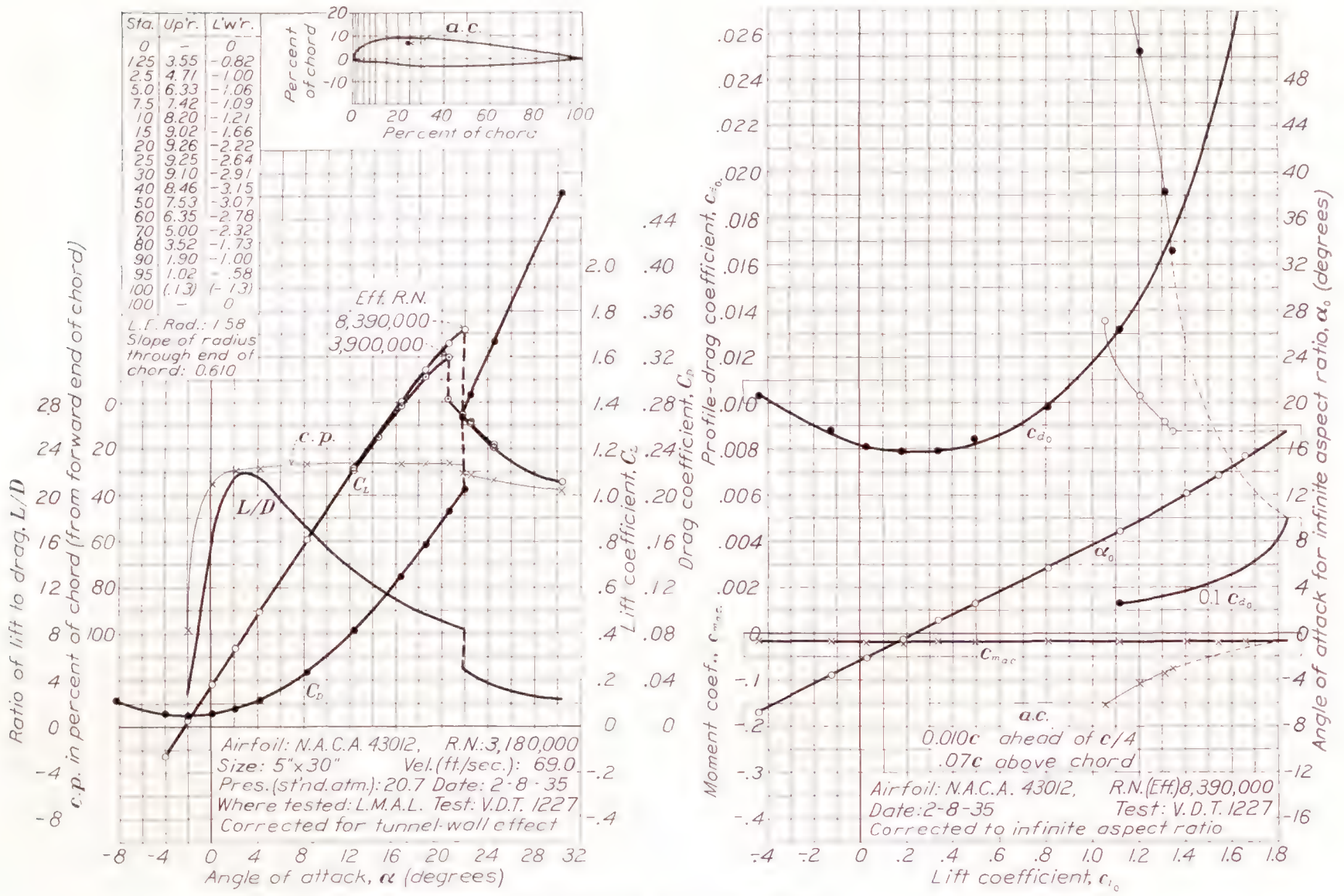

FIGURE 29.—N. A. C. A. 43012 airfoil.

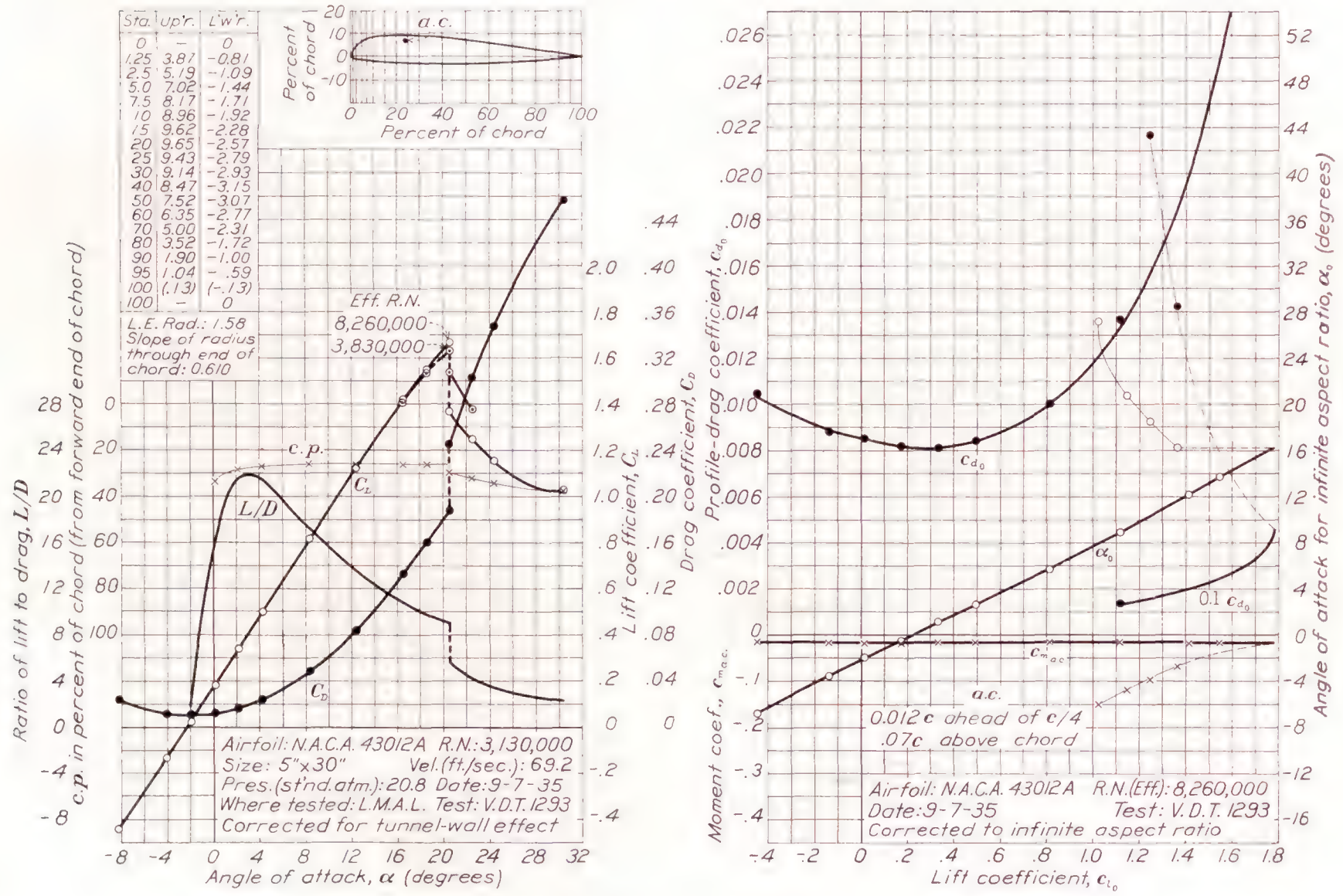

FIGURE 30.—N. A. C. A. 43012A airfoil.

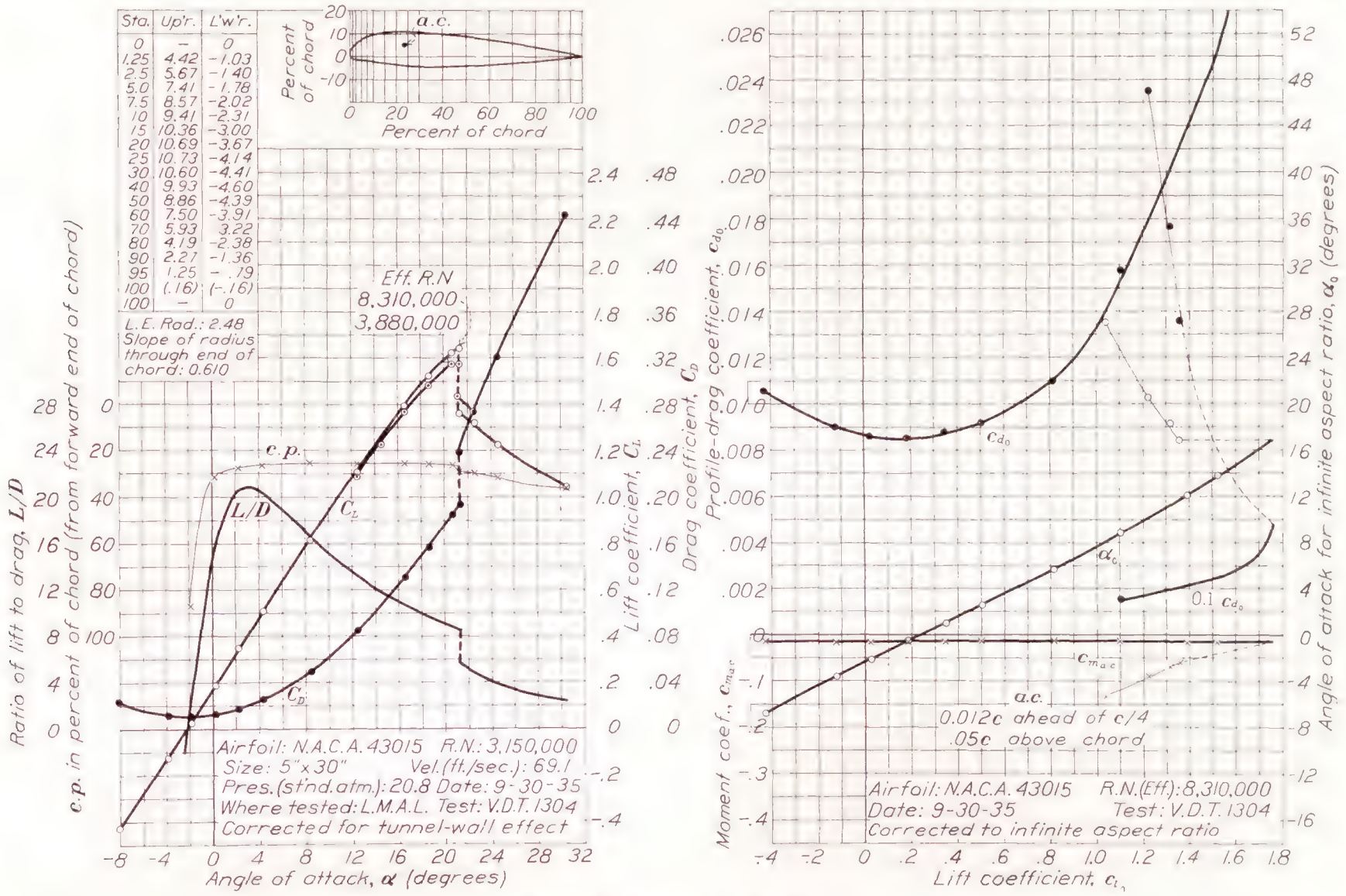

FIGURE 31.—N. A. C. A. 43015 airfoil.

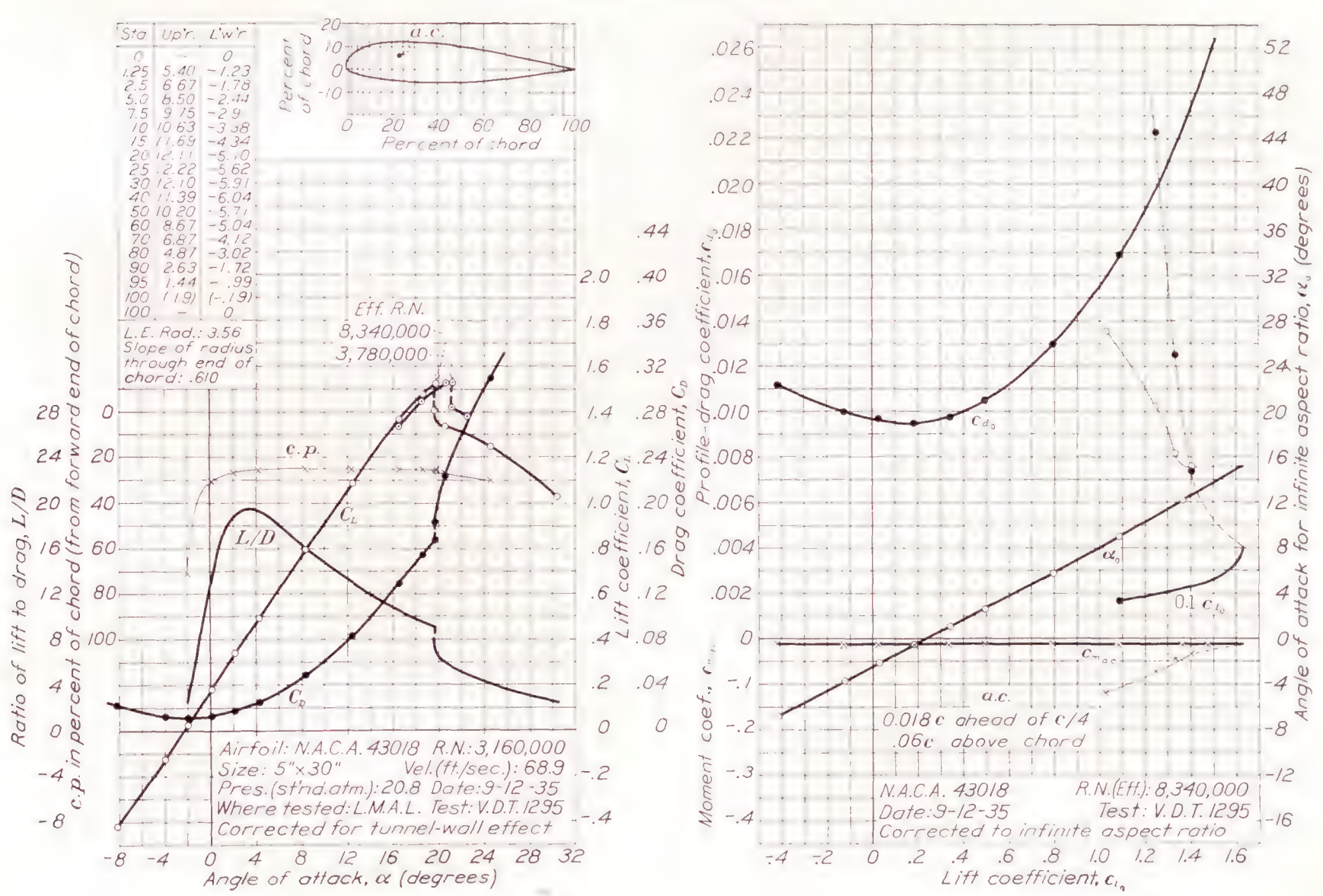

FIGURE 32.—N. A. C. A. 43018 airfoil.

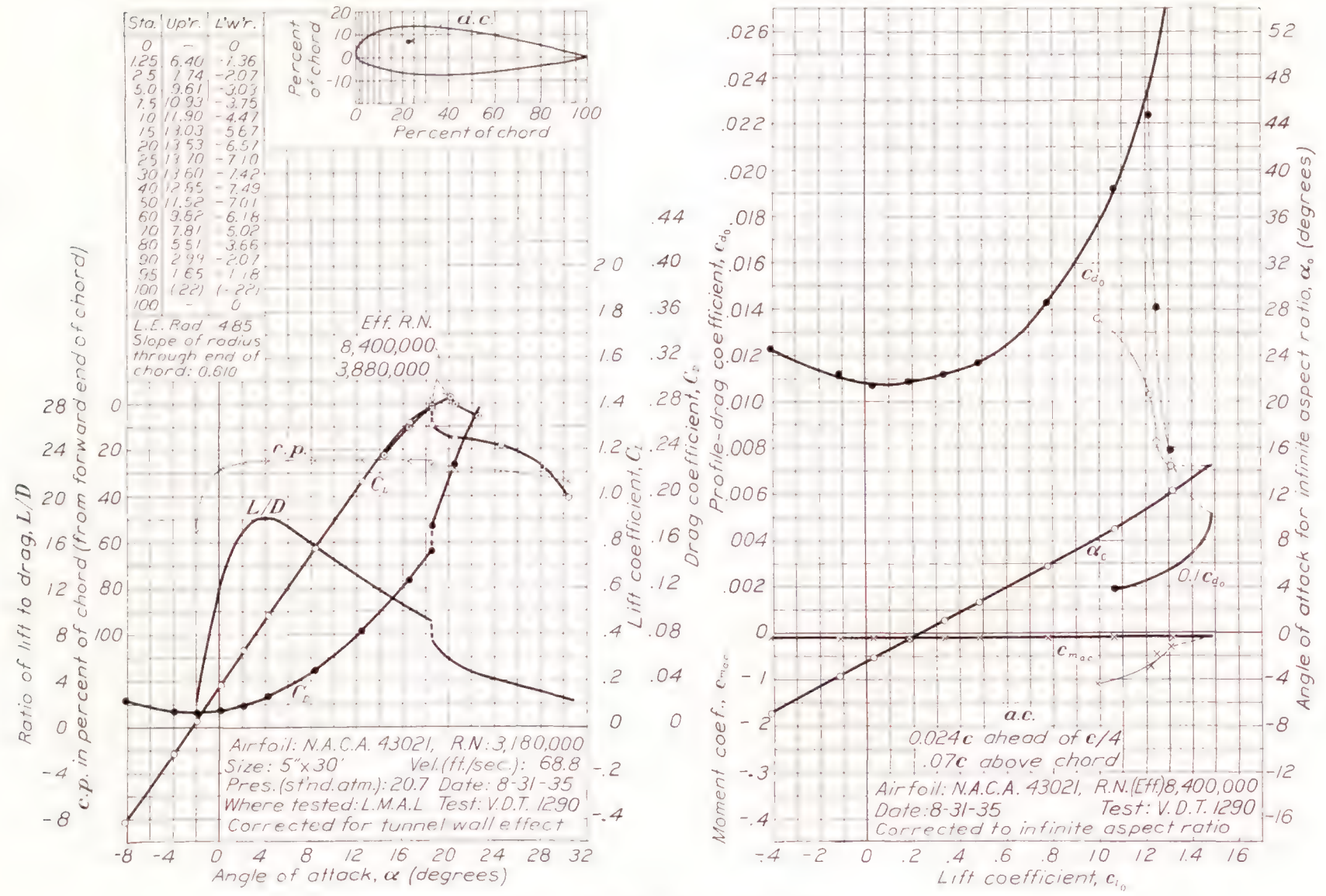

FIGURE 33. N. A. C. A. 43021 airfoil.

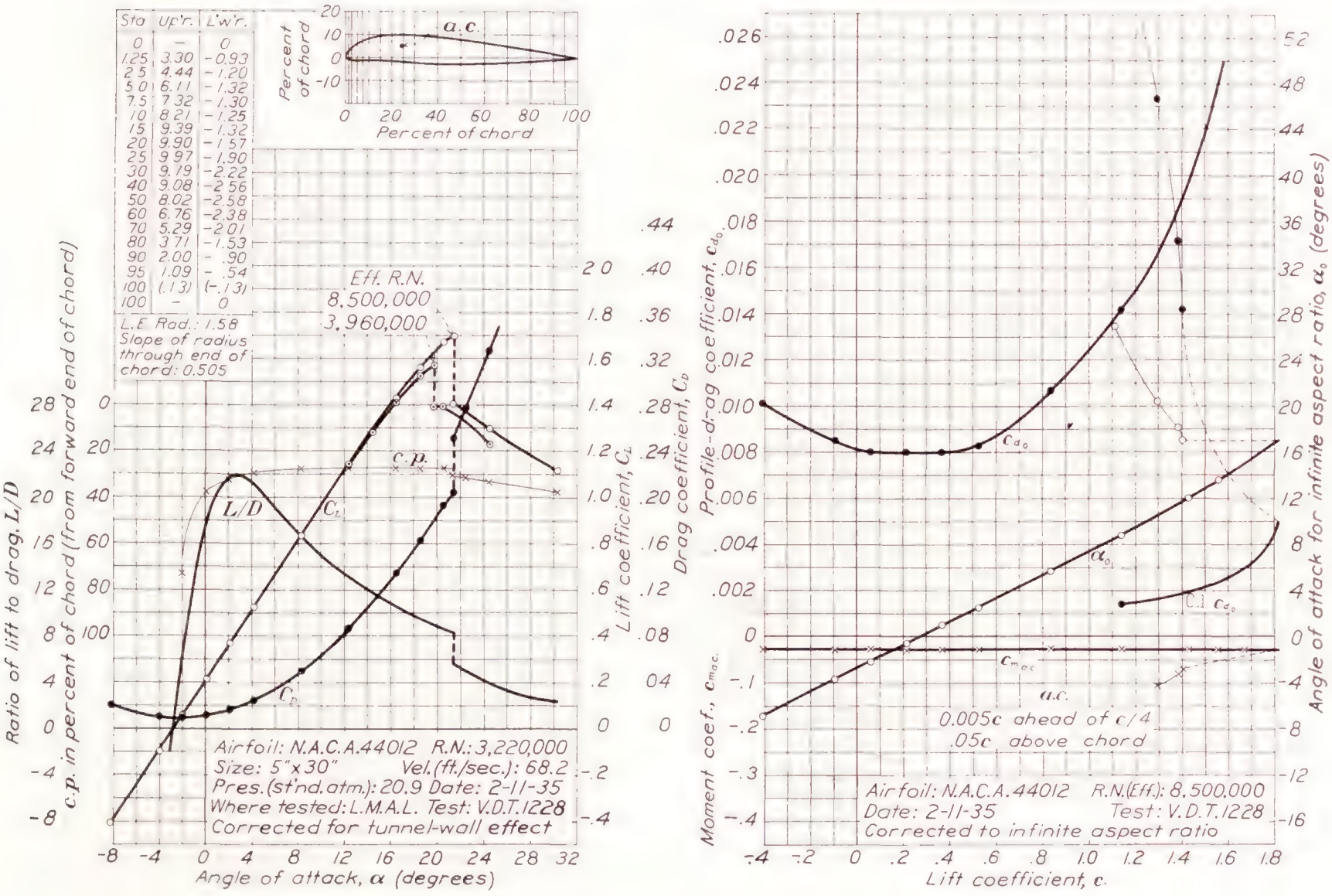

FIGURE 34.—N. A. C. A. 44012 airfoil.

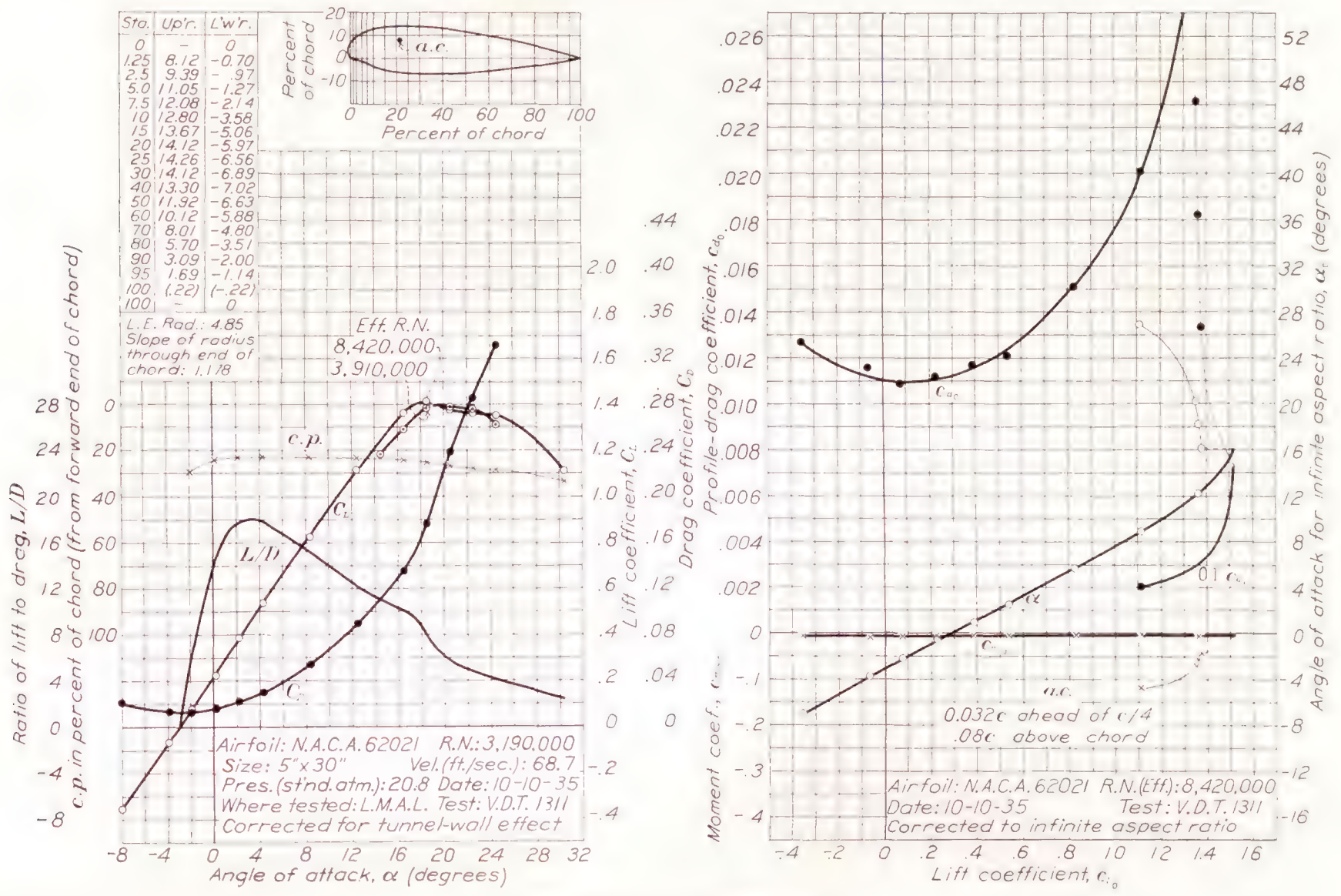

FIGURE 35.—N. A. C. A. 62021 airfoil.

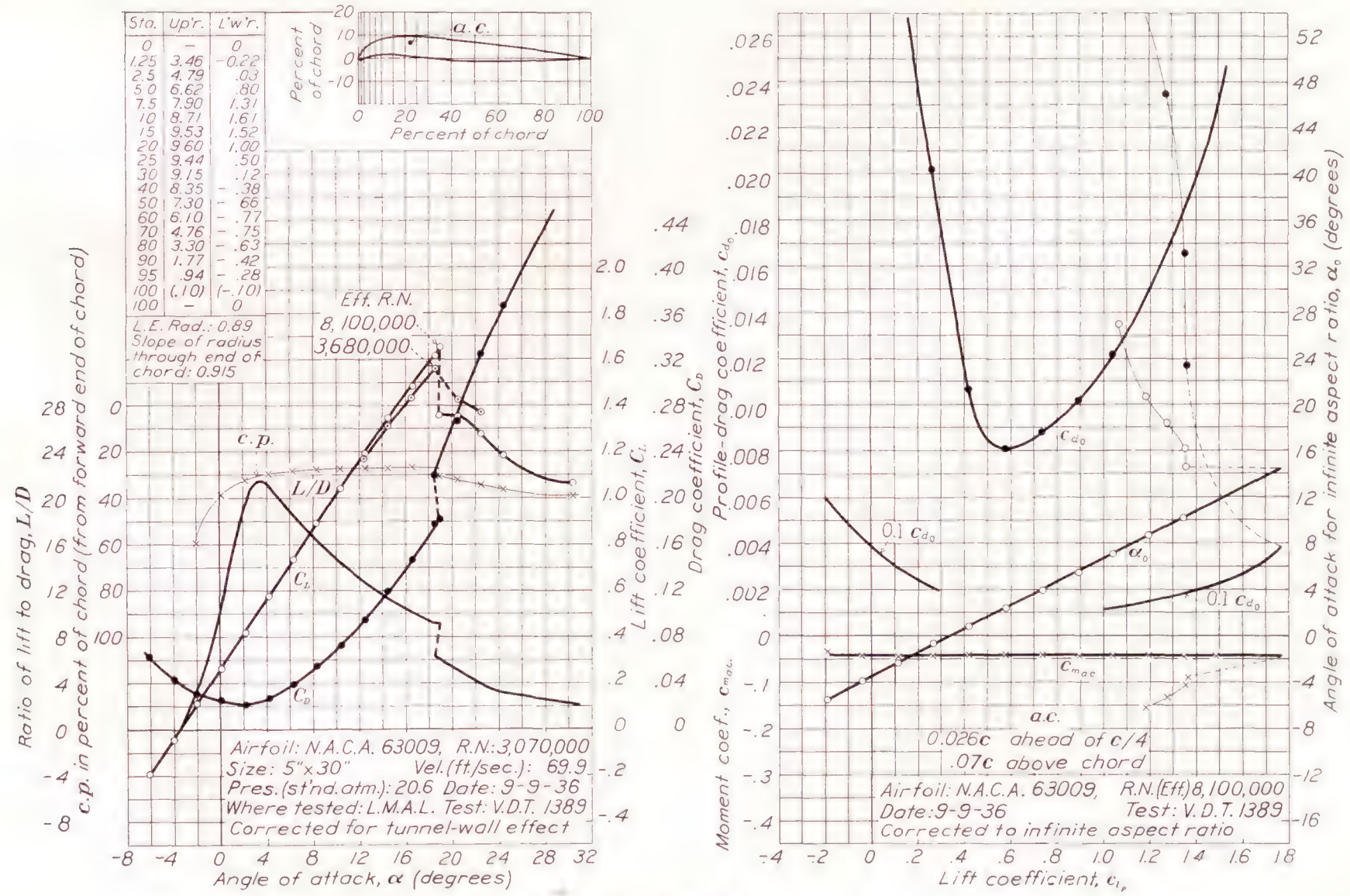

FIGURE 36.—N. A. C. A. 63009 airfoil.

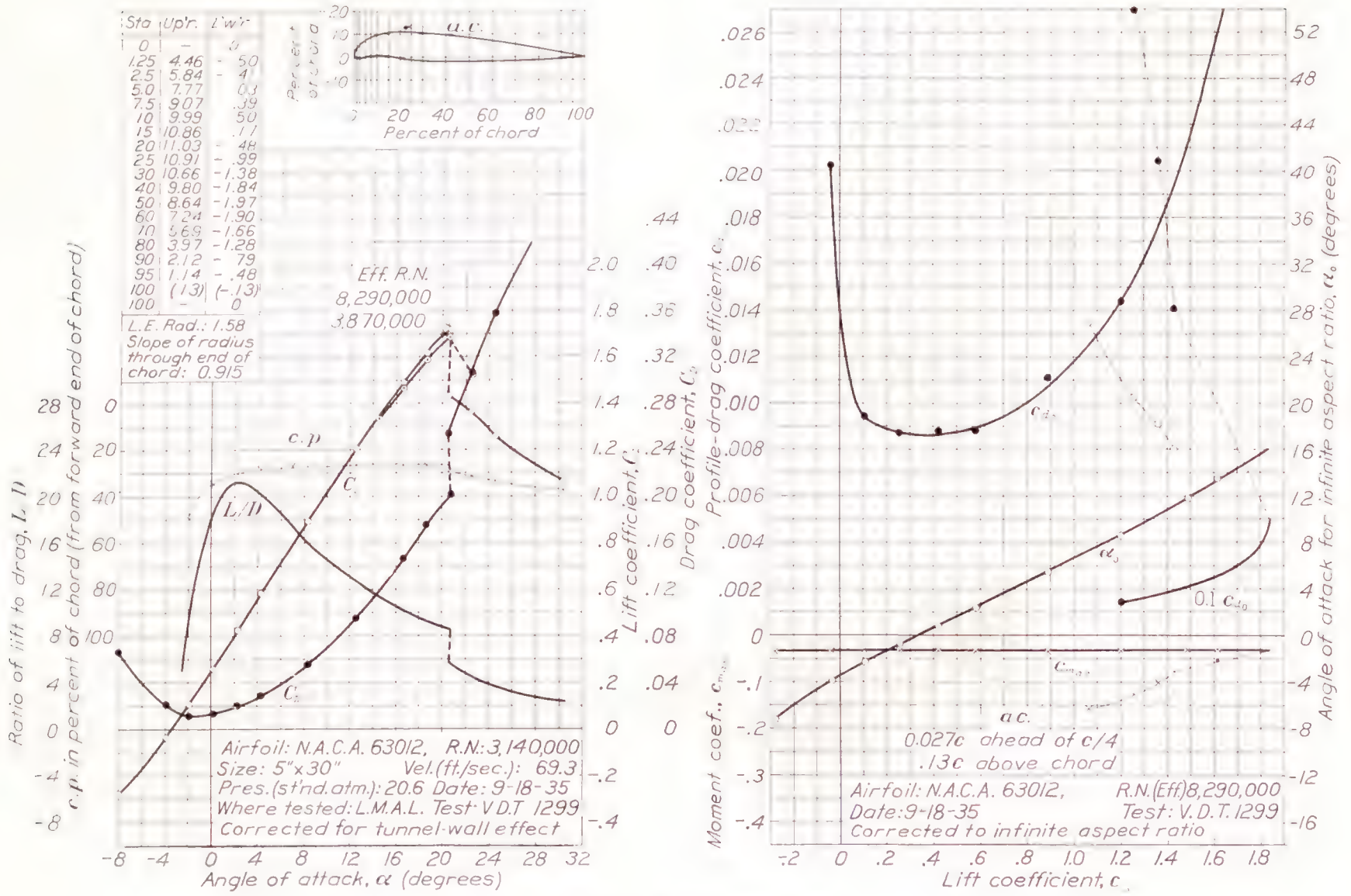

FIGURE 37.—N. A. C. A. 63012 airfoil.

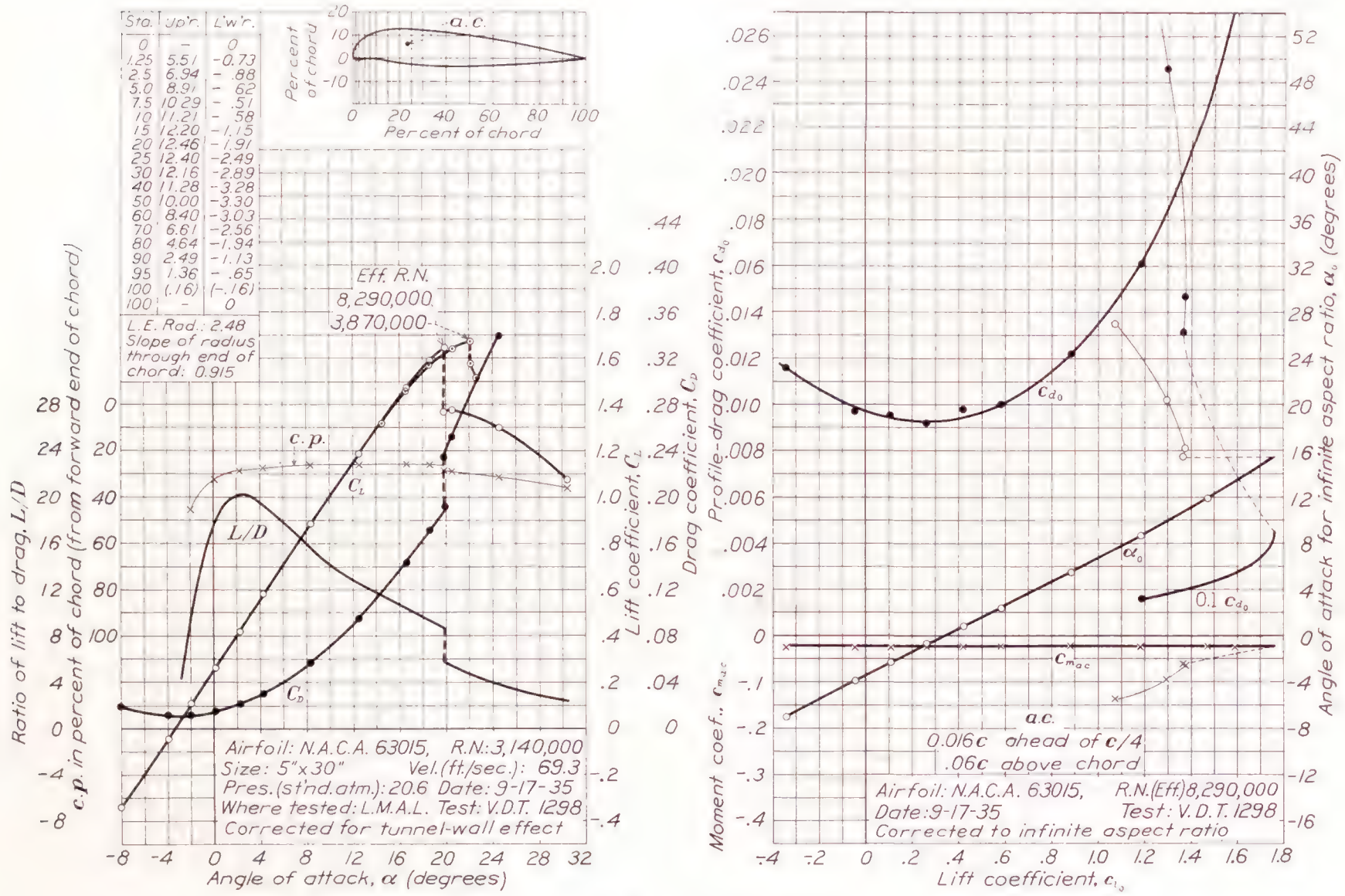

FIGURE 38.—N. A. C. A. 63015 airfoil.

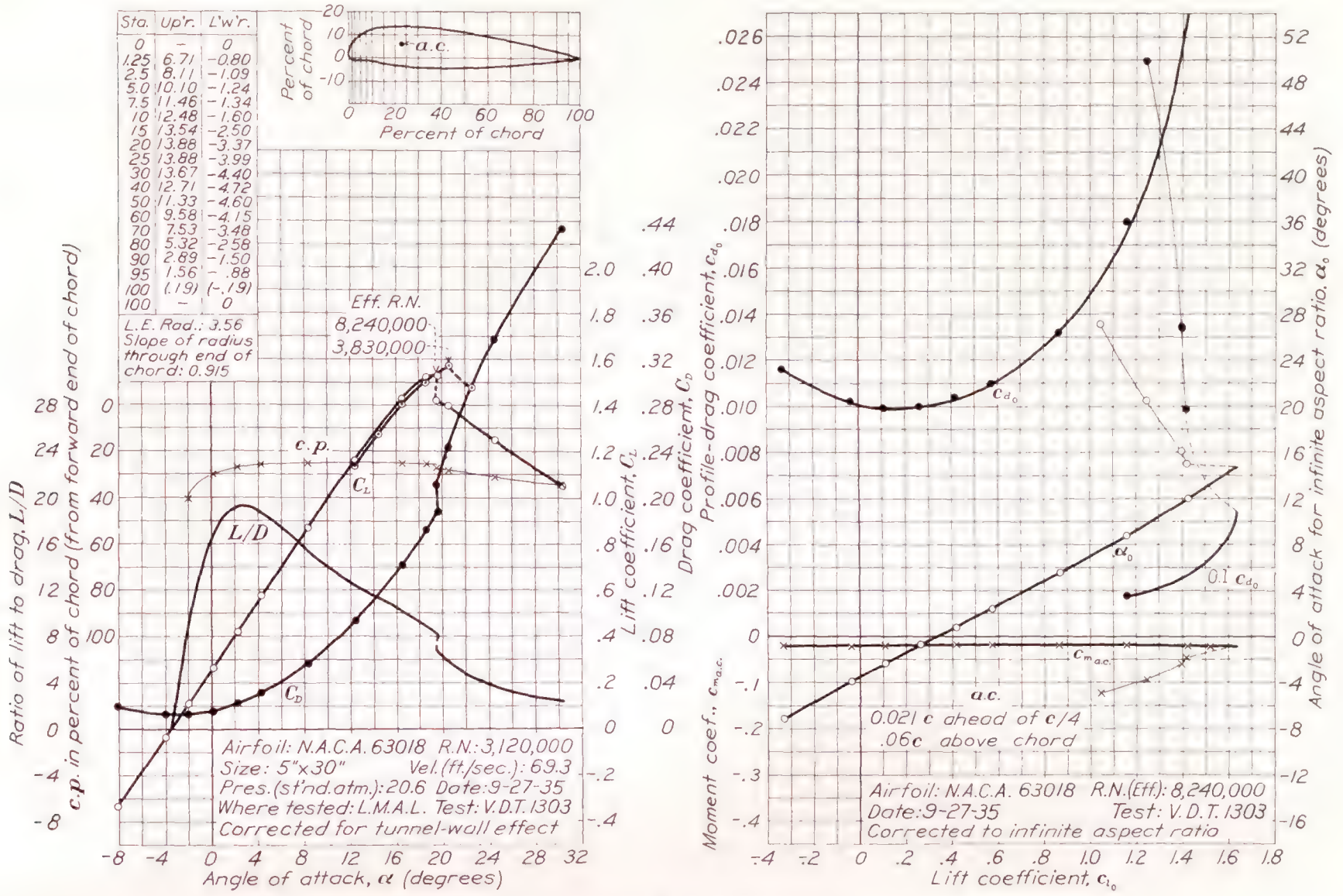

FIGURE 39.—N. A. C. A. 63018 airfoil.

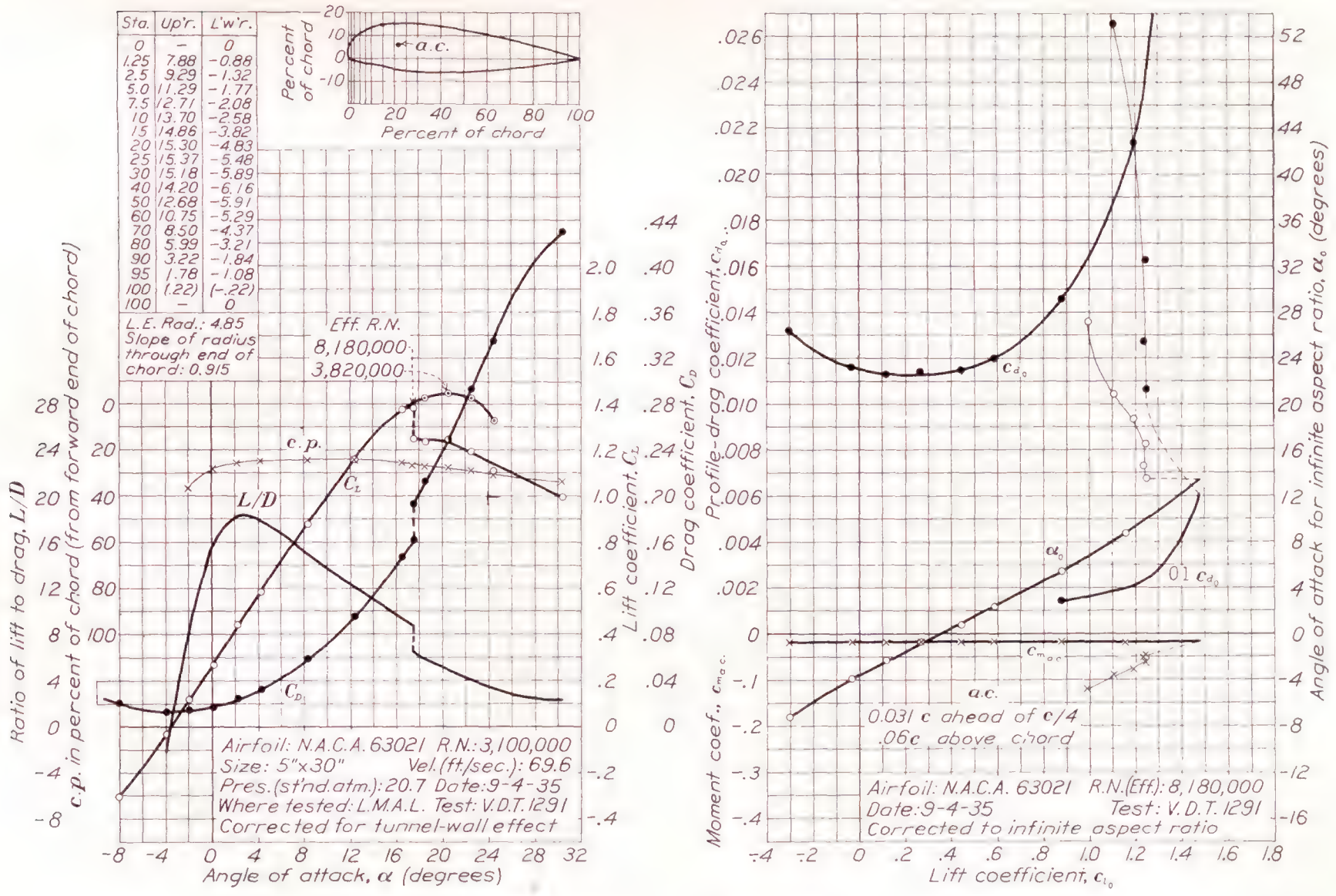

FIGURE 40.—N. A. C. A. 63021 airfoil.

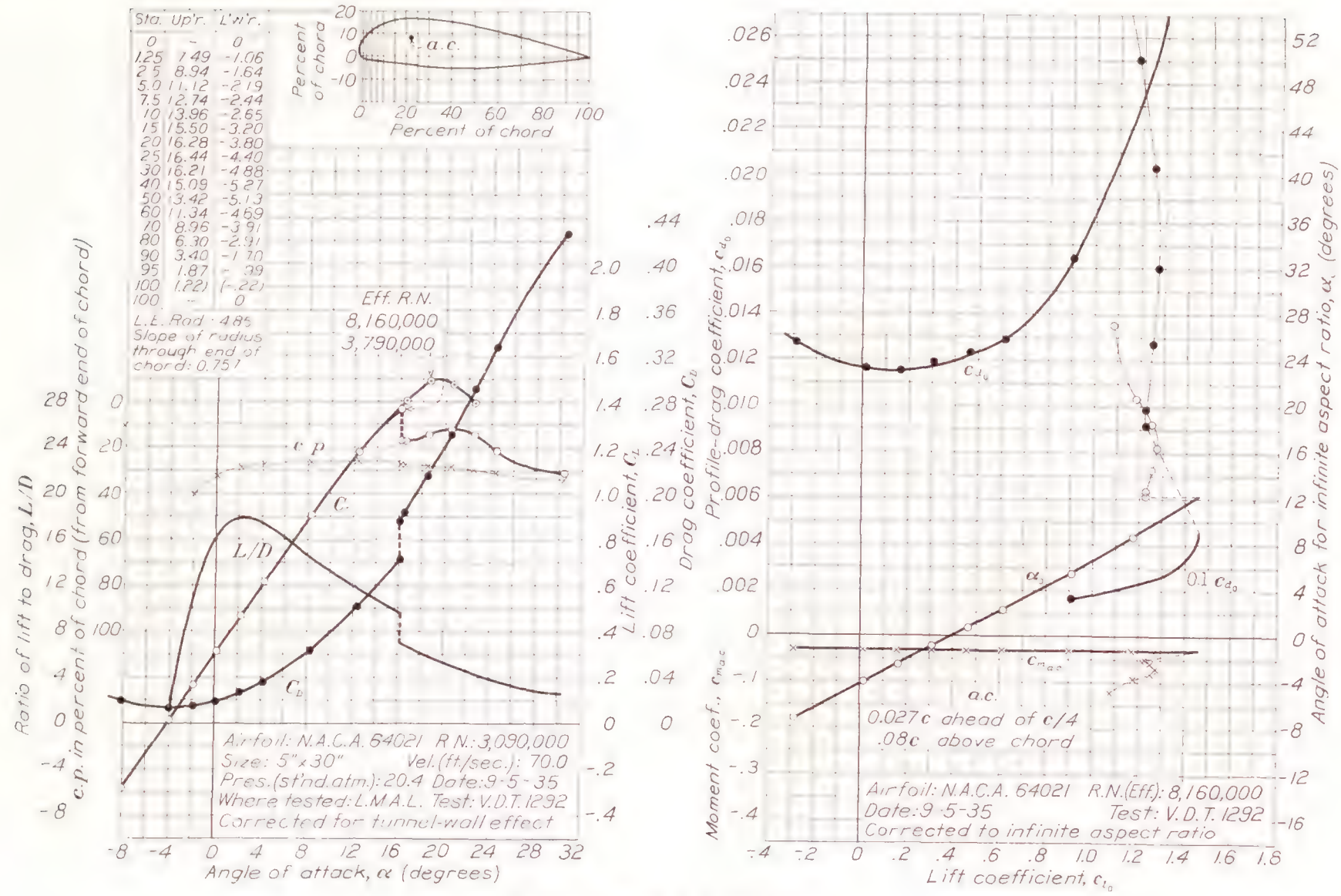

FIGURE 41.—N. A. C. A. 64021 airfoil.

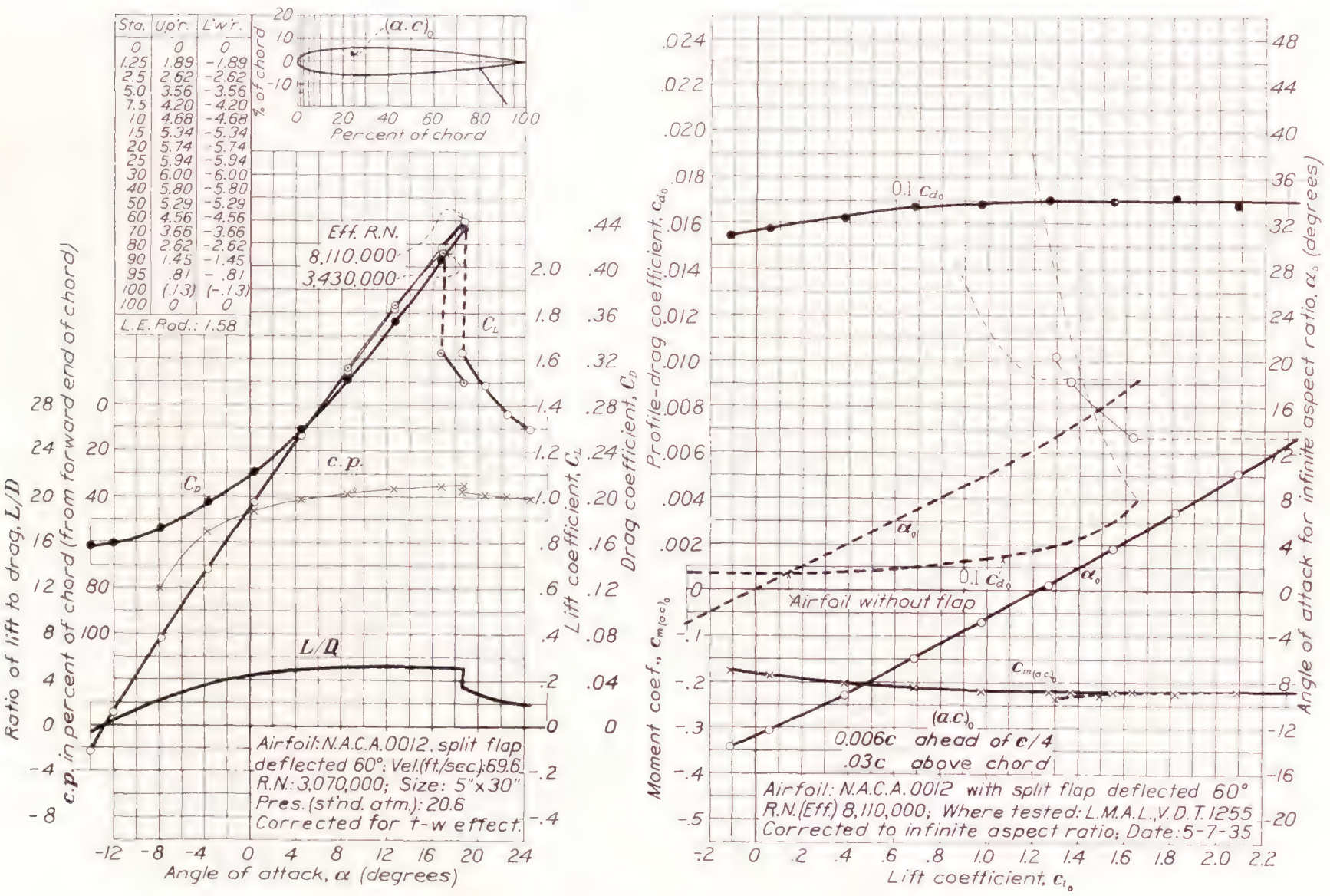

FIGURE 42.—N. A. C. A. 0012 airfoil with 0.2c split flap deflected 60°.

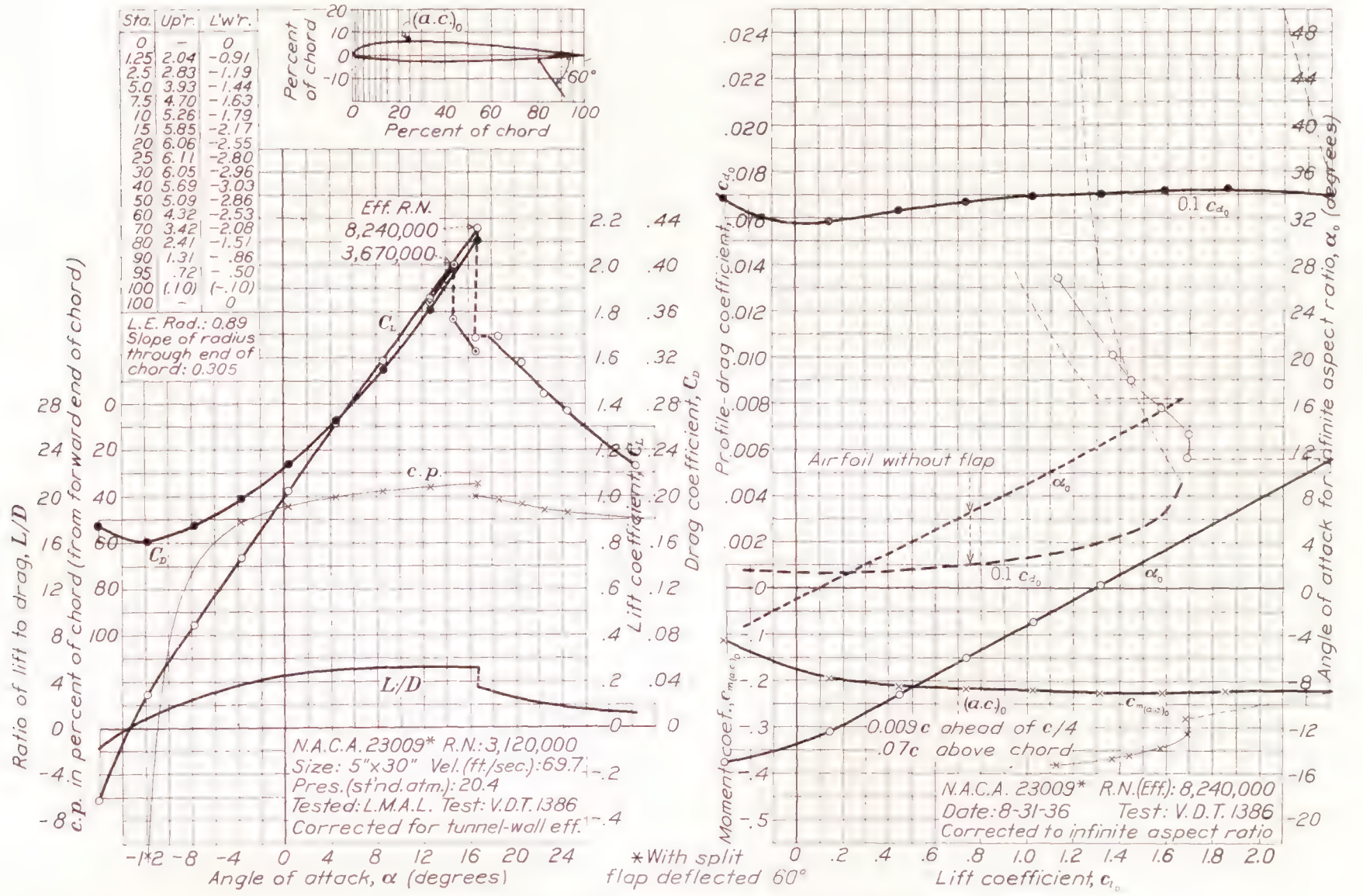

FIGURE 43.—N. A. C. A. 23009 airfoil with 0.2c split flap deflected 60°.

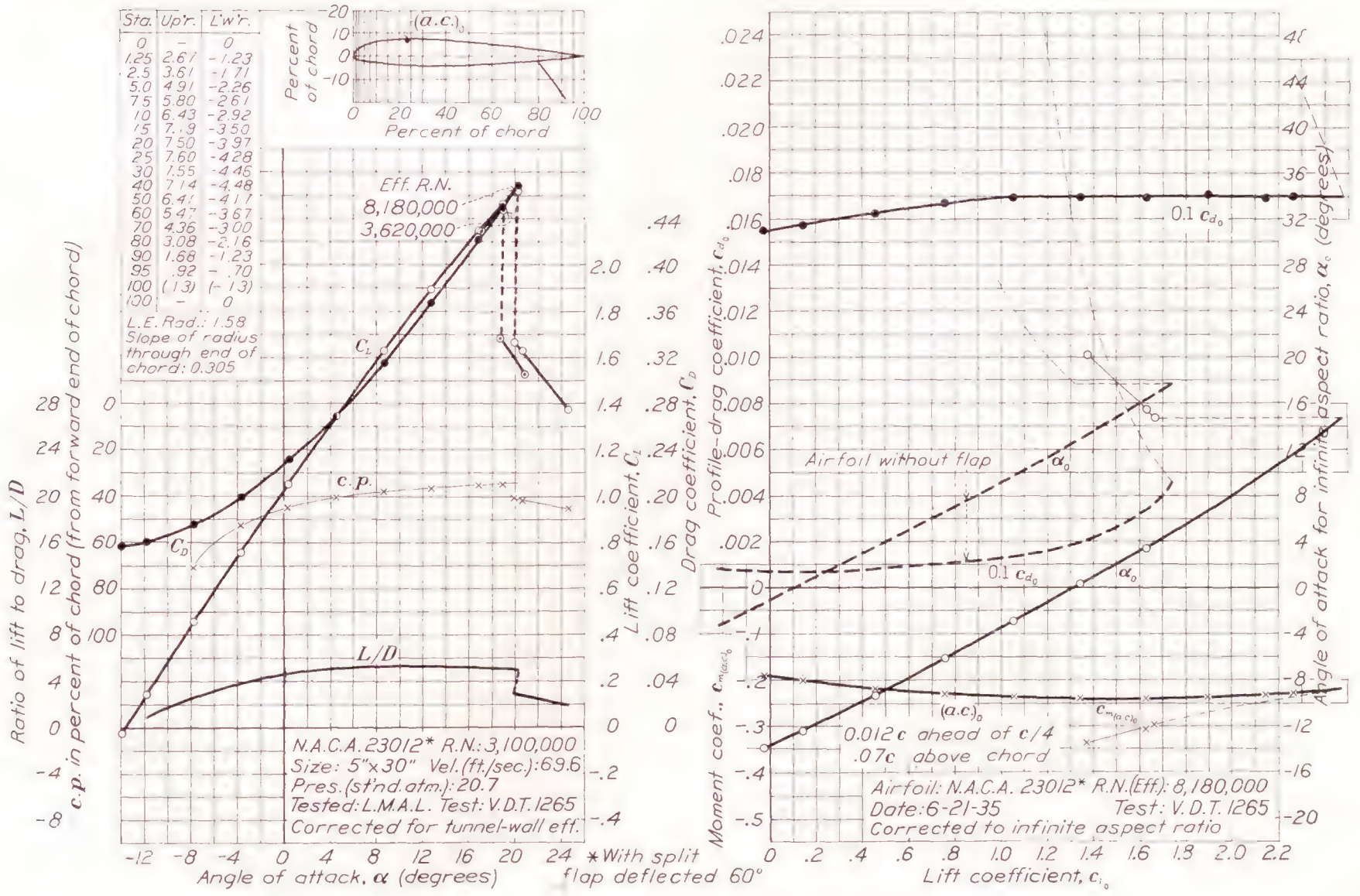

FIGURE 44.—N. A. C. A. 23012 airfoil with 0.2c split flap deflected 60°.

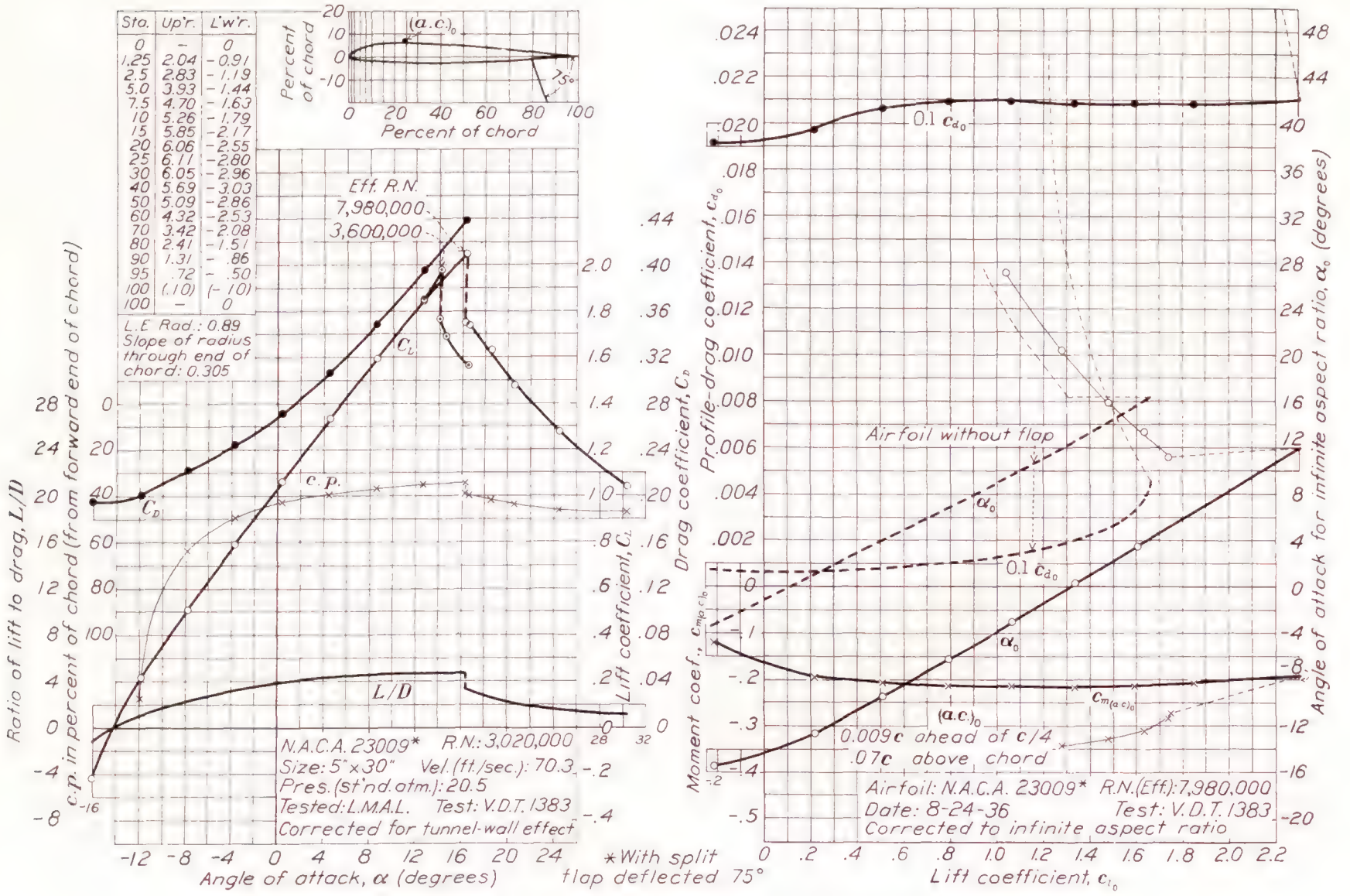

FIGURE 45.—N. A. C. A. 23009 airfoil with 0.2c split flap deflected 75°.

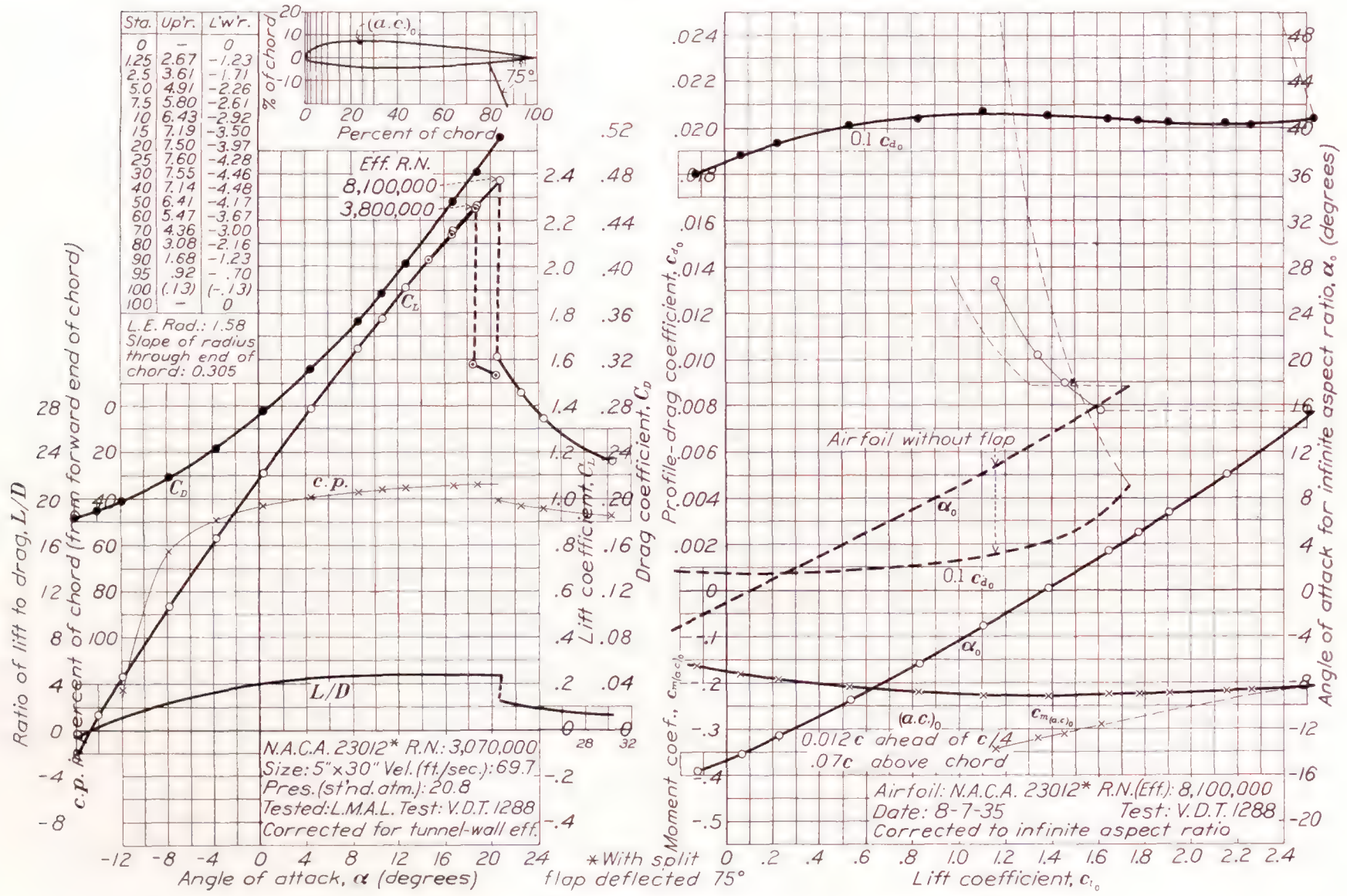

FIGURE 46.—N. A. C. A. 23012 airfoil with 0.2c split flap deflected 75°

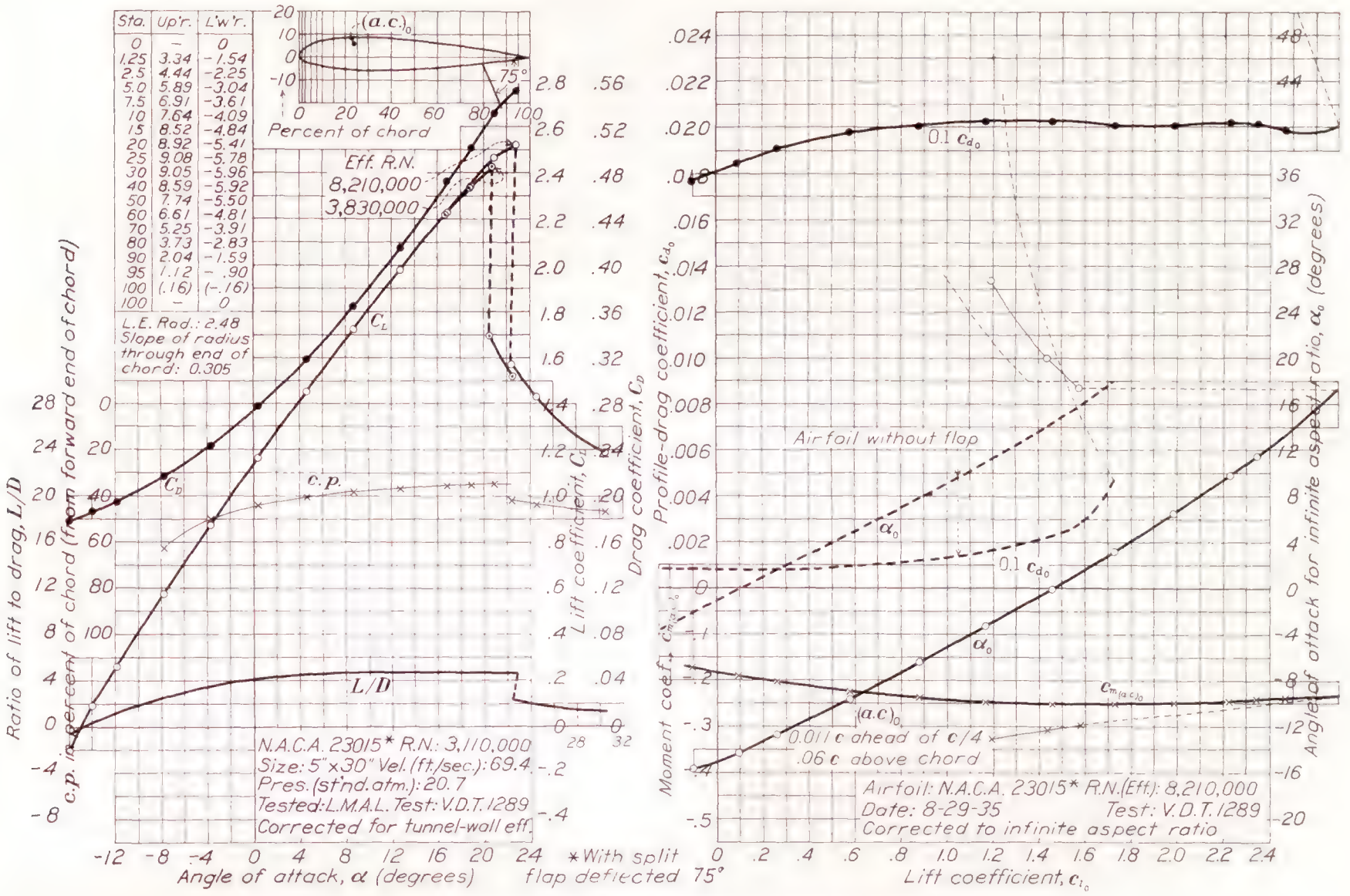

FIGURE 47.—N. A. C. A. 23015 airfoil with 0.2c split flap deflected 75°.

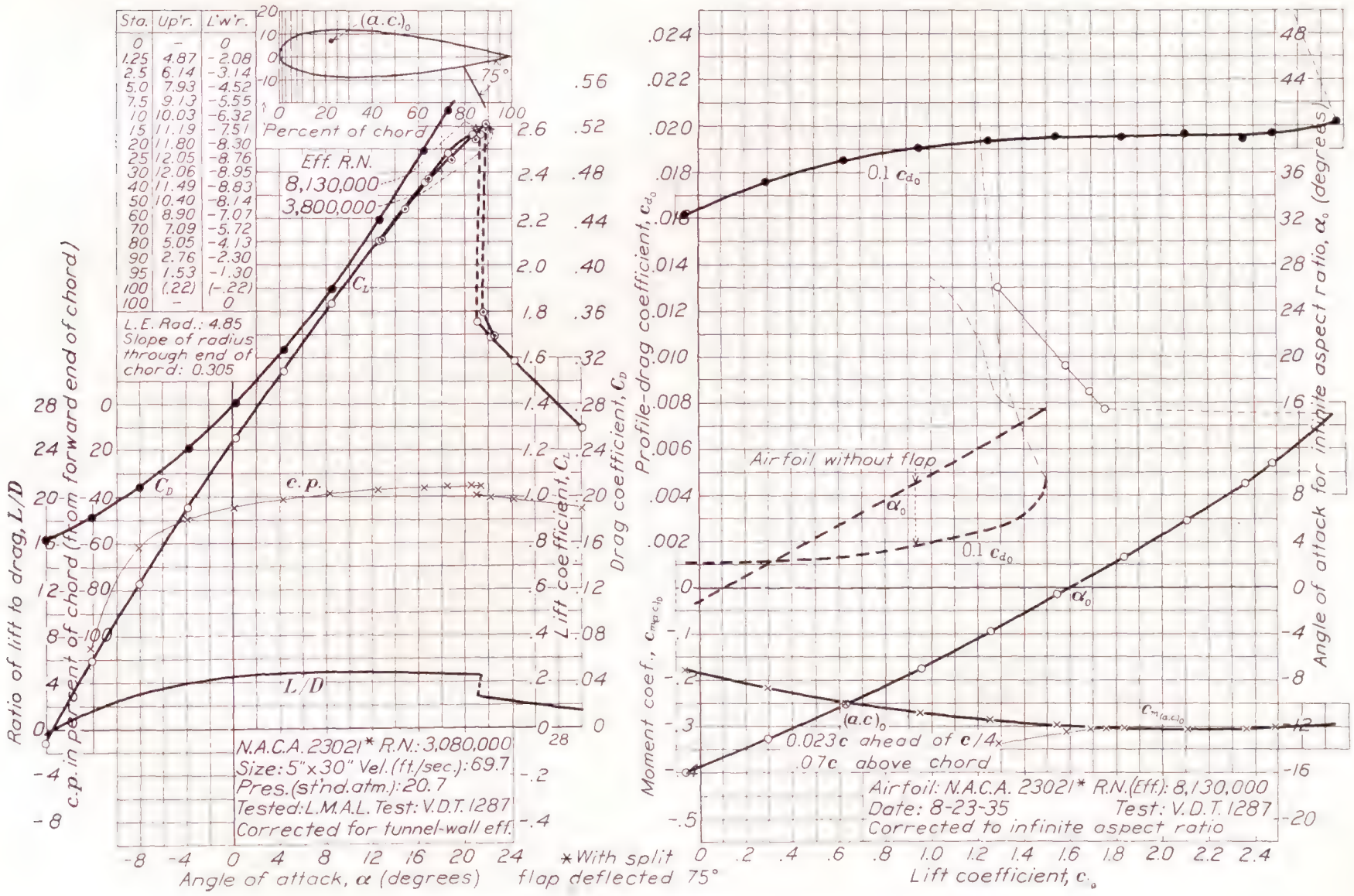

FIGURE 48.—N. A. C. A. 23021 airfoil with 0.2c split flap deflected 75°

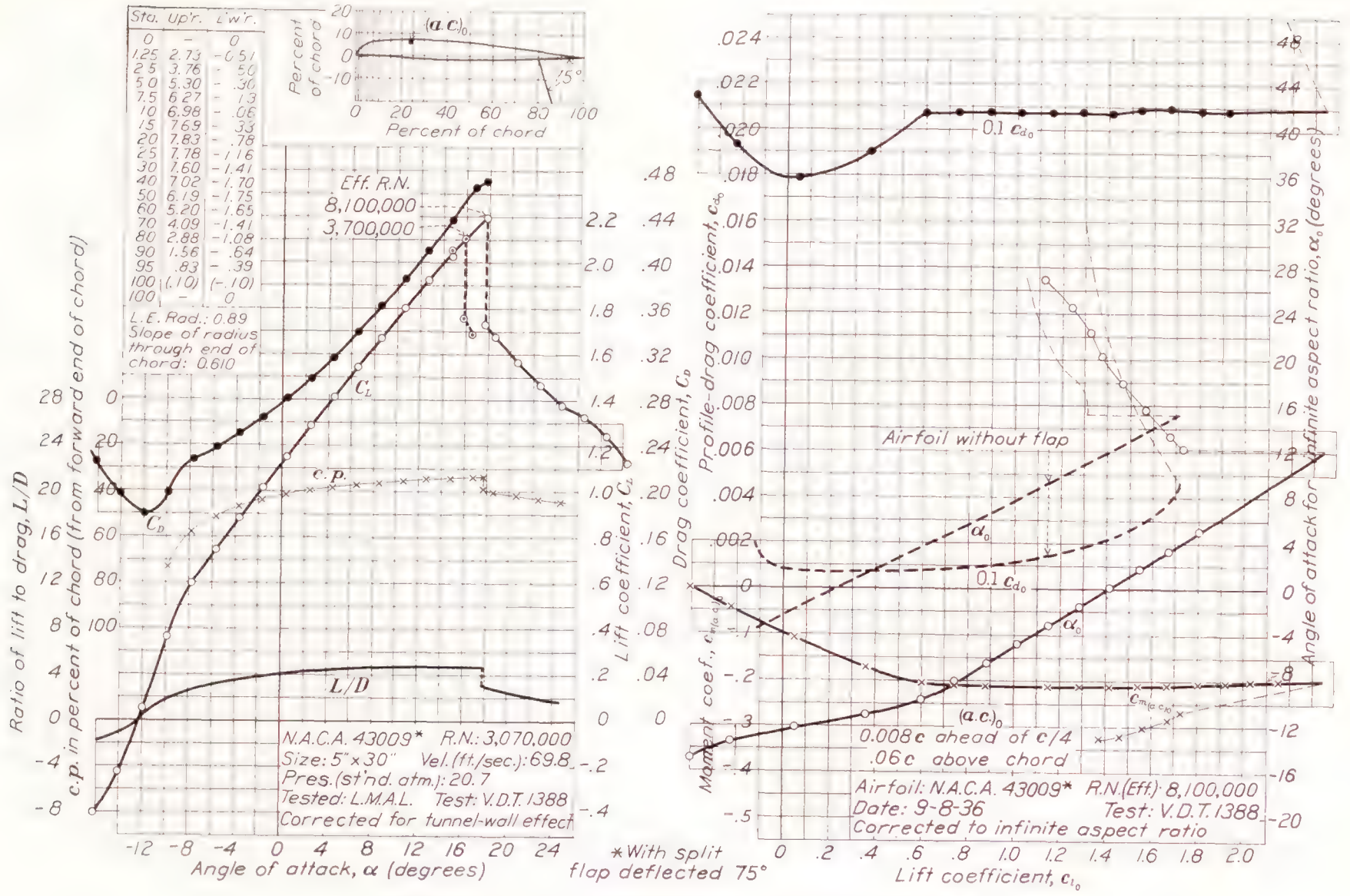

FIGURE 49.—N. A. C. A. 43009 airfoil with 0.2c split flap deflected 75°.

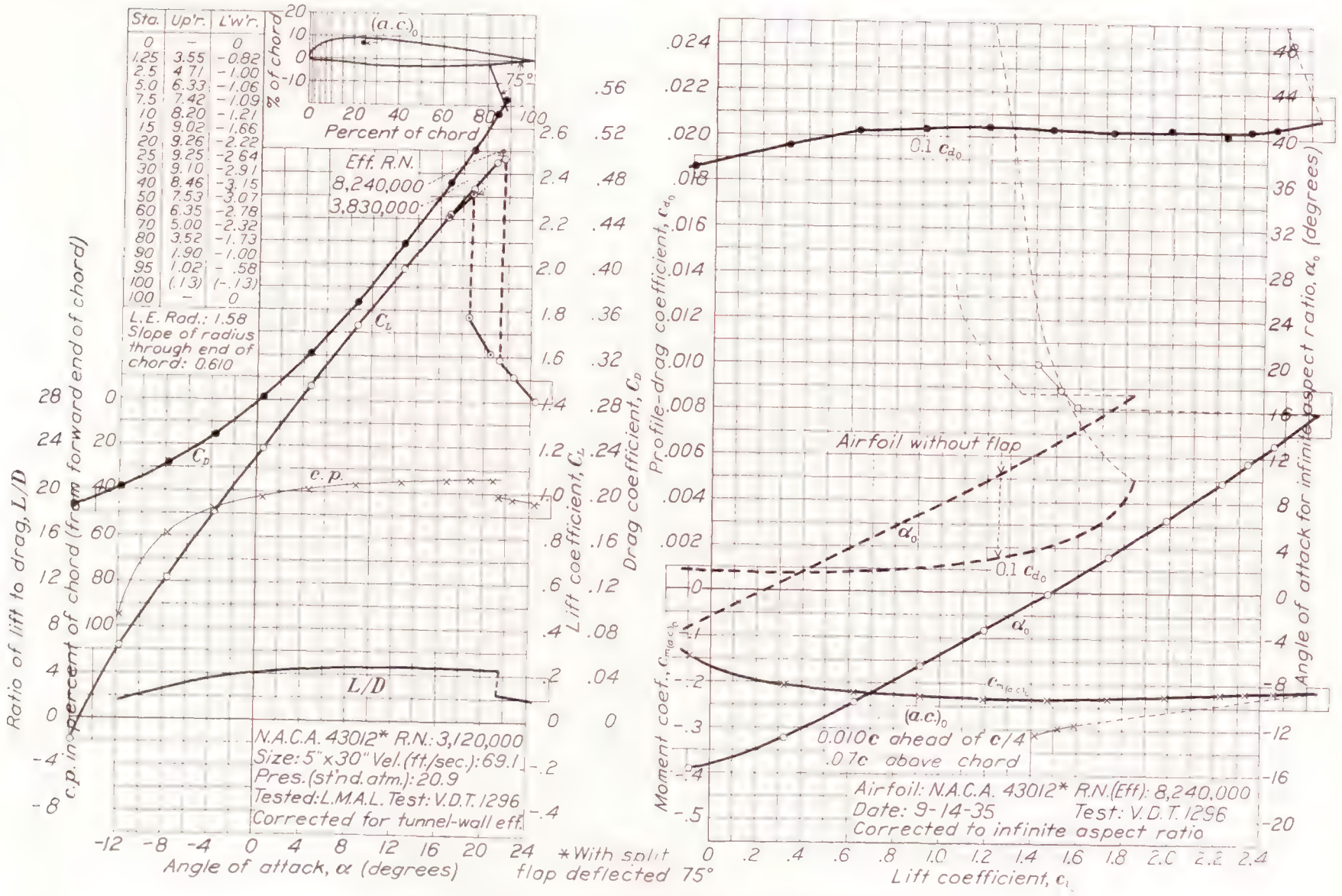

FIGURE 50.—N. A. C. A. 43012 airfoil with 0.2c split flap deflected 75°.

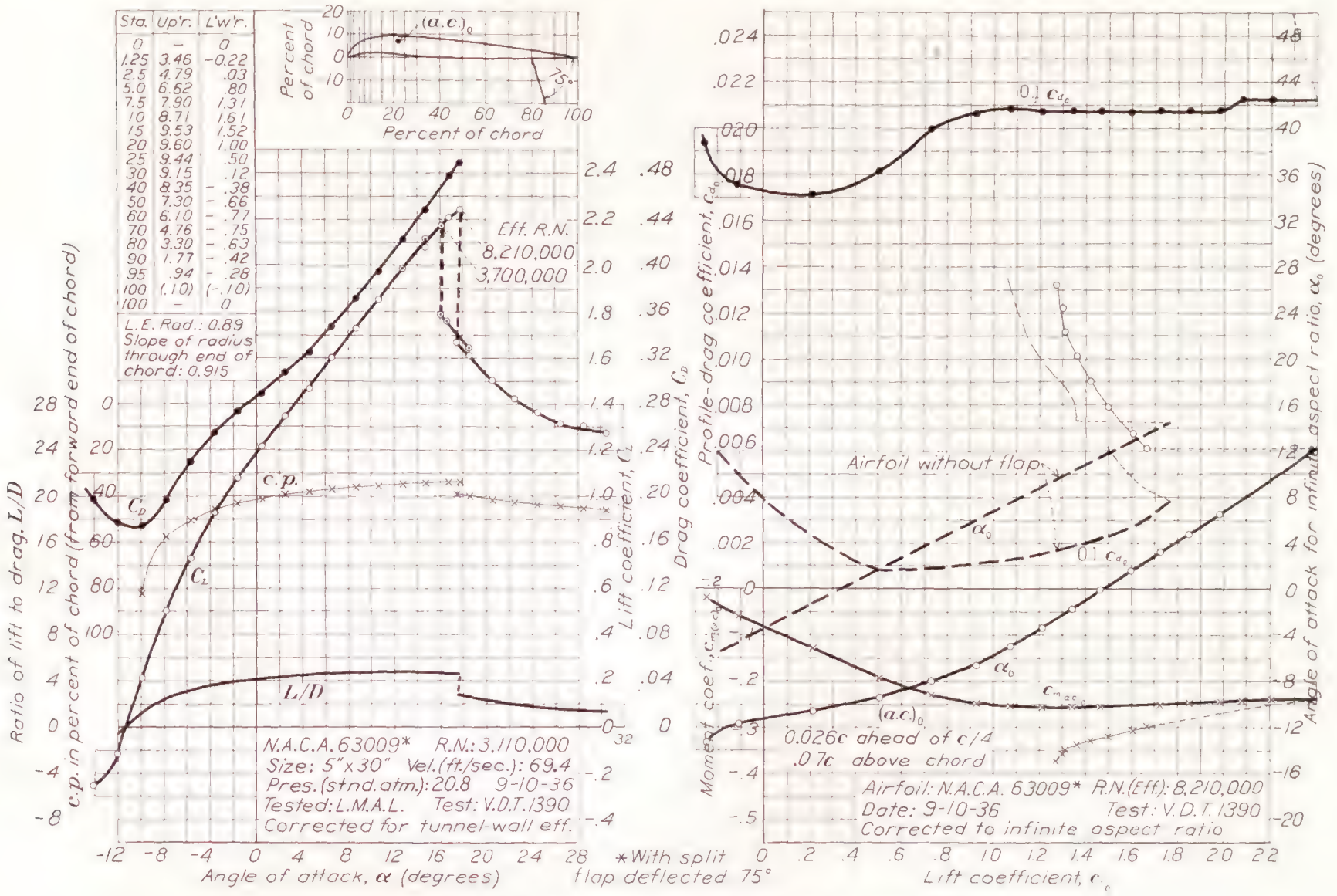

FIGURE 51.—N. A. C. A. 63009 airfoil with 0.2c split flap deflected 75°.

CHOICE OF BEST CAMBER POSITION

The first results of an investigation of the effects of placing the camber forward of normal positions were reported in reference 2. These results showed that airfoils with the camber well forward had improved characteristics and that the 0.15c position was probably the best except for the apparently high maximum lift of the N. A. C. A. 21012 airfoil. (See fig. 15 and table II of reference 2.) Subsequently, the investigation was extended to higher cambers. These results (fig. 52) indicate that the 0.15c position is best for airfoils of moderate thickness (12 percent c). Furthermore, when the data for this report (including the data in references 2 and 3) were being prepared, an error was discovered in figure 15 and table II of reference 2. The value of the uncorrected maximum lift for the N. A. C. A. 21012 airfoil plotted in figure 15 should have been 1.52 instead of 1.62 and the corresponding value of C_{Lmax} in table II corrected for the tip effect should have been 1.57 instead of 1.67. The basis for the qualified conclusion of reference 2 that stated the maximum lift coefficient of simple mean-line airfoils to be unaffected by positions of camber less than 0.15c is thus removed. The optimum position of camber may now be definitely placed at 0.15c; that is, the position corresponding to the mean-line shape designation 30.

The rest of this discussion will therefore be concerned with the effects of airfoil shape on the aerodynamic characteristics of those airfoils whose camber position

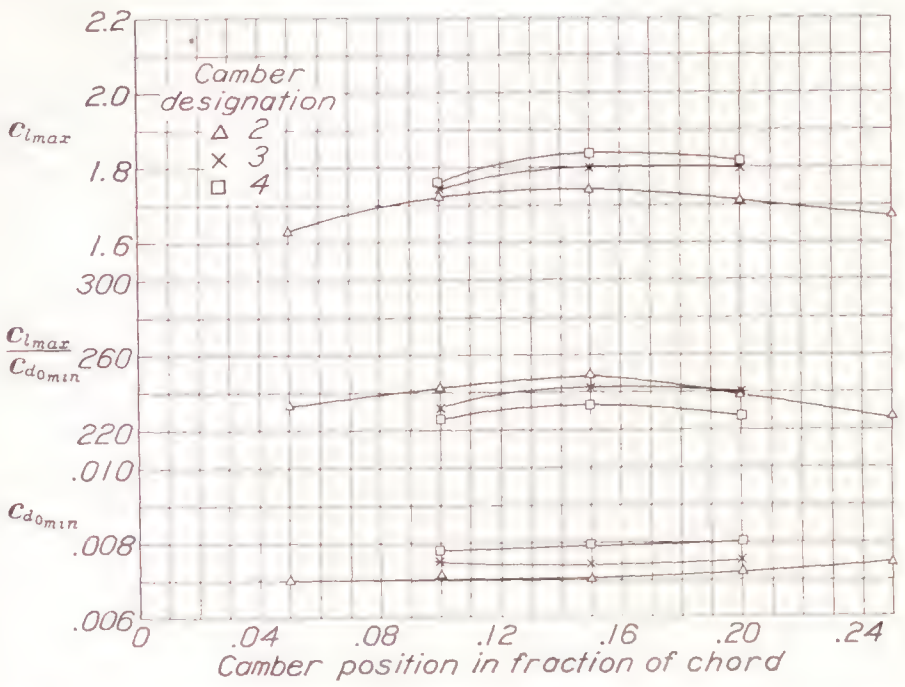

FIGURE 52.—Variation with camber position of maximum lift, minimum drag, and the ratio of maximum lift to minimum drag for the 12 percent thick airfoils.

is at 15 percent of the chord back of the leading edge and will be concluded with a discussion of the choice of the best thickness and camber.

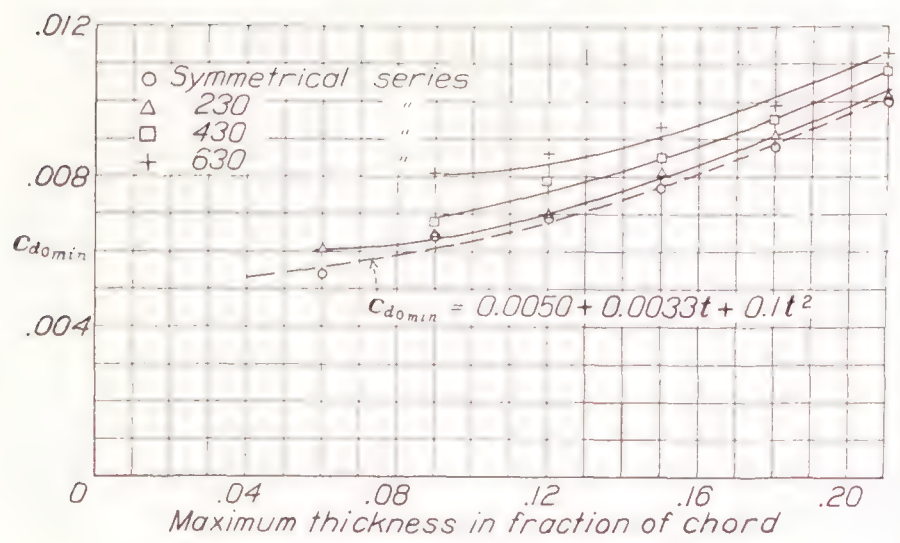

FIGURE 53.—Variation of minimum drag with thickness.

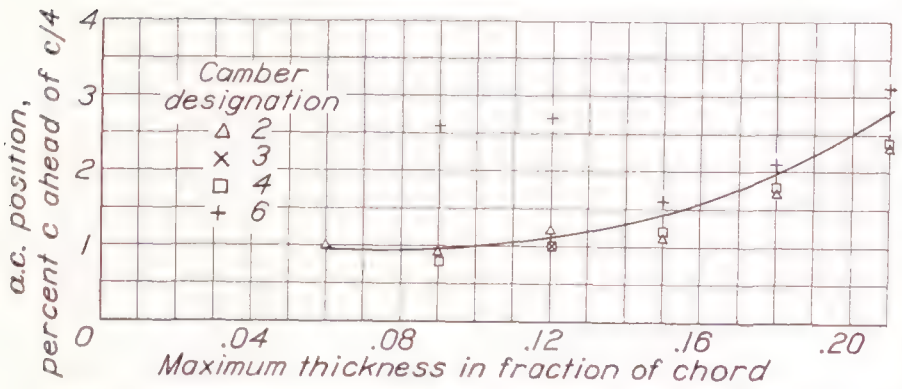

FIGURE 54.—Variation of position of aerodynamic center with thickness.

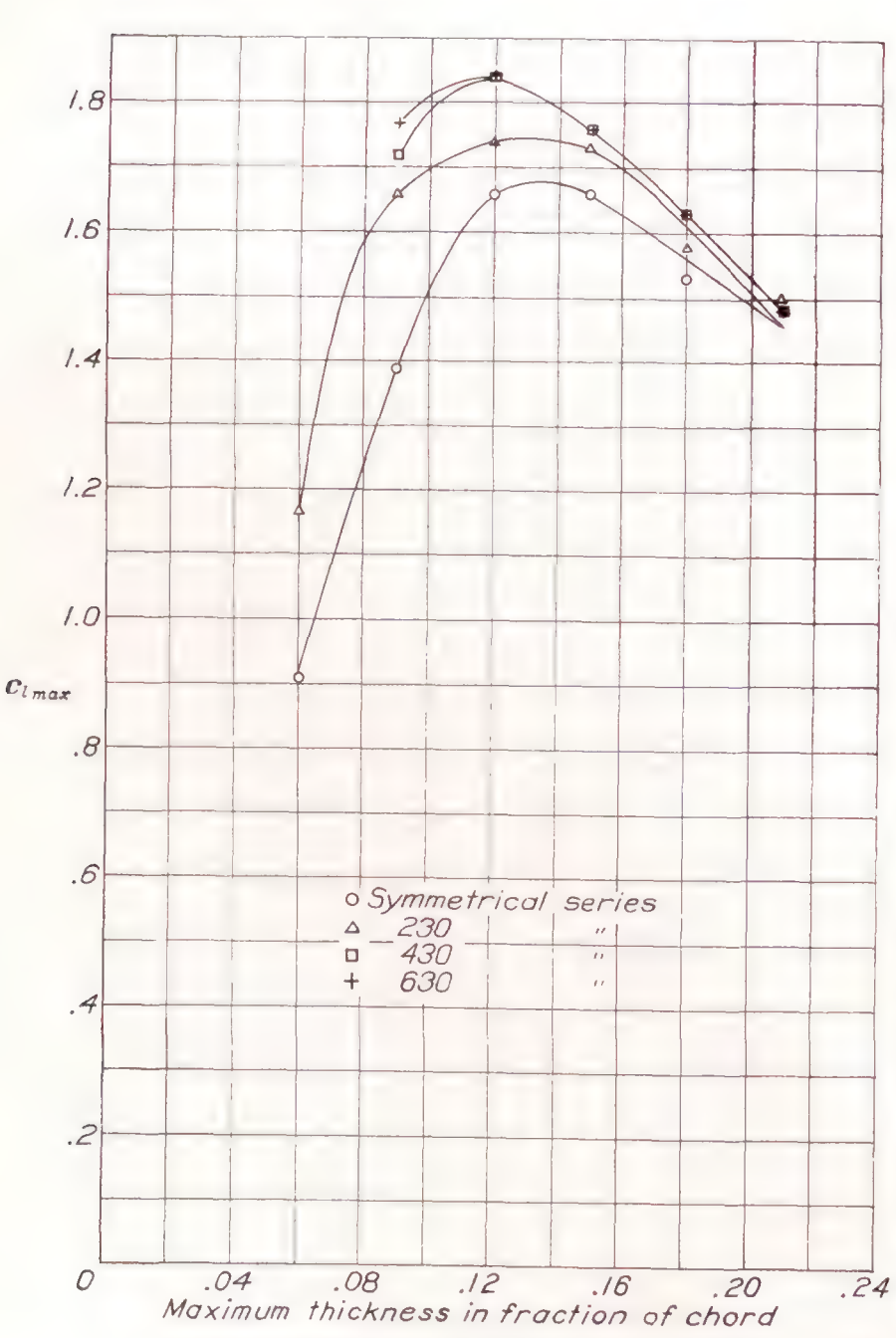

FIGURE 55.—Variation of maximum lift with thickness.

VARIATION OF AERODYNAMIC CHARACTERISTICS WITH SECTION SHAPE

The variation with thickness of the characteristics of the airfoils reported herein agrees approximately with previous findings, although the present results are slightly different owing to their greater accuracy. The added accuracy of the section characteristics is principally the result of corrections for turbulence and tip effects (reference 6), which may also be applied to the results presented in reference 1. The minimum drag coefficient increases in accordance with the relation $c_{d_{0_{min}}} = k + 0.0050 + 0.0033t + 0.1t^2$ (fig. 53), where t is the thickness ratio and k (which is approximately constant for sections having the same mean line) represents the increase in $c_{d_{0_{min}}}$ above that of the symmetrical section of corresponding thickness. The lift-curve slope decreases slightly for the thicker airfoils, and the position of the aerodynamic center moves slightly forward with increasing thickness (fig. 54). The pitching-moment coefficient and the optimum lift coefficient decrease numerically with increasing thickness.

The maximum lift coefficient is highest for moderately thick sections, as shown in figure 55. The greatest value of maximum lift occurs at a thickness near 13 percent for the symmetrical and 230 series but at a lower thickness for the 430 and 630 series.

Tests made to determine the optimum position of maximum thickness for an airfoil showed that the usual N. A. C. A. thickness distribution is better than thickness distributions having positions of maximum thickness farther back. This conclusion is substantiated by the results shown in figure 56.

The effect of filling out the concave portion of the lower surface near the nose of the N. A. C. A. 43012 airfoil and thickening the upper surfaces so that the mean line is unchanged may be seen by examining the data given in table I. The N. A. C. A. 43012 is seen to be aerodynamically better than the N. A. C. A. 43012A. A comparison of the results given in table I for the N. A. C. A. 23012 with the N. A. C. A. 23012–33 and those for the N. A. C. A. 23012–64 with the N. A. C. A. 23012–34 shows that the effect of decreasing the leading-edge radius below its normal value is to decrease the maximum lift, which confirms the results of reference 1.

The effects of camber changes upon the aerodynamic characteristics of the airfoils shown in figure 1 also agree with previous findings. The minimum drag increases with camber. (See fig. 53.) The angle of zero lift is proportional to camber and agrees with the theoretical value (see reference 1) to within 0.2° for airfoils of moderate thickness. The comparison of the angle of zero lift with the computed theoretical value is shown in figure 57. The diving moment is proportional to the camber and increases with a rearward movement of the position of the camber as predicted by

theory but is smaller in magnitude than the theoretical value (fig. 58). These and other differences between theory and experiment agree with the findings in reference 1 but have since been adequately explained. (See reference 10.)

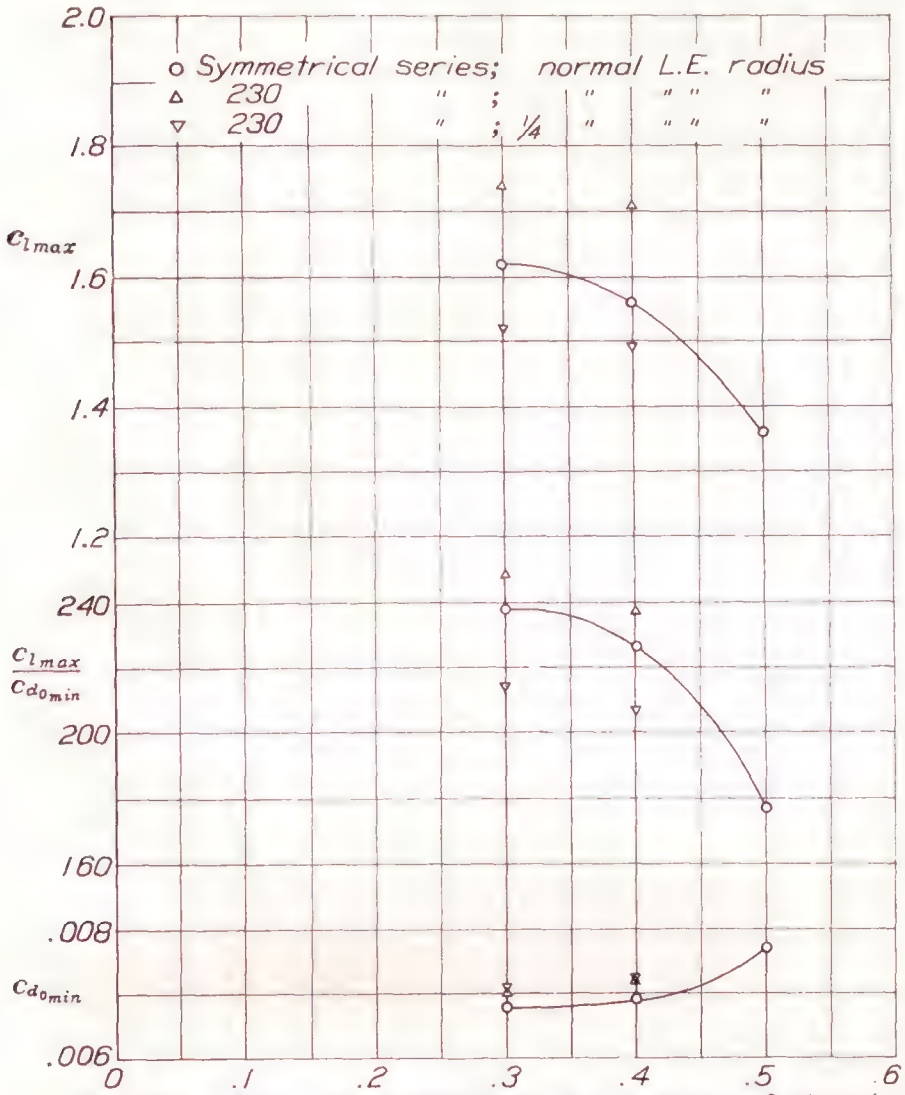

FIGURE 56.—Variation with position of maximum thickness of maximum lift, minimum drag, and the ratio of maximum lift to minimum drag.

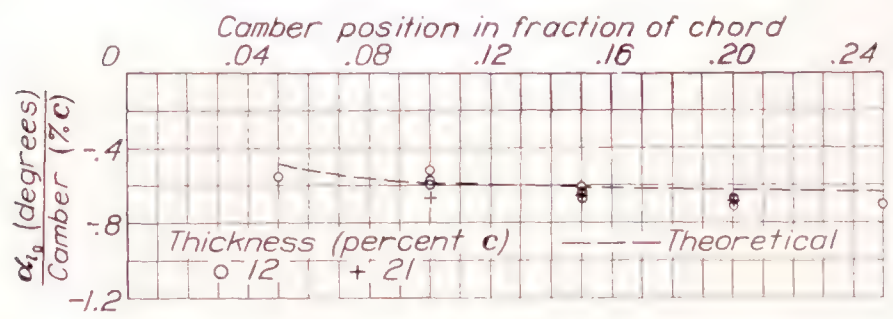

FIGURE 57.—Variation of angle of zero lift with camber position.

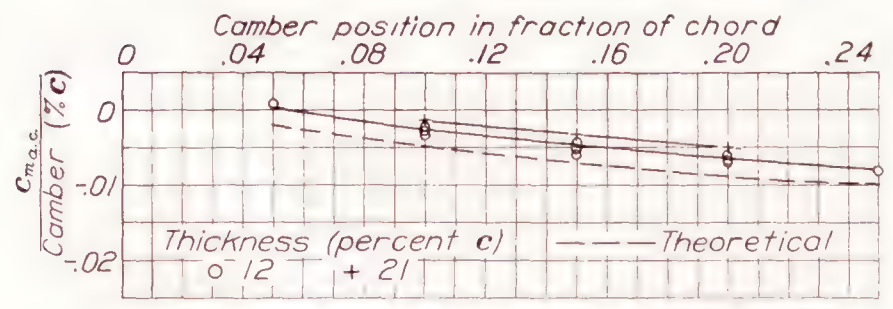

FIGURE 58.—Variation of pitching moment with camber position.

The maximum lift increases for moderate amounts of camber, but this effect is less noticeable with thicker airfoils (fig. 59). It may be mentioned that the increase of maximum lift with camber is more pronounced at reduced values of the Reynolds Number. (See reference 6.)

38548—38——47

The addition of the split flap may be considered as giving a maximum-lift increment. This maximum-lift increment increases with thickness, as shown in figure 60, but does not change appreciably with camber.

CHOICE OF BEST THICKNESS AND CAMBER

In the selection of a member of this airfoil family for a given application, the choice of the best thickness and camber to be used depends on several factors. The Reynolds Number at which the airfoil is to be used will be one of these factors. By means of the scale-

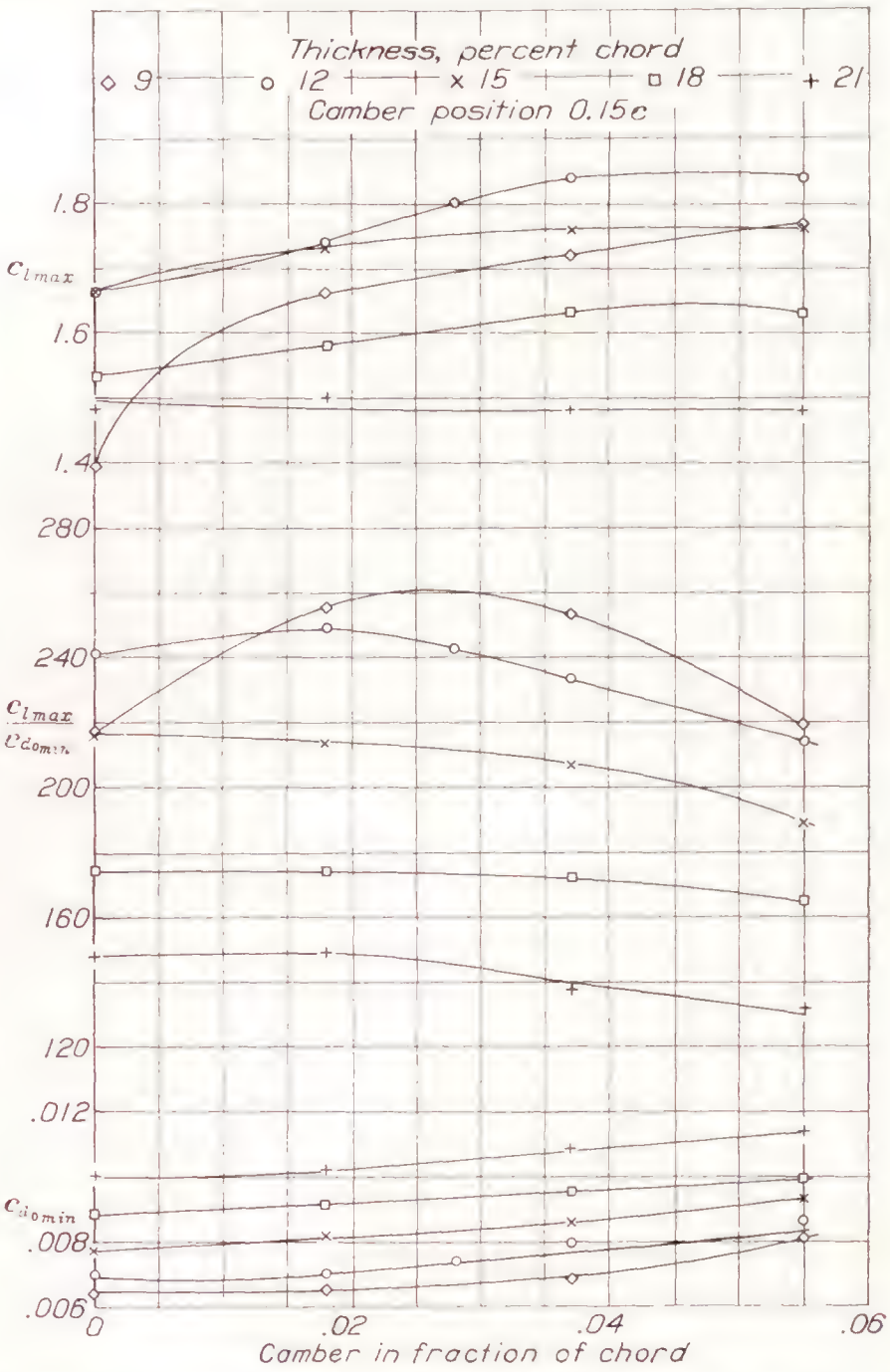

FIGURE 59.—Variation with camber of maximum lift, minimum drag, and the ratio of maximum lift to minimum drag.

effect classification given in table I and explained in references 6 and 9, the variation of maximum lift and other characteristics with Reynolds Number for any airfoil can be found.

For simplicity, the following discussion is based on airfoil section characteristics corresponding to the standard conditions (effective Reynolds Number, 8,000,000). Such an analysis will apply approximately to an airplane such as a medium-size transport, which lands at Reynolds Numbers near 8,000,000.

If a high cruising speed for a given landing speed is of primary importance, the ratio of maximum lift to the drag at cruising speed $c_{l_{max}}/c_{d_0}$, known as the "speed-range index," is a useful criterion of airfoil efficiency.

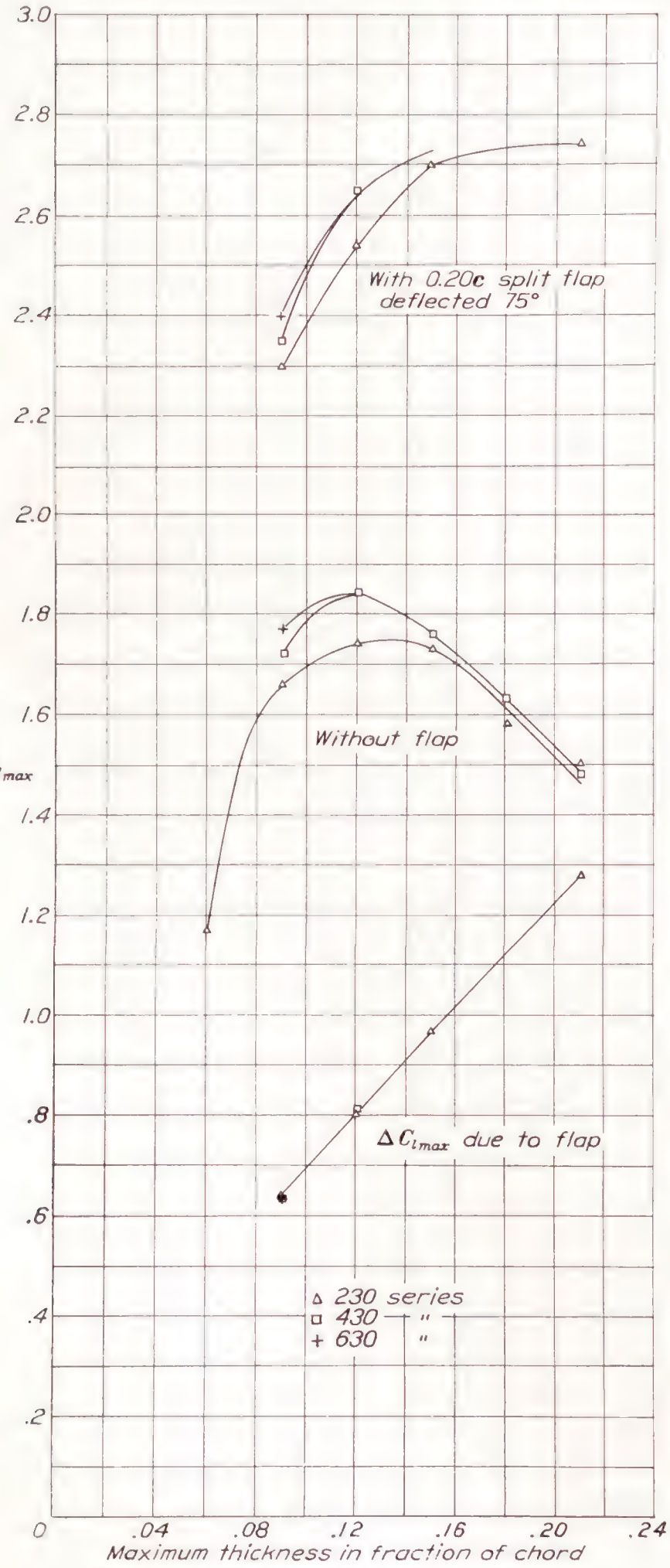

FIGURE 60.—Variation of maximum lift with thickness.

Although other performance characteristics, such as rate of climb and length of take-off run, depend less on the airfoil section characteristics than does the speed range, the same criterion may also serve as a rough indication of these characteristics. In such cases, the drag coefficient in the ratio $c_{l_{max}}/c_{d_0}$ should be taken at a lift coefficient corresponding to the best rate of climb or to the shortest take-off run, respectively.

Inasmuch as the cruising speed generally occurs near the lift coefficient corresponding to the attitude of minimum profile drag, the ratio $c_{l_{max}}/c_{d_{0_{min}}}$ may be used as a measure of merit. The variation of this ratio with thickness and camber is shown in figure 61, which indicates that for thicknesses near the optimum (that is, somewhat less than 12 percent c) the N. A. C. A. airfoils can be arranged in the following decreasing

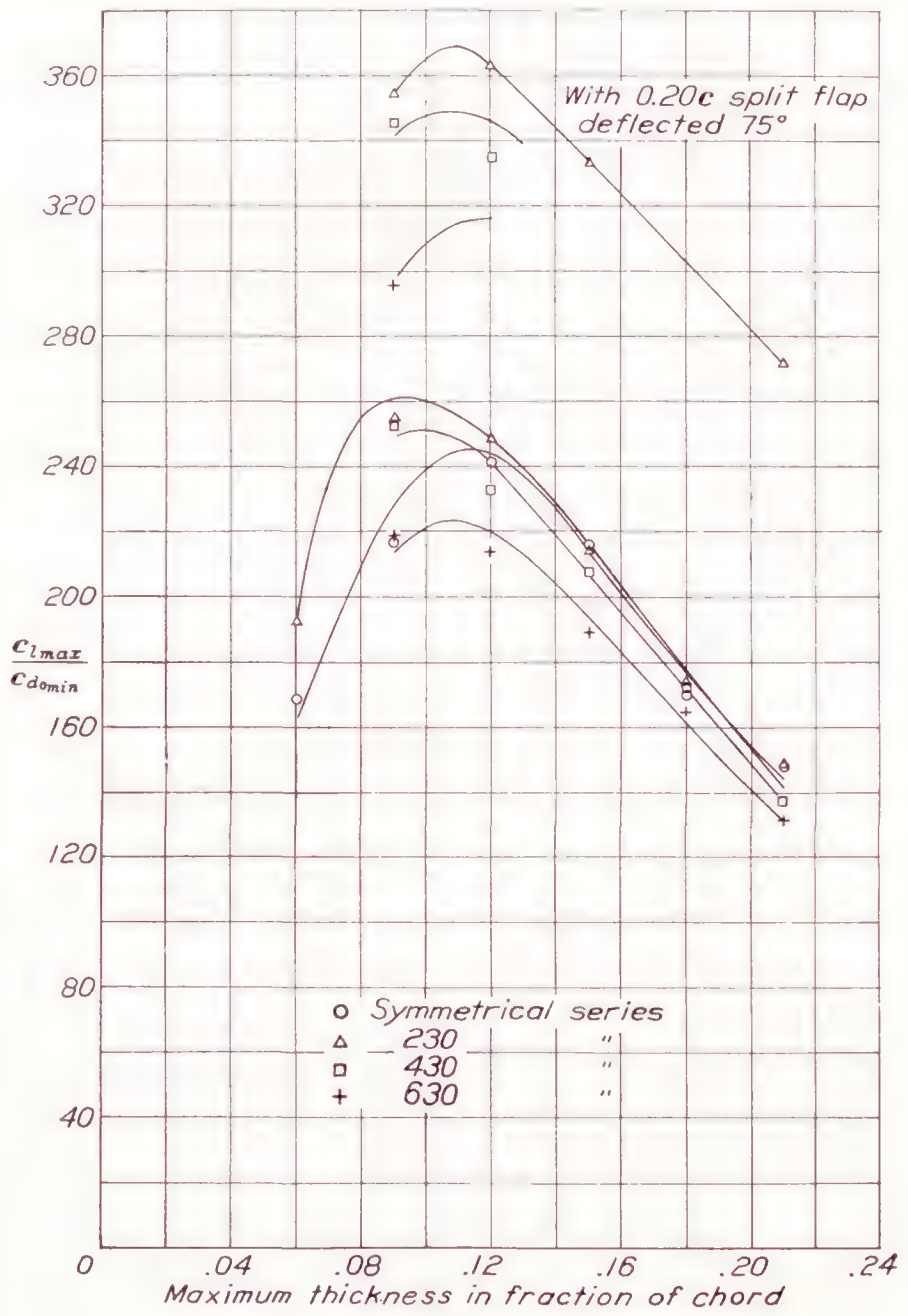

FIGURE 61.—Variation of $c_{l_{max}}/c_{d_{0_{min}}}$ with thickness.

order of merit as shown by the speed-range index: 230 series, 430 series, symmetrical series, and 630 series. For thicknesses only slightly greater than the optimum, however, the index for the symmetrical series becomes greater than for the 430 series and nearly equal to that of the 230 series. Attention should perhaps be called to the fact that the curves presented in figures 61, 62, and 63 are drawn to agree with cross plots of the characteristics against thickness. Points are included to show the experimental values.

Owing to the wide use of split flaps and other high-lift devices in landing, the speed-range index should preferably be derived from the maximum lift coefficient with the high-lift device. Figures 61, 62, and 63 each include curves showing the ratio of the maximum lift coefficient with flap deflected to the drag coefficient with flap neutral. The addition of split flaps does not affect the optimum camber of the airfoils since the maximum-lift increment is practically independent of camber at flap deflections of 60° and 75°. The addition of split flaps will tend, however, to increase the optimum thickness of the airfoils, since the maximum-lift increment with flaps increases with thickness. (See fig. 60.) Thus the thickness for the highest value of $c_{l_{max}}/c_{d_{0_{min}}}$ for the 230 series increases from 9 to 11 percent (approximately) with the addition of the flap. (See fig. 61.)

Particular design conditions, such as high-altitude flight, high wing loadings, and long-range flight, require that the airplane fly most efficiently at a certain lift coefficient that may be higher than $c_{l_{opt}}$. For such applications the useful criterion is the ratio $c_{l_{max}}/c_{d_0}$ where c_{d_0} is taken as the value corresponding to this certain lift coefficient.

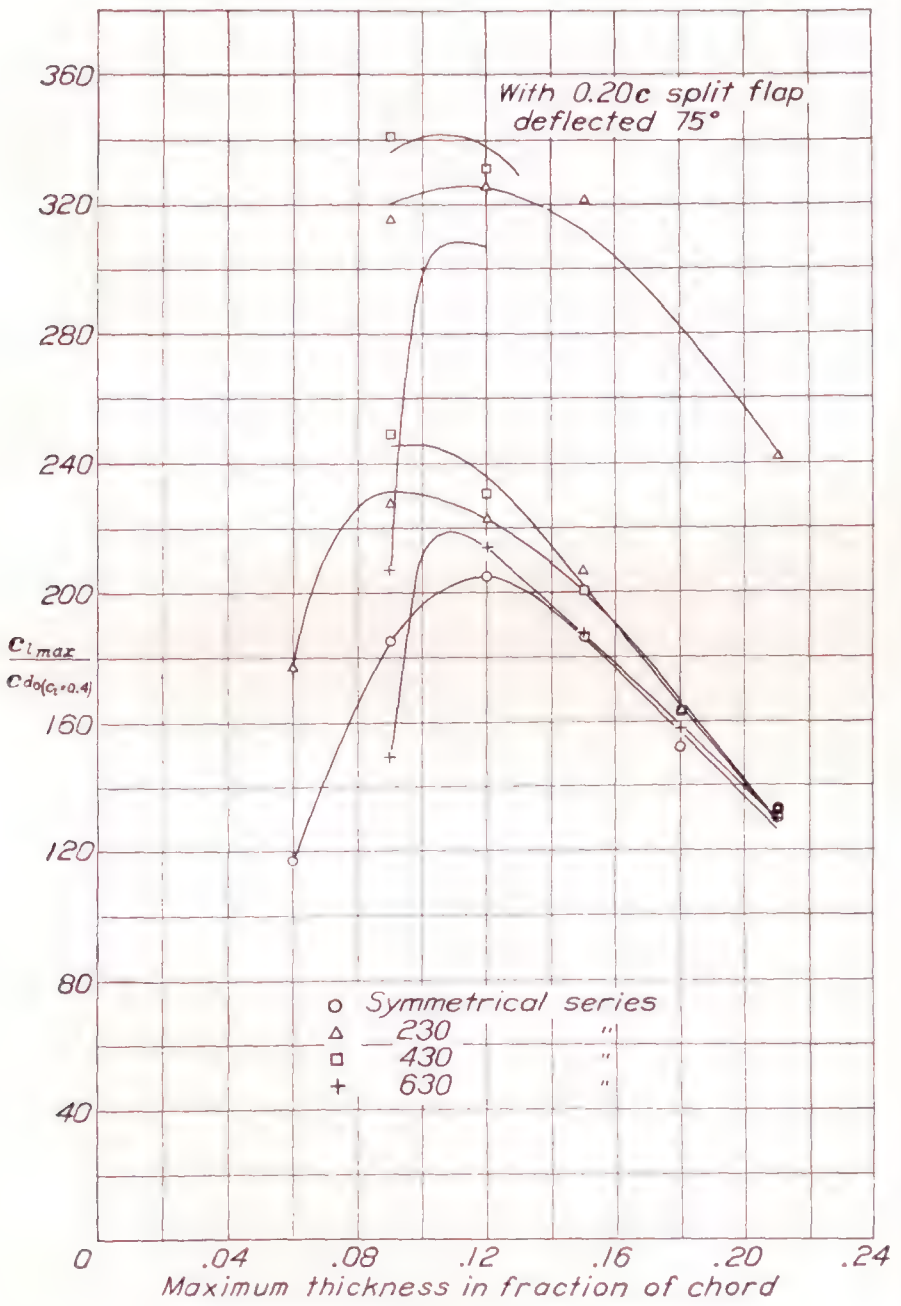

FIGURE 62.—Variation of $c_{l_{max}}/c_{d_{0(c_l=0.4)}}$ with thickness.

A comparison of the N. A. C. A. forward-camber airfoils, based on their drags at a lift coefficient of 0.4, is given in figure 62. The order of decreasing merit for thicknesses between 10 and 12 percent is then changed and becomes 430 series, 230 series, 630 series, and symmetrical series. As before, the addition of a flap will not markedly affect the relative merit of the airfoils for any given thickness but will increase the value of optimum thickness for any given camber.

It may also be desirable to compare these airfoils on the basis of a cruising speed corresponding to a lift coefficient of 0.6. The results, which are shown in figure 63, indicate that the 430 series now becomes superior to the 230 series over the entire range of thicknesses tested and the symmetrical series becomes definitely inferior.

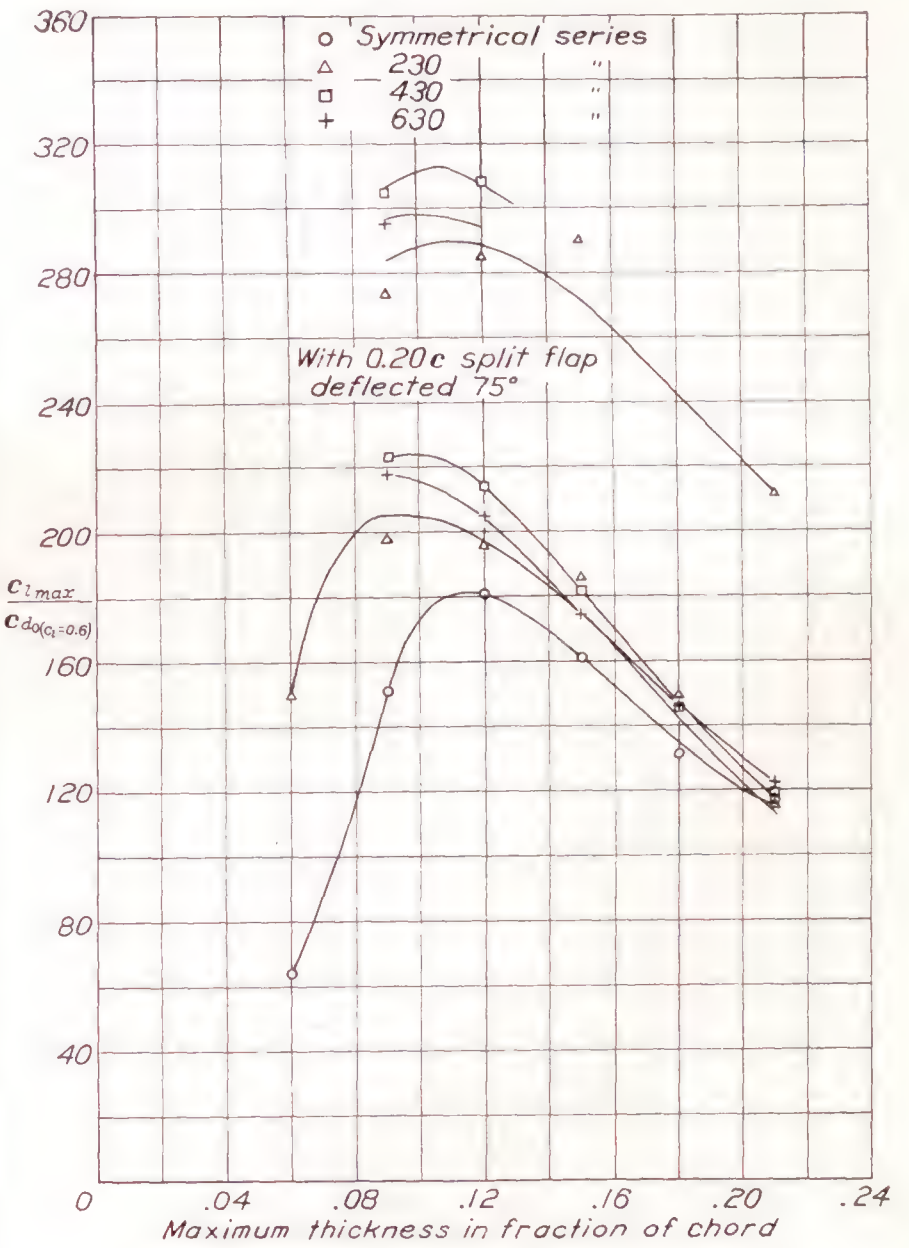

FIGURE 63.—Variation of $c_{l_{max}}/c_{d_{0(c_l=0.6)}}$ with thickness.

Finally, structural considerations will dictate the choice of an airfoil thickness and a wing shape that will efficiently support the aerodynamic loads. This requirement will lead to the choice of an airfoil that is thicker, in general, than one selected solely on the basis of aerodynamic requirements. The final selection of the best thickness and camber will result in a compromise between the demands of aerodynamic and structural efficiency.

The general factors determining the choice of the best thickness and camber have been only briefly discussed. The requirements of any particular airplane design will determine exactly what airfoil will be best suited to that application. It should be emphasized, for instance, that for small airplanes landing at Reynolds Numbers much below 8,000,000, section characteristics should be corrected by means of the method given in reference 6 to the design Reynolds Number before comparisons to determine the optimum sections are made. Such a comparison will show that the optimum camber is considerably higher at the lower Reynolds Number than that indicated by the preceding analysis. For most purposes, a camber of 2 to 4 percent and a thickness slightly above that of the maximum speed-range index will usually be chosen. Some unpublished investigations of particular cases indicate that it is inadvisable, in any case, to depart very much from the optimum airfoil shape dictated by purely aerodynamic considerations unless structural considerations definitely justify the departure.

LANGLEY MEMORIAL AERONAUTICAL LABORATORY,
NATIONAL ADVISORY COMMITTEE FOR AERONAUTICS,
LANGLEY FIELD, VA., *December 5, 1936.*

REFERENCES

1. Jacobs, Eastman N., Ward, Kenneth E., and Pinkerton, Robert M.: The Characteristics of 78 Related Airfoil Sections from Tests in the Variable-Density Wind Tunnel. T. R. No. 460, N. A. C. A., 1933.
2. Jacobs, Eastman N., and Pinkerton, Robert M.: Tests in the Variable-Density Wind Tunnel of Related Airfoils Having the Maximum Camber Unusually Far Forward. T. R. No. 537, N. A. C. A., 1935.
3. Jacobs, Eastman N., and Pinkerton, Robert M.: Tests of N. A. C. A. Airfoils in the Variable-Density Wind Tunnel. Series 230. T. N. No. 567, N. A. C. A., 1936.
4. Jacobs, Eastman N., and Clay, William C.: Characteristics of the N. A. C. A. 23012 Airfoil from Tests in the Full-Scale and Variable-Density Tunnels. T. R. No. 530, N. A. C. A., 1935.
5. Platt, Robert C.: Turbulence Factors of N. A. C. A. Wind Tunnels as Determined by Sphere Tests. T. R. No. 558, N. A. C. A., 1936.
6. Jacobs, Eastman N., and Sherman, Albert: Airfoil Section Characteristics as Affected by Variations of the Reynolds Number. T. R. No. 586, N. A. C. A., 1937.
7. Stack, John, and von Doenhoff, Albert E.: Tests of 16 Related Airfoils at High Speeds. T. R. No. 492, N. A. C. A., 1934.
8. Jacobs, Eastman N., and Abbott, Ira H.: The N. A. C. A. Variable-Density Wind Tunnel. T. R. No. 416, N. A. C. A., 1932.
9. Jacobs, Eastman N., and Rhode, R. V.: Airfoil Section Characteristics as Applied to the Prediction of Air Forces and Their Distribution on Wings. T. R. to be published, N. A. C. A., 1938.
10. Pinkerton, Robert M.: Calculated and Measured Pressure Distributions over the Midspan Section of the N. A. C. A. 4412 Airfoil. T. R. No. 563, N. A. C. A., 1936.

TABLE I.—CHARACTERISTICS OF FORWARD-CAMBER AIRFOILS

Airfoil	Classification				Effective Reynolds number (millions)	Fundamental section characteristics								Derived and additional characteristics that may be used for structural design							
	Chord	PD	SE	$C_{L_{max}}$		$c_{l_{max}}$	α_{l_0} (deg.)	a_0 (per deg.)	$c_{l_{opt}}$	$c_{d_{0_{min}}}$	$c_{m_{a.c.}}$	a. c. (percent c from c/4)		$\frac{c_{l_{max}}}{c_{d_{0_{min}}}}$	c. p. at $c_{l_{max}}$ (percent c)	Wing characteristics $A=6$, round tips		Thickness (percent c) at			Camber (percent c)
												Ahead	Above			m_6 (per radian)	$C_{D_{min}}$	0.15c	0.65c	Maximum	
N. A. C. A.	(1)	(2)	(3)	(4)	(5)	(6)		(6)	(6)	(6)											
0006	A	A10	A	D	8.47	0.91	0	0.098	0.00	0.0054	0	0.7	2	169	35	4.28	0.0054	5.35	4.13	6	0
0009	A	B10	B0	A	8.29	1.39	0	.098	.00	.0064	0	1.0	5	217	26	4.28	.0064	8.02	6.20	9	0
0012	A	C10	C0	A	8.37	1.66	0	.099	.00	.0069	0	.6	3	241	26	4.32	.0069	10.69	8.27	12	0
0012-63	A	C10	C0	A	7.87	1.62	0	.098	.00	.0068	0	1.0	6	238	25	4.28	.0068	10.82	8.58	12	0
0012-64	A	C10	C0	C	7.95	1.56	0	.094	.00	.0069	0	1.5	5	226	24	4.14	.0069	9.72	9.87	12	0
0012-65	A	C10	B8	C	8.21	1.36	0	.084	.00	.0077	0	3.5	6	177	23	3.78	.0077	9.01	11.22	12	0
0015	A	D10	D0	A	8.61	1.66	0	.097	.00	.0077	0	1.2	4	216	25	4.24	.0077	13.36	10.33	15	0
0018	A	E10	E0	A	7.84	1.53	0	.096	.00	.0088	0	1.7	4	174	25	4.20	.0088	16.04	12.40	18	0
0021	A	F10	E1	A	8.34	1.48	0	.093	.00	.0100	0	3.0	6	148	24	4.11	.0100	18.71	14.46	21	0
21012	A	C12	D3	C	8.37	1.63	−.6	.099	.04	.0070	.001	1.5	6	233	25	4.32	.0070	10.69	8.26	12	1.1
22012	A	C12	D2	C	8.32	1.72	−.9	.100	.10	.0071	−.005	1.3	5	242	25	4.34	.0072	10.69	8.24	12	1.5
23006	A	A12	A	D	8.29	1.17	−1.2	.100	.15	.0061	−.012	1.0	8	192	26	4.34	.0062	5.34	4.13	6	1.8
23009	A	B12	C2	A	8.26	1.66	−1.1	.099	.08	.0065	−.009	.9	7	255	25	4.32	.0066	8.02	6.21	9	1.8
23012	A	C12	D2	A	8.37	1.74	−1.2	.100	.08	.0070	−.008	1.2	7	249	25	4.34	.0071	10.69	8.25	12	1.8
23012-33	A	B12	B6	B	8.53	1.52	−1.2	.097	.25	.0071	−.010	.7	7	214	27	4.24	.0073	10.48	8.60	12	1.8
23012-34	A	B12	B3	C	8.60	1.49	−1.2	.094	.13	.0072	−.011	.9	4	207	26	4.14	.0073	8.98	9.87	12	1.8
23012-64	A	C12	D2	A	8.40	1.71	−1.0	.095	.10	.0072	−.010	1.0	4	237	26	4.18	.0073	9.72	9.88	12	1.8
23015	A	D12	D2	A	8.37	1.73	−1.1	.098	.10	.0081	−.008	1.1	6	214	24	4.28	.0082	13.36	10.35	15	1.8
23018	A	E12	E2	B	8.16	1.58	−1.2	.097	.08	.0091	−.006	1.7	6	174	24	4.24	.0091	16.04	12.39	18	1.8
23021	A	F12	E2	B	8.21	1.50	−1.2	.092	.07	.0101	−.005	2.3	7	149	24	4.07	.0102	18.70	14.44	21	1.8
24012	A	C12	C3	C	8.26	1.71	−1.5	.100	.08	.0072	−.013	1.3	6	238	26	4.34	.0073	10.71	8.25	12	2.1
25012	A	C12	C3	C	8.24	1.67	−1.6	100	.10	.0074	−.019	1.1	7	226	27	4.34	.0075	10.72	8.28	12	2.3
32012	A	C12	D3	A	8.40	1.74	−1.2	.100	.15	.0075	−.005	1.1	6	232	24	4.34	.0077	10.69	8.23	12	2.3
33012	A	C12	D3	A	8.37	1.80	−1.7	.099	.10	.0074	−.014	1.0	6	243	25	4.32	.0075	10.68	8.28	12	2.8
34012	A	C12	D3	A	8.37	1.80	−2.1	.100	.20	.0075	−.022	.6	5	240	27	4.34	.0077	10.71	8.25	12	3.1
42012	A	C12	D4	A	8.42	1.76	−1.8	.100	.20	.0078	−.009	1.1	6	226	26	4.34	.0079	10.72	8.28	12	3.1
43009	A	B12	B4	A	8.08	1.72	−2.4	.100	.18	.0068	−.021	.8	6	253	26	4.34	.0073	8.02	6.21	9	3.7
43012	A	C12	D4	A	8.39	1.84	−2.3	.100	.26	.0079	−.019	1.0	7	233	27	4.34	.0081	10.69	8.26	12	3.7
43012A	A	C12	E4	A	8.26	1.78	−2.2	.102	.29	.0081	−.017	1.2	7	220	26	4.41	.0085	11.90	8.26	12	3.7
43015	A	D12	D4	A	8.31	1.76	−2.3	.101	.18	.0085	−.015	1.2	5	207	26	4.37	.0086	13.36	10.32	15	3.7
43018	A	E12	E4	C	8.34	1.63	−2.4	.096	.16	.0095	−.013	1.8	6	172	26	4.20	.0097	16.03	12.40	18	3.7
43021	A	F12	E6	A	8.40	1.48	−2.4	.093	.10	.0108	−.010	2.4	7	137	25	4.11	.0108	18.70	14.50	21	3.7
44012	A	C12	D4	A	8.50	1.82	−2.8	.098	.25	.0080	−.028	.5	5	227	28	4.28	.0081	10.70	8.24	12	4.2
62021	A	F12	E4	D	8.42	1.52	−3.1	.094	.12	.0110	−.006	3.2	8	138	25	4.14	.0111	18.73	14.47	21	4.6
63009	A	B12	C6	A	8.10	1.77	−3.5	.098	.57	.0081	−.042	2.6	7	219	27	4.28	.0204	11.05	6.22	9	5.5
63012	A	C12	D6	A	8.29	1.84	−3.5	.100	.40	.0086	−.033	2.7	13	214	26	4.34	.0100	11.03	8.27	12	5.5
63015	A	D12	E6	A	8.29	1.76	−3.5	.098	.25	.0093	−.024	1.6	6	189	26	4.28	.0097	13.35	10.33	15	5.5
63018	A	E12	E7	A	8.24	1.63	−3.4	.097	.15	.0099	−.020	2.1	6	165	26	4.24	.0100	16.04	12.44	18	5.5
63021	A	F12	E8	A	8.18	1.48	−3.6	.097	.21	.0113	−.018	3.1	6	131	25	4.24	.0115	18.68	14.52	21	5.5
64021	A	F12	E11	A	8.16	1.46	−4.2	.094	.13	.0115	−.031	2.7	8	127	26	4.14	.0116	18.68	14.53	21	6.2
							(7)	(8)		(9)	(10)				(11)						
0012; 60°, 0.2c split flap	A		C0	A	8.11	2.35	−13.1	.091		.167	−.220	.6	3	341	35	4.04		10.69	8.27	12	0
23009; 60°, 0.2c split flap	A		C2	A	8.24	2.31	−14.0	.092		.166	−.223	.9	7	355	35	4.07		8.02	6.21	9	1.8
23012; 60°, 0.2c split flap	A		D2	A	8.18	2.48	−14.3	.088		.166	−.236	1.2	7	354	35	3.93		10.69	8.25	12	1.8
23009; 75°, 0.2c split flap	A		C2	A	7.98	2.30	−15.1	.089		.205	−.210	.9	7	354	34	3.96		8.02	6.21	9	1.8
23012; 75°, 0.2c split flap	A		D2	A	8.10	2.54	−15.6	.085		.201	−.228	1.2	7	363	34	3.82		10.69	8.25	12	1.8
23015; 75°, 0.2c split flap	A		D2	A	8.21	2.70	−16.2	.086		.198	−.245	1.1	6	333	35	3.86		13.36	10.35	15	1.8
23021; 75°, 0.2c split flap	A		E2	A	8.13	2.74	−16.5	.094		.191	−.300	2.3	7	271	35	4.14		18.70	14.44	21	1.8
43009; 75°, 0.2c split flap	A		B4	A	8.10	2.35	−17.5	.080		.207	−.208	.8	6	346	34	3.64		7.52	6.20	9	3.7
43012; 75°, 0.2c split flap	A		D4	A	8.24	2.65	−17.3	.082		.200	−.225	1.0	7	335	34	3.72		10.68	8.26	12	3.7
63009; 75°, 0.2c split flap	A		C6	A	8.21	2.40	−19.0	.078		.207	−.230	2.6	7	295	34	3.57		11.05	6.23	9	5.5

[1] Type of chord. A refers to a chord defined as a line joining the extremities of the mean line.
[2] Type of pressure distribution. See reference 9.
[3] Type of scale effect on maximum lift. A signifies practically no scale effect.
For other designations see reference 6, fig. 44.
[4] Type of lift-curve peak as shown in the sketches.

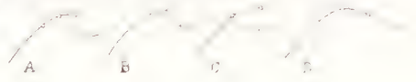

[5] Turbulence factor is 2.64.
[6] These data have been corrected for tip effect.
[7] Angle of zero lift obtained from linear lift curve approximating experimental lift curve.
[8] Slope obtained from linear lift curve approximating experimental lift curve.
[9] Value of the drag that applies approximately over the entire useful range of lift coefficients.
[10] The value of $c_{m_{a.c.}}$ is taken about the aerodynamic center of the airfoil without the flap.
[11] Values of $c_{d_{0min}}$ used in computing this ratio are taken from tests of the airfoil without the flap.

REPORT No. 611

WIND-TUNNEL INVESTIGATION OF TAPERED WINGS WITH ORDINARY AILERONS AND PARTIAL-SPAN SPLIT FLAPS

By Carl J. Wenzinger

SUMMARY

An investigation was made in the N. A. C. A. 7- by 10-foot wind tunnel to determine the aerodynamic properties of tapered wings having partial-span flaps for high lift and ordinary ailerons for lateral control. Each of two Clark Y wings, tapered 5:1 and 5:3, was equipped with partial-span split flaps of two lengths and with ordinary ailerons extending from the outboard ends of the flap to the wing tips. Measurements of wing forces and moments and of aileron hinge moments were made for the two conditions of flaps neutral and deflected.

With split flaps of equal length both wings had practically the same C_{Lmax}. If 30 percent of the flap outer span were removed for the installation of ailerons, a reduction in C_{Lmax} of the tapered wings with flaps might be expected of the order of 4 to 7 percent.

Ailerons of the same span were found to give higher rolling-moment coefficients together with greater adverse yawing-moment coefficients on the 5:3 tapered wing than on the wing tapered 5:1. In addition, ailerons of the same span on the tapered wings tested gave greater rolling-moment coefficients and smaller adverse yawing-moment coefficients at the same lift coefficient when the partial-span flaps were deflected than when they were neutral.

INTRODUCTION

Full-span high-lift devices are seldom used on airplanes at the present time because of the difficulty of obtaining satisfactory lateral control with the lift-increasing device extending along the entire trailing edge of the wing. Several control devices adaptable to wings with a full-span flap have been investigated (references 1 and 2) and a few have shown considerable promise. However, each one has apparently had some disadvantage sufficient to prevent its general use. An arrangement commonly used in practice consists of partial-span flaps extending along the inner portion of the wing span for increasing lift combined with ordinary ailerons extending from the outboard ends of the flap to the wing tips for lateral control. Naturally, such an arrangement does not take advantage of the full potential value of the flap in decreasing the landing speed and steepening the gliding angle at landing.

Some research has already been completed concerning the aerodynamic effects of flaps extending along different portions of the wing span for both rectangular and tapered wings (references 3, 4, and 5). In addition, considerable data are available concerning the characteristics of different sizes of ordinary ailerons on wings of various plan forms (references 6, 7, and 8). There is a scarcity, however, of information regarding the aerodynamic characteristics of wings combined with partial-span flaps and ordinary ailerons.

The investigation described in the present report was made to determine the aerodynamic effects of combinations of flaps and ailerons of various spans. The tests included wings of medium and high taper having split flaps and ordinary ailerons of different spans.

APPARATUS

MODELS

The two models used have been previously tested in connection with the wind-tunnel research described in references 4 and 8. One wing is tapered 5:1 and the other 5:3, the slopes of the leading and trailing edges being equal (figs. 1 and 2). The Clark Y profile is used at all sections along the span, and the maximum ordinates of all the sections are in a horizontal plane on the upper surface. The models are constructed of laminated mahogany; each has a span of 60 inches and a geometrical aspect ratio of 6.0.

The ailerons tapered with the wings, the chord of each aileron at any longitudinal section being 25 percent of the wing chord (c_w) at the same section. The spans of the ailerons first tested were the same as those used in previous tests, 50 percent $b/2$ and 41 percent $b/2$ for the wings tapered 5:1 and 5:3, respectively. The spans were then reduced to 30 percent $b/2$ for each aileron tested, this latter length being considered the shortest desirable. Since earlier tests (reference 6) had shown that the moments caused by both the right and left ailerons could be separately found and added to give the total effect with satisfactory accuracy, the present models were equipped with ailerons only at the right wing tip.

All the ailerons were arranged to lock rigidly to the wing at a given deflection or to rotate freely about their hinge axes, the gap between aileron and wing being sealed with a light grease. Hinge moments of the ailerons were measured by the calibrated twist of a long slender steel rod extending along the hinge axis

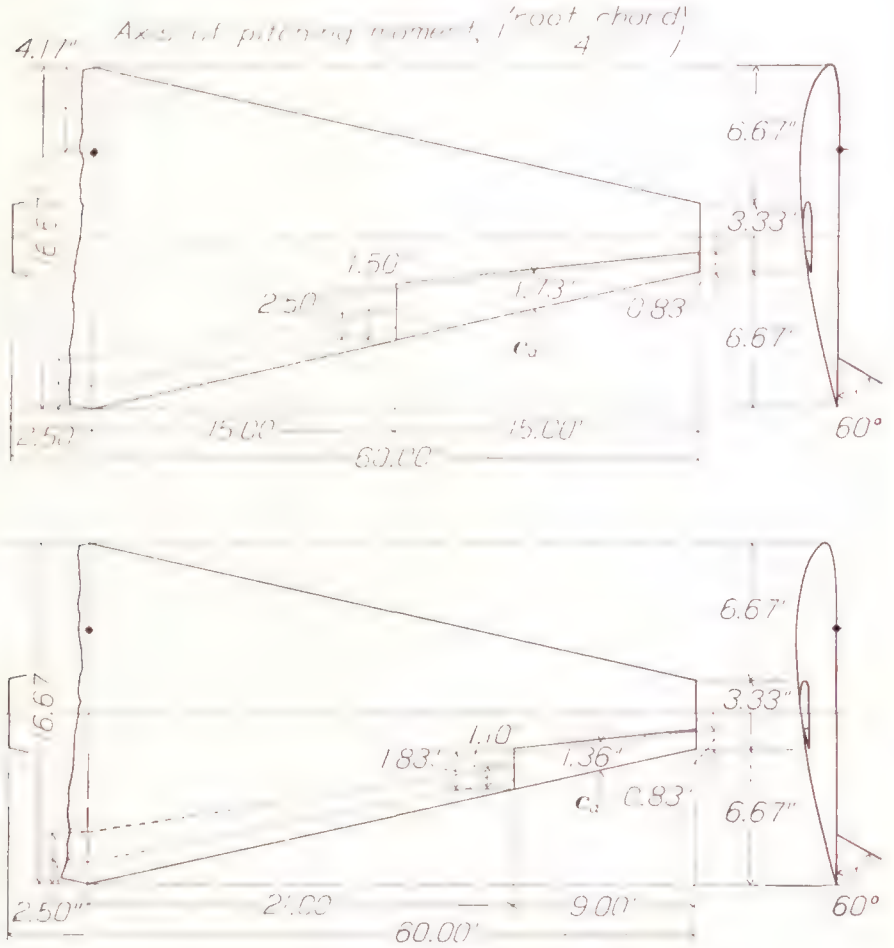

FIGURE 1.—The 5:1 tapered Clark Y wing with $0.25c_w$ tapered ordinary ailerons and $0.15c_w$ tapered partial-span split flaps.

from the aileron to the balance frame outside the air stream.

Simple split flaps that tapered with the wing were used with each model, the flap chord at any longitudinal section being $0.15c_w$ at the same section. In each case the flaps extended along the trailing edge of the wing from the center section to the inboard end of the ailerons, so that partial-span flaps of 0.50, 0.59, and $0.70b$ were used. Each of the flaps was built of $\frac{1}{16}$-inch steel plate and was fastened to the wing model by screws and blocks at an angle of 60°. This angle was the one that gave the highest $C_{L_{max}}$ with the $0.15c_w$ tapered flap in earlier tests (reference 4).

WIND TUNNEL

The N. A. C. A. 7- by 10-foot wind tunnel in which the tests were made had an open jet and a closed return passage. The tunnel and regular 6-component balance are described in detail in reference 9. On this balance the six components of aerodynamic forces and moments are independently and simultaneously measured with respect to the wind axes of the model.

TESTS

The dynamic pressure was maintained constant throughout the tests at 16.37 pounds per square foot corresponding to an air speed of 80 miles per hour at standard sea-level conditions. The average test Reynolds Number was 609,000 based on the mean wing chord of 10 inches; the effective Reynolds Number (test Reynolds Number×the turbulence factor of the wind tunnel) was 609,000×1.4=853,000. (See reference 10.) The angle-of-attack range covered from zero lift to beyond the stall of the wing. Aileron deflections covered from 30° to −30° and were measured in a plane perpendicular to their hinge axes. (Positive deflections are downward and negative, upward.)

Force tests were made first with full-span flaps on the wings as a basis for comparison with the partial-span flaps. Lift, drag, and pitching-moment coefficients were measured for flap deflections of 0° and 60°. The flaps were next cut to the shortest spans used so that the longest ailerons could be tested first. With this arrangement no alterations to the original models were required. Lift, drag, and pitching-moment coefficients were again measured for flap angles of 0° and 60°, ailerons neutral, and then rolling-, yawing-, and hinge-moment coefficients of the ailerons were measured for the same two flap deflections. In all these tests the aileron gaps were sealed with a light grease to prevent any leakage because even a small gap considerably reduces the aileron effectiveness.

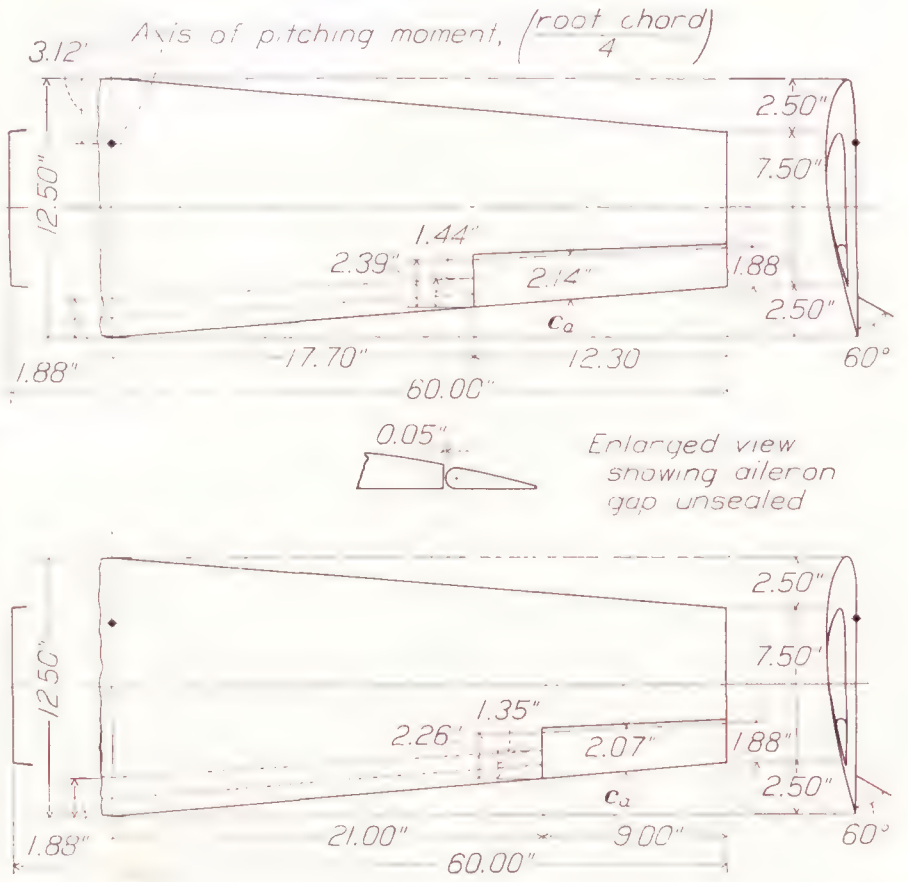

FIGURE 2.—The 5:3 tapered Clark Y wing with $0.25c_w$ tapered ordinary ailerons and $0.15c_w$ tapered partial-span split flaps.

For comparison with results for the aileron gap sealed, a few tests were made with the long aileron having the gap unsealed on the 5:1 tapered wing. In this case rolling-, yawing-, and hinge-moment coefficients of the aileron were measured only for the flap-neutral condition. These data also served for comparison with similar data from the same model obtained about 3 years earlier.

The ailerons were then cut to the shorter spans and the flaps were lengthened. Tests similar to those for the longer ailerons were again made, except that the aileron gaps were always kept sealed.

RESULTS AND DISCUSSION

FORM OF PRESENTATION OF DATA

The test results are given in the form of absolute coefficients of lift and drag, and of pitching, rolling, yawing, and hinge moment:

$$C_L = \frac{\text{lift}}{qS}$$

$$C_D = \frac{\text{drag}}{qS}$$

$$C_{m_{(a.c.)_0}}{}' = \frac{\text{pitching moment about aerodynamic center [of plain wing}}{qcS}$$

$$C_l' = \frac{\text{rolling moment}}{qbS}$$

$$C_n' = \frac{\text{yawing moment}}{qbS}$$

$$C_h = \frac{\text{hinge moment}}{qc_aS_a}$$

where S is the wing area.
b, the wing span.
c, the mean geometric chord of the wing.
S_a, the area of one aileron.
c_a, the root-mean-square chord of a tapered aileron; i. e., the square root of the mean of the squares of the aileron chords along its span.
q, the dynamic pressure.

All coefficients, except those of hinge moment, were obtained directly from the balance and refer to the wind (or tunnel) axes.

The data were corrected for tunnel effects to aspect ratio 6.0. The standard jet-boundary corrections were applied,

$$\Delta\alpha = \delta\frac{S}{C}C_L \times 57.3, \text{ degrees}$$

$$\Delta C_D = \delta\frac{S}{C}C_L{}^2$$

where C is the jet cross-sectional area. A value $\delta = -0.165$ for the open-jet 7- by 10-foot wind tunnel was used in correcting the test results. An additional correction to the drag data was necessitated by the static-pressure gradient in the open jet. This gradient produced an additional downstream force on the model corresponding to ΔC_D of 0.0019 for the wing tapered 5:1 and ΔC_D of 0.0017 for the wing tapered 5:3.

EFFECT OF FLAP SPAN ON WING CHARACTERISTICS

Lift and drag coefficients for the 5:1 tapered wing with various spans of tapered split flap are given in figure 3, and pitching-moment coefficients in figure 4. Similar data for the 5:3 tapered wing are given in figures 5 and 6. Values of $C_{L_{max}}$ and of C_D and L/D

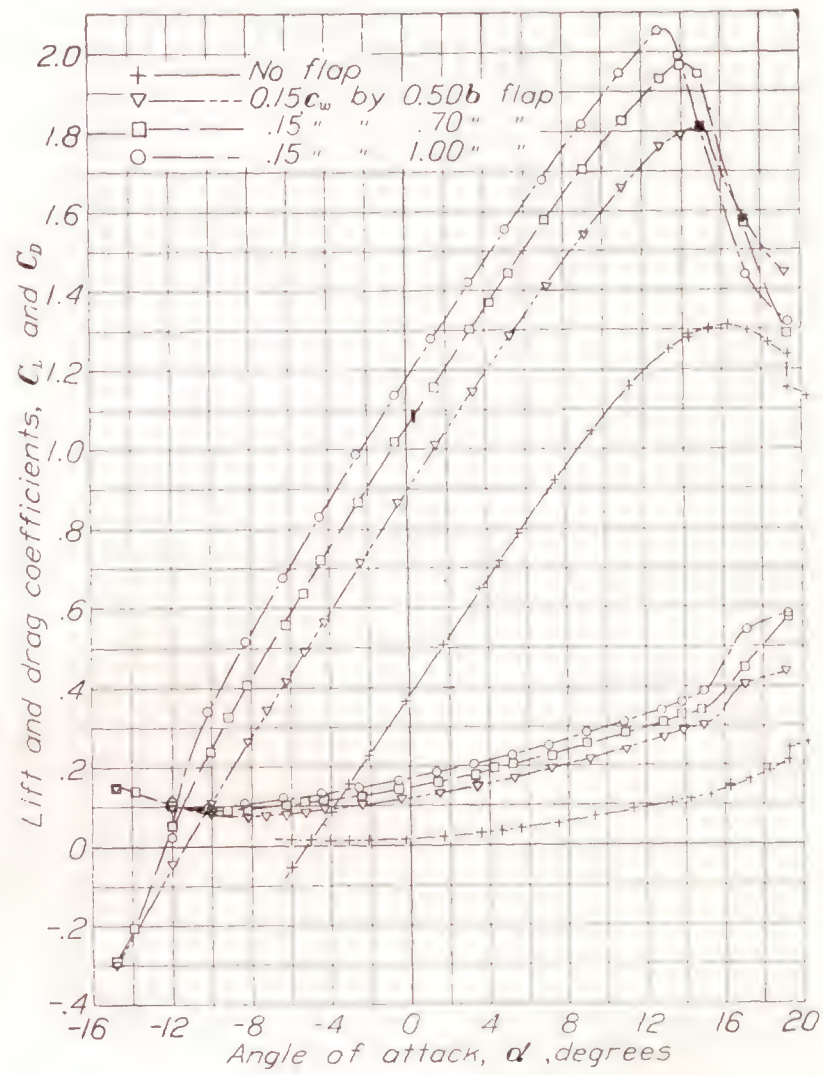

FIGURE 3.—Lift and drag coefficients of 5:1 tapered wing with tapered split flaps of various spans deflected 60°. Aileron neutral.

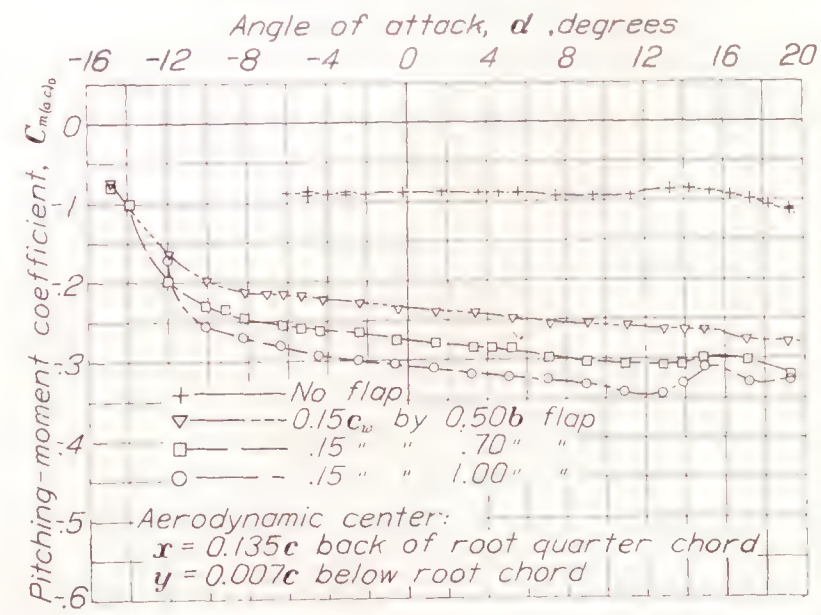

FIGURE 4.—Pitching-moment coefficients of 5:1 tapered wing with tapered split flaps of various spans deflected 60°. Aileron neutral.

at $C_{L_{max}}$ for different flap spans on both the 5:1 and 5:3 tapered wings are plotted in figure 7.

Some aerodynamic characteristics of the tapered wings with split flaps of various spans are compared in table I with similar data for a rectangular wing. (The data for the rectangular wing were taken from reference 3 and corrected for tunnel effects.) It will be noted

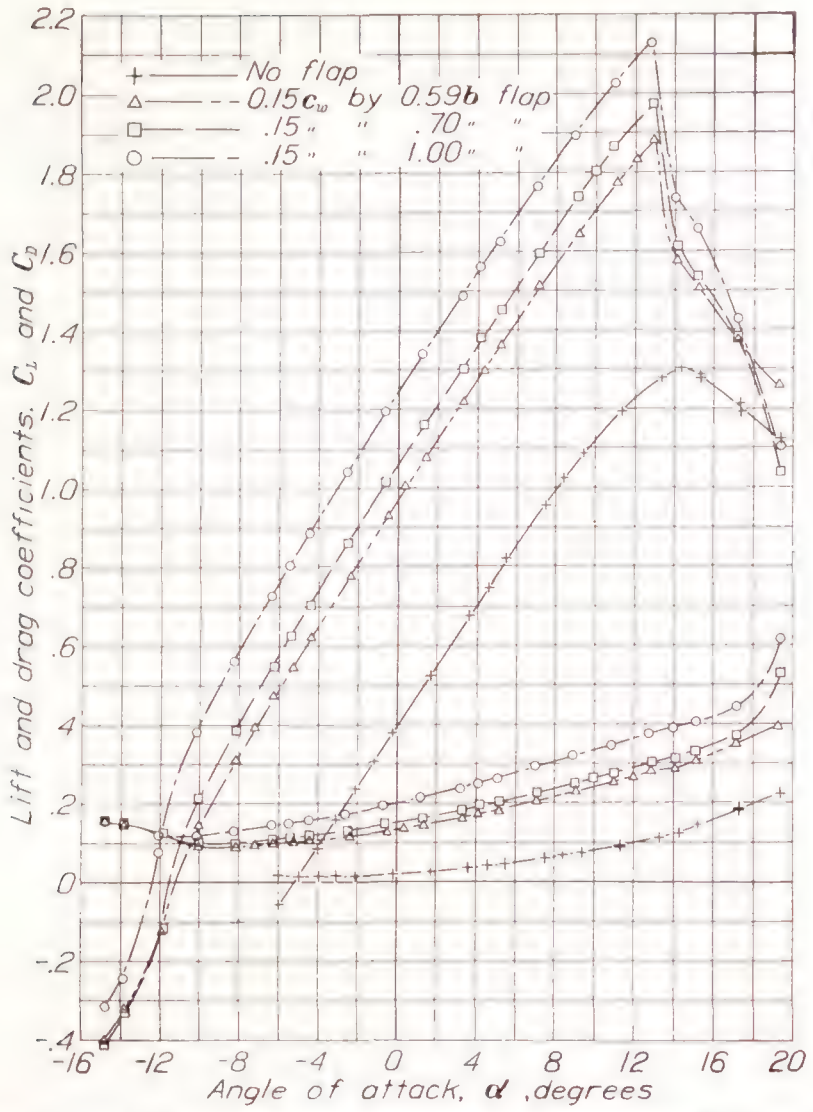

FIGURE 5.—Lift and drag coefficients for 5:3 tapered wing with tapered split flaps of various spans deflected 60°. Aileron neutral.

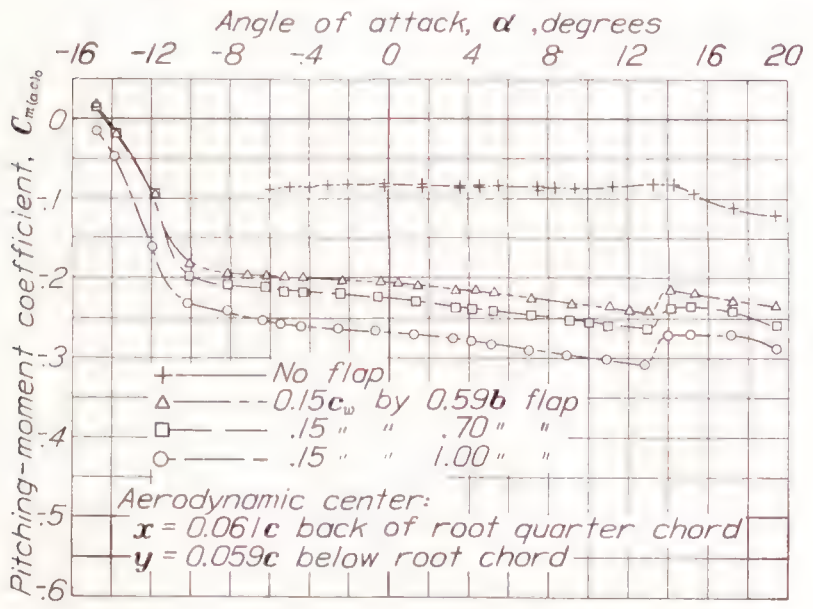

FIGURE 6.—Pitching-moment coefficients for 5:3 tapered wing with tapered split flaps of various spans deflected 60°. Aileron neutral.

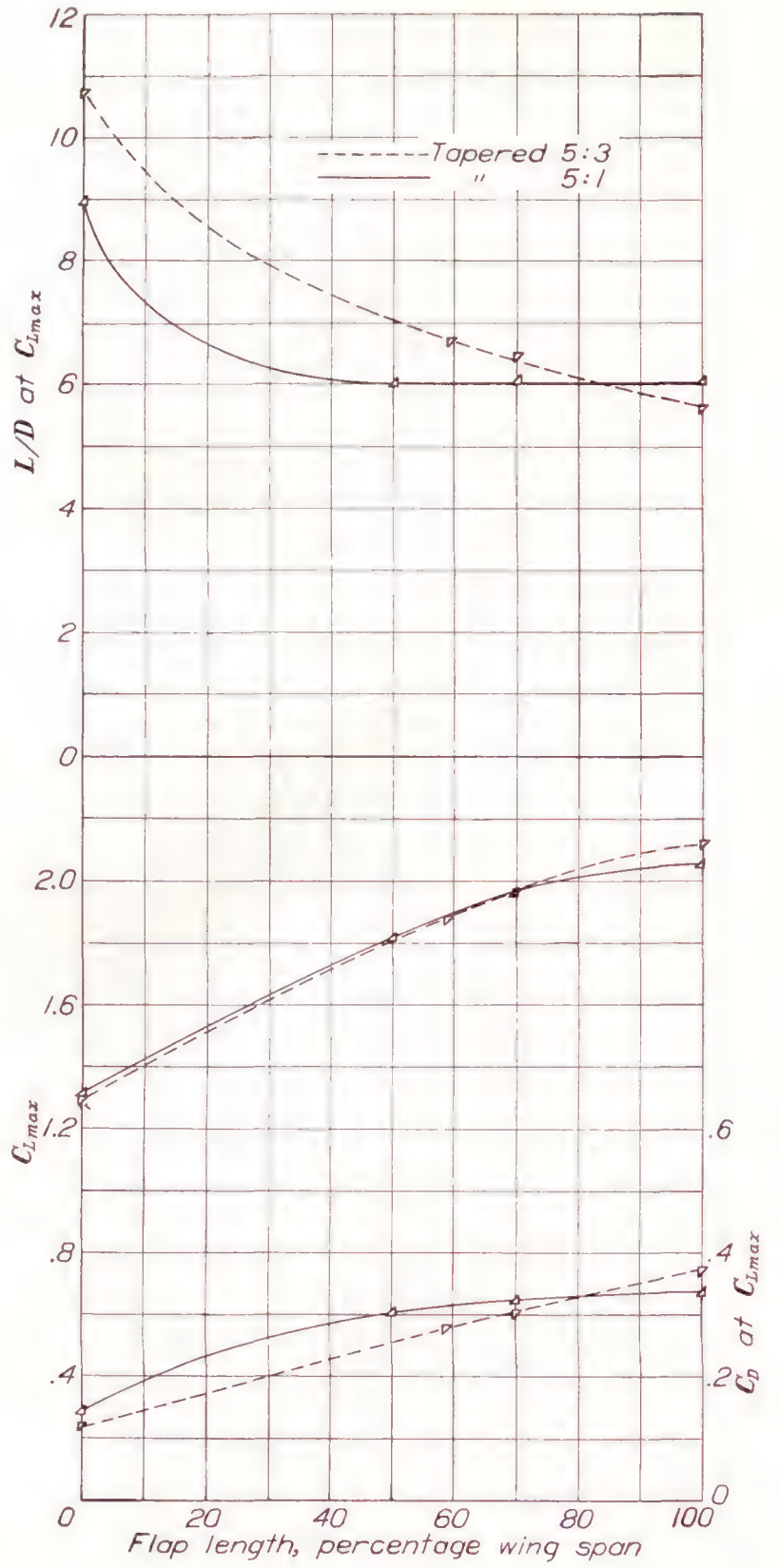

FIGURE 7.—Effect of partial-span split flaps on $C_{L_{max}}$ and on C_D and L/D at $C_{L_{max}}$. The 5:1 and 5:3 tapered wings with 0.15 c_w tapered split flaps deflected 60°.

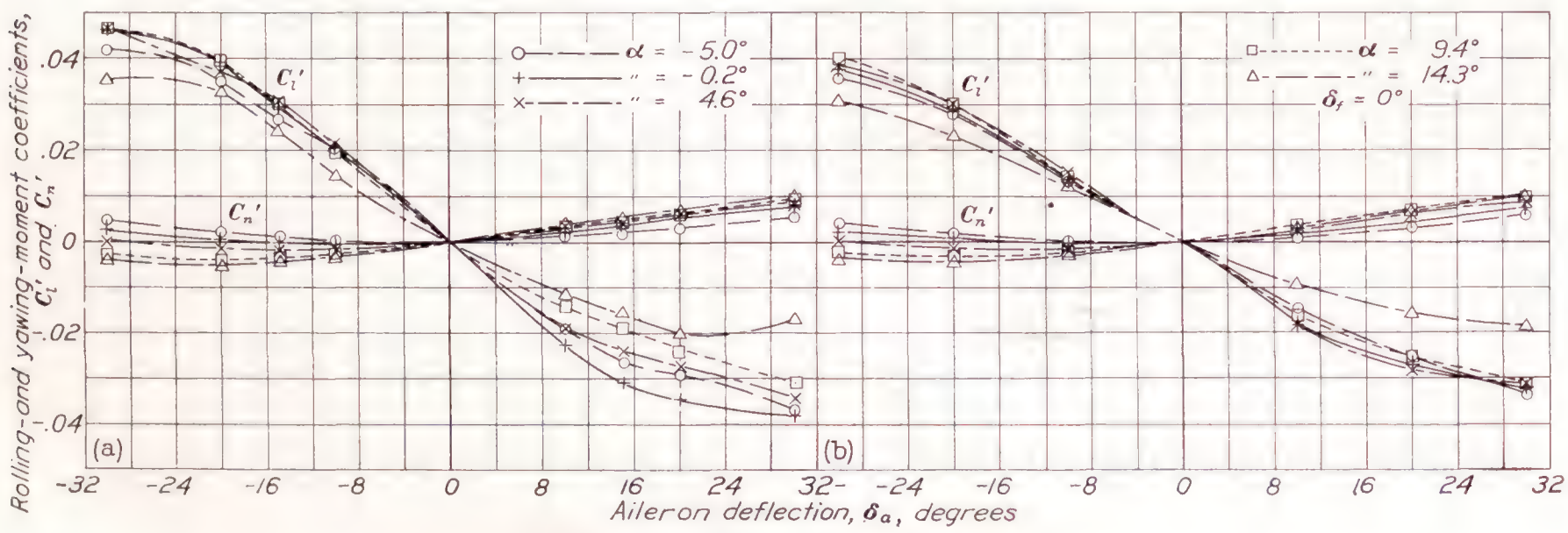

(a) Aileron gap closed. (b) Aileron gap open.

FIGURE 8.—Rolling- and yawing-moment coefficients of 0.25c_w by 0.50 $\frac{b}{2}$ tapered aileron on 5:1 tapered wing. Flaps neutral.

that the $C_{L_{max}}$ of the plain wings increases slightly with increasing taper but, with full-span flaps deflected, the $C_{L_{max}}$ decreases slightly with increasing taper.

Reducing the flap span from 100 to 70 percent on the 5:1 tapered wing reduced the lift increment $\Delta C_{L_{max}}$ by about 11.5 percent although the actual $C_{L_{max}}$ was reduced about 4 percent. On the 5:3 tapered wing and on the rectangular wing the values are roughly 17 percent reduction in $\Delta C_{L_{max}}$ and 7 percent in $C_{L_{max}}$.

AILERON CHARACTERISTICS, 5 : 1 TAPERED WING

Rolling- and yawing-moment coefficients due to the $0.25c_w$ by 0.50 $b/2$ tapered aileron, gap closed, are given in figure 8 (a) at five angles of attack for the flap-neutral condition. The results for the gap open between aileron and wing are plotted in figure 8 (b). Comparison of these two figures shows that the rolling-moment coefficient for a given aileron deflection is decreased when the gap is left unsealed, indicating that no leakage should be permitted between aileron and wing for the maximum rolling effect. Comparison of the data for the unsealed aileron (fig. 8 (b)) with those obtained with the same aileron in tests made about 3 years earlier (reference 8) shows good agreement.

The effect on aileron rolling- and yawing-moment coefficients due to deflecting the $0.15c_w$ by $0.50b$ split flap 60° is shown in figure 9. For the two conditions

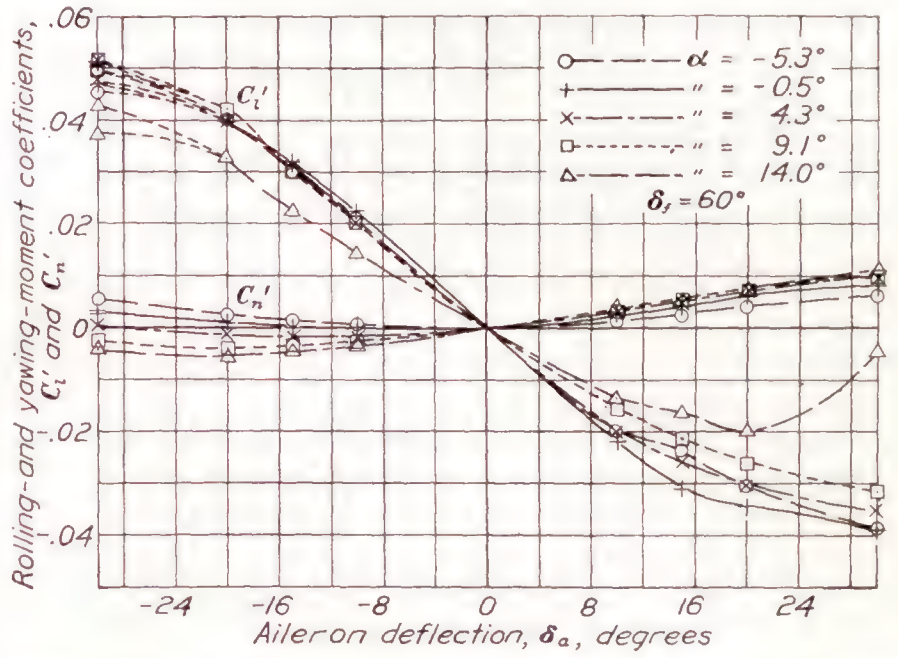

FIGURE 9.—Rolling- and yawing-moment coefficients of $0.25c_w$ by $0.50\frac{b}{2}$ tapered aileron on 5:1 tapered wing. The $0.15c_w$ by $0.50b$ tapered split flaps deflected 60°.

of flap neutral and flap deflected, the rolling moments due to the up aileron increase directly with aileron deflection to about 20° after which they taper off.

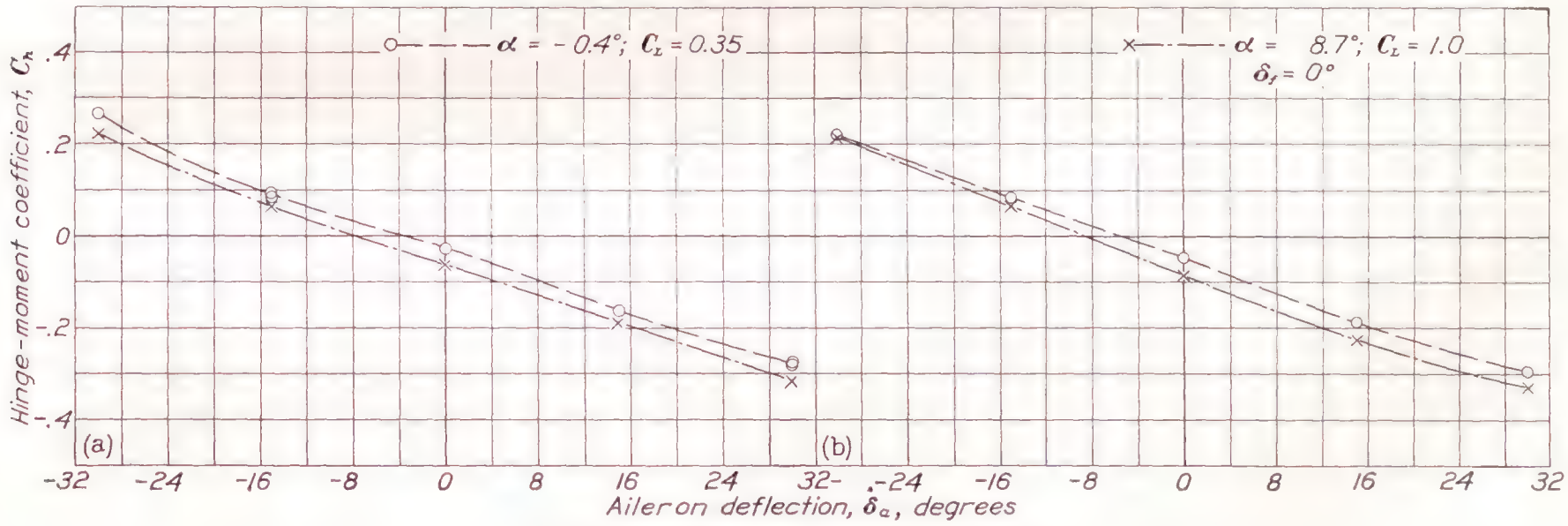

(a) Aileron gap closed. (b) Aileron gap open.

FIGURE 10.—Hinge-moment coefficients of $0.25c_w$ by $0.50\frac{b}{2}$ tapered aileron on 5:1 tapered wing. Flaps neutral.

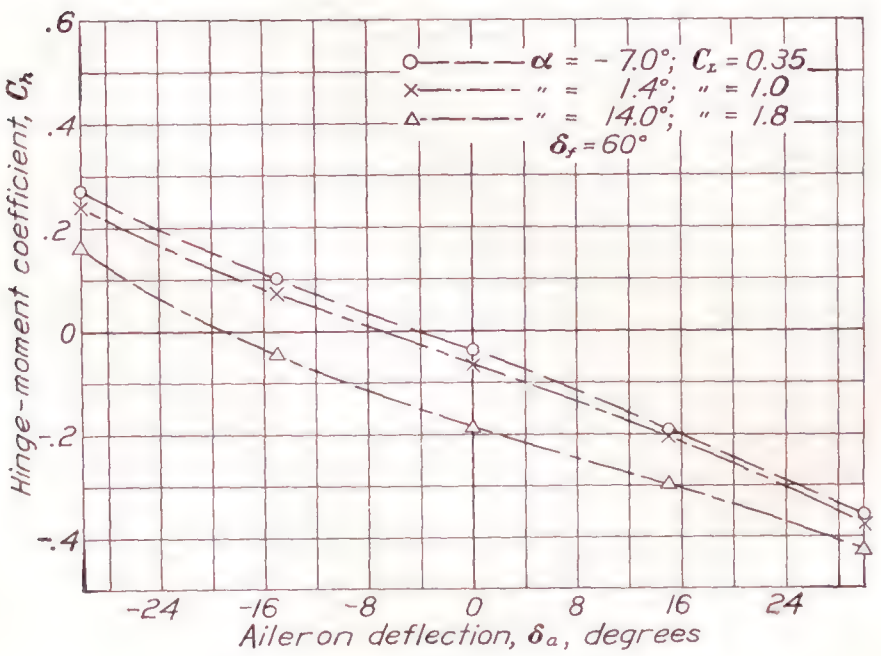

FIGURE 11.—Hinge-moment coefficients of $0.25c_w$ by $0.50\frac{b}{2}$ tapered aileron on 5:1 tapered wing. The $0.15c_w$ by $0.50b$ tapered split flaps deflected 60°.

The moments due to the down aileron increase directly to an aileron angle of about 15° after which they also begin to fall off. In general, when the flap is deflected, the rolling-moment coefficients are increased above the values for the flap-neutral condition. Hinge-moment coefficients of these ailerons increase almost directly with aileron deflection (figs. 10 (a), 10 (b), and 11) for the range tested.

Rolling- and yawing-moment coefficients due to the $0.25c_w$ by 0.30 $b/2$ tapered ailerons are given in figure 12 for the flap-neutral condition and in figure 13 for the $0.15c_w$ by $0.70b$ split flap deflected 60°. Hinge-moment coefficients for the two conditions are given in figures 14 and 15. The variation of rolling moment with aileron deflection is quite similar for these ailerons to that of the longer ones, but the values are considerably less for a given deflection at a given angle of attack. In fact,

the reduction in rolling-moment coefficient is almost directly proportional to the decrease in the span of the aileron.

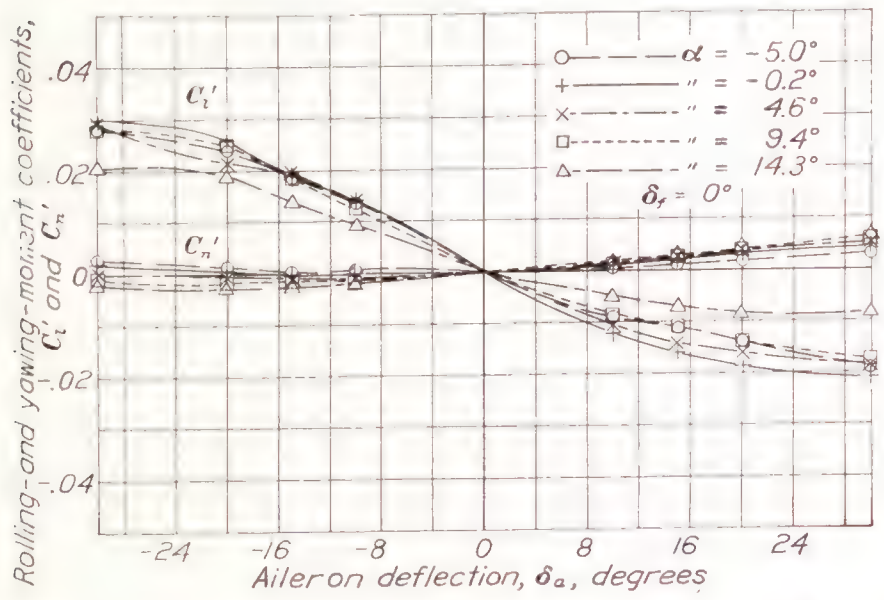

FIGURE 12.—Rolling- and yawing-moment coefficients of $0.25c_w$ by $0.30\frac{b}{2}$ tapered aileron on 5:1 tapered wing. Flaps neutral.

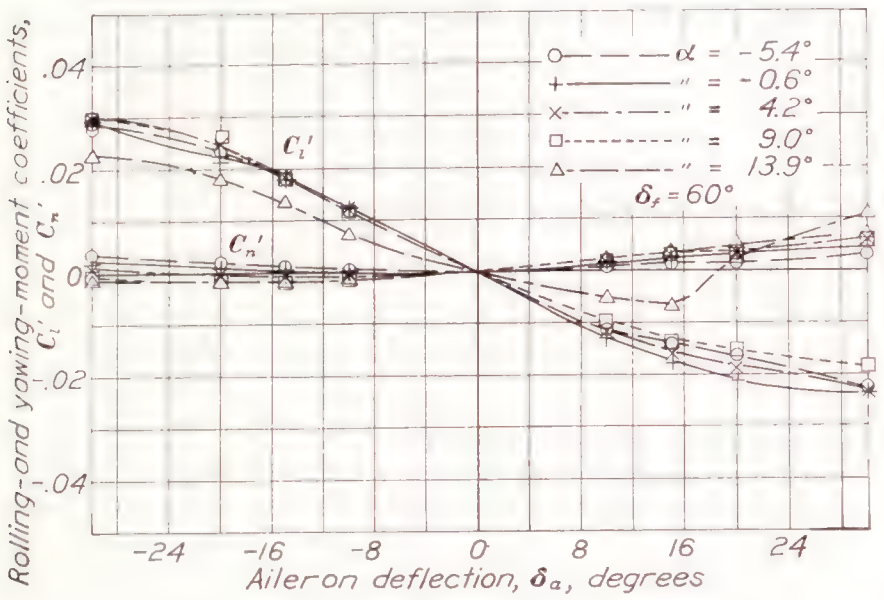

FIGURE 13.—Rolling- and yawing-moment coefficients of $0.25c_w$ by $0.30\frac{b}{2}$ tapered aileron on 5:1 tapered wing. The $0.15c_w$ by $0.70b$ tapered split flaps deflected 60°.

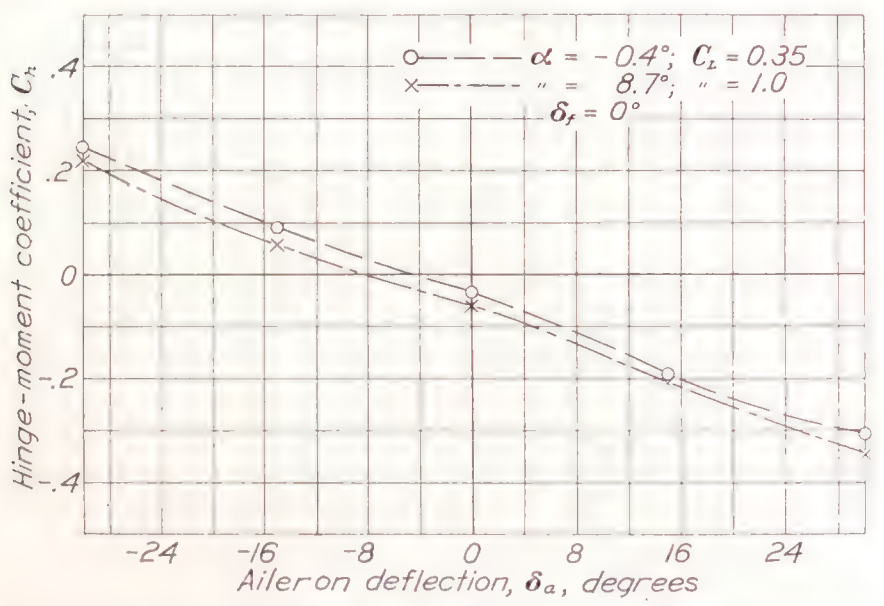

FIGURE 14.—Hinge-moment coefficients of $0.25c_w$ by $0.30\frac{b}{2}$ tapered aileron on 5:1 tapered wing. Flaps neutral.

AILERON CHARACTERISTICS, 5 : 3 TAPERED WING

Rolling-, yawing-, and hinge-moment coefficients of the $0.25c_w$ by 0.41 $b/2$ tapered aileron are given in figures 16, 17, 18, and 19 for various aileron deflections at several angles of attack, the $0.15c_w$ by $0.59b$ tapered split flap both neutral and deflected 60°. Similar plots for the shorter aileron, $0.25c_w$ by 0.30 $b/2$, with the

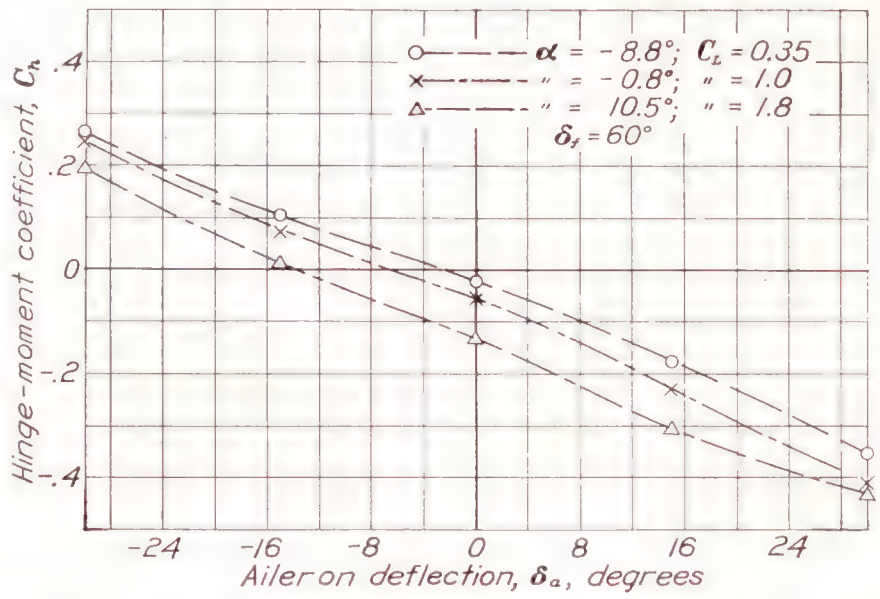

FIGURE 15.—Hinge-moment coefficients of $0.25c_w$ by $0.30\frac{b}{2}$ tapered aileron on 5:1 tapered wing. The $0.15c_w$ by $0.70b$ tapered split flaps deflected 60°.

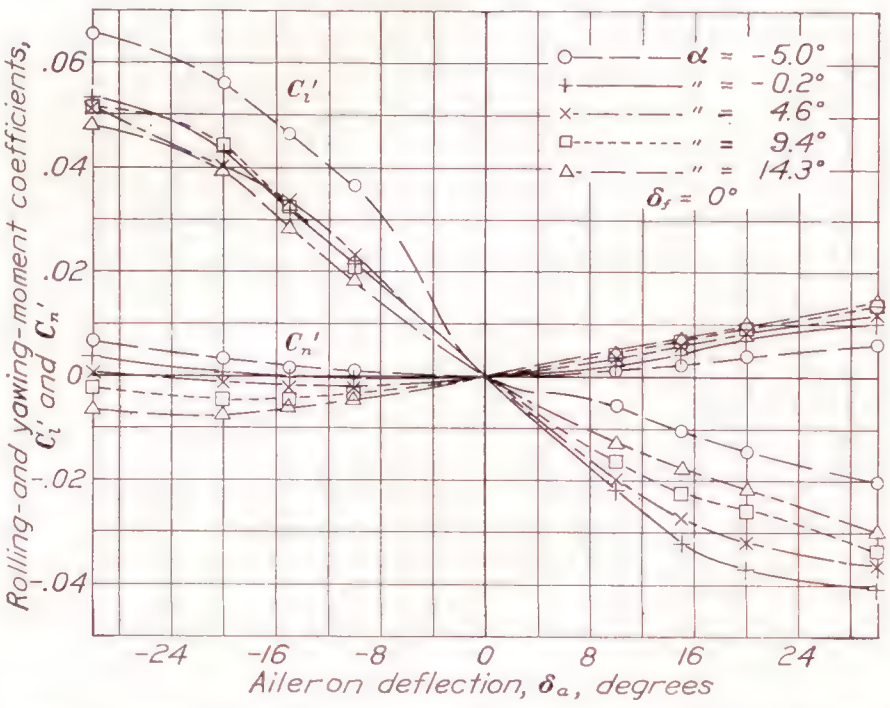

FIGURE 16.—Rolling- and yawing-moment coefficients of $0.25c_w$ by $0.41\frac{b}{2}$ tapered aileron on 5:3 tapered wing. Flaps neutral.

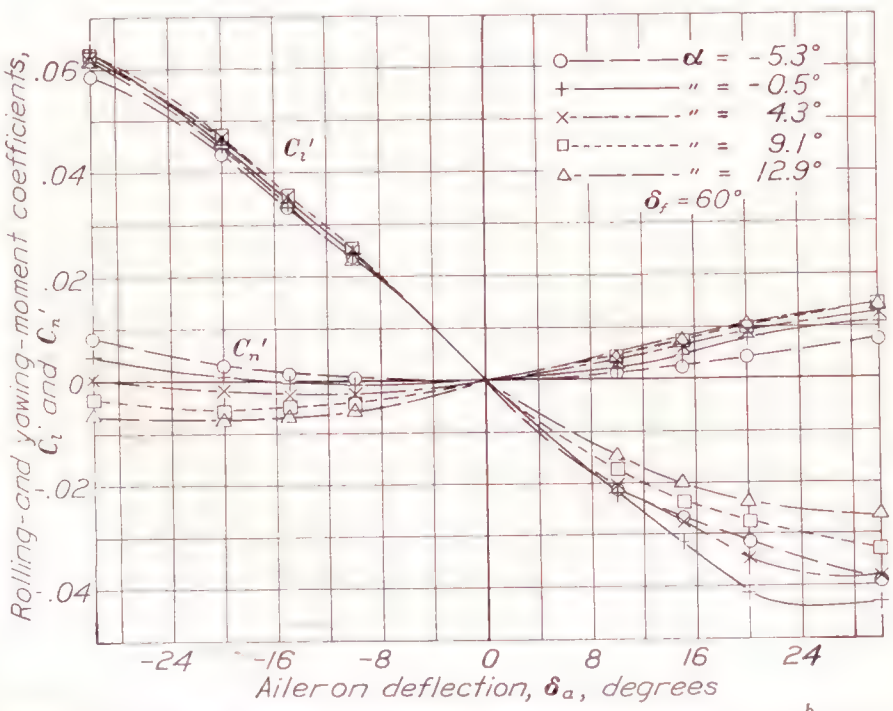

FIGURE 17.—Rolling- and yawing-moment coefficients of $0.25c_w$ by $0.41\frac{b}{2}$ tapered aileron on 5:3 tapered wing. The $0.15c_w$ by $0.59b$ tapered split flaps deflected 60°.

longer flap, $0.15c_w$ by $0.70b$, are given in figures 20, 21, 22, and 23.

For the 5:3 tapered wing, the variation of rolling moment with aileron deflection is much the same as that of the ailerons on the 5:1 tapered wing except for the case of the up aileron when the flap is deflected.

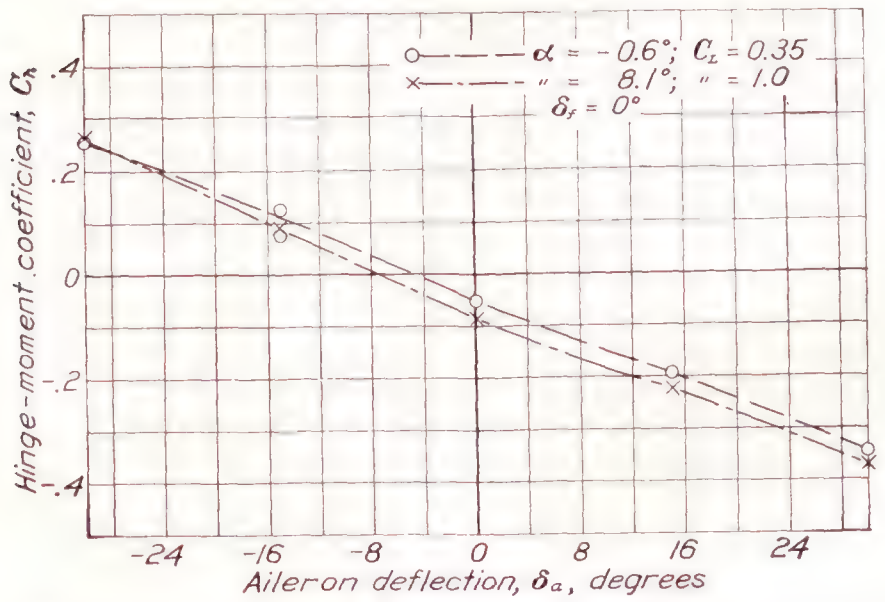

FIGURE 18.—Hinge-moment coefficients of $0.25c_w$ by $0.41\frac{b}{2}$ tapered aileron on 5:3 tapered wing. Flaps neutral.

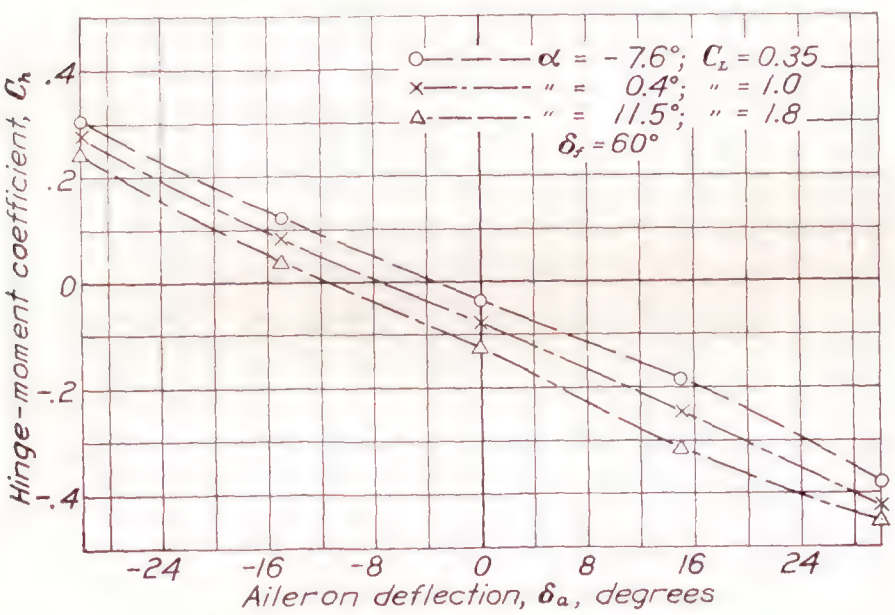

FIGURE 19.—Hinge-moment coefficients of $0.25c_w$ by $0.41\frac{b}{2}$ tapered aileron on 5:3 tapered wing. The $0.15c_w$ by $0.59b$ tapered split flaps deflected 60°.

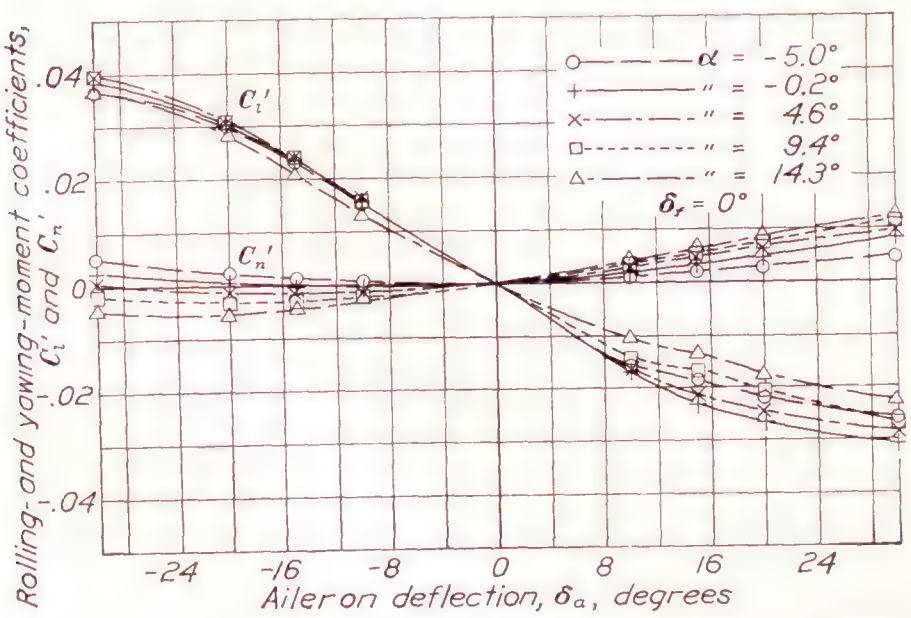

FIGURE 20.—Rolling- and yawing-moment coefficients of $0.25c_w$ by $0.30\frac{b}{2}$ tapered aileron on 5:3 tapered wing. Flaps neutral.

In this condition on the 5:3 tapered wing the rolling moments due to the up aileron increase almost directly without falling off over the range of deflections tested (0° to 30°). The moments due to the down aileron, however, vary in a manner similar to those on the 5:1 tapered wing. As in the case of the ailerons on the 5:1 tapered wing, the rolling-moment coefficients for the ailerons on the 5:3 tapered wing are somewhat

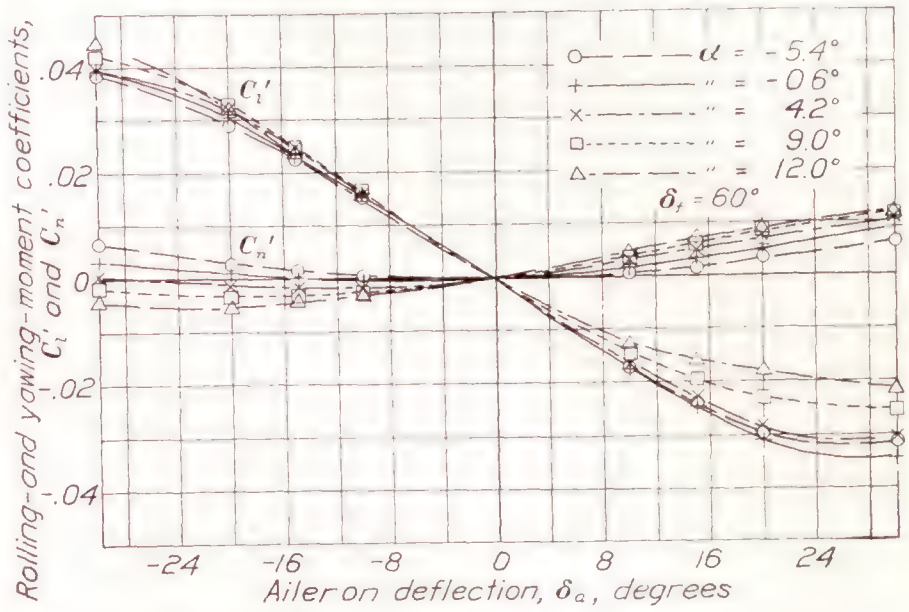

FIGURE 21.—Rolling- and yawing-moment coefficients of $0.25c_w$ by $0.30\frac{b}{2}$ tapered aileron on 5:3 tapered wing. The $0.15c_w$ by $0.70b$ tapered split flaps deflected 60°.

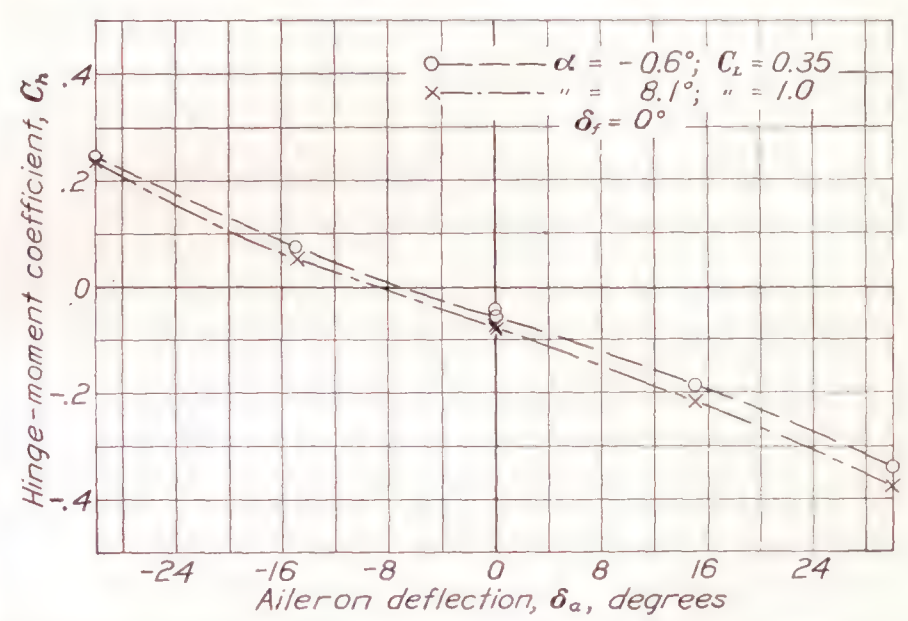

FIGURE 22.—Hinge-moment coefficients of $0.25c_w$ by $0.30\frac{b}{2}$ tapered aileron on 5:3 tapered wing. Flaps neutral.

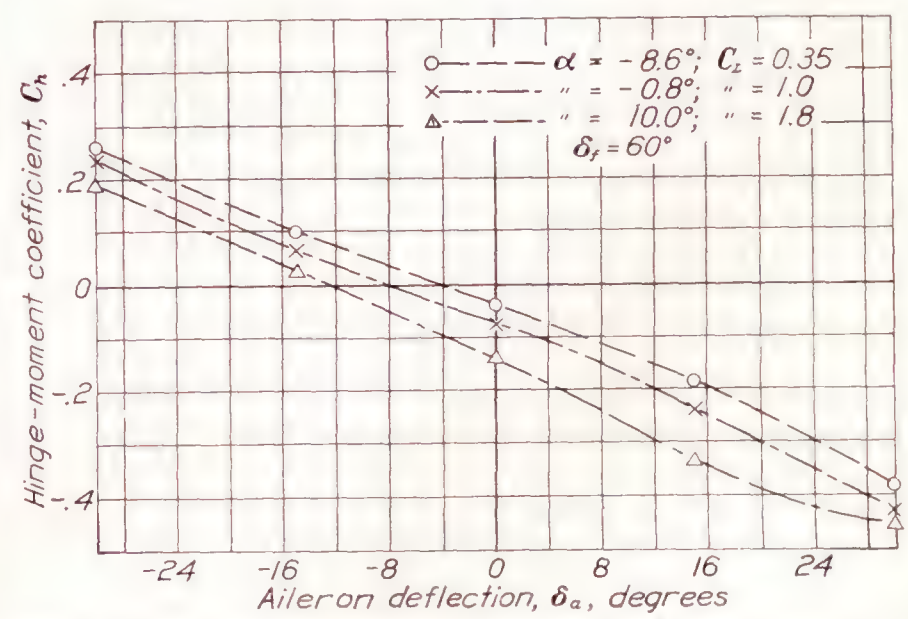

FIGURE 23.—Hinge-moment coefficients of $0.25c_w$ by $0.30\frac{b}{2}$ tapered aileron on 5:3 tapered wing. The $0.15c_w$ by $0.70b$ tapered split flaps deflected 60°.

increased when the flap is deflected. In addition, the reduction in rolling-moment coefficient with decreased aileron span is also directly proportional to the decrease in span.

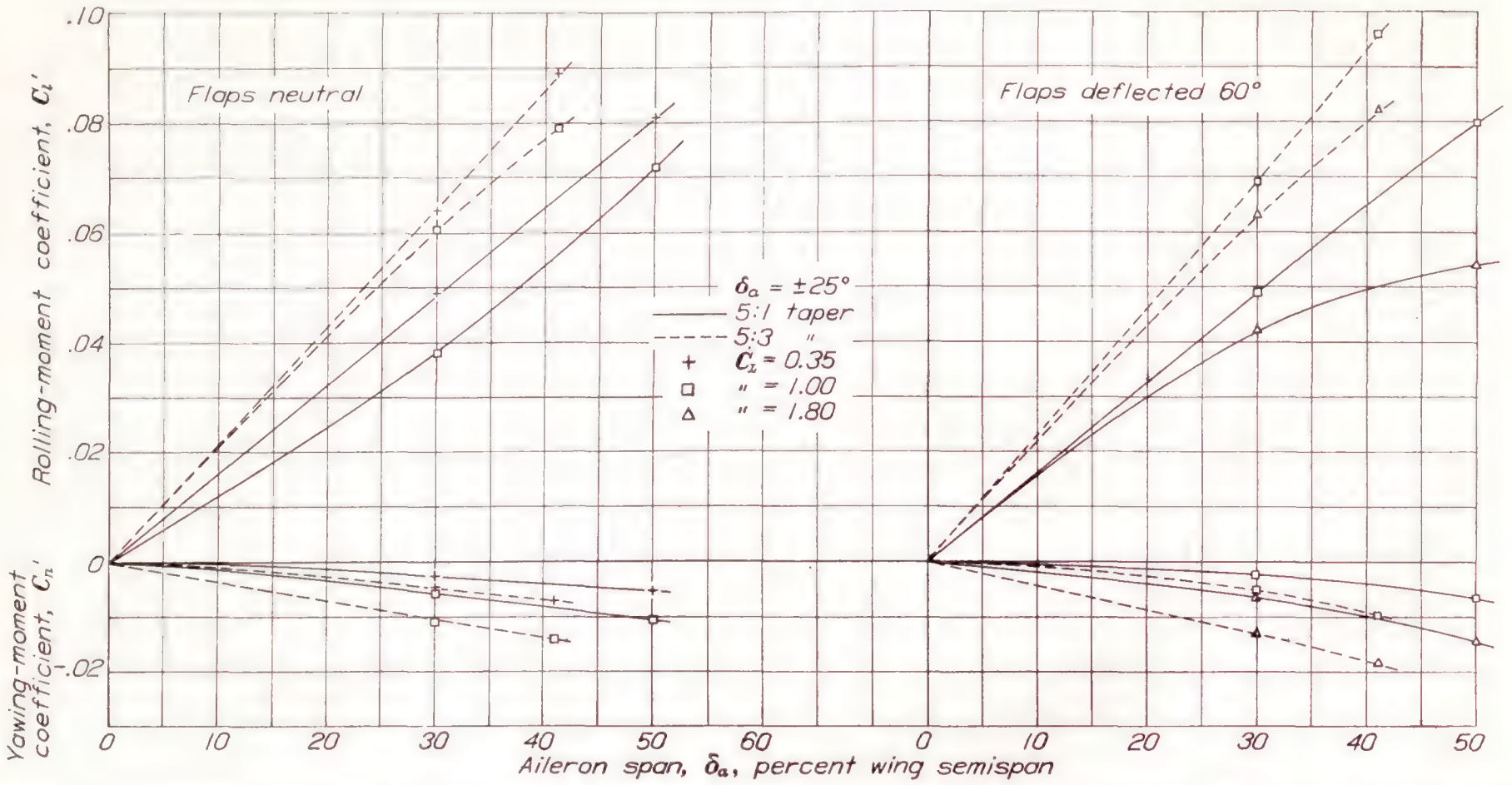

FIGURE 24.—Effect of aileron span on rolling- and yawing-moment coefficients. The $0.25c_w$ tapered aileron with equal up-and-down deflection on tapered Clark Y wings The $0.15c_w$ partial-span split flaps neutral and deflected.

COMPARISON OF THE TAPERED AILERONS ON TAPERED WINGS

The effect of aileron span on rolling- and yawing-moment coefficients with equal up-and-down deflection is shown in figure 24, with the partial-span flaps both neutral and deflected. With the arrangements shown it is evident that ailerons of the same span on the 5:3 tapered wing are capable of giving higher rolling-moment coefficients, together with more adverse yawing-moment coefficients, than those on the 5:1 tapered wing, flaps neutral or deflected. This characteristic may be attributed almost entirely to the difference in area of the ailerons for the sizes investigated on the two wings. The chords of the ailerons are the same percentage of the wing chord so that, since the wings have the same span and area, the aileron on the 5:3 tapered wing has a larger area than an aileron of equal span on the 5:1 tapered wing. At the same lift coefficient of the wing, deflecting the flap has the same general effect as in the case of single ailerons; i. e., the rolling-moment coefficients are increased and the adverse yawing-moment coefficients are decreased for the same aileron deflection.

Previous tests showed (reference 8) that the long tapered ailerons on both the 5:1 and 5:3 tapered wings, flaps neutral, gave rolling moments equal in magnitude to an assumed value that would provide satisfactory lateral control up to the stall. At and beyond the stall, however, the indicated control was poor.

The rolling-moment coefficient corresponding to the foregoing conditions is approximately 0.065 at a lift coefficient of 1.0 for the tapered ailerons and wings in question. In addition, flight tests have shown that in some cases $C_l'=0.04$ gives satisfactory rolling control (reference 11) so that the value of $C_l'=0.065$ may be too high for most of the usual flight conditions.

Decreasing the span of the tapered ailerons to 0.30 $b/2$ gives an aileron that just meets the requirement of the lower rolling-moment coefficient on the 5:1 tapered wing, which is probably the highest taper likely to be dealt with in practice. The use of the highly tapered wing is accompanied by a decreased damping in roll compared with the medium tapered or rectangular wings, so that it seems likely that lower aileron rolling moments will suffice to give the same degree of control. In addition, the reduction in $C_{L_{max}}$ with partial-span flaps is small (about 4 percent), so that the combination appears promising from considerations of both high lift and rolling control.

CONCLUSIONS

1. There was practically no difference in $C_{L_{max}}$ obtained with Clark Y wings tapered 5:1 or 5:3 with equal lengths of split flap.

2. A reduction in $C_{L_{max}}$ of tapered wings with split flaps might be expected of the order of 4 to 7 percent, if 30 percent of the flap outer span were removed for ailerons.

3. Ailerons of the same span on the 5:3 tapered wing gave higher rolling-moment coefficients but also greater adverse yawing-moment coefficients than those on the 5:1 tapered wing, flaps neutral or deflected.

4. Ailerons of the same span gave greater rolling-moment coefficients and smaller adverse yawing-moment coefficients at the same lift coefficient on the tapered wings tested when partial-span split flaps were deflected than when neutral.

LANGLEY MEMORIAL AERONAUTICAL LABORATORY,
NATIONAL ADVISORY COMMITTEE FOR AERONAUTICS,
LANGLEY FIELD, VA., *January 14, 1937.*

REFERENCES

1. Soulé, H. A., and McAvoy, W. H.: Flight Investigation of Lateral Control Devices for Use with Full-Span Flaps. T. R. No. 517, N. A. C. A., 1935.
2. Weick, Fred E., and Shortal, Joseph A.: Development of the N. A. C. A. Slot-Lip Aileron. T. N. No. 547, N. A. C. A., 1935.
3. Wenzinger, Carl J.: The Effect of Partial-Span Split Flaps on the Aerodynamic Characteristics of a Clark Y Wing. T. N. No. 472, N. A. C. A., 1933.
4. Wenzinger, Carl J.: The Effects of Full-Span and Partial-Span Split Flaps on the Aerodynamic Characteristics of a Tapered Wing. T. N. No. 505, N. A. C. A., 1934.
5. Le choix des parametres de l'aile à fente. Cahiers Aérotechniques, No. 13, 1934.
6. Weick, Fred E., and Wenzinger, Carl J.: Wind-Tunnel Research Comparing Lateral Control Devices, Particularly at High Angles of Attack. I.—Ordinary Ailerons on Rectangular Wings. T. R. No. 419, N. A. C. A., 1932.
7. Weick, Fred E., and Shortal, Joseph A.: Wind-Tunnel Research Comparing Lateral Control Devices, Particularly at High Angles of Attack. VIII.—Straight and Skewed Ailerons on Wings with Rounded Tips. T. N. No. 445, N. A. C. A., 1933.
8. Weick, Fred E., and Wenzinger, Carl J.: Wind-Tunnel Research Comparing Lateral Control Devices, Particularly at High Angles of Attack. IX.—Tapered Wings with Ordinary Ailerons. T. N. No. 449, N. A. C. A., 1933.
9. Harris, Thomas A.: The 7 by 10 Foot Wind Tunnel of the National Advisory Committee for Aeronautics. T. R. No. 412, N. A. C. A., 1931.
10. Platt, Robert C.: Turbulence Factors of N. A. C. A. Wind Tunnels as Determined by Sphere Tests. T. R. No. 558, N. A. C. A., 1936.
11. Soulé, Hartley A., and Wetmore, J. W.: The Effect of Slots and Flaps on Lateral Control of a Low-Wing Monoplane as Determined in Flight. T. N. No. 478, N. A. C. A., 1933.

TABLE I.—COMPARISON OF RECTANGULAR AND TAPERED CLARK Y WINGS WITH SPLIT FLAPS OF VARIOUS SPANS

Flap span	Flap chord	$C_{L_{max}}$	$\Delta C_{L_{max}}$	$C_{L_{max}}/C_{D_{min}}$	L/D at $C_{L_{max}}$
Rectangular wing [1]					
No flap		1.282		86.7	9.98
Full span	$0.20c_w$	2.188	0.906	148.0	4.86
$0.70b$	$.20c_w$	2.040	.758	138.0	6.03
$0.59b$	$.20c_w$	1.940	.658	131.1	6.45
$0.50b$	$.20c_w$	1.845	.563	124.7	6.76
5:3 tapered wing					
No flap		1.300		95.5	10.74
Full span	$0.15c_w$	2.129	0.829	156.6	5.68
$0.70b$	$.15c_w$	1.973	.673	145.0	6.50
$0.59b$	$.15c_w$	1.881	.581	138.4	6.70
$0.50b$	$.15c_w$	1.810	.510	133.1	7.15
5:1 tapered wing					
No flap		1.312		96.5	9.01
Full span	$0.15c_w$	2.055	0.743	151.1	6.05
$0.70b$	$.15c_w$	1.970	.658	144.9	6.05
$0.59b$	$.15c_w$	1.895	.583	139.4	6.05
$0.50b$	$.15c_w$	1.816	.504	133.5	6.05

[1] Values obtained from data in reference 3, corrected for tunnel effects.

AERONAUTIC SYMBOLS

1. FUNDAMENTAL AND DERIVED UNITS

	Symbol	Metric		English	
		Unit	Abbreviation	Unit	Abbreviation
Length	l	meter	m	foot (or mile)	ft. (or mi.)
Time	t	second	s	second (or hour)	sec. (or hr.)
Force	F	weight of 1 kilogram	kg	weight of 1 pound	lb.
Power	P	horsepower (metric)		horsepower	hp.
Speed	V	kilometers per hour	k.p.h.	miles per hour	m.p.h.
		meters per second	m.p.s.	feet per second	f.p.s.

2. GENERAL SYMBOLS

W, Weight$=mg$

g, Standard acceleration of gravity$=9.80665$ m/s^2 or 32.1740 ft./sec.^{2}

m, Mass$=\frac{W}{g}$

I, Moment of inertia$=mk^2$. (Indicate axis of radius of gyration k by proper subscript.)

μ, Coefficient of viscosity

ν, Kinematic viscosity

ρ, Density (mass per unit volume)

Standard density of dry air, 0.12497 kg-m^{-4}-s^2 at 15° C. and 760 mm; or 0.002378 lb.-ft.$^{-4}$ sec.^{2}

Specific weight of "standard" air, 1.2255 kg/m^3 or 0.07651 lb./cu. ft.

3. AERODYNAMIC SYMBOLS

S, Area

S_w, Area of wing

G, Gap

b, Span

c, Chord

$\frac{b^2}{S}$, Aspect ratio

V, True air speed

q, Dynamic pressure$=\frac{1}{2}\rho V^2$

L, Lift, absolute coefficient $C_L=\frac{L}{qS}$

D, Drag, absolute coefficient $C_D=\frac{D}{qS}$

D_0, Profile drag, absolute coefficient $C_{D_0}=\frac{D_0}{qS}$

D_i, Induced drag, absolute coefficient $C_{D_i}=\frac{D_i}{qS}$

D_p, Parasite drag, absolute coefficient $C_{D_p}=\frac{D_p}{qS}$

C, Cross-wind force, absolute coefficient $C_C=\frac{C}{qS}$

R, Resultant force

i_w, Angle of setting of wings (relative to thrust line)

i_t, Angle of stabilizer setting (relative to thrust line)

Q, Resultant moment

Ω, Resultant angular velocity

$\rho\frac{Vl}{\mu}$, Reynolds Number, where l is a linear dimension (e.g., for a model airfoil 3 in. chord, 100 m.p.h. normal pressure at 15° C., the corresponding number is 234,000; or for a model of 10 cm chord, 40 m.p.s., the corresponding number is 274,000)

C_p, Center-of-pressure coefficient (ratio of distance of c.p. from leading edge to chord length)

α, Angle of attack

ϵ, Angle of downwash

α_0, Angle of attack, infinite aspect ratio

α_i, Angle of attack, induced

α_a, Angle of attack, absolute (measured from zero-lift position)

γ, Flight-path angle

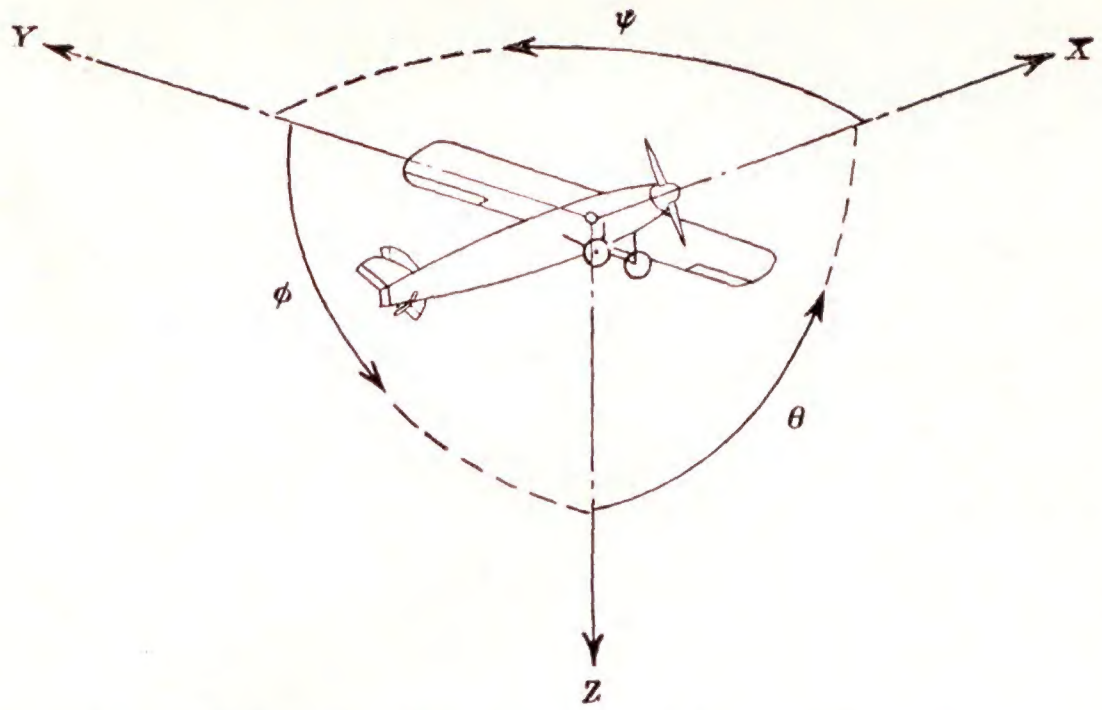

Positive directions of axes and angles (forces and moments) are shown by arrows

Axis		Force (parallel to axis) symbol	Moment about axis			Angle		Velocities	
Designation	Symbol		Designation	Symbol	Positive direction	Designation	Symbol	Linear (component along axis)	Angular
Longitudinal	X	X	Rolling	L	$Y \longrightarrow Z$	Roll	ϕ	u	p
Lateral	Y	Y	Pitching	M	$Z \longrightarrow X$	Pitch	θ	v	q
Normal	Z	Z	Yawing	N	$X \longrightarrow Y$	Yaw	ψ	w	r

Absolute coefficients of moment

$C_l = \frac{L}{qbS}$ (rolling) $\quad C_m = \frac{M}{qcS}$ (pitching) $\quad C_n = \frac{N}{qbS}$ (yawing)

Angle of set of control surface (relative to neutral position), δ. (Indicate surface by proper subscript.)

4. PROPELLER SYMBOLS

D, Diameter

p, Geometric pitch

p/D, Pitch ratio

V', Inflow velocity

V_s, Slipstream velocity

T, Thrust, absolute coefficient $C_T = \frac{T}{\rho n^2 D^4}$

Q, Torque, absolute coefficient $C_Q = \frac{Q}{\rho n^2 D^5}$

P, Power, absolute coefficient $C_P = \frac{P}{\rho n^3 D^5}$

C_s, Speed-power coefficient $= \sqrt[5]{\frac{\rho V^5}{P n^2}}$

η, Efficiency

n, Revolutions per second, r.p.s.

Φ, Effective helix angle $= \tan^{-1}\left(\frac{V}{2\pi r n}\right)$

5. NUMERICAL RELATIONS

1 hp.=76.04 kg-m/s=550 ft-lb./sec.

1 metric horsepower=1.0132 hp.

1 m.p.h.=0.4470 m.p.s.

1 m.p.s.=2.2369 m.p.h.

1 lb.=0.4536 kg.

1 kg=2.2046 lb.

1 mi.=1,609.35 m=5,280 ft.

1 m=3.2808 ft.

38548—38——48

SMITHSONIAN INSTITUTION LIBRARIES

SMITHSONIAN INSTITUTION LIBRARIES

SMITHSONIAN LIBRARIES
3 9088 01800 8581